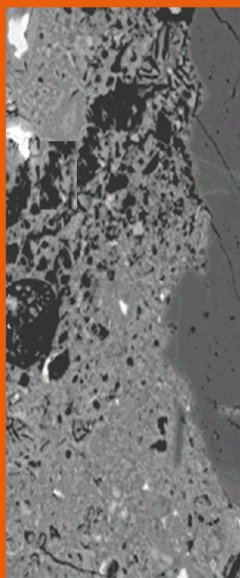


# Construction Materials and Structures

ICCMATS-1



## *Editors*

Stephen O. Ekolu

Morgan Dundu

Xiaojian Gao

**IOS**  
Press

# CONSTRUCTION MATERIALS AND STRUCTURES

This page intentionally left blank

# Construction Materials and Structures

Proceedings of the First International Conference on  
Construction Materials and Structures



*Editors*

Stephen O. Ekelu

Morgan Dundu

and

Xiaojian Gao

**IOS**  
Press

Amsterdam • Berlin • Tokyo • Washington, DC

© 2014 The authors and IOS Press.

All rights reserved. No part of this book may be reproduced, stored in a retrieval system, or transmitted, in any form or by any means, without prior written permission from the publisher.

ISBN 978-1-61499-465-7 (print)

ISBN 978-1-61499-466-4 (online)

*Publisher*

IOS Press BV

Nieuwe Hemweg 6B

1013 BG Amsterdam

Netherlands

fax: +31 20 687 0019

e-mail: [order@iospress.nl](mailto:order@iospress.nl)

*Distributor in the USA and Canada*

IOS Press, Inc.

4502 Rachael Manor Drive

Fairfax, VA 22032

USA

fax: +1 703 323 3668

e-mail: [iosbooks@iospress.com](mailto:iosbooks@iospress.com)

LEGAL NOTICE

The publisher is not responsible for the use which might be made of the following information.

PRINTED IN THE NETHERLANDS

## Preface

The first International Conference on Construction Materials and Structures (ICCMATS2014) was held in Johannesburg, South Africa from 24–26 November 2014. The event was locally considered to be a major onset for promotion and stimulation of research and engineering applications in the fields of materials and their structural implications on physical infrastructure. The core value of the conference was embedded on science and engineering as a necessary vehicle for addressing infrastructure needs and related modern socio-economic concerns, of the global community. The event also served to strengthen existing relationships and to establish new directions between South Africa as a country and research leader in the African continent, and other countries within and outside the continent including Europe, China, North America, to mention but a few.

The Proceedings of this conference contain about two hundred peer-reviewed papers from fifty-one countries, making this a truly international event. They include ten keynote speeches by some of the leading academics, researchers and international experts from *Canada, USA, Turkey, United Kingdom, Uganda, New Zealand, South Africa, Qatar, and Japan*.

The geographical location and timing of this event demanded special consideration on issues of developing countries where the severe lack of a critical mass of academics, research scientists and engineers undermines efforts to attain sustainable development. In developing countries, the fast population growth promotes rapid urbanization; resulting in high poverty and mortality, aggravation of poor housing conditions, disproportionately high energy demands and environmental degradation due to human activity, among other social ills. Besides these negative issues, most of these countries are on a significant economic growth trajectory, but remain in dire need for impactful and sustainable physical infrastructure. In an attempt to confront these concerns, the International Conference on Construction Materials and Structures was organized to bring together international experts from several countries to discuss scientific research and share advances in technology. Against this backdrop, ICCMATS 2014 was used as a platform for sharing of cutting-edge theories, techniques and scientific advances by some of the foremost scientists and researchers worldwide. The event provided insights for addressing issues of modern local infrastructure, and inspired future advancements, innovations and emerging researchers.

Consistent with the technical focus of the conference, high quality papers presented in these Proceedings covered a range of fields, categorized into nine (9) sub-topics and five (5) main themes viz. materials and characterization, durability of construction materials, structural implications and service life, sustainability and the environment, building science and construction. All the papers that were submitted for ICCMATS 2014 were fully peer-reviewed, a task undertaken by the International Scientific Committee (ISC). The acceptance of the papers for publishing in these Proceedings was based on the recommendations provided in the reviewer reports. Sincere gratitude is due to the individual members of the ISC and all reviewers for their important contribution of ensuring the high quality of these Proceedings.

The following organizations are gratefully acknowledged for their significant financial and technical support to the conference: The National Research Foundation of South Africa, Council of Geoscience (South Africa), Concrete Society of Southern Africa, Johannesburg Convention Bureau, The American Concrete Institute and RILEM.

On behalf of the Organising Committee, the Editors of the Proceedings wish to extend special thanks to all authors for the technical contribution of their high quality research, expertise and knowledge through these Proceedings. In addition, the dilemmas of resource planning for participation in the conference, placed high demands on the authors; for which collective applause is in order for all authors who participated in the event.

Finally, thanks are due to all members of the Conference Organizing Committee, the Conference Secretarial team, the Dean of the Faculty of Engineering and the Built Environment at the University of Johannesburg (UJ), academic and technical staff of the UJ Department of Civil Engineering Science, partners from Harbin Institute of Technology, research students and all those who contributed to the running and success of the event. It was a rewarding programme to all those involved, not excluding the wider scientific community. In that regard, this event's continuity into the future is anticipated.

Editors:  
Stephen O. Ekolu  
Morgan Dundu  
Xiaojian Gao

# ICCMATS 2014 Committees

## **Organizing Committee**

Prof. Morgan Dundu (Co-Chair)

*University of Johannesburg*

Dr. Stephen O. Ekolu (Co-Chair/Coordinator)

*University of Johannesburg*

Prof. Xiaojian Gao

*Harbin Institute of Technology (Co-Chair)*

Mnr. John Sheath

*The Concrete Society of Southern Africa*

Dr. Alvin Masarira

*Anglo-American (pty) Ltd*

Dr. Felix Okonta

*University of Johannesburg*

Engr. Deon Kruger

*University of Johannesburg*

Dr. Harry Quainoo

*University of Johannesburg*

Dr. Jean-Bosco Kazurikanyo

*The Advanced Cement Institute*

## **Local Advisory Committee**

Engr. Balu Tabaaro

*GEOengineering, Uganda*

Mnr. Lucky Aluge

*Lucky Links Consult, Nigeria*

Mnr. Firehiwot Azene

*Council of Geoscience, South Africa*

Mnr. Johan de Koker

*University of Johannesburg, South Africa*

Mnr. Pierre van Tonder

*University of Johannesburg, South Africa*

Mnr. Bruce Raath

*B.A. Raath and Associates Johannesburg, South Africa*



**International Scientific Committee**

Prof. Hakim Abdelgader  
*Tripoli University, Libya*

Dr. Hamid Akbarazadeh  
*McGill University, Canada*

Prof. Mark Alexander  
*University of Cape Town, South Africa*

Prof. Henry Alinaitwe  
*Makerere University, Uganda*

Dr. Janis Anderson  
*University of Latvia, Latvia*

Prof. Nicolae Angelescu  
*Valahia University, Romania*

Prof. Abdul Awal  
*University of Technology, Malaysia*

Prof. Hans Beushausen  
*University of Cape Town, South Africa*

Prof. Billy Boshoff  
*University of Stellenbosch, South Africa*

Dr. Souleymane Diop  
*Council of Geoscience, South Africa*

Dr. Sydney du Plessis  
*University of Johannesburg, South Africa*

Prof. Amr S. El-Dieb  
*United Arab Emirates University, United Arab Emirates*

Prof. George Fanourakis  
*University of Johannesburg, South Africa*

Prof. David W. Fowler  
*The University of Texas at Austin, United States of America*

Prof. Suresh B. Gholve  
*Nagpur University, India*

Prof. Douglas Hooton  
*University of Toronto, Canada*

Prof. Kei-chi Imamoto  
*Tokyo University of Science, Japan*

Dr. Maria Kaszynska  
*University of Szczecin, Poland*

Prof. Agnieszka J. Klemm  
*Caledonian University, United Kingdom*

Prof. M. Iqbal Khan  
*King Saud University, Saudi Arabia*

Prof. Baoguo Ma  
*Wuhan University of Technology, China*

Dr. Jeffrey Mahachi  
*Centre for Research and Housing Innovation, NHBRC, South Africa*

Dr. Olumide O. Ojuri  
*Federal University of Technology, Akure, Nigeria*

Dr. Ioan Pepenar  
*ICECON Res Inst. for Construction Equipment, Romania*

Prof. Wassim Raphael  
*Saint-Joseph University, Lebanon*

Prof. Ali Rizwan  
*National University of Science and Technology, Pakistan*

Prof. Marios Soutsos  
*Queen's University, United Kingdom*

Dr. Shaikh Faiz Uddin Ahmed  
*Curtin University of Technology, Australia*

Dr. Celeste B. Viljoen  
*University of Stellenbosch, South Africa*

Prof. Keijin Wang  
*Iowa State University, United States of America*

Prof. Nadia Fahim Youssef  
*Housing & Building National Research Center, Egypt*

Prof. Yamei Zhang  
*Southeast University, China*

Prof. Alphose Zingoni  
*University of Cape Town, South Africa*

This page intentionally left blank

# Contents

Preface	v
<i>Stephen O. Ekolu, Morgan Dundu and Xiaojian Gao</i>	
ICCMATS 2014 Committees	vii
<b>Keynote papers</b>	
Achieving concrete durability for specified service-life in chloride exposures	3
<i>R. Doug Hooton</i>	
Nanoparticle modified concrete materials: opportunities, challenges and prosperities	16
<i>Kejin Wang and Gilson R. Lomboy</i>	
Low-damage earthquake-resistant structures achieved through movability and ductility	27
<i>Nawawi Chow</i>	
Severe plastic deformation as a new processing for enhancing the performance of metallic components	35
<i>Hiroyuki Miyamoto, Rifai Muhammad and Hiroshi Fujiwara</i>	
Optimizing coefficient of thermal expansion of concrete and its importance on concrete structures	47
<i>Md Sarwar Siddiqui and David W. Fowler</i>	
Superabsorbent polymers in cementitious composites with fly ash cements – selected aspects	57
<i>Agnieszka J. Klemm, Karol S. Sikora and David E. Wiggins</i>	
Steel hysteretic damper featuring displacement dependent hardening for seismic protection of structures	68
<i>Murat Dicleli and Ali Salem Milani</i>	
Failure of structure in East Africa with focus on the causes of failures in the construction phase	76
<i>Henry Mwanaki Alinaitwe and Stephen Ekolu</i>	
Design and properties of ultra-high performance concrete	86
<i>Caijun Shi, Zemei Wu, Dehui Wang and Linmei Wu</i>	
Green road construction using discarded materials: a holistic overview from the Middle East	99
<i>Ramzi Taha</i>	

## 1. Materials and characterisation

### Cementitious materials and concrete

- Structural and mechanical characterization of high alumina additivated cement based on high refractory mineralogical compounds 113  
*Nicolae Angelescu, Cristina Stancu and Vasile Bratu*
- Investigation on the suitability of borrow pit sand as fine aggregate for structural concrete 121  
*Amadou Adamou and Munachi U. Nnebe*
- Concreting method that produces sustainable concrete 127  
*H.S. Abdelgader, A.M. Othman, A.S. El-Baden and N. Angelescu*
- Reuse of non-metallic residues from aluminium recycling industry in production of porous building materials 136  
*Diana Bajare, Girts Bumanis, Aleksandrs Korjakins and Laura Sele*
- Study of properties of steel fiber reinforced concrete for possible applications in Pakistan 145  
*Asad-ur-Rehman Khan and Tatheer Zahra*
- Blended cement utilizing ceramic wall tiles waste 152  
*Dina M. Sadek, Sh.K. Amin and N.F. Youssef*
- Estimation of concrete properties at early age by thermal stress device 162  
*Sang Lyul Cha and Jin Keun Kim*
- Effects of recycled aggregates on the properties of fresh and hardened concrete 168  
*B.N. Makhathini, A. Dawneerangen and A.T. Shohniwa*
- An examination of natural pozzolans in Uganda for low-strength construction applications 175  
*Dans N. Naturinda and Anthony G. Kerali*
- Mechanical properties and microscopic structure of cement based materials with very low water-cement ratio 183  
*Xiqiang Lin, Zhongnan Song, Tao Zhang and Liang Huo*
- Experimental research on mechanical properties of engineered cementitious composites 189  
*Guoyou Li, Liang Huo, Tao Zhang and Hang Yao*
- Study on drying shrinkage cracking characteristics of steel chip reinforced polymer cementitious composite 196  
*Sunhee Hong, Shinya Kimura, Yuichi Sato and Yoshio Kaneko*
- The effect of steel and polypropylene fibres in the mechanical properties of structural lightweight concrete 202  
*S.P. Yap, Ubagaram Johnson Alengaram and Mohd Zamin Jumaat*
- Utilization of ceramic wastes as replacement of portland cements 208  
*Viviana Rahhal, Edgardo Irassar, Cristina Castellano, Zbyšek Pavlík and Robert Černý*

Rheology of portland cement pastes with siliceous mineral additions <i>Viviana Rahhal, César Pedrajas, Edgardo Irassar and Rafael Talero</i>	214
Cement calorimetry with different condition of calcium sulfate and water reducer admixture <i>Horacio Donza and Viviana Rahhal</i>	220
Foam concrete landfill use in landslide hazardous area in West Şırnak Road <i>Yıldırım İ. Tosun</i>	226
Pozzolans as a binder for affordable building materials in Uganda <i>William Balu-Tabaaro</i>	232
Effect of temperature on rheological performances of fresh SCC mixture <i>Huan Ye, Xiaojian Gao and Hui Wang</i>	240
Assessing the effect of procurement source of scoria rocks on the pozzolanic properties of the cementitious system <i>Galal Fares, A. Alhozaimy, A. Al-Negheimish and Omer A. Alawad</i>	247
Potential South African standard sand for cement mortar testing and research <i>Stephen O. Ekolu</i>	253
A study of thermal conductivity of wood ash blended cement mortar <i>Akeem Ayinde Raheem, Ibrahim Akinyemi Akinteye and Saheed A. Lasisi</i>	261
Behavior of high-volume fly ash concrete in mass concrete applications <i>Anton K. Schindler and Kevin P. Keith</i>	268
Microstructure and durability characteristics of self-curing concrete <i>Amr S. El-Dieb, Tamer A. El-Maaddawy and Abdelrahman Al-Sallamin</i>	276
Palm Kernel Incinerated Ash as low cost concrete component <i>Emem-Obong Emmanuel Agbenyeku and Felix Ndubisi Okonta</i>	284
Ultrasonic pulse velocity used to predict the compressive strength of structural sand lightweight concrete <i>J. Alexandre Bogas, M. Glória Gomes, Sofia Real and Jorge Pontes</i>	293
Influence of different grinding types on granulometry of recycled glass <i>Karel Dvořák, Marcela Fridrichová and Petr Dobrovolný</i>	305
Material properties of bottom ash and welding slag as fine aggregates in concrete <i>Karthikeyan Jayakumar and Ananthi Arunachalam</i>	311
The use of waste materials for the production of an hydraulic mortar based on slacked lime <i>Bartolomeo Megna, Laura Ercoli and Giovanni Rizzo</i>	320
Effects of polycarboxylate-based superplasticizer on rheological and mechanical properties of concrete <i>Samer Al-Martini, Omar F. Najim and Waddah Al Hawat</i>	327
Influence of a new viscosity modifying admixture on the performance of different superplasticizers <i>Stephen O. Ekolu and Jean-Bosco Kazurikanyo</i>	333

Effect of microfines mineral admixtures on rheology of blended cement paste <i>Maulik M. Panseriya, U.V. Dave and A.K. Tiwari</i>	339
Research on a novel technology of FRP bonded to concrete substrate without adhesive <i>Ming Li, Yunpeng Liu, Muyu Liu and Fazhou Wang</i>	347
Fundamentals of plastic settlement cracking in concrete <i>Riaan Combrinck and William Peter Boshoff</i>	354
Initial study to determine the tensile material properties of fresh concrete <i>Jan Diederick Dippenaar, Riaan Combrinck and William Peter Boshoff</i>	362
Blended cements based on C&DW: its influence in the pozzolanicity <i>E. Asensio, C. Medina, M.I. Sánchez de Rojas and M. Frias</i>	370
Use of crushed brick aggregate in structural concrete: properties and performance <i>Sunanda Paul and Gopinandan Dey</i>	378
Study of particle packing in self-consolidating mortar systems <i>Syed Ali Rizwan, Qamar uz Zaman and Thomas A. Bier</i>	384
Nearly 20 years of the EN 197 cement standards in South Africa <i>Sibusiso Hlatshwayo and Reinhold Amtsbüchler</i>	391
An investigation into the use of Piliostigma Thonningii Pod Ash as an admixture in mortar <i>Suleiman Mannir</i>	398
Material selection and mix design of radiation shielding concrete <i>Stephen Ekolu and Mokgobi A. Ramushu</i>	404
A new structural sand lightweight concrete mix design <i>J. Alexandre Bogas, M. Glória Gomes, Sofia Real and Jorge Pontes</i>	411
Effect of partial replacement of sand in concrete with steel-file particles <i>Musibau Ajibade Salau, Kolawole Adisa Olonade and Oyesola Sunday Ajiboye</i>	420
Mechanical properties of green concrete with Palm Nut Shell as low cost aggregate <i>Emem-Obong Emmanuel Agbenyeku and Felix Ndubisi Okonta</i>	427
New proposed direct tensile strength test for concrete <i>M. Iqbal Khan and Shehab Mourad</i>	436
The effect of different PPC binders, partially replaced by fly ash properties, on self-compacting concrete <i>Omar Almuwbbber, Rainer Haldenwang and Irina Masalova</i>	445
Lowering the embodied CO <sub>2</sub> by using fly ash concrete internally cured with recycled ceramic tile aggregates <i>Mohammed S. Meddah, T. Nukushina, S. Seiki and R. Sato</i>	453

## Geopolymers and polymers

- Polyfurfuryl alcohol – a waste from sugarcane bagasse as a construction material 461  
*Rakesh Kumar*
- Geopolymer concrete: a practical approach 466  
*Cyril Attwell*
- Development of geopolymer mortar using palm oil fuel ash-blast furnace slag-fly ash-as binders 475  
*Azizul Islam, U. Johnson Alengaram, Mohd Zamin Jumaat and Iftekhair Ibnul Bashar*
- The development of sustainable geopolymer mortar from fly ash-palm oil fuel ash based binder and manufactured sand 481  
*Iftekhair Ibnul Bashar, Ubagaram Johnson Alengaram, Mohd Zamin Jumaat and Azizul Islam*
- Cementless concrete using ceramic waste powder 487  
*Amr S. El-Dieb and Ehab E. Shehab*
- Engineering properties of Class-F fly ash-based geopolymer concrete 495  
*M. Albitar, P. Visintin and M.S. Mohamed Ali*
- Engineering properties of slag-based geopolymer concrete 503  
*M. Albitar, M.S. Mohamed Ali and P. Visintin*
- Steel-slag and activators ratio impacts on the shrinkage of alkaline activated ultrafine palm oil ash-steel slag paste/mortar 511  
*Moruf O. Yusuf, Megat A.M. Johari, Zainal A. Ahmad and M. Maslehuiddin*
- Use of self-compacting geopolymer concrete in a precast environment – a case study 518  
*Warren McKenzie*
- EVA/intumescent agent flame retardant composite materials using organic/inorganic hybrid filler 526  
*Ji-Won Park, Jung-Hun Lee, Hee-Chun Choi, Hyun-Joong Kim, Hyun-Min Jang and Jung-Yun Choi*
- Evolution in physical modeling of structural built-up in polymer concrete and in polymer-cement concrete 532  
*Dionys Van Gemert*
- Natural fibre reinforced polymer-concrete composite for future bridge structures in earthquake regions 544  
*Libo Yan and Nawawi Chow*

## Bituminous materials and pavements

- Road conditions and engineering performance of subgrade soils in part of South-Western Nigeria 553  
*N.O. Adebisi, S.A. Adeniji and F.O. Akintayo*



The application of polymer coated aggregates in flexible pavement <i>Reshma Rughooputh and Najeeb Ahmad Fokeerbux</i>	560
Use of waste plastics and scrap rubber tyre in the wearing course of a bituminous pavement <i>Reshma Rughooputh and Nishley Ravikesh Gunesh</i>	568
Influence of curing time and compaction on black cotton soil stabilized with fly ash, ground-granulated blast furnace slag and lime <i>A. Maneli, W.K. Kupolati, J.M. Ndambuki and O.S. Abiola</i>	575
Analysis of coarse aggregate microtexture in polishing process <i>Marta Wasilewska</i>	581
Response modelling of recycled concrete and masonry in pavements <i>F. Barisanga, C. Rudman and K. Jenkins</i>	587
The effects of residual moisture on asphalt concrete strength <i>Nura Usman</i>	595
Effect of different additives on fatigue behavior of asphalt mixtures <i>Amin Daghighi and Ali Nahvi</i>	601
Characterization of lateritic soils/gravels for their suitability as a pavement material – a review <i>D.R. Biswal, S.R. Dash and U.C. Sahoo</i>	608
Proposing a realistic frequency for fatigue tests using Artificial Neural Network <i>Ali Khodaii and Attila Hassanzadeh Zonouzy</i>	613
Polymer modified bitumen asphalt, a proposed solution for UAE pavement deterioration <i>Reem Sabouni and Ahmed Al-Ghazali</i>	620
Investigating the packing condition of porous asphalt mixture using Discrete Element Method <i>Mengjia Chen and Yiik Diew Wong</i>	629
Comparison of in-situ and lab-measured void contents for a bituminous pavement of a carriageway <i>Lewis Kabwe Kizyalla and Stephen Ekolu</i>	637
<b>Brick and block masonry</b>	
Flexural strength of low density blockwork <i>A. Ahmed</i>	647
Properties of conventional cement and thin layer mortars <i>A. Ahmed</i>	655
Improving physical properties of red clay from Morapalala Village, Limpopo Province <i>Nthabiseng Portia Mahumapelo</i>	662

Physical, chemical and pozzolanic properties of bricks of X-X zone of Karacahisar castle, Turkey	668
<i>İnci Güldoğan, Yücel Güney and Erol Mehmet Altinsapan</i>	
Cement stabilization of laterite-quarry dust mixture for interlocking brick production	676
<i>Amana Ocholi and Manasseh Joel</i>	
Effect of wetting and air curing durations on strength of stabilized sands	683
<i>Lerato J. Moatlhodi and Felix N. Okonta</i>	
<b>Material science and nanotechnology</b>	
Phase transitions and microstructural characterization of martensite in copper based shape memory alloys	691
<i>O. Adiguzel</i>	
Using carbon nanotubes in self-compacting paste systems	697
<i>Afshan Naz, Syed Ali Rizwan, Naveed Z. Ali, Thomas A. Bier and Hameed Ullah</i>	
Influence of the characteristic of input materials on formation and properties of sintered fly ash body	703
<i>Vit Cerny and Rostislav Drochytka</i>	
Thin spray rock liners with different concentrations of nanoclays	709
<i>P. van Tonder and C.J. Booyesen</i>	
Effects of multi-walled carbon nanotubes on strength and interfacial transition zone of concrete	718
<i>P. Van Tonder and T.T. Mafokoane</i>	
Molecular dynamics research of triple junctions structure of tilt and mixed-type grain boundaries in nickel	728
<i>Gennady Poletaev, Darya Dmitrienko, Vadim Diabdenkov, Vladimir Mikrukov and Mikhail Starostenkov</i>	
Analysis of elongation variance of tendons using stress-strain graphs	734
<i>Morgan Dundu and Sebastian Rupieper</i>	
Limits of elongation variation of tendons in post-tensioning	740
<i>Morgan Dundu and Sebastian Rupieper</i>	
<b>2. Durability of construction materials</b>	
Performance of corrosion inhibiting admixtures in a marine environment	749
<i>Ian N. Robertson</i>	
Effect of superplasticizers on concrete durability indexes	758
<i>Stephen O. Ekolu</i>	

Effects of sulphuric acid on the compressive strength of blended cement-cassava peel ash concrete <i>Kolawole Adisa Olonade, Akinropo Musiliu Olajumoke, Ayoade Oluwaseun Omotosho and Funso Ayobami Oyekunle</i>	764
Properties of self-consolidating concrete containing limestone filler <i>Daman Panesar and Mohammad Aqel</i>	772
Evaluation of sulphate attack on concrete incorporating high volume palm oil fuel ash <i>I.A. Shehu, A.S.M.A. Awal, S. Mohammad and A. Sulaiman</i>	780
Sulphate corrosion behaviour of high volume slag concrete <i>Stephen O. Ekolu and Adam Ngwenya</i>	788
Sulphate resistance of concrete made with moderately high alumina slag <i>Stephen O. Ekolu and Adam Ngwenya</i>	797
Simple criteria for evaluating sulphate attack in concrete <i>Stephen Ekolu</i>	806
Comparison of moisture equilibrium of cement-based materials in presence of slag and silica fume in different wetting and drying cycles <i>M. Seaidpour and L. Wadsö</i>	813
Chloride penetration into concrete with compressive load-induced cracks <i>M.Y. Balqis, H.M. Jonkers and E. Schlangen</i>	819
Indicative tests on the effect of fly ash- $\beta$ cyclodextrin composite on mortar and concrete permeability, sorptivity and porosity <i>B.D. Ikotun, G.C. Fanourakis and S. Mishra</i>	825
Durability of mortars and concretes containing scoria-based blended cements <i>Aref Mohammad Alswaidani and Samira Dib Aliyan</i>	835
Effect of surface treatments on abrasion and permeation properties of clay concretes <i>Fitsum Solomon and Stephen Ekolu</i>	848

### **3. Structural implications, performance and service life**

#### **Reinforced concrete and structural composites**

Impact of environmental exposure on concrete strength in highway bridges in Uganda <i>Hilary Bakamwesiga, Jackson Mwakali, Stephen Sengendo and Sven Thelandersson</i>	861
Strength and behaviour of steel fibre reinforced self-compacting rubberised concrete beams under flexure <i>Bharati Raj, N. Ganesan and A.P. Shashikala</i>	871
Effects of pit-sand on shear capacity of reinforced concrete space framed structures: case study of a building at Oba – Ile Akure <i>Lekan Makanju Olanitori and Joseph Olaseinde Afolayan</i>	881

An experimental study on acoustic emission of a notched three point bending concrete beams	888
<i>Zohra Dahou and Abdelkhalek Benmiloud</i>	
Flexural tests of Mi Panels	893
<i>G.M. Bukasa and M. Dundu</i>	
Compression tests of Mi Panels	899
<i>G.M. Bukasa and M. Dundu</i>	
Infrared thermography as a diagnostic tool for subsurface assessments of concrete structures	904
<i>Matthew Scott and Deon Kruger</i>	
The stress-related material damping of rigid frame bridge with corrugated steel webs	910
<i>Liu Baodong, Li Weilong, Li Pengfei and Lv Wenjuan</i>	
Evaluating concrete with high-performance steel fibers using double-punch testing	917
<i>Aaron P. Woods, Richard Klingner, James Jirsa, Shih-Ho Chao, Netra Karki and Oguzhan Bayrak</i>	
Relationship between the wide-flange steel and the long-term deformation of steel-reinforced concrete columns	925
<i>Gyeong-Hee An and Jin-Keun Kim</i>	
Experimental bond behaviour between textile reinforced cement and concrete: Review of the existing test methods and the analysis of the results of a modified double-lap shear test	932
<i>Maciej Wozniak, Tine Tysmans, John Vantomme and Sven De Sutter</i>	
Relation between crack width and corrosion degree in elements of concrete with crushed sand	939
<i>Oscar A. Cabrera, Néstor F. Ortega, Luis P. Traversa and Horacio Donza</i>	
Investigation of prestressed hollow core concrete slabs at elevated temperatures	946
<i>Ehab Ellobody</i>	
Behaviour of reinforced concrete slabs strengthened by concrete overlays	956
<i>Wael Ibrahim, Mohamed El-adawy and Gouda Ghanem</i>	
Study on the mechanical property recovery of concrete subjected to elevated temperatures	963
<i>Qingtao Li, Guanglin Yuan and Qianjin Shu</i>	
Shear behavior of ultra-high-strength steel fiber-reinforced self-compacting concrete beams	972
<i>Amr S. El-Dieb, Tamer A. El-Maaddawy and Omar Al-Rawashdah</i>	
Static and dynamic testing of RC-slabs with high strength concrete overlay	980
<i>Norbert Randl and Csaba Simon</i>	

Effect of the loading condition on the restoring force characteristics of the rigid frame RC pier with the shear wall <i>Wenjun Gao, Hisanori Otsuka and Yukihide Kajita</i>	989
A study on behavior of reinforced concrete columns subjected to axial compression <i>P.K Gupta and V.K Verma</i>	998
Parametric study of non-uniform thickness rectangular concrete filled steel tube in pure bending <i>P.K. Gupta and S.K. Katariya</i>	1007
Load-deflection curve prediction of RC beams strengthened by externally bonded CFRP wraps and strips <i>Asad-ur-Rehman Khan and Fawwad Masood</i>	1015
New investigations of butt-jointed precast and in-situ concrete columns <i>Daniel Wolff, Manuel Koob, Markus Blatt and Jens Minnert</i>	1022
Innovative structural frame using composite precast concrete components, the SMART frame <i>Won-Kee Hong, Chaeyeon Lim, Joongsoo Park and Sunkuk Kim</i>	1030
Flexural behavior of RC Beams with local steel – experimental investigation <i>Shehab Mourad, Abdelhamid Charif and M. Iqbal Khan</i>	1038
Experimental study of time dependent bond transfer length under pure tension in slabs <i>Behnam Vakhshouri and Felix Shami Nejadi</i>	1044
Condition assessment of a Johannesburg skyscraper <i>Willem F. van Ede and Stephen Ekolu</i>	1052
Understanding the influence of marine microclimates on the durability performance of RC structures <i>Olukayode O. Alao, Mark Alexander and Hans Beushausen</i>	1060
Concrete filled double skin circular tubes: a review <i>Yoosuf Essopjee and Morgan Dundu</i>	1068
Flexural failure modes of steel plate-strengthened reinforced concrete elements <i>Akinropo Musiliu Olajumoke and Morgan Dundu</i>	1074
Methods for flexural strengthening of reinforced concrete elements using steel plates <i>Akinropo Musiliu Olajumoke and Morgan Dundu</i>	1080
<b>Structural steel and other metals</b>	
Behaviour and design of a double track open timber floor plate girder railway deck steel bridge <i>Ehab Ellobody</i>	1089

Kinetic study of steel emissivity and its effect on steel behaviour under fire condition	1100
<i>Han Fang, Man Biu Wong and Yu Bai</i>	
Low cycle fatigue performance of integral bridge steel H-piles subjected to earthquakes	1107
<i>Murat Dicleli and Semih Erhan</i>	
Buckling behavior of 6082-T6 aluminum alloy columns with box-section and L-section under eccentric compression	1116
<i>Ximei Zhai, Lijuan Sun and Yuanzheng Zhao</i>	
A different approach to the design of steel columns	1125
<i>Anthony F. Gee and Primus V. Mtenga</i>	
A critical review on current and proposed structural fire engineering codes for steelwork in South Africa	1134
<i>Richard Walls, Celeste Viljoen, Hennie De Clercq and Johan Retief</i>	
Factors that influence friction in tendons of unbonded post-tensioning systems	1141
<i>Morgan Dundu and Michelle Ward</i>	
Cold-formed circular hollow sections under axial compression	1148
<i>Morgan Dundu and Vongani Chabalala</i>	
<b>Structural masonry and timber</b>	
Assessment of the unreinforced masonry shear wall stiffness	1157
<i>Nebojša Mojsilović</i>	
A complete timber building system for multi-storey buildings	1164
<i>Per-Anders Daerga, Ulf Arne Girhammar and Bo Källsner</i>	
Sheathing-to-framing fasteners in light wood-framed buildings as finite beam element	1172
<i>Michał Baszeń and Czesław Miedzialowski</i>	
Repair of masonry arch bridges with respect to longitudinal cracking and load assessment	1181
<i>Triona Byrne and Dermot O'Dwyer</i>	
The conservation state of the wooden roof of the National Museum in Phnom Penh	1190
<i>Bartolomeo Megna and Giovanni Liotta</i>	
<b>Modelling, simulation and computation</b>	
Macro vs mesoscale modelling of fracture in concrete beams: size effect and crack openings	1201
<i>N. Aissaoui, S. Ghezali and M. Matallah</i>	
Review of the strength theories	1207
<i>Ilmir Valiakmetov</i>	

Analysis of hopper eccentricity effect on granular flow in three-dimensional silos using discrete element method <i>M. Benyammine, N. Fezzioui, O. Hami, M. Djermame and A. Slimani</i>	1215
A constitutive model for shape memory alloys, visualizing internal deformability mechanism <i>Seyed Amirodin Sadrnejad</i>	1223
Brittle material damage pro-elasticity model for rock made structures <i>Seyed Amirodin Sadrnejad</i>	1233
Target column overdesign factor of steel frames considering system reliability <i>Yan-Gang Zhao, Zhao-Hui Lu and Mohammad Sharfuddin</i>	1242
Effect of shear wall in improving the reliability of RC frame buildings subjected to seismic loading <i>Mohamed A. Dahesh, Ahmet Tuken and Nadeem A. Siddiqui</i>	1249
Prediction on short-term burst pressure of plastic pipe reinforced by cross-winding steel wires <i>Xiangpeng Luo, Jinyang Zheng, Ping Xu, Weican Guo and Jianfeng Shi</i>	1256
Neural network model for predicting deterioration of bridge components using visual inspection data <i>Md Saeed Hasan, Sujeeva Setunge and David W. Law</i>	1264
Information-based formulation of a creep model using a new experimental database <i>Wassim Raphael, Laurent Touma and Alaa Chateauneuf</i>	1274
Testing and nonlinear numerical modelling of fibre pull-out mechanism from cementitious materials <i>Faisal Abdulle and Robert Xiao</i>	1287
Parameter identification for supports and cracks in beams with non-classical boundary conditions <i>Ljubov Feklistova and Helle Hein</i>	1295
Effect of proximity on wind loads on tall buildings <i>Ashok Kumar Ahuja and Ritu Raj</i>	1303
Evaluation of the scale effect for the tensile strength of aligned flax fiber-reinforced composites <i>Jānis Andersons</i>	1310
Flexural behavior of RC beams with local steel: analytical investigation <i>Abdelhamid Charif, Shehab Mourad and M. Iqbal Khan</i>	1317
Simplified torsional strength of reinforced and prestressed concrete beams <i>Khaldoun N. Rahal</i>	1325
Effect of clay-concrete lining on canal seepage towards the drainage region – an analysis using Finite-Element method <i>Fitsum Solomon and Stephen Ekolu</i>	1331

#### 4. Sustainability, waste utilization and the environment

- Achieving building sustainability using sustainable building envelope 1345  
*Joseph Iwaro and Abrahams Mwasha*
- On-site concrete waste minimization in the UK 1352  
*Amir B. Meibodi and H. Kew*
- Moisture transfer in three hemp concretes 1358  
*Ines Othmen, Philippe Poullain and Nordine Leklou*
- Foam concrete production with şırnak mine waste claystone and fly ash 1364  
*Yıldırım İ. Tosun*
- Reducing CO<sub>2</sub> in concrete by half 1370  
*Michiel Haas*
- Embedded LCA information in BIM models 1377  
*Joaquín Díaz, Laura Álvarez Antón and Kareem Tarek Anis*
- Compressive strength and durability of fly ash stabilized dolomitic waste as a lightweight construction material 1386  
*Ikechukwu F. Aneke and Felix N. Okonta*
- Preliminary study of strength of coal composites 1395  
*Lerato J. Moatlhodi and Felix N. Okonta*
- Use of ground waste glass in concrete production 1401  
*Salim Barbhuiya, Aminul Laskar and Arnesh Das*
- Radiological assessment of high density shielding concrete for neutron radiography 1409  
*Stephen Ekolu and Mokgobi A. Ramushu*
- Permeable reactive barriers for acid mine drainage treatment: a review 1416  
*Ayanda N. Shabalala, Stephen O. Ekolu and Souleymane Diop*
- Bottom ash and fly ash wastes as alkalinising reagents for neutralising acid mine drainage 1427  
*Stephen O. Ekolu, Souleymane Diop and Firehiwot Azene*
- Potentiodynamic polarization study of the corrosion characteristics of acid mine drainage 1436  
*Stephen O. Ekolu, Souleymane Diop and Firehiwot Azene*

#### 5. Building science and construction

- Comparison of simple linear regression and multiple linear regression for estimating fuel use and emission rates for excavators 1445  
*Heni Fitriani and Phil Lewis*
- The effects of natural and artificial UV exposure on the physical properties of synthetic turf used for various sports fields 1453  
*Adriano Coutinho Zuzarte and Deon Kruger*



Thermal characterization of heat reflective coating for building application <i>Bal Mukund Suman</i>	1461
Impact of traditional and modern building materials on the thermal behavior and energy consumption of a courtyard house in the hot and dry climate <i>Naiima Fezzioui, Mébirika Benyamine, Saleh Larbi, Belkacem Draoui and Claude-Alain Roulet</i>	1468
Assessment of the involvement of qualified professionals in building supervision in Nigeria: Lagos and Ondo states as case studies <i>Catherine Mayowa Ikumapayi, Chinwuba Arum and Reuben P. Omale</i>	1475
Thermal insulation of crumb-rubber mortar for building walls application <i>Mukaila Yinka Sanni, Ocholi Amana and Pinder Ejeh Stephen</i>	1481
Precast concrete fencing units in low cost domestic housing in South Africa – a case study <i>Stella M. Mlasi</i>	1489
The environmental performance of a reinforced precast concrete slab with void forming system <i>Magdalena Hajdukiewicz, Jérémy Lebrêne and Jamie Goggins</i>	1495
Foam geopolymers: state of the art and preliminary experimental results <i>Zahra Abdollahnejad, F. Pacheco Torgal and J.L. Barroso De Aguiar</i>	1503
Quality assurance in low-cost housing construction projects in the metropole <i>Manelisi Rarani and Stanley Fore</i>	1510
Performance measurement of quality of houses: development of a building quality index for houses <i>Jeffrey Mahachi</i>	1517
Subject Index	1525
Author Index	1533

## Keynote papers

This page intentionally left blank

# Achieving concrete durability for specified service-life in chloride exposures

R. Doug HOOTON<sup>1</sup>

*Department of Civil Engineering, University of Toronto*

**Abstract.** Obtaining durability for a known service life in chloride exposures requires knowledge of the concrete properties, relevant transport processes, depth of cover as well as minimization of cracking and construction defects. For example, imperfect curing can result in depth-dependent effects on resistance to chloride ingress. Several service life models with various levels of sophistication exist for prediction of time-to-corrosion of concrete structures exposed to chlorides. The model inputs have uncertainty associated with them such as boundary conditions (level of saturation and temperature), cover depths, diffusion coefficients, time-dependent changes, and rates of buildup of chlorides at the surface. The performance test methods used to obtain predictive model inputs as well as how models handle these properties have a dramatic impact on predicted service lives. Very few models deal with the influence of cracks or the fact that concrete in the cover zone will almost certainly have a higher diffusion coefficient than the bulk concrete as the result of imperfect curing or compaction. While many models account for variability in input properties, they will never be able to account for extremes in construction defects. Therefore, to ensure the reliability of service life predictions and to attain a concrete structure that achieves its predicted potential, designers, contractors and suppliers need to work together to ensure proper detailing, minimize defects, and adopt adequate, yet achievable, curing procedures. As well, concrete structures are often exposed to other destructive elements in addition to chlorides (eg frost, ASR) and this adds another level of complexity since regardless of cause, cracks will accelerate the ingress of chlorides. These issues are discussed along with the need to use performance-based specifications together with predictive models.

**Keywords.** Chloride ingress, diffusion, construction defects, cracks, performance specifications, uncertainty

## Introduction

Concrete is a durable material and the most widely used construction material. Reinforced concrete structures can be designed to be resilient to severe storms, fire and earthquakes as well as to be durable in severe environmental exposures. Whether from marine or de-icing salts, chloride corrosion of steel reinforcement is the biggest challenge for both builders and owners of concrete structures. In addition to using materials and mix designs that will resist chloride ingress, construction detailing and practices have a large impact on durability. Achievement of concrete durability in-place

---

<sup>1</sup>Corresponding author: Dept. of Civil Engineering, University of Toronto, Toronto, ON, Canada, M5S1A4, [hooton@civ.utoronto.ca](mailto:hooton@civ.utoronto.ca)

is more likely with the use of appropriate performance specifications since temperature control, adequate compaction, protection of fresh concrete, and curing need to be detailed in specifications as well as requirements for sufficient inspection and testing to ensure that the specifications are being met.

In order to quantify the service life in severe environments, numerous predictive models have been developed over the last 25 years, especially related to the time-to-corrosion of reinforced concrete exposed to marine or de-icer salts. While early chloride ingress models, based on Fick's second law of diffusion were overly simplistic, newer models account for time-dependent changes in diffusion, the time to build up of surface chloride concentration, chloride binding and, in some cases, depth-dependent diffusion. However, diffusion is only one mechanism of ingress of fluids including aggressive ions such as chlorides. Other mechanisms including capillary absorption, permeability, and wick action can greatly accelerate ingress of chlorides, and some models have added terms to account for their effects. Taking a different approach, more fundamental multi-species models have been developed (such as STADIUM [1, 2]) that use effective diffusion values for different ions and account for their interactions and the nature of the pore structure and transport processes. In addition, deterministic models only provide average predictions which are not realistic given the level of uncertainty in concrete composition, rebar placement, and transport properties. However some models, such as DuraCrete [3] and LIFE-365 Version 2 [4] are at least semi-probabilistic and typically standard deviations as well as average values for each input value are used. The *fib* 2010 model code has incorporated some aspects of the Duracrete model [5]. Aspects of modelling will be discussed in more detail.

## 1. Design of durable concrete mixtures

Concrete mixtures that will be durable in aggressive exposures need to have low water/binder ratio, low unit water content, and contain appropriate levels of supplementary cementing materials. Typically, in order to minimize concrete permeability, a w/b of no higher than 0.40 is required. Using optimized total aggregate gradations and water-reducing admixtures, the unit water content can often be reduced to 135-140 L/m<sup>3</sup>, minimizing the paste volume fraction, thus reducing permeability while reducing thermal and drying shrinkage. Appropriate levels of supplementary cementing materials have many benefits in reducing paste permeability, reducing the porosity of the interfacial transition zones surrounding aggregates. Slag and fly ash will improve permeability at later ages, and silica fume improves properties at early ages, so ternary mixtures will work synergistically to improve initial properties and provide long-term benefits. In addition, SCMs improve the chloride binding capacity of the matrix, due to the lower Ca/Si ratio of the C-S-H and the incorporation of alumina into the hydrates, forming C-A-S-H [6, 7, 8].

Binder contents should be minimized, consistent with obtaining workable concrete, in order to minimize volume changes due to hydration temperatures and due to shrinkage. This will help minimize early-age cracking potential.

## 2. Types of performance testing

Tests are or can be performed at various stages in construction.

- **Pre-qualification Tests:** Used by producers to demonstrate that a concrete mixture, when placed and cured under defined conditions, can meet the specification requirements and, if needed, provide input data for service life prediction. These tests often require significant lead time to complete and may include tests needed as inputs to service life models.
- **Identity Tests:** Performed when the concrete arrives on-site but before concrete is placed to demonstrate that the concrete being supplied is equivalent to the mixture that was pre-qualified (Similar to a DNA test). Unfortunately the range of identity tests that can be performed prior to acceptance of the truck load of concrete are quite limited. Typically, slump or slump flow is measured, and air content is determined. Useful information on concrete uniformity and air content can also be obtained from measuring the fresh density of the concrete, and some owners, such as the New York/New Jersey Port Authority have adopted the AASHTO microwave test to determine the water content of the delivered concrete [9] (as a partial check on w/cm (assuming that the cementitious materials are typically batched accurately) related to unintentional or deliberately added water).
- **Quality Control:** To document that the concrete supplied meets strength and other specification limits (a) at the change of ownership (the point of discharge from the truck) and (b) at the point of placement to demonstrate that pre-qualified placing practices are being followed.
- **In-Place Testing:** Using NDT and/or tests on cores extracted from the structure to ensure that the combination of the concrete supplied and the placement and curing methods used resulted in achieving the owner-defined performance levels. This is required in the End Result Specifications (ERS) used by several highway agencies.

Traditionally, concrete producers and contractors are often just interested in prequalification and quality control testing. However, owners are interested in performance of the hardened concrete in the structure, a number of highway agencies in North America have adopted or are currently considering the use of ERS where contractors are paid based on consistently meeting specified performance requirements using in-place testing of concrete in the structure. A number of these agencies have developed ERS with defined financial bonuses for consistently meeting performance, and penalties for failure to meet the in-place requirements. If performance is lower than a certain threshold, removal can be required. Regardless, of the type of performance specification adopted, the acceptance criteria and the responsibilities of the various parties in cases of failure need to be clearly defined.

While there are many types of aggressive exposures which could potentially require a multitude of durability tests, for resistance in all aggressive exposures the “permeability” or fluid penetration resistance of concrete needs to be minimized. Therefore, adoption of one or more tests for measuring fluid penetration resistance is fundamental to ensuring durable concrete.

Most deterioration processes involve two stages. Initially, aggressive fluids (water, ionic solutions with dissolved salts, gases) need to penetrate or be transported through the capillary pore structure of the concrete to reaction sites (e.g., chlorides penetrating to reinforcement, or sulfates penetrating to reactive aluminates) prior to the actual chemical or physical deterioration reactions. Therefore, a standard acceptance test or

tests to measure rates of ingress of aggressive fluids, or a related rapid index test, is fundamental to the development of performance-based durability specifications. However, before tests are adopted in specifications, they must not only be shown to be useful and reliable, they must also be standardized and should include precision data based on interlaboratory evaluations (as is required for ASTM test methods), in order to set realistic specification limits that take account of test variability. Many tests have been proposed by researchers, but only a few have been found to be sufficiently robust to be adopted in recognised standards. Some interlaboratory data on non-destructive tests of concrete cover quality have been published [10, 11].

However, to be effective, the relevant mechanisms of fluid ingress for the environmental exposure of the structure or of specific structural elements need to be determined and appropriate test methods need to be adopted. Potential transport mechanisms include capillary absorption, diffusion, permeability and wick action, all of which are time-dependent. Many service life models only account for diffusion, but that is only one mechanism of chloride ingress. Capillary absorption into unsaturated near-surface zones can allow rapid ingress of dissolved ions in the so-called convection zone of the concrete cover. In some cases, pressure heads are also involved so permeability will also accelerate ingress. In the cases of tunnel liners, pipes, and slabs-on-grade, wick action from the air boundary can evaporate water from the near-surface capillary pores, leaving behind a buildup of precipitated chloride salts [12, 13, 14].

Test methods related to measurement of various durability properties exist in various standards (e.g. CSA, ASTM, AASHTO, US Corps of Engineers (CRD), and individual Departments of Transportation (DOT) in North America). Limits based on some of these test methods are specified in ACI, CSA and individual DOT specifications, amongst many others. Currently, standard test methods and/or limits do not exist for all of the relevant durability or performance concerns. As well, existing test methods are not always sufficiently rapid, accurate, or repeatable, nor do they necessarily adequately represent any or all of the in-situ exposure conditions. The lack of adequate performance-related test methods for concrete is one of the main factors that inhibit the move from prescriptive to performance specifications.

Limits on specific penetration resistance properties such as bulk chloride diffusion (ASTM C1556 [15], Nordtest NT Build 443 [16]), and water sorptivity (ASTM C1585 [17]) may be suitable for adoption in HPC specifications during pre-qualification and as inputs into predictive service life models, they are too time consuming to be used for acceptance purposes. For acceptance testing, a rapid permeability-index test should also be tested during prequalification and limits set that relate to the desired limits in the diffusion and sorptivity tests. Such rapid index tests include the ASTM C1202 [18] (adopted in CSA A23.1 [19]), the Rapid Chloride Migration Test (Nordtest NT492 [20] or AASHTO TP-64 [21]), a resistivity test [22, 23], or a chloride conductivity test [24]. Because it is relatively simple, rapid and due to familiarity with its use, the ASTM C1202 test has become widely used for this purpose in North America. However, there is current activity at ASTM to adopt much simpler surface and bulk resistivity tests that may eventually replace the C1202 test. Many of these test methods are discussed by Lane et al [25]

In 2004, the Canadian CSA A23.1 concrete standard introduced limits for the ASTM C1202 rapid chloride penetration test for prequalification of concrete mixtures to meet (a) C-1 exposure conditions (concrete exposed to freezing in a saturated condition with de-icer salts, 35 MPa, air-entrained, 0.40 w/cm max.) of 1500 coulombs at 56 days, and (b) C-XL exposure (similar exposure as the C-1 but where extended

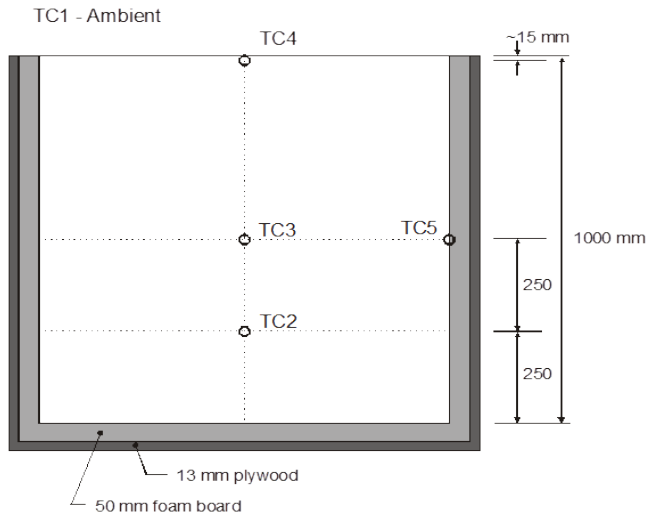
service life is required, 50 MPa, air-entrained, 0.37 w/cm max.) of 1000 coulombs at 56 days. These limits effectively mandated the use of either blended cements or SCM's in all such concretes since 100% Portland cement concretes would be unable to meet these limits. The limits were set at 56 days of age to allow concretes containing slag or fly ash, that develop their properties more slowly, to be able to meet them.

In 2009, CSA A23.1 [19] was revised to include statistical limits for acceptance purposes. The CSA coulomb limits were originally intended for prequalification, so notes were added that the 1500 coulomb requirement for Exposure Class C-1 an average value with no single result to be greater than 1750 coulombs. Similar wording was added for the high-performance C-XL Exposure Class concrete, except with different coulomb values (average of 1000, with no single value to exceed 1250). The 2014 revision has moved these notes into the body of the specification. It is expected that the next revision will include a much simpler and less costly bulk resistivity test method and limits that will likely replace the C1202 test.

### **3. Identity tests and the monolith approach**

A challenging issue in implementation of performance specifications is the establishment of identity tests to confirm, at the start of a contract, that the concrete mixture being delivered is the correct one. Of necessity, these tests need to be done at the point of discharge from the truck and provide immediate confirmation that the mixture is essentially the same as the pre-qualified one. So how can it be determined that the measured slump, density, and air content, even if they are in the approved range, actually represent the concrete pre-qualified by the supplier to meet the specified strength and durability criteria? In connection with pre-qualification and constructability tests made by the authors for a proposed nuclear power station, casting of a pre-concreting monolith test procedure has been used [26]. A similar performance approach was also developed for a series of underground transit stations. In these trials an insulated one cubic meter cube, suitably instrumented with thermocouples, was used as a pre-construction approval process. Specified performance criteria based on data and cores extracted from the monolith, were compressive strength, impermeability, freeze-thaw resistance, maximum temperatures, and temperature gradients. There are no instant tests for most of these properties so the monolith approach allows the Owner's design professional to check all the specified properties of the mixture that the contractor proposes to use. The sketch in Figure 1 shows a cross-section of the monolith with locations of thermocouples (TC). If needed to better determine thermal gradients, additional thermocouples can be added. The form is insulated so that curing is similar to the internal conditions in the mass concrete base slab. For this project compression tests up to 120 days were required, plus testing of in-place entrained air void systems, in-place rapid chloride permeability, and temperature gradients and maxima at all locations. The in-place tests were made on cores drilled from the monolith at different ages. On behalf of the owner the fabrication, concrete placing, compaction and curing can be witnessed. The owner can then make the tests on the concrete listed above and confirm that the concrete meets all strength and durability requirements. From then on, the total responsibility for the quality of concrete delivered placed and cured rests with the contractor and the concrete supplier. This approach requires significant lead time, typically in excess of 3 months, but on most major contracts this is typically not a problem.





**Figure 1.** Sketch of insulated one cubic metre monolith used for pre-qualification of concrete mixtures, showing locations of thermocouples (TC) [26]

#### 4. Roles and responsibilities in performance specifications

Adoption of true performance-based specifications presupposes that we have a clear understanding of all the performance issues that can affect concrete. It also assumes that there are appropriate performance test methods in place to evaluate all of the performance issues for: concrete materials, fresh concrete, hardened concrete, and durability. It also assumes that performance can either be measured in time to affect the outcome, and/or can be used to pre-qualify concrete mixtures. Most parties to construction are familiar with testing for fresh properties and strength of concrete, but the biggest challenges in this regard relate to requirements for durability [27, 28, 29].

While there are many types of aggressive exposures which might require a multitude of durability tests, the common element is that most aggressive exposures require that the permeability or fluid penetration resistance of concrete be minimized. Therefore adoption of one or more tests for penetration resistance is fundamental to ensuring durable concrete.

The Canadian concrete standard CSA A23.1-09 [19] outlines the requirements and responsibilities for use in performance-based concrete specifications. The responsibilities of the various parties need to be clearly defined with a performance specification. This has been documented in CSA A23.1-09, as shown in Table 1. In addition, Annex J to that standard explains each of the table items in more detail.

#### 5. Implementation of performance specifications

The onus for meeting performance clearly rests with the producer up to point of placement. Since in-place performance is also affected by the contractor's placement methods, the producer must work with the contractor to ensure the owner's performance requirements are achieved: eg. the contractor (not the owner/specifier)

should set the target slump to allow for proper placement and compaction for the situation, and the producer needs to design and provide this without reducing the intended performance of the hardened concrete.

Even if performance requirements are clearly stated in a specification, experience suggests that the successful implementation of a contract depends significantly on a dialogue between the contractors bidding for a contract and the Owner's design professional. Recent experience on a major HPC project suggests that where this requirement is established as an absolute and where there is constant and open communication across the construction team, all members will come to recognize the benefits of this approach.

A few important points are as follows:

- Require all contract bidders to attend a pre-bid meeting to hear about special requirements—so they cannot complain afterwards that they missed some of the performance requirements.
- Make contractors, including subcontractors, detail in their bid how they intend to meet the special requirements part of the bid submittal. eg. Concrete placement methods, protection, curing, hot/cold weather provisions.
- Do not accept low-price bids that are not responsive to the special requirements.
- Once work has commenced, require pre-pour meetings for important placements: The contractors, the suppliers, the subcontractors, including the finishers need to be aware of what needs to be done to ensure that the concrete can be delivered, placed, compacted, protected, finished, and cured to achieve the performance objectives. Even the person who will be fog misting, or applying other protective measures needs to be there to understand why it is important.
- During construction, the owner must be notified of any errors or problems without delay together with documentation and communication of the action being taken to rectify the problem.

Achieving the owner's performance requirements requires more cooperation between the concrete suppliers, the contractors, and concrete finishers than often exists in typical practice. This type of information is detailed in Annex J of CSA A23.1-09 [19].

## **6. Minimizing construction defects**

Construction detailing and practices as well as defects can significantly affect actual penetration rates of aggressive ions and fluids, but are rarely quantified or modeled. Almost no current service life prediction models can deal with the influence of cracks or the fact that concrete in the cover zone will almost certainly have a higher diffusion coefficient than the bulk concrete as the result of imperfect curing or compaction. An example of the variation in properties of similar bridge structures is given by Tikalsky et al [30].

It is the unpredictable areas of poorly compacted, poorly cured, or cracked concrete with less than the design depth of cover which will severely shorten the predicted time to corrosion, regardless of what model is used. Therefore, one of the most effective ways to obtain the model-predicted service life of a structure is to

address these site issues prior to and during construction. Pre-construction and pre-pour meetings mentioned previously are effective in ensuring that the contractor and sub-contractors understand the issues and have the required labor, materials and equipment on site to ensure best practices are followed.

As well, inspection of formwork placement and reinforcement cover depths prior to each placement of concrete can be used to correct areas of low cover deficiencies. In probability-based models, a common approach is to assume an average and range of properties such as concrete cover depth. But by correcting cover deficiencies prior to concrete placement, the variability in predicted service life can be significantly reduced. For example at the newest parking garage at Toronto’s Pearson airport, this process of inspection prior to placement led to a standard deviation in cover depth of only 3 mm over a huge deck area (Figure 2) (the specified cover was 40 mm), significantly below the CSA A23.1 [19] allowable variation of 10 mm [31].

The ability to adequately place, vibrate and compact concrete in areas of congested reinforcement also needs to be established, preferably with test of mock ups but also by letting the contractor select the required workability required for the situation given the available equipment and labour. The concrete supplier can then design appropriate mixtures for the contractor’s required workability. To address compaction and curing, cores extracted from the in-place concrete can be tested to assess the in-place performance of the final structural element (to avoid drilling cores from precast elements, extra elements for coring can be cast with the structural elements).

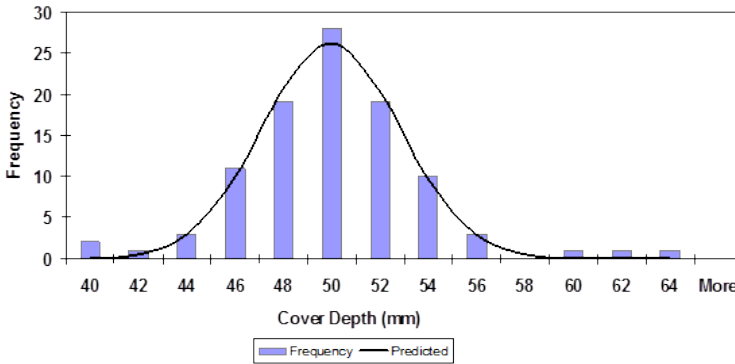


Figure 2. Range of measured in-place concrete cover on parking garage deck slab when inspected before placement (Specified cover = 40 mm) [31]

### 6.1 Predictive Models

Since corrosion of reinforcement is the largest single cause of deterioration of reinforced concrete structures, most models have focused on this, and mainly due to chloride ingress. The earliest chloride ingress models assumed that diffusion is the only mechanism of chloride ingress. Crank's solution [32] to Fick's second law can be used to determine the diffusion constant (Dc) of the concrete from chloride concentration profiles.

$$C(x, t) = C_s \left[ 1 - \operatorname{erf} \left( \frac{x}{2\sqrt{D_c t}} \right) \right] \quad \dots \text{Eqn. 1}$$

where  $C(x,t)$  = the chloride concentration at depth (x) and time (t)  
 $C_s$  = the chloride concentration at the concrete surface  
 $\text{erf}[\ ]$  = the error function (values can be obtained from standard tables for various values of the number within the brackets).

Typically, chloride profiles are obtained from a particular concrete which has been exposed to a solution of known chloride concentration after a fixed length of time. Careful use of a milling machine can provide samples for chloride concentration profiles at 0.5 to 1 mm intervals. Such tests have been standardized as Nordtest NT Build 443 [16] and ASTM C 1556 [15]. The numeric solution to Fick's 2nd law can then be used with  $D_c$  and  $C_s$  as inputs to predict the time to critical chloride concentration,  $C(x,t)$  at the depth of cover,  $x$ .

Later models included time-dependent ( $m$ ) [33] and depth-dependent [34, 35] diffusion coefficients and time-dependent buildup of surface chlorides ( $C_s(t)$ ) [36], and chloride binding [6, 8, 37]. Some models use apparent or bulk diffusion coefficients ( $D_a$ ) based on total (acid soluble) chloride penetration profiles and make corrections for chloride binding while others have used effective diffusion coefficients ( $D_e$ ). It is far easier to obtain reliable measurements of total chloride content (acid soluble chloride contents) by dissolving samples in nitric acid. Unfortunately, this includes any bound chlorides and if not accounted for, this has a significant impact on service life predictions [37]. While it is only the water-soluble chlorides that will act to depassivate the steel reinforcement, the methods for obtaining water-soluble chlorides are somewhat arbitrary and are difficult to define. Under some conditions, such as carbonation [8], almost all bound chlorides can be released. Another issue is that all materials contain some chlorides and there will be a background level of chloride throughout the concrete. For example, in Toronto and Chicago, the crushed limestone coarse aggregates typically contain significant chlorides, but unless the aggregate is crushed to powder, these chlorides are effectively insoluble as they are encased inside the coarse particles. If the background chloride in concrete is effectively insoluble, then a correction should be made to subtract these background values when acid soluble chlorides are being determined; for models, this typically has to be done anyway as diffusion rates are impacted by the chloride gradient.

Some models have included terms that also account for permeability and absorption while a few can account for conditions where pore systems are less than saturated throughout the thickness of the element. As stated earlier, it is important to consider other mechanisms of chloride ingress than diffusion such as absorption into unsaturated surfaces is a rapid process with time spans in the order of minutes or hours while diffusion ingress is measured in time spans of years. As well, evaporation due to wick action [12, 13, 14] can act to concentrate deleterious levels of precipitated salts in pores below the evaporative surfaces (although that mechanism becomes less important with concretes having a discontinuous capillary pore structure. ie. at  $w/c < 0.45$ ). Wick action is also important for damage due to physical sulfate and other types of salt attack.

Cracks wider than 0.05 to 0.10 mm accelerate chloride ingress [38, 39] but predictive models have not progressed to the point where the impacts of cracks on chloride ingress can be quantified. In practice, the emphasis must be placed on minimizing cracking as well as the width of cracks.

It is known that there is variability in all properties of reinforced concrete, so models, such as DuraCrete [3], and Version 2 of LIFE-365 [4] have taken probabilistic approaches using inputs of both average and standard deviation for each input value. A

typical example of input values needed in LIFE-365 is shown in Table 2. More simplistic stochastic models only give average time predictions that are well beyond the decision point required for structural repair since repairs are often initiated when only 5 or 10% of surfaces are exhibiting corrosion damage.

**Table 1.** Prescriptive vs performance specification responsibilities (adapted from CSA A23.1-09) [19].

	<b>The owner shall specify</b>	<b>The contractor shall</b>	<b>The supplier shall</b>
<p><b>(1) Performance:</b> When the owner requires the concrete supplier to assume responsibility for performance of the concrete as delivered and the contractor to assume responsibility for the concrete in place.</p>	<p>(a) required structural criteria including strength at age;                      (b) required durability criteria including class of exposure;                      (c) additional criteria for durability, volume stability, architectural requirements, sustainability, and any additional owner performance, pre-qualification or verification criteria;                      (d) quality management requirements (Annex J)                      (e) whether the concrete supplier shall meet certification requirements of concrete industry certification programs; and                      (f) any other properties they may be required to meet the owner's performance requirements.</p>	<p>(a) work with the supplier to establish the concrete mix properties to meet performance criteria for plastic and hardened concrete, considering the contractor's criteria for construction and placement and the owner's performance criteria;                      (b) submit documentation demonstrating the owner's pre performance requirements have been met; and                      (c) prepare and implement a quality control plan to ensure that the owner's performance criteria will be met and submit documentation demonstrating the owner's performance requirements have been met.</p>	<p>(a) certify that the plant, equipment, and all materials to be used in the concrete comply with the requirements of this Standard;                      (b) certify that the mix design satisfies the requirements of this Standard;                      (c) certify that production and delivery of concrete will meet the requirements of this Standard;                      (d) certify that the concrete complies with the performance criteria specified;                      (e) prepare and implement a quality control plan to ensure that the owner's and contractor's performance requirements will be met if required;                      (f) provide documentation verifying that the concrete supplier meets industry certification requirements, if specified; and                      (g) at the request of the owner, submit documentation to the satisfaction of the owner demonstrating that the proposed mix design will achieve the required strength, durability, and performance requirements.</p>
<p><b>(2) Prescriptive:</b> When the owner assumes responsibility for the concrete.</p>	<p>(a) mix proportions, including the quantities of any or all materials (admixtures, aggregates, cementing materials, and water) by mass per cubic metre of concrete;                      (b) the range of air content;                      (c) the slump range;                      (d) use of a concrete quality plan, if required; and                      (e) other requirements.</p>	<p>(a) plan the construction methods based on the owner's mix proportions and parameters;                      (b) obtain approval from the owner for any deviation from the specified mix design or parameters; and                      (c) identify to the owner any anticipated problems or deficiencies with the mix parameters related to construction.</p>	<p>(a) provide verification that the plant, equipment, and all materials to be used in the concrete comply with the requirements of this Standard;                      (b) demonstrate that the concrete complies with the prescriptive criteria as supplied by the owner; and                      (c) identify to the contractor any anticipated problems or deficiencies with the mix parameters related to construction.</p>

**Table 2.** Example of average values and standard deviations inputs to LIFE-365 [4]

Variable	Units	Average Value	Standard Deviation	Coefficient of Variation, %
Chloride Bulk Diffusion, $D_a$ at 28 days	$m^2/s$	$8.87 \times 10^{-12}$	$2.22 \times 10^{-12}$	25
Time-dependent coefficient, $m$	-	0.20	0.05	25
Max. Surface [Cl], $C_s$	% Cl	1.0	0.30	30
Background [Cl], $C_t$	% Cl	0.05	0.01	20
Cover Depth	mm	60	5	8

More sophisticated models, such as STADIUM [1, 2], use a more materials science-based approach and account for multi-species ionic movements (since chlorides are not the only potentially damaging ions entering pore solutions and also to maintain charge balance, there must also be cations present: the presence of different cations can impact the rate of diffusion).

Once the transport processes are modeled, another area that needs further attention is the critical chloride threshold for initiation of corrosion. Published values vary by more than an order of magnitude. More recent work has recognized the usefulness of the chloride to hydroxyl ion ratio as being more meaningful (taking into account different cement contents and types of cementing materials), but even these values vary by more than an order of magnitude [an extensive review is given in [40]. This subject is the current subject of study by RILEM committee CTC.

Lastly, to increase confidence in their use, model predictions need to be calibrated against chloride ingress in structures. A series of 8-15 year old parking and bridge decks exposed to de-icer salts were cored and chloride profiles were compared to model predictions; it was generally found that the Life-365 model predictions were conservative [41].

## 7. Summary

Achieving durability requires more than selecting an appropriate concrete mixture, construction practices and details also impact durability. In addition, performance specifications, making use of appropriate durability tests and limits, can help in the achievement of durable structures. While not perfect, performance approaches to durability design are being used successfully in large infrastructure projects and focus attention to the whole construction process and not just to the concrete mixture being supplied. To quantify durability in chloride exposures, there have been impressive achievements in the development of predictive service-life models in the last 25 years. This is especially true in the area of time to onset of reinforcement corrosion where models have developed beyond application of very simplistic Fick's 2<sup>nd</sup> Law methods to much more sophisticated multi-mechanistic, time-dependent, probabilistic transport models. Test methods have been developed to provide input values for these models, but often these tests are time-consuming, making them unsuitable beyond prequalification purposes. Some of these tests also suffer from high levels of variability. Faster, more reliable test methods will provide better predictions and will be better suited for quality assurance purposes during construction. In the meantime, rapid index tests can be used for that purpose.

## References

- [1] Marchand, J., Samson, E. Maltais, Y. Lee R. J. and Sahu, S., 'Predicting the performance of concrete structures exposed to chemically aggressive environment—Field validation', *Materials and Structures* 35 (10) (2002) 623-631.
- [2] Maltais, Y. Marchand, J. Samson, E., 'Predicting the durability of Portland cement systems in aggressive environments – Laboratory validation', *Cement and Concrete Research* 34 (9) (2004) 1579-158.
- [3] DuraCrete, '*Duracrete Probabilistic Performance Based Durability Design of Concrete Structures*', Final Technical Report, EU-Project-Euram III Document No. BE95-1347/R17, (2000).
- [4] Ehlen, M.A., Thomas, M.D.A., and Bentz, E.C., 'Life-365 Service Life Prediction Model Version 2.0', *Concrete International* 31(2) (2009) 41-46.
- [5] *fib Model Code for Concrete Structures*, International Federation for Structural Concrete Switzerland (2010)
- [6] Zibara, H., Hooton, R.D., Thomas, M.D.A., and Stanish, K., Influence of the C/S and C/A ratios of hydration products on the chloride ion binding capacity of lime-SF and lime-MK mixtures, *Cement and Concrete Research*, 38 (3) (2008), 422-426.
- [7] Hooton, R.D., Thomas, M.D.A., and Ramlochan, T., Use of Pore Solution Analysis in Design for Concrete Durability, *Advances in Cement Research*, 22 (4) (2010), 203-210.
- [8] Thomas, M.D.A., Hooton, R.D., Scott, A. and Zibara, H., The Effect of Supplementary Cementing Materials and W/CM on the Chloride Binding Capacity of Cement Paste, *Cement and Concrete Research* 42 (1) 2012, 1-7.
- [9] Bognacki, C. J., Pirozzi, M., Marsano, J. and Scriffiano, A., Increasing the services lives of concrete pavements, *Concrete International* 34(1) (2012), 27-33.
- [10] Rilem TC 189-NEC, Non-destructive evaluation of the concrete cover, Part I-Comparative test of penetrability methods, *Materials and Structures* 38 (2005), 895-906.
- [11] Rilem TC 189-NEC, Update of the recommendation of Rilem TC 189-NEC, Non-destructive evaluation of the concrete cover, Part I - Comparative test of penetrability methods, *Materials and Structures* 41 (2008), 443-447.
- [12] Buenfeld, N.R., Shurafa-Daoudi, M-T. and McLoughlin, I.M., 'Chloride Transport due to Wick Action in Concrete,' in Chloride Penetration into Concrete, *Proceedings, RILEM International Workshop*, St-Remy-les-Chevreuse, France, October (1995) 315-324.
- [13] Nokken, M.R. and Hooton, R.D., 'Evaporative Transport of Chlorides in Concrete', *Proceedings, Concrete Under Severe Environments*, CONSEC'01, Vancouver, 1 (2001) 357-364.
- [14] Aldred, J.M., Rangan, B.V., and Buenfeld, N.R., 'Effect of Initial Moisture Content on Wick Action through Concrete', *Cem Conc Res.*, 34 (2004) 907-912.
- [15] ASTM C1556-11a, Standard Test Method for Determining the Apparent Chloride Diffusion Coefficient of Cementitious Mixtures by Bulk Diffusion, ASTM Annual Book of Standards, V.04.02, ASTM International, 100 Barr Harbor Dr., P.O. Box C-700, West Conshohocken, PA USA (2013).
- [16] Nordtest NT Build 443, *Accelerated Chloride Penetration*. P.O. Box 116, FIN-02151 Espoo Finland.
- [17] ASTM C1585-13, Standard Test Method for Measurement of Rate of Absorption of Water by Hydraulic-Cement Concretes, ASTM Annual Book of Standards, V.04.02, ASTM International, 100 Barr Harbor Dr., P.O. Box C-700, West Conshohocken, PA USA (2013).
- [18] ASTM C1202-12, Standard test method for electrical indication of concrete's ability to resist chloride ion penetration, ASTM Annual Book of Standards, V.04.02, ASTM International, 100 Barr Harbor Dr., P.O. Box C-700, West Conshohocken, PA USA (2013).
- [19] CSA A23.1/A23.2-09, Concrete materials, methods of concrete construction, test methods and standard practices, Canadian Standards Association, Mississauga, Ontario, Canada, L4W5N6, (2009).
- [20] Nordtest NTBuild 492, Chloride Migration Coefficient from Non-Steady-State Migration Experiments, P.O. Box 116, FIN-02151 Espoo Finland (1999).
- [21] AASHTO TP64-03, Standard Test Method for Predicting Chloride Penetration of Hydraulic Cement Concrete by the Rapid Migration Procedure, American Association of State Highway Transportation Officials, Washington, DC (2003).
- [22] Hooton, R. D. and Karkar, E., Evaluating durability of concretes using rapid measurements for fluid penetration resistance, Proceedings, *Concrete Structures for Sustainable Community*, FIB, Stockholm (2012), 315-318.
- [23] AASHTO TP 95-11, Standard Method of Test for Surface Resistivity Indication of Concrete's Ability to Resist Chloride Ion Penetration, American Association of State Highway Transportation Officials, Washington, DC (2003).

- [24] Alexander, M. G., Ballim, Y. and Stanish, K., A framework for use of durability indexes in performance-based design and specifications for reinforced concrete structures, *Materials and Structures* 41(5) (2008), 921-936.
- [25] Lane, D. S., Detwiler, R. J. and Hooton, R. D., Testing transport properties in concrete, *Concrete International* 32(11) (2012), 33-38.
- [26] Hooton, R. D. and Bickley, J. A., Prescriptive versus performance approaches for durability design - The end of innocence? *Materials and Corrosion* 63(12) (2012), 1097-1101.
- [27] Bickley, J.A., Hooton, R.D., and Hover, K.C., Preparation of a Performance-Based Specification for Cast-In-Place Concrete, Report, RMC Research & Education Foundation, (2006), 168p. <http://www.nrmca.org/p2p>
- [28] Hooton, R.D., Hover, K.C., and Bickley, J.A., "Performance Standards and Specifications for Concrete for Promotion of Sustainable Construction", *Proceedings, CONSEC'07*, Tours, France, June 4-6, 2007, Vol. 1, pp. 815-830.
- [29] Hooton, R.D., Bickley, J.A., and Hover, K.C., Specifying and Achieving High Performance in Concrete Structures, *e-Proceedings, 9th International Conference on High Performance Concrete*, Rotorua, New Zealand, (2011).
- [30] Tikalsky, P., Pustka, D. and Marek, P. Statistical Variations in Chloride diffusion in concrete Bridges, *ACI Structural Journal* 102(3) (2005), 481-486.
- [31] Hooton, R.D. and Bickley, J.A., Design for Durability: The Key to Improving Concrete Sustainability, *Proceedings, First International conference on Concrete Sustainability (ICCS'13)*, Tokyo (2013).
- [32] Crank, J., *The Mathematics of Diffusion*, 2nd Edn, Clarendon, Oxford, (1975).
- [33] Mangat, P.S. and Malloy, B.T., Prediction of Long Term Chloride Concentration in Concrete, *Materials and Structures* 27 (1994) 338-346.
- [34] Bentz, D.P., Feng, X. and Hooton, R.D., Time-Dependent Diffusivities: Possible Misinterpretation due to Spatial Dependence, In RILEM Proceedings, PRO19, *Testing and Modelling the Chloride Ingress into Concrete*, (2000) 2250-234.
- [35] Hooton, R.D., Geiker, M.R. and Bentz, E.C., "Effects of Curing on Chloride Ingress and Implications of Service Life", *ACI Materials Journal* 99 (2002) 201-206.
- [36] Weyers, R.E., Service Life Modeling for Concrete Structures in Chloride Laden Environments, *ACI Materials Journal* 95 (4) (1998) 445-453.
- [37] Martin-Perez, B., Zibara, H., Hooton, R.D. and Thomas, M.D.A., 'A Study of the Effect of Chloride Binding on Service Life Predictions', *Cement and Concrete Research* 30 (2000) 1215-1223.
- [38] Garces Rodriguez, O. and Hooton, R.D., Influence of Cracks on Chloride Resistance of Concrete, *ACI Materials Journal*, 100 (2) (2003) 120-126.
- [39] Reinhardt, H-W. and Jooss, M., Permeability and Self-Healing of Cracked Concrete as a Function of Temperature and Crack Width, *Cement and Concrete Research* 33 (2003) 981-985.
- [40] Angst, U., Elsener, B., Larsen, B.K. and Vennesland, O., Critical Chloride Content in Reinforced Concrete—A Review, *Cement and Concrete Research* 39 (2009), 1122-1138.
- [41] Hooton, R.D., Bentz, E.C., and Kojundic, T., Long-Term Chloride Penetration Resistance of Silica Fume Concretes Based on Field Exposure, RILEM e-Proceedings, *Service Life Design for Infrastructure 2010*, TUDelft (2010).



# Nanoparticle modified concrete materials: opportunities, challenges and prosperities

Kejin WANG<sup>1</sup> and Gilson R. LOMBOY

*Department of Civil, Construction and Environmental Engineering,  
Iowa State University, Ames, IA 50010, USA*

**Abstract.** Research and applications of nanoparticles in concrete materials are rapidly increasing because fundamental properties of concrete (such as rheology, strength, transport properties, fracture behavior, etc.) are strongly influenced by the material properties at the nanoscale. Use of nanomaterials in concrete can also enhance sustainability and reduce negative environmental impact through reduction in cement use, energy and natural material consumptions during production and service. In this paper, the needs and opportunities of use of nanoparticle modified concrete are highlighted. The challenges in nanoparticle processing (such as dispersion and stabilization) are addressed. Recent developments in characterization methods (such as Raman spectroscopy, nanoindentation, modulus mapping, peak-force quantitative nanomechanical mapping and atomic force microscopy) are reviewed. Effects of nanoparticles (such as nanosilica, nanolimestone and nanoclay) on concrete rheology, hydration, microstructure development, mechanical properties, and durability are discussed.

**Keywords.** Nanoparticles, Processing, Characterization, Rheology, Hydration, Strength, Durability

## Needs and opportunities

Concrete has been the most widely used construction material since 1800s when Portland cement was invented. Today, rapid globalization and technological change are demanding modern infrastructures to meet the growing needs for quality of life, global competitiveness, and sustainability. As a result, the standards for functionality, constructability, serviceability, durability, environmental impacts, and life-cycle assessment of concrete are rising.

Recently, many breakthroughs of concrete technology have been made from the use of nanomaterials in concrete, which facilitates meeting the above-mentioned growing needs [1,2]. Some examples include (a) super-performance concrete featured with enhanced strength, fracture resistance, and ductility by using carbon nanotubes, nanosilica, etc., (b) sustainable cementitious materials featured with energy conservation and CO<sub>2</sub> emission reduction by using nanolimestone, nanoclay, etc., (c) microbial protection and air purification resulting from photoactivation of titanium

---

<sup>1</sup>Corresponding author: Iowa State University, Department of Civil, Construction and Environmental Engineering, 492 Town Engineering, Ames, IA 50010, USA; E-mail. [kejinw@iastate.edu](mailto:kejinw@iastate.edu)

dioxide nanoparticles; and (d) advanced concrete remediation obtained from the formation of nanoparticle barriers for transport control. Nanotechnology is opening new doors for the new era of concrete construction.

**Table 1.** Effects of various nanoparticles on compressive and flexural strength of cement-based materials

	Dosage <sup>†</sup> (%)	Size (nm)	w/b	Compress- ion <sup>‡</sup> (%)	Flexure <sup>‡</sup> (%)	Sample	Sources
Silica	0.25-13.5	5-40	0.35-0.50	10-169	19-37	mortar	[3-8]
	1-5	15-20	0.40-0.48	30	5-57	concrete	Behfarni et al. (2013), Najjigivi et al. (2013)
Alumina	1-1.25	13-15	0.40	4-15	51	mortar	Nazari et al. (2011) Oltulu et al. (2013)
	1.5-3	8-25	0.25-0.48	8-55	-	concrete	Shekari et al. (2011) Behfarnia et al. (2013)
Limestone	4	25	0.50	6-8	(-7)-(-17)	mortar	D.Wang (2013)
	2.5-5	5	0.25	(-10)-(-7)		concrete	Camiletti et al (2013)
Palygorskite*	1	10×1500	0.40	7	-	paste	K.Wang, et al. (2011)
Montmorillonite	0.6	0.1×100	0.55	22	-	paste	Chang, et al. (2007)
Titanium dioxide	1-5	15-25	0.25-0.40	11-54	(-5)-43	concrete	Nazari et al. (2010/11) Jala, et al. (2013)
	1	15	0.40	13	2	concrete	Nazari et al. (2011)
Copper oxide	1-5	15	0.40	4-44	25	concrete	Nazari et al. (2011)
Iron Oxide	0.5	60	0.40	5	-	mortar	Oltulu et al. (2013)
	1-5	15-25	0.25-0.40	20-72	12-76	concrete	Shekari et al. (2011) Khoshakhlagh et al. (2012)
Zinc peroxide	1-5	15	0.40	5-42	(-7)-59	concrete	Nazari et al. (2011/12)
Zirconia	1-5	15-25	0.25-0.40	6-51	0-57	concrete	Rafieipoura (2011) Nazari et al. (2010/11)

\* highly purified magnesium aluminosilicate; <sup>†</sup> % of cementitious materials; <sup>‡</sup> 28-day value, % increase of samples without nanomaterial additions.

## 1. Nanoparticles used in cement-based materials

Nanoparticles are materials with dimensions less than 100nm. At the nanoscale, the proportion of atoms on the surface increases relative to those inside which leads to novel properties. At the nanometer size, the classical mechanics cross over into quantum mechanics; different things start to happen, e.g. gravity becomes unimportant, electrostatic forces take over and quantum effects kick in [9]. There is a great interest for use of nanoparticles in cement-based materials because of its wide and almost exclusive use in construction, and the potential for nanoscale manipulation has profound ramifications for altering performance of cement based materials [10]. Having extreme small particle size and large surface area, nanomaterials are often reactive and show great potential for improving concrete properties such as compressive strength and permeability. Table 1 lists different nanoparticles that have been incorporated in concrete and/or being studied. Typically, the addition of nanoparticles increases compressive and flexural strengths by 5% to 50%. However, there are cases when adding nanoparticles reduces mechanical strength. In these cases, further investigation on dispersion and hydration products may be necessary to explain the reduction in strength. For the case of adding nanolimestone in ultra-high performance concrete, Camiletti, et al. [11] suggested that packing conditions prevent nanoparticles from creating nucleation sites.

## 2. Nanoparticle dispersion and stabilization

Agglomeration of nanoparticles is natural in an aqueous system because of the relatively high adhesion forces between these small particles. Physical, chemical and mechanical measures (such as use of dispersion agents and sonication, and mechanical milling) are often required for proper dispersion of nanoparticles. Clusters of nanoparticles due to any improper dispersion may introduce air through vapor-gas nuclei trapped in crevices [12] and form unreacted pockets in the cement matrix [3], thus resulting in weak zones in concrete.

It shall be pointed out that well-dispersed nanoparticles can naturally re-agglomerate with time, and the stability of the nanoparticles in a suspension is equally important to the initial dispersion [13]. Generally, dispersion concerns how effectively the aggregated nanoparticles can be broken up into primary particles or primary aggregates, and stability describes how well the nanoparticles can remain dispersed.

### 2.1. Dispersion

Proper dispersion of nanomaterials often requires use of dispersion agents, sonication, and/or mechanical milling. Surfactants are often used as both dispersion and stabilization agents. These chemicals generally position themselves on the interfaces between two phases (e.g., solid-liquid interfaces). Through electrostatic repulsion resulting from the electrical double layers around the electrically charged particles, stable dispersions can be obtained. A recent study has shown that a good dispersion of nanolimestone can be achieved in water with polycarboxylate superplasticizer [14].

Ultrasonication has been considered as the most effective for dispersing nanoparticles homogeneously in suspensions. A number of studies have evaluated the effectiveness of the technique on nanopowders, including silica, titania and alumina nanopowders [15,16]. Kawashima, et al. [17] studied the influence of ultrasonication and blending dispersion protocols of nanolimestone and found that ultrasonication led to a higher acceleration in rate of hydration and a greater improvement in early-age compressive strength of pastes with 30% fly ash replacement, compared to blending.

Recent research has showed that high energy vibratory and planetary ball mills are especially suited for fine and ultra-fine grinding of hard and brittle materials down to the nanometer size range [18]. They have also been used in co-grinding of cementitious materials to drive a wide range of mechano-chemical reactions [19]. During milling, solid–solid, solid–liquid and solid–gas reactions are initiated through repeated deformation and fracture of powder particles. Besides blending and reducing particle size, they can effectively change morphology of the cementitious materials [19].

### 2.2. Stabilization

Surfactants are often used for stabilization through electrostatic repulsion, steric hindrance, or a combination of both. The bonds that exist between particles depend on their shape, size and surface properties. Therefore, selection of appropriate surfactants often varies depending upon types of nanoparticles used. Generally, surfactants are anionic, cationic, or non-ionic. They differ in the charge of the hydrophilic head: negative for anionic, positive for cationic, and neutral for non-ionic. Anionic surfactants have been found to disperse limestone particles [13]. On the other hand, cationic surfactants are known to induce flocculation of calcium. For polymeric

surfactants, the adsorption and dispersion capabilities can be varied by the molecular weight of the polymer chains [20].

Kawashima, et al. [17] investigated polycarboxylate ether and naphthalene-based superplasticizers, anionic surfactants and non-ionic polymeric surfactant to determine their ability to stabilize the limestone nanoparticles. Stability was tested by centrifugation and sedimentation and was quantitatively measured through optical absorbance spectroscopy. PCE-based superplasticizers were found to be the most effect surfactant at stabilizing nanolimestone in dilute aqueous suspension. However, the amount of nanoparticles that reaggregate and settle is still relatively high.

### 3. Characterization

Advanced analytic tools (such as characterization methods and modelling) are a key factor for achieving prominence. Using advanced characterization methods, researchers are able to identify the changes in hydration kinetics, hydration products, nanostructure and nanomechanical properties, to connect nano-, micro-, meso-, and macro-scale properties, and to further understand the mechanisms of nanoparticle modification in concrete [21]. Table 2 provides a summary the various characterization methods. The following sections describe the various measurement techniques that have often been employed in characterizing the effects of nanoparticles on concrete materials.

#### 3.1. Hydration process and chemistry

Addition of nanoparticles to a cementitious system is found to have interesting effects on hydration, such as reduction in induction period, time shifts in peak heat of hydration and development of new types of hydration products. Hydration process of a cement-based system is often monitored using semi-adiabatic and isothermal calorimetry technique, which measures the heat and rate of hydration; thermo-gravimetric and x-ray diffraction analysis, which identify the phase changes of the hydrating materials. Garg et al. recently characterized cementitious materials (cement and fly ash) using Raman spectroscopy [22]. They showed the evolution of sulfoaluminate and hydroxyl phases in pastes and gradual disappearances of gypsum in parallel with the formation of ettringite (AFt). Raman spectroscopy has been applied to multiple aspects of cement research, ranging from the study of hardened concrete surfaces to the understanding of the structure of C-S-H gel [23].

#### 3.2. Microscopy and tomography

Technical advances in microscopy and tomography and complementary techniques have allowed the visualization and analysis of structures of hydration products at the nanoscale. Because of the very small size of nanoparticles, their sizes and shapes are often viewed through a transmission electron microscope (TEM). TEM has also been instrumental in imaging C-S-H structures. Some examples are shown in [24].

Monteiro et al [25] has extensively utilized high resolution full-field soft X-ray imaging to view in-situ hydration of cementitious particles in the water window. They had observed the early growth of calcium hydroxide (CH) and evaluated the supersaturation ratio of solution, growth rates, both kinetic and diffusion coefficients, and concentrations of solute molecules at facets of the CH crystals. They had also shown nucleation process with nanosilica using full-field soft X-ray imaging.

**Table 2.** Characterization methods

Method	Hydration/ Chemistry	Microscopy/ Tomography	Mechanical/ Permeability
Atomic Absorption Spectroscopy (AAS)	✓		
Atomic Force Microscopy (AFM)	✓	✓	✓
Atom Probe Tomography (APT)	✓	✓	
BET Nitrogen Adsorption			✓
Differential Scanning Calorimeter (DSC)	✓		
Differential Thermal Analysis (DTA)	✓		
Fourier Transform Infrared Spectroscopy (FTIR)	✓		
Energy-Dispersive X-Ray Spectroscopy (EDS, EDX, XEDS)	✓		
Inductively Coupled Plasma Mass/Atomic Emission (ICP-MS/AES) Spectrometry	✓		
Ion Chromatography	✓		
Isothermal Calorimetry	✓		
Mercury Intrusion Porosimetry (MIP)			✓
Micro-Indentation / Nano-Indentation			✓
Magnetic Resonance Imaging (MRI)	✓	✓	
Modulus Mapping		✓	✓
Nano-Scratch			✓
Nuclear Magnetic Resonance Spectroscopy (NMR)	✓	✓	
Optical Microscopy		✓	
Petrographic Microscopy / Polarized Light Microscopy	✓	✓	
Raman Spectroscopy	✓	✓	
Scanning Electron Microscopy (SEM)		✓	
Thermogravimetric Analysis (TGA)	✓		
Time-of-Flight Secondary Ion Mass Spectrometry (ToF-SIMS)	✓	✓	
Transmission Electron Microscopy (TEM)		✓	
X-Ray Diffraction (XRD) And Quantitative XRD	✓		✓
X-Ray Fluorescence (XRF)	✓		
X-Ray Photoelectron Spectroscopy (XPS)	✓	✓	
X-Ray Computed Tomography (X-Ray CT)	✓	✓	
Zeta Potential (electrophoretic mobility)	✓		

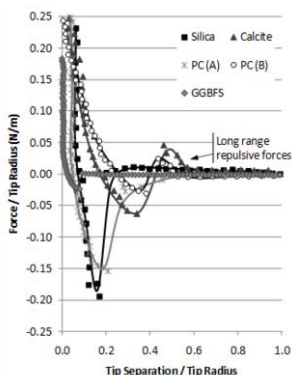
Atomic force microscopy (AFM) is another very useful tool in visualizing and analyzing the formation of different hydration products [26], providing insight on to concrete microstructure development [27], distinguishing between CSH particles and crystals of CH [28], identifying the carbonation process of CH [29], and quantifying interparticle forces. Wang, et al. [30,31] used AFM to investigate the adhesion properties and coefficient of friction of various cementitious particles. [Figure 1](#) shows the force interaction curves of selected cementitious materials with silicon nitride [30] and [Figure 2](#) shows the coefficient of friction between different cementitious materials [31].

### 3.3. Mechanical properties and permeability

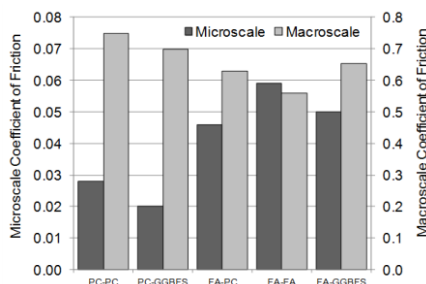
Studies have shown that nanomaterials can change mechanical properties of hydration products at the nanoscale. This has been observed by the increase in proportion of high stiffness C-S-H in nanoindentation tests [32]. Li, et al. [33] studied and compared three methods of measuring the nanomechanical properties of cement hydration products. They were nanoindentation, modulus mapping and peak force qualitative nanomechanical mapping (QNM). Nanoindentation is widely used for determining modulus and hardness [34]. Modulus mapping uses the same tools as a nanoindenter,

but the normal loads are much lower than indentation tests that it should not damage the surface and a higher resolution of surface modulus can be obtained. Peak Force QNM uses an AFM to measure the surface modulus.

Another novel experimental approach was also utilized by Oh, et al. [35] on determining the bulk modulus of CSH (14 Å tobermorite). They used a high-pressure synchrotron X-ray diffraction (up to 4.8 GPa) with a diamond anvil cell to measure the bulk modulus. They had also used the same method to study the mechanical properties of alkali-silica reaction gel, tetracalcium aluminum carbonate hydrates and ettringite.



**Figure 1.** Force interaction curves of silica, calcite, Portland cement (PC) and ground granulated blast furnace slag (GGBFS) with silicon nitride probe.



**Figure 2.** Micro and macroscale coefficients of friction of various cementitious materials.

## 4. Effects of nanomaterials on concrete properties

The key properties of concrete materials include workability/rheology, strength and durability. Use of nanoparticles in concrete can significantly affect all these properties.

### 4.1. Rheology

Table 3 shows the effects of nanoparticles on rheological properties (flowability-yield stress and viscosity, thixotropy, and stability) of cementitious systems. Although many nanomaterials reduce concrete flowability by increasing yield stress and viscosity, a study [36] at Iowa State University (ISU) indicated that small dosage of nanolimestone addition ( $\leq 1.5\%$  by weight of cement) slightly increased viscosity and yield stress, while a larger dosage ( $> 1.5\%$ ) of the addition decreased viscosity without significantly changing yield stress of cement pastes.

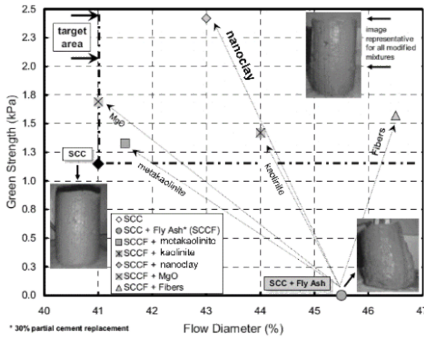
Recently, thixotropic behavior of cementitious materials is attracting much attention due to its important applications in concrete practice, such as formwork pressure, multi-lift casting, slip form paving, pumping, and segregation. Wang and Shah et al. [37] extensively studied the use of nanoclay made from highly purified magnesium aluminosilicate to improve the shape stability of semi-flowable self-consolidating concrete (SFSCC) that was to be used for slip-form construction of a concrete pavement. They had found that 0.75 to 1.0% addition of this type of nanoclay was sufficient to a shape-stable extruded slab (Figure 3). Quanji [38] subsequently

investigated the influence of the same type of clay on thixotropic behavior, particularly the structural rebuilding of fresh cement pastes. It was found that at a low dosage ( $\leq 1.3\%$  by weight of cement), nanoclay addition increased the structure rebuilding rate, while at a higher dosage, it decreased the rate of structural rebuilding (Figure 4).

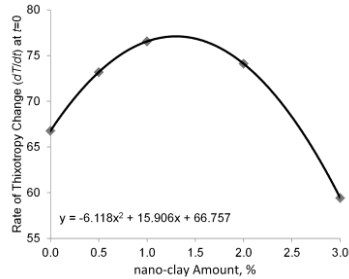
**Table 3.** Effects of various nanoparticles on rheological properties of cement-based materials

	Dosage (%)	Viscosity	Yield Stress	Thixotropy	Slump	Flow	Sample	Sources
Silica	0.5-1.5	↑	↑				paste	Wang et al. (2013)
	1-2.5	↑	↑				mortar	Senff et al. (2009)
	0.8-3.8	↑	↑				paste	Berra et al. (2012)
Alumina	0.5-2.0				↓		concrete	Najigivi et al. (2013)
	0.5-2.0				↓		concrete	Nazari, Riahi (2011)
Limestone	0.5-1.5	↑/↓	↑				paste	K.Wang et al. (2013)
	2.5-5.0					↑	concrete	Camiletti et al. (2013)
Palygorskite	0.5-2.5	↑					paste	Sun (2013)
	0.5-3.0	↑	↑	↑			paste	K.Wang et al. (2013)
	0.45	↑	↑	↑	↓	↓	mortar	K.Wang et al. (2011)
Titanium dioxide	0.45	↑	↑	↑	↓	↓	concrete	K.Wang et al. (2011)
	2.6-5.2	↓	↑				paste	Senff et al. (2012)
Iron Oxide	0.5-2.0				↓		concrete	Nazari, Riahi (2011)
Zinc peroxide	0.5-2.0				↓		concrete	Nazari, Riahi (2011)

Note: (↑ – increase, ↓ – decrease)



**Figure 3.** Effect of different additives on green strength and flowability for SFSCC



**Figure 4.** Effect of nanoclay amount on rate of thixotropy change

#### 4.2. Hydration and strength

Mechanisms attributed to accelerated rate of hydration and shortened induction period are nucleation for the case of nanosilica [39] and seeding effect in the case of nanolimestone [40]. Addition of colloidal silica results in acceleration of  $C_3S$  dissolution and rapid formation of C-S-H phase in cement paste [39]. Hydration products of cement, deposit on the nanoparticles due to their higher surface energy. Sato and Diallo [40] proposed that nanolimestone either broke down the protective layer on  $C_3S$  grains during hydration to shorten the induction period, or accelerated C-S-H nucleation.

The improvement in strength due to the addition of nanosilica may result from (a) pozzolanic reaction, (b) nanoparticles fill the nanosize pores [41], (c) improvement in the mechanical properties of the C-S-H gel itself (e.g., greater alumina-content, longer silicate chains) [42], (d) solid, dense, and stable bonding framework [43], (e) formation of denser microstructures through growth of silica chains in C-S-H [44], (f) crystal orientation degree, and crystal size of portlandite crystals [8,45]. A combined effect of the above mechanisms produces a uniform dense microstructure with improvement not only in the cement paste but also in the interfacial transition zone.

### 4.3. Durability

The durability of concrete is largely related to concrete permeability. The intrusions of gas, liquid and ions may cause harmful stresses and chemical changes in concrete that will affect its integrity. Nanoparticles can contribute to reducing permeability by creating a denser nanostructure such as by pozzolanic reaction and by possibly longer chains in C-S-H and/or by filling pores and acting as barriers, thus increasing concrete durability and service life.

Reduction in water penetration depth, gas permeability, and diffusion depth has been observed in concrete with nanosilica [41]. Cervellati et al. [46] found that concrete made with nanolimestone had high water vapor permeability but low liquid water permeability. Hydrophobic organo-modified montmorillonites nanoparticles around capillary pores can obstruct the diffusion of pore solution and aggressive chemicals, thus reducing permeability [47, 48]. Wang, et al. found that 1% nanolimestone addition improved freezing-thawing (F-T) resistance and decreased free-drying shrinkage [36]. Behfarnia and Salemi [49] found that the residual strength of concrete made with nanosilica and nanoalumina (without air entrainment) ranged in 70-90%, while concrete samples without nanoparticles did not survive after 300 F-T cycles.

## 5. Concluding remarks

Nanoparticles can improve rheological, mechanical and durability properties of concrete materials. Although some nanomaterials reduce concrete flowability, other nanomaterials, such as nanolimestone and nanoclays, can increase flowability and thixotropy, providing concrete mixtures with better flowability and stability. Nanoparticles accelerate cement hydration and early age strength development. This acceleration often results from a combined effect of seeding for nucleation of hydration products, high degree pore refinement, and rapid chemical (such as pozzolanic) reactivity. Nanoparticles can also lengthen CSH chains and produce a denser nanostructure for both strength and durability enhancement. There are still many challenges in using nanomaterials in concrete practice. One is the particle dispersion and stabilization. Another challenge is the understanding of the mechanisms involved in the interaction between nanoparticles and cementitious materials. Studying the behavior of nanoparticle modified concrete materials often requires interdisciplinary knowledge to use of various advanced characterization methods and simulation tools and to analyze chemistry, morphology and mechanical properties of the materials at multiple scales. An additional challenge, which was not addressed in this paper, is the potential impact on health and safety during handling a large quantity of nanomaterials. In brief, nanotechnology has opened new doors for production of functional,



economical, eco-friendly, and sustainable concrete, and more research is needed to address the challenges and to meet the growing demands of modern infrastructure.

## Acknowledgements

The authors would like to acknowledge the contributions and references from the works of Professor Surendra P. Shah of Northwestern University and the contributions of former and current students at Iowa State University, Zhuojun Quanji, Nishant Garg and Xin Wang. Some of the works presented are part of research projects funded by the Tennessee Valley Authority and Oak Ridge Associated Universities (Award 105866), National Science Foundation (GRANT NO. 0927660), and pool fund by IA, KS, NE, NY, WA departments of transportation, Federal Highway Administration, National Center of Concrete Pavement Technology and concrete admixture companies.

## References

- [1] J. Grove, S. Vanikar, and G. Crawford, Nanotechnology – New tools to address old problems, *Jo. of the TRB* **2141** (2010), 47–51.
- [2] B. Birgisson, P. Taylor, J. Armaghani, and S.P. Shah, American road map for research for nanotechnology-based concrete materials, *J. of the TRB* **2142** (2010), 130–137.
- [3] H. Li, et al, Microstructure of cement mortar with nano-particles, *Compos Part B* **35** (2004), 185–189.
- [4] K. Sobolev, et al. Engineering of SiO<sub>2</sub> Nanoparticles for Optimal Performance in Nano Cement-Based Materials. In: 3rd Intl Sym on Nanotechnology in Const, Prague, Czech Republic. (2009) 139-148.
- [5] B.W. Jo, C.H. Kim, G.H. Tae, J.B. Park, Characteristics of cement mortar with nano-SiO<sub>2</sub> particles, *Constr Build Mater* **21** (2007), 1351–1355.
- [6] L. Senff, J.A. Labrincha, V.M. Ferreira, D. Hotza, W.L. Repette, Effect of nano-silica on rheology and fresh properties of cement pastes and mortars, *Constr Build Mater* **23** (2009), 2487–2491
- [7] M. Aly, et al., Effect of colloidal nano-silica on the mechanical and physical behavior of waste-glass cement mortar, *Mater Design* **33** (2012), 127–135
- [8] P. Hosseini, A. Booshehrian, and S. Farshchi, Influence of Nano-SiO<sub>2</sub> Addition on Microstructure and Mechanical Properties of Cement Mortars for Ferrocement, *J. of the TRB* **2141** (2010), 15–20.
- [9] S. Mann, *Nanoforum Report: Nanotechnology and Construction*, Institute of Nanotechnology, 2006
- [10] D. Lange, *Book Review: Nanomaterials in Concrete: Advances in Protection, Repair, and Upgrade*, by Henry E. Cardenas, DEStech Publications, Inc., PA, USA, 2013
- [11] J. Camiletti, A.M. Soliman, M.L. Nehdi, Effects of nano- and micro-limestone addition on early-age properties of ultra-high-performance concrete, *Mater Struct* **46** (2013), 881–898
- [12] C. Sauter, et al., Influence of hydrostatic pressure and sound amplitude on the ultrasound induced dispersion and de-agglomeration of nanoparticles, *Ultrasonics Sonochemistry* **1** 5(4) (2008), 517-523.
- [13] P. Panya, O. Arquero, G.V. Franks, Dispersion stability of a ceramic glaze achieved through ionic surfactant adsorption, *Journal of Colloid and Interface Science* **279** (1) (2004), 23-35.
- [14] S. Kawashima, et al., Modification of Cement-based Materials with Nanoparticles, *Cem. and Concr Composites*, **36** (2013), 8-15
- [15] K.A. Kusters, S.E. Pratsinis, S.G. Thoma, et al., Ultrasonic fragmentation of agglomerate powders, *Chem. Engg. Sci.* **48** (24) (1993), 4119-4127
- [16] V.S. Nguyen, D. Rouxel, R. Hadji, Effect of ultrasonication and dispersion stability on the cluster size of alumina nanoscale particles in aqueous solutions, *Ultrasonics Sonochemistry* **18** (1) (2011), 382-388.
- [17] S. Kawashima, J. Seo, D. Corr, Dispersion of CaCO<sub>3</sub> nanoparticles by sonication and surfactant treatment for application in fly ash-cement systems, *Materials and Structures* (2013), 1-13
- [18] S. Rosenkranz, S. Breitung-Faes, and A. Kwade, “Experimental investigations and modelling of the ball motion in planetary ball mills,” *Powder Technology* **212** (2011), 224–230
- [19] P. M. Babiain, et al., “Effect of Mechano-Chemical Activation on Reactivity of Cement Kiln Dust-Fly Ash Systems,” *ACI Material J.*, **100** (2003), 55–62

- [20] F. Winnefeld, et al., Effects of the molecular architecture of combshaped superplasticizers on their performance in cementitious systems, *Cem and Conc Comp* **29** (4) (2007), 251-262.
- [21] A. Porro, J.S. Dolado, J.J. Gaitero, Nanotechnology and Concrete - Concepts and Approach, *Jo. of the TRB*, **2142** (2010), 127-129.
- [22] N. Garg, K. Wang, S.W. Martin, A Raman spectroscopic study of the evolution of sulfates and hydroxides in cement-fly ash pastes, *Cem. and Conc. Res.* **53** (2013) 91-103
- [23] M. Chollet, M. Horgnies, Analyses of the surfaces of concrete by Raman and FT-IR spectroscopies: comparative study of hardened samples after demoulding and after organic post-treatment, *Surf. Interface Anal.* **43** (2011), 714-725.
- [24] R.J.M. Pellenq, N. Lequeux, H. van Damme, Engineering the bonding scheme in C-S-H: The iono-covalent framework, *Cem. and Conc. Res.* **38** (2008), 159-174
- [25] P.J.M. Monteiro, A.P. Kirchheim, S. Chae, et al., Characterizing the nano and micro structure of concrete to improve its durability, *Cem. & Conc. Comp.* **31** (2009), 577-584
- [26] L. Ferrari, J. Kaufmann, F. Winnefeld, et al., Reaction of clinker surfaces investigated with atomic force microscopy, *Const. and Bldg Mats* **35** (2012) 92-96
- [27] V.G. Papadakis, E.J. Pedersen, An AFM-SEM investigation of the effect of silica fume and fly ash on cement paste microstructure, *Jo. Of Mats Sci.* **34**(1999), 683- 690
- [28] A. Peled, J. Weiss, Hydrated cement paste constituents observed with Atomic Force and Lateral Force Microscopy, *Const. and Bldg Mats* **25**(2011), 4299-4302
- [29] T. Yang, et al, Direct observation of the carbonation process on the surface of calcium hydroxide crystals in hardened cement paste using an AFM, *Jo. Of Mats Sci* **38** (2003), 1909-1916
- [30] G.R. Lomboy, S. Sundararajan, et al., A test method for determining adhesion forces and Hamaker constants of cementitious materials using AFM, *Cem. and Conc. Res.* **41** (11) (2011), 1157-1166
- [31] G.R. Lomboy, S. Sundararajan, K. Wang, Micro- and macroscale coefficients of friction of cementitious materials, *Cem. and Conc. Res.* **54** (2013), 21-28
- [32] P. Hou, S. Kawashima, D. Kong, et al., Modification effects of colloidal nanoSiO<sub>2</sub> on cement hydration and its gel property, *Composites Part B: Engineering* **45**(1)(2013), 440-448
- [33] S.P. Shah, S. Kawashima, W. Li, G.R. Lomboy, Controlling Properties Of Concrete Through Nanomodification, in *Proceedings of the FraMCoS-8, Workshop on Nanotechnology and Sustainability in Construction*, S.P. Shah, G. Ruiz, R.C. Yu, X.X. Zhang, C. Andrade editors, Toledo Spain, 2013
- [34] P. Mondal, S.P. Shah, L. Marks, A reliable technique to determine the local mechanical properties at the nanoscale for cementitious materials, *Cem. and Conc. Res.* **37** (10) (2007), 1440-1444
- [35] J.E. Oh, S.M. Clark, H.R. Wenk, P.J.M. Monteiro, Experimental determination of bulk modulus of 14 Å tobermorite using high pressure synchrotron X-ray diffraction, *Cem & Conc Res* **42** (2012), 397-403
- [36] X. Wang, K. Wang, J. Li, N. Garg, S.P. Shah, Properties of self-consolidating concrete containing high volume supplementary cementitious materials and nano-limestone, Proceedings of the The Fifth North American Conference on the Design and Use of Self-Consolidating Concrete, May 12-15, 2013, Chicago
- [37] K. Wang, S.P. Shah, P. Taylor, et al., *Self-Consolidating Concrete-Applications for Slip-Form Paving: Phase II*. National Concrete Pavement Technology Center, Iowa State University, 2011.
- [38] Z. Quanji, *Thixotropic behavior of cement-based materials: effect of clay and cement types*, Master Thesis, Iowa State University, 2011
- [39] J. Bjornstrom, et al., Accelerating Effects of Colloidal Nanosilica for Beneficial Calcium-Silicate-Hydrate Formation in Cement, *Chemical Physics Letters*, **392** (1-3) (2004), 242-248.
- [40] T. Sato, F. Diallo, Seeding Effect of Nano-CaCO<sub>3</sub> on the Hydration of Tricalcium Silicate, *Jo of the TRB* **2141** (2010), 61-67.
- [41] K. Sobolev, M. Ferrada-Gutiérrez, How Nanotechnology Can Change the Concrete World, *American Ceramic Society Bulletin* **10** (2005), 14-17.
- [42] J.J. Gaitero, I. Campillo, A. Guerrero, Reduction of the Calcium Leaching Rate of Cement Paste by Addition of Silica Nanoparticles, *Cem. and Conc. Res.* **38** (8-9) (2008), 1112-1118.
- [43] J.Y. Shih, T.P. Chang, T.C. Hsiao, Effect of Nanosilica on Characterization of Portland Cement Composite, *Materials Science and Engineering A* **A424**(1-2)(2006), 266-274.
- [44] J.S. Dolado, I. Campillo, E. Erkizia, et al., Effects of Nanosilica Additions on Cement Pastes. *Proc., International Conference on Applications of Nanotechnology in Concrete Design* (2005), 87-96.
- [45] Y. Qing, Z. Zenan, K. Deyu, Influence of Nano-SiO<sub>2</sub> Addition on Properties of Hardened Cement Paste as Compared with Silica Fume, *Construction and Building Materials* **21**(3)(2007), 539-545
- [46] G. Cervellati, R. Rosa, Use of calcium carbonate particles with high surface area in production of plaster, cement, mortar and concrete. *PCT Int. Appl.* WO 2006134080 **40** (2006)

- [47] T.P. Chang, J.Y. Shih, K.M. Yang, T.C. Hsiao, Material Properties of Portland Cement Paste with Nano-Montmorillonite. *Journal of Material Science* **42** (17) (2007), 7478–7487.
- [48] W.Y. Kuo, J.S. Huang, C.H. Lin, Effects of Organo-Modified Montmorillonite on Strengths and Permeability of Cement Mortars. *Cement and Concrete Research* **36** (5) (2006), 886–895.
- [49] K. Behfarnia, N. Salemi, The effects of nano-silica and nano-alumina on frost resistance of normal concrete, *Constr Build Mater* **48** (2013) 580–584

# Low-damage earthquake-resistant structures achieved through movability and ductility

Nawawi CHOUW<sup>1</sup>

*The University of Auckland, Department of Civil and Environmental Engineering,  
Auckland Mail Centre, Private Bag 92019, Auckland 1142, New Zealand*

**Abstract.** In current seismic design, structures are typically assumed to be fixed at the base. Separation at the base during earthquakes is thus avoided, in order to avoid the possibility instability or even overturning. In contrast to this conventional approach, the structures described in this paper subscribe to a low-damage design philosophy in which the structures are indeed allowed to move and uplift while responding to earthquake loading. Whenever there is partial separation of the structure from the supporting ground, earthquake energy induced into the structure will be temporarily cut off. Consequently, the structures experience less loading and less or even zero damage can be anticipated. This paper presents an overview of current research on innovative seismic design approaches that could be implemented in low-damage earthquake-resistant structures of the future.

**Keywords.** Earthquake, uplift, relative movement, interlocking block, mortar free

## Introduction

In conventional design structures are assumed to be fixed at the base. This is mainly because of the intrinsic difficulty in incorporating the dynamic behaviour of the supporting soil in the analysis of the structural response. The other reason is that structural uplift is considered as a source of possible collapse due to overturning of the structure. Hence, any temporary separation at the foundation-soil interface should be avoided, no matter how small or brief. In this respect current design specifications worldwide have remained the same for decades. To reduce the impact of earthquake loading and at the same time to minimize the costs of construction, in current design specifications minor damage to the structure is tolerated, in the form of controlled plastic hinge development at predefined locations.

The 2011 Christchurch earthquake showed that well-designed structures indeed behaved as anticipated. Damage occurred at the beam-column joints as the designer intended and the safety of the occupants was ensured. However, current design philosophy assumes that the structure will experience a strong one-off earthquake event with the estimated return period. This assumption ignores the possibility of a sequence of strong aftershocks, such as that observed in Canterbury, New Zealand, during late 2010 and early 2011 (Chouw and Hao, 2012).

---

<sup>1</sup> Corresponding author: Director of the University of Auckland Centre for Earthquake Engineering Research

Observations of damage in structures in the Christchurch CBD showed that in many cases the repair costs were as high as 90% of what would be the replacement cost of the building. In addition to this, cost is incurred due to the down time that is required to carry out the repairs to the building and surrounding infrastructure – and this can be very difficult to predict. Also, it should be noted that just because a structure has been repaired, it could still be difficult to convince previous tenants to move back into the building, especially when it is unknown when the whole CBD will be restored again.

Observations of structural behaviour in major earthquakes showed that temporary and partial separations of structures from the supporting ground can be beneficial. Because of these separations, some of these structures suffered significantly less damage. These observations have been incorporated in a very small number of structures. One example is the South Rangitikei Viaduct in New Zealand (Beck and Skinner, 1973). Instead of rigidly securing the bridge piers to the ground, the bridge can rock in the out-of-plane direction. A large chimney at Christchurch airport (see Figure 1) is another example of a movable structure that is designed to rock under a strong earthquake (Sharpe and Skinner, 1983). Over the past three years since the February 2011 main earthquake, the Canterbury region has experienced more than eleven thousands aftershocks, with a number of these consisting of strong shakings. An inspection of the chimney more than one year after the February 2011 Christchurch earthquake showed that despite undergoing a large number of these strong aftershocks, no damage has been observed (Chouw and McCue, 2012).

Research on low-damage earthquake-resistant structures with capability to perform relative movements without causing damage is still very limited. This is also because a holistic consideration of the structure-footing-soil system is necessary. This paper presents an overview of some recent research at the University of Auckland, New Zealand.



**Figure 1.** Chimney with rocking ability.

## **1. Low-damage earthquake-resistant design approach**

In low-damage earthquake-resistant design, temporary separations can take place not only at the interface between foundation and the ground, but also at wall-foundation interface or between structural members. In the first case the structure is allowed to rock and part of the footing is permitted to separate from the base. The uplift behaviour will be controlled, typically by having the centre of the gravity low enough so that the structure will re-centre by itself. In the second case each structural member can

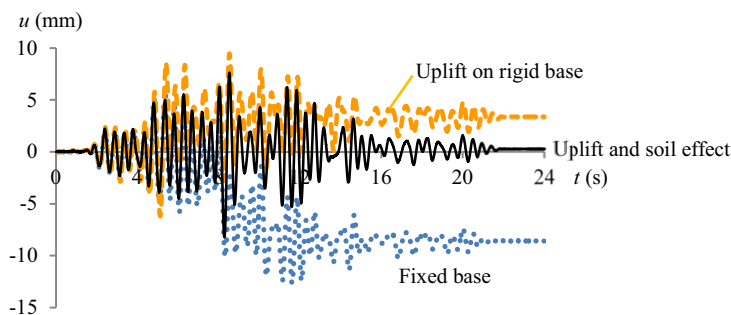
separate from its adjacent members. Temporary separations can also take place along the height and throughout the structure. Four examples of the new design approach are presented.

### 1.1. Multi-storey buildings

Figure 2 shows a model of a multi-storey building founded on sand. The building is designed according to current design specification with possible plastic hinge development at the beam-column joints and at the base. The earthquake excitations based on Japanese design spectrum (JSCE, 2000) are simulated by a shake table. To ensure the repeatability of the experiments Teflon washers were used to enable artificial plastic hinging (see Qin et al. 2013; Qin and Chow, 2013).



**Figure 2.** Multi-storey building model.



**Figure 3.** Influence of uplift and flexible soil on nonlinear structural responses.

Figure 3 shows the consequence of temporary uplifts at the base, on horizontal displacements at the top of the model building. Under the current design approach the building will suffer significant permanent displacement,  $u$ , due to plastic deformation at the joints (see fixed-base result, dotted line). However, when uplifts are permitted the residual displacement can be reduced by more than 50% (dashed line). This result is achieved with a rigid base. When the soil deformation is considered, the impact of the earthquake can be further reduced, as indicated by the thin solid line, with the building suffering minimal plastic deformation.

1.2. Liquid storage tanks

Figure 4 shows the model of a liquid storage tank. To incorporate the effects of the supporting ground it is placed on sand within a laminar box (Qin and Chow, 2013). The box has the capability to conform to the deformation of the mass of sand, and thus a more realistic simulation of the soil condition can be achieved. Instead of anchoring the tank on a rigid base, the tank should be able to uplift on a flexible base. The interaction between liquid, tank, footing uplift, and soil deformation plays a significant role in the response of the tank to the ground excitations.

Figure 5 shows the development of the axial stress along the height of the tank. The left, middle, and right results are caused by the tank with the aspect ratio  $H/R = 1, 2$  and  $3$ , respectively.  $H$  and  $R$  are the water level and radius of the tank, respectively. The excitation used was that of the 1940 El-Centro ground motion. As anticipated, with an increasing aspect ratio the maximum stress at the base becomes larger.

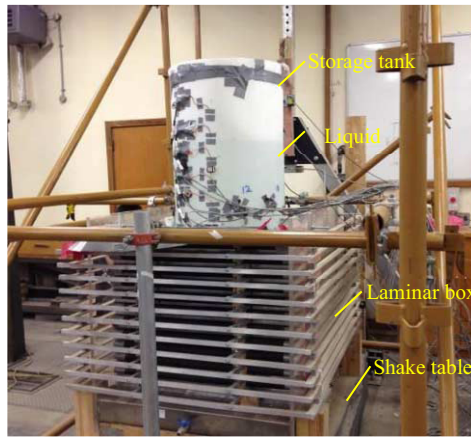


Figure 4. Fluid-structure-soil system.

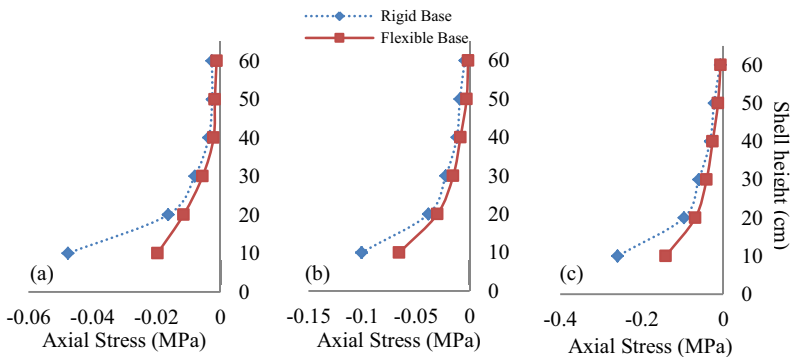


Figure 5. Influence of uplift of flexible ground on the development of the maximum axial compressive stress. (a)  $H/R = 1$ , (v)  $H/R = 2$  and (c)  $H/R = 3$

The most significant insight is that uplift on deformable soils can significantly reduce the impact of the earthquake, compared with that observed from the experiments with the tank on the shake table directly. The stress development in the

upliftable tank on sand (solid line) is smaller in comparison with that on rigid base (dotted line). More information is provided by Ormeño et al. (2012a and b, 2013).

### 1.3. Timber shear walls

To control the uplift movement during an earthquake, slip-friction connectors are used as hold-downs in what would otherwise be a rigid timber shear wall in Figure 6. Whenever uplift takes place friction forces will be activated and thus earthquake-induced vibration energy will be dissipated. To resist the shear forces activated at the base, shear-keys are installed. The location of the shear-keys will significantly determine the moment resistance at the base. For simplicity the earthquake loading is simulated by quasi-static cyclic movements at the top left corner of the wall using the hydraulic actuator attached to the adjacent strong wall.

Figure 7(a) shows the relationship between the ratio of the restraining moment  $M_{rp}$  to the overturning moment  $M_r$  and the angle of shear-key contact surface.  $\mu$  is the friction coefficient. The relationship displays the effect of  $\mu$  and  $\phi$  on the percentage contribution of the shear-key to the overall moment resistance of the wall (Loo et al., in print).

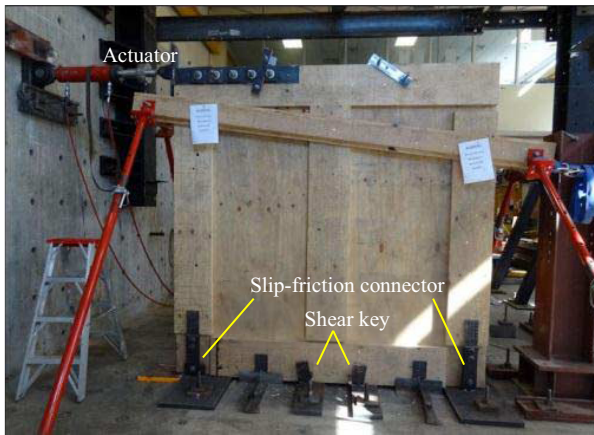


Figure 6. Rigid timber shear wall with slip-friction connectors and shear keys.

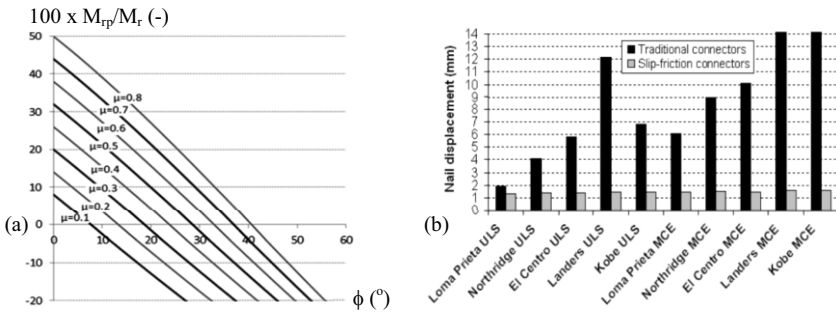


Figure 7. Influence of uplift, slip-friction connectors and shear-keys on (a) restoring moment and (b) nail displacements from numerical analysis of a flexible timber shear wall.



Figure 7(b) shows the results obtained from numerical analyses, this time on a *flexible* timber shear wall of plywood sheathing nailed to timber framing. The impact on the nail connections from various earthquake simulations demonstrates the effectiveness of including slip-friction connectors as hold-downs, versus the use of the traditional hold-down. The results clearly show that conventional hold-down connectors, fixing the wall to the foundation, will cause an immense stress to the nail within the wall. In contrast, allowing the wall to uplift activates the wall rotation, and base shear is capped. Consequently, deformation of the wall is avoided and nails within the wall will not bear the impact of the earthquake loading. The slip-friction connectors will further reduce the induced energy due to activated friction forces. The results also show that the proposed approach can cope with ground motions of different characteristics and magnitudes. Details of the research can be found in (Loo et al., 2012a and b).

#### 1.4. Structures with multiple uplifting components

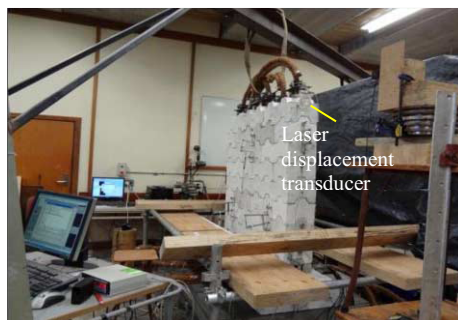
Figure 8 shows a mortar-free wall made of interlocking blocks. Since no mortar is used, each block can move relative to the blocks adjacent to it. Consequently, mutual movement among all the blocks take place throughout the entire wall. Whenever the wall experiences a strong earthquake, relative movements are activated and energy induced into the wall will be cut off through at multiple locations and times at different spatial block interfaces.

To enhance the block performance, coconut fibre reinforced concrete is used. Coir is selected mainly because of its high energy absorption capability. Inclusion of fibres will also more evenly distribute the minor crack development and thus increase the damping of the coil-concrete composite. To limit the amount of uplift of each block, coir ropes are used as restraints. Since natural fibres are used instead of steel reinforcement, the structure is environmentally friendly.

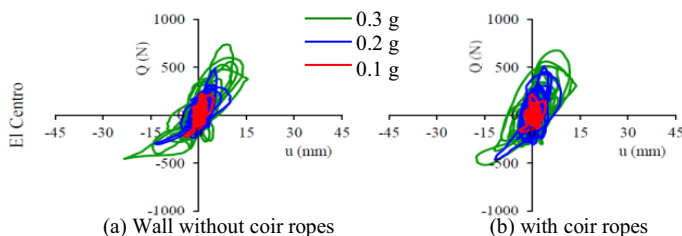
Because the block has predefined keys and no mortar is used, the structure can be constructed rapidly without the requirement of special engineering techniques. This feature will not only reduce the total construction cost, but could be particularly suitable for use in developing countries, especially in tropical regions with abundant coconut fibres.

Figure 9 shows the relationship between the base shear  $Q$  and the top displacement  $u$  of the wall due to the 1940 El-Centro earthquake. Three peak ground accelerations are considered, i.e. 0.1 g, 0.2 g and 0.3 g. In the case considered the influence of coir ropes on the wall response are marginal. In total more than 40 ground motions of different characteristics and magnitudes were applied. When stronger earthquakes were considered, relative movements of larger magnitudes occurred. Despite experiencing a large number of ground excitations no damage to the wall was observed. The results confirmed the effectiveness of the design philosophy, i.e. activating rigid body movements by allowing separation at the block interfaces to enable significant reductions in the impact felt from earthquakes.

To examine the strength of the blocks after a large sequence of earthquake loadings, and thus to compare with the strength prior to loading, compressive tests were performed. The blocks showed little reduction in strength from the original. Details are given in (Ali et al., 2013 a and b; Ali and Chow, 2013, Ali et al., 2012a and b).



**Figure 8.** Interlocking wall.



**Figure 9.** Influence of load magnitudes and multiple uplifts on the wall response.

A similar concept has been considered for bridge structures subjected to near-source earthquakes with strong pulse-type vertical ground motions. The preliminary results show that temporary and partial uplifts can also be used to reduce the effects of combined strong vertical and horizontal ground motions on the structural response (see e.g. Chen et. al, 2013 and Kun et al., 2013).

## 2. Conclusions

An overview of ongoing research at the University of Auckland on low-damage earthquake resistant design approaches, with the potential for implementation in structures of the future, is presented. The design philosophy is based on the activation of rigid body motions. Instead of resisting the earthquake loading within the structure, the structural members are able to move relative to one another, and also relative to the soil foundation. The temporary isolation of the structure from earthquake induced energy, due to rigid body movement significantly reduces the possibility of large inelastic deformations in the structural members. Consequently, the development of stresses within the structural members is reduced, if not essentially eliminated. Since the overall structure will resist less loading, less damage to the structure can be anticipated.

The other advantage of this design philosophy is that low-damage structures under strong earthquakes will more likely ensure not only the safety of occupants, but also the functionality of the structure during and immediately after the earthquake. Thus, down times after a major earthquake, which have been a problem in structures built according to current design specifications, can be considerably shortened or even avoided.

## Acknowledgements

The author would like thank to the Ministry of Business, Innovation and Employment for their support through the Natural Hazards Research Platform under the Awards 3703249.

## References

- [1] N. Chow, H. Hao, Pounding damage to buildings and bridges in the 22 February 2011 Christchurch earthquake. *International Journal of Protective Structures* **3(2)** (2012), 123-139.
- [2] J. Beck, R. Skinner, The seismic response of a reinforced concrete bridge pier designed to step, *Earthquake Engineering and Structural Dynamics*; **2 (4)** (1973), 343-358
- [3] R.D. Sharpe, R.I. Skinner, The seismic design of an industrial chimney with rocking base. *Bulletin of the New Zealand Society for Earthquake Engineering* **16(2)** (1983), 98-106.
- [4] N. Chow, K. McCue, An upliftable structure in the 2010-2012 Canterbury earthquake swarm, *Newsletter of the Australian Earthquake Engineering Society*, [http://www.aees.org.au/Newsletters/AEES\\_2012\\_3.pdf](http://www.aees.org.au/Newsletters/AEES_2012_3.pdf). September 2012
- [5] Japan Society of Civil Engineers (JSCE), Earthquake resistant design codes in Japan, Maruzen, Tokyo (2000).
- [6] X. Qin, Y. Chen, N. Chow, Effect of uplift and soil nonlinearity on plastic hinge development and induced vibrations in structures, *Advances in Structural Engineering* **16 (1)** (2013), 135-147
- [7] X. Qin, N. Chow, Prediction of seismic induced forces in an upliftable structure, *Proceedings of the Australian Earthquake Engineering Society Conference*, Hobart, Tasmania, Australia, 15 - 17 November 2013.
- [8] X. Qin, N. Chow, N. Effect of SFSI on the response of soil. In: *Soil Liquefaction during Recent Large-Scale Earthquakes* (Eds. R. Orense, I. Towhata, N. Chow), the University of Auckland, Auckland, 2 - 3 December 2013, 197-204
- [9] M. Ormeño, T. Larkin, N. Chow, Comparison between standards for seismic design of liquid storage tanks with respect to soil-foundation-structure interaction and uplift, *Bulletin of the New Zealand Society for Earthquake Engineering* **45 (1)** (2012a), 40-46.
- [10] M. Ormeño, T. Larkin, N. Chow, Influence of uplift on liquid storage tanks during earthquakes, *Journal of Coupled Systems Mechanics* **1 (4)** (2012b), 311-324.
- [11] M. Ormeño, T. Larkin, N. Chow, Experimental investigation of the stresses in a tank shell resulting from uplift during earthquakes. *Proceedings of the 10<sup>th</sup> International Conference on Urban Earthquake Engineering*, Tokyo Institute of Technology, Tokyo, Japan, 1 - 2 March 2013.
- [12] W.Y. Loo, P. Quenneville, N. Chow, A numerical approach for simulating the behaviour of timber shear walls, *Structural Engineering and Mechanics* **42(3)** (2012a): 383-407
- [13] W.Y. Loo, P. Quenneville, N. Chow, A numerical study of the seismic behaviour of timber shear walls with slip-friction connectors, *Engineering Structures* **34** (2012b), 233-243
- [14] W.Y. Loo, C. Kun, P. Quenneville, N. Chow, Experimental testing of a rocking timber shear wall with slip-friction connectors, *Earthquake Engineering and Structural Dynamics* (in print), DOI: 10.1002/eqe.2413
- [15] M. Ali, R. Briet, N. Chow, Dynamic response of mortar-free interlocking structures, *Construction and Building Materials* **42** (2013a), 168-189
- [16] M. Ali, X. Li, N. Chow, Experimental investigations on bond strength between coconut fibre and concrete, *Materials and Design* **44** (2013b), 596-605
- [17] M. Ali, N. Chow, Experimental investigations on coconut-fibre rope tensile strength and pullout from coconut fibre reinforced concrete, *Construction and Building Materials* **41** (2013), 681-690
- [18] M. Ali, R.J. Gultom, N. Chow, Capacity of innovative interlocking blocks under monotonic loading. *Construction and Building Materials* **37** (2012a), 812-821.
- [19] M. Ali, A. Liu, S. Hao, N. Chow, Mechanical and dynamic properties of coconut fibre reinforced concrete, *Construction and Building Materials* **30** (2012b), 814-825.
- [20] Y. Chen, C. Kun, N. Chow, T. Larkin, The experimental investigation of bridge with footing uplift under near-fault earthquake. *Proceedings of the Australian Earthquake Engineering Society Conference*, Hobart, Tasmania, Australia, 15 - 17 November 2013.
- [21] C. Kun, Y. Chen, T. Larkin, N. Chow, An experimental investigation of the seismic response of a bridge due to simultaneous horizontal and vertical excitations, *Proceedings of the Australian Earthquake Engineering Society Conference*, Hobart, Tasmania, Australia, 15 - 17 November 2013.

# Severe plastic deformation as a new processing for enhancing the performance of metallic components

Hiroyuki MIYAMOTO<sup>a,1</sup> Rifai MUHAMMAD<sup>b</sup> and Hiroshi FUJIWARA<sup>a</sup>

<sup>a</sup>*Department of Mechanical Engineering, Doshisha University, Kyotanabe Japan*

<sup>b</sup>*Graduate School of Science and Engineering, Doshisha University, Kyotanabe Japan*

**Abstract.** Severe plastic deformation emerged as new processing to fabricate ultrafine grain metallic materials with a grain size under one micron meter, or nanocrystalline metals in a bulk form. It was found that such ultrafine grain (UFG) and nanocrystalline metals have superior mechanical properties with high strength and relatively high ductility as well as corrosion properties. On the other hand, they also exhibit unique mechanical, physical and thermal properties ascribing to large fraction of grain boundaries and triple junctions, which may reach to more than 50 %. In this paper, equal-channel angular pressing (ECAP) and mechanical, corrosion and thermal properties of UFG Fe-20%Cr steel fabricated by ECAP are presented.

**Keywords.** Severe plastic deformation (SPD), equal-channel angular pressing (ECAP), ultrafine grain structure, nanocrystalline structure

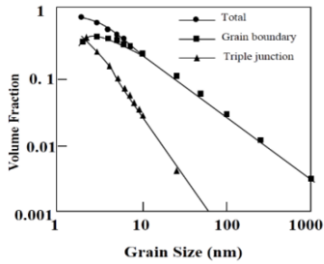
## Introduction

Since severe plastic deformation (SPD) emerged as a processing to fabricate bulk nanocrystalline (NC) or ultrafine grain (UFG) metallic materials almost 30 years ago, it has widely been recognized worldwide in materials science [1]. Grain refinement was recognized as one of the method to strengthen metallic materials with less sacrifice of ductility as compared to other approaches such as precipitation hardening and solid solution hardening. When grain size is reduced to nano-scale, the volume fraction of grain boundary (GB) and triple-junction (TJ) reach to more than 10 % as shown in Figure 1 [2]. Such high volume fraction of GB and TJ may cause unique and unexpected mechanical or physical, chemical properties, which are not observed in materials having conventional grain size. By grain size reduction to nano-scale, one can expect some favorable effect on properties; one is stress homogenization when the materials is subjected to load or stress. In conventional grain size, dislocations tend to accumulate and form pile-ups at the grain boundaries, and they cause local stress concentration as expressed by  $n\tau$ , where  $n$  is the number of dislocations and  $\tau$  is applied shear stress. These local stress concentration may cause intergranular fracture under cyclic stress or static tensile stress in high temperature or corrosive environment. When

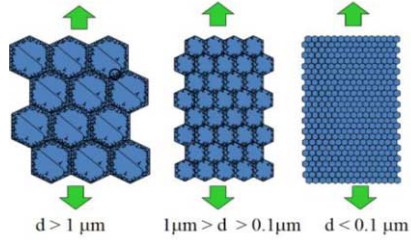
---

<sup>1</sup>Corresponding author: [hmiyamot@mail.doshisha.ac.jp](mailto:hmiyamot@mail.doshisha.ac.jp)

grain size reduce to nano-scale or under microscale, dislocations cannot stay and accumulate inside grain and stress distribution become more homogeneous as shown in Figure 2. The other



**Figure 1.** Volume fraction of GB and TJ[2]

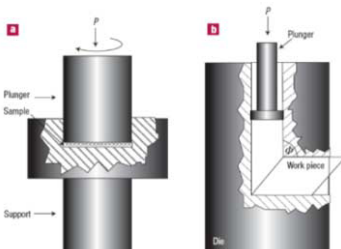


**Figure 2.** Schematic diagram of inhomogeneous dislocations accumulation under applied stress

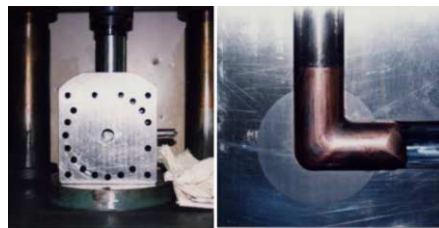
important but yet demonstrated favorable effect is dilution of impurity segregation at GBs. The impurity segregation may cause intergranular brittle fracture under impact, cyclic stress or/and static tensile stress in high temperature or corrosive environment. According to the simple estimation, impurity segregation at grain boundaries is 1000 times higher than that of bulk concentration in grain size of  $10 \mu\text{m}$  while it is reduced to 10 times when grain size become  $20 \text{ nm}$ . Therefore one can expect that NC materials are potentially ideal materials for structural or construction application with high resistance to degradation. With the advent of SPD processing, we can obtain a new class of metallic materials for these application.

## 1. Equal channel angular pressing (ECAP)

Two major processing methods widely recognized in SPD community is equal-channel angular pressing (ECAP) and high pressure torsion (HPT) as illustrated in Figure 3 [1]. In HPT, a disk-shape material is given torsion straining under high hydrostatic pressure. The materials are in principle given infinitive strain by a number of rotations. Grain refinement to nanoscale in a range of materials has been reported [3]. The drawback of this processing is that the magnitude of shear strain decrease in the vicinity of the center of the disk, and that sample size is limited. In ECAP, a billet is simple-sheared in the corner intersecting the two channels. When the angle between the two channels is 90 degrees, equivalent plastic strain is estimated to be about 1 [4]. Figure 4 shows a ECAP die with a round channel owned by the present authors wherein a copper billet is pressed.



**Figure 3.** Schematic diagram of HPT and ECAP



**Figure 4.** Photos of ECAP die in our group.

In general, several pressing, usually more than 8 passes, is needed to obtain UFG microstructures. Several deformation route is reported according to the rotation of billet before each pass (Figure 5) [5]. It is frequently reported that route Bc, where a billet is rotated 90 degrees in an alternative direction around the longitudinal axis between passes, is most efficient deformation route to obtain UFG structures [6]. ECAP is generally applied for billet, but recently been tried to be applied to processing of metallic plate [7], or sheets [8]; later case require higher technology, in order to obtain high strength or texture control (Figure 6). The present authors reported the effect of one-pass ECAP prior to cold-rolling on the final texture, and on alleviating ridging of ferritic stainless sheet [8,9]. The drawback of ECAP, and most other SPD processes, is low productivity, and therefore is not still introduced in the industry for commercialization. Currently, UFG by SPD processing such as ECAP and HPT is considered for the application of biomaterials such as pure titanium bone, where strengthening by alloying such as V elements is difficult for human body. On the other hand, several continual processes of ECAPs were proposed for future application (Figure 7) [10-12].

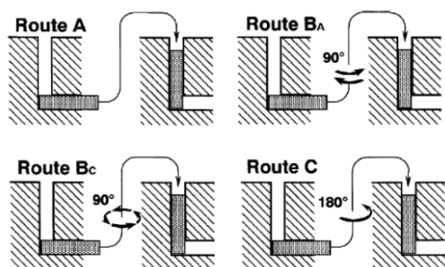


Figure 5 Illustration of deformation routes of ECAP[5]



Figure 6. Photo of ECAP die for sheets

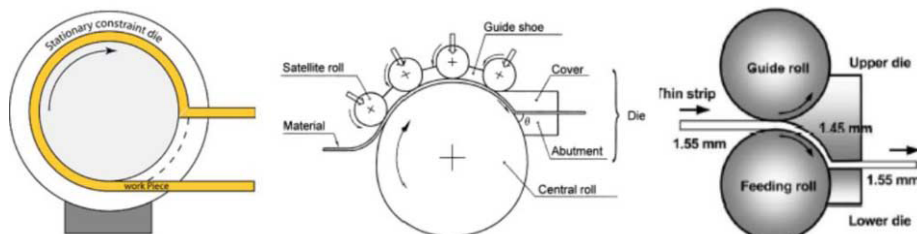


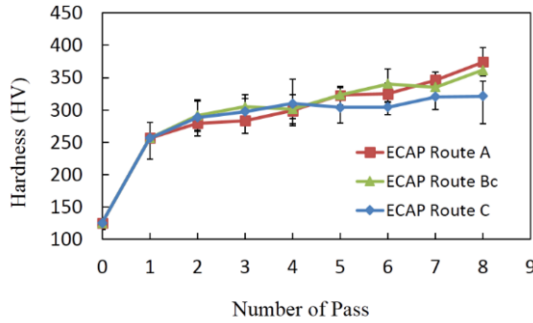
Figure 7. Continual ECAP process proposed by (a) Raab et al. [10], (b) Usumomiya et al. [11] and (c) Lee et al. [12]

## 2. Microstructural development during ECAP

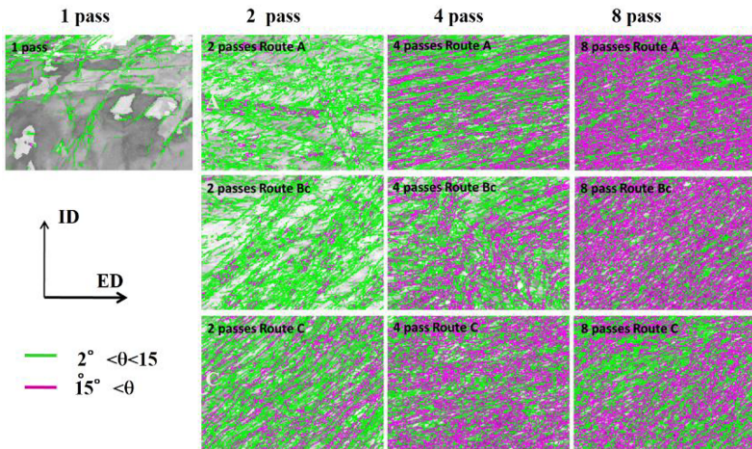
Figure 8 shows variation of hardness of Fe-20%Cr steel as a function of number of passes. Considerable increase of hardness was observed after one pass, followed by the moderate increase after second pass and more. As shown in the figure, the degree of hardening differs in three different deformation routes described in the previous section. Route A and Bc showed the same level of hardness followed by route C. It is suggested that the degree of dislocation accumulation and resultant grain size reduction differs in different deformation routes. Namely, in route C where billet is sheared forward and

reverse direction in alternative passes, dislocations formed in previous pass have high chance to meet other dislocations with opposite sign leading to annihilation. Thus, shear strain is redundant and ineffective in dislocation accumulations. Less accumulation of dislocations cause the delay of grain subdivision and UFG formations.

Figure 9 shows GB misorientation map obtained by electron back-diffraction (EBSD). In the first and second passes, low angle grain boundaries (LAGB) are mostly developed. With an increase of passes, the fraction of high angle grain boundary



**Figure 8.** Variation of hardness as a function ECAP in route A, Bc and C



**Figure 9.** GB misorientation maps after 1, 2, 4, 8 passes by route A (upper), route B (middle) and C (bottom)

(HAGB) increased replacing the LAGB. In grain subdivision mechanism, it is considered that grains are subdivided by cell boundary in the beginning stage. Then these cell boundaries developed into LAGBs by next stage. With further straining, LAGBs increase their misorientation by absorbing lattice dislocations into GBs. Such GBs developed during high plastic strain have extrinsic GB dislocations, and are called nonequilibrium GBs. Variation of HAGB fraction with an increase of ECAP pass is shown in Figure 10. As shown in hardness variation, HAGB fraction is relatively lower in route C where strain is reversed in the same parallel shear plane with the previous pass, and most strain is redundant. In route A and C, billets are sheared in near parallel plane in successive passes, GBs tend to array in parallel manner, and become anisotropic, and this was manifested as a different HAGB fraction in the three

orthogonal plane as shown in Figure 10. Namely, HAGB fraction is relatively low on Z plane in route A and C whereas they are the same level in all planes in route Bc where billets are sheared along different shear planes in successive passes. In summary, dislocation accumulation and UFG formation is most effective in route Bc, and microstructure is isotropic in this deformation route.

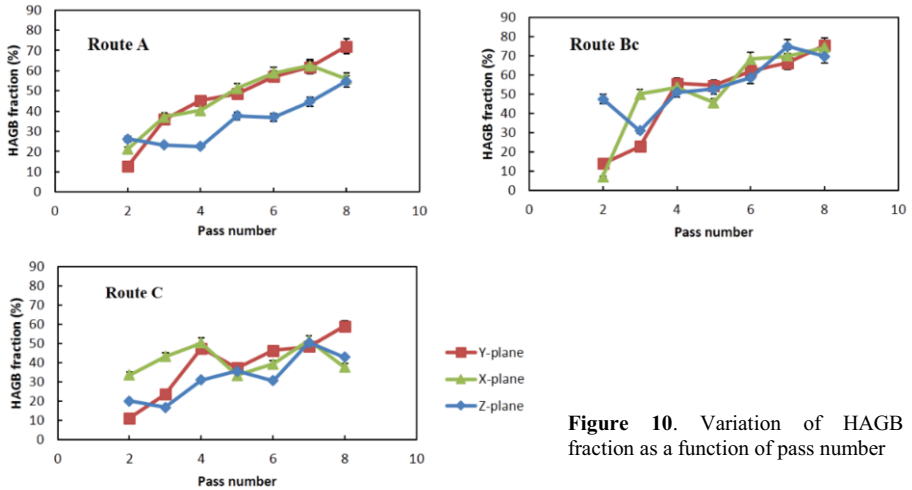


Figure 10. Variation of HAGB fraction as a function of pass number

### 3. Properties of UFG metals by ECAP

#### 3.1. Mechanical properties

Figure 11 shows stress-strain curves obtained by tensile tests. The maximum tensile stress exhibits drastic increase after one pass, and moderate increase after the second pass and more as is shown in hardness. ECAPed samples exhibited little or no strain hardening behavior. If one compares 8 pass samples in route A and Bc, (Data of route

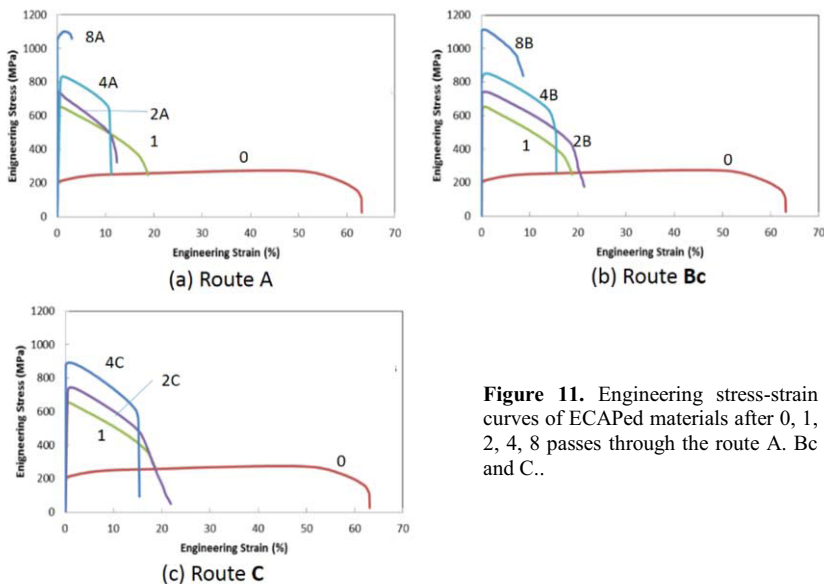


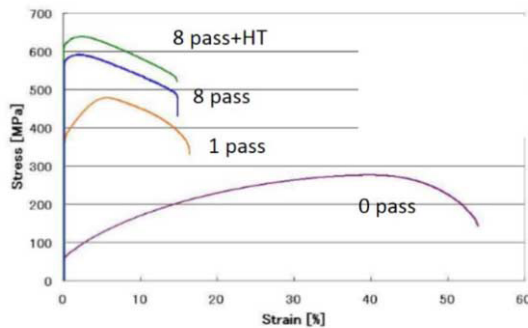
Figure 11. Engineering stress-strain curves of ECAPed materials after 0, 1, 2, 4, 8 passes through the route A, Bc and C..



**Table 1.** Mechanical properties of commercial and ECAPed materials of selected materials

Materials	Type	Hardness (HV)	Yield stress (MPa)	Tensile stress (MPa)
$\alpha$ Fe	ECAP	300	850	980
	Commercial	90	200	350
Cu(99.98%)	ECAP	155	400	480
	Commercial	55	100	240
Ni(99.86%)	ECAP	310	600	920
	Commercial	70	170	400
Pure Ti	ECAP	280	650	810
	Commercial	180	250	380
Au-12.5Ag-12.5Cu	ECAP	270		880
	Commercial	155		550

C is not available because of fracture during 8 pass of ECAP), route Bc showed higher stress and ductility. It is because of isotropic microstructure. Mechanical properties of other ECAPed materials reported elsewhere are summarized in Table 1. Yield stress of ECAPed materials show in general three to four times higher than the commercial counterparts. With regards to the mechanical properties of ECAPed materials, unique properties were observed after post-ECAP annealing at relatively moderate temperature and short times before recrystallization and grain growth occurs. Figure 12 shows tensile stress-strain curves of pure copper after ECAP, and both ECAP and annealing at 200°C for 90s. It is interest to note that pure copper after post-ECAP annealing showed higher flow stress than that after ECAP alone. This unique phenomena is also reported in UFG aluminum, and is considered that recovery and dislocation extinction during annealing prior to the grain growth is the main cause of hardening [13]. Indeed, Tsuji et al [14] reported that UFG pure aluminum fabricated by accumulative roll bonding (ARB) showed higher flow stress after annealing, and become softer by additional straining. This “*hardening by annealing and softening by deformation*” is also considered to be associated with UFG structure formed by deformation [14]. Similarly, it is reported that UFG steels fabricated by SPD show no brittle-ductile transition temperature (DBTT) [15].



**Figure 12.** Engineering stress-strain curves of pure copper after ECAPed for 1 and 8 passes, and heat treatment at 200°C for 90 seconds

### 3.2. Annealing of ECAPed materials

Figure 13 shows softening behavior Fe-20%Cr steels and pure copper after 8 pass ECAP as a function of annealing temperature. The former materials started to soften at about 700 K and finish at about 1000K. This drastic softening corresponds with grain growth as shown in orientation image maps as shown in Figure 14. It should be pointed out that in this drastic softening stage, grain growth seems to be uniform with no abnormally large grain, and it is contrasted with that occurred in ECAPed FCC metals such as copper and aluminum [16,17]. In UFG FCC metals, it was observed that limited grains became “nucleus” and grow preferentially replacing other deformation induced grains during

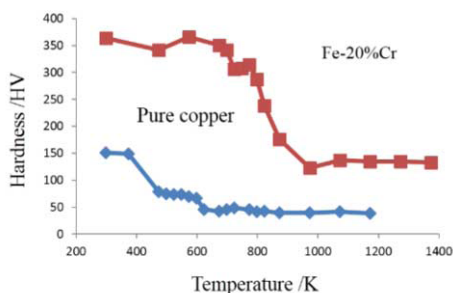


Figure 13. Hardness variation as a function of annealing temperature

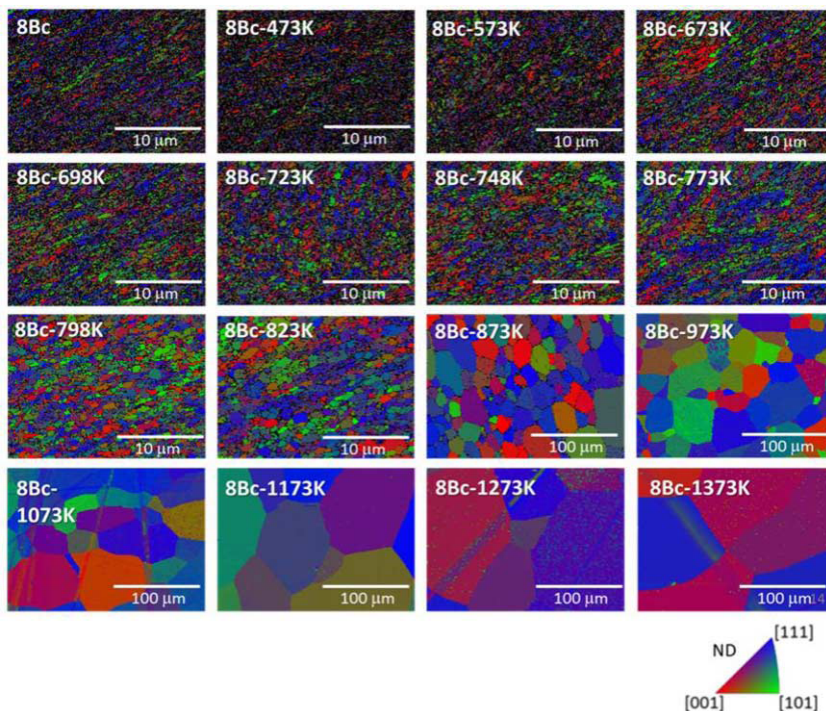
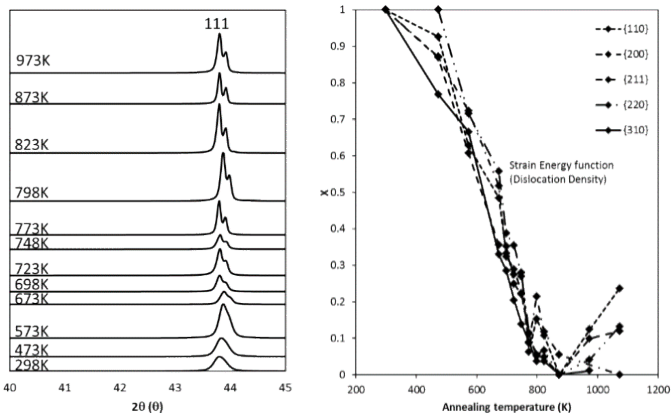


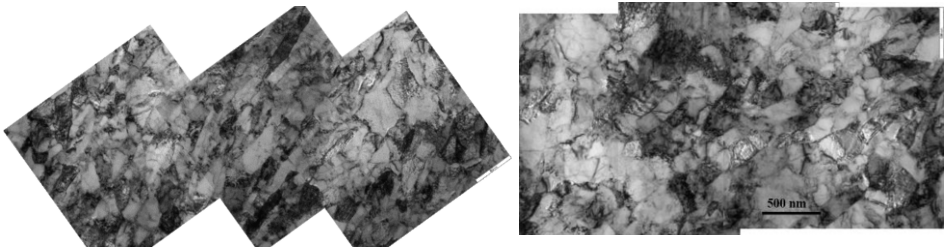
Figure 14. EBSD OIMs after annealing at various temperatures

annealing [16,17]. It is, phenomenologically, similar to static recrystallization. Figure 15 shows X-ray diffraction peak and the parameter X as a function of temperature. X is a measure of plastic strain energy and defined by  $X=(W_x-W_o)/(W_d-W_o)$ , where  $W_x$  is the width at temperature X,  $W_o$  is width at fully recrystallized state,  $W_d$  is width before annealing. With an increase of temperature,  $\{111\}$  peaks became sharper by a recovery of strain energy. It is interesting to note that recovery started, i.e., X started to decrease, at much lower temperature than the softening started (Fig.15b). It means that deformation-induced UFG structures after ECAP contains dislocation inside or along the grain boundaries, and that these dislocations disappeared by recovery process at lower temperature than the softening started with grain size unchanged.



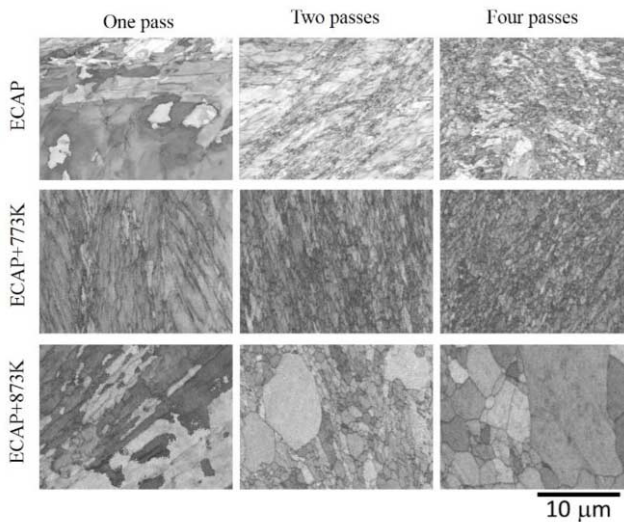
**Figure 15.** (a)  $\{111\}$  X-ray diffraction peaks after annealing and (b) variation in X parameter as a function temperature

Figure16 shows TEM micrographs after ECAP and annealing at 698K. Grain size is essentially the same in both micrographs, but difference in dislocation is not clear. Early recovery prior to softening and related uniform grain growth is indeed contrasted with annealing behavior



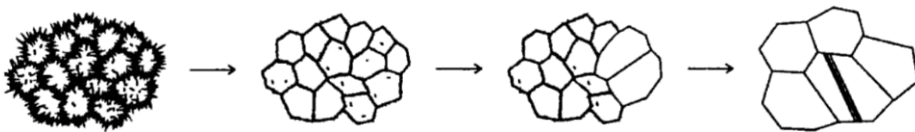
**Figure 16.** TEM micrographs (a) after ECAP for 8 passes, and (b) after annealing at 698 K before grain growth occurs

after moderate deformation with 1, 2 and 4 pass as shown in Figure 17. It is evident that usual recrystallization process with nucleation and growth of nucleus replacing the deformed structures occurs in moderate deformed billets. It was recognized that deformation-induced UFG structures have nonequilibrium grain boundaries [18], and the nonequilibrium grain boundaries become equilibrium ones in early stage of annealing as



**Figure 17.** Image quality maps of 1, 2 and 4 pressed samples after annealing.

illustrated in Figure 18 [18]. During this stage, softening does not yet start. After this recovery stage, limited grains start to grow replacing other grains accompanying drastic softening. This softening is again phenomenologically similar to recrystallization if one can regard this grains as “nucleus”, but is also viewed as abnormal grain growth in that driving force is grain boundary energy, and not dislocations (strain energy).

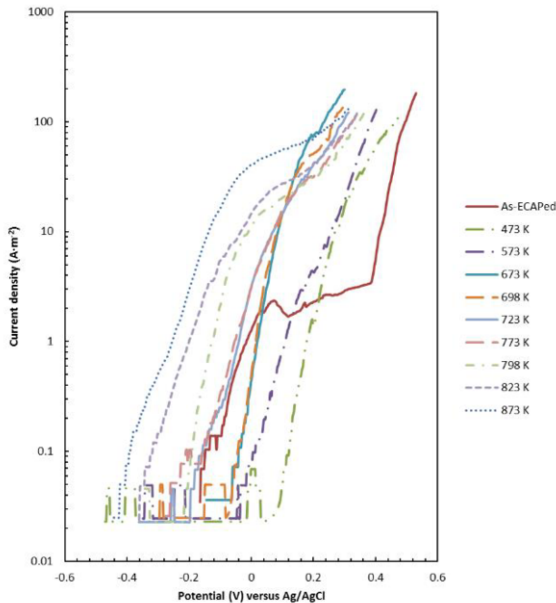


**Figure 18.** Schematic diagrams of recovery and grain growth of UFG structures during annealing [18]

### 3.3. Corrosion of ECAPed materials

Corrosion properties are also important properties of construction materials. Figure 19 shows pitting corrosion tests of ECAPed Fe-20%Cr steels and annealed ones after ECAP in NaCl solutions. ECAPed samples show anomalous behavior with two stages

increase of anodic currents, but the potential at second increase of current is higher than any other samples. With an increase of annealing temperature, breaking potential (pitting potential) become lower indicating the resistance to pitting formation decreased with increasing temperature. It is important to note that the breaking potential decreased by annealing at 473-698K, at which grain size remained constant, but dislocation density is supposed to decrease. Therefore, it is considered that stability of passivation and resistance to pitting corrosion is strongly affected by such low-temperature annealing, and dislocation density in spite of the same grain size. Figure 20 shows the relation between pitting potential and annealing temperature and XRD parameter as defined in the previous section. It is evident that pitting potential increases in proportion to  $X$  parameter. In Fe-Cr steels, it is considered that passivation occurs as a result of preferential dissolution of Fe atoms and surface concentration of Cr atoms [19,20]. It is reported that pitting potential of ferritic stainless steel becomes higher with decreasing of grain size because Cr atoms can be supplied by higher grain boundary diffusion than lattice diffusion and enhance the Cr concentration on the surface. Similarly, with an increasing dislocation density inside the grains, Cr diffusion become higher through the so-called pipe diffusion along these dislocations. Effect of grain size on corrosion behavior seems to be different in different materials. In pure copper, corrosion rate of UFG copper by ECAP is higher than that of conventional grain size [21]. Therefore it is difficult to establish the universal law on the effect of grain size on corrosion. However, with regards to materials which form passivation, in materials whose alloying elements form passivation such as Fe-Cr alloy, grain refinement and dislocation accumulation work favorably whereas in materials whose host element form passivation such as copper and aluminum, the corrosion resistance seems to be degraded by grain size reduction. It may be because the passivation film become defected structure, and may be broken easily by aggressive environment.



**Figure 19.** Anodic polarization curves of pitting potential of ECAPed and annealed samples at various temperature

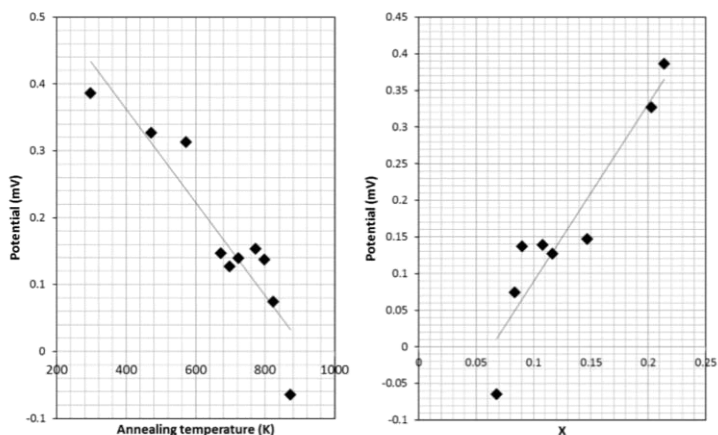


Figure 20. (a) Effect of annealing temperature, and (b) X-ray parameter on pitting potentials

#### 4. Summary and conclusions

Grain size reduction into submicron or nanocrystalline range may introduce several favorable effect for mechanical and electrochemical properties of materials for structural applications through uniform stress distribution and dilution of impurity element which otherwise segregate in grain boundaries. This two effects do work especially for the application where stress is applied in aggressive corrosive environments. In this paper, microstructural development of Fe-Cr steels by ECAP is reviewed focusing on the BCC structures. Favorable effect of UFG structures for corrosion properties is demonstrated, which may be attributed to high diffusion rate of Cr elements facilitated by the high-density grain boundaries and dislocation structures.

#### Acknowledgements

The authors gratefully acknowledge the financial support of a Grant-in-Aid for Scientific Research on Innovative Areas “Bulk nano metals,” MEXT Japan

#### References

- [1] Valiev, R.Z., R.K. Islamgaliev, and I.V. Alexandrov, *Bulk nanostructured materials from severe plastic deformation*. Progress in Materials Science, 2000. **45**(2): p. 103-189.
- [2] Palumbo, G., S.J. Thorpe, and K.T. Aust, *On the contribution of triple junctions to the structure and properties of nanocrystalline materials*. Scripta Metallurgica et Materialia, 1990. **24**: p. 1347-1350.
- [3] Hohenwarter, A., C. Kammerhofer, and R. Pippan, *The ductile to brittle transition of ultrafine-grained Armco iron: an experimental study*. Journal of Materials Science, 2010. **45**(17): p. 4805-4812.
- [4] Iwahashi, Y., et al., Principle of equal-channel angular pressing for the processing of ultra-fine grained materials. Scripta Materialia, 1996. **35**: p. 143-146.
- [5] Iwahashi, Y., et al., An investigation of microstructural evolution during equal-channel angular pressing. Acta Metallurgica et Materialia, 1997. **45**: p. 4733-4741.
- [6] Iwahashi, Y., et al., Microstructural characteristics of ultrafine-grained aluminum produced using equal-channel angular pressing. Metallurgical and Materials Transactions, 1998. **29A**: p. 2245-2252.

- [7] Kamachi, M., et al., *Equal-channel angular pressing using plate samples*. Materials Science and Engineering, 2003. **A361**: p. 258-266.
- [8] Miyamoto, H., et al., Effect of simple shear deformation prior to cold rolling on texture and ridging of 16% Cr ferritic stainless steel sheets. ISIJ International, 2010. **50**(11): p. 1653-1659.
- [9] Xiao, T., H. Miyamoto, and T. Uenoya, Equal-channel angular pressing as a new processing to control the microstructure and texture of metallic sheets. Materials Science and Applications, 2012. **3**: p. 600-605.
- [10] Raab, G.J., et al., *Continuous processing of ultrafine grained Al by ECAP*. Materials Science and Engineering: A, 2004. **A382**: p. 30-34.
- [11] Utsunomiya, H., et al., *Continuous grain refinement of aluminum strip by conshearing*. Materials Science and Engineering, 2004. **A372**: p. 199-206.
- [12] Lee, J.C., H.K. Seok, and J.Y. Suh, Microstructural evolutions of the Al strip prepared by cold rolling and continuous equal channel angular pressing. Acta Materialia, 2002. **50**(16): p. 4005-4019.
- [13] Huang, X., N. Hansen, and N. Tsuji, Hardening by annealing and softening by deformation in nanostructured metals. Science, 2006. **312**(14): p. 249-251.
- [14] Huang, X., N. Hansen, and N. Tsuji, Hardening by annealing and softening by deformation in nanostructured metals. Science, 2006. **312**(14): p. 249-251.
- [15] Kimura, Y., et al., Inverse temperature dependence of toughness in an ultrafine grain-structure steel. Science, 2008. **320**: p. 1057-1059.
- [16] Komura, S., et al., Influence of stacking fault energy on microstructural development in equal-channel angular pressing. Journal of Materials Research, 1999. **14**(10): p. 4044-4050.
- [17] Neishi, K., Z. Horita, and T.G. Langdon, *Grain refinement of pure nickel using equal-channel angular pressing*. Materials Science and Engineering a-Structural Materials Properties Microstructure and Processing, 2002. **325**(1-2): p. 54-58.
- [18] Valiev, R.Z., V.Y. Gertsman, and O.A. Kaibyshev, *Non-equilibrium state and recovery of grain boundary structure*. Physica status solidi (a), 1983. **78**: p. 177-187.
- [19] Sieradzki, K. and R.C. Newman, *Percolation model for passivation in stainless steels*. Journal of The Electrochemical Society, 1979. **133**: p. 1979-1980.
- [20] Qian, S., R.C. Newman, and R.A. Cottis, *Validation of a percolation model for passivation of Fe-Cr alloys: Two-dimensional computer simulation*. Journal of The Electrochemical Society, 1990. **137**(2): p. 435-439.
- [21] Miyamoto, H., et al., Corrosion of ultra-fine grained copper fabricated by equal-channel angular pressing. Corrosion Science, 2008. **50**: p. 1215-1220.

# Optimizing coefficient of thermal expansion of concrete and its importance on concrete structures

Md Sarwar SIDDIQUI<sup>1</sup> and David W. FOWLER

*Department of Civil, Architectural and Environmental Engineering, The University of Texas at Austin, Austin, TX, USA*

**Abstract.** Thermal stress development in concrete structures is significantly influenced by the coefficient of thermal expansion (CTE) of concrete. Optimizing concrete CTE can reduce the thermal stress, which will eventually reduce the cracking potential of concrete structures. At early age, when concrete has low strength, it is much more vulnerable to cracking. Early-age cracking has a detrimental effect on the durability of concrete structures. This study presents the importance of concrete CTE on the thermal stress development in concrete structures as well as three techniques to reduce the CTE of concrete. Replacing high CTE coarse aggregates with low CTE coarse aggregates is the most effective method for reducing concrete CTE. Concrete CTE can also be reduced by reducing cement paste volume. However, if the cement paste reduction increases the void content in the concrete system, saturated concrete CTE is likely to increase.

**Keyword.** Coefficient of thermal expansion, concrete, thermal stresses, pavement, bridge, mass concrete, cte optimization, durability

## Introduction

Coefficient of thermal expansion (CTE) is an important concrete property that is responsible for some distresses in concrete structures. Thermal deformations take place when concrete is subjected to temperature change. These deformations are responsible for thermal stresses when the structure is restrained. The magnitude of thermal stress depends on change in temperature, property of materials, and degree of restraint of the concrete member. If the developed thermal stress is greater than the tensile strength of the concrete, cracks occur. At early age, concrete is more prone to thermal cracking due to low strength [1]. In addition, a high amount of early age relaxation may occur. Higher CTE generates higher thermal stress at a given temperature difference. Optimizing the CTE of concrete is likely to reduce the distress potential of concrete structures. According to Mallela et al. [2] it might not be cost effective to optimize concrete CTE by changing the constituents of concrete mixture. However, optimizing the CTE of concrete according to the need of a given structure can result in a

---

<sup>1</sup>Corresponding author: Department of Civil, Architectural and Environmental Engineering, The University of Texas at Austin, 10100 Burnet Road, PRC 18B, Austin, TX 78758, e-mail: [mssidiqui@utexas.edu](mailto:mssidiqui@utexas.edu)



significant savings in repair and rehabilitation cost and increases the durability and longevity of the structure.

## 1. Background

CTE is the strain development due to a unit change in temperature. Thermal stress is one of the major causes of pavement distresses including slab cracking, joint faulting, punchouts, and delamination. A small variation in CTE can significantly affect the design pavement thickness by the Mechanistic-Empirical Pavement Design Guide (MEPDG) [2–6]. Mallela et al. [2] and Tanish et al. [6] studied the effect of CTE on slab cracking, joint faulting, and ride quality of jointed plain concrete pavements (JPCP). They both agreed that CTE significantly affects pavement performance. The Texas Department of Transportation (TxDOT) has recognized the thermal incompatibility between cement paste and aggregates as one of the major causes of continuously reinforced concrete pavement (CRCP) distresses. Won and coworkers [7,8] identified CTE as the major reason of CRCP horizontal cracking. Many districts of TxDOT have limited the CTE of CRCP concrete to avoid pavement distresses. Spalling has virtually been eliminated after the Houston District limited the CTE of CRCP concrete [9]. Recently, TxDOT started to implement a statewide CTE maximum of  $5.5 \times 10^{-6}$  strain/ $^{\circ}\text{F}$  ( $9.9 \times 10^{-6}$  strain/ $^{\circ}\text{C}$ ) on CRCP concrete.

Krauss and Rogalla [10] studied the early age cracking of bridge decks in the U.S. and observed over 10,000 bridge decks that exhibited early age cracking. Early age cracking has a detrimental effect on the long term performance of concrete bridges. One of the reasons of early age cracking is thermal loading [1]. Temperature change influences the girder axial force, girder moment, pole lateral force, pile moment, and pile head movement [11]. Bridge joint and bearing distresses can also occur from thermal movement [12]. Several bridge failures were reported due to a lack of design consideration to accommodate thermal movement [13,14]. Im and Chang [15] studied thermal stress development in a composite box-girder bridge and observed that daily temperature cycles can generate significant tensile and compressive stresses.

Mass concrete can experience significant temperature rise due to the heat of hydration of cementitious materials. Bentz et al. [16] presented a real world situation where severe cracking occurred in mass concrete due to excessive temperature rise generated from heat of hydration.

It can be concluded from the previous discussions that thermal stress plays a major role on the durability and longevity of concrete structures. Optimizing CTE of concrete can diminish these unwanted thermal distresses and improve the service life of the structures, and reduce the repair cost.

## 2. Numerical model for thermal stress development

This section will develop a basic model of thermal stress development in a fully restrained concrete member. Thermal strain developed in a concrete body can be expressed as follows:

$$\varepsilon_T = CTE \times \Delta T \quad (1)$$

Where:

$\epsilon_T$  = thermal strain

CTE= coefficient of thermal expansion of concrete

$\Delta T$ = temperature change

So, the thermal stress can be expressed as,

$$\sigma_T = \epsilon_T \times E_c \tag{2}$$

Where:

$\sigma_T$  = thermal stress

$E_c$  = modulus of elasticity

According to ACI 318 [17] modulus of elasticity  $E_c$  can be expressed as,

$$E_c = 57,000\sqrt{f'_c} \text{ (psi)} \tag{3}$$

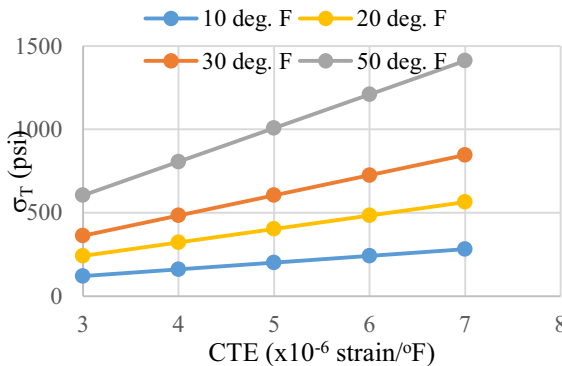
Where:

$f'_c$  = compressive strength of concrete

From Equations 1, 2, and 3, Equation 4 can be written

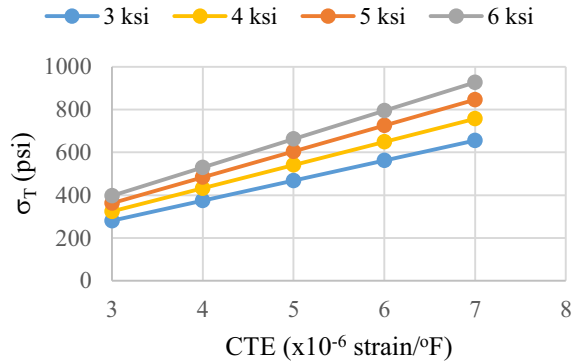
$$\sigma_T = CTE \times \Delta T \times 57,000\sqrt{f'_c} \text{ (psi)} \tag{4}$$

Equation 4 was used to develop Figures 1 and 2. Figure 1 shows the influence of concrete CTE on the stress development due to temperature change. Concrete compressive strength was assumed to be 5 ksi (34.5 MPa), which is a typical compressive strength for normal concrete. Thermal stress was determined for temperature changes ( $\Delta T$ ) of 10, 20, 30, and 50°F (5.5, 11, 16.7, and 27.8°C). The thermal stress vs CTE lines are not parallel and the slopes of line are increasing with the increased temperature change. This represents that at higher temperature, CTE has larger influence on thermal stress development, which can be explained by Equation 4. It can be noted from Equation 4 that, for a given concrete strength, the rate of change of thermal stress as a function of CTE is proportional to temperature difference. Therefore, higher temperature change results in higher rate of thermal stress increase for increasing CTE.



**Figure 1.** Effect of CTE on thermal stress development at 10, 20, 30, and 50°F (5.5, 11, 16.7, and 27.8°C) temperature change for 5 ksi (34.5 MPa) concrete.

Figure 2 represents the influence of CTE on thermal stress development on concrete with different compressive strengths ( $f'_c$ ) of 3, 4, 5, and 6 ksi (20.5, 27.5, 34.5, and 41.5 MPa). Temperature change was assumed to be 30°F (16.7°C). The CTE of concrete has a more predominant effect on the thermal stress increase of high strength concrete than low strength concrete, which can be explained considering Equation 4. For a given temperature change, rate of change of thermal stress as a function of CTE is proportional to the modulus of elasticity, which in turn is proportional to the square root of concrete strength. This results in higher thermal stress increases for high strength concrete than low strength concrete with increasing CTE.



**Figure 2.** Effect of CTE on thermal stress development for 3, 4, 5, and 6 ksi (20.5, 27.5, 34.5, and 41.5 MPa) concrete, while subjected to 30°F (16.7°C) temperature change.

From the previous discussion it can be concluded that, CTE has a significant effect on the thermal stress development in concrete structures. Reducing concrete CTE can have significant benefits in reducing thermal distresses.

### 3. Optimizing concrete coefficient of thermal expansion

Concrete consists of aggregates and cement paste. Aggregates can be divided into two components, coarse and fine. The CTE of all these constituents affect the CTE of concrete. Reducing the CTE of each component will reduce the CTE of concrete. Siddiqui and Fowler[18] showed that blending low CTE coarse aggregate with high CTE coarse aggregate can reduce the CTE of concrete compared to concrete made with high CTE coarse aggregate. This section will discuss the influence of the CTE of each constituent on the overall CTE of concrete.

### 3.1. Materials

An ASTM C 150 [19] type I/II cement was used for all concrete mixtures. Coarse and fine aggregates were collected from various locations around Texas. One limestone (LS) and one river gravel (RG) coarse aggregate were used in this study. Both aggregates met ASTM 57 [20] aggregate gradation. Three different sand sources were used, including silica river sand (RS), limestone (LSS), and slate (SLS). RS met ASTM C33 [20] requirements, but LSS and SLS did not.

### 3.2. Test procedure

Three optimization techniques were evaluated in this study including blending low CTE coarse aggregates with high CTE aggregates, blending low CTE sand with high CTE sand, and reducing cement content. Concrete was proportioned according to Tex-428-A [21] for coarse aggregate blending. Concrete proportioning for 0.75 ft<sup>3</sup> (0.02 m<sup>3</sup>) of concrete is shown in Table 1. Mortar was used to determine the effect of sand blending on CTE. Mortar was also proportioned according to Tex-428-A, by excluding the coarse aggregate. Then concrete specimens were made according to Tex-428-A to evaluate the effect of replacing high CTE sand with low CTE sand on the CTE of concrete. Concrete was proportioned according to a proportioning method suggested by Siddiqui et al. [22] for cement paste reduction. This proportioning technique was used since this method presented a rational procedure to reduce cement content. Concrete and mortar were mixed according to ASTM C192 [23] and ASTM C305 [24], respectively. Two 4-in. x 8-in. (200-mm x 400-mm) cylinders were made from each mixture. The CTE was determined according to Tex-428-A [21] test procedures. Each cylinder was trimmed to a 7-in. (350-mm) length. Cylinders were submerged under water for at least 48 hours to achieve complete saturation. Each cylinder was subjected to three cycles of heating and cooling for testing purposes. Heating and cooling cycling started with cooling to 50°F (10°C) and maintaining that isothermal state for at least 1 hour, then heating to 122°F (50°C) followed by a 1-hour isothermal state at 122°F (50°C) and then cooling to 50°F (10°C). The cooling and heating rate was adjusted so that it took at least 2 hours to reach 50°F (10°C) to 122°F (50°C) and vice versa.

**Table 1.** Mixture proportioning for 0.75 ft<sup>3</sup> (0.02 m<sup>3</sup>) concrete [21]

Materials	Weight in lb (kg)
Cement	23.45 (10.63)
Water	11.49 (5.21)
Coarse aggregate	85.20 (38.64)
Fine aggregate	51.40 (23.31)

### 3.3. Results and discussions

Three different CTE optimization techniques are presented in this paper. Findings are presented in the following sections.

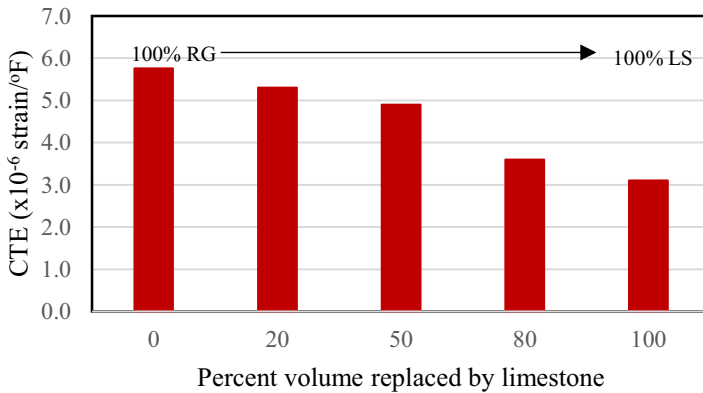
#### 3.3.1. Replacing low CTE coarse aggregate with high CTE coarse aggregate

Coarse aggregate occupies about 40 to 50% of concrete volume and has the most influence on the CTE of concrete. Concrete CTE can be significantly reduced by

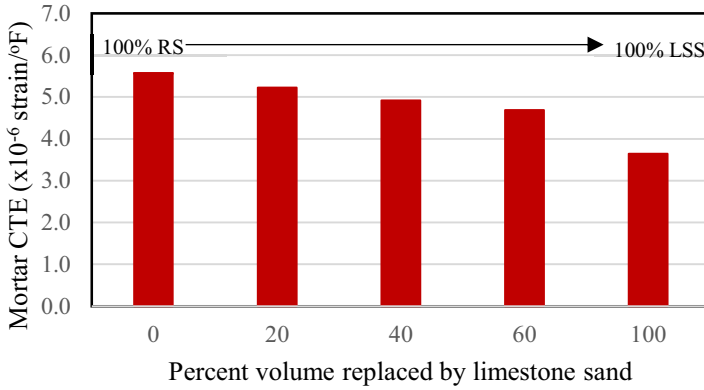
reducing the CTE of the coarse aggregate. RG has high and LS has low CTE. Likewise, given that the concrete proportions are same, concrete with RS yields a higher CTE than concrete with LS. In this study 0, 20, 50, 80, and 100% of RG is replaced by LS aggregate, and concrete mixtures were prepared. Measured CTE of concrete mixtures are presented in Figure 3. Concrete with 100% RG and 100% LS yielded highest and lowest CTE, respectively. Measured CTE of 100% RG is about  $6 \times 10^{-6}$  strain/ $^{\circ}$ F ( $10.8 \times 10^{-6}$  strain/ $^{\circ}$ C) and of 100% LS is about  $3 \times 10^{-6}$  strain/ $^{\circ}$ F ( $5.4 \times 10^{-6}$  strain/ $^{\circ}$ C). The CTE of concrete decreased with increasing volume of LS. Therefore, it can be observed that concrete CTE can be reduced by replacing high CTE coarse aggregate with low CTE coarse aggregate.

### 3.3.2. Replacing low CTE sand with high CTE sand

Mortar occupies about 40 to 50% of concrete. Concrete CTE can be reduced by reducing the CTE of mortar. Mortar cylinders were made using RS and LSS. RS was replaced by LSS at levels of 0, 20, 40, 60, and 100% by volume. Measured CTE is presented in Figure 4. Mortar with 100% RS had the highest CTE of about  $5.5 \times 10^{-6}$  strain/ $^{\circ}$ F and 100% LSS had the lowest CTE of about  $3.5 \times 10^{-6}$  strain/ $^{\circ}$ F. The CTE of mortar decreased as the LSS volume increased. CTE can be reduced by replacing high CTE sand with low CTE sand.

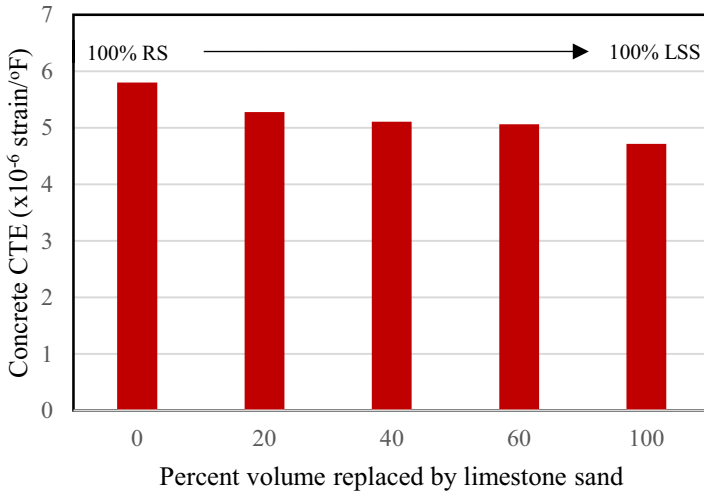


**Figure 3.** Optimizing concrete CTE by blending low CTE coarse aggregate with high CTE coarse aggregate.



**Figure 4.** Effect of blending low CTE sand with high CTE sand to optimize mortar CTE

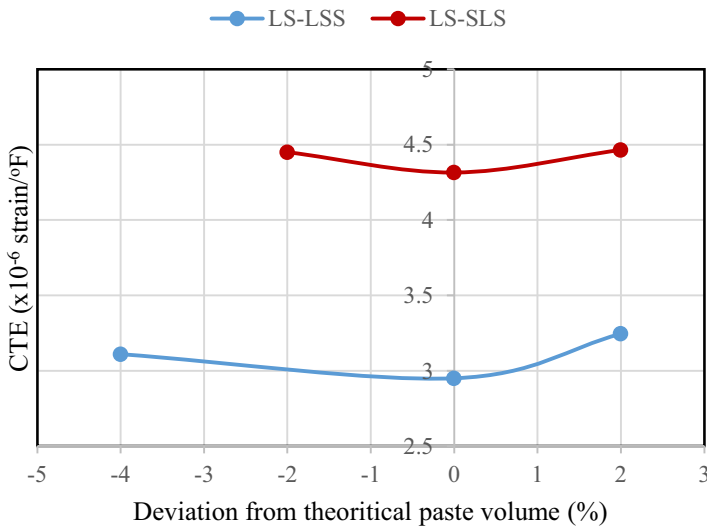
Concrete samples were made with the same mortar composition as described in the previous section. Measured CTE values of concrete samples are presented in Figure 5. Concrete with 100% RS had the highest CTE of  $5.8 \times 10^{-6}$  strain/ $^{\circ}$ F ( $10.5 \times 10^{-6}$  strain/ $^{\circ}$ C) and the lowest CTE of  $4.7 \times 10^{-6}$  strain/ $^{\circ}$ F ( $8.5 \times 10^{-6}$  strain/ $^{\circ}$ C) was measured for 100% LSS concrete. The CTE of concrete decreases with increasing volume of LSS. Therefore, the CTE of concrete can be reduced by replacing high CTE sand with low CTE sand.



**Figure 5.** Effect of blending low CTE sand with high CTE sand on concrete CTE

### 3.3.3. Reducing cement paste volume

Figure 6 shows the effect of cement paste volume on the CTE of concrete. Concrete was first proportioned for the cement content equivalent to theoretical paste volume that can be defined as the paste volume required to fill the voids of the combined aggregate. The paste volume was deviated (increased and decreased) from the theoretical paste volume to determine the effect on concrete CTE. The CTE of concrete decreased as the cement paste volume decreased up to the theoretical paste volume, but increased when paste volume decreased beyond the theoretical paste volume. The increase in CTE below theoretical paste volume can likely be explained by the effect of internal water pressure. When the paste content is below the theoretical paste volume, the concrete does not have enough paste to fill all the voids between aggregates. Therefore, a paste volume below the theoretical paste requirement introduces additional voids into the concrete system. Higher voids in concrete means higher amounts of liquid in the saturated concrete. The liquid phase has a higher CTE than the solid phase which is the reason for higher CTE in saturated concrete with a higher void content [25].



**Figure 6.** Effect of cement paste volume on the CTE of concrete

## 4. Conclusions

CTE of concrete plays an important role on the durability and longevity of concrete structures. Concrete, when exposed to temperature change, experiences thermal movements that when restrained produce thermal stresses. Optimizing the CTE can alleviate the thermal stress and eventually reduce structural distresses. The major findings of this study are listed below.

- CTE is one of the important material properties that significantly affects thermal stress development.
- A significant reduction of concrete CTE can be achieved by replacing high CTE coarse aggregate with low CTE coarse aggregate.
- Replacing high CTE sand with low CTE sand can also reduce the CTE of mortar, which eventually reduces the CTE of concrete.
- Reducing cement content to the theoretical paste volume can also reduce CTE. Reducing the cement paste volume below the theoretical paste volume introduces voids in the concrete system, which leads to a higher CTE for saturated concrete.

## Acknowledgement

Authors like to acknowledge the help and support of the colleagues in the Construction Material Research Group (CMRG) at the University of Texas at Austin, particularly David Whitney and Michael Rung.

## References

- [1] Schindler, A., and B. F. McCullough. Importance of Concrete Temperature Control During Concrete Pavement Construction in Hot Weather Conditions. Transportation Research Record: *Journal of the Transportation Research Board*, Vol. 1813, No. -1, Jan. 2002, pp. 3–10.
- [2] Mallela, J., A. Abbas, T. Harman, C. Rao, R. Liu, and M. Darter. Measurement and Significance of the Coefficient of Thermal Expansion of Concrete in Rigid Pavement Design. Transportation Research Record: *Journal of the Transportation Research Board*, Vol. 1919, No. 1, Jan. 2005, pp. 38–46.
- [3] Chung, Y., and H.-C. Shin. Characterization of the coefficient of thermal expansion and its effect on the performance of Portland cement concrete pavements. *Canadian Journal of Civil Engineering*, Vol. 38, No. 2, Feb. 2011, pp. 175–183.
- [4] Jahangirnejad, S., N. Buch, and A. Kravchenko. Evaluation of Coefficient of Thermal Expansion Test Protocol and Its Impact on Jointed Concrete Pavement Performance. *ACI Materials Journal*, Vol. 106, No. 1, Jan. 2009, pp. 64–71.
- [5] Kannekanti, V. N., and J. T. Harvey. Sensitivity Analysis of 2002 Design Guide Distress Prediction Models for Jointed Plain Concrete Pavement. Transportation Research Record: *Journal of the Transportation Research Board*, Vol. 1947, No. 1, Jan. 2006, pp. 91–100.
- [6] Tanesi, J., M. Kutay, A. Abbas, and R. Meininger. Effect of Coefficient of Thermal Expansion Test Variability on Concrete Pavement Performance as Predicted by Mechanistic-Empirical Pavement Design Guide. Transportation Research Record: *Journal of the Transportation Research Board*, Vol. 2020, No. 1, Dec. 2007, pp. 40–44.
- [7] Choi, S., S. Ha, and M. C. Won. Horizontal cracking of continuously reinforced concrete pavement under environmental loadings. *Construction and Building Materials*, Vol. 25, Nov. 2011, pp. 4250–4262.
- [8] Kim, S., and M. C. Won. Horizontal Cracking in Continuously Reinforced Concrete Pavements. *ACI Structural Journal*, Vol. 101, No. 6, Nov. 2004, pp. 784–791.
- [9] Naranjo, A. Two Lift Concrete Paving -TxDOT Perspective. Two-lift Concrete Paving Workshop. *The University of Texas*, Austin, TX, May 23, 2013.
- [10] Krauss, P. D., and E. A. Rogalla. Transverse Cracking in Newly Constructed Bridge Decks. Publication 380. *Transportation Research Board*, Washington D.C., 1996, p. 132.
- [11] Kim, W., and J. A. Laman. Integral Abutment Bridge Response under Thermal Loading. *Engineering Structures*, Vol. 32, No. 6, Jun. 2010, pp. 1495–1508.
- [12] Moorty, S., and C. W. Roeder. Thermal Responses of Skewed Bridges. Presented at the Developments in Short and Medium Span Bridge Engineering. *Third International Conference on Short and Medium Span Bridges*, Toronto, Canada, 1990.
- [13] Paul, V. *Composite Construction and Bearings*. In Design of Steel Bridges, No. H. Evans, ed., London, England, 1981, pp. 10.68–10.70.



- [14] Imbsen, R. A., D. E. Vandershaf, R. A. Schamber, and R. V. Nutt. Thermal Effects in Concrete Bridge Superstructures. Transportation Research Board, *National Research Council*, Washington, DC, 1985.
- [15] Im, C. K., and S. P. Chang. Thermal behaviour of composite box-girder bridges. *Proceedings of the ICE - Structures and Buildings*, Vol. 140, No. 2, Jan. 2000, pp. 117–126.
- [16] Bentz, D. P., C. J. Bognacki, K. A. Riding, and V. H. Villarreal. Hotter Cements, Cooler Concretes. *Concrete International*, Vol. 33, No. 1, Jan. 2011, pp. 41–48.
- [17] ACI Committee 318. *Building Code Requirements for Structural Concrete (ACI 318-11)*. American Concrete Institute, Farmington Hills, MI, 1991, 2011, p. 503.
- [18] Siddiqui, M. S., and D. W. Fowler. Optimizing the COTE of Concrete by Blending High and Low COTE Aggregates to Meet TxDOT Limit. Presented at the 2nd T&DI Green Street, *Highways and Development 2013*, Austin, TX, 2013.
- [19] ASTM C150 / C150M - 12. *Standard Specification for Portland Cement*. ASTM International, 100 Barr Harbor Drive, PO Box C700, West Conshohocken, PA 19428-2959, United States, 2012, p. 9.
- [20] ASTM C33 / C33M - 13. *Standard Specification for Concrete Aggregates*. ASTM International, 100 Barr Harbor Drive, PO Box C700, West Conshohocken, PA 19428-2959, United States, 2013, p. 11.
- [21] Tex-428-A. *Determining the Coefficient of Thermal Expansion of Concrete*. Texas Department of Transportation, Austin, Tx, Jun. 2011, p. 8.
- [22] Siddiqui, M. S., M. Rached, and D. W. Fowler. A Rational Mixture Design for Pavement Concrete. Transportation Research Record: *Journal of the Transportation Research Board*, 2014, p. 13. In press.
- [23] ASTM C192 / C192M - 12a. *Standard Practice for Making and Curing Concrete Test Specimens in the Laboratory*. ASTM International, 100 Barr Harbor Drive, PO Box C700, West Conshohocken, PA 19428-2959, United States, 2012, p. 8.
- [24] ASTM C305-13. *Standard Practice for Mechanical Mixing of Hydraulic Cement Pastes and Mortars of Plastic Consistency*. ASTM International, 100 Barr Harbor Drive, PO Box C700, West Conshohocken, PA 19428-2959, United States, Jun. 2013, p. 3.
- [25] Siddiqui, M. S., and D. W. Fowler. Effect of Internal Water Pressure on the Measured Coefficient of Thermal Expansion of Concrete. *Journal of Materials in Civil Engineering*, 2014, p. 13. In press.

# Superabsorbent polymers in cementitious composites with fly ash cements – selected aspects

Agnieszka J KLEMM<sup>a,1</sup>, Karol S SIKORA<sup>b</sup> and David E WIGGINS<sup>a</sup>

<sup>a</sup>*Glasgow Caledonian University, School of Engineering and Built Environment, UK*

<sup>b</sup>*National University of Ireland, College of Engineering & Informatics, Ireland*

**Abstract.** In an attempt to address future construction requirements a clear focus is necessary on development of new technologies addressing the need for safer and more cost-effective infrastructure. The paper aims to summarise the current state-of-the-art on application of superabsorbent polymers (SAP) in cementitious composites as internal curing agents. The effect of SAP type, cement type and fly ash content on performance of cement mortars is briefly discussed. The importance of adequate selection of SAP with water absorption/desorption characteristics compatible with hydration process is highlighted.

**Keywords.** Superabsorbent polymers, internal curing, supplementary cementitious materials

## Introduction

Despite worldwide popularity as construction materials, cementitious composite materials (i.e. mortars and concrete) suffer from various deteriorative processes. Reported instances of in service materials failure, as well as the ever expanding requirement to upgrade and refresh existing infrastructure has led to the need to address two interlinked and related problems. Firstly to cost-effectively improve and increase the lifespan and safety of existing infrastructure. Secondly to enhance the performance and safety of new infrastructure provision.

The key issue in the technology of cementitious composites is in the optimal management of water supply during the hydration process. Practically, additional free water available to enable correct mixing, placing, compacting and ensure time for transporting has highly significant effects on performance. It results in increased porosity, shrinkage and creep, reduction in strength and durability in general. Conversely, high performance concretes made with extremely low water to cement ratios (in range of 0.21-0.33), may develop self-desiccation and in consequence increased autogenous shrinkage and crack propagation resulting in significantly compromised mechanical properties and durability. Only a proper curing process of concrete is a practical solution for prevention of these negative effects.

---

<sup>1</sup>Corresponding author: Glasgow Caledonian University, SEBE, 70 Cowcaddens Road, Glasgow, G4 0BA, UK, Email: [a.klemm@gcu.ac.uk](mailto:a.klemm@gcu.ac.uk)

There are two general philosophies of curing cementitious materials: external curing and internal curing. Despite the diversity of external curing methods, many drawbacks and limitations resulting in serious problems are encountered. Firstly, for the purpose of external curing, extra labour needs to be provided, increasing costs of the final product. In addition, even well trained and equipped staff may not ensure a high quality of service and uniform distribution of water. A further limitation of external curing is accessibility of the concrete surface. Extra water supply is more problematic in complex formworks. The final issue is the low permeability of cementitious materials, especially in high performance concretes, which reduces water movement from the surface inside the matrix, leading to uneven water distribution of composite subsequent layers.

The reason for external curing generally is that there is no need to apply any additional materials to the cementitious matrix, unlike in internal curing. So it has no implications on price of a composite mix production. Nevertheless, due to the requirement of extra labour during external curing process, the overall cost of the finished product is likely to be higher than if internal curing is used. Therefore, the above issues suggest that implementation of internal curing instead of external curing might be more beneficial. Internal curing (IC) is defined, according to American Concrete Institute (ACI), as: "supplying water throughout a freshly placed cementitious mixture using reservoirs, via pre-wetted lightweight aggregates, that readily release water as needed for hydration or to replace moisture lost through evaporation or self-desiccation." In order to ensure sufficient water supply various types of internal curing agents have been proposed. One of the promising solutions is modification of cementitious matrix by superabsorbent polymers (SAP).

The use of SAP as an admixture for concrete has been widely researched and published in the last two decades [1-15]. In spite of comprehensive documentation in the literature, SAP suitability for general use is still not clearly understood. A majority of authors suggest that SAPs could be introduced as an internal curing agent to cementitious matrix [4,8,9,11,12]. Due to the complex kinetics of absorption/desorption processes the effect of SAPs on the behaviour of composites may notably differ. The vast majority of produced SAPs are based on cross-linked acrylic acid and acrylamide, along with their modifications. They hydrate in contact with water, forming a swollen polymer gel. As this process is reversible, removal of water leads to a collapsed state of SAP and formation of air-filled pores. It is generally accepted that SAPs increase a degree of hydration and can prevent concrete from self-desiccation. Consequently a denser paste phase is obtained and propagation of microcracks may be prevented. Since SAP increases porosity of hardened cement paste by creation of voids in its collapsed state, these pores may lead to temporary loss of strength. However, it has been argued that, if polymers are carefully selected, the volume of swollen SAP can be replaced by hydration products at later ages and actually increase the strength of cementitious materials. Some authors [14-15] suggest that the differences in pores sizes and their numbers do not have any significant effect on strength development due to the predominant role of air pores over the polymer pores formed in the collapsed state. Since tensile strength depends on microcrack occurrence, the effect of SAP on tensile strength may not be of the same rate as that on compressive strength. Prevention of self-desiccation may therefore significantly improve tensile properties. Relatively high number of reports confirmed shrinkage reduction resulting from SAP addition to mixes. The common view is that water captured by SAP in whole volume leads to reduction of self-desiccation and results in a decrease in autogenous shrinkage [4, 8, 12].

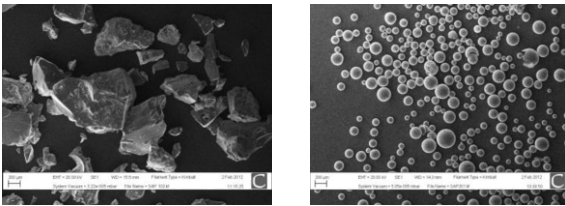
Degradation of cementitious composites by frost action is another issue, which can be potentially counteracted by SAP addition. This view is based on an assumption that SAP forms a system of fine, evenly distributed pores, which are filled with swollen polymers in fresh or young concrete [13]. Over time these pores empty (the ‘collapsed state’) and can act similarly to air-entrained pores. The main advantage of SAP in comparison to the use of air entraining agents (AEA) is the higher robustness of SAP pore system, resulting in highly predictable properties. Air bubbles formed by the AEA may be relatively easily destroyed during concrete transport or processing (pumping, compaction, spraying). Nevertheless, the type of SAP and its absorption/desorption characteristics may have stronger effect than originally anticipated. Different polymers may therefore offer different degree of protection [16]. It should be noted that there are no published reports indicating the negative effect of SAP on F/T performance of cementitious composites.

Despite of a number of studies on the effects of SAP on concrete rheological behaviour, its shrinkage and strength development, the findings are somewhat controversial. To some extent, this can be ascribed to the sensitivity of the results on the type of SAP, the amount of additional mix water and other variations in the examined concrete compositions. More critically the efficiency of SAP products and their applicability to a wide range of blended cements has not been systematically investigated. It should be stressed that the previously published studies were predominantly focused on the effect of SAP in composites based on Portland cements (CEM I type) without any supplementary cementitious materials (SCM).

## 1. Effect of cement type on SAP modified mortars

As reported previously in [16] cement type may have a noticeable effect on autogenous shrinkage in mortars modified by the superabsorbent polymers (Fig 1). Two different types of cement: CEM I 52.5 and CEM II/B-V 32.5 (BS EN 197-1) (LAFARGE) have been used in this study. CEM II/B-V 32.5 is the Portland-fly ash cement containing maximum 30% of fly ash.

It was apparent that application of SAPs in samples containing CEM I resulted in reduction of shrinkage (ASTM C 1698-09), while in CEM II an adverse effect was recorded (Fig. 2-3). It was argued that the SAP ability to absorb water is reduced in the presence of fly ash in blended cements or fly ash particles get surrounded by SAP gel (Fig 4) leading to increase availability of water in the system or indeed combination of both processes. SAP 2 (smaller spherical particles) (Fig 1- right) with the higher affinity to water was capable of small reduction of shrinkage in both cements.



**Figure 1.** SEM images of dry SAP 1 and SAP 2

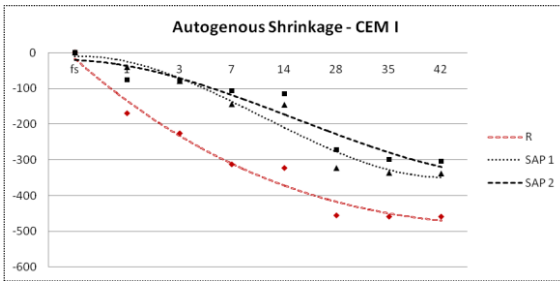


Figure 2. Autogenous Shrinkage for CEM I

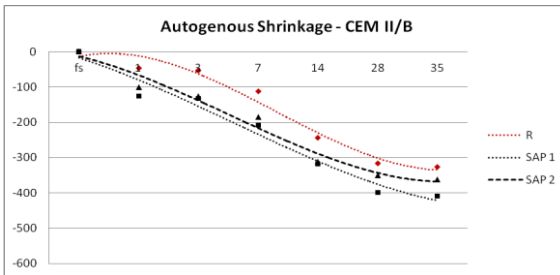


Figure 3. Autogenous Shrinkage for CEM II

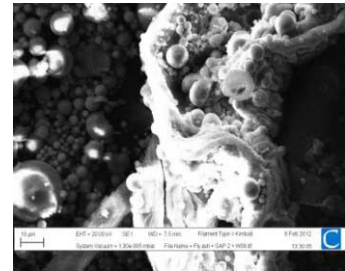


Figure 4. Fly ash in SAP gel

It should be noted that fly ash cement resulted in increased total porosity and decreased average pore diameter (Table. 1). Influence of SAPs, regardless their affinity to water, was of the secondary importance although small increase in porosity was identified.

Table 1. Total porosity [%] and Average pore diameter [nm] at 28 days

Cement Type	Mix	Total porosity	Average pore diameter
CEM II 32.5	R	12.78	13.3
	SAP1	12.90	14.8
	SAP2	13.96	12.2
CEM I 52.5	R	9.02	19.7
	SAP1	9.71	17.9
	SAP2	10.40	16.8

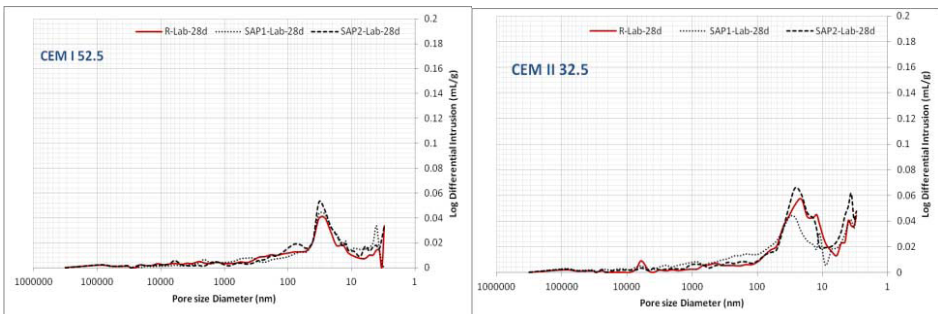


Figure 5. Pore size distribution for CEM I and CEM II mortars

Figure 5 presents pore size distributions in composites with CEM I and CEM II. Formation of smaller pores in SAP mortars is a complex process as normal hydration processes are accompanied by formation of pores after collapsing SAP gel. In blended cement pozzolanic reactions of fly ash with newly created CH lead to densification of microstructure with some delay. The difference between composites containing SAP1 and SAP2 can be attributed to variations in their absorption characteristics, swelling ratios and stabilities. This process is represented by the data shown in Paragraph 2.

## 2. Effect of SAP type on mortars

The effect of three different superabsorbent polymers on mortars has been investigated in the previous study [17]. All SAPs had absorption capacity in demineralised water of 200-250 ml/g. However, their absorption characteristics in cement paste solution differ significantly; approximately 10 g/g for SAP A, 5 g/g for SAP B and 25-30 g/g for SAP C. (Fig 6). The studied composites contained Portland-fly ash cement CEM II/B-V 32.5 (BS EN 197-1) (LAFARGE).

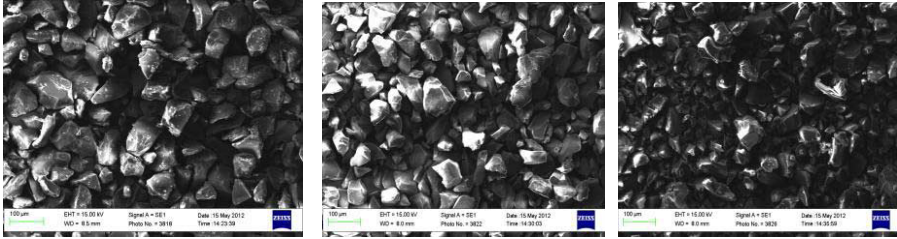


Figure 6. SEM images of SAP A, SAP B and SAP C

As it was demonstrated the effects of SAPs on rheology, autogenous shrinkage and microstructure strongly depend on SAP type and water absorption/desorption kinetics. The ability to absorb water is determined by swelling ratio. The swelling ratio and strength of the network are directly determined by the degree of cross-linking, the chemical structures of the monomers forming the SAP network, and external stimuli such as pH and ionic concentration in the surrounding. The presence of supplementary cementitious materials such as fly ash may also influence their efficiency in water supply.

In general, SAPs with the high water absorption capacity (min 10g of water per 1g of polymer in pore solution) proved to be efficient in diminishing autogenous shrinkage (SAP A and C). These polymers were able to retain part of the absorbed water and release it gradually during a period of four weeks. SAPs with low water absorption capacity (5g of water per 1g of the polymer) had a limited effect on microstructure alteration and hence autogenous shrinkage (SAP B). Vast majority of the absorbed water was released during the first hours after mix preparation. Non-uniform distribution of water and/or permanent retention of some water molecules inside polymer network may lead, in some cases, to a small increase in autogenous shrinkage. The autogenous shrinkage measurements have been performed on mortars with different proportion of sand to cement (1:1 and 2:1) as well as cement pastes. W/C was maintained at 0.45. Figures 7-9 presents recorded values over the period of 42 days.

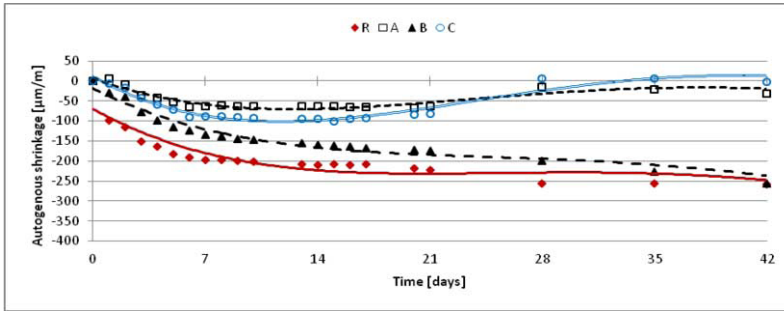


Figure 7. Autogenous shrinkage in mortar 1:1

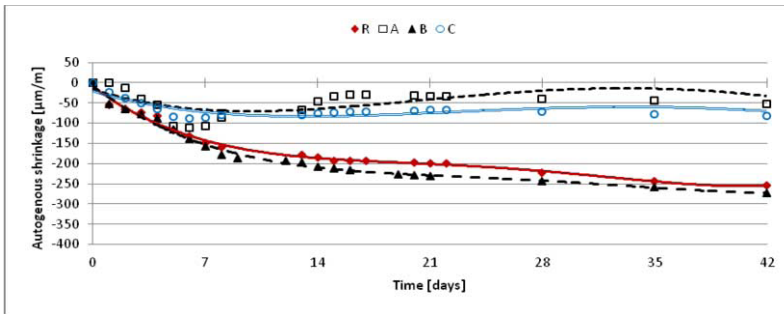


Figure 8. Autogenous shrinkage in mortar 2:1

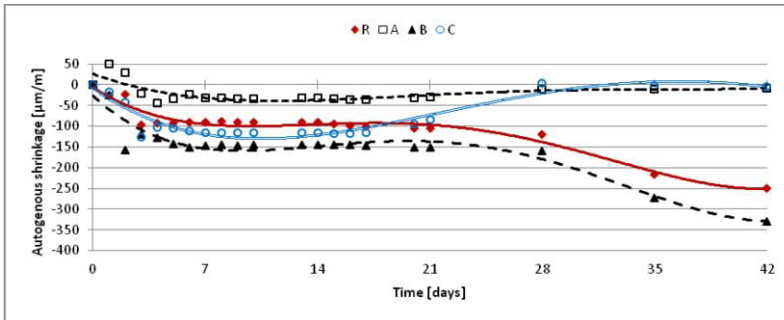


Figure 9. Autogenous shrinkage in cement paste

Based on experiment it was deduced that modification by SAP A and C may mitigate autogenous shrinkage of mortars. Approximately between the second and the fourth week some swelling has been recorded in samples A and C in different compositions. In turn, shrinkage trend of specimens containing SAP B have been similar to the reference samples in different mix compositions. SAP B with lower absorption capabilities was not able to provide sufficient protection. It should be also noted that inadequately selected SAPs may have a negative effect on shrinkage behavior as indicated by samples B.

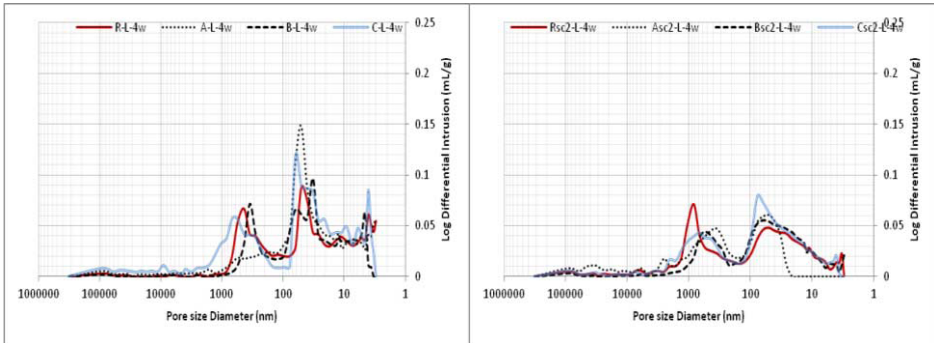
Total water absorption capacity is not a sole criterion for selection of appropriate SAP in cementitious systems. The kinetics of the process and its compatibility with hydration process is of a paramount importance. Despite higher full water absorption

capacity (WAC) for SAP C (25 - 30g of water per 1g of polymer in pore solution) the process of water absorption/desorption was delayed in the studied cementitious mixes, resulting in smaller flow reduction than for SAP A (10 grams of water per 1 gram of the polymer). (see Table 2)

**Table 2.** Flow value for mortar mixes [mm]

Sand/cement ratio	1:1				2:1			
	R	A	B	C	R	A	B	C
Flow before jolts	217.5	100	192.5	103.8	105	100	100	100
After 15 jolts	>250	197.5	>250	202.5	185	112.5	165	113.5

Figure 10 presents pore size distributions in 28 days mixes. In all studied cases a clearly defined bimodal distributions have been identified. The bigger differences appeared in higher cement contents and hence higher SAP contents. As expected more similarities were observed for samples R and B (low absorption capacities).



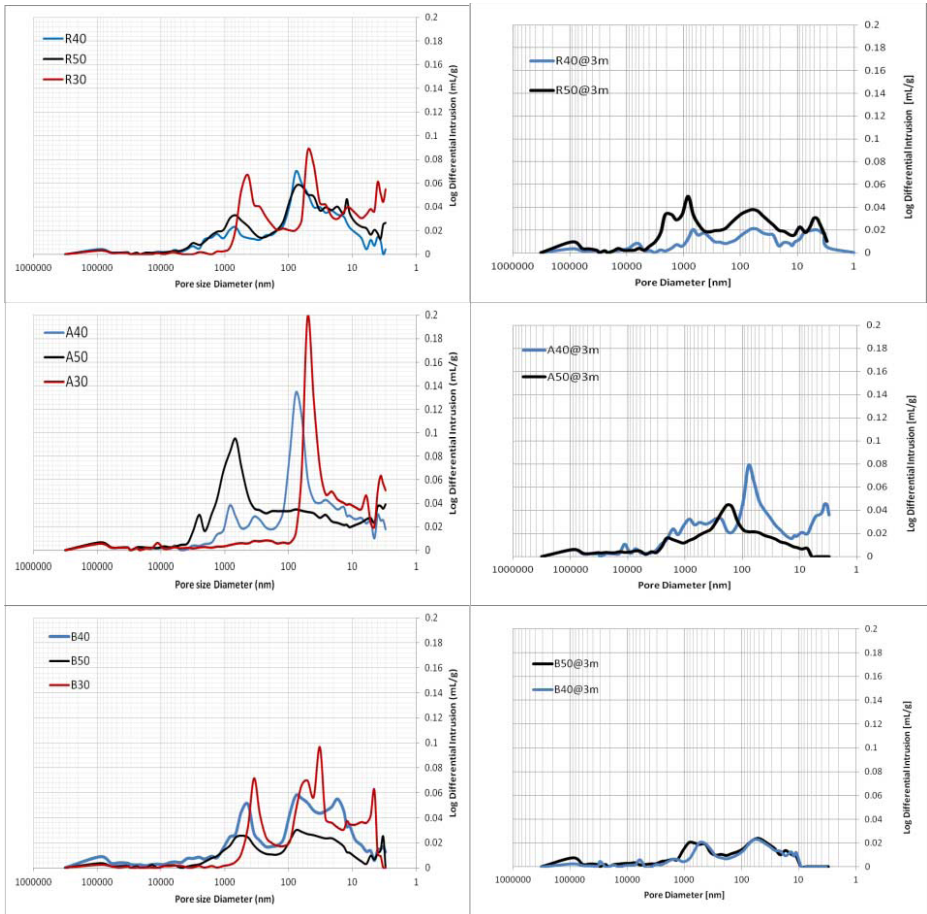
**Figure 10.** Pore size distributions for 28 days mortars with 1:1 and 2:1 sand to cement ratios

The vast majority of pores created by SAP are ‘ink-bottle’ and/or closed and have at least a few thousands nanometres diameters. SAP promotes creation of a dense network of CSH in a collapsed state consequently leading to pores closures. The phenomenon is much more pronounced in samples containing SAPs with a high water absorption capacity. When ‘ink-bottle’ pores are intruded the higher pressure need to be applied giving an indication of higher percentage of smaller pores. In reality these pores may be larger. This may be particularly true in immature mortars with higher cement content. However, most of these SAP pores are being progressively filled with CSH and CAH phases. Hence the initial increase in porosity is followed by its reduction.



### 3. Effect of fly ash content on SAP modified mortars

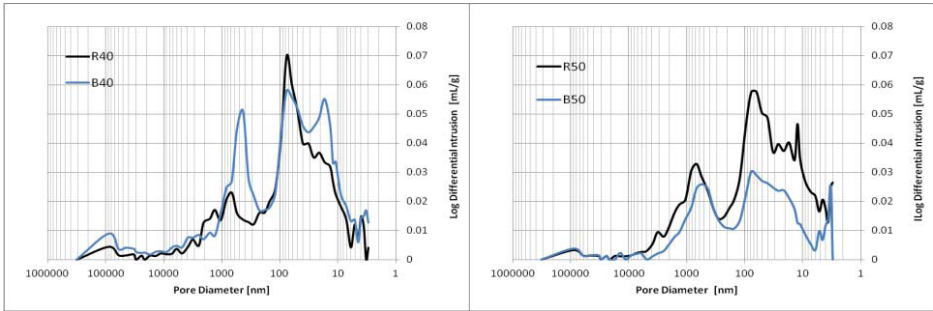
As noted earlier, supplementary cementitious materials (SCM) may have a strong effect on microstructural features of SAP mortars due to modification of the kinetics of hydration process and hence alteration of internal microstructure. The results presented below have been obtained for mortar samples (2:1) modified by two SAPs (A and B, same as in study 2 above). Water/cement ratio for all samples was maintained at 0.45. Pore size distributions of cement-fly ash mortars for 1 and 3 months laboratory cured samples are presented in Fig. 11. The most pronounced effect has been observed in mortars containing SAP A, with higher affinity for water. Higher substitution of cement by fly ash resulted in an increase of both total porosity and proportion of larger pores. Predominant range of pores moved from approx. 30–70nm (for 30% cement substitution) to 40–150nm (40% cement substitution) and 400–1500nm (50% cement substitution). SAP A not only rapidly absorbed a large amount of water (10g/g) but released it quickly too.



**Figure 11.** Pore size distribution in mortars containing 30, 40 and 50% of fly ash after 1 month (left) and 3 months (right); Samples R – no SAP, A – with SAP A, B – with SAP B.

This fast desorption process in high fly ash mortars resulted in formation of larger number of pores after SAP collapsing. Excess of water from SAP was available too soon before the pozzolanic reaction was initiated.

A certain degree of similarity has been observed for reference R and B samples with lower water absorption capacity (5g/g). Bimodal distribution of pores with peaks at 20-100nm and 200-800nm range was observed in all R and B samples. Figure 12 presents MIP results for samples R and B containing respectively 40% and 50% of fly ash. It appears that an increase in fly ash content (50%) results in more pronounced differences. Despite a similar shape of the differential intrusion curves a drop in total porosity has been recorded in samples containing SAP B. Slow release of SAP water facilitated hydration process over the longer period of time and manifested itself in some densification of microstructure.



**Figure 12.** Pore size distribution in mortars R and B containing 40 and 50% of fly ash after 1 month

It appears that in high fly ash cements an extended supply of water plays a more important role than the amount of water. In fact too early desorption may lead to increased porosity particularly in the range of pores between 400 -1200nm.

Similarities between R and B samples have been also recorded after 3 months of curing. Pore size distribution patterns are very alike although total porosities are substantially different (Table 3). Samples R and B containing 40% cement replacement exhibited decrease in total porosities while the higher replacement (50%) did not result in any change.

**Table 3.** Total porosities for samples after 1 and 3 months of lab curing [%]

	40% fly ash		50% fly ash	
	1 month	3 months	1 month	3 months
<b>R</b>	16%	9%	18%	18%
<b>B</b>	19%	9%	10%	10%
<b>A</b>	19%	19%	22%	14%

Samples A behaved differently; here the reduction of porosity was observed only for 50% cement replacement. Release of larger amount of water over the longer period of time facilitated continuity of pozzolanic reaction of fly ash. Due to the higher content of fly ash densification of microstructure was delayed. The higher total porosities measured after 1 month of lab curing for A50 samples could be attributed to the formation of larger number of “SAP pores”. These empty spaces after collapsed

polymer were then gradually filled with CSH leading to densification of microstructure. It is also possible that some of these larger “SAP pores” have been converted to a larger number of partially closed off smaller pores. This would result in further reduction of mercury penetration and hence lower value of measured porosity.

#### 4. Summary

The authors of this study contend that despite interaction complexity between various types of SAPs and supplementary cementitious materials (SCM), superabsorbent polymers may prove to be very effective to facilitate internal curing (IC). Careful selection of the SAP with desorption characteristics compatible with the hydration process is the most critical issue. Diversity in the types of commercially available cements leads to differences in the kinetics of the hydration process, and hence different water requirements. Since water absorption capacity and the rate of both water uptake and release depend on the SAP type, the adjustment to certain cements is of prime importance. Comprehensive laboratory analyses of these phenomena are therefore essential before any recommendations for industrial applications are made.

From the on-going research it is evident that these new materials may have a revolutionary **impact on economics, environment, and structural durability of infrastructure**. These are highly significant commercially to those organisations at the forefront of their introduction. From the perspective of the general public, these materials promise increased infrastructure affordability as well as a higher degree of performance and safety of that infrastructure in operation. Specific benefits include:

- Enhancement of the quality of cementitious materials by improving the material strength and durability by reduction of autogenous shrinkage and crack formation
- Reduced maintenance and construction cost by reducing the need for laborious curing procedures
- Development of high performance repair material which will produce durable, aesthetically pleasing and cost-effective repairs
- Development of new types of blended cements containing SAPs for specific applications and climatic conditions.

#### References

- [1] Brüderm, A.-E. & Mechtcherine, V. 2010. Multifunctional use of SAP in strain-hardening cement-based composites, *Use of Superabsorbent Polymers*: 11-22. Lyngby: RILEM Publications S.A.R.L.
- [2] Esteves, L. P. 2010. Water-entrained cement-based materials by superabsorbent polymers: on the fundamentals..., *International RILEM Conference on Use of Superabsorbent Polymers*, 85-91. Lyngby: RILEM Publications S.A.R.L.
- [3] Hasholt, M. T., Jespersen, M. H., Jensen, O. M. 2010. Mechanical properties of concrete with SAP. Part I: Development of compressive strength. *International RILEM Conference on Use of Superabsorbent Polymers and Other New Additives in Concrete*: 127-136. Lyngby: RILEM Publications S.A.R.L.
- [4] Igarashi, S.-i., Aragane, N., Koike, Y. 2010. Effects of spatial structure of superabsorbent polymer particles on autogenous shrinkage behaviour of cement paste, *International RILEM Conference on Use of Superabsorbent Polymers*: 137-147. Lyngby: RILEM Publications S.A.R.L.
- [5] Jensen, O. M. & Hansen P. F. 2001. Water-entrained cement-based materials I. Principles and theoretical background, *Cement and Concrete Research* 31: 647-654.
- [6] Klemm, A. J. 2011. The influence of superabsorbent polymers on the microstructural features and mechanical properties of cementitious mortars subjected to freezing and thawing conditions, *9<sup>th</sup> Symposium on High Performance Concrete*. Rotorua.

- [7] Lura, P., Durand, F., Loukili, A., Kovler, K., Jensen, O. M. 2006. Compressive strength of cement pastes and mortars with superabsorbent polymers, *Volume Changes of Hardening Concrete: Testing and Mitigation*. Lyngby.
- [8] Ribeiro, A. B., Vinagre, M., Goncalves, A. 2010. Shrinkage of mortars with a suspension of superabsorbent polymers, *International RILEM Conference on Use of Superabsorbent Polymers*: 213-222. Lyngby: RILEM Publications S.A.R.L.
- [9] Siramanont, J., Vichit-Vadakan, W., Siriwatwechakul, W. 2010. The impact of SAP structure on the effectiveness of internal curing, *International RILEM Conference on Use of Superabsorbent Polymers*: 243-252. Lyngby: RILEM Publications S.A.R.L.
- [10] Siriwatwechakul, W., Siramanont, J., Vichit-Vadakan, W., Superabsorbent polymer structures, *International RILEM Conference on Use of Superabsorbent Polymers*: 253-262. Lyngby: RILEM Publications S.A.R.L.
- [11] Schlitter, J., Barrett, T., Weiss, W. J. 2010. Restrained shrinkage behaviour due to combined autogenous and thermal effects in mortars containing Super Absorbent Polymer (SAP), *International RILEM Conference on Use of Superabsorbent Polymers* 233-242. Lyngby: RILEM Publications S.A.R.L.
- [12] Zhutovsky, S. & Kovler, K. 2010. Combined effect of internal curing and shrinkage-reducing admixture on cracking potential of high-strength concrete, *International Conference on Material Science and 64th RILEM Annual Week in Aachen - MATSCI*. Aachen.
- [13] Reinhardt, H. W., Assmann, A., Mönnig, S. 2008. Superabsorbent Polymers (SAPS) - an admixture to increase the durability of concrete, *Microstructure Related Durability of Cementitious Composites*. Nanjing.
- [14] Reinhardt H. W. & Assmann, A. 2009. Enhanced durability of concrete by Superabsorbent Polymers, *Brittle Matrix Composites 9*: 291-300. Warsaw.
- [15] Reinhardt, H. W. & Assmann, A. 2010. Application of superabsorbent polymers in lightweight concrete with porous matrix, *International RILEM Conference on Use of Superabsorbent Polymers*: 207-212. Lyngby: RILEM Publications S.A.R.L.
- [16] Klemm A.J., Sikora K. 2012, The effect of cement type on the performance of mortars modified by superabsorbent polymers, *3<sup>rd</sup> ICCRRR*, Cape Town, South Africa
- [17] Sikora K.S. 2013. The effect of Superabsorbent Polymers on the properties of cementitious mortars containing fly ash", *PhD Thesis*, GCU, Glasgow, UK

# Steel hysteretic damper featuring displacement dependent hardening for seismic protection of structures

Murat DICLELI<sup>1</sup> and Ali Salem MILANI  
*Middle East Technical University, Turkey*

**Abstract.** In this paper, a summary of analytical and experimental studies into the behavior of a new hysteretic damper, designed for seismic protection of structures is presented. The Multi-directional Torsional Hysteretic Damper (MTHD) is a recently-patented invention in which a symmetrical arrangement of identical cylindrical steel cores is so configured as to yield in torsion while the structure experiences planar movements due to earthquake shakings. The new device has certain desirable properties. Notably, it is characterized by a variable and controllable-via-design post-elastic stiffness. The mentioned property is a result of MTHD's kinematic configuration which produces this geometric hardening, rather than being a secondary large-displacement effect. Additionally, the new system is capable of reaching high force and displacement capacities, shows high levels of damping, and very stable cyclic response. The device has gone through many stages of design refinement, multiple prototype verification tests and development of design guidelines and computer codes to facilitate its implementation in practice. Practicality of the new device, as offspring of an academic sphere, is assured through extensive collaboration with industry in its final design stages, prototyping and verification test programs. Analytical and experimental progress made so far in this on-going research is summarized in this paper.

**Keywords.** Damper, seismic, structure

## Introduction

Major bridge structures when threatened by earthquake hazard, often require special seismic protection to meet the design objectives of controlled displacement and limited or no damage. This is usually a combination of isolation/dissipation devices integrated into an isolation system of the bridge. While isolators reduce the force demand on superstructure by increasing the effective period and bringing the structure to low-energy region of the design spectrum, energy dissipaters absorb and dissipate part of the energy that has already swept into the structure and reduce the displacement and ductility demand on structural components. However, the added energy dissipation capacity due to addition of energy dissipaters is accompanied by increased effective stiffness owing to the added reaction force of the damper, necessary for it to function. This is an effect in contrast to that of an isolator. Depending on project specifics and

---

<sup>1</sup>Corresponding author: [mdicleli@metu.edu.tr](mailto:mdicleli@metu.edu.tr)

design demands, usually an appropriate combination of these two different but complimentary mechanisms is sought to provide an effective design.

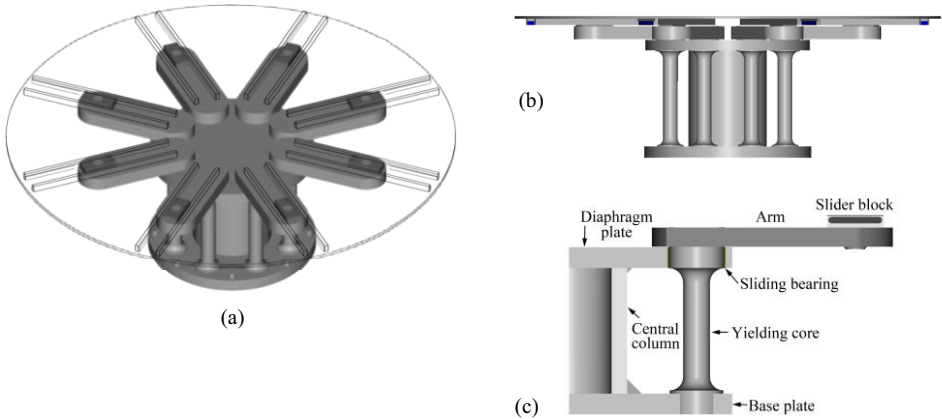
The first appearance and application of steel hysteretic dampers during late 60s and early 70s came about as the outcome of a study in the Engineering Seismology Section of the Physics and Engineering Laboratory, DSIR, [1,2,3]. Ever since, hysteretic dampers have come under increasing attention as an effective and economical means for response control for important structures. Compared to buildings, deployment of hysteretic dampers in bridges encounters the additional difficulties of multidirectional displacements and presence of service-condition temperature-induced displacements which are not supposed to engage the dampers. Multi-directionality of displacements demands that the device be both mechanically capable of displacement at all planar directions and also provide a uniform response irrespective of displacement direction. Consequently, bridge hysteretic dampers are not as diverse as the building ones. A thorough review of bridge dissipation and isolation devices can be found in [4]. The focus of this paper is a newly developed bridge hysteretic damper, Multi-directional Torsional Hysteretic Damper (MTHD). MTHD is capable of large force/displacement capacities and the combination of geometric and material hardening gives it a variable post-elastic stiffness which is believed to be necessary in displacement control of highway bridges. MTHD has passed most phases of necessary analytical and design optimization studies and a 200 kN, 120 mm-capacity prototype of MTHD has recently been tested in the laboratory of the Institute of Structural Engineering at the University of the German Armed Forces in Munich (UniBwM) and also in the Mechanics Laboratory of Engineering Sciences Department at METU. Further experimental investigations which focus on low-cycle fatigue endurance of energy dissipaters are currently in progress in the Middle East Technical University.

## 1. Basic mechanisms and working principle of MTHD

MTHD is designed to dissipate energy by torsionally-yielding cylindrical cores. These are energy dissipater units of the device. Eight of these identical yielding cores, each attached to a torsion arm, are arranged in a symmetric configuration to create the MTHD device, as depicted in Figure 1. To convert translational motion of the structure to twisting in the cylindrical cores, each arm is coupled with a guiding rail, which through a low-friction slider block guides the motion of the arm. The arms are thus restrained to move along a predetermined path regardless of the direction of the imposed displacement on the rail system, relative to the base, creating a guided roller hinge connection. The yielding cores are configured in an upright position around a central column to which they are attached through a thick plate (see Figure 1-c). The plate functions as a diaphragm in transmitting the shear and bending forces imposed by the arms to the top part of the corresponding yielding cores, into the central column, base plate and base anchorage; thus protecting the uniform part of the yielding core below from significant bending and its associated shear force. The uniform part of the yielding cores is where energy dissipation due to torsional yielding occurs.

As a general rule in shape design of a yielding dissipater, optimized design principle requires that plasticization and energy dissipation should be obtained at a minimum expense to the device, that is, minimum damage or plastic straining. Assuming that the objective is to minimize the largest strain value irrespective of the extent and distribution, this leads to uniform strain criterion. The shape should thus be

designed so as to result in uniform strains over the body of the dissipater. For a dissipater working based on pure twist/torsion, this criterion suggests a uniform cylinder as the optimum shape. As the shape is optimized for pure twist/torsion, unwanted bending and shear will upset the desired uniformity in strains and thus the minimum damage objective, as laid out above. Proper functioning of base plate-central column-diaphragm plate as a rigid support for yielding cores against bending is thus crucial to stable and reliable performance of the device. A more detailed description of the system is presented in [5,6].



**Figure 1.** Multi-directional Torsional Hysteretic Damper (MTHD): (a) Isometric view showing the rail system and base device underneath; (b) side view; (c) energy dissipation unit of MTHD: A yielding core, as attached to other components of the device.

## 2. Force-displacement response features of MTHD

A distinguishing feature in force-displacement response of MTHD is the geometric hardening behavior which is the outcome of translation-to-rotation motion conversion mechanism in MTHD. As depicted in Figure 2, this mechanism, working at individual energy dissipater level, magnifies the reaction force required to balance the torque in yielding cores. Reaction force of the device is the sum of projections of all eight forces at slider-rail interface. Since the projection angles are independent of displacement and depend only on orientation of rails, the hardening behavior at eight energy dissipater level directly translates to similar behavior in global response of the device. The same mechanism also offers the possibility of controlling the desired level of hardening in force-displacement response, through adjustment of the arm length to maximum displacement ratio. This is depicted in Figure 3. Varying levels of hardening obtained as such, leads to hysteresis loops of different shapes as shown in Figure 4; As indicated on these graphs, the parameter used to characterize hardening in MTHD is termed ‘Hardening Index’, defined as:

$$HI = \frac{F_{max}}{F_Y} \quad (1)$$

where  $F_{max}$  and  $F_y$  stand for maximum force capacity (force at  $D_{max}$ ) and effective yield force of MTHD, respectively. Analytical formulation of force-displacement response of MTHD leads to complicated equations unfit for hand calculations. Nevertheless, simulations have shown that assuming a certain material model for energy dissipaters (steel grade), properly normalized form of force-displacement curves, categorized by their  $HI$  values, are universal and can be established as the scalable response curves for any MTHD with a specific  $HI$ , regardless of component dimensions and force/displacement capacity. Graphs in Figure 4 represent such curves obtained for C45 steel. Furthermore, component friction is found to have negligible impact on the shape of normalized loops and equations for frictionless MTHD can reliably be used to construct the curves.

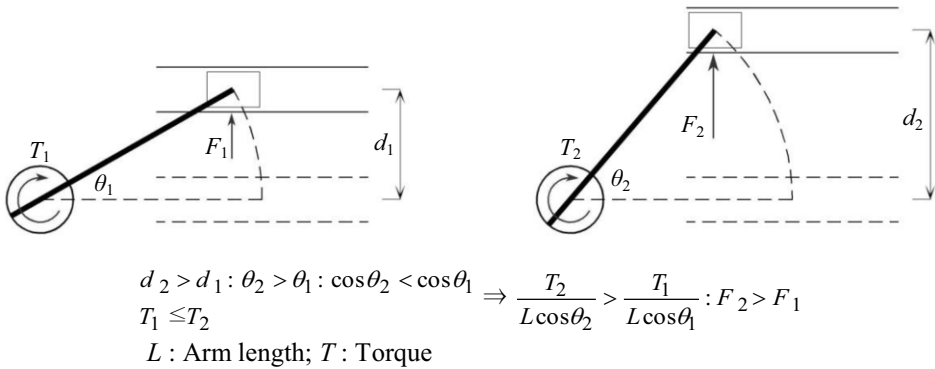


Figure 2. Working mechanism of MTHD responsible for geometric hardening.

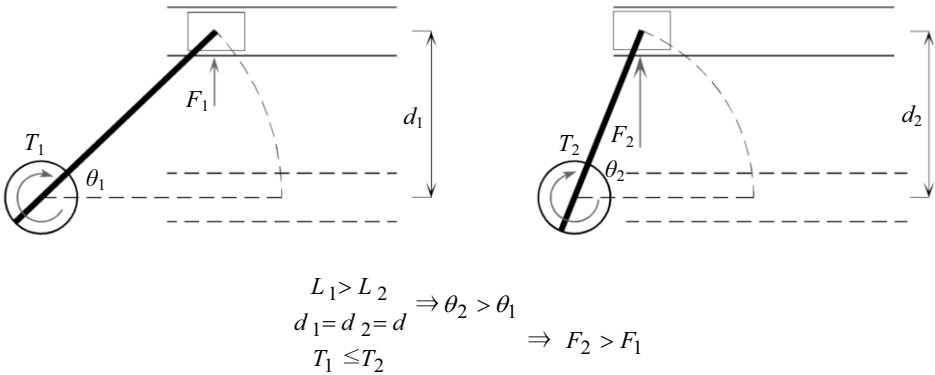
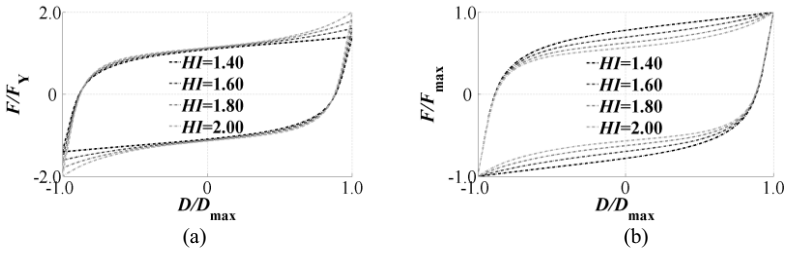


Figure 3. Target hardening index is obtained by adjusting the arm length.

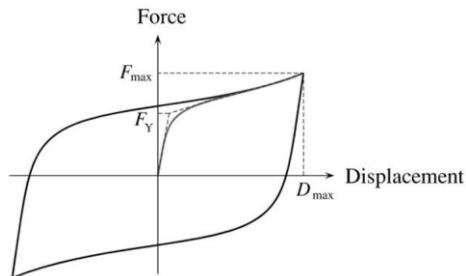




**Figure 4.** MTHD response for different design hardening indices ( $HI=F_{max}/F_Y$ ). (a) force values are normalized to  $F_Y$  to emphasize variation in  $F_{max}$  among loops; (b) force values are normalized to  $F_{max}$  to emphasize shape variation of hysteresis loops among MTHDs designed for the same maximum force.

### 3. Characteristic properties of MTHD as relevant to structural analysis

For implementation of isolation/dissipation devices in practice, modeling issues which arise in the course of the structural design should be addressed. Although quality and accuracy of computer modeling is constantly improving with advancements in computing technology, the kinds of models used in engineering practice are usually simpler than research-oriented models. One reason for this is the tendency to have less number of input parameters in model. In a time history dynamic analysis model whereby the damper is represented by its hysteretic force-displacement rule, usually in form of a phenomenological model, the least parameters necessary to define the model include (elastic stiffness, yield force, post-elastic stiffness) or its equivalent. In case of MTHD, similar number of parameters are necessary and must be enough to characterize the force displacement behavior: either  $(F_{max}, F_Y, D_{max})$  or  $(F_{max}, D_{max}, HI)$ .  $HI (F_{max}/F_Y)$  is used to define the normalized curve (see Figure 4) and  $F_{max}, D_{max}$  are used as scale factors. In the parameter sets listed above, yield displacement could be an alternative to  $D_{max}$ . However, since  $D_{max}$  is more relevant in design of both the MTHD and the structure and is a more concretely-defined point on force-displacement curve, it is preferred over the yield point (see Figure 5). Once a hardening index is chosen by the structural engineer, based on requirements of design, geometric properties of MTHD can be easily adjusted to obtain the demanded level of hardening, as indicated in the preceding section and depicted in Figure 3. This is done in design phase of the MTHD itself, which follows the structural design of the bridge. The three parameters are therefore enough for the structural engineer to proceed with the design without any knowledge or assumption on design specifics of the device itself.



**Figure 5.** Characteristic properties of MTHD.

#### 4. Prototype testing

A 200kN, 120mm-capacity MTHD was designed for prototype testing, as shown in Figure 6. Since design and configuration of the MTHD allows for easy replacement of the yielding cores (energy dissipaters of MTHD), four sets of replaceable yielding cores were produced out of S355J2+N, C45 (two sets), 42CrMo4+QT steel grades. The device is considered a low-capacity version of its kind, as in real practice much higher force/displacement capacity devices are employed. Experiments on prototype MTHD, consist of fully-reversed cyclic quasi-static displacement-controlled tests at varying amplitudes:  $1/4 D_{max}$ ,  $1/2 D_{max}$  and  $1.0 D_{max}$ . After completing the test with one steel grade, the eight yielding cores were replaced for the next phase of tests. The most sought-after results in a quasi static cyclic test on a seismic device are:

- General shape of force-displacement response loops, force measurements, effective stiffness and damping of the device,
- Observations on stability of response expressed in terms of the extent of variation in force-displacement response loops, the maximum force and enclosed loop area at a certain displacement range of response,
- Consistency of measured response with theoretical predictions.



(a)

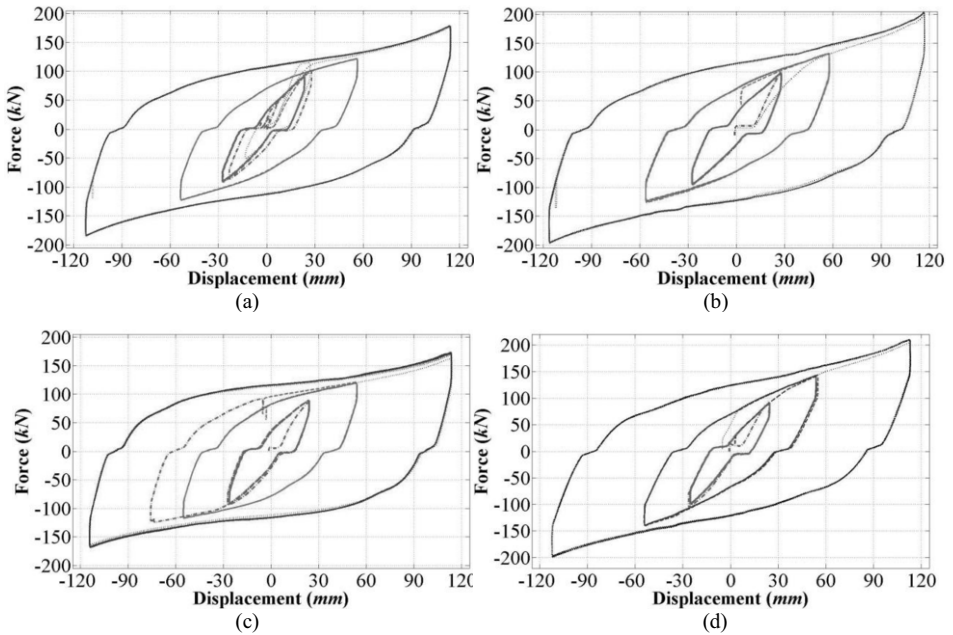


(b)

(c)

**Figure 6.** 200kN, 120mm-capacity prototype MTHD, as tested at METU: (a) un-displaced position, (b),(c) two extreme strokes of  $\pm 120\text{mm}$ .

Force-displacement response loops for nearly all tests are plotted in separate figures for each type of steel used as energy dissipaters, in Figure 7. The graphs show a very stable cyclic response and little variation in force levels which do not exceed %4.0 the mean value, at worst. This is considerably smaller than the %15 limit prescribed by EN-15129, ASCE 07-05 and ASCE 41-06. Higher hardening in the MTHD with 42CrMo4+QT steel and the second set of C45 steel is clearly attributed to higher material hardening, since the rate of geometric hardening is the same for tests with the same displacement amplitudes. Small segments are seen near (force) zero-crossing points with a sharp drop in stiffness. These appear as sloped lines with lower slope than the main unloading branch of the curve, and resemble the behavior characteristics of systems with gap. The behavior is attributed to the clearances at certain components of MTHD. Lowering of the manufacturing tolerances will reduce the size of these segments. Table 1 contains the summary of two main properties of the damper, force and effective damping coefficient. The values in this table are average of all loops at the described displacement. An objective comparison between theoretical predictions and experimental results could not have been performed at this stage, because cyclic material characteristics of steels used in production of the energy dissipaters are yet unavailable.



**Figure 7.** Cyclic response of prototype MTHD with yielding cores made of three different steels: (a) C45-set 1 (b) C45-set 2 (c) S355J2+N (d) 42CrMo4+QT.

**Table 1.** Measured maximum force and effective damping coefficient.

Steel grade	$D_{\max}$ (mm)	$F_{\max}$ (kN)	$\beta_{\text{eff}}$ at $D_{\max}$
C45-set 1	-113,+114	-184,+178	0.33
C45-set 2	-116,+117	-196,+204	0.33
S355J2+N	-114,+114	-168,+172	0.38
42CrMo4+QT	-112,+113	-198,+210	0.32

## 5. Summary and conclusions

A summary of analytical and experimental studies into the behavior of a new hysteretic damper, Multi-directional Torsional Hysteretic Damper (MTHD) is presented. A 200kN, 120mm-capacity version of the device was built and tested in UniBw/Munich and also at METU. The new system is capable of reaching high force and displacement capacities, shows high levels of damping, controllable post-elastic stiffness and very stable cyclic response. A design methodology for the device has also been completed recently. The work so far, has demonstrated the prospects of the system. To further establish the new device as a technically proven anti-seismic system, and also to optimize the design process of the device, more tests on larger-capacity MTHDs will be required.

## Acknowledgements

Full sponsorship of the experimental phase of this work by the international construction firm, MAURER SÖHNE, and provided technical assistance has been instrumental in progress of the research. This contribution is hereby acknowledged. The second author gratefully acknowledges the financial support provided by the Scientific and Technological Research Council of Turkey (TÜBİTAK), under the PhD fellowship program 2215.

## References

- [1] Skinner R. I., Robinson W. H., and McVerry G. H., *An Introduction to Seismic Isolation*, John Wiley & Sons, Chichester, England, 1993.
- [2] Kelly J. M., Skinner R.I. and Heine, A. J., Mechanisms of Energy Absorption in Special Devices for Use in Earthquake Resistant Structures, *Bull. N.Z. Soc. Earthquake Engrg.*, 5(1972), 63-88.
- [3] Skinner R. I., Kelly J. M. and Heine A. J., Hysteretic dampers for earthquake-resistant structures, *Earthquake Engineering and Structural Dynamics*, 3 (1974), 287-296.
- [4] Casarotti C. *Bridge isolation and dissipation devices: state of the art review in bridge isolation, structural seismic response and modeling of modern seismic isolation and dissipation devices*. ROSE School, MSc Dissertation, 2004.
- [5] Dicleli M. and Salem Milani A. Multi directional hysteretic damper with adaptive post-elastic stiffness for seismic protection of bridges in near fault zones. *Proceedings of the 5th International Conference on Bridge Maintenance, Safety and Management (IABMAS2010)*, July 11-15, 2010, Philadelphia, USA, CRC Press, (2010), 615-615.
- [6] Dicleli M. and Salem Milani A. Multi-Directional Hysteretic Damper with Geometrically Hardening Post-Elastic Stiffness for Seismic Protection of Bridges. *2011 World Congress on Advances in Structural Engineering and Mechanics (ASEMI1+)*, Seoul, Korea, Paper No. 329, (2011).

# Failure of structures in East Africa with focus on the causes of failures in the construction phase

Henry Mwanaki ALINAITWE<sup>a,1</sup> and Stephen EKOLU<sup>b</sup>

<sup>a</sup>College of Engineering, Design, Art & Technology, Makerere University, Uganda

<sup>b</sup>Department of Civil Engineering Science, University of Johannesburg, South Africa

**Abstract.** Despite the relatively well-established concrete practice in the East African region, there are frequent incidents of construction failures, resulting into heavy loss of lives and property. The main objective of this paper was to examine structures that have failed during the construction phase, in East Africa, since the start of the 21<sup>st</sup> century; identify and discuss the primary causes and sources of failures. A classic failure case of building collapse, herein referred to as *BBJ* building, has been used to examine the most important issues related to construction failures. Following the analysis of reports of technical investigations undertaken on the collapsed structure, it was found that failures in reinforced concrete (RC) structures during construction, result from five primary causes of: (1) poor materials and workmanship, (2) design and construction errors, (3) absence of professional supervision of site-works, (4) wrong implementation of construction methods, (5) neglect of design approval procedures. Secondary issues that are complicit to construction failures are:- attempts to severely minimize construction cost, neglect of inspection and monitoring by local authorities, influence peddling by proprietors. It is evident that construction failures can be minimized if the right procedures are followed in the design, construction and operation of the structures; a matter that is of interest to stakeholders of the Built Environment.

**Keywords.** Construction failures, causes and sources, reinforced concrete structures, concrete, steel, East Africa, Uganda

## Introduction

In the recent past, there has been a general public outcry over the low quality of physical infrastructure being constructed countrywide. The relatively frequent failure of bridges, road pavements and collapse of buildings at construction sites are some of the major occurrences that have drawn particular attention from the public. The Government of Uganda spends a significant proportion of the national budget on physical infrastructure development and so the failure of such infrastructure means direct loss of financial investment; also involve fatalities. Re-construction of collapsed structures increases the whole life cycle cost, and diminishes the monetary value of the investment.

<sup>1</sup>Corresponding author: College of Engineering, Design, Art and Technology, Makerere University, P. O. Box 7062, Kampala-Uganda; Email. [alinaitwe\\_h@tech.mak.ac.ug](mailto:alinaitwe_h@tech.mak.ac.ug)

This paper gives some of the major recent failures in the EA region which have occurred since the start of the 21<sup>st</sup> century. It gives this background while emphasizing the generally high number of incidents that have been reported, and presents the need for concern by the built environment professionals and all stakeholders. The paper then attempts to isolate some specific causes and issues that likely led to the observed failures. Owing to space limitations in the paper, only one carefully selected case study analysis (*BBJ* building collapse) is presented. The case study contains perhaps all the primary and universal causes of failures that could occur in reinforced concrete (RC) construction. Discussion of these issues are based on technical reports of investigations conducted by professional engineers, architects and construction professionals, as commissioned by the relevant statutory authorities.

## 1. Recent building failures in the East African region

### 1.1 Collapse of structures in Uganda

A number of building structures have exhibited premature failure in the recent past. Some of the notable incidents of failures in Uganda that have occurred within the past 10 years, include:

- *BBJ* building construction accident of 1<sup>st</sup> September, 2004 where 11 deaths and over 26 injuries were reported [1] (also Figure 2)
- St. Peter's Naalya Senior Secondary School building construction accident where 11 deaths and over 10 serious injuries were recorded [2]
- 27 deaths and 86 serious injuries which occurred in 2006, when a church collapsed upon the congregation during a service. This occurred in Kalerwe, a Kampala city suburb
- Collapse of a building that housed a shoe shop (Mini Price Bata) on Ben Kiwanuka Street in the city centre of Kampala, in 2007, killing three people [3],
- Collapse of a building on Lumumba Avenue in Kampala, in 2008, killing two (2) people [4]

### 1.2 Collapse of structures in other East African countries

Similar to the failure incidents experienced in Uganda, quite a few structures have collapsed in other East African countries. Some of major recent cases are [7]:

- Colossal collapse of a 12 storey building that occurred in Kariakoo, Dar es Salaam, Tanzania. This occurred in 2013 killing 36 people and leaving many others injured [5].
- Building collapse in Kiambu town, Kenya in October 2009. This was followed by another building collapse during construction, as seen in Figure 1
- Collapse on Langata Southern Bypass (Kenya) which occurred in June 2011
- Building collapse at Embakasi, Kenya in July 2011
- Building collapse in Ngara Nairobi City, Kenya
- Matigari building collapse at Mathare North, which occurred in September 2011
- Another building collapse in Luanda, Vihiga Western Kenya.

Reports [6] on collapse of buildings in Kenya pointed to the absence of supervision services of a registered architect and Engineers to have been a common denominator. In other parts of Africa, the situation regarding collapse of buildings is similar or even worse. Tanko et al. [7] gave an extensive list of building failures in Nigeria since 1974, which showed that there were 64 reported failures over the 37 year period. Figures 1 and 2 show typical scenes of collapse of structures during construction.



**Figure 1.** Building collapse in Kiambu District, Kenya



**Figure 2.** BBJ building collapse, Uganda [1]

## 2. Implications of skills shortage on construction failures

Architects and engineers are core professions of the construction industry. Capacity deficit in these professions impact construction industry in different ways, one of these consequences being construction failures. A study by Zawdie and Langford [8] on the challenges of construction in sub-Saharan, found materials, skills shortage and lack of training to be predominant issues for African countries, as summarised in Table 1. These issues place more weight on the human factor than on technology or equipment. It is a matter that can be addressed through education and training. These concerns are consistent with other detailed studies conducted on skills shortage in the engineering profession. The gravity of the lack of high-level engineering skills among African countries has been established to be of a very high scale [9]. The population served by a single engineer in Africa is up to 13,000 persons compared to 100 to 300 persons in most developed and emerging economies. For the civil engineering profession, the number of engineers serving a given population is even much smaller. For example, one civil engineer in local government in South Africa serves a population of 33,000. These numbers are again much higher for other African countries [10]. It can be safely estimated that the national engineering skills gap is about 30 to 50% across Africa.

Unfortunately, neither technology nor any form of legislation is capable of compensating for human skills shortage. Improving the skills gap in the built environment requires concerted and targeted effort by governments along with the support by the industry.

**Table 1.** Capacity deficits in the Africa's construction industry

Country	Evidence of Capacity Deficit
Kenya	Shortage of, and high prices of building materials
Tanzania	Reliance on foreign owned large firms for large projects
Ghana	Skills shortage due to absence of training Reliance on importation of building materials especially cement
Nigeria	Inadequate training Inadequate local capacity to produce building materials (cement and concrete)
Ethiopia	Shortage of engineering expertise Lack of equipment and machinery

### 3. Failures at the construction phase

#### 3.1 Ensuring proper construction delivery

Modern construction can be sophisticated and highly technical depending on the size, use and type of structure. The construction stage itself can be critical and delicate, elaborate and demanding, and never satisfactory without highly technical and professional inputs. A properly executed construction program would involve four stages that must be satisfactorily achieved. They consist of: (1) architectural planning and concept design, (2) engineering /structural design and specifications, (3) construction planning and works including, planning and management of resources especially materials, technologies and equipment, workforce and labour, (4) adherence to the governing laws and regulations.

The construction phase is a stage at which concepts and ideas are turned into a tangible physical asset. It is often the most interesting stage to all stakeholders involved but is also a point where important technical errors may result or manifest. The effect of foregone errors at planning and design stages may or may not manifest at the construction phase but they usually have an effect, regardless. More importantly, errors made at the construction stage can be catastrophic. The construction phase can be viewed as the borderline that may technically determine success or failure of the program. Problems that may have accrued from the architectural, tendering and design phases may accumulate and manifest into a failure at construction stage. For example, a tender awarded based on a very low bid would urge the contractor to seek means of severely limiting the construction costs. The contractor may be constrained to use less costly and poor quality materials, low quality cement and less cement content in the concrete mix, eventually leading to low concrete strength. Also, the contractor may not be well-positioned to hire or acquire necessary construction equipment such as concrete mixer and would instead replace such equipment with hand-mixing while chemical admixtures may be replaced by adding more water into the concrete at mixing stage. More importantly, the contractor may be unable or may not have enough capacity to employ professional services and experienced labour force. A typical case would be a decision by the contractor to employ a foreman with experience so as to pay a lower remuneration, rather than retaining a professional engineer or architect, who may charge professional fees.

#### 3.2 Causes of failures at the construction phase of RC structures

The important factors typically responsible for failures during the construction phase are quite numerous. These causes range from design and specification errors to poor



decisions and human related factors. A classic case of construction failure, which depicts nearly all the important failure causes which can occur in construction, is the 5-storey *BBJ new hotel building* which collapsed in September 2004 while construction was taking place at its third floor level (Figure 2). The collapse was fatal leaving 11 people dead and 26 injured. An independent technical committee commissioned by government authority, the Ministry of Works, Housing and Communications [1], conducted investigations and determined the causes of failure. Investigations were also conducted by the Uganda National Bureau of Standards (UNBS) [11]. The two reports reached similar conclusions on the causes and sources of the failure, as subsequently discussed in detail.

### 3.2.1 Poor materials and workmanship

Investigations conducted on the BBJ building collapse, found that the design specifications required C25 concrete strength grade, which is generally appropriate for design of medium height storey RC structures. However, the insitu concrete strengths were determined to be C15 [1] at the age of 3 to 5 months. Flexural members (beams and slabs) exhibiting the lowest strengths. Similarly, the UNBS report [11] found that the compressive strengths of concrete in columns varied widely, from as low as 7 MPa to 20 MPa. It was determined that the materials of construction (especially cement, aggregates, steel) were of adequate quality, conforming to the national standard specifications. However, their technical use appears to have been a critical problem area, due to incorrect implementation of concrete technology onsite which in turn led to the low concrete strength ranging from 30 to 78% of the specified design strength. It was established that Portland pozzolan cement (PPZ) CEM IIB 32.5 was used in the construction. This is the lowest cement strength grade of all cement types that are available in the market and specified based on EN 197-1 [12]. To obtain 25 MPa strength using CEM IIB 32.5 requires very careful mix design verified by testing. According to EN 196-1, CEM IIB 32.5 contains about 20-35% pozzolan. It is important to note that pozzolans characteristically give low early age strength of concrete and gradually and consistently increase later strength, but not necessarily higher than plain concrete mixes containing ordinary Portland cement (OPC). If mixes designed for OPC were used with PPZ cement without mix adjustments, the latter would give lower strengths.

Although the investigations [1,11] approved the quality of concrete materials, it is their implementation in mix design that would determine the insitu concrete strength. A prescribed mix design of 1:2:4 (commonly employed in most RC concrete structures in the EA region) was reportedly used, however, such prescribed mix ratios are often misunderstood by construction workers to mean volume ratios rather than weight quantities. On construction sites, wheelbarrows are often used to measure mix quantities yet more dimensionally defined measuring gauges would be appropriate to use. This issue was discussed in detail in [1] as it happens to be a common problem in most construction sites in the region. Another issue which is often overlooked with prescribed mixes is that the amount of water to be added to the mix is not known, and is normally left to the discretion of site workers. Now, in construction sites where there are no quality control measures (as the case was with the *BBJ* building) such as slump and strength tests etc., the final mixtures become subjective to the concrete mixing experience of workers or foreman who then decides on the amount of water to be added based on “eye-ball” observations. It is no surprise that the concrete mixes observed in

the construction of the *BBJ* building would have been non-uniform and gave highly variable strength.

Another important consideration is that PPZ cement requires longer and more efficient curing than OPC cements, a factor which is not favoured under typical site conditions. This factor, along with lack of adequately skilled workforce on site is reason enough for poor handling and processing of concrete which then leads to low concrete strength.

The problems observed at *BBJ* site went further into workmanship, which again is related to the concerns regarding skills employed on site. There was evidence of severe honey-combing especially at the joints [1,11]. This would have been a result of various processing factors especially poor mixtures and casting methods, resulting in segregation and honey-combing, as seen in Figure 3.

### 3.2.2 Inadequate design capacity of structural elements

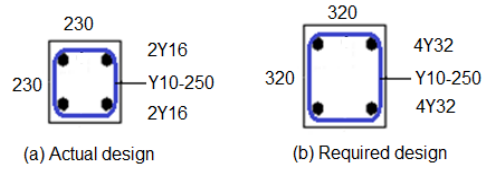
An evaluation of the capacity of structural elements found that, based on the specified 25 MPa concrete grade, the design for RC beams (230x450 mm spanning 5.23m, reinforced with 3Y20 tension and compression reinforcements; Y10-250 mm links, 40 mm cover) would be adequate. Similarly, the 150-mm thick suspended maxpan ribbed slab with 100 mm solid concrete topping would be adequate over a span of 5.23 m. However, with the actual low insitu strength of 7 to 20 MPa, clearly the capacity of the flexural members would be severely diminished perhaps to a point of failure. However, this was not verified with detailed structural calculations.

The design capacity of the columns was however found to have been inadequate. The square (presumably short) columns 230x230 mm were reinforced with 4Y16 mm steel bars and Y10-250 mm links. Design analysis showed that for this size of columns and 25 MPa concrete, 4Y40 mm reinforcement bars would be required for the ground floor columns of the 5-storey RC structure to support the 2000 kN load that would result upon completion of the five-storeys. But as already stated, simply Y16 reinforcement steel bars were provided during construction. A recommended column design would be 320x320 mm with 4Y32 steel bars, as shown in Figure 4. At the time of collapse, and considering the 15 MPa concrete strength and 4Y16 reinforcement bars, the column capacity was 600 kN, about 30% lower than the actual load from the upper two floors supported by the internal columns. This inadequate load carrying capacity of the columns was the critical and defining cause of the building collapse which occurred on the morning of September 1<sup>st</sup>, 2004.

Evidently (and besides the failure of concrete to attain the specified strength of 25 MPa in structural members) there were critical design errors. This is consistent with findings of the investigation, that there were no approved designs and drawings for the buildings, as discussed later. Usually, structural designs include design calculations that have to be checked by a Professional Engineer who would be an employ of the relevant municipal or government authority. During such a process, design errors would have been uncovered and corrected before commencement of building construction would be approved. Figure 5 shows the failure of one of the columns. The buckling failure mode confirms the determination of design capacity analysis, which showed that at the time of collapse, the columns were under excessive loadings, well above their design and constructed capacity.



**Figure 3.** Honey-combed concrete at the column base [11]



**Figure 4.** Column design capacity (units in mm) [1]



**Figure 5.** Buckling failure of the under-designed column [1]

### 3.2.3 Wrong implementation of construction methods

Timber formwork and scaffolds are typically used for construction of RC structures in developing countries. There is limited use of heavy equipment in favour of labour intensive construction, for reasons of high equipment cost and the need for employment creation in the populations faced high unemployment rates. The case of *BBJ* building was no different to this typical scenario. It must be mentioned that there are numerous cases of successful construction of RC structures of low to medium storey sizes, that are daily built using these labour intensive methods and with limited use of equipment. A large proportion of multi-storey structures in major cities in the EA region have been constructed using this approach. It can therefore be confidently emphasized that the approach of using intensive labour and limited equipment is effective and appropriate. However, the required skills appear to gain more significance and influence with use of less advanced construction technology. Once the skills are poor, lacking or compromised due to inadequate knowledge, training or experience, the construction methods employed are likely to develop serious flaws, as observed in the *BBJ* building collapse.

It was found that the construction process employed in the *BBJ* building also involved an error of judgment on the part of the construction workforce. The construction process was programmed speedily. Construction of the structural frame elements (beams, slabs, columns) continued unhalting from 1<sup>st</sup> to the 3<sup>rd</sup> floor i.e. the formwork and scaffolding was kept in place while the subsequent upper floors were cast-in-place. While the procedure is not in itself erroneous, it was blindfolding in the absence of quality control testing of concrete. The process gave the impression that the structural form was formidable as it was supported by the proppings. Hurriedly conducted construction has the danger of not giving time and attention to quality control testing and inspection of newly constructed elements, prior to progression of

casting for the subsequent upper floors. It has been determined that there is a direct link between uncontrolled speedy construction delivery and poor workmanship [13]. This appears to have been a contributing factor in the case of the *BBJ* building collapse.

### 3.2.4 Neglect of design and building approval procedures

Building construction is typically regulated by the city or town council authorities. It is a normal procedure that before a permanent building construction is commenced on a site within the city, its architectural and structural drawings, and bill of quantities are submitted to the local authorities for approval by a professional engineer. Normally, such documents will have been prepared by a professional architect and/or engineer. Construction works that are conducted without undertaking this approval process would normally be deemed illegal.

In developing countries, two challenges arise from implementing these legal procedures. Firstly, the municipal or town authorities may not have sufficient capacity of professionally qualified engineers needed to approve sophisticated structural designs. This alludes to the shortage of scarce skills generally, as discussed in Section 2. Another issue is associated with neglect of procedures, whereby the required approval process may be circumvented by a proprietor through influence peddling or other means. A well-meaning proprietor would appreciate the importance of proper checking of designs, however, financial pressures which come with the need to cut down costs often lead to flawed decisions such as neglecting design approval procedures since it involves engaging professional services of architects and engineers. This, however, may be considered to be a warning sign of embedded flaws that may result in potential failure problems at the construction stage.

In the *BBJ* building case, the investigation [1] found that the design approval process was simply not undertaken. Moreover for a 5-storey RC building, there were no structural drawings and no bills of quantities prepared. These strong signs of non-conformity with approval procedures would have been reason enough for the municipal authorities to query the construction at its early stages and interrogate their lack of approved documents. Interestingly, the municipal authorities did not undertake any such action to inspect and monitor the site construction, and by so doing the authorities too passively contributed to the tragic collapse.

### 3.2.5 Absence of professional supervision of site works

A brief discussion of the lack of adequate qualified professionals of the Built Environment was given in Section 2. It was discussed that Africa has a severely low number of qualified engineers but in addition, most of the young engineering graduates may venture into construction practice without endeavouring to acquire professional registration. But this in itself is not a technical source of failures observed. Economic factor is also an issue which often appears to influence proprietor decisions in retaining professional services. In order to save funds, a proprietor or building owner may resort to employ a less qualified person who may claim to have an extensive experience, instead of hiring a professional who would charge professional fees.

The *BBJ* building collapse is a case in point. The investigation [1] found that there was no professional architect or engineer, retained to be responsible for supervision of the construction work. The site workers who were regarded as ‘engineers’ were only technicians and artisans, and not qualified engineers. Surely, the case of *BBJ* building

cannot be attributed to lack of professional engineers in the City as there are several practicing professional consulting firms. In the same vein, no formal contracting firm with experience and capacity to deliver such heavy construction was used in the construction work. Rather, informal arrangements were made with some construction workers to conduct the construction, without any professional supervision. No wonder that all the early signs of problems and impending failures, which would have been detected, went unnoticed prior to the collapse. These early signs included design errors and low concrete strength, as discussed in Sections 3.2.1 and 3.2.2.

#### **4. Conclusions**

The foregone discussion has highlighted reported cases of structures, particularly buildings, which have collapsed in the East African region since the start of the 21<sup>st</sup> century. Major recent failures that have occurred in Kenya, Uganda and Tanzania are highlighted along with their fatal consequences. But the focus of the paper has been on only those structures that have collapsed during the construction phase or structures whose failure may be traced to new construction works. A classic case of construction failure in Uganda, the *BBJ* building collapse has been analysed as a case study. The case study contained almost all the possible sources and causes of failures that could happen in the construction phase. It was therefore used to identify and discuss the most important, universal or primary failure causes that would result in collapse of any reinforced concrete structure, more so in developing countries.

Five primary causes of construction failures were identified, as follows:- poor materials and workmanship, design errors, absence of professional supervision of site works, wrong implementation of construction methods, neglect of design approval procedures. Secondary factors that are complicit in construction failures include attempts to severely minimize construction costs, neglect of inspection and monitoring by council authorities, influence peddling by proprietors.

Based on the analysis of the findings of investigations conducted on collapsed structures, it can be concluded that construction failures can be prevented or at least minimized, if the right procedures are followed in the design, construction and operation of the structures. There is need to sensitize stakeholders in construction industry on aspects of design and construction that would minimize failures. Local government authorities and relevant government departments have the responsibility to oversee that structures are adequately designed and well-constructed by qualified persons who are capable of meeting standards, methods and procedures required in sound construction practice.

#### **Acknowledgements**

I would like to acknowledge the support from colleagues who provided the data and reports that were necessary in writing this paper. I particularly thank the Chairman of the Engineers Registration Board of Uganda who gave access to the reports on some of the buildings that had collapsed in the period 2004 to 2008. I also thank Sida for the financial report for doing the field activities.

## References

- [1] J.A. Mwakali .... *BBJ Building Accident Report (Main Report)*, Report for the Ministry of Works, Housing and Communications, Entebbe, Uganda, 2004 (confidential report).
- [2] J. Namutebi and H. Sempogo: Four die as Kampala building collapses. *New Vision*, 1<sup>st</sup> January 2008.
- [3] H. Sempogo, , S. Candia, N. Kajoba, F. Ouma, and A. Wasike: Survivors rescued after 24 hours, *New Vision newspaper*, Friday 1 February, 2008, Vol. 23, N<sup>o</sup> 023, page 1, available at <http://www.newvision.co.ug/D/8/12/609440> (accessed 4 August 2010).
- [4] J.A. Mwakali ...*Report of the Technical Investigation into ... (Main Report)*, Report for the Ministry of Works and Transport, Entebbe, Uganda, 2008 (confidential report).
- [5] Fumbuka Ng'wanakilala, James Macharia and Sophie Hares: Death toll hits 36 in Tanzania building collapse, 2013. *Reuters* 1<sup>st</sup> April 2013
- [6] F. Githuhi: Why buildings collapse in Kenya, 2011. <http://www.a4architect.com/2011/09/18/why-builsings-collapse-in-Kenya/> . Accessed on April 20, 2014.
- [7] Joseph A. Tanko, Felix A. Ilesanmi and Sunday K. Balla, Building failure causes in Nigeria and mitigating roles by Engineering Regulation and Monitoring, *Engineering*, 2013, 5, 184-190. doi:10.4236/eng.2013.52026 Published Online February 2013 (<http://www.scirp.org/journal/eng>)
- [8] G. Zawdie, D.A Langford, The state of construction and infrastructure in Sub-Saharan Africa and strategies for a sustainable way forward, *Dept of Civil Engrg, Univ of Strathclyde*, 107 Rottenrow, Glasgow G4 ONG, Scotland, UK, 13p.
- [9] A. Lawless (2005), *Numbers and needs: addressing imbalances in the civil engineering profession*, SAICE, Johannesburg, RSA
- [10] A. Lawless (2007), *Numbers and needs in local govt: civil engrg the critical profession for service delivery*, SAICE, JHB, RSA
- [11] UNBS (2004), *Preliminary report on the collapse of the building ...*, Uganda National Bureau of Standards, Plot M217 Nakawa, Industrial Area, P.O. Box 6329, Kampala, Uganda (confidential report).
- [12] EN 197-1:2000 Cement composition, specifications and conformity criteria for common cements
- [13] Giray Ozay, The most common defects on housing surfaces in Northern Cyprus, Department of Civil Engineering Eastern Mediterranean University, Magusa, Via Mersin 10, Turkey. Paper presented at the *XXXIII IAHS World Congress on Housing*, 27-30 September 2005, "Transforming Housing Environments through Design", University of Pretoria

# Design and properties of ultra-high performance concrete

Caijun SHI<sup>1</sup>, Zemei WU, Dehui WANG and Linmei WU  
*College of Civil Engineering, Hunan University, Changsha 410082, PR China*

**Abstract.** Ultra high performance concrete (UHPC) is a composite material that consists of Portland cement, silica fume, ultra-fine quartz powder, superplasticizer and small sized steel fibers with low water to binder ratio and absence of coarse aggregates. Compared to conventional concrete, UHPC has superior properties such as strength, toughness and durability. In this paper, the principles for mixture design and properties including mechanical properties, dimensional stability and durability of UHPC were reviewed.

**Keywords.** UHPC, mixture design, mechanical properties, dimensional stability, durability

## Introduction

Reactive powder concrete (RPC) is an advanced cement-based material, which was developed by Richard et al. in France using components of increased fineness and reactivity via thermal treatment [1,2]. De Larrard [3] introduced the term “ultra high performance concrete” (UHPC). It is a material characterized by high binder content, very low water-to-binder ratio, use of silica fume, fine quartz powder and superplasticizer, and/or fine ductile fibers [4]. It generally gave of over 150 MPa for compressive strength, 7-15 MPa for uniaxial tension strength and 25-40 MPa for bending strength [5]. Furthermore, it exhibited high toughness and excellent durability [6]. In addition, it possesses possess ultra-high static dynamic strength, high fracture capacity, low shrinkage and excellent durability under severe condition. With these merits, UHPC has been wildly applied in Europe, North America, Australia, Asia and New Zealand [7]. However, the production of UHPC often uses thermal curing at 90°C or higher, which result in high energy consumption and low production efficiency [8]. Therefore, more and more researches have been conducted on the selection of raw materials and properties of UHPCs to facilitate their production and applications [9,10].

---

<sup>1</sup>Corresponding author: [caijunshi@yahoo.com](mailto:caijunshi@yahoo.com)

However, one of the big challenges before wide implementation of UHPC is lack of commonly accepted standards for the selection of the materials and test methods, design guides for engineers and quality control methods in manufacturing facilities. In this paper, mixture design and properties including mechanical properties, dimensional stability and durability of UHPC were reviewed. Four basic principles for UHPC design were summarized. It is the purpose to summarize the recent progress, and to provide some insights and suggestions for further research and development of UHPC.

## 1. Mixture design

### 1.1 Mixture design principles for UHPC

#### (1) Reduction in porosity

It is well known that the strength of concrete is dependent on its porosity. The granular raw materials of UHPC generally include cement, silica fume, quartz powder, quartz sand and so on. Their proportions can be optimized by applying close packing models to achieve low initial porosity. Superplasticizers used in UHPC can significantly reduce the required w/b for a given workability, thus effectively reducing the initial porosity [11,12]. In addition, the pozzolanic effect between  $\text{Ca}(\text{OH})_2$  and pozzolanic materials can obtain more hydration products thus decreasing the porosity of hardened UHPC [13].

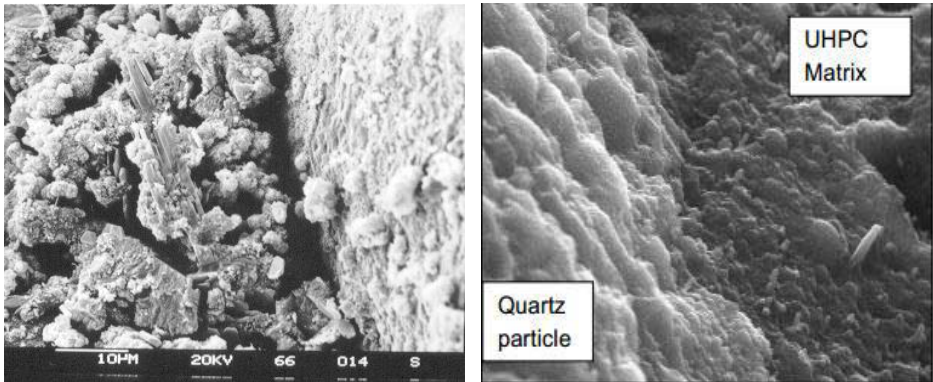
#### (2) Improvement in microstructure

UHPC has a very dense and uniform microstructure due to physical, chemical and adhesion optimization. It is believed that the low w/b results in low porosity that restricts the space available for the growth of  $\text{Ca}(\text{OH})_2$  (CH) crystals. Use of elevated temperature curing accelerates the hydration of cement and promotes the pozzolanic reactions, which is beneficial for reduction of defects and a high packing density of the microstructure. The internal microstructure of UHPC is mainly comprised of unhydrated cement clinker particles, quartz sand and hydration products such as C-S-H [14]. There are almost no pores observed in the nanoporous range with pore sizes up to 100 nm and no significant CH was detected by XRD [15]. The C-S-H in UHPC mainly belongs to high density type characterized by intrinsic higher stiffness and hardness than low density type that dominates in conventional concrete.

The interfacial transition zone (ITZ) between aggregates and paste matrix has high porosity and CH content, and is the weakest part in conventional concrete. SEM



pictures of ITZ in conventional cement mortars and UHPC are shown in Fig.1 [16,17]. It can be seen that a very porous ITZ can be observed in the conventional portland cement mortar. However, owing to the low w/b and the pozzolanic reaction reactions between CH and pozzolanic mineral admixture, the ITZ in UHPC seems as dense as the matrix [2, 18]. The homogenous structure will endorse UHPC's excellence performance.



(a) ITZ in Conventional Mortar [16]

(b) ITZ in UHPC [19]

**Figure 1.** Comparison of SEM observations of ITZ between conventional cement mortar and UHPC

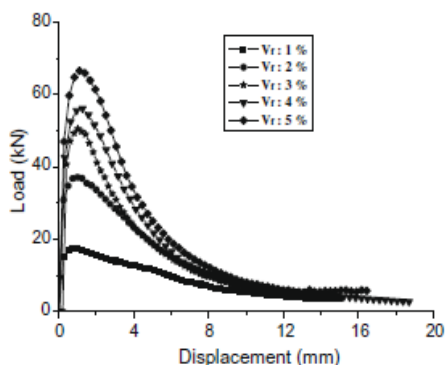
### (3) Enhancement in homogeneity

Coarse aggregates in conventional concrete usually have higher hardness than cement paste and act as a skeleton in concrete. However, due to the difference in thermal and mechanical properties between aggregates and paste matrix, shear and tensile stresses may occur and result in micro-cracks at the ITZ. The crack size is proportional to the size of aggregates. The use of quartz sand with diameter of 400  $\mu\text{m}$  instead of coarse aggregates, would significantly decrease the size of micro-cracks in UHPC [2]. Meantime, the reduction in aggregate size also decreases the probability of its own defect; thereby reduces the inhomogeneity of concrete. As discussed above, the ITZ looks the same as matrix, which indicates the homogeneity of microstructure in UHPC.

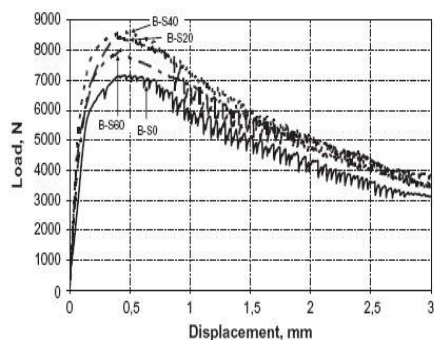
### (4) Increase in toughness

Toughness is a measure of the energy absorption capacity of a material and is used to characterize its ability to resist fracture [20]. Concrete is a typical quasi-brittle material with low tensile strength, strain capacity and fracture toughness. Incorporation of fibers into concrete can prevent and control the initiation, propagation, or coalescence of cracks. When a load acts on fiber reinforced concrete, the fibers do not sustain the load

directly, but the matrix does. It is transferred to the fibers through the interface between the fibers and the matrix[21]. The high loading carrying capacity of UHPC after the peak load was attributed to the addition of steel fiber and improved toughness. Usually, flexural loading capacity of UHPC increases with its fiber content as shown in Fig. 2. The use of slag could increase the maximum bending loads of mixtures considerably, as shown in Fig 3 [22].



**Figure 2.** Effect of fiber content on the on flexural loading of UHPC [23]



**Figure 3.** Effect of slag content load-displacement curves of UHPC [22]

## 1.2 Mixture design methods

Mixture design is a selection of raw materials in optimum proportions to give concrete of required properties in fresh and hardened states for particular applications. The design of UHPC aims to achieve a densely compacted cementitious matrix with good workability and strength. Different closing packing models and softwares have been used for mixture design of UHPC [24-26]. People often use modified Andreasen and Andersen model as a target function for the optimisation of the composition of mixture of granular materials [24,27]. The Equation is shown as follows:

$$P(D_i) = \frac{D_i^q - D_{\min}^q}{D_{\max}^q - D_{\min}^q} \quad (1)$$

where  $P(D_i)$  is a fraction of the total solids being smaller than size  $D_i$ ,  $D_i$  is the particle size ( $\mu\text{m}$ ),  $D_{\max}$  and  $D_{\min}$  is the maximum and minimum particle size ( $\mu\text{m}$ ) respectively, and  $q$  is the distribution modulus. Considering the amount of fine particles in UHPC, the value of  $q$  is about 0.23 [24]. The proportions of each individual ingredient in the mixture are adjusted until an optimum fit between the composed mixture and the target

curves is reached, using an optimization algorithm based on the Least Squares Method (LSM), as presented in Eq. (2). When the deviation between the target and the composed mixture curves, expressed by the sum of the squares of the residuals (RSS) at defined particle sizes, is minimized, the composition of the concrete is treated as the best one.

$$RSS = \sum_{i=1}^n [P_{mix}(D_i) - P_{tar}(D_i)]^2 \rightarrow \min \quad (2)$$

where  $P_{mix}$  is the composed mixture,  $P_{tar}$  is the target grading calculated from Eq. (1).

After that, the components of UHPC are mixed, cast and vibrated as like conventional concrete. The mixing procedure is shown in Fig. 4.

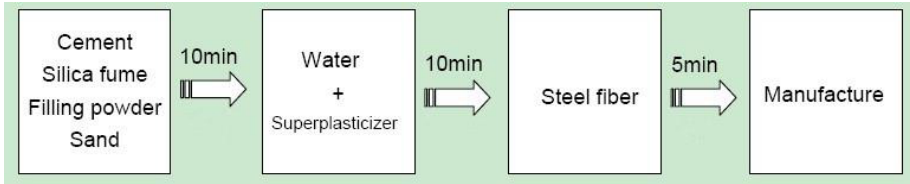


Figure 4. Mixing procedure of UHPC

## 2. Properties of UHPC

### 2.1. Mechanical properties

UHPC has high compressive and flexural strengths, elastic modulus, as shown in Table 1. The following sections describe the properties in more details.

Table 1. Typical performance of UHPC [36]

Item	RPC 200	RPC 800	HPC
Compressive strength (MPa)	170-230	490-680	60-100
Flexural strength (MPa)	25-60	45-102	6-10
Elastic modulus (GPa)	62-66	65-75	30-40
Fracture Energy (J/m <sup>2</sup> )	20000-40000	1200-2000	140

#### 2.1.1 Compressive and flexural strengths

Curing regimes, steel fiber content and curing age has significantly influence on mechanical properties of UHPC. It was found that the compressive strength started to

develop at approximately 32 h after the addition of water to the mixture [28]. At 7 days, the concrete compressive strength amounted to 81% of the final strength. The development of the mechanical properties virtually stopped after 90 days. Zhang [29] investigated the compressive strengths of various green reactive powder concrete (GRPC) made with different matrices, fiber content, curing regimes and curing time. The results showed that the compressive strength of GRPC improved with the increase of steel fiber content. Depending on the fly ash content, strengths of UHPC after steam curing are between 89% and 126% of those strengths after autoclave curing [30]. The compressive strength reached over 200 MPa after 3h of autoclaving curing at 180°C [31]. Kang et al. [32] studied the tensile fracture properties of UHPFRC with fiber volume ratio varying from 0% to 5% through notched 3-point bending tests and found that the flexural tensile strength of UHPFRC linearly increases with increasing fiber volume ratio. The flexural strength reached over 30 MPa after 3h of autoclave curing at 180°C [33]. Steam and autoclave curing decreased the flexural strength of UHPC, and steam curing resulted in considerably lower flexural strength than autoclave curing did [34]. Wille et al. [35] recently produced strain hardening behavior, with 14.2 MPa post-cracking strength and 0.24% strain capacity, by using only 2.5% short, smooth steel fibers ( $d_f = 0.2$  mm,  $L = 13$  mm) in an UHPC matrix. They reported good tensile performance of UHPFRCs with 2% high strength deformed steel fibers such as hooked and twisted steel fibers. Fiber geometry has obvious effect on tensile properties of UHPC. It was reported that UHP-HFRC produced with twisted macro -fibers showed the best performance with respect to post-cracking strength, strain capacity and multiple micro-cracking behaviors, whereas UHP-HFRC produced with long, smooth macro-fibers exhibited the worst performance [36].

### *2.1.2 Dynamic properties*

Dynamic properties are important for hydraulic structures, offshore structures, explosion and penetration resistant structures, protective shelter of military engineering and nuclear waste treatment [37]. The dynamic compressive behavior of the UHPCC is significantly sensitive to the strain rate. Under the same compressive loading, the sample of UHPFRC matrix was crushed while the sample made of UHPFRC with 3% or 4% of steel fibers by volume fraction remained essentially intact. Rong [38] investigated the dynamic compression behavior of UHPFRC with different fiber volume fraction using split hopkinson pressure bar (SHPB). Results show that impact resistance of UHPFRC was improved with an increase of fiber volume fraction.

UHPFRC is sensitive to strain rate. It has excellent strain rate stiffening effects under dynamic load. Its peak stress, peak strain and the area under strain-stress curve increased with the increasing of strain rate. Its fracture pattern changed from brittleness to toughness under high strain rates. The threshold value of strain rate was  $50^{-8}$ , beyond which the strength, ductility and elastic modulus of UHPFRC is remarkably increased with the increase of fiber volume fractions. The dynamic tensile strength increases obviously with increasing of impact velocity, which showed high strain rate sensitivity. The minimal dynamic tensile strength was higher than quasi-static strength, especially for GRPCs with high fiber content. What's more, the dynamic tensile strength of fiber reinforced GRPC was much larger than that of GRPC matrix without fiber [38].

### *2.1.3 Fatigue behavior*

Fatigue process of FRC is actually the cause of cracks, propagation and recovery under repeated load. UHPFRC has a longer fatigue life than ordinary FRC at higher fatigue stress levels. The cracking state under fatigue load is an important factor for fatigue resistance of UHPFRC [39]. Makita et al. [40] conducted tensile fatigue tests on R-UHPFRC elements for the determination of fatigue behavior. Experimental results showed a fatigue endurance limit of 10 million cycles at a solicitation level of  $S = 0.54$  for  $S$  being the ratio between the maximum fatigue force and the ultimate strength. There is little information available on the fatigue behavior of UHPFRC.

## **2.2 Dimensional stability**

### *2.2.1 Autogenous shrinkage*

Autogenous shrinkage is affected by several factors such as cement type, water-to-binder ratio, temperature, mineral admixture type and adding dosage. A low water/binder ratio and a high binder content in UHPC can lead to a large early autogenous shrinkage and cracking. Experimental investigation using factorial design showed that steel fiber content had the most significant effect on the cracking resistant behavior of UHPC, but the influence of sand-to-binder ratio and water-to-binder ratio on the cracking behavior of UHPC was not obvious [41].

### *2.2.2 Drying shrinkage*

Mixtures with retardation or high superplasticizers dosages showed increased drying

shrinkage and crack tendency. Shrinkage strain rate linearly increases with cementitious material content, paste-to-void ratio (by volume), and clay content of fine aggregate. Concrete with low water-to-binder ratios had low drying shrinkage, as shown in Fig. 5 [42]. In general, the drying shrinkage of UHPC after steam curing is very low because of the incorporation of steel fiber [43]. Higher shrinkage rates were developed from 1 to 14 days for UHPC. The shrinkage rate increased steadily from 14 to 100 days, and then gradually reduced from 100 to 130 days.

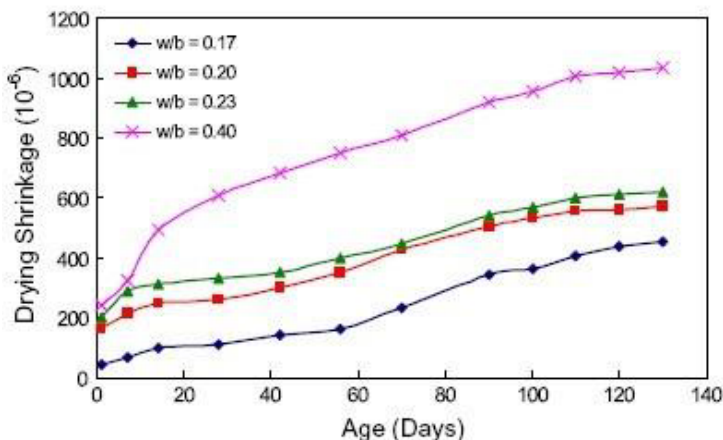


Figure 5. Drying shrinkage of UHPC with different water-to-binder ratios [42]

### 2.2.3 Creep cracking resistance

The cracking of concrete affects the integrity and durability of concrete structures. Therefore, it is important to evaluate the cracking resistance of concrete. Garas et al. [44] investigated the effects of three different thermal treatment regimes on tensile and compressive creep performance of UHPC. Results showed that UHPC creeps phenomenologically differentiated in tension and compression. The specific tensile creep in UHPC with no thermal treatment was  $176 \mu\epsilon/\text{MPa}$  at 1 year while it was  $54 \mu\epsilon/\text{MPa}$  with  $90^\circ\text{C}$  treatment. The specific compressive creep with no thermal treatment was  $8.3 \mu\epsilon/\text{MPa}$  at 1 year while that with  $90^\circ\text{C}$  treatment was  $3.3 \mu\epsilon/\text{MPa}$ . It is suggested that the quality of the fiber/matrix interface is a major contributor to the measured increased creep of non-thermally treated UHPC as compared to UHPC treated at  $60^\circ\text{C}$  or  $90^\circ\text{C}$ .

## 2.3. Durability

### 2.3.1 Permeability

Permeability is used for assessing the overall movement of fluids into and through concrete. Due to a very low porosity, the typical permeability coefficient of UHPC was about 0.0005 at 98 days; whereas the typical permeability coefficient of ordinary concrete was about 0.0015 at 98 days, which differs by an order of magnitude. In hydrated cement paste, the size and continuity of the pores at any point during the hydration process would control the permeability coefficient. Therefore, the low permeability of UHPC might be explained by the small and discontinuous pores that presented in the very homogenous, compacted and dense pastes. As hydration proceeds, the capillary network became increasingly tortuous as interconnected pores were blocked by the formation of C-S-H, which lead to continuous decrease in permeability [42].

Use of superplasticizer reduced the macroporosity as they made concrete more flowable and compaction easier. Insufficient superplasticizer dosage would make UHPC compaction difficult and lead to high level of porosity. However, there existed an optimal superplasticizer dosage which resulted in the lowest permeability [42]. Excessive superplasticizer dosage could lead to chemical incompatibility problems and segregation, resulting in higher porosity and consequently higher water permeability.

The chloride penetration resistance is one of the important durability degradation indexes of concrete. The permeability coefficient and diffusion coefficient of chloride ion in HPC and UHPC were much lower than that of ordinary concrete, and the diffusion coefficient of chloride ion in UHPC was much lower than that of HPC[45].

### 2.3.2 Carbonation resistance

Carbonation of concrete can reduce the alkaline of concrete and destruct passive film of surface of reinforcing steel, and as a result, make the reinforcing steel easy to rust. The water/binder ratio of UHPC is very low, and the internal structure of UHPC is very dense, which is difficult for CO<sub>2</sub> to penetrate into concrete. Therefore, UHPC has an excellent carbonation resistance. Other study found that there was no carbonation in UHPC system, no matter after sealed, standard and heat-curing condition. Another one found that the 28d mean depth of the carbonation of UHPC was less than 0.30mm [46].

### 2.3.3 Frost action

Freezing-thawing is the main reason for the deterioration of concrete structure in cold regions. The internal structure of UHPC is so dense that it is difficult for external water to penetrate into UHPC. In addition, the incorporation of steel could inhibit propagation of cracking. After 600 freeze-thaw cycles, the durability coefficient of UHPC was larger than or equal to 100, and the mass loss was almost zero [46]. After 1000 freeze-thaw cycles, the relative dynamic modulus of regular concrete (RC), high strength mortar (HSM) and reactive powder concrete (RPC) reduced by 61%, 22% and 10% respectively; their compressive strengths reduced by 57%, 16% and 6% respectively; the bond strength between steel and them decreased by 35%, 23% and 5% respectively; the bond strength between RC and them decreased by 69%, 44% and 3% respectively. Therefore, it could be concluded that the freezing resistance of RPC was better than that of RC and HSM [47]. However, specimens incorporating steel fibers revealed an increased surface scaling especially in the vicinity of the fibers.

### 2.3.4 Fire resistance

During fire endurance temperature studies, it was found that the explosive spalling of HPC specimens occurred near 600°C, Ordinary concrete (OC) specimens at around 690°C, and UHPC at about 790°C [48]. The compressive strength of UHPC gradually increased when specimens were heated to 200~300°C, but started to decrease as temperatures further increased [49]. After fire duration test at a constant temperature of 500 ± 50°C, the compressive strengths of UHPC, HPC and OC dropped dramatically and their residual compressive strength reduced to 62.2, 46.7 and 58.5% respectively after 60 min of fire. After 120 min fire, their residual compressive strengths maintained 55.6, 34.6 and 52.7% of their original compressive strengths. It was also found that the inner temperatures of UHPC specimens were consistently higher than those of HPC and ordinary concrete specimens when they were subjected to the same fire temperature and duration. This means that the differential temperature between the center and peripheral surface of each UHPC was lower, leading to a lower internal thermal stress. The total mass losses of HPC and OC were consistently more than those of UHPC when they were subjected to the same temperature and duration of fire. Hence, the fire resistances of UHPC and OC are better than HPC.



### 3. Conclusions

UHPC exhibits very high strength, good toughness and excellent durability. Based on the literature review and discussions above, it can be summarized as follows:

(1) The main principles for UHPC design include reduction in porosity, improvement in microstructure, enhancement in homogeneity and increase in toughness.

(2) The compressive, tensile and flexural strengths of UHPC could reach from 200 to 800 MPa, 25 to 150 MPa and 30 to 141 MPa respectively depending on compositions, production process and curing conditions. Heat curing could increase the compressive strength of UHPC.

(3) The application of heat-curing, incorporation of fibers, and the use of coarse aggregates can decrease the drying shrinkage of UHPC. The permeability coefficient and diffusion coefficient of UHPC are much lower than that of conventional concrete. The 28d carbonation depth of UHPC is very low. The freezing resistance of UHPC is better than that of ordinary concrete and high strength concrete. The fire resistance of UHPC is better than that of ordinary concrete and HPC.

### Acknowledgements

The research was financially supported by National Science Foundation of China under contract Nos. U1305243 and 51378196.

### References

- [1] Richard P, Cheyrezy M. Reactive powder concretes with high ductility and 200-800 MPa compressive strength. *ACI Mater J* 1994; 144 (3): 507-518.
- [2] Richard P, Cheyrezy M. Composition of reactive powder concretes. *Cem Concr Res* 1995; 25(7): 1501-1511.
- [3] De Larrard F, Sedran T. Optimization of ultra-high-performance concrete by the use of a packing model. *Cem Concr Res* 1994; 24(6): 997-1009.
- [4] Buck JJ, McDowell DL, Zhou M. Effect of microstructure on load-carrying and energy-dissipation capacities of UHPC. *Cem Concr Res* 2013; 43: 34-50.
- [5] Spasojevic A. Structural implications of ultra-high performance fiber reinforced concrete in bridge design. *Ph.D. thesis, EPFL*; 2008.
- [6] Habel K, Gauvreau P. Response of ultra-high performance fiber reinforced concrete (UHPRFC) to impact and static loading. *Cem Concr Res* 2008; 30(10): 938-946.
- [7] Rebetrost M, Wight G. Experience and applications of ultra-high performance concrete in Asia. In: Proceedings of the 2nd International Symposium on Ultra-High Performance Concrete. Kassel, Germany: Kassel University Press GmbH. 2008. p. 19-30.
- [8] Feylessoufi A, Crespin M, Dion P, et al. Controlled rate thermal treatment of reactive powder concretes. *Adv Cement Based Mater* 1997; 6(1): 21-27.
- [9] Reda MM, Shrive NG, Gillott JE. Microstructural investigation of innovative UHPC. *Cem Concr Res* 1999; 29(3): 323-329.

- [10] Yunsheng Z, Wei S, Sifeng L, et al. Preparation of C200 green reactive powder concrete and its static-dynamic behaviors. *Cem Concr Compos* 2008; 30(9): 831-838.
- [11] Yoshioka K, Tazawa E, Kawai K, et al. Adsorption characteristics of superplasticizers on cement component minerals. *Cem Concr Res* 2002; 32(10): 1507-1513.
- [12] Golaszewski J, Szwabowski J. Influence of superplasticizers on rheological behaviour of fresh cement mortars. *Cem Concr Res* 2004; 34(2): 235-248.
- [13] Park CK, Noh MH, Park TH. Rheological properties of cementitious materials containing mineral admixtures. *Cem Concr Res* 2005, 35(5): 842-849.
- [14] Sorelli L, Constantinides G, Ulm FJ, et al. The nano-mechanical signature of ultra high performance concrete by statistical nanoindentation techniques. *Cem Concr Res* 2008; 38(12): 1447-1456.
- [15] Reda MM, Shrive NG, Gillott JE. Microstructural investigation of innovative UHPC. *Cem Concr Res* 1999; 29(3): 323-329.
- [16] Shi C. Strength, pore structure and permeability of alkali-activated slag mortars. *Cem Concr Res* 1996; 26(12): 1789-1799.
- [17] Shmidt M, Fehling E. Grundlagen der Betontechnologie von Hochund Ultra Hochleistungs beton und Anwendung von UHPC im Bruckenbau. In: Ultra high performance concrete - 10 years of research and development at the University of Kassal. Kassal, Germany. 2007, p. 70-81.
- [18] Chan YW, Chu SH. Effect of silica fume on steel fiber bond characteristics in reactive powder concrete. *Cem Concr Res* 2004; 34(7): 1167-1172.
- [19] Michael Shmidt, Ekkehard Fehling. Grundlagen der Betontechnologie von Hochund Ultra Hochleistungs beton und Anwendung von UHPC im Bruckenbau. Ultra high performance concrete - 10 years of research and development at the University of Kassal. Kassal, pp. 70-81, 2007.
- [20] Prabha SL, Dattatreya JK, Neelamegam M, et al. Study on Stress-Strain Properties of Reactive Powder Concrete under Uniaxial Compression. *International Journal of Engineering Science and Technology*, 2010; 2(11): 6408-6416.
- [21] Zollo RF. Fiber-reinforced concrete: an overview after 30 years of development. *Cem Concr Compos* 1997, 19(2): 107-122.
- [22] Halit Yazıcı, Mert Y. Yardımcı, Hüseyin Yiğ'iter, Serdar Aydın, Selcuk Türkel. Mechanical properties of reactive powder concrete containing high volumes of ground granulated blast furnace slag. *Cement & Concrete Composites*. 32 (2010): 639-648.
- [23] Su-Tae Kang, Yun Lee, Yon-Dong Park, Jin-Keun Kim. Tensile fracture properties of an Ultra High Performance Fiber Reinforced Concrete (UHPRFC) with steel fiber. *Composite Structures* 92 (2010) 61-71
- [24] Yu R, Spiesz P, Brouwers HJH. Mix design and properties assessment of Ultra-High Performance Fibre Reinforced Concrete (UHPRFC). *Cem Concr Res* 2014; 56: 29-39.
- [25] Van VTA, Ludwig HM. Proportioning Optimization of UHPC Containing Rice Husk Ash and Ground Granulated Blast-furnace Slag. In: *Proceedings of the 3rd International Symposium on UHPC and Nanotechnology for High Performance Construction Materials*. Kassal, Germany, 2012.
- [26] Gong JQ. Study on grading effects of Ultra-high Performance concrete (in Chinese). *PhD thesis, Hunan University, China*, 2007.
- [27] Peng Zhouyan. Study on Composition, Structure and Properties of Reactive powder Concrete Containing Steel Slag powder. *PhD thesis, Wuhan university of technology, China*, 2009.
- [28] Habel K, Viviani M, Denarié E, et al. Development of the mechanical properties of an ultra-high performance fiber reinforced concrete (UHPRFC)[J]. *Cement and Concrete Research*. 2006, 36(7): 1362-1370.
- [29] Zhang YS, Sun W, Liu SF, Jiao CJ, Lai JZ. Preparation of C200 green reactive powder concrete and its static-dynamic behaviors. *Cem Concr Compos* 2008;30:831-8.
- [30] Halit Yazıcı. The effect of curing conditions on compressive strength of ultra high strength concrete with high volume mineral admixtures. *Building and Environment*, 42 (2007): 2083-2089.
- [31] Massidda L, Sanna U, Cocco E, Meloni P. High pressure steam curing of reactive - powder mortars, ACI SP200-27, 2001; 200: 447-64.
- [32] Kang S T, Lee B Y, Kim J, et al. The effect of fibre distribution characteristics on the flexural strength of steel fibre-reinforced ultra high strength concrete[J]. *Construction and Building Materials*. 2011, 25(5): 2450-2457.
- [33] Massidda L, Sanna U, Cocco E, Meloni P. High pressure steam curing of reactive-powder mortars, ACI SP200-27, 2001; 200: 447-64.
- [34] Yazıcı H, Yardımcı MY, Aydın S, Karabulut AS. Mechanical properties of reactive powder concrete containing mineral admixtures under different curing regimes. *Constr Build Mater*

- 2009;23(3):1223–31.
- [35] Wille K, Naaman A E, Parra-Montesinos G J. Ultra-High Performance Concrete with Compressive Strength Exceeding 150 MPa (22 ksi): A Simpler Way.[J]. *ACI Materials Journal*. 2011, 108(1).
- [36] Park S H, Kim D J, Ryu G S, et al. Tensile behavior of ultra high performance hybrid fiber reinforced concrete[J]. *Cement and Concrete Composites*. 2012, 34(2): 172-184.
- [37] Lee M, Wang Y, Chiu C. A preliminary study of reactive powder concrete as a new repair material[J]. *Construction and Building Materials*. 2007, 21(1): 182-189.
- [38] Rong Z, Sun W, Zhang Y. Dynamic compression behavior of ultra-high performance cement based composites[J]. *International Journal of Impact Engineering*. 2010, 37(5): 515-520.
- [39] Zhang J, Li V C. Monotonic and fatigue performance in bending of fiber-reinforced engineered cementitious composite in overlay system[J]. *Cement and Concrete Research*. 2002, 32(3): 415-423.
- [40] Makita T, Brühwiler E. Tensile fatigue behaviour of Ultra-High Performance Fibre Reinforced Concrete combined with steel rebars (R-UHPFRC)[J]. *International Journal of Fatigue*. 2014, 59: 145-152.
- [41] Tao Ji, Cai-Yi Chen, Yi-Zhou Zhuang. Evaluation method for cracking resistant behavior of reactive powder concrete. *Construction and Building Materials*, 28 (2012) : 45–49.
- [42] C.M. Tam, Vivian W.Y. Tam, K.M. Ng. Assessing drying shrinkage and water permeability of reactive powder concrete produced in Hong Kong. *Construction and Building Materials*, 26 (2012) : 79–89.
- [43] Acker P , Behloul M. Ductal Technology: A Large Spect rum of Properties, A Wide Range of Application (C), *Proceedings of the International Symposium on Ultra High Performance Concrete*. Germany, 2004: 11-23.
- [44] V.Y. Garas , K.E. Kurtis , L.F. Kahn. Creep of UHPC in tension and compression: Effect of thermal treatment. *Cement & Concrete Composites*,2012,34,493-502
- [45] Hooton RD, Titherington MP. Chloride resistance of high-performance concretes accelerated curing. *Cem Concr Res* 2004;34:1561–7.
- [46] Liu sifeng, Sun wei, Lin wei, Lai jianzhong. Preparation and durability of a high performance concrete with natural ultra-fine particles (J). *Journal of the Chinese ceramic society*. 2003, 11, 31, 11: 1080~1085.
- [47] Ming-Gin Lee, Yung-Chih Wang, Chui-Te Chiu. A preliminary study of reactive powder concrete as a new repair material. *Construction and Building Materials*, 21(2007): 182–189.
- [48] Chin-Tsung Liu, Jong-Shin Huang. Fire performance of highly flowable reactive powder concrete. *Construction and Building Materials*. 23 (2009): 2072–2079.
- [49] Yuh-Shiou Tai, Huang-Hsing Pan and Ying-Nien Kung. Mechanical properties of steel fiber reinforced reactive powder concrete following exposure to high temperature reaching 800 [J]. *Nuclear Engineering and Design*, 2011, 241: 2416-2424.

# Green road construction using discarded materials: a holistic overview from the Middle East

Ramzi TAHA<sup>1</sup>

*Department of Civil Engineering, Qatar University, Doha, Qatar*

**Abstract.** Various wastes and by-product materials are generated in the Middle East including reclaimed asphalt pavement (RAP) aggregate, demolition concrete, excavation waste, steel and aluminum slags, cement by-pass dust (CBPD), copper slag, petroleum-contaminated soils (PCS), waste tires, incinerator ash, and others. Recycling of such materials for road construction is not practiced. Research data and field studies on the potential use of selected materials in road construction applications are limited. This paper presents an overview of the different waste materials generated in many countries in the Middle East, their potential applications in road construction and the impediments to recycling initiatives. Representative results of several laboratory studies on the use of PCS in asphalt concrete mixtures; the utilization of CBPD in soil stabilization; and the recycling of RAP aggregates in road bases and sub-bases will be presented. The Laboratory data indicated that it is feasible to partially reuse some of these materials in road construction provided that economic incentives and environmental concerns are taken into consideration.

**Keywords.** Recycling, waste, by-products, materials, road, construction

## Introduction

Environmental protection is of great concern in many countries. Environmental regulations are getting more stringent and the tolerance in allowing old techniques of waste disposal in landfills, open dumps, waste piles, etc. is getting narrower. Recycling of certain waste and by-product materials has become a viable option to be considered in road construction. There is a wealth of data available in the literature on the use of by-product materials in various applications [1-12].

Countries in the Middle East are no exception. Population growth and increased infrastructure construction and rehabilitation are generating many waste and by-product materials including food and organic products, glass, plastic, metal, paper and cardboard, construction and demolition waste, cement by-pass dust, petroleum-contaminated soils, oily sludge, wastewater sludge, various slag forms, reclaimed asphalt pavement aggregates, incinerator and bottom ash, and much more. However, only small amounts of such materials are recycled back in road construction.

<sup>1</sup>Corresponding author: [ramzitaha@qu.edu.qa](mailto:ramzitaha@qu.edu.qa)

## 1. Impediments to recycling initiatives

Impediments to recycling materials in the Middle East are many. There are generally limited experiences and studies available concerning the use of such materials as potential substitutes for virgin aggregates, cement, or sand. Economics of recycling may not work well in every country as some countries are rich in mineral and aggregate resources. Also, many countries have no laws or regulations that specifically encourage the reuse of such materials. Furthermore, there are limited standard specifications regarding the use of non-traditional materials such as copper and steel slags, cement by-pass dust, reclaimed asphalt pavement aggregates and others in road construction. Finally, contractors are reluctant to use such materials if there are no incentives to do so or have no prior experience with their performance. Successful recycling of solid and industrial wastes in the Middle East would require comprehensive and detailed economic, environmental and field-based studies. In addition, specifications changes, laws to encourage or mandate recycling, and provision of incentives for reuse are necessary elements to consider in the final analysis.

## 2. Case study from Qatar

Qatar is an arid country located in the Arabian Peninsula. It has an area of 11,571 km<sup>2</sup> with a total population close to 2 million people. Qatar is currently experiencing a massive construction growth including major hotels, roads, bridges, metro, tunnels, etc. However, the country has limited resources of natural aggregates and has to import most of the coarse aggregates (gabbro) from the United Arab Emirates for use in asphalt and concrete. Bitumen is also imported from Bahrain and concrete sand is being depleted at a fast rate.

However, massive amounts of construction and demolition waste (between 60 and 80 million tons) as shown in Figure 1, incinerator bottom ash, steel slag, waste tires, etc. are available in the country.



**Figure 1.** Construction and demolition waste [13].

Recycling of such locally available materials will reduce dependence on imported aggregates resulting in cost savings, the protection of the environment and prevention of unnecessary project delays. Anticipated aggregates' demand in Qatar for the next five years is presented in Figure 2.

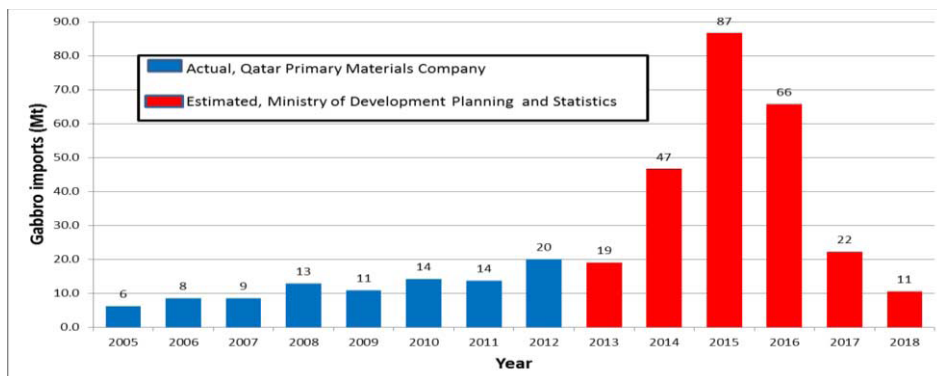


Figure 2. Anticipated aggregates' consumption in Qatar [13].

### 3. Sample laboratory results

The results from several laboratory studies into the use of petroleum-contaminated soils (PCS) in asphalt concrete mixtures; utilization of cement by-pass dust (CBPD) in soil stabilization; and reclaimed asphalt pavement aggregates (RAP) in road bases and sub-bases were presented in the following sections.

#### 3.1. Use of PCS in asphalt concrete

Petroleum-contaminated soils (PCS) consist of natural sands, silts, and clays mixed with petroleum products. In oil-producing countries, PCS are produced as a result of oil spills on clean sand or from the clean-up of oil tanks. For example, in Oman more than 19,000 tons of PCS are generated annually. The present method of treating such materials is land farming. Sludge farms have been provided at Fahud and Marmul oil fields. The objective of this process is to reduce the oil content below 3%. However, land farming is not entirely efficient as this oil content target in the treated soil is not always met.

In this application, PCS were investigated for use as fine aggregates in hot mix asphalt concrete (HMAC) mixtures. Initially, aggregate blending was performed as to meet the Omani specifications for a Class B asphalt concrete wearing course. Figure 3 shows various aggregate blending curves for the three mixtures (0, 10, and 20% PCS) along with the upper and lower limits band requirements for a class B HMAC. The use of up to 20% PCS in the mix did not pose any problems in meeting aggregate blending requirements.

The Marshall mix design method (ASTM D1559) was used in the preparation of HMAC samples. Three samples were prepared for each asphalt content. Tests conducted include bulk specific gravity, Rice specific gravity, stability, and flow.

Parameters calculated include unit weight, percent air voids (AV), percent voids in mineral aggregate (VMA), and percent voids filled with asphalt (VFA). A summary of test results is presented in Table 1. The stability of the control mix (0% PCS) was higher than the 10 and 20% PCS-substituted mixes. However, such mixes still met the minimum stability requirement of 14 kN for a Class B HMAC wearing course. The flow values for the PCS mixes were higher than the control mix but still within the allowable specifications. The VMA for the 20% PCS mix (14.8%) was slightly lower than an allowable minimum specification value of 15%. The optimum asphalt content for the 20% PCS mix was 3.7%, which is lower than the control mix (4.3%). This could result in cost savings per ton of asphalt concrete produced. The mix design data generally indicate that it would be feasible to use petroleum-contaminated soils in asphalt concrete mixtures.

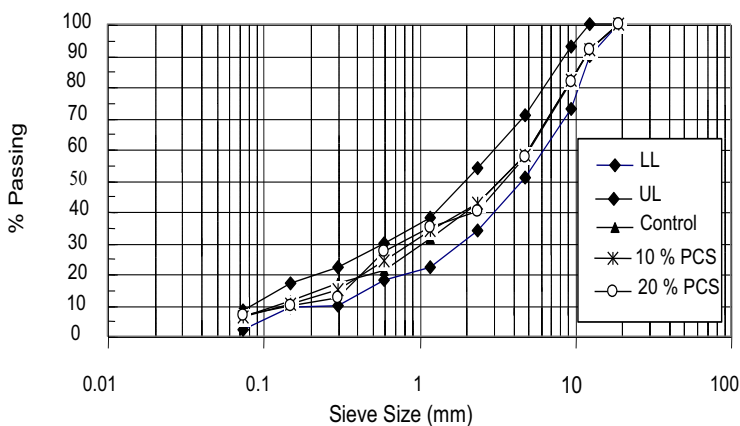


Figure 3. Blending curves for PCS-asphalt concrete mixtures [14].

Table 1. Summary of PCS-asphalt concrete mix design [14].

Asphalt Concrete Property	Allowable Specifications <sup>a</sup>	Control	10% PCS	20% PCS
Density, g/cm <sup>3</sup>	None	2.490	2.480	2.485
Stability, kN	14 (min.)	20.2	18.0	17.0
AV, %	3.5 – 5.5	5.0	4.1	5.0
VMA, %	15 (min.)	15.2	15.5	14.8
VFA, %	63 – 75	67	72	65
Flow, mm	2 – 4	3.1	4.0	4.0
Optimum AC, (%)	3.5 – 5.5	4.3	4.4	3.7

<sup>a</sup>Omani specifications for a Class B asphalt concrete wearing course.

### 3.2. Use of CBPD in soil stabilization

Cement by-pass dust (CBPD) or cement kiln dust is a by-product of the manufacture of Portland cement. It is generated during the calcining process in the kiln. Total lime (CaO) constitutes more than 60% of CBPD composition. Oman Cement Company (OCC) generates about 25,000 to 30,000 tons of CBPD every year. Some CBPD is recycled back with the clinker. However, most of the material is disposed of on-site without any further reuse or reclamation.

In this application, CBPD was investigated for use as a stabilizing material for inorganic silt with high plasticity (MH). The soil is also classified as A-7-6 soil in accordance with the AASHTO classification system (AASHTO M145). The soil consists of 40% gravel and sand, 40% silt, and 20% clay. The soil showed a relatively high plasticity index of 20.4% and a clay activity of 1.03. The soil is also characterized by the presence of high content of montmorillonite clay minerals (~ 43%), high cation exchange capacity (~ 70 meq/100g), high content of sodium cation (~ 41%), and low content of calcium cation (~ 6%).

The soil was stabilized with 0, 3, 6, and 9% CBPD. Mixtures were subjected to the following tests: (1) Atterberg limits, (2) pH, (3) compaction, (4) California Bearing Ratio (CBR), (5) swell percent, and (6) swell pressure. Table 2 presents the pH and Atterberg limits data obtained on the four mixtures. Tests were conducted in accordance with ASTM D4318 (2010). The data indicate that as CBPD content increases, the pH values tend to increase although not significantly. The initial increase in pH from 9.3 (untreated soil) to 10.9 (3% CBPD) is appreciable. This is primarily due to the lime presence in CBPD. The addition of dust to the soil also seems to increase the liquid and plastic limits while the plasticity index tends to decrease. The only exception is the soil stabilized with 3% CBPD where there was an increase in the plasticity index value. This indicates that higher percentages of CBPD would be more beneficial in stabilizing expansive soils. This is probably due to the higher release rate of  $\text{Ca}^{++}$ ,  $\text{Si}^{++}$ , and  $\text{Al}^{+++}$  cations with increased CBPD usage.

**Table 2.** Physical properties of CBPD-stabilized soil mixtures [3].

Mixture	pH	Liquid Limit (%)	Plastic Limit (%)	Plasticity Index (%)
Untreated soil	9.3	49.9	29.5	20.4
3% CBPD	10.9	65.2	37.6	27.6
6% CBPD	11.0	60.4	40.7	19.7
9% CBPD	11.1	56.3	38.9	17.4



Modified Proctor compaction tests (ASTM D1557) were conducted on the four mixtures (Figure 4). Generally, there is a slight decrease in the optimum moisture content and maximum dry density values with the addition of CBPD. A reduction in dry unit weight is generally expected for soil-lime mixtures when compared with untreated soils [15]. CBPD stabilized soil exhibited a similar trend.

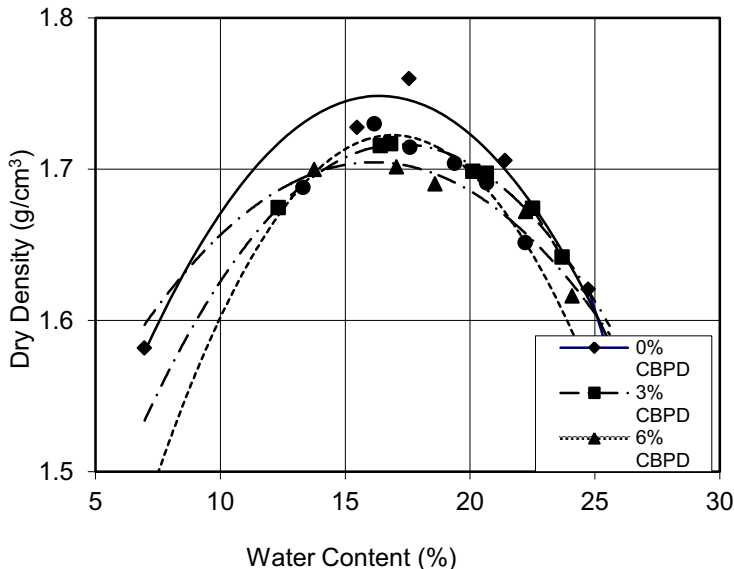


Figure 4. Compaction curves for CBPD-stabilized soil mixtures [3].

The California Bearing Ratio (CBR) test (ASTM D1883) was conducted on the four mixtures. In this test, the CBR of a compacted soil is determined by comparing the penetration load of the tested soil to that of a standard high quality crushed stone rock. A summary of the CBR and swelling results are presented in Table 3. The data indicate that as CBPD content was increased, there was an increase in the CBR and a decrease in swelling.

There is no standard procedure acceptable universally for carrying out swell percent and swell pressure testing. However, the loaded-swell and constant volume methods are commonly referred to for determining swell percent and swell pressure, respectively. Swell percent is a measure of the vertical deformation of a soil sample when its' moisture content increases. Swell pressure is the pressure needed to bring the soil sample back to its' original height after swelling or the pressure needed to keep the sample's volume constant when water is added to it. A summary of the swell percent and swell pressure data is presented in Table 4. The untreated soil exhibited a relatively high swell percent (~ 11.6%). Generally, there is a decrease in swelling as CBPD content is increased. Soil stabilized with 9% CBPD produced the least swelling (a reduction of 65%). This is primarily due to the release of more silica, alumina, and calcium oxide at higher CBPD contents. Also, for the soil sample stabilized with 9% CBPD, the swell pressure value was lower than those soil samples stabilized with 3 and 6% CBPD and significantly lower than the value obtained for the untreated soil.

**Table 3.** California Bearing Ratio test results for CBPD-stabilized soil mixtures [3].

Mixture Type	California Bearing Ratio (%)	Swelling (%)
Untreated soil	0.7	3.8
3% CBPD	4.5	2.3
6% CBPD	10.9	0.2
9% CBPD	13.1	0.1

**Table 4.** Swelling potential test results for CBPD-stabilized soil mixtures [3].

Mixture	Swell Percent	Total Swell Pressure (kPa)
Untreated soil	11.6	249.0
3% CBPD	5.1	259.2
6% CBPD	6.9	261.6
9% CBPD	4.1	202.3

### 3.3. Use of RAP aggregates in road bases and sub-bases

Reclaimed asphalt pavement (RAP) is a bituminous pavement that have been recovered, usually by milling, and used in part or as a whole in a new pavement by mixing it with other virgin aggregate or asphalt, cement, lime, or other materials. Recycling of RAP in Qatar and neighboring countries could be become economically attractive because of aggregate shortage in certain regions and because of major road rehabilitation, which would provide the RAP aggregate for reuse.

In this application, RAP and virgin aggregate blends were evaluated for use as road base and sub-base materials for highway construction. Sieve analyses were performed on RAP and virgin aggregates in accordance with AASHTO T27. Testing showed that RAP was classified as well-graded gravel (GW), whereas virgin aggregate was a mixture of well-graded sands and gravelly sands with little or no fines (SW). Both RAP and virgin aggregates were essentially non-plastic. Table 5 presents a summary of the moisture content, specific gravity, water absorption, sand equivalent, and toughness data obtained on both materials.

**Table 5.** Physical properties of RAP and virgin aggregates [14].

Property	RAP	Virgin Aggregate
Moisture Content (%)	0.23	0.86
Specific Gravity (SSD)	2.12	---
Water Absorption (%)	1.0	---
Sand Equivalent (%)	97	67
Los Angeles Abrasion (%)	33.6	18.8

Various blends were prepared using 100/0, 80/20, 60/40, 20/80, and 0/100 percent RAP to virgin aggregates. Compaction testing was performed by the modified Proctor testing procedure (AASHTO T180). The relationships between dry density and moisture content for all mixes were presented in Figure 5. As more RAP aggregate is added to a blend, the maximum dry density tends to decrease. The maximum dry density of 100% RAP aggregate was about 83% of the maximum density of 100% virgin aggregate.

California Bearing Ratio (CBR) testing was also conducted on the above blends. The objective of this test is to determine the bearing value of soils and soil-aggregate mixtures when they are compacted in the laboratory at their optimum moisture contents. The test was performed in accordance with AASHTO T193. However, the test was conducted on unsoaked specimens and CBR values were calculated based on the standard virgin aggregate used in the testing program. CBR values obtained on all blends are presented in Figure 6. A low CBR value of 11% was determined for 100% RAP aggregate. As the percentage of virgin aggregate in the mix increases, the CBR value increases. When 20% virgin aggregate is added to RAP, the CBR value increases to 26%. Possible reasons for this increase in CBR may be due to better load transfer among between particles of the virgin aggregate and the slip surfaces developed between the asphalt-coated particles of the RAP. Furthermore, as virgin aggregate content in the blend increases, better interlocking between aggregate particles will develop. This leads to further increases in the shear strength of the blend.

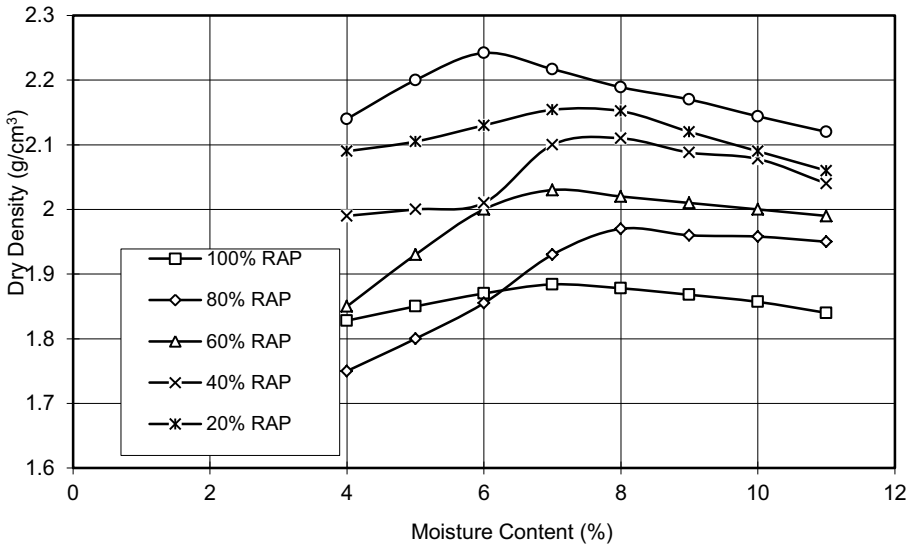
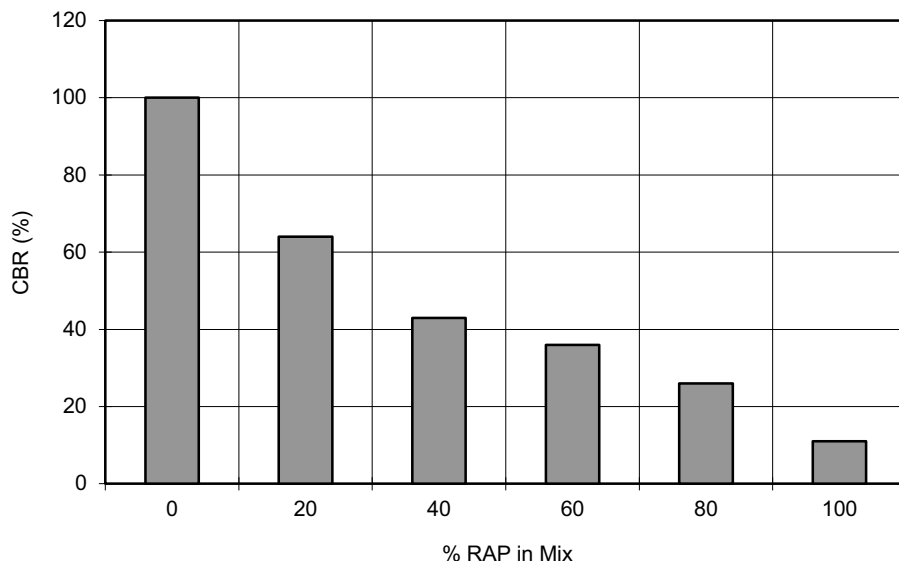


Figure 5. Compaction curves for various RAP/virgin aggregates mixtures [14].



**Figure 6.** California Bearing Ratio (CBR) test results for various RAP/virgin aggregates mixtures [14].

#### 4. Conclusions

There are various types of waste and by-product materials generated in the Middle East. Many of these materials are not efficiently used in road construction because of the absence of aggressive governmental regulations and policies to mandate the reuse of such materials. However, there are promising signs that changes are forthcoming in many Middle Eastern countries whereby many of the discarded materials such as demolition waste, slags, reclaimed asphalt pavement aggregates and others will find their way into the road construction industry.

#### References

- [1] Al-Amoudi, O.B., Maslehuddin, M. and Asi, I.M. *Performance and Correlation of the Properties of Fly Ash Cement Concrete*. Cement, Concrete and Aggregate Journal, CCAGDP, Vol. 18, No. 2, ASTM International, 1996.
- [2] Al-Harthy, A. and Taha, R.A. *Effect of Cement By-Pass Dust on Fresh and Engineering Properties of Concrete*. Proceedings of the International Conference on "Challenges of Concrete Construction," Dundee, Scotland, UK, September, 2002.
- [3] Al-Rawas, A., Taha, R.A., Nelson, J.D., Al-Shab, T.B. and Al-Siyabi, H. *A Comparative Evaluation of Various Additives Used in the Stabilization of Expansive Clays*. Geotechnical Testing Journal, GTJODJ, Vol. 25, No. 2, ASTM International, June, 2002.
- [4] Garg, N. and Thompson, M.R. *Lincoln Avenue Reclaimed Asphalt Pavement Base Project*. Transportation Research Record 1547, TRB, National Research Council, Washington, D.C., 1996.
- [5] Konsta-Gdoutos, M.S., Shah, S.P. and Battacharja, S. *Development and Performance of Cement Kiln Dust-Slag Cement*. Proceedings of the International Conference on "Challenges of Concrete Construction," Dundee, Scotland, UK, September, 2002.

- [6] Lin, C. and Zhang, X. *Use of Cement Kiln Dust, Fly Ash, and Recycling Technique in Low-Volume Road Rehabilitation*. Transportation Research Record 1345, TRB, National Research Council, Washington, D.C., 1992.
- [7] Maher, M.H. and Popp, Jr. W. *Recycled Asphalt Pavement as Base and Sub-base Material*. ASTM STP 1275, American Society of Testing and Materials, New Orleans, Louisiana, 1997.
- [8] Meegoda, J.N. and Muller, R.T. *Petroleum Contaminated Soils in Highway Construction*. Proceedings of the U.S. Federal Highway Administration Symposium on "Recovery and Effective Reuse of Discarded Materials and By-Products for Construction of Highway Facilities," Denver, Colorado, USA, October, 1993.
- [9] Rivard-Lentz, D.J., Sweeney, L.R. and Demars, K. *Incinerator Bottom Ash as a Soil Substitute: Physical and Chemical Behavior*. Proceedings of the Symposium on Testing Soil Mixed with Waste or Recycled Materials, ASTM STP 1275, New Orleans, Louisiana, USA, September, 1997.
- [10] Taha, R.A., Delwar, M., Ali, G., Al-Harthy, A. and Al-Oraimi, S. *Use of Municipal Solid Waste Incinerator Ash in Portland Cement Concrete*. Proceedings of the 4<sup>th</sup> International Symposium on Environmental Geotechnology and Global Sustainable Development, Vol. 1, Boston, Massachusetts, USA, August, 2000.
- [11] Taha, R.A., Ba-Omar, M., Pillay, A.E., Ross, G. and Al-Hamdi, A. *Recycling of Petroleum-Contaminated Sand*. Journal of Environmental Monitoring, JEM, Vol. 3, Issue 4, August, 2001.
- [12] Taha, R.A., Al-Harthy, A., Al-Shamsi, K. and Al-Zubeidi, M. *Cement Stabilization of Reclaimed Asphalt Pavement Aggregate for Road Bases and Sub-bases*. Journal of Materials in Civil Engineering, Vol. 14, No. 3, American Society of Civil Engineers, ASCE, May/June, 2002.
- [13] Hassan, K. *Workshop on the Use of Construction Waste in Buildings, Roads, Infrastructure and Construction Industries in Qatar*. Doha, Qatar, November, 2013.
- [14] Taha, R.A., Al-Rawas, A., Al-Jabri, K., Al-Harthy, A., Hassan, H. and Al-Oraimi, S. *An Overview of Waste Materials Recycling in the Sultanate of Oman*. Resources, Conservation and Recycling Journal, RCR, Vol. 41, Issue 4, pp. 293-306, 2004.
- [15] Little, D.N., Thompson, M.R., Terrell, R.L., Epps, J.A. and Barenberg, E.J. *Soil Stabilization for Roadways and Airfields*. Final Report, ESL-TR-86-19, Engineering and Services Laboratory, Air Force Engineering and Services Center, Florida, 1987.

# 1. Materials and characterisation

This page intentionally left blank

# Cementitious materials and concrete



This page intentionally left blank

# Structural and mechanical characterization of high alumina additivated cement based on high refractory mineralogical compounds

Nicolae ANGELESCU<sup>a,1</sup>, Cristina STANCU<sup>b</sup> and Vasile BRATU<sup>a</sup>

<sup>a</sup>VALAHIA Univ of Targoviste, 2 Carol I Blvd., Code 130024, Targoviste, Romania

<sup>b</sup>S.C. CEPROCIM S.A., 6 Preciziei Blvd., Code 062203, Sect. 6, Bucharest, Romania

**Abstract.** High alumina cements are widely used in refractory industry, mainly for the manufacture of refractory concrete. It is known fact that from the components of refractory concrete, high alumina cement is the fondant component of the system due to the lower melting point of the mineralogical compounds contained, compare to the refractory aggregates used. To improve the behaviour at high temperature of high alumina cement, we will try to obtain high alumina cements based on calcium-aluminates compounds with higher refractory toward the usual high alumina cement based on monocalcium monoaluminate and dicalcium monoaluminate. However, because with the improvement of refractoriness of calcium-aluminates compounds form high alumina cement, the hydraulically properties decrees, we will try to increase the hydraulically properties with an accelerator additive, such as calcium sulphoaluminate. This paper aims to present the structural and mechanical behaviour of high alumina additivated cement based on high mineralogical refractory compounds such as dicalcium monoaluminate and monocalcium hexa aluminate in comparison with the usual high alumina cement, at normal temperature and after treatment at high temperature heat, too.

**Keywords.** High alumina cement, monocalcium monoaluminate, dicalcium monoaluminate, monocalcium hexa aluminate, accelerators admixtures.

## Introduction

The binder matrix of hard refractory concrete is developed by the hydration of the main mineralogical constituents of high alumina cement [monocalcium monoaluminate (CA) and monocalcium dialuminate (CA<sub>2</sub>) with embedding of the fine aggregates and specific additions [1].

To make refractory concrete with high pyroscopic strength, is important to choose very carefully the binder matrix and the specific aggregates.

A less inspired choice of a lower refractory binder matrix will adversely affect the final properties of refractory concrete, even if it was used in making concrete some aggregates with high pyroscopic resistant. This is due to the fact that in the refractory concrete the binder matrix is the component with lower refractoriness.

---

<sup>1</sup>Corresponding author: [nicolae.angelescu@yahoo.com](mailto:nicolae.angelescu@yahoo.com)

For this fact to achieve a refractory concrete that can be used at very high temperature, it must be use high refractory hydraulic binders such as high alumina cement with a content of alumina  $\geq 70\%$ . An alternative technological option that can have the same result, and which it is the aim of this paper, is to design a binder matrix whose value of molar ratio  $\text{Al}_2\text{O}_3/\text{CaO}$  is higher than the one corresponding to monocalcium dialuminate [1, 2]. The types of binder matrix (high alumina cements) used in these papers are base on monocalcium hexaluminate ( $\text{CA}_6$ ) and monocalcium dialuminate ( $\text{CA}_2$ ), or only on monocalcium dialuminate ( $\text{CA}_2$ ). But once the value of molar ratio  $\text{Al}_2\text{O}_3/\text{CaO}$  increase the interaction with water of the mineralogical compounds decrease, and with it the mechanical properties are lower. To counteract this deficiency it can be use some additive with acceleratory properties.

From the great variety of high alumina cement accelerators the authors chose one to improve the physical and mechanical properties at room temperature and which did not affected refractoriness. This accelerator was calcium sulfoaluminate [3, 4].

## 1. Materials characterization

The raw materials used in the present works were:

- reactive alumina ( $\text{Al}_2\text{O}_3$  content = 99.50%) and calcium carbonate ( $\text{CaCO}_3$  content = 99.70%) for prepared the high alumina cements based on  $\text{CA}_6$  and  $\text{CA}_2$ , or based only on  $\text{CA}_2$ ;
- reactive alumina ( $\text{Al}_2\text{O}_3$  content = 99.50%), calcium carbonate ( $\text{CaCO}_3$  content = 99.70%) and dehydrate calcium sulphate ( $\text{CaSO}_4 \cdot 2\text{H}_2\text{O}$  content = 99.98%) for the calcium sulfoaluminate obtaining.

From on the  $\text{CaO}-\text{Al}_2\text{O}_3$  binary system we choose the composition of mixtures of raw materials and heat treatment temperatures for the specific high alumina cements based on  $\text{CA}_2$  and  $\text{CA}_6$  and respectively based on  $\text{CA}_2$ , see Figure 1.

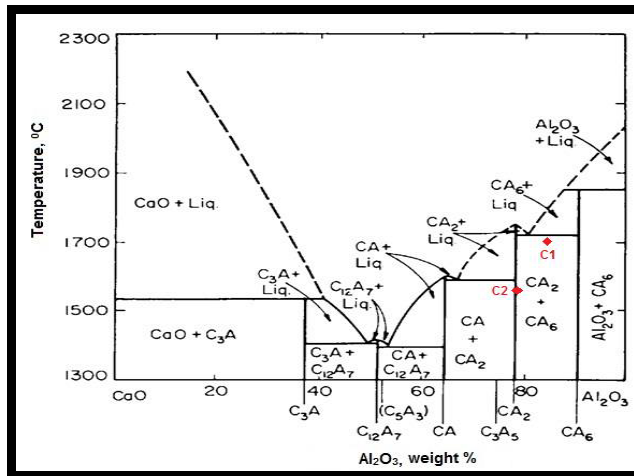


Figure 1. Phase diagram of  $\text{CaO}-\text{Al}_2\text{O}_3$  system.

The point noted in Figure 1 by C1 corresponds to the mineralogical composition of high aluminous cement based on  $\text{CA}_2$  and  $\text{CA}_6$ . The C2 point corresponds to the

mineralogical composition of high aluminous cement based on  $CA_2$ . Regarding the location of industrially high aluminous cement composition, it is known only the fact that it can be located in CA and  $CA_2$  subsystem [5].

For obtaining calcium sulphoaluminate the mixture of raw materials was intimately mixed, pressed using a uniaxial press and subjected to heat treatment at a temperature of 1250°C.

For characterization of the high alumina cement were used the chemical analysis and the X-ray diffraction.

Chemical analysis of high alumina cement samples reveals content in  $Al_2O_3$  that exceeds 70% (Table 1). This high alumina content will influence favourably the refractoriness. In the same time, the absence of free CaO from the high alumina cement compositions makes them ideal for using in the refractory domain.

**Table 1.** Oxide composition of high alumina cements

Cement type	$Al_2O_3$ [%]	CaO [%]	$SiO_2$ [%]	$Fe_2O_3$ [%]	Alkalis [%]	$SO_3$ [%]	MgO [%]	CaO <sub>free</sub> [%]
$CA_6+CA_2$	85.33	14.24	0.15	0.12	0.03	0.00	0.13	0.00
$CA_2$	77.60	22.20	0.10	0.09	0.02	0.00	0.08	0.00

X-ray diffraction spectrum (Table 2) obtained for high alumina cement revealed the characteristic diffraction lines of specific mineralogical components:

- $CA_2$ ,  $CA_6$  and  $\alpha-Al_2O_3$  in the spectrum of high alumina cement based on  $CA_2$  and  $CA_6$ ;
- $CA_2$ ,  $\alpha-Al_2O_3$  and CA in the spectrum of high alumina cement based  $CA_2$ .

**Table 2.** Diffraction lines of specific mineralogical compounds from high alumina cements

Cement type	Calcium alumina compounds			
	$CA_6$	$CA_2$	CA	A
$CA_6+CA_2$	+++	+++	-	+
$CA_2$	-	+++	+	+

## 2. Results and discussions

The high alumina cements based on high refractory compound were characterized in parallel with the sample with additive. The percent in which the additive (calcium sulphoaluminate -  $C_4A_3\check{S}$ ) was added to the cement was 5%.

Blaine specific surface area values are typical for high alumina cements based on high alumina mineralogical compounds, exceeding 3000  $cm^2/g$  [6]. In the case of sintered cements (the sample without additive) we tried to grind the clinkers at a specific surface area as close as possible so the amounts of water content of standard consistency to be equal.

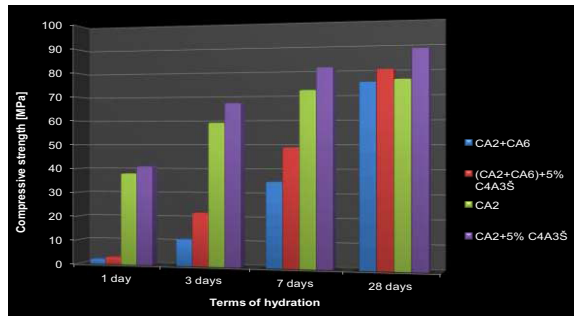
For a better understating of the properties of the new high alumina cements, the results obtained after the physical and mechanical characterisation will be presented versus the ones obtained on the same cements but with 5% additive. Regarding the water content for standard consistency for the high alumina cements types studied in this paper is correlated with specific surface area (Table 3) and complies with the recommended values (see [4, 6, 7]). Setting time of high alumina cements is related with the mineralogical composition, i.e. setting time increases as increases the amount of less basic mineralogical compounds. As it was anticipated from the moment of choosing the compositions of sintered alumina cement based on  $CA_2$  and  $CA_6$ , the

initial setting time and final setting time are much longer than those of high alumina cement based on  $CA_2$  that has a higher basicity.

**Table 3.** Physical properties of high alumina cements

Cement type	Water content for standard consistency [%]	Setting time [min.]	
		initial	final
$CA_2+CA_6$	28.0	415	1200
$(CA_2+CA_6)+5\% C_4A_3\check{S}$	28.0	150	240
$CA_2$	28.0	320	960
$CA_2+5\% C_4A_3\check{S}$	28.0	120	150

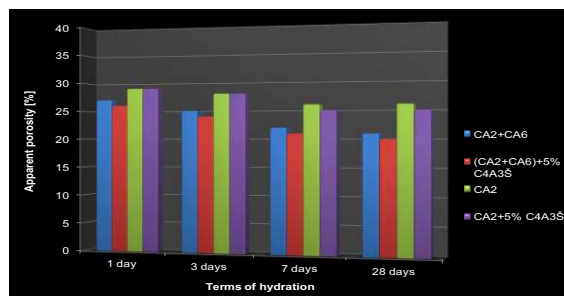
With the addition of 5%  $C_4A_3\check{S}$  the initial and final setting times of high alumina cement whit additive were significantly shortened. The initial setting time was reduced by approx. 63% - 64% and final setting time was reduced by approx. 84% for both high alumina cements with additive versus the samples without additives. The characterization of the high alumina cements with and without additive took place after to exposure at the elevated temperature. Temperatures selected for exposure were: 110<sup>0</sup>C, 600<sup>0</sup>C, 800<sup>0</sup>C, 1000<sup>0</sup>C, 1200<sup>0</sup>C, 1400<sup>0</sup>C and 1600<sup>0</sup>C, to understand the behaviour of cements both start-up and during actual use. The structural properties (compressive strength and apparent porosity) at normal temperature after different periods of time are presented in Figures 2 and 3.



**Figure 2.** The compressive strength of high alumina cements at different terms of hydration.

Like it can be seen from the Figure 2 the compressive strength obtained for high alumina cement based on  $CA_2$  and  $CA_6$  present higher growth at 7 days, compared with developed one of cement based on  $CA_2$  that present significant values since 1 day. One should be noted that the values reported for high alumina cement based on  $CA_2$  and  $CA_6$  were anticipated from the moment of choosing mineralogical composition. However, the supposed strength at high temperature is to be aimed with the improved characteristics at room temperature, especially at long hydration time (28 days).

In the case of high alumina cements with 5%  $C_4A_3\check{S}$  the values of the compressive strength, at the same period of hydration, were better toward the cements without additive, and that because the interaction with water of the mineralogical compounds intensified due to the percent of 5%  $C_4A_3\check{S}$ . Like it can be seen from the Figure 3 the values of the apparent porosity were better (are decreasing) with the time pass, especially at 28 days. The best behaviour is reported for the cement based on  $CA_2$  and  $CA_6$  and especially when was added the additive, toward the cement based on  $CA_2$ . This phenomenon may be can be put on the fact that the cement based  $CA_2$  shows a higher reactivity to water, which lead to a higher porosity even at short terms of hydration.

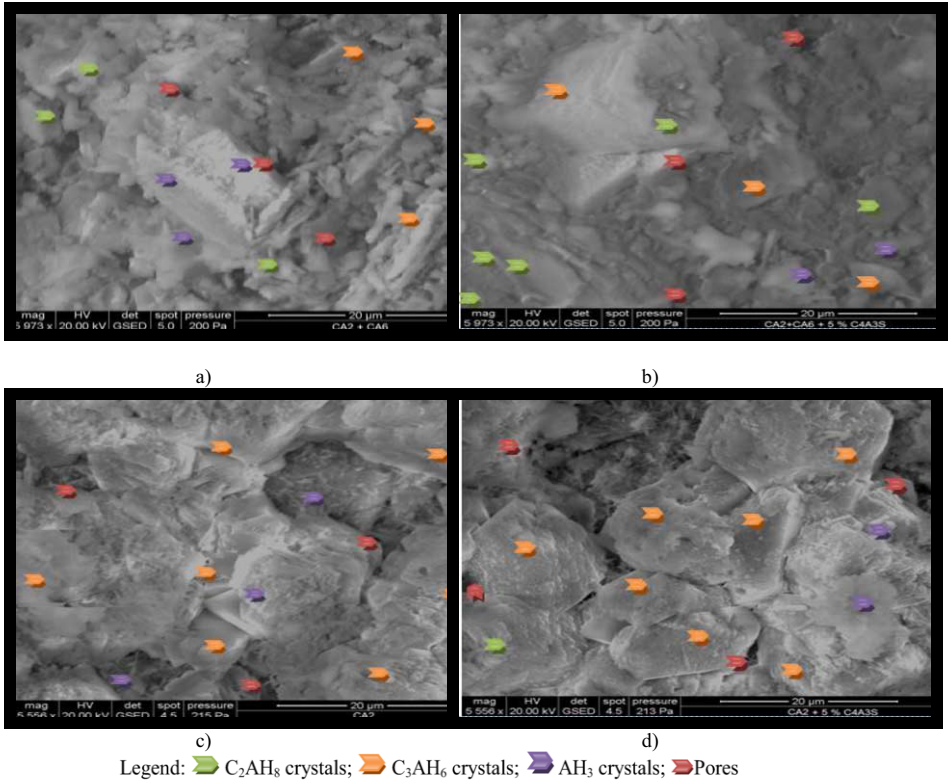


**Figure 3.** The apparent porosity of high alumina cements at different terms of hydration

Regarding the samples in which were added additive, the best porosity values were obtained especially at longer hydration terms compared with those of samples without additives, its can be explained by the fact that present of additive led to greater amounts of mineralogical compounds which filled pores in the hydrated cement paste obtained after compaction or interaction with water in the initial stages [4].

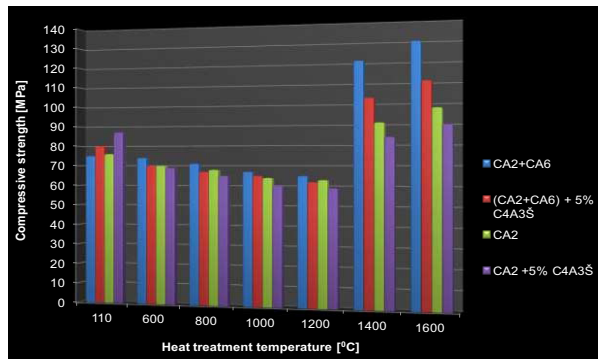
The high values of the compressive strength and apparent porosity obtained in the case of additivated cements are sustained by the electron micrographs made after the samples were hydrated 28 days in water at 20<sup>0</sup>C, Figure 4. It can be seen from the Figure 4 b) and d) that samples with 5% C<sub>4</sub>A<sub>3</sub>S presented bigger and better contoured crystals, the structure was better densified with pores with smaller size toward the cements without additive. The compressive strength and apparent porosity values of high alumina cements (see Figures 5 and 6) showed a strong influence to the temperature treatment at which they were exposed. All high alumina cements showed a decrease in compressive strength and an increase in apparent porosity in the temperature range 110<sup>0</sup>C - (1000<sup>0</sup>C) 1200<sup>0</sup>C, due to structural reorganization that occurs in the critical temperature range. Instead in the range 1000<sup>0</sup>C (1200<sup>0</sup>C) - 1600<sup>0</sup>C, the values of compressive strength, Figure 5, are improved, while the apparent porosity, Figure 6, were lower than those recorded in the critical temperature range, this being due to the formation of ceramic binding between mineralogical compounds present at high temperature. Concerning the samples with additive, the compressive strength was found to be lower than those register for the sample without additive. This fact was explained by the stronger hydration of the samples with additive and the additive behaviour at high temperature.

The apparent porosity values of high alumina cement based on CA<sub>2</sub> and CA<sub>6</sub> with additive at all heat treatment temperatures were very close to those of the sample without additive. In the case of high alumina cement based on CA<sub>2</sub>, the apparent porosity values were approx. 12% lower than those recorded on samples without additive, in the whole temperature range. The high values of the compressive strength and lower values of the apparent porosity obtained in the case of cements without additive, especially by the sample based on CA<sub>2</sub> and CA<sub>6</sub>, are sustained by the electron micrographs made after the samples were exposed at 1600<sup>0</sup>C, Figure 7. The better compoment of the sample based on CA<sub>2</sub> and CA<sub>6</sub> at high temperature is due the fact that this sample contains a component that present a very good refractoriness, this were CA<sub>6</sub>. It can be seen from the Figure 7 a) and c) that samples without additive present bigger and better contoured crystals, the structure was better densified, the pores were smaller in size toward the cements without additive.



**Figure 4.** The electron micrographs of high alumina cements based on: a) CA<sub>2</sub> and CA<sub>6</sub>, without additive; b) CA<sub>2</sub> and CA<sub>6</sub>, with 5% C<sub>4</sub>A<sub>3</sub>S additive; c) CA<sub>2</sub>, without additive; d) CA<sub>2</sub>, with 5% C<sub>4</sub>A<sub>3</sub>S additive hydrated 28 days in water at 20°C

The smaller crystals and the low densification of the samples observed in the case of cements with additive, Figure 7 b) and d), were due to the fact that those samples contain a component (the additive) with a low refractoriness.



**Figure 5.** The compressive strength of high alumina cements heat treated after 28 days of strength and dried at 110°C

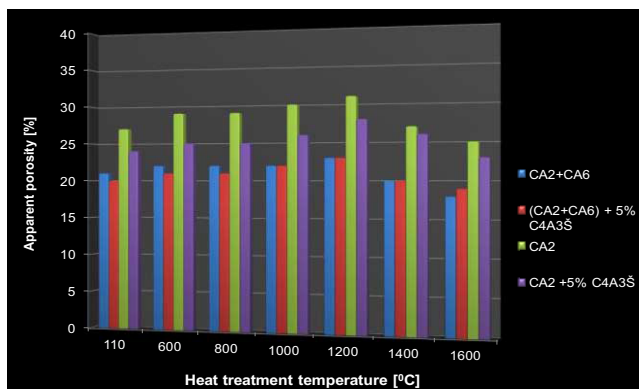


Figure 6. The apparent porosity of high alumina cements heat treated after 28 days of strength and dried at 110°C

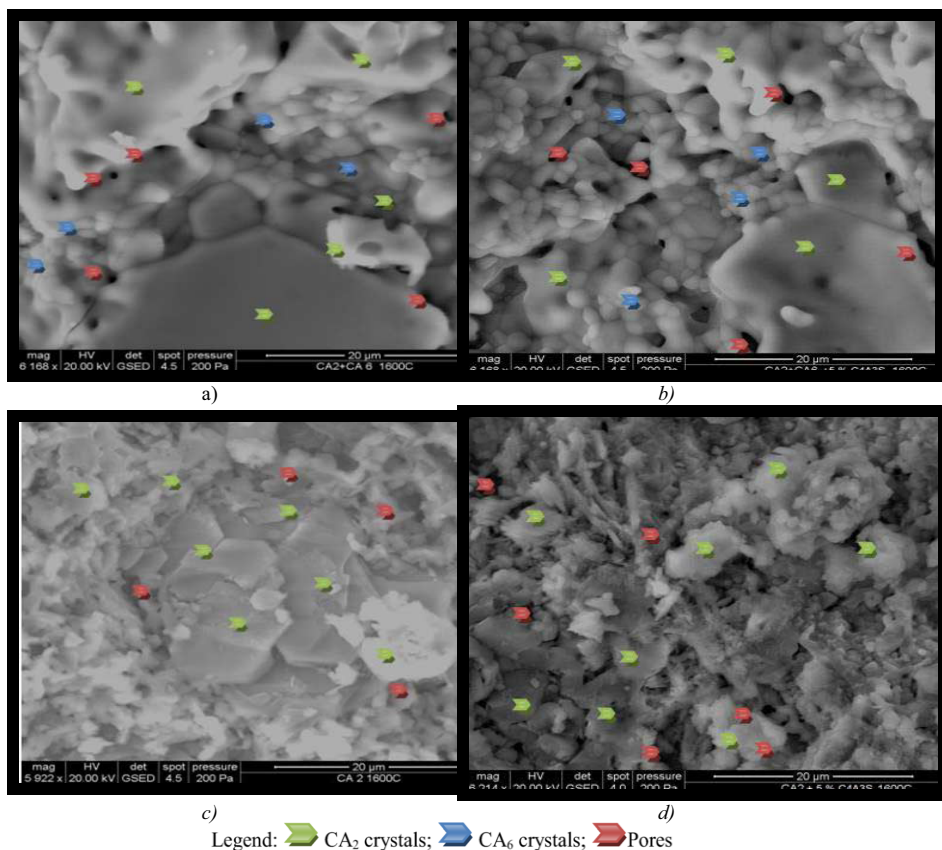


Figure 7. Electron micrographs of the high alumina cements based on: a) CA<sub>2</sub> and CA<sub>6</sub>, without additive; b) CA<sub>2</sub> and CA<sub>6</sub>, with 5% C<sub>4</sub>A<sub>3</sub>S additive; c) CA<sub>2</sub>, without additive; d) CA<sub>2</sub>, with 5% C<sub>4</sub>A<sub>3</sub>S additive after the exposure at 1600°C



### 3. Conclusions

The investigations made on the high alumina cement studied in this paper based on the two mineralogical compounds with the best refractoriness from the  $\text{Al}_2\text{O}_3$ -CaO system let us to the following conclusions:

- Samples of high alumina cement containing the mineralogical compounds with high refractoriness didn't presented a very structural and mechanical behaviour at short interval of hidratation, especially when the  $\text{CA}_6$  was presented in the samples. This was due to the fact that  $\text{CA}_6$  need a long period of time to interact with water;
- Using an accelerator additive lead to improved structural and mechanical behaviour at short period of hidratation of high alumina cements based on highly refractory mineralogical compounds, maintaining in the same time the good behaviour at high temperature.
- Samples of high alumina cement containing the mineralogical compounds such as  $\text{CA}_2$  and  $\text{CA}_6$  present a very good structural and mechanical behaviour at high temperature then those based only on  $\text{CA}_2$ .

### References

- [1] N. Angelescu, C. Ionita, Calcium hexa aluminate as possible mineralogical compound in alumina cements, *Metallurgy and New Materials Researches* **19** (2011), Special Bramat No, ISSN 1221 - 5503, 11-13;
- [2] I. Teoreanu, N. Ciocca, *Lianti, mase si betoane refractare* (Binders, refractory masses and concrete - in Romanian), Ed. Tehnica, Bucharest, 1977.
- [3] M. Muntean, A. Ionescu, I. Ropota, O. Muntean, Hydration of calcium aluminates in the presence of yeelenite, *Proceeding of the Centenary Conference of Calcium Aluminate Cements*, Avignon, France, 30 June-2 July 2008, HIS BRE Press (2008), 429-434.
- [4] C. Ionita (Stancu), *Doctorate Thesis*, Valahia University Targoviste, 2013.
- [5] C. Stancu, N. Angelescu, H. Abdelgader, V. Bratu, D. Stanciu, I. Ion, The influence of hydration on the mechanical strength of the high aluminous cement, *Advances in Cement and Concrete Technology in Africa - ACCTA 2013*, Johannesburg, South Africa (2013), 961 – 968.
- [6] P. Hewlett, *Lea's Chemistry of Cement and Concrete 4th edition*, Elsevier Science & Technology Books, 2002.
- [7] M. A. Taher, H. W. Chandlert, A. Anderson, Factors influencing consistency of strength of high alumina cement, *Construction and Building Materials*, **10** (7) (1996), 491-500.

# Investigation on the suitability of borrow pit sand as fine aggregate for structural concrete

Amadou ADAMOU<sup>1</sup> and Munachi U. NNEBE

*Department of Civil Engineering, University of Nigeria Nsukka, Nigeria*

**Abstract:** This paper investigated the suitability of the use of borrow pit sand locally known as Obimo sand in structural concrete. The physical properties of the unwashed Obimo sand (UOS) and the washed Obimo sand (WOS) were first investigated and compared to those of the conventional river sand (RS). Concrete cubes made from the three samples (UOS, WOS and RS) were crushed for their compressive strength. It was found out that the specimens fall within the acceptable limits of fine aggregates for structural concrete works given in both IS: 383 – 1970 and BS 882: 1973. The chemical composition obtained by elemental analysis using X-ray fluorescence spectrometry proved Obimo sand samples free of sulfate and saline contents. Also the concrete made from the WOS gave 6.5% more strength than that made from RS at 28 days age, while the UOS produced a concrete of slightly lower compressive strength. Specifically, the compressive strength ranged from 29.5 to 33 N/mm<sup>2</sup> for the alternative Obimo sand. Conclusively, a cost analysis carried out showed a reduction of 1.42% and 0.43% for the WOS and UOS concretes respectively when compared to that of RS.

**Keywords.** Concrete, Obimo sand, physical properties, compressive strength

## Introduction

Aggregates have a significant influence on both rheological and mechanical properties of mortars and concrete. Their specific gravity, particle size distribution, shape and surface texture influence markedly the properties of concrete in the fresh state. On the other hand, the mineralogical composition, toughness, elastic modulus and degree of alteration of aggregates are generally found to affect the properties of concrete in the hardened state [1]. River sand is the most commonly used fine aggregate in the production of concrete and this poses the problem of its acute shortage in many areas. Its continuous use has started posing serious problems with respect to availability, cost and environmental impact [2]. To overcome the stress and demand for river sand, researchers and builders in the construction industries have identified some alternatives namely laterite, quarry dust, limestone powder and siliceous stone powder [3]. A lot of attempts have been made to provide local alternatives to the use of conventional river sand as fine aggregate in concrete. There has been an increase in the use of local lateritic sand referred to as “sharp-sharp” sand by building construction industries in some areas in southern Nigeria.

<sup>1</sup>Corresponding author: [adamou.amadou@unn.edu.ng](mailto:adamou.amadou@unn.edu.ng)

The sand usually gotten from borrow pits around the areas is used in block molding and concrete works. The practice has continued, despite the surge of building collapses in some major cities of the country. Research efforts are directed towards enhancing the use of locally and readily available fine aggregates such as lateritic soils and quarry dust [4].

Ilangovan and Nagamani [2] reported that Natural Sand with Quarry Dust as full replacement in concrete is possible with proper treatment of Quarry Dust before utilization. The utilization of Quarry rock dust which can be called as manufactured sand has been accepted as a building material in the industrially advanced countries of the west for the past three decades [5]. Recent developments in the building construction industry in Nsukka, southern Nigeria and its environs, have witnessed an increased use of local lateritic sand and generally sand from borrow pits at Obimo, Mkpologwu and Ama-Oshabe for block molding and concrete works in construction of low-cost buildings, farm structures and other rural infrastructures. Some builders combine the sandy laterite with quarry dust and this practice has continued without any reliable data on the structural integrity of the resulting structures. This is worrisome given the spate of building collapses in some major cities of the country.

The knowledge of structural characteristics of fine aggregates and performance of concrete made with these materials is necessary for the accurate design of structural elements in buildings and bridges. Compressive strength is arguably the most widely used strength parameter for concrete [6].

The objective of the study is to investigate Obimo sand as complete replacement of river sand for structural concrete in terms of its physical properties, chemical properties and the structural behavior of concrete made with it.

## **1. Materials and method**

### *1.1 sources of materials*

The Obimo sand used for this investigation was obtained from a borrow-pit in Obimo, a town in Nsukka area of Enugu State. The DANGOTE brand cement used in this work was purchased in Nsukka and taken to the laboratory in sealed 50 kg bags. The cement was well protected from dampness to avoid lumps and its properties conform to BS 12 part 2 of 1970 [7]. The coarse aggregate was obtained from piles of natural earth gravel and transported to the laboratory. Portable water directly from the tap was obtained in the materials laboratory of the Department of Civil Engineering, University of Nigeria Nsukka.

### *1.2 sample preparation*

The coarse aggregate was passed through sets of sieves, the portion passing through sieve (19.05 mm) and retained on sieve (4.75 mm) was used. The water used complied with BS 5328 [8]. The concrete samples used for the compressive strength test were 100 mm cubes. The tests were carried out at the materials laboratory of the University of Nigeria, Nsukka. The materials were air dried in the laboratory. Sieve analysis was carried out on the sands. The samples used for the study were those passing sieve (4.75 mm) and retained on sieve (150  $\mu\text{m}$ ). The Obimo sand used was separated into two

portions: one portion was washed to remove any organic material that may be deleterious to concrete produced while the other was used as obtained from the borrow pit to accommodate the effect of organic matter (if present). The Physical properties of both the washed and unwashed specimens were investigated by obtaining the particle size distribution, moisture content and specific gravity. The results were compared to that of conventional river sand. Chemical composition of the Obimo sand specimen was determined based on Elemental Analysis using the X-Ray fluorescence spectrometry carried out at the National Geosciences Research Laboratory (NGRL), Kaduna. All tests were conducted according to the relevant British Standard (e.g. BS 1881 [9]). The materials were specified according to BS 882 [10], BS 5328 [8], and BS 8110 [11].

### *1.3 Batching and mixing*

The pre-determined concrete mix proportion of 1:2:4, which is used for general reinforced concrete work, was used for this report [12]. Water-cement ratio of 0.6 was used for this mix proportion. Batching was by weight using Avery weighing scale. Same mixtures of cement, fine aggregate soil and gravel were prepared and “worked” manually using shovel to stir. The working process involved the gradual addition of predetermined quantity of water to the mixtures already obtained and a continuous stirring with a shovel until a homogeneous mix was obtained. Mix proportion was first generated “on paper” as a starting point which was used to prepare trial batches required to verify proportions. The freshly mixed concrete was filled into moulds in 3 equal layers with each layer given 25 strokes of the tamping rod. The concrete was leveled off to be at the same level with the top of the mould using the trowel, then stored in the laboratory for 24 hours at room temperature before de-moulding and curing in water for the required curing age. A total of 27 cubes were made. Testing of the hardened cubes were carried out after 7 days, 14 days, and 28 days, respectively using a universal testing machine

## **2. Results and discussions**

### *2.1 Physical properties of specimens*

From the results presented in Table 1, it can be clearly seen that the specific gravity and moisture content of the specimens fall within acceptable overall limits of fine aggregates [13]. Also the particle size distribution of the samples classified the Obimo and river sands as zones 3 and 2 fine aggregates respectively [14, 15]. Fineness modulus may not have effect on the strength of concrete but may have a great effect on the workability of concrete. The result clearly shows that the UOS and WOS are finer than the conventional river sand but suitable for structural concrete production [16]. Despite the variation in the zones, the specimens all fall within acceptable limits of fine aggregate for structural concrete work given in BS 882:1973 [14] as well as in IS 383: 1970 [15].

## 2.2 Chemical composition of specimen

The absence of sulfur from the results (Table 2) shows that the concrete produced using Obimo sand will not produce sulphates when it reacts with oxygen. Also, the absence of chlorine, fluorides, iodides etc. indicates low saline content and absence of salts. These sulphates and salts which, if present would cause a great damaging effect on concrete such as spalling, shrinkage and loss of structural integrity.

## 2.3 Variation of compressive strength of concrete with age

The relationship between strength and age of concrete using WOS, UOS and RS as fine aggregate is shown in Figure 1. Mix proportion of 1:2:4 and water/cement ratio of 0.6 were used. The overall compressive strength for the washed sample reported 6.5% more strength than the river sand for both the 7-day and 28-day ages and conformed (with acceptable accuracy) to MacGregor's equation for strength prediction with age [17] given by Eq. (1).

$$f(t) = 158.5 + 40.4 \ln(t) \quad (1)$$

where  $f(t)$ , in  $\text{KN}/\text{cm}^2$ , is the compressive strength at age  $t$ , in days.

The concrete produced using the unwashed sample indicated 4.8% compressive strength less than that produced using the river sand. However the compressive strength is within range when compared with MacGregor's equation for both the 7-day and 28-day ages and thus, the sample can be used for structural concrete.

## 2.4 Cost analysis

The cost analysis (Table 3) showed a slight cost benefit when using UOS and WOS as fine aggregate comparatively to the use of river sand. Specifically the unwashed sample produces a concrete 1.42% cheaper than that produced from river sand while a cost saving of 0.43% is achieved when the washed sample is used. However the cost profit may be substantial when large volumes of concrete are involved due cumulative effect.

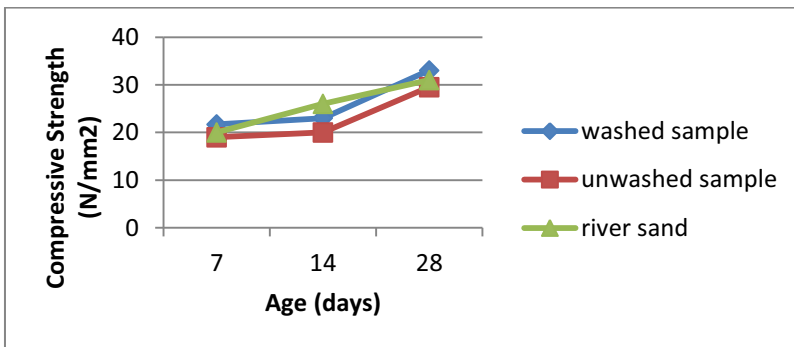


Figure 1. Variation of compressive strength of specimen concrete with age

**Table 1.** Physical properties ofswashed Obimosand (UOS), Washed Obimosd (WOS) and(RS)

Properties	UOS	WOS	RS	Test Method
Specific Gravity	2.65	2.64	2.73	BS 812-2-1995
Moisture Content %	0.76	0.72	1.5	BS 812-109-1990
Sieve Analysis	Zone 3	Zone 3	Zone 2	BS 812-102-1984
Fineness Modulus	2.25	2.25	1.32	BS 812-102-1984
Uniformity	2.33	2.36	2.56	BS 812-102-1984
Coefficient, Cu				

**Table 2.** Chemical composition of Obimo sand by X-ray Fluorescence Spectrometry

Elements	Composition (%)	Elements	Composition (%)
Al	3.48	Cu	0.015
Si	84.9	As	0.02
K	0.049	Sr	0.014
Ca	0.43	Zr	0.369
Ti	2.48	Ru	0.568
V	0.078	Pd	0.49
Cr	0.022	Ag	1.12
Mn	0.013	Eu	0.099
Fe	4.75	Re	0.002
Se	0.45	Au	0.38
Os	0.004	Pb	0.013
Ge	0.041		

**Table 3.** Cost analysis for the production of 1 m<sup>3</sup> of concrete using the UOS, WOS and RS

Component	Mass (Kg)	Volume (m <sup>3</sup> )			Cost (₦) <sup>a</sup>		
		UOS	WOS	RS	UOS	WOS	RS
Cement	315.79	0.2193			12,000		
Fine aggregate	631.58	0.2383	0.2392	0.2313	240	400	470
Coarse aggregate	1263.16	0.477			1,000		
Water	189.89	0.19			200		
Labour	-	-			2530		
Total Cost	-	-			15,970	16,130	16,200

\*Nigerian Naira

### 3. Conclusion

The need to find suitable alternatives to replace the conventional river sand in the production of concrete structures is necessary. Therefore any alternative chosen must be economic and result in structures with reasonable structural characteristics. Based on the results obtained from this work, the following conclusions can be deduced:

- The Physical properties of Obimo sand which include specific gravity, moisture content; particle size distribution, aggregate grading and zoning are within the overall acceptable limits specified for concrete works.
- The elemental analysis indicates the absence of sulphate and chloride salts which are deleterious to concrete durability. This encourages the use of Obimo sand for replacement of conventional river sand in structural concrete.

- The densities of hardened concrete obtained before crushing the cubes were within the range of 2360-2482 kg/m<sup>3</sup>. This is within the range for normal weight concrete.
- The compressive strength of the concrete was found to increase with age as of normal concrete. The 28-day strength of the washed sample showed greater strength than the river sand while the unwashed sample gave a concrete with slightly lesser compressive strength but within an acceptable range. This also encourages the replacement of river sand by Obimo sand.
- The cost analysis also advocates for the use of Obimo sand as fine aggregate for structural concrete.

## References

- [1] Gonçalves J P, Tavares L M, Toledo Filho R D, Fairbairn E M R & Cunha E R, *Cement and Concrete Research*, 37 (2007) 924–932.
- [2] Ilangovana R, Mahendrana N & Nagamanib K 2008, *ARPN Journal of Engineering and Applied Sciences*, 3 (2008) 20-26.
- [3] Manasseh J, *Leonardo Electronic Journal of Practices and Technologies*, 17 (2010) 85-96
- [4] Osadebe N N & Nwakonobi T U, *Nigerian Journal of Technology*, 26 (2007) 12-17.
- [5] Nisnevich M, Sirotin G & Eshel Y, *Magazine of Concrete Research*, 55 (2003) 313-320.
- [6] Ukpata J O, Ephraim M E & Godwin A A, *ARPN Journal of Engineering and Applied Sciences*, 7(2012) 81-92
- [7] BS 12: part 2, *Method of Testing Concrete*, British Standards Institution, London (1970).
- [8] BS 5328: Part 1, *Guide to Specifying Concrete*, British Standards Institute, London (1997).
- [9] BS 1881 – 125, *Mixing and Sampling Fresh Concrete in the Laboratory*, British Standards Institute, London (1983).
- [10] BS 882, *Specification for Aggregates from Natural Sources for Concrete*, British Standards Institute, London (1992)
- [11] BS 8110-1, *Structural Use of Concrete-Code of Practice for Design and Construction*. British Standards Institute, London (1997).
- [12] Reynolds C E and Steedman J C, *Reinforced concrete designer's handbook* (E & F N Spon, London), 1981.
- [13] Neville A M & Brooks J J, *Concrete technology* (Prentice Hall, Harlow), 2010.
- [14] BS 882, *Specification for Aggregates from Natural Sources for Concrete*, British Standards Institute, London (1973).
- [15] IS: 383, *Specification for Coarse and Fine Aggregates from Natural Sources for Concrete*, Bureau of Indian Standards, New Delhi (1970).
- [16] *Concrete Technology*, Indian Railways Institute of Civil Engineering, Pune, 2007.
- [17] MacGregor J G, *Load and resistance factors for concrete design*. ACI Journal, 80(1983): 279-287

# Concreting method that produces sustainable concrete

H. S. ABDELGADER<sup>a,1</sup>, A. M. OTHMAN<sup>a</sup>, A. S. EL-BADEN<sup>a</sup> and N. ANGELESCU<sup>b</sup>

<sup>a</sup>*Department of Civil Engineering, University of Tripoli, Libya*

<sup>b</sup>*Valahia University, Targoviste, Romania*

**Abstract.** For the last decades, concrete materials and technology have been widely developing in many ways in order to achieve an economic and high quality product. But from the other hand concrete offers a wide range of capabilities to achieve a good balance between human needs and earth's capacity which is known as the sustainability. Two stage concrete (TSC) known sometimes as preplaced aggregate concrete (PAC) is a relatively as a new concrete type which has ability to satisfy the requirements of performance and sustainability. Its main concept depends on pre-packing the coarse aggregates in the formwork, then injecting cement mortar grout into the voids in between the aggregates. TSC differs from conventional concrete in having a higher percentage of coarse aggregates which are placed in direct contact with each other resulting in fewer voids that are to be filled with the cement mortar/grout. This low percentage of voids should have a positive impact on the concrete properties both on short and long term basis. The behaviour of TSC in compression has been well documented, but there are little published data on its behaviour in tension and modulus of elasticity. This paper presents results of experimental testing of TSC made with two types of coarse aggregates and three different mix proportions of grout. It was found that the modulus of elasticity of two-stage concrete is equivalent or higher than that of conventional concrete for the same compressive strength. Relationships of stress versus strain and modulus of elasticity versus compressive strength were statistically derived and elaborated.

**Keywords.** Two-stage concrete, modulus of elasticity, compressive strength.

## Introduction

Two-stage concrete is unlike conventional concrete, being made by first placing coarse aggregate in the formwork and then injecting cement grout to fill the voids between coarse aggregate particles. Mechanical properties of TSC are thus influenced by the properties of the coarse aggregate, the properties of the grout, and the effectiveness of the grouting process. When placed properly, TSC has beneficial properties such as low drying shrinkage, high bonding strength, high modulus of elasticity, and excellent durability.

---

<sup>1</sup>Corresponding author: [hakimsa@poczta.onet.pl](mailto:hakimsa@poczta.onet.pl)



The method of TSC has proved particularly useful in a number of applications like underwater construction, concrete and masonry repair, situations where placement by usual methods is extremely difficult, mass concrete where low heat of hydration is required, tunnel and sluiceway plugs to contain water at high pressure where very low shrinkage is important. It is also useful in the manufacture of high density concrete for atomic radiation shielding where steel and heavy metallic ores are used as aggregate [1, 2]. TSC differs from conventional concrete not only in the method of placement but also in its higher proportion of coarse aggregate. TSC compressive strength is also different from conventional concrete because of the different means of stress transmission that occurs in TSC. The closely packed coarse aggregate exhibits contact areas in all directions, whereas in normal concrete, the aggregate is usually smaller in size, and rather dispersed. The stress distribution in TSC gives higher shear stresses and stress concentration in the aggregate contact areas. The modulus of elasticity is particularly important from the design point of view in plain or reinforced concrete, since it represents the concrete mechanical behaviour. The elastic modulus and the failure properties of TSC differ from those of normal concrete [3, 4]. While the mechanical properties of TSC in compression have been well documented, there remains little published data on tensile strength and modulus of elasticity. The objective of this investigation was to study the behaviour of TSC subjected to compressive stresses using different grout mixtures. From the experimental data, relationships of stress versus strain and modulus of elasticity versus compressive strength, were statistically derived.

## **1. Experimental programme**

### *1.1 Materials*

Two types of high quality aggregates having angular and round shapes were used, and referred in the text as crushed and round aggregates. The rounded aggregate was sieved out in three fractions of 16/32 mm (34%), 32/50 mm (60%), and 50/63 (6%) by mass. The compositions of the rounded aggregate consisted of mainly granite and basalt. The crushed aggregate was also sieved in three fractions of 16/32 mm (46%), 32/50 mm (49%), and 50/63 mm (5%) by mass. The crushed aggregate was composed only of basalt. The mixed aggregates were a 50/50 mixture by volume of the rounded and crushed aggregate. The fine aggregate used in the manufacture of the grout was clean sand having a maximum particle size of less than 2 mm and water absorption value of 1.05% by mass. The sand was divided into three fractions of 0/0.25 mm (20%), 0.23/1.0 mm (67%), and 1.0/2.0 mm (13%) by mass. Both fine and coarse aggregate properties were determined according to ASTM methods [4]. Some basic characteristics of coarse aggregate presented in Table 1. Through-out the study ordinary Portland cement (Type I) was used. Its 28-day compressive strength and Blaine fineness were 41.4MPa and {3155 cm<sup>2</sup>/g} respectively. The cement properties were conformed to ASTM standard [5, 6]. The admixture used was super-plasticizer of the naphthalene formaldehyde sulfonate type added to all of the mixtures at adosage rate of 2% by mass of cement.

**Table 1.** Some physical properties of the coarse aggregate

Aggregate Type	Bulk density (Kg/m <sup>3</sup> )	Specific gravity	Void ratio (%)	Absorption (%)	Grain size (mm)
Round	1540	2.607	43	0.62	16-63
Crushed	1430	2.687	47	0.34	16-63

### 1.2 Mixture proportions

The mix proportions of the grout were prepared using three water/cement ratios (w/c) of 0.45, 0.5, 0.55, and three cement/sand (c/s) ratios: 1/1.5, 1/1.0 and 1/0.8. The mixing of the grout was done by a mixer of 120 to 130 liter capacity. The rotor speed was 3000 rpm. The grout was mixed for four minutes after all the ingredients had been added. Table 2 shows sample of mix proportions, for more details see reference [7].

**Table 2.** Sample of mix proportions

Cement:Sand ratio	Water	Admixture	Cement	Sand
	Unit quantities : kg/m <sup>3</sup>			
1/1.5	131.10	5.826	291.34	437.01
	149.09	5.421	271.09	406.63
1/1	152.61	6.782	339.14	339.14
	171.60	6.240	312.01	312.01
1/0.8	163.33	7.259	362.97	290.37
	182.63	6.641	332.06	265.64

### 1.3 Specimen preparation

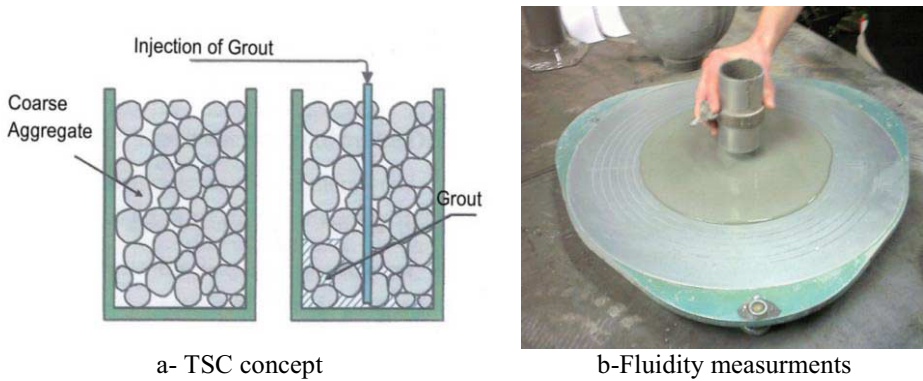
First, clean and saturated-surface dry coarse aggregate was introduced to the moulds. Then the grout was introduced through a funnel to the bottom of the sample under gravity pressure using a hard plastic injection pipe 20 mm in diameter and height of 2.0 m placed in the coarse aggregate as shown in Figure 1. One hundred and eight (108) cube specimens (300x300x300 mm) were prepared and tested for compressive strength for both concrete and grout. Three cube samples were tested to obtain the concrete compressive strength for each mix proportion and type of aggregate while another three cube samples were used for testing grout compressive strength. Stress-strain relations using compressive stresses were analyzed using cylinder specimens (196 mm in diameter and 392 mm in length) of the same nine different grout proportions and types of aggregate (see Table 1). There were fifty four (54) cylinder specimens prepared in total (three cylinders per mix composition). After 24 hours of curing time, concrete specimens were removed from the moulds and covered with wet burlap for 7 days. Specimens were then stored in open air (in the laboratory) at 18°C for 28 days.

### 1.4. Concrete and grout testing

#### 1.4.1 Fluidity test

The test method measures the flow of the injected grout placed in a cylinder of 0.25L volume when poured onto a scaled plate from a height of 10 mm as shown in Figure 1. The measurement of grout fluidity is the diameter of the spread. Three readings of

fluidity were made in all measurement series [8, 9]. Table 3 presents sample of results from this test.



**Figure 1.** TSC concept and grout fluidity measurements

**Table 3.** Average results of sedimentation, fluidity and compressive strength of grout

c/s	w/c	Sedimentation (%)	Fluidity (cm)	Compressive strength (MPa)	
				Grout	Concrete
1/1.5	0.45	1.09	7.37	43	31
1/1		1.80	9.67	44	30
1/0.8		3.05	9.70	45	32
1/1.5	0.55	3	10.47	32	24
1/1		4	12.00	32	23
1/0.8		5.1	13.30	35	21

#### 1.4.2 Sedimentation tests

Sedimentation causes decrease in the adherence forces between the grout and the stone aggregate grains. The grout is poured in quantities of about 500 ml into three graded cylinders of 1000-mL volume. After 3 h, the depth of the water layer on the grout is measured. Sedimentation is the ratio of the depth of the water layer to the height of the grout after pouring into the cylinders [3, 9]. Three readings of sedimentation were made in all measurement series, gave the results presented in Table 3.

#### 1.4.3 Concrete strength tests

The compressive strength of grout ( $\bar{f}_g$ ) was tested by using a hydraulic machine of 1600kN capacity. Measurements on the compressive strength of TSC ( $\bar{f}_c$ ) were done using a hydraulic testing machine of the load range 0 to 4000 kN. The rate of loading was 0.74 MPa/sec. Samples of average results are presented in Table 3.

## 2. Results, analysis and discussions

### 2.1 Compressive strength

As described earlier, the compressive strength of TSC was measured by using the 300 mm cube specimens. On the basis of the results relations for  $\bar{f}_c$  have been obtained for all concrete mixes made using both types of aggregates [10]. Empirical equations for  $\bar{f}_c$  in terms of w/c and c/s for each round and crushed aggregates are presented in Eq. (1) and Eq. (2) respectively as follows:

$$\bar{f}_c = 64.27 - 75.25(W/c) - 0.06(C/s) \quad (1)$$

$$\bar{f}_c = 62.08 - 71.00(W/c) + 0.52(C/s) \quad (2)$$

Results and observations indicated that TSC compressive strength was different in comparison with the strength value describing the traditional concrete [11]. This can be explained by the direct transmission of stresses, occurring in the TSC. The closely packed stone aggregate exhibit contact areas in all directions, where as in normal concrete the aggregate is usually smaller in size and rather dispersed as shown in Figure 2. For this reason, the compressive stresses in the stone aggregate of TSC and in the grout cannot be equal. The compressive stresses are mainly transmitted by the stone aggregate in TSC. The rigid close-packed grains do not allow for significant growth of the grout strains and the corresponding stresses. The other mechanism is that distribution of stress produces stress concentration points in the contact areas. These stresses are responsible for fracture of some particular stones and cause a tearing away action of the aggregate grains from the grout. Unlike ordinary concrete, tested samples showed considerable cracks formed on the surface, and extensive lateral deformations prior to failure. The failure in general was not explosive [10].

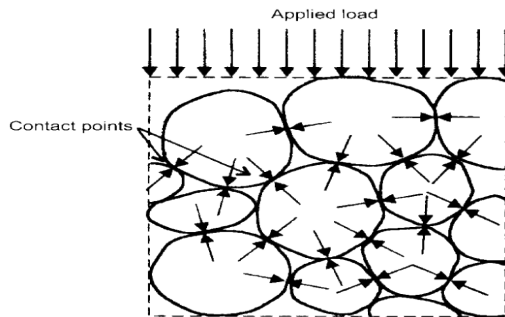


Figure 2. Mechanism of stress- transmission in TSC

### 2.2 Stress-Strain Relations

Stress-strain relations were determined using cylinder specimens. Following a period of 28 days of air curing, the specimens were subjected to the compressive tests. During the loading procedure, the vertical deformations were measured on three sides of the specimen

versus the axial force increment. The results obtained from the cylinder specimens were used to derive the stress-strain relations (see Figure 3) and the modulus of elasticity for the two-stage concrete.

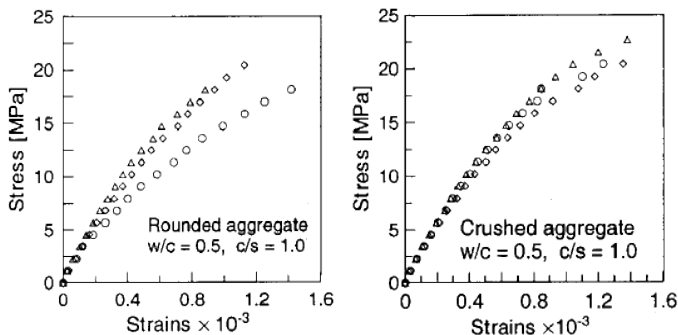


Figure 3. Sample of stress –strain relations for TSC

The obtained results are statistically analysed to estimate equations for the compressive strain-stress relations of various two-stage concrete types. The statistical analysis was performed by use of the MINITAB program [12]. The Minitab Regress Package fits an equation to the experimental data by the least square method. The calculation can be divided into the following steps: assumption of the mathematical relation, estimation of the equation coefficients, testing of the assumed equation and choice of the best model. The statistical analysis of the TSC test data was performed in two successive phases. First, equations for stress-strain relations for type of coarse aggregate and different grout proportions were estimated. In this step, the data consisted of 27 (3×9 samples) stress-strain sets of experimental results obtained from cylinder compressive tests. After various trials the following simple relation for all concrete types was obtained:

$$\hat{\sigma} = a\varepsilon_1^3 + b\varepsilon_1^2 + c\varepsilon_1 \quad [\text{MPa}] \quad (3)$$

In the above formulae  $\hat{\sigma}$  stands for the estimated concrete stresses, and  $\varepsilon_1 = \varepsilon \times 10^3$ . Where  $\varepsilon$  denotes the concrete strain. The constants  $a$ ,  $b$ , and  $c$  in Eq.(3) for each concrete type are statistically obtained. In Table4 some results (6 out of 18 test data sets) for  $c/s=1/1.5$  and various  $w/c$  ratios are presented. Equation (3) gives reliable results at strain range of: ( $0 \leq \varepsilon \leq 0.001$ ).

**Table 4.** Constants  $a$ ,  $b$ ,  $c$  of equation (3) for coarse aggregate type and  $c/s = 1/1.5$ 

Aggregate type	w/c	a	b	c	Correlation coefficient
Crushed	0.45	9.15	-27.0	34.9	0.9846
	0.50	0.08	-17.2	33.3	0.9931
	0.55	5.84	-23.4	36.2	0.9983
Round	0.45	18.2	-32.5	34.0	0.9941
	0.50	1.00	-9.4	28.5	0.9978
	0.55	5.81	-22.0	32.1	0.9861

In the second step the statistical analysis is used to obtain the two-stage concrete stress-strain relations as function of water-cement ( $\omega = w/c$ ) and cement-sand ( $\zeta = c/s$ ) ratios [11]. After a complex analysis the functions:  $a = a(\omega, \zeta)$ ,  $b = b(\omega, \zeta)$  and  $c = c(\omega, \zeta)$  in Eq. (3) are assumed as follows:

(a)- For crushed aggregate:

$$\begin{aligned}
 a(\omega, \zeta) &= 14.9 - 17.1\omega + 1.89\zeta, \\
 b(\omega, \zeta) &= -28.7 + 1.0\omega + 9.63\zeta, \\
 c(\omega, \zeta) &= 37.9 + 4.0\omega - 7.82\zeta,
 \end{aligned} \tag{4}$$

(b)- For round aggregate:

$$\begin{aligned}
 a(\omega, \zeta) &= 38.9 - 51.2\omega - 7.59\zeta \\
 b(\omega, \zeta) &= -40.8 + 30.1\omega + 5.80\zeta \\
 c(\omega, \zeta) &= 40.7 - 11.1\omega - 4.46\zeta
 \end{aligned} \tag{5}$$

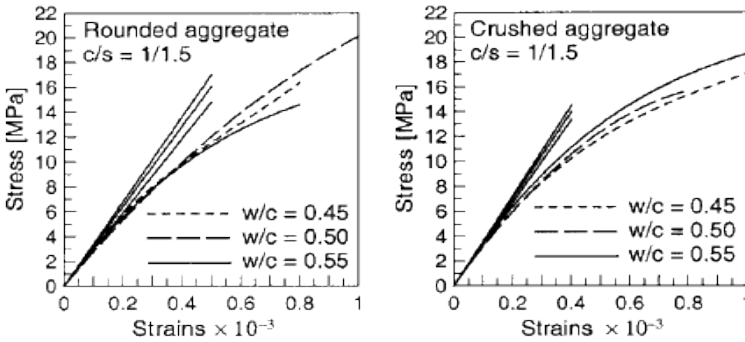
Some estimated results for concrete stresses obtained according to Eq.(3) by use of Eq. (4) and (5) are presented in Table 5. The values of the correlation coefficient reveal that using the function:  $a(\omega, \zeta)$ ,  $b(\omega, \zeta)$ , and  $c(\omega, \zeta)$  the test results and their estimators are more dispersed (compare Table 4 and 5). The analysis proved that the obtained stress-strain curves of the two-stage concrete are mainly affected by the physical properties of the coarse aggregate, and in particular by its compressive strength (Table 3). The influence of the grout content used is not significant. This relation may result from good contact between the aggregate particles. Therefore, it can be assumed that the applied load is distributed mainly through the aggregate skeleton. The test observations and the statistical analysis have demonstrated that the linear part of the stress-strain curve in the two stage concrete may reach as much as 40–60% of the compressive strength of the specimens

**Table 5.** Constants calculated for Equations (4 &5)

Aggregate type	w/c	$a(\omega, \zeta)$	$b(\omega, \zeta)$	$c(\omega, \zeta)$	Correlation coefficient
Crushed	0.45	8.47	-21.83	34.49	0.808.
	0.50	7.61	-21.78	34.69	0.814
	0.55	6.76	-21.73	34.89	0.735
Round	0.45	10.8	-23.39	32.73	0.827
	0.50	8.24	-21.88	32.18	0.797
	0.55	5.68	-20.38	32.62	0.652

2.3 Tangent modulus of elasticity

The experimental data analysis and the statistically obtained stress-strain relations allow formulation of the relationship between the static modulus of elasticity and the compressive strength of the two-stage concrete  $\bar{f}_c$  at 28 days (see Eq. 1&2). As the linear part of the stress-strain curves obtained for each type of the two-stage concrete reached at least 40% of its compressive strength, the tangent modulus of elasticity was derived. The tangent line is drawn along the stress-strain curve at its starting point (see some examples presented in Figure 4). The values of the moduli are computed from stress-strain curves for the examined cases of aggregate types and grout mixes, and are given in Table 6.



**Figure 4.** Graphical presentation of estimated TSC modulus of elasticity

Making use of the statistical analysis of the experimental data expressions describing the relationship between the TSC elastic modulus and its cube compressive strength  $\bar{f}_c$  can be derived for round and crushed aggregate as presented in Eq. (6) and (7) respectively:

$$(For Round Agg.) \gggg E_{TSC} = 28.7 + 0.080\bar{f}_c \quad (GPa) \quad (6)$$

$$(For Crushed Agg.) \gggg E_{TSC} = 33.9 - 0.049\bar{f}_c \quad (GPa) \quad (7)$$

**Table 6.** Modulus of elasticity for different TSC (GPa)

c/s	w/c	Type of Aggregate	
		Round	Crushed
1/1.5	0.45	34	34.9
1/1		33.7	32.9
1/0.8		27.1	29.8
1/1.5	0.55	32.1	36.2
1/1		30.4	31.7
1/0.8		-	30.9

### 3. Conclusions

The following conclusions can be drawn from this study:

(a)- Results and observations indicated that TSC compressive strength was different in comparison with the strength value describing the traditional concrete [11]. This can be explained by the specific transmission of stresses, occurring in the TSC.

(b)-The stress-strain relationships for different grout mixes (of varied water/cement ratios and cement/sand ratios) do not show a big difference. The initial stress-strain curves can be estimated by linear relations. This may result from the stresses distributed mainly by the particles of stone aggregate (skeleton of stones).

©-The modulus of elasticity as a function of compressive strength of the TSC is elaborated. The modulus of elasticity values for specific type of aggregate is described by linear constant functions. The obtained equations may allow engineers to design the TSC according to the algorithms presented in [13].

### References

- [1] ACI Committee 304, Guide for The Use of Preplaced Aggregate Concrete for Structural and Mass Concrete Applications, *ACI 304.1 R-92*, (1997), 21-24.
- [2] H.S Abdelgader, Effect of Quantity of Sand on The Compressive Strength of Two-Stage Concrete, *Magazine of Concrete Research*, **48**(1996), 353-360.
- [3] H.S Abdelgader, How to design Concrete Produced by a Two-Stage Concreting Method, *Cement and Concrete Research*, **3**(1999), 331-337.
- [4] ASTM. C33, Specification for concrete aggregates: *American Society for Testing and Materials*. Philadelphia: Pennsylvania, 1997.
- [5] ASTM C150, Specification for Portland cement: *American Society for Testing and Materials*. Philadelphia: Pennsylvania. 1994.
- [6] British Standard Institution: BS 882, Water for making concrete, BSI, London, 1985.
- [7] H.S Abdelgader and A. A Elgalhud, Effect of Grout Proportion on Strength of Two-Stage Concrete," *Structural Concrete*, **3**(2008),.163-170.
- [8] ASTM C230, Standard specification for flow table for use in tests of hydraulic cement, *American Society for Testing and Materials*, Philadelphia, Pennsylvania, (2001), 129-133.
- [9] ASTM C939, Standard Test Method for flow of Grout for Preplaced Aggregate Concrete (Flow Cone Method), *American Society for Testing and Materials*, Philadelphia, Pennsylvania, (2010), 134-136.
- [10] H.S. Abdelgader and J. Górski, Influence of Grout Proportions on Modulus of Elasticity of Two-Stage Concrete, *Magazine of Concrete Research*, **4**(2002), 251-255.
- [11] A.M. Neville, Properties of concrete, *Pitman Books Limited*, London, Third Edition, (1981), 779 pp.
- [12] R.L. Schaefer and R.B. Anderson, The students edition of MINITAB statistical software adapted for education, *Addison-Wesley Company*, (1989), 5-23.
- [13] H.S. Abdelgader and J. Górski, Stress-Strain Relations and Modulus of Elasticity of Two-Stage Concrete, *ASCE J. Mat. Civ. Eng.*, **4**(2003), 251-255.



# Reuse of non-metallic residues from aluminium recycling industry in production of porous building materials

Diana BAJARE<sup>1</sup>, Girts BUMANIS, Aleksandrs KORJAKINS and Laura SELE  
*Riga Technical University, Kalku str. 1, LV-1658, Riga, Latvia*

**Abstract.** The aim of this study was to find a new method for usage of the hazardous waste coming from the aluminium scrap recycling factories. It is generally considered that non-metallic residues (NMR) are process waste and subject to disposal after residual metal has been recovered from primary dross. NMR are impurities, which are removed from the molten metal in the process of dross recycling, and it could be defined as a hazardous waste product. Processing of NMR created in the aluminium scrap recycling companies is one of the most challenging tasks due to its toxic nature - in accordance with the Basel Convention, Annex III, marking of this waste is H 4.3 (reaction with water results in highly inflammable substances) and H 10 (reaction with water results in increased concentration of toxic gases, for instance, ammonia). The new alkali activated materials, which could be defined as porous building materials, were created by using calcined illite clay from local site and NMR. Solution of sodium silicate ( $\text{Na}_2\text{SiO}_3 + n\text{H}_2\text{O}$ ) modified by commercially available alkali flakes (NaOH) was used as an activating solution. Polymerization mechanism of raw materials in alkaline media was investigated by using FTIR and XRD. Physical and thermal properties of the obtained materials were tested. Density of the obtained materials was in the range 550-675 kg/m<sup>3</sup>, but the total porosity was from 73 to 78%. The compressive strength of the materials was in range from 1.4 to 2.0 MPa. The thermal conductivity of porous alkali activated building materials was between 0.14 and 0.15 (W/(m·K)).

**Keywords.** Aluminium scrap recycling waste, alkali activation, porous building material, insulation material

## Introduction

Alkali-activated binders (AAB) are receiving increasing attention as an alternative to Portland cement because of their high strength and durability and low environmental impact. AAB or geopolymers are made by mixing solid aluminosilicate powders such as fly ash, blast furnace slag, metakaolin or other with an alkaline activating solution [1]. Unlike Portland cement, the solid component of AAB can be entirely waste-stream materials, particularly fly ash and blast furnace slag as well as scrap recycling waste, used with very limited further processing. It has been estimated that substituting AAB for Portland cement in concrete can reduce CO<sub>2</sub> emissions up to 80% [2]. A key attribute of geopolymer technology is the robustness and versatility of the

---

<sup>1</sup>Corresponding author. [Diana.Bajare@rtu.lv](mailto:Diana.Bajare@rtu.lv)

manufacturing process; it enables products to be tailor-made from a range of aluminosilicate raw materials so that they have specific properties for a given application at a competitive cost [2]. It is clear that alkali activated materials (AAM) (alkali activated binder with fillers) can exhibit performance properties such as high compressive strength [3]; high level of resistance to a range of different acids and salt solutions [4]; high resistance to freeze–thaw [4]; not subject to deleterious alkali–aggregate reactions [4]; low shrinkage [5]; low thermal conductivity [6]; good adhesion to steel [7]; inherent protection of steel reinforcing due to high residual pH and low chloride diffusion rates [8]; high stability when exposed to high temperatures [4]; effective solution for the stabilization of industrial by-products and the immobilization of heavy metals [9]. Although several researchers demonstrated an excellent durability of AAB in their experiments, the major unsolved problem in the development and application of alkali activation technology is still related to the durability, because it seems to depend strongly on the application of adequate curing regimes and composition. It should be noted that, contrary to the assertions of some researchers, high-temperature curing is not required for high strength development in AAB [10]. A correctly formulated AAB can set and harden at the room temperature or even below it. Also carbonation can be quite problematic in these systems, as there is no reservoir of available calcium to provide a pH buffer, and so durability performance is critically dependent on the development of a compact and refined pore structure [8].

The focus in this paper will be on finding an effective solution for the utilization of industrial by-products, namely, aluminium scrap recycling waste by using geopolymer technology, i.e., to integrate this waste into aluminosilicate system activated with mixture of sodium hydroxide and silicate solution.

The consumption of aluminium recycling waste has been rising continuously worldwide, which is a great stimulus for developing non-waste technology [11]. Aluminium dross represents a residue from primary and secondary aluminium production. Dross is classified according to the aluminium metal content into white and black dross. Typically, white dross is produced when melting using salt flux. It has a high metal content and is compacted in large clotted lumps or blocks. It consists almost entirely of  $Al_2O_3$  and aluminum metal trapped by the surface tension of the oxide skin. In contrast, black dross is granular with a high metal content in coarse fraction and chiefly oxides and salts in the fines [11]. Black dross typically contains a mixture of aluminium oxides and slag with recoverable aluminium content ranging between 12–18% [12]. The conventional rotary furnaces heated with a fuel or gas burners are used to recover the extra aluminium from black or white dross. This treatment process produces the residual oxide mix called aluminium recycling waste containing alumina, salts, impurities and a small amount (3–5%) of metallic aluminium. This case study investigates the use of aluminium scrap recycling waste (NMR) generated from the secondary dross processing.

The composition of NMR is highly variable and usually unique to the plant generating the waste, hence finding potential application for this material is often seen as a difficult task. The task becomes more challenging due to the toxic nature of aluminium recycling waste. It emits flammable gases, such as acetylene, or it is liable to give off toxic gases, such as ammonia, in dangerous quantities in contact with water. In accordance with the Basel Convention, Annex III, marking of this waste is H 4.3 (reaction with water results in highly inflammable substances) and H 10 (reaction with water results in increased concentration of toxic gases, for instance, ammonia). Beside this, the waste contains compounds like soluble salts, oxides, carbides and sulphides as

well as metallic aluminium. Its landfill disposal is forbidden in most of the European countries and it should be recycled [11]. After conventional treatment of salt slag the non-metallic residue (NMR) can be acquired and it could be used in a variety of applications, such as the production of cements, in ceramic and refractory applications, in chemical and metallurgical industry [12], [11], [13].

The aim of this study is to find a new method for usage of the hazardous waste coming from the aluminium scrap recycling factories and Illite clay. The AAB obtained in this research was a low calcium system containing X-ray amorphous gel binder with porous structure. A limited amount of literature is available on porous geopolymer materials. However, some of the researchers have tried to incorporate lightweight aggregates in the structure of geopolymer binder [14] or aerated the fresh mixture [15]. In current research waste from aluminium scrap recycling industry will be used as pore creating agent to obtain porous building materials.

## 1. Experimental materials and methods

### 1.1. Test methods

Raw materials, AAB and AAM, which consist from AAB and fillers, were tested. Chemical composition of the raw materials was determined according to LVS EN 196-2 with precision  $\pm 0.5\%$ . Analysis of the elements was carried out with a help of inductive coupled plasma optical emission spectrometry (ICP-OES), atomic absorption spectroscopy (AAS) and potentiometer titration technique. Specific surface area was detected by BET method ("Nova 1200 E-Series, Quantachrome Instruments"). Effective diameter was detected by Zeta potential ("90 Plus" and "MAS ZetaPALS Brookhaven Instr").

The mineralogical composition of NMP, IC and AAB was determined by using the X-Ray diffractometer "RIGAKU ULTIMA+". Structural characterization of the different functional groups for AAB pastes were performed by using Fourier transform infrared (FTIR) spectrometer (VARIAN 800 FT-IR) between 400 and 4000  $\text{cm}^{-1}$ . Microphotographs of AMM were obtained by SEM "Tescan" "Mira/LMU Schottky".

The flexural and compressive strength of AAM were tested according to LVS EN 1015-11 using specimens with dimensions 40x40x160 mm. The density of AAM was measured in accordance with EN 1097-7, but the water absorption was determined according to EN 1097-6. The open porosity was determined by water absorption against the volume of prepared samples. Samples were immersed in water for 72h. Total porosity was obtained from specific gravity obtained by Le Chatelier flask (ASTM C188).

The thermal conductivity was measured with heat flow meter instrument LaserComp FOX 660 using air-dry A10 sample with dimensions 300x300x50mm. The upper and lower plate temperatures were 0°C and 20°C with average temperature of 10°C.

All instrumental investigations were carried out at Riga Biomaterial Innovation and Development Centre of RTU.

## 1.2. Raw materials

The raw materials used in the current study were calcined illite clay (IC), industrial waste received from aluminium scrap recycling industry (NMR) and fillers: quartz sand (Q) and dolomite powder (D) with particle size 0-0.3 mm. IC, NMR, Q and D were ground in the laboratory planetary ball mill Retsch PM 400 for 30 min with speed 300 rpm. Alkali-activation of raw material composition was done by modifying sodium silicate solution with an addition of sodium hydroxide.

### 1.2.1. Calcined illite clay (IC)

The IC was taken from a local brick production site. Calcination of IC was sintered at 800 °C in an air atmosphere for approximately 30 min in rotary furnace with maximum temperature. Specific surface area of ground IC was 21.42 m<sup>2</sup>/g, but effective diameter– 709.5 nm. Calcined IC has little crystalline structure and beside quartz (SiO<sub>2</sub>) and illite K(AlFe)<sub>2</sub>AlSiO<sub>3</sub>O<sub>10</sub>(OH)<sub>2</sub>·H<sub>2</sub>O it also contains microcline (KAlSiO<sub>3</sub>) in a small amount. Chemical composition of calcined IC is given in Table 1.

### 1.2.2. Non-metallic residues from the aluminium scrap recycling factories (NMR)

Analysis of the NMR elements was carried out with the help of ICP-OES, AAS and potentiometer titration technique. The results showed the following content of NMR: aluminium (Al) – 34.40%, silicon (Si) – 4.40%, magnesium (Mg) – 2.44%, calcium (Ca) – 1.32%, sodium (Na) – 1.69%, potassium (K) – 2.31%, sulphur (S) – 0.07%, chlorine (Cl) – 4.23%, iron (Fe) – 3.60%, copper (Cu) – 0.99%, lead (Pb) – 0.14% and zinc (Zn) – 0.6%. This data corresponds to the chemical composition of NMR, which is given in Table 1.

**Table 1.** Chemical composition of NMR, IC, Q and D (w %)

Chemical component	NMR	IC	Q	D
Al <sub>2</sub> O <sub>3</sub>	63.19	14.60	1,42	-
SiO <sub>2</sub>	7.92	73.84	96,8	-
CaO	2.57	0.91	-	-
SO <sub>3</sub>	0.36	-	-	-
TiO <sub>2</sub>	0.53	0.63	-	-
MgO	4.43	1.10	-	-
Fe <sub>2</sub> O <sub>3</sub>	4.54	4.08	0,34	-
Na <sub>2</sub> O	3.84	0.06	-	-
K <sub>2</sub> O	3.81	2.75	-	-
CaCO <sub>3</sub> ·MgCO <sub>3</sub>	-	-	-	97,0
Other	2.60	1.05	0,49	-
LOI, 1000°C	6.21	0.98	-	-

With regard to chemical composition, the analyzed NMR also contained aluminium nitride (AlN) – on average 5 w%, aluminium chloride (AlCl<sub>3</sub>) – on average 3 w%, potassium and sodium chloride (NaCl +KCl) – total 5 w% and iron sulphite (FeSO<sub>3</sub>) – on average 1 w%.

According to the XRD analysis data, the NMR contained metallic aluminium (Al), iron sulphite (FeSO<sub>3</sub>), aluminium nitride (AlN), corundum (Al<sub>2</sub>O<sub>3</sub>), aluminium iron oxide (FeAlO<sub>3</sub>), magnesium dialuminium (MgAl<sub>2</sub>O<sub>4</sub>), quartz (SiO<sub>2</sub>), aluminium chloride (AlCl<sub>3</sub>) and aluminium hydroxide (Al(OH)<sub>3</sub>).

### 1.3. Mixture design and sample preparation

The paste of AAB was obtained by mixing IC and NMR in various ratios with activator. Two types of filler were added to AAB with propose to increase the mechanical properties of AAM. Sodium silicate solution/paste ratio was constant 0.75. Mixture composition is given in Table 2. Additional water was added to ensure equal workability. As a result materials with different density were obtained.

**Table 2.** Mixture composition of AAM

Mixture composition	IC	NMR	Total paste mass	Filler/paste ratio	Sodium silicate solution/paste ratio
B10-0.1A-Q	1.0	0.1	1.1		
B10-0.5A-Q	1.0	0.5	1.5		
B10-1.0A-Q	1.0	1.0	2.0		
B10-0.1A-D	1.0	0.1	1.1	1.0	0.75
B10-0.5A-D	1.0	0.5	1.5		
B10-1.0A-D	1.0	1.0	2.0		

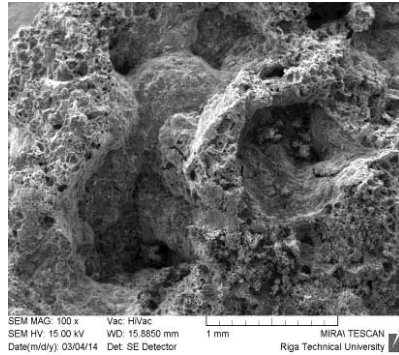
Then sodium silicate solution with  $M_s=1.67$  was added to dry composition and mixed for 1 minute. The amount of mixture poured into mould ( $4 \times 4 \times 16$  cm) was calculated according to the expansion of each mixture. The mass ratio of moulded material for mixture compositions with 1.0A, 0.5A and 0.1A was 1:1.1:1.5 accordingly. Moulds were covered and then heated in  $80^\circ\text{C}$  for 24 h. The density of porous AAM can be controlled by amount of NMP incorporated in the mixture design.

After demoulding specimens (AAB and AAM) were cured at room environment until the testing day. Microstructural photographs of porous AAM and AAB, which are similar no regard to composition, are shown in Figures 1 and 2.

Instrumental methods, such as XRD, SEM and FTIR, were used to characterize the geopolymerisation process of AAB pastes without micro-fillers.



**Figure 1.** Photography of AAM with NMR ratio 0.1 and ground quartz sand (B10-0.1A-Q)



**Figure 2.** Microphotography of AAB paste with NMR ratio 0.1 (B10-1.0A). without micro-fillers

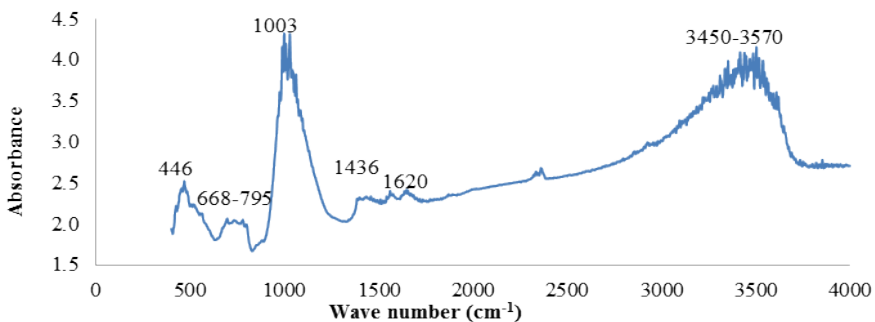
## 2. Results

### 2.1. XRD

The X-ray diffractograms for AAB pastes without micro-fillers cured at room environment for 28 days show they typically are „x-ray amorphous”. XRD patterns have halo in the  $2\theta=15\text{--}35^\circ$  region, which demonstrates the formation of new amorphous phases, usually described as geopolymeric gels [16]. Generally speaking, the only crystalline phase, which is possible to be clearly identified by XRD analysis, is quartz coming from the calcined IC. According to the results of XRD analysis, significant difference of mineralogical composition among AAB with different amount of NMR was not detected.

### 2.2. FTIR

The infrared spectra (FTIR) for AAB pastes without micro-fillers were studied and the data are reproduced in Table 3. There is not difference between infrared spectras (FTIR) for AAB pastes with different amount of NMR. Wavenumber  $446\text{ cm}^{-1}$  corresponds to Si–O–Si [16], [17] (Figure 3). Wavenumber  $540\text{ cm}^{-1}$  is associated to Si–O–Al bonds, where Al is present in octahedral co-ordination [18]. The small wavenumbers at  $668$  and  $730\text{ cm}^{-1}$  could be attributed also to Si–O (zeolite species) bond band or Si–O symmetrically stretching vibration [18], [17]. In the FTIR spectrums shoulder at  $777\text{--}795\text{ cm}^{-1}$  is attributed to Si–O–Si bonds recognized as quartz [19], [17]. Shoulder at  $1000\text{ cm}^{-1}$  corresponds to Si–O–T stretching vibration which moves towards lower frequencies ( $1080\text{ cm}^{-1}$ ) as a result of alkali activation of calcined clay [16]. This band shift is usually considered to occur due to the formation of geopolymers, although it is also observed in the formation of zeolites from disordered aluminosilicate precursors [16]. The wavenumber  $1436\text{ cm}^{-1}$ , which corresponds to the stretching vibration of O–C–O bonds in the carbonate group ( $\text{CO}_3^{2-}$ ), appears only after prolonged curing time of specimens [22], [19], [17], [16]. The shoulder at  $3450\text{--}3470\text{ cm}^{-1}$  and wavenumber  $1620\text{ cm}^{-1}$  are associated to the stretching and deformation vibrations of OH and H–O–H groups from the water molecules [19], [22].



**Figure 3.** FTIR spectra of 28 days old AAB B10-1.0A

**Table 3.** Interpretation of bands from FTIR spectra of AAM

Band number and wavelength	Bands interpretation
446 cm <sup>-1</sup>	Bending vibration of Si–O–Si or Al–O–Si bonds
540 cm <sup>-1</sup>	Si–O–Al bonds, where Al is present in octahedral co-ordination
668, 730 cm <sup>-1</sup>	O–Si–O (zeolite species) bond band
696, 777 and 795 cm <sup>-1</sup>	Quartz
~1000 cm <sup>-1</sup>	Si–O–T stretching vibration (calcined clay) moves towards lower frequencies as a result of alkali activation
1436 cm <sup>-1</sup>	Sodium carbonate
Shoulder 3450-3470 cm <sup>-1</sup> and 1620 cm <sup>-1</sup>	Stretching and deformation vibrations of OH and H-O-H groups from the water molecules

### 2.3. Physical and mechanical properties

Mechanical and physical properties of AAM are given in Table 4. The density of hardened samples depends from NMR concentration in AAM and type of filler used. Lowest density is observed in samples with highest NMR ratio – from 540-550 kg/m<sup>3</sup>. Density slightly increases to 555-585 kg/m<sup>3</sup> for samples with NMR ratio of 0.5. This negligible increase could be explained by the relative expansion of alkali-activated paste. Close to maximum increase could be achieved for AAM with NMR concentration of 0.5. Further increase of NMR ratio results in slightly increased volume. However, due to high NMR density (3.65g/cm<sup>3</sup>), further density decrease of the material was not observed. Material without NMP has a denser structure with density up to 1900kg/m<sup>3</sup> (Figure 4). Density for samples with NMR 0.1 increased to 655-675 kg/m<sup>3</sup>. This could be explained with the low NMR rate in mixture and lower pore developing gas release from NMR.

**Table 4.** Physical and mechanical properties of porous AAM

Mixture design	Density kg/m <sup>3</sup>	Water absorption,%	Open porosity, %	Total porosity, %	f <sub>c</sub> , MPa	f <sub>m</sub> , MPa
B10-0.1A-Q	655±16	41.5±2.5	33.4±0.8	73.6±1.2	1.9±0.13	1.0±0.08
B10-0.5A-Q	585±12	49.0±3.7	31.0±2.8	76.8±1.5	1.5±0.06	0.7±0.03
B10-1.0A-Q	540±27	52.8±2.7	29.7±1.6	78.6±1.8	1.7±0.10	0.6±0.05
B10-0.1A-D	675±17	41.5±1.7	30.3±1.3	73.0±1.3	2.0±0.13	0.9±0.02
B10-0.5A-D	555±16	55.2±3.2	33.0±0.7	78.0±2.0	1.4±0.04	0.6±0.03
B10-1.0A-D	550±16	54.4±4.7	29.4±0.8	78.4±1.5	1.7±0.10	0.6±0.02

Lowest water absorption by mass was obtained for AAM with NMR ratio of 0.1 (41.5%). The higher density leads to relative water absorption decrease comparing to AAM with NMR ratio from 0.5 to 1.0. For mixtures with high NMR ratio water absorption was in range from 49.0-55.2%. The open porosity was similar for all samples and was in range from 29.4-33.4%. The total porosity was slightly lower for mixture composition with low NMR rate – 73.0% and 76.8-78.6% for mixtures with high amount of NMR.

Mechanical properties of porous AAM were affected by the high porosity of material which leads to compressive strength (f<sub>c</sub>) of material from 1.4-2.0 MPa. Highest f<sub>c</sub> was observed for AAM with highest density (B10-0.1A-Q or D) – 1.9-2.0 MPa. Significant decrease of f<sub>c</sub> was obtained for samples with NMR 0.5– 1.4-1.5 MPa but with NMR content 1.0 (B10-1.0A-Q or D) f<sub>c</sub> increased to 1.7 MPa. Lower strength for AAM composition with NMR ratio 0.5 could be contributed to the decreased aluminium ratio in mixture composition comparing to the samples with NMR ratio 1.0;

however density of all composition is comparable. This phenomenon must be investigated. The choice of micro-fillers does not contribute to the strength change for AAM.

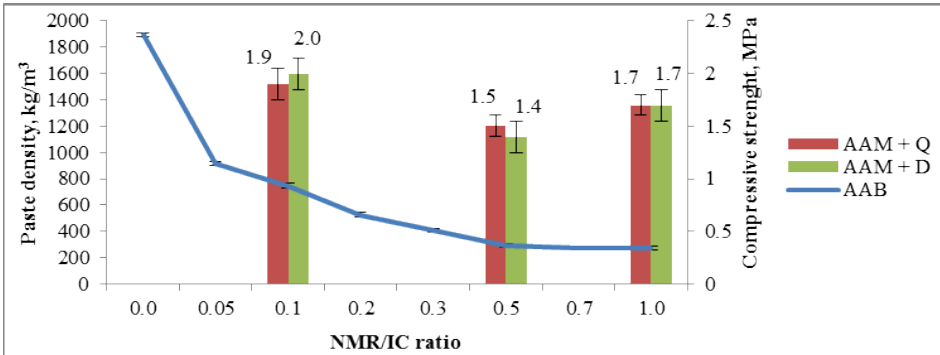


Figure 4. AAB paste density and AAM compressive strength related to NMP/IC ratio

Similar results were obtained for the flexural strength  $f_m$ . The highest results were achieved from AAM with NMR 0.1 – 0.9 to 1.0MPa. Decrease of  $f_m$  was observed for lower density samples – 0.6-0.7MPa.

The thermal conductivity of porous alkali activated building materials was between 0.14 and 0.15 (W/(m·K)).

### 3. Conclusions

The NMR in combination with alkali-activated geopolymer paste contributes to the creation of a new porous building material having similar properties to those of aerated concrete. According to FTIR and XRD analyses alkali activation of calcined illite clay and formation of geopolymer gel is approved.

This mixture design approach allows reusing NMR effectively and is a step forward in lightweight AAM research society. Material with low density (from 540-675kg/m<sup>3</sup> in this research) could be created having similar porosity (open porosity 29-33%; total porosity 73-78%), water absorption (41-55%) and mechanical properties ( $f_c$  1.4-2 MPa;  $f_m$  0.6-1.0 MPa) as similar competing materials. The choice of micro-fillers does not contribute to the strength change for porous AAM. The thermal conductivity of porous alkali activated building materials was between 0.14 and 0.15 (W/(m·K)) therefore it could be regarded as a material with thermal insulation properties.

To ensure sustainability of material during its life cycle the durability must be tested. Microstructural investigation revealed efflorescence as salt spots on pore surface, therefore leaching tests should be performed.

### Acknowledgement

The research work was carried out in the frame of the Latvian Council of Science Project: "Development of sustainable effective lightweight construction materials based on industrial waste and local resources" (No. Z12.0412).



## References

- [1] M. C. G. Juenger, F. Winnefeld, J. L. Provis, and J. H. Ideker, "Advances in alternative cementitious binders," *Cem. Concr. Res.*, vol. 41, no. 12, pp. 1232–1243, Dec. 2011.
- [2] P. Duxson, J. L. Provis, G. C. Lukey, and J. S. J. van Deventer, "The role of inorganic polymer technology in the development of 'green concrete,'" *Cem. Concr. Res.*, vol. 37, no. 12, pp. 1590–1597, Dec. 2007.
- [3] W. K. W. Lee and J. S. J. van Deventer, "The effect of ionic contaminants on the early-age properties of alkali-activated fly ash-based cements," *Cem. Concr. Res.*, vol. 32, no. 4, pp. 577–584, Apr. 2002.
- [4] F. Pacheco-Torgal, Z. Abdollahnejad, A. F. Camões, M. Jamshidi, and Y. Ding, "Durability of alkali-activated binders: A clear advantage over Portland cement or an unproven issue?," *Constr. Build. Mater.*, vol. 30, pp. 400–405, 2012.
- [5] a. Elimbi, H. K. Tchakoute, and D. Njopwouo, "Effects of calcination temperature of kaolinite clays on the properties of geopolymer cements," *Constr. Build. Mater.*, vol. 25, no. 6, pp. 2805–2812, Jun. 2011.
- [6] R. Arellano Aguilar, O. Burciaga Díaz, and J. I. Escalante García, "Lightweight concretes of activated metakaolin-fly ash binders, with blast furnace slag aggregates," *Constr. Build. Mater.*, vol. 24, no. 7, pp. 1166–1175, Jul. 2010.
- [7] J. Temuujin, A. Minjigmaa, W. Rickard, M. Lee, I. Williams, and A. van Riessen, "Preparation of metakaolin based geopolymer coatings on metal substrates as thermal barriers," *Appl. Clay Sci.*, vol. 46, no. 3, pp. 265–270, Nov. 2009.
- [8] R. R. Lloyd, J. L. Provis, and J. S. J. van Deventer, "Pore solution composition and alkali diffusion in inorganic polymer cement," *Cem. Concr. Res.*, vol. 40, no. 9, pp. 1386–1392, Sep. 2010.
- [9] L. Zheng, C. Wang, W. Wang, Y. Shi, and X. Gao, "Immobilization of MSWI fly ash through geopolymerization: effects of water-wash.," *Waste Manag.*, vol. 31, no. 2, pp. 311–7, Feb. 2011.
- [10] P. Duxson, G. C. Lukey, and J. S. J. van Deventer, "The thermal evolution of metakaolin geopolymers: Part 2 – Phase stability and structural development," *J. Non. Cryst. Solids*, vol. 353, no. 22–23, pp. 2186–2200, Jul. 2007.
- [11] P. E. Tsakiridis, "Aluminium salt slag characterization and utilization—a review.," *J. Hazard. Mater.*, vol. 217–218, pp. 1–10, May 2012.
- [12] M. C. Shinzato and R. Hypolito, "Solid waste from aluminum recycling process: characterization and reuse of its economically valuable constituents.," *Waste Manag.*, vol. 25, no. 1, pp. 37–46, Jan. 2005.
- [13] D. Bajare, a. Korjakins, J. Kazjonovs, and I. Rozenstrauha, "Pore structure of lightweight clay aggregate incorporate with non-metallic products coming from aluminium scrap recycling industry," *J. Eur. Ceram. Soc.*, vol. 32, no. 1, pp. 141–148, Jan. 2012.
- [14] H.-C. Wu and P. Sun, "New building materials from fly ash-based lightweight inorganic polymer," *Constr. Build. Mater.*, vol. 21, no. 1, pp. 211–217, Jan. 2007.
- [15] K. Okada, A. Ooyama, T. Isobe, Y. Kameshima, A. Nakajima, and K. J. D. MacKenzie, "Water retention properties of porous geopolymers for use in cooling applications," *J. Eur. Ceram. Soc.*, vol. 29, no. 10, pp. 1917–1923, Jul. 2009.
- [16] Z. Zhang, H. Wang, J. L. Provis, F. Bullen, A. Reid, and Y. Zhu, "Quantitative kinetic and structural analysis of geopolymers. Part 1. The activation of metakaolin with sodium hydroxide," *Thermochim. Acta*, vol. 539, pp. 23–33, Jul. 2012.
- [17] M. Criado, a Palomo, and a Fernandezjimenez, "Alkali activation of fly ashes. Part 1: Effect of curing conditions on the carbonation of the reaction products," *Fuel*, vol. 84, no. 16, pp. 2048–2054, Nov. 2005.
- [18] Z. Yunsheng, S. Wei, C. Qianli, and C. Lin, "Synthesis and heavy metal immobilization behaviors of slag based geopolymer.," *J. Hazard. Mater.*, vol. 143, no. 1–2, pp. 206–13, May 2007.
- [19] Z. Baščarević, M. Komljenović, Z. Miladinović, V. Nikolić, N. Marjanović, Z. Žujović, and R. Petrović, "Effects of the concentrated NH<sub>4</sub>NO<sub>3</sub> solution on mechanical properties and structure of the fly ash based geopolymers," *Constr. Build. Mater.*, vol. 41, no. 3, pp. 570–579, Apr. 2013.
- [20] I. Biljana, M. Aleksandra, and M. Ljiljana, "Thermal treatment of kaolin clay to obtain metakaolin," *Hem. Ind.*, vol. 64, no. 4, pp. 351–356, 2010.
- [21] Y. M. Liew, H. Kamarudin, a. M. Mustafa Al Bakri, M. Luqman, I. Khairul Nizar, C. M. Ruzaidi, and C. Y. Heah, "Processing and characterization of calcined kaolin cement powder," *Constr. Build. Mater.*, vol. 30, pp. 794–802, May 2012.
- [22] S. a. Bernal, R. M. de Gutierrez, J. L. Provis, and V. Rose, "Effect of silicate modulus and metakaolin incorporation on the carbonation of alkali silicate-activated slags," *Cem. Concr. Res.*, vol. 40, no. 6, pp. 898–907, Jun. 2010.
- [23] S. S. Legodi, M.A., de Wall, D., Potgieter, J.H., Potgieter, "Technical Note Rapid Determination of CaCO<sub>3</sub> in Mixtures Utilizing FT-IR Spectroscopy," *Miner. Engineering*, vol. 14, no. 9, pp. 1107–1111, 2001.

# Study of properties of steel fiber reinforced concrete for possible applications in Pakistan

Asad-ur-Rehman KHAN<sup>1</sup> and Tatheer ZAHRA

*NED University of Engineering and Technology, Karachi-75270, Pakistan*

**Abstract.** Steel fibers have been used worldwide to enhance properties of concrete but have not yet gained popularity in Pakistan. An experimental study was conducted to study the mechanical properties of steel fiber reinforced concrete that would lead to recommendation for possible use in Pakistan. Steel fibers conforming to recommendations of ACI Committee 544 were used with cement, sand and silica fume to cast samples for testing. Coarse aggregates were not used in order to compare the properties with famous Ultra High Performance ductile Concrete (UHPdC). Three different mixes were made with 2.5%, 5% and 8% of steel fibers by total weight of batch mix. Water cement ratio was kept as low as 0.25 to obtain high strength. Super plasticizer was added to increase workability. Reduction in flowability of concrete was observed with increasing percentage of fibers. Compressive, splitting tensile and flexural strengths were defined by testing standard cylinders and beams made up of different mixes of SFRC. Highest compressive, splitting tensile and flexural strengths were observed for steel fiber content of 8% followed by 5% and then 2.5% fiber contents as expected. Achieved compressive, splitting tensile and flexural strengths were much higher than the conventional concrete strengths used in Pakistan. Results of the study indicate that SFRC has the potential to be used in Pakistan in structures where high strength and is desired. Durability aspects of SFRC have to be looked into before it can be used in structures exposed to aggressive environments or located in coastal areas.

**Keywords.** Steel fibers, ductility, high strength, flowability, Ultra high performance ductile concrete

## Introduction

Addition of steel fibers in normal strength concrete could enhance its strength, ductility and durability. Ultra high performance ductile concrete (UHPdC) is one example for that. Many researchers have worked on this concrete to attain concrete strength as high as 25,000 psi [1-3]. Inspiration was taken from this newly evolved high performance concrete and steel fiber reinforced concrete (SFRC) was developed using indigenous materials available in Karachi. The constituents used were ordinary Portland cement, sand, Silica fume and steel fibers. Silica fume was added to increase flowability and particle packing [1-4]. Coarse aggregate were not used primarily to reduce the inter-

---

<sup>1</sup>Corresponding author: NED University of Engineering and Technology, Karachi-75270, Pakistan, [asadkhan@neduet.edu.pk](mailto:asadkhan@neduet.edu.pk)

particle space, resultantly increasing the durability of the final product. Steel fibers in proportion of 2.5%, 5% and 8% were added to enhance strength and ductility.

Compressive strength, splitting tensile strength and flexural strength were determined through ASTM standard testing procedures. Increasing percentages of fiber resulted in increased strength and reduced workability. Highest strength was achieved for mix design with 8% steel fibers. SFRC performed much better than normal strength concrete (NSC) due to its higher strength and ductile behavior. High strength and ductility will result in lighter sections which could be proportioned appropriately in structures like bridges where heavy loads are to be incorporated [5]. However, more detailed and comparative studies are needed before it can be used with confidence in construction industry where high strength, ductility and durability are major concerns.

## 1. Experimental program

Constituents used to produce SFRC were more or less similar in contrast to conventional concrete used within Pakistani Construction Industry. Constituents used to produce SFRC included Ordinary Portland cement (OPC), Silica Fume (SF), water, sand and steel fibers. Super plasticizer (Poly-Carboxylate Ether based) was used to elevate the workability in lieu of reduced water-to-cement ratio. This resulted in a densely packed matrix that elevates the rheological and mechanical properties with reduced permeability [1,6]. Among the changes were the elimination of coarse aggregate to reduce the inter-particle space, and finally increasing the durability.

OPC was used as primary binder within SFRC. Water to cement (w/c) ratio was kept at 0.25. Silica fume was added to increase flowability due to spherical nature and it served the purpose for particle packing. Fine aggregate was the largest constituent within SFRC, size selection for sand was #14 sieve passing and #30 sieve retained, this implies that the particle size was kept within range of 1.41 mm to 0.595 mm. The rationale being that the mix was intended to be kept as fine as possible. Length of steel fibers was kept at 30 mm and diameter of 0.461 mm, this resulted into an aspect ratio of 65. The proportion of steel fibers was kept between 2.5% to 8%.

Consistency test was performed immediately after mixing the constituents. Compressive and splitting tensile strengths were determined at 7, 14 and 28 days while flexural strength was determined at 28 days only.

### 1.1 Manufacturing of SFRC

Three mix designs were used with varying steel fibers percentages to study the implications incurred as a result of variation in steel fibers proportion. All other constituents were kept the same including the curing regime.

- Mix Design # 1 (M1) with steel fibers proportions of 2.5%
- Mix Design # 2 (M2) with steel fibers proportion of 5%
- Mix Design # 3 (M3) with steel fibers proportion of 8%

Quantities used in three mix designs with varying steel fibers proportion are shown in Table 1. Number of samples prepared for each mix design is shown in Table 2. A dry premix of Portland cement, silica fume and sand was obtained by allowing them to mix under dry condition within the mixer for 3 minutes to homogenize the mix and

remove any clumps formed within the constituents. After obtaining a homogenized dry premix, half of the required water and super plasticizer were added into the premix. Water and super plasticizer were allowed to mix thoroughly. A time came where balls of concrete mix commenced to form, after which the remaining water and super-plasticizer were added into the mix and allowed to mix to a point where a workable concrete mix was obtained. Steel fibers were the last to be mixed within concrete mix. It is noteworthy that the time varied with the variation in the proportion of steel fibers.

**Table 1.** Composition of SFRC mix designs M1, M2, M3

Constituents	Kg	% of total batch weight
	M1, M2, M3	M1, M2, M3
Portland Cement	80.94, 79.40, 80.94	34.02, 33.09, 32.11
Sand	99.50, 97.50, 99.50	41.82, 40.65, 39.46
Silica Fume	23.00, 22.5, 23.00	9.66, 9.38, 9.10
Super Plasticizers	2.50, 2.50, 2.50	1.05, 1.04, 1.01
Steel Fibers	5.94, 12.50, 20.16	2.50, 5.0, 8.0
Water	26.00, 25.50, 26.00	10.92, 10.62, 10.30

**Table 2.** Specimen tested for different mechanical properties of each batch

Curing Regime	Specimen age at Testing (Days)	Number of specimen		
		Compressive Strength	Tensile Strength	Flexural Strength
Water cured	7	5	3	-
	14	5	3	-
	28	5	3	2

### 1.2 Tests for determining consistency, compressive strength, splitting tensile strength and flexural strength

Consistency of mix designs was determined as per ASTM C1437 immediately after mixing was completed. Freshly mixed SFRC was placed within the steel cone resting on the impact table. Steel cone was then lifted to allow the mix evenly spread onto the impact table. After that the impact table was allowed to drop by 12.5 mm for 25 times, the extent to which the mix had spread was measured using a Vernier Caliper to quantify its consistency.

The initial diameter was taken that of steel cone which is 4 in. The flowability was evaluated using Eq. (1).

$$\text{Flowability}(\%) = \frac{\text{FinalDia.} - \text{InitialDia.}}{\text{InitialDia.}} \times 100 \quad (1)$$

Cylindrical specimens measuring 100 mm × 200 mm were tested as per ASTM C39. Loading was applied by Compression Testing Machine (CTM) under controlled rate of loading till the specimen had failed in compression.

Cylindrical specimens measuring 150 mm × 300 mm were tested as per ASTM C496. Specimen was longitudinally aligned with the CTM. Specimens were loaded till the specimens splitted into two.

Testing was conducted on a sample beam of 114 mm × 114 mm × 356 mm in accordance with ASTM C1018. Loads were applied at third points on the beams. Beams were placed on supports at the offset of 25 mm from the edges, and two point loads were applied at the one-thirds of the span of the beams. Rate of loading was maintained at 0.5 mm/min. Calculation of modulus of rupture depends upon the propagation of cracks. If cracks remained within one-third of specimen Eq. (2) is used, while Eq. (3) is to be used if cracks propagate beyond one-third length of the specimen.

$$R = \frac{PL}{bd^2} \quad (2)$$

$$R = \frac{3Pa}{bd^2} \quad (3)$$

where,

$R$  = Modulus of Rupture, MPa or psi.

$P$  = maximum applied load indicated by the testing machine, N or lb.

$L$  = Span length, mm or in.

$b$  = average width of specimen, mm or in., at the fracture.

$d$  = average depth of specimen, mm or in., at the fracture, and

$a$  = average distance between the fracture and the nearest support measured on tension surface of the beam, mm or in.

## 2 Results and discussion

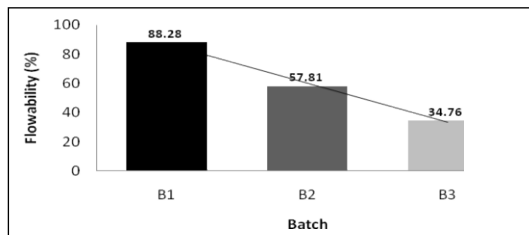
### 2.1 Consistency test results

Flowability of mix designs is shown in Figure 1. It can be seen in Figure 1 that workability of SFRC decreases linearly with an increase in steel proportion, indicating that workability is inversely proportional to steel proportion used.

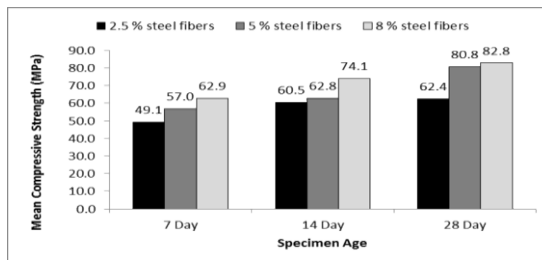
### 2.2 Compressive strength test results

Figure 2 shows the average compressive strength of samples at 7, 14 and 28 days with comparison of varying steel fibers percentages. Highest strength was achieved by the mix design with 8% steel fibers (82.8 MPa) followed by 5% steel fibers (80.8 MPa) and 2.5% steel fibers (62.4 MPa). Gain in compressive strength achieved by all mix designs is significant as compared to normal strength concrete used in the construction industry and followed the general trend reported in literature ([7-8]) that increase in proportion of steel fibers consequently elevates the compressive strength. Increased strength of SFRC would result in reduced cross sectional area and lighter sections since strength has inverse relation with the cross sectional area. Since this study is aimed towards exploring the potential of SFRC for use in Pakistan, only three fiber contents

were used. However, optimum fiber content needs to be defined before the material can be used in practical applications.



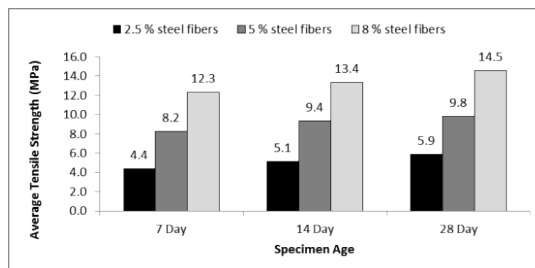
**Figure 1.** Flowability of SFRC for different steel fibers proportions



**Figure 2.** Compressive Strength of SFRC for different steel fibers proportions

### 2.3 Splitting tensile test results

Splitting tensile strength of specimens are shown and compared in Figure 3. Trend similar to that of compressive strength can be seen in this case also. Specimens with 2.5% steel fiber have the lowest strength (5.9 MPa) at 28 days followed by specimen with 5% steel fibers (9.8 MPa) and 8% steel fibers (14.5 MPa). Normally NSC has a tensile strength in the range of 2.76–3.1 MPa. However, with the addition of steel fibers the tensile strength has increased to 14.5 MPa making it almost 5 times the tensile strength of NSC. This trend is in line with the results reported in literature that steel fibers greatly add to SFRC ductility and superior tensile strength ([8-9]).



**Figure 3.** Splitting Tensile Strength of SFRC for different steel fibers proportions

## 2.4 Flexural strength test results

For flexural strength test, two beams for each mix design were tested at 28 days only. Eq. (2) was used to evaluate modulus of rupture as all the propagated cracks were within one-third of the beam length. Modulus of rupture respectively for mix designs 1, 2 and 3 were observed to be 7 MPa, 11.06 MPa and 15.55 MPa respectively which are in comparison to 5.9 MPa, 9.8 MPa and 14.5 MPa splitting tensile strengths. SFRC for each mix design exhibited ductile behavior and improved serviceability in post cracking regime, unlike NSC, by carrying further load after first crack had occurred.

## 3 Conclusions and recommendations

Following conclusions can be drawn from the study:

- Compressive strength of SFRC was found to be higher than NSC for all the mix designs used in the study, with mix design having 8% steel fibers showing the maximum strength of 82.8 MPa.
- Splitting tensile strengths and modulus of rupture of SFRC were also found to be higher, as much as 5 times, than that of conventional concrete, making it more ductile and resistant to cracking.
- Results indicate that SFRC has potential to be used in high rise buildings and bridge construction where ductility and high strength are to be met.
- Optimum fiber content, modulus of elasticity and Poisson's ratio need to be defined in order to quantify the serviceability of SFRC elements.
- Durability aspects of SFRC need to be explored before it can be used in areas where structures are exposed to aggressive environments.

## Acknowledgement

The authors are indebted to the Department of Civil Engineering at NED University of Engineering & Technology, Karachi, Pakistan and the University itself, in the pursuit of this work.

## References

- [1] T.M. Ahlborn, E.J. Peuse and D.L. Misson, *Ultra-High-Performance Concrete for Michigan Bridges Material Performance-Phase I*, Research Report RC-1525, Michigan Tech, Center for Structural Durability, Michigan Tech Transportation Institute, 2008.
- [2] B. Nematullahi, M.R. Saifulnaz, M.S. Jafer and Y.L. Voo, A review of ultra-high performance 'ductile' concrete (UHPdC) technology, *International Journal of Civil and Structural Engineering*, **2**(2012), 1003–1018.
- [3] Y. L. Voo, Ultra-High performance 'ductile' concrete technology towards sustainable construction, *International Journal of Sustainable Construction Engineering and Technology*, **1** (2010), 105–126.
- [4] P. Richard and M. Cheyrezy, Composition of reactive Powder Concretes, *Cement and Concrete Research*, **25** (1995), 1501-1511.
- [5] Y.L. Voo, P.C. Augustin and T.A.J. Thamboe, Design and construction of a 50m single span ultra-high performance ductile concrete composite road bridge, *International Journal of Sustainable Construction Engineering and Technology*, **3** (2012), 1–17.

- [6] M. Schmidt and E. Fehling, Ultra-High-Performance Concrete: Research, Development and Application in Europe, Seventh International Symposium on the Utilization of High-Strength/High-Performance Concrete, *ACI Special Publication*, Washington, D.C., USA, 228 (2005), 51-7.
- [7] M.C. Nataraja, N. Dhang and A.P. Gupta, Stress-strain curves for steel fiber reinforced concrete in compression, *Cement and Concrete Composites*, **21** (1999), 383–390.
- [8] P.S. Song and S. Hwang, Mechanical properties of high-strength steel fiber-reinforced concrete, *Construction and Building Materials*, **18** (2004), 669–673.
- [9] G. Batson, Steel fiber reinforced concrete, *Material Science and Engineering*, **25** (1976), 53-58.



# Blended cement utilizing ceramic wall tiles waste

Dina M.SADEK<sup>a</sup>, Sh.K. AMIN<sup>b</sup>, and N.F. YOUSSEF<sup>a,1</sup>

<sup>a</sup>*Housing and Building National Research Center (HBRC), Dokki, Giza, Egypt.*

<sup>b</sup>*Chemical Engineering and Pilot Plant Department, NRC, Dokki, Giza, Egypt*

<sup>a,1</sup>*Building Materials Technology and Processing Research Institute, (HBRC), Egypt*

**Abstract.** In order to reduce the footprint over the environment, regarding the great energy consumption required to produce cement, it was allowed in the International, European and Egyptian standards to produce the blended cement known as CEMII. This work could successfully utilize the fired ceramic wall tiles waste rejected in industry to partially replace cement up to 35% by weight to produce one of the allowed types of CEMII, depending on the fact that Egyptian standards of ceramic wall tiles allows only the 1<sup>st</sup> grade to be delivered to the market. The obtained blended cement was found to be in good conformity to the standards.

In the present work, the fired ceramic tiles waste was very fine ground up to particle size of 70  $\mu\text{m}$ . It was replacing ordinary Portland cement (OPC) known as CEMI42.5N in different proportions, then mixed with sand and water to form mortar. Standard test methods of cement mortar were applied, then the best ratios of additions were investigated. Tools as XRD, XRF, particle size distribution and SEM with EDAX were used to assess both raw materials and the suggested mixtures as well.

**Keywords.** Blended cements, fired ceramic tiles waste

## Introduction

The cost of construction materials is increasing day by day because of high demand, scarcity of raw materials, and high price of energy. The use of alternative constituents in construction materials is now a global concern [1]. The building material industry could easily play a significant role in attaining the goal of substitution of natural raw materials by utilizing the wastes of some industries.

Other than recycling of fired wastes as cullet or grog, which improves the properties of the product, (like reducing shrinkage of ceramic tiles) [2], utilizing some of these industries wastes will save not only natural raw materials for cement production and waste landfill disposal, but also reduces clinker production. In fact, cement industry is considered worldwide, together with iron and steel industry, as a main CO<sub>2</sub> producer due to the high-temperature processes (1500°C) and the high use of calcium carbonate, although it could be reduced on 2009 [3]. The production of one ton of cement generates 0.55 ton of CO<sub>2</sub> and requires 0.39 tons of CO<sub>2</sub> in fuel emissions, accounting for a total of 0.94 tons of CO<sub>2</sub> [4]. So, two environmental strategies were considered, one of them is "blended cement" [5].

<sup>1</sup>Corresponding author: [dr\\_n\\_faheem@hotmail.com](mailto:dr_n_faheem@hotmail.com), [nadiaf.youssef@gmail.com](mailto:nadiaf.youssef@gmail.com)

Suggesting mixing more than one partial replacement of the Supplementary Cementitious Materials (SCMs) was also discussed [6].

Utilization of both fired red and white ceramic wastes and their combination as a substitute of raw materials in the manufacture of clinker itself was investigated. The results showed that they were technically viable, and have higher reactivity and burnability than a conventional mix, providing that the particle size of the waste used is lower than 90  $\mu\text{m}$  [7]. Broken glass and ceramics are considered as non-hazardous waste that can be also utilized [8]. The recycling practice has been adopted in Europe by enforcing specific standards that allow the use of waste (fly-ashes, blast furnace slag, silica fume ( $\text{SiO}_2$ ), respectively, in blended cements, according to EN 197-1. [9]. The Egyptian Standards of cement, which is fully harmonized with European Standards of cement allows it too [10].

Ceramic wastes were utilized in concrete in two phases: (phase A) for partial replacement of cement by ceramic fine powder, and (phase B) for replacement of traditional aggregates by ceramic sand and aggregates. The results insured the pozzolanic properties of the cement replacement powder [11]. In a distinguished work about utilizing the polishing and glazing ceramic wastes, produced as a sludge, in Italian factories, they were utilized as a partial replacement of CEMI52.5 successfully up to 25%, with some important differences in their behavior [12]. In another work, the ceramic factory wastes known as masonry rubble, were also classified as activated clays from industrial waste with pozzolanic properties. A substitution ratio of cement by the fired ceramic waste of 15-20% was found satisfactory [13]. Utilization of powdered roof tile, of cracked or broken ceramic bodies, not accepted as commercial products, as pozzolanic addition, in the manufacture of blended cements was achieved. The calcined clay wastes are found suitable for partial replacement (up to 20–30% weight) of cement without a detrimental effect on the strength [14]. Studies have been carried out in order to investigate the viability of partially substituting cement by using ceramic rejects or masonry rubble as raw materials in prefabricated concrete, exploiting their pozzolanic properties [15] [16]. Ceramic masonry rubble must be suitably fine, with a Blaine value of around 3500  $\text{cm}^2/\text{g}$ , in order to be used as a pozzolanic additive in cement. Calcined clay waste, from Spanish paper industry, in the form of slurry with 29% organic materials, was utilized in blended cements [17]. New blended cements containing 10% and 20% ceramic sanitary ware (SW), and construction and demolition waste (C&DW) were investigated. The results showed that the addition of ceramic sanitary ware waste reduced shear yield stress and retarded the hydration reactions [18].

Other wastes as future possible additives to blended cements such as: bottom ashes derived from municipal solids waste incinerators after a simple thermal treatment, showed a promising pozzolanic binder [19]. Untreated bottom ashes have shown scanty pozzolanic activity and they thus appear to be unsuitable to be used directly in cementitious composites [20]. Attempts to utilize other inorganic wastes in blended cements were carried on, such as ground glass [21] [22] and ferroalloy industry waste [23]. Organic wastes were also put under investigation, but they must be treated (mostly by burning) to obtain them in the form of silica residue. Examples are: rice husk ash [24], and sugar cane bagasse ash [25]. The environmental problems of bamboo leaf wastes, specially existing in Latin America, motivated Brazilian researchers to utilize them after thermal treatment at 600°C as calcinations temperature, reducing its size to 5% only, with grinding to below 45 $\mu\text{m}$  [26]. This

work was supported by Indian researchers utilizing Indian bamboo leaves ashes, who reported good pozzolanic effect [27] [28].

In a recent work of Egyptian authors, to improve Egyptian ordinary Portland cement blended with granulated blast furnace slag, nano silica was added. The blended cement of 45% blast furnace slag and 3-4% nano silica caused the highest improvement of cement pastes and mortars properties [29].

### **Aim of this work**

Cement industry in Egypt, which is very promising, suffers from lack of energy. A debate is taking place in Egyptian society about saving energy to this industry as soon as possible. It consists 5% of the national income of Egyptian industry, and 2% of the total national income. There are 24 factories producing cement, owned by 21 Egyptian and international companies with 60 milliard Egyptian pounds investments and producing 68 million metric tons of cement [30]. Due to the efforts of EEAA to control the pollution coming out of this industry, seven cement companies were financed, supplied and supervised by the EEAA during the year 2012 [31].

On the other hand, Ceramic tiles industry is also a promising industry in Egypt. There are 32 Ceramic tiles and sanitary ware factories, owned by around 22 investors, other than new factories under establishing [30]. The ceramics and refractory industries constitutes 7% of all the Egyptian industries, being one of the most important 7 promising Egyptian industries. The wastes of 3 different ceramics industries were investigated by the EEAA[32].

The Egyptian standards of Ceramic wall and floor tiles [33], is fully harmonized with International standards [34]. In their scope, both allow only the best commercial quality (first quality) tiles to be delivered to the market. So, the rejects of defected fired tiles may cause a waste problem.

As long as the standards allows blending with burnt shale, from 21 up to 35% by weight known as CEMII/B-T [9], this work is very ambitious to utilize the wall ceramic tiles waste, up to this ratio, insuring its conformity to standards, to save energy required for clinker production, materials to cement manufacturing and to fulfill both environmental and economical targets. The choice of OPC CEMI 42.5N to be blended with this waste, was because it is the most common type of cement production in Egypt.

### **1. Materials and methods**

The used cement in all pastes and mortar mixtures was CEMI 42.5N from El-Suez cement company, Egypt. Its fineness is expected to be around 90  $\mu\text{m}$  as standardized. It complies with the British Standards BS EN 197-1:2011 [9]. Fired glazed wall ceramic tiles waste, as a reject from the production line of "Venus Ceramic Tiles Factory" in 10<sup>th</sup> of Ramadan industrial new city was used as a supplementary cementing material to replace part of cement. Its original raw materials are: plastic clay and ball clay, two types of potash feldspars, limestone, kaolin, bentonite and glass sand (quartz). It was crushed and finely ground to around 70  $\mu\text{m}$  as nominal particle size.

Both cement and ceramic waste powders were analyzed by X-ray fluorescence technique (XRF) where the chemical analysis was carried out using Axios (PW4400) WD-XRF Sequential Spectrometer (Panalytical, Netherlands), using (Rubidium) Rb-

ka radiation tube at 50 kV and 50 mA. The mineralogical composition of the studied components was determined by powder X-ray diffractometry analysis.

Both raw materials fineness were investigated through Laser Scattering Particle Size Distribution Analyzer apparatus (Horiba LA950). The measurements were volume distribution base. The effect of using ground ceramic waste powder on the properties of blended cement in the fresh and hardened states was investigated. Natural siliceous sand conforming the requirements of the British Standards BS EN 196-1:2005 [35] was used as fine aggregate for casting mortar mixtures and results were compared with the limits set out in the British Standards of cement BS EN 197-1:2011 [9]. Hence, the experimental work was divided into two parts: the first part is the determination of the properties of cement pastes containing ground ceramic waste powder such as standard water required for standard consistency, initial and final setting times and soundness. While the second part is the determination of the properties of cement mortars, containing ground ceramic waste powder, such as flexural and compressive strengths at the ages of 2 and 28 days using 4x4x16 cm prisms, as well as the determination of bulk density and water absorption at the age of 28 days using 2.5 cm cubic specimens. The mortars of these small cubes were prepared using commercial sand and tap water.

In each part during the experimental work, ground ceramic waste was used to replace 0% to 35% by weight of cement with an interval of 5% increase. The water required for the paste to have a standard consistency as well as the initial and final setting times of cement pastes were determined according to the British Standards BS EN 196-3:2005 [36] using Vicat apparatus. The soundness of cement pastes was determined according to Standards [36] using Le Chatelier apparatus. The 2 and 28 days compression and flexural strengths of cement mortars were determined according to the British Standards BS EN 196-1:2005 [35] using a compression-testing machine. The ratio between cement : sand : water in mortar mixtures was 1 : 3 : 0.5 (by weight).

Depending upon results, the blank sample, 20% replacement sample and 35% sample were investigated using XRD and XRF beside the analytical techniques of a scanning electron microscopy (SEM) and energy dispersive X ray spectroscopy (EDAX) of a magnification power of up to 100000x. Mortar samples for XRD, XRF and SEM analysis were obtained from cutting the cubes used for water absorption measurements by sawing into 2 thirds in size. The fresh-fractured surfaces of the third were subjected to SEM, while the other two thirds of the cubes were ground for XRD and XRF.

## 2. Discussion of results

### 2.1. Assessment of raw materials

The chemical composition of cement contained 3.15% SO<sub>3</sub>, 0.02% Cl and 3.84% LOI while ground fired ceramic tiles waste powder contained 0.23% SO<sub>3</sub>, 0.1% Cl and 0.26% LOI. Loss on ignition, chloride and sulfate contents for the suggested blends of pure cement and pure ceramic waste powders are calculated by mass balance. As shown in Figure 1.

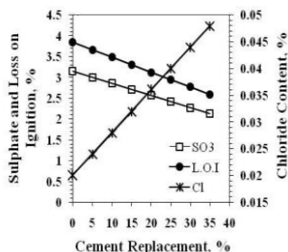


Figure 1. Effect of blending

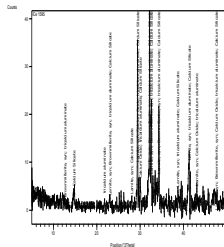


Figure 2. XRD of CEM142.5N

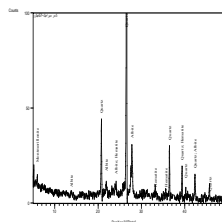


Figure 3. XRD of the ceramic waste

It is expected that SO<sub>3</sub> and LOI decrease ,while Cl, increases as the replacement of cement by the fired ceramic tile waste increases. But, in all cases it did not exceed the limit specified in table 4 of the standards [9]. The correlations of these straight line relationships R<sup>2</sup> = 1. The XRD results of both raw materials are shown in Figure 2 and Figure 3. Chemical analysis of the used raw materials is in good agreement with the XRD analysis. Cement contains : Larnite, syn(Ca<sub>2</sub>SiO<sub>4</sub>), Brownmillerite, syn(Ca<sub>2</sub> ( Al , Fe +3 )<sub>2</sub>O<sub>5</sub>), Calcium Oxide(CaO), tricalcium aluminate(Ca<sub>3</sub>Al<sub>2</sub>O<sub>6</sub>) and Calcium Silicate(Ca<sub>3</sub>SiO<sub>5</sub>). The fired ceramic wall tiles waste contains: Quartz (SiO<sub>2</sub>), Albite(Na AlSi<sub>3</sub>O<sub>8</sub>), Montmorillonite(( Na, Ca )<sub>0.3</sub> ( Al, Mg )<sub>2</sub> Si<sub>2</sub>O<sub>10</sub> (OH)<sub>2</sub>·nH<sub>2</sub>O), Hematite(Fe<sub>2</sub>O<sub>3</sub>).

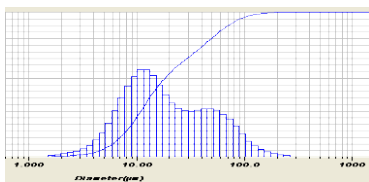


Figure 4. Particle size distribution of CEM142.2N

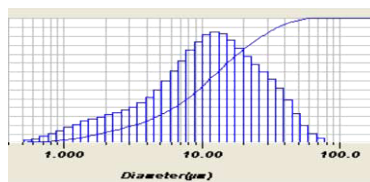


Figure 5. Particle size distribution of the ceramic waste

Figure 4 and Figure 5 show the Particle Size Distribution Analysis of cement and ceramic waste respectively. The differences in skewness of both curves is explained by the direct and calculated parameters as follows:

The mean size of cement is 28.97 μm while that of ceramic waste is 14.78 μm.  
 The median size of cement is 16.29μm while that of ceramic waste is 11.27μm.  
 The mode size of cement is 12.32μm while that of ceramic waste is 12.39μm.  
 The range of the particle size of cement started at 1.73μm and ended at 262.4 μm while that of ceramic waste ranged from 0.58 μm to 77.34 μm. The diameter on cumulative of 10% for cement is 6.25μm while that of ceramic waste is 2.45μm, and the diameter on cumulative of 90% for cement is 68.96 μm while that of ceramic waste is 32.58μm. From the above results, the mode of the particle size of the two powders are almost the same, with the fact that the ceramic waste is more fine than cement, with a better and normal grain size distribution.

2.2. Properties of cement pastes containing fired ceramic tiles waste

Figure 6 showed that the standard water required for consistency of cement increased as the % replacement by the ceramic waste increases, but in a very limited range.

Figure 7 showed both initial and final setting times of the blends. It is observed that as the % replacement increases, the setting times are increasing showing a trend.

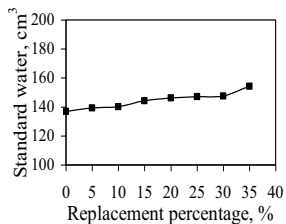


Figure 6. Standard water

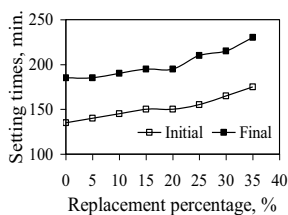


Figure 7. Setting times

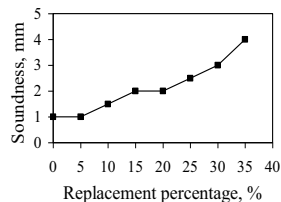


Figure 8. Soundness

Comparing to table 3 of the standards [9] which limits initial setting time > 60 min, all the tested blends are in conformity. Figure 8 shows the effect of blending with the waste on the soundness. The expansion increases as the waste % increases, but it did not exceed 4 mm at the 35% replacement ratio. Referring to table 3 of the standards [9], the highest limits=10 is still very far from the obtained results. No differences were observed between 0 and 5% replacement, and also between 15 and 20% replacement.

2.3. Properties of cement mortars containing fired ceramic tiles waste

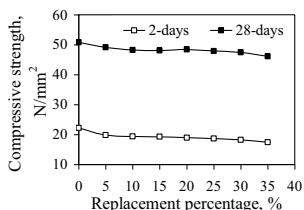


Figure 9. Compressive strength

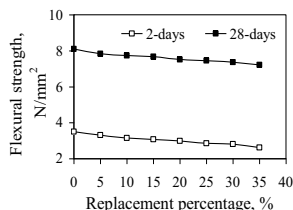


Figure 10. Flexural strength

Figure 9 shows both early and standard compressive strength of the cement-ceramic waste blends mortars. A decrease took place as the % replacement increases, but in a small range compared to the pure cement mortar (0% replacement). Comparing with table 3 of the standards [9], the early strength in its worst case is greater than required (10 MPa). The standard compressive strength has the same trend and conformity. Same trend is shown in Figure 10 of the flexural strength of the same blended cement samples.

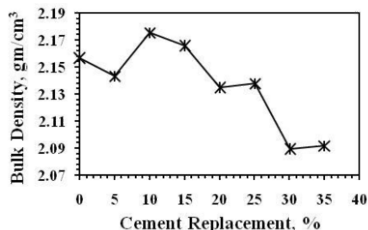


Figure 11. bulk density

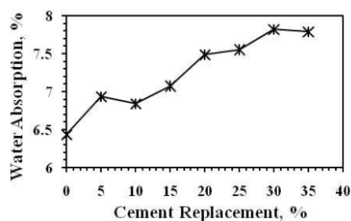


Figure 12. water absorption

For research purposes, Bulk density and water absorption of cement blends mortars after 28 days curing were measured. It is clear that bulk density gets lower as the % replacement increases, which means lighter weight mortar, as shown in Figure 11. From Figure 12, the water absorption increases as the % replacement increases. It is observed that 20, 25% replacements are almost identical while the 30% and the 35% samples are also almost identical. It must be noted that these samples contain non standard sand and water.

#### 2.4. Investigations of 0%, 20% and 35% replacements mortar samples

From previous discussion, The samples 20% and 35% replacements, after 28 days curing, needed monitoring and more investigations compared to the blank sample (0% replacement). They were all exposed to XRF, XRD and SEM with EDAX.

Chemical composition of mortar samples containing fired ceramic tiles waste after 28 days showed that for 0%, 20% and 35% Replacements respectively,  $SO_3$  was 1.49%, 1.27% and 1.19%, while Cl was 0.094%, 0.096% and 0.0832%. LOI was 4.55%, 4.28% and 3.85% respectively.

Referring to table 4 of the standards [9], All the obtained values of those important 3 elements are in good compliance, although it allows CEMII/B-T with over 20% replacement to contain 4.5% sulfate as  $SO_3$  instead of 3.5% as a maximum.

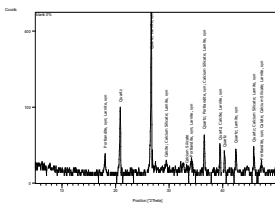


Figure13. 0% replacement

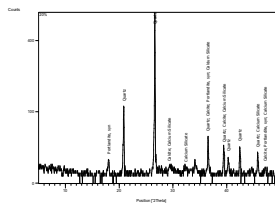


Figure14. 20 % replacement

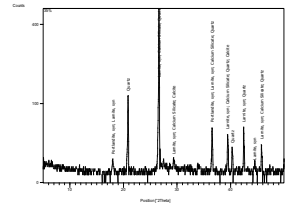


Figure15. 35% replacement

Figures 13, 14 and 15 show XRD of 0%, 20% and 35% replacements respectively. The blank sample and the 35% replacement sample have the same mineralogical composition. They have: Quartz ( $SiO_2$ ), Portlandite, syn( $Ca(OH)_2$ ), Calcite( $CaCO_3$ ), Calcium Silicate( $Ca_3SiO_5$ ) and Larnite, syn( $Ca_2SiO_4$ ). The 20% replacement sample has the same first 4 minerals, but Larnite, syn did not show up. Comparing with Figures 2 and 3, it is clear that the elements that are found in the fired ceramic wall tiles, not to mention those of the glaze, did not affect the mineral composition of the cement mortars.

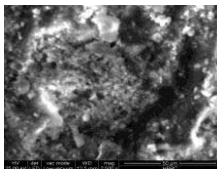


Figure16 (a). 0 % replacement

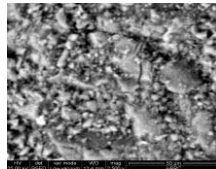


Figure17 (a). 20% replacement

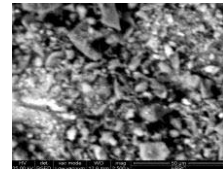
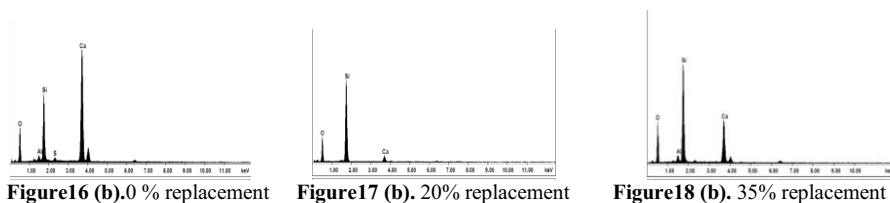


Figure18 (a). 35% replacement



Figures 16(a,b), 17(a,b) and 18(a,b) show the SEM micrographs of 2500x magnification and its EDAX pattern for the mortar samples of 0%, 20% and 35% replacements respectively. From Figure 16 of the blank cement mortar sample, the aluminum silicates crystals are shown. The elements analysis showed that it is composed of 53.08% O<sub>2</sub>, 1.53% Al, 16.21% Si, 28.32% Ca and 0.87% S. From Figure 17 of the 20% replacement mortar sample, less aluminum silicates crystals are shown. The elements analysis showed that it is composed of 54.22% O<sub>2</sub>, 41.64% Si and 4.14% Ca. There should be Al as it has Al Silicates as mineral, but may be spotting was not an adequate position. From Figure 18 of the 35% replacement mortar sample, the aluminum silicates crystals are shown again. The elements analysis showed that it is composed of 55.71% O<sub>2</sub>, 2.14% Al, 28.12% Si and 14.03% Ca. Comparing with the blank cement, the 35% replacement may contain slightly more silica and alumina, but less calcium oxides, and of course much less sulfur. These results seem to be compatible with previous work on ceramic waste [12]. Any differences from results of a previous work [14] can be due to manufacturing process, where the ceramic waste was fired at 930 °C, while the waste used in this work was fired at 1100 °C.

### 3. Conclusions

On blending OPC of type CEMI 42.5N with fired ceramic tiles waste powder, starting from 5% till 35%, it did not exceed the limit specified in table 4 of the standards [9] for Cl, SO<sub>3</sub> and LOI. Properties of both cement pastes and cement mortars containing fired ceramic tiles waste, such as soundness and setting times, early and standard compressive strength were compared to table 3 of BSI EN 197-1, 2011 [9] and found in good conformity.

The measured water absorption increases as the % replacement increases, and accordingly the bulk density decreases but both are in a small range. Investigations of 0%, 20% and 35% replacements mortar samples after 28 days curing, showed that SO<sub>3</sub>, Cl and LOI are decreasing as the % replacement increases. Obtained values of those important 3 elements are in good compliance to table 4 of the standards [9]. The XRD showed that both plain cement mortar and 35% replacement mortar have Quartz, Portlandite, Calcite, Calcium Silicate and Larnite as identical minerals and that the other materials such as glaze of the fired tiles did not affect the blended cement as approved by SEM and EDAX.

It can be concluded that replacement of 21% up to 35% by weight of CEMI 42.5N by fired ceramic wall tiles waste produces a blended cement whose properties are in good conformity to both BSI EN 197-1, 2011 and the Egyptian standards of cement.



## References

- [1] M. Safiuddin, M. Z. Jumaat, M. A. Salam, M. S. Islam, R. Hashim, Utilization of solid wastes in construction materials, *International Journal of the Physical Sciences* Vol. 5(13), (2010) 1952-1963,
- [2] M.F. Abadir, *Elements of ceramic technology*, 6<sup>th</sup> edition, Faculty of Engineering, Cairo University press, 2012
- [3] EPA 430-R-11-005. Inventory of U.S. greenhouse gas emissions and sinks: (1990–2009), APRIL 15, 2011, U.S. Environmental Protection Agency homepage, <http://www.epa.gov>
- [4] G.Ellis, Industrially interesting approaches to low- CO<sub>2</sub> cements, *Cement and concrete research*, 34 (2004) 1489-98
- [5] G. Habert, N. Roussel, [Study of two concrete mix-design strategies to reach carbon mitigation objectives](#), *Cement and Concrete Composites*, Volume 31, Issue 6, (July 2009), 397-402
- [6] R.J Flatt, N. Roussel, C.R.Cheesman, Concrete: An eco-material that needs to be improved, *Journal of the European Ceramic Society*, 32(2012) 2787-2798
- [7] F. Puertas, I. Garcia-Diaz, A. Barba, M.F. Gazulla, M. Palacios, M.P. Gomez, S. Martinez-Ramirez, Ceramic wastes as alternative raw materials for Portland cement clinker production, *Cement & Concrete Composites*, 30 (2008) 798–805
- [8] A. Pappu, M.Saxena, SR. Asolekar SR. Solid wastes generation in india and their recycling potential in building materials, *Building and Environment*, 42: (2007)2311-2320
- [9] BSI EN 197-1, 2011. Composition, specifications and conformity criteria for common cements. BSI Standards Publication, London, UK
- [10] ES 4756-1, 2013. Composition, Specifications and conformity criteria for common cements, Egyptian Organization for Standardization and Quality, (EOS), Cairo, Egypt
- [11] F. Pacheco –Torgal, S. Jalali, Reusing ceramic wastes in concrete, *Construction and Building Materials*, 24(2010) 832-838
- [12] F. Andreola, L. Barbieri, I. Lancellotti, M. C. Bignozzi, F. Sandrolini, New blended cement from polishing and glazing ceramic sludge, *Int. J. Appl. Ceram. Technol.* 7 [4] 5 (2010), 546–55
- [13] A. Juan, C. Medina, M. Ignacio Guerra, J. M. Morán, P. J. Aguado, M. I. Sánchez de Rojas, M. Frías, O. Rodríguez, Re-use of ceramic wastes in construction, *Ceramic Materials* 10(2010)197-214, Wilfried Wunderlich (Ed.), ISBN: 978-953-307-145-9, InTech,
- [14] A.E. Lavat, M. A. Trezza, M. Poggi, Characterization of ceramic roof tile wastes as pozzolanic admixture, *Waste Management* 29 (2009) 1666–1674
- [15] M.I. Sánchez de Rojas, M., Frías, J. Rivera, F.P. Marín, Waste products from prefabricated ceramic materials as pozzolanic addition. *Proceedings of 11<sup>th</sup> International Congress on the Chemistry of Cement*, (2003). 935-943, Alpha, Durban.
- [16] M.I. Sánchez de Rojas F.P., Marín, J. Rivera, M. Frías, Morphology and properties in blended cements with ceramic waste materials recycled as pozzolanic addition. *Journal of the American Ceramic Society*, Vol. 89, No. 12, (2006), 3701-3705
- [17] M. Frías, O. Rodríguez, I. Vegas, R. Vigil, Properties of calcined clay waste and its influence on blended cement behavior, *Journal of the American Ceramic Society*, Vol. 91, No. 4, (2008), 1226-1230.
- [18] C. Medina, M. I. Sánchez de Rojas, P. F. G. Banfill, M. Frías, Rheological and calorimetric behaviour of cements blended with containing ceramic sanitary ware and construction/demolition waste, *Construction and Building Materials*, (2013) 40 822-831.
- [19] A. Saccani, F. Sandrolini, F. Andreola, L. Barbieri, A. Corradi, I. Lancellotti, Influence of the pozzolanic fraction obtained from vitrified bottom-ashes from MSWI on the properties of cementitious composites, *Materials and Structures* 38 (April 2005) 367-371.
- [20] Filipponi, P., Poletti, A., Pomi, R., Sirini, P., Physical and mechanical properties of cement-based products containing incineration bottom ashes, *Waste Management* 23 (2) (2003) 145-56.
- [21] T.D. Dyer, R. K. Dhir, “Chemical Reactions of Glass Cullet Used as Cement Component,” *J. Mater. Civ. Eng.*, 13(2001) 412–417
- [22] C. Shi, Y. Wu, C. Riefler, H. Wang, characteristics and pozzolanic reactivity of glass powders, *Cem. Concr. Res.*, 35 (2005) 987–993
- [23] M. Frías, C. Rodríguez, “Effect of incorporating ferroalloy industry wastes as complementary cementing materials on the properties of blended cement matrices,” *Cem. Concr. Compos.*, 30 (2008) 212–219
- [24] M. Anwar, T. Miyagawa, M. Gaweesh, “Using rice husk ash as a cement replacement material in concrete, *Waste Manage. Ser.* 1(2000) 671–684.
- [25] G.C. Cordeiro, R.D. Toledo Filho, L.M., Tavares, E.M.R. Fairbairn, [Pozzolanic activity and filler effect of sugar cane bagasse ash in Portland cement and lime mortars](#), *Cement and Concrete Composites*, Volume 30, Issue 5, (2008), 410-418.

- [26] M. Frias ,H. Savastano, E. Villar, M. I.Sanchez de Rojas, S.Santos, Characterization and properties of blended cement matrices containing activated bamboo leaf waste, *Cement & Concrete Composites* 34 (2012) 1019–1023
- [27] NB. Singh, SS .Das, NP .Singh, VN .Dwivedi. Hydration of bamboo leaf ash blended Portland cement. *J Eng Mater Sci* (2007) 14 69–76.
- [28] VN .Dwivedi, NP .Singh, SS .Das, NB. Singh, A new pozzoolanic material for cement industry: bamboo leaf ash. ( 2006) **1**,106–111.
- [29] M. Heikal,S. Abdelaleem,W.M.Morsi, Characteristics of blended cements containing nano-silica, *HBRC Journal*,vol9,issue 3,december2013,243-255
- [30] Federation of Egyptian Industries, Chamber of Building Materials Industries, [www.cbmegypt.com](http://www.cbmegypt.com)
- [31] Annual environmental status report 2012, part10, Egyptian Environment Authority Agency, AAEE website.
- [32] EEAA, Control of Industrial Pollution Project, Inspection Guide of Ceramics, (2002), Cairo, Egypt,5-6 (in Arabic language)
- [33] ISO 13006 /2012, “Ceramic tiles –Definitions, classification, characteristics and marking”, (2012),. International Organization for Standardization.
- [34] ES 3168 – 6 / 2005, “Dry pressed ceramic tiles with water absorption > 10% (group BIII)”, (2005) Egyptian Organization for Standardization and Quality (EOS), Cairo, Egypt,.
- [35] BS EN 196-1:2005,Methods of testing of cement-Part1:Determination of strength, BSI Standards Publication, London,UK
- [36] BS EN 196-3:2005,Methods of testing of cement-Part3: Determination of setting times and soundness, BSI Standards Publication, London,UK

# Estimation of concrete properties at early age by thermal stress device

Sang Lyul CHA<sup>1</sup> and Jin Keun KIM

*Korea Advanced Institute of Science and Technology*

**Abstract.** The properties of concrete should be estimated in order to simulate the behavior of concrete structures at early age. However, it is difficult to estimate properties of concrete at early age because they change with time, temperature history, humidity and etc. In this study, a new approach is suggested in estimation of concrete properties such as final autogenous shrinkage, final creep coefficient and thermal expansion coefficient. Properties of concrete at early age are estimated by comparing between the results of analysis and experiments considering the effects of mixing material, temperature history and humidity by using thermal stress device which is able to get stress history in a chamber with various temperature history because each step of the analysis has the best values of concrete properties which would result in similar stress results between the analysis and the experiments. The results show that properties of concrete change with time at very early age which is within 1 day and then are converged to constant values.

**Keywords.** Concrete property, thermal stress, early age, thermal stress device

## Introduction

As concrete strength becomes higher and concrete structures become larger, the cracks induced by thermal stresses and restraints occur frequently and are more important. However, it is difficult to predict the possibility of the cracks induced by thermal stresses and restraints in concrete structures because the cracks occur at early age when concrete properties change with time, curing condition, which are temperature and humidity, and mixing materials. Even though the factors, which influence on concrete properties, can be considered by using existing models and analysis, not only the results should be verified through various experiments, but it is also difficult to perform various experiments considering curing condition.

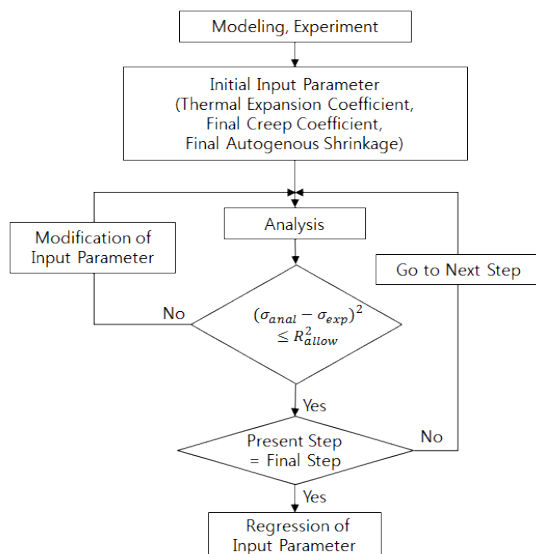
In this study, a new approach is suggested in estimation of concrete properties at early age which can be used in structural analysis to improve the accuracy of the possibility of the cracks at early age.

## 1. A new approach in estimation of concrete properties

As shown in Fig. 1, concrete properties are estimated by comparing between the stress results of analysis and experiments considering the effects of mixing material, tempera-

<sup>1</sup>Corresponding author: [maikuraki@kaist.ac.kr](mailto:maikuraki@kaist.ac.kr)

-ture history and humidity by using thermal stress device which is able to obtain thermal stresses in a chamber with various temperature history when each step of the analysis has the best values of concrete properties which would result in similar stress result between the analysis and the experiments.



**Figure 1.** Procedure of the suggested approach

### 1.1. Experiment

Experiment is performed using thermal stress device. Shape and dimension of the device are shown as Fig. 2. This device can obtain thermal stresses considering mix proportion, temperature and humidity. Used mix proportion and the results of the experiments are shown in Table 1 and Fig. 3 respectively. There are three results of the experiments from different thickness of constraint materials by which the device can simulate various degree of restraint[1]. In this study, the results within only 2 day, when concrete properties change with time rapidly, are considered.

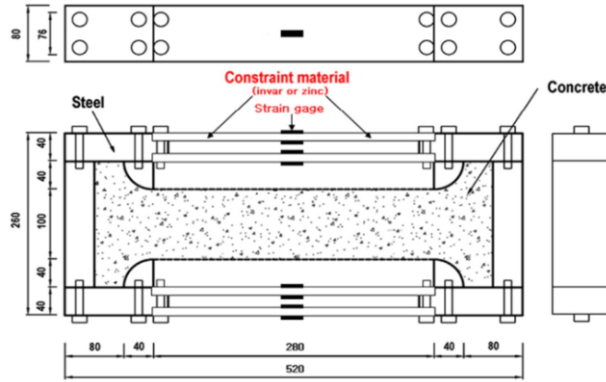


Figure 2. Shape and dimension of thermal stress device[1]

Table 1. Mix proportion

W/B (%)	Material (kg/m <sup>3</sup> )							
	W	C	FA	G	S	WRA	AEA	HWRA
40	185	375	94	961	692	0.7059	0.0844	2.551

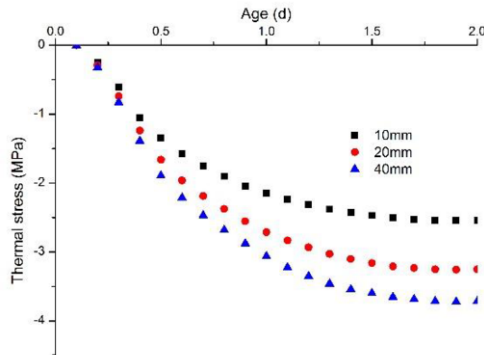


Figure 3. Thermal stresses from the experiments using thermal stress device

1.2. Analysis program

Two programs, hydration heat analysis program based on finite element method and regression program based on Levenberg-Marquardt method, are united to compare the stress results between analysis and experiments. In this study, uncertain concrete properties are thermal expansion coefficient, final creep coefficient of ACI model[3] and final autogenous shrinkage of B3 model[4] and elastic modulus is used based on the results of compressive strength and elastic modulus experiments.

- Uncertainties and compared stresses  
 Even though regression program can find the exact values of concrete properties which would result in same stresses between analysis and experiments when number of uncertainties and number of compared stresses are same, the program is performed, as shown in Fig. 4, with three

uncertainties and nine compared stresses from three step's results to avoid meaningless results induced by experimental and analytical errors, such as negative values.

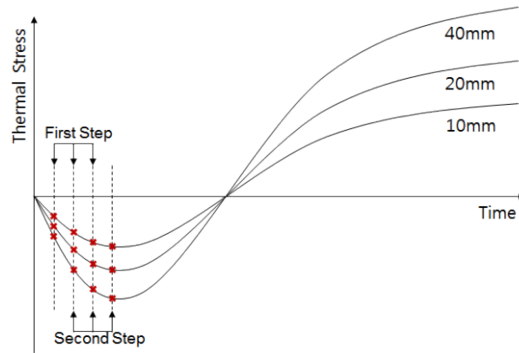
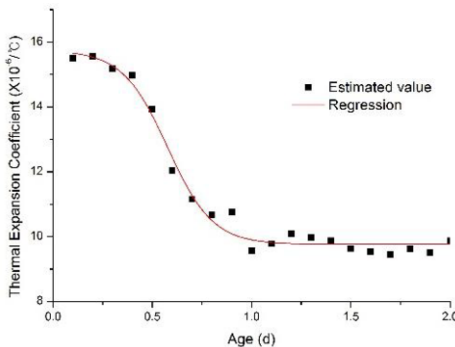


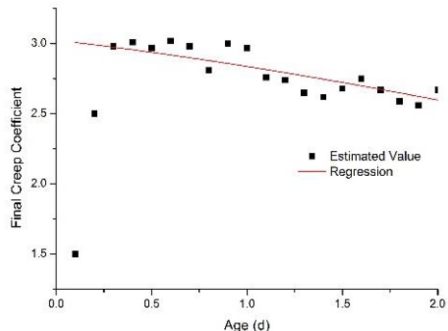
Figure 4. Compared stresses in each step

- Weight factor  
 The best value of concrete properties, which would result in similar stresses between the analysis and the experiments, cannot be the best values of concrete properties in each step because regression analysis determine the values when sum of R-square in three steps has the least value. In this study, the stress results of the first step in each step are weighted using a weight factor to avoid large difference in the stresses of the first step in each step.

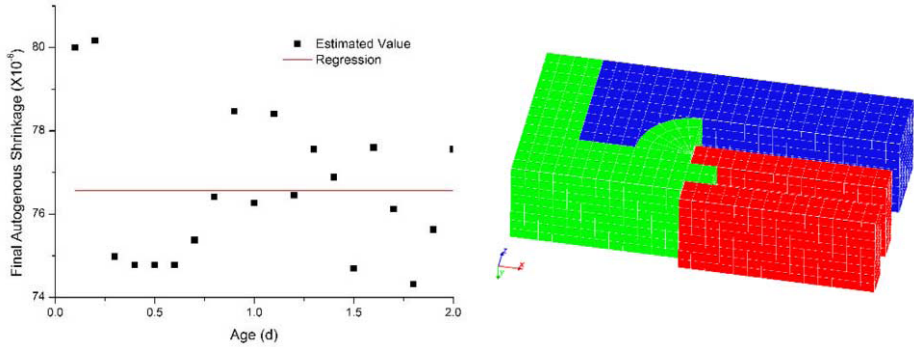
The results of regression analysis are shown in Fig. 5. Final autogenous shrinkage is almost constant through all steps, however final creep coefficient decrease continually and thermal expansion coefficient lower rapidly at very early age and then reach to a constant value. The results at 0.1 and 0.2 day should be neglected because thermal stresses at very early age are so small as not to neglect experimental errors.



(a) Thermal expansion coefficient



(b) Final creep coefficient

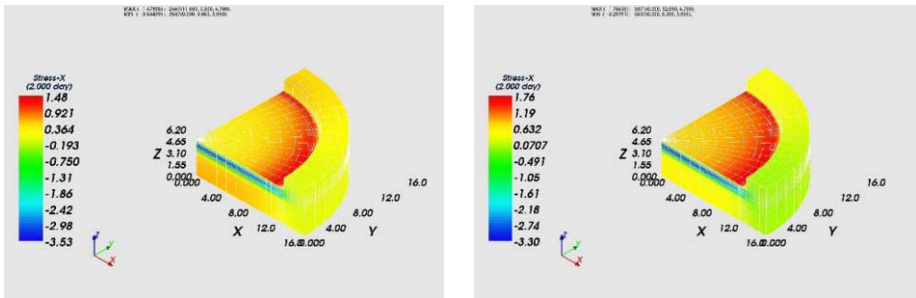


(c) Final autogenous shrinkage (d) Modeling of thermal stress device

Figure 5. Estimated concrete properties and modeling of thermal stress device

2. Structural analysis using estimated concrete properties

Structural analysis is performed using estimated concrete properties from suggested approach. Fig. 6 shows different results of structural analysis at 2 day using time dependent concrete properties and time independent concrete properties which are average values. There is small difference between the results because time independent concrete properties are average values of time dependent concrete properties and elastic modulus is small at very early age. However, the possibility of cracks should be evaluated using both time dependent and independent concrete properties because a small difference of stress results can cause cracks on concrete structures due to small strength at early age.



(a) Time dependent properties (b) Time independent properties

Figure 6. Stresses of mat foundation by analysis

3. Conclusion

The accuracy of structural analysis depends on input parameters, such as thermal properties and mechanical properties. Therefore, it is very important to estimate concrete properties appropriately. Even if further study needs to be performed to verify the estimated values of concrete properties, suggested approach can estimate concrete properties at early age considering environmental condition of concrete so that it will help out to increase the accuracy of structural analysis.

## Acknowledgments

This work was supported by the Nuclear Power Core Technology Development Program of the Korea Institute of Energy Technology Evaluation and Planning(KETEP), granted financial resource from the Ministry of Trade, Industry & Energy, Republic of Korea. (No. 20111520100090)

## References

- [1] M. N. Amin, Simulation of the Thermal Stress in Mass Concrete Using a Thermal Stress Measuring Device, *Cement and Concrete Research* **39**(2009) 154-164
- [2] E. Tazawa, *Autogenous Shrinkage of Concrete*, E & FN SPON, London and New York, 1999
- [3] ACI Committee 207 (2009), Report on Thermal and Volume Change Effects on Cracking of Mass Concrete, *ACI Manual of Concrete Practice 2009*, Part 1, 207.2R, 22-28
- [4] Z.P. Bazant and S. Baweja, Creep and Shrinkage Prediction Model for Analysis and Design of Concrete Structures: Model B3, ACI Concrete International ACI 23, Jan.2001



# Effects of recycled aggregates on the properties of fresh and hardened concrete

B.N. MAKHATHINI<sup>1</sup>, A. DAWNEERANGEN and A.T. SHOHNIWA  
*AfriSam South Africa (Pty) Ltd, Centre of Product Excellence, Roodepoort 1725*

**Abstract.** Construction and Ready-Mix waste constitutes one of the increasing waste potentially useful material is disposed of as landfill. The environmental and economic implications of these are no longer considered sustainable and, as a result, the construction industry is experiencing challenges to overcome this practise. This investigation was aimed at examining the effects of recycled aggregates, ready-mix waste and laboratory waste on the properties of fresh and hardened concrete. Demolished material exhibited lower compressive and flexural strength and high initial slump. Laboratory waste on the other hand, showed a slight decrease in compressive and flexural strength, it however had a constant initial slump and good durability properties. The returned ready mix stone and sand material showed more positive results in most properties as compared to the other two waste materials. This work has demonstrated that there is a potential in utilising recycled aggregate in producing concrete although the actual percentage of substitution has to be determined by the intended application.

**Keywords.** Recycled aggregates, fresh and hardened properties, waste management

## Introduction

For many years globally, the use of natural resources and the abuse of the environment have been seen as necessary “costs of development”, but recently the drive for a greener, more sustainable construction industry has been on the rise worldwide. The introduction of green building rating with systems such as the ones employed by Leadership in Energy and Environmental Design in the United States of America and the Green Star rating system in South Africa have changed the global view of green technology[1]. This change in public perceptions has led to the demand, and subsequently, the prices of “green” properties increasing.

This international trend has resulted in a rethink of the construction industry as a whole worldwide, resulting in what is known as sustainable development, which the Brundtland Report defines as: “*Development that meets the needs of the present, without compromising on the ability of the future generations to meet their needs.*”[2]

Concrete in various forms has been used as a construction material for around 7000 years [3]. Concrete is the most widely used construction material in the world, it is said to be the second most consumed substance on the planet after water [4] with

---

<sup>1</sup>Corresponding author: [bheki.makhathini@za.afrisam.com](mailto:bheki.makhathini@za.afrisam.com)

more than 1 ton being used worldwide per capita per year, this makes it a natural starting point for consideration when a rethink in the manner in which the construction industry conducts itself is necessary.

Concrete is generally made-up of about 12% cement and 80% aggregate, this means that the population is using around 10 billion tons of sand, gravel and crushed stone per year and subsequently having a truly massive effect on our surrounding environment [5].

The idea of recycling of concrete and demolished waste is not a new one, but one that many, more developed, countries such as those in the European Union and Japan have implemented very successfully for a number of years now. The work presented in this investigation considers the possibility of reusing waste materials from demolished buildings and returned ready-mix concrete as construction materials.

## 1. Experimental work

In this investigation of the effect of incorporating the following waste materials, demolished waste sand, laboratory waste stone, returned concrete stone and returned concrete sand on the various properties of concrete were studied.



**Figure 1.** Demolished waste sand



**Figure 2.** Recycled laboratory stone waste



**Figure 3.** Returned Ready-Mix concrete



**Figure 4.** Returned Ready-Mix concrete (dry)

The tests were done in triplicates at the laboratory by casting 100 x 100 mm cubes for each mix for compressive strength test and 500 x 100 x 100 mm beams for testing flexural strength. Extra four cubes were cast for core drilling for durability index tests.

All the test specimens were cast under laboratory conditions, temperature of between 22-25<sup>0</sup>C and cured at the same temperature with % Relative Humidity of >90.

The waste materials were used to replace traditional materials in the reference mix at 25%, 50%, 75% and 100% replacement levels (see Table 1, Table 2, Table 3 and Table 4 for mix designs).

**Table 1.** Mixes A to D, cumulative replacement of traditional sand with demolished waste sand.

MIX	A	B	C	D
REPLACEMENT MATERIAL	25% Demolished waste sand	50% Demolished waste sand	75% Demolished waste sand	100% Demolished waste sand

**Table 2.** Mixes E to H, cumulative replacement of traditional stone with waste laboratory stone.

MIX	E	F	G	H
REPLACEMENT MATERIAL	25% Laboratory waste stone	50% Laboratory waste stone	75% Laboratory waste stone	100% Laboratory waste stone

**Table 3.** Mixes Q to L, cumulative replacement of traditional stone with returned ready-mix concrete stone.

MIX	Q	J	K	L
REPLACEMENT MATERIAL	25% Returned concrete stone	50% Returned concrete stone	75% Returned concrete stone	100% Returned concrete stone

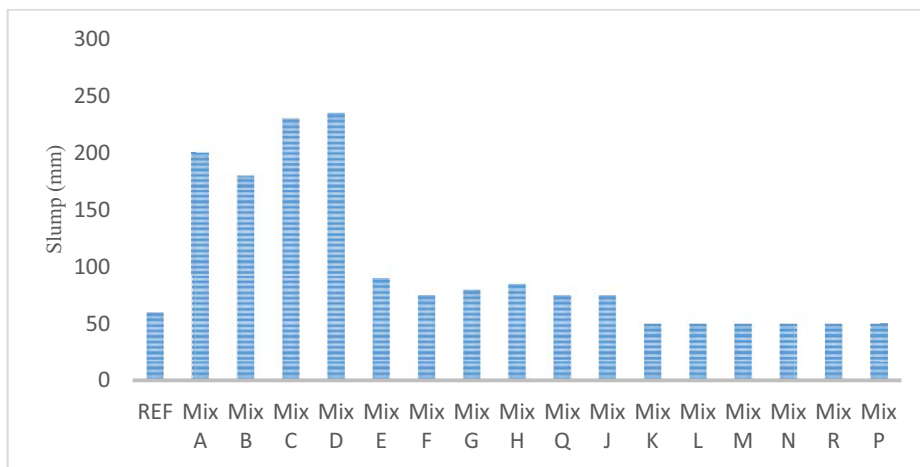
**Table 4.** Mixes M to P, cumulative replacement of traditional sand with returned concrete sand.

MIX	M	N	R	P
REPLACEMENT	25% Returned	50% Returned	75% Returned	100% Returned
MATERIAL	concrete sand	concrete sand	concrete sand	concrete sand

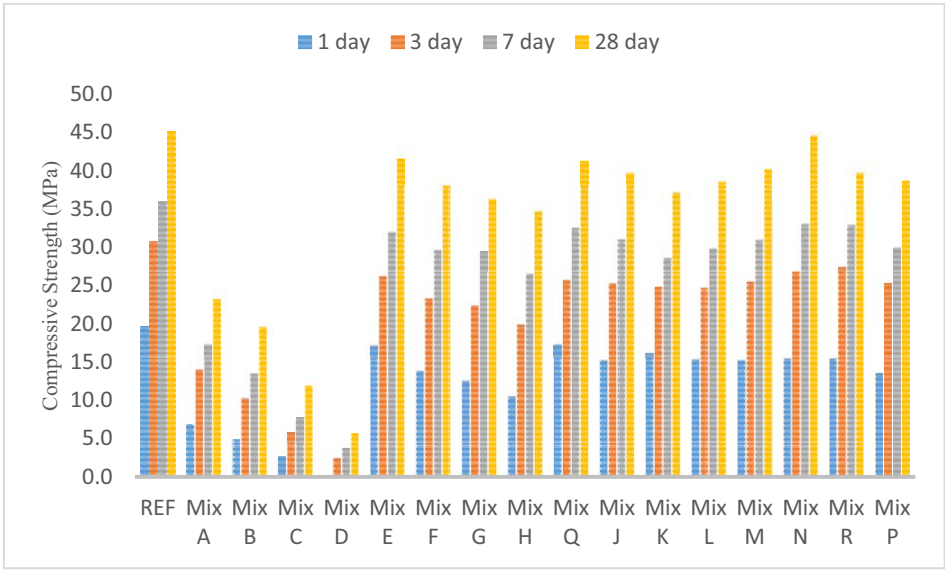
The following fresh and hardened concrete properties were determined on the above mixes (A to mix P) see Figure 5 to Figure 8 for results.

- Slump (mm) [6-9]
- Average Concrete compressive strength (MPa) [6-10]
- Average Flexural Strength (MPa) [6-11]
- Average Oxygen Permeability Index [k(m/s) [12]
- Average Water Sorptivity (mm/hr0.5) [12] and
- Average Chloride Conductivity Index (mS/cm) [12]

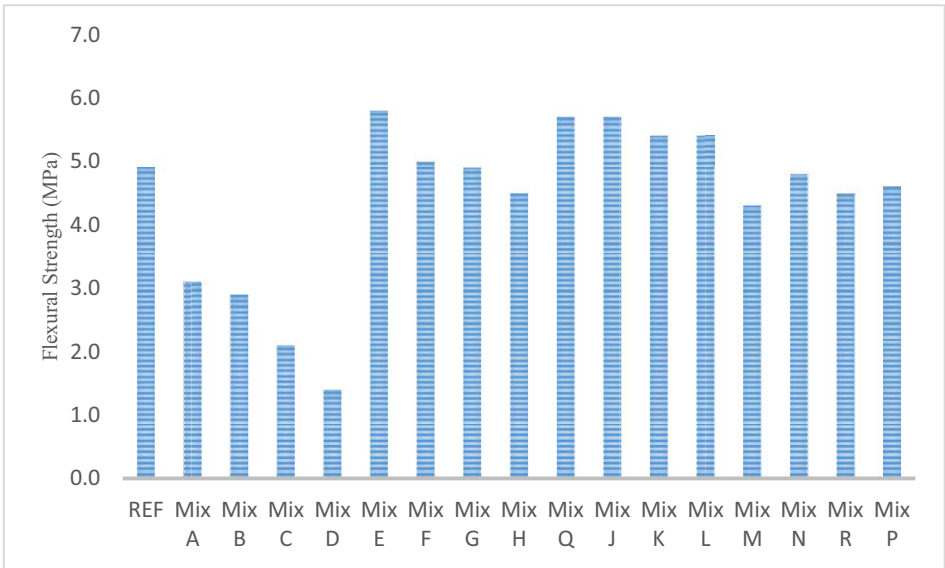
## 2. Results



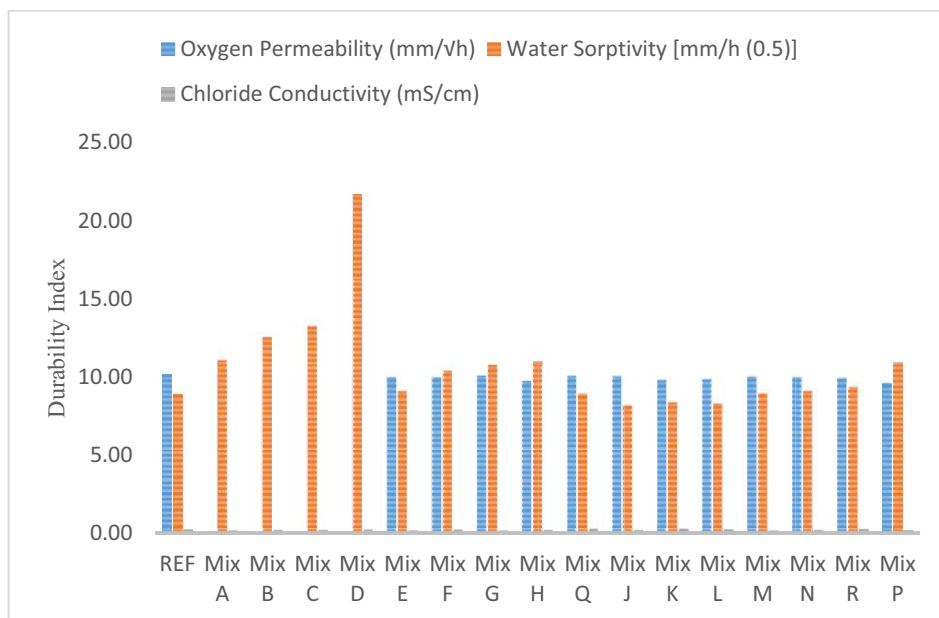
**Figure 5.** Slump test results for mixes A to P, cumulative replacement of traditional sand with demolished waste sand, laboratory waste stone, returned concrete stone and sand.



**Figure 6.** Compressive strength test results for mixes A to P, cumulative replacement of traditional sand with demolished waste sand, laboratory waste stone, returned concrete stone and sand.



**Figure 7.** Flexural strength test results for mixes A to P, cumulative replacement of traditional sand with demolished waste sand, laboratory waste stone, returned concrete stone and sand.



NB: SANRAL Specification : Oxygen Permeability >9.2, Water Sorptivity <10, Chloride Conductivity <0.25

**Figure 8.** Durability Index test results for mixes A to P, cumulative replacement of traditional sand with demolished waste sand, laboratory waste stone, returned concrete stone and sand.

### 3. Discussion

From the results above the following points can be noted:

- Demolished waste sand results in lower compressive, flexural strength and high initial slump at all replacement levels. The high slump values of the demolition sand material could be attributed to the pre-soaking of the material. Because the material was not left to dry adequately and the effect of the increased capillary action of the finer material that would make it difficult for excess water to drain off after the pre-soaking, the material was not in a proper saturated surface dry condition and most likely had a large degree of surface water present. This surface water is exacerbated by the materials small particle size, which means that the percentage water retained by the recycled material is much higher for the fine material than it would have been for a larger particle size.
- Laboratory waste stone gives good compressive and flexural strength as well as slump retention only up to 25% replacement level and beyond that it results in low strength values.
- The returned ready mix stone and sand material gives good compressive and flexural strength results up to 50% replacement levels. This can be a result of an extra paste left on the aggregate which adds to the bond strength in the concrete.
- Only demolished waste sand material has a negative effect on Oxygen permeability and Water Sorptivity, all mixes above the threshold. Due to the

nature of the demolished waste sand, the concrete was very porous and easily absorbed water through capillary action.

- All materials, however do not have detrimental effect on Chloride conductivity.

#### 4. Conclusion

This work has demonstrated that there is a potential in utilising laboratory waste stone, returned concrete stone and sand in producing concrete although the actual percentage of substitution has to be determined by the intended application.

Thus, the possibility for growth in the recycling of concrete waste material in South Africa looks bright and hope to see great development in this field soon.

#### References

- [1] U.S. Environmental Protection Agency. (October 28, 2009). Green building basic information. Retrieved December 10, 2009, from <http://www.epa.gov/greenbuilding/pubs/about.htm>
- [2] Brundtland Commission (1987). *Report of the World Commission on environment and development*. United Nations.
- [3] Amorim, P., de Brito, J. & Evangelista, L., 2012. Concrete made with coarse concrete aggregate: influence of curing on durability. *ACI Materials Journal*, 109(March-April), pp.195-204.
- [4] M. Kawamura, K.T.K.T. et al., 1983. Properties of recycling concrete made with aggregate obtained from demolished pavement. *Journal of the Society of Materials Science*, 32(353).
- [5] Lauritzen, E.K., 2004. Recycled Concrete - An overview of development challenges.
- [6] SANS 5861-1: 2006 Concrete tests – Mixing fresh concrete in the laboratory
- [7] SANS 5861-2: 2006 Concrete tests – Sampling of freshly mixed concrete
- [8] SANS 5861-3: 2006 Concrete tests – Making and curing of test specimens
- [9] SANS 5862-1: 2006 Concrete tests – Consistence of freshly mixed concrete
- [10] SANS 5863: 2006 Concrete tests – Compressive strength of hardened concrete
- [11] SANS 5864: 2006 Concrete tests - Flexural strength of hardened concrete
- [12] Alexander MG, Ballim Y, Mackechnie JM, 'Concrete durability index

# An examination of natural pozzolans in Uganda for low-strength construction applications

Dans N. NATURINDA<sup>1</sup> and Anthony G. KERALI

*Department of Construction Economics & Management, Makerere University, Uganda*

**Abstract.** A pozzolan is a material that contains reactive silica or silica and alumina. When finely ground and mixed with lime in the presence of water, pozzolans react to form a cement-like product. Uganda has a vast potential for natural pozzolans especially in the rift valley areas. These can be used to produce a cheaper alternative material to Ordinary Portland Cement (OPC). However, limited investigations have been done in the past on their quality and potential to reduce the cost of housing especially for the low-income earners in Uganda. This study was aimed at generating data to determine their suitability for use in low-strength construction applications. The study established diverse physical and chemical properties of natural pozzolans in Uganda. The findings indicate a strong bearing between pozzolan grading and strength development. Due to the cost implications of attaining the finest grades, the ratio of pozzolan to lime in the blend was varied to attain optimum grades that can provide adequate strength for a number of low-strength construction applications without escalating the cost. The study recommends further investigation of strength variations of pozzolan-lime blends to generate products for specific applications at a reasonable cost.

**Keywords.** Natural pozzolan, pozzolanicity, low-strength application

## Introduction

According to the American Standards for Testing and Materials (ASTM C125), a pozzolan is defined as “a siliceous or siliceous and aluminous material, which in itself possesses little or no cementitious value, but will, in finely divided form and in the presence of moisture, chemically react with calcium hydroxide at ordinary temperatures to form compounds possessing cementitious properties”. The material is usually inert in its natural state. However, when it is finely ground and mixed with lime in the presence of water, it reacts to form a cement-like product [1]. The degree of reaction, also known as pozzolanicity, is dependent on the nature and content of the reactive silica or alumina in the pozzolan. Materials whose pozzolanicity does not need any activation are categorized as natural pozzolans. Artificial pozzolans are the ones that require calcination to activate pozzolanicity.

Hydrated lime ( $\text{Ca(OH)}_2$ ) is a by-product of OPC hydration, and is known to contribute to the deterioration of concrete, as it is soluble in water [2]. Pozzolans are usually added to OPC to enhance its performance by reacting with the residual

---

<sup>1</sup> Corresponding author: [dnaturinda@cedat.mak.ac.ug](mailto:dnaturinda@cedat.mak.ac.ug)



hydrated lime to form an extra cementitious material. Pozzolans can also be used as a substitute to OPC when mixed with lime. This would help to reduce the cost of construction and would be a major step towards the quest for affordable housing. However, there is need to generate sufficient evidence of their structural properties and cost-saving benefits, through comprehensive tests and examination of the pozzolan properties to give confidence in their use as a major construction material.

In Uganda, pozzolans occur naturally in rift valley areas in the south-western, western, eastern, and north-eastern parts of the country. These are mainly a result of volcanic deposits and other natural earth deposits of similar origin. Currently, the pozzolans are used by cement manufacturers to blend OPC. Rudimentary methods have been tried to exploit and use pozzolans in rural areas. However, their extensive use has been hindered by the suspect quality of their products.

Pozzolans by their diverse nature, have widely varying characteristics and chemical compositions depending on the source [3]. These need to be assessed to understand the ability of the material to meet the desired building performance, and to determine the most appropriate production method and technology. This is important in setting the stage for the use of pozzolan-based materials to boost the housing situation in Uganda by providing alternative materials for low-cost housing.

## **1. Research problem and aim**

Construction cost is considered the main hindrance to adequate housing and improved quality of life and better living standards, especially for the rural population in Uganda. Construction materials constitute the biggest component of this cost accounting for up to 50% of the cost in some cases. Most building material specifications use ordinary Portland cement as the main binder because of its proven performance with respect to structural strength. However, it is relatively expensive and makes construction unnecessarily expensive when used especially for building applications that do not require strength grades of ordinary Portland cement. The use of alternative binders that can provide adequate strength at a lower cost and better durability has been limited by lack of adequate information on their performance.

There is a vast potential for pozzolans in several parts of Uganda that may be used in construction. However, there has been limited research on their quality in relation to their potential to substitute OPC in low-strength applications and lower the cost of housing. This has led to little interest in their appropriate application in construction to exploit their cost saving possibilities and other associated benefits.

This study was carried out to assess natural pozzolans in Uganda and generate data required to determine their suitability for use in construction especially for low-strength applications. This involved review of different constituent compounds and properties of natural pozzolans, and identification of those that have influence on the behaviour of pozzolans in engineering functions to which the pozzolans are applicable.

## **2. Key engineering properties of pozzolans**

The engineering performance of a pozzolan-based binder can be judged from its compressive strength, workability, serviceability, and durability [3]. These are essential parameters for production of good pozzolan-based building elements. The United

States Bureau of Mines (1969)[4] developed four performance classes based on petrographic examination and ASTM physical test methods given in Table 1 below.

**Table 1.** Performance classification of pozzolans (US Bureau of Mines, 1969)[4]

Class	Pozzolanic Activity Index with OPC, % (Strength)	Water Requirement, % (Workability)	Drying Shrinkage, % (Serviceability)	AAR, % Improvement wrt Control (Durability)
1	>80	<112	<0.03	>75
2	75 – 80	112 – 115	0.03 – 0.037	65 – 75
3	70 – 75	115 – 118	0.037 – 0.045	55 – 65
4	<70	>118	>0.045	<55

This classification is appropriate for applied research as it addresses the elements essential for good pozzolan-based building applications, and the parameters considered can easily be assessed in most materials laboratories. However, it has been established that the achievable compressive strength from pozzolans is a function of the glass content, nature of the glass, other minerals, and fineness of the material [5].

The glass component for natural pozzolans is mainly silicate glass modified by aluminium and iron compounds; i.e.  $\text{SiO}_2$ ,  $\text{Al}_2\text{O}_3$  and  $\text{Fe}_2\text{O}_3$ . The nature of the glass can either be amorphous or crystalline and is measured by the degree of disorder of the glass. The higher the degree of disorder, the more reactive the pozzolan material. Various minerals, especially zeolitic or opaline crystalline material influence the short-term pozzolanic activity shortly after contact with water [3].

It has also been demonstrated that the pozzolan activity and their filler effect depend on particle size or fineness [6]. The reactive glass component can be activated by lime in the presence of water. However, excess lime would make the product less durable, since it dissolves in water. As such the lime content is critical to ensure minimum residual lime after the reaction with the pozzolan. The fineness of the pozzolan material determines the total surface area per unit weight of the material that is available for reaction with lime in the presence of water.

Natural pozzolans need to be ground to the required level of fineness. The level of grinding is determined by the physical properties of the raw material and has an influence on the cost of the product. Therefore, there is need to determine the physical properties of the material, and hence the particle size that would provide adequate structural performance at an optimum cost.

This study examined both chemical and physical parameters of natural pozzolans from different locations in Uganda. The key chemical and physical parameters that influence the engineering performance of pozzolan materials and considered under the study, are summarized in Tables 2a and 2b below.

**Table 2a.** Chemical properties of pozzolans that influence engineering performance

Parameter	Purpose
$\text{SiO}_2$ , $\text{Al}_2\text{O}_3$ , $\text{Fe}_2\text{O}_3$	This is the glassy material of the pozzolan, the <b>content</b> of which determines its strength improvement potential
Pozzolanicity	Determines the <b>nature</b> of the glass content, whether crystalline or disordered
$\text{SO}_3$ , CaO, MgO	The rate of pozzolanic <b>reaction after gauging</b> depends more on the minor minerals present, while the long term rate of reaction depends more on the nature of the bulk glassy material

**Table 2b.** Physical properties of pozzolans that influence engineering performance

Moisture content	Has influence on reaction of pozzolans with lime and should not exceed 5% (Indian Standard - IS 4098)
Particle size distribution	Extent of grinding required hence cost
Loss on Ignition (LOI)	Measures the amount volatile components of the material that should not exceed 20% (IS 4098)

The tests carried out helped to characterize the pozzolan materials in Uganda on the basis of these parameters, and lay a foundation for further experimentation on their use in construction.

### 3. Approach and methodology used

Sampling of materials was guided by ASTM C 311-11B Sections 7 and 8. Samples were picked from 18 prospective sites in western, south-western and eastern parts of Uganda, and the respective characteristics examined. The samples included volcanic ash, pozzolanic rocks, and soil sediments.

The ASTM C 311-77 standard was adopted for laboratory examination. Macroscopic observations were carried out to determine physical and chemical properties of the samples required for mineral identification. Chemical tests were applied on all the samples to determine the presence of various minerals.

The compressive tests were guided by the test procedure prescribed in ASTM C311 specified in Test Method C109/C109M.

### 4. Research findings and discussion

The degree of reaction of pozzolans with lime in the presence of water is the main defining factor of the relevance of pozzolans in construction. This is influenced by both the chemical constituents of the pozzolan and its physical properties.

#### 4.1. Pozzolanicity and chemical composition

Pozzolanicity is reflected in the glass content, and the nature of the glass, whether crystalline or amorphous. Its mineral components influence the short-term and long-term pozzolanic activity after contact with water. Table 3 below presents the chemical composition of the examined pozzolans and the nature of the glass content.

While pozzolans from the same region seem to be similar in type, the composition and nature varies from site to site. Generally samples from all the sites exhibited a high content of pozzolanic constituents, making them worth consideration for appropriate applications in construction. However, a number of sites had materials with a more crystalline structure which is a limiting factor to pozzolanicity. These include sites LD02875, LD02878, LD02894, and LD02892. All the other sites had pozzolans with more amorphous structures and hence pass for consideration for further investigation to establish their suitability in construction applications.

**Table 3.** Chemical composition and nature of glass content

Sample ID	Location	% CaO	% MgO	% Al <sub>2</sub> O <sub>3</sub>	% Fe <sub>2</sub> O <sub>3</sub>	% SO <sub>3</sub>	% SiO <sub>2</sub>	Nature of Glass
LD02872	Mudege, Kisoro	4.13	3.11	16.10	12.71	<0.01	64.00	Compact vesicular
LD02873	Nyagishenyi	5.48	3.96	11.6	10.95	1.70	61.75	Porous friable tuff
LD02874	Muko Mutare	4.84	4.97	5.94	12.68	1.71	65.35	Porous friable tuff
LD02875	Muko	9.33	1.20	12.00	14.94	0.12	50.00	Grey crystal ash
LD02876	Kikombe	4.14	5.03	12.23	14.79	0.03	58.42	Homogenous porous
LD02878	Bunyaruguru	10.2	5.75	14.85	12.68	<0.01	52.48	Glassy crystal tuff
LD02879	Queen Elizabeth	4.55	7.49	12.50	13.52	0.22	61.00	Grey buff schists
LD02880	Nyamunuka	4.02	3.82	15.83	13.68	0.04	55.77	Grey porous ash
LD02881	Lake Katwe	1.69	3.61	2.53	7.91	<0.01	75.75	Mineral salt complex
LD02883	Lake Katwe	1.52	2.02	5.05	0.72	<0.01	60.10	Friable porous
LD02891	Kapchorwa Rd	9.68	5.12	15.15	15.59	0.05	51.00	Compact vesicular
LD02892	Kapchorwa	8.05	2.55	20.53	9.29	1.72	52.00	Compact crystalline
LD02893	Kaserem	4.55	1.98	25.25	12.94	1.80	56.57	Glassy grown crystals
LD02885	Kibede Mugusu	2.11	1.92	10.00	9.25	<0.01	75.00	Friable porous
LD02889	Kwapa Tororo	2.62	0.74	16.83	1.37	<0.01	69.70	Phenocrystic
LD02890	Kapchorwa	8.75	3.80	24.75	14.09	<0.01	48.62	Vitrophylic
LD02894	Bulunga	2.45	4.85	17.33	11.27	1.23	73.27	Grey crystal ash
LD02895	Katarara	4.08	4.97	24.50	11.16	0.71	63.37	Grey porous ash
LD02898	Kisoro	5.49	0.31	4.48	0.72	4.91	4.00	Grey porous ash
LD02901	Harugongo	3.12	1.98	14.43	12.31	0.08	51.70	Grey buff schists

#### 4.2. Physical parameters

The key physical properties considered include free moisture content, natural particle size distribution, and loss on ignition (LOI). This is because of their influence on the performance of the pozzolan materials used in construction. Table 4 below presents the moisture content and LOI results of the examined pozzolans.

**Table 4.** Moisture content and loss of ignition

Sample ID	Description	% LOI @ 1000°C	% Moisture Content
LD02872	Volcanic Ash	0.25	3.42
LD02873	Volcanic Ash	0.43	6.20
LD02874	Volcanic Ash	0.03	0.40
LD02875	Volcanic Ash	0.68	0.30
LD02876	Volcanic Ash	2.09	1.00
LD02878	Volcanic Tuff	12.03	3.53
LD02879	Soil Sediments	1.74	1.10
LD02880	Volcanic Ash	4.23	1.50
LD02881	Soil Sediments	7.28	2.99
LD02883	Soil Sediments	25.28	3.29
LD02891	Volcanic Rock	7.56	2.69
LD02892	Volcanic Rock	10.17	3.79
LD02893	Volcanic Rock	8.64	2.11
LD02885	Soil Sediments	5.38	1.79
LD02889	Rock Sample	5.89	0.50
LD02890	Rock Sample	10.56	2.99
LD02894	Volcanic Ash	0.81	0.10
LD02895	Volcanic Ash	1.00	0.40
LD02898	Volcanic Tuff	41.19	0.20
LD02901	Volcanic Ash	25.87	3.80

The Indian Standard (IS 4098 – 1967) was used to gauge the suitability of the materials under investigation as it is more relevant to the local settings and more

suitable for compliance with local requirements. According to the standard, the LOI should not exceed 20% for the material to be suitable for use in construction. Materials from all the sites, except LD02883, LD02898, and LD02901, were found suitable. The guideline for natural moisture content is 5% and samples from all the sites passed based on this criterion.

The natural particle size distribution for volcanic ash and tuffs determines the level of grinding required to attain a suitable pozzolan grade, and hence the cost of production. Sieve analysis was carried out only on pozzolan samples with a wide disparity of particle sizes. Some of the materials had single peak log-normal distributions and hence homogenous, while others had more than one peak, and hence are heterogeneous. Figure 1 below illustrates each category.

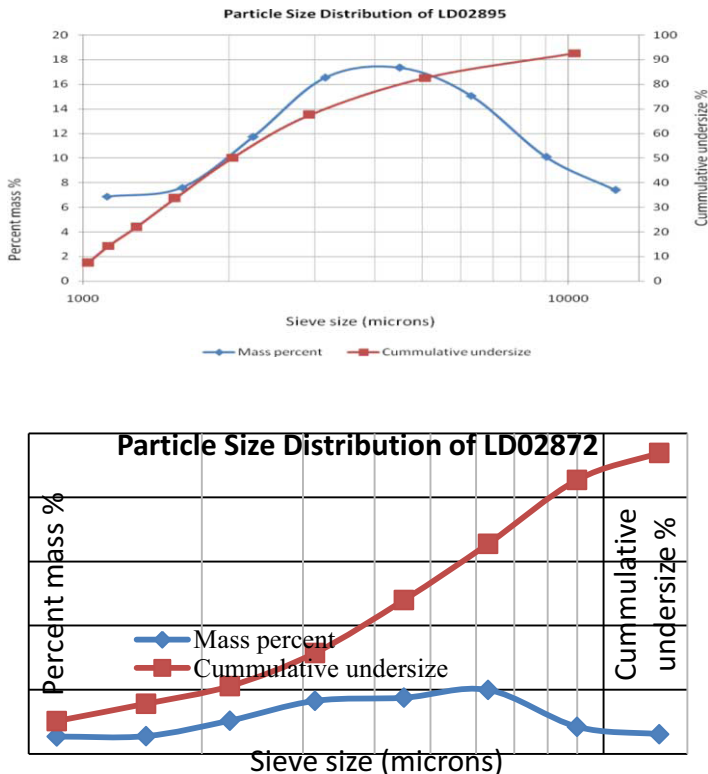
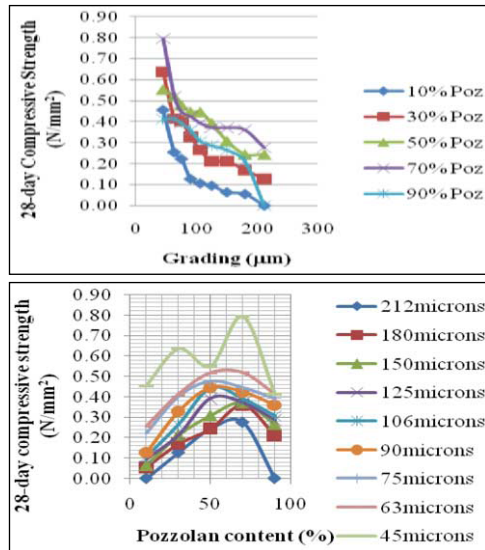


Figure 1. Particle size distribution of selected pozzolan samples

Heterogeneous materials require a versatile production process to deliver a consistent product. The homogenous ones are preferred for consistent production design and planning as it would be easier to design a production process that will be consistent with the available material. One such material selected for trial tests for compressive strength variation with grading and content was from Kataraara Site (sample LD02895) which was selected for further investigations.

### 4.3. Variation of compressive strength with pozzolan grading and content

Experimental tests on samples from the selected site of Kataraara examined the strength development of pozzolan–lime mortars with respect to pozzolan grading (fineness) and pozzolan content, to determine the optimum pozzolan–lime blend that can yield adequate strength for use in low-strength construction applications. The mixture varied from 10% to 90% pozzolan, while nine different grades varying between 45 $\mu\text{m}$  and 213 $\mu\text{m}$  were considered. Sample preparation and testing was guided by the procedure prescribed under ASTM C311 under test method C109/C109M. The results are presented in Figure 2 below.



**Figure 2.** Variation of mortar strength with pozzolan grading and content

The results indicate a strong inverse relationship between pozzolan grading and strength development. However, the finer the pozzolan the higher the cost of grinding it. As such, there is need to determine the optimum grade that would give adequate strength for construction applications without cost escalation. From the test results, the variation of the pozzolan–lime ratio in the blend yields an increase in strength development up to a certain point beyond which the strength starts to reduce. The maximum strength attained for the various grades can serve as a guide to decide on the optimum grade that will yield compressive strength required for specific applications by blending the pozzolan with the given content of lime. For instance in this particular case, according to the Indian Standard IS4098-1967 Specification for Pozzolan – Lime Mixture, mortar grade 150 $\mu\text{m}$  with 70% pozzolan content would be suitable for Lime-Pozzolan material type LP7 for mortars up to Grade MM0.5 and mass concrete which require 28 day compressive strength of 0.68N/mm<sup>2</sup>.

## 5. Conclusions and recommendations

Most of the natural pozzolans in Uganda possess physical and chemical properties that are suitable for use in construction. Hence they can be used to develop a cheaper alternative material to OPC, for use especially in low-strength construction applications. The quality of the pozzolans varies from site to site, which makes it difficult to develop a general guiding standard to process the material for the wide range of relevant applications. But rapid testing methods can be developed to determine the desired properties of the natural pozzolans for use in a given construction context.

The strength development capability of pozzolans is significantly enhanced by finer grading. However, this has a bearing on the cost of production of the material. The variation of the pozzolan-lime ratios can facilitate the determination of the optimum grade that can provide adequate strength for construction applications.

Further examination of strength variations is needed to generate an array of products for specific construction applications, and appropriate production methods. The focus need not to be on attaining a high strength material per se, but to generate products whose strength is adequate for low-strength applications.

## References

- [1] A.G. Kerali, J.A. Mwakali and M.E Okure. *Development and application of construction materials in Uganda*. Fountain Publishers, Kampala, 2007.
- [2] V.N. Dwivedi, N.P Singh, S.S. Das, and N.B. Singh, A new pozzolanic material for the cement industry. *International Journal of Physical Sciences*, Vol. 1 (3) pp 106-111, November 2006, Lagos, Nigeria.
- [3] R. L. Day, Pozzolans for use in low-cost housing. A report for the International Development Research Centre (1990), Ottawa, Canada.
- [4] US Bureau of Mines, Pozzolanic raw material resources in the central and western United States. US Department of the Interior, Bureau of Mines, Information Circular 8421, p117, 1969.
- [5] P. K. Mehta, Pozzolanic and cementitious byproducts as mineral admixtures for concrete, a critical review. *American Concrete Institute*, 1983
- [6] G.C. Cordeiro, R.D. Toledo Filho, and R.F. Morales, E. *Use of ultrafine rice husk ash with high-carbon content as pozzolan in high performance concrete*. *Materials and Structures* (2009). 42(7), 983–992.

# Mechanical properties and microscopic structure of cement based materials with very low water-cement ratio

Xiqiang LIN<sup>1</sup>, Zhongnan SONG, Tao ZHANG and Liang HUO  
*China State Construction Co. Ltd. Technology Center, Beijing, China*

**Abstract.** The sealing anchor mortar is a special cement-based engineered material with water-cement ratio (W/C) less than 0.18 and early (1 day) compressive strength greater than 40 MPa. It used high frequency shock pressure molding prepared mortar material with W/C of 0.09-0.18 and pure cement as the gelling material. Among them, the early (1 day) compressive strength of the mortar with W/C of 0.13 and 0.18 being more than 65MPa, and a high late (56 days) strength of 102.4MPa. SEM analysis showed when the W/C was 0.09, only the surface of the cement particles with early hydration (3 days) was hydrated, appearing a loose form and failed to stick together as a whole. The material with W/C of 0.13 and 0.18 produced more C-S-H gel phase and the overall cement particles cemented together whose microstructure was compact and uniform. Unhydrated cement particles mainly played the role of filling and micro-aggregates in the material.

**Keywords:** Very low water-cement ratio, mechanical properties, microscopic structure, hardening mechanism

## Introduction

It needs a very low water-cement ratio to make cement-based materials of ultra-high strength (compressive strength greater than 100 MPa). There are mainly three coordinated technical means to reduce water-cement ratio: it is to reduce water consumption by superplasticizer [1,2,3], adding superfine powder compaction to improve the degree of accumulation of cementitious materials [4,5,6] and use of pressure molding material to increase the degree of compaction [7,8]. It is also widely researched to make excellent preparation of low water-cement ratio of cement-based materials by a certain pressure means.

Xu [9] prepared a water-cement ratio of 0.09 for the low porosity of pure cement-based materials by the 300 MPa high pressure molding method. The study found that the material had an initial porosity of 26.9%, its degree of 1day hydration reached 21%, 3 day was 31%, and 28 d hydration degree reached 45%. Vladimír Živica [8] respectively prepared the water-cement ratio of pure cement cementitious materials of 0.115, 0.095 and 0.075 by using 46 MPa, 102 MPa and 210 MPa high pressure molding.

---

<sup>1</sup>Corresponding author: NO.15, Lin He Street, Shunyi, Beijing, China, 101300, [bjlinxiqiang@163.com](mailto:bjlinxiqiang@163.com), CSCEC-2010-Z-01



The study found the strength of 28 days could reach 187 MPa, 229.4 MPa and 262.8 MPa respectively. They [10] analyzed the hydration of ash cement materials under the compression molding and found that it significantly reduced the rate of hydration of cementitious material. Tiny calcium hydroxide grains, unhydrated cement clinker minerals and calcium silicate hydrate gel wrapped with each other.

The sealing anchor mortar cement-based material has a very low water-cement ratio (0.15 to 0.18) prepared by the impact of repression. It is to further improve the strength of the material through high impact pressure molding method and study mechanical properties and microstructure of low water-cement ratio (0.09 to 0.18) of cement-based materials.

## 1. Materials and test methods

### 1.1. Materials

Cement: The experiment used PO42.5 Cement which was produced by Tangshan Jidong company, its chemical composition as shown in Table 1.

**Table 1.** Chemical compositions of cement, wt%

CaO	SiO <sub>2</sub>	Al <sub>2</sub> O <sub>3</sub>	MgO	Fe <sub>2</sub> O <sub>3</sub>	TiO <sub>2</sub>	SO <sub>3</sub>
59.45	20.98	9.38	2.14	3.64	0.40	2.50

Aggregate: The experiment used 20 to 40 mesh and 40-70 mesh of silica sand.

Superplasticizer: The experiment used polycarboxylate superplasticizer (PC) which was produced by BASF SE

### 1.2. Test methods

Materials were weighed according to the experiment, then slowly stirred for 1 minute and stirred quickly for 4 minutes after put in the forced planetary mixer. The system were filled to 4 cm×4 cm×16 cm triple test mode. The experiment then used molding equipment including an air compressor whose power was greater than 3 KW and the exhaust pressure was greater than 0.3 MPa, vibrating hammer whose impact frequency was greater than 1000 Hz and has a forming end for compaction molding. Then the mortar was put into the standard curing oven to be cured for 1d and the form was removed. The compressive strength of mortar were tested in accordance with GB17671-1999 which is mortar strength test method (ISO method). Microstructural features test done using Hitachi S-3400 scanning electron microscopy and spectroscopy analyzer.

## 2. Results and discussion

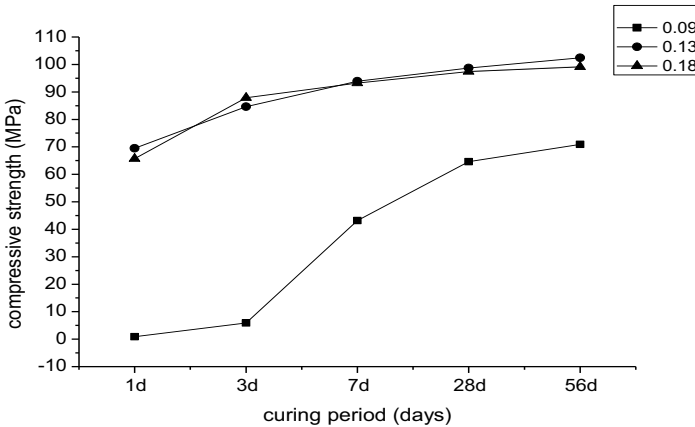
### 2.1. Effect of low W/C on the mechanical properties of mortar

Selected W/C of 0.18, 0.13 and 0.09 were used to do comparison. The results of the experiments are shown in Table 2.

**Table 2.** The mortar mixing proportion of only cement as cementitious material

	W/C	Cement (g)	20-40 Mesh Quartz sand	40-70 Mesh Quartz sand	PC (%)	Water (g)
A	0.09	1000	500	500	1.0%	90
B	0.13	1000	500	500	0.2%	130
C	0.18	1000	500	500	/	180

Under pressure, low W/C of cement is different from cement hydration of normal W/C, because in the low W/C and dense environment, the hydration of cement mainly affected by the diffusion of water including diffusion of water from the outside of samples and the internal water diffusion [11]. Figure 1 shows the compressive strength of specimens with different water-cement ratio. When the W / C is 0.09 in the system, it has a low resistance compressive strength of 5.6 MPa. As it needs a small amount of water in the early hydration (3 days), much polycarboxylate superplasticizer is added which made the hydration of cementitious material to be very slow. As hydration progresses, more adequate water moves to the system which promote the strength of late hydration (56 days) to be 71.5 MPa. When the W/C is 0.15 and 0.18 in the system, it has relatively high moisture content and more cement hydration. The compressive strength of one day hydration is more than 65 MPa and it generates gel phase in the initial hydration of the system which makes the system itself achieve higher compactness. With the increase of hydration, so the strength grows steady and the compressive strength of 7 days' hydration reached 90 MPa.



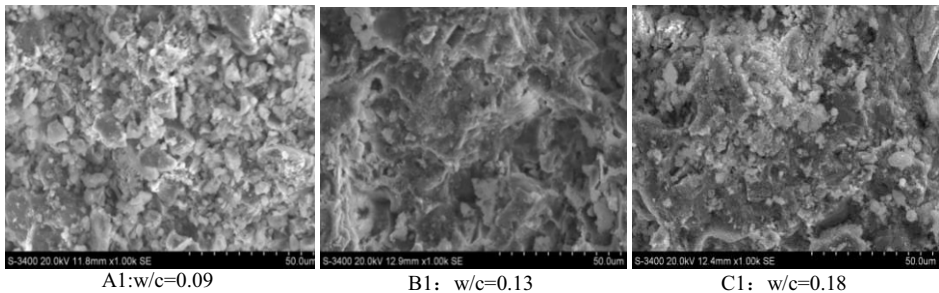
**Figure 1.** Mortar compressive strength of pure cement as cementitious material

## 2.2. Effect of low W/C on the microstructure

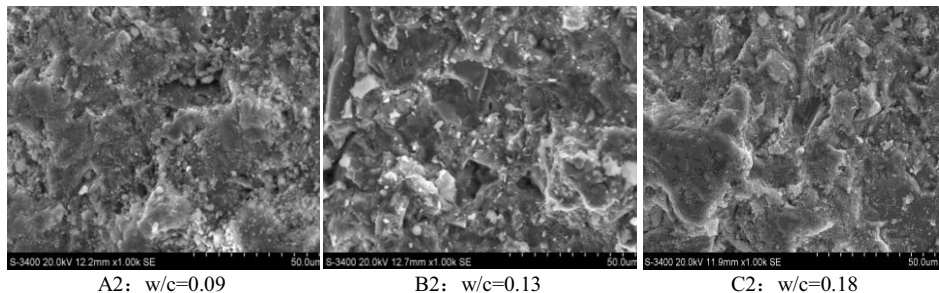
Mechanical properties of the material are macroscopic performance and the microstructure of material plays a decisive role on the macroscopic properties. By observing the morphology at different hydration time of cement, it could analyze the effect of different low water-cement ratio. The experiment used SEM to observe the morphology of early hydration (3 days) and late hydration (90 days) of pure cement with different water-cement ratio. The microstructure features are as shown in Figure 2 and Figure 3.

Figure 2 show that the microstructure of hydration of cement with W/C of 0.09 is different from the sample of W/C of 0.13 and 0.18 of with hydration time of 3 days. Water cement ratio of 0.09 sample only cement particle surface hydration, hydration particles loose and there is no condensation together closely. But the water cement ratio of 0.13 and 0.18 of the surface of the sample hydration degree is high, hydration products solidifies into a whole, the microstructure is more compact.

Figure 3 shows the microstructure of hydration of cement with hydration time of 56 day, it could see the loose hydration particles which only distribute in the edge reduce apparent, replaced by solid-phase gel cemented together. It is because the free water outside goes into the interior through the pores of materials during process of hydration, so the early unhydrated cement particles continue to be hydrated and cemented together to form hydration gel with low porosity. It is also the reason of why the compressive strength of 56 day hydration mortar with W/C of 0.09 has been greatly improved.



**Figure 2.** Microstructure of hydration of cement with curing time of 3 day



**Figure 3.** Microstructure of hydration of cement with curing time of 56 day

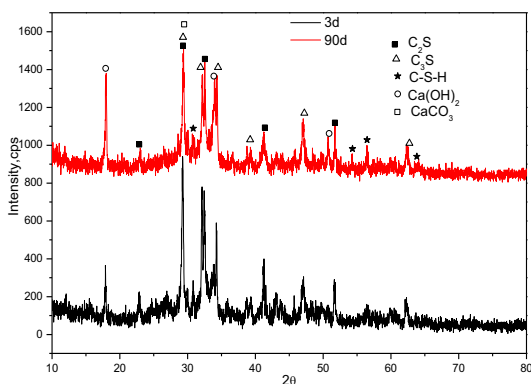
With hydration of 3 days, the compactness of mortar with W/C of 0.13 and 0.18 is better than that with W/C of 0.09. It could suggest that with the increase of W/C, the

early hydration of cement is easier and the density of materials is greater, so that the compressive strength of mortar is higher. With the increase of curing time, external migration of water promote the hydration of cement and more C-S-H gel phase is generated and overall cemented with cement particles. So the uniformity of microstructure is denser and material has good strength in late curing time. Unhydrated cement particles mainly play the role of filling and micro-aggregates in the material.

When the concrete is sufficiently dense, the compressive strength increases with lower water-cement ratio. But when little or a lot of water, the concrete can't be "sufficiently dense" [12]. In these very low w/c ratio of cement-based materials can't reach the condition, the inversely proportional relationship between the strength and water-cement ratio is not fully applicable to the change of strength of cement-based materials with low water-cement ratio.

### 2.3. Hydration products are affected to very low W/C

XRD was used to characterize the type and content of the crystalline phase changes in the hydration products. Figure 4 shows the w/c of 0.13 cement hydration results being analyzed by XRD.



**Figure 4** water cement ratio of 0.13 cement hydrates XRD analysis diagram

Figure 4 shows the  $C_3S$ ,  $C_2S$  diffraction peaks are relatively highest, indicating that there are several unhydrated particles of  $C_3S$ ,  $C_2S$  in hardening cement;  $Ca(OH)_2$  content change is also evident;  $Ca(OH)_2$  content change is also evident; As part of the C-S-H gel hydration products are amorphous substances, so the diffraction peak is smaller. As the curing period from 3 days to 90 days growth, X-ray diffraction peak of hydration products C-S-H gel phase and  $Ca(OH)_2$  becomes higher at the very low water-cement ratio of hardened cement, indicating that their content has increased. Unhydrated clinker phases  $C_3S$ ,  $C_2S$  diffraction peak decreases with the increase of curing period, but unhydrated clinker phase content remains the largest in the hardened cement. The main hydration product C-S-H gel phase and  $Ca(OH)_2$  content is increased.

XRD diffraction analysis showed that it has a consistent correspondence between unhydrated mineral phase content, mechanical properties of the mortar and degree of hydration of cement. There is a low degree of hydration of cement under conditions of low water-cement ratio, and the largest phase is unhydrated cement particles. The

degree of hydration of the material under dense conditions of low water-cement ratio with increasing age shows a slight increase.

### 3. Conclusions

- (1) The super early age (1 day) compressive strength of the mortar with W/C of 0.13 and 0.18 is more than 65 MPa, and it has high late (56 days) strength of 102.4 MPa. W/c of 0.09 mortar water consumption is low, its compressive strength is lower than the strength of other tow mortars.
- (2) When the W/C was 0.09, only the surface of the cement particles at early age (3 days) was hydrated. The mortar appears loose and failed to stick together as a whole. And the W/C 0.13 and 0.18, the hydration cement produced more C-S-H gel phase and the overall cement particles cemented in one piece, with compact and uniform microstructure. Unhydrated cement particles mainly played the role of filling and micro-aggregates in the material.
- (3) In standard curing and very low W/C conditions, the C-S-H gel phase and  $\text{Ca}(\text{OH})_2$  content increased with the growth of the curing period. The clinker phase  $\text{C}_3\text{S}$ ,  $\text{C}_2\text{S}$  content decreases with the growth of the curing period, but the  $\text{C}_3\text{S}$ ,  $\text{C}_2\text{S}$  content was still the largest in the hardened cement.
- (4) When the water-cement ratio is 0.13 and 0.18, it has a consistent correspondence between unhydrated mineral phase content, mechanical properties of the mortar and degree of hydration of cement.

### References

- [1] Tang MC. High performance concrete-paste, present and future. In: *Proceedings of the international symposium on ultra high performance concrete*. Kassel: University of Kassel. 2004. P.3~10.
- [2] de Larrard F, Sedran T. Mixture-proportioning of high-performance concrete. *Cement and Concrete Research*. 2002;32:1699~704.
- [3] Chong Wang, Changhui Yang. Preparation of Ultra-High Performance Concrete with common technology and materials. *Cement & Concrete Composites*. 34 (2012) 538~544
- [4] Matte V, Moranville M. Durability of reactive powder composites: influence of silica fume on the leaching properties of very low water/binder pastes. *Cement & Concrete Composites*. 1999;21(1):1~9.
- [5] Halit Yazici. The effect of curing conditions on compressive strength of ultra high strength concrete with high volume mineral admixtures [J]. *Build Environ*. 2007. 42(5):2083~2089.
- [6] Rougeau P, Borys B. Ultra high performance concrete with ultra fine particles other than silica fume. In: *Proceedings of the international symposium on ultra high performance concrete*. Kassel: University of Kassel; 2004. p. 213~26.
- [7] Richard P, Cheyrezy M. Reactive powder concrete with high ductility and 200–800 MPa compressive strength. *ACI SP 1994*.144:507~518.
- [8] Vladimír Živica, Effects of the very low water/cement ratio [J]. *Construction and Building Materials*. 2009, 23: 3579~3582
- [9] Zhongzi Xu. Low porosity cementitious material composition, structure and mechanical properties of the relationship and its modified (D). *Nanjing Institute of Chemical Technology PhD thesis*. 1988.3
- [10] Jiachun Wang, Peiyu Yan. Molding conditions of low water-cement ratio of small silicate hydration of cement - fly ash system [J]. *Bulletin of the Chinese ceramic society*. 2005 (1), 87 -90
- [11] Kudsén T. The dispersion model for hydration of Portland cement (I): general concepts. *Cement and Concrete Research*. 1984, 14: 622~632
- [12] Zhongwei Wu, Huizhen Lian. *High-performance concrete* [M] Beijing: China Railway Press,1999:22~23

# Experimental research on mechanical properties of engineered cementitious composites

Guoyou LI<sup>a,1</sup>, Liang HUO<sup>a</sup>, Tao ZHANG<sup>a</sup> and Hang YAO<sup>b</sup>

<sup>a</sup>Technical Center, China State Construction Engineering Corporation, Beijing, China

<sup>b</sup>Liaoning Product Quality Supervision and Inspection Institute, Shenyang, China

**Abstract.** Engineered cementitious composites (ECC) with the excellent tensile strain capacity was made of domestic raw materials except PVA-fiber. The effect of water-binder ratio, fiber content and silica fume content on the mechanical properties was investigated in this paper. While the ECC microstructure was also investigated by Scanning Electron Microscope (SEM). The results showed that high water-binder ratio and larger amount of PVA-fiber will help to improve tensile property of ECC with adding a moderate amount of silica fume. While the compressive strength of ECC was 35.4 MPa to 57.6 MPa, the tensile strain capacity attended to 2.59% to 4.77%. SEM analysis showed that large amount of spherical non-hydrated fly ash could improve the matrix and fiber interface structure. The water-binder ratio has a great effect on the structure compactness of the hydration products and fiber abrasion degrees.

**Keywords.** Engineered cementitious composites, mechanical properties, tensile strain capacity, microstructure

## Introduction

Engineered Cementitious Composite (ECC) is a new kind of fiber-reinforced material, which is a micromechanically designed material, and has the characteristic of pseudo-strain hardening and multiple cracking [1-4]. ECC overcomes the brittleness of traditional cement-based materials and it has broad prospects in the areas of building structure seismic resistance, repair and reinforcement.

Li [5-7] prepared engineered cementitious composites with the tensile strain capacity of 3%-5% through the design and screening of the matrix material and polyvinyl alcohol (PVA) fibers. But until now little reports that the tensile strain capacity is more than 3% have been observed in china. In this paper, with the use of domestic raw material base, the compressive strength and uniaxial tensile performance of ECC were tested and the effects of water-binder ratio, fiber content and silica fume on the performance of ECC were investigated. In addition, the test results were analyzed through the micro-mechanics model and SEM morphology.

---

<sup>1</sup> Corresponding author: [liguoyou1986@126.com](mailto:liguoyou1986@126.com)

## 1. Experimental procedure

### 1.1. Materials and test mix

The cement used was from JiDong Cement Plant and conformed to PO 42.5 for Ordinary Portland Cement. The fly ash used was Class I fly ash. The active SiO<sub>2</sub> of silica fume was higher than 95%. The chemical composition of cement and the mineral admixtures used are shown in Table 1.

Polyvinyl alcohol fibers (PVA) of the type KURALON K-II RECS15 were produced by Kuraray of Japan and their performance properties are shown in Table 2. Ordinary quartz sands with the particle size of 96-180μm were used in the experiment. The Superplasticizer in this experiment was from MuHu Group.

**Table 1.** Chemical composition of raw materials (%)

Items	SiO <sub>2</sub>	Al <sub>2</sub> O <sub>3</sub>	Fe <sub>2</sub> O <sub>3</sub>	CaO	MgO	SO <sub>3</sub>	Loss
Cement	28.16	8.11	3.37	52.35	2.53	2.40	2.10
Fly ash	58.24	25.18	6.18	4.69	1.12	0.40	2.23
Silica fume	95.2	0.49	1.07	0.56	0.70	/	1.8

**Table 2.** Properties of PVA fibers

Length mm	Diameter mm	Modulus of elasticity GPa	Ultimate elongation %	Tensile strength MPa	Density kg/m <sup>3</sup>
12	0.039	40	6	1600	1300

The total amount of binder (including cement, fly ash and silica fume) was fixed at 1217.2 kg/m<sup>3</sup>. The mass ratio of fly ash and cement was 3:2, and sand-binder ratio was 0.36. When the fiber volume content was 2% and not mixed with silica fume, the effects of water-binder ratio (0.30, 0.33, 0.36 and 0.39 respectively) on ECC tensile properties were studied. When the water-binder ratio was 0.36 and not mixed with silica fume, the effects of fiber volume content (1%, 1.4%, 1.7%, 2% and 2.5% respectively) on ECC tensile properties were studied, and when the water-binder ratio was 0.33 and fiber volume content was 2%, the effects of silica fume content (0%, 3%, 6%, 9% and 12% respectively) on ECC tensile properties were also studied.

### 1.2. Molding and curing methods

The cementitious materials, quartz sand and chemical admixtures that were weighed accurately were mixed into blender and stirred for 1min; and then the water was added slowly and stirred for 2 to 3 minutes. The mortar fluidity was tested according to the present national standard "test method for fluidity of cement mortar"(GB/T 2419-2005). Superplasticizer and aquasorb content was adjusted so that the mortar fluidity was around 360mm and there was no segregation and bleeding. At last, the mortar was kept in rapid stirring and the pre-dispersed PVA fibers were added slowly.

Uniaxial tensile testing used coupon plate specimens with dimensions of 175 ×50 ×15 mm. The compressive properties were obtained from cuboid specimens with dimensions of 160 ×40 ×40 mm. The fresh ECC specimens were covered with plastic sheets and demolded after 24h. ECC specimens were cured for 6 days in a standard curing room where temperature and relative humidity are 20 ± 2 °C and 95 ± 5%

respectively. The two ends of the uniaxial tensile specimen was reinforced with the aluminum sheet (aluminum sheet size was 50×50×1 mm) and then cured in the standard curing room until testing ages.

### 1.3. Test methods

The uniaxial tensile performance was tested by CMT5305 Electric Universal Testing Machine and the loading rate was 0.2 mm/min, the extensometer gauge with length of 50mm was used to measure tensile strain. The compressive strength was tested according to the present national standard “method of testing cements-determination of strength”(GB/T 17671-1999). The scanning electron microscopy with the type of Hitachi S-3400 was used to observe the morphology of tensile specimen sections.

## 2. Results and discussion

Uniaxial tensile stress-strain curves of partial mix at 7 and 28 days are shown in Figure 1. The specimen with each mix proportion exhibited the significant pseudo-strain hardening and multiple cracking characteristics. After reaching the peak tensile stress, the stress could maintain a high level over a substantial range of strain. the tensile strain capacity was defined as the corresponding tensile stress dropped to 80% of the peak tensile stress in this paper. Table 3 shows the tensile properties and compressive strength results. In order to improve the reliability of test results, the data in Table 3 was the average of the test results of three specimens.

**Table 3.** Strength and tensile properties of ECC

Mix	Compressive Strength,MPa		First crack stress,MPa		Peak tensile Stress,MPa		Peak tensile Strain,%		Tensile strain capacity,%	
	7d	28d	7d	28d	7d	28d	7d	28d	7d	28d
0.30-2%-0%	28.5	49.5	2.82	3.62	3.53	4.25	2.79	1.66	3.92	2.60
0.33-2%-0%	28.0	49.3	2.46	3.03	3.30	4.15	3.40	2.27	4.81	2.96
0.36-2%-0%	24.6	46.1	1.94	2.78	2.77	3.90	4.17	2.10	4.85	2.89
0.39-2%-0%	18.8	35.4	1.80	2.34	2.73	3.70	4.15	3.37	4.93	4.77
0.36-1%-0%	29.2	50.4	1.45	1.51	2.44	2.30	2.22	0.69	3.05	1.45
0.36-1.4%-0%	28.4	48.3	1.73	3.02	2.80	3.35	4.04	0.87	4.74	1.91
0.36-1.7%-0%	25.8	46.9	1.88	2.80	3.15	3.82	4.45	2.12	5.49	2.57
0.36-2.5%-0%	24.0	44.3	1.78	2.85	2.87	4.23	2.99	1.73	5.13	3.10
0.33-2%-3%	33.4	59.1	2.03	2.27	3.16	3.56	2.82	0.97	4.09	2.25
0.33-2%-6%	37.3	59.6	2.45	3.56	4.16	4.75	3.56	1.01	4.58	1.58
0.33-2%-9%	36.3	57.6	2.16	2.62	3.95	4.05	3.89	1.82	4.25	2.59
0.33-2%-12%	37.1	57.1	2.25	2.81	3.98	3.34	3.98	0.65	4.93	1.53

Note: the figures in mix represented the water/binder ratio – fiber volume content – silica fume content respectively.



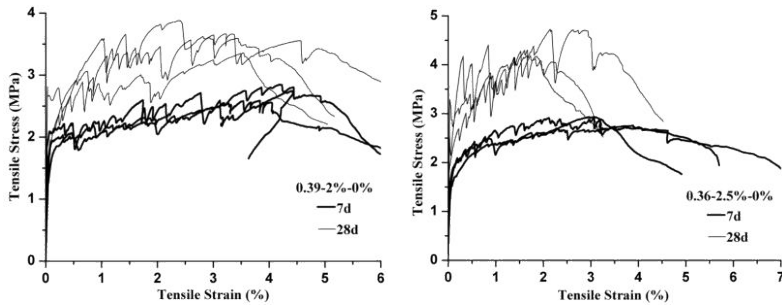


Figure 1. Uniaxial tensile stress-strain curves of ECC with part of the mix

### 2.1. Effects of water-binder ratio on ECC properties

It can be seen from Table 3, the mechanical properties of ECC decreased with the water-binder ratio increased. When the water-binder ratio increased from 0.30 to 0.39, the compressive strength at 28 days decreased from 49.5 MPa to 35.4 MPa. The first crack stress and the peak tensile stress ratio were 0.85, 0.73, 0.71 and 0.63 with the specimen water-binder ratio of 0.30, 0.33, 0.36 and 0.39 at 28 days respectively. According to the micro-mechanical model<sup>[2-4]</sup>, the ratio of first crack stress and peak tensile stress decreased, which could lead to the energy increase of multi-point cracking and improvement of the ductility of ECC. When the water-binder ratio is 0.30, the tensile strain capacity at 28 days was 2.60% and when the water-binder ratio rose to 0.39, the tensile strain capacity at 28 days reached 4.77%.

### 2.2. Effects of fiber content on ECC properties

It can be seen from Table 3, with the fiber content increasing, compressive strength of ECC specimens decreased. When the fiber content increased from 1% to 2.5%, the compressive strength at 28 days decreased from 50.4 MPa to 44.3 MPa. When the fiber content was 1%, the peak tensile stress of each age was low. When the fiber content was more than 1.4%, the peak tensile stress of 28 days age was increased with the fiber content increasing significantly. When the fiber content increased from 1% to 2.5%, the tensile strain capacity at 7 days was all greater than 3% and the tensile strain capacity at 28 days age were 1.45%, 1.91%, 2.57%, 2.89% and 3.10% respectively. So increasing the fiber content could improve the ECC ductility significantly.

Because the matrix strength of ECC specimen at 7 days was low, the fibers with low content can dissipated energy to improve the ductility of the specimen during the extraction process. With the increase of curing period, the chemical adhesion between matrix and fiber increased and the proportion of damaged fiber pulled off increased, so low fiber content made it difficult to maintain a high ductility of the specimen. High fiber content in per unit area of the specimen could bear more bridging stress and the tensile stress was transmitted to the surrounding uncracked matrix, which promoted the generation of multiple cracking. However, increasing the fiber content made the matrix defects increased and resulted in lower matrix strength. Through the micro-mechanical model, it showed that ECC specimens with high fiber content had higher fiber bridging stress and lower matrix strength, which was conducive to the improvement of ductility. However, excessive fiber content was not conducive to specimen forming and fiber dispersion. It not only resulted in low compressive strength, but also enhance cost of

ECC. So it should be reasonable to determine the fiber content based on the actual project needs.

### 2.3. Effects of silica fume content on ECC properties

Table 3 showed that when the silica fume content was 3%, the specimens compressive strength at 28 days was 59.1 MPa which was higher than results of those without silica fume by 9.8 MPa. When the silica fume content was at 3%-12%, the compressive strength at 28 days was between 57.1 MPa and 59.6 MPa. The peak tensile stress reached the maximum when the silica fume content was 6% and the stress at 7 and 28 days were 4.16 MPa and 4.75 MPa respectively. When silica fume content was 9%, the tensile strain capacity was 2.59%, slightly lower than the specimens without silica fume, but the compressive strength was higher by 8.3 MPa.

Silica fume has high specific surface area and pozzolanic activity. It could increase the density of the ECC matrix and improve the interface characteristics of cementitious materials and aggregates, so the strength was increased. Part of the silica fume particles that could play a role as balls attaches to the surface of the fiber, which reduced the friction between matrix and the fiber in the process of the tensile experiments. Therefore the ECC ductility was improved.

### 2.4. Morphology analysis of ECC

The uniaxial tensile properties of the specimens with the water-binder ratio of 0.33 and 0.39 were tested at 28 days and then the specimen sections were sliced, soaked with alcohol to terminate hydration. After drying, vacuuming and spraying, the cross-section morphology was observed. Combined with the micro-mechanical model, the effects of water-cement ratio on matrix structure and fibers morphology were studied.

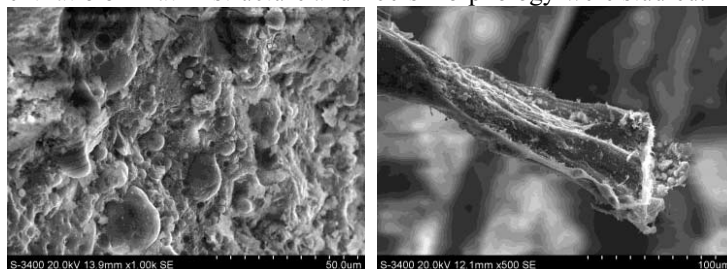


Figure 2. Morphology of 0.33-2%-0% (28days)

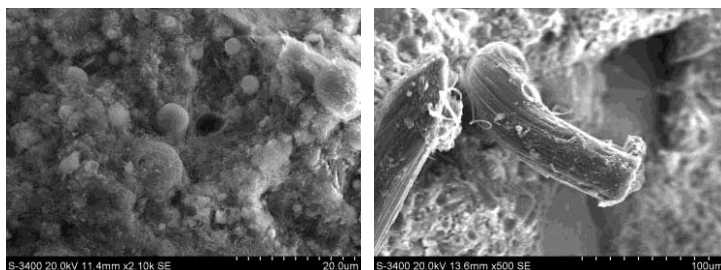


Figure 3. Morphology of 0.39-2%-0% (28days)

As can be seen from the matrix microstructure, the main hydration products were calcium silicate hydrate, and the flaky crystals of  $\text{Ca}(\text{OH})_2$  were undetected in the vision. This was because the  $\text{Ca}(\text{OH})_2$  crystals of hydration products reacted with high active  $\text{SiO}_2$  and  $\text{Al}_2\text{O}_3$  that was in the surface of fly ash, and generated the hydrated aluminum silicate and hydrated calcium aluminate. Meanwhile, in the part of fly ash surface, hydration products formed micro-crystals apparently. Due to the incorporation of large ash in ECC, a large matrix of unhydrated ash particles the distributed in the matrix, which made the internal structure more dense.

When the water-binder ratio was low, the matrix of specimens was dense and when the water-binder ratio was 0.39, the matrix structure was loose. By comparing fibers morphology of Figure 2 and Figure 3, it can be found the specimen surface with low water-cement ratio had a serious corrosion, which showed the typical tearing. When the water-cement ratio of specimens was high, fibers were pulled out and the appearance was kept intact, only the surface had a slight edge wear. In the extraction process, the fibers played the role of bridging and consumed a lot of energy to help materials to achieve multiple cracking.

### 3. Conclusions

With the increase of water-cement ratio, the peak tensile stress and compressive strength of ECC decreased and ultimate tensile strain tended to increase. When the water-cement ratio was 0.39, compressive strength at 28 days was 35.4MPa and the tensile strain capacity was 4.77%.

Increasing the fiber content reduced the compressive strength of the specimens, but peak tensile stress and ultimate tensile strain at 28 days were significantly increased. When the fiber content was 2.5%, 28 days compressive strength was 44.3MPa and the tensile strain capacity was 3.10%. So it should be reasonable to determine the fiber content based on the actual project needs.

When the appropriate amount of silica fume was mixed into the matrix, the silica fume had a morphological effect and had ash activity, which improved the density and interface characteristics of matrix. So the matrix ductility and strength of ECC were all improved. The suitable silica fume content was 9%. The compressive strength at 28 days was 57.6MPa and the tensile strain capacity was 2.59%.

As can be seen from the tensile fracture morphology, the main hydration products of the specimen was calcium silicate hydrate and a large amount of unhydrated fly ash particles improved the interface structure of the matrix and fibers. The water-binder ratio had a greater impact on the density of hydration products and the degree of fiber abrasion, which affected the performance of multi-cracking of ECC materials.

### References

- [1] V.C. Li, C.K.Y. Leung, Steady state and multiple cracking of short random fiber composites, *Journal of Engineering Mechanics* 188 (1992) , 2246-2264.
- [2] C.K.Y. Leung, Design criteria for pseudo-ductile fiber reinforced composites, *ASCE Journal of Engineering Mechanics* 122 (1996) , 10-18.
- [3] Z. Lin, V.C. Li, Crack bridging in fiber reinforced cementitious composites with slip-hardening interfaces, *Journal of Mechanics and Physics of Solids* 45 (1997) , 763-787.

- [4] J.K. Kim, J.S. Kim, et al, Tensile and fiber dispersion performance of ECC (engineered cementitious composites) produced with ground granulated blast furnace slag, *Cement and Concrete Composites* 37 (2007), 1096-1105.
- [5] V.C. Li, S. Wang, C. Wu, Tensile strain-hardening behavior of polyvinyl alcohol engineered cementitious composite(PVA-ECC), *ACI Materials Journal* 98 (2001), 483-492.
- [6] V.C. Li, Large volume high-performance applications of fibers in civil engineering, *Applied Polymer Science* 83 (2002), 660-686.
- [7] V.C. Li, On engineered cementitious composites(ECC) a review of the material and its applications, *Adv Concrete Technol* 1(2003), 215-230.

# Study on drying shrinkage cracking characteristics of steel chip reinforced polymer cementitious composite

Sunhee HONG<sup>1</sup>, Shinya KIMURA, Yuichi SATO and Yoshio KANEKO  
*Department of Architecture and Architectural Engineering, Kyoto University, Japan*

**Abstract.** Fiber reinforcement cementitious composite can efficaciously improve the toughness shrinkage and durability of cementitious composite. This study is to clarify the drying shrinkage and shrinkage cracking characteristics of steel chip reinforced polymer cementitious composite (SCRPPCC). In this study, free shrinkage of SCRPPCC, drying shrinkage and shrinkage cracking of SCRPPCC reinforced with deformed bars were examined. Test results shows that (1) the free shrinkage of SCRPPCC is smaller than that of polymer cement mortar (PCM) at the outside; (2) the restrained shrinkage of PCM specimens was reduced by reinforcing with steel chip; (3) average crack width of PCM specimen with low reinforcement ratio was greatly declined by reinforcing with steel chip.

**Keywords.** Fiber reinforcement cementitious composite, steel chip, reuse, polymer, drying shrinkage

## Introduction

Since the adoption of Kyoto Protocol in 1997, reducing of CO<sub>2</sub> emission became important tasks in the entire industry. Among others, iron and steel industry represents one of the major constituents of industrial waste. Therefore, the reuse of these steel materials, can contribute to reducing the environmental load.

On research about steel chip reinforced cementitious composite (SCRCC), there is a study in the literature on the shape memory alloy machining chips used in reinforcing smart composites [1]. But the application of SCRCC to building structures is not economically practical. So, steel chip which is an industrial waste produced in iron works is economically efficient and environmentally sound because of industrial waste reduction.

Drying shrinkage, when restrained, contributes to nearly all the cracking observed in concrete members before loading. A free shrinkage test cannot give the true potential of fiber reinforcement to resist restrained shrinkage stresses and to control shrinkage cracking [2]. Therefore, it is necessary to examine not only free shrinkage, but also restrained drying shrinkage. So far, the authors have conducted a pilot experimental investigation of the free and restrained drying shrinkage of SCRCC made of ordinary Portland cement binder [3]. To enhance strength, adhesion, waterproofness and

---

<sup>1</sup>Corresponding author: Building C1-4, Kyoto University, Nishikyō-Ku, Kyoto, 615-8540, Japan; E-mail: [sunhee.hong1128@gmail.com](mailto:sunhee.hong1128@gmail.com)

durability of building structures, the usage of polymer cement mortar is one of the promising solutions [4]. Hence, this research investigates the drying shrinkage properties and the cracking characteristics of the newly developed SCRPPCC with large scale wall specimens [5, 6].

## 1. Experimental programs

### 1.1. Materials

#### 1.1.1. Steel chip

Steel chip produced when a steel plate is precisely machined on the NC (Numerical Controlled) lathe which is a machine tool for metal working was used in this study. The steel grade was SS400, and the density of steel chip was  $7.86 \text{ g/cm}^3$ . All these steel chips formed during machining are being buried as wastes.

#### 1.1.2. Mix proportion

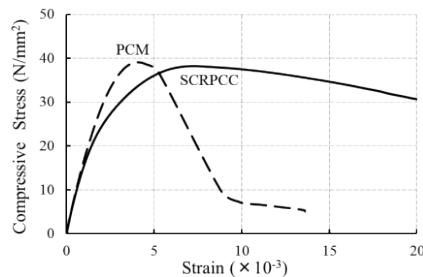
The mix proportions of cementitious composites used in this study are given in Table 1. Polymer cement mortar was used as a binder. Ordinary Portland cement was used as a cement. Polymeric admixture used is ethylene vinyl acetate (EVA) emulsion which is a fluid milk-white solution with a solid content of 45% and the density  $1.07 \text{ g/cm}^3$ . An antifoaming agent was used to control the entrained air with 1% by mass on polymer. River sand was used as a fine aggregate. Steel chip contents of 3% by volume were used in this study.

**Table 1.** Mix proportion of cementitious composites

	PCM	SCRPPCC
Water-cement ratio, W/C (%)	30	
Cement :Sand (by mass)	1:2	
Polymer-cement ratio, P/C (%)	10	
Steel chip (Vol. %)	0	3

#### 1.1.3. Material properties

Physical properties of cementitious composites used were shown in Figure 1.



**Figure 1.** Relationship between compressive stress and strain of cementitious composite

1.2. Test specimens

Specimens for free shrinkage test were beam specimens of size 100×100×500 mm. On the other hand, four large specimens of 2,500 mm length for restrained drying shrinkage test are prepared as shown in Figure 2. The parameters of specimens are listed in Table 2.

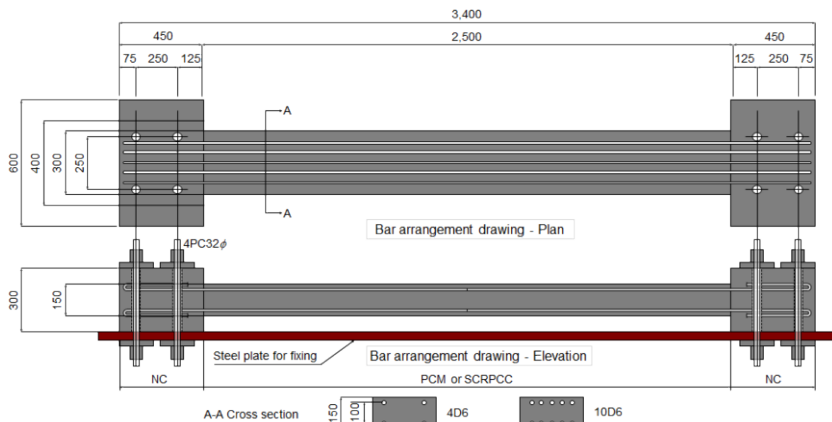


Figure 2. Specimens of restrained drying shrinkage test

Table 2. Parameters of specimens

Specimen	Curing condition	Restrain	Mortar	Bar
PCM-In	20°C, 60% R.H	Free	PCM	-
SCP-In	20°C, 60% R.H	Free	SCRPPC	-
PCM-Out	Outdoor	Free	PCM	-
SCP-Out	Outdoor	Free	SCRPPC	-
PCM4	Outdoor	Restrained	PCM	4D6
SCP4	Outdoor	Restrained	SCRPPC	4D6
PCM10	Outdoor	Restrained	PCM	10D6
SCP10	Outdoor	Restrained	SCRPPC	10D6

1.3. Test procedure

Firstly, the casting form was arranged and restraining steel bars were placed. The steel bars consisted of four or ten deformed bars of 6mm diameter with 180°hooks at the both ends. Secondly, the restraining block (450×600×300 mm) was cast with normal concrete (NC,  $f_c = 58.6 \text{ N/mm}^2$ ). Each block was fixed with four prestressing bars of 32 mm diameter, to which 250 kN tensile force was applied. Thirdly, the center part (2500×300×150 mm) was cast with PCM or SCRPPC.

After the casting form was removed (curing 5 days), beam specimens (100×100×500 mm) for free shrinkage and large specimens (300×150×2500 mm) for restrained drying shrinkage were cured for 5 days at the each curing conditions. Then 25 measuring targets were bonded on the surface of specimen with every 100mm. And initial measurement was started after curing for 7 days. Then this point was fixed as a standard point (drying period 0 day). The measuring of strains and the observation of crack patterns were conducted every 7 days during first 56 days, every 14 days after the 56 days, and every 28 days after 112 days.

## 2. Test results and discussion

### 2.1. Curing and drying condition

Two beam specimens for the free shrinkage test (PCM-In and SCP-In) were subjected to a constant temperature and humidity condition of 20°C and 60 R.H. On the other hand, two beam specimens (PCM-Out and SCP-Out) and four wall specimens (PCM4, SCP4, PCM10 and SCP10) were subjected to the outdoor condition and kept from the rain. Average daily temperature and humidity of the outdoor that specimens were exposed to during drying period are shown in Figure 3 and Figure 4.

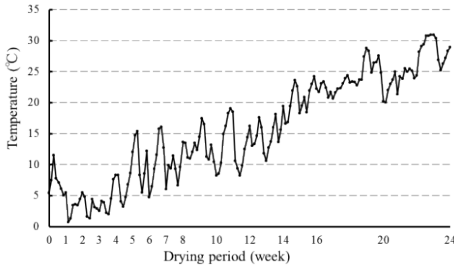


Figure 3. Average daily temperature

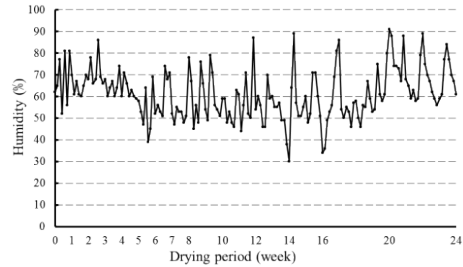


Figure 4. Average daily humidity

### 2.2. Shrinkage strains and crack patterns

#### 2.2.1. Free shrinkage

Figure 5 represents the relationship between drying shrinkage of free shrinkage specimens and drying period. Overall, drying shrinkage of all specimens was increased with drying period. And the drying shrinkage was decreased by reinforcing with steel chip at the outside condition. However, the shrinkage of SCRPPC was slightly larger than that of PCM at the indoor condition. Effect of curing condition is that the drying shrinkage of specimens in the outdoor condition was decreased as compared with that of indoor specimens. This is explained by the reason that the temperature and humidity of outdoor were irregular, and the temperature was always below 20°C until 14 weeks, however, indoor was always maintained constant condition of 20°C, 60% R.H.

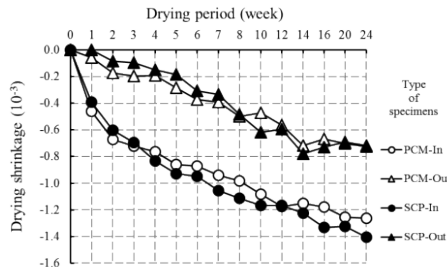


Figure 5. Relationship between drying shrinkage of free shrinkage specimens and drying period

#### 2.2.2. Restrained shrinkage and cracking characteristic

Figure 6 show the drying shrinkage and crack patterns for three sides of each specimen. Drying shrinkage of restrained PCM specimens was inclined to decrease due to



reinforcing with steel chip. The reason for this decrease is because the bridging effect was provided by reinforcing with steel chip, and the bond strength of binder was increased in the cement matrix.

Cracking characteristic is that in the case of specimens with high reinforcement ratio (PCM10, SCP10), the occurrence of cracks of the restrained specimen made of SCRPPC was less than that of PCM, and in the case of specimens with low reinforcement ratio (PCM4, SCP4), there is not so much difference on the number of cracks of both specimens.

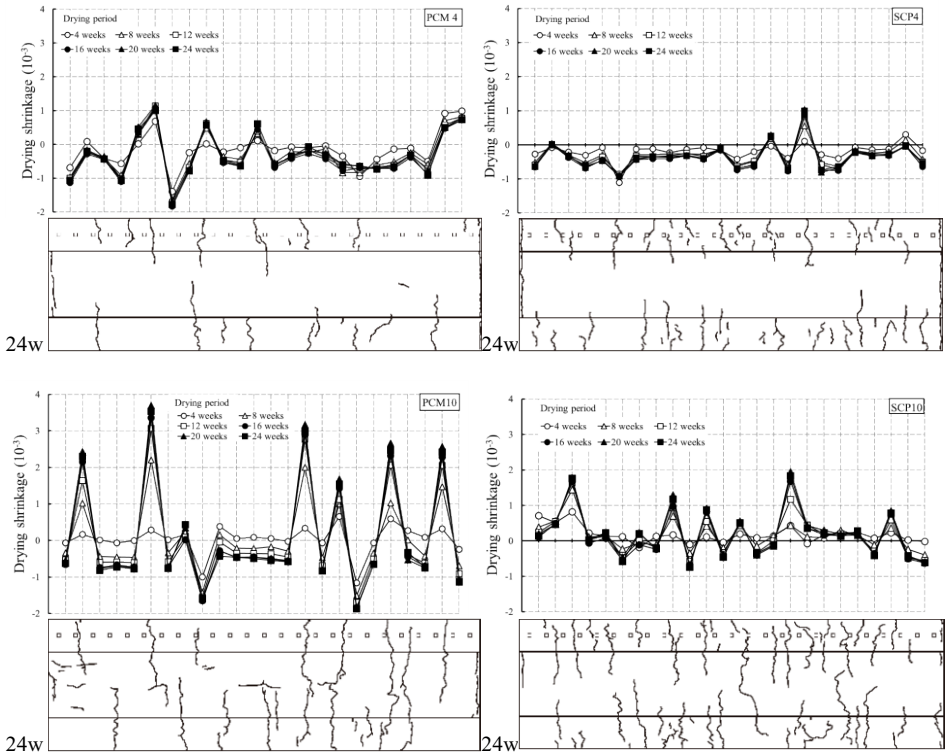


Figure 6. Drying shrinkage and crack patterns of specimen PCM4, SCP4, PCM10 and SCP10

Figure 7 shows relationship between average crack width and drying period. In order to calculate  $w_{crs}$ , first of all, equivalent number of cracks was calculated by Eq. (1). After that, average crack width was calculated by Eq. (2). The number of cracks  $N_{cre}$  is defined as total lengths of cracks on the top surface of the specimen divided by the width (300 mm). Equivalent number of cracks  $N_{cre}$  is used since only a few cracks penetrate the entire width of the specimen.

$$N_{cre} = \sum(l_{cr}) / 300 \tag{1}$$

$$w_{cr} = (L \times \epsilon_{cd}) / N_{cre} \tag{2}$$

$N_{cre}$  : equivalent number of cracks

$l_{cr}$  : length of a crack on the top surface of the specimen (mm)

$w_{cr}$  : average crack width of restrained specimen (mm)

$L$  : length of a restrained specimens (= 2500 mm)

$\epsilon_{cd}$  : free drying shrinkage strain of outdoor specimen

Overall, average crack width of restrained specimens was decreased by increasing of the amount of reinforcing bar. In the case of specimens with low reinforcement ratio (PCM4, SCP4), average crack width of PCM specimen was decreased by reinforcing with steel chip. And average crack width of specimens with high reinforcement ratio (PCM10, SCP10) was that PCM specimen was lower than SCP specimen.

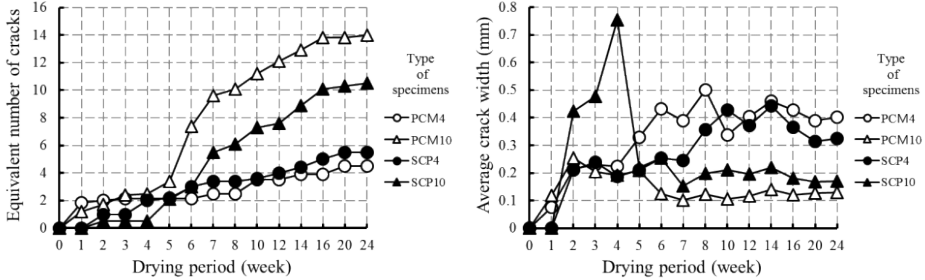


Figure 7. Relationship between average crack width and drying period

### 3. Conclusions

In this paper, the drying shrinkage properties and the cracking characteristics of the newly developed SCRPPCC with large scale wall specimen were investigated. The following conclusions can be obtained.

(1) Drying shrinkage of all free shrinkage specimens increased with drying period. And the drying shrinkage was decreased by reinforcing with steel chip at the outdoor condition. Influence of curing and drying condition on drying shrinkage is that drying shrinkage of outdoor specimens was lower than that of indoor specimens.

(2) Drying shrinkage of restrained PCM specimens was reduced by reinforcing with steel chip. And in the case of specimens with high reinforcement ratio, the occurrence of cracks of restrained SCRPPCC specimen was less than that of PCM specimen.

(3) Average crack width of restrained specimens was decreased by increasing of the amount of reinforcing bar. And in the case of specimens with low reinforcement ratio, average crack width of PCM specimen was declined by reinforcing with steel chip.

### References

- [1] T. Wakatsuki et al., Development of Fe-Mn-Si- Cr Shape Memory Alloy Machining Chips Reinforced Smart Composite, *Journal of the Iron and Steel Institute of Japan* 92(2006), 562-566. (in Japanese)
- [2] R.N. Swamy and H. Stavrides, Influence of Fiber Reinforcement on Restrained Shrinkage and Cracking, *ACI Journal*, 76(1979), 443-460.
- [3] S. Hong, Experimental Study on Drying Shrinkage Cracking Characteristics of Steel Chip Reinforced Cementitious Composite, *the Proceeding of JCI*, 35(2013), 601-606.
- [4] Y. Ohama, Principle of Latex Modification and Some Typical Properties of Latex-Modified Mortars and Concretes, *ACI Materials Journal*, 84(1987), 511-518.
- [5] M. Koyanagi, Y. Masuo and S. Nakane, A Study on Shrinkage Cracks in Reinforced Concrete Walls (Part 4) Prediction Analysis of Cracking Widths due to Restrained Volume Change in One-Way Concrete Members", *Report of Obayashi Corporation Technical Research Institute*, 41(1990), 73-79. (in Japanese)
- [6] G.F. Kheder, A New Look at the Control of Volume Change Cracking of Base-Restrained Concrete Walls, *ACI Structural Journal*, 94(1997), 262-270.

# The effect of steel and polypropylene fibres in the mechanical properties of structural lightweight concrete

S. P. YAP, Ubagaram Johnson ALENGARAM<sup>1</sup>, and Mohd Zamin JUMAAT  
*Department of Civil Engineering, University of Malaya, Kuala Lumpur*

**Abstract.** The effect of fibres in the structural lightweight concrete made from palm kernel shell (PKS) as coarse aggregate and to enhance the mechanical properties of palm kernel shell concrete (PKSC) was investigated. The crushed PKS was used to replace the conventional crushed granite wholly and thus it falls under the category of sustainable construction; the use of PKSC as the structural lightweight concrete could lead to a reduction in the construction cost and also environmentally beneficial as PKS causes land pollution. In this paper, steel fibres of aspect ratio 65 and fibrillated polypropylene (PP) fibres were added in the PKSC. The compressive and flexural strengths of palm kernel shell fibre-reinforced concrete (PKSFRC) were evaluated. The experimental results show that steel fibres produced significant improvement on the mechanical properties of PKSFRC. The enhancement on compressive and flexural strength are 23% and 27%, respectively higher than control mix. However, the compressive strength and the tensile strength increment in PKSFRC containing PP fibres was lower than the steel fibres. In addition, the addition of fibres in PKSFRC reduced the brittleness of the PKSC significantly. Hence the role of fibres in enhancing the mechanical properties and brittleness of PKSC is evident.

**Keywords.** Polypropylene fibres, mechanical property, lightweight concrete

## Introduction

The researches on the utilization of palm kernel shell (PKS) as lightweight aggregates to produce lightweight concrete (LWC) has been reported for few decades (Alengaram et al 2013). PKS is a waste material from the palm oil industry which generated after the extraction of palm oil from the palm oil fruits (Fig. 1). As the second largest palm oil production country, Malaysia produced 2.4 million tons of PKS as waste (MPOB, 2011) and these wastes are generally dumped in open air. This eventually results in environmental pollutions such as contamination of underground water and soil, as well as increased costs to manage the waste. Therefore the application of PKS as coarse aggregate to replace the rapid depleting granite aggregates paves way to produce a more sustainable concrete.

---

<sup>1</sup>Corresponding author: Faculty of Engineering, University of Malaya 50603, Kuala Lumpur, Malaysia; Email: [johnson@um.edu.my](mailto:johnson@um.edu.my)



**Figure 1.** Palm Oil Fruits (left) and PKS (right)

In addition to the environmental benefits, the lightweight characteristic of PKS enables the production of LWC. The use of LWC in the construction industry enables the dead load reduction on buildings and this eventually allows for greater design flexibility and cost savings on structural members and foundation construction (Yap et al. 2013). The early published researches on OKS reported that LWC called PKS concrete (PKSC) with a density and compressive strength in the range of 1700-1850 kg/m<sup>3</sup> and 5-25 MPa, respectively (Basri et al. 1999; Mannan & Ganapathy 2002) could be produced with 100% coarse aggregate replacement by PKS.

However the low mechanical properties, especially the compressive and tensile strengths, and high brittleness of LWC including PKSC compared to the normal concrete have held the development of PKSC in the structural applications (Domagala 2011). One of the methods to improve the mechanical properties of the PKSC is by the inclusion of fibres as the construction industry is now aware of the benefits of fibers in enhancing the concrete properties. The main advantages of fibres in concrete are enhanced flexural capacity, toughness, ductility, crack control, impact strength and others (Hassanpour *et al.* 2012).

In this study, two different fibres, steel and polypropylene (PP) fibers were added into PKSC to produce PKS fibre-reinforced concrete (PKSFRC). This paper aims to improve the mechanical properties of the PKSFRC to meet the structural requirements of the LWC to widen the applications of PKSC. This study serves as a preliminary research on future evaluation of other properties of PKSFRC.

## **1. Materials and methods**

### *1.1. Materials*

#### *1.1.1. Cement & supplementary cementitious material*

Ordinary Portland Cement (OPC) with a Blaine specific surface area and specific gravity of 335 m<sup>2</sup>/kg and 3.10, respectively and 10% (of cement weight) silica fume were used in all the mixes.

### 1.1.2. Coarse aggregate

PKS were collected from the local crude palm oil mill (Fig. 1). The PKS was sieved using a 9 mm sieve and the OPS retained on the 9 mm sieve were crushed to obtain the PKS with maximum size of 9 mm. The physical properties of PKS are shown in Table 1. It should be noted that the effect of high water absorption of PKS (Table 1) was compensated by using PKS in saturated surface dry condition during the mixing.

**Table 1.** Comparison of physical properties between PKS and crushed granite

Physical properties	OPS	Crushed granite (Mannan & Ganapathy 2002)
Compacted bulk density, kg/m <sup>3</sup>	658	1470
Specific gravity	1.35	2.61
24-hours water absorption, %	19.1	0.76
Aggregate Impact Value (AIV), %	2.63	17.29

### 1.1.3. Fine aggregate

Mining sand was used as fine aggregate with the specific gravity and fineness modulus of mining sand were found to be 2.65 and 2.71, respectively.

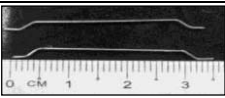
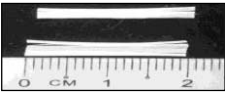
### 1.1.4. Water and superplasticizer

Potable water with a pH value of 6.4 was used for all mixes. A polycarboxylate-based superplasticizer was used in all mixes to improve the workability of the mixes.

### 1.1.5. Fibers

Two types of fibers were added into OPSC: (i) steel fiber and (ii) PP fibers. The basic properties of the fibers are displayed in Table 2.

**Table 2.** Properties of steel and polypropylene (PP) fibers

Fiber	Geometry	Length (mm)	Diameter	Specific gravity	Tensile strength (MPa)	
Steel		Hooked-end	35	0.55 mm	7.90	1100
PP		Fibrillated	19	1000 denier	0.90	400

## 1.2. Mix proportions

A total of 3 mix proportions were prepared (Table 3). All the constituent materials were kept constant while the differences between the mixes are the type of fibers. A fiber content of 0.5% (of concrete volume) was used in the PKSFRCC mixes.

**Table 3.** Mix proportions

Mix	Description	Constituent Materials (kg/m <sup>3</sup> )				Fiber (%vol.)	
		OPS	Sand	Cement	Water	Steel	PP
PKSC	Control					0	0
PKSFRC-ST	0.5% steel fiber	335	980	500	160	0.5%	0
PKSFRC-PP	0.5% PP fiber					0	0.5%

### 1.3. Specimen preparation and testing procedures

The workability (slump) of all mixes was measured in accordance to the ASTM C143 (2010). For each mix, fifteen 100 mm cubes and three 100 x 100 x 500 mm prisms were prepared to be tested for corresponding testing: compressive strength (BS EN 12390-3, 2000) and flexural strength (ASTM C78) respectively. After the de-moulding, all the specimens were cured in water and all of the samples were tested the age of 28-day except the cubes. The cubes were tested at the age of 1-, 3-, 7-, 28- and 56-day.

## 2. Results and discussions

### 2.1. Slump

The addition of fibers into concrete generally causes significant loss in concrete workability, attributed to larger surface area of fibers than aggregates which results in the requirement of more cement paste to wrap around the fibres (Chen and Liu 2005). From Table 4, PKSFRCC-PP produced the lowest slump; It produced 50% slump reduction relative to the control mix. However, the PKSFRCC-ST produced a slump value of 40 mm with 33% slump reduction. The difference between the slump values of the steel and PP fibers is due to the larger surface area in PP fibers which requires a huge amount of cement paste to wrap around to form the fibre-matrix interfacial bonding, eventually reduced the flow ability of the fresh cement matrix. Despite the low slump values, all three mixes attained good compaction and finishing.

### 2.2. Oven-dry density

The EN 206-1 defined lightweight concrete (LWC) as concrete having an oven-dry density (ODD) of not less than 800 kg/m<sup>3</sup> and not more than 2000 kg/m<sup>3</sup> which is produced using lightweight aggregate for all or part of the total aggregate. Hence all the PKSC and PKSFRCC mixes from Table 4 fulfilled the requirement to be considered as LWC with the ODD within the range of 1725-1810 kg/m<sup>3</sup>.

The PKSFRCC-ST showed higher ODD than other two mixes, due to the high specific gravity of steel fibres of about 8.

**Table 4.** Mechanical properties of OPSC and OPSFRCC

Mix	Slump (mm)	Oven-dry density (kg/m <sup>3</sup> )	Compressive strength (MPa)				Flexural strength (MPa)	Brittleness*
			1-day	3-day	7-day	28-day		
PKSC	60	1725	18.6	29.3	30.3	31.6	4.74	7.3
PKSFRCC-ST	40	1810	23.6	29.1	35.9	38.8	6.03	6.4
PKSFRCC-PP	30	1740	20.9	28.2	31.8	33.8	5.15	6.6

\* brittleness = compressive to flexural strengths ratio

### 2.3. Compressive strength

The compressive strengths at the age of 1-, 3-, 7- and 28-day are reported in Table 4. The control mix produced 28-day compressive strength of 32 MPa, while the PKSFRCC

reinforced with steel fibers showed the highest compressive strength of about 39 MPa, which was 23% higher than control concrete. Further, PKSFRC-PP showed slight improvement of compressive strength.

The beneficial effect of fibers on enhancing compressive strength of concrete is mainly due to the crack bridging effect. Under an increasing compression loading, cracks will initiate and advance. When the advancing crack approaches a fiber, the debonding at the fiber-matrix interface begins due to the tensile stresses perpendicular to the expected path of the advancing crack. As the advancing crack reaches the interface, the crack tip stress concentration is reduced and thus the propagation of crack is blunted and blocked (Yap et al. 2013). In the crack bridging, the additional stress taken by the fibers is governed by the tensile strength of the fibers. Steel fibers possess high tensile strength and hence it provided high improvement on the compressive strength of PKSC. While marginal effect of PP fibers on compressive strength of PKSC might due to the low stiffness of PP fibres which resulted in less crack bridging effect to be induced in the fibre-matrix network.

Other than that all the mixes achieved high early strength (Table 4). At the age of 3-day and 7-day, the mixes produced 70-90% and 80-95%, respectively of their corresponding 28-day compressive strength. The high early strength of OPSC is the high reactivity and micro filler effects of silica fume added into OPSC (Yap et al. 2013).

#### *2.4. Flexural strength*

The flexural strengths were investigated and shown in Table 4. However the low tensile strength in PKSC arises the use of fibres in PKSC. In this study, the control mix without any fibers produced 4.7 MPa in the flexural strengths.

In comparison to the PP fibres, steel fibers produced the highest flexural strength of 6 MPa and it was found 27% higher than the PKSC mix. The tensile strengths enhancement is significant. However the improvement of flexural strengths in PKSFRC-PP mix was only 9%. Judging for the smaller beneficial effects of PP fibers compared to steel fibers, the situation might be attributed to the lower tensile strength of PP fibers. This caused a smaller tensile stress taken by PP fibers during crack bridging, compared to the steel fibers.

#### *2.5. Brittleness*

The high brittleness is also another concrete of LWC and PKSC. In this study, the brittleness is taken as the ratio of compressive to flexural strengths (Sun & Xu, 2009). A high brittleness ratio indicates that the concrete material fractures and loses the load bearing capacity under tensile stress at a much lower loading, compared to the compressive strength. Based on results from Table 4, the control mix produced a brittleness ratio of about 7.3, while the PKSFRC reduced the brittleness significantly to 6.4-6.6. The presence of fibres in the cement matrix contributes a restraining effect on the matrix and this eventually allows the concrete to sustain higher deflection after the cracking commences. The crack bridging effect also aids in holding the concrete together. Therefore the inclusion of both steel and PP fibres significantly reduced the brittleness of PKSFRC.

### 3. Conclusions

The following conclusions could be drawn:

- Addition of fibers into the PKSFRC significantly reduced the slump.
- Both PKSC and PKSFRC fulfilled the requirement of LWC with oven-dry density 1725-1810 kg/m<sup>3</sup>. The addition of 0.5% steel fibers increased the dry density by 5% but PP fibers have negligible effect on dry density of OPSC.
- Steel PKSFRC experienced significant enhancements of both the compressive and tensile strengths of PKSC.
- PP fibers slightly improved on compressive and flexural strengths of PKSC, with only marginal enhancement of about 9% on the flexural strength of PKSC.
- The addition of both steel and PP fibres reduced the brittleness of PKSC.
- The use of steel fibers is highly recommended to enhance the mechanical properties of PKSC.

### Acknowledgement

The authors are grateful to University of Malaya for the financial support through the University of Malaya Research Project RP018-2012B: Development of geo-polymer concrete for structural application.

### References

- [1] Alengaram, U. J., Al Muhit, B. A., and Jumaat, M. Z. 2013. Utilization of oil palm kernel shell as lightweight aggregate in concrete – A review, *Construction and Building Materials*, 38: 161-172.
- [2] ASTM C78 *Standard test method for flexural strength of concrete (using simple beam with third-point loading)*. American Society for Testing and Materials (ASTM), 2002.
- [3] Basri, H. B., Mannan, M. A., and Zain, M. F. M. 1999. Concrete using waste oil palm shells as aggregate. *Cement and Concrete Research*, 29: 619-622.
- [4] BS EN 12390: Part 3 *Testing hardened concrete- Compressive strength of test specimens*. British Standard Institution, 2000.
- [5] Chen, B. and Liu J. 2005. Contribution of hybrid fibers on the properties of the high-strength lightweight concrete having good workability. *Cement and Concrete Research*, 35: 913-917.
- [6] Domagala, L. 2011. Modification of properties of structural lightweight concrete with steel fibres. *Journal of Civil Engineering and Management*, 17(1): 36-44.
- [7] Hassanpour M., Shafiq P. and Mahmud H. 2012. Lightweight aggregate concrete fiber reinforcement – A review. *Construction and Building Materials*, 37: 452-461.
- [8] Mannan, M. A.; Ganapathy, C. 2002. Engineering properties of concrete with oil palm shell as coarse aggregate. *Construction and Building Materials*, 16: 29-34.
- [9] MPOB, Malaysia Palm Oil Board (2011). Production of Palm Kernel and Palm Kernel Cake. Website: [http://econ.mpop.gov.my/economy/ei\\_monproduction.htm](http://econ.mpop.gov.my/economy/ei_monproduction.htm)
- [10] Sun, Z. and Xu, Q. 2009. Microscopic, physical and mechanical analysis of polypropylene fiber reinforced concrete. *Materials Science and Engineering A*, 527: 198-204.
- [11] Yap, S. P., Alengaram, U. J. & Zamin, M. Z. 2013. Enhancement of mechanical properties in polypropylene- and nylon-fibre reinforced oil palm shell concrete. *Materials and Design*, 49: 1034-1041.



# Utilization of ceramic wastes as replacement of portland cements

Viviana RAHHAL<sup>a,1</sup> Edgardo IRASSAR<sup>a</sup>, Cristina CASTELLANO<sup>a</sup>  
Zbyšek PAVLÍK<sup>b</sup> and Robert ČERNÝ<sup>b</sup>

<sup>a</sup> *Departamento de Ingeniería Civil Facultad de Ingeniería UNCPBA, Argentina*

<sup>b</sup> *Faculty of Civil Engineering, Czech Tech Univ in Prague, Czech Republic*

**Abstract.** The possible applicability of ceramic waste as partial replacement of Portland cement was studied. For this purpose, two ceramic wastes and two Portland cements of different countries (Argentina and Czech Republic) were analysed. After characterization of the materials used (chemical and mineralogical composition and specific surface), the effect of ceramic waste replacement (8, 16, 24, 32 and 40 % by mass) was analyzed. The pozzolanic activity, the heat released rate and the hydration products were determined at 2, 7 and 28 days. Results show that ceramic wastes have pozzolanic activity with both portland cements. At early age, the dilution effect governs the properties and finally the pozzolanic reaction improves the performance of blended cements.

**Keywords.** Portland cement, ceramic waste, heat of hydration, XRD-ray

## Introduction

In the cement industry, the manufacture of one ton of portland clinker requires 1.7 tons of raw materials that causes a large consumption of non-renewable mineral resources and a serious depletion of quarrying areas. Furthermore, the high temperature process requires high energy consumption and also releases a large volume of CO<sub>2</sub> to the atmosphere as a result of decarbonation of limestone in the furnace and the combustion of fossil fuels [1].

Additionally, the growth of industrial activity also produced a large volume of solid waste that annually increases in several industrial sectors, becoming an environmental issue add its final deposition. Among this industrial sector, the ceramic brick industry grows due to its high heat-efficient envelop for building. In Europe, the amount of wastes from different production stages of the ceramic industry reaches to 3-7 % of its global production, meaning millions of tons of calcined-clays per year [2]. The same values of scrap are reported for the Latin-American ceramic industry.

The cement production companies have begun to implement a series of measures to reduce their environmental impact and transform the portland cement into a material with sustainable development. In order to find economic, technological and solutions primarily friendlier to the environment, there has been widespread use of industrial by-products or waste material [3-4], during the manufacture of portland cement. In this

---

<sup>1</sup>Corresponding author: Av. del Valle 5737 (B7400JWI) Olavarría; Email. [vrahhah@fio.unicen.edu.ar](mailto:vrahhah@fio.unicen.edu.ar)

paper the potential of using ceramic wastes as partial replacement of portland cement is studied.

## 1. Materials and methodology

Two portland cements (ArgPC and CzPC) and two ceramic wastes (ArgCW and CzCW) were used. Portland cements meet the composition of CEM I according to EN197:1 and ceramic wastes come from a red brick factor were they are calcined at about 850-1050°C. The ArgCW is the scrap and it was crushed and ground in a ball grinding mill. The CzCW is the ceramic dust obtained after the grinding treatment made on the face of the bricks to calibrate its heights. The characteristics of all materials, chemical and mineralogical composition, density and specific surface (Blaine) are given in Table 1. The chemical composition was determined by X-ray fluorescence and the mineralogical composition of cements was calculated by Bogue's formulate and the main crystalline minerals of ceramic waste was determined by XRD.

**Table 1.** Characteristic of materials

Parameters	Portland Cements		Parameters	Ceramic Wastes	
	ArgPC	CzPC		ArgCW	CzCW
SiO <sub>2</sub> , %	21.5	18.9	SiO <sub>2</sub> , %	64.6	51.3
Al <sub>2</sub> O <sub>3</sub> , %	3.8	4.2	Al <sub>2</sub> O <sub>3</sub> , %	17.0	20.0
Fe <sub>2</sub> O <sub>3</sub> , %	3.8	3.8	Fe <sub>2</sub> O <sub>3</sub> , %	5.6	6.0
CaO, %	64.3	62.4	CaO, %	2.5	11.5
MgO, %	0.8	1.0	MgO, %	1.5	4.5
SO <sub>3</sub> , %	2.6	2.3	SO <sub>3</sub> , %	-	1.0
Na <sub>2</sub> O, %	0.1	0.0	Na <sub>2</sub> O, %	4.2	1.3
K <sub>2</sub> O, %	1.1	0.0	K <sub>2</sub> O, %	2.9	3.2
TiO <sub>2</sub> , %	-	0.8	TiO <sub>2</sub> , %	0.7	0.8
Loss on ignition	2.1	1.5	Loss on ignition	0.6	1.1
Density	3.15	3.10	Density	2.70	2.72
SS Blaine, m <sup>2</sup> /kg	315	330	SS Blaine, m <sup>2</sup> /kg	590	512
C <sub>3</sub> S, %	60.0	50.5		Quartz	Quartz
C <sub>2</sub> S, %	16.4	19.2	Mineralogical	Feldspar	Feldspar
C <sub>3</sub> A, %	3.8	8.8	composition	Hematite	Mica
C <sub>4</sub> AF, %	11.5	11.6			
Gypsum, %	5.5	7.2			

Regarding the mineralogical composition of cements, ArgPC has more C<sub>3</sub>S than the CzPC, but the last-one has more C<sub>3</sub>A and more gypsum that the ArgPC; with respect to their C<sub>2</sub>S and C<sub>4</sub>AF content they are similar. The mineralogical composition of ceramic wastes was glassy phase, quartz, feldspars (mainly anorthite in ArgCW; albite and orthoclase in CzCW), high content of muscovite in CzCW and hematite in ArgCW. The CW was incorporated to blended cement with 8, 16, 24, 32 and 40 % of replacement by weight of cement. For all blended cements, the pozzolanic activity, the heat liberation rate and hydrated compounds identification by XRD were determined.

Pozzolanic activity was determined by Frattini test according the procedure described in EN196-5 at 2, 7 and 28 days. The method consists in the determination of the amount of Ca<sup>2+</sup> and OH<sup>-</sup> in the water of contact with the samples stored at 40 °C. The ceramic wastes may be considered as an active pozzolan when the [CaO] and [OH<sup>-</sup>] of their solution are located below the solubility isotherm of calcium hydroxide.

The heat released rate was determined for 48 hours in an isothermal calorimeter operating at 20 °C, the amount of blended cement was 20 g and the water-to-cementitious ratio was 0.50. XRD analysis was made on ground pastes cured in sealed condition at 2, 7 and 28 days. The determinations were performed on Philips PW 3710 diffractometer with Cu K $\alpha$  operating radiation 40 kV and 20 mA using carbon monochromator.

## 2. Results and discussion

Figures 1 and 2 show the results of Frattini test on the [CaO] vs [OH] plot for the blended cement ArgPC-ArgCW and CzPC-CzCW at 2, 7 and 28 days, of respectively.

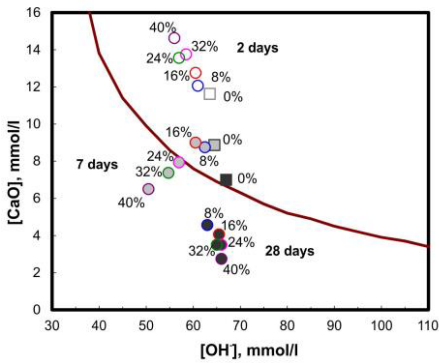


Figure 1. Frattini test of ArgPC with ArgCW

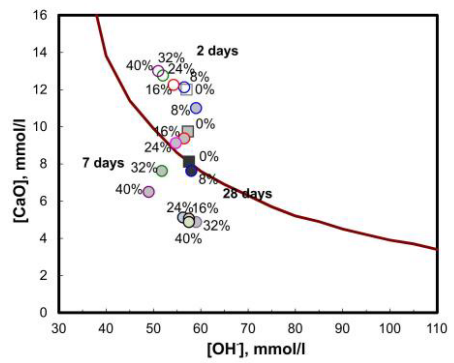


Figure 2. Frattini test of CzPC with CzCW

At 2 days, both cements with 8 to 40 % of ceramic waste have not pozzolan activity, because all points are above the calcium solubility isotherm at the super saturation zone. The [CaO] increases when increase the level of replacement showing the stimulation effect on the hydration of cement. At 7 days, the reduction of [OH<sup>-</sup>] and [CaO] shows that ceramic wastes have pozzolanic reactivity and the blended cement with high replacement level became below the solubility isotherm at the calcium sub saturation zone. At 28 days, all blended cements appear with good pozzolanic activity and this is more evident when the replacement level of CW increases.

The results of calorimetric test for ArgPC-ArgCW and CzPC-CzCW blended cements are given in Figures 3 and 4, respectively. For both systems, it can be observed that the increase of replacement level from 8 to 40 % produces a low heat liberation rate and low accumulated heat. This observation can be attributed to the dilution effect [5]. For the ArgPC-ArgCW blended cements, the acceleration slope of the second peak in the calorimetric curve is reduced and it remains with slight changes for the CzPC-CzCW blended cements. The high C<sub>3</sub>A content of the CzPC produces the third peak, which is not revealed in pastes with the ArgPC (low C<sub>3</sub>A). From the CzPC-CzCW, it can be observed that the CW-addition stimulates the cement hydration, specially the aluminic phase, because the intensity of the second peak decreases more than the intensity of the third peak when the replacement level of CW increases.

All blended cements exhibited the maximum of the hydration heat at approximately 14 hours revealing that CW acts without interference in the cement

hydration. Therefore, the kinetics of the early hydration reaction for both systems behaves in similar way. From the practical point of view, this behavior can lead to a reduction of hydration heat that is beneficial for casting and production of high volume structures, but can be a shortcoming for the early strength development of these blended cements.

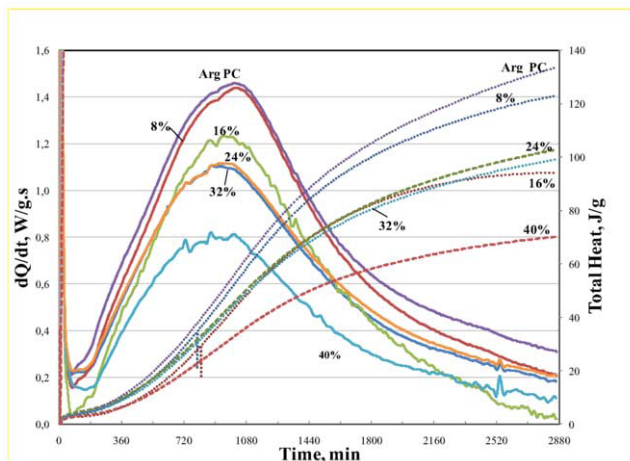


Figure 3. Heat released rate and accumulated heat of ArgPC-ArgCW blended cements

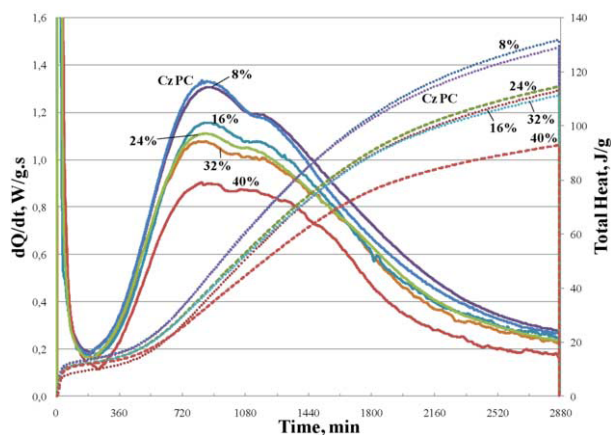
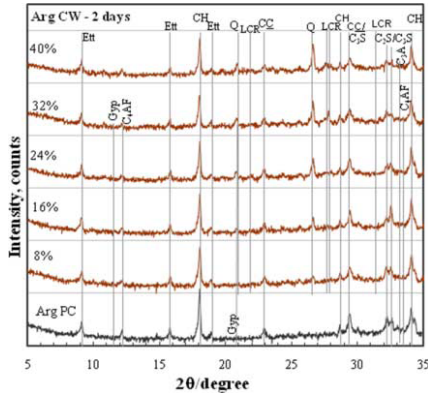
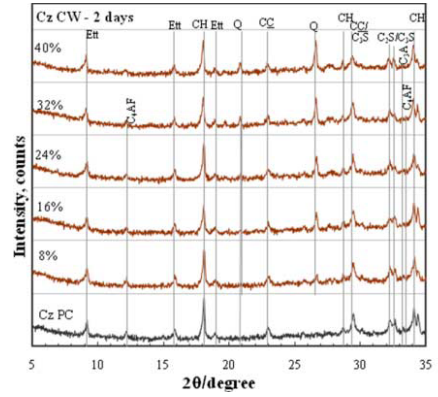


Figure 4. Heat released rate and accumulated heat of CzPC-CzCW blended cements

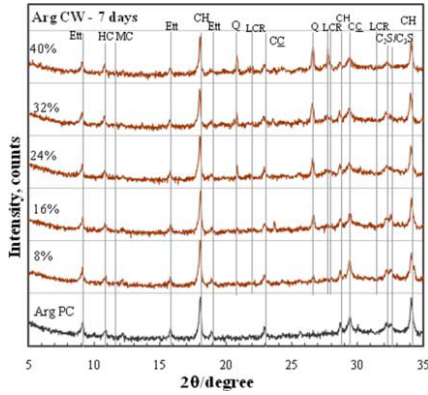
Figures 5 and 6 show the XRD patterns for the hydrated paste at 2, 7 and 28 days of ArgPC-ArgCW and CzPC-CzCW blended cements, respectively. At 2 days (Figs. 5a and 6a), the ArgPC and CzPC show the presence of ettringite (Ett) and calcium hydroxide (CH). For all blended cements (8 to 40% ArgCW and CzCW), the intensity of Ett and CH peaks have similar value to those of corresponding PCs instead of the dilution effect caused by CW-addition. These observations are evidences of the cement that hydration stimulation caused by the incorporation of CW due to the filler effect, the heterogeneous nucleation and the large amount of free water [5]. In blended cements, quartz (Q) is identified form ceramic wastes and consequently its peak intensity increases when increasing the replacement level.



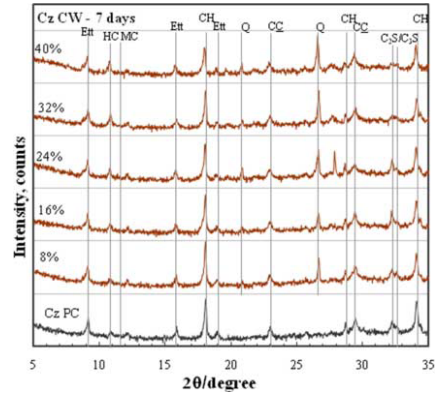
(a)



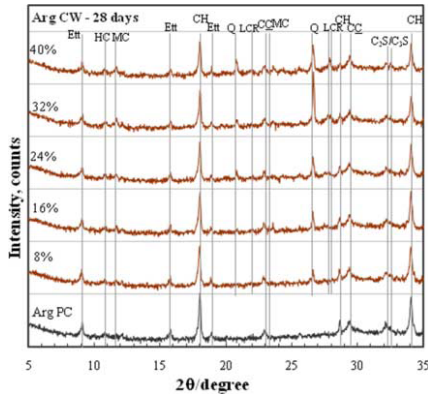
(a)



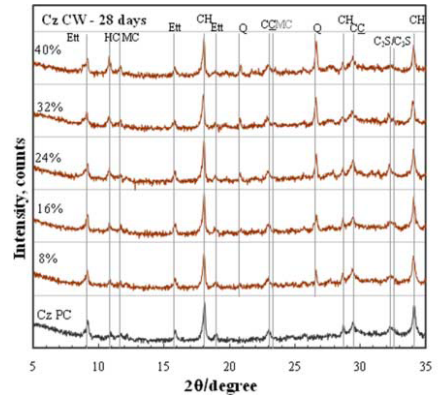
(b)



(b)



(c)



(c)

**Figure 5.** XRD pattern for hydrated paste of ArgPC –ArgCW blended cement: (a) 2 days, (b) 7 days and (c) 28 days

**Figure 6.** XRD pattern for hydrated paste of CzPC – CzCW blended cement: (a) 2 days, (b) 7 days and (c) 28 days

At 7 days (Figs 5b and 6b), the Et and CH are accompanied by hemi-carboaluminate (HC) and the incipient formation of monocarboaluminate (MC). The HC and MC formation is promoted by the calcium carbonate (CC) present in PCs. At 28 days, the intensity of CH and Et peaks decreases and the peaks intensity of MC increases. This effect appears more remarkable for blended cements with high

replacement level. The significant decrease of the CH peak is attributed to the progress of the pozzolanic reaction of CW as commented in results of Frattini test. The transformation of HC into MC is attributed to the presence of limestone filler as minor component in the PCs.

Summarizing, it can be observed that both CW combinations with different PC behave in similar way. At early ages, the incorporation of CW produces the dilution of PC and the stimulation of PC hydration due to the increase of effective water to cement ratio in the system and their role as nucleation sites for calcium hydrated products [4]. This can be observed in the Frattini test results at 2 days where the [CaO] increases for incremental levels of CW replacement. It can be corroborated in the calorimetric test because the characteristic peaks on the heat released curve do not reveal advances or delays for all blended cement tested and the cumulative heat is higher than the proportional to cement reduction. Finally, the XRD shows similar intensity of CH peak at 2 days. At later ages, the CW became to develop its pozzolanic reaction as reveals the Frattini test and it can be corroborated by the decrease of CH peaks in XRD patterns at 7 and 28 days.

### 3. Conclusions

Based on the results present here, it can be concluded that:

The ceramic wastes providing from the brick ceramic industry have a very good pozzolanic activity at 28 days. However, ceramic wastes can be classified as a slow reactive pozzolan.

The addition of ceramic waste (from 8 to 40 %) does not produce significant changes on the mechanisms and kinetics of PC hydration at early ages has reveals the calorimetric curve. At later ages, the mechanism of hydration is the same as revealed the compounds products assembly detect by XRD.

### References

- [1] G Habert, C Billard, P Rossi, C Chen, N Roussel. Cement production technology improvement compared to factor 4 objectives. *Cement and Concrete Research*. 40 (2010) 820–826.
- [2] Z.Pavlik, J. Fořt, M.Pavliková, T.Kulovaná, J.Studnička, R.Černý, V.F.Rahhal, E.F.Irassar, H.A.Donza, Reusing of ceramic waste powder in concrete production, *Proceedings 18 th International Meeting of Thermophysical Slovak Republic* 2013.
- [3] F.Puertas, I.García-Díaz, A.Barba, M.F.Gazulla, M.Palacios, M.P.Gomez, Ceramic wastes as alternative raw materials for Portland cement clinker production, *Cement and Concrete Composite* 30 (2008), 798–805.
- [4] A. Lavat, M.A.Trezza, M. Poggi, Characterization of ceramic roof tile wastes as pozzolanic admixture *Waste Management* 29 (2009), 1666-1674.
- [5] C.Zhang, A.Wan, M.Tang, X.Liu, The Filling Role of Pozzolanic Material, *Cement and Concrete Research* 26 (1993), 856-890.

# Rheology of portland cement pastes with siliceous mineral additions

Viviana RAHHAL<sup>a,1</sup> César PEDRAJAS<sup>b</sup>, Edgardo IRASSAR<sup>a</sup> and Rafael TALERO<sup>b</sup>

<sup>a</sup>*Departamento de Ingeniería Civil Facultad de Ingeniería UNCPBA. Av. del Valle 5737 (B7400JWI) Olavarría. Argentina*

<sup>b</sup>*Instituto Eduardo Torroja CSIC. Serrano Galvache 6 (28033) Madrid. España*

**Abstract.** In this paper, the rheological behaviour of pastes of Portland cement and different siliceous mineral additions was analyzed. For this purpose, two Portland cements with different mineralogical composition (low  $C_3A$  and high  $C_3S$  content and low  $C_3S$  and high  $C_3A$  content) combined with different replacement percentages of three minerals additions of siliceous nature (quartz, diatomite and silica fume) are used. Mineral admixtures have similar chemical composition, but they have different crystallinity and morphology: the quartz is fully crystalline; diatomite and the silica fume are vitreous with a small fraction of cristobalite. The vitreous phase content in the mineral additions gives the pozzolanic properties. All determinations were performed on Haake Roto Viscosimeter at 25° C, at the time corresponding to the minimum in  $dQ/dt$  calorimetric curve during the dormant period. The results show that portland cement with low  $C_3A$  content and high  $C_3S$  content presents a great shear resistance and the replacement by siliceous mineral addition affect the rheological behavior of paste depending on the water demand and the pozzolanic reactivity.

**Keywords.** Rheology, portland cement pastes, pozzolanic non-pozzolanic additions

## Introduction

When portland cement is mixed with water, the hydration reactions start realising a lot of heat during 15 minutes. Then, the rate of hydration drastically decays during the dormant period and the paste has a plastic consistency. This period extends until the reactions have produced enough hydrated compounds that links the particles and the setting begins. These phenomena can be clearly observed in the calorimetric curve.

The rheological properties of the cement pastes, during the dormant period, are modified by the incorporation of mineral additions. The initial shear stress and viscosity of cement pastes are very important for mix, transport, placement and compaction of concrete. The shear stress and viscosity and their evolution with the time may be determined by rheological test [1, 2].

In a previous paper, the influence of the rotation rate and the duration of each cycle in the test on the rheological parameters of paste were analyzed. It can be observed a great difference between the shear response during the acceleration and deceleration when crystalline mineral additions were incorporated [3].

---

<sup>1</sup>Corresponding author: [vrahhall@fio.unicen.edu.ar](mailto:vrahhall@fio.unicen.edu.ar)

In this paper, the rheological behaviour of pastes made with two different portland cements and three different siliceous mineral additions were analyzed.

## 1. Materials and methodology

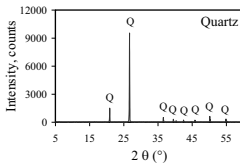
Two Portland cement were used: PC1 and PC2. The physical characteristics and the mineralogical composition of both portland PC are given in Table 1.

**Table 1.** Characteristic of materials

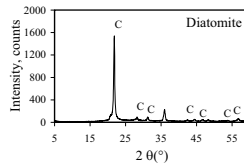
Parameters	Portland Cements		Parameters	Mineral Additions		
	PC1	PC2		Q	D	SF
C <sub>3</sub> S, %	51	79	SiO <sub>2</sub> , %	99.9	91.8	92.0
C <sub>2</sub> S, %	16	2	Density	2.70	2.59	2.10
C <sub>3</sub> A, %	14	0	SSB*, m <sup>2</sup> /kg	395	-	-
C <sub>4</sub> AF, %	5	10	BET, m <sup>2</sup> /kg	-	720	22100
Alkalis eq., %	1.5	0.4	Humidity absorption 1 day, %	0.41	0.04	5.59
Density	3.08	3.21	Fratini test 7 days, %	negative	negative	positive
SSB*, m <sup>2</sup> /kg	319	301	Fratini test 28 days, %	negative	positive	positive
			d 90, μm	84.051	26.203	17.662
			d 50, μm	29.696	11.996	8.402
			d 10, μm	4.687	4.598	3.026

\*SSB: Specific Surface Blaine

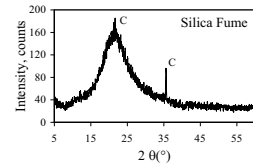
Three mineral additions with more than 90% SiO<sub>2</sub> in its chemical composition were used. Quartz (Q) is totally crystalline (Fig. 1a) and it has not pozzolanic activity. Diatomite (D) and silica fume (SF) have pozzolanic activity, but diatomite presents some part of SiO<sub>2</sub> as cristobalite (Fig. 1b) and powdered silica fume is completely amorphous (Fig. 1c) having very high reactivity. The shape of particles is angular for Q, frustules for D and microspheres for SF.



**Figure 1a.** XRD-ray SF addition



**Figure 1b.** XRD-ray D addition



**Figure 1c.** XRD-ray Q addition

For Q and D additions, the replacement percentages were 20 and 40% by mass of cement (called: 20% Q and 40% Q for Q-addition and 20% D and 40% D for D-addition). For the SF addition, the replacements were 5 and 15% by mass of cement (5% SF and 15% SF). Table 2 reports the water demand and the setting times of pastes determined according to the EN 196-3 procedure.

**Table 2.** Water demand and setting time of pastes

Sample	PC1	20% Q	40% Q	20% D	40% D	5% SF	15% SF
Water demand, w/b	0.31	0.32	0.32	0.54	0.90	0.33	0.41
Initial set, minutes	200	165	195	225	270	145	60
Final set, minutes	310	270	285	340	---	265	240
Sample	PC2	20% Q	40% Q	20% D	40% D	5% SF	15% SF
Water demand, w/b	0.28	0.29	0.30	0.54	0.86	0.32	0.40
Initial set, minutes	270	305	300	410	440	335	250
Final set, minutes	375	420	480	540	600	520	550



The water demand of PC1 paste was greater than that of the corresponding to PC2 paste. It is due to the greater ability to form AFt phase in PC1 that requires a large amount of water in their constitution. Therefore, the initial and final setting times of PC1 paste were shorter than that of PC2 paste.

The water demand of pastes with Q-addition is similar to the corresponding PC used. These results could be attributed to the low humidity absorption and the null pozzolanic activity of Q. However, the setting times were earlier than plain paste for PC1-cement and they were later than plain paste for PC2-cement. This behavior could be attributed compensation between the stimulation effect on the  $C_3A$  hydration (mainly for PC1) and the dilution effect on the  $C_3S$  (mainly for PC2).

For both PCs, the replacement by D and SF additions increase the water demand when the replacement level increases. It could be due to the small size of particles and their morphology that reduces the free water at early time. For D addition, the setting times increase for both replacement level used due to the large inter-particles space caused by the high water demand. On the hand, the setting times of pastes containing 5% of SF have the same tendency that those reported by Q-addition: it occurs in advance for PC1 and it is delayed for PC2. For 15% of SF, the setting times decreased, except for the final set of PC2. The stimulation effect on hydration is due to the small particles size and the high pozzolanic activity of SF.

The rheological tests were made on pastes with similar flowability. Using the minislump test, the spread-diameter was determined for PC1 and PC2 pastes with w/c of 0.50 ( $100 \pm 10$  mm). For pastes with siliceous additions, the water to binder-ratio (w/b) was varied to obtain this spread diameter. For this objective, the w/b was 0.5 for 20 and 40% replacement of Q addition; 0.75 and 1.00 for 20 and 40% replacement by D addition, respectively; and w/b of 0.56 and 0.69 for 5 and 15% replacement by SF addition, respectively. The water content to obtain the same spread-diameter in the pastes with siliceous additions has the same tendency that those determined by water demand test. After mixing, pastes were stored at 25 °C until the time reported in Table 3. This time corresponds to the minimum of heat released during the dormant period in the calorimetric curve determined previously on paste with the same w/b [4]. Additionally, the XRD-analyses were performed at this time to determine the crystalline compounds presents in the paste.

The rheological test was carried using a Haake rotational viscometer, compound by a viscometer Rotovisco 1, a profiled rotor Z38 DIN 53018, a glass Z43 DIN 53018, a control temperature unit for coaxial cylinders and a circulation thermostat DC 30-B3 [5]. The mixing sequence of paste is showed in Figure 2. It consisted of a ramp up to 45 rad/s staying 30 s, following by a ramp down from 45-to-0 rad/s with two steps down of 10 s and a ramp up from 0-to-45/s with the same step. Then, the paste staying 30 s at 45rad/s and finally down to 0 in 10 s without step [6]. Shear stress was measured at singular points (A1, B1, C1, C2, A2, B2, and C3).

## 2. Results and discussion

Table 3 summarizes the shear stress of the singular points (A1, B1, C1, C2, A2, B2, and C3) for all studied pastes. Figures 3 and 4 show the XRD-pattern for plain and blend pastes containing PC1 and PC2 cement, respectively.

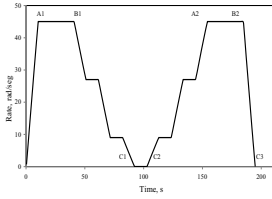


Figure 2. Mixing sequence

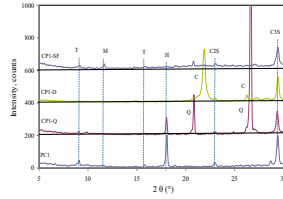


Figure 3. XRD-ray PC1 samples

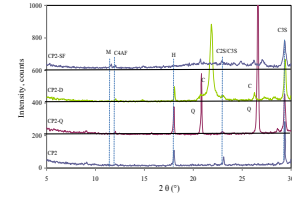


Figure 4. XRD-ray PC2 samples

Table 3. Shear Stress at singular points

Sample	w/b ratio	Minimum of dormant period, min	Shear Stress, Pa						
			A1	B1	C1	C2	A2	B2	C2
PC1	0.50	120	91.91	54.07	11.48	12.30	47.20	46.15	11.35
20% Q	0.50	100	78.50	55.34	12.81	13.90	36.97	34.77	12.76
40% Q	0.50	125	122.7	74.48	15.09	13.60	48.06	44.98	13.75
20% D	0.75	110	106.7	65.34	10.76	10.13	60.21	55.23	9.30
40% D	1.00	165	45.62	30.99	3.27	3.72	38.52	36.74	4.10
5% SF	0.56	100	116.4	71.34	25.27	27.24	47.86	45.22	22.4
15% SF	0.69	110	180.3	97.25	53.78	65.56	60.16	56.06	39.2
PC2	0.50	100	162.5	75.78	13.44	12.04	46.15	42.87	12.83
20% Q	0.50	180	138.7	77.92	12.99	12.77	48.77	45.19	10.58
40% Q	0.50	95	119.4	74.46	11.19	11.30	47.37	44.77	11.36
20% D	0.75	125	59.31	28.27	2.92	3.56	27.49	26.82	3.53
40% D	1.00	160	51.63	32.89	2.19	3.10	34.39	31.83	2.32
5% SF	0.56	160	164.5	97.7	25.96	25.81	51.27	45.54	18.13
15% SF	0.69	155	209.9	122.6	55.5	61.37	62.85	55.13	34.91

At the minimum in the dormant period, the PC1 paste has an initial shear stress of 91.91 Pa (A1 point); this value may be due to the ettringite formation (see Fig. 3) that occurs in this high C<sub>3</sub>A-content cement. After 30 s at 45 rad/s, the paste shows a thixotropic behavior causing a significant decrease of shear stress (B1 point). When the rotor stop (C1 point), the paste shows a remaining shear stress, and 10 s later it recovers part of stress (C2 point) reaching to 12.3 Pa. At A2 point, the shear stress is reduced about 50% with respect to the value obtained at A1 point. On the other hand, the shear stress at B2 point is reduced about 15% compared to the value at B1 point after that paste remains 30 s at 45 rad/s. Finally, the value of shear stress at C3 point remains with similar value that obtained at C1 point. For PC1 paste, all results show a high thixotropic recovery.

For PC2 paste at the minimum in the dormant period, the initial shear stress is 162.5 Pa at A1 point. It is observed that the shear stress is higher than that of CP1 due to the different mineralogical composition of cement. For PC2, the high content of C<sub>3</sub>S produces a different nature of reaction products at early stages of hydration (Fig. 4). After 30 seconds at 45 rad/s, the paste shows a thixotropic behavior with a significant decrease in the shear stress (B1 point) approximately a half as occurs in PC1 paste. When the rotor stop (C1 point), the paste has a residual stress (13.44 Pa) that decays up to 12.04 Pa after 10 seconds (C2 point). At the A2 point, the shear stress is reduced about 75% with respect to A1 point; while this stress reduction was about 45% between the B2-point and B1-point. Finally, the residual stress at C3 point was lower than that determined at C1 point. For PC2 paste, all results show some difficulty for the thixotropic recovery.

When PC1 was replaced by Q addition, the shear stress was greater in the most of singular points and it also increases when the level replacement increases. This behavior could be partly attributed to the mineralogical composition of the cement and partly to the acidic nature of the addition. For PC1 with high  $C_3A$ -content, the Q-addition stimulates the hydration of aluminic phases of cement due to its particle size and acidic nature, and it also increases the available water for reaction due to the dilution effect. Both effects contribute to the rapid recovery of links due to the renewed ettringite formation. From the PC1-results, it can be inferred that the incorporation of Q addition specifically stimulates the hydration of aluminic phases of cement.

When PC2 was replaced by 20 and 40% of Q addition, the shear stress was lower in the most of the singular points and it was reduced when the level replacement increases, unlike as occurred for PC1. This behavior reveals the low interaction between the Q-addition and PC with low  $C_3A$ -content making very obvious the dilution effect. After 30 seconds at 45rad/s, the shear stress decreased about 40% (B1 point). When the rotor stop (C1 point), the pastes have a residual stress and 10 s later (C2 point) the shear stress decreases. Regarding Q addition-PC2 interaction, it has a low capacity to remake the links between particles, unlike as occurred for CP1 at the same points. At the A2 point, the shear stress is reduced about 60% with respect to A1 point; while this stress reduction was about 40% between the B2-point and B1-point. Finally, the residual stress at C3 point increases when increase the replacement level. Comparing the residual stress at C3 point with the value at C1 point, it was lower for 20% of Q and similar for 40% of Q.

The D addition has a high water demand and also low pozzolanic reactivity causing an excess of free water that is employed to wet the particles. The incorporation of 20% addition to PC1 causes an increase of shear stress in the most of the singular points. However, the incorporation of 40% causes a decreased of shear stress at all measured points. The increment of shear stress may be partially attributed to the stimulation effect on the cement hydration caused by the high available water to react and the increase of hydration degree of cement phases produced by the particle addition acting as extra nucleation sites for the calcium hydroxide in the system (Fig. 3). For 40% of D-addition, the lower shear stress may be due to the dilution effect caused by the lower amount of cement and the big increase of water available in the system.

The incorporation D addition to PC2 produces a reduction of shear stress in all singular points. The decrease of shear stress is attributed to the high demand of water and the poor pozzolanic reactivity of addition that causes an excess of free water.

When PC1 was replaced by the SF addition, the shear stress was higher in all the singular points and it also increases when the replacement level increases. When the rotor stops (C2 point), the shear stress has a drastic increment of 121 and 433% for 5 and 15% replacement, respectively. This increase of shear stress produced by the incorporation of SF addition could be partly attributed to the mineralogical composition of the cement, the very high specific surface and the high reactivity of SF. As occurred for Q-addition, the high  $C_3A$  content of PC1 contributes to the rapid recovery of links. The hydration of silicate phases of cement are also stimulated by SF addition contributing to the calcium hydroxide formation that it is consumed for their highly reactive grains and consequently increasing the amount of calcium silicate hydrate. From the results, it can be inferred that the incorporation of SF addition stimulates the hydration of both phases ( $C_3A$  and  $C_3S$ ) of cement.

When the SF addition is incorporated to PC2, the shear stress was higher in all singular points and it increases with increasing the replacement level as observed for

PC1. The increment of shear stress was more significant when the speed is lower (C2 points) attaining to 114 and 410 % for 5 to 15% replacement, respectively. It was somewhat lower than that of the same points for PC1 cement. These results highlight the very high reactivity of SF and the stimulation effect on the cement hydration caused by the physical effect (filler action and heterogenous nucleation) and the chemical effect (pozzolanic reaction). The high shear stress caused by the incorporation and increased level of SF addition is attributed to the same reasons described for the PC1, with the exception of the C<sub>3</sub>A stimulation

### 3. Conclusions

From the results of rheological tests the following conclusions can be drawn:

For pastes made with portland cements, the initial shear stress was higher for PC2 (high C<sub>3</sub>S), but both cement pastes show a similar reduction (~ 50%) after 30 s at 45 rad/s. Then, the residual shear stress shows the high capacity to remake the links between particles for the PC1 (high C<sub>3</sub>A) due to the renewed ettringite formation.

For the same flowability after mixture, the rheological behavior of pastes was different depending on addition used:

- The Q addition (crystalline, not pozzolanic, regular water demand) produces an increased of shear stress on high C<sub>3</sub>A cement; while on high C<sub>3</sub>S cement produces a decreased of shear stress.
- The D addition (pozzolan low reactivity, siliceous chemical character and high water demand) tends to increase the shear stress in high C<sub>3</sub>A cement, but when the replacement increases the shear stress decays. However, for high C<sub>3</sub>S cement, the shear stress always decreases.
- The SF addition (pozzolan very high reactivity, siliceous chemical character, and high water demand) increases the shear stress for both cements (CP1 and CP2) and the increase of stress is higher when increases the replacement level.

### References

- [1] B. Caufin, A. Papo, Rheological behaviour of cement pastes *Zement-Kalk-Gips*, **12** (1984), 656-661.
- [2] P. Banfill, M. Frias, Rheology and conduction calorimetry of cement modified with calcined paper sludge *Cement and Concrete Research*, **37** (2007), 184-190.
- [3] V. Rahhal, C. Pedrajas, E. Irassar, R. Talero Reologia de pastas de cemento con incorporación de adiciones cristalinas *XII Congreso Latinoamericano de Patología de la Construcción, XIV Congreso de Control de Calidad en la Construcción CONPAT*, ISBN 978-958-58030-1-7 (2013), 424-433.
- [4] V. Rahhal, R. Talero Calorimetry of Portland cement with silica fume, diatomite and quartz additions *Construction and Building Materials* **23** (2009), 3367-3374.
- [5] M. Criado Sanz, A. Palomo Sánchez, A. Fernández Jiménez, *Nuevos materiales cementantes basados en cenizas volantes. Influencia de los aditivos en las propiedades reológicas* Monografía 413 Instituto de Ciencias de la Construcción Eduardo Torroja, Madrid, España, 2006.
- [6] C. Pedrajas, V. Rahhal, R. Talero Determination of characteristic rheological parameters in Portland cement pastes *Construction and Building Materials* **51** (2014), 484-491.

# Cement calorimetry with different condition of calcium sulfate and water reducer admixture

Horacio DONZA<sup>a,1</sup> and Viviana RAHHAL

*Departamento de Ingeniería Civil Facultad de Ingeniería UNCPBA  
Av. del Valle 5737 B7400JWI) Olavarría, Argentina*

**Abstract.** Heat development during portland cement hydration is affected by the type of cement used, by the presence of additions and admixtures, by "water / binder material" ratio, by the calcium sulfate state, and others. Hydration process can be monitored by calorimetric techniques which permits to evaluate from the time that cement comes into contact with water, the paste behavior through the release rate of heat produced by the interpretation of acceleration or delay of hydration reactions as well as the intensity of the heat release occurring.

In this paper the influence of water-reducing admixtures in cement with low C<sub>3</sub>A content, which was previously heated to remove partially and totally the combination water of calcium sulfate, are evaluated. Through a calorimeter, hydration development under isothermal conditions (20 and 30 °C) was studied. Results show that in general increasing the dose of admixtures the hydration reactions are delayed, and on the other hand because of the prior heating of cement significant changes are produced in the acceleration of these reactions. With increasing temperature, the hydration reactions occur earlier with higher intensity peaks.

**Keywords.** Cement, water reducers, calcium sulfate, calorimetric techniques, temperature effect

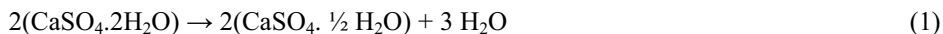
## Introduction

Portland cements hydration is an exothermic process and the amount of heat released per gram until full hydration is defined as "heat of hydration". To determinate its value several methods are available including ASTM C-186, IRAM 1852 standard, which establish methodologies for evaluating hydration heat in a given period of time; EN 196-9 standard, establishes the test methods to determinate the heat of hydration by the semi adiabatic Langavant calorimeter until 120 hours of hydration.

Heat release rate is proportional to the reaction rate of the process, which not only depends on the cement composition, but also the presence of additions, admixtures and temperature conditions. Gypsum (C<sub>2</sub>S $\cdot$ H<sub>2</sub>) is used in cement production as a setting regulator agent that particularly affects C<sub>3</sub>A hydration. Often happens that during clinker and gypsum inter grinding heat is generated. If the heat generated is enough to produce partial dehydration of gypsum, a hemihydrate (bassanita) can be produced according to the reaction shown in Equation 1.

---

<sup>1</sup>Corresponding author: hdonza@fo.unicen.edu.ar , Tel/Fax 54-2284 451055



When the temperature is enough, total dehydration of gypsum may occur becoming anhydrite (Equation 2).



Both forms (hemihydrate and anhydrite) are very avid of water; when they come into contact, gypsum refreezes in needle forms which stiffen the paste. This stiffening is known as false set. The solubility of different forms of sulphates present in cements is not the same, and also can be strongly modified by the presence of water-reducing admixtures or superplasticizers. This can lead to an imbalance between  $\text{C}_3\text{A}$  and calcium sulfate solubility modifying the set to an unexpected time [1].

Water reducers (reduce by more than 5% water content mixing), particularly superplasticizers (reduce water content greater than 12%) [2,3] are used for various purposes [4]: increased workability without changing in the mixture composition, reducing water content to reduce water/cement ratio in order to increase strength and/or durability and reduce the water and cement contents to reduce costs, minimize creep, drying shrinkage and thermal deformation caused by heat of hydration, etc. These admixtures are surfactants which are adsorbed on the cement particles and disperse them. Their solubility is given by the presence of hydroxyl and carboxylic groups or sulfonate attached to an organic chain, which is usually anionic [5]. The main synthetic active compounds are polymers [6] which can be classified into: condensate of melamine sulfonate - formaldehyde (SMF), condensates of naphthalene sulfonate - formaldehyde (SNF), modified lignosulfonates, and other synthetic polymers, such as polyesters, carboxylic, vinyl, hydroxylated polymers and copolymers dispersions, alone or in combination.

Superplasticizers affect portland cement hydration: on the one hand may delay and on the other can affect the morphology and microstructure of products reaction [1, 5]. Molecules can be absorbed in  $\text{C}_3\text{S}$  which causes a delay in the development of heat [1, 7]. Besides decreasing heat, it may also occur a delay in the setting time of concrete when higher proportions of admixtures are used. As a rule [1], for a given portland cement, the amount of superplasticizer required to get certain fluidity, increases with the specific surface of cement. In warm environments, the higher concrete temperature causes more mixing water evaporation, plastic shrinkage cracking, excessive slump loss during transportation and application, premature setting time and loss of strength by poor hydration or retraction phenomena, etc. The heats of hydration problems are greater when very fine cements are used, when high cement contents are employed for high-strength concrete, over reinforced sections, and the need to not stop concreting even in very unfavorable conditions, among others.

In light of the foregoing, in this work by a conduction calorimeter, the effect of different doses of superplasticizer admixture at two different temperatures: 20 and 30 °C on a commercial cement with low  $\text{C}_3\text{A}$  content, (which was heat-treated to convert the gypsum into hemihydrate and anhydrite), are studied.

## 1. Materials and methodologies

Portland cement used had an oxides composition that is shown in Table 1. The major phases are 68.5%  $C_3S$ , 6.9 %  $C_2S$ , 1.8%  $C_3A$ , 14.2%  $C_4AF$ , and 1.1% of equivalent alkalis.

**Table 1.** Cement oxides composition

Oxides	Cement with low $C_3A$
LOI	2,68
SiO <sub>2</sub>	20,42
Al <sub>2</sub> O <sub>3</sub>	3,57
Fe <sub>2</sub> O <sub>3</sub>	4,68
CaO	64,26
MgO	0,73
SO <sub>3</sub>	2,53
K <sub>2</sub> O	1,03
Na <sub>2</sub> O	0,1

To transform gypsum into hemihydrates (bassanite), the cement was heated up to 140 °C and to transform into anhydrite, it was heated up to 200 °C. A water reducer of a polycarboxylates admixture base was used. The doses used were 0.35, 0.6, 1.0 and 1.5 % by weight of cement, being recommended by the manufacturer from 0.35 to 1.0 % dose. The mixing water was network water. All the tests were performed under isothermal conditions at 20 and 30 °C, in a conduction calorimeter, with water/cement ratio equal to 0.35. Twenty grams of cement was used as sample and mixing was carried out manually in a plastic bag to prevent loss of water.

## 2. Results and discussion

The obtained results are shown in Figures 1 to 8, which are plotted against time the heat release rate per gram of cement. Figure 1 shows the behavior developed by the sample without admixture. The most significant difference appears in the occurrence and intensity of the second maximum. The second maximum occurs earlier when treatment temperature increased: 14:00, 12:25 and 10:40 h: min, accompanied by an increase in the intensity of the heat release rate, being 1.45, 1.72 and 1.81 mW/grams to 20, 140 and 200 °C, respectively. Both parameters show a stimulation of reactions, which also corresponds to the slopes of the curves (Figure 1) between the first minimum and second maximum. This behavior can be attributed to the avidity of hemihydrates and anhydrite to retrieve water combination that was extracted by heat treatment. Analyzing the accumulated heat from time zero to the second maximum of the three samples, similar values are obtained, approximately 43 J/g, confirming a real stimulation of reactions to generate the same amount of hydration products.

When test temperature reaches 30 °C, a general acceleration of reactions is produced (Figures 2). An increase in the intensity of the second peak is observed, the dormant period is shorter and the slope to reach the second maximum is higher.

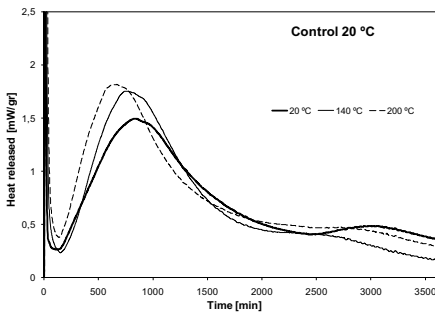


Figure 1. Heat released for control at 20 °C

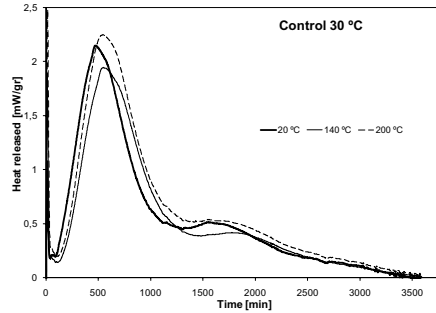


Figure 2. Heat released for control at 30 °C

On the other hand, the appearance of the second peak is not dependent on the heat treatment performed on cement and the three curves tend to stick together.

The use of superplasticizer in lowest dose (0.35%, Figure 3) shows significant variations between treated and untreated samples. Thus, the second maximum is reached at 28:30, 23:50 and 19:00 h: min with peak heat release rate of 1.52, 1.54 and 1.67 mW/g for the untreated and treated samples at 140 and 200 °C, respectively. Moreover, the total amount of heat released from the beginning and second maximum peak was 50.6, 55.9 and 59.3 J/g for the untreated sample and the treated samples at 140 to 200 °C, respectively. This may be due in part to the contribution of heat generated in the pre-peaks (that appearing in the beginning minutes) and contributes to the synergistic action mentioned above. Once the dormant period finished the slopes of three curves are similar, indicating that the acceleration of reaction are similar.

As in the case of cement without admixture, when the temperature rise was 30 °C, and admixture dose is equal to 0.35 %, a general acceleration of reactions is produced and also the three curves tend to remain together, although the untreated cement does not show the long delay that occurs at 20 °C and is located to the left of the other curves.

When dosage reaches 0.6 % and 1% (Figure 5 and 7) the behavior is very similar to a lower dose, but delays are accentuated. For example to 1 % dose the second peak appear at 55:15, 37:30 and 30:00 h:min (Figure 7). The intensity is similar to those obtained with the lower dose: 1.26, 1.41 and 1.65 mW/g for untreated samples and those treated at 140 and 200 °C, respectively. The total heat released from the beginning until the second peak was 54, 58 and 59.6 J/g for the untreated sample and the treated at 140 and 200 °C, respectively. These values are very similar to those obtained with the lowest dose, and can be attributed to the reasons already mentioned.

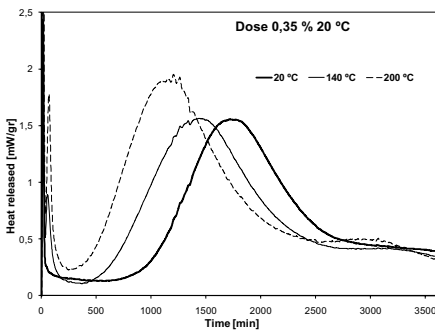


Figure 3. Heat released for 0,35 % admixture at 20°C

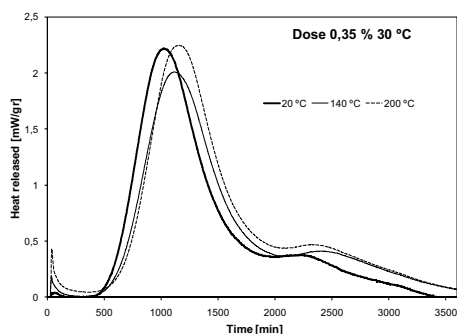


Figure 4. Heat released for 0,35 % admixture at 30°C



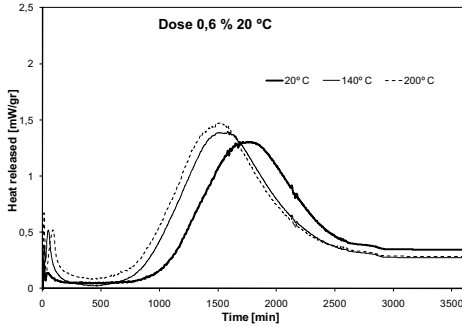


Figure 5. Heat released for 0,6 % admixture at 20°C

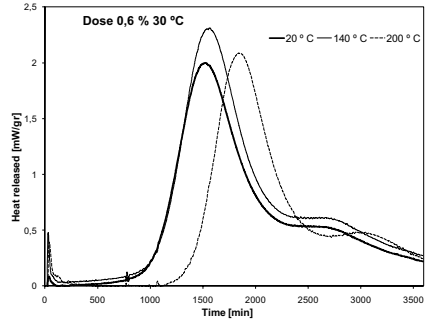


Figure 6. Heat released for 0,6 % admixture at 30°C

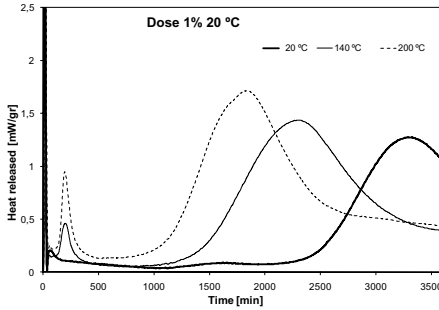


Figure 7. Heat released for 1 % admixture at 20°C

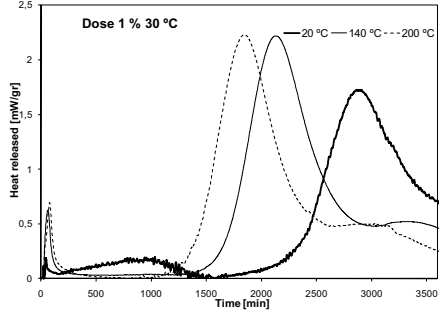


Figure 8. Heat released for 1 % admixture at 30°C

If an overdose is used (1.5%) the trend observed is similar to lower doses, producing the second maximum at 75:00, 54:30 and 45:50 h: min respectively. The rest of behavior is similar to that described for the previous dose.

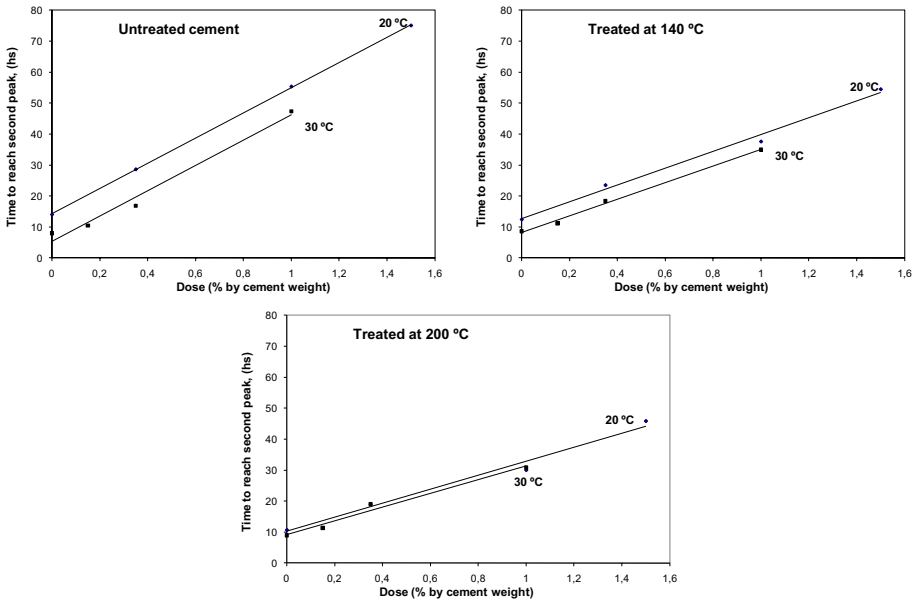


Figure 9. Time to reach 2<sup>nd</sup> peak vs % superplasticizer. a) Untreated, b) treated at 140 °C c) treated at 200 °C

In tests at 30°C significant changes were observed (Figure 4, 6 and 8). For 0.35 % of dose, in average the second peak is delayed about 5 hours relative to control but its intensity is similar. When dose was 0.6% delays are higher with the same trend.

When dose reaches 1%, delays are increasing even more, but the order is altered; untreated sample is the most delayed, the following is the treated at 140°C and finally the treated at 200°C. Figures 9 a), b) and c) shows the time required to reach the second peak as a function of admixture dose for temperatures test of 20 and 30°C. When admixture dose increases, in all cases the time of occurrence of second peak is longer.

When test temperature reaches 30°C and the cement is untreated, delays are somewhat smaller than 20 °C (Figure 9 a). With the loss of water in gypsum, the delays are smaller, but in anhydrite presence, the curves virtually overlap for both temperatures (Figure 9 c).

In summary, when temperature test is 30°C, an attenuation in the delays from 9 hours to 4 hours occurs when gypsum was changed to bassanite and from 4 hours to 1.5 hours when bassanite was changed to anhydrite.

### 3. Conclusions

Based on the results obtained from the tests and materials used in the present work, it can be concluded that:

- The effects of partial dehydration of gypsum in the absence of admixtures can be assessed through conduction calorimetric technique: the dehydration of gypsum causes the second peak to appear between 3 and 4 hours before. However the amount of heat involved is similar up to that time.

- The use of such superplasticizers in cement with low C<sub>3</sub>A causes delays in the development of the heat release rate, reaching second maximum at shorter times as a function of gypsum dehydration.

- New superplasticizers may cause significant delays in the reactions even at lower doses. Overdoses can cause delays incompatible with the behavior of concrete at early ages.

- Increasing the test temperature up to 30 °C, produces a general acceleration of reactions, making less sensitive the previous heat treatment of cement.

### References

- [1] Aïtcin P. *Concrete de alto desempeño*. First edition, (2008), 650 p.
- [2] Norma *ASTM C-494*, Standard specification for chemical admixtures for concrete
- [3] Norma *ASTM C-1017*: Standard specification for chemical admixtures for use in producing flowing concrete
- [4] ACI SP 186, High-performance concrete: performance and quality of concrete structures– *Proceedings Second Connet/ACI international conference* Editors: Malhotra V., Helene P., Prudencio L., Dal Molin D. Gramado Brazil 1999.
- [5] Puertas F. y Vazquez T. Hidratación inicial del cemento. Efecto de aditivos superfluidificantes. *Materiales de construcción*, Vol 51 nº 262, Abril/mayo/junio, España, 2001
- [6] Ramachandran V. *Concrete admixtures handbook*, second edition, Noyes publications, (1995)
- [7] Spiratos N., Pagé M., Mailvaganam N., Malhotra V. and Jolicoeur C. *Superplasticizers for concrete: fundamentals, technology and practice*. Segunda edición, (2006) 322 p.

# Foam concrete landfill use in landslide hazardous area in West Şırnak Road

Yıldırım İ. TOSUN<sup>1</sup>

*Faculty of Engineering, Şırnak University, Şırnak, Turkey*

**Abstract.** There are steeper slopes, sliding large land masses or rocks in Şırnak City and the surrounding areas. Underground water and harsh climatic conditions contain high risk hazard areas in urban living site with higher population density. In order to eliminate landslides and related events, significant precautions should be taken. The mapping of landslide risk may ease to take precautions. Even the application of landfill rock may reduce water content of soil. In this research, fly ash and Mine Waste shale stone were used with low density foam concrete. Waste mixture at certain proportions decreased cement use. Shale stone as fine aggregate instead of fly ash in specific proportions improved mechanical strength and porosity. Hence landslide hazardous area could be safer for urban living.

**Keywords.** Foam concrete, lightweight concrete, foam mortar, fly ash, clay stone

## Introduction

Slope stability and landslide problem dealing with the ground have been closely worked for many years by geotechnical engineers. For this reason, the deep disorder of land masses and slope instability are known as natural disasters such as flood, hurricanes, similar to leading to serious loss of life and property [1-10]. The civil engineers are much interested in the foundation issues regarding the earth soil, surface created by the nature, the slope geometry and design of the structures built on land [11-13]. The technological development parallel to the housing needs the high embankment, dams, large and deep excavations along with stability problems. Each year, few flood and landslide damages may cause to heavy loss of life. They also cause to loss of the millions of pounds in the world. The landslide in Turkey is one of the most important geotechnical hazards [11-13].

In this study, Şırnak city and the surrounding area were studied by geological mapping at 1/1000 scale and the soil units. The properties of every unit soil were determined. Landslide hazardous area provisionally was concerned in the first region's landslide area. The soil properties worked promotes the construction distributions in the future in Şırnak City, promoting winter tourism, one of the popular south eastern Anatolian lands. The importance of civil constructions under the threat of landslide intended to draw attention to the urbanization of the area. In order to minimize the landslide hazard, geological and geotechnical analysis of the land slopes were needed to be studied.

<sup>1</sup>Corresponding author: [yildirimismailtosun@gmail.com](mailto:yildirimismailtosun@gmail.com)

In this study, in the area of south Şırnak City (Figure 1) 2 km circled from the center of the slopes S2 was investigated as much critical hazardous area due to some mass sliding occurred in the district. Geotechnical properties soils of four different locations were determined for examining the stability analysis. This project was carried out for urban use, which will open workspace and environment covering the engineering geological mapping of the field of 4 km<sup>2</sup> area at 1/10.000 scale. The laboratory studies followed by the polar coordinate system using a field study with the topographic maps and cross-sections of four slopes were prepared.

**1. Method**

Alluvium soil, muddy shale occurs in wide urban living area of Şırnak City at the south, which field as seen in Figure 1 extends to the study area. In field observations, the Miocene aged limestone and dissociated limestone were determined. Thickness of this formation is highly variable among 2-30m. Decrease in the slope of the land shows that a relatively small outcrop occurs.

The study area to the north of the city contains fundamentally higher land slopes in the urban location. The observations of sorting and grading of unseen alluvial fill show a thickness varies between 10-35 m. The high slope massive fills are concerned as active and potential hazardous landslide areas and are requiring for various examinations.

The representative contents of drilling logs were taken from the rectangular fields as seen from Figure 1. The representative samples of soil were taken from each different location over the slopes. The experiments conducted to determine the geotechnical characteristics regarding the American Standards (ASTM 3080) [13-15]. The mechanical properties of soils are given in Table 1.

In the study area of fine-grained portions of alluvium samples were taken from slopes as undisturbed and disturbed sample logs. The results of the experiments conducted on the samples of disturbed soil grain distribution curve, unit weight and consistency limit grain sizes are given in Table 1 [16-18]. With the help of Shear box tests on undisturbed samples, the effective cohesion (c') and effective shear resistance angle ( $\phi^\circ$ ) belonging to the representative logs was found.

**Table 1.** Properties soil formation in Şırnak City.

Slope Specimen No	S1	S2	S3	S4
Level (m)	1225	1221	1233	1227
Wopt,%	15,9	13,7	10,8	11,4
c'(kPa)	1,2	4,7	5,3	2,5
$\phi'$	12,5	22,5	21	20
LI(%)	26	15	28	17
PI(%)	19	11	18	22
Ip (%)	10	9	8	12
$\gamma_{sat}$ g/cm <sup>3</sup>	2,4	2,5	2,4	2,3
$\gamma_{an}$ g/cm <sup>3</sup>	1,65	1,6	1,78	1,6
$\gamma_{dry}$ g/cm <sup>3</sup>	1,82	1,76	1,9	1,7
$\gamma_s$ g/cm <sup>3</sup>	2,02	1,84	2,0	1,8
Wopt %	15,9	15,8	12,3	13,0
Permeability (k) (mD)	0.56	0.38	0.31	0.56



**Figure 1.** Satellite image of the study area and the slopes in Şırnak City.

## 2. Results and discussion

According to the classification of the soils in S1 and S2 landslide hazardous areas, the soils were determined as less plastic and non plastic group, even the soils of S3 and S4 in the landslide hazardous area were determined as less plastic.

Fly ash and Mine Waste Shale stone thrown as waste in Şırnak City of Turkey were used with foam concrete. Waste mixture at certain proportions of fly ash and shale stone were decreasing the use of cement. Fine shale aggregate in specific proportions were decreasing the use of fly ash. Certain proportion of fly ash and fine shale aggregate mixture used improved mechanical strength and porosity. Fine aggregate was reducing porosity rather than fly ash. Three different methods are performed in foam concrete production. Firstly, only foam concrete was used as binder of mixture fill. Secondly, foam concrete included fly ash. Thirdly, foam concrete included fly ash and fine shale stone. Effects of foam concrete on mechanical properties of fly ash and fine shale stone aggregate were studied intensively. The results contributed the widely efficient use of high amount of shale stone and fly ash, better workability of the foam concrete and the improved curing time. For this purpose, in the mixture of foam concrete fine shale aggregate was added 5 %, 10%, 20% and 30% weight rates, fly ash was added 5%, 10%, 20% and 30% weight rates, respectively. Water / cement ratio were kept constant 3/1-4/1 volume rate. The prepared laboratory 10x10x10 cm cubic blocks was tested as the foam concrete mixture blocks. In conclusion, depending on the amount of the fly ash in foam concrete mixture, workability significantly improved and even significant the pressure increase was observed.

Compression strength values depending on the increasing amount of fly ash and foam concrete reduced. Increase in fly ash amount used in the foam concrete mixture by curing time was found to reduce the porosity.

The representative rock fill samples were taken from the construction foundation and strengths with the bulk density are shown in Table 2. For determination of rock types based on logging were carried out and the results showed poor and good rock classification as given in Table 2.

Evaluation of the test results to determine the level of soil permeability regarding Table 1, for S1, S2, S3 and S4 slopes may be critically hazardous on land constructions. It is observed that low permeable ground under construction as seen in Figure 2 caused sliding tension cracks and soil land slide.

Landfill of foam concrete performed was compared with the soil samples taken from the test results as given in Table 2. The pore pressure parameters foam concrete landfill at the optimum water content and maximum dry unit weight were determined and used in the calculation of the stability of slopes. A natural slope does not affect the stability of the compression parameters. These parameters of the soil were improved by compacted landfill in the desired manner. Artificial compression parameters used directly on the slopes [19-21]. If there is a risk of landslide hazard in a natural layer, compression case using these parameters are used in stability analysis. The use of anchorage or pile applications should be taken in consideration against to the any possible hazard of landslide in the front slope or the slope should be gradually compacted [22-25]. In this study, an amount of the natural ground is excavated and compressed and foundation was filled by certain foam concrete and rock fill. The pore

parameters were improved against to the hazard. In this case, the stability analysis of these improved parameters was used in the stability analysis of compressed ground [22-25].

c' and  $\phi'$  values are taken as given in Table 1. In addition, the safety coefficient values were used as 1.3-1.5 in GEO5 program. The probable circular sliding surfaces were determined using the methods such as landslide, according to Fellenius, Bishop and Janbu calculations [22-25].

**Table 2.** The resulting strength of foam concrete landfill.

Mixture in Foam Concrete	$\sigma$ , Strength MPa	Water Discharge (%)	$\gamma_{ap}$ Unit Weight, g/cm <sup>3</sup>
Claystone,5%	8.9-9.9	88.2	1.540
10%	12.4-13.9	85.5	1.620
20%	14.5-17.5	82.4	1.790
30%	19.1-20.3	77.7	1.850
Fly Ash,5%	9.6-9.9	64.3	1.250
10%	11.5-12.5	62.7	1.380
20%	13.4-13.9	61.2	1.420
30%	14.3-14.9	60.3	1.580



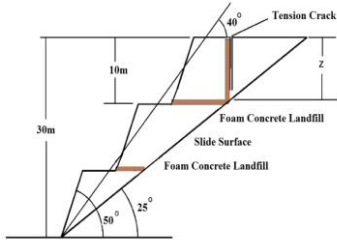
**Figure 2.** Sliding land soil and foam concrete landfill study area.

This kind of soil conditions in this study provide a circular or non- circular sliding close quarters to the top of the slope begin as a deep developing and ongoing planar surfaces. In this type of instabilities developed along the sliding surface in order to investigate the stability of the slope the Bishop method is commonly used [26-28].

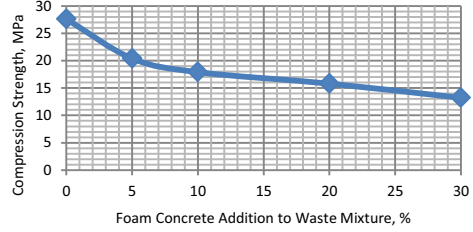
At the construction site foundation the foam concrete wells in 2 m diameters were excavated at elevation 1210 m to 10 m depth to sliding face. At creeping slopes hazard of mass slide may be prevented by rock fill. Even 1 meter depth foam concrete landfill horizontal columns constructed as seen in Figure 3.

With performed the foam concrete landfill application as constructed in Figure 3, hydraulic works at high rate water discharge through the foam concrete structure of landfill, even separately improved compression strength obtained by waste shale stone and fly ash use. Shale stone in the foam concrete mixture provided higher water discharges. According to landfill construction seen from the Figure 4, the landfill length varies from 3 to 10 m horizontal length. Shale stone and fly ash concrete covered foam concrete tunnels and wells could easily provide the sliding face dry.

The landslide S2 maximum elevation difference between the top and the heel point 35 m, 30 m maximum height of the slope divided three faces by excavation, surface slope angle is 43 °. Any slope in the floor was too weak, rock fill mass covered weak material properties of the slope along so that circular 10m mass sliding was avoided. However water drainage was almost varied. At that point, the floor - rock interface with a certain water holding structural feature needed the foam concrete application so that in the mass, reaching low shear strength planar levels were auger bored and tunneled and foam concrete -rock fill were applied as seen in Figure 3.



**Figure 3.** Foam concrete landfill application cross-section.



**Figure 4.** Compression strength of foam concrete landfill.

In this study, the compression strength of the foam concrete applied landfills for the slopes in the area is illustrated in Figure 4. The stability analysis for S2 slope in terms of active and potential hazardous areas of landfill was carried out. The applied foam concrete on the soil surface improved the strength and eliminated hazard of sliding. According to studies of the stability without landfill, the land mass slope area there was relative movement designated as the active landslide area. Relative movements are determined by making use of tension cracks on the surface. From this point of view, the foam concrete landfill of horizontal column improved water level under sliding surfaces and the safety factor values reached over 1.5 and 1.8.

### 3. Conclusions

The studied area of potential landslide hazard around the active site of stress, cracking displacement of relative motion could be observed, but changed regarding the field.

Soil samples performed on the laboratory test results in the slope material permeable that the cohesion value of 1.2 - 4.7 kPa, angle of internal friction of the 17.5 - 22.4° varied between unified soil classifications. Stability analysis performed in the light of this information, S1, S2 and S3 were unstable hillsides. By use foam concrete application the hazardous slopes were concluded that the stable condition.

Landfill porosity thus reduces the retaining force which stabilizes the slopes. For this reason, the vegetation of landslide hazardous areas is preventive enrichment an important parameter in the region. However, up to 30 m depth to the sliding surfaces of vegetation stability effect will be minimal. Weathering of rocks varies greatly in to undergo, to the weakening of the bond between grains and leads to total extinction. In the study area weakened by weathering rocks are easily eroded and slope angle of inclination of the slope is changing with height. Dissociation observed in rocks in the study area also offers a negative contribution to stability problems.

As a result of this work performing of the geotechnical analysis, hazardous conditions would not be expected of a very large landslide. However, the urban living areas and the urban development areas at certain land slopes for the possibility of landslide hazard should need further technological improvements.

## References

- [1] Anderson, M.G., Richards, K.S., 1982, *Slope Stability*, John Wiley and Sons Ltd., New York.
- [2] Bishop, A.W., 1955, The use of the slip circle in the stability analysis of earth slopes, *Geotechnique*, Vol. 5, 7-17.
- [3] Cernica, J.N., 1995, *Geotechnical Engineering: Soil Mechanics*, John Wiley and Sons Inc., Canada.
- [4] Das, B.M., 1994, *Principles of Geotechnical Engineering*, PWS Publishing Company, USA
- [5] Höek, E., 1970, *Estimating the Stability of Excavated Slopes in Opencast Mines*, Institution of Mining and Metallurgy, A105, A132
- [6] Höek, E. ve Bray, J.W., 1977, *Rock Slope Engineering*, Stephen Austin and Sons Ltd, Hertford, 402 s.
- [7] Hoek, E., 2013. *Practical Rock Engineering*, Hoek notes by Evert Hoek. <http://www.rocksience.com>
- [8] Hutchinson, J.N., 1995 "Landslide Hazard Assessment. Keynote paper. In: Bell DH (ed) *Landslides, Proceeding of 6th International Symposium on Landslides*", Christchurch, New Zealand, vol 1. Balkema, Rotterdam, pp 1805–1841,
- [9] Anonymous a, 2013, GEO5 - Engineering Manuals - Part 1, Part 2. <http://www.finesoftware.eu/geotechnical-software/>
- [10] Anonymous b, 2009, GEO5 - FEM - Theoretical Guide <http://www.finesoftware.eu/geotechnical-software/>
- [11] Anonymous c, 2011, "Türkiye Deprem Bölgeleri Haritası", Afet ve Acil durum Yönetimi Başkanlığı Deprem Dairesi Başkanlığı, Ankara
- [12] Anonymous d, 2012, Şırnak İl Özel İdare Raporları, Şırnak
- [13] ASTM, 1990, "Standard Test Method for Direct Shear Test of Soils Under Consolidated Drained Condition", D3080-90,
- [14] ASTM, 1985, "Standart Specifications For Fly Ash And Raw Or Calcined Natural Pozzolan For Use As Mineral Admixture in Portland Cement Concrete", ASTM Philadelphia, ASTM C 618-85.
- [15] ASTM, 1999, "Standard Test Method for Time of Setting of Concrete Mixtures by Penetration Resistance", Pennsylvania, ASTM C 403.
- [16] Chen, B., Liu, J., 2008, "Experimental Application Of Mineral Admixtures in Lightweight Concrete With High Strength And Workability", *Construction and Building Materials* 22 , pp 655–659.
- [17] Dramis, F., Sorriso-Valvo, M., 1994 "Deep-Seated Gravitational Slope Deformations, Related Landslides and Tectonics", *Engineering Geology*, 38, 231- 243..
- [18] Görög P & Török Á, 2006, Stability Problems of Abandoned Clay Pits in Budapest, *IAEG2006* P295, The Geological Society of London
- [19] Görög P & Török Á, 2007 Slope stability assessment of weathered clay by using field data and computer modeling: a case study from Budapest ,*Natural Hazards and Earth System Sciences*, 7, 417–422, [www.nat-hazards-earth-syst-sci.net](http://www.nat-hazards-earth-syst-sci.net)
- [20] Pruška, J., 2009, Comparison of geotechnical softwares - Geo FEM, Plaxis, Z-Soil , *XIII ECSMG*, Vaníček et al. (eds). CGtS, Prague, ISBN 80-86769-01-1, (Vol. 2)
- [21] Güz, H , 1987, "Geoteknikte Gelişmeler", DSİ Yamaç ve Şevlerin Stabilitesi ve Dayanma Yapıları Semineri, Samsun
- [22] Lambe, W.T. ve Whitman, R.V., 1969, *Soil Mechanics*, John Wiley and Sons, New York
- [23] Langan, B. W. , K. Weng, M. A. Ward, Effect Of Silica Fume And Fly Ash On Heat Of Hydration Of Portland Cement. *Cement And Concrete Research*. 2002. 1045-1051.
- [24] Paşamehmetoğlu, A.G., Özgenoğlu, A., Karpuz, C., 1991, *Kaya Şev Stabilitesi*, 2. Baskı , T.M.M.O.B Maden Müh. Odası Yayınları, Ankara, Mayıs.,
- [25] Park, C. K., Noh, M. H., Park, T. H, 2005, Rheological Properties Of Cementitious Materials Containing Mineral Admixtures, *Cement And Concrete Research*. 2005. 842-849
- [26] Sata, V., Jaturapitakkul, C., Kiattikomol, V., 2007, Influence Of Pozzolan From Various By-Product Materials On Mechanical Properties Of High-Strength Concrete, *Construction And Building Materials*. pp. 1589-1598.
- [27] TSE, 1991, "Yamaç ve Şevlerin Dengesi ve Hesap Metodları-Zeminde", TS 8853, Ankara.
- [28] TSE a, 2002, TS EN 12350-3, Beton – Taze Beton Deneyleri- Bölüm 3: Ve-Be Deneyi, Ankara.
- [29] TSE b, 2002, TS EN 12350-2, Beton – Taze Beton Deneyleri- Bölüm 2, Ankara, 2002.
- [30] TSE c, 2002, TS EN 12390-3 2003. Beton-Sertleşmiş Beton Deneyleri- Bölüm 3: Deney Numunelerinde Basınç Dayanımının Tayini. TSE, Ankara.
- [31] TSE, 1985, TS 802 *Beton Karışımı Hesap Esasları*. TSE, Ankara
- [32] Ulusay, B 1982, Şev Açılarının İlk Yaklaşım Olarak Hesaplanmasında İki Yeni Pratik Yöntemin Konya-Çumra Manyezit Sahasına Uygulanışı, *Jeoloji Müh.Der.*, Ocak 30-41
- [33] Vaneckova, V , Laurin J, Pruska J, 2011, Sheeting Wall Analysis by the Method of Dependent Pressures, *Geotech Hanoi*, ISBN 978 - 604 - 82 - 000 - 8 ID No./ pp. 7
- [34] Wiley, L., 1987 "Slope Stability Geotechnical Engineering and Geomorphology", England,



# Pozzolans as a binder for affordable building materials in Uganda

William BALU- TABAARO<sup>1</sup>

*GEOengineering Technologies, Entebbe, Uganda*

**Abstract.** Due to the rapid increase in population in Uganda demand for housing has outstripped housing availability. This is largely due to the high cost of building materials most of which are imported at high cost. The majority of the population of Uganda many of whom live in rural areas cannot afford these high cost materials and hence cannot build durable and decent houses. Traditional building materials like burnt bricks are getting more expensive due to shrinking availability of fuel energy resources, especially firewood. The cutting down of large chunks of forests to generate firewood is creating a lot of environmental problems, such as degradation, soil erosion and weather uncertainties. Hope therefore lies in the development of alternative building materials that are cheaper and that have little impact on the environment.

One such alternative building material is the natural pozzolans based on the abundant volcanic ashes in the Kisoro and Kabale areas. The Kisoro, and Kabale, Volcanic Ashes (Pozzolans) have been extensively studied and found to be cementitious when activated with cement or lime. Once converted into pozzolan cement, they can be used to manufacture produce binders, blocks, wall panels, etc. to provide a cheap alternative building material that will assist in increasing low cost housing in Kisoro and Kabale and in Uganda. The need to reduce the excessive dependence on imported materials and rather concentrate on the production and use of durable local cementitious materials for housing delivery is therefore essential. This would greatly reduce on the cost of the key building material and thereby make housing affordable to majority of the citizens. The successful commercialization and popularization of the pozzolanic materials will create employment for the majority poor in these areas. Provision of cheaper building materials will also enable them get cheaper binders.

**Keywords.** Pozzolans, binder, mineralogical composition, volcanic ash

## Introduction

According to results of the 2002 Population and Housing Census, Uganda is presently estimated to have a population of about 24.7 people with an average household size of 5.7. The same results gave an occupancy density of 1.05 and hence an estimated housing stock of 2,690,900 units and a backlog of 235,914 units in the country.

Uganda also has a lot of pozzolanic materials based on volcanic ashes found in Kisoro and Kabale districts that could be used elsewhere to produce low cost building materials. It is known that technologies based on these materials have been developed and commercialized in other countries. Uganda has the potential to develop similar technologies locally and get them commercialized in order to provide low cost effective building materials to solve the housing problem.

<sup>1</sup>Corresponding author: [balutabaro@gmail.com](mailto:balutabaro@gmail.com)

One of the ways to improve both the quality and quantity of housing is to increase the availability of low cost effective building materials. Building materials and construction are very important inputs to the housing sector, but suffer from dependence (60%, 1992) on imports, poor distribution, shortage, lack of local skills and equipment, lack of standardization of both locally manufactured and imported materials and equipment, and low production capacities by the factories. Shortage and importation of materials is the cause of their high prices and high construction costs. In general the building materials industry in Uganda suffers from:

- High cost of materials and construction due to the unfavorable economic factors and performance, and overall shortage of the materials, tools, equipment and skills.
- Lack of standardization of materials and their quality control
- Local building materials are usually in short supply due to the fact that the factories have low production and cater for a high demand.
- The traditional building materials and building techniques are not allowed to be used in urban areas. There is too much dependence on imports, there is poor distribution and high transportation costs add to the problem.
- Related services such as consultancies are also in short supply and unevenly distributed.

The majority of Uganda's population lives in poor and non-durable housing. In most cases, there is barely anything called housing as some live in mud walled huts. The main problem to access to decent housing is due to high cost of building materials, which are not affordable by the majority poor. Lack of appropriate technology to harness some abundant local raw materials also hinders access to low cost housing. Although there are abundant local reserves of pozzolanic materials that could be developed into building materials at lesser cost than other traditional materials, there is need to use low cost technologies to develop cheap building materials that will lead to enhancement of low cost housing in Uganda.

## **1. Background**

In Uganda, most of the pozzolans are derived from the abundant volcanic ashes in the Kabale, Kisoro and Kapchorwa areas (See map Fig.1). These geological materials were formed many years ago and large quantities of these materials have accumulated over the years. Samples from these areas were collected, characterized and some test work on their pozzolanicity, grindability, reactivity, have been carried out. Their conversion into building materials (blocks, wall panels) have yet to be carried out.

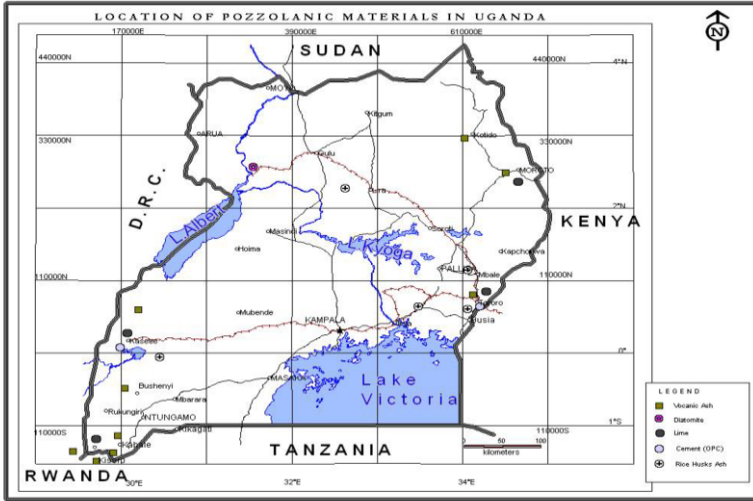


Figure 1. Map Showing Location of Pozzolans in Uganda

## 2. Experimental programme

### 2.1. Materials

#### 2.1.1. Mineralogical tests

Table 1. Glass state of the volcanic ash: Source University of Toronto cements

Sample No.	Location	% Glass
1-	Kisoro clinic quarry	45
2-	Kwasembi – Busanza Road	30
3-	Nyagishenyi - Chamke Road	00
4-	Chamka 1 ½ miles to Rwanda Border	33
5-	Hakitembe – Nyakabande county	30
6-	Hamugeza – Mulumdwa	35
7-	Kasheregyenyi – Mulumdwa	15
9-	Junction: Kashenyi – Muko	30
9A-	Junction: Kashenyi Road	20
10-	To Junction: Kashenyi - Road	20

#### 2.1.2. Pozzolanicity tests

The pozzolanicity tests give indications of the reactivity of a pozzolan with lime. The procedure followed was in accordance to the European standard EN 196. In the tests, comparison is made of calcium hydroxide present in aqueous solution in contact with the hydrated cement after a period of time, 8 to 15 days, with the quality of calcium hydroxide capable of saturating a solution of the same alkalinity. The test is positive when the concentration in the solution is lower than the saturation concentration. Results of the pozzolanicity tests are shown in Table 2.

**Table 2.** Pozzolanicity Tests

Pozzolan	Sample No.	Hydroxyl ion conc. (moles/litre)	CaO conc (moles/litre)
Bunagana	2	3.96	8.05
Burnt clay -		26.73	6.04
Hakitembe	5	32.67	10.06
Nyagishenyi	3	1.58	8.68
Rubanda	12	3.96	7.47

### 2.1.3. Mineralogical composition

The mineralogical compositions of the Uganda pozzolan were determined by X-ray diffraction .

**Table 3.** Uganda pozzolan mineralogical composition

Sample No.	Minerals identified by X-ray Diffraction
1-	Augite (24-203)* and possibly Halloysite - 10A (9-451)
2-	Augite, Aluminium (24-202) and possibly Pyrophanite (29-902)
3-	Augite (24-203) and possibly quartz (5-490)
4-	Diopside, Aluminium (38-466) and Forsterite (4-768)
5-	Diopside (11-654) and Forsterite (4-768)
6-	Forsterite, Ferroan (33-675) and possibly Augite (24-201)
7-	Forsterite, Ferroan (33-657) and possibly Pyrophanite (29-902)
8-	Quartz (5-490) and Muscovite - 2M1 (19-814)
9-	Augite (24-203), Forsterite (7-74) and possibly Kutnohorite (11-345)
9A-	Diopside (19-239)
10-	Augite (24-203) and Forsterite (4-768)
11-	Quartz (33-1161) and Kaolinite - 1MD (6-221)
12-	Quartz (5-490) and Calcite (5-586)
13-	Calcite (24-27) and Aragonite (5-453)

\* Numbers in parenthesis refer to JCPDS powder index files. Source: University of Toronto.

## 2.2. Chemical analysis

### 2.2.1. Pozzolanic activity index

The Chemical compositions of a selection of the pozzolans were analysed. The Chemical compositions of the pozzolans were compared with the requirements prescribed by ASTM C618 for Class N material.

According to ASTM C618, natural pozzolans shall conform to the chemical requirements presented in Table 4 to be classified as a Class N material. Class N covers raw or calcined natural pozzolans for use as mineral admixtures in concrete.

**Table 4.** Chemical requirements for class N according to ASTM C618.

	Class N
SiO <sub>2</sub> + Al <sub>2</sub> O <sub>3</sub> + Fe <sub>2</sub> O <sub>3</sub> , min %	70.0
Loss on Ignition, max %	10.0
Alkalis (optional), requirement Na <sub>2</sub> O-content, max %	1.5
Moisture content*, max %	3.0
SO <sub>3</sub> , max %	4.0

\* Equivalent Na<sub>2</sub>O = Na<sub>2</sub>O + 0.658 K<sub>2</sub>O

The chemical composition, i.e. the content of the major oxides of the pozzolans was determined by ICP. The following oxides were quantified: Al<sub>2</sub>O<sub>3</sub>, CaO, Fe<sub>2</sub>O<sub>3</sub>, K<sub>2</sub>O, MgO, Na<sub>2</sub>O, and SiO<sub>2</sub>.

The results of the analysis are summarized in Table 5.

**Table 5.** Chemical analysis (all values are presented in % by volume)

Pozzolan No.	SiO <sub>2</sub>	Al <sub>2</sub> O <sub>3</sub>	Fe <sub>2</sub> O <sub>3</sub>	MgO	CaO	Na <sub>2</sub> O	Ka <sub>2</sub> O	LOI*	NC**
1	42.72	11.66	13.97	7.89	12.10	1.22	2.74	2.35	65
7	45.03	15.02	13.55	5.44	8.32	2.48	3.63	1.10	85
9	45.75	15.79	12.27	4.28	7.42	2.62	4.01	1.62	65
19	42.22	9.77	12.60	10.34	13.32	1.60	2.78	1.47	60
21	45.07	11.16	12.11	11.13	10.51	2.05	2.49	0.24	55
22	34.49	5.76	10.81	8.67	14.37	0.18	3.03	15.19	5
25	47.31	7.15	7.53	6.26	10.57	0.36	3.39	12.14	5
27B	47.33	8.23	7.44	5.70	9.77	0.30	3.56	13.56	5

\*Loss on Ignition

\*\*Estimated Non crystalline Matter (Content of Glass)

### 3. Test programme

#### 3.1. Development of the pozzolanic cement

##### 3.1.1. Grinding tests

After the chemical and pozzolanicity tests, samples of pozzolans were subjected to grinding tests, after size analysis. Using past tests, a range of sizes were targeted. For each grind size, the fineness was determined and mortar cubes made for subsequent tests for compression strength, initial and final setting, water ratios and durability. The grinding tests were also used to determine optimal grinding costs using work indices.

**Table 6.** Natural particle size of volcanic ash

Sample	Distribution function	Sieve size in microns ( $\mu$ )			
		12.5mm	6.3mm	2.8mm	150 $\mu$ m
2	Cumm % undersize	74.7	41.4	14.4	0.9
3	Cumm % undersize	74.3	51.9	25.1	5.4
5	Cumm % undersize	99.4	92.9	61.8	11.9
12	Cumm % undersize	95.2	64.3	26.6	3.3
9	Cumm % undersize	99.8	90.1	46.2	5.3

No.2 - Bunagana road

No.3 - Nyagishenyi (Katarara)

No.5 - Hakilembe (Gihinga)

No.12 - Kikombe (Rubanda)

No.9 - Muko

**Table 7.** Sieve size with 80% and 50% passing for volcanic ash in natural state

Sample No.	Sieve size in mm	
	80% Passing	50% Passing
2	14,000	76,000
3	15,200	6,000
5	4,700	2,350
12	9,000	4,800
9	5,200	3,300

After size analysis, the volcanic ash had their specific gravities determined and the results are shown in Table 8.

**Table 8.** Specific gravities of volcanic ash samples

Sample No.	Specific Gravity
2	2.22
3	2.30
5	2.02
12	2.40
9	2.38
Average specific gravity	2.9

### 3.1.2. Work index

Using the grinding tests, the work index was used to determine power consumption, a factor that would help in evaluating costs of production. The work index was calculated using the formula:

$$W = W_i (10/P^{1/2} - 10/F^{1/2}) \quad (1)$$

Where Work Index denoted by  $W_i$ , is the amount of work required in Kwh/short ton to reduce a material from infinite size to 80 percent passing 100 microns and is calculated from the above formula where:

- F = 80 percent passing size in the feed, expressed in microns
- P = 80 percent passing size in the product, expressed in microns
- W = Work required in Kwh/short ton to reduce a material from F to P

The work index (Kw-h/ton) was determined by grinding silica sand whose comminution energies are known, and the same conditions were used for volcanic ash in a 220mm × 200mm ball mill at 45% ball charge and 72 rpm. The resultant particle size distribution was determined. The experimental variables for work index determination are time of grind and particle size. The calculated work indices for volcanic ash samples are shown in Table 9.

**Table 9.** Work Index of volcanic ash

Sample No.	Specific Gravity	Work Index (Ei (KW-hr/ton))
2	2.22	10.16
3	2.30	12.23
5	2.43	11.72
12	2.40	8.77
9	2.38	9.49
Average		10.49

After grinding, various surface areas were determined and the results are as shown in Table 10.

**Table 10.** Specific surface area of ground volcanic ash

Sample No.	Specific surface area (Blaine cm <sup>2</sup> /g)		
	4 hrs	5hrs	6hrs
Hakilembe No.5	3300	4400	4800
Bunagana No.2	4000	4400	4900
Rubanda No.12	3800	4200	4400

### 3.1.3. Mixing trials

After all the grinding tests, mixing trials were carried out. The mixing involved additives of Ordinary Portland Cement and lime. But due to low quality lime from Uganda, a lime from Kenya was used. (see table for chemical and physical properties).

The different sizes of ground pozzolans were activated with Ordinary Portland Cement and lime in various proportions from 10% to 40% i.e. ratios of 1:10 to 1:2.5 (cement: pozzolans). The various mix ratios were then subjected to various tests (i.e. water ratios, compression strengths etc.) to determine various characteristics of the cement.

### 3.1.4. Determination of compressive strength

The results of compression tests are shown in the Tables 11 – 14 below.

**Table 11.** Portland-pozzolan cement characteristics

Mix ratio OPC*/Ash* %	Standard Consistency	Setting Time (min)		Compressive strengths 7 days water (cured MPa)*
100/00	27.6	100	165	56.72
90/10	27.2	98	160	55.93
80/20	26.6	92	175	56.00
70/30	25.2	135	170	49.16
60/40	24.3	125	183	46.18
50/50	23.8	120	229	38.61
40/60	23.9	160	250	37.02

Ash Type\*: "Sample 2" ground for 4 hours in 220 x 200 mm ball mill.

OPC\*: wiga Brand., Specimen\*: 8 x 4 cylinders.

**Table 12.** Compressive strength of OPC- pozzolan cements

Mix ratio OPC*/Ash*%	Compressive Strengths (MPa)* 7 days		Cured Air/water 28 days	
	Air	Water	Air	Water
100/00	46.58	55.93	43.20	75.72
90/10	40.50	50.16	40.20	56.72
80/20	39.60	48.77	30.25	69.67
70/30	35.20	46.77	40.00	68.67
60/40	33.64	45.98	32.44	52.15
50/50	26.90	32.64	25.44	44.79
40/60	25.10	36.22	23.69	40.21
30/70	18.91	21.22	18.90	31.85
20/80	11.35	15.13	13.14	24.88
10/90	5.90	9.30	5.00	11.74

Ash Type\*: "Sample 3" No. 2, OPC\*: Twiga Brand (Tanzania), Specimen\*: 8 x 4 Cylinders

**Table 13.** Compressive strengths of OPC – pozzolan cement mortars

Mix ratio OPC*/Ash* %	Compressive strength (MPa) * Water cured	
	7 days	28 days
100/00	26.0	38.4
90/10	22.0	29.3
80/20	18.0	25.4
60/40	9.4	13.2
50/50	6.4	13.5
40/60	4.1	8.2
30/70	2.7	5.8

Ash Type\*: "Sample 4", OPC\*: Twiga Brand (Tanzania), Specimen\*: 100 mm cubes, cement: sand: 1:3  
W/C = 0.53

**Table 14.** Compressive strength of OPG-pozzolan cement mortars

Mix Ratio OPC*/Ash* %	Compressive Strength (MPa)* Water cured	
	7 days	28 days
100/00	26.0	38.4
90/10	16.3	25.6
80/20	10.5	24.7
70/30	10.2	21.9
60/40	4.8	13.6
50/50	3.9	10.3

Ash Type\*: "Sample 5" No. 12

OPC\*: Twiga Brand (Tanzania)

Specimen\*: 100 mm cubes, cement: sand, 1:3 W/C = 0.53

#### 4. Conclusions

Tests carried out identified pozzolanic materials that proved reactive when activated. It was established that these pozzolanic materials can be used as binders to produce building materials and at a price cheaper than Ordinary Portland Cement.

This shows that low cost buildings can be constructed especially for low income and rural populations. There is need to carry out socio-economic studies.

#### References

- [1] S.S. Byamugisha, W. Balu-Tabaaro, The western rift valley volcanic fields, and their association and role in the lime-pozzolana cement manufacture in Uganda, *UGSM unpub. Report*, UGSM; Entebbe, Uganda, No. SSB/12, WBT/1(1986).
- [2] L. Day Robert, *Pozzolans for use in low cost housing: state of the art report*, Department of Civil Engineering. Universidad de Calgary. Investigacion reportada No. CE92-1. Enero 1992.
- [3] M. Heikal et al., Limestone filled pozzolanic cement, *Cement & Concrete Research*, Vol. 30, Issue No.11( 2000).
- [4] V.M. Malhotra and P.K. Mehta, *Pozzolanic and cementitious materials*, Publicado por Gordon and Breach, Inglaterra, 1996.
- [5] G. Ndwula, The potential for use of volcanic ash pozzolan based cements in Kisoro District, . *UGSM unpub. Report*, UGSM, Entebbe, Uganda, No. GN/1 (1992).
- [6] J. Martirena and S. Betancourt, Notes on a Book for Technology for the manufacture of Lime Pozzolana Binders.
- [7] J.F. Martirena, The Development of Pozzolanic Cement in Cuba, *Journal of Appropriate Technology*, vol. 21, No.2 (September 1994), Intermediate Technology Publications, U.K.
- [8] F.A. Kabagambe-Kaliisa, Possible Sources of pozzolana in Uganda, *UGSM unpub. Report*, UGSM, Entebbe, Uganda, No. FAKK/14 (1998).
- [9] A.W. Groves, Report on the prospects of using the volcanic tuff of the Fort Portal District for the manufacture of cement, *UGSM unpub. Report*, UGSM; Entebbe, Uganda, No. AWG/-3 (1929)



# Effect of temperature on rheological performances of fresh SCC mixture

Huan YE<sup>1</sup>, Xiaojian GAO, Hui WANG

*School of Civil Engineering, Harbin Institute of Technology, Harbin 150090, China*

**Abstract.** This paper shows the study of effects of different testing temperatures ranging from 10°C ~30°C, on the rheological behavior of fresh self-compacting concrete mortars by using RCAD 400 rheometer. To begin with, the temperature of raw materials was firstly regulated before mixing, and then a water bath system linked to rheometer was used to remain the temperature of the mortar within a designated range during the test. The tested rheological parameters included shear stress, viscosity, yield stress, and the evolution of these parameters over time. Material mixing fraction factors considered in this analysis included water-to-binder ratio (w/b) and the fractions of mineral admixtures. The results show that for most of the studied mortar, a higher temperature leads to a lower initial viscosity and a lower growth rate of shear stress with shear rate, and afterwards the yield stress and the evolution rates of these parameters over time are intensified gradually. The effects of temperature on the shear stress and viscosity of the mortar samples are alleviated by the increased w/b ratio and the addition of mineral admixtures. However, an observation of reduced shear stress and viscosity when increasing w/b ratio and adding mineral admixtures seemingly indicated that the rheological properties of the mortars may be also associated with the w/b ratio and mineral admixture.

**Keywords.** SCC, rheological performance, temperature, mixing proportion

## Introduction

The rheological behavior of fresh self-compacting concrete is always described by Bingham model (Eq.(1)) with two parameters, the yield stress and the viscosity [1, 2]. Fresh SCC behaves as liquid when the stress applied to it is beyond the yield stress, and when below, it has a solid viscoelastic behavior [3].

The addition of superplasticizer (SP) leads the yield stress of SCC to be much smaller than traditional concrete, almost approaching zero, which makes the yield stress of SCC extrapolated by Bingham model turn out to be negative in cases, which is impossible [4]. Some modified models have been proposed to solve this conflict, such as the modified Bingham model (Eq.(2)) [4, 5].

The rheological behavior of fresh SCC is affected by many factors such as the amount and type of SP, fine fillers, w/b ratio, mixture proportions, particle size distribution of cement and the temperature. The rheological behavior is influenced by fine fillers as the addition of fine fillers may change the powder content and the water film thickness of SCC [6, 7].

<sup>1</sup>Corresponding author: [646519546@qq.com](mailto:646519546@qq.com), [xjgao2013@gmail.com](mailto:xjgao2013@gmail.com)

The influences of fine fillers are inconformity in different studies, due to the different characteristics of fine fillers and the coupled effects of other parameters, like SP and temperature. The rheology of SCC can be strongly influenced by a little change of mixture temperature as the SP efficiency and incompatibility with cement are affected by temperature [8]. For most SCC, an increase of mixture temperature leads to a higher yield stress and a lower plastic viscosity [9] and a higher loss rate of workability. There is few studies on the influence of temperature on the rheological properties of SCC with different admixtures. And it is very difficult to reach a general conclusion on the influence of temperature on the rheological properties of different SCCs due to the coupled effect of temperature and other material or mixing proportion factors.

$$\tau = \tau_0 + \mu \cdot \partial\gamma / \partial t \tag{1}$$

$$\tau = \tau_0 + \mu \cdot \partial\gamma / \partial t + c \cdot (\partial\gamma / \partial t)^2 \tag{2}$$

where:  $\tau$ ---shear stress (Pa),  $\tau_0$ ---yield shear stress (Pa),  $\mu$ ---plastic viscosity (Pa·s),  $\partial\gamma / \partial t$ ---shear rate (1/s),  $c$ ---second order parameter (Pa·s<sup>2</sup>).

In this paper, the results obtained from the study of rheological properties of fresh SCC mortars were discussed and attempts to draw a conclusion of the coupled effects of mixing ratios, curing and testing temperature and rest time on the rheological behavior of the mortars.

### 1. Materials and methods

A RCAD400 rheometer, made in France, was used to measure the rheological parameters of mortars as showed in Figure 1. The identical test procedure was applied to every sample. This type of rheometer requires the maximum diameter of particle to be less than 10 mm. Although this requirement is mostly based on cement paste, the rheological transient behaviors of concrete, cement paste or mortar are very similar [10]. Therefore, the rheological parameters in this paper were measured on the mortar samples formulated from SCC mixtures.

The cementitious materials used in this study were Type I Portland cement according to Chinese standard, ground granulated blast-furnace slag (GGBS) and fly ash (Class F). The information of their material compositions is showed in Table 1. The SP here represented a polycarboxylate-based superplasticizer liquid with solid content of 40% and specific density of 1.07. The size distribution of sand is showed in Table 2.

**Table 1.** The chemical characteristics of cementitious materials (%)

Oxide	Cement	Fly ash	GGBS
SiO <sub>2</sub>	19.5	42.47	33.52
Al <sub>2</sub> O <sub>3</sub>	4.7	26.01	14.42
Fe <sub>2</sub> O <sub>3</sub>	2.80	8.44	0.29
CaO	64.2	14.01	42.8
MgO	2.50	3.15	5.91
SO <sub>3</sub>	2.6	1.57	0.8

The mixture proportion of SCC is showed in Table 3. Four mortar samples were prepared according to the SCC mixtures and each mortar samples were tested under three different temperatures, 10 °C, 20 °C and 30 °C, as shown in Table 4. All concretes in this study can meet the requirement of a slump flow between 640 mm and 720 mm and V-funnel flow time between 10 s and 15 s.

**Table 2.** The size distribution of sand (%)

<b>Sieve size (mm)</b>	9.5	4.75	2.36	1.18	0.6	0.3	0.15	0.075
<b>Passing percent</b>	100.0	99.3	89.1	74.8	56.7	21.1	2.6	0.6

**Table 3.** Mixture proportion of SCC (units in kg/m<sup>3</sup>)

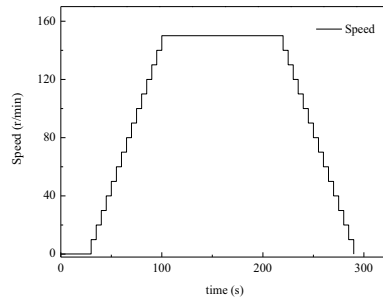
Mixture	Cement	Water	Fly ash	GGBFS	Sand	Gravel	SP	Retarder
SCC11,12,13	530	180	0	0	800	880	4.24	0.53
SCC21,22,23	530	191	0	0	800	880	4.24	0.53
SCC31,32,33	424	180	106	0	800	880	4.24	0.53
SCC41,42,43	371	180	0	159	800	880	4.24	0.53

**Table 4.** Temperature of the tested mortar sample

Temperature	10°C	20°C	30°C
<b>Mixture</b>	SCC11	SCC12	SCC13
	SCC21	SCC22	SCC23
	SCC31	SCC32	SCC33
	SCC41	SCC42	SCC43



**Figure 1.** RCAD 400 rheometer

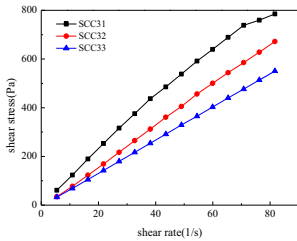


**Figure 2.** Increasing and decreasing sequence of shear rates

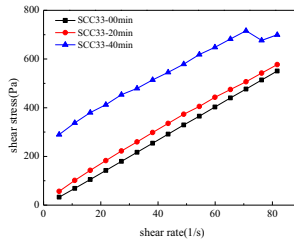
The mortar was prepared using a planetary mixer, and immediately after finishing the blending it was tested by the rheometer for the initial test. This operation was finished within 5 minutes. To measure the rheological parameters of mortar, the rotational speed was set in an optimum way: at a low speed of 0.1 rev/min for 30 s (step 1), to measure the static yield stress, and stepwisely increased to 150 rev/min in 75 s by 15 steps (step 2), then kept at 150 rev/min for 120 s (step 3), and finally stepwisely decreased to 0 rev/min in 75 s by 15 steps (step 4). On these stages, every step of the increasing and decreasing process of rotational speed was 5 s, as showed in Figure 2. After the initial test, the mortar sample was tested again with an interval of 20 min within a total time duration of one hour. These tests were to study the influence of rest time on rheological behavior. However, some mortars set too fast during rest time to be tested for all the 4 times. The temperature of raw materials was firstly regulated before mixing, and then a water bath system linked to rheometer was used to remain the temperature of the mortar within a designated range during the test.

## 2. Results and discussion

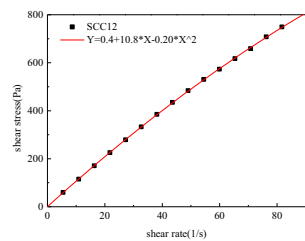
The results mainly show the way in which the shear stress changed with the decreasing shear rate (step 4), which can be indicative of the rheological performance of mortar by the modified Bingham model. In this part, SCC22-20min means the rheological data of SCC22 mortar sample at the rest time of 20 min. Figure 3 and Figure 4 shows the initial test results of the mortar sample from SCC3 mixtures under different temperature and the influence of rest time on mortar sample SCC33. Furthermore, the experimental results from other samples tested in this work indicated similar influences of temperature and rest time on rheological performance as those from SCC33.



**Figure 3.** The data of shear stress of the mortars at different temperature against shear rate.



**Figure 4.** The data of shear stress of the mortar at different rest time against shear rate.



**Figure 5.** The rheological parameters obtained by the modified Bingham model.

Table 5 presents the initial rheological parameters of fresh mortars extrapolated by the modified Bingham model. The  $c$  values for most mortar samples ranges between -0.03 and 0.024. The growth rate of shear stress increased with the increasing of shear rate when  $c$  is a positive value, and it decreased when  $c$  is a negative value. The influence of the parameter  $c$  on the shear stress is moderate when the shear rate is low.

The relationship between shear stress and shear rate is associated with plastic viscosity,  $\mu$ . However, when the shear rate increases to and over a certain value, the way in which shear stress changes with shear rate changing may be altered by the  $c$  value. The rheological behaviors of mortar was also altered by the rest time because it is found that the values of yield stress ( $\tau_0$ ) and viscosity ( $\mu$ ) for all mixtures increased with the rest time and the  $c$  values decreased with it.

**Table 5.** The rheological parameters of fresh SCCs modeled by modified Bingham model

mixture	SCC11	SCC12	SCC13	SCC21	SCC22	SCC23	SCC31	SCC32	SCC33	SCC41	SCC42	SCC43
$c(\text{Pa}\cdot\text{s}^2)$	0.015	-0.020	-0.030	0.024	0.013	0.005	0.014	-0.005	-0.011	0.015	0.016	0.018
$\mu(\text{Pa}\cdot\text{s})$	11.3	10.8	7.5	8.7	7.9	7.4	13.6	8.9	6.8	14.3	9.7	6.5
$\tau_0(\text{Pa})$	0.2	0.4	3.3	0.2	0.2	1.3	0.1	0.3	0.8	0.3	1.2	3.8

From the testing results of SCC1 mortar (control mixture) sample under different temperatures (SCC11, SCC12 and SCC13), it is found that increasing temperature from 10 °C to 30 °C led to a lower viscosity and higher yield stress, and a lower growth rate of shear stress with shear rate. The yield stress of mortar increased slightly, from 0.2 Pa to 0.4 Pa, when the temperature was from 10 °C to 20 °C, but increased significantly to 3.3 Pa under the temperature of 30 °C. The viscosity of mortar decreased from 11.3 Pa.s to 7.5 Pa.s along with the sample temperature increasing from 10 °C to 30 °C. The higher temperature decreased the  $c$  value from 0.015 to -0.030, and changed the mortar from shear thickening to shear thinning. The rising rate of yield stress and viscosity

with rest time became much higher when temperature increased. This effect explain the influence of temperature on the activity of powders and SP efficiency.

At the room temperature (20°C), the w/b ratio increasing from 0.34 (SCC12) to 0.36 (SCC22) led to decrease the yield stress and slower the growth rate of the shear stress with shear rate. Furthermore, it has been observed that the mortar changed from shear thinning to shear thickening when the *c* value increased from -0.020 to 0.013. At the same time, the viscosity of SCC22, 7.9 Pa.s was much lower than SCC12. During the rest time of one hour, the rheological parameters of SCC22 changed much more slowly than SCC12 did. This can be explained by the higher w/b ratio of SCC22 since more content of free water would resulted in an increased distance and decreased friction among particles in the mortar.

Along with the temperature increasing, the yield stress increment of mortar with the w/b ratio of 0.36 (SCC21, SCC22 and SCC23) was much lower than the mortar with the w/b ratio of 0.34. The *c* value of three mortars maintained positive. The occurrence of this implied that the mortar with w/b of 0.36 was kept shear thickening with the increasing temperature from 10 °C to 30 °C; while the intensity of its shear thickening decreased. The viscosity of the mortar samples generally decreased from 8.7 Pa.s to 7.4 Pa.s with the increasing temperature, and the viscosity difference was much smaller than the control mortar mixture. As expected, the influence of rest time on rheological behavior of mortar became stronger as temperature increased. Comparing to the reference mortar tested under the standard temperature, the effect of temperature on the rheological properties of the mortars was reduced when the w/b ratio was higher.

At the same temperature of 20 °C, the addition of 20% fly ash increased the *c* value of mortar from -0.020 to -0.005, reduced the viscosity from 10.8 Pa.s to 8.9 Pa.s. And the influence of rest time on the rheological behavior was weakened by the addition of fly ash. As the testing temperature increased from 10 °C to 30 °C, the yield stress of the fly ash mortar increased from 0.1 Pa to 0.8 Pa, the increment was much lower than that of the reference mortar. Along with the temperature changing, the viscosity reduced from to 13.6 Pa.s to 6.8 Pa.s, which had a bigger decrease than control mortars.

At the testing temperature of 10 °C, the viscosity of SCC31 was higher than SCC11, but when the temperature increased, the viscosity of SCC31 became lower than SCC11. The addition of fly ash increased the *c* value of mortar at the temperatures of 20 °C and 30 °C, but the *c* value was kept negative for both of the temperatures. The results suggested the changing temperature would has less interference to the effect to the rest time on the rheological properties of the mortar when the mortar has been added in fly ash than when mortar without fly ash. This may be because the lower reacting activity of fly ash than that of cement. On the other hand, the shape of round fly ash particle is beneficial for the lubrication among the solid particles in mortar and subsequently increases the flowing ability of the mortar. Therefore, for the sample contained round fly ash, the growth rate of shear stress with shear rate decreased and the yield stress became smaller when fly ash was added in mortar.

At the same temperature of 20 °C, the addition of 30% of GGBS increased the yield stress of fresh mortar from 0.2 Pa to 1.2 Pa, and increased the *c* value from -0.020 to 0.013. The mortar became much shear thickening with the addition of GGBS, and the viscosity was lower than the control mortar. The addition of GGBS led to a higher growth rate of shear stress with shear rate and the weakened effect of the rest time on the rheological parameters of mortar.

As the testing temperature increased from 10 °C to 30 °C, the yield stress of fresh mortar became much higher, while the viscosity decreased dramatically with testing temperature increasing. The  $c$  value increasing with the increasing of temperature, meant that the increasing temperature changed the mortar more shear thickening when GGBS substituted cement at 30%. With the testing temperature increased, the rest time presented an increased effect on rheological parameter. The effect of GGBS can be attributed to the irregular particles of GGBS which reduced the flow ability of the mortar. The effect of rest time on the rheological parameters of SCC became more significant after the addition of GGBS.

### 3. Conclusion

- 1) The increasing temperature from 10 °C to 30 °C results in a higher initial yield stress and a lower growth rate of shear stress with shear rate for all mortar mixtures. The addition of 20% fly ash, the addition of 30% GGBS or a higher w/b ratio reduces the influence of testing temperature on the initial yield stress and slows the increasing of the growth rate of shear stress with shear rate.
- 2) The rise of the temperature from 10 °C to 30 °C leads to a lowering initial apparent viscosity for all the fresh mortar mixtures. Along with the increasing of temperature, the GGBS mortar becomes slightly more shear thickening, and other mixtures become more shear thinning.
- 3) The initial yield stress and the increasing rate of yield stress with rest time goes up with the higher temperature. Under a higher w/b ratio, the addition of 20% of fly ash diminishes the influence of temperature on the increasing rate of yield stress with rest time, while the addition of 30% of GGBS works in an opposite way in which temperature has a larger influence on the increasing rate of yield stress with rest time. The effects of the temperature on the rheology of mortar mostly is associated with the moving activity and the hydration rate of particles since a higher temperature increases the kinetic energy of the particles, which increases the movement of the particles, and consequently decreases the viscosity of the mortar. Moreover, a higher hydration rate caused by heating leads to a quick loss of fluidity.

### References

- [1] G H Tattersall. The rationale of a two-point workability test[J]. Magazine of Concrete Research, 1973, 25(84): 169-172.
- [2] J E Wallevik. Rheology of particle suspensions: fresh concrete, mortar and cement paste with various types of lignosulfonates[D]. Norwegian University of Science and Technology, 2003.
- [3] L Nachbaur, J C Mutin, A Nonat, et al. Dynamic mode rheology of cement and tricalcium silicate pastes from mixing to setting[J]. Cement and Concrete Research, 2001, 31(2): 183-192.
- [4] D Feys, R Verhoeven, G De Schutter. Fresh self compacting concrete, a shear thickening material[J]. Cement and Concrete Research, 2008, 38(7): 920-929.
- [5] A Yahia, K H Khayat. Analytical models for estimating yield stress of high-performance pseudoplastic grout[J]. Cement and concrete research, 2001, 31(5): 731-738.
- [6] I Mehdipour, M S Razzaghi, K Amini, et al. Effect of mineral admixtures on fluidity and stability of self-consolidating mortar subjected to prolonged mixing time[J]. Construction and Building Materials, 2013, 40: 1029-1037.
- [7] B Felekoğlu, K Tosun, B Baradan, et al. The effect of fly ash and limestone fillers on the viscosity and

- compressive strength of self-compacting repair mortars[J]. *Cement and concrete research*, 2006, 36(9): 1719-1726.
- [8] J Gołaszewski, J Szwabowski. Influence of superplasticizers on rheological behaviour of fresh cement mortars[J]. *Cement and Concrete Research*, 2004, 34(2): 235-248.
- [9] J Y Petit, E Wirquin, B Duthoit. Influence of temperature on yield value of highly flowable micromortars made with sulfonate-based superplasticizers[J]. *Cement and concrete research*, 2005, 35(2): 256-266.
- [10] N Roussel. A thixotropy model for fresh fluid concretes: theory, validation and applications[J]. *Cement and Concrete Research*, 2006, 36(10): 1797-1806.

# Assessing the effect of procurement source of scoria rocks on the pozzolanic properties of the cementitious system

Galal FARES<sup>1</sup>, A. ALHOZAIMY, A. AL-NEGHEIMISH and Omer A. ALAWAD  
*Center of Excellence for Concrete Research and Testing (CoE-CRT), Department of Civil Engineering, College of Engineering, King Saud University, Saudi Arabia*

**Abstract.** Arabian Peninsula possesses large deposits of scoria rocks (SR) of different grain sizes around pyroclastic volcanic cones along the Arabian shield. SR grains are commonly used as lightweight aggregates in the production of lightweight concrete. Mineral admixtures from local resources are unavailable in the Arabian Peninsula; therefore, searching for local alternatives becomes a necessity. In this study, SR is proposed for the use as natural pozzolan. Three SR samples procured from different sources, defined by GPS international coordinates, were characterized using stereomicroscope and FESEM techniques. SR samples were then ground for a definite time of 120 min. The SR powders obtained were investigated using laser particle size, X-ray diffraction analysis (XRD), X-ray fluorescence (XRF) and field emission scanning electron microscope -energy dispersive X-ray spectroscopy (FESEM-EDS) analyses. The strength activity indices of mortars with water-to-binder (W/B) ratio of 0.5 and a replacement level of 20% ground SR powders at curing ages of 28 and 180 days were determined. The strength activity index was found to depend on SR physico-chemical properties. FESEM analysis has shown how SR particles react in the cementitious system. It is concluded that SR particles react according to the chemical and physical nature of their constituting phases (silicic, aluminic and ferric). The particle size is not the only parameter that controls the pozzolanic activity of SR powders. It is verified that SR grain surface contamination greatly affects the microstructure of the cementitious system. SR samples are found to provide different latent pozzolanic properties. SR3 powder has shown the best potential for use as an alternative supplementary cementitious material in the Arabian Peninsula.

**Keywords.** Scoria rocks, volcanic cones, particle size, strength activity indices, microstructure

## Introduction

Arabian Peninsula has large deposits of scoria rocks (SR), which formed during volcanic eruptions millions years ago [1]. Different SR of various grain sizes are found around pyroclastic volcanic cones broadened along the Arabian shield. This zone covers non-urban area of approximately 90,000 km<sup>2</sup> [2]. In this study, SR is proposed for the use as a natural pozzolan. Natural pozzolan has been the first known hydraulic cement in history [3-5].

<sup>1</sup>Corresponding author: Tel. +966-560-830-754, Fax. +966(1)4696342, E-mail. [galfares@ksu.edu.sa](mailto:galfares@ksu.edu.sa)



Recently, several studies on the potential incorporation of SR in concrete have been reported [6, 7]. It has been proven that the presence of SR in concrete, as a partial cement replacement, has promising durability benefits [8]. Three 120-min ground SR samples were procured from different sources defined by GPS international coordinates and characterized using stereomicroscope and FESEM techniques. These powders were further investigated using laser particle size, XRD, XRF analyses. The strength activity indices of mortars with a water-to-binder (W/B) ratio of 0.5 and a replacement level of 20% ground SR powders cured at ages of 28 and 180 days were determined. The strength activity index is an indication to the pozzolanic activity. The microstructure of corresponding paste mixtures was performed at 180 days. The aim of this study was to investigate the potential use of SR powders from different procurement sources as alternative local supplementary cementitious materials.

## 1. Materials

General use type I cement complying with the requirements of ASTM C 150 was used. Scoria rocks samples were procured from different places along the Arabian Peninsula. Table 1 shows the GPS international coordinates for the procured SR samples (SR1, SR2 and SR3). SR samples were ground for 120 minutes. SR powders were found to be approximately 2.5 to 3 times finer than cement. Natural dune sand with specific gravity of 2.59 was used as fine aggregate for mortar.

**Table 1.** Location and nomenclature of the SR samples collected from three regions

Region	Sample	Nomenclature	GPS coordinates	
			Latitude (N)	Longitude (E)
R1	S1	SR1	23° 11.9103	39° 56.9014
R2	S2	SR2	25° 37.7778	37° 73.1667
R3	S3	SR3	26° 91.7778	42° 35.1389

## 2. Experimental program

The samples procured from three different sources were ground for 120 minutes using Fritsch pulverisette 6 planetary mono Mill (320 RPM). The particle size analysis of the fine powders was determined using Horiba LA-950 laser diffraction particle size analyzer. XRD analysis was performed using Panalytical Empyrean with Cu K $\alpha$  radiation of 45 kV and 40 mA with scan speed of 20/minutes. The X-ray patterns of samples were obtained in the  $2\theta$ -range from 5° to 60°. The chemical analysis of cement and SR samples was measured by PANalytical AXIOS XRF machine using pressed powder pellets made from approximately 12 g of sample. The strength activity indices of mortar mixtures prepared with a water-to-binder (W/B) ratio of 0.5 and a replacement level of 20% ground SR powders cured at ages of 28 and 180 days were determined according to ASTM C 311. In the same way, cement pastes of same mortar composition were prepared for microstructural studies.

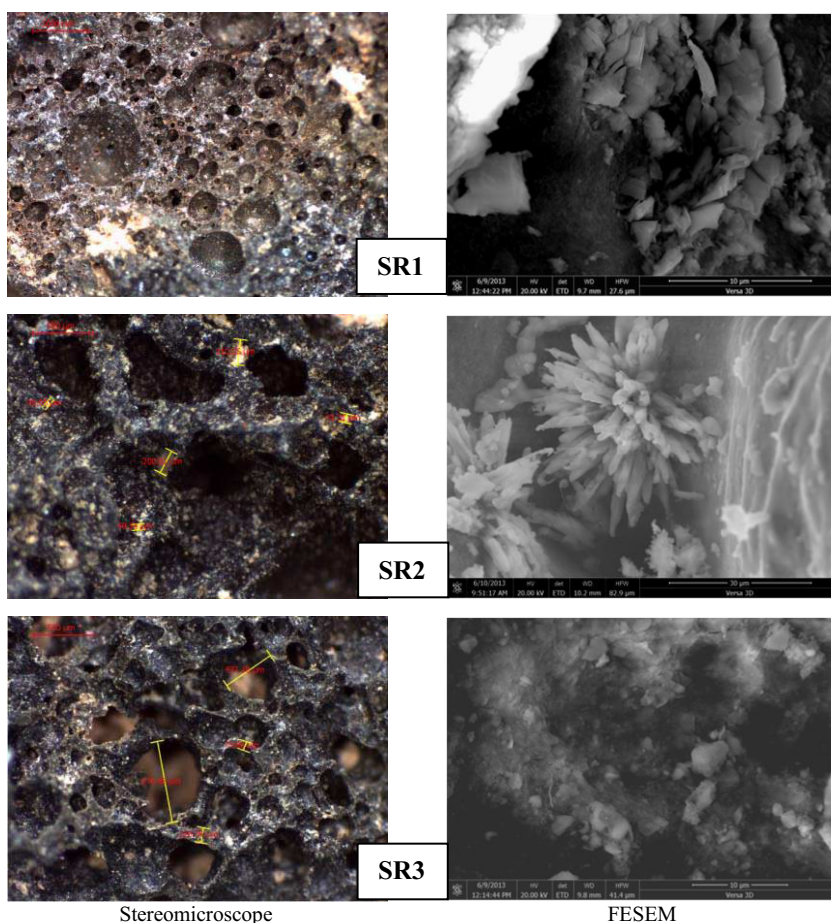
Microstructural analysis was performed using field emission dual beam Versa 3D scanning electron microscope (FESEM) from Field Emission Inc (FEI). FESEM was performed to investigate the microstructure of pastes and their morphology at 180 days.

The microstructural analysis performed was used to explain the effect of incorporating SR powder in enhancing the microstructure of cement pastes.

### 3. Results and discussions

#### 3.1. Microstructural, physical, mineralogical and chemical analyses of SR powders

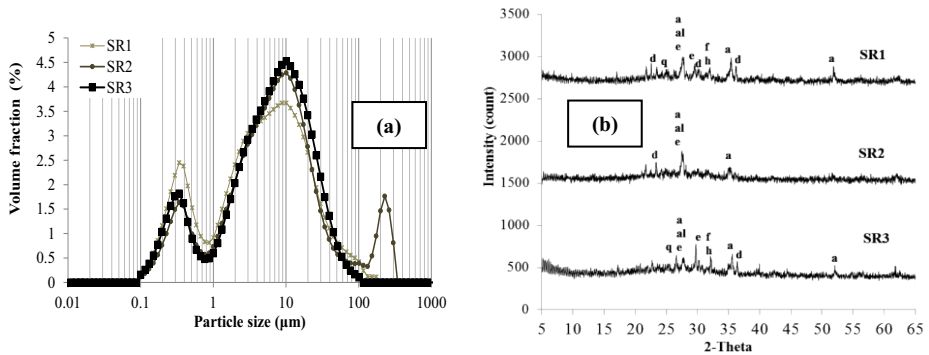
The stereomicroscopic investigation illustrates that SR1 and SR2 grains had sintered and dense structures of variable porosity while SR3 had much less dense network of porous structure, as shown in Figure 1. The microstructural analysis of SR grains reveals that SR 1 is contaminated with siliceous compounds while SR2 is contaminated with sulfate-bearing compounds and SR3 has less contamination, as shown in Figure 1.



**Figure 1.** Stereomicroscopic investigation and FESEM microstructural analysis of SR grains (SR1, SR2 and SR3)

Figure 2 (a&b) shows particle size distribution (PSD) and XRD analyses of SR powders, respectively. It is shown that SR1 and SR3 powders have a bimodal

distribution peak while SR2 has multimodal distribution peaks (3 modes) which depend on the nature of their particles. This might reflect the effect of sample source and composition on the PSD results.



a: Anorthite      al: Albite                      e: Enstatite      f: Frosterite      d: diopside

**Figure 2.** PSD (a) and XRD analyses of SR powders (b)

The chemical analysis in Table 2 shows that SR powders have comparable chemical analysis except for the lower MgO content in SR2. The main particle size distribution parameters (D10, D50, and D90) of SR powders seem to be also similar except for the lower median particle size of SR1. As per ASTM C 618, SR1 and SR2 comply with the sum of elemental oxides (> 70%) while SR3 is at the border line.

**Table 2.** Chemical analysis of different SR samples from different regions

Oxides (%)	SR1	SR2	SR3	PC
SiO <sub>2</sub>	43.31	44.74	43.68	20.41
Al <sub>2</sub> O <sub>3</sub>	15.41	16.44	14.62	5.32
Fe <sub>2</sub> O <sub>3</sub>	12.48	12.96	11.09	4.1
CaO	9.26	9.64	9.66	64.14
MgO	10.1	7.29	9.26	0.71
SO <sub>3</sub>	0.06	0.06	0.07	2.44
TiO <sub>2</sub>	2.19	2.19	2.1	0.3
Na <sub>2</sub> O	2.95	3.53	3	0.1
K <sub>2</sub> O	0.75	0.94	1.53	0.17
L.O.I	0.95	1.21	2.33	2.18
Σ (SiO <sub>2</sub> +Al <sub>2</sub> O <sub>3</sub> +Fe <sub>2</sub> O <sub>3</sub> )	71.1	74.1	69.4	NA
D10 (μm)	0.30	0.40	0.30	2.34
Median size (μm)	4.6	5.7	5.8	14.4
D90 (μm)	24.70	25.0	25.9	44.84

### 3.2. Compressive strength development and strength activity index

Figure 3(a) shows the development of compressive strength of mortar mixtures with time. The rate of the development of compressive strength of SR3 mixture at 28 and 180 days is faster than these of SR1 and SR2 mixtures. The strength activity index of each mixture with respect to the control mixture was calculated as shown in Figure 3(b). The strength activity index at later curing age of 180 days was found to vary between

71 to 95%. Since the SR powders have similar particle sizes as it can be deduced that particle size is not the only parameter that controls their pozzolanic activity.

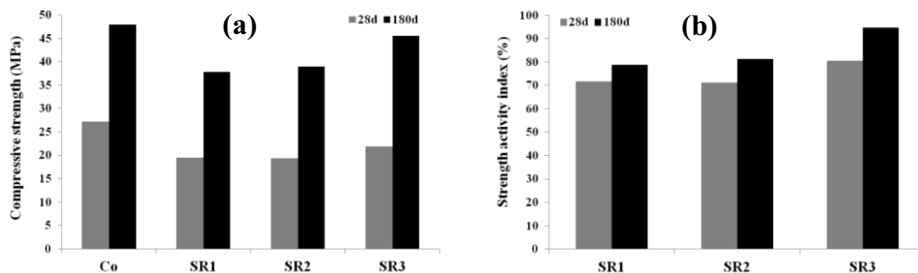


Figure 3. Development of compressive strength with time (a), calculated strength activity index (b)

### 3.3. Microstructure of pastes

Microstructural analysis is presented in Figure 4. The microstructure of the control mixture (Co) reveals the presence of regular hydration products such as ettringite and portlandite. The microstructure of SR1 shows the abundant presence of portlandite crystals while SR 2 shows the formation of abundant ettringite needles attributed to the pre-existence of sulfate-bearing compounds in its grains. However, the microstructure of SR3 proves the presence of advanced type of C-S-H microfibrils that improve the physic-chemical properties of its paste. Therefore, the microstructure is affected by the constituting phases of SR powders (silicic, aluminic and ferric). Each of these phases seem to have different rates of reactivity.

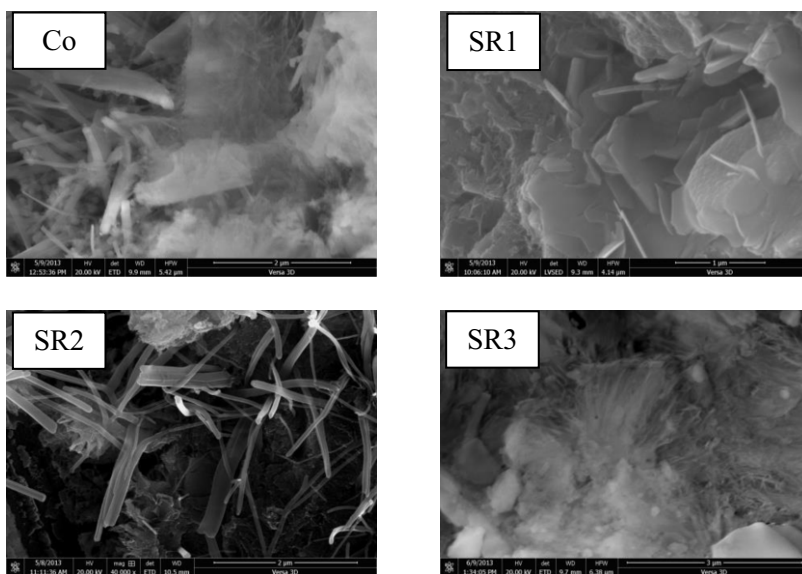


Figure 4. FESEM photomicrographs of control and SR paste mixtures

#### 4. Conclusions

The pozzolanic activity of the SR powders was found to depend on their physico-chemical properties. FESEM analysis has shown how SR particles react in the cementitious system. It is concluded that SR particles react according to the chemical and physical nature of their constituting phases (silicic, aluminic and ferric). The particle size is not the only parameter that controls the pozzolanic activity of SR powders. It is verified that SR grain surface contamination greatly affects the microstructure of the cementitious system. SR samples were found to provide different latent pozzolanic properties. SR3 powder showed the best potential for use as an alternative and efficient supplementary cementitious material in the Arabian Peninsula.

#### Acknowledgment

This research was supported by the National Plan for Science and Technology at King Saud University, Project No.08-ENV 314-02.

#### References

- [1] Wohletz KH. Mechanisms of hydrovolcanic pyroclast formation: size, scanning electron microscopy, and experimental studies, *J Volcanol Geotherm Res* 1983,17(1): 31-63.
- [2] Moufti M, Sabtan A, El-Mahdy O, Shehata W. Assessment of the industrial utilization of scoria materials in central Harrat Rahat, Saudi Arabia, *Eng geolog* 2000,57:155-162.
- [3] Malhotra VM, Mehta PK, Pozzolanic and cementitious materials, London: *Taylor and Francis*, 1996.
- [4] Hewlett P. Lea's chemistry of cement and concrete. Butterworth-Heinemann, 2003.
- [5] Mindess S, Young JF, Darwin D., *Concrete. 2nd ed.* NJ: Prentice-Hall, Englewood Cliffs, 2003.
- [6] Khan KI, AlhozaimyAM. Properties of natural pozzolan and its potential utilization in environmental friendly concrete, *Canad J Civ Eng* 2010,38:71-78.
- [7] Celik K, Meral C, Mancio M, Mehta PK, and Monteiro PJ. A comparative study of self-consolidating concretes incorporating high-volume natural pozzolan or high-volume fly ash, *Constr Build Mater* 2013. <http://dx.doi.org/10.1016/j.conbuildmat.2013.11.065>
- [8] Celik K, Jackson M, Mancio M, Meral C, Emwas A-H, Mehta PK, Monteiro PJ. High-volume natural volcanic pozzolan and limestone powder as partial replacements for portland cement in self-compacting and sustainable concrete, *Cem Concr compo* 2014,45:136-147.

# Potential South African standard sand for cement mortar testing and research

Stephen O. EKOLU<sup>1</sup>

*Department of Civil Engineering Science, University of Johannesburg, South Africa*

**Abstract.** Mortars are used extensively in accelerated methods of testing the physical properties of cementitious materials. Mortar strength is invariably used to determine cement strength grade of cements and for general evaluation of material behavior, as typically employed in research and testing. Presently, the South African (SA) cement industry imports standard from Europe for cement testing purposes. This study was conducted to formulate South African standard sand that could be used to conduct mortar strength tests for compliance to specifications and for general research purposes.

Two formulations of local South African silica sands, referenced as SA513S and SA413S, were developed to suit standard gradings. The formulated South African standard sands (SASS) were tested in comparison with European standard sand (ENSS) of EN196-1 and American graded standard sand (GSS) of ASTM C-778. Following the formulation and grading of SASS, mortar mixtures of 1:3:0.5 cement to sand to water were cast in 50 mm cubes and tested for compressive strength for ages up to 90 days. Two types of cements were employed in the tests, the ordinary Portland cement CEM 1 42.5N and pozzolanic cement CEM V 32.5N. Comparison of the 28-day compressive strength results between the four SS types showed an excellent agreement, giving standard deviations of 1.96 and 2.51 for CEM I and CEM V. The flow results for the standard sand types varied, with EN196-1 giving the highest mortar flow followed by GSS sand and SA413S. The GSS and SA513S gave precisely the same flow results. The investigation indicates the SASS may be suitable for use with SA standard specifications for mortar strength tests.

**Keywords.** Standard sand, compressive strength, mortars, grading

## Introduction

The testing of Portland cements and various cementitious systems for strength are usually based on mortar test methods rather than concrete tests. These approaches play a crucial role in evaluating material performance and have gained universal international acceptance, through the ASTM methods, European test methods and other international standards. Specifically formulated silica sand, referred to as “standard sand” (SS) is prescribed in specifications for use in the accelerated mortar tests and is a crucial ingredient. Accordingly, the SS is required to meet specific quality and grading requirements. Internationally, SS is produced and packaged commercially for specific use in the cement industry.

<sup>1</sup>Corresponding author: University of Johannesburg, Department of Civil Engineering, P.O. Box 524, Auckland Park, 2006, South Africa; E-mail. [sekolu@uj.ac.za](mailto:sekolu@uj.ac.za), [sekolu@gmail.com](mailto:sekolu@gmail.com)

However in South Africa (SA), there is no such standard sand that is locally produced and prepackage for use by the cement industry for mortar testing and research. The standard sand (SS) used in SA is imported, usually from Europe. The importation of standard sand generally brings about difficulties associated with SS availability; it also adds to the costs of testing and research, as experienced by the local industry and academic institutions. For this reason, it is essential to investigate and develop locally available silica sand for potential use as standard sand in cement and mortar specifications, material performance evaluation, testing and research. Such SS could in future be considered for incorporation into the SANS (South African National Standards) standard specifications.

## 1. International specifications and requirements for Standard Sand

### 1.1 Standard mixtures for mortar strength testing

ASTM C 109 [1] is a standard mortar test method for determining the compressive strength grade of Portland cement. It specifies the use of graded standard sand according to the requirements of C 778 [2] and recommends mortar mixes of 1: 2.75: 0.485 cement to sand to water, for OPC and non-air entrained cement mortars. In case of non-OPC or air entrained cements, the amount of water used is determined on the basis of the water quantity required to achieve a flow of  $110 \pm 5$  mm. Similarly, the European method EN 196-1 [3] for strength testing of cement, specifies its grading requirements (table 1) and mix proportions of 1: 3: 0.5 cement to sand to water but does not state the chemical criteria for sand quality.

### 1.2 Grading requirements

The grading requirements for the standard sand for mortar strength tests, vary widely with different countries or regions, as given in Table 1 for ASTM C 778 [1-2], EN 196-1 [3] and Indian standard IS 650 [4].

**Table 1.** International specifications for standard sand grading

ASTM C 778		EN 196-1		IS 650 [4]	
Sieve Size (mm)	Cumulative passing (%)	Sieve Size (mm)	Cumulative passing (%)	Sieve Size (mm)	Cumulative passing (%)
1.18	100	2.00	100	2.00 -100	100
0.85	100	1.60	88-98	1.00-0.50	67
0.60	96-100	1.00	62-72	0.50 -0.09	33
0.425	65-75	0.50	28-38	<0.09	0
0.30	20-30	0.16	8-18		
0.15	0-4	0.08	0-2		

Evidently, size distribution of the sand can be vastly different but the size range of the sand is from about  $80 \mu\text{m}$  for the finer particles to no more than 2 mm particle size. The predominant sizes are between 0.5-1.0 mm for EN and Indian standard, and 0.30-0.425 mm for ASTM sand. It may also be noted the minimum size for the GSS is  $150 \mu\text{m}$  compared to  $80\text{-}90 \mu\text{m}$  for the European and Indian standards. These size ranges and particle size distributions have significant influence on the mechanical interlock of the

grains and pore structure of the mortars; both of these factors being of impact on compressive strength [5].

### *1.3 Chemical requirements*

ASTM C 778 [2] defines standard sand as “silica sand, composed almost entirely of naturally rounded grains of nearly pure quartz, used for preparing mortars in the testing of hydraulic cements”. However, both the ASTM and EN standards [1-3] do not pay attention to the chemical composition, other than a brief mention in C 778 that the SS should be nearly pure quartz or silica. The EN 196-1 on the other hand emphasizes the verification testing of sand through a certification process. The Indian standard IS 650 [4] also is non-specific on the quartz purity level. It simply gives its chemical and physical requirements as “quartz of grey or whitish variety” and angular sand grains with small or negligible quantities of elongated, round or spherical particles. IS 650 does not state the composition or silica content requirement for SS, however, it specifies a requirement for hydrochloric acid testing of SS, which is an indicative test for purity. The acid test evaluates the amount of organic matter, which may impact setting of cement and its hydration, eventually affecting the strength development. A maximum of 0.25% mass loss under acid test is required.

### *1.4 Sources*

It appears the standards deem it important to recommend specific deposits from which the standard sand may be obtained within particular countries or geographical regions. C 778 [2] recommends that standard sand used in North America should be obtained from Ottawa, Illinois or LeSuer, Minnesota. The Indian standard IS 650 also recommends a specific supplier while the EN 196-1 applies the use of CEN (European Committee for Standardization) certification process to verify the approval of SS producers within the European Union.

Natural sand is generally abundant and is available at various sources in most countries, yet its physical features and quartz quality can be vastly variable to the extent that perhaps much of the abundant sand may not be suitable for use as standard sand. Recommendation of verified sand sources would therefore embed uniformity of quality into the supply chain and minimize variability of test results. In testing for compliance to specification, these factors can have major implications in the industry.

## **2. Local South African standard sand**

As mentioned earlier, South Africa presently does not have specified, commercially produced standard sand for use in mortars for cement testing, evaluation of materials or for research purposes. Instead, local cement producers import standard sand from European producers.

However, since as early as 1970s, there was recognition for the need to have a local source of sand for cement and mortar testing. The early SABS method 749:1971 [6], gave some recommendations on the quality and local source of standard sand in South Africa. The standard [6] recommended the use of naturally occurring, single size sand of 0.85 mm with not less than 10% passing 0.6 mm sieve. It also specified the acid test



similarly as the Indian standard [4]. The source of the sand was stated to be at Philippi in the Cape Province. The sand supplier was also given. Comparing these specifications with the modern standard grading requirements for standard sand (see Section 1.2), it is evident that the requirements in the old SA standard [6] are quite different and likely to give vastly different results compared to modern SS (Table 1). Lim et al. [5] found that apart from higher water demand of finer, single sized sand gradings, it may give lower strengths compared to coarser sand sizes. Similar observations are echoed by Reddy and Gupta [7]. These issues underscore the need to update or develop a suitable modern SANS specification for local standard sand. In the context of SA standard sand requirements, there would be demand for SS for use in cement testing and research in Southern Africa. Such uses are conducted by cement manufacturing companies in the region, commercial laboratories and academic institutions that are engaged in cement and concrete research. There would therefore be a sufficiently large market for locally produced standard sand, which at present is occupied by imported SS.

### 3. Experimental

#### 3.1 SA sand grading formulation

Having considered the various gradings and other requirements from established international standards, the specifications in EN 196-1 were used to prepare the SASS formulation used in this investigation. Commercially available, high quality silica sand containing 98% SiO<sub>2</sub> was purchased as sold in different particle sizes and gradings. Following various trials, the sand sizes were divided into coarse (C), medium (M) and fine (F). Various trials of C:M:F combinations were then made to obtain gradings comparable to the EN 196-1 requirements. The two C-M-F formulations *SASS4-1-3* and *SASS5-1-3*, were found to satisfy grading requirements and were then used for mortar preparation

#### 3.2 Mortar mixtures and physical tests

Mortar mixes of 1:3:0.5 cement to sand to water were made using the different sand types: (i) *SASS4-1-3* and *SASS5-1-3*, (ii) GSS and (iii) ENSS. Mortar specimens consisted of 40x40x160 mm prisms, cast and cured in water until testing. Flexural strength and compressive strength were tested at ages of 3, 7, 28 and 90 days. Two types of cements, ordinary Portland cement CEM I 42.5 N and CEM V 32.5 N, were used in the mortar mixture preparations. Other tests included density and flow. During casting of the mixtures, a flow test was performed on each mix as per ASTM C 1437 [8].

### 4. Results and discussion

#### 4.1 Grading of formulated standard sands

Figure 1 shows six (6) different sand gradings that were formulated during the investigation, along with the grading envelope of EN196-1 [2], plotted as CEN-LL for

the lower limit and CEM-UL for the upper limit. Also plotted is the mean grading of the reference EN sand (CEN-avrg). It can be seen that all the six sand formulations satisfied the grading requirement as they all fell within the specified envelope. However, it is notable that the locally formulated sands (SASS) had relatively less coarser fractions than the ENSS sand, as the curves tended to lie towards the upper limit especially at the mid-range fractions of 0.5 to 1.5 mm. Scrutiny of the gradings for the various trial formulations led to refinement of the combinations; the two final formulations *SASS4-1-3* and *SASS5-1-3* were then considered to be more likely to yield performance more closer to that of ENSS. The grading of the selected SASS and ENSS were compared as seen in Figure 2. The curves are generally very close all along the particle size distribution curve. However, there are some disparities in particle sizes, with the SASS showing more fine particles at the size ranges of 0.5 to 1.5 mm and more coarser fractions at higher sizes of greater than 1.5 mm.

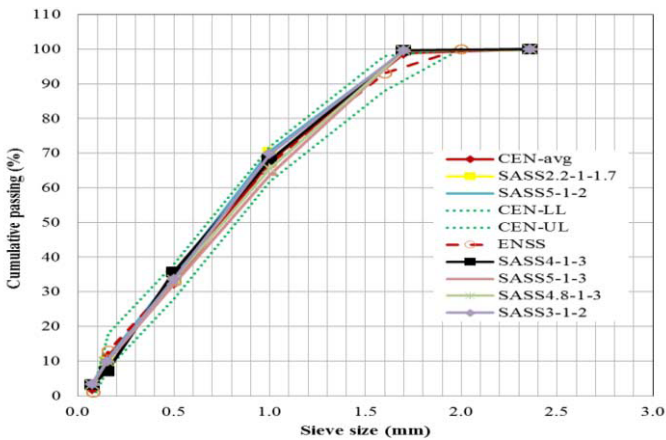


Figure 1. Various combinations of standard sand formulations (CEN-LL = lower limit of envelope, CEN-UL=upper limit of envelope, CEN-avrg = mean of envelope, ENSS = EN196 standard sand, SASS = South African Standard Sand)

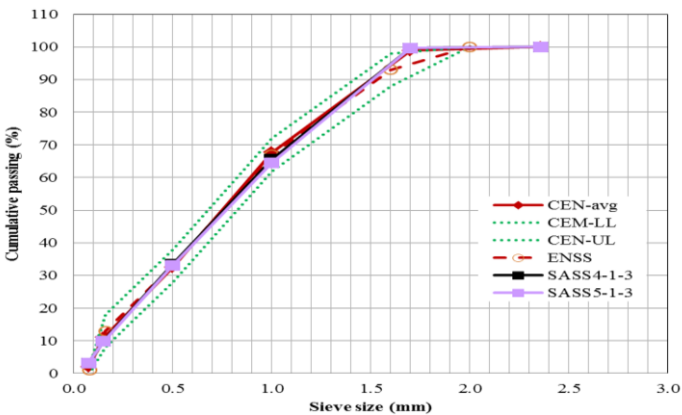


Figure 2. Comparison of SASS sands versus ENSS

### 4.2 Flow

A fixed water-cement ratio of 0.5 was used in all the mixes as explained in Section 4.2. Therefore the variations in the flow measurements should indicate the relative water demand of the mortar mixtures made with the different standard sand types. Figure 3 shows the flow results conducted for three batches of mortar mixtures, using CEM V 32.5 N and CEM I 42.5 N. As expected, the flow measurements for CEM V are generally higher, being in the range of 112 to 142 mm compared to the flow values of 102 to 118 mm for CEM I. The higher flow measurements in CEM V are attributed to the effect of extenders, given the high proportions of about 30% slag and 30% fly ash [9]. Incorporation of fly ash and ground granulated blast furnace slag (GGBS) is known to result in improved workability.

Regardless of the cement type, it can be seen that ENSS had the highest workability, giving flow measurements of 118 mm and 142 mm for CEM I and CEM V respectively. Among the SASS types, SASS4-1-3 gave a higher flow of 111 and 121 mm for CEM I and CEM V, compared to the respective flow values of 107 and 113 mm for SASS5-1-3. GSS had the lowest flow, measuring 102 and 112 for CEM I and CEM V respectively. As pointed out in Section 4.1, the SASS sand types had more finer fractions than ENSS which would increase the water demand of the former over the latter, leading to lower workability for the SASS types. The differences in grading may also explain, to a certain extent, the relatively low workability given by the GSS sand type.

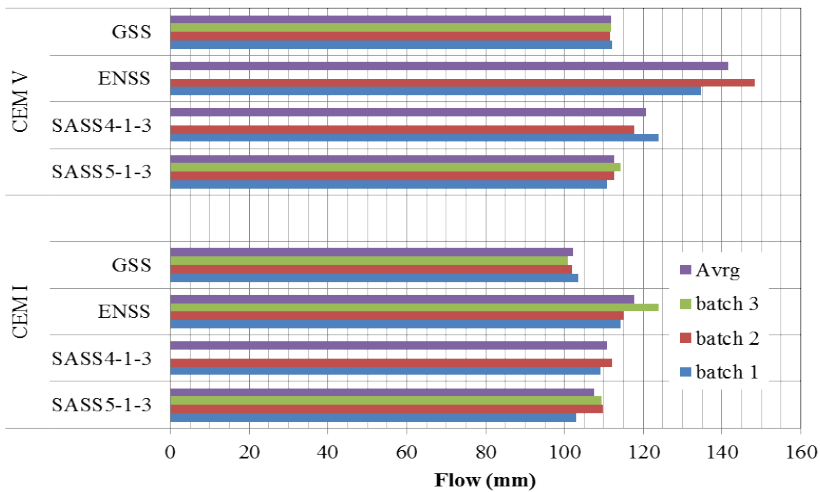


Figure 3. Flow of mortar mixes made with different standard sand types

### 4.3 Flexural strength

The flexural strength results of mortars made from the various standard sand types are shown in Figure 4. It can be seen that the two sand types that gave the highest results were ENSS and SASS4-1-3. The two sand types gave practically similar values of flexural strength at 28 days, as evident in both CEM I and CEM V mortar mixes. The

CEM I strength values for ENSS and SASS were 8.5 MPa and 8.9 MPa while the corresponding values for CEM V were respectively 6.0 and 6.2 MPa.

The higher flexural strengths for ENSS and SASS4-1-3 may be attributed to the good workability of these mixes over their counterparts. Unlike mixtures with lower flow, better workability allows good compaction to be achieved. The GSS sand appeared to give relatively higher early strengths but there was no sufficient data to verify this performance over the long-term.

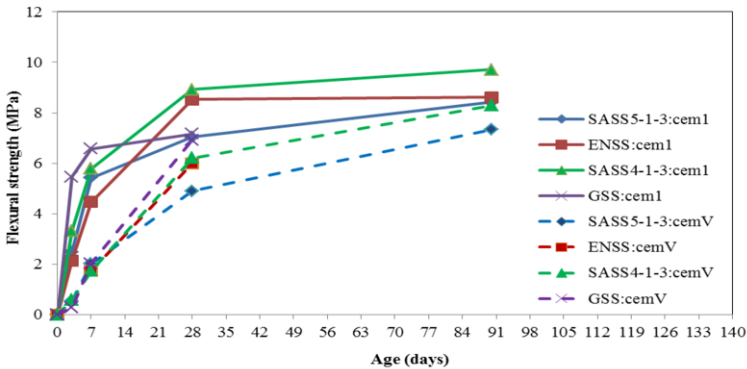


Figure 4. Flexural strength of mortar mixes made with different standard sand types

#### 4.4 Compressive strength

Figure 5 gives a plot of the compressive strength development in the various mortar mixtures made using different standard sand types. Again, it can be seen that the two sand types ENSS and SASS4-1-3 gave higher strength growth for ages of up to 90 days. Also, the strength curves of the sand types were very close. For CEM I mortars, the ENSS sand gave compressive strengths of 29 and 32.7 MPa at 28 days and 90 days respectively, compared to the respective strength values of 29.5 and 33.8 MPa for SASS4-1-3. GSS gave lower strengths than all the other sand types (ENSS and SASS).

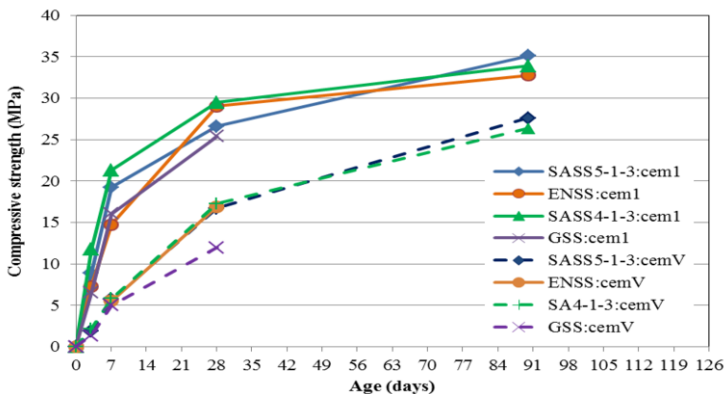


Figure 5. Compressive strength of mortar mixes made with different standard sand types

## 5. Conclusions

The foregone investigation was conducted to formulate potential SA standard sand for mortar strength testing. Following the formulation of six (6) sand types that satisfied the grading requirements, two refined gradings were selected for mortar strength testing. The selected SASS sand types were compared to the relevant EN standard sand and ASTM standard sand. The following conclusions have been drawn:

There is potential for developing suitable standard sand from locally available sources of silica sand in South Africa, for purposes of cement mortar testing and for research.

Whereas EN196 sand consistently gave the highest flow, the South African formulated sand types also showed good workability, better than the ASTM sand type.

It was found that the strength performance of the EN and one of the SASS sand types (SASS4-1-3) were similar, with the latter giving seemingly better flexural and compressive strength than the EN sand.

Although further investigations may be needed to exhaust this investigation, it may be postulated that the SASS formulated in this study has the full potential for use as standard sand for mortars.

## References

- [1] ASTM C 109-13, Standard Test Method for Compressive Strength of Hydraulic Cement Mortars (Using 2-in. or 50-mm Cube Specimens), *ASTM International*, 100 Barr Harbor Drive, PO Box C700, West Conshohocken, PA 19428-2959, USA
- [2] ASTM C 778-13, Standard Specification for Standard Sand, *ASTM International*, 100 Barr Harbor Drive, PO Box C700, West Conshohocken, PA 19428-2959, USA
- [3] SABS EN 196-1: 1994 Methods for testing cement, Part 1: determination of strength, *South African Bureau of Standards*, Private Bag X191, Pretoria
- [4] IS 650, Standard Sand for Testing Cement – Specification, Amendment No.1, May 2000, *Bureau of Indian Standards*, Manak Bhavan, 9 Bahadur Shah Zafar Marg, New Delhi 110 002
- [5] Siong Kang Lim, Cher Siang Tan, Kah Pin Chen, Min Lee Lee, Wah Peng Lee Effect of different sand grading on strength properties of cement grout, *Construction and Building Materials*, Vol. 38 (January 2013) 348–355
- [6] SABS Method 749:1971, Compressive strength of mortars, Section 2: Standard sand for cement testing, *South African Bureau of Standards*, Private Bag X191, Pretoria
- [7] B.V. Venkatarama Reddy and A. Gupta, Influence of sand grading on the characteristics of mortars and soil–cement block masonry, *Construction and Building Materials*, Vol. 22, Issue 8 (August 2008) 1614–1623
- [8] ASTM C 1437 – 13, Standard Test Method for Flow of Hydraulic Cement Mortar, *ASTM International*, 100 Barr Harbor Drive, PO Box C700, West Conshohocken, PA 19428-2959, USA
- [9] SABS EN 197, Methods for testing cement, Part 1: determination of strength, *South African Bureau of Standards*, Private Bag X191, Pretoria

# A study of thermal conductivity of wood ash blended cement mortar

Akeem Ayinde RAHEEM<sup>1</sup>, Ibrahim Akinyemi AKINTEYE and Saheed A. LASISI  
*Civil Engineering Department, Ladoke Akintola University of Technology, Nigeria*

**Abstract.** This paper reports the result of research aimed at assessing the thermal conductivity of wood ash blended cement mortar. Wood ash obtained from bread bakery, was used as partial replacement for ordinary Portland cement in mortar production with replacement ranging from 5% to 25%. Mortar specimen with no wood ash content served as the control. The physical and chemical properties of fly ash were reviewed to evaluate the possible effect on cement properties. Mortar specimens were prepared using cementitious material to sand ratios 1:1, 1:2 and 1:3. The mortar specimens were air-cured for 15 days and oven-dried for 24 hours for complete removal of moisture before thermal conductivity test was carried out on them. For mix ratio 1:1, the thermal conductivity results obtained were 1.399, 1.175, 1.129, 1.040, 1.019 and 1.039 (W/m<sup>0</sup>C) for the control, 5%, 10%, 15%, 20% and 25% fly ash replacement respectively. Similar trends were observed for 1:2 and 1:3 mix ratios. The results showed that the thermal conductivity decreases as the wood ash percentage increases. The thermal conductivity of the control cubes for mix ratio 1:1 gave the highest value. It was concluded that the replacement of cement by wood ash reduces the thermal conductivity of mortar.

**Keywords.** Wood ash, ordinary portland cement, mortar, thermal conductivity

## Introduction

The search for alternative binder or cement replacement materials led to the discovery of the potentials of using industrial by-products and agricultural wastes as cementitious materials. Fly ash is an industrial by-product collected from a practical combustion device after the fuel is consumed. The disposal of this ash usually constitutes an environmental problem. The use of this waste product in cement production is an environmental friendly method of disposal of large quantities of the material that would otherwise pollute land, water and air.

The fly ashes that have been widely studied are those obtained from power plants where coal is used as a fuel [1-6]. This study sought an alternative source of fly ash by investigating the properties of wood ash obtained from bread bakeries, which are located in every nooks and cranny of the country to cater for the high demand of the product. These bakeries use wood as fuel for their operation thereby resulting in high volume of ash as by-product. The ash particles solidify as microscopic, glassy spheres that are collected from the bakery's exhaust before they can "fly" away, hence the product's name – fly ash [7]. Previous research efforts on wood ash concentrated on the determination of the workability and compressive strength of concrete and mortar [8-12].

<sup>1</sup> Corresponding author: [raheemayinde@yahoo.com](mailto:raheemayinde@yahoo.com), [araheem@lautech.edu.ng](mailto:araheem@lautech.edu.ng)

Literature is however scarce on the effect of wood ash on thermal conductivity of concrete or mortar. The thermal conductivity of concrete is of interest due to its relevance to the development of temperature gradients, thermal strains and cracking in the very early life of concrete, as well as the thermal insulation provided by concrete during its service life. The major cause of the temperature differential in a concrete element is the generation of heat by the hydration of cement. It is possible to reduce this heat by choosing a Portland cement with a chemical composition that leads to a low rate of heat development. Blended cements have been known to possess this trait depending on the particular type of pozzolan incorporated [13-15]. There are various testing devices for measuring thermal conductivity. The three-blocks-of-brass method in [16, 17] was adopted for this research due to its availability and simplicity of application. The method employs steady state heat flow in which the heat flux does not change with time.

This study investigated the thermal conductivity of fly ash blended cement mortar with a view to ascertaining its insulation characteristics.

## **1. Materials and method**

### *1.1 Materials*

The fly ash used for this study was collected from Ladoke Akintola University of Technology Ogbomosho, Nigeria, bread bakery located behind Food Science and Engineering Laboratory (Owodunni Building). The ash was carefully collected at the exhaust of the bakery, after the fuel had burned out, with the aid of hand scoop. It was sieved to separate the ash from any unwanted material. The ash was then ground to fine powdery form and only that passing through 425  $\mu\text{m}$  sieve was used for the experiments. The ordinary Portland cement (Elephant Brand) used was obtained from a local retailer in Ogbomosho. Sharp sand obtained from river bed was used as fine aggregates and it was also obtained from Ogbomosho, Nigeria.

### *1.2 Chemical composition of wood ash*

The wood ash was taken to Lafarge Cement, West Africa Portland Cement Company (WAPCO) Sagamu, Ogun State, Nigeria, for chemical analysis. The analysis of the ash was carried out using X-ray Fluorescence Analyser (Model QX 1279).

### *1.3 Sieve analysis of wood ash and fine aggregates*

The particle size distribution of the wood ash and fine aggregates used were determined in accordance with the procedure in BS 1377 (1990)[18].

### *1.4 Specimen preparation*

Specimen preparation for thermal conductivity test was performed using 100 x 100 x 20mm mortar specimens with cementitious material to sand ratios 1:1, 1:2 and 1:3. Wood ash was used to replace 5% - 25% by weight of cement in the mortar. Mortar with no wood ash content served as the control. The water binder ratio ranged between 0.25 and 0.30. The specimens were cast in wooden moulds in pairs, de-moulded after 24hours, air-cured for 15 days and oven-dried for 24hours to ensure complete removal of their water content.

### 1.5 Thermal conductivity test

The steady state heating method involving the use of three – blocks of brass as employed by [16, 17] was used for conducting the test. The three blocks of brass (labeled L, C, R) have the dimensions 100mm x 100mm each, and a thickness of 20mm, 40mm and 20mm respectively. A heater, made of nichrome wire wound round a ceramic rod was used. The experimental set up for the test is shown in Figure 1.

The heater was connected in series to the ammeter, voltmeter, rheostat, power supply and key as shown in Figure 1. The power supply used was a 12 volt car battery. The rheostat was adjusted until a minimum current of 1 ampere was supplied for the heating. The final temperature difference obtained over a period of continuous heating for eight hours was used in determining the thermal conductivity (k) using Equation 1.

$$k = \frac{V \cdot I \cdot d}{A [\Theta_1 - \Theta_2]} \quad (1)$$

where:

V	=	Voltage (volts)
I	=	Current (ampere)
k	=	Thermal Conductivity (W/m <sup>0</sup> C)
A	=	Cross sectional area of sample (mm <sup>2</sup> )
[ $\Theta_1 - \Theta_2$ ]	=	Temperature difference between the faces ( <sup>0</sup> C)
d	=	Thickness of sample (mm)

## 2. Results and discussion

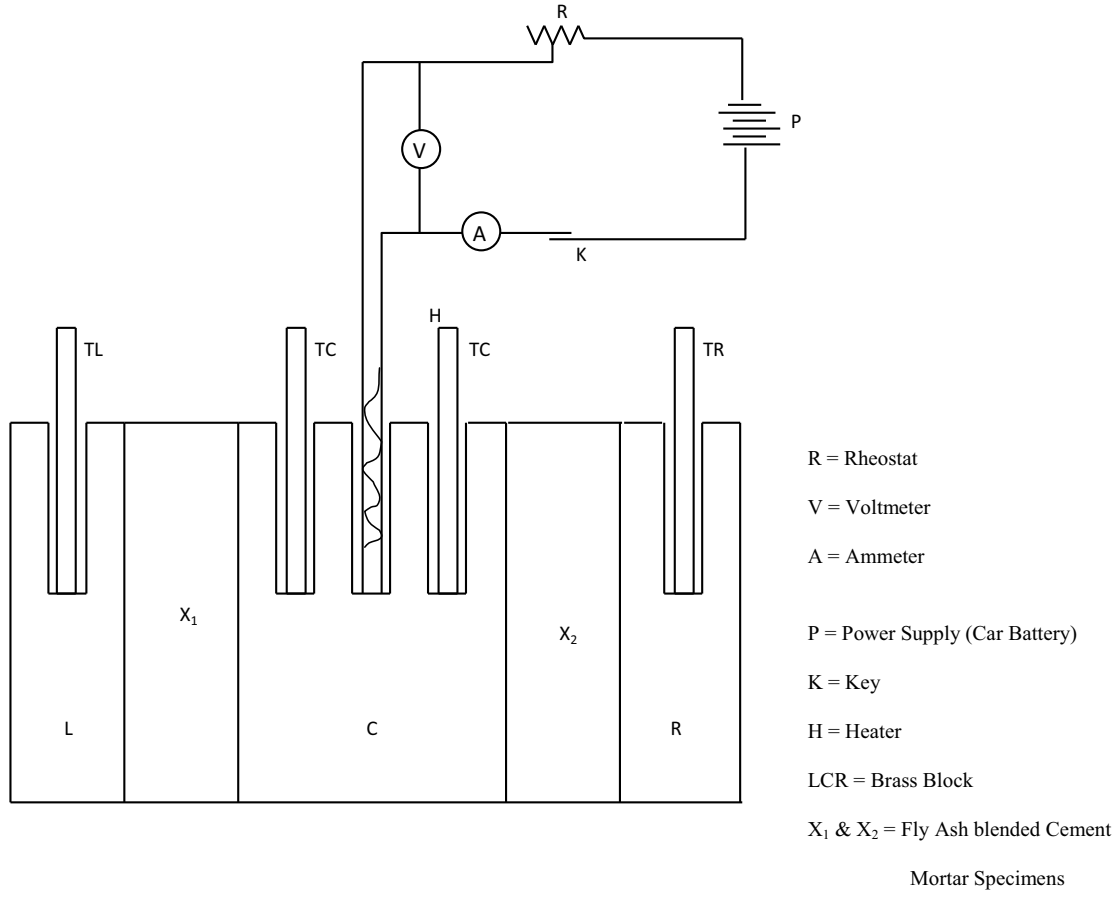
### 2.1 Chemical composition of wood ash

The elemental oxides present in the wood ash are shown in Table 1. The results showed that the wood ash had combined percentages of SiO<sub>2</sub>, Al<sub>2</sub>O<sub>3</sub> and Fe<sub>2</sub>O<sub>3</sub> of more than 70% (73%). This indicates that it is a good pozzolanic material in accordance with the requirements in ASTM C 618 [16]. As reported by [17], wood ash from bread bakery falls under the category of Class F fly ash since the sum of (SiO<sub>2</sub> + Al<sub>2</sub>O<sub>3</sub> + Fe<sub>2</sub>O<sub>3</sub>) is greater than 70%.

### 2.2 Physical properties of wood ash and fine aggregates

Figure 2 shows the grading curve for the wood ash used. The fraction of particles retained on 425 $\mu$ m sieve was 5.53%. The coefficient of uniformity (C<sub>u</sub>) and coefficient of curvature (C<sub>c</sub>) were 3.15 and 0.70 respectively. These indicated that the wood ash is well graded. The wood ash had a specific gravity of 2.0 which is lower than that of the ordinary Portland cement used that is 3.14. The grain size distribution curve of the fine aggregate is also presented in Figure 2. The values of C<sub>u</sub> and C<sub>c</sub> were 5.14 and 1.40 respectively. Thus, the fine aggregate was also well graded.





**Figure 1.** Experimental set-up for thermal conductivity test

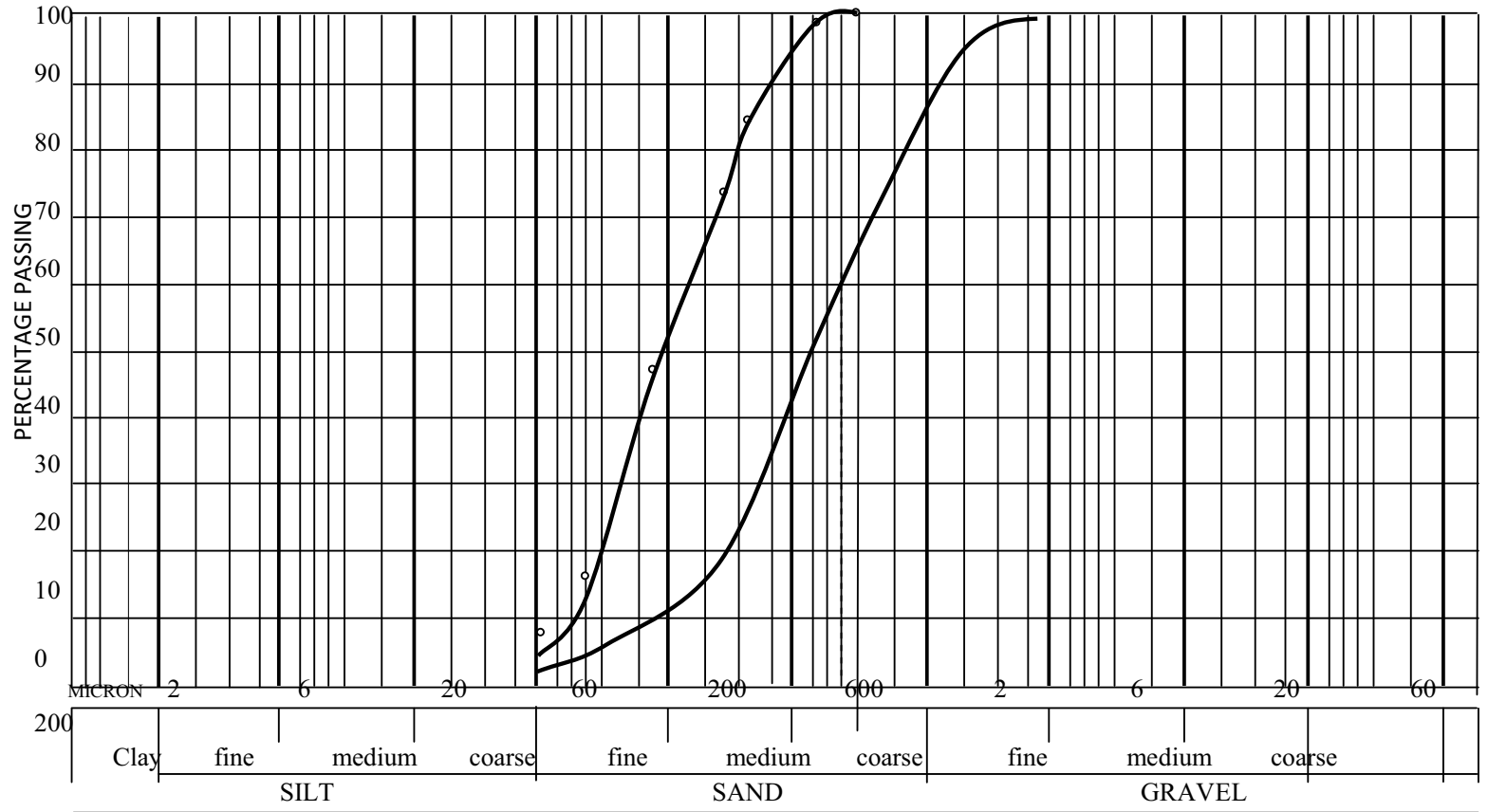


Figure 2. Grading curve for the wood ash and fine aggregates used

**Table 1.** Chemical composition of wood ash

Chemical Constituents	Percentage Composition (%)			
	Sample 1	Sample 2	Sample 3	Average
SiO <sub>2</sub>	61.12	62.75	61.74	61.18
Al <sub>2</sub> O <sub>3</sub>	7.05	7.95	7.57	7.52
Fe <sub>2</sub> O <sub>3</sub>	3.22	2.91	3.44	3.19
CaO	10.56	12.94	11.80	11.77
MgO	2.34	2.00	3.11	2.48
SO <sub>3</sub>	1.84	1.80	1.82	1.82
Na <sub>2</sub> O	1.15	1.00	1.11	1.09
K <sub>2</sub> O	3.56	4.11	3.75	3.81
CaCO <sub>3</sub>	6.12	6.22	6.31	6.22
LOI	2.95	3.20	2.99	3.05
LSF	1.20	1.37	1.27	1.28
SR	4.15	4.25	4.56	4.32
AR	7.48	7.56	7.62	7.55
Total SiO <sub>2</sub> + Al <sub>2</sub> O <sub>3</sub> + Fe <sub>2</sub> O <sub>3</sub>	71.39	73.61	72.75	72.58

### 2.3 Thermal conductivity of wood ash mortar

The results of the thermal conductivity of wood ash blended cement mortar cubes for the three mix proportions considered are presented in Tables 2. Generally, a decrease in thermal conductivity was observed as the wood ash percentage replacement increases.

**Table 2.** Thermal conductivity of mortar specimens

Wood Ash Content (%)	Thermal Conductivity (w//m <sup>0</sup> C)		
	1:1	1:2	1:3
0	1.399	1.282	1.309
5	1.175	1.322	1.349
10	1.129	1.249	1.240
15	1.040	1.182	1.194
20	1.019	1.124	1.129
25	1.039	1.200	1.212

Table 2 indicates that for 1:1 mix proportion, the thermal conductivity decreased from 1.175 W/m<sup>0</sup>C to 1.019 W/m<sup>0</sup>C when the wood ash percentage replacement increased from 5% to 20% as against the control value of 1.399 W/m<sup>0</sup>C. At 25% wood ash replacement, the value of the thermal conductivity increased slightly to 1.039 W/m<sup>0</sup>C. Similar trend was observed for 1:2 mix proportion. The thermal conductivity decreased from 1.322 W/m<sup>0</sup>C to 1.124 W/m<sup>0</sup>C as the wood ash percentage replacement increased from 5% to 20%. The value for 25% replacement also increased slightly to 1.200 W/m<sup>0</sup>C. For 1:3 mix proportion, the thermal conductivity decreased from 1.349 W/m<sup>0</sup>C to 1.129 W/m<sup>0</sup>C when the wood ash percentage replacement increased from 5% to 20%. A slight increase was also observed at 25% replacement with a value of 1.212 W/m<sup>0</sup>C.

The reduction in thermal conductivity in all cases could be attributed to the presence of wood ash in the cement used. This is in line with the findings of [15, 19, and 20] which stated that thermal conductivity decreases with the addition of pozzolanic materials in concrete. According to [21], the reduction in thermal conductivity is partly due to the high silica content of the pozzolan (wood ash in this

case). This could be confirmed from the result of chemical composition of wood ash in Table 1 as silica alone represents 61.18% of the entire composition.

### 3. Conclusion

From the results of the tests performed, it could be concluded that the incorporation of fly ash in blended cement mortar decreases thermal conductivity and improves the insulation properties of the specimens. The implication of this is that the use of fly ash blended cement in mortar used for plastering and floor screeding, would improve the thermal comfort in buildings thereby reducing the cost of energy required for cooling thus, leading to energy conservation.

### References

- [1] S. Antiohos, K. Maganari and S. Tsimas, Evaluation of blends of high and low calcium fly ashes for use as supplementary cementing materials, *Cement & Concrete Composites*, 27 (2005), 349-356.
- [2] R. Siddique, Performance characteristics of high-volume Class F fly ash concrete, *Cement and Concrete Research*, 34 (3) (2004), 487-493.
- [3] C. S. Poon, X. C. Qiao and Z. S. Lin, Pozzolanic properties of reject fly ash in blended cement pastes, *Cement and Concrete Research*, 33 (2003), 1857-1865.
- [4] N. Bouzoubaa, M. H. Zhang and V. M. Malhotra, Mechanical properties and durability of concrete made with high-volume fly ash blended cements using a coarse fly ash, *Cement and Concrete Research*, 31 (10), (2001), 1393-1402.
- [5] M. N. Hague and O. Kayali, Properties of high-strength concrete using a fine fly ash, *Cement and Concrete Research*, 28(10) (1998), 1445-1452.
- [6] T. R. Naik, S. S. Singh and M. Hossain, Enhancement in mechanical properties of concrete due to blended ash, *Cement and Concrete Research*, 26(1) (1996), 49-54.
- [7] V. N. Dwivedi, N. P. Singh, S. S. Das and N. B. Singh, A new pozzolanic material for cement industry: Bamboo leaf ash, *International Journal of Physical Science*, 1(3) (2006), 106-111.
- [8] A. U. Elinwa and Y. A. Mahmoodb, Ash from timber waste as cement replacement material, *Cement and Concrete Composites*, 24(2) (2002), 219-222.
- [9] A. U. Elinwa and S. P. Ejeh, Effects of the incorporation of sawdust waste incineration fly ash in cement pastes and mortars, *Journal of Asian Architecture and Building Engineering*, 3(1) (2004), 1-7.
- [10] A. U. Elinwa, S. P. Ejeh and A. M. Mamuda, Assessing of the fresh concrete properties of self-compacting concrete containing sawdust ash, *Constr and Building Mats.*, 22(6) (2008), 1178-1182.
- [11] A. A. Raheem, B. S. Olasunkanmi and C. S. Folorunso, Saw dust ash as partial replacement for cement in concrete, *Organization, Tech and Mgt in Construction an Inter Jour.*, 4 (2) (2012), 472-478.
- [12] A. A. Raheem and O. A. Adenuga, Wood ash from bread bakery as partial replacement for cement in concrete, *Inter Jour of Sustainable Construction Engineering and Tech*, 4(1) (2013), 75-81.
- [13] X. Fu and D. D. L. Chung,. "Effect of admixtures on the thermal and thermomechanical behaviour of cement paste", *ACI Materials Journal*, 96(4) (1999), 455-461.
- [14] A. M. Neville, *Properties of Concrete*, 4th ed. Longman: London, UK, 2000.
- [15] R. Demirboga, Influence of mineral admixtures on thermal conductivity and compressive strength of mortar, *Energy Building*, 35 (2003), 189-192.
- [16] ASTM C 618, Standard specification for fly ash and raw or calcined natural pozzolan for use as a mineral admixture in portland cement concrete, *Annual Bk of ASTM Stds*, Philadelphia, USA, 1991.
- [17] S. Jerath and N. Hanson, Effect of fly ash content and aggregate gradation on the durability of concrete pavement, *Journals of Material in Civil Engineering*, 19(5) (2007), 367-375.
- [18] BS 1377, Methods of test for the classification of soil and for the determination of basic physical properties, *British Standard Institution*, London, 1990.
- [19] K. Kim, S. Jeon, J. Kim and S. Yang, An experimental study on thermal conductivity of concrete, *Cement and Concrete Research*, 33(3) (2003), 363-371.
- [20] A. A. Raheem and D. A. Adesanya, A study of thermal conductivity of corn cob ash blended cement mortar, *Pacific Journal of Science and Technology*. 12(2) (2011), 106-111.
- [21] R. Demirboga and R. Gul, The effects of expanded perlite aggregate, silica fume and fly ash on the thermal conductivity of lightweight concrete, *Cement and Concrete Research*, 35(5) (2003), 723-727.

# Behavior of high-volume fly ash concrete in mass concrete applications

Anton K. SCHINDLER<sup>a,1</sup> and Kevin P. KEITH<sup>b</sup>

<sup>a</sup>*Department of Civil Engineering, Auburn University, Alabama, U.S.A.*

<sup>b</sup>*Tennessee Valley Authority, Chattanooga, Tennessee, U.S.A.*

**Abstract.** Concrete produced with high fly ash replacement levels is considered high volume fly ash (HVFA) concrete. One of the main limitations to the increased usage of HVFA concrete is the lack of familiarity with its setting time and strength development at various curing temperatures. A laboratory testing program was developed to quantify the effect of fly ash dosage, fly ash chemical composition, cement chemical composition, and environmental conditions on the hydration development, setting times, and compressive strength development of HVFA concrete. Concretes were made with 35% and 50% fly ash replacement levels (by volume) with four fly ash sources (two Class C and two Class F). Setting times are delayed with an increase in fly ash dosage and when the fly ash CaO content is increased for a given fly ash dosage. As the fly ash dosage is increased, the heat generated per volume of concrete decreases. An increase in the fly ash CaO content for a given fly ash dosage, results in increased in-place temperatures. HVFA concrete made with Class C fly ash exhibits a higher rate of early-strength development when compared to the Class F fly ash concrete. HVFA concrete can be produced to have comparable setting times and early-age compressive strength development to conventional concrete.

**Keywords.** hydration, calorimetry, setting, strength

## Introduction

Concrete produced with high fly ash replacement levels is considered high volume fly ash (HVFA) concrete. HVFA concrete has many benefits, including reduced concrete production cost, reduced greenhouse gas emissions, and improved sustainability. One of the main barriers to the increased use of HVFA concrete is the concern over retarded set times, especially when cold curing conditions are encountered. Retarded set times can cause delays to concrete finishing operations, causing HVFA concrete to be undesirable. Similarly, there are concerns over slow early-age compressive strength development for HVFA concrete. Reduced early-age compressive strength development can delay formwork removal times, and negatively impact construction sequencing. In this paper, in-place setting and compressive strength development are estimated for HVFA concretes under varying placement conditions.

Delayed ettringite formation (DEF) is a potential long-term durability concern in mass concrete applications. DEF is defined as the “formation of ettringite in a

---

<sup>1</sup>Corresponding author: Department of Civil Engineering, 237 Harbert Engineering Center, Auburn University, Alabama, 36849, U.S.A.; Email: [schinak@auburn.edu](mailto:schinak@auburn.edu)

cementitious material by a process that begins after hardening is substantially complete and in which none of the sulfate comes from outside the cement paste” [1]. For DEF to occur, the concrete must be subjected to high temperatures early in the curing process. The critical temperature for DEF to occur in concrete made with only portland cement is 70 °C [1]. Folliard et al. [2] recommend a maximum in-place concrete temperature of 85 °C when at least 25% Class F or 35% Class C fly ash dosages are used. When fly ash is used to replace cement in portland cement concrete, the rate of heat development and overall heat of hydration is altered [3]. In some cases, the total heat of hydration is reduced, which can be very beneficial in mass concrete construction. In this paper, the maximum in-place concrete temperatures are estimated for HVFA concretes under varying placement conditions.

## 1. Experimental work

Twenty different concretes (two control concretes and HVFA concretes per cement source) were tested under laboratory conditions. Two portland cement sources and four fly ash sources were investigated. Two control concretes at water-to-cementitious materials ratio ( $w/cm$ ) of 0.42 and 0.44 were developed for each cement source. These concretes are representative of those commonly used in bridge deck applications in Alabama. In addition to the two control concretes for each cement source, two concretes were evaluated for each fly ash source at 35% and 50% fly ash replacement by volume.

When proportioning HVFA concrete, Bilodeau et al. [4] recommended that “the proportion of fly ash should be as high as possible and the  $w/cm$  as low as possible to provide adequate early-age strength and durability.” A preliminary mortar cube study was conducted to determine the  $w/cm$  required to provide adequate early-age strength for the 35% and 50% fly ash concretes. From this study, it was determined that the  $w/cm$  should be 0.34 and 0.39 for the 50% and 35% fly ash concretes, respectively. Ravina and Mehta [5] found that HVFA concrete will experience delayed set times as compared to a control concrete with no fly ash; therefore, an accelerating admixture was used for all HVFA concretes.

### 1.1 Fly ash properties

Four fly ash sources, two Class C and two Class F, were selected for laboratory testing to represent the range of fly ash chemical compositions available to the concrete industry in the United States. The four fly ash sources were differentiated based on their calcium oxide content. The chemical composition of each fly ash is a function of the coal burnt during their production. The chemical analysis results and specific gravity values for each of the fly ashes as tested by an independent laboratory are presented in Table 1.

## 2. Modeling approach

The ConcreteWorks software program [7] was used to estimate in-place temperature profiles for HVFA concrete under various placement conditions. For each concrete

mixture investigated, iterations were completed within ConcreteWorks at a range of placement temperatures to generate a set of in-place concrete temperature profiles. The HVFA concretes were varied based on fly ash type and dosage. Fly ash dosages of 0%, 35%, and 50% by volume of cementitious materials were investigated. For each fly ash dosage, iterations were completed using the four fly ashes shown in Table 1. Activation energy values for the concretes were determined from isothermal calorimetry. Semi-adiabatic calorimetry tests were conducted to quantify the hydration behavior of HVFA concrete. All these tests results are presented by Keith [6].

Mass concrete elements were modeled by considering three square column sizes. The column members were modeled with a two-dimensional horizontal cross section. The plan dimensions for the three column sizes considered were:  $0.9 \times 0.9$  m,  $1.8 \times 1.8$  m, and  $3.0 \times 3.0$  m. The ConcreteWorks inputs used for this analysis are defined in Keith [6].

The ConcreteWorks software program includes a historical environmental condition database (temperature, wind speed, percent cloud cover, solar radiation, atmospheric pressure, and relative humidity) based on 30-year average data for selected locations. A 12:00 p.m. placement time was used for all analysis. The fresh concrete temperature was assumed to be equal to the ambient air temperature from the ConcreteWorks historical database. Using this assumption, iterations were completed for concrete placement temperatures equal to 4.4, 10, 15.5, 21.1, 26.7, 32.2 and 35 °C.

**Table 1.** Fly ash properties

Parameter	Fly Ash Type			
	28%CaO	24%CaO	15%CaO	1%CaO
Calcium Oxide, CaO (%)	27.08	23.07	15.34	1.01
Silicon Dioxide, SiO <sub>2</sub> (%)	35.64	39.17	51.61	59.56
Aluminum Oxide, Al <sub>2</sub> O <sub>3</sub> (%)	15.88	18.48	20.16	27.30
Iron Oxide, Fe <sub>2</sub> O <sub>3</sub> (%)	6.47	7.06	4.83	5.02
Magnesium Oxide, MgO (%)	6.45	5.04	3.05	1.06
Sulfur Trioxide, SO <sub>3</sub> (%)	2.14	1.24	0.71	0.05
Equivalent Alkali, Na <sub>2</sub> O <sub>eq</sub> (%)	2.47	1.99	1.47	2.08
Loss on Ignition (%)	0.35	0.17	0.23	0.17
Specific Gravity	2.71	2.63	2.47	2.17
Amount retained on the 45 μm sieve (%)	18.6	12.3	27.2	27.2

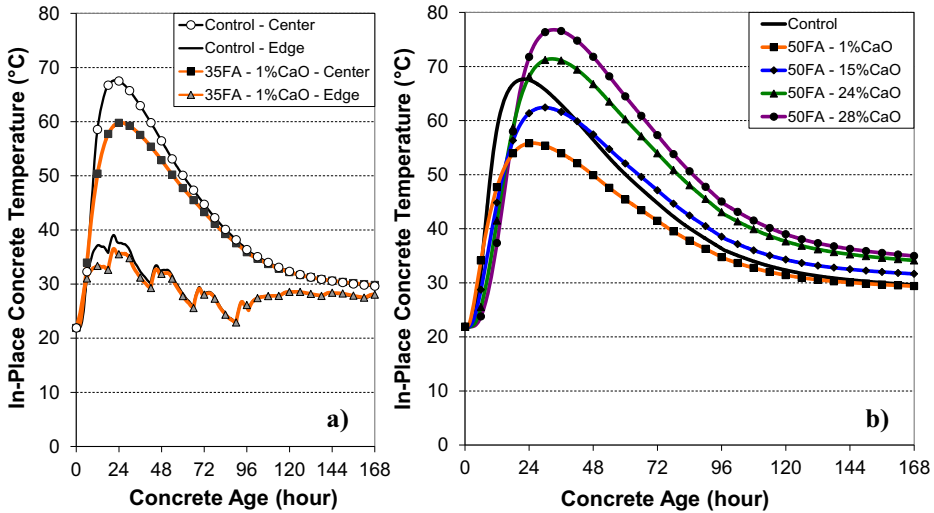
### 3. Sample in-place temperature profiles from concreteness analysis

All in-place temperature profiles presented herein were generated using similar baseline conditions. An example of the predicted temperature profiles at the center and the edge of the  $1.8 \times 1.8$  m column element placed at 21.1 °C is shown in Figure 1a.

The general effect of fly ash type on the maximum in-place temperature development for the  $1.8 \times 1.8$  m columns is presented in Figure 1b. The results presented in this figure represent the estimated temperature development at the center node of the column element when the concrete placement temperature is 21.1 °C.

In Figure 1b, it is shown that as the fly ash CaO content increases, for a given fly ash dosage, the maximum in-place concrete temperature also increases. For the  $1.8 \times 1.8$  m columns placed at 21.1 °C, an increase in fly ash CaO content from 1% to 28% resulted in an increase in the maximum in-place concrete temperature of 21 °C. Also,

the HVFA concretes proportioned with 50% of either Class C fly ash and lower  $w/cm$  reached a much higher in-place concrete temperature than the control concrete. The results obtained for the Class C fly ash concretes are attributed to the combined effect of the increased Class C fly ash heat of hydration and the low  $w/cm$  of the concrete. The same trend was observed for the  $3.0 \times 3.0$  m columns; however, the maximum in-place concrete temperature increased by  $25^\circ\text{C}$  as the fly ash CaO content increased from 1% to 28%. The results presented in Figure 1b agree with past research conducted by Langley et al. [8].



**Figure 1.** a) Center and edge temperatures and b) maximum concrete temperatures for  $1.8 \times 1.8$  m columns placed at  $21.1^\circ\text{C}$

## 4. Evaluation of in-place performance of HVFA Concrete

### 4.1 Maximum in-place concrete temperature

Maximum in-place concrete temperature versus concrete placement temperature for  $1.8 \times 1.8$  m columns is presented in Figure 2. DEF temperature limits for concrete proportioned with portland cement (PC) and supplementary cementitious materials (SCMs) are also indicated on each figure. In this figure, the results for the control concrete and HVFA concretes proportioned with the 1%, 15% and 28% CaO content fly ashes are presented. The temperature development for the HVFA concretes proportioned with 24% and 28% CaO Class C fly ashes were very similar; therefore, only the results for the 28% CaO Class C fly ash concretes are presented in this section.

In Figure 2, it is shown that the maximum in-place concrete temperature increases linearly with an increase in the concrete placement temperature. For all column sizes, there is a range of maximum in-place temperature results for the HVFA concretes at each placement temperature. The maximum in-place concrete temperature for the Class C fly ash concretes exceed the maximum in-place temperature for the control concrete at all placement temperatures. Also, the results for the 35FA-15% concrete were very similar to the results for the control concrete at all placement temperatures.



For the HVFA concretes proportioned with the Class F fly ashes, the maximum in-place concrete temperature for the 50% dosages were lower than the results for the concretes proportioned with 35% fly ash at all placement temperatures. These results were also observed for all other column sizes evaluated. The results presented in this figure illustrate that an increase in fly ash dosage does not translate to reduced maximum in-place temperature development when high-calcium Class C fly ashes are used for large concrete elements.

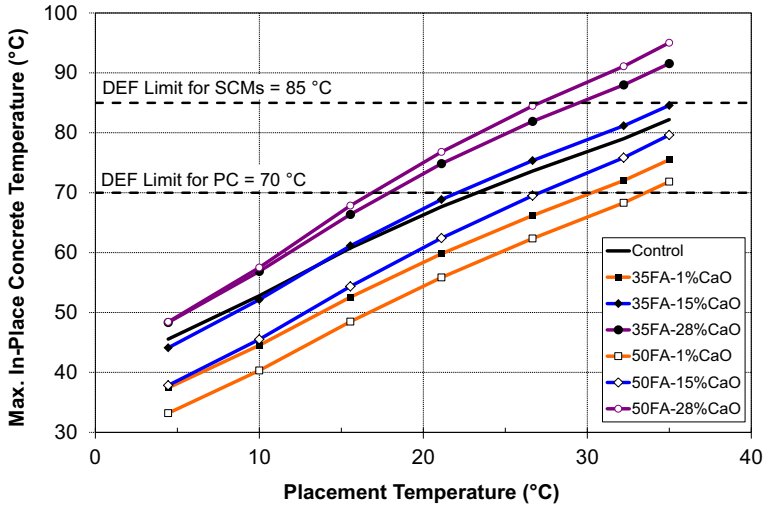


Figure 2. Maximum in-place concrete temperature versus concrete placement temperature for 1.8 × 1.8 m columns

4.2 Initial set time

The in-place temperature profiles from the ConcreteWorks analysis were used to estimate the time required to reach initial set for each of the HVFA concretes. During the laboratory testing phase of this project, the equivalent age at initial and final set was determined for each concrete mixture. The equivalent ages at initial set are summarized in Table 2 for the HVFA concretes. Since the equivalent age at initial set was known for each concrete, the time required to reach initial set was determined with the equivalent age maturity method and the estimated in-place concrete temperature profiles from ConcreteWorks. The temperature profile at the surface of each element was used to estimate the time required to reach initial set, because the maturity of the concrete at this location drives finishing operations.

Table 2. Equivalent age at initial set for concretes considered

Concrete Type	Equivalent Age at Initial Set (hrs)	Concrete Type	Equivalent Age at Initial Set (hrs)
Control (w/c = 0.44)	4.38	50FA-1%CaO	3.61
35FA-1%CaO	3.54	50FA-15%CaO	4.12
35FA-15%CaO	4.57	50FA-24%CaO	5.78
35FA-24%CaO	5.15	50FA-28%CaO	5.73
35FA-28%CaO	4.73		

In Figure 3, the time required to reach initial set versus concrete placement temperature for the HVFA concretes proportioned with the 1, 15, and 28% CaO fly ash sources are presented for both the 35% and 50% fly ash concretes. The results indicate that unlike the results obtained for maximum in-place concrete temperature, a linear relationship between initial setting time and concrete placement temperature does not exist. As expected, for all concrete elements investigated, the range in initial setting times was largest at the coldest placement temperature and smallest at the highest placement temperature.

Initial set times for the HVFA concretes are delayed as the fly ash CaO content increases. The concretes proportioned with the high-calcium Class C fly ashes exhibit the longest initial set times at all placement temperatures. This finding matches those reported by Ravina and Mehta [5]. The initial set times for the 1% CaO Class F fly ash concretes were shorter than the control concrete set times for all placement conditions.

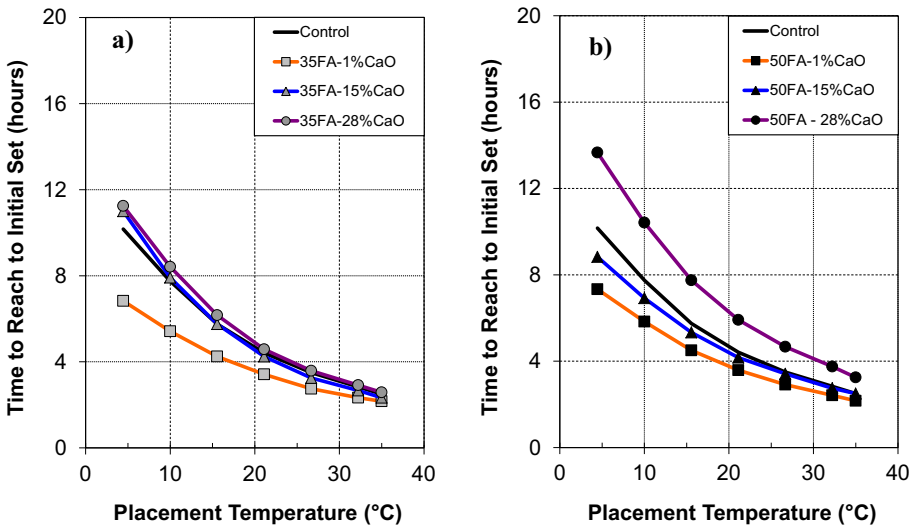


Figure 3. Time to reach initial set for a) 35% fly ash and b) 50% fly ash concretes in  $1.8 \times 1.8$  m columns

#### 4.3 Early-age compressive strength development

Formwork removal times are often based on the requirement of reaching 70 % of the 28-day design compressive strength. In this paper the time required to reach 70 % of the 28-day strength of the control concrete was used. The in-place compressive strength development was determined by using the equivalent age maturity method and the *surface* temperature history from ConcreteWorks. The strength-maturity parameters for each concrete were determined by laboratory testing and are presented in Keith [6]. The activation energy was determined from mortar cube testing as per ASTM C 1074.

The time to reach 70% of the 28-day strength versus concrete placement temperature results for  $1.8 \times 1.8$  m columns are presented in Figure 4. All times shown are limited to 14 days, as a time beyond 14 days will significantly delay subsequent construction activities. The compressive strength development results are similar in form to the initial setting results. As the placement temperature increases, the results converge, indicating the difference in the strength behavior of these concretes is reduced when placed under hot weather conditions. Also, in general the time required

to reach 70% of the control concrete 28-day strength decreased as the fly ash dosage was reduced.

In general an increase in fly ash CaO content results in less time required to reach 70 % of the 28-day compressive strength. Typically, HVFA concretes proportioned with Class C fly ashes exhibit increased early-age compressive strengths when compared to similar Class F fly ash concretes due to an increased rate of reaction at early ages [9]. The 28% CaO fly ash concretes required less time to reach 70% of the 28-day strength than all other HVFA concretes. The 35FA-15%CaO, 35FA-28% CaO, and 50FA-28% CaO concretes performed similar to the control concrete. For example, the average delay in time required to reach 70% of the 28-day strength for the 50FA-28% CaO concrete when placed in this column element was only 8 hours.

The largest delays in compressive strength development were associated with the 1% CaO Class F fly ash concretes when placed under *cold* weather conditions. For example, the average delay in compressive strength development for the 35FA-1% CaO concrete when compared to the control was about 8.4 days at 4.4 °C. These results indicate that high dosages of low-calcium Class F fly ashes should not be used under *cold weather conditions* when the time to achieve sufficient early-age compressive strengths is of concern.

Based on the results presented in this section, it is concluded that HVFA concrete can be proportioned to have similar compressive strength development to that of conventional portland cement concrete.

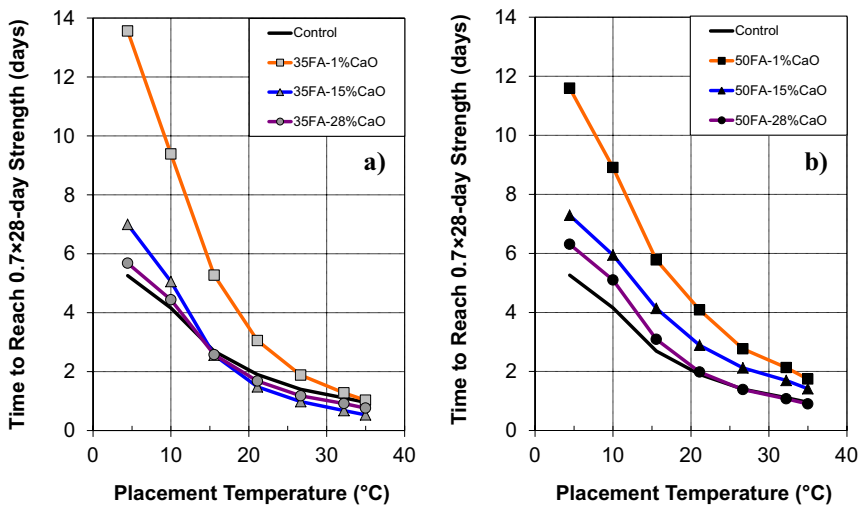


Figure 4. Time to reach 70% of the 28-day strength for a) 35% fly ash dosage and b) 50% fly ash concretes when placed in a 1.8 × 1.8 m column

## 5. Conclusions

The results presented in this paper are intended to provide guidance on the maximum in-place temperature development, time to reach initial set, and compressive strength development of HVFA concrete placed in some mass concrete elements. The results presented herein are only valid for the baseline conditions described. If the baseline conditions are not met, a new ConcreteWorks analysis should be completed with

mixture-specific inputs for the activation energy, hydration parameters, and proportions. Additionally, to accurately estimate the in-place behavior it is required to perform laboratory testing to establish the equivalent age at initial set and strength-maturity parameters. The results of the study support the following primary conclusions:

- An increase in fly ash CaO content, for a given fly ash dosage, causes an increase in the maximum in-place concrete temperature, regardless of the placement conditions.
- For both Class F fly ash concretes, an increase in fly ash dosage from 35 % to 50 % resulted in a decreased maximum in-place temperature, despite the lowered  $w/cm$  used for the HVFA concretes.
- An increase in fly ash dosage does not translate to reduced maximum in-place concrete temperatures when high-calcium Class C fly ashes are used at a reduced  $w/cm$  for mass concrete elements.
- HVFA concrete may be proportioned to have similar, if not reduced, initial set times than conventional portland cement concrete when low-calcium Class F fly ashes are used with accelerating admixtures.
- Unless very low concrete placement temperatures (4.4 to 10 °C) are expected, HVFA concrete may be used in mass concrete elements without encountering excessive delays in initial set times, regardless of the fly ash type.
- HVFA concrete may be proportioned to have similar in-place compressive strength development to that of conventional portland cement concrete.

## References

- [1] H.F.W. Taylor, C. Famy, and K.L. Scrivener, Review: Delayed Ettringite Formation, *Cement and Concrete Research* 31, 683-693, 2001.
- [2] K.J. Folliard, M.C. Juenger, A.K. Schindler, K. Riding, J. Poole, L. Kallivokas, S. Slatnick, J. Whigham, and J.L. Meadows, *Prediction Model for Concrete Behavior – Final Report*, Research Report No. 0-4563-1, Center for Transportation Research, The University of Texas at Austin. 65 pages, 2008.
- [3] A.K. Schindler and K.J. Folliard, Heat of Hydration Models for Cementitious Materials, *ACI Materials Journal* 102 (1), 24-33, 2005.
- [4] A. Bilodeau, V.M. Malhotra, and P.T. Seabrook.. Use of High-Volume Fly Ash Concrete at the Liu Centre. International Centre for Sustainable Development of Cement and Concrete (ICON), Materials and Research Laboratory, CANMET, Natural Resources Canada, Ottawa, Canada, 21 pages, 2001.
- [5] D. Ravina and P.K. Mehta, Properties of Fresh Concrete Containing Large Amounts of Fly Ash, *Cement and Concrete Research* 16 (6), 227-238, 1986.
- [6] K.P. Keith, *Characterization of the Behavior of High Volume Fly Ash Concrete*, M.S. Thesis, Auburn University, Alabama, 2011.
- [7] K.A. Riding, *Early Age Concrete Thermal Stress Measurement and Modeling*, PhD Dissertation, The University of Texas at Austin, Austin, Texas, 2007.
- [8] W.S. Langley, G.G. Carette, and V.M. Malhotra, Strength Development and Temperature Rise in Large Concrete Blocks Containing High Volumes of Low-Calcium (ASTM Class F) Fly Ash, *ACI Materials Journal* 89 (4), 362-368, 1992.
- [9] R.L. Smith, C.F. Raba, and M.A. Mearing, Utilization of Class C Fly Ash in Concrete, *Sixth International Fly Ash Utilization Symposium*. Reno, Nevada. March, 31 pages, 1982.

# Microstructure and durability characteristics of self-curing concrete

Amr S. EL-DIEB<sup>1</sup>, Tamer A. EL-MAADDAWY and Abdelrahman AL-SALLAMIN  
*Civil and Environmental Engineering Department, United Arab Emirates Univ, UAE*

**Abstract.** Efficient curing of concrete requires high water demand which is not available in many practical situations. Therefore, the need of self-curing concrete becomes more demanding. In this study, polyethylene glycol (PEG) and polyacrylamide (PAM) have been used as water soluble polymers to develop self-curing concrete. The main microstructural and durability characteristics of the developed self-curing concrete mixture were examined and compared to those of conventional concrete mixtures with no self-curing agents under different curing regimes. One batch of the self-curing and the conventional mixtures were left in the lab air-cured to act as non-water-cured control samples. The water curing regimes for conventional mixture included continuous moist-curing (water-immersion) for 3, 7 and 28 days and periodical moist-curing by means of wetted burlaps for 3 and 7 days. Curing regimes for the self-curing mixtures included 3 days of moist-curing and periodical curing using wetted burlaps for 3 and 7 days. The microstructure characteristics of the concrete mixtures were investigated by a scanning electron microscope. The durability performance of the concrete mixtures was evaluated by measuring the rapid chloride permeability and water permeability. Self-curing concrete mixtures showed better microstructure development and durability performance than those of the air-cured conventional concrete mixtures. A short 3 days moist-curing significantly improved the performance of the self-curing concrete mixture to a level almost similar to that of the conventional concrete mixture that was water-immersed for 28 days. Self-curing concrete represents a step towards a new construction material due to its lower water demand needed for curing, and hence can reserve the limited water resources in many parts in the world.

**Keywords.** Self-curing concrete, water-soluble polymers, moist-curing, periodic curing, microstructure, durability, RCPT, water permeability

## Introduction

Curing of concrete plays a major role in developing the concrete microstructure. According to the ACI 308R [1], Guide to Curing Concrete, “the term “curing” is frequently used to describe the process by which hydraulic cement concrete matures and develops hardened properties over time as a result of the continued hydration of the cement in the presence of sufficient water and heat”. Curing is essential for the continuation of hydration of the cement, and consequently the development of concrete microstructure and pore structure. Nevertheless, good curing is not always practical in many cases.

---

<sup>1</sup>Corresponding author: Civil and Environmental Engineering Department, College of Engineering, United Arab Emirates University, P.O. Box 15551, Al Ain, UAE; E-mail. [amr.eldieb@uaeu.ac.ae](mailto:amr.eldieb@uaeu.ac.ae)

Producing self-curing concrete is very important from the point of view that water resources are getting valuable every day, especially in desert areas where water is not adequately available. Self-curing concrete can be produced by incorporating self-curing agents in the concrete mixtures [2 - 7]. The integration of self-curing agents, such as water-soluble polymers, in the mixtures can reduce the water evaporation thus increasing the water retention capacity of concrete [8, 9]. Water-soluble polymers have been successfully used by El-Dieb et al. (2012) [10] to produce self-curing cement pastes. The use of these water-soluble polymers to produce self-curing concrete, rather than cement pastes, would represent a new trend in the concrete construction. In this study, the performance of self-curing concrete mixtures has been evaluated and compared to that of conventional concrete mixtures under different curing regimes.

## 1. Study objectives

The main objectives of the study are to develop self-curing concrete mixtures and examine their main microstructural characteristics and evaluate key durability indices. The self-curing concrete mixtures have been developed by incorporating the water-soluble polymers; polyethylene glycol (PEG) and polyacrylamide (PAM). The durability performance of the concrete mixtures has been evaluated by measuring the 28-day rapid chloride permeability test (RCPT) and water permeability test.

## 2. Experimental work

### 2.1. Materials and concrete mixtures

Cement used in this study was ordinary Portland cement. The coarse aggregate was natural crushed stone from Ras Al Khaima with nominal sizes of 10 and 19 mm (mixed in 1:1 by mass), a specific gravity of 2.65, and absorption of 1.0%. Two types of sand, mixed in 1:1 by mass, were used in the mixture namely crushed natural sand from Ras Al Khaima with a fineness modulus of 3.5 and specific gravity of 2.63, and dune sand from Al Ain area with a fineness modulus of 0.9 and specific gravity of 2.63. The concrete mixture was designed to have a slump ranging from 50 to 60 mm and to yield a nominal compressive strength of 25 MPa. Table 1 shows the concrete mixture design used in the study.

**Table 1.** Concrete mixtures proportions for (1 m<sup>3</sup>).

Cement	Fine Aggregate	Coarse Aggregate	Water (W/C)
328 kg	716 kg	1121 kg	210 lit (0.64)

The water-soluble polymers polyethylene glycol (PEG) and polyacrylamide (PAM) synthesized in the laboratory, have been used in the present study as self-curing agents. Table 2 gives the main properties of both polymers. As a first alternative, PEG was used solely with a dosage of 0.025% by weight of cement (mixture SCC-PEG100). A higher dosage of PEG would result in a dry mixture with low workability and cement hydration [8 - 10]. Polyacrylamide (PAM) was used in conjunction with PEG as another alternative. The dosage of PEG+PAM together was kept at 0.025% by weight of cement. The weight ratios of the PEG and PAM in the dosage were varied; the first

ratio was 80% PEG and 20% PAM (SCC-PEG80-PAM20) and the second ratio was 60% PEG and 40% PAM (SCC-PEG60-PAM40). All self-curing mixtures had fresh concrete slump in the designed range of 50-60 mm except for SCC-PEG60-PAM40, the mix was dry and sticky with a slump ranging from 20-30 mm. This was also observed and reported by Sun and Xu [11] for mixtures with a high dosage of PAM.

**Table 2.** Properties of water-soluble polymers

Polymer Type	Molecular Weight (g/mol)	Property			
		Appearance	Moisture %	SG***	pH
PEG*	6000	White Flakes	0.1% Max.	1.08 – 1.09	5 – 7
PAM**	9000000	White Crystalline Powder	0.1% Max.	0.75	5 – 7
*	Polyethylene glycol				
**	Polyacrylamide				
***	Specific Gravity in 50% aqueous sol.				

## 2.2. Curing regimes

The curing regimes of the conventional concrete mixtures included air-curing, continuous moist-curing (i.e. water-immersion) for 3, 7 and 28 days and periodic moist-curing using wetted burlaps for 3 and 7 days. The self-curing concrete mixtures were air-cured, periodically moist-cured for 3 and 7 days using wetted burlaps, or continuously moist-cured (i.e. water-immersed) for 3 days. Table 3 summarizes the curing regimes adopted in this study.

**Table 3.** Concrete mixtures proportions for (1 m<sup>3</sup>)

Concrete Mixture I.D.	Curing Regimes					
	Air-Curing	3 days Periodic	7 days Periodic	3 days Moist	7 days Moist	28 days Moist
Conventional	✓	✓	✓	✓	✓	✓
SCC-PEG100	✓	✓	✓	✓	-----	-----
SCC-PEG80-PAM20	✓	✓	✓	✓	-----	-----
SCC-PEG60-PAM40	✓	✓	✓	✓	-----	-----

## 2.3. Specimen and testing

Chloride ions permeability and water permeability were used as durability indices of the concrete which mainly depends on the microstructure of the concrete [12]. The rapid chloride permeability test (RCPT) and the water permeability test were conducted at 28 days of age. Both tests were conducted on disc specimens cut from concrete cylinders, with a diameter of 100 mm and thickness of 50 mm. Figure 1 shows the water permeability test. Tests were conducted on 3 to 5 replicates and the average values were used in the analysis. The RCPT was conducted according to ASTM C1202. The water permeability test was conducted using a pressure head ranging from 10-20 bars and sides of the concrete specimens were sealed using a sealer material. The microstructure characteristics were examined using JOEL scanning electron microscope. The tested specimens were freshly fractured pieces.



**Figure 1.** Water permeability test

### 3. Results and discussions

#### 3.1. Rapid chloride permeability test (RCPT)

The RCPT was conducted to evaluate the concrete durability with respect to its resistance to chloride attack and chloride induced corrosion. Figure 2 shows the RCPT values of tested mixtures for different curing regimes. Moist-curing resulted in the lowest charge passing for conventional mixture with the 28 days moist-curing having the lowest value, which is ranked as moderate permeability according to ASTM C1202. The periodic curing regimes as well as the 3-day continuous moist-curing did not change the permeability category of the conventional mixture significantly, where the mixture was still in the “high permeability” category. The conventional mixtures needed a minimum of 7 days of continuous moist-curing to achieve a permeability ranking similar to that achieved at 28 days of continuous moist-curing. A minimum moist-curing period of 7 days is stipulated in the ACI 318 [13].

Similar to the conventional mixture, the periodic moist-curing was not effective in improving the chloride permeability ranking of all self-curing mixtures, except for the mixture SCC-PEG100. Continuous moist-curing for 3 days was sufficient to reduce the RCPT values of all self-curing mixtures to be in the “Moderate” permeability category according to ASTM C1202. The self-curing mixture SCC-PEG80-PAM20 exhibited the lowest RCPT values among all mixtures that were either air-cured or subjected to 3 days of periodic moist-curing. This indicates that the self-curing mixture SCC-PEG80-PAM20 was able to produce a denser microstructure within a very short curing period owing to the water retention of such mixture by the inclusion of two types of water-soluble polymers and adjusting the mixing ratio of these polymers [10]. Increasing the time of the periodic moist-curing from 3 to 7 days did not result in a further improvement in the performance of the mixture SCC-PEG80-PAM20 but significantly reduced the RCPT value of the mixture SCC-PEG100. Similarly, the mixture SCC-PEG100 exhibited the best performance after 3 days of continuous moist-curing. This demonstrates that the self-cured mixture containing PEG only is more sensitive to curing time and regime relative to other mixtures.

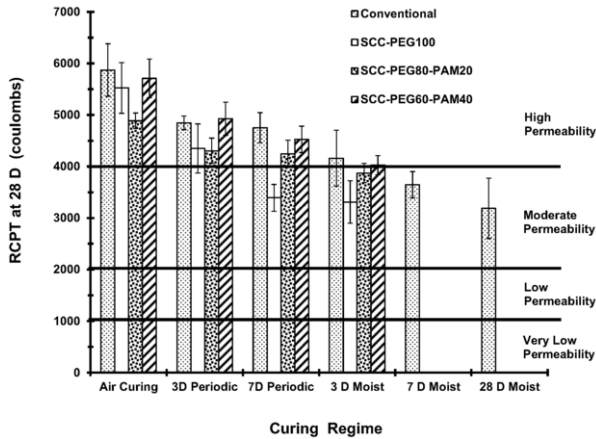
#### 3.2. Water permeability test

Figure 3 shows the 28 days water permeability of the tested mixtures. Similar to the RCPT results, the water permeability values of the conventional mixtures was significantly reduced by increasing the moist-curing period. Conventional mixture exposed to periodic curing with wet burlap did not show significant effect on



permeability results. The permeability value started to be significantly affected when applying 7 days of moist-curing.

All self-curing concrete mixtures showed lower permeability with respect to air-cured conventional mixture. The reduction is around 50% in the permeability values. Exposure to 3 days moist-curing resulted in a significant reduction in the permeability similar to the value of 28 days moist-cured conventional mixture. Periodic curing did affect the permeability values of self-curing concrete mixtures, but the values were slightly higher than that of the 28 days moist-cured conventional mixture. The improvement in water permeability could be attributed to the discontinuity of pores as a function of cement hydration.



**Figure 2.** RCPT results of tested mixtures under different curing regimes

### 3.3. Microstructure characteristics

Microstructure investigation was conducted at 28 days of age. Microstructure investigation was conducted on conventional concrete mixture exposed to air-curing, 28 days moist-curing and all self-curing concrete mixtures exposed to air-curing and 3 days moist-curing in order to show the main microstructural characteristics. Microstructural investigation of 28 days moist-cured conventional concrete mixture exhibited denser microstructure compared to the same mix air-cured, owing to better hydration and densification of the microstructure. Figure (4-a) and (4-b) show SEM micrographs of conventional mixture air-cured and 28 days moist-cured respectively. For the air-cured mixture, larger voids were observed compared to those of the 28 days moist-cured. Also, several microcracks, up to 9.0  $\mu\text{m}$  width, were observed in the air-cured conventional mixture, while the width of microcracks was up to 2.0  $\mu\text{m}$  for 28 days moist-cured conventional mixture.

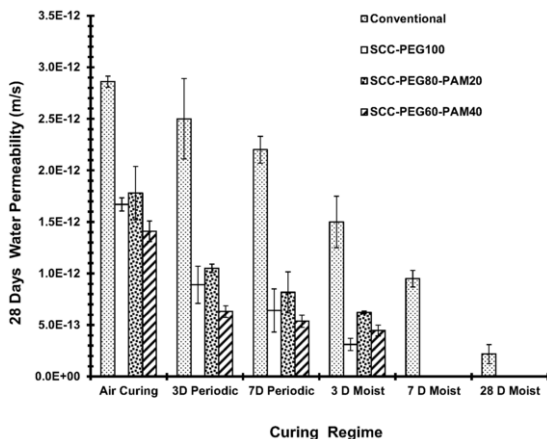


Figure 3. Water permeability results of tested mixtures under different curing regimes

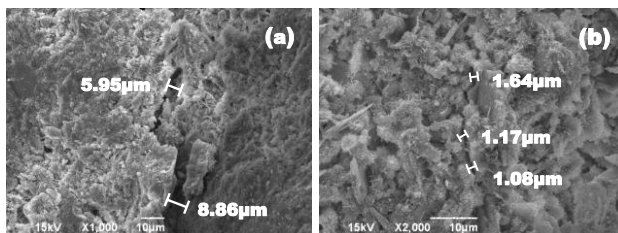


Figure 4. Microstructure of conventional concrete mixture; (a) air cured, (b) 28 days moist-curing

Figure (5-a), (5-b) and (5-c) shows the SEM micrographs of air-cured self-curing mixtures SCC-PEG100, SCC-PEG80-PAM20 and SCC-PEG60-PAM40 respectively. Generally, microstructure of all self-curing concrete mixtures was not as dense as that of the conventional 28 days moist-cured mixture but is denser than the air-cured conventional mixture. It was observed that crystalline hydration products such as  $Ca(OH)_2$  did not have obvious edges and corners in all self-curing mixtures which could be attributed to the un-availability of space for crystal to grow and well develop due to dense microstructure as a result of the continuation of hydration. Similar observations were previously reported in the literature [4, 11]. Also, the width of microcracks observed in all self-curing mixtures ranged from 2.0  $\mu m$  to 5.0  $\mu m$  which is smaller than those observed in air-cured conventional mixture.

Figure (6-a), (6-b) and (6-c) shows the SEM micrographs of 3 days moist-cured self-curing mixtures SCC-PEG100, SCC-PEG80-PAM20 and SCC-PEG60-PAM40 respectively. The microstructure of all self-curing concrete mixtures exposed to 3 days of moist-curing exhibited a dense microstructure similar to that of 28 days moist-cured conventional mixture. The C-S-H cross-links with the crystalline hydration products forming a discrete skeleton network. The width of microcracks observed in all self-curing mixtures ranged from 1.0  $\mu m$  to 3.0  $\mu m$  which is comparable to those observed in 28 days moist-cured conventional mixture. This explains the results obtained in the RCPT and water permeability tests.

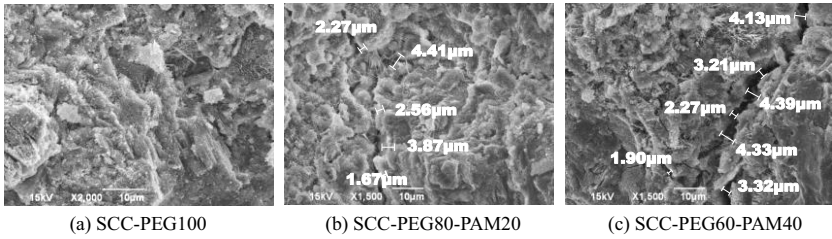


Figure 5. Microstructure of air-cured self-curing concrete mixtures

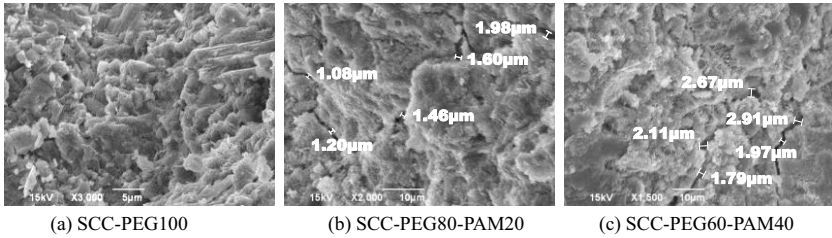


Figure 6. Microstructure of 3 days moist-cured self-curing concrete mixtures

The examination of the aggregate matrix interfacial transition zone (ITZ) showed that the ITZ zone for self-curing mixtures is dense and contains less size and not well-formed crystalline hydration products similar to the air-cured conventional mixture as shown in Figure 7.

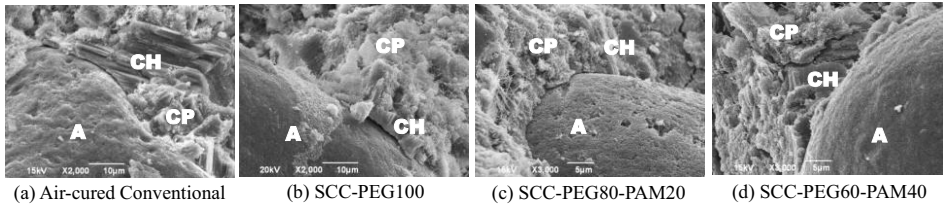


Figure 7. Microstructure of aggregate matrix interfacial transition zone (ITZ), A=aggregate, CH=calcium hydroxide, CP=cement paste

#### 4. Conclusions

The following are the main conclusions based on the test results obtained in this study:

- Production of self-curing concrete is viable with the use of water-soluble polymers; polyethylene glycol (PEG) and polyacrylamide (PAM), with a very low dosage (i.e. 0.025% by weight of cement).
- High dosage of water-soluble polymers has an adverse effect on the mixture fresh properties. Replacing 40% of the PEG dosage by PAM impaired the mixture workability.
- Water-soluble polymers with high molecular weight should not be used solely and should be used in conjunction with low molecular weight polymers.

- Self-curing mixtures tested in this study have better durability performance as measured by RCPT and water permeability tests compared with those of air-cured conventional mixtures.
- Adopting a short moist-curing of 3 days to self-curing mixtures significantly improved its durability indices to a level similar to that of conventional mixtures continuously cured for 28 days.
- Periodic curing with wet burlap up to 3 or 7 days have the same effect on RCPT and water permeability for all self-curing mixtures.
- Microstructure of self-curing concrete mixtures exhibited denser microstructure with a smaller width of microcracks and reduced size of crystalline hydration products compared to air-cured conventional mixture.
- Microstructure characteristics of 3 days moist-cured self-curing concrete resembles those of conventional mixtures continuously moist-cured for 28 days.

## 5. Acknowledgment

This work was financially supported by the UAEU-NRF Research Grant # UAEU-NRF-20911. Also, the manufacturing of the polymers used in the study at Ain Shams University, Faculty of Engineering by Dr. Ahmed Adel Mahmoud is very much appreciated.

## References

- [1] ACI 308R-01, Guide to Curing Concrete. *ACI Manual of Concrete Practice*, (2008).
- [2] R.K. Dhir, P.C. Hewlett, J.S. Lota and T.D. Dyer, An Investigation into the Feasibility of Formulating 'Self-Curing' Concrete, *Materials and Structures* 27 (1994), 606-615.
- [3] R.K. Dhir, P.C. Hewlett and T.D. Dyer, Durability of Self-Cured Concrete, *Cement and Concrete Research* 25 (1995), 1153-1158.
- [4] R.K. Dhir, P.C. Hewlett and T.D. Dyer, T. D., The Influence of Microstructure on the Physical Properties of Self-Curing Concrete, *ACI Materials Journal* 93 (1996), 1-7.
- [5] H.W. Reinhardt and S. Weber, Self-Cured High Performance Concrete, *ASCE Journal of Materials in Civil Engineering* 10 (1998), 208-209.
- [6] B. Mather, Self-Curing Concrete, Why not?, *Concrete International* 23 (2001), 46-47.
- [7] D.P. Bentz, P. Lura and J.W. Roberts, Mixture Proportioning for Internal Curing, *Concrete International* 27 (2005), 35-40.
- [8] R.K. Dhir, P.C. Hewlett and T.D. Dyer, Mechanism of Water Retention in Cement Pastes Containing a Self-Curing Agent, *Magazine of Concrete Research* 50 (1998), 85-90.
- [9] A.S. El-Dieb, Self-Curing Concrete: Water Retention, Hydration and Moisture Transport, *Construction and Building Materials* 21 (2007), 1282-1287.
- [10] A.S. El-Dieb, T.A. El Maaddawy and A.A. Mahmoud, Water-Soluble Polymers as Self-Curing Agents in Cement Mixes, *Advances in Cement Research* 24 (2012), 291-299.
- [11] Z. Sun and Q. Xu, Micromechanical Analysis of Polyacrylamide-Modified Concrete for Improving Strengths, *Materials Science and Engineering A* 490 (2008), 181-192.
- [12] L. Basheer, L. Kropp and D.J. Cleland, Assessment of the Durability of Concrete from its Permeation Properties: A Review, *Construction and Building Materials* 15 (2001), 93-103.
- [13] ACI-318M-08, Building Code Requirements for Structural Concrete and Commentary, (2008).

# Palm Kernel Incinerated Ash as low cost concrete component

Emem-Obong Emmanuel AGBENYEKU<sup>1</sup> and Felix Ndubisi OKONTA

*Department of Civil Engineering Science, University of Johannesburg, South Africa*

**Abstract.** The incorporation of commercially available fly ash (FA) as low cost material in concrete has long been established. Large quantities of FA are utilized for research and field applications because of the pozzolanic characteristics. One of many pozzolanic materials is palm kernel incinerated ash (PKIA). The abundance of PKIA as an agricultural waste material in West Africa obtained by the incineration of palm kernel husk and shells in milling boilers paved way for this study. Specimens containing 50%PKIA were cast and cured both in water and air and their compressive strength and shrinkage behaviours were investigated with and without the addition of superplasticizer (hydroxylated carboxylic (HC) acid) in comparison with controlled specimens containing 100%OPC. Results showed that the strength development in PKIA green concrete at all ages of curing; 7,14 and 28days were lower than OPC concrete. On the addition of superplasticizer, strength of 36.9N/mm<sup>2</sup> was observed for specimens with superplasticizer as against 31.7N/mm<sup>2</sup> for specimens without superplasticizer on the 28day. The water curing method produced the best results while the predicted shrinkage strain of the green concrete in accordance to ACI 209R-92 standard was higher than the control specimens.

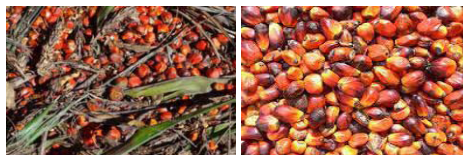
**Keywords.** Lightweight green concrete, palm nut shell, compressive strength, workability

## Introduction

The use of supplementary cementitious materials (SCMs), such as fly ash (FA), rice husk ash (RHA), slag and silica fume (SF) in concrete has attracted considerable interest over the past decades. The generation of SCMs is vital to developing countries as low-cost construction constituents in self-sustaining means of shelter. The unrelenting rise in the prices of conventional materials has triggered the search for locally available resources as alternatives [1]. These alternatives are to supplement the costly conventional materials partly or fully, particularly in mortar and concrete. The pulverized fuel ash or FA as recorded by [2] is considered the most widely used in concrete construction amongst other silicon by-products. Apart from industrial waste, ashes from agricultural origin [3] such as; rice husk, cassava peels, coconut husk, corn cob, groundnut shell etc. have been identified as SCMs in many parts of the world. One of such pozzolanic materials is palm kernel incinerated ash (PKIA); an agricultural waste material derived by the combustion of palm oil husk and/or palm kernel shell in palm oil milling factories.

<sup>1</sup>Corresponding author: [kobitha2003@yahoo.com](mailto:kobitha2003@yahoo.com)

The oil palm is a tall or short-stemmed tree belonging to the palm family-Palmea with palm nut as its fruit (see Figures 1 and 2).



**Figure 1.** Palm nuts



**Figure 2.** Palm trees

As reported by [4] Benin Republic, Colombia, Ecuador, Nigeria, Zaire, Malaysia and Indonesia are amongst the countries in the equatorial belt that cultivate oil palm and palm oil products. These by-products are commonly used as fuel in the boilers of palm oil mills which become ashes in the form of PKIA (see Figures 3 and 4). The use of SCM such as PKIA does not only improve concrete properties but protects and conserves the environment by saving energy and natural resources [5].



**Figure 3.** Oil palm husk and kernel shells



**Figure 4.** Palm kernel incinerated ash (PKIA)

In West Africa the PKIA is popularly regarded as waste material in which case it is openly dumped creating risks of soil and groundwater contamination leading to environmental pollution. However, PKIA has been identified to possess good pozzolanic properties that can be used as substitute for cement in mortar and concrete mixes. In light of this, researchers have investigated the utilization of PKIA as a SCM and have examined various properties of the fresh and hardened concrete made from PKIA based on short and long-term laboratory investigations [6]. The PKIA as recorded by [6] has not only enabled the replacement of Ordinary Portland Cement (OPC) but has been found to play an effective role in producing strong and durable concrete. Considering the availability of PKIA in West Africa, this study opted to investigate the short-term properties of concrete containing 50% by mass of PKIA as it is within the limit to which cement be replaced for quality and economy for a targeted 28days strength, effects of admixture and curing process on the strength development of this concrete type; alongside the strength and drying shrinkage behaviour in comparison to the conventional OPC concrete set as control.

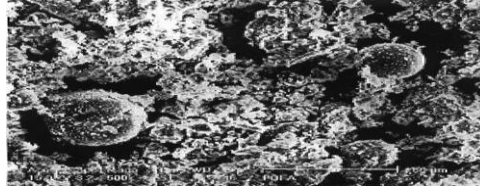
## 1. Materials and methods

### 1.1. Palm kernel incinerated ash (PKIA)

The PKIA used in this study is the combustion product of oil palm husk and palm kernel shells in oil milling boilers 220-300<sup>0</sup>C collected from Ikoritungko Oil Milling

Factory located around Calabar, Nigeria. The collected ash as shown in Figure 4 was oven dried for 24hours at a constant temperature of 100<sup>0</sup>C.

The dried ash was passed through 300- $\mu$ m sieve to remove dirt and ash lumps/clinkers. It was then finely ground in a modified Los Angeles abrasion machine using steel bars (12mm diameter and 800mm long). The PKIA appeared grayish in color due to low carbon content as well as relatively spherical as seen in the electron micrograph in Figure 5.



**Figure 5.** Scanning electron micrograph of PKIA

Table 1 shows the results of the chemical analysis carried out on PKIA which clearly revealed that the necessary chemical composition qualifying PKIA as a pozzolana was met and places it in between Class-C and Class-F in conformance to ASTM C618-94a standard [7].

**Table 1.** Chemical constituents of PKIA

Chemical Composition	Fe <sub>2</sub> O <sub>3</sub>	SiO <sub>2</sub>	Al <sub>2</sub> O <sub>3</sub>	CaO	MgO	TiO	LIO	SiO <sub>2</sub> +Al <sub>2</sub> O <sub>3</sub> +Fe <sub>2</sub> O <sub>3</sub>
PKIA	7.22	55.9	8.49	9.30	2.88	-	14.9	70.61

### 1.2. Concrete production

The materials used in this study are portable tap water for mixing and curing the concrete, Burham- an ASTM Type I Ordinary Portland Cement, crushed granite with particle size distribution in a range of 10-12mm and sharp river sand with particle size distribution in a range of 2-4mm having a fineness modulus of 2.4m<sup>2</sup>/kg used as coarse and fine aggregate respectively. Their relative density on oven-dry basis in accordance to BS 812: Part 2 [8] was gotten as 2.72 and 2.65 while their corresponding water absorption values were 0.77% and 1.42% respectively. The Adva-cast trade name Superplasticizer (hydroxylated carboxylic (HC) acid) used in this study as shown in Figure 6 was added at the rate of 1% by mass of total binder content in the respective concrete mixes. In conformance to DOE [9] mix design, the control sample was targeted for a mean strength of 40MPa with 50  $\pm$  10mm slump.



**Figure 6.** Powdery and solvent forms of Adva-cast hydroxylated carboxylic (HC) superplasticizer

A water-binder ratio of 0.40 on the introduction of superplasticizer to the mix was adopted maintaining a similar workability through the entire test. The PKIA concrete was prepared by replacing 50% by mass of OPC in the concrete with a mix ratio of 1:1.45:2.42. Details of the mix proportions for OPC and PKIA concrete are given in Table 2. The specimens were demoulded and cured by air and total submergence in a water bath for periods of 7, 14 and 28days respectively. To investigate the effect of curing condition on strength development, three curing schedules were initiated in this study namely; continuous submergence in water, 7days submergence plus air curing (7days submergence + air curing) and continuous air curing. Specifications in BS 1881: Part 110 [10] for preparation of cylindrical specimens of 150mm x 300mm dimensions was conformed to. An average laboratory temperature (T) of 25-27°C and Relative Humidity (RH) of 60 ± 5% was maintained through the testing period.

**Table 2.** Constituent mix of OPC and PKIA concrete

Material (kg/m <sup>3</sup> )	OPC	PKIA	Coarse Aggregate	Fine Aggregate	Water
<b>OPC Concrete</b>	420	-	1020	610	200
<b>PKIA Concrete</b>	210	210	1020	610	200

## 2. Test approach

The strength tests carried out in this study involved the determination of the splitting tensile and compressive strength tests over hydration periods of 7, 14 and 28days in accordance to BS 1881: Part 116 [11] and part 117 [12] respectively. The shrinkage of concrete in this study was measured using the cylindrical specimens after the initial 7days curing by submergence in water although, there are several other methods by which concrete shrinkage is measured based on sample sizes. Three specimens for each concrete mix were cast such that an average was taken to ensure consistency in results while the shrinkage strains were measured on four vertical gauge lines by flexible mechanical strain gauges spaced uniformly around the edge of the specimens and having a gauge length of 150mm. Readings from the strain gauge were recorded daily over a duration of 7days and once weekly afterwards.

## 3. Discussion of results

### 3.1. Tensile strength

The tensile strength of concrete was determined over the 7, 14 and 28days hydration periods. The conventional concrete is generally known to be weak in tension however; the study found the need to compare the tensile strengths of normal OPC concrete to that of PKIA concrete. A similar trend was observed for tensile strength development in both OPC normal concrete and the PKIA concrete as shown in Figure 7. The tensile strengths of OPC normal concrete were found to be 2.61, 2.77 and 3.34N/mm<sup>2</sup> which were higher than the PKIA concrete with values of 2.36, 2.43 and 2.98N/mm<sup>2</sup> over the different hydration periods respectively. Nevertheless, the general rate of early age strength gain was observed to be slow notwithstanding, there was increased strength development at later hydration periods.



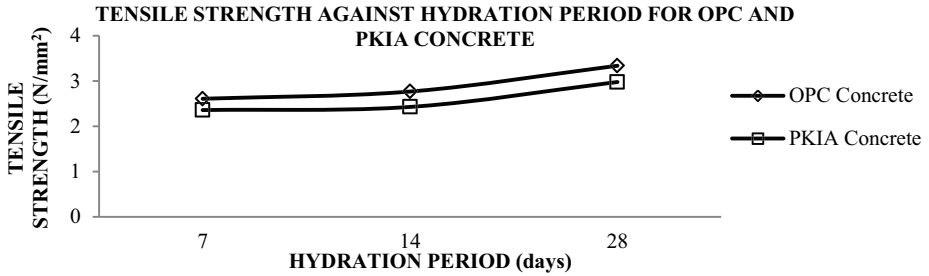


Figure 7. Tensile strength comparison between OPC and PKIA concrete

3.2. Effect of PKIA fineness on compressive strength of concrete

As in the case of conventional cement, the fineness of waste ash has been recorded to influence concrete strength development. Hence, this work investigated three different PKIA size fractions to determine their respective effects on compressive strength of concrete specimens crushed after 28days hydration period by complete submergence in water. From Figure 8, it can be seen that at 28days the concrete made with raw coarse PKIA had a strength of 17.9N/mm<sup>2</sup> whereas concrete made with fine ash (passing 45µm) had almost twice the strength i.e. 31.7 N/mm<sup>2</sup> over the same hydration period. This is a clear indication that the higher the PKIA fineness, the higher the strength expectancy. It is generally understood that hydration starts at the surface of the particles, and it is the total surface area that represent the material available for hydration. The higher development of strength in concrete with the fine PKIA was therefore due to a higher surface area of the particles in reaction which enhanced the pozzolanic activity thereby, leading to a strength increase.

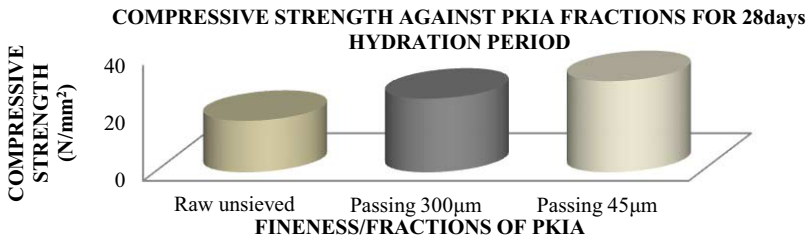


Figure 8. Effect of PKIA size fractions/fineness on compressive strength of concrete

3.3. Effect of hydration schedules on compressive strength of PKIA concrete

Results for the relative strength development of PKIA concrete based on the three different curing schedules is shown in Figure 9. Although the tests in this study was short-termed it however, clearly revealed differences in the curing sensitivity of concrete specimens. The strength values attained over the 7days water, water+air and air curing schedules had strengths of 23.5N/mm<sup>2</sup>, 21.7N/mm<sup>2</sup> and 19.2N/mm<sup>2</sup> respectively; the continuous curing in water had the highest strength whereas, the air cured specimens attained the lowest strength. After the 28days of hydration for the respective curing schedules, a more definite trend in the compressive strength

development was observed such that; the compressive strength of water cured PKIA concrete attained a strength value of  $31.7\text{N/mm}^2$ .

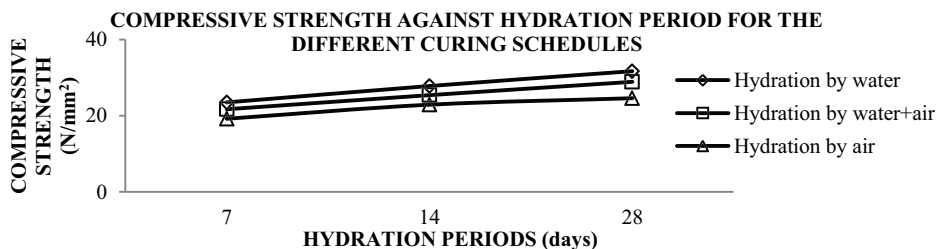


Figure 9. Effect of hydration schedule on the compressive strength of PKIA concrete

The samples cured for 7 days in water and subsequently in air attained a strength value of  $28.9\text{N/mm}^2$  while a lowest value of  $24.6\text{N/mm}^2$  was recorded for samples cured in air alone. The lower strength from air curing alone can be accounted for since hydration of cement and pozzolanic concretes takes place in water filled capillaries and the RH in the laboratory could not offer sufficient moisture to enhance the pozzolanic reaction. It is therefore, due to this reason as reported by [13] that the strength development of concrete containing pozzolans is affected by short hydration periods when submerged in water as compared to OPC since pozzolans continually require moisture for strength development. Hence, the observations herein are concurrent with findings on other pozzolanic materials as reported by [14].

### 3.4. Effect of HC superplasticizer on compressive strength of PKIA concrete

The concrete specimens were prepared containing superplasticizer added at the rate of 1% by mass of total binder content. The resultant product was compared to the samples without admixture as well as with OPC concrete (control sample). Figure 10 shows the respective strength behaviours of OPC concrete, PKIA concrete with and without the hydroxylated carboxylic superplasticizer.

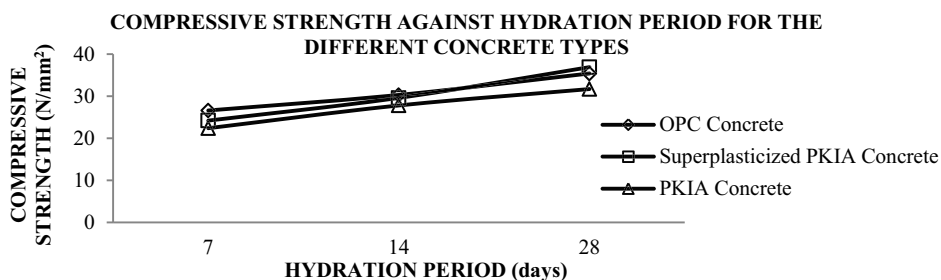


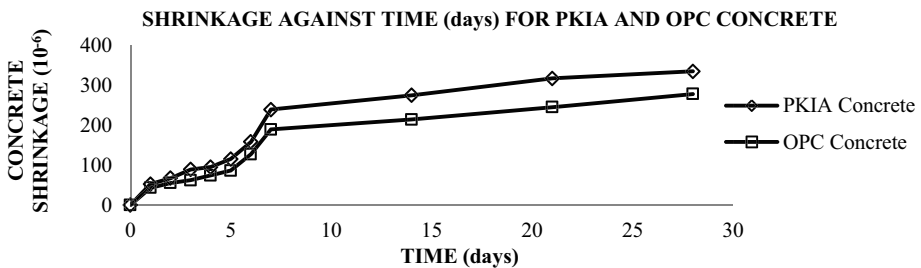
Figure 10. Effect of superplasticizer on the compressive strength development of PKIA concrete

From the comparison, it was evident that over the various hydration periods the superplasticizer had a positive effect on compressive strength development of PKIA concrete. A significant difference in the development of strength was noticed at later ages of curing however, the recorded difference in the rate of early age strength development was low. The measured compressive strength of PKIA concrete without the admixture at age 7, 14 and 28 days were  $22.4$ ,  $27.8$ , and  $31.7\text{N/mm}^2$  while

corresponding values for the samples with superplasticizer were measured at 24.2, 29.6 and 36.9N/mm<sup>2</sup> respectively. Close values of 35.4 and 36.9N/mm<sup>2</sup> at 28days of hydration were measured for OPC concrete and the superplasticized PKIA concrete respectively. The pozzolanic reaction plus the reduced water content effect triggered by the hydroxylated carboxylic superplasticizer in the PKIA concrete mix explains the higher strength development over the PKIA concrete mix without superplasticizer. Similar observations in RHA, SF and FA concretes by [13,15,16] have been recorded such that; the use of superplasticizer is vital in concrete possessing high proportions of pozzolans.

### 3.5. Concrete shrinkage

The concrete shrinkage test carried out was recorded over a 28days period and the measured values are expressed in Figure 11. The test results show the shrinkage strain of PKIA to be higher than that of OPC normal concrete. The magnitude of shrinkage of PKIA concrete was gotten as  $335 \times 10^{-6}$  while that of OPC concrete was gotten to be  $278 \times 10^{-6}$  with a difference of about 20.5% lower than the shrinkage value measured for the PKIA concrete. Findings close to the one herein were reported by [17] who recorded 40% palm oil fuel as (POFA) to exhibit higher shrinkage values in drying condition.



**Figure 11.** Shrinkage for PKIA and OPC concrete measured daily for 7days and weekly till 28days

The reason for a higher value according to [17] was due to the differences in the rate of moisture diffusion caused by the different porosity and pore size distribution. Observations made by [18] confirms the findings in this study such that [18] demonstrated that a constant water-cement ratio for high proportion of FA concrete resulted in a 20% higher shrinkage magnitude when compared to normal OPC concrete.

### 3.6. Concrete shrinkage prediction

The time dependent predictions of shrinkage strain development in concrete have been expressed by different equations amongst which, the equation generated by ACI 209R-92 [19] is mostly considered where structural or non-structural emphases are required. Although the equation is used to estimate ultimate shrinkage of wide ranges of water cured concretes, the prediction of concrete shrinkage using this equation is subjected to significant changes. An improvement in the accuracy of prediction of shrinkage was therefore made by [20] where long-term shrinkage values can be obtained by extrapolating the short-term 28day tests period. Eq. (1) was therefore applied to predict one-year shrinkage of PKIA and OPC concrete.

$$S_h(t, \tau_0) = S_{h,28} + 100[3.61 \log_e(t - \tau_0) - 12.05]^{1/2} \quad (1)$$

Where;  $S_h(t, \tau_0)$  = long-term concrete shrinkage ( $10^{-6}$ ) at an age  $t$ , after dried at age  $\tau_0$

$S_{h,28}$  = shrinkage ( $10^{-6}$ ) after 28days

$(t - \tau_0)$  = time difference since the start of drying must be greater than 28days (>28days)

Thus, the one-year values computed from the concrete shrinkage prediction using Eq. (1) are:

$S_{h,365}$  for PKIA concrete =  $633 \times 10^{-6}$ ,

$S_{h,365}$  for OPC concrete =  $576 \times 10^{-6}$

The predicted magnitude of shrinkage for PKIA concrete was computed as  $633 \times 10^{-6}$  while that of OPC concrete was computed as  $576 \times 10^{-6}$  with a difference of about 9.9% lesser than the predicted shrinkage value for the PKIA concrete over a one-year period.

#### 4. Conclusions

This study investigated the strength and shrinkage behaviours of concrete made by replacing 50% by mass of OPC with PKIA. The availability of PKIA generated by the processing of palm oil from milling boilers in West Africa paved way for the study of PKIA as a constituent in low cost concrete production. From results and analysis presented, the following conclusions were drawn;

- That the finer the ash, the higher the compressive strength of concrete due to the high surface area of the particles enhancing pozzolanic activity.
- The tensile and compressive strength of the 50%PKIA concrete were found to be lower than those of normal concrete. However, on the addition of superplasticizer, a significant improvement in compressive strength development due to the reduced water content triggered by the hydroxylated carboxylic superplasticizer in the PKIA concrete mix was recorded.
- The curing of PKIA concrete in water had a positive effect on the strength; the water curing schedule revealed the best result when compared to water+air and air alone.
- The shrinkage strain development values of PKIA concrete were higher than the values obtained for OPC concrete. However, from the extrapolated short-term test values a long-term concrete shrinkage effect was predicted.
- This paper finally demonstrated the use of PKIA as an option in transforming cheap and abundantly available agricultural waste into a useful end product which can be utilized in developing countries. As such, the green concrete product can be used in the construction of simple foundations and masonry walls with less structural complexities while further investigations are recommended to be carried out on the effect of prolonged curing of up to 120days on the concrete durability.

## References

- [1] Tay, J. H., Ash from oil-palm waste as concrete material, *Journal of Materials in Civil Engineering*, Vol. 2, No. 2, 1990, pp. 94-105.
- [2] Nimityongskul, P. and Daladar, T.U., Use of coconut husk, corn cob and peanut shell as cement replacement, *Proceedings of the International Symposium on Urban Housing Issues on Environment and Technology*, Asian Institute of Technology, Thailand, 1993, pp.353-362.
- [3] Salihuddin, R. S., Relationships between Engineering Properties and Microstructural Characteristics of Mortar Containing Agricultural Ash, *Ph.D. Thesis, Universiti Teknologi Malaysia*, 1993.
- [4] Rashid, M. and Rozainee, M., Particulate emissions from a palm oil mill plant—a case study, *Journal Teknologi*, Universiti Teknologi Malaysia, Vol. 22, December, 1993, pp.19-24.
- [5] Elinwa, A.U. and Mahmood, Y.A., Ash from Timber Waste as Cement Replacement Material, *Cement and Concrete Composites*, V. 24, No. 2, 2002, pp. 219-222.
- [6] Awal, A.S.M.A. and Hussin, M.W., Some aspects of durability performances of concrete incorporating palm oil fuel ash, *Proceedings of the 5th International Conference on Structural Failure, Durability and Retrofitting*, Singapore, Nov. 1997, pp.210-218.
- [7] American Society for Testing and Materials, Standard Specification for Fly Ash and Raw or Calcined Natural pozzolan for Use as a Mineral Admixture in Portland Cement Concrete, *Annual Book of ASTM Standards, ASTM C618-94a*, 1994.
- [8] British Standards Institution, *Methods for Determination of Physical Properties*, BS 12: Part 2:1975.
- [9] Teychenné, D C, Franklin, R E and Erntroy, H C. Design of normal concrete mixes. Department of the Environment. HMSO, 1997, Report 331, ISBN 9781860811722
- [10] British Standards Institution, *Method for Making Test Cylinders from Fresh Concrete*, BS 1881: Part 110: 1983.
- [11] British Standards Institution, *Method for Determination of Tensile Splitting Strength*, BS 1881: Part 117: 1983.
- [12] British Standards Institution, *Method for Determination of Compressive Strength of Concrete Cubes*, BS 1881: Part 116: 1983.
- [13] Neville, A.M., *Properties of Concrete*, Fourth Edition, Longman Group UK Ltd, 1995.
- [14] Malhotra, V.M., Carrette, G.G. and Sivasundaram, V., Role of silica fume in concrete: a review, *Advances in Concrete Technology, CANMET*, Ottawa, 1994, pp.925-991.
- [15] Sirivatnanon, V., Cao, H.T., Khatri, R.P. and Bucea, L., *Guidelines for Use of High Volume Fly Ash Concretes, Technical Report 7R95/2*, Division of Building, Construction and Engineering, CSIRO Australia, 1995.
- [16] Habeeb, G.A. and Mahmud, H.B., Experimental investigation on the mechanical properties of Grade 40 concrete incorporating rice husk ash (RHA), *Proceedings of the 7th Asia Pacific Structural Engineering and Construction Conference and 2nd European Asian Civil Engineering Forum*, Vol.2, August 2009, pp. 678-682.
- [17] Ishida, T., Creep and Shrinkage of Palm Oil Fuel Ash Concrete, *M. Eng. Thesis, Universiti Teknologi Malaysia*, 1999.
- [18] Brooks, J.J. and Neville, A.M., Creep and shrinkage of concrete as affected by admixtures and cement replacement materials, *Creep and Shrinkage of Concrete: Effect of Materials and Environment, ACI Publication SP-135*, 1992, pp. 19-36.
- [19] American Concrete Institute, Prediction of Creep, Shrinkage and Temperature Effects in Concrete Structures, *ACI Manual of Concrete Practice*, Part 1: Materials and General Properties of Concrete, ACI 209R-92, 1994.
- [20] Neville, A.M. and Brooks, J.J., *Concrete Technology*, Longman Group UK Ltd, 1987.

# Ultrasonic pulse velocity used to predict the compressive strength of structural sand lightweight concrete

J. Alexandre BOGAS<sup>1</sup>, M. Glória GOMES, Sofia REAL and Jorge PONTES  
*DECivil/ICIST, Instituto Superior Técnico,  
Technical University of Lisbon, Av. Rovisco Pais, 1049-001 Lisbon, Portugal*

**Abstract.** This paper aims at evaluating the compressive strength of structural sand lightweight aggregate concrete (LWC) by the non-destructive ultrasonic pulse velocity method. To this end, a comprehensive experimental study was carried out involving more than 70 different compositions tested between 3 and 180 days with mean compressive strengths ranging from about 30 to 80 MPa and density classes from D1.6 to D2.0. The influence of several factors on the relation between the ultrasonic pulse velocity (UPV) and compressive strength was examined, including the type and binder content, type and volume of aggregates. It is found that lightweight and normal weight concretes (NWC) are affected differently by mix design parameters. NWC is more affected by the volume of aggregate and the dispersion effect caused by concrete heterogeneity tends to be lower in LWC. The prediction of the concrete's compressive strength by means of the non-destructive UPV test is analysed. Based on the dependence of the UPV on the density and elasticity of concrete, a simplified expression is proposed to estimate the compressive strength, regardless of the type of concrete and its composition. High correlation coefficients were obtained taking into account several results for different types of aggregates and concrete compositions.

**Keywords.** Sand lightweight concrete, non-destructive method, ultrasonic pulse velocity, compressive strength prediction

## Introduction

Old lightweight concrete structures that have been built since the 50s, especially in North America and Europe, now represent a major issue in terms of maintenance and rehabilitation. Non-destructive ultrasound pulse velocity tests have proved to be helpful in the inspection of old structures. However, the experience acquired in this field and the correlations that have been built between the quality of concrete and its UPV are essentially limited to normal weight concrete (NWC) [1-3].

Based on the theory of elasticity applied to homogeneous and isotropic materials, the pulse velocity of compressional waves (P-waves) is directly proportional to the square root of the dynamic modulus of elasticity,  $E_d$ , and inversely proportional to the square root of its density,  $\rho$ , according to Eq. 1 [3, 4].  $\nu_d$  is the dynamic Poisson's ratio.

<sup>1</sup>Corresponding author: [abogas@civil.ist.utl.pt](mailto:abogas@civil.ist.utl.pt)

$$UPV = \sqrt{\frac{E_d}{\rho} \cdot \frac{(1-\nu_d)}{(1+\nu_d)(1-2\nu_d)}} \quad (1)$$

According to Eq. 1, the relevant physical properties of materials that influence pulse velocity are the density, elastic modulus and  $\nu_d$ . Thus, EN 1992-1-1 [5] suggests the expression Eq. 2 to relate the modulus elasticity of concrete,  $E_c$  and the compressive strength of concrete,  $f_c$ , where  $\rho$  is the oven-dry density.

$$E_c \approx 22 \cdot \left(\frac{f_c}{10}\right)^{0.3} \cdot \left(\frac{\rho}{2200}\right)^2 \text{ [GPa]} \quad (2)$$

However, the relation between UPV and  $f_c$  is not unique and can be affected by factors such as the type and size of aggregate, physical properties of the cement paste, curing conditions, mixture composition, concrete age and moisture content [4, 6-11]. Thus, although in situ estimation of  $f_c$  from UPV is covered in EN 13791 [12], there is no standard correlation between these properties. Nonetheless, several relationships between UPV and  $f_c$  have been proposed, especially for NWC [1, 2, 7, 9, 13].

Most investigations have focused on NWC behaviour. Published studies involving LWC are still limited. Nasser and Al-Manaseer [14] reported expressions of the type  $f_c = a \cdot UPV^b$  for NWC and LWC produced with expanded clay aggregates. Chang et al. [15] established exponential relationships between UPV and  $f_c$  for LWC with two types of lightweight aggregates (LWA). Hamidian, et al [16] found poor correlations when several LWC mixes were analyzed together.

This study investigates the use of the non-destructive ultrasonic pulse velocity method to assess the compressive strength of LWC produced with different types of expanded clay aggregates. Based on the dependence of UPV on density and elasticity (Eq. 1) and taking into account the empirical relationship between  $f_c$  and  $E_c$  (Eq. 2), a general simplified expression is proposed and assessed that relates  $f_c$  and UPV, irrespective of the type of concrete, mixture composition and test age.

## 1. Experimental program

### 1.1. Materials

Three Iberian expanded clay lightweight aggregates were analyzed: Leca and Argex from Portugal and Arlita from Spain (Table 1). A more detailed microstructural characterization of these aggregates is found elsewhere [17-19].

For the reference NWC, two crushed limestone aggregates of different sizes were combined so as to have the same grading curve as Leca (20% fine and 80% coarse gravel). Fine aggregates consisted of 2/3 coarse and 1/3 fine sand. Their main properties are listed in Table 1. The two fractions of Argex were also combined to have the same grading curve as Leca (35% 2-4 and 65% 3-8F, Table 1). Cement type I 52.5 R, I 42.5 R, II-A/L 42.5, II-A/D 42.5 (8% of silica fume (SF) by weight), II-A/V 42.5 (20% of fly ash (FA) by weight) and IV-A 42.5 (8% SF and 20% FA) according to EN 197-1 [20], were considered. For low w/b ratios, a polycarboxylate based

superplasticizer (SP) was used. A water dispersed RHEOMAC VMA 350 nanosilica (NS) with an average density of 1.1 and about 16.1% solids content was also tested.

**Table 1.** Aggregate properties

Property	Normal weight aggregates				Lightweight aggregates				
	Fine sand	Coarse sand	Fine gravel	Coarse gravel	Leca 0-3	Leca 4-12	Argex 2-4	Argex 3-8F	Arlita AF7
Particle dry density, $\rho_p$ (kg/m <sup>3</sup> )	2620	2610	2631	2612	1060	1068	865	705	1290
Loose bulk density, $\rho_b$ (kg/m <sup>3</sup> )	1416	1530	1343	1377	562	613	423	397	738
24h water absorpt., $w_{abs,24h}$ (%)	0.2	0.5	1.4	1.1	-	12.3	22.9	23.3	12.1
Granulometric fraction ( $d_i/D_i$ )	0/2	0/4	4/6.3	6.3/12.5	0.5/3	4/11.2	4/8	6.3/12.5	3/10
Los Angeles coefficient (%)	-	-	33.3	30.5	-	-	-	-	-

### 1.2. Concrete mixing and compositions

Based on an extensive study of the durability and mechanical characterization of LWC produced with different types of aggregates that was conducted at the Instituto Superior Técnico [17], the UPV of about 74 different compositions were measured. The compositions varied in terms of type and volume of aggregate (150 to 450 L/m<sup>3</sup>), different effective water/binder (w/b) ratios (0.3 to 0.65), types and amounts of cement (300 to 525 kg/m<sup>3</sup>), types and volumes of mineral admixtures (22 and 40% of FA, 8% of SF, 1.3% of NS) and also the partial replacement of natural sand by the lightweight sand (Leca 0-3) indicated in Table 1 (lightweight sand concrete - LWSC).

The concretes were produced in a vertical shaft mixer. The LWA was pre-soaked for 24h to better control the workability and effective water content of the concrete. The main characteristics of each composition are summarized in Table A.1 in appendix. All these mixtures are listed in detail elsewhere [17, 21]. The denominations 'NA', 'L', 'A' and 'Argex' correspond to the mixes with normal weight aggregate (NA), Leca, Arlita and Argex. The compositions were basically variations of a reference mixture with 450 kg/m<sup>3</sup> of binder, w/b ratio of 0.35 and 350 L/m<sup>3</sup> of coarse aggregate.

### 1.3. Specimen preparation and test setup

For each mix at each age, three 150 mm cubic specimens were tested for ultrasonic pulse velocity and then for compressive strength according to EN 12390-3 [22]. After demolding at 24 h, specimens were kept in water until testing.

The ultrasonic pulse velocity was obtained by direct transmission according to EN 12504-4 [11]. The equipment used was the *portable ultrasonic non-destructive digital indicating tester* (PUNDIT), shown in Figure 1 [4]. The time taken by a pulse to travel through the concrete,  $t_{us}$ , is measured with accuracy up to 0.1  $\mu$ s by a receiver transducer on the opposite side. The 54 kHz transducers were positioned in the middle of each opposing face, orthogonal to the direction of concreting. Finally, UPV is the ratio between the length traveled by the pulse (150 mm) and the measured time,  $t_{us}$ .

For all mixes ultrasonic pulse velocity was measured at 28 days. Tests were also performed at 1, 3, 7, 90 and 180 days on certain selected mixtures (Table A.1).



2. Test results and discussion

Figure 2 summarizes the mean values of  $UPV$  and  $f_c$  obtained for each mixture, between 3 and 90 days (about 200 results, ranging from about 30-80 MPa and  $UPV$  from 3.5- 5.2 km/s). As expected, when different compositions, types of aggregate and test ages are considered simultaneously there is a poor correlation between  $UPV$  and  $f_c$ .

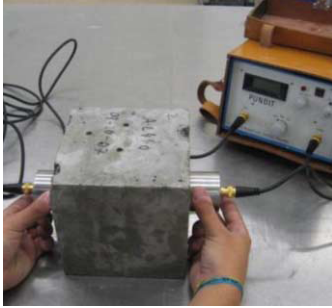


Figure 1. Scheme of the ultrasonic pulse velocity measurement in concrete.

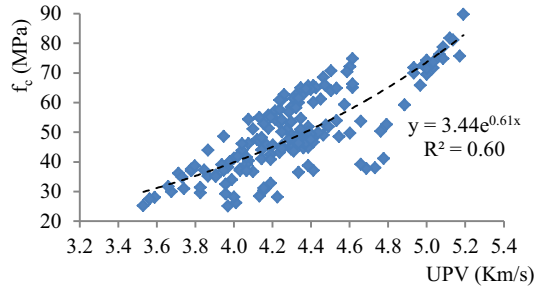


Figure 2.  $UPV$  versus  $f_c$  for different concrete compositions and different types of aggregate at ages between 3 and 90 days.

2.1. Influence of type of aggregate

When the mixtures with different types of aggregate are analyzed separately, there is a natural increase of the correlation coefficient (Figure 3). For similar values of  $UPV$ , the strength is higher in LWC of higher density. Conversely, the lower the density of the LWA the higher the  $UPV$  for a given compressive strength.

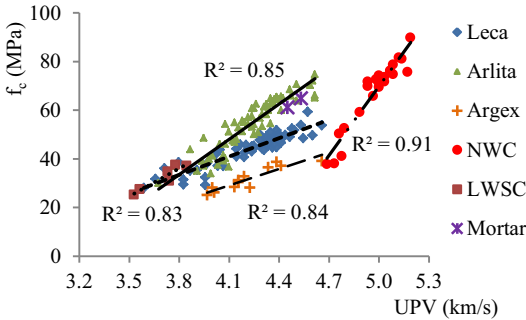


Figure 3.  $UPV$  versus  $f_c$  for each type of aggregate, considering different compositions at ages between 3 and 90 days.

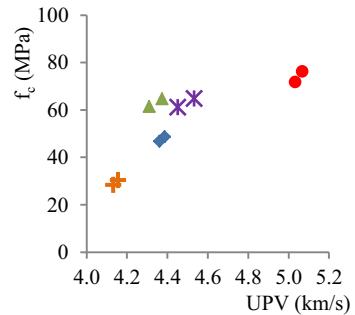


Figure 4.  $UPV$  versus  $f_c$  in reference concrete and in the respective mortar of equivalent composition at 7 and 28 days (same sand/cement ratio, w/b ratio of 0.35 and 350 L/m<sup>3</sup> of coarse aggregate).

This trend is likely to be primarily related to the: lower increment of  $UPV$  in relation to  $f_c$ , for higher strength levels; simultaneous reduction of density and stiffness in LWC, which means a smaller variation of  $UPV$  (Eq. 1); slight variation of  $f_c$  for LWC with rich mortars and more porous aggregates; higher compacity of richer mortars in more porous LWC of the same strength; small differences between the

ultrasonic pulse velocities of lightweight aggregates,  $UPV_{ag}$ ; higher water content in LWC with lower density aggregates.

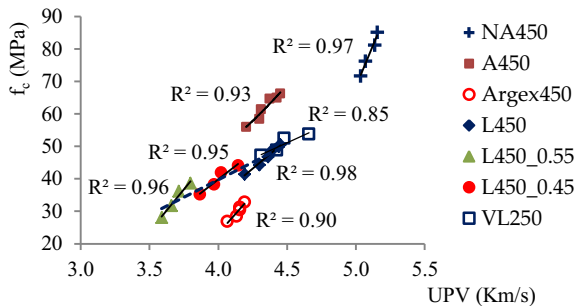
In Figure 4, the  $UPV$  in reference mixes with a w/b ratio of 0.35 is compared with that obtained for a mortar with an equivalent composition (Mortar\_0.35, Table A.1). The absence of coarse aggregates leads to a reduction of  $UPV$  in NWC and the opposite effect in LWC. The difference is higher in NWC, which means the aggregate and its volume has greater influence on this type of concrete.

On the other hand, since the NWC strength is essentially controlled by the mortar, the  $UPV$  decreases with the decrease in the volume of aggregate without a significant variation of  $f_c$ , i.e., the  $UPV$ - $f_c$  relation strongly depends on the aggregate proportion in the mix. Thus, a new correlation between  $f_c$  and  $UPV$  in NWC has to be defined for a given volume of NA. The same is concluded by Lin, et al. [8] and Popovics, et al [6].

LWC behaves differently. The strength is also affected by LWA, and hence both  $UPV$  and  $f_c$  decrease as the volume of aggregate increases. Therefore, one would expect the relation between  $UPV$  and  $f_c$  to be less affected. However, although  $UPV$  varies in the same direction as  $f_c$ , they may progress differently. Since the  $UPV$  in LWA and in mortar are similar, the variation of  $f_c$  can be higher than that of  $UPV$ . Moreover, the compressive strength of LWC is affected by the strength level, whereas  $UPV$  is not. That is why the regression curves of Figure 3, for different types of LWA, diverge from each other with the increment of  $f_c$ . As expected,  $UPV$  and  $f_c$  decrease with the partial replacement of natural sand by lightweight sand.

### 2.2. Influence of concrete age

As expected,  $UPV$  and  $f_c$  increase with curing time [7, 23]. In fact, the greater the paste hydration the lower the volume of pores and the greater the  $UPV$  [23]. The concrete strength tends to increase faster than  $UPV$ , especially in NWC, where  $f_c$  is not limited by the aggregate strength (Figure 5, Table A.1). The same is reported in [8, 15, 13]. The  $f_c$  trend in LWC is less steep and hence less sensitive to small changes in  $UPV$ .



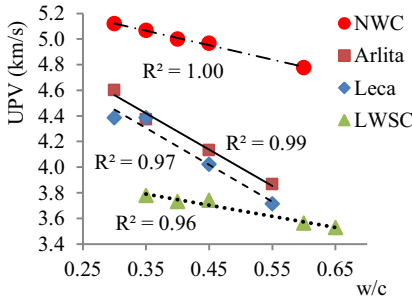
**Figure 5.**  $UPV$  versus  $f_c$  at different ages (between 1 and 180 days) for different w/b ratios (0.35, 0.45, 0.55), types and volumes of aggregate (250 and 350 L/m<sup>3</sup>).

Strong correlations are obtained when each concrete composition is individually assessed. However, the correlation decreases when different compositions are analyzed together. For example, there is a greater dispersion when different w/b ratios are considered in LWC with Leca (dashed line in Figure 5). In fact, whereas  $UPV$  tends to increase faster with age than  $f_c$ ,  $f_c$  increases more with the w/c ratio than  $UPV$  does.

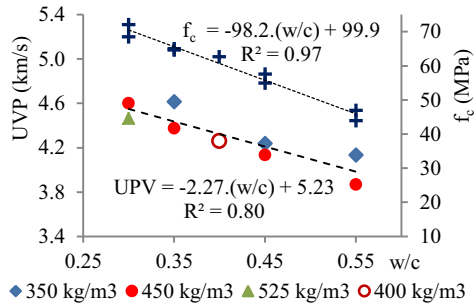
2.3. Influence of the w/c ratio

In Figure 6 mixes with the same volume of coarse aggregate and the same type and cement content were considered in LWC with Leca or Arlita. Different w/c ratios were obtained by varying the amount of water and the respective volume of sand. Mixes with the same volume of water and coarse aggregate were considered in NWC, where different w/c ratios were obtained by varying the amount of cement and the respective volume of sand. This is why the *UPV* trend with the w/c ratio is less pronounced in NWC (the higher w/c ratio is partially offset by the greater volume of sand).

When the regression analysis takes different water and cement contents into account at the same time, there is a reduction of the correlation coefficient (Figure 7). As shown in Figure 7,  $f_c$  tends to be less affected by different amounts of water, sand and cement than *UPV*, for a given w/c ratio. Therefore, the relation between *UPV* and  $f_c$  also depends on how the w/c ratio is changed. Furthermore, moisture content helps the *UPV* propagation in concrete [17, 24] but may affect  $f_c$  negatively.



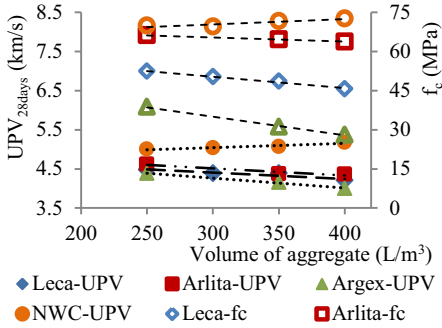
**Figure 6.** *UPV* versus the w/c ratio for different types of aggregate at 28 days (w/c by varying the amount of water – LWC with Leca or Arlita; w/c by varying the cement content – NWC).



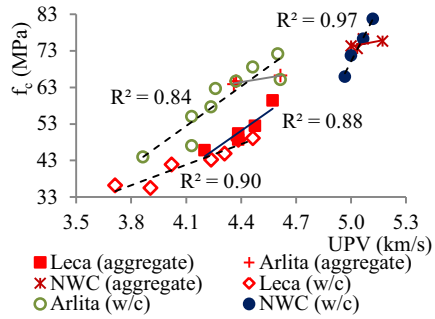
**Figure 7.**  $f_c$  and *UPV* versus the w/c ratio for LWC with Arlita and different water and cement contents at 28 days (CEM I 52,5).

2.4. Influence of the volume of aggregate

For LWC,  $f_c$  and *UPV* decrease as the volume of LWA increases (Figure 8). But *UPV* increases with the volume of aggregate in NWC. The  $f_c$  also increases, albeit only slightly, with the volume of NA. An opposite trend is reported by other authors [8, 10], which may explain the better correlation obtained in this work for NWC (Figure 3).



**Figure 8.** UPV and  $f_c$  for different volumes of aggregate at 28 days.

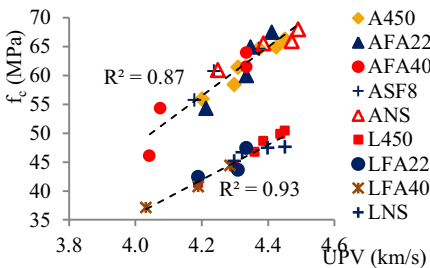


**Figure 9.** UPV versus  $f_c$  for different w/c ratios (0.3, 0.35, 0.4, 0.45, 0.55) and volumes of aggregate (150, 250, 300, 350, 400 L/m³) at 28 days.

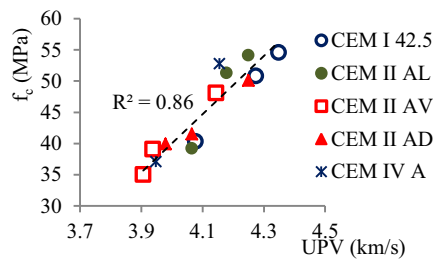
As expected, differences are higher when different w/c ratios and volumes of aggregate are considered at the same time (Figure 9). Since the compressive strength of LWC is also affected by the aggregate, the variation of  $f_c$  with w/c is lower in LWC with Leca than in NWC and LWC of higher density. Moreover, the strength of LWC is more affected by the volume of aggregate than that of NWC. Therefore, there is a greater interdependence between UPV and  $f_c$  in LWC than in NWC. However, when LWC reaches its ceiling strength the behavior may change. After a given strength level a further increase of  $f_c$  is not meaningful, contrary to what happens with UPV.

### 2.5. Influence of the type of binder

There is a high correlation between UPV and  $f_c$  regardless of the type of cement or mineral admixture (Figures 10 and 11). It is thus shown that when a given type of binder is used without interfering with the other constituents of concrete, there appears to be little effect on the relationship between  $f_c$  and UPV. The densification of the porous structure was not detected in LWC with silica fume or nanosilica, which was less efficient than expected. It is likely that there was no effective dispersion of such admixtures. Moreover, the strength limitation imposed by LWA and the better quality of the aggregate-paste transition zone in LWC also play a part in the lower efficiency of SF and NS. It is also shown that the replacement of cement by fly ash leads to less dense microstructures at early ages. However, this recovers over time (Table A.1).



**Figure 10.** Relationship between UPV and  $f_c$  for LWC produced with different types of admixtures and tested at different ages (7 to 180 days).



**Figure 11.** Relation between UPV and  $f_c$  for LWC with Arlita and different types of cement and w/b ratio (28 days).

2.6. Suggested expression to estimate LWC compressive strength from UPV

Taking into account Eq. 1, which relates  $UPV$  to  $E_d$  and  $\rho$ , and the expression suggested by EN1992-1-1 [5] that relates  $E_c$  with  $f_c$  and  $\rho$  (Eq. 2), the equation Eq. 8 can be obtained. The parameters A, B and  $K_{UPV}$  are constants. The reasonable accuracy of Eq. 2 applied to LWC is demonstrated in [17, 25, 26]. The application of Eq. 8 leads to a significant improvement of the correlation coefficient, even taking different compositions into account (Figure 12). Wet density at 28 days was assumed, but better correlations should be obtained for dry densities. The correlation is determined by forcing the regression line to cross the origin. Although better correlations can be obtained without this condition, the physical meaning is distorted.

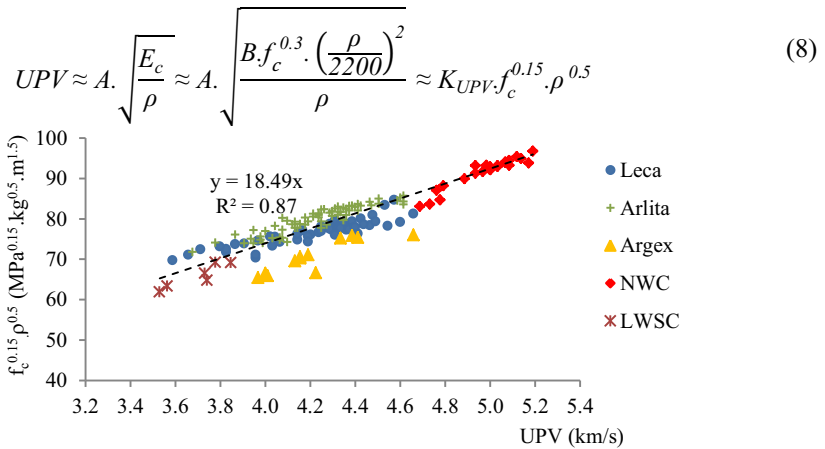


Figure 12. UPV as a function of  $f_c$  and  $\rho$  for different concrete compositions at ages between 3 and 90 days.

The approximation for LWC with more porous aggregates (Argex) is poorer. This is probably because these concretes work near their ceiling strength. For that reason, the correlation coefficient indicated in Figure 12 (0.87) only takes into account the LWA with density above  $1000 \text{ kg/m}^3$ . Therefore, expressions similar to Eq. 9 allow a better estimation of  $f_c$  from  $UPV$  and are practically independent of the type of concrete. In Eq. 9,  $UPV$  is in  $\text{m/s}$  and  $\rho$  in  $\text{kg/m}^3$ . According to the regression analysis, the  $K_{UPV}$  is 54.6 or 54.3  $\text{m}^{2.5} \cdot \text{MPa}^{-0.15} \cdot \text{kg}^{-0.5} \cdot \text{s}^{-1}$ , depending on whether Argex is included or not.

$$f_c \approx \left( \frac{UPV}{K_{UPV} \cdot \rho^{0.5}} \right)^{0.15} \text{ [MPa]} \tag{9}$$

3. Conclusions

The compressive strength of LWC was estimated by the non-destructive  $UPV$  method. Based on a comprehensive experimental investigation the main conclusions are:

- Calibrating curves for each type of concrete with a given type of aggregate must be previously established when  $f_c$  is to be directly estimated from  $UPV$ .

- LWCs with less porous aggregates are associated with lower ultrasonic pulse velocity for a given  $f_c$  and higher  $f_c$  for a given  $UPV$ .
- The relationship between  $UPV$  and  $f_c$  tends to be less affected by the aggregate volume in LWC than in NWC. However, in LWC with more porous aggregates and rich mortars there is a greater relative variation of  $UPV$  than  $f_c$ .
- In LWC,  $f_c$  is little affected by the changes in w/c ratio, unlike  $UPV$ , which also depends on the proportion of mortar constituents.
- The  $UPV$  versus  $f_c$  relation was little affected by different types of binder.
- A new simplified expression was defined that allows a more accurate estimate of  $f_c$  from  $UPV$ , regardless of the type of concrete and its composition.

## Acknowledgements

The research work presented herein was supported by the Portuguese Foundation for Science and Technology (FCT), under grant PTDC/ECM-COM1734/2012. The authors also wish to thank ICIST-IST for funding the research and the *Argex, Saint-Gobain Weber Portugal, BASF* and *SECIL* for supplying the materials used in the experiments.

## References

- [1] R. S. Ravindrarajah, Strength evaluation of high-strength concrete by ultrasonic pulse velocity method, *NDT and E Int.* 30 (4), (1997), 262-262.
- [2] W. F. Price, J. P. Haynes, In situ strength testing of high strength concrete, *Mag. Concr. Res.* 48 (176), (1996), 189-197.
- [3] S. Nazarian, M. Baker, K. Crain, Assessing quality of concrete with wave propagation techniques, *ACI Mater. J.* 94-M35 (1997), 296-305.
- [4] Pundit, *Pundit manual for use with the portable ultrasonic non-destructive digital indicating tester*, C.N.S. Electronics LTD, 1991.
- [5] EN 1992, Eurocode 2: *Design of concrete structures - Part 1-1: General rules and rules for buildings*, European Committee for standardization CEN, 2004.
- [6] S. Popovics, J. L. Rose, J. S. Popovics, The behavior of ultrasonic pulses in concrete, *Cement Concrete Res.* 20, (1990), 259-270.
- [7] K. K. Phoon, T. H. Wee, C. S. Loi, Development of statistical quality assurance criterion for concrete using ultrasonic pulse velocity method, *ACI Mater. J.* 96-M70 (1999), 568-573.
- [8] Y. Lin, S.-F. Kuo, C. Hsiao, C.-P. Lai, Investigation of pulse velocity-strength relationship of hardened concrete, *ACI Mat. Journal* 104-M38 (2007), 344-350.
- [9] A. E. Ben-Zeitun, Use of pulse velocity to predict compressive strength of concrete, *Int. J. Cem. Compos. Lightweight Concrete*, 8 (1), (1986), 51-59.
- [10] G. Trtnik, F. Kavcic, G. Turk, Prediction of concrete strength using ultrasonic pulse velocity and artificial neural networks, *Ultrasonics* 49 (2009), 53-60.
- [11] EN12504-4, *Testing concrete-Part 4: Determination of pulse velocity*, European Committee for Standardization CEN, 2004.
- [12] EN 13791, *assessment of in-situ compressive strength in structures and precast concrete components*. European Committee for Standardization CEN, 2007.
- [13] V. Sturup, F. Vecchio, H. Caratin, Pulse velocity as a measure of concrete compressive strength, *Situ/Nondestructive Testing of Concrete, ACI SP-82* (1984), 201-227.
- [14] K. W. Nasser, A. A. Al-Manaseer, Comparison of Nondestructive testers of hardened concrete, *ACI Mater. J.* 84-M38 (1987), 374-380.
- [15] T.-P. Chang, H.-C. Lin, W.-T. Chang, J.-F. Hsiao, Engineering properties of lightweight aggregate concrete assessed by stress wave propagation methods, *Cem. Concr. Compos.* 28 (1), (2006), 57-68.

- [16] M. Hamidian, M. Shariati, M. M. K. Arabnejad, H. Sinaei. Assessment of high strength and light weight aggregate concrete properties using ultrasonic pulse velocity technique. *International Journal Phys. Sci.* 6 (22), (2011), 5261-5266.
- [17] J. A. Bogas. Characterization of structural lightweight expanded clay aggregate concrete. PhD thesis in civil engineering, Technical University of Lisbon, Instituto Superior Técnico, Portugal, 2011.
- [18] J. A. Bogas, A. Mauricio, M. F. C. Pereira, Microstructural analysis of Iberian expanded clay aggregates, *Microsc. Microanal.* 18 (5), (2012), 1190-1208.
- [19] J. A. Bogas, A. Gomes, M. G. Gloria, Estimation of water absorbed by expanding clay aggregates during structural lightweight concrete production. *Mater. Struct.* 45 (10), (2012), 1565-1576.
- [20] EN 197-1, *Cement - Part 1: Composition, specifications and conformity criteria for common cements*. European Committee for Standardization CEN, 2011.
- [21] J. A. Bogas, A. Gomes. Compressive behavior and failure modes of structural lightweight aggregate concrete – Characterization and strength prediction. *Materials & Design* 46 (2013), 832-841.
- [22] EN 12390-3, *Testing hardened concrete - Part 3: Compressive strength of test specimens*, European Committee for Standardization CEN, 2009.
- [23] A. A. Ikpong, The relationship between the strength and non-destructive parameters of rice husk ash concrete, *Cement and Concrete Research* 23 (1993), 387-398.
- [24] E. Ohdaira, N. Masuzawa. Water content and its effect on ultrasound propagation in concrete – the possibility of NDE, *Ultrasonics* 38 (2000), 546– 552.
- [25] T. Faust, *The behaviour of structural LWC in compression*, Second International Symposium on structural lightweight aggregate concrete, 18-22 June. Kristiansand, Norway: Editors: S. Helland et al (2000), 512-521.
- [26] J. A. Bogas, A. Gomes. Static and dynamic modulus of elasticity of structural lightweight and modified density concrete with and without nanosilica – Characterization and normalization. *International Journal of Civil Engineering* (2014), accepted.

Appendix

Table A.1. Mix proportions, ultrasonic pulse velocity, compressive strength and wet density

Mixtures	w/b	c.a. <sup>a</sup> (L/m <sup>3</sup> )	binder (kg/m <sup>3</sup> )	f <sub>c,7days</sub> (MPa)	UPV <sub>7d</sub> (km/s)	f <sub>c,28days</sub> (MPa)	UPV <sub>28d</sub> (km/s)	f <sub>c,90days</sub> (MPa)	UPV <sub>90d</sub> (km/s)	ρ <sub>28days</sub> (kg/m <sup>3</sup> )
L350	0.45	350	350	-	-	43.1	4.2	44.4/45.1 <sup>b</sup>	4.2/4.3 <sup>b</sup>	1899
L394	0.4	350	394	-	-	44.9	4.3	46.4/46.3 <sup>b</sup>	4.4/4.4 <sup>b</sup>	1893
L450	0.35	350	450	46.7	4.4	48.6	4.4	49.8/50.4 <sup>b</sup>	4.4/4.5 <sup>b</sup>	1915
L525	0.3	350	525	-	-	50.0	4.3	51.0	4.3	1917
L350_0.55	0.55	350	350	31.4	3.8	35.5	3.9	37.0	4.1	1870
L350_0.35	0.35	350	350	44.8	4.4	49.1	4.5	48.5	4.5	1913
L450_0.55	0.55	350	450	31.7	3.7	36.1	3.7	38.6	3.8	1791
L450_0.45	0.45	350	450	38.2	4.0	41.9	4.0	44.1	4.1	1868
L450_0.30	0.3	350	450	49.3	4.4	51.8	4.4	51.8	4.5	1927
Leca										
VL150	0.35	150	450	53.9	4.5	59.3	4.6	-	-	2106
VL250	0.35	250	450	48.8	4.4	52.4	4.5	53.7	4.7	2000
VL300	0.35	300	450	47.4	4.3	50.3	4.4	49.7	4.6	1944
VL400	0.35	400	450	43.8	4.0	45.7	4.2	46.7	4.4	1839
L42,5IIAL	0.35	350	450	-	-	45.3	4.3	46.3	4.3	1913
LFA22	0.35	350	450(22%FA)	-	-	42.4	4.2	43.6/47.4 <sup>b</sup>	4.3/4.3 <sup>b</sup>	1862
LFA40	0.35	350	450(40%FA)	-	-	37.1	4.0	40.7/44.4 <sup>b</sup>	4.2/4.3 <sup>b</sup>	1820
LSF8	0.35	350	450(8%SF)	45.8	4.2	47.6	4.3	49.3/51 <sup>b</sup>	4.4/4.4 <sup>b</sup>	1888
LNS	0.35	350	450(13%NS)	45.1	4.3	46.7	4.3	47.5/47.6 <sup>b</sup>	4.4/4.5 <sup>b</sup>	1908
L295_I42,5	0.65	350	295	-	-	29.2	4.0	-	-	1801
L345_I42,5	0.6	350	345	-	-	32.4	4.0	-	-	1780
LWSC										
LS450	0.35	350	450	-	-	37.5	3.8	37.2	3.8	1618
LS295_I42,5	0.65	350	295	-	-	25.2	3.5	-	-	1458
LS345_I42,5	0.6	350	345	-	-	27.5	3.6	-	-	1487
LS440_I42,5	0.45	350	440	-	-	30.9	3.7	-	-	1501
LS460_I42,5	0.4	350	460	-	-	34.8	3.7	-	-	1529
Normal weight aggregates (NA)										
NA350	0.45	350	350	-	-	65.8	5.0	71.4	5.0	2396
NA394	0.4	350	394	-	-	71.6	5.0	74.7	5.1	2387
NA450	0.35	350	450	71.6	5.0	76.2	5.1	81.1/85.1 <sup>b</sup>	5.1/5.2 <sup>b</sup>	2411
NA525	0.3	350	525	-	-	81.6	5.1	89.7	5.2	2430
NA42,5AL	0.35	350	450	71.7	4.9	75.8	5.1	78.7	5.1	2409
VNA250	0.35	250	450	69.9	4.9	74.2	5.0	-	-	2333
VNA300	0.35	300	450	69.5	5.0	73.5	5.0	-	-	2382
VNA400	0.35	400	450	72.6	5.0	75.6	5.2	-	-	2405
NA295_I42,5	0.65	350	295	-	-	38.0	4.7	-	-	2351
NA345_I42,5	0.6	350	345	-	-	41.1	4.8	-	-	2353
NA440_I42,5	0.45	350	440	-	-	52.6	4.8	-	-	2368
NA460_I42,5	0.4	350	460	-	-	59.2	4.9	-	-	2378
NA394_IVA	0.55	350	394	-	-	37.8	4.7	-	-	2323
NA420_IVA	0.45	350	420	-	-	50.3	4.8	-	-	2340

a - c.a. - coarse aggregate; b - Results obtained at 180 days



**Table A.1.** (cont.) Mix proportions, ultrasonic pulse velocity, compressive strength and wet density

Mixtures	w/b	c.a. <sup>d</sup> (L/m <sup>3</sup> )	binder (kg/m <sup>3</sup> )	f <sub>c,7days</sub> (MPa)	UPV <sub>7d</sub> (km/s)	f <sub>c,28days</sub> (MPa)	UPV <sub>28d</sub> (km/s)	f <sub>c,90days</sub> (MPa)	UPV <sub>90d</sub> (km/s)	ρ <sub>28days</sub> (kg/m <sup>3</sup> )	
Argex	VArgex250	0.35	250	450	37.1	4.4	38.7	4.4	39.2	4.7	1924
	Argex450	0.35	350	450	30.4	4.2	31.2	4.2	32.8	4.2	1776
	VArgex400	0.35	400	450	26.2	4.0	28.1	4.0	28.2	4.2	1631
	A350	0.45	350	350	51.1	4.1	57.6	4.2	58.2	4.3	1942
	A394	0.4	350	394	57.1	4.2	62.6	4.3	62.9	4.4	1964
	A450	0.35	350	450	61.4	4.3	64.6	4.4	64.9/66.2 <sup>b</sup>	4.4/4.5 <sup>b</sup>	1982
	A525	0.3	350	525	65.7	4.4	68.5	4.5	70.3	4.6	1995
	A350_0.55	0.55	350	350	37.6	4.0	46.9	4.1	-	-	1907
	A350_0.35	0.35	350	350	-	-	65.0	4.6	-	-	1995
	A450_0.55	0.55	350	450	37.0	3.8	43.9	3.9	48.6	3.9	1862
	A450_0.45	0.45	350	450	46.2	4.1	54.9	4.1	55.1	4.2	1892
	A450_0.30	0.3	350	450	70.6	4.5	72.1	4.6	74.7	4.6	2014
	VA250_I42,5	0.35	250	450	-	-	66.2	4.6	-	-	2022
	VA400_I42,5	0.35	400	450	-	-	63.8	4.4	-	-	1884
	A42,5IIAL	0.35	350	450	53.4	4.3	60.0	4.4	64.4	4.4	1974
	AFA22	0.35	350	450(22%FA)	54.3	4.2	60.0	4.3	64.9/67.5 <sup>b</sup>	4.3/4.4 <sup>b</sup>	1959
	AFA40	0.35	350	450(40%FA)	46.1	4.0	54.3	4.1	61.5/63.9 <sup>b</sup>	4.3/4.3 <sup>b</sup>	1941
	ASF8	0.35	350	450(8%SF)	55.7	4.2	60.8	4.2	64.6	4.4	1931
	ANS	0.35	350	450(13%NS)	60.9	4.2	65.5	4.4	65.9/68 <sup>b</sup>	4.5/4.5 <sup>b</sup>	1976
Arlita	A295_I42,5	0.65	350	295	-	-	36.7	4.1	-	-	1872
	A345_I42,5	0.6	350	345	-	-	40.3	4.1	-	-	1872
	A440_I42,5	0.45	350	440	-	-	50.8	4.3	-	-	1901
	A460_I42,5	0.4	350	460	-	-	54.6	4.3	-	-	1913
	A345_IIAL	0.6	350	345	-	-	39.2	4.1	-	-	1890
	A440_IIAL	0.45	350	440	-	-	51.3	4.2	-	-	1896
	A460_IIAL	0.4	350	460	-	-	54.1	4.2	-	-	1904
	A345_IIAV	0.6	350	345	-	-	35	3.9	-	-	1882
	A394_IIAV	0.55	350	394	-	-	39.1	3.9	-	-	1876
	A420_IIAV	0.45	350	420	-	-	48.1	4.1	-	-	1891
	A345_IIAD	0.6	350	345	-	-	39.9	4.0	-	-	1854
	A394_IIAD	0.55	350	394	-	-	41.5	4.1	-	-	1833
	A420_IIAD	0.45	350	420	-	-	50.1	4.2	-	-	1868
	A394_IVA	0.55	350	394	-	-	37.1	3.9	-	-	1852
	A420_IVA	0.45	350	420	-	-	52.8	4.2	-	-	1886
	Mortar_0.35	0.35	0	702	61.1	4.5	64.8	4.5	71.2	4.7	2216

a - c.a. - coarse aggregate; b - Results obtained at 180 days

# Influence of different grinding types on granulometry of recycled glass

Karel DVOŘÁK<sup>1</sup> Marcela FRIDRICHOVÁ Petr and DOBROVOLNÝ  
Brno Univ. of Technology, Faculty of Civil Engineering, Brno, 602 00 Czech Republic

**Abstract.** This paper is dedicated to reducing CO<sub>2</sub> emissions by using the production of Portland cement with admixtures II species. It explores the possibility of using recycled glass as hydraulically active substance dependent on pozzolanity on progress and specific surface grinding. Recycled glass prepared in standart grinding device, for example ball or vibration mill, does not reach required qualities to participate in high rate of hydrating reaction of cement. Disadvantage of glass grain is their sharp-edge morphology. After grinding, they create conglomeration, which despite a large specific surface it does not adequately react and will behave as inert admixture. This work is an opening study in issue of potential utilization of high-speed mill for recycled glass grinding. The article deals with comparison of the influence of traditional ball mill with high-speed mill on shape and size of grains and on increase of Pozzolanic activity. The resulting products are examined from the chemical, mineralogical and technological perspective.

**Keywords.** Recycled glass, blended cement, pozzolanity, specific surface area, grinding, high speed mill

## Introduction

The building industry, particularly the area for the production of binders, is a manufacturing industry that significantly impacts the environment. However, it is also a very important waste processor for re-use in manufacturing.

The actual issue is the problem of CO<sub>2</sub> emissions during the production of construction materials and when constructing buildings. At present, this issue is particularly important with regard to the negative aspects of global climate change and from the viewpoint of the Kyoto Protocol. Taking into consideration the energy-climate package "20-20-20", approved by the European Parliament and the Council in 2008 and legitimation in June 2009, it concerns an issue closely related to the long-term basic research objectives of EU countries in the area of reducing the energy intensity of building structures, the use of renewable sources of raw materials and advanced building materials with a high utility value [1]. Potential ways of reducing emissions seriously addresses the lime and cement industry, which during the manufacturing process is a significant CO<sub>2</sub> producer from the thermal decomposition of limestone and from fuel combustion.

---

<sup>1</sup>Corresponding author: [Dvorak.k@fce.vutbr.cz](mailto:Dvorak.k@fce.vutbr.cz)

In the area of cement production, it can be stated that in standard cases, where there is approximately 75% of  $\text{CaCO}_3$  in raw meal, then when the clinker is burnt, approximately half a ton of  $\text{CO}_2$  per each ton of the produced single-component cement is released. A further reduction in the ratio of  $\text{CO}_2$  emissions can be achieved by modifying the cement through blending. Within the standards, it is possible to consider substitution permission-based and emission high demanding clinker by latent hydraulic, pozzolanic, as well as various inert substances. It is stated that in this procedure it is possible to decrease the ratio of  $\text{CO}_2$  emissions by 10 to 15% per unit of the blended cement produced. When searching for potential substitute materials it is recommended to focus on substances that will act in the cement both physically mechanically as filler, physico-chemical as a pozzolan and other alternative could be residual hydraulicity substances in the hardened cement stone. Active pozzolans currently represent well researched and high temperature and fluidized ash [2-11]. The raw material, which in this area also appears to be very promising, is recycled glass. This material should act in hydraulic binders as a substance with pozzolanic properties and as microfiller. There are many relative sources of this material, mainly recycled from dismantled screens and flat and colour glass packaging [12].

The limiting factors for the use of these materials in other industries are especially the contents of various impurities. In the case of a glass screen, which is characterized as hazardous waste, these impurities are various heavy metals. For some fractions of package and flat recycled glass in other areas of the building industry, the limiting factor is the content of various, usually organic substances [13].

By using this material in the mixed cements, possibly as a replacement for part of the raw materials in the preparation of raw meal for cement production, the most negative features can be eliminated [14-15].

The disadvantage of recycled glass is its low grindability. This technological difficulty can currently be solved by using modern milling equipment, such as a combination of traditional mills and high-speed disintegrators, which to a certain degree, use the principle of mechanical-chemical activation which significantly results in the milling process. The optimising of milling processes can improve the technical and economic usability of the mentioned material [16-17].

This work aims to ascertain the influence of grinding in high-speed mill, so called desintegrator. This type of mill uses exchangeable grinding rotors for attainment of large specific surfaces and modification of grain morphology. The effect of grinding rotors on morphological properties of grains and pozzolanic properties of recycled glass, has been researched [18-19].

## 1. Methodology

In order to conduct the tests, a sample of silicious soda lime glass was taken from a producer of recycled glass. Recycled glass was ground to constant specific surface area in ball mill. This initial specific surface area was determined to be  $296 \text{ m}^2/\text{kg}$  by Blaine air. This sample was used as referential and it was used for next step of milling in a high speed mill.

In cooperation with the Research and Development center in Moravský Beroun, research was done on the effects of different rotors in high-speed mill, on final recycled glass properties. For selection of optimal grinding rotor there were measurements of the maximum reached specific surface by Blaine air and the change of morphology grain

form. Finally for better comparison, the initial sample was also milled in a traditional ball mill to the same specific surface area which was reached by high speed mill. Reading of measured specific surface areas of all samples are illustrated in table 1.

**Table 1.** Dependency of specific surface on chosen type of rotor

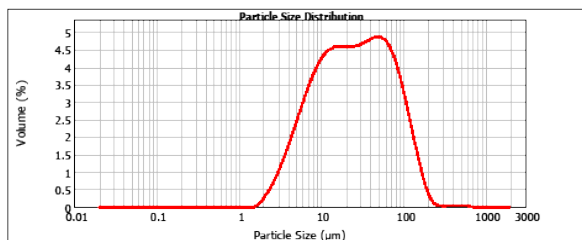
Sample	Specific surface area [ $\text{m}^2/\text{kg}$ ]
recycled glass (ref)	296
recycled glass 2×ČR	355
recycled glass 1×GR	322
recycled glass 1×HR	324
recycled glass 1×SR	321
recycled glass Ball mill	364

## 2. Evaluation of grinding rotors effect

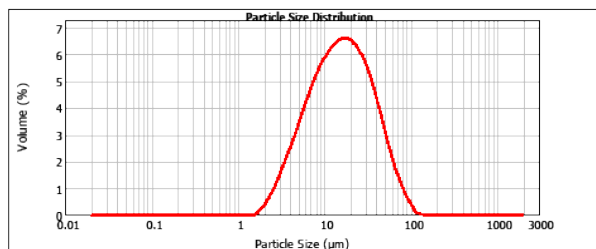
On the basis of results obtained, it is possible to observe that the largest specific surface area and the largest reaction surface relating with it, was reached by using ČR type of rotor. This type is characteristic of cuboidal protrusions which are arranged into concentric circles. On the basis of previous experiences of Research and Development center in Moravský Beroun, it was assumed that the modification of grain forms is not ball-shaped. For this purpose the GR rotors were chosen which are convenient for removing sharp-edge morphology. These rotors have wavy protrusions where individual grains abrade and their form is changed into spherical form.

### 2.1. Effects on particle size

Particle size of milled samples was measured by laser granulometry device Mastersizer 2000. For comparison of the effects of particle size, the chosen samples were ref. (initial sample), 2×ČR, 1×GR and sample milled in ball mill, see fig. 1-4.



**Figure 1.** Recycled glass REF



**Figure 2.** Recycled glass 2×ČR

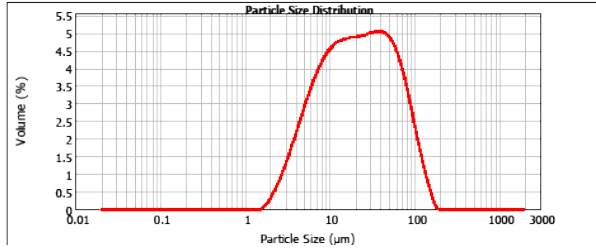


Figure 3. Recycled glass 1×GR

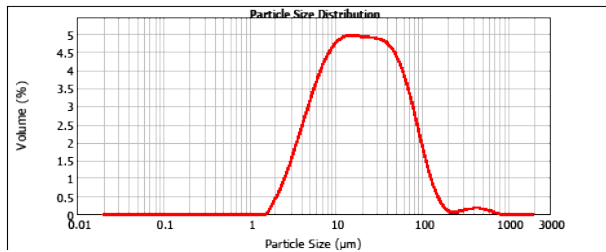


Figure 4. Recycled glass Ball mill

The particle size of samples milled in the ball mill (fig. 4) and in high speed mill with GR rotor (fig.3) are very similar. Values which represent the minimum, average and maximum grain sizes reached, were similar values. Conversely, sample milled in high speed mill with ČR rotor (fig.2) shows similar minimum grain size as the previous two samples, but had smaller average particle size and smaller maximum grain. From these results, it is apparent that this kind of rotor, grinds the sample of recycled glass to narrower fraction than the previous two samples.

## 2.2. Effects on morphology

Effect of type of mill on grains morphology was evaluated by SEM. It was confirmed that there was uneven representation measurement of particles and sharp-edge morphology in recycled glass of reference sample, which was prepared with specific surface  $300 \text{ m}^2/\text{kg}$  by Blaine in a ball mill (fig. 5 and 6).

Eliminating this unsuitable morphology was achieved by GR rotors. This type of rotor made grain edges smoothed and grains form was completely better. But grains created agglomerates which are unsuitable because of reduction of reactive surface and subsequent reduction of hydration (fig 7 and 8). Grains ground in a ball mill do not evince change of grain form in comparison with reference sample and also evince formation of agglomerated particles (pic. 9 and 10).

Using ČR rotors appears very convenient. This rotors gave the highest increase of specific surface, and grain forms are very close to samples from GR rotors but it is obvious that the distribution of particles is even in fraction without agglomerates (fig .11 and 12).

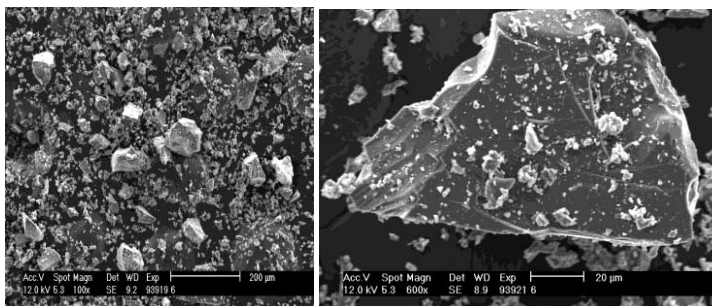


Figure 5-6. Recycled glass - Ref

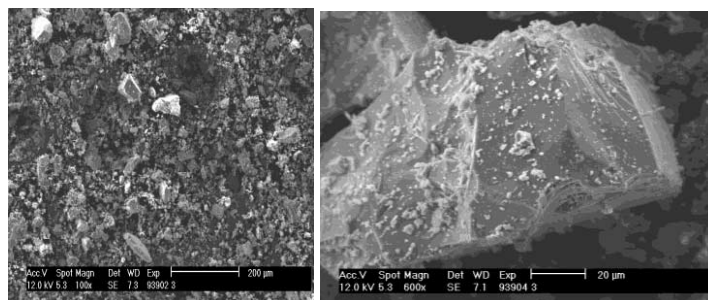


Figure 7-8. Recycled glass 1×GR

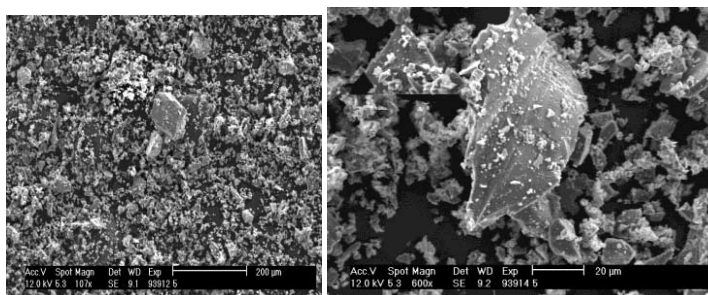


Figure 9-10. Recycled glass Ball mill

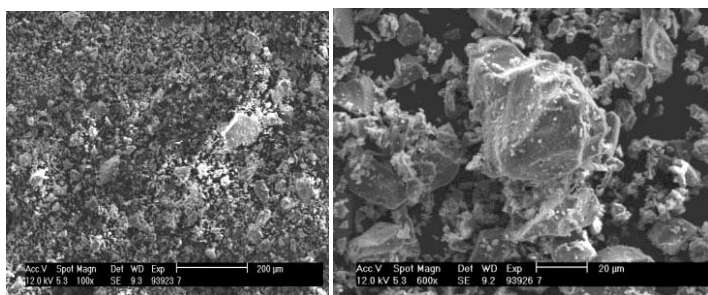


Figure 11-12. Recycled glass 2×ČR

### 3. Conclusion

Recycled glass is typical for sharp-edge morphology which produces conglomerations and this way it decreases reactive surface. That is why it was considered to use advanced method of grinding in high-speed mill on different types of rotors, which has minimalized this negative property. In comparison with sample ground in a ball mill, considerable improvement of recycled glass grain morphology happened as shown by samples ground in the mill with GR rotor. Using CR rotor seems to be the most advantageous, as they reached the largest increase of specific surface, considerably narrow fraction of recycled glass and improvement of grain morphology.

### Acknowledgements

This work was financially supported by the FAST-S-12-25/1671. This paper was also elaborated with the financial support of the European Union's "Operational Programme Research and Development for Innovations", No. CZ.1.05/2.1.00/03.0097, as an activity of the regional Centre AdMaS "Advanced Materials, Structures and Technologies".

### References

- [1] García-Díaz I., Palomo J.G., Puertas F.: *Cem.Concr.Comp.* 33,1063 (2011)
- [2] Diouri A., Boukhari A., Aride J., Puertas F., Vázquez T.: *Materiales de Construcción* 48, 23 (1998)
- [3] Kacimi L., Cyr M., Clastres P.: *J.Haz.Mat.* 181,593 (2010)
- [4] Beretka J., Vito B., Santoro L., Sherman N., Valenti GL.: *Resour. Conserv.Recycl.* 9, 179 (1993)
- [5] Beretka J., Vito B., Santoro L., Sherman N., Valenti GL.: *J.Cem.Concr.Res.* 23,1205 (1993)
- [6] Sahu S., Majling J.: *J.Cem.Concr.Res.* 24,1065 (1994)
- [7] Singh M., Upadhyay SN., Prasad PM.: *J.Waste Manag* 16,665 (1996)
- [8] Öztürk A., Suyadal Y., Oguz H., *J.Cem.Concr.Res.* 30,967 (2000)
- [9] Raupp-Pereira F., James Ball R., Rocha J., Labrincha J.A., Allen G.: *J.Cem.Concr.Res.*38, 511 (2008)
- [10] Shi Huing-Sheng, Deng Kai, Yuan Feng, Wu Kai.: *J.Hazarded.Mater.* 169, 551 (2009)
- [11] Zapata A., Bosch P. A.: *J.Am.Ceram.Soc.* 93, 987 (2010)
- [12] Bouška, V. et al.: *Přírodní skla. Pragur* : Academia, (1987)
- [13] Meyer C., Baxter S.: *Final report to New York state energy research and development authority*, 98–18 (1998)
- [14] Corinaldesi V., Gnappi G., Moriconi G., Montenegro A.: *Wast. Manag.* 25, 197–201 (2005)
- [15] Figg J. W.: *Proc. 5th Int. Conf. on AAR in concrete*, Cape Town, South Africa, S252/7 (1981)
- [16] Balaz, P.: *Mechanochemistry in Nanoscience and Mineral Engineering*, Springer-Verlag Berlin Heidelberg, (2008)
- [17] DINTER, O., *drcení a mletí nerostných surovin, sntl praha* 1984, 244 s
- [18] MEYER, C., BAXTER, S.: *Use of recycled glass and fly ash for precast concrete, Final Report to New York State Energy Research and Development Authority*, Rep. 98-18, Albany, NY, Oct. 1998
- [19] GAZDIČ, D.: *Slag-Sulphate Binder Preparation, Advanced Materials Research*, 2013. 2013(818). p. 68 - 71. ISSN 1022-6680

# Material properties of bottom ash and welding slag as fine aggregates in concrete

Karthikeyan JAYAKUMAR<sup>1</sup> and Ananthi ARUNACHALAM

*National Institute Technology, Tiruchirappalli, Tamilnadu, 620015, India*

**Abstract.** This paper highlights the use of industrial waste such as bottom ash and two types of welding slag (WS) such as Steel WS and Stainless Steel WS, as the partial replacements for fine aggregates in concrete. This Paper presents the chemical analysis and strength properties of industrial solid waste consisting of Bottom ash, Steel WS and Stainless Steel WS. Their chemical compositions were identified by X-ray powder diffraction (XRD) analysis. The results shows that the 7-day compressive strength of concrete containing 10% bottom ash increases by about 1.2 N/mm<sup>2</sup> and at 28 days, it increases by about 1.5 N/mm<sup>2</sup> and Similar changes were noted for Stainless Steel WS. The enhancement of concrete strength in bottom ash and Stainless steel WS was due to the presence of calcium and silica. The compressive strength of concrete containing 10% Steel WS at 7 days was the same as that of control mix but at 28 days, its compressive strength decreased by about 1.8 N/mm<sup>2</sup>. In the Steel WS concrete, later the strength is decreased due to the presence of chromium and magnesium in the slag.

**Keywords.** X-ray powder diffraction (XRD) analysis, EDX Analysis, Compressive strength

## Introduction

Rapid industrialization generates numerous amounts of industrial solid waste. The disposal of this solid waste is a tedious process causing various threats to the environment. Environmental, economic and technical problems have led to increasing attention towards recycling of solid waste materials in the construction [1]. Industrial wastes can be divided into two types: industrial by-products and recycled wastes. The first type includes coal ash, various slags from metal industries, industrial sludge, waste from industries like pulp and paper mills, mine tailings, food and agriculture, and leather. The second type includes different plastic and rubber wastes [2]. Slags are produced in a very large amount in pyro metallurgical processes, and are major sources of waste, if not properly recycled and utilized. With rapid growth of industrialization, the available landfill of large quantities of metallurgical slags is diminishing all over the world and, correspondingly, the disposal cost becomes increasingly higher. The global warming effect and natural resource saving are the general environmental issues of importance nowadays. In addition, the landfills used for waste materials, tend to

---

<sup>1</sup>Corresponding author: [karthi1212@gmail.com](mailto:karthi1212@gmail.com), Fax. 91-431-2500133, Tel. 91-9487359908



become a significant source of pollution of air, water and soil, and further adversely affect human health, growth of plants and vegetation etc. From the viewpoint of preservation and protection of the global environment, slag recycling has attracted the attention of scientists in recent years [3].

Furnace bottom ash (FBA) is a waste material from coal-fired thermal power plants. In India over 75% of the total installed power generation is coal-based. FBA with high ash contents varying from 30% to 50% are generated during the power generation. More than 110 million tonnes of ash is generated every year in India. Presently 65,000 acres of land are occupied by ash ponds [4].

Submerged-arc welding is a well-established process capable of producing quality welds in a wide range of thicknesses in ferrous, stainless steels and even some non-ferrous metals. The process consists of an arc that is formed when an electric current passes continuously between a welding wire and the work piece. The arc, the tip of the welding wire, and the weld joint are fully covered by a layer of a powdered flux, which protects the welding operation from atmospheric contamination, preventing flash and glare, and avoids smoke and fumes. During the welding process, the flux is partially melted, resulting in a liquid protective slag layer that is solidified during the sequence, generating a waste material known as submerged-arc welding slags [5]. This slag is normally disposed of as waste. This poses the problem of environmental pollution and needs landfill space which in turn exhausts of non-renewable resources. Re-using of this slag would not only solve these problems but would also be economical. This paper highlights the use of these industrial wastes such as bottom ash and welding slag in concrete.

## **1. Literature review**

### *1.1. Bottom ash*

In 2005, Y.Bai et al [6] of UK, experimentally investigated the replacement of furnace bottom ash as fine aggregates in concrete. The experimental work was carried out in two series, A and B. For both series, the natural sand was replaced with the FBA sand at replacement levels of 0%, 30%, 50%, 70% and 100% by mass, and the cement content was fixed at 382 kg/m<sup>3</sup>. He concluded that 30% of the natural sand can be beneficially replaced with the FBA sand to produce concrete in the compressive strength range from 40 to 60 N/mm<sup>2</sup>.

Experimental investigations [7] were carried out by replacing sand in concrete with bottom ash. The proportions of fine aggregate replaced ranged from 20% to 50%. The compressive strength, splitting tensile strength and flexural strength tests were performed at 7, 28, 56, 90 days. He concluded that the compressive strength of concrete containing 50% bottom ash is acceptable for most structural applications since the observed compressive strength is more than 20 MPa at 28 days.

In 2009, an experimental study [8] was done on the concrete mixes in which natural river sand was replaced by the crushed fine stone (CFS), furnace bottom ash (FBA) and fine recycled aggregates (FRA) at replacement levels of 0%, 25%, 50%, 75% and 100% by mass, and the cement content was fixed at 386 kg/m<sup>3</sup>. He reported that concrete containing FBA as fine aggregates had higher compressive strength, lower drying shrinkage and higher resistance to the chloride-ion penetration.

Kim and Lee [9] conducted an experimental study to evaluate the feasibility of utilizing bottom ash as fine and coarse aggregates in high-strength concrete of compressive strength in a range of 60 to 80 MPa. Fine and coarse bottom ash were used to replace with normal sand and gravel in varying percentages of 25%, 50%, 75% and 100%. The mechanical properties, consisting of compressive strength, modulus of elasticity and flexural strength were evaluated for about 100% replacement of fine and coarse bottom ash. The 7 day and 28 day compressive strengths were around 60 MPa and 70 MPa and were not strongly affected by the replacement of FBA and CBA.

Research was also done by Wongkoe et al [10] on replacing cement with bottom ash (BA) in making autoclave concrete blocks. The binder /sand /calcium hydroxide ratio (B-S-CH ratio) of 55-40-5% by weight were used in the mix. The water to solid ratio used was 0.29. BA was used to replace part of Portland cement at 10%, 20% and 30% by weight and aluminium powder was added at 0.2% by weight of solid, respectively. The results show that the compressive strength, flexural strength and thermal conductivity increased with increased BA content

Experimental research was carried out by Bajare et al [11] on replacing cement with 20% and 40% Coal Combustion Bottom ash (CCBA). Four different mixes with CCBA were prepared, two of them with CCBA grinded ground for 4 minutes and other two with CCBA ground for 15 minutes. They found that ground CCBA could effectively replace up to 20% cement without reducing compressive strength of concrete. By replacing 40% of cement with CCBA, the compressive strength of concrete reduced significantly.

### *1.2. Welding slag*

In 2009, Viana et al [12] investigated the potential use of Welding Flux (SWF) waste, the Submerged Arc Welding (SAW) as an alternative raw material for manufacturing of clay bricks. Four mortar samples were prepared: 1) reference mortar made with conventional fine aggregate, 2) acid SWF mortar, 3) neutral SWF mortar and 4) basic SWF mortar. For the three SWF mortars, natural sand was totally replaced by the corresponding SWF waste. It was demonstrated that the properties of the bricks incorporating with up to 10 wt. % of SWF waste as clay replacement were similar to those specified for ceramic bricks.

In 2013, Ramesh et al [13], investigated the furnace and welding slags as a replacement of fine aggregates in concrete. For mixes containing WS, the 7-day compressive strength of concrete cubes increased from 10% to 15% and the 28 days compressive strength increased from 5% to 15%. It was concluded that 5% of WS and 10% FS replacement with fine aggregates is effective for practical purpose.

## **2. Materials**

- The cement used was an ordinary Portland cement (OPC) of 53 grade conforming to IS 12269-1987 specifications.
- The aggregate used were with 12 mm nominal size and river sand conforming to IS 383-1970.
- Potable water used conforming to IS 456-2000 specifications.

- Steel and Stainless Steel slags were obtained from local steel fabrication industries and ground to powder to meet the IS 383-1970 specifications.
- Bottom ash was obtained from the Neyveli Lignite Power Plant, Tamilnadu.

### 3. Mix proportions and preparation of specimen

Two concrete mixes were prepared using bottom ash and welding slag replacing 10% fine aggregates. Control mix was prepared as per Indian Standard Specifications IS 10262-2009 and cured for 7 and 28 days. M35 grade concrete was adopted and the mixtures were cast in cube moulds of size 100×100×100 mm. Afterwards, the specimens were demoulded and incurred at the room temperature for 7 days and 28 days and then tested under compression. The Compressive strength test was carried out as per the IS 516-1959. The material properties for concrete mix are listed in the table 1.

**Table 1.** Material properties for concrete mix

Properties	Coarse aggregates	Fine aggregates	BA	Steel WS	Stainless steel WS
Specific gravity	2.64	2.61	2.66	2.98	2.76
Fineness Modulus	7.88	2.74	2.00	2.05	1.93

### 4. Results and discussion

#### 4.1 Physical properties

The physical appearance of the bottom ash, Steel Welding slag (Steel WS) and Stainless steel welding slag (Stainless Steel WS) are shown in the figures 1 to 3.



**Figure 1.** Bottom ash



**Figure 2.** Steel WS



**Figure 3.** Stainless steel WS

#### 4.2 XRD analysis

The chemical composition of the bottom ash, Steel WS and Stainless Steel WS was identified by X-ray diffraction. The prepared samples were exposed to X-ray with the  $2\theta$  angle varying between  $10^\circ$  and  $80^\circ$  with Cu radiation. The applied voltage and current were 40 kV and 30 mA, respectively. The chemical composition of the bottom ash, Steel WS and Stainless Steel WS are listed in Tables 2 to 4. The XRD curves given in Figures 4 to 6 shows that calcium and silica are predominant in bottom ash and Stainless steel WS whereas calcium, magnesium and chromium silicide are predominant in Steel WS.

**Table 2.** Chemical composition of bottom ash

S.No	Compound Name	Chemical Formula
1	Silicon Oxide	Si O <sub>2</sub>
2	Quartz low	O <sub>2</sub> Si
3	Magnesioferrite	Fe <sub>2</sub> Mg O <sub>4</sub>
4	Cobalt Dinitrate	Co N <sub>2</sub> O <sub>6</sub>
5	Chromium Nitride	Cr <sub>2</sub>
6	Calcium Duo-dicarbide	C <sub>2</sub> Ca

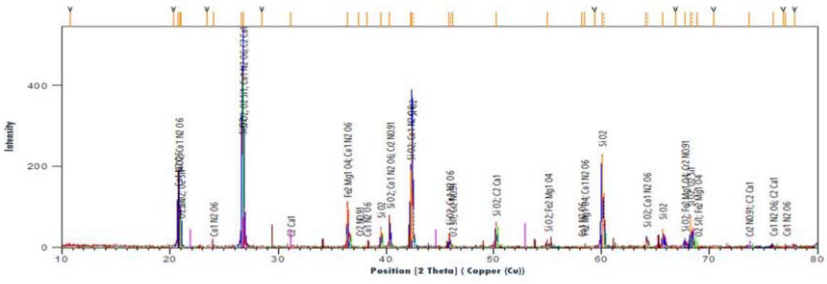


Figure 4. XRD of bottom ash

Table 3. Chemical composition of steel WS

S.No	Compound Name	Chemical Formula
1	Calcium Carbonate	CaCO <sub>3</sub>
2	Manganese oxide	Mn <sub>3</sub> O <sub>4</sub>
3	Calcium	Ca
4	Calcium Magnesium	Ca Mg <sub>2</sub>
5	Chromium Silicide	CrSi <sub>2</sub>

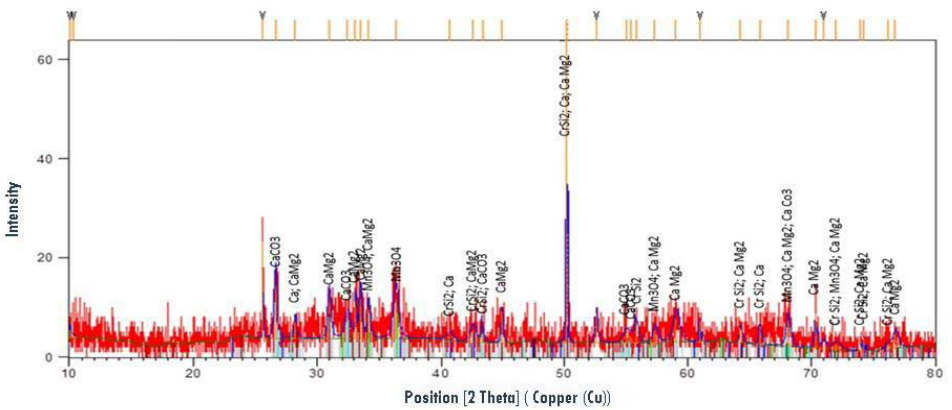
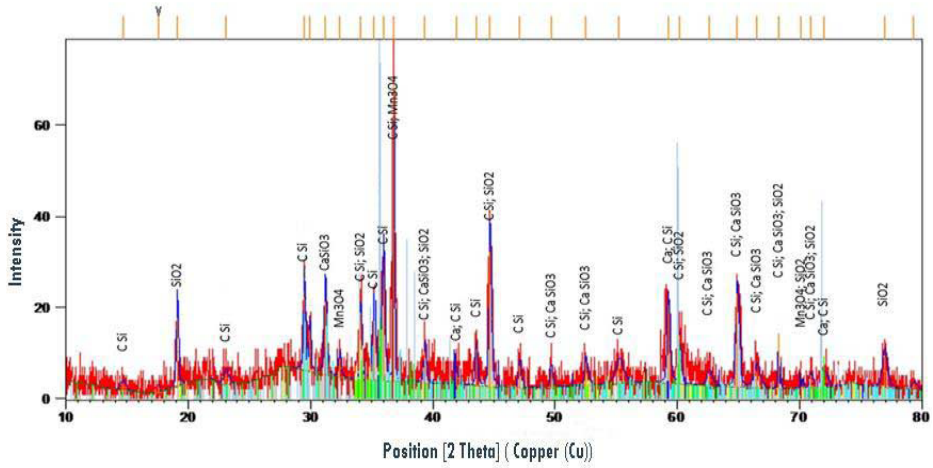


Figure 5. XRD of steel WS

**Table 4.** Chemical composition of stainless steel WS

S.No	Compound Name	Chemical Formula
1	Calcium	Ca
2	Moissanite	C Si
3	Wollastonite	CaSiO <sub>3</sub>
4	Manganese oxide	Mn <sub>3</sub> O <sub>4</sub>
5	Silica	SiO <sub>2</sub>



**Figure 6.** XRD of stainless steel WS

4.3 EDX analysis

The chemical composition of BA particles was analysed using EDX. According to the results of EDX analysis, porous and comparatively large particles could be particles of partially burned pieces of coal, consisting of 88.78% carbon (C) and 10.44% oxygen (O). Finer particles with higher density distributed on the surface of larger particles contained Al and Si, as well as other chemical elements such as Mg, S, Ca, Fe .

According to the results of EDX analysis for Stainless steel WS, the atomic weight% of silica was 41.92% and of manganese is 40.9%. The calcium content constituted about 17.18%. The EDX analysis for steel WS consists mostly of CaCO<sub>3</sub> particles.

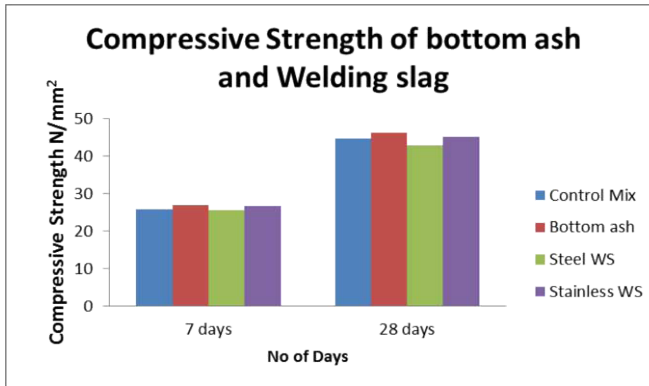
4.4 Compressive strength

Compressive strength for 10% replacement of fine aggregates with bottom ash and welding slag were measured for 7 days and 28 days given in figure 7 and table 5. The strength was then compared with the reference mix of 7 days and 28 days. The

Compressive strength due to the addition of bottom ash and Stainless Steel WS show similar increases in strength whereas Steel WS addition reduces the 28<sup>th</sup> day strength.

**Table 5.** Compressive strength of concrete

<b>Compressive Strength</b>	<b>7 days (N/mm<sup>2</sup>)</b>	<b>28 days (N/mm<sup>2</sup>)</b>
Control mix	25.8	44.7
Bottom ash	27.0	46.2
Stainless Steel WS	26.8	45.0
Steel WS	25.63	42.9



**Figure 7.** Compressive strength of bottom ash and welding slag

## 5. Conclusions

- The 7-day compressive strength of concrete, obtained by replacing 10% bottom ash increased by about 1.2N/mm<sup>2</sup> and at 28 days increased to about 1.5 N/mm<sup>2</sup>.
- The 7-day compressive strength of concrete, obtained by replacing 10% Steel WS was the same as that of the control mix but at 28 days, the compressive strength decreased by about 1.8 N/mm<sup>2</sup>.
- The 7-day compressive strength of concrete by replacing 10% Stainless steel WS increased by about 1 N/mm<sup>2</sup> and at 28 days increased by about 0.3 N/mm<sup>2</sup>.
- The enhancement of strength in bottom ash and Stainless steel WS is due to the presence of calcium and silica.
- The Welding slag achieves early compressive strength but later the strength is decreased due to the presence of chromium and magnesium.

## Acknowledgements

The authors are grateful to the Department of Civil Engineering, National Institute of Technology Tiruchirappalli, Tamilnadu. The authors would like to express their thanks to the director of the National Institute of Technology Tiruchirappalli, Tamilnadu for approving the project.

## References

- [1] Marco Pasetto, Nicola Baldo, Performance comparative analysis of stone masticasphalts with electric arc furnace steel slag: a laboratory evaluation, *Materials and Structures* 45, (2012), 411–424.
- [2] Industrial Waste Aggregates, Chapter 2.
- [3] REUTER, M., XIAO, Y., and BOIN, U. Recycling and environmental issues of metallurgical slags and salt fluxes, VII International Conference on Molten Slags Fluxes and Salts, *The South African Institute of Mining and Metallurgy*, 2004.
- [4] S. Geetha, K. Ramamurthy, Properties of sintered low calcium bottom ash aggregate with clay binders *Construction and Building Materials* 25, (2011), 2002–2013.
- [5] R. Annoni et al. Submerged-arc welding slags: Characterization and leaching strategies for the removal of aluminium and titanium, *Journal of Hazardous Materials* , (2013), 335– 341.
- [6] Y. Bai et al. Strength and drying shrinkage properties of concrete containing furnace bottom ash as fine aggregate, *Construction and Building Materials* 19, (2005),691–697.
- [7] P. Aggarwal, Y. Aggarwal, S.M. Gupta, Effect of bottom ash as replacement of fine aggregates in concrete, *Asian journal of civil engineering* (building and housing) vol. 8, (2007), 49-62.
- [8] S.-C. Kou, C.-S. Poon, Properties of concrete prepared with crushed fine stone, furnace bottom ash and fine recycled aggregate as fine aggregates, *Construction and Building Materials* 23, (2009), 2877–2886.
- [9] H.K. Kim, H.K. Lee, Use of power plant bottom ash as fine and coarse aggregates in high-strength concrete, *Construction and Building Materials* 25, (2011), 1115–1122.
- [10] W. Wongkeo et al. Compressive strength, flexural strength and thermal conductivity of autoclaved concrete block made using bottom ash as cement replacement materials, *Materials and Design* 35, (2012), 434–439.
- [11] Diana Bajare et al. Coal Combustion Bottom Ash as Microfiller with Pozzolanic Properties for Traditional Concrete *Procedia Engineering* 57, (2013) 149 – 158.
- [12] Viana, C. E., Dias, D. P., Holanda, J. N. F., Paranhos, R. P. R., , The Use of Submerged-Arc Welding Flux Slag as Raw Material for the Fabrication of Multiple-Use Mortars and Bricks, *Soldagem Insp.* Sao Paulo, Vol. 14, No. 3, 2009, p.257-262.
- [13] Ramesh et al. Use of furnace slag and welding slag as replacement for sand in concrete, *International Journal of Energy and Environmental Engineering*, (2013).



# The use of waste materials for the production of an hydraulic mortar based on slacked lime

Bartolomeo MEGNA<sup>1</sup>, Laura ERCOLI and Giovanni RIZZO

*Laboratory of Materials for Restoration and Conservation, Dipartimento di Ingegneria Civile, Ambientale, Aerospaziale, dei Materiali, Università di Palermo*

**Abstract.** This paper deals with the production of crushed brick mortars using waste materials from a brick factory. Part of the quarried material is unsuited to the production line, because of the high plasticity of the clay, it is discharged as waste, causing both additional costs and environmental issue. Experimental work has been performed to investigate if, instead of being disposed, the fat clay can be used as a reactive aggregate to produce hydraulic mortars based on slacked lime. In previous work [5] the clay was fired in a muffle furnace at three different temperatures and then ground to obtain powders with different particle size distributions, to investigate the influence of both processing temperature and specific surface area on the reactivity of the aggregates with respect to the slacked lime. Hardened samples of selected mortars underwent standard compression and wash out tests in order to evaluate their properties as compared to the properties of samples made of both a commercial hydraulic lime and a Portland cement. The results encourage the reuse of the fat clay to produce such environmental friendly hydraulic binders, as an interesting option with respect to the use of traditional hydraulic limes and cements.

**Keywords.** Crushed bricks, hydraulic mortars, CO<sub>2</sub>, restoration

## Introduction

The use of pozzolanic materials to improve the mechanical properties and durability of lime mortars is very well known since ancient time. As reported by Vitruvius, the use of ground fired clay product such as bricks, was very common in the Roman Empire in order to obtain more resistant and impermeable mortars [1]. These hydraulic mortars have been considered obsolete as a results of discovering of hydraulic lime and cement in the XIX century. Particularly Portland Cement became the most commonly used binder in building products, ranging from concrete to plasters. In the last few decades both environmental problems and compatibility issues in restoration intervention have led to reassessment of using hydraulic mortars which are based on air hardening lime. In fact, production of cement is responsible for about 5% of man-made CO<sub>2</sub> resulting to be one of the most important causes of CO<sub>2</sub> emission in the atmosphere [2]. Furthermore, its use in the restoration of masonry buildings is incompatible due both to

---

<sup>1</sup>Corresponding author: [bartolomeo.megna@unipa.it](mailto:bartolomeo.megna@unipa.it); mobile 00393336243062

the higher Young modulus and to the risks related to formation of alteration products (ettringite, thaumasite, soluble salts).

The production of hydraulic mortars based on air hardening lime and crushed bricks could reduce the CO<sub>2</sub> emission [3], as a cement kiln operates at 1450°C whereas a lime kiln operates around 1000°C and clay is fired at about 700°C to obtain a reactive pozzolanic material. Moreover such a binder could offer a higher compatibility to masonry mortars with respect to cement due to its lower mechanical properties.

## 1. Materials and methods

The lime used in this work was a standard CL90 hydrated lime [3]. A 32,5R Portland cement and a Natural Hydraulic Lime were also used as reference of hydraulic binders. The clay belongs to the formation “Terravecchia”, Messinian Low-Tortonian Era, consisting of Kaolin, Montmorillonite, Illite in order of relative abundance as clay minerals, and carbon frustules, carbonates and quartz as other phases [4]. In order to produce a reactive pozzolanic material, the clay was fired at 700°C in an electric muffle.

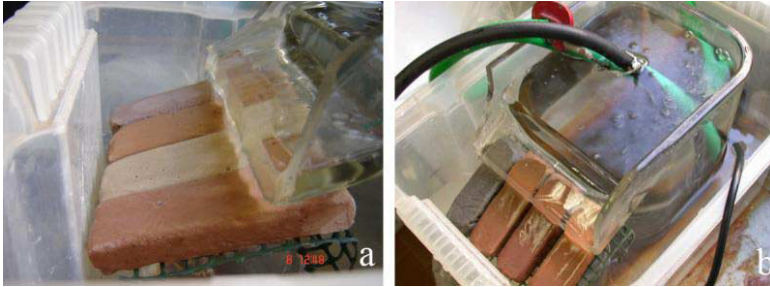
According to the results of preliminary mechanical characterization, as reported in table 1, the fired clay was ground in order to obtain a particle size lower than 100 microns. At a first step three different grain size distributions were selected, i.e. maximum grain size 500, 250 and 100 microns respectively. Mortar samples were prepared by mixing binder and aggregates with a volume ratio 1:1. The samples were then cured for 60 days at 40°C and 100% of relative humidity. The cured samples underwent static compression test, in order to evaluate the influence of aggregate grain size. As shown in table 1, a dramatic increase in resistance is achieved as effect of grain size reduced from 500 to 250 microns, and a slight increase is still obtained by grinding aggregates to 100 microns. According to these preliminary results all the samples prepared in this work used only the smallest grain size to ensure the highest mechanical properties of the hydraulic mortars.

**Table 1.** Preliminary mechanical characterization of mortars obtained with different granulometric distribution of fired clay aggregates

	< 500 $\mu\text{m}$	<250 $\mu\text{m}$	<100 $\mu\text{m}$
Compressive strenght [MPa]	1.0	3.9	4.2
Standard deviation [MPa]	0.2	0.4	0.4

A quartz sand, with silica content higher than 95%, was used to prepare some mortar samples with inert aggregate. The sand particle size distribution was selected to fit the Fuller curve. Only deionized water with conductivity lower than 1 $\mu\text{S}/\text{cm}$  was used to prepare the mortars, in order to avoid any influence of the water quality on the results. Mechanical test were performed using a Controls 50-C9030 machine, working at different load rates in order to ensure a test duration ranging from 60 to 200 seconds for all the samples.

The washout test was performed in an *ad-hoc* apparatus consisting of two vessels, shown in figure 1. The smaller one is properly designed to let water flow as thin film over the samples; carbon dioxide is bubbled into the water at a constant flow rate to settle the pH in the range of 5.5 to 6.5.



**Figure 1.** Wash out test apparatus: a) detail of water film on the samples; b) CO<sub>2</sub> mixing with water

### 1.1. Samples preparation

Two different kinds of samples were prepared:

- 2 cm cube, for static compression test;
- rectangular parallel piped 10.5x3.5x1 cm, for accelerated wash out test.

All the samples were prepared using 1:3 binder to aggregate ratio. Both hydraulic lime and cement were mixed with the inert quartz sand, whereas for air hardening lime two different sets of samples were prepared: i) mixing only the fired clay as aggregate; ii) mixing one part of lime, one part of fired clay and two parts of quartz sand.

All the samples were cured for at least 90 days at 30°C and 99±1% RH.

Thermal analysis of the cured materials was performed on the mortars in order to evaluate their hydraulicity [5-9] by means of a Netzsch STA 409. The analysis was performed in static air, in the range 30-1000°C at a heating rate of 10°C/min.

## 2. Results and discussion

The samples are indicated after the binder used, as follows:

- Ce = cement samples;
- CI = Hydraulic Lime;
- CA1\_1 = Lime/fired clay/quartz sand ratio 1/1/2 ;
- CA1\_3 = Lime/fired clay ratio 1/3.

### 2.1. Mechanical tests

The compressive test was performed on at least 10 samples for each of the four kinds of mortars prepared and the strength and standard deviation are reported in figure 2. The hydraulic mortars based on air hardening lime definitely show higher value in compressive strength than the hydraulic lime, but significantly lower than Portland cement one. It can be also highlighted that, on increasing the ratio between slaked lime and fired clay, the compressive strength slightly decreases, see sample CA1\_3, probably due to lack of quartz sand, which has higher mechanical properties than clay fired at 700°C.

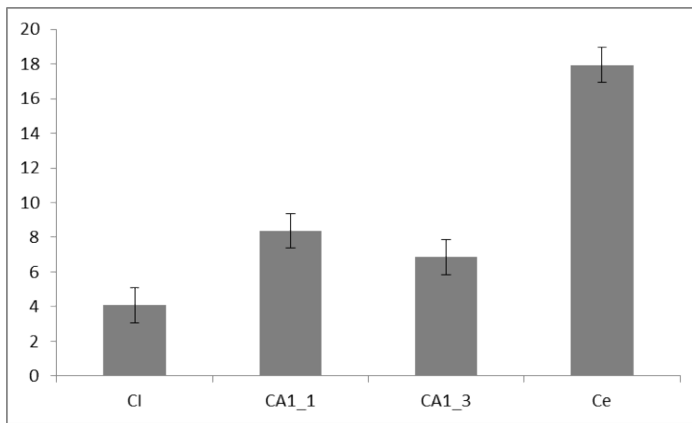


Figure 2. Compressive strength of mortars

2.2. Accelerated wash-out tests

All the mortars underwent three consecutive wash-out cycles for 96 hours.

In figure 3 the weight loss versus time is plotted. To measure weight loss, after each cycle the samples were oven dried till constant weight.

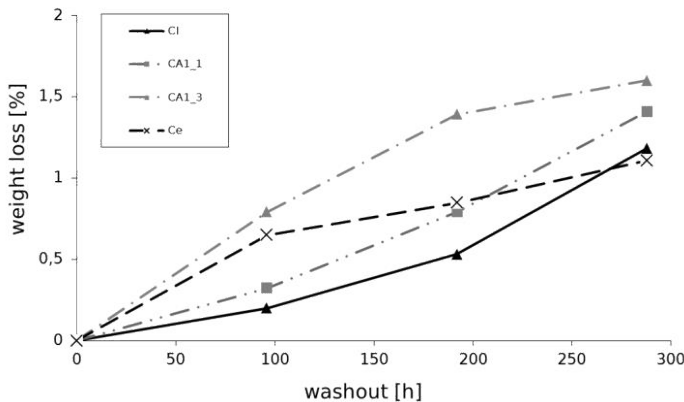


Figure 3. Weight loss versus wash-out time

The apparently poor behaviour of cement samples is due to the detachment of micro particles from of the surface during the first cycle, the weight loss during the successive cycles show a very low increase. As for the mortars of air hardening lime, the presence of quartz sand seems to induce positive effects on the wash-out resistance as well. As a general comment, the hydraulic binder proposed in this work, i.e. a mixture of air hardening lime and crushed brick powder, can offer a washout resistance comparable to the commercial hydraulic lime.

### 2.3. Thermal analysis

The mortars were also characterized by means of Simultaneous Thermal Analysis in order to verify their hydraulicity.

As proposed in the literature [7] the temperature range was divided into four parts and the weight loss occurring in every range was associated to a different decomposition phenomenon:

- 30-120°C: loss of free water in capillary pores and humidity [H<sub>2</sub>O];
- 120-200°C: loss of water due to dehydration of hydrated salts;
- 200-600°C: loss of water due to the decomposition of hydraulic products [H<sub>2</sub>O<sub>idr.</sub>];
- >600°C: loss of CO<sub>2</sub> due to the decomposition of Calcite.

According to this classification the results of thermal analysis are summarized in table 2.

**Table 2.** Weight loss % of different mortars for each interval of temperature range in Simultaneous Thermal Analysis

Temperature range	CI	CA1_1	CA1_3	Ce
30-120°C	0.7	2.4	2.8	1.4
120-200°C	0.5	0.8	0.9	1.2
200-600°C	2.7	1.4	3.0	2.0
>600°C	19.9	18.2	8.4	17.4

It's worth pointing out that the highest weight loss associated with hydraulic products (200-600°C) was measured for the mixture between lime and fired clay at high ratio CA1\_3, even if this mortar showed poorer mechanical properties than CA1\_1, containing quartz.

The hydraulicity of a mortar can also be evidenced by the ratio between CO<sub>2</sub> and the hydraulic water weight, called inverse hydraulicity index [7-9] or by the ratio between hydraulic water and free water [6], called direct index of hydraulicity. In figures 4 and 5 the results of mechanical test and thermal analysis are plotted versus such parameters.

In figure 5, the direct index of hydraulicity shows a very good correlation between mechanical properties and hydraulic behaviour for all of the mortars analysed in this work.

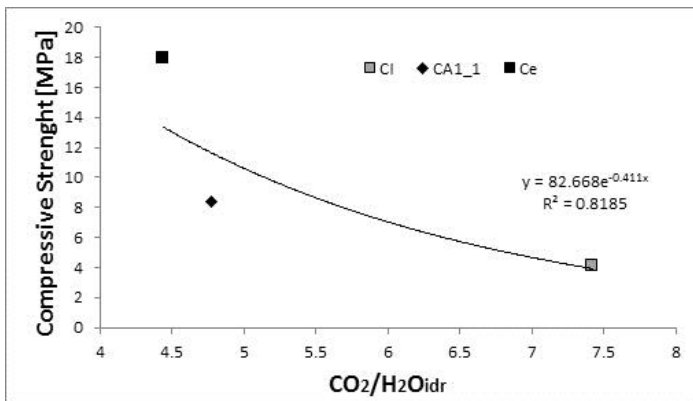


Figure 4. Compressive strength versus inverse hydraulicity index

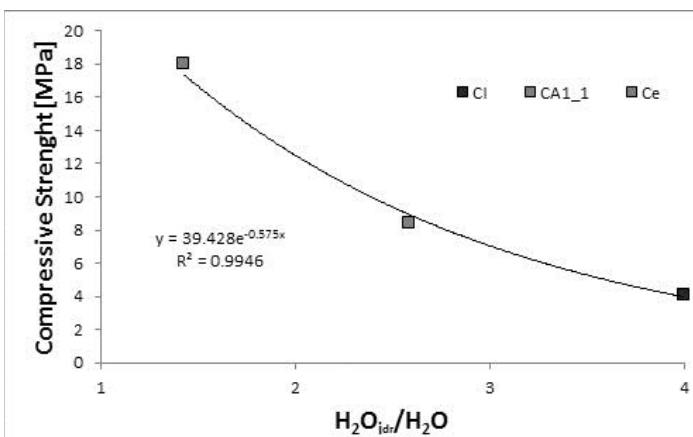


Figure 5. Compressive strength versus direct hydraulicity index

### 3. Concluding remarks

In this paper the use of a fat clay, unsuitable for bricks production, as pozzolanic admixtures for air hardening lime was tested. The experimental results show that an interesting hydraulic binder can be produced by mixing slaked lime and metakaolin produced by firing at 700°C the fat clay. Such binder can be used to prepare mortars using as aggregate the same crushed brick or quartz sand. The best results, in terms of both mechanical resistance and durability, are achieved using the quartz sand. However, the mortars proposed in this work show a compressive strength slightly higher than the commercial hydraulic lime used but quite lower than the cement.

According to the results obtained, it seems that the hydraulic system proposed in this work could be used an alternative cement in all the cases where high mechanical properties are not required, i.e. for plasters and laying mortars in non-load bearing walls. For such use, it could be even more compatible than the commercial hydraulic binders. Furthermore, it is more eco-friendly, as a rejected raw material is used and fired at lower temperature.

Finally, the index of hydraulicity seems to describe the behaviour of the binder more effectively than the inverse index. It's a preliminary result that has to be verified in a larger number of samples. These results encourage further experimental work on such material in order to identify the best lime to clay ratio for different purposes.

## References

- [1] M. P. Vitruvio, *De architectura*, Einaudi, Italy, 1997
- [2] N. Tanaka B. Stigson, World Business Council for Sustainable Development and International Energy Agency, *Cement Technology Roadmap*, 2009
- [3] E. Gartner Low energy cement systems, *Proceedings of 31st Cement and concrete science conference*, London, 2011, paper 15.
- [4] UNI EN 459-1 *Calci da costruzione. Definizioni, specifiche e criteri di conformità*, UNI, Italy, 1996.
- [5] B. Megna, The use of waste materials from a brick kiln to produce hydraulic mortars based on slaked lime: evaluation of materials reactivity. *Meccanica dei Materiali e delle Strutture*, **3**, (2010), 146-157
- [6] G. Rizzo, B. Megna, Characterization of hydraulic mortars by means of simultaneous thermal analysis, *Journal of Thermal Analysis and Calorimetry*, **92**, (2008), 173-178.
- [7] A. Moropoulou, A. Bakolas and K. Bisbikou, Characterization of ancient, byzantine and later historic mortars by thermal and X-ray diffraction techniques, *Thermochimica Acta*, **269/270**, (1995), 779-795.
- [8] J. Pires, A. J. Cruz, Techniques of thermal analysis applied to the study of cultural heritage, *Journal of Thermal Analysis and Calorimetry*, **87**, (2007), 411-415.
- [9] A. Moropoulou, A. Bakolas, K. Bisbikou, Investigation of the technology of historic mortars, *Journal of Cultural Heritage*, **1**, (2000), 45-58.

# Effects of polycarboxylate-based superplasticizer on rheological and mechanical properties of concrete

Samer AL-MARTINI<sup>1</sup>, Omar F. NAJIM and Waddah AL HAWAT  
*Department of Civil Engineering, Abu Dhabi University, Abu Dhabi, UAE*

**Abstract.** Ready mix concrete in hot weather countries, such as United Arab Emirates (UAE), is usually subjected to high temperature during its transportation to construction sites. In some cases, due to traffic and location of construction sites, concrete mixing may be prolonged. As such, concrete under such harsh environments (as high temperature and prolonged mixing) suffers from severe slump loss, which may affect its mechanical properties. In this paper, the effect of polycarboxylate-based superplasticizer on rheology and compressive strength of concrete under hot weather was investigated. Ordinary portland cement and fly ash (FA) were used as cementitious materials. Concrete mixtures were made with a water/binder ratio of 0.36. The concrete mixtures were mixed in a walk-in environmental chamber using a drum mixer. The investigated temperature was 40 °C. The compressive strength of concrete was taken at 3, 7 and 28 days. The results show that both rheological parameters and compressive strength are influenced by variation of superplasticizer dosage. While compressive strength increased when superplasticizer dosage increased, torque resistance and flow resistance decreased.

**Keywords.** Superplasticizer, compressive strength, rheology, polycarboxylate

## Introduction

With high public and private investments in United Arab Emirates (UAE), the construction industry in UAE continues to require major research and development (R&D) efforts to increase its productivity and leadership. The competitive situation of concrete industry is crucially affected by cost factors, productivity, and quality of the final product. This environment is characterized by demand for ever-shorter construction times, rising labor costs, and increased requirements for challenging placement conditions. From a design perspective, this includes the construction of more intricate and densely reinforced structural elements, as well as growing requirements for greater development of early strength, better surface finish, lower deformation and cracking, and longer service life.

---

<sup>1</sup>Corresponding author. [samer.almartini@adu.ac.ae](mailto:samer.almartini@adu.ac.ae)



Hot weather environment, which is typical during summer in UAE, causes serious problems in the placement of fresh concrete due to the acceleration of cement hydration and faster water evaporation. Fresh concrete mixtures at high temperature tend to stiffen much faster with time compared to similar mixtures placed at moderate temperatures, and significant slump loss is usually experienced under high temperature [1,2]. This presents a real challenge in hot weather concreting, because concrete does not remain workable long enough to allow time for its transport, placement, compaction, and finishing [3]. Excessive slump loss does not usually occur in moderate temperature concreting, but it becomes more significant in hot weather conditions. The preferable condition for placing concrete is generally when the ambient temperature ranges from 20 to 23 °C [4]. The ACI guidelines for hot weather concreting specify that ambient temperature is considered high when above 27 °C [4].

In this paper, the effect of the dosage of polycarboxylate-based superplasticizer (PCS) on rheological properties and compressive strength of concrete with a w/b = 0.36 was studied at an ambient temperature of 40°C. The w/b was selected to be 0.36 because for a higher w/b, the effect of chemical admixtures on rheological properties is diminished, whereas very low w/b and high temperature combinations need focus in future research.

## 1. Experimental program

### 1.1. Materials

Ordinary portland cement (Type I) and fly ash (FA) were used as cementitious materials. Locally produced well-graded crushed coarse and fine aggregates were used. The coarse aggregate had a nominal size equal to 10 mm. Polycarboxylate-based superplasticizer (PCS), complying with ASTM C-494 Type F HRWR was used. The superplasticizer was in liquid form with solid concentration of 41%, and its recommended dosage range was from 0.4% to 0.6% by mass of cementitious materials.

### 1.2. Apparatus

A drum concrete mixer was used throughout this investigation. Mixing of the concrete was conducted in a temperature-controlled walk-in environmental chamber. A portable concrete rheometer was used to measure the rheological parameters of the fresh concrete (Fig. 1). The rheometer consists of a steering handle, a drive shaft, two probes (inner and outer), a concrete container, a personal digital assistance (PDA) and a personal computer. As the drive shaft rotates at variable angular velocity, the two probes measure the torque resistance  $T$  of concrete at each rotational speed. The PDA then transfers the measured data to a computer, where the data is imported to an excel sheet and the flow curves are plotted. The torque resistance typically increases linearly with the increase of the flow rate. This relationship is expressed by:

$$T = G + HN \quad (1)$$

Where,  $T$  (Nmm) is the torque resistance,  $G$  (Nmm) is the flow resistance,  $H$  (Nmm·s) is the viscosity factor, and  $N$  is the rotational speed (m/s). The torque resistance  $G$  is the intercept of the T-N line with the torque axis (y axis), and it

represents the force necessary for concrete to start flowing;  $H$  is the slope of this line and is a measure of the resistance of the concrete to an increased speed of flow [5].



**Figure 1.** Illustration of the concrete rheometer used: (a) rheometer assembled, (b) rheometer during testing rheology of fresh concrete

### 1.3. Rheometer calibration

Before conducting the rheology testing, the rheometer was calibrated to ensure accuracy of the measurements. The calibration included defining the distances of the probes from the shaft, calculating the torque constant and calibrating the two sensors using the torque constant. The first step in calibration was to determine the distance of each sensor from the shaft (radius of rotation). The radius of rotation of the inner probe was 75 mm and the radius of rotation of the outer probe was 175 mm. The torque constant (the value of torque corresponding to the weight used in calibration) was the reference torque used in the rheological measurements. To determine the torque constant, the sensors had to be loaded with a weight of 1591 gm (as specified by manufacturer). The weight was hanged on the probe using a thin wire at a distance of 6 mm from the probe's edge (Fig. 2). The rheometer was then set to start reading normal measurement option and the drive shaft was rotated to full rotation. Then, the value of the torque constant was calculated using the equations below (2652 N.mm):

$$F = W * g \quad (2)$$

$$T = F * L_e \quad (3)$$

Where,  $W$  is the weight applied on the sensor in kg,  $G$  is the gravitational acceleration (about  $9.806 \text{ m/s}^2$ ),  $F$  is the force in Newtons,  $T$  is torque constant in N.mm, and  $L_e$  is the effective length of the probe = 170 mm as given by the manufacturer.

After calibration, a trial measurement was conducted by applying the same weight on the two sensors at the same time and the measured torque was to be equal to that calculated and specified by the manufacturer (2652 N.mm), which indicated that rheometer was ready to perform reliable rheological testing.

### 1.4. Mixing and test procedures

The experiments were conducted in a walk-in hot room under a controlled temperature of  $40 \text{ }^\circ\text{C}$ . The percentages of fly ash (FA) were 33% and 25% of the binding materials and superplasticizer dosage ranged from 0.4 to 0.6% by mass of cementitious materials.



**Figure 2.** Illustration of probes calibration

Before the start of mixing, the fine aggregates were first placed in a drum mixer followed by the coarse aggregates. Coarse and fine aggregates were mixed together for 1 minute, then the cementitious materials were added then a third of the total water was poured and mixing continued for 2 minutes. Subsequently, the second third of water was added. After 5 minutes of mixing, the last third of water mixed with half amount of superplasticizer was poured gradually and uniformly in the concrete mixture. The other half of the superplasticizer was injected uniformly onto the concrete batch after 8 minutes of mixing. The procedure used for mixing corresponds to the ASTM C 685-02 guidelines (Standard Test for Concrete Made by Continuous Mixing) [6] and that reported by Ferraris and de Larrad for concretes incorporating superplasticizers [7]. The compressive strength at 3, 7, 28 days was determined using  $150 \times 150$ -mm cubes according to British Standard 8110. For rheology testing, the mixer was stopped and a concrete sample was taken and placed into the container of the rheometer and concrete was leveled. Then, the drive shaft was rotated full rotation. The total rheological testing takes around 2 minutes.

## 2. Results and discussion

### 2.1. Effect of superplasticizer dosage on rheological parameters

Figure 3 illustrates the influence of PCS dosage on the rheological behavior of fresh concrete incorporating 25% FA at 40 °C. Figure 3a shows the flow curve of concrete incorporating 0.5% PC and figures b and c show the flow curves of concrete incorporating 0.55% and 0.6% PC, respectively. It can be seen that the torque resistance of fresh concrete increases linearly with higher rotational speed. It can be further observed that when the PC dosage increases both the flow resistance ( $G$ ) and viscosity factor ( $H$ ) decrease. As shown in Fig. 3, the flow resistance decreased from 279.21 to 108.06 Nmm when the dosage of PCS was increased from 0.5% to 0.6%. The viscosity factor dropped from 5080.6 to 1815 Nmm.s when the dosage of PCS increased from 0.5% to 0.6%. This is due to the dispersion effect of PCS that involves both electrostatic repulsion and steric hindrance. As such, cement particles were more dispersed with a higher PCS dosage, which led to the drop in the flow resistance ( $G$ ) and viscosity factor ( $H$ ).

### 2.2. Effect of superplasticizer dosage on compressive strength

Figure 4a illustrates the compressive strength values at different ages (of 7 and 28 days) for concrete mixtures incorporating 25% FA and two dosages of PC (0.5 and

0.6%). Figure 4b shows the compressive strength of concrete made with 33%FA and incorporating three dosages of PC namely 0.4, 0.5, and 0.6% then cured for 3, 7, 28 days. It can be observed that, in general, the compressive strength for all ages increased by about 10% with increasing PCS dosage. This is likely due to the improvement in the rheological parameters observed in the previous section, when PC dosage increased which made the concrete with a higher workability. As such, the consolidation of concrete with higher dosage of PC was better, because less compaction energy needed to compact fresh concrete with a higher workability.

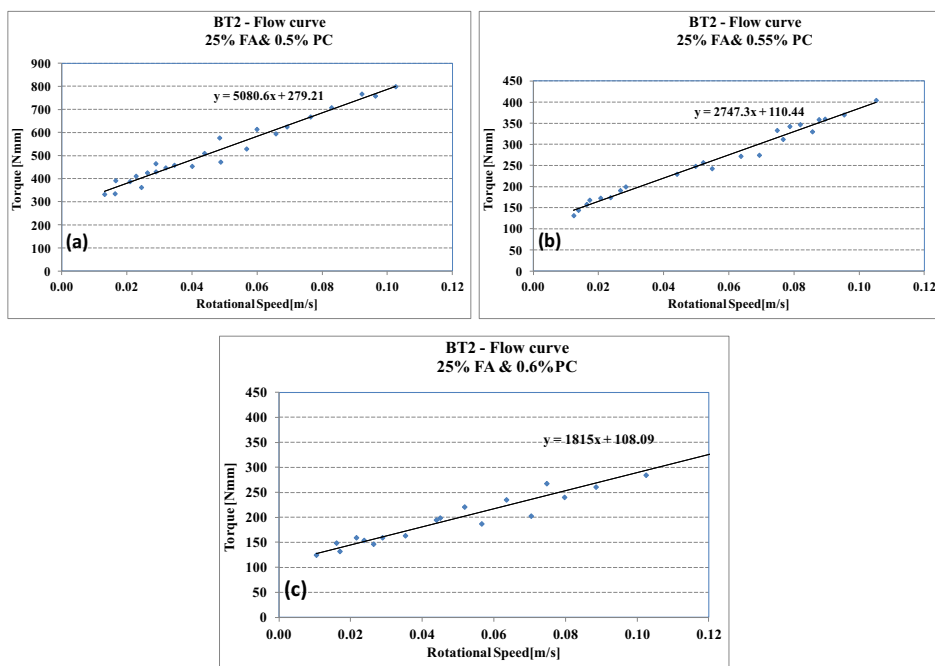


Figure 3. Torque versus rotational speed for concrete mixtures incorporating 25% FA and different PCS dosages (a) 0.5%PCS, (b) 0.55%PCS, and (c) (a) 0.6%PCS

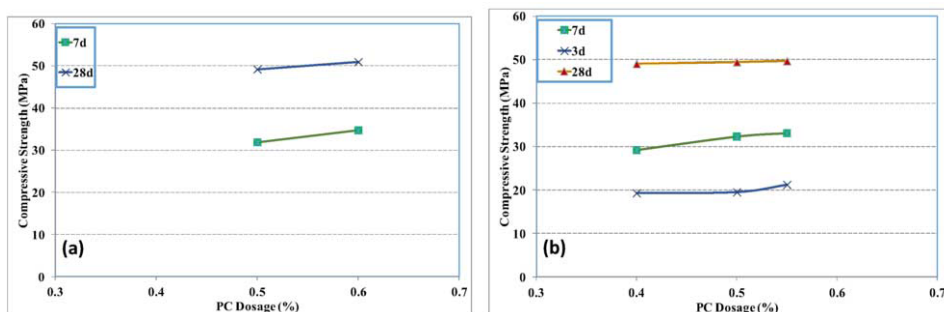


Figure 4. Relation between polycarboxylate dosage and compressive strength at different ages for concrete incorporating (a): 25 % FA and (b): 33% FA

### 3. Conclusions

The present study explores how the PCS dosage affect the rheology and compressive strength of concrete. Based on the results obtained, the following conclusions can be drawn:

- a) The flow curves of fresh concrete followed linear function, where the torque increased linearly with increasing rotational speed.
- b) Both flow resistant ( $G$ ) and viscosity factor ( $H$ ) decreased with increasing PC dosage.
- c) Compressive strength of concrete, in general, increased with increasing PC dosage.

### Acknowledgments

The authors would like to acknowledge the financial support of The .Abu Dhabi University (ADU), Grant number CRGS/SERG/1920096. Thanks are also due to a number of admixtures, additives and aggregates suppliers who contributed materials used in this investigation.

### References

- [1] Soroka, I. and Ravina, D, Hot Weather Concreting with Admixtures, *Cement and Concrete Composites*, **20** (1998), 129–136.
- [2] Thomas, J. J., Rothstein, D., Jennings, H. M., and Christensen, B. J, Effect of Hydration Temperature on the Solubility Behavior of Ca-, S-, Al-, and Si-Bearing Solid Phases in Portland Cement Pastes,” *Cement. Concrete Research*, **33**(2003), 2037–2047.
- [3] Berge, O, Improving the Properties of Hot-Mixed Concrete Using Retarding Concrete Admixtures, *ACI Journal*, **73**, (1976) 394–398.
- [4] ACI Committee 305, “Recommended Practice for Hot Weather Concreting (ACI 305R-77),” American Concrete Institute, Farmington Hills, MI, 1977.
- [5] Geiker, M. R.; Brandl, M.; Thrane, L. N.; Bager, D. H.; and Wallevik, O., The Effect of Measuring Procedure on the Apparent Rheological Properties of Self-Compacting Concrete, *Cement and Concrete Research*, **32**( 2002), 1791-1795.
- [6] ASTM C 685, Standard Specification for Concrete Made by Volumetric Batching and Continuous Mixing, *Annual Book of American Society for Testing Materials*, **4**(2002), West Conshohocken, PA.
- [7] Ferraris, C. and de Larrard, F. Testing and Modeling of Fresh Concrete Rheology, NISTIR 6094, National Institute of Standards and Technology, 1997.

# Influence of a new viscosity modifying admixture on the performance of different superplasticizers

Stephen O. EKOLU<sup>a,1</sup> and Jean-Bosco KAZURIKANYO<sup>b</sup>

<sup>a</sup>Department of Civil Engineering Science, University of Johannesburg

<sup>b</sup>Advanced Cement Training & Projects (ACTP) The Advanced Cement Institute

**Abstract.** An investigation was conducted on a new viscosity modifier, herein referred to as *VMA*, to determine its effects and compatibility with commercially available superplasticizers and local cements. Marsh cone tests were conducted on cement pastes to compare saturation points and the influence of the viscosity modifying admixture.

It was found that the *VMA* gave improved results when used with a polycarboxylate-based superplasticizer and also reduces the required dosage of the superplasticizer needed to achieve specific fluidity. However, it was observed that the *VMA* showed no influence whatsoever, when used with the phosphonate based-superplasticizer. These findings underscore the importance of establishing compatibilities and interactions when more than one admixture is used in fresh concrete.

**Keywords.** Marsh cone test, viscosity modifying agent, saturation point, polycarboxylate, phosphonate superplasticizer

## Introduction

The chemical admixture technology for use in concrete has developed since the early 1930s [1], and as the technology continued to evolve over the years, admixtures have become a vital part of concrete. Presently, there exist a vast variety of admixtures, all fulfilling different functions. The common types of commercially available admixtures are: air-entrainers, plasticizers/superplasticizers, retarders, accelerators, shrinkage reducers, and viscosity modifiers. Gołaszewski [2] investigated the functionality and influence of the combined use of viscosity enhancing agents (VEA) with different superplasticizers (SP's) and found that  $C_3A$  content in cement had a significant effect; high  $C_3A$  cements require higher dosages of SPs. To achieve the high flow requirements for SCC, superplasticizers are added into concrete, in order to reduce the yield stress and increase fluidity. But by the same action, there is the unintended consequence of high wetness as the mix becomes less viscous (high flowing paste) and may cause segregation. A viscosity modifier is added in order to increase plastic

---

<sup>1</sup>Corresponding author: University of Johannesburg, Department of Civil Engineering, P.O. Box 524, Auckland Park, 2006, South Africa; E-mail. [sekolu@uj.ac.za](mailto:sekolu@uj.ac.za), [sekolu@gmail.com](mailto:sekolu@gmail.com)

viscosity without much effect on the yield stress (fluidity), consequently making the mix to be cohesive.

The purpose of this research was to assess the effects and compatibility of a new viscosity modifying agent, *VMA*, with commercially available superplasticizers and cements in the South African market.

## 1. Background

The use of admixtures has taken place since the days of the ancient civilizations. Originally, these admixtures were made from organic matter and were predominantly used as: water resistant and tinting surface coats and set retarders for mortar [1]. Some natural admixtures used throughout history were; “milk and lard by the Romans; eggs during the middle ages in Europe, and extracts from elm soaked in water and boiled bananas by the Chinese” [1]. Pozzolanic materials, (also referred to as mineral admixtures) were first used by the ancient Greeks during the period 700-600 B.C. The ancient Greeks used these materials in constructing water-storage tanks [3]. These construction techniques were then passed on through the ages and adapted for different purposes by the Romans, the French and the Spanish. Most recently, after the invention of Portland cement, natural pozzolan has been used as a concrete strengthening additive to improve engineering characteristics [3]. Modern use of chemical admixtures started around 1900’s with different admixture types emerging over different periods of the century as shown in Figure 1.

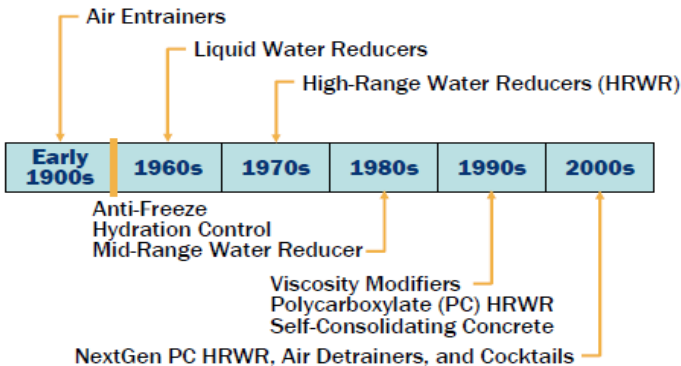


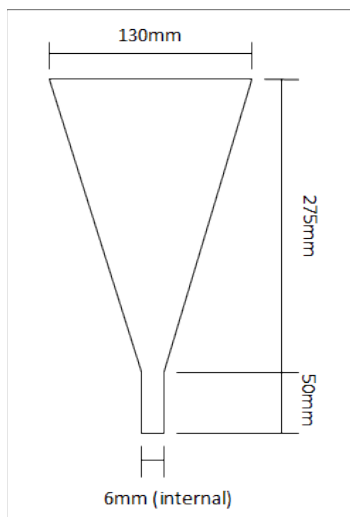
Figure 1. Different admixture types emerging over different periods of the century

## 2. Experimental

The Marsh Cone tests were used to evaluate the fluidity of the mixes and also to determine the saturation points for different superplasticizers with and without the addition of *VMA* and silica fume.

The Marsh Cone used in this investigation was fabricated inhouse. Although the dimensions of the fabricated apparatus were different from those required by BS EN 445:2007 [4], the side slope of the fabricated cone was made to be almost identical with that of the standard specifications [4]. It was built using an adhesive glue, a

plastic funnel with appropriate nozzle shape and diameter, and a plastic vacuum jug of an approximate 2-litre volume. Figure 2 shows the dimensions of the Marsh Cone size that was fabricated for conducting the experiment.



**Figure 2.** Dimensions of the fabricated Marsh Cone

The investigation was conducted using two superplasticizers of different chemical bases i.e the modified polycarboxylate (SPS) and the modified phosphonate (SPC). Paste mixes were prepared at water/cementitious ratio (w/c) of 0.4. By varying the recommended dosages of the superplasticizers, it was possible to establish the saturation points (SatP) with and without incorporation of the *VMA*. An extension of the study included the incorporation of 10% silica fume (SF) into the mixtures. Table 1 gives the various sets of Marsh Cone tests conducted on paste mixtures.

**Table 1.** The various Marsh Cone tests

Constituent	SPS	SPC	SPS	SPC	SPS	SPC	SPS+SF	SPC+SF
Cement	X	X	X	X	X	X	X	X
Water	X	X	X	X	X	X	X	X
Silica Fume			X	X			X	X
VMA (%)			0.05- 0.25	0.05- 0.25	0.1	0.1		
SP dosage (%)	0.6-3	0.6-3	1.5	1.8	0.6-3	0.6-3	0.6-3	0.6-3

The experiment was conducted in three stages: (i) First, the dosages of admixtures (SPS/SPC) were varied in order to obtain its saturation point (SatP), then (ii) *VMA* dosage was varied for a fixed dosage of admixture at its saturation point, finally (iii) the dosage of admixture was varied at a constant dosage of *VMA*.



### 3. Discussion of results

#### 3.1 Saturation points of the different admixtures

The results of the Marsh Cone test are shown in Figures 3 to 6. In Figure 3, it can be seen that the modified polycarboxylate SPS gave a lower saturation point of 1.5% compared to 1.8% of the modified phosphonate SPC. However, SPS gave a greater flow efficiency than SPC.

#### 3.2 Effect of the viscosity modifying admixture on saturation points of superplasticisers

In order to examine the effect of *VMA* on the paste mix, a test series with SPS and with SPC was carried out. In this series, the dosage of the admixtures was fixed at its predetermined SatP while the dosage of *VMA* was varied from 0.05% to 0.25% by mass of cement, i.e the SPS dosage was fixed at 1.5% while that of SPC was kept at 1.8%. For SPS, the optimum dosage of *VMA* was established to be 0.1%, with higher or lower dosages giving higher flow times, as shown in Figure 4. Similarly, it shown that the optimal dosage for SPC was 0.05-0.1%, both of which gave similar results. While dosages lower than 0.1% did not increase or lower the flow time, it was clear that raising the dosage of *VMA* to above 0.1% led to a dramatic increase in flow time, implying reduced workability.

Having established the SatPs of admixtures and optimum dosages for use of *VMA*, a test series was conducted in which *VMA* was introduced into the mixture at a fixed (optimum) dosage while the admixture dosage was varied. The results of this test series are shown in Figure 5. Clearly, in the presence of *VMA* there is a significant effect characterized by reduction of the amount SPS required to maintain the same level of fluidity. However, the SatP of the SPS remained unchanged by the use of *VMA*. Interestingly, however, the use of *VMA* with SPC had no effect on the performance of SPC, with both curves remaining in the same position with or without the *VMA* (Figure 5). The factor that was found to be common to the interaction of *VMA* and both superplasticizers, was that the SatP's of the superplasticizers (SPS/SPC) remained unchanged.

#### 3.3 Effect of silica fume

Using silica fume in the mixtures had a strong influence on the SatP of both superplasticizers (SPS and SPC). It can be seen in Figure 6 that the SatP of SPS shifted from 1.5% to 2%, while that of SPC increased from 1.8 to 2.4%, when 10% SF was incorporated into the mixtures.

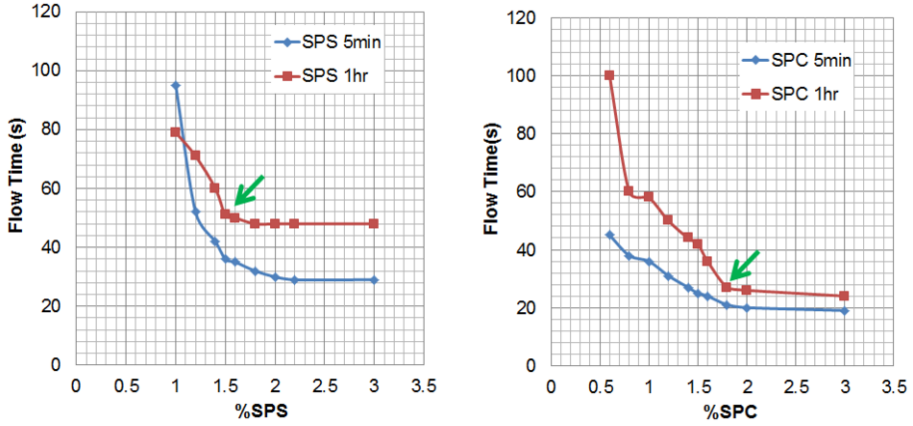


Figure 3. Saturation points (SatP) of the superplasticisers

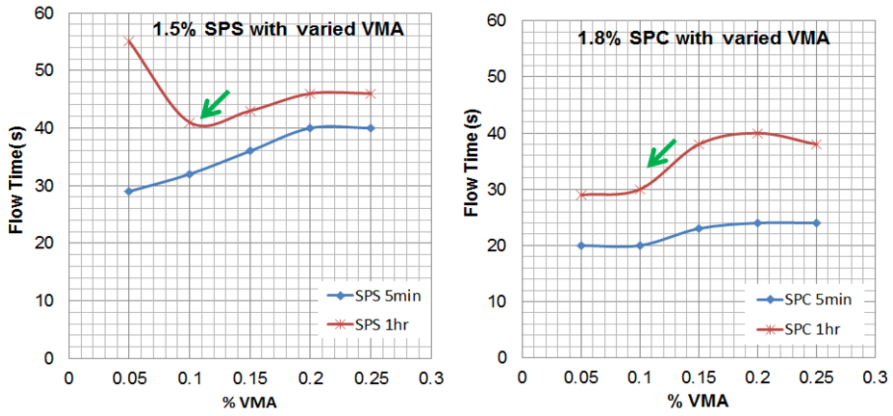


Figure 4. Optimum dosage of VMA

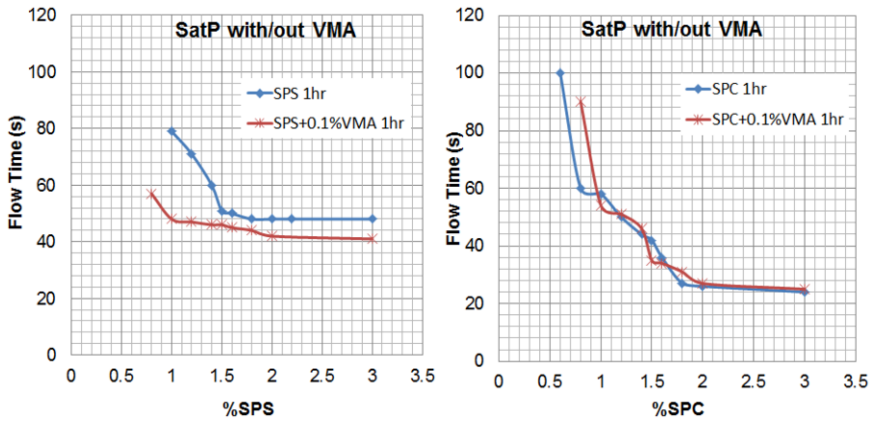


Figure 5. Influence of VMA on flow and SatP

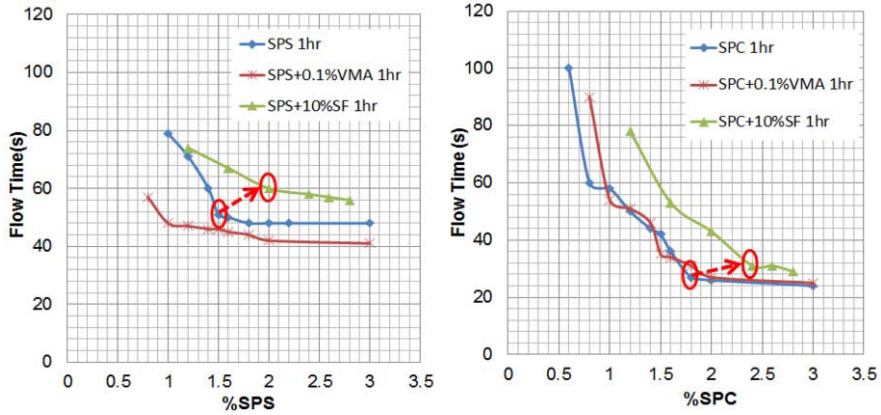


Figure 6. Influence of silica fume on flow and SatP

#### 4. Conclusions

From the foregoing results and analysis presented, the following conclusions were drawn:-

- The modified polycarboxylate superplasticizer gave a lower saturation point of 1.5% compared to 1.8% of the modified phosphonate superplasticizer. However, the latter had greater flow efficiency than the former.
- The *VMA* reduces the amount of a modified polycarboxylate superplasticizer needed to maintain the same paste fluidity.
- On the other hand, the *VMA* does not seem to affect positively nor adversely the use of modified phosphonate superplasticizer, as the viscosity modifier shows no impact on the saturation point or fluidity of cement paste.

#### Acknowledgement

The work presented in this paper was based on the final year investigation project of Mr. Sebastian Burwitz and Mr. Stephen Panagiotou.

#### References

- [1] American Concrete Institute, *Chemical Admixtures for Concrete*, ACI Committee E-701, ACI Education Bulletin E4-03.
- [2] Gołaszewski J., Influence of viscosity enhancing agent on rheology and compressive strength of superplasticized mortars, *Journal of Civil Engineering and Management*, Vol. 15, no2, 2009, pp.181-188.
- [3] Wilson, J.W. and Ding, Y.C., *A Comprehensive Report on Pozzolanic Admixtures*, the Cement Industry, Market and Economic Trends and Major Companies Operating in the FarEast, with Referenceto Pagan Island, Department of Public Lands, Commonwealth of Northern Mariana Islands, 2007
- [4] British Standards Institution. (2007). BS EN 445:2007 Grout for prestressing tendons — Test methods. London: Standards Policy and Strategy Committee.

# Effect of microfines mineral admixtures on rheology of blended cement paste

Maulik M. PANSERIYA<sup>a</sup>, U.V.DAVE<sup>a</sup> and A. K. TIWARI<sup>b,1</sup>

<sup>a</sup>Department of Civil Engineering Nirma University

<sup>b</sup>Central R&D Ultratech Cement LTD, India

**Abstract.** Rheological tests on cement paste were used to successfully select the type and dosage of micro-fine mineral admixtures that improved concrete workability. Among the seven different micro-fine mineral admixtures tested, the classified fly ash (CFA, P-100) was determined to give the best results by reducing the yield stress and viscosity. These improved rheological properties were not achieved by increasing the water demand or the high-range water reducer dosage. Therefore, the replacement of classified fly ash improved the rheological property of cement paste without a decrease of the hardened properties or an increase in cost. The cement paste rheological data were also compared using a simpler test, the minislump. The conclusion is that this simpler test is reliable for certain cases to co-relate slump flow with yield stress.

**Keywords.** Rheology, cement paste, micro fine, mini slump, viscosity.

## Introduction

Concrete pumping is extensively used worldwide for the construction of sky scrapers and long span bridges. This technique offers notable advantages such as allowing concrete casting in difficult to access locations, and reducing casting process durations or allowing for a continuous concrete casting process. The property that allows concrete to be pumped is called pumpability or flow ability [1].

Concrete workability is usually quantified by the slump test. Studies have shown that slump value is a necessary but not a sufficient measurement to characterize the fundamental rheological properties of concrete, namely plastic viscosity and yield stress. Concrete is a yield stress fluid and many constitutive equations have been proposed in the literature to predict their rheological behavior. For normal slump concrete, Bingham material model has been shown to fit very well with experimental data and is defined by

$$\zeta = \zeta_0 + \mu\dot{\gamma} \quad (1)$$

Where  $\zeta$  is the shear stress (Pa),  $\zeta_0$  the yield stress (Pa),  $\eta$  the plastic viscosity (Pa.s) and  $\dot{\gamma}$  the shear strain rate (1/s) [2].

---

<sup>1</sup>Corresponding author: UltraTech Cement Limited, Central R&D Taloja Unit, NB1, Plot No. 1 &1-A/1, MIDC Taloja, Navi Mumbai 410 208, India; Email. [ashok.k.tiwari@adityabirla.com](mailto:ashok.k.tiwari@adityabirla.com)

## 1. Background

### 1.1 Research Significance

The objective of the present study was in relation to high-performance concrete (HPC). HPC is a complex mixture often containing different materials. Interaction between the various materials can cause wide variations in workability. This makes it very challenging to predict and optimize the rheological characteristics of fresh concrete in order to meet specific requirements. The decision to study the effect of micro-fines mineral admixture for improved concrete durability and economics along with environmental considerations have also played a role in the growth of mineral admixture usages [3].

### 1.2. Role of fine powder on workability

Ferris et al. [3]. reported that, if the volume concentration of a concrete is held constant, the addition of mineral admixtures improves concrete performance but reduces workability. The most common reason for poor workability is that the addition of a fine powder will increase the water demand due to the increase in surface area.

A popular hypothesis put forward to explain the workability enhancement due to the use of certain fine mineral admixtures, especially fly ash, is that the spherical particles easily roll over one another, reducing inter particle friction [4].

The spherical shape also minimizes the particle's surface to volume ratio, resulting in low fluid demands. Out of all 3D shapes, a sphere gives the minimum surface area for a given volume [5].

Karthik H. Obla et al. [4]. reported that a higher packing density increased sphericity in theory, and should result in lower water retention in the spherical case and subsequently, lower water demand for a specific workability.

## 2. Material mixing and testing details

### 2.1 Materials

The cement used was ordinary portland cement conforming to IS 12269 whose composition is described in Table 1. This cement was used for all rheological tests of cement paste. The micro-fine mineral admixtures used are also shown on Table 1 with their chemical composition. The particle size distribution was measured using a laser diffraction particle size analyzer, as shown in fig 1.

The cement paste composition was varied to explore the influence of mineral admixture dosage and type on the rheological properties. The performance differences in the pastes, due to the replacement of mineral admixture by mass, were determined by measuring their rheological properties at four different water contents. The compositions of the cement pastes can be summarized as follows:

- Water/Cement ratio: 0.45, 0.5, 0.55, 0.6
- Dosages of mineral admixtures: 5%, 7.5% and 10% of cement, replacing cement by mass.

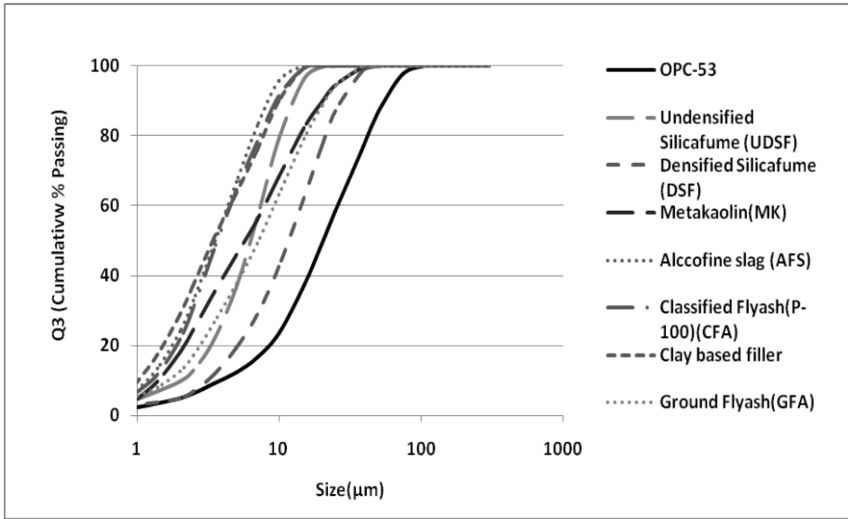


Figure 1. Particle size distribution of micro-fines with OPC-53 cement.

Table 1. Chemical Composition of all micro fine materials with OPC-53 cement

Chemical Composition (% by mass)	Micro fines Mineral Admixtures							
	OPC-53 (Cement)	UDSF	DSF	MK	AFS	GFA	CFA (P-100)	Clay based Filler
Loss of Ignition(LOI)	2.06	2.29	2.4	2.35	0.43	1.09	0.58	43.18
Insoluble Residue(IR)	2.37			86.67	0.79	93.95	92.93	2.58
Silica dioxide(SiO <sub>2</sub> )	22.65	93.96	94.64	51.78	33.28	59.11	55.94	1.66
Aluminum Oxide (Al <sub>2</sub> O <sub>3</sub> )	4.65	0.42	0.38	42.66	21.24	30.53	32.17	0.65
Ferric Oxide (Fe <sub>2</sub> O <sub>3</sub> )	4.46	0.17	0.18	0.55	0.9	3.45	4.89	0.16
Calcium Oxide (Cao)	60.43	0.36	0.24	0.21	34.01	1.41	1.38	48.34
Magnesium Oxide (Mgo)	0.8	0.59	0.53	0.12	5.79	0.51	0.73	5.07
Sulfur Trioxide (So <sub>3</sub> )	2.22			0.03	0.22	0.23	0.23	-
Equivalent alkali (as Na <sub>2</sub> O)	1.11	1.63	0.38	1.18	1.73	3.09	3.31	0.48

DSF = Densified Silica fume, UDSF = Undensified Silica fume, AFS = Alcco fine slag, MK = Metakaolin, CFA = Classified Fly Ash, GFA = Ground Fly Ash

### 2.2 Cement paste preparation

The cement paste preparation is very important because the shear history of a mixture will influence its rheological behavior. Digital mortar type of mixers was therefore considered. The cement paste was mixed using a digital mortar mixer according to the procedure of ASTM C305, except that no sand was added. [6]

### 2.3 Cement paste testing details

Fresh cement paste specimens were tested first in a Viskomat NT fluid rheometer and then using the mini slump. The testing details are given below.

#### 2.3.1 Viskomat NT rheometer

The Viskomat NT rheometer was used to determine the yield stress and the plastic viscosity as defined by Bingham model [7]. The probe of the Viskomat NT rheometer should be selected based on the type of fluid. For cement paste, the stirrer type cement paste probe is used. All samples were pre-sheared for 5 min at 120 rpm. This reduced substantially the torque; close enough to a plateau value to consider the sample to have been well preconditioned in which a steady state had been reached. The rotation frequency was then reduced at logarithmically spaced steps (120, 100, 80, 60, 40,  $\text{min}^{-1}$ ), each step lasting 5 min. Flow curves were established with data corresponding to steady state only.

It is generally agreed that during a rheology test, the attractions and agglomerations of the particles in the tested sample are broken down during the period of the increased shear rate (up curve of the test result). After the attractions and agglomerations of the particles in the tested sample have fully broken down, the rheological behavior of the tested material generally agrees with the Bingham model, as shown by the down curve of the test result. Due to the complicated flow pattern applied to the tested cement paste by the probe, it is difficult to obtain the exact value of shear stress and shear rate of the tested cement paste. Therefore, the torque and the speed of the probe were reported during the cement paste rheology tests and their relationship was plotted. A typical Viskomat NT test result is shown in Fig.2. The following equation was used to fit the down curve from a Viskomat NT rheology test based on Bingham model:

$$T = G + H \times N \quad (2)$$

Where T was the torque acting on the probe, and N was the rotation speed of the impeller. G was the interception of the linear portion of a Viskomat NT down curve and the y-axis. H was the slope of the linear portion of the Viskomat NT down curve.

The device does not allow direct calculation of yield stress and plastic viscosity in fundamental units due to the complicated flow pattern, the down curves of the torque-rotation speed were found to fit well with Bingham pattern. The slope (H) and interception (G) obtained from Viskomat NT measurements were considered to be directly proportional to yield stress and viscosity of cement paste respectively. In the present paper, G is therefore used to describe the yield stress and H is used to describe the plastic viscosity of the tested cement paste. [7]

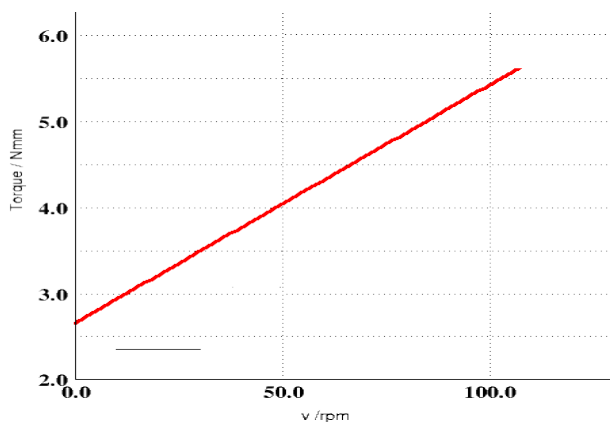


Figure 2. Typical Viskomat NT Flow curve.

### 2.3.2 Mini slump test detail

The Mini slump test was conducted as follows:

- A square piece of flat glass on which the diagonals and the median were traced.
- The mini slump cone was placed in the center of the glass plate and filled with the cement paste.
- The cone was gently lifted and after one minute, the diameter of the pad formed was measured along the marked line on the glass in four directions.
- All four diameters were recorded and the average diameter was calculated.[8]

## 3. Result and discussion

In Figures 3, 4 & 5, the yield stress and viscosity are shown for mixtures composed of cement paste with the same W/C ratio of 0.45. The amounts of the various micro-fine mineral admixtures by mass as replacement of cement were 5%, 7.5% and 10%. It is clear that the replacement of cement with classified flyash (P-100) leads to a decrease in yield stress and viscosity over the control sample (no mineral admixtures). In contrast, the replacement of cement by Undensified silicafume significantly increases the given yield stress and viscosity. The possible reason for increasing in rheological parameter is its extreme fineness and very high amorphous silicon dioxide content, which makes silica fume highly reactive pozzolanic material while flyash having lower silicon dioxide content makes fly ash less reactive. Increasing the fineness of flyash particles by grinding improves reactivity but eventually increases its water demand due to irregularly shaped ground flyash particles, while increasing the fineness of flyash by air classification techniques improves reactivity of flyash without impact on spherical shape of particles.



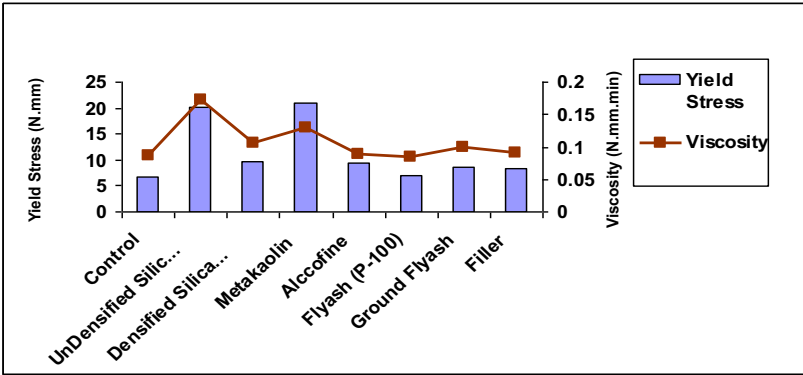


Figure 3. Effect of micro fine mineral admixture on rheology of cement paste with 5% replacement level at w/c-0.45.

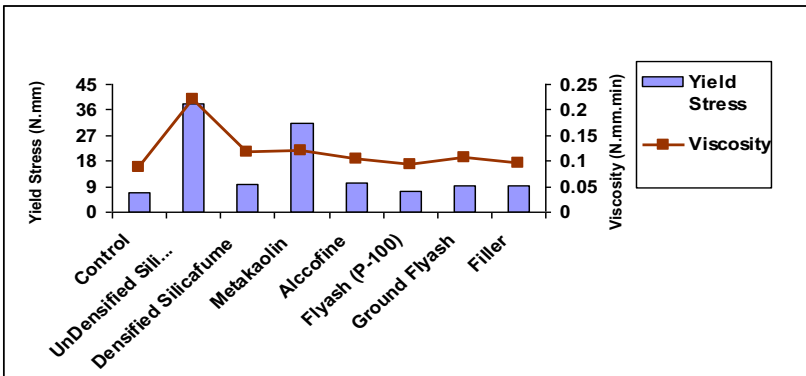


Figure 4. Effect of micro fine mineral admixture on rheology of cement paste with 7.5% replacement level at w/c-0.45.

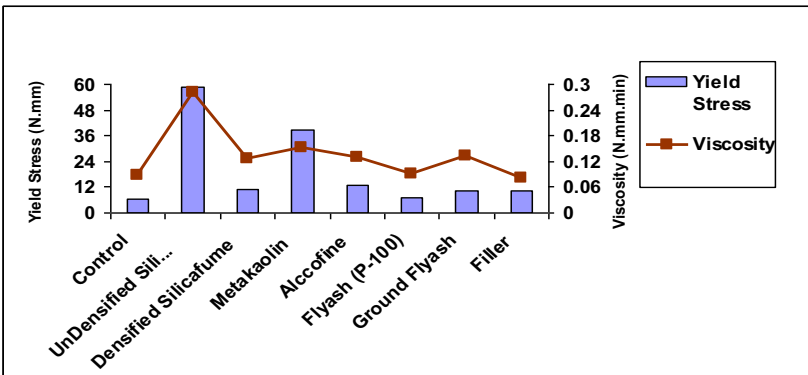


Figure 5. Effect of micro fine mineral admixture on rheology of cement paste with 10% replacement level at w/c-0.45.

#### 4. Relation between minislump flow and Viskomat NT yield stress

A fluid rheometer for cement paste is not widely available in the construction industry because of two main reasons is: (1) the instrument is relatively expensive and (2) the knowledge of using such a device for cement paste is limited. Therefore, it is advantageous to use simpler tests such as the minislump test. The plot of yield stress vs. minislump spread diameter (Fig.6) shows a good correlation for all micro-fines mineral admixtures except Metakaoline at 5% replacement level and Undensified Silicafume at 7.5% and 10% replacement levels; higher yield stress corresponds to a lower spread in the minislump. This result shows that the cement paste in a minislump test will only flow if the stress due to the weight of the cement paste contained in the cone is high enough, i.e., higher than the yield stress of the cement paste. An approximation of the yield stress could be obtained by fitting a straight line through the data.

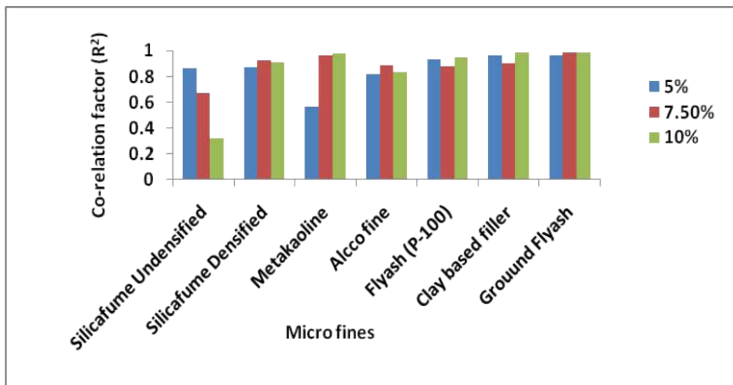


Figure 6. Co-relation factor of yield stress and spread diameter of minislump flow of all micro fines.

#### 5. Conclusion

The purpose of this research was to determine effect of microfine admixtures, being commonly used today to improve the performance of concrete on the rheological properties of mixtures.

In cement paste, which affects the pumpability of resulting concrete, provided other parameters remains same, several mineral admixtures were examined and it was found that classified flyash (P-100) improves the rheology while Silicafume and metakaolin changes the same negatively. It was observed that the replacement of cement by Silicafume results in an increase in the water demand and requires high range water reducer dosage to maintain the rheological properties. In contrast the replacement of cement by classified fly ash (P-100) resulted in a reduction of the water demand and lower HRWR dosage to maintain the same rheological properties of the control. The other mineral admixtures, Alcco fine, Densified Silicafume, and Ground fly ash, gave results in between the Undensified Silicafume and Classified fly ash (P-100) and, therefore, were not as extensively studied as Silica fume and fly ash. Simpler

tests such as the minislump test shows a good correlation with rheological tests, for all micro-fine mineral admixtures except Undensified Silicafume at 7.5 and 10%; metakaolin at 5% replacement level.

## References

- [1] Myoungsung Choi, Nicolas Roussel, Youngjin Kim, Jinkeun Kim, Lubrication layer properties during concrete pumping, *Cement and Concrete Research* 45 (2013) 69–78.
- [2] F. Mahmoodzadeh, S.E. Chidiac, Rheological models for predicting plastic viscosity and yield stress of fresh concrete, *Cement and Concrete Research* 49 (2013) 1–9.
- [3] Chiara F. Ferrarisa, Karthik H. Obla, Russell Hill, The influence of mineral admixtures on the rheology of cement paste and concrete, *Cement and Concrete Research* 31 (2001) 245–255.
- [4] Karthik H. Obla, Russell L. Hill, Michel D.A. Thomas, Surali G. Shashiprakash, and Olga Perebatova, Properties of Concrete Containing Ultra-Fine Flyash, *ACI Material Journal* September/October (2003).
- [5] G. Polya, G. Szego, *Isoperimetric Inequality in Mathematical Physics*, Princeton Univ. Press, Princeton, NJ, 1951
- [6] ASTM C305-94, Standard Practice for Mechanical Mixing of Hydraulic Cement Pastes and Mortars of Plastic Consistency, vol.04.01, 1998
- [7] Robert J. Flatt, Domenico Larosa a, Nicolas Roussel, Linking yield stress measurements: Spread test versus Viskomat, *Cement and Concrete Research* 36 (2006) 99-109.
- [8] ACI 238.1R-08, Report on Measurements of Workability and Rheology of Fresh Concrete, pp 43-44.

# Research on a novel technology of FRP bonded to concrete substrate without adhesive

Ming LI<sup>a</sup>, Yunpeng LIU<sup>b</sup>, Muyu LIU<sup>b</sup> and Fazhou WANG<sup>a,1</sup>

<sup>a</sup>State Key Laboratory of Silicate Materials for Architectures, Wuhan University of Technology, Wuhan 430070, China

<sup>b</sup>Hubei Key Laboratory of Roadway Bridge and Structure Engineering, Wuhan University of Technology, Wuhan 430070, China

**Abstract.** Without any treatment for concrete surface, a novel technology of FRP bonded to concrete substrate without adhesive was developed, in which the porous lightweight aggregate was used as bridge material between FRP sheet and concrete. Base on that technology, a prefabricated rough FRP sheet which can be used accompanying with concrete pouring was presented with the aim to improve the durability of concrete, which has a great potential to be widely used in the area of reinforcement, surface decoration and protection for concrete construction. The durability of rough FRP sheet was preliminarily evaluated by pull-off test and chloride ion penetration test. Results indicated that bond strength between rough FRP sheet and concrete substrate was 2.17MPa, chloride ion permeability coefficient at 30 days was  $8.41 \times 10^{-4}$  mg/d·cm<sup>2</sup>. Microstructure analysis showed that the bond strength was mainly determined by mechanical interlocking and interfacial structure between lightweight aggregate and cement paste, an equation based on the bond model was put forward to optimize the design of rough FRP sheet.

**Keywords.** FRP sheet, durability, bond

## Introduction

Owing to the excellent performance of corrosion resistance, fatigue resistance, high strength and stiffness to weight ratio, fiber reinforced polymer (FRP) composites have been widely applied in retrofitting and rehabilitating the concrete structures in civil engineering. Externally Bonded Retrofit (EBR) using FRP sheet or plate is most popular method for flexural retrofit of concrete member. However, problems like drop-out in epoxy parts have been reported in many cases due to insufficient development of bond strength between FRP sheet or plate and concrete substrate [1]. In recent years, Near Surface-Mounted Retrofit (NSMR) method was developed and has been proven to be an efficient technique for strengthening concrete members [2-4]. Recent studies [5-6] have shown that the adhesive layer play a relevant role in the behavior of

---

<sup>1</sup>Corresponding author: fzhuwang@whut.edu.cn, Tel. +86 27 8764, Fax. +86 27 8765 1779

adhesive joints. However, in NSMR method, concrete surface treatment and adhesive were needed, thus lead the process to be more complex.

To improve such problems, a novel technology of FRP bonded to concrete substrate was developed by the use of rough material instead of adhesive, a prefabricated rough FRP sheet was manufactured based on that technology, and became a unit with concrete construction after concrete is casted, without any treatment for concrete surface, which has a great potential to be widely used in the area of reinforcement, surface decoration and protection for concrete construction. In this study, lightweight aggregate was used as rough material to prepare the rough FRP sheet, bond behavior and durability of rough FRP sheet were preliminarily discussed.

## 1. Materials and methods

### 1.1. Materials

Ordinary Portland cement (OPC) was used with a blaine fineness of  $318\text{m}^2/\text{kg}$ , the fly ash (FA) with a fineness (vacuum sieve,  $>45\mu\text{m}$ ) of 7.8% and blast furnace slag (BFS) with the activity coefficient of S95 were added as dry powder, the chemical composition were shown in Table 1. The natural river sand (S) with a maximum size of 4.75mm and limestone with a size distribution ranging from 5mm to 20mm were used as the fine and the coarse aggregate, respectively. A polycarboxylate-based superplasticizer (SP) with 20% solid content was used. The mix proportion of concrete was listed in Table 2 and several concrete specimens with the size of  $100\times 100\times 100\text{mm}$  were cast.

**Table 1.** Chemical composition of cementitious materials ( in wt. %)

Parameters (%)	SiO <sub>2</sub>	Al <sub>2</sub> O <sub>3</sub>	Fe <sub>2</sub> O <sub>3</sub>	CaO	MgO	SO <sub>3</sub>	K <sub>2</sub> O	TiO <sub>2</sub>
OPC	21.46	5.64	2.95	60.59	1.64	2.75	-	-
FA	50.93	33.51	3.33	3.69	0.66	0.51	1.49	1.60
BSF	29.89	16.20	0.41	35.53	10.96	3.32	0.36	1.27

**Table 2.** Mix proportion of concrete ( $\text{kg}/\text{m}^3$ )

W/B	C	FA	BSF	W	S	G	SP
0.35	275	50	135	160	700	1100	6.4

The FRP composite consisted of glass fiber fabric in epoxy resin matrix. In this study, the glass fiber fabric was provided by CPIC company, a commercial epoxy resin that formulated in bisphenol A resin with modified amine where a mix ratio was 100:29 (bisphenol A resin: modified amine) was used to fabricate the FRP composite. The thickness of FRP composite was 1.5 mm. Lightweight aggregate (LWA) was used as rough material to prepare rough FRP sheet, two different kinds of LWA with the specific gravity grade at 0.5 and 0.9 ( $>500\text{kg}/\text{m}^3$  and  $>900\text{kg}/\text{m}^3$ , respectively), and with the particle size at 3.15~4.75 mm (marked with L0.5-3-4, L0.9-3-4 respectively) were prepared and then distributed evenly on the FRP by gravel within the epoxy resin curing. The preparation process of rough FRP sheet was shown in Fig. 1

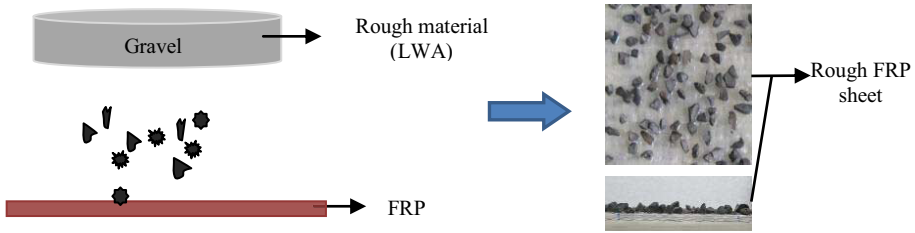


Figure 1. The preparation process of rough FRP sheet

## 1.2. Methods

### 1.2.1. Texture depth

Texture depth (TD) was tested by fine sand with a 0.1mm maximum size to evaluate the average depth of rough FRP sheet caused by rough material, according to the Chinese national standard field test methods of subgrade and pavement for highway engineering (JTG E60-2008). The fine sand was poured in the test area, and paved into round shape evenly. Subsequently, two vertical diameters ( $D$ ) were measured and the volume of sand ( $V$ ) was obtained by measuring cylinder at the same time. The texture depth of rough FRP sheet can be calculated according to Eq. (1). For each of the rough FRP sheet specimens, the same test was carried out 6 times to minimize experimental errors by averaging the results.

$$TD = \frac{V}{\pi D^2 / 4} \quad (1)$$

### 1.2.2. Pull off bond strength

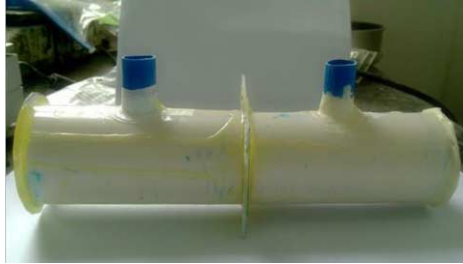
Pull off bond strength between the concrete and the rough FRP sheet was determined according to the Chinese national standard corrosion prevention technical specifications for concrete structures of marine harbor engineering (JTJ275-2000 analogous with ASTM D7522). Pull-off bond was measured by using a rectangular loading fixture normal to the bottom surface of the retrofitting materials. After curing for 28 days, a tension force was loaded to the test surface by gradually increasing the force until failure occurred along the weakest plane between rough FRP sheet and concrete substrate. For each composite specimen, four pull off tests were carried out to minimize experimental errors by averaging the results.

### 1.2.3. Chloride ion penetration test

Chloride ion penetration of rough FRP sheet was evaluated according to the Chinese national standard corrosion prevention technical specifications for concrete structures of marine harbor engineering (JTJ275-2000). Rough FRP sheet was cut to a specimen with diameter of 60mm, the side of specimen with LWA toward the distilled water, another side toward the salt water with mass concentration of 3%. Silicon rubber and

epoxy resin were used to effectively ensure the sealing performance of the device. After 30d, the chloride ion in distilled water ( $m$ ) and the inner diameter ( $d$ ) were measured. Activity layer of chloride ion penetration test was shown in Fig 2. Chloride ion penetration ( $C$ ) can be calculated according to Eq. (2). Four activity layer of chloride ion penetration tests were carried out to minimize experimental errors by averaging the results.

$$C = \frac{m}{30 \cdot (\pi D^2 / 4)} \quad (2)$$



**Figure 2.** Activity layer of chloride ion penetration test

#### 1.2.4. Microstructure analysis

Extra specimens including composite specimens and RFC were prepared for scanning electron microscope (SEM) analysis. The interfacial transition zone between cement paste and rough material and that between rough material and FRP were observed, respectively.

## 2. Results and discussion

### 2.1. Bond strength

Three failure modes, which were rough FRP sheet failure (cohesive failure in FRP substrate), adhesive failure between rough FRP sheet and concrete substrate, and mixed mode failure including rough FRP sheet failure and interface failure, were observed during pull off test,. This research result was similar to the findings of other researchers [7]. First, cohesive failure in FRP substrate, representing poor adhesion system, was shown in Fig 3(a). Complete de-bonding failure occurred in the interface layer between FRP and rough materials. Next, the desired failure mode, as shown in Fig 3(b) was: concrete was seriously destroyed and great amount of rough materials were pulled off from concrete substrate. Finally, mixed failure mode was observed that the rough materials were partially pulled off from concrete substrate, as shown in Fig 3(c).

The result of texture depth test and pull off bond strength test were listed in Table 3. The specimen treated with L0.5-3-4 resulted in a pull-off bond strength of 1.36MPa, which is lower than the standard requirement that should not be less than 1.5MPa.

However, the specimen treated with L0.5-3-4 resulted in a pull off bond strength of 2.17MPa, which is higher than the standard requirement. Here we assumed that the strength of LWA was  $\sigma_1$ , the bond strength between LWA and cement paste was  $\sigma_2$ , and the bond strength between LWA and FRP sheet was  $\sigma_3$ , respectively.

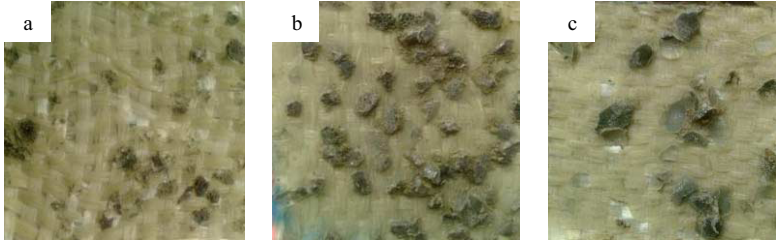


Figure 3. Failure modes

Once  $\sigma_1$  was lower than  $\sigma_2$  and  $\sigma_3$ , LWA would be mainly destroyed at the interface between LWA and cement paste or FRP sheet, showing a bad bond strength, and was corresponding to the rough FRP sheet failure or adhesive failure between rough FRP sheet and concrete substrate, as shown in Fig 3(a) and Fig 3(b), respectively. Once  $\sigma_1$  was higher than  $\sigma_2$  or  $\sigma_3$ , bond failure would also occur at interface between LWA and cement paste or FRP sheet, however, maybe showing excellent bond strength, and corresponding to the entire failure mode. In this study, LWA with the specific gravity grade at 0.5 was more fragile and thus resulted in lower bond strength, while LWA with the specific gravity grade at 0.9 resulted in higher bond strength. It can be concluded that the strength of rough materials have a significant influence on the bond property.

Table 3. TD and average SH of rough FRP sheet

Parameters	L0.5-3-4	L0.9-3-4
TD (mm)	2.40	2.72
Bond strength (MPa)	1.36	2.17

## 2.2. Chloride ion penetration

Chloride ion penetration of three groups was considered in activity layer of chloride ion penetration test, which include L0.5-3-4, L0.9-3-4 and the control group without LWA. There was significant difference among the three groups, as shown in Fig 4. Chloride ion penetration of control group was not detected, indicating that the FRP sheet manufactured was effective, chloride ion penetration of L0.5-3-4 was lower than that of L0.9-3-4 probably due to the factor of specific gravity, lighter rough materials seem to make fewer defects on the surface of FRP sheet, and increase the effective protect thickness of FRP sheet. Both chloride ion permeability coefficient of L0.5-3-4 and L0.9-3-4 were lower than the standard requirement that is less than  $5.0 \times 10^{-3} \text{mg/d}\cdot\text{cm}^2$ , indicating that the rough FRP sheet primarily prepared have good resistance to permeation of chloride ion.



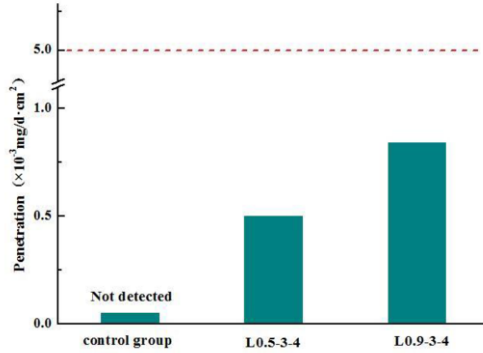


Figure 4. Chloride ion penetration test

### 2.3. Microstructure analysis

Previous work has suggested that the lightweight aggregate interlocks with the cement paste boundary, the hydrated calcium silicate gels fill in the micro defects and cracks of lightweight aggregate [8]. In this study, on the one hand, the rough material interlocks with the cement paste and resin matrix, as can be seen in Fig 5. On the other hand, pre-wetted rough material could act as an internal curing agent, optimizing the structure of interface transition zone, repairing the defects and cracks. In addition, the surface pores of the rough materials shell absorbed the water built-up at the cement/aggregate transition zone, thus resulting in lower water content at the transition zone, and thus improving the bond strength of rough material/cement.

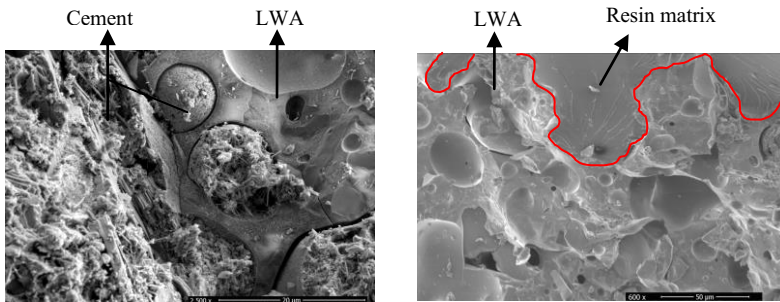


Figure 5. Interlocks effect

The profile of RFC bonded to concrete substrate was shown in Fig 6. Our study shows that higher bond strength was obtained from the adhesive failure between rough FRP sheet and concrete substrate, as shown in Fig 3(b). Therefore, it was concluded that bond strength was mainly determined by mechanical interlocking and interfacial structure between rough material and cement paste. In this study, we assumed that the average failure bond force  $F$  could be formulated by the Eq. (3), where the interlock force  $F_1$  was caused by interlock between cement paste and structure formed through rough materials, and bond force  $F_2$  was caused by the interlock and chemical bond between rough material and cement paste.

$$F = F_1 + F_2 \quad (3)$$

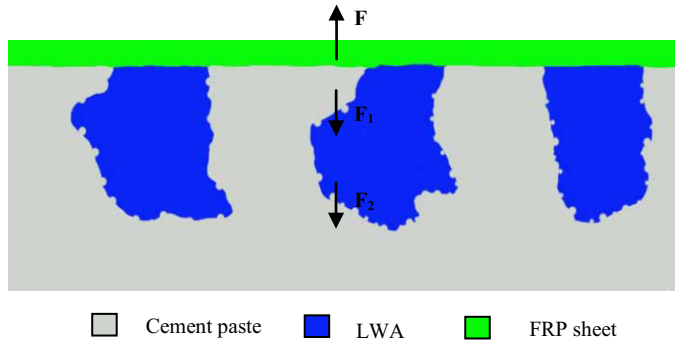


Figure 6. Bond model

It is obvious that the interlock force  $F_1$  was determined by texture depth, grain size and density of rough material on FRP sheet surface. While the bond force  $F_2$  was affected by the factors such as roughness, porosity of rough material and cement paste strength. Therefore, further studies are needed to achieve excellent bond performance and durability.

### 3. Conclusion

- Rough FRP sheet prepared by LWA and FRP could bond to concrete substrate without adhesive, the pull off bond strength of L0.9-3-4 reaches 2.17MPa, and chloride ion permeability coefficient of 30 days is  $8.41 \times 10^{-4} \text{ mg/d} \cdot \text{cm}^2$ .
- Bond strength of the rough FRP sheet between concrete substrate systems is mainly determined by mechanical interlocking and interfacial structure between rough material and cement paste. Rough material such as LWA has many advantages including light weight, optimizing the structure of interface transition zone, and repairing the defects and cracks based on the internal curing effect.
- Bond behavior mainly is related to the grain size, density, roughness, porosity of rough material and texture depth, further studies are needed to achieve excellent bond performance and durability.

### References

- [1] S.Y. Seo, Bond strength of near surface-mounted FRP plate for retrofit of concrete structures. *Compos Struct* 95 (2013), 719 - 727.
- [2] X.Z. Lu, Bond-slip models for FRP sheets/plates bonded to concrete. *Eng Struct* 27 (2005), 920 - 937.
- [3] M.A. Mashrei, Application of artificial neural networks to predict the bond strength of FRP-to-concrete joints. *Constr Build Mater* 40 (2013), 812 - 821.
- [4] I. Iovinella, Influence of surface roughness on the bond of FRP laminates to concrete. *Const. Build. Mater* 40 (2013), 533 - 542.
- [5] F. Ascione, Mechanical behaviour of FRP adhesive joints: a theoretical model. *Composites Part B* 40 (2009), 116 - 24.
- [6] H. M. Diab, Bond strength and effective bond length of FRP sheets/plates bonded to concrete considering the type of adhesive layer, *Composites: Part B*, 58 (2014) 618 - 624.
- [7] S.K. Ha, Bond characteristics of sprayed FRP composites bonded to concrete substrate considering various concrete surface conditions, *Compos. Struct.* 100 (2013) 270 - 279.
- [8] S.G. Hu, Interface structure between lightweight aggregate and cement paste. *J Chin Ceram Soc* 33(2005), 713 - 717.

# Fundamentals of plastic settlement cracking in concrete

Riaan COMBRINCK<sup>1</sup> and William Peter BOSHOFF

*Department of Civil Engineering, Stellenbosch University, South Africa*

**Abstract.** The durability of flat concrete elements such as floor slabs and bridge decks remains a concern. One of the main causes of durability issues is the corrosion of reinforcing steel in the concrete. Since the presence of cracks significantly accelerates the corrosion process it is of utmost importance to prevent cracking if the expected service life of concrete is to be reached. This paper investigates the crack formation due to plastic settlement, since plastic settlement cracking is the earliest form of cracking in concrete it arguably has one of the highest potentials to reduce the service life of a concrete structure. Plastic settlement cracking occurs once the concrete has been cast up to the initial setting time which indicates that the concrete is no longer in a plastic state. The mechanism of cracking is differential settlement of the concrete due to vertical restraints in the form of imbedded reinforcing steel or a non-uniform depth. Once these cracks have formed they act as locations for further crack growth due to volume changes such as drying shrinkage. Although plastic settlement cracks can be mitigated through the re-vibration or the sequential placement of the concrete, both methods are practically difficult to implement for large concrete pours. Due to the early occurrence and difficulty associated with mitigating these cracks it is imperative to fundamentally understand the behaviour of these cracks, if they are to be prevented. The results identified three distinctly different defects due to plastic settlement cracking described as follows: 1) Shear cracks starting from the bottom upwards at an angle at both the left and right outermost points of the reinforcing steel bar; 2) Tensile cracks starting from the surface downward; 3) Water pockets beneath the reinforcing steel bar. The results also showed that the severity of the cracking increases with a decrease in cover depth and spacing of reinforcing steel. The shear cracks tend to approach the behavior of tensile cracks as cover depth decreases.

**Keywords.** Plastic settlement, cracking, cover depth, spacing.

## Introduction

The durability of flat concrete elements such as floor slabs and bridge decks remains a concern in the construction industry [1-3]. One of the main causes of durability issues is the corrosion of reinforcing steel in the concrete. The corrosion is accelerated by the lowering of the pH of the concrete through carbonation and chloride ingress which in

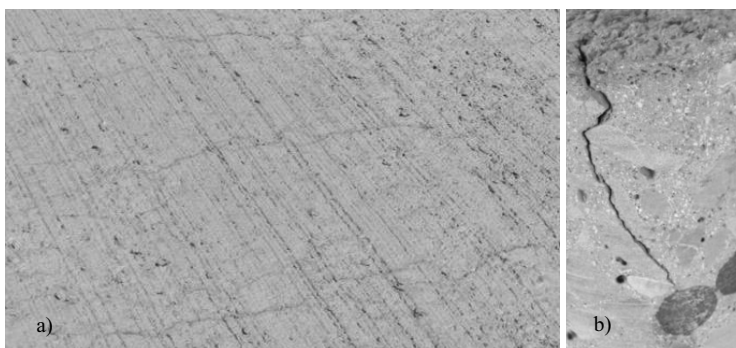
---

<sup>1</sup>Corresponding author: Civil Engineering Department, Private Bag X1, Stellenbosch, 7602, South Africa; E-mail. [rcom@sun.ac.za](mailto:rcom@sun.ac.za)

turn destroys the protective passivation layer around the reinforcing steel. The process of corrosion is significantly aggravated by the presence of cracks, which not only results in the deeper penetration of chloride ions and carbon dioxide but in several cases directly exposes the reinforcing steel to the environment [4]. This highlights the importance of preventing cracking in concrete elements if the expected service life of concrete is to be reached without expensive repair costs. With this in mind, this paper investigates the crack formation due to plastic settlement, since plastic settlement cracking is the earliest form of cracking in concrete it arguably has one of the highest potentials to reduce the service life of a concrete structure.

Plastic settlement cracking can occur once the concrete has been cast up to the initial setting time of the concrete which indicates that the concrete is no longer in a fluid state. The mechanism of cracking is differential settlement of the concrete due to vertical restraints in the form of imbedded reinforcing steel or a non-uniform sectional depth in the form of T- and/or L-beams [2,5]. The crack pattern is almost always linked to the location of the elements causing the vertical restraint. Figure 1 a) shows an example of plastic settlement cracks that coincides with the spacing of the reinforcing steel within a concrete slab. Figure 1 b) shows a core that was drilled from the slab which illustrates that the crack can penetrate to the exact depth and location of the reinforcing steel.

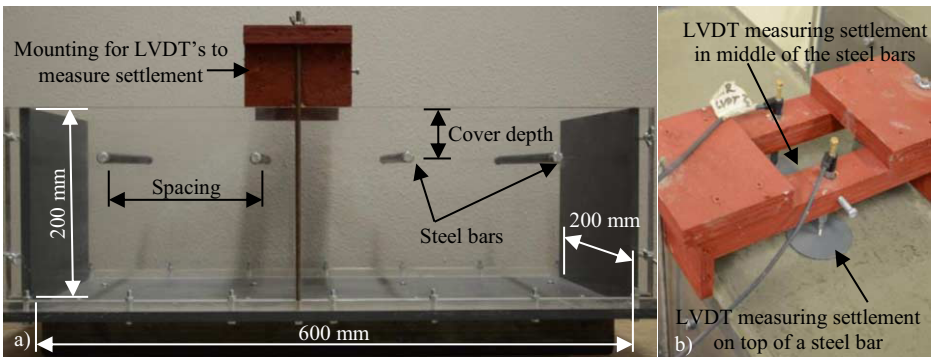
Once plastic settlement cracks have formed they act as locations for further crack growth due to future volume changes such as plastic-, thermal-, chemical- and drying shrinkage [6]. These future volume changes can be minimised and controlled by applying curing techniques, while plastic settlement cracks cannot. Although plastic settlement cracks can be mitigated through re-vibration or the sequential placement of the concrete, both these methods are practically difficult to implement for large concrete pours and may result in concrete with reduced strength and quality if implemented incorrectly [7,8]. Due to the early occurrence and difficulty associated with mitigating these cracks it is imperative to fundamentally understand the behaviour of these cracks. This will help engineers and contractor alike to understand when and how these cracks are formed and what are the critical factors that influence the severity of these cracks. This paper aims to provide the description of the formation of plastic settlement cracks based on experimental observations and measurements. The influence of the cover depth and the spacing of the reinforcing steel on the behaviour and severity of the cracks are also discussed.



**Figure 1. a)** Plastic settlement cracks in concrete slab that coincides with the reinforcing steel layout. **b)** Drilled core of slab showing the penetration of the crack to the depth and location of the reinforcing steel.

## 1. Test setup

Two special moulds were built to study the behaviour of plastic settlement cracks in flat concrete elements containing reinforcing steel. These moulds have transparent Perspex side panels to allow the observation of cracks below the surface. Both moulds have dimensions of 600 x 200 x 200 mm (length x width x height) and contains reinforcing steel bars with a diameter of 10 mm. The spacing and cover depth of the reinforcing steel bars were varied as these two parameters were identified as the factors that have the biggest influence on plastic settlement cracking behaviour [2]. The spacing of reinforcing steel was chosen as 150 mm in one of the moulds and 200 mm in the other. Cover depths of 15, 30 and 45 mm were investigated for both spacing's, resulting in a total of six tests. Figure 2 a) shows a side view of the mould with a 150 mm spacing and a 45 mm cover depth. Figure 2 b) shows the attachment used to mount the LVDT's that measured the vertical settlement on top of a reinforcing steel bar as well as in the middle between two reinforcing steel bars. The ends of the LVDT's were attached to circular disks that rest on the surface of the concrete.



**Figure 2.** a) Side view of mould with 150 mm spacing and 45 mm cover depth. b) Attachment used to mount LVDT's that measures the vertical displacement.

The proportion and constituents of the concrete mix used for the tests are given in Table 1. The mix has a w/c ratio of 0.62 and is estimated to reach an average 28-day compression strength of 40 MPa. The slump was 90 mm and there were no signs of segregation. A relatively fine local quarry sand with FM of 1.5 was used together with a 13 mm Greywacke stone and CEM I 52.5N OPC cement. The mix was chosen because it is suitable for use in a large flat concrete element such as a warehouse floor where plastic settlement cracking is often problematic. The initial and final setting times of the mix were 180 and 270 minutes respectively and were determined with a Vicat penetration apparatus in accordance with SANS 10196-3 [9]. Note that the large aggregates were sieved out to obtain a mortar that was suitable for testing.

**Table 1.** Mix proportions and constituents.

Content	kg/m <sup>3</sup>
Water	205
Cement - CEM I 52.5N	331
13mm Greywacke stone	993
Natural quarry sand	800

Prior to mixing, a thin layer of mould oil was applied to all the moulds to minimise the effect of side friction on the settlement. After mixing and compaction the concrete filled moulds were placed in a climate controlled room with a temperature of 23°C, relative humidity of 65% and no wind. These conditions gave a low enough evaporation rate to ensure no capillary pressure build up and therefore no plastic shrinkage cracking. In addition, all moulds were monitored to ensure that there was a clear water film at the surface due to bleeding up to the final setting time after which the moulds were de-moulded. During all the tests the formation of the cracks were continuously monitored by eye and through high resolution pictures at both the surface and from the sides.

## 2. Results and discussion

### 2.1. Crack behavior

Three distinctly different types of cracks or defects were observed through the Perspex side covers during the experiments. A vertical crack was formed from the concrete surface downwards above the reinforcing steel, while angled cracks formed upwards from the sides of the reinforcing steel well below the concrete surface. Finally, a water pocket was formed below the steel reinforcing. Figures 3 a) and b) show an illustration of the different settlement zones as well as the different types of cracks or defects. The figure also shows two pictures taken of the three defects. Figure 3 c) shows an image taken through the Perspex covers at the initial setting time while Figure 3 d) shows an image taken after the Perspex cover was removed just after the final setting time. A discussion on each of the three defects as well as the influence of cover depth and spacing follows:

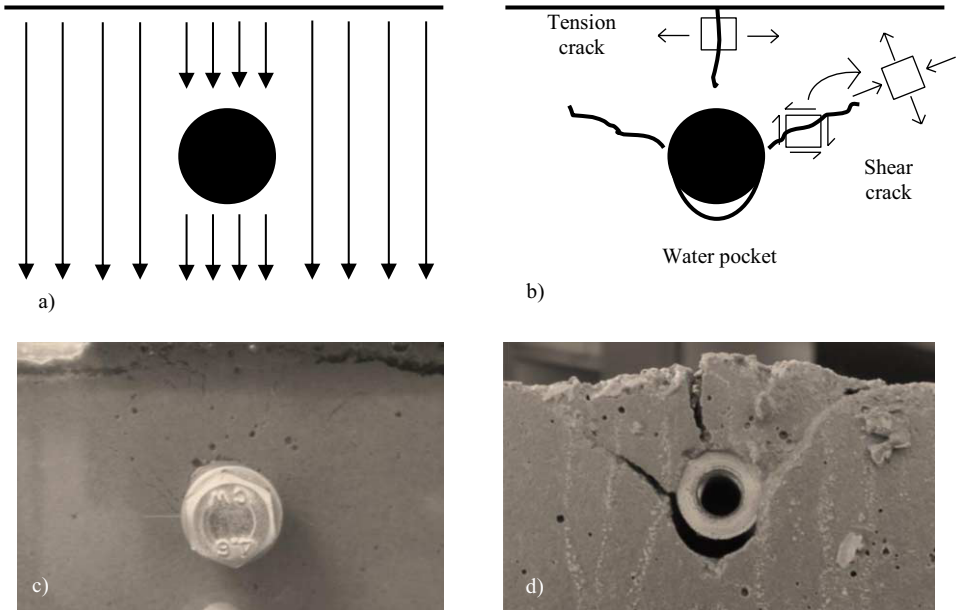
### 2.2. Shear cracks

Angled cracks developed at the most left and most right points of the reinforcing steel bars as can be seen in Figures 3 b), c) and d). The starting location of the cracks coincides with the boundary between the different settlement zones as shown in Figure 3 a). Figure 3 b) shows the shear stresses on a small block at the crack location as well as the rotation of the block to principal normal stresses. Although these cracks were formed by tensile stresses as illustrated by the principal stresses on the rotated block, the origin of these tensile stresses remain shear stresses caused by differential settlement. These cracks will therefore further be referred to as shear cracks. In general, the shear cracks formed first from the bottom upwards and were not visible from the surface. This indicates that shear cracks may be present below the surface of concrete elements even if not visible from the surface. These cracks form natural weak spots that may be widened by loading or shrinkage later in the life of the structure.

### 2.3. Tensile cracks

Vertical cracks developed at the concrete surface and propagated downward towards the reinforcing steel as can be seen in Figures 3 b), c) and d). These cracks were formed due to the large difference in settlement between the concrete in the middle of the

reinforcing steel bars and the concrete above the reinforcing steel bars. This differential settlement was also responsible for the shear cracks discussed in the previous section, although in this case it resulted in a direct tensile stress situation as illustrated by the small block just below the surface of the concrete in Figure 3 b). These cracks normally appeared after the shear cracks and are further referred to as tensile cracks. These tensile cracks were visible on the concrete surface.



**Figure 3.** a) Illustration of different settlement zones caused by a reinforcing steel bar. b) Illustration of defects caused by differential settlement. c) Image of defects caused by differential settlement taken at initial setting time. d) Image of defects caused by differential settlement taken just after final setting time.

#### 2.4. Water pocket

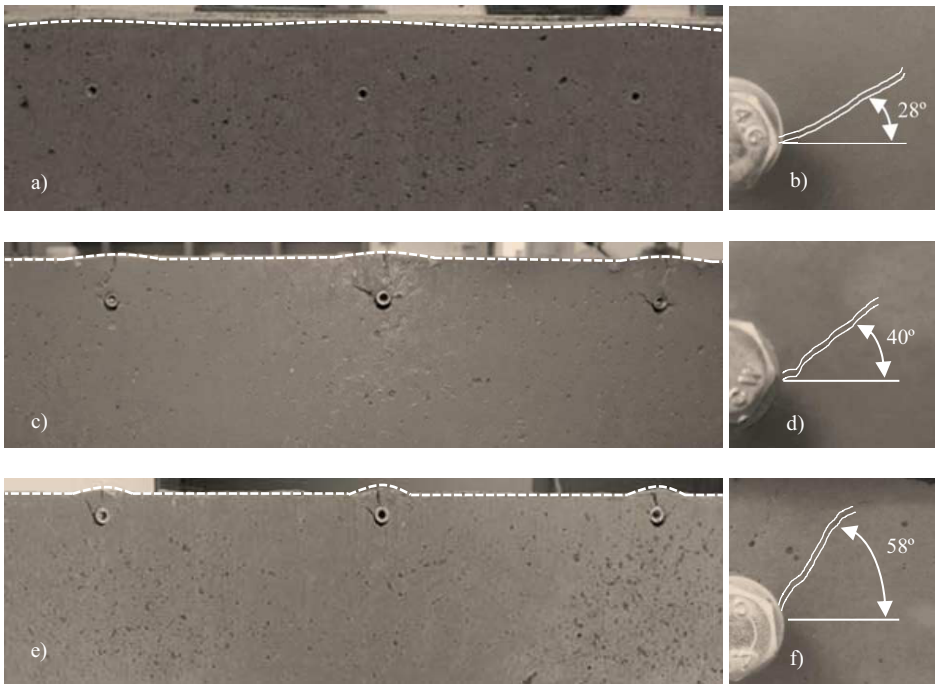
Bleeding water was trapped just beneath the reinforcing steel bars. This created water pockets which formed due to the settlement of the concrete below the reinforcing steel bars. The water pocket is not clearly visible in Figure 3 c) as it was still filled with water at that stage. Figure 3 d) clearly shows the void left by the water pocket not filled with water after the Perspex side panel was removed. The voids left by these water pockets not only decrease the concrete strength and durability but also reduces the mechanical bond between the concrete and the reinforcing steel.

#### 2.5. Influence of cover depth

The cover depth is the clear distance between the surface of the concrete and the top most point of the reinforcing steel embedded in the concrete. The cover depth is specified by the design engineer based on the durability and/or fire resistance requirements of the structure and is normally specified to be around 30 mm. However in practice, a uniform cover depth is hard to achieve and inadequate cover depths far less than 20 mm are often reality [10]. This can be due to imperfect construction or

flexural deflections of the reinforcing steel bars which causes sagging and hogging zones. This results in a reduced cover depth in the hogging zone. Figure 4 shows the results of tests conducted on cover depths of 15, 30 and 45 mm with 200 mm spacing. Figures 4 a), c) and e) show a side view of the cracks over the entire mould with the Perspex covers removed just after the final setting time, while Figures 4 b), d) and f) only show the cracks formed at the middle reinforcing steel bar at the initial setting time with the Perspex covers not removed.

From Figure 4 it is clear that the smaller the cover depth the more severe the cracking. The figures also show that the angle of the shear cracks increases as the cover depth decreases. This means that the smaller the cover depth the more the shear cracks tend to behave like a tensile crack. It is also notable that only the tensile cracks of the 15 mm cover depth mould penetrated to the depth of the reinforcing steel bars. Figures a), c) and e) also show the wave-like shape of the surface of the concrete after settlement. The smaller the cover depth the more pronounced the wave-like shape, which shows that the influence zone of the reinforcing steel on the settlement of the concrete above it reduces as the cover depth decreases.



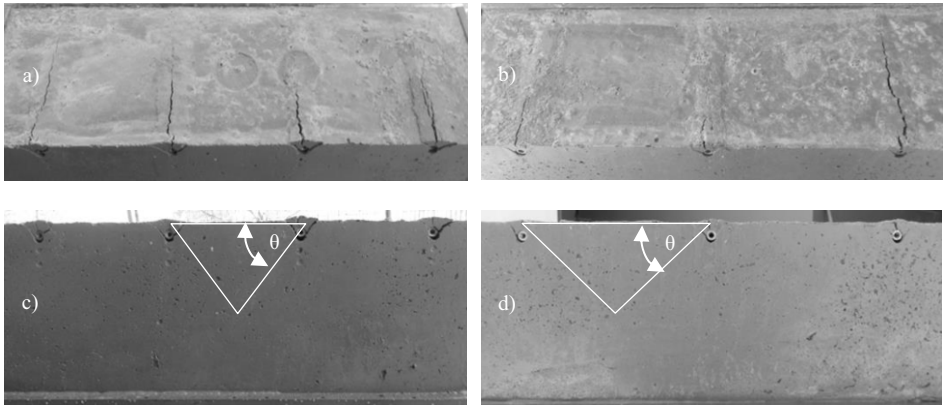
**Figure 4.** a,c,e) Images of all the cracks formed for the 200 mm spacing mould with the Perspex covers removed just after the final setting time for cover depths of 45, 30 and 15 mm respectively. b,d,f) Images of cracks formed at the middle reinforcing steel bar of the 200 mm spacing mould at the initial setting time with the Perspex covers not removed for cover depths of 45, 30 and 15 mm respectively.

## 2.6. Influence of spacing

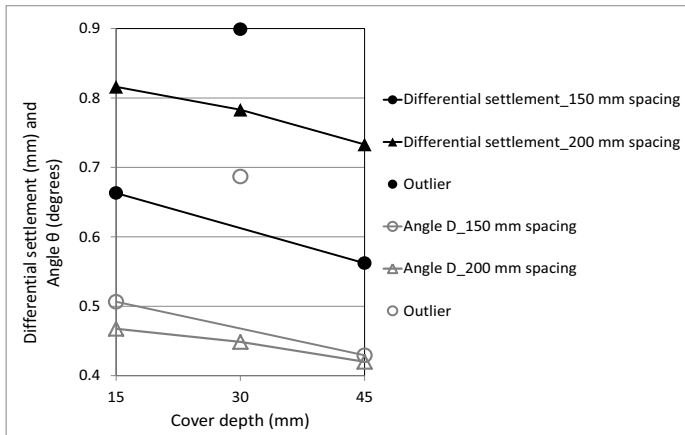
The spacing of reinforcing steel is the horizontal distance between the center points of parallel and adjacent steel bars. The spacing of top reinforcing steel, which has the biggest influence on plastic settlement cracking of concrete, is specified by the design



engineer and is normally within the range of 100 to 400 mm. The top reinforcing steel mainly resists tensile forces due to negative bending moments and/or to control cracking due to volume changes such as drying shrinkage or temperature deformations. Figure 5 shows the cracking for both the 150 and 200 mm spacing moulds at 15 mm cover depth after de-moulding just after the final setting time. It should be noted that the moulds with 30 and 45 mm cover depths showed similar results. From the figure it appears that the smaller the spacing the more severe the cracking. One possible reason for this is found in the differential settlement results as shown in Figures 6. This figure shows the difference in settlement between the measured settlement directly above the reinforcing steel and the settlement in the middle between reinforcing steel bars. The figure also shows an ignored outlier result which is thought to be due to a malfunctioning LVDT. Figure 6 also shows the Angle  $\theta$  (illustrated in Figure 5) that is calculated using the differential settlement and half the spacing value. The results show that the smaller the spacing the bigger the Angle  $\theta$ . This could be a reason for the higher cracking severity since it is believed that the bigger this Angle  $\theta$  the higher the tensile stresses and therefore the more severe the cracking.



**Figure 5.** a,c) Images of cracking for the 150 mm spacing mould with a 15 mm cover depth taken with the Perspex covers removed just after the final setting time. b,d) Images of cracking for the 200 mm spacing mould with a 15 mm cover depth taken with the Perspex covers removed just after the final setting time.



**Figure 6.** Graph showing the influence of cover depth on differential settlement and the Angle  $\theta$ .

### 3. Conclusions

This paper describes the formation of plastic settlement cracks based on experimental observations and measurements. The following significant conclusions can be drawn:

- The settlement of fresh concrete around a reinforcing steel bar leads to the following three distinctly different defects: 1) Shear cracks starting from the bottom upwards at an angle at both the left and right outermost points of the reinforcing steel bar; 2) Tensile cracks starting from the surface downward; 3) Water pockets, forming voids later on, beneath the reinforcing steel bar.
- As the cover depth above the reinforcing steel decreases the orientation of the shear cracks becomes more vertical. Also the influence zone of the reinforcing steel on the settlement of the concrete above reduces as the cover depth decreases.
- The smaller the cover depth as well as the spacing of the reinforcing steel bars the more severe the cracking.

### 4. Acknowledgments

This work is based on the research supported in part by the National Research Foundation of South Africa for the Grant: “Minimising the early age cracking of concrete in South African environmental conditions”. Any opinion, finding and conclusions or recommendation expressed in this material is that of the author(s) and the NRF does not accept any liability on this regard.

### References

- [1] V. Slowik, M. Schmidt, T. Hubner and B. Villmann, Simulation of capillary shrinkage cracking in cement-like materials, *Cement & Concrete Composites* **31** (2009), 461-469.
- [2] R.E. Weyers, J.C. Conway and P.D. Cady, Photoelastic analysis of rigid inclusions in fresh concrete. *Cement and Concrete Research* **12** (1982), 475-484.
- [3] P.J. Uno, Plastic Shrinkage Cracking and Evaporation Formulas, *ACI Materials Journal* **95** (4) (1998), 365-375.
- [4] M.B. Otieno, M.G. Alexander and H. –D. Beushausen, Corrosion in cracked and uncracked concrete – influence of crack width, concrete quality and crack reopening, *Magazine of Concrete Research* **62** (6) (2010), 393-404.
- [5] H.-G. Kwak and W.J. Weiss, Experimental and Numerical Quantification of Plastic Settlement in Fresh Cementitious Systems, *Journal of Materials in Civil Engineering* **22** (10) (2010), 951-966.
- [6] E. Holt and M. Leivo, Cracking risks associated with early age shrinkage, *Cement and Concrete Composites* **26** (2004), 521-520.
- [7] H.-G. Kwak and S.-J. Ha, Bleeding and evaporation in concrete slabs with sequential placement, *Magazine of Concrete Research* **60** (10) (2008), 769-783.
- [8] R. Combrinck and W.P. Boshoff, The origin of plastic settlement cracking and the effect of re-vibration, *Research and Applications in Structural Engineering, Mechanics and Computation*, Proceedings of the Fifth International Conference on Structural Engineering, Mechanics and Computation, Cape Town, South Africa, September 2013, 1107-1113 (CRC Press, London).
- [9] SANS 50196-3, *Methods for testing cement Part 3: Determination of setting times and soundness*, 2nd Edn, Standards South Africa, Pretoria, 2006.
- [10] A.V. Monteiro and A.F. Goncalves, Assessment of concrete cover in structures Part 1 –Statistical tolerance analysis approach, *Performance-based Specifications for Concrete*, Proceedings of International Workshop, Leipzig, Germany, June 2011, 220-229 (MFPA, Leipzig).

# Initial study to determine the tensile material properties of fresh concrete

Jan Diederick DIPPENAAR, Riaan COMBRINCK<sup>1</sup> and William Peter BOSHOFF  
*Department of Civil Engineering, Stellenbosch University, South Africa*

**Abstract:** The early age cracking of concrete often occurs in flat concrete elements such as bridge decks and slabs exposed to conditions with high evaporation. These cracks, which include plastic shrinkage and plastic settlement cracks, have a premature detrimental effect on the durability of concrete structures. Cracking occurs when mechanisms such as differential settlement and capillary pressure cause the development of tensile stresses in the concrete which exceeds the tensile strength of the concrete. A fundamental understanding of the tensile properties of fresh concrete and the variables that affect them are imperative in order to understand and reduce the risk of early age cracking. In addition, the tensile properties such as ultimate tensile strength, tensile strain capacity and Young's modulus all as a function of time are also required as input parameters for the numerical analysis of early age cracking of fresh concrete which can ultimately be used to predict and prevent cracking. This paper gives a summary of the most significant work done in this field over the last few decades. This is followed by the description of initial results achieved with a newly built test setup which aims to measure the tensile material properties of fresh concrete specimens at ages from 1 hour after mixing and onwards. Although the new test setup showed promise it still encountered several issues which are discussed in the paper. These issues were mainly due to the difficulty of handling and testing plastic concrete at such an early age. Finally, an improved test setup is proposed based on the knowledge gained from the initial test setup as well as the literature study. This improved test setup is currently under construction and forms part of a larger ongoing research project at Stellenbosch University aimed at controlling the early age plastic cracking of concrete.

**Keywords.** Fresh concrete, early age cracking, tensile material properties.

## Introduction

The early age cracking of concrete typically occurs within half an hour to six hours after placing and finishing the concrete. These cracks, which include plastic shrinkage and plastic settlement cracks, are primarily caused by differential settlement and capillary pressure build up, which are the mechanisms responsible for the development of stress in plastic concrete [1-3]. Crack onset occurs once the tensile stresses developed in the concrete exceed its ultimate tensile strength or, equivalently, when the restrained shrinkage strain exceeds the tensile strain capacity of the concrete [4-6].

Early age cracking commonly occurs in flat concrete elements like slabs and bridge decks which are exposed to environments that are conducive to high evaporation

---

<sup>1</sup>Corresponding author: Civil Engineering Department, Private Bag X1, Stellenbosch, 7602, South Africa; E-mail. [rcm@sun.ac.za](mailto:rcm@sun.ac.za).

rates. These cracks can have a premature detrimental effect on the durability and strength of concrete structures as it allows destructive fluids and ions to penetrate the concrete which causes the attack of cement paste and promotes the corrosion of reinforcing steel [7]. For this reason a fundamental understanding of the tensile properties of fresh concrete and the variables that affect them are imperative in order to understand and reduce the risk of early age cracking. Ultimate tensile strength, tensile strain capacity and Young's modulus, all as a function of time, are the essential properties to be determined as they are required as input parameters for the numerical analysis of fresh concrete behavior. This can ultimately be used to prevent and predict the early age cracking of concrete.

This paper first provides a review of the more significant research conducted over the past few decades in the field of tensile material properties of fresh concrete and its measurement. This is followed by a description of a newly built test setup which aims to allow for the testing of concrete at the ages of 1 hour, while it is still plastic and onwards. The results obtained with the new test setup are analyzed and discussed critically. Finally, an improved test setup is proposed based on the knowledge gained from the current tests as well as the literature study.

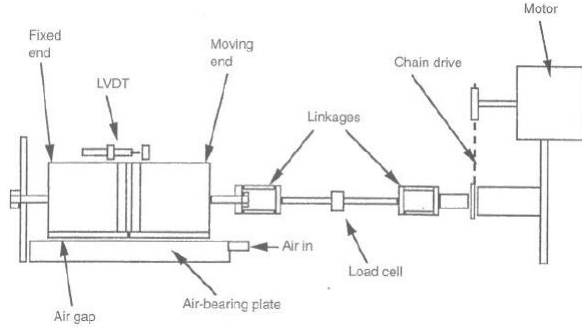
## **1. Literature review on field of tensile material properties of fresh concrete**

Fresh concrete is a very challenging material to handle and test. At the instant of mixing concrete displays Newtonian-like behaviour, with an increase in time changing to Bingham-like behaviour and eventually the concrete becomes a brittle solid with considerable tensile stiffness and strength [8]. Any test apparatus has to take into account these rheological changes that concrete undergoes during its first few hours after mixing. The cement hydration products, responsible for concrete's strength, are also fragile during this period and can easily be disturbed by the slightest material deformation or shock [4, 5, 9]. Due to the considerable practical difficulties that need to be overcome in the determination of the tensile material properties of fresh concrete, there is only limited literature available on this topic. A discussion regarding the state of the art in the field of tensile material properties testing follows.

In 1998 Abel and Hover [10] conducted tensile test on fresh concrete by using a test apparatus consisting of moulds formed by two halves. These mould halves made use of grips to impose a tensile load on the concrete specimen inside the moulds. Ball-bearing slides were used to minimize friction during the linear motion of the two halves being pulled apart. Concrete mix designs with w/c ratios varying from 0.3 to 0.7 were tested using this experimental assembly. These tests found that the tensile strength of concrete specimens initially developed slowly, finally reaching strengths between 10 and 100 kPa at ages up to 5 hours.

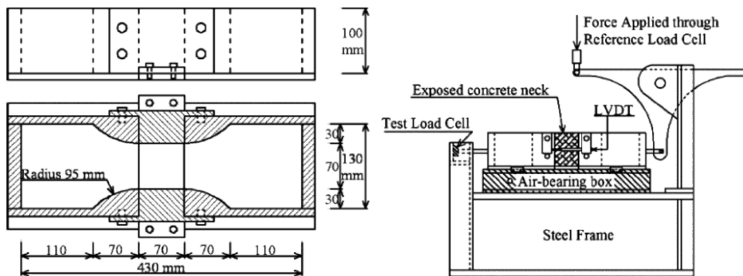
The first description of the complete stress-displacement curve of fresh concrete was done by Hannant et al. in 1999 [9]. A schematic of the apparatus used is shown in the Figure 1. A major improvement from previous test assemblies was the use of an air bearing which allowed virtually frictionless movement of the mould. A strength of 1 to 9 kPa for concrete with an age of 1 hour was observed in this study. Two concrete mix designs were tested at hourly intervals from 1 to 5 hours of age. A displacement rate of 0.75 mm/min was applied for all tests. The results showed that fresh concrete's tensile strength increased at a slow rate initially up to an age of approximately 3 hours, after which an exponential increase was measured. The results also showed a rapid decrease

in the strain at peak stress as age increased [9]. In 2002 Branch et al. [4] used the exact same test assembly to conduct tensile tests on high-strength concrete. Tests were done on specimens that were sealed from the atmosphere and specimens with their surfaces exposed to a wind of a 4 km/h. The wind was found to have a negligible effect on the stress-displacement curve of the tested specimens for up to a 5 hour specimen age.



**Figure 1.** Tensile testing assembly as used by Hannant et al. [9].

Doa et al. [5] made further progress in the field of the tensile testing of fresh concrete. Most significantly they improved the mould design of the concrete specimens. The curved transitions, as can be seen in the plan view in the left of Figure 2, promote failure in the middle section of the specimen. In contrast to the grips used in previous tensile test moulds, the use of this mould design allows for a tensile load to be transmitted to the specimen while eliminating any significant stress concentrations that could cause unintended cracking outside of the middle section. A range of typical concrete mixes were tested with an aggregate size of 10 mm. During tests a displacement rate of 0.05 mm/min was used. This was considerably slower than any of the displacement rates used in previous studies. Tests were conducted from 1.5 hours after mixing and onwards. A schematic of the complete test assembly is shown in the right of Figure 2. This study found that the tensile strength of the fresh concrete initially increased slowly, with a strength of approximately 10 kPa at an age of 3 hours, where after it increase rapidly, reaching approximately 100 kPa at an age of 6 hours. There was found to be a near linear relationship between the Young’s modulus and the tensile strength of concrete.



**Figure 2.** Steel tensile test mould and test setup as used by Doa et al. [5].

## 2. Initial test setup and results

Keeping in mind that the early age cracking of concrete can occur as early as 30 minutes after the concrete has been placed, an initial test setup was designed and built with the aim of determining the tensile material properties of fresh concrete specimens at ages from 1 hour after mixing and onwards. This section describes the entire test setup including the tensile test mould, supporting structures and procedures used during testing as well as the critical evaluation of the results achieved.

### 2.1. Description of initial test setup

The tensile test mould, shown in Figure 3, was specifically designed to transfer a tensile force to a concrete specimen while plastic and still deformable under its own weight. The mould is based on the mould designed by Doa et al. [5], with the major design difference being the use of 1 mm thick steel plates on the sides and bottom of the 100 mm gauge length section in the center of the specimen. The bottom plate is connected to the fixed mould half while the side plates are connected to the moving mould half, overlapping by 50 mm in the center of the gauge length. The mould parts were manufactured from aluminum using a CNC (computer numerical control) milling machine with an accuracy of 8 micro meters, allowing for a perfect fit of the two mould halves. Another significant change to the design of Doa et al. [5] is the size of the mould. This mould was enlarged to allow a gauge length of 100 mm and a cross-section over this length of  $100 \times 140 \text{ mm}^2$ , allowing concrete mix designs that incorporate 19 mm aggregate to be tested.

Figure 4 shows the supporting structure of the tensile testing assembly: For the test to be successfully conducted and to gather reliable data, this structure must have high stability and stiffness. The moving half of the mould is supported on four adjustable roller bearings which are mounted on a wooden box. The other half of the mould is fixed to another wooden box. The bearings, together with the two wooden boxes can be adjusted to ensure that the mould is supported evenly and level. A pulley system, in the form of a bicycle chain and gear, was used to convert a vertical force exerted by the load source to a horizontal force acting in on the concrete specimen. Since the forces measured during these test were very small and the displacement rate was extremely slow, slack or a sudden jerk action in the pulley system would cause the material to fail abruptly. The pulley system was connected to a load cell which measured the force exerted on the concrete specimen as shown in the top right hand corner of Figure 4. To ensure sufficient stiffness, the base of the supporting structure is a PC260 x 90 steel channel section. All the components of the test assembly were firmly mounted to this ridged base and the ridged base in turn was firmly mounted to a Zwick Z250 uniaxial testing machine which was used to apply the load.

Linear variable differential transformers (LVDT's) were used to measure the average, resultant displacement over the gauge length of the concrete specimen. Four LVDT's were connected to the surface of the concrete as shown in Figure 5. Since the material of the specimen at the moving and fixed sides of the gauge length deform, it is necessary to measure the displacement of both ends of the gauge length as the relative displacement between the points needs to be determined in order to calculate the strain of the specimen. The two pairs of LVDT's were connected to freely rotating lightweight PVC pipes as shown in Figure 5.

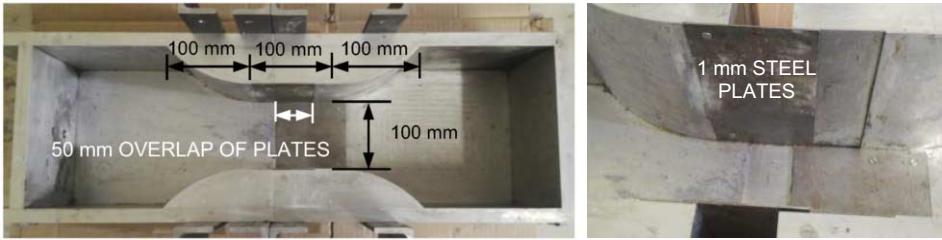


Figure 3. Tensile test mould.

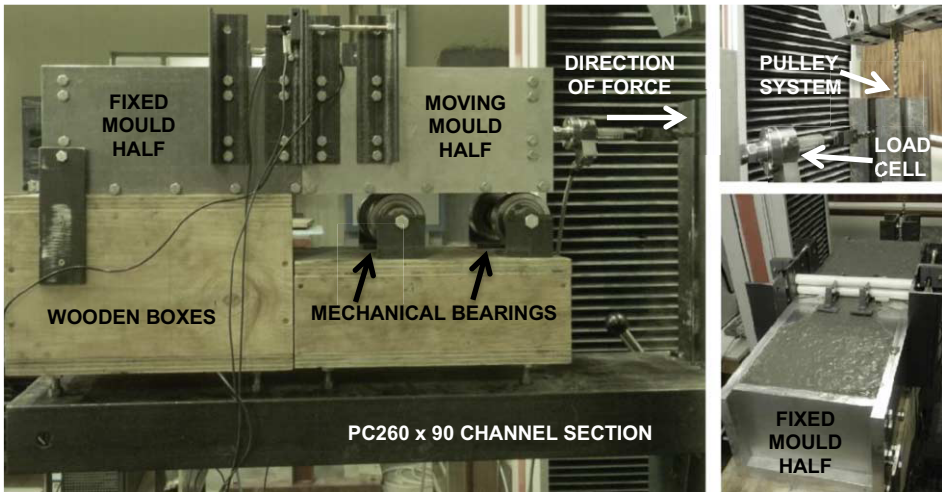


Figure 4. Supporting structure.



Figure 5. LVDT displacement measurement setup over gauge length.

## 2.2. Test procedure

Prior to testing, all the constituents of the concrete mix were placed overnight in the testing room with a controlled temperature of 23 °C and a relative humidity of 60 %. After the constituents were mixed sufficiently, the fresh concrete was placed in the prepared mould and compacted on a vibration table until air bubbles were no longer visible on the specimen surface. The mould was then carefully placed on the wooden box and mechanical bearings, after which the LVDT's and load cell were connected to the specimen. During tests, a slow displacement rate of 0.05 mm/min was used. The slow testing rate does however lead to undesirably long testing times. Initial test were conducted using the concrete mix design as shown in Table 1. This mix had a w/c ratio of 0.4, a slump of 80 mm and was designed for minimum segregation and bleeding.

**Table 1.** Mix proportions and constituents.

Content	kg/m <sup>3</sup>
Water	205
Cement - CEM I 52.5N	513
13mm Greywacke stone	631
Natural quarry sand	1105

### 2.3. Test results

Tensile test were conducted on two specimens; one at an age of 1 hour after mixing, still in a plastic state, and another at an age of 4 hours after mixing, the age at which final set for this concrete mix had occurred. The mould performed well during testing of the 1 hour specimen and provided the needed support to the plastic concrete specimen while ensuring cracking somewhere along the gauge length of the mould (see Figure 5). However, the hydrostatic force that the plastic concrete exerted on the inside of the mould combined with the weight of the pulley system, caused the slightest movement of the mould halves just before the test was initiated. The one hour test could therefore not be completed on an undisturbed specimen. A more rigid method of applying the load that eliminates the effect of hydrostatic forces is required. The stress-displacement curve of the test conducted on the 4 hour specimen is shown in Figure 6.

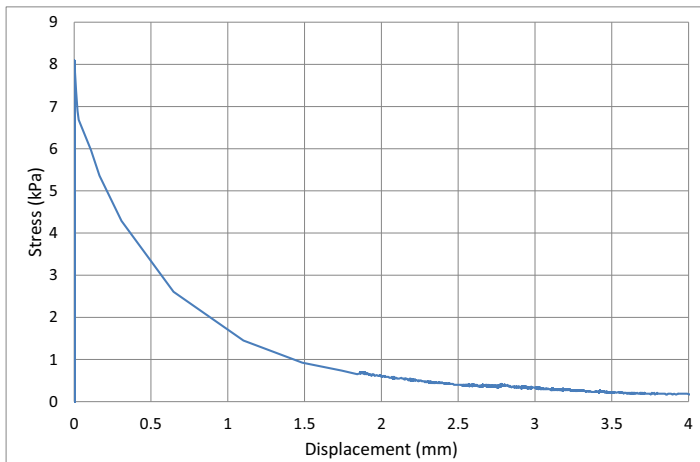
**Figure 6.** Stress-displacement curve for 4 hour specimen.

Figure 6 shows that failure occurred before adequate data could be captured in the linear elastic region. The Young's modulus of the concrete specimen could thus not be determined. It is believed that the hydrostatic forces, although much smaller than for the 1 hour test, was also responsible for the difficulty in capturing data in the elastic region. Another possible reason could be due to the method of displacement measurement i.e. the LVDT's which were only connected to the concrete surface does not account for any significant deformation or cracks that may have occurred far below the concrete surface. Such deformation and cracks may have occurred before the LVDT's measured any deformation on the surface. However, despite this the specimen did show a maximum measured tensile strength of 8.1 kPa which is comparable to the results as reported in the literature [4, 5, 9, 10].



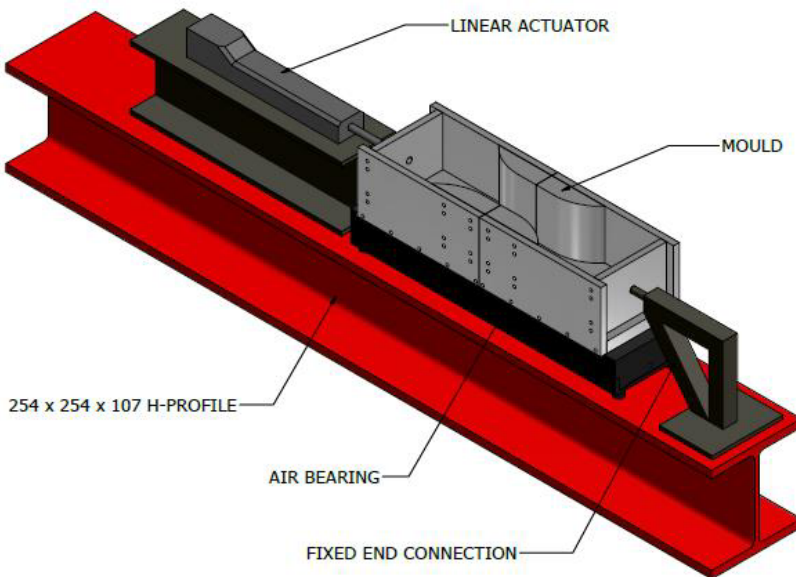
## 2.4. Evaluation of initial test setup

After critically evaluating the initial test setup and the results obtained the following shortcomings were identified:

- The method of load application through the uniaxial tensile testing machine and pulley system could not account for the influence of hydrostatic forces.
- The fixed location of the uniaxial testing machine does not allow for testing in other climatic environments.
- The method of displacement measurement only accounts for deformation and cracking near the surface of the concrete.
- The wooden boxes provided insufficient stiffness and caused slippage during testing that resulted in inaccurate results.
- It was cumbersome to align and level the fixed half of the mould on the wooden box with the moving half of the mould on the four mechanical bearings.

## 3. Proposed improved test setup

Figure 7 shows the proposed improved test setup that is currently under construction at Stellenbosch University.



**Figure 7.** Proposed improved test setup layout.

The proposed test setup consists of a rigid load application system by using a linear actuator powered by a brushless DC servomotor, which allows for smooth continuous motion at a constant rate. This will eliminate the effect of the hydrostatic forces exerted by the fresh concrete. Both mould halves will rest on a steel air bearing, specifically designed for the tensile testing mould. The air bearing can be perfectly levelled by treaded levelers at the bottom corners and will ultimately ensure a nearly

frictionless motion during tests. A 2 meter long 254x254x107 steel H-profile will be used as base for the test setup and ensure that all the assembly components can be rigidly fixed in place. In addition the entire test setup can be moved to allow for testing to occur in different climatic conditions.

#### 4. Conclusions

This paper provided a literature review on the more significant, although limited, research available on the field of tensile material properties of fresh concrete and its measurement. The results of a newly built initial test setup design to measure the tensile material properties of fresh concrete as early as one hour after mixing was critically evaluated. Although the new mould was able to support the fresh concrete the supporting structure and method of load application did not allow for the influence of hydrostatic force, which resulted in unreliable results. Finally, the lessons learned from literature and the initial tests were used to propose an improved test setup that accounts for the shortcomings of the initial test setup. This improved test setup is currently under construction and forms part of a larger ongoing research project at Stellenbosch University aimed at controlling the early age cracking of concrete.

#### Acknowledgments

This work is based on the research supported in part by the National Research Foundation of South Africa for the Grant: “Minimising the early age cracking of concrete in South African environmental conditions”. Any opinion, finding and conclusions or recommendation expressed in this material is that of the author(s) and the NRF does not accept any liability on this regard.

#### References

- [1] F.H. Wittmann, On the Action of Capillary Pressure in Fresh Concrete, *Cement and Concrete Research* 6 (1976), 49-56.
- [2] V. Slowik, M. Schmidt, and R. Fritzsche, Capillary pressure in fresh cement-based materials and identification of the air entry value, *Cement and Concrete Composites* 30 (2008), 557-565.
- [3] R.E. Weyers, J.C. Conway and P.D. Cady, Photoelastic analysis of rigid inclusions in fresh concrete. *Cement and Concrete Research* 12 (1982), 475-484.
- [4] J. Branch, D.J. Hannant and M. Mulheron, Factors affecting the plastic shrinkage cracking of high strength concrete, *Magazine of Concrete Research* 54 (2002), 347-354.
- [5] V.N.T. Dao, P.F. Dux and P.H. Morris, Tensile Properties of Early-Age Concrete, *ACI Materials Journal* 106 (2009), 483-492.
- [6] W.P. Boshoff and R. Combrinck, Modelling the severity of plastic shrinkage cracking in concrete, *Cement and Concrete Research* 48 (2013), 34-39.
- [7] C. Qi, *Quantitative assessment of plastic Shrinkage cracking and its effect on the corrosion of steel reinforcement*, PhD thesis, Purdue University, Indiana, United States of America (2003).
- [8] G. Owens (ed), *Fulton's Concrete Technology*. Midrand, South Africa: Cement and Concrete Institute (2009).
- [9] D.J. Hannant, J. Branch and M. Mulheron, Equipment for tensile testing of fresh concrete, *Magazine of Concrete Research* 51 (1999), 263-267.
- [10] J. Abel and K. Hover, Effect of Water/Cement Ratio on the Early Age Tensile Strength of Concrete, *Transportation Research Record* 1610 (1998), 33-38.

# Blended cements based on C&DW: its influence in the pozzolanicity

E. ASENSIO<sup>a,1</sup>, C. MEDINA<sup>b</sup>, M. I. SÁNCHEZ DE ROJAS<sup>a</sup> and M. FRÍAS<sup>a</sup>

<sup>a</sup>*Eduardo Torroja Inst. for Constr. Sciences, Serrano Galvache 4, 28033, Spain*

<sup>b</sup>*Escuela Politécnica de Cáceres (UEX), Dpto. Construcción, Cáceres, Spain*

**Abstract.** Construction sector is in constant research and innovation, and in this way is the search of new cementitious materials that it can be used in construction to achieve a more sustainable and eco-efficient industry. Actually, the construction and demolition waste (C&DW) has low percentages of recycling, with a correct management by the recycling plants and a minimum previous conditioning it can be used as pozzolanic addition in cement. In view of its mineralogical and chemical composition have been chosen three different wastes from all the samples collected and used for making blended cements for the study of their pozzolanicity. Good results have been obtained and show that this kind of materials can be useful for pozzolanic additions in cements.

**Keywords.** C&DW, ceramic, recycling, pozzolan, blended cement

## Introduction

Construction sector has been considered historic unrespect with the environmental due to the high environmental impact as consequence of the activities derivate from it. This sector has a lot of influence from cement industry since the use of the quarry for obtaining raw materials needed for the manufactured process to the final production of the cement for its sale. With the idea of decrease this impact, cement industry use several materials and industrial wastes in the whole process (raw materials, fuel, correctors, additions, etc.) trying to decrease the amount of clinker for obtaining all the types of cement that are sold what have economic and energetic save and environmental advantages as the reduction of greenhouse gases emission to the atmosphere (i.e CO<sub>2</sub>).

It is very important the introduction of wastes from previous activities, achieving in the same time reduction, reuse and valorization of wastes that due to low recycle percentages goes to landfill [1] and in a second step take advantage of these wastes as cement additions, then with the decrease of the materials and fuel required and the emission to the atmosphere.

One of these different wastes are construction and demolition wastes (C&DW), wastes that nowadays have a lot of importance because they are one of principal flows of wastes in Europe Union [2] and they are from construction and demolition activities and from wastes from manufacturing industries of ceramic materials (tiles, bricks, etc.)

---

<sup>1</sup>Corresponding author: [eloyadl@ietcc.csic.es](mailto:eloyadl@ietcc.csic.es)

that due to problem in the manufacturing process (they are raw or burn, for default or excess of cooking) is impossible to sale [3 – 7]. These wastes arrive to the recycling plants and there are various fractions, which highlights a clean waste of concrete and a ceramic mix fraction [8] plus other wastes as plastics, wood, metal, paints, grease, etc.

The study is based on the use of the mix ceramic fraction from construction and demolition wastes as pozzolanic addition, studying their chemical and mineralogical composition, carrying out if it is possible their reduction, reuse and valorization.

## 1. Experimental procedure

### 1.1. Materials

The materials used were cement and construction and demolition wastes.

- a) Cement used as reference was a CEM I 42.5 R type, with a content unless 95 % of Clinker and up to 5 % of minority components, based on UNE – EN 197 – 1:2011 Standard [9].
- b) Construction and demolition wastes from Spanish recycling plants. Twenty were the samples collected. The wasted selected have unless 20 % of ceramic material and up to 100 % with undesirable products as paint, mortar, grease, etc. And looking for the optimization of the process were collected the samples with minor particle size in order to decrease the cost of the conditioning that consists on a) drying during 24 hours in an oven at 105 °C, b) grinding and sieving until a particle size of 63 µm, trying to obtain a homogenous sample with a particle size similar to cement for it use as pozzolanic addition.

### 1.2. Characterization of the wastes

The characterization was carried out in order to study the viability as pozzolanic addition.

- a) Chemical composition  
X-ray fluorescence (XRF) was used to know the chemical composition of the wastes; it was observed a very similar composition between the samples collected from different plants. In table 1 it is shown the media composition of all the wastes.  
Silicon oxide is the major component in all the samples and with more than 25 % of reactive silica, besides there are acid compounds as alumina and iron oxides, components of the pozzolanic materials that agree with the Standard; UNE – EN 197 – 1:2011.
- b) Mineralogic composition  
X-ray diffraction (XRD) was the technique used for the mineralogical characterization of the wastes. It is observed that the most important

mineralogical phases present in this kind of wastes are quartz, calcite, dolomite, illite and another kind of oxides. In the figure 1, is shown as example one of the diffraction pattern of one of the samples.

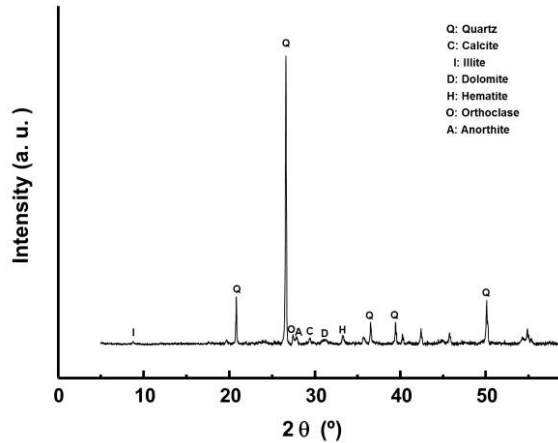


Figure 1. X- ray diffraction pattern of one of the wastes

Table 1. Chemical media composition by XFR of the C&DW

Components* (%)											
SiO <sub>2</sub>	Al <sub>2</sub> O <sub>3</sub>	Fe <sub>2</sub> O <sub>3</sub>	MnO	MgO	CaO	Na <sub>2</sub> O	SO <sub>3</sub>	K <sub>2</sub> O	TiO <sub>2</sub>	P <sub>2</sub> O <sub>5</sub>	LOI
45,84	9,83	3,43	0,06	3,59	18,20	0,60	1,19	2,13	0,42	0,14	14,55

\* 100 % is completed with minor components

## 2. Results and discussion

Once the conditioning of the samples collected and the characterization was carried out and it shows that all the wastes have a similar composition both mineralogical and chemical from the quantitative point of view, binder cements were prepared using three different wastes from the recycling plants with various percentages of ceramic material; 20, 40 and 100 % (S1, S2 and S3 respectively) and three ratios of waste in the cement (10, 20 and 30 %) obtaining 9 binder cements in order to study the influence of the percentage of ceramic material in the waste and the percentage of substitution in the pozzolanicity and compared it with the reference cement. In table 2, is shown the names of the different samples are going to be studied in the present work.

**Table 2.** Nomenclature of the samples in which the work is based on.

% Substitution of C&DW in cement	% Ceramic Material in C&DW		
	S1	S2	S3
	20	40	100
10	M1	M4	M7
20	M2	M5	M8
30	M3	M6	M9

First of all, it was studied the chemical and physical properties of the binder cements to know if they fit with the European standard.

a) Chemical composition

Besides of the compositional intervals of the Clinker and additions, that are going to vary depends on the kind of cement, they are extremely important the chloride (Cl) and sulfates (SO<sub>3</sub>) contents which limits are establish by the normative (UNE – EN 197 – 1:2011)

In table 3, are indicated both limitant values from the standard and values from the samples and reference cement.

In view of the results, it can be possible to say that cements made with addition of construction and demolition wastes in different percentages from Spanish management plants are according to the normative.

b) Physical characteristics

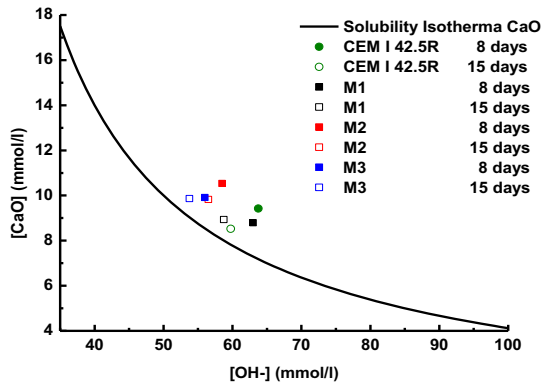
Setting times and volume stability were measured for all the samples studied. In both cases the values are according with the normative (UNE – EN 197-1:2011) with times higher than 60 minutes and volume expansions less than 10 mm.

**Table 3.** Chloride and sulfates contents in reference cement, in blended cements and allowed by the Standard.

	Cl <sup>-</sup> (%)	SO <sub>3</sub> (%)
<b>Cement*</b>	0.000	3.7
<b>M1</b>	0.002	3.6
<b>M4</b>	0.004	3.5
<b>M7</b>	0.006	3.4
<b>M2</b>	0.005	3.6
<b>M5</b>	0.010	3.5
<b>M8</b>	0.015	3.4
<b>M3</b>	0.002	3.4
<b>M6</b>	0.004	3.0
<b>M9</b>	0.006	2.7
<b>UNE – EN 197-1:2011</b>	≤ 0.100	≤ 4.0

\* Taking into account cement employed

After that the fit of properties of the cements with the normative have been corroborated, it was continued with the study of the pozzolanic activity. All the pozzolanic cements (CEM IV/A and CEM IV/B) must meet the test described in the norm: UNE – EN 196-5:2006 [10], pozzolanicity test. In figure 2, it is shown the pozzolanicity test for the blended cements using S1 waste in different ratios of substitution and compared with the reference cement. In the same way for S1 in figures 3 and 4 it is shown for S2 and S3 wastes respectively.



**Figure 2.** Pozzolanicity for cements with S1 waste for 8 and 15 days curing

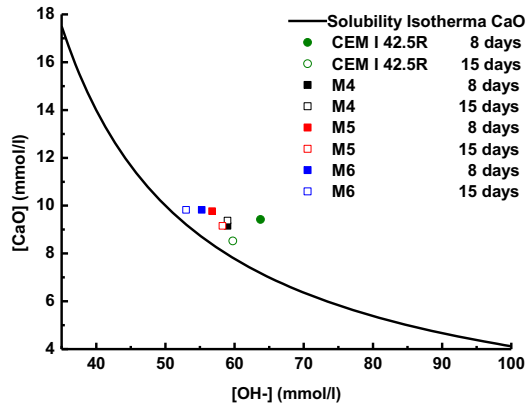


Figure 3. Pozzolanicity for cements with S2 waste for 8 and 15 days curing

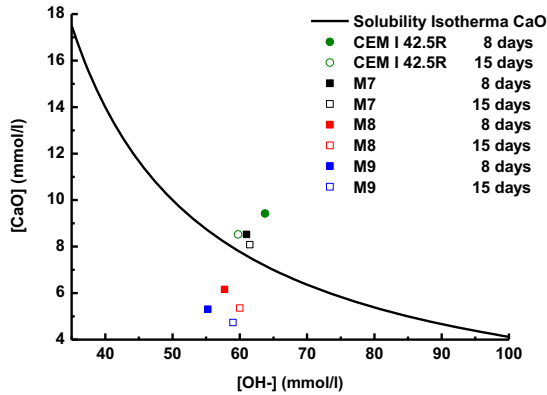
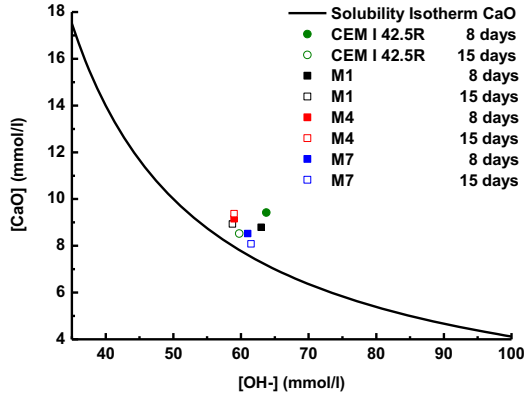


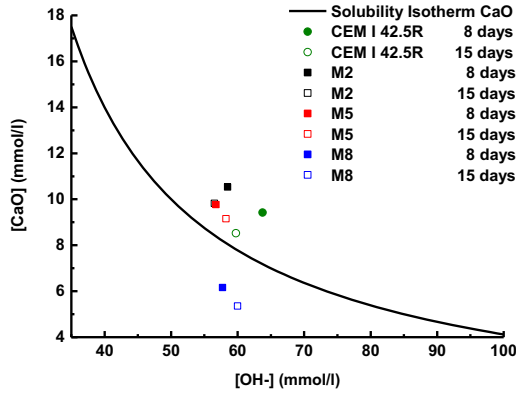
Figure 4. Pozzolanicity for cements with S3 waste for 8 and 15 days curing

In view of the results shown in the figures it can be observed that the percentage of addition in these new cements has a direct relation with pozzolanicity and it is demonstrated that the higher is the percentage of addition, the higher is the pozzolanic activity in the cements. In figure 5, it is shown the representation of the pozzolanicity for cements with the three wastes in the same percentage of substitution (10%). In the same way in figures 6 and 7, are represented the addition percentages of 20 and 30 % respectively. The pozzolanic activity is directly related with the percentage of ceramic material in the waste. The higher is the ceramic material the higher is the pozzolanic activity. This way, cements made with S3 as addition are more pozzolanic than made with S1 or S2.

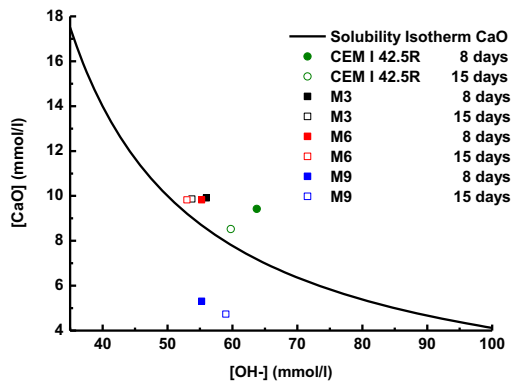




**Figure 5.** Pozzolanicity for cements with 10% of addition for 8 and 15 days curing



**Figure 6.** Pozzolanicity for cements with 20% of addition for 8 and 15 days curing



**Figure 7.** Pozzolanicity for cements with 30% of addition for 8 and 15 days curing

### 3. Conclusions

Several wastes from construction and demolition management plants were collected for studying their characteristics and properties in order to can use them as pozzolanic addition in cements.

The chemical and mineralogical compositions have been studied in all the wastes and all the samples have similar composition and they are comparable. Three of the wastes were used to prepare blended cements in different ratios of addition (10, 20 and 30 %) in order to study their pozzolanic activity and compare it with the cement used as reference.

The chloride and sulfate contents were studied and all the cements fit with the Standard. Setting times and volume stability meet with the Standard too. The pozzolanic activity was evaluated in 9 blended cements and in the reference by the European normative: UNE – EN 196-5:2006. In the view of the pozzolanic activity obtained it can be possible to say that:

- The higher ceramic material in the wastes (from 20 to 100 %), the higher is the pozzolanic activity in cements.
- The higher percentage of addition (from 10 to 30 %) in cements, the higher is the pozzolanic activity shown.

### Acknowledgment

The present study could be possible thanks to Spanish Ministry of Science and Innovation under the coordination of the research project (BIA2010–21194–C03–01).

### References

- [1] VITO, BIO. 2007. Institute for European Environmental Policy and IVM. Data gathering and impact assessment for a review and possible widening of the scope of the IPPC Directive in relation to waste treatment activities. Potential amendment E3-Sorting of construction and demolition waste
- [2] EIONET (European Environment Information and Observation Network), *European Topic Centre on Resource and Waste Management*. www.eionet.europa.eu
- [3] Ministerio de la Presidencia. RD 105/2008, de 1 de febrero, por el que se regula la Producción y Gestión de los Residuos de Construcción y Demolición. 2008
- [4] Ministerio de Medio Ambiente. PNRC D 2001-2006. Plan Nacional de Residuos de Construcción y Demolición. 2001
- [5] Ministerio de Medio Ambiente.. PNIR 2008-2015. Plan Nacional Integrado de Residuos. 2009
- [6] M. I. SÁNCHEZ DE ROJAS et al. *J. Am. Ceram. Soc.* Vol. 89, No. 12, pp. 3701 – 3705. 2006
- [7] M. I. SÁNCHEZ DE ROJAS et al. *Materiales de Construcción*. Vol. 51, No. 261. 2001
- [8] GERD, Ministerio de Agricultura, Alimentación y Medio Ambiente. Spanish Guide of recycled aggregates from C&DW. Project GEAR. 2012
- [9] AENOR. Cement. Part 1: “ Composition, specifications and criteria of conformity for common cements”. *UNE – EN 197-1*. 2011
- [10] AENOR. Method of essay in cements. Part 5: “Essays of pozzolanicity for pozzolanic cements”. *UNE – EN 196-5*. 2006

# Use of crushed brick aggregate in structural concrete: properties and performance

Sunanda PAUL<sup>1</sup> and Gopinandan DEY

*Department of Civil Engineering, National Institute of Technology, Agartala*

**Abstract.** A comprehensive test program was conducted to investigate upon the use of crushed brick aggregate in structural concrete. In Tripura, a tiny state in the North-eastern India and some places of West Bengal, India and in Bangladesh where there is a scarcity of natural stone aggregates, burnt clay bricks are used as a potential source of coarse aggregate and performance of concrete made with broken brick as coarse aggregate has been found quite extensive and satisfactory (M.A.Rashid et al.). But the current designs for brick aggregate concrete are based on existing nominal mix concrete codes for natural stone aggregates and experience. The presented paper depicts an effort to establish a proper mix design procedure which would satisfy the requirements of using such aggregate whereas the Indian Standard code of recommended guidelines for concrete mix design suggests only the use of naturally occurring crushed or uncrushed aggregates. Based on physical standard and strength criteria, a comparative study was conducted among concrete properties made with brick aggregate in different saturation conditions as well as with natural stone aggregate. Test results were satisfactory for strength criteria and suggestions are proposed to promote the suitability of using crushed brick aggregate in concrete for structural use.

**Keywords.** Brick aggregate, mechanical properties, water absorption, compressive strength

## Introduction

Concrete is a versatile engineering material consisting essentially of cementing substance, aggregates and water. Its strength is developed from the hydration due to the reaction between cement and water. The products, mainly calcium silicate hydrate, calcium aluminates and calcium hydroxide are relatively insoluble and bind the aggregate in a hardened matrix. The raw materials consisting of cement and aggregates, affect both the quality and cost of construction. Aggregates constitute over 70% by volume of concrete. The availability of aggregate in any region also affects the cost of construction.

At present, the most commonly used coarse aggregates for concrete production in the state of Tripura is the broken stone aggregate obtained from quarries in Kachar district in the neighboring state of Assam, India. As these are not readily available in local areas, the cost of transportation tends to increase the cost of construction. This necessitates the use of alternative coarse aggregates which can be locally obtained. One of such coarse aggregates is crushed clay bricks. In spite of extensive use of brick

---

<sup>1</sup> Corresponding author: [sunandapaul@gmail.com](mailto:sunandapaul@gmail.com)

aggregate concrete in Bangladesh and the apparent satisfactory performance of the structures built, there is little investigation work conducted and documented [1]. Previous researchers have shown that a linear relationship exists between the compressive strength of the parent bricks and the impact value of aggregates produced from them [2]. The low quality of bricks in comparison with natural rocks is due to production process of such bricks [3]. The stronger the original bricks; the higher the compressive strength of the concrete made with aggregates produced by crushing these bricks and the higher the density of the brick aggregates, the higher the concrete strength achieved [4].

## **1. Research significance**

This research investigates the possibility of using concrete made with brick aggregates as coarse aggregate in new construction as well as the justification and proper documentation of wide use of crushed brick aggregate concrete in the state of Tripura and West Bengal, India and Bangladesh. The low range of compressive strength of bricks available in this area restricts the strength of brick aggregates as well. As far as the physical properties such as specific gravity, water absorption, abrasion resistance, impact value and crushing strength are concerned, brick aggregates show lower potential in comparison with natural stone aggregates.

A comparative analysis was done between crushed brick and natural stone aggregate used in this region based on the standard test for workability and compressive strength. There was also a scope to check whether or not brick aggregate concrete could be used as light-weight concrete. So the unit weight of each set/batch of concrete was noted. Guidelines laid down in the Indian Standard code of Mix design (IS 10262:2009) is mainly used for concrete made with aggregate obtained from natural rock and it restricts the use of coarse aggregate which absorbs more than 10 % water by mass (IS 456:2000). Due to high water absorption (10 to 20%) and low strength of brick aggregates, those provisions are not fully applicable to concrete made with brick aggregate. This research work will shed some light on the possibility of developing an executable standard procedure of mix design which will satisfy the prerequisites of good structural concrete made with brick aggregate.

## **2. Materials investigation**

The cement used was ordinary Portland cement of 43 grade (OPC 43) conforming to IS 8112:1989. The grading curve of the fine aggregate obtained from sieve analysis fitted the limits set in IS 383:1970 for grading zone IV, the finest among all the grading zones as per Indian standard, and its specific gravity was found to be 2.27. New clay bricks of 250x115x70 mm working sizes were used in this investigation. The compressive strength of the whole brick was found to be 12.10 MPa. The whole bricks were crushed into aggregates of sizes ranging from 600  $\mu$ m to 25 mm and manually sieved to 20 mm nominal size as per Indian standard code IS 383:1970.

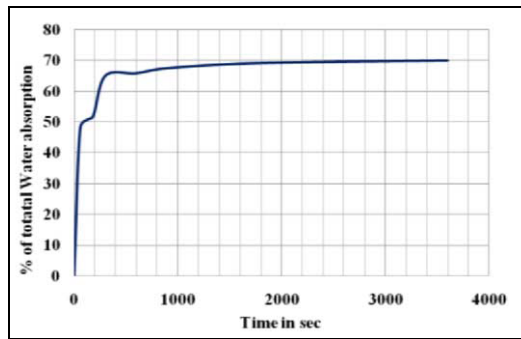
One of the major contributing factors to the quality of concrete is the aggregate property used therein. To assess the qualities of aggregate used in concrete, the physical and mechanical tests were conducted according to IS 2386:1963, as given in

Table 1. It can be seen that the water absorption property for aggregates obtained by crushing locally available brick was higher than that of crushed natural stone aggregate.

**Table 1.** Basic tests conducted on crushed brick and stone aggregate

Properties	Brick aggregate	Crushed stone aggregate
Specific Gravity	2.125	2.66
Water Absorption (%)	11.60	1.84
Aggregate Crushing Value (%)	38.90	22.40
Impact Value (%)	39.25	21.82
Abrasion Value (Los Angeles) (%)	43.36	31.40

The water absorption property for aggregates obtained by crushing locally available brick was different from that of crushed natural stone aggregate.



**Figure 1.** Water absorption percentage as total water absorption for brick aggregate

Figure 1 shows that the absorption rate of brick aggregate is quite high in initial stage and after 3 to 5 minutes, the absorption rate decreases. Superplasticizing admixtures BASF-MASTER Rheobuild 1100i (SNF) and FORSOC Conplast SP430 IT(PQ) conforming to IS 9103:1999 were used in this investigation, in order to improve workability and to study the effect of admixtures on the properties of fresh and hardened concrete.

### 3. Test program

The basic guideline for mix design of concrete as per the Indian code IS 10262:2009 was followed for concrete of grade M25 i.e., for the designed mix, expected characteristic strength as per the standard is  $f_{ck}' = f_{ck} + 1.65S = 31.6$  MPa. According to the guideline stated in standard code, saturated and surface dry (SSD) aggregates are used and either moist or dried condition adjustment is done accordingly. Most of the researches are done on aggregates in SSD condition, but in real field projects, it is almost impossible to prepare SSD aggregate. So investigation was done upon concrete made in different moisture conditions of aggregates. Concrete using brick aggregates

were made at w/c ratios of 0.45, 0.40 and 0.35. Test properties included slump, unit weight and compressive strength. The tests were all performed according to the Indian standard testing methodology. The investigation was executed for three different brick aggregate moisture state and one natural stone aggregate viz. with Saturated Surface Dry brick aggregates, with normal (air dry) condition brick aggregate, but with the mixing of extra water that aggregates would have absorbed in 24 hours soaking, with normal (air dry) condition brick aggregate, but with the mixing of extra water that aggregates would have absorbed in 3 minutes soaking and with Saturated Surface Dry natural stone aggregates.

Standard tests were performed as follows:

1. Slump test according to IS 1199:1959 for workability
2. Compressive strength as per IS 516:1959

#### 4. Results and discussion

Compressive strength for the concrete mixes made with SSD brick aggregates (designated as Mix1), normal (air dry) aggregate with additional mixing of 24 hour soaking water (Mix2), normal (air dry) aggregate with additional mixing of 3 min soaking water (Mix3) and SSD stone aggregate (Mix4) were found to be satisfactory as far as the 28 day characteristic compressive strength is concerned for w/c ratios 0.45 and 0.40, whereas at w/c ratio 0.35, it was found to follow an unusual trend in accordance with different saturation conditions as can be seen from figures 2 and 3 respectively.

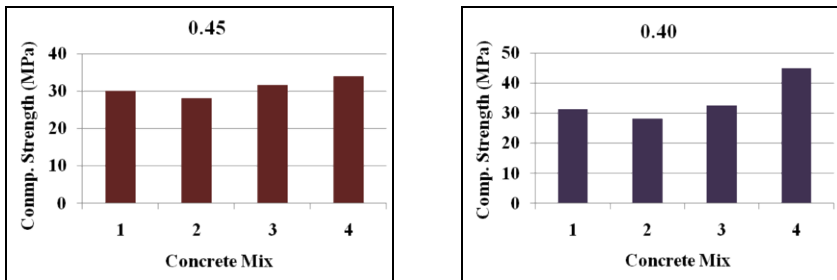


Figure 2. Comparison of compressive strength with different saturation conditions of aggregate

It is evident that saturation condition matters in terms of compressive strength i.e., unlike code provisions, the added extra water to adjust the dry condition of coarse aggregates on the sheer supposition that during mixing, adding the amount of water aggregates would have absorbed in 24 hours (as per the definition of saturated surface dry condition) can be detrimental to the strength property of concrete.

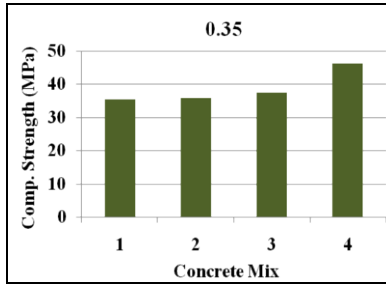


Figure 3. Trend for a lower w/c ratio mix in different saturation conditions

However, figures 2 and 3 also points up that concrete made with normal dry condition aggregate with the addition of 3 min soaking water during mixing (concrete Mix3) resulted in more strength in comparison with 24 hour soaking (concrete Mix2). This trend can be attributed to the fact that brick aggregates absorb roughly 60 % of the total water absorption ( of 24 hours) in initial 3 to 5 minutes (figure 1), which makes the aggregates reasonably saturated and apparently an ideal condition to be used in concrete production. The variation of unit weight with respect to different saturation conditions and w/c ratios is shown in figure 4.

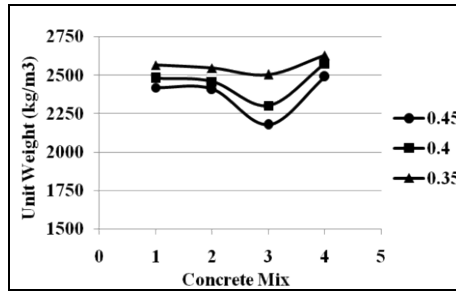


Figure 4. Unit weight observation

The only wide range of variation is observed in 3 min saturated brick aggregate concrete (Mix 3), which indicates that this phenomenon can be used in concrete making for design of varying weight of structural elements. As far as workability is concerned, slump values were satisfactory for all batches of concrete mixes except for the second mix, which had 24 hour soaking extra water for dry aggregate and gave higher slumps as shown in figure 5. This phenonmenon can be attributed to the provision of adding water in excess of calculated water content on a mere assumption basis.

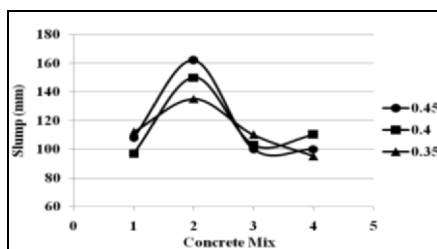


Figure 5. Workability observation

## 5. Conclusion and future scope

The present study concludes that brick aggregate used as coarse aggregate in structural concrete satisfies the standard for compressive strength as of the designed mix of concrete. The practice of mixing as much quantity of water as 24 hour absorption should be restricted based on in-situ moisture content determination. For general practice, 3 min absorption water can be used as correction since it was found to be producing both workable and strong concrete. There is a future scope to investigate upon the tensile strength and bond characteristics of brick aggregate concrete. Moreover, there is inevitability for proper documentation for the application of crushed brick aggregate in structural concrete.

## References

- [1] Mohammed Abdur Rashid, T.Hossain, and M.Ariful Islam (2009), "Properties of higher strength Concrete made with crushed brick as coarse aggregate". *Journal of Civil Engineering (IEB)*.
- [2] Fouad M. Khalaf and Alan S. DeVenny (2005), "Properties of New and Recycled Clay Brick Aggregates for Use in Concrete". *Journal of Materials in Civil Engineering(ASCE)*.
- [3] Jafar Bolouri Bazaz, Mahmood Khayati and Navid Akrami (2006), "Performance of concrete produced with crushed bricks as the coarse and fine aggregate". *IAEG2006 Paper number 616*, The Geological Society of London.
- [4] Fouad M. Khalaf (2006), "Using Crushed Clay Brick as Coarse Aggregate in Concrete". *Journal of Materials in Civil Engineering (ASCE)*.
- [5] IS: 383 (1997), "Specification for Coarse and Fine Aggregates from Natural sources for Concrete"
- [6] IS: 1199 (1959), "Methods of Sampling and Analysis of Concrete"
- [7] IS: 516 (1959), "Methods of Tests for Strength of Concrete "
- [8] Neville, A. M. and Brooks, J. J. (2002), *Concrete Technology*, Pearson Education.
- [9] J.H. Bungey and S.G. Millard. (1996), *Testing of Concrete in Structures*.
- [10] Khaloo, A. R. (1994), "Properties of concrete using crushed clinker brick as coarse aggregate" *ACI Mater. J.*, 91(2), 401-407.
- [11] Neville, A. M. (1995), *Properties of concrete*, Longman's, London.
- [12] Farid Debieb and Said Kenai (2007), "The use of coarse and fine crushed bricks as aggregate in concrete". *Construction and Building Materials (Elsevier)*.
- [13] Paulo B. Cachim (2008), "Mechanical properties of brick aggregate concrete". *Construction and Building Materials (Elsevier)*.
- [14] Mohammad Abdur Rashid, Md. Abdus Salam, Sukanta Kumar Shill and Md. Kowsur Hasan (2012), "Effect of Replacing Natural Coarse Aggregate on the Properties of Concrete". *Dhaka University of Engineering and Technology Journal, Vol.1, Issue 3*.



# Study of particle packing in self-consolidating mortar systems

Syed Ali RIZWAN<sup>a,1</sup>, Qamar uz ZAMAN<sup>a</sup> and Thomas A. BIER<sup>b</sup>

<sup>a</sup>National University of Sciences and Technology (NUST), Islamabad, Pakistan

<sup>b</sup>Technische Universität, Bergakademie, Freiberg, Germany

**Abstract.** This paper reports the results of self-consolidating cementitious systems using Dinger & Funk (D & F) particle packing model which is a refinement of Anderson & Andreassen model (A & A) in the sense that it contains both minimum and maximum particle sizes in the expression for cumulative percent finer than a given size “d” (CPFT-percent passing a given sieve size “d”). D & F packing model seems to be fairly applicable to the particle packing in cementitious systems using fine mineral admixtures. Better particle packing results in reducing voids and hence total paste volume requirement of self-compacting cementitious systems is also reduced translating into improved economy, durability and volume stability. Several formulations based on such models were designed and tested. Flow of self-consolidating mortar (SCM) systems was found to be depending on particle size distribution of the matrix. The self-consolidating mortar system incorporating mineral admixtures showed better packing at distribution modulus ‘q’ = 0.205 and displayed improvement in strengths. It appears that with the additions of fine powders the value of ‘q’ reduces.

**Keywords.** Andersen & Andreassen model, optimized grading curve, packing density and self-consolidating mortars (SCM)

## 1. Introduction

Concrete systems contain particles of varying sizes and shapes and therefore show characteristics which are largely dependent on the way the particles pack themselves inside the matrix. Particle packing in cementitious systems is random and packing density of a system can be improved by incorporating suitable contents of various size groups of aggregates and fine mineral admixtures. Packing density is key to performance of cementitious systems and is defined as volume fraction randomly arranged in confined space [1]. The optimum packing value of randomly packed mono sized spheres is around 0.64 [2]. However, introducing finer and finer particles in the system a dense particle packing can be achieved.

Particle packing is the art and science of arranging particles in confined space [3], and depends upon particle size distribution (PSD) of a mix [4]. In cementitious systems different combinations of materials are used [5]. Paste defines binding properties, acts as lubricant and fills the cavities between aggregate particles. According to Shilstone, mortar is the most important part of the mixture as it controls many properties of concrete [6].

<sup>1</sup>Corresponding author: [syedalirizwan@hotmail.com](mailto:syedalirizwan@hotmail.com)

Secondary raw materials (SRMs) act as filler and possibly binder as well in the cementitious mix and improve packing of binder phase and of smaller aggregate particles provided those are about two orders less than the size ( $D_{50}$ ) of binder particle. SRMs reduce the voids and are used in high performance concrete (HPC)/self-consolidating concrete (SCC) to obtain improved microstructure and durability [7]. The role of SRMs is to improve packing, facilitate placements and increase durability of system [8]. With continuously graded aggregates, the use of SRM's in the presence of super-plastizer usually results in minimizing the voids, paste and hence the cement requirement [9]. Poorly graded aggregates typically have a lower packing density [10]. Reduced cement content due to SRMs achieves environmental benefits in terms of overall reduction in cement production and hence reduced emission of  $CO_2$  and saving in energy.

## 2. General concepts in study of particle packing

### 2.1 Definitions of special concretes

Particle packing models give a basis for mix designs not only for traditional concrete but for special concretes like HPC, SCC and high strength concrete (HSC) [11]. American Concrete Institute (ACI) defines HPC as “the concrete that meets special performance and uniformity requirements that may not always be obtained using conventional ingredients, normal mixing procedures and typical curing practices” [7]. ACI 237R – 07 defines SCC as “a highly flow able, non-segregating concrete that can spread into place, fill the formwork, and encapsulate the reinforcement without any mechanical consolidation” [12]. Self-consolidating mortar (SCM) systems are kind of concrete systems which require higher powder content to increase its flow-ability and stability [13].

### 2.2 Packing models

Füller & Thompson (F&T) in 1907, Andreasen & Andersen (A&A) in 1930 and Dinger & Funk (D&F) proposed continuous PSD curves for the purpose of achieving higher workability of mixes at low water content [14]. F&T worked on fixed value of distribution modulus ‘q’ at 0.5, whereas floating value of q was used by A&A which seems logical owing to the fine particles used in various modern concrete systems. Particle packing models or characteristics equations of F&T and A&A do not consider the effect of smallest size particles used in the system.

D&F Model is used in this work. D&F, towards the end of last century, incorporated minimum size of particles in their equation as shown in Table 1. The value of distribution modulus ‘q’ is a function of particulate structure in the mix. In general, the more the powder content or very fine sand particles with size less than  $125\mu\text{m}$ , the smaller is the ‘q’ the best is the characterization of the PSD of the mix [15]. Characteristics equations of various researcher's along with best value of suggested distribution modulus ‘q’ are presented in Table 1.

In Table 1, ‘CPFT’ is cumulative percent finer than a given size, ‘d’ and ‘q’ is the value of distribution modulus and ‘ $d_{\text{max}}$ ’ and ‘ $d_{\text{min}}$ ’ are maximum and minimum size of particles in the mix respectively.

**Table 1.** Continuous particle packing models [16]

Researcher	Characteristics Equation	Best Value of Distribution Modulus
Fuller & Thompson (F&T)	$CPFT = \left[ \frac{d}{d_{max}} \right]^{0.5} \times 100$	q = 0.5
Andreasen & Andersen (A&A)	$CPFT = \left[ \frac{d}{d_{max}} \right]^q \times 100$	q = 0.37 less fines q = 0.25 more fines q = 0.45 for coarse particles
Dinger & Funk (D&F)	$CPFT = \left[ \frac{d^q - d_{min}^q}{d_{max}^q - d_{min}^q} \right] \times 100$	q = 0.30

### 3. Experimental program

#### 3.1 Materials

Ordinary Portland Cement CEM1 42.5R produced by Lafarge and local natural siliceous sand available in Freiberg was used in this study. Sand was sieved and size fractions were separated and designated as tabulated in Table 2.

**Table 2.** Fine aggregate size distribution

Designation	Upper Size Limit (Microns) - passing	Lower Size Limit (Microns) – Retained on
S1	2000	1000
S2	1000	500
S3	500	250
S4	250	125
S5	125	63

Silica fume and fly ash were used as mineral admixtures; binder to aggregate ratio was 1:1.33. Further proportions of each material constituent are detailed in Table 3. A fixed w/c ratio of 0.38 was used in this study.

**Table 3.** Material constituent in each mix (mass %)

Material %	Mix Designation				
	Q1	Q2	Q3	Q4	Q5
Cement	43.0	43.0	43.0	38.0	38.0
Silica Fume	-	-	-	2.5	2.5
Fly Ash	-	-	-	2.5	2.5
S1		14.9	17.6	14.9	17.6
S2		12.9	13.7	12.9	13.7
S3	57	11.2	10.7	11.2	10.7
S4		9.7	8.4	9.7	8.4
S5		8.3	6.6	8.3	6.6

Mix Q1 was prepared taking weighted proportion of cement and local siliceous Sand. Mix Q2 and Q4 were prepared in weighted fraction as obtained from curve plot of D&F model at 'q' of 0.205 and mix Q3 and Q5 were prepared in weighted fractions as obtained from gradation curve plot of D&F at 'q' of 0.35. All five SCM mixes were cast using super-plasticizer content required for target flow of  $30 \pm 1$  cm measured with  $6 \times 7 \times 10 \text{ cm}^3$  using Hagerman's mini-slump cone.

### 3.2 Determination of suitable distribution modulus 'q'

After having sieved and separated into various size groups, PSD of various fine aggregate size groups, binder and mineral admixtures was determined using Beckmann Coulter LS 230 Laser Granulometer. Figure 1 shows the PSD of binder and fine aggregates. Figure 2 shows the gradation plot of A&A and D&F at distribution modulus of 0.2 and 0.5. Gradation curves of D&F model were plotted taking various values of distribution modulus (from 0.2 to 0.5) and considering available materials particle range. Value of distribution modulus 'q' at 0.205 was found suitable from Figure 2 to maintain the binder to aggregate ratio of 1:1.33. Figure 3 shows modeled and actual gradation curve. It can be clearly seen that it is difficult to achieve the modeled gradation plots especially for the powder particles due to the difficulty in separating extremely fine powder particles. Figure 4 shows the availability of 43% mass of particles below 63 microns to maintain binder to aggregate ratio of 1:1.33.

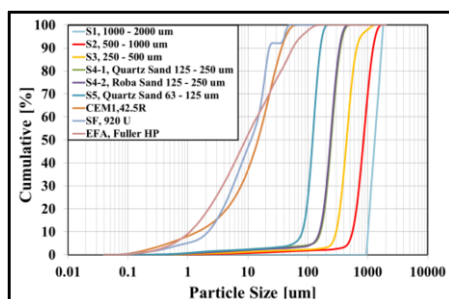


Figure 1. PSD of binder and fine aggregate

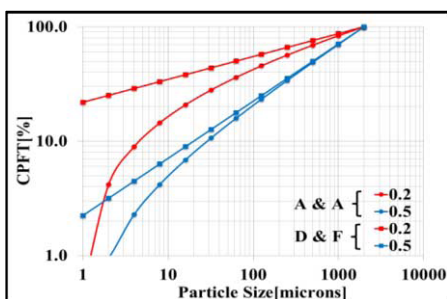


Figure 2. Gradation Curve of A&A and D&F

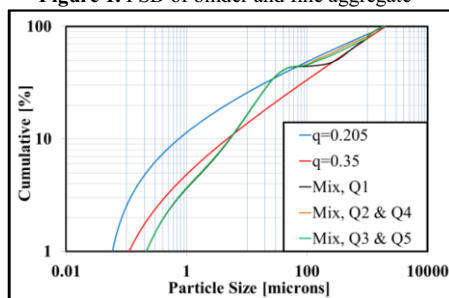


Figure 3. modeled and actual gradation curve

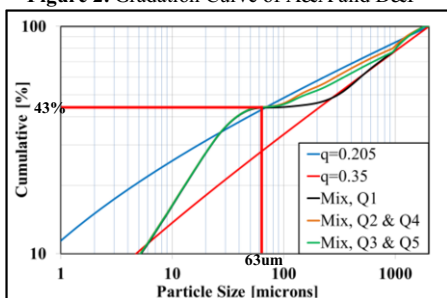


Figure 4. Selection of optimum value of 'q'

### 3.3 Material Characteristics and gradation requirements

In this study five mixes of self-consolidating mortar (SCM) system designated as Q1 to Q5, as detailed in Table 3, were prepared to test the effects of various values of

distribution modulus 'q'. The whole range of particles present in fine aggregate, cement and mineral admixtures was considered to formulate the mix. A minimum particle size of 0.1 micron was assumed for plotting gradation curves. A value of distribution modulus 'q' at 0.205 was selected based on D&F model. The other value of distribution modulus 'q' of 0.35 was used as suggested in the literature [5] for better degree of packing of aggregate phase only. Q1 is the SCP system with cement and source sand (Siliceous) and is a control mix in this study. Q4 and Q2 are the mixes modeled at distribution modulus 'q' at 0.205 with and without SRMs respectively. Q5 and Q3 are the SCM mixes modeled at distribution modulus 'q' at 0.35 with and without SRMs respectively. Proportions of binder and aggregates were taken as detailed in Table 3. It is also interesting to note that gradation curve of Q1 mix constituting locally available siliceous sand can be viewed following the gradation curve of D & F at distribution Modulus 'q' of 0.35 up to particle size of 125 microns.

## 4. Results and discussion

### 4.1 Flow

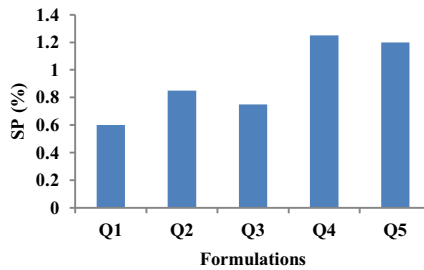


Figure 5. Super-plasticizer requirement to produce target flow of formulations

### 4.2 Strength test results

- Flexure Strength. Figure 6 and 7 show the flexural and compressive strength of all the five mixes at 2, 7, 28 and 56 days respectively. Flexural strength results for the modeled SCM mix Q2 were consistent. Whereas Q3 results were inconsistent. Q4 mix also displayed good results as compared to Q5 mix.
- Compressive Strength. The compressive strength results of the SCM mix 'Q2' modeled at distribution modulus 'q' at 0.205 of D & F model are consistent and improved as compared to other mixes formulated without SRMs. However, mix Q4 and Q5 formulated incorporating SRMs displayed almost similar trends. The parity in results of Q4 and Q5 may be due to the filler and pozzolanic effects of Fly Ash and Silica Fume used in equal proportions in both the mixes.

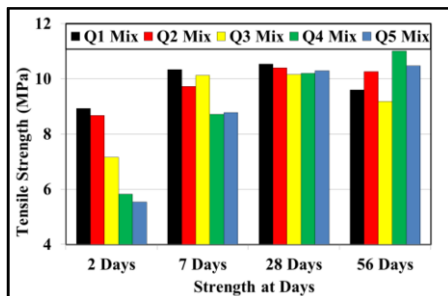


Figure 6. Flexure strength of various mixes

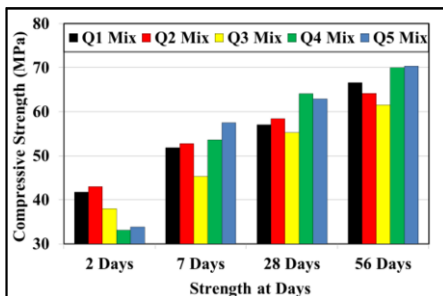


Figure 7. Compressive strength of various mixes

### 4.3 Mercury Intrusion Porosimetry

MIP analysis was carried out using Pascal 440 Porosimeter. Contact angle was 140° and mercury surface tension was 480 dyne/cm. Figure 7 shows the results of MIP for all five mixes at seven days. The threshold diameters of all the SCM formulations (Q1 to Q5) were measured as 39.89, 48.47, 52.15, 32.46 and 29.17 respectively. It is evident that Q2 has displayed good performance attributes as compared to other SCM mixes without SRMs i.e. Q1 and Q3. SCM Mixes Q4 and Q5 incorporated SRMs, displayed comparatively better strength results due to packing of both aggregate and binder phases resulting in improved microstructures. It must be kept in mind that due to constant mixing water content, formulations having higher fines (SF & FA) had lower effective water cement ratio and this also resulted in higher strengths.

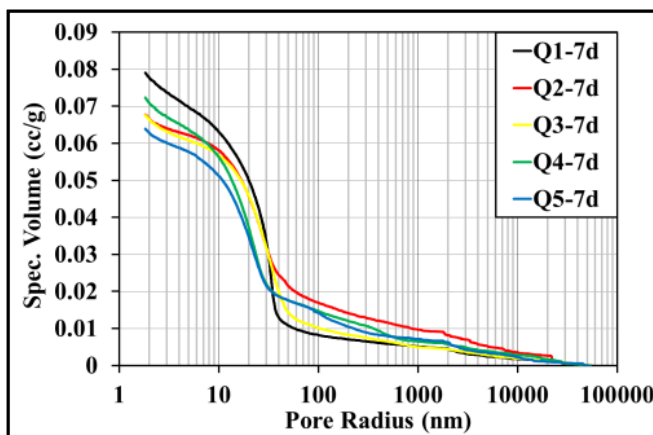


Figure 8. MIP results of various SCM mixes.

## 5. Concluding remarks

Dinger & Funk Model is useful for the improved response of the normal as well self-consolidating cementitious systems. Value of distribution modulus 'q' plays an important role in defining system attributes and thus depends on many factors especially on the presence of fine mineral admixtures for a selected mix of self-consolidating mortar systems. From this study; a value of distribution modulus 'q' at 0.205 seems to give better packing density for self-compacting mortar systems. It may be possible that reducing the mixing water content for the improved packing density systems gives still better results.

## 6. Acknowledgements

The authors are thankful to DAAD for partially sponsoring this research work.

## References

- [1] SHRP-C-340, *Concrete Components Packing Handbook*, 1993.
- [2] K. Sobolev and A. Amirjanov, The Development of a Simulation Model of the Dense Packing of Large Particulate Assemblies, *Powder Technology*, Vol. 141, 2004, (155-160).
- [3] X. Jia, R.A. Williams, A packing algorithm for particles of arbitrary shapes, *J. Powder Technology*, 120 (2001), (175-186).
- [4] Mirza A., Study of Packing concepts in SCCS using different SRMs and Mixing Regimes, *MS Thesis, NICE, National University of Sciences and Technology*(NUST), Islamabad, Pakistan (2013).
- [5] Ahmad S., A Study of Packing Density Effects on Self-Consolidating Mortar Systems, *MS Thesis, NICE, National University of Sciences and Technology*(NUST), Islamabad, Pakistan (2011).
- [6] P. N. Quiroga, D. W. Fowler, The effects of aggregates characteristics on the performance of Portland cement concrete, *ICAR 104-1F*(2003).
- [7] Rizwan S.A. ,High performance mortars and concrete using Secondary Raw Materials, *PhD Thesis, Technical University Freiberg*, Germany, ISBN 978-3-639-17878-4, VDM Verlag, Dr. Muller, Germany, 2006.
- [8] Rizwan, S.A, Bier, T.A and Ahmad, H., Self-Compacting Concrete -A Useful Technology, Paper No. 670, *70<sup>th</sup> Annual Session Proceedings of Pakistan Engineering Congress*, Vol 70, pp 293-318, December 2-4, 2006, Lahore, Pakistan.
- [9] Rizwan S. A.and Bier T. A., Self-Compacting Mortars using various Secondary Raw Materials, *ACI Material Journal*, Volume 106 No. 1, January-February 2009, PP 25-32.
- [10] Marc Rached, David Fowler, and Eric Koehler., Use of Aggregates to Reduce Cement Content in Concrete, *Second International Conference on Sustainable Construction Materials and technologies*, 30 June 2013 ISBN 978-1-4510-1487-7.
- [11] Mohammed H. Mohammed, Mats Emborg, Roland Pusch, Sven Knutsson, Packing Theory for Natural and Crushed Aggregate to Obtain the Best Mix of Aggregate: *Research and Development, World Academy of Science, Engineering and Technology* 67 2012.
- [12] ACI 237R – 07; Self Consolidating Concrete, Report by ACI Committee 237, Published April 2007.
- [13] B. Benabed, E. Kadri, L. Azzouz, S. Kenai, Properties of self-compacting mortar made with various types of sand, *Cement and Concrete Composites, Volume 34, Issue 10*, November 2012, Pages 1167-1173.
- [14] Rizwan, S.A, Ahmad, S. and Bier, T. A., *Application of Packing Concepts to High Performance Self-Consolidating Mortar Systems*, ACI SP-289.22, USA PP 299-315, Special 2012
- [15] H. J. H. Brouwers, SCC, The Role of Particle Size Distribution, *First International Symposium on Design, Performance and Use of Self-Consolidating Concrete SCC'2005 - China*, 26 - 28 May 2005, Changsha, Hunan, China (109-118).
- [16] Rizwan, S.A, Zaman, Q. and Bier, T. A., Study of Packing Concept in Self-Consolidating Mortar Systems, *International Conference on Advanced Concrete Technology and its Applications* (ACTA-2012). Islamabad, Pakistan, November 6-7, 2012 (125-134).

# Nearly 20 years of the EN 197 cement standards in South Africa

Sibusiso HLATSHWAYO<sup>1</sup> and Reinhold AMTSBÜCHLER  
*Lafarge Industries South Africa*

**Abstract.** The 1994 version of the EN 197 standard was first adopted in South Africa in 1996. This was after a major change in South Africa's political and social landscape. Before the EN standard, South Africa had a few standards for cement. They included SABS 471, 831, 626, and 1466. These standards broadly allowed for only 8 types of cement and 2 strength classes. The EN 197 however, catered for 27 types of cement and 6 strength classes. The EN 197 continues to evolve to expand the types and strength classes of cement with the latest edition being CEM III with "L" strength classes and SR cements to mention some. In 2007, the EN 197 standard was made a compulsory specification by the Minister of Trade and Industry. The National Regulatory of Compulsory Specifications ensures compliance to this specification to ensure fair trade and consumer protection. Was it a prudent decision to switch from the old SABS standard to the EN 197? What are the current challenges with the EN 197 standard?

The paper aims to explore the broad impact of the adoption of EN 197 on the manufacturing industry, construction industry, the government, and the general consumer. It will also address some of the challenges posed by this specification and the readiness of South Africa to keep up with the development path and changes of this particular standard.

**Keywords.** SABS cement standards, European cement standards

## Introduction

Specifications are key drivers for any industry. Even after research has proven any innovation and need for change for the better, the next challenge is always the influence of the governing specifications. It is necessary therefore to review the history and current state of this key driver of the cement industry in South Africa and discuss historic changes, impact, and challenges for the future.

From 1971 to 1996, South Africa used four standards to regulate the production and performance characteristics of cements sold. The European Cement Standard EN 197-1 & 2 was adopted in the country in 1996. This was still the voluntary version of the standard. Before 1996, only seven cement types could be manufactured and sold. Only 3 and 7 days compressive and flexural strength (referred to as transverse strength in SABS 471) were specified. Only Slag was allowed to be blended or interground at more than 15% (with 70% as a maximum) until 1988 when the fly ash specification was introduced. Fly ash addition was limited to 35%. Some specifications for these cements were left to an agreement between the seller and purchaser with 28 days

---

<sup>1</sup>Corresponding author: [sibusiso.hlatshwayo@lafarge.com](mailto:sibusiso.hlatshwayo@lafarge.com)



compressive strength as an example. Fineness of the cement was also specified. Nevertheless, many buildings and other types of infrastructure were constructed using these cements between 1971 and 1996.

In 1996, two years after the historic political change of 1994 in the South African context, the ENV 197 specification for common cements was adopted. This specification replaced the previous four SABS standards. The ENV 197 combined all cement types and six strength classes. Also, the EN 413 was adopted though it is not part of this review. There were glaring differences between the set of the four SABS standards and the EN 197-1. The key differences were the number of cement types that could now be made. From only 7 cement types, now South Africa could potentially make 27 cement types across 6 strength classes. The test methods had to change also to EN tests methods. This adoption was set to change the landscape of cement production and sales in the country. It was also set to pose some challenges later for the manufacturers and the consumers. How fast would stakeholders be educated in this new standard? How quickly would consumers let go the Ordinary Portland Cement and embrace all other types of cements that were now available. What would the impact be on the environment? How would this change impact the competition among industry players? The paper aims to review some of these impacts, and also discuss some future challenges with regards to the 1996 decision to adopt ENV 197 in South Africa.

## **1. The history of SABS cement standards: 1971 to 1996**

In 1971, three standards were introduced. They covered 6 cement types as detailed in Table 1. The fly ash cement standard was introduced later in 1988. These standards detailed the chemical and physical requirements, the packaging requirements, test methods, and the quality control and conformance assessment criteria. There were no constituent requirements.

### *1.1. Chemical requirements*

Referring to Table 1:  $\text{SO}_3$  was dependent on  $\text{C}_3\text{A}$  level. Loss on Ignition (LOI) for even the OPC was 4% whereas clinker is normally below 1%. Sulphide (S) was specified. For some cements, chemical ratios were also specified. Processing additives were limited to 0.25% versus today's 1.0%.  $\text{C}_3\text{A}$  level was limited for sulphate resisting cements versus today's seven different options for sulfate resisting cements.

### *1.2. Physical requirements*

VMC was used, therefore direct comparison of results to EN prism strength is not possible since a different water/cement ratio and a different standard sand is used. In the previous cements (1971 – 1996), 28 days was optional and done only at customer's request. Also the expansion limit was 5 mm versus today's 10 mm.

**Table 1.** Summary of chemical and physical requirements of SABS standards

Standard	471			626	831		1466
Year	1971			1971	1971		1988
Portland Cement	Ordinary	Rapid-	Sulphate	Blast	Ordinary	Rapid-	Fly ash
MgO	5.0	5.00	5.00		5.00	5.00	5.00
SO <sub>3</sub> a) <7%C <sub>3</sub> A	3.0	3.00	2.50	3.00	3.00	3.00	3.00
SO <sub>3</sub> b) >7%C <sub>3</sub> A	3.5	3.50					
C <sub>3</sub> A max (%)			3.50				
LOI max (%)	4.5	4.50	4.50	4.00	2.50	2.50	4.00
Sulphide	1.0	1.00	1.00	1.50			1.00
SiO <sub>2</sub> +Al <sub>2</sub> O <sub>3</sub> +Fe <sub>2</sub> O <sub>3</sub>					70.00	70.00	
SiO <sub>2</sub> /(Al <sub>2</sub> O <sub>3</sub> +Fe <sub>2</sub> O <sub>3</sub> )					2.00	2.00	
Al <sub>2</sub> O <sub>3</sub> /Fe <sub>2</sub> O <sub>3</sub>					3.00	3.00	
Fineness +212 um	1.2	0.50	1.20		1.00	0.50	1.00
SSA minimum	2250	3250	2250	2750	2500	3500	2750

**Compressive strength (VMC – Vibrated Mortar Cube)**

3 days	16.0	21.00	16.00	14.00	16.00	21.00	14.0
7 days	24.0	28.00	24.00	23.00	24.00	28.00	23.0
28 days++				35.00			35.0

**Transverse strength (VMC – Vibrated Mortar Cube)**

3 days	1.8	2.80	1.80	1.50	1.80	2.80	1.50
7 days	2.8	3.80	2.80	2.60	2.80	3.80	2.60
28 days++				4.00			4.00

Initial set minimum (min)	45.0	45.00	45.00	45.00	45.00	45.00	
Final set (hrs)	10.0	10.00	10.00	10.00	10.00	10.00	

Soundness (mm expansion)	5.0	5.00	5.00		5.00	5.00	5.00
Autoclave expansion				0.50			

Addition (%)				15-70	5 – 15*	5 - 15*	25 - 35
--------------	--	--	--	-------	---------	---------	---------

(\* ) Originally, only Slag and Calcined Shale was allowed, fly ash was later approved.

**Interesting**

Low alkali content (LA)	0.6	0.60	0.60				
Clinker LSF - Lime Saturation Factor	0.8-1.02	0.8-1.02	0.8-1.02				
Processing additive max (%)	0.25						

## **2. 1996: The adoption of ENV 197**

### *2.1 Main differences: SABS 471, 626, 831, 1466 versus ENV 197-1*

There were some glaring differences between the SABS specifications and the ENV 197-1. The number of cement types that could be manufactured was a major change. Less than 10 different types of products could be manufactured before 1996. A total of 27 common cement types could now be manufactured based on EN 197. - The compressive strength assessments had to be included in the conformance assessments of all the cement types. There was a further distinction in terms of early strength development. The new ENV 197-1 now allowed for Normal and Rapid early strength development. It is still a challenge however, for the general consumer to understand the difference between the N and R notations on the cement descriptions.

Another key difference was the introduction of statistical conformance for early and standard compressive strength. The statistical criteria used in the conformance analysis favours higher frequency of testing and a lower standard deviation. This meant that more care has to be taken by the manufacturer when adjusting performance parameters of the cement even in cases where the compressive strength was increased. This was good for the consumers because it ensured a more uniform product would be supplied to the market. The tests performed had to comply to EN tests as well.

### *2.2 Reasons for adoption*

The EN specification was seen as a modern specification allowing the wider use of constituent materials, and providing the customer with a more consistent product (statistical conformance). The set of SABS standards were “stand alone”. Many African countries were moving or mooting to move towards the ENV specifications. This would have facilitated some ease of trading barriers.

## **3. Evaluation of the impact of adoption**

### *3.1 Manufacturing*

Manufacturing process and quality control procedures had to be updated and improved; constituent compliance was implemented and detailed customer information had to be introduced. Quality control had to focus not only on meeting the strength requirements but on uniformity. Since more cement types could now be manufactured and sold, an innovative period followed the adoption thus allowing manufacturers to develop products that were addressing the needs of the customers more directly and that were more environmentally friendly.

### *3.2 Consumers*

Customer seminars had to be undertaken; partially with the help of the then C&CI (Cement and Concrete Institute) to educate the general public on what the new standard entailed. It would be fair to state that even after almost 20 years, more education and awareness campaigns are required in various customer segments. The customers had

more choices in terms of cement types available in the market. New industries like third party blenders were established and gave customers more choices and increased competition in the market place.

### *3.3 Government*

The government, via SABS, had to ensure that it understood how to regulate the new ENV197 standards. The market place was also poised for the increased competition as the cement producers could now differentiate themselves better than before.

### *3.4 Environment*

Preservation of limestone resources with positive impact on CO<sub>2</sub> emission is a major environmental benefit of adopting EN 197. Materials such as fly ash were now more widely used thus reducing their environmental footprint.

### *3.5 Market competition*

There was more competition due to a wider variety of cement types and strength classes. The varying combinations of extenders also meant that the cost structures of the products from various suppliers were more varied. In addition, the new products were aimed at certain segments thus increasing competition and prompting more innovation.

### *3.6 Durability of structures*

Blended cements made it possible for bag and “one silo” customers to achieve better durability in aggressive environments. Some of the technologies developed to make the blended cements perform, for example, grinding aids and strength enhancers, found their way to concrete thus removing generally accepted limits of extenders in some structures.

### *3.7 CEM I cement type*

One of the interesting observations is that South Africa immediately adopted a 42,5N whilst in Europe a CEM I 32,5N was not uncommon. This meant that the South African customer had access to a high strength class CEM I from the beginning. The volume percentage of the CEM I has declined over the years mainly as a result of preference for blended cements due to the preference for blended cements due to their lower carbon footprint and the durability advantages.

### *3.8 Engineers and specifiers*

There was a huge impact due to the fact that some specifiers often used “the same” documentation when specifying cement, and it took a very long time to get the old specifications out of the system. The specifiers also had to capacitate themselves to understand what type of cement they had to specify that would best suit the intended application. The choice of different cement types was and still is to the advantage of the

specifier as now the specific needs can be met more adequately with the various options of cement types available.

#### **4. Challenges for the future?**

##### *4.1 New cement types*

As more and more cement types are introduced in Europe, South Africa will have to continuously adapt. The latest example being the imminent introduction of a CEM VI cement type and discussions about a CEM II/C already. A significant observable point will be when South Africa can have a greater influence and contribution of the continuous development of EN 197 instead of the current passive role where the newer versions are adopted.

##### *4.2 Education of consumers*

Can the consumers keep up with the different cement types? Do the producers have to do more? These are the relevant questions to be asked when one looks at the rate of the introduction of new cement types into the market. As the world faces off the challenge of reducing the carbon footprint, the continuous development of the EN standard will be central to the role that the cement industry do to preserve the environment. This in turn will mean more and more variations of cement types which will require more education of the consumer.

##### *4.3 Researchers*

The scholars also face a tough time in terms of adapting their research amid all the various cement types available in the market. Whilst the researchers prefer to use a CEM I and vary the extenders, it is becoming more difficult to draw conclusions that could readily assist the industry. The rate at which new products are introduced that have different compositions also pose a challenge to the researchers.

#### **5. Was it prudent to adopt ENV 197 in 1996?**

After reviewing some benefits for the various sectors of society, it can be said that the decision taken in 1996 was a prudent one. The adoption of ENV 197 specification has had a positive impact in South Africa. There are still challenges that need to be overcome though to ensure that the continuous adoption of the revised standards is beneficial to all sectors and that consumers can understand the value that it brings.

#### **6. A call for greater participations in the development of standards in South Africa**

As highlighted in the introduction, the standard of a country determines which types of cements can be made and which extenders can be used. It therefore, makes sense that

all stakeholders to participate in the development and adoption of these standards. The SABS has a standard for making standards in the South Africa which details a clear and consensus based process for the development and adoption of standards.

## 7. Conclusions

It can be concluded that the industry decision to switch from the old SABS standards to SANS 50197 based on the EN 197 standard was prudent.

The EN standard provided for a wider variety of different types of cements and strength classes. The extension levels allowed the industry to significantly reduce the carbon footprint linked to cement manufacturing. In addition, it gave the user a better choice to select a product that is suitable for specific applications.

There is still a need for better understanding of the overall benefits this specification has provided for the manufacturers, the specifiers and the end users.

## References

- [1] SABS Standards Division, *SANS 50197-1:2013*, SABS, Pretoria, 2013.
- [2] SABS Standards Division, *SABS ENV 197-1:1996*, SABS, Pretoria, 1996.
- [3] SABS Standards Division, *SABS 471*, SABS, Pretoria, 1971.
- [4] SABS Standards Division, *SABS 626*, SABS, Pretoria, 1971.
- [5] SABS Standards Division, *SABS 831*, SABS, Pretoria, 1971.
- [6] SABS Standards Division, *SABS 1466*, SABS, Pretoria, 1988.

# An investigation into the use of Piliostigma Thonningii Pod Ash as an admixture in mortar

Suleiman MANNIR

*Department of Civil Engineering, College of Engineering, Hassan UsmanKatsina Polytechnic, P.M.B. 2052. Katsina, Nigeria*

**Abstract.** This research presents the findings of an investigation into the use of PiliostigmaThonningii pod ash as an admixture in mortar. The investigation was conducted on cement sand mortar and also on cement paste using varying percentage addition of piliostigma thonningii pod ash (PTA) of 0%, 0.2%, 0.4%, 0.6%, 0.8% and 1.0% respectively. The result of the investigation shows that the predominant oxides of PTA were  $\text{Fe}_2\text{O}_3$  and  $\text{K}_2\text{O}$  with 35.7% and 25% on standard consistency test, it was found that the water requirement ranged from 120ml to 160ml for 0.0% and 1.0% of PTA. This represents 6.7% to 35% as percentage increase in water requirement. The study also shows that the use of PTA in cement paste decreases the initial and final setting times with increase in percentage addition of PTA. The strength with 0% PTA was 3.2 N/mm<sup>2</sup>, 6.8 N/mm<sup>2</sup>, 7.1 N/mm<sup>2</sup>, and 13.0 N/mm<sup>2</sup> and the compressive strength obtained with 1.0% addition of PTA were 6.6 N/mm<sup>2</sup>, 9.6 N/mm<sup>2</sup>, 11.0 N/mm<sup>2</sup> and 14.9 N/mm<sup>2</sup> at 3days, 7days, 14days and 28days respectively. This represent percentage increase of 106.25%, 41.2%, 54.9% and 20.2% respectively.

**Keywords.** Piliostigma Thonningii (PTA), admixture, compressive strength, mortar

## Introduction

Admixture refers to the materials other than water aggregates, hydraulic cement and fiber reinforcement used as an ingredient of a cementitious mixture to modify its freshly mixed, setting, or hardened properties and that is added to the batch before or during its mixing, [1]. Sand cement mortar is created by mixing cement with sand and water. It is further stated that, modern Portland cement was patented on 18<sup>th</sup> December, 1824 largely as a result of various scientific effort to develop stronger mortars existed at the time [2]. Many researches have been conducted by professionals for the purpose of providing a cheap and locally available material that can be used as an admixture in concrete or soil. Locally produced admixtures are being developed to reduce the use of expensive imported admixtures in concrete. These include research on the effect of locust bean pod powder on strength properties of concrete, [3], Gum Arabic as an admixture in concrete [4], and the use of pilliostigmathonningii pod powder as an admixture in concrete [5].

<sup>1</sup>Corresponding author: [smgafai@gmail.com](mailto:smgafai@gmail.com)

Considering the above, it can be seen that most of the researches conducted on local additives involve concrete strength improvement, thus, this paper tends to unveil the investigation in the use of pilliostigmathonningii pod ash(PTA) as an admixture in mortar.

## **1. Materials**

### *1.1 PiliostigmaThonningii*

Piliostigmathonningii is found in abundance in West Africa, it is a leguminous plant belonging to the family Caesalpiniacea, a family that comprises trees, shrubs or very rarely scramblers. The tree is perennial in nature and its petals are white to pinkish colour produced between November and April, [6]. While the fruits, which is a hairy, hard, flattish pod which turns rusty brown, woody and twisted and splits upon ripening. It is usually persistent on the tree and produced between June and September, [7]. It is found growing abundantly as a wild uncultivated tree in many parts of Nigeria such as Zaria, Bauchi, Ilorin, Plateau, Lagos, and Abeokuta, [8].

The local builders use the pod powder as strength improving agent in mud for walling and rendering. Piliostigmathonningii pod is rich in Potassium (56.39%), Nitrogen (26.61%), Calcium (6.66%) Magnesium (4.15%) and other elements in minute quantities, [9]. The cost of this pod is about \$0.06 per Kg which makes it cheaper than any locally available material of its kind. The Piliostigmathonningii pod ash (PTA) used in this research was burnt at a controlled temperature of 100<sup>0</sup>C.

### *1.2 Cement*

The type of cement use for the study was ordinary Portland cement popularly known as “Dangote cement” produce in Dangote cement industry in Kogi State Nigeria. The cement strength is 32.5N.

### *1.3 Sand*

Clear and air-dried sand was obtained from Batagarawa Local Government Area, Katsina state Nigeria.

### *1.4 Water*

Portable water fit for drinking was used for this research.

## **2. Methodology**

In order to study the effect of Pilliostigma Thonnigii pod ash as an admixture in mortar. A cement sand mortar with water cement ratio of 0.5 and assumed slump of 10-30min was prepared. Various percentage additions of PTA of 0%, 0.2%, 0.4%, 0.6%, 0.8% and 1.0% respectively by weight of cement were added to the dry mix. The materials



were batched and 40 x 40 x 160mm mortar prism were cast and cured in water in normal laboratory conditions for 3 days, 7 days, 14 days and 28 days. A total of 72 prisms were tested to determine the compressive strength at various percentage additions of PTA. The test was in accordance with BS EN 196- (1994), [10].

Moreover, the setting time tests were conducted using vicat apparatus in accordance with BS1377: part 2 (1990), [11] on cement paste with various percentage additions of PTA.

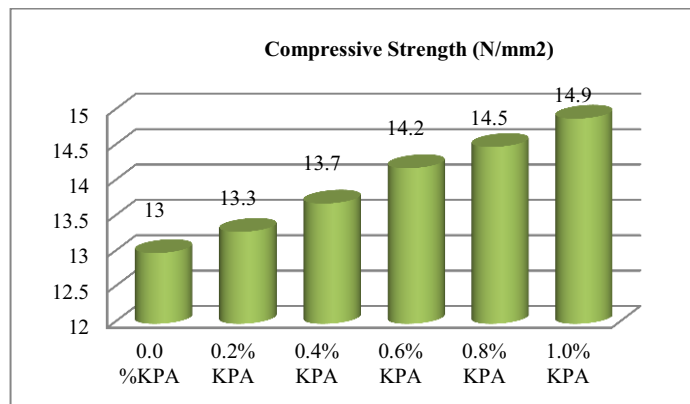
### 3. Result and discussion

#### 3.1 Compressive strength

As mentioned in the previous section, a total of 72 prisms were cast. At each testing date 12 prisms were taken to the compression machine for compressive test. The specimen was placed at the centre between platens to hold it in position. The machine was switch on to apply load until failure. Then the maximum load was recorded and the appearance of the specimen was noticed. The result of the compressive strength of mortar prisms are shown in table 1; and summarized in fig 1.

**Table 1.** Compressive strength of various percentage of PTA cement paste with curing age

% of PTA	3 days (N/mm <sup>2</sup> )	7 days (N/mm <sup>2</sup> )	14 days (N/mm <sup>2</sup> )	28 days (N/mm <sup>2</sup> )
0.0	3.2	6.8	7.1	13.0
0.2	4.1	7.1	7.4	13.3
0.4	4.6	7.6	8.0	13.7
0.6	5.2	8.2	8.7	14.2
0.8	6.0	9.3	10.5	14.5
1.0	6.6	9.6	11.0	14.9



**Figure 1.** Compressive strength of cement paste with various PTA additions

From the table 1 and figure 1, the result shows an increase in compressive strength with increase in percentage addition of PTA up to 1.0%, the strength obtained were

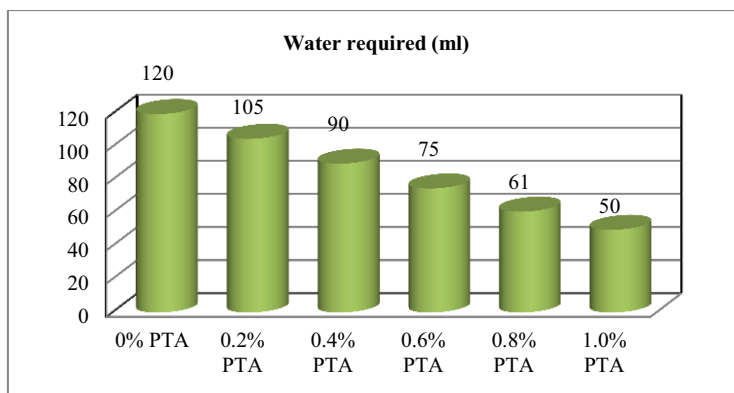
6.6N/mm<sup>2</sup>, 9.6N/mm<sup>2</sup>, 11.0N/mm<sup>2</sup> and 14.9N/mm<sup>2</sup> at 3 days, 7 days, 14 days and 28 days respectively. This represents percentage strength increase of 106.25%, 41.2%, 54.9% and 20.2% with 1.0% addition of PTA at 3 days, 7 days, 14 days and 28 days respectively. Considering the early strength of mortar, it can be noticed that 106.25% obtained at age of 3 days recorded the highest increase in strength compared to 54.9% and 20.2% at 14 days and 28 days respectively. As such the PTA could be categorized as accelerating admixture.

### 3.2 Setting time test

Three types of tests were conducted under the above mentioned test. They are standard consistency test, initial and final setting time of cement paste for 0%, 0.2%, 0.4%, 0.6%, 0.8%, and 1.0% PTA paste. The tests were conducted in accordance with BS 1377: part 2:1990. Tables [2,3] and figures [2-4] below show the result of consistency and setting time of cement paste.

**Table 2.** Consistency of various addition of PTA cement paste

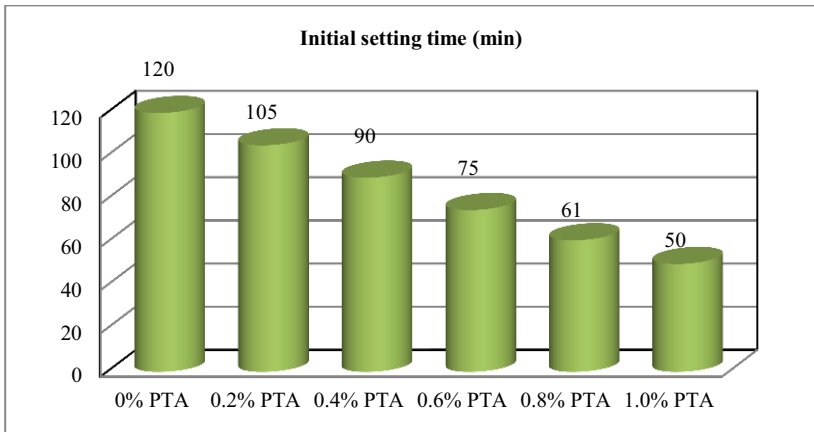
% PTA	W/C Ratio	Water Required (ml)	% Increase
0.0	0.30	120	0.00
0.2	0.32	128	6.70
0.4	0.34	137	14.2
0.6	0.36	145	20.8
0.8	0.38	153	27.5
1.0	0.40	160	35.0



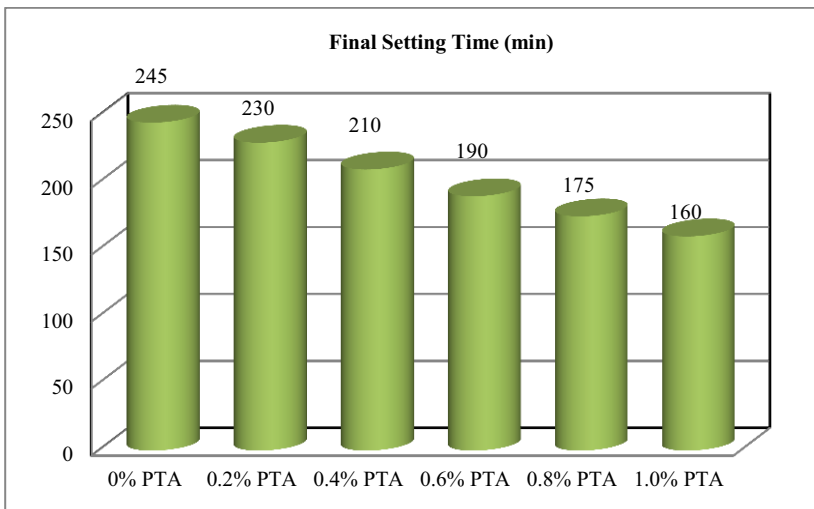
**Figure 2.** Consistency of various addition of PTA cement paste

**Table 3.** Initial and final setting time of various addition of PTA cement paste

% PTA	Initial Setting Time (min)	Final Setting Time (min)
0.0	120	245
0.2	105	230
0.4	90	210
0.6	75	190
0.8	61	175
1.0	50	160



**Figure 3.** Initial setting time of various addition of PTA cement paste



**Figure 4.** Final setting time of various addition of PTA cement paste

Table 3 indicates the increase in W/C ratio ranging from 0.3 to 0.4 as a result of increase addition of PTA. Also water requirements to achieve standard consistency were found to be 120 ml, 145 ml, and 160 ml for 0.0%, 0.6% and 1.0% addition of PTA at various percentages. This represents percentage increase of between 6.7% to 35.0% compare to control sample.

Looking at the table 3 one can understand that, the time required for cement paste to harden decreases with the increase in addition of PTA for both the initial and final setting time. The initial and final setting time of 1.0% addition of PTA was found to be 50 min, and 160 min, which is lower than 120 min. and 245 min respectively 0.0% addition of PTA. The total quantity of heat generated in the complete hydration will depend upon the relative quantities of major compounds present in cement, [12].

#### 4. Conclusion

This research work “An investigation in to the use of Piliostigma Thonningii pod ash as an admixture in mortar” was conducted and the following conclusions were drawn:

1. The use of PTA in cement paste decreases setting time with the increase in percentage addition of PTA. Also the water requirement increases with the increase in percentage addition of PTA in order to achieve standard consistency.
2. Piliostigma Thonningii Pod ash (PTA) is therefore performs satisfactorily as an admixture in mortar at various percentage additions of 0.2% to 1.0% tested.
3. The compressive strength of mortar increases with increase in percentage addition of PTA of up to 1.0%.
4. PTA could be considered as an accelerating admixture when used at 1.0% addition or more.

#### References

- [1] ACI 212-3R: *Chemical admixture for concrete*, ACI. Education bulletin E4 — 03. Retrieved from www.sciencedirect.com science. (2009)
- [2] Wikipedia Encyclopedia retrieved May,: properties of mortar first. Edition London, England. (2010)
- [3] Baffa M.J. The effect of locust Bean pod powder on the strength properties of concrete: *B Eng research project, Civil Engineering Department, Bayero University Kano*, Nigeria (1995).
- [4] Ominije P.W Gum Arabic as an admixture in concrete: *M Eng Thesis, Civil Engineering Department, Bayero University Kano*, Nigeria (2003).
- [5] Ogork, EN and Rimi, M.K: “Karlgo” (piliostigmathonningii) Fruits powder as an admixture in concrete. *Journal of Engineering and Technology*, New Series Vol. 2 No. 1, Bayero University, Kano, Nigeria.(2007) 9 — 11.
- [6] Jimoh, F.O and Oladiji, A. T: Preliminary studies on piliostigmathonningii seeds: proximate analysis. mineral composition and Phytochemical Screening. *Journal of Engineering and Technology (JET) VOL.2, No. 1, Nigeria Metrological Agency, Makia. Kano, Nigeria.* (2005)
- [7] Lock JT, Simpson MJ. Legumes of West Tropical Asia.3<sup>rd</sup> ed. *Academic Press Inc*, London.(1999) 216—220.
- [8] Schultes RE, Hofmann A. *The Botany and Chemistry of Hallucinogens*, Charles C Thomas, Spring Fields 111.(1973). 267.
- [9] Rimi M.K An investigation into the admixture properties of PiliostigmaThonningii fruits powder in concrete. *M Eng Thesis, Civil Engineering Department, Bayero University Kano, Nigeria* (2005).
- [10] British Standard, BS EN 196-1: *Methods of determining strength of mortar*. Published by British standard institute.BSI Linford wood, Milton Keynes MK 146 LE. (1994)
- [11] British Standard, BS1 181-119: *Method of testing hardened concrete for compressive strength*. (1993)
- [12] Shetty, S. and Chand, S.: *Concrete technology, theory and practice*. Published by S.Chand& Company Ltd. 7361, Ram Nagar, New Delhi -110055. (2005)

# Material selection and mix design of radiation shielding concrete

Stephen EKOLU<sup>a</sup> and Mokgobi A. RAMUSHU<sup>b,1</sup>

<sup>a</sup>*Department of Civil Engineering Science, University of Johannesburg, South Africa*

<sup>b</sup>*Sasol Synfuels, Private Bag X1000, Secunda 2302, South Africa*

**Abstract.** Based on the compiled literature and the availability of materials that could be used, concrete was selected as the best shielding material. Further work was carried out to develop a specific mixture that would shield the radioactive energies. The important special concrete ingredients that were considered in the mix design were high density aggregates and boron-containing aggregates. Various high density concrete mixtures of w/c (water/cementitious ratio) = 0.42, 0.45, 0.5 and 0.6, were prepared and adjusted appropriately in order to obtain the desired mix characteristics.

The final (high density shielding concrete) mix produced was workable and cohesive with average 28-day compressive cube strength of 30 MPa, w/c = 0.51 and density of 4231 kg/m<sup>3</sup>. The concrete had high slump with a height and spread of 230 mm and 510 mm respectively. It was composed of CEM 52.5 N, silica fume, water, hematite sand, hematite stones, steel shots, colemanite and chemical admixtures.

**Keywords.** Radiation shielding, curing, retardation, workability

## Introduction

The nuclear industry has traditionally been regarded as the originator of high density concrete where it is used for radiation shielding. Early work of the 1950s in USA, resulted in the development of some of these shielding materials. Further significant gains were made during the 1980s, mainly at the Sella field reprocessing site where a range of concrete relative densities between 3.4 and 8.75 together with a range of grouts between 2.8 and 6.6 were successfully designed and used in significant quantities [1]. In general the shielding effectiveness is proportional to the concrete density and is used where space is premium; however, it can additionally be affected by the nature of radiation though this is a very specialist topic beyond the realm of the concrete technologist.

The typically used aggregate in shielding (high density) concrete may be naturally occurring or they may be materials used in other industries for various purposes. The common aggregate types used include: Barytes (naturally occurring barium sulphate mineral ore), magnetite and haematite (Iron ores), iron and steel shots, various sizes and types of scrap iron and steel, ferrosilic, iron silicon slag, lead shots.

<sup>1</sup>Corresponding author: Sasol Synfuels, Private Bag X1000, Secunda 2302, South Africa, [ramushuma@gmail.com](mailto:ramushuma@gmail.com)

The advantages of using concrete as a shielding material are related to its good compromise thickness requirements for neutron and photon shielding; it can also be cast into almost any complex shape [2]. Its use as a radiation shielding material is well-established as indicated by the availability of existing knowledge and literature [1-3]. Other benefits of using concrete include the local availability of the required high density aggregates, its versatility, composite nature, economic savings, low maintenance, ease of manufacture and structural integrity. Concretes are highly durable and provide permanent shielding installations [3], unlike materials such as lead which may lack structural integrity, or use of water that might cause complications such as rusting and leakage of containers. Materials have different shielding properties for different types of radiation and therefore the selection of shielding material is a function of the radiation type and the energies of the specific radiation.

This paper is limited to discussion and identification of suitable raw materials for high density shielding concrete (HSDC), its mix design and optimization, testing of mechanical properties. The evaluation of the shielding properties of HSDC is presented in another paper [4].

## **1. Use of concrete for radiation shielding**

### *1.1 Galena aggregates*

In a study conducted by Mortazavi, et al. [5], where the focus was on production of an economic high-density concrete for shielding of megavoltage radiotherapy room and nuclear reactors, galena was used as the only heavy-weight aggregate in the mix. In their investigation, two types of concrete mixes were produced. These were the control and galena mixes of w/c (water/cementitious ratio) of 0.53 and 0.25 respectively. The galena used in this study had a density of  $7400 \text{ kg/m}^3$  and was obtained from a mine in Firouzabad in Iran. It was reported that while the control mix yielded a density of  $2350 \text{ kg/m}^3$  and 30 MPa, the galena high density concrete had a density of  $4800 \text{ kg/m}^3$  and 50 MPa. It was reported that the galena concrete gave good shielding properties.

It is well known from nuclear physics that only lighter element such as hydrogen and boron are capable of shielding neutrons. Neutrons penetrate through lead quite easily, and since lead was the only special aggregate used in the mix [5], the concrete would not be able to stop the neutrons. The reason for the good shielding properties obtained in the Mortazavi et al. study [5] is that a gamma ray source in form of a narrow beam emitted from a cobalt-60 therapy unit was used. The results were therefore exceptional since lead is good in shielding gamma rays but inadequate for neutron shielding.

### *1.2 Effect of colemanite*

Gencil, et al. [6] conducted a study on the effect of colemanite on physical and mechanical properties of concrete, when used as a replacement aggregate. Concretes containing different ratios of 10, 20, 30, 40 and 50% colemanite were incorporated into the mix as fine and as coarse aggregate. Concrete mixes of cement content  $400 \text{ kg/m}^3$  and w/c = 0.42 were used in the experiments. It was found that the slump of concrete significantly decreased with addition of colemanite into the mix. Further still, the

concrete tended to flocculate upon addition of colemanite into the mixes. The slump reduction and related flocculation, were attributed to a possible chemical reaction between colemanite and the cement paste. The overall conclusion of this study was that using 10 to 50 % colemanite as aggregates in concrete negatively affects the concrete in respect to both its physical and mechanical properties. Colemanite is a water soluble boron-containing material, and is known to delay the setting of concrete even when added in small quantities [4].

### *1.3 Iron ore and steel shots*

Iron ore and steel shots are normally included in the HSDC mixes in order to obtain the desired high density which helps in attenuation of photons and slowing down of fast neutron. Several studies and developments have been carried out using these aggregates where magnetite and hematite have been used as the main sources of natural iron.

In a study carried out by Dubrovskii, et al. (1970) [7], hematite was used as the natural source of iron and was incorporated in concrete as fine and coarse aggregate. The mix design had a density of 3030 kg/m<sup>3</sup> and showed good shielding properties. In another study by Kharita, et al. (2007) [8], hematite was used together with black coastal sand to produce special shielding concrete that was tested using two different gamma sources and a neutron source. At the conclusion of the study, hematite samples were considered the best for shielding gamma rays as compared to those mixes which contained no hematite. It was also found that the samples showed good results for shielding neutrons and this was suspected to have resulted from the high iron content of hematite and the presence of iron hydroxide (Kharita, et al., 2007) [8]. Mahdy, Speare and Abdel-Reheem (2002) [9] conducted a study to investigate the effect of transient high temperature on magnetite based heavy-weight and high strength concrete. In their study, twelve mixes with slumps of over 100 mm and strengths of 140 Mpa at 180 days were used. The mixes contained combinations of cement, silica fume, coarse magnetite with a maximum size of 16 mm, fine magnetite and natural fine sand. It was found that concrete strength decreased when temperatures were raised to 100°C. With further increase in temperature, the loss in strength recovered and reached peak strength of 10 % to 30% above the corresponding strength at room temperature. At temperatures of 500 and 700 °C, the strength dropped sharply (Mahdy, Speare & Abdel-Reheem, 2002) [8].

Warnke, et al. (2001) [10] used steel granules to develop a concrete shielding material for casting of low cost, storage concrete containers for waste management. The iron granules were used in the concrete mix at a proportion of 50%. The iron aggregates raised the mix densities from the normal 2400 kg/m<sup>3</sup> to 4000 kg/m<sup>3</sup>; and gave concrete compressive strengths reaching up to 65 MPa.

## **2. Special concrete ingredients for high density shielding concrete**

Most of material considerations for HSDC have physical and chemical property requirements which can be challenging to traditional mix design methods. Therefore careful evaluation of these issues is necessary both before and during use of the concretes and grouts. Designers and specifiers of HDSC need to be aware that aggregate grading, will frequently fail to comply with more traditional specifications but high quality concrete can still be produced using these materials. It is generally

appropriate to design HDSC mixes starting from basics of the mix characteristics in terms of aggregate/cement ratios and fines content, which will often appear to be extreme and unconventional. Water contents need to be minimized to prevent segregation and full use of superplasticisers is normally recommended (in order to achieve workable mixes), though magnetite has been used to produce self-compacting concrete.

The HDSC concrete developed in this research was required to be of sufficient high density to be of a special type needed to fulfill the purpose of neutron and gamma-rays shielding. Normal weight concrete would be too thick if it was considered for this purpose, which would result in an excessive shield size well beyond the space limitations available; it would also be uneconomical. Each identified ingredient used in the mix development had a certain role to play. The following materials were identified for use in this investigation:

- Ordinary Portland cement (OPC), CEM 52.5 N.
- Hematite (natural high density aggregate).
- Iron/steel shots (artificial high density aggregate).
- Municipal water.
- Colemanite (boron containing aggregate).
- Galena (natural high density Lead containing aggregate).

The aggregates were divided into two categories consisting of:- high density aggregates which produce HDSC, attenuate (absorbs) photons (gamma-rays) and scatters neutrons (change the energy from fast to thermal), and the boron containing aggregate that attenuates thermal neutrons.

### **3. Chemical analyses of aggregates**

Small samples were obtained from the identified suppliers and tested for chemical compositions. The purpose of this testing was to ensure that ingredients that could become radioactive due to elements that have long decaying half-lives (i.e. Cobalt, Copper, Nickel, Zinc etc.) were not significantly present in the concrete mix. These tests were also used to confirm the guarantees presented on the suppliers' product data sheets. The chemical composition analyses of aggregates were conducted using ICP (Inductively Coupled Plasma) and XRF (X-ray Fluorescence methods). It was confirmed that none of the selected aggregates for mix design of HDSC had long half-life elements.

### **4. Practical mix design of high density concretes**

Various trial concrete mixtures of w/c's of 0.42, 0.45, 0.5 and 0.6 were prepared. In the process of developing a suitable HDSC, adjustments were made to the various mixtures so as to obtain the desired material properties, especially:- workability, cohesion, density and compressive strength. The various mixtures and their results are shown in Table 1. As indicated in table, the TM1 was too stony and lacked cohesion. The mix was therefore modified and colemanite was also introduced. It was decided to start with two different proportions of 5 % colemanite (TM1) and 10 % colemanite (TM3), thus



satisfying the requirements of the Monte Carlo Neutron Particle (MCNP) simulation outputs [4]. In addition to the above results, a delay in setting time of TM2 was also noticed. As a result of this retardation effect of colemanite, cubes disintegrated when placed under water after they had been demoulded (see Figure 1). The results of TM3 were similar to those obtained for TM2. The mix (TM3) yielded no slump, was not workable nor cohesive, and had delay in setting time. However, the early strength of TM3 was much higher than that obtained for TM2. This resulted due to the different demoulding times of the cubes. The TM2 cubes were demoulded after 24 hours while the TM3 cubes were demoulded after 48 hours. It was evident that the use of colemanite in the mix resulted in the two effects of very low workability with zero slump and delay in setting time of the concrete, which confirms findings in the literature [6].



**Figure 1.** Disintegrated cubes after being placed under water following the use of colemanite

Given the two difficulties posed by use of colemanite in mixtures, it was decided to introduce two admixtures to improve results. In order to achieve a high slump, a superplasticiser was introduced. To improve the setting time of concrete, an accelerator was added into the mix. This accelerator needed to be free from chlorides due to the high percentage of steel shots used in the mix. A 1 % dosage of accelerator was used in TM 4.

## 5. Further mix adjustments

The 10 mm slump obtained from TM4 indicated that the dosage of the superplasticiser was not effective enough. In addition to the 10 mm slump obtained, the mix lacked finer aggregates and as a result, its cohesion was poor. The delay in setting time of the TM4 mix, still posed a problem. TM4 mix was therefore modified by adjusting the stone/sand blends from 55/45 (percent ratio of superfine to fine aggregates) in TM 4 to 60/40 blend into TM5. The dosages of chemical admixtures were also adjusted.

As a result, the slump improved to 25 mm for TM5, and the mix was generally cohesive and workable. The required high slump was however still not achieved. From TM5, it was determined that increasing the finer particles of FA (fine aggregates) and reducing the high content of the CA (coarse aggregate) had an influence on the consistency, workability and cohesion of the mix. TM5 mix was further modified to

TM 6 by replacing 60/40 FA blend with 70/30 blend and reducing the w/c and stone content as shown in Table 1. The dosages of the superplasticiser and accelerator used in TM 5 were also increased. Due to the extended setting of the concrete, cubes were cast and only demoulded after 48 hours, cured at 23°C and 65% RH for the first seven days and then under water for the rest of the 28 days. At demoulding of the cubes at 48 hours, it was noticed that the concrete had not completely set. This was attributed to the high dosages of the chemical admixtures. TM 6 was modified into TM7 by changing the type of superplasticizer and using it at a lower dosage, incorporating silica fume and high alumina cement (HAC); no accelerator was used. The TM7 mix gave satisfactory results, setting fully within 24 hours. It also had good cohesion and strength gain at both, the early and late ages. Further adjustments were done on TM7 by removing HAC from the mix and re-introducing the accelerator. This gave TM 8, which required three days for proper setting of the mix samples before demoulding. Use of HAC in the mixtures was not favoured due to its potential to cause *conversion*, a chemical alteration process leading to long-term strength loss in concretes made with HAC. TM8 was considered to be the suitable mix design. The results of its evaluation for radiation shielding are presented in [4].

Table 1. HDSC concrete mix design

		TM1	TM2	TM3	TM4	TM5	TM6	TM7	TM8	
Ingredients mass %	CEM I 52.5N- PPC	8.75	8.98	8.48	8.07	8.07	10.39	7.96	7.88	
	Water	4.38	4.03	4.24	4.86	4.86	4.41	4.41	4.36	
	Hematite Stones	46.02	44.89	43.58	37.22	33.52	28.96	28.96	28.66	
	Hematite Sand	21.77	21.39	20.97	19.65	23.38	19.73	19.73	19.53	
	Steel shots	19.08	18.62	18.37	27.92	27.93	35.77	35.77	35.40	
	Colemanite	-	2.30	4.36	2.07	2.07	2.31	2.31	2.28	
	Superplasticiser 1	-	-	-	0.06	0.05	0.27	0.17	0.12	
	Superplasticiser 2	-	-	-	-	-	-	0.14	0.05	
	Accelerator	-	-	-	0.16	0.12	0.36	-	0.19	
	Silica fume	-	-	-	-	-	-	0.69	0.69	
	High alumina cement	-	-	-	-	-	-	1.73	-	
	W/C	0.5	0.45	0.5	0.5	0.6	0.42	0.42	0.51	
Results	Density (kg/m <sup>3</sup> )	4514	4421	4071	4287	4292	4372	4220	4231	
	Slump	Height (mm)	50	No slump	No slump	10	25	190	210	230
		Spread (mm)	-	-	-	-	-	530	510	
	Cohesion	Poor	Poor	Poor	Poor	Good	Good	Good	Good	
	7day strength (Mpa)	39.35	2.64	12.6	-	-	2.6	20	2.51	
	28day strength (Mpa)	54	41.1	33.8	-	-	38.9	48	29.94	

## 6. Conclusions

The final mix design of the high density shielding concrete was workable and cohesive with average 28- day compressive cube strength of 30 MPa, water to cement ratio of 0.51 and density of 4231 kg/m<sup>3</sup>. The concrete had a high slump with a height and spread of 230 mm and 510 mm respectively. The main special aggregates used in the mix were hematite, steel shots and colemanite. It was observed that colemanite had a strong effect of retarding the setting of concrete. The retardation could be offset by use of high alumina cement, however, consideration should be given to potential

*conversion* of concrete as a result of using high alumina cement. It may be appropriate to avoid using high alumina cement in shielding concrete and instead compensate for set retardation by allowing a long period of setting before demoulding or removal of formwork.

## Acknowledgements

The authors acknowledge the National Research Foundation of South Africa for funding of the project, and are also grateful to NECSA (Nuclear Energy Corporation of South Africa) for supporting the MSc study program of the second author.

## References

- [1] Miller E., *High density and radiation shielding concrete and grout*, Advanced concrete Technology – Processes Chapter 5, Newman & Seng Choo, Elsevier Press., 2003.
- [2] Callan E.J., *Concrete radiation shielding: nuclear physics, concrete properties, design and construction*. 2<sup>nd</sup> edition. United States of America: American concrete institute.
- [3] Kaplan M.F., *Concrete radiation shielding: nuclear physics, concrete properties, design and construction*. United Kingdom: Longman group.
- [4] Ekolu S.O and Ramushu M.A, Radiological assessment of high density shielding concrete for neutron radiography, *Proc. Intl Conf. on Construction Materials and Structures (ICCMATS)*, 24-26 November 2014, Johannesburg, South Africa.
- [5] Mortazavi SMJ, Mosleh-Shiraz MA, Maheri MR, Yousefnia H, Zolghadri S. and Haji-poue A. (2007) Production of economic high-density concrete for shielding megavoltage radiography rooms and nuclear reactors. *Iran.J.Radiat.Res* Vol 5(3), pp. 143-146.
- [6] Gencil O., Brostow W., Ozel C. and Filiz M. (2010) An investigation on concrete properties containing colemanite. *International journal of physical science* Vol 5(3), pp. 216-225.
- [7] Dubrovskii V.B, Ibragimov Sh.Sh, Korenevsii V.V, Ladygin A. Ya; Pergamenschik V.K and Perevalov V.S. (1970) Hematite concrete for shielding against high neutron fluxes. *Atonmnaya Energiya* Vol. 28(3), pp.258-260, March. New York: Consultants Bureau.
- [8] Kharita MH, Takeyeddin, M, Alnassar M. and Yousef S. (2007), Development of special radiation shielding concrete using natural local materials and evaluation of their shielding characteristics. *Progress in nuclear energy* 50, pp.33-36, Elsevier.
- [9] Mahdy M, Speare, PRS and Abdel-Reheem, AH. (2002) Effect of transient high temperature on heavyweight, high strength concrete. *15th ASCE engineering mechanics conference, June 2-5*. New York: University of Columbia.
- [10] Warnke EP, Wienert R, Kramm K and Bounin D. (2001) A new concrete shielding material for waste management. *SMiRT 16*, August. Washington DC

# A new structural sand lightweight concrete mix design

J. Alexandre BOGAS<sup>1</sup>, M. Glória GOMES, Sofia REAL and Jorge PONTES  
*DECivil/ICIST, Instituto Superior Técnico,  
Technical University of Lisbon, Av. Rovisco Pais, 1049-001 Lisbon, Portugal*

**Abstract.** A simplified design method is proposed for structural Lightweight aggregate concrete (SLWAC) made with natural sand. The major advantages of the proposed method are that it is easy to apply and it can be generalized to any type of lightweight aggregate (LWA). For this, three additional design parameters are needed: the strength of LWA in concrete; the limit strength; the SLWAC potential strength. At most, two experimental mixtures are needed to determine these parameters. A biphasic model to estimate the strength of SLWAC is evaluated and high correlations are obtained. The good performance of the suggested method is demonstrated by the comparison with experimental results reported by the authors.

**Keywords.** Lightweight aggregate, lightweight aggregate concrete, mix design, limit strength, potential strength

## Acronyms:

LWA - lightweight aggregate

NA - natural aggregates

NWC - normal weight concrete

SLWAC - structural Lightweight aggregate concrete

$f_{cs}$  - ceiling strength

$f_{cm}$  - compressive strength

$f_L$  - limit strength

$\rho_f$  - fresh density

$\rho_d$  - dry density

$v_m$  - relative volume of cement

$v_{LWA}$  - relative volume of LWA

*LWA strength in concrete,  $f_{LWA}$*

## Introduction

Current design methods for structural lightweight aggregate concrete (SLWAC) are usually only valid for a limited range of concrete compositions that have previously been subjected to trial tests. The SLWAC mix design is more complex than that of normal weight concrete (NWC) as more parameters need to be determined [1-3].

<sup>1</sup>Corresponding author: [abogas@civil.ist.utl.pt](mailto:abogas@civil.ist.utl.pt)

In addition to the mortar strength (w/c ratio) and quality of the aggregate-paste transition zone, the SLWAC strength depends on the volume and properties of lightweight aggregate (LWA) [4, 5]. Design methods based on the w/c ratio alone are therefore unreasonable, contrary to what happens with NWC. Moreover, the SLWAC mechanical behaviour depends on the concrete strength level for a given type of aggregate [6-8]. Some design methods have been suggested for SLWAC [1, 3, 4, 9, 8]. But most of them are just based on experimental results obtained for a certain type of concrete, and these depend on the specific characteristics of the selected materials, particularly on the type of LWA.

Chandra and Berntsson [4] have proposed a semi-empirical method for SLWAC mix design which makes it clear that the concrete strength depends on the strength and volume of its constituents. Based on a biphasic model, the authors proposed the expression (Eq.1) to estimate the strength of SLWAC, which is a function of the volume and strength of the mortar and the LWA. In (Eq.1)  $f_{cm}$  is the mean compressive strength of the concrete and  $f_m$  is the mean compressive strength of the mortar, whose composition is the same as that of the mortar in the concrete;  $v_m$  and  $v_{LWA}$  are the relative volumes of cement and LWA in the mix;  $f_{LWA}$  is the strength of the aggregate in the concrete, estimated from empirical relations.

$$\log(f_{cm}) = v_{LWA} \cdot \log(f_{LWA}) + v_m \cdot \log(f_m) \quad (\text{Eq.1})$$

The compressive behavior of LWAC is strongly dependent on the limit strength,  $f_L$ , and the ceiling strength,  $f_{cs}$ .  $f_L$  corresponds to the strength for which the modulus of elasticity is similar to that of the aggregate [2, 10]. Above  $f_L$  the strength of concrete is also affected by LWA and is lower than the mortar strength.  $f_{cs}$  corresponds to the highest bearing strength of LWAC, beyond which an increment of the mortar strength has little influence on the concrete strength [5, 11]. Because of the relevance of  $f_L$  in SLWAC, as studied in [6, 7], some methods have been proposed to predict concrete strength based on this concept [10]. Basically,  $f_L$  may be calculated based on the relationship between the strength development in concrete and in identical mortar samples of the same composition [7, 10]. Above  $f_L$ , it is assumed that the strength of concrete varies linearly with that of the mortar, which is not true.

Taking into account the above-mentioned distinct contributions of Chandra and Berntsson [4] and Chen et al [10], an easy design approach for SLWAC produced with natural sand is suggested and experimentally validated in this paper.

## 1. Materials and experimental procedure

### 1.1. Materials

Three Iberian expanded clay LWA were analyzed: Leca and Argex from Portugal and Arlita from Spain (Table 1). A more detailed microstructural characterization of these aggregates is found elsewhere [6, 12]. Fine aggregates consisted of 2/3 coarse and 1/3 fine sand. The two fractions of Argex were combined to have the same grading curve as Leca (35 % 2-4 and 65 % 3-8F). The cement types CEM I 52.5 R and CEM I 42.5R and a polycarboxylate based superplasticizer, SP, were also used.

**Table 1.** Aggregate properties

Property	natural sand		lightweight aggregates			
	Fine sand	Coarse sand	Leca 4-12	Argex 2-4	Argex 3-8F	Arlita AF7
Particle dry density, $\rho_p$ (kg/m <sup>3</sup> )	2620	2610	1068	865	705	1290
Loose bulk density, $\rho_b$ (kg/m <sup>3</sup> )	1416	1530	613	423	397	738
24h water absorption, $w_{abs,24h}$ (%)	0.2	0.5	12.3	22.9	23.3	12.1
Total porosity, $P_T$ (%)	-	-	60	67	73	52
Granulometric fraction ( $d_i/D_i$ )	0/2	0/4	4/11.2	4/8	6.3/12.5	3/10

### 1.2. Specimen preparation and tests

For each mix, 150 mm cubic specimens were cast for compressive strength tests according to EN 12390-1 [13]. After demolding at 24h, the specimens were kept in water until testing. The relevant compositions for the mix design procedure presented in section 3 and their slump, fresh density,  $\rho_f$ , and compressive strength,  $f_{cm}$ , are listed in Table 2. Sp/c is the percentage of SP by cement weight. The denominations ‘M’, ‘L’, ‘A’ and ‘Argex’ correspond to the mixes with only mortar, Leca, Arlita and Argex. The  $w/c_{ef}$  concerns only the effective water, not the mixing water absorbed by LWA.

**Table 2** Mix proportions and slump, compressive strength and fresh density (350 L/m<sup>3</sup> of LWA)

Mixes	sand (kg/m <sup>3</sup> )	cement (kg/m <sup>3</sup> )	Sp/c (%)	$w/c_{ef}$	fresh density $\rho_f$	compressive strength (MPa)				
						3 days	7 days	28 days	90 days	
Concrete I42.5	L450_0.5	677	450	0.0	0.50	1763	17.1/22.2/24.3 <sup>a</sup>	29.1	35.2	36.0 <sup>c</sup>
	Argex450_0.5	676	450	0.0	0.50	1686	14.2/17.7/19.5 <sup>a</sup>	22.0	26.8	25.5 <sup>c</sup>
	L450_0.35	847	450	0.7	0.35	1897	44.2	46.7	48.6	49.8
	A450_0.35	833	450	0.7	0.35	1942	55.1/60.5/61.3 <sup>a</sup>	62.8	64.7 <sup>b</sup> /65.8	67.4 <sup>c</sup>
Concrete I52.5	Argex450_0.35	846	450	0.7	0.35	1776	28.4	30.4	31.2	32.8
Mortar CEM I52.5	M0.30	1403	703	0.6	0.30	2213	-	69.8	75.0	-
	M0.35	1322	702	0.4	0.35	2244	55.1/60.3/59.9 <sup>a</sup>	64.4	66.6 <sup>b</sup> /69.6	72.4 <sup>c</sup>
	M0.40	1226	705	0.2	0.40	2237	-	56.6	62.2	-
	M0.45	1143	702	0.0	0.45	2215	-	50.7	59.2	-
	M0.5	1055	702	0	0.50	2168	-	44.1	50.6	-
Mortar CEM I42.5	M0.35	1322	702	0.4	0.35	2279	-	60.6	71.2	-
	M0.40	1226	705	0.2	0.40	2251	-	49.5	64.0	-
	M0.45	1143	702	0.0	0.45	2230	-	42.7	54.4	-
	M0.5	1055	702	0	0.50	2161	20.9/24.7/27.2 <sup>a</sup>	32.6	46.2	53.2 <sup>c</sup>

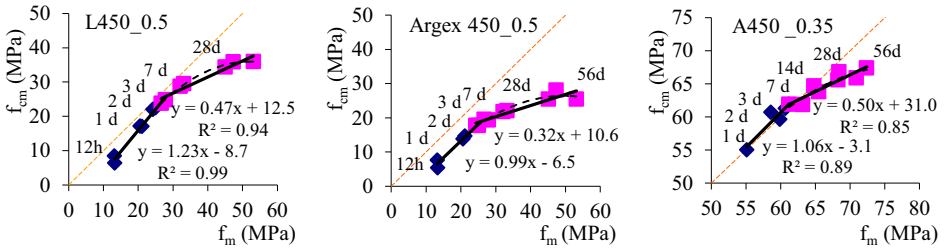
<sup>a</sup> compressive strengths at 1,2 and 3 days; <sup>b</sup> at 14 days; <sup>c</sup> at 56 days

**2. Mix design procedure for SLWAC made with natural sand**

A simple method is proposed to obtain the starting composition for the production of SLWAC, which can be applied to different compositions, LWA types and strength levels. The following must be pre-established for the SLWAC mix design: the strength, density, durability and workability requirements; the density, strength (2.2) and grading of LWA; the density and grading of fine aggregates; type and density of the binder; characteristics of additives; absorption and initial water content of aggregates (2.10).

*2.1. Limit strength,  $f_L$*

As mentioned,  $f_L$  can be determined by producing one experimental mixture of concrete and another with the mortar used to make that concrete. This is exemplified in Figure 1. For each LWA,  $f_L$  was estimated, based on the L/Argex450\_0.5, A450, M0.35 and M0.5 mixes in Table 2.  $f_L = 24\text{-}28$  MPa is obtained for Leca and  $f_L = 61\text{-}63$  MPa for Arlita. It was not possible to identify the limit strength for Argex, which is lower than the minimum strength usually required in structural concrete.



**Figure 1.** Limit strength of SLWAC with Leca (left), Argex (center) and Arlita (right).

*2.2. LWA strength in concrete,  $f_{LWA}$*

It is recognized that the strength of LWA in concrete benefits from the confinement of the matrix around them [14, 15]. The estimation of  $f_{LWA}$  from tests on concrete is therefore justified. Based on (Eq.1),  $f_{LWA}$  can be obtained from (Eq.2). Based on mixtures L/A/Argex450 and M0.35,  $f_{LWA}$  was found to be 25 MPa (Leca), 59.2 MPa (Arlita) and 7 MPa (Argex). The strength of these mixes must be greater than  $f_L$  (2.1) otherwise the biphasic model that depends on  $f_{LWA}$  and  $f_m$  is not valid.

$$f_{LWA} = 10^{\left( \frac{\log(f_{cm}) - v_m \cdot \log(f_m)}{1 - v_m} \right)} \tag{Eq.2}$$

*2.3. Estimation of the SLWAC strength*

The expression (Eq.3) can be used to estimate the SLWAC strength,  $f_{cm}$ . This requires prior knowledge of the mortar strength,  $f_m$ , of equal composition and tested under the same conditions as concrete (identical specimens' geometries and curing conditions). The expression (Eq.3) was evaluated taking into account several mixtures produced with the aggregates listed in Table 1 (Figure 2). Figure 2 only shows the results for

which (Eq.3) is valid, i.e.  $f_{cm} > f_L$ . Differences between the experimental and design values were generally less than 2% - 3%.

$$f_{cm} = 10^{(V_{LWA} \cdot \log(f_{LWA}) + V_m \cdot \log(f_m))} \tag{Eq.3}$$

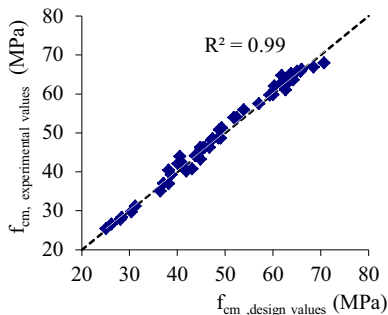


Figure 2. Experimental and design strengths of SLWAC with Leca, Argex and Arlita [6,7].

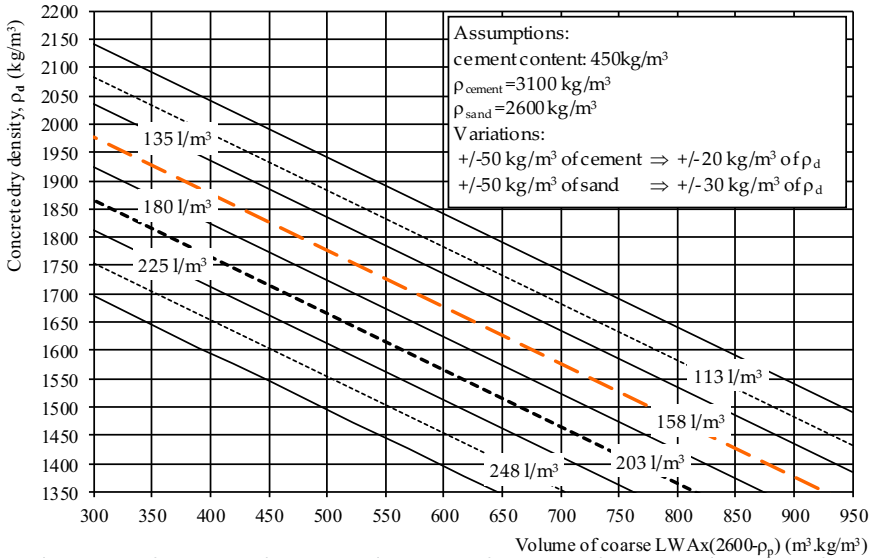
#### 2.4. Concrete density

The dry density of SLWAC,  $\rho_d$ , can be approximately estimated according to (Eq.4), [8, 16, 11].  $m_d$ ,  $m_{LWA}$  and  $m_c$  are the weight, in kg, of sand, LWA and cement.  $V_B$  is the volume of concrete in  $m^3$ .  $a$  takes into account the water chemically bonded after total cement hydration, which is assumed to be about 0.25 [15, 16].  $\alpha$  is a coefficient related to the degree of cement hydration that is conservatively taken to be 0.8 [16, 17].

$$\rho_d = \frac{m_d + m_{LWA} + (1 + \alpha \cdot a) \cdot m_c}{V_B} \quad [kg/m^3] \tag{Eq.4}$$

Alternatively, the dry density can be estimated by the abacus shown in Figure 3. The curve of 158 L/m<sup>3</sup> of effective water (about 0.3 m<sup>3</sup>/m<sup>3</sup> of paste volume) allows a first estimate of the SLWAC dry density (3.7).





**Figure 3.** Dry density,  $\rho_d$ , as a function of the LWA volume and particle density,  $\rho_p$ , for different amounts of effective water.

2.5. Choice of the type and volume of aggregate

SLWAC is characterized by a maximum strength level above which greater mortar strength leads to insignificant increases in the strength of concrete [5, 8, 11]. Its determination makes it possible to define the domain of application of a certain type of aggregate. Table 3 indicates the potential strength associated with each LWA listed in Table 1. These strengths were estimated based on the compressive strengths reported in [6, 7] for SLWAC with a w/c ratio of less than 0.35 and 250-400 L/m<sup>3</sup> of LWA. Faust [5] built regression curves in which the potential strength is estimated as a function of the LWA density (Table 3). The similarity of the approaches means that it seems reasonable to estimate the SLWAC potential strength from the LWA density.

**Table 3.** Potential strength and recommended limits of SLWAC studied

agregates	potential strength (MPa)		recomended limits (MPa)	domain of dry density, $\rho_d$ (kg/m <sup>3</sup> )
	experimental	Faust [5]		
Argex	30-35	35	25-35	1400-1750
Leca	50-55	53	45-55	1550-1850
Arlita	70-75	70	70-75	1650-1950

Table 3 summarizes the recommended upper limits for the LWAs listed in Table 1. The listed aggregates fall into three quite distinct classes of application. Argex is suitable for low strength concrete where the density is an important factor, while Arlita can be used in a wide field of applications, maintaining high efficiency levels.

In [6, 7] is shown that increasing the volume of coarse LWA is the most effective way to reduce the density of concrete. It was also found that except for very porous LWA there is no loss of structural efficiency with the increased volume of LWA. It is thus desirable to use larger volumes of LWA, just for density reasons. But higher LWA

volumes increase the risk of concrete segregation. Taking all into account, 300-400 L/m<sup>3</sup> of LWA are recommended, with amounts of 350-400 L/m<sup>3</sup> preferred.

2.6. Workability and mixing water

The volume of paste should be around 0.29 to 0.34 m<sup>3</sup>/m<sup>3</sup> [4, 8], especially when concrete slumps higher than about 150 mm are wanted. Knowing the desired w/c ratio and having admitted a volume of paste within this range, the amount of water can be estimated by means of (Eq.5), where  $\rho_c$  is the cement density, in kg/m<sup>3</sup>, and  $V_p$  is the volume of paste per m<sup>3</sup> of concrete. The first mixture can be taken to 0.3 m<sup>3</sup>/m<sup>3</sup> for  $V_p$ . The concrete workability aimed at can be adjusted with the aid of a high range SP.

$$w = \frac{V_p \cdot \rho_c \cdot \left(\frac{W}{C}\right)}{1000 + \rho_c \cdot \left(\frac{W}{C}\right)} \cdot 1000 \text{ (kg/m}^3\text{)} \tag{Eq.5}$$

2.7. Estimation of the mortar strength

The mortar strength,  $f_m$ , for the intended concrete compressive strength,  $f_{cm}$ , can be estimated by (Eq.6) that is only valid for  $f_{cm} > f_L$ . For  $f_{cm} < f_L$ , which occur in some SLWACs with Arlita, the mortar strength can be directly obtained from Figure 1, taking into account the first regression line under  $f_L$ .

$$f_m = 10^{\left(\frac{\log(f_{cm}) - v_{LWA} \log(f_{LWA})}{1 - v_{LWA}}\right)} \tag{Eq.6}$$

2.8. Cement content and w/c ratio determination

The w/c ratio can be estimated in the same way as for NWC [2, 18]. The graphs of Figure 4 were thus built (for mixtures with cement types I 52.5 and I 42.5 at 7 and 28 days). The mortar strength was obtained from 150 mm cubic specimens that underwent the same test and curing conditions as the concrete of identical composition.

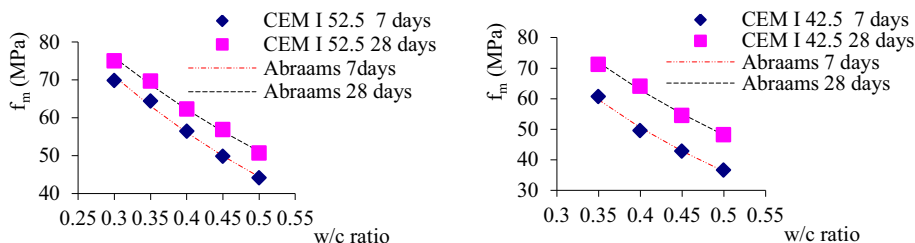


Figure 4. The mortar strength,  $f_m$ , versus the w/c ratio: CEM I 52.5 (left); CEM I 42.5 (right)

The w/c ratio for each cement type can be estimated from the simplified expression (Eq.12), based on the Abrams law [18]. Note that  $f_L$ ,  $f_{LWA}$  and the potential strength do not depend on the type and amount of binder. Finally, knowing the w/c ratio and taking into account the amount of water estimated in 2.6, the cement content can be calculated.

$$\frac{w}{c} = \frac{\ln\left(\frac{K_1}{f_c}\right)}{\ln(K_2)} \quad (\text{Eq.12})$$

### 2.9. Volume of sand

The volume of sand ( $V_s$ ) can be estimated from (Eq.13), based on the absolute volume of the rest of the concrete ingredients.  $V_{LWA}$ ,  $V_b$ ,  $V_{air}$ ,  $V_w$  and  $V_{SP}$  are the absolute volumes of LWA, binder, air, water and superplasticizer. For LWA with  $D_{max}$  of 9.5 to 12.5 mm, the volume of air can be simply taken as 30 L/m<sup>3</sup> [6, 7].

$$V_s = 1 - V_{LWA} - V_b - V_{air} - V_w - V_{SP} \quad (\text{Eq.13})$$

### 2.10. Correction of the mixing water because of the LWA water absorption

The EN 206-1 [19] suggests that the water absorbed during concrete mixing should correspond to 1 h of absorption by the LWA in pure water. Chandra and Berntsson [4] generalize the aggregate absorption in fresh concrete as about 75-100% of the first 30 minutes to 1 hour of absorption in water. Although there is some controversy, the difference between the absorption at 30 and 60 minutes tends to be negligible [12, 20].

Bogas [20] proposes a new method to estimate the LWA absorption,  $w_{abs,ag}$ , more accurately. This approach considers the key parameters that affect absorption by LWA in concrete, such as the presence of broken particles, the characteristics of the surrounding mortar and the initial water content in LWA. According to that study, the LWA absorption in concrete can generally be estimated by (Eq.14).  $K_{LWA}$  is a dimensionless experimental coefficient that takes into account the LWA water absorption in mortar. This coefficient ranges from about 1.1 to 1.25 depending on the type and physical characteristics of aggregates and their percentage of broken particles [20].  $w_{R48h}$  is the relative water content at 48 h, given by  $w_0/w_{s,48h}$ , where  $w_0$  is the initial water content and  $w_{s,48h}$  is the saturation water content of the aggregate at 48 h.  $w_{abs,w0=0\%}$  is the LWA water absorption with  $w_0 = 0\%$ . The great advantage of this method is its validity for different types of LWA.

$$w_{abs,ag} (\%) = K_{LWA} \times \frac{116-1,14 \cdot w_{R48h}}{100} \times w_{abs,w0=0} \quad (\text{Eq.14})$$

## 3. Conclusions

A simple design method has been proposed with the aim of expeditiously defining the composition of a first trial mixture. Contrary to current design procedures, the method can simultaneously take into account: the dependence of the SLWAC compressive behaviour on the concrete composition and strength level; the influence of the volume and strength of each concrete constituent; the concrete density; the absorption of LWA.

In addition to the usual properties, such as the density of materials, absorption of aggregates and cement type, three other parameters are introduced: the strength of LWA in concrete,  $f_{LWA}$ ; the limit strength,  $f_L$ ; the potential strength of SLWAC. Only

two experimental mixtures are needed to determine them: a concrete mix with the aggregates that are to be characterized; a mix with only the mortar fraction used to produce that concrete. One more mixture may be needed if the potential strength of the SLWAC made with a certain LWA is too high. However, these trial mixtures are only needed if a new type of aggregate, whose properties are still not known, is introduced.

For the validity domain of the model ( $f_{cm} > f_L$ ), and taking different compositions with different types of aggregate, high correlations of over 0.95 were obtained between design and experimental results reported by the authors.

## Acknowledgements

The research work presented herein was supported by the Portuguese Foundation for Science and Technology (FCT), under grant PTDC/ECM-COM1734/2012. The authors also wish to thank ICIST-IST for funding the research and the *Argex, Saint-Gobain Weber Portugal, BASF* and *SECIL* for supplying the materials used in the experiments.

## References

- [1] K. Dhir, RGC. Mays, HC. Chua. Lightweight structural concrete with Aglite aggregate: mix design and properties . *Int. J. Cem. Compos. Lightweight Concrete* 6 (4), (1984), 249-61
- [2] RN. Swamy, GH. Lambert. Mix design and properties of concrete made from PFA coarse aggregates and sand. *Int. J. Cem. Compos. Lightweight Concrete* 3 (4), (1983), 263-75
- [3] ACI 211.2. *Standard Practice for Selecting Proportions for SLWC*. American Concrete Institute, 1998
- [4] S. Chandra, L. Berntsson. *Lightweight aggregate concrete. Science, Technology and applications*. Noyes publications-Wiliam Andrew Publishing, USA, 2003.
- [5] T. Faust. Properties of different matrixes and LWAs and their influences on the behaviour of structural LWAC. *Second Internat. Symp. on structural LWC*, 18-22 June , Kristiansand, Norway. Helland et al (Eds.), (2000), 502-11
- [6] JA. Bogas. Characterization of structural lightweight expanded clay aggregate concrete. *PhD dissertation in civil engineering*, Technical University of Lisbon. Instituto Superior Técnico, 2011
- [7] JA. Bogas, A. Gomes (2013). Compressive behaviour and failure modes of structural lightweight aggregate concrete – characterization and strength prediction. *Mater. Des.* 46 (2013), 832-41
- [8] FIP manual of LWC. Fédération internationale de la précontrainte, Surrey University Press, 1983.
- [9] G. Dreux. Composition des bétons légers. In: Granulats et betons legers. Arnould et Virlogeux. *Presses de l'école nationale des ponts et chaussées* (1986), 425-37
- [10] HJ. Chen, T. Yen, TP. Lai. A new proportion method of LWC based on dividing strenght . *Int Symp structural LWC*, 20-4 June, Sandefjord, Norway. Holand et al (Eds.), (1995): 463-71
- [11] ACI 213R. *Guide for Structural Lightweight Aggregate Concrete*. American Concrete Institute, 2003
- [12] JA. Bogas, A. Mauricio, MFC. Pereira. Microstructural analysis of Iberian expanded clay aggregates. *Microsc. Microanal.* 18(5), (2012), 1190-208
- [13] EN 12390-1. *Testing hardened concrete - Part 1: Shape, dimensions and other requirements for specimens and moulds*. Eurpean committee for standardization, 2000.
- [14] MH. Zhang, OE. Gjörv. Mechanical properties of high-strength lightweight concrete. *ACI Mater. J.* 88(29), (1991): 240-47
- [15] M. Virlogeux. Fabrication, controle et mise en oeuvre du béton léger de structure. In: Granulats et betons legers. Arnould et Virlogeux. *Presses de l'école nationale des ponts et chaussées* (1986), 457-504
- [16] EuroLightCon R14. *Structural LWAC: Specification and guideline for materials and production*. European Union – Brite EuRam III, BE96-3942/R14, 2000.
- [17] M. Cervera, R. Faria, J. Olivera, T. Prato. Numerical modelling of concrete curing, regarding hydration and temperature phenomena. *Comput. Struct.* 80 (2002), 1511-21
- [18] PC. Aïtcin, J. Baron. Les adjuvants normalisés pour bétons. In: Les bétons. *Bases et données pour leur formulation* (1999), 88-131.
- [19] EN206-1. Concrete – part 1: Specification, performance, production and conformity. CEN/TC104, 2009.
- [20] JA. Bogas, A. Gomes, MG Gloria. Estimation of water absorbed by expanding clay aggregates during structural lightweight concrete production. *Mater. Struct.* 45 (10), (2012), 1565-76.

# Effect of partial replacement of sand in concrete with steel-file particles

Musibau Ajibade SALAU<sup>a,1</sup>, Kolawole Adisa OLONADE<sup>b</sup>  
and Oyesola Sunday AJIBOYE<sup>a</sup>

<sup>a</sup>*Dept of Civil and Environmental Engineering, University of Lagos, Nigeria*

<sup>b</sup>*Dept of Civil Engineering, Obafemi Awolowo University, Ile-Ife, Nigeria*

**Abstract.** In this paper, results of study on the effect of partial substitution of sand with steel-file particles (SFP) on properties of concrete are presented. Steel-file particles were used to replace sand at replacement levels of 5, 10, 15, 20, 25 and 30% to produce concrete of mix ratio 1:2:4 using water-cement ratio of 0.65. Physical and grading properties of the aggregates were investigated. Also, workability, density and compressive strength of SFP/sand concrete specimens were determined using standard procedures. The concrete specimens were cured in water for 3, 7, 14, 21 and 28 days. Results showed that SFP could be classified as heavy weight aggregate with bulk density of 7800 kg/m<sup>3</sup>, compared to those of sand (1520 kg/m<sup>3</sup>) and granite (1690 kg/m<sup>3</sup>). It also has the lowest fineness modulus (0.4). The slump value reduces as the ratio of SFP/sand increases while both the density and compressive strength increase with an average increase in strength of about 15% at 28 days. However, an optimum performance could be said to have occurred when not more than 20% of sand is replaced by steel-file particles. The study concluded that SFP is a potential material for use as partial replacement of sand in concrete.

**Keywords.** Steel filing particle, compressive strength, sand, concrete, workability

## Introduction

Steel file particles are by-products of filing and grinding of steel. It is produced in large quantity where these activities take place and are often disposed off as waste affects the environment. Meanwhile, effective management of solid waste has been a major worry of all the countries of the world. One interesting area that has been attracting attention of researchers is to utilize these wastes as partial replacement of sand in concrete production. More so, the use of natural sand is not sustainable.

Review of literatures shows that quite number of solid wastes are used as partial replacement of natural sand to produce concrete with positive results. In the work of Aggarwal and Gupta in [1], performance of bottom ash as a replacement for fine aggregates was investigated. Their results showed that strength development for various percentage (0-50%) replacements of fine aggregates with bottom ash was comparable to strength of normal concrete. Yuksel et al. [2] studied the use of ground

---

<sup>1</sup>Corresponding author: [ajibsalau@yahoo.co.uk](mailto:ajibsalau@yahoo.co.uk)

granulated blast furnace slag as fine aggregate in concrete. The study concluded that the ratio of GGBS/sand was a major governing criterion for the observed effects on the strength and durability characteristics.

Olonade et al. [3] also studied the effect of utilization of steel slag, produced from melting metal scrap, to replace sand on the mechanical properties of concrete. They showed that the 28-day compressive strength of concrete containing 25 and 50% slag were 9.8% (23.59N/mm<sup>2</sup>) and 11.5% (23.95N/mm<sup>2</sup>) higher than that of the normal concrete (21.48N/mm<sup>2</sup>), which showed that steel slag has appreciable influence on the compressive strength of concrete when up to 50% of sand was replaced with slag. Textile mill sludge was equally used as fine aggregate in concrete production. Their results showed that concrete containing textile mill sludge (32%) and fly ash (20%) could be used to produce concrete whose strength is above 20 N/mm<sup>2</sup> and that increase in the sludge content reduces the workability [4]. However, the durability of the concrete was not reported. Al-Otaibi [5] also studied use of recycling steel mill as fine aggregate in cement mortars. The replacement of 40% steel mill scale with that of fine aggregate increased compressive strength by 40%, drying shrinkage was lower when using steel mill scale. However, the effect of the steel mill on concrete was not considered. Sheet glass powder [6], electric arc furnace slag [7] and welding slag [8] are some of the industrial waste materials that have been found to be appropriate as replacements for sand in concrete production.

This study investigated the strength properties of concrete when steel filing particles are used to replace natural sand. The effect of the steel filing particles on the size distribution, density and workability were studied. If found acceptable, the volume of steel filing particles disposed indiscriminately would reduce; consequently saving landfill space for other beneficial uses. Also, sustainable construction would be ensured as scarce natural sand will be preserved.

## 1. Materials and method

The materials used for this study were Portland cement (as binder), river sand and granite (as aggregates) of nominal maximum particle sizes of 3.18 mm and 12.5 mm respectively. Steel- file particles were obtained from the general workshop of the University of Lagos, Nigeria while potable water was used for mixing. A sample of the steel-file particles is shown in Figure 1.

## 2. Mixing and testing

Concrete mix of ratio 1:2:4 (cement: sand and STP: granite) by weight was prepared with STP as partial substitutes of sand at the replacement levels of 5, 10, 15, 20, 25, and 30% by weight of sand. The physical properties of the materials were tested. Sieve analysis of the aggregates was conducted in accordance with American Society for Testing and Materials standard (ASTM C136-06) and the subsequent grading coefficients were determined. Also, slump test was conducted on all the concrete mixes to determine the effect of STP on the workability of fresh concrete. This was performed in line with the provision of British Standard BS 1881 (2).



**Figure 1.** Sample of steel-file particles

Ninety (90) concrete cubes of size 150 mm were cast and cured in water for 3, 7, 14, 21 and 28 days, when compressive strength were measured. Prior to the crushing test, the densities of the concrete specimens were determined and average of three readings was recorded.

### 3. Results and discussion

#### 3.1 Properties and size-distribution of aggregates

The results of the tests, conducted on the physical properties of granite, sand and steel-file particles, are presented in Table 1. It is shown that the specific gravity of granite was 2.68 while that of steel-file particles was about three times the specific gravity of sand, indicating that steel file particles are heavier relative to sand. This result is evident in their bulk densities with steel file particle having a value of  $7800 \text{ kg/m}^3$ , which is about six times that of the sand ( $1520 \text{ kg/m}^3$ ) meaning that steel particles could contribute to concrete density as it replaces sand. When compared to the standard (ASTM C136), steel file particle may be categorized as heavy weight aggregate while both sand and granite have densities within the range of normal weight aggregate ( $1200$  to  $1750 \text{ kg/m}^3$ ). However, steel file particle has relatively low water absorption relative to sand and granite. The likely effect of replacing sand with STP in concrete, depending on the replacement level, is that less water would be required to produce the same quantity of normal concrete.

**Table 1.** Physical properties and grading coefficients of aggregates

Parameters	Granite	Sand	Steel File Particle
Specific Gravity	2.68	2.45	7.56
Water Absorption (%)	14.20	22.50	9.35
Bulk Density ( $\text{kg/m}^3$ )	1690	1520	7800
Fineness Modulus	5.45	4.81	0.40

The grading characteristics of the aggregates, expressed as particle size distribution curves, are shown in Figure 2. It is observed that more than 90% of the granite stone was retained above 4.75 mm sieve size, the upper bound for aggregate to be categorized as fine aggregate, while above 98% of the sand passes 4.75 mm and less than 0.35% was retained on 0.075 mm sieve size. Hence, both sand and granite are

within the specified requirements for fine and coarse aggregates, respectively (ASTM C136). However, steel file particles size curve behaves differently as more fine particles are present with about 99% of it passing through sieve No. 30 (0.6 mm) while 32% was retained on sieve No. 200 (0.075) compared to sand, which retained only 0.35%. This trend is evident in their different fineness moduli. The fineness moduli (FM) of sand and granite SFP are 4.81 and 5.45 respectively while steel-file particles have FM of 0.40. According to ASTM C 125, the higher the value of FM, the coarser the material is and vice-versa. Since SFP is finer than sand, substitution of sand with SFP, depending on the replacement level, will have significant effect on gradation of the mixture of sand and SFP, and consequently on concrete properties. The likely effects of the STP are increase in surface area and reduction of void between the aggregates because fine particles tend to fill the voids.

### 3.2 Workability

In order to determine the effect of substituting sand with steel file particles on the workability of fresh concrete, slump test was conducted on all the concrete mixes produced at a constant water-cement ratio of 0.65. Results obtained are presented in Table 2. It is seen that slump reduces as the percentage of SFP in concrete increases; with normal concrete (0% SFP) having highest slump value of 126 mm followed by 5% SFP (73 mm slump) and 10% SFP (61 mm slump). However, at 15% SFP and above, the change in slump decreases compared to changes at 5 and 10% SFP. It is equally observed that *True* slump was obtained with 5 and 10% SFP while at 15% SFP and above, the slump was *Shear* type.

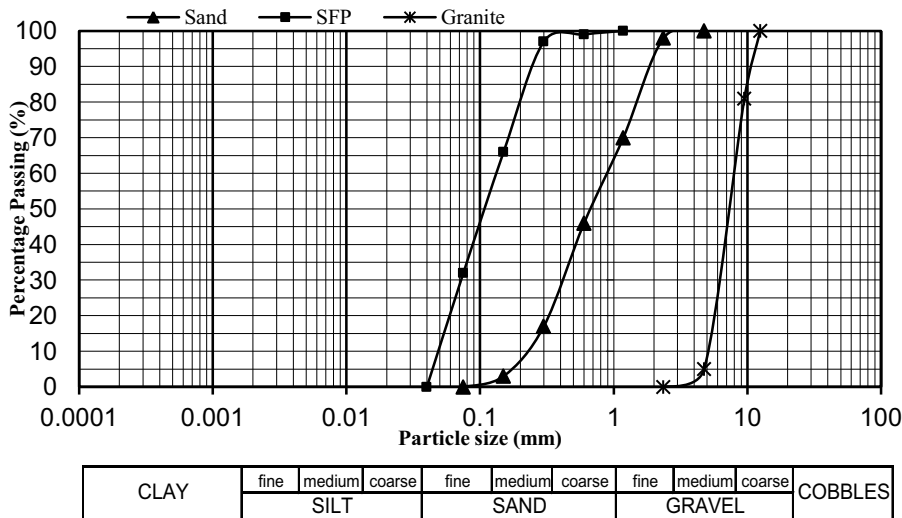


Figure 2. Particle-size distribution of the aggregates (sand, granite and SFP)

This behaviour (decrease in slump with increase amount of SFP) could be attributed to low fineness modulus of SFP, which contributes to increase in surface area of the fine aggregate in the mix, depending on the quantity of SFP. Shear slump achieved at 15% of SFP and above is an indication that the mix was *drier* and so more water was needed to make the mix plastic as obtained in the case of 0 to 10% SFP. Interesting to note that, all the slump values were within the medium workability [9].



**Table 2.** Slump of fresh concrete at different contents of SFP

Amount of Sand Replacement with SFP (%)	Slump (mm)	Type of Slump	Class of Workability
0	126	True	Medium
5	73	True	Medium
10	61	True	Medium
15	48	Shear	Medium
20	43	Shear	Medium
25	40	Shear	Medium
30	35	Shear	Medium

### 3.3 Density and compressive strength

#### 3.3.1 Density

Density of concrete is a measure of its compaction and is a function of many factors in which the constituent material is significant. In Table 3, the density of concrete mix containing various proportions of steel file particles, as substitute for sand, at different curing ages is presented. All the concrete mixes could be classified as normal weight concrete as the densities range from 2330 to 2645 kg/m<sup>3</sup> with concrete without SFP having the lowest value while concrete containing 30% SFP gave the highest value. It is equally observed that curing ages appear not to be significant as no definite pattern is observed as the age increases. For instance densities of 0% SFP concrete at ages 3, 7, and 14 days are 2370, 2340 and 2365 kg/m<sup>3</sup> respectively while 2345 and 2330 kg/m<sup>3</sup> are densities at ages 21 and 28 days respectively. However, density increases with increase in quantity of SFP in the mix for all the ages. At 28 days, normal concrete had density of 2330 kg/m<sup>3</sup>, which is about 97% (2410 kg/m<sup>3</sup>), 94% (2552 kg/m<sup>3</sup>), 91% (2568 kg/m<sup>3</sup>) and 90% (2590 kg/m<sup>3</sup>) of densities of the concrete containing 5, 10, 15 and 20% SFP respectively, while 25 and 30% SFPs concrete had corresponding densities of 2620 and 2645 kg/m<sup>3</sup> respectively.

The reason for this performance could be attributed to the inclusion of SFP in the mix. Since the specific gravity of SFP (7.8) is relatively high compared to that of sand (2.45), it is an indication that it has potential to increase the weight of the concrete, hence increased density. Also, inclusion of SFP tends to fill voids within the aggregates making it uniformly graded, which lead to higher packing resulting in concrete with higher density and less permeability.

**Table 3.** Density of SFP Concrete at different curing ages

Amount of Sand Replacement with SFP (%)	Density (kg/m <sup>3</sup> )				
	Curing Age (Days)				
	3	7	14	21	28
0	2370	2340	2365	2345	2330
5	2430	2450	2400	2445	2410
10	2465	2475	2430	2455	2552
15	2485	2530	2525	2510	2568
20	2532	2565	2545	2565	2590
25	2580	2578	2577	2585	2620
30	2605	2628	2615	2625	2645

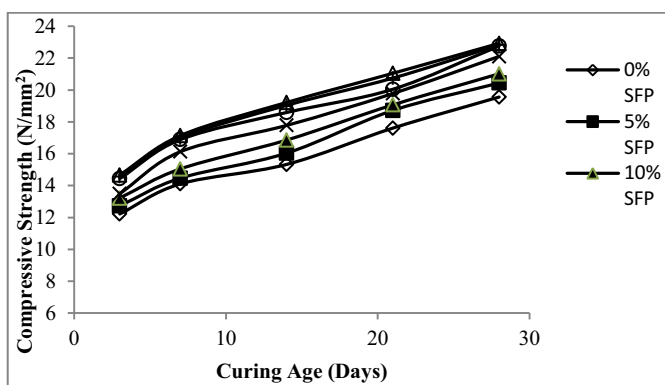
### 3.3.2 Compressive strength

Table 4 summarizes the compressive strength of concrete containing various SFP/Sand ratios at different curing ages. It shows that SFP/sand concrete had higher strength, compared to the normal sand concrete, and it increases with increase in SFP for all the curing ages (Figure 3). Considering 28-day strength, the normal concrete had the least strength having a value of  $19.56 \text{ N/mm}^2$ , about 95% of the strength of concrete with 5% SFP. Similarly, strength of normal concrete is 93%, 88% and 86% of the strength of 10, 15 and 20% SFP concrete, respectively. At 25 and 30% SFP content, strength of normal concrete was 85.6 and 85% of the SFP concretes. It can be observed that the difference in strength tends to merge when the amount SFP is 20% and above. This could have been that the presence of SFP in concrete in quantities above 20% may not perform better than when 20% SFP is used. In the same vein, if a larger quantity of SFP is used, there could be possibility of corrosion occurring, which adversely affects the durability of the concrete. In view of this, there is need to carry out long-term study of the effect of SFP on concrete durability vis-à-vis corrosion effect.

**Table 4.** Compressive of SFP concrete at different curing ages

Amount of Sand Replacement with SFP (%)	Compressive Strength ( $\text{N/mm}^2$ )				
	Curing Age (Days)				
	3	7	14	21	28
0	12.22	14.11	15.33	17.61	19.56
5	12.73	14.47	16.04	18.72	20.44
10	13.22	15.05	16.86	19.07	21.02
15	13.49	16.13	17.78	19.78	22.11
20	14.44	16.89	18.59	20.05	22.76
25	14.56	16.98	19.04	20.75	22.83
30	14.67	17.14	19.22	21.05	22.93

The trend shows that steel-file particles contribute to the strength development of concrete when it is used as partial replacement of sand. The reason for this performance could be partly attributed its grading properties because of its finer particles, which minimize voids. It is known that if voids are minimized, the amount of paste required for filling these voids is also minimized contributing to improved strength compared to the river sand control mix.



**Figure 3.** Compressive strength of concrete mixes with different quantities of SFP

#### 4. Conclusion

Effect of partial replacement of sand with steel-file particles on some properties of concrete was studied using standard procedures. The study concludes as follow:

- i. Steel-file particles are heavy material with specific gravity of 7.80 compared to that of sand, of specific gravity of 2.45. Its bulk density ( $7800 \text{ kg/m}^3$ ) is higher than the maximum density recommended for normal weight aggregate. Hence, it can be categorized as heavy weight aggregate. This makes SFP concrete denser than normal sand concrete.
- ii. The increase in SFP/sand ratio leads to increase in fineness modulus indicating that SFP affects the grading properties of the mixture. It also brings about increased surface area, which has effect on workability of the concrete mix; the higher the quantity of SFP the lower the slump value.
- iii. SFP particles contribute to increase in density and compressive strength of SFP/sand concrete. However, the effect is more pronounced when not more than 20% SFP replaces sand in the concrete mix.
- iv. Steel-file particles are a potential material for use as partial replacement of sand in concrete production.

#### Reference

- [1] Aggarwal V., Gupta S.M. and Sachdeva S.N. High volume fly ash concrete: A green concrete, *J. Environ. Res. Develop.*, **6**(2012), 884-887.
- [2] Yuksel, I. Ozkan, O. and Bilir T. Use of Granulated Blast Furnace Slag in Concrete as Fine Aggregate, *ACI Materials Journal*, **103**(2006), 203-208.
- [3] Olonade K. A., Kadiri, M. B. and Aderemi P. O. Performance of Steel Slag as Fine Aggregate in Structural Concrete, 12<sup>th</sup> Arab Structural Engineering Conference, University of Tripoli, Tripoli, (2013), 430 – 436.
- [4] Kulkarni, G.J., Dwivedi, A.K., Jahgirdar, S.S. Textile mill sludge as fine aggregate in concrete, *Global Journal of Researches in Engineering*, **12**(2012), 20 – 26.
- [5] Al-Otaibi, S. “Recycling Steel Mill Scale as Fine Aggregate in Cement Mortars,” *European Journal of Scientific Research*, **24**(2008), 332-338.
- [6] Gautam S.P., Vikas S. and Agarwal V.C. Use of glass wastes as fine aggregate in Concrete, *J. Acad. Indus. Res.*, **1**(2012), 320 – 322.
- [7] Manso, J. M. Gonzalez J. J. and Polanco J. A. Electric Arc Furnace Slag in Concrete, *ASCE Journal of Materials in Civil Engineering*, **16**(2004), 639- 645.
- [8] Sreekrishnaperumal T. R., Rajan G, PuthiyaV., Shanmugam R. and Subramani P. Use of furnace slag and welding slag as Replacement for sand in concrete *Rameshetal International Journal of Energy and Environmental Engineering*, **4**(2013),1 – 6.
- [9] Domon, P.L. “Fresh concrete” contribution in *Advanced Concrete technology – concrete properties*, Elsevier Ltd., 2003.

# Mechanical properties of green concrete with Palm Nut Shell as low cost aggregate

Emem-Obong Emmanuel AGBENYEKU<sup>1</sup> and Felix Ndubisi OKONTA

*Department of Civil Engineering Science, University of Johannesburg, South Africa*

**Abstract.** The cost saving benefits of aggregate replacement in concrete works are well documented. The utilization of Supplementary Aggregate Materials (SAMs) in concrete engineering without compromising standards in concrete works remain very attractive to both infrastructure developers and design engineers. However, there is continual search for low cost beneficial substitute materials. The mechanical properties of green concrete produced from Palm Nut Shell (PNS) as coarse aggregate was investigated. The abundance of PNS (light weight waste product of palm oil production) in West Africa created the impetus for the study. Series of laboratory tests such as; Slump, Compaction factor, Density, Schmidt hammer and Compressive strength tests were conducted on specimens of 10, 20, 30, 40 and 50% replacements of dry weight of PNS as coarse aggregate and specimens of natural aggregate as control sample. The specimens were cured at relative humidity (RH) of 95-100% and temperature (T) of 22-25°C in a chamber for periods of 7, 14, 21 and 28 days. The results showed the PNS samples to have relatively medium to high workability ranging from 24-47 mm for slump height and values of 0.85 to 0.90 for compaction factors. A general strength development was observed across the different samples with the PNS sample reaching strength of 48.7 N/mm<sup>2</sup> at 28 days curing. The 50% replacement specimens which mobilized UCS of 28.7 N/mm<sup>2</sup> met the requirement for lightweight concrete however, 30% is the optimum for a partial aggregate replacement in green concrete as UCS of 39.2 N/mm<sup>2</sup> was mobilized in 28 days. Thus PNS is a suitable concrete constituent and can be a major cost reduction factor especially in low cost rural projects with streamlined loading requirements.

**Keywords.** Lightweight green concrete, palm nut shell, compressive strength, workability

## Introduction

The construction industries in many developed countries have identified and resorted to the utilization of natural waste materials, particularly agricultural wastes as potential alternatives to conventional aggregates without compromising standards of structural members with less construction complexities [1]. This has led to the drastic transformation in the development and construction of light weight green concrete (LWGC) to serve as structural members. Nevertheless, the advantageous use of LWGC in Africa and most parts of the developing world by the construction industries have not been sufficiently recorded. Conventionally, the insistent rise in the demand for concrete in construction industries have led to a rapid depletion in the natural gravelly

---

<sup>1</sup>Corresponding author: [kobitha2003@yahoo.com](mailto:kobitha2003@yahoo.com)

and granitic stone deposits such that it has resulted in the excessive usage of natural stone deposits [2]. This is increasingly causing environmental challenges ranging from gulling to severe erosion problems and ground instability thereby affecting ecological balance. The need to source and explore natural alternative waste materials that could serve as partial or total substitutes to the very scarce and costly conventional aggregates have gained attention in recent times [3]. Aggregates constitute over 60 to 80% of the total volume of concrete. Having this large proportion of the concrete mass occupied by aggregate, it is expected for aggregate to have a significant effect on the general behavioral performance of the concrete product and its properties. Aggregates are essential in concrete production especially when needed as engineering materials for structural emphasis. They possess a unified influence on moisture reduction with respect to related deformations (i.e., shrinkages) and additionally, provide concrete with volumetric stability [3].



**Figure 1.** Palm nuts

**Figure 2.** Palm trees

Palm Nut Shell is a by-product from the manufacturing process of palm nut fruits, dumped as agricultural waste in palm oil producing localities. Palm nut is the fruit from a palm tree (see Figures 1 and 2). Palm trees are grown in regions with long and heavy down pours as well as very hot temperatures such as the case of Nigeria, Benin Republic, Ecuador, Colombia, Malaysia e.t.c. Currently Malaysia is known to be the largest producer of palm oil and its related products. The palm nut fruit consists of two major sections as shown in Figure 3: a yellowish fruit called the Pulp and when crushed, palm oil is produced and the Kernel which is covered in the shell of the seed which produces palm kernel oil when crushed. The demand for palm oil as a significant part of West Africa's diet is continually on the rise as such, there is increased cultivation of oil palm to meet the pressing demand. However, one significant challenge in oil palm processing as recorded by [3] is the vast quantities of waste generated in the forms of; Palm Nut Shells (PNS), Oil Palm Mill Effluent (OPME) and Empty Fruit Bunches (EFB). These waste products are stockpiled and openly dumped. It creates a ghastly site and constitutes a nuisance to the environment and the vicinity of the factories as large quantities of these wastes are generated daily.

## 1. Brief review of related studies

It has been established by [4] that PNS aggregates are capable of producing concrete with compressive strengths of over 25 MPa. Outside the environmental friendliness of utilizing PNS in the production of concrete, this aggregate further offers an option as partial or total substitutes to the scarce and expensive conventional concrete aggregates. This is an indication of the cost benefits from its use in the production of LWGC for rural low cost housing and development. For instance, the use of this new concrete type in West Africa is yet to be largely tested. However, as recorded by [4] a model low-cost housing of 58.68 m<sup>2</sup> area was built in Sarawak-Malaysia using 'PNS hollow blocks' for walls and 'PNS concrete' for footings, lintels and beams. These LWGC components

are presently performing well and no structural deficiencies have at yet been experienced or recorded. Nevertheless, it was noted by [4] that fly ash (FA) used as cement replacement for PNS concrete had negative effects on the compressive strength of the concrete product with a strength reduction of up to 29%. It was also revealed that the compressive strength of PNS concrete was found to be within the range acceptable for structural LWGC, which was about 50% lower than the ordinary concrete, and that the PNS concrete gained its highest strength within a 56days hydration period. The use of PNS therefore, as coarse aggregate in LWGC production with different hydration schedules over a 56days period will have effects on compressive strength, density and workability of the LWGC product.

Certain established methods such as; ACI method for normal weight concrete and other similar methods as recorded by [5, 6 and 7] could not be applied as mix design for PNS concrete. A trial mix design for concrete with PNS aggregate as coarse aggregate yielded a compressive strength of 24 N/mm<sup>2</sup> for a hydration period of 28 days [5]. Fly ash as mineral admixture and calcium chloride as an accelerator were also used to study the improvement in strength of the concrete. Meanwhile, High Strength Concrete according to [8] is set to achieve 40 Mpa (6000psi) compressive strength over 28 days hydration period although, it should be taken into cognizance that it depends on geographical and concreting conditions. Hence, the abundance of PNS in West Africa has paved way for PNS to be studied as replacement for coarse aggregate in green concrete where series of laboratory tests are conducted on the fresh and hardened LWGC specimens.

## 2. Materials and methods

The materials used in this study are portable tap water for mixing and curing the concrete, ASTM Type I Ordinary Portland Cement, coarse aggregate with particle size distribution between 5 to 14mm, PNS were obtained in sufficient quantities from Ikoritungko Oil Milling Factory located around Calabar, Nigeria (see Figure 4). All impurities and injurious contents such as oil remains and dirt were removed from PNS by a thermal process. The PNS was left in the oven under high temperatures of about 150-170<sup>0</sup>C for close to 24 hours. Series of laboratory works were conducted to investigate the effects of PNS on workability and compressive strength of the new concrete type, when used as partial replacements for coarse aggregates. The tests carried out included; the slump test which was done in accordance to B.S. 1882 part II, the compaction factor test was done in conformance to B.S. 1881:1970 part II to test the workability of concrete, the Schmidt hammer or Surface Hardness-rebound test based on BS 1881 Part 202 and the compressive strength test which was done according to BS 1881 Part 116 for strength determination of concrete.

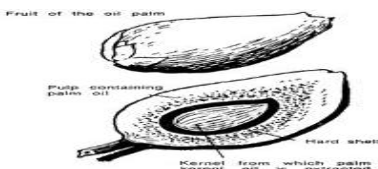


Figure 3. Inner cot of palm



Figure 4. PNS collected as waste

All the samples were cured at relative humidity (RH) of 95-100% and temperature (T) of 22-25 °C in a chamber for different hydration ages of 7, 14, 21 and 28 days [9]. A mix proportion for LWGC as earlier stated is different from the mix proportion of high strength concrete or normal strength concrete. For the LWGC, which is to be produced from using PNS as aggregate partially replacing the conventional coarse aggregate, requires an average cement/water ratio as indicated by [6]. Thus, a cement/water ratio of 0.5 was initiated in this study with mixing ratio of 1:2:4. The cubic samples were cast in metal moulds with dimensions of 100 x 100 x 100 mm<sup>3</sup>. For every batch of PNS concrete mix, Table 1 shows the weight of cement, the fine sand and the crushed aggregates used.

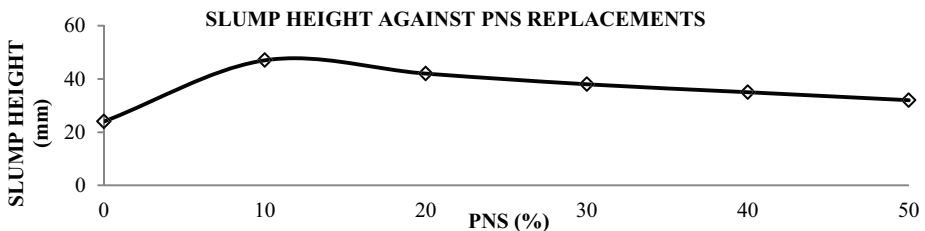
**Table 1.** Quantities of concrete constituents in every batch of PNS concrete mix

Samples	%PNS	OPC	Sand	Gravel	PNS	Total
P <sub>0</sub>	0	1.157	2.314	4.63	0.0	8.101
P <sub>10</sub>	10	1.157	2.314	4.17	0.43	8.101
P <sub>20</sub>	20	1.157	2.314	3.70	0.93	8.101
P <sub>30</sub>	30	1.157	2.314	3.24	1.39	8.101
P <sub>40</sub>	40	1.157	2.314	1.39	3.24	8.101
P <sub>50</sub>	50	1.157	2.314	2.32	2.32	8.101
<b>Total</b>		<b>6.942</b>	<b>13.884</b>	<b>19.45</b>	<b>8.31</b>	<b>48.61</b>

### 3. Discussion of results

#### 3.1. Slump test

The workability of concrete batches for the respective percentages of PNS mix using the slump test was presented in Figure 5. The mix samples with constant w/c ratios of 0.5 were found to display medium to high workability. It further showed that as the percentage replacement of PNS increased, workability of LWGC reduced except for 10%PNS where it showed a spike in workability. The specific surface was also found to increase as the PNS content increased. The plausible explanation to these behaviours can be because the control aggregate was denser than the PNS aggregate and the replacement in this study was done by weight. This led to more cement paste been required to lubricate the aggregate as such, reduced the entire fluidity of the mix which subsequently reduced the height of the slump.



**Figure 5.** Effects of PNS replacements on slump height of respective mixes

Consequently, the decreased slump height in the 20, 30, 40 and 50% mixes as the percentage of PNS increased was attributed to w/c ratio; having w/c ratio of 0.5 used for the respective mixes, the hydrated cement paste became more watery and less viscous. This process allows the penetration of cement into the PNS aggregate.

Additionally, it reduces the amount of cement paste available for lubrication and hydration which resulted in decreased free flow of cement paste in the mix and thereby, causing a decreased slump. A test by [2] was conducted using Palm Kernel Shells (PKS) as replacement for the control aggregate which displayed similar behaviours recorded by PNS aggregate in this study. As the percentage of PKS increased, the workability of the concrete was reported to reduce as such, the height of slump reduced.

### 3.2. Compaction factor test

The compaction factor test was conducted to check the workability of the respective concrete mixes. Although the workability of the concrete was first checked by slump test however, the compaction factor test was further conducted to validate the accuracy of the results. The compaction factor of the concrete mixes for the respective percentages of PNS as replacement for the coarse aggregate was shown in Figure 6.

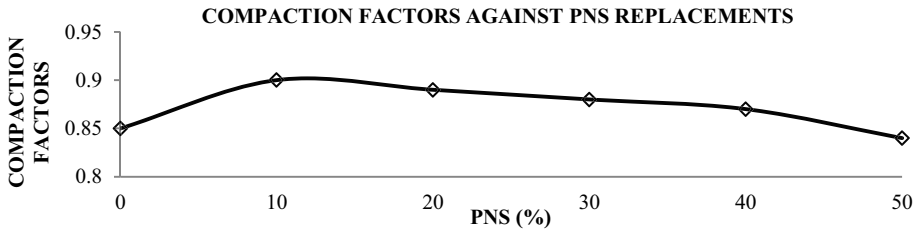


Figure 6. Effects of PNS replacements on compaction factors of respective mixes

From the results gotten from the compaction factor test, it was observed that the 10%PNS sample had the highest compaction factor of 0.9. It can also be seen that similar to the slump test, after the 10%PNS replacement, the compaction factor decreases. The decrease in the compaction factor value after a steep rise from 0-10% PNS replacement may have resulted from the sensitivity of workability test or because the control aggregate was denser than the PNS aggregate and the replacement in this study was done by weight. Furthermore, it was seen that all compaction factor values for the entire sample mixes were within the acceptable ranges from medium to high workability.

### 3.3. Density of specimens

The densities of the tested samples were determined to find the possibility of using LWGC as a structural element. Average densities of three specimens were determined as the actual density of each percentage mix. Table 2 shows the densities of the samples with the respective percentage of PNS replacements. Figure 7 shows the densities to reduce as the percentage of PNS increases vice versa, with the range of densities for PNS concrete for 28 days to be between 2278–1975 kg/m<sup>3</sup>, while the 0%PNS concrete (as control) had a density of 2473 kg/m<sup>3</sup>. The highest density, 2473 kg/m<sup>3</sup>, was recorded for 0%PNS, while the least density 1975 kg/m<sup>3</sup> was recorded for 50%PNS.

As established in hypothesis of this study, concrete strength was expected to decrease as the %PNS increases. This contributes to the properties of LWGC from PNS aggregates having a density lesser than 2000 kg/m<sup>3</sup>. This became approximately 60%

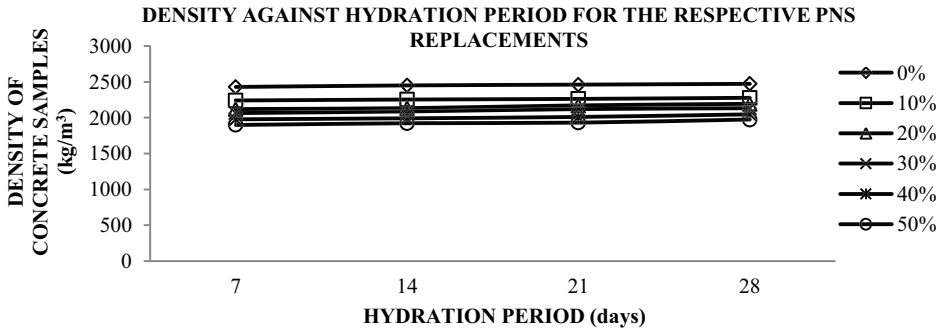


lighter as reported by [4 and 7] in comparison to the conventional crushed stone aggregate, which then results in the production of LWGC. The LWGC having a density lesser than 2000 kg/m<sup>3</sup> indicated that the 40 and 50%PNS samples are considered LWGC with densities of 2047 and 1975 kg/m<sup>3</sup> respectively. An expected density for control sample was in the range of 2400 kg/m<sup>3</sup> as such, the 0%PNS concrete was considered a normal weight concrete.

**Table 2.** Density of respective specimens

Hydration period	0% PNS	10% PNS	20% PNS	30% PNS	40% PNS	50% PNS
7	2430	2241	2121	2065	1978	1899
14	2451	2254	2134	2088	1992	1923
21	2462	2263	2172	2120	2011	1932
28	2473	2278	2194	2133	2047	1975

The 40 and 50%PNS is been considered a lightweight concrete for the fact that the 10,20, and 30%PNS had a higher coarse aggregate to PNS aggregate ratio. This shows that coarse aggregate has a larger volume in the mix than PNS aggregate, and since coarse aggregate is heavier than PNS aggregate, the concrete specimen was denser.



**Figure 7.** Density of samples with respect to hydration periods

The LWGC maybe have been produced due to the amount of w/c ratio used in the study. An increase in w/c ratio resulted in a decrease in cement content and increased the water content which reduced the overall weight of the concrete. An additional possibility could be the actual weight of coarse and PNS aggregate used. Hence, the Table 2 and Figure 7 show that an increase in PNS aggregate led to a decrease in the density of the product. Nonetheless, since PNS aggregate is lighter in weight, the replacement of coarse aggregate at different percentages resulted to a lesser amount of coarse aggregate in the mix; the absorption of cement paste was reduced as PNS aggregate do not firmly bond with cement thereby, reducing the overall density of concrete and then creating a LWGC.

**3.4. Schmidt hammer test**

The Schmidt hammer test was conducted to determine the strength of samples by measuring the surface hardness of concrete. Schmidt hammer test results for PNS samples showed that the strength of the samples increased with age as seen in Figure 8. This test is very similar to the compressive strength test. The results from the test revealed a substantial extension in concrete strength as the hydration period extended and as the %PNS in each sample reduced, with 0%PNS recording the highest strength

and 50%PNS had the least concrete strength 47.3 N/mm<sup>2</sup> and 22.7 N/mm<sup>2</sup> at 28 days. In the case of the Rebound hammer test however, the concrete strength depreciated when compared to the compressive strength test results in Figure 9. The difference was accounted for by the concrete surface area which is affected by its rough surface due to the presence of PNS in the sample.

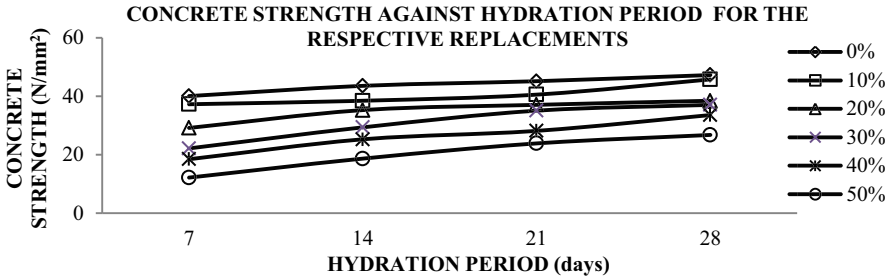


Figure 8. Concrete strength of samples with respect to hydration periods

Inclusive factors maybe in relation to the angle of inclination or the Schmidt hammer. It is clear from the results that both Schmidt hammer and compressive strength test have a strong correlation which can be the reason 0%PNS had a higher strength and 50%PNS is made of higher quantity of organic materials that happen to be lighter and less stronger than the conventional coarse aggregate.

### 3.5. Compressive strength test

The compressive strength of the crushed specimens in this work is reciprocal to the %PNS used. From Table 3 and Figure 9 respectively, the compressive strength development of concrete with age is observed.

Table 3. Compressive strength of respective specimens

Hydration period	0% PNS	10% PNS	20% PNS	30% PNS	40% PNS	50% PNS
7	42.3	37.1	33.6	22.8	18.6	13.7
14	49.6	39.6	37.3	33.1	26.3	22.5
21	54.4	42.5	39.5	36.7	29.8	24.8
28	59.5	48.7	41.6	39.2	32.1	28.7

It shows the effect of the different amount of PNS on the strength of the concrete. The rate of strength gain was pronounced as the hydration period increased i.e., as the %PNS increased, the compressive strength of the concrete decreased, vice versa. While the strength of the concrete decreased as the %PNS increased. The 0%PNS had the highest strength although, as PNS replaced the coarse aggregate the concrete strength gradually decreased. The plausible explanation is the fact that PNS are organic materials lighter and less strong than the conventional coarse aggregate. It also could be attributed to the highly irregular shapes of PNS, which prevented full compaction with normal coarse aggregate hence, affecting the strength of the concrete. Furthermore as recorded by [5], the weak bond between PNS and cement paste as compared to the control samples may have caused the reduction in strength due the smoothness of the sample.

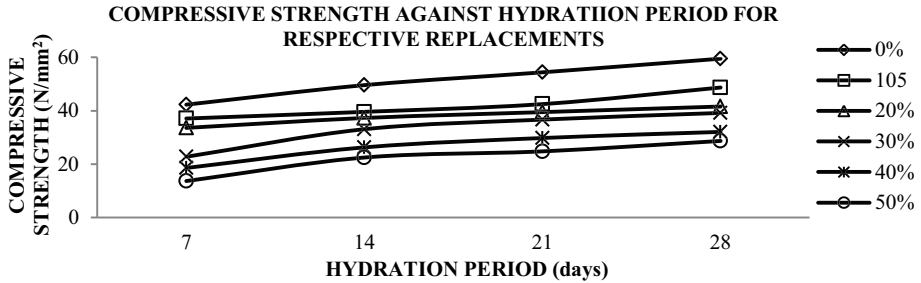


Figure 9. Compressive strength of samples with respect to hydration periods

Nevertheless, with respect to the general strength of samples, it was observed that all mixes produced high strength concrete at age 28 days. As defined by [8] a high strength concrete generally is a high performing concrete with specific compressive strength of up to 40 MPa (6000psi) and beyond. Considering the 28 days in reference to hydration periods; 0, 10 and 20% PNS satisfied the requirements of high strength concrete. Even though at 7 days early hydration stages, some concrete samples obtained very high strength values. The compressive strength developed for 50% PNS in 28 days, was above the range of 20.10–24.20 N/mm<sup>2</sup> requirement for structural LWGC elements.

#### 4. Conclusions

This study illustrated some mechanical properties of green concrete produced from PNS as coarse aggregate. The abundance of PNS in West Africa paved way for PNS to be studied as replacement for coarse aggregate in green concrete. From a perspective of strength and workability, and in conformance to waste recycled materials, PNS aggregate was founded to be a good substitute of coarse aggregate in concrete production. From results and analysis however, the following conclusions were reached;

- The PNS samples had relative medium to high workability ranging from 24–47mm for slump height, and 0.85–0.90 for compaction factor.
- Not all PNS concrete samples fully satisfied the structural light weight concrete requirement, with only 28 days 50% PNS concrete sample been within the density limit of 2000 kg/m<sup>3</sup> for structural lightweight concrete although, 10, 20, 30 and 40% PNS samples could be considered as partial lightweight concrete.
- The general strength of 10, 20 and 30% PNS concrete samples produced high strength concrete with compressive strength reaching up to 48.7 N/mm<sup>2</sup> for 28 days, which satisfied the requirement for high strength concrete. The 30% PNS is therefore, the ideal percentage of PNS which is in the boundary limit for the production of high strength concrete, however it is considered as partial lightweight concrete.
- The samples with 10% PNS and 50% PNS had the highest and least compressive strength respectively, which signified that the compressive strength of PNS concrete samples is dependent on the amount of PNS aggregate in the sample; although, the strength of the samples are dependent on the amount of PNS and

the hydration period, the least desirable structural requirement for light weight concrete was met.

- Finally, this paper demonstrates how the use of PNS as yet another option in transforming abundantly available cheap agricultural waste into useful resource for developing countries. Hence, the green concrete product can at the moment be utilized in the construction of light weight simple foundations and masonry walls while further investigations are recommended to be carried out on the effect of admixtures on PNS concrete over an extended hydration period of up to 120days.

## References

- [1] Alengaram U.J., Hilmi Mahmud and Mohd Zamin Jumaat, Comparison of Mechanical and Bond Properties of Oil Palm Kernel Shell Concrete with Normal Weight Concrete, *International Journal of Physical Science*, Vol. 5(8), pp.1231-1239, 2010.
- [2] Teo D.C.L., Mannan, and V.J. Kurian , Flexural behaviour of Reinforced Lightweight Concrete Beams made with Oil Palm Shell, *Journal of Advanced Concrete Technology*, Vol. 4, No. 3, pp. 459-468, 2006.
- [3] Alexander M.G. and Sydney Mindness, *Aggregates in Concrete*, Taylor and Francis Publication, Abingdon, 2005.
- [4] Teo D.C.L., Man.nan, and V.J. Kurian , Structural Concrete Using Oil Palm Shell (OPS) as Lightweight Aggregate, *Turkish J. Eng. Env. Sci*, Vol 30, pp. 1-7, 2006.
- [5] Mannan M.A, Ganapathy C. 2001, Mix Design for Oil Palm Shell Concrete, *Cement and Concrete Research* Vol-31, Issue (2001), pp. 1323-1325.
- [6] Mannan M.A., Ganapathy C. 2004, Concrete from an agricultural waste-Oil Palm shell, *Building and Environment* Vol-39, Issue (2004), pp. 441-448.
- [7] Payam Shafiqh, Mohd Zamin Jumaat and Hilmi Mahmud, Mix Design and Mechanical Properties of Oil Palm Shell Light Weight Aggregate Concrete: A Review Paper, *International Journal of the Physical Science*, Vol. 5, No. 14, pp. 2127-2134, 2010.
- [8] *Portland Cement Association*, Concrete Technology Today, High Strength Concrete, Vol. 15, No. 1, March 1994.
- [9] TMH1. 1986. *Standard Methods of Testing Road Construction Material*, Technical Methods for Highways. Vol. 11.

# New proposed direct tensile strength test for concrete

M. Iqbal KHAN<sup>1</sup> and Shehab MOURAD

*Department of Civil Engineering, College of Engineering  
King Saud University, Saudi Arabia*

**Abstract.** The evaluation of the tensile strength and determination of the tensile stress-strain curve using indirect tests becomes approximate hence there is a necessity for exploring direct tensile strength measurement. This investigation is part of ongoing research on the development of direct tensile strength measurement. In this paper direct tensile strength test has been proposed and the results obtained have been compared with compressive strength and flexural strength. It has been found that results obtained are well comparable and relationships are similar to that proposed in earlier findings.

**Keywords.** Direct tensile strength, flexural strength, compressive strength

## Introduction

Tensile strength of concrete is of prime importance in case of water retaining structures, runway slabs, pre-stressed concrete members, bond and shear failure of reinforced concrete members and cracking of mass concrete works. Practicing Engineers working with reinforced concrete ignore the low value of the tensile strength of concrete and use steel to pick up tensile loads. With massive concrete structures, such as dams, it is impractical to use steel reinforcement. Therefore, a reliable estimate of the tensile strength of concrete is necessary, especially for judging the safety of dam under seismic loadings [1].

The tensile strength of concrete is much lower than its compressive strength, largely because of the ease with which cracks can propagate under tensile loads. Although tensile strengths are usually not considered directly in design (being assumed to equal zero), they are quite important, since cracking in concrete tends to be a tensile failure. However, the relationship between tensile and compressive strengths is not a simple one. It depends on the age, strength of the concrete, the type of curing, the type of aggregate, the amount of air entrainment, and the degree of compaction.

Present research work has been mostly done on the evaluation of tensile strength of concrete by indirect methods and comparatively fewer efforts have been made for its determination by direct methods. The behavior of concrete under tension has not been extensively investigated because of its limited tensile strength and extensibility [2].

---

<sup>1</sup>Corresponding author: [miqbal@ksu.edu.sa](mailto:miqbal@ksu.edu.sa)

Although concrete is never made to carry tension, yet tensile cracking of concrete limits the usefulness as well as life of several structures. For such cases formulation of the behavior of concrete under tension is needed for the development of structural theory. There is the need of standard methods and size of specimen for the determination of tensile strength of concrete [3]. None of the existing methods for determination of tensile strength of concrete compare favorably as regards reproducibility or reliability with compression test [4].

The determination of tensile strength and the stress-strain curve in tension for brittle materials such as cement mortar and concrete is not a straight forward affair. Arrangement of suitable loading and gripping devices to create uniform tensile stress in a test specimen encounters major problems which resulted in accepting indirect tensile measurements to be a practical alternative measurement. The indirect tests do not create a strictly uniform tension on the failure surface and often the stresses on the failure surface are not uniaxial. Therefore, determination of the tensile strength becomes approximate and in addition, determination of the tensile stress-strain curve from the above mentioned indirect tests is difficult. Hence there is a necessity for exploring direct tensile strength measurement.

## 1. Experimental program

### 1.1. Materials and mix design

Cement Type I complying with the requirements of the ASTM C150 was used in this investigation. Fine and coarse aggregates available in the laboratory were used for this investigation. Grading limits of fine and coarse aggregates were in accordance with ASTM C 33. Both the fine and coarse aggregates were air-dried before use, and allowance was made for absorption when calculating batch weights. Water to cement (w/c) ratios at 0.30, 0.40 and 0.50 were used. The dosage of superplasticizer was maintained to attain an initial slump between  $120 \pm 20$  mm. The mix design used in this study is as per ACI 211.1-91. The summary of the mix proportions are given in Table 1. The measurements were taken at 7 and 28 days, in accordance to ASTM standards. Triplicate samples were tested for each age and the mean value is reported as the result.

**Table 1.** Design of mixes with different water-cement ratios

Materials	Mix 1	Mix 2	Mix 3
Cement (kg/m <sup>3</sup> )	520	446	350
Fine aggregates (kg/m <sup>3</sup> )	600	600	780
Coarse aggregates (kg/m <sup>3</sup> )	1040	1040	1050
Superplasticizer dosage	Maintained initial slump at $120 \pm 20$ mm		
w/c	0.30	0.40	0.50

### 1.2. Testing procedure

There is no standard method for measurement of direct tensile strength. In this investigation directed tensile test measurement is proposed which is based on pullout direct tension.

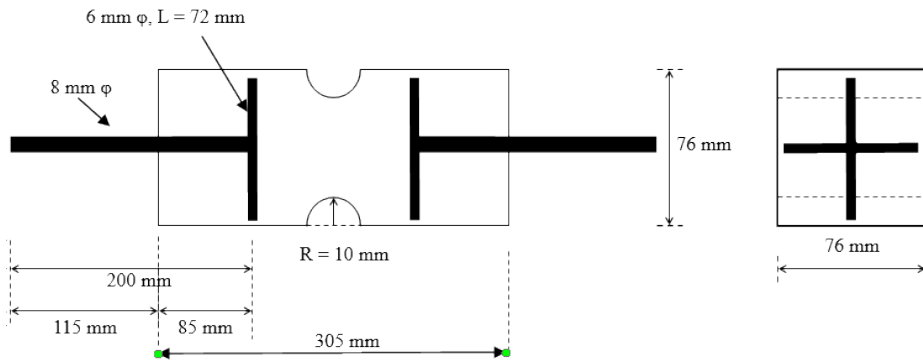
The specimen used for this test method was 76 x 76 x 305 mm as shown in the Schematic Diagram, Figure 1. The specimens are notched at mid-height, providing for a nominal cross section at the failure zone of 51 x 76 mm [5], by using two pieces of wood to reduce the cross section of the material at the middle as shown in Figure 2. To apply the tensile force to the concrete two pieces of reinforcement steel (8 mm bar) were placed as shown in Figure 3. The total length of each piece was 200 mm and 100 mm was placed inside the concrete. One end of the rod was fixed with plus shaped anchor (6 mm bar) to get the grip in the concrete. The concrete was casted in these specially prepared molds as show in Figure 4. The final shape of the specimen is presented in Figure 5. Testing arrangement and typical failure modes are shown in Figures. 6 and 7, respectively.

This test method involves the measurement of the force required to pull out a previously cast-in steel bar. Because of the shape of the specimen, the steel bar assembly is pulled out with a crack on its body. The pull out strength is calculated as the ratio of the force to the area of the cross section, the strength being close to that of the shearing strength of concrete. This test comprises of a concrete prism with embedded steel. The steel bars are connected to the clutches of the pullout machines and at the failure the maximum load upon fracture and the location of the failure is noted down. Then the tension resistance is calculated as:

$$f_t = \frac{P}{A} \quad (1)$$

where:  $f_t$  = Direct tensile strength;  $P$  = Load of the web at failure point  
 $A$  = Area of web at failure point

In order to validate the results obtained for the tensile strength of concrete, compressive strength, and flexural strength measurements were also conducted in accordance to ASTM standards.



**Figure 1.** Schematic diagram of direct tension arrangement



**Figure 2.** Shape of specimen



**Figure 3.** Shape of pullout rod



**Figure 4.** Mould arrangement





Figure 5. Shape of direct tension specimen



Figure 6. Direct tension test in progress



Figure 7. Typical direct tensile failure

## 2. Results and discussion

### 2.1 Compressive strength

The compressive strength development of concrete is shown in Figure 8. It is evident from this figure that compressive strength decreases with increase in w/c ratio, as expected. Mix-1 having w/c ratio 0.30 attained compressive strength 72.4 MPa and 82.9 MPa at 7 and 28 days, respectively. At 7 days, Mix-2 and Mix-3, having w/c ratios of 0.40 and 0.50 are 41% and 46% lesser than the Mix-1, respectively. At the age of 28 days Mix 3 is 41% and Mix-2 is 32% lesser than the Mix-1.

## 2.2 Flexural strength

Figure 9 demonstrates the flexural strength development of concrete. The trend of the results of flexural strength is similar to that of compressive strength. As expected, Mix-1 attained maximum flexural strength at both ages investigated. Mix-1 had a flexural strength gain of 12% from 7 to 28 days whilst Mix-2 and Mix-3 gained 33% and 17%, respectively.

## 2.3 Direct tensile strength

The direct tensile strength development of concrete is demonstrated in Figure 10. It clearly shows the similar pattern of strength development as in case of compressive and flexural strengths (Figures. 8 and 9). As w/c ratio increases the direct tension decreased uniformly, as expected. Direct tensile strength development of Mix-1 having w/c ratio 0.30 showed 4.81 MPa and 5.37 MPa at 7 and 28 days, respectively. As being an indirect tensile measurement, flexural strength showed 8.32 MPa and 9.33 MPa which is at least 40% higher than that of direct tensile measurements. For Mix-2 (w/c 0.40) and Mix-3 (w/c 0.50) the flexural strength were also higher at both ages investigated, however, the rate of increase in the flexural strength is between 30 and 20%. It is evident for the results that the flexural strength measurement shows higher results than that of direct tensile measurements. This trend of increase can be seen from Figure 11 which shows the relationship between direct tensile strength and flexural strength.

The empirical relationship for the direct and indirect tension is as follow:

$$f_t = 1.57(f_f)^{0.55} \quad (2)$$

where:  $f_t$  - is direct tensile strength (MPa)  
 $f_f$  - is flexural strength (MPa)

Similarly, relationship between direct tensile strength and compressive strength has been shown in Figure 12 for the sake of comparison and its empirical relationship is as follow:

$$f_t = 0.50(f_{cu})^{0.54} \quad (3)$$

where:  $f_{cu}$  - is compressive strength (MPa)  
 Equation 3 is similar to that proposed by ACI which is as follows;

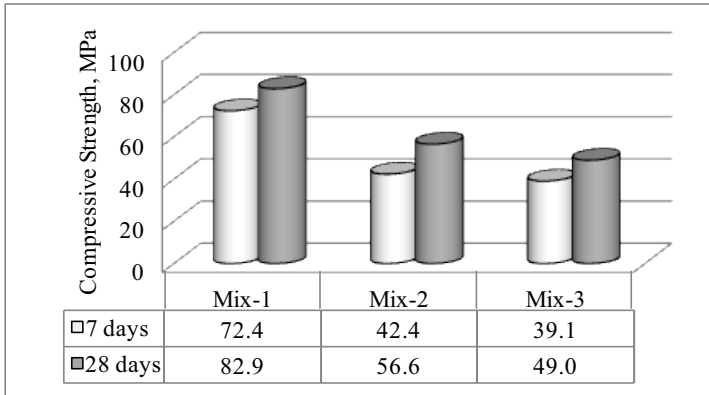
$$\sigma_t = 0.62(\sigma_c)^{0.5} \quad (4)$$

where:  $\sigma_t$  - is direct tensile strength (MPa)  
 $\sigma_c$  - is compressive strength (MPa)

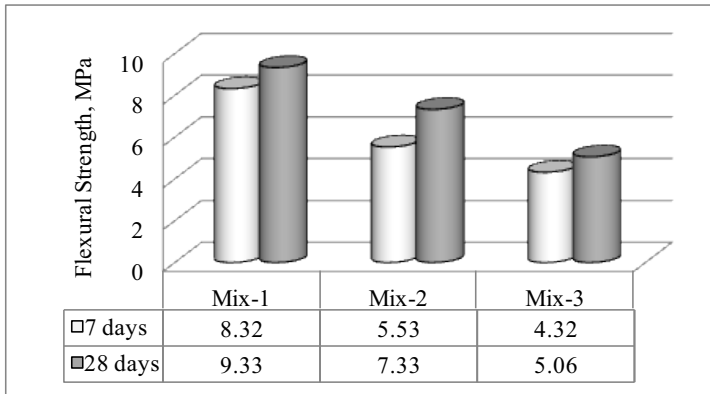
Equations 2 and 3 are limited to within the scope of this investigation. As mentioned earlier that this investigation is part of ongoing research on the development

of direct tensile strength measurement. It is expected that wider scope of this measurement will be published in due course of time.

Generally, the ratio of the direct tensile strength to the compressive strength ranges from about 0.07 to 0.11. Since splitting tension values tend to be slightly higher than direct tension values. Flexural tests (which are the most common way of estimating tensile strengths) give results that are substantially higher than direct tension tests, and the ratio of flexural to compressive strength ranges from about 0.11 to 0.23.



**Figure 8.** Compressive strength development of concrete



**Figure 9.** Flexural strength development of concrete

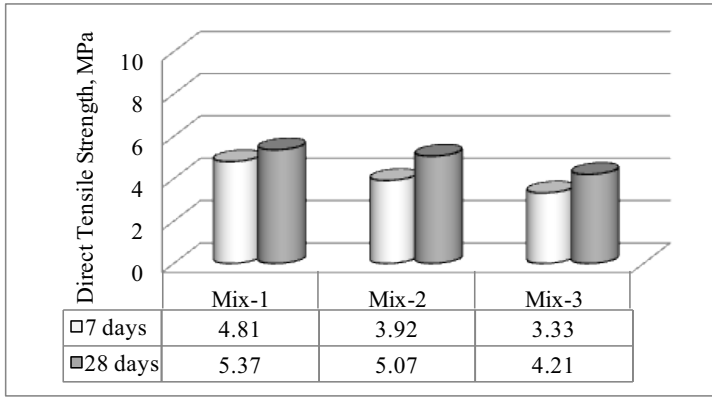


Figure 10. Direct tensile strength development of concrete

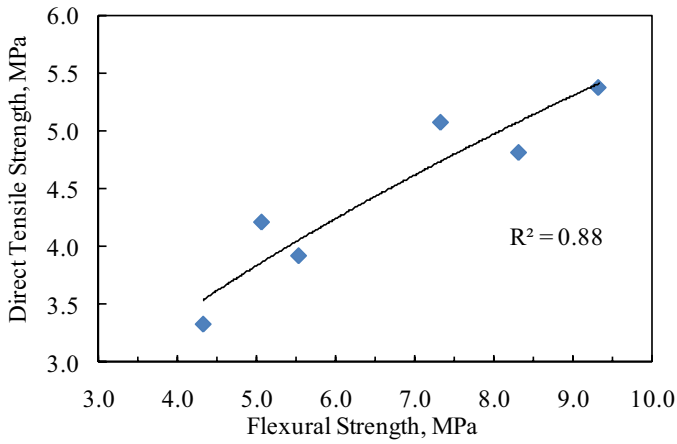


Figure 11. Relationship between direct tensile strength and flexural strength of concrete

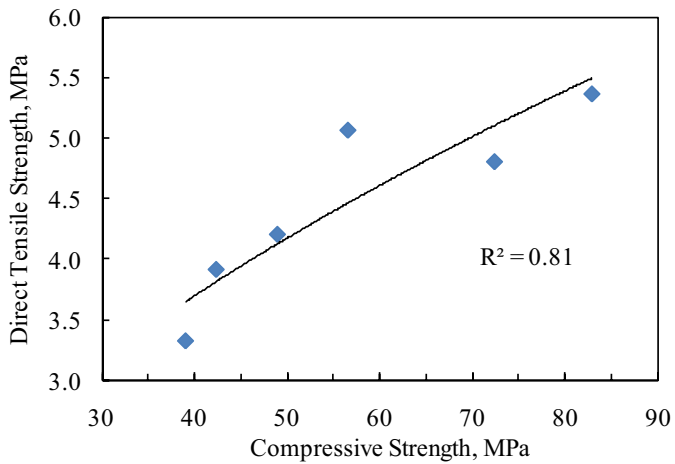


Figure 12. Relationship between direct tensile strength and compressive strength of concrete

### 3. Conclusions

Direct tensile strength test has been proposed and the results obtained are well comparable and similar to that proposed in earlier findings. The relationship between direct tensile strength and compressive strength is similar to that in ACI.

### References

- [1] S.H. Kosmatka, B. Kerkhoff, and W.C. Panarese, *Design and control of concrete mixtures*; 14th Edition, Portland Cement Association, 2002.
- [2] V.A. Yerlici, Behavior of plain concrete under axial tension, *ACI Journal*, 62(8), p. 987-992, 1965.
- [3] V.M. Malhotra, Effect of specimen size on tensile strength of concrete, *ACI Journal*, June, pp. 467-469, 1970.
- [4] G.S. Pandit, Discussion on the paper, concrete rings for determining tensile strength of concrete, *ACI Journal*, October, 847-848, 1970.
- [5] R.W. Poston, K. Kesner, J.E. McDonald, A.M. Vaysburd, and P.H. Emmons, Concrete repair material performance–laboratory study, *ACI Materials Journal*, 98(2), pp. 137-147, 2001.

# The effect of different PPC binders, partially replaced by fly ash properties, on self-compacting concrete

Omar ALMUWBBER<sup>1</sup>, Rainer HALDENWANG and Irina MASALOVA  
*Department of Civil Engineering and Survey, Cape Peninsula Univ of Technology*

**Abstract.** The effect of different CEM I 52.5N cements produced at different factories on Self-Compacting Concrete (SCC) is currently not well understood. The effect of four cements tested and one type of superplasticiser (SP) and partially replaced with two types of fly ash on an SCC mix were studied. Mix design and tests were done according to the European Specification and Guidelines for Self Compacting Concrete (2005). The cements reacted differently with addition of the SPs and partial replacement of fly ash. Although the differences can be distinguished from the SCC tests, it is not yet understood what causes these differences.

**Keywords.** SCC (self-compacting concrete), fly ash, superplasticiser, compressive strength, workability, segregation ratio

## Introduction

SCC is a special type of concrete that can settle into heavily reinforced, deep and narrow sections by its own weight, can consolidate itself without necessitating internal or external vibration and can keep its cohesion (stability) without leading to segregation and bleeding [1]. SCC was developed in the 1980's in Japan and has since become widely used all over the world. It has been hailed as a really novel development. The development in superplasticiser technology has greatly contributed to the formation and improvement of SCC [2–4]. Superplasticisers are essential in SCC mixes and in order to avoid separation of large particles, pozzolanic admixtures or fillers are used to increase the viscosity [5]. SCC demands a large amount of powder content compared to conventional vibrated concrete. This is necessary to produce a homogeneous and cohesive mix [6]. It was reported that SCC often contains powder in the order of 450–600 kg/m<sup>3</sup> of concrete [7]. Due to its rheological requirements, fillers (both reactive and inert) are commonly used in SCC to improve and maintain the workability, to regulate the cement content and to reduce the heat of hydration. Part of this powder content can be effectively replaced by mineral admixtures like fly ash. Even though SCC consists basically of the same components as normal vibrated concrete, there are distinct differences in the concrete composition in order to achieve the desired “self-compacting properties”.

<sup>1</sup>Corresponding author: [omarlb17@yahoo.com](mailto:omarlb17@yahoo.com)

On the one hand, SCC has to reach a high segregation resistance and on the other hand a high deformability. Therefore, the content of ultra-fine materials in SCC is essentially higher [8]. One of the disadvantages of SCC is its cost, associated with the use of chemical admixtures and use of high volumes of cement. One alternative to reduce the cost of SCC is the use of mineral admixtures such as fly ash. The use of fly ash provides benefits in the production of SCC such as reduction in the water requirements with increased workability and increased strength at later ages of curing, which cannot be achieved through the use of additional cement. It is also known that fly ash increases the workability, durability and long-term properties of SCC [9].

## 1. Materials

The Four Ordinary Portland cements were used in this study, were produced in different PPC factories according to the European Standards EN-197-1 and labelled as CEMI 52.5N. The maximum size of coarse aggregate was selected as 13 mm in order to avoid any blocking effect. The fine aggregate used was Malmesbury sand which is a river sand with a good grading. Limestone filler was used as a viscosity modifying filler in the mix. The mix design was for a 28 day 50 MPa compressive strength, according to European Standards EN-196-1. Tables 1-3 give the chemical and physical properties of the cements and SPs used in this research.

Table 1. Physical properties of cements

Physical properties	Designation of the cement samples			
	C1	C2	C3	C4
Relative density	3.05	3.03	3.04	2.99
Specific surface, cm <sup>2</sup> /g	3750	3650	4250	3850
consistence, %	25	31	25	33
Initial set, min	170	180	190	315
Final Set, h	3.25	3.75	3.75	6
45 µm residue, %	11.7	0.6	3.9	1.8
90 µm residue %	1.1	0	0.5	0.1
212 µm residue, %	0.2	0	0	0

## 2. Methods

One control and several mixes with mineral admixtures were prepared and tested to quantify the properties of SCC. In some of the the mixes, cement was replaced with flyash contents of 10%, 20%, 30% and 40% all by mass. After some preliminary investigations, the water–cement ratio (w/c) was selected as 0.45 and the cement content was fixed at 418 kg/m<sup>3</sup>. A new generation superplasticiser (SP), the modified vinyl polymer-based super-plasticiser was used.

**Table 2.** Chemical Properties – mineralogical composition of the cement

Chemical components	Designation of the cement samples			
	C1	C2	C3	C4
SiO <sub>2</sub> (%)	20.8	21.5	20.9	22.3
Al <sub>2</sub> O <sub>3</sub> (%)	3.8	4.1	4	4.7
Fe <sub>2</sub> O <sub>3</sub> (%)	2.9	2.8	3	3.3
Mn <sub>2</sub> O <sub>3</sub> (%)	0.1	0.7	0.6	0.4
TiO <sub>2</sub> (%)	0.2	0.3	0.3	0.5
CaO(%)	64	62.7	62.7	61.3
MgO(%)	1.2	3.3	2.9	2.6
P <sub>2</sub> O <sub>5</sub> (%)	0.17	0.1	0.03	0.12
SO <sub>3</sub> (%)	2.33	2.47	2.81	2.95
Cl(%)	0	0	0	0
K <sub>2</sub> O(%)	0.66	0.36	0.24	0.25
Na <sub>2</sub> O(%)	0.34	0.19	0.15	0.18
LOI(%)	4.11	1.83	2.83	1.74
Total(%)	100.5	100.3	100.5	100.2
FCaO(%)	1	1.3	0.95	1.43
Calcium Silicate (C3S)	59.92	50.8	52.74	54.19
Larnite (C2S)	13.99	20.43	18.76	17.95
Calcium Aluminium Oxide (C3A)	3.95	2.75	1.84	2.63
Brownmillerite (C4AF)	14.54	18.46	20.49	17.15
Periclase	1	2.92	2.08	2.49
Lime	0.35	0.41	0.51	0.4
Arcanite	1.37	0.78	0.31	1.34
Gypsum	1.62	2.74	2.92	1.29
Bassanite	3.28	0.63	0.35	2.58

Note: The mineralogical composition of the cement was determined by XRD Analysis with Rietveld refinement method Topas.

**Table 3.** SP characteristics

Characteristics	Composition of SP
Consistency	Liquid
Colour	Amber
Density according to ISO 758 (g/cm <sup>3</sup> )	1.07
	± 0.02
Dry content according to EN 480-8 (%)	26
	± 1.3
Chlorides soluble in water according to EN 480-10 (%)	< 0.1
Alkali content (Na <sub>2</sub> O equivalent) according to EN 480-12 (%)	< 2.5



### 3. Casting, curing and testing

For each mixture, six 100 mm cubes were prepared to determine the 7 and 28 day compressive strength. The slump-flow test, T50 test, and L-box test and segregation test were conducted to characterise the workability of the fresh concrete and to determine the filling and passing abilities as well as the segregation ratio. During the slump-flow test, the required time for the SCC to reach 500 mm diameter i.e., slump-flow radius (T500), and the final diameter of the concrete flow circle in two directions, were measured. In the L-box test, the test was started by lifting the control gate to allow the flow of SCC through the re-bars into the horizontal part of the L-box. When the flow of fresh SCC stopped, the heights of the concrete at the end ( $h_2$ ) and the beginning ( $h_1$ ) of the horizontal section were measured. The blocking ratio was calculated as the ratio " $h_2/h_1$ ". Specimen cubes were then cast in plastic moulds and were not subjected to any compaction other than their own self-weight. The specimens were kept covered in a controlled chamber at  $20 \pm 2^\circ\text{C}$  for 24 hours until demolding. Thereafter, specimens were placed in water pre-saturated with lime at  $20^\circ\text{C}$ . Hardened concrete compression testing was conducted at 7 and 28 days.

### 4. Discussion of results

Figure 1 presents the slump flow and T50 results, which are related to viscosity, for different cements with SP.

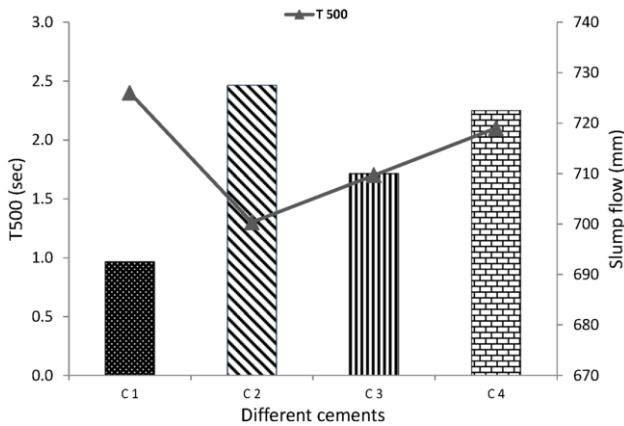


Figure 1. Slump-flow and T500 time of SCC mixes with 4 different cements and SP

In terms of slump flow, all optimised SCC mixes exhibited satisfactory slump flows in the range of 640–800 mm, which is an indication of a good flowability. With SP, C2 and C4 produced higher slump-flow values than C1 and C3.

The V-Funnel results are an indication of the flowability of the mixture. The V-Funnel results are displayed in Figure 2, and indicate that all cement types were within the VF1 limit, below 10 seconds. Additional testing was done and it was confirmed that

the mixture achieved the required segregation resistance to be within the SR2 limits as shown in Figure 3. Figure 4 shows the variation in compressive strength of SCC mixes with SP at 28 days.

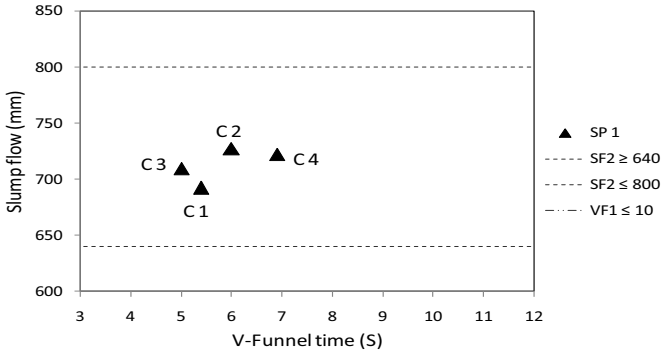


Figure 2. Slump flow results relative to V-funnel results for SP

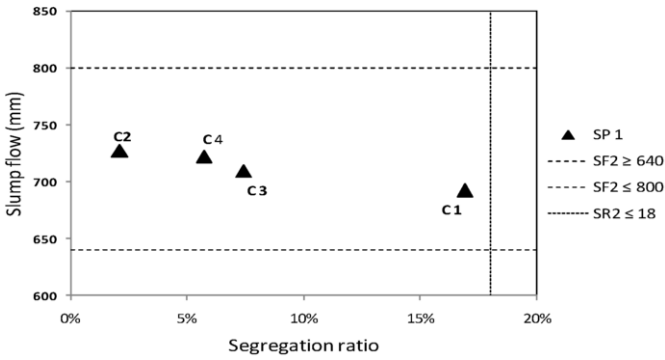


Figure 3. Slump flow results relative to segregation ratio results for SP

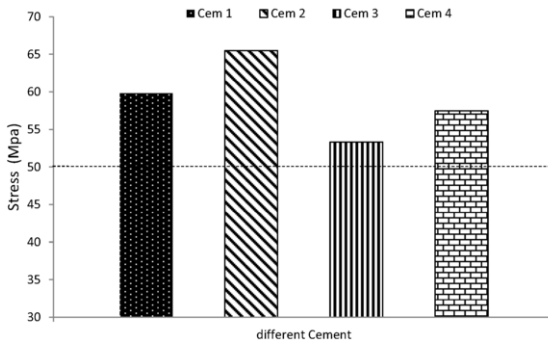


Figure 4. 28 day Compressive strength (MPa) of different cement samples with SP

4.1 Effect of fly ash on cements with SP

Figure 5 shows the effect of replacing cement with fly ash on slump flow. Increasing the fly ash resulted in reduced workability for cements C2 and C3 compared to C1 and C4. The fineness of the four cements were within the range of 3650-4250 cm<sup>2</sup>/g (Table 1). The slump of the mixes increased as the fineness of the cement decreased, C2 cement which was the coarsest cement, had the lowest slump flow, whereas the C4 cement, which was the finest cement, had the highest slump flow.

It was also observed that the workability (slump flow) of mixes prepared with the low-alkali cements was reduced compared to that of the mixes with higher alkali cements [11]. We can see from Table 4 that C3 and C2 respectively has the lower alkali content which resulted in the lower slump – (Figure 5).

Table 4. C<sub>3</sub>A and K<sub>2</sub>SO<sub>4</sub> content for different cements

Cement	C <sub>3</sub> A	K <sub>2</sub> SO <sub>4</sub>
C3	1.84	0.31
C2	2.75	0.78
C4	2.63	1.34
C1	3.95	1.37

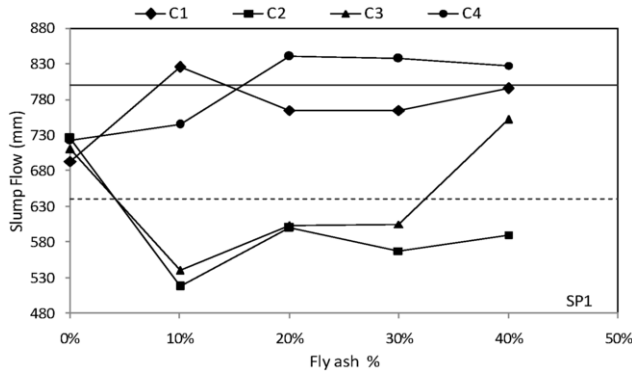
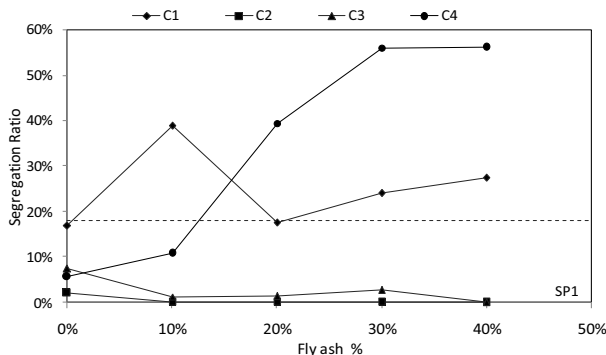


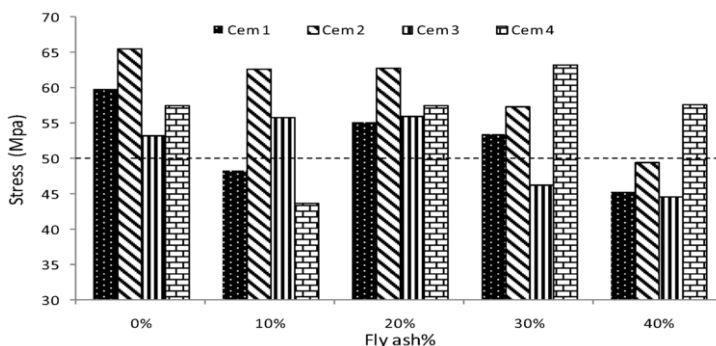
Figure 5. Slump-flow of SCC versus fly ash at different replacement rates for different cements using SP

From Figure 6, (sieve segregation test) the cement types that performed best were C2 and C3. Mixes with C1 and C4 replaced with 10%, 20%, 30% and 40% fly ash were outside the required SR2 limit of 18.0% segregation ratio. From the segregation results, it is evident that the addition of fly ash had a positive effect on C2 and C3 reducing the segregation resistance over the range that the cements were replaced by fly ash. C1 and C4 were negative effected by the addition of fly ash.



**Figure 6.** Segregation ratio of SCC versus Fly ash at different replacement rates for different cements using SP

The compressive strength generally, decreased with increase in the percentage of the fly ash. Replacing OPC with 10, 20, 30 and 40% fly ash caused a reduction in the compressive strength after 28 days as would be expected. The effect at 7 days was even more pronounced. The long term effect on compressive strength was not evaluated.



**Figure 7.** Compressive strength (MPa)at different fly ash replacement rates for different cements with SP

### 5. Conclusions

This study illustrated some mechanical properties of self-compacting concrete to achieve a base mix with the optimum amount of superplasticiser for four CEM I 52.5 N cements produced at different factories. Local materials were used to design an optimised base mix with a 28 day compressive strength of 50MPa. The second objective of this project was to determine the effect of extending the cements with fly ash at different percentages. The effect of the extender was expressed in terms of the effect it had on the SCC properties. The properties considered were the flowability, viscosity, passing ability, segregation resistance and compressive strength at seven and twenty-eight days.

Cements C2 and C1 show respectively the highest and lowest slump flows followed by C4 and C3. These differences could be caused by the variation in  $C_3A$  and alkali-sulphate ( $K_2SO_4$ ) content in the cements. It has been shown that cements produced at different factories have variations in cement chemistry and physical properties which can affect the flowability and segregation resistance of an SCC mix.

## Acknowledgement

We would like to thank PPC for funding this research, making laboratories available and sponsoring most of the material and new test instruments.

## References

1. Alyamac, K.E., Ince, R. (2009). Preliminary concrete mix design for SCC with marble powders. *Construction Building Material*.23:1201–10.
2. Okamura, H., Ouchi, M. (1999) Self-compacting concrete: development, present use and future. The first international RILEM symposium on SCC. Bagnoux: RILEM Publications SARL. p. 3–14.
3. Siddique, R. (2011) Properties of self-compacting concrete containing class F fly ash. *Mater Design*.32:1501–7.
4. Melo, K.A., Carneiro, A.M. (2010) Effect of Metakaolin's finesses and content in self-consolidating concrete. *Construction Building Material*.24:1529–35.
5. Nishio A, Tamura H, and Ohashi M. (1998) Self-compacting concrete with high-volume crushed rock fines. In: Malhotra VM, editor. *Fourth CANMET/ACI/JCI international symposium on advances in concrete technology*. Tokushima: ACI. p. 617–30.
6. Topcu I.B., Uygunoglu T, (2010) Effect of aggregate type on properties of hardened self-consolidating lightweight concrete (SCLC). *Construction Building Material*.24:1286–95.
7. Vengala J, Sudarshan M.S. and Ranganath R.V. (2003). Experimental Study for Obtaining Self-Compacting Concrete. *The Indian Concrete Journal*, Vol. 77, No. 8, August 2003, pp. 1261 – 1266.
8. Sukumar B, Nagamani K, Raghavan RS. (2008) Evaluation of strength at early ages of self-compacting concrete with high volume fly ash. *Construction Building Material*.22:1394–401.
9. Bouzoubaa N, Lachemi M. (2001) Self-compacting concrete incorporating high volumes of class F fly ash preliminary results. *Cement and Concrete Research* 31:413–20.
10. The European Project Group, May 2005. The European Guidelines for Self-Compacting Concrete Specification, Production and Use.
11. Flatt, R.J. & Houst, Y.F. 2001. A simplified view on chemical effects perturbing the action of superplasticizers. *Cement and concrete research*, 31(8): 1169–1176.

# Lowering the embodied CO<sub>2</sub> by using fly ash concrete internally cured with recycled ceramic tile aggregates

Mohammed S. MEDDAH<sup>a,1</sup>, T. NUKUSHINA<sup>b</sup>, S. SEIKI<sup>c</sup> and R. SATO<sup>d</sup>

<sup>a</sup>Department of Civil & Architectural Engineering, Sultan Qaboos University, Oman

<sup>b</sup>Kajima Construction Corporation, Japan

<sup>c</sup>Technical Research Center, Chugoku Electric Power Co., Inc, Japan

<sup>d</sup>Department of Social and Environmental Engineering, Hiroshima University, Japan

**Abstract.** Large quantities of recycled materials, including waste aggregates and supplementary cementing materials (SCMs), such as fly ash (FA) are used in concrete mixtures to reduce environmental impact. Recent studies have proven that Recycled Porous Ceramic (RPC) coarse aggregates could successfully be used as an internal curing agent to enhance mechanical properties and mitigate autogenous shrinkage in silica fume high-performance concrete (HPC). This paper discusses the effectiveness of internal curing provided by the RPC in concrete made with 20% of FA as a partial replacement of Portland cement and cured under three different curing systems, namely: sealed, dry and underwater. A single water-to-binder ratios (*w/b*) of 0.30 was selected; and a single partial replacement level of 40% of natural coarse aggregate (NCA) by the RPC was adopted. Concrete performance was investigated in terms of compressive and splitting tensile strengths, and modulus of elasticity up to 91 days, and autogenous and drying shrinkage. The results showed a significant improvement in the compressive and splitting tensile strengths, and a slight decrease in the modulus of elasticity of RPC concrete compared to the control mixture. It has been found that FA-concrete needs extended wet curing (internal or external) to achieve its potential. Additionally, the use of RPC in FA-concrete seems to be very effective in shrinkage reduction.

**Keywords.** Curing conditions, fly ash, internal curing, mechanical properties, recycled aggregate, waste ceramic aggregate

## Introduction

Sustainability in concrete industry has gained a wide acceptance and is a key issue in the 21<sup>st</sup> century. Over the years of Portland cement manufacturing, extensive use of natural mineral resources and increasing amount of solid wastes dumped in landfills are continuously damaging the environment. Thus, exploring alternative materials based on recycling and industrial by-products has to be promoted. The concept of sustainable construction involves mainly reducing environmental charges by minimizing CO<sub>2</sub> emissions and preserving raw materials through the use of various recycled and

---

<sup>1</sup>Corresponding author: Department of Civil & Architectural Engineering, Sultan Qaboos University, P.O. BOX: 33, P.C:123-Al-Khod, Muscat, Oman; E-mail: seddikm@squ.edu.om

by-product materials, as aggregates or cementing materials in concrete. Indeed, various SCMs, such as silica fume (SF) and FA used in replacement of PC, and recycled aggregates as substitute of natural aggregate has become a common component in today's concrete production.

Using FA in concrete can improve workability, reduce heat of hydration and drying shrinkage, increase long-term strength [1,2] and durability [3]. Several studies have been conducted to design a more sustainable and durable FA-concrete [4-7]. However, FA-concrete is also known by its low early-age strength and the need for prolonged wet curing period compared to Portland cement or silica fume-concretes.

Over the past years, the interest in use of pre-soaked lightweight aggregates in HPC as an internal curing agent has increased rapidly [6-9]. Internal wet curing can, not only limit the risk of early-age cracking induced by autogenous shrinkage, but it could also significantly improve the long-term mechanical performance of concrete, decreasing its permeability, and enhancing concrete's durability [9,10-12]. Recently, it has been proven that waste porous ceramic coarse aggregate, derived from the fragments of clay tile used as roof material in Japan, embedded in SF-HPC as an internal curing agent is very effective in reducing (even to neutralizing) autogenous shrinkage, the self-induced stress as well as long-term compressive strength improvement [9,10].

This study investigates the effectiveness of partial replacement of NCA by RPC as an internal curing agent in flyash-concrete designed with a w/b of 0.30 and subjected to three curing regimes.

## 1. Experimental

### 1.1. Materials

Portland cement (PC) and blended cement containing 20% of FA as partial replacement of PC were used. Crushed quartz (QS) and limestone (LS) sand were used as fine aggregates. Hard sandstone was employed as natural coarse aggregate while 40% (by volume) of recycled porous ceramic coarse aggregates were incorporated as a partial substitute of NCA for internal curing purpose. Both the fine and coarse aggregates including the RPC were used in saturated surface-dry (SSD) conditions. An appropriate dosage of Polycarboxylate-based superplasticizer was added to obtain the desired workability. Materials' properties are given in Table 1.

### 1.2. Mixture proportioning and testing methods

Table 2 provides the mix proportions and fresh properties of the HPC investigated. Blended cement concretes were designed with 20% FA (FA20) as a substituted pozzolanic material of PC while NC designate the PC concrete. Concretes internally cured with 40% RPC were denoted as G40 where the number 40 represents the replacement level of NCA by the RPC. Fresh concrete properties were determined before concrete placement in the moulds and the specimens were then covered with plastic sheet and wet jute to avoid early drying. For the first 24 hours, the specimens were kept in their moulds in environmental chamber ( $60 \pm 2\%$  of RH and  $20 \pm 1^\circ\text{C}$ ) and then demoulded and stored in a specific curing condition until the time of testing.

Cylindrical specimens, 100 × 200 mm were used for compressive strength tests. Autogenous shrinkage was measured on prismatic sealed specimens while drying shrinkage was measured on unsealed specimens after 7 days of sealed curing conditions. Three curing regimes were selected. i) Sealed conditions: specimens were covered with adhesive aluminum foil to prevent moisture loss and stored in environmental chamber at 20 ± 1°C of temperature and 60 ± 2% of RH. ii) dry-air: concrete specimens were kept unsealed in the environmental chamber at T = 20 ± 1°C and 60 ± 2% of RH. iii) Water curing regime: specimens were submerged in a water tank at T = 20 ± 1°C. All specimens were kept in the designated curing regime until the testing time (7, 28 and 91 days for mechanical testing). All measurements were carried out in accordance with the JIS test specifications.

**Table 1.** Materials proprieties

Materials	Type	Properties	Label
Cementing materials	Normal Portland cement	Specific gravity: 3.16 Specific surface area: 3260 cm <sup>2</sup> /g	NC
	Fly ash	Specific gravity: 2.13 Specific surface area: 3200 cm <sup>2</sup> /g	FA
Chemical admixtures	Air entraining and water reducing agent	Lignosulphonate Polymer	LSP
	High range water reducing agent	Polycarboxylate Polymer	HRWRA
Coarse aggregates	Crushed sandstone aggregate	Surface-dry Specific gravity: 2.67 Water absorption: 0.56% Crush rate: 12% Aggregate size: 5-20 mm	NCA
	Recycled porous ceramic coarse aggregate	Surface-dry Specific gravity: 2.24 Water absorption: 8.58% Crushing value: 21% Aggregate size: 5-20 mm	RPC
Fine aggregates	Crushed quartz	Surface-dry Specific gravity: 2.60 Water absorption: 1.13%	QS
	Crushed limestone	Surface-dry Specific gravity: 2.70 Water absorption: 0.93%	LS

**Table 2.** Mixture compositions of concrete designed with 0.3 w/b

Mixture label	W/(C+FA)	Unit amount (kg/m <sup>3</sup> )								Slump flow (mm) (d <sub>1</sub> ×d <sub>2</sub> )	Air (%)
		W	C	FA	QS	LS	QS+LS	NCA	PC		
NC	0.30	165	550	-	532	368	900	795	-	590 × 610	1.3
FA20		165	440	110	508	352	860	795	-	710 × 680	0.4
G40NC		165	550	-	510	353	864	477	269	540 × 540	1.3
G40FA20		165	440	110	508	352	860	477	269	590 × 640	0.6



## 2. Experimental results

### 2.1. Compressive strength

Figure 1 shows that the curing regime applied has significant effect on the compressive strength development of concrete produced with and without FA and coarse RPC aggregate. Both at early and later-ages, the lowest compressive strength values were achieved by the concretes cured in dry-air while generally; the sealed concrete specimens have exhibited the highest compressive strength. A significant gap could be seen in Figure 1 between the concrete mixtures subjected to dry-air and their corresponding mixtures cured under sealed or water curing regimes.

The results indicated that, for all mixes investigated and cured in dry-air, no significant strength gain was obtained when extending the curing time from 28 to 91 days. For each curing regime applied, the FA20 mixes showed the lowest compressive strength compared to their corresponding mixes NC, G40NC and G40FA20. In fact, due to its low and slow reactivity, the addition of FA to concrete tends to decrease its early-age compressive strength. Except the dry-air curing regime, all FA mixes have exhibited the lowest compressive strength at 7 days; however, and generally, the same FA mixtures have exhibited the highest compressive strength after 91 days of curing.

It is well established that, FA needs additional water for its pozzolanic reaction with portlandite to produce secondary C-S-H and hence, long-term strength enhancement.

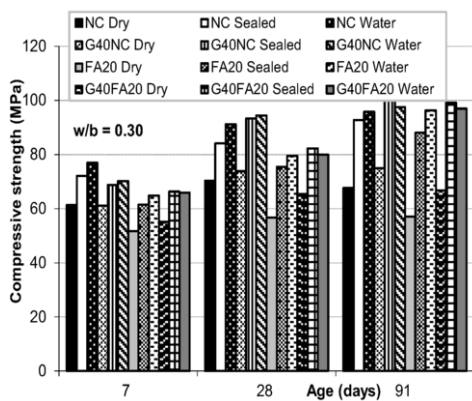
On the other hand, the use of FA was found to be more effective when it is combined with the RPC aggregates as an IC agent. In fact, using the RPC as an IC agent in the four concrete mixes studied did not affect the compressive strength development at early-age, while beyond 28 days; the mixes with the RPC, especially those cured under sealed or water conditions showed noticeable strength improvement. For the same mix design, no significant difference in a strength gain was observed between specimens cured under sealed conditions and those cured underwater.

At early age (7 days) and for both sealed and water cured concrete specimens, quite a similar strength gain varying from 5 to 23% was recorded. Moreover, for both curing regimes (sealed and water), the strength gain became more noticeable beyond 7 days, especially after 91 days of curing. In fact, sealed and water curing of concrete specimens have resulted in a substantial enhancement of the compressive strength of up to 32% and 45% at 28 and 91 days, respectively.

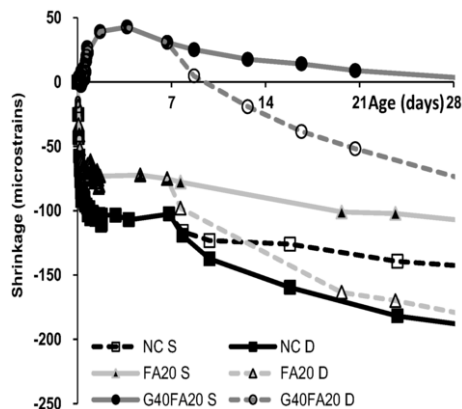
### 2.2. Free deformation

Figure 2 shows the development of autogenous shrinkage (solid line) measured on sealed specimens up to 28 days as well the drying shrinkage (dotted line) measured on specimens subjected to dry air after the first 7 days on sealed conditions.

The use of 20% FA as a partial substitute of PC could reduce both the autogenous and drying shrinkage magnitude at early and later-ages. It seems that the effect of FA on autogenous shrinkage reduction is more perceptible compared to its slight effect on drying shrinkage measured after 7 days. Meanwhile, the results clearly indicate that substituting 40% of the NCA by the RPC in the FA-concrete mixtures has led to a total elimination of autogenous shrinkage (a non-shrinking concrete up to 28 days).



**Figure 1.** Effect of the curing regime on the compressive strength development up to 91 days.



**Figure 2.** Autogenous and drying deformations development over time for the four mixtures investigated (Sealed and air-dry curing regimes).

In fact, this internally cured mixture (G40FA20) has shown an important early-age expansion (around 50 microstrains). However, the same mixture subjected to dry-air after 7 days has generated a quite significant drying shrinkage strains of around 78 microstrains at 28 days. It could be speculated that the combination of 20% FA with 40% RPC is very effective in shrinkage reduction (autogenous and drying).

### 3. Discussion

Water curing and sealed conditions regimes have proven to be efficient in enhancing concrete compressive strength. In fact, the sealed curing system is able to prevent moisture loss while water curing system could provide an external water supply to the cementitious system which ensures a continuous cement hydration process and hence, mechanical properties enhancement.

Concrete cured in dry-air is subjected to a rapid evaporation of pore water and a slow progress of cement hydration which results in low strength development. The combination of internal and external drying would result in low mechanical properties.

Meanwhile, the presence of soaked RPC aggregate as an IC agent in concrete mixtures has greatly contributed to compressive strength development due to their effect in cement hydration enhancement. This contribution is linked to the external curing conditions. Mixes treated with the RPC and cured in sealed conditions or underwater were more efficient compared to those cured in dry-air. Moreover, the reduction in autogenous shrinkage of FA-concrete mixture internally cured with the RPC aggregates is due to the slow reaction of FA and water supply by the RPC which keeps the pore network saturated and avoid internal drying during cement hydration.

#### 4. Conclusions

Based on the experimental results obtained, the following conclusions can be drawn:

1. The RPC was successfully used as an internal water curing agent in FA-concrete.
2. Sealed condition seems to be the appropriate curing system that could enhance mechanical properties of concrete, especially at long-term. This curing system resulted in 15 to 30% of strength gain compared to dry environment.
3. It was concluded that FA-concretes need wet curing to achieve its potential of strength development, particularly at long-term.
4. A significant shrinkage reduction was obtained for the hybrid mix G40FA20.
5. This mix G40FA20 results not only in an environmentally friendly concrete and may address sustainability issue in concrete industry but also provides a substantial mechanical performance enhancement and shrinkage reduction.

#### References

- [1] JSCE, 1999, "Recommendation for Construction of Concrete Containing Fly Ash as a Mineral Admixture," *Concrete Engineering Series*, 94.
- [2] M.S. Meddah, and A. Tagnit-Hamou, Effect of Mineral Admixtures on Shrinkage Measured on Massive Concrete Elements, *Proceeding of the 8th Int. Conf. on creep, shrinkage and durability of concrete and concrete structures*, 2008, Ise-Shima, Japan, Tanabe et al. (eds), Taylor & Francis, London, 381-386.
- [3] L. Jiang, Z. Liu, and Y. Ye, Durability of Concrete Incorporating Large Volumes of Low-Quality Fly Ash, *Cement and Concrete Research*, 34(8) (2004), 1467-1469.
- [4] A. Bilodeau, V. Sivasundaram K.E, Painter and V.M, Malhotra, Durability of Concrete Incorporating High Volumes of Fly Ash from Sources in the USA, *ACI Materials Journal*, 1994, 91(1), 3-12.
- [5] V.M. Malhotra, Making Concrete Greener with Fly Ash, *Concrete International*, 1999, 21(5), 61-66.
- [6] V.M. Malhotra, *Role of Supplementary Cementing Materials in Reducing Greenhouse Gas Emissions*, in: Gjorv OE, Sakai K, Editors, *Concrete Technology for a Sustainable Development in the 21st Century*. London: E& FN Spon, 2000, 251-261.
- [7] V.M. Malhotra, High-performance high-volume fly ash concrete, *Concrete International*, 24(7), 2002, 30-39.
- [8] CEMBUREAU, *Activity Report 2007*, The European Cement Association, Brussels, 2008, 44p.
- [9] M. Suzuki, M.S. Meddah, and R. Sato, Use of porous ceramic waste aggregates for internal curing of high-performance concrete, *Cement and Concrete Research*, 39(5), 2009, 373-381.
- [10] M.S. Meddah, R. Sato, Effect of curing methods on autogenous shrinkage and self-induced stress of high-performance concrete," *ACI Materials Journal*, 107(1), 2010, 65-74.
- [11] P. Lura, and K. Breugel van, The influence of moisture flow from the LWA to the paste on the early-age deformations, *6<sup>th</sup> Inter Symposium on High Strength/High Performance Concrete*, 1149-1160, 2002
- [12] D.P. Bentz, P. Lura, P and J.W. Roberts, Mixture proportioning for internal curing, *Concrete International*, 27(2), 2005, 35-40.

# Geopolymers and polymers

This page intentionally left blank

# Polyfurfuryl alcohol - a waste from sugarcane bagasse as a construction material

Rakesh KUMAR<sup>1</sup>

*Department of Applied Chemistry,*

*Birla Institute of Technology, Mesra, Patna Campus, Patna - 800014, India*

**Abstract.** Furfuryl alcohol is extracted from the waste of sugarcane bagasse. Polyfurfuryl alcohol (PFA), as a matrix, is obtained from the acid catalysed polymerization of furfuryl alcohol. The difficulties encountered in the conversion of furfuryl alcohol as monomers into polyfurfuryl alcohol by homopolymerization are attributed to the exothermic reaction often leading to dangerous explosion, which can be overcome by the approach presented in the South African and World Patents [4,5] filed by the author. The processes provided herein can be used to prepare various shapes and sizes of reinforced or unreinforced molded products that can also be used in construction sectors.

PFA based biopolymer shows tensile strength and tensile modulus of 15-17 MPa and 2.0-2.6 GPa, respectively with almost 100% water resistance. Glass transition temperature of polyfurfuryl alcohol is 117-118 °C. Interestingly, the biopolymer is thermally stable with maximum degradation temperature of 475 °C with a char yield of 63%. The thermal properties of the PFA based biopolymer prepared by this method are similar or somewhat higher than that of phenolics which are widely used in construction sectors.

To be used as in construction sectors, the commercial development of this technology requires a specification of the conditions for the synthesis of large biopolymer sheets with definite thickness and surface area. High-temperature treatment effects on polymers are highly dependent on the primary effects of thickness, and surface area on the relevant thermodynamic and transport properties of polymerization process. Thickness and temperature as a fundamental state variable drastically influences the processing parameters of PFA based sheets. In this work, biopolymers sheets have been developed focusing on scale-up of the process using the three parameters thickness, temperature and the surface area.

**Keywords.** Furfuryl alcohol, scaling, time, temperature, thickness

## Introduction

The potential, challenges and feasibility of using biopolymers such as polylactic acid, soy protein isolate (SPI) as well as polyfurfuryl alcohol (PFA) based thermoset resins as plastics have been explored. There are a few reports available for PFA, a hydrophobic polymer obtained from sugarcane bagasse [1-3]. The formation of conjugated sequences in this thermoset polymer responsible for black coloured PFA, is due to acid-catalysed self-condensation of furfuryl alcohol (FA) [2].

Researchers have observed the difficulties encountered in the conversion of FA as monomers into PFA.

<sup>1</sup>Corresponding author: Tel. +91-9709474061. Email. [krakesh72@gmail.com](mailto:krakesh72@gmail.com)

They are due to the exothermic reaction often leading to dangerous explosion, which can be overcome by the approach presented in the South African patent [4] and World Patent [5] filed by the authors. The processes provided herein can be used to prepare various shapes and sizes of reinforced or unreinforced molded products that can also be used in construction sectors.

In this work, the effect of temperature, time and thickness on the curing characteristics of PFA based sheets will be discussed. The objective of this work will be to optimize the conditions so that blistering of the PFA based final products can be prevented.

## 1. Experimental

### 1.1 Materials

Furfuryl alcohol (FA) and p-toulenesulphonic acid (PTSA) monohydrate were purchased from Sigma-Aldrich, and were used as received. The density of FA as mentioned in the manufacturer's data sheet is 1.135 gm/ mL. Circular silicon based mold of 10 cm diameter was used for molding the products. The area of the silicon mold was 78.5cm<sup>2</sup>.

### 1.2 Methods

A solution of PTSA monohydrate (0.3 phr with respect to the resin) prepared in 5 ml water was added dropwise to FA at room temperature in order to catalyse the FA.

In the first case, temperature and catalyst concentration were kept constant at 50°C and 0.3 parts per hundred (phr), respectively. The thickness of PFA sheet was varied in order to optimize the thickness. In the second case, temperature and thickness of PFA based sheet were kept constant as 50 °C and 5 mm and the contents of catalyst were varied. Lastly, at optimized thickness and catalyst concentration, temperature to cure PFA based sheet was varied.

## 2. Results and Discussions

In results and discussion part, a report is given on the optimized temperature, thickness and catalyst concentration above which blistering in PFA takes places.

### 2.1 Effect of thickness on the curing characteristics at constant temperature and constant amount of PTSA

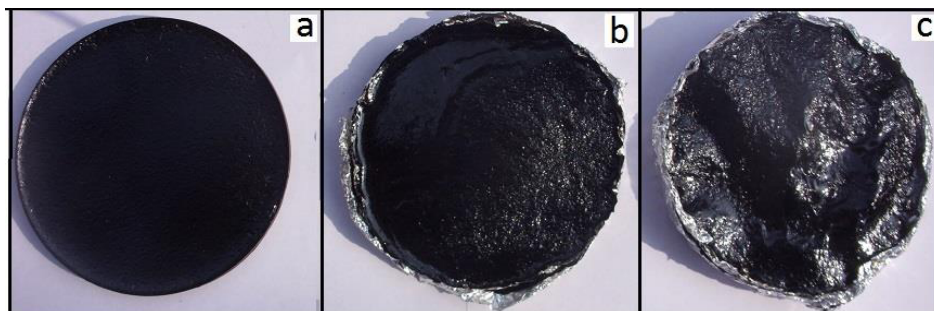
Table 1 shows the effect of thickness on the curing characteristics of PFA sheets. The thickness was varied from 5 mm to 10 mm. The amount of catalyst concentration of 0.3 phr was kept constant in all the cases. As the thickness increased, the differences in the

theoretical weight i.e. weight of FA taken for polymerization and weight of PFA sheets after polymerization increased.

**Table 1.** Effect of thickness on the curing characteristics at  $50\pm 2^\circ\text{C}$  of furfuryl alcohol by incorporating constant amount of PTSA

Thickness (mm)	Furfuryl alcohol (ml)	PTSA (phr)	Theoretical weight (gm) of FA before curing	Experimental weight (gm) of FA after curing	Difference in weight (%)
5	50		56.75	47.79	15.7
7.5	70	0.3	79.45	62.06	21.8
10	90		102.15	78.6	23.05

Figure 1 shows the photograph of PFA sheets. At lower thickness (5 mm), PFA sheet possesses smooth surface but with the increase in thickness from 5 mm to 10 mm, blistering in PFA sheets was clearly observed. This means that if the thickness of the PFA sheets increases to 10 mm, the curing reaction tends towards explosion and hence blistering takes place.



**Figure 1.** Photograph of PFA sheets at thickness of 5 mm (a), 7.5 mm (b) and 10 mm (c).

## 2.2 Effect of catalyst content on the curing characteristics at constant temperature and constant thickness

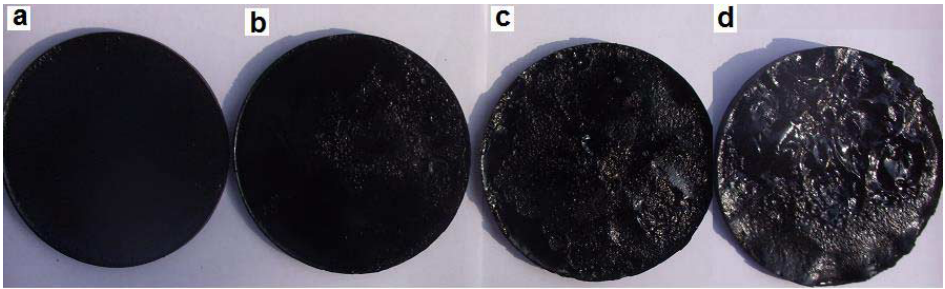
Table 2 shows the effect of concentration of catalyst on the curing characteristics of PFA sheets. The concentration of catalyst was varied from 0.3 phr to 0.5 phr. The thickness of PFA sheet was kept constant in all the cases. As the concentration of the catalyst increases, there are no differences in the theoretical weight i.e. weight of FA taken for polymerization and weight of PFA sheets after polymerization increased. The weight of cured PFA sheets, with different contents of PTSA, was in the range of  $15\pm 5$  mg.



**Table 2.** Effect of concentration of catalyst on the curing characteristics at  $50\pm 2^\circ\text{C}$  of furfuryl alcohol at constant thickness

Furfuryl alcohol (ml)	PTSA (phr)	Thickness (mm)	Theoretical weight (gm) of FA before curing	Experimental weight (gm) of FA after curing	Difference in weight (%)
50	0.3	5	56.75	47.79	15.7
	0.4		56.75	47.14	15.7
	0.45		56.75	47.25	14.9
	0.5		56.75	47.51	14.5

Figure 2 shows the photograph of PFA sheets at different contents of PTSA. At lower concentration of catalyst i.e. 0.3 phr, PFA sheet possesses smooth surface but with the increase in concentration of catalyst from 0.4 phr to 0.5 phr, blistering in PFA sheets was clearly observed. This means that if the concentration of catalyst increases to 0.5 phr, the curing reaction tends towards explosion and hence blistering takes place.

**Figure 2.** Photograph of PFA sheets at 0.3 phr (a), 0.4 phr (b), 0.45 phr (c) and 0.5 phr (d) of PTSA

### 2.3 Effect of temperature on the curing characteristics at constant thickness and constant amount of PTSA

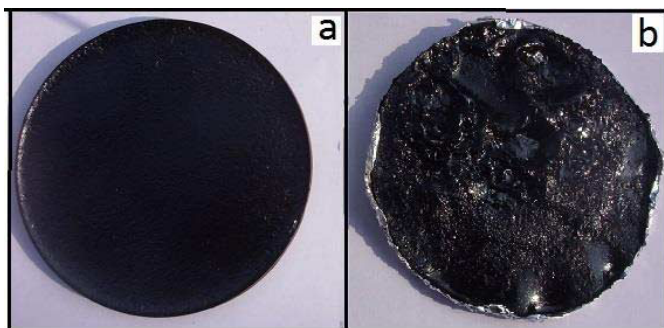
Table 3 shows the effect of temperature on the curing characteristics of PFA sheets. The temperature was varied from  $50^\circ\text{C}$  to  $60^\circ\text{C}$ . The thickness of PFA sheet and concentration of catalyst was kept constant in all the cases. As the temperature increases, the weight of PFA sheets after polymerization decreased. This may be due to loss of PFA due to blistering.

**Table 3.** Effect of temperature on the curing characteristics of furfuryl alcohol at constant thickness and constant catalyst concentration

Furfuryl alcohol (ml)	Temperature ( $^\circ\text{C}$ )	Thickness (mm)	Theoretical weight (gm) of FA before curing	Experimental weight (gm) of FA after curing	Difference in weight (%)
50	$50\pm 2$	5	56.75	47.79	15.7
	$60\pm 2$		56.75	46.40	18.14

Figure 3 shows the photograph of PFA sheets. At lower temperature i.e.  $50^\circ\text{C}$ , PFA sheet possesses smooth surface but with the increase in temperature to  $60^\circ\text{C}$ , blistering in PFA sheets was clearly observed. This means that if the temperature of

curing increases to 60 °C in the first step, the curing reaction tends towards explosion and hence blistering takes place.



**Figure 3.** Photograph of PFA sheets at 50 °C (a) and at 60 °C (b)

### 3. Conclusions

PFA based sheets without blistering can be fabricated provided one controls temperature of curing as well as thickness of PFA based sheets. The optimum temperature for the first stage of curing was found to be  $50 \pm 2$  °C and the optimum thickness was found to be 5 mm. Even at high concentration of acid catalyst (more than 0.3 phr), one can see blistering in PFA based sheets. From this work, mathematical models for biopolymers sheets focusing on scale-up of the process will be discussed using the three parameters thickness, temperature and the surface area.

### Acknowledgement

I am grateful to the University Grant commission (UGC), New Delhi, India for granting me the Start-Up-Grant-Research-Fund (No. F 20-2(19)/2012 (BSR)) to deliver the oral presentation in this conference (ICCMATS 2014).

### References

- [1] L. Pranger, R. Tannenbaum, Biobased nanocomposites prepared by in situ polymerization of furfuryl alcohol with cellulose whiskers or montmorillonite clay, *Macromolecules*, **41** (2008), 8682–8687.
- [2] M. Choura, N. M. Belgacem, A. Gandini, Acid-catalyzed polycondensation of furfuryl alcohol: mechanisms of chromophore formation and cross-linking. *Macromolecules* **29** (1996), 3839–3850.
- [3] W. G. Trindade, W. Hoareau, I. A. T. Razera, R. Ruggiero, E. Frollini, A. Castellan, Phenolic thermoset matrix reinforced with sugar cane bagasse fibers; Attempt to develop a new fiber surface chemical modification involving formation of Quinones flowed by reaction with furfuryl alcohol. *Macromol. Mater. Eng.*, **289** (2004), 728–736.
- [4] R. Kumar, R.D. Anandjiwala, Polyfurfuryl Alcohol Products, *South Africa Patent Application ZA2011/01976*, (2011).
- [5] R. Kumar, R.D. Anandjiwala, Process for Preparing Polyfurfuryl Alcohol Products, *WIPO*, WO 2012/123902 A1, (2012).

# Geopolymer concrete: a practical approach

Cyril ATTWELL

*Concrete Centre of Excellence, Murray & Roberts (pty) Ltd, South Africa*

**Abstract.** High production costs of concrete in combination with the high CO<sub>2</sub> footprint of cement has instigated the research, development and application of concrete utilizing by-products and wastes as partial or entire binder replacements. The literature research progressed through the myriad of definitions and theses available to define two distinct paths of activation, notably alkali- and acid-activations. The alkali-activated path was chosen as the operating risks with alkali materials within the construction industry are known. Experimental work progressed in the laboratory using this base concept to achieve a predictable material with properties similar to both resin and concrete systems depending on the balance of chemistry. The experimentally-defined chemical system has been applied in trials for concrete slabs to study the properties in dry and wet plastic states and their respective hardened properties. The hardened properties tested include shrinkage, durability, compressive and flexural strengths under different curing regimes. Plastic properties were reviewed through the placing, consolidation and finishing of the products. Differences in consolidation and finishing were established with wet-plastic applications. The majority of hardened state properties were improved except for a marginal decrease of flexural strength. Due to the benefits in the plastic and hardened state of the geopolymer concrete, further applications on several sites with improvements to the chemical process are being considered to evaluate the viability of replacing conventional portland cement concrete with the geopolymer concrete on a structural basis.

**Keywords.** Geopolymer, shrinkage, durability

## Introduction

Alkali-activated material has a recorded history from 1939; the material is generally referred to as geopolymer after classification by Davidovits in 1979. Significant strides in the material have been achieved by several authors as given in table 1.

In South Africa, CO<sub>2</sub> tax will be implemented from 2015 [1] and as such alternatives to the use of high CO<sub>2</sub> emission material like Portland concrete must be investigated for application in the construction industry.

The production of cement is estimated to attribute 5-8% of total CO<sub>2</sub> emissions worldwide [2]. The reduction of the CO<sub>2</sub> footprint of concrete is considered a priority in the South African construction industry.

Due to the reliance on coal-fired power stations for the majority of electricity in South Africa and the large metal resources available, both pulverized flue ash (PFA), and slag materials are available in large quantities.

<sup>1</sup>Corresponding author: [cyril.attwell@murrob.com](mailto:cyril.attwell@murrob.com)

The efficient use of this by-product/waste can assist in economic growth by decreasing the material costs of construction and increasing the durability of the structures built. These efficiencies can be complimented further by better utilization of non-virgin aggregates. These non-virgin aggregate such as slag and bottom ash are generally not used as concrete aggregates due to their density and vesicular nature.

**Table 1.** Bibliographic History of some important events about alkali-activated cements [3]

Author	Year	Significance
Feret	1939	Slags used for cement.
Purdon	1940	Alkali-slag combinations.
Glukhovskiy	1959	Theoretical basis and development of alkaline cements.
Glukhovskiy	1965	First called "alkaline cements".
Davidovits	1979	"Geopolymer" term.
Malinowski	1979	Ancient aqueducts characterized.
Forss	1983	F-cement (slag-alkali-superplasticizer).
Langton and Roy	1984	Ancient building materials characterized.
Davidovits and Sawyer	1985	Patent of "Pyrament" cement.
Krivenko	1986	DSc thesis, $R_2O-RO-SiO_2-H_2O$ .
Malolepsy and Petri	1986	Activation of synthetic melilite slags.
Malek et al.	1986	Slag cement-low level radioactive wastes forms.
Davidovits	1987	Ancient and modern concretes compared.
Deja and Malolepsy	1989	Resistance to chlorides shown.
Kaushal et al.	1989	Adiabatic cured nuclear wastes forms from alkaline mixtures.
Roy and Langton	1989	Ancient concretes analogs.
Majundar et al.	1989	$C_{12}A_7$ -slag activation.
Talling and Brandstetr	1989	Alkali-activated slag.
Wu et al.	1990	Activation of slag cement.
Roy et al.	1991	Rapid setting alkali-activated cements.
Roy and Silsbee	1992	Alkali-activated cements: an overview.
Palomo and Glasser	1992	CBC with metakaolin.
Roy and Malek	1993	Slag cement.
Glukhovskiy	1994	Ancient, modern and future concretes.
Krivenko	1994	Alkaline cements.
Wang and Scivener	1995	Slag and alkali-activated microstructure.
Shi	1996	Strength, pore structure and permeability of alkali-activated slag.
Fernández-Jiménez and Puertas	1997	Kinetic studies of alkali-activated slag cements.
Katz	1998	Microstructure of alkali-activated fly ash.
Davidovits	1999	Chemistry of geopolymeric systems, technology.
Roy	1999	Opportunities and challenges of alkali-activated cements.
Palomo	1999	Alkali-activated fly ash – a cement for the future.
Gong and Yang	2000	Alkali-activated red mud-slag cement.
Puertas	2000	Alkali-activated fly ash/slag cement.
Bakharev	2001–2002	Alkali-activated slag concrete.
Palomo and Palacios	2003	Immobilization of hazardous wastes.
Grutzeck	2004	Zeolite formation.
Sun	2006	Sialite technology.
Duxson	2007	Geopolymer technology: the current state of the art.
Hajimohammadi, Provis and Deventer	2008	One-part geopolymer.
Provis and Deventer	2009	Geopolymers: structure, processing, properties and industrial applications.

In this work, investigations into the standard methodology of alkali-activation through the use of excessive sodium silicate (water-glass), and sodium hydroxide resulted in a material that set rapidly with significant shrinkage which would be economically and structurally unfeasible. Through the evaluation of the crystallography of the PFA and slag monomers and polymers which tend to trap water molecules in the polycondensation phase, a different approach to the design process was adopted and implemented initially for laboratory testing. After successful trials in the laboratory, a site application was recommended for further data analysis regarding the implementation of the material as an alternative to Portland concrete. The standard plastic and hardened properties of the material required verification on site.

The elements chosen for the application were 450 mm thick surface beds without reinforcement, these elements were purposely chosen due to the ease of access when the container terminal would be operational in case any of the alkali-activated material would fail prematurely and need to be replaced. Compressive strengths of 40MPa and flexural strengths of 3.5MPa were required by the project specification.

Site testing was done to ensure that the alkali-activated concrete achieves a workability which allows the material to be placed with ease within a certain time period (3hours).

The plastic and drying shrinkage properties of the concrete were evaluated by eliminating all environmental protection and the concrete was air-cured with no curing membrane or moisture curing.

Further concrete specimen testing was conducted by a SANAS-accredited laboratory to evaluate the shrinkage based on of SANS 6085.

Durability testing was conducted on cores that were taken from the finished slab in areas of any cracks or surface weakness visible.

## **1. Theory**

The theory of alkali-activation is not new and has being reviewed and utilized in concrete from 1960 in USSR [4] and several other spheres of influence, i.e. medical technology is currently utilizing alkali-activation in research of IRR (insulin receptor-related receptor ) [5]. However, little work has being conducted in studying the optimal balance of alkali-activator and by-products/wastes in the formation of a thermal and volumetric stable binder that is economically feasible and safe to use.

Shrinkage values in excess of the standard 0.06% of Portland cement concretes are often attained which inhibits the use of geopolymeric materials in structural and most non-structural applications. The effect of accelerating the natural carbonation that occurs on the surface of the material was also reviewed on a larger scale to attempt to inhibit the shrinkage to a value below 0.06%.

## **2. Experimental methods**

The following tests were conducted on the alkali-activated material on site at the City Deep Container Terminal;

- Initial drying shrinkage and wetting expansion of concrete – SANS 6085:2006
- Testing of Hardened Concrete – for compressive strength – SANS 5863
- Testing of Hardened Concrete – for flexural strength – SANS 5864
- Drilling, preparation and testing of cores – SANS 5865
- Concrete durability – SANS 3001-CO3

The following methods were adhered to;

- Sampling of freshly mixed concrete – SANS 5861-2
- Consistence of freshly mixed concrete, slump test – SANS 5862-1
- Consistence of freshly mixed concrete, flow test – SANS 5862-2
- Making and curing of test specimen – SANS5861-3. It may be noted that due to the experiment related to the carbonation, additional test specimens were cured in ambient conditions of 22-25°C with humidity below 45%.

### 3. Results

A total of 32 laboratory trials done using the aggregate available at site were compiled. Some of the results are summarized below;

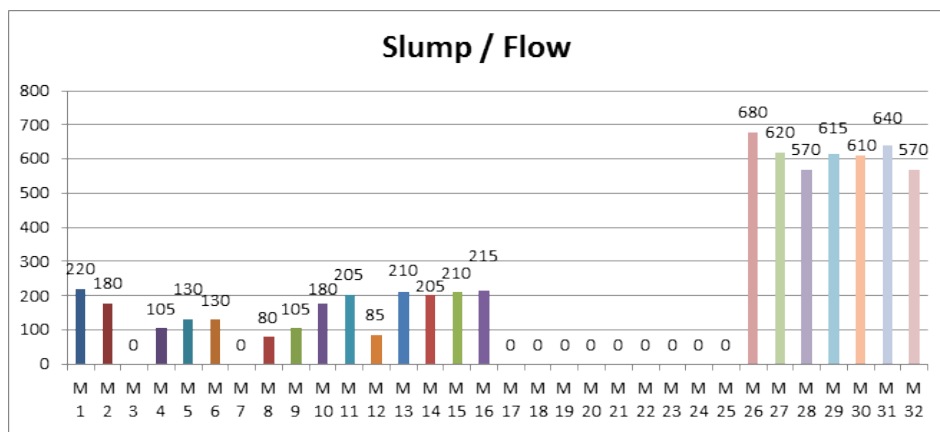


Figure 1. A slump/flow graph of the workability achieved in the laboratory trials, SANS 5862-1 &-2.

As can be seen by the above graph, several of the mixes achieved a flash set or no workability. The choice of which design to apply on site was based on several criteria, notably:-

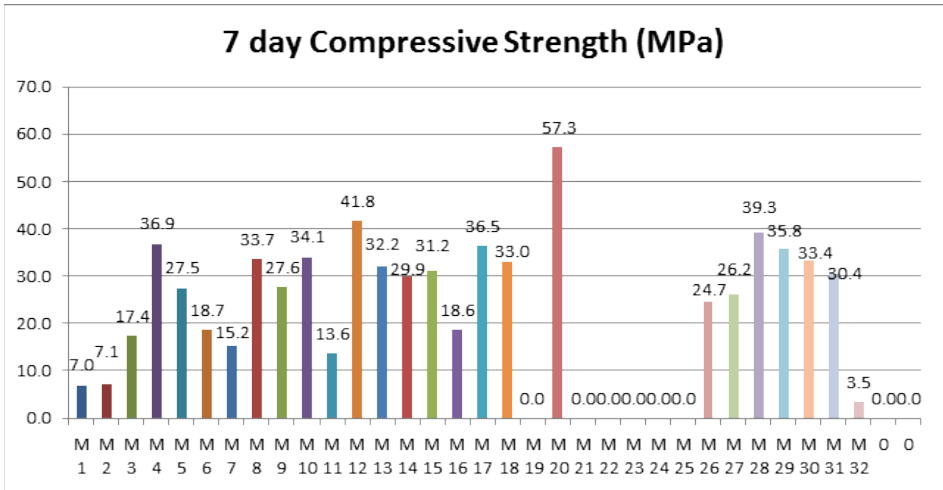
- Compressive strength: 40 MPa minimum at 28 days
- Workability: 150 mm slump minimum
- Workability retention: 2 hours in excess of 75 mm slump
- Costs: Similar or reduced material costs

Seven of the above concrete mix designs represented in figures 1-3 complied with the above parameters, six of the concrete mix designs, (M26-M31), were based on the most feasible original design, (M10).

The six filtered concrete mix designs did not optimize the original M10 any further when taking all the parameters into consideration and as such design M10 was chosen as the concrete mix design to apply to site.

**Table 2.** Geopolymer concrete mix design (M10), finally used at the City Deep Container Terminal.

City Deep - Container Depot - Geopolymer Mix 10								
M 10	22mm Stone	Crusher Sand	Filler Sand	PFA (Lethabo)	GGBS (Slagment)	Water	Polymer	Catalyst
Kg / Mix	925	480	185	240	360	200	20	20
							slump / flow	180
Strength	24 Hrs	3 Days	7 days	14 days	21 days	28 days	56 days	84 days
Mpa	1.7	18.4	34.1	39.4	42.1	44.7	0.0	0.0



**Figure 2.** Compressive strength summary achieved at 7 days in the laboratory trials.

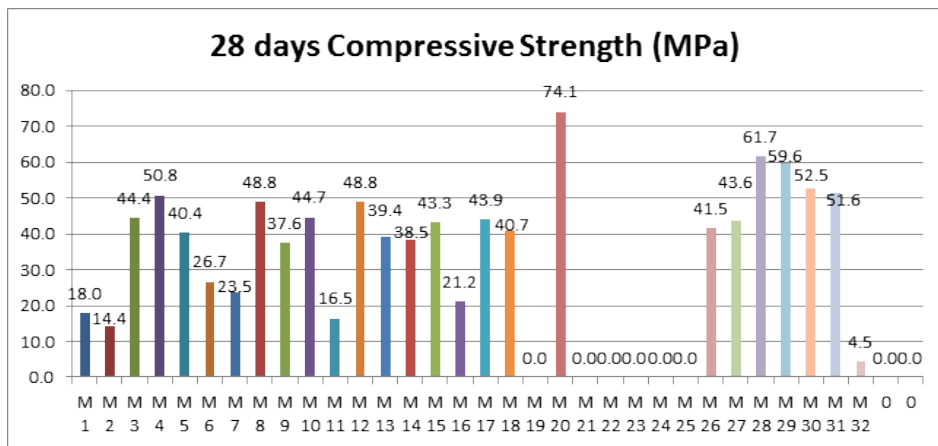


Figure 3. Compressive strength summary achieved at 28 days in the laboratory trials.



Photo 1. Application of Geopolymer concrete on site at Transnet’s City Deep Container Terminal.

Initial temperature and the time taken for the material to achieve ambient temperatures were measured in addition to the normal criteria to understand the consequences of batching varying volumes. As such the 1<sup>st</sup>, 2<sup>nd</sup>, and 3<sup>rd</sup> ready-mix trucks were batched with 2m<sup>3</sup>, 4m<sup>3</sup> and 6m<sup>3</sup> respectively. The 4<sup>th</sup> batch was the required final of 3m<sup>3</sup>.



**Table 3.** Summary of plastic properties achieved on site at the City Deep Container Terminal.

Truck no.	Volume of material (m <sup>3</sup> )	Workability (mm)	Initial Temperature (°C)	Time to Ambient (min)
1	2	165	31.4	38
2	4	180	32.6	43
3	6	190	33.7	46
4	3	185	32.3	42

**Photo 2.** Geopolymer concrete on site at the City Deep Container Terminal after 3 days

The hardened properties were tested by 3 different laboratories;

- The site laboratory – SANS 5863
- Afrisam laboratory – SANS 5865 & SANS 3001-CO3
- SANAS-accredited independent laboratory – SANS 6085 & SANS 5864

**Table 4.** Summary of hardened properties achieved on site at the City Deep Container Terminal

Tests	Results	Parameters
Compressive Strength (MPa)	51.0	40 minimum
Flexural Strength (MPa)	4.2	3.5 minimum
Shrinkage (%) SANS 6085	0.028	0.045 maximum
Shrinkage (%) reduced humidity, (45%) SANS 6085	0.022	0.045 maximum
Oxygen Permeability Index	9.7	9.4 minimum
Chloride conductivity	0.43	2.5 maximum

Additional test specimen were taken and cured at lower humidity, (below 45%) and tested further as per SANS 6085.



**Photo 3.** Alkali-activated concrete test specimen from site tested for shrinkage.

#### 4. Analysis

Both the plastic and hardened properties of the geopolymeric material complied with the required project and SANS specifications and had conformed to all the SANS test procedures listed in the experimental methods.

Marginal increases in the initial temperature were measured on site as was discussed; however, all batches of material achieved ambient temperature within an hour, confirming the minimal effect of mass on temperature.

The carbonation film-forming occurred between 15-20 minutes after casting and prevented plastic shrinkage cracks from occurring. In addition, this protective layer increased the estimated workability retention established in the laboratory. Due to the strength of the carbonation layer, the concrete placement team could walk on top of the material within approximately 15 minutes after casting without penetrating the surface. When reconsolidated through poker vibrators, the protective layer was broken and the fluid material beneath was easily reconstituted with the fresher material above without any type of layered differences. This was verified on the cores drilled for the durability testing.

The low heat in mass indicates a benefit of using the geopolymeric material in comparison to higher hydration heats experienced in Portland concrete. The shrinkage results were approximately 40 to 50% of the shrinkage generally achieved in good concrete. The percentage ratio of flexural strength to compressive strength was 8.2% was achieved on site. This proportion is comparable to that of Portland concrete.

Compressive strengths at 7 days were approximately 75% of 28 day strengths, similar to the ratio achieved in the laboratory. Durability results show an inclination of high resistance to chemical attack, with service life expected to be in excess of 50 years.

## 5. Conclusions

Some of the benefits of using alkali-activated by-products/wastes are;

- Lower heat of mass
- Limited plastic shrinkage due to the protective carbonation layer
- Air curing of the material
- Low potential drying shrinkage
- High chemical resistance
- Lower labour costs due to protective carbonation layer
- Low material costs
- Lower CO<sub>2</sub> footprint in comparison to Portland concrete

The benefits of using alkali-activated by-products/wastes are numerous and the material is similar or superior to Portland concrete on several technical aspects.

### Suggestions for further research

Further research should be continued to understand the reaction kinetics of the protective carbonation layer and its limitations, i.e. underwater concreting.

An additional aspect that must be tested is the creep of this material. It may be possible through the addition of other chemicals to enhance the flexural strength to compressive strength ratio by changing the resultant crystallography of the geopolymer.

### References

- [1] Carbon Tax Policy Paper, Reducing greenhouse gas emissions and facilitating the transition to a green economy, *Department of National treasury*, (May 2013)
- [2] The effect of activator concentration on the residual strength of alkali-activated fly ash pastes subjected to thermal load, *Construction and Building Materials*, (2011)
- [3] Alkali-activated Cements: Opportunities and Challenges, *Chem.Concr.Res.*, pgs 249-254, (1999)
- [4] High Strength Slag Alkaline cements, *7<sup>th</sup> International Congress on the Chemistry of Cement*, Glukhovsky (1980)
- [5] Structural Determinants of the Insulin Receptor-related Receptor Activation by Alkali, Deyev, Mitrofanova, Zhevlenov, Radionov, Berchatova, Popova, Serova and Petrenko, (2013)

# Development of geopolymer mortar using palm oil fuel ash-blast furnace slag-fly ash-as binders

Azizul ISLAM, U. Johnson ALENGARAM<sup>1</sup>, Mohd Zamin JUMAAT, and Iftekhair  
Ibnul BASHAR

*Department of Civil Engineering, University of Malaya, Kuala Lumpur, Malaysia*

**Abstract.** Geopolymer mortar can be produced from industrial by products rich in alumina-silicate. This paper presents the development of novel geopolymer mortar developed using palm oil fuel ash (POFA) (waste from palm oil industry), blast furnace slag (BFS) and fly ash (FA) as binders and manufactured sand as conventional sand replacement. A combination of sodium silicate and sodium hydroxide solution was used as alkaline activator of 12 molar. The compressive strength of the geopolymer mortar with POFA:BFS:FA ratios of 100:0:0, 0:100:0, 0:0:100, 50:50:0, 0:50:50, 50:0:50 and sodium silicate to sodium hydroxide solution by mass of 2.5 and 1.0 was investigated on 50 mm cube specimens. Specimens were cured at room temperature and heat curing at 65°C for 24 hours. The compressive strength test result shows that using POFA and BFS as binder maximum cube compressive strength of 56 MPa could be produced.

**Keywords.** Geopolymer, palm oil fuel ash, blast furnace slag, manufactured sand, compressive strength

## Introduction

The depletion of natural sand due to quarrying activities has already caused flooding in many parts of the world; the need for alternative materials to reduce natural sand through the use of recycling of old mortar [1] has also been investigated; however there have been efforts to utilize the manufactured sand (MS), commonly known as M-sand from the waste of crushed granite aggregates. Therefore, CO<sub>2</sub> emission from clinker production amounts to about 0.5 kg/kg. The CO<sub>2</sub> emission per ton of cement depends on the ratio of clinker to cement. This ratio varies normally from 0.5 to 0.95 [2].

The utilization of industrial by-products such as fly ash (FA), silica fume, blast furnace slag (BFS), rice husk ash etc., as the cement replacement or as the additional cementitious materials has had a constructive effect in minimizing greenhouse gas emissions. The term “geopolymer” was first applied by Davidovits in 1979 [3]. Geopolymer concrete is well-suited to manufacture precast concrete products that can be used in infrastructure developments [4] and structural application as well [5].

---

<sup>1</sup> Corresponding author: Faculty of Engineering, University of Malaya, 50603 Kuala Lumpur, Tel. +6 03 7967 7632, Fax. +6 03 7967 5318, E-mail address: [johnson@um.edu.my](mailto:johnson@um.edu.my)

FA has pozzolanic properties which mainly consists of reactive silicon dioxide ( $\text{SiO}_2$ ) and aluminium oxide ( $\text{Al}_2\text{O}_3$ ). It can be obtained by electrostatic or mechanical precipitation of dust-like particles from the flue gases of power station furnaces fired with pulverized bituminous or other hard coal [6]. The government of Malaysia decided that by 2010 the share of coal in the fuel mix for electricity generation would rise to about 40% [7]. Bakharev et al. [8] reported that alkali-activated slag concrete had lower resistance to carbonation and alkali-aggregate than that of OPC concrete of similar grade. Another locally abundant waste material from palm oil industry is palm oil fuel ash (POFA), which is about 5% of solid waste product, have the potentiality to be used as pozzolanic materials in concrete industry [9].

Quarrying of natural sand has a great irreversible environment impact [10] as it causes reduction in the ground water that affects the moisture content of the soil. Sand mining causes erosion of nearby land leading to instability in the ecosystem [11]. During the year 2010, Malaysia consumed 2.76 billion metric tons of natural aggregate of this amount 1.17 billion metric tons or 42.4%, was sand [11]. In many regions of the world, the extraction of sand and gravel is heavily taxed or banned completely to try to preserve remaining deposits [12].

The main objective of this research was to investigate the development of the compressive strength of geopolymer mortar using four locally available waste materials such as FA, POFA and BFS as binders and M-sand as fine aggregate.

## 1. Experimental program

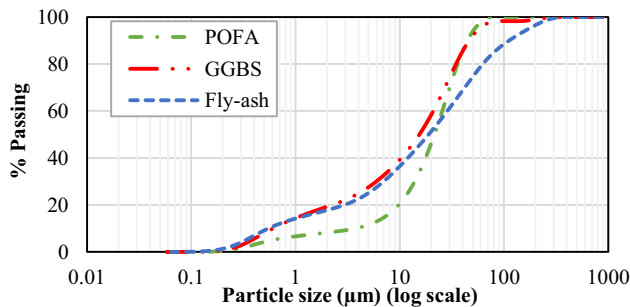
### 1.1. Materials

#### 1.1.1. Blast furnace slag

Blast furnace slag (BFS) or ground granulated blast furnace slag (GGBS) was obtained from YTL Cement Marketing Sdn Bhd, Malaysia. The specific gravity of BFS was  $2.89 \text{ g/cm}^3$ . The chemical composition of BFS is shown in Table 1.

**Table 1.** Chemical composition (wt %) of the raw materials, X-ray Fluorescence (XRF) analysis

Chemical	CaO	SiO <sub>2</sub>	Al <sub>2</sub> O <sub>3</sub>	MgO	Na <sub>2</sub> O	SO <sub>3</sub>	P <sub>2</sub> O <sub>5</sub>	K <sub>2</sub> O	TiO <sub>2</sub>	MnO	Fe <sub>2</sub> O <sub>3</sub>	SrO	Cl	CuO	LOI
GGBS	45.83	32.52	13.71	3.27	0.25	1.80	0.04	0.48	0.73	0.35	0.76	0.08	0.02	-	0.60
FA	5.31	54.72	27.28	1.10	0.43	1.01	1.12	1.00	1.82	0.10	5.15	0.36	0.01	0.01	6.80
POFA	4.34	63.41	5.55	3.74	0.16	0.91	3.78	6.33	0.33	0.17	4.19	0.02	0.45	6.54	6.20



**Figure 1.** Particle size distribution of BFS, POFA and Fly ash

1.1.2. Palm oil fuel ash

Palm oil fuel ash (POFA) collected from factory was then dried in an oven for at least 24 hours at 100 °C to remove the moisture and then it was sieved through 300 μm sieve. ASTM: C618-12a [13] stipulates that the mass of fly ash and natural pozzolan passing through 45-μm by wet sieving shall be at least 66% and POFA exceeded this target as 88% passed through the sieve. Its particle size distribution and chemical composition are shown in Figure 1 and Table 1, respectively.

1.1.3. Fly ash

Fly ash (FA) was obtained from Lafarge Malayan Cement Bhd, Malaysia. According to ASTM C 618, FA is divided into two distinct categories i.e., low-calcium FA (Class F, CaO<10%) and high-calcium FA (Class C, CaO>10%) [13].

1.1.4. Manufactured-sand

Generally, the quarry dust (QD) obtained during the crushing of granite aggregate is considered waste and sometime used in land filling. Thus, the QD is processed through centrifuge action to smoothen the angular edges and the resulting particles are rounded and it is used to replace for natural sand (Figure 2). The processed QD is christened as manufactured sand (MS) and widely used in Singapore, India and some other countries to replace conventional sand. The MS has a wide range of particles as shown in the distribution curve (-sand production and collection Figure 3).

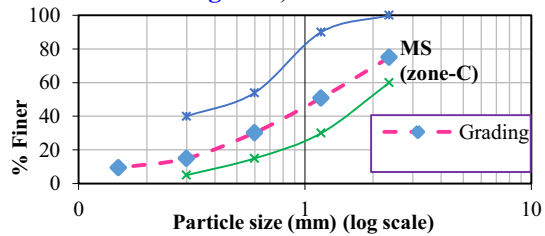


Figure 2. M-sand production and collection Figure 3. Particle size distribution of M-sand (BS 882:1992)

From the particle-size distribution curve shown in -sand production and collection Figure 3,

$$D_{10} = 0.17 \text{ mm}; D_{60} = 1.60 \text{ mm}; D_{30} = 0.60 \text{ mm}; Cu = (D_{60} / D_{10}) = 9.41$$

$$Cc = (D_{30})^2 / (D_{10} \times D_{60}) = 1.32 \tag{1}$$

It is observed that *Cu* (uniformity co-efficient) is greater than 6 and *Cc* (co-efficient of gradation) is between 1 and 3. Hence, the MS is well graded and it is under zone-C [BS 882:1992].

1.2. Specimen preparation and curing

1.2.1. Activator solution and preparation of mortar

The alkaline activator used was from the combination of sodium silicate and sodium hydroxide solution. The activator from the sodium silicate solution (Na<sub>2</sub>O=12%, SiO<sub>2</sub>=30%, and water = 57% by mass) and sodium hydroxide (NaOH) in flakes or pellets form with 99% purity was prepared according to the reference [14]. The

concentration of the sodium hydroxide solution used was 12 molarity (M) and the mixture contained additional water. A total 6 mixtures were prepared by varying the POFA, FA and GGBS contents. The sand and activators contents were kept constant to investigate the effect of the binders. The proportion of binder to sand ratio was 1: 4. The mixture proportions and experimental parameters for mortar are given in Table 2 and Table 3, respectively.

**Table 2.** Mixture proportion (kg/m<sup>3</sup>)

Mix	Binding raw materials					
	GGBS <sup>a</sup>		POFA <sup>b</sup>		FA <sup>c</sup>	
	(%)	Weight (kg/m <sup>3</sup> )	(%)	Weight (kg/m <sup>3</sup> )	(%)	Weight (kg/m <sup>3</sup> )
M1	100	460	0	0	0	0
M2	0	0	100	460	0	0
M3	0	0	0	0	100	460
M4	50	230	50	230	0	0
M5	0	0	50	230	50	230
M6	50	230	0	0	50	230

<sup>a</sup> Ground granulated blast furnace slag; <sup>b</sup> Palm oil fuel ash; <sup>c</sup> Class F fly ash

**Table 3.** Experimental parameters

Binder : M-sand	Binder	M-sand	Activators (1 : 2.5)		Added water	s/b	w/b	Curing Temp. (°C)
			NaOH solution	Na <sub>2</sub> SiO <sub>3</sub>				
			(kg/m <sup>3</sup> )					
1:4	460	1840	53	131	184	0.4	0.4	65° C

s/b: solution to binder weight ratio, w/b: water to binder weight ratio

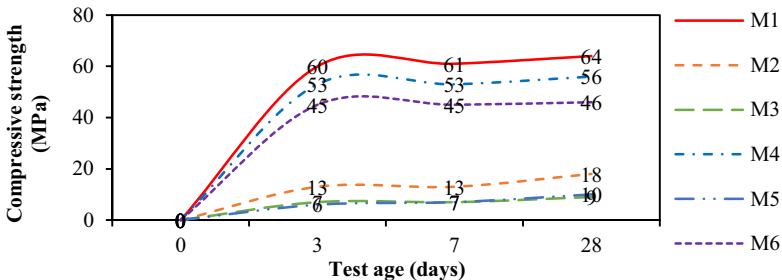
### 1.2.2. Curing

Immediately after casting, the test specimens were covered with plastic film to minimise the water evaporation during curing at an elevated temperature. The test specimens were cured in an oven at 65°C for 24-h. After the curing period, the test specimens were left in the moulds for at least six hours and demoulded.

## 2. Results and discussion

### 2.1. Development of compressive strength

The development of compressive strength at the age of 3-, 7- and 28-day are shown in Figure 4. It can be observed from Figure 4 that the mixture M3 that contains 100% FA and cured at 65 °C for 24-h produced the lowest compressive strength.

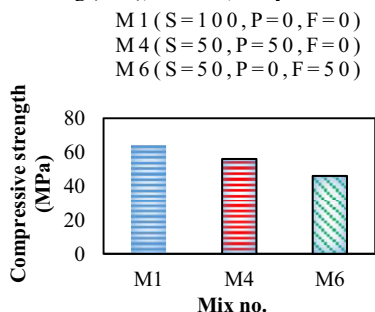


**Figure 4.** Development of compressive strength of mortar with varying binder content ratio

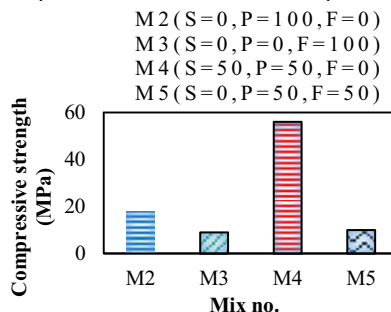
## 2.2. Effect of activator and BFS on the compressive strength of the mortar

The blast furnace slag (BFS) employed is a latent hydraulic product, which can be activated by suitable activators. Without an activation, the development of the strength of the BFS is extremely slow and the development of the slag necessitates a  $\text{pH} \geq 12$  [15]. BFS plays an important role in the development of the compressive strength (Figure 5).

Legend: S-Slag (BFS), P-POFA, F-Fly ash and mix compositions are shown in bracket in percentage (%)



**Figure 5.** The effect of BFS on the compressive strength of mortar.



**Figure 6.** The effect of POFA on the compressive strength of mortar

## 2.3. Effect of POFA on the compressive strength of the mortar

Figure 6 shows the effect of POFA content on the compressive strength at the age of 28-day. The compressive strengths of the mixes M2 and M3 that contain 100% POFA and 100% FA, respectively shows that the later produced about 50% lower compressive strength than the mix M2. Safiuddin et al. [16] reported that a POFA content higher than 40% may adversely affect the properties and durability of concrete which was reflected in the geopolymer mortar as well.

## 2.4. Analysis of chemical composition

The mix M3 achieved the lowest strength. The ratios of  $\text{SiO}_2/\text{Al}_2\text{O}_3$  and  $\text{CaO}/\text{Al}_2\text{O}_3$  for M1 and M3 are 2.37, 3.34 and 2.01, 0.19, respectively. The lowest compressive strength of mix M3 that contains 100% FA might be attributed to the lowest  $\text{SiO}_2/\text{Al}_2\text{O}_3$  and  $\text{CaO}/\text{Al}_2\text{O}_3$  ratios of 2.01 and 0.19, respectively as seen from Table 4.

**Table 4.**  $\text{SiO}_2/\text{Al}_2\text{O}_3$  and  $\text{CaO}/\text{Al}_2\text{O}_3$  ratios for the mixes

Mix No.	M1	M2	M3	M4	M5	M6
$\text{SiO}_2/\text{Al}_2\text{O}_3$	2.37	11.43	2.01	4.98	3.60	2.13
$\text{CaO}/\text{Al}_2\text{O}_3$	3.34	0.78	0.19	2.60	0.29	1.25

## 3. Conclusions

The following conclusions can be drawn from this experimental study:

- The compressive strength of geopolymer mortar increases as the BFS content increases.



- The addition of POFA by 50% with BFS achieved in compressive strength of about 56 MPa.
- It was found from the study that the POFA could be the ideal substitute pozzolanic material of fly ash since the 28-d compressive strength of the mix prepared using POFA was found about 50% higher compared to the mix prepared with FA.

The results are valid for the materials used with the stated chemical and physical properties. It is noticed that the behaviour of POFA is varying to the sources and manufacturing process, e.g. burning procedures and temperature, particle sizes and shapes etc.

### Acknowledgement

The authors are grateful to University of Malaya for the financial support through the Research Project “UM.C/625/1/HIR/206: *Synthesis of Energy Redeemable Material from Local Wastes for Buildings*”.

### References

- [1] Kou S-C, Poon C-S. Effects of different kinds of recycled fine aggregate on properties of rendering mortar. *Journal of Sustainable Cement-Based Materials*, UK 2 (2013), 43-57.
- [2] Ernst Worrell, Lynn Price, Nathan Martin, Chris Hendriks, Leticia Ozawa Meida. Carbon dioxide Emissions from the Global Cement Industry. *Annu. Rev. Energy Environ.*, US: Lawrence Berkeley National Laboratory, Berkeley, California 94720; 2001. p. 303-29.
- [3] Davidovits J. 30 Years of successes and failures in geopolymer applications. Market trends and potential breakthroughs. *Geopolymer 2002 conference*. Melbourne, Australia 2002.
- [4] Lloyd N, Rangan BV. Geopolymer Concrete with Fly Ash. In: Zachar JaC, P. and Naik, T. and Ganjian, G., editor. *Second International Conference on Sustainable Construction Materials and Technologies*. Ancona, Italy: UWM Center for By-Products Utilization; 2010. p. 1493-504.
- [5] Aldred J, Day J. Is geopolymer concrete a suitable alternative to traditional concrete? *37th Conference on our world in concrete & structures*, Singapore 2012. p. 29-31.
- [6] BS 3892 : Part 1. Pulverized-fuel ash. Specification for pulverized-fuel ash for use with Portland cement. London, UK: BSI; 1997.
- [7] Kupaei RH, Alengaram UJ, Jumaat MZ, Nikraz H. Mix design for fly ash based oil palm shell geopolymer lightweight concrete. *Construction and Building Materials* 43 (2013), 490-6.
- [8] Bakharev T, Sanjayan JG, Cheng YB. Resistance of alkali-activated slag concrete to alkali-aggregate reaction. *Cement and Concrete Research* 31 (2001), 331-4.
- [9] Sata V, Jaturapitakkul C, Rattanashotinunt C. Compressive strength and heat evolution of concretes containing palm oil fuel ash. *Journal of Materials in Civil Engineering @ ASCE, USA* 22 (2010), 1033-8.
- [10] Andrew Short, William Kinniburgh. *Lightweight concrete*. 3 ed. UK: Applied Science Publishers; 1978.
- [11] Ashraf MA, Maah MJ, Yusoff I, Wajid A, Mahmood K. Sand mining effects, causes and concerns: a case study from Bestari Jaya, Selangor, Peninsular Malaysia. *Scientific Research and Essays* 6 (2011), 1216-31.
- [12] Sreenivasa G. Use of manufactured sand in concrete and construction an alternate to river sand. NBMCW, India 2012.
- [13] ASTM C 618. Standard Specification for Coal Fly Ash and Raw or Calcined Natural Pozzolan for Use as a Mineral Admixture in Concrete. Philadelphia, USA: ASTM International; 2008.
- [14] Wallah SE, Rangan BV. Low-Calcium Fly Ash-Based Geopolymer Concrete: Long-Term Properties. Perth, Australia: Curtin University of Technology; 2006.
- [15] Davidovits J. *Geopolymer chemistry and applications*. 3 ed. France: Geopolymer Institute; 2011.
- [16] Safiuddin M, Abdus Salam M, Jumaat MZ. Utilization of palm oil fuel ash in concrete: a review. *Journal of Civil Engineering and Management, UK* 17 (2011), 234-47.

# The development of sustainable geopolymer mortar from fly ash-palm oil fuel ash based binder and manufactured sand

Iftekhair Ibnul BASHAR, Ubagaram Johnson ALENGARAM<sup>1</sup>, Mohd Zamin JUMAAT and Azizul ISLAM

*Department of Civil Engineering, University of Malaya, Kuala Lumpur, Malaysia*

**Abstract.** The use of alternative binder from industrial waste product, namely palm oil fuel ash (POFA) to replace conventional fly ash (FA) and the effect on the use of processed quarry waste, alternatively known as manufactured sand (M-sand) as fine aggregate replacement for conventional mining sand (N-sand) in the development of compressive strength of POFA-FA based geopolymer mortar is investigated. The variable investigated includes the quantities of replacement levels of M-sand with N-sand. The alkaline solution, water, POFA/FA ratio and curing condition remained constant. The results show that the silica rich POFA and FA increased the rate of strength development of the mortar and an average of 76% of the 28-day compressive strength was found at the age of 3-day. Based on the compressive strength, it can be seen that the use of alternative addition of 100% M-sand shows that comparable strength as that of mortar prepared with mixes of 100% N-sand. The particle size of fine aggregates play significant role in the strength development due to the filling and packing ability. The use of industrial waste materials such as POFA-FA and M-sand as binders and fine aggregate, respectively could be viable alternative to conventional concrete that could lead to sustainable geopolymer material.

**Keywords.** Palm oil fuel ash, fly ash, geopolymer mortar, mining sand, manufactured sand, quarry dust, compressive strength

## Introduction

Millions of tons of industrial wastes are generated every year and these wastes cause environmental issue due to shortage of storage facility; this subsequently leads to land and water pollution in the vicinity of factories. The quarry industries produce millions of tons of wastes in the form of quarry dust (QD); it is produced as waste after crushing granite for the use of coarse aggregates. About 25% QD is produced from the coarse aggregate production by stone crusher [1]. These wastes are dumped in the factory yards and hence reuse of QD might help in reducing the overuse of mining and quarrying. The end product by removing flaky and sharp edges of QD is known as manufactured sand (M-sand). The use of M-sand and QD is in the right direction to achieve sustainable material.

---

<sup>1</sup>Corresponding author: Faculty of Engineering, University of Malaya 50603, Kuala Lumpur, Malaysia; Email: [johnson@um.edu.my](mailto:johnson@um.edu.my)



**Figure 1.** (a) M-sand, (b) QD, (c) POFA and (d) FA.

Besides the depletion of natural resources, another environmental problem is the Greenhouse effect. One of the main reasons for the greenhouse effect is the emission of carbon dioxide ( $\text{CO}_2$ ) from the ordinary Portland cement (OPC) based concrete production. The development of cement less concrete is a big challenge to the researchers now-a-day. Davidovits, J. [2] is the pioneer in introducing geopolymer concrete which emits no  $\text{CO}_2$ . Silica and Alumina are the main compounds to activate the geopolymerization process. The raw materials consisting Silica and Alumina are known as pozzolanic material. Rukzon, S. and Chindapasirt, P. [3] reported that palm oil fuel ash (POFA), fly ash (FA) and rice husk ash (RHA) have a potentiality to be pozzolanic material. Since about 85% of world's palm oil is being produced in Indonesia and Malaysia [4], the development of green concrete using these two industrial by-products could enhance the use of the local waste material to develop sustainable material.

The POFA-FA based geopolymer mortar was developed and the effect of M-sand has been analyzed in this article in comparison with N-sand and QD.

## 1. Materials and methods

### 1.1. Properties of POFA, FA, N-sand, M-sand and QD

X-ray fluorescence (XRF) analysis (Table 1) shows that the percentages of  $\text{SiO}_2$ ,  $\text{Al}_2\text{O}_3$  &  $\text{Fe}_2\text{O}_3$  are 76.14 and 87.15 in POFA and FA respectively. According to ASTM C618, pozzolans containing at least 70% of  $\text{SiO}_2$ ,  $\text{Al}_2\text{O}_3$  &  $\text{Fe}_2\text{O}_3$  are categorized as class F. The ratio of POFA to FA used in this investigation was 1:1; therefore,  $\text{SiO}_2:\text{Al}_2\text{O}_3$  in POFA & FA was 3.95:1. The particle size of POFA and FA were below 45 and 110  $\mu\text{m}$  (Figure 2), respectively.

**Table 1.** Chemical composition & physical properties of POFA and FA

	Chemical compounds (%)													Physical properties		
	CaO	$\text{SiO}_2$	$\text{Al}_2\text{O}_3$	MgO	$\text{Na}_2\text{O}$	$\text{SO}_3$	$\text{P}_2\text{O}_5$	$\text{K}_2\text{O}$	$\text{TiO}_2$	$\text{Cr}_2\text{O}_3$	MnO	$\text{Fe}_2\text{O}_3$	Cl	LoI	Color	S.G. (S.S.A)
POFA	5.57	67.72	3.71	4.04	0.16	1.07	4.13	7.67	0.27	-	0.11	4.71	0.65	6.20	Black	2.2 (3.49)
FA	5.31	54.72	27.2	1.10	0.43	1.01	1.12	1.00	1.82	0.04	0.10	5.15	0.01	6.80	Grey	2.4 (1.72)

S.G. = Specific gravity; S.S.A. = Specific surface area,  $\text{m}^2/\text{g}$

**Table 2. Mortar mix design**

Mortar Designation	Variables (kg/m <sup>3</sup> )		
	N-Sand	M-Sand	QD
N100	1029 (100 <sup>a</sup> )		
M100	1029 (100)		
Q100	1029 (100)		
N50-M25-Q25	514 (50)	257 (25)	257 (25)
N25-M50-Q25	257 (25)	514 (50)	257 (25)
N25-M25-Q50	257 (25)	257 (25)	514 (50)
Constants			
Binder : fine aggregate = 1 : 1.5; POFA : FA = 1 : 1;			
Water / binder = 0.2; Alkaline activator / binder = 0.4			
14M NaOH : liquid Na <sub>2</sub> SiO <sub>3</sub> = 2.5			
Modulus of Na <sub>2</sub> SiO <sub>3</sub> = ratio of SiO <sub>2</sub> /Na <sub>2</sub> O = 2.5			
<sup>a</sup> Proportion in percent in bracket ( )			

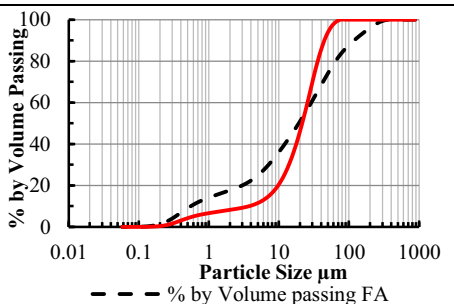


Figure 2. Particle size distribution of POFA&FA

Specific gravity, and absorption of N-sand, M-sand and QD were found in range of 2.61 – 2.79 and 0.81 – 0.92, respectively (Table 3) and according to BS 882-1992 [5], N-sand, M-sand and QD are classified as Grade C based on the particle size distribution (Figure 3).

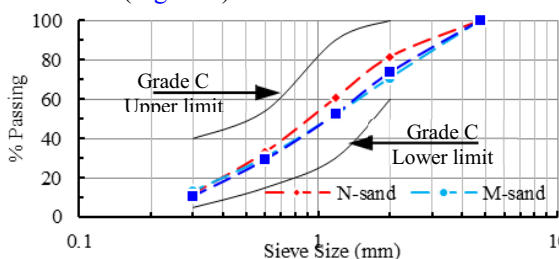


Figure 3. Particle size distribution curve for N-sand, M-sand and QD.

**Table 3. Properties of N-sand, M-sand and QD**

	Fineness Modulus	W.A.	S.G.
N-sand	2.88	0.81	2.79
M-sand	2.66	0.91	2.63
QD	2.67	0.92	2.61

W.A. = water absorption (%)  
 S.G. = Specific gravity in saturated surface dry condition

### 1.2. Mix design, specimen preparation and testing

The mix proportions are shown in Table 2. The alkaline activator using sodium hydroxide (NaOH) and sodium silicate (Na<sub>2</sub>SiO<sub>3</sub>) was prepared 24 hours before the casting. The binder was mixed with the fine aggregates at slow speed (140 ± 5 r/min) in the mixture. The alkaline activator was then added with binder and fine aggregates. The additional water was gradually added to the mixture for good workability. The mortar was cast in the 50- mm cube mold and vibrated. The mortar molds were kept in an oven at 650C for 24 hours. After removal of the molds, the specimens were kept in a room temperature and relative humidity of 280C and 79%, respectively. The compressive strength tests were carried on at the age of 3-, 7-, 14- and 28-day according to ASTM C 109/C 109M-12 [6].

## 2. Results and discussion

### 2.1. Development of compressive strength

The compressive strengths for different mix proportions at the ages of 3-, 7-, 14-, and 28-day are shown in Figure 4. The 28-day compressive strength for the mixes varied between 21 and 28 N/mm<sup>2</sup>. The average 3-day compressive strength of all mixes was found to be 76% of the 28-day strength. The pattern of early age strength development supports the findings reported by previous researchers [2, 7]. The variation of compressive strength may be due to the effect of shape, texture and particle size distribution [8] of N-sand, M-sand and QD since all other ingredients and conditions remain consistent.

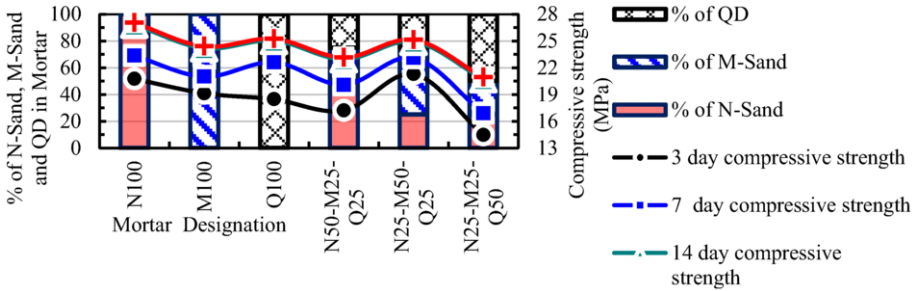


Figure 4. Compressive strengths for different mix design

### 2.2. Role of POFA-FA on the development of compressive strength

The binders, POFA and FA were kept at equal proportion for all the mixes. The silica/alumina ratio and the total contents of silica, alumina and Fe<sub>2</sub>O<sub>3</sub> in the POFA-FA mixture affect the strength development [2] and it was noted as 3.95 and 82%, respectively. The high content of pozzolanic silica and alumina [9] in POFA and FA causes the silica based geopolymerization in presence of alkaline solution. The finer particle and curing in high temperature increase the reactivity in the geopolymerization process [10] As seen from Figure 2, 90% particles of POFA and FA were found below 38.27 and 101.74 μm, respectively. About 76% of 28-day compressive strength was achieved at the age of 3-day due to the larger surface area of fine particles (Figure 6). The filling and packing ability of fine particles also effect on the development of compressive strength. The finer particles decrease the capillary pore effectively [11]. The pores generated due to the angularity and irregular shape of QD particles might be filled by the fine FA and POFA and thus enhanced the compressive strength [12].

### 2.3. Effect of molarity of alkaline activated solution on development of compressive strength

The effect of molarity of alkaline activated solution (NaOH solution) on the 28-day compressive strength is shown in Figure 6. The early age compressive strength at the age of 3-day for the mix with 14 M was found between 55 and 77% of the 28-day strength and this is higher than the corresponding strength of mixes with 12M. It might be due to the rate of geopolymer reaction. The NaOH solution performs the dissolution process and bonding of solid particles in the geopolymeric environment [13]. The use

of high concentration of NaOH solution leads to greater dissolution and increases the geopolymerization reaction [14] by leaching silica and alumina in high rate [15].

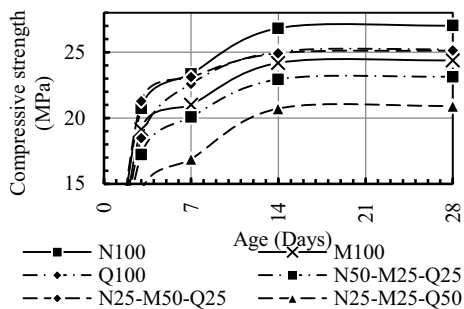


Figure 5. Compressive strength (MPa) vs age (days)

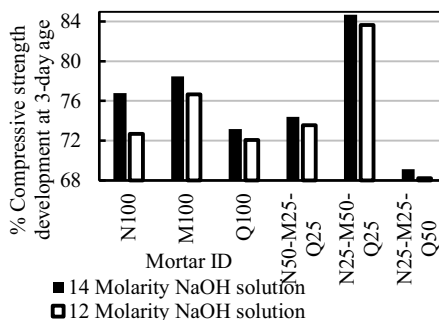


Figure 6. Early-age compressive strength

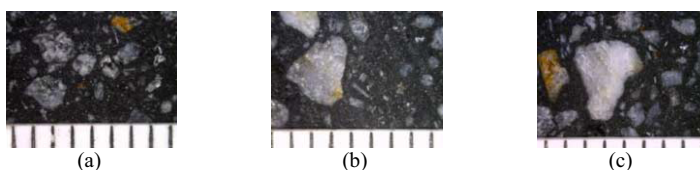


Figure 7. N-sand/ M-sand/ QD interlocking in geopolymer mortar

#### 2.4. Effect of N-sand, M-Sand and QD on development of compressive strength

The compressive strengths at different ages are shown in Figure 5. M100 and Q100 show comparable strength development with N100. N100 contains rounder and smoother particle than M100 and Q100 [8]. Hudson, B.P. [16] reported that rough aggregates have a propensity for increasing water demand for a given workability. Thus, for a given water content, N100 is more workable than M100 and Q100 [8]. The rough surface of M100 demands more water than N100. Since the water and binder content was kept constant in this study M100 absorbs water from the alkali-solution and this might have affected the reactivity of binder in alkali solution and reduces the compressive strength. Q100 shows better strength development than M100, because of the angular particle shape of QD. The angularity of aggregates has a positive effect on the compressive strength [8, 17] and enhances the bond between the matrix and the aggregates due to its surface texture [18]. It was noted that the compressive strength was reduced slightly for the combinations of N-sand, M-sand and QD. The voids due to the semi-rounded, rounded and rough shape may influence in reducing strength by reason of demanding more water for a given workability and as required for better geopolymer reaction. Dumitru, I. et al. [19] also reported the slight reduction of compressive strength in normal concrete due to the usage of M100 and Q100. Since M100 and Q100 develop comparable strength, M100 and Q100 could be viable replacement of conventional N-sand as a sustainable material.

### 3. Conclusions

M-sand and QD are replaceable material with N-sand. The usage of 100% M-sand or QD produces comparable strength as using N-sand. The shape and water demand of

aggregate in mortar effects on the strength development of POFA-FA based geopolymer mortar due to filling and packing ability of POFA and FA. The high concentration of sodium hydroxide solution increases the compressive strength. The mixes with more fine particles require more paste to cover the surface areas; but for the mixes with constant binder content, the influence of the finer particles can't be ignored.

## Acknowledgement

The authors are grateful to University of Malaya for the financial support through the University of Malaya Research Project ER010-2013A: Flexural & Bond Behaviour of Palm Shell Lightweight Geopolymer Concrete.

## References

- [1] Appukutty, P., Murugesan, R. Substitution of quarry dust to sand for mortar in brick masonry works. *International Journal on Design and Manufacturing Technologies*. 2009;3:59-63.
- [2] Davidovits, J. *Geopolymer chemistry & application*. 3rd ed. 16 rue Galilee, F-02100 Saint-Quentin, France: Institute Géopolymère; 2008.
- [3] Rukzon, S., Chindaprasirt, P. Use of disposed waste ash from landfills to replace Portland cement. *Waste Management & Research*. 2009;27:588-94.
- [4] Nagiah, C., Azmi, R. A review of smallholder oil palm production: Challenges and opportunities for enhancing sustainability-A Malaysian perspective. *Journal of Oil Palm & the Environment*. 2012;3:114-20.
- [5] British Standard BS 882. Specification for Aggregates from natural sources for concrete. British Standards Institute; 1992.
- [6] International, A. C 109/C 109M. Standard Test Method for Compressive Strength of Hydraulic Cement Mortars (Using 2-in or [50-mm] Cube Specimens): ASTM International, West Conshohocken, PA, 2003; 1999.
- [7] Lloyd, N., Rangan, V. Geopolymer Concrete-Sustainable Cementless Concrete. *ACI Special Publication*. 2009;261:33-54.
- [8] Quiroga, P.N., Fowler, D.W. The effects of aggregates characteristics on the performance of Portland cement concrete. 1 University Station C1755, Austin, TX 78712-0277: International Centre for Aggregates Research (ICAR), The University of Texas at Austin; 2004.
- [9] Autfef, A., Joussein, E., Gasgnier, G., Rossignol, S. Role of the silica source on the geopolymerization rate: A thermal analysis study. *Journal of Non-Crystalline Solids*. 2013;366:13-21.
- [10] Somna, K., Jaturapitakkul, C., Kajitvichyanukul, P., Chindaprasirt, P. NaOH-activated ground fly ash geopolymer cured at ambient temperature. *Fuel*. 2011;90:2118-24.
- [11] Chindaprasirt, P., Jaturapitakkul, C., Sinsiri, T. Effect of fly ash fineness on microstructure of blended cement paste. *Construction and Building Materials*. 2007;21:1534-41.
- [12] Ashtiani, M.S., Scott, A.N., Dhakal, R.P. Mechanical and fresh properties of high-strength self-compacting concrete containing class C fly ash. *Construction and Building Materials*. 2013;47:1217-24.
- [13] Álvarez-Ayuso, E., Querol, X., Plana, F., Alastuey, A., Moreno, N., Izquierdo, M. et al. Environmental, physical and structural characterisation of geopolymer matrixes synthesised from coal (co-) combustion fly ashes. *Journal of hazardous materials*. 2008;154:175-83.
- [14] Guo, X., Shi, H., Dick, W.A. Compressive strength and microstructural characteristics of class C fly ash geopolymer. *Cement and Concrete Composites*. 2010;32:142-7.
- [15] Chindaprasirt, P., Jaturapitakkul, C., Chalee, W., Rattanasak, U. Comparative study on the characteristics of fly ash and bottom ash geopolymers. *Waste Management*. 2009;29:539-43.
- [16] Hudson, B.P. Concrete workability with high fines content sands. *Quarry*. 1999;7:22-5.
- [17] Kaplan, M. The Flexural and Compressive Strength of Concrete as Affected by the Properties of Coarse Aggregates. National Building Research Institute, Council for Scientific and Industrial Research (CSIR); 1960.
- [18] Galloway, J.E. *Grading, Shape and Surface Properties*: ASTM International; 1994.
- [19] Dumitru, I., Zdrilic, T., Smorchevsky, G. The use of manufactured quarry fines in concrete. Proc 7 th Annual Symposium on Aggregates-Concrete, Bases and Fines, Austin: International Centre for Aggregates Research (ICAR); 1999. p. C1.5.1-12.

# Cementless concrete using ceramic waste powder

Amr S. EL-DIEB<sup>1</sup> and Ehab E. SHEHAB

*Civil and Environmental Engineering Department, United Arab Emirates University*

**Abstract.** Concrete is the main construction material worldwide. The cement production is well known to significantly contribute to the world carbon dioxide emission, around 7% of the global green-house gas produced annually. Worldwide the replacement of cement by supplementary cementing materials has been used as a step to reduce the consumption of cement quantities in concrete mixtures. Geopolymer concrete represents a new alternative in making concrete by utilizing materials mainly composed of silica and alumina which could be alkali-activated to form a CaO-free aluminosilicate binder. Different materials were used in producing geopolymer concrete such as fly ash, metakaolin and slag. The ceramic industry produces significant amount of ceramic waste powder. The ceramic waste powder is characterized by its high percentage of silica (SiO<sub>2</sub>) and alumina (Al<sub>2</sub>O<sub>3</sub>), which is more than 70%. It represents a potential material to be utilized in making geopolymer concrete. In this study, ceramic waste powder was used in a preliminary investigation to produce geopolymer concrete. The study investigated the effect of using sodium hydroxide as alkali activation solution, the pH concentration of the alkali solution (i.e. 8M, 10M, 12M, 14M and 16M) and applying curing temperature of 60°C. Compressive strength, water absorption, electrical resistivity and microstructure of the produced geopolymer were investigated. Preliminary results showed that ceramic waste powder represents a very good potential to be used in producing cementless concrete.

**Keywords.** Ceramic powder, geopolymer, sodium hydroxide activator, compressive strength, water absorption, electrical resistivity, microstructure

## Introduction

Green environment is a challenging concern to accomplish in today's world. This could be achieved through a beneficial recycling procedure that aims at reusing solid waste materials. Concrete industry can play a huge role in sustainable development of the UAE. Production of 1 ton of Portland cement is an energy intensive process and also generates about 1 ton of CO<sub>2</sub> [1,2], which represents about 7% of the global green-house gas produced annually. With Abu Dhabi development plans, there will be an increasing demand on cement and therefore an expected increase in CO<sub>2</sub> emission which will have negative impact on the environment. Usage of substitution materials as partial or complete replacement of cement is considered an efficient solution. Silica fume, fly ash and slag are used as supplementary cementing materials (SCM) in daily concrete production [3]. This step has made its effect on reducing the CO<sub>2</sub> emission.

---

<sup>1</sup>Corresponding author: Civil and Environmental Engineering Department, College of Engineering, United Arab Emirates University, P.O. Box 15551, Al Ain, UAE; E-mail: [amr.eldieb@uaeu.ac.ae](mailto:amr.eldieb@uaeu.ac.ae)



With the current practice which involves the use of SCM in the range of 20% to 50% replacement of OPC, the CO<sub>2</sub> emission from cement production is reduced by around the half [3].

The alkali-activated binders have emerged as an alternative [4-6] sometimes referred to as inorganic-polymer concrete or geopolymer concrete. In geopolymer concrete, cement is completely replaced by alkali activated alumino-silicate materials. This new concrete type started to attract several investigators. The geopolymer concrete utilizes any material composed of silica and aluminum which can be alkali-activated to form a CaO-free alumino-silicate binder. During the last decade increased research was directed to the development of this new material due to the wide range of potential applications [7]. The performed investigations utilized different prime (i.e. source or binder) materials such as metakaoline, blast-furnace slag, fly ashes, mixtures of fly ashes and metakaoline, mixtures of fly ashes and slag [8].

As seen from these investigations, the prime materials used are mainly solid waste byproducts; therefore the geopolymer technology has the potential to reduce the CO<sub>2</sub> emission by about 80% [9]. Ceramic tiles are widely used in structures and other applications. In Abu Dhabi, the ceramic waste powder produced from one company is estimated at 10,000 tons/year. This brings a major challenge with respect to its environmental impact. On the other hand, it represents a good opportunity as an alternative concrete ingredient if it could be utilized in making concrete. In the literature, one study [10] investigated the use of ceramic waste powder in geopolymer concrete; this study will evaluate the feasibility of using ceramic waste powder in making geopolymer concrete.

## 1. Study objectives

The main objective of this preliminary study was to investigate the use of ceramic waste powder in producing geopolymer concrete. The main parameter was the pH value of the sodium hydroxide solution used as the alkali activation, mainly 8M, 10M, 12M, 14M and 16M. Curing temperature of 60°C was applied. The produced geopolymer concrete was evaluated by measuring the compressive strength, water absorption, electrical resistivity and main microstructure characteristics. All tests were conducted at 28-days of age.

## 2. Experimental work

### 2.1. Materials and mixture

The ceramic waste powder was obtained from the polishing process of final ceramic products from a ceramic factory in Abu Dhabi, UAE. The ceramic powder was delivered as wet powder as produced from the factory. The as delivered ceramic powder was dried in an oven at 110°C for 24 hours. The average moisture content was 36% by mass. Due to the process of producing the ceramic waste powder many dried ceramic powder particles coagulated together in several large particles, which could be manually subdivided back into powder particles. Figure 1 shows the dried ceramic powder after being sieved on different sieves. In this study only the ceramic powder which passes the 300 µm sieve was used in order to be sure that no powder particles are

coagulated together. The average percentage of ceramic powder passed the 300  $\mu\text{m}$  was 19%. The compacted and free flow bulk densities were 1228 and 922  $\text{kg/m}^3$  respectively.

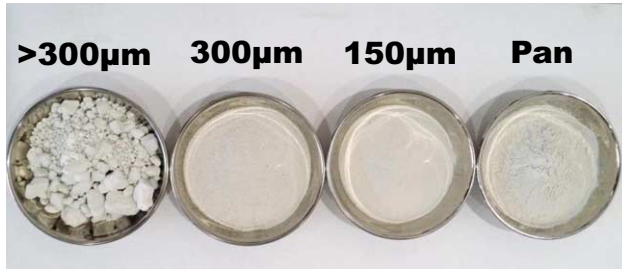


Figure 1. Sieved dried ceramic powder.

Table 1 shows the average chemical analysis and the standard deviation of thirteen samples of the ceramic powder over a period of 45 days. It should be noted that the main composition was  $\text{SiO}_2$  and  $\text{Al}_2\text{O}_3$ . They represent more than 80% by mass. Also, the ceramic powder included very small mass percentages of calcium oxide ( $\text{CaO}$ ), magnesium oxide ( $\text{MgO}$ ), sodium oxide ( $\text{Na}_2\text{O}$ ) and potassium oxide ( $\text{K}_2\text{O}$ ), the average mass percentages are 1.65%, 1.80%, 4.34% and 1.37% respectively. Figure 2 shows scanning electron microscope (SEM) image of the ceramic powder which consists of irregular and angular particles that resembles cement particles in shape. Energy dispersive spectroscopy (EDS) was used to study the chemical composition of the ceramic powder; Figure 3 shows the EDS analysis of two ceramic waste powder samples which confirmed that more than 80% is  $\text{SiO}_2$  and  $\text{Al}_2\text{O}_3$ .

Table 1. Chemical composition of ceramic powder.

Sample	Main Oxides (mass %)							
	LOI*	$\text{SiO}_2$	$\text{Al}_2\text{O}_3$	$\text{Fe}_2\text{O}_3$	$\text{CaO}$	$\text{MgO}$	$\text{Na}_2\text{O}$	$\text{K}_2\text{O}$
Result	1.78	70.79	17.43	0.88	1.10	1.07	4.47	0.98
Standard Deviation	0.26	0.68	0.35	0.40	0.15	0.34	0.52	0.10

\*Loss on Ignition at 1000°C

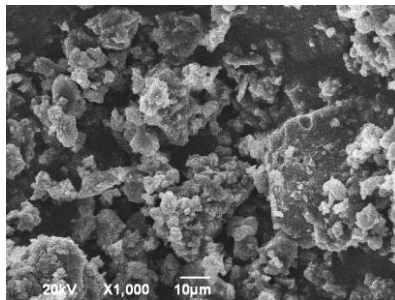


Figure 2. SEM image of used ceramic powder.

Sodium hydroxide (laboratory grade) was used as reagent. The sodium hydroxide solution was prepared 24 hours before being used in the mixture. The sodium hydroxide solutions were prepared at different molarities; 8M, 10M, 12M, 14M and 16M to investigate the effect of solution alkalinity on the produced geopolymer.

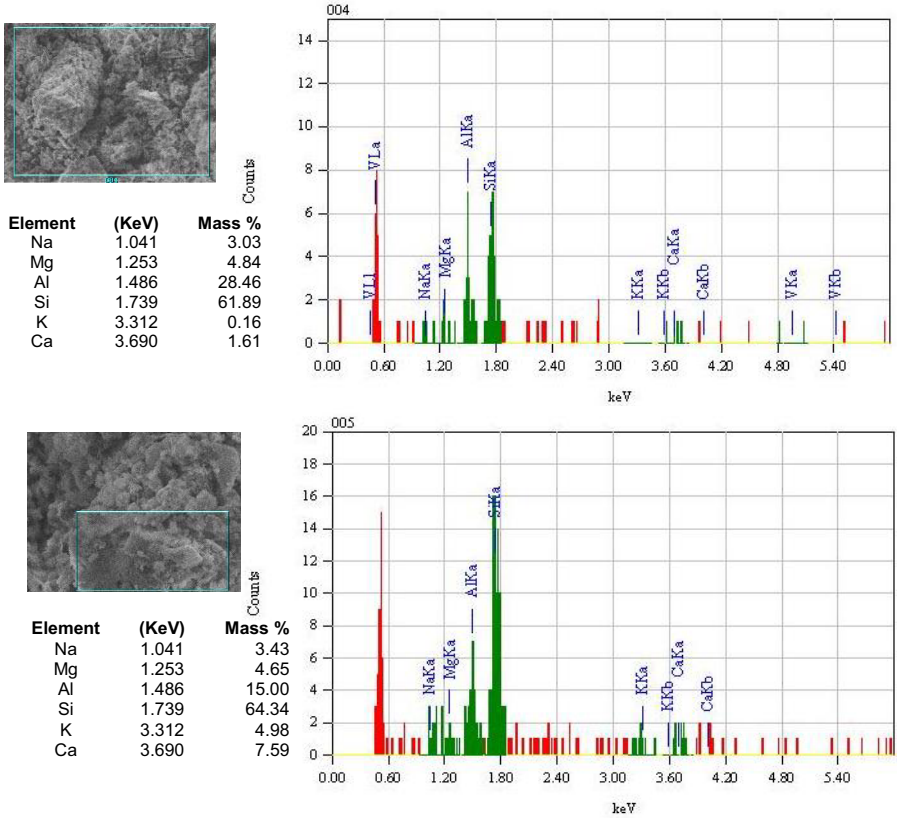


Figure 3. EDS analysis of two ceramic powder samples used in the study.

### 2.2. Geopolymer synthesis and curing

The geopolymer paste was synthesized by mixing ceramic powder with the NaOH activating solutions with a liquid/solid ratio of 0.4. The mixture was mixed for 5 minutes followed by casting the paste in cubic steel molds of 50x50x50 mm and then vibrated for 2 minutes to remove entrained air. The molds were then sealed with polyethylene film and were kept in an oven at a temperature of 60°C and under ambient pressure. After 72 hours the specimens were de-molded and then continued to be cured at the desired temperature until testing date.

### 2.3. Specimens and testing

The compressive strength was measured at 28-days of age using cubic specimens with dimensions 50x50x50 mm. The water absorption and resistivity were used to evaluate the durability. The water absorption and electrical resistivity were measured at 28-days of age using cubic specimens of 50x50x50 mm. The resistivity test was conducted on saturated specimens. All tests were conducted on three replicates and the average values of test results were used in the analysis. A JOEL scanning electron microscope (SEM) was used to study microstructural characteristics of a freshly fractured surface

of the geopolymer. The microstructure investigation was performed at the age of 28-days.

### 3. Results and discussions

#### 3.1. Compressive strength

Figure 4 shows the 28-days compressive strength of the produced ceramic waste powder geopolymer. The geopolymer paste achieved compressive strength of more than 35 MPa, which satisfies the BS-EN 197-1-2000 [14] requirements for CEM I-32.5N. The strength of the geopolymer paste increased from 28 MPa to 38 MPa when the alkalinity of the activation solution increased from 8M to 12M. When the alkalinity increases over 12M the strength decreases.

Similar results were obtained in previous studies on fly ash and ground blast furnace slag geopolymer [11–13]. It was noted that the compressive strength increased as the alkalinity of the NaOH solution increased for up to 10M to 14M and as the alkalinity was increased beyond these values the compressive strength of the fly ash and slag geopolymer decreased. This could be attributed to the fact that the solubility or leaching of silica and alumina ions increases as the alkalinity of the activating solution increases up to certain concentration after which the dissolution decreases. As the silica and aluminate ions are diffused into the solution it lead to the formation of thin layer of reaction products on the surface of the particles and the thickening of the NaOH solution. This reduces the leaching of more ions and thus inhibits further activations. Though a large concentration of OH is available in the solution at higher NaOH concentration, the rate of further hydration growth would be slower as the ceramic powder particles are partially or completely encapsulated by the aluminosilicate gel. Therefore, at higher concentration of the activating solution, the ceramic powder particles might not be completely utilized and the degree of reaction remains moderate.

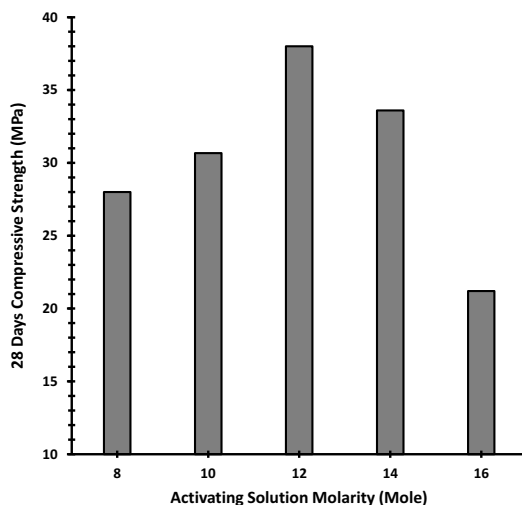
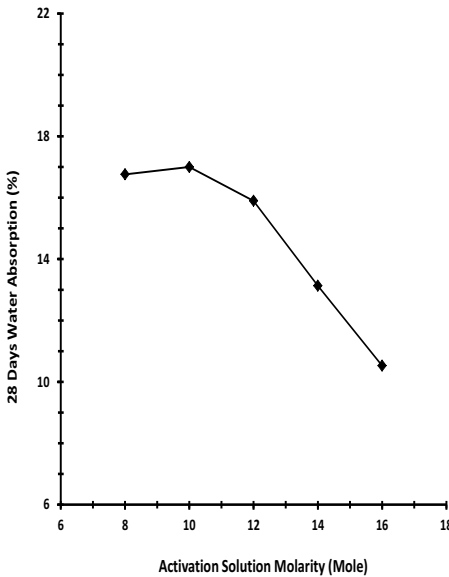


Figure 4. 28-days compressive strength.

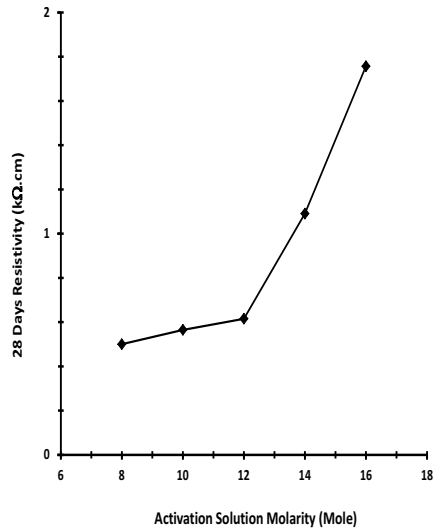
### 3.2. Water absorption and electrical resistivity

Figure 5 shows the 28-days water absorption of the tested geopolymer mixtures. The water absorption decreased as the activation solution alkalinity increased. The reduction was 37% for activation solution with molarity 16M compared to the 8M solution. The reduction could be attributed to either lower porosity or discontinuity of the pores. The reduction in water absorption indicated better durability characteristics of the produced geopolymer as the alkalinity of the activation solution increased.

The electrical resistivity results are shown in Figure 6. The resistivity increased as the alkalinity of the activating solution increased. The resistivity test was conducted on saturated specimens. The increase in resistivity could be attributed to lower connected pores thus limiting the path for electrical current flow. This was confirmed by the water absorption test results, showing decrease in absorption as activating solution molarity increases. The increase in resistivity indicates better corrosion protection to reinforcing steel.



**Figure 5.** Effect of activation solution pH value on water absorption of produced geopolymer.



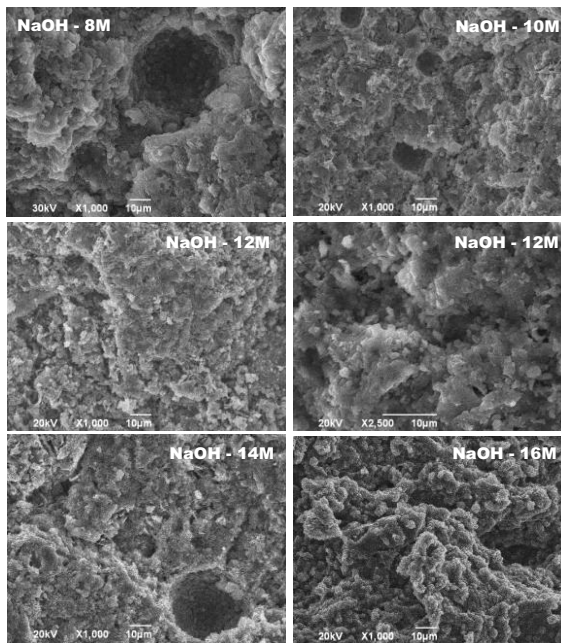
**Figure 6.** Electrical resistivity for different activation solution molarity.

### 3.3. Microstructure characteristics

Microstructure investigation was conducted at 28 days of age. Figure 7 shows SEM micrographs of produced ceramic powder geopolymer at 28-days of age for different concentrations of the NaOH solution. It was observed for all mixtures that there is few if none of the crystalline hydration products. The matrix is mainly formed of continuous homogeneous hydration product mainly aluminosilicate gel as shown in the higher magnification SEM micrograph of the NaOH – 12M, which shows that the microstructure is comprised of both homogeneous and porous regions of gel.

As the alkalinity of the NaOH solution increases it was observed that the microstructure becomes more compact with fewer pores, which may be explained by the formation of amorphous gel being the major component of the paste. At low NaOH concentration of 8M some unreacted ceramic powder particles were observed. Also, at high concentration of 14M and 16M few unreacted ceramic powder particles were observed which confirms that with very high alkaline solution some particles might not be completely utilized.

Lower alkalinity of the solution was found to create a microstructure that is more porous than higher alkalinity solutions. At alkalinity of 12M, the structure of the paste experienced more gel growth and becomes denser and more compact which contributed to the highest compressive strength at 28-days. For low alkalinity mixtures (i.e. 8M and 10M), pore sizes  $>10\mu\text{m}$  are observed in the microstructure. For the mixture with 12M NaOH solution the pore size was in the order of  $5\mu\text{m}$  or smaller. While for mixtures made with 14M and 16M NaOH solution pores were  $>10\mu\text{m}$ . For all geopolymer paste mixtures, it was also observed that pores are mostly isolated and not connected which explains the reduction in the water absorption and increase in resistivity.



**Figure 7.** Microstructure of ceramic waste geopolymer paste made with different concentration of NaOH activating solution.

#### 4. Conclusions

The following are the main conclusions based on the test results obtained in this study:

- Ceramic waste powder has potential for producing geopolymer concrete.
- Increase in NaOH solution concentration enhanced strength development of ceramic powder geopolymer paste, but excess OH ion concentration causes aluminosilicate gel precipitation at the very early stage resulting in lower strength. Sodium hydroxide solution with pH value 12M produced the highest compressive strength.
- Water absorption continued to decrease as the pH value of the sodium hydroxide increases.
- Electrical resistivity increases as the molarity of the activation solution increases.
- Different curing temperatures and activating solution type need to be investigated.

#### 5. Acknowledgment

This work was financially supported by the UAEU-College of Engineering Individual Research Grant # 03\_34\_07\_11/13 (21N144). The donation of the ceramic waste powder for the study by PORCELLAN (ICAD II MUSSAFAH – ABU DHABI) and the cooperation of Mr. Dilip Kumar Borah are highly appreciated.

#### References

- [1] P. Chindapasirt, T. Chareerat and V. Sirivivatnanon, Workability and Strength of Coarse High Calcium Fly Ash Geopolymer, *Cement and Concrete Composites* 29 (2007), 224-229.
- [2] F. Pacheco-Torgal, Z. Abdollahnejad, A.F. Camões, M. Jamshidi and Y. Ding, Durability of Alkali-Activated Binders: A Clear Advantage over Portland Cement or an Unproven Issue?, *Construction and Building Materials* 30 (2012), 400-405.
- [3] J.S.J. Van Deventer, J. Provis and P. Duxson, Technical and Commercial Progress in the Adoption of Geopolymer Cement, *Minerals Engineering* 29 (2012), 89-104.
- [4] F. Pacheco-Torgal, J. Castro-Gomes and S. Jalali, Alkali-Activated Binders: A Review Part 1. Historical Background, Terminology, Reaction Mechanisms and Hydration Products, *Construction and Building Materials*, 22 (2008), 1305-1314.
- [5] C. Shi, A.F. Jiménez and A. Palomo, New Cements for the 21<sup>st</sup> Century: The Pursuit of an Alternative to Portland Cement, *Cement and Concrete Research* 41 (2011), 750-761.
- [6] P. Duxson, J.L. Provis, G.C. Lukey and J.S.J. Van Deventer, The Role of Inorganic Technology in the Development of 'Green Concrete', *Cement and Concrete Research* 37 (2007), 1590-1597.
- [7] K.A. Komnitsas, Potential of Geopolymer Technology towards Green Buildings and Sustainable Cities, *Procedia Engineering* 21 (2011), 1023-1032.
- [8] F. Pacheco-Torgal, J. Castro-Gomes and S. Jalali, Alkali-Activated Binders: A Review Part 2. About Materials and Binders Manufacture, *Construction and Building Materials* 22 (2008), 1315-1322.
- [9] D.L.Y. Kong and J.G. Sanjayan, Damage Behavior of Geopolymer Composites Exposed to Elevated Temperatures, *Cement and Concrete Composites* 30 (2008), 986-991.
- [10] Z. Sun, H. Cui, H. An, D. Tao, Y. Xu, J. Zhai and Q. Li, Synthesis and Thermal Behavior of Geopolymer-Type Material from Waste Ceramic, *Construction and Building Mat.* 49 (2013), 281-287.
- [11] U. Rattanasak, P. Chindapasirt, Influence of NaOH Solution on the Synthesis of Fly Ash Geopolymer, *Minerals Engineering* 22 (2009), 1073-1078
- [12] D. Ravikumar, S. Peethamparan, N. Neithalath, Structure and Strength of NaOH Activated Concrete Containing Fly Ash or GGBS as the Sole Binder, *Cement and Concrete Composites* 32 (2010), 399-410.
- [13] K. Somna, C. Jaturapitakkul, P. Kajitvichyanukul, P. Chindapasirt, NaOH-Activated Ground Fly Ash Geopolymer Cured at Ambient Temperature, *Fuel* 90 (2011), 2118-2124.
- [14] BS EN 197-1:2000; Cement - Part 1 Part 1: Composition, specifications and conformity criteria for common cements.

# Engineering properties of Class-F fly ash-based geopolymer concrete

M. ALBITAR<sup>1</sup>, P. VISINTIN, and M.S. Mohamed ALI

*School of Civil, Envir and Mining Engineering University of Adelaide, Australia*

**Abstract.** Concrete is the most utilized building material in the world. Ordinary Portland Cement (OPC) is a core ingredient in the manufacturing process of concrete. For every tonne of OPC produced, approximately one tonne of carbon dioxide is released into the atmosphere. Increasing environmental awareness means alternative binders are being considered in the ever growing demand for building construction. The development of geopolymer concrete aims to reduce the need for OPC concrete by using constituents that would otherwise be considered as industrial waste to form a binder. This study presents an experimental program aimed to develop an optimum mix design using fly ash. The engineering properties of this mix was tested, analyzed and compared with prediction models developed for OPC-based concrete. The comparison suggests that existing OPC models provide reasonably accurate predictions of the elastic moduli and stress-strain relationships, whereas they slightly underestimate flexural and splitting tensile strengths.

**Keywords.** Fly ash, geopolymer, workability, tensile strength, elastic modulus

## Introduction

Climate change is becoming an increasing concern as the population continues to rise. Carbon dioxide (CO<sub>2</sub>) is considered the primary driver of climate change, contributing to around 65% of the global warming phenomena [1]. Ordinary Portland Cement (OPC) produces approximately one tonne of carbon dioxide per tonne produced [2], raising significant environmental concerns.

Geopolymer concrete (GPC) is a relatively new class of building material, with the potential to become an alternative to conventional OPC concrete. GPC is formed through a polymerization reaction when the silicon and aluminum components of a geologically sourced material or by-product, such as fly ash, is activated by an alkaline liquid to form a binder [3-7]. The production of GPC produces significantly less CO<sub>2</sub> emissions while possessing some superior mechanical properties to that of OPC concrete [8-11]. Although still vastly under-researched, the development of GPC has the potential to revolutionize the construction industry as the demand for an alternative to OPC becomes greater.

---

<sup>1</sup>Corresponding author: Tel. +61 8 8313-1575; fax. +61 8 8313-4359. E-mail address [mohammad.albitar@adelaide.edu.au](mailto:mohammad.albitar@adelaide.edu.au)



## 1. Experimental program

A total of 15 mixes described in Table 1 were carried out to quantify the influence of naphthalene sulphonate polymer-based superplasticizer and water on workability and strength of fly ash-based geopolymer concrete. In this study, low-calcium Class-F (ASTM C618-08 [12]) fly ash produced at Port Augusta Power Station in South Australia was used. For all of the mixes, the alkaline solution phase consisted of a sodium silicate ( $\text{Na}_2\text{SiO}_3$ ) and 14M sodium hydroxide (NaOH) pre-mixed at a ratio of  $\text{Na}_2\text{SiO}_3$ -to-NaOH of 1.5.

**Table 1.** Experimental mix designs

Mix no	w:b	sp:b	Quantity ( $\text{kg}/\text{m}^3$ )						Results	
			Coarse aggregate	Sand	Fly ash	NaOH + $\text{Na}_2\text{SiO}_3$	SP	Water	Slump (mm)	Com. strength
1	0	0.0203	1200	600	424.8	158.4	8.64	0	4	53.8
2	0	0.0331	1197.12	598.5	424.8	158.4	13.92	0	6	34.8
3	0	0.1146	1179.84	589.9	424.8	158.4	48	0	70	29.4
4	0.0525	0.1129	1168.8	584.4	424.8	158.4	48	22.32	210	36.3
5	0.0079	0.0576	1192.8	594.4	424.8	158.4	24	3.36	5	74.5
6	0.0169	0.0576	1192.8	587.5	424.8	158.4	24	7.2	15	67.6
7	0.0225	0.0576	1192.8	584.1	424.8	158.4	24	9.6	25	64.4
8	0.0960	0	1180.8	580.8	424.8	158.4	0	40.8	125	55.6
9	0.0887	0.0197	1185.6	585.6	424.8	158.4	0.84	35.28	200	44.4
10	0.0225	0.0745	1183.2	585.6	424.8	158.4	31.68	9.6	65	66.9
11	0.0225	0.0858	1183.2	585.6	424.8	158.4	36.48	9.6	85	62.4
12	0.0225	0.0971	1183.2	585.6	424.8	158.4	41.28	9.6	125	57.1
13	0.0225	0.1129	1183.2	585.6	424.8	158.4	48	9.6	165	40.9
14	0.1073	0	1183.2	585.6	424.8	158.4	0	45.6	165	46.2
15	0.1412	0	1183.2	585.6	424.8	158.4	0	60	230	27.2

w:b = water-to-binder ratio, sp:b = superplasticiser-to-binder ratio, sp = superplasticizer, Com. strength = 3 day compressive strength MPa (heat cured 24 hr).

### 1.1. Compressive strength and workability

Primary measurement of workability was based on a slump test. Testing was undertaken in accordance with Australian Standards [13] for all mix designs. Compressive tests were performed using the “Seidner Form+Test” UCS apparatus by means of hydraulic force. Testing was undertaken in accordance with Australian Standards [14].

### 1.2. Curing conditions and applicability

To investigate the effect of curing conditions on the strength progression of the optimum mix (mix 13), heat and ambient cured specimens were tested comparatively over 3, 7, 14, 28, 56 and 240 days. The heat curing was done by placing specimens in an oven for 24 hours at 70°C.

### 1.3. Short term mechanical properties of the optimum mix

The stress-strain relationships for both ambient and heat-cured specimens of mix 13 were determined at 28 days using strain gauges and Linear Variable Data Transformers (LVDTs), which measured the displacement of the concrete under a compressive load. Strain gauges were attached to a standard 100 x 200 mm long cylinder 24 hours prior to testing, using a polymer to ensure full contact was made during adhesion to the concrete. The Modulus of Elasticity was then determined from the data using the linear elastic portion of stress, as given in Eq. 1.

$$E = \sigma/\varepsilon \quad (\text{MPa}) \quad (1)$$

The indirect tensile strength of the concrete was tested at 28 days for both ambient and heat-cured specimens. Testing was done in accordance with Australian Standards [15]. The split strength upon failure was then converted into an indirect tensile strength, as given in Eq. 2.

$$T = 2P/\pi LD \quad (\text{MPa}) \quad (2)$$

The flexural strength of the concrete was determined by finding the modulus of rupture ( $f'_{cf}$ ). Specimens with dimensions of 100 x 100 x 500 mm long unreinforced beams were tested in flexure with two points of loading at 28 days for both ambient and heat curing. Testing was performed in accordance with Australian Standards [16]. The load upon failure was converted to the modulus of rupture using Eq. 3.

$$f'_{cf} = PL/(BD^2) \quad (\text{MPa}) \quad (3)$$

## 2. Experimental results

### 2.1. Effect of admixtures on workability

To investigate the influence of the water-to-binder (w:b) and superplasticizer-to-binder (sp:b) ratios on workability, slump tests were performed on each mix design. The results are presented in Table 1 and represented graphically in Figure 1. It is shown that the addition of superplasticizer leads to increase the concrete slump. This increase can be expressed mathematically through a linear regression of the data, as shown in Figure 1(a), which yields Eq.4.

$$\text{slump} = 2112(w:b) + 1275(sp:b) - 61 \quad (4)$$

A clear indication of the influence of the superplasticizer on the workability can be seen in Figure. 1(b) in which the solid superplasticizer-to-binder (solid sp:b) ratio and total water-to-binder (total w:b) ratio are plotted. Repeating the regression analysis for the data in Figure 1(b) gives Eq. 5.

$$slump = 2112(total\ w:b) - 279.8(solid\ sp:b) - 60.1 \tag{5}$$

When the reactive component of superplasticizer is considered only to be its solid contents, which makes up 35% of the total quantity of the superplasticizer, it becomes clear that the reactive component of naphthalene sulphonate polymer-based superplasticizer has little to no effect on the workability of geopolymer concrete and the influence on the workability is raised due to the free water in the superplasticizer.

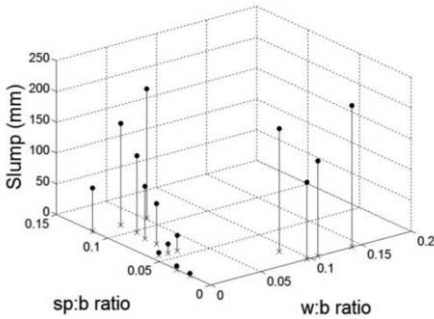


Figure 1a. Superplasticiser-to-binder ratio versus water-to-binder ratio

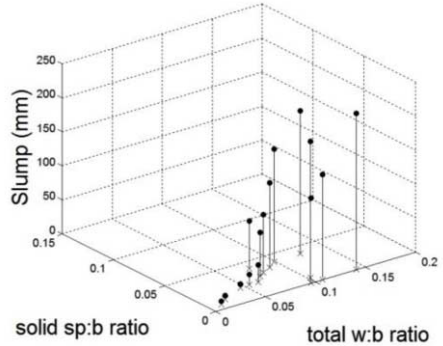


Figure 1b. Solid superplasticiser-to-binder ratio versus total water-to-binder ratio

2.2. Compressive Strength progression

The effect of different curing conditions on the strength progression was investigated using the optimum mix design, mix 13. The compressive strength developments of heat- and ambient-cured specimens are shown in Figure 2. It can be seen that the strength development of ambient-cured cylinders is slower than that of the heat-cured cylinders, reflecting the process of the polymerization reaction, which can be accelerated with heat curing.

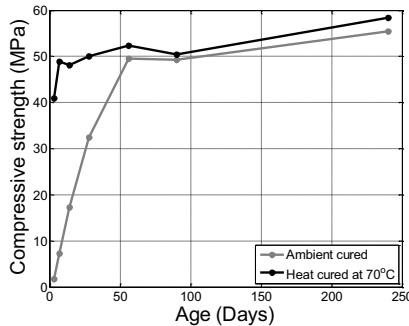


Figure 2. Compressive strength developments of ambient and heat cured

2.3. Short term properties of the optimum mix

The full stress-strain relationships for both heat and ambient cured specimens are shown in Figure 3, together with Hognestad [17] and Collins et al. [18]’s expressions. It is evident that the expressions provide reasonable accuracy for fly ash-based geopolymer concrete stress-strain relationships.

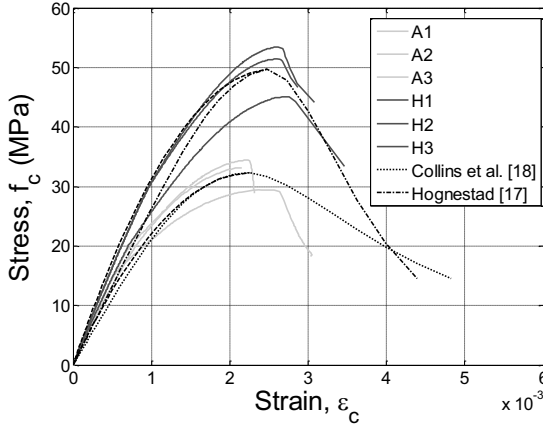


Figure 3. Stress-strain relationships

The results of the splitting tensile strength are shown in Figure 4, together with available results in the open literature on geopolymer concrete [2, 8, 19-22], and compared with predictions models developed for OPC-based concrete and GPC, including ACI 318-08 [23], Eurocode [24] and Sofi et al. [8]. It can be seen that the majority of the experimental data fell above the prediction models of OPC, indicating the higher tensile strength exhibited in GPC. Therefore, a regression analysis was then performed to estimate the splitting tensile strength from the compressive strength, Eq. 6.

$$f'_{ct} = 0.6 \sqrt{f'_c} \quad (\text{MPa}) \tag{6}$$

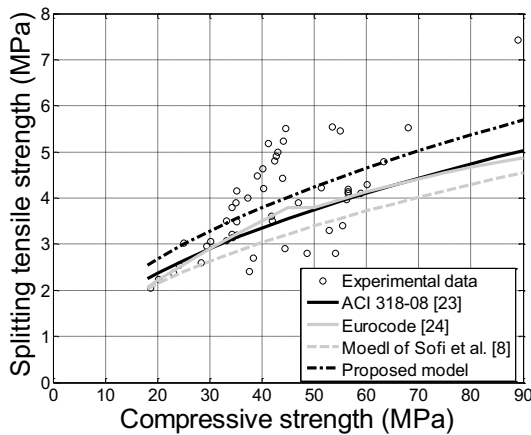


Figure 4. Splitting tensile strength versus compressive strength

Figure 5 shows the results of the flexural tensile tests conducted in the present study, as well as available results on class-F fly ash-based geopolymer concrete [8, 19, 21-22], and compared with predictions models developed for OPC-based concrete and GPC, including ACI 318-08 [23]; Sofi et al. [8]; Ivan Diaz-Loya et al. [22]. In addition, results on class-C fly ash [22] were also included for comparison purpose. It is evident that the expressions set for conventional OPC concrete, such as ACI [23], underestimate the values of class-F fly ash-based geopolymer concrete, yet they accurately estimate the values of class-C fly ash-based geopolymer concrete, as can be seen in Figure 5. This indicates that the mechanical properties of class-C fly ash-based geopolymer concrete are similar to those of conventional OPC-based concrete. Thus, a regression analysis was performed to estimate the flexural strength of class-F fly ash from the compressive strength, Eq. 7.

$$f'_{cf} = 0.75 \sqrt{f'_c} \quad (\text{MPa}) \tag{7}$$

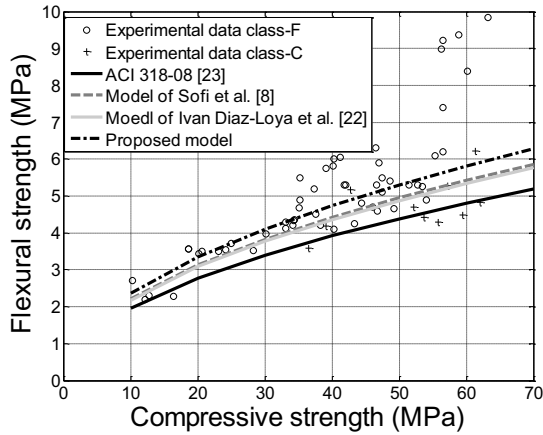


Figure 5. Flexural strength versus compressive strength

The results of modulus of elasticity ( $E_c$ ) are shown in Figure 6, together with results from database of available test data for comparison purpose, including class-C [22, 25] and class-F [2, 20-22, 25] fly ash-based geopolymer concrete. As seen in Figure 6, while there is a large scatter of experimental results, the expression of the ACI 318-08 [23] for OPC provides a reasonable estimate of the mean test results. Moreover, the upper and lower bounds of Australian Standards AS 3600 [26] capture the scatter of the results.

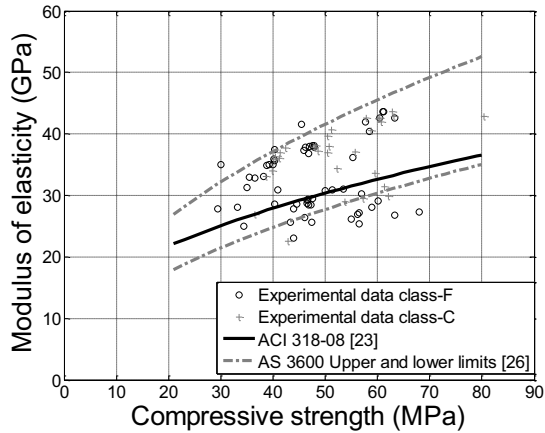


Figure 6. Modulus of elasticity of fly ash (Class-F and Class-C)

### 3. Conclusion

This paper has presented the results of an experimental study that was conducted to obtain a greater understanding of the behavior of typical Class-F fly ash-based geopolymer concrete. The results from the current study augmented the existing database of geopolymer concrete, as it involved compressive strength development, flexural strength, tensile strength, elastic modulus and the stress-strain relationship. The following conclusions can be drawn based on the results and discussions reported in this paper.

1. The polymerization reaction can be accelerated with heat curing, as the compressive strength can be developed at an early age.
2. Naphthalene sulphonate polymer-based superplasticiser has little to no effect on the slump.
3. The experimentally determined values of splitting tensile and flexural strength were higher than those in the expressions prescribed by national standards for OPC-based concrete, indicating that class-F fly ash-based geopolymer concrete exhibits higher tensile strength than the OPC-based concrete.
4. Elastic modulus of class-F fly ash-based geopolymer concrete was found to be similar to those of conventional OPC-based concrete.
5. Stress-strain expressions developed for conventional OPC-based concrete can be applied with reasonable accuracy for determination of fly ash-based geopolymer concrete stress-strain relationships.
6. The results have shown that geopolymer-based concrete using Class-F fly ash has a great potential for utilization in construction industries as a replacement for OPC-based concrete, as it has comparable structural properties.

## References

- [1] McCaffrey, R 2002, 'Climate Change and the Cement Industry,' *Global Cement and Lime Magazine (Environmental Special Issue)*, pp. 15-19.
- [2] Hardjito, D & Rangan, BV 2005, 'Development and Properties of Low-Calcium Fly Ash-based Geopolymer Concrete,' Faculty of Engineering, Curtin University of Technology, Perth, Australia.
- [3] Davidovits, J 1991, 'Geopolymers Inorganic polymeric new materials,' *Journal of Thermal Analysis*, vol. 37, pp. 1633-1656.
- [4] Davidovits, J 1994, 'Global warming impact on the cement and aggregates industries,' *World Resource Review*, vol. 6, no. 2, pp. 263-278.
- [5] Davidovits, J 1994, 'Properties of Geopolymer Cements,' *First International Conference on Alkaline Cements and Concretes*, vol. 1, pp. 131-149.
- [6] Palomo, A, Grutzeck, MW & Blanco, MT 1999, 'Alkali-activated fly ashes: a cement for the future,' *Cement and Concrete Research*, pp. 1323-1329.
- [7] Duxson, P, Provis, JL, Lukey, GC & van Deventer, JSJ 2007, 'The role of inorganic polymer technology in the development of 'green concrete,' *Cement and Concrete Research*, vol. 37, pp. 1590-1597.
- [8] Sofi, M, van Deventer, JSJ, Mendis, PA & Lukey, GC 2007, 'Engineering properties of inorganic polymer concretes (IPCs),' *Cement and Concrete Research*, vol. 37, pp. 251-257.
- [9] Izquierdo, M, Querol, X, Phillipart, C, Antenucci, D & Towler, M 2010, 'The role of open and closed curing conditions on the leaching properties of fly ash-slag-based geopolymers,' *Journal of Hazardous Materials*, vol. 176, pp. 623-628.
- [10] Shi, C, Jiménez, AF & Palomo, A 2011, 'New cements for the 21st century: The pursuit of an alternative to Portland cement,' *Cement and Concrete Research*, vol. 41, pp. 750-763.
- [11] van Deventer, JSJ, Provis, JL & Duxson, P 2012, 'Technical and commercial progress in the adoption of geopolymer cement,' *Minerals Engineering*, vol. 29, pp. 89-104.
- [12] ASTM C618-08 (2008), 'Standard Specification for Coal Fly Ash and Raw or Calcined Natural Pozzolan for Use in Concrete,' Philadelphia: American Society for Testing and Materials.
- [13] Standards-Australia (1998), 'Methods of testing concrete - Determination of properties related to the consistency of concrete slump test,' AS 1012.3.1-1998.
- [14] Standards-Australia (1999), 'Methods of testing concrete - Determination of the compressive strength of concrete specimens,' AS 1012.9-1999.
- [15] Standards-Australia (2000), 'Determination of indirect tensile strength of concrete cylinders ('Brazil' or splitting test),' AS 1012.10 - 2000.
- [16] Standards-Australia (2000), 'Methods of testing concrete - Determination of the modulus of rupture,' AS 1012.11-2000.
- [17] Hognestad, EN 1951, 'A study of combined bending and axial load in reinforced concrete members,' *University of Illinois at Urbana-Champaign*, vol. 49, no. 22, USA.
- [18] Collins, MP, Mitchell, D, and MacGregor, GJ 1993, 'Structural design considerations for high strength concrete,' *ACI Concrete International*, vol. 15, no. 5, pp. 27-34.
- [19] Raijiwala, DB, and Patil, HS 2010, 'Geopolymer concrete: a green concrete,' *2nd International Conference on Chemical, Biological and Environmental Engineering*, pp. 202-206.
- [20] Nguyen, NH, Smith, SM, Staniford, MD, and van Senden, MF 2010, 'Geopolymer concrete - concrete goes green,' Research report, School of Civil, Environmental and Mining Engineering, The University of Adelaide, Adelaide, Australia.
- [21] Olivia, M, and Nikraz, H 2011, 'Properties of fly ash geopolymer concrete designed by Taguchi method,' *Materials and Design*, pp. 1-27.
- [22] Ivan Diaz-Loya, E, Allouche, EN, Vaiday, S 2011, 'Mechanical properties of fly-ash-based geopolymer concrete,' *ACI Materials Journal*, pp. 300-306.
- [23] ACI Committee 318 (2008), 'Building code requirements for structural concrete (ACI 318-08) and commentary,' *American Concrete Institute*, Farmington Hills, MI.
- [24] European Standard (2002), 'Eurocode 2: Design of Concrete Structure - Part 1: General Rules and Rules for Buildings,' ref. no. prEN 1992-1-1.
- [25] Yildirim, H, Sümer, M, Akyüncü, V, and Gürbüz, E 2011, 'Comparison on efficiency factors of F and C types of fly ashes,' *Construction & Building Materials*, vol. 25, no. 6, pp. 2939-2947.
- [26] AS 3600 (2001), 'Concrete structure,' Australian Standards, ISBN: 0-7337-3931-8.

# Engineering properties of slag-based geopolymer concrete

M. ALBITAR, M.S. Mohamed ALI<sup>1</sup> and P. VISINTIN

*School of Civil, Envir and Mining Engineering University of Adelaide, Australia*

**Abstract.** Geopolymer concrete is manufactured from high-volume waste materials, such as fly ash from coal-burning power stations and can be altered by adding mineral admixtures, such as ground granulated slag or granulated lead smelter slag. The addition of these admixtures may lead to increase the compressive strength of fly ash, or reduce the amount of cementitious material in the binder, which in turn reduces costs and offers further environmental benefits. This paper presents an experimental study on the behavior of slag-based geopolymer concrete. The experimental program included 25 mix designs which were used to examine several parameters. The key parameters considered were the slag-to-fly ash ratio, slag-to-river sand ratio, alkaline solution-to-binder ratio and curing method. The mechanical properties were tested, analyzed and compared to the American Concrete Institute and Australian Standards set for ordinary Portland cement concrete in order to determine the similarities and differences. The results show that using partially slag as a binder of up to 75% can provide a normal concrete strength. The results concluded that the mechanical properties of the slag-based geopolymer concrete were similar to that of fly ash-based geopolymer concrete.

**Keywords.** Fly ash, geopolymer, workability, tensile strength, elastic moduli

## Introduction

Climate change is becoming an increasing concern as the population continues to rise. Carbon dioxide (CO<sub>2</sub>) is considered the primary driver of climate change, contributing to around 65% of the global warming phenomena [1]. Manufacturing one tonne of Ordinary Portland Cement (OPC) produces approximately one tonne of carbon dioxide [2], raising significant environmental concerns.

Fly ash-based geopolymer concrete has been demonstrated to possess comparable mechanical properties to that of OPC [3-7], and it is used to reduce the Greenhouse footprint. Granulated lead smelter slag (GLSS) can partially replace the fly ash to produce slag-based geopolymer concrete. Utilizing GLSS as a binder provides further reduction to the Greenhouse footprint while maintaining the comparable mechanical properties. Furthermore, it reduces the demand and reliance on fly ash. This study aims to develop a mix design of slag geopolymer concrete based on GLSS and fly ash, as well as study the engineering properties of the optimum mix design. Granulated lead smelter slag (GLSS) is a by-product waste material that is significantly produced from heavy metal extraction during lead smelting process.

<sup>1</sup>Corresponding author: Tel.: +61 8 8313-1575; fax. +61 8 8313-4359. E-mail address [mohammad.albitar@adelaide.edu.au](mailto:mohammad.albitar@adelaide.edu.au)



## 1. Experimental program

### 1.1. Materials

In this study, low-calcium class-F (ASTM C618-08) fly ash produced at Port Augusta Power Station in South Australia and granulated lead smelter slag (GLSS) known as black sand from Nystar in Port Pirie were used. The chemical compositions of the fly ash and GLSS were determined by x-ray fluorescence (XRF) and are summarized in Table 1. For all mixes, the alkaline solution phase used consisted of sodium silicate ( $\text{Na}_2\text{SiO}_3$ ) and 14M sodium hydroxide (NaOH) pre-mixed at a ratio of  $\text{Na}_2\text{SiO}_3$ -to-NaOH of 1.5 .

**Table 1.** Chemical compositions of the binder materials

Chemical Composition (%)	Fly ash	GLSS
Calcium oxide, CaO	5.4	19.43
Silicon dioxide, $\text{SiO}_2$	49	27.5
Aluminum oxide, $\text{Al}_2\text{O}_3$	31	7.38
Ferric oxide, $\text{Fe}_2\text{O}_3$	2.8	33.79
Magnesium oxide, MgO	2.5	2.1
Titanium dioxide, $\text{TiO}_2$	2.1	0.36

### 1.2. Mix proportions

The mix proportion of this project was designed to develop an optimum mix design that contains high volume of reactive slag, such as GLSS. In order to achieve that, 25 mix designs, prescribed in Table 2, were designed to examine the influence of (i) particle size of GLSS (mixes 1-8), (ii) river sand replacement with GLSS as fine aggregate (mixes 13-16), (iii) fly ash replacement with GLSS as a binder (mixes 21-25), and (iv) activator-to-binder (*a/b*) ratio (mixes 2, 7, 17-20). The core components were binder  $424.8 \text{ kg/m}^3$ , coarse aggregate  $1180.8 \text{ kg/m}^3$ , fine aggregate  $595.2 \text{ kg/m}^3$ , NaOH with  $\text{Na}_2\text{SiO}_3$   $156.7 \text{ kg/m}^3$  (except for mixes 17 & 19, which had  $212.4 \text{ kg/m}^3$  and mixes 18 & 20, which had  $318.4 \text{ kg/m}^3$ ), superplasticiser  $31.2 \text{ kg/m}^3$  and water  $9.84 \text{ kg/m}^3$ .

### 1.3. Optimum mixture

A total of 42 slag-based geopolymer concrete cylinder specimens of the optimized mix, mix 24, were manufactured and tested under either compression or tension. Twenty one (21) specimens were cured in an oven for 24 hours at a temperature of  $70^\circ\text{C}$ , and the remaining 21 specimens were cured at ambient temperature. Moreover, 4 prisms were manufactured and tested under flexural. To allow a meaningful comparison, the same testing procedure was done on 100% fly ash geopolymer concrete (mix 16).

### 1.4. Test methods

Compressive, tensile and flexural tests were performed in accordance with Australian Standards [8-10], and then the results were compared to several standards [11-14]. The

stress-strain relationships were determined at 28 days using strain gauges and Linear Variable Data Transformers (LVDTs), which measured the displacement of the concrete under a compressive load.

**Table 2.** Mix designs

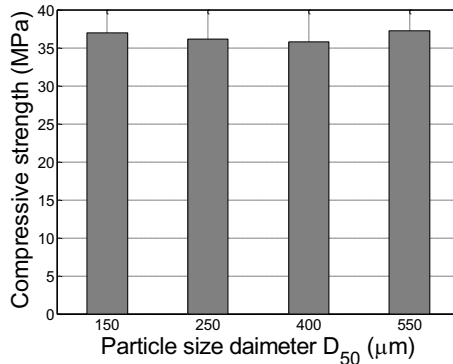
Mix No	Binder		Fine aggregates			GYP	a:b	Heat-curing period (Hour)	Slump (mm)	Strength at 7 days (MPa)
	FA Ratio	GLSS		RS	GLSS					
		Ratio	D <sub>50</sub> (μm)							
1	0.5	0.5	550	1	0	-	0.37	24	75	37.2
2	0.5	0.5	400	1	0	-	0.37	24	27	35.8
3	0.5	0.5	250	1	0	-	0.37	24	50	36.1
4	0.5	0.5	150	1	0	-	0.37	24	50	37.4
5	0.5	0.5	550	0	1	-	0.37	24	180	51.9
6	0.5	0.5	400	0	1	-	0.37	24	130	46.0
7	0.5	0.5	250	0	1	-	0.37	24	75	50.1
8	0.5	0.5	150	0	1	-	0.37	24	100	49.5
9	0.5	0.5	250	1	0	5%	0.37	24	0	13.6
10	0.5	0.5	250	1	0	10%	0.37	24	0	1.1
11	0.5	0.5	250	1	0	15%	0.37	24	0	3.1
12	0.5	0.5	250	1	0	-	0.37	48	80	36.4
13	1	0	-	1	0	-	0.37	24	155	66.8
14	1	0	-	0.5	0.5	-	0.37	24	140	63.8
15	1	0	-	0.25	0.75	-	0.37	24	200	62.5
16	1	0	-	0	1	-	0.37	24	200	63.2
17	0.5	0.5	250	1	0	-	0.50	24	235	28.9
18	0.5	0.5	250	1	0	-	0.75	24	270	16.8
19	0.5	0.5	250	0	1	-	0.50	24	240	40.8
20	0.5	0.5	250	0	1	-	0.75	24	275	23.2
21	1	0	-	0	1	-	0.37	48	155	63.7
22	0.75	0.25	550	0	1	-	0.37	24	200	62.4
23	0.5	0.5	550	0	1	-	0.37	24	200	51.1
24	0.25	0.75	550	0	1	-	0.37	24	130	31.5
25	0	1	550	0	1	-	0.37	24	-	6.7

FA = fly ash, GLSS = lead smelter slag, RS = river sand, a/b = activator/binder ratio, GYP = gypsum, D<sub>50</sub> = grainsize of which 50% material passes.

## 2. Results and discussions

### 2.1. Effect of particle size of GLSS

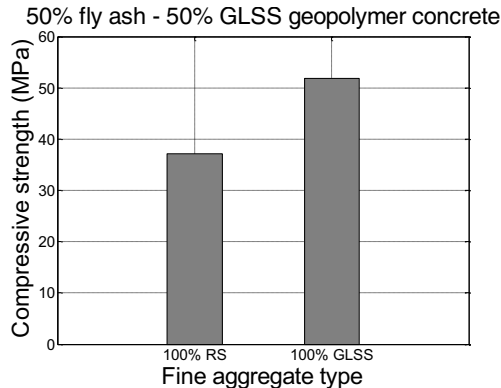
Mixes 1, 2, 3 and 4 were designed to investigate the effect of particle size of GLSS incorporated as 50% partial replacement of the fly ash binder. Four different particle sizes  $D_{50}$  (grain size of which 50% material passes) were examined, including 550  $\mu\text{m}$ , 400  $\mu\text{m}$ , 250  $\mu\text{m}$ , and 150  $\mu\text{m}$ . The results show that the particle size used in the experiment had no influence on the compressive strength, as can be seen in Figure 1. This can be attributed to the significant difference in the particle sizes of fly ash and GLSS, as 150  $\mu\text{m}$  is relatively coarse compared to that of fly ash, which is 12  $\mu\text{m}$ .



**Figure 1.** Effect of particle size on the compressive strength

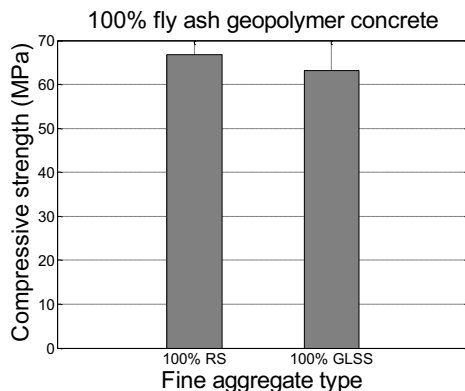
### 2.2. Effect of GLSS as fine aggregate replacement

The effect of utilizing GLSS as slag reactive filler can only be significant when the volume of fly ash is reduced. Figure 2 shows the influence of river sand (RS) replacement with GLSS as fine aggregate on 50% fly ash - 50% GLSS geopolymer concrete. It is evident from Figure 2 that the compressive strength increased when the river sand was completely replaced with GLSS. This increase can be attributed to the improvement of polymerization reaction provided by the reactive slag.



**Figure 2.** Effect of GLSS as filler on compressive strength of 50% fly ash and 50% GLSS binder

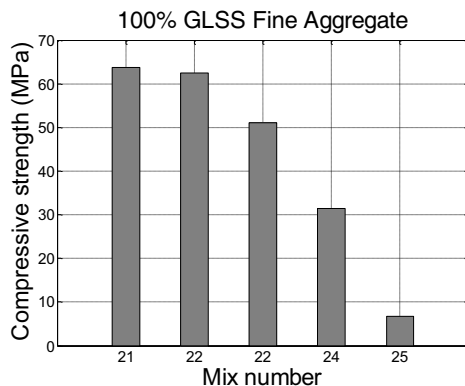
On the other hand, the utilization of GLSS as fine aggregate did not have any influence on 100% fly ash geopolymer concrete, as can be seen in Figure 3.



**Figure 3.** Effect of GLSS as filler on compressive strength of 100% fly ash geopolymer concrete

### 2.3. Effect of GLSS as binder replacement

Figure 4 shows the influence of fly ash replacement with GLSS as a binder. The fly ash was gradually replaced with GLSS and the ratios of fly ash-to-GLSS were 1, 0.75, 0.5, 0.25, and 0 (mixes 21-25, respectively). It is evident from these results that the compressive strength of concrete mixtures decreased with an increase in GLSS content. It can be seen that mix 24, which contains 75% GLSS and 25% fly ash as a binder, obtains a compressive strength of 31 MPa, which is in the range of normal concrete strength.



**Figure 4.** Effect of the proportion of GLSS as a binder on compressive strength

### 2.4. Effect of activator to binder ratio

Six mixtures were designed to investigate the influence of activator-to-binder ( $a/b$ ) ratio. The  $a/b$  ratios were varied between 0.37, 0.5, and 0.75. Each ratio was examined with two different filler types, river sand and GLSS. The results show a reduction in the

compressive strength with increasing the  $a/b$  ratio. This is due to the fact that the solid silicate content was less than the liquid silicate content, which hinders the leaching of the silica and alumina, resulting in a lesser degree of polymerization reaction [15].

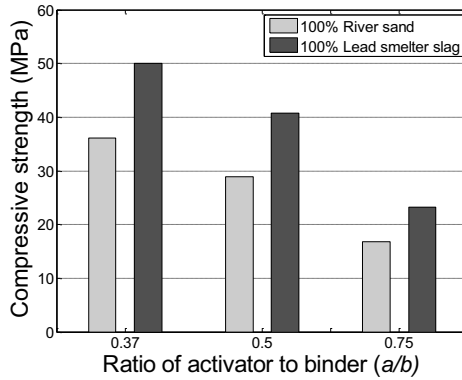


Figure 5. Effect of activator to binder ( $a/b$ ) ratio

2.5. Mechanical properties of the optimum mix

Mix 24 was chosen to be the optimum mix design due to the lowermost of cementitious material, meanwhile achieving adequate compressive strength. Figure 6 shows the compressive strength gain profile with curing time. Figures 7, 8 and 9 show the tensile strength, flexural strengths and elastic modulus, respectively. The results were compared to that of 100% fly ash geopolymer concrete (mix 16). It is shown that slag-based geopolymer concrete possesses mechanical properties similar to that of fly ash geopolymer concrete.

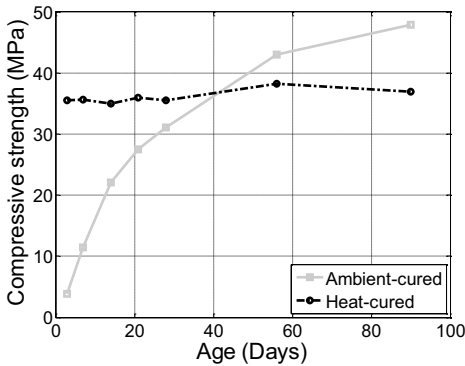


Figure 6. Compressive strength vs. curing time

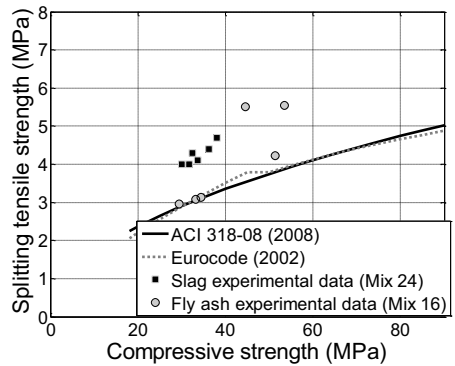


Figure 7. Tensile strength

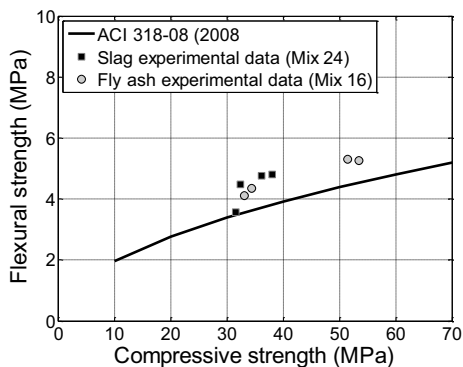


Figure 8. Flexural strength

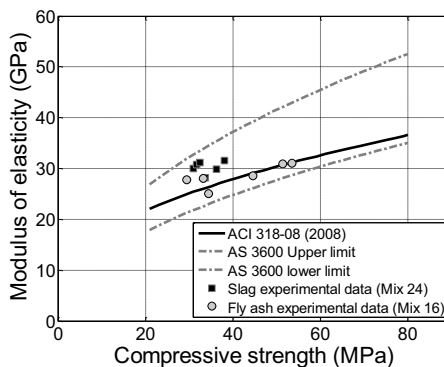


Figure 9. Elastic modulus

### 3. Conclusion

This paper has presented the results of an experimental study that was undertaken to investigate the influence of granulated lead smelter slag (GLSS) on the mechanical properties of fly ash-based geopolymer concrete. The investigation involved the influence of (i) particle size of GLSS, (ii) river sand replacement with GLSS as fine aggregate, (iii) fly ash replacement with GLSS as a binder, and (iv) activator-to-binder ( $a/b$ ) ratio. The following conclusions can be drawn based on the results and discussions reported in this paper:

1. The particle size used of GLSS did not have any influence on the compressive strength.
2. The influence of utilizing GLSS as fine aggregate was only observed when the volume of fly ash was reduced, as there was no effect on 100% fly ash geopolymer concrete.
3. The compressive strength was reduced with increasing the replacement of fly ash with GLSS.
4. A reduction in the compressive strength was observed with increasing the activator-to-binder ratio.
5. The mechanical properties of the optimum mix design, which contained 25% fly ash and 75% GLSS as a binder were found to be similar to that of 100% fly ash-based geopolymer concrete.

### References

- [1] McCaffrey, R 2002, 'Climate Change and the Cement Industry,' *Global Cement and Lime Magazine (Environmental Special Issue)*, pp. 15-19.
- [2] Hardjito, D. & Rangan, BV 2005, 'Development and Properties of Low-Calcium Fly Ash-based Geopolymer Concrete,' Faculty of Engineering, Curtin University of Technology, Perth, Australia.
- [3] Davidovits, J 1991, 'Geopolymers Inorganic polymeric new materials,' *Journal of Thermal Analysis*, vol. 37, pp. 1633-1656.
- [4] Davidovits, J 1994, 'Global warming impact on the cement and aggregates industries,' *World Resource Review*, vol. 6, no. 2, pp. 263-278.

- [5] Davidovits, J, 1994, 'Properties of Geopolymer Cements,' *First International Conference on Alkaline Cements and Concretes*, vol. 1, pp. 131-149. 1994.
- [6] Palomo, A, Grutzeck, MW & Blanco, MT 1999, 'Alkali-activated fly ashes: a cement for the future,' *Cement and Concrete Research*, pp. 1323-1329.
- [7] Duxson, P, Provis, JL, Lukey, GC & van Deventer, JSJ 2007, 'The role of inorganic polymer technology in the development of 'green concrete,' *Cement and Concrete Research*, vol. 37, pp. 1590-1597.
- [8] Standards-Australia (1999), 'Methods of testing concrete - Determination of the compressive strength of concrete specimens,' *AS 1012.9-1999*.
- [9] Standards-Australia (2000), 'Determination of indirect tensile strength of concrete cylinders ('Brazilian' splitting test),' *AS 1012.10 - 2000*.
- [10] Standards-Australia (2000), Methods of testing concrete - Determination of the modulus of rupture, *AS 1012.11-2000*
- [11] *AS 3600*, Concrete structure, Australian Standards (2001)
- [12] American Concrete Institute (ACI) Committee 363 (1992), State of the Art Report on High-Strength Concrete, *American Concrete Institute*, Detroit, USA.
- [13] European Standard, *Eurocode 2: Design of Concrete Structure – Part 1: General Rules and Rules for Buildings*, ref. no. prEN 1992-1-1, July 2002, p. 29.
- [14] Shah, SP and Ahmad, SH 1985, Structural properties of high strength concrete and its implication for precast prestressed concrete, *Portland Cement Inst. J.* 30, no. 6, pp. 92-119.
- [15] Sathonsaowaphak, A, Chindapasirt, P & Pimraksa, K 2009, 'Workability and strength of lignite bottom ash geopolymer mortar,' *Journal of Hazardous Materials*, vol. 168, pp. 44-50.

# Steel-slag and activators ratio impacts on the shrinkage of alkaline activated ultrafine palm oil ash-steel slag paste/mortar

Moruf O. YUSUF<sup>a,c,1</sup>, Megat A.M JOHARI<sup>a</sup>, Zainal A. AHMAD<sup>b</sup> and M. MASLEHUDDIN<sup>c</sup>

<sup>a</sup>*School of Civil Engineering, Universiti Sains Malaysia, 14300 Nibong Tebal Pinang*

<sup>b</sup>*School of Materials and Mineral Resources Engineering, Universiti Sains Malaysia*

<sup>c</sup>*Center for Engineering Res., King Fahd Univ of Petroleum & Minerals, Saudi Arabia*

**Abstract** The ground steel slag (GSS) was used in synergy with ultrafine-palm oil fuel ash (UPOFA) to study the shrinkage of alkaline activated GSS-UPOFA (AAGU) products, which were oven-cured for 24 h at 60 °C and relative humidity of 50%. The GSS (G)/(GSS+UPOFA) varied from 0 to 0.8 and 0 to 0.4 for pastes and mortars, respectively with the use of the two activators - Na<sub>2</sub>SiO<sub>3aq</sub> (SiO<sub>2</sub>/Na<sub>2</sub>O=3.3) and 10 M NaOH<sub>aq</sub>. The findings showed that steel slag inclusion decreased the shrinkage of AAGU mortars and pastes due to its larger pore volume, and its enhancement of bulk modulus of the solid skeleton (C-(A)-S-H) through infusion of a network-modified Ca<sup>2+</sup>. The shrinkage was also found to decrease with the increase in the NaOH<sub>aq</sub> / Na<sub>2</sub>SiO<sub>3aq</sub> mass ratio from 1 to 2.5. The 90-day shrinkage of the product prepared with GSS/(GSS+UPOFA) of 0.2 were found to be 25.88x10<sup>3</sup> and 8.20x10<sup>3</sup> µε in the paste and mortar, respectively.

**Keywords.** Palm-oil-fuel-ash, steel-slag, geopolymers, shrinkage, solid waste, alkaline activated binder

## Introduction

The environmental consideration has necessitated the need to find an alternative material of construction other than ordinary Portland cement (OPC). The reason being that in addition to the proliferation of CO<sub>2</sub>, there is a great deal of energy required in the breaking down of limestones and transportation of raw materials during the manufacturing of OPC. The alkaline activated products had been proven to show better performance in terms of shrinkage [1,2]. There are few other studies recently on the shrinkage characteristics of alkaline activated binders (AAB). For instance, the shrinkage of oven-cured flyash-based geopolymers revealed that initial shrinkage was accelerated by oven-curing but the eventual network formation within the product reduced the total shrinkage [1].

<sup>1</sup>Corresponding author: [moruff@gmail.com](mailto:moruff@gmail.com), [moy12\\_civ023@student.usm.my](mailto:moy12_civ023@student.usm.my)



The alkaline-activator ratio and NaOH concentration control the AAB shrinkage, in addition to the curing temperature and liquid-to-ash ratio [2]. However, the shrinkage characteristics of the alkaline activated ground slag/ultrafine palm oil fuel ash (AAGU) pastes/mortars are not yet understood. This study reports the shrinkage of the novel products and also consolidates the advantage of using the solid wastes as alternative materials to OPC products in the construction industry.

## 1. Materials and methods

### 1.1 Pozzolanic base materials

The materials used were the palm oil fuel ash (POFA) and the steel slag (SS) which were obtained from the United Palm Oil Company and Southern Steel Malaysia, respectively. The POFA and GSS were ground for 16h to achieve ground SS (GSS) and ultrafine POFA (UPOFA), respectively. The POFA was ground in two phases, first, for 8 h, then calcined for 90 min at 500 °C, and then comminuted for additional 8 hr to produce UPOFA. The specific gravity of GSS and UPOFA were 2.9 and 2.6, respectively while the specific surface areas were 14.9 and 13.4 m<sup>2</sup>/g, respectively. The oxide compositions of PMs were determined using the XRF techniques (Table 1). The Microtrac (Turbotrac) instrument model S3500 was used for the determination of particle size distributions (PSDs) while the Micromeritics ASAP 2020 was used to determine surface areas and the pore volumes of the GSS and UPOFA as shown in Table 2. The X-ray diffractions (XRD) of the raw pozzolanic materials (PMs) was done using Bruker instrument model D2-Phaser while the scanning was done from 10° to 80° of 2θ angle as shown in Fig.1. The results were analyzed using the X'PERT analytical software.

**Table 1.** Oxide percentage compositions of UPOFA and GSS

Oxides	SiO <sub>2</sub>	Al <sub>2</sub> O <sub>3</sub>	Fe <sub>2</sub> O <sub>3</sub>	CaO	Na <sub>2</sub> O	MgO	K <sub>2</sub> O	P <sub>2</sub> O <sub>5</sub>	SO <sub>3</sub>	C	LOI
GPOFA	46.00	3.10	2.45	8.46	0.13	4.40	4.08	3.95	0.3	26.44	21.60
UPOFA	60.42	4.26	3.34	11.00	0.18	5.31	5.03	4.48	0.45	4.86	2.55
GSS	25.78	4.42	1.94	53.54	0.03	9.50	0.05	0.04	3.85	0	2.05

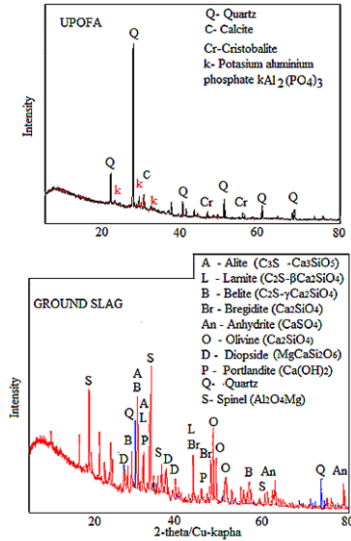
**Table 2.** The pore and surface area characteristics of the ground steel slag (GSS) and UPOFA

Material properties	GSS	UPOFA
Median particle size, d <sub>50</sub> (μm)	1.098	1.069
BJH adsorption average pore width (Å)	133.849	117.603
BJH desorption average pore width (Å)	83.012	76.332

### 1.2 Alkaline activators

The activators used were Na-silicate (NS) of silica modulus of 3.3 and the prepared 10 M-NaOH (NH), which contained the dissolved 404 g of pellets in 1 liter of solution [3]. The reaction was exothermic and solution was allowed to cool down. The combined

alkaline activator (NS+NH)/PMs ratios of 0.35 and 0.5 were used for pastes and mortars, respectively but at varied NS/NH ratios as shown in Table 3a and 3b.



**Figure 1.** Diffractogram ground steel slag and ultrafine palm oil fuel ash

### 1.3 Mixture design proportions and preparation of specimens

The mixture proportions for the paste and mortar specimens were as shown in Table 3a and 3b, respectively. The mixing was done using 4.7L mixer such that the pozzolanic materials was first added, followed by the free mixing water and the activators –  $10MNaOH_{aq}$  and  $Na_2SiO_{3aq}$  – were then subsequently added. The prismatic specimens were cast in 25x25x285 mm moulds in triplicate and the average measurement was then recorded. The change in length ( $L_o-L_f$ ) was obtained from data logger by deducting the new length from gauge length (250 mm) and the shrinkage (microstrain ( $\mu\epsilon$ )) was then computed as shown in Eq.1.

$$\text{Strain}(\mu\epsilon) = (L_o - L_f) / L_o \times 10^6 \quad (1)$$

**Table 3a.** Mix proportions for the paste specimens

Total Binder	UPOFA (kg/m <sup>3</sup> )	Slag (kg/m <sup>3</sup> )	Free water (kg/m <sup>3</sup> )	CAA/PMs (kg/m <sup>3</sup> )	Na <sub>2</sub> SiO <sub>3</sub> <sub>aq</sub> (kg/m <sup>3</sup> )	10MNaOH <sub>aq</sub> (kg/m <sup>3</sup> )
AAGU0R2.5	1313.87	0.00	26.28	0.35	328.47	131.38
AAGU0.2R2.5	1051.09	262.77	26.28	0.35	328.47	131.38
AAGU0.4R2.5	788.32	525.55	26.28	0.35	328.47	131.38
AAGU0.6R2.5	534.53	779.21	26.28	0.35	328.47	131.38
AAGU0.8R2.5	291.43	1022.10	26.28	0.35	328.47	131.38

R=Na<sub>2</sub>SiO<sub>3</sub>/NaOH<sub>aq</sub> (by mass), AAGUx; x=G/U+G, G=Ground steel slag, U=ultrafine palm oil fuel ash

**Table 3b.** Mix proportions for the mortar specimens

Total binder	UPOFA (kg/m <sup>3</sup> )	Slag (kg/m <sup>3</sup> )	Sand (kg/m <sup>3</sup> )	Free water (kg/m <sup>3</sup> )	CAA/PMs (kg/m <sup>3</sup> )	Na <sub>2</sub> SiO <sub>3</sub> <sub>aq</sub> (kg/m <sup>3</sup> )	10MNaOH <sub>aq</sub> (kg/m <sup>3</sup> )
AAGU0R2.5	722.8	0	1301.2	14.5	0.5	258.2	103.3
AAGU0.2R1.0	578.3	144.6	1301.2	14.5	0.5	258.2	103.3
AAGU0.2R2.5	578.3	144.6	1301.2	14.5	0.5	180.7	180.7
AAGU0.4R2.5	433.7	289.2	1301.2	14.5	0.5	258.2	103.3
AAGU0.6R2.5	289.2	433.7	1301.2	14.5	0.5	258.2	103.3

R=Na<sub>2</sub>SiO<sub>3</sub>/NaOH<sub>aq</sub> (by mass), AAGUx; x=G/U+G, G=Ground steel slag, U=ultrafine palm oil fuel ash

## 2. Discussions of results

From Table 1, it was observed that the pre-treatment of the PMs reduced the materials carbon content and loss on ignition. These contributed to the reactivity of POFA materials. The reactivity of GSS mainly depended on its finely divided nature and its richness in Ca<sup>2+</sup> content [4]. Fig. 1 reveals the chemical compounds present in the two materials. The presence of alite, belite, and spinel coupled with higher composition of SiO<sub>2</sub> in UPOFA and the higher CaO in GSS (Table 1). These minerals in addition to the contribution of OH<sup>-</sup>, Na and Si from the alkaline activators (NS and NH) signified the possibility of the formation of calcium-silicate-hydrate (C-S-H) or Na/Ca modified aluminosilicate products (C/N-(A)-S-H) as the dominant products. The NH also plays the role of dissolution of silicates and alumina complexes in the PMs thereby resulting in the mobility of the active monomers that later condensed to form a solid skeleton.

Table 2 shows the larger diameter of GSS pores compared to that of UPOFA. The pore diameter (pore volume) and pore relative humidity (RH) had been reported by [5, 6] to affect the products shrinkage due to the increase in the surface tension of the pore liquid and their corresponding tensile stresses as shown in Eq.2 and 3 [7, 8]. The

smaller the pore diameters or micropores; the higher the tensile stress would be. Hence, it is expected that the shrinkage of AAGU0 (slag-free) products would be higher than that of the GSS blended products (AAGU<sub>x</sub>).

$$\sigma = R^*T/V_m \ln(RH/x_w) \quad (2)$$

$$\epsilon = S^*\sigma / (3(K-K_s)) \quad (3)$$

Where  $S$  is the volumetric saturation degree,  $x_w$  is the mole of water/ mole of pore solution,  $V_m$  is pore volume,  $K$  and  $K_s$  are the moduli of the entire volume and the solid skeleton ( $C$ -( $A$ )- $S$ - $H$ ), respectively.

From Fig. 2, the shrinkage of paste specimens was reduced due to the addition of the GSS in the mixture. The specimens with zero-GSS was found to have the highest shrinkage such that the 0.5-h post curing (initial) paste shrinkage was  $24 \times 10^3 \mu\epsilon$  while the 90-d shrinkage was equal to  $60.80 \times 10^3 \mu\epsilon$ . Upon adding 20%, 40%, 60% and 80% of steel slag, the initial (0.5-h) shrinkage was reduced by 62.5%, 78.5%, 80.0% and 65.7%, respectively while the 90-d shrinkage was reduced by 57.4%, 77.0%, 98.3% and 95.3%, respectively. In other words, AAGU<sub>0.6</sub> gave the highest shrinkage performance. For the mortar specimens (Fig.3), the highest 0.5-h and 90-d shrinkage of AAGU0R2.5 were  $5.24 \times 10^3 \mu\epsilon$  and  $11.82 \times 10^3 \mu\epsilon$ , respectively. The values were then reduced to  $4.04 \times 10^3 \mu\epsilon$  and  $8.20 \times 10^3 \mu\epsilon$ , respectively upon adding 20%-GSS. The initial (0.5-h) and 90-d shrinkage values further reduced to  $0.324 \times 10^3$  and  $2.71 \times 10^3 \mu\epsilon$ , respectively in AAGU<sub>0.4</sub>. Meanwhile, there was an insignificant change in the 0.5-h and 90-d shrinkages upon changing the NS/NH ratio from 1.0 to 2.5 (Fig.3). The 90-d shrinkage for NS/NH of 2.5 ( $8.20 \times 10^3 \mu\epsilon$ ) was found to be better than that of NS/NH of 1.0 ( $8.74 \times 10^3 \mu\epsilon$ ). It should be noted that addition of excessive amount of slag had previously been reported to have debilitating effects on the product strength [9, 10]

### 3. Conclusions

The study examined the contribution of steel-slag to the shrinkage performance of the alkaline activated ground slag- ultrafine palm oil fuel ash (AAGU) pastes and mortars. The results showed that the decrease in the shrinkage of the products emanated from the higher pore-volume and pore diameter of the steel-slag, which caused the increase in the bulk modulus of the solid skeleton. The shrinkage obtained in the mortar specimens were almost 2.5 to 5 times lesser the corresponding values in the paste specimens. At a workable alkaline activator/pozzolanic materials ratio, the alkaline activator ( $\text{Na}_2\text{SiO}_{3\text{aq}}/\text{NaOH}_{\text{aq}}$ ) ratios in the range of 2.5:1 to 1.0:1.0 were insignificantly affected the shrinkage of AAGU pastes and mortars.

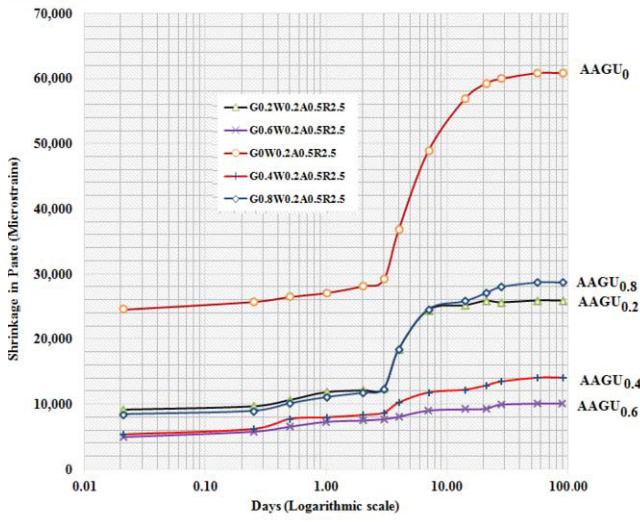


Figure 2. Variation of drying shrinkage of AAGU paste specimens

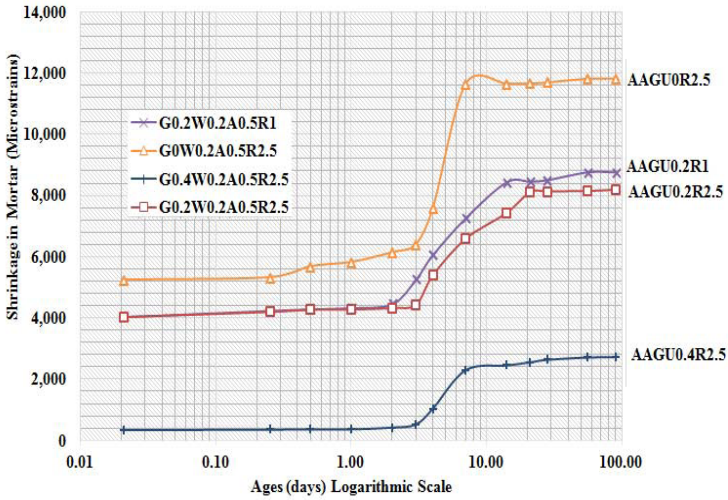


Figure 3. Variation of drying shrinkage of AAGU mortar specimens

## References

- [1] K. Sagoe-Crenstil, T. Brown, A. Taylor, Drying shrinkage and creep performance of geopolymer concrete, *Journal of Sustainable Cement-Based Materials* 2 (2013) 35-42.
- [2] C. Ridthirud, P. Chindapasirt, K. Pimraksa, Factors affecting the shrinkage of fly ash geopolymers, *International Journal of Minerals, Metallurgy and Materials* 18 (2011) 100-104.
- [3] M.O. Yusuf, M.A. Megat Johari, Z.A. Ahmad, M. Maslehuddin, Influence of curing methods and concentration of NaOH on strength of the synthesized alkaline activated ground slag-ultrafine palm oil fuel ash mortar/concrete, *Constr Build Mater* In press (2014).
- [4] H. Wan, Z. Shui, Z. Lin, Analysis of geometric characteristics of GGBS particles and their influences on cement properties, *Cem. Concr. Res.* 34 (2005) 133-137.
- [5] V. Slowik, M. Schmidt, B. Villman, Capillary shrinkage cracking – experiments and numerical simulation, in: e.a. B. H. Oh (Ed.), *Fracture Mechanics of Concrete and Concrete Structures- Assessment, Durability, Monitoring and Retrofitting of Concrete Structures*, Korea Concrete Institute, Seoul, 2010.
- [6] G.W. Scherer, Aging and Drying of Gels, *Journal of Non-Crystalline Solids* 100 (1988) 77-92.
- [7] A.W. Adamson, A.P. Gast, Physical Chemistry of Surfaces, 6th Ed., *Wiley-Interscience*, New York., 1997
- [8] D.P. Bentz, E.J. Garboczi, D.A. Quenard, Modeling drying shrinkage in reconstructed porous materials: Application to porous Vycor glass, *Modeling and Simulation in Materials Science and Engineering* 6 (1998) 211-236.
- [9] M.O. Yusuf, M.A. Megat Johari, Z.A. Ahmad, M. Maslehuddin, Evolution of alkaline activated ground blast furnace slag–ultrafine palm oil fuel ash based concrete, *Materials & Design* 55 (2014) 387-393.
- [10] M.O. Yusuf, M.A. Megat Johari, Z.A. Ahmad, M. Maslehuddin, Strength and microstructure of alkali-activated binary blended binder containing palm oil fuel ash and ground blast-furnace slag, *Construction and Building Materials* 52 (2014) 504-510.

# Use of self-compacting geopolymer concrete in a precast environment - a case study

Warren MC KENZIE<sup>1</sup>

*Murray and Roberts (pty) Ltd, South Africa*

**Abstract.** This paper serves as a case study for the potential use of geopolymer based concrete in the precast environment, paying specific attention to self-compacting properties. Based on site trials and results obtained from within the laboratory, the production of SCGC and the application thereof in the precast environment was proven feasible with positive results.

**Keywords.** Self-compacting geopolymer concrete (SCGC), binder, pulverized fuel ash (PFa), ground granulated blast furnace slag (GGBS), sodium (Na), silicate (Si), hydroxide (OH)

## Introduction

Self-compacting concrete was first developed in the late 1980's by Prof. Okamura at Ouchi University, Japan, to compensate for the decrease in the skilled labour sector [1]. Since its inception, the industry has reaped the benefits thereof. The South African construction industry/ market is one where by very deliberate and methodical steps are required to ensure that technology is firstly applied correctly, then utilized correctly and finally accepted. The use of SCGC is only different to conventional Self-Compacting Concrete (SCC) due to the reduction / elimination of Portland cement as a binder. Therefore, in an effort to gain trust within the industry, the desires and concerns of engrossed parties will be addressed; this paper will discuss use of SCGC within the precast environment.

## 1. Understanding geopolymer

The term "Geopolymer" was coined by French Prof. Joseph Davidovits in the 1970's and defines geopolymers as "mineral polymers resulting from geochemistry or geosynthesis" which are typically "amorphous to semi-crystalline three-dimensional silico-aluminate materials" [2,3].

<sup>1</sup>Corresponding author: [wwmckenzie@gmail.com](mailto:wwmckenzie@gmail.com)

Although alumino-silicate based research has been conducted since the early 1930's, it is only of late, in the past decade that serious consideration has been given to the use of this technology, with approximately 40 papers published in 2004 containing the word geopolymer as to the over 400 papers published in 2013. In order to streamline the "practical applications" in South Africa, "geopolymer" herewith refers to all mixes that contain zero Portland cement as a binder. However, the use of multiple waste materials as a binder is to be referred to as geopolymer binder.

### 1.1. Typical binders

PFa was used as the predominant binder as it contained the required chemical properties for polymerization to take place, whilst utilizing the hydraulic properties of GGBS to facilitate the control of strength development. *Table 1* lists the average chemical compositions of PFA. *Table 2* contains the average chemical compositions of GGBS within local proximity.

**Table 1.** Average chemical compositions of PFA within South Africa

Chemical Name	Chemical Formula	Avg Percentage
Alumina	Al <sub>2</sub> O <sub>3</sub>	28.5 – 29.5
Calcium Oxide	CaO	6.0 – 9.5
Ferric Oxide	Fe <sub>2</sub> O <sub>3</sub>	2.0 – 3.0
Magnesium Oxide	MgO	2.0 – 2.5
Manganese Oxide	MnO	Unavailable
Potassium Oxide	K <sub>2</sub> O	< 1.0
Silica	SiO <sub>2</sub>	36.1 – 39.8
Sodium Oxide	Na <sub>2</sub> O	< 1.5
Titanium Oxide	TiO <sub>2</sub>	1.5 – 2.0

**Table 2.** Average chemical compositions of GGBS within South Africa

Chemical Name	Chemical Formula	Avg Percentage
Alumina	Al <sub>2</sub> O <sub>3</sub>	12.0 – 12.9
Calcium Oxide	CaO	30.0 – 35.4
Ferric Oxide	Fe <sub>2</sub> O <sub>3</sub>	0.32 – 0.84
Magnesium Oxide	MgO	9.7 – 12.7
Manganese Oxide	MnO	0.97 – 1.68
Potassium Oxide	K <sub>2</sub> O	0.73 – 0.99
Silica	SiO <sub>2</sub>	36.1 – 39.8
Sodium Oxide	Na <sub>2</sub> O	0.23 – 0.49
Titanium Oxide	TiO <sub>2</sub>	0.61 – 0.69

### 1.2. Alkali-based activators

The use of alkali metals such as potassium, calcium and sodium, to name a few, are used for the activation of the binder. For the purpose of this case study, sodium silicate (Na<sub>2</sub>SiO<sub>3</sub>) with a solids content of approximately 45 %, in conjunction with sodium hydroxide (NaOH), at a ratio of 1:1 was deemed best suited. The Na<sub>2</sub>SiO<sub>3</sub> was

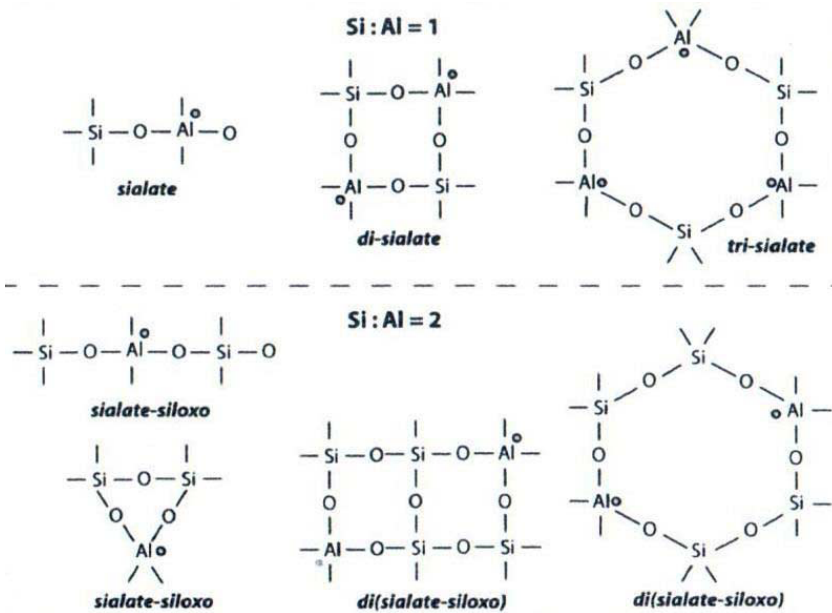


considered the main activator. The function of NaOH was to control the setting time and early strength development, whilst aiding workability.

### 1.3. Morphology, dissolution and polymerization

PFA, consisting of mostly thin walled glassy spherical particles, are best suited for use in geopolymer. Essentially PFA particles share a similar shape and size distribution with a smooth surface texture, however variations do occur. These occurrences can be traced to (a) source of coal and (b) the combustion process (i.e. temperature of firing and oxygen supply).

The term sialate is as an abbreviation for alkali silicon-oxo-aluminate, where the alkali is an earth metal as described in point 1.2 (i.e. potassium, calcium, sodium etc). *Figure 1* shows some examples of sialate molecular structures. Si:Al = 1, poly(sialate) & Si:Al = 2, poly(sialate-siloxo).



**Figure 1.** Reference to the molecular structures that are present in geopolymer

The average Si:Al ratio of PFA seemed appropriate for the synthesis of poly(sialate), Si:Al = 1, and poly(sialate-siloxo) Si:Al = 2. Adequate mixing of PFA and/or the addition of small quantities of inexpensive industrial materials presented the mix required for synthesis.

## 2. Mix design and rheology

The following design parameters were set out by the client to achieve increased daily production, with the intention of reducing costs associated with accelerated curing.

- A slump flow of 650 – 700 mm.

- 5 MPa in 6 hours.
- Gravity fed discharge.

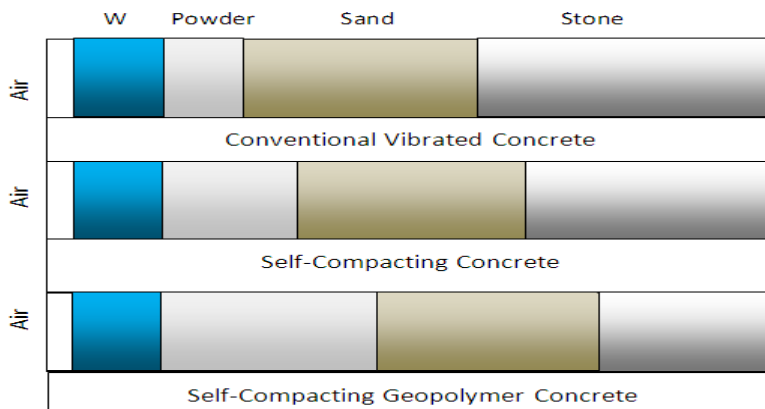
### 2.1. Mix design

The fundamental principles applied to that of conventional SCC have been incorporated into the mix design process, baring subtle changes to the material proportioning. A water reducing plasticizer was not used as it typically has little to no benefit within geopolymer concretes. *Figure 2* illustrates the different material proportions between conventional vibrated concrete, conventional SCC and SCGC.

About 80 % of the PFA was used as binder, enabling polymerization to take place; the remaining 20 % was used to replicate the characteristics of viscosity modifying admixtures (VMA). The increased binder content, with high surface area, resulted in a mix that was more thixotropic than its counterparts. As a result, the mix tended to have an amplified resistance to segregation.

Granite, being the parent rock of both the coarse and fine aggregates, was selected as it was a relatively inert material. Subsequently, materials with a chemical base of calcium (Ca), such as Dolomite, tend to produce erratic and unquantifiable results.

The coarse aggregate make up 31.6 % of the dry constitutes by volume and 26.8 % of the total mix design. The fine aggregate dry volume was 36.7 % and 31.1 % respectively. A blend of 60 % PFA with 40 % GGBS make a dry volume of 31.7 % and 26.9 % of total mix design. The total liquid content of the mix was 15.3 %, and was comprised of 7.7 % water (H<sub>2</sub>O), 3.8 % sodium silicate (Na<sub>2</sub>SiO<sub>3</sub>) and 3.8 % sodium hydroxide (NaOH).



**Figure 2.** Theoretical comparison illustrating the difference between concrete mix proportions. To be used as a visual aid only; it does not reflect accurate percentages of each constitute

## 2.2. Rheology

The use of a slump-flow,  $T_{500}$  and J-ring, as prescribed in EFNARC [3], were elected to measure the rheology of the SCGC. *Table 3* indicates the number of available test methods and the properties they evaluate. The results of which are tabled under point 4.

**Table 3.** List of test methods for workability properties of SCC [3]

No.	Method	Properties
1	Slump-flow	Filling ability
2	$T_{500}$ Slump-flow	Filling ability
3	J-ring	Passing ability
4	V-funnel	Filling ability
5	V-funnel at T 5 minutes	Segregation resistance
6	L-box	Passing ability
7	U-box	Passing ability
8	Fill-box	Passing ability
9	GTM screen stability test	Segregation resistance
10	Orimet	Filling ability

## 3. Mixing, casting and curing

A 750 ltr pan mix, with a counter current mixing action, was utilized on site during the trials. Dry materials were batched by mass and discharged into the mixer, as per the standard operating procedures of the client.

### 3.1. Mixing

Moisture content of both the coarse and fine aggregates was recorded and the appropriate adjustments applied.

GGBS was not a common material on site; as a result bagged samples were supplied. The required mass of GGBS was placed with caution into the aggregate hopper to allow for easy dispensing and improved dispersion during mixing. This was followed by the addition of PFA, discharged from a silo attached to the batch plant. The dry materials were mixed for approximately 30 seconds to ensure a homogeneous mix, at which point water was added. Following the addition of the total mixing water, the mix stiffened and clumped during the subsequent stage of mixing (approximately 60 seconds).

The total required volume of  $\text{Na}_2\text{SiO}_3$  was gradually discharged into the mixer allowing for uniform distribution throughout the mix. With minimum delay the final constitute, NaOH, was discharged into the mixer (at this stage of the process the addition of NaOH performed similarly to a plasticizer, as well as, assisting in the control of setting). Following the addition of all materials, the mix was allowed to blend for a further 2 minutes thereby ensuring adequate integration before being discharged.

### 3.2. Casting

Upon completion of mixing, the SCGC was transferred to banana shoots, as shown in *Figure 3*, via a conveyor belt system. The banana shoot allowed the operator to control the rate of discharge, whilst maintaining a constant state of energy transfer during the process. Once the casting of a product was initiated, it was completed in a single process to prevent irregularities from occurring; i.e. pour joints (not to be confused with cold joints).



**Figure 3.** Banana shoot used for gravitational feed casting of SCGC

### 3.3. Curing

This SCGC was designed to achieve 5 MPa, within 6 hours, under ambient temperatures. Once the products were cast and the desired effects attained, the moulds were left uncovered and exposed to the environment, taking care to prevent water from coming into contact with the product.

Allowing the SCGC to be exposed to the atmosphere accelerated the polymerization process and facilitated in the accomplishment of the required strength as illustrated in *Figure 4*.



**Figure 4.** Following the completion of casting, elements were placed in a pre-designated area, and allowed to cure

#### 4. Results

The results pertaining to this paper are tabled below:

- Slump-flow – *Table 4*
- $T_{500}$  Slump-flow – *Table 4*
- J-ring – *Table 4*
- Compressive strength – *Table 5*

**Table 4.** Test results of fresh concrete

Slump-flow	$T_{500}$ Slump-flow	J-ring
685 mm	1.5 – 2.0 sec	625 mm

**Table 5.** Compressive strengths

Age	Cube Dimension (mm)	Avg Cube mass (g)	Avg Load Kn	Avg MPa	Standard Deviation
3 Hrs	100 X 100	2235	24.1	2.4 MPa	0.1 MPa
4 Hrs	100 X 100	2160	30.8	3.1 MPa	0.1 MPa
5 Hrs	100 X 100	2210	35.3	3.5 MPa	0.1 MPa
6 Hrs	100 X 100	2195	39.4	3.9 MPa	0.1 MPa
24 Hrs	100 X 100	2180	105.1	10.5 MPa	0.5 MPa
3 Days	100 X 100	2190	196.4	19.6 MPa	1.7 MPa
7 Days	100 X 100	2200	295.4	29.5 MPa	2.6 MPa
28 Days	100 X 100	2165	481.4	48.1 MPa	4.2 MPa

## **5. Conclusion**

The following conclusions can be drawn based on site trials and results obtained from within the laboratory:

- The production of SCGC and the application thereof in the precast environment was proven feasible with positive results.
- Subsequent trials will be conducted, to assist in identifying diverse handling methods for assorted products (i.e. box culverts and railway sleepers).
- Financial benefits are anticipated as a result of reduction in energy costs (i.e. steam curing).

In conclusion, further advancements and applications of SCGC will be the subsequent technological leap in the field of concrete technology as we incessantly strive to lessen our carbon footprint on earth.

## **References**

- [1] Prof. Okamura, Ouchi University , (1986)
- [2] Prof. Joseph Davidovits, *Geopolymer Chemistry & Applications*, (2011), 6, 11, 30, 285, 286.
- [3] Prof. Joseph Davidovits, <http://www.geopolymer.org/science/world-wide-increase-in-geopolymer-research>, (2014)
- [4] EFNARC. 2002. Specifications and guidelines for self-compacting concrete. <http://www.efnarc.org/pdf/SandGforSCC.PDF> (2012)

# EVA/intumescent agent flame retardant composite materials using organic/inorganic hybrid filler

Ji-Won PARK<sup>a,1</sup>, Jung-Hun LEE<sup>a</sup>, Hee-Chun CHOI<sup>a</sup>, Hyun-Joong KIM<sup>a,b</sup>  
Hyun-Min JANG<sup>c</sup>, and Jung-Yun CHOI<sup>c</sup>

<sup>a</sup>Laboratory of Adhesion & Bio-Composites, Seoul National Univ, Republic of Korea

<sup>b</sup>Research Institute for Agric & Life Science, Seoul National Univ, Republic of Korea

<sup>c</sup>Korea Environment Merchandise Testing Institute, Republic of Korea

**Abstract.** Ethylene vinyl acetate copolymer as the ethylene vinyl acetate (EVA) is used in various fields, because EVA has wide selection of properties. Recently, eco-friendly flame retardants have been actively researched. Securing of flame retardants is very important, especially for the purpose of expanding the polymer. In this study, in order to develop a category of non-halogen flame retardants, intumescent agent system was introduced. Intumescent agent system - Ammonium phosphate monobasic (APP), Pentaerythritol (PER), Melamine (MEL) consisting of three substances - has demonstrated good miscibility with EVA, and the composite excellent flame-retardant properties to be implemented. By the hybrid system, mechanical properties of intumescent agent composite are dramatically increased. Polypropylene (PP) hybrid system is very useful method for improving mechanical properties

**Keywords.** EVA (ethylene vinyl acetate), intumescent agent, blowing system, flame retardant, hybrid composite

## Introduction

EVA (Ethylene Vinyl Acetate) is copolymer with vinyl acetate ethylene (VA) and ethylene. Properties of EVA depend on the ratio of VA and ethylene, and the properties have widely variation. When ethylene structure is increased, EVA have almost same properties with polyethylene that was a structure have high stiffness and good mechanical properties. But this structure has low viscosity and low melt index, so processing characteristics of the EVA is very poor. There are so many kinds of general applications of EVA such as film, sheet, modifier of petroleum goods and hot melt adhesives. Recently, using of EVA was dramatically increased by energy industries.

As above mentioned, properties of the EVA depend on their own structure. More specifically, the factor include all of the following items: vinyl acetate content, vinyl acetate distribution, crosslinking density, molecular weight and crystallinity. By introducing VA, crystallinity of EVA reduced and EVA get other properties such as optical properties (transparency, glossy), flexibility and cold resistance.

<sup>1</sup>Corresponding author: [roorouny@gmail.com](mailto:roorouny@gmail.com)

Vinyl Acetate distribution, resin, molecular weight, molecular weight distribution, crystallinity. Qualitatively reduced by the introduction of Vinyl Acetate crystalline, optical (transparency, gloss, etc.), flexibility and low temperature resistance, such as the nature of the grant which Moreover, because of Vinyl Acetate with polar properties, printability, adhesion, etc. will be granted.



Figure 1. Intumescent agent blowing system (a) polymer process (b) blowing situation

Because carbon polymeric materials are easy to burn, flame-retardant treatment is important process to polymer used in some kinds of industries. The retardant materials are used in electric area - computer / VTR / TV - , automobile, construction and transportation. Flammability regulations within the specifications of set forth in the world, wide in standards such as UL, CSA, JIS, ASTM and DIN [1,2].

In recent years, the world is interested in the environmental issues. Especially, brominated dioxins and furans that arise from brominated flame retardant are treated to bio-hazard compounds, so using of the retardant are prohibited by some countries in the world [2-4].

Table 1. Properties table of EVA

Properties	Standard	Unit	Result
Melt Index	ASTM D1238	g/10min	6
Vinyl Acetate	HPC	wt.%	28
Density	ASTM D1505	g/cm <sup>3</sup>	0.95
Melting Point	HPC	℃	71
Hardness	ASTM D2240	D scale	26
Vicat Softening Point	ASTM D1525	℃	42

In this study, it is performed that basic research on the applicability of the industry in performance and evaluation of flame-retardant composite materials using EVA. To prepare Intumescent agent polymer, blowing agent and a crosslinking agent are used. State of foaming and foaming ratio are closely related with the foaming agent of type and usage. In addition, blowing point of the agent are depending on the chemical composition, the point are should be important at polymer prepare process and application.



## 1. Preparation and evaluation of intumescent system

### 1.1. Optimized material selection for intumescent system

EVA can be broadly divided into four grades, the different types of materials are selected by process requirement that depending on the melting characteristics and the final stage of the product characteristics. These kinds of distinctions are separated according to the difference of these ratios of melt index (MI) and VA content. When MI increased, polymer flow are increased too. So MI represent typically the workability. To set high process ability, high VA content VA are selected. And MI of the EVA is over 4~5g/10min. EVA that has low MI is not well mixed in the extruder.

Figure			
Sample	MONO - PENTAERYTHRITOL	DI- PENTAERYTHRITOL	TRI - PENTAERYTHRITOL
Blowing Size	16 (um)	18	17
Forming Carbide	o	⊙	o
Figure			
Sample	GUANIDINE	GLYCINE	MELAMINE
Blowing Size	5	6	7.5
Forming Carbide	X	Δ	o
Figure			
Sample	AMMONIUM POLYPHOSPHATE	MELAMINE PHOSPHATE	AMMONIUM PHOSPHATE
Blowing Size	19	16	14
Forming Carbide	o+	Δ+	Δ

**Figure 2.** Blowing and Forming characteristic of intumescent agent (350°C)

Intumescent system is composed of carbide forming agent, blowing agent and acid catalyst. The carbide form and blowing layer are formed through mechanisms such as given in Figure 2, the flame retardant is maximized through the system. Carbide forming agent has thermal stability from the carbon skeleton. And when exposed to heat, the agent reacts with acid the catalyst and form the carbide. Mono- pentaerythritol, Dipentaerythritol, Tri-pentaerythritol, polyurethane, phenol formaldehyde resins are

used to carbide forming agent. Nitrogen-based compounds are mainly used as the blowing agent. Acid catalyst form the carbide with the carbide forming agent, and generates flame retardant gas/inorganic acid. There are many kinds of acid catalyst, such as mono ammonium phosphate, di-ammonium phosphate, ammonium poly phosphate, melamine phosphate, and so on [5-7].

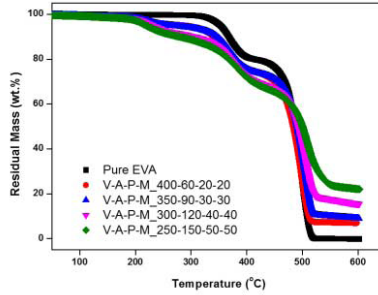
### 1.2. Flame retardant properties of Intumescent system

To evaluate flame retardant properties UL94 method [8] and cone calorimeter are used. UL94 serves as a preliminary indication of a plastic's acceptability for use as part of a device or appliance with respect to its flammability. It is not intended to reflect the hazards of a material under actual fire conditions. At UL94 test, grade rating can be categorized V0, V1 and V2, if composites used as a flame retardant material that required to be a rating of V0. When use the amount of intumescent agent over than 40%, class V0 appears (Figure 3). In particular, ignition of sample that has over 50% intumescent agent is not progress. In the specimen, a bit of a carbide are progressed and composites are maintained with stable condition. The results show that if blocks the heat transfer mechanism of intumescent agent and high applicability for flame retardant materials.



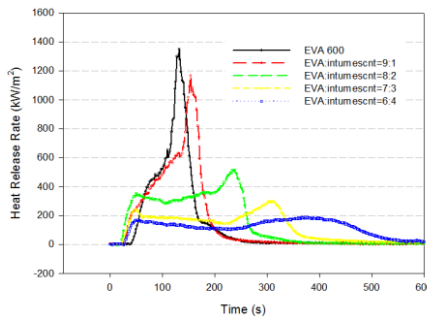
**Figure 3.** Combustion sample of flame retardant test by UL 94

Flaming performance was characterized by cone calorimeter (Fire Testing Technology LTD., UK) according to standard ISO 5660-1. Specimens (100 mm x 100 mm x 4 mm, W x L x T) were irradiated horizontally at a heat flux of 50 kW/m<sup>2</sup>. Figure 5 in this experiment the results of the test specimen EVA and a sample that is composed of intumescent agent and EVA (w/ratio 1:9) looks almost similar results.



**Figure 4.** Thermal degradation properties of intumescent agent composite

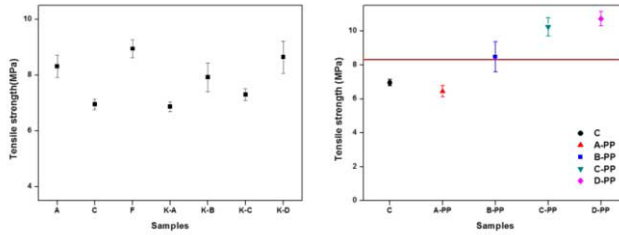
This test results similar to thermal gravimetric analysis results in figure 4, the addition of about 10% of the intumescent agent do not affect heat transfer, weight loss and additional characteristics. If more than 20%, MHR (maximum heat release rate) are sharply reduced. Containing more than 40%, especially, shows less than 15% MHR and very slow progresses of weight loss, and intumescent agent delay reaching of MHR. Reaction of intumescent agent prevent the progression to fire or grow on the surface. And intumescent agent form a carbide layer, the layer work heat transfer delaying too. This two mechanisms has synergies effect. Delaying of heat transfer is very important, because personal injury in fire accident occurred during very short time after ignition. Life can be rescued by the short delaying time.



**Figure 5.** Result of cone calorimeter (Heat Release Rate)

### 1.3. Improving the mechanical properties of intumescent system via hybrid composite

A filler to strengthen properties require high aspect ratio and high mechanical properties themselves. Typical fibers have not also a high aspect ratio but high strength that can be used to reinforce the system. The most utilizes filler of recent polymer system are glass fiber, carbon fiber, basalt fiber, and etc. Especially, Natural fibers, the price is very cheap and lighter as well as the general fiber furthermore it has high strength properties. So that fiber can be expected to enhance the composite system. Thus, by utilizing these natural fibers, the strength of EVA resin are reinforced. And for comparison, polymer blend system was introduced in this study. The range of utilizing of the system is very wide and that can be easily introduced by simple methods. However, increasing the amount of blending material has effect on the polymer process, so there are some limitations of blending ratios



**Figure 6.** Tensile strength of hybrid composite (left) with kenaf (right) with PP

In polymer blending hybrid system, tensile strength and modulus are dramatically increased by proportion of PP. Mechanical properties of hybrid composites are higher than for pure EVA. PP has higher process condition, but in this system, just a small amount of PP is used. So PP properties do not effect on the whole process (Figure 6). Natural hybrid composites are show higher properties than pure EVA at high amount of kenaf fiber. At small amount of fiber, the properties are located between pure intumescent agents system and PP hybrid system.

## 2. Conclusion

Intumescent agent system has demonstrated good miscibility with EVA, and the composite excellent flame-retardant properties. The methods are very simple way to implement flame retardant properties. But physical properties of the composite are too low application on industries such as plastic case, electrical line and so on. By the hybrid system, mechanical properties of intumescent agent composite are dramatically increased. PP hybrid system is very useful methods for improve mechanical properties. There are possibly of improving properties of natural fiber composites with intumescent agent. Further research will be continue in the future in the area.

## References

- [1] Beyer G. Nanocomposites: a new class of flame retardants for polymers. *Plast Addit Compd* 2002
- [2] Landrock AH. *Handbook of plastics flammability and combustion toxicology*. Park Ridge, NJ: Noyes Publications; 1983
- [3] Lu SY, Hamerton I. Recent developments in the chemistry of halogen-free flame retardant pol-ymer. *Progr Polym Sci* 2002
- [4] Irvine DJ, McCluskey JA, Robinson IM. Fire hazards and some common polymers. *Polym Degrad Stabil* 2000
- [5] Lomakin SM, Haslam E. *Ecological aspects of polymer flame retardancy* (new concepts in polymer science). Leiden, The Netherlands: Brill Academic Publishers; 1999.
- [6] Crummett WB. *Decades of dioxin*. Princeton, NJ: Xlibris Corp; 2002.
- [7] Bourbigot S, Le Bras M., Fundamentals: flame retardant plastics. In: Troitzsch J, editor. *Plastics flammability handbook: principles, regulation, testing and approval*. Munich, Germany/Cincinnati, OH: Hanser Publishers/Hanser Gardner Publications Inc.; 2004
- [8] UL 94 V Test (Vertical Burning Test)

# Evolution in physical modeling of structural built-up in polymer concrete and in polymer-cement concrete

Dionys VAN GEMERT<sup>1</sup>  
*KU Leuven, Triconsult n.v., Belgium*

**Abstract.** The evolution of the microstructure models with time shows a growing understanding of the microstructure formation during hydration and hardening, as well as a better knowledge of the morphology and behavior of the polymer phase within the composite material. Development and improvement of SEM analysis techniques supported better understanding of microstructure formation, and further integration of the time scale in the models was enabled by ESEM analysis during hydration and hardening of fresh mixes. Enhancement of SEM resolution and magnification capabilities also enabled to study the effect of very low amounts of polymer on the microstructure.

The paper deals with the physical mechanisms, described by the models, and shows the improvements added in the successive models, leading to a better understanding of the synergies realized by the interaction and collaboration of polymers and hydraulic cement.

**Keywords.** PCC, PC, microstructure, modeling, hydration, hardening, SEM

## Introduction

The use of polymers in combination with cement concrete dates back to 1924, when Victor Lefebure [1] used natural rubber latex to produce latex cement. Parallel to the use of polymers in combination with cement, polymer concrete was developed in which the polymer was used as full replacement for the cement binder. Most of the earlier work utilized epoxy, polyester, and furan resins. In the 1960s also methyl methacrylate and styrene monomers were used [2].

Because of the benefits of using a combination of hydraulic cement and polymer, several researchers have attempted to describe and model the formation of the complex microstructure of polymer-cement mortar and concrete (PCM, PCC). They all give a description of the hardened material consisting of two interpenetrating matrices of polymer phase and hydrated cement with random dispersion of the aggregates.

The First International Congress on Polymer Concretes was organized in London in 1975, by The Concrete Society, under chairmanship of Owen Nutt. Already at this first congress in 1975 H. R. Sasse [3] reported on the interaction between polymer admixtures and cement hydrates. He assumed that the polymers formed extremely thin

---

<sup>1</sup>Corresponding author: [dionys.vangemert@bwk.kuleuven.be](mailto:dionys.vangemert@bwk.kuleuven.be)

resin films or net-like structures on the hydrate surfaces, that are penetrated and swallowed up by the new hydration products and thus lose their effectiveness. However, that assumption only holds for the low polymer/cement ratios ( $< 2$  w%) applied in his study.

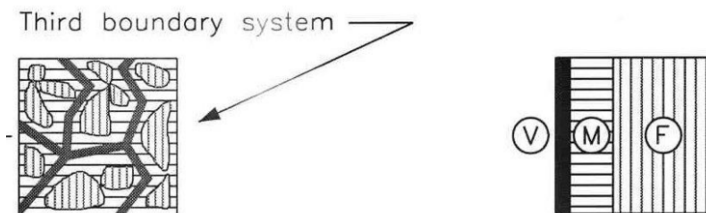
At first, the models only envisaged the interaction of polymer, cement paste and aggregates in the hardened state [4]. The starting three-step model proposed by Y. Ohama already in 1987 [5], was the first model that took into account the hardening process of the polymer phase. Afterwards, numerous specifications and modifications to this model have been proposed: Bijen and Su (1995) [6], Puterman and Malorny (1998) [7], Schorn and Schiekel (2001) [8], Beeldens e.a. (2005) [9], Dimmig-Osburg (2007) [10], Ye (2011) [11].

Latest research results on process and phasing of the film forming process of latex dispersions in cement pore solution were presented at ICPIC XIV in Shanghai (2013) [13]. Enhancement of SEM resolution and magnification capabilities also enabled to study the effect of very low amounts of polymer on the microstructure, Knapen and Van Gemert (2009) [17].

### 1. Basic classification according to R. Bareš [4]

In PCC, the binder consists of a polymer cement co-matrix. During hardening and curing, cement hydration and polymer hardening take place resulting in a co-matrix in which the polymer phase is intermingled with cement hydrates. R. Bareš (1985) introduced the concept of super-structurality of a material, i.e. the geometric distribution of the different phases in the volume. Both super-structurality and the inner specific surface of the material determine the interaction between the phases. He distinguished 4 different types of composite materials and 5 boundary situations or systems, starting from the pure binder as material (first boundary system) up to the pure filler (fifth boundary system). Figure 1 shows the third boundary system, in which the pore system becomes continuous throughout the material, enabling interaction at the interior with the environment. But also allowing impregnation of a fluid into the material structure. The Bareš model applies to polymer concrete (PC) as well as to PCC and polymer impregnated concrete (PIC).

It is obvious that this model originates from a structural engineering approach, in which properties of the composite are derived from a certain rule of mixtures. However, the model enabled to estimate the strength and stiffness increase, obtained by impregnation of polymer in cement mortar and cement concrete.

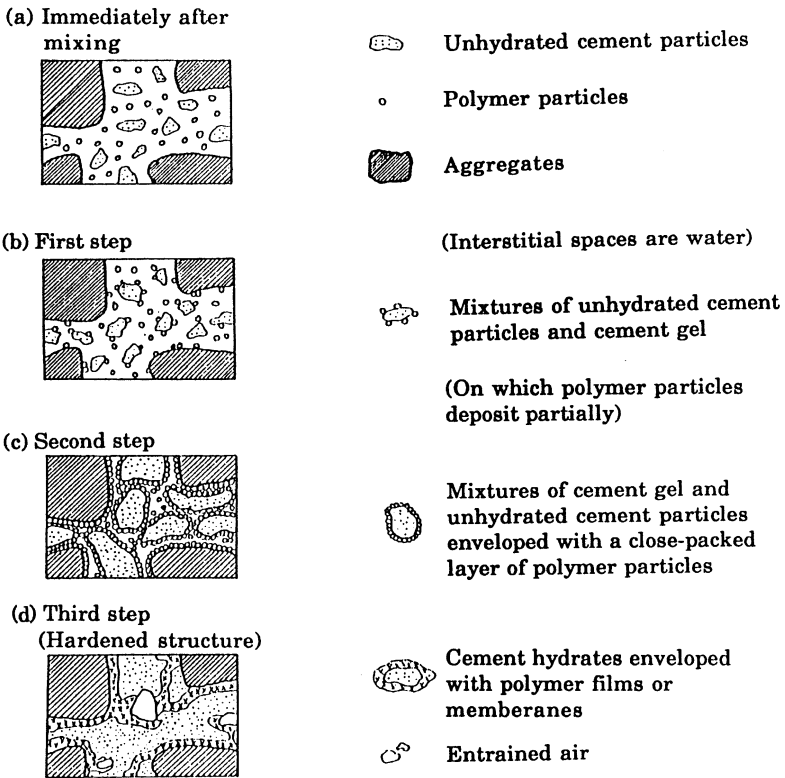


**Figure 1.** Bareš structural model: 3<sup>rd</sup> boundary system. (Void – Matrix – Filler) (1985) [4]

## 2. Microstructure models

### 2.1. Three-step model proposed by Y. Ohama [5]

The first physical model of microstructure formation in PCC was presented by Prof. Yoshihiko Ohama in 1987, Figure 2. Since then, it served as a basis for most of the later models.



**Figure 2.** Simplified Model of Formation of Polymer-Cement Co-matrix in Polymer-Modified Mortar and Concrete (Ohama, 1987) [5]

Immediately after mixing the polymer dispersion with fresh concrete, the polymer particles are uniformly dispersed in the cement paste, the mixture of cement and water. During the first step, CSH-gel is gradually formed by cement hydration, and polymer particles partially deposit on the surfaces of the cement gel and of the unhydrated cement particles.

In the second step, the polymer particles are gradually being confined in the capillary system. Water consumption at cement hydration reduces the amount of capillary water, and the polymer particles flocculate to form a continuous layer on the surfaces of unhydrated cement and of cement gel mixture, as well as at the interface between aggregates and polymer-cement paste. In the third step, water is further withdrawn due to progressing hydration, and inter-molecular attraction forces make the

polymer particles coalesce into a continuous film. A monolithic network can be formed in which the polymer phase interpenetrates throughout the cement hydrate phase.

### 2.2 Modifications of the three-step model proposed by Bijen and SU [6]

Bijen and Su [6] studied the particle size distribution of styrene-acrylic and polyvinylidene chloride polymer dispersion before and directly after mixing with cement and water. They observed that part of the polymer was immediately adsorbed on the cement particles. The adsorbed amount depends on polymer type, dispersing agents, type of cement and polymer/cement ratio. That situation remained over a number of hours before setting. At higher p/c ratio the adsorbed polymer caused agglomeration of particles and loss of workability. They also studied the hydration process by environmental scanning electron microscopy (ESEM) which became commercially available in 1988. By ESEM it was observed that through and on the adsorbed polymer layer hydration products start to grow. At increasing polymer content, the moment that hydrates are observed on and through the polymer layer is delayed: the polymer layer act as a barrier against water ingress into the cement particle. At progressing hydration, cement particles are growing and hydration products are formed directly on the cement grains and in the inner core of the original cement grains. As a consequence of hydration and crystallization the total volume of cement and water is reduced: an underpressure is created in the system by which water is sucked up in the grains. This phenomenon is known as imbibition.

The remaining free water with the polymer withdraws into areas where the capillary forces are the highest, e.g. in the narrow contact areas between cement particles and not in the larger pores. Progressing hydration consumes more water, and when the interspace between polymer particles has decreased sufficiently, the particles will coalesce. They will form a film at the places where they are most effective, namely in the contact zones between cement particles.

The polymer is highly non-uniformly distributed in the hardened material. This finding will allow to drastically decrease the amount of polymer in PCC, as shown further.

### 2.3 Modification of the three-step model proposed by Puterman and Malorny [7]

Puterman and Malorny (1998) investigated the interaction of the polymer dispersion and the cement particles at an early stage of hydration. They formulated several questions, part of which has only been answered by later researches:

- At what stage do the polymer particles of the dispersion deposit on the various mineral surfaces?
- Do polymer particles remain dispersed in the water as long as water phase is available in the mix?
- Do the deposited coalesced particles form a continuous film?
- Is the hydration reaction of cement hindered by the adsorbed particles or by the polymer film?
- Is flocculation and film formation localized in some favorable sites like aggregate surfaces, or is the polymer uniformly distributed in the material?

Based on SEM investigation, Puterman and Malorny proposed a first modified three-step model. The first stage is similar to the first step in de Ohama model. In the second stage, the polymer particles which are closely packed together at the surfaces



coalesce into a film, providing the minimum film forming temperature (MFT) is lower than the hydration temperature. Simultaneously cement hydration starts, wherever the water reaches the cement surface. An external layer of hydration products is thus formed on some parts of some of the cement grains. Other cement grains remain unhydrated because they are fully covered by the polymer. In the final stage cement hydration continues, hydrates grow and may even penetrate through the polymer film. The resulting structure is hydrated cement in which the polymer film, which initially coated the cement particles, is incorporated and contained within the cement phase.

Puterman and Malorny also show the importance of the minimum film forming temperature (MFT). They claim that if the MFT is above the curing temperature, the polymer layer will not form a continuous film, but it will remain as a layer of stacked droplets on the surface. That might influence permeability properties, as well as strength and toughness of the hardened material.

#### *2.4 Investigations by Schorn and Schiekol [8]*

Schorn and Schiekol (2001) deepened the ideas of Puterman and Malorny, and studied the binder structure of PCC with limited aggregate fraction using ESEM. If the MFT of the polymer emulsion is lower than the working temperature, a quasi homogeneous film surface without any distinctly visible structures was formed from the beginning of observation in the electron microscope. This complies with the idea that film formation indeed can take place immediately after mixing and prior to cement hydration.

They also studied the behavior of a polymer dispersion with MFT as high as 38 °C, thus well above working temperature. If the sample was stored in conditions preventing water loss, both film formation and hydration processes took place already in a short time after mixing. After some period, cement hydration prevailed. In strongly filmed regions, no hydrate products were formed. In the case the curing temperature was lower than the MFT of the polymer dispersion, the polymer particles were displaced and moved to the pores and to the crystal gaps, showing no interactions with the cement hydrates. This confirmed the observations of Bijen and Su [6].

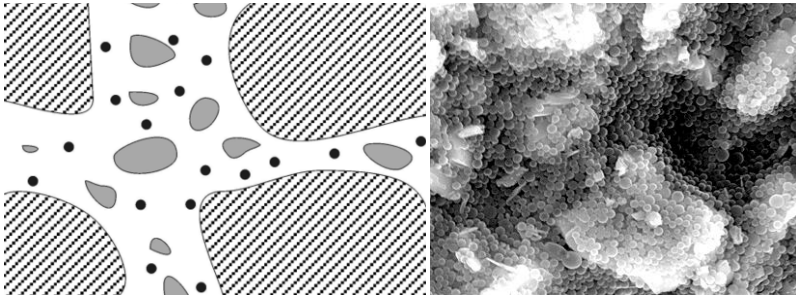
#### *2.5 Integrated model proposed by Beeldens-Ohama-Van Gemert [9]*

The influence of the polymer modification is twofold. Due to the presence of the polymers and the surfactants, a retardation of the cement hydration can be noticed, delaying compressive strength build up. On the other hand, due to the film formation or due to the interaction between the cement hydrates and the polymer particles, the tensile strength of the binder matrix as well as the adhesion strength between the aggregate and the binder increase.

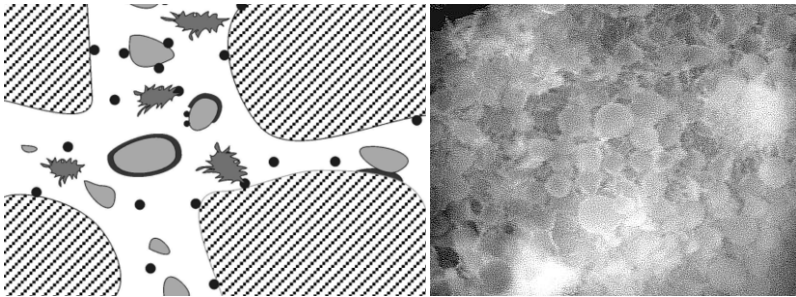
The cement hydration is retarded when the polymer-cement ratio is increased, illustrated by a decrease of compressive strength. This shows the existence, already at an early stage of curing, of a polymer film or at least it shows the interaction between polymer particles and cement particles. No influence of the polymer modification on the flexural strength is noticed in the case of standard cured and water cured samples as long as no dry curing period is applied.

The mutual influences between the cement hydrates and the polymer particles and films are incorporated in an integrated model of structure formation. The model is based on the three-step model as proposed by Ohama [7], but puts the mechanisms on the time scale and focuses on the interaction between the different components.

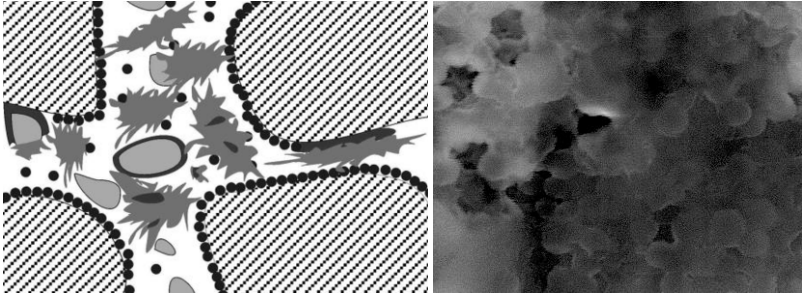
The formation of the polymer film can take place from the moment two polymer droplets have sufficient energy to overcome the repulsion forces originating from the surfactants. In other words, if the temperature is high enough to cause sufficient Brownian motion, or if additional forces are working on the liquid layer around the polymer droplets, such as capillary forces or water withdrawal by further cement hydration, two droplets can approach to each other and can coalesce to form a polymer film. This process simultaneously can take place with the cement hydration mechanism, especially in the case of dry curing conditions. Therefore, partial or full encapsulation of the cement hydrates is possible, which retards the hydration process. The different steps of the conclusive model are presented in Figure 3 to Figure 6.



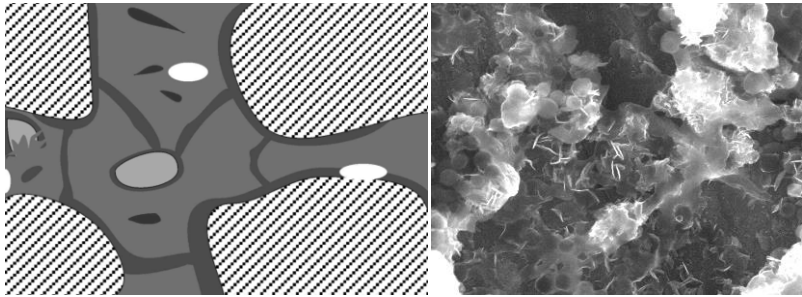
**Figure 3.** Step 1, immediately after mixing, aggregates, unhydrated cement particles, polymer particles and mixing water – small ettringite needles are formed



**Figure 4.** Step 2, after mixing, the polymer particles interact with the cement particles and the aggregates. In the case a dry curing period is introduced, a continuous film may be formed – polymer particles flocculate together, on restricted places, no coalescence has taken place at this stage



**Figure 5.** Step 3, cement hydration proceeds, polymer film formation starts on specific spots – polymer particles coalesce into a continuous film



**Figure 6.** Final step, cement hydration continues, the polymer particles coalesce into a continuous film – cement particles are hydrated

The integrated Beeldens-Ohama-Van Gemert model illustrates the effect of different curing conditions. Optimal conditions towards the strength development are a wet curing period followed by a dry curing period.

The relative humidity of the surrounding atmosphere has a large influence on the film formation and especially on the drying rate. The higher the relative humidity of the surrounding atmosphere, the lower the drying rate becomes. The slower the drying process, the lower the amount of energy needed for the polymer particles to coalesce into a continuous film. Therefore, at low drying rate, the polymer can form a film at a lower temperature. Tests indicated that even at laboratory circumstances, i.e., 20°C, a polystyrene-acrylic ester (SAE) dispersion with a MFT of 32°C, could form a continuous film, as long as the drying rate was low enough.

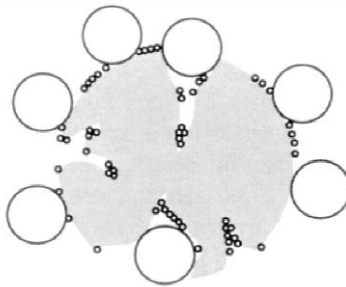
This model accentuates two important changes towards the original model of Ohama. First of all, a relation to the time scale of the different processes is made. Second, the formation of an interstitial phase, consisting of inorganic and organic precipitates in the bulk phase is pointed out. This is important towards an optimal benefit of polymer modification since the polymers present in this interstitial phase are contributing less to the final properties of the material. The optimum conditions come forward from these findings, i.e., a long period of water or moist curing (up to 28 days) during which the cement hydrates develop, followed by a period of curing at lower relative humidity during which the polymer film formation is promoted.

## 2.6 Modifications proposed by Dimmig-Osburg [10]

An extensive research was executed by A. Dimmig-Osburg (2007) on coagulation (flocculation) and film formation. In the previous models it is assumed that film formation of the polymer happens in step 4, from and by the polymer particles remaining in the pore water. However, part of the polymer is assumed to be adsorbed on the cement particles already just after mixing. Dimmig-Osburg tried to find out how much of the polymer could be adsorbed.

The surface that can be occupied by the dispersion particles depends on the size of the dispersion particles, i.e. on whether they can penetrate or not to the inner surface of the cement particles (cracks and holes), Figure 7.

Small dispersion particles can occupy a much greater part of the cement particle, with a denser packing, but with a much smaller amount of polymer needed. It is obvious that a dense and also multi-layer occupation of the cement surface can take place with very small particle sizes, with a large portion of the dispersion particles still remaining in the liquid phase to finally settle on the walls of the pores and narrows in the mortar structure. Larger dispersion particles could be completely adsorbed on the cement surface, without covering the cement surface completely. In such case the adsorption does not interfere much with the hydration processes, as only part of the particle surface is covered.



**Figure 7.** Adsorption of small or big dispersion particles on the cement surface (by courtesy of Prof. A. Dimmig-Osburg)

As most dispersions used in PCC are milky white, the size of the polymer droplets will be about 0.1 to 1  $\mu$ . The effects, studied by A. Dimmig-Osburg, will occur to a smaller or greater extent in the microstructure formation process.

The models will have to be adapted, according to the size of the polymer dispersion particles. Dimmig-Osburg observed in the experiments with a styrene acrylic acid ester at  $p/c = 0.15$  that already after 3 days the composition of the pore solution in PCC corresponded to the composition of the pore solution of conventional Portland cement, indicating that all the polymer had precipitated from the pore water solution.

This means that at normal  $p/c$  ratios of 10-20 % there is a real chance that the whole polymer fraction is rapidly adsorbed on the cement particles, and that the hydration phases penetrate through the polymer layer, or/and grow in the non-covered parts of the surface. In such case step 4 in the integrated model could be skipped. For dispersions with very small particles, there can be full coverage of the cement particles,

with a fraction of polymer still remaining in the pore solution. Step 3 in the integrated model would be skipped in such case. The drying period will cause the condensation of the polymer film and the enhancement of adhesion. Polymer precipitation and film formation already happened in an earlier phase.

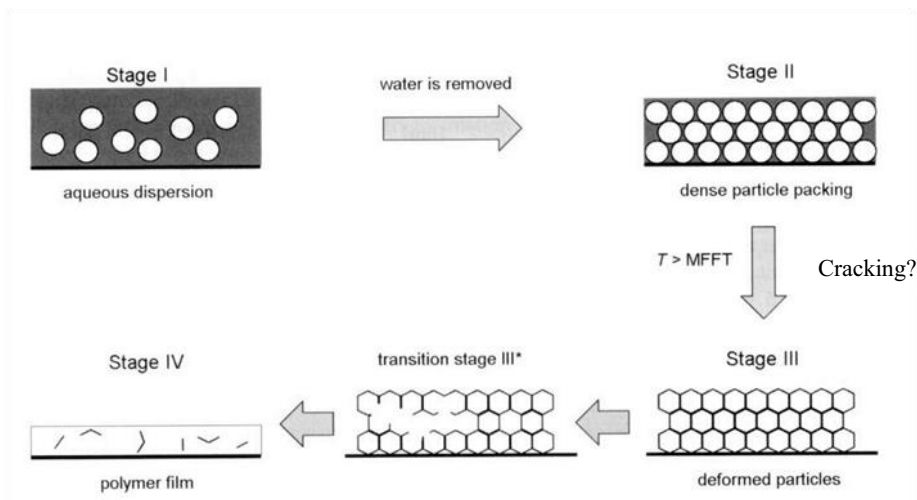
### 2.7 Modifications proposed by Ye Tian e.a. (2011)

Y. Tian e.a. [11] observed that polyacrylate (PA) polymer dispersion in PCC will deposit and flocculate in big groups at localized areas. The uniform distribution throughout the microstructure, which is assumed in the previous models, seems to be broken down. The authors call this phenomenon ‘localization of polymer modification’. This might open the possibility of purposely designed polymer latexes that could enhance PCC properties in a more effective way, at limited polymer consumption.

Flocculations may be caused by surfactant breakdown, but also by drying effects. Such drying effects also happen inside the cement paste by water consumption due to hydration, causing a suction effect inside the paste. This imbibition effect was already mentioned by Bijen [6].

### 2.8 Research on polymer film forming, presented at ICPIC XIV, Shanghai 2013 [13]

The film forming process of a nonionic ethylene-vinyl acetate (EVA) (MFT 3°C;  $T_g$  19°C) dispersion was studied in deionized water (DI) and in synthetic cement pore solution (SCPS) [13]. Generally, the film forming process can be viewed as a succession of 4 steps, shown in Figure 8: water removal by evaporation or cement hydration, leading to a dense packing of latex particles; deformation of the particles due to capillary pressure and finally formation of a homogeneous polymer film.



**Figure 8.** Successive stages I to IV during the film formation process from aqueous latex polymer dispersion (by courtesy of Prof. J. Plank, TU Munich/Garching) [13]

At transition from stage II to stage III the particles deform, until the voids between the particles have completely closed. If the particles are not flexible enough, cracking may be initiated. In that case, the particles deform and even fuse to some extent, but the generated cohesion is not good enough to withstand the drying induced tensile stress. Finally, different particles fuse together, which involves the rupture of the surfactant membranes in-between different particles, and interdiffusion of polymer chains across the interparticle boundaries.

Latex film formation was first studied on the dispersion in DI with 5 wt. % polymer content. Direct observation of the kinetics of film formation under the ESEM is not possible, because to initiate film formation, water has to be removed from the sample. Therefore, the samples were first stored under room conditions to dry, and then monitored via ESEM imaging at specific time intervals. After one hour, already a dense packing of the latex particles was observed, but no homogeneous polymer film was detected, even not after five days of storage at room temperature (RT). The authors suggest that the polyvinylalcohol (PVOH) stabilizer of the EVA latex inhibits film formation. It was also possible to redisperse the latex in water, to become the initial latex particles again.

At high pH ( $\sim 12.5$ ) and in cement pore solution, film formation occurs rapidly and produces a homogeneous film, due to the removal of the stabilizer from the surface of the particles by precipitation of PVOH in SCPS. The authors found that  $\text{Ca}^{2+}$  ions present in SCPS interact with nonionic EVA, and suggest that the presence of PVOH introduces a lightly negative surface charge to the latex particles.

Opposite results were found at studying film forming of anionic styrene/n-butylacrylate latex (FMT  $18^\circ\text{C}$ ;  $T_g$   $30^\circ\text{C}$ ) in DI and in SCPS [14]. Droplets of latex at 5 wt. % dispersed in DI and SCPS were put on an aluminium disk and allowed to dry at  $40^\circ\text{C}$  and 25 % RH over a period up to 3 days. In DI water evaporation at temperatures above MFT causes particle deformation and subsequent polymer interdiffusion. The latex spheres attain a hexagonal shape and form an ordered array, similar to honeycombs. The styrene/n-butylacrylate latex is hydrophobic by nature, but the particles are separated via hydrophilic membranes existing on their surface. Fragmentation of the hydrophilic layers and beginning coalescence could be observed after 60 min of storage. At that time the latex is in stages III\* and IV of the film forming process, Figure 8. Film formation of the aqueous polymer dispersion was completed after about 4 hours.

Dispersed in SCPS, the transition from stages II and III to stage III\*, which comprises particle coalescence to achieve a continuous polymer film is significantly retarded. After  $\sim 3$  hours, only minor particle deformation (stage II  $\rightarrow$  stage III) was observed. After 24 hours of drying, a gradual onset of latex deformation and film formation was observed, but still a large number of latex particles maintained their spherical shape and did not coalesce into a film. Only after  $\sim 3$  days film formation was completed. The authors suggest that surface adsorption of cations, particularly  $\text{Ca}^{2+}$ , onto the latex particles contributes a lot to the delay in film formation.

The findings at TU Munich provide answers to some questions, put by Puterman and Malorny [7], especially about the film formation at temperatures lower than MFT, and about the coalescence of individual particles into a film. The findings also confirm the necessity of a drying period, to initiate and finally to obtain complete film formation.

X. Yue and R. Wang reported on the effect of SBR latex on the formation of CSH in a synthetic  $C_3S$  paste [15]. They found that SBR delays hydration, changes morphology of the CSH crystals, as well as the Ca/Si ratio of the CSH phase.

At combined use of superplasticizer (SP) and latex (SAE and PAE), researchers found an important mutual interaction [16]. Depending on type (naphthalene formaldehyde or polycarboxylic) and dosage of SP (0.3 or 1 %), the adsorption was reduced from 5 up to more than 50 %. This corresponds to the findings at TU Munich, because the SP have similar effects on the cement particles, as the stabilizers on the polymer dispersion particles.

### *2.9 SEM investigations by Knapen on water soluble polymers [17]*

PCC normally involves polymer emulsions at a p/c ratio above 4-5 %. Water soluble polymers are being used already long time in adhesive mortars [4]. The idea has always been that water soluble polymers act as concrete admixtures, whose effect disappears at hardening. However, recent research demonstrates that very low amounts of water soluble polymers (p/c < 1 %) are able to considerably change the microstructure and properties of PCC [17].

The water-soluble polymers provide an improved dispersion of the cement particles in the mixing water. The tendency of certain water-soluble polymers to retard the flocculation of the cement particles minimizes the formation of a water-rich layer around the aggregate surfaces. They also provide a more uniform distribution of unhydrated cement particles in the matrix, without significant depletion near aggregate surfaces. Both effects enable to reduce the ITZ. The polymers provide a more cohesive microstructure, with a reduced amount of microcracks in the interfacial transition zones.

## **3. Conclusions**

Modeling microstructure formation in concrete-polymer composites proves to be a continuous process, guided and supported by enhanced investigation technologies, e.g. improved resolution of SEM and development of ESEM, EDX, calorimetric and particle size analysis tools. Whereas initially modeling concerned the hardened composite material, research focus moved gradually to the microstructure built up process out of the fresh mix. Based on the basic three step model developed by Y. Ohama, successive researchers introduced different modifications to the model: non-uniform distribution of polymer, imbibitions, simultaneity of hydration and polymer hardening, interaction between hydration and hardening, adsorption and film forming, early flocculation of polymer. All these modifications present improvements and better understanding of different aspects in the Ohama three step model. Although the modifications do not bring down the concepts of the three step model, they provide better understanding of the phenomena, and offer possibilities to better exploit synergies between cement and polymer by optimizing their interaction.

## References

- [1] V. Lefebure, Improvements in or relating to concrete cements, plasters and like, British patent 217.279, 1924
- [2] J. Dikeou, *Review of worldwide developments and use of polymers in concrete*, Proceedings of First International Congress on Polymer Concretes. The Construction Press, 1975, p 2-8
- [3] H.R. Sasse, *Water-soluble plastics as concrete admixtures*, Proceedings of First ICPC Congress. The Construction Press, 1975, p 168-173
- [4] R. Bareš, R. A. *conception of a structural theory of composite materials*, Brittle Matrix Composites I, Eds Brandt A. and Marshall I., 1985, p 25-48
- [5] Y. Ohama, *Principle of latex modification and some typical properties of latex modified mortars and concretes*. ACI Materials Journal, 1987, p 511-518
- [6] J. Bijen, Z. Su, *Polymer cement concrete: a contribution to modeling of the microstructure*. Proceedings of RILEM TC 113, Oostende. Ed. Van Gemert D., 1995, p 19-27
- [7] M. Puterman, W. Malorny, *Some doubts and ideas on the microstructure formation of PCC*. Proceedings of the 9<sup>th</sup> ICPC Congress, Bologna, ed. Sandrolini F., 1998, p. 165-178
- [8] H. Schorn, M. Schiekkel, *Shape and distribution of polymer particles in PCC, investigated by ESEM*. Proceedings of 10<sup>th</sup> ICPC, Hawaii, Ed. Fowler D., on CD-rom, 2001
- [9] A. Beeldens, D. Van Gemert, H. Schorn, Y. Ohama, L. Czarniecki, *From microstructure to macrostructure: an integrated model of structure formation in polymer modified concrete*. RILEM Materials and Structures, vol 38, nr 280, 2005, p 601-607
- [10] A. Dimmig-Osburg, *Microstructure of PCC – Effects of polymer components and additives*. Proceedings of 12<sup>th</sup> ICPC, Chuncheon, Korea, 2007, p 239-248
- [11] Y. Tian, Z. Li, H. Ma, N. Jin, *An investigation on the microstructure formation of polymer modified mortars in the presence of polyacrylate latex*. Proceedings of International RILEM Conference on Advances in Construction Materials through Science and Engineering, Eds. Leung C. and Wan K., Hong Kong, 2011, p 71-77
- [12] R. Wang, Z. Yang, *Progress in Polymers in Concrete*. Proceedings of ICPC XIV, April 17-20, Shanghai, 2013, Trans Tech Publications Inc.
- [13] T. Pavlitschek, Y. Jin, J. Plank, *Film formation of a non-ionic ethylene-vinyl acetate latex dispersion in cement pore solution*, Proceedings of ICPC XIV, Shanghai, 2013, Trans Tech Publications Inc., p 316-321
- [14] T. Pavlitschek, M. Gretz, J. Plank, *Effect of Ca<sup>2+</sup> ions on the Film formation of an anionic styrene/nbutylacrylate latexpolymer in cement pore solution*, Proceedings of ICPC XIV, Shanghai, 2013, Trans Tech Publications Inc., p 322-328
- [15] X. Yue, R. Wang, *Influence of SBR latex on the formation of CSH in C<sub>3</sub>S paste*, Proceedings of ICPC XIV, Shanghai, 2013, Trans Tech Publ. Inc., p 329-334
- [16] D. Han, J. Li, W. Chen, S. Zhong, *Influences of superplasticizer on the interaction between latex particles and cement grains*, Proceedings of ICPC XIV, Shanghai, 2013, Trans Tech Publications Inc., p 335-340
- [17] E. Knapen, D. Van Gemert, *Cement hydration and microstructure formation in the presence of water-soluble polymers*. Cement and Concrete Research Vol 39, Issue 1, 2009, p 6-13



# Natural fibre reinforced polymer-concrete composite for future bridge structures in earthquake regions

Libo YAN and Nawawi CHOUW<sup>1</sup>

*The University of Auckland, Department of Civil and Environmental Engineering,  
Auckland Mail Centre, Private Bag 92019, Auckland 1142, New Zealand*

**Abstract.** In comparison to glass/carbon fibres, natural fibre is environmentally friendly and can be used as reinforcement in polymer-concrete composites. The pre-fabricated flax fibre reinforced polymer (FFRP) serves as a permanent formwork and confines the coconut fibre reinforced concrete (CFRC) core. Coir in concrete enhances ductility due to a fibre bridging effect, and increases the damping due to frictions at interfaces of widely distributed cracks. This study shows the performance of FFRP-CFRC composite bridge pier models under earthquake loading. The experimental results show the potential of this new composite material for use in structures built in earthquake prone regions.

**Keywords.** Flax fibre, coir, bridge, polymer-concrete composite, seismic response

## Introduction

Glass or carbon fibre reinforced polymers (G/CFRP) have seen wide use in the automobile and aerospace industries. In addition to their non-corrosive properties, high strength and stiffness characterize their beneficial properties. These characteristics make G/CFRP a possible alternative for replacing steel as a reinforcing material [1]. Because of their high cost, the use of these polymers in civil infrastructure, to date, has been mainly limited to the retrofitting of earthquake-prone structures. In contrast, natural fibres are a low-cost alternative with no compromise in strength. In civil infrastructure prefabricated FRP tube can serve as lightweight permanent formwork of fresh concrete. At the same time it can act as non-corrosive reinforcement of the concrete. The usage of pre-fabricated FRP components can simplify the planning, accelerate the construction and thus reduce the total cost of a project [2]. Since corrosion is not an issue, the cost for long-term maintenance can also be reduced significantly. Under compressive loadings the outer FRP confinement, e.g. in the form of a tube, impedes the lateral deformation of the concrete core and thus enhances the load bearing capacity and the ductility of the composite. Under bending the inner concrete core provides internal constraint against expansion of the FRP. Consequently, local buckling of the FRP confinement can be avoided. In addition, the concrete also enhances the strength of the compressive zone and thus increases the total strength and bending stiffness of the composite [3].

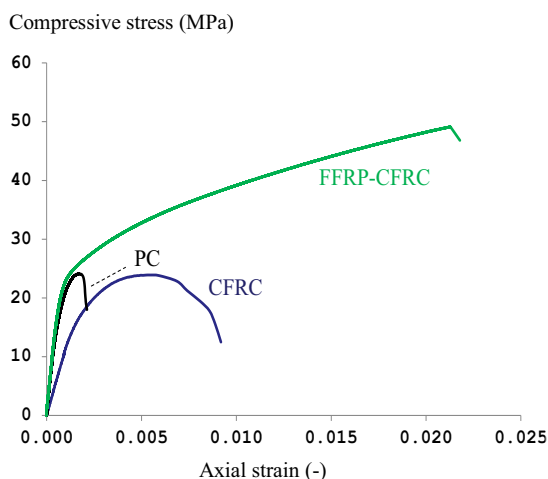
---

<sup>1</sup>Corresponding author: Director of the University of Auckland Centre for Earthquake Engineering Research, Email. [n.chouw@auckland.ac.nz](mailto:n.chouw@auckland.ac.nz)

For use as reinforcement, of the various natural fibres, flax fibre provides the best combined properties, in terms of low cost, lightweight, high strength and stiffness. As reinforcement of concrete, coir reveals its suitability since it is the toughest among other natural fibres. Coconut fibre also has the benefits of being readily available and abundant, particularly in tropical regions. Thus, flax and coconut fibres have been selected for use in the studies.

Figure 1 shows the influences of coconut fibre, used as reinforcement of the concrete core (CFRC), and the outer flax fibre reinforced polymer (FFRP) on the compressive strength of the composite. In the case considered the compressive strength of the plain concrete cylinder is about 22 MPa. The coconut fibre reinforcement does not increase the compressive strength. However, it increases the ductility of the coir-concrete composite significantly. The outer FFRP confinement more than doubles the compressive strength and also increases the ductility significantly [4].

A comprehensive review of flax fibre composites is provided in the references [5]. The bond strength between coconut fibre and the surrounding concrete has been described by Ali et al. [6]. The static and dynamic behaviour of FFRP-CFRC composite structures, the bond strength between flax fibre and polymer as well as the interface bonding between FFRP and CFRC, have all been investigated in a series of experiments at the University of Auckland [5-11].



**Figure 1.** Influence of coconut fibre reinforced concrete (CFRC) and flax fibre reinforced polymer (FFRP) constraint on composite strength

In contrast to current conventional seismic design of steel reinforced concrete structures, the use of natural fibre reinforced polymers instead of steel reinforcement will reduce the total structural mass significantly, and also avoid the long-term corrosion problems associated with steel – as observed in some of the infrastructure of large cities in coastal regions, e.g. in Toronto. Because of the lower mass and the corrosion-free materials the new FFRP-CFRC composite bridge structures can withstand higher load and require less cost to maintain.

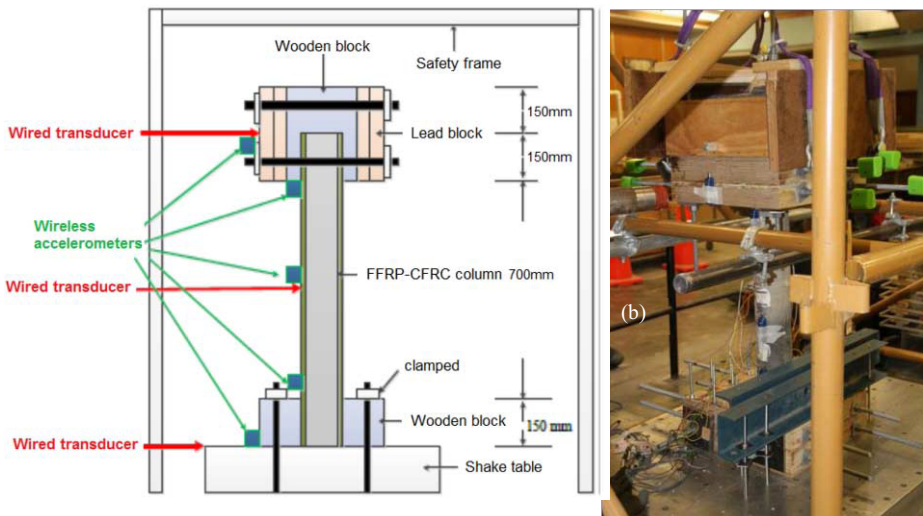
## 1. Bridge pier under earthquake loadings

This research focuses on engineering design of new composite structural members and assembled structures. Flax fibre reinforced polymer (FFRP) and coconut fibre reinforced concrete (CFRC) are used to carry the activated tensile and compressive stresses, respectively. In the laboratory a scale model bridge has been constructed. The seismic performance of a FFRP-CRFC bridge pier is investigated using a shake table.

Figure 2(a) shows a sketch of the bridge pier model. The bridge deck is simulated by a mass of 240 kg at the top. To fabricate FFRP commercial bi-directional woven flax fabric of 550 g/m<sup>2</sup>, SP high modulus 22 resin and slow hardener were used. An aluminium mould was covered with a layer of infusion sheet to enable the easy detachment of FFRP. Six layers of flax fabric were used. Each ply of the fabric has a thickness of about 1 mm. The bridge pier had a height of 1 m and the inner diameter of the concrete core was 100 mm. The mix ratio of CFRC by weight was 1 : 0.68 : 3.77 : 2.96 for cement : water : gravel : sand, respectively. The length of the coconut fibre was 50 mm, and the weight content was 1% by mass of the cement.

The FFRP-CFRC model was fixed to the shake table through a wooden foundation. To record the induced accelerations five wireless accelerometers were mounted uniformly along the height of the column. In addition, an accelerometer was attached at the top of the model. To measure the displacements three wired transducers were attached to the top, middle height and base. Figure 2(b) shows the test set-up.

To determine the dynamic properties of the model, snap-back tests were performed. From the free vibrations, the fundamental frequency and the damping ratio of the model were determined. To estimate the effect of accumulated damage under earthquake loading, subsequent snap-back tests were performed after the shake-table tests. Figure 3 shows the time history of the ground acceleration. It is simulated based on the Japanese design spectrum for medium soils.



**Figure 2.** Set-up of the experiments. (a) Instrumentation and (b) bridge pier model on shake table

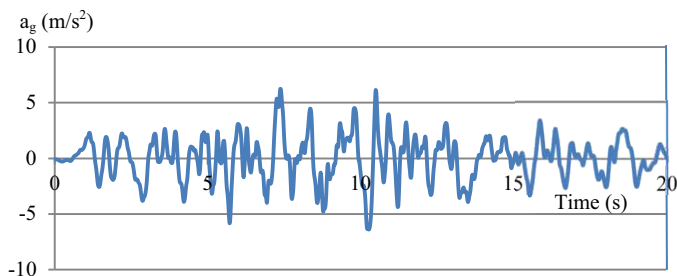


Figure 3. Ground accelerations

## 2. Experimental results

In the snap-back tests the top of the model was pulled and the setup deflected, and then released suddenly. Figure 4 shows the free vibrations initiated. The influence of the earthquake loading on the overall behaviour of the bridge pier model can be clearly seen from the longer vibration period (see dotted line in comparison with the solid line). Prior to being subjected to the earthquake loading the fundamental frequency was 3.45 Hz and the damping ratio was 11.7%. After the earthquake loading the frequency decreased to 2.09 Hz and the damping ratio increased to 21.6%. This change in the dynamic properties indicates damage to the structural components.

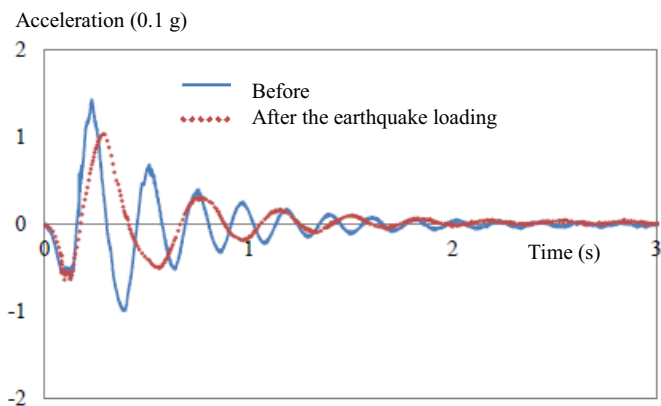


Figure 4. Earthquake impact on the dynamic property of the structure

Examination of the outer FFRP showed no macro-cracks. The damage could take place within the concrete core, and at the interface between coconut fibre and surrounding concrete, and between CFRC and FFRP. To further examine the damage the FFRP cover was partially removed by using a hand saw (see Figure 5(a)). A major horizontal crack was observed at the base of the pier next to the foundation (note the wooden block of Figure 2). This damage significantly reduced the bending stiffness of the pier and consequently the fundamental frequency of the model. The CFRC core itself did not suffer much damage, with only minor cracking as shown in Figure 5(b). The closing and opening of the micro cracks at the base dissipated the vibration energy. This resulted in a higher damping ratio compared with that observed in the snap-back induced free vibrations.

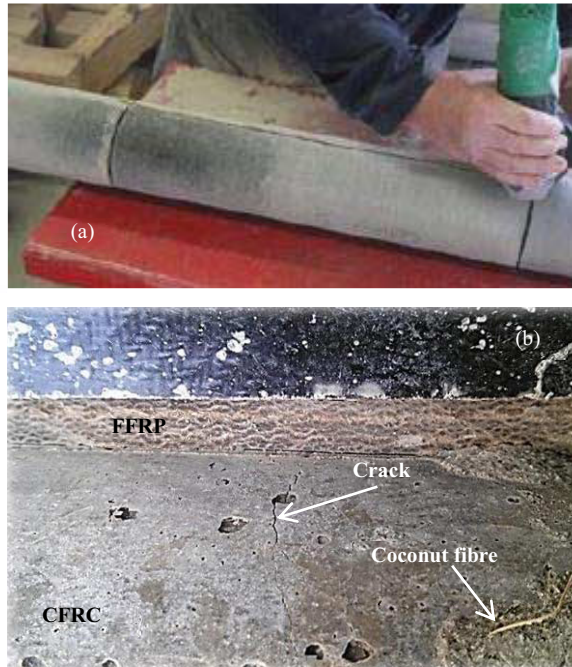


Figure 5. Observation following shake-table test. (a) Removal of FFRP and (b) crack of CFRC

### 3. Conclusions

Flax-fibre reinforced polymer (FFRP) and coconut fibre reinforced concrete (CFRC) were investigated as possible environmentally-friendly construction materials for use in civil infrastructure. In particular, the performance of a FFRP-CFRC bridge pier under earthquake loadings was investigated through a series of shake table tests.

The results of this preliminary study were promising. Despite a large number of repeated loadings no macro cracks of the outer FFRP were observed, and only minor cracking of the CFRC core occurred.

However, detailed studies are necessary to have a deeper understanding of the relationship between the seismic performance of FFRP-CFRC composite structures and the characteristics of the earthquake loadings before recommendations for seismic design using this new composite material can be derived.

### Acknowledgements

The authors would like to thank the University of Auckland for supporting this research under the FRDF Award 3702507 and for the Doctoral Scholarship to the first author. The support of the Ministry of Business, Innovation and Employment through the Natural Hazards Research Platform under the Award UoA3701868 is acknowledged.

## References

- [1] L. Yan, N. Chouw, Behaviour and analytical modelling of natural flax fibre reinforced polymer tube confined plain concrete and coir fibre reinforced concrete. *Composite Material* **47(17)** (2013a), 2133-2148.
- [2] T. Ozbakkaloglu, Compressive behaviour of concrete-filled FRP tube columns: Assessment of critical column parameters, *Engineering Structures* **51** (2013), 188-199.
- [3] L. Yan, N. Chouw, Experimental study of flax FRP tube encased coir fibre reinforced concrete composite column. *Construction and Building Materials* **40** (2013b), 1118-1127.
- [4] L. Yan, N. Chouw, Dynamic and static properties of flax fibre reinforced polymer tube confined coir fibre reinforced concrete, *Journal of Composite Materials* (in print).
- [5] L. Yan, N. Chouw, K. Jayaraman, Flax fibre and its composites - A review, *Composites Part B: Engineering* **56** (2014a), 296-317.
- [6] M. Ali, X. Li, N. Chouw, Experimental investigations on bond strength between coconut fibre and concrete, *Materials and Design* **44** (2013a), 596-605.
- [7] L. Yan, N. Chouw, X. Yuan, Improving the mechanical properties of natural fibre reinforced epoxy composites by alkali treatment. *Reinforced Plastic Composite* **31(6)** (2012a), 425-437.
- [8] L. Yan, N. Chouw, Effect of alkali treatment on vibration characteristics and mechanical properties of natural fabric reinforced composites. *Reinforced Plastic Composite* **31(13)** (2012b), 887-896.
- [9] L. Yan, N. Chouw, Compressive and flexural behaviour and theoretical analysis of flax FRP tube encased coir fibre reinforced concrete composite beams. *Materials and Design* **52** (2013c), 801-811.
- [10] L. Yan, A. Duchez, N. Chouw, Effect of bond on compressive behaviour of flax fibre reinforced polymer tube-confined coir fibre reinforced concrete. *Reinforced Plastic Composite* **32 (4)** (2013d), 273-285.
- [11] L. Yan, N. Chouw, K. Jayaraman, Effect of column parameters on flax FRP confined coir fibre reinforced concrete, *Construction and Building Materials* **55** (2014b), 299-312
- [12] L. Yan, N. Chouw, K. Jayaraman, On energy absorption capacity, flexural and dynamic properties of flax/epoxy composite tubes. *Journal of Fibers and Polymers* (in print)
- [13] M. Ali, A. Liu, S. Hao, N. Chouw, Mechanical and dynamic properties of coconut fibre reinforced concrete. *International Journal of Construction and Building Materials* **30** (2012), 814-825.
- [14] M. Ali, R. Briet, N. Chouw, Dynamic response of mortar-free interlocking structures. *Construction and Building Materials* **42** (2013b), 168-189.
- [15] Japan Society of Civil Engineers (JSCE), Earthquake resistant design codes in Japan, Maruzen, Tokyo (2000).

This page intentionally left blank

# Bituminous materials and pavements



This page intentionally left blank

# Road conditions and engineering performance of subgrade soils in part of South-Western Nigeria

N.O ADEBISI<sup>a,1</sup>, S.A. ADENIJI<sup>b</sup>, and F.O. AKINTAYO<sup>c</sup>

<sup>a</sup>*Department of Earth Sciences, Olabisi Onabanjo University, Nigeria*

<sup>b</sup>*OyoState Agricultural Development Programme (OYSADEP) Ibadan, Nigeria*

<sup>c</sup>*Department of Civil Engineering, University of Ibadan, Oyo State, Nigeria*

**Abstract.** Studies on subgrade performance and failure of road pavement in parts of Southwestern Nigeria have been carried out. However, an enquiry on native subgrade soils which combines geotechnical data with drainage system in establishing causes of road failure is yet to be made. In a reconnaissance survey, major outcrops, stable and failed (unstable) portions of roads in Ago-Iwoye were identified. Disturbed and undisturbed samples of subgrade soils were obtained by hand auger and U-4 tubes respectively from 18 burrowed pits. Grading, consistency, specific gravity and strength properties of the soils were evaluated through the laboratory, British conventional procedures.

For comparison at stable and failed (unstable) sections of the roads, subgrade soils at failed portions of the roads have higher clay (35%) and fines (11%) content with inconsistent plasticity characteristics compared to subgrade soils at stable portions. It is also observed that lower cohesive strength and unsoaked CBR apparently instigated failure of the roads pavements at Ago-Iwoye locality. In addition, the drainage system combined with soils' moisture-density enhances road failure against the axial loading.

**Keywords.** Subgrade, failed, strength, road and drainage

## Introduction

The layers of profiles developed on crystalline rocks underlie the roads in most parts of Southwestern Nigeria. Failures like cracks and waviness in rigid pavement are ubiquitous on certain parts of roads in the area. Information regarding the behavior of subgrade soils in the area had been presented [1-3.]. Previous studies found subgrade soils in the stable sections of Lagos – Ibadan expressway to have higher strength as against those underlain failed (unstable) sections [4,22]. In another report, the clay on the highway route in Bangkok are found to have higher density ( $1808 \text{ kg/m}^3$ ) and moisture content (15.50 %) compared to lateritic soils with density of  $2050 \text{ kg/m}^3$  and moisture content of 8.30% [5]. A contribution unraveled changes in grading and compaction characteristics of a residual laterised soil using fly ash [6]. Some factors which led to failures at certain sections of roads were revealed, but could not considerably exploit reasons for variation in their engineering performance [7].

<sup>1</sup>Corresponding author: [noadebisi@yahoo.com](mailto:noadebisi@yahoo.com)

Identification of clay type in the subgrade soils as the root cause of road failure at critical locations along Sylhet-Sunamganj road of Bangladesh was made [8].

In this study, hydrological factor is combined with specific geotechnical properties in the assessment of performance of subgrade soils in part of Southwestern Nigeria. Numerical data from geotechnical testing of 12 different subgrade materials for 4 trial pits are employed in the mechanistic determination of subgrade failure criteria for pavements. The study area is around Ago-Iwoye, between longitudes  $03^{\circ} 55' - 03^{\circ} 56'$  E and latitudes  $06^{\circ} 52' - 07^{\circ} 00'$  N in a tropical environment [9]. The drainage pattern is dendritic as influenced by the crystalline rocks that underlain the area, and controlled by its undulating topography as well as the land gradient. Geologically, the area is underlain by variably Migmatized Gneissic rocks of Precambrian age, which structurally trend in the SW - NE direction [10].

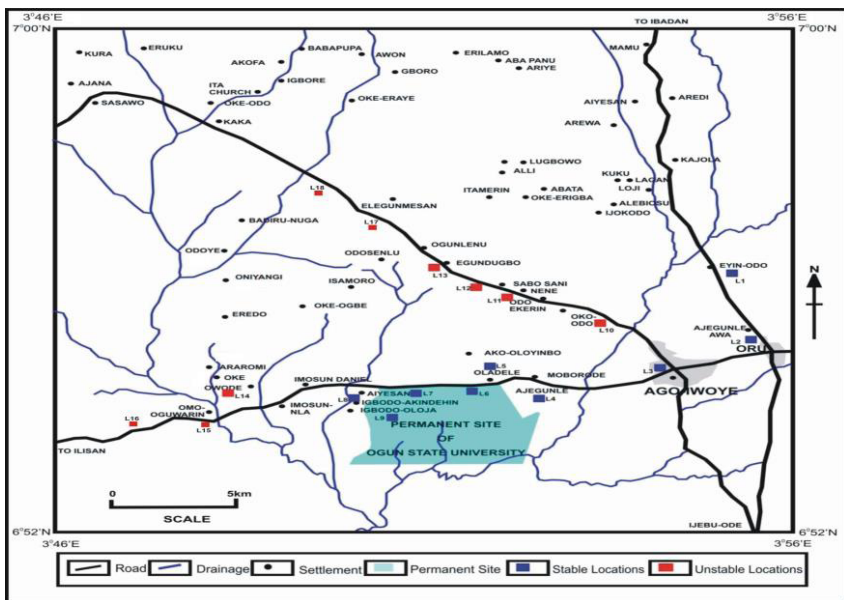


Figure 1. Map of Ago-Iwoye showing sampling points on the studied roads

## 1. Reconnaissance survey, sampling and testing

Reconnaissance survey for locating major outcrops of major rock types, which underlain the study area was followed by identification of locations where roads are stable and failed. Soils selected for this project reflect the common subgrade materials found throughout the areas underlain by Precambrian rocks of Southwestern Nigeria. Prior to laboratory testing, the disturbed and undisturbed soils were obtained by hand auger and U-4 tubes respectively, from 18 burrow pits already established. Consistency limits, specific gravity and California Bearing Ratio (CBR) tests on the soils were carried out through the British Standards, BS 1337 (1990) for civil engineering purposes. Determination of grain-size analyses and moisture-density relationship were

in accordance with the methods of Head [12], while the undrained triaxial testing followed [13].

## 2. Results and discussion

### 2.1 Index properties

The index properties of the subgrade soils are summarized in table 1. It is obvious that soils from failed sections of the roads have lower specific gravity ( $G_s$ ) values than soils from the stable sections of the roads. Selected grading curves for every pair of a stable section and an unstable section are presented in Figures 2 and 3. All the curves cover several log cycles of the semi-log paper. This is characteristic of well-graded soils as they composed of various particle sizes. Further observation of the grading characteristics reveals that the soils' composition is closely related to the range of specific gravity of grains.

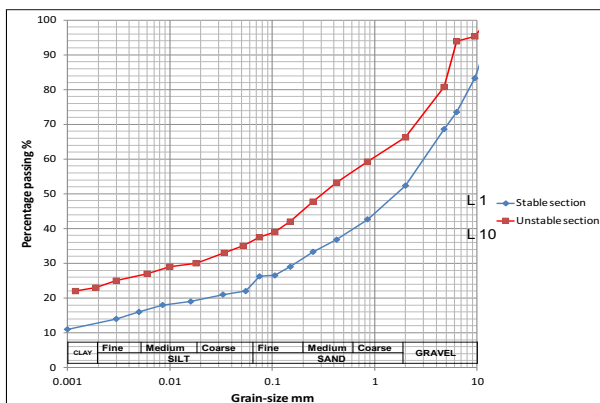


Figure 2. Grading curves for samples from locations 1 & 10

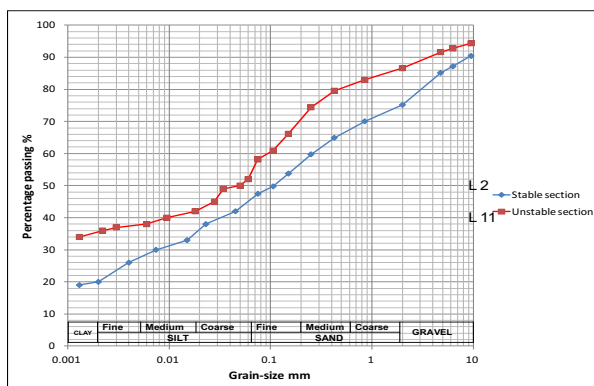
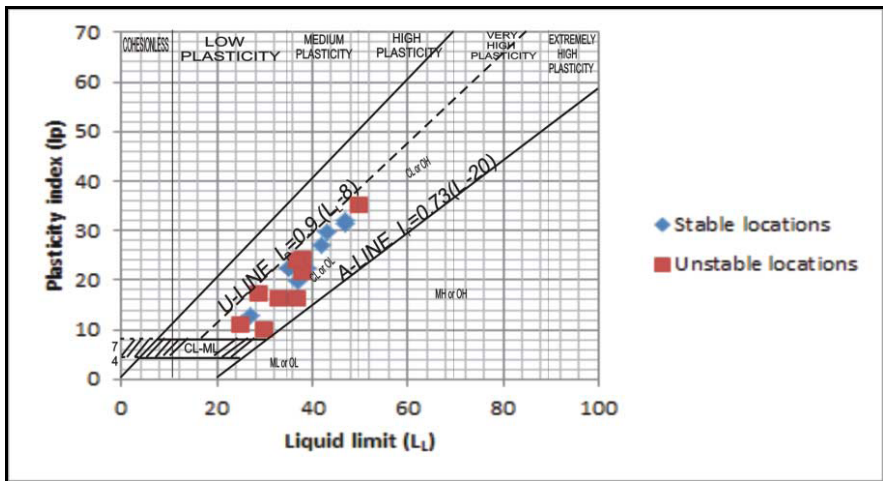


Figure 3. Grading curves for samples from locations 2 & 11

The soils have varying liquid limits ( $L_L$ ) and the plastic limit ( $L_P$ ), which also reflect in their plasticity index ( $I_P$ ). The Casagrande chart (Figure 4) shows that the soils contained inorganic clays of low plasticity to medium plasticity with a maximum liquid limit of 50%. Following the Unified Soil Classification System for British Standard [14], and the American Association of State Highway and Transportation Officials [15] classification systems. The soils are well-graded, low to medium clayey sand with gravelly silt mixtures in the group of A-4 materials. Lower  $I_P$  soils at failed sections of the roads attest to poor engineering performance of the soils [21].

**Table 1.** Index properties of the studied subgrade soils

Road	Specific Gravity		Grain-size Distribution				Consistency Limits			
			% Clay-sized Particles		% Fines		Liquid Limit ( $L_L$ ) %		Plasticity Index ( $I_P$ ) %	
	Range	Mean	Range	Mean	Range	Mean	Range	Mean	Range	Mean
Stable	2.64-2.83	2.71	4-22	14.56	2-9	6	27-47	39.1	13-32	24.4
Unstable	2.54-2.88	2.66	4-35	18.33	1-11	5.1	25-50	35.2	10-29	19.4



**Figure 4.** Casagrande chart for soil classification

*2.2 Strength properties*

Results of moisture-density relationship at West African level compactive effort, CBR and undrained shear strength parameters are summarized in Table 2. Information regarding moisture-density relationship of a subgrade soil is critical to road construction [16,20.]. Soils from stable sections of the roads show higher Maximum Dry Density (MDD) and lower average Optimum Moisture Content (OMC) than soils from unstable sections. Thus able to better support loads transmitted from the pavement structure, which in turn enhanced the degree of compaction without excessive deformation.

The mechanical strength of road subgrades is usually accessed via the California Bearing Ratio (CBR) values [17]. Lower CBR values are peculiar to subgrade soils from failed locations, indicating low bearing and weak subgrade soils. Two types of resistance are applicable to lateritic soils; cohesion (C) and friction ( $\phi$ ) [18,19]. Soils from unstable sections show wider variation in cohesive strength (5-50 kN/m<sup>2</sup>) than those from stable sections (10 - 45 kN/m<sup>2</sup>). The angles of internal friction values range between 1<sup>o</sup> and 6<sup>o</sup>, reflecting silty-clayey laterised soils.

**Table 2.** Results of moisture-density relationship

Road Con- dition	Moisture-Density Relationship				California Bearing Ratio				Shear Strength Parameters			
	Maximum Dry Density $\times 10^3$ (kg/m <sup>3</sup> )		Optimum Moisture Content (%)		Soaked CBR (%)		Unsoaked CBR (%)		Undrained Cohesion (C <sub>u</sub> ) kN/m <sup>2</sup>		Angle of Internal Friction ( $\phi$ ) Degrees	
	Range	Mean	Range	Mean	Range	Mean	Range	Mean	Range	Mean	Range	Mean
Stable	1.79-2.15	1.97	6.9-18.3	13.62	5.3-51.1	22.94	4.1-74.6	28.57	10- 45	20.56	1-5	3
Unstable	1.66-2.03	1.87	9.5-21.5	15.44	7.2-51.1	23.64	6.9-59.4	22.08	5 -50	20.33	2- 6	4

### 2.3 Hydrologic interconnection

Taking cognizance of surface water flow as an important component of road construction project, drainage systems are of several categories depending on the **topography** and **geology** of an area [23]. The dendritic drainage pattern developed in the study area (Fig. 1) is as a result of the crystalline bedrock types which are impervious and non-porous. In this case, the environmental factor responsible for failure of the roads is the drainage system. Field observation revealed that the subgrade material failed against the axial loading. Cracks of inadequate joint sealant allowed water to penetrate through the sub base into the subgrade. This tends to soften the subgrade soils inducing poor bearing capacity into them.

### 3. Conclusions and recommendations

Key geotechnical properties of the subgrade soils from failed sections indicated substandard paving properties for Nigerian roads. Higher amount of fines with low plasticity index in soils from failed sections is unfavorable for pavement construction. Strength properties deduced from subgrade soils from both sections to an extent, attest to the basis for stability and failure on the roads. The drainage system is against the axial loading aiding surface water infiltration into the subgrade to enhance failure. The remedial measure against failure in this case would be proper alignment or redesign of the roads.

### References

- [1] Gidigas M.D. (1976). *Laterite soil engineering*, Elsevier Scientific Publishing Co, New York.
- [2] Gidigas, M.D. (1984). Variability of Geotechnical Properties of Subgrade Soils in a Residual Profile Over Phyllite. *Proceedings of the Seventh Regional Conference for Africa on Soil Mechanics and Foundation Engineering*. Accra, Ghana. 1:95-104.
- [3] Omotoso, O. A., Mamodu, M. O. and Ojo, O. J. (2011). Evaluation of geotechnical properties of laterite soils in Asa-Dam area, Ilorin, Southwestern Nigeria. *World Journal of Applied Science and Technology*. Vol.3. No. 2, pp. 1 – 9
- [4] Adeyemi,G.O. and Oyeyemi, F. (2000). Geotechnical basis for failure of sections of Lagos-Ibadan expressway, Southwestern Nigeria. *Bulletin of engineering geology and the environment*. Vol. 59, No. 1, pp. 39 – 45.
- [5] GERD, (2008). *Improvement of clay and lateritic soil by using stabilizer admixture*. Report by Geotechnical Engineering Research and Development Center (GERD), Department of Civil Engineering, Faculty of Engineering Kasetsart University to Asia group international Co., LTD.
- [6] Amadi, A. (2010). Evaluation of changes in index properties of lateritic soil stabilized with Fly Ash. *Leonardo Electronic Journal of Practices and Technologies*. ISSN 1583-1078 Issue 17, pp. 69-78
- [7] Adeniji, .AS. (2011). *The physical environment and geotechnical properties of subgrade soils in Ago-Iwoye, Southwestern Nigeria*. M.Sc. Dissertation in Environmental Science, Faculty of Science, OOU, Ago-Iwoye.
- [8] Ahmed, M.Y., Nury , A. H., Islam, F. and Alam M. J. B. (2012). Evaluation of geotechnical properties and structural strength enhancing road pavement failure along Sylhet Sunamganj highway, Bangladesh. *Journal of Soil Science and Environmental Management.t.* Vol. 3, No.5, pp. 110-117.
- [9] Akanni, C.O. (1992). Aspects of climate: In *Ogun State in maps*. Onakomaya, S. O., Oyesiku, K., and Jegede, J. Edited. Rex Charles and Connel publications, pp. 18 - 19.
- [10] Oyinloye, A.O. (2011). *Geology and geotectonic setting of the Basement Complex rocks in Southwestern Nigeria: Implications on provenance and evolution*. 'Earth and Environmental sciences' Imran Ahmad Dar and Mithas Ahmad Dar, edited, pp. 97-118, ISBN 978-953-307-468-9
- [11] British Standard BS 1377. (1990). *Methods of tests for soils for civil engineering purposes*. British Standards Institutions, London, UK.
- [12] Head, K.H. (1994a) . *Manual for soil laboratory testing*. Vol. I. Soil classification and compaction tests. Halsted Press, New York, NY, USA.
- [13] Head, K.H. (1994b). *Manual of soil laboratory testing*. Permeability, shear strength and compressibility tests. Vol. 2, 2nd ed., Pentech Press, London, England, UK.
- [14] British Standard BS 5930, (1981). Code of Practice for Site Investigation. *British Standard Institution*. Unified Soil Classification System(USCS).
- [15] American Association of State Highway and Transportation Officials (AASHTO, 1982). *Standard specifications for transportation materials and methods of testing and sampling*.
- [16] Arya, L.M., and Paris, J.F., (1981). A physicoempirical model to predict the soil moisture characteristic from particle-size distribution and bulk density data. *Soil Science Society of America Journal*. Vol.45, pp.1023-1030.
- [17] Madu, R. M. (1975). Some Nigerian residual lateritic soil, their characteristics and relative road building properties on Group Basis. *Proceedings of 6th Regional Conference for Africa Soil*

- Mechanics and Foundation Engineering. Durban, South Africa. International Society for Soil Mechanics and Foundation Engineering*, pp. 121- 129.
- [18] Bowles, J. E. (1990). *Physical and geotechnical properties of soil* (2nd ed.). Mc Graw-Hill, Inc. 478 p.
- [19] Das, B.M. (2008). *Fundamentals of geotechnical engineering*. International SI Edn, Thompson Learning, Toronto.
- [20] Mayne, P. W., Christopher, B.R., and DeJong, J., (2002). *Subsurface Investigations-Geotechnical Site Characterization*, Publication No. FHWA NHI-01-031, National Highway Institute, Federal Highway Administration, Washington, DC, 300 p.
- [21] Nigerian General Specification (NGS) for Roads and Bridges, (1997). Federal Ministry of Works and Housing, Abuja, Nigeria.
- [22] Oyediran A.T., (2001) Primary cause of highway failure in Southwestern Nigeria and lasting solution. *Technical Transactions of the Nigerian Society of Engineers*, Vol. 36, No.3, pp.54 - 62.
- [23] Gupta S. C. and Larson W. E. (1979). Estimating soil water retention characteristics from particle-size distribution, organic matter percent, and bulk density. *Water Resour. Res.* Vol. 15, pp.1633-1635.



# The application of polymer coated aggregates in flexible pavement

Reshma RUGHOOPTH<sup>1</sup> and Najeeb Ahmad FOKKEERBUX

*Department of Civil Engineering, University of Mauritius, Réduit, Mauritius*

**Abstract.** The road construction industry in Mauritius has experienced a boom continuously for the past five to eight years to date. Moreover, since existing roads need maintenance and rehabilitation; these indeed result in costly investment. From literature, it has been found that for bituminous pavements, polymer can be added in the bituminous mix of the wearing and base courses either as Polymer Modified Bitumen Binder (PMBB) or as Polymer Coated Aggregates (PCA) in order to improve performance of the road and achieve longer life-span. Since only around 4% of plastic wastes in Mauritius are being recycled annually, an investigation on the use of recycled Low Density Poly-Ethylene (LDPE) to pre-treat aggregates for use in flexible pavement construction in the form of PCA was carried out. Different percentages of the polymer by weight of the same aggregates were tested for their strength properties using the i) Aggregate Crushing Value (ACV), ii) Aggregate Impact Value (AIV); and the iii) Los Angeles Abrasion (LAA) Test. It was found that the use of recycled LDPE as PCA improved the strength properties of the aggregates, giving higher resistance to loads, impact, and abrasion. As a solid waste management strategy, it was found that by using 2% polymer by weight of aggregates, approximately 7.8 tonnes of LDPE could be used in a road 1km long  $\times$  3.75 m  $\times$  55 mm thick wearing/base course(s). There would be an insignificant increase in the price of the pavement cost as a proportion of the project cost, due to the aggregate-polymer processing.

**Keywords.** Polymer coated aggregates (PCA), flexible pavement, low density polyethylene (LDPE), strength tests of aggregates, solid waste management (SWM)

## Introduction

Aggregates from non-conventional sources are gaining increasing interest. With the concept of *reduce, reuse and recycle* gaining importance, aggregates derived from industrial by-products and from the construction and demolition wastes, are of increasing interest to researchers and engineers.

Aggregates are basically defined as coarse particulate materials for use in the construction sector in the form of gravel, sand, crushed stones, slag, and recycled concrete, amongst others. Aggregate uses can either be in a composite mix or as base material.

<sup>1</sup>Corresponding author: [reshma@uom.ac.mu](mailto:reshma@uom.ac.mu)

Studies suggest that Polymer Modified Bitumen Binder and Polymer Coated Aggregates exhibit better properties for road construction in flexible pavement than conventional ones. A conventional bituminous mix consists of only aggregates and bitumen. PCA can be a form of recycled aggregate [6], since various studies show that the processing and use of PCA is done similarly as crumb rubber or scrap tyre. It is estimated that some 1200 tonnes of waste are produced daily in Mauritius distributed as follows as per the Ministry of Environment and Sustainable Development and the National Development Unit in their fact sheet on Solid Waste Management (SWM) [11]. Furthermore, it was forecasted [11] on SWM that due to increase in solid waste produced in Mauritius, the need for facilities for disposal of these solid wastes is being felt and new facilities have to be set-up. It was also found that there was a loss in economic value of recyclable solid wastes such as plastic, metal, and others.

Research [14] stated that India already uses plastic wastes such as carry bags, cups and thermocols to coat stone aggregates to be used in road construction. Moreover, tyres as wastes converted into powdered form, are blended with bitumen binder to be used together with the coated aggregates in road construction. It was observed that for a road of 1 km long by 3.375 m wide, 1 million plastic bags were used as PMBB and PCA. It was observed that at softening temperatures (of between 100 and 160°C), PE (Polyethylene), PP (Polypropylene) and PS (Polystyrene) did not emit hazardous or toxic substances/gasses, an aspect which is important for health and safety. In addition, all three polymers were insoluble in water, which is a beneficial indication for the durability of the materials with respect to water since roads are often subject to aqueous environments. The performance of a pavement related to hydrophobic properties, is confirmed by [9], stating that the mechanical strength and serviceable life of a road are reduced if water permeates the pavement structure.

Scrap tyres [8] are used in road construction through the wet and dry processes. The wet process is to apply the scrap tyre as a bitumen modifier and the dry process is to coat the aggregates with the scrap tyre. Furthermore, recycled plastic can be used in road construction similarly to scrap tyres; either as bitumen binder or for partial aggregate replacement. Moreover, [7] noted that up to 50% of asphalt pavement could be recycled for use in road construction. Recycled pavement can be used for the wearing course and the base course by controlling the flow properties and homogeneity of the mix to produce “high-performance mixtures”. Additionally, it was found that with the use of additives such as polymers, natural rubber and crumb rubber (waste tyres), when mixed in bitumen to obtain Modified Bitumen, up to 100% of life of surfacing could be obtained depending on the type of additives and the modification process used [13].

Different testing methods have been identified based on different principles used:

a) the empirical approach based on laboratory testing of properties of aggregates against specifications; and b) the understanding of mechanical and physical properties of various conditions and properties involved through the Finite Element Modelling (FEM) method.

## 1. Methodology

### 1.1. Polymer choice

LDPE, in pellet form, was chosen as the suitable polymer due to its availability on the local market and numerous findings in the Literature which gave evidence of LDPE being suitable for use as polymer coating in pre-treatment of aggregates. LDPE has a softening point below 170°C.

### 1.2. Testing of PCA

The following steps were adopted for manufacturing of PCA prior to testing: aggregates (passing 14 mm and retained on 10 mm) in batches of 1500 g were measured. Polymers in half required weight were measured. 1500 g of aggregates were placed over a sufficiently large tray so as to completely fill the tray base with one layer of aggregate batch. Half of required weight of polymers was spread over the aggregates. Thereafter, another 1500 g of aggregates were dispersed over the aggregate-polymer sample. Finally, the remaining half weight of polymer was poured over the whole sample. The oven was preheated to a temperature of 170°C and maintained for this temperature throughout the process. The tray filled with the aggregates and the polymers was placed in the oven for around 30 to 45 minutes, till the polymer softened and became translucent. The tray was removed from the oven after the aggregates have coated and, using a trowel, the aggregate-polymer mix was mixed together for 15 to 30 seconds. The mix was allowed to cool for 1 hour, resulting in PCA.

Since, primarily, the aggregates were being coated and thus, pre-treated, direct tests on aggregates were identified as follows [10]:

- Aggregate Crushing Value (ACV), [2]
- Aggregate Impact Value (AIV), [3]
- Los Angeles Abrasion (LAA), [1]

Test results were analysed against specified requirements as given in Table 1, displaying the required properties for Hot Mixed aggregates (HMA) from [10] as displayed in Table 1.

**Table 1.** Extract of strength properties of HMA aggregates [10]

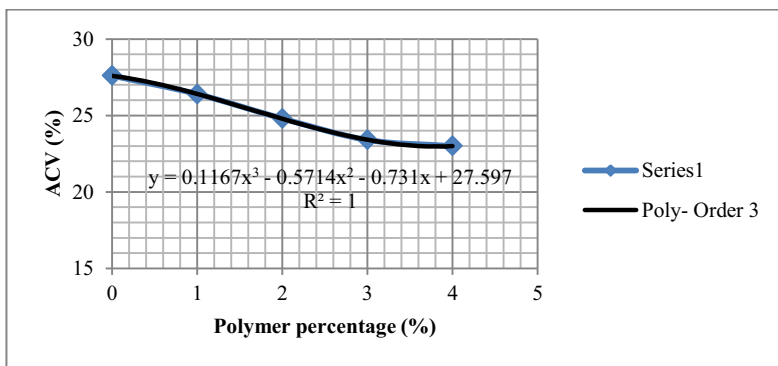
Property	Test	Properties	
		Wearing Course	Binder Course
Strength	Aggregate Crushing Value (ACV)	<25	
	Aggregate Impact Value (AIV)	<25	
	10% FACT (dry) kN	>160	
	Los Angeles Abrasion (LAA)	<30	<35

### 1.3. Benefit and Cost (B/C) analysis

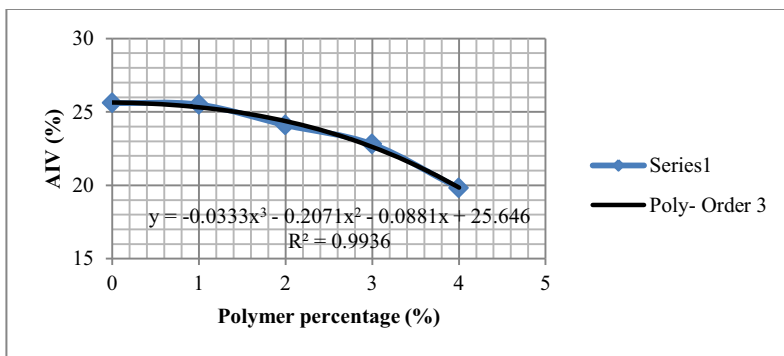
Based on assumed 5% optimum bitumen content as witnessed from the literature, coupled with prices of aggregates, polymers, and bitumen, reduced to approximate proportions, cost estimates were derived.

## 2. Test results and analysis

Different percentages of polymer by weight of the aggregates were tested for their strength properties using the i) Aggregate Crushing Value, ii) Aggregate Impact Value; and the iii) Los Angeles Abrasion (LAA) Test. Respective graphs were obtained for the mentioned tests as displayed in Figure 1 through 3. Correspondingly good correlation values have been obtained for the ACV, AIV and LAA tests. ACV values were found to decrease with increasing polymer content. This signified that mixing aggregates with polymer did improve the ACV of the aggregates.

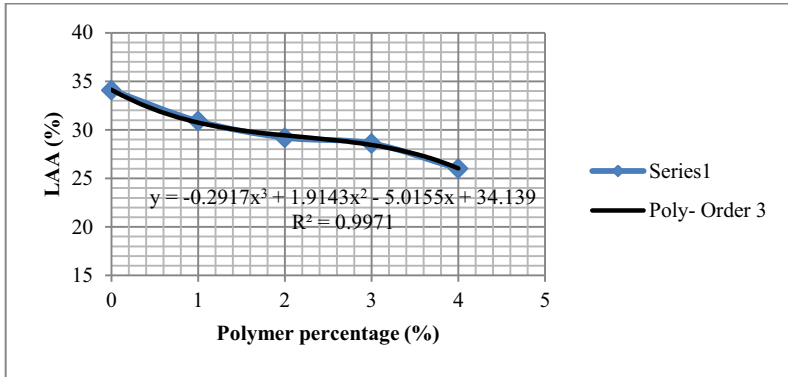


**Figure 1.** Variation of ACV (y) with varying % of polymer by weight of aggregate (poly-order 3 line of fit equation shown)



**Figure 2.** Variation of AIV(y) with varying % of polymer by weight of aggregate (poly-order 3 line of fit equation shown)

The AIV decreased with increasing polymer content. This signified that mixing aggregates with polymer improves the AIV of the aggregates; that is, the aggregates became more resistant to sudden shock or impact. From ORN 19, the wearing course and binder course need to have ACV and AIV values less than 25% respectively; hence a minimum polymer content of 2 % satisfied this requirement for both the ACV and AIV.



**Figure 3.** Variation of LAA(y) with varying polymer by weight of aggregate (poly-order 3 line of fit equation shown)

A decreasing trend was obtained for LAA with increasing polymer content. This signified that mixing aggregates with polymer improved the LAA of the aggregates; that is, the aggregates became more resistant to abrasion. For the Ten % Fines Value (TFV) [15], the 10%FACT was not obtained through experiments due to testing limitations. Instead, two equations shown below from [15] and [10] respectively were used to generate graphs (Figures 4).

BS 812: Part 111: 1990 uses the equation [15]:

$$\text{Required Force (RF)} = 4000 \div AIV \quad (1)$$

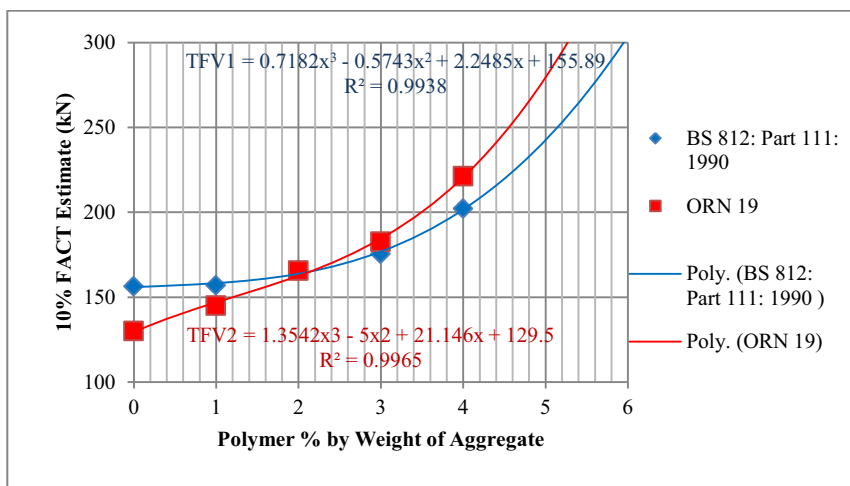
Where, RF is the force required (in kN) to produce fines in the range of 7.5% to 12.5% after doing the TFV test.

ORN 19 uses the equation:

$$ACV = 38 - (0.08 \times 10\%FACT) \quad (2)$$

Where, ACV is the Aggregate Crushing Value (in %)

10% FACT is the force required to produce 10% fines after carrying out the TFV test.



**Figure 4.** Polynomial Variation (order 3) of 10%FACT Estimate (y) with varying polymer by weight of aggregate (line of fit equation shown TFV1 for BS812; TFV2 for ORN19)

The  $R^2$  values displayed in Figure 4, suggest that a good correlation was derived from the experimental results. In fact, after 2% polymer by weight of aggregate, the 10%FACT value is greater than 160 kN for all curves; implying better crushing resistance to loads. The general formula to estimate the different proportions of bitumen aggregates and polymer for a volume of 1 m<sup>3</sup> to be used has been derived as follows.

Volume balance:

$$V_{agg.} + V_{pol.} + V_{bit.} = 1m^3 \tag{3}$$

Where,  $V_{agg.}$  is the Volume of aggregate in m<sup>3</sup>  
 $V_{pol.}$  is the Volume of polymer in m<sup>3</sup>  
 $V_{bit.}$  is the Volume of bitumen in m<sup>3</sup>

Thus,

$$\frac{M_{agg.}}{\rho_{agg.}} + \frac{M_{pol.}}{\rho_{pol.}} + \frac{M_{bit.}}{\rho_{bit.}} = 1 m^3 \tag{4}$$

Where,  $M_{agg.}$  is the Mass of aggregates in kg =  $M_{agg.}$   
 $M_{pol.}$  is the Mass of polymer in kg =  $x\% \times M_{agg.}$   
 $M_{bit.}$  is the Mass of bitumen in kg =  $5\% \times M_{agg.}$   
 $\rho_{agg.}$  is the Density of aggregates in kg/m<sup>3</sup> = 2,430 kg/m<sup>3</sup>  
 $\rho_{pol.}$  is the Density of polymer in kg/m<sup>3</sup> = 902 kg/m<sup>3</sup>  
 $\rho_{bit.}$  is the Density of bitumen in kg/m<sup>3</sup> = 1,010 kg/m<sup>3</sup>  
 $x,$  is the Polymer content for PCA

*Note: The 5% of bitumen content by weight of aggregate is due to optimum bitumen content being assumed to be 5% of weight of bitumen.*

Thus, the general equation:

$$\frac{M_{agg.}}{2430} + \frac{x\% \times M_{agg.}}{902} + \frac{5\% \times M_{agg.}}{1010} = 1 \text{ m}^3 \quad (5)$$

Table 2 summarises the proportions and costing for 1m<sup>3</sup> of bituminous mix at 5% bitumen content.

**Table 2.** Cost estimates of various mixtures

Polymer (%)	Aggregates(t) 500MUR/t	Polymer Weight(kg) 30MUR/kg	Bitumen(kg) 35MUR/kg	Total Cost (MUR)
0	2.169	0	108.5	<b>4882.00</b>
1	2.119	21.2	106.0	<b>5405.50</b>
2	2.071	41.4	103.6	<b>5903.50</b>
3	2.026	60.8	101.3	<b>6382.50</b>
4	1.982	79.3	99.1	<b>6838.50</b>

From the above, it is observed that the cost of the bituminous mix increases with increasing polymer percentage despite a decrease in use of the amount of bitumen. This is because the amount of polymer used increases at a rate which is around 8 times more than the decrease in bitumen content; and the slight variation in the prices of the polymer and bitumen used. For a road of the length by width by depth of 1 km long x 3.5 m x 50 mm using 2% polymer content, the amount of polymer absorbed in road construction is around 7.8 tonnes.

### 3. Conclusion and recommendation

The following main points can be highlighted i) addition of polymer (LDPE) in aggregates improved the strength and impact resistance of aggregates, ii) for the aggregates investigated, the minimum percentage polymer by weight of aggregate needed was 2%; and iii) the results obtained from testing are consistent with observations from previous researches in the literature.

More studies prior to the manufacturing of PCA locally for the application of PCA for road maintenance need to be carried out. Despite the increase in costs when using PCA, the implementation of PCA through pre-fabrication at crushing plants need to be investigated so as to provide for mass production of PCA, which could result in lower cost implications ; PCA could then be economically produced.

## References

- [1] ASTM C131: 2006. *Standard Test Method for Resistance to Degradation of Small Size Coarse Aggregate by Abrasion and Impact in the Los Angeles Machine*. American Society of Testing and Materials (ASTM).
- [2] BS 812: Part 110:1990. *Methods for determination of aggregate crushing value (ACV)*. British Standard Institute.
- [3] BS 812: Part 112:1990. *Methods for determination of aggregate impact value (AIV)*. British Standard Institute.
- [4] BS 812: Part 112:1990. *Methods for determination of aggregate Los Angeles Abrasion Test (LAA)*. British Standard Institute.
- [5] BS 812: Part 111:1990. *Methods for determination of ten per cent fines value (TFV)*. British Standard Institute.
- [6] CCA, 2008. *Use of recycled aggregates in construction*. Australia: Cca.
- [7] CELAURO, C., CELAURO, B. AND BOSCAINO, G., 2010. Production of innovative, recycled and high-performance asphalt for road pavements. *Resources, conservation and recycling*. 54 (2010), 337–347.
- [8] HUANG, Y., BIRD, R.N. AND HEIDRICH, O., 2007. A review of the use of recycled solid waste materials in asphalt pavements. *Resources, Conservation and Recycling*. 52 (2007), 58–73.
- [9] HUNTER, R.N., 1994. *Bituminous mixtures in road construction*. London: Thomas Telford Services Ltd.
- [10] ORN 19, 2002. *A guide to the design of hot mix asphalt in tropical and sub-tropical countries*. London: dfid.
- [11] MOE & SD, [no date]. *Fact sheet on solid waste management* [online]. Mauritius, Government of Mauritius. Available from: <http://www.gov.mu/portal/goc/menv/files/fsheet1.pdf> [Accessed 05 November 2012].
- [12] MOF & ED, 2010. *Public sector investment programme 2010* [online]. Mauritius, Government of Mauritius. Available from: [http://mof.gov.mu/English/Documents/Budget%202010/PSIP\\_2010\\_2014.pdf](http://mof.gov.mu/English/Documents/Budget%202010/PSIP_2010_2014.pdf) [Accessed 01 November 2012].
- [13] ROCKADE, S., 2012. Use of waste plastic and waste rubber tyres in flexible pavements. *2012 International Conference on Future Environment and Energy, ICBEE*. Vol. 28.
- [14] VASUDEVAN, R., NIGAM, S.K., VELKENNEDY, R., RAMALINGA, CHANDRA SEKAR, A. AND SUNDARAKANNAN, B., 2007. Utilisation of waste polymers for flexible pavement and easy disposal of waste polymers. *Proceedings of the International Conference on Sustainable Solid Waste Management*, 5 - 7 September 2007, Chennai, India. 105-111.



# Use of waste plastics and scrap rubber tyre in the wearing course of a bituminous pavement

Reshma RUGHOOPUTH<sup>1</sup> and Nishley Ravikesh GUNESH

*Department of Civil Engineering, University of Mauritius, Réduit, Mauritius*

**Abstract.** Large amount of wastes are produced that are incinerated, put in landfill or recycled. Many of these are non-biodegradable such as plastics and rubber. Waste materials can be used as a polymer in bitumen for road surfacing, thereby resulting in a more sustainable way for disposing of waste materials.

This paper aims at highlighting the use and effect of waste materials, namely scrap rubber tyre (SR), high density polyethylene (HDPE), polypropylene (PP) and polystyrene (PS) as polymers in modified bituminous mix production for use in the wearing course of pavements.

PP coated aggregates were found to be more durable as compared to SR. Only scrap rubber tyre coating treatment was found to be the suitable polymer, based on the laboratory tests on modified binder. The other waste plastics had some limitations regarding their chemical properties. Some of the properties of the modified bituminous mixes were improved with the use of the scrap rubber tyre and the others were within limits. The results revealed that 6% scrap rubber content yielded most favourable test results with regards to polymer modified bituminous binder.

**Keywords.** Modified bituminous mix, polymer, Los Angeles abrasion test, Marshall stability, penetration test, softening point test

## Introduction

With the growing population of Mauritius, traffic is increasing. It has also been noted that road surfaces need more frequent repair and maintenance. Larger amount of waste products is also being produced, that are incinerated, put in landfill or recycled. Many of the wastes are non-biodegradable such as plastics polymers and rubber. Recycling remains, however less common. A conventional bituminous mix consists of coarse aggregates, fine aggregates and bitumen. Studies have shown that waste materials can be used in a bituminous mix for road surfacing which provides a more sustainable way of disposing of waste materials [11]. Bituminous binders are extensively used by the paving industry. There are almost 100 Megatonnes of bitumen being produced annually in the world of which 95% is being utilized by paving industries. There is however a global change in climatic conditions which is affecting the performance of conventional bituminous pavements [7], hence justifying the need to develop sustainable bituminous mixes with enhanced properties.

---

<sup>1</sup>Corresponding author: [reshma@uom.ac.mu](mailto:reshma@uom.ac.mu)

Moreover, the green pavement concept is being adopted worldwide, whereby efforts are being made to conserve natural resources through recycling and re-use of waste materials. Indeed, many governmental bodies throughout the world have introduced a number of policies to sensitise people on the importance of preserving our natural resources and also encouraging the use of recycled materials [6].

This research work was primarily to: i) assess the physical, mechanical and chemical properties of plastic wastes and scrap rubber as modifiers in bituminous mixes and compare these with the conventional bituminous mix, ii) investigate an appropriate method for the replacement of conventional materials with the polymers.

## 1. Methodology

In an attempt to assess the effects of waste polymers produced on a bituminous mix, the methodology involved: selection of waste materials and the desired properties, investigations on the compatibility of the resulting binder, processing of scrap rubber tyre and waste plastics to produce polymer modified bituminous mix and the aggregates, defining and proportioning the control and test mixes, carrying out laboratory tests according to various standards including the British Standards, Eurocode and American Standards for Testing and Monitoring.

The aggregates chosen were in accordance to the specifications [10] provided by the Road Development Authority (RDA), for the strength, porosity and water absorption of the aggregates. For the polymer coated aggregate (PCA), the aggregates were heated to 170°C and the polymer was sprayed over it, ensuring uniform coating. Conversely, for the polymer modified bitumen, the PCA was mixed with 35/50 bitumen which was at 160 °C. This type of sample preparation was used for the Marshall stability test, Marshall flow test and Los Angeles test.

Sample preparation for the modified binders involved the melt blending technique. The bitumen about 300 grams was heated till fluid condition and polymer was slowly added while speed of mixer was at 1300 rpm and temperature 160-170 °C. The concentration of polymers used was varied by 0%, 2%, 4% and 6% by weight of blend. Mixing was continued for 30 minutes to produce homogeneous mixture. The empirical tests that is penetration test, softening point and ductility were then conducted on these samples. The laboratory work comprised first, the preliminary investigations on polymer coated aggregates and the modified bitumen, followed by the design, batching and testing of four types of mixes containing Polystyrene (PS), Polypropylene (PP), High density polyethylene (HDPE) and Scrap Rubber (SR) respectively. The mixture proportions for each bituminous mix type were determined in accordance to the following conditions: same bitumen grade 35/50, same type of aggregates, as well as particle size distribution, different type and quantity of polymers. Pellets of the PS, PP and HDPE were used and compared to shredded SR. These aspects allowed the investigation of the effect of polymers (type and proportions) on bituminous mixes while keeping other factors constant. Main tests carried out included the:

- Los Angeles abrasion test [1]: This test is a common method used to indicate aggregate toughness and abrasion characteristics. Its importance lies in evaluating the resistance of the constituent aggregates to crushing, degradation and disintegration in order to produce high quality bituminous mix. A lower Los Angeles value indicates aggregate that is tougher and more resistant to wear and tear [9].

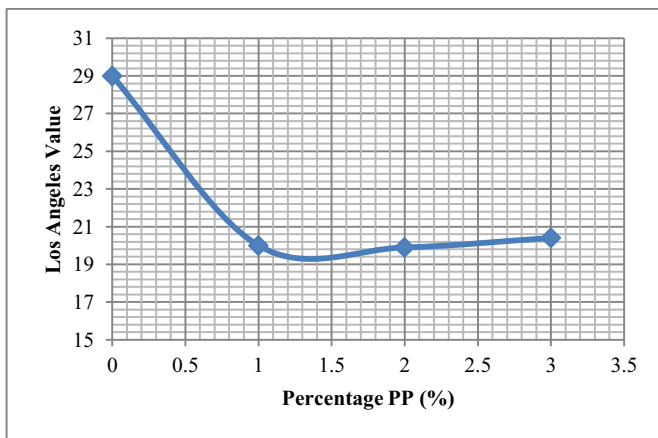
- Softening point [5]: The softening test indicates how resistant a material is to rutting and sliding.
- Penetration value [2]: The penetration test determined the hardness of bitumen by measuring the depth in decimillimetre (dmm) to which a standard loaded needle penetrated vertically in 5 seconds. A lower penetration value means the harder the material, and in hot climates a lower penetration grade is preferred [8].
- Stability and flow (Marshall) tests [4]: The test measures the maximum load that can be sustained by a bituminous material.
- Bitumen extraction test [3]: Bitumen content is important as it influences significantly the permeability, durability and stability of the bituminous mix, thereby affecting the performance of the binder.

## 2. Results and discussion

### 2.1. Los Angeles abrasion test values for polymer coated aggregates

In this test, the PP percentage was varied. Figure 1 displays the trend in Los Angeles abrasion values obtained for the aggregate and polymer coated aggregate used. Thermal degradation occurred for the polystyrene and HDPE which were in pellets form, when it was heated at a temperature of 120°C and hence did not coat onto the aggregates. A similar problem was also experience with shredded SR. It was also noted that PP used, was thermally stable at a temperature of 160°C.

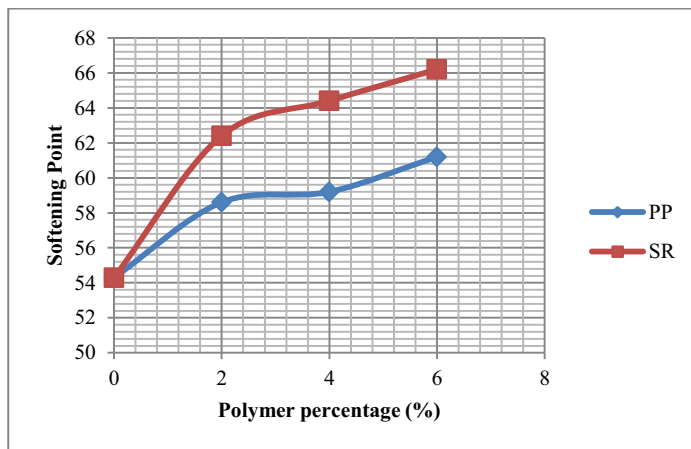
The decreasing Los Angeles values for PCA as compared to the aggregate not coated (NC) with polymer, suggests that PCA has a better resistance to wear and tear. Hence, polymer coated aggregates are expected to be more durable and less susceptible to moisture content in actual field.



**Figure 1.** Los Angeles value of plastic coated aggregate

## 2.2. Softening point test for modified binder

Figure 2 shows the variation in softening points obtained after the polymers (PP and SR) were mixed with different percentages of bitumen. PS and HDPE tests were not possible as these additives disintegrated very quickly under heat.



**Figure 2.** Softening point tests for PP and SR modified bitumen

The softening point values for the modified bitumen mixes increased with an increase in the percentage of polymer in the mix, for both the PP and SR additives. However, the softening point for the rubber modified bitumen mix has higher as compared to the PP modified mix. The results indicate that pavements using modified bituminous mix with polypropylene and scrap rubber tyre will have less deformation at high temperatures, when subjected to traffic. As the polymers dissolve in the bitumen, there is a stronger bonding which increases its resistance to temperature.

## 2.3. Penetration test for modified binder

The penetration values for both polymer modified bitumen mixes of PP and PR decrease with increasing percentage of the polymers, as indicated by the graph in Figure 3. The variations were quite similar for both the PP and the SR. The HDPE and PS pellets could not be tested as they did not soften and dissolve in the bitumen, and therefore did not mix properly. These results indicate that the modified bitumen mixes are stiffer and more viscous than the conventional mix. Thus the rutting resistance is expected to be higher, and so is the resistance to cracking.

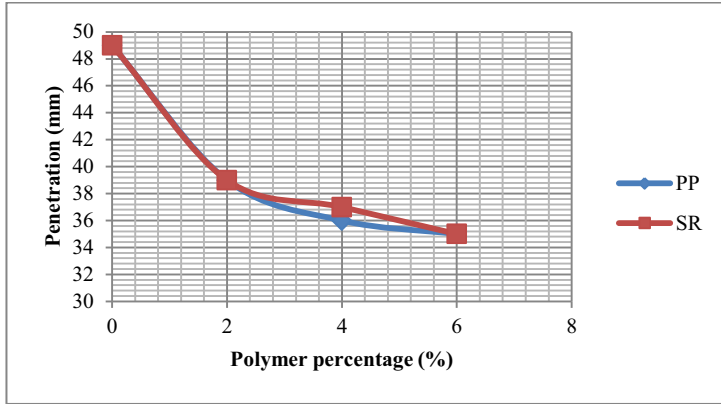


Figure 3. Penetration tests for PP and SR modified bitumen

#### 2.4. Marshall stability test for modified bituminous mixes

An increase in stability can be observed for the 2%, 4% and 6% rubber in the asphalt mixture compared to the control mix, as indicated in Figure 4. The Marshall stability value for the wearing course remained in the limit of above 9.0 kN as defined by the local authority [10].

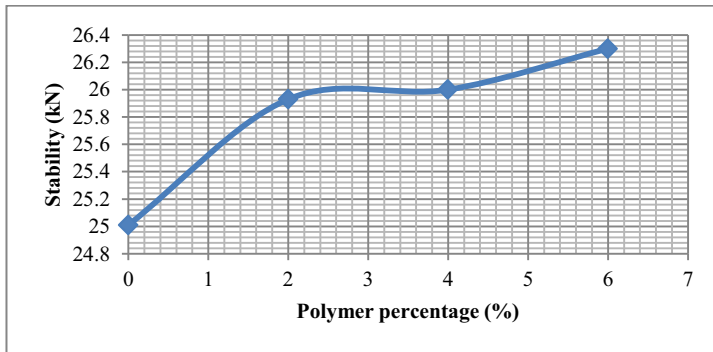


Figure 4. Marshall stability test for SR bituminous mix

#### 2.5. Marshall flow test for modified bituminous mix

A decreasing trend in the flow values of the SR mixes was observed (Figure 5). This test was not carried out on the PP modified asphalt mixture as segregation occurred. It was observed that the flow remained within limits of 1 to 4 mm, specified by the local authority [10] for wearing course for flexible pavements.

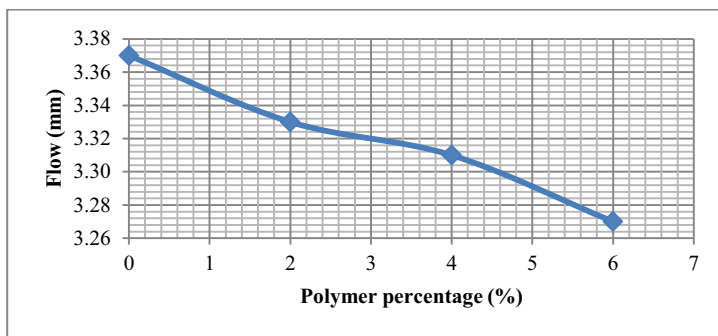


Figure 5. Marshall flow test for SR bituminous mix

### 2.6. Bitumen extraction of SR modified bituminous mixes

This test was carried out to obtain the bitumen content in the sample of bituminous mixes, and hence determine if the aggregates and bitumen had good bonding.

Table 1. Bitumen extraction results

Rubber (%)	Bitumen added in mix (% in mix)	Bitumen extracted (%in sample)	Percentage extracted
0	5.7	5.3	93
2	5.6	4.5	81
4	5.1	4.8	88
6	5.4	5.2	97

From Table 1, it can be seen that the percentage of bitumen extracted was lower for the mix containing the 2% and 4% rubber, as compared to the conventional bituminous mix. However, the percentage of bitumen extracted from the 6% rubber modified bituminous mix was higher than that of the control mix. Mixes having the 6% rubber content in the modified asphalt, had 97% bitumen extracted which implies that the binder was well mixed with aggregates and also that the bonding was quite strong.

### 3. Conclusion

The most effective polymer found in this study was the scrap rubber tyre as all tests could be carried out on the rubber modified bitumen. Above all, the values obtained when using rubber as a polymer were within the limits specified by the local authority for the wearing course of the pavement. The Los Angeles results on PP modified aggregates found that PCA had a better resistance to wear and tear.

In this study, the 6% rubber in modified bituminous mix yielded the most stable

results compared to other mixes. The properties that improved due to use of the 6% rubber in bituminous mix were the penetration value and softening point of the modified bitumen.

The results above confirm that bituminous mixes would be more resistant to the climatic effects and hence would have a longer lifespan compared to the conventional mix. Moreover, this type of bituminous mix is more sustainable than a conventional mix in the following ways:

- It makes use of waste materials and avoids dumping and incineration which causes pollution.
- It increases the lifespan of pavement and hence less repair and maintenance needed.
- It reduces the amount of bitumen used which is a non-renewable material.
- There would be a reduction in fuel consumption and carbon dioxide emission during the pavement use.

## References

- [1] British Standard European Norm 1097-2: 2010. *Tests for mechanical and physical properties of aggregates. Methods for the determination of resistance to fragmentation*. British Standard Institute.
- [2] British Standard European Norm 1426: 2007. *Penetration of bituminous materials*. British Standard Institute.
- [3] British Standard European Norm 12697 – 1: 2005. *Test methods for HMA-binder content*. British Standard Institute.
- [4] British Standard European Norm 12697 -34: 2004. *Test methods for HMA-Marshall test*. British Standard Institute.
- [5] British Standard European Norm 1427: 2007. *Softening point of bitumen (Ring and ball apparatus)*. British Standard Institute.
- [6] Epa.gov (2012) *Ground Rubber Applications | Scrap Tires | US EPA*. [online]. Available from: <http://www.epa.gov/osw/conservematerials/tires/ground.htm> [Last accessed: 10 January 2013].
- [7] Noor Zainab Habib, Ibrahim Kamaruddin, Madzalan Napiah and Isa Mohd Tan. (2011). Rheological Properties of Polyethylene and Polypropylene Modified Bitumen. *International Journal of Civil and Environmental Engineering*. Vol.2 part 3, pp. 99-100.
- [8] Mathew and Krishna Rao (2006) *Pavement materials: bitumen* [Online]. Available from: [http://www.cdeep.iitb.ac.in/nptel/Civil%20Engineering/Transportation%20Engg%201/23-Ltexthtml/nptel\\_ceTEI\\_L23.pdf](http://www.cdeep.iitb.ac.in/nptel/Civil%20Engineering/Transportation%20Engg%201/23-Ltexthtml/nptel_ceTEI_L23.pdf) [Accessed 23 February 2013].
- [9] Pavement Interactive. (2011) *Los Angeles Abrasion* [Online]. Available from: <http://www.pavementinteractive.org/article/los-angeles-abrasion> [Accessed 03 February 2013].
- [10] Specification manual of Road Development authority (RDA), 2010.
- [11] Vasudevana, R., Ramalinga, A., Chandra Sekara, Sundarakannana, B. and Velkenn, R., 2012. *A technique to dispose waste plastics in an ecofriendly way – Application in construction of flexible pavements* [Online]. Available from: <http://www.sciencedirect.com/science/article/pii/S0950061811004648> [Accessed 12 Jan 2013]

# Influence of curing time and compaction on black cotton soil stabilized with fly ash, ground-granulated blast furnace slag and lime

A. MANELI, W. K KUPOLATI, J. M NDAMBUKI and O. S ABIOLA<sup>1</sup>

*Department of Civil Engineering, Faculty of Engineering and the Built Environment  
Tshwane University of Technology, Pretoria, South Africa*

**Abstract:** The influence of curing time and compaction efforts on black cotton soil stabilized with optimum percentages of two industrial wastes activated with lime were evaluated in this paper. Fly ash (FA), ground granulated blast furnace slag (GGBFS) and lime at 12%, 8% and 1-9% respectively were used to stabilize black cotton soil in accordance to South Africa standards. Atterberg's limit, compaction and California bearing ratio (CBR) tests were conducted on the specimens. All the mixtures were compacted at optimum moisture content to different degrees of compaction and cured for 7, 28, 60 and 90 days before testing. The result showed that stabilized soil with 12% FA, 8% GGBFS and 6% lime improved the soil to be used as subgrade material. Both maximum dry density and optimum density increases as lime increased up to 6% and then decreased. It was observed that for all the curing days, there is an increase in CBR values as the compaction increased. The 60<sup>th</sup> day of curing at 100% modified AASHTO compaction effort produced the highest CBR value while the lowest CBR was recorded at 28 days at 90% compaction.

**Keywords.** Black cotton oil, compaction, curing time, industrial waste, stabilization

## Introduction

Black cotton soils undergo large amounts of heaving and shrinking due to seasonal moisture changes; and as a result, geotechnical problems arise in construction works owing to its low strength, low durability and high compressibility. Problems associated with structures on expansive soils include swelling, cracking and spalling of pavements. Practical methods for pavement construction on expansive soil are either realignment, construction of adequate drainage systems or stabilization. Soil stabilization is a technique with the aim of making the soils capable of meeting the standard requirements [1]. Engineering properties of sub-grade material including plasticity, compaction, volume stability and strength may be enhanced by adding stabilizing agents such as lime, fly ash, cement, sodium chloride and ground granulated blast furnace slag (GGBFS).

---

<sup>1</sup>Corresponding author: [AbiolaOS@tut.ac.za](mailto:AbiolaOS@tut.ac.za)



The changes in properties of the soils primarily depend upon the type and amount of binder, curing conditions and time, organic matter content and the percentage of clay. Stavridakis [2] examined the influence of curing time, compaction and composition of clayey soils on the development of their engineering properties. Unconfined compressive strength test was carried on two groups of bentonite-kaolin-sand mixtures stabilized with 4% cement and compacted at 100%, 95%, 90% relative density and cured for 7 and 28 days.

Liquid limit and maximum dry density showed strong influence on the strength and durability from the empirical equations. Kenai et al [3] investigated the effect of natural pozzolana, lime and their combinations on compaction and strength of soft clayey soils. Maximum dry density (MDD) of lime stabilized soils decreased with increase in lime content, in contrast with natural pozzolana stabilized soils, while the combination of lime-natural pozzolana increased the MDD for grey soil but decreases that of the red soil. It was concluded that the addition of lime improved the strength, especially at long term, whereas the increase was very low with the addition of natural pozzolana. Nwaiwu et al [4] evaluated the effects of compactive efforts on the compaction characteristics and California bearing ratio (CBR) of quarry dust-black cotton soil mixtures as well as the changes in swelling characteristics of the soil mixtures. It was reported that the variations in the values of the properties investigated with respect to differences in compactive efforts and quarry dust content were significant at 5% level of significance.

Utilization of waste products with soil has gained attention as a result of sustaining natural resources and the increasing problems of industrial waste management. Many industrial by-products alone or in a combination with cement and lime have been investigated, such as blast furnace slag [5], ground granulated blast furnace slag [6], lime and plastic jute [7], Rice husk ash and lime [8], lime and quarry dust [9], lime and natural pozzolana [3]. This research evaluate the influence of curing time and compaction on the engineering properties of expansive soil stabilized with fly ash (FA), ground granulated blast furnace slag (GGBFS) and lime as subgrade material.

## **1. Experimental program**

### *1.1 Material*

Black cotton soil (BCS) sample for the research was obtained from N4 road North West of South Africa. The road lies on black cotton soil. Sampling and sample preparation guidelines stipulated in TMH1 [10] of the South African standard was used while fly ash (FA), ground granulated blast furnace slag (GGBFS) and lime were obtained commercially.

### *1.2 Testing procedure*

Index properties and all other laboratory tests such as compaction characteristics, strength were conducted on the black cotton soils and treated BCS in accordance with TMH 1 - Standard Methods of Testing Road Construction Materials [10]. Stabilization of BCS with FA and GGBFS was carried out separately to determine the optimum percentage. At combined optimum percentages of FA and GGBFS, lime was added to

BCS between 1-9% at step of 1%. The moisture-density relationship of BCS and stabilized BCS and California bearing ratio (CBR) test were carried out using modified Association of American highway and transportation official (AASHTO) relative density method. The specimens were then capped with a high-strength gypsum compound to provide a flat surface on each end necessary to ensure uniform load distribution during testing. All the mixtures were compacted at optimum moisture content (two hours delay after the mixing) and cured for 7, 28, 60 and 90 days before testing.

## 2. Results and discussion

### 2.1 Index properties

Index properties of BCS, FA and GGBFS are presented in Table 1. Over 77% of BCS composed of clay and silt thus making the material to be fine graded. The material is classified as A-7-6 (15) according to AASHTO (2008) classification. In accordance with the Technical Recommendations for Highway design 4 (TRH 4) [11], the plasticity index (PI) value of a subgrade material must be equal or less than 16; the material thus qualify for modification or stabilization.

Figure 1 show the variations of plasticity index for FA and GGBFS and the optimum percentage is achieved at 12% and 8% respectively. The index properties of BCS stabilized with 12% FA, 8% GGBFS and different percentages of lime are presented in Table 2. Plasticity index was reduced to 16 at 6% lime showing an improvement in the properties of the soil thus making it suitable for use as subgrade material.

**Table 1.** Engineering properties of BCS and Characteristics of FA and GGBFS

BCS	(%)	FA	(%)	GGBFS	(%)
Liquid limit	58	Reactive CaO	< 10	LOI	0.42
Plastic limit	30	Chloride	< 0.1	SiO <sub>2</sub>	38.9
Linear shrinkage	13	SO <sub>4</sub> <sup>2-</sup>	< 2.5	Al <sub>2</sub> O <sub>3</sub>	13.6
Gravel (> 2.36 mm)	7.0	F/CaO	< 1 max	Fe	0.61
Sand (> 0.425mm)	16.0	H <sub>2</sub> O req.	< 95	CaO	37.1
Silt & clay	77.0	Soundness	< 10	MgO	8.67
Classification	Fine	Activity index 28d	> 75	K <sub>2</sub> O	1.03
		A-7-6(15) Activity index 90d	> 85	TiO <sub>2</sub>	0.76
		Reactive SiO <sub>2</sub>	> 25	MnO	0.78
OMC (%)	15.3	Particle density	2-2.4g/cm <sup>3</sup>	SO <sub>3</sub>	0.63
MDD	1704 kg/m <sup>3</sup>			Free H <sub>2</sub> O	0.39
Specific gravity	2.58	Sulphide	0.98		

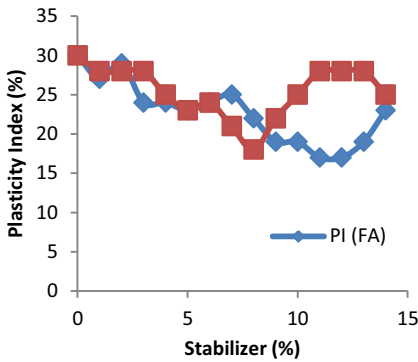


Figure 1. Variation of plasticity index with percent of FA & GGBFS

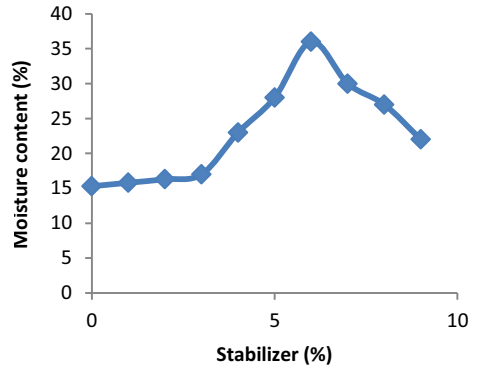


Figure 2. Variations of lime and optimum moisture content

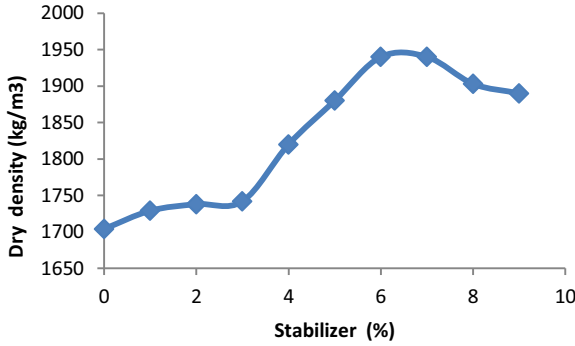


Figure 3. Variations of lime with maximum dry density

Table 2. Physical properties of BCS stabilized with 12%FA & 8% GGBFS and percentages of lime

Soil properties	BC S	A+1% B	A+2% B	A+3% B	A+4% B	A+5% B	A+6% B	A+7% B	A+8% B	A+9% B
LL (%)	58	55	60	64	60	57	59	66	64	65
PI (%)	31	18	18	17.5	17	16.5	16	17	17.5	18
LS (%)	13.7	9	9	9	9	8	9	9	10	9
MDD(kg/m³)	1704	1729	1738	1746	1820	1880	1940	1940	1903	1890
OMC (%)	15.3	15.8	16.3	17	23	28	36	30	27	22
G.M	0.38	0.49	0.49	0.49	0.49	0.49	0.49	0.49	0.49	0.49

A= 12%FA+8%GGBFS , B= lime

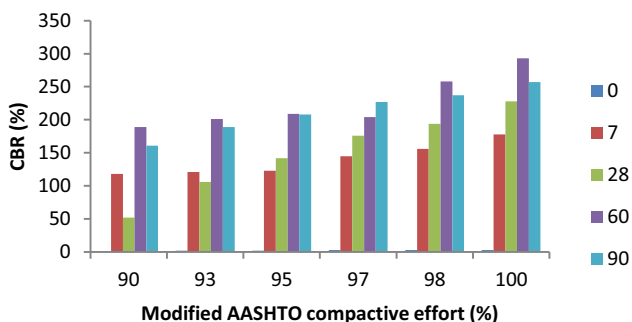
There is an increase in both maximum dry density (MDD) and optimum moisture content as shown in figures 2 and 3, as lime is been added from 1-6%, further increase shows a decline. The trend can be attributed to dissociation of admixtures with  $\text{Ca}^{2+}$  and  $\text{OH}^-$  ions to supply more  $\text{Ca}^{2+}$  for the cation exchange reaction and increase in surface area which required water for lubrication of the matrix [12].

## 2.2 Effect of curing time and compaction effort on CBR

The result of CBR is shown in Table 3 and figure 4. It was observed that there is an increase in CBR as the curing time increases till the 60<sup>th</sup> day and then decreases. While, curing period at 7days, 28days, and 60days show considerable increase of CBR value. The 60<sup>th</sup> day of curing at 100% modified AASHTO compaction effort produce the highest CBR value while the lowest CBR is recorded at 28days and at 90% compaction. Curing allows the chemical reaction between the soil and the stabilizers. Applying curing for samples for 7 days, 28 days, 60days or 90days may help the pozzolanic reactions which occur within the clay and stabilizers. Curing may have resulted in a more cementitious soil matrix thus providing more resistance against swelling. The reason for the improvement in CBR could be attributed to the occurrence of time-dependent pozzolanic reactions. Generally, it was observed that for all the curing days, there is an increase in CBR values as the relative compaction increases. There is an improvement of the soil from G9 to equivalent C4 material.

**Table 3.** BCS stabilized with additives at different level of compactive effort

Mod AASHTO Density (%)	0	7	28 (%)	60	90 days
90	1	118	52	189	161
93	2	121	106	201	189
95	2	123	142	209	208
97	3	145	176	204	227
98	3	156	194	258	237
100	3	178	228	293	257



**Figure 4.** Relationship between CBR and Modified AASHTO relative compaction level

### 3. Conclusion

This paper presents the results of the black cotton soil stabilized with a combination of fly ash, ground granulated blast furnace slag and hydrated lime. Index properties and California bearing ratio test were conducted on the black cotton soil and modified soil at optimum moisture content at various levels of compactive effort in accordance with South Africa standard. Optimum percentages of fly ash and ground granulated blast furnace slag were blended with lime at 1-9%. The combination of 12% fly ash, 8% ground granulated blast furnace slag and 6% lime improves the soil for use as subgrade material. The specimens were cured for 7days, 28days, 60days and 90days which promote the pozzolanic reactions between the clay and the stabilizers. Both the optimum moisture content and maximum dry density increases as the percentage of lime increases up to a point and then decreases. California bearing ratio increases both at different curing time and levels of compaction. Black cotton soil modified with combination of fly ash, ground granulated blast furnace slag and lime shows a significant improvement when compared with virgin soil. Thus curing time and different levels of compaction has significant roles in improving the engineering properties of expansive soil stabilization. The soil showed an improvement from G9 to equivalent C4 material.

### References

- [1] S. Koliass, V. Kasselouri-Rigopoulou, A. Karahalios. Stabilization of clayey soils with high calcium fly ash and cement. *CemConcr Compos* **27** (2005), 301–313.
- [2] E.I. Stavridakis. Influence of curing time and composition of clayey-soils on their Engineering and cement stabilization parameters. *12<sup>th</sup> Conference of International Association for computer methods and advances in Geo-mechanics* (2008)1-6 Oct, India.
- [3] S. Kenai, M. Ghrici, and K. Harichane. Effect of the combination of lime and pozzolana on the compaction and strength of soft clayey Soil: a preliminary study. *Environ Earth Sci* **66** (2012), 2197-2205.
- [4] C. M. O. Nwaiwu, S. H. Mshelia, and J. K. Durkwa. Compactive effort influence on properties of quarry dust-black cotton soil mixtures. *Int J. Geotech. Eng.* **6** (2012), 91-101.
- [5] T. Noorinaand R. K. Yadav. Influence of Blast furnace slag on the consistency limits of the black cotton soil. *Int. J. Scientific & Engr Res.* **4**(4), (2013), 456-458.
- [6] K. V. Manjunath, H. Shekhar, M. Kumar, P. Kumar and R. Kumar. Stabilization of black cotton soil using ground granulated blast furnace slag. *Proc. of Int. conf. on Advances in Architecture and Civil Engineering*, 21<sup>st</sup> -23<sup>rd</sup> June, 2012
- [7] D. Neeraja. Influence of lime and plastic jute on Strength and CBR characteristics of soft clayey soil. *Global J. Researches in Engineering*, **10**(1), (2010), 16-24.
- [8] D. K. Rao, G. V.V. Rao Rameswara, and P. R. T. Pranav. A laboratory study on the affect of rice husk ash & lime on the Properties of Marine Clay. *Int. J. Eng& Innovative Tech.*, **2**(1), (2012), 345-353.
- [9] K. S. Akshaya. A study on some geotechnical properties of lime stabilised expansive soil-quarry dust mixes. *Int. J. Emerging trends in Eng. & dev.* **1**(2), (2102), 42-49.
- [10] Standard Methods of Testing Road Construction Materials, South Africa, 1986.
- [11] Structural design of flexible pavements for Interurban and Rural Roads, 1996.
- [12] Akinmade. The Effects of Locust Bean Waste Ash on the Geotechnical Properties of Black Cotton Soil. *M.Sc. Thesis, Department of Civil Engineering, Ahmadu Bello University, Zaria*, 2008.

# Analysis of coarse aggregate microtexture in polishing process

Marta WASILEWSKA<sup>1</sup>

*Bialystok University of Technology, Faculty of Civil and Environmental Engineering*

**Abstract.** Road surface microtexture is essential for pavement skid resistance. Microtexture depends on the changes of coarse aggregate surface used for wearing course during the actual traffic conditions. Due to the fact that microtexture exists on a microscopic scale, it is very difficult to assess. An indirect method of assessing microtexture is PSV (Polished Stone Value) of coarse aggregates. However, it is difficult to explain the changes on aggregate surface during polishing process on the basis of PSV. The aim of experiment is to assess changes in the coarse aggregate microtexture with the polishing process based on the analysis of digital images, which are made by optical microscopy. Coarse aggregates from dolomite, granodiorite, gabbro, dolorite, sandstone were chosen for the tests. The polishing process of aggregate was divided into two phases and carried out in the accelerated polishing machine. The standard deviation  $\sigma_n$  from the histogram of intensities digital image of the surface is a measure of microtexture. During the polishing the asperities of microtexture change specific for each type of rock. It was noted that aggregates which included minerals of similar hardness (granodiorite, dolomite, dolorite) were more prone to polishing than others. Regeneration of the microtexture, the recovery to its original asperity, occurred in the case of sandstone.

**Keywords.** Coarse aggregate, microtexture, wearing course, skid resistance

## Introduction

Skid resistance plays an important role in reducing road accidents in wet conditions. Skid resistance is related to pavement surface texture. Pavement surface texture is specified in the three-level scale, each defined by the wavelength ( $\lambda$ ) and peak – to peak amplitude (A) of its components. According to the division, which was established in 1987 by the Permanent International Association of Road Congresses (PIARC) there are: megatexture ( $\lambda = 50$  to 500 mm;  $A = 0.1$  to 50 mm), macrotexture ( $\lambda = 0.5$  to 50 mm;  $A = 0.1$  to 20 mm), microtexture ( $\lambda < 0.5$  mm;  $A = 1$  to 500  $\mu\text{m}$ ). Especially macrotexture and microtexture influence skid resistance. Macrotexture depends on asphalt mixture properties (shape, size and gradation of aggregate) and has an effect on skid resistance especially at high vehicle speed. Microtexture depends on polishing resistance of coarse aggregate in wearing course. In actual conditions the phenomenon of polishing of the exposed coarse aggregate is caused by traffic [1]. Polishing properties of coarse aggregate influence seasonal variation of skid resistance, which are higher in

---

<sup>1</sup>Corresponding author: Bialystok University of Technology, Faculty of Civil and Environment Engineering, Wiejska 45 E, 15-351 Bialystok, Poland, e-mail:marta.wasilewska@pb.edu.pl

falls and winters and lower in springs and summers. Season when measurements are taken can quite significantly influence skid resistance data [2]. Different aggregates also vary in their tendency to lose microtexture, that is to polish or become smoother, under the abrasion of traffic. These changes depend on the hardness of minerals, texture, structure of rocks which the aggregate was made from. Because of this fact it is important to determine aggregate polishing resistance before its application for wearing course. It has an effect on safety. The test method is standardized and widely known as the PSV (Polished Stone Value) test. It is used as an indirect method to assess microtexture of coarse aggregates for wearing course. However it is difficult to explain microtexture only on the basis of PSV. Direct methods for better understanding of evolution of microtexture due to traffic polishing are being developed. Do et al. [3] developed the model which based on the description of geometry of microtexture on the grain surface [4]. Huang presented an analysis of changes in microtexture based on laser measurement of aggregate surface [5]. The advance in opto-electronics contributed of the analysis of surface aggregate in polishing process based on digital images. Slimane et al [6] proposed a methodology based on a photometric stereovision. They showed that the characterization of road microtexture obtained through a geometrical and frequential analysis of images, leads to descriptors related to the shape and the density of surface asperities technique and a surface photometric model. Dunford et al. [7] showed that the use three-dimensional surface measurement of aggregate profile ensures accurate analysis of changes in microtexture. Presently, most of researchers use Wehner/Schulze machine for simulation of polishing. The test procedure allows to evaluate of resistance to polishing of aggregates and aggregates in the asphalt mixture, and thus evaluate the skid resistance of wearing course on the stage of selecting proper materials [7, 8]. The study done showed good correlation between results from PSV test and Wehner/Schulze test. Despite the fact that PSV test allows only to assess aggregates, the use of this procedure evaluates changes of aggregates surface under the influence of two different abrasives, which are used in polishing procedure. The tests proved that the type of polishing emery influences significantly the changes of aggregates relief [9].

In this paper the possibility of using digital images for qualitative and quantitative assessment of microtexture under polishing process is presented.

## 1. Program research

### 1.1. Materials

The selection of coarse aggregates depends both on petrographic characteristics of rocks and on their PSV. The aggregate characteristics are shown in Table 1.

**Table 1.** Aggregate characteristics

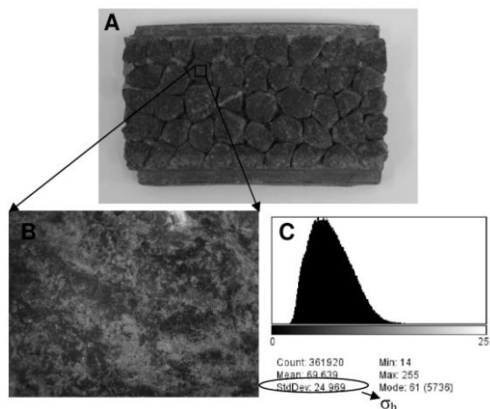
Rock type	Genetic classification	Structure	Range of PSV
Dolomite	sedimentary	crystalline	40 - 43
Granodiorite	igneous	holocrystalline	47 - 49
Gabbro	igneous	holocrystalline	52 - 55
Doleryt	igneous	hypocrystalline	49 - 52
Quartz sandstone	sedimentary	sandstorm	56 - 58

## 1.2. Test procedure

There were made two specimens of each aggregates. Polishing process was conducted according to the standard PN-EN 1097-8:2009. Specimens were clamped round the periphery of the road wheel of polishing machine and were brought to speed 315 rev/min. The outer surface of the specimens form a continuous strip of particles with periphery of 406 mm diameter, upon which rubber tire rode freely without bumping or slipping Test lasted 6 hours and consisted of two three-hour stages. In the first stage water and corn emery were fed continuously on to the road wheel and in the second stage water and emery flour were fed.

Images of the aggregate surface were taken with the optical microscope in the reflection mode either before polishing as well as after the first and the second stage. Specimen surfaces were registered using a CCD camera under controlled lighting conditions. The 30 images (3.2x magnification) from randomly selected locations were taken for each of the specimen.

The images of aggregates from the optical microscope are raster images having a finite set of digital values, called pixels. Each image contains a fixed number of rows and columns of pixels. Such image may be a subject of digital image processing which primary goal is to improve the visual quality and obtain quantitative information (image analysis). Image analysis involves the determination of numerical descriptors calculated on the basis of various statistical characteristics for a set of pixels that make up digital images. Modern technology includes many tools for image processing and analysis. Most descriptions are used by the statistical method. Each of the pixels in an image, holding quantized values that represent the brightness of a given grey level at any specific point. A statistical distribution of brightness of pixels is described as a histogram of intensities. This histogram is a graph showing the number of pixels in an image at each different intensity value found in that image. In our case the image was saved to 8-bit grayscale image. There were characterized by 256 different possible intensities, and so the histogram graphically displayed 256 numbers showing the distribution of pixels amongst those grayscale values. Grayscale variations represent local surface-relief variations. The value of the  $\sigma_h$  parameter from the histogram of intensities was assumed as a measure of microtexture (Figure 1).



**Figure 1.** Exemplary specimen of the aggregate, their digital image surface and their grey level histogram



## 2. Results and analysis

Average values, STD (standard deviations), maximum, minimum, median and V (coefficient of variation) from  $\sigma_h$  are presented in Tables 2 – 4.

**Table 2.** Parameter  $\sigma_h$  and its statistic before polishing process

Statistic	Dolomite	Granodiorite	Gabbro	Dolerite	Quartz sandstone
Average	31.57	38.79	39.69	29.40	32.21
STD	4.33	3.91	6.30	2.83	2.96
Max	41.23	58.91	56.54	46.47	26.01
Min	23.97	30.08	25.71	23.67	44.36
Median	31.37	38.89	39.34	29.20	31.98
V (%)	10.81	10,05	15.85	9.65	9.20

**Table 3.** Parameter  $\sigma_h$  and its statistic after the first stage of polishing process

Statistic	Dolomite	Granodiorite	Gabbro	Dolerite	Quartz sandstone
Average	23.09	28.82	34.25	26.04	37.16
STD	2.59	8.46	8.29	5.85	10.51
Max	32.97	53.84	53.64	44.34	71.10
Min	17.81	17.61	19.83	15.94	20.07
Median	22.35	27.25	32.50	25.54	31.38
V (%)	11.48	29.34	24.13	30.73	22.17

**Table 4.** Parameter  $\sigma_h$  and its statistic after the second stage of polishing process

Statistic	Dolomite	Granodiorite	Gabbro	Dolerite	Quartz sandstone
Average	22.77	22.37	29.73	23.79	31.95
STD	6.07	6.80	8.17	14.21	2.98
Max	46.37	41.70	47.11	40.56	44.36
Min	9.67	5.54	14.81	10.08	26.01
Median	23.14	23.03	18.38	24.25	31.98
V (%)	26.65	30.43	27.46	29.84	9,02

Before polishing microtexture depends on the structure of the rocks and the mechanical properties of particular minerals (cleavage or fracture). Aggregates with holocrystalline structure - gabbro and granodiorite are characterized by the most different relief. The highest average values of  $\sigma_h$  before polishing were received for those rocks. The lowest value of  $\sigma_h$  was obtained for dolerite.

The intensity of polishing of the aggregates depend on petrographic characteristics. In the first phase corn emery was fed to a road wheel. This simulates both phenomena: abrasion and polishing. The highest decrease of  $\sigma_h$  were recorded in dolomite and granodiorite. Dolomite contains only one soft mineral. Granodiorite is holocrystalline rocks and it contains minerals of similar hardness. It was noted that aggregates which included minerals of similar hardness are prone to polishing although the conditions for abrasion were in favor. It could be seen that their surfaces have also been smoothed at the edges of some minerals. In particular, the images of granodiorite and dolomite at the edges of individual minerals are specifically glossy. On the surface minerals of gabbro

are visible scratches, not smooth relief. This holocrystalline rock contains mineral of varied hardness and it has got good resistance of polishing.

In the second phase emery flour was fed, which simulated only polishing. In this phase the highest loss of  $\sigma_h$  was observed for gabbro. But its parameter  $\sigma_h$  is still higher than  $\sigma_h$  of other aggregates (granodiorite, dolomite, dolerite) after polishing. On the surface of the aggregates can be seen glassy gloss. It means the deformation of crystalline structure of minerals in polishing process [2]

The differences on the surfaces of aggregates are shown in Figures 2- 4.

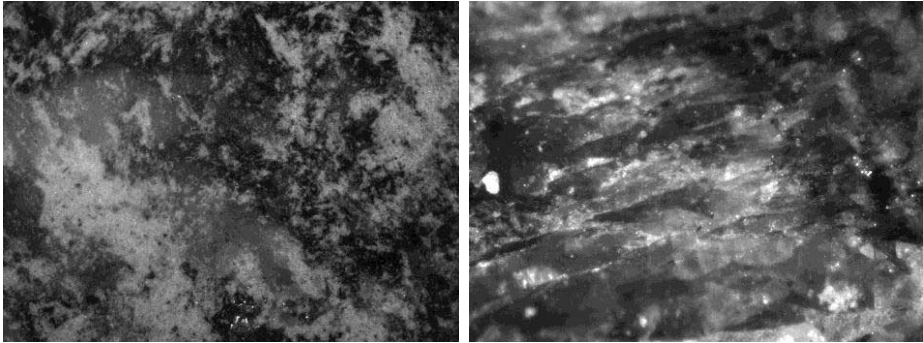


Figure 2. Surface of gabbro before and after polishing

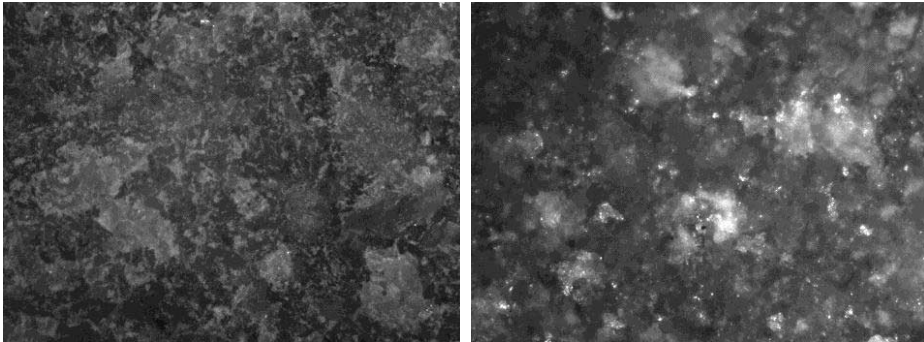


Figure 3. Surface of dolomite before and after polishing

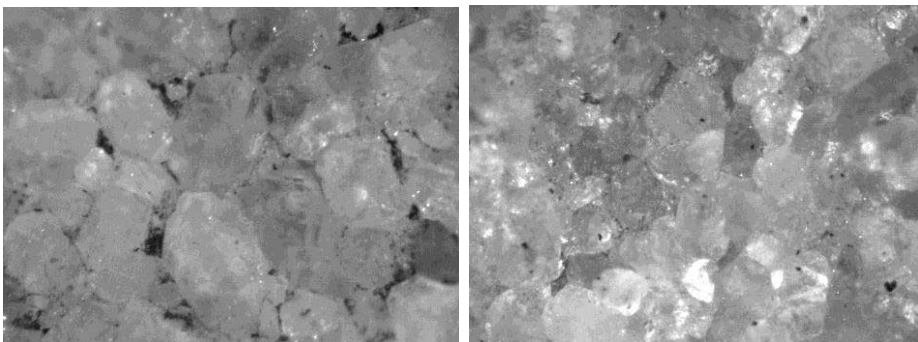


Figure 4. Surface of quartz sandstone before and after polishing

Quartzite sandstone has got possibility to regenerate its microtexture. Quartz minerals were ripped out from soft mastics surface of sandstone grains as result of abrasion and in this way the regeneration of asperities took place. This is confirmed by the mean values of  $\sigma_h$  which were higher compared to values before polishing in the second phase. The slight decrease of  $\sigma_h$  after polishing is the result of polishing of quartz minerals.

It should also be noted that the coefficients of variation in all groups of aggregates are larger in the phase I and II compared then before test. This is a proof that the polishing process does not occur uniformly over the entire surface of the grain. In some areas are no changes because of lack of contact between grain and tire. Significant differences between minimum and maximum values testify for this fact.

Gabbro and sandstone are the best aggregates for wearing coursing on the based test results. This result confirms PSV results but analysis of digital images allow to understand phenomena occurring during polishing process.

### 3. Conclusion

Because of the fact that microtexture existis on a microscopic scale, it is very difficult to assess it. To get a better insight into the evolution of the microtexture due to polishing, digital images were taken by optical microscopy. It was noted that aggregates which included minerals of similar hardness (granodiorite, dolomite, dolerite) are prone to polishing. Gabbro and quartz sandstone are the best aggregates for wearing coursing Using digital images analysis techniques to assess the microtexture can be made directly. It was determined that the standard deviation  $\sigma_h$  of the histogram received from images of aggregate surface from the optical microscope can provide a basis for quantitative evaluation of microtexture changes of aggregate surface occurring during polishing.

### References

- [1] J. Hall, K. L. Smith, L. Titus-Glover, J. C. Wambold, T.J. Yager, Z. Rado, *Guide for pavement friction. NCHRP*. Web-only document 108. Contractor's Final Report NCHRP Project 01-43. Transportation Research Board of the National Academes., 2009.
- [2] P.G. Roe, S. A Hartshorne, The Polished Stone Value of aggregates and in-service skidding resistance. TRL Report 322. Crowthorne,1998.
- [3] M.-T. Do, M. Kane, Z. Tang, F. Larrard, Physical model for the prediction of pavement polishing. *Wear* 267 (2009) 81-85.
- [4] M. Kane, J. M. Piau, M.-T. Do, Modeling of the road surface polishing based on contact-mechanics approach. *Road Materials and Pavement Design*, 9 (2008) 305-318.
- [5] Ch. Huang, Texture characteristics of unpolished and polished aggregate surfaces, *Tribology International* 43 (2010), 188-196
- [6] A.B. Slimane, M. Khoudeir, J. Brochard, M.T. Do, Characterization of road microtexture by means of image analysis. *Wear* 8 (2008), 264-464
- [7] A. M.Dunford, A. R.Parry, P. H.Shipway, H. E. Viner, Three-dimensional characterization of surface texture for road stones undergoing simulated traffic wear. *Wear* 292-293 (2012)188-196.
- [8] M.-T. DoZ. Tang, M. Kane, F. Larrard Pavement polishing – Development of dedicated laboratory test and its correlation with road results. *Wear* 263 (2007) 36-42.
- [9] ARG.Van de Wall The polishing of aggregate used in road construction. The relation between the Polished Stone Value and the petrography and mechanic properties of road aggregate. Faculty of Mining and Petroleum Engineering, Section of Engineering Geology. No 96. Delft,1992

# Response modelling of recycled concrete and masonry in pavements

F. BARISANGA, C. RUDMAN<sup>1</sup>, and K. JENKINS

*Department of Civil Engineering, Stellenbosch University*

**Abstract.** An increasing need for sustainable development has made recycling a priority in many countries. In South Africa, due to rapid urbanisation, millions of tons of construction and demolition waste (CDW) are generated and significant percentages end up in landfills. Many international studies have shown that CDW (in this context consisting of a mixture of concrete and masonry rubble) could be a viable road construction material within the structural layers of the pavement.

In this research, a laboratory experimental program was developed to assess the physical and mechanical behavior of CDW. Through monotonic and dynamic testing the shear strength and resilient response was tested. Experimental variables such as mix composition (ratio of concrete to masonry), mixing and compaction moisture and degree of compaction with regard to its Maximum Dry Density (MDD) were evaluated.

The laboratory results revealed that the failure behaviour, i.e the shear strength showed to be dependent on composition and degree of compaction but less on the compaction moisture. Moreover, the stress history significantly affected the shear behaviour of CDW as indicated by the difference in the obtained results for the shear parameters on “virgin” samples and samples preloaded by cyclic loading through resilient modulus testing. In addition, the material composition and compaction moisture were found to have a relative distinctive effect on the resilient response.

**Keywords.** Construction demolition waste, pavement materials, monotonic tests, resilient modulus tests

## Introduction

In South Africa, more than 4,725,542 tonnes of construction and demolition waste (CDW) were generated in 2011, but only 16% were recycled [1]. Possibilities exist in using construction demolition waste (waste constituting builder’s rubble of masonry and concrete) in road building. Considering the fact that the construction industry is responsible for more than 50% of all resources used and generates large amounts of construction waste, alternatives to conventional building materials are imperative.

To date, no technical guidelines within the South African industry for the use of CDW in pavements have been established. Typical specifications for standard pavement materials include characterisation and empirical tests which do not allow for the analysis of a material and pavement performance beyond their range of validity.

---

<sup>1</sup>Corresponding author: [rudman@sun.ac.za](mailto:rudman@sun.ac.za)

The key factor with recycled materials is variability, which can significantly affect the physical characteristics and mechanical performance of pavement layers. This variability results from construction materials preferences and specifications for different regions, which in return, influence the composition of demolition waste and thus the composition of recycled aggregates [2]. As a result, a number of recycling processes have been proposed by various researchers [3, 4] aimed at minimising contaminants and controlling the recycled materials composition. Despite these recycling methods, variability in recycled materials performance characteristics still prevails. Consequently, O'Mahony *et al.* [5] suggested that proper guidelines on production and quality of recycled materials should be adopted.

This ubiquitous presence of variability substantiates the importance of understanding the performance of this material on a fundamental level, including which parameters govern its behaviour (such as stresses, mix composition, saturation and compaction level). This paper focussed on some of these parameters and its influence on the shear failure and resilient response.

## 1. Materials

A laboratory experimental program was undertaken which included characterising of the physical and mechanical properties of the aggregates. This included an evaluation of the shear strength (cohesion and friction angles) and resilient response by means of triaxial tests.

### 1.1 Preparation of the material

Concrete and masonry rubble for the study was obtained by acquisition of demolished floors and partition walls, respectively. A two stage crushing process was implemented, aimed at reducing aggregates to a desired laboratory size (<19mm) and minimising flaky aggregates. In order to facilitate blending, the material was sieved separately into five fractions (<19-13.2mm, <13.2-6.7mm, < 6.7- 4.75 mm, <4.75 – 0.425 mm, < 0.425- 0.075 mm, < 0.075 mm). This method for separating fractions and reconstitution was followed rather than the standard method of sampling (and quartering) of stockpiles. This would limit variability in the grading and ensure quality.

A target grading was designed as illustrated in Figure 1. The target grading was an optimisation from the optimum packing of the particles (Fuller curve) and percentages of fractions obtained through the original crushing process. During blending, the fraction (<19mm-6.7) comprised only of 70% concrete and 30% masonry while fractions below 6.7mm were blended either to a 70% concrete and 30% masonry mix (Labelled - 70C:30M) or 30% concrete and 70% masonry (Labelled - 30C:70M) by mass. A testing moisture of 65% Optimum Moisture Content (OMC) was selected. This moisture content index was established by Emery [6], who characterized it with regards to the ratio of the pavement Equilibrium Moisture Content in relation to the AASTHO Optimum Moisture Content ( $EMC/OMC_m$ ). Specimens for shear and resilient response testing were compacted using a vibratory hammer in a split mould measuring 150mm internal diameter and 300mm height. For uniform density and

interlock through the specimen, each specimen was compacted into equal 60mm height five layers with light scarification of the compacted layer before adding a new layer.

1.2 Testing parameters

Various aggregate characterisation tests were carried out, prior to the material performance investigation. Material characterisation test results are reported in Table 1(a). The performance based laboratory study was designed to evaluate the influence of three factors; the Mix Composition (M), Degree of Compaction (DOC) and Compaction Moisture (CM) on the shear strength and the resilient response. Table 1(b) provides the design matrix for the performance tests (includes duplicates). The compaction moistures as noted in these tables were constituted as a ratio of the measured Modified AASTHO OMC, whilst the degree of compaction of 100% and 102% of Maximum Dry Density (MDD) was applied.

The monotonic triaxial tests were carried out at three different confining pressures: 50 kPa, 100 kPa and 200 kPa and a strain rate of 3mm/min [7]. The combination of three stresses (with duplicates) at failure corresponding to three different confinements was fitted into the Mohr-Coulomb model using a linear regression analysis in order to obtain the shear parameters (C,  $\phi$ ). Monotonic tests on preloaded cyclic samples were also performed at two confining pressures (50 and 200kPa). During resilient triaxial testing, a haversine-shaped load (0.1 sec loading duration and 0.9 sec rest period) pulse was applied. After conditioning, a loading sequence that included varying the confining pressure as well as the deviator stresses was implemented. The detailed testing sequence is stipulated in Barisanga [8].

Table 1(a): Physical and Mechanical Properties:

Physical Properties				
	70C:30M		30C:70M	
	>4.75mm	<4.75mm	>4.75mm	<4.75mm
Grading Modulus (GM)	2.39		2.39	
Flakiness Index (%)	10.8		11.02	
Atterberg Limit	None plastic		None plastic	
Bulk Relative Density (BRD)	2.52	2.51	2.51	2.49
Apparent Relative Density (ARD)	2.55	2.57	2.54	2.56
Water Absorption (%)	1.22	1.40	1.32	1.92
Mechanical Properties				
Density	g= 1829 (kg/m <sup>3</sup> )		g= 1807 (kg/m <sup>3</sup> )	
Moisture	w=14.1 (%)		w=15.5 (%)	
10% Fines Aggregate Crushing Value(FACT) (kN)	Dry	131		
	Wet	89		
	Ratio	68%		

Table 1(b): Test Plan:

Test Run	Mix Composition (M)	Compaction Moisture (CM)	Degree of Compaction (DOC)
1	70 <sup>(a)</sup>	80	102 <sup>(b)</sup>
2	30	80	102
3	70	70	102
4	30	70	102
5	70	80	100
6	30	80	100
7	70	70	100
8	30	70	100

Note:  
 (a) Percentage Concrete in Small Fraction  
 (b) Percentage Degree of Compaction of Mod AASTHO

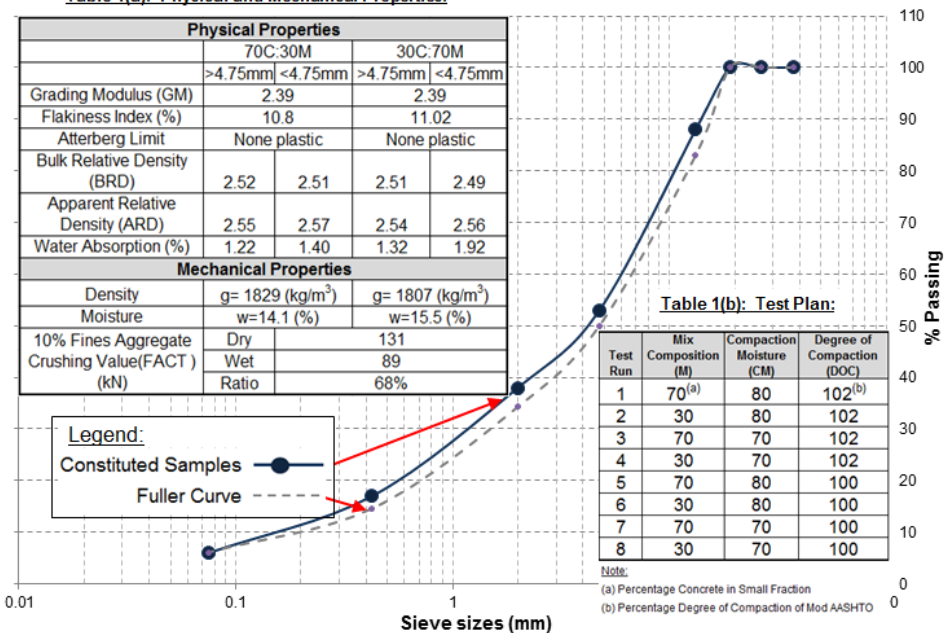


Figure 1. Grading of CDW used in study

## 2. Results and interpretation

### 2.1 Processing and material characteristics

Secondary crushing has proven to reduce flaky aggregates in the mix and contribute to increase fines. In addition, it reduces the amount of soft concrete mortar attached to the aggregates, which in return enhances the resistance on breakdown of the aggregates due to wear and tear.

It was observed that the reported flakiness indexes (Table 1a) are present predominantly in the large aggregates sizes of the masonry mixes (< 19mm-13.2mm). However, all the aggregates types and mixtures met requirements as recommended by the Technical Recommendations for Highways Part 8 (TRH 8) [9] and Part 14 (TRH 14) [10]. Maximum limits of 20% and 35% are specified in these two documents, for base course materials, respectively.

In addition, Table 1a includes results of the crushing resistance obtained from the 10% fines aggregate crushing test (10% FACT). It can be seen from this table that the results are the same for both mixtures since the aggregate fraction type (<13.2mm - >9.5mm) specified for this test is both constituted from the same ratios material. The results of 131 kN for dry 10% FACT and 89 kN for wet conditions were obtained. This indicates that the material exhibits good resistance to crushing in dry conditions because the result obtained is higher than that of the required (110 kN) for base course material as specified in the TRH 14 and South African Pavement Engineering Manual (SAPEM) [11]. However, the obtained dry-wet ratio of 68% failed to meet the minimum of 75% specified. This can be explained by the fact that when these aggregates are soaked, the water softens the mortar attached to the aggregates and weakens the clay bricks granulate. When these soft constituents are crushed during the 10% FACT test, they generate more fines at low forces. This reiterates the benefits of secondary crushing.

### 2.2 Mechanical behaviour test results

The equation for the Mohr-Coulomb Theory was used to establish the shear parameters for monotonic tests. Figure 2 reports on the obtained C and  $\phi$  values for virgin and preloaded samples (which were previously subjected to the resilient modulus test). Friction angle results were lower for higher quantities of masonry in the mix (values below 45°). Increase in cohesion results with DOC is evident, especially when specimens have been preloaded. This increase can be related to the increase in contact points between particles and the concrete content that could generate bonding through self-cementing due to hydration of residual cement comprise in concrete. Consequently, higher shear strength is obtained at higher compaction levels and higher concrete content in the mix. In addition, a significant increase in the shear stress due to stress history is observed.

### 2.3 Resilient response test results

Resilient triaxial tests results were analysed according to the Mr- $\Theta$  model. The Mr- $\Theta$  is also known as K- $\Theta$  model which was developed by Hicks & Monosmith [12]:

$$Mr = k1\Theta^{k2} \quad (1)$$

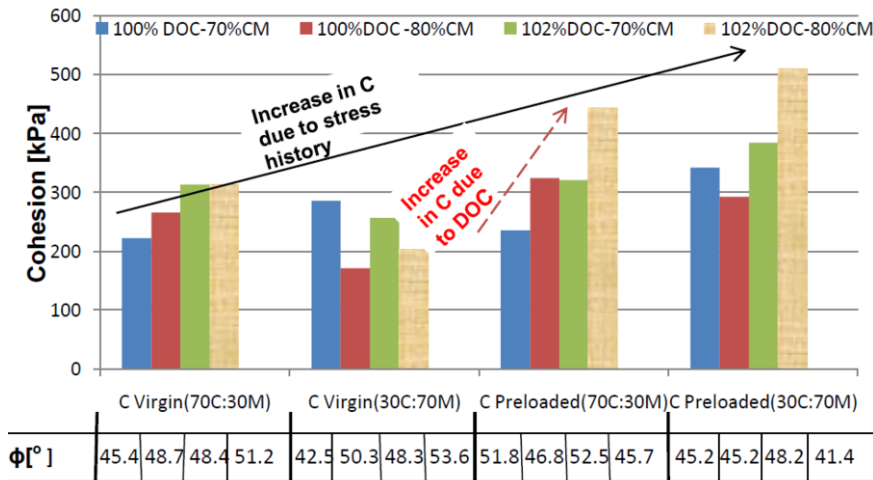


Figure 2. Shear behavior of virgin and preloaded specimens

It should be noted that this formulation is not fundamentally correct because it predicts an increase in resilient modulus when the material is close to failure. Nevertheless, as stated by Molenaar [13], this model could be used for practical purposes in a state of low and medium stresses, which is the case of the current study. The resilient modulus of each variable was analysed at 300 kPa, 900 kPa and 1500 kPa bulk stresses ( $\sigma_1 + \sigma_2 + \sigma_3$ ), respectively. These stresses represent more or less the minimum, medium and high stress ranges that materials in this study were subjected to. Figure 3 through Figure 5 show the trends for the variation in resilient modulus with the change of the degree of compaction, compaction moisture and mix composition as indicated by the shift of the model lines and the arrows.

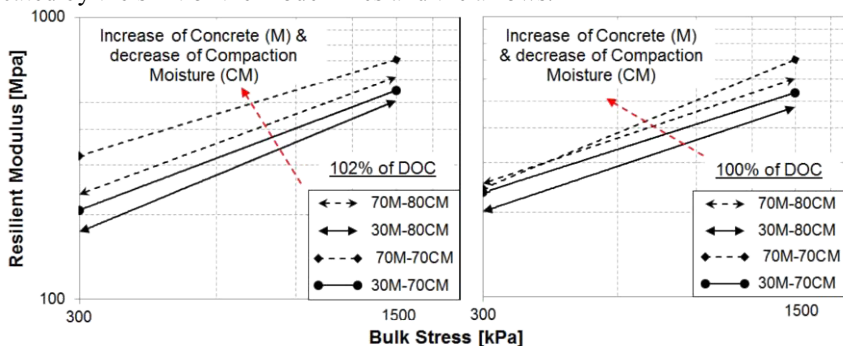


Figure 3. Variation in resilient modulus due to change in mix composition (M) and compaction moisture (CM) for 102%DOC (left) and 100%DOC (right)

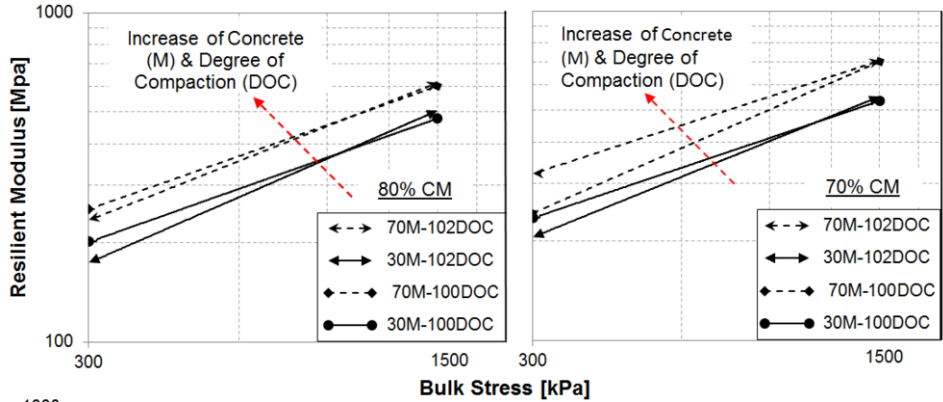
The stress dependency of the resilient response are evident for all results (Figure 3-5) There is a strong agreement in studies on the significant impact of stress on the resilient response of granular materials and this is observed in this study i.e the behaviour of CDW as well. Figure 3 shows the increase in resilient modulus as the concrete addition increases from 30% to 70% and compared between 102% and 100% DOC of Modified



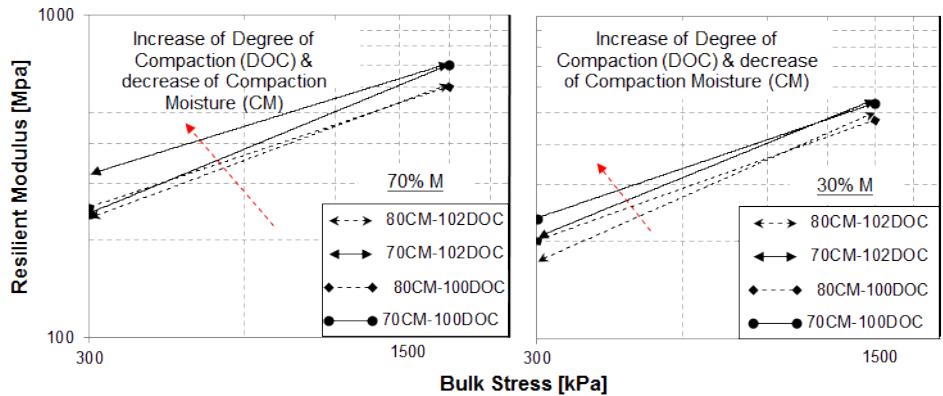
AASTHO Maximum Dry Density (MDD). There is a notable difference in the magnitude of this upward shift between 102% and 100%DOC, especially for the 70% concrete mix.

Figure 4 shows an increase of the resilient modulus with an increase in concrete content and compared between 80% and 70% CM. It seems that the decrease in CM shows a small increase of resilient modulus for low additions of concrete. However, for higher additions of concrete the increase in resilient modulus is more pronounced at high bulk stresses.

In addition, the DOC seems to have negligible effect at 80%CM when compared to the mix composition.



**Figure 4.** Variation in resilient modulus due to change in mix composition (M) and degree of compaction (DOC) for 80 % CM (left) and 70%CM (right)



**Figure 5.** Variation in resilient modulus due to change in compaction moisture (CM) and degree of compaction (DOC) for 70 % M (left) and 30% M (right)

Figure 5 indicates a noteworthy upward shift of the model lines with a decrease in compaction moisture at high bulk stresses. This is less pronounced for the mix with only 30% concrete. However, at lower bulk stresses some disparity exists in the upward shift with 70% compaction moisture, between the two mixes. This could be due to the high influence of the mix composition.

For all comparisons the results revealed that the mix composition (apart from stress dependency) had the most notable effect. The development of a strong aggregate skeleton due to strong concrete aggregates is the probable cause of this behaviour.

### 3. Conclusions

CDW failed to meet some of the characterisation tests. However, its shear strength and resilient response showed satisfactory results for an alternative road building material, although it does not meet empirical test regimes.

The shear properties and particularly the cohesion were found to be affected significantly by the stress history. This was observed comparing the shear properties of the virgin specimens and the cyclic preloaded specimens.

From the resilient modulus results it was observed that the degree of compaction exhibited less distinctive effect than other investigated factors. It was concluded that in this study, the predominant factors to the resilient response were the mixture composition and the compaction moisture. This substantiates quality control in the the mixture selection and compaction procedure (and addition of moisture) with regard to CDW.

### References

- [1] DEAT Rep-154171. National Waste Management Strategy, First Draft for Public comment. *Department of Environmental Affairs*, Pretoria, 2012.
- [2] Barbudo A, Agrela F, Ayuso J, Jiménez JR, Poon CS. Statistical analysis of recycled aggregates derived from different sources for sub-base applications, *Construction and Building Material*, 2011, 28(1): 129-138.
- [3] Schulz R, Hendricks F. Recycling of masonry rubble. Recycling of demolished concrete and masonry. In: Hansen TC, editor. Report of technical committee – demolition and reuse of concrete, vol. 37. London: *RILEM*, 1992.
- [4] Xing W. Quality improvement of granular secondary raw building materials by separation and cleansing techniques, *MSc Thesis, Delft University of Technology*, 2004.
- [5] O'Mahony MM, Milligan GWE. Use of recycled materials in subbase layers. *Transportation Research Record*, 1991:1310:73-80.
- [6] Emery CJ. The prediction of moisture content in untreated pavement layers and an application to design in Southern Africa. *CSIR Research Report 644*, Pretoria, 1988.
- [7] Mgangira MB, Jenkins KJ, Paige-Green P, Theyse HL. Proposed protocol for triaxial testing of resilient modulus and permanent deformation characteristics of unbound and bound granular materials. *CSIR and Stellenbosch University*, Pretoria and Stellenbosch, South Africa, 2011.
- [8] Barisanga F. Material characterisation and response modelling of recycled concrete and masonry in pavements, *MSc Thesis, University of Stellenbosch*, 2014.
- [9] TRH Part 8. Technical Recommendations for Highways: Design and use of hot-mix in pavements, *Department of Transport*, Pretoria, 1987.
- [10] TRH Part 14. Technical Recommendations for Highways: Guidelines for road construction materials, *Department of Transport*, Pretoria, 1984.

- [11] South African Pavement Engineering Manual (SAPEM). South African Pavement Engineering *Manual 1<sup>st</sup> ed. Republic of South Africa*, 2013.
- [12] Hicks R, Monosmith C. Factors influencing the resilient properties of granular materials, *Highway Research Record* 1973:345:15-31.
- [13] Molenaar AAA. Cohesive and non-cohesive soils and unbound granular materials for bases and sub-bases in roads. *Lecture Notes, Delft University of Technology*, 2005.

# The effects of residual moisture on asphalt concrete strength

Nura USMAN<sup>1</sup>

*Department of Civil Engineering, Hassan Usman Katsina Polytechnic, Nigeria*

**Abstract.** This research was conducted to evaluate the effect of residual moisture in asphalt concrete mixture. Superpave method of mix design was adopted; two laboratory tests (i.e. resilient modulus and indirect tensile strength tests) were conducted on two different set of samples. One set was prepared using well dried aggregates while the other set was prepared with poorly dried aggregates (2% moisture). The results obtained shows that, specimens prepared with well dried aggregates are stronger compared to specimens prepared with poorly dried aggregates.

The result shows that the resilient modulus of specimens produced with well dried aggregates doubles that of specimens produced with poorly dried aggregates. Tensile strength of specimens with well dried aggregates is higher which is an indication of resistance to fatigue damage. In general, specimens produced with dried aggregates are better in strength hence better performance.

**Keywords.** Residual moisture, resilient modulus, indirect tensile strength, poorly dried aggregates, strength

## Introduction

The presence of water (or moisture) often results in premature failure of asphalt pavements in the form of isolated distress caused by de-bonding of the asphalt film from the aggregate surface, or early rutting/fatigue cracking due to reduced mix strength. Sometimes moisture might not be due to the post laid environmental conditions, but due to inability of the drying process to produce moisture free aggregates for asphalt mix at the mixing plant, thus residual moisture.

As the concept of perpetual pavements and long life pavements become more popular, engineers must focus on how to minimize the detrimental effects of moisture damage.

## 1. Residual moisture in hot mix asphalt concrete

Residual moisture in hot mix asphalt concrete is thought to adversely affect pavement performance. It is also believed that residual moisture prevents full development of asphalt aggregate bonds thereby reducing mix strength and thus pavement strength [1].

<sup>1</sup>Corresponding author: [nuragafai@gmail.com](mailto:nuragafai@gmail.com)

The significance of the problem created by residual moisture is debatable, the level at which residual moisture begins to be detrimental to pavement performance is also debatable. In USA, specifications on allowable residual moisture content vary from state to state ranging from 0.5 to 2% [1]. Table 1 lists states and their allowable moisture content for HMA in the United States of America.

Residual moisture tends to escape in form of steam which disrupts and prevents proper coating and weakens asphalt-aggregate bond. The weakened bonds are susceptible to the detrimental influence of water and thus stripping. This theory is somewhat substantiated by laboratory retained tensile strength testing of asphalt mixes as means of assessing susceptibility to stripping. Research conducted by [2-3] shows that, when aggregate is well dried (no residual moisture) for preparation of laboratory samples, retained tensile strength ratios are higher than expected for mixes with high stripping potential. In addition, tensile strength ratio (TSR) results from samples prepared from a laboratory mix with controlled residual moisture and field mix [2], suggest a decrease in TSR as residual moisture content increases.

**Table 1.** Limited state HMA moisture content specification in the United States [1]

State	Year	Specification
Alabama	1995	0.5% Moisture Content at Mixer
Arkansas	1993	0.75% Moisture Content Limit at Mixer
Arizona	1990	1% Moisture content Limit at Paver
California	1992	1% Moisture content Limit at Paver
Connecticut	1988	1% Moisture Content Limit at Truck
Mississippi	1991	0.5% for surface mixes, 0.75 for base , leveling
Missouri	1993	0.5% Moisture Content at Mixer
N. Dakota	1992	1% Moisture Content for drum plants & 0.5% batch plants
Oklahoma	1988	0.75% Moisture Content Limit at Mixer
Texas	1993	1.0% Moisture Content at Limit at Mixer
Washington	1991	2% Moisture Content at Mixer
Wyoming	1987	0.5% Moisture Content at Drum

## 2. Methodology

### 2.1. Materials selection

The first stage in asphalt production is material selection followed by mix design. Several parameters need to be considered in a mix design to ensure that the final mix has optimized properties. The aggregates and binder selected for this research conformed to AASHTO standard specifications. Tables 2, 3 and 4 show a summary of aggregates properties test, binder test and volumetric properties of asphalt concrete used.

**Table 2.** Properties of aggregates used

Aggregate Property Test	Test Value (%)
Flakiness Index	15
Elongation Index	17
Aggregate Impact Value	21
Aggregate Crushing Value	21

**Table 3.** Properties of bitumen used

Bitumen test	Temperature ( $^{\circ}$ C)
Penetration Test at 25 $^{\circ}$ C	83
Softening Point ( $^{\circ}$ C)	43

**Table 4.** Volumetric properties of asphalt concrete produced

Volumetric Property	Value Obtained (%)
Optimum Bitumen Content	7
Air Voids	4
Voids in Mineral Aggregates	17
Voids Filled with Asphalt	76

## 2.2 Hot mixed asphalt (HMA) mixture design

The HMA mixtures were prepared in accordance to Superpave system. The adoptability of the Superpave system in this research considers current practices in qualitative production of asphalt concrete.

Superpave (Superior Performing Asphalt Pavements) mix design was first introduced in 1993 in the USA, with the completion of the Strategic Highway Research Program (SHRP) [4]. This new design system was not an evolution in mix design but a revolution. The Superpave system introduced a new compactor, the Superpave Gyratory compactor for densifying mixes in the lab. In addition the new design system introduced aggregate and binder requirements and mixture compactive effort tied to traffic [4]. The procedure used to develop Superpave specimens followed in this research is AASHTO T312 procedure published by Asphalt Institute's Superpave Mix Design, SP-2, third edition.

The mixture was blended at OBC of 7% that yielded acceptable volumetric properties at 4% air voids based on the established Superpave criteria at design number of gyrations i.e. 100. The projected traffic level chosen in this study was medium to high traffic load which is equivalent to 3 to <30 million ESALs. The Superpave Gyratory Compactor (SGC) was used to compact the Superpave specimens. The compatibility estimation of the mixture was determined at  $N_{ini}$  after 8 gyrations. At 160 gyrations or  $N_{max}$ , the mixture properties are established as a check to help guard against plastic failure caused by traffic in excess of the design level. The mix was batched out in appropriate quantities to produce a final mix specimen of approximately 1200g. Six percent of bitumen content was used as the first trial, followed by 7% and

finally 10%. Three replicate samples were prepared for each bitumen contents. Prior to mixing, aggregates for control samples were heated in an oven set approximately 15°C higher than the mixing temperature (165°C) for approximately four hours to achieve 0% moisture. The binder was also heated to mixing temperature of 165°C to enable a homogenous coating of binder and aggregates in the mixing process.

### 2.3 Conditioning of aggregates (poorly dried aggregates)

To achieve the objective of this study, coarse aggregates were considered under different moisture conditions, since stripping occurs due to adhesive failures in aggregate-asphalt inter-face as a result of moisture effect [5]. Coarse aggregates were saturated in water for 24 hours. To obtain consistent moisture content for all conditioned samples, 2 sets of saturated aggregates were placed in oven at 100°C in which the moisture content was checked for interval of every ten minutes in the first hour, then at 2 hours, 5 hours, 6 hours, 7 hours and 24 hours.

Figure 1 shows a graphical illustration of moisture content against time at 100°C. Average moisture content of 2% was selected at 20 minutes; therefore all saturated aggregates were placed in oven 20 minutes prior to the mixing time.

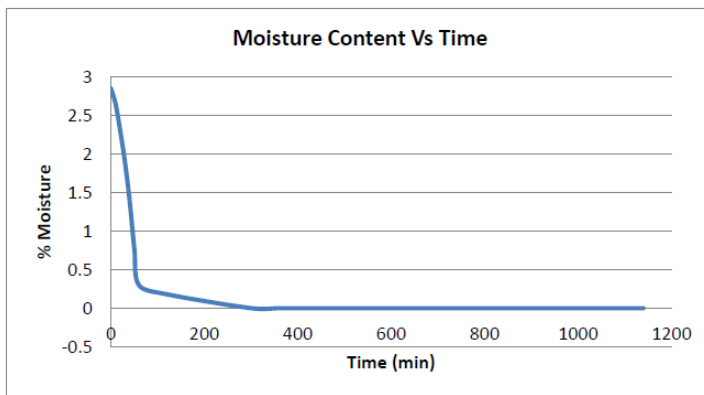


Figure 1. Variation of moisture content with time at 100°C

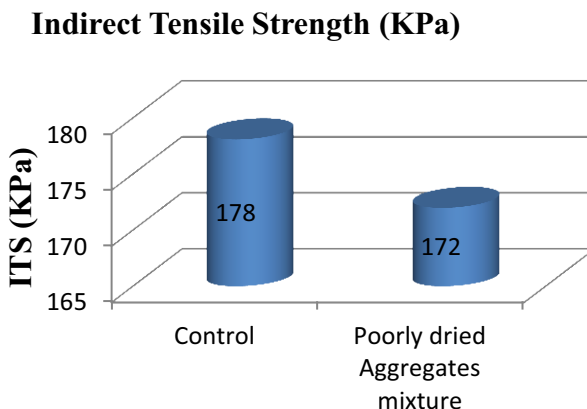
## 3. Result and discussion

This research involved preparation of sample in two sets, one set was prepared with well dried aggregate as a control using optimum bitumen content of 7%, in which the aggregates were completely dried (i.e. 0% moisture) at 110°C for 24 hours in oven. The other set was prepared using poorly dried aggregates of 2% moisture content. The two sets were tested to find their performances under loading. The tests involved were: Resilient modulus (MR) and Indirect Tensile strength tests.

### 3.1 Indirect tensile strength (ITS) test

Indirect Tensile Strength (ITS) test is an indicator of the tensile strength of HMA mix. In figure 2, it is clear that tensile strength of control specimen is stronger than specimen

produced with poorly dried aggregates. This implies that moisture has effect on tensile strength of asphalt concrete. It can be seen that the tensile strength of poorly dried aggregates was 172 KPa while tensile strength of mixture with well dried aggregates was 178 KPa.



**Figure 2.** Indirect tensile strength of asphalt concrete with well dried and poorly dried aggregates

### 3.2 Resilient modulus (MR) test results

Resilient modulus is an important variable used to measure pavement response in terms of dynamic stresses corresponding to strains. This test was performed to compare and characterize two different set of mixtures, one set was produced with dried aggregates as a control and the other was produced using poorly dried aggregates. The test was conducted at 25°C and 40°C. From this characterization test the behavior of HMA mix can be predicted as corresponding to test temperature. At 25°C, the resilient modulus is an indication of mixture resistance to fatigue whereas resilient modulus at 40°C indicates mixture resistance to rutting.

Table 5 shows resilient modulus values of control mixture and of mixture with conditioned aggregates at different temperatures with highest values at 25°C and lowest at 40°C. It also shows that as the pulse repetition period during loading time increases from 1000ms to 3000ms, the resilient modulus values decreases. As temperature increases, the difference in resilient modulus is more noticeable with a decline in stiffness at 40°C. At high temperature the samples of dried aggregates shows higher resilient modulus values compared to samples produced with moist-conditioned aggregates. This indicates that mixtures with dried aggregates are least susceptible to rutting than mixture with poorly dried aggregates. In conclusion, moisture in aggregates plays a vital role in rutting of asphalt concrete pavement.



**Table 5.** Resilient modulus (MR) of all mixtures

Pulse Repetition period (ms)	Mixture with dried aggregate		Mixture with poorly dried aggregates	
	Average MR at 25°C (MPa)	Average MR at 40°C (MPa)	Average MR at 25°C (MPa)	Average MR at 40°C (MPa)
1000	2194	567	907	296
2000	1947	479	759	269
3000	1729	438	660	243

From Table 5, the resilient modulus of control sample is about twice the resilient modulus of sample produced with poorly dried aggregates for both temperatures and under all pulse repetition periods. The higher resilient modulus of the control sample at the temperature of 25°C is an indication of its least susceptibility to fatigue. The higher stiffness of asphalt concrete mixture gives it the ability to absorb or withstand stresses without causing much horizontal strain at the bottom of asphalt which is among the factors responsible for fatigue cracks in pavement structure.

#### 4. Conclusion

This study confirms that moisture has effect on the strength of asphalt concrete, the research results indicates useful findings on the pavement durability and performance due to presence of residual moisture in its aggregates. Based on the research work described above, the conclusions of this study are as follows:

- 1) Moisture induces damage to asphalt concrete mixture but has limited effect on its tensile strength. As indicated by tensile test in this study, the difference in tensile strength between control sample and poorly dried aggregate sample is minimum (only 3.5%). This may be influenced by the temperature at which the test was conducted i.e. 25°C.
- 2) The strength of asphalt concrete containing poorly dried aggregates worsens more with increase in temperature compared to asphalt concrete containing dried aggregates. In Resilient modulus test, the percentage reduction in resilient modulus value with increase in temperature on samples with poorly dried aggregates is higher compared to that of control samples.
- 3) Resilient modulus value of asphalt concrete containing well dried aggregates was found to be about twice than resilient modulus for asphalt concrete with poorly dried aggregates.

#### References

- [1] Frazier Parker: Residual Moisture in Hot Mix Asphalt Concrete, *Auburn University Highway Research Center*, 238 Harbert Engineering Center Auburn, AL 36849-5337 (1996).
- [2] Parker, F.: A Field Study of Stripping Potential of Asphalt Concrete Mixtures, *Final Report, Alabama Department of Transportation*, Research Project ST 2019-6 (1989).
- [3] Powell, R.L. and L. Lockett: A Study of Moisture Absorption Characteristics of Chert River Gravel Aggregate in Hot Mix Asphalt, *Alabama Department of Transportation*, Bureau of Research and Development (1994).
- [4] Superpave Mix Design and Gyrotory Compaction Levels, *U.S. Department of Transportation*, Federal Highway Administration (2010).
- [5] Shah, B.D.: Evaluation of moisture damage within asphalt concrete mixes, *PhD dissertation*, Texas A & M University, College Station, Texas (2003).

# Effect of different additives on fatigue behavior of asphalt mixtures

Amin DAGHIGHI<sup>1</sup> and Ali NAHVI

*School of Civil Engineering, College of Engineering,  
University of Tehran, Tehran, Iran*

**Abstract.** Fatigue failure is a common problem of asphaltic concrete pavements which can lead to damage. Fatigue cracking has been recognized as one of the main forms for structural damage in asphalt concrete pavements. Under the action of repeated vehicular loading, deterioration of the asphalt concrete materials in pavements, caused by the accumulation and growth of micro- and macro-cracks, gradually takes place. This paper studies the beneficial properties of modified asphalt mixtures in resistance to fatigue of mixtures with different additives of crumb rubber (CR), reclaimed rubber (RR) and styrene-butadiene-styrene SBS. Laboratory asphalt mixture samples were fabricated then compacted into slabs and sawed to beam samples. Asphalt mixture beams were tested under four point bending (4PB) universal testing machine. Stress controlled testing protocol simulates the same situation as in the pavement structure. As the stress remains constant during load cycles the measured strain increases continuously. Beam fatigue results compared to each other and results showed that modified mixtures had performed better in different conditions.

**Keywords.** Asphalt concrete, fatigue behavior, additives, crumb rubber, reclaimed rubber, SBS

## Introduction

In order to provide comfortable ride and withstand the effects arising from traffic loading and climate, pavement materials should be designed to achieve a certain level of performance and the performance should be maintained during service life of the pavement[1,2]. Asphalt concrete (AC) is the most commonly used material in pavement because of its superior service performance in providing driving comfort, stability, durability and water resistance [3,4]. AC mixture is subject to many external forces during its service life which could eventually lead to failure. Different types of failures have been observed in asphalt mixtures such as permanent deformation (rutting), fatigue failure, and low temperature cracking. Fatigue failure is a common damage in AC mixtures which mostly appears in the form of cracking (alligator cracking).

The fatigue resistance of AC mixtures is its ability to withstand repeated bending without fracture. Fatigue manifests itself in the form of cracking from repeated traffic loading. What appears to be minor cracking on highway and airport runway may mean the start of serious damage failure. Most analyses utilize flexure stresses or strains on

---

<sup>1</sup>Corresponding author: [Amin.Daghighi@ut.ac.ir](mailto:Amin.Daghighi@ut.ac.ir), Tel.: +989124588969

the underside of the AC pavement layers to assess the pavement lives[5] and fatigue behavior of the AC mixtures is characterized by the slope and the relative level of the stress or strain versus the number of load repetition to failure [6,7].

Fatigue resistance is the ability of the asphalt mixture to resist repeated bending forces without fracture and cracking. In asphalt concrete pavements, fatigue cracking is caused by successive tensile strains due to repeated traffic loading. According to structural analysis fatigue cracks are produced at the bottom of asphalt layer where the maximum tensile strains occurred, thereafter these cracks propagate to the surface of asphalt mixtures. Fatigue life of AC mixtures has negative correlation with the loads applied by vehicles on road pavements. Besides, fatigue life differs significantly among types of AC mixtures. Using additives and modifiers is a common way to improve fatigue life of AC mixtures.

This approach is inherently complex and the fracture mechanistic concept in fact does not describe the gradual deterioration of asphalt concrete material strength under cyclic loading [8]. In fact, damage can be defined as a continuum of change in the material subject to unfavorable mechanical and environmental conditions that result in a decrease in strength [9,10].

Utilization of additives in asphalt mixture can improve fatigue properties of AC, in many cases road construction cost increases considerably. Thus in this study, many investigations were conducted on the mixtures containing waste materials as additives to improve asphalt mixture characteristics while reducing imposed additional charges by usage of virgin materials. Furthermore, this would be an alternative solution for environmental pollution by utilizing waste materials as secondary materials in road construction projects. Waste glass, steel slag, tires and plastics (polymers) are examples of waste materials which have been used in AC mixtures in previous studies [11]. Among waste materials waste tire and recycled polymer have received prominent utilization [12–17]. The main objective of this study was to investigate fatigue properties of hot mix asphalt (HMA) mixtures containing different percentages of crumb rubber, reclaimed rubber and SBS.

## **1. Experimental procedure**

### *1.1. Materials*

The aggregates used in this study were the continuously graded with 19 mm of nominal maximum aggregate size of the AASHTO standard as presented in Table 2 [18].

The properties of the aggregate used are given in Table 1. Limestone aggregate particles were obtained from “Asb Cheran” in Iran. The aggregate was sampled from the quarry and transported to the lab where it was dried in an oven at 170 °C, then mechanically sieved into the individual sizes.

Furthermore, in this study for HMA mixture, the amount of aggregates passing sieve 0.075 mm (filler) was 5% by weight. The asphalt mixture was designed in accordance with the standard Marshall mix design procedure. Pure bitumen grade of 60/70 was used in the preparation of the samples. The characteristics of the bitumen were controlled according to the ASTM D946.

**Table 1.** Physical properties of the aggregate

Properties	Standard	Specification Limits	Coarse	Fine	Filler
Abrasion loss (%) (Los Angeles)	ASTM D 131	Max 30	28	-	-
Frost action (%) (with Na <sub>2</sub> SO <sub>4</sub> )	ASTM C 88	Max 10	5.2	-	-
Flat and elongated particles (%)	ASTM D 4791	Max 10	5		
Water absorption (%)	ASTM C 127	Max 2	1.59		
Specific gravity (g/cm <sup>3</sup> )	ASTM C 127		2.613	-	-
Specific gravity (g/cm <sup>3</sup> )	ASTM C 128		-	2.622	-
Specific gravity (g/cm <sup>3</sup> )	ASTM D 854		-	-	2.711

**Table 2.** Continuous type gradation for HMA, Topeka layer

Sieve size	19 mm (3/4 in.)	12.5 mm (1/2 in.)	9.5 mm (3/8 in.)	4.75 mm (#4)	2.36 mm (#8)	0.3 mm (#50)	0.075 mm (#200)
Passing (%)	100	90-100	-	44-74	28-58	5-21	2-10

Four SBS polymer modified bitumen (PMBs) types were prepared. The polymer contents ranged from a low polymer modification of 2% to higher degrees of modification, up to 5%, with a 1% increment. To produce asphalt rubber, the crumb rubber and reclaim rubber must be cut, scraped into small particles and reduced to powder size. It is then added into the conventional asphalt. Processing scrap tires into crumb rubber and reclaim rubber can be accomplished through either ambient grinding or cryogenic grinding technologies. In ambient ground rubber processing, scrap tire rubber is ground or processed at or above ordinary room temperature. Cryogenic processing uses liquid nitrogen to freeze tire chips or rubber particles prior to size reduction (120 °C) [19]. The crumb rubber (CR) and reclaim rubber (RR) used in this study was obtained by an ambient process.

Four tire rubber modified bitumen types were prepared. The crumb rubber contents ranged from 4% to 10%, with a 2% increment and the reclaim rubber contents ranged from 6% to 12%, with a 2% increment. The modified bitumen binders were mixed at a temperature of 180 °C for one hour at a rotation speed of 1000 rpm. The asphalt mixture was designed in accordance with the standard Marshall mix design procedure.

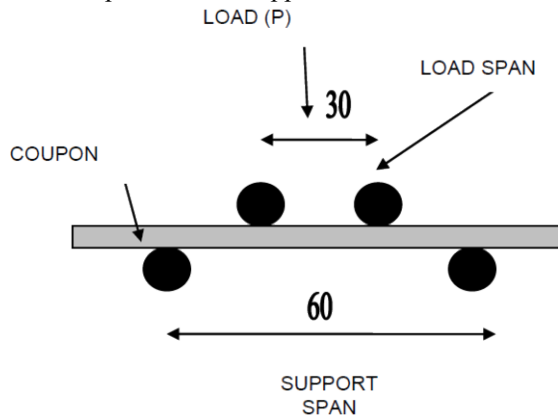
The optimum bitumen content was found to be 5.0% by weight of aggregate for the unmodified asphalt mixes. This ratio was chosen for all mixtures so that the amount of bitumen would not confound the analysis of the test data. For the mechanical tests, SBS-modified mixtures were prepared with 2%, 3%, 4%, and 5% SBS modified bitumen and CR modified mixtures were prepared with the 4%, 6%, 8%, and 10% CR modified bitumen, RR modified mixtures were prepared with the 6%, 8%, 10% and 12% RR modified bitumen. The physical properties of the mixtures such as air voids (Va), voids filled with asphalt (Vfa), voids in mineral aggregates (Vma), Marshall stabilities and flow values are given in Table 3.

**Table 3.** Physical properties of the mixtures

Mixture type	Mixing temp. (°C)	Compaction tempt. (°C)	Va (%)	Vma (%)	Vfa (%)	Marshall stability (Kn)	Flow (mm)
Base	150	138	4.06	14.89	72.68	17.2	2.88
4% CR	172	158	4.15	15.31	72.77	17.4	2.74
6% CR	181	168	4.13	15.25	72.86	17.8	2.79
8% CR	196	182	4.14	15.23	72.91	18.1	2.82
10% CR	210	194	4.09	15.19	72.98	18.8	2.69
6% RR	169	157	4.17	15.30	72.64	17.6	2.87
8% RR	178	164	4.15	15.26	72.71	18.2	2.91
10% RR	192	178	4.14	15.21	72.79	18.6	2.96
12% RR	203	188	4.10	15.18	72.85	19.3	2.84
2% SBS	162	149	4.07	14.98	72.78	17.5	2.84
3% SBS	176	164	4.10	15.05	72.69	18.4	2.72
4% SBS	189	173	4.15	15.11	72.61	19.6	2.81
5% SBS	201	187	4.12	15.06	72.67	21.1	3.06

### 1.2. Indirect tensile–fatigue test

Fatigue is considered to be one of the most significant distress modes in pavements associated with repeated traffic loads [20]. In this study, a constant-stress indirect tensile–fatigue test was conducted by applying cyclic constant loads of 270 kPa with a 0.1 second loading followed by a 1.4 second rest period. The test was carried out at 25 °C. A universal testing machine (UTM) was used for this purpose. The machine has a servohydraulic test system. The loading frame was housed in an environmental chamber to control temperature during the test. The desired load level, load rate and load duration were controlled by a computer. The deformation of the specimen was monitored through linear variable-differential transducers (LVDTs). The LVDTs were clamped vertically onto the diametrical opposite side of the specimen. A repeated dynamic compressive load was applied to specimens across the vertical cross-section along the depth of the specimen using two loading strips 12.5 mm in width. The resulting total deformation parallel to the applied force was measured.

**Figure 1.** Schematic illustration of a composite coupon loaded in four point bending (4PB)

## 2. Results and discussion

### 2.1. Indirect tensile-fatigue test

Based on results of the fatigue test, the number of load repetitions to failure was determined for the base, SBS, CR and RR modified mixtures. Figs. 3, 4 and 5 show examples of the changes in accumulated deformation versus load repetitions. It is readily observed that, at first, the accumulated deformations increased rapidly as the air voids were compressed by the load repetition. Later, the accumulated deformations of the mixture increased linearly. Because the test was performed in stress controlled mode, the deformations finally increased rapidly after initial cracking occurred. The crack growth of SBS, CR and RR modified mixtures exhibited the same trends, except for the 10% CR modified mixture and 12% RR modified mixture. It can be concluded that among the modified mixtures, the 10% CR and 12% RR mixture had low resistance to crack growth. The number of load cycles to fracture induction of the different mixtures are given in Fig. 2. The values ranged from low to high; thus, the relative performances of the mixtures can be compared along the horizontal axis of the graph.

The presented data are the mean values of three specimens. It is seen from the figure that the minimum 4% CR modification used gave better results than the minimums of 2% SBS and 6% RR modification used. The 6% CR modification gave better results than the 2% and 3% SBS and 6%, 8% and 10% RR modification. The 8% CR modifications gave better results than the 2%, 3% and 4% SBS and 6%, 8% and 10% RR modifications. The 10% CR modifications gave better results than the 2%, 3% and 4% SBS and 6%, 8%, 10% and 12% RR modifications. The 10% RR modifications gave better results than the 2% and 3% SBS and 4% CR modifications. The 12% RR modifications gave better results than the 2%, 3% and 4% SBS and 4%, 6% and 8% CR modifications. None of the CR and RR modified mixtures could reach the performance of a 5% SBS modified mixture. As to 10% CR and 12% RR modified mixtures showed a high deformation rate after initial cracking, the 8% crumb rubber and 10% reclaim rubber modification was determined to be the maximum useful crumb rubber and reclaim rubber content. The load cycle number of the mixture modified with 8% CR, which determined to be the effective CR content, was 5 times greater than that of the base mixture and, the load cycle number of the mixture modified with 10% RR, which determined to be the effective RR content, was 3.5 times greater than that of the base mixture

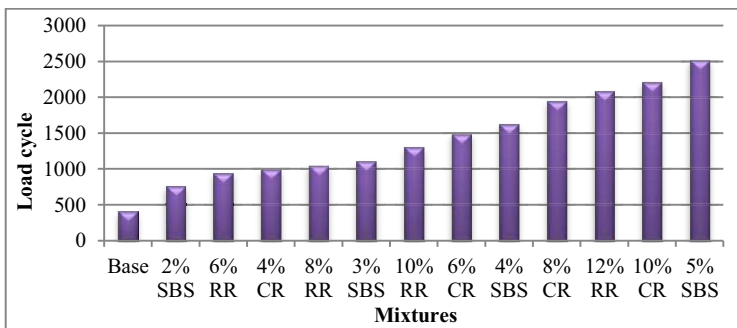


Figure 2. Load cycle numbers of the mixtures

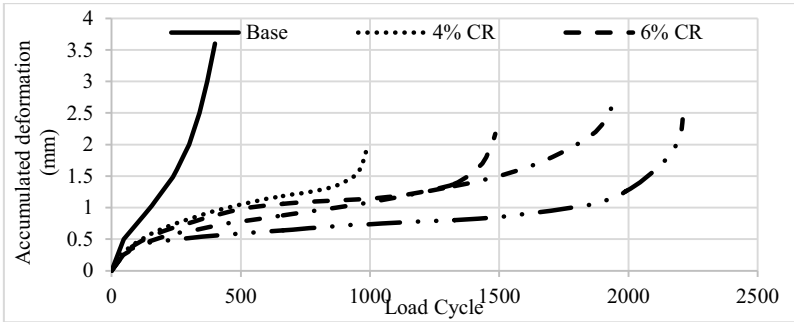


Figure 3. Accumulated deformation versus load repetitions for CR modified mixtures

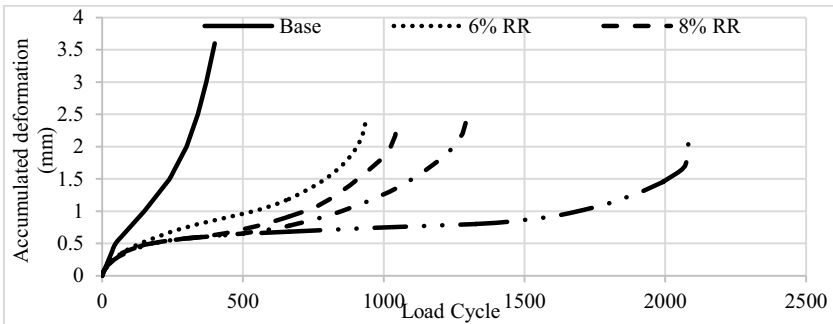


Figure 4. Accumulated deformation versus load repetitions for RR modified mixtures

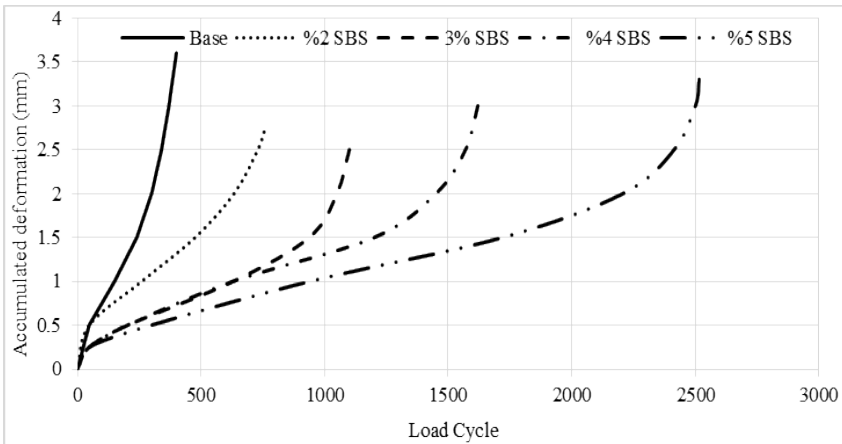


Figure 5. Accumulated deformation versus load repetitions for SBS modified mixtures

### 3. Conclusion

The experimental results of this study show the effect of using crumb rubber, reclaim rubber and SBS for modification of hot mix asphalt mixtures. The fatigue performances of crumb rubber, reclaim rubber and SBS asphalt mixtures were compared to determine

if the use of crumb rubber and reclaim rubber can replace SBS as an additive with respect to the tested properties of the bitumen and mixtures.

The fatigue test results showed that the crack growth of the SBS, CR and RR modified mixtures exhibited similar trends. As to 10% CR and 12% RR modified mixtures showed a high deformation rate after initial cracking, the 8% crumb rubber and 10% reclaim rubber modification was determined to be the maximum useful crumb rubber and reclaim rubber content. An 8% CR modification gave better results than the 2%, 3% and 4% SBS modifications and, 10% RR modification gave better results than the 2% and 3% SBS modifications. The 8% CR yielded a load cycle number 5 times that of the base mixture and 10% RR yielded a load cycle number 3.5 times that of the base mixture. None of the CR and RR modified mixtures could reach the performance of a 5% SBS modified mixture.

## References

- [1] Sadananda K, Vasudevan AK. Analysis of fatigue crack growth behavior in polymers using the unified approach, *Mater Sci Eng* 2004;A:387–9. 536–541.
- [2] Brown ER, Cooley LA. Designing stone matrix asphalt mixtures for rut-resistant pavements. NCHRP Report 425, *Transportation Research Board*; 1999.
- [3] Conner BP, Lindley TC, Nicholas T. Application of a fracture mechanics based life prediction method for contact fatigue, *Int J Fatigue* 2004;26:511–20.
- [4] Siddharthan R, Krishnamenon N, El-Mously M, Sebbaly PE. Investigation of tire contact stress distributions on pavement response, *J Transport Eng* 2002;128(2):136–44.
- [5] Brown SF, Rowlett RD, Boucher JL. Asphalt modification, in highway research: sharing the benefits. In: Proceedings of the conference The United States strategic highway research program, *Institute of Civil Engineers*, London; 1990. p. 181–203.
- [6] SHRP, A-404. Fatigue response of asphalt–aggregate mixer, *Strategic highway research program. National Research Council*, 1994.
- [7] Brown ER, Kandhal PS, Zhang J. Performance testing for hot mix asphalt. In: NCAT Report No. 2001–05. Alabama: *National Centre for Asphalt Technology*; 2001.
- [8] Suo Z, Wong WG. Analysis of Fatigue Crack Growth Behavior in Asphalt Concrete Material in Wearing Course, *Int J Constr Build Mater* 2009;23:462–8.
- [9] Arnold JC. Sasobit: characterization of properties and effects on binder and asphalt. in: *41<sup>st</sup> Conference of the association of road and traffic engineers*, Saxonia, Leizig, Germany; 2005.
- [10] Suo Z, Wong WG. Nonlinear properties analysis on rutting behavior of bituminous materials with different air void contents, *Int J Constr Build Mater* 2009;23(12):3492–8.
- [11] Huang Y, Bird RN, Heidrich O. A review of the use of recycled solid waste materials in asphalt pavements, *J Resour Conserv Recy* 2007;52:58–73.
- [12] Arabani M, Mirabdolazimi SM, Sasani AR. The effect of waste tire thread mesh on the dynamic behaviour of asphalt mixtures, *J Constr Build Mater* 2010;24:1060–8.
- [13] Katman HY, Karim MR, Mahrez A, Ibrahim MR. Performance of wet mix rubberised porous asphalt, *Proc Eastern Asia Soc for Transport Stud* 2005;5:695–708.
- [14] Katman HY, Karim MR, Ibrahim MR, Mahrez A. Effect of mixing type on performance of rubberised porous asphalt, *Proc Eastern Asia Soc for Transport Stud* 2005;5:762–71.
- [15] Casey D, McNally C, Gibney A, Gilchrist MD. Development of a recycled polymer modified binder for use in stone mastic asphalt, *J Resour Conserv Recy* 2008;52:1167–74.
- [16] Hinshog'lu S, Ag'ar E. Use of waste high density polyethylene as bitumen modifier in asphalt concrete mix, *J Mater Lett* 2004;58:267–71.
- [17] Li J, Zhang Y, Zhang Y. The research of GMA-g-LDPE modified Qinhuangdao bitumen, *J Constr Build Mater* 2008;22:1067–73.
- [18] *AASHTO guide for design of pavement structures*; 1993.
- [19] Fontes Liseane PTL, Trichês G, Pais JC, Pereira Paulo AA. Evaluating permanent deformation in asphalt rubber mixtures, *Construct Build Mater* 2010;24: 1193–200.
- [20] Ye Q, Wu S, Li N. Investigation of the dynamic and fatigue properties of fiber-modified asphalt mixtures, *Int J Fatigue* 2009;31:1598–602.



# Characterization of lateritic soils/gravels for their suitability as a pavement material- a review

D. R. BISWAL, S. R. DASH and U. C. SAHOO<sup>1</sup>

*School of Infrastructure, Indian Institute of Technology,  
Bhubaneswar, 751013, India*

**Abstract.** Lateritic soils are formed by intensive weathering and decomposition of rocks in the tropical and subtropical climate. These are secondary oxides of iron, aluminum and silicon with some calcium and/or magnesium and usually formed as a result of leaching of free silica and bases and accumulation of oxides of iron and aluminum due to heavy rains and high temperatures. Therefore the mineralogical, chemical and geotechnical characteristics of lateritic soils are largely dependent on the place of their origin. Shortage of crushed rock aggregates for pavement base and sub-bases along with the scope for using substandard gravels for low volume roads have prompted the need to explore the possibility of using locally available materials for pavement construction. In developing countries like India, Brazil and Nigeria, lateritic gravels are extensively used in road works as a sub-base material. Even though these materials are widely used, in majority of the cases, these do not meet the conventional pavement material specifications. Limited studies related to the engineering characterization of lateritic soils and gravels have been done. This paper critically reviews the studies carried out for mineralogical chemical and geotechnical characteristics of lateritic soils/gravels to present a brief overview of such materials available in different parts of the world. The paper also proposes a rational characterization process of lateritic gravels for use in mechanistic design of pavements.

**Keywords.** Laterite, gravel, characterization, pavement, subbase, resilient modulus

## Introduction

Shortage of crushed rock aggregates and good quality road construction materials for pavement base and sub base have prompted to explore the possibility of using locally available granular soils to use in pavement construction. In developing countries like India, Brazil, Nigeria, lateritic gravels are extensively used in road works as a sub-base material.

Lateritic soils are reddish soils formed by in-situ intensive weathering and decomposition of rocks in the tropical and subtropical climate [1,3]. The characteristics of these lateritic soils are mostly dependent on the place of their origin, climate, drainage, chemical and mineralogical composition and degree of weathering. Many studies have been carried out on lateritic soils of Nigeria, Ghana, Brazil and Australia to find their characteristics [1-3].

<sup>1</sup>Corresponding author: [ucsaahoo@iitbbs.ac.in](mailto:ucsaahoo@iitbbs.ac.in)

In most of the developing countries, road construction is sometimes done with little attention to norms and standards [4]. Road design needs to be based on realistic knowledge or objectives information of local materials characteristics, the gravel lateritic soil specifically. To carry out the pavement analysis using elastic layered approach, material properties in terms of elastic modulus and Poisson's ratio are the major input parameters. Resilient modulus which represents elastic modulus of pavement materials under dynamic loading is determined from the repeated load triaxial tests. This test covers a very tedious procedure and also it is not available with many highway organizations in developing countries. Hence, there is a need for detailed characterization of these soils/gravels and establish relationships between resilient modulus and other routinely evaluated geotechnical properties of lateritic soils/gravels. Also, in majority of the cases, lateritic soils/gravels do not meet the conventional pavement material specification requirement and hence there is a need to develop suitable stabilization methods to make them suitable as a base or sub-base material [4].

### 1. Mineralogical and chemical characteristics

The chemical compositions of lateritic soils / gravels vary widely based on genesis, climatic conditions, age of laterisation. Some lateritic soil contain more than 60%  $\text{Fe}_2\text{O}_3$  and little of  $\text{Al}_2\text{O}_3$  and where as some contain more than 60%  $\text{SiO}_2$  and little of  $\text{Al}_2\text{O}_3$  and  $\text{Fe}_2\text{O}_3$ . Iyer and Williams [3] studied the lateritic soils of Green swamp Australia and reported the chemical compositions as  $\text{Fe}_2\text{O}_3$ (16%),  $\text{SiO}_2$ (66%) and  $\text{Al}_2\text{O}_3$ (10%). It has been reported by many studies [4] that there is a general relationship between altitude and the chemical composition of lateritic soils. The soils on the higher areas are generally more acidic than the low lying areas. The chemical analysis of Indian soils shows that these soils are rich in iron, and aluminum but poor in nitrogen, potash, potassium, lime and organic matter.

A number of researchers [2, 3, 5, 6] have carried out X-Ray diffraction analysis to find out the mineralogical composition of lateritic soils. These soils are mainly composed of weathering minerals such as hematite, goethite, kaolinite, gibbsite etc. Iyer and Williams [3] found that the soil contains kaolinite, haematite, goethite and quartz. Various researchers use the silica/sesquioxide ratio to define the lateritic soil. Some authors suggest that this ratio should be more than 2 whereas other authors question the role of silica/sesquioxide in defining the degree of laterisation [1]. The high silica / sesquioxide ratio is due to the presence of quartz [3,7].

Alexander and Candy [8] reported that the hardness of a lateritic soil is controlled by the arrangement of iron oxide in relation to other minerals. Iyer and Williams [3] stated that the iron oxide and aluminum oxide bind the clay particles leading to the change of micro-structure of the clay particles. Some researchers have studied the micro-structure of lateritic soil by scanning electron microscope (SEM). The microstructure gives an idea about the state of laterisation. Lateritic soil and a microscopic view of lateritic soil are given in Figure 1 [3].



**Figure 1.** (a) Lateritic soil/gravel (b) Microstructure of lateritic soil

## 2. Geotechnical characterization of lateritic soils

The geotechnical properties of lateritic soils such as index properties, compaction characteristics and strength parameters are mostly influenced by the climate, parent rock, degree of laterisation, mineralogy and micro structure of the soil [3, 9]. Several studies have been carried out to find out the geotechnical properties of these soils [10-12]. Specific gravity of the lateritic soils found in various parts of the world varies between 2.35 and 3.1. Nwaiwu et al. [5] has studied the iron stone laterites and have found that water absorption values of ironstone lateritic gravels vary from 5.41% to 11.5% [4]. They have also reported that the soil having highest gravel percentage possess lowest optimum moisture content (OMC). According to their investigation lateritic gravels having specific gravity more than 2.85, water absorption less than 4%, aggregate impact value (AIV) less than 30% and Los Angeles Abrasion value less than 40% will give good performance.

Badmus [2] studied the plasticity and compressibility characteristics of South-western Nigerian soil and reports that the most important parameter of parent rock is the coefficient of compressibility followed by amount of fines, plasticity index and specific gravity. Nwaiwu et al. [5] calculated parameters like grading modulus, activity ratio, plasticity modulus and shrinkage modulus of lateritic soils of Nigeria and reported that these soils satisfy the requirements for paved and unpaved roads. The compacted lateritic specimen shows very little shrinkage and it may be due to the low clay content and its micro structure [3].

Osulale et al. [13] investigated the effect of pH on geotechnical properties of lateritic soils and reported that the consistency limits decrease with increase with time at various pH values. MDD decreases and OMC increases with increase in number of days and the increase in OMC may be due to the increase in surface area and texture as a result of activities of acids and base. The CBR of the soils also decreased with increase in number of days for each pH solution. The author attributes the decrease in CBR (strength of soil) to the leaching of iron oxide by the acids and the base which cause the reduction in the bonding forces in between the soil particles.

Many of the researchers studied the compaction characteristics of lateritic soils. The OMC for these soils vary between 11% and 26% and maximum dry density (MDD) for lateritic gravels vary between 18.5 KN/m<sup>3</sup> and 20.3 KN/m<sup>3</sup>. Various researchers observed that the maximum dry density of compacted lateritic soil increases with the compaction energy imparted to soil specimen [2,3,14].

Iyers and Williams [3] reported that the angle of shearing resistance increases from 35° at 11.0% to 49° at 7.7% moisture content and concluded that the high shear strength is due to the high angle of shearing resistance and high suction. Omotoso et. al. [15]

measured shearing angle from direct shear test and found it to be  $33^{\circ}$  at cohesion 75 kPa. The study reported California bearing ratio (CBR) values of the lateritic soil to be in the range of 35 - 90%. Bello [16] has studied the unconfined compressive strength of Nigerian soils at varying water contents and observed unconfined compressive strength (UCS) values more than 200 kN/m<sup>2</sup> corresponding to water content of 13.9-18.1%.

Fall et al. [12] have studied lateritic soil of Senegal in West Africa and have reported that the un-drained shear strength depends on the initial dry density and the initial consolidation pressure. They have also carried out tests on lateritic gravels under static and dynamic loading. Fall et al. [12] and Molenaar [17] has conducted repeated load tests and have studied the resilient modulus characteristics of lateritic soils and gravels. The resilient modulus obtained from repeated load CBR can be compared with resilient modulus obtained from triaxial load at confining pressure 24 kPa [18].

### 3. Discussion and conclusion

Lateritic soils/gravels have been proved to be a potential pavement material to be used in base and subbase layers [3, 5]. Researchers in the field have unanimously opined that the property of lateritic soils depends on the geographical location of lateritic soils, genesis, degree of laterisation, vegetation, drainage and chemical composition. Lateritic soils available in many parts of the world are mostly composed of minerals such as hematite, goethite, kaolinite, gibbsite etc. The specific gravity of lateritic soils varies between 2.31 gm/cc to 3.1 gm/cc. (OMC) has been found to vary widely from 11 to 26%. The liquid limit of most lateritic soils ranges between 35 to 50 which exceeds the criteria for pavement material as per specification of Indian Road Congress (IRC) and American Association of State Highway and Transportation Officials (AASHTO). To control the liquid limit and plasticity index, these soils need to be stabilized. CBR values of these gravels vary widely from 10% to 90%.

Properties of base materials have mostly been evaluated by laboratory tests such as CBR, which do not represent the nature of repeated dynamic traffic load. Recognizing this, the AASHTO guide for design of pavement structures [19] incorporated the resilient modulus for characterizing pavement materials in flexible pavement design. Very few studies are available on characterization of lateritic gravels / soils using the resilient modulus. Resilient modulus is usually determined with repeated load triaxial test which is a very tedious process. Hence there is a need to evaluate the resilient moduli for lateritic gravels and establish correlations with other routinely determined geotechnical parameters such as UCS, CBR etc. Also, resilient modulus and poisons ratio of stabilized lateritic soil needs to be determined in order to go for mechanistic-empirical design of pavements. This type of work need to be carried out on laterites obtained from various places, as the properties of this soil are largely dependent on the place of origin.

### References

- [1] Gidigasu, M. D. (1976) "Laterite Soil Engineering: Pedogenesis and Engineering Principles", Elsevier, Amsterdam, Netherlands.
- [2] Badmus, B. S., (2010) "Plasticity and Compressibility Characteristics of Lateritic soil From South Western Nigeria." *J. Nat. Sci. Engr. Tech*, Nigeria, 9(1), p.14-22.

- [3] Iyer, U. M. and Williams, D. J., (1997). "Properties and performance of lateritic soil in road pavements." *Engineering Geology*, St.Lucia, Queensland 4072, Australia, 46, p.71-80.
- [4] Joel, M. and Agbade, I. O., (2010). "Mechanical-Cement Stabilisation of Laterite for Use as Flexible Pavement Material." *Journals of Materials in Civil Engineering*, Vol. 23, No.2.
- [5] Nwaiwu, C. M. O., Alkali, I. B. K. and Ahmed, U. A., (2006). "Properties of ironstone lateritic gravels in relation to gravel road pavement construction." *Geotechnical and Geological Engineering*, Nigeria, 24, p.283-298.
- [6] Alao, D. A., (1982/83). "Geology and Engineering Properties of lateritic from Ilorin, Nigeria." *Engineering Geology*, Elsevier Science Publishers, B.V. Amsterdam, Houghton MI 49931(U.S.A.), p.111-118.
- [7] De Graft-Johnson, J. W. S., Bhatia, H. S., and Hammond, A. A. (1972). "Lateritic gravel evaluation for road base." *J. Soil Mech. Div., ASCE*, 98(11), 1245-1265.
- [8] Alexander, L.T and Candy, J.G (1962) "Genesis and Hardening of Laterite in soils", *U.S.D.A Technical Bulletin* No.1282,pp 90
- [9] Bayewu, O. O., Olountola, M. O., Mosuro, G. O. and Adeniyi, S.A., (2012). "Petrographic and Geotechnical Properties of Lateritic Soils developed over different parent rocks in Ago-Iwoye area, South-western Nigeria." *International Journal of Applied Sciences & Engineering Research*, Nigeria, Vol.1, Issue 4, p.584-594.
- [10] Vargas M. (1953) "Some Engineering Properties of Residual Clay Soils occurring in Southern Brazil", *Proc. Int. Conf. SMFE 3<sup>rd</sup> Zurich*, 1: 67-71.
- [11] Ogunsanwo, O. (1985) "Variability in the shear strength characteristics of an amphibolite derived laterite soil." *Bull. I.A.E.G.* No.32: 111-115.
- [12] Fall, M., Tisot, J. P. and Ciss, I. K., (1997) "Undrained behaviour of compacted gravel lateritic soils from western Senegal under monotonic and cyclic triaxial loadings." *Engineering Geology*, Senegal, 47, p.71-87.
- [13] Osulale, O. M., Falola, O. D. and Ayoola, M. A., (2012). "Effect of pH on Geotechnical Properties of Lateritic Soil Used in Highway Pavement Construction." *Civil and Environmental Research*, Ogbomoso, Nigeria, Vol.2, No.10, p.23-28.
- [14] Alayaki, F.M., (2012). "Water Absorption Properties of Lateritic Soil in Road Pavement: A Case Study Ife-Ilesha Highway, South Western Nigeria." *International Journal of Emerging Technology and Advanced Engineering*, Vol.2, Issue11, p.51-57.
- [15] Omotoso, O. A., Ojo, O. J. and Adetolaju, E. T., (2012). "Engineering Properties of Lateritic Soils around Dall Quarry in Sango Area, Ilorin, Nigeria." *Earth Science Research*, Vol.1, No.2, p.71-81.
- [16] Bello, A. A., (2011) "Analysis of Shear Strength of Compacted Laterite Soils." *The Pacific Journal of Science and Technology*, Vol-12, 1.
- [17] Molenaar, A. A. A., (2007). "Characterization of Some Tropical Soils for Road Pavements", *Transportation Research Record*, No. 1989, Vol. 2, pp. 186-193.
- [18] Samb, F., Fall, M., Berthaud, Y and Makhaly, B. (2013) " Resilient Modulus of Compacted Lateritic Soils from Senegal at OPM Conditions", *Geomaterials*, Vol. 3, pp. 165-171 .
- [19] AASHTO, (1993) "Design of Pavement Structures", American Association of State Highway and Transport Officials, USA.

# Proposing a realistic frequency for fatigue tests using Artificial Neural Network

Ali KHODAII<sup>1</sup> and Attila Hassanzadeh ZONOUZY

*Amirkabir University of Technology, Iran*

**Abstract.** Among many factors affecting fatigue life estimation of hot mix asphalt pavement materials are loading frequencies, rest period, test temperature and obviously constituent material properties. An over or under estimation of fatigue life could lead to an early destruction of pavement or an over design which is naturally not desirable. It is therefore essential that a realistic loading frequency be used that corresponds to the actual speed; headway and the traffic wander across the lane. The actual data collected from a weight in motion system at a major road from Tehran to Qum was used and analyzed employing an artificial neural network. A prediction model is proposed that show 89% goodness of fit and 0.296 errors in predicting the loading frequency. This model can be used for selection of realistic loading time and the rest period which has an important impact on many properties of asphaltic materials including fatigue, relaxation and self-healing properties of such pavement materials.

**Keywords.** Loading frequency, fatigue test, Artificial Neural Network, headway, Traffic Wander

## Introduction

Life time estimation of asphalt concrete pavements due to fatigue failure is one of the engineer's responsibilities. Fatigue failure in asphalt materials almost happens as a consequence of repetitive loads applied with a magnitude well below the strength of asphalt mix. Fatigue phenomenon can be studied using traditional and Dissipated Energy methods [1-3]. Traditional method uses models based on stress and strain relations to determine the fatigue life, another method uses dissipated energy to assess the fatigue lifelong [2,4]. Fatigue phenomenon can be examined under stress and strain hysteresis loops in loading cycles [5,6]. There are some parameters such as loading frequency, rest periods, loading amplitudes, pavement thicknesses etc., that can influence fatigue life [7]. The number of loading cycles applied on the specimen in a unit of time, is called loading frequency. Epps and Monsmith in 1972 [8] investigated the loading frequency impact. They changed loading frequency with different rest periods, and concluded that in strain-control circumstances, increasing frequency from 3 to 30 loads per minute, has no effect on specimen life, although increasing from 30 to 100 would decrease fatigue life. In strain-controlled tests increasing the frequency decreases the fatigue life, because of reduction in healing time [8] and increasing dissipated energy[9]; however, increasing the frequency while

---

<sup>1</sup>Corresponding author. [akhodaii@gmail.com](mailto:akhodaii@gmail.com), Tel. +982164543000

decreasing the loading periods can increase fatigue life. In stress-controlled tests increasing the frequency can improve fatigue life. Fakhri et al and Alkhatib tests conducted in strain-control and stress-control experiments proves these statements [9-16].

In order to achieve optimized design and assess fatigue life of materials subjected to moving loads, appropriate loading history like in actual conditions should be applied on specimen [17,18]. Investigation of loading frequency effect on asphalt mixes is really a hard work; since it is related to both loading and unloading periods [19]. Speed of moving vehicle on asphalt pavements is recognized as one of the effective parameters on determining loading frequency [4,20]. As a result, it is observed that speed and frequency changes have same trend. In addition to speed, traffic headway and wander have fundamental effect on the rest and loading periods of pavement materials; hence, in this study both traffic headway and wander are used to define loading model in frequency of fatigue tests. Traffic headway is the time interval between two vehicles passing a specific section. Traffic wander is a parameter describing the actual location of vehicle in road lane. Because of larger width of road lanes than vehicles' width, moving in different locations is natural for vehicles. This study uses these parameters based on the records collected from WIM (Weight In Motion) system installed in Tehran to Qum road, near Hassan-Abad as inputs to develop a model with ANN (Artificial Neural Network).

There are many researches in modeling the traffic headway in the literature. In 1936 traffic flow was described as random nature phenomenon [21]. Adams described the traffic headway by Poisson distribution, fitting highly with actual records. Some years later, in 1966, Greenberg described headway by Log-Norm distribution [22]. In 1990 and 1993, Heidman described headway in accordance with flow density. However, there is no definite inference about capability of Heidman's model in comparison with Greenberg's [23,24]. In 1981 Akcelik proposed exponential distribution to describe headway [25]. Researchers after Akcelik were focused on effect of car groups on statistical distribution of headway [26,27]. In 1997, Hoogendorn used Fourier Series and introduced Pierson's third kind to describe headway [28, 29]. In 1999 and 2003, Luttinen, studied traffic flow in single and trop forms and introduced exponential distribution as best fitted distribution for headway [30, 31]. Al-Ghamdi, contrary to conventional literature trend described headway with Gamma and Erlong distributions, respectively for urban streets and highways. Other researchers investigated the relations between headway and other traffic parameters [32]. For instance, Arason and Koshy worked on the relation between headway and vehicles dimensions [33]. Zhang et al. observed relation between headway and high occupancy vehicles [34]. Shariat et al. studied headway in Tehran [35]. In other research Khodayari et al simulated car following behavior by ANN [36].

Pavement material laboratory investigators are always looking for a way to eliminate the difference between estimated and actual life. As a result, Pell et al proposed 22 and 10 as the correction coefficients, respectively for traffic wander and headway [10]. In this study, an optimized model is investigated to achieve loading frequency in fatigue tests; since, it would reduce the gap between estimated and actual life time. The writers used two variables, traffic headway and wander as inputs in Artificial Neural Network model to obtain fatigue frequency.

## 1. Artificial Neural Network (ANN)

ANN is inspired from human mind structure [37]. This method develops models by imitating the process of mind in learning new issues, and generalizing the concept to similar situations [38]. The simple unit neural network is shown in Figure 1. schematically[39].

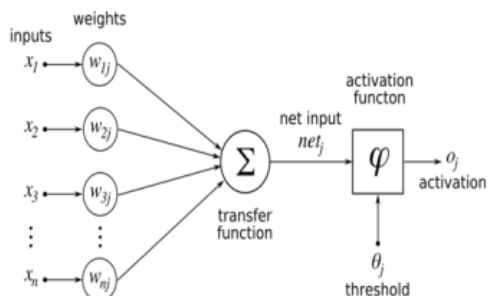


Figure 1. Unit neuron in ANN network schematically

The neurons adjustment can be done by means of Equations 1 and 2.

$$U_k = \sum_{j=1}^m w_{kj} x_j \quad (1)$$

$$Y_k = f(u_k + b_k) \quad (2)$$

In which  $x_j$ - are input variables.  $w_{jk}$ - are weights related to  $k^{\text{th}}$  neuron.  $u_k$ - is input combinatory.  $b_k$ - is bias.  $f_k$  is transferring function.  $Y_k$  neuron output. The network is developed by Matlab software in 4 stages:

### 1. Developing configuration

In this step; firstly, a number of layers, hidden layers and neurons in hidden layers are created; secondly, is training the algorithm, including feed-forward and/or back-propagation and; finally, training, activation and error functions are determined [40].

### 2. Training stage

Training neural networks is carried out by adjusting the weights considered in each neuron. Weight adjustment is done in two steps: first, inputs are subjected to the network and output evaluated, then according to difference in actual and evaluated outputs, in the second step the software begins to reform weighs [37].

### 3. Test

Test stage is performed to check the prediction ability of networks. The error deviation will show the capability of model in predicting similar situations [37].

### 4. Validation

Validation module is done to check the generalization capability of models and to stop training process, unless it reaches significant development training process.



1.1 Input data

Input data included traffic headways and wanders taken from WIM system in Tehran-Qum highway. By a random selection, 300 records were used in forms of  $300 \times 2$  matrix as input to the system. Rows of matrix represented different kinds of input variables and matrix columns introduced number of observations.

1.2 ANN Model construction

In this study, various combinations of networks with different training functions and neuron numbers in hidden layer were used to obtain the best fitted model. All networks had one input layer. As shown in Figure 2, the networks had 4 layers totally. All networks configurations were feed-forward. Activation functions in hidden layers were sigmoid function. Different kinds of training functions such as tansig, purelin logsig were used. Linear neurons in outer layers played a role. The networks were trained under Back-Propagation Levenberg-Marquart algorithm by Matlab software. All errors were examined by Mean Squared Error (MSE) index.

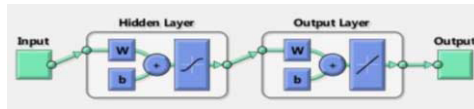


Figure 2. Schematic view of network configuration

In this study, 10 to 30 neurons in hidden layers were built with respect to input and output variables, computation time, duration and accuracy needed. Table 1 shows the networks which were built. Input data, as defined matrixes, was inserted to the models. 70% (210) of input data was used to train networks. Networks were trained due to errors obtained from train data. 15% (45) of data were used to test validate networks. Afterward, Matlab software was set and the modeling results were speculated to find optimized solution.

Table 1. Networks detailed structures and results

Neuron in hidden layer	training function	R	error amount
20	TANSIGN	0,89025	0,283
22	TANSIGN	0,86373	0,446
24	TANSIGN	0,88733	0,373
26	TANSIGN	0,87671	0,318
28	TANSIGN	0,085	0,446
30	TANSIGN	0,86	0,6159
20	PURELIN	0,88	0,2275
22	PURELIN	0,8761	0,3338
24	PURELIN	0,87911	0,3195
26	PURELIN	0,87844	0,3172
28	PURELIN	0,85062	0,3015
30	PURELIN	0,88164	0,3257
20	LOGSIG	0,88126	0,3854
22	LOGSIG	0,87437	0,3811
24	LOGSIG	0,86939	0,3399
26	LOGSIG	0,89208	0,2963
28	LOGSIG	0,89782	0,381
30	LOGSIG	0,89529	0,2959

## 2. Results and discussion

“R” and amount of errors are reported in Table 1. “R” shows the correlation between models calculated outputs and real field outputs. This quantity ranges between 0 and 1. Zero means the complete random relation and 1 means, full dependence of two outputs and may be sign of overtraining, that means the network does not train well, but just memorizes inputs and related outputs. This index shows the probability of cases predicted correctly by the model. The error amount is the difference between actual and computed output in final stage. Given below are the findings:

- The optimized network had 30 neurons in its hidden layer with logsign training function, sigmoid activation function, MSE error function, which was trained by Levenberg-Marquart feed-forward algorithm, totally in four (4) layers. In this network R was 89% and error amount was 0.296, this R showed that the model can predict frequencies in almost 90% situations correctly. The error amount quantity can be negligible in asphalt fatigue test.
- Selecting of optimized network is based on two criteria changing in opposite trends. Greater R, and lower error amount are desired. In this study, firstly; error amount was considered, then the network with greater than an R value was chosen.
- Reported R values, show that overtraining did not happen in these networks.
- According to the model selected, 5 Hz loading is a good representation of actual loading that the pavement material is subjected to and can be used for fatigue testing. Of-course, this finding can only be applied to the pavements experiencing similar traffic flow and drivers' behavior as in the case used in this study and further investigation will be needed before any generalization of the results.
- High accuracy, low amount and duration of calculation and the capability of coping with different kinds of actual data, are the ANN strength points. Additionally, ANN algorithm is developed in a way that, it can easily purify raw data. As a result, there is no need for data preparation process in projects [41]. This spatiality brings high calculation speed to ANN method.

## 3. Conclusion

The aim of this study was to determine the appropriate fatigue test frequency representing the actual field condition to estimate fatigue life of asphalt correctly in laboratory. The models were made by ANN method and the final model was selected with 90% probability of correct predictions.

## Acknowledgement

Authors wish to acknowledge their special thanks to Eng. A. Mehrara and Eng. F. Farokhzadeh, for their help in gathering data and software development.

## References

- [1] Boudabbous M, Millien A, Petit C. Energy approach for the fatigue of the viscoelastic materials: application to asphalt materials in pavement surface layers. *Int J Fatigue* 2013;47:308–18.
- [2] Ghuzlan K, Carpenter SC. Energy-derived, damage-based failure criterion for fatigue testing. *J Transport Res Board (TRB)* 2000;9:141–9 [Transportation Research Record No. 1723, National Research Council, Washington, DC, USA].
- [3] Monismith CL, Deacon JA. Fatigue of asphalt paving mixtures. *Transport Eng J, Proc Am Soc Civil Eng (ASCE)* 1969;95(TE2).
- [4] Guide for mechanistic-empirical design of new and rehabilitated pavement structures, final report, *NCHRP 1-37A, Part Three Design Analysis*, ARA Inc., ERES Consultants Division; 2004.
- [5] Al-Khateeb G, Shenoy A. A distinctive fatigue failure criterion. *Assoc Asphalt Pav Technol (AAPT) J* 2004;73:585–622.
- [6] Al-Khateeb G, Shenoy A. A simple quantitative method for identification of failure due to fatigue damage. *Int J Damage Mech (IJDM)* 2011;20:3–21.
- [7] Baburamani, Pud. Asphalt fatigue life prediction models: A literature review . No. ARR 334, 1999
- [8] Epps JA, Monismith CL. Fatigue of asphalt concrete mixtures-summary of existing information. Fatigue of compacted bituminous aggregate mixtures, *ASTM STP508. American Society for Testing Materials*; 1971. p. 19–45.
- [9] Al-Khateeb G, Stuart K, Mogawer W, Gibson N. Fatigue performance: asphalt binders versus mixtures versus full-scale pavements. *Can J Transport (CJT)* 2008;2(Part 1):13–33.
- [10] Pell, P. S.. "Characterization of Fatigue Behavior," in Structural Design of Asphalt Concrete Pavements to Prevent Fatigue Cracking. *Special Report 140, Highway Research Board*, 1973, 49-64.
- [11] Deacon JA. Fatigue of asphalt concrete. Engineering Doctor of Philosophy Dissertation. Berkeley, USA: *Transport Engineering Division, University of California*; 1965.
- [12] Pell PS, Taylor IF. Asphaltic road materials in fatigue. In: *Proceedings of the association of the asphalt pavement technologists (AAPT)*, vol. 38, Los Angeles, California, USA; 1969. p. 577–93.
- [13] Raithby KD, Sterling AB. The effect of rest periods on the fatigue performance of a hot-rolled asphalt under reversed axial loading. In: *Proceedings of the asphalt paving technologists (AAPT)*, vol. 39, Kansas City, USA; 1970. p. 134–47.
- [14] Al-Khateeb, G. G., & Khalid, A. G.. The combined effect of loading frequency, temperature, and stress level. *International Journal of Fatigue*, 2013 254-261.
- [15] Al-Khateeb, G. G., & Khalid, A. G.. The combined effect of loading frequency, temperature, and stress level. *International Journal of Fatigue*, 2013, 254-261.
- [16] Fakhri, M., Hassani, K., & Ghanizadeh, A.. Impact of loading frequency on the fatigue behavior of SBS. *Procedia - Social and Behavioral Sciences* (pp. 69-78). India: Elsevier Ltd, 2013.
- [17] Heuler, P. and Kl'atschke, H. Generation and use of standardised load spectra and load-time histories. *Int. J. Fatigue* 27, 974–990. 2005
- [18] Oelmann, B. Determination of load spectra for durability approval of car drive lines. *Fatigue Fract. Eng. Mater. Struct.* 2002, 25, 1121–1125.
- [19] Porter BW, Kennedy TW. Comparison of fatigue test methods for asphalt materials. Research Report 183–4, Project 3-9-72-183. Austin, USA: Center for Highway Research, *the University of Texas*; 1975.
- [20] Barksdale RD. Compressive stress pulse times in flexible pavements for use in dynamic testing. *Highway Research Record*, No. 345, Washington DC; 1971
- [21] Adams, W. F., 'Road traffic considered as a random series', *Journal of the Institution of Civil Engineers*, 1936 4(1), 121–130.
- [22] Greenberg, I., 'The log-normal distribution of headways', *Australian Road Research*, 1966 2(7), 14–18.
- [23] Heidemann, D., A theoretical model to calculate time-headway distributions as a function of traffic density, in M. Koshi, ed., 'Transportation and Traffic Theory', *Proceedings of the Eleventh International Symposium on Transportation and Traffic Theory*, held July 18–20, 1990, in Yokohama, Japan, Elsevier, New York, 1990, pp. 1–17.
- [24] Heidemann, D., A theoretical model for distributions of speeds and timeheadways on two-lane roads, in C. F. Daganzo, ed., 'Transportation and Traffic Theory', *Proceedings of the 12th International Symposium on Transportation and Traffic Theory*, Berkeley, California, USA, 21–23 July, 1993, Elsevier, Amsterdam, 1993, pp. 523–537
- [25] Akcelik, R.. Traffic Signals: Capacity and Timing Analysis. *Australian Road Research Board Research Report* ARR No. 123 (5th reprint: 1993).
- [26] Akcelik, R. and TROUTBECK, R. Implementation of the Australian roundabout analysis method in SIDRA. In: U. Brannolte (ed.) *Highway Capacity and Level of Service*, *Proc. of the International Symposium on Highway Capacity*, Karlsruhe, A.A. Balkema, Rotterdam, 1991, pp. 17-34

- [27] Akcelik, R. & Chung, E, 'Calibration of the bunched exponential distribution of arrival headways', *Road & Transport Research* 3(1), 1994, 42– 59.
- [28] Serge P. Hoogendoorn and Hein Botma, "Modeling and Estimation of Headway Distributions", *Transportation Research Record: Journal of the 13 Transportation Research Board, No.1591*, TRB, National Research Council, Washington D.C. 1997.
- [29] Serge P. Hoogendoorn and Piet H. L. Bovy, "New Estimation Technique for Vehicle-Type-Specific Headway Distributions", *Transportation Research Record: Journal of the Transportation Research Board, No.1646*, TRB, National Research Council, Washington D.C. 1998.
- [30] Luttinen, R.T. Properties of Cowan's M3 headway distribution. *Transportation Research Record* 1678, 1999, pp 189-196.
- [31] Luttinen, R.T.. Capacity of Unsignalised Intersections. TL Research Report No. 3.TL Consulting Engineers, Lahti, Finland. 2003.
- [32] Ali S. Al-Ghamdi, , "Analysis of Time Headways on Urban Roads: Case Study from Riyadh", *Journal of Transportation Engineering: Journal of the American Society of Civil Engineering*, ASCE. 2001
- [33] V. Thamizh Arasan and R. Z. Koshy, "Headway Distribution of Heterogeneous Traffic on Urban Arterials", *IE (I) Journal-CV*, 2003, Vol. 84.
- [34] Guohui Zhang, Yin Hai Wang, Heng Wei, and Yanyan Chen, , "Examining Headway Distribution Models Using Urban Freeway Loop Event Data, *TRB 2007 Annual Meeting CD-ROM, TRB, National Research Council*, Washington D.C. 2007.
- [35] Shariat Mahmini, A, Arman, M, Kalantari, N, 'Estimation of Vehicle headway', *International Tehran Traffic Conference*, Tehran Municipality, 2012
- [36] Khodayari, A, Ghaffari, A, Kazemi, R, and Alirezaiee, M, 'Simulation and Prediction of Car Following Behavior on the Basis of Drivers Lateness' 18<sup>th</sup> International Mechanic Engineers of Iran, 2011.
- [37] Menhaj, M, 'Arteficial Network' 1<sup>th</sup> Volume, AmirKabir University of Technology Publication Center.
- [38] Kaveh, A, Servati, H, 'Arteficial Neural Networks in Analysis and Design of Structures' Markaze Tahghigat Sakhteman o Maskan, 2002.
- [39] Hola, J., and Schabowicz, K. "Application of artificial neural networks to determine concrete compressive strength based on non-destructive tests", Feb 21, 2005.
- [40] Giri, A.K. "Pigeaud's Curves Modeling By Using Artificial Neural Networks", March, 2006 pp-25.
- [41] Hensher, A. D., & Ton, T. T. A comparison of the predictive potential of artificial neural networks and nested logit models for commuter mode choice. *Transportation Research Part E*, 1999, 155-172.

# Polymer modified bitumen asphalt, a proposed solution for UAE pavement deterioration

Reem SABOUNI<sup>1</sup> and Ahmed AL-GHAZALI

*Department of Civil Engineering, ALHOSN Univ., Abu Dhabi, United Arab Emirates*

**Abstract.** The traffic volume in the United Arab Emirates (UAE) has tremendously risen in the last decade due to the fast-pace development of the country. This increase in traffic volume combined with the harsh environment of the UAE causes the deterioration of asphalt pavements to accelerate all around the country, especially in areas of congested traffic. To understand the main mechanisms of pavement deterioration present in UAE roads a field examination of asphalt pavements in congested areas in the UAE was performed. The field examination recognized six main problems in UAE pavements: mix rutting, subgrade rutting, fatigue cracking, bleeding, raveling, and potholes. Then an investigation was been carried out to evaluate the effectiveness of using Styrene-Butadiene-Styrene (SBS) polymer modified bitumen (PMB) asphalt to help improve the deterioration problems. A group of standard experiments were performed on both standard asphalt and polymer modified asphalt samples. The experimental investigation shows that, the SBS-PMB asphalt had favorable stability, stiffness, flow and density results. Based on the field observations and the experimental investigation, polymer modified bitumen asphalt is proposed to be used in new constructed roads to help reduce the amount of deterioration and maintenance cost in the UAE.

**Keywords.** Polymer modified bitumen, asphalt pavements, pavement deterioration

## Introduction

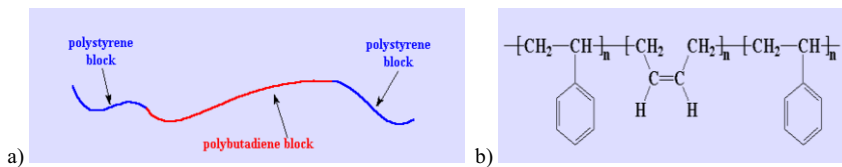
Due to the fast pace of development in the United Arab Emirates in the last decay, the traffic volume has tremendously increased. The harsh environment of the UAE combined with this traffic increase has accelerated the deterioration of asphalt pavements in congested traffic areas all around the country. Some of the pavement performance enhancers to improve bitumen characteristics that have been adopted by other countries encountering similar problems include: additives modification, polymer modification and chemical reaction modification [1]. Polymer modification was found to be among the most commonly used binder modifications. In general, two types of polymers are used to modify bitumen for road construction: plastomers and elastomers. Examples of commonly used plastomers are Ethene-Vinyl-Acetate (EVA) and Polyethylene, while Styrene-Butadiene-Styrene (SBS) is the most used elastomer and

---

<sup>1</sup>Corresponding author: Department of Civil Engineering, ALHOSN University, Abu Dhabi, United Arab Emirates, P.O.Box: 38772, email. [r.arsabouni@alhosnu.ae](mailto:r.arsabouni@alhosnu.ae)

probably the most appropriate polymer for bitumen modification. Basically, plastomers increase the stiffness and viscosity of bitumen while elastomers improve the elastic behavior of bitumen [2].

The UAE has taken the lead in producing SBS polymer modified bitumen (PMB) in the region by using the Sealoflex technology- A manufacturing facility has been built in the capital city Abu Dhabi [3]. SBS is a unique material which creates a three dimensional network with the polystyrene blocks at the ends of the SBS while the polybutadiene forms the mid-block, which gives the material its exceptional elasticity (Figure 1). The SBS structure acts as a skeleton to the bitumen [4].



**Figure 1.** Styrene-Butadiene-Styrene (SBS): a) Block and b) Structure [5]

Several researchers have carried out studies on the characteristics and performance of SBS as a polymer modified bitumen. Tayfur et.al. [6] carried out an investigation of rutting performance of asphalt mixtures containing five different polymer modifiers. SBS mixtures were found as the most resistant of the five mixtures with respect to rutting [6]. Gorkem and Sengoz [7] conducted a study to determine the effect of additives such as hydrated lime as well as elastomeric (SBS) and plastomeric (EVA) PMB on stripping and moisture induced damage of hot mixed asphalt. It was found out from this study that the samples prepared with SBS-PMB exhibited more resistance to water damage compared to other samples [7]. Kok and Yilmaz [8] also investigated the effect of using lime and SBS on the properties of hot mix asphalt. The investigation results indicated that the application of lime as mineral filler and SBS modified binders, each on its own, improved the stability, stiffness and strength characteristics of hot mix asphalt [8]. Sengoz and Isikyakar [1,2] evaluated the properties and microstructure of SBS and EVA polymer modified bitumen. The results showed that the polymer modification improved the mechanical properties such as Marshall and ITS, as well as, the conventional properties of penetration, softening point and temperature susceptibility [1,2].

In the course of this research a field study was conducted at UAE's capital Abu Dhabi to identify the common asphalt problems. Based on the identified problems in the field and the fact that an SBS manufacturing facility is available in Abu Dhabi, the SBS-PMB was proposed as a solution for these problems in areas of high traffic volumes. To justify this proposal an experimental investigation was conducted in this research to compare the conventional asphalt to SBS-PMB asphalt mixes using locally available materials and accounting for local weather conditions.

## 1. Typical asphalt pavement problems in the UAE

To identify the common asphalt pavement problems in UAE a field study was conducted in UAE's capital city (Abu Dhabi). This field study recognized six main problems in Abu Dhabi pavements. These problems are discussed in details in the following paragraph.

The first two problems recognized were rutting problems which are kinds of deformations that are common in pavements that experience high traffic volumes. This deformation can be seen on Abu Dhabi roads with high intensity of truck traffic, such as Al Salam Street where hundreds of trucks are passing daily. The first rutting problem is mix rutting which occurs before the subgrade ruts but the surface deforms from a compaction problem or a mix design problem. Figure 2a shows examples of mix rutting in Al Salam Street in Abu Dhabi. The second rutting type noticed is subgrade rutting which occurs when the subgrade ruts (wheel path depression) due to heavy loading or poor pavement structure. Therefore, the pavement settles into the subgrade resulting in depression of surface in the wheel path. Figure 2b shows examples of subgrade rutting in Al Salam Street. The third problem recognized is the fatigue cracking which is a series of cracks caused by the fatigue failure of the hot mix asphalt surface which occurs from the repeated traffic loading and asphalt pavement aging. Thermal fatigue cracking is a common type of fatigue cracking in the UAE. It occurs on the pavement's surface due to the large fluctuation in daily temperatures (very high during the day and low during the night). Examples of fatigue cracking in Abu Dhabi's roads can be seen in Musaffah (M10) (Figure 2c). Bleeding is the fourth problem that was recognized in the field study. Bleeding happens when the asphalt binder fills all the voids in the aggregates and expands till it reaches the pavement surface during the high temperature periods, then during the low temperature period the asphalt binder is not able to return to its origin location, therefore the asphalt binder accumulates at the surface of the pavement over time which eventually leads to bleeding. Figure 2d shows examples of bleeding on Abu Dhabi roads in Mohammad Bin Zayed. Raveling, which was the fifth identified pavement problem in Abu Dhabi, happens when the aggregate particles are separated from the surface of the pavement. Usually, the finer aggregates wears out first and leave small holes called pothole on the surface. As raveling continues larger particles start to brake free and the pavement becomes rough as shown in Figure 2e taken in Musaffah (M15). Potholes are small bowl shape holes that occur on the surface of the pavement and extend inwards until it reaches the base course. Potholes were recognized as the sixth problem in Abu Dhabi pavements. Examples of pothole are shown in Khalidiyah Street in Figure 2f.

To reduce most of the pavement problems identified in the field study and to produce long lasting pavements with better operational and maintenance efficiency, PMB asphalt pavements are recommended to be used. The most commonly used PMB material for hot mix asphalts is the SBS. The use of this material results in an increase in the initial cost of the pavements that would be offset by the reduction in the long term costs (operation and maintenance). In the following parts of the paper the results of an experimental program that was conducted to compare between the properties (stability, flow, stiffness and bulk density) of a typical asphalt mix and of several SBS-PMB mixes, will be discussed.

## 2. Experimental program

Modified bituminous materials are proposed to solve pavement problems in UAE. To validate this proposal an experimental program was conducted to compare the characteristics of the modified bituminous material to those of the typical asphalt material.



**Figure 2.** Pavement problems field study in Abu Dhabi, UAE: a) Mix rutting (Al Salam Street), b) Subgrade rutting (Al Salam Street), c) Fatigue cracking (Musaffah M10), d) Bleeding (Mohammad Bin Zayed) e) Raveling (Musaffah M15) and f) Potholes (Khalidiyah Street).



## 2.1. Materials

A common asphalt mix (with unmodified bitumen) design from a project in the western region of Abu Dhabi, UAE was adopted in this research to compare the performance of conventional asphalt to polymer modified asphalt. Based on this mix design, samples for Marshall test were prepared using standard aggregates of weight 1220 g needed to achieve the required thickness. Table 1 shows the sample combination aggregate weights. The typical asphalt sample, which was used as a reference mix, was prepared with the optimum asphalt percentage indicated in the adopted mix design of 4% asphalt content, and a performance grade of PG76 [3]. This grade was selected to match the Abu Dhabi traffic condition, which consists of slow and heavy traffic in most places [3, 9]. For the PMB samples, five different percentages of SBS (Sealoflex SFB3 polymer) of 3%, 3.5%, 4%, 4.5% and 5% were used to find the optimum percent of SBS materials needed. The specifications of the used SBS are shown in Table 2. Three identical samples were prepared from each mix and the average result from each three samples was taken as a single result.

**Table 1.** Sample combination aggregates weights

Sieve	3/4	1/2	3/8	#4	#8	#16	#30	#50	#100	#200	filler
Combination aggregate of gradation	100	83	70	56	39	30	18	14	10	5	0
Retained %		17	13	14	17	9	12	4	4	5	0
Aggregate weight (g)		207.4	158.6	170.8	207.4	109.8	146.4	48.8	48.8	61	61
Total aggregate weight (g)		207.4	366	536.8	744.2	854	1000.4	1049.2	1098	1159	1220

**Table 2.** Styrene-Butadiene-Styrene polymer (Sealoflex SFB3 polymer) specifications from product data sheet

Description	Test method	Specification
<b>Basic properties</b>		
Penetration at 25 °C	ASTM D5	35-70 [0.1 mm]
Softening Point R&B	ASTM D36	≥ 65 oC
Faass breaking point	EN 12593:1999	≤ -10 oC
Elastic recovery at 25 °C	ASTM D6084	≥ 70%
Superpave performance grade	AASHTO MP1:1998	At least PG76-16
Viscosity at 135 °C	ASTM D4402	1 000-3000 mPa.s
Viscosity at 185 °C	ASTM D4402	150-250 mPa.s
Storage stability difference R&B <sub>top</sub> – R&B <sub>bottom</sub>	ASTM D7173	≤ 3°C
Flash point	ASTM D92	> 300 °C
<b>Rutting resistance</b>		
Zero shear viscosity		
$\eta_0$ at 40 °C	prEN 15325	≥ 2.5x10 <sup>6</sup> Pa.s
$\eta_0$ at 40 °C		≥ 0.5x10 <sup>6</sup> Pa.s
<b>Cracking resistance</b>		
Force-ductility at 5 °C		
Elongation at fracture	EN 13589:2003	≥ 25 cm
Total energy till fracture	EN 13589:2003/EN 13703:2003	≥ 10 J

## 2.2. Experimental procedure

The Marshall specimens were prepared in accordance to ASTM D 1559 (see Figure 3), with the typical asphalt material heated to 150°C and the SBS asphalt heated to 185°C. Two days after preparing the specimens, they were weighed first in air then in water and the bulk densities of the specimens were determined. Then before testing, they were heated in a water bath to 60°C to match the UAE expected weather conditions. The Marshall test was conducted on these specimens after towel drying them. The stability ring and the flow meter readings were recorded and stability, stiffness and the flow were calculated as shown in Table 5. To check that the tested materials match the adopted mix properties, a bitumen extraction test was conducted. The results of this test are shown in Tables 3 and 4. The results showed that the aggregates are within the specified design limits for the adopted mix.



**Figure 3.** Marshall specimen preparation: a) Material mix after heating, b) Specimen compaction, c) Specimens in water bath and d) Marshall test machine.

**Table 3.** Weights from extraction of bitumen test

Extraction of bitumen	Units	
Weight of samples	gm	3149
Weight of filter + cylinder before test	gm	278.2
Weight of filter + cylinder after test	gm	303.2
Weight of fines/filler	gm	25
Weight of extracted agg. + container	gm	5606.7
Weight of container only	gm	2622.4
Weight of extracted aggregate	gm	2984.3
Total wt. of extracted aggregate	gm	3009.3
Weight of loss material	gm	139.7
Bitumen content by wt. of mix	%	4.64
Bitumen content by wt. of aggregate	%	4.64
Approved design value	%	4.2
Tolerances for bitumen/specified	%	-0.2

Table 4. Combination aggregate gradation

Sieve size	3/4" aggregate		3/8" aggregate		3/16" aggregate		Filler	Obtained gradation	Target	Design mix limits	Specific limit
	%used	31%	%used	16%	%used	47%					
3/4"	100	31	100	16	100	47	100	6	100	100	100
1/2"	48.4	15	100	16	100	47	-	6	84.0	83.0	78-98
3/8"	6.0	1.9	96.9	15.5	100	47	-	6	70.4	70.0	65-75
#4	0.0	0	18.9	3.0	100	47	-	6	56.0	56.0	51-61
#8			1.2	0.2	71.4	33.6	-	6	39.8	39.0	35-43
#16					49.1	23.1	-	6	29.1	29.1	26-34
#30					24.2	11.4	-	6	17.4	17.4	14-22
#50					15.8	7.4	98	5.9	13.3	13.3	10-18
#100					9.4	4.4	87.4	5.2	9.6	9.6	6-14
#200					2.9	1.4	67.5	4.1	5.5	5.5	3.5-6.5

### 3. Results and discussion

In order to determine the optimum binder content of SBS-PMB mixes, and to compare the characteristics of the modified bituminous material to the conventional asphalt, the stability, flow, stiffness and bulk density of both materials were studied by conducting Marshall tests on the prepared specimens.

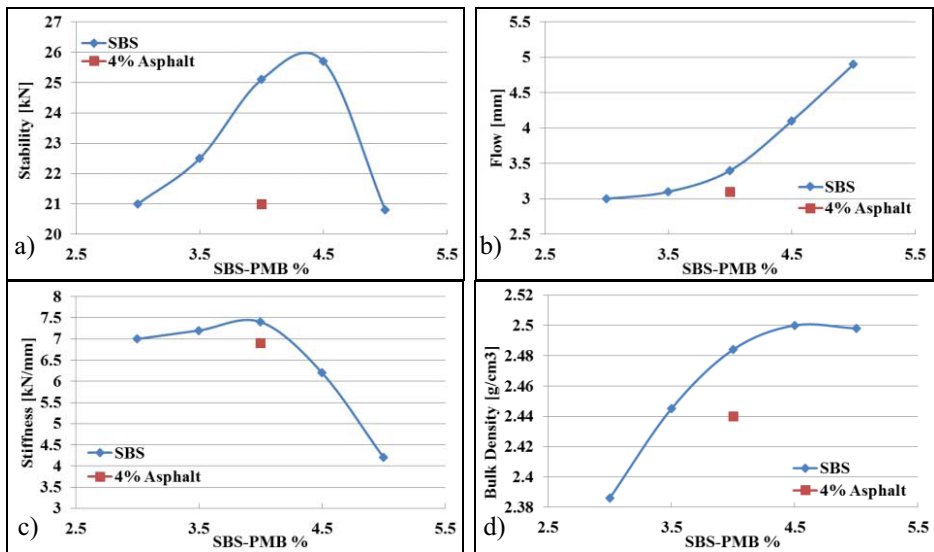
The test results are presented in Table 5 and Figure 4. The results shown in Figure 4 indicate that the optimum binder content for SBS-PMB is 4.5%. Comparing the experimental results for both conventional and SBS asphalts at 4% binder content, showed that the replacement of the conventional bitumen by SBS-PMB increased the stability by 19.5%, the stiffness by 7.3%, the flow by 9.7% and the bulk density by 1.8%. Comparison of the results of both binder types at their optimum binder contents of 4% for conventional asphalt and 4.5% for SBS asphalt, showed even more favorable results for the SBS-PMB asphalts. When the stability increased by 22.4%, the flow increased by 32.3% , the bulk density increased by 2.5% and the stiffness decreased by 10%.

Table 5. Marshall test results

Mi	SBS x [%]	SSD weight [gm]	Weight of specimen		Density		Stability			Flow [MM]	Stiff. [kN/mm]
					Bulk Vol. [cc]	Bulk [gm/cc]	Measured		Adjusted		
			In air [gm]	In Water [gm]			RD	KN*			
S0	0	1246.3	1246	735.7	510.6	2.440	810	21	21	3.1	6.9
S1	3	1256.7	1255.5	730.5	526.2	2.386	812	21	21	3	7
S2	3.5	1264.8	1263.9	747.9	516.9	2.445	868.3	22.5	22.5	3.1	7.2
S3	4	1262.3	1261.4	754.5	507.8	2.484	970	25.1	25.1	3.4	7.4
S4	4.5	1265.5	1265.2	756.5	509	2.5	993.3	25.7	25.7	4.1	6.2
S5	5	1274.1	1273.8	764.1	510	2.498	803.3	20.8	20.8	4.9	4.2

\* Ring factor = 0.0259

\*\* Correction factor = 1



**Figure 4.** Marshall test results: a) Stability vs. SBS %, b) Flow vs. SBS, c) Stiffness vs. SBS and d) Bulk density vs. SBS.

These results also demonstrate that thinner cross-sections are required for SBS-PMB asphalt pavements compared to conventional asphalt pavements, due to their characteristically higher values of the former. This reduction in cross-section thickness would offset the higher price of the SBS PMB material. When comparing prices of both SBS-PMB and conventional asphalt pavements, the long-term operation and maintenance costs have to be accounted for also. The available literature [3] shows that these costs are lower for SBS-PMB asphalt compared to conventional asphalt.

#### 4. Summary and conclusions

The harsh environment of the UAE combined with the high traffic volume increase in the last decay has accelerated the deterioration of asphalt pavements in congested traffic areas of the country. In the course of this research a field study was conducted in UAE's capital city (Abu Dhabi) to identify the common asphalt pavement problems in the country. The field study recognized the following six main pavement problems: mix rutting, subgrade rutting, fatigue cracking, bleeding, raveling, and potholes.

The use of SBS-PMB asphalt in newly constructed pavements, especially in heavy traffic areas, is proposed in this research to reduce the pavement problem in the UAE. To validate this proposal, an experimental program was conducted to compare the characteristics of the modified bituminous material to typical asphalt material and to obtain the optimum binder content of SBS-PMB asphalt. A common asphalt mix design (with unmodified bitumen) from a real life project in the western region of Abu Dhabi, UAE was adopted in this research to carry out the comparison. This mix was used as a reference mix and had a 4% optimum asphalt percentage. The test results showed the optimum binder content for SBS PMB to be 4.5%. It also showed that the SBS-PMB asphalt had more favorable characteristics in terms of stability, stiffness, flow and density. The results indicated that the replacement of conventional bitumen

with SBS PMB in asphalt pavements would produce more durable pavements with less problems and longer lifespan.

## References

- [1] Sengoz, B. and Isikyakar, G., Evaluation of the properties and microstructure of SBS and EVA polymer modified bitumen, *Construction and Building Materials* 22 (2008), 1897–1905.
- [2] Sengoz, B. and Isikyakar, G., Analysis of styrene-butadiene-styrene polymer modified bitumen using fluorescent microscopy and conventional test methods, *Journal of Hazardous Materials* 150 (2008), 424–432.
- [3] Al Hajjaj, A, *Sealoflex PG76 (Polymer modified bitumen) for improvement of Abu Dhabi roads network*, Al Jaber Bitumen Ooms JV, Abu Dhabi, UAE, 2009.
- [4] Airey, G., Fundamental binder and practical mixture evaluation of polymer modified bituminous materials, *The International Journal of Pavement Engineering* 5 (2004), 137–151.
- [5] Polymer Science Learning Center, Department of polymer science, [The University of Southern Mississippi](http://pslc.ws/macrog/tpe.htm) (2005), [http://pslc.ws/macrog/tpe.htm].
- [6] Tayfur, S., Ozen, H. and Aksoy, A., Investigation of rutting performance of asphalt mixtures containing polymer modifiers, *Construction and Building Materials* 21 (2007), 328–337.
- [7] Gorkem, C. and Sengoz, B., Predicting stripping and moisture induced damage of asphalt concrete prepared with polymer modified bitumen and hydrated lime, *Construction and Building Materials* 23 (2009), 2227–2236.
- [8] Kok, B. V. and Yilmaz, M., The effects of using lime and styrene-butadiene-styrene on moisture sensitivity resistance of hot mix asphalt, *Construction and Building Materials* 23 (2009), 1999–2006.
- [9] Hanson, D.I, Mallick, R.B. and Foo, K., Strategic highway research program properties of asphalt cement, *Transportation Research Record Journal* 1488 (1995), 40–51.

# Investigating the packing condition of porous asphalt mixture using Discrete Element Method

Mengjia CHEN<sup>1</sup> and Yiik Diew WONG

*School of Civil and Environmental Engineering, Nanyang Technological University, Singapore*

**Abstract.** Packing condition is an important factor to asphalt mixture's capacity in carrying traffic loads and resisting deformation, which is directly dependent on aggregate gradation. Porous Asphalt Mixture (PAM), with a characteristic feature of open-graded design, is advantageous in improving drainage, lowering noise level, and generating cooling effect, making it an appropriate material for a tropical country like Singapore. However, current gradation design methods are mostly based on dense asphalt mixtures, and little research has been conducted in providing explicit and direct parameters to represent the packing condition in a mixture. In this study, six PAMs were designed and relevant parameters were obtained from both laboratory experiments and Discrete Element Method (DEM) simulation. From four types of DEM models for each PAM group, it was found that particle-to-particle interlocking among coarser particles is affected by both size and amount of finer particles. In essence, DEM simulations showed that the development of packing condition among an assembly of particles is not only related to the percentage of fines fraction, but also the proportions of particles within various size ranges, and this finding corroborated with laboratory measurements of air voids content in the PAMs. This study indicates that DEM is an effective tool in analysing the packing condition in a mixture, and the findings should be a useful guide in PAM gradation design.

**Keywords.** Aggregate packing, porous asphalt mixture, Discrete Element Method (DEM), coordination number

## Introduction

Asphalt mixture's capability in bearing traffic loads is mainly attributed to aggregate gradation, aggregate shape and surface texture, amount and type of asphalt binder, compaction effort, etc., among which aggregate gradation is the most unstructured factor and deserves more attention [1]. For Porous Asphalt Mixture, the most distinct feature is the open-graded design, namely coarse aggregates accounts dominantly in aggregate blend which are up to 70 to 80% by mass [2], resulting in the high content of air voids greater than 18% by volume. Advantages from the high inter-connected air voids content of PAM material include improving drainage, enhancing skid resistance,

---

<sup>1</sup> Corresponding author: [c110021@e.ntu.edu.sg](mailto:c110021@e.ntu.edu.sg)

lowering noise level, generating cooling effect etc. [3, 4], making it a suitable type of paving material for a tropical country like Singapore.

Given the high content of coarse aggregates in PAM, packing is mostly created by the stone-to-stone skeleton formed by coarse aggregates. However, most aggregate gradation designs and packing theories are based on dense mixture [1 and 5], which cannot necessarily lead to an adequate aggregate structure [6 and 7]. Also, conventional design method is a trial-and-error process and requires substantial laboratory work. For PAM, the main components are coarse aggregates and mastic, thus it can be regarded as discrete material. Discrete Element Method (DEM) thereby was used, which is good at modelling the particle-to-particle interaction in the aspect of micro-mechanism [8].

## 1. Research methodology

### 1.1. PAM gradation design

For PAM material, higher air voids content is generally related to lower strength but higher permeability, which is achieved by lower proportion of fines. Based on PAM gradations by [9, 10, 11], six PAM gradations were designed (Table 1).

**Table 1.** Design of six PAM gradations

sieve size (mm)	passing, % by mass					
	G1	G2	G3	G4	G5	G6
19	100	100	100	100	100	100
13.2	80	85	95	85	90	95
9.5	72	70	51	75	66	59
6.3	40	60	40	60	30	50
4.75	35	30	24	44	21	42
2.36	15	10	20	20	15	10
1.18	13	9	17	17	13	9
0.6	11	8	14	14	11	8
0.3	9	7	11	11	9	7
0.15	7	6	8	8	7	6
0.075	5	5	5	5	5	5

### 1.2. Laboratory experiments

#### 1.2.1. Preparation of PAM specimens

Granite and PG76 asphalt were used in this study as raw materials. Cylindrical PAM specimens were fabricated using gyratory compactor. Binder content was initially estimated by aggregate surface area [13], and subsequently adjusted by draindown test and Cantabro test, whose upper limits are 0.3%, and 20%, respectively [2].

#### 1.2.2. Volumetric measurement

Bulk density and theoretical maximum density (TMD) were measured in the laboratory to gain air voids content for each PAM design.

#### 1.2.3. Performance tests

Permeability is the basic function for PAM, which reflects the drainage capability. However, the increase in permeability is generally at the cost of mixture's strength.

Permeameter by Florida method was used to obtain coefficient of permeability [14], while Marshall stability was measured as well [15].

### 1.3. Discrete Element Method (DEM) simulation approach

Particle Flow Code in 3 Dimensions (PFC3D), which is a kind of software based on DEM [16], is used to simulate the packing condition in PAM groups. The configuration of the PC for computation work was: CPU of Core™ i7, RAM of 8.0 GB, and Operating System of 64-bit.

#### 1.3.1. Generation of PAM model

In the PFC3D model, a cylindrical mould was established with radius of 50 mm and height of 200 mm. For each PAM in Table 1, an assembly of particles according to designed PAM was generated in the mould with a total mass of 1,000 g. Particles smaller than 2.36 mm were not created so as to gain adequate computational efficiency (see Figure 1). Particles were represented by spheres. The contact model used was Hertz model, which is suitable to describe contact behaviour among granular material without bonds [16]. The input parameters set in the model were based on previous research on granite, whose elastic modulus and friction coefficient of the mould were 300 GPa and 0, respectively; shear modulus and Poisson ratio of the particles were 25 GPa and 0.2, respectively. The aggregate friction coefficient was set at 0.5 to simulate the aggregate surface roughness and particle-to-particle sliding behaviour [18~22].

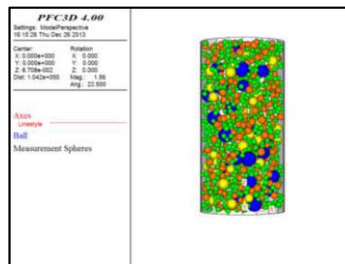


Figure 1. PAM model generated in PFC3D model

#### 1.3.2. Compaction by magnification gravitation

A magnified gravitation method with magnification factor (MF) of 1,000 was used to quickly realise adequate interlocking condition since: (1) computation efficiency for an assembly to get compacted increases with the magnitude of applied gravitation, and a MF of 1,000 will not result in breakage; (2) Applying gravitation can be regarded consolidation and the pressure exerted on each particle is linearly proportionate to the weight of particles above it. Hence, taking particles in the mid-height of the assembly as an average case, then the average pressure  $P$  can be obtained according to Eq. (1), which equals to 625 kPa, very close to the recommended pressure of 600 kPa by [12].

$$P=G/A=(M_{half} \times g \times MF)/(\pi \times R^2) \quad (1)$$

Here,  $M_{half}$  is the half mass of particles in PFC3D model, which equals to 0.5 kg,  $g$  is the normal gravitation ( $9.81 \text{ m/s}^2$ ), and  $R$  is the mould radius i.e. 0.05 m.



1.3.3. Simulation parameters

The four simulation parameters traced are: (1) unbalanced force (UF), which is the mean value of out-of-balance force in assembly; (2) contact force (CF), which is the mean value of normal force among effective contacts; (3) porosity (n), which is the proportion of voids by volume; and (4) coordination number ( $C_n$ ), which is the mean number of effective contacts around per particle.

2. Results and discussion

2.1. Experimental results

2.1.1. Determination of binder content

The final selected binder content (%) was 4.3, 4.3, 4.7, 4.8, 4.2, 3.9 for G1, G2, G3, G4, G5, and G6, respectively.

2.1.2. Volumetric parameters and performance of PAM groups

Volumetric and performance parameters of the PAMs are given in Table 2 and 3. G1, G3, and G4 possessed relatively lower permeability and higher strength, which can be ascribed to the lower air voids. The lower air voids content in G3 and G4 can be attributed to the higher proportion in fines; the percentage of particles finer than 2.36 mm in the two PAM groups was 20% while that in the other groups was 15% or 10%. For G1, although the percentage of particles finer than 2.36 mm was 15%, which was the same as that in G5, the percentage of particles within 4.75-2.36 mm was 20%, which was 6% higher than that in G5, thereby rendering the lower air voids content. It was further found, air voids content is not only attributed to the percentage of fines fraction, but also the proportions of particles in various size ranges.

Table 2. Volumetric parameters of PAM groups

PAM group	bulk density (g/cm <sup>3</sup> )	TMD (g/cm <sup>3</sup> )	air voids content (%)
G1	2.02 (± 0.002)	2.42 (± 0.060)	16.5
G2	1.90 (± 0.001)	2.45 (± 0.005)	22.4
G3	2.05 (± 0.011)	2.44 (± 0.005)	16.0
G4	2.08 (± 0.005)	2.43 (± 0.003)	14.4
G5	1.96(± 0.019)	2.59 (± 0.012)	24.3
G6	1.93 (± 0.001)	2.46 (± 0.010)	21.5

Note: value in parenthesis refers to standard deviation.

Table 3. Permeability and Marshall stability of PAMs

PAM group	Coefficient of permeability, k (cm/s)	Marshall stability (kN)
G1	0.13 (± 0.043)	7.6 (± 1.2)
G2	0.27 (± 0.005)	5.2 (± 0.2)
G3	0.07 (± 0.076)	8.6 (± 0.3)
G4	0.04 (± 0.012)	7.4 (± 0.8)
G5	0.21 (± 0.008)	5.5 (± 0.9)
G6	0.23 (± 0.052)	5.2 (± 0.7)

## 2.2. DEM simulation results and discussion

To evaluate the development of packing within particle-to-particle framework, for each PAM group, four types of PFC3D models were established, which are Model(19.0-9.5), Model(19.0-6.3), Model(19.0-4.75), and Model(19.0-2.36), presenting the model constituting particles in size ranges of 19.0-9.5 mm, 19.0-6.3 mm, 19.0-4.75 mm, and 19.0-2.36 mm, respectively.

### 2.2.1. Stability and equilibrium of compacted PAM groups

In PFC3D, stability and equilibrium should be evaluated in advance to ensure the rationality of later analysis. For the six PAM groups, the coordination number was all able to converge to an approximately constant value, indicating that the stability condition could be realised in the PAM groups along the process of compaction. Meanwhile the UF/CF values for the six groups were less than 0.001, which is the upper limit suggested by [16], meaning the six PAM groups achieved equilibrium.

### 2.2.2. Porosity of PAM groups

Porosity, which is a simulation parameter that possesses similar meaning to voids content measured in lab, is an important parameter to describe aggregate interlocking. Table 4 gives the resultant porosity in each type of PFC3D. For each PAM group, porosity generally decreases as finer particles are added in, indicating the process of packing development. This can be attributed to the fact that the void sizes are reduced due to the rearrangement of particles as finer particles are added in, and large and/or medium voids are partially filled by the finer particles as well.

**Table 4.** Porosity in PAM groups in PFC3D models

PAM group	Model (19.0-9.5)	Model (19.0-6.3)	Model (19.0-4.75)	Model (19.0-2.36)
G1	42.8	42.0	41.1	38.1
G2	45.0	41.3	39.1	38.3
G3	43.3	42.7	39.9	41.7
G4	41.0	41.0	38.5	37.6
G5	41.4	42.3	42.6	39.9
G6	44.9	42.7	41.0	36.7

### 2.2.3. Coordination number of PAM groups

Coordination number (CN) reflects the situation of effective contacts around each particle, thus it is a significant parameter to describe particle-to-particle skeleton in an assembly of particles. For each PAM group, the coordination number within various size ranges in the four types of PFC3D model were recorded as shown in Table 5.

In each PAM group, with the addition of finer particles, the coordination number generally increased, indicating a further compacted model was achieved, which is similar to the finding in the porosity value. Also, for the same size range in each PAM group, taking 19.0-9.5 mm as an example, coordination number was generally reduced as next-size-down finer particles were added in, indicating the particle-to-particle framework initially created by coarser particles (e.g. 19.0-9.5 mm particles) was being jeopardised by the finer particles, whereby contacted coarser particles were being shoved apart by the next-size-down finer fraction.

It was found that the impact of finer particles in the coarser model is related to both size and amount of finer particles. In terms of the size of finer particles, the coarser particles tend to be pushed apart by the particles of closer size much more significantly than by particles of much smaller size range. For example, in G1 group, coordination number among 19.0-9.5 mm particles was reduced from 4.22 to 1.41 as 9.5-6.3 mm particles were added, indicating that the previous particle-to-particle skeleton created by coarser particles (i.e. 19.0-9.5 mm particles) was severely impaired by the subsequent next-size-down finer particles (i.e. 9.5-6.3 mm particles) and all the particles in Model(19.0-6.3) functioned mostly as creating the skeleton instead of the smaller ones filling the voids. In contrast, the finer fraction within the smaller size range, e.g. 4.75-2.36 mm particles, exerted much less impact on the established skeleton by coarser particles. This is reflected that, in the six PAM groups, coordination number generally decreased less harshly as 4.75-2.36 mm particles were added in as compared with the reduction generated by 9.5-6.3 mm particles.

**Table 5.** Coordination number (CN) developed within various size ranges

PAM group	size range (mm)	model			
		Model (19.0-9.5)	Model (19.0-6.3)	Model (19.0-4.75)	Model (19.0-2.36)
G1	19.0-9.5	4.22	1.41	1.59	0.84
	19.0-6.3		4.33	3.83	2.55
	19.0-4.75			4.33	2.75
	19.0-2.36				4.47
G2	19.0-9.5	4.12	2.77	1.53	0.93
	19.0-6.3		4.19	1.95	1.27
	19.0-4.75			4.45	2.98
	19.0-2.36				4.51
G3	19.0-9.5	4.26	3.31	2.45	2.32
	19.0-6.3		4.31	3.09	2.93
	19.0-4.75			4.40	3.98
	19.0-2.36				4.38
G4	19.0-9.5	4.16	2.05	1.54	0.85
	19.0-6.3		4.27	2.60	1.66
	19.0-4.75			4.43	2.57
	19.0-2.36				4.54
G5	19.0-9.5	4.16	2.01	1.44	1.11
	19.0-6.3		4.33	3.64	3.14
	19.0-4.75			4.32	3.78
	19.0-2.36				4.34
G6	19.0-9.5	4.24	3.35	2.83	1.34
	19.0-6.3		4.32	3.48	1.74
	19.0-4.75			4.34	2.11
	19.0-2.36				4.52

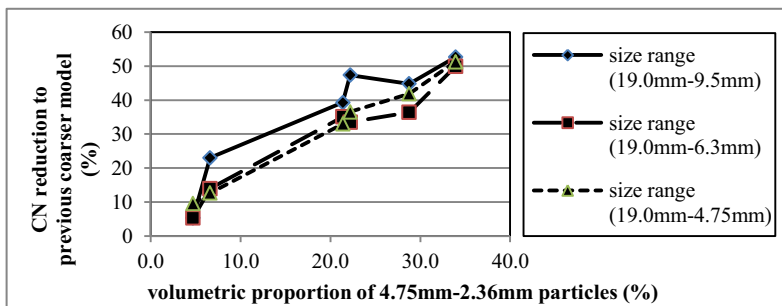
It should be noted that, in G6, the harshest reduction in coordination number was upon the addition of 4.75-2.36 mm particles as compared with other PAM groups, while the reduction generated by 9.5-6.3 mm particles was smaller. This can be attributed to the other effect of finer particles on the interlocking condition in a mixture, namely the relative amount of finer particles. The volumetric proportion of particles within each size range in PFC3D model according to the gradation design is given in Table 6. With the various proportions of 4.75-2.36 mm particles in the six PAM groups, the reduction of coordination number by percentage to the previous coarser PFC3D model within the three size ranges (i.e. 19.0-9.5 mm, 19.0-6.3 mm, and 19.0-4.75 mm) are given in Figure 2. With the increasing volumetric percentage of finer particles (i.e.

4.75-2.36 mm particles) being added, the coarser particles retained on different sieve sizes generally were being de-attached more severely. It can be explained that a high amount of fine particles can make the skeleton created by coarse particles to be disrupted and even make coarse particles to be dispersed amongst a mixture of fine particles without interlocking among coarse fraction.

Therefore, it can be concluded that the packing condition in PAMs is attributed to the size of finer fraction in terms of aggregate gradation, and the proportion of fine aggregates as well, which agrees with the findings of the air voids content of the six PAMs as measured in the laboratory.

**Table 6.** Volumetric proportion of particles within each size range in PFC3D model

PAM group	size range (mm)				
	19.0-13.2	13.2-9.5	9.5-6.3	6.3-4.75	4.75-2.36
G1	24.1	9.7	38.4	5.6	22.2
G2	17.4	17.4	11.6	32.2	21.4
G3	6.4	56.1	14.0	18.8	4.7
G4	19.5	13.0	19.5	19.2	28.8
G5	11.9	28.7	42.8	9.9	6.6
G6	5.8	41.5	10.3	8.5	33.9



**Figure 2.** Coordination number reduction by the addition of 4.75-2.36 mm particles

### 3. Conclusion

This research was conducted to evaluate the packing condition within PAM material using DEM simulation. Six PAMs were designed, and relevant volumetric properties and performance parameters were obtained in the laboratory, and the development of particle-to-particle interlocking mechanism was evaluated via PFC3D models.

According to the experimental results, performance in permeability for PAM material increases with air voids content, but it is at the expense of mixture strength. On the other hand, air voids content is dependent on the amount of fine aggregates (those smaller than 2.36 mm), and the proportion of aggregates in other size range as well (those within 4.75-2.36 mm).

Four types of PFC3D models were established for the six PAM groups, which represented the assemblies composed of particles within different size ranges, i.e. 19.0-9.5 mm, 19.0-6.3 mm, 19.0-4.75 mm, and 19.0-2.36 mm. It was found that, for each PAM group, compacting condition is further enhanced as finer particles are added based on the observation of two simulation parameters, namely porosity and coordination number. Furthermore, according to the coordination number within various size ranges for each PAM group, it was found that the particle-to-particle

skeleton created by coarser particles is affected by both size and amount of finer particles added in, which agrees with the finding of the air voids content as measured in the laboratory.

On the whole, the research has provided new insights into the development of packing condition in PAM material, and DEM is found to be an effective tool to evaluate the development of particle-to-particle interlocking among an assembly of particles with specific gradation design. The findings in this study can be a helpful guide in gradation design for PAM material.

## References

- [1] Vavrik, W. R., Huber, G., Pine, W. J., Carpenter, S. H., & Bailey, R. (2002). Bailey Method for Gradation Selection in HMA Mixture Design. *Transportation Research Record*.
- [2] Rajib, B. M., Prithvi, S. K., Cooley, L. A., & Donald, E. W. (2000). *Design, Construction, and Performance of New-Generation Open-Graded Friction Courses (NCAT Report 00-01)*: National Center for Asphalt Technology.
- [3] Fabb, T. R. J. (1993). *The Case for the Use of Porous Asphalt in the UK*: Institute of Asphalt Technology.
- [4] Khalid, H., & Jimenez, P. F. K. (1995). *Performance Assessment of Spanish and British Porous Asphalts Performance and Durability of Bituminous Materials*: London : Spon Press.
- [5] Fuller, W. B., & Thompson, S. E. (1907). The Laws of Proportioning Concrete. *Journal of Transportation Division, American Society of Civil Engineering.*, 59.
- [6] Shen, S. H., & Yu, H. N. (2011). Characterize Packing of Aggregate Particles for Paving Materials: Particle Size Impact. *Construction and Building Materials*, 25(3), 1362-1368.
- [7] Sungho, K., Roque, R., Birgisson, B., & Guarin, A. (2009). Porosity of the Dominant Aggregate Size Range to Evaluate Coarse Aggregate Structure of Asphalt Mixtures. *Journal of Materials in Civil Engineering*, 21(1), 32-39.
- [8] Cundall, P. A. (1971). A Computer Model for Simulating Progressive, Large-scale Movements in Blocky Rock Systems. Paper presented at the *The International Symposium on Rock Mechanics* Nancy, France.
- [9] Boving, T., Stolt, M., and Augenstern, J. (2004). Investigation of the University of Rhode Island, Kingston, RI, Porous Pavement Parking lot and Its Impact on Subsurface Water Quality. *Annual Meeting, International Association of Hydrologists, Zacatecas, Mexico*.
- [10] LTA. (2010). *Engineering Group Materials & Workmanship Specification for Civil & Structural Works*. Singapore: Land Transport Authority.
- [11] PennDOT. (2006). *Pennsylvania Stormwater Best Management Practices Manual*. The Department of Transportation. Pennsylvania.
- [12] AI. (1996). *Superpave Mix Design*: Lexington, KY : Asphalt Institute.
- [13] AI. (1997). *Mix Design Methods for Asphalt Concrete and Other Hot-Mix Types*: Lexington, KY : Asphalt Institute.
- [14] Florida DOT. (2004). *Florida Method of Test for Measurement of Water Permeability of Compacted Asphalt Paving Mixture (FM5-565)*. Florida: Department of Transportation.
- [15] ASTM D6927 (2006): Standard Test Method for Marshall Stability and Flow of Bituminous Mixtures: *American Society for Testing and Materials*.
- [16] Itasca. (2008). *PFC3D Version 4.0*. Minneapolis, Minnesota: Itasca Consulting Group Inc.
- [17] Liu, Y., & You, Z. P. (2011). Accelerated Discrete-Element Modeling of Asphalt-Based Materials with the Frequency-Temperature Superposition Principle. *Journal of Engineering Mechanics*, 137(5), 355-365.
- [18] Abbas, A., Papagiannakis, A.T., Masad, E., & Shenoy, A. (2005). A Modelling Asphalt Mastic Stiffness Using Discrete Element Analysis and Micromechanics Based Models. *International Journal of Pavement Engineering*, 6(2), 137-146.
- [19] Kim, H., & Buttlar, G. (2009). Discrete Fracture Modelling of Asphalt Concrete. *International Journal of Solids and Structures*, 69, 2716-2723.
- [20] Lu, M., & McDowell, G. R. (2007). The Importance of Modelling Ballast Particle Shape in the Discrete Element Method. *Granular Matter*, 9, 69-80.
- [21] Shen, S. H., & Yu, H. N. (2011b). Analysis Gradation and Packing for Easy Estimation of Hot-Mix Asphalt Voids in Mineral Aggregate. *Journal of Materials in Civil Engineering*, 23(5), 664-672.
- [22] You, Z. P., Adhikari, S., & Dai, Q. L. (2008). Three-Dimensional Discrete Element Models for Asphalt Mixtures. *Journal of Engineering Mechanics*, 134(12), 1053-1062.

# Comparison of in-situ and lab-measured void contents for a bituminous pavement of a carriageway

Lewis Kabwe KIZYALLA<sup>1</sup> and Stephen EKOLU

*Department of Civil Engineering, University of Johannesburg, South Africa*

**Abstract.** In situ air voids are a function of mix design (aggregate type and gradation, and bitumen content), manufacture and the level of compaction achieved during construction and subsequent traffic [1-2]. During the improvement of N12-19 highway construction project between Snake road interchange and Kingsway interchange in Johannesburg, South Africa, the quality control (QC) of a bitumen treated base layer was done according to Committee of Land Transport Officials (COLTO) specifications where compliance is a statistical judgment of three parameters namely, the relative compaction, binder content (lab binder) and voids in the mix (lab air voids).

The focus of this paper is to analyse only one of the three parameters namely, voids content obtained from the laboratory and from in-situ field measurements. It was found that for a given random sample, there is a considerable difference between in-situ void and lab void for the same material. Therefore, it becomes interesting to statistically evaluate the random sample results of in-situ air voids in order to decide on its compliance with quality control requirements. The study concluded that QC evaluation based on lab void results might be accepted but use of in-situ air voids values may lead to rejection decision, for the same bituminous mixtures.

Keywords: Marshall compaction, core density, air voids

## Introduction and background

There has been some concern that the voids in the mix aggregate (VMA) attained in the field can be somewhat different than the laboratory measured VMA for a given mix. The proportion of air voids in a compacted asphalt mix is a critical performance characteristic [3]. The bitumen random sample (BTB166) examined herein displays differences between in-situ voids and lab voids but the routine statistical judgment is usually done with lab voids. In the past, many researches have been done to find the relationship between lab voids and in-situ voids, yet there is still not proper relationship between the two parameters to date [4]. Through this paper, the statistical judgment is done with in-situ air voids as well as in-situ voids are directly linked to the pavement designed life. The outcome of the two judgments are compared to finally decide on the compliance of the BTB166 random sample. Marshall mix design testing methodology often called "Full Marshall" was employed as it widely used over the other more

---

<sup>1</sup>Corresponding author : jlsacrekiz@yahoo.fr

fundamental methods and is the most widely used mix design method in South Africa [5].

It is important to point out the fact that a Hot Mix Asphalt mixture produced in laboratory may have all the desired mix properties but the same mix may perform poorly under subjected traffic loading if the mix is not compacted to the proper level of density on the roadway [1]. The performance of bituminous layer after construction is influenced by volumetric properties resulting from mixing and compacting at high temperature. Compaction provides adequate lubrication for aggregates to stick each other, therefore high quality [6].

Compaction is the process by which the volume of an asphalt mixture is reduced, leading to an increase of the mixture in interlock among aggregate particles [7]. Compaction increases the service life of a bituminous pavement in many ways. It reduces rutting, increases mix stability and enable the pavement to carry traffic for longest period. Compaction is achieved by forcing the aggregate in the mix into close contact with each other. Consequently, the air voids content in the mix is reduced [8]. Excessive air voids content is undesirable as it may cause a pavement premature failure [9]. With air voids reduced, the pavement will have three important properties of:

**(a) Cohesion:** With fewer voids, the pavement is also more cohesive. Cohesion is the ability of the bituminous materials to hold together. Asphalt and filler are blended into a binder that holds the aggregate in place.

**(b) Impermeability:** This refers to the resistance of a pavement to the passage of air and penetration of water. Properly compacted bituminous material is dense enough to prevent connecting voids that would allow moisture to penetrate through the compacted material. The resulting pavement is durable and impermeable.

**(c) Stability:** Stability refers to the resistance of a pavement against internal movement. Even under high traffic loads, a properly compacted roadway will be stable. Stability depends on the internal friction between aggregate particles. Compaction, forces the aggregate into close contact with each other, interlocking the mixture together and improving its internal friction.

The aim of this paper is to calculate and compare in-situ voids content with laboratory voids values (referred to as 'lab voids'), apply statistical evaluation of data from lab voids and from in-situ void measurements. The two sets of results are then examined on the basis of QC decision that may be reached using lab void results vis-a-vis in-situ measurements.

## 1. Literature review

The two most common asphalt mixture design methods, namely Marshall and Superpave, use air void content (AVC) as the main controlling element that determines binder content. The design AVC represents the ultimate level desired in situ as a result of compaction efforts [10]. AVC is commonly considered by the pavement engineering community to be the single most important factor that affects mixture behaviour and pavement performance. In the typical Marshall testing method, the design AVC ranges between 3 and 5%. In the Superpave methodology, the design AVC is fixed at 4%. A study by Khatri et al [8] re-evaluated this target value for the Superpave system. The

study concluded that a design AVC in the range of 3 to 5% is adequate for all Superpave mixture types, for all aggregate gradations, and for all binder grades.

With high air void content, the asphalt becomes permeable to water and air, which causes reduced service life. With a very low air void content, the asphalt becomes rutted and deforms under traffic. Thus, for the mix to perform as expected, the contractor must be able to compact the mix to the desired level of density or air-void content [11].

### *1.1 Influence of air voids on asphalt performance*

Asphalt consists of four main materials: bitumen, aggregate, fillers (fine particles) and air. Asphalt without sufficient air entrapped in the layer will deform under traffic and result in a rutted and rough surface. Field (in-situ) air voids represent the amount of entrapped air in an asphalt layer that has been placed on-site [12].

### *1.2 Variability in the determination of Void Mineral Aggregate (VMA)*

The overall precision of the VMA calculation depends on the precision of many parameters of the compacted mixture. All laboratory tests performed on similar materials will have some variability due to inherent random testing errors. Other causes of variability are sampling procedures, operator experience, equipment, etc. [11].

### *1.3 Effect of variability on VMA*

To calculate VMA, it is necessary to determine the Bulk Relative Density (BRD) and Theoretical Maximum Relative Density (TMRD) of the compacted mixture. The greater the variability among these two properties, the greater the variability of the VMA. Yildirim et al [7] stated that the variability of measured TMRD of the aggregate and compacted specimens can significantly affect the variability of VMA, regardless of whether the same asphalt content is used.

### *1.4 Influence of air voids on compliance*

The Committee of Land Transport Officials (COLTO) considers air voids to be one of the major factors influencing the compliance based on a statistical analysis called "Judgment plan B" [13]. In this judgment, the variability of the values of tests is calculated and applied where acceptance limits for sample means are determined. Despite acceptance of those properties judged by this statistical method, the materials or work submitted will be rejected when other properties which aren't controlled statistically fail to comply with the requirements of the specifications, or where there are other causes of rejection.

## **2. Results presentation**

### *2.1 Results*

Samples were prepared according to Marshall Mix design method to determine all the engineering mix parameters (Air voids, Bulk Relative Density, Theoretical Maximum



Relative Density, binder content, indirect tensile strength, stability and flow of the mix. The results obtained for the N12-19 carriageway, were analysed for a random sample referred to as BTB 166. Core densities, laboratory voids content and binder content are the three Marshall parameters used for the statistical judgement summarized; the other properties which aren't controlled statistically did comply with the requirements of the specifications before proceeding with the statistical method.

Throughout this paper, the focus is on the difference between lab voids and in-situ voids. For  $n = 8$  positions, voids<sub>LAB</sub> and voids<sub>IN-SITU</sub> of the BTB 166 random sample are calculated as follows:

$$\text{Void}_{\text{LAB}} [\%] = [(\text{TMRD} - \text{BRD}_{\text{Marshall}}) / \text{TMRD}] * 100$$

$$\text{Void}_{\text{IN-SITU}} [\%] = [(\text{TMRD} - \text{BRD}_{\text{IN-SITU}}) / \text{TMRD}] * 100$$

Where:-TMRD is the theoretical maximum relative density of the mix, BRD is the bulk relative density of the mix, BRD<sub>in-situ</sub> is the core bulk relative density.

Table 1 and Figure 1 show results of the lab AVC and insitu AVC determined for BTB 166. It can be seen that there are significant differences between field and lab void contents of the bituminous mix.

## 2.2 Statistical judgment

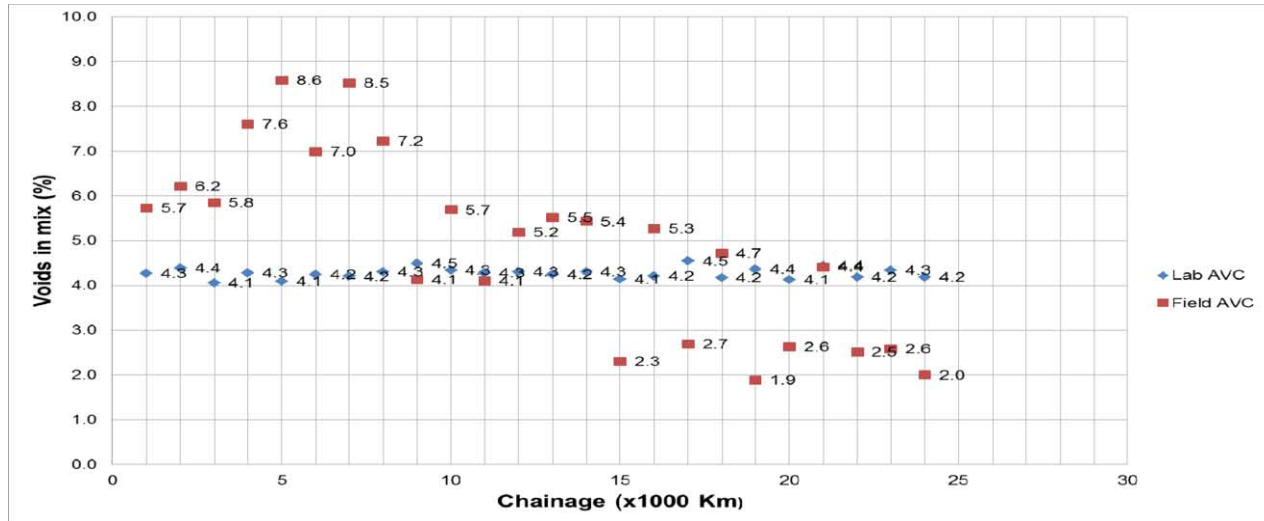
Statistical calculations were conducted on parameters for the judgment i.e. core densities, binder content and lab voids, as per COLTO [13]. The Judgement Plan B was done for Lab void content and for insitu void content. The evaluation returned 'accepted' result for Lab AVC but 'rejected' for insitu AVC.

## 3. Discussion

Examining the judgment plan B herein called "lab judgment", one can see that the statistical method combines lab parameters and in-situ parameters to accept or reject a random sample [14]. Among the three parameters of the judgment, core densities are field parameters. The binder content by definition, is the mass of binder expressed as a percentage of the total mass of the mix[15-16] .Throughout this paper, binder content laboratory measurements are assumed to be more or less equal to field values.

**Table 1.** Lab voids and In-situ voids comparison based on Marshall Test results for a random sample BTB 166

Section	East Bound	East Bound	East Bound	East Bound	East Bound	East Bound	East Bound	East Bound
Position (8 positions)	25+880	26+029	25+947	26+111	26+307	26+220	26+614	26+766
Offset	9.5 R	10.5 R	10.1 R	9.3 R	10 R	8.5 R	9.2 R	9.5 R
Marshall Density = BRD (kg/m <sup>3</sup> )	2623	2620	2625	2619	2627	2620	2622	2623
Core density = BRD <sub>IN-SITU</sub> (kg/m <sup>3</sup> )	2583	2570	2576	2528	2504	2545	2504	2543
Rice Density =TMRD (kg/m <sup>3</sup> )	2740	2740	2736	2736	2739	2736	2737	2741
<b>Voids LAB (%)</b>	<b>4.3</b>	<b>4.4</b>	<b>4.1</b>	<b>4.3</b>	<b>4.1</b>	<b>4.2</b>	<b>4.2</b>	<b>4.3</b>
<b>Voids In-situ (%)</b>	<b>5.7</b>	<b>6.2</b>	<b>5.8</b>	<b>7.6</b>	<b>8.6</b>	<b>7.0</b>	<b>8.5</b>	<b>7.2</b>



**Figure 1.** Comparison between Lab and in-situ air void values for BTB166

Therefore, binder content values used for statistical judgments in lab and in-situ values are assumed to be equal. An additional research might be needed to assess the correlation (if any) between the binder contents of in-situ and lab values.

Voids content for the lab judgment are lab values. In-situ VC are different from lab VC as seen in figure 1 that there isn't correlation between lab and in-situ parameters.  $BRD_{BRIQUETTE(LAB)}$  is more or less constant (see table 1) because all the briquettes are compacted under same conditions in the lab (same effort-75 blows, same temperature etc.) whereas in-situ compaction ( $BRD_{IN-SITU}$ ) is influenced by many variable factors such as the temperature (ground temperature, air temperature, wind speed, changing solar flux, etc.), the roller type (speed and timing, number of passes, etc.), the haul distance, haul time, handling time etc.), driver behavior, etc.

For the "in-situ judgment" all the three parameters are in-situ parameters directly linked to the pavement life and may therefore be more realistic. Lab VC parameters aren't linked to the pavement life and behavior, and since there isn't correlation between lab and in-situ VC, decisions made based on lab VC may be misleading.

#### 4. Conclusions

Quality control, Marshall parameters determined from construction of N12-19 Carriageway, were evaluated in comparison of laboratory results and in-situ measurements. It was shown that there is no correlation between the laboratory-measured void and in-situ measured void content of the bituminous mixtures.

Statistically analyzed results of a random sample led to *accepted* judgment for lab void content results but gave *rejection* judgment for the in-situ void content results. Based on current practice, the quality control results would approve these results even through the in-situ measurements give rejection judgment. This leads to the need to give consideration on the implications of in-situ measured void content, since the designed life of a pavement depends on in-situ parameters and are directly linked to the designed life and behavior of the pavement.

#### Acknowledgments

The authors wish to express their appreciation to The South African National Road Agency Limited representative for the N12-19 rehabilitation project and Mr. Estime Mukandila of The South African AURECON for granting the publication of the project results.

#### References

- [1] Mix Design Methods for Asphalt Concrete and Other Hot-Mix Types, Manual Series No. 1. Asphalt Inst. 1962
- [2] Mix Design Methods for Asphalt Concrete and Other Hot-Mix Types, Manual Series No. 2. Asphalt Inst. 1974.
- [3] Bahia, H. U., W. P. Hislop, H. Zhai, and A. Rangel. Classification of Asphalt Binders into Simple and Complex Binders. *Journal of the Association of Asphalt Paving Technologists*, Boston, Massachusetts, 1998.
- [4] Gudimettla, J. M., A. L. Cooley, Jr., R. E. Brown. Workability of Hot-Mix Asphalt, Report No. 03-03. National Center for Asphalt Technologies, Auburn, Ala., April 2003.

- [5] Hugo, F. A critical review of asphalt paving mixes in current use with proposals for a new mix. *Proceedings of the first conference on Asphalt Pavements for Southern Africa*, Durban, 1969.
- [6] Bahia, H.U., D. Hanson, M. Zeng., H. Zhai, and A. Khatri. NCHRP Report 459: Characterization of Modified Asphalt Binders in Superpave Mix Design. *TRB*, National Research Council, Washington, D.C., 2001.
- [7] Yildirim, Y., W. T. Kennedy, and M. Solimanian. Mixing and Compaction Temperatures for Modified Asphalt Binders. South Central Superpave Center Newsletter, 1999.
- [8] Khatri, A., H. U. Bahia, and D. Hanson. Mixing and Compaction Temperatures for Modified Binders using the Superpave Gyrotory Compactor. *Journal of the Association of Asphalt Paving Technologists*, Vol. 70, 2001.
- [9] Hensley, J., and A. Parmer. Establishing Hot Mix Asphalt Mixing and Compaction Temperatures at the Project Level. *Asphalt*, Vol. 12, No. 2. pp 368-395, 1998.
- [10] Yildirim, Y., M. Solaimanian, and T. Kennedy. Mixing and Compaction Temperatures for Superpave Mixes. *Journal of the Association of Asphalt Paving Technologists*, Vol. 69, 2000.
- [11] Shenoy, A. Determination of the Temperature for Mixing Aggregates with Polymer-Modified Asphalts. *International Journal of Pavement Engineering*, Nottingham, U.K., 2001.
- [12] Salomon, D., and H. Zhai. Ranking Asphalt Binders by Activation Energy for Flow. *Journal of Applied Asphalt Binder Technology*, October 2002.
- [13] Standard Specifications for Road and Bridge Works for State Road Authorities, Committee of Land Transport Officials (COLTO), pp 8200-1 - 8200-9, 1998
- [14] Standard Specifications for Road and Bridge Works for State Road Authorities, Committee of Land Transport Officials (COLTO), Table 8206/1, pp8200-7, 1998
- [15] Reinke, G. OnAlaska, Mathy Construction Company, 2004. Personal Communication.
- [16] Bahia, H. U., T. P. Friemel, P. A. Peterson, J. S. Russel, and B. Poehnelt. Optimization of Constructibility and Resistance to Traffic: A New Design Approach for HMA Using the Superpave Compactor. *Journal of the Association of Asphalt Paving Technologists*, Vol. 67, 1998, pp. 189–213.

This page intentionally left blank

# Brick and block masonry

This page intentionally left blank

# Flexural strength of low density blockwork

A. AHMED<sup>1</sup>

*Civil Engineering Group, Leeds Metropolitan University, UK*

**Abstract.** In this study, the characteristic flexural strength of low density aircrete wallettes incorporating both conventional and thin layer mortar is verified. The wallettes were tested in accordance with British and European standards. The flexural strength of aircrete wallettes was derived from the strength of small specimens tested to destruction under four-point loading. The strengths of the wallettes are high with impressive repeatability with the maximum strength being reached for thin layer wallettes within 7 days curing time. In general the strengths of both conventional mortar and thin layer mortar wallettes compare favourably to values reported in the standards.

**Keywords.** Autoclaved aerated concrete, aircrete, flexural strength, low density blockwork

## Introduction

Aircrete (AAC) was first used in the late 1950's [1-4] as an alternative to building with timber. Currently over 30 million m<sup>3</sup> of the material is produced annually. It is so extensively used that aircrete now accounts for a third of all concrete blocks in the UK. The porous cellular structure and durability [2,5] make AAC a recognised alternative for walls and floors in buildings. Aircrete's superior thermal performance in most cases eliminates the need for expensive cavity insulation. Aircrete is comprised of cement and/or pulverised fuel ash (PFA), lime, sand, water and aluminium oxide powder. The final process involves autoclaving for approximately 10 hours at a high temperature and pressure, hence, the name autoclaved aerated concrete. Aircrete is comprised of 60 to 85 % of air by volume, however, the pores are evenly dispersed throughout the material. for this reason, low density aircrete is sufficiently strong for use in construction of dwellings in spite of its high porosity [6-8].

**Table 1.** Physical properties of aircrete blocks

Aircrete density	Compressive strength (N/mm <sup>2</sup> )	Density (Kg/m <sup>3</sup> )	Thermal conductivity (W/mK)
Low	2.0 – 3.5	450	0.09 - 0.11
Medium	4.0 – 4.5	620	0.15 – 0.17
High	7.0 – 8.5	750	0.19 – 0.20

<sup>1</sup>Corresponding author: Leeds Metropolitan University, Civil Engineering Group, Northern Terrace, Civic Quarter, Leeds, LS2 8AG, UK. E-mail: [ash\\_ahmed@icloud.com](mailto:ash_ahmed@icloud.com)



Low density aircrete has outstanding thermal insulation properties [5,9-19] as shown in Table 1. In the UK compressive strengths greater than 3 N/mm<sup>2</sup> are commonly used, however, in Europe lower strength aircrete has been successfully utilised for construction of dwellings [1-4,9,13,16] implying that lower compressive strength will be adequate. With the drive to reducing greenhouse gas emissions, one way of achieving this is by constructing buildings with better thermal insulation, as this would require less heating energy. This paper reports the findings of a study undertaken to verify the characteristic flexural strength of low density aircrete wallettes with both conventional and thin layer mortar.

## 1. Experimental

This paper describes the results achieved for verifying the characteristic flexural strength of low density aircrete wallettes built using 2.8 and 2 N/mm<sup>2</sup> compressive strength blocks (provided by H + H Celcon). Aircrete is typically comprised of sand, cement, lime, pulverised fuel ash and aluminium oxide; the precise mixture proportions are not disclosed by the manufacturers. Wallettes were prepared using designation (iii) and (iv) mortars in accordance with BS 5628 [20], and using two different makes of thin layer mortar. Wallettes were tested in accordance to BS EN 1052; Part 2 [21]. The size of blocks were 440 x 215 x 150mm for 2.8 N/mm<sup>2</sup> blocks and 620 x 215 x 150mm for 2 N/mm<sup>2</sup> blocks. The flexural strength of aircrete wallettes was derived from the strength of small specimens of size 1100 x 860mm for 2.8 N/mm<sup>2</sup> blocks, 930 x 645mm for 2 N/mm<sup>2</sup> blocks tested to destruction under four-point loading, with the load applied such that the flexural stress was increased at a rate between 0.03 and 0.3 N/mm<sup>2</sup>/min. The maximum load achieved was recorded. The value calculated from the maximum stresses achieved by the samples was considered to be the flexural strength of the blockwork. The characteristic strength values were calculated as specified in BS EN 1052; Part 2 [21]. A matrix of the different block and mortar combinations built and tested was given in Table 2. The wallette thickness is 150mm unless otherwise specified.

**Table 2.** Matrix of specimens tested

Aircrete block strength (N/mm <sup>2</sup> )	Mortar designation		Thin layer mortar	
	iii	iv	A	B
2.0	5B	5B	5B	15B*
2.0	5P	5P	5P	
2.8	x	x	5B	15B*
2.8	x	x	5P	

B wallettes = flexural strength for a plane of failure parallel to the bed joints. P = Flexural strength for a plane of failure perpendicular to the bed joints. Designation iii = cement: lime: sand ratio of 1: 1: 6 (vol). iv = cement: lime: sand ratio of 1: 2: 8. \*15 wallettes, comprising three sets of five wallets each, and each set being used for 1, 7 and 28 days curing using thin layer mortar B.

Given the accelerated setting time for thin layer mortar, it has been suggested that early age (of up to 7 days curing) flexural testing on thin layer wallettes could provide some useful results. Professional blocklayers used different thin layer mortars, either **type A** (provided by H + H Celcon) or **type B** (provided by Clan). All specimens were tested at either 1, 7 or 28 days curing as given in Table 2.

## 2. Results and discussion

Results obtained for 2 and 2.8N/mm<sup>2</sup> thin layer wallettes (after 28 days curing) constructed using type A and B mortars are summarised in Tables 3 and 4. Tables 5 and 6 show the effect of curing time (ageing) on flexural strength for Thin Layer wallettes. Table 7 provides statistical analysis of results obtained for both Thin Layer mortars. Results obtained for 2N Designation iii and iv wallettes are summarised in Tables 8 and 9. Table 10 provides statistical analysis of results obtained for conventional mortars.

**Table 3(a).** Flexural strength of thin layer wallettes of Type A Mortar and 2 N/Mm<sup>2</sup> aircrete (after 28 days curing (28d))

Aircrete block strength (N/mm <sup>2</sup> )	Failure stress (N/mm <sup>2</sup> ) B	Failure stress (N/mm <sup>2</sup> ) P
2	0.31	0.27
2	0.30	0.29
2	0.28	0.27
2	0.32	0.28
2	0.28	0.30

**Table 3(b).** Flexural strength of thin layer wallettes of Type A Mortar and 2.8 N/mm<sup>2</sup> aircrete (28 d)

Aircrete block strength (N/mm <sup>2</sup> )	Failure stress (N/mm <sup>2</sup> ) B	Failure stress (N/mm <sup>2</sup> ) P
2.8	0.51	0.39
2.8	0.43	0.41
2.8	0.46	0.36
2.8	0.50	0.37
2.8	0.48	0.40

**Table 4(a).** Flexural strength of thin layer wallettes of Type B Mortar and 2 N/mm<sup>2</sup> aircrete (28 d)

Aircrete block strength (N/mm <sup>2</sup> )	Direction	Failure stress (N/mm <sup>2</sup> )
2	B	0.35
2	B	0.29
2	B	0.29
2	B	0.33
2	B	0.31

**Table 4(b).** Flexural strength of thin layer wallettes of Type B Mortar and 2.8 N/mm<sup>2</sup> aircrete (28d)

Aircrete block strength (N/mm <sup>2</sup> )	Direction	Failure stress (N/mm <sup>2</sup> )
2.8	B	0.51
2.8	B	0.46
2.8	B	0.47
2.8	B	0.51
2.8	B	0.46

**Table 5.** Flexural strength of thin layer wallettes of Type B Mortar and 2 N/mm<sup>2</sup> aircrete (1,7 & 28 Days)

Aircrete block strength (N/mm <sup>2</sup> )	Direction	Failure stress (N/mm <sup>2</sup> )		
		1d curing	7d curing,	28d curing
2	B	0.24	0.31	... 0.35.....
2	B	0.24	0.28	... 0.29.....
2	B	0.26	0.29....	0.29 ...
2	B	0.22	0.30..	0.33
2	B	0.26	0.29..//	0.31

**Table 6.** Flexural strength of thin layer wallettes of Type B Mortar and 2.8N/mm<sup>2</sup> aircrete (1,7 & 28 d)

Aircrete block strength (N/mm <sup>2</sup> )	Direction	Failure stress (N/mm <sup>2</sup> )		
		1d curing	7d curing	28d curing
2.8	B	0.23	0.46	.....0.51.....
2.8	B	0.19	0.42	0.46
2.8	B	0.22	0.48	0.47
2.8	B	0.21	0.45	0.51
2.8	B	0.24	0.48	0.46

**Table 7.** Statistical analysis of flexural strength of Thin Layer wallettes

Aircrete block strength (N/mm <sup>2</sup> )	Curing time (days)	Thin layer mortar	Direction	Average failure $\sigma$ (N/mm <sup>2</sup> )	Standard deviation	Characteristic strength (N/mm <sup>2</sup> )
2	28	A	B	0.30	0.017	0.27
2	28	B	B	0.31	0.023	0.27
2	28	A	P	0.28	0.013	0.26
2	1	B	B	0.24	0.015	0.22
2	7	B	B	0.30	0.010	0.28
2.8	28	A	B	0.48	0.032	0.42
2.8	28	B	B	0.48	0.023	0.44
2.8	28	A	P	0.39	0.021	0.35
2.8	1	B	B	0.22	0.017	0.19
2.8	7	B	B	0.46	0.022	0.42

**Table 8.** Flexural strength of wallettes of type designation iii Mortar and 2 N/mm<sup>2</sup> Aircrete (28d).

Aircrete block strength (N/mm <sup>2</sup> )	Failure stress (N/mm <sup>2</sup> ) B	Failure stress (N/mm <sup>2</sup> ) P
2	0.16	0.22
2	0.18	0.20
2	0.16	0.22
2	0.19	0.23
2	0.18	0.24

**Table 9.** Flexural strength of wallettes of type designation iv Mortar and 2 N/mm<sup>2</sup> Aircrete (28d)

Aircrete block strength (N/mm <sup>2</sup> )	Failure stress (N/mm <sup>2</sup> ) B	Failure stress (N/mm <sup>2</sup> ) P
2	0.19	0.17
2	0.17	0.20
2	0.15	0.22
2	0.15	0.23
2	0.18	0.21

**Table 10.** Statistical analysis of flexural strength of wallettes Made with Conventional Mortar

Aircrete block strength (N/mm <sup>2</sup> )	Mortar designation	Direction	Average failure $\sigma$ (N/mm <sup>2</sup> )	Standard deviation	Characteristic strength (N/mm <sup>2</sup> )
2	iii	B	0.17	0.013	0.15
2	iii	P	0.22	0.014	0.20
2	iv	B	0.17	0.018	0.14
2	iv	P	0.21	0.023	0.17

### 2.1 Thin layer wallettes

From the results obtained (Table 7), it can be seen that there is very good repeatability as reflected by low standard deviation values. In BS 5628 [20] the characteristic flexure strength obtained using 7 N/mm<sup>2</sup> blocks with designation iv mortar is 0.2 and 0.45 N/mm<sup>2</sup> for B and P wallettes respectively. In comparison to the data presented in this paper, the flexural strength of both the B wallettes (thin layer with 2 and 2.8 N/mm<sup>2</sup> blocks) is substantially higher, giving 0.30 and 0.48 N/mm<sup>2</sup> respectively. There is remarkable consistency in the results with regards to both thin layer mortars giving characteristic strengths of 0.27 and 0.26 N/mm<sup>2</sup> for 2N/mm<sup>2</sup> aircrete and 0.44 and 0.35? N/mm<sup>2</sup> for 2.8N/mm<sup>2</sup> aircrete. The normal trend in masonry is that the flexural strengths of P wallettes are higher than that of B wallettes, however, the trend here is to

the contrary. This is not altogether surprising given the very thin (3mm) and excellent bond strength of the mortar, the B wallettes behave as a large plate. This seemed to be the case as failure was not just confined to the mortar bed but also there was significant material failure, as shown in Figure 1. This is clearly an advantage considering that even when there is significant material failure (in comparison to wallettes using conventional mortar) a much larger stress is required to initiate failure. Further, as the bond in the perpendicular joints is likely to be inferior to that in the bed joints, it will initiate failure at a lower load in that direction. The results (tables 5 & 6) also show that for thin layer wallettes, maximum strength is usually reached within 7 days curing time. The characteristic flexural strengths for both 2 and 2.8N/mm<sup>2</sup> aircrete after 7 days is in most cases precisely the same as after the standard 28 days curing time. After 1 day curing time for the 2N/mm<sup>2</sup> aircrete wallettes reach 80% of ultimate strength, for 2.8N/mm<sup>2</sup> aircrete only 45% of ultimate strength was reached in 1 day. Figure 2 shows that after 1 day curing time, the failure mode is predominantly confined to the mortar bed as opposed to the failure after 7 and 28 days curing (Figure 1), thus, suggesting that the bond between mortar and material wasn't yet well-developed at 1 day.

## 2.2 Conventional mortar wallettes

In BS 5628 [20] the characteristic strength of B wallettes for 2.8 to 7 N/mm<sup>2</sup> blocks of 250 mm thickness, are given as 0.15 and 0.1N/mm<sup>2</sup> respectively for designations (iii) and (iv) mortar. The strength of 250 mm thick P wallettes for 2.8 to 3.5 N/mm<sup>2</sup> blocks are 0.25 and 0.2 N/mm<sup>2</sup> respectively for designations iii and iv. Therefore, the values achieved for 2 N/mm<sup>2</sup> wallettes of 0.15 and 0.20 N/mm<sup>2</sup> in the B and P directions respectively, are consistent with standard specification requirements. The strength of these wallettes are in keeping with the normal trend in masonry, i.e P wallettes are stronger than B ones. Designation iii wallettes are stronger than designation (iv) wallettes, however, the difference is not substantial, especially in the B direction. Furthermore, the failure mode is different to thin joint wallettes, where cleavage occurs along the mortar with negligible material failure, as shown in Figure 3,. This observation supports results showing that the strength in conventional mortar wallettes is much lower than in thin layer wallettes.



**Figure 1.** Typical failure of a low density aircrete thin layer (mortar) walette in the B direction showing predominantly material failure



**Figure 2.** Typical failure of a low density aircrete thin layer wallette (after 1 day curing) in the B direction showing failure occurring along the bed joint.



**Figure 3.** Typical failure of a low density aircrete designation iii wallette in the B direction showing failure occurring along the bed joint.

### 3. Conclusions

The characteristic flexural strength of low density aircrete wallettes made of 2.8 and 2 N/mm<sup>2</sup> blocks using thin layer mortar and conventional mortar, was determined.

- The values of B wallettes in particular are relatively high with impressive repeatability, especially for the thin layer mortar wallettes.
- The maximum strength for thin layer mortar wallettes is reached within 7 days curing time.
- In general conventional mortar wallettes were weaker than thin layer wallettes. However, the strengths of both wallette types compare favourably to values reported in BS5628.
- The mode of failure for thin layer and conventional mortar wallette specimens were different.

### Acknowledgement

The author would like to acknowledge the funding and support for the Low-Density Aircrete project given by the EPSRC and industrial collaborators (AACPA).

## References

- [1] H+H Celcon Ltd, [www.hhcelcon.co.uk](http://www.hhcelcon.co.uk) [accessed 24.11.13].
- [2] The UK Aircrete Association, 2013, *Code of Best Practice for the Use of AAC*, [www.aircrete.co.uk](http://www.aircrete.co.uk).
- [3] Ahmed, A., Fried, A., Roberts, J.J., Advantages and Implications of High Performance Low Density Aircrete Products for the UK Construction Industry, *13th International Brick and Block Masonry Conference (IBBMac)*, Amsterdam, Netherlands 2004.
- [4] Bright, N., Ahmed, A., Concentrated Loads on Aircrete Thin Joint Blockwork, *14th International Brick and Block Masonry Conference (IBBMac)*, Sydney, Australia 2008.
- [5] Dubral, W., 1992, YTONG AG, Munich, Germany, *Advances in Autoclaved Aerated Concrete*, Wittmann (ed.) © Balkema, Rotterdam. ISBN 90 5410 086 9.
- [6] Mitsuda, T., and Kiribayashi, T., 1992, Hydrothermal properties of autoclaved aerated concrete, *Advances in Autoclaved Aerated Concrete*, Wittmann (ed.) © Balkema, Rotterdam. ISBN 90 5410 086 9.
- [7] Callister, W., Jr., 2006, Department of Metallurgical Engineering, The University of Utah, *Materials Science and Engineering – An Introduction*, Seventh Edition, John Wiley and Sons, Inc, ISBN 9780471736967.
- [8] Ungkoon et al, A study of hygrothermal performance of AAC blocks under humid climate of Thailand. *International Conference “Passive and Low Energy Cooling for the Built Environment”*, Santorini, Greece 2005
- [9] Thermalite, Hanson Heidelberg Cement Group, [www.heidelbergcement.com](http://www.heidelbergcement.com) [accessed 18.3.14].
- [10] Design for Homes, Application of Aircrete Blocks, [www.designforhomes.org](http://www.designforhomes.org) [accessed 18.03.14].
- [11] Lippe, K., 1992, YTONG AG, R + D Centre, Schrobenhausen, Germany, The effect of moisture on the thermal conductivity of AAC, *Advances in Autoclaved Aerated Concrete*, Wittmann (ed.) © Balkema, Rotterdam. ISBN 90 5410 086 9.
- [12] Liu, C., and Wang, J., 1992, An experimental study on thermal transmission properties of AAC panels, *Advances in Autoclaved Aerated Concrete*, Wittmann (ed.) © Balkema, Rotterdam. ISBN 90 5410 086 9.
- [13] Tarmac Building products, AAC Blocks, [www.tarmacbuildingproducts.co.uk](http://www.tarmacbuildingproducts.co.uk) [accessed 18.1.14].
- [14] Quan, Y., Nianxiang, Y., Applications of AAC block in new energy-saving building structure, *Electric Technology and Civil Engineering (ICETCE) Conference*, 1066-1069, Lushan, China 2011.
- [15] Yuplng, Z., Dedong, L., Guokuang, S., Investigation into the Carbonation of Autoclaved Aerated Concrete, *8th International Congress on the Chemistry of Cement*, 1996;5:93-98
- [16] Wittman, F.H., 1993a, Autoclaved Aerated Concrete: Properties, Testing and Design, RILEM Recommended Practice, *RILEM Technical Committees 78 – MCA and 51 – ALC*.
- [17] Tada, S., 1992, Texte, Inc. and Nihon University, Japan. *Advances in AAC*, Wittmann (ed.) © Balkema, Rotterdam. ISBN 90 5410 086 9.
- [18] Jacobs, F., and Mayer, G., 1992, Institute for Building Materials, ETH Zurich, Switzerland, *Advances in Autoclaved Aerated Concrete*, Wittmann (ed.) © Balkema, Rotterdam. ISBN 90 5410 086 9.
- [19] Schober, G., Hebel AG, Emmering, 1992, Germany, Effect of size distribution of air pores in AAC on compressive strength, *Advances in AAC*, Wittmann (ed.) © Balkema, Rotterdam. ISBN 90 5410 086 9.
- [20] British Standards a, BS 5628: Part 1: – Structural use of Unreinforced Masonry.
- [21] British Standards b, BS EN 1052: Part 2: 1999 – Determination of Flexural Strength. Now incorporated into Eurocode 6.

# Properties of conventional cement and thin layer mortars

A. AHMED<sup>1</sup>

*Civil Engineering Group, Leeds Metropolitan University, UK*

**Abstract.** Mortar for masonry is important because it provides the linkage between masonry units so enabling the composite to behave as a single material. The type of mortar used determines the flexural and compressive strength of the masonry, so in this paper, a range of mortars are examined. These include traditional designation (iii) (1 cement : 1 lime : 6 sand), designation (iv) (1 cement : 1 lime : 9 sand) mortars as defined in BS 5628: Part 1 [ref], and two thin layer mortars. The conventional mortars were formed using both CEM I 42.5N or CEM I 32.5N PC (Portland Cement) to BS EN 197: Part 1 in order to ascertain the difference these two cements have on the properties of mortar. The thin layer mortars show remarkably high compressive strength.

**Keywords.** Mortar, thin layer mortar, masonry, compressive strength

## Introduction

Mortar is a very important material in civil engineering as it bonds together bricks and blocks in dwellings. Traditionally there are two different types of mortars: lime and cement. Lime mortar is the oldest type and has been used for centuries. This was the preferred type of mortar until cement mortars were developed. The disadvantage with lime mortars is that it gains maximum strength after 90 days, this can delay construction time which can confer negative economic implications. The main advantage with cement based mortars is that it reaches maximum strength in only 28 days. There are four different designations of cement mortars as shown in Table 1.

**Table 1.** Different designations of cement based mortars and respective mean and minimum compressive strength at 28 days, as per BS 5628 [1].

Mortar Designation	Cement:Lime Ratio	Sand Ratio	Known as	Compressive strength (N/mm <sup>2</sup> )
(i)	1:0 to 0.25 <sup>1</sup> / <sub>4</sub>	3	1:3	16.0
(ii)	1: <sup>0.5</sup>	4	1: <sup>1</sup> / <sub>2</sub> :4	6.5
(iii)	1:1	6	1:1:6	3.6
(iv)	1:2	8/9	1:2:9	1.5

<sup>1</sup>Corresponding author: Leeds Metropolitan University, Civil Engineering Group, Northern Terrace, Civic Quarter, Leeds, LS2 8AG, UK. E-mail: [ash\\_ahmed@icloud.com](mailto:ash_ahmed@icloud.com)



With decreasing strength, there is increased flexibility, i.e. designation (iv) has the greatest flexibility. Typically, designations (iii) and (iv) are used with low density blockwork, however, over the last 15 years or so, thin layer mortars have become increasingly popular as they provide greater flexural strength for the wall [2]. Thin layer mortar, as the name implies, is a special type of adhesive mortar with a mortar thickness of only 3 mm (in comparison to 10 mm for conventional mortars, including lime). Although the layer is very thin, the mortar forms a very strong bond with the blocks. Furthermore, as the greatest heat loss through a wall is through the mortar layer, reducing the mortar bed thickness can improve the thermal insulation of the dwelling [3]. This paper reports the findings of a study undertaken to verify the mechanical properties of different conventional cement and thin layer mortars as this can to an extent, explain why only 3mm joint thickness is required for thin layer mortars.

## 1. Experimental

Experimental work was undertaken to establish the mechanical properties of three mortars types (designations (iii), (iv) and thin layer). A series of tests were carried out to evaluate the cube compressive, tensile and flexural strengths of conventional mortar prepared using CEM I 32.5N and CEM I 42.5N Portland cement and two types of thin layer mortar designated type **A** and **B**. The two cements were selected as there is no guidance on cement choice in the British code although there is some data on mortar strengths in Table 1 of BS5628:Part 1 [1], the relevant parts of which are reproduced as Table 1 of this paper. Flow properties of these mortars were also established. Sample preparation and testing were carried out in accordance with appropriate Standards as documented in this paper.

The paper is divided into two main parts. The first part gives details of test materials and mortar properties and this is followed by the test results.

### 1.1 Test Materials

#### 1.1.1 Cement

The first set of tests were carried out using 42.5N PC to BS EN 197: Part 1- CEM I [4], these being repeated using 32.5N PC to BS EN 197: Part 1- CEM I.

#### 1.1.2 Lime

Bulk hydrated lime was used in the mortar production. It contained between 95.0 to 97.0% calcium hydroxide.

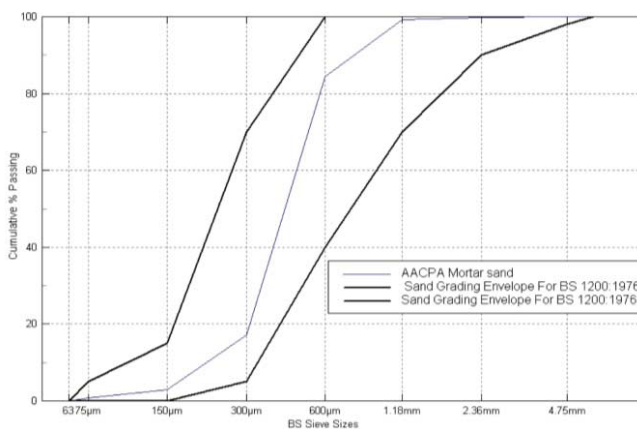
#### 1.1.3 Sand

Soft building sand was used. The particle size distribution of the sand is given in Table 2 and schematically shown plotted in Figure 1. Tests were carried out in

accordance with BS 1200 [5] and the results indicate that the sand used complies with the requirements of the BS 1200:1976 [5].

**Table 2.** Sand grading test results

Sieve Aperture Size	Mass of sand passing sieve (g)	Mass of sand retained by sieve (g)	Cumulative sand passing sieve (%)
6.30mm	1160.5	0.4	99.97
5.00mm	1160.5	0.0	99.97
2.36mm	1158.7	1.8	99.81
1.18mm	1151.3	7.4	99.17
600 $\mu$ m	980.2	171.1	84.43
300 $\mu$ m	199.4	780.8	17.18
150 $\mu$ m	34.2	165.2	2.95
75 $\mu$ m	8.2	26.0	0.71



**Figure 1.** Particle size distribution of sand (cumulative passing v sieve size).

## 1.2 Specimen preparation

### 1.2.1 Conventional mortar

Conventional mortar samples of designations (iii) and (iv) were produced to establish fresh and mechanical properties. Water was added so that the workability was consistent and corresponded to a 10mm penetration of the dropping ball test as suggested in BS 5628. The flow properties were determined in accordance with EN 1015; Part 3 [6]. The flow values obtained for all mixes fell within a range of between 186 to 188 mm.

### 1.2.2 Thin layer mortar

Again, mortar samples were produced to establish fresh and mechanical properties. Different thin layer mortars, either type A (provided by H + H Celcon) or type B (provided by Clan). Manufacturer's mixing guidelines, given in Table 3 were strictly followed - the mixture was stirred for approximately 10 minutes until a lump free paste was obtained and the workability was consistent and corresponded to a 9.5 mm penetration of the dropping ball test. The flow values obtained for all mixes fell within a range of between 154 to 156 mm. Both thin layer mortars were manufactured in accordance with EN 998-2:1997 [7].

**Table 3.** Mortar mixing preparation

	<b>Mortar A (H + H Celcon)</b>	<b>Mortar B (Clan)</b>
<b>Mortar Weight (kg)</b>	25	25
<b>Water Content (litres)</b>	4.4	5 / 5.5

### 1.2.3 Properties examined

A range of properties were examined during experimental work as shown in Table 4. In all testing, three specimens were broken at each test age (Table 4). Tests were carried out in accordance with EN 1015:Part 11 [8].

**Table 4.** Mortar properties and testing regimes

<b>Mortar Property</b>	<b>Specimen</b>	<b>Test Age</b>
Compressive cube strength	100 x 100 x 100 mm	1 - 28 days
Tensile strength	Dog bone	28 days
Flexural strength	40 x 40 x 160 mm	28 days

Test specimens were demoulded after 24 hours of casting and then transferred into an Environmental Chamber where a constant temperature of 20 °C and relative humidity of 95% was maintained throughout.

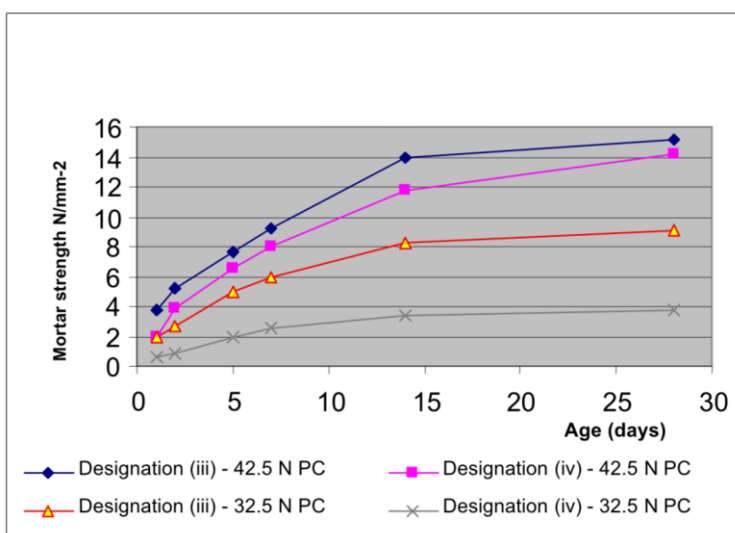
## 2. Results and discussion

### 2.1 Compressive strength development of mortar

The compressive strength development of both conventional mortars (designations (iii) and (iv)) for both cement types are given in Table 5 and Figure 2 while Table 6 summarises the 28-day cube compressive, flexural and tensile strength test results of both designations (iii) and (iv) mortars.

**Table 5.** Compressive strength results for designations (iii) and (iv) mortars

Curing Age (Days)	Compressive Cube Strength (N/mm <sup>2</sup> )			
	42.5N PC		32.5N PC	
	Designation (iii)	Designation iv	Designation iii	Designation iv
1	3.7	1.9	1.9	0.6
2	5.2	3.9	2.7	0.9
5	7.6	6.6	5.0	2.0
7	9.2	8.0	6.0	2.5
14	13.9	11.8	8.2	3.4
28	15.2	14.2	9.1	3.8



**Figure 2.** Strength development of conventional mortars

**Table 6.** 28-day strength results of designations (iii) and (iv) mortars

Cement Type	Mortar Designation	Compressive Strength (N/mm <sup>2</sup> )	Flexural Strength (N/mm <sup>2</sup> )	Tensile Strength (N/mm <sup>2</sup> )
42.5 N PC	iii	15.2	5.1	4.8
	iv	14.2	4.8	4.5
32.5 N PC	iii	9.1	2.9	2.5
	iv	3.7	1.5	2.0

*2.2 Discussion*

With 42.5 N PC, the compressive strengths for designations (iii) and (iv) mortars are approximately 5 times greater than that specified in BS 5628. With the 32.5 N PC

cement mortar, the 28 day strength is 2.5 times that specified in the code. Variations are probably due to different mortar consistencies and possibly type of sand used.

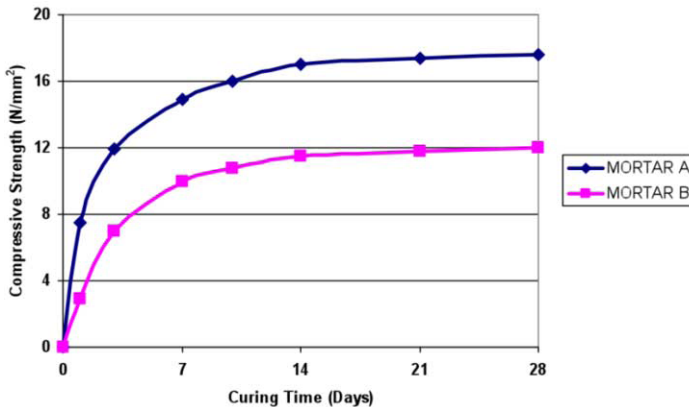
### 2.2.1 Thin layer mortar

The compressive strength results of thin layer mortars cured up to 28-days are given in Table 7 and plotted on Figure 3 while Table 8 summarises 28-day compressive cube, flexural and tensile strength test results of these mortars.

**Table 7.** Compressive strength results of thin layer mortar)

Curing Age (Days)	Compressive Cube Strength (N/mm <sup>2</sup> )	
	A (n*)	B (n)
1	7.5 (2.08)	2.9 (0.81)
3	11.9 (3.31)	5.8 (1.61)
7	14.9 (4.14)	8.6(2.39)
10	16.0 (4.44)	10 (2.78)
14	17.0 (4.72)	11.5 (3.19)
21	17.4 (4.83)	11.8 (3.27)
28	17.6 (4.88)	12 (3.33)

\*n: bracketed numbers indicate how many times the thin joint mortars are stronger than the BS5628 : Part 1[1] specification for a designation (iii) mortar.



**Figure 3.** Compressive strength development for thin layer mortars.

**Table 8.** 28-day strength results of thin layer mortars

Thin Joint Mortar	Compressive Strength (N/mm <sup>2</sup> )	Flexural Strength (N/mm <sup>2</sup> )	Tensile Strength (N/mm <sup>2</sup> )
A	17.6	4.6	1.9
B	12.0	3.6	1.7

Thin Layer Mortar **A** had a compressive strength nearly 50% greater than Mortar **B** but both mortars exceed the strength requirement of designation (iii) mortar as specified in BS 5628:Part 1[1] by significant amounts. The bracketed numbers in Table 7 indicate how many times stronger these mortars are over the 28 day strength of designation (iii) mortar. Mortar A at one day, is twice the 28day BS 5628 specified strength, whilst mortar B at one day is 0.85 the BS 5628 28-day strength and at 3 days, it is 1.6 times the 28 day strength. Both mortars give remarkably consistent flexural strength results using wallettes despite their discrepancy in strength [2]. For the conventional mortars reported in this paper, the strength development is approximately 60% after 7 days, however, for the thin layer mortars, nearly 75% of the final strength is reached after 7 days curing.

### 3. Conclusions

- Key strength properties of three mortar types (designations iii, iv produced using 32.5N and 42.5N PC) and thin joint-mortar have been established.
- Strengths of mortars produced using CEM .. 32.5N PC are considerably lower than those obtained for 42.5N PC mortars.
- Mortar strengths from both CEM .. 32.5PC and CEM .. 42.5PC mortars exceed the values given in BS 5628; Part 1.
- The Thin Layer Mortar type **A** was stronger than Thin Layer Mortar type **B** at all ages.
- With both thin layer mortars 70% of the total strength was reached after 7 days curing.
- With both thin layer mortars, the strength at 3 days was at least 1.6 times (3.3 for mortar A) the 28-day strength for designation (iii) mortar as required in Table 1 of BS 5628:Part 1.

### Acknowledgement

The author would like to acknowledge the funding and support for the Low-Density Aircrete project given by the EPSRC and industrial collaborators Autoclaved Aerated Concrete Products Association (AACPA).

### References

- [1] BS 5628-1:1992 – *Code of practice for use of masonry* – Part 1: Structural Use of Un-reinforced Masonry.
- [2] Ahmed, A., Flexural strength of low density blockwork, *International Conference on Construction Materials and Structures*, ICCMATS 2014, Johannesburg, South Africa.
- [3] Ahmed, A., Fried, A., Roberts, J.J., Advantages and Implications of High Performance Low Density Aircrete Products for the UK Construction Industry, *13th International Brick and Block Masonry Conference (IBBMaC)*, Amsterdam, Netherlands 2004.
- [4] BS EN 197; Part 1- Cement Composition, Specifications and Conformity Criteria for Common Cements.
- [5] BS 1200:1976 – Specifications for Building Sands from Natural Resources.
- [6] BS EN 1015-3:1999 – Methods of Test for Mortar for Masonry – Part 3: Determination of consistence of fresh mortar (by flow table).
- [7] BS EN 998-2:2003 - Specification for mortar for masonry. Masonry mortar.
- [8] BS EN 1015-11:1999 - Methods of Test for Mortar for Masonry. Determination of Flexural and Compressive Strength of Hardened Mortar.

# Improving physical properties of red clay from Morapalala village, Limpopo Province

Nthabiseng Portia MAHUMAPELO<sup>1</sup>

*MINTEK, Small Scale Mining and Beneficiation Division, Randburg, South Africa*

**Abstract.** This paper is based on a preliminary evaluation that was conducted on red clay from Morapalala village, Limpopo Province. The objective of the study was to improve the physical characteristics of the red clay by adding bentonite to the sample. Red clay is currently being mined and used for brickmaking. The following tests were conducted on the samples: linear shrinkage, water absorption and modulus of rupture. Major and trace elements were determined using Inductively Coupled Plasma-Optical Emission Spectroscopy. The addition of bentonite to red clay improved its quality making it suitable for brickmaking. The mixing ratio of 90:10 was found suitable to achieve the required results.

**Key words.** Red clay, bentonite, brickmaking

## Introduction

The Mintek's Small Scale Mining and Beneficiation (SSMB) Division has been involved in the development of rural pottery and ceramic programmes in South Africa. Extensive work has been done in clay assessments for pottery and brickmaking. Through this programme, SSMB has been able to set-up pottery and brickmaking businesses in many parts of the country.

This study is based on the red clay (RC) from Morapalala Village in Limpopo Province of South Africa. The RC is currently being used to make bricks. The standard of the bricks was found to be poor in that the bricks had cracks after firing. Mintek personnel participated in a study by visiting Morapalala bricks co-operative site, situated in Morapalala village to obtain red clay sample for analysis. The RC sample collected from the village was then tested, processed and beneficiated at Mintek laboratories. The findings were as follows: The RC clay sample was not suitable for brick and pottery manufacture, because the fired samples had cracks, and low unfired strengths, which are important properties in brick manufacturing. It was recommended that a more plastic or fine material be added to the RC clay sample to improve its physical characteristics [1]. In order to improve the properties of the RC clay received from Morapalala bricks co-operative 10 % bentonite clay was added to the 90 % RC clay sample and the final mixed sample was named RB clay sample. The main clay mineral of bentonite is montmorillonite.

<sup>1</sup>Corresponding author: [portiama@mintek.co.za](mailto:portiama@mintek.co.za)

This makes the clay take up water readily and swell to four or five times its dry volume. It is extremely plastic, has a low fusion point and gives a coloured product. The chief use of bentonite is as a plasticiser. Addition of 1 % bentonite may improve plasticity more than 10 % ball clay would, making it particularly useful for brick making [2].

## 1. Method

Large lumps of clay were crushed with a mallet. The sample was dried at 110°C for 24 hours and then crushed to <3 mm in a mill. Of the crushed material 500 grams was milled and sieved to minus 75 µm. 100 g sample was weighed from the sieved material and the chemical analysis by Inductive Coupled Plasma (I.C.P) was determined.

The remaining <3 mm crushed samples were mixed in a pan mixer and then small briquettes were formed in a Germatec Laboratory vacuum extruder (Type VP 0). The extruded samples (H: 26mm x W: 50 mm x L: 150 mm) were air dried for five days. The briquettes were fired respectively at 950°C, 1000°C and 1050°C using an electrically powered laboratory furnace. After removing the briquettes from the electric furnace the length of each sample was measured using a digital Vernier calliper and the shrinkage was recorded. Water Absorption tests were conducted to determine the amount of water absorbed by the samples. The samples were immersed in clean water at a temperature of 22-25°C for 24 hours. The samples were removed from the water, dried with a damp cloth and the mass was recorded [3].

The Modulus of Rupture (M.o.R) tests were conducted on the miniature clay bricks to determine their unfired and fired strength values using a Kingtest Auto 200 Press Machine. A comparison was made between RC and RB clay samples. Criteria used for comparison was the change in: chemical analysis, linear shrinkage, water absorption and strength results.

## 2. Results

Currently the South African Bureau of Standard does not have standards on clay testing specification to ensure quality in brick formation. Therefore Mintek uses its own specifications based on the outcome of the results obtained from different clays tested in Mintek's clay testing laboratory. The results which will be discussed in the sections below are compared with Mintek's specifications.

### 2.1 Chemical analysis

It is important to know the percentage of the elements found in clays because they can contribute to the outcome of the final product. The chemical analysis results of the clay samples that were tested are listed in the table 1.

The RC clay sample had high content of silica (81.5 %) and according to Mintek's requirements it means the clay sample is coarse and cannot form good quality products. Fine or plastic material should be added to the coarse clay. When 10 % bentonite was added to RC clay sample the silica content decreased by 6 % and the RB sample



became 75.5 %. This was a good outcome because the samples will not crack after firing. The Aluminium Oxide content remained the same 11.7% in RC and RB samples. This indicates that when bentonite was added to RC sample the Aluminium Oxide content was not affected. Slight differences were recorded in elements such as MgO, CaO, TiO<sub>2</sub>, Cr<sub>2</sub>O<sub>3</sub>, MnO, Na and K. The Loss on ignition (L.O.I) increased by 2.14 per cent in RB sample and it became 7.61 % and this is not a problem because the loss on ignition must be less than 10 % according to Mintek's requirements. From this result it is recommended that only 10 % bentonite should be added to RC sample because excess amount of bentonite can cause the samples to bloat. Bloating is the defect observed as spongy swollen mass over the surface of burned bricks is caused due to the presence of excess carbonaceous matter and sulphur in brick-clay [4].

**Table 1.** Chemical analysis results

Elements	RC (%)	RB (%)	Difference (%)
MgO	0.4	0.88	0.48
Al <sub>2</sub> O <sub>3</sub>	11.7	11.7	0.00
SiO <sub>2</sub>	81.5	75.5	-6.00
CaO	0.12	0.24	0.12
TiO <sub>2</sub>	0.67	0.74	0.07
Cr <sub>2</sub> O <sub>3</sub>	0.07	0.07	0.00
MnO	0.12	0.12	0.00
FeO	5.52	5.73	0.21
Na	0.78	0.29	-0.49
K	1.84	0.98	-0.86
L.O.I	5.47	7.61	2.14

## 2.2 Linear shrinkage

The linear shrinkage result was calculated from the average of four miniature bricks to ensure reliability of the results. Table 2 indicates the percentages at which the miniature bricks decreased in length at different temperatures.

The linear shrinkage of RB clay sample is higher than that of RC sample; this is an indication that samples shrink more when bentonite is added to it. High amounts of bentonite will dramatically slow down the drying rate. Bentonite makes bodies more plastic and dry harder but this comes at a cost, they shrink more during drying and thus potentially crack more [5].

The highest shrinkage value of RB samples is 7.30 % and this is acceptable. The shrinkage values must not exceed 10 % because the samples will crack after firing according to Mintek's requirements.

**Table 2.** Linear shrinkage results

Temperature (°C)	RC (%)	RB (%)	Difference (%)
950	2.90	6.93	4.03
1000	3.69	7.82	4.13
1050	5.23	7.30	2.07

### 2.3 Water absorption

The water absorption result was calculated from the average of four miniature bricks to ensure reliability of the results. Table 3 indicates the percentage water absorbed by the different samples after soaking them in cold water for 24 hours. The water absorption results of RB clay sample are low compared to the RC clay sample and this is an improvement. High percentages of water absorption can result in leakage especially when there are floods or heavy rains.

**Table 3.** Water absorption results

Time in H <sub>2</sub> O	Temperature (°C)	RC Sample W/A (%)	RB Sample W/A (%)	Difference (%)
24 hrs soaked in cold water	950	14.41	13.43	-2.03
	1000	16.63	11.97	-7.54
	1050	15.38	10.82	-6.5

### 2.4 Strength

The strength result was calculated from the average of four miniature bricks to ensure reliability of the results. The average M.o.R results of the samples are given in table 4. The strength results of RB sample were higher than RC sample, which indicates an improvement. According to Mintek's requirements, when the unfired strength is less than 1% the samples will break during handling.

**Table 4.** Strength results of RC and RB

Temperature (°C)	RC (MPa)	RB (MPa)	Difference (%)
110 (Unfired)	0.60	3.08	2.48
950	2.55	6.14	3.59
1000	1.69	7.97	5.61
1050	2.13	7.30	5.84

### 2.5 RC and RB Briquettes

The RC and RB briquettes were fired at 950 °C. Figure 1 shows the briquettes after firing. RC is labelled 2, and RB is labelled 3. The RC clay had cracks after firing of the samples. The RB briquettes were without cracks and resulted in smooth texture.



Figure 1. RC and RB briquettes comparison

### 3. Conclusions

The addition of bentonite improved the performance and quality of red clay. RB clay sample was found to be suitable for pottery and brick manufacturing, because it had high unfired and fired strength, low water absorption values and briquettes without cracks.

A 10 per cent addition of bentonite to red clay was found suitable to improve its characteristics. With that mixing ratio, shrinkage values increased. Adding more

bentonite may result in cracking, thus making it unsuitable for brickmaking. High percentages of bentonite may also result in bloating.

## References

- [1] P Mahumapelo & A van Niekerk (2013), Mintek Technical Report no: 41191, *Preliminary evaluation of clay from Morapalala Village*, 2012, p 1-15
- [2] F Singer & S Singer. 1963. The raw materials. *Industrial Ceramics*. Chapman & Hall Ltd. London. pp.30.
- [3] South African Bureau of Standards, SABS 227-2002, Burnt Clay Masonry Units, p13-14
- [4] The constructor, Identifying defects in bricks. <http://theconstructor.org/building/identifying-defects-in-bricks/6941> [Accessed 13 June 2014]
- [5] Ceramic Materials Database, Bentonite: [http://digitalfire.com/4sight/material/bentonite\\_106.html](http://digitalfire.com/4sight/material/bentonite_106.html), date [Accessed 17 March 2014]

# Physical, chemical and pozzolanic properties of bricks of X-X zone of Karacahisar castle, Turkey

Inci GÜLDOĞAN <sup>a,1</sup>, Yücel GÜNEY <sup>b</sup> and Erol Mehmet ALTINSAPAN <sup>c</sup>

<sup>a</sup>Department of Architecture, Anadolu University

<sup>b</sup>Earth and Space Science Institute, Anadolu University

<sup>c</sup>Faculty of Art, Anadolu University

**Abstract.** The objective of this study was to analyze the similar and different properties of historic bricks used in X-X zone of old Byzantium Castle Karacahisar Castle and according this knowledge to provide a reference for the bricks which will be used for the restoration here in the future. In order to perform this research, physical, pozzolanic and chemical analyses were carried out to structural adobe bricks. According to the analysis, it was found that water absorption percentage by weight under atmospheric pressure is between 11,8-25,3%, apparent porosity and water absorption by volume percent is between 22,2-38,2%. Apparent density of bricks is between 1,51- 1,89 gr/cm<sup>3</sup> and real density is between 2,37-2,61 gr/cm<sup>3</sup>. According to the ignition loss analysis, the CaCO<sub>3</sub> content percent is between 1-19,4 % and the bricks do not have good pozzolanic properties.

**Keywords.** Karacahisar castle, historic brick, physical property, pozzolanic activity of bricks, ignition loss of bricks, brick characterization.

## Notation

$A_b$	water absorption by mass under atmospheric pressure, expressed as a percentage;
$A_h$	water absorption by volume under atmospheric pressure, expressed as a percentage;
$\rho_b$	apparent density, expressed as gr/cm <sup>3</sup> ;
$\rho_r$	real density, expressed as gr/cm <sup>3</sup> ;
$p_0$	open porosity, expressed as a percentage;
$\Delta EC$	difference between electrical conductivity, expressed in $\mu S/cm$ ;
SB X	Structural brick group name and number from X-X site

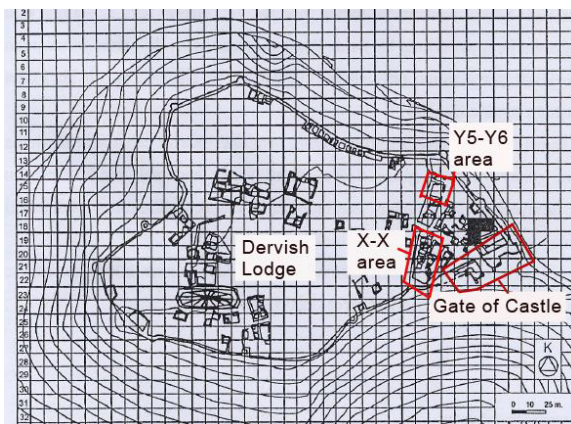
## Introduction

Historic buildings and sites are important cultural heritage for all of humanity. First step in conservation is understanding the historic place correctly and for this reason the

<sup>1</sup> Corresponding author: [iguler@anadolu.edu.tr](mailto:iguler@anadolu.edu.tr)

building materials and structural properties of the place should be carefully investigated by different approaches.

Karacahisar Castle is located in the southwest of the Eskişehir, on the plateau which has 1010 m in height above sea level and 7 km far from the city. It was constructed in the Medieval Age, known as a Byzantium Castle and covers around 60 acres (200 m x 300 m) in area. The original name of the castle is uncertain. Karacahisar Castle was conquered in 1288 by Osman Bey, the founder of Ottoman Empire, and renamed afterward as a “Karacahisar Castle”. Today the castle is located within the military borders, so it is not possible to visit the historic place without permission [1]. Archaeological excavations at the site began in 1999. The excavations are ongoing in four areas: The Gate, X-X, Y-Y and Dervish Lodge areas as seen in Figure 1.



**Figure 1.** Locations of investigated areas in the Castle [2]

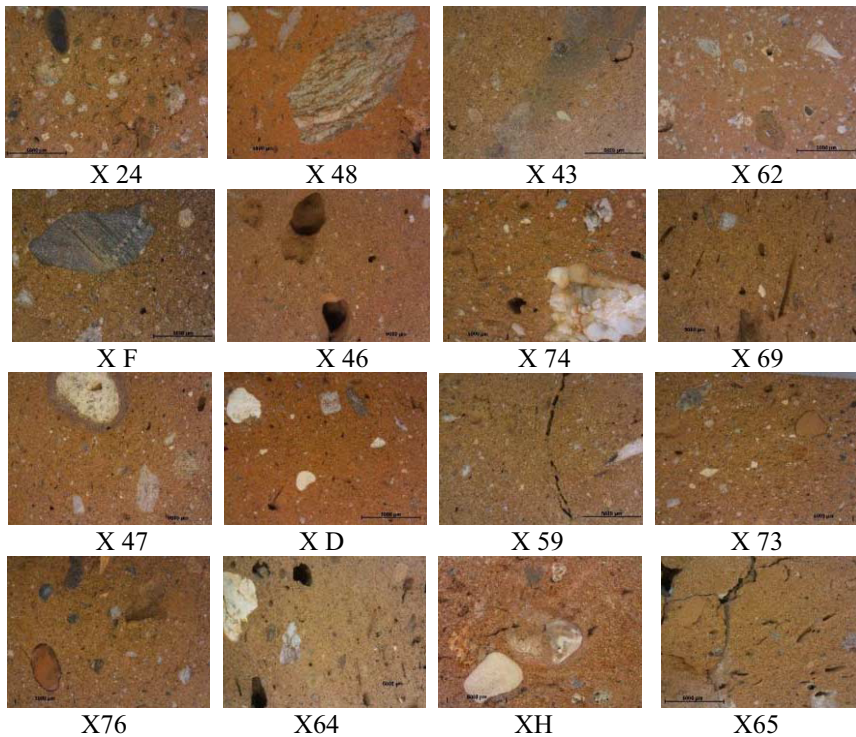


**Figure 2.** View 3of X-X Area

Bricks analysed in this study, were collected in 2012 and 2013 years from the X-X (Figure 2) area, which consisted of rectangular and two-parted spaces. At the beginning of excavation, the whole area was under the soil and all the bricks were extracted from this deep earth layer. In order to define the characteristic features of the thirty historic bricks, water absorption percentage by mass and volume (%), open porosity percent (%), apparent and real densities ( $\text{gr}/\text{cm}^3$ ), pozzolanic activities of bricks and  $\text{CaCO}_3$  based impurities were investigated in the study.

## 1. Test methods and results

After bricks were transported to the laboratory from the Castle, they were cleaned and photographed. Following, they were cut as possible as cube prisms, in 50 mm ( $\pm 3$  mm) or 40 mm ( $\pm 3$  mm) dimensions, like mentioned in the standards (TS EN 699, RILEM, 1980). Afterwards they were washed with wire brush under pressurized water and then dried until constant mass at 70°C in the oven during 4 days. Then the bricks were classified according to their thicknesses. The bricks thicker than 30 mm which were used in the walls, so they were classified as Structural Brick Group and they were named with "SB" code in front of the group name of bricks. Bricks thinner than 30 mm were classified as Non-Structural Brick Group and they were mostly used as floor or roof tiles. Bricks were examined visually; the colors, surface textures, porosity types, shapes of pores, shapes and amount and colors of impurities were considered during examination.



**Figure 3.** Stereomicroscope views of some brick matrixes from X-X zone

Structural bricks, which were used in the wall construction, have different thicknesses:

- h= 31-35 mm: X36, X47, X13, X70;
- h= 36-40 mm: X64, X65, X74;
- h= 41-45 mm: XM, X43, XC, X69, XD, X49, XB, XH, X22, X76.
- h= 46-50 mm: X24, XA, XE, X48, X26, X46, XF, X 62, X59, X73, X60, XG, XX, XK, Xi, X45.

1.1. Physical properties of the bricks

Experiments for definition the basic physical properties were carried out according to TS EN 699 [3], TS EN 13755: 2008 [4] and TS EN 1936 (2010) [5] standards and the results are shown in Figures 4 and 5. Water absorption percentage, open porosity and apparent density were identified according to Archimedes method. After drying the bricks until to constant mass at 70°C temperature, they were left in the water tank for 72 hours until they were saturated with water. Then the samples were dried with wet towel and weighted both in air and in water at 20-25°C temperature on 0,01 gram sensitive balance. Real density was determined by pycnometer method by using powdered brick samples.

Water absorption percentage by weight under atmospheric pressure differs between 11,8-25,3%, open porosity and water absorption percent by volume differs between 22,2-38,2% (Fig.4). It was seen that, bricks which are thinner than 45 mm have more porous structure than thicker bricks. X24 brick has minimum open porosity percent and water absorption percent by mass. This brick has the highest apparent density and one of the lowest real density.

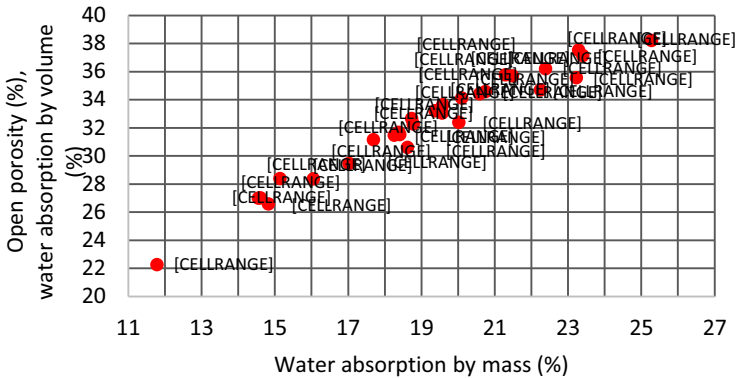


Figure 4. Water absorption percent by weight and volume of bricks of X-X zone

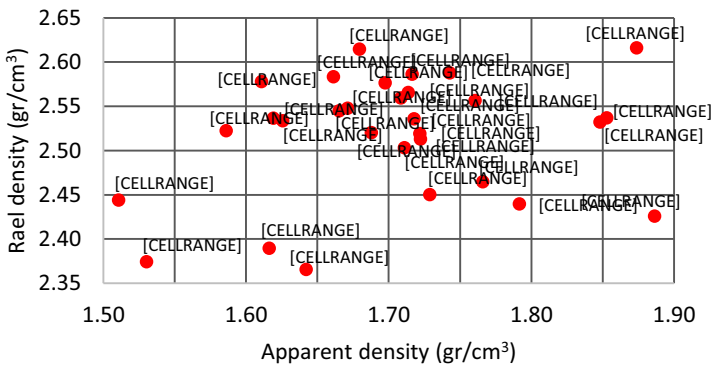


Figure 5. Apparent density (gr/cm³) and real density (gr/cm³) of bricks of X-X zone



Apparent density of bricks differs between 1,51- 1,89 gr/cm<sup>3</sup> and real density differs between 2,37-2,61 gr/cm<sup>3</sup> (Figure 5). Figure 6. shows that there is a negative strong relationship between open porosity percentage and apparent density of the bricks. Bricks which have higher percent of open porosity, have lower apparent density. The correlation coefficient R<sup>2</sup>=0,7442. On the other hand, there is not any relation between open porosity percent and real densities of historic bricks. For example, X24 has 22%, X65 brick has 38% open porosity, but their real densities are very close to each other (Figure 7).

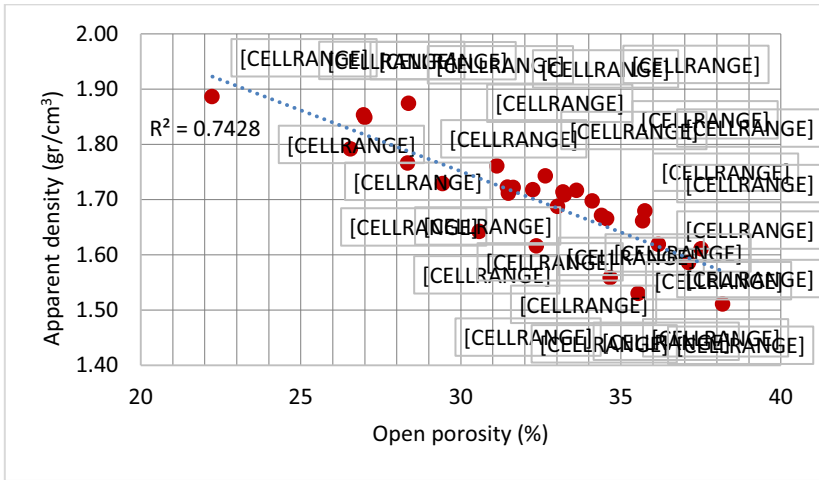


Figure 6. Relation between open porosity and apparent density

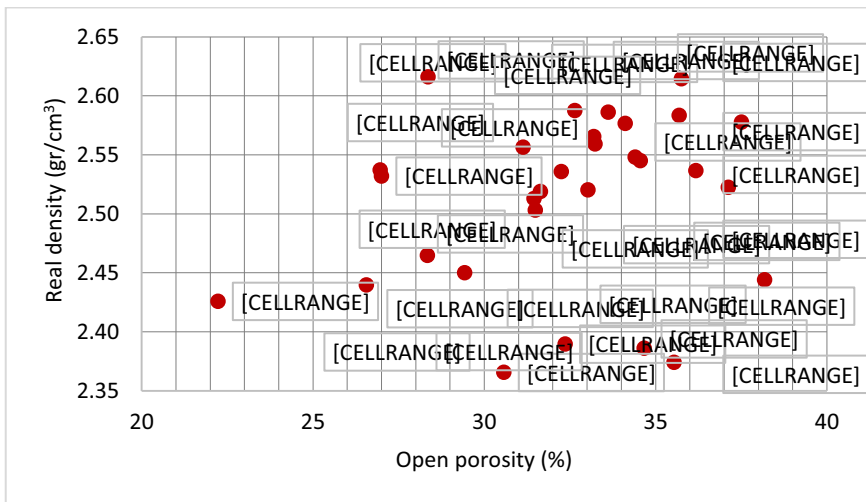


Figure 7. Relation between open porosity and real density

### 1.2. Ignition loss (calcination) analysis

In the characterization of historic bricks another distinctiveness is the carbonated impurity content in the brick matrixes. In order to define the percent of  $\text{CaCO}_3$  content, calcination analysis was carried out. Two sets of powdered samples of 1 gr were heated at  $105^\circ\text{C}$  temperature for 15 hours, at  $550^\circ\text{C}$  for a hour, at  $1050^\circ\text{C}$  for 30 min. in porcelain crucibles in the Protherm PLF 120 muffle furnace [6]. The weight losses measured after heating have been used for calculation of percentage of free water or moisture content (%) at  $105^\circ\text{C}$ , bound water and organic matter at  $550^\circ\text{C}$  and  $\text{CO}_2$  content at  $1050^\circ\text{C}$  to define  $\text{CaCO}_3$  content. The average of two sets were calculated at the end and results are given in Figure 8. According to the ignition loss analysis, the  $\text{CaCO}_3$  content percent ranges between 1-19,4%. The maximum  $\text{CaCO}_3$  content is in X36 brick. Bricks, which thickness is 45-50 mm. contain between 0-7%  $\text{CaCO}_3$  and their ignition loss is less than 5%. The other bricks with smaller thickness contain 7-12% of  $\text{CaCO}_3$  and have around 12% ignition loss.

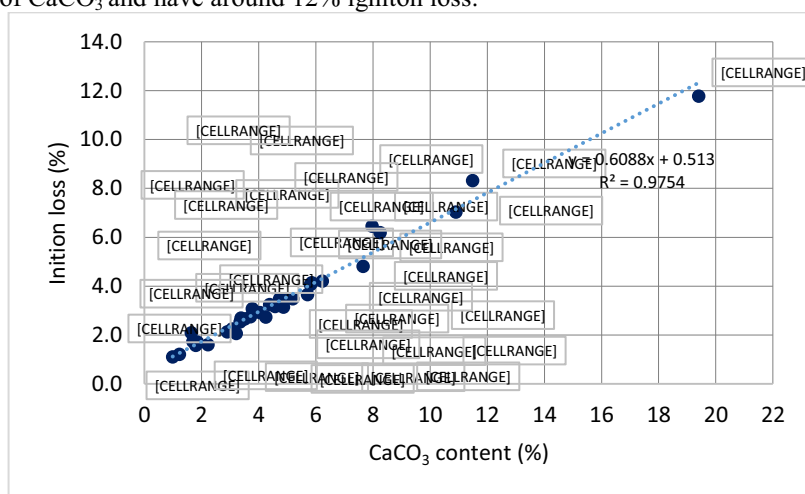


Figure 8. Ignition loss (%) and  $\text{CaCO}_3$  content (%) relation of bricks

### 1.3. Pozzolanic properties of the bricks

Pozzolanic activity of fine bricks ground to fineness less than  $63\ \mu\text{m}$  were determined by electrical conductivity measurement test procedure recommended by Luxan et al [7]. Firstly, the conductivity of 40 ml. saturated calcium hydroxide solution was measured and later 1 gr of brick powder was added into solution and was stirred for 2 minutes. The conductivity of new solution was measured once more. If the difference in conductivity is more than  $1,2\ \mu\text{S}/\text{cm}$ , this means the material is a good pozzolana. If conductivity difference is between  $0,4$ - $1,2\ \mu\text{S}/\text{cm}$ , that means the material is pozzolanic, if there is a change less than  $0,4\ \mu\text{S}/\text{cm}$ , that means the material is not pozzolanic.

Pozzolanic properties of bricks give an idea about used clay type and internal structure of the brick. The best pozzolanicity occurs between  $550$ - $600\ ^\circ\text{C}$  firing temperatures and enough amount of clay type necessary for pozzolanicity. Generally, pozzolanicity decreases with increasing firing temperature, but the clay type should be taken into account also [8].

Difference in conductivity change of the historic bricks was between 0,1-0,88  $\mu\text{S}/\text{cm}$  as seen at Figure 9. Difference in electrical conductivity for most of the bricks between 31-40 mm. is bigger than 0,4  $\mu\text{S}/\text{cm}$ , so these bricks have pozzolanic properties, but not good enough, because difference is less than 1,2  $\mu\text{S}/\text{cm}$ . Brick XH has a maximum pozzolanicity effect, and X26 has minimum one. Non pozzolanic bricks contain 1-5%  $\text{CaCO}_3$ , Similar bricks tend to show similar pozzolanic activities and  $\text{CaCO}_3$  content percent, so the Figure 7 actually shows the similar bricks at the same time. For example XC and X69, XA and X48, but also these bricks should be investigated mineralogically.

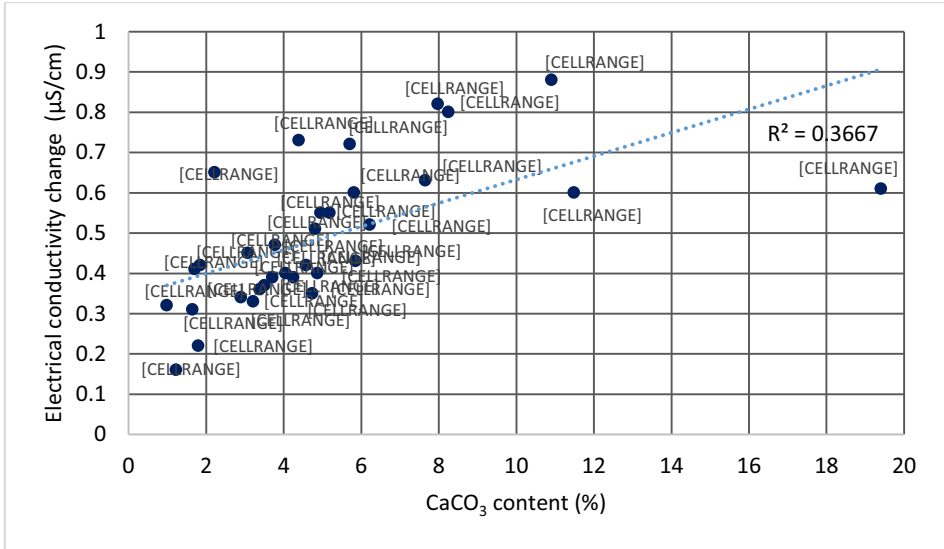


Figure 9. Relation between pozzolanicity and  $\text{CaCO}_3$  percent contents in bricks

## 2. Conclusion

As a conclusion of this study, it was seen that there is a large variety of bricks used in X-X area. Thirty bricks from X-X area were analyzed and it was seen that although bricks have different matrixes, their physical properties are close to each other. Water absorption by mass mostly differs between 14-24%, open porosity percent and water absorption by volume differs between 26-38%. As given in the literature, apparent density of bricks is between 1,51-1,89  $\text{gr}/\text{cm}^3$  and real density differs between 2,37-2,61  $\text{gr}/\text{cm}^3$ . Apparent densities of bricks decreases with increasing open porosity percentage, but real densities do not respect with open porosities. For example, X46, X59, X70 and XH bricks have open porosity between 30-35% but their real densities are less than 2,40 $\text{gr}/\text{cm}^3$ , but real densities of the bricks with same porosity are between 2,50-2,60  $\text{gr}/\text{cm}^3$ . This shows that some of the historic bricks, like X46, X59, X70 and XH, include fully close pores inside themselves.

As a result of pozzolanic activity experiment, it was seen that the bricks do not have good pozzolanic properties. Most of thick bricks are not pozzolans, thinner bricks are pozzolans, but not good enough. There could be two reasons for non-pozzolanicity of the thick bricks: they could be fired in higher degrees than 900°C degree or they do not

contain kaoline clay as raw material. Also the relationship between pozzolanity and carbonated content is seen during the study, pozzolan activity increases with increasing CaCO<sub>3</sub> impurity. Bricks which include higher percent of CaCO<sub>3</sub>, also have more ignition loss. Bricks contain mostly less than 7% of CaCO<sub>3</sub> and they have less than 5% ignition loss.

When compared the bricks of X-X zone with the bricks of Ktahya Castle [9] from Ktahya, the neighbor city of Eskiřehir, it was seen that the bricks of X-X zone have less porous structure and bigger apparent densities than the bricks of Ktahya Castle. This means, although being located in close cities, there were using different productions techniques and raw materials in the past for the bricks used in Castles.

## Acknowledgements

This study is supported by Anadolu University Scientific Research Projects Commission under the grant no: 1306F237.

## References

- [1] Dođru, Halime (2001), Karacahisar Castle and It's Importance at the Foundation of Ottoman State, Anadolu University, *Journal of Social Sciences*, 1/1, p.106.
- [2] Parman, E. (2003), Eskiřehir – 2001 Year Excavation Studies of Karacahisar Castle, 24. *Excavation Results Meeting*, Vol.2, 27-31 May 2003, Ankara, pp. 69-80
- [3] TS EN 699, (2009), Natural building stones - Methods of inspection and laboratory testing, *Turkish Standards Institution*, Turkey
- [4] EN 13755:2008 Standard; Determination of water absorption at atmospheric pressure, *Turkish Standards Institution*, Turkey
- [5] TS EN 1936 (2010), Natural Stones –Test Methods– Standard for Determination Real Density, Apparent Density, Total and Open Porosity, *Turkish Standards Institution*, Turkey.
- [6] Walter E., Dean Jr. (1974) Determination of Carbonate and Organic Matter in Calcareous Sediments and Sedimentary Rocks by Loss of Ignition; Comparison with Other Methods, *Journal of Sedimentary Petrology*, Vol. 44.
- [7] Luxan M.P, Madruga F. and Saavedra J. (1989), Rapid Evaluation of Pozzolan Activity of Natural Products by Conductivity Measurement, *Cement and Concrete Research*, Vol. 19, pp. 63-69.
- [8] Bke, H., Akkurt, S., İpekođlu, B., (2004), Properties of Horasan Mortar and Plasters Used in Historic Structures, *Yapı 269*, April, p.92.
- [9] Kurugl, S. (2010), Investigation of Mechanical Properties and Pozzolan Activities of Historical Ktahya Castle Bricks, *Firat Univ. Journal of Engineering* 22 (1), pp. 13-26.

# Cement stabilization of laterite-quarry dust mixture for interlocking brick production

Amana OCHOLI<sup>a,1</sup> and Manasseh JOEL<sup>b</sup>

<sup>a</sup>*Civil Engineering Department, Ahmadu Bello University, Zaria.*

<sup>b</sup>*Civil Engineering Department, Univ of Agriculture Makrudi, P.M.B 2373, Makurdi*

**Abstract.** The suitability of laterite mixed with 0 %, 10 %, 20 % and 30 % Quarry dust, stabilized with 0 %, 2%, 4 %, 6 % and 8 % cement content by dry weight of laterite for interlocking brick production was investigated. Grain size analysis, was performed on natural laterite, while Atterberg's limits test, was performed on laterite, mixed with quarry dust and cement. Compressive strength test and water absorption test were performed on bricks produced using different combination of laterite, quarry dust and cement. The 28 day compressive strength of bricks produced with untreated laterite increased from 0.92 N/mm<sup>2</sup> to peak value of 5.66 N/mm<sup>2</sup> when stabilized with a combination of 30 % quarry dust and 8 % cement content. Water absorption value of bricks decreased from a state of saturation to a minimum value of 5.16% at a combination of 30% quarry dust plus 8 % cement. Results of tests clearly showed that the use of quarry dust will enhance the compressive strength and water absorption values of interlocking brick. Its usage will provide an effective way of disposing quarry dust left as wastes at quarry sites.

**Keywords.** Stabilization, cement, quarry dust, interlocking bricks

## Introduction

Over the ages, the use of earth in the production of adobe bricks, and clay in the production of burnt bricks is well known all over the world, the quest for more reliable walling material has led to the development of new walling materials such as Sandcrete blocks, concrete, pre-cast walling materials, and iron sheets, which are seen as signs of modernity and progress. The costs of the new modern walling materials however, are beyond the reach of most rural dwellers. To help overcome the problem of inadequate strength arising from substandard blocks and high cost of technological advancements has led to the production of interlocking bricks. Interlocking bricks are made from a mixture of soil and a stabilizing agent, with provision for bricks to key into each other without bonding with cement mortar and compressed by different types of manual or motor-driven press machines.

The main challenge with interlocking brick production is the availability of suitable material for its production, as locally available soil deposits in most cases may not satisfy the minimum requirement for their usage in brick production.

<sup>1</sup>Corresponding author: [amanaocholi@yahoo.com](mailto:amanaocholi@yahoo.com), Phone. +234803 428 2019; [manassehjoel@yahoo.com](mailto:manassehjoel@yahoo.com), Phone. +234803 210 4329

To make locally available material suitable for interlocking brick production, what readily comes to mind is soil stabilization. Soil stabilization as defined by [1] is the treatment of natural soil to improve its engineering properties, using mechanical or chemical agents. Mechanical stabilization according to [2] refers to either the blending of soils or the application of mechanical energy to ensure compaction. In the production of bricks the blending of different grades of soils to obtain a required grade, and compaction of soil using mechanical press to ensure densification can be described as mechanical stabilization. The blending of chemical agents with the natural soil is referred to as chemical stabilization. Such agents include, cement, lime, bitumen, fly ash, rice husk ash or a combination of chemical agents. According to [3] soil stabilization as it applies to interlocking brick production is the application of additional supplements or forces to the soil in order to make them water resistant and stronger. Such strength is dependent on the properties and mix of soil types, the measure/amount of force applied to achieve compaction, in addition to chemical or natural products used as stabilizers.

When laterite, which is readily available in most areas, is treated with cement, strength development is normally attributed to the effect of the hydration of cement; however where available materials seem to have a high plasticity index, the use of admixtures such as lime is normally recommended. In Nigeria, lime is very expensive, as it costs four times more than the same quantity of ordinary Portland cement. This observation was reported by [4]. To ensure economy in plasticity index reduction, the use of quarry dust instead of lime has been proposed in this study.

Quarry dust as described by [5] is the residue or non-valuable waste material after the extraction and processing of rocks to form fine particles less than 4.75 mm. Although the utilization of quarry rock dusts as a building material in the industrially advanced countries of the west, for the past three decades, was reported by [6], large heaps of quarry dusts deposits are found at different aggregate quarry sites in Benue state of Nigeria. The successful utilization of quarry dust in the production of interlocking bricks will provide an effective way of disposing off the waste, and ensuring economy in the production of bricks where there is shortage of laterite and abundance of quarry dust. The aim of the study was to investigate the effect of quarry dust addition on the properties of lateritic interlocking bricks.

## 1. Materials and methods

Materials used in the production of the interlocking bricks comprises of laterite, cement and water. The laterite used was obtained from Ikpayongo, a distance of 22km from Makurdi the capital of Benue State, along Makurdi-Aliade road, at a distance of 800 m from the centre line of the road and a bearing of N085°W, where an outcrop of laterite showing the relics of Makurdi sand stone was observed. Quarry dust as obtained from the building material market located at the Wurukum area of Makurdi was used. Ordinary Portland cement as obtained from the open market at Makurdi was used for this work. Potable tap water as obtained in the Civil Engineering Department Laboratory was used. The laterite sample admixed with 0 %, 10 %, 20 %, and 30 % quarry dust was stabilized with 0 %, 2 %, 4 %, 6 % and 8 % cement, by dry weight of laterite.

The stabilized samples were then used to produce interlocking bricks which were subjected to compressive strength and water absorption test. All the processes were carried out with reference to [7-9], guideline on the production of interlocking bricks.

### *1.1. Preparation of laterite sample*

The laterite sample were air –dried for seven days in a cool, dry place before samples were taken for sieve analysis test and Atterberg's limits test, which were performed in accordance with specification of [10]. The sample for brick production was sieved using a wire mesh screen with aperture of about 6 mm in diameter. Fine materials passing through the sieve were collected for use in brick production, while those retained were discarded.

### *1.2. Production of lateritic interlocking bricks*

Interlocking bricks were produced using a locally fabricated press machine, fitted with mould to produce bricks with dimension of 230 x 230 x 120 mm. The production process comprises of batching, mixing and compaction of Laterite. The prescribed quantity of dry Laterite and cement were thoroughly mixed together using shovels on a clean concrete platform. The dry mixture was spread again to receive water which was added gradually while mixing, using a watering can, until the optimum moisture content of the mixture was attained in addition to a uniform consistency. The optimum moisture content (OMC) of the mixture was determined by progressively wetting the soil and taking handful of the soil, compressing it firmly in the fist and allowing it to drop on a hard and flat surface from a height of about 1.10 m. When the soil breaks into 4 or 5 parts, the water was considered sufficient [11]. The mixture of cement, laterite quarry dust and water was then poured into the lubricated mould of the interlocking brick moulding machine, and was compressed at a pressure of 100kpa, after which the brick was ejected from the machine. The green bricks were cured by covering of bricks with tarpaulin after sprinkling of water twice a day (morning and evening) this exercise started twenty four (24) hours after moulding in line with the recommendations of [12] for effective curing of bricks. According to [13], the primary aim of curing is to ensure that moisture is retained within the bricks for effective hydration reactions of cement. The exercise continued until the bricks were due for testing.

Bricks produced using the different combination of cement and quarry dusts were cured for 7, 14, and 28 days and subjected to compressive strength and water absorption tests. Compressive strength test was performed at 7, 14, and 28 days of curing. For each age five bricks were removed from the curing area to the laboratory, two hours before the test was conducted to normalize the temperature and make the brick relatively dry or free from moisture. The weight of each brick was determined before the test, which was performed using an ELE compressive testing machine. The brick was sand witched between two plates such that the top and bottom as moulded lie on a flat metal plate and the recessions filled with metal plate of the exact size to prevent shearing of the brick during testing. The brick sand witched between the two metal plates was then inserted into the compartment of the compressive machine before being subjected to load. The load at failure was recorded and divided by the sectional area of the brick to arrive at the compressive strength.

Water absorption test was performed on bricks cured for 28 days. The air dried weight of each brick was measured using a balance, after which the bricks were then immersed completely in water for 24 hours, The percentage water absorption was estimated as presented in Eqn. (1).

$$Wa = \frac{Ws - Wd}{Wd} \times 100 \tag{1}$$

Where: Wa is the percentage moisture absorption, Ws is weight of soaked brick, and W<sub>d</sub> is the weight of dry brick.

**2. Discussion of results**

Particle size distribution curve of Laterite and quarry dust used in brick production is as presented in Figure 1. Atterberg’s limits test result given in Table.1, clearly show that liquid limit, plastic limit and plasticity index of laterite, decreased, with increase in cement and quarry dust content. Reduction in Atterberg’s limits indices can be attributed to the reduction in the clay fraction as quarry dust was added to laterite due to the hydration of cement. Liquid limit, plastic limit and plasticity index decreased from 40.0 %, 25.0%, and 23.0 % for the natural Laterite to a minimum value of 21.0%, 11.0%, and 10.0 % respectively when treated with 8 % cement, plus 30 % quarry dust. The use of both cement and quarry dust greatly enhanced the suitability of Ikpayongo Laterite for brick production, as reflected in the attainment of plasticity index value range of 10 to 15 % suggested in [5] for economic brick production.

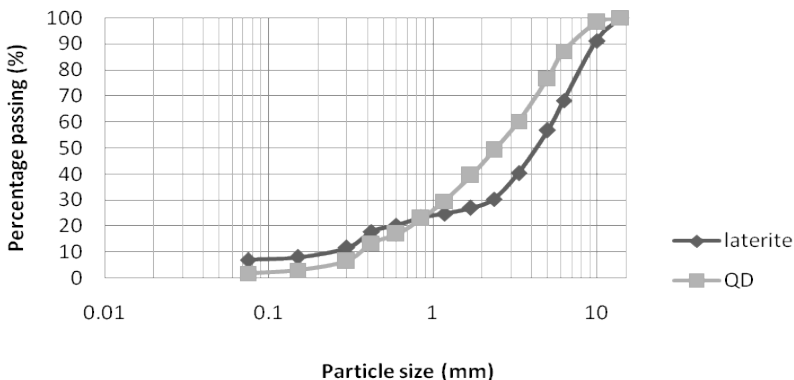


Fig.1: Particle size distribution curve of laterite and quarry dust (QD)

*2.1 Compressive strengths*

The compressive strengths of bricks produced using laterite treated with cement and quarry dust as presented in Table 2, showed that the compressive strength of bricks increased with cement and quarry dust content and with age. This observation can be attributed to the product of cement hydration which helps to bind sand, clay and silt particles of laterite and quarry dust together.



**Table 1.** Atterberg's Limits test result of laterite stabilized with cement and quarry dust

Cement content (%)		0	2	4	6	8
0 % Quarry Dust	LL	48.0	44.0	42.0	39.0	36.0
	PL	25.0	24.0	23.0	22.0	21.0
	PI	23.0	20.0	19.0	17.0	15.0
10 % Quarry Dust	LL	44.0	41.0	38.0	35.0	32.0
	PL	23.0	22.0	21.0	20.0	19.0
	PI	21.0	19.0	17.0	15.0	13.0
20 % Quarry Dust	LL	41.0	36.0	32.0	30.0	26.0
	PL	21.0	19.0	17.0	16.0	14.0
	PI	20.0	17.0	15.0	14.0	12.0
30 % Quarry Dust	LL	34.0	31.0	27.0	24.0	21.0
	PL	19.0	17.0	15.0	13.0	11.0
	PI	15.0	14.0	12.0	11.0	10.0

Decrease in compressive strength observed with the singular use of quarry dust is due to the reduction in the clay fraction of laterite, which served as the bonding agent in the absence of cement, when quarry dust partially replaced Laterite. The 28 day compressive strength of bricks produced with untreated laterite increased from 0.92 N/mm<sup>2</sup> to peak value of 5.66 N/mm<sup>2</sup> when laterite used for production was treated with a combination of 30 % quarry dust plus 8 % cement content. Results of compressive strength test clearly showed that quarry dust slightly enhanced the compressive strength of lateritic interlocking bricks, hence the recommendation of 30 % quarry dust plus 8 % cement content for brick production as the minimum 28 day dry compressive strength value of 2.0 N/mm<sup>2</sup> recommended by [8], was satisfied, using this combination.

**Table 2.** Compressive strength test result of laterite stabilized with cement and quarry dust

Cement content (%)		0	2	4	6	8
0 % Quarry Dust	7days	0.90	1.94	2.10	2.93	3.16
	14 days	0.91	2.20	2.58	3.00	3.37
	28 days	0.92	2.62	3.12	3.75	3.90
10 % Quarry Dust	7days	0.77	1.97	2.27	3.10	3.30
	14 days	0.78	2.21	2.61	3.24	3.90
	28 days	0.79	2.64	3.26	3.91	4.21
20 % Quarry Dust	7 days	0.66	1.98	2.44	3.00	3.52
	14 days	0.67	2.40	2.90	3.26	4.06
	28 days	0.68	2.67	3.55	4.58	5.40
30 % Quarry Dust	7 days	0.56	1.91	2.97	3.15	3.60
	14 days	0.57	2.49	2.96	3.56	4.10
	28 days	0.58	2.70	3.61	4.60	5.66

## 2.2 Correlation between compressive strength, stabilizer content and plasticity index.

The relationship between 28 day compressive strength, quarry dust and cement content is as presented in Eq. (2).

$$CS = 0.90 + 0.483C + 0.12QD \dots \dots R^2 = 0.909 \dots \dots (2)$$

Where CS = 28 day compressive strength, C= cement content,(%) QD = Quarry dust content (%).

It showed that natural laterite accounted for 0.90N/mm<sup>2</sup> of interlocking bricks strength, cement and quarry dust accounted for 0.483 and 0.12 multiplied by the respective quantity of cement and quarry dust used in brick production. The equations R<sup>2</sup> value of 0.909 showed that the model provides a good relationship between strength and the different additives content as R<sup>2</sup> value normally lies between -1 and +1.

### 2.3 Water absorption test result

Water absorption is a measure of the pore space in hardened specimen, occupied by water in saturation condition. Water absorption result presented in Table 3, showed that water absorption value of bricks decreased with cement and quarry dust content. This can be attributed to low water absorption associated with quarry dust, and the product of cement hydration which serves as bonding agent, which help reduce voids in the bricks, resulting in low water absorption.

Test results also showed that all bricks produced without cement disintegrated, 24 hours after immersion in water. This can be attributed to the absence of cement hydration product that binds and enhance water resistance of bricks. Water absorption values obtained using different percentages of cement and quarry dust is lower than the maximum acceptable value of 12 % recommended by [14].

**Table 3.** Water Absorption test result of laterite stabilized with cement and quarry dust.

Cement content (%)	0	2	4	6	8
0 % Quarry Dust	D	6.90	6.83	5.78	5.44
10 % Quarry Dust	D	6.71	6.59	6.48	6.36
20 % Quarry Dust	D	6.48	5.87	5.75	5.52
30 % Quarry Dust	D	6.09	5.63	5.27	5.16

D=Disintegrated inside curing tank

### 3. Conclusion

Based on the findings from this study, it can be concluded that:

- The use of quarry dust greatly enhanced the suitability of laterite for use as interlocking brick production material.
- The plasticity index of untreated laterite decreased from 23 % to a minimum value of 10 % when treated with a combination of 30 % quarry dust and 8 % cement.
- The compressive strength of interlocking bricks increased with days, quarry dust and cement content as reflected in the 28 day compressive strength of brick which increased from 0.92 N/mm<sup>2</sup> for bricks produced with natural laterite to 5.66 N/mm<sup>2</sup> when the laterite was treated with a combination of 30 % quarry dust plus 8 % cement.
- Water absorption value of bricks increased from 0% for bricks made with untreated laterite to a minimum value of 5.16 % when bricks were produced with laterite treated with a combination of 30 % quarry dust and 8 % cement.

## References

- [1] Garber, J.N. and Hoel, A.L. *Traffic and Highway Engineering*, S.I. Edition, RRD-Crawfordsville, USA. (2010)
- [2] O'Flaherty, C.A.O. *Highways*; fourth edition, Butterworth Heinemann, Oxford. (2002)
- [3] Tibaijuka, K.A. Interlocking Stabilized Soil Bricks; Appropriate Earth Technologies in Uganda, United Nations Human Settlements Programme. *Unon Publishing Services*, Section, Nairobi, Kenya. [www.unhabitat.org](http://www.unhabitat.org). (2009)
- [4] Raheem, A.A, Bello, A.O, Makinde O.A. A comparative study of cement and Lime Stabilized Lateritic Interlocking bricks. *The pacific Journal of science and Technology*. (2010). 11 (2) 27-34.
- [5] Ilangovana, R., Mahendrana, N. and Nagamanib, K. Strength and Durability properties of concrete containing quarry dust as fine aggregate. *Asian Research Publishing Network (ARPN)*. (2008). Vol.3, 5 20-26. [www.arpn-journals.com](http://www.arpn-journals.com).
- [6] Nisnevich, M., Sirotin, G. and Eshel, Y. Light weight concrete containing Thermal power station and stone quarry waste. *Magazine of concrete research*. (2003), 313-320.
- [7] International Labour Organisation. Small scale manufacture of Stabilized soil bricks, technical memorandum No 12. *International Labour office*: Switzerland. (1987)
- [8] NBRRI. Nigerian Building and Road Research Institute Interlocking Brick making machine" *NBBRI Newsletter I* (1). (2006) 15 -17.
- [9] Hydraform. Hydraform Brick making Machine Manual, *Hydraform Group*.(2004) [www.hydraform.com](http://www.hydraform.com)
- [10] BS 1377. Methods of Testing Soils for Civil Engineering Purpose. *British Standards Institution*, London (1990)
- [11] National Building Code. *Building Regulations*. Lexis Nexis: Butterworths, OH . (2006)
- [12] Adam, A. E. *Compressed Stabilized earth brick manufactured in Sudan*. Grapho print, for UNESCO, Paris, France. (2001)
- [13] Kerali, G.A. Durability of compressed and cement-stabilized building bricks: *unpublished PhD dissertation* University of Warwick. (2001)
- [14] Nigerian Industrial Standard. *Standard for Sandcrete Bricks ICS 91. 100.20*, NIS: Abuja, Nigeria. (2004)

# Effect of wetting and air curing durations on strength of stabilized sands

Lerato J. MOATLHODI<sup>1</sup> and Felix N. OKONTA

*Department of Civil Engineering Science, University of Johannesburg, South Africa*

**Abstract.** Low cost houses in most developing countries are constructed from sandcrete blocks manufactured from sand-cement mortar. In South Africa, failure of many of these blocks has been experienced leading to collapse of the structures. Lack of sufficient compressive strength in the manufactured blocks was attributed as the main cause of the failures. The unconfined compressive strength (UCS) of sandcrete blocks can however be improved by curing the blocks under different conditions. Therefore the objective of this study was to evaluate the effect of different wetting and air drying durations would have on the strength and the stiffness of the cubes produced. Weakly cemented sand cubes, with different cement contents and cement-fly ash binder ratios compacted at the optimum moisture content, were prepared. The 28 days UCS was determined, modulus of elasticity and moisture contents of sample specimen was also determined. The results showed that curing cubes under water for 7 days and then air curing for 21 days yield maximum UCS and modulus of elasticity for sands cemented by plain Portland cement, and that 3 days under water curing produced maximum results for sands stabilized by cement-fly ash binder. It was however found that under water for 28 days results in minimum strength. Therefore the longer the cubes are cured under water minimum strengths were achieved.

**Keywords.** Sandcrete, fly ash, cement, unconfined compressive strength, stiffness

## Introduction

Sandcrete blocks are widely used for the construction of low cost housing in many developing countries and are manufactured by mixing sand, cement and water in some predetermined proportion. The South African government with the aim to improve the living conditions of many of its people, contracts to build millions of low cost housing subsidised by the government under the Reconstruction and Development Programme (RDP) were issued to various contractors. As these are low cost houses, sandcrete blocks became the building bricks of choice by virtue of their low retail price. Failure of these blocks has been witnessed in varied applications with some even failing as they were being stacked post production, some while in transit, and many during construction. About three million low-cost houses have been built since 1994 using sandcrete blocks and the blocks were cured by sprinkling water once a day for seven days [3]. This method of curing has failed to consistently produce desired compressive strength for the blocks.

<sup>1</sup>Corresponding author: [ljmoatlhodi@uj.ac.za](mailto:ljmoatlhodi@uj.ac.za)

The common use of this material as the main building block for these housing units remains the current reality and will arguably remain, into the immediate foreseeable future. Therefore, this large scale use gives rise to the need to study and understand the various factors affecting the development of compressive strength of these blocks and stiffness, and in particular the influence that different wetting and air curing durations and the mixing of fly ash in the cement have on their compressive strength development and stiffness. It has been proven that by 28 days under appropriate curing conditions concrete will gain above 95% of its strength, this study seeks to evaluate whether sandcrete cubes under the similar curing conditions would yield maximum strength or would require different curing conditions be used. The sandcrete failure has largely been attributed, in other studies, to the inadequate quality and quantities of the materials used in the manufacturing process, i.e sand aggregate, Portland cement and water. However the use of inappropriate methods for curing, further contributes to low strength blocks by failure to provide conducive conditions for adequate strength development. Several studies have been conducted and methods developed to analyse the effect of curing on the strength of cement mixes. Park [5] analysed the effect of wetting duration on unconfined compressive strength of cemented sands, and moisture conditions and temperatures for curing cemented sands. He found that when sprinkling curing is used on cemented sand, wetting for one day on the last day of twenty eight days decreased the strength while wetting for one day in the middle of 28 days curing, resulted in an increased strength. He also found wetting and drying over three cycles to be the most optimum period to increase strength, beyond which the strength decreased. This paper is subdivided into six parts, namely: introduction; materials and methods; results and discussions; conclusions and recommendations.

## **1. Materials and methods**

Sandcrete blocks can be described as solid material made up of cement, sand and water which can be shaped into different sizes. A sandcrete block can be hollow or solid and can be utilized as load-bearing or non-load-bearing units [4]. These blocks are usually made up of cement to sand ratio of 1:6 and are supposed to have a minimum compressive strength of 2.5 – 3.45MPa as specified by the Nigerian Industrial Standard [2] and 3.2MPa according to the South African National Standards (SANS) 2001-CM1:2007, is required for masonry units used for wall building. Similar to normal concrete, sandcrete blocks are weak in tension and strong in compression.

A textural classification of sands, according to the Unified Soil Classification System (USCS), is soils with particle size smaller than 4.75mm but greater 0.075mm. Sands are primarily sourced from river and stream banks as they are predominantly transported through these mediums. Sands can also be produced through the process where rocks weather over many years caused by the prevailing climatic conditions into sand sized particles. Portland Cement is a fine mineral powder which chemically reacts when mixed with water to form a paste that sets and hardens; forming a rigid mass that binds aggregates together and AfriSam 52.5R cement was used. Fly ash is a product of pulverised coal combustion; fly ash rises with flue gases through the exhaust chamber and removed by electrostatic precipitators. The class F fly ash was used in this study. A



**2. Results and discussions**

The grading analysis of the soil depicts a poorly graded soil in Figure 1 where over 95% of the sample grain sizes are between #10 (2.0mm) and #200 (.075mm) sieve. The coefficient of uniformity of less than 4 as it is shown corroborates the soils' uniformity [1]. The sand is non-plastic with low shrinkage limit making the soil suitable for sandcrete block production see Table 3.

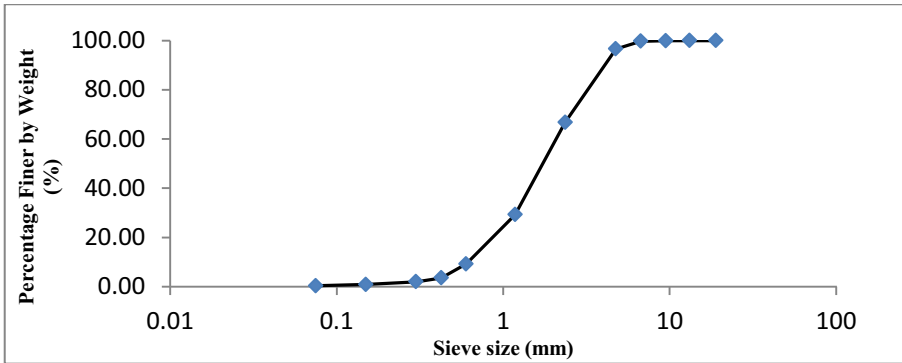


Figure 1. Particle size distribution

Table 3. Sand properties

Cu	Cc	D <sub>50</sub> (mm)	D <sub>10</sub> (mm)	LL (%)	PI (%)	SL (mm)	G <sub>s</sub>	OMC (%)	MDD (g/cm <sup>3</sup> )
3.55	1.24	1.7	0.6	18.9	0.45	0.63	2.63	7	1620

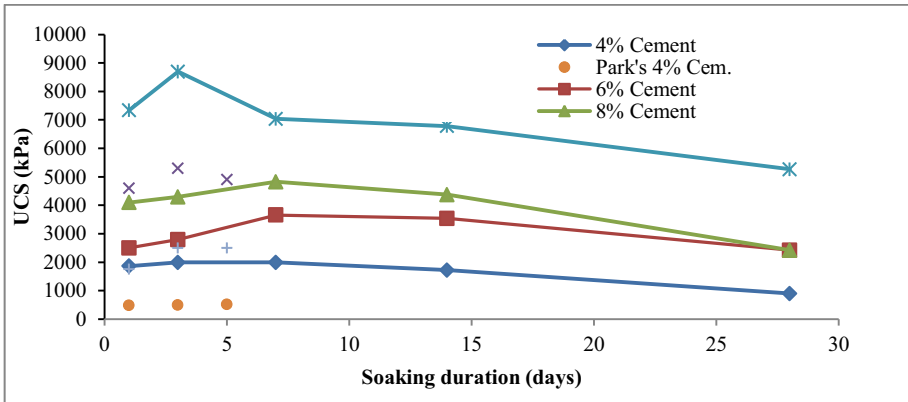


Figure 2. UCS and soaking durations for cement content

There is a gradual increase in strength as the number of days underwater curing increase reaching a maximum value on day 7 Figure 2. A more significant jump in strength is witnessed as the cement ratio increases to 12%, the strength of the lower cement ratio remained slightly steady until about day 14 was reached underwater and a gradual decrease in strength is shown beyond. The cubes soaked in water for the whole

28 days show the least strength, even at higher cement ratio. Because there exists an optimum water moisture content for a given cement ratio that will mobilize complete hydration necessary to facilitate cementation of sand grains under conducive curing conditions, however a further excess ingress of water may wash away the cementing material especially in higher cement ratio mixes [5]. Equation (1) describes the approximate statistical relationship developed from these results of the binder content (BC) and soaking days (SD) to the UCS. The coefficient of determination is 0.856 and the closeness of the UCS values to the predicted in Figure 3 further depicts the quality of the fit. According to the SANS 2001- CM1:2007, a minimum compressive strength of 3200kPa is required for masonry units used for wall building. As a result model (1) is valid for values of BC no less than 6%, and SD from 0 – 28 days for the minimum strength to be achieved. Though peak strength is reached at day 7 for plain cement, addition of Class F Fly ash (replacing 40% plain cement) using equation (1), samples reach similar strength values in just 3 days for 8-12% BC. Class F fly ash is a pozzolan material that reacts with the calcium hydroxide produced during the hydration of Portland cement to form additional cementitious compounds thereby assisting the hydrated Calcium Silicates to bind sand particles. Park's results [5] are incorporated in some of these figures to make some comparison, as seen in Figures 2 the 3 and 5 day wetting strength of Park's study is less than the current work's UCS value even at 12% cement ratio. It is worth noting however that the curing methodology and conditions, along with the cube sizes were different between the 2 studies.

$$\text{UCS} = - 46.301 \text{ SD} + 884.583 \text{ BC} - 2163.677 \quad (R^2 = 0.856) \quad (1)$$

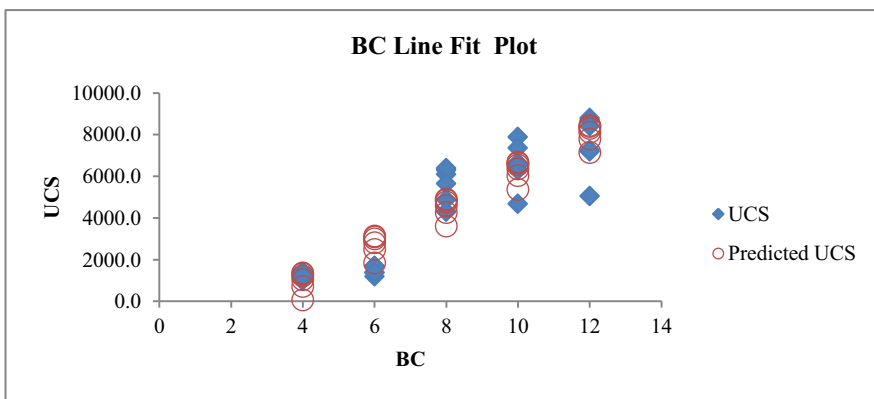


Figure 3. BC best fit plot

Modulus of elasticity (E) is a measure of stiffness of the stabilized sand obtained as the ratio of uniaxial stress over the uniaxial strain from the unconfined compressive strength tests. The result E versus Soaking duration showed a similar trend to the UCS in that for plain cement it peaked in 7 days at 290 MPa and for BC in 3 days at 321MPa.



### 3. Conclusions

The large scale use of sandcrete blocks construction in low cost housing in South Africa, necessitates a study to understand how sands can be stabilized to effect sufficient strength gain and efficiently. Sandcrete blocks gain most of their strength by soaking for 7 days when stabilized by plain cement. The replacement of 40% of the cement with Class F shortens the time required to gain strengths to 3 days for BC of 8-12%, while slightly improving the strength. The reuse of waste fly ash in stabilization is recommended to be practiced along with cement stabilization. This would enhance utilizing of local resources, improved energy management, reduced land disposal and environmental sustainability. Soaking the cubes with plain cement underwater for consecutive days produces higher strength than when it removed from the water in cycles. However, that increases the amount of water beyond that which is required for hydration process, resulting in weakly cemented sandcrete blocks. From the study, we can conclude that the quality of sandcrete blocks used for constructing low cost houses can be improved by curing them under water for 7 days, and the strength development can further be accelerated by replacing 40% of the cement with Class F Fly ash. Equation (1) with a coefficient of determination of 0.856 is proposed as an approximate expression to predict the compressive strength by SD and BC, which is defined for BC greater 6% and SD of 0 – 28days, to achieve minimum strength required for masonry units intended for wall building.

### Acknowledgements

The authors would like to acknowledge Mukovhe C Tshilande and Nozipho L Ngomane for their involvement in data collection.

### References

- [1] B.M. Das, *Principles of Geotechnical Engineering 7th Edition*, Cengage Learning, Stanford USA, 2009.
- [2] D.E. Ewa & J.O. Ukpata, Investigation of the compressive strengths of commercial sandcrete blocks in Calabar Nigeria, *International Journal of Engineering and Technology Vol3 No 4*, (2013), 477 – 482.
- [3] E. Green, Fact Sheet, [Web:] [http://www.bop.org.za/BOP\\_Lab/Publications\\_files/Reciprocity\\_iShack.pdf](http://www.bop.org.za/BOP_Lab/Publications_files/Reciprocity_iShack.pdf). [Date of access] November 2013
- [4] M.N. Anosike, A.A Oyebade, Sandcrete blocks and quality management in Nigeria Building Industry, *Journal of Engineering, Project and Production Management* (2012), 37–46.
- [5] S. Park, Effect of wetting on unconfined strength of cemented sands, *Journal of Geotechnical and Geoenvironmental Engineering* (2010), 1714 – 1720.

# Material science and nanotechnology

This page intentionally left blank

# Phase transitions and microstructural characterization of martensite in copper based shape memory alloys

O. ADIGUZEL<sup>1</sup>

*Firat University, Department of Physics, 23169 Elazig, Turkey*

**Abstract.** Shape memory effect is a peculiar property exhibited by certain alloy system, and shape memory behaviour is evaluated by the structural changes in microscopic scale. Shape-memory effect is based on martensitic transformation, which occurs on cooling from high-temperature parent phase region with the cooperative movements of atoms on {110}-type close-packed planes of parent austenite phase by means of shear-like mechanism. The material changes its internal crystalline structure with martensitic transition, and the ordered structure or super lattice structure is essential for the shape memory quality of the material. Copper based alloys exhibit this property in metastable  $\beta$ - phase field which has bcc-based high symmetric structure at high temperature parent state. These structures turn into non-conventional stacking ordered structure with low symmetry following two ordered reactions on cooling from high temperatures

**Keywords.** Martensitic transition, shape memory effect, twinning, detwinning, inhomogeneous shear, Bain distortion, layered structures.

## Introduction

A series of alloy systems exhibit a peculiar property which involves the repeated recovery of macroscopic shape of material at different temperatures. The origin of this phenomenon lies in the fact that the material changes its internal crystalline structure with changing temperature. The basis of this phenomenon is the stimulus-induced phase transformations, martensitic transitions, which govern the remarkable changes in internal crystalline structure of the materials [1-5]. In the shape memory alloys, the austenite lattice has a higher order of symmetry than that of martensite. Martensite variants have identical crystal lattice, but are oriented in different directions [2]. Shape memory alloys are easily deformed at low temperature martensitic phase, and recover the original shape on heating over the reverse transformation temperature.

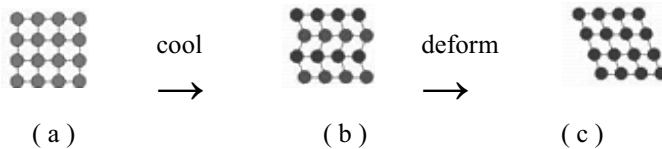
On the other hand, martensitic transformations have diffusionless character, and product martensite inherits the order of the parent phase [3, 4]. The martensitic transformation is a shear-dominant solid-state phase transformation, and, shape memory materials transform from the parent phase to one or more of the different variants of the martensitic phase in thermal induced manner [6, 7]. The variants of the martensite usually arrange themselves in a self-accommodating manner through twinning [6, 7].

<sup>1</sup>Corresponding author: [oadiguzel@firat.edu.tr](mailto:oadiguzel@firat.edu.tr)

The shape memory effect is based on martensitic transformation, and shape memory properties are intimately related to the microstructures of the material. In particular, orientation relationship between the various martensite variants has great importance [6, 7].

Twinning and detwinning processes can be considered as elementary processes activated during the transformation. These processes are responsible for shape memory effect, as well as martensitic transformation. In particular, the detwinning is essential as well as martensitic transformation in reversible shape memory effect [6, 7]. By applying external stress, the martensitic variants are forced to reorient into a single variant leading inelastic strains.

Deformation of shape memory alloys in martensitic state proceeds through a martensite variant reorientation or detwinning of twins. The basic mechanism of shape memory effect is schematically illustrated in Figure 1 [6]. As seen from this figure; the ordered parent phase turns into twinned martensite in thermal manner on cooling from high temperature, and the twinned martensites turn into the detwinned martensites or oriented martensites in stress-induced manner by applying external forces.



**Figure 1.** Schematic illustration of the mechanism of the shape-memory effect: (a) atomic configuration on  $\{110\}$ -type planes of parent austenite phase, (b) twinned martensite phase occurring thermally on cooling, (c) detwinned martensite occurring with deformation[6].

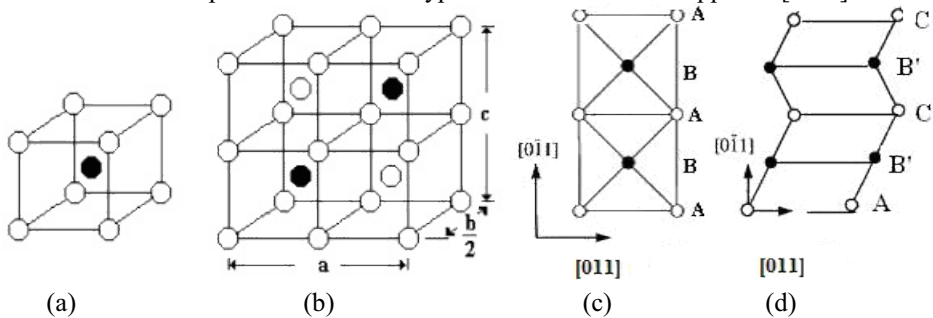
Copper-based alloys exhibit shape memory effect in metastable beta-phase region. Beta phases of copper-based alloys have the A2-type disordered structures at high temperatures and undergo the ordered structure with B2 or DO3 - type superlattice with disorder-order transition on cooling, and these ordered structures also transform into martensite with further cooling. The basic ordered  $\beta$ -phase structures are schematically illustrated in Figure 2 (a, b).

Martensitic transformations occur in a few steps in Copper-based alloys. The first one is Bain distortion and second one is lattice invariant shear. Bain distortion consists of an expansion of 26% parallel to the  $[001]$  - axis and a compression of 11% parallel to the  $[110]$  and  $[1\bar{1}0]$  directions. Lattice invariant shear occurs on a  $\{110\}$ -type plane of austenite matrix, which is basal plane of martensite. With these distortions, 9R (or 18R)-type layered structures occur in the material.

The  $\beta$ -type martensites have the layered structures which consist of an array of close-packed planes. Formation of the layered structures and sequence of  $\beta$  to 8R martensite transformation is shown in Figure 2 (c, d). The layered structures are characterized by the stacking sequences depending on the order in parent phase. Internally faulted martensites in Cu-Zn-Al alloys are characterized by a long period stacking order such as the 9R or 18R type structures, depending on the number of close-packed layers in the unit cell.

Copper based ternary alloys have the DO3 (or B2)-type superlattice prior to the transformation, and stacking sequence is  $AB'CB'CA'CA'BA'BC'BC'AC'AB'$  (18R) in martensitic case. Monoclinic distortion takes place in some cases and 18R structure is modified as M18R [4, 8]. It has been reported that the basal plane of 18R martensites

originates from one of the  $\{110\}\beta$  planes of the matrix and the inhomogeneous shear occurs on the basal plane in  $\langle 1\bar{1}0 \rangle$  - type directions and their opposite [8-10].



**Figure 2.** Basic ordered beta-phase structures; (a) CsCl-type unit cell (B2), (b)  $\text{Cu}_3\text{Al}$  - (DO3) - type unit cell; (c) stacking of  $(110)\beta$  planes viewed from  $[001]\beta$  direction, (d) inhomogeneous shear and formation of layered structures.

The  $\{110\}\beta$  planes have six special planes;  $(110)$ ,  $(1\bar{1}0)$ ,  $(101)$ ,  $(10\bar{1})$ ,  $(011)$ ,  $(0\bar{1}\bar{1})$ ; and 24 martensite variants with inhomogeneous shears different directions and different sides of these planes.

## 1. Experimental

Two copper based ternary shape memory alloys were selected for investigation; Cu-26.1%Zn 4%Al and Cu-11%Al-6%Mn (in weight). The martensitic transformation temperature of these alloys is over the room temperature and both alloys are entirely martensitic at room temperature. Specimens obtained from these alloys were solution treated for homogenization in the  $\beta$ -phase field (15 minutes at  $830^\circ\text{C}$  for the Alloy 1 and 20 minutes at  $700^\circ\text{C}$  for the Alloy 2), then quenched in iced-brine to retain the  $\beta$ -phase and aged at room temperature after quenching (both alloys).

Powder specimens for X-ray examination were prepared by filling the alloys. These specimens were then heated in evacuated quartz tubes at  $830^\circ\text{C}$  for 15 minutes and immediately quenched into iced-brine for homogenization. X-ray diffraction profiles were taken from the quenched specimens using Cu- $K\alpha$  radiation with wavelength  $1.5418 \text{ \AA}$ . The scanning speed of the Geiger counter was chosen as  $2^\circ$ ,  $20/\text{min}$  for the diffractograms.

Specimens for TEM examination were prepared from 3mm diameter discs and thinned down mechanically to 0.3mm thickness. These specimens were heat-treated for homogenization at  $830^\circ\text{C}$  for 15 minutes and quenched into iced-brine to obtain  $\beta$ -type martensite. The quenched disc-shaped specimens were electropolished in a Struers Tenupol-2 instrument at  $-20^\circ\text{C}$  in a solution of 20% nitric acid in methanol, and examined in a JEOL 200CX electron microscope operated at 160 kV.

## 2. Results and discussion

When the copper based beta-phase alloys are cooled below a critical temperature called martensite start temperature,  $M_s$ , the martensitic transformation occurs and martensite

forms as plates in groups of variants. It enables the shape memory alloys to deform under low stresses by variant coalescence because the total shape change on transformation becomes nearly zero for the group [6]. Product martensite phase including 24 variants undergoes the single crystal of martensite by means of reorientation mechanism on stressing in martensitic condition, and deformed single crystal of martensite undergoes the single crystal of parent phase as a reverse transformation on heating over the austenite finish temperature. This single crystal retransform to the 24 martensite variants on cooling below Ms. The mechanism of this formation has been given elsewhere [9,10]. On the other hand, a single variant can not have a coherent interface with the austenite. However a region consisting of fine twins of two martensitic variants can form a coherent interface with the parent austenite [11]. It has been reported that some copper based ternary alloys (cubic  $\rightarrow$  monoclinic transformation) exhibit an undeformed interface between austenite and a single variant of martensite [12].

A typical X-ray powder diffraction profile taken from CuZnAl alloy specimen in as-quenched case is shown in Figure 3. This diffractograms which exhibits superlattice reflection has been indexed on the monoclinic M18R basis. Two electron diffraction patterns taken from the quenched samples of CuZnAl and CuAlMn Alloys are also shown in Figure 4. Both X-ray diffractograms and electron diffraction patterns reveal that both alloys exhibit superlattice reflections.

A series of x-ray diffractograms have been taken from both of the alloy samples in a long time interval and some changes in peak characteristics on the diffractograms with aging duration have been observed. Although all of the diffractograms exhibit similar properties, it was observed that peak locations of some diffraction planes have changed. In particular, some of the successive peak pairs have moved toward each other.

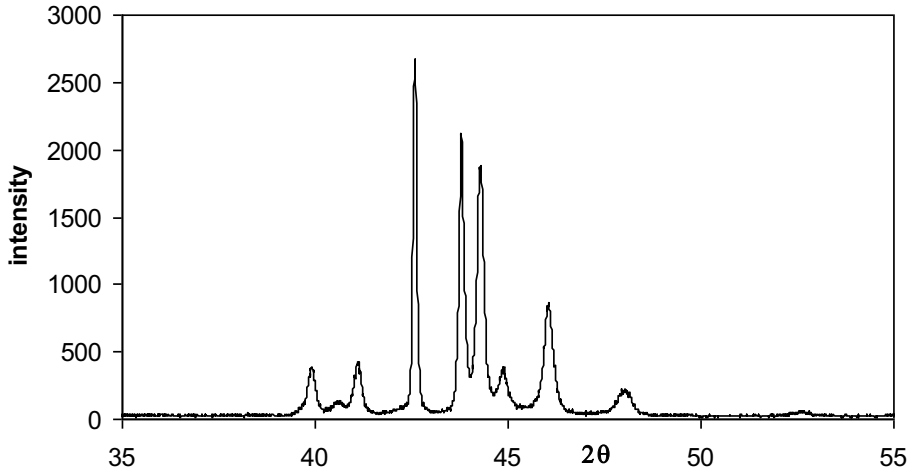
It is interesting that miller indices of these plane pairs provide a special relation;

$$\left(h_1^2 - h_2^2\right) / 3 = \left(k_2^2 - k_1^2\right) / n$$

where  $n=4$  for 18R martensite [4]. These plane pairs can be listed as follow; (122)-(202), (128)-(208), (1 2 10) – (2 0 10), (040)- (320). This observation can be attributed to a relation between interplane distances of these plane pairs. When the martensite is transformed from the parent phase with differently ordered states such as B2 or DO3, the close-packed plane may consist of atomic sites with different sizes due to the ordering arrangement. The different sizes of atomic sites lead to a distortion of the close-packed plane from an exact hexagon and thus a more close-packed layered structure may be expected.

The martensitic phase in copper-based  $\beta$ -phase alloys is based on one of the  $\{110\}\beta$  planes of parent phase called basal plane for martensite. The lattice invariant shears occurs, in two opposite directions,  $\langle 110 \rangle$ -type directions on the  $\{110\}$ -type planes of austenite matrix.  $\{110\}$ - plane group has the following planes; (110), (1  $\bar{1}$ 0), (101), (10 $\bar{1}$ ), (011) and (01 $\bar{1}$ ). With the lattice invariant shears in two opposite directions on both sides of these planes, 24 martensite variants occur. On the other hand, (110) – type planes of the parent phase have rectangular shape in original case, and these planes turn into hexagon with hexagonal distortion. The detailed explanation and illustration related to these distortions has been given elsewhere [4]. Structural ordering is one of the important factors for the formation of martensite, and atom sizes have an important effect on formation of ordered structures [9, 10].

The martensite basal plane  $(110)\beta$  has an ideal hexagonal form in case atom sizes of alloying elements are equal, and it undergoes a hexagonal distortion in case atom sizes are different.



**Figure 3.** An x-ray powder diffractogram of CuZnAl alloy.

In the disordered case, lattice sites are occupied randomly by different atoms, and the basal plane becomes ideal hexagon taking the atomic sizes approximately equal. In the ordered case, sub-lattices are occupied regularly by certain atoms which have different atomic sizes, and basal plane undergoes a hexagonal distortion owing to the differences in atom sizes.

Metastable phases of copper-based shape memory alloys are very sensitive to the ageing effects, and any heat treatment can change the relative stability of both martensite and parent phases. Martensite stabilization is closely related to the disordering in martensitic state. Although martensitic transformations are diffusionless, the transitions occurring during the ageing in the martensitic condition have a diffusive character because this transition requires a structural change and this also gives rise to a change in the configurational order.



**Figure 4.** Electron diffraction patterns taken from CuZnAl and CuAlMn alloy samples



### 3. Conclusion

On the basis of austenite-martensite relation, the basal plane of 9R (or 18R) martensite originates from one of the  $\{110\}$ - planes of the parent phase, which have six different planes, and inhomogeneous shears occur in two opposite directions. The basal plane of martensite is subjected to the hexagonal distortion by means of Bain distortion with martensite formation on which atom sizes have important effect. In case the atoms occupying the lattice sites have the same size, the basal plane of martensite becomes regular hexagon. Otherwise the deviations occur from the hexagon arrangement of the atoms in case atom sizes are different. In the light of this knowledge, the atom sizes can be taken approximately equal, in the disordered lattice case, and basal plane becomes nearly ideal hexagon. In the superlattice case, the sizes of atoms occupying the hexagonal lattice sites are different, and the hexagon deviates from regular one.

In conclusion, the changes in the location of the above mentioned plane pairs reveal the rearrangements of the atom in displacive manner; and this result provides us information on the degree of ordering in the martensitic state of the material.

### References

- [1] R.D. James and K.F. Hane, Martensitic Transformations and Shape Memory Materials, *Acta Materialia* 48 (2000), 197- 222.
- [2] J.J. Zhu and K.M. Liew, Description of Deformation in Shape Memory Alloys from DO3 Austenite to 18R Martensite by Group Theory, *Acta Materialia* 51 (2003), 2443-2456.
- [3] J. Pons, et al., Crystal Structure of Martensitic Phases in Ni-Mn-Ga Shape Memory Alloys, *Acta Materialia* 48 (2000), 3027-3038.
- [4] O. Adiguzel, Smart Materials and the Influence of Atom Sizes on Martensite Microstructures in Copper-Based Shape Memory Alloys, *Journal of Materials Processing Technology* 185 (2007), 120-124.
- [5] Y. Sutou, et al., Effect of Grain Size and Texture on Pseudoelasticity in Cu-Al-Mn-Based Shape Memory Wire, *Acta Materialia* 53 (2005), 4121-4133.
- [6] J. Ma, I. Karaman and R.D. Noebe, High Temperature Shape Memory Alloys, *International Materials Reviews* 55 (2010), 257-315.
- [7] Y. Liu, Detwinning Process and Its Anisotropy in Shape Memory Alloys, Smart Materials, *Proceedings of SPIE* 4234 (2001), 82-93.
- [8] T. Uhera and T. Tamai, An Atomistic Study on Shape Memory Effect by Shear Deformation and Phase Transformation, *Mechanics of Advanced Materials and Structures* 13 (2006), 197-204.
- [9] Y.F.Guo et al., Mechanisms of Martensitic Phase Transformations in Body-Centered Cubic Structural Metals and Alloys: Molecular Dynamics Simulations, *Acta Materialia* 55 (2007), 6634-6641.
- [10] A. Aydogdu, Y. Aydogdu, O. Adiguzel, Long-Term Ageing Behaviour of Martensite in Shape Memory Cu-Al-Ni Alloys, *Journal of Materials Processing Technology* 153-154 (2004), 164-169.
- [11] C. Lexcelent, P. Blanc, Phase Transformation, Yield Surface Determination for Some Shape Memory Alloys, *Acta Materialia* 52 (2004), 2317- 2324.
- [12] K.F. Hane, Bulk and Thin Film Microstructures in Untwined Martensites, *J. Mech. Phys Solids* 47 (1999), 1917-1939.

# Using carbon nanotubes in self-compacting paste systems

Afshan NAZ<sup>a</sup>, Syed Ali RIZWAN<sup>a,1</sup>, Naveed Z. ALI<sup>b</sup>, Thomas A. BIER<sup>b</sup>  
and Hameed ULLAH<sup>a</sup>

<sup>a</sup>*Department of Chemistry, Hazara University, Mansehra, Pakistan*

<sup>a</sup>*Structural Engineering Dept, National Univ of Sciences & Tech, Pakistan*

<sup>b</sup>*National Centre for Physics, Islamabad, Pakistan*

<sup>b</sup>*Construction Materials Technology, IKGB, Technical Univ. Freiberg, Germany*

**Abstract.** Dispersions of carbon Nanotubes (CNTs) with different surfactants were prepared and were used in self-compacting paste (SCP) systems with a view to observe improvement in their response under fresh and hardened state. Different surfactants were tried and the better ones were used on the basis of dispersion time of CNTs solutions and other properties compatible with those of SCP systems. The flow and strength response of SCP system using CNTs dispersed in solution of acacia gum obtained from a plant in Pakistan showed an overall improved performance in terms of strength gain due to CNTs dispersed solutions.

**Keywords.** Carbon nanotubes, self-compacting paste systems, microstructure and super-plasticizer demand

## Introduction

Secondary raw materials (SRMs) and chemical admixtures have been used by many researchers in self-consolidating cementitious systems to achieve enhanced strength, economy, durability and environment friendliness [1]. Self-compacting concrete (SCC) is a new technology and is defined by ACI 237R – 07 as “a highly flow-able, non-segregating concrete that can spread into place, fill the formwork, and encapsulate the reinforcement without any mechanical consolidation. Nanotechnology is yet again a new technology and use of Carbon Nanotubes (CNTs) in cementitious systems has attracted the researchers due to its excellent potential as reinforcement in a wide range of composite systems and exciting intrinsic mechanical and other functional properties [2-5]. Raw carbon Nanotubes are strongly hydrophobic due to high Van der Waals forces and hence are not dispersible in aqueous solution [6]. Covalent and non-covalent modifications are used for obtaining dispersed Carbon Nanotubes solutions. In covalent modification, chemical attachment of the groups occurs to the Nanotubes while in non-covalent approach there is adsorption of the groups on the surface of the Nanotubes [7].

---

<sup>1</sup>Corresponding author: Structural Engineering Department, NICE/National University of Sciences and Technology H-12, Islamabad, [syedalirizwan@hotmail.com](mailto:syedalirizwan@hotmail.com)

Introducing CNTs dispersed solutions to cement matrix reduces the crack initiation and propagation [8] and results in improved post cracking response and reduced crack widths. These aspects add to ductility and durability of cement based composites. Nano-Carbons [9] mostly CNTs have been used by researchers to enhance the tensile strain of cement based composites due to its higher Young's modulus and tensile strength. CNTs also exhibit elastic behavior [10] and show excellent thermal properties [11]. CNTs can act as fillers to produce a denser, less porous material. The similar kind of role is also played by secondary raw materials [12]. It is believed that CNTs produce more high density C-S-H gel [13], thus impart higher strengths which may indirectly reduce shrinkage.

## 1. Experimental

### 1.1 Characterization and dispersion of carbon nanotubes

Multi walled Carbon Nanotubes (MWCNTs) were obtained from a local organization. Acacia gum, a common *ooze-out* of the local acacia tree in Pakistan, was selected after trials for dispersion of CNTs in water after sonication. Carbon Nanotubes were characterized by Ultra-violet visible spectroscopy using Perkin Elmer spectrophotometer for the evaluation of the degree of dispersions of different surfactants while Fourier transformed infrared spectroscopy was used to depict the functional groups attached with Carbon Nanotubes. Scanning electron microscopy was used for particle characterization and surface morphology of CNTs and x-ray diffraction was used to ascertain the phase purity and the nature of CNTs. Size of CNTs was analyzed by particle size analysis. As received MWCNTs were taken and functionalized firstly by using  $\text{HNO}_3$  and  $\text{H}_2\text{SO}_4$ . Acid functionalization of CNTs was confirmed by FTIR analysis. As MWCNTs were to be used in cement based composites, amino acids and surfactants were used for debundling of carbon Nanotubes [14]. Surfactants including Sodium dodecyl sulfate (SDS), Triton X-100, Triton X-45, Cetyltrimethyl ammonium 4 vinyl bromide (CTAB) and acacia gum (AG) were used. SDS, CTAB and Acacia gum showed good dispersibility. Finally for preparing self-compacting paste samples as per EN196, local acacia gum 1:1 weight per cent of AG and CNTs was selected while with CTAB this ratio was 1:10. Literature suggests that sodium dodecyl sulfate may hinder in the development of the desired properties of cement matrix [14]. Moreover CTAB based SCPs showed low strength and significant surface foaming so it has not been finally recommended for making self-compacting paste systems.

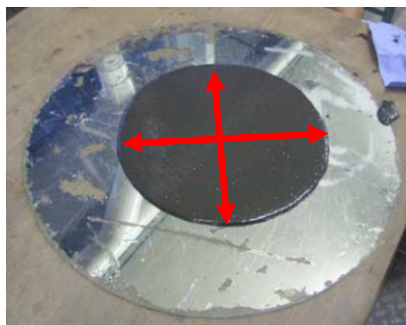
### 1.2 Fabrication of self-compacting paste systems

Carbon Nanotubes, Acacia gum (AG), CTAB, ordinary Portland cement having brand name of Bestway of grade 43 and Melflux 2651F super plasticizer of BASF was used to make samples of self-compacting paste samples having size of  $4 \times 4 \times 16 \text{ cm}^3$ . Flow was measured by Hagerman's  $6 \times 7 \times 10 \text{ cm}^3$  mini-slump cone. The flow target was  $30 \pm 1 \text{ cm}$ . The flow test measured T25 cm [12] and T  $30 \pm 1 \text{ cm}$  time in addition to total flow values. This was followed by compressive strength tests as per EN 196. Both control and those having functionalized CNTs self-compacting cement paste samples were

prepared at the systems water demand of 26.5%. These were water cured after demoulding at the age of one day and were tested for strength at 3, 7 and 28 days of age in saturated surface dry (SSD) condition as per EN 196. Flow test was done on self-compacting pastes using Hagerman's mini-slump cone apparatus as shown in Fig 1(a). Flow is defined as the average of two orthogonal diameters of a spread formulation shown in Fig. 1(b). T 25cm time is a flow time that a SCP formulation takes to reach a spread of 25 cm [18]. Similarly T 30 cm time is the time taken by the formulation to reach a spread of  $30\pm 1$  cm.



**Figure 1(a).** Hagerman's mini-cone flow apparatus [18]



**Figure 1(b).** Flow spread after removal of cone [18]

## 2. Results and discussions

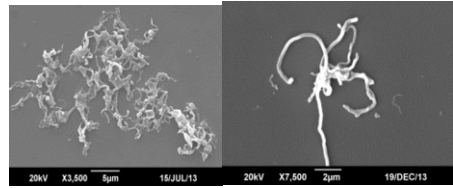
### 2.1 Dispersions of CNTs

Different dispersions of Carbon Nanotubes prepared were left in test tubes at room temperature to check their dispersibility. Carbon Nanotubes were sonicated for different periods of time to check the effect of sonication time on dispersions which was thereafter measured by characterization tools. Fig 2 shows different de-agglomerated Carbon Nanotubes after 6 months. It is evident that acid functionalized and also surfactant treated Carbon Nanotubes showed good dispersibility. After preparing these dispersions, self-compacting cement paste specimens were prepared and tested to see the strength enhancement due to CNTs with respect to water based control formulation.



[A] [B] [C]

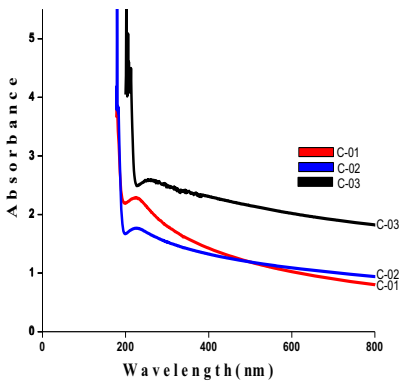
**Figure 2.** Functionalized CNTs with acid(A), Acacia gum (B), Amino acids(C)



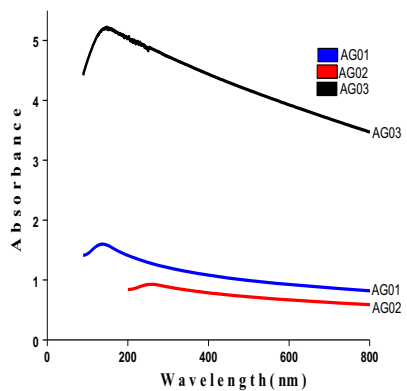
(a) Pristine CNTs (b) Dispersed CNTs

**Figure 3.** SEM images of CNTs-Non-functionalized (a) and functionalized (b)

Scanning electron microscopy of pristine and dispersed CNTs was done to check its morphology. From the SEM images it is clear that the CNTs have been debundled in acids and different surfactants as shown in Fig 3. UV measurements of various dispersions were taken for maximum absorption and are shown in Fig 4 and 5 respectively.



**Figure 4.** UV spectra of CTAB



**Figure 5.** UV spectra of acacia gum

Raw CNTs are normally non-active in characteristic UV visible region due to quenched photoluminescence tunneling between the Nanotubes [15-16] whereas CNTs as individual tubes in dispersions will give characteristic peaks, shown in Fig 3 and 4, in the corresponding wavelength region attributed to additional absorption due to 1D Van Hove singularities [17]. Maximum wavelength for CTAB and acacia gum dispersions were measured at 250-260 nm which illustrate its stability and optimum concentrations for further study in self-compacting cement paste systems.

## 2.2 Flow test

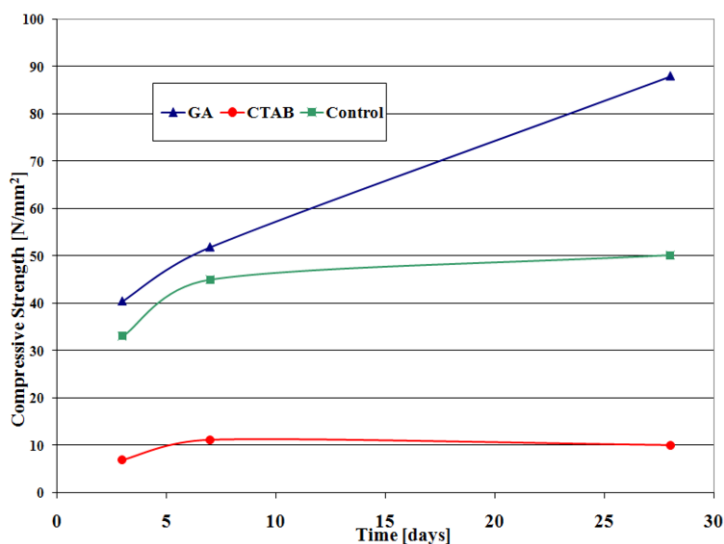
**Table 1.** Shows the flow properties of control and functionalized SCP formulations

SCP Formulation	Cement (gm)	Water (gm)	SP Demand (%)	T25 cm (sec)	T 30±1 cm (sec)
Control	750	199	0.15	2.18	14.09
With AG	750	199	1.0	5.03	20.78
With CTAB	750	199	0.16	7.88	22.98

The results show that SCP systems made with CTAB functionalized solution, the flow times are more probably because of the higher concentration of CTAB functionalized solution than that of AG functionalized solution.

## 2.3 Compressive strength

CTAB composites of SCP showed a poor result for its strength. SCP formulations made with water and AG dispersions as shown in Fig 6. It is clear from Fig 6 that the strength of SCP system increases with the addition of carbon Nanotubes dispersions.



**Figure 6.** Age strength relation of SCP Systems (Control and those based on AG and CTAB dispersions)

### 3. Conclusions

1. Good dispersion of CNTs can be obtained by using locally available acacia gum powder, which is a complex material of poly saccharides and oligo saccharides, as surfactant solution. Same comment regarding dispersion is true for CTAB.
2. CTAB functionalized solution, when used in SCP systems, may achieve correct flow values at proper solution concentration, however at higher concentrations as used in this study resulted in higher flow times.
3. Functionalized CNTs dispersions with AG used in self-compacting paste systems enhanced the compressive strength significantly.
4. SCP samples made with CTAB functionalized solution at 1:10 concentration showed poor strength as compared to even control samples possibly due to higher solution concentration. Surface foaming was observed in fresh state, however, in hardened state samples looked normal.
5. In order to clarify the mechanisms of strength increase, additional experiments involving phase and porosity development with time are needed.

### References

- [1] Rizwan, S.A and .Bier, T.A.,” Blends of limestone powder and fly ash enhance the response of self-compacting mortars”, *Construction and Building Materials* **27** (2012) 398-403
- [2] Thostenson ET, Ren ZF, Chou TW , Advances in the science and technology of carbon Nanotubes and their composites: a review, *Composites Science and Technology*, **61** (2001) 1899-1912
- [3] Shaffer MSP, Sandler JKW (2006) In: Processing and properties of Nano-composites, *World Scientific*, Singapore,
- [4] Lau KT, Hui D (2002) *Compos B Eng* 33(4):263
- [5] Harris PJ., Carbon Nanotubes and related structures, *Cambridge University Press*, Cambridge (2002).
- [6] I .Capek, Dispersions, novel nonmaterial sensors and nanoconjugates based on carbon Nanotubes, *Advances in Colloid and Interface Science* **150** (2009 ) 63–89. ELSEVIER.
- [7] Li Zhang , Qing-Qing Ni ,, Yaqin Fu , Toshiaki Natsuki One-step preparation of water-soluble single-walled carbon Nanotubes, *Applied Surface Science* **255** ,(2009,) pp7095–7099. ELSEVIER.
- [8] G. Ferro, J.M. Tulliani, S. Musso, carbon nano tubes cement composites, ( 2011) 49-59
- [9] Raki L, Beaudoin J, Alizadeh R, Makar J, Sato T. Cement and concrete nanoscience and Nanotechnology, *Materials* **3** (2010),918–42.
- [10] Walters DA, Ericson LM, Casavant MJ, Liu J, Colbert DT, Smith KA, Elastic strain of freely suspended single-wall carbon nanotube ropes, *ApplPhysLett* **74** (1999), 3803–5.
- [11] See CH, Harris AT. A review of carbon nanotube synthesis via fluidized-bed chemical vapor deposition, *IndEngChem Res* **46** (2007), 997–1012.
- [12] Rizwan.S.A and Bier,T.A., Self-Compacting Mortars using Various Secondary Raw Materials, *ACI Material Journal*, vol **106**, No.1,Jan-Feb 2009, pp 25-32.
- [13] Konsta-Gdoutos MS, Metaxa ZS, Shah SP. Highly dispersed carbon nanotube reinforced cement based materials, *Cem Concr Res* **40** (2010)1052–9.
- [14] Surendra P. Shah, Maria S. Konsta-Gdoutos, Zoi S. Metaxa/ US patent, Highly dispersed carbon nanotubes-reinforced cement-based materials, *Pub no.US 2009/0229494 A1*
- [15] Junrong Yu , Nadia Grossiord , Cor E. Koning , Joachim Loos , *Carbon* **459** (2007) 618–623.
- [16] Laurent Js, Voisin C, Cassabois G, Delalande C, Roussignol P, Jost O, *Phys Rev Lett* **90**(2003):057404-1–4,
- [17] N Hamada, Sawada S, Oshiyama A. New One-Dimensional Conductors: Graphitic Microtubules, *Phys Rev Lett*;**68**, (1992)1579–81.
- [18] Rizwan,S.A., High Performance Mortars and Concretes Using Secondary Raw Materials- *PhD thesis, TU Freiberg*, 2006. Germany. ISBN 978-3-639-17878-4,VDMVerlag Dr.Muller, Germany.

# Influence of the characteristic of input materials on formation and properties of sintered fly ash body

Vit CERNY<sup>1</sup> and Rostislav DROCHYTKA

<sup>1</sup>Faculty of Civil Engineering, Brno University of Technology, Czech Republic

**Abstract.** Artificial aggregate from sintered fly ash is an example of material, which can be used solely on the basis of fly ash without any additions. However, to ensure optimal progress of firing and high quality aggregate, it is necessary to study influence of the characteristic of fly ash on properties of fly ash body. The aim of the research work is evaluation of influence of characteristic of fly ash on formation, structure and properties of sintered fly ash body using laboratory firings of testing samples and also using the heating microscopy. The main difference as regards behavior is between fly ash originating from high temperature and fluidized bed combustion. While the first type of fly ash contains mainly mullite and other high temperature minerals, fluidized bed combustion fly ash contains mainly anhydrite and free lime. These increase for example manipulation strength of fly ash mix, but they also increase the amount of mixing water, emissions, content of extractable sulphur and weaken the sintered fly ash body.

Content of  $\text{Fe}_2\text{O}_3$  and its modifications and proportion of  $\text{SiO}_2$  in amorphous phase or mullite are important parameters for evaluation of various types of high temperature combustion fly ash. Content of  $\text{Fe}_2\text{O}_3$  together with carbon caused reduction to  $\text{FeO}$ , which consequently works as a very effective fluxing agent. Thus, the surface of the specimen was sintered and swelling was considerable due to product gases  $\text{CO}$  and  $\text{CO}_2$ . After exceeding the melting point, melting begins. Higher proportion of  $\text{SiO}_2$  contained in amorphous phase increase strength and quality of fly ash body.

**Keywords.** Fly ash, power plant, artificial aggregate, clinkering

## Introduction

European and world trends in new technology development in the building industry make a sustained pressure on provision of production of quality light artificial aggregates, its application has a rising trend namely in advanced countries. Only Poland in Central and Eastern Europe reacted to this trend by construction of a factory for artificial aggregates production from sintered fly ash in Gdansk, the factory is equipped by license process equipment from Lytag, UK. However, the technology level of this production process is even older than the Corson technology.

---

<sup>1</sup> Corresponding author: Institute of Technology of Building Materials and Components, Faculty of Civil Engineering, Brno University of Technology, Czech Republic, cerny.v@fce.vutbr.cz, tel. +420 541 147 463, fax. +420 541 147 502.



The production technology of artificial aggregates by burning are frequently operated in original format using quality black coal fly ash containing optimal amount of unburned residues and without necessary correction of the fuel. There is no competition within this field in the world and thus the involved companies do not dedicate to development and innovations. On that ground the questions of artificial aggregates from sintered fly ash are relatively lowly explored and only minimum scientific work dedicated to the process of production of fly ash body creation at burning exist. Therefore if we consider the possibility to restoration of the production in inland conditions it is necessary not only to innovate the existing technology but also in particular to dedicate to study of reaction processes in solid phase and creation of fly ash aggregates.

## **1. Characterization of tested ashes**

To present characteristic of fly ash produced in the Czech Republic, following samples were selected: there is sample of fly ash produced by high temperature combustion of black and brown coal as well as fly ash from fluidized bed combustion. Here, it is necessary to repeat that high temperature ash are produced during combustion of ground coal at temperatures of 1200 – 1600 °C, desulphurization takes place after separators by means of lime solution. Fluidized bed combustion takes place at temperatures around 850 °C; desulphurization is located directly in the furnace by means of combustion lime together with coal. [1] High quality fly ash from anthracite (FA) and brown coal fly ashes are also represented (BFA1 and BFA2). There is also one sample of fly ashes produced by brown coal fluidized bed combustion technology (FBC). There is the same coal base as BFA2.

### *1.1. Physico-mechanical and physico-chemical parameters*

Physico-mechanical and physico-chemical parameters are very important for basic evaluation of fly ash. Following parameters were selected: loss of ignition showing unburned residues, bulk density and specific gravity, showing density of fly ash and specific surface area, which is a complement for screen analyses. Following table shows test results of individual samples of fly ash.

**Table 1.** Parameters of tested ashes

	Loss of ignition [%]	Bulk density [kg.m <sup>-3</sup> ]	Specific gravity [kg.m <sup>-3</sup> ]	Specific surface area [m <sup>2</sup> .kg <sup>-1</sup> ]	Rest on the sieve 0.063 mm [%]
FA	1.26	1190	2250	359	30.2
BFA1	1.07	1110	2160	224	64.5
BFA2	1.19	990	1992	329	48.8
FBC	2.08	770	2189	352	47.7

Analysis of unburned residues in tested fly ash shows that all samples fulfill the requirements of the standard CSN 72 2072-6 [4] for maximal loss on ignition maximally 15%. Determination of bulk density shows that fly ash from high temperature combustion reach higher values than fly ash from fluidized bed combustion. All values of high temperature fly ash samples and bottom ash fulfill the requirements of the Standard CSN 72 2072-6 [4] form minimal value of loose bulk weight 600 kg.m<sup>-3</sup> and tapped 800 kg.m<sup>-3</sup>. Evaluation results of determination rest on the 0.063 mm sieve shows that the finest ashes are FA1 and FBC. Evaluation results of determination rest on the 0.063 mm sieve shows that the finest ashes is the sample marked FA1. By using the fly ash BFA1 it will be probably made less solid structure of ash body.

### 1.2. Chemical and mineralogical analysis of the samples

Chemical and mineralogical analyses were selected for the main comparison of the characteristics of the tested samples. As far as the physical-mechanical properties are concerned, those were not evaluated in this section.

**Table 2.** Chemical composition of tested ashes

	Chemical composition [%]								
	SiO <sub>2</sub>	Al <sub>2</sub> O <sub>3</sub>	Fe <sub>2</sub> O <sub>3</sub>	SO <sub>3</sub>	CaO	MgO	K <sub>2</sub> O	Na <sub>2</sub> O	P <sub>2</sub> O <sub>5</sub>
FA	58.20	27.30	7.06	0.43	<b>6.04</b>	2.62	<b>3.21</b>	0.55	0.46
BFA1	47.60	25.00	<b>12.70</b>	0.54	2.29	1.37	1.35	0.33	1.23
BFA2	47.70	28.20	5.61	0.13	1.10	0.81	1.04	0.23	0.14
FBC	42.70	26.80	5.05	<b>2.98</b>	<b>10.20</b>	0.86	0.86	0.35	0.18

It is obvious that BFA1 may behave differently during firing than the other representatives of fly ashes due to increased Fe<sub>2</sub>O<sub>3</sub>. Fly ash from black coal combustion has slightly higher content of Fe<sub>2</sub>O<sub>3</sub> and also CaO. In the interaction with the K<sub>2</sub>O it can cause faster sintering of the sample or its surface. Fluidized bed ashes will be affected during annealing by a higher percentage of CaO and SO<sub>3</sub>.

## 2. Sample annealing test

In order to monitor the behavior of the samples during the firing process, a special type of picture-analysis was chosen. Cylinders of about 2x3 mm in cross-section were made of the samples. They were placed into an annealing chamber equipped with a camera

and backlight to capture changes in the sample cross-section during annealing. Current temperature and changes to the sample cross-sectional area were primarily recorded. Figure 1 shows the changes to the sample cross-sectional area during gradual annealing of the samples. There is noticeable shrinkage, subsequent swelling, to the final melting of some of them.

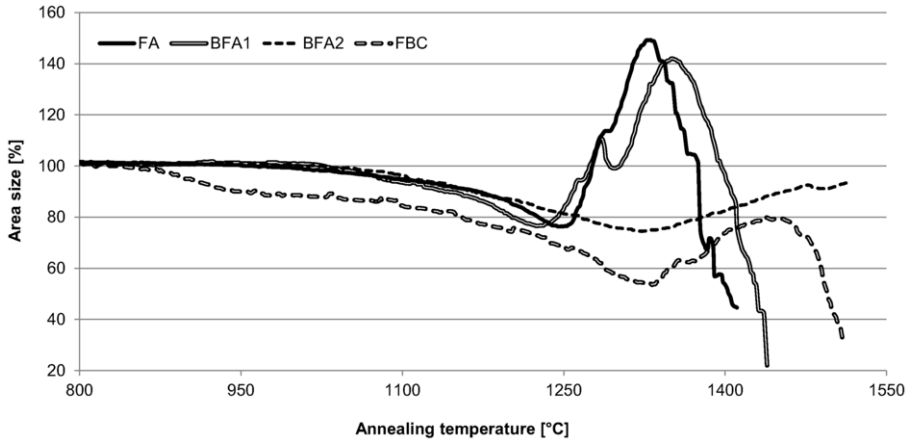


Figure 1. Changes to the sample cross-sectional area during annealing

The graphs confirm the previous assumptions. The samples (FA and BFA1) with a higher content of fluxes went through a certain sintering phase, followed by swelling caused by generated gases. The content of  $\text{Fe}_2\text{O}_3$  (BFA1), together with the carbon, causes the reduction to FeO, which then functions as a highly effective flux. [2] This leads to the sintering of the sample surface and subsequent significant swelling caused by generated gases CO and  $\text{CO}_2$ . After crossing the melting point, melting follows. Annealing of fluid fly ash is significantly affected by the presence of  $\text{CaSO}_4$ ,  $\text{CaCO}_3$  or CaO alone. The first two minerals show their degradation during firing and the subsequent percentage of CaO significantly lowers the melting point of the other minerals.

The following images show the main stages of annealing the selected fly ash samples.

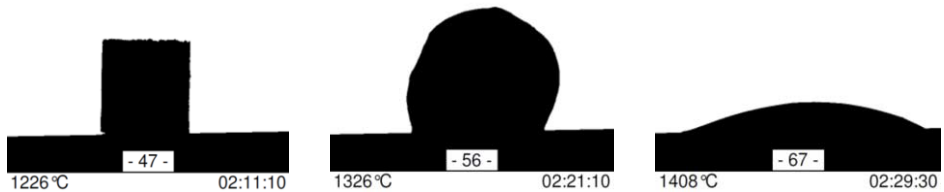


Figure 2. Sample FA at maximum sintering, swelling and melting

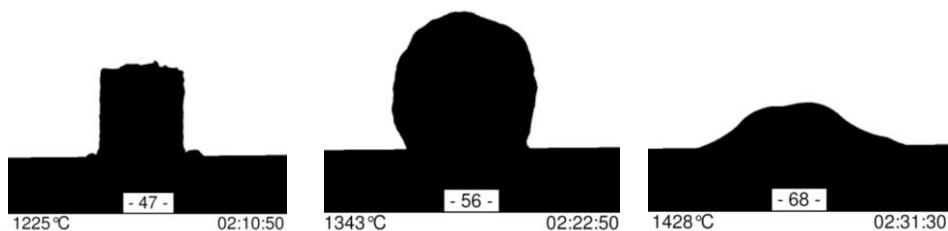


Figure 3. Sample BFA1 at maximum sintering, swelling and melting



Figure 4. Sample BFA2 at maximum sintering and maximum swelling at the end of the test

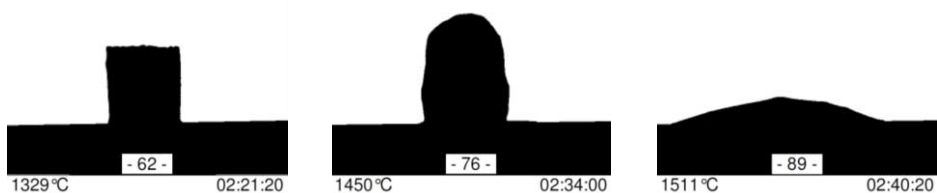


Figure 5. Sample FBC at maximum sintering, swelling and melting

Figure 2 and Figure 3 show the main states of the samples (FA and BFA1) cross-section from the maximum sintering, through swelling to the final melting moment. Figure 4 shows much better progress of annealing of the sample BFA2, which has no swelling or melting phase and is much stable. Figure 5 shows much similar progress of the sample (FBC) cross-section as you can see by the samples FA and BFA1. However, the sample FBC has lower swelling and the melting moment about 70 °C higher.

### 3. Firing tests

For better comparison of quality next artificial aggregate were made some samples (20x20x100 mm) from testing ashes. For preparing of these samples were the ashes mixed with some content of water. It was found that FBC ash due to the characteristic of the structure and chemical composition needs twice more water content as the fly ashes for the same consistency. The samples were fired 24 hours after the mixing. The temperature was set on 1150 °C, the growth rate of temperature was 600 °C per hour and the isothermal holding time was 10 minutes. It can better simulate the clinkering

process in the technology furnace. In the Figure 6 you can see the results of compressive strength of the samples.

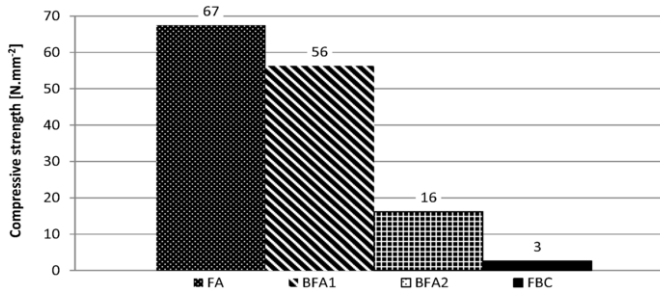


Figure 6. Compressive strength of the samples

As you can see in the Figure 6, the samples FA and BFA1 have the highest strength. The fluxes help them to get more solid structure. The sample BFA2 needs higher temperature to get more solid. The sample FBC fails to create a solid and regular structure ash body due to the higher proportion of CaO and sulphates.

#### 4. Summary

The paper showed the influence of fly ash characteristic on its behaviour during clinking process. The higher percentage of Fe<sub>2</sub>O<sub>3</sub>, CaO and sulphates in fly ash significantly affects its stability during the clinking process. Content of fluxes increases the sintering and swelling of the ashes and by the temperatures more than 1400 °C causes melting of the samples. If there is use the firing temperature 1150 °C get these samples solid structure. Fly ash without fluxes (like Fe<sub>2</sub>O<sub>3</sub>) needs the higher temperature than 1150 °C to get higher strength. However, it is more stable by the annealing process and does not swelling or melting. Higher content of CaO and sulfur causes, that the FBC ashes get no solid structure and it is not stable.

#### Acknowledgements

This paper was elaborated with the financial support of the Czech Science Foundation Project P104-13-30753P "Study of the process of creating fly ash body" and the European Union's "Operational Programme Research and Development for Innovations", No. CZ.1.05/2.1.00/03.0097, as an activity of the regional Centre AdMaS "Advanced Materials, Structures and Technologies".

#### References

- [1] J. Hlavac, *Zaklady technologie silikatu*, SNTL, Bratislava, Slovakia, 1988. (in Czech)
- [2] R. Sokolar, *Keramika*, Publishing house VUTIUM, Brno, Czech Republic, 2006. (in Czech)
- [3] C.L. Verma, S.K. Handa, S.K. Jain, R.K. Yadav, *Techno-commercial perspective study for sintered fly ash light-weight aggregates in India*, Construction and Building Materials, 12, 341-346. 1998
- [4] ČSN 72 2072-6, *Fly ash for building industry purposes - Part 6: Fly ash for the production of artificial aggregates by clinking*, Czech Standards Institute, Prague, 2013.

# Thin spray rock liners with different concentrations of nanoclays

P van TONDER<sup>1</sup> and CJ BOOYSEN

*Department of Civil Engineering Science, University of Johannesburg*

**Abstract.** This study investigates the possibility of effectively replacing polymers in thin sprayed liners (TSL's) with nanoclay particles. In the industry Nano particles are used in many different products to enhance their properties. The strength properties was analysed to see if the addition of nanoclays improve the strengths of the TSL product. Different concentrations of nanoclay were added to a standard TSL mixture in the place of polymer particles. The different composites were tested for Tensile Strength, Compression Strength, Shear Strength and Shear Bond Strength. Though there are other parameters to be tested, the study will only focus on those mentioned above, as they were considered to be the most important. The materials used for testing these characteristics were supplied by Oxyfibre. The mixtures have consisted of four different composites that included the standard mixture, 2% nanoclays, 4% nanoclays and 6% nanoclays.

**Keywords.** Nanoclays, thin spray rock liner, compressive strength, tensile strength, shear strength, shear bond strength

## Introduction

In the mining industry one of the major causes of instability in underground excavations and the resulting of rock-related accidents is the lack of proper support coverage between support units in these excavations [1]. This is the reason for introducing different products such as thin spray rock liners (TSL) to support the rock fragments which can move or fall due to gravity, seismic activity or blasting-induced vibrations.

This study looks at some ways how polymers can be replaced in the mix design with different concentrations of mineral clays like Kaolinite, Montmorillonite, and Illite etc. The reason for this is to see if the product (TSL) can be more cost effective and also get better structural strengths. Figure 1 to 4 illustrates a rock liner being sprayed to the rock surfaces. This process is quick and easy to do with all the relevant tools and safety gear. The equipment used is a simple mixer pump arrangement having a positive displacement type pump [2]. The delivery hose should be about seven metres for best effect. Compressed air is added at the nozzle to spray the fresh mix. Cleaning of the equipment is easy by simply flushing thoroughly with water after the application is complete [2].

<sup>1</sup>Corresponding author: [pierrevt@uj.ac.za](mailto:pierrevt@uj.ac.za)



Figure 1. Thin sprayed rock liner being sprayed[4]



Figure 2. TSL layer easily applied by one person[4]



Figure 3. White TSL product[4]



Figure 4. Finished tunnel with the TSL product[4]

The thin sprayed liners are widely used in today's industry all over the world for different situations. The polymer-based liner, which is known as thin spray lining or TSL, was originally designed to stabilize the surface between rock bolts, but mine operators have different valuable additional features. "Typical uses which have been successfully found for TSL below ground are in the stabilization of friable ground, sealing sensitive rock types against water and humidity, preventing the unraveling of fractured ground by holding key blocks in place, and sealing dams, sumps and drains"[5].

## 1. Material properties

### 1.1 Testing and mix design

Test specimens were prepared with the TSL mix and tested for tensile strength and elongation, shear bond strength and compression strength. Table 1 shows the basic tests that would be done on TSL's rock liners to look at the different properties that would have an effect on the design of a specific mixture. But to test all these properties would take a long time and would not be relevant for this investigation. Only the most relevant tests have been chosen that would give us the basic answers we seek. The relevant tests selected are the tensile test, compression test, shear bond strength test and shear strength test.

**Table 1.** Relevant standards for testing TSL's[1]

Test type	Standard No	Description
Tensile Strength and Elongation	ASTM D638	Tensile properties of plastics
	ASTM D1708-84	Tensile properties of plastics by use of microtensile specimens
Tear Strength	ASTM D1004-90*	Initial tear resistance of plastic film and sheeting.
	ASTM D1922-89*	Propagation tear resistance of plastic film and thin sheeting by pendulum method.
	ASTM D5884-99*	Determining tearing strength of internally reinforced geomembranes.
	BS 903-A3-3.2:1997, ISO 34-2: 1996	Physical testing of rubber. determination of tear strength. section 3.2 small (delft) test pieces
	BS 903-A3:1995, ISO 34-1: 1994	Physical testing of rubber. method for determination of tear strength
Shear Strength	ASTM D732-90	Shear strength of plastics by punch tool
Adhesion Strength	ASTM D4541	Pull-off strength of coatings
Toxicity	ASTM E1619-95	Standard test method for chronic oral toxicity study in rats
Flammability	ASTM E162	Surface flammability of materials using a radiant heat energy source
	ASTM D568-74	Flammability of flexible plastics
	ASTM E84	Surface burning characteristics
	IEC 707	The determination of the flammability of solid electrical insulating materials when exposed to an igniting source
	CAN/UCL S102-M88	Standard method for test for surface burning characteristics of building materials and assemblies
Water Absorption	ASTM C827	Change in height at early ages of cylindrical specimens from cementitious mixtures
	ASTM D570	Water absorption of plastics
Abrasion	ASTM D4060	Abrasion resistance of organic coatings by the taber abraser
	ASTM D1242	Resistance to abrasion of plastic materials

\*: applicable after modification

## 1.2 Mix design

The original mix design supplied by Oxyfibre (Pty) Ltd can be seen in Table 2. The mix design uses 2.5% Polymers. The amount of Polymers was removed from the mix design and later replaced by nanoclays. The nanoclays were added at three different ratios of 2%, 4% and 6%. With the different, ratios the sand in the mix design was changed accordingly and the water/cement ratio was changed from 20% to 25% as to ensure the workability stay more or less the same as the original mix design from Oxyfibre.

**Table 2.** The original mix design for TSL's

Thin Spray Liner	%
Cement	52
Fibres	0.2
Accelerator	2.5
Sand	42.68
Polymer	2.5
Thickner	0.02
Plasticiser	0.1
Water/cement ratio	20



## 2. Experimental programme and results

### 2.1 Tensile strength testing

The shape and dimensions of an ASTM D638 Type I test specimen can be seen in Figure 5. The shape and dimensions of Type IV specimen mentioned in the same standard are considered to be more suitable for testing TSLs with high elongation capacities[6]. The thickness of the TSL specimens is determined by taking the field applications as a reference. This thickness is generally accepted to be around 5 mm. The test specimen was placed in an Instron 1195 testing machine that applies a vertical tension load at a constant rate of 2.5 N/s up to 100 N (40 seconds) and then tensioning at a constant loading rate of 5 N/s up to failure. Failure normally occurred in the smaller middle section of test specimen. The results was obtained and statistically analysed and shown in Table 3.

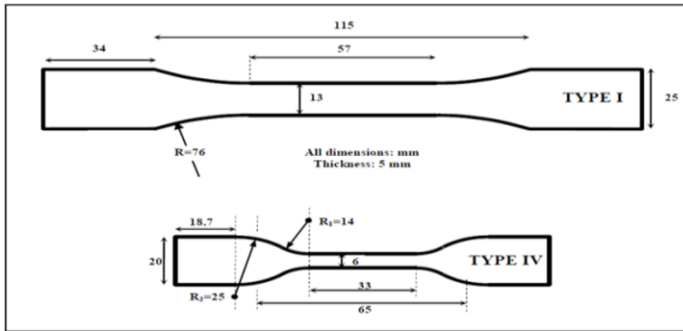


Figure 5. Dimensions of the dog-bone specimens [1]

Table 3. Statically analysed results for tensile test

Sample Number	Concentrations			
	0% Strength(MPa)	2% Strength(MPa)	4% Strength(MPa)	6% Strength(MPa)
1	2.56	4.32	4.11	4.02
2	4.53	4.60	4.77	5.27
3	3.95	3.14	2.74	6.08
4	4.13	3.69	2.85	3.13
5	2.78	3.26	2.23	3.68
6		3.61	2.71	
Mean value	3.59	3.77	3.23	4.44
Sample Variance	0.76	0.34	0.96	1.46
Std deviation	0.87	0.58	0.98	1.21
95% Confidence Intervals (MPa)				
Minimum	2.95	3.38	2.58	3.54
Maximum	4.23	4.16	3.89	5.33
Final Mean values(MPa)	4.04	3.65	2.77	4.33

The 6% nanoclay mixture performed the best. The strength gained for this mixture was 4.33MPa. The original mix design performed second best with a strength of 4.04MPa. Third and fourth were the 2% and 4% nanoclay mixtures with recorded strengths of 3.65MPa and 2.77MPa respectively. The inclusion of nanoclay into the

mixture decreases the tensile strength of TSL's but not for the concentration of 6% nanoclays.

### 2.2 Shear bond testing

A 20 mm thick steel-ring with a 52.5 mm diameter inner hole is used for housing the TSL and a rock core of 27.5 mm diameter as seen in Figure 6. The rock core is centrally positioned in the steel-ring. The gap between the steel-ring and the rock core is filled with TSL. After curing of the TSL for the predetermined period, the specimen is placed on a base which offers support to the steel-ring and the TSL but not to the rock core. A compressive load was applied on the rock core, displacing the core on the rock/TSL contact towards the void in the support base. The loading and failure of the TSL take place due to shear movement at the rock/TSL contact. Load deformation characteristics were observed until the TSL has failed[1]. The results was obtained and statistically analysed and shown in Table 4.

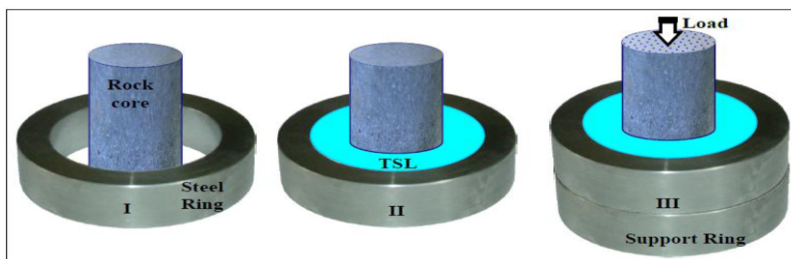


Figure 6. Steps followed during specimen preparation in shear-bond strength testing[1]

Table 4. Statically analysed results for shear bond test

	Concentrations			
	0%	2%	4%	6%
Sample Number	Strength(MPa)	Strength(MPa)	Strength(MPa)	Strength(MPa)
1	14.03	32.50	16.53	3.34
2	7.58	23.67	9.61	5.12
3	8.93	27.02	4.00	11.76
Mean value	10.18	27.73	10.05	6.74
Sample Variance	11.57	19.87	39.39	19.69
Std deviation	3.40	4.46	6.28	4.44
	95% Confidence Intervals (MPa)			
Minimum	6.33	22.69	2.94	1.72
Maximum	14.03	32.77	17.15	11.76
	90% Confidence Intervals (MPa)			
Minimum	6.94	23.48	4.07	2.51
Maximum	13.42	31.98	16.03	10.97
	85% Confidence Intervals (MPa)			
Minimum	7.35	24.03	4.83	3.05
Maximum	13.01	31.44	15.26	10.43
Final Mean values(MPa)	8.26	27.02	9.61	4.23

The results are not reliable due to the flaws in the testing method. The following flaws were observed: rock cores sheared away with large differences in strengths, rock core surfaces are smooth and lastly it was difficult to mould the rock cores exactly in the middle of the steel rings. They do however give a rough idea of how the different

nanoclay mixtures respond to shear bond testing. The 2% nanoclay mixture performed the best with a strength of 27.02MPa. This is a significant improvement of the strength which was around 227.12% higher than the original mix. The decrease in strengths is then followed by the 4% nanoclay and the original mixture and lastly by the 6% nanoclay mixture. The values recorded for these tests ranged from 4.23MPa to 9.61MPa.

### 2.3 Shear strength test

The steel ring in Figure 7 is used for the purpose of housing the TSL which bonds onto the inner surface of the steel ring. The dimensions are the same as the steel ring used for the shear-bond strength testing. The TSL-ring has a depth of 20 mm. The steel punch is used to apply the shear load on the TSL. The diameter of the steel punch is 29.6 mm and is smaller than the holes (30 mm) on the clamping fixture. The difference in the diameters leaves a spacing of 0.2 mm along which TSL is sheared[1]. The clamping fixture is designed to accommodate the prepared specimen consisting of the TSL and steel ring. Two steel plates with overlaying holes are pressed against the surface of the TSL-steel ring using two screws. The purpose of using a single clamping fixture is to ensure continuity of clamping all around the TSL material and for the prevention of rotation and premature failure.

The results obtained from this test also showed a significant improvement in strength when adding the nanoclays to the mixture as seen in Table 5. The mixture that clearly stood out was the one of the 2% nanoclay addition. The strength gained for this mixture was 50.01MPa. This is a significant improvement of the strength which is 20.21% higher than the original mix design from Oxyfibre. The original mix strengths only reached a stress of 41.6MPa and were also the lowest. Second and third were the mixtures of the 4% and 6% nanoclay additions. The values recorded for the tests range from 45.15MPa to 43.44MPa respectively. This shows also an increase of strength by a percentage of 8.53% and 4.42% respectively.

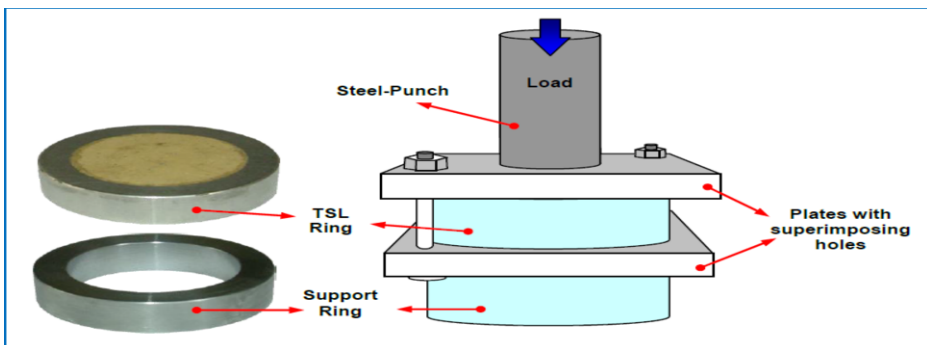


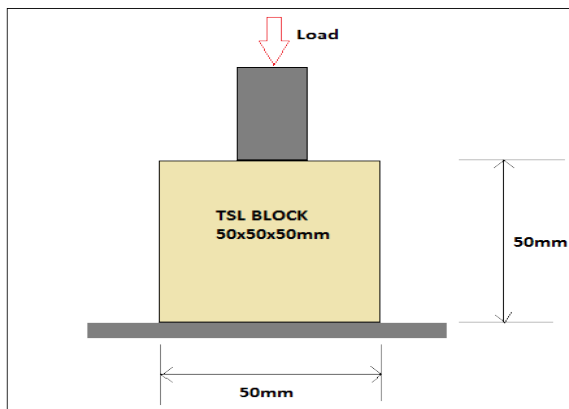
Figure 7. Shear strength test setup[4]

**Table 5.** Statically analysed results for shear strength test

	Concentrations			
	0%	2%	4%	6%
Sample Number	Strength(MPa)	Strength(MPa)	Strength(MPa)	Strength(MPa)
1	34.59	49.63	48.02	41.61
2	41.29	49.59	46.54	42.35
3	41.70	51.73	40.64	44.53
4	41.81	50.82	43.75	44.67
Mean value	39.85	50.44	44.74	43.29
Sample Variance	12.34	1.06	10.60	2.38
Std deviation	3.51	1.03	3.26	1.54
95% Confidence Intervals (MPa)				
Minimum	36.41	49.43	41.55	41.78
Maximum	43.29	51.45	47.93	44.8
90% Confidence Intervals (MPa)				
Minimum	36.95	49.59	42.05	42.02
Maximum	42.75	51.29	47.42	44.56
Final Mean values(MPa)	41.60	50.01	45.15	43.44

### 2.4 Compression strength test

A Perspex mould with dimensions of 50 x 50 x 50mm is used to cast the TSL compression block test specimen as shown in Figure 8. After sufficient curing time, the TSL block was placed in an Instron 1195 compression machine and tested. The test was over when the pressure has reached its maximum load and suddenly decreased.



**Figure 8.** Compression test setup

The mixture that performed the best in this regard was that of the 2% nanoclay mixture. The strength gained for this mixture was 36.70MPa. This is a significant improvement of the compression strength which was 43.49% higher than the original mix design from Oxyfibre. Second and third were the mixtures of the 4% and 6% nanoclay mixtures. The values recorded for these tests ranged from 34.28MPa to 34.79MPa respectively. This also shows an increase of strengths by a percentage of

31.7% and 33.65% respectively. The mix design given by Oxyfibre performed the worst. The strength recorded was around 26.21MPa and was the lowest. The analysed data is summarised in Table 6. All of these cubes have broken in the range from 22MPa to just over 26MPa.

**Table 6.** Statically analysed results for compression test

Sample Number	Concentrations			
	0% Strength(MPa)	2% Strength(MPa)	4% Strength(MPa)	6% Strength(MPa)
1	22.50	35.00	32.29	28.97
2	25.78	34.43	31.92	35.37
3	26.64	38.76	35.94	35.20
4	26.20	38.41	34.61	33.79
Mean value	25.28	36.65	33.69	33.33
Sample Variance	3.56	5.06	3.67	8.96
Std deviation	1.89	2.25	1.92	2.99
95% Confidence Intervals (MPa)				
Minimum	23.43	34.44	31.81	30.40
Maximum	27.13	38.85	35.57	36.27
90% Confidence Intervals (MPa)				
Minimum	23.72	34.79	32.11	30.86
Maximum	26.84	38.50	35.27	35.80
Final Mean values(MPa)	26.21	36.70	34.28	34.79

### 3. Conclusion

Four TSL rock liner mixtures were investigated, namely: Original TSL mixture, 2% nanoclay, 4% nanoclay and 6% nanoclay TSL Mixtures. The replacement of nanoclays into TSL products appears to have a significant impact on the strengths gained for the certain test done in this investigation.

The use of the most optimal concentration nanoclay added to TSL's will be determined by cost purposes and also the best desired use of the product. The TSL's strength does not increase by mere adding of nanoclays; it decreases the strengths slightly but still performs better than the mix design given by Oxyfibre. This investigation proves that it would be a much better option to replace polymers with nanoclays. But product wise, nanoclays are much more expensive to use over polymers. As the need increases for the production of nanoclays all over the world, the cost to purchase nanoclays in the future might decrease and this will certainly make nanoclays more favorable over polymers.

The replacement of nanoclays in the mixtures will increase the water demand. It changes the w/c ratio from 20% to 25%. This means that in the industry mines will need to accommodate for larger volumes of water to be used for this mixtures. Further investigations should be done to investigate if maybe admixtures would influence the strengths gained and to ensure the workability does not change.

## References

- [1] H. Yilmaz., *Development of testing methods for comparative assessment of thin spray-on liner (TSL) shear and tensile properties*. PhD Thesis. Johannesburg: University of Witwatersrand Faculty of the Engineering and the Built Environment, 2011.
- [2] Technicrete Murray & Roberts Company. [Online] Available at: <http://www.hellotrade.com/technicrete-murray-roberts-company/tsl-sprayed-liner.html>, HelloTrade, 10 March 2013.
- [3] Strata Mine Services for Underground & Surface. [Online] Egeland Wood & Zuber, Inc Available at: <http://s247784952.onlinehome.us/images/mine-services/basf-tsl-application510.jpg>, Strata, 10 March 2013.
- [4] P.H. Ferreira, A. Piroddi, *The Application of GRP and Thin Spray Liner Support Products in a Typical Block Cave Mining Method to Enhance Safety and Productivity*. The Southern African Institute of Mining and Metallurgy 6th Southern African Base Metals Conference 2011.
- [5] Pray on liner binds friable rock surfaces. [Online] Available at: <http://www.technicrete.co.za/downloads/downloads.html>. Concor, 9 March 2007.

# Effects of multi-walled carbon nanotubes on strength and interfacial transition zone of concrete

P. Van TONDER<sup>1</sup> and T.T. MAFOKOANE

*Department of Civil Engineering Science, University of Johannesburg*

**Abstract.** Multi-walled carbon nanotubes (MWCNTs) were used to try and eliminate the aggregate interfacial transition zone. Different concrete mixes were used in fixed proportions along with varying concentrations of CNTs. The CNTs were applied in different concentrations, namely, 0.05 wt%, 0.1 wt% and 0.2 wt%, per dry weight. CNTs were dispersed using sonication. Concrete specimens were tested for compressive, flexural and split-tensile strengths. For each test, thirteen mix designs were investigated which included untreated aggregates and CNTs, and treated aggregates and CNTs. The results were compared with the results of the control concrete. The results showed that the use of CNTs improves the compressive, flexural and split-tensile strengths. It was concluded that CNTs minimize the ITZ.

**Keywords.** Multi walled carbon nanotubes, interfacial transition zone, concrete, compressive strength, flexural strength, split-tensile strength, sonication

## Introduction

Concrete is the most widely utilised material in the construction industry. However, concrete is generally very brittle and is characterized by a very low tensile strength and strain [1]. Tensile strength of concrete can be tested indirectly by flexural and split-tensile tests. Compressive strength of concrete is its indexing property as concrete has its maximum strength in compression. Concrete strength depends on various factors of which the ITZ is one variable. The Interfacial transition zone (ITZ) is a region in the concrete between the aggregate and hydrated cement paste. It is not a definite zone but rather a region of transition. The transition zone exists on a thin shell, typically 10-15  $\mu\text{m}$  thick around large aggregates. It is generally weaker than the other main components of concrete. This weaker zone can have an influence on the mechanical behaviour of concrete [2].

Nanotechnology is an emerging field of science and engineering. It is the new alternative of re-engineering concrete design and offers extraordinary environmental benefits. Nanotechnology promises significant enhanced material strength which is critical in constructions. Nano-materials improve particle packing capacity and concrete durability. According to Yamabe et al [3], CNTs were first synthesized in arc-discharge as a by-product of fullerene. There are two types of CNTs namely SWCNTs (single-walled carbon nanotubes) and MWCNTs. SWCNTs are synthesised under precisely controlled conditions in the presence of a catalyst.

<sup>1</sup>Corresponding author: [pierrevt@uj.ac.za](mailto:pierrevt@uj.ac.za)

In case of deviation from the production route of SWCNTs, MWCNTs are formed. They are made of 2 to 30 concentric graphic sheets (hexagonal, pentagonal or heptagonal) rolled into overlapping cylinders. Their diameters vary from 10 to 50nm and their length is greater than 10 $\mu$ m. CNTs have a modulus of elasticity of approximately 5 times higher, a tensile strength 100 times larger and elastic strain 60 times greater than steel. Tyson et al [1] performed an investigation using untreated and treated MWCNTs as reinforcement for cementitious materials. The samples were tested for both compression and flexural strengths. Treated CNTs produced compressive and flexural strengths respectively 2.7MPa and 0.4MPa higher than that of untreated CNTs.

Research by Ferro et al [4] shows that CNTs have a potential for crack bridging and enhanced stress transfer. Shah et al [5] investigated the effect of MWCNTs' length and concentration on the fracture properties of the nanocomposites with constant weight ratio. The fracture mechanics test results showed that the flexural strength of cement matrix significantly increased through the use of small amounts of MWCNTs (0.048 wt% and 0.08 wt%). In another study by Ximba [6], a series of compression tests were performed with different mix designs. The overall best mix design was found to be 0.2% treated aggregates and treated CNT. Luo [7] conducted a research on nanocomposites with different concentrations MWCNTs and different concentrations and combinations of surfactants. When comparing 0.5 wt% of MWCNTs to plain cement paste, it was found that pristine and annealed MWCNTs greatly improve flexural and compressive strengths. Reduced strength was achieved when using carboxyl functionalized MWCNTs.

## 1. Material properties and preparation

### 1.1 Material used

Table 1 lists the materials used to prepare the specimens. Material properties of the MWCNTs used are shown in Table 2.

**Table 1.** List of material used and their purposes

Material	Purpose
CEM IV 32.5R "Buildcrete" 13mm stone Washed crusher sand Fine sand Water	Standard concrete ingredients
MWCNTs	Reinforcement
Oil	Mould release agent

**Table 2.** Characteristics of the MWCNTs used

Property	Unit	Value	Method of Measurement
Average Diameter	Nanometers	9.5	TEM
Average length	Microns	1.5	TEM
Carbon Purity	%	90	TGA
Metal Oxide	%	10	TGA
Amorphous Carbon	-	Pyrolytically deposited carbon on the surface of the NC7000	HRTEM
Surface Area	m <sup>2</sup> /g	250-300	BET



The following mix designs were used namely Control mix, Untreated aggregates and untreated CNT mix (UAUC), Untreated aggregates and treated CNT mix (UATC), Treated aggregates and untreated CNT mix (TAUC) and Treated aggregates and treated CNT mix (TATC). A total of 13 mix designs were investigated. Over 39 specimens were cast and tested.

### *1.2 Crypsination and sonication*

Crypsination is a technology owned by Oxyfibre (Pty) Ltd. CNTs have a tendency to aggregate in an aqueous solution and repel water molecules. Crypsination is a process whereby aggregates and CNTs are treated to improve the bond between aggregates, CNTs and water. It is a gaseous process using fluorine as catalyst to modify the molecular structure on the surface of Polypropylene (or other exposed materials). The process renders the surface permanently wettable and adhesive. In the context of this study, treated aggregates and CNTs refer to crypsinated aggregates and CNTs, and untreated aggregates and CNTs refers to standard aggregates and CNTs.

For CNTs to be effectively utilized within materials, they must be properly dispersed. CNTs have a tendency to self-associate into micro-scale aggregate. Dispersion separates the bundles of CNTs into individual filaments within a matrix. Required amount of CNTs were sonicated for 30 minutes before mixing the solution with the concrete.

## **2. Experimental programme**

### *2.1 Mixing of concrete and slump test*

The amount of all required materials were weighed and measured. All the apparatus were cleaned and made ready. Stones and washed crusher sand were mixed for 2 minutes until the mixture had a uniform colour. The fines were added to the mixture and were mixed for a minute. Cement was added and mixed together with the mixture for 2 minutes. Sonicated solution of CNTs was added to the mixture in the drum and mixed for 5 minutes. The remaining amount of water required was further added and mixed until the concrete appeared homogeneous.

For all the concrete mixes prepared, slump tests were performed in accordance with SANS 5862-1:2006 standards [8]. All the tools were cleaned and wiped with a damp cloth prior to performing the slump test. The slump mould was placed on the steel plate with the narrow end at the top. With the two feet standing on the foot piece, the slump mould was filled with three layers of freshly mixed concrete. Each layer of about equal depth was tamped 25 times with a steel rod. After tamping the last layer, the excess concrete was stroked off with a steel rod. The slump mould was slowly lifted straight up and off. The distance between the bottom of the tamping rod and the highest point of the concrete was measured.

### *2.2 Moulding and curing of the specimens*

The moulds were assembled and cleaned with a damp cloth. The internal surfaces of the moulds were coated with a thin layer of oil to prevent leakage of water through the

joints and to prevent the adhesion of the concrete to the moulds<sup>[8,9]</sup>. During moulding, concrete was compacted using a steel rod to avoid honeycombing. Both beam moulds and cube moulds were filled with concrete in approximately 50mm layers. Each layer was stamped at least 45 times with the rod. A steel float was used to strike off excess concrete and to level the last layer. Each specimen was labelled and left overnight. The specimen were covered in a plastic sheet and stored in a cool place to avoid moisture loss.

After 24 hours, the specimens were removed from the moulds. The specimens were stored in a curing pond until they gained 28 days strength. The water in the curing pond was kept clean, at a temperature of  $\pm 23^{\circ}\text{C}$ .

### *2.3 Compression strength test*

The compression test was performed according to the guidelines from SANS 5863:2006<sup>[10]</sup>. The cube specimens were taken out of the curing pond after 28 days. The surface water and grit were removed and the mass of the cubes were determined and recorded. Prior to testing, the bearing surfaces of the plates of the compression testing machine were wiped clean. The cube specimens were crushed one cube at a time. The cube in the machine was positioned to allow for the load to be applied on the opposite as-cast faces of the specimen. The corresponding cube mass and volume were entered on the data recording monitor and the load was gradually applied at the rate of 0.3MPa/s until the specimen failed. The maximum load applied was recorded and the appearance of the specimen was photographed. The compressive strength was calculated using the maximum failure load and the cross-sectional area of the specimen on which the compressive force acts.

### *2.4 Flexural strength test*

Tensile strength is an important property of concrete because concrete structures are highly vulnerable to tensile cracking. Due to difficulty in applying uniaxial tension to concrete specimens, the tensile strength of the concrete is determined by indirect test methods, flexural and split-tensile tests. Only the flexural test was performed in the study and the split-tensile test was performed by another person and the results were used to analyse and evaluate the proposed mix designs. The flexural strength test was conducted on a computer controlled INSTRON compression testing machine with 250kN cell loader in the laboratory air atmosphere. The two-point loading method was used. The test was performed in accordance with SANS 5863:2006 [11]. The beam specimens were prepared similar to the cube specimens. A beam specimen was placed centrally on the supporting rollers. Prior to loading, it was ensured that the loading and supporting rollers are evenly in contact with the specimen. The load was applied uniformly without shock at the rate of 0.2mm/min until the beam specimen failed. The various applied loads together with the maximum failure load and deflections were recorded by the computer. The distance between the line of fracture and the position of the nearer supporting roller, along the centre-line of the bottom surface, was measured. The flexural strength was calculated using maximum failure load, the distance between the axis of the supporting rollers, the width and depth of the specimen.

## 2.5 SEM observations

A sample of about a cubic centimetre was extracted from the failed specimens for each mix design tested. The samples were left in the oven overnight to dry. The following day, the samples were taken out of the oven and were allowed to cool for 10 minutes. The samples were placed on the sample stubs/holders and were held in place by an adhesive tape. The coating process was performed in order to make the samples conductive. Most of the samples were coated twice due to poor electron conductivity. Gold coat was used because of irregular surface of the concrete samples. When coating process was completed, the samples were stored in the Glass Vacuum Desiccator until the SEM was available for use. The TESCAN Scanning Electron Microscope was used to observe the microstructure of various concrete samples. A high voltage of 20kV was used for most of the samples. An accelerating voltage of 10kV was used on some samples to reduce surface charging.

## 3. Results and discussion

### 3.1 Compressive strength test

The compression strength of each specimen was calculated using the Eq.(1).

$$f_{cc} = \frac{F}{A_c} \quad (1)$$

where  $f_{cc}$  = compressive strength (MPa); F = maximum load at failure (N);  $A_c$  = cross-sectional area of the specimen ( $\text{mm}^2$ ).

The control mix had an average strength of 14.533. The average strength of the other mix designs, and the strength increase/reduction in comparison to the control mix design are shown in Table 3. Positive and negative percentages for the strength improvement respectively indicate an increase or decrease in strength.

From the results obtained, it was noted that the addition of 0.1 wt% TAUC, 0.05 wt% TATC and 0.1 wt% TATC greatly increased the compressive strength. The 0.05% UAUC, 0.1 wt% UAUC, 0.2 wt% UATC and 0.2 wt% TATC mix designs, reduced the compressive strength. This is as a result of poor dispersion and large amount of CNTs added.

**Table 3.** Average compressive strength and strength improvements for different mix designs

Mix Design	Concentration(%)	Average Strength(MPa)	Strength Improvement(%)
UAUC	0.05	13.617	-6
	0.1	14.347	-1
	0.2	15.711	8
TAUC	0.05	16.579	13
	0.1	18.056	20
	0.2	16.006	9
UATC	0.05	16.009	9
	0.1	16.692	13
	0.2	13.559	-7
TATC	0.05	17.751	18
	0.1	18.762	23
	0.2	13.121	-11

Figure 1 shows a graphical comparison of the mean compressive strengths from the different mix designs. A notable mix design is TAUC. It always yielded an increased compressive strength regardless of the concentration.

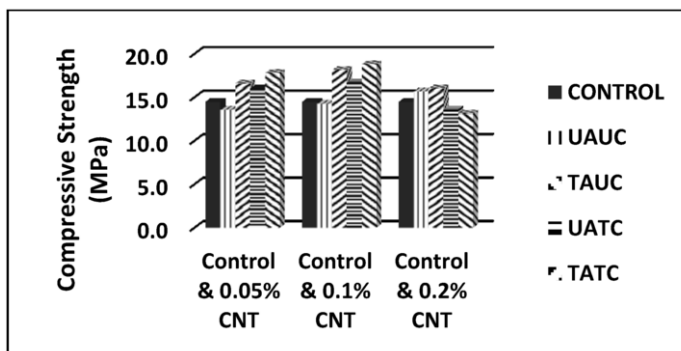


Figure 1. Comparison of average compressive strength per concentration of CNTs

Generally, 0.1 wt% concentration yielded an increased strength for almost all the different aggregate and CNTs combinations. The 0.05 wt% concentration produced moderate results. Poor results were achieved with 0.2 wt% concentration of CNTs. With high concentrations, the CNTs tend to self-associate into a micro-scale aggregates. This resulted in insufficient or poor dispersion. The more CNTs added, the less workable the concrete became. Concrete mixes with 0.2% CNTs concentration were very dry, hard to compact and mould by hand. These left voids within the concrete, thus weakening the strength of the specimens.

### 3.2 Flexural strength test

Eq. (2) was used to calculate the flexural strength of each specimen

$$f_{cf} = \frac{F \times \ell}{b \times d^2} \quad (2)$$

where  $f_{cf}$  = flexural strength (MPa);  $F$  = maximum load at failure (N);  $\ell$  = distance between the axis of the supporting rollers (mm);  $b$  = width of the specimen (mm);  $d$  = depth of the specimen (mm)

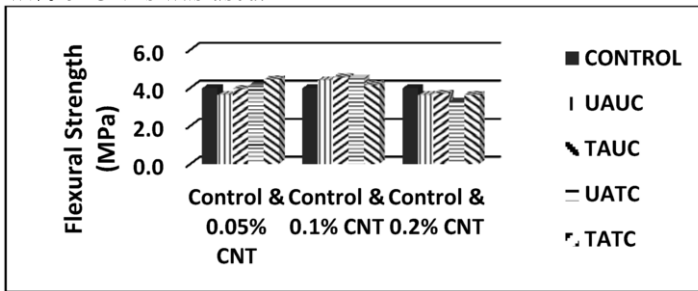
According to SANS 5863 standards, the calculated results from Eq. (2) are considered valid only if the tension surface (bottom surface) is within the middle third of the span length<sup>[12]</sup>. All the results were considered valid because the lines of fracture were always between 100mm and 200mm for all the specimens.

The control mix had an average strength of 3.969. The average strength of the other mix designs, and the strength increase/reduction in comparison to the control mix design are shown in Table 4. Most mix designs on Table 4 show negative impact of CNTs on concrete flexural strength. Greatest improvement was found when 0.1 wt% concentration of untreated CNTs was added to treated aggregates. Addition of 0.2 wt% of treated CNTs to untreated aggregates produced the worst results.

**Table 4.** Average flexural strength and strength improvement for different mix designs

Mix Design	Concentration(%)	Average Strength(MPa)	Strength Improvement(%)
UAUC	0.05	3.619	-11
	0.1	4.371	8
	0.2	3.606	-11
TAUC	0.05	3.938	-2
	0.1	4.550	12
	0.2	3.683	-9
UATC	0.05	4.104	3
	0.1	4.486	11
	0.2	3.249	-23
TATC	0.05	4.420	10
	0.1	4.154	4
	0.2	3.623	-10

Graphical comparison of the different mixes per concentration is shown in Figure 2. Overall, 0.1 wt% of CNTs is the best concentration of the three. An improved flexural strength was achieved for all possible aggregate and CNTs combination for this concentration. The best mix design is 0.1 wt% TAUC with 4.7MPa average strength, and 12% strength increase. No improvement was shown when 0.2 wt% of CNTs was added to concrete. Only UATC and TATC showed an increase in flexural strength when 0.05 wt% of CNTs was used.

**Figure 2.** Comparison of average flexural strength per concentration of CNTs

### 3.3 Split-tensile test

Similar mix designs were considered and specimens were prepared the same way as the compressive and flexural tests. A total of 39 cylindrical specimens, with dimensions 300mm long and 150mm diameter were prepared.

**Table 5.** Average split-tensile strength and strength improvement for different mix designs

Mix Design	Concentration(%)	Average Strength(MPa)	Strength Improvement(%)
UAUC	0.05	1.359	26
	0.1	1.292	23
	0.2	1.215	18
TAUC	0.05	1.411	29
	0.1	1.213	18
	0.2	1.336	25
UATC	0.05	1.269	21
	0.1	1.456	31
	0.2	1.229	19
TATC	0.05	1.202	17
	0.1	1.296	23
	0.2	0.978	-2

Tables 5 shows the average strengths achieved for the different mix designs. The control mix had an average strength of 1.038MPa. The highest strength improvement achieved was 31% with the 0.1 wt% UATC mix design. Only 0.2 wt% TATC mix yielded a decreased strength.

The results in Table 5 were plotted as shown in Figure 3. The TAUC mix produced the highest strength when 0.05 wt% and 0.2 wt% concentrations of CNTs per dry weight were applied. When 0.1 wt% of CNTs was utilised, a combination of untreated aggregates and treated CNTs showed the greatest strength improvement.

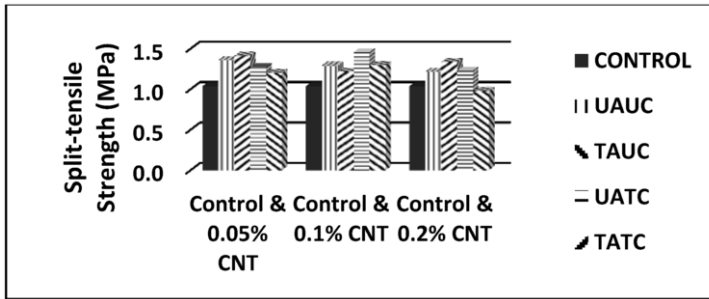


Figure 3. Comparison of average split-tensile strength per concentration of CNTs

### 3.4 SEM observations

The SEM was used to observe the impact the CNTs had on the ITZ. Figure 4 to 9 show micrographs of the fractured samples from four different mix designs.

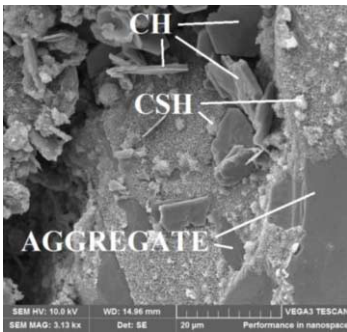


Figure 4. SEM image from the control mix

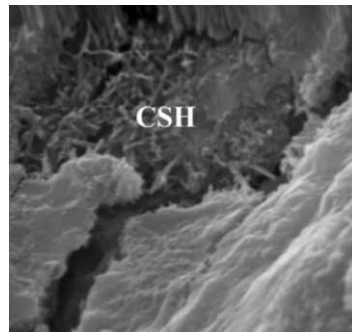


Figure 5. SEM image for 0.1% TATC, (mag: 2µm)

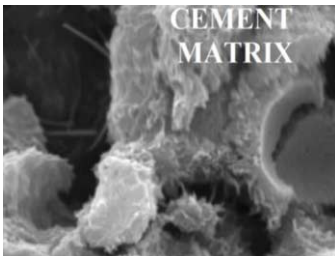


Figure 6. SEM image for 0.1% UATC sample (mag: 2µm)

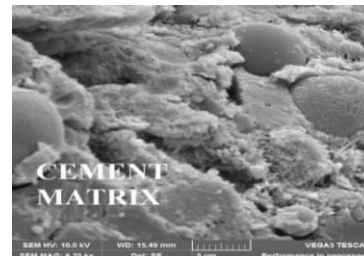
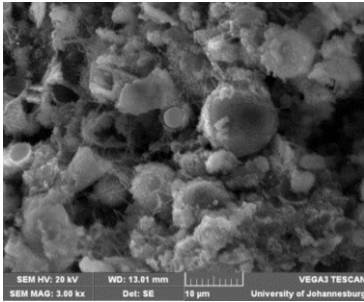
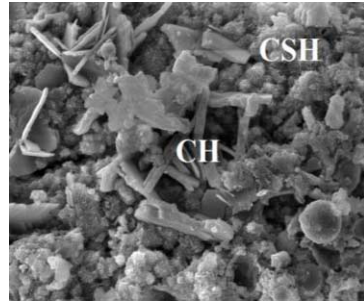


Figure 7. SEM image for 0.1% UAUC sample



**Figure 8.** SEM image for 0.2% UAUC



**Figure 9.** SEM image for 0.05% UATC sample (mag: 20µm)

The high concentration of CH is evident in the control sample in Figure 4. Other samples with reinforcement, were dominated by crystals of CSH and Ettringite. However, on some of the images it was not clear if the needle-like particles are the CNTs or the ettringite.

#### 4. Conclusion

The CNTs improve the properties of concrete due to the effect the increased surface has on reactivity and through filling the micro- and nanopores of the ITZ. It was found that different concentrations of CNTs have different impacts on concrete strength. On average, the 0.1 wt% concentration improved the three tensile strengths better than 0.05 wt% and 0.2 wt% concentrations. When CNTs were applied in large amounts, the concrete lost its workability due to difficulty of nano-particles to disperse uniformly. These increased the voids within the concrete, leading to decreased strength especially the flexural strength.

Different combinations of treated and untreated aggregates and CNTs improved the concrete strength differently. The UATC and TATC combination worked well for most tests under different concentrations of CNTs. The overall best design mix is 0.1 wt% UATC. For compressive strength, 0.1 wt% TATC performed the best. For flexural strength, 0.1 wt% TAUC showed the greatest results, and 0.1 wt% UATC improved the split-tensile strength greatly.

During the SEM observation, it was hard to spot the CNTs because of similarities between CNTs and some of the concrete/cement particles such as Ettringite. The absence of CNTs in some samples was due to poor dispersion, and only a cubic centimetre samples were analysed. But the improved strengths achieved shows that CNTs bonded well with cement and this can possibly be because the ITZ was minimised. Further studies is under way to verify the position of these CNTs exactly. However, addition of large amount of CNTs worsened the voids because of poor workability and compaction. Though promising, several challenges have to be solved before introducing CNTs to the public through concrete technology. The challenges of using CNTs include: proper dispersion, high water demand, manufacturing methods, safety, handling issues and high costs.

## References

- [1] B.M. Tyson, Carbon nanotube and nanofiber reinforcement for improving the flexural strength and fracture toughness of portland cement paste. Texas: Texas A&M University, 2010.
- [2] P.K. Mehta, P.J.M. Monterio, *Concrete: Structure, Properties, and Materials* (Prentice-Hall International Series in Civil Engineering and Engineering Mechanics). New York: Prentice-Hall International, 1993.
- [3] T. Yamabe, K. Fukui, K. Tanaka., *The Science and Technology of Carbon Nanotubes*. Abiko City: Elsevier, pp. 2-11, 1999.
- [4] G. Ferro, J.M. Tulliani, S. Musso, Carbon nanotubes cement composites. *The International Journal of the Italian Group of Fracture*, 18: 34-44, 2011.
- [5] S.P. Shah, M.S. Konsta-Gdoutos, Z.S. Metaxa, Highly-dispersed carbon nanotube-reinforced cement based materials. Patent US 20090229494A1, 2009.
- [6] S.I. Ximba, Procedures to eliminate aggregate interfacial transition zone. Johannesburg: University of Johannesburg, 2012.
- [7] J.L. Luo, Fabrication and functional properties of multi-walled carbon nanotube/cement composites. *PhD thesis. Harbin: Harbin Institute of Technology*, 2009.
- [8] SABS Standards SANS 5862-1:2006: Concrete tests - Consistence of freshly mixed concrete - Slump test. Pretoria: *SABS Standards Division*, 2006.
- [9] SABS Standards SANS 5861-3:2006: Concrete tests - Part 3: Making and curing of test specimens. Pretoria: *SABS Standards Division*, 2006.
- [10] SABS Standards SANS 5864:2006: Concrete tests - Flexural strength of hardened concrete. Pretoria: *SABS Standards Division*, 2006.
- [11] K.L. Scrivener, A.K. Crumbie, P. Laugesen, The Interfacial Transition Zone (ITZ) Between Cement Paste and Aggregate in Concrete. *Interface Science*, 12: 411-421, 2004.



# Molecular dynamics research of triple junctions structure of tilt and mixed-type grain boundaries in nickel

Gennady POLETAEV<sup>1</sup>, Darya DMITRIENKO, Vadim DIABDENKOV,  
Vladimir MIKRUKOV and Mikhail STAROSTENKOV

*Altai State Technical University, Barnaul, Lenin st. 46, 656038, Russia*

**Abstract.** The atomic structure and the diffusion permeability of triple junctions of high-angle tilt boundaries and mixed-type grain boundaries in nickel have been investigated using the molecular dynamics method. It has been shown that equilibrium triple junction has no structural features, which ably single it out as a special defect among its constituent grain boundaries. The diffusion permeability of triple junctions does not exceed the permeability of the boundaries. The effective diffusion radius of the considered triple junctions and the width of the grain boundaries are determined.

**Keywords.** Molecular dynamics, triple junction, grain boundary, tilt boundary, mixed-type boundary, nickel, grain boundary dislocation

## Introduction

The triple junction of grains is a linear defect, along which three variously oriented grains i.e. three grain boundary surfaces are conjugated. Despite the fact that the triple junctions are the main defects of polycrystals along the grain boundaries, researchers started to be interested in them comparatively recently. In some articles, the difference in the properties of triple junctions and their constituent grain boundaries is indicated. It is considered that the diffusion along triple junctions is more intensive than along the grain boundaries [1-3]. However, in the comparatively recent studies [4, 5] performed using computer simulation, the conclusion is made that the diffusion permeabilities of the grain boundaries and the triple junctions can have the same order of magnitude. The question relative to the effective width of the grain boundaries and the radius of the triple junctions, the knowledge of which would give the notion on the permeability of the “diffusion channels” in polycrystals, also remains open. For the grain boundaries, the width is usually accepted to be equal to 5Å [3, 4], and there is substantially fewer data on the triple junctions.

<sup>1</sup>Corresponding author: [genphys@mail.ru](mailto:genphys@mail.ru), [gmpoletaev@mail.ru](mailto:gmpoletaev@mail.ru)

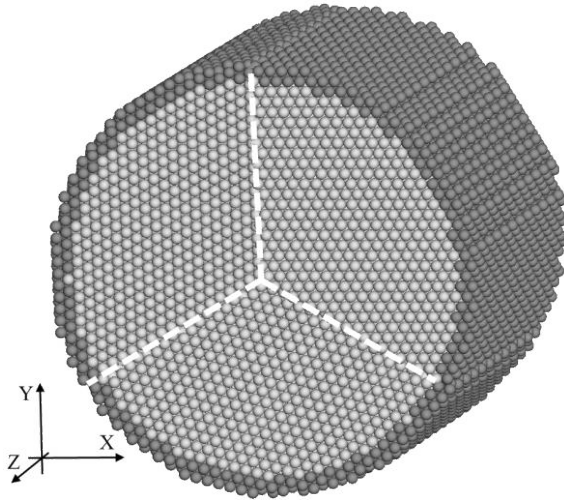
This study is devoted to the investigation of the atomic structure and the diffusion permeability of triple junctions of high-angle tilt boundaries  $\langle 111 \rangle$  and  $\langle 100 \rangle$  and mixed-type grain boundaries in nickel using the method of molecular dynamics.

## 1. Description of the model

A triple junction of tilt boundaries was formed in a center of the computational block by means of conjugation of three grains misoriented relative to each other using the rotation around the axis parallel to the line of the triple junction. In this study, two misorientation axes were considered:  $\langle 111 \rangle$  and  $\langle 100 \rangle$ . When constructing the computational block, initially three parallelepiped-shaped crystals were formed. Then they were rotated for the angle around axis  $\langle 111 \rangle$  or  $\langle 100 \rangle$  specified for each grain. The next stage was cutting the segment of each grain according to the specified angles between the grain boundaries in the junction. In this study, the angles between the boundaries in the joint were specified to be equal to  $120^\circ$ . After cutting the segments, the conjugation of the grains was performed, during which the atoms situating at a distance shorter than  $0.5\text{\AA}$  from the neighboring atom were removed. The final stage was cutting the final cylinder-shaped computational block. The number of the atoms in the computational block was about 40000 (Figure 1). The periodic boundary conditions were specified at the cylinder ends (the infinite repetition of the cylindrical computational block along axis  $Z$  was specified). The rigid conditions were specified at the side cylinder surface, and the atoms near the side surface were not allowed to move during the computer experiment (in Fig. 1, the rigidly fastened atoms are shown dark-gray).

In this study, two triple junctions of the tilt boundaries were considered: with the misorientation of the grains by angles  $15^\circ$ ,  $15^\circ$ , and  $30^\circ$  relative to axis  $\langle 111 \rangle$  and by angles  $18^\circ$ ,  $18^\circ$ , and  $36^\circ$  relative to axis  $\langle 100 \rangle$  (at the construction of the triple junction of  $\langle 111 \rangle$  tilt boundaries in the model three crystal grains were rotated around the axes  $\langle 111 \rangle$  on angles  $0^\circ$ ,  $15^\circ$ ,  $30^\circ$ ; at the construction of the junction of  $\langle 100 \rangle$  tilt boundaries - on angles  $0^\circ$ ,  $18^\circ$ ,  $36^\circ$ ).

When constructing the triple junction of the mixed-type boundaries, three variously oriented crystals were formed so that the  $(111)$  plane of the first crystal, the  $(100)$  plane of the second crystal, and the  $(110)$  plane of the third crystal corresponded to the  $XY$  plane. Then, to create a less ordered structure of the conjugated grain boundaries, the grains were additionally rotated by angles  $5^\circ$ ,  $15^\circ$ , and  $35^\circ$ , correspondingly, relative to axis  $Z$ , after which, similarly to the formation of the junctions of the tilt boundaries, the segments  $120^\circ$  each were cut from them and conjugated. In this case, the boundary conditions on all the surfaces of the obtained cylinder were specified rigid.



**Figure 1.** Computational block containing the triple junction of the  $\langle 111 \rangle$  tilt boundaries.

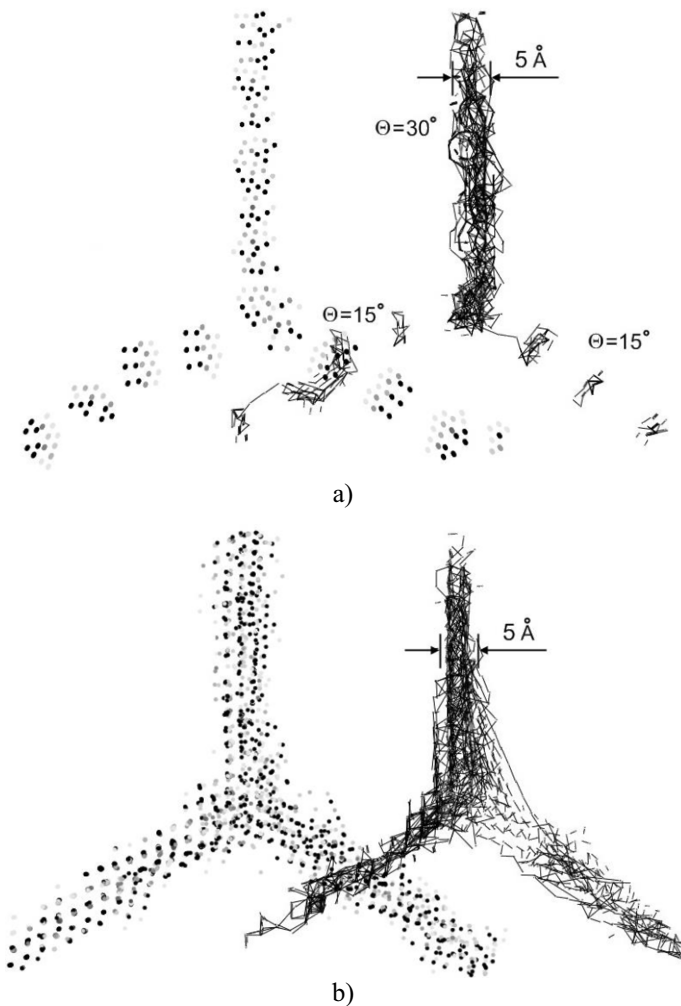
In Figure 1, the atoms that are shown dark-gray remained immobile during the computer experiment (the rigid boundary conditions). The periodic boundary conditions were specified at the cylinder ends. The grain boundaries are denoted by the bright dashed lines.

To present the structure of the computational block into the equilibrium state (in these conditions), the block was held for 100ps at a constant temperature of 1500K. After then the computational block was cooled to 0 K. Thus obtained computational blocks were starting when simulating the self-diffusion. The integration step over time in the molecular dynamics method was varied from 5 to 10fs. The interaction of the nickel atoms with each other was described by the Cleri-Rosato tight binding potential [6]. The action radius of the potentials was limited by five coordination spheres.

For the research own computer programs were used (in particular MDR1.5), creation and modernization of which is held by the research team for more than fifteen years.

## 2. Results and discussions

Visualization of the structure of the triple junctions was carried out by estimating of the free volume distribution in the computational block. Figure 2 shows the distribution of the free volume in the computational block (on the left) containing the triple junction of the  $\langle 111 \rangle$  tilt boundaries with misorientation angles  $15^\circ$ ,  $15^\circ$  and  $30^\circ$  (Figure 2a) and the triple junction of the mixed-type boundaries (Figure 2b) (the darker atoms have more free volume near himself). In all cases (including the junction of the mixed-type boundaries) was not observed any structural features that distinguish the triple junction as a specific defect. In other words, the equilibrium triple junctions of any configuration (formed by tilt or mixed-type boundaries) did not contain any excess defects compared with the grain boundaries forming the junctions, and were, in fact, a continuation of these boundaries.



**Figure 2.** Distribution of the free volume (on the left) and atomic displacements in the process of self-diffusion (on the right) near the triple junction of the  $\langle 111 \rangle$  tilt boundaries with misorientation angles 15°, 15° and 30° (a) and the triple junction of the mixed-type boundaries (b).

In order to investigate the self-diffusion near the triple junctions, the simulation of the process 300 ps long at various temperatures was performed. The temperature during the process was held constant. Upon finishing the computer experiment, the computational blocks were cooled to 0 K in order to avoid the influence of the thermal atomic vibrations on the computations of the diffusion characteristics. The character of displacements of the atoms during the self-diffusion was investigated using the visualizer of the atomic displacement [7]. These displacements were depicted by the segments connecting the initial and final locations of the atoms. Insignificant displacements were not imaged in this case.

Fig. 2 (on the right) shows the patterns of the atomic displacements near the triple junctions of the  $\langle 111 \rangle$  tilt boundaries and the mixed-type boundaries during the

computer experiment for 300 ps at a temperature of 1500 K. For the triple junction of the  $\langle 100 \rangle$  tilt boundaries, the pattern was obtained similar to that one observed for the  $\langle 111 \rangle$  boundaries.

Despite a relatively high temperature, the diffusion atomic displacements in all cases occurred in comparatively narrow channels along the grain boundaries having the visual diffusion width of about 5 Å according to the acquired patterns. This agrees with the convenient width of the grain boundaries [3, 4]. For the  $\langle 111 \rangle$  grain boundaries with the misorientation angle of  $15^\circ$  (Fig. 2a), despite the fact that such boundaries are often referred to high-angle boundaries, it was found that the “pipe” diffusion (the diffusion along the grain boundary dislocations) which is characteristic of the low-angle tilt boundaries [8], is clearly followed.

When comparing the intensity of atomic displacements along the grain boundaries and the triple junctions, no specific prevalence of the diffusion along the junctions was observed. According to the acquired patterns, the comparable intensities were of approximately the same order of magnitude. The diffusion radius of the triple junctions can be evaluated visually using the acquired patterns of the atomic displacements. It is seen from Fig. 2a that the radius for the junction formed by the  $\langle 111 \rangle$  tilt boundaries is small and does not exceed 3 Å. The radius for the junction formed by the mixed-type boundaries (Fig. 2b) is larger and equals approximately 5 Å.

### 3. Summary

Thus, as shown by the molecular dynamics simulation, equilibrium triple junction (non-containing of additional defects) has no structural features, which ably single it out as a special defect among grain boundaries forming this junction. The diffusion intensity along the equilibrium triple junctions has the same order as the diffusion intensity along the grain boundaries. The diffusion radius, i.e. the effective radius of the diffusion channel, oscillates in limits of 3–5 Å depending on the type of the grain boundaries forming the junction, and the junction radius becomes smaller with its formation by the tilt boundaries. The effective diffusion width of the considered boundaries was 5 Å. Moreover, the diffusion intensity in the boundary region is distributed nonuniformly and higher in the channel center as a rule.

It should be noted that the conclusions made in this article are referred to the equilibrium triple junctions. It is known that similarly to the grain boundaries themselves, the junctions of the boundaries in actual metals can serve as the accumulation place of the different defects (disclinations, dislocations, point defects and others) as a result of the recrystallization, grain boundary sliding, the capture of the lattice dislocations, the deformations, etc. In this case the triple junctions already can have the structural energy features which differ their properties from the properties of the grain boundaries forming these joints.

### Acknowledgements

The reported study was partially supported by RFBR, research projects No. 13-02-00301\_a, No. 14-02-98000-r\_sibir\_a.

## References

- [1] G. Palumbo, K.T. Aust, A coincident axial direction (CAD) approach to the structure of triple junctions in polycrystalline materials, *Scripta Metallurgica et Materialia* **24** (1990), 1771-1776.
- [2] S.G. Protasova, V.G. Sursaeva, L.S. Shvindlerman, Study of the motion of individual triple junctions in aluminum, *Physics of the Solid State* **45** (2003), 1471-1474.
- [3] Yu.R. Kolobov, A.G. Lipnitskii, I.V. Nelasov, G.P. Grabovetskaya, Investigations and computer simulations of the intergrain diffusion in submicro- and nanocrystalline metals, *Russian Physics Journal* **51** (2008), 385-399.
- [4] T. Frolov, Y. Mishin, Molecular dynamics modeling of self-diffusion along a triple junction, *Physical Review B* **79** (2009), 174110.
- [5] A.G. Lipnitskii, I.V. Nelasov, Yu.R. Kolobov, Self-diffusion parameters of grain boundaries and triple junctions in nanocrystalline materials, *Diffusion and Defect Data Pt. A: Defect and Diffusion Forum* **309-310** (2011), 45-50.
- [6] F. Cleri, V. Rosato, Tight-binding potentials for transition metals and alloys, *Physical Review B* **48** (1993), 22-33.
- [7] G.M. Poletaev, M.D. Starostenkov, [Dynamic collective displacements of atoms in metals and their role in the vacancy mechanism of diffusion](#), *Physics of the Solid State* **51** (2009), 727-732.
- [8] M.D. Starostenkov, D.V. Sinyaev, R.Yu. Rakitin, G.M. Poletaev, Diffusion mechanisms near tilt grain boundaries in Ni<sub>3</sub>Al intermetallide, *Diffusion and Defect Data Pt. B: Solid State Phenomena* **139** (2008), 89-94.

# Analysis of elongation variance of tendons using stress-strain graphs

Morgan DUNDU<sup>1</sup> and Sebastian RUIEPER

Department of Civil Engineering Science, University of Johannesburg, South Africa

**Abstract.** The South African design standards (SANS 2001-CC1 and COLTO) prescribes an elongation variation limit of  $\pm 6\%$  and an average variation limit of  $\pm 3\%$ . Most often these limits are exceeded in practice. If the elongation variation of a tendon falls outside the prescribed elongation limits it must be assessed by the engineer. This paper analyses data of bonded tendons from post-tensioned structures. The aim of this study is to explain the elongation variance of tendons in post-tensioned structures using selected stress-strain graphs. These structures include a reservoir (Mthatha 1-10) and a viaduct (Gautrain Jean Avenue P80).

**Keywords.** Elongation, variation, elastic modulus, tendon, friction, wobble.

## Introduction

Post-tensioning is a process of reinforcing (strengthening) concrete with high-strength steel strands or bars, typically referred to as tendons. There are two main types of post-tensioning systems; unbonded and bonded (grouted). In an unbonded tendon the mono-strand tendon consists of a seven-wire strand that is coated with a corrosion-inhibiting grease and encased in an extruded plastic protective sheathing, as shown in Figure 1(a). The plastic sheathing acts as a bond breaker between the concrete and the pre-stressing strands. It also serves as a barrier that prevents moisture and chemicals from reaching the strand and provides protection against damage by mechanical handling. In bonded systems, two or more strands are inserted into a metal or plastic duct that is embedded in the concrete. A large, multi-strand jack is used to stress the strands. After the strands have been anchored, the duct is filled with a cementitious grout, as shown in Figure 1(b). The grout provides corrosion protection to the strand and bonds the tendon to the concrete surrounding the duct.

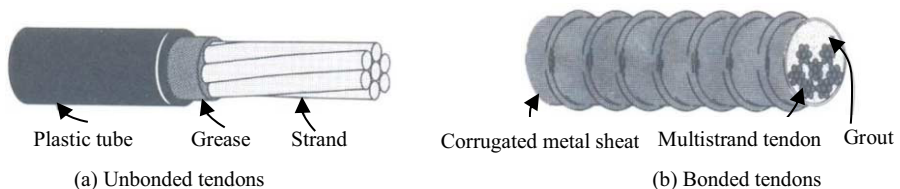


Figure 1. Bonded and unbonded tendons

<sup>1</sup>Corresponding author: University of Johannesburg, Department of Civil Engineering Science, P.O. Box 524, Auckland Park, 2006, South Africa; E-mail: [mdundu@uj.ac.za](mailto:mdundu@uj.ac.za)

The tendons reported in this paper were all bonded. The average areas and elastic moduli of these tendons are given in Table 1. Table 1 show that the values of the elastic modulus and cross-sectional area of the strand tend to be greater than the assumed values of 195 GPa and 150 mm<sup>2</sup>, respectively. This causes a slight reduction in the elongation of the average tendon. Since the value of the elastic modulus and cross-sectional area vary along the length of the strand, the elongation will vary too. The average and standard deviation in Table 1 gives a combined average elastic modulus of 195.49 GPa for the 15.7mm strand and an average elastic modulus of 191.61 GPa for the 15.24 mm. Based on these elastic modulus results it is recommended that the average elastic modulus of 195 GPa be maintained, however the elastic modulus should range from 195±5 GPa, for locally manufactured strands. This range is more stringent than the elastic modulus range of 195±10 GPa, suggested by BS 5896 [1] and EN1992-1-1 [2]. Such a reduction in the elastic modulus range will impact the elongation variation positively.

**Table 1.** Average areas and elastic modulus for the strand

Strand	Project	Tendons	Average material properties		Standard deviation	
			Area (mm <sup>2</sup> )	E (GPa)	Area (mm <sup>2</sup> )	E (GPa)
15.70mm	K71 Beams	11	154.05	196.93	0.94	6.07
	Coega to Colchester	42	153.79	192.23	0.98	6.22
	Mthatha	100	153.89	196.14	1.34	5.30
	Jean Ave. P76	24	150.70	196.61	0.98	2.94
	Jean Ave. P77	18	150.54	193.99	1.10	5.01
	Jean Ave. P80	16	150.00	196.52	0.00	3.78
	John Vorster P6	18	150.28	195.63	0.70	3.00
	John Vorster P7	16	150.04	195.74	0.10	3.29
	John Vorster P8	20	150.00	195.42	0.00	4.46
	John Vorster P10	6	150.13	195.68	0.15	1.69
	Average			151.34	195.49	0.63
15.24mm	K46	70	143.86	191.61	0.86	4.91

## 1. Elongation variations

To explain the elongation variance of tendons in post-tensioned structures, selected stress-strain graphs of the tendons from two post-tensioned structures are presented and discussed in this section. These structures include a reservoir (Mthatha 1-10) and a viaduct (Gautrain Jean Avenue P80). A summary of the elongation variations for these structures is given in Table 2.

**Table 2.** Summary of elongation variation results

Project	Tendons	Average (%)	Std. Deviation (%)	Max. Value (%)	Min. Value (%)	Var.range (%)
Mthatha 1-10	50	+0.73	5.38	+10.84	-13.21	+7.43
Jean Ave. P80	16	+6.55	3.97	+11.88	-2.08	+5.72



1.1. Mthatha 1-10 tendons

The stress-strain graphs for Mthatha 1-10 set of tendons is shown in Figure 2. The length of the tendons tensioned is 15.85 m and the elongation variation is given in the legend (and this applies to the two stress-strain graphs discussed in the paper). Over-elongation variations are positive and under-elongation variations are negative. Positive elongation means that the tendons exceeded the required elongation and the reverse is true for negative elongation. Since a small average elongation variation of 0.73% was obtained for the fifty (50) Mthatha 1-10 tendons (Table 2), the elongation can be regarded as balanced. These average elongation variation is also well below the limit of 3%, provided by SANS 2001-CC1 [3] and COLTO [4]. The corresponding standard deviation of 5.38% indicates a large dispersion of elongation results; however, they are below the limit of 6%, provided by these standards. Further evidence of the large dispersion of the elongation variation is shown by the maximum and minimum values in Table 2.

Over-elongation variations do not pose problems in post-tensioning; however, under-elongation can be problematic. Over-elongation is either caused by the plastic deformation of the strand, low strand strength or less than expected friction, wobble, elastic modulus and cross-sectional area, or any combination of these. If the strand deform plastically, then the gradient of the stress-strain graph will decrease. This is immediately apparent to an experienced jack operator since the jack would carry on extending at the same jacking pressure. Better tension distribution is achieved if there is less than expected friction and wobble or any combination of these, and this is the most desirable case in post-tensioning. A larger than expected friction or wobble causes under-elongation, and might indicate that the tension in the tendon is not distributed evenly. This is a cause for concern since some sections of the tendon might be tensioned more than the others. It should be noted that under-elongation can be caused by higher values of the elastic modulus and cross-sectional area of the strand.

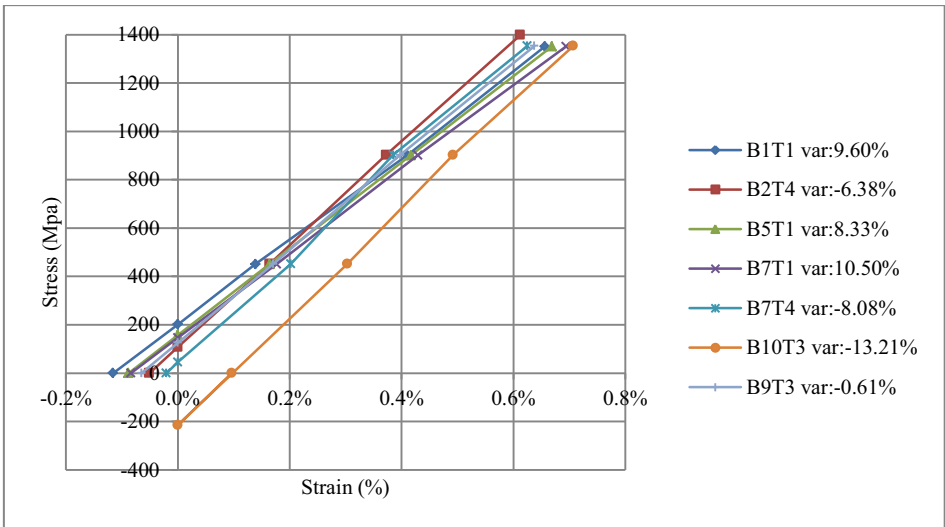


Figure 2. Selected stress-strain graph of Mthatha 1-10 Tendons

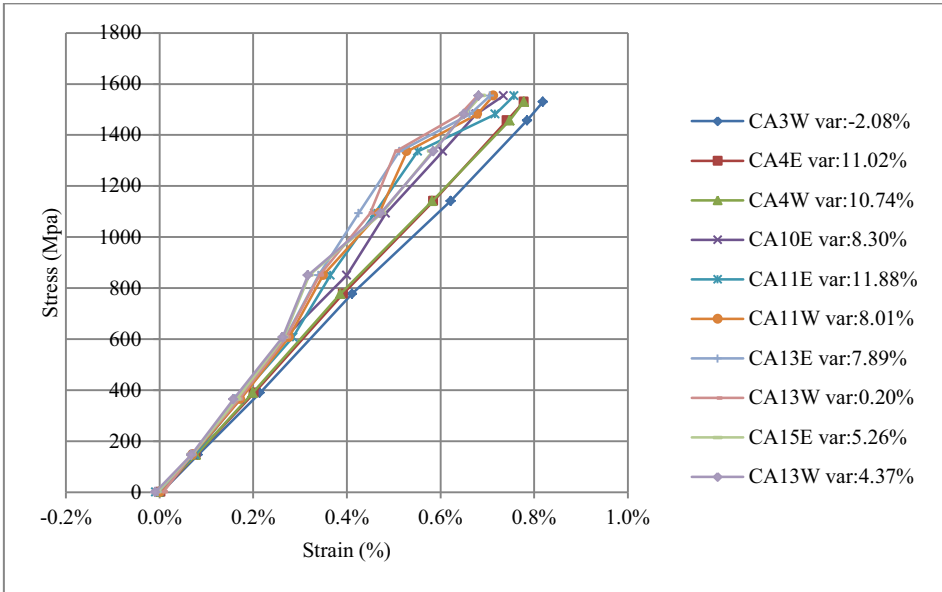
Although the elongation variation results of Mthatha 1-10 tendons vary considerably, the stress-strain gradients of most tendons are almost the same. Tendon B9T3 (Figure 2) can be regarded as a perfect elongation result, since it has a small elongation variation of -0.61%. Tendons B10T3 and B2T4, in Figure 2, have steeper stress-strain gradients than the other tendons, and this is usually evidence of higher friction or significant wobble experienced by the tendons. None of the strand certificates showed an elastic modulus or cross-sectional area that is high enough to cause such a drastic change in gradient. Steeper gradient means more force is required to attain a pre-determined elongation. Friction increases the tensile force and reduces the resultant elongation; this increases the stiffness of the tendon. A lower friction will have the reverse effect, causing greater elongation than theoretically predicted. The slight difference in the gradient of the other tendons is most likely due to the variable nature of both the elastic modulus and the area of the strand along its length.

The positive strain of tendon B10T3 at zero pressure shows that there might have been loose strands in the tendon or slippage in the anchor. Such a tendon should be checked for signs of slippage to explain the shift to the right of the stress-strain graph. All the other tendon graphs crossed the zero x-axis at a positive stress. A shift to the right of the stress-strain graph of a tendon is usually caused by the slack of the tendon in the sheath, before the tendon is tensioned. When a force is applied to the strand, the slack disappears, however this also elongate the strand slightly, hence elongation occurs beyond the zero strain point. COLTO [4] and SANS 10100-1 [5] recommends that 10% of the tensioning force be applied to the tendon before re-setting the jack to zero-elongation. In compliance with the specifications, the stresses achieved are almost 10% of the tension force.

Tendon B7T4 (Figure 2) differ from the other tendons in that they show alternate stages of over-elongation and under-elongation. This behaviour is referred to as “slip-stick” and is attributed to the squeeze effect of strands in the tendon on each other during tensioning [6]. It occurs when localized friction holds tension and then releases it at the next stressing increment. A final negative or positive elongation variation is evidence that the magnitudes of under-elongation and over-elongation were different. When higher localized friction occur the tendons usually under-elongate as is the case with Tendon B7T4.

### 1.2. Gautrain Jean Avenue P80 tendons

The long tendons for the Gautrain Jean Avenue segment P80 (length ranging from 83.86 m to 111.09 m), in Figure 3, were only linear at low stress levels, and non-linear at high stress levels. The non-linear or slip-stick (over and under-elongation) behaviour exhibited by these tendons was caused by friction, as discussed previously. The high friction is due to the squeezing of tendons on each other over regions of large curvature [6]. All tendons in this range were stressed from both ends, starting with the live-end, and then the dead-end. A cable is double-end stressed when the length of the cable is long and the frictional forces along the tendon are expected to be large. In this situation, the stress-strain plot only shows the stressing from the live-end since only the live end's stressing is done in increments. The other end of the tendon is stressed in one increment; this is termed “top-up” in the industry. It is important to note that although the tendons experienced alternate over and under-elongations during tensioning, the tendons still over-elongated, which indicate that the force was uniformly distributed along the length of the cable.



**Figure 3.** Selected stress-strain graph of Gautrain Jean Avenue P80 tendons

## 2. Conclusions

Table 1 gives a combined average elastic modulus of 195.49 GPa for the 15.7mm strand and an average elastic modulus of 191.61 GPa for the 15.24 mm. From these elastic modulus results it is recommended that the average elastic modulus of 195 GPa be maintained, however the elastic modulus should range from  $195 \pm 5$  GPa, for locally manufactured strands. This range is more stringent than the range suggested by BS 5896 [1] and EN1992-1-1 [2]. Such a reduction in the elastic modulus range will impact the elongation variation positively.

Elongation variations are dependent on the assumed friction and wobble coefficients. Over-elongation is caused by less than expected friction, wobble, elastic modulus and cross-sectional area, or any combination of these. When these factors are large they favour negative elongation. A larger than expected friction or wobble might indicate that the tension in the tendon is not distributed evenly. This is a cause for concern since some sections of the tendon might be under-tensioned and others over-tensioned.

It has been shown that the slip-stick behaviour that occurred in numerous tendons in this study is due to high localized friction. This behaviour is caused by squeezing effect of strands in a tendon during tensioning [6], and occurs when localized friction holds tension and releases it at the next stressing increment. Longer tendons show greater non-linear behaviour than shorter tendons. This is due to numerous zones of friction. Stressing of the tendon from both ends (live and dead-end) ensures uniform tension distribution in the strand.

## References

- [1] BS 5896, *Specification for high tensile steel wire and strand for the pre-stressing of concrete*, British standard, UK, 2012.
- [2] EN 1992-1-1, *Design of concrete structures - Part 1-1: General rules and rules for buildings*, Brussels, European Committee for Standardization, 2004.
- [3] SANS 2001-CC1, *Construction works - Part CC1: Concrete works (structural)*, South African Bureau of Standards, Pretoria, South Africa, 2007.
- [4] COLTO, *Standard specification for road and bridge works*, Committee of Land and Transport Officials, Department of Transport, South Africa, 1998.
- [5] SANS 10100-1, *Standardised specification for the structural use of concrete*, South African Bureau of Standards, Pretoria, South Africa, 2000.
- [6] IFP, *Tensioning of tendons: force-elongation relationship*, International Federation for Prestressing, Thomas Telford Ltd, London, UK, 1986.

# Limits of elongation variation of tendons in post-tensioning

Morgan DUNDU<sup>1</sup> and Sebastian RUIEPER

*Department of Civil Engineering Science, University of Johannesburg, South Africa*

**Abstract.** This paper analyses tensioning data obtained from a variety of projects that have been completed in South Africa in recent years in order to determine the causes of variation in elongation and suggest practical elongation limits. Current limits, prescribed by the South African standards (SANS 2001-CC1 and COLTO), of elongation variation limit of  $\pm 6\%$  and an average elongation variation limit of  $\pm 3\%$  are causing huge problems to the post-tensioning industry. The scatter of tendon elongation results is often greater than the range prescribed by these standards. This usually requires the contractor to re-tension the tendons at huge financial costs. In most cases the results obtained after re-tensioning are the same.

**Keywords.** Elongation variation, post-tensioning, tendon, tension, friction, wobble.

## Introduction

In South Africa, guidelines for post-tensioning are provided by SANS 2001-CC1 [1] and COLTO [2]. In these standards the specification for high tensile steel wire and strand for the pre-stressing of concrete comply with the requirements of BS 5896 [3] and the mechanical tests for post-tensioning systems (including anchorages and couplers) comply with the requirements of EN 13391 [4]. According to these specifications the measured extension on individual tendons should be within 6% of the theoretical extension and the average of the measured extensions of all the tendons in a unit should not deviate from the theoretical extension by more than 3%. The accomplishment of these limits is causing problems in the South African post-tensioning industry because some elongation variations do not fall within these specifications. Such tendons are normally re-stressed (at the cost of the post-tensioning contractor); however, it has been found that after re-stressing the elongations do not change. This paper seeks to study post-tensioning data on several projects constructed in South Africa in order to solve this puzzle. The data was provided by Freyssinet, South Africa.

## 1. Presentation and discussion of tendon results

A total of 402 tendons from various projects, done by Freyssinet, were studied. Table 1 summarizes the average, standard deviation, maximum, minimum and range of the

---

<sup>1</sup>Corresponding author: University of Johannesburg, Department of Civil Engineering Science, P.O. Box 524, Auckland Park, 2006, South Africa; E-mail. mdundu@uj.ac.za

elongation results for the 402 tendons that were considered. The data was divided into groups, and these groups were split according to the type of project, date of stressing and type of jack. This ensured that tendons in the same group were stressed under similar conditions. Tendons of the same project, but stressed at different dates are numbered differently. For instance, Mthatha 1-10 tendons are from the same project as those of Mthatha 11-20, however these tendons were stressed at different dates. As can be seen from Table 1, the average value of +4.06% for all tendons is high, considering that the expected average elongation variation is  $\pm 3\%$  (SANS 2001-CC1 [1] and COLTO [2]). Since only five of the sixteen tendon groups met this requirement, this requirement can be considered to be too stringent. The positive average elongation variation also shows that post-tensioning tendons tend to over-elongate during stressing.

**Table 1.** Summary of elongation variation results

Project	Tendons	Average (%)	Std. Deviation (%)	Max. Value (%)	Min. Value (%)	Var.range (%)
Coega-Colchester (1-14)	28	+6.07	2.27	+10.18	+1.04	+8.30
Coega-Colchester (15-21)	14	+5.03	2.09	+7.41	+1.39	+8.22
Kwa-Mashu	14	+0.78	5.02	+9.83	-5.94	-3.03
K46 15.24mm (1-9)	18	-8.38	4.10	+0.49	-15.29	+6.85
K46 15.24mm (17-32)	52	-3.87	6.00	+3.70	-22.85	-2.43
Malendela	54	-0.14	3.60	+8.12	-7.69	-2.90
Mthatha 1-10	50	+0.73	5.38	+10.84	-13.21	+7.43
Mthatha 11-20	50	+0.11	5.16	+9.99	-13.21	+7.38
Jean Ave. P76	24	+2.53	8.82	+14.46	-22.81	+4.46
Jean Ave. P77	18	+5.70	5.04	+16.00	-1.10	+4.28
Jean Ave. P78	4	+8.76	4.19	+14.09	+4.12	-
Jean Ave. P80	16	+6.55	3.97	+11.88	-2.08	+5.72
John Vorster P6	18	+10.17	5.40	+19.17	+3.00	+4.43
John Vorster P7	16	+6.50	5.13	+16.75	-1.00	+3.74
John Vorster P8	20	11.00	3.75	+16.70	+4.81	+5.58
John Vorster P10	6	+13.43	2.92	+16.39	+9.33	-
Mean		+4.06%	4.55%	11.63	-5.09	+5.56

The standard deviation from Table 1 of 4.55% indicates a high degree of scatter of elongation variation results. It means that the majority of elongation variation results will occur in the region of 4.55% on either side of the average value. Since this standard deviation is the average value of the standard deviations of a group of tendons, the tolerance range can be taken as two standard deviations combined, from the average value. Hence, a standard deviation of 4.55% would give an elongation variation of  $\pm 9.1\%$  (rounded to 9%), which is about 50% greater than the current limit of  $\pm 6\%$ . Since none of the tendons considered in this paper failed when subjected to the prescribed tension, an elongation variations of  $\pm 9\%$  can be considered to be safe. The limit of elongation variation of  $\pm 6\%$  is too stringent, and do not reflect site conditions. All the tendons in Table 1 were stressed to their target tension forces.

To illustrate how the elongation variations of tendons compare with standards, selected elongation variation graphs of tendons are presented and discussed in this section. These graphs help to show the actual scatter of variation data from 0% and how these results relates to the limits provided by SANS 2001-CC1 [1] and COLTO [2]. The results considered in this section includes tendons that predominantly experienced balanced elongation (Mthatha 1-10 and Mthatha 11-20), over-elongation (Coega to Colchester 1-14 and John Vorster P8) and under-elongation (K46 (1-9)). The variation in elongation was calculated as the difference between the theoretical and the real elongation.

1.1. Mthatha 1-10 and Mthatha 11-20 tendons

Mthatha 1-10 and Mthatha 11-20 tendons, in Figures 1 and 2, are examples of projects that experienced balanced elongation variations. This is due to the fact that the corresponding average elongation variations of +0.73% and +0.11% are small (close to 0%) and well below the average elongation variation of  $\pm 3\%$  (Table 1). In addition standard deviations of 5.38% and 5.160% are below the limit elongation variation of  $\pm 6\%$ , provided by the standards. In both groups of tendons the scatter of elongation results is almost the same about the datum (Figure 1 and 2), which clearly shows that there was a balance between under and over-elongation results. Despite the fact that the length of these two groups of tendons were the same (15.85 m) Mthatha 1-10 tendon elongation results vary from a minimum of -13.21% to a maximum of 10.84%, and Mthatha 11-20 from a minimum of -13.21% to a maximum of 9.99%. According to the SANS 2001-CC1 [1] and COLTO [2] specifications, 13 out of 50 of Mthatha 1-10 tendons (26%), and 14 out of 50 tendons of Mthatha 11-20 (28%) fall outside of the limit of  $\pm 6\%$  (Figures 1 and 2).

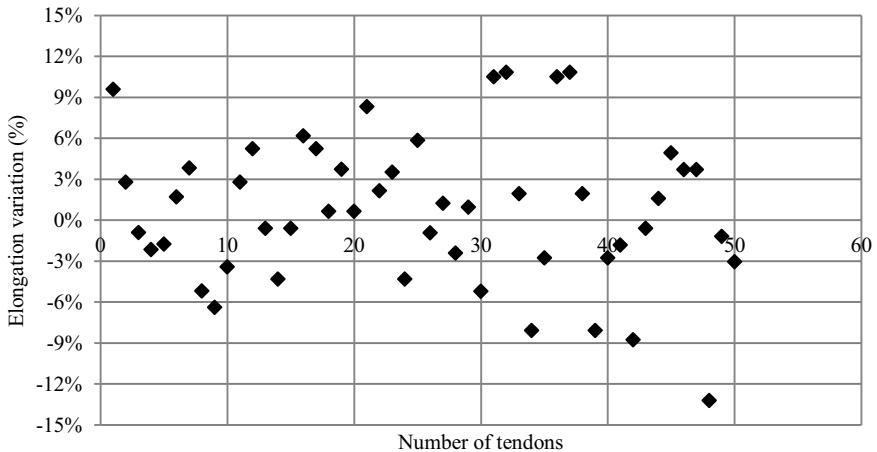
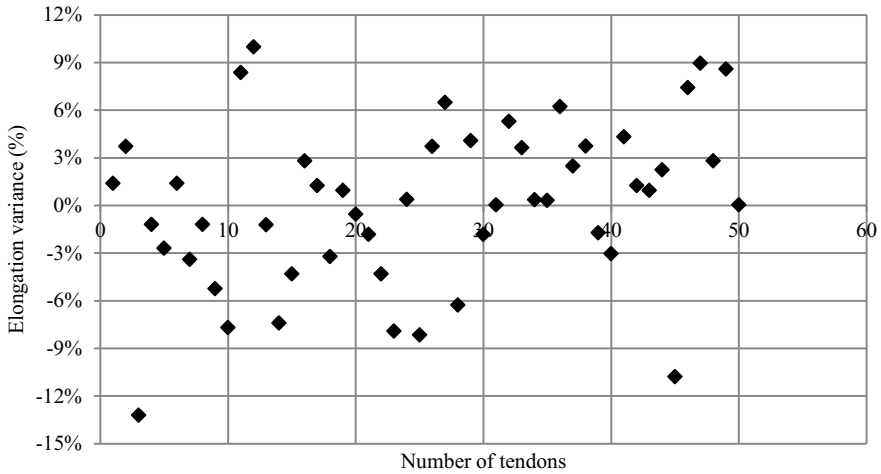


Figure 1. Elongation variations of Mthatha 1-10 tendons



**Figure 2.** Elongation variations of Mthatha 11-20 tendons

If the recommended elongation variation range of  $\pm 9\%$  is applied then only six Mthatha 1-10 and 3 Mthatha 11-20 would fall out of the specification limits. Tendons with significantly higher negative elongations show evidence of higher friction or wobble experienced by the tendons. None of the strand certificates showed an elastic modulus or cross-sectional area that is high enough to cause such a drastic change in gradient. Negative elongation variations imply that more force is required to attain a pre-determined elongation. Friction increases the tensile force and reduces the resultant elongation; this increases the stiffness of the tendon. A lower friction will have the reverse effect, causing greater elongation than theoretically predicted.

### 1.2. Coega to Colchester 1-14 and John Vorster P8 tendons

The Coega to Colchester 1-14 (Figure 3) and John Vorster P8 (Figure 4) set of tendons produced average elongation variations of 6.07% and 11.00%, respectively, which are completely outside of the limit of 3%. However, their corresponding standard deviation of 2.27% and 3.75% are low, which indicates that there is little deviation from the average values of 6.07% and 11.00%, respectively. The large average elongation variations occurred despite the fact that the prescribed tensile force was achieved in the tendons. The positive maximum and minimum elongation values for the two groups of tendons (+10.18% and +1.04% for Coega to Colchester 1-14, and +16.70% and +4.81% for John Vorster P8) shows that the tendons experienced significant over-elongation. The shift in the elongation results was probably caused by reduced friction in the sheathing or by assuming too high friction and wobble factors. It is interesting to note that if the average value in these graph was taken as the datum, then all the elongation variations for Coega to Colchester 1-14 tendons will fall within the  $\pm 6\%$ , specified by SANS 2001-CC1 [1] and COLTO [2]. If such a shift in noticed earlier, re-stressing of the tendons can be avoided. It is also important to note that if the proposed limit of  $\pm 9\%$  was applied, then both Coega to Colchester 1-14 and John Vorster P8 tendons will be within the specified limits.



As indicated before, a shift in elongation results could also be caused by the loose “lay” of the strands in the tendons. Loose, outer wires tend to have a greater length than a normal tight strand. When a force is applied to the strand, the outer wires are tightened, causing the strand to lengthen, under a small tensile force from the jack. This elongation shifts the stress-strain plots to the right of the graph. Loose wires can also result in a lower initial elastic modulus in the strand. This situation is caused by the uneven distribution of tension in the 7-wire strand. When the strand is tightened the centre wire immediately resists the tension whilst the outer wires lag behind. Such a tendon would experience over-elongation during the initial tensioning increments.

Loose wires in a strand increase the variability of the elongation results, however, they do not seem to have affected Coega-Colchester (1-14) and John Vorster tendons much, because the elongation standard deviations of 2.27% and 3.75 are small. It should be noted that over-elongation was not caused by the material properties since the actual average elastic moduli and areas of these two groups of tendons did not differ much from the assumed values of 195 GPa and 150 mm<sup>2</sup>.

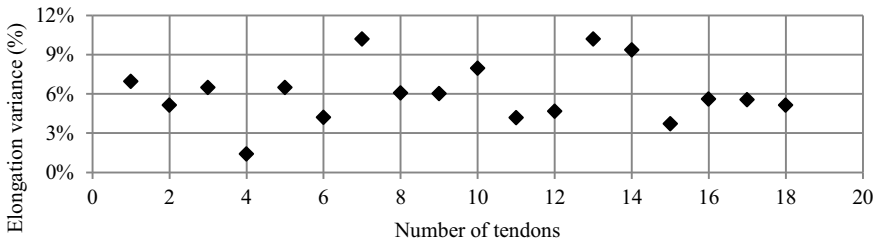


Figure 3. Coega to Colchester 1-14 tendons

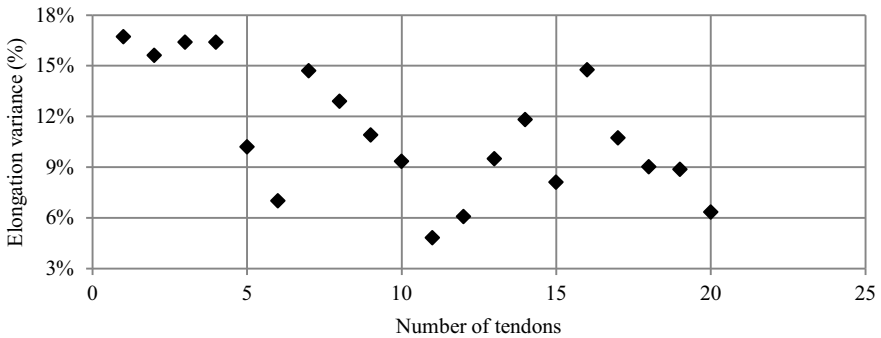


Figure 4. John Vorster P8 tendons

1.3. K46 (1-9) tendons

Except one, all K46 (1-9) tendons (Figure 5) experienced under-elongation. The tendons are 16.22 m long, and can be accommodated by the proposed elongation variation limit of ±9% if the datum is shifted downwards. Since the material properties of each group of tendons are almost the same, it can be assumed that under-elongation was either caused by higher than expected friction, wobble, elastic modulus and cross-sectional area, or any combination of these. A larger than expected friction or wobble

might indicate that the tension in the tendon is not distributed evenly. This is a cause for concern since some sections of the tendon might be tensioned more than the others.

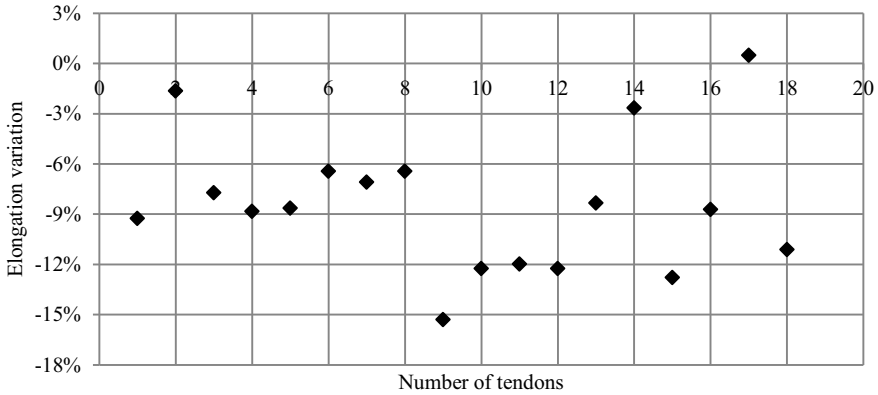


Figure 5. K46 (1-9) tendons

## 2. Summary and conclusions

The aim of this paper was to determine if the SANS 2001-CC1 [1] and COLTO [2] limits for elongation variation of  $\pm 6\%$  are too stringent or not. To achieve this selected elongation variation graphs of tendons are presented and discussed. The following conclusions are deduced from this study:

- Elongation variations are dependent on the assumed friction and wobble coefficients. Over-elongation is caused by less than expected friction, wobble, elastic modulus and cross-sectional area, or any combination of these. When these factors are large they favour negative elongation. A larger than expected friction or wobble might indicate that the tension in the tendon is not distributed evenly. This is a cause for concern since some sections of the tendon might be under-tensioned and others over-tensioned.
- It is also noted that when larger values of friction and wobble are assumed during the calculation of the tendon elongation then there is a positive shift of results. This means that the results would shift in the negative side if the friction and wobble values are small. In interpreting the results, the engineer must consider the shift and judge the elongation results of the tendons accordingly.
- The average elongation variations of the tendons range from a minimum of  $-8.38\%$  to a maximum of  $+13.43\%$ . An average elongation variation of  $4.06\%$  shows that tendons tend to over-elongate during stressing. Over-elongation reflects a better distribution of tension in the strand due to lower friction encountered by the strand [5]. The average elongation variation also exceeds the average elongation variation limit of  $\pm 3\%$ , provided by SANS 2001-CC1 [1] and COLTO [2]. It can be seen from Table 1 that only five out of sixteen tendon groups met this requirement.
- The standard deviation from Table 1 of  $+4.55\%$  indicates a high degree of scatter of elongation variation results. This scatter occurred despite the fact that the

correct tension was applied to all the tendons considered in this paper. Since this standard deviation is the mean of the average standard deviation for all groups of tendons, the elongation variation of tendons can be expected to extend two standard deviations from the average value. Hence, it is recommended that the limit  $\pm 6$  be adjusted to  $\pm 9\%$ . This gives an average elongation variation of  $\pm 4.5\%$ .

## References

- [1] SANS 2001-CC1, *Construction works - Part CC1: Concrete works (structural)*, South African Bureau of Standards, Pretoria, South Africa, 2007.
- [2] COLTO, *Standard specification for road and bridge works*, Committee of Land and Transport Officials, Department of Transport, South Africa, 1998.
- [3] BS 5896, *Specification for high tensile steel wire and strand for the pre-stressing of concrete*, British standard, UK, 2012.
- [4] EN 13391, *Mechanical tests for post-tensioning systems*, Brussels, European Committee for Standardization, 2004.
- [5] Concrete Society, *Loss of prestress*, Concrete, 2P/19/1 No. 43, UK, 1979.

## 2. Durability of construction materials

This page intentionally left blank

# Performance of corrosion inhibiting admixtures in a marine environment

Ian N. ROBERTSON  
*University of Hawaii at Manoa*

**Abstract.** Corrosion of reinforcing steel is a major contributor to early deterioration of concrete structures in a coastal environment. This paper presents the results of an eight year field study involving 25 reinforced concrete panels exposed to a marine tidal zone. Seven different corrosion inhibiting admixtures and two pozzolans were used to compare their effectiveness at preventing or delaying onset of corrosion. This study was funded by the Hawaii Dept. of Transportation, Harbors Division, in order to evaluate commercially available corrosion inhibiting admixtures when used in concretes made with basalt aggregates common to Hawaii and other Pacific Islands. The corrosion-inhibiting admixtures included in this project were Darex Corrosion Inhibitor (DCI), Rheocrete CNI, Rheocrete 222+, FerroGard 901, Xypex Admix C-2000, Latex-modifier, Kryton KIM, and the pozzolans were fly ash and silica fume.

This paper presents an assessment of the amount of corrosion on the reinforcing steel in the field panels and compares the results with companion laboratory specimens with the same concrete mixtures. It was found that DCI, CNI, fly ash and silica fume all provided improved corrosion protection compared with the control specimens. Kryton KIM performed well in a field panel, but was not included in the laboratory study. As expected, the control mixture with lower water-cement ratio (0.35) performed better than a control mixture with higher water-cement ratio (0.40). Concrete mixtures using Rheocrete 222+, FerroGard 901, Xypex Admix C-2000 or Latex-modifier showed mixed results. Some mixtures exhibited improved performance compared with the control mixtures, while others did not. Based on the results of this study, these corrosion inhibiting admixtures cannot be recommended for concrete using Hawaiian aggregates in a marine environment.

**Keywords.** Corrosion, marine exposure, admixtures, corrosion inhibitors

## Introduction

Reinforced concrete structures exposed to a marine environment often experience corrosion of the reinforcing steel, which may require that the structure be rehabilitated to remain in service. This study was intended to identify effective and reliable corrosion inhibiting measures that will delay the onset of corrosion, prolong the service lives of future structures, and reduce maintenance costs for deteriorating structures.

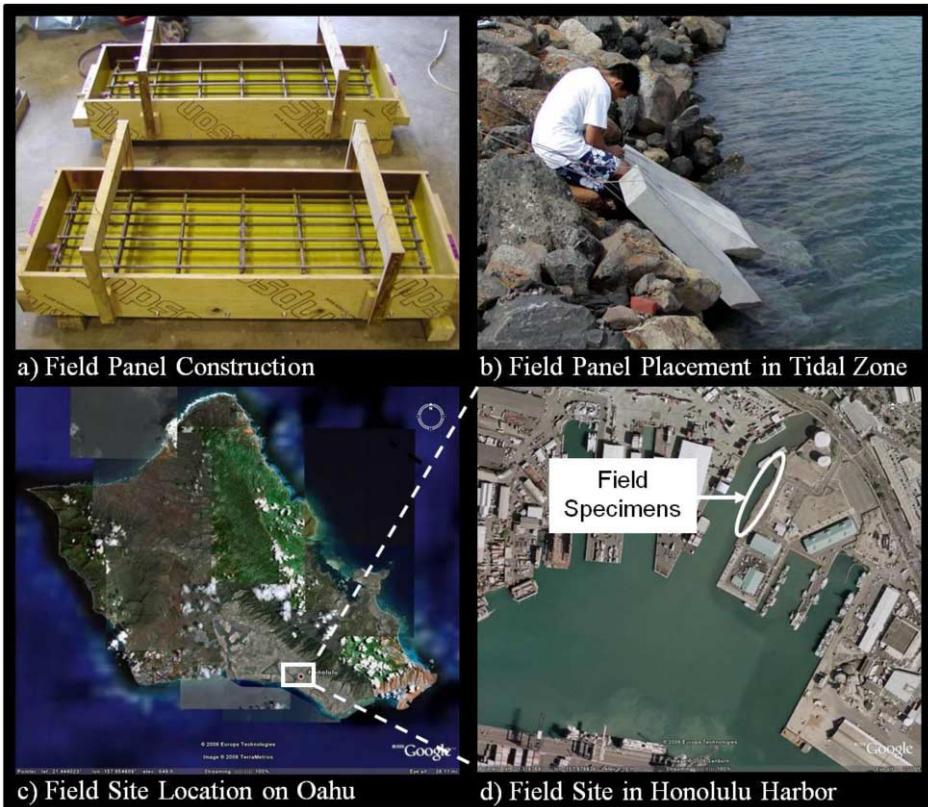
The study was conducted in three phases. The first phase was a field investigation aimed at evaluating the effectiveness of corrosion inhibiting measures in existing structures along Hawaii's shoreline. Results of this phase are not discussed here, but are available in [1].

<sup>1</sup>Corresponding author: [ianrob@hawaii.edu](mailto:ianrob@hawaii.edu)

Phase II of the research included a laboratory study to investigate the corrosion inhibiting effects of mixture proportions using corrosion inhibiting admixtures and pozzolanic materials. Detailed information on materials and methods used, and results of this phase are presented in [2, 3, 4 available online].

Phase III of the investigation was a long-term field exposure program to assess the performance of panels produced using some of the inhibiting methods identified in the laboratory study (Figure 1). Table 1 provides details of the 25 field panels located in the tidal zone at Honolulu harbor. Coarse and fine aggregates were obtained from both main quarries on the Hawaiian island of Oahu, namely Kapaa and Halawa quarries. Additional details on this study are available in [5, 6, 7 available online, and 8].

This paper provides a final analysis of the field specimens after 8 years of marine exposure. The specimens were removed from the field site, tested for half-cell potential, chloride concentration and pH at the level of the reinforcing steel, and dissected to recover the reinforcing steel for mass loss measurements [9]. A final assessment of the corrosion inhibiting admixtures is provided based on both field and laboratory results.



**Figure 1.** Fabrication and location of Phase III field corrosion panels in a marine environment.

## 1. Reinforcing steel inspection

After approximately 8 years exposure in a marine environment, all panels were removed and returned to the laboratory for dissection. Unfortunately three specimens (P1, P3 and P16) had broken loose and fallen to the bottom of the harbor, so could not be recovered.

**Table 1.** Field specimen details

Panel	w/c Ratio	Aggregate Source	Inhibiting Admixture	Admixture Dosage	Mass Loss (%)
7	0.35	Kapaa	None	Control	0.53
2	0.4	Halawa	None	Control	3.79
4	0.4	Halawa	DCI	10 l/m <sup>3</sup>	2.33
3A	0.4	Kapaa	DCI	20 l/m <sup>3</sup>	0.00
5	0.4	Kapaa	CNI	10 l/m <sup>3</sup>	0.66
6	0.4	Kapaa	CNI	10 l/m <sup>3</sup>	0.92
5A	0.4	Kapaa	CNI	20 l/m <sup>3</sup>	0.00
15	0.4	Kapaa	Rheocrete	5 l/m <sup>3</sup>	0.57
17	0.4	Halawa	Rheocrete	5 l/m <sup>3</sup>	1.08
17A	0.4	Halawa	Rheocrete	5 l/m <sup>3</sup>	0.52
18	0.4	Halawa	FerroGard	15 l/m <sup>3</sup>	1.45
19	0.4	Halawa	FerroGard	15 l/m <sup>3</sup>	0.37
20	0.4	Kapaa	FerroGard	15 l/m <sup>3</sup>	0.52
14	0.4	Kapaa	Latex-mod.	5%	1.57
21	0.4	Kapaa	Xypex	2%	1.27
22	0.4	Kapaa	Kryton KIM	2%	0.16
8	0.36	Kapaa	Silica Fume	5%	0.00
9	0.36	Kapaa	Silica Fume	5%	0.63
10	0.36	Kapaa	Silica Fume	5%	0.35
11	0.36	Kapaa	Fly Ash	15%	0.00
12	0.36	Halawa	Fly Ash	15%	0.11
13	0.36	Halawa	Fly Ash	15%	0.00



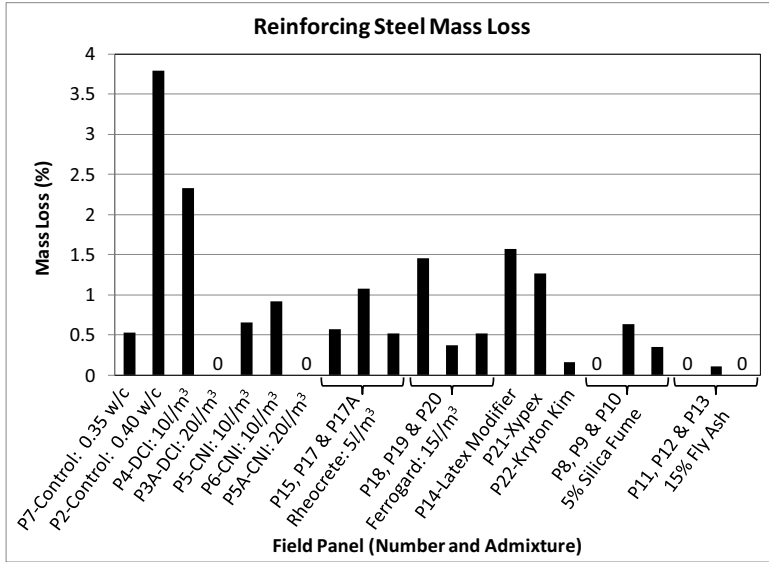
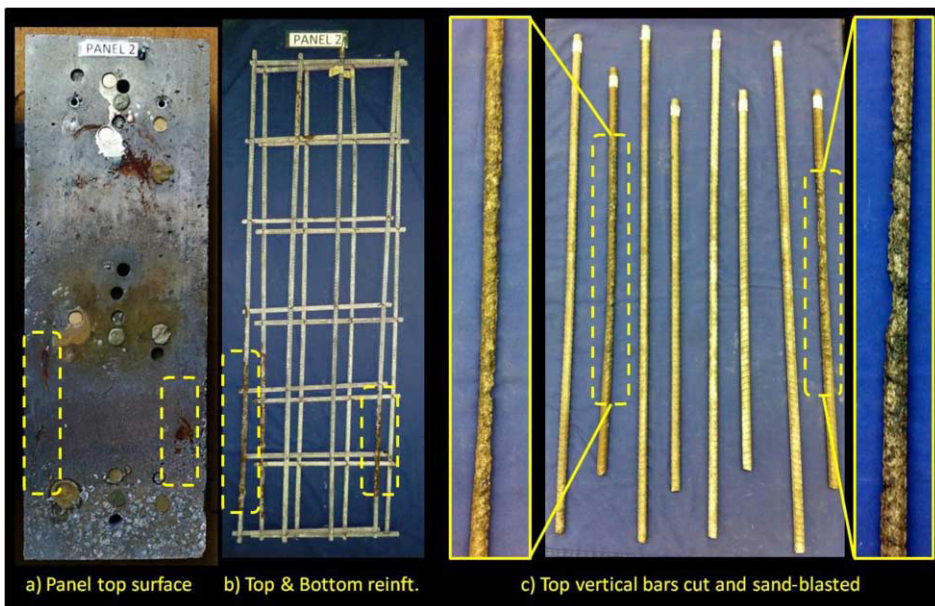


Figure 2. Mass loss due to corrosion of top layer reinforcing steel

Final half-cell readings were taken and a core removed for chloride and pH testing, before the panels were demolished, salvaging the reinforcing bars. The top layer of reinforcing steel was then cut in half (so as to fit in the sandblasting chamber), sandblasted and weighed to determine the mass loss due to corrosion. Table 1 and Figure 2 show the mass loss as a percentage of the total mass of the four top reinforcing bars. Only the top longitudinal layer of top steel was considered for the mass loss evaluation since these bars were at a clear cover of 38 mm (1.5 in.) from the top surface of the concrete panel, designated as the test face. All other reinforcing bars had a clear cover of at least 51 mm (2 in.). However, corrosion was observed on some of the transverse top steel and on the bottom steel, particularly at the edges of the panel where chloride ingress is possible in two directions.

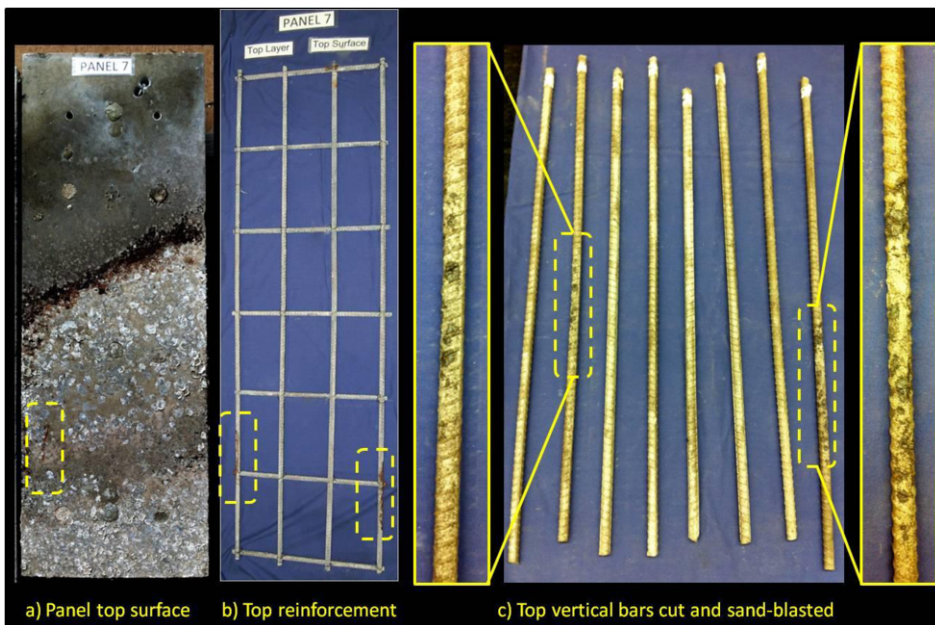
### 1.1. Control specimens

Figure 3 shows the progression of autopsy applied to Control Panel 2 (0.40 w/c ratio); exterior surface prior to demolition (left), salvaged reinforcing layers (center), and top layer of reinforcing steel after cutting in half, sandblasting and weighing for weight loss (right). Cracking and rust stains on the panel were evidence of corrosion towards the bottom of the left and right edge bars (Figure 3, left). This corrosion was obvious once the concrete was removed and the corroded steel exposed (Figure 3, center). After sandblasting the top four test reinforcing bars, the extent of steel lost due to corrosion on the bottom portion of the left and right bars was obvious (Figure 3, right). The total weight loss for the four top bars was approximately 3.79%, but the section loss at the heavily corroded areas exceeded 50% of the original bar cross-section.



**Figure 3.** Control Panel 2 with 0.4 w/c ratio before and after reinforcing steel recovery

Control Panel 7 (0.35 w/c ratio) performed much better, but still exhibited the initiation of surface corrosion towards the bottom of the two edge bars (Figure 4). Cracking and rust staining was only visible on the panel surface due to the left bar corrosion. The right bar corrosion was evident from the half-cell readings and after concrete removal. The total weight loss for the four top bars was approximately 0.53%. The level of corrosion represented moderate surface pitting.



**Figure 4.** Control Panel 7, with 0.35 w/c ratio, before and after reinforcing steel recovery

### 1.2. Admixtures designed to protect the steel surface

DCI and CNI with dosage of  $10 \text{ l/m}^3$  did not protect the reinforcing steel from corrosion. Panels 4, 5 and 6 all exhibited moderate to severe corrosion with mass loss of 2.33%, 0.66% and 0.92% respectively (Table 1). However, at a dosage of  $20 \text{ l/m}^3$ , these additives were able to prevent corrosion almost entirely in Panels 3A and 5A. There was zero mass loss for these specimens and only minor evidence of surface corrosion (Figure 5).

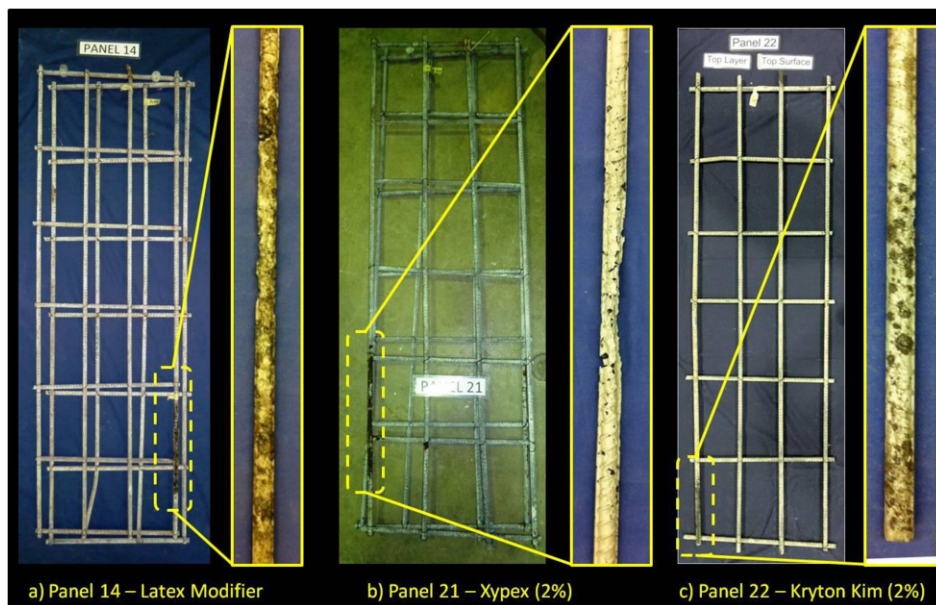
Rheocrete 222+ (at  $5 \text{ l/m}^3$ ) and FerroGard 901 (at  $15 \text{ l/m}^3$ ) were unable to prevent corrosion of the reinforcing steel. All six specimens using these admixtures had moderate to severe corrosion on portions of the reinforcing steel, resulting in mass loss values ranging from 0.37% to 1.45% (Table 1 and Figure 2).

### 1.3. Admixtures designed to reduce permeability

Latex-modifier, Xypex Admix C-2000 and Kryton KIM are admixtures designed to reduce the concrete permeability so as to limit the chloride ingress to the steel reinforcing, thereby delaying the onset and rate of corrosion. Figure 2 shows that neither the Latex-modifier (Panel 14) nor Xypex (Panel 21) was able to prevent corrosion similar to that observed on the control specimens. Mass loss for these specimens was 1.57% and 1.27% respectively. Panel 22 with Kryton KIM performed considerably better with only minor corrosion initiation on one reinforcing bar resulting in 0.16% mass loss. Figure 6 shows the location and extent of corrosion in each of these specimens.



Figure 5. Top reinforcing steel recovered from Panels 3A and 5A with  $20 \text{ l/m}^3$  of DCI and CNI respectively



**Figure 6.** Corrosion on reinforcing in Panels 14 (Latex Modifier), 21 (Xypex) and 22 (Kryton KIM)

Silica fume and fly ash are common concrete additives derived as byproducts from other industrial processes. Both serve as pozzolans providing both cementitious effects and reduced permeability for the concrete. Three panels contained silica fume replacing 5% of the cement (Panels 8, 9 and 10), while another three panels contained fly ash at 15% cement replacement (Panels 11, 12 and 13). Table 1 and Figure 2 show that the mass loss for the three fly ash specimens was virtually zero. Two of the silica fume specimens exhibited corrosion representing 0.35% and 0.63% mass loss for the top reinforcing steel bars. In one of these specimens pockets of silica fume powder were evident during coring and demolition, indicating poor mixing of the silica fume during panel construction.

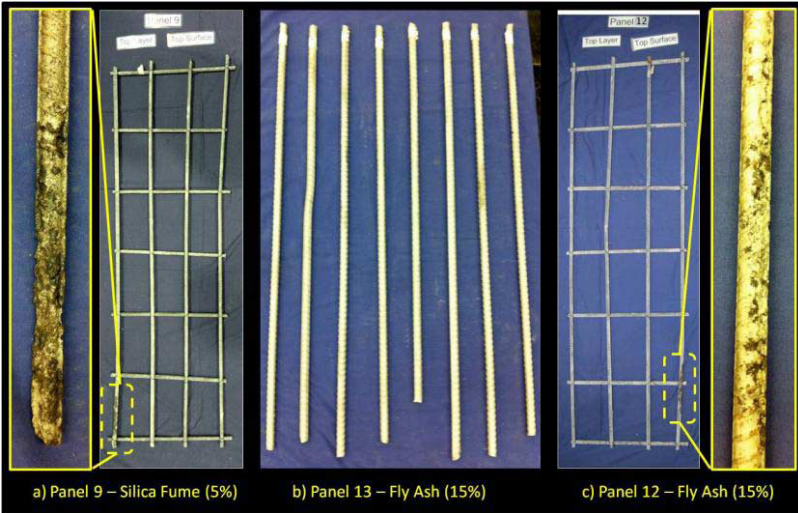


Figure 7. Corrosion on reinforcing in Panels 9 (Silica Fume) and 12 and 13 (Fly Ash)

## 2. Summary and conclusions

This paper is based on results from a multi-year field investigation of the performance of various corrosion inhibiting admixtures when used in concrete made with Hawaiian aggregates and exposed to a marine environment. Based on observations after 8 years of the field study, and 10 years of the companion laboratory tests, the following conclusions were drawn:

1. The control mixture with water/cement ratio of 0.35 showed improved corrosion protection compared with the control mixtures with 0.40 water/cement ratio.
2. Mixtures with DCI or Rheocrete CNI at doses of 20 liters per cubic meter showed superior corrosion inhibiting performance compared with the corresponding control specimens. The same admixtures at doses of 10 liters per cubic meter had less satisfactory performance in both laboratory and field specimens.
3. Mixtures with 15 percent replacement of cement with Fly Ash showed superior corrosion inhibiting performance compared with the corresponding control specimens.
4. Mixtures with 5 percent replacement of cement with Silica Fume showed superior corrosion inhibiting performance compared with the corresponding control specimens, provided the Silica Fume was fully dispersed during mixing.
5. A field panel containing Krytron KIM showed significantly better performance than the control specimen.
6. Mixtures using Rheocrete 222+, FerroGard 901, Xypex Admix C-2000 or Latex-modifier showed mixed results. Some mixtures exhibited improved performance compared with the control mixtures, while others did not.

7. A recommended concrete mixture for use in marine environments in Hawaii would have a 0.35 w/c ratio with either DCI or CNI at 20 l/m<sup>3</sup> and either Fly Ash at 15% cement replacement or Silica Fume at 5% cement replacement. Although this combination was not tested in this study, it is believed that the admixture attributes will complement each other when combined in a concrete mixture.

## Acknowledgements

The author would like to thank Prof. Craig Newton who initiated this project, and the numerous graduate and undergraduate students at the University of Hawaii who have worked on the project over the past 12 years. This research project was funded by a grant from the Hawaii Department of Transportation. This funding is gratefully acknowledged. The findings and observations made in this paper are those of the author and do not necessarily reflect those of the funding agency.

## References

- [1] Bola, M. M. B., and Newton, C. M. (2000). "Field Evaluation of Corrosion in Reinforced Concrete Structures in Marine Environment," *Department of Civil Engineering Research Report*, [UHM/CE/00-01](#).
- [2] Pham, P.A., and Newton, C. M. (2001). "Properties of Concrete Produced with Admixtures Intended to Inhibit Corrosion," *Dept of Civil Eng Research Report*, [UHM/CE/01-01](#).
- [3] Kakuda, D., Robertson, I. N. and Newton, C. M. (2005). "Evaluation of Non-Destructive Techniques for Corrosion Detection in Concrete Exposed to a Marine Environment," *Dept of Civil and Environmental Eng Research Report*, [UHM/CEE/05-04](#).
- [4] Okunaga, G. J., Robertson, I. N., and Newton, C. M. (2005). "Laboratory Study of Concrete Produced with Admixtures Intended to Inhibit Corrosion," *Dept of Civil and Environmental Eng Research Report*, [UHM/CE/05-05](#).
- [5] Uno, J., Robertson, I. N., and Newton, C. M. (2004). "Corrosion Susceptibility of Concrete Exposed to a Marine Environment," *Dept of Civil and Environmental Eng Research Report*, [UHM/CEE/04-09](#).
- [6] Cheng, H., and Robertson, I. N. (2006). "Performance of Admixtures Intended to Resist Corrosion in Concrete Exposed to a Marine Environment," *Dept of Civil and Environmental Eng Research Report*, [UHM/CEE/06-08](#).
- [7] Robertson, I. N., and Newton, C. M. (2008). "Performance of Corrosion Inhibitors in Concrete Exposed to Marine Environment," *2<sup>nd</sup> International Conference on Concrete Repair, Rehabilitation and Retrofitting*, ICCRRR 2008, Cape Town.
- [8] Robertson, I. N. (2012). "Improving Concrete Durability through the use of Corrosion Inhibitors," *3<sup>rd</sup> International Conference on Concrete Repair, Rehabilitation and Retrofitting*, ICCRRR 2012, Cape Town.
- [9] Gatdula, R.M.R., and Robertson, I.N. (2012). "Final Analysis of Reinforced Concrete Specimens after Ten Years of Marine Exposure", *Dept of Civil and Environmental Eng Research Report*, [UHM/CEE/18-08](#).

Note: All reports are available online at the UH Civil and Environmental Engineering Department website at: [www.cce.hawaii.edu/content/resreport.htm](http://www.cce.hawaii.edu/content/resreport.htm)

# Effect of superplasticizers on concrete durability indexes

Stephen O. EKOLU<sup>1</sup>

*Department of Civil Engineering Science, University of Johannesburg*

**Abstract.** Use of durability index (DI) is one of the several approaches that have been used or advanced through various test methods for the purpose of evaluating the durability of concrete mixtures. In South Africa, use of DI's has developed through testing and research over the past years. A consortium of three tests of oxygen permeability index (OPI), water sorptivity and chloride conductivity are employed.

This paper presents an investigation conducted to determine the effect that superplasticizers may have on durability indexes of concrete. Concrete mixtures of strengths ranging from 30 to 50 MPa were cast using two types of commercially available superplasticizers, herein referred to as *GL* and *RSP*. The admixtures were of different chemical bases with *RSP* being a sulphonated naphthalene superplasticizer while *GL* was a polycarboxylate ether superplasticizer. The tests conducted were compressive strength, oxygen permeability and water sorptivity.

It was found that use of *GL* increased the compressive strength of concrete by about 10 MPa over the strengths of mixes made using *RSP*. Correspondingly, *GL* had an adverse effect on durability performance, as it decreased the OPI and increased the sorptivity indexes. The results implied the possible coarsening of the pore structure of the hardened concrete which could have resulted from the use of *GL*. Results also showed that the influence of chemical admixtures on hardened concrete properties and durability characteristics of high strength concretes may be less significant for high strength concretes.

**Keywords.** Marsh cone test, viscosity modifying agent, saturation point, superplasticizer

## Introduction

The assessment of concrete durability is principally based on methods and techniques that attempt to represent the ingress of aggressive agents into concrete. As such, the transport properties of concrete are perhaps the most important but not the only crucial factors that influence durability. Nearly all aggressive agents that lead to deterioration of concrete through non-mechanical processes, will involve external ingress of at least one of the agents that is involved in the attack process [1,2]. To illustrate this point, we may consider some chemical attack processes: chloride/carbonation attack arises from ingress of  $\text{Cl}^-/\text{CO}_2$  and the presence or ingress of moisture, external/internal sulphate attack involves ingress of either sulphate ions and/or moisture. Although the reactive

---

<sup>1</sup>Corresponding author: University of Johannesburg, Department of Civil Engineering, P.O. Box 524, Auckland Park, 2006, South Africa; E-mail. [sekolu@uj.ac.za](mailto:sekolu@uj.ac.za), [sekolu@gmail.com](mailto:sekolu@gmail.com)

agents for alkalis-silica reaction (ASR) attack are usually part of the concrete matrix i.e alkalis in the pore solution and reactive aggregates, it takes an external ingress or supply of moisture for ASR attack to evolve and remain sustained. Similarly, freeze-thaw attack requires saturation of the concrete with water from the environment. Clearly, evaluating the permeation characteristics of concrete is probably one of the most important considerations in attempting to assess durability. Over the past years of research, different techniques have been proposed in the literature, for the purpose of evaluating durability.

In South Africa, index methods based on oxygen permeability, sorptivity and chloride conductivity have been the foremost techniques used for durability evaluation of concretes [3]. A recent study comparing some SA-index tests with international standard methods showed good agreement which adds credence to the local index tests [4].

## 1. Background

As mentioned in the prior section, durability Index testing is a South African approach that has been in development through research, in response to the need for innovation and improvements in evaluation of the durability of concretes exposed to aggressive environments. For conditions in Southern Africa, it is generally accepted that for specification of reliably good quality concrete that is capable of effectively resisting attack and ingress of deleterious ions, use of the three tests of Oxygen Permeability Index (OPI), the Water Sorptivity Test and the Chloride Conductivity Test is essential. These tests measure the transport properties of concretes and are expected to reflect the integrity and microstructural characteristics of hardened concretes. The use of these three tests is increasingly being specified in construction. They form the basis for the performance-based specifications currently being advanced for evaluation of the quality of concrete for construction in South Africa [5,6]. Substantial research on Durability Index (DI) has been generated over the past 15 years, and several aspects involving the tests have been investigated including the influence of cementitious materials, curing, temperature, relative humidity, repeatability and reproducibility of the tests [7-10]. However, hardly any investigations have been conducted on the intrinsic effects of plasticizing admixtures on DI. Such information is necessary in aiding further scientific understanding of the potential and limitations of the techniques, especially considering that chemical admixtures are used extensively in concretes.

Plasticizing admixtures may influence both concrete workability and its performance properties, in some cases adversely. There are many variables that can affect their effectiveness including its chemical base, dosage rates, timing of admixture addition into the concrete mix, incompatibility with cementitious materials, field conditions during concrete placement, interaction with other admixtures, among others. The characteristics of cementitious materials that often interact with chemical admixtures have long been identified in the literature as fineness, tricalcium aluminate ( $C_3A$ ), alkalis ( $Na_2O$ ), and sulphates ( $SO_3$ ) [11]. Chemical admixtures containing triethanolamine and/or lignosulfonates are known to cause incompatibility problems. The air content of concrete is also affected, depending on the slump of concrete and chemical formulation of the superplasticizing admixture. Investigations have shown that naphthalene-based superplasticizers have the tendency to increase air content. Melamine-based superplasticizers may in some cases reduce air content in concretes



[12]. Investigations (reported in [13]) on the influence of different superplasticizers on the pore structure of hardened concretes have shown mixed results. Chemical admixtures also variably affect creep and drying shrinkage of concretes [14]. In addition, new generation plasticizing admixtures continue to enter the market. The long-term influence of these admixtures may be unknown.

This paper investigates the potential influence of superplasticizers on concrete durability indexes. As mentioned earlier, there is presently little or no work in the literature concerning the influence of chemical admixtures on durability indexes.

## 2. Experimental

This investigation consisted of eight concrete mixes of varied compressive strengths and water-cementitious ratio (w/cm). The design strengths of the concretes were 25, 30, 35, 40 MPa. Two mixes were prepared for each design strength category, as shown in table 1 of the mix parameters.

**Table 1.** Concrete mix parameters

Mix ID	1,8	2,7	3,6	4,5
Design strength (MPa)	25	30	35	40
w/cm*	0.55	0.54	0.49	0.47

w/cm = water-cementitious ratio

The main variable in the investigation was the use of different types of chemical admixtures. Two types of commercially available superplasticizers were used in the mixes. *RSP* was a sulphonated naphthalene-based superplasticizer and was applied in mixes 1 to 4. *GL* was a polycarboxylate ether superplasticizer and was used in mixes 5 to 8. Cube samples of 150 mm size were prepared and cured for 28 days prior to testing. Compressive strength tests and the durability tests of oxygen permeability index and sorptivity index were measured [3].

The durability index tests comprising oxygen permeability and water sorptivity, were tested using 68 dia x 30 mm discs extracted from the concrete cube samples. The discs were subjected to oven-dry conditioning at 50°C for seven days, prior to testing.

## 3. Results and discussion

### 3.1 Durability index results

Altogether, sixteen (16) disc samples were prepared then tested for oxygen permeability and sorptivity. The results for the index tests have been plotted in Figures 1 and 2, respectively showing the OPI and sorptivity values for the various samples. From the charts, individual results can be related across all samples while trends can be easily identified. The individual sorptivity results for all mixes generally ranged from 6 to 9 mm/hr<sup>0.5</sup>, which falls within the good durability class. The OPI results of mixes made with *RSP* gave values exceeding 10, meeting the criteria for excellent durability.

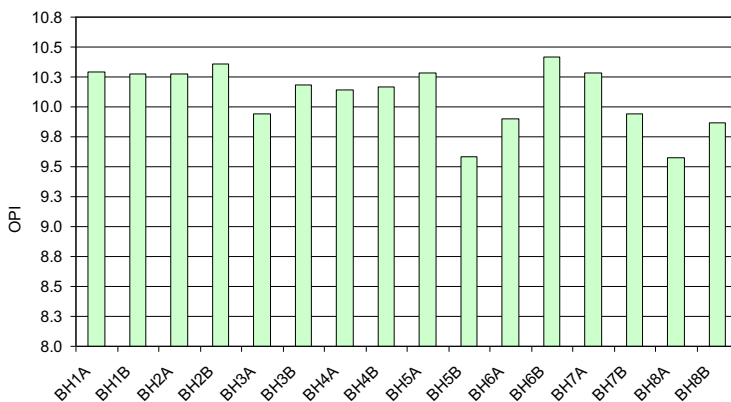


Figure 1. Oxygen permeability indexes

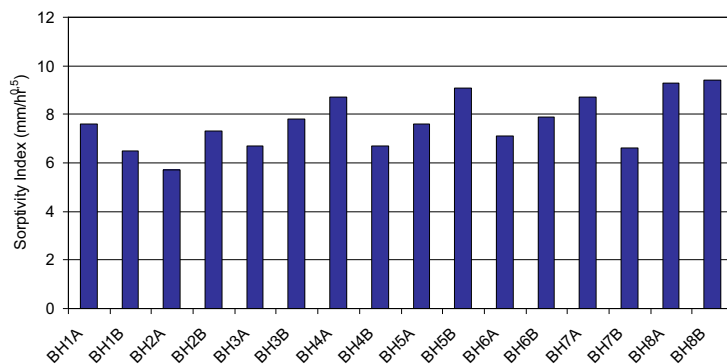


Figure 2. Sorptivity indexes

### 3.2 Discussion

The durability index test results obtained for the various mixes, as influenced by the two different superplasticizers, *RSP* and *GL*, are given in Table 2. It is interesting to note that the use of *GL* consistently led to increase in the compressive strength of concrete (mixes 5-8) by about 10 MPa over the strength of mixes (1-4) made using *RSP*. However, for high strength concretes (mixes 2 and 5) of strengths greater than 50 MPa, the difference in results (due to use of the chemical admixtures), diminished and was negligible.

The corresponding effect of the superplasticisers on durability indexes is also evident. It can be seen in Table 2, that mixes made using *GL* and which gave higher compressive strengths, also exhibited higher water sorptivity indexes relative to their counterparts made using *RSP*. Mixes made with the former, gave sorptivity indexes that were 0.2 to 2.3 mm/hr<sup>0.5</sup> higher than the corresponding indexes of mixes made using the latter. This effect of the different superplasticizer was also clear with OPI

results. It can be seen that the OPI values of mixes made using *GL* were generally 0.2 to 0.6 units lower than the corresponding values for mixes made using *RSP*.

**Table 2.** Durability index results of the various concrete mixtures

Mix ID	Compressive strength (MPa)	OPI	Water Sorptivity (mm/hr <sup>0.5</sup> )
Mix 1	35.0	10.3	7.1
Mix 8	43.5	9.7	9.4
Mix 2	37.0	10.3	6.5
Mix 7	48.0	10.1	7.7
Mix 3	43.5	10.1	7.3
Mix 6	52.5	10.2	7.5
Mix 4	54.5	10.2	7.7
Mix 5	55.0	9.9	8.4

Clearly, the differences in strengths and durability of concrete, as a result of using the two superplasticizers, indicates an alteration in the pore characteristics of the hardened concrete. It is postulated that *GL* may cause acceleration of cement hydration which in turn results in higher rate of strength gain. Such effects could be related to temperature increase and could have implications leading to coarsening of the pore structure of the hardened concrete. This may explain the observed results of mixes containing *GL*, which gave higher compressive strengths and corresponding reduction in durability performance.

#### 4. Conclusions

In the foregone investigation, the effect of superplasticizers on durability indexes was investigated. Two different types of plasticizers were used in the concrete mixes, whose strengths ranged from 30 to 50 MPa.

Results show that superplasticizers can differently affect the durability indexes of concretes. This, however, will depend on the type of the admixture. *GL* was found to have the effect of increasing the compressive strength of hardened concrete by about 10 MPa over the results obtained by using *RSP*. There was, however, a related adverse effect of correspondingly lower durability index performance of mixes containing the *GL*.

#### References

- [1] BS EN 1504-9:2009, Products and systems for the protection and repair of concrete structures. Definitions, requirements, quality control and evaluation of conformity. General principles for use of products and systems, British Standards Institution, 32p
- [2] *Fulton's Concrete Technology*, 9<sup>th</sup> Edition, Cement & Concrete Institute 2009, ISBN Number: 9780958477918
- [3] Alexander M.G., Ballim Y. and Mackechnie J.M., *Concrete durability index testing manual*, Research Monograph no. 4, Departments of Civil Engineering, University of Cape Town and University of the Witwatersrand, March 1999
- [4] Beushausen H. and Alexander M.G, The South African durability index tests in an international comparison. *Journal of the South African Institution of Civil Engineering*, Vol 50 No 1, 2008, Pages 25–31, Paper 671

- [5] Gouws, S.M., and Ballim, Y. (2003), Towards performance-based specifications for concrete durability, *Proceedings of the 2nd International Conference of the African Materials Research Society*. Johannesburg, South Africa. University of the Witwatersrand, Dec. 2003. pp.115-116.
- [6] Grieve, G.R.H. (2005), Design of concretes to meet durability requirements; Development towards a performance specification in South Africa, *Proceedings of the International Conference on Concrete Repair, Rehabilitation and Retrofitting (ICRRR)*, Cape Town, South Africa. University of Cape Town, Nov. 2005, pp.12-13.
- [7] Griesel, E.J., and Alexander, M.J.(2001), Effect of controlled environmental conditions on Durability Index parameters of Portland cement concretes, *Cement, Concretes and Aggregates*, Vol. 23, No.1, pp.44-49.
- [8] Gouws, S., Alexander, M.G., and Maritz, G. (2001), Use of Durability Indexes for concrete in marine conditions, *Materials and Structures*, Vol. 37, No. 267, April 2004, pp. 146-154.
- [9] Du Preez, A.A., and Alexander, M.G. (2004), A site study of Durability Indexes for concrete in marine conditions, *Materials and Structures*, Vol. 37, No. 267, April 2004, pp. 146-154.
- [10] Stanish, K., Alexander, M.G., and Ballim, Y. (2005), *Durability Index inter-laboratory test results-statistical analysis of variance*, Technical Report, Department of Civil Engineering, University of Cape Town, January 2005, 87p.
- [11] Bruere, G.M. (1975), Actions of admixtures in plastic concrete and cement-admixture interactions, *Workshop on the Use of Chemical Admixtures in Concrete*, The University of New South Wales, Dec., 1975, pp. 29-41.
- [12] Whiting, D. and Dziedzic, W. (1992), Effects of Conventional and High-Range Water Reducers on Concrete Properties, Technical Report, RD107T, Portland Cement Association, 1992.
- [13] Khatib, J.M., and Mangat, P.S., (1999), Influence of superplasticizer and curing on porosity and pore structure of cement paste, *Cement and Concrete Research*, Vol. 21, pp. 431-437.
- [14] Morgan, D.R., (1975), Effects of chemical admixtures on creep and shrinkage in concrete, *Workshop on the Use of Chemical Admixtures in Concrete*, The University of New South Wales, Dec., 1975, pp. 113-148.

# Effects of sulphuric acid on the compressive strength of blended cement-cassava peel ash concrete

Kolawole Adisa OLONADE<sup>a,1</sup>, Akinropo Musiliu OLAJUMOKE<sup>a,b</sup>  
Ayoade Oluwaseun OMOTOSHO<sup>a</sup> and Funso Ayobami OYEKUNLE<sup>a</sup>

<sup>a</sup>Department of Civil Engineering, Obafemi Awolowo University, Ile-Ife, Nigeria

<sup>b</sup>Department of Civil Engineering Science, University of Johannesburg, South Africa

**Abstract.** Influence of sulphuric acid on compressive strength of concrete made with blended cement-cassava peel ash was investigated in this study. This is with a view to determining the level of resistance of such concrete to acidic exposure. Cassava peel ash (CPA) prepared from uncontrolled burning was used to substitute cement at 5, 10, 15 and 20% by weight of cement as binder. Concrete mix proportions of 1:2:4 (batching by weight) were prepared with the slump value within  $60 \pm 10$  mm while water-binder ratios (w/b) were being noted. A total of 90 cubes of the concrete mixture of sizes 150 mm were cast and cured in fresh water (as control), 0.5, 1.0 and 1.5 M concentrations of sulphuric acid solution ( $H_2SO_4$ ) for 7, 28, 56 and 90 days. The compressive strength was determined at the expiration of each curing age. The results showed that the w/b increased with increase in the quantity of CPA in the mixture. Compressive strength of concrete made with cement-CPA as binder and cured in fresh water was comparable to that of normal concrete when up to 15% CPA was used, but relatively low strength was obtained when cured in  $H_2SO_4$  solutions, depending on the quantity of CPA. Leaching of Portlandite in the concrete cubes was observed with worse condition in the case of concrete containing 20% CPA in sulphuric acid solution of 1.5 M. The compressive strength reduced with increase in concentrations of the acid as well as with increase in the content of the CPA. It is concluded that CPA did not mitigate the adverse effects of sulphuric acid on the compressive strength of blended cement-CPA concrete.

**Keywords.** Blended cement-cassava peel ash, water-binder ratio, compressive strength, sulphuric acid solution, acid concentration, slump

## Introduction

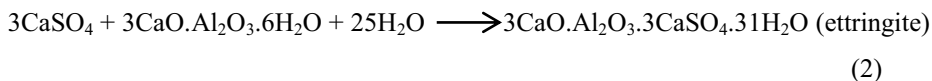
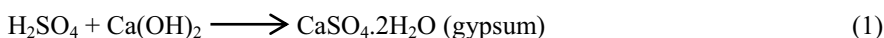
The use of industrial and agricultural wastes as pozzolan or as supplementary cementitious materials (SCMs) in concrete production is becoming popular and attracting attention of many researchers. However, the durability of such concrete in an unfriendly environment has been a major concern. Durability of concrete, as defined by

---

<sup>1</sup>Corresponding author: [makkolawole@yahoo.com](mailto:makkolawole@yahoo.com)

ACI Committee 201[1], is its ability to resist weathering action, chemical attack, abrasion, or any other process of deterioration. A durable concrete will retain its original form, quality and serviceability when exposed to the environment. One of such environment, which concrete could be exposed to, is acidic. According to Zivica et al, [2], acid attack on concrete may come from different sources such as air pollution and bacterial contamination.

It is well established in literatures [2 - 6] that acidic environment is deleterious to concrete durability because acid neutralizes the alkalinity of concrete by reacting with the hydration products of the concrete matrix to form gypsum and ettringite. The chemical reaction of this neutralization phenomenon with sulphuric acid is given by Zivica and Bajza [3] as in Equations (1) and (2). Both gypsum and ettringite possess little structural strength, yet they have larger volumes than the compounds they replace. This results in internal pressures, formation of cracks and eventually, the loss of strength [7]. Consequently, the concrete becomes vulnerable to aggressive exposure.



Adesanya and Raheem [8] studied the effects of  $\text{H}_2\text{SO}_4$  and  $\text{HCl}$  on the concrete produced with different proportions of corn cob ash (CCA) blended with cement. Their results showed that CCA was responsible for the reduced water absorption of the concrete, and when up to 15% of CCA replaced cement, the resistance to chemical attack was improved. Also, the performance of fly ash (FA) and stone dust (SD) blended concrete in acidic environment was investigated by Verma et al [9]. They found that the residual strength of concrete containing FA and SD was comparable with that of normal concrete, when the mixture of about 40% stone dust and up to 30% FA were used.

In the recent past, cassava peel ash (CPA) has been found to be pozzolanic [10]. Salau et. al [11, 12] studied the strength characteristics and effect of elevated temperature on the concrete produced with partial replacement of cement with cassava peel ash. They reported that performance of concrete containing up to 15% CPA was comparable with that of normal concrete and recommended that up to 10% could be used in the case of structures exposed to 400°C. Olonade et al. [13] also used cassava peel ash, derived from uncontrolled burning, blended with cement to produce sandcrete blocks with positive results. However, the performance of concrete made with blended cement-CPA concrete in acidic environment has not been reported. Therefore, the thrust of this paper is to investigate the effect of sulphuric acid on the strength properties of the concrete containing cassava peel ash as partial substitute for cement.

## 1. Materials and methods

### 1.1 Materials

The cement used for the study was ordinary Portland cement (CEM I). Cassava peels were burnt into ashes in an incinerator and sieved through 150 sieve size. It was used to replace cement, partially, to produce the binder for the concrete. The chemical composition of both the cement and CPA was determined. River sand and granite of

maximum nominal sizes of 3.18 mm and 19 mm were used as fine and coarse aggregate respectively. Potable water was used for mixing. The sulphuric acid was procured from the Department of Chemistry, Obafemi Awolowo University, Ile-Ife, and different concentrations of its solution were prepared in the laboratory.

### 1.2 Mixing, curing and testing concrete specimens

Concrete mix proportion of 1:2:4 (cement/CPA: sand: granite) was batched by weight. Cement was substituted with CPA in the proportions of 5, 10, 15 and 20% of the weight of cement. In order to maintain the same consistency, water-binder ratio was varied until slump was within  $60 \pm 10$  mm. The choice of the slump was to achieve medium workability for general concrete work [14]. Seventy-two (72) concrete cubes of sizes 150 mm were cast, and moulds were removed after 24 hours and cured by total immersion in sulphuric acid ( $H_2SO_4$ ) solutions of different concentrations of 0.5, 1.0 and 1.5 M for 7, 28, 56 and 90 days. At the expiration of each curing age, cubes were tested for compressive strength. Another 18 cubes were cast and cured in fresh water for the same ages to serve as controls. Average of three readings was recorded for each curing age result. All the concrete cubes were cured under the laboratory conditions, with average minimum and maximum temperatures within  $25^{\circ}C$  and  $35^{\circ}C$  respectively.

## 2. Results and discussion

### 2.1 Chemical composition of cement and CPA

The chemical composition of both the cement and CPA is presented in Table 1. It is observed that the dominant oxide in the cement and CPA are CaO and  $SiO_2$  respectively. CaO is the main source of binding and hardening compound in cement, when reacted with water (hydration reaction), which is very low in CPA. But, the  $SiO_2$  in CPA reacts with  $Ca(OH)_2$  (by product of cement hydration) to produce more binding property (Pozzolanic reaction). The advantage of reduction in the consumption of cement leading to reduction in the greenhouse effects of cement usage is being exploited by the use of pozzolan in concrete production.

**Table 1.** Chemical composition of the cement and cassava peel ash

Material	Oxides (%)								LOI
	$SiO_2$	$Al_2O_3$	$Fe_2O_3$	CaO	MgO	Na <sub>2</sub> O	K <sub>2</sub> O	SO <sub>3</sub>	
Cement	20.80	3.10	2.50	64.50	1.70	0.23	0.85	2.50	3.40
CPA	36.79	7.57	2.23	8.20	2.9	1.37	18.74	1.52	15.10

### 2.2 Effect of CPA on Water-Binder Ratio

In order to maintain standard consistency for all the concrete mixes, the slump value was kept within the range  $60 \pm 10$  mm and the water-binder ratio (w/b) to achieve this was determined for each concrete mix. The results of the w/b at different content of CPA are presented in Table 2. It is observed that the w/b increases with increase in CPA content. A w/b of 0.60 was obtained in case of normal concrete (0% CPA) while concrete containing 5%, 10%, 15% and 20% have w/b of 0.63, 0.68, 0.73 and 0.76, respectively. The reason for this behaviour could be attributed to higher water absorption potential of cassava peel ash [11]. The implication is that more water would

be required to produce concrete containing CPA depending on the amount used. However, the amount of water in a concrete matrix is a major factor that influences most engineering properties of concrete, it is expected that the inclusion of cassava peel ash would have effect on the performance of concrete.

**Table 2.** Water-binder ratios at constant slump of cement-CPA concrete

CPA Content (%)	Water-binder ratio at slump $60 \pm 10$ mm
0	0.60
5	0.63
10	0.68
15	0.73
20	0.76

### 2.3 Effect of curing cement-CPA concrete in $H_2SO_4$ solution on compressive strength

Concrete cubes produced from various proportion of CPA as replacement for cement were cured in sulphuric acid solution of different concentrations. The compressive strength of the cubes was determined at the end of each curing age. The results are presented in Table 3 along with those cured in fresh water. Considering the compressive strength of the cubes cured in fresh water, it is observed that the strength increases with age and reduces with increase in CPA content. However, the strength of cement-CPA concrete tends to merge up with those of normal concrete, especially at later age (56 days and above) when not more than 15% CPA is used. For instance, 28-day strength of normal concrete is  $19.84 \text{ N/mm}^2$  while 5% CPA concrete has strength of 18.56 representing about 94% of the normal concrete strength. Similarly, the strength of 10, 15 and 20% CPA concrete are 17.26 (87%), 14.74 (75%) and  $12.78 \text{ N/mm}^2$  (65%), respectively. These results agree with what Salau et al [12] reported.

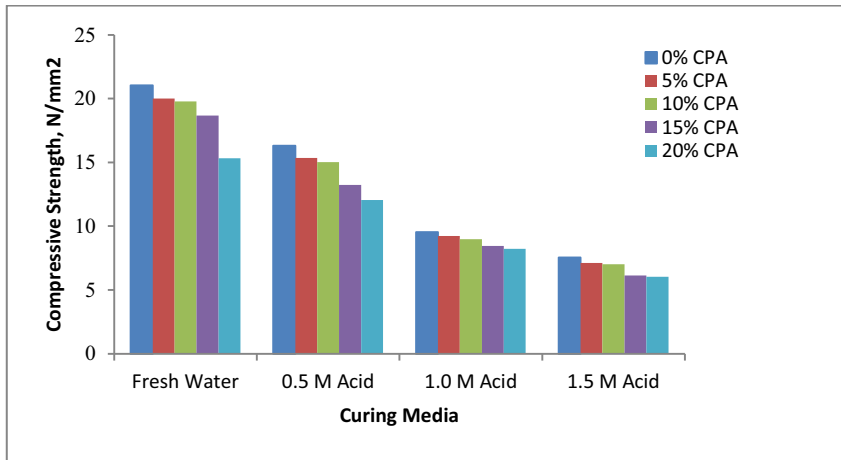
**Table 3.** Compressive strength of cement-CPA blended concrete at different curing ages

Curing Media	Curing Ages (Days)	Residual Strength ( $\text{N/mm}^2$ )				
		Amount CPA (%)				
		0	5	10	15	20
Fresh Water	7	14.59	13.53	13.37	12.87	10.63
	28	19.84	18.56	17.26	14.74	12.78
	56	20.80	19.58	18.87	17.18	14.30
	90	21.03	20.00	19.78	18.67	15.31
0.5M $H_2SO_4$	7	13.98	13.12	12.28	11.99	11.78
	28	18.48	17.56	16.07	14.77	14.35
	56	17.51	16.61	15.78	13.91	12.91
	90	16.31	15.34	15.01	13.23	12.05
1.0 M $H_2SO_4$	7	12.39	11.76	11.05	10.88	9.66
	28	11.39	10.57	10.28	9.34	9.07
	56	10.01	9.93	9.22	9.05	8.76
	90	9.52	9.23	8.98	8.45	8.21
1.5M $H_2SO_4$	7	10.51	10.48	9.36	8.74	7.78
	28	10.13	9.25	9.04	8.25	7.03
	56	8.99	7.49	7.34	6.82	6.20
	90	7.53	7.12	7.01	6.12	6.02

On the other hand, compressive strength of concrete cubes cured in  $H_2SO_4$  solution differs considerably from those obtained when cured in fresh water. The trend is that



the strength reduces with increase in concentrations of the acid and the duration of curing. Figure 1 shows the typical trend at age 90 days. For instance, compressive strength (CS) of concrete cubes cured in 0.5, 1.0 and 1.5 M  $H_2SO_4$  solution are 16.31, 9.52 and 7.53  $N/mm^2$  respectively for normal concrete, while the CS of 5 and 10% CPA, cured in the same media for the period (90 days), are 15.34, 9.23, 7.12 and 15.01, 8.98 and 7.01 respectively. At the same age, least strength is obtained in concrete with the binder containing 20% CPA, and when cured in 1.5 M for 90 days (6.02  $N/mm^2$ ). Of interest is the marginal decremental change observed in CS due to the effects of the sulphuric acid at the same concentration for each of the concrete made with up to 15% CPA replacement. At 90-day curing age, taking the CS of concrete cured in fresh water as reference, the percentage reduction in CS for 0.5M  $H_2SO_4$  solution at 0, 5, 10 and 15% CPA replacement ranges basically between 22 and 24%. For 1.0M of the acid, the percentage reduction in CS ranges between 53 and 55%, while the CS, when cured in 1.5M  $H_2SO_4$  solution, ranges essentially between 64 and 65%, respectively.



**Figure 1.** Compressive strength of cement-CPA concrete in different curing media at age 90 days

Similarly, mass of the concrete cubes is observed to be gradually reducing. This effect may be attributed to the effect of curing in sulphuric acid solution. Figure 2 shows the plot of average mass of the concrete cubes against the curing ages in different media. It is shown that the mass of the concrete cured in fresh water is almost the same (standard deviation is about 0.03). This result is comparable with what Salau et al (11) reported. The reason for this may be due to the relative low specific gravity of CPA compared to that of cement. However, gradual reduction in mass is observed in the concrete cubes cured in  $H_2SO_4$  solution. This effect shows that  $H_2SO_4$  solution causes reduction in the mass of concrete. The pattern is that, at early age of 7 days, there appear to be minimal change in the mass of the concrete cubes cured in all the media, but as the age increases, the mass also decreases. It is shown that concrete loses more weight (about 20%) between the ages 7 and 90 days, when cured in 1.5 M  $H_2SO_4$  solution compared to the concrete cured in fresh water (0.6%). Moreso, about 4% and 10% of the mass were lost, when cured in 0.5M and 1.0M  $H_2SO_4$  solution, respectively. The progressive reduction in mass may be attributed to weaker compound (gypsum) that is formed as a result of neutralization reaction between  $H_2SO_4$  and  $Ca(OH)_2$ , consequently leading to lowering of the compressive strength (Equation 1).

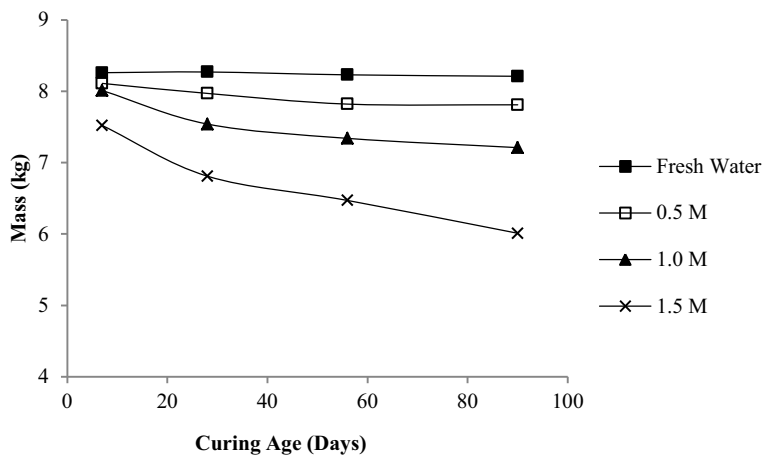


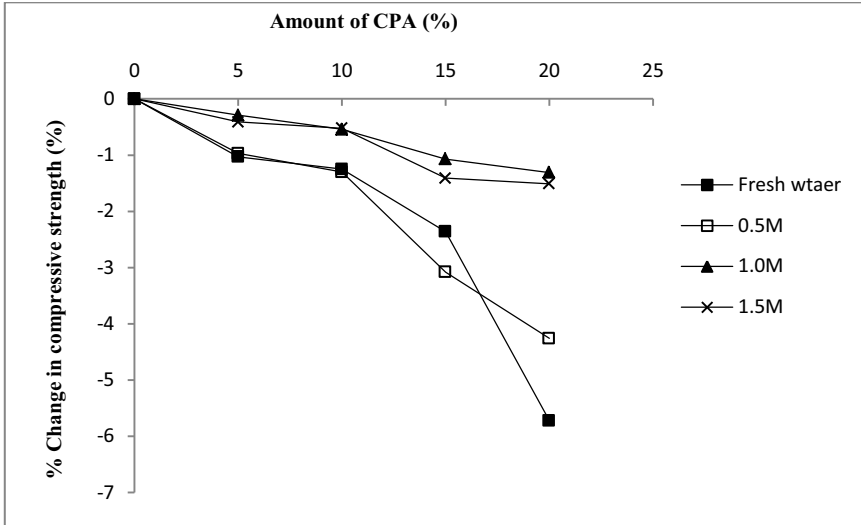
Figure 2. Effect of acid concentration on the mass of cement/CPA concrete



Figure 3. Typical leaching of  $\text{Ca}(\text{OH})_2$  from concrete cubes in the  $\text{H}_2\text{SO}_4$  solutions at 90-day curing age

These results suggest that the concentration of sulphuric acid had appreciable effect on the performance of cement-CPA concrete and presence of CPA does not improve concrete resistance to sulphuric acid attack. This may be because sulphuric acid leaches and neutralizes calcium hydroxide  $\text{Ca}(\text{OH})_2$ , a by-product of cement hydration, which was to react with the silica in the CPA for later strength development (pozzolanic reaction). This reaction tends to produce *fragile* concrete that contains several pores (Figure 3). It can be deduced also, that the sulphuric acid inhibits the pozzolanic reaction of CPA in the mix and made the concrete to be more permeable with low strength, when compared to the control. Therefore, concrete made with blended cement - CPA may not be used to make facilities for wastewater disposal and treatment, where there are high chances of  $\text{H}_2\text{SO}_4$  solution generation. Nevertheless, there is the need to investigate the effect of sulphuric acid solution on cement-CPA concrete cured in fresh water for a longer period to permit pozzolanic reaction.

In addition, Figure 4 shows comparative rate of strength reduction of the concrete over that of normal concrete at 90 days curing age. The rate appears very high in concrete cured in fresh water and 0.5M while it is very low in the concrete cured in 1.0M and 1.5M of  $H_2SO_4$  solution, respectively. This shows that other secondary products may be forming at higher concentrations of  $H_2SO_4$  solution that reduces the rate of deteriorating effects of the acid over the curing ages.



**Figure 4.** Change in comparative strength of concrete made with binder of different percentages of CPA in varying concentration of  $H_2SO_4$  at 90-day curing age

### 3. Conclusions

The effect of curing blended cement-cassava peel ash concrete in different concentrations of sulphuric acid has been studied and the following conclusions were reached:

1. Water-binder ratio (w/b) increases with increase in the quantity of CPA in the mixture.
2. Sulphuric acid solution causes reduction in the mass of cement-CPA concrete due to the leaching effect of the acid.
3. Concrete made from blended cement-cassava peel ash possesses relative low compressive strength, when cured in sulphuric acid.
4. Sulphuric acid solution inhibits pozzolanic reaction between CPA and calcium hydroxide (by-product of cement hydration) to take place. Thus, making CPA to be inactive in the mixture.
5. This research is on-going. There is need to further study the effect of sulphuric acid solution on cement-CPA concrete cured in fresh water for longer period to allow pozzolanic reaction to take place.

## References

- [1] ACI Committee 201: *Guide to durable concrete*, American Concrete Institute, Report of ACI Committee, Detroit, 2001.
- [2] Zivica V., M. Palou, M. Krizmaand L. Bagel, L.: Acidic attack of cement based materials under the common action of high ambient temperature and pressure. *Construction and Building Materials*, **36**(2012), 623 – 629.
- [3] Zivica V. and A. Bajza. Acidic attack of cement based materials – a review. Part 1: principle of acidic attack. *Construction and Building Materials*, **15**(2001), 331 – 340.
- [4] Neville A.M. *Properties of concrete*. Fourth edition, Pearson Prentice Hall, 2008.
- [5] Larreur-Cayol, S.,Bertron, A and G. Escadeillas. Degradation of cement-based materials by various organic acids in agro-industrial wastewaters. *Cement and Concrete Research*; **41**(2011), 882 – 892.
- [6] Yuan, H. Dangla, P., Chatellier, P. and T. Chaussadent: Degradation modelling of concrete submitted to sulphuric acid attack. *Cement and Concrete Research*, **53**(2013) 267 – 277.
- [7] Monteny N., Debelie E., Vinke V. And Taerwe L. Chemical and microbiological tests to simulate sulphuric acid corrosion of polymer-modified concrete. *Cement and Concrete Research*, **31**(9) 2001, 1359–1365.
- [8] Adesanya, D.A. and Raheem, A.A. A study of the permeability and acid attack of corn cob ash blended cements. *Constr. Build. Mater.* **24**(3) 2010. 403-409.
- [9] Verma, A, Shukla, M., and Sahu, A. K. Performance of Fly Ash and Stone Dust Blended Concrete in Acidic Environment, *Concrete Research Letters*, **4**(1) 2013.
- [10] Salau, M.A. and Olonade, K.A. “Pozzolanic Potentials of Cassava Peel Ash” *Journal of Engineering Research*, **16**(1) 2011, 10-21.
- [11] Salau M.A., Ikponmwosa, E.E. and Olonade, K.A. “Structural Strength Characteristics of Cement-Cassava Peel Ash Blended Concrete”, *Civil and Environmental Research*, **2**(2) 2012, 68-77.
- [12] Salau M.A., Ikponmwosa, E.E. and Olonade, K.A. “Effect of elevated temperature on cassava peel ash concrete”, *America Journal of Materials Science*, **3**(5) 2013, 142 – 148.
- [13] Olonade, K.A.,A.M. Olajumoke and Oladokun, A.B. ‘Engineering properties of sandcrete blocks using cassava peel ash as pozzolan’ *Proceedings*, International Conference on Advances in Cement and Concrete in Africa (ACCTA), Emperor’s Palace, Johannesburg, South Africa. 28 – 30th, 2013.
- [14] Domon, P.L “*Fresh concrete*” *contribution in Advanced Concrete technology* – concrete properties, Elsevier Ltd. (2003). 1-27.

# Properties of self-consolidating concrete containing limestone filler

Daman PANESAR<sup>1</sup> and Mohammad AQEL

*Department of Civil Engineering, University of Toronto, Ontario, Canada*

**Abstract.** Fillers such as limestone filler (LF) can be used to replace the cement and thus reduce the cement content in concrete. However, in applications where early age strength is critical such as precast and prestressed applications increased amount of fillers could cause a challenge due to dilution effect. This paper investigates the influence of LF on early age hydration and strength of steam cured SCC made with CSA general use cement (type GU) and high early strength cement (type HE). The reactivity of LF was also evaluated using thermal analysis. Durability tests including rapid chloride permeability test (RCPT), freeze thaw and salt scalings were conducted on SCC mixtures made with and without LF. The results showed improved early age hydration and strength in SCC mixtures containing LF compared to SCC mixtures without LF. The chloride permeability was lower in SCC mixtures containing LF compared to SCC mixtures without LF. The durability performance of SCC mixes made with and without LF was similar under freeze thaw and salt scaling cycles.

**Keywords.** Concrete, general use cement, high early strength cement, limestone filler, self-consolidating concrete, steam cured

## 1. Introduction

Over the past 25 years self-consolidating concrete (SCC) has advanced and is considered to be a solution to many challenges associated with concrete construction around the world and also gained attention in the precast industry. At the same time there is pressure to incorporate supplementary cementing materials and fillers as cement replacement without compromising material properties and performance. For precast products, beyond the necessity for long term durability, it is also required that the desired early age properties are achieved in order to meet production demands through timely demoulding and prestressing operations. High early strength is typically achieved through application of high temperature curing and or the use of high early strength (HE) cement.

Although many hydration studies have been conducted on cement-based materials containing limestone filler few studies have considered the effect of limestone filler combined with HE cement for precast applications. Studies have been reported which investigate the influence of limestone filler on the hydration kinetics, and properties of concrete [1-3]. Addition of fine non-reactive filler to cement affects the rate of hydration through physical and chemical processes, namely, (i) dilution, (ii)

---

<sup>1</sup>Corresponding author: [d.panesar@utoronto.ca](mailto:d.panesar@utoronto.ca)

heterogeneous nucleation, and (iii) modification of the particle size distribution. Although the reactivity of limestone filler has been debated, at low concentrations, limestone (calcite) reacts to form various carboaluminate phases and the extent of reactivity is dependent on the sulphates present in the system [4,5].

Conflicting observations are reported on the impact of limestone filler on later age compressive strength. Some researchers indicate that the 28-day strength is reduced owing to the dilution effect [6,7] while others report no observable difference. The use of limestone filler when blended with Ordinary Portland Cement (OPC) alone has been reported to have implications related to durability problems particularly sulfate attack (thaumasite formation) and ion diffusion, depending on the level of limestone addition [8].

The focus of this study is to determine the interplay between the concentration of limestone filler (up to 15%), and cement type (general use (GU) and high early (HE) strength), on early age hydration, evolution of mechanical properties, transport properties and durability performance of self-consolidating concrete containing limestone filler designed for precast applications.

## **2. Experimental program**

### *2.1 Materials, mix design and curing*

The main mix design variables in this study are cement type (CSA GU (general use) and CSA HE (high early strength)), limestone filler content (0% and 15%). All self-consolidating concrete mixtures contain: a cementing material content of 450 kg/m<sup>3</sup>, a water-to-binder ratio of 0.34, and a fine-to-coarse aggregate ratio of 0.895 and 5% silica fume as cement replacement. The four mix design names are: 100%GU; GU+15%LF; 100%HE; and HE+15%LF.

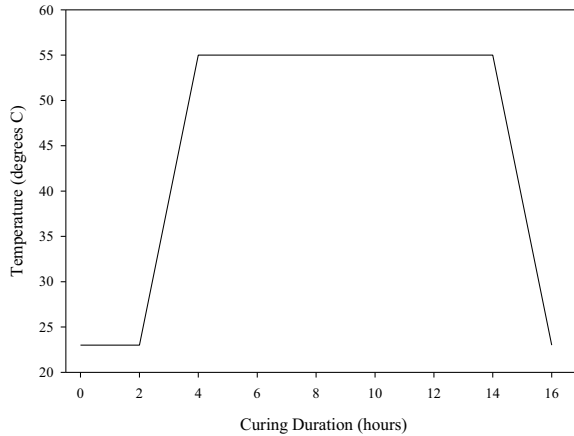
The GU and HE strength cement which have a blaine fineness of 417 and 514 m<sup>2</sup>/kg, respectively, were supplied by Holcim Canada and the silica fume was supplied by SKW Canada Inc., Quebec Canada. The limestone filler was supplied by Omya Canada. The nominal limestone particle size for all mixtures used was 3µm with a blaine fineness of 1125 m<sup>2</sup>/kg.

After casting, all specimens were steam cured in an environmental chamber for 16 hours following the profile presented in Figure 1. After the 16 hours steam curing in the chamber, specimens were moist curing in lime water at 23°C until tested.

### *2.2 Test methods*

*Initial setting time:* The normal consistency and initial setting time was measured according to ASTM C187-11 and ASTM C191-08 [9,10].

*Heat of hydration:* For each mix design, three cement paste samples were tested for heat of hydration over a period of 72 hours. The test was conducted at 23°C in accordance with ASTM C1702-09 Method B. A TAM Air isothermal calorimeter manufactured by Thermometric was used [11]. Before mixing the cement pastes, all materials were preconditioned at 23±1°C.



**Figure 1.** Steam curing regime

*Compressive strength:* The compressive strength of mortar samples was measured in accordance to ASTM C109 and for each mix design, three replicate specimens were tested per test age [12].

*Reactivity of LF:* The reactivity of LF was measured using Thermal Gravimetric Analysis/Differential Thermal Analysis (TGA/DTA). Approximately 100 mg of cement paste was heated to 1145°C at a rate of 10°C/min. The mass loss between 680 and 800°C was used to measure the content of LF unreacted in each mix using stoichiometry as presented in the Eq. (1) [13]. The theoretical CaCO<sub>3</sub> content was calculated using Eq. (2). The difference between the measured and the theoretical CaCO<sub>3</sub> content is assumed to be the percentage of reacted LF in each mix.

$$\text{Measured CaCO}_3 \text{ Content (\%)} = \text{Mass loss (680 – 800°C)} \times \frac{\text{Molar Mass of CaCO}_3}{\text{Molar Mass of CO}_2} \quad (1)$$

$$\text{Theoretical CaCO}_3 \text{ Content (\%)} = \frac{\text{Mass of LF}}{\text{Mass of Cement} + \text{Mass of LF} + \text{Mass of Water}} \quad (2)$$

*Fresh properties:* The SCC mix designs were tested for various plastic properties including: Column Segregation Method (MTO LS-442), Slump Flow (MTO LS-438), T-50 (MTO LS-438), J-Ring (MTO LS-439), Visual Stability Index (MTO LS-438) and L-Box (MTO LS-440) [14-17].

*Mechanical, transport and durability properties:* Hardened properties including: compressive strength (MTO LS-437), rapid chloride penetration test (RCPT) (ASTM C 1202), rapid freeze/thaw test (ASTM C666), and de-icer salt scaling (MTO LS-412) were investigated [18-21].

### 3. Results and discussion

The initial setting time was 94 minutes for the 100%GU mix and 91 minutes for the 100%HE mix. The presence of 15% limestone in the mixtures reduced the initial setting time to 81 minutes and 77 minutes for the GU and HE mixtures, respectively. Therefore, the presence of 15% limestone reduced the initial setting time by 14 to 18%.

Figure 2 shows the heat of hydration for the four mix designs. The data presents the influence of GU vs. HE cementing material, and also the impact of 15% limestone filler on the heat of hydration. As expected, mixtures consisting of HE cement exhibited greater heat of hydration peaks and these peaks occurred earlier than the corresponding peaks observed for the GU cement based mixtures. Closer examination also indicates that the 15% limestone filler yields a higher and earlier hydration peak for both GU and HE mixtures. The reactivity of LF at 16 hours and 28 days is presented in Figure 3. It should be noted that the 100%GU cement has 2.5% interground  $\text{CaCO}_3$ , and 100% HE cement mixtures have 3.5% interground  $\text{CaCO}_3$ . As expected, the reactivity of the limestone filler increases with age, use of HE cement instead of GU cement, and increase in blended limestone from 0 to 15%.

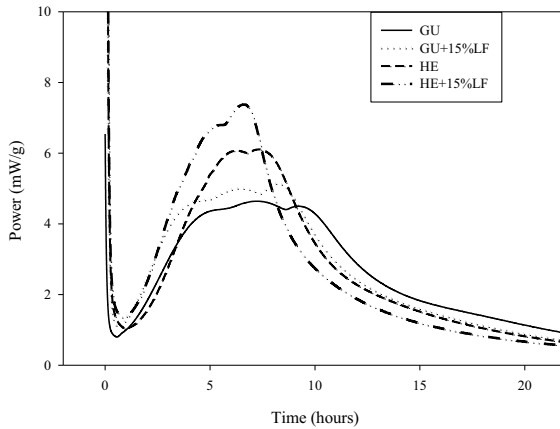


Figure 2. Effect of LF on heat of hydration of cement paste

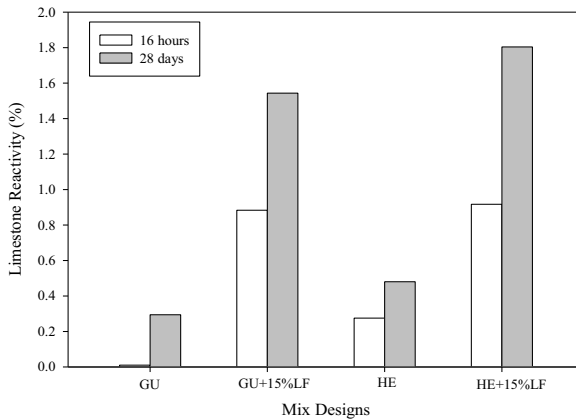


Figure 3. Reactivity of LF



To further assess the role of the limestone filler in context with limestone reactivity, Figure 4 presents the calculated limestone reactivity at 16 hours plotted against the hydration peak for the GU and HE based mixtures. In general it is observed that the HE and HE+15%LF exhibit more of an increasing linear relationship of increasing LF reactivity with increasing hydration peak value in contrast the GU mixtures. Data for more mix designs are needed in order to further populate the figure and analyze the relationship.

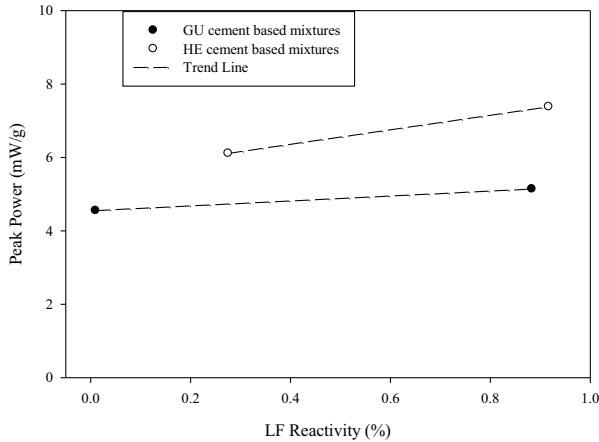


Figure 4. Reactivity of LF vs. hydration peak

The compressive strength of the mortar cubes is presented in Figure 5. The data presents the average of three tests whereby the coefficients of variation were low, below 7%. The results clearly show that HE cement based mixtures have a greater 16 hour compressive strength compared to the corresponding GU mixtures with and without 15%LF. The results also show that the addition of 15% limestone filler also increased the 16 hour compressive strength but did not impact the 28 day compressive strengths. The early age (16 hour) strength varied widely from 57 to 70 MPa, in contrast to the 28 day strength which narrowly fell between 80 and 84 MPa. It is clear from the data and in particular the regression lines in Figure 6, that the early age (16 hour) compressive strength is more influenced by the presence and reactivity of the limestone filler

The plastic properties of the self-consolidating concrete all fell within the required ranges based on CSA and or MTO standards with the exception of the L-box test. Given that the application of the concrete would be in cold climates all mixtures had an entrained air content of 5.0 to 5.6%. The rapid chloride penetration test (RCPT) showed that the influence of HE cement and or the presence of 15% limestone filler could reduce the RCPT value as presented in Figure 7. However, it should be noted that all mixtures did exhibit low RCPT values which were measured to be less than 616 Coulombs. This low penetration resistance also proved to indicate strong resistance against freeze-thaw damage when tested in accordance with ASTM 666, and also good resistance to de-icer salt scaling. Irrespective of the cement type used or the presence of limestone filler, all mixtures had a durability factor of greater than 97% after 300 freeze thaw cycles, and de-icer salt scaling mass losses after 50 freeze thaw cycles less than  $0.38 \text{ kg/m}^2$ . The freeze thaw and deicer salt scaling properties were not impacted by the cement type used or the presence of 15% limestone filler.

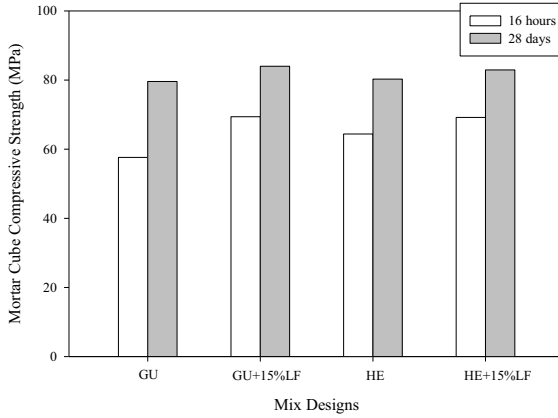


Figure 5. Mortar cube compressive strength

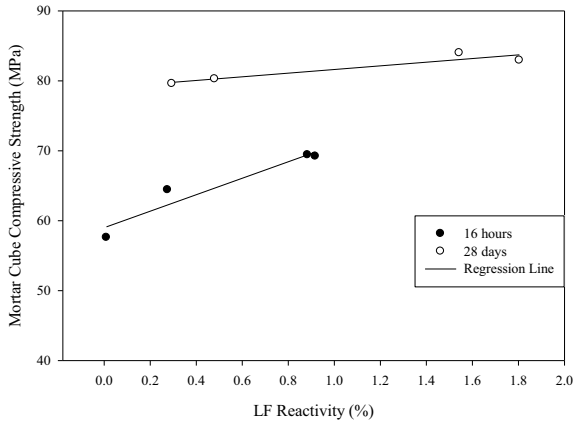


Figure 6. Reactivity of LF vs. mortar cube compressive strength

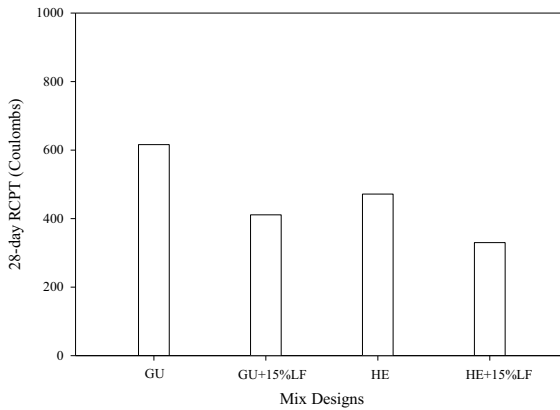


Figure 7. RCPT of concrete at 28 days

#### 4. Conclusions

- Mortar and concrete mixtures made with 15% LF exhibit higher compressive strength at 16 hours compared to mortar and concrete mixtures made without LF. In contrast at 28 days, the presence of heat of hydration results show that the LF and cement type have relatively less of an impact.
- The influence of LF on the RCPT of concrete was greater than the influence of cement type. Concrete mixture made with 15% LF showed similar freeze thaw and salt scaling resistance compared to GU and HE concrete mixtures made without LF.

#### 5. Acknowledgment

The authors acknowledge the MTO HIIFP (2011-2013) program for support of this research.

#### 6. References

- [1] G. Kakali, S. Tsivilis, E. Aggeli, M. Bati, Hydration products of  $C_3A$ ,  $C_3S$  and Portland cement in the presence of  $CaCO_3$ , *Cement and Concrete Research* **30** (2000) 1073 – 1077.
- [2] E. F. Irassar, D. Violinib, V. F. Rahhala, C. Milaneseb, M. A. Trezzaa, V. L. Bonavettia, Influence of limestone content, gypsum content and fineness on early age properties of Portland limestone cement produced by inter-grinding, *Cement and Concrete Composites* **33** (2011), 192–200.
- [3] A. M. Poppe, G. De Schutter, Cement hydration in the presence of high filler contents, *Cement and Concrete Research* **35** (2005), 2290-2299.
- [4] D. Hooton, M. Nokken, M. Thomas, Portland-limestone cement: state of the art report and gap analysis for CSA A3000, *Report to Cement Association of Canada*.
- [5] B. Lothenbach B., G. Le Saout, E. Gallucci, K. Scrivener, Influence of limestone on the hydration of portland cements, *Cement and Concrete Research* **38** (2008), 848-860.
- [6] G. Ge, X. Liu, G. De Schutter, A. Poppe, L. Taerwe, Influence of limestone powder as filler in SCC on hydration and microstructure of cement pastes. *Cement and Concrete Composites* **29** (2007) 94-102
- [7] G. Menendez, V. Bonavetti, E. Irassar, Strength development of ternary blended cement with limestone filler and blast-furnace slag, *Cement and Concrete Composites* **25** (2003), 61-67.
- [8] P. Mounanga, M. Khokhar, R. El Hachem, A. Loukili, Improvement of early-age reactivity of fly ash and blast furnace slag cementitious systems using limestone filler, *Materials & Structure* **44** (2011), 437-453.
- [9] ASTM C187, Standard test method for normal consistency of hydraulic cement, *American Society for Testing and Materials*. Philadelphia, USA, 2010.
- [10] ASTM C191, Standard test method for time of setting of hydraulic cement by Vicat needle, *American Society for Testing and Materials*. Philadelphia, USA, 2004.
- [11] ASTM C1702, standard test method for measurement of heat of hydration of hydraulic cementitious materials using isothermal conduction calorimetry, *American Society for Testing and Materials*. Philadelphia, USA, 2013.
- [12] ASTM C109, standard test method for compressive strength of hydraulic cement mortars (using 2-in. or [50-mm] cube specimens), *American Society for Testing and Materials*. Philadelphia, USA, 2013.
- [13] F. Maria, Handbook of thermogravimetric system of minerals and its use in geological practice, *Geological Institute of Hungary* (2011), 13-55.
- [14] MTO LS-442, Segregation and settlement of freshly mixed self-consolidating concrete by the column method. *Ministry of Transportation, Ontario Laboratory Testing Manual*, 2007.
- [15] MTO LS-438, Method for evaluation of freshly mixed self consolidating concrete by slump flow. *Ministry of Transportation, Ontario Laboratory Testing Manual*, 2007.
- [16] MTO LS-439, Method of test for evaluation of open time of freshly mixed self consolidating concrete. *Ministry of Transportation, Ontario Laboratory Testing Manual*, 2007.
- [17] MTO LS-440, Evaluation of freshly mixed SCC with the L-box. *Ministry of Transportation, Ontario Laboratory Testing Manual*, 2007.

- [18] MTO LS-437, Making and curing freshly mixed self-consolidating concrete compression test specimens. *Ministry of Transportation, Ontario Laboratory Testing Manual*, 2012.
- [19] ASTM C1202, Standard test method for electrical indication of concrete's ability to resist chloride ion penetration. *American Society for Testing and Materials*. Philadelphia, USA, 2012.
- [20] ASTM C666, Standard test method for resistance of concrete to rapid freezing and thawing. *American Society for Testing and Materials*. Philadelphia, USA, 2008.
- [21] MTO LS-412, Method of test for scaling resistance of concrete surfaces exposed to de-icing chemicals. *Ministry of Transportation, Ontario Laboratory Testing Manual*, 1997.

# Evaluation of sulphate attack on concrete incorporating high volume palm oil fuel ash

I.A. SHEHU, A.S.M.A. AWAL<sup>1</sup>, S. MOHAMMAD and A. SULAIMAN  
*Faculty of Civil Engineering, Universiti Teknologi, Malaysia*

**Abstract.** In recent years, the requirement of sustainability has given rise to application of high volume industrial waste in the production of building materials. Fly ash has been found to perform satisfactorily in this regard, and this development is expected to continue in the years ahead because of technological, economical and ecological advantages of the material. This study focuses the potentials of high volume palm oil fuel ash (HVPOFA) replacement of ordinary Portland cement (OPC) and presents experimental results on the effect of sulphate attack. Concrete cube specimens containing 50, 60 and 70% POFA were made alongside with mortar bars made of the same material composition were immersed in 10% magnesium sulphate ( $MgSO_4$ ) solution. Mass and strength loss of concrete cube as well as expansion of mortar bars were studied using wet and drying circle method. The results obtained and observations made were compared with those of 100% OPC specimens. It has been found that the expansion and mass loss significantly decreased with the increase in POFA content, which clearly demonstrates that the replacement of cement with high volume POFA is advantageous particularly in aggressive sulphate environment.

**Keywords.** Concrete, high volume, palm oil fuel ash, sulphate attack, weight and strength loss.

## Introduction

The pressing need for the preservation of natural resources and reduction of carbon dioxide emission due to the rise of construction industry have fuelled the search for alternative solution to produce environment-friendly construction materials. During the past decades, numerous research works have been carried out on the use of agro waste ashes as supplementary cementing materials in concrete construction. The utilization of these wastes contributes to reduce the cost and negative impact to the environment [1-3]. Among others, palm oil fuel ash (POFA) is relatively a new member of the ash family, and is obtained on burning palm oil husk and palm oil kernel shells in palm oil mill boilers. Despite its application as a pozzolanic material in concrete, the problem of ash disposal still persists as major portion of the ash remains unused even after its maximum use of up to 30% as cement substitute [4,5]. With the expansion of palm oil plantation in South-East Asian regions, the production of palm oil and the consequent ash generation in the mills are expected to increase, posing further problems. Although palm oil fuel ash has been identified to be a good supplementary cementing material,

---

<sup>1</sup>Corresponding author: H/P. +60167489357, email. [abdulawal@utm.my](mailto:abdulawal@utm.my)

research work and published data on sulphate resistance of concrete containing high volume palm oil fuel ash are not many. This paper presents experimental results of evaluation of sulphate attack on concrete incorporating high volume palm oil fuel ash.

## 1. Materials and test methods

### 1.1 Preparation of ash and concrete materials

Palm oil fuel ash used in this study was obtained from Kilangsawit PPNJ Kahang of Johor, Malaysia. The ash was collected at the foot of the flue tower where all the fine ashes are trapped while escaping from the burning chamber of the boiler. The ash was sieved through BS standard sieve to remove larger particles as well as reducing the carbon content. Materials passing through 150 $\mu$ m sieve were pulverized using Los Angeles milling machine having 10 stainless bars of 12mm diameter x 800mm length.

Ordinary Portland cement conforming to ASTM C150 [6] was used in the study. A saturated surface dry river sand with fineness modulus of 2.9 passing through 4.75mm ASTM sieve with specific gravity and water absorption of 2.6 and 0.7% respectively was used as fine aggregate. The coarse aggregate was crushed granite of 10mm maximum size with specific gravity of 2.7 and water absorption of 0.5%.

### 1.2 Mix proportion

The mix proportions of the concrete are shown in Table 1. Ordinary Portland cement (OPC) was replaced by POFA at replacement levels of 50, 60 and 70% by weight. Superplasticizer (SP) of sulfonated naphthalene formaldehyde type conforming to ASTM C 494 [7] was added to concrete mix at 2% by weight of cementitious material, to obtain a moderate slump (80-160mm) for the concrete mix.

**Table 1.** Mix characteristics of OPC and POFA concrete

Materials	OPC	50% POFA	60% POFA	70% POFA
OPC (kg/m <sup>3</sup> )	380	190	152	114
POFA (kg/m <sup>3</sup> )	--	190	228	266
Coarse aggregate(kg/m <sup>3</sup> )	1024	1024	1024	1024
Fine aggregate (kg/m <sup>3</sup> )	741	741	741	741
Water (kg/m <sup>3</sup> )	171	171	171	171
Slump (mm)	160	140	110	80

### 1.3 Preparation of specimens and testing of concrete

This test was performed to assess the physical characteristics and response of concrete to attack by sulphate solution. Concrete cubes and mortar bar specimen were cast and the assessment for sulphate action was made in terms of length change for mortar bars; while mass change, visual observation and strength deterioration factor were used to assess the concrete cubes.

Specimen for measurement of linear change was prepared in accordance with the procedures outline in ASTM C 1012 [8], using a bar size of 25 x 25 x 250 mm. Mortar was cast in a metal mould in three layers, each layer was compacted using vibrating

table. After casting, the surface of the specimen was protected by a plastic sheet against evaporation.

After 28 days of moist curing, the surface of the mortar bar was first made smooth by sand paper and cleaned with acetone. Two gauge studs were fixed with glue on the surface of specimen bars with effective length between the gauge studs of 150 mm. The strain was then measured using comparator meter and this was noted as the reference strain with respect to the subsequent strain readings during immersion.

Similarly, cube specimens were wiped to surface dry condition and weighed with an electronic weighing balance to the nearest gram and this was noted as reference weight with respect to subsequent weight during immersion. Specimens made of 100% Portland cement and those replaced by 50, 60 and 70% POFA were submerged in a solution containing 10%  $MgSO_4$  with 12-hour alternate wet and dry cycle using JAB SUBMERSIBLE PUMP as shown in Figure 1. The pH of the solution was not controlled; however, the solution was replaced at a regular interval of 5-6 weeks.

#### 1.4 Strength deterioration factor

The deterioration of concrete specimens was investigated by measuring the strength distortion factor expressed in percentage and was measured after 56 weeks of immersion and calculated using equation 1.

$$SDF = \frac{F_{cw} - F_{ca}}{F_{cw}} \quad [1]$$

Where:

$SDF$  = Strength deterioration factor

$F_{cw}$  = The average compressive strength of companion specimen cured in water

$F_{ca}$  = The average compressive strength of the specimen after immersion in sulphate solution.



**Figure 1.** Specimen in sulphate solution with alternate wet and dry cycle arrangement.

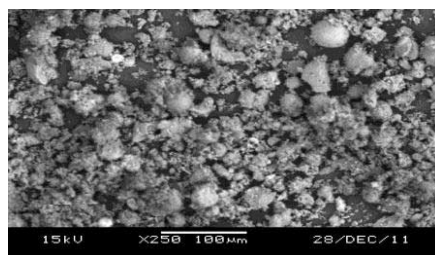
## 2. Results and discussion

### 2.1 Physical and chemical properties of palm oil fuel ash

The chemical composition and physical properties of ordinary Portland cement and palm oil fuel ash (POFA) are presented in Table 2. The POFA contains high amount of silica ( $\text{SiO}_2$ ) of 62.60%, and very small proportions of other chemical compositions. Clearly the presence of higher silica content influences the pozzolanic reaction when it reacts with free lime thus creating extra C-S-H gels, which is beneficial to strength development of the POFA concrete. Specific gravity of Portland cement (3.15) is higher than that of POFA (2.42), which makes it more water demanding than Portland cement. Blaine fineness of POFA ( $4935 \text{ cm}^2/\text{g}$ ) is also more than that of Portland cement ( $3990 \text{ cm}^2/\text{g}$ ). The result suggested that POFA can be classified between class C and F based on ASTM 618 [9] recommendation. The SEM micrograph of POFA at magnification of x250 is illustrated in Figure 2. It can be seen that POFA contains round, angular and irregular shaped particles with clustered arrangement and some air space between particles.

**Table 2.** Chemical composition and physical properties of OPC and POFA

Chemical composition (%)	OPC	POFA
$\text{SiO}_2$	20.4	62.6
$\text{Al}_2\text{O}_3$	5.2	4.7
$\text{Fe}_2\text{O}_3$	4.7	8.1
CaO	62.4	5.7
MgO	1.6	3.5
$\text{K}_2\text{O}$	0.005	9.1
$\text{Na}_2\text{O}$	0.75	0.8
$\text{P}_2\text{O}_5$	0.3	3.9
CL	0.001	0.5
$\text{SO}_3$	2.1	1.2
LOI	2.4	6.3
Physical properties		
Specific gravity	3.15	2.42
Particle retained on $45\mu\text{m}$ sieve	4.58	4.98
Median particle $d_{10}$	--	1.69
Median particle $d_{50}$	--	14.58
Blaine fineness ( $\text{cm}^2/\text{g}$ )	3990	4935
Soundness (mm)	1.0	2.0
Strength Activity Index at 28-day (%)	--	112



**Figure 2.** Scanning electron micrograph of POFA



## 2.2 Mortar bar expansion

The values of the expansion of mortar bars immersed in 10% magnesium sulphate solution for the period of 56 weeks is presented in Figure 3. From the figure it can be seen that with increase in the duration of immersion in  $MgSO_4$  solution, the mortar bar expansion increased. It is clearly evident that mortar bar made with ordinary Portland cement showed considerably higher expansion throughout the period of immersion as compared to the specimen with HVPOFA. It is interesting to note that the expansion progressively decreases with an increase in the POFA replacement. For example, at 56 weeks the expansion attained by bars containing 50, 60 and 70% POFA are 22, 19.2 and 14.2 micro strain. Earlier findings show that gypsum development during sulphate attack is expansive [10, 11], whereas ettringite might develop afterwards, contributing to expansion within the paste matrix. High volume ash application also reduces the presence of  $Ca(OH)_2$  which would have otherwise influenced the expansion in HVPOFA specimens.

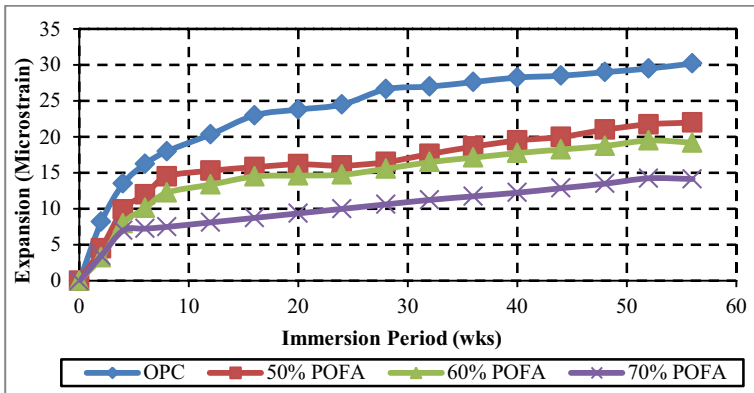


Figure 3. Expansion of mortar bar exposed to magnesium sulphate solution

## 2.3 Loss of mass

The result of change in mass versus time of exposure of the specimen is illustrated in Figure 4. It can be observed that the entire specimen exhibited the same behaviour (increase in weight). Initially, there was no change in weight of the specimen up the period of 4 weeks.

At the period of 6 weeks, OPC, 50 and 60% POFA specimen developed a gradual change in mass. In the same solution, specimen made of 70% POFA experienced no change in mass up to the period of 24 weeks. It was also observed that concrete containing 70% POFA suffered less on the effect of changing mass throughout the period of immersion. Application of HVPOFA in concrete is therefore advantageous under sulphate environment due to the discontinuous pore structure of the ash concrete and reduced amount of calcium hydroxide present in the concrete [12].

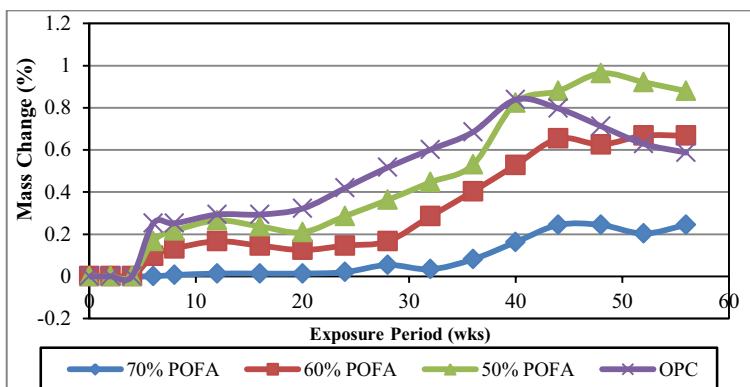


Figure 4. Mass variation of concrete cube specimen exposed to sulphate solution

### 2.4 Loss of strength

Comparisons between strength loss of companion specimen and specimen immersed in sulphate solution are illustrated in Figure 5. While the test specimen suffers attack due to sulphate, the companion specimens enjoyed curing in water at room temperature. At the end of 56 weeks the strength of concrete specimens immersed in sulphate solution is compared with that of companion concrete. The difference in the strength between the companion specimen and those immersed in solution is regarded as the strength loss.

From the figure, it is apparent that the entire specimen suffered strength loss. The loss was observed to be more in the OPC specimen as compared to those of high HVPOFA. For example a strength loss of 10.5, 8.8, 6.8 and 2.2MPa were observed for OPC, 50, 60 and 70% POFA concrete respectively. The strength loss associated with the entire sample is understood to be the consequence of the prolonged immersion into sulphate solution. Whereas, OPC specimen developed fine cracks on the surface showing the effect of deterioration as explained earlier. Earlier findings, however, shows dissimilarity where an increase in compressive strength of concrete containing large amount of low calcium fly ash immersed in 5% and 10% Na<sub>2</sub>SO<sub>4</sub> solution was observed [12,13].

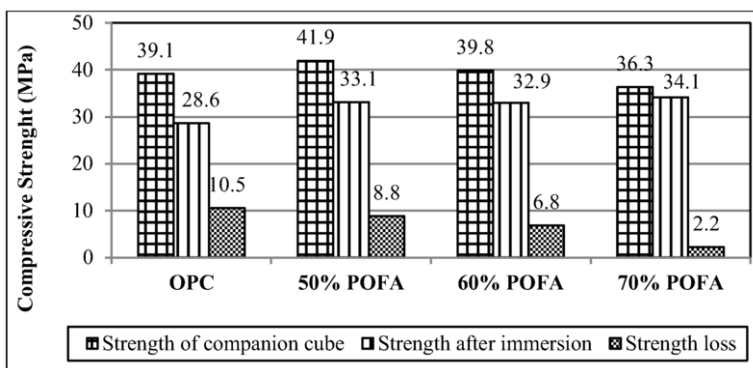


Figure 5. Strength losses between companion and test specimen in magnesium sulphate solution

### 2.5 Strength deterioration factor

The compressive strength deterioration of OPC specimen and those of high volume POFA due to sulphate attack was expressed in the form of strength deterioration factor (SDF). Figure 6 shows the SDF after 56 weeks immersion in sulphate. The entire specimens are affected by the sulphate action and generally developed SDF. The values are found to be higher in OPC, while minimal SDFs were observed in POFA specimen under the same condition and decreased with increase in cement replacement with POFA. The reason of SDF feature in the test specimens is similar to those stated earlier in strength loss.

This is to note that considerably higher  $C_3A$  content in the control specimen should in theory make it more prone to sulphate attack. High volume POFA thus chemically binds the CH in the form of calcium silicate hydrate making it unavailable for sulphate, gypsum and ettringite, thus reduces the specimen permeability and sulphate ion from penetrating into the concrete. Although there are very few test data on the influence of high volume POFA concrete in sulphate solution, the results obtained in this study are however in agreement with the findings of Donatello *et al.*, ; Jiang *et al.*, and Torii *et al.*, [12-14] on high volume fly ash concrete which has successfully been practiced since the last decade.

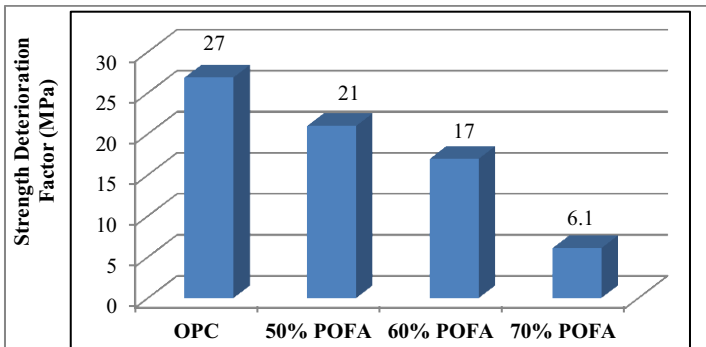


Figure 6. Strength deterioration of OPC and high volume POFA concrete

### 3. Conclusion

The results obtained and observation made in the study demonstrates that high volume palm oil fuel ash has potentials of reducing the effect of sulphate of concrete. The performance of high volume POFA is influenced by its lower calcium content which is consumed in the pozzolanic reaction, thus making the mixture free of expansive chemical when it come into contact with sulphate; while the control specimen suffers expansion due to high calcium oxide content. This infers that incorporating high volume POFA in concrete will offer credible advantage in performance of concrete in aggressive environment. Longer period of study on the behaviour of concrete containing higher amount of palm oil fuel ash, however, has been put forward as a recommendation for future investigation.

## Acknowledgement

The authors wish to acknowledge the help and co-operation received from the technical staff of the Structure and Materials Laboratory of the Universiti Teknologi Malaysia (UTM) in conducting the experimental work. The financial support from the Research University Grant (GUP 01J81) is also gratefully acknowledged.

## References

- [1] J.J. Brooks, J.G. Cabrera, M. El-Badari, Properties of clay/PFA bricks. In *Proc. 8<sup>th</sup> Int. Bricks/Blocks Masonry Conference*, Ireland. **1**(1998), 64-75.
- [2] R.L. Day, J.W. Bergmen, Fly ash as substitute for clay in brick manufacture. In *Proc. 8<sup>th</sup> Int. Bricks/Blocks Masonry Conference*, Ireland. **1**(1998), 14-25.
- [3] J.H. Tay, Ash from oil-palm waste as concrete materials, *Journal of Materials in Civil Engineering*, **2**(2) (1990):94-105.
- [4] R.S. Salihuddin, Relationship between engineering properties and microstructural characteristics of mortar containing agricultural ash, *PhD Thesis. Universiti Teknologi*, Malaysia, 1993.
- [5] A.S.M.A. Awal, K.N.A. Siew, A short-term investigation on high volume palm oil fuel ash (POFA) concrete. In *Proc. 35<sup>th</sup> Conference on Our world in Concrete and Structure*, Singapore, August 25-27 (2010), 185-192.
- [6] ASTM, C 150. Standard specification for portland cement. *Annual Book of ASTM Standards, American Society for Testing and Materials* (2004).
- [7] ASTM C 494. Standard specification for chemical admixtures for concrete. *Annual Book of ASTM Standards, American Society for Testing and Materials* (2005).
- [8] ASTM C 1012. Standard test method for length change of hydraulic-cement mortars exposed to a sulphate solution. *Annual Book of ASTM Standards, American Society for Testing and Materials* (2003).
- [9] ASTM C 618. Standard specification for coal fly ash and raw or calcined natural pozzolan for use as a mineral admixture for concrete. *Annual Book of ASTM Standards, American Society for Testing and Materials* (2005).
- [10] M. Santhanam, M. D. Cohen and J. Olek. Modelling the effect of solution temperature and concentration during sulphate attack on cement mortars. *Cement and Concrete Research*. **32** (2003), 585-592
- [11] B. Tian and M. D. Cohen. Does gypsum formation during sulphate attack on concrete leads to expansion? *Cement and Concrete Research* **30** (2000), 117-123.
- [12] Torii, K., Taniguchi, K. and Kawamura, M. Sulfate resistance of high fly ash content concrete. *Cement and Concrete Research*. **25**(4) (1995), 759-768.
- [13] L. Jiang, Z. Liu and Y. Ye. Durability of concrete incorporating large volumes of low-quality fly ash. *Cement and Concrete Research*. **34**(8) (2004), 1467-1469.
- [14] S., Donatello, A. Palomo and A. Fernández-Jiménez. Durability of very high volume fly ash cement pastes and mortars in aggressive solutions. *Cement and Concrete Composites*. **38**(0) (2013), 12-20.

# Sulphate corrosion behaviour of high volume slag concrete

Stephen O. EKOLU<sup>a,1</sup> and Adam NGWENYA<sup>b</sup>

<sup>a</sup>Department of Civil Engineering Science, University of Johannesburg, South Africa

<sup>b</sup>ABB South Africa (pty) Ltd ABB Campus, South Africa

**Abstract.** Concrete mixes of water-cementitious ratio (w/c's) = 0.45, 0.5, 0.65 were used to prepare 100 mm cubes and 75 x 75 x 285 mm prisms. Moderately high alumina slag was incorporated in proportions of 50 or 70% and the specimens immersed in sodium sulphate or magnesium sulphate solutions of 50 g/L as SO<sub>4</sub>. Emphasis in the study was to assess sulphate resistance using concrete samples and other non-conventional methods. Expansion measurements, mass loss and corrosion attack or physical deterioration of concrete were monitored for 69 weeks. It was found that the results of expansion, mass gain and corrosion were consistent for Na<sub>2</sub>SO<sub>4</sub> solution, showing improved sulphate resistance with increase in ground granulated blast-furnace slag (GGBS) incorporation. The expansion observations under MgSO<sub>4</sub>, while showing increased resistance with use of GGBS, gave conflicting results between expansion on one hand and, mass gain and corrosion on the other with the most severe corrosion occurring in concrete containing the high 70% GGBS. The corrosion test method appears to give a more realistic indicator of physical damage under MgSO<sub>4</sub> attack compared to expansion measurement.

**Keywords.** Sulphate resistance, high alumina slag, corrosion, mass loss, sodium sulphate, magnesium sulphate attack

## Introduction

Past studies and field experiences with sulphate attack have generally established that the mechanism is associated with two processes of: (i) expansive chemical reactions within the pore structure of concrete resulting in ensuing pressures, that lead to the next process of (ii) physical degradation associated with cracking and delamination. Low alumina slags are considered to be those containing less than 11% Al<sub>2</sub>O<sub>3</sub> in accordance ASTM C 989. Such slags are known to consistently increase sulphate resistance. High alumina slags have been found to show adverse effects and this understanding can be traced to an early South African study [1]. The South African slag used in the present study is of moderately high alumina content, being 13.4% Al<sub>2</sub>O<sub>3</sub>.

---

<sup>1</sup>Corresponding author: University of Johannesburg, Department of Civil Engineering, P.O. Box 524, Auckland Park, 2006, South Africa; E-mail. [sekolu@uj.ac.za](mailto:sekolu@uj.ac.za), [sekolu@gmail.com](mailto:sekolu@gmail.com)

## 1. Literature

### 1.1. Accelerated test methods

It is recognised that while accelerated test methods play an important role in determining early indications of potential long-term behaviour, their results may not provide confirmatory observations for various reasons: (a) the experimental conditions are typically severe than actual site environments, (b) the specimens are much smaller creating a different micro-climate and specimen responsiveness that may deviate widely from a finite element within the typically large-scale concrete element, (c) material characteristics of mortars used in the test may not adequately represent similar concrete properties, (d) overly severe tests may induce attack mechanisms different from those intended to develop in the deterioration process.

Sulphate attack in concrete is usually associated with ettringite formation within the cement paste matrix. It is generally observed that the attack increases with proportional growth in the amount of ettringite formed but there is no direct correlation between expansion observed in laboratory tests and the amount of ettringite formed. Infact, non-expansive systems may contain similar or more ettringite amounts as found in expansive systems [2]. In discussing sulphate attack, Idorn et al. [3] explained that the effect of ettringite formation, which usually causes expansions in laboratory tests, is not usually reflected with field concretes in form of expansions. In view of the range of experimental variations from real-life exposure conditions, it is typical to require that experimental results be related or calibrated against field observations to establish reliability of the accelerated test method. Often times, it is found that useful accelerated test methods provide a means for screening of potential material behaviour over short test time periods for which results must be obtained. But in many cases, the accelerated test methods typically tend towards severity and may fail materials that in real life exposure conditions would not exhibit failure under the mechanism of attack being examined. These fears have been recognised by researchers and in certain fields, confirmatory test methods conducted over relatively longer periods are devised to provide more reliable observations.

### 1.2. Some past studies on sulphate attack in concrete

In comparison to the mortar prism test of ASTM C 1012, relatively limited literature is available where sulphate resistance evaluation has been conducted using concretes. Khatri and Sirivivatnanon [4] used 75 x 75 x 285 mm prisms to monitor expansion in concrete of 35 MPa and 40 MPa strength grades made with ordinary Portland cement and sulphate resisting Portland cement, with or without 7% silica fume and 60% slag. In their study, mortar prism expansion tests were also conducted but emphasis in the study assessed the possibility of permeability playing a role in influencing sulphate resistance behaviour of the concretes. Specimens were stored in 5% sodium sulphate solution with a pH being maintained constant through automated addition of sulphuric acid. They found that the permeability property influenced expansion results in concretes but does not fully account for the observations made which they attributed to the chemical resistance in the cementitious systems. Some studies [5] along this approach recognise that a complete evaluation for sulphate resistance should adequately consider both the physical and chemical resistance properties of the

cementitious system. In this approach, permeability is favoured as a dominant parameter to represent physical ingress of sulphate into concrete and a method is proposed to rapidly measure sulphate permeability in a manner similar to the Rapid Chloride Permeability Test in accordance with ASTM C 1202.

### *1.3. Sulphate and magnesium sulphate attack processes*

Studies have long established the difference in attack processes between the two different sulphate salts. In the case of external sulphate attack, ions from soils or water sources react with calcium hydroxide in concrete forming gypsum and soluble sodium hydroxide. The gypsum formed in turn converts calcium monosulphoaluminate hydrate into ettringite. The formation of ettringite structure results in large volume increase, leading to infilling of the existing pores and causing expansion in the hardened concrete with its continuous accumulation. In a similar manner, magnesium sulphate forms gypsum and magnesium hydroxide or brucite. But the difference arises from the insoluble nature of  $Mg(OH)_2$ . It has been reported that at advanced stages of the attack, brucite may replace the calcium component of the calcium silicate hydrate (C-S-H) forming a non-cementitious product M-S-H [6]. A combination of the expansive gypsum reactions to form ettringite and de-calcification of the C-S-H may be responsible for typically devastating physical attack by magnesium sulphate in comparison to sodium sulphate.

## **2. Experimental**

### *2.1. Mixtures*

The present study was conducted using concrete mixtures of w/c's = 0.45, 0.50, 0.65 made using CEM I 42.5N normal strength Portland cement and GGBS, as given in Tables 1 and 2. Ground granulated blast-furnace slag was incorporated as a cement extender in proportions of 50 or 70%. Concrete prisms 75 x 75 x 285 mm and 100 mm cubes were cast then water-cured for 28 days prior to immersion of the specimens in 50 g/L storage solutions of  $Na_2SO_4$  and  $MgSO_4$ . No air entrainment or other chemical admixtures were used in the concrete mixtures.

**Table 1.** Chemical compositions of the cementitious materials

	SiO <sub>2</sub>	Al <sub>2</sub> O <sub>3</sub>	Fe <sub>2</sub> O <sub>3</sub>	CaO	MgO	K <sub>2</sub> O	TiO <sub>3</sub>	Mn <sub>2</sub> O <sub>3</sub>	Na <sub>2</sub> O	SO <sub>3</sub>	Cl-	LOI
CEM1 42.5N	21.7	5.3	2.0	62.5	4.6	0.6	0.3	0.9	0.1	2.0	0.02	2.9
GGBS	38.3	13.4	0.8	35.3	7.5	1.0	0.9	1.1	0.3	12.4	0.02	0.7

### *2.2. Test methods*

The test methods employed included conventional measurement of length change (expansion) of the prisms. Mass change was determined for prisms and cubes. In an attempt to quantify physical attack effects on the concretes, a method referred to as

corrosion assessment on cubes, was employed. The measurements were determined at intervals of 0, 2, 8, 13, 17, 25, 29 and 69 weeks.

**Table 2.** Concrete mixtures used to prepare specimens stored in Na<sub>2</sub>SO<sub>4</sub> and MgSO<sub>4</sub> solutions (sg – slag)

Mix	Initial compressive strength upon immersion in sulphate solution (MPa)	GGBS (%)
0.45w/c-CEM I	52.4	0
0.45w/c-50sg	38.3	50
0.45w/c-70sg	28.6	70
0.5w/c-CEM I	48.3	0
0.5w/c-50sg	31.4	50
0.5w/c-70sg	24.0	70
0.65w/c-CEM I	36.5	0
0.65w/c-50sg	22.8	50
0.65w/c-70sg	20.0	70

Corrosion assessment was done by recording the cube diagonals at the top and bottom surfaces using a metric ruler. The ruler was placed on the diagonal across the face and the extent of loss of material or cracking at the corner was recorded in mm. A mean value (d) for each of these two corners was then calculated as:

$$d = (141 - D)/2 \quad (1)$$

Where, D is the length of “unattacked” area visible across the diagonal of the face measured.

The top and bottom faces of each cube as cast were measured in this way. The mean of the d values for the two faces of two cubes i.e. a total of 8 measurements was then considered the corrosion value for a particular mix and age of testing.

### 3. Results and discussions

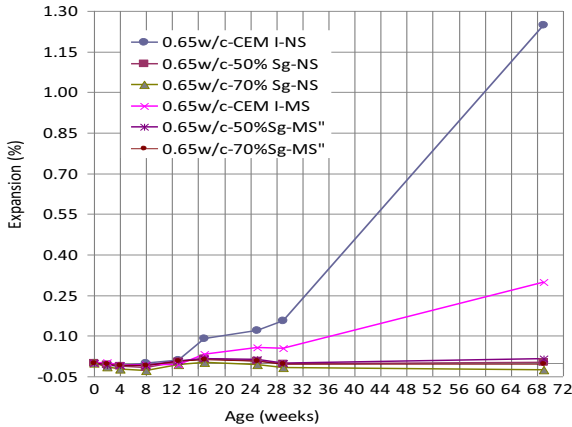
#### 3.1. Expansion of prisms

Following 69 weeks of specimen storage in sulphate solutions, expansion occurred only in control prisms while the concretes containing extenders had not exhibited expansion, as seen in Table 3. The effect of water-cement ratio is notable, with mixes of high w/c's giving correspondingly higher expansions. In all cases, the expansion in Na<sub>2</sub>SO<sub>4</sub> was always higher compared to the corresponding expansion in MgSO<sub>4</sub>, as also seen in Figure 1 for 0.65 w/c concrete. Similar observations were exhibited in the 0.45 w/c and 0.50 w/c concretes, given in Figure 2. In all the blended cement mixes, the difference in expansion between the 50% and 70% slag concretes was small, but the surface deterioration of the 70% slag concrete was found to be quite severe, more especially for the specimen stored in MgSO<sub>4</sub> solution.

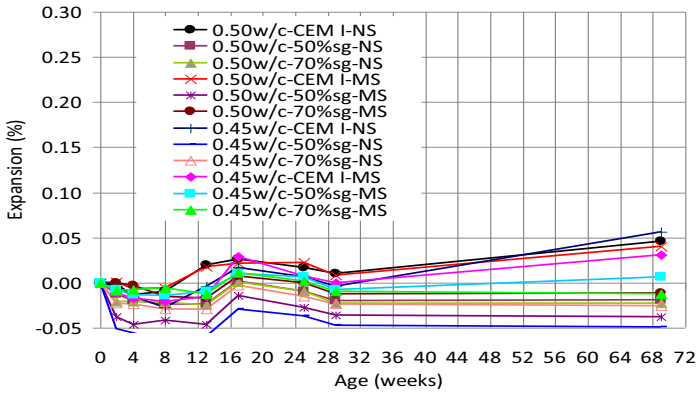


**Table 3.** Expansion of concrete prisms stored in Na<sub>2</sub>SO<sub>4</sub> and MgSO<sub>4</sub> solutions

Mix	Expansion (%) after 69 weeks of storage in	
	Na <sub>2</sub> SO <sub>4</sub>	MgSO <sub>4</sub>
0.45w/c-CEM I	0.06	0.03
0.45w/c-50sg	0.00	0.01
0.45w/c-70sg	0.00	0.00
0.5w/c-CEM I	0.05	0.04
0.5w/c-50sg	0.00	0.00
0.5w/c-70sg	0.00	0.00
0.65w/c-CEM I	1.25	0.30
0.65w/c-50sg	0.00	0.02
0.65w/c-70sg	0.00	0.00



**Figure 1.** Expansion of 0.65 w/c concrete prisms in Na<sub>2</sub>SO<sub>4</sub> and MgSO<sub>4</sub> solutions (NS-sodium sulphate, MS-magnesium sulphate, sg-slag)

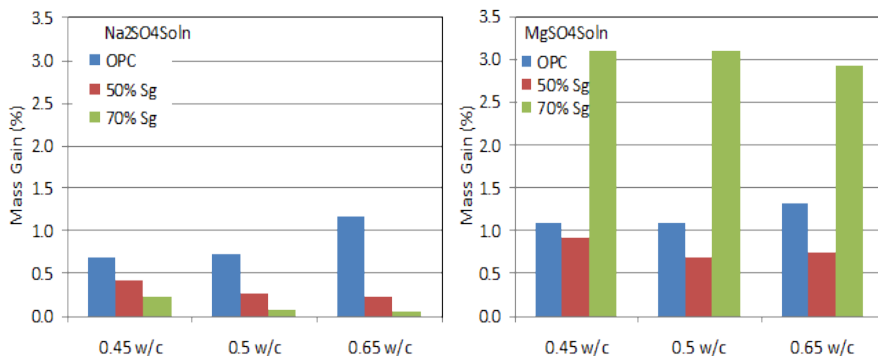


**Figure 2.** Expansion of 0.50 and 0.45 w/c concrete prisms in Na<sub>2</sub>SO<sub>4</sub> and MgSO<sub>4</sub> solutions (NS-sodium sulphate, MS-magnesium sulphate, sg-slag)

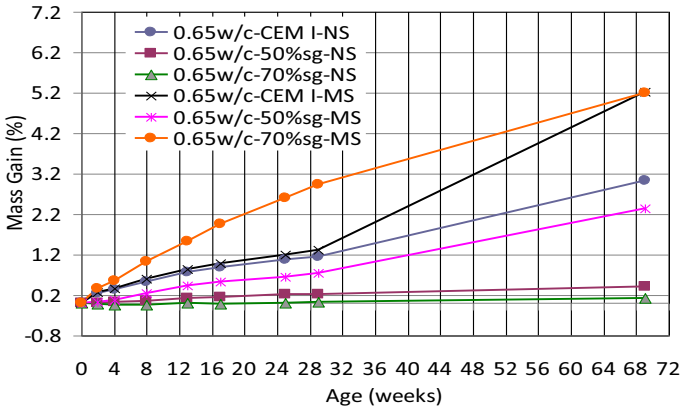
### 3.2. Mass change

The graphs in Figure 3 show the mass gain trends of prisms stored in Na<sub>2</sub>SO<sub>4</sub> and MgSO<sub>4</sub> solution for duration of 69 weeks. The mass gain is related to growth of reaction products responsible for deterioration. It can be seen that their deterioration is generally more severe in MgSO<sub>4</sub> solution than in Na<sub>2</sub>SO<sub>4</sub> solution, contrary to observations in expansion results where the former shows lesser effect than the latter attack solution. Regardless of the lower values observed in sodium sulphate, CEM I mixes are the ones that gained more weight than the slag blended mixes. Comparing the prisms expansion rate and mass gain of the same prisms, it can be observed in Figures 1 and 4, that the rate of mass gain is initially faster than the expansion rate, this being presumably contributed by immediate water uptake upon immersion of prisms in solution.

Under both the Na<sub>2</sub>SO<sub>4</sub> and MgSO<sub>4</sub> storage, the 70% slag replacement mixes expanded the least. The 70% GGBS concrete also gave the least mass gain under Na<sub>2</sub>SO<sub>4</sub> but it exhibited the highest mass gain and most severe physical deterioration than all the other mixes when subjected to magnesium sulphate attack. This contrast in behaviour of magnesium sulphate relative to sodium sulphate is related to the formation of brucite in the former, as already explained in the foregone. At the age of 29 weeks of sample storage in MgSO<sub>4</sub>, the 50% slag concrete of 0.45 w/c had 0.90% mass gain in comparison to 3.1% for 70% slag concrete and 1.31% mass gain for CEM I (see Figure 3). On the basis of mass gain and expansion alone, it would appear that the 50% slag concretes showed better performance in the magnesium sulphate solution than the CEM I or the 70% slag concretes. While in the Na<sub>2</sub>SO<sub>4</sub> solution, performance improved with increase in proportion of slag incorporated into the mix.



**Figure 3.** Mass change of concrete prisms after 29 weeks of storage in Na<sub>2</sub>SO<sub>4</sub> and MgSO<sub>4</sub> solutions (OPC = CEM I Portland cement)



**Figure 4.** Mass change of 0.65 w/c concrete prisms after 29 weeks of storage in  $\text{Na}_2\text{SO}_4$  and  $\text{MgSO}_4$  solutions

### 3.3. Corrosion

The Figures 5 and 6 give the corrosion results for cubes that were exposed in  $\text{Na}_2\text{SO}_4$  and  $\text{MgSO}_4$  solutions for a period of 69 weeks. For specimens exposed to  $\text{Na}_2\text{SO}_4$  solution, there is a clear separation between the corrosion results of CEM I mix samples on one hand, and the results of mixes containing GGBS extender, considering all the three w/c mixtures. It is evident that corrosion attack occurred only in the plain CEM I concrete cubes containing no extenders. The CEM I mixes of 0.45, 0.50, 0.65 w/c's gave respective corrosion values of 9.8%, 12%, 13.6% as compared to 2 to 3% corrosion in the mixes incorporating GGBS extender. There was no significant difference between the corrosion values of 50% and 70% slag mixes.

The corrosion results for mixes stored in  $\text{MgSO}_4$  solution gave a different and contrary behavior from that observed under  $\text{Na}_2\text{SO}_4$  storage. Figure 6 shows that for the cube samples stored in  $\text{MgSO}_4$  solution, plain CEM I concretes gave better corrosion performance than slag blended mixes. The corrosion increased with increase in the proportion of GGBS incorporated and with increase in w/c ratio. After 69 weeks of storage, the corrosion in the plain CEM I mixes was in the range of 3 to 5% compared to 7 to 17% in slag blended mixes, depending on the w/c and slag proportion. The disintegration of concrete was already excessive just in five months of exposure of the 70% slag mix in  $\text{MgSO}_4$ , while the corresponding CEM I mixes showed no significant deterioration over the same period. In comparison of expansion results and the corrosion observations under  $\text{Na}_2\text{SO}_4$  storage, it is quite interesting to note that both methods were in good agreement, showing the same tendencies in behavior of the mixes. Only the plain CEM I mixes showed expansion and also showed corrosion attack. The blended mixes showed neither expansion nor corrosion. But under the  $\text{MgSO}_4$  attack, it was found that the expansion results showed a different behavior from the corrosion results. The expansion of prisms in the magnesium sulphate solution was less compared to corresponding expansions in sodium sulphate, but the reverse was true for corrosion, with deterioration being severe in magnesium sulphate than in

sodium sulphate solution. The behaviour of the two solutions emphasizes the need to know the type of sulphate present in the soil, groundwater or the exposure environment before deciding on the suitable mix design.

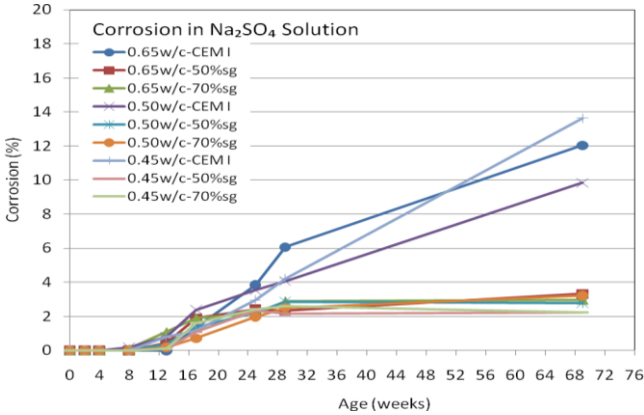


Figure 5. Corrosion of concrete cubes stored in Na<sub>2</sub>SO<sub>4</sub> solution

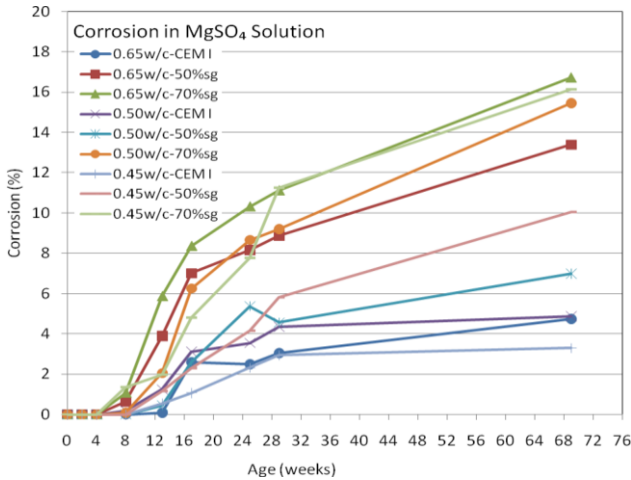


Figure 6. Corrosion of concrete cubes stored in MgSO<sub>4</sub> solution

#### 4. Conclusions

In the foregone investigation, both conventional and some non-conventional methods were used to assess the sulphate corrosion behavior of high volume slag concrete subjected to two different forms of sulphate solutions namely, Na<sub>2</sub>SO<sub>4</sub> and MgSO<sub>4</sub> solutions.

Basing on the expansion measurements conducted up to 29 weeks, it was found that the moderately high alumina slag was effective in increasing the resistance of cementitious systems against both magnesium and sodium sulphate attack but the expansions under sodium sulphate were far greater than corresponding results under magnesium sulphate solution.

For sodium sulphate attack, the corrosion results were in agreement with expansion results. However, for magnesium sulphate attack, the corrosion and mass change results contradict expansion results with systems containing slag exhibiting greater corrosion in proportion to the amount of slag incorporated. The 70% slag extender was found to be especially vulnerable to significant physical deterioration from magnesium sulphate attack. The use of 50% slag blend in conjunction with a low water-cementitious ratio  $\leq 0.5$ , appears to exhibit a combination of generally good chemical and physical resistance to both sodium and magnesium sulphate attack processes. It can be concluded that the expansion method alone is not capable of representing the physical resistance of concretes under magnesium sulphate attack.

### Acknowledgement

The authors wish to thank Afrisam (pty) Ltd for providing technical support used to undertake this investigation.

### References

- [1] Aardt and Visser., The behaviour of mixtures of milled granulated blast-furnace slag and Portland cement in sulphate solutions, *National Building Research Institute (NBRI)*, Bulletin 47, South Africa, 1967.
- [2] Famy, C., Expansion of heat-cured mortars, *Ph.D. Thesis, Dept of Materials, University of London*, Sept (1999), 00. 256.
- [3] Idom, G.M., Johansen V., and Thaulow., Research innovations for durable concrete, *Concrete International*, July 1992, pp. 19-24.
- [4] Khatri , P. and Sirivivatnanon V., Role of permeability in sulphate attack, *Cement and Concrete Research*, V. 27, No.8, 1997, pp. 1179-1189.
- [5] Cement, Concrete and Aggregates Australia, *Sulfate resisting concrete*, Technical Note, CCA ,Sep. 2007, pp. 8.
- [6] Dewah H.H., Effect of sulphate concentration and associated cation type on concrete, deterioration and morphological changes in cement hydrates, *Construction and Building Materials*, Vol. 21, 2007, pp. 29-39.

# Sulphate resistance of concrete made with moderately high alumina slag

Stephen O. EKOLU<sup>a,1</sup> and Adam NGWENYA<sup>b</sup>

<sup>a</sup>Department of Civil Engineering Science, University of Johannesburg, South Africa

<sup>b</sup>ABB South Africa (pty) Ltd ABB Campus, South Africa

**Abstract.** This paper reports findings of ongoing investigation into the effect of high alumina ground granulated blast furnace slag (GGBS) on sulphate resistance of concrete. Slags used in most countries contain low alumina contents and provide high resistance to sulphate attack among other durability improvements. It is however known that slags of high alumina contents do not necessarily improve sulphate resistance but may otherwise adversely influence concrete performance. South African slags have moderately high alumina contents but hardly any studies have been conducted to determine its influence on sulphate resistance of concretes. In this investigation, commercially available slag widely used in South Africa was used. Mortar prisms 25 x 25 x 285 mm of 0.5 water-binder ratio incorporating 30%, 50%, 70% GGBS were prepared and immersed in sodium sulphate solutions of different concentrations of 28 g/L and 50 g/L as SO<sub>4</sub>.

Expansion and mass change of the cementitious systems were monitored. Variables examined were compressive strengths prior to immersion in Na<sub>2</sub>SO<sub>4</sub> solution, slag replacement levels, concentrations of sulphate solutions. It was found that the moderately high alumina slag improved resistance to sulphate attack in correspondence with increase in the replacement levels of the extender. Mixtures that were not cured to develop 20 MPa initial strength prior to exposure in Na<sub>2</sub>SO<sub>4</sub> solution, showed elevated early age expansion while their cured counterparts did not expand. The long-term expansions of mixtures that had not been cured were much higher than expansions of the respective cured mixes. Interestingly, the use of GGBS in proportions exceeding 50% mitigated the adverse effects of early age expansions giving no long-term expansions in any of the mixtures containing the extender.

**Keywords.** Sulphate resistance, mortar expansion, initial compressive strength, South African slag, sulphate concentration

## Introduction

In South Africa, sulphate attack is not a dominant problem like other deterioration mechanisms such as alkali-silica reaction, and research towards sulphate attack has in the past not received much attention locally. However, sulphates do occur in soils and ground water in significant proportions in and around some brownfields, and naturally in some parts of the country, mostly in the western provinces. Besides natural sources of sulphate ions, urban occupancy, domestic lifestyles and industrial effluents also discharge sulphate laded wastes into existing infrastructure.

<sup>1</sup>Corresponding author: University of Johannesburg, Department of Civil Engineering, P.O. Box 524, Auckland Park, 2006, South Africa; E-mail. [sekolu@uj.ac.za](mailto:sekolu@uj.ac.za), [sekolu@gmail.com](mailto:sekolu@gmail.com)

Sulphate attack may therefore occur in sewer pipes and sewage storage tanks among other structures. As such, it is of interest to develop clear scientific understanding of the potentials and implications associated with use of extenders including local slag extenders in situations where sulphate attack is possible.

## 1. Background

### 1.1. An early South African study

This paper is first in a series of reports of an ongoing study of the effect of ground granulated blast-furnace slag produced in South Africa on sulphate resistance of concrete. The extender is widely used and typically incorporated in proportions of 50% but higher levels of up to 70% may also be used for special applications. It contributes significantly to the concrete industry due to major benefits ranging from its influence on engineering properties to environmental impact. While the contribution of the GGBS to engineering properties and durability of concrete are generally accepted to be significantly beneficial, little is known about their effect on sulphate resistance of concrete.

Emphasis in this investigation was placed on the potential ability of South African GGBS to mitigate sulphate attack in concrete. The practice of using GGBS to provide high sulphate resistance to concrete is well established for slags in Europe, North America and other countries where sulphate attack can be prevalent and an extensive body of knowledge in this regard has been accumulated. Research knowledge available in the mainstream literature may lead to the somehow erroneous view that GGBS does always provide improved sulphate resistance in concrete regardless of its source or type. Emerging research now appears to indicate that not all slags are capable of improving sulphate resistance of concrete.

### 1.2. High alumina slags

ASTM C 989 [1] recognises that there is an exception to contribution of high alumina slags to sulphate resistance. Alumina content of slags not exceeding 11% is considered to be low  $\text{Al}_2\text{O}_3$  while high alumina contents can be as much as 18%  $\text{Al}_2\text{O}_3$ . However, the influence of alumina content is not necessarily an overriding factor in the different cementitious systems containing slags. Alumina affects sulphate resistance in conjunction with its interaction with the  $\text{C}_3\text{A}$  levels present in cement. ASTM C 989 stipulates that high replacement levels exceeding 60% slag should increase sulphate resistance irrespective of the composition of slag or cement while low  $\text{Al}_2\text{O}_3$  content of slag should ensure improved sulphate resistance in cementitious systems.

Van Aardt and Visser [2] while conducting a study of South African slags in sulphate solutions, were among the first to show that alumina content of slags played an important role in determining the influence of the extender on sulphate resistance. Their study was conducted using mortars cured in water for 28 days prior to immersion in 5% magnesium sulphate or 5% sodium sulphate solutions. Expansion and the dynamic modulus of specimens were monitored. The cementitious materials used were ordinary Portland cements of 0, 6.6, 6.9%  $\text{C}_3\text{A}$  contents; milled GGBS of 10.1, 15.5,

18.4%  $\text{Al}_2\text{O}_3$ ; and one sulphate resisting Portland cement (SRPC). Cement /slag blends used in the experiment consisted of 30%, 50% and 70% slag. They found that the performance of the blends was dependent on the  $\text{Al}_2\text{O}_3$  of the slags. The slag with 10.1%  $\text{Al}_2\text{O}_3$  increased sulphate resistance of the mixture. Increase in the  $\text{Al}_2\text{O}_3$  content of slags reduced sulphate resistance with the slag containing a high 18.4%  $\text{Al}_2\text{O}_3$  giving results poorer than Portland cement alone. Use of higher slag contents led to relatively improved sulphate resistance but in all cases, worse than results of control mix. These NBRI findings somehow disagree with ASTM C 1012 which stipulates that use of high replacement levels exceeding 60% should, by implication improve sulphate resistance even for high  $\text{Al}_2\text{O}_3$  slags.

The findings of the National Building Research Institute (NBRI) study were mentioned in the earlier edition of Fulton's Concrete Technology [3]. Later, an independent Australian study [4] made reference to these NBRI findings, pointing out that some of the Australian slags also had similarly high  $\text{Al}_2\text{O}_3$  contents in the range of 17%, and so an investigation into their performance was conducted. In their experiment, cylindrical specimens 31.5 mm dia x 63 mm long were prepared using mortars of 1: 3 cement to sand, and water-cement ratio (w/c) of 0.5. Specimens were cured in water for 28 days before immersion in 5% sodium sulphate solution. Length change was monitored. The slag studied contained 17%  $\text{Al}_2\text{O}_3$  and was blended in proportions of 50% with Portland cements of 3.8% and 8%  $\text{C}_3\text{A}$  contents. Their results showed the cement/slag blends to be highly expansive in sulphate solutions than the control mix containing Portland cement alone, confirming the findings of Van Aardt and Visser [2].

The current scientific understanding appears to suggest that slags with low  $\text{Al}_2\text{O}_3$  contents significantly increase sulphate resistance when used as extender in concrete. North American slags have low alumina contents of 8 to 11%, and are used to mitigate sulphate attack in concrete but in the pacific rim, slags of high  $\text{Al}_2\text{O}_3$  of 12 to 18% have been reported. While these slags are known to provide high durability improvement against deterioration due to attack mechanisms such as corrosion and alkali-silica reaction, they generally show poor resistance to sulphate attack. Their high  $\text{Al}_2\text{O}_3$  content is clearly the main influential factor, but it has also been suggested that this alone does not fully account for the observed behaviour [5]. Further research is needed to establish fully the critical factors responsible for the differing behaviours between high and low alumina slags under sulphate environments.

The objective of this investigation was to assess the performance of proprietary cementitious materials incorporating South Africa slags under sulphate environments. This was done against the background of the early NBRI study [2]. Experimental details of the investigation, results, discussion of findings and conclusions are presented in the subsequent sections.

## 2. Experimental

### 2.1. Mixtures

CEM I 42.5N normal strength Portland cement was used in the study with normal cured mortars. The extender used was a commercially available slag incorporated in cement in varied proportions of 30%, 50%, and 70%. Table 1 shows the composition of the cementitious materials used. Mortar bars 25 x 25 x 285 mm were prepared according to ASTM C 1012 and either moist-cured in water for 21 days or immersed



immediately in sulphate solutions. Mortar mixtures consisting of 1: 2.25: 0.5 cement to sand to water were made using South African silica sand. No air entrainment or admixtures were used in the mortar mixtures.

## 2.2. Curing and storage

ASTM C 1012 requires attainment of 20 MPa compressive strength prior to immersion of specimens in sulphate solution. In this study, two sets of mortar mixtures were cast for each mixture. One set designated with 'X', was allowed to develop minimum required strength which was achieved at around 21 days of curing in water. The other set of mortar mixes designated with 'i' were those immersed in sulphate solutions immediately after demoulding of specimens i.e. without curing. Two different concentrations of sodium sulphate solution of 28 g/L and 50 g/L as SO<sub>4</sub> were used. Length change measurements were monitored at regular intervals. In Table 2 are given the mix combinations used including the initial compressive strengths at time of immersion of the mortar specimens in sulphate storage solutions, binder proportions, and the concentrations of the storage solutions for each mix.

**Table 1.** Chemical compositions of the cementitious materials

	CEM1 42.5N	GGBS	50/50 CEM/GGBS
SiO <sub>2</sub>	21.7	38.3	30.1
Al <sub>2</sub> O <sub>3</sub>	5.3	13.4	9.4
Fe <sub>2</sub> O <sub>3</sub>	2.0	0.8	1.4
CaO	62.5	35.3	48.4
MgO	4.6	7.5	6.1
K <sub>2</sub> O	0.6	1.0	0.8
TiO <sub>3</sub>	0.3	0.9	0.6
Mn <sub>2</sub> O <sub>3</sub>	0.9	1.1	1.0
Na <sub>2</sub> O	0.1	0.3	0.2
SO <sub>3</sub>	2.0	12.4	2.3
Cl-	0.02	0.02	0.02
LOI	2.9	0.7	1.1
C <sub>3</sub> A	10.7		
C <sub>3</sub> S	45.3		
C <sub>2</sub> S	28.3		
C <sub>4</sub> AF	6.1		
Blaine fineness (m <sup>2</sup> /kg)	337.5	384.1	364.1
45 µm sieve residue (%)	14.9	14.8	14.7

## 3. Results

Expansion results were examined on the basis of variables consisting of the initial compressive prior to exposure of specimens to sulphate solutions, concentrations of Na<sub>2</sub>SO<sub>4</sub> solution, and the replacement levels of GGBS. All the samples were made of CEM 1N 42.5 of 10.7% C<sub>3</sub>A and GGBS of 13.4% Al<sub>2</sub>O<sub>3</sub> (see Table 1). Figures 1 to 3 give the results of expansion measurements observed for the various mixtures and storage conditions.

**Table 2.** Mortar mixtures, binders and storage solutions

Description	Mix	Initial compressive strength (MPa)	GGBS (%)	Na <sub>2</sub> SO <sub>4</sub> (g/L)
Mortars immersed in sulphate solutions immediately i.e. at one day, without water curing (i-mixes)	0-28g/L-i	11.5	0	28
	0-50g/L-i	11.5	0	50
	50%-28g/L-i	6.4	50	28
	50%-50g/L-i	6.4	50	50
	70%-28g/L-i	4.2	70	28
	70%-50g/L-i	4.2	70	50
Mortars immersed in sulphate solutions after 21 days of curing in water (x-mixes)	0-28g/L-x	29.3	0	28
	0-50g/L-x	29.3	0	50
	30%-28g/L-x	26.3	30	28
	50%-28g/L-x	22.8	50	28
	50%-50g/L-x	22.8	50	50
	70%-28g/L-x	17.3	70	28
	70%-50g/L-x	17.3	70	50

### 3.1. Effect of minimum compressive strength at immersion of mortars in sulphate solution:

The compressive strengths at one day and at 21 days are shown in Table 2 for mixtures containing varied replacement proportions of GGBS. As expected, the mixtures incorporating GGBS developed lower early strengths with increase in the proportion of the extender. Mixtures containing 70% GGBS were able to achieved only 17 MPa after 21 days. However, this was considered substantial enough to relatively avoid or significantly minimize undue effects of low early strengths. The significance of 20 MPa as a requirement in conduct of the ASTM C 1012 compressive strength is intended to allow adequate initial tensile strength to develop within the cementitious matrix for resistance of expansive pressures. The requirement is considered important with regard to the relatively slower early strength development in the mixtures containing extenders. Without adequate strength development it has been argued that the dilution effect of using extenders can result in undue penalization of mixtures incorporating extenders, resulting in poorer results.

Figure 3 gives the initial development of expansions in the cured and non-cured prisms. It can be seen that the non-cured specimens of low strengths prior to immersion in Na<sub>2</sub>SO<sub>4</sub> solution exhibited relatively elevated early-age expansion values in the range of 0.05% compared to 0.0% expansion for their water-cured counterparts. Despite the initial 'shock effect' due to low early strengths in non-cured specimens, resulting in their early-age elevated expansions, the long-term results indicate that the mitigating effect of GGBS against sulphate expansion was not affected as mixes containing 50 or 70% GGBS showed no expansion whatsoever (Figure 1). In fact, it is evident that after about 3 months of storage, the use of GGBS caused a reversal of the early age elevated expansions in the non-cured mixtures, reducing the early age expansion of 0.05% to a level of 0% in the long-term.

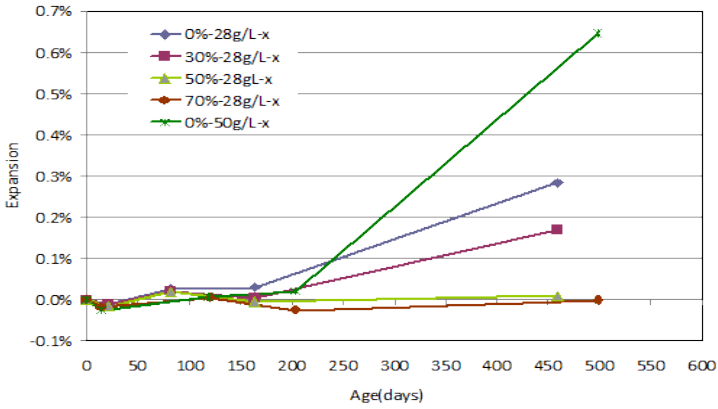


Figure 1. Expansion of mortar prisms not cured prior to storage in 28 g/L and 50 g/L Na<sub>2</sub>SO<sub>4</sub> solutions i.e. immersed at the low one-day compressive strengths

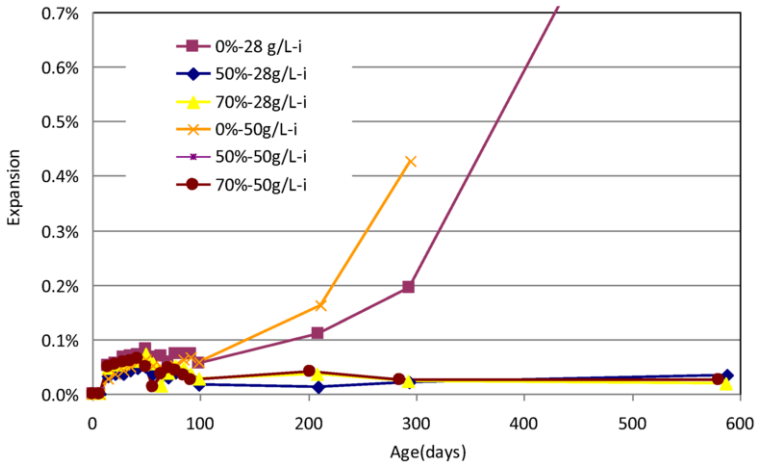


Figure 2. Expansion of mortar prisms cured in water to attain high compressive strengths prior to storage in 28 g/L and 50 g/L Na<sub>2</sub>SO<sub>4</sub> solutions

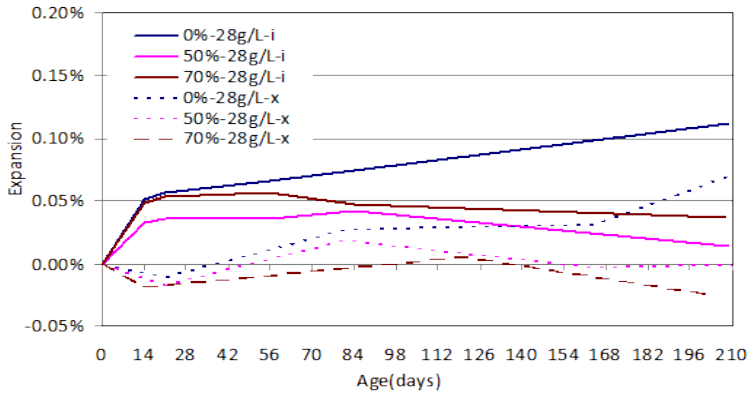


Figure 3. Early – age expansion results for cured and non-cured mortar prisms stored in 28 g/L Na<sub>2</sub>SO<sub>4</sub> solution

For plain /control mixtures (not incorporating GGBS), the long-term expansions were much greater in the non-cured mixes i.e. of lower initial compressive strengths compared to their water-cured counterparts. At the age of 500 days, the expansions of non-cured and water-cured prisms were 1.29% and 0.28% respectively for specimens stored in 28 g/L  $\text{Na}_2\text{SO}_4$ . Similar results were observed for 50 g/L  $\text{Na}_2\text{SO}_4$  storage solution (see also Table 3).

The mass change results of the cured mortar mixes are given in Figure 4, showing similar tendency as the expansion results (Figure 2) with the plain mortars giving greater mass gain relative to the mortars containing extenders. Generally, the mass gain decreased with increase in proportion of GGBS incorporated. Expansive mortars broke after about 2 to 6 % mass increase.

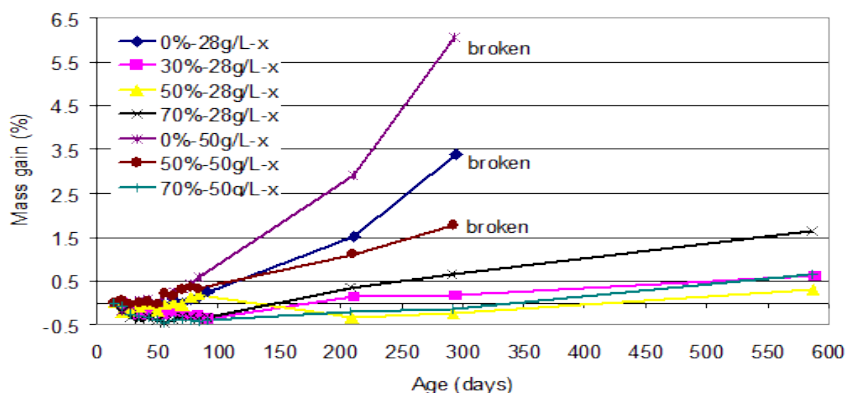


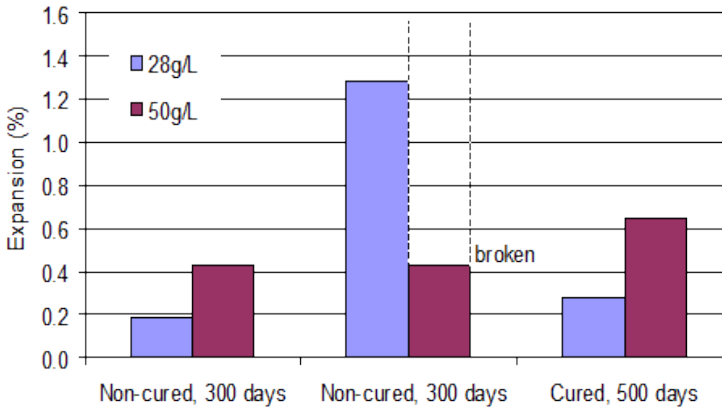
Figure 4. Mass change results for the cured mortar prisms stored in 28 g/L or 50 g/L  $\text{Na}_2\text{SO}_4$  solution

### 3.2. Effect of the concentration of $\text{Na}_2\text{SO}_4$ storage solution

Two solution concentrations of 28 g/L and 50 g/L  $\text{Na}_2\text{SO}_4$  were used in the study. Some past studies [6] have reported that higher  $\text{Na}_2\text{SO}_4$  concentrations may give lower expansions than lower  $\text{Na}_2\text{SO}_4$  concentrations. In this study, the effect of solution concentration can be seen from Table 3, showing that the expansions observed were greater the higher the  $\text{Na}_2\text{SO}_4$  concentration, also plotted in Figure 5 for the ages of 300 and 500 days. The graph does not include mixtures containing GGBS as no expansions resulted from these specimens.

Table 3. Influence on  $\text{Na}_2\text{SO}_4$  concentration on expansion of control mixes

Specimen	Age (days)	Expansion (%)
0%-28g/L-i	300	0.19
0%-28g/L-i	500	1.29
0%-28g/L-x	500	0.28
0%-50g/L-i	300	0.43
0%-50g/L-i	500	broken
0%-50g/L-x	500	0.65



**Figure 5.** Influence of initial compressive strengths and storage solution concentrations on long-term expansion

### 3.3. Effect of GGBS content on sulphate resistance

It is evident in Figure 2, that the sulphate resistance of the mixtures increased with increase in the proportion of GGBS incorporated. For specimens stored in 28 g/L  $\text{Na}_2\text{SO}_4$  solution, the expansions at 460 days for mixes incorporating 0%, 30%, 50, 70% were 0.28%, 0.17%, 0.01%, 0.00% respectively. The results showed some expansion at 30% GGBS but no expansions were observed for 50 or 70% GGBS. The results are consistent with the well established understanding in the literature, that higher GGBS proportions are required to effectively control sulphate resistance.

## 4. Conclusions

The effectiveness of South African slag of moderately high alumina content of 10.7%  $\text{C}_3\text{A}$  and 13.4%  $\text{Al}_2\text{O}_3$ , was investigated along with the influence of initial strength requirements and solution concentrations.

Basing on the observations of up to 600 days, it was found that the moderately high alumina slag was effective in increasing the sulphate resistance of cementitious systems. Incorporation of at least 50% GGBS was effective in preventing sulphate expansion. The results that did not meet the initial compressive strength requirement of 20 MPa gave relatively high long-term expansion measurements, in those mixtures not containing GGBS. For mixtures containing  $\geq 50\%$ , the low initial strength had no effect on the long-term results as no expansion resulted. But in all cases, the non-cured specimens with low initial strengths showed relatively elevated early age expansion measurements compared to their water-cured counterparts. For the limited  $\text{Na}_2\text{SO}_4$  solution concentrations used, mortar expansions increased with increase in sulphate concentration of the storage solution.

## Acknowledgement

The author wishes to thank Afrisam (pty) Ltd for providing technical support used to undertake this investigation.

## References

- [1] American Society for Testing and Materials, Standard specification for ground granulated blast-furnace slag for use in concrete and mortars, *Annual Book of ASTM Standards, ASTM C989*, 2006.
- [2] Aardt and Visser., The behaviour of mixtures of milled granulated blast-furnace slag and Portland cement in sulphate solutions, *National Building Research Institute (NBRI), Bulletin 47*, 1967, USA.
- [3] Fulton., *Fulton's Concrete Technology*, Second edition, Portland Cement Institute, Midrand, South Africa, 1974, pp. 956.
- [4] Heaton B.S., Down F.W. and Emery J.J., Properties of ground granulated slag in cement blends, *National Slag Association (NSA)*, pp. 181 – 12.
- [5] Hooton, R.D., A review of different forms of sulphate attack, *Dept of Civil Engineering, University of Toronto*, 35 St George Str., Toronto, Canada.
- [6] Hooton R.D. and Emery J.J., Sulfate resistance of a Canadian slag cement, *ACI Materials Journal*, V. 87, No. 6, 1990, pp. 547-555.

# Simple criteria for evaluating sulphate attack in concrete

Stephen EKOLU<sup>1</sup>

*Department of Civil Engineering Science, University of Johannesburg, South Africa*

**Abstract.** This paper attempts to analyse results from the standard test methods employed for sulphate attack and evaluates their correlations, consistency and contrasts, as well as physical observations. Data from expansions and mass change of 25 x 25 x 285 mm mortar prisms and 75 x 75 x 285 mm concrete prisms were used. Mortar mixtures consisted of 1: 2.25: 0.5 cement to sand to water while concrete mixtures were of water-cementitious ratio (w/cm) of 0.45, 0.50, 0.65. Mixtures were made using CEM I 42.5N with or without 30, 50, 70% ground granulated blast furnace slag (GGBS) and stored in sodium sulphate solutions of 28 g/L and 50 g/L as SO<sub>4</sub>. Results show that ASTM C 1012 mortar expansion criteria of 0.10% corresponds to 1.2% mass gain. Similarly, concrete prism expansion criteria of 0.05% is equivalent to 0.75% mass gain. It is proposed that in the absence of expansion monitoring, the use of mass gain criteria of 1.2% mass in mortar prisms or 0.75% in concrete prisms may be sufficient for evaluating sulphate attack.

**Keywords.** Sulphate attack, mass gain, expansion, mortar/concrete prisms

## Introduction

The existing accumulated wealth of knowledge concerning sulphate attack has led to well-established current understanding of the mechanism of attack. Through this scientific understanding, some standard methods have been developed such as ASTM C1012 currently used in evaluating external sulphate attack. However, there remain major shortfalls concerning current techniques that fuel researchers to continue efforts towards better and improved methods as evident from the wide range of attempts published [1-3]. But it is evident that much attention has been given to simulation of chemical resistance of the cementitious system and using this measure as the overriding criteria for evaluating the sulphate resistance of the system. But there is growing recognition that chemical resistance evaluation may be relevant but not sufficient in certain cases to fully assess the effect of sulphate attack. Magnesium sulphate ions attack process, for example, is characterised by more severe physical deterioration rather than expansion. Therefore techniques for evaluation of cementitious systems for resistance to physical deterioration are of interest.

---

<sup>1</sup>Corresponding author: University of Johannesburg, Department of Civil Engineering, P.O. Box 524, Auckland Park, 2006, South Africa; E-mail. [sekolu@uj.ac.za](mailto:sekolu@uj.ac.za), [sekolu@gmail.com](mailto:sekolu@gmail.com)

In [4], it was reported that permeability of concretes influenced expansion behaviour but the parameter on its own was insufficient to account for full effects. Use of other transport properties in the sulphate attack evaluation, including water absorption and diffusion, have been given consideration by researchers [5].

## 1. Background

Most developing countries would seek to use reliable but simple techniques, in view of the requirements of monitoring equipment. There are few experiments where sulphate research has been conducted extensively on the basis of properties other than length change [6,7]. The equipment needed to monitor weight or physical examination of the specimens are all but basic and simple, while length change monitoring apparatus are often costly and found mostly in well equipped, specialised cement and concrete laboratories. However, while mass change and physical damage are generally monitored in sulphate attack studies, it is rare to find studies where these properties have been given focussed attention as a criteria in evaluation of sulphate attack. The work presented here was conducted with the intention of primarily examining these simple properties with potential to utilize them as key indicators of potential sulphate attack.

A key consideration of interest in using weight change and physical deterioration characteristics is the potential to evaluate effects of different sulphate salts by using the same methodology. In the present test methods, it is not possible to evaluate both sodium and magnesium sulphate attack using the same standard method. Yet in field situations, mixed salt types are possible as can be found in soils and water, which may result in combined sulphate attack on concrete [8]. A hypothetical but meaningful situation is explained by Neville [8] in which a house or structure can be within the proximity of a garden or farm where fertilizers are used. Fertilizers and greening agents may contain potassium, magnesium and ammonium sulphates that can attack foundations and walls of the structure. Each of these salt types may have different attack mechanisms but the common feature to their manifestation is physical damage, although this may take different forms which some researchers have categorised as acid type, expansive type, and onion peeling type [2]. It has been suggested that where mixed sulphates salt types may exist, the magnesium sulphate attack is the controlling attack mechanism, which primarily results through severe physical softening deterioration as opposed to expansion-induced damage [9].

The research question addressed in this paper is whether standard tests can be based on physical degradation analyses or combined forms of simple physical and chemical indicators of deterioration. In 1969, Neville [8] remarked that his work on sulphate attack consisting of monitoring length change, weight change and resonance frequency led to the conclusion that they do not all reflect the same pattern of behaviour. In the present investigation, this question is highlighted in view of scientific understanding that has come a long way.



## 2. Experimental

The data used in this paper is based on experimental work presented in separate investigations involving evaluation of sulphate resistance using:- (a) the conventional ASTM C 1012 accelerated mortar expansion test method, (b) Concrete prism expansion test [4]. In the mortar study, expansion and mass change were monitored in the experiment. Similarly in the concrete study, expansion and mass change of prisms were measured. Concrete prisms 75 x 75 x 285 mm were also used to monitor physical damage and related changes in the samples. Further details regarding the mixtures, materials and methods employed in the investigations are found in other papers [10,11].

**Table 1.** Chemical compositions of the cementitious materials [10]

	CEM1 42.5N	GGBS	50/50 CEM/GGBS
SiO <sub>2</sub>	21.7	38.3	30.1
Al <sub>2</sub> O <sub>3</sub>	5.3	13.4	9.4
Fe <sub>2</sub> O <sub>3</sub>	2.0	0.8	1.4
CaO	62.5	35.3	48.4
MgO	4.6	7.5	6.1
K <sub>2</sub> O	0.6	1.0	0.8
TiO <sub>3</sub>	0.3	0.9	0.6
Mn <sub>2</sub> O <sub>3</sub>	0.9	1.1	1.0
Na <sub>2</sub> O	0.1	0.3	0.2
SO <sub>3</sub>	2.0	12.4	2.3
Cl-	0.02	0.02	0.02
LOI	2.9	0.7	1.1
C <sub>3</sub> A	10.7		
C <sub>3</sub> S	45.3		
C <sub>2</sub> S	28.3		
C <sub>4</sub> AF	6.1		
Blaine fineness (m <sup>2</sup> /kg)	337.5	384.1	364.1
45 µm sieve residue (%)	14.9	14.8	14.7

## 3. Results

### 3.1. Assessment of chemical resistance

#### 3.1.1. Monitoring expansion

Tests for length change using prisms are generally regarded to be evaluation of the chemical resistance of the cementitious system. In the data presented, expansion was determined using both mortars and concretes.

The durations and trends in development of expansion monitored by the standard mortar prism method and by the concrete prisms are given Figure 1. In the legend of the graph, 'M' stands for mortars of 0.5 w/cm made in accordance with ASTM C 1012, while 'C' represents concrete. Hence M-CEM I are mortars made using plain CEM I Portland cement and C-0.5w/c-CEM I are 0.5 w/c concretes made using CEM I only.

It is seen in Figure 1 that both the mortars and the prisms took several weeks to develop significant expansion. The typical sulphate resistance criteria for 0.5 w/c

mortar expansion is 0.10% after one year of storage in 0.5% sodium sulphate. According to the results presented, it can be seen that CEM I would be such cement that could be regarded susceptible to sulphate attack. However, based on 0.5 w/c concretes, the development of expansion is expectedly far more subdued in the concrete prisms than mortar prisms of 0.5 w/c. Once expansion initiates, it progresses more rapidly in the small mortar prisms than in the concretes. At 69 weeks, the 0.50 w/c concrete prisms gave 0.05% expansion compared to 0.65% for the corresponding mortar prisms. However, by increasing the w/cm ratio of the mix to 0.65, expansion of about 0.10% was attained in four to six months, potentially reducing the duration to failure significantly. Other conditions that have the potential to accelerate the attack are elevated temperature, maintaining constant pH of the sulphate solution, wet-drying cycles, although it ought to be recognized that some of these factors may alter the nature of the attack [12,13]. Nonetheless, incorporation of these factors into the test methods could result in significantly improved rapid evaluations.

### 3.2. Mass change

While expansion in sulphate attack is primarily attributed to volume increase from the ettringite product formation within the pore structure of the cementitious system, the product also leads to increase in mass, although the initial weight gain within the first week would be attributed to water uptake by the unsaturated concrete. Thereafter, the increase in weight would mainly be expected from the reaction products, consisting of ettringite and gypsum in the case of sodium sulphate attack. The monitoring of mass change is usually done or recommended as part and parcel of the test requirement during expansion monitoring using prisms. However, lesser importance is generally attached to weight change relative to length change parameters. Basically, the standard methods of this category including ASTM C 452, C 1038, C 1012, use length change as the failure criteria and typically give no similar or parallel failure criteria on the basis of weight change. Few standards such as the Chinese standards GB 2420, GB 749 specify flexural strength criteria. Perhaps one of the reasons for attachment of comparatively less value to weight change may be related to its distant association with physical deterioration. Typically, it is the expansion-induced stresses that lead to cracking and ultimately, cause structural disintegration of concrete.

Weight change on the other is only indicative of the internal expansive reactions and in addition, it may be difficult to account for initial weight change from initial water uptake by the samples. Despite the relatively lower place usually assigned to weight change, it is evident that this parameter is consistent and could as well be a fairly reliable indicator of expansive cementitious systems. In situations, such as found in most developing countries, where laboratory facilities are limited or lacking, the simplicity of using weight change as an evaluation parameter can be an attractive option.

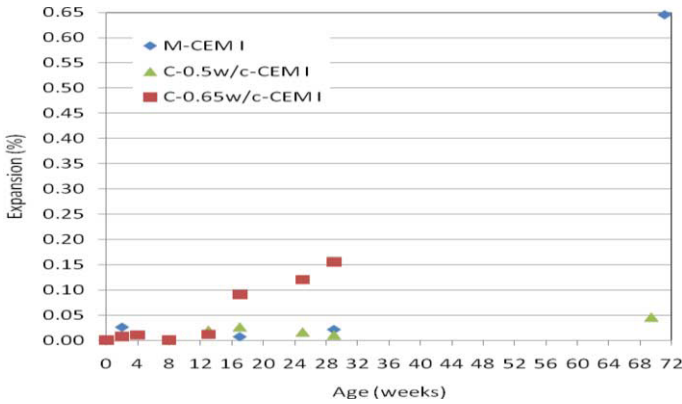


Figure 1. Expansion development in mortar and concrete prisms stored in Na<sub>2</sub>SO<sub>4</sub> solution

Figure 2 is a plot of results relating the length change and weight gain for mortar prisms that expanded as well those that did not show expansion. It can be seen that those specimens that showed expansion, had greater weight gain such that 0.10% mortar expansion corresponds to about 1.2% of their mass gain. Hence all specimens that exceeded 1.2% weight gain showed expansion but there was one exception 50%-28g/L-i that exhibited up to 3% mass gain but showed no expansion. Figure 3 gives similar results for concrete prisms. Here all the concrete prisms that did not expand, never exhibited more than 1.0% mass gain. It can be seen that 0.10% concrete expansion corresponds to 1.0% of their mass gain and 0.05% expansion relates directly to 0.75% mass gain. These criteria were satisfied by all the concrete specimens without exceptions.

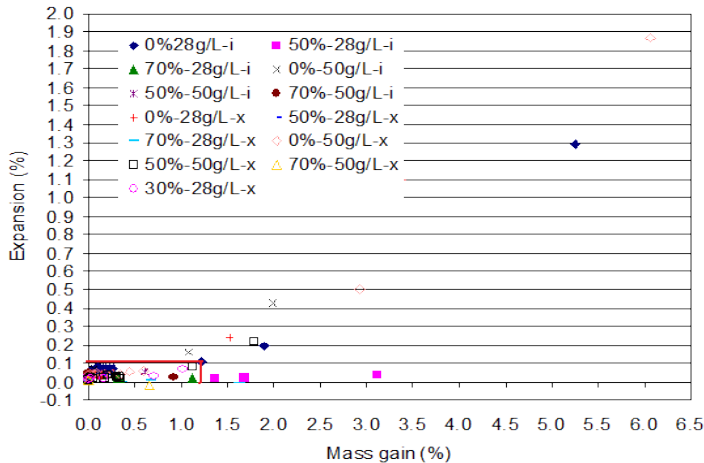
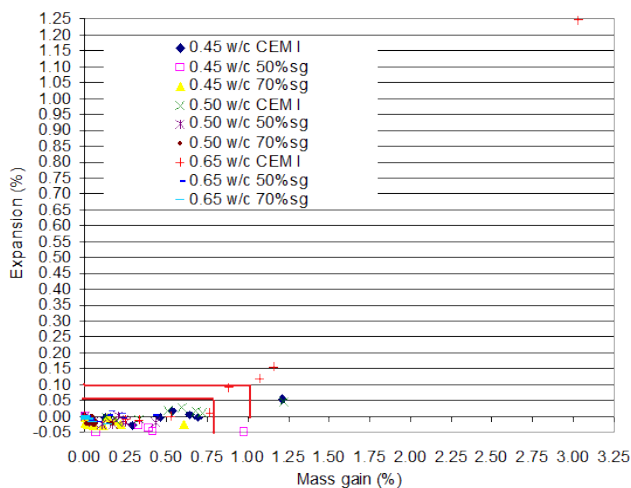


Figure 2. Relationship between expansion and mass gain of 25x25x285mm mortar prisms stored in Na<sub>2</sub>SO<sub>4</sub> solution for up to 69 weeks



**Figure 3.** Relationship between expansion and mass gain of 75x75x285 mm concrete prisms stored in  $\text{Na}_2\text{SO}_4$  solution for up to 69 weeks

#### 4. Conclusions

The results generated through standard test methods for sulphate resistance have been compared in the foregone analyses. The following findings have been reached, keeping consideration of the limitations of this study which was conducted with only one type of slag and one type of cement. The results are, however, generated based on wide ranging parameters of varied w/c ratios, curing periods, sulphate types and concentrations.

Both the standard mortar ASTM C 1012 test method and concrete prisms required extended durations of at least 6 months to develop significant expansion adequately notable for use as criteria. However, use of increased water-cement ratio such as 0.65w/c has the potential to give accelerated results within 3 months. Further research is needed to consider other test conditions such as pH, temperature, wet-dry cycles, that may lead to greater acceleration of results.

When using mortar and concrete prisms stored in  $\text{Na}_2\text{SO}_4$  solution, it was found that 0.10% mortar prism expansion corresponds to 1.2% mass gain and 0.05% concrete prism expansion relates directly to 0.75% mass gain. In the absence of expansion monitoring, the use of this mass gain criteria appears to be an adequate evaluation parameter. Further work in this regard is being undertaken by the authors.

#### Acknowledgement

The authors wish to thank Afrisam (pty) Ltd for providing technical support used to undertake this investigation.

## References

- [1] Cement Concrete and Aggregates Australia, Sulfate resisting concrete, Technical Note, CCA, Sep. 2007, pp. 8.
- [2] Al-Amoudi, O.S.B., Attack on plain and blended cements exposed to aggressive sulphate environments, *Cement and Concrete Composites*, V.24 , 2002, pp. 305-316.
- [3] Aimin, Xu., Shayan A. And Baburamani P., Test Methods for Sulphate Resistance of Concrete and Mechanism of Sulphate Attack, A state-of-the-art review, ARRB Transport Research Ltd, Review Report, 1999, pp. 44.
- [4] Khatri R.P. and Sirivivatnanon V., Role of permeability in sulphate attack, *Cement and Concrete Research*, V. 27, No.8 , 1997, pp. 1179-1189.
- [5] Ferraris C.F., Stutzman P.E. and Snyder, K.A., Sulfate Resistance of Concrete – a new approach, Portland Cement Association, 5420 Old Orchard Road, Skokie Illinois, 60077-1083, PCA R&D Serial No. 2486, 2006.
- [6] Bircik H., Akozi F. and Berkday I., Resistance to magnesium and sulphate attack of mortars containing wheat straw ash, *Cement and Concrete Research*, Vol.30 ,2000, pp. 1189-97.
- [7] Lee S.T., Lee D.H., Kim S.S., Park K.P., Jung H.S., Kim D.K. and Kim B.Y., Magnesium sulphate attack of mortars containing GGBFS with different fineness levels, The 3rd ACF International Conference – ACF/VCA, 2008, pp. 1069-1073.
- [8] Neville A., The confused world of sulphate attack on concrete, *Cement and Concrete Research*, Vol.34, 2004, pp. 1275-1296.
- [9] Al-Amoudi O.S.B., Performance of 15 reinforced concrete mixtures in magnesium-sodium sulphate environment, *Construction and Building Materials*, V.9, No.3, 1995, pp. 149-159.
- [10] Ekolu S.O. and Ngwenya A., Sulphate Corrosion Behaviour of High Volume Slag Concrete, *Proc.of the International Conference on Construction Materials and Structures (ICCMATS)*, Johannesburg, 2014, 9p.
- [11] Ekolu S.O., Chokoe T.S. and Cele A.A. Sulphate Resistance of South African Slag of Moderately High Alumina Content, *Proc.of the International Conference on Construction Materials and Structures (ICCMATS)*, Johannesburg, 2014, 9p.
- [12] Clifton J.R., Frohnsdorff G. and Ferraris C., Standards for evaluating the susceptibility of cement-based materials to external sulphate attack, National Institute of Standards and Technology, Published in *Material Science of Concrete – Sulfate Attack Mechanisms*, Special Volume (proceedings from Seminar on Sulfate Attack Mechanisms, Quebec, Canada, October 5-6 1998, American Ceramic Society, 1999, p.337-355 .... (1998).
- [13] Akoz F., Turker F., Koral S. And Yuzer N., Effects of raised temperature of sulphate solutions on sulphate resistance of mortars with and without silica fume, *Cement and Concrete Research*, Vol.29, 1999, pp. 537-544.

# Comparison of moisture equilibrium of cement-based materials in presence of slag and silica fume in different wetting and drying cycles

M. SEIDPOUR<sup>1</sup> and L. WADSÖ

*Building Materials, Lund University, Lund, Sweden*

**Abstract.** Water vapor sorption isotherms are essential data in models to predict the service life of the cement based structures. The knowledge about sorption isotherms in the presence of supplementary cementitious materials (SCMs) is limited. This study investigates the influence of water to cement ratio (0.4, 0.5 and 0.6), and the presence of two SCMs (70% slag and 10% silica fume) on sorption isotherm in hygroscopic and above hygroscopic RH ranges for paste and mortars. Dynamic vapor balance in hygroscopic range and pressure plates above hygroscopic range are used to generate sorption isotherms. Based on Jennings model (CM-II) for C-S-H structure, desorption isotherms are divided to different parts in which different pores are emptied. The samples with silica fume and slag have higher moisture content than OPC, but, with higher amount of gel pores and lower amount of capillary pores. At low RH intervals all samples have very similar desorption curves and introduction of SCMs induce slightly increase on BET surface area. Above 30% RH, samples have different desorption curves and the initial desorption is higher than following desorption for all samples.

**Keywords.** Water vapor sorption isotherms, supplementary cementitious materials

## Introduction

The durability of cement and concrete structures depends on transport and sorption of moisture. All physiochemical processes that are responsible for durability issues in concrete, such as carbonation, chloride initiated corrosion, sulfate attack, freeze and thaw cycles, and alkali silica reaction (ASR), are moisture dependent [1]. To be able to predict the rates at which these processes occur, or to prevent them altogether, transport and sorption data are needed. Water vapor absorption and desorption isotherms are the equilibrium water contents of the material as a function of relative humidity (RH) at a constant temperature. These data are used in computer models to predict the service life of structures [2] and are essential to understand moisture distribution in cement based structures [3].

The first sorption isotherms on cement pastes were reported by Powers and Brownyard in 1948 (see references [4,5]). The sorption isotherms of pastes, mortars

---

<sup>1</sup>Corresponding author: [Mahsa.saeidpour@byggttek.lth.se](mailto:Mahsa.saeidpour@byggttek.lth.se)

and concretes made with ordinary Portland cement (OPC) have been measured; see for example references [6-8]. However, these results are difficult to compare due to a number of factors being different between studies and in some cases not well described.

In contrast to OPC, the knowledge about sorption isotherms for materials made with blended cements is much more limited; such knowledge is needed because today there is a general trend of using more blended cements with supplementary cementitious materials (SCMs) as a way to limit the CO<sub>2</sub> emissions associated with the cement production. The presence of SCMs change the amount and kind of hydrates formed during the hydration, especially the calcium silicate hydrate (C-S-H), which is the main product of cement hydration [9]. This also changes the internal surface and pore structure, and thus the sorption and transport properties.

In this study, the influence of w/b-ratio (0.4, 0.5 and 0.6) and the presence of two SCMs (70% slag and 10% silica fume) on the microstructure and water vapor isotherms of paste and mortar samples were studied in a systematic way. Care was taken so that the samples were exposed to the same treatment before the measurements, and the sorption balance method was used to avoid carbonation.

## 1. Materials

Nine pastes and six mortars with different binders have been used in this study. The binders were ordinary Portland cement OPC (CEM I), OPC with 10% silica fume, and OPC with 70% slag (CEM III). Three water/binder-ratios (w/b), 0.4, 0.5 and 0.6, for paste samples and two w/b ratios, 0.4 and 0.5, for mortar samples were used. Both paste and mortar materials were mixed with water according to EN 196-1. The samples were seal cured for 90 days and then crushed to pieces of approx. 5 mm. The crushed pieces were kept in contact with wet cloth to become capillary saturated, then they were crushed to 1-2 mm pieces before being placed in a sorption balance. The samples were prepared for pressure plate testing, were cement pastes pieces of approx. 20×15×3 mm. Samples were vacuum saturated before the test and were placed in contact with wet membrane in two different pressure cells. The measurements were done more than one year after the time of casting the samples.

## 2. Experimental techniques

### 2.1. Water vapor sorption balance

Approximately 20 mg of water saturated samples were crushed and placed in a DVS Advantage (Surface Measurement Systems, UK) sorption balance. In these instruments mass of the small sample is continuously measured with an analytical balance, while it is exposed to an RH-program. Measurements made with an RH-program consisting of desorption (95-90-80-....40-30), absorption (30-40-....-80-90-95), desorption (95-90-80-....-10-5-0). Each RH step was ended when the mass change rate was lower than 0.0001% of the initial mass per minute, or if a maximum time of 2000 min had been exceeded; except for final drying that was continued for up to 6000 min.

The moisture content of the sample at equilibrium in each relative humidity was expressed as mass of water per mass of dry material. The mass for each step was curve

fitted using an exponential function and then extrapolated to infinite time to evaluate the final (equilibrium) mass [10].

## *2.2. Pressure plate*

The sorption isotherm above the hygroscopic range can be measured with a pressure plate instrument [11]. Samples were vacuum saturated and were put in contact with wet membrane in two different pressure cells. 3 and 1MPa pressure which are corresponding to 97.81 and 99.26 %RH were applied to pressure plates until equilibrium is reached in the water menisci in the material. At this point the experiment was stopped and the samples were weighted. The samples were dried at 105°C and the moisture contents at hygroscopic range and also vacuum saturated were reported as mass of water per mass of dry sample at 105°C.

## **3. Results**

The sorption isotherms measured for different w/b and different binders for both cement paste and mortars are shown in Figure 1. The data connected by lines are for the sorption balance measurements. The three data points shown at high RHs are the pressure plate results for 97.81 and 99.26 % RH, and the vacuum saturation moisture content (drew at 100% RH).

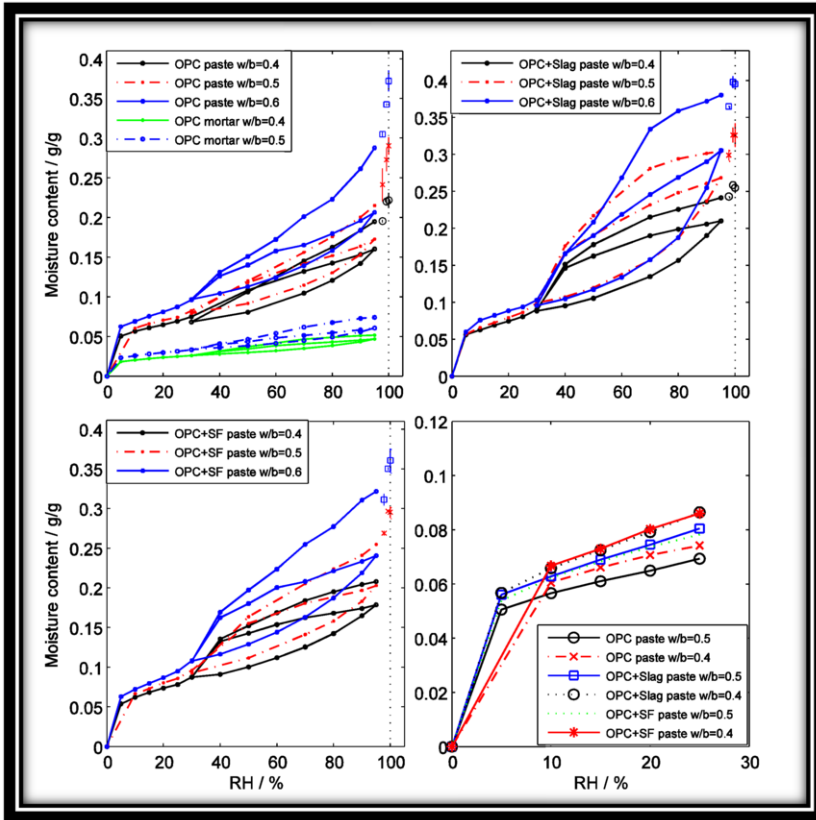
## **4. Discussion**

Figure 1 shows that all desorption-absorption-desorption curves have similar qualitative appearances; however, the OPC samples absorb less moisture than the samples with silica fume and slag. Further, the curve shapes follow a complex pattern that can be summarized in the following points:

- The initial desorption is higher than the following desorption above 30-40% RH, and the level decreases for every consecutive cycle.
- All desorption curves merge at about 30-40% RH. Below this, they follow same path for the same binder.
- Desorption isotherms show a significant change in slope between 40 and 30% RH.
- Absorption isotherms show a smooth increase over the whole RH range.

From above we can see that the desorption curves were more complex than the absorption curves. We will in the following focus on the desorption curves. We use the Jennings model (CM-II) [12] and results from recent studies done with 1H Nuclear Magnetic Resonance (NMR) relaxometry techniques [13, 14] to describe the shape of the desorption isotherms. The CM-II model describes the C-S-H structure based on combination of nitrogen and water vapor sorption isotherms.





**Figure 1.** The sorption isotherms of cement paste and mortars with different w/b and different binders

In this model, the basic units of C-S-H are globules that have layered sheet-like structure. In CMI, the size of the globules is 4.2 nm and in the structure three different pores can be differentiated. Pores within the globules are referred to as interglobular pores (IGP) (pore size less than 1 nm), small gel pores (SGP) (pore size 1-3 nm) are formed between the globules, and large gel pores (LGP) (pore size 3-12 nm) are formed between flocs of globules. With NMR technique two well defined pore sizes have been found (0.85 nm and 2.5 nm [13]). These correspond to interlayer pores (IGP) and small gel pores (SGP), interhydrate spaces around 10 nm corresponding to large gel pores (LGP) were also found, but decreased in volume as C-S-H grows. Based on these studies we divided the desorption isotherms into four parts. First, from saturated condition to 90% RH, where capillary pores are emptied; second from 90 to 80% RH, where interhydrate spaces dry out; third, from 80 to 30% RH where gel pores are emptied; and, finally, from 30 to 0% RH where interlayer pores in the C-S-H structure are emptied (Fig. 2).

At low RH intervals (0-30%), desorption takes place in the interlayer C-S-H pore structure[14]. It can be seen in Fig. 1 that cement based materials with different binders and different w/b have similar sorption curves. The amount of water in this RH-range is a function of the C-S-H globules surface area, while increase in w/b ratio and the presence of SCMs induces small and almost negligible increase in moisture content.

In desorption from 80 to 40% RH, the gel pores are emptied. In the presence of slag and silica fume the amount of gel pores (30-80 % RH) is higher than for OPC samples with the same W/b. By applying this to the CMII model we find that the C-S-H in the tested blended cement pastes especially in presence of slag is less dense than OPC and there is thus more space between globule flocs. From 80% to 90 %RH the interhydrate spaces are emptied, and above 90% the capillary pores are emptied.

There is a hysteresis between absorption and desorption over the whole ranges for all samples. The hysteresis is more significant above 40% RH and it is larger between the first desorption (main desorption) and the following absorption than between the subsequent desorption-absorption cycle. The presence of the two SCMs tested increased the hysteresis, especially the presence of 70% slag.

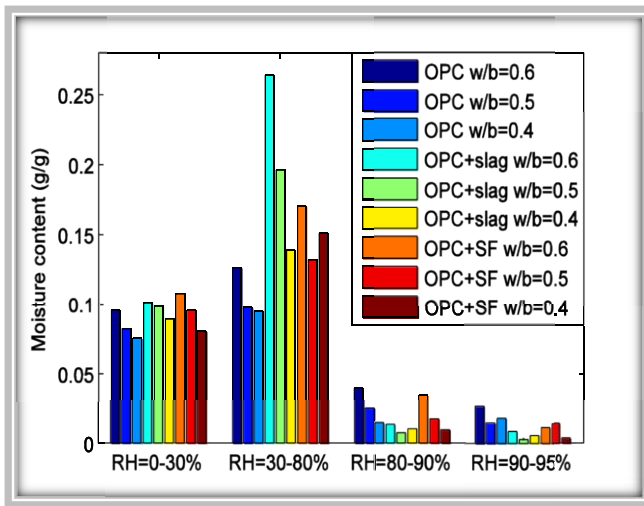


Figure 2. The sorption isotherms of cement paste and mortars with different w/b and different binders.

## 5. Conclusion

- Desorption isotherms at low RH (0-30%) for different binders and different w/b ratios are similar. The increase in w/b ratio and/or presence of SCMs induces small increases in calculated BET (Bruanuar, Emmett and Teller) surface area in this range.
- The moisture content in samples with same w/b is higher in presence of slag and silica fume than the OPC in the whole RH range. The samples with silica fume and slag have higher amount of gel pores and lower amount of capillary pores than OPC.

## Acknowledgment

The research leading to these results has received funding from the European Union Seventh Framework Program (FP7/2007-2013) under grant agreement 264448.

## References

- [1] L.O. Nilsson, On the role of moisture in degradation of concrete structures, in: International Congress - Global Construction: Ultimate Concrete Opportunities, Dundee, Scotland, United Kingdom, 2005, pp. 15 - 24.
- [2] A. Ait-Mokhtar, R. Belarbi, F. Benboudjema, N. Burlion, B. Capra, M. Carcassès, J.B. Colliat, F. Cussigh, F. Deby, F. Jacquemot, T. de Larrard, J.F. Lataste, P. Le Bescop, M. Pierre, S. Poyet, P. Rougeau, T. Rougelot, A. Sellier, J. Séménadisse, J.M. Torrenti, A. Trabelsi, P. Turcry, H. Yanez-Godoy, Experimental investigation of the variability of concrete durability properties, *Cement and Concrete Research*, 45 (2013) 21-36.
- [3] M.S. Åhs, Sorption scanning curves for hardened cementitious materials, *Construction and Building Materials*, 22 (2008) 2228-2234.
- [4] H.J.H. Brouwers, The work of Powers and Brownyard revisited: Part 1, *Cement and Concrete Research*, 34 (2004) 1697-1716.
- [5] H.J.H. Brouwers, The work of Powers and Brownyard revisited: Part 2, *Cement and Concrete Research*, 35 (2005) 1922-1936.
- [6] R.M. Espinosa, L. Franke, Influence of the age and drying process on pore structure and sorption isotherms of hardened cement paste, *Cement and Concrete Research*, 36 (2006) 1969-1984.
- [7] J. Hagymassy Jr, I. Odler, M. Yudenfreund, J. Skalny, S. Brunauer, Pore structure analysis by water vapor adsorption. III. Analysis of hydrated calcium silicates and portland cements, *Journal of Colloid and Interface Science*, 38 (1972) 20-34.
- [8] V. Baroghel-Bouny, Water vapour sorption experiments on hardened cementitious materials: Part I: Essential tool for analysis of hygral behaviour and its relation to pore structure, *Cement and Concrete Research*, 37 (2007) 414-437.
- [9] B. Lothenbach, K. Scrivener, R.D. Hooton, Supplementary cementitious materials, *Cement and Concrete Research*, 41 (2011) 1244-1256.
- [10] H.H. Willems, K.B. Van Der Velden, A gravimetric study of water vapour sorption on hydrated cement pastes, *Thermochimica Acta*, 82 (1984) 211-220.
- [11] M. Fredriksson, L. Wadsö, P. Johansson, Small resistive wood moisture sensors: a method for moisture content determination in wood structures, *Eur J Wood Prod*, 71 (2013) 515-524.
- [12] H.M. Jennings, Refinements to colloid model of C-S-H in cement: CM-II, *Cement and Concrete Research*, 38 (2008) 275-289.
- [13] A.C.A. Muller, K.L. Scrivener, A.M. Gajewicz, P.J. McDonald, Densification of C-S-H Measured by <sup>1</sup>H NMR Relaxometry, *The Journal of Physical Chemistry C*, 117 (2012) 403-412.
- [14] A.C.A. Muller, K.L. Scrivener, A.M. Gajewicz, P.J. McDonald, Use of bench-top NMR to measure the density, composition and desorption isotherm of C-S-H in cement paste, *Microporous and Mesoporous Materials*, 178 (2013) 99-103.

# Chloride penetration into concrete with compressive load-induced cracks

M.Y. BALQIS<sup>a,b,1</sup>, H.M. JONKERS<sup>a</sup> and E. SCHLANGEN<sup>a</sup>

<sup>a</sup>*Delft University of Technology, The Netherlands*

<sup>b</sup>*Universiti Teknologi MARA, Malaysia*

**Abstract.** In this study, a new experimental approach of chloride penetration in concrete specimens under compressive load was projected. The influence of chloride transport in concrete with cracks was investigated by varying the compression load levels and the period of contact with chloride solution containing 3% of sodium chloride. The concrete specimens were set in paired and parallel direction to the compressive load. Circulation of chloride solution was realized through a container that was attached on one of the moulded surfaces of the specimens. The chloride profiles and chloride content were measured using highly energetic laser pulse of so-called LIBS method. The modification on concrete pore structure by an applied compressive load was confirmed by the MIP determination. The results shows penetration of chloride in concrete becomes more significant at higher load levels with increased time of contact with salt solution. It can be concluded that chloride diffusivity in cement-based materials was influenced by time and very much affected by an applied load, thereby limiting the service life of concrete structures.

**Keywords.** Service life of concrete, combined load, chloride penetration, compressive load

## Introduction

Micro-cracking is a general feature of ordinary concrete. Their occurrence is not harmful as long as the cracks are stable. However, if micro-cracks form a continuous network of cracks they may substantially contribute to the permeability of the concrete, thus reducing the concrete's resistance against ingress of aggressive substances [1]. There is currently considerable interest in investigation the deterioration of concrete during crack initiation and further propagation. One of the most significant current discussion in concrete structures deterioration is the service life design are based on simple laboratory test results which run without applying the load, thereby overestimating service life of real structures considerably [2]. There are several factors which may contribute to this remark. A main contribution is the effects of mechanical stress since under loading new micro-cracks are being developed along with the growth of existing cracks. This, in turn, results in modification on concrete pore structure

---

<sup>1</sup>Corresponding author: Delft University of Technology, Room 6.72, Building 23 ( CITG ) , Stevinweg 12628CN Delft, P.O. Box 5048, 2600 GA Delft, The Netherlands; E-mail. [B.BintiMdYunus@tudelft.nl](mailto:B.BintiMdYunus@tudelft.nl)

which affect the ingress rate of aggressive substance. Another reason to the observed is predictions of chloride ingress are based on the assumption of a homogenous uncracked concrete [3] – [6].

This paper describes experiments of concrete under coupled effects of chloride penetration at different compressive load level. The chloride profiles were analysed and the diffusion rate was determined with respect to the percentage of the cement mortar. This process is done by Laser-Induced Breakdown Spectroscopy (LIBS) method. Additionally, Mercury Intrusion Porosimetry (MIP) analyses were employed to analyse the total porosity and pore size distribution of the concrete.

## 1. Materials and method

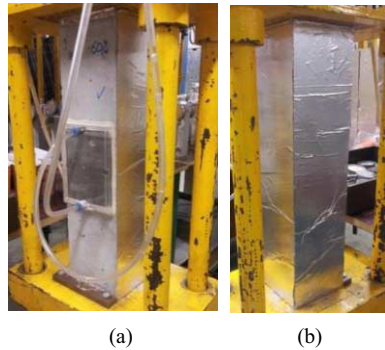
Investigation was carried out by casting concrete prisms of size 100 mm x 100 mm x 400 mm. The concrete was composed of Ordinary Portland Cement type I, 42.5 with water/cement ratio of 0.45. Crushed gravel with nominal maximum size 16 mm was used. A small amount of super-plasticizer has been added to achieve 12 – 15 cm of slump value. The whole materials were mixed using tap water. The fresh concrete proportions are listed in Table 1 with the compressive strength tested on prism at the age of 28 days. The concrete was poured in two layers and compacted using a vibrating needle.

Table 1. Mix proportion of fresh concrete (kg/m<sup>3</sup>)

w/c	Portland cement	Sand	Coarse aggregates	Tap water	Super-plasticizer	Compressive strength (N/mm <sup>2</sup> )
0.45	368	840	1027.5	165.5	2.6	37.74

### 1.1 Specimen under combined load

After casting, the specimens were covered with plastic sheets. All mixing and casting were carried out in a standard laboratory condition at  $23 \pm 2^\circ\text{C}$  and  $50 \pm 5\%$  RH. The specimens were demoulded on the following day and saturated under water for 28 days. The free water was removed from the surface of the specimens with a dry cloth. The surfaces were sealed with self-adhesive aluminum foil except one from the moulded surface that is fixed by the chloride solution container. The specimens were subjected to compression with the load levels of 0, 30 % and 60 % of the ultimate load. The specimens were set in paired and parallel direction to an applied load. The chloride solution containing 3% of sodium chloride was circulated through the transparent container which was attached on moulded surface of the specimens. The specimens were left under combined environmental mechanical loads for 6 and 18 weeks. Figure 1(a) and (b) illustrates the testing setup of the materials.



**Figure 1.** (a) Front view and; (b) rear view of concrete exposed to chloride attack and loading

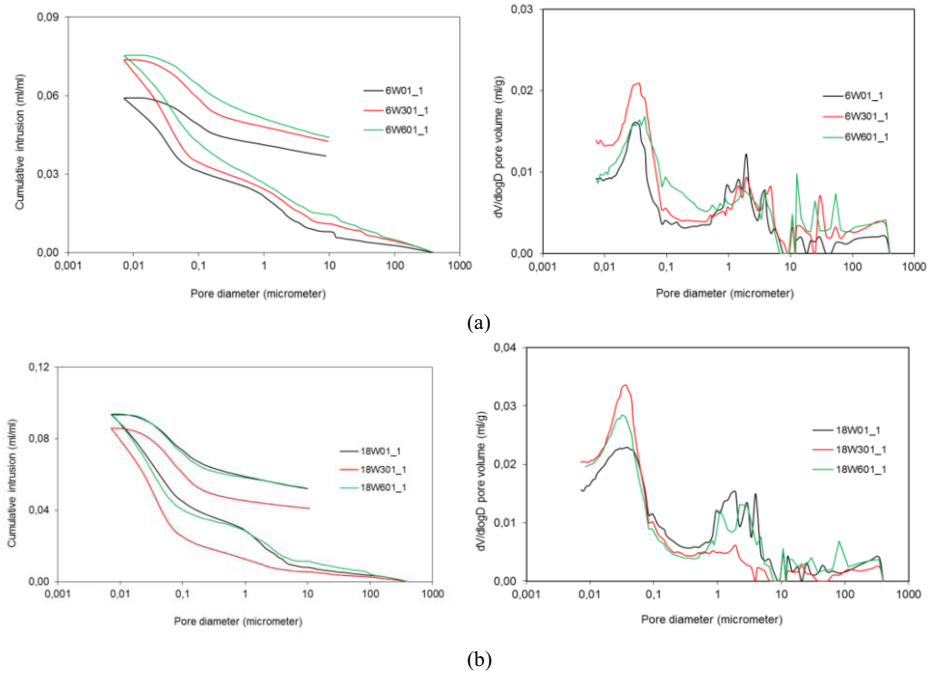
### 1.2 Determination of chloride profiles

Chloride profiles of different specimens have been determined by cutting with a special liquid, which was in contact with chloride solution in two parts. The surface from one half was used for LIBS measurements [7]. Line scans of 0.5 mm interval with a resolution of about 0.5 mm were applied. The exposure time of the detector was 0.05 s for all measurements. In addition, MIP testing was performed with a 210 MPa mercury intrusion porosimeter, which determines the pore size range from 7 nm to 400  $\mu\text{m}$ . A non-uniform size (around 5 mm diameter) sample of approximately three grams is assembled in the sample cell for pressure measurements.

## 2. Results and discussions

### 2.1 MIP determination

Figure 2 (a) and (b) illustrate the pore size distribution of concrete specimen from the MIP examination. For better comparison of the modification of the microstructure during loading, the change of total porosity is used as parameter [8]. It is defined as the total porosity after loading exposure divided by the total porosity of samples without load. The porosity and change of total porosity at 6 weeks and 18 weeks are listed in Table 2. It is observed that at 6 weeks, the damage process of concrete has taken place when the total porosity increased with the increasing of load applied. Interestingly, samples at 18 weeks show an autogenous-healing phenomenon for load levels of 30% and 60%. The material becomes less compact compared with samples without load. At this stage duration, damage induced into the composite structure of concrete by an applied load can be reduced again by self-healing. However, the overall total porosity of 18 weeks was still higher than that of 6 weeks. Although there was a reduction in the porosity of concrete at 18 weeks of loading and impedes the diffusion process, the MIP observation proved mechanical loading contributes to a major affect to the modification of pores structures.



**Figure 2.** Pore size distribution at (a) 6 weeks and; (b) 18 weeks under coupling function of loading and chloride penetration

**Table 2.** The porosity and change of total porosity of 6 weeks and 18 weeks samples

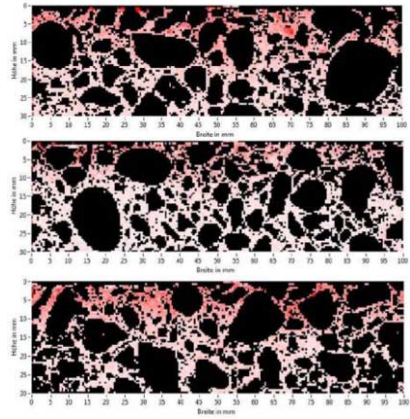
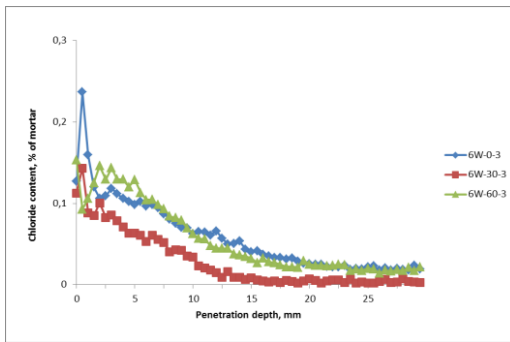
	6 weeks			18 weeks		
	0	30%	60%	0	30%	60%
Porosity (ml/g)	0.059	0.074	0.075	0.094	0.086	0.093
Change of total porosity (%)	-	125	127	-	92	99

### 2.2 Ingress of chloride ions

After 6 and 18 weeks being under compressive load and chloride penetration, the chloride profiles and chloride content were measured. Figure 3 (a) shows the influence of different load level on concrete chloride penetration under the circumstances of same exposure duration of 6 weeks. It can be seen that load level of about 30 % makes the concrete surface denser thus, delay the chloride penetration. The degree of chloride penetration starts to increase with the increasing of load level. However, it was observed that the chloride profiles of specimen with load level of about 60 % were comparable with the profiles of undamaged specimen. Although the role of damage has been detected, the permeability of the concrete at this stage is still lower.

The difference of profiles change has been observed in Figure 4 (a) for the specimen with the extension of exposure time of 18 weeks. It shows that load level of about 30 % and 60 % have a similar chloride penetration into the pore space of concrete. Although the undamaged specimen shows higher penetration at the beginning depth of 1.5 mm to 7.5 mm, it drops after passing the 10 mm depth consistently.

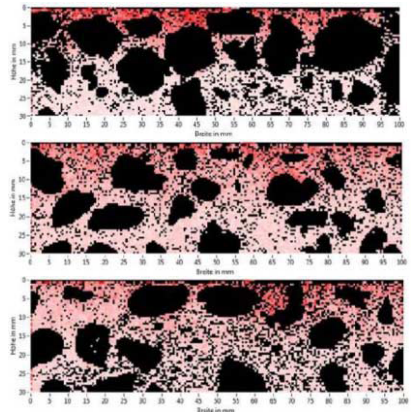
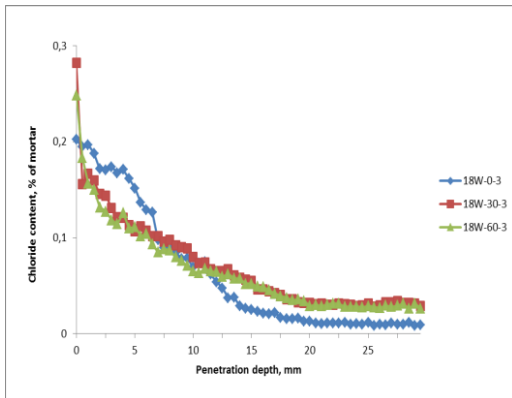
Comparing the two results illustrated in Figure 3 (a) and Figure 4 (a), it can be observed that the ingress of chloride ions at the top surface of the concrete of 18 weeks were higher than that of the 6 weeks, as well as the depth of the chloride penetration. Results also indicated that the applied stresses contribute to the percentage increase of penetrated chloride into pore space of concrete by initiating or developing microcracks [9]. This observed become larger is partly due to internal crack and changes of pores connectivity as described previously. Figure 3 (b) and Figure 4 (b) show images of chlorine distribution over the surface of samples with aggregates excluded captured from LIBS measurement.



(a)

(b)

**Figure 3.** (a) Chloride profiles determined after 6 weeks of contact with salt solution of specimens without load (6W-0-3) and of specimens loaded with 30 % (6W-30-3) and 60 % (6W-60-3); and (b) chlorine distribution over sample surface (aggregates excluded)



(a)

(b)

**Figure 4.** (a) Chloride profiles determined after 18 weeks of contact with salt solution of specimens without load (18W-0-3) and of specimens loaded with 30 % (18W-30-3) and 60 % (18W-60-3); and (b) chlorine distribution over sample surface (aggregates excluded).



### 3. Conclusions

The following conclusions can be drawn on the basis of the test results from the present study. Results for concrete under higher compressive load level have shown high chloride penetration. The ingress is particularly sensible to porosity and pores connectivity changes occurring, for instance due to load induced cracking. In addition, penetrations of chloride into concrete were also influence by the exposure duration. For realistic service life design this effect has to be taken into consideration. In general, therefore, it seems that ingress of chloride ions in concrete has significant relationship with the compressive load level. However, the compressive loads are small compared with the concrete compressive strength, so the rate of ion transport processes is not obvious. It is suggested that the association of these factors is investigated in future studies. Further research will investigate the chloride ingress at higher stress level and also to consider a tensile stress applied on the concrete.

### Acknowledgements

This work is part of an ongoing research project. The authors would like to express their appreciation to RILEM TC-TDC as this paper is part of their present study. In kind support of Bundesanstalt für Materialforschung und – prüfung (BAM) and other respective contributions on tests performed are gratefully acknowledged.

### References

- [1] A.M. Neville, *Properties of Concrete*, Pearson Higher Education, 4th edition, Prentice Hall, New Jersey, 1995
- [2] F.H. Wittmann and Y.V. Zaytsev, Application of Fracture Mechanics to Investigate Durability of Concrete Under Load, VIII International Conference on Fracture Mechanics of Concrete and Concrete Structures, FraMCoS-8 (2013).
- [3] F.H. Wittmann, T-J Zhao, P. Zhang and F-X. Jiang, 2010, Service Life of Reinforced Concrete Structures under Combined Mechanical and Environmental Loads, *Proceeding of 2<sup>nd</sup> International Symposium on Service Life Design for Infrastructures* (2010), 91 – 98.
- [4] F.H. Wittmann, T-J. Zhao, F-X. Jiang and P. Zhang, Service Life of Combined Mechanical and Environmental Loads, *Proceeding of International RILEM Conference on Advances in Construction Materials Through Science and Engineering* (2011), 998 – 1004.
- [5] Q-W. Cao, X-M. Wan, T-J. Zhao and X-H. Wan, 2008, Effect of Mechanical Loading on Chloride Penetration into Concrete, *Proceedings of the International Conference on Durability of Concrete Structures* (2008), 283 – 288.
- [6] F-X. Jiang, F.H. Wittmann and T-J. Zhao, Influence of Mechanically Induced Damage on Durability and Service Life of Reinforced Concrete Structures, *International Journal for Restoration of Buildings and Monuments* **17** (2011), 25 – 32.
- [7] G. Wilsch, F. Weritz, D. Schaurich and H. Wiggenhauser, Determination of chloride content in concrete structures with laser-induced breakdown spectroscopy, *Construction Building Material* **19** (2005), 724-730.
- [8] G.Ye, G.De Schutter and L.Taerwe, Study of Vapor Pressure of High Performance Concrete and Self-Compacting Concrete Slabs subjected to Standard Fire Conditions, *2<sup>nd</sup> International RILEM Workshop on Concrete Spalling due to Fire Exposure* (2011), 79 – 86.
- [9] R. Gao, Q. Li and S. Zhao, Concrete deterioration Mechanisms under Combined Sulfate Attack and Flexural Loading, *Journal of Materials in Civil Engineering* **25** (2013), 39 – 44.

# Indicative tests on the effect of fly ash- $\beta$ -cyclodextrin composite on mortar and concrete permeability, sorptivity and porosity

B.D. IKOTUN<sup>a,1</sup>, G.C. FANOURAKIS<sup>b</sup> and S. MISHRA<sup>c</sup>

<sup>a</sup>Department of Civil Engineering, University of South Africa, Johannesburg, RSA

<sup>b</sup>Department of Civil Engineering Technology, University of Johannesburg, RSA

<sup>c</sup>Department of Applied Chemistry, University of Johannesburg, Johannesburg, RSA

**Abstract.** The focus of this research is to modify fly ash (FA) structure using  $\beta$ -cyclodextrin ( $\beta$ -CD) to increase its pozzolanic function in concrete. A previous study by the authors has shown that a composite is formed due to structural changes of fly ash by its interaction with cyclodextrin [1]. The objective of this paper was to assess the effect of fly ash- $\beta$ -cyclodextrin composite (FA- $\beta$ -CD) on the transport properties (durability performance) of mortar and concrete, with a view to optimise its incorporation in concrete. The durability performance of mortar and concrete were assessed from the measurement of oxygen gas permeability, sorptivity and porosity using the South Africa durability index approach. Six mixtures were tested, comprising a control mixture (100% Portland Cement, PC), and five mixes containing the FA- $\beta$  CD composite. All the composite mixes included 30 % FA by mass. The  $\beta$ -CD was mixed with the FA, in separate mixtures, in proportions of 0.1 %, 0.2 % and 0.5 %. Two sample preparation procedures were followed for FA- $\beta$ -CD composites mixtures; firstly, physical mixtures of a pre-weighed amount of  $\beta$ -CD and FA were adopted for the dry mixtures and secondly, 0.0103M, 0.0206M and 0.0516M  $\beta$ -CD solutions were added to the concrete at the mixing stage for solution mixtures. The results indicated that FA- $\beta$ -CD composite improved the flowability and durability performances when  $\beta$ -cyclodextrin ( $\beta$ -CD) was used at a lower percentage (0.1% and 0.2%).

**Keywords.**  $\beta$ -cyclodextrin, concrete, FA- $\beta$ -CD composite, fly ash, mortar, permeability, porosity and sorptivity

## Introduction

The global interest in optimising and improving concrete performances with reduction in environmental pollution caused by cement production has inspired many researchers into exploring the inclusion of different by-products from industrial processes into concrete technology [2-3]. The industrial by-products that have been proven to be pozzolanic and improve concrete performance include ground granulated blast furnace slag (GGBS), fly ash (FA) and condensed silica fume (CSF) [4-9].

<sup>1</sup>Corresponding author: Tel. +27 11 4712145, [ikotubd@unisa.ac.za](mailto:ikotubd@unisa.ac.za)

FA, a by-product of coal combustion, which is in abundance in South Africa, has been of great use in blended cement [8, 10-15]. Fly ash has the characteristics of improving concrete workability, reducing heat of hydration, and improving late strength and durability [8, 16-17]. Apart from the advantages of using FA in blended cement, reduction in disposal costs and minimization of its impact on the environment are part of the main reasons for further research towards increasing the use of FA [14, 18-23]. The research focus that is of interest to the authors and some researchers [20, 22, 24] is the modification of FA structure to aid its function in concrete technology. A previous study by the authors [1] has shown that a composite is formed, due to structural changes, by the interaction of FA with  $\beta$ -cyclodextrin ( $\beta$ -CD) (oligosaccharides formed by the enzymatic modification of starch). This composite provides promising application in concrete technology. The incorporation of the composite formed by fly ash-  $\beta$ -cyclodextrin (FA- $\beta$ -CD) interaction in concrete production is a very new area in research. Hence, limited information is available and indicative tests are required to give guidance for on-going research.

The key durability assessment of concrete is based on the factors that affect concrete transport mechanisms [3, 25-27]. This paper presents the indicative tests results of the effect of FA- $\beta$ -CD composite on the durability behaviour of mortar and concrete. The durability performance of mortar and concrete were assessed from the measurement of oxygen gas permeability, sorptivity and porosity using the South Africa durability index approach [28]. Two major parameters that are related to transportation mechanisms, which aid these tests, are permeation and absorption.

## 1. Materials

The materials used in this study were class F FA,  $\beta$ -CD, Portland cement (CEMI52.5N), silica sand, crusher sand and coarse aggregate. FA was obtained from one of the South African ESKOM power stations through Ash Resources, South Africa.  $\beta$ -CD from Wacker chemie were obtained from Industrial Urethanes (Pty) Ltd, South Africa and the CEMI52.5N cement was obtained from Pretoria Portland Cement (PPC), South Africa. Granite crusher sand and coarse aggregate with a nominal size of 22 mm were obtained from Afrisam, South Africa. Silica sand sized within the ranges of 0.8-1.8 mm (coarse), 0.4–0.85 mm (medium) and 600  $\mu$ m (fine), produced by Rolfes silica, South Africa, was used in mortar mixes. Standard silica sand was prepared with the available size ranges in accordance with the SANS 50196-1 [29] and used for mortar mixes. The characteristics of  $\beta$ -CD, as supplied by the producer and the chemical analysis of the fly ash used, are presented in Tables 1 and 2, respectively.

Two samples preparation procedures were followed for FA- $\beta$ -CD composites mixtures. Firstly, physical mixtures of pre-weighed amount of  $\beta$ -CD and FA were adopted for the dry mixtures and secondly, 0.0103M, 0.0206M and 0.0516M  $\beta$ -CD solutions were added to the mortar and concrete at the mixing stage in the case of the solution mixtures. A proportion of 30% FA was maintained in the mixtures proportions. Furthermore, 0.1% and 0.2 %  $\beta$ -CD, in both dry and solution mixtures were used together with FA.

**Table 1.** General characterisation of  $\beta$ -CD used

Property	$\beta$ CD
Empirical formula	C <sub>42</sub> H <sub>70</sub> O <sub>35</sub>
Bulk density	400-700 kg/m <sup>3</sup>
Solubility in water at 25 °C	18.5 g/l
Content (on dry basis)	Min. 95 %

**Table 2.** Chemical composition of the FA

Content in oxide form.	% mass
SiO <sub>2</sub>	50.26
Al <sub>2</sub> O <sub>3</sub>	31.59
Fe <sub>2</sub> O <sub>3</sub>	3.08
MgO	2.04
CaO	6.78
Na <sub>2</sub> O	0.56
K <sub>2</sub> O	0.81
TiO <sub>2</sub>	1.64
SO <sub>3</sub>	0.55
LOI	1.42
SiO <sub>2</sub> /Al <sub>2</sub> O <sub>3</sub>	1.59

## 2. Experimental procedures

### 2.1. Mixes and curing of mortar

A total of six mortar mixtures were designed, in accordance with the mixture proportions shown in Table 3. The mortar samples were prepared and mixed in accordance with SANS 50196-1 [29] without any alteration in the case of dry mixes.

In the case of the solution mixes, the 0.0103M and 0.0206M  $\beta$ -CD solutions for F/0.1CD/S and F/0.2CD/S samples, respectively, were added after the standard silica sand had been introduced to the mix. 100 mm cubic moulds were prepared and demoulded in accordance with SANS 50196-1 [29]. The samples with  $\beta$ -CD were kept covered with polythene sheets for three days before demoulding because of the nature of the material. After demoulding, the samples were placed in a water bath maintained at 23°C  $\pm$  2°C for curing until the testing ages.

The mix proportion used for the mortar production is as shown in Table 3. To maintain relative consistency with the control sample, the samples were prepared with varied w/b ratios. This approach was adopted to assess the behaviour of  $\beta$ -CD on fresh mortar and to establish a relationship that will form a basis for proper mixture design for on-going research. The flow test was conducted on mortars according to ASTM C 1437 [30] immediately after mixing.

**Table 3.** Mortar mixture proportion per 1m<sup>3</sup> of mortar

Samples	Cement (kg)	Silica sand (kg)	Fly ash (kg)	CD (kg)	CD solution (litres)	Water (kg)	w/b	Flow
Control (100 % Cement)	586.00	1758.00	0.00	0.00	0.00	293.00	0.5	101
FA/C (30%FA + Cement)	410.20	1758.00	175.80	0.00	0.00	293.00	0.5	106
F/0.1 CD/D (29.9% FA + 0.1% CD dry + Cement)	410.20	1758.00	175.21	0.59	0.00	275.42	0.47	115
F/0.2 CD/D (29.8% FA + 0.2% CD dry + Cement)	410.20	1758.00	174.63	1.17	0.00	246.12	0.42	120
F/0.1 CD/S (29.9% FA + 0.1% CD in solution (0.0103M) + Cement)	410.20	1758.00	174.63	0.00	50.00	226.01	0.47	120
F/0.2 CD/S (29.8% FA + 0.2% CD in solution (0.0206M) + Cement)	410.20	1758.00	172.87	0.00	50.00	197.29	0.42	125

## 2.2. Mixes and curing of concrete

During mixing, the rotary mixer with a 100 litre capacity was charged with coarse aggregate, fine aggregate, cement, FA and  $\beta$ -CD, respectively. These materials were mixed in their dry state for one minute. Thereafter, water was introduced into the mix over the period of one minute and mixing continued for a further minute. In the case of the solution mixtures, the  $\beta$ -CD solution was added, over a 30 second period, after the dry material was mixed for one minute. Thereafter, the remaining water was added after a period of 30 seconds and mixing continued for a further minute.

Immediately after each mixture was produced, the slump test was performed (according to SANS 5862-1:2006 [31]) and 100 mm cubic moulds were cast and compacted (using a vibrating table). The curing procedures explained in Section 2.1 were followed. Table 4 presents the mixture proportions used for the concrete production. The samples were prepared with varied w/b ratio for the same reason as explained in Section 2.1.

## 2.3. Permeability, sorptivity and porosity tests

The oxygen permeability and sorptivity tests were performed at the AFRISAM laboratory in Roodepoort, South Africa. The South African durability index approach which was developed by Ballim and Alexander [32-34] was adopted in this study. The approach was developed to cater for the practical durability tests that could be site-applicable. Measurements of oxygen permeability and sorptivity/porosity were used in this study to assess the durability performance of the samples. The oxygen permeability index (OPI) test gives an indication of the degree of pore connectivity in a concrete

matrix, while sorptivity measures the rate of movement of a water front through the concrete under capillary suction. These tests were conducted on discs samples with a diameter of 68mm and thickness of  $30 \pm 2$  mm which were core drilled from the cover zone of the 100 mm cubes samples, after being cured for 14 and 28 days. The disc samples were preconditioned in an oven at  $50^{\circ}\text{C}$  for 7 days before testing. The detailed procedures, which have been previously described and documented [33, 35-39] were followed.

**Table 4.** Mixture proportions for  $1\text{m}^3$  of concrete

Samples	Cement	Crusher sand (kg)	Coarse aggregate (kg)	FA (kg)	CD (kg)	CD solution (litres)	Water (kg)	w/b	Slump (mm)
Control	410.00	788	980	0.00	0.00	0.00	205	0.5	50
FA/C	287.00	788	980	123.00	0.00	0.00	205	0.5	90
F/0.1 CD/D	287.00	788	980	122.59	0.41	0.00	192.7	0.47	95
F/0.2 CD/D	287.00	788	980	122.18	0.82	0.00	172.2	0.42	120
F/0.1 CD/S	287.00	788	980	122.59	0.00	35.00	192.29	0.47	150
F/0.2 CD/S	287.00	788	980	122.18	0.00	35.00	171.38	0.42	150

### 3. Results and discussion

#### 3.1. Flow of mortar and workability of concrete samples

The flow of mortar and workability of Concrete Samples as shown in Tables 3 and 4 respectively showed that  $\beta$ -CD increased both flow and workability with reduced water content. The characteristic of  $\beta$ -CD of enhancing wettability in water [40-41] contributes to this behaviour, with a higher dissolution being experienced in the solution mixed samples. The reduction of water content in the mix and increased flow/workability is an advantage to FA- $\beta$ -CD composite in improving mortar and concrete quality.

#### 3.2. Effect of $\beta$ Cyclodextrin on the permeability of fa/c mortar

The oxygen permeability index (OPI) test is sensitive to the amount and continuity of larger pores and voids where most of the flow will occur [28]. The coefficient of permeability (k) and oxygen permeability index (OPI) values for mortar samples are presented in Figures 1 and 2, respectively. The results for concrete samples were not reported because of some invalid values, which are anomalous. It is evident from Figure 1 that all the samples showed decrease in permeability at increased curing age. The highest permeability was exhibited by the FA/C sample at 14 days curing age. However, a decrease in permeability was observed in the case of the FA/C mortar sample relative to the control sample at 28 days curing age. It is evident in Figure 2 that, in general, the higher the OPI, the less permeable the concrete. This is in

agreement with the findings of Ballim and Alexander [28], who stated that the OPI provides an indication of the degree of pore connectivity in the matrix and how permeable the samples are.

The samples containing the FA-β-CD composite exhibited lower permeability than the control sample and FA/C sample, for both curing ages. The β-CD solution was more effective in decreasing permeability, compared to the dry β-CD. When considering both dry and solution β-CD mixes, no general correlation was established between the quantity of β-CD and its effectiveness in reducing permeability. The mixtures containing the β-CD solutions resulted in the greatest relative reductions in permeability, being 64.8 % and 62.8 % in the case of the F/0.2 CD/S and F/0.1 CD/S, respectively.

This showed that despite the dissolution observed with the solution mixed samples, a positive effect on sample permeability was observed. The results confirmed the previous observation by the authors [1] that cyclodextrins in solution will try to occupy the pores. This will thereby limit continuous pores and in turn reduce permeability. Generally, the results indicated that FA-β-CD composite boosted the pozzolanic reaction with evidence of permeability reduction at both 14 and 28 days after curing period, compared to control sample.

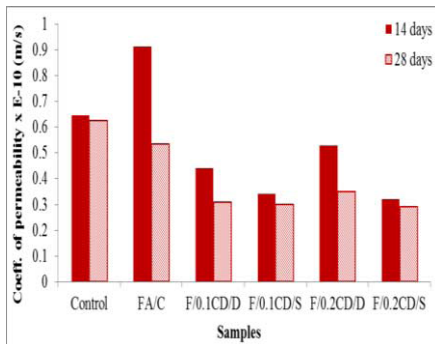


Figure 1. Permeability of mortar samples

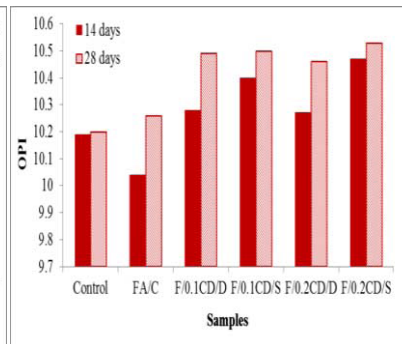


Figure 2. Oxygen permeability index (OPI) values of mortar samples

### 3.3. Effect of βCyclodextrin on the sorptivity of FA/C mortar and concrete

The water sorptivity test measures the rate of movement of a water front through the exposed face of the mortar or concrete samples, under capillary suction. The lower the water sorptivity index, the better the potential durability of the concrete [28]. Figures 3 and 4 present the sorptivity results of mortar and concrete samples, respectively. A decrease in sorptivity was observed with an increase in curing age for all samples for both mortar and concrete. The reason for this is that as the curing age increased; the mortar or concrete became denser, starting from the exposed face, which resulted in decrease in sorptivity. A higher sorptivity was observed for FA/C mortar compared to the control samples at both curing ages due to the slow pozzolanic reaction, which

might have not been completed to result in a denser mortar at these ages. However, a lower sorptivity was observed for FA/C concrete relative to the control sample at a curing age of 14 days. This is attributed to the presence of coarse aggregate, which resist to a smaller extend the movement of water under capillary suction. However, the slower pozzolanic reaction resulted in higher soptivity of FA/C concrete relative to the control sample at a curing age of 28 days.

The mortar and concrete samples with FA- $\beta$ -CD composite exhibited a lower sorptivity than the control sample and FA/C sample at both curing ages. The mortar samples showed lower sorptivity compared to concrete samples. This is based on the understanding that cyclodextrin will have more space of reactivity in mortar than concrete, since there is no coarse aggregate in mortar that can stand as a barrier to the reaction.

The results showed that the F/0.1CD/D sample exhibited highest reduction in sorptivity compared with FA/C, with approximately 29 % reduction at a 28 day curing period. Furthermore, the FA- $\beta$ -CD composite dry mixes proved to be more effective in reducing the sorptivity than their corresponding solution mixes, in the case of both curing ages. This is attributed to the dissolution ability of the solution mix samples, which resulted in less dense mortar/concrete at the water front compared to the dried mix samples. Cylcodextrins in solution will try to occupy the pores as explained earlier, resulting in lower permeability, but its presence will cause the material at the space it occupies to be less dense and consequently increases sorptivity. In general, the sorptivity results agree with the permeability results in that FA- $\beta$ -CD composite boosted the pozzolanic reaction.

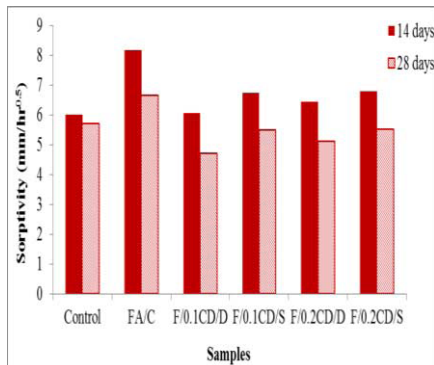


Figure 3. Sorptivity of mortar samples

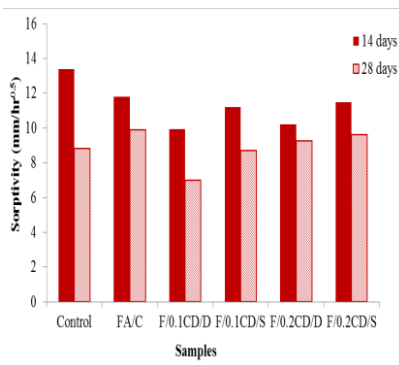


Figure 4. Sorptivity of concrete samples

### 3.4. Effect of $\beta$ Cyclodextrin on the porosity of FA/C mortar and concrete

The porosity results are reflection of what was observed in both the permeability and sorptivity tests. The trend of results observed in sorptivity was also observed in porosity results as shown in Figures 5 and 6. As curing age increased, porosity decreased. The samples with FA- $\beta$ -CD composite exhibited lower porosity than the control sample and FA/C sample for both curing ages. A higher porosity was observed for FA/C mortar relative to the control samples at both curing ages, due to the slow



pozzolanic reaction. In the case of the concrete samples, a lower porosity was observed for FA/C mix compared to the control sample at a curing age of 14 days, while higher porosity was observed for FA/C concrete compared to the control sample at a curing age of 28 days. As reflected in sorptivity results, the FA- $\beta$ -CD composite dried mix samples showed lower porosity compared to FA/C sample than their corresponding solution mix samples for both curing ages. The above observations might be as a result of the explanation given for sorptivity results. The porosity results further buttressed the fact that FA- $\beta$ -CD composite boosted the pozzolanic reaction.

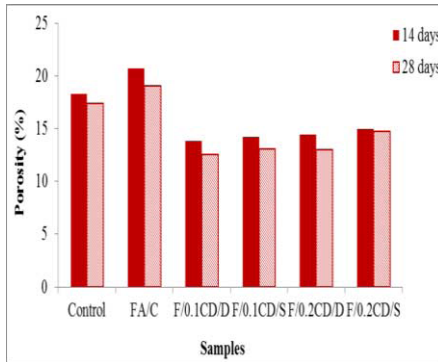


Figure 5. Porosity of mortar samples

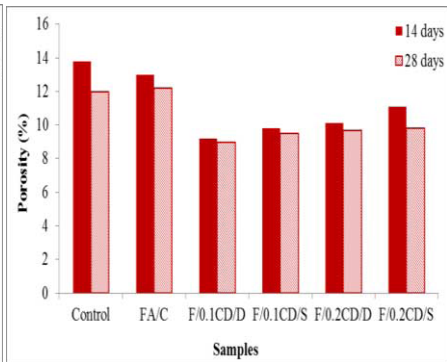


Figure 6. Porosity of concrete samples

#### 4. Conclusions

The durability performance of FA- $\beta$ -CD composite on mortar and concrete was investigated using oxygen permeability, sorptivity and porosity tests, based on the South African durability index tests. The FA- $\beta$ -CD composite improved the flow of mortars and workability of concrete. The results obtained for the three tests indicated that FA- $\beta$ -CD composite boosted the pozzolanic reaction, with the dried mix samples showing better sorptivity and porosity than solution mixed samples. Improved durability performance of pozzolanic concrete can be achieved when used as a composite with  $\beta$ -CD.

#### References

- [1] B.D Ikotun., S.Mishra, G.C Fanourakis., Study on the synthesis, morphology and structural analysis of fly ash-cyclodextrin composite, *Journal of Inclusion Phenomena and Macrocyclic Chemistry*, ISSN 1388-3127. Imprint: Springer, Online first, DOI 10.1007/s10847-013-0353-7, (2013).
- [2] A. André, J. de Brito, A. Rosa, D. Pedro., Durability performance of concrete incorporating coarse aggregates from marble industry waste, *Journal of Cleaner Production* (2013), 1-8.
- [3] F. Gameiro., J. De Brito, D. Correia da Silva, Durability performance of structural concrete containing fine aggregates from waste generated by marble quarrying industry, *Engineering Structures* **59** (2014), 654–662.
- [4] P. Chindaprasirt, C. Jaturapitakkul, T. Sinsiri, Effect of fly ash fineness on compressive strength and pore size of blended cement paste, *Cement & Concrete Composites* **27** (2005), 425–428.
- [5] H. Binici, H. Temiz, M.M. Kose, The effect of fineness on the properties of the blended cements incorporating ground granulated blast furnace slag and ground basaltic pumice, *Construction and Building Materials* **21** (2007), 1122–1128.

- [6] P. Pipilikaki, M. Katsioti, Study of the hydration process of quaternary blended cements and durability of the produced mortars and concretes, *Construction and Building Materials* **23** (2009), 2246–2250.
- [7] S. Ogawa, T. Nozaki, K. Yamada, H. Hirao, R.D. Hooton, Improvement on sulfate resistance of blended cement with high alumina slag, *Cement and Concrete Research* **42(2)** (2012), 244–251.
- [8] M. Uysal, V. Akyuncu, Durability performance of concrete incorporating Class F and Class C fly ashes, *Construction and Building Materials* **34** (2012), 170–178.
- [9] K. Githachuri, M.G. Alexander, Durability performance potential and strength of blended Portlandlimestone cement concrete, *Cement & Concrete Composites* **39** (2013), 115–121.
- [10] N. Bouzoubaa, M.H. Zhang, V.M. Malhotra, Laboratory-produced high-volume fly ash blended cements Compressive strength and resistance to the chloride-ion penetration of concrete, *Cement and Concrete Research* **30** (2000), 1037–1046.
- [11] N. Bouzoubaa, M.H. Zhang, V.M. Malhotra, Mechanical properties and durability of concrete made with high-volume fly ash blended cements using a coarse fly ash, *Cement and Concrete Research* **31** (2001), 1393–1402.
- [12] P. Chindaprasirt, C. Jaturapitakkul, T. Sinsiri, Effect of fly ash fineness on microstructure of blended cement paste, *Construction and Building Materials* **21** (2007), 1534–1541.
- [13] F. Deschner, B. Lothenbach, F. Winnefeld, J. Neubauer, Effect of temperature on the hydration of Portland cement blended with siliceous fly ash, *Cement and Concrete Research* **52** (2013), 169–181.
- [14] D. Mainganye, T.V. Ojumu, L. Petrik, Synthesis of Zeolites Na-P1 from South African Coal Fly Ash: Effect of Impeller Design and Agitation, *Materials* **6** (2013), 2074–2089.
- [15] Z. Yu, G. Ye, The pore structure of cement paste blended with fly ash, *Construction and Building Materials* **45** (2013), 30–35.
- [16] G. Grieve, Cementitious materials, Fulton's Concrete Technology, Edited by Gill Owens, 9<sup>th</sup> edition, Cement and Concrete Institute Midrand, South Africa. ISBN 978-0-9584779-1-8(2009), 1-16.
- [17] R. Siddique, Compressive strength, water absorption, sorptivity, abrasion resistance and permeability of self-compacting concrete containing coal bottom ash, *Construction and Building Materials* **47** (2013), 1444–1450.
- [18] C.D. Woolard, K. Petrus, M. Van der Horst, The use of a modified fly ash as an adsorbent for lead, *Water SA* **26(4)** (2000), 531–536.
- [19] J. Marrero, G. Polla, R.J. Rebagliati, R. Plá, D. Gómez, P. Smichowski, Characterization and determination of 28 elements in fly ashes collected in a thermal power plant in Argentina using different instrumental techniques, *Spectrochimica Acta Part B* **62** (2007), 101–108.
- [20] F. Skvara, L. Kopecky, V. Smilauer, Z. Bittnar, Material and structural characterization of alkali activated low-calcium brown coal fly ash, *Journal of Hazardous Materials* **168** (2009), 711–720.
- [21] O. Babajide, L. Petrik, N. Musyoka, B. Amigun, F. Ameer, Use of coal fly ash as a catalyst in the production of biodiesel, *Petroleum & Coal* **52(4)** (2010), 261–272.
- [22] M. Komljenovic, Z. Bascarevic, V. Bradic, Mechanical and microstructural properties of alkali-activated fly ash Geopolymers, *Journal of Hazardous Materials* **181**, (2010), 35–42.
- [23] J.S. Mahlaba, E.P. Kearsley, R.A. Kruger, Physical, chemical and mineralogical characterisation of hydraulically disposed fine coal ash from SASOL Synfuels, *Fuel* **90**(2011), 2491–2500.
- [24] H. Justnes, L. Elfgren, V. Ronin, Mechanism for performance of energetically modified cement versus corresponding blended cement, *Cement and Concrete Research* **35** (2005), 315–323.
- [25] W. Kubissa, R. Jaskulski, Measuring and Time Variability of The Sorptivity of Concrete, 11th International Conference on Modern Building Materials, Structures and Techniques, MBMST 2013, *Procedia Engineering* **57** (2013), 634 – 641.
- [26] K.K. Sideris, N.S. Anagnostopoulos, Durability of normal strength self-compacting concretes and their impact on service life of reinforced concrete structures, *Construction and Building Materials* **41** (2013), 491–497.
- [27] W. Wang, J. Liu, F. Agostini, C.A. Davy, F. Skoczylas, D. Corvez, Durability of an Ultra High Performance Fiber Reinforced Concrete(UHPFRC) under progressive aging, *Cement and Concrete Research* **55** (2014), 1–13.
- [28] Y. Ballim, M.G. Alexander, Towards a performance-based specification for concrete durability, *African Concrete Code Symposium* (2005), 206–218.
- [29] SANS 50196-1, Methods of testing cement, Part 1: Determination of strength (2006), 4–14.
- [30] ASTM C 1437, Standard Test Method for Flow Table for Flow of Hydraulic Cement Mortar, Annual Book of ASTM Standards, **4(01)** (2006), 614–615.
- [31] SANS 5862-1:2006, Concrete tests-compressive strength of hardened concrete, Pretoria: South Africa Bureau of Standards, (2006).
- [32] M.G. Alexander, Y. Ballim, J.M. Mackechnie, Concrete durability index testing manual, Research monograph no. 4, Departments of Civil Engineering, University of Cape Town and University of the Witwatersrand (1999).

- [33] M.G. Alexander, J.R. Mackechnie, Y. Ballim, Guide to the use of durability indexes for achieving durability in concrete structures, Research monograph no 2, published by the Department of Civil Engineering, University of Cape Town in collaboration of University of the Witwatersrand (2001), 5-25.
- [34] M.G. Alexander, Durability indexes and their use in concrete engineering, International RILEM Symposium on Concrete Science and Engineering: A Tribute to ArnonBentur. Print-ISBN: 2-912143-46-2, e-ISBN: 2912143586, Publisher: RILEM Publications SARL(2004), 9 – 22.
- [35] Y.A. Ballim, Low cost, falling head permeameter for measuring concrete gas permeability, Concrete/Beton, *Journal of the Concrete Society of Southern Africa* **61**(1991), 13-18.
- [36] P.E. Streicher, M.G. Alexander, A chloride conduction test for concrete, *Cement and Concrete Research* **25** (1995), 1284-1294.
- [37] P.E. Streicher, M.G. Alexander, Towards standardisation of a rapid chloride conduction test for concrete, *Cement, Concrete and Aggregates* **21**(1999), 23-30.
- [38] S.M. Gouws, M.G. Alexander, G. Maritz, Use of durability index tests for the assessment and control of concrete quality on site, *Concrete Beton* **98** (2001), 5-16.
- [39] M.G. Alexander, Y. Ballim, K. Stanish, A framework for use of durability indexes in performance based design and specifications for reinforced concrete structures, *Materials and Structures* **41** (2008), 921–936.
- [40] T. Bajor, L. Szente, J. Szejtli, Methods for Characterization of the Wettability of Cyclodextrin Complexes, *Proceedings of the Fourth International Symposium on Cyclodextrins, Advances in Inclusion Science* **5** (1988), 237-241.
- [41] R. Singh, N. Bharti, J. Madan, S.N. Hiremath, Characterization of Cyclodextrin Inclusion Complexes – A Review, *Journal of Pharmaceutical Science and Technology* **2(3)** (2010), 171-183.

# Durability of mortars and concretes containing scoria-based blended cements

Aref Mohammad ALSWAIDANI<sup>a,1</sup> and Samira Dib ALIYAN<sup>b</sup>

<sup>a</sup>*Faculty of Architectural Engineering, Arab International Univ, Damascus, Syria*

<sup>b</sup>*Syrian Arab Organization for Standardization and Metrology, Damascus, Syria*

**Abstract.** A lot of reinforced concrete (RC) structures in Syria went out of service after a few years of construction. This was mainly due to reinforcement corrosion or chemical attack on concrete. The use of blended cements is growing rapidly in the construction industry due to economical, ecological and technical benefits. Syria is relatively rich in scoria. In this study, mortar/concrete specimens were produced with seven types of cement: one plain Portland cement (control) and six blended cements with replacement levels ranging from 10 to 35%. Rapid chloride penetration test (RCPT) was carried out according to ASTM C 1202 after two curing times of 28 and 90 days. The effect on the resistance of concrete against damage caused by corrosion of the embedded steel has been investigated using an accelerated corrosion test (ACT) by impressing a constant anodic potential. The variation of current with time and the time to failure of RC specimens were determined at 28 and 90 days curing. The specimens were also monitored periodically. In addition, effects of aggressive acidic environments on mortars were investigated through 100 days of exposure to 5% H<sub>2</sub>SO<sub>4</sub>, 10% HCl, 5% HNO<sub>3</sub> and 10% CH<sub>3</sub>COOH solutions. Evaluation of sulfate resistance of mortars was also performed by immersing in 5% Na<sub>2</sub>SO<sub>4</sub> solution for 52 weeks. Test results reveal that the resistance to chloride penetration of concrete improves substantially with the increase of replacement level, and the concretes containing blended cements, especially CEM II/B-P, exhibited corrosion initiation periods several times longer than the control mix. Moreover, a definite correlation is observed between RCPT and ACT. An increase in scoria addition improves the chemical resistance of mortar, especially in the early days of exposure, whereas after a long period of continuous exposure all specimens show the same behavior against the chemical attack. According to results of sulfate resistance, CEM II/B-P can be used instead of SRPC in sulfate-bearing environments.

**Keywords.** Durability, corrosion resistance, blended cement, natural pozzolans, chemical attack, scoria, sulfate attack

## Introduction

Use of natural pozzolan in production of blended Portland cements makes important effects on physical, chemical, mechanical and durability properties of mortar and concrete [1-4]. In addition, since these materials enter the cement production after kiln process, they also provide important economical and ecological benefits [5]. This study is part of the first detailed research in Syria to investigate the potential utilization of scoria as cement replacement in producing Portland-pozzolan cements, and its effects on the performance of mortar and concrete. The study is of particular importance not only for the country but also for other areas of similar geology, e.g. Harrat Al-Shaam, a volcanic field covering a total area of some 40 000 km<sup>2</sup>, third of which is located in the country. The rest is covering parts from Jordan and Saudi Arabia.

<sup>1</sup>Corresponding author: aydlswardani@yahoo.fr; a-swardani@aiu.edu.sy

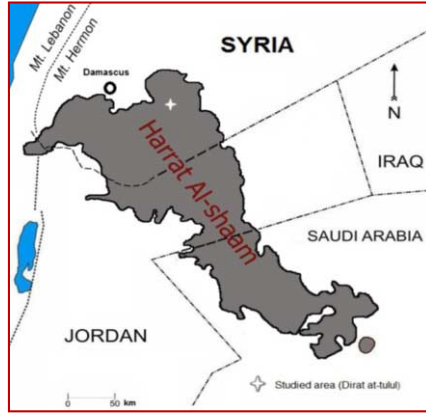
The objective of this paper is to report a part of this ongoing research on the effect of different amount of scoria when adding as cement replacement on some durability-related properties. Penetrability of chloride ions, corrosion of reinforcing steel, acid and sulfate attacks have been particularly investigated. Some chemical, physical and mechanical properties have been also reported.

## 1. Materials and methods

The scoria used in the experiments was collected from a Tal Dakwa' quarry, at 70 km southeast of Damascus as shown in the Figure 1. Figure 2 shows thin sections of the used scoria. The chemical analysis of scoria used in the study is summarized in Table 1. This analysis was carried out by means of wet chemical analysis specified in EN 196-2. Three types of scoria-based cement were prepared, one plain Portland cement CEM I-42.4 (control), and two blended cements: CEM II/A-P and CEM II/B-P (EN 197-1), each of them with 3 replacement levels of scoria: (10%, 15% and 20%) and (25%, 30%, 35%), respectively. 5% of gypsum was added to all these cements. The clinker used for producing the cements was obtained from Adra Cement Plant, Damascus, Syria. Table 2 shows the chemical and physical properties of the cements produced. Eight mortar mixtures were prepared using these cements and sand meeting the requirements of ASTM C 778. Seven concrete mixes were prepared using a grading of aggregate mixtures kept constant for all concretes.

**Table 1.** Chemical composition of the used materials

	Materials				
	Scoria	Clinker	Gypsum	Dolomite aggregate	Natural sand
SiO <sub>2</sub>	46.52	21.30	0.90	0.42	93.39
SiO <sub>2(reactive)</sub>	42.22	-	-	-	-
Al <sub>2</sub> O <sub>3</sub>	13.00	4.84	0.07	0.38	0.57
Fe <sub>2</sub> O <sub>3</sub>	11.40	3.99	0.10	0.10	0.24
CaO	10.10	65.05	32.23	31.40	1.70
CaO <sub>F</sub>	-	2.1	-	-	-
MgO	9.11	1.81	0.20	20.46	0.20
SO <sub>3</sub>	0.27	0.25	45.29	0.18	1.15
Loss on ignition	2.58	-	21.15	46.48	2.52
Na <sub>2</sub> O	2.14	0.60	-	0.06	0.06
K <sub>2</sub> O	0.77	0.28	-	0.30	0.05
Cl <sup>-</sup>	<0.1	0.05	-	0.021	0.017
Pozzolan activity index (ASTM C 618)	79 (at 7 days) 85 (at 28 days)				



a. Map of Harrat Al-Shaam and the studied area.



b. The studied scoria quarry, some volcanic scoria cones are shown behind. c. The studied scoria aggregate.

**Figure 1.** Map of Harrat Al-Shaam, photo of the studied quarry & the used scoria aggregate.



a.

b.

**Figure 2.** Thin sections of the scoria. a). Microphenocryst of Olivine in volcanic glass matrix with vesicles, some of which are filled with white minerals. b). Microphenocrysts of elongated plagioclase in volcanic glass matrix with vesicles, some of which are filled with white minerals.

Aggregates used in the study were crushed dolomite with river bed natural sand added. Both aggregates were obtained from local sources. Their chemical compositions are shown in Table 1. Their quantities in  $1\text{m}^3$  concrete mix based on oven-dry condition

are as follows: 565.5 kg of coarse aggregate, 565.5 kg of medium-size aggregate, 447.5 kg of coarse sand and 286.5 kg of natural sand. All concrete mixes were designed to have a water-binder ratio of 0.6 and a slump of  $150\pm 20$  mm. Concrete cubes (150 mm), plain and reinforced concrete cylinders (100mm $\times$ 200 mm) were cast for evaluating the compressive strength, penetrability of chloride ions and corrosion resistance. The compressive strength development was determined on 150 mm cubic concrete specimens, according to ISO 4012 [6], at ages of 2, 7, 28, 56, 90 days. The rapid chloride penetrability test has been conducted in accordance with ASTM C 1202 [7]. The corrosion performance of concretes containing scoria-based cements was evaluated by impressing a relatively high anodic potential of 12 V to accelerate the corrosion process. The experimental set-up and view for the accelerated corrosion test are illustrated in Figure 3. The relative acid resistance was determined in accordance with ASTM C 267-01 [8]. The aggressive acid environmental conditions were: 5% H<sub>2</sub>SO<sub>4</sub>, 10% HCl, 5% HNO<sub>3</sub> and 10% CH<sub>3</sub>COOH. The evaluation of sulfate attack resistance of mortars containing scoria-based cements was performed in accordance with [ASTM C 1012-04] [9].

## 2. Results and discussion

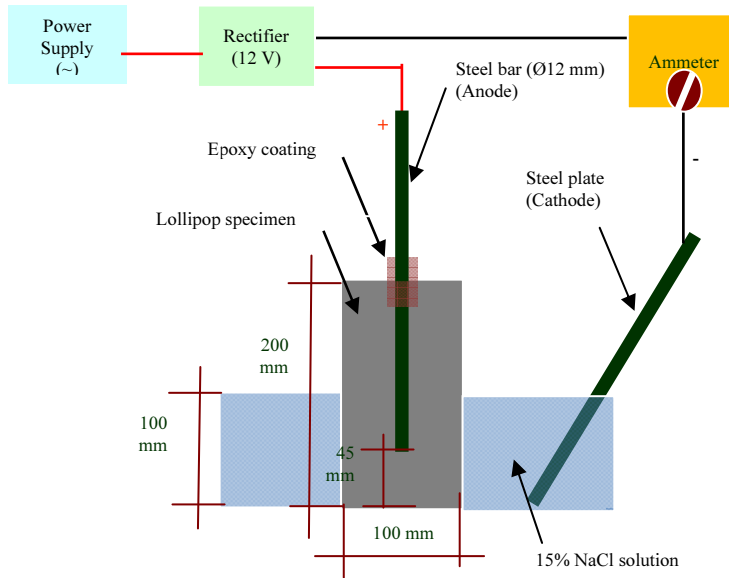
Scoria is considered as suitable material for use as pozzolan. It satisfied the American and European standard requirements. The chemical and physical properties of cements containing scoria are also in conformity with the standard requirements ASTM C595 [10]. Results of compressive strength test are summarized in Table 3. As expected, the compressive strengths of scoria-based cement concretes are lower than that of the plain Portland cement at 28 days curing. Scoria-based concrete mixes have low compressive strengths at early ages which gradually increase at longer ages. This reduction in the early strengths of blended cements is mainly due to the slowness of pozzolanic reaction between pozzolan and calcium hydroxide (CH) released during cement hydration [11]. However, due to the continuation of this reaction and the formation of a secondary C-S-H, a greater degree of hydration is achieved resulting in strengths after 90 days curing which are comparable to those of CEM I specimens. The resistance to chloride penetration was greatly increased with the use of scoria-based cement concretes as displayed in Figure 4.

The concretes containing CEM II/B-P with scoria contents of 25, 30 and 35%, showed the best performance among all the specimens. According to ASTM C1202 [7], these concretes can be considered as low chloride permeable after 90 days curing. This enhanced performance can be due to the secondary pozzolanic reaction which contributes to make the microstructure of concrete denser [12-14]. If a higher volume of scoria is added, much lower penetrability can be achieved. In addition, a good correlation between resistance to chloride penetration and alumina content in cements used was also observed as shown in Figure 5.

**Table 2.** Chemical and physical properties of plain and blended cements

Chemical composition (%)	Chemical properties of plain and blended cements								
	C1/CEMI %	C2/I0 %	C3/I5 %	C4/20 %	C5/25 %	C6/30 %	C7/35 %	C8/SRPC %	
SiO <sub>2</sub>	20.69	21.59	22.35	23.25	24.00	24.33	24.61	20.72	
Al <sub>2</sub> O <sub>3</sub>	5.09	5.20	5.68	5.73	6.55	6.80	7.39	4.33	
Fe <sub>2</sub> O <sub>3</sub>	4.23	4.75	4.79	5.15	5.43	5.47	6.31	5.79	
CaO	60.62	58.21	55.18	53.05	50.30	48.00	44.84	61.69	
MgO	2.46	2.66	3.23	3.39	3.87	4.11	4.63	1.21	
SO <sub>3</sub>	2.26	2.31	2.20	2.20	2.30	2.26	2.55	2.13	
Loss on ignition	1.41	1.40	1.43	1.37	1.47	1.48	1.60	2.90	
Na <sub>2</sub> O	0.60	0.71	0.83	0.94	1.07	1.16	1.31	0.21	
K <sub>2</sub> O	0.35	0.39	0.43	0.46	0.50	0.53	0.57	0.19	
Cl <sup>-</sup>	0.023	0.021	0.022	0.019	0.018	0.019	0.019	0.022	
Insoluble Residue	1.03	1.58	2.09	2.51	3.48	4.08	5.33	0.36	
Main compounds of clinker used in cement specimens «Based on Bogue composition »	C <sub>3</sub> S	53.36	50.55	47.74	44.94	42.13	39.32	36.51	50.16
	C <sub>2</sub> S	17.76	16.82	15.89	14.95	14.02	13.08	12.15	21.58
	C <sub>3</sub> A	5.78	5.47	5.17	4.86	4.56	4.26	3.95	1.69
	C <sub>4</sub> AF	11.53	10.93	10.32	9.71	9.11	8.50	7.89	17.60
	C <sub>3</sub> S/C <sub>2</sub> S	3.0	3.0	3.0	3.0	3.0	3.0	3.0	2.32
<b>Physical properties of plain and blended cements</b>									
Density (g/cm <sup>3</sup> )	3.13	3.09	3.05	3.02	2.99	2.98	2.96		
Initial setting (min)	151	153	153	153	152	153	158		
Final setting (min)	178	179	180	180	179	181	188		
Water demand (%)	25.1	25.2	25.2	25.4	25.4	25.4	25.5		
Soundness (mm)	0.6	0.7	0.8	0.8	0.9	1.1	0.9		
Residue on 45 µm sieve (%)	13.6	14.3	14.8	15.2	16.1	17.0	17.9		
Residue on 90 µm sieve (%)	6.4	6.2	6.4	6.5	6.7	6.9	6.8		
Strength of mortars at 28 days curing (MPa)	45.6	44.2	42.3	40.6	37.1	33.7	30.6		





a. Setup for the accelerated corrosion test



b. View of the experimental setup

**Figure 3.** Schematic representation and view of experimental setup for the accelerated corrosion test

Increasing the alumina content in cement reduces the total charge passed. This could be due to the capability of alumina to bind chloride ions [15]. However, this relationship should be investigated further with a wide range of cement types.

Figure 6 & 7 present the typical curves of corrosion current versus time for the 90-day cured concrete specimens and the average corrosion times required to crack the specimens, respectively. As seen from Figure 6, current-time curve initially descended till a time period after which a steady low rate of increase in current was observed, and after a specific time period a rapid increase in current was detected until failure. Almost a similar variation of the corrosion current with time has also been observed by other researchers [16, 17]. The sudden rise of the current intensity coincided with the cracking of the specimen. As shown in Figure 7, time to cracking in CEM I concrete specimens was in the range of 70-106 h (3-5 days), whereas that in CEM II/B-P was in the range of 120-370 h (5-16 days), depending on the replacement level and age at testing. This delay in corrosion time when using blended cements may be related to the pozzolanic reaction of scoria which contributes to fill the voids and pores in concrete with an additional C-S-H gel. This leads to decrease of pore size and to a smaller effective diffusivity for chloride. [16, 18]. It was also observed that there is a good correlation between corrosion initiation times and total charge passed through concrete specimens, with a regression coefficient ( $R^2 \approx 0.92$ ), as shown in Figure 8. According to Montgomery [19] a regression coefficient,  $R^2$ , of more than 0.85 indicates an excellent correlation between the fitted parameters. Increasing the total charge passed through concrete specimens reduces the time to initiate corrosion.

**Table 3.** Compressive strength of concrete cubes.

Sample	Compressive strength (MPa)-Normalized				
	2 days	7 days	28 days	56 days	90 days
C1/CEM I (Control)	13.6-100%	24.9-100%	35.0-100%	40.6-100%	42.3-100%
C2/10%	12.8-94%	24.4-98%	33.6-96%	39.8-98%	41.6-98%
C3/15%	11.8-87%	21.0-84%	30.1-86%	37.0-91%	39.3-93%
C4/20%	11.0-81%	20.1-81%	29.5-84%	35.1-86%	38.3-91%
C5/25%	9.9-73%	17.6-71%	26.5-76%	31.8-78%	36.5-86%
C6/30%	8.9-65%	16.5-66%	24.6-70%	29.6-73%	33.1-78%
C7/35%	8.5-63%	16.0-64%	23.4-67%	28.0-69%	30.9-73%

The resistance to acid solutions was measured by means of the weight loss of the mortar cubes. Typical curves of weight losses as a function of time of 90 days-cured mortars exposed to 5% sulfuric attack are illustrated in Figure 9. The number of days needed to register a 10% loss in weight is considered in the evaluation. As shown in Table 4, the 10% weight loss was obtained with the C7/35% mix at up to 6.2 & 6.70 days of exposure to sulfuric acid; 4.6 & 5.2 days of exposure to hydrochloric acid at 28 and 90 days curing, respectively. The SRPC and CEM I mixes, however, reached the same weight loss at only 3.0 & 3.5 days when exposed to sulfuric acid; at 3.2 & 2.9 days and 3.7 & 3.2 days when exposed to hydrochloric acid at 28 and 90 days curing, respectively. None of CEM II/B mixes lost 10% weight even after 100 days of exposure to nitric and acetic acids. The better performance of scoria-based cements can be due to the pozzolanic reaction which dilutes  $\text{Ca}(\text{OH})_2$ ; the most vulnerable product of cement hydration in so far as acid attack is concerned [20]. Contrary to expectation, the weight loss of SRPC mortars was very similar to that of CEM I mortars under similar conditions.

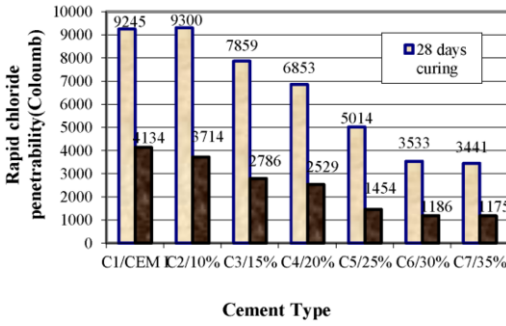


Figure 4. Influence of scoria content on chloride penetrability of concrete

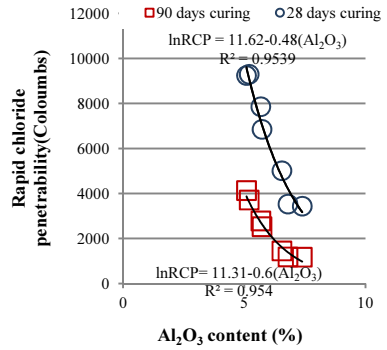


Figure 5. Influence of alumina content in cements on chloride penetrability of concretes

This is possibly because SRPC and CEM I mortars both contain lime and calcium silicates in large proportions. Generally, all acid attacks on mortars were associated with erosion and softening due to leaching of Ca and decalcification of C-S-H [21]. As generally expected, none of all cements used can provide a long-term resistance to strong acids.

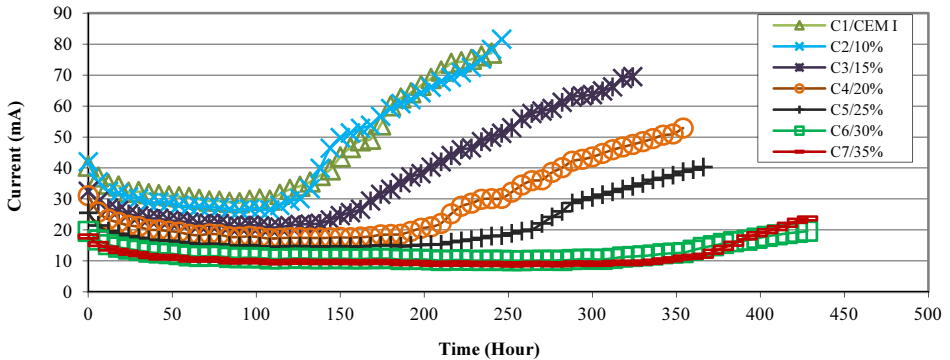


Figure 6. Typical curve of corrosion current versus time of concrete specimens tested after 90 days curing

It should be noted that, contrary to expectation, there was a strong correlation between  $H_2SO_4$  and  $HCl$  attacks ( $R^2 \approx 0.95$ ), as shown in Figure 10. This was despite the different mechanisms of deterioration. In the sulfuric acid attack, expansive calcium salts of lower solubility are formed and followed by cracking and eventual transformation of mortar into a mushy or non-cohesive mass [22], whereas in the hydrochloric acid attack the calcium salts are highly soluble, and may be easily leached away [23]. The 5%  $H_2SO_4$  solution was found to be, at early days of exposure, less corrosive than 10%  $HCl$  solution. This case can be due to the formation of gypsum

which covers the surface, thereby blocking further reactions [24, 25]. Later, a similar behavior was observed in both attacks. However, if the concentrations were changed, different behavior might be observed.

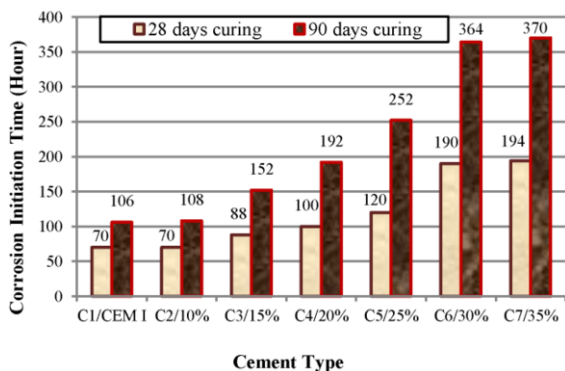


Figure 7. Average corrosion times of specimens at 28 and 90 days curing

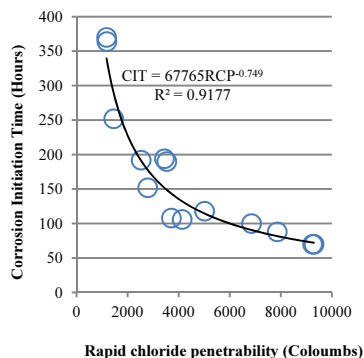


Figure 8. Variation of corrosion initiation time with rapid chloride penetrability

Another stronger linear correlation ( $R^2=0.97$ ) was also observed between hydrochloric and acetic acids, as illustrated in Figure 11. The HCl attack is much more corrosive than  $CH_3COOH$  attack. The weaker attack of acetic acid can be due to the higher pH values of the acetic acid owing to its low dissociation degree, and due to its buffering effect, when compared to that of HCl solutions [26, 27].

The results of the expansion test of bars immersed in 5%  $Na_2SO_4$  solution for 26 and 52 weeks are illustrated in Table 5. The results showed that the use of scoria reduced expansion of the mortar bars. This reduction in expansion increased with increase in the scoria replacement level. At 26 & 52 weeks, the amount of expansion of the CEM II/B mortar bars ranged from 0.10% to 0.11% and from 0.18% to 0.19%, respectively, whereas the expansion of SRPC was 0.09% and 0.16%, respectively. This was despite the lack of  $C_3A$  in SRPC. The slightly elevated expansion noted in SRPC used in the study, which made it unsuitable for severe exposure, is possibly because the SRPC mortar contains lime and  $C_4AF$  in large proportions when compared to the CEM II/B mortars. These results confirmed earlier findings that the presence of  $C_3A$  is not the only cause of expansion due to sulfate attack [28, 29]. The improvement of sulfate resistance by adding scoria as cement replacement can be mainly explained by the pore size refinement, the removal of lime by the pozzolanic reaction and the  $C_3A$  dilution [30-33]. According to the results obtained, blending a CEM I of about 6%  $C_3A$  content with 25% scoria content or more usually resulted in a performance similar to that of SRPC.

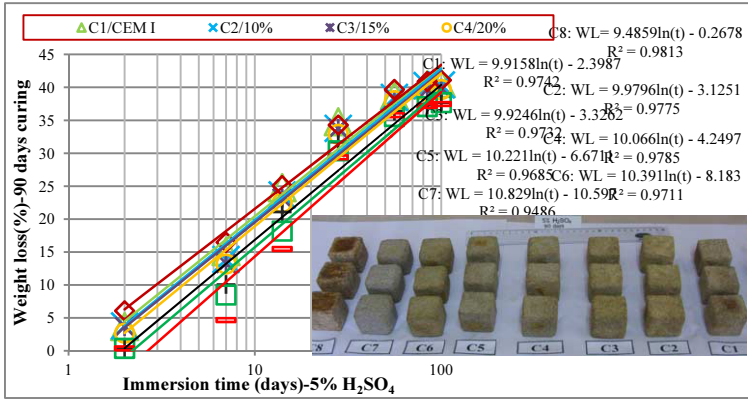


Figure 9. Weight losses over time of 90 days-cured mortars immersed in 5% H<sub>2</sub>SO<sub>4</sub> solution

Table 4. Number of days needed to register a 10% weight loss of mortar cubes

Cement type	Number of days to register 10% weight loss							
	5% H <sub>2</sub> SO <sub>4</sub>		10% HCl		5% HNO <sub>3</sub>		10% CH <sub>3</sub> COOH	
	28 days curing	90 days curing	28 days curing	90 days curing	28 days curing	90 days curing	28 days curing	90 days curing
C1/CEM I	3.5	3.5	3.7	3.2	22.5	25.9	NR	NR
C2/10%	3.7	3.7	3.7	3.1	25.4	22.8	NR	NR
C3/15%	3.8	3.8	3.8	3.6	55.5	48.9	NR	NR
C4/20%	4.0	4.1	3.9	3.7	79.1	97.3	NR	NR
C5/25%	4.7	5.1	4.1	4.3	NR	NR	NR	NR
C6/30%	5.2	5.8	4.4	4.9	NR	NR	NR	NR
C7/35%	6.2	6.7	4.6	5.2	NR	NR	NR	NR
C8/SRPC	3.0	3.0	3.2	2.9	20.1	18.8	NR	NR

NR: 10% weight loss was not reached.

Table 5. Expansion of mortar bars immersed in Na<sub>2</sub>SO<sub>4</sub> solution at 26 and 52 weeks of exposure

	C1/CEM I %	C2/10 %	C3/15 %	C4/20 %	C5/25 %	C6/30 %	C7/35 %	C8/ SRPC, %
26 weeks	0.19	0.17	0.13	0.12	0.11	0.11	0.10	0.09
52 weeks	0.41	0.36	0.26	0.23	0.19	0.18	0.18	0.16

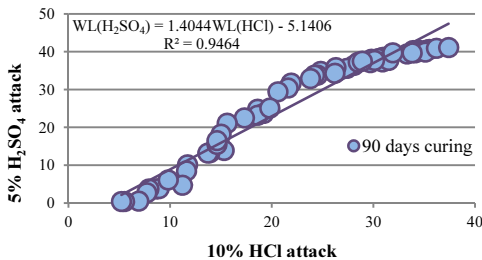


Figure 10. 5% H<sub>2</sub>SO<sub>4</sub> attack versus 10% HCl attack - 90 days cured mortars.

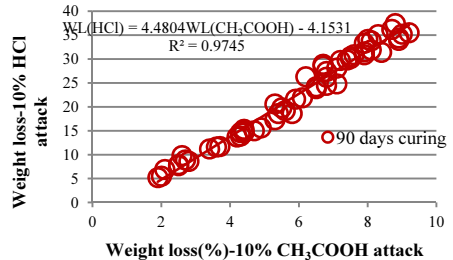


Figure 11. 10% HCl attack versus 10% CH<sub>3</sub>COOH attack - 90 days cured mortars

### 3. Conclusion

From the experimental results, the following conclusions can be drawn:

- The studied scoria is a suitable material for use as a natural pozzolan.
- At 90 days curing, the compressive strengths of scoria-based cement concretes are comparable to those of plain cement concrete.
- The chloride penetrability of scoria-based concrete mixes is much lower than that of plain concrete, especially at high replacement levels of scoria.
- Use of scoria at 30% cement replacement level makes the service life of a RC structure under chloride-bearing environments longer twice or thrice compared with that of the control.
- A definite correlation was observed between the rapid chloride penetrability test and the accelerated corrosion test, such that one can be estimated from knowledge of the other.
- There is no advantage in recommending SRPC in highly acidic environments.
- Blending of CEM I of 6 %  $C_3A$  content, with 25% scoria content or more, resulted in a performance similar to that of SRPC and an enhanced acid resistance, as well.
- Adding scoria as cement replacement reduces the expansion of the mortar bars exposed to  $Na_2SO_4$  attack. More reduction occurs with increasing the replacement level.
- Based on the results, the assumption that 'strong concrete is durable concrete' is not always true. Scoria-based cement concretes have lower compressive strengths, but greater resistance to chloride penetration, longer corrosion initiation times, greater resistance to acid attack and lower expansion in sodium sulfate solution compared with plain cement concretes after 28 and 90 days curing. So, it would be erroneous to predict durability based on strength.
- According to the results obtained, it is suggested that scoria can be used up to 30% as a partial substitute for Portland cement in production of blended cements. This addition ratio can reduce the quantity of  $CO_2$  released by Syrian cement plants by about 1.5 million tonnes, and the consumed energy by about 30% annually. So, production of a green concrete could be promoted.

### Acknowledgement

The authors gratefully acknowledge the technical and financial support of this research from the management of General Organization for cement & Building Materials/Adra Cement Plant. Thanks are also expressed to Chemist Nazeer Adarnaly, Eng. M. Eid Dyab (Order of the Syrian Engineers) and Prof. Tamer al-Hajeh, Vice-President of AIU for their help in some experiments.

### References

- [1] Al-Chaar G.K., Al-Kadi M., Asteris P.G., Natural pozzolan as a partial substitute for cement in concrete, *The Open Construction and Technology Journal*, Vol. 7(2013)33-42.
- [2] Senhadji Y., Escadeillas G., Khelafi H., Mouli M. and Benosman A.S., Evaluation of natural pozzolan for use as supplementary cementitious material, *European Journal of Environmental and Civil Engineering*, Vol. 16(1)(2012)77-96.

- [3] Hossain K.M.A., Resistance of scoria-based blended cement concrete against deterioration and corrosion in mixed sulfate environment, *Journal of Materials in Civil Engineering*, ASCE, Vol. 21(7)(2009)299-308.
- [4] Ghrici M, Kenai S, Meziane E. Mechanical and durability properties of cement mortar with Algerian natural Pozzolana. *Journal of Material Science*, Vol. 41(2006)6965-6972.
- [5] Mehta PK, Monteiro PJM, Concrete: *Microstructure, properties, and Materials*, 3<sup>rd</sup> edition. McGraw-Hill, ISBN 0-07-146289-9, 2006.
- [6] ISO 4012/1978, *Concrete – Determination of compressive strength of test specimens*.
- [7] ASTM C 1202. (*Electrical Indication of Concrete's Ability to Resist Chloride Ion Penetration, RCPT*)
- [8] ASTM C-267, *Standard test methods for chemical resistance of mortars, grouts, and monolithic surfacings and polymer concretes*, 2001.
- [9] ASTM C 1012, *standard test method for length change of hydraulic-cement mortars exposed to a sulfate solution*, 2004.
- [10] ASTM C595, Standard specification for blended hydraulic cements, *American Society for Testing and Materials*, Vol. 04.01, 2001.
- [11] Mindess S., Young J.F., Darwin D., *Concrete*, 2<sup>nd</sup> Edition, Prentice Hall, 2003.
- [12] Rukzon S, Chindaprasirt P. Effect of grinding on chemical and physical properties of rice husk ash. *Int J Miner Metal Mater*, Vol. 16(2)(2009) 242-247.
- [13] Chindaprasirt P, Chotithanorm C, Cao HT, Sirivivatnanon V. Influence of fly ash fineness on the chloride penetration of concrete. *Construction and Building Materials*, Vol. 21(2007)356-361.
- [14] Gastaldini ALG, Isaia GC, Gomes NS, Sperb JEK. Chloride penetration and carbonation in concrete with rice husk ash and chemical activators. *Cement and Concrete Composites*, Vol. 21(2007)356-361.
- [15] Lewis R., Sear L., Wainwright P., Ryle R., *Cementitious additions, Advanced Concrete Technology: Constituent Materials*, Edited by Newman J. & Choo B.S., Elsevier Ltd., 2003, pp:3/14.
- [16] E. Guneyisi et al., A study on reinforcement corrosion and related properties of plain and blended cement concretes under different curing conditions, *Cement & Concrete Composites*, Vol. No. 27(2005) 449-461.
- [17] Horsakulthai V., Phiuvanna S., Kaenbud W., Investigation on the corrosion of bagasse-rice husk-wood ash blended cement concrete by impressed voltage, *Construction and Building Materials*, Vol. 25(2011) 54-60.
- [18] Hossain K.M.A., Blended cement using volcanic ash and pumice, *Cement and Concrete Research*, Vol. 33(2003)1601-1605.
- [19] Montgomery D.C.& Peck E.A., *Introduction to linear regression analysis*. New York: Wiley; 1982.
- [20] Neville A.M., *Properties of concrete*, fifth edition, Pearson Education 2011.
- [21] H.T.Cao, I.Bucea, A.Ray, S.Yozghatlian, The effect of cement composition and pH of environment on sulfate resistance of Portland cements and blended cements, *Cement and Concrete Composites*, Vol. Nr. 19(2)(1997)161-171.
- [22] J. Monteny, N.De Belie, E. Vincke, W. Verstraete, L. Taerwe, Chemical and microbiological tests to simulate sulfuric acid corrosion of polymer-modified concrete, *Cement and Concrete Research*, Vol. Nr. 31(2001)1359-1365.
- [23] D. Israel, D.E. Macphee, E.E. Lachowski, Acid attack on pore-reduced cements, *Journal of Material Science*, Vol. Nr. 32(1997)4109-4116.
- [24] M. Alexander and S. Mindess, *Aggregates in concrete*, Taylor & Francis, 2005.
- [25] A.K. Tamimi, High performance concrete mix for an optimum protection in acid conditions, *Materials and structures*, Vol. Nr. 30(1997)188-191.
- [26] V. Pavlik, Corrosion of hardened cement paste by acetic and Nitric acids; Part II: Formation and chemical composition of the corrosion products layer, *Cement and Concrete Research*, Vol. Nr. 24(1994)1495-1508.
- [27] A. Allahverdi, F. Skvara, Acidic corrosion of hydrated cement based materials; Part 1.: Mechanism of the phenomenon, *Ceramics-Silicaty*, Vol. Nr. 44(3)(2000)114-120
- [28] H.T.Cao, I.Bucea, A.Ray, S.Yozghatlian, The effect of cement composition and pH of environment on sulfate resistance of Portland cements and blended cements, *Cement and Concrete Composites*, Vol. Nr. 19(2)(1997)161-171.
- [29] W. Tangchirapat, C. Jaturapitakkul, P. Chindaprasirt, Use of palm oil fuel ash as a supplementary cementitious material for producing high-strength concrete, *Construction and Building Materials*, Vol. Nr. 23(7)(2009)2641-2646.
- [30] E.F.Irassar, M.A.Gonzalez, V. Rahhal, Sulfate resistance of type V cements with limestone filler and natural pozzolan, *Cement and Concrete Composites*, Vol. Nr. 22(5)(2000)361-368.
- [31] R.D. Hooton, J.J. Emery, Sulphate resistance of a Canadian slag cement, *ACI Material Journal*, Vol. Nr. 87(1990)547-555.

- [32] O.S.B. al-Amoudi, Attack on plain and blended cements exposed to aggressive sulfate environments, *Cement and Concrete Composites*, Vol. Nr. 24(2002)304-30-316.
- [33] S.U.al-Dulaijan, M. Maslehuddin, M.M. al-Zahrani, A.M. Sharif, M. Shameem, M. Ibrahim, Sulfate resistance of plain and blended cements exposed to varying concentrations of sodium sulfate, Vol. Nr. 25(2003)429-437.



# Effect of surface treatments on abrasion and permeation properties of clay concretes

Fitsum SOLOMON<sup>1</sup> and Stephen EKOLU

*Department of Civil Engineering Science, University of Johannesburg, South Africa*

**Abstract.** The resistance of concrete surfaces to various types of wear can be a defining performance characteristic in certain applications. Some concrete structures are required to be abrasion-resistant; among them are dams, canals, roads, floors, footpaths, parking lots, and paths in parks.

The work reported in this paper is based on a laboratory study of the concrete-surface treatments (CSTs) consisting of dry shake and screeding. Four control concrete mixtures were prepared with ordinary Portland cement (OPC), having a cement content (CC) of 350 kg/m<sup>3</sup> at water-cementitious ratio (w/cc) = 0.70, 0.75; and 280 kg/m<sup>3</sup> CC of w/cc = 0.80, 0.85. Other concrete mixtures were then prepared by substituting OPC in the control mixtures with 10, 20, 30, and 40% local raw clay.

Compressive strength, abrasion resistance, and air permeability of the surface-treated concretes were measured at the ages of six months, while drying shrinkage was monitored for up to year. Drying shrinkage of concrete reduced with decrease in w/cc ratio and increased with increase in raw clay content. Among all the mixtures, the control concrete of w/cm ratio = 0.70 and the clay-cement concrete containing w/cm=0.80 at 70% OPC/30% raw clay showed the least and highest shrinkage increments respectively. Abrasion resistance of concrete, measured by the rotating-cutter method, increased with increasing clay content and decreasing compressive strength. However, abrasion performance results of clay-cement concrete mixtures with CSTs were generally higher. Air permeability of the concretes was measured and its relationship with the depth of abrasion of the concrete was examined.

**Keywords.** Abrasion resistance, drying shrinkage, air permeability, dry shake, screed

## Introduction

The use of clay in concrete as partial replacement for cement is not common. In spite of heavy competition from industrial by-products, clays may still be good alternatives as mineral additives or blending for concrete in many places of the world. Incorporation of clay soil into concrete mixtures is one means of designing low-cost, low-strength construction materials. However the influence of clay on material properties should be understood as it affects engineering performance. Previous laboratory experimental work showed that clay-cement mixtures with a maximum of w/cc = 0.80 and 20 to 30% clay replacement can be suited to fulfill the requirement of strength and workability for low-cost, low-strength applications [1].

---

<sup>1</sup>Corresponding author: [Fitsummoa@gmail.com](mailto:Fitsummoa@gmail.com)

In clay concretes, it is clear that the presence of more voids reduces the strength of clay concrete compared with ordinary concrete, but in many applications high strength is not essential. Light weight concrete, for example, provides very good thermal insulation and has satisfactory durability but is not highly resistant to abrasion. Researchers on abrasion resistance recommend that concrete can be made more abrasion resistant by several factors among them being surface treatments [2]. In the present work, the tests done include compressive strength, drying shrinkage, abrasion resistance and air permeability.

## **1. Background**

Partial or complete substitution of cementing agents with clay binder can be done in sandy-clay and clay-mortar material. The use of such cementing materials is limited by availability, cost, susceptibility to local climatic conditions, mixing, placing, and densification with the available resources at the site of construction. This leaves large quantities of unutilized local sands usually containing a significant clay fraction exceeding the acceptable limits for use in normal concrete. The increased global use of traditional supplementary cementitious materials is still favoured over other natural resources that may be locally available for use in construction [3]. In general, clay concrete is cheaper than ordinary concrete. Also, direct water permeability tests can be conducted on clay concrete, unlike normal concrete of low w/cc whose permeability can be too low for practical measurement of water permeability. By using selected aggregates and fine mineral additives such as raw clay and concrete surface treatments, the properties of clay-cement concrete can be improved greatly.

Abrasion tests are destructive and will damage the test area permanently. For this reason, attempts have been made to predict non-destructively the abrasion resistance of concrete floors, with contradictory conclusions drawn [4]. There is an accepted view that the permeation properties of the 'cover' concrete are related to quality and hence performance, particularly durability [5]. The establishment of quantitative relationships between the permeation properties and the abrasion resistance of concrete, and how closely this type of durability can be established by means of permeation measurement would be of practical value. The aim of this investigation was to explore this possibility.

At present time, the initial surface absorption test (ISAT) is the best method of predicting the abrasion resistance of concrete non-destructively. Whilst the ISAT is somehow arbitrary, it does have acceptance by practising engineers [6].

## **2. Experimental**

### *2.1. Clays*

The research started with collection of undisturbed raw soil samples within Gauteng province guided by maps in the areas of Springs (RD) and Soweto (S2M). The soil samples were tested to determine their engineering properties such as Atterberg limits, ASTM soil group classification, Casagrande's soil classification systems and particle specific gravities. The two types of clays and commercially available bentonite were incorporated into concrete mixtures in various proportions. Soils were not oven-dried

since an elevated temperature can permanently alter the properties of the clay. The two raw soil samples were rich in clay content, found to be between 35 to 45%.

## 2.2. Mixture proportions

Ordinary Portland cement (42,5N grade) was used. Four control concrete mixtures were prepared with ordinary Portland cement (OPC), having a cement content (CC) of 350 kg/m<sup>3</sup> at water-cementitious ratio (w/cc) = 0.70, 0.75; 280 kg/m<sup>3</sup> CC and w/cc = 0.80, 0.85. Further concrete mixtures were prepared by substituting ordinary Portland cement with 10, 20, 30, 40 and 60% raw clay in all control mixtures, as shown in Table 1. The workability of fresh concrete was measured for each mix and compressive strength of the hardened concretes was reported in the previous paper [1]. Further mixtures were prepared for the compressive strength and abrasion resistance testing at ages of six months, drying shrinkage monitoring for up to one year, and air permeability measurement for the selected mixtures and their concrete-surface treatments.

**Table 1.** Mix proportions of the cement, clay- cement Concretes (kg/m<sup>3</sup>) and local stone (19mm) used

Mix	w/cc	Clay (%)	Density (Kg/m <sup>3</sup> )	Cement (Kg)	Clay (Kg)	Water (Kg)	Bldg Sand (Kg)	River sand (Kg)	Local stone (Kg)
CM1	0.70	0	2235	350	0	245	380	380	880
CM2	0.75	0	2253	350	0	263	380	380	880
CM3	0.80	0	2144	280	0	224	380	380	880
CM4	0.85	0	2158	280	0	238	380	380	880
RD1	0.70	10	2235	315	35	245	380	380	880
RD2	0.70	20	2235	280	70	245	380	380	880
RD4	0.70	40	2235	210	140	245	380	380	880
RD7	0.75	20	2253	280	70	263	380	380	880
RD9	0.75	40	2253	210	140	263	380	380	880
RD12	0.80	20	2144	224	56	224	380	380	880
RD13	0.80	30	2151	196	84	224	380	380	880
RD14	0.80	40	2158	168	112	224	380	380	880
RD17	0.85	20	2158	224	56	238	380	380	880
RD19	0.85	40	2158	168	112	238	380	380	880
S2M2	0.70	20	2235	280	70	245	380	380	880
S2M4	0.70	40	2235	210	140	245	380	380	880
S2M5	0.70	60	2235	140	210	245	380	380	880
S2M7	0.75	20	2253	280	70	263	380	380	880
S2M9	0.75	40	2253	210	140	263	380	380	880
S2M12	0.80	20	2144	224	56	224	380	380	880
S2M14	0.80	40	2144	168	112	224	380	380	880
S2M17	0.85	20	2158	224	56	238	380	380	880
S2M18	0.85	30	2158	196	84	238	380	380	880
S2M19	0.85	40	2158	168	112	238	380	380	880
*BM 2	0.70	20	2235	280	70	245	380	380	880
BM17	0.85	20	2158	224	56	238	380	380	880

\*BM-bentonite mixes.

## 2.3. Concrete-surface treatments (CSTs) preparation

Two types of surface treatments were applied namely, dry shake and screed. The surface treatments were prepared using OPC 42.5N. The dry shake finish consisted of the cement: crusher sand ratio of 1:2. The screed finish comprised a blend of 4 parts of

crusher sand and 1 part building sand; in a mix of 3.5 blended sand and 1 part of cement by mass. Sufficient water was added to achieve a plastic and workable sand mix.

2.4. Specimens preparation and casting

100 mm concrete cubes were cast for compressive strength, 100 mm x 100 mm x 200 mm for drying shrinkage, 60 mm x 120 mm x 380 mm slabs for abrasion resistance. Cores were extracted from the slabs for air permeability testing. For surface abrasion test, core samples were extracted from the slab and surface treatments were applied. The treatments consists of screed surface finish of 15 mm and dry shake surface of 15 mm. This test was done to compare the permeation performance of surface finish treatments relative to plain concrete. Samples were cut and polished before transferring to a 50 °C ventilated oven to be dried for 7 days before being tested.

2.5. Testing

Tests for compressive strength and drying shrinkage were conducted in accordance with SABS 863: 1976 and SABS 0100: 1992 respectively. Abrasion resistance test was performed as per ASTM C944-99:2005 [7]. The intrinsic air permeability was measured on specimens (cored from the test slabs) by using Blight apparatus [8].

Abrasion test samples were removed after 6 months of water curing then oven dried for 7 days. The abrasion mass loss or depths measurements were made by using a laboratory balance (mass loss) to the nearest 0.01 g or by vernier calliper to the nearest 0.01mm depth of wear, following 2 minutes abrasive wear for plain concretes and 8 minutes for surface finish treatments. A constant 100 N spindle load and 200 rpm speed of rotation were applied in abrasion test.

3. Results and discussion

3.1. Compressive strength

The strength results obtained are shown in Table 2. It was required that the substrate concrete on which the screed or dry shake is to be laid should be hard and strong. Weak, friable concrete is not suitable as the substrate for a screed or topping may fail [9]. For this reason, the surface finishes were applied on the limited samples of CM1, S2M2, CM2, and S2M7.

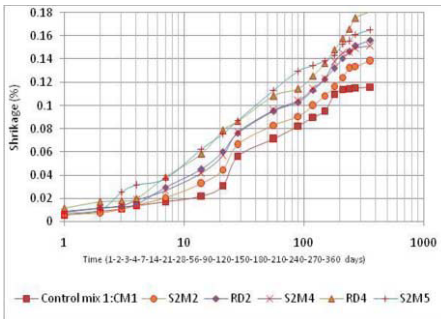
Table 2. Compressive strength of 6 months samples

Type of concrete	CM1	RD1	S2M2	S2M4	CM2	S2M7	CM3	S2M14	CM4	S2M18
Compressive Strength (MPa)	37.6	30.7	23.6	17.8	33.0	22.8	32.3	15.0	31.0	14.6

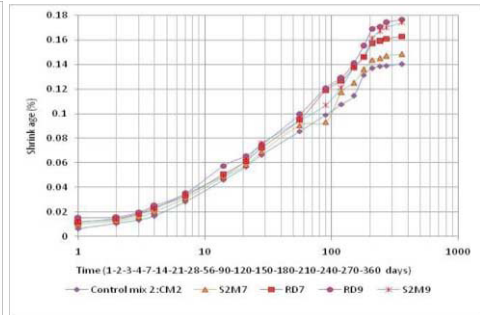
### 3.2. Drying shrinkage

Drying shrinkage can be defined as the volumetric change due to drying of the concrete. Normal concrete usually shrinks between 300 – 600 micro-strains in one year of drying [10] but the cement concrete made from control mixes CM1 to CM4 gave shrinkage of 711, 855, 919, and 1135 micro-strains respectively, as shown in Figures 1 to 4. This drying shrinkage levels were larger, probably due to high water content in the clay-concrete mixes as they contained relatively high fines. This is not necessarily a problem in itself since concrete in compression can with stand up to 2000 micro-strains. So when determining whether this material is suitable for applications of concrete, these shrinkage movements need to be considered. For pre-made concrete blocks, provided the drying shrinkage has already occurred, it is expected that these concrete blocks can be used.

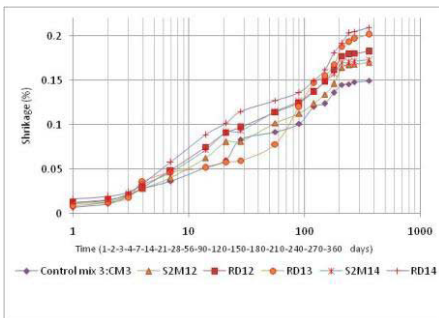
Figures 1 to 4 show that shrinkage of the clay-cement concretes is significantly greater than shrinkage of normal concretes. Clay concrete shrinkage of samples RD13, RD14, RD17, RD19 and S2M19 are extremely high, giving 2015, 2095, 2159, 2328 and 2094 micro-strains respectively, as shown in Figures 3&4. This would lead to unacceptably high tensile strains at the interface with the substrate, with the consequence of potential cracking and adhesion failures.



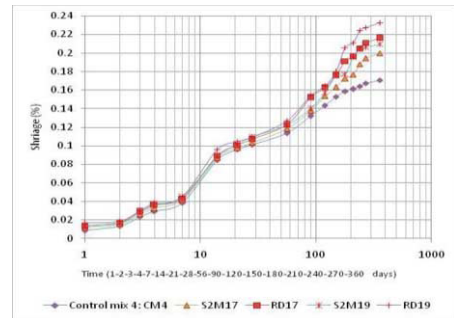
**Figure 1.** Drying shrinkage of clay concretes of  $w/cc = 0.70$  and cementitious content  $350 \text{ Kg/m}^3$ .



**Figure 2.** Drying shrinkage of clay concretes of  $w/cc = 0.75$  and cementitious content  $350 \text{ Kg/m}^3$ .



**Figure 3.** Drying shrinkage of clay concretes of  $w/cc = 0.80$  and cementitious content  $280 \text{ Kg/m}^3$ .



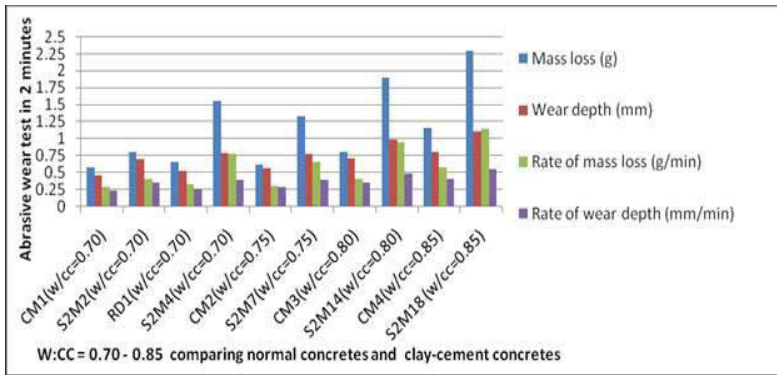
**Figure 4.** Drying shrinkage of clay concretes of  $w/cc = 0.85$  and cementitious content  $280 \text{ Kg/m}^3$ .

### 3.3. Abrasion resistance of normal concretes

The results for abrasion resistance of normal concretes are shown in Table 3 and Figure 5. The abrasion mass loss, wear depth, the rate of mass loss and rate of wear depth is highest for S2M18 (w/cc=0.85 with mass loss 2.2 g (1.14 g/min), 1.11 mm) followed by S2M14. The lowest abrasion value was shown by CM1 (w/cc=0.70 with 0.57 g abrasion loss and 0.46 mm wear depth), followed by CM2, CM3 and CM4.

**Table 3.** Abrasive mass loss and depth rate of normal (non-treated surface) concretes

Type of concrete	CM1	RD1	S2M2	S2M4	CM2	S2M7	CM3	S2M14	CM4	S2M18
Abrasive mass loss rate (g/min)	0.28	0.33	0.40	0.77	0.30	0.66	0.40	0.95	0.58	1.14
Abrasive depth rate (mm/min)	0.23	0.26	0.35	0.39	0.28	0.39	0.35	0.49	0.40	0.55



**Figure 5.** Abrasive wear of depth and mass loss of plain concretes

### 3.4. Abrasion of treated surface finishes

The results of abrasion (mass loss in g/min and wear depth) of treated surfaces are shown on Table 4 and Figure 6. The highest rate of mass loss and wear depth was given by S2M7 dry shake (DS) and screed (SCR) finish. The lowest rate of mass loss occurred on CM1 dry shake topping which gave 0.05 g/min. The lowest rate of wear depth was exhibited by screed surface finishes CM1, S2M2 screed giving 0.05mm/min.

**Table 4.** Abrasion of surface treatment finishes

Abrasion	CM1	CM1	CM1	S2M2	S2M2	S2M2	CM2	CM2	CM2	S2M7	S2M7	S2M7
2&8 mins	NIL	DS	SCR	NIL	DS	SCR	NIL	DS	SCR	NIL	DS	SCR
RML* (g/min)	0.28	0.05	0.11	0.4	0.07	0.11	0.3	0.10	0.13	0.66	0.18	0.15
RWD** (mm/min)	0.23	0.07	0.05	0.35	0.07	0.05	0.28	0.06	0.05	0.39	0.05	0.05

\*RML=Rate of mass loss, \*\*RWD= Rate of wear depth. DS= Dry Shake. SCR= Screed

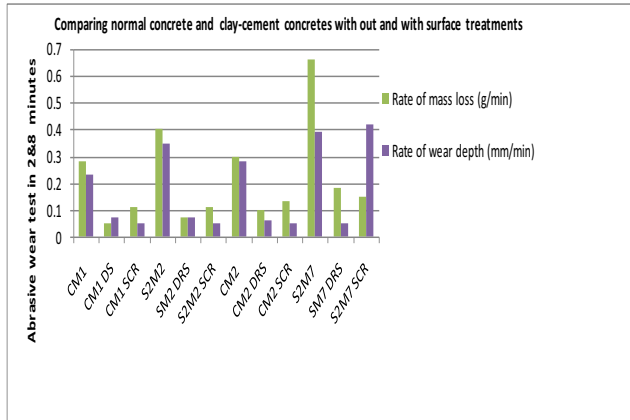


Figure 6. Abrasive wear of on plain and surface-treated concretes

3.5. Intrinsic permeability and relationship with abrasion

The intrinsic permeability was measured on specimens cored from the slabs. Air was used as a flow gas. The intrinsic permeability was obtained using the equation (1) given below. The coefficient of permeability values obtained are shown in Table 5.

The coefficient of permeability (m/s) is calculated using the equation [11]:

$$K = WVg/RA (d/(\theta.t))\ln(Po/P) \tag{1}$$

Where

- k = coefficient of permeability (m/s)
- W = molecular mass of air = 28.97g/mol
- V = volume of air under pressure in permeameter (m<sup>3</sup>)
- g = acceleration due to gravity (9.81m/s<sup>2</sup>)
- R = Universal gas constant = 8.313 (Nm/kmol)
- A = superficial cross-sectional area of sample (m<sup>2</sup>)
- θ = absolute temperature (K)
- t = time (s) for pressure to decrease from Po to P
- Po = Pressure at the beginning of test (KPa)
- P = Pressure at the end of test

Table 5. Intrinsic permeability (m<sup>2</sup>) plain concretes and concrete surface-treatments

Sample	(K*10E-17m <sup>2</sup> ) Plain	(K*10E-17m <sup>2</sup> ) Dry shake	(K*10E-17m <sup>2</sup> ) Screed finish
CM1	21.3	16.2	16.0
S2M2	38.1	28.8	28.5
CM2	23.2	17.6	17.4
S2M7	22.1	16.8	16.5

Figures 7 and 8 show an attempt to relate abrasion mass loss rate and intrinsic permeability. There is a general trend showing a significant linear relationship between the two parameters. The close relationship between the abrasion resistance and intrinsic permeability can be attributed to the fact that both parameters are influenced largely by

the quality of surface matrix. The practical implication of these results is that fluid permeability has the potential of being used to non-destructively assess the abrasion resistance of concrete slabs. For testing in situ slabs, an air-drying method can be adopted for pre-conditioning purposes.

It was anticipated that a significant relationship would be found between abrasion resistance and the absolute properties of intrinsic permeability. While there exists a general linear relationship, there is wide data scatter (Figures 7&8) which shows that the correlation between abrasion depth and permeation characteristics may be weak. The reasons for these differences are however not clear.

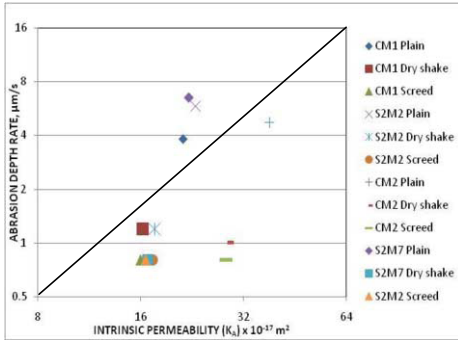


Figure 7. Relationship between abrasion depth rate and permeability.

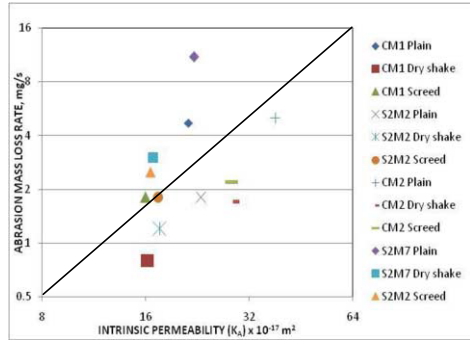


Figure 8. Relationship between abrasion mass loss rate and permeability.

#### 4. Conclusions

The following conclusions are based on the experimental results reported in this paper. Drying shrinkage is greater for clay concretes which contain RD raw clay. In all cases, most of the shrinkage occurs within the first 56/90 days and remains relatively stable beyond that age.

Abrasion resistance was found to be influenced by the water-cement ratio and strength of concrete. The concrete having the highest water-cement ratio showed lower abrasion resistance [1]. The use of concrete surface treatment was found to be effective in offsetting this problem. Concrete surface treatment with dry shake was found to have a reduced abrasion resistance than screed finish. The abrasion resistance of the normal concretes was found to be similar to that of surface treated clay-cement concretes. A relationship between intrinsic permeability and abrasion test was found to exist.

#### References

- [1] F.Solomon and S.Ekolu, Strength behaviour of clay-cement concrete and quality implications for low-construction materials, *proceedings of the 3<sup>rd</sup> international conference on concrete repair, rehabilitation and retrofitting*, Cape town, South Africa, September 3-5, 2012.
- [2] J.P. Nicolas, *Abrasion wear, abrasion resistance, and related strength characteristics in concrete, with special reference to concrete pavers*, PhD thesis, University of the Witwatersrand, Johannesburg, 2002.
- [3] V.A. Ferenandes et al, The effect of clay content in sands used for cementitious materials in developing countries, *Cement and concrete research* 37(2007), 751-758.



- [4] M. Sadegzadeh and R.Kettle, 'indirect and non-destructive methods for assessing abrasion resistance of concrete', *Magazine concrete Research* **38**(137) (1986).
- [5] R.K. Dhir, P.C. Hewlett and Y.N. Chan, Near-surface characteristics of concrete: Intrinsic permeability, *Magazine of Concrete Research* **41**(147) (1989), 87-97.
- [6] British Standard Institution, BS1881 Part 202: 1986, 'Method of testing concrete, surface hardness'.
- [7] ASTM C944-99: 2005, 'Abrasion resistance of concrete or mortar surfaces by rotating-cutter method'.
- [8] G.E Blight, A falling head permeameter for testing asphalt, *Trans. of the S.A. Institute of Civil Engineers*, June 1977, 123-126.
- [9] Cement & concrete Institute, Sand-cement screeds and concrete toppings for floors, Cement & concrete Institute, Midrand, 2006.
- [10] J.M. Illuston, Construction Materials, 2<sup>nd</sup> Edition, Chapman and Hall, 1994, 155-157, 129-132.
- [11] Y.A. Ballim, A low cost, falling head permeameter for measuring concrete Gas permeability, *Concrete/ Beton*, Journal of the Concrete Society of South Africa, No.61, 13-18.

### 3. Structural implications, performance and service life

This page intentionally left blank

# Reinforced concrete and structural composites

This page intentionally left blank

# Impact of environmental exposure on concrete strength in highway bridges in Uganda

Hilary BAKAMWESIGA<sup>a,1</sup>, Jackson MWAKALI<sup>a</sup>, Stephen SENGENDO<sup>a</sup> and Sven THELANDERSSON<sup>b</sup>

<sup>a</sup>*Department of Civil and Environmental Engineering, Makerere University*

<sup>b</sup>*Division of Structural Engineering, Lund University*

**Abstract.** Deterioration of concrete structures is a worldwide problem. Environmental exposure is known to affect concrete strength in structures. While moisture affects rebound values by lowering them, carbonation does the opposite. The aim of the study was to determine the in-situ concrete strength of three bridge elements, namely, pier, abutment and deck and evaluate the environmental conditions such as moisture and abrasive forces on the near surface of concrete. Acknowledging that destructive tests on concrete are expensive and time consuming, this research used rebound hammer test – a non-destructive test (NDT) method. The easiness, simplicity and portability of the rebound hammer made it possible to cover all 13 highway bridges in a period of two months. All the study sites were under the management of Uganda National Roads Authority (UNRA). The choice of test locations was based on BS 1881: Part 202. Rebound hammer tests were done on main elements of bridges namely, decks, piers and abutments. Where possible a maximum of 3 test points were chosen for every single test location. In addition to the universal machine calibrations, the rebound values were correlated to the standard concrete cube compressive strength using old concrete factors. Preliminary results show that although there is significant variation in concrete strength in both pier and abutment, the variation is relatively more pronounced in latter. The paper recommends a combined methodology involving the use of several NDTs to come up with sufficiently reliable results. In conclusion, the development of a formal Bridge Management System (BMS) to enable collection of data through regular monitoring and inspection programs would facilitate prioritization of Maintenance, Repair and Rehabilitation (MR&R) strategies.

**Keywords.** Highway bridges, concrete, environmental exposure, structural integrity, rebound hammer

## Introduction

Deterioration of concrete structures is a worldwide problem. The actual environmental exposure depends on the local conditions of concrete structures [1]. Environmental exposure is known to affect concrete strength in structures. Moisture affects rebound values by lowering them while carbonation does the opposite.

Bridge structures are critical components of infrastructure which take a significant part of the budget. Concrete is the world's most widely used construction material in structures. The physical and chemical characteristics of concrete make it ideal as a

---

<sup>1</sup>Corresponding author: [hbakamwesiga@yahoo.com](mailto:hbakamwesiga@yahoo.com)

construction material. Due to its versatility, strength and durability, concrete is used in most of construction including buildings, roads, bridges, airports, subways, and water resource structures [2]. It is also envisaged that the use of concrete is expected to double in the next thirty years [3]. However, reinforcement concrete structures such as road bridges undergo loss in structural integrity overtime as a result of physical and chemical processes [4].

Following several years of neglect due to tumultuous times between 1970s and 1980s, there is renewed enthusiasm in Uganda to reclaim the ageing and dilapidated infrastructure, in addition to constructing new developments [5]. With a vision to be a middle income country by 2040, sustainable infrastructure growth and environmental reforms are now prioritized with emphasis on capacity development for vulnerability assessment and development of early warning systems to increase resilience to environmental vulnerability [6].

With such national plans in the offing, coupled with the rapid economic growth (5.96%), burgeoning population growth and the changing climate, it is a shared responsibility by all stakeholders to ensure that the critical structures such as bridges are maintained in a good condition throughout their life cycle. Moreover, to fulfill future traffic demands, bridge management agencies such as Uganda National Roads Authority (UNRA) and the Ministry of Transport and Work (MoWT) have to increase durability of bridge stock, their life spans as well as lower the costs of maintenance. This may be done through regular and planned inspections and monitoring of bridges using non-destructive testing (NDT) methods.

This study was motivated by several factors, first, the lack of a formal bridge management system; second, the bridges under study are linkages in crucially important roads which facilitate trade with neighbouring countries, and thirdly, the fact that in the last decade there has been several incidences of bridge failures and collapses in Uganda.

NDT methods provide ideal means to evaluate various structural elements without affecting their functionality and serviceability [4]. The term “nondestructive” is therefore given to any test that does not damage or affect the structural behavior of the elements and also leaves the structure in acceptable condition for bridge managers [7]. The main advantage of NDT methods is that they do not damage or affect the structural performance of building components. In addition, they offer simplicity and rapidity in use: test results are readily obtained on site after the test, it provides the possibility of testing concrete strength in structures where cores cannot be drilled, and the equipment used is less expensive [8]. Indeed a rebound hammer is known to be portable, easy to use and reliable. Acknowledging the aforementioned advantages, this research used rebound hammer test, a NDT method.

The present investigation therefore sought to evaluate the surface concrete strength after being subjected to field environmental conditions for many years. The aim of the study was to evaluate the in-situ concrete strength of three bridge elements, namely the pier, abutment and deck which have been maintained under similar structural and environmental conditions such as moisture and abrasive forces on the near surface. The results can be of interest to bridge managers and can be used to incorporate compressive strength in planning, monitoring and inspection of road bridges. They can also be used as a basis for developing a formal computerized Bridge Management System (BMS). The BMS further provides strategic information to facilitate prioritization of Maintenance, Repair and Rehabilitation (MR&R) of critical bridge elements on highways.

### 1. Study area and scope

A total of 13 sites located along 3 highways were studied (Figure 1). The three highways are Kampala-Karuma-Gulu (GUL) road to the northern region; Kampala-Masaka-Mbarara-Kabale (MBA) road to south-western Uganda and Kampala-Mubende-Fort Portal-Kasese (KAS) road to the Western region. The study sites and highways are among the 22 road bridges located on five highways which are under an ongoing PhD study programme of the author. Table 1 shows a list of study sites, age, type, and location. A big proportion of bridges (77%) were constructed in the 1950s and 1960s. The bridge age range is 52 years. The scope of this study was limited to concrete and steel-concrete composite bridges which comprise the majority of road bridges in Uganda.

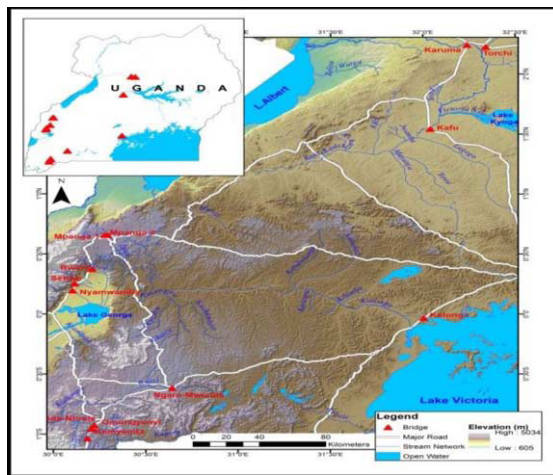


Figure 1. Map of Western Uganda showing study sites.

Table 1. Bridge characteristics, age, location and elevation

Bridge name	Bridge Code	HWY Code	Age	Bridge type	Latitude	Longitude	Height (above Sea level)
Kafu	KAF	GUL	48	Composite	32.0418	1.5422	1038.04
Karuma	KAR	GUL	48	Composite	32.2398	2.2425	1001.64
Torchi	TOR	GUL	48	Composite	32.3420	2.2271	1034.20
Mpanga 1	MP1	KAS	59	Concrete	30.2953	0.2953	1422.51
Mpanga 2	MP2	KAS	58	Composite	30.2782	0.6569	1489.56
Rwimi	RWI	KAS	7	Concrete	30.2113	0.3733	1388.78
Sebwe	SEB	KAS	7	Composite	30.1168	0.2520	1087.18
Nyamwamba	NYA	KAS	24	Composite	30.1050	0.1944	967.29
Katonga	KAT	MBA	46	Concrete	32.0075	-0.0342	1140.56
Ngaro-Mwenda	NGM	MBA	45	Composite	30.6440	-0.6182	1388.78
Katinda-Ntinde	KAN	MBA	46	Composite	30.2231	-0.9271	1375.91
Omungyenyi	OMU	MBA	46	Composite	30.2070	-0.9584	1359.50
Kemyenda	KEM	MBA	46	Composite	30.1848	-0.0378	1406.06



## 2. Methodology

In this section, the rebound hammer test for determining the strength of concrete components of road bridges has been described. The procedures used are mentioned and the techniques of conducting in-situ tests are also discussed.

### 2.1 Field tests

As described in [7] the rebound test gives a relationship between hardness and strength of concrete. The relationship is dependent upon factors affecting the concrete surface such as carbonation, the degree of saturation, surface preparation and location, and type of surface finish [9]. For better results, concrete surface areas that exhibit scaling, rough texture or high porosity were avoided. The hardness tests were aimed at establishing the impact of moisture on the quality of the concrete surface. All rebound hammer tests results presented in Table 4 were done on piers, abutments and decks of highway bridges within the test region.

### 2.2 Strength evaluation using Schmidt Hammer

Initial conditions on superficial bridge damages obtained using visual inspection are documented [10]. The superficial damages, recorded and supplemented with photographs, formed a basis for identification of the test region for every bridge element, namely, deck, abutment and pier.

Rebound (Schmidt) hammer tests using a Proceq<sup>®</sup> N-34 Schmidt hammer were conducted at various test locations of the bridge elements to determine surface structural integrity of concrete. The assumption made was that rebound number as read from the Schmidt rebound hammer, is proportional to the compressive strength and hence the relative condition of the surface of the concrete cover [11]. The purpose of the test was to determine the in-situ concrete strength of the various bridge elements and evaluate the impact of environmental conditions such as moisture and abrasive forces on the near surface structural integrity of concrete. To minimize local variations (which are a source of error that can dramatically affect the measured rebound number values due to hard and soft individual aggregate particles, air voids and surface imperfections [12]), an abrasive stone was used to clean the surface first. Also, maximum care was taken to strike perpendicularly to the surface of the concrete in order to avoid inclination of the hammer which would, in turn, affect the results [9].

The choice of tests locations was based on BS 1881: Part 202 [7]. Wherever possible, a minimum of 3 test points were chosen for every bridge element. A maximum of 10-12 readings were conducted at each test point [9] on a single test location. Care was taken to avoid striking on same point to reduce the influence of local aggregates [13] distribution, and the rebound number was obtained by averaging the results. However, the inability to access some groups of structural elements deterred the latter. There is a tendency to place too much reliance on the calibration curve supplied with the equipment since the manufacturer develops this curve using standard cube specimens. But this could be a source of error as the mixes used by the manufacturer could be different from the mixes being tested [8]. It is also known that rebound hammer index is only indicative of compressive strength of concrete up to a limited depth from the surface and moreover the rebound numbers does not indicate heterogeneity across the cross section.



**Figure 2.** Schmidt Hammer test is done horizontally on a pier column, just above the flood level

To overcome the above limitations, the correction factors were used to transform strength intervals obtained from Schmidt Hammer test for concrete older than 90 days. The factors are shown in Table 2. The strength values obtained from the correlation chart of the rebound hammer were multiplied by the old concrete factor numbers [14] to provide estimated concrete strength values.

**Table 2.** Strength transform factors for Schmidt Hammer test used in old concrete [14]

Strength Interval (Mpa)	Factor number
<10	0.51
10 - 15	0.62
15 - 20	0.67
20 - 25	0.72
25 - 30	0.75
30 - 35	0.78
35 - 40	0.80
40 - 45	0.81
45 - 50	0.82

Source: Adopted from [14]

### 3. Results and discussion

#### 3.1 Introduction

The factors affecting the relationship between hardness and strength of the concrete surface include degree of saturation, carbonation, temperature, surface preparation, and the type of surface finish [14].

#### 3.2 Strength distribution in bridge elements

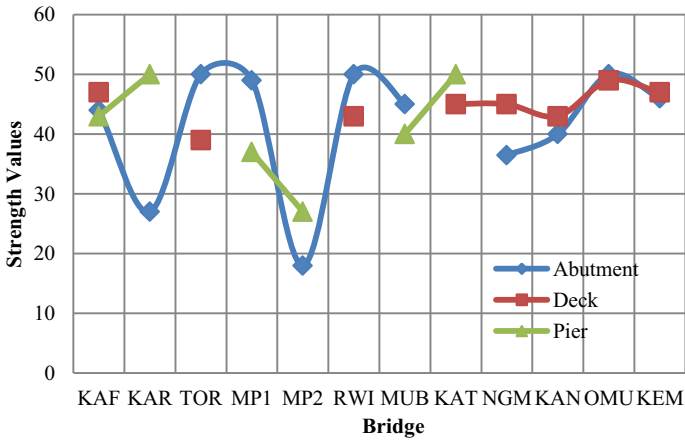
Results show that average concrete strength is lower in the piers and abutments than in the decks (Table 3). Except deck, there is high variation in concrete strength for abutments and piers as illustrated in Figure 3. Two probable reasons, age and location of bridges, may explain the lower concrete strength values in abutments and piers. Mpanga-1 and Mpanga-2 bridges which presented the lowest strength values as illustrated in Figure 3 are the oldest among the sample bridges. The bridge location at foot of Rwenzori highlands in Western Uganda (Figure 1) means that that abutments

and piers are constantly subjected to abrasive forces of high speed water in rivers originating from the mountains ranges.

**Table 3.** Average strength values of different bridge elements

	K A F	T O R	K A R	M P 1	M P 2	R W I	M U B	K A T	N G M	K A N	O M U	K E M	M e a n	St. D e v
Abut*	44	50	27	49	18	50	45		36.5	40	50	46	40.1	10.2
Deck	47	39				43		45	45	43	49	47	44.8	3.1
Pier	43		50	37	27		40	50					41.2	8.7

\*abutment



**Figure 3.** Strength (rebound values) distribution for bridge elements

### 3.3 Comparison of bridge age and the strength of its elements

Very little negative correlation was found between bridge age and the strength of its elements. A 40.5% negative correlation degree was obtained between the abutments' strength values and age as shown in Figure 4a. A higher value of -18.9% (Figure 4b) was obtained for pier values while deck values showed no bearing to bridge age. Generally all deck rebound values were high irrespective of the bridge age. However, in this case, it is clear that there is no change in compressive strength as a result of age. These observations are contrary to the ideal - concrete should progress in compressive strength with time [15]. Although this observation could have changed by using combined methodology, the observations may probably be an indicator that long term exposure of concrete to environmental conditions of moisture and abrasion leads to creation of superficial delaminations [10] which cause low rebound values. Other environmental factors such as acidic rain and wetting and drying cycles have been previously reported [15] to cause reduction in compressive strength of surface concrete.

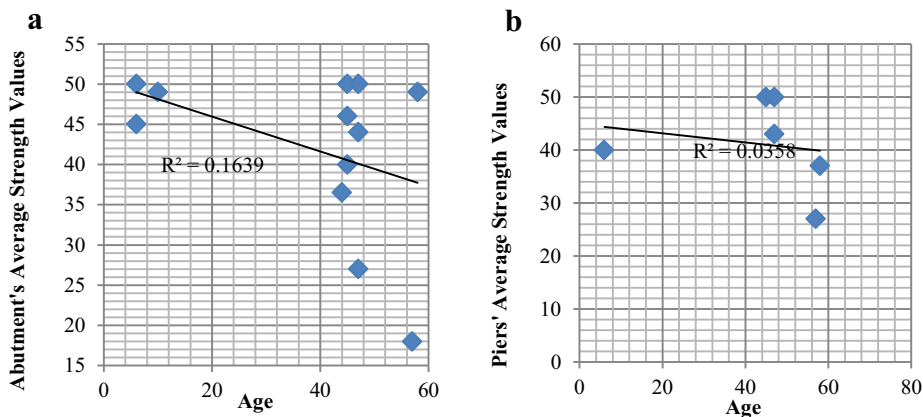


Figure 4. Correlation of bridge age and average rebound hammer value: a) abutments; b) piers

High strength values for the bridge elements of old bridges can be attributed to carbonation. Carbonation reduces the porosity of concrete because  $\text{CaCO}_3$  which is the product of carbonation, occupies a greater volume than  $\text{Ca(OH)}_2$ . As a result, the progressive reduction of porosity with age leads to increase in strength and hardness of concrete [13]. Obviously, new bridges such as Rwimi and Mubuku presented high strength values. This is expected of new bridges because there is less likelihood of existence of delaminations on recently constructed structures. As noted earlier, due to their exposure to the best combination of moisture, temperature and relative humidity, decks experience less variability in concrete strength (Figure 3) compared to substructure elements. ON the other hand, the high variability in concrete strength substructure elements could be due to changes in seasonal flood levels. The surface concrete deterioration may be a consequence of the intermittent exposure to water content and temperature during the wet and dry seasons [16].

### 3.4 Correlation of strength between bridge elements

Figure 5a shows correlation of strength between bridge deck and sub-structural elements, abutment and pier. R-squared value of 0.0003 is an indicator that for every single bridge, there is no relation in variation of deck vs abutment or pier values. A zero correlation ( $R = 0.284$ ) was also found in the relationship between rebound values taken in different directions (Figure 5b). A probable reason for an insignificant correlation in strength values between bridge elements can be explained by the similarity in environmental conditions such as relief and climatic conditions, as well as structural design. Furthermore, in this study two assumptions were made. First, both old and new bridges were constructed of the same grade. Second, the properties of concrete in the test region are distributed in the same way [17].

### 3.5 Impact of vegetation

Prominent among the study sites is the seemingly dilapidated bridge elements due to vegetation overgrowth in river channels under the road bridges, lichens and algae on concrete surfaces (Figure 6). These create dampness by consistently hindering the free flow of water. The resulting poor drainage promotes chemical activities between reactive agents and cement oxides as a result of consistent dampness [15].

Nevertheless, vegetation may not be as serious as cracks. Cracks in a bridge element may arise as a result of structural movements, fatigue, overload and poor construction materials and workmanship [10, 15]. Worse still a combination of dampness and cracks may facilitate is seepage of acidic rain water through cracks. The resulting corrosion of reinforcement embedded in the concrete may seriously affect the strength of bridge structures [15]. Other causes of reinforcement corrosion have been previously reported [10].

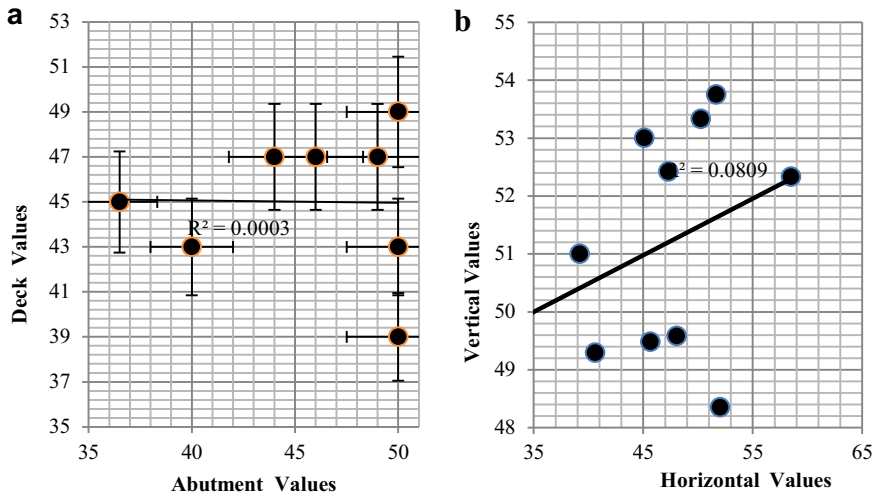


Figure 5. Correlation of compressive strength between bridge elements: a) deck and abutment; b) horizontal and vertical strength rebound hammer values



Figure 6. Growth of vegetation, lichens and algae

#### **4. Conclusions and recommendations**

The Schmidt rebound hammer test method has widely been used to determine concrete strength. The similarity of the bridges coupled with the difficulty of acquiring the appropriate correlation data and the need to rapidly survey of a large area [12] endeared the use of rebound hammer. The following conclusions have been drawn:

1. The rebound hammer results and absence of rust stains in all study sites is an indication that the highway bridges had good quality of concrete. Indeed, if in the order of 50 years the concrete is still good, the bridges could have been built to high standard specifications.
2. Although, the Schmidt hammer test readings for existing concrete can be greatly influenced by several factors including the moisture condition, surface carbonation and researcher's ability to properly read and record the values, results show that the environmental conditions were similar for all study sites.
3. Whereas monitoring can provide information on a particular bridge element for entire service life, inspection provides information of the entire bridge structure at a specific time. Combining various methods will lead to obtaining maximum information about the performance of the bridge.
4. It is of paramount importance to provide strategic information to facilitate prioritization of MR&R of bridge stock to avoid costly interventions of repairs and maintenance, and/or reduced lifespan of bridges. This situation strains the already limited resources.

All in all, this study was limited to a small number of highway bridges in Western Uganda. It can be extended to the whole country for a more extensive and exhaustive investigation of impact of environmental conditions on MR&R. The study would reveal vulnerable areas, damage types and behaviours for highway bridges in aggressive environments [18]. Furthermore, the methodology and results of this study provide a basis for modelling and development of BMS for Uganda. The database of information on bridges will enable well-informed decisions on strategic maintenance of highway bridges. This will not only minimize future maintenance costs of bridge stock but greatly improve their durability.

#### **5. Limitations and suggested further research**

A couple of limitations resulted in less sampling and limited information. These are access restrictions due to permanently flooded deep rivers and the avoidance of destructive methods, especially, coring. In addition to visual inspection and rebound hammer tests, further research should include both hammer tapping and cores taken from bridge elements. The combined methodology will obtain quantitative and qualitative assessment of the surface hardness [16] which should be able to provide a direct correlation with the condition of concrete in road bridges.

#### **Acknowledgements**

The authors wish to acknowledge the financial support by the Swedish International Development Cooperation Agency (Sida) and Makerere University. Also, the support

from the staff of Makerere and Lund Universities, particularly, the Departments of Civil and Environmental Engineering and Division of Structural Engineering, respectively, is gratefully acknowledged.

## References

- [1] Wang, X., Nguyen, M., Stewart, M. G., Syme, M., and Leitch, A., Analysis of climate change impacts on the deterioration of concrete infrastructure – Synthesis Report. Published by CSIRO, Canberra, 2010, ISBN978 0 643 103641.
- [2] Ashley, E. and Lemay, L., Concrete's Contribution to Sustainable Development. *The Journal of Green Building*, **3** (4) (2008), 37-49.
- [3] Lounis, Z. and Daigle, L., Environmental benefits of life cycle design of concrete bridges. National Research Council Canada. 3<sup>rd</sup> *International Conference on Life Cycle Management*, Zurich, Switzerland, Aug. 27-29 (2007), 1-6.
- [4] Goel, A., Gupta, A., Verma, R., and Das A. M., Structural Health Evaluation of concrete road bridges – an NDT Approach. Available on <http://creativecommons.org/licenses/by-nd/3.0>.
- [5] Mwakali, J. A., Kiggundu, B. M., Gadenya, W. and Haavaldsen, T., Failures of reinforced concrete structures in Uganda. In T. W. Leong (ed.) Proceedings, Third International Conference on Inspection, Appraisal, Repairs & Maintenance of Buildings & Structures, Bangkok, Thailand, 1994, pp. 175-182.
- [6] State of the Environment Report for Uganda 2010, National Environment Management Authority (NEMA), Kampala, 2010.
- [7] Qasrawi, H. Y., Concrete strength by combined nondestructive methods simply and reliably predicted. *Cement and Concrete Research*, **30**(5) (2000), 739-756.
- [8] Hobbs, B. and Kebir, M. T., Non-destructive testing techniques for the forensic engineering investigation of reinforced concrete buildings. *Forensic Science International*, **167** (2007) 167–172.
- [9] BS 1881: Part 202, Recommendations for Surface Hardness Tests by the Rebound Hammer, BSI, U.K., 1986.
- [10] Bakamwesiga, H., Mwakali, J. and Thelandersson, S., 2014, Nondestructive condition assessment of highway bridges for safety enhancement. Proceedings of 7<sup>th</sup> *International Conference on Bridge Maintenance, Safety and Management (IABMAS)*. Taylor & Francis Group. <http://www.crcnetbase.com/doi/abs/10.1201/b17063-270>.
- [11] Rens, K. L. and Kim, T., Inspection of Quebec Street Bridge in Denver, Colorado: Destructive and Nondestructive Testing, (June) (2007), 215–224.
- [12] Long, A. E., Henderson, G. D., & Montgomery, F. R., Why assess the properties of near-surface concrete? *Construction and Building Materials*, **15** (2-3) (2001), 65–79.
- [13] Kim, J., Kim, C., Yi, S. and Lee, Y., Effect of carbonation on the rebound number and compressive strength of concrete. *Cement and Concrete Composites*, **31** (2009), 139-144.
- [14] Aydin, F. and Saribiyik, M., Correlation between Schmidt Hammer and destructive compressions testing for concretes in existing buildings. *Scientific research and essays*, Turkey, **5**(13) (2010), 1644-1648.
- [15] Mmusi, M. O., Alexander, M. G. and Beushausen, H. D., Determination of critical moisture content for carbonation of concrete, Department of Civil Engineering, University of Cape Town, South Africa, Concrete Repair, Rehabilitation and Retrofitting II – Alexander et al (eds), Taylor & Francis Group, London, 2009, ISBN 978-0-415-46850-3359.
- [16] Tay, D. C. K. and Tam, C. T., *In situ* investigation of the strength of deteriorated concrete, *Construction and Building Materials*, **10** (1996), 17-26.
- [17] Thelandersson, S., Assessment of material property data for structural analysis of nuclear containments. Report TVBK-3051, ISSN 0349-4969.
- [18] Enright, P. M. and Frangopol, M. D., Survey and evaluation of damaged concrete bridges, *Journal of Bridge Engineering*, **5** (2000), 31-38.

# Strength and behaviour of steel fibre reinforced self-compacting rubberised concrete beams under flexure

Bharati RAJ<sup>a,1</sup>, N. GANESAN<sup>b</sup> and A.P. SHASHIKALA<sup>b</sup>

<sup>a</sup>Structural Engineer, Noida, Uttar Pradesh

<sup>b</sup>Department of Civil Engineering, National Institute of Technology Calicut, Kerala

**Abstract.** Past studies indicate that addition of shredded rubber to concrete improves its ductility significantly. Also, the incorporation of steel fibres enhances the ductile and engineering properties remarkably. Considering these aspects, a sustainable composite having improved ductility has been developed by adding shredded scrap rubber to Self Compacting Concrete (SCC) as a partial replacement of fine aggregate. The flexural behaviour of Self Compacting Rubberised Concrete (SCRC) beams under monotonic loads has been studied. Besides this, the effect of adding steel fibres to SCRC to obtain Steel Fibre Reinforced Self Compacting Rubberised Concrete (SFRSCRC) has also been studied. The experimental investigation consists of casting and testing of 18 beams of 100 x 150 x 1200 mm size under flexure. Three specimens were tested for each mix and the average results were taken for analysis. The results were analysed based on first crack load and ultimate load, load deflection behaviour and energy absorption capacity. The analysis results indicate that the SCRC and SFRSCRC specimens showed better load carrying capacity, crack resistance and ductility than the SCC specimens under monotonic and cyclic loads.

**Keywords.** Beams, crack pattern, flexure, self compacting concrete, shredded rubber, steel fibres

## Introduction

An emerging field for the reuse of scrap tyres is in the production of concrete, where tyre rubber can be used as a partial replacement to natural aggregates. Since the production of shredded tyre rubber is well advanced, the reuse of scrap rubber in concrete leads to both environmental and economic advantages. Past investigations on rubberised concrete [1,2] indicate that the partial replacement of coarse or fine aggregate of concrete with waste tyre can improve properties such as resistance to abrasion, absorption of shocks and vibrations and ductility and hence, make a move towards achieving sustainable concrete.

The development of Self Compacting Concrete (SCC) with the unique property of flowing under its own weight by Okamura [3] was with the prime aim of solving the problem of honeycombing and giving better finishes to structures, especially where congestion of reinforcement occurs [4]. The possibility of developing SCC incorporating shredded scrap rubber aggregates was a novel approach to combine the advantages of both SCC and rubberised concrete. Even though this seemed to be a promising technology in controlling the microstructure of concrete to obtain more versatile and innovative mechanical behaviour, very few studies have been carried out so far on Self Compacting Rubberised Concrete (SCRC) [5,6]. Past studies have revealed that the use of steel fibres in SCC improves the engineering properties such as ductility, post crack resistance, energy absorption capacity etc [7].

<sup>1</sup>Corresponding author: [bharatiraj83@gmail.com](mailto:bharatiraj83@gmail.com)



The concepts of sustainability and sustainable development are receiving greater attention nowadays as the causes of global warming and climatic change are discussed in various forums. Since, concrete is the most widely used construction material, sustainable technologies for concrete construction allow for reduced cost, conservation of resources, utilization of waste materials and development of eco-friendly durable concrete. Considering these aspects, a sustainable composite having improved ductility has been developed by adding shredded scrap rubber to SCC as a partial replacement of fine aggregate. One of the barriers of the application of SCRC in construction is the lack of adequate information regarding the behaviour of structural elements with this material. The application of SCRC to structural members has not been studied so far. Hence, an attempt has been made to investigate strength and behaviour of SCRC and Steel Fibre Reinforced SCRC (SFRSCRC) flexural members subjected to monotonic and cyclic loading.

## 1. Experimental programme

### 1.1. Materials and mix proportions

The materials used in this study include Ordinary Portland cement conforming to IS: 12269-1987 [8], flyash with a normal consistency of 45% obtained from Neyveli Lignite Power Plant conforming to Type F as per ASTM C618 [9], river sand passing through 4.75mm IS sieve conforming to grading zone II of IS: 383-1970 [10] having specific gravity of 2.54 and coarse aggregate with a maximum size of 12mm and specific gravity of 2.77.

The mix design adopted is based on the method proposed by Nan et.al [11] which gives an indication of the target strength after 28 days of curing. The water powder ratio (w/p) was adjusted so as to obtain the SCC mix of grade 50MPa and then was checked for the self compactability as per the EFNARC [12] acceptance criteria for SCC. Naphthalene based super plasticizer Structuro 201 and viscosity modifying admixture (VMA) Calcium Sulphate dihydrate were added to impart better workability and viscosity to the mix in order to avoid segregation.

Fine rubber was obtained by shredding the worn out scrap tyres accumulated in the rubber waste industry and sieved to get rubber particles with a maximum size of 4.75mm. The specific gravity of fine rubber thus obtained was 1.14. In Self Compacting Rubberised Concrete (SCRC), the fine aggregate was partially replaced by fine rubber and the percentage volume of replacement ( $R_r$ ) was 15%. Steel Fibre Reinforced Self Compacting Rubberised Concrete (SFRSCRC) was obtained by adding 30mm long crimped steel fibres having 0.45mm diameter (aspect ratio 66) at volume fractions ( $V_f$ ) of 0.50% to the SCRC mixes.

As the partial replacement of fine aggregate with fine rubber increased, the mix was found to be less workable and hence, the amount of super plasticizer was increased, so that the mixes satisfy the acceptance criteria of SCC. The viscosity modifying admixture was also added at the rate of 0.01% of the water content for imparting better workability and viscosity to the mixes in order to avoid segregation. In order to offset the loss of strength due to the addition of scrap rubber, Poly Vinyl Alcohol (PVA) of 2.35% of water content was added.

The details of the constituents of the mix are given in Table 1. The self compactability of the mixes was verified by Flow test, V-funnel test and L-Box test. The fresh properties of the mixes are given in Table 2. Along with test specimen, 100 mm cubes were also cast and cured under the same conditions. The compressive strength of the mixes is also given in Table 2.

**Table 1.** Mix proportions for SCC, SCRC and SFRSCRC

Material	SCC	SCRC	SFRSCRC
Cement (kg/m <sup>3</sup> )	430.00	430.00	430.00
Fly ash (kg/m <sup>3</sup> )	170.00	170.00	170.00
Coarse Aggregate (kg/m <sup>3</sup> )	720.00	720.00	720.00
Fine Aggregate (kg/m <sup>3</sup> )	720.00	612.00	612.00
Shredded Rubber (kg/m <sup>3</sup> )	-	41.20	41.20
Steel Fibres (kg/m <sup>3</sup> )	-	-	45.04
Super Plasticiser (% of powder content)	5.83	7.80	7.80
Water (kg/m <sup>3</sup> )	247.00	256.00	256.00
PVA (kg/m <sup>3</sup> )	-	5.80	5.80
Water Powder Ratio (w/p)	0.412	0.427	0.427
VMA (kg/m <sup>3</sup> )	-	0.81	0.81

**Table 2.** Fresh and hardened properties of the mixes

Mix Designation	Slump flow (mm)	V-funnel time (s)	L-box Value	Compressive Strength (MPa)
SCC	750	8	0.92	58.89
SCRC	750	9	0.89	51.04
SFRSCRC	750	12	0.88	54.22

### 1.2. Details of specimens

The experimental work consisted of casting and testing 18 beams of size 100 x 150 x 1200mm. Out of these 18 beams, 9 beams were tested under monotonic loading and the remaining were tested under cyclic loading. In each series, three beams were cast using SCC, three beams using SCRC and the remaining three using SFRSCRC. Beams were reinforced with two 10 mm diameter high yield strength deformed bars at bottom and two 6 mm diameter bars at top. Two legged stirrups of 6 mm diameter @ 85mm c/c have been used as shear reinforcement. The shear reinforcement is designed to ensure flexural failure. Properties of reinforcing bars used are given in Table 3. The overall dimensions and reinforcement details are given in Fig 1. Three specimens were tested in each series and average results were taken for analysis.

**Table 3.** Mechanical properties of steel reinforcement bars

Nominal diameter of bar (mm)	Actual diameter of bar (mm)	Yield Strength (N/mm <sup>2</sup> )	Ultimate Strength (N/mm <sup>2</sup> )	Modulus of Elasticity (N/mm <sup>2</sup> )
10	9.97	426	570	2.32 x 10 <sup>5</sup>
6	6.09	433	678	2.44 x 10 <sup>5</sup>

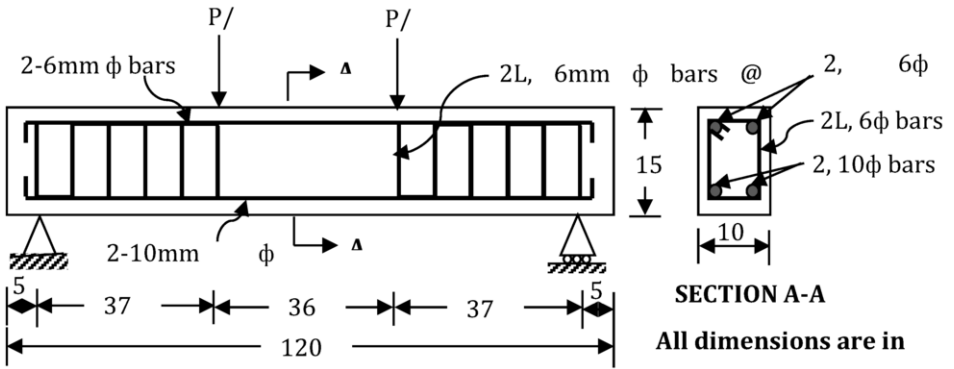


Figure 1. Details of specimen

1.3. Testing

A two point flexural bending system was adopted for the test in such a way that the shear span to effective depth ratio was greater than 2.5. The specimens were tested in a Universal Testing Machine (UTM) of 2943kN (300t) capacity with an effective span of 1100mm. Fig 2 shows the schematic diagram of test set up and Fig 3 shows the photograph of test setup.

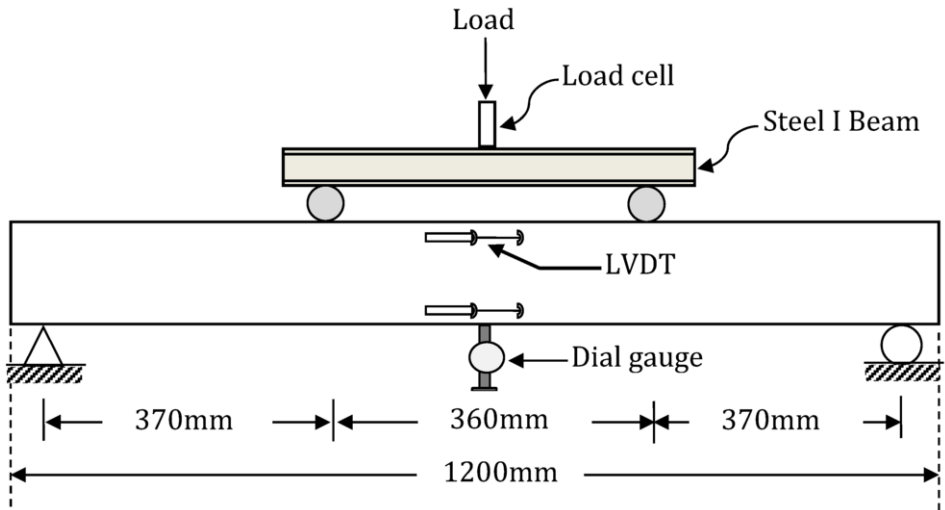


Figure 2. Schematic diagram of test setup



**Figure 3.** Test setup for monotonic and cyclic loading test on beams

### *1.3.1. Monotonic loading*

The load applied on the specimen was increased in stages at a uniform rate till the failure of the specimen, and at each stage of loading, following measurements were made.

- i. Deflection at mid-span using a dial gauge having least count of 0.01mm and 25 mm travel.
- ii. Deformations at mid-span using LVDTs having least count of 1 micron across the depth of the beam at 20mm below the top and 20mm above the bottom. The deformations obtained from LVDT readings were used to calculate strains.
- iii. Crack widths at ultimate load using a microscope of 25X magnification (Crackscope).

### *1.3.2. Cyclic loading*

In the case of cyclic loading, specimens were loaded up to 9.81kN (1t) then unloaded and subsequently reloaded to the next increment of 9.81kN. This procedure was carried out till the failure of the specimen and at each stage of loading, measurements was taken as mentioned in the case of monotonic loading.

## **2. Behaviour of specimens**

All the beams were tested under two point loading (four point bending) both in monotonic and cyclic loading. In all the specimens as the loading was increased, cracks appeared in the flexural span and further increase in load, resulted in additional cracks and widening of some of the earlier cracks. In the case of SCRC specimens, a large number of finer cracks developed in the flexure span and it started widening when the load increased. At higher loads, some of the cracks propagated up the beam, deflections were large and tension steel started yielding at this stage. At ultimate stage, all the cracks traversed towards the top and some of the cracks got widened. A slight improvement in the load carrying capacity under cyclic loading was observed. This may be due to the rubber particles absorbing the energy during loading and suitably releasing it during unloading. The first crack load, ultimate load and deflection at ultimate load increased considerably with the addition of steel fibres to SCRC.

Figs. 4 to 6 show the crack pattern in SCC, SCRC and SFRSCRC beams. From the figures it can be observed that in the case of SCC and SCRC specimens, cracks are uniformly distributed and are almost parallel to each other. But in the case of SFRSCRC specimens, large number of finer cracks occurred without any uniform pattern. This may be due to the steel fibre bridging effect. After the formation of cracks, steel fibres intercept them and widening of cracks gets reduced. As and when micro cracks develop in the matrix, the steel fibres in the vicinity of such micro cracks try to arrest these cracks and prevent further propagation. Hence, the cracks appearing inside the matrix have to take a meandering path, resulting in the demand for more energy for future propagation, which in turn increases the ultimate load. Behaviour of specimens under cyclic loading was similar to those specimens under monotonic loading. However under cyclic loading, deviation of cracks occurred quite often and cracks were distributed over a wider area.

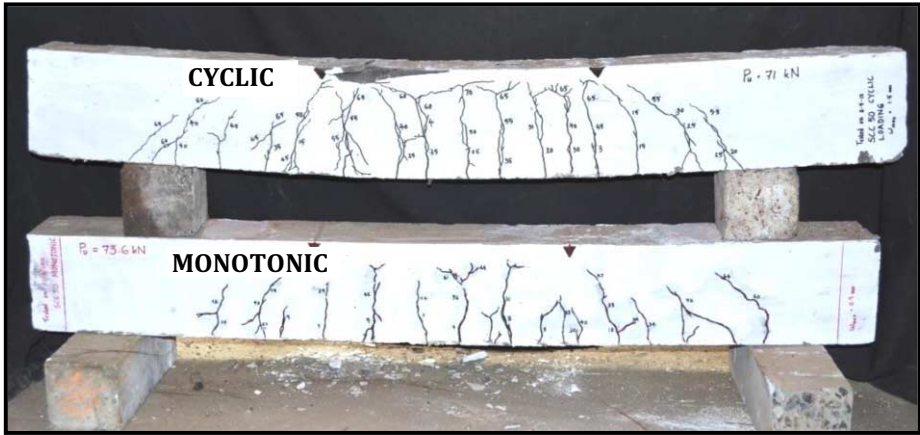


Figure 4 . Crack pattern in SCC beams under monotonic and cyclic loading

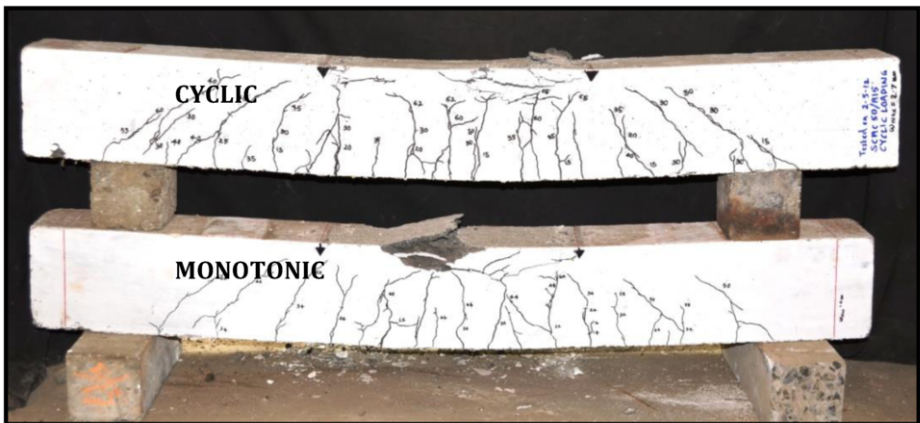


Figure 5. Crack pattern in SCRC beams under monotonic and cyclic loading



Figure 6. Crack pattern in SFRSCRC beams under monotonic and cyclic loading

### 3. Analysis of test results

#### 3.1. Load deflection behaviour

Load deflection plots for all the tested specimens were drawn. The comparison of load deflection curves is shown in Fig 7. From the figure it can be observed that all the curves are linear up to first crack load. Further application of load, caused multiple cracks and the curve deviated from linearity into a nonlinear region. Beyond the multiple cracking stage, the  $P-\delta$  curve became more or less flat till the ultimate load was reached. In the case of SCC specimens, a sudden drop in the load was noticed beyond the peak load while for SCRC, the reduction was observed to be more gradual. SFRSCRC specimens exhibited more or less a flat descending portion of the curve beyond peak load. This indicates the improvement in the dimensional stability and structural integrity of the specimen even beyond peak load when steel fibres are added. The addition of steel fibres led to an increase in the peak load and resulted in a more ductile softening behaviour.

The  $P-\delta$  plots for SCC, SCRC and SFRSCRC specimens under cyclic loading are given in Figs 8 to 10. The envelope curves of load deflection plots obtained by joining the peak points of each cycle are shown in Fig 11. From the figure, it can be seen that the load deflection curve is linear up to first crack load. Further application of load, caused multiple cracks and the curve deviated from linearity and entered into a nonlinear region. Beyond the multiple cracking stages, the  $P-\delta$  curve became more or less flat till the ultimate load is reached with slight increase in load.

From Fig 11, it may be noted that peak load, deflection at peak load, area under the  $P-\delta$  curve are found to be higher for SCRC and SFRSCRC beams than that of SCC specimens and this behaviour is similar to the results obtained for specimens subjected to monotonic loading. This enhancement in peak load, deflection at peak load and area under the  $P-\delta$  curve of SCRC and SFRSCRC beam specimens could be attributed to the elastic nature that rubber exhibits when subjected to stress reversals. Since rubber aggregates have the ability to undergo large elastic deformation before failure, they tend to show more strain at the time of fracture.

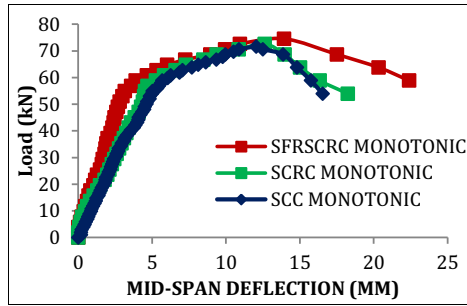


Figure 7. Comparison of load-deflection curves under monotonic loads

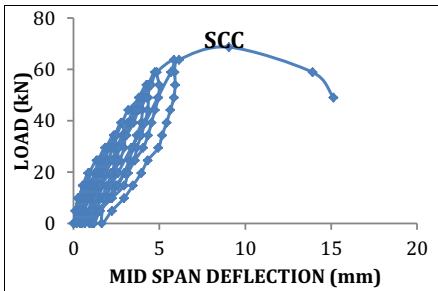


Figure 8. Load deflection plot for SCC under cyclic load

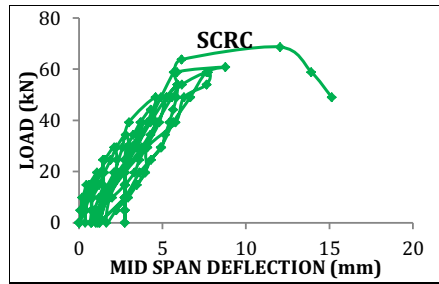


Figure 9. Load deflection plot for SCRC under cyclic load

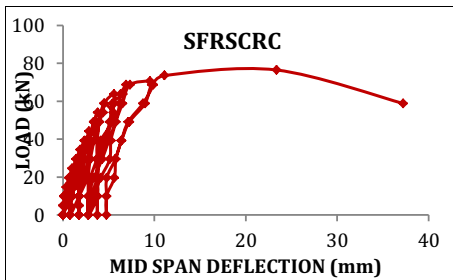


Figure 10. Load deflection for SFRSCRC under cyclic load

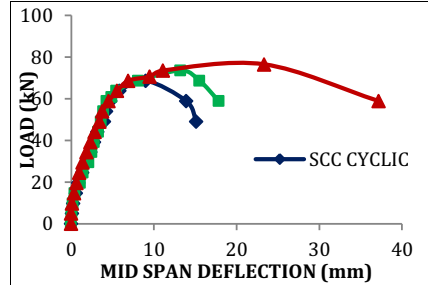


Figure 11. Comparison of envelope plots

### 3.2. First crack load and ultimate load

Average values of test results of three specimens for each mix are given in Table 4. First crack load was determined from the load deflection plot corresponding to that point on the curve at which the curve deviated from linearity. From the table it can be observed that first crack load under monotonic loading increased with addition of rubber and steel fibres, which may be due to the increase in tensile strain carrying capacity of concrete in the neighbourhood of rubber and steel fibres. Ultimate load also gradually increased with addition of rubber and steel fibres. When steel fibres are added to concrete, crack propagation gets arrested which results in requirement of more energy. This leads to improvement in load carrying capacity. The results indicate an increase of up to 9% in first crack load and 1% in ultimate load for SCRC specimens under monotonic loading. With the addition of 0.5% steel fibres, the increase in first crack load and ultimate load was 10% and 6% respectively.

**Table 4.** Comparison of test results

Loading Designation	MONOTONIC			CYCLIC		
	First crack load (kN)	Ultimate load (kN)	Deflection at ultimate load (mm)	First crack load (kN)	Ultimate load (kN)	Deflection at ultimate load (mm)
SCC	11.7	71.60	12.05	9.8	69.70	12.47
SCRC	12.7	72.59	12.62	10.8	73.58	13.23
SFRSCRC	17.6	74.56	13.93	14.7	76.52	14.35

SFRSCRC beams under cyclic loading showed an increase of 50% in the first crack load over SCC beams while the increase was around 10% in the case of SCRC beams. This may be due to the increase in the tensile strain carrying capacity of concrete in the neighbourhood of rubber and steel fibres. Comparing with SCC beams, the ultimate load was found to increase by 6% and 10% for SCRC and SFRSCRC beams respectively. This may be attributed to the following reason. When steel fibres are added to concrete, they intercept the cracks and causes deviation of cracks from its initial propagation. This results in the demand of more energy, which in turn improves the load carrying capacity. When specimens are subjected to cyclic loading, cracks form as and when the tensile stress in concrete exceeds modulus of rupture and the partial crack closure occurs during unloading. When the reloading takes place new cracks need not develop from the tip of the earlier cracks because the tip becomes blunt during unloading. Such deviation of cracks demands higher energy for further propagation resulting in higher ultimate load.

### 3.3. Energy absorption capacity

The area under the load deflection curve indicates the energy absorption capacity. Due to inherent limitations of the testing machine, full load deflection curve could not be obtained. Therefore load deflection behaviour up to 80 % of peak load in the descending branch was noted. Energy absorption capacity was calculated as the area under the load deflection curve up to peak load and up to 80% peak load in the descending branch. Results obtained for monotonic and cyclic loading are given in Table 5. From the Table, it can be seen that energy absorption capacity under monotonic loading consistently increases and the increase is about 23% for SCRC specimens and 88% for SFRSCRC specimens when compared to SCC specimens.

The energy absorption capacity under cyclic loading was increased by 1.29 times and 3.02 times respectively for SCRC and SFRSCRC specimens. The relative values show an increase under cyclic loading for SCRC and SFRSCRC specimens and it is about 29% higher for SCRC specimens and three times higher for SFRSCRC specimens than that of SCC specimens. These improved qualities can be attributed to the low stiffness of rubber particles which impart relatively high flexibility and hence absorbs considerable amount of energy. Enhanced elasticity and energy absorption capacity of rubberised concrete greatly reduces the damage incurred by collisions. The further enhancement noted in SFRSCRC specimens is due to the bridging action of the steel fibres.

**Table 5.** Energy absorption capacity

Designation	Energy absorption capacity (kNm)			
	Monotonic		Cyclic	
	Absolute	Relative	Absolute	Relative
SCC	1.22	1.00	0.818	1.00
SCRC	1.50	1.23	1.059	1.29
SFRSCRC	2.29	1.88	2.474	3.02



#### 4. Conclusions

The load deflection characteristics, energy absorption capacity, first crack load, ultimate load and crack pattern of SCC, SCRC and SFRSCRC flexural members were investigated. The results indicate that SCRC and SFRSCRC could bring about drastic improvement in the flexural behaviour under monotonic loading and the following conclusions were arrived at:

1. The reinforced beams cast with SCRC exhibited better flexural behaviour compared to SCC. There was reduction in the ultimate load taken by SCC under cyclic loading compared to the monotonic load applied to the composite. However, SCRC specimen did not show any variation with cyclic and monotonic loading.
2. SCRC and SFRSCRC specimens exhibited numerous finer cracks and showed enhanced ultimate deflection than SCC specimens. The first crack load increased with the addition of scrap rubber and steel fibres. While there was a marginal increase (1%) in the ultimate load of SCC with the addition of shredded rubber (SCRC beams), significant improvement (6%) was obtained with the addition of shredded rubber and steel fibres in the case of SFRSCRC specimens.
3. The energy absorption capacity consistently increased for rubberised concrete specimens and the increase was about 23% for SCRC and 88% for SFRSCRC specimens when compared to SCC specimens.

#### References

- [1] Topçu İ.B, and Avcular N (1997), "Analysis of rubberized concrete as a composite material", *Cement and Concrete Research*, Vol. 27, No. 8, pp. 1135-1139.
- [2] Gregory Marvin Garrick B.S (2005), "Analysis and testing of waste tyre fibre modified concrete", *MS Thesis, Louisiana State University*.
- [3] Okamura H (1997), "Self-Compacting High-Performance Concrete", *Concrete International*, Vol. 19, No. 7, pp. 50-54.
- [4] Gettu R, Shareef S.N, and Ernest K.J.D (2009), "Evaluation of the robustness of SCC", *Indian Concrete Journal*, Vol. 83, No. 6, pp. 13-19.
- [5] Najim K.B, and Hall M.R (2010), "A review of the fresh/hardened properties and applications for plain- (PRC) and self-compacting rubberised concrete (SCRC)", *Construction and Building Materials* No. 24, pp. 2043–2051.
- [6] Mehmet G, and Erhan G (2011), "Permeability properties of self-compacting rubberized concretes", *Construction and Building Materials*, Vol. 25, pp. 3319–3326.
- [7] Grunewald S, and Walraven J.C (2001), "Parameter-study on the influence of steel fibres and coarse aggregate content on the fresh properties of self-compacting concrete", *Cement and Concrete Research* Vol. 31, pp. 1793–1798.
- [8] IS 12269: 1987, Indian Standard Specification for 53 Grade Ordinary Portland Cement, *Bureau of Indian Standards*, New Delhi.
- [9] ASTM C618 - 08a, Standard Specification for Coal Fly Ash and Raw or Calcined Natural Pozzolan for Use in Concrete.
- [10] IS 383:1970 (R2002), Indian Standard Specification for coarse and fine aggregates from natural sources for concrete, *Bureau of Indian Standards*, New Delhi.
- [11] Nan S, Kung-Chung H, His-Wen C (2001), "A simple mix design method for self-compacting concrete", *Cement and Concrete Research*, Vol. 31, pp. 1799–1807.
- [12] European Federation of Producers and Contractors of Specialist Products for Structures (EFNARC), "Specifications and Guidelines for Self Compacting Concrete", February 2002. [www.efnarc.org](http://www.efnarc.org)

# Effects of pit-sand on shear capacity of reinforced concrete space framed structures: case study of a building at Oba - Ile Akure

Lekan Makanju OLANITORI<sup>1</sup> and Joseph Olaseinde AFOLAYAN

*Dept of Civil Engineering, Federal Univ. of Technology, Akure, Ondo State, Nigeria*

**Abstract.** In the Nigerian construction industry today, there were instances when the prescribed concrete strength by the consultant structural engineer is not achieved during construction, due to the poor quality of available sand. This paper evaluates the existing formulae used in estimating the shear capacity of reinforced concrete structures and assesses the effect of concrete produced from pit-sand in Akure metropolis, on the shear capacity of a collapsed building in Oba-Ile, Akure. Site inspections were carried out on the collapsed building, and concrete samples were taken. Both destructive and non-destructive methods were used to determine the structure's concrete strength. Many of the structural members were exposed, so as to determine the number of reinforcements in each structural element. The shear capacity of the structure was estimated using existing formulae and, compared it with the structure's actual shear capacity. The average concrete strength was 8.5 N/mm<sup>2</sup> which is less than 20 N/mm<sup>2</sup>, the prescribed concrete strength for construction of the building. The estimated shear capacity based on 8.5 N/mm<sup>2</sup> and 20 N/mm<sup>2</sup> concrete strengths were 93.9 kN and 118 kN respectively, while the actual shear capacity at collapse was 18.88 kN. The actual shear capacity is less than the estimated shear capacity of the collapsed building, because of the reduced concrete strength due to the poor quality of pit-sand used for the concrete work; hence the collapse of the building was by shear failure induced by the reduction in concrete strength.

**Keywords.** Structure, collapse, load capacity, shear capacity, concrete

## Introduction

In Nigeria, concrete specifications are based on CP 114 [1], which states that concrete mixes of 1:2:4, 1:1½:3 and 1:1:2 will produce concrete with compressive strength of /mm<sup>2</sup>, 25.5 N/mm<sup>2</sup> and 30 N/mm<sup>2</sup> respectively at 28 days. However, Olanitori and Olotuah [2] show that these compressive strengths might not be attained due to the clay/silt content of sand, which negatively affects the compressive strength of concrete produced from them.

---

<sup>1</sup>Corresponding author: [lekanolanitori@gmail.com](mailto:lekanolanitori@gmail.com)

In the past few years a considerable improvement had taken place in the understanding of structural concrete and has been incorporated in the revised codes of practice. The British Standard CP110 [3], Code of Practice for the Structural Use of Concrete, has superseded the British Standard Codes of Practice CP114 [1], for reinforced concrete. Similarly, in America the ACI Standard ACI 318-71[4] has replaced the previous standard ACI 318-63 [5]. The major aspects of the revised codes is the limit state approach for designing reinforced concrete structures and the separation of methods of concrete mix design procedures from that of concrete design considerations. With the publication of BS8110 in 1985 [6], CP110 [3] was withdrawn. The publication of CP110 [3] and BS8110 [6] were accompanied with several BS standards which dealt with different aspects of concrete production.

The quality of concrete produced depends on the quality of its constituent materials and their mix ratios, the higher the percentage of clay/silt contents of sand, the lower the characteristic strength [2]. To mitigate the effect of clay/silt content of sand on the strength of concrete produced from it, there is need to increase the cement content of the concrete, depending on the clay/silt percentage [7]. Olanitori [8] determines the cost implication of mitigating the effect of clay/silt content of sand using mathematical models.

The collapse of most reinforced concrete structures is by shear failure at the beam-column joint and sudden in nature [9]. In 1962, Joint ACI-ASCE Committee 326[10] published a report regarding the design and behavior of beams failing due to shear and diagonal tension and design equation was formulated and is included in ACI 318-05 [11] and presented as Eq.1.

$$V_c = \left( \sqrt{f_c'} + 120\rho_w \frac{V_u d}{M_u} \right) \frac{b_w d}{7} \leq 0.3(f_c') b_w d \quad \text{Eq.1}$$

Where  $V_c$  is the nominal shear strength provided by concrete;  $f_c'$  is the specified compressive strength of concrete;  $\rho_w$  is the ratio  $A_s/b_w d$ ;  $V_u$  is the factored shear force at section;  $M_u$  is the factored moment at section;  $b_w$  is the web width;  $d$  is the effective depth of section; and  $A_s$  is the area of tension reinforcement. By neglecting the term  $\frac{Vd}{M}$  in Eq.1 a simplified but conservative version could be derived and presented as Eq.2.

$$V_c = \frac{1}{6} \sqrt{f_c'} b_w d \quad \text{Eq.2}$$

To include the effects of loading type and shear span to depth ratio into current code provisions, for members in which more than 1/3 of the factored shear at the critical section results from concentrated load located between 2d and 6d of the face of the support, Brown *et al* [12], proposed Eq.3:

$$V_c = \frac{1}{12} (f_c') b_w d \quad \text{Eq.3}$$

According to Arslan [13], the nominal shear strength provided by concrete can be estimated using Eq. 4.

$$V_{cr} = V_{crt} + V_{crd} = 0.15(f_c)^{0.5} b_w d + 0.02(f_c)^{0.65} b_w d$$

Eq.4

Where:  $V_{cr}$  is the cracking shear strength,  $V_{crt}$  is the diagonal tension cracking strength and  $V_{crd}$  is the dowel strength.

Based on the principal shear strength  $V_o$  carried in the compression zone, considering the influence of parameters; the slenderness ratio ( $a/d$ ) and size effect ( $1/d$ ), Arslan [14] expresses the diagonal cracking strength of RC slender beams without stirrups as given in Eq.5.

$$V_c = [0.2 f_c^{2/3} (\frac{c}{d})(1 + 0.032 f_c^{1/6})(\frac{4}{a/d})^{0.15} (\frac{400}{d})] b_w d$$

Eq.5

Where  $c$  is the depth of the neutral axis.

Other existing shear strength models for slender beams without stirrups proposed by Kim and Park (1996) [15], Rebeiz [16] and, Khuntia and Stojadinovic [17] are presented in Table 1. The ACI 318-08 [18] design shear strength is a simple superposition of transverse reinforcement and concrete strength. The design strength is independent of whether flexural yield has occurred prior to shear failure. For members, design shear strength is calculated using Eq.6.

$$V_n = V_c + V_s = \frac{\sqrt{f_c}}{6} b_w d + \frac{A_w f_y d}{s}$$

Eq.6

Where  $V_n$  is the design shear strength,  $V_c$  and  $V_s$  are the nominal shear strength provided by concrete and shear reinforcement,  $f_c$  is compressive strength of concrete;  $f_y$  is characteristic strength of steel;  $b_w$  is the web width;  $d$  is the effective depth of section; and  $A_w$  is the area of shear reinforcement.

In their work, Arslan and Polat [19], show that there exists a significant amount of contribution of concrete to the shear strength (18 - 69%), however, noted further experiments should be conducted with a wider range of shear reinforcement ratio, shear span-to-depth ratio, concrete strength and various loading schemes in order to obtain more reliable assessments. Since the mid-1980s, there has been an increasing amount of experimental evidence showing that the underlying concepts of the provisions of current codes (for example, BS 8110-1985 [6] and ACI 318-05 [11]) for the shear in particular and, to a certain extent for the flexural design of reinforced concrete (RC) structures are in conflict with fundamental properties of concrete at both the material and the structural levels [20].

## 1. Materials and methods

The materials used for this study were structural detailing, portable rotary drilling machine, 15 samples of 75 mm diameter cores of concrete, PUNDIT6 equipment, and a manually operated universal testing machine. Exposing the structural elements such as slab, beams and columns, numbers of reinforcements provided were determined. The slab thickness was 150 mm and provided Y12 reinforcements at 300mm center to center. The beam section was 250 mm by 400 mm and provided with 2Y16 bars (bottom and top steel), while the column section was 250 mm by 250 mm and provided with 4Y16 bars. The column grid was 4 m by 4m.

Fifteen samples of 75 mm diameter cylindrical cores of concrete were taken from slabs, beams and columns. Five samples each were taken from each structural element. The retrieved cores were tested for strength using universal testing machine in accordance with BS 1881-120 (1983) [21]. Also non-destructive tests were carried out on parts of the building that are yet to collapse. The compressive strengths from universal testing machine and the PUNDIT 6 are presented in Table 2, and the characteristic strengths results from universal testing machine and the PUNDIT6 were determined to be  $8.2 \text{ N/mm}^2$  and  $8.8 \text{ N/mm}^2$  respectively, with the average value of  $8.5 \text{ N/mm}^2$ . This value is less than  $20 \text{ N/mm}^2$ , the prescribed concrete strength for the construction of the collapsed building.

Using equations in the code and existing shear strength models, shear capacity of the building was estimated, and compared with the actual shear capacity. The shear capacity of the collapsed building based on the existing shear strength models for slender beams without stirrups are presented in Table 3, while Figure 1 shows the collapsed building.



Figure 1. Collapsed part of the building

## 2. Shear capacity ( $v_n$ )

### 2.1 Estimated shear capacities, of the collapsed building

Using Eq. 6 above, and taking  $f_{cu}$  to be  $8.5 \text{ N/mm}^2$  and  $20 \text{ N/mm}^2$ , the prescribed and actual concrete strengths, we have:

$$\begin{aligned} V_{NACS} &= V_{CACS} + V_S = 45.2 + 48.7 = 93.9kN; V_{NPCS} = V_{CPCS} + V_S \\ &= 69.3 + 48.7 = 118kN \end{aligned}$$

Where  $V_{NPCS}$  and  $V_{NACS}$  - shear capacity due to the prescribed and actual strength of concrete,  $V_{CPCS}$  and  $V_{CACS}$  - concrete shear strength due to prescribed and actual strength of concrete,  $V_s$  - contribution of shear reinforcement to shear strength.

**Table 1.** Some of the existing shear strength models for slender beams without stirrups

Investigator	Shear strength models
Kim and Park [15]	$V_u = [3.5 f_c^{\alpha/3} \rho^{3/8} (0.4 + \frac{d}{a}) (\frac{1}{\sqrt{1 + 0.008d}} + 0.18)] b_w d$ $\alpha = 2 - (a / d) / 3 \text{ for } 1.0 \leq \frac{a}{d} < 3.0 ; \alpha = 1 \text{ for } \frac{a}{d} \geq 3.0$
Rebeiz [16]	$V_c = [0.4 + \sqrt{f_c \rho} \frac{a}{d} (2.7 - 0.4 A_d)] b_w d$ $A_d = \frac{a}{d} \text{ for } (\frac{a}{d}) < 2.5 \text{ and } A_d = 2.5 \text{ for } (a / d) \geq 2.5$
Khuntia and Stojadinovic [17]	$V_c = [0.54 \sqrt[3]{\rho (f_c \frac{Vd}{M_u})^{0.5}}] b_w d ; \frac{M_u}{Vd} = \frac{a}{d} - 1$

2.2 Actual shear capacity, of the collapsed space framed building

At collapse, the load acting on the structure is estimated as follows:

Slab load = 0.15 x 24 = 3.6 kN/m<sup>2</sup>. Live load during construction = 1.5 kN/m<sup>2</sup>. Collapse slab load  $n_s = 1.4 \times 3.6 + 1.6 \times 1.5 = 7.44$  kN/m<sup>2</sup>. Load due to beam weight = 0.25 x (0.4 – 0.15) x 24 x 1.4 = 2.1 kN/m. Hence collapse beam load

$$w_c = \frac{1}{4} n l_x + 2.1 = 7.44 + 2.1 = 9.44 \text{ kN/m}$$

While the actual shear capacity of the collapsed building can be estimated by:

$$V_{NA} = \frac{wl}{2} = \frac{9.44 \times 4}{2} = 18.88 \text{ kN.}$$

Where  $w$  is the uniformly distributed load on beam and,  $l$  is the beam span.

3. Analysis and discussion of results

Table 2 shows the results of universal testing machine and the PUNDIT 6, from which the characteristic strength of the concrete of the collapsed building was determined to

be 8.8 N/mm<sup>2</sup> and 8.2 N/mm<sup>2</sup> for PUNDIT 6 and Universal Machine respectively, resulting in an average characteristic strength of 8.5 N/mm<sup>2</sup>. The prescribed concrete strength for the building was 20 N/mm<sup>2</sup>. This shows a 60% reduction in the concrete strength.

Estimated shear capacities of the collapsed building from the actual concrete strength of 8.5N/mm<sup>2</sup> ( $V_{NACS}$ ) and prescribed concrete strength of 20 N/mm<sup>2</sup> ( $V_{NPCS}$ ) were 93.9 kN and 118 kN respectively, while the actual shear capacity ( $V_{NA}$ ) of the collapsed building was 18.8 kN. The contribution of concrete to the estimated shear capacities was 45.2 kN and 69.3 kN for actual and prescribed concrete strength respectively, while the contribution of shear reinforcement was 48.7 kN. The actual shear capacity of 18.8 kN of the collapsed building is over five times lesser than the estimated values of 93.9 kN and 118 kN respectively. This large reduction in the actual shear capacity when compared with the estimated values caused the building to collapse even, when it was still under construction.

Table 3 shows shear capacities determined from existing shear strength models. Only the shear strength models of Brown *et al.* [12] and Kim and Park [15] give shear capacities of 22.6 kN and 20.4 kN respectively, which compares favorably with the actual shear capacity of the collapsed building which equals 18.88 kN. The shear capacities from Brown *et el* and Kim and Park, defers from that of the actual shear capacity by 8.1% and19.7% respectively.

**Table 2.** Results from universal testing machine and the PUNDIT 6

SM	Slab (N/mm <sup>2</sup> )					Beam (N/mm <sup>2</sup> )					Column (N/mm <sup>2</sup> )				
PD6	11.5	10.2	11.0	9.8	10.2	10.5	9.3	9.5	10.2	9.8	10.4	10.6	9.1	9.9	8.5
UTM	10.0	9.8	9.4	9.0	9.7	9.2	10.5	7.9	8.8	10.8	9.4	9.6	10.2	10.4	8.2

**Table 3.** Shear capacities determined from existing shear strength models

Investig/ Con Shear Capacity	ACI [11]	Brown <i>et al.</i> [12]	Arslan [13]	Arslan [14]	Kim and Park [15]	Rebeiz [16]	Khuntia and Stojadinovic [17]
$V_{NACS}$ (kN)	45.2	22.6	48.2	13.2	20.4	84.6	12.56
$V_{NPCS}$ (kN)	69.4	34.7	75.4	35.3	28.3	109.9	14.56

$V_{NACS}$  – shear capacity, determined using actual concrete strength  
 $V_{NPCS}$  – shear capacity, determined using prescribed concrete strength

#### 4. Conclusion

From the discussion above, the following conclusions can be drawn:

- i. The collapse of the building was caused by shear failure which is sudden in nature.
- ii. There are discrepancies between the estimated values of shear capacity, using shear design formulae in the codes and other existing shear strength models in the literature.
- iii. Shear strength models of Brown *et el* [12] and Kim and Park [15] give the most accurate value of shear capacity of reinforced concrete at failure.

## 5. Recommendations

- i. Current shear design formulae should be reviewed, to properly reflect the effect of concrete strength on shear capacity.
- ii. Effect of the reduction of the characteristic strength of concrete should be investigated and appropriate measures should be put in place so as to produce safe reinforced concrete structures.

## References

- [1] CP 114 (1957). The structural use of reinforced concrete in buildings (amended in 1965), *British Standards Institution*, London.
- [2] Olanitori L.M. and Olotuah A.O. (2005). The effect of Clayey impurities in sand on the crushing strength of concrete (a case study of sand in Akure metropolis, Ondo State, Nigeria). *Proceedings of 30<sup>th</sup> Conference on 'Our World in Concrete and Structures'*. Singapore, 23-24 August. Pp 373-376.
- [3] CP 110 (1972). Code of practice for structural use of concrete: Part I – Design, materials and workmanship. British Standards Institution, London.
- [4] ACI Committee 318 (1971). Buildings code requirement for reinforced concrete, *American Concrete Institute*, Detroit, USA.
- [5] ACI Committee 318 (1963). Buildings code requirement for reinforced concrete, *American Concrete Institute*, Detroit, USA.
- [6] BS 8110 (1985). Structural use of concrete: Part – I: Code of practice for design and construction, British Standards Institution, London.
- [7] Olanitori, L.M. (2006). Mitigating the effect of clay content of sand on concrete strength. *31<sup>st</sup> Conference on Our World in Concrete and Structures*; 15- 17 August 2006, Kaula Lumpur, Malaysia; pp 344 – 352.
- [8] Olanitori, L.M. (2012). Cost implication of mitigating the effect of clay/silt content of sand on concrete compressive strength, *Journal of Civil Engineering and Urbanism*, Vol. 2, Issue 4, pp 143 – 148.
- [9] Olanitori, L.M. (2011). Causes of structural failures of a building: Case study of a building at Oba – Ile Akure. *Journal of Building Appraisal*, Vol. 6 , Issue ¾, pp 277 – 284.
- [10] Joint ACI-ASCE Committee 326, 1962a. shear and diagonal tension, *ACI Journal Proceedings* 59 (1) : 1 – 30 .
- [11] ACI Committee 318,(2005). Building code requirements for structural concrete and commentary (ACI 318R-05), *American Concrete Institute*, Farmington Hills, Mich.
- [12] Brown M.D., Bayrak O, and Jirsa J. O, (2006). Design for shear based on loading conditions, *ACI Structural Journal*, Vol. 103, No. 4. Pp 541-550.
- [13] Arslan, G. (2008): Cracking shear strength of RC slender beams without stirrups, *Journal of Civil Engineering and Management*, Vol. 14, Issue 3. Pp 177-182.
- [14] Arslan, G. (2012): Diagonal tension failure of rc beams without stirrups, *Journal of Civil Engineering and Management*, Vol. 18, Issue 2. Pp 217-226.
- [15] Kim, J.K. and Park, Y.D. (1996). Prediction of shear strength of reinforced concrete beams without web reinforcement, *ACI Materials Journal* 93(3): 213–222.
- [16] Rebeiz, K.S.(1999). Shear strength prediction for concrete member, *Journal of Structural Engineering ASCE* 125(3): 301–308.
- [17] Khuntia, M.; Stojadinovic, B. (2001). Shear strength of reinforced concrete beams without transverse reinforcement, *ACI Structural Journal* 98(5): 648–656.
- [18] ACI Committee 318,( 2008). building code requirements for structural concrete and commentary (ACI 318R-05), *American Concrete Institute*, Farmington Hills, Mich.
- [19] Arslan G. and Polat, Z. (2013): Contribution of concrete to shear strength of rc beams failing in shear, *Journal of Civil Engineering and Management*. Vol. 19. Issue 3. Pp 400-408.
- [20] Kotsos, M.D. (2007). Concepts underlying reinforced concrete design: time for reappraisal, *ACI Structural Journal*, Vol. 104, No 6, pp 675-684.
- [21] BS 1881( 1983 ) Testing concrete – Part 120: Method for determination of the compressive strength of concrete cores, London: British Standards Institution .



# An experimental study on acoustic emission of a notched three point bending concrete beams

Zohra DAHOU<sup>1</sup> and Abdelkhalek BENMILOUD  
*Laboratory Mechanics of Structures –LMS-  
University of Bechar, BP n° 417, Bechar, Algeria*

**Abstract.** In this present study, notched three-point concrete bend specimens were tested and the accompanying acoustics emissions (AE) were recorded using a four channel AE monitoring system. The specimens were tested at various ages. A quantitative signal analysis is proposed for following the crack evolution until failure. The AE absolute energy, the number of events, the variation of amplitude and the counts are used for presenting our results.

**Keywords.** Acoustic emission, concrete, bending test, cracking, fracture

## Introduction

Among the nondestructive testing (NDT) techniques based on acoustic waves, the acoustic emission (AE) monitoring and ultrasonic testing (UT) are now often used in the field of civil engineering [6,7]. AE and UT are passive and active techniques respectively. UT is implemented to assess previously existing damages or more generally the mechanical integrity of the propagation medium while AE monitoring allows detecting an ongoing damaging phenomenon. Acoustic emission (AE) waves are elastic waves [3] caused by irreversible changes, such as dislocation movement, twinning, phase transformations, crack initiation, and propagation. The AE technique detects high frequency energy waves, which are emitted by the material itself when damage occurs. Consequently, different phases of the cracking process and different failure modes can be detected.

In this paper three-point bending strength loading test was done on concrete prisms having different maturity. There was no reinforcement and therefore only cracking processes should cause acoustic emission. During testing, the acoustic emission activity was acquired. The differences in reading and analysing acoustic emission signal and its behavior during the loading until the concretes specimens fractured are presented.

---

<sup>1</sup>Corresponding author: [dzohra@gmail.com](mailto:dzohra@gmail.com), Tel/ Fax +21349819024

## 1. Materials and tests

### 1.1. Concrete proprieties and specimens

Concrete was prepared using an ordinary Portland cement and natural siliceous sand. Two types of coarse aggregates were used, with a maximum aggregate size of 15 mm. Mixture proportion is shown in Table 1. Cubes of 100x100 mm were used to evaluate compressive strength. Prisms specimens of 100x100-mm section with 400-mm span were tested under three point bending condition, according to the EN 12390-5 standard [1]. All specimens were cast with the same batch of concrete. They were removed from their moulds 24 h after casting and stored at least 28 days in a controlled environment ( $T^{\circ}= 20^{\circ}\text{C}$ ,  $\text{RH}\%= 60\%$ ) until . At 28 days the compressive strength was 37,4MPa.

**Table 1.** Mixture proportions ( $\text{kg}/\text{m}^3$ )

Component	Weight (kg)
CEM II/B 42.5 N NA, Lafarge	380
Sand 0/5	601,8
Gravel 3/8	208,3
Gravel 8/15	1060,5
Water	205,4

The prisms specimens were tested in bending with concurrent acoustic emission monitoring in two different maturities: two and nine months. A central notch was saw-cut in each test specimen before testing. The notch width and depth were 2 mm and 20mm respectively. The test set-up consisted of a bending machine of 150 kN capacity.

### 1.2. AE equipment

The AE monitoring setup consisted 4 AE sensors and a PCI-DSP-4P channel monitoring system  $\text{AE}_{\text{win}} \text{DP4}$  manufactured by Mistras Group Inc. The AE transducers (R15a) were resonant type with a natural resonant frequency 150 kHz [4]. The operating frequency of the AE sensor is 50 kHz – 200 kHz. The threshold for detecting AE was fixed at 30 dB to ensure a high signal to noise ratio. A preamplifier 2/4/6 was used. It is supplied with 20/40/60 dB gain (switch selectable) and operates with either a single ended or differential sensor. It has AST (auto-sensor test) capability of self pulsing the sensor for test of a single sensor or groups of sensors on the same structure. The preamplifier gain was set to 40 dB.

AE signals due for example to micro-cracks are detected by AE sensors. Figure 1 show some parameters, for a typical AE signal, as, count, duration time, amplitude, energy, and rise time.

In order to obtain a bi-dimensional location of AE-events, four AE-sensors were mounted on one face of the specimen as shown in Figure 2. To fix the sensors on the surface we used a coupling agent (high vacuum silicon grease). AE hits (including waveforms) were recorded with a sampling rate of 5 MHz.

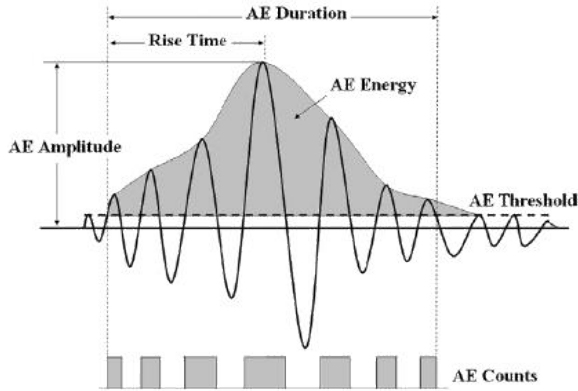


Figure 1. Parameters of a typical AE signal [9]

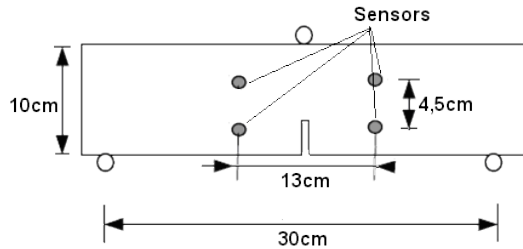


Figure 2. AE sensor location

## 2. Results and discussion

During the formation of a crack, energy is emitted as an elastic wave and propagates from the crack location to the AE transducers at the specimen surface. The Figure 3, show the variation of the amplitude versus absolute AE energy from the AE data of the beams tested at two and nine months. For each one, it clarifies the fact that same absolute AE energy level shows different amplitudes and vice versa. This is in adequacy with what is known [5] that the absolute AE energy is an appropriate parameter to represent an event. It's noted that the amplitudes and the reached AE energy are independent from the maturity of the concrete.

The maximum loads and corresponding results from AE tests at peak and failure are given in Table 2. The number of events corresponding to the greatest maturity of concrete, and then the higher strength, are the smallest. Its well knows that the brittleness of concrete is affected by the strength [2,8]. So, the number of AE events can use in acoustic emission for characterizing this behavior of concrete.

At failure, the number of counts corresponding to 9 months is the largest one (Table 2), but the less dispersed one (Figure 4).

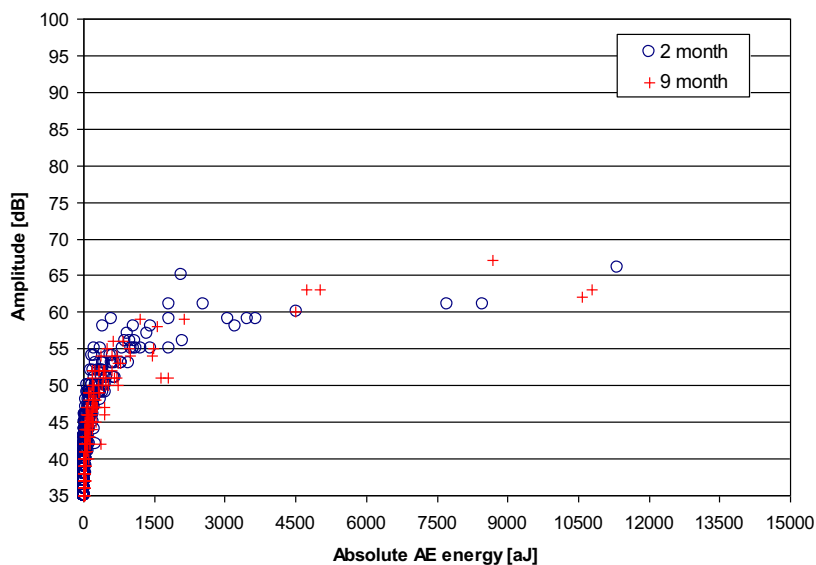


Figure 3. Variation of the amplitude versus absolute AE energy

Table 2. AE events and counts obtained from testing

Concrete age [months]	Peak load (kN)	Number of AE events at peak load	Number of AE events at failure	Number of AE counts at peak load	Number of AE counts at failure
2	9.4	937	979	30725	37615
9	10.2	412	451	84076	158736

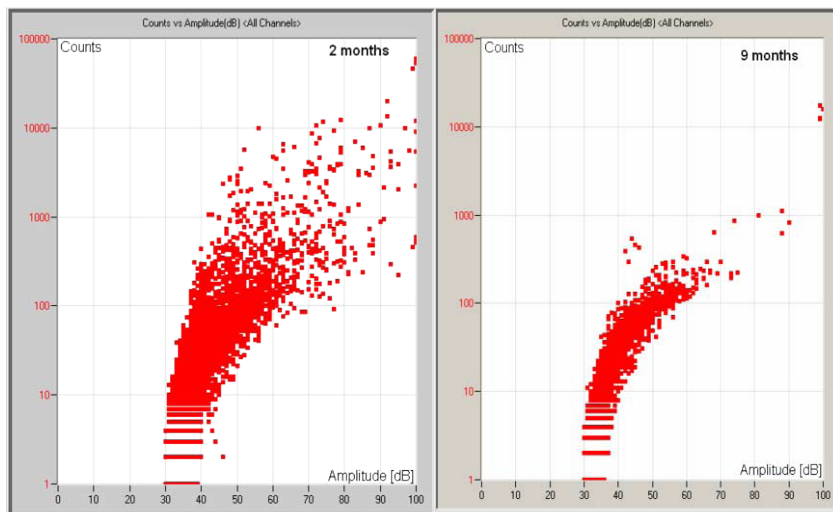


Figure 4. Counts versus amplitude for all channels – Variation with maturity-

### 3. Conclusions

In this study, the acoustic emission (AE) technique has been used for monitoring the crack progress to failure fatigue in plain concrete specimens. Beam specimens of same sizes are prepared and tested under three-point bending at different age. The evolution of crack is continuously monitored using four AE-sensors mounted on the specimens. The results found show that the number of events decreases with the increase of the maturity of concrete.

### References

- [1] Afnor, NF EN 12390-5, « Essai pour béton durci, Partie 5 : Résistance à la flexion sur éprouvettes », Afnor, Octobre, 2001.
- [2] Gettu R., Garcia-Alvarez V.O., Aguado A., Effect of aging on the fracture characteristics and brittleness of a high-strength concrete, *Cement and Concrete Composites*, 28 (1998), 349-355.
- [3] Grosse, C.U.; Ohtsu, *Acoustic Emission Testing, Basics for research-Applications in Civil Engineering*, Springer – Verlag Berlin Heidelberg, 2008.
- [4] Mistras Group INC, *Products & Systems Division, PAC Part # : 6320 – 1001, DiSP with AEwin USer's Manual Rev 4*, Princeton Junction, NJ USA, 2011.
- [5] Muralidhara S., Raghu Prasad B.K.b, Eskandari H., Karihaloo B.L., Fracture process zone size and true fracture energy of concrete using acoustic emission, *Construction and Building Materials* 24 (2010), 479–486.
- [6] Ohtsu, M., Basics of acoustic emission and applications to concrete engineering, *Materials Science Research International*, 4 (1998), 131-140.
- [7] Ohtsu S., M., Sakata, Y., NDE of defects in concrete by quantitative acoustic emission and ultrasonics, *Ultrasonics* 36 (1998), 187-197.
- [8] Shah S.P., Fracture toughness for high-strength concrete, *ACI Materials Journal*, 87 (1990), 260-265.
- [9] Shah S. G., Chandra Kishen J.M., Use of acoustic emissions in flexural fatigue crack growth studies on concrete, *Engineering Fracture Mechanics* 87 (2012), 36–47.

# Flexural tests of Mi Panels

G. M. BUKASA and M. DUNDU<sup>1</sup>

*Department of Civil Engineering Science, University of Johannesburg, South Africa*

**Abstract.** Two series of flexural tests on 2700x600x75 mm Mi Panels are presented. The inner core of these lightweight panels is made from mixing polystyrene beads called Neopor, high strength cement, and water. A chemical is used as binding agent to bond the inner core to the external fibre cement sheets of 4.5 mm thickness. The experimental programme consists of two series of tests with different loading conditions; the first series has line loads at one-third point from each end support and the second series has line loads, at quarter and three quarter span of the panels. All flexural tests are performed to simulate the behaviour of the wall, when subjected to wind loads. Although the panels failed by fracturing, the tests showed that the panels are capable of carrying the required loads.

**Keywords.** Mi Panel, flexure, fibre cement, polystyrene.

## Introduction

Mi Panels are lightweight, ease to construct and requires far less construction materials than conventional building technology, which makes them an excellent choice for remote construction projects. The panels have been used as structural elements in building structures ranging from single (ordinary houses, sheds, factory and warehousing developments) to multi-storey buildings. Mi Panels exists in two different dimensions; 2700x600x75 mm for wall panels and 3000x600x50 mm for roof panels. The interlocking panels comprises of 4.5mm-thick fibre-cement sheeting compressed on either side of an inner core of expanded graphite impregnated polystyrene beads called Neopor, high strength cement, and three proprietary chemicals mixed together, as shown in Figure 1. Delamination of the fibre-cement sheeting is prevented by the chemicals and the method of production. Mi Panels have tongue and groove joints to allow interlocking during construction. All joints are secured with polyurethane glue and are then sealed with a fibre tape membrane.

The South Africa building regulation, SANS 10 400 XA [1], recognizes Mi Panels as alternative building systems among others. The regulation concerning alternative systems, defines that building systems different from the traditional building can be used on condition that it is proved by experimental tests. The aim of this investigation is to determine the flexural strength of similar panels, manufactured by MIBT, South Africa. Preliminary flexural tests of these panels have produced positive results [2].

---

<sup>1</sup>Corresponding author: University of Johannesburg, Department of Civil Engineering Science, P.O. Box 524, Auckland Park, 2006, South Africa; E-mail. [mdundu@uj.ac.za](mailto:mdundu@uj.ac.za)

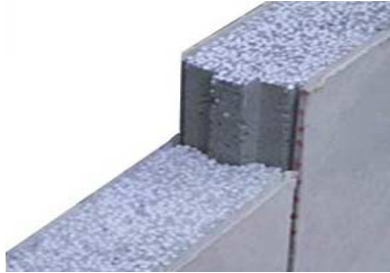


Figure 1. Mi panel

## 1. Experimental Investigations

Flexural tests were conducted on 2700x600x75 mm Mi Panels using two-point loads to examine the strength. The tests were performed to simulate the behaviour of the wall, when subjected to wind loads. In all the tests carried out, the panels used had the same mix proportion. The test system consists of specially designed supporting rigs and load spreader beams. This test configuration simulates a distributed load, applied to the panel. The tests were carried out using an Instron machine with an actuator capacity of 250 kN, at the rate 1mm/minute. Figure 2 illustrates the flexural test set-up.



Figure 2. Test set-up of panels

The panels were instrumented so that in-plane deflection and strains at mid-span could be measured. The deflection and longitudinal strains were measured by means of a linear variable displacement transducer (LVDT) and strain gauges, respectively. Strains were recorded in order to determine the moment curvature behaviour of the panels. Two strain gauges were used for each panel; one placed on the compression side, and another one on the tension side. The Data-logger was set and connected to computer system in order to record the readings. Each panel was incrementally loaded

at the rate of 1mm/min, so that the behaviour and failure patterns of the panel could be well observed.

## 2. Test results

The panels failed by fracturing. For the first six tested panels, with the load applied at one-third of the span (Series 1), failure occurred at mid-span, whilst for the 4 panels, with the load applied at one-quarter from each support (Series 2), half of the panels failed at mid-span and the other half failed at the point where loads were applied. No visible cracks were observed before global flexural failure and no debonding occurred between the inner core and the external fibre cement sheeting during the bending test. In addition, no considerable in-plane deflection was experienced in all tested panels until global failure occurred.

Tables 1 and 2 shows the total load, line load, experimental (Exp.) moment and experimental pressure, applied on the 2700x600x75 mm panels, and the expected maximum unfactored wind pressure. The failure load value exhibited by the specimen varied from 2.48 kN to 2.97 kN when the specimens were subjected to one-third loading condition (Series 1) and from 3.60 kN to 4.87 kN when one-quarter loading was applied (Series 2). It is obvious that the load increased as the applied point loads moved towards the supports. These loads generated experimental pressure values greater than the theoretical wind pressure values. The maximum unfactored wind pressure is determined based on SANS 10160 [3], as shown in Equation 1.

$$\begin{aligned}
 p_z &= K_p V_z^2 \times (C_{pe} - C_{pi}) \\
 &= K_p (K_r K_z V)^2 \times (C_{pe} - C_{pi})
 \end{aligned}
 \tag{1}$$

where,  $K_p$  is site altitude above sea level (taken as 0),  $V_z$  is the characteristic wind speed at height  $z$  (m/s),  $K_r$  is the mean return period correction factor (taken as 50 years),  $K_z$  is the wind speed multiplier,  $V$  is the wind speed,  $C_{pe}$  is the external wind pressure coefficient and  $C_{pi}$  is the internal wind pressure coefficient. The calculation in Eq. (1) assumes that the height is 5m and the terrain category is 3 (suburbs, towns, suburbs, wooded areas, industrial areas). Based on the results from Eq. (1), it is clear that the theoretical wind pressure is far much smaller than the experimental pressure (Exp. Pressure), resisted by the panels.

**Table 1.** Flexural loads of Series 1 tests

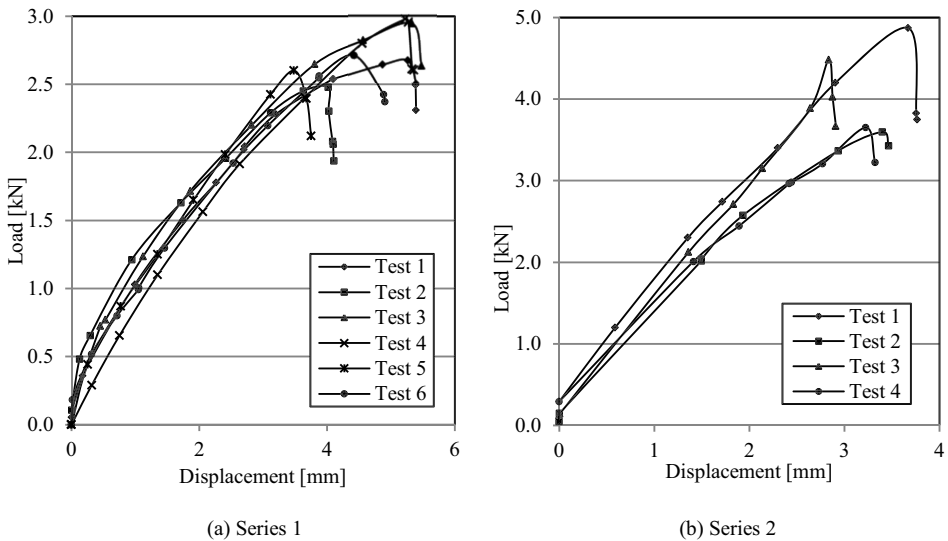
Test	Total load (kN)	Line loads (kN/m)	Exp. Moment (kNm)	Exp. Pressure (kN/m <sup>2</sup> )	Wind Pressure (kN/m <sup>2</sup> )
1	2.68	4.47	1.11	1.79	0.55
2	2.48	4.13	1.03	1.65	0.55
3	2.94	4.90	1.22	1.96	0.55
4	2.97	4.95	1.23	1.98	0.55
5	2.60	4.33	1.08	1.73	0.55
6	2.71	4.52	1.12	1.81	0.55



**Table 2.** Flexural loads of Series 2 tests

Test	Total load (kN)	Line loads (kN/m)	Exp. Moment (kNm)	Exp. Pressure (kN/m <sup>2</sup> )	Wind Pressure (kN/m <sup>2</sup> )
1	4.87	8.12	1.52	3.25	0.55
2	4.48	7.47	1.40	2.99	0.55
3	3.65	6.08	1.14	2.43	0.55
4	3.60	6.00	1.13	2.40	0.55

Figure 3 shows the in-plane load-deflection graphs of the panels. It is evident from Figure 3(a) that Series 1 graphs are largely non-linear. The behaviour of Series 2 graphs consists firstly of a linear response followed by a non-linear response. The small inelastic behaviour in Series 2 is only exhibited as the applied load approaches the maximum capacity of the panels. Since the composition of all the panels are the same, this load-deflection response was influenced by nothing else except the loading positions.



**Figure 3.** Load-deflection graphs

The moment-curvature relationships of Series 1 and 2 panels are shown in Figure 4. Notice that the moment-curvature for Test 3 and 6 were removed from Figure 4(a), since they were significantly distorted. Curvature was calculated from the strain readings at the top and bottom fibre cement sheets. Series 1 graphs are non-linear and Series 2 graphs are linear. Non-linearity only became visible in Series 2 graphs when the applied load approached the capacity of the panels. These characteristics are similar to the load-deflection curves in Figure 3. In general, the maximum moments were achieved at low strain values because the panel could not sustain a significant vertical deflection.

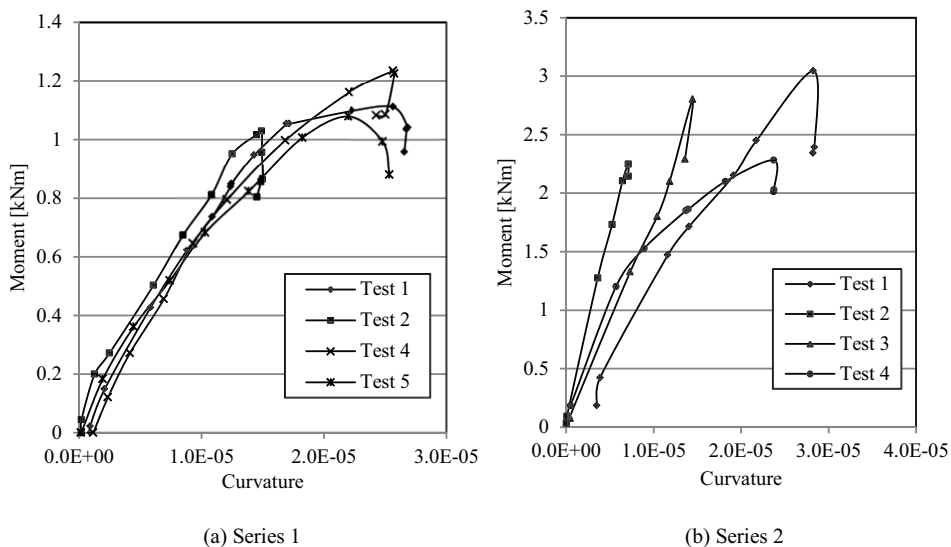


Figure 4. Moment-curvature graphs

### 3. Conclusions

This paper presents experimental studies on the flexural strength and behaviour of 2700x600x75 mm Mi Panels. Based on the results from the tests, it is clear that the theoretical wind pressure, calculated using the South African loading code, is far much smaller than the experimental pressure, resisted by the panels. The maximum deflections at mid-span as well as strains are small. This has negative implications on the ductility of the panels. Despite this deficiency, Mi Panels possess the required strength and can be used as alternative building system.

### Acknowledgments

The authors wish to express their appreciation to MIBT South Africa for their generous donation of Mi Panels without which these tests could not have been conducted.

**References**

- [1] SANS 10400, South African standard code of practice for the application of the national building regulations, South African Bureau of Standards, Pretoria, South Africa, 2011.
- [2] M. Dundu and G.M. Bukasa, Compression and flexural tests of Mi Panels. *International Conference on Civil and Environmental Engineering (CEE'2013)*, Nov. 27-28, Johannesburg, South Africa, 2013.
- [3] SANS 10160, South Africa standard code of practice for the general procedures and loadings to be adopted in the design of buildings. South African Bureau of Standards, Pretoria, South Africa, 1989.

# Compression tests of Mi Panels

G. M. BUKASA and M. DUNDU<sup>1</sup>

*Department of Civil Engineering Science, University of Johannesburg, South Africa*

**Abstract.** A number of compression tests of Mi Panels are presented. The use of lightweight Mi Panels as building system allows the reduction of construction time and waste in the building environment. The compression tests are performed to simulate the behaviour of the wall, when subjected to vertical loads from the roof. Two LVDTs were placed at mid-height of the panels during the compression tests, to record the lateral displacement. Mi Panels failed by fracturing into two parts at mid-height. No cracks in the panel were observed before overall flexural buckling failure. The tests showed that the panels are capable of carrying the required loads, and can be used in place of brick walls.

**Keywords.** Mi Panel, compression, fibre cement, Polystyrene, high strength cement.

## Introduction

The increasing housing demand and the increasing costs due to the use of conventional bricks structures has become motivations for the building industry to use alternative building systems that can reduce the construction time and waste in the building environment. This reduction can be achieved by using lightweight materials, such as Mi Panels. Mi Panels are produced locally in South Africa and can offer rapid construction compared to conventional construction. Mi Panels are composed of high strength cement, polystyrene beads that are graphite impregnated, and a special blend of binding agents that allows adhesion between the inner core and the external fibre cement sheets. Since this building system is still new in South Africa and its demand has slowly started increasing, there is a need for a better understanding of their buckling behaviour and strength. The aim of this experimental study is to determine the compressive strength of Mi Panels, and its failure patterns. Preliminary compression tests of these panels have produced good results [1].

## 1. Experimental programme

The test set-up for the compression tests is shown in Figure 1. The test simulates the behaviour of the wall, when subject to vertical loads from the roof. In the set-up, thick flat plates were placed at the top and bottom ends of the panel so as to distribute the load uniformly along the width of the panel.

---

<sup>1</sup>Corresponding author: University of Johannesburg, Department of Civil Engineering Science, P.O. Box 524, Auckland Park, 2006, South Africa; E-mail. [mdundu@uj.ac.za](mailto:mdundu@uj.ac.za)

The panels were instrumented so that lateral deflection could be measured. Lateral deflection, at mid height of the panel, was measured by means of a linear variable displacement transducer (LVDT). Two LVDTs were used so that the readings of one LVDT could be checked against the other.

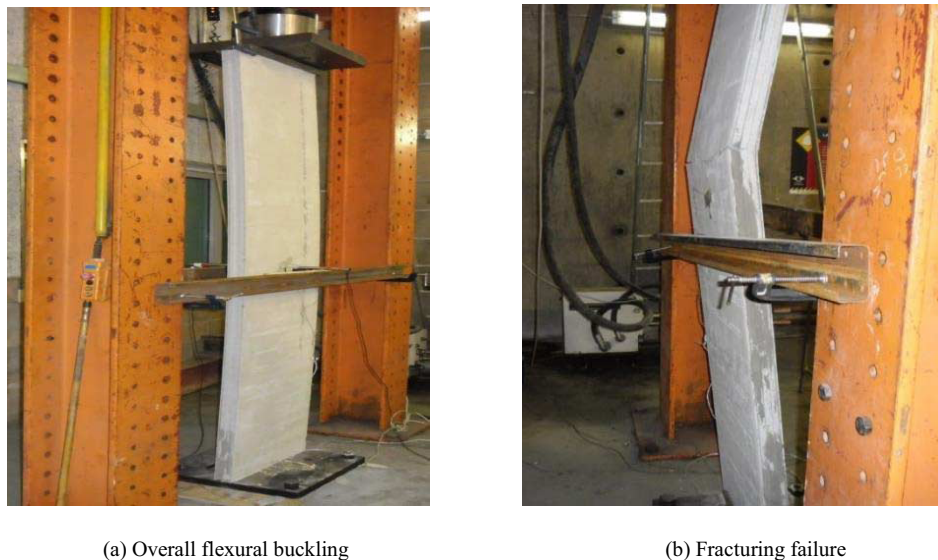
After settings and calibration of all measuring devices have been completed and the load value zeroed, the load was applied using a 500 kN Instron. All measurements (lateral deflection and load) were recorded automatically as the test was performed. Each panel was incrementally loaded at the rate of 1mm/min, so that the behaviour and failure patterns of the panel could be well observed.



**Figure 1.** Panel specimens

## **2. Test results**

In all the tested panels, it was observed that failure occurred around mid-height, by sudden fracturing. There was no debonding observed of the fibre sheeting from the inner core, after failure. Figures 2(a) and (b) shows a panel deflecting under vertical load before failure and fracture failure of the panels, respectively. This sudden failure is due to the lack of reinforcing steel inside the inner core.

**Figure 2.** Failure mode

The experimental results are summarized in Table 1. These results include the ultimate loads achieved by the panels, the corresponding distributed loads, and the lateral deflection. The failure load value exhibited by the specimen varied from 107.57 kN to 136.28 kN. Notice that Test 5 was removed Table 1 and Figure 3, since it was significantly distorted. The lateral deflection was used to calculate the secondary moment. Values of this second order effect are also given in Table 1. The lateral deflection and subsequent secondary moment are too small to warrant any further consideration.

**Table 1.** Compression loads

Test	Load (kN)	Distributed load (kN/m)	Lateral deflection (mm)	Secondary moment (kNm)
1	136.28	227.13	7.44	1.01
2	116.05	193.42	7.18	0.83
3	107.57	179.29	7.32	0.78
4	133.42	222.37	6.98	0.93
6	127.16	211.93	6.32	0.80

Figure 3 shows the load-deflection graphs of the tested panels. The load-deflection graphs clearly show that all the tests were initially elastic, but became progressively inelastic as the applied load approached the maximum capacity of the panels.

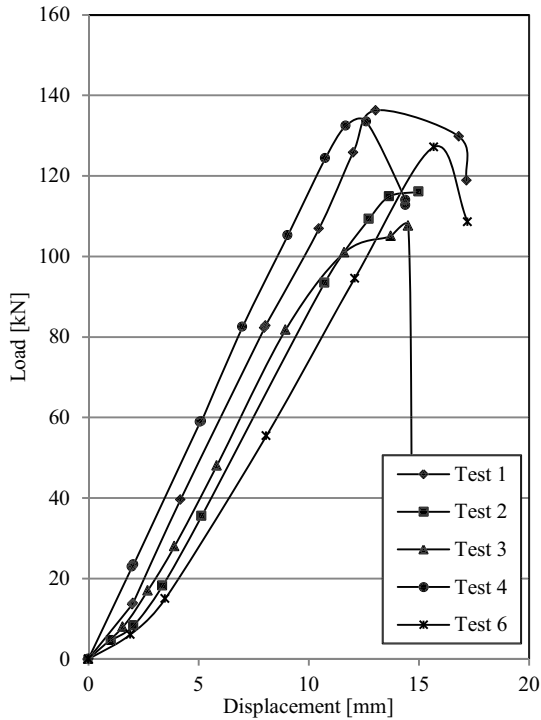


Figure 3. Load-deflections

### 3. Conclusions

This paper has described experimental studies on the compressive strength and behaviour of Mi-Panels tested in compression. From the tests the following conclusions are made:

- The panels achieved substantially large loads, considering that they are made of very light materials. These loads range from 107.57 kN to 136.28 kN, and far much exceeds the 80 kN load, expected of this type of panels.
- The tested panels achieved all the maximum loads at small lateral deflections. This lack of ductility is due to the absence of steel reinforcements, which can sustain the load before global failure occurs.
- The failure mode observed in all the tested panels was a sudden fracturing failure, which occurred either at mid-height for some panels or close to mid-height for others.

Based on the strengths obtained in these compression tests, it can be concluded that Mi Panels are strong enough in compression, and can meet the requirements required by South African code, SANS 10400 [2].

## **Acknowledgments**

The authors wish to express their appreciation to MIBT South Africa for their generous donation of Mi Panels without which these tests could not have been conducted.

## **References**

- [1] M. Dundu and G.M. Bukasa, Compression and flexural tests of Mi Panels. *International Conference on Civil and Environmental Engineering (CEE'2013)*, Nov. 27-28, Johannesburg, South Africa, 2013.
- [2] SANS 10400, South African standard code of practice for the application of the national building regulations, South African Bureau of Standards, Pretoria, South Africa, 2011.



# Infrared thermography as a diagnostic tool for subsurface assessments of concrete structures

Matthew SCOTT<sup>1</sup> and Deon KRUGER

*Department of Civil Engineering Science, University of Johannesburg, South Africa*

**Abstract.** This paper presents on-going research into the application of infrared (IR) thermography as a means of diagnosing the presence of delaminations in concrete structures. Infrared thermography, as a diagnostic tool, has demonstrated the potential to detect and visually display areas of delamination in concrete structures, offering a feasible supplement to the traditional techniques used for delamination surveys. However, the thermal gradients that develop in the concrete, and that are essential for the detection of the delaminations, are the result of the prevailing ambient conditions that surround the structure. Depending on the nature of these conditions, certain delaminations may be more visible than others while some may not be visible at all. Solar radiation has a significant effect on these thermal gradients and consequently, the temperature contrasts that develop between the areas of delaminated and intact concrete. This paper addresses the effect that solar radiation has on the ability of infrared thermography to detect and reveal areas of delamination in concrete structures. This effect has been studied by quantifying the temperature contrasts that developed at the surface of a concrete panel into which delamination type defects were intentionally embedded at different depths.

**Keywords.** Infrared, thermography, delamination, concrete, diagnostic, thermal, gradients, ambient, solar, radiation, temperature, contrasts

## Introduction

As a non-destructive, two dimensional means of evaluation, infrared thermography has demonstrated the potential to detect, and in real time, visually display areas of delamination in concrete structures. The application of this technology has seen a significant increase in recent years as infrared cameras have become increasingly sophisticated and far better suited to the civil practitioners needs. In addition to this, the costs of these instruments have reduced considerably, making them more accessible and thus a more feasible means of evaluation. However, there are associated limitations with infrared thermography, most significantly, its reliance on the prevailing ambient conditions that surround the structure to provide the necessary thermal gradients needed in the concrete for delamination detection [1].

---

<sup>1</sup>Corresponding author: Department of Civil Engineering Science, Faculty of Engineering and the Built Environment, University of Johannesburg, PO Box 524 Auckland Park 2006 Johannesburg South Africa; E-mail: [200714792@student.uj.ac.za](mailto:200714792@student.uj.ac.za).

In order to detect areas where delaminations of the concrete cover have occurred, a thermal gradient must be present in the concrete so as to initiate the flow of heat through the concrete itself. In the presence of a delamination, this flow of heat is disrupted [2], the consequence of which reveals itself at the surface of the concrete. The disruption in heat flow manifests in an observable variation in temperature at the surface of the concrete relative to areas of concrete that are intact [1]. That is to say, temperature contrasts develop on the surface between those areas of concrete that are intact and those above the subsurface locations of the delaminations. It is these surface temperature variations that are detected by infrared cameras which in turn reveal the presence and areas of delamination.

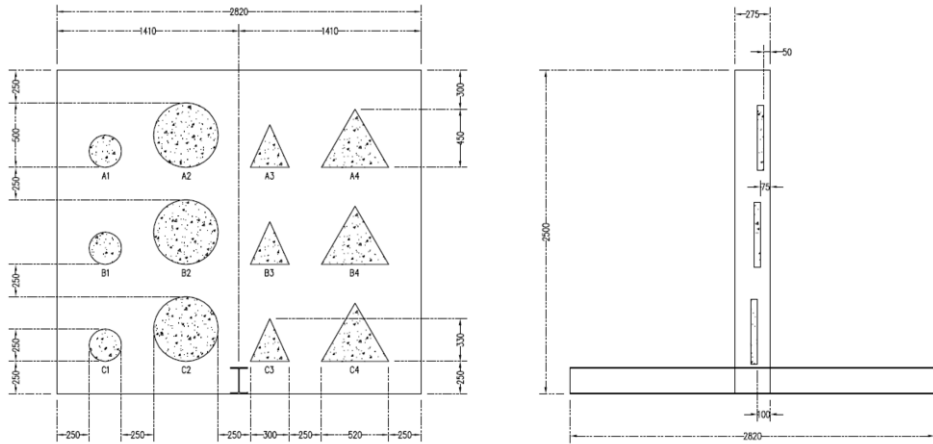
The thermal gradient that drives the flow of heat through the concrete is the result of the prevailing ambient conditions that surround the structure [3]. Solar radiation provides the radiant heating that warms the surface of the concrete, establishing the thermal gradient necessary for delamination detection. The ability to detect areas of delamination is heavily influenced by the intensity and duration of radiant heating absorbed by the concrete. Meteorological conditions such as cloud cover reduce the intensity of radiant heating received from the sun and thus hinder the ability to detect areas of delamination. Atmospheric attenuation, perpetuated by factors such as air temperature and relative humidity, is compensated for through camera settings and input parameters of these meteorological phenomena.

It is important to understand what ambient conditions are required in order to provide optimum surface temperature contrasts between areas of concrete that are intact and any potential areas of delamination. However, it is also important to understand how the prevailing ambient conditions on any given day may influence the outcome of a delamination survey using infrared thermography. The research presented in this paper focused on addressing the effect that solar radiation has on the ability of infrared thermography to detect and reveal areas of delamination in concrete structures. To quantify this effect, a concrete panel was constructed, into which delamination type defects were intentionally embedded at different depths, simulating the presence of delaminations that would disrupt the flow of heat through the concrete.

## **1. Background**

As it has previously been established, areas of delamination in concrete structures reveal themselves at the surface of the concrete in observable variations in temperature relative to areas of concrete that are intact [1]. The cause of this is the influence the delamination has on the rate at which the concrete, anterior to the delamination, warms and cools under the prevailing ambient conditions surrounding the structure. The effect of the delamination is to increase the rate of warming or cooling of the anterior concrete depending on the direction of heat transfer. The delamination increases the rate of warming or cooling as the air void, created by the delamination, acts as an insulating discontinuity reducing the ability of heat to conduct through and beyond the delamination.

When the ambient conditions begin to warm after sunrise, a positive thermal gradient develops in the concrete resulting in an increased rate of warming of the anterior concrete, leading to higher surface temperatures of the areas of concrete above the subsurface locations of the delaminations. Conversely, when the ambient conditions begin to cool following solar noon, a negative thermal gradient develops in the



**Figure 1.** Diagram of the concrete panel with embedded targets at depths of 50 mm (A1, A2, A3, A4), 75 mm (B1, B2, B3, B4) and 100 mm (C1, C2, C3, C4)

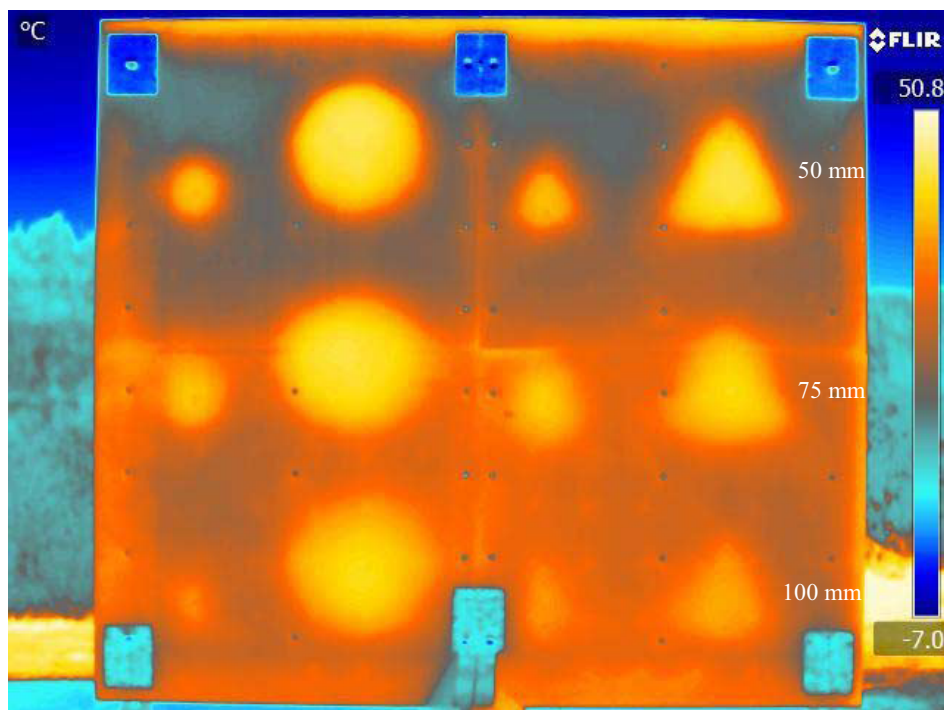
concrete, resulting in an increased rate of cooling of the anterior concrete, leading to lower surface temperatures of the areas of concrete above the subsurface locations of the delaminations. However, if the concrete finds itself in a state of equilibrium with the prevailing ambient conditions, the thermal gradient in the concrete will cease to exist and any potential areas of delamination will go undetected.

## 2. Experimental

A concrete panel was constructed as shown in Figure 1. Resting on a circular footing, the panel was 2.82 m x 2.5 m with thickness of 0.275 m. To provide stability against overturning a universal beam (I-section) was cast through the panel at mid-base as shown in Figure 1. Circular and triangular sheets, cut from 50 mm thick high density expanded polystyrene, were used as embedded targets to provide subsurface features that would disrupt the flow of heat through the concrete. The targets were placed at depths of 50 mm (A1, A2, A3, A4), 75 mm (B1, B2, B3, B4) and 100 mm (C1, C2, C3, C4) from the north facing elevation of the panel.

A FLIR SC620 infrared camera which monitored the panel was positioned in an observation enclosure located 8 m from the panel. Thermal images of the panel were captured at 30 minute intervals over duration of approximately 11 hours, a period governed by the local rising and setting times of the sun. In addition to this, global horizontal irradiance was measured and logged during the observation of the panel. The global horizontal irradiance was measured using a horizontally mounted pyranometer. Irradiance is the instantaneous value of radiation, or the flux of radiation, expressed in watts per square meter ( $W/m^2$ ).

Figure 2 details a thermal image of the north facing elevation of the concrete panel. From the image it is evident that all of the embedded targets, at all three depths, are clearly visible with twelve distinct temperature contrasts appearing on the surface of the concrete. In order to obtain quantitative data from these visual contrasts, the apparent temperature differences, inferred by the thermal images, between the



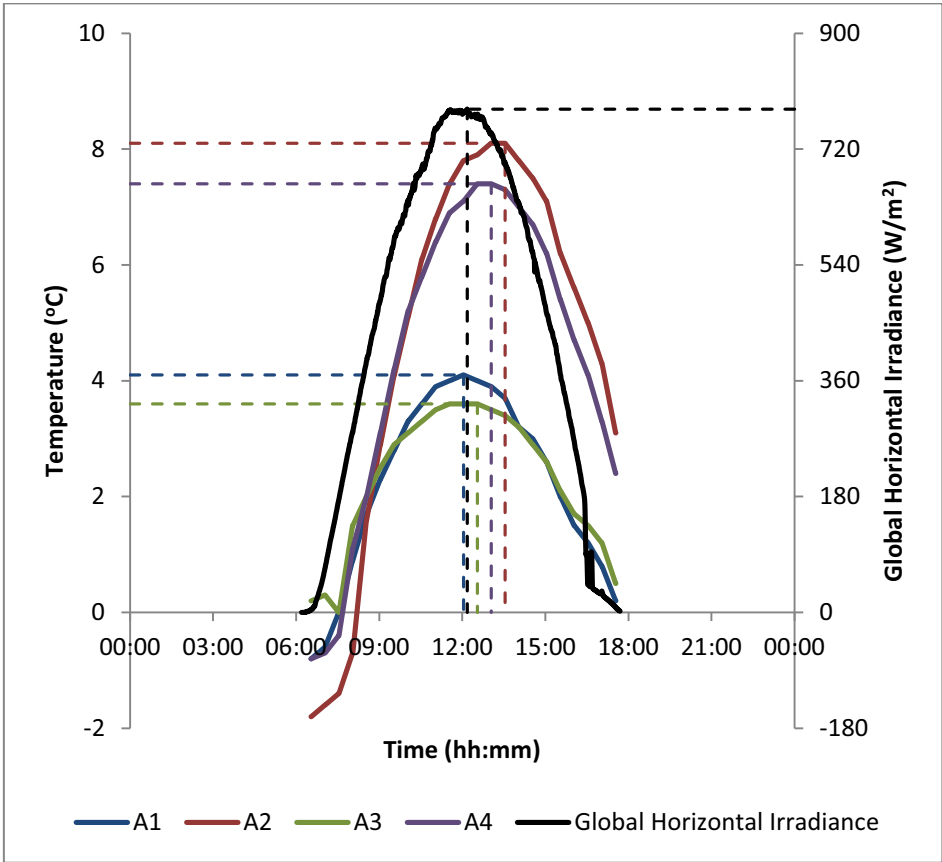
**Figure 2.** Thermal image of the concrete panel showing the embedded targets at depths of 50 mm, 75 mm and 100 mm

embedded targets and the surrounding intact concrete were measured and analysed. The temperature differences were measured for each target over the complete duration of observation.

### 3. Results

The actions of this experimental work are reported herein with results that were used to evaluate the degree to which the 50 mm deep delamination type defects (A1, A2, A3, A4) affect the relative time period during which the observable variations in temperature that manifested at the surface of the concrete panel are optimized under local conditions in Johannesburg, South Africa. Observations of the north facing elevation of the concrete panel were conducted with data collected over the winter months of May and June 2013. This data included the apparent temperature differences between the embedded targets and the surrounding intact concrete as well as local on-site measurements of global horizontal irradiance.

Figure 3 illustrates the temporal distribution of global horizontal irradiance over a 12 hour period on a particular day in May 2013. It is a graphical representation of the power of the solar radiation per unit area incident on a horizontal surface. It serves as a site reference, quantifying the local solar energy resources on that particular day. In addition to this, Figure 3 illustrates the temporal distribution of the temperature contrasts that developed at the surface of the concrete panel over the same period, on



**Figure 3.** Effects of solar radiation on the temperature contrasts created by the embedded targets at a depth of 50 mm (02/05/13)

the same day, for each of the 50 mm deep embedded targets. The figure shows the similarities between the development of the temperature contrasts and the pattern of global horizontal irradiance, as illustrated by the shape of each temporal distribution.

It shows a delay between the peak temperature contrasts for Target’s A2 and A4 and the maximum irradiance for that particular day, leading to the conclusion that the delay between maximum solar radiation and peak temperature contrast increases for an increased target size. Moreover, the peak temperature contrasts suggest that larger targets develop larger contrasts. The temperature contrasts for Target’s A1, A2, A3 and A4, at maximum, are 4.1°C, 8.1°C, 3.6°C and 7.4°C, occurring at approximately 12:00, 13:30, 12:30 and 13:00 respectively. This in contrast to the maximum irradiance occurring at approximately 12:00. The smaller targets reached their maximum contrasts at roughly the same time as maximum irradiance whereas the larger targets reached their maximum temperature contrasts approximately one hour later.

Data over the two months of observations were analysed in this manner to quantify the time of day and duration after sunrise that each target reached its maximum temperature contrast. It was found that the duration after sunrise for maximum temperature contrast to occur for Target’s A2 and A4 were identical at roughly six

hours, 30 minutes after sunrise, with a standard deviation of approximately 25 minutes. Target A1 reached its maximum temperature contrast in the shortest space of time, roughly four hours, 30 minutes after sunrise, with a standard deviation of approximately 20 minutes. Sunrise on this particular day occurred at approximately 06:30 which suggests that the optimum time to conduct the delamination survey would have been between 11:00 and 13:00.

#### **4. Conclusions**

This paper has reported selected results from on-going research into the application of infrared thermography as a means of diagnosing the presence of delaminations in concrete structures. A concrete panel was constructed to address the effect that solar radiation has on the ability of infrared thermography to detect and reveal areas of delamination in concrete structures. The paper focused on evaluating the degree to which a 50 mm deep delamination would affect the relative time period during which the observable variations in temperature that manifested at the surface of the concrete panel, relative to areas of intact concrete, created by the presence of the delamination, are optimised under local conditions in Johannesburg, South Africa.

Observations of the north facing elevation of the concrete panel were made over a period of two months during winter. Data collected included thermal images of the panel which were used to extract quantitative data of the apparent temperature differences between the embedded targets and the surrounding intact concrete. In addition to this, global horizontal irradiance was measured and logged to provide a site reference of local solar energy resources. This data was analysed in order to quantify the time of day and duration after sunrise that a 50 mm deep delamination would reach its maximum temperature contrast. The results suggested that optimum contrasts would be achieved during a late morning, early afternoon survey.

#### **Acknowledgments**

This author wishes to acknowledge Glenn Washer (Assistant Professor, University of Missouri), Richard Fenwick and Naveen Bolleni (Graduate Research Assistants, University of Missouri) for their research presented in the manuscript entitled "Effects of Solar Loading on Infrared Imaging of Subsurface Features in Concrete". The paper, published in the *Journal of Bridge Engineering*, provided this author with the inspiration to pursue this line of research for a Master of Engineering (MEng: Civil). An attempt has been made to replicate the experimental study reported in the paper for the purpose of evaluating how their results and the conclusions at which they arrived would differ for observations in the Southern Hemisphere.

#### **References**

- [1] Washer, G., R. Fenwick & N. Bolleni 2010: Effects of Solar Loading on Infrared Imaging of Subsurface Features in Concrete. *Journal of Bridge Engineering*, 15, 384-390.
- [2] Kipp, J.S. & J.T. Kunz 1983: Thermographic investigation of a bridge deck. *Public works*, 70-73. Ridgewood, N.J.
- [3] Roddis, W.M.K. 1987: Concrete bridge deck assessment using thermography and radar. M.S. thesis. Massachusetts Institute of Technology: Department of Civil Engineering.

# The stress-related material damping of rigid frame bridge with corrugated steel webs

Liu BAODONG<sup>1</sup>, Li WEILONG, Li PENGFEI and Lv WENJUAN

*Department of Civil Engineering, Beijing Jiaotong University, Beijing 100044, China*

**Abstract:** The inelastic behavior of the materials leads to the energy dissipation. The amplitude of the stress is the main affect factor for the energy dissipation capacity of solid materials such as metal and concrete. Based on the loss energy per unit volume of the metal material and reinforced concrete material, the stress-related material damping of the steel concrete composite structure are calculated. Combined with the finite element methods, an iterative algorithm is proposed to calculate the material damping of the rigid frame bridge with corrugated steel webs. Based on a model of rigid frame bridge with corrugated steel webs and the equivalent concrete web bridges, the material damping of the structure under different seismic intensity are calculated and compared. The analysis and comparison show that the stress-related material damping increased with the seismic intensity. Different damping ratios should be considered under different seismic intensities for the seismic response analysis of the bridge.

**Keywords.** Energy dissipation, stress-related material damping, rigid frame bridge with corrugated steel webs, iteration, seismic intensity

## Introduction

Box girder with corrugated steel webs represents a new innovative system which has emerged in the past decade for short and medium span bridge. The new system usually combines the usage of corrugated steel plates as webs and reinforced/prestressed concrete slabs as flanges for plate or box girders [1].

This bridge type has been widely applied since the French built the first box girder bridge with corrugated steel webs in 1986[2]. Currently this bridge type has been mainly used in continuous bridges and continuous rigid frame bridges.

Damping ratio has a great influence on the dynamic response of structures. Large numbers of measured data show that, the structural damping ratio is different under different loading conditions, and the difference has a great gap. Under different seismic intensities, Newmark did a lot of research work to determine the damping ratio of the nuclear reactor in 1971, and got the experimental results that the damping ratio could had magnitude difference in different working stresses[3]. Hart identified the first three modes of damping ratio according to the earthquake records data of 12 high-rise buildings[4]. He found that the damping ratio of the structure increase when the ground

---

<sup>1</sup>Corresponding author: Tel. +86-10-51687252, Fax.+86-10-51687248, baodongliu@vip.sina.com

motion got stronger. Celebi collected five structural damping data under Loma Prieta Earthquake in San Francisco on October 17, 1989, and the damping data measured in part of the buildings before and after the earthquake under low amplitude of vibration [5]. The analysis results showed that the structure damping ratio in strong earthquake ground motion was significantly larger than that under the low amplitude of vibration.

Considering the structural characteristic of the rigid frame bridge with corrugated steel webs, this paper introduce a stress-related damping ratio formula based on the loss energy per unit volume of metal material [6] and reinforced concrete material [7]. Meanwhile, an iterative algorithm is proposed and the damping ratios under different seismic intensities are iteratively calculated based on a model of rigid frame bridge with corrugated steel webs and the equivalent concrete web bridges.

**1. Stress-related damping formulas**

Lazan B J (1968) [6] proposed the relationship between the unit volume loss energy  $\Delta u_1$  and the maximum stress amplitude for most metal materials as Eq. (1):

$$\Delta u_1(\sigma_s) = 0.006895(\sigma_s / \sigma_f)^{2.3} + 0.041360(\sigma_s / \sigma_f)^8 \tag{1}$$

Where  $\sigma_f$  is the fatigue limit stress of metal,  $\sigma_s$  is the average maximum shear stress amplitude of every metal unit.

Wen Jie[7] established an unit volume loss energy  $\Delta u_2$  of reinforcement concrete considering the working conditions. It can be written as Eq. (2):

$$\Delta u_2(\sigma_c, f_c, r, ac) = \frac{0.0193013 \sigma_c^{3.88} \cdot (1+r)^{-31.93}}{(1-41.66 \cdot f_c - 0.57 \cdot f_c^2) \cdot (1-56977.5 \cdot ac + 44634.7 \cdot ac^2)} \tag{2}$$

Where  $\sigma_c$  is the average maximum bending stress amplitude of each concrete unit,  $r$  is the longitudinal reinforcement ratio,  $f_c$  is the standard value of concrete compressive strength,  $ac$  is the axial compression ratio.

In the rigid frame bridge with corrugated steel webs, the bending moment mainly undertook by the concrete slabs and the shear force mainly undertook by corrugated steel webs. Using the finite element discrete form, after obtaining the maximum stress of each element under different working conditions using finite element method, the loss factor could be calculated as Eq. (3)[8]:

$$\eta = \frac{1}{2\pi} \frac{\Delta U}{U} = \frac{1}{\pi} \cdot \sum_{i,j} \frac{A \sigma_i^{3.88} V_i + \left[ B \left( \frac{\tau_j}{\sigma_f} \right)^{2.3} + C \left( \frac{\tau_j}{\sigma_f} \right)^8 \right] V_j}{\left( \frac{\sigma_i^2}{E} V_i + \frac{\tau_j^2}{G} V_j \right)} \tag{3}$$

where  $A = \frac{0.0193013(1+r)^{-31.93}}{(1-41.66 \cdot f_c - 0.57 \cdot f_c^2) \cdot (1-56977.5 \cdot ac + 44634.7 \cdot ac^2)}$ ,  $B$  is 0.006895,



$C$  is 0.04136,  $\sigma_i$  is the average maximum bending stress of  $i$ -th element at two nodes of concrete unit,  $\tau_j$  is the average maximum shear stress of  $j$ -th steel plate unit,  $V_i$ 、 $V_j$  is the volume of each unit,  $E$  is the elastic modulus of concrete,  $G$  is the shear modulus of steel.

The value of equivalent damping ratio could be calculated according to the loss factor using Eq. (4) [9-10]:

$$\xi = \frac{\eta}{2} \tag{4}$$

**2. Calculation of damping ratio under different seismic intensities**

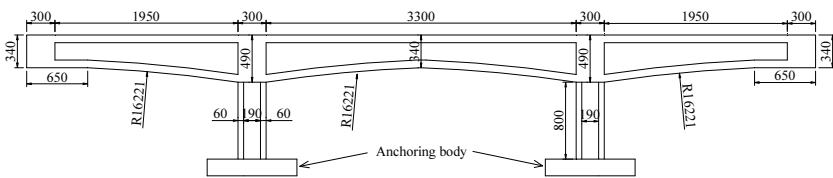
*2.1. Iteration algorithm*

In order to get the stress-related damping ratio of rigid frame bridge with corrugated steel webs and concrete web bridge under different seismic intensities, the longitudinal seismic response is calculated using response spectrum method by the Chinese Guidelines for Seismic Design of Highway Bridges (MCPRC 2008) [11]. Assume the site type is Class II. The seismic fortification category is class B.

By assuming an initial damping ratio  $\zeta_0$  in the finite element model, the stress of every unit can be calculated using mode-decomposition response spectrum method. Then, use the stress of every unit, the equivalent damping ratio  $\zeta$  of the bridge can be calculated by Eq. (1) to Eq. (4). If the  $\zeta$  is not equal to  $\zeta_0$ , make  $\zeta_0$  equal to the  $\zeta$  and calculated again by the steps above. Using this iteration algorithm, until the final  $\zeta$  is equal to  $\zeta_0$ , the equivalent damping ratio can be got.

*2.2. Establish and verification of FEM for rigid frame bridge*

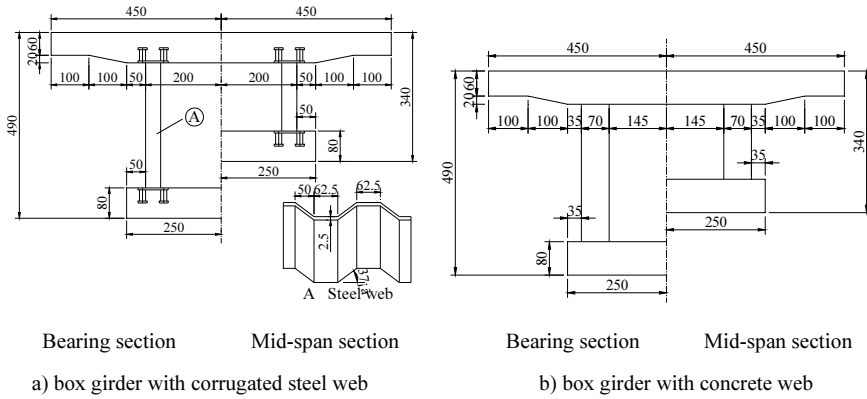
Two comparison models of continuous rigid frame bridge with corrugated steel webs and equivalent concrete continuous rigid frame bridge were designed and constructed. The structural diagram of the two bridges is shown in Figure 1.



**Figure 1.** Geometric size of the bridge ( mm )

The corrugated steel webs using Q235 steel, the thickness of them is 2.5mm. According to the equivalence principle that the webs can withstand the same shear force under the same load, the thickness of concrete web is 70mm. Both of the two kinds of webs are in straight web form. The concrete used in both of the two girders is

C40 grade concrete. The cross sections of the two kinds of bridge are showed in Figure2.



**Figure 2.** Section of box girder (mm)

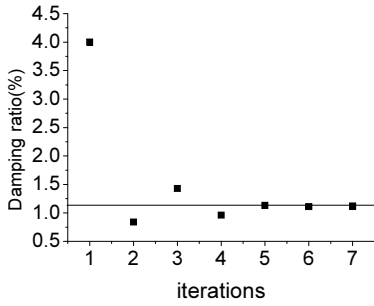
The finite element models of the bridges was built by MIDAS / CIVIL. The plate element was used in corrugated steel webs. 8-node solid element was used in concrete web rigid frame bridge and the other parts of the rigid frame bridge with corrugated steel webs. The finite element model of rigid frame bridge with corrugated steel webs had a total of 7304 solid elements and 312 plate elements. The finite element model of concrete web rigid frame bridge had a total of 3296 solid elements. All of the degrees of freedom at the bottom of piers were constrained. The vertical and lateral translational degrees of freedom of the side spans of the bridges were constrained.

Pulsation test was adopted in testing natural frequencies of the bridges. The measured longitudinal frequency of the concrete web rigid frame bridge was 14.279Hz and the calculated frequency was 14.554Hz. The measured longitudinal frequency of the concrete rigid frame bridge with corrugated steel webs was 10.935Hz and the calculated frequency was 11.172Hz. So, the finite element model is with sufficient precision and can be used to calculate the seismic response of the bridge.

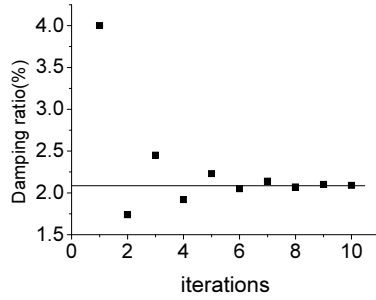
### 2.3. Iterative results and analysis

On the basis of Guidelines for Seismic Design of Highway Bridges, the number of vibration mode considered in mode-decomposition response spectrum analysis should make the modal mass participation ratio more than 90% in the calculation direction. Based on the finite element model in front, by combining the first 20 modes, the modal mass participation ratio is more than 90% in the longitudinal directions.

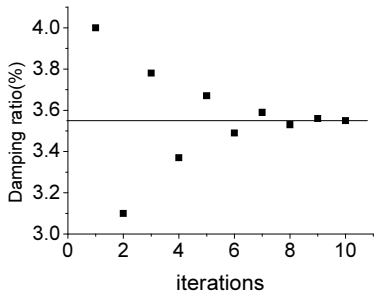
In order to discuss the stress-related damping ratio under different seismic intensities, the peak ground acceleration (PGA) is assumed as 0.05g, 0.10g, 0.20g and 0.40g. The initial damping ratio  $\zeta_0$  is assumed as 0.04. The iterative processes under different PGA are shown in Figure 3. and Figure 4.



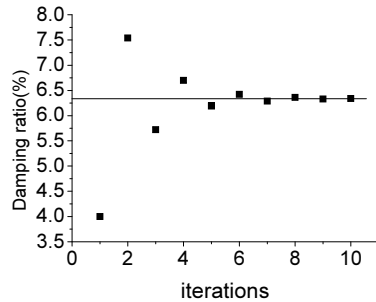
a) Iteration of damping ratio when PGA is 0.05g



b) Iteration of damping ratio when PGA is 0.10g

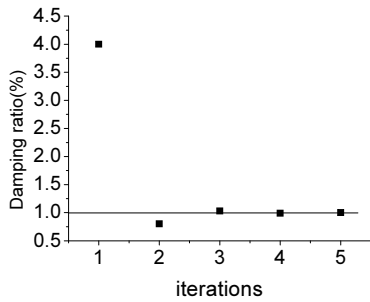


c) Iteration of damping ratio when PGA is 0.20g

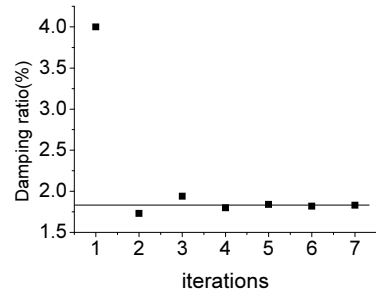


d) Iteration of damping ratio when PGA is 0.40g

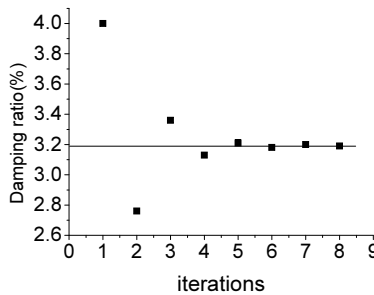
Figure 3. Damping ratio of the rigid frame bridge with corrugated steel webs



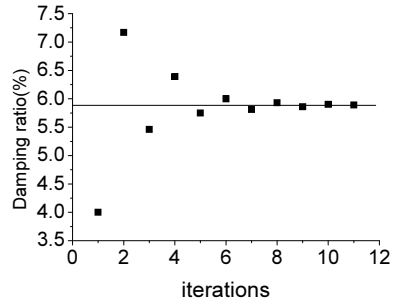
a) Iteration of damping ratio when PGA is 0.05g



b) Iteration of damping ratio when PGA is 0.10g



c) Iteration of damping ratio when PGA is 0.20g



d) Iteration of damping ratio when PGA is 0.40g

Figure 4. Damping ratio of the equivalent concrete web rigid frame bridge

As can be seen from figure 3 and figure 4, after several iterations, the final equivalent stress-related damping ratios under different PGA of the two bridges can come close to a fixed value. This method of calculating the stress-related damping ratio of rigid frame bridge is effective. The damping ratios under different PGA are different. With the increasing of the PGA, the damping ratio of the both kinds of bridges increased.

According to the response spectrum method, the seismic response of the structure depends on the spectrum value and mass of the structure. Because of the large stiffness of the two models in this paper, the vibration period located at ascent stage of the response spectrum. The spectrum value of the rigid frame bridge with corrugated steel webs is 15.1% larger than the spectrum value of the equivalent concrete web bridge when the PGA is same. The rigid frame bridge with corrugated steel webs is at a higher stress level than the equivalent concrete web bridge. So, the calculated damping ratios of the rigid frame bridge with corrugated steel webs are larger than that of the equivalent concrete web bridge. It is certified that the damping ratio of the bridge is related with the stress level.

### 3. Conclusions

(1) The stress-related damping ratio formula of rigid frame bridge with corrugated steel webs is introduced, which considered the loss energy of both the concrete slabs and the corrugated steel webs.

(2) The stress-related damping ratios of the rigid frame bridge with corrugated steel webs and the equivalent concrete web bridge change along with the seismic intensities. The higher the seismic fortification intensity is, the larger the damping ratios. The stress level of the structure determined the equivalent damping ratio of structure. Therefore, we suggest that different damping ratios should be considered under different seismic intensities for the seismic response analysis of the bridge.

### Acknowledgment

This research is sponsored by the China Natural Science Foundation No.50278031.

### Reference

- [1] Sayed-Ahmed E Y, Behavior of steel and (or) composite girders with corrugated steel webs, *Canadian Journal of Civil Engineering*, 2001,28,656-672.
- [2] Johnson R P, Cafolla J, Corrugated Webs in Plate Girders for Bridges, *Proceedings of the Institution of Civil Engineers, Structures and Buildings*, 1997,122(2),157-164.
- [3] Newmark N M. Earthquake Response Analysis of Reactor Structures, *Nuclear Engineering and Design*,1972,20,303-322.
- [4] Hart Gary C, Random damping in buildings, *Journal of Wind Engineering and Industrial Aerodynamics*,1996,59,233-246.
- [5] Celebi M., Comparison of damping in buildings under low-amplitude and strong motions, *Journal of Wind Engineering and Industrial Aerodynamics*, 1996,59, 309-323.
- [6] B J Lazan, *Damping of material and members in structural mechanics*, London, Pergamon Press, 1968.
- [7] Wen Jie, Wang Yuanfeng, Computation And Formula For Material Damping Of Concrete Components Under Axial Cycle Load, *Journal of Vibration and Shock*,2007,26(6),14-16.

- [8] Li Bo, Liu Baodong, Li Pengfei, Wang Yuanfeng, Stress-related damping characteristic of a composite box-girder with corrugated steel webs, *Journal of Vibration and Shock*, 2012,31(6),68-71.
- [9] Liang Chaofeng, Ou Jinping, Relationship between structural damping and material damping, *Earthquake Engineering and Engineering Vibration*, 2006,26(1),49-55.
- [10] Zhu Jingqing, On the Two Basic Problems of Complex Damping Theory, *Acta Mechanica Sinica*, 1992,13(2),113-118.
- [11] JTG/T B02-01-2008, *Guidelines for Seismic Design of Highway Bridges*.

# Evaluating concrete with high-performance steel fibers using double-punch testing

Aaron P. WOODS<sup>a,1</sup>, Richard KLINGNER<sup>a</sup>, James JIRSA<sup>a</sup>, Shih-Ho CHAO<sup>b</sup>, Netra KARKI<sup>b</sup> and Oguzhan BAYRAK<sup>a</sup>

<sup>a</sup>University of Texas at Austin, United States

<sup>b</sup>University of Texas at Arlington, United States

**Abstract.** In order to quantify steel fiber-reinforced concrete (SFRC) mixtures for field applications, a material test capable of predicting the performance of SFRC for various fiber content and types is required. However, current test methods used to evaluate the structural properties of FRC (such as residual strength and toughness) are widely regarded as inadequate and complicated; a simple, accurate, and consistent test method is needed. It was determined that the Double-Punch Test (DPT), originally introduced for plain concrete, could be extended to fiber-reinforced concrete to satisfy this industry need. Like most conventional methods, in the DPT, a specimen is stressed in indirect tension. A concrete cylinder is compressed vertically by steel punches located concentrically on the top and bottom cut surfaces. Initial tests showed distinct advantages in simplicity, reliability, and repeatability over current test methods for FRC. Benefits were largely due to the loading procedure and load distribution which resulted in multiple failure surfaces that captured the random distribution of fibers more effectively than current standardized test methods for FRC. Several variables including fiber manufacturer, fiber content, and testing equipment were evaluated to refine the testing procedure for straightforwardness and accuracy. In this paper, the results of over 350 double-punch tests are summarized.

**Keywords.** Concrete, Double-Punch Test, fiber-reinforced concrete, high-performance steel fibers, strength, durability

## Introduction

The main topic of this paper is the use of double-punch testing to evaluate the effectiveness of different types of high-performance steel fibers in concrete. The procedures proposed here offer end users a simple and reliable way to convert the results of tests involving one type of high-performance fiber, to the probable test results that would be obtained with other types of high-performance fibers. In addition to comparative purposes, experimental results indicate the DPT can be standardized by national and international agencies, such as the American Society of Testing and Materials (ASTM), as a method to evaluate the mechanical behavior of FRC in general.

## 1. Background on Double-Punch Testing

The tensile strength and toughness of fiber-reinforced concrete can be determined from indirect tensile tests on cylinders [1], flexural tests on beams [2, 3], centrally load-tested panels [4, 5], or direct tensile tests on dog-bone specimens [6].

<sup>1</sup>Corresponding author: [awoods@mka.com](mailto:awoods@mka.com)

Unfortunately, each of these tests suffers from a lack of simplicity, reliability, or reproducibility (alone or in combination). An improved test method is needed. That need may be satisfied by the Double-Punch Test (DPT), originally proposed by Chen in 1970 [7].

At the time of its introduction, the DPT was recommended as an alternative to the splitting tensile test for determining the tensile strength of plain concrete. As shown in Figure 1, in the Double-Punch Test, a concrete cylinder is placed vertically between the loading platens of the test machine and compressed by two steel punches located concentrically on the top and bottom faces of the cylinder [7, 8]. The simplicity of this test and the fundamental fracture mechanics underlying it suggest that it would be useful for evaluating the performance of fiber-reinforced concrete (FRC).

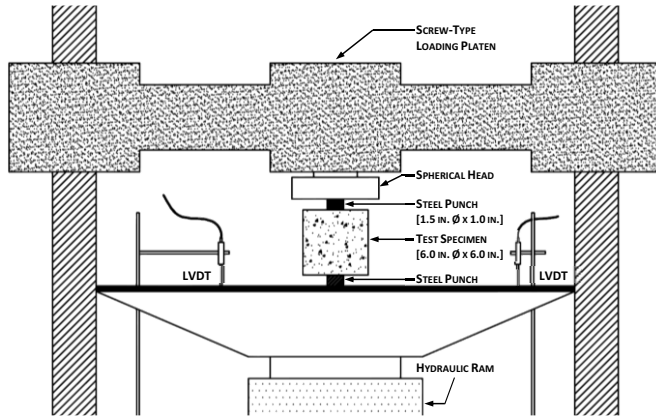


Figure 1. Apparatus and loading schematic for the Double-Punch Test [8]

## 2. Theory and mechanics of the Double-Punch Test

The fundamental theory and mechanics of the Double-Punch Test are based on the bearing capacity of concrete blocks [9]. A formula for computing the tensile strength of indirect tensile tests was obtained from the theory of linear elasticity and combined with a plasticity approach for concrete. This approach was based on the assumption that sufficient local deformability of concrete in tension and in compression existed such that generalized theorems of limit analysis could be applied to concrete idealized as a perfectly plastic material [7].

Because the behavior of a concrete block during a bearing capacity test is closely related to the behavior of a Double-Punch test, the formula for the DPT was obtained directly from a simple modification of results reported for concrete blocks [9, 10]. The formula for computing the tensile strength in a Double-Punch Test is given by Eq. (1).

$$f_t' = \frac{Q}{\pi(1.20 bH - a^2)} \quad (1)$$

Where:  $f_t'$  = tensile strength, psi [kgf/cm<sup>2</sup>],  $Q$  = ultimate load, lb [kg],  $H$  = cylinder height, in. [cm]  
 $b$  = cylinder radius, in. [cm], and  $a$  = punch radius, in. [cm]

As shown in Figure 2, the ideal DPT failure mechanism of a test specimen consists of three to four major radial tension cracks as well as various micro-cracks.

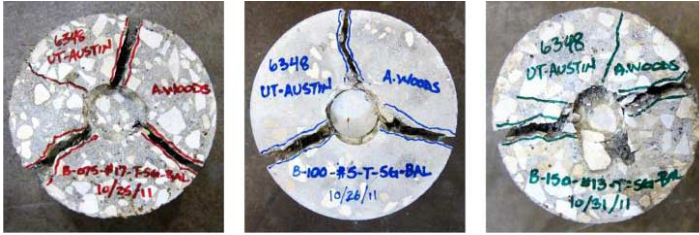


Figure 2. Typical damage and cracking pattern of DPT specimens with steel fibers [8]

### 3. Extension of DPT testing to evaluate the mechanical properties of FRC

The extension of DPT testing to FRC is a novel application of this test method. At the time of writing this paper, the earliest research of DPT for FRC that the authors are aware of was reported in 2006 [11]. Previous research showed that the Double-Punch Test resulted in lower coefficients of variation compared to beam tests on FRC [12]. However, further experimental and theoretical work was recommended to determine the usefulness of this test in characterizing the tensile properties of fiber-reinforced concrete.


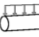
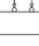
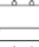
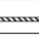



The Double-Punch Test is particularly useful for testing FRC for two main reasons: 1) it involves a relatively simple test setup and procedure; and 2) it produces failure by radial cracking at unconstrained angular orientations, which is consistent with the random dispersion and orientation of high-performance steel fibers in concrete.

The Double-Punch Test is conducted using an easily handled 6- x 6-in. [15.30- x 15.30-cm] cylinder specimen weighing about 15 lb [6.80 kg]. Because specimens are tested in compression, any universal testing machine can be used (hydraulic or screw-type), and servo-controlled testing machines are unnecessary.

The multiple radial cracks at random orientations produced by DPT increases the probability that fibers will intersect crack planes, permitting the effects of fiber reinforcement to be captured. One measure of this is the specific failure surface ( $\beta$ ) of the test specimen, defined as the total failure surface area per unit volume of a test specimen. Numerically, it represents the fracture plane or planes that form at failure for a given test method. Table 1 gives the ratios of specific failure surface for the DPT compared with other standardized test methods for FRC. It is evident that the DPT is superior to all other methods in terms of  $\beta$ , in some cases as much as an order of magnitude [8].



**Table 1.** Comparison of the specific failure surface of DPT vs. test specimens for current FRC test methods

TEST INFORMATION <sup>1</sup>		TEST SPECIMENS				
Designation	Layout	Volume (in. <sup>3</sup> )	Number of Failure Planes	Failure Surface Area (in. <sup>2</sup> )	Specific Failure Surface, $\beta$	$\beta_{DPT} / \beta_{TEST}$
Double-Punch Test		170	3	54.0	0.318	1
ASTM C496		101	1	12.6	0.125	3
ASTM C1609		720	1	36.0	0.050	6
ASTM C1609		224	1	16.0	0.071	4
ASTM C1399		224	1	16.0	0.071	4
ASTM C1550		2338	3	141.8	0.061	5
EFNARC Panel Test		2304	3	144.0	0.063	5
Uniaxial Direct Tensile Test		524	1	16.0	0.031	10

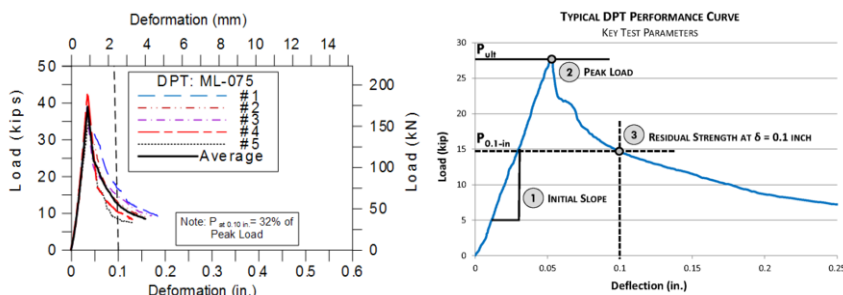
<sup>1</sup>Test layouts modified from Molins (2006) [11]

#### 4. Results from Double-Punch Testing of fiber-reinforced concrete

In the research program described here, Double-Punch tests were carried out at the University of Texas at Arlington (UT Arlington), and at the University of Texas at Austin (UT Austin). Additional information is provided in the final report for this project [13], and in individual references cited below for each university.

##### 4.1. Evaluation criteria for DPT results

When a concrete specimen reinforced with high-performance steel fibers is subjected the Double-Punch test, the resulting curves of applied load versus axial deformation are typified by those given in Figure 3, with a nearly linear ascending branch, a peak load, and a non-linear descending branch.



**Figure 3.** Typical DPT results in concrete with high-performance steel fibers

The load-deformation curves can be characterized by three key parameters: the slope of the ascending branch; the peak load; and the value of load on the descending branch at a deformation of 0.1 in. (2.5 mm).

4.2. Results from DPT testing of FRC at UT Arlington

In this section, results from Double-Punch tests at UT Arlington are summarized. Details of test procedures and results are provided in Appendix F in [13]. Additional information is given in [6, 14].

The first three phases of double-punch testing at UT Arlington emphasized the validation of DPT methods in terms of peak strengths and residual strengths. Tests were carried out using a simple 60-kip universal machine on concrete made with three types of high-performance steel fibers: Type 1 (Royal with a single end hook); Type 2 (Baekert short, with double end hooks), and Type 3 (Baekert long, with double end hooks). Volume fractions ranged from 0 to 2%. Volume fractions less than 0.5% did not enhance the performance of concrete significantly. Volume fractions greater than 1.5% caused mixing problems particularly for long fibers.

Phase 1 of double-punch testing at UT Arlington showed significant variability in elastic stiffness and post-peak behavior, even though 10 replicates were used. In contrast, this variability was much lower in Phase 3, even though the number of replicates was reduced to four. This was due to the introduction of an initial “shakedown” loading.

In Phase 4 of double-punch testing at UT Arlington, the variability in residual strength at 0.1-in. deformation was further reduced by carrying out tests at 28 days rather than at early ages. As shown in Table 2, COVs for peak strength and for residual strength at 0.10-in. deformation were less than 15%, which is lower than those for other material test methods.

**Table 2.** Average COVs for Phases 1 through 4 of Double-Punch testing done at UT Arlington

Type of Specimen	Peak Load				Residual Load (at 0.1 in. Deformation)			
	Phase 1	Phase 2	Phase 3	Phase 4	Phase 1	Phase 2	Phase 3	Phase 4
PC	5.2%	12.7%	5.2%	5.2%	-	-	-	-
SFRC-R-Type 1	5.7%	9.9%	4.1%	4.2%	11.6%	11.9%	13.7%	15.8%
SFRC-BS-Type 2	5.2%	7.3%	4.5%	3.7%	14.8%	19.8%	16.9%	14.9%
SFRC-BL-Type 3	8.3%	6.2%	4.5%	4.5%	20.0%	21.4%	25.9%	14.4%
SFRC-HX-Type 4	-	-	-	5.4%	-	-	-	12.3%

As shown in Table 3, although COVs for residual strength and toughness from the DPT were greater than 10%, these values were still less than half the corresponding COVs from bending and direct tensile tests. Similarly, individual load-deformation curves from bending tests and direct tensile tests show more scatter around their average curves.

**Table 3.** Average COVs for Double-Punch test, bending test, and direct tensile test done at UT Arlington

Type of test	Peak load	Residual Strength	Toughness
Double punch test (DPT)	5.7%	14.8%	9.2%
Bending test (ASTM C1609 )	16.8%	32.0%	24.2%
Direct tensile test (DTT)	17.8%	32.0%	24.8%

Applying the criteria of equal peak strength and equal residual strength at 0.1-in. deformation, the volume fractions necessary to achieve equivalent performance is approximately (Royal: Short Bekaert: Long Bekaert) = (2.4: 1.55: 1.0). For example, a mixture with a volume fraction of 1% Long Bekaert fibers will have the same performance as a mixture with 1.55% short Bekaert fibers, and as a mixture with 2.4% Royal fibers.

#### 4.3. Results from DPT testing of FRC at UT Austin

The emphasis of the double-punch testing conducted at the UT Austin was the development of testing protocols that would give reliable intra- and inter-laboratory results, and thereby permit the DPT to be used to compare the effectiveness of concrete mixtures reinforced with different types and volume fractions of high-performance steel fibers. Experiments addressed the fabrication of specimens, preparation of specimens for testing, test setup, testing procedures, and evaluation of test data. Details are given in [8, 13].

More than 240 Double-Punch tests were conducted at UT Austin using two different high-performance steel fibers. For the five (5) batches of samples tested, coefficients of variation for initial slope, peak load, and residual load obtained using the developed protocol were 10%, 5%, and 20%, respectively. As discussed in Appendix B in [8], these findings were consistent across different fiber types, volume fractions, surface preparation (grinding or Hydro-stone), test machine, and cylinder portion (top or bottom).

## 5. Significance of results and conclusions

DPT performance curves (raw data) show that the Double-Punch Test can reliably distinguish between the effects of different fiber types and volume fractions on steel fiber-reinforced concrete (SFRC); indicating that the DPT is useful for comparing SFRC mixtures. Various statistical analyses (derived data), substantiate the validity of the DPT for such comparison purposes. DPT can also be used to characterize other aspects of the mechanical performance of SFRC, such as resistance to cracking, residual strength, and toughness.

The following conclusions are based on the results of the DPT Research and Testing Program [8]. Conclusions are categorized based on their relation to the simplicity, reliability, and reproducibility of the Double-Punch Test.

### 5.1. Simplicity of the DPT

- The *specimens* required to conduct the Double-Punch Test can be fabricated using basic cylinder molds. They are lightweight, and can be placed into the testing apparatus without the need for special fixtures.
- The *test setup* and *support conditions* are simple and it is quite easy to ensure concentric load is applied to the test specimen.
- As for the *test machine*, any Universal Testing Machine can be used to conduct the DPT; a closed-loop, servo-controlled machine is not required.
- The *test procedure* is quick and simple; the average Double-Punch Test takes less than 20 minutes to perform.

### 5.2. Reliability of the DPT

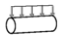
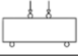





- The *test results* reflect the desired role of steel fibers, being to improve the toughness and ductility of concrete. The DPT is an effective way to compare the post-cracking ductility and performance of mixtures containing different fiber types (manufacturer and geometry) as well as different fiber volume fractions (% fiber).
- The *failure mechanism* produced by the DPT occurs along multiple planes, with the typical damage being concentrated along three or four radial planes. Thus, test results represent an averaged mechanical behavior.
- The *within-batch, single-laboratory precision (COV)* for key test parameters is generally low and comparable to or better than other current test methods for FRC:  $\pm 10\%$  Initial Slope;  $\pm 5\%$  Peak Load; and  $\pm 20\%$  Residual Strength at 0.1 in. deflection.

### 5.3. Reproducibility of the DPT

- The *inter-laboratory precision (COV)* for key test parameters was not determined in this study.

Table 4 provides a comparison of the complexity, reliability, and reproducibility of current test methods (for FRC) vs. DPT. It is clear that the Double-Punch Test can be extended to SFRC with similar precision and less complexity compared to other tests.

**Table 4.** Simplicity, reliability, and reproducibility of current FRC testing procedures vs. DPT

TEST INFORMATION <sup>1</sup>		SIMPLICITY <sup>2</sup>				RELIABILITY <sup>3</sup>		REPRODUCIBILITY <sup>3</sup>
Designation	Layout	Specimen Fabrication & Handling	Test Setup & Support Fixtures	Test Procedure	Test Machine	Failure Mechanism	Within-Batch Precision (COV)	Inter-Laboratory Precision (COV)
ASTM C496		Easy	Easy	Easy	Standard	Single Major Crack	± 5% PL	Not Available
ASTM C1609		Moderate	Difficult	Moderate	Closed-Loop	Single Major Crack	± 8% PL ± 20% RS	Not Available
ASTM C1399		Moderate	Difficult	Difficult	Standard	Single Major Crack	± 20% RS	± 40% RS
ASTM C1550		Difficult	Difficult	Difficult	Closed-Loop	Multiple Cracks	± 6% PL ± 10% RS	± 9% PL ± 9% RS
EFNARC Panel Test		Difficult	Difficult	Moderate	Closed-Loop	Multiple Cracks	Not Available	Not Available
Uniaxial Direct Tensile Test		Difficult	Moderate	Moderate	Closed-Loop	Single Major Crack	Not Available	Not Available
<b>Double-Punch Test</b>		<b>Easy</b>	<b>Easy</b>	<b>Easy</b>	<b>Standard</b>	<b>Multiple Cracks</b>	<b>± 10% Initial Slope ± 5% Peak Load ± 20% Residual Strength</b>	<b>Not Available</b>

<sup>1</sup> Test layouts modified from [11].

<sup>2</sup> Complexity levels assigned based on literature and personal communication with researchers [6].

<sup>3</sup> Reliability and reproducibility data obtained from industry standards and research literature [1, 2, 3, 4, 6]. COVs for peak load and residual strength (toughness) are denoted (PL) and (RS), respectively.

**References**

[1] ASTM C496. "Standard Test Method for Splitting Tensile Strength of Cylindrical Concrete Specimens." 2011.

[2] ASTM C1609. "Standard Test Method for Flexural Performance of Fiber-Reinforced Concrete (Using Beam with Third-Point Loading)." 2010.

[3] ASTM C1399. "Standard Test Method for Obtaining Average Residual-Strength of Fiber-Reinforced Concrete." 2010.

[4] ASTM C1550. "Standard Test Method for Flexural Toughness of Fiber Reinforced Concrete (Using Centrally Loaded Round Panel)." 2010.

[5] EFNARC. "European Specification for Sprayed Concrete." 1996.

[6] Chao, Shih-Ho. "FRC Performance Comparison: Uniaxial Direct Tensile Test, Third-Point Bending Test, and Round Panel Test." *ACI Special Publication 276: Durability Enhancements in Concrete with Fiber Reinforcement*, 2011: 5.1-5.20.

[7] Chen, W.F. "Double Punch Test for Tensile Strength of Concrete." *ACI Journal (American Concrete Institute)*, December 1970: 993-995.

[8] Woods, Aaron P. "Double-Punch Test for Evaluating the Performance of Steel Fiber-Reinforced Concrete." *MS Thesis. University of Texas at Austin*, 2012.

[9] Chen, W.F. "Bearing Capacity of Concrete Blocks or Rock." *ASCE Proceedings. American Society of Civil Engineers*, 1969. 955-978

[10] Bortolotti, Lionello. "Double-Punch Test for Tensile and Compressive Strengths in Concrete." *ACI Materials Journal (Jan-Feb 1988)*: 26-32.

[11] Molins, C. "Quality Control Test for SFRC to be used in Precast Segments." *Tunneling and Underground Space Technology* 21 (2006): 423-424.

[12] Molins, Climent and A. Aguado. "Double Punch Test to Control the Energy Dissipation in Tension of FRC (Barcelona Test)." *Materials and Structures* (2009): 415-425.

[13] Bayrak, Oguzhan, et al. *Bridge Deck Reinforcement and PCP Cracking: Final Report. TX-DOT 6348 Report. Austin: Texas Department of Transportation*, 2013.

[14] Karki, N.B. "Flexural Behavior of Steel Fiber Reinforced Prestressed Concrete Beams and Double Punch Test for Fiber Reinforced Concrete." PhD Dissertation. December 2011.

# Relationship between the wide-flange steel and the long-term deformation of steel-reinforced concrete columns

Gyeong-Hee AN and Jin-Keun KIM<sup>1</sup>

*Department of Civil and Environmental Engineering, KAIST, Republic of Korea*

**Abstract.** In high-rise buildings, column shortening due to creep and shrinkage of concrete is an important issue because it can cause serious problem when it does not considered properly. Moisture diffusion is one of the main reasons of this long-term deformation of concrete. In case of steel-reinforced concrete (SRC) columns which have been widely used for high-rise buildings, however, the moisture diffusion process is quite different from the ordinary RC columns because of the wide-flange steel located inside the column. Wide-flange steel hinders the moisture diffusion, and the long-term shortening of the column is delayed due to the slower diffusion. This research is focused on the relationship between the wide-flange steel and the long-term deformation of SRC columns. In order to find the relationship, the analysis method which adopts the moisture diffusion process is suggested and some parametric study is conducted by using the analysis method. Parameters that can affect the moisture diffusion and the long-term deformation are the size of the column, the geometry of the wide-flange steel, and thickness of concrete cover.

**Keywords.** Long-term deformation, steel-reinforced concrete, moisture diffusion

## Introduction

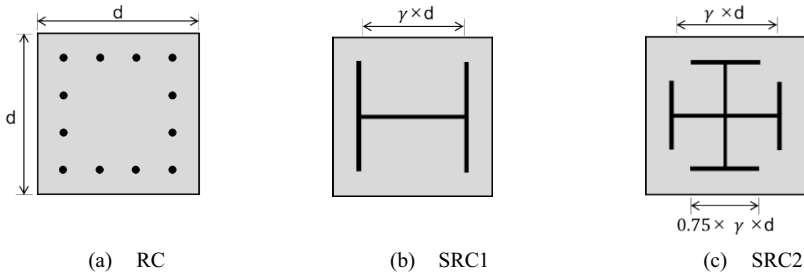
Creep and shrinkage are important time-dependent properties of concrete. One of the main reasons of the long-term deformation is the moisture diffusion. In other words, any factors that can affect the moisture diffusion of concrete can affect the long-term deformation. Therefore, the long-term deformation of SRC column is different from that of RC column because the wide-flange steel in SRC column affect the moisture diffusion of concrete. This phenomenon was pointed in the paper of Seol et al (2008). In this paper, the difference will be analyzed quantitatively by using some criteria such as starting age of the distinction and the equivalent age of SRC at the same level of deformation. This will be very helpful to identify the different long-term deformation of SRC column intuitively. Analysis method and results of the parametric study are also suggested.

---

<sup>1</sup>Corresponding author: [kimjinkeun@kaist.ac.kr](mailto:kimjinkeun@kaist.ac.kr)

**1. Long-term deformation analysis considering the moisture diffusion**

Overall procedure is as in the following. First, the sections for analyzing are chosen and meshes are generated. Fig. 1 shows the sections and their marks roughly. Then, the four parameters which affect the long-term shortening of concrete columns are chosen by literature study. These parameters are the maximum diffusion coefficient  $D_I$ , the surface factor  $f$ , the ultimate free shrinkage  $\epsilon_s^0$ , and the constant for shrinkage  $r$  and they remain constant during the whole parametric studies. The equations for the maximum diffusion coefficient  $D_I$ , the surface factor,  $f$ , and the order of the magnitude of the ultimate free shrinkage,  $\epsilon_s^0$ , and constant for shrinkage,  $r$  can be found in CEB-FIP('90), papers by Sakata(1983), and papers by Bazant(2002). The main purpose of this research is to identify the relationship between the wide-flange steel and the long-term deformation of SRC column. Therefore, the value of those parameters are not important if they are within the reasonable region.



**Figure 1.** Column section layout

Then, moisture diffusion analysis is conducted for SRC column and humidity information of each node in the section at every time step is stored. Using this humidity information, shrinkage and creep during one time step at each node are calculated as each element is under free of restraint. Finally, the deformation of the section is acquired by considering the restraint between the elements based on the assumption that plane remains plane after the deformation.

All the parameters except the wide-flange steel are fixed to see the effect of the wide-flange steel on the long-term deformation of column. Also, the area of the steel is decreased to be almost zero to demonstrate the effect on concrete only. In other words, the wide-flange-steel can affect the moisture diffusion only.

*1.1. Moisture diffusion analysis*

Eq.(1) is the nonlinear moisture diffusion equation and Eq.(2) represents the boundary condition. Important parameters that affect the moisture diffusion are the moisture diffusion coefficient and surface factor as shown in Eqs. (1) - (2). (Kim,1998)

$$\frac{\partial h}{\partial t} = \text{div}(D \text{ grad } h) \tag{1}$$

$$D \left( \frac{\partial h}{\partial n} \right)_s = f(h_{en} - h_s) \tag{2}$$

where  $h$  is the pore relative humidity,  $D$  is the moisture diffusion coefficient,  $f$  is the surface factor,  $h_{en}$  is the environmental humidity, and  $h_s$  is the relative humidity on the exposed surface. In CEB-FIP('90) model code, for isothermal conditions, the moisture diffusion coefficient is expressed as Eq. (3).

$$D(h) = D_1 \left( \alpha + \frac{1 - \alpha}{1 + [(1 - h) / (1 - h_c)]^n} \right) \tag{3}$$

where  $D_1$  is the maximum of  $D(h)$  for  $h=1.0$ ,  $\alpha = D_0/D_1$ ,  $D_0$  is the minimum of  $D(h)$  for  $h=0$ ,  $h_c$  is the pore relative humidity at  $D(h)=0.5D_1$ , and  $n$  is an exponent. In this paper,  $\alpha=0.05$ ,  $h_c=0.8$ ,  $n=15$ ,  $D_1=3.6 \times 10^{-6}/(f_{ck}/10\text{MPa})$  are fixed as suggested in CEB-FIP ('90) and surface factor,  $f$ , is chosen based on the paper of Sakata.

### 1.2. Long-term deformation analysis

Long-term deformation of the concrete can be divided into three parts, drying shrinkage, basic creep and drying creep. B3 model is used for the basic creep coefficient and Eq.(4) is used for the drying shrinkage and drying creep. Eq.(4) is appropriate for calculating shrinkage of each mesh from humidity variation at restraint-free condition.

$$\Delta \varepsilon_{drying} = \varepsilon_s^0 g_s(t) (1 + r\sigma(t)) \Delta f_s(h) \tag{4}$$

where  $\varepsilon_s^0$  is the ultimate free shrinkage,  $g_s(t) = E_c(t_0)/E_c(t)$ , and the function  $f_s(h) = 1 - h$  is chosen in this paper. As expected, the result of Eq.(4) is dependent on the humidity of each node.

The restraint stress due to the free shrinkage can be calculated as in Eq.(5) as the definition of restraint stress. The restraint stress is dependent on the  $\Delta \varepsilon_{drying}$ , therefore it depends on the humidity of each node.

$$\Delta \sigma_{restraint}(t_i, t_{i-1}) = - \frac{E_c(t_{i-1})}{1 + \phi_{basic}(t_i, t_{i-1})} \left( \sum_{j=1}^{i-2} \frac{\Delta \sigma_c(t_{j+1}, t_j)}{E_c(t_j)} (\phi_{basic}(t_i, t_j) - \phi_{basic}(t_{i-1}, t_j)) + \Delta \varepsilon_{drying}(t_i, t_{i-1}) \right) \tag{5}$$

Summing up this restraint stress, and applying it to the section in the opposite direction, one can get the final shrinkage of the interesting section. Schematic explanation of the calculation process is as shown as Fig.2.



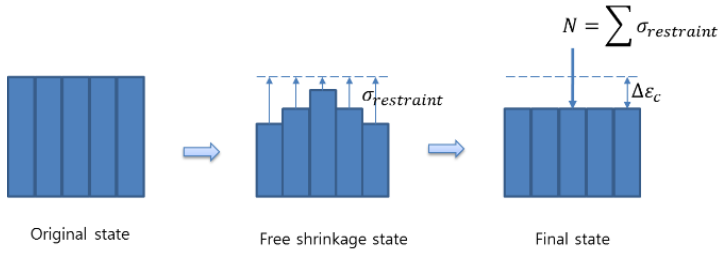


Figure 2. Calculation of strain during a time step

**2. Relationship between the wide-flange steel and the long-term deformation of steel-reinforced concrete columns**

Fig.3 shows the analysis results of three types of columns whose sizes are 500mm, 1000mm and 1500mm. They are the sections whose thickness of concrete cover are 5 percent of the sectional size. In other words,  $\gamma$  is 0.9. Environmental temperature is 20 degree and relative humidity is 50%.

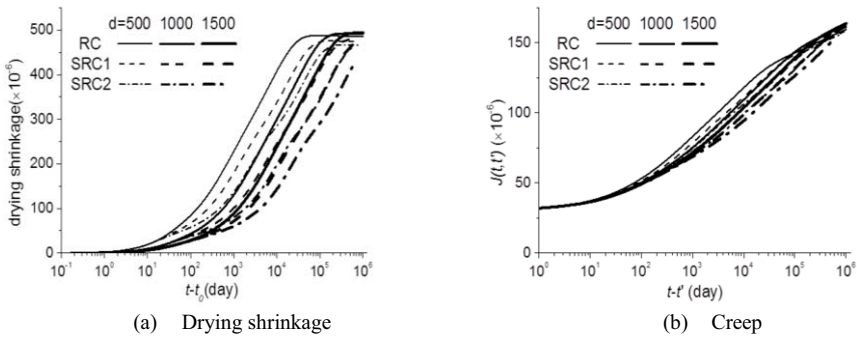


Figure 3. Long-term deformation of RC and SRC columns

If the long-term deformation of SRC column starts to show difference from RC at time  $t_1$ ,  $t_1$  for the drying shrinkage and creep are as in Fig.4.

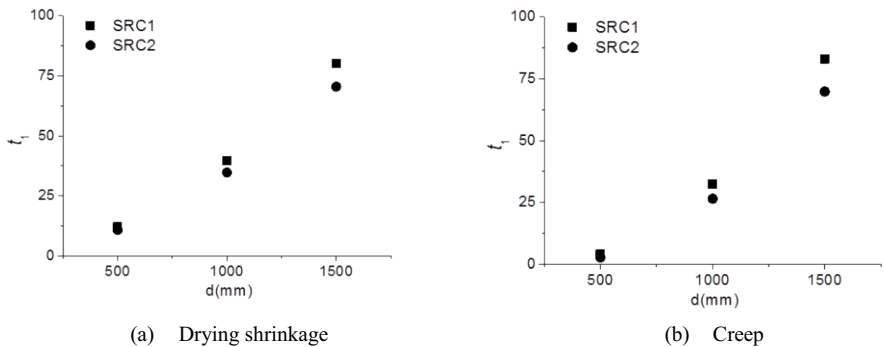


Figure 4. Starting age of distinction between SRC and RC column

As shown in Fig.4, the starting age becomes earlier when the wide-flange steel disturbs the moisture diffusion more. Therefore,  $t_1$  for SRC2 section is smaller than  $t_1$  for SRC1. Also,  $t_1$  becomes bigger as the sectional size increases because the ratio  $\gamma$  is fixed and consequently the thickness of concrete cover is thicker when the sectional size increases. Starting age,  $t_1$ , of 1000 mm section with various  $\gamma$  are represented in Fig.5.

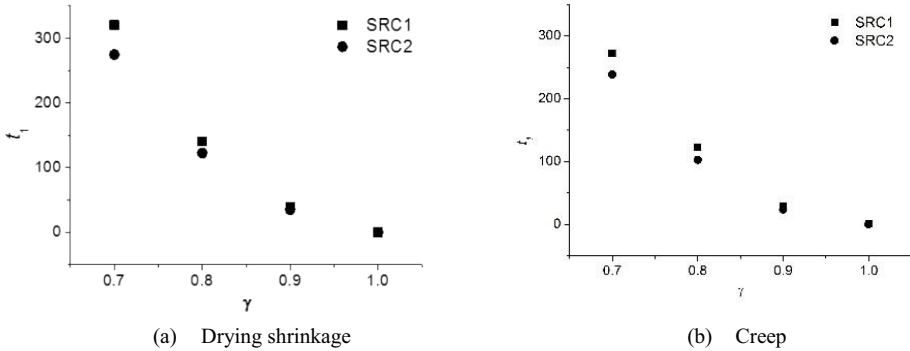


Figure 5. Starting age of 1000 mm section with various  $\gamma$

For a section with various thickness of concrete cover, the starting age increases as the thickness increases which means  $\gamma$  decreases. The equivalent age ratio is presented in Fig.6.

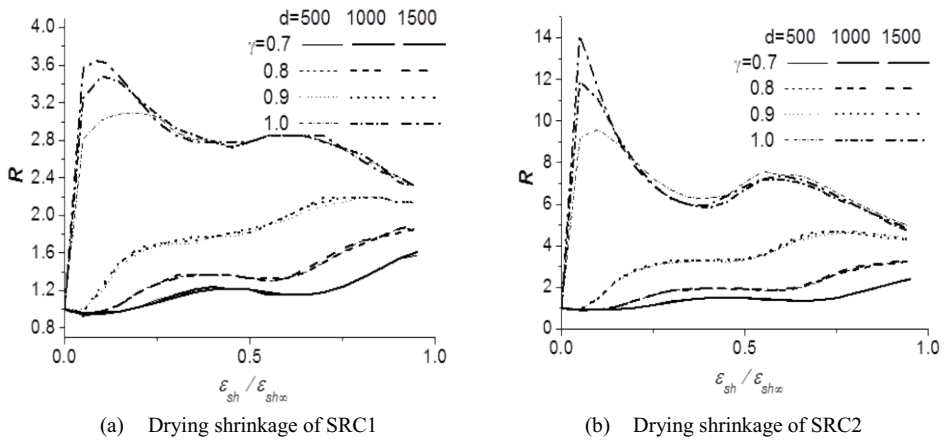


Figure 6a & b. Equivalent age of SRC columns

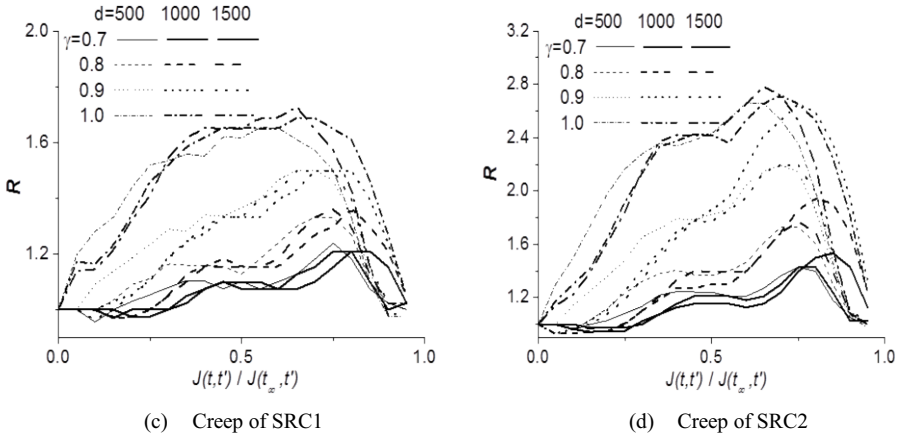


Figure 6c & d. Equivalent age of SRC columns

If the ratio,  $\alpha$ , is 2, for example, it means that it takes twice the time for SRC column to reach the same deformation of RC column. In other words, the ratio represents the amount of horizontal shift of deformation curve of SRC column in comparison with RC column. The ratio,  $\alpha$  becomes larger when the wide-flange steel disturbs the moisture diffusion more. Therefore,  $\alpha$  for SRC2 section is larger than  $\alpha$  for SRC1.

In conclusion, the long-term deformation of SRC columns starts to be different after  $t_1$  and the deformation develops  $\alpha$  times slower and both values are closely related the wide-flange-steel geometry in SRC column.

### 3. Conclusion

As observed so far, the inner configuration of the section affects moisture diffusion and long-term behavior of concrete consequently. If the wide-flange-steel geometry of the section disturbs moisture diffusion, the drying related strain develops slower as a result of diffusion speed. Therefore, the long-term deformation of SRC column should be predicted by considering the effect of the wide-flange steel. The difference in the long-term deformation of SRC columns caused by the wide-flange steel becomes significant as the steel disturbs the moisture diffusion more. More researches are needed to modify model equations commonly used in practice.

### Acknowledgement

This work was supported by the National Research Foundation of Korea(NRF) grant funded by the Korea government(MEST) (No. 2013R1A2A2A01016604).

## References

- [1] Bažant, Z.P. and Baweja, S., Creep and shrinkage prediction model for analysis and design of concrete structures—Model B3. *Mater. Struct.*, **28**(6)(1995), 357–365.
- [2] Bažant, Z.P. and Xi, Y., Drying creep of concrete: constitutive model and new experiments separating its mechanisms, *Mater. Struct.*, **27**(1994), 3–14.
- [3] Bažant, Z.P., *Mathematical Modeling of Creep and Shrinkage of concrete*, John Wiley, New York, 1988.
- [4] Bažant, Z.P. and Chern, J.C., Stress-induced thermal and shrinkage strains in concrete, *J. Eng. Mech.*, *ASCE*, **113**(10)(1987), 1493-1511.
- [5] Kim, J.-K. and Lee, C.-S., Prediction of differential drying shrinkage in concrete, *Cement Concrete Res.*, **28**(7)(1998), 985-994.
- [6] Kim, J.-K. and Lee, C.-S., Moisture diffusion of concrete considering self-desiccation at early ages, *Cement Concrete Res.*, **29**(12)(1999), 1921-1927.
- [7] Sakata K, A study on moisture diffusion in drying and drying shrinkage of concrete, *Cement Concrete Res.*, **13**(2)(1983), 216-224.
- [8] Seol, H.-C., Kwon, S.-H., Yang, J.-K., Kim, H.-S., and Kim, J.-K., Effect of differential moisture distribution on the shortening of steel-reinforced concrete columns, *Mag Concr Res.*, **60**(5)(2008), 313-322.

# Experimental bond behaviour between textile reinforced cement and concrete

Review of the existing test methods and the analysis of the results of a modified double-lap shear test

Maciej WOZNIAK<sup>a,1</sup>, Tine TYSMANS<sup>a</sup>, John VANTOMME<sup>a,b</sup>, and Sven DE SUTTER<sup>a</sup>

<sup>a</sup>*Dept of Mechanics of Materials & Constructions, Vrije Universiteit Brussel, Belgium*

<sup>b</sup>*Dept of Civil & Materials Engineering, Royal Military Academy, Brussels, Belgium*

**Abstract.** Utilisation of high-strength fibres (such as carbon, glass or aramid) is becoming an interesting alternative for reinforcing structures in the building industry. Textile reinforced cement (TRC) composites, which combine the high tensile strength of fibres with the high compressive strength and stiffness of cement-based materials, are widely investigated for their various applications: strengthening and retrofitting of existing concrete structures, stay-in-place formwork, prefabrication of slabs, seismic design, etc. The weak point of such mixed concrete – TRC composite structures is the insufficient knowledge of the mechanical behaviour of the interface between both materials, preventing their effective utilisation. To facilitate understanding of the materials' interaction, we present a state-of-art on the direct bond tests between fibre-reinforced cement composites and concrete, as well as new experimental results achieved by our research group. The literature review shows that the problem is widely investigated in the scientific community, however, due to its complexity it is still an unresolved issue. New bond experiments were performed based on a modified double-lap shear test as proposed by D'Ambrisi et al. As the results show, the test set-up eliminates the influence of parasitical bending and allows continuous monitoring of the entire strain field at the interface. The results of the experiments are promising and validate the proposed bond test set-up. The test results can be used for creating a numerical bond model and contribute to future design recommendations.

**Keywords.** Fibre-reinforced cement composites, bond test, bond-slip diagram

## Introduction

Fibre-Reinforced Mortar (FRM), Fibre-Reinforced Cement Composite (FRCC), Textile Reinforced Mortar (TRM) and Textile Reinforced Cement or Concrete (TRC) are all terms used for a cementitious matrix reinforced by fibres. Depending on the fibre structure (discontinuous chopped fibres mixed in the concrete, or continuous fibres in the form of textiles) and the matrix used, a new family of building materials (named TRC hereafter) can be obtained with different properties. The tensile strength and stiffness of the materials are mainly determined by the fraction of fibres, their orientation and distribution.

---

<sup>1</sup>Corresponding author: [mwozniak@vub.ac.be](mailto:mwozniak@vub.ac.be)

TRC is being researched in a variety of construction applications, among which the vastest is the shear and flexural strengthening of existing concrete structures [1-4]. Besides strengthening, TRC is also studied as stay-in-place formwork [5-6], seismic reinforcement [7], prefabrication of slabs and shells [8-9], exterior facades panels [10] and many others. Despite the high potential benefit of using TRC, its application currently remains limited. One of the reasons for this is the lack of understanding the behaviour of the bonding between the TRC and the concrete. Similar to Fibre-Reinforced Polymers (FRP), for effective utilisation of TRC as reinforcement for concrete, the bond properties must be well established.

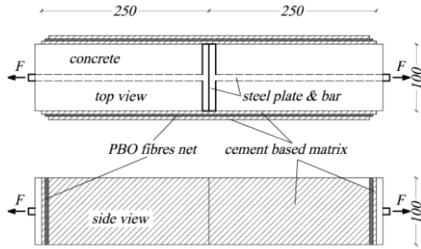
This paper is divided into two parts. The first part presents the state-of-the-art on the bond tests performed by four different research groups. Their results are given and commented upon. The second part describes the test performed by our research group. The review focuses on the precise topic of the bond test between the TRC and the concrete. Due to the different combinations of fibres, textile and the matrix used in the literature and in our research, the results differ strongly, signifying the importance of the determination of these parameters with an appropriate and unified bond test.

## **1. State-of-the-art on bond test methods**

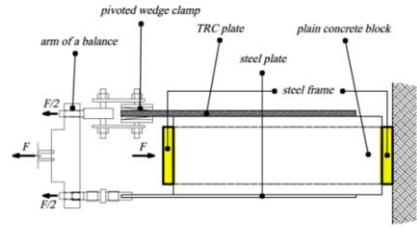
All of the presented research groups applied TRC to concrete posteriori as a simulation of strengthening of reinforced concrete members. In all of the reviewed cases, a thin layer of the cement-based matrix was applied to the treated surface of concrete and a fibre grid was pressed into the surface with the intention of impregnation. Additionally, the second presented research group tested a different method of application of a fibre grid. The first presented research group, under the leadership of A. D'Ambrisi, performed a direct bond test by means of double-lap shear (Figure 1). The TRC was made of a grid textile of poliparafenilenbenzobisoxazole (PBO) fibres embedded in a cement-based matrix [11-12]. The twelve specimens tested varied in anchorage length (from 50 to 250 mm) and number of layers of PBO grid (1 or 2).

The second group, Curbach and Ortlepp from Dresden University of Technology, also performed the double-lap shear test with a different test set-up (Figure 2) [13-14]. The analysed TRC was made of alkali-resistant glass fibres with two different textile grids with mesh size of 3.6 x 3.6mm and 7.2 x 7.2mm.

The second research was mainly focused on (i) determining the effective bond length by varying this bond length in the experiments, (ii) the preparation of the sub-concrete (surface of old concrete to which TRC is applied) by sandblasting, and (iii) the application method of the TRC layer by laminating, spraying or using adhesive bond agent.



**Figure 1.** The double-lap test set-up of D'Ambrisi et al.



**Figure 2.** Double-lap shear set-up by Curbach and Ortlepp

The third group, under supervision of C. Carloni, performed the single-lap shear test [15]. Similar to the first mentioned group (D'Ambrisi et. al), a PBO fibre grid was applied to strengthen the concrete. However, a cement-based adhesive was used only over the bond length, while the rest of fibre grid was left bare. The variables in the twenty-one tested specimens were bond length, bond width and the thickness of the top layer of composite.

The fourth research group performed an indirect bond test – the four-point bending beam test [16]. Once again PBO fibres were used as reinforcement for TRC. The research focused on the correlation between the bond length and the debonding failure mode. Six beams were tested with a different number of fibre layers (from 0 to 3).

## 2. Conclusions drawn after state-of-art on bond test

The results achieved from the different tests from literature are difficult to compare due to the different TRC compositions, however, general remarks can be made. To begin with, all of the tests ended up with a delamination of the fibre textile from the cement matrix and not with the delamination in the concrete substrate as is the case for FRP-concrete structures. The FRP-concrete structures utilize additional adhesives whose strength is generally higher than concrete substrate causing the tensile failure of the latter. Secondly, the effective bond length was estimated to be over 250 mm by D'Ambrisi et al. [17] and confirmed by Carloni et al. [15] as both research groups used the same fibres. Furthermore, Ombres indicated that 200 mm was insufficient length in the case of 4-point bending. However, Curbach and Ortlepp implied that it equalled 120 mm for the fine grid textile (mesh size 3.6 mm) and 50 mm for the coarse grid textile (mesh size 7.2 mm) [18]. The difference found by the research group relates to use of the alkali-resistant glass fibres instead of PBO and the fact that with a coarser mesh grid, the contact area increased between yarns and matrix, resulting in better bonding. Nevertheless, the slippage that occurred before debonding had a wide scatter of values (0.2 mm [14] up to 1.54 mm depending on the bonded length and the number of fibre grid layers [12]). Finally, the shear strength was the parameter to differ the most in each of the tests. The values varied from 0.6 MPa [12] to 3.5 MPa [14].

Besides the common tests results, additional data were reported. Curbach and Ortlepp indicated non-continuous strain distribution along the bonded TRC [14]. The analysis of the crack angles is widely reported in the research [13]. However, no transverse cracks were noticed in other experiments. Carloni et al. indicated the width effect on the bond between TRC and concrete, but highlighted that it needs further

investigation [15]. Ombres reported intermediate crack debonding as the most common failure in the four-point bending beam test, provided sufficient bond length is available, which is impossible to achieve in a shear test [16].

### 3. Double-lap shear test set-up

The test set-up, developed by our research group, was adapted after/from D'Ambrisi et al. [17]. Our adaptation includes the changes in:

- Application of the TRC on the concrete substrate
- Strain measurement
- Composition of TRC
- Dimensions of the specimens

Considering the fact that one of the promising applications of the TRC currently studied is the stay-in-place formwork that functions as (partial) reinforcement for the new concrete structures, the specimens were prepared by casting concrete onto TRC laminates. This differs from the classical application of FRP where additional adhesives are used or strengthening of existing concrete structures with TRC where fibre grids are laminated directly on the concrete surface by inorganic mortars/cements.

Strain measurement was done by two systems – four strain gauges on the sides of the specimens and the Digital Image Correlation (DIC) system. The strain gauges were used to determine if the parasitical bending had been eliminated by the set-up and to compare the strains at the outer TRC surface with the strain across the thickness. DIC is a continuous strain measuring technique, analysing the displacement of a previously applied speckle pattern on the specimen surface for increasing load steps frame by frame [19]. The function of DIC was to measure the strain field across the whole region of interest, allowing also the calculation of the relative displacements between concrete and TRC.

The TRC used in the experiment was made from Inorganic Phosphate Cement (IPC), reinforced by randomly oriented E-glass fibres strand mats [20]. Such TRC is being successfully investigated by the team of the department of Mechanics of Materials and Constructions at Vrije Universiteit Brussel.

Finally, dimensions of the specimens were changed so that debonding/failure occurred in the area of interest investigated by DIC. This was achieved by decreasing the bond length of TRC to concrete to 90 mm in the upper part of the specimen, while the bottom part had a bonded length of 120 mm, making the specimen asymmetric (Figure 3).

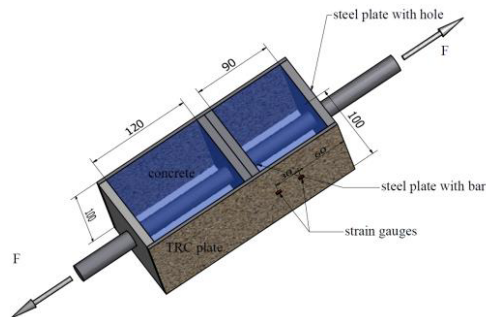


Figure 3. Double-lap shear test set-up



### 4. Test results

The aim of the tests was, by means of three identical specimens (Figure 3), to verify the correctness of the test set-up as well as to check the feasibility of measuring important parameters such as strains and slippage. The tests results confirm the utility of the experimental method.

The first conclusion of the test is that the set-up totally eliminates parasitical bending from the experiment. This is illustrated in Figure 4, where the results of the strain gauges on the both sides of the specimen are in good agreement. Hence, we can assume that the results of the test are correct and we can compare our results to the results from the literature review.

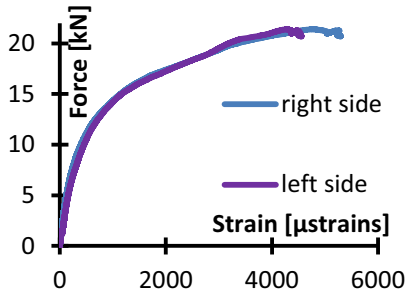


Figure 4. Strains measured by strain gauges at the left and right side of the specimen, showing no bending of the specimen

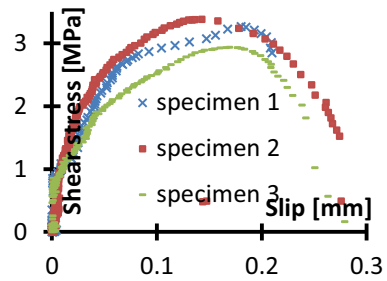


Figure 5. Bond-slip diagram of TRC-concrete interface

Similar to the reviewed tests, the failure of the specimens didn't occur in the concrete substrate as in the FRP-concrete structures; instead the delamination happened at the interface of TRC-concrete with the pull out of some fibres from the first layer of the fibre grid. Maximum slippage, achieved during the test of the third specimen and described as relative displacement between TRC and concrete substrate, was 0.38 mm. This is in the same range as the slippage achieved by D'Ambrisi with the bond length of 100 mm: 0.56 mm for one layer, 0.55 mm and 0.62 mm for two layers of fibre grid [17]. Shear strength was estimated between 2.5 and 3.4 MPa, similar to that found by Ortlepp et al. [14]. The shear stress was calculated from the strains measured by the strain gauges, as well as by the DIC in the corresponding locations. The locations of the strain gauges were in the middle of the TRC plate at a distances of 10 and 40 mm from the debonding initiation (concrete to steel plate with bar noted in Figure 3), leading to a strain measuring interval  $\delta = 30$  mm. From this strain the average shear stress was calculated according to equation (1) [21]

$$\tau = \frac{\varepsilon_{i+1} - \varepsilon_i}{\delta} \cdot E \cdot t \tag{1}$$

where  $t$  is the thickness of the TRC plate. The shear stress-strain relation is assumed to be linear and it is determined by the secant Young modulus  $E$ . The bond-slip diagrams are also generated and are shown in Figure 5.

The shear strength, as well as the maximum slippage, is where the TRC bond-slip and the FRP bond-slip tests differ mostly. In both cases the values were lower for TRC compared to the FRP. The diagrams for the TRC tests performed are shown in Figure 5. The generalisation, however, is very difficult to establish since the observed values depend on the properties of the adhesive used.

## 5. Conclusion

This paper analyses the bond between the TRC and the concrete by comparing bond tests performed by four different research groups to the own work, following common conclusions can be drawn:

- Delamination of the TRC is different to the delamination of the FRP since the debonding occurs in the first layers of fibre reinforcement, and not in the concrete substrate;
- The bond strength between the TRC and the concrete depends on the composition of the TRC material;
- There exists an effective bond length but it depends largely on the materials used;
- The presented double-lap shear test set-up is well-designed, eliminating the influence of parasitical bending.

Nevertheless, the solution to the problem is not exhausted, and there is a need for additional experiments, which will enable the constructing a reliable model for simulating the bond behaviour between the TRC and the concrete.

## Acknowledgements

The authors gratefully acknowledge the funding of Fonds Wetenschappelijk Onderzoek-Vlaanderen (FWO) through a scholarship for the first author, and the funding of the Brussels Capital Region through the Innoviris Strategic Platform Brussels Retrofit XL.

## References

- [1] A. Si Larbi, R. Contamine, E. Ferrier, and P. Hamelin, Shear strengthening of RC beams with textile reinforced concrete (TRC) plate, *Constr. Build. Mater.*, vol. 24, no. 10, pp. 1928–1936, Oct. 2010.
- [2] a. Brückner, R. Ortlepp, and M. Curbach, Textile reinforced concrete for strengthening in bending and shear, *Mater. Struct.*, vol. 39, no. 8, pp. 741–748, Sep. 2006.
- [3] T. Triantafyllou and C. Papanicolaou, Shear strengthening of reinforced concrete members with textile reinforced mortar (TRM) jackets., *Mater. Struct.*, vol. 39, no. 1, pp. 93–103, 2006.
- [4] S. Verbruggen, J. Wastiels, T. Tysmans, O. Remy, and S. Michez, The influence of externally bonded longitudinal TRC reinforcement on the crack pattern of a concrete beam, in *Proceedings 3rd International Conference on Concrete Repair, Rehabilitation and Retrofitting*, 2012, no. Kamada, pp. 1259–1265.
- [5] O. Remy, S. Verbruggen, J. Wastiels, and T. Tysmans, Cement composite stay-in-place formwork: A concept for future building system, in *18th International Conference on Composite Materials*, 2011.
- [6] C. G. Papanicolaou and I. C. Papantoniou, Mechanical Behavior of Textile Reinforced Concrete (TRC) / Concrete Composite Elements, *J. Adv. Concr. Technol.*, vol. 8, no. 1, pp. 35–47, 2010.
- [7] G. Parra-Montesinos, High-performance fiber-reinforced cement composites: an alternative for seismic design of structures, *ACI Struct. J.*, vol. 102, no. 5, pp. 668–675, 2005.
- [8] K. Holschemacher, Y. Klug, S. Kobisch, B. Weiße, and H. Zscheile, Textile reinforced slabs and prefabricated double walls, in *1st International Conference Textile Reinforced Concrete (ICTRC)*, 2006, pp. 319–330.
- [9] T. Tysmans, S. Adriaenssens, H. Cuyper, and J. Wastiels, Structural analysis of small span textile reinforced concrete shells with double curvature, *Compos. Sci. Technol.*, vol. 69, no. 11–12, pp. 1790–1796, Sep. 2009.
- [10] E. Engberts, Large-size façade elements of textile reinforced concrete, in *1st International Conference Textile Reinforced Concrete*, 2006, pp. 309–318.

- [11] A. D'Ambrisi, L. Feo, and F. Focacci, Experimental analysis on bond between PBO-FRCM strengthening materials and concrete, *Compos. Part B Eng.*, vol. 44, no. 1, pp. 524–532, Jan. 2013.
- [12] A. D'Ambrisi, L. Feo, and F. Focacci, Bond-slip relations for PBO-FRCM materials externally bonded to concrete, *Compos. Part B Eng.*, vol. 43, no. 8, pp. 2938–2949, Dec. 2012.
- [13] R. Ortlepp, U. Hampel, and M. Curbach, A new approach for evaluating bond capacity of TRC strengthening, *Cem. Concr. Compos.*, vol. 28, no. 7, pp. 589–597, Aug. 2006.
- [14] R. Ortlepp and M. Curbach, Bonding behaviour of Textile Reinforced Concrete strengthening, in *High Performance Fibre Reinforced Cement Composites - 4th International RILEM Workshop*, 2003, pp. 517–527.
- [15] C. Carloni, L. H. Sneed, and T. D. Antino, Interfacial bond characteristics of fiber reinforced cementitious matrix for external strengthening of reinforced concrete members, *VIII International Conference on Fracture Mechanics of Concrete and Concrete Structures*, FraMCoS-8, 9p
- [16] L. Ombres, Debonding analysis of reinforced concrete beams strengthened with fibre reinforced cementitious mortar” *Eng. Fract. Mech.*, vol. 81, pp. 94–109, Feb. 2012.
- [17] A. D'Ambrisi, L. Feo, and F. Focacci, Experimental and analytical investigation on bond between Carbon-FRCM materials and masonry” *Compos. Part B Eng.*, vol. 46, pp. 15–20, Mar. 2013.
- [18] R. Ortlepp, S. Ortlepp, and M. Curbach, 137. Stress transfer in the bond joint of subsequently applied textile reinforced concrete strengthening *6th International RILEM Symposium on Fibre Reinforced Concretes*, pp. 1483–1494, 2004.
- [19] D. Lecompte, Elastic and Elasto-Plastic Material Parameter Identification by Inverse Modeling of Static Tests using Digital Image Correlation, 2007.
- [20] S. Verbruggen, O. Remy, J. Wastiels, and T. Tysmans, Stay-in-Place Formwork of TRC Designed as Shear Reinforcement for Concrete Beams, *Adv. Mater. Sci. Eng.*, vol. 2013, pp. 1–9, 2013.
- [21] J. Dai, T. Ueda, and Y. Sato, Development of the nonlinear bond stress–slip model of fiber reinforced plastics sheet–concrete interfaces with a simple method, *J. Compos. Constr.*, no. February, 2005.

# Relation between crack width and corrosion degree in elements of concrete with crushed sand

Oscar A. CABRERA<sup>a,1</sup>, Néstor F. ORTEGA<sup>b</sup>, Luis P. TRAVERSA<sup>c</sup> and Horacio DONZA<sup>a</sup>

<sup>a</sup>Universidad Nacional del Centro de la Provincia de Buenos Aires, Argentina

<sup>b</sup>Departamento de Ingeniería, Universidad Nacional del Sur, Argentina

<sup>c</sup>Laboratorio de Entrenamiento Multidisciplinario para la Investigación Tecnológica (CIC-LEMIT), Argentina

**Abstract.** The development of cracks due to corrosion products depends on the quality of the concrete, the concrete cover thickness, etc. The link between the rate of growth of crack width and the evolution of corrosion, can predict the safety and suitability for service residual of reinforced concrete structures. In this sense, this work assesses the impact of the influence of the type of fine aggregate and water/cement ( $w/c$ ) ratio on the evolution of the "crack width" regarding the "concrete cover/diameter of the steel" relation. Then, two series of beams were made with  $w/c$  ratio of 0.45 and 0.50. The results show that the type of sand and the  $w/c$  ratio significantly influence the growing mechanism of crack width, and the obtained information is compared to results obtained by other authors.

**Keywords.** Fine aggregates, corrosion, crack width, corrosion rate

## Introduction

The durability of reinforced concrete structures subject to corrosion can be enhanced by controlling cover thickness and crack width. Cracks caused by corrosion show the progress of dissolution of the steel. For reasons of durability, the width of cracks due to applied loads is limited in some codes according to the environment, to values of 0.40, 0.15 and 0.10 mm for dry environments, seawater or water retaining structures, respectively [1, 2]. It is considered that limiting the crack width by durability is controversial, as they accelerate corrosion, and those less than 0.40 mm are sealed with calcium hydroxide or corrosion products. On the other hand, mechanical properties and durability of concrete containing crushed sand depend on paste composition, the paste volume, the physical characteristics of the sand particles, and the nature of the "paste-fine aggregate" interface. Since fine aggregates occupy about 25-30 percent of the volume of a concrete, they can be expected to exert an important influence on the mechanical and durable properties of the composite material.

As for the concrete cover cracking, due to the expansion of the corrosion products are numerous theoretical and experimental research, and *in-situ* observations. It was concluded that, in general, the beginning of the cracking depends mainly on the

---

<sup>1</sup>Corresponding author: [ocabrera@fio.unicen.edu.ar](mailto:ocabrera@fio.unicen.edu.ar)

characteristics of the concrete and the relation "concrete cover/diameter of the bar". The degradation of a concrete structure by the corrosion is clearly a very complex phenomenon which involves multiple causes and effects. Although aspects of the mechanism of cracking that are essential for the prediction of durability are uncertain [3, 4, 5]. The progress of corrosion damage of the reinforcement can be analyzed by measuring the crack width. The maximum crack width not always increases in the same area, but varies from the beam area. In the corrosion of steel, the "penetration of corrosion in time", ( $P_x$ , in mm), [3, 6] was calculated based on Faraday's law (Equation 1). In addition, there are other equations that link the cracking of concrete cover to the advancement of corrosion; this relationship is not unique since it depends on the exposure environment, quality of concrete and type structural element; and in laboratory of the accelerated corrosion method employed. To evaluate the crack width values ( $w$ , in mm) caused by corrosion, it has been used by several authors a simple empirical equation, Eq. (2) [3, 4].

$$P_x = R_o - R_t = 0.032 * i_{corr} * t \quad (1)$$

$$w = k * P_x / (C/\phi) + b \quad (2)$$

where  $R_o$  is original radius (mm),  $R_t$  (mm) is radius in time  $t$  (days),  $i_{corr}$  is current density ( $\mu\text{A}/\text{cm}^2$ ), 0.032 is the conversion factor ( $\mu\text{A}/\text{cm}^2$  a mm/day),  $k$  is a factor of proportionality without dimensions, " $C/\phi$ " is the relation "concrete cover/diameter of the bar" (mm/mm), and  $b$  is another constant (mm).

The purpose of the study is to assess the behavior of two series of reinforced concrete beams, made with different crushed sands, and two  $w/c$  ratios, which were subjected to accelerated corrosion testing galvanostatically. In particular, the evolution of the crack width as a function of corrosion progress is analyzed using Eq. (2), and the results are compared with those obtained by other authors.

## 1. Materials, mix proportioning and methodology

*Concrete and steel:* The concrete was made with Portland cement with calcareous filler (CPF30, IRAM 50000 standard) [7]. Crushed granite stone with a maximum size of 13 mm was used as coarse aggregate. Four fine aggregates from different mineralogical sources and similar fineness modulus were used. Natural siliceous river sand ( $S$ ), having rounded and smooth particles, was used as reference sand. Crushed sands were selected from different petrography characteristics (granite, limestone and dolomite) with a similar grading curve. Table 1 reports the characteristics of fine aggregates. The surface texture and particle shape classification according BS 812 standard are presented [8]. Two series of concrete (Table 2) were dosed. In this study, the  $w/c$  ratio, the proportions of materials and the fineness modulus of the sand remained constant, so that the only variable was the type of sand. The tensile strength of the bars was 855 MPa.

*Beams and accelerated corrosion method:* Concrete beams (110 x 10 x 15 cm) contained four bars of steel with 4.2 mm of diameter, and stirrups at 100 mm spacing. To accelerate corrosion, a nominally constant anodic current density was impressed on

the anode ( $100 \mu\text{A}/\text{cm}^2$ ), through a counter electrode in the central area of the beams. Above counter electrode, a sponge to moisten was placed with a solution of 0.30% NaCl in weight. This technique was used in previous investigations [6, 9, 11].

**Table 1.** Characteristics of fine aggregates

Type of sand:	Limestone (L)	Dolomite (D)	Granite (G)	Siliceous (S)
Fineness modulus	3.48	3.38	3.15	3.33
Apparent specific density	2.68	2.77	2.69	2.64
Dust content, %	10.6	13.3	10.7	0
Particle shape (BS 812)	Angular	Elongated	Angular	Rounded
Surface texture (BS 812)	Rough	Rough	Crystalline	Smooth

**Table 2.** Mixture proportions ( $\text{kg}/\text{m}^3$ ), compressive strength (MPa) and capillary suction speed

Mixture/ Materials	Series 1 ( $w/c=0.45$ )				Series 2 ( $w/c=0.50$ )			
	HL-1	HD-1	HG-1	HS-1	HL-2	HD-2	HG-2	HS-2
Cement <i>CPF30</i>	400	400	400	400	400	400	400	400
Water	180	180	180	180	200	200	200	200
Fine aggregate	798	825	801	786	745	770	747	733
Coarse aggregate	1000	1000	1000	1000	1000	1000	1000	1000
Superplasticizer	0.50%	0.60%	0.50%	---	---	---	---	---
Slump, cm	6	6	6	14	6	8	6	15
Strength, 28 days,	40.4	38.8	38.2	31.9	33.7	35.2	32.3	28.5
CSS ( $\text{g}/\text{m}^2 \cdot \text{s}^{0.50}$ )	4.32	3.75	3.56	5.06	7.87	7.71	8.30	11.0

## 2. Analysis and discussion of results

### 2.1. Evolution of cracks in concrete beams subjected to accelerated corrosion

Table 2 shows the relationship between strength and capillary suction speed (CSS) [12]. As the concrete is more porous the CSS is greater, behavior observed in other studies [6]. On the other hand, Figures 1 and 2 show curves "maximum crack width" versus "penetration corrosion in time" for the two series of concrete. In general, major cracks occurred in the sides of the beams, and in the direction of the main reinforcement. The values of the maximum crack width at the end of the test, in both series, were higher for natural sand concrete with respect to crushed sand concrete.

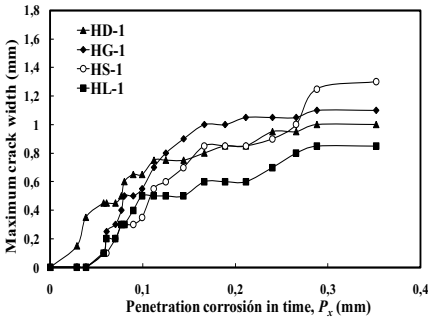


Figure 1. Maximum crack width for Series 1

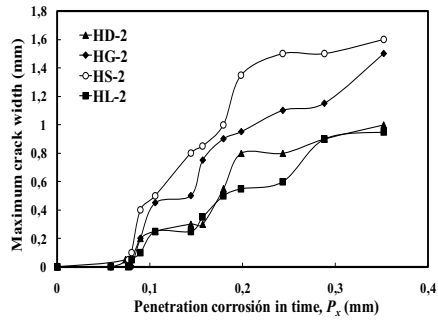


Figure 2. Maximum crack width for Series 2

The initiation of cracking was later in the Series 2 (~7 days), that is the cracks were generated for increased steel consumption. This is associated with the increased porosity of the concretes of the Series 2 (higher  $w/c$  ratio), which allows the corrosion products initially fill the pores, and no pressure increase caused by the increasing volume of oxides. For a  $P_x$  value of 0.35 mm (110 days of test), the range of values of the maximum crack width was 153 and 168% (respect to average) for Series 1 and 2, respectively. This behavior is due to the effect of sand type on corrosion cracking.

2.2. Analysis of the application of the equation “ $w = k * P_x / (C/\phi) + b$ ”

Figures 3 and 4 were obtained with the experimental results and using Eq. (2). In the two referred figures, curves belonging to studies of other authors [3, 4, 10, 11], are taken by way of comparison in order to analyze the factors that influence the different behaviors.

Experiences of other authors as references: Table 3 shows the characteristics of concrete and accelerated corrosion methods, used as reference papers. The last two reference curves [11], were obtained with the same methodology as that used in this paper. The curves “ $Rm_4$ ” and “ $Rm_5$ ”, correspond to concretes made with crushed sand (CS) and natural sand (NS), respectively. The fineness modulus of CS was 2.88, and the module of the NS, 2.80.

Table 3. Characteristics of concrete and accelerated methods used as reference

Curve	Ref.	w/c ratio	Cemento (kg/m <sup>3</sup> )	C (mm)	φ (mm)	Chloride ions	f <sub>c</sub> (MPa)	Current density (μA/cm <sup>2</sup> )
"Rm <sub>1</sub> "	[3]	0.70	360	30	12	3% CaCl <sub>2</sub> (*)	---	(**)
"Rm <sub>2</sub> "	[4]	0.50	350	24	16	3% CaCl <sub>2</sub> (*)	---	100
"Rm <sub>3</sub> "	[10]	0.50	389	30	10	3% NaCl (*)	37	80
"Rm <sub>4</sub> "	[11]	0.60	300	10	4.2	0.30% NaCl	38	100
"Rm <sub>5</sub> "	[11]	0.60	300	10	4.2	0.30% NaCl	25	100

(\*) in the mixing water – (\*\*) exposed to the atmosphere de Madrid, Spain

Analysis of the results by applying the Eq. (2): In Figures 3 and 4 shows the differential behavior regarding “w” versus “ $P_x/(C/\phi)$ ” for each type of sand. Equations

of the lines corresponding to the concretes studied had correlation coefficients between 0.78 and 0.96.

The concrete of the first three curves ( $Rm_1$ ,  $Rm_2$  and  $Rm_3$ ) containing chloride ions (1.82-1.92%) in excess of the threshold of corrosion (0.40%), were incorporated in the mixing water. In the case of the concretes  $Rm_4$  and  $Rm_5$ , the chloride ions (0.18%) were entered from the outside, through the cover of concrete. In the latter case, there was a time to form the protective oxide coating. Analyzing the results based on Eq. (2), the  $Rm_1$ ,  $Rm_2$  and  $Rm_3$  curves have an almost coincidental development (Figures 3 and 4) despite the difference in  $w/c$  ratio. Instead, the  $Rm_4$  and  $Rm_5$  curves are for a certain value of " $P_x/(C/\phi)$ ", an order of magnitude of five times lower than the remaining reference curves. Namely, that the effect of inclusion in the mixing water of high chloride ions concentration, is an interesting fact for the experimental design of test.

This difference between the two groups of reference curves can be based on another paper [9], which compares the effect of corrosion on specimens (with  $C/\phi = 2.5$  to 5.5) with chlorides incorporated in its mass, and other, entering them from the outside. They conclude that in the first case, at the time of the test the reinforcement present a certain state of activation (corroborated by their corrosion potentials), the appearance of the first cracks begins previously, and higher maximum width of cracks, those receiving external chloride can be seen. In addition, the gravimetry showed a greater loss of reinforcement material when chlorides were incorporated during the mixing.

The experimental curves for the Series 1, are more clustered than those of Series 2. In relative terms, for the curves corresponding to beams with identical methodology ( $HD$ ,  $HL$ ,  $HG$ ,  $HS$ ,  $Rm_4$  and  $Rm_5$ ), for a given " $P_x/(C/\phi)$ " ratio, thereof are located according to a crack width thus decreasing with the  $w/c$  ratio. First are the curves of Series 1 ( $w/c = 0.45$ ), then the curves of Series 2 ( $w/c = 0.50$ ) and followed the curves  $Rm_5$  and  $Rm_4$  ( $w/c = 0.60$ ).

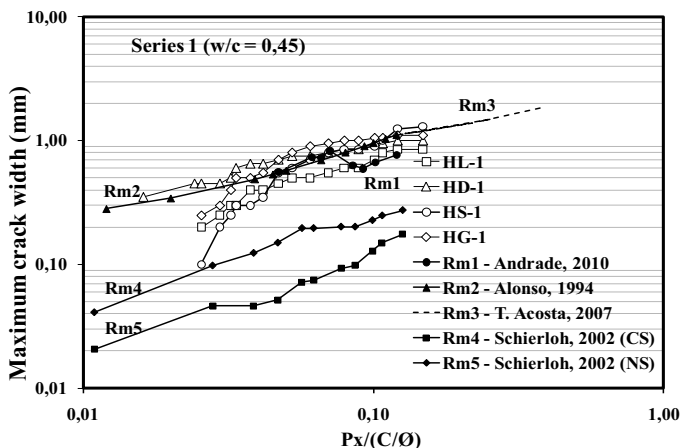


Figure 3. Maximum crack width versus  $P_x/(C/\phi)$  for the beams of Series 1



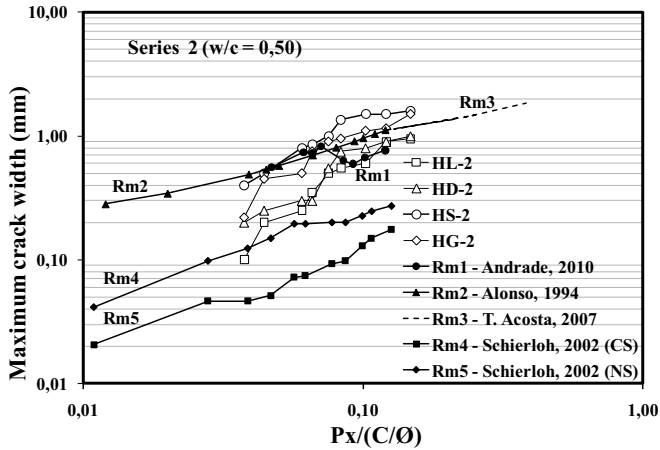


Figure 4. Maximum crack width versus  $P_x/(C/\phi)$  for the beams of Series 2

Finally, the results of accelerated methods where chlorides are incorporated in the mixing water are not affected by the thickness of concrete cover, or by the  $w/c$  ratio. Therefore, the results are difficult to extrapolate to the real structures, and will require further studies aimed at the practical application of these results.

### 3. Conclusions

The experiences and studies in beams made with different types of fine aggregates (natural and crushed), and with a  $w/c$  ratios between 0.45 and 0.50, allow to reach the following considerations:

- The equation studied ( $w = k \cdot P_x / (C/\phi) + b$ ) is simple and sensitive to changes in the type of fine aggregate, the  $w/c$  ratio, and the entry mode (or of incorporation) and concentration of chlorides.
- This equation for a set of materials can predict the relationship between the progress of corrosion through the crack width, based on the diameter and thickness of concrete cover. Although, it is difficult to extrapolate these results to real structures.
- This equation linearly superimposed the results in the case where chloride ions are introduced during the mixing, in concentrations above the threshold of corrosion (0.40% by weight of cement), regardless of the  $w/c$  ratio and the concrete cover thickness. In the case of chloride ions that ingress from the outside, the  $w/c$  ratio and the type of sand, establish a differential behavior between reinforced concrete beams tested with the same methodology.

### References

- [1] ACI 224, Control of cracking in concrete structures, *ACI Manual of Concrete Practice*, Farmington Hill, USA, (2002).
- [2] EHE, Instrucciones del hormigón estructural, *Ministerio de Fomento*, España, (2008).
- [3] Andrade, C., Muñoz, A. & Torres-Acosta, A., Relation between crack width and corrosion degree in corroding elements exposed to the natural atmosphere, *Proc. Fracture Mechanics of Concrete and Concrete Structures – Assessment, Durability, Monitoring and Retrofitting of Concrete Structures*, B.H. Oh, et al (Eds), Korea Concrete Institute, Seoul, (2010), 853-858.

- [4] Alonso, C. et al., Evaluación experimental de la fisuración del hormigón producida por la corrosión de las armaduras, *Hormigón y Acero* **194** (1994), 29-43.
- [5] Shodja, H.M., Kiani, K., & Hashemian, A., A model for the evolution of concrete deterioration due to reinforcement corrosion, *Mathematical and Computer Modelling* **52** (2010), 1403-1422.
- [6] Cabrera, O.A., Caracterización de la durabilidad de hormigones con arenas de trituración, *Thesis doctoral, Universidad Nacional del Sur, Departamento de Ingeniería*, Bahía Blanca, Argentina, (2013).
- [7] Norma *IRAM 50000*. Cemento. Cemento para uso general. Composición, características, evaluación de la conformidad y condiciones de recepción (2000).
- [8] *BS 812*. Part 1: Methods for sampling and testing of mineral aggregates, sands and filler: sampling, shape, size and classification (1975).
- [9] Aveldaño, R.R. & Ortega, N.F., Acción de cloruros incorporados dentro de la masa del hormigón armado o desde el exterior, *Proc. CINPAR 2010*, Tópico 1, en CD, Córdoba, Argentina, (2010), 1-15.
- [10] Torres-Acosta, A.A., Structural consequences of corrosion for reinforced concrete, *Revista Técnica de la Facultad de Ingeniería, Universidad de Zulia* **30** Ed. Especial, (2007), 245-251.
- [11] Schierloh, M.I., Corrosión de armaduras. Características que debe tener el hormigón para aumentar la protección, *Tesis de Magíster, Universidad Nacional del Sur, Departamento de Ingeniería*, Bahía Blanca, Argentina, (2002).
- [12] Norma *IRAM 1871*. Hormigón. Método de ensayo para determinar la capacidad y la velocidad de succión capilar de agua del hormigón endurecido (2004).

# Investigation of prestressed hollow core concrete slabs at elevated temperatures

Ehab ELLOBODY<sup>1</sup>

*Department of Structural Engineering, Faculty of Engineering, Tanta University, Tanta, Egypt*

**Abstract.** This paper investigates the behaviour and design of full-scale prestressed hollow core one-way spanning concrete slabs under fire conditions. The hollow core slabs were simply-supported and reinforced with 9.3mm nominal diameter seven-wire mono-strand tendons. Nonlinear 3-D finite element models were developed for the analysis of prestressed hollow core concrete slabs at elevated temperatures. The finite element models were based on a nonlinear finite element modelling approach adopted by the author over the last eight years for the analysis of different structures under fire conditions. The mechanical and thermal material nonlinearities of the concrete and prestressing tendons have been carefully inserted into the model. The interface between the tendon and surrounding concrete was also modelled, allowing the tendon to retain its profile shape during the deformation of the prestressed hollow core slab. In addition, gap elements were used to model the thermal behaviour of the hollow cores, which ensures, for the first time, correct temperature distributions in the regions surrounding the cores. The temperature distribution throughout the prestressed hollow core concrete slab, time-deflection behaviour, time-longitudinal expansion and failure modes of the slabs were predicted by the model and verified against test data. A parametric study was conducted to investigate the effects on the global structural behaviour due to the change in the prestressed hollow core slab geometries, hollow core shapes, load ratios during fire and different fire curves.

The study has shown that the failure of the prestressed hollow core concrete slabs investigated study was due to tensile splitting with longitudinal cracks along the slab directly above and inline with the tendons developed between 15-25 minutes from the start of heating. It was also shown that no shear failure was observed. The fire resistances of the prestressed hollow core concrete slabs obtained from the finite element analyses were compared with the design values obtained from the British Standards (BS) and European Code (EC) for concrete structures at elevated temperatures. The comparisons have shown that the BS were generally conservative for the prestressed hollow core concrete slabs investigated in the parametric study, except for the slabs heated using the standard fire curve under a higher load ratio of 0.7, while the EC predictions were conservative for all the slabs investigated in this study.

**Keywords.** Design, FE modelling, fire, prestressed, hollow core concrete slabs

## Introduction

Prestressed hollow core concrete floors are commonly used in the construction market owing to many advantages including high strength, self-weight-to-depth ratio, larger span-to-depth ratio, high durability and good thermal and sound insulations. Walraven and Mercx [1] identified four different failure modes of prestressed hollow core

---

<sup>1</sup>Corresponding author, [ehab.ellobody@f-eng.tanta.edu.eg](mailto:ehab.ellobody@f-eng.tanta.edu.eg)

concrete slabs at ambient temperatures and these are flexure, anchorage, shear tension and shear compression. However, when prestressed hollow core slabs are exposed to fire, their structural performance becomes quite complicated owing to the presence of the prestressing tendons and hollow cores, which is addressed by this investigation.

Limited experimental investigations were found in the literature on prestressed hollow core slabs at elevated temperatures. Andersen and Lauridsen [2] conducted three furnace tests on prestressed hollow core concrete slabs. The main failure mode of the slabs was vertical shear. The vertical shear failure mode observed in [2] was discussed by Van Acker [3]. It was shown that due to the non-linear thermal gradient through a prestressed hollow core concrete slab at elevated temperatures, thermal stresses are induced through the cross-section. Materazzi and Breccolotti [4] presented preliminary results of full scale furnace tests on prestressed hollow core concrete slabs. It was shown that the fire resistance of the tested specimens was affected by explosive spalling. Recently, Torić et al. [5] detailed a full-scale fire test on prestressed hollow core concrete slab exposed to ISO fire curve. The prestressed hollow core slab had a width of 1.2 m and a length of 8.28 m. The study [5] provided useful information regarding the time-temperature distributions within the slabs, time-mid-span deflection behaviour, time-longitudinal strain relationships and failure modes of the slabs at elevated temperatures. Also, very limited numerical investigations, with limited success, were found in the literature highlighting the structural performance of prestressed hollow core concrete slabs at elevated temperature. Fellingner et al. [6] presented a 2-D finite element model to study shear and anchorage behaviour of fire exposed prestressed hollow core concrete slabs. The model was calibrated against small-scale fire tests loaded in shear, reported by the first author [7]. Two separate plane stress models were developed in the finite element package DIANA [8]. Materazzi and Breccolotti [4] presented a 2-D finite element model to evaluate temperature distribution across prestressed hollow core concrete slabs and to use the distributions to refine the analytical evaluation of the fire resistance of the slabs. Chang et al. [9] presented a simplified 3-D finite element model to simulate the behaviour of an entire prestressed hollow core floor system including the surrounding structural members such as columns and beams. To date there is no detailed nonlinear 3-D finite element model highlighting the structural behaviour of prestressed hollow core concrete slabs under severe fire conditions, which is credited to the current study.

Recent investigations on composite beams exposed to fire [10, 11], investigations on composite columns exposed to fire [12] as well as investigations on post-tensioned concrete slabs exposed to fire [13, 14] have proposed a consistent and robust 3-D finite element modelling approach for analyzing different structures in fire. The approach [10-14] will be implemented in this study. Overall, efficient nonlinear 3-D finite element model investigating the behaviour of prestressed hollow core concrete slabs exposed to different fires were reported in this paper. The model was developed using ABAQUS [15] and was validated against published experimental results of full-scale prestressed hollow core concrete slabs at elevated temperatures [4, 5]. A parametric study was performed to investigate the effects of different prestressed hollow core slab geometries, load ratios during fire and fire curves on behaviour and fire resistance of the prestressed hollow core concrete slabs. The fire resistances of the hollow core slabs investigated in the parametric study were compared with the design values calculated using BS 8110-2 [16] and EC2 (BS EN 1992-1-2) [17].

## 1. Summary of experimental investigation

The full-scale fire tests reported in [4, 5] on prestressed hollow core concrete slabs were used to verify the 3-D finite element models developed in this study. Table 1 summarizes the measured dimensions and main parameters of the prestressed hollow core concrete slab fire tests. The definitions of symbols for the prestressed hollow core concrete slabs are shown in Figs. 1 and 2, respectively, for the full-scale tests reported in [4, 5]. The full-scale test detailed in [5] is denoted as T1, with the general layout shown in Figs. 1 and 3. The prestressed hollow core concrete slab T1 was 8.28m long, 1.2m wide, and 200mm deep. Each slab had eight longitudinal tendons with a nominal diameter ( $d$ ) of 9.3mm and an area of  $52\text{mm}^2$ , see Fig. 1. The tendon was a monostrand with seven high-strength steel wires. The distance from the bottom of the slab to the axis of the tendon was 25mm. The prestressed hollow core slab had a compressive concrete strength and Young's modulus at ambient temperatures of 65 MPa and 44 GPa, respectively. The prestressed hollow core concrete slab was loaded in thirds of span, uniformly and transversely, with the load ratio during fire equal to 0.5 of the design load. The design load was approximately the same as that calculated using BS8110-1 [18]. In order to use a consistent definition, the load ratio during fire is defined in this study as the applied static load divided by the design capacity of the prestressed hollow core concrete calculated according to BS8110-1 [18]. The slab was exposed to fire at the bottom surface as shown in Fig. 1. The slab was heated with the aim of following the standard time-temperature curve specified in BSEN1991-1-2 [19]. The dimensions of the furnace were  $7.6 \times 1.4 \times 1.2$  m and the thickness of the walls was 200mm. Thermocouples were used to measure the temperatures at different locations in the slab comprising the upper surface of concrete slab, prestressing tendons, and in the middle of the hollow core.

**Table 1.** Specimen dimensions of tests and prestressed hollow core concrete slabs investigated in this study.

Group	Specimen	Fire curve	Load ratio	Hollow core	Dimensions (mm)			
					$L$	$h$	$h_2$	$d$
Test [5]	T1	Test [5]	0.5	Figs. 1, 3	8280	200	25	9.3
Test [4]	T2	Test [4]	0.6	Figs. 2, 4	4000	200	44	9.3
G1	S1	ST	0.3	Fig. 3	8280	200	25	9.3
	S2	ST	0.5	Fig. 3	8280	200	25	9.3
	S3	ST	0.7	Fig. 3	8280	200	25	9.3
G2	S4	SH	0.3	Fig. 3	8280	200	25	9.3
	S5	SH	0.5	Fig. 3	8280	200	25	9.3
	S6	SH	0.7	Fig. 3	8280	200	25	9.3
G3	S7	LC	0.3	Fig. 3	8280	200	25	9.3
	S8	LC	0.5	Fig. 3	8280	200	25	9.3
	S9	LC	0.7	Fig. 3	8280	200	25	9.3
G4	S10	P	0.3	Fig. 3	8280	200	25	9.3
	S11	P	0.5	Fig. 3	8280	200	25	9.3
	S12	P	0.7	Fig. 3	8280	200	25	9.3
G5	S13	ST	0.3	Fig. 4	4000	200	44	9.3
	S14	ST	0.5	Fig. 4	4000	200	44	9.3
	S15	ST	0.7	Fig. 4	4000	200	44	9.3
G6	S16	SH	0.3	Fig. 4	4000	200	44	9.3
	S17	SH	0.5	Fig. 4	4000	200	44	9.3
	S18	SH	0.7	Fig. 4	4000	200	44	9.3
G7	S19	LC	0.3	Fig. 4	4000	200	44	9.3
	S20	LC	0.5	Fig. 4	4000	200	44	9.3
	S21	LC	0.7	Fig. 4	4000	200	44	9.3
G8	S22	P	0.3	Fig. 4	4000	200	44	9.3
	S23	P	0.5	Fig. 4	4000	200	44	9.3
	S24	P	0.7	Fig. 4	4000	200	44	9.3

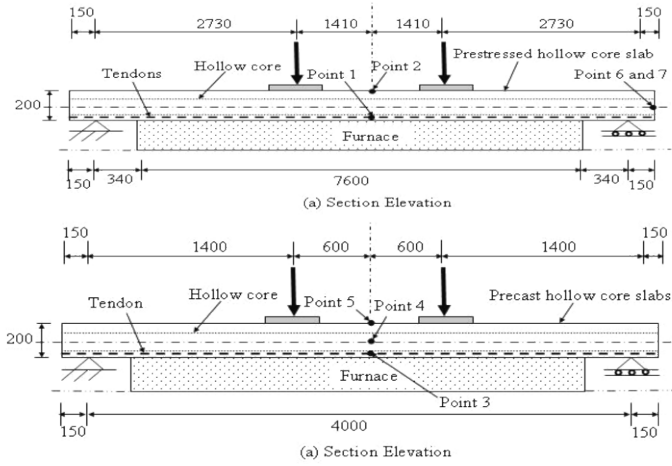


Figure 1. General layout of the test T1 detailed in [5].

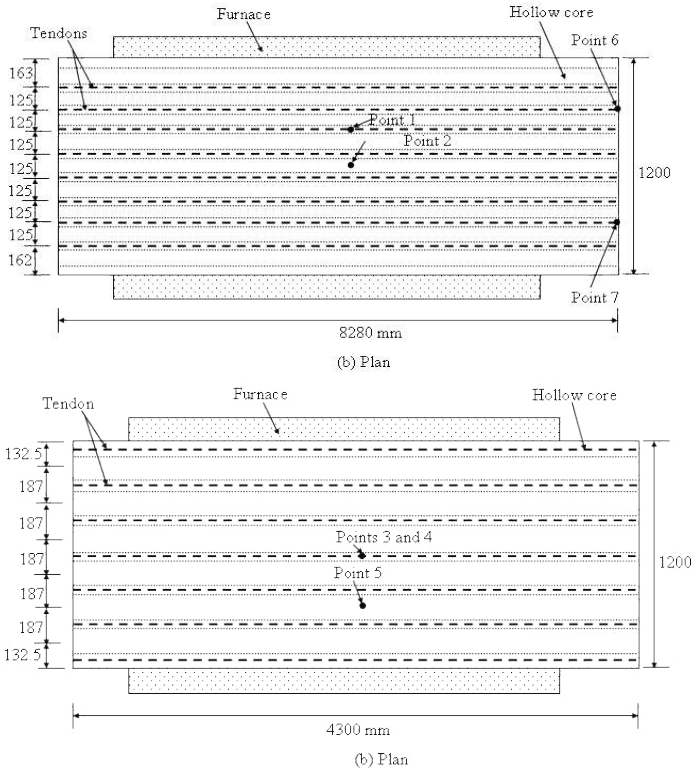
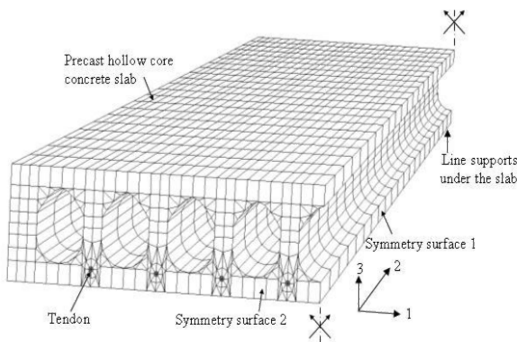


Figure 2. General layout of the test T2 detailed in [4].

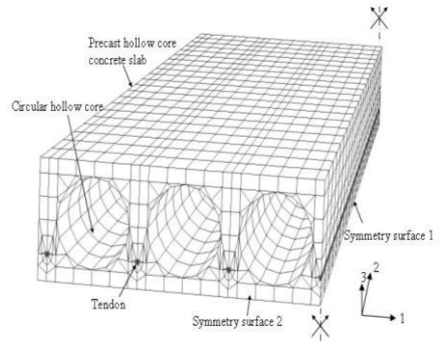
The full-scale fire test reported in [4] on prestressed hollow core concrete slabs was also used to verify the 3-D finite element models developed in this study. Table 1 summarizes the measured dimensions and main parameters of the slab fire test. The definition of symbols for the prestressed hollow core concrete slab (denoted as T2) is shown in Figs. 2 and 4. The prestressed hollow core concrete slab T2 was 4.0m long, 1.2m wide, and 200mm deep. Each slab had seven longitudinal tendons with a nominal diameter of 9.3mm and an area of 52mm<sup>2</sup>. The distance from the bottom of the slab to the centre of the tendon was 44mm. The prestressed hollow core slab had a compressive concrete strength and Young's modulus at ambient temperatures of C48/58 MPa and 33 GPa, respectively. The prestressed hollow core concrete slab was loaded, as shown in Fig. 2, uniformly and transversely, with the load ratio during fire equal to 0.6 of the design load. The slab was heated, see Fig. 2, with the aim of following the standard time-temperature curve specified in BSEN1991-1-2 [19].

## 2. Finite element model

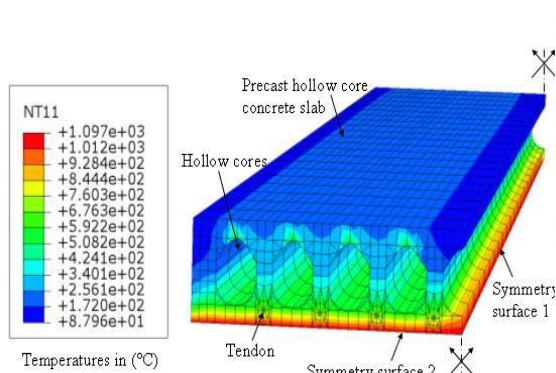
Two finite element models were developed to investigate the nonlinear behaviour of the full-scale prestressed hollow core concrete slab fire tests reported in [4, 5]. A combination of 3-D solid elements (C3D8 and C3D6) available within ABAQUS [15] were used to model the concrete slab and tendons. Due to symmetry, only quarters of the slabs were modelled (Figs. 3 and 4). The prestressing tendons had a nominal Young's modulus of 198-200 kN/mm<sup>2</sup>, a proportional limit ( $\sigma_{0.01}$ ) of 1620-1650 N/mm<sup>2</sup>, a yield stress ( $\sigma_{0.02}$ ) of 1770-1780 N/mm<sup>2</sup> and an ultimate stress ( $\sigma_u$ ) of 1870-1900 N/mm<sup>2</sup>. The investigations reported in [20] accurately measured the tendon stress-strain curves at ambient temperature, therefore it is used in this study. For the fire tests the applied load remained constant and the temperature within the slab increased. For the modelling of the fire tests a thermal analysis was conducted to evaluate the temperature distribution throughout the slabs, based on the measured furnace curve from the test. A constant convective coefficient ( $\alpha_c$ ) of 25w/m<sup>2</sup>k was assumed for the exposed surface and 9w/m<sup>2</sup>k was assumed for the unexposed surface. The radiative heat flux was calculated using a concrete emissivity ( $e$ ) value of 0.7. Fig. 5 shows the temperature contours predicted from the heat transfer analysis for the slab T1.



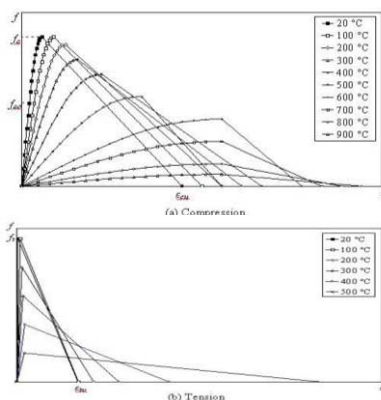
**Figure 3.** Finite element mesh for quarter of the test T1.



**Figure 4.** Finite element mesh for quarter of the test T2.



**Figure 5.** Temperature distribution within a prestressed hollow core slab after three hours of exposure to the standard fire



**Figure 6.** Stress-strain curves of concrete at elevated temperatures.

Concrete was modelled using the damaged plasticity model implemented within ABAQUS [15]. Under uniaxial compression the response is linear until the value of the proportional limit stress, ( $f_{co}$ ) is reached, as shown in Fig. 6a. Under uniaxial tension the stress-strain response follows a linear elastic relationship until the value of the failure stress. The softening stress-strain response, Fig. 6b, past the maximum tensile stress, was represented by a linear line defined by the fracture energy and crack band width. The fracture energy  $G_f$  was taken as 0.16N/mm, which is recommended by ABAQUS [15] and CEB [21]. The stress-strain-temperature curves for concrete in compression and tension are shown in Fig. 6. The curves were based on the reduction factors given in BSEN1992-1-2 [17]. The stress-strain curves of the tendon at elevated temperatures were predicted adopting the reduction factors given in BSEN1992-1-2 [17].

### 3. Verification of the FE model

The developed finite element models were used to analyse the full-scale fire tests reported in [4,5]. Fig. 7 plotted the time-temperature relationships obtained experimentally and numerically for slab T1. The relationships were plotted at the tendon level and the cold surface. It can be seen that generally good agreement was achieved between experimental and numerical results. The time-central deflection curves obtained from the full-scale tests and the finite element analysis were also compared, with an example shown in Fig. 8 for slab T1. Generally, it can be seen that good agreement existed between experimental and numerical results. The failure mode of the prestressed hollow core concrete slab T1 observed experimentally was also compared with that predicted from the finite element analysis as shown in Fig. 9. The figure shows the failure mode observed experimentally at the end of fire exposure together with the plastic strain contours in direction 1-1 predicted from the finite element analysis. Longitudinal cracks along the slab T1 directly above and inline with the tendons developed between 15-25 minutes from the start of heating as shown in Fig. 9(a). If we consider the modelling of T1 we can see that tensile stresses occurred above the tendons, as shown in Fig. 9(b).



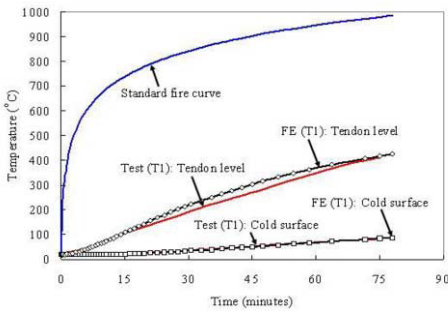


Figure 7. Comparison of time-temperature curves for slab T1.

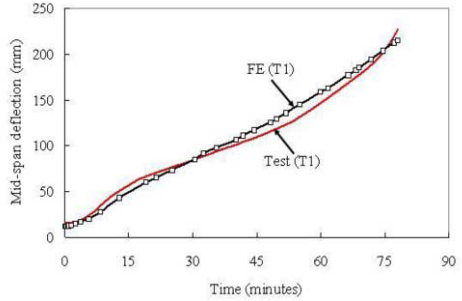
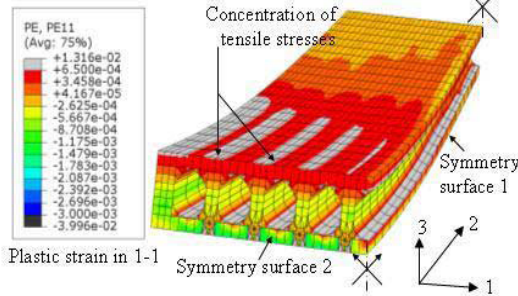


Figure 8. Comparison of time-deflection curves for slab T1.



(a) Experimental [5]



(b) Numerical

Figure 9. Comparison of failure modes for slab T1 at the end of fire.

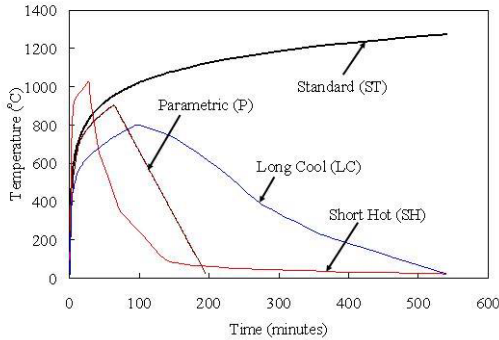


Figure 10. Fire curves considered in the parametric study.

#### 4. Parametric studies and discussions

The verified finite element models were used to investigate the effects of the change in the geometries, load ratios during fire and fire curves on the global structural behaviour of prestressed hollow core one-way concrete slabs in fire, see Table 1. To investigate the effects of different types of fire scenarios, see Fig. 10, on the structural response of prestressed hollow core concrete slabs, the standard fire curve (ST) specified in [19] together with three natural fires defined as a ‘short hot’ fire (SH), a ‘long cool’ fire

(LC) and an average parametric fire (P) were assumed. Details regarding the characteristics of the fires could be found in reference [21]. Three load ratios during fire were considered, which are 0.3, 0.5 and 0.7. A total of 24 prestressed hollow core concrete slabs were analysed in this study, which were classified to eight groups (denoted G1-G8). Groups G1-G4 and G5-G8 had prestressed hollow core concrete slabs with identical dimensions to that tested in Refs. [5] and [4], respectively. The coarse aggregate used was granite having a thermal expansion coefficient (K) of  $8.6 \times 10^{-6}/^{\circ}\text{C}$  as recommended in [22]. The maximum and residual deflections, fire resistances and failure modes of the slabs investigated in the parametric study were predicted using the finite element model as summarised in Table 2. It can be seen from Table 2 that the slabs heated using the natural fire curves did not fail and survived the whole duration of fire exposure. On the other hand, the slabs heated using the standard fire curve underwent tensile splitting failure mode and had fire resistances varied from 59 to 122 minutes. The prestressed hollow core concrete slabs S1-S12 had an axis distance of the tendons of 25mm, which according to BS8110-2 [16] and EN1992-1-2 [17] should achieve 60 and 30 minutes fire resistance, respectively. On the other hand, the slabs S13-S24 had an axis distance of the tendons of 44mm, which according to BS8110-2 [16] and EN1992-1-2 [17] should achieve 90 and 60 minutes fire resistance, respectively. It can be seen that the BS8110-2 [16] conservatively estimated the fire resistances of the prestressed hollow core concrete slabs investigated, except for the slabs heated using the standard fire curve under a higher load ratio of 0.7. On the other hand, the EN1992-1-2 [17] conservatively estimated the fire resistances of all the prestressed hollow core concrete slabs.

**Table 2.** Finite element results and design predictions for the hollow core concrete slabs investigated.

Group	Specimen	Fire curve	Load ratio	Finite element analysis			BS	EC4
				Maximum deflection (mm)	Residual Deflection (mm)	Fire resistance (minutes)	Fire resistance (minutes)	Fire resistance (minutes)
Test [5]	T1	Exp. [5]	0.5	215.0	215.0	78	60	30
Test [4]	T2	Exp. [4]	0.6	136.0	136.0	75	90	60
G1	S1	ST	0.3	237.9	237.9	122	60	30
	S2	ST	0.5	490.7	490.7	85	60	30
	S3	ST	0.7	592.8	592.8	59	60	30
G2	S4	SH	0.3	132.4	58.1	540	60	30
	S5	SH	0.5	202.2	127.4	540	60	30
	S6	SH	0.7	210.9	140.6	540	60	30
G3	S7	LC	0.3	153.8	65.7	540	60	30
	S8	LC	0.5	318.0	225.0	540	60	30
	S9	LC	0.7	360.1	265.1	540	60	30
G4	S10	P	0.3	153.5	86.0	195	60	30
	S11	P	0.5	270.5	201.4	195	60	30
	S12	P	0.7	297.5	231.5	195	60	30
G5	S13	ST	0.3	109.2	109.2	93	90	60
	S14	ST	0.5	178.9	178.9	92	90	60
	S15	ST	0.7	207.3	207.3	59	90	60
G6	S16	SH	0.3	74.3	34.0	540	90	60
	S17	SH	0.5	112.9	73.3	540	90	60
	S18	SH	0.7	174.3	135.0	540	90	60
G7	S19	LC	0.3	101.6	49.3	540	90	60
	S20	LC	0.5	140.2	86.8	540	90	60
	S21	LC	0.7	187.5	133.3	540	90	60
G8	S22	P	0.3	93.9	68.1	195	90	60
	S23	P	0.5	143.7	117.8	195	90	60
	S24	P	0.7	206.7	135.5	195	90	60

## 5. Conclusions

Nonlinear 3-D finite element models, for the analysis of prestressed hollow core concrete slabs at elevated temperatures have been developed. The temperature distribution throughout the slab, time-deflection behaviour, fire resistances and the failure modes of the slabs have been predicted by the model and verified well against full-scale fire test results.

The study has shown that the failure of the prestressed hollow core concrete slabs investigated was due to tensile splitting, with longitudinal cracks developing along the slab directly above and inline with the tendons, between 15-25 minutes from the start of heating. No shear failure was observed and the fire resistance of the slabs was mainly dependent on the tensile splitting failure. The model developed was used to investigate the effects on the global structural behaviour due to the change in the slab geometries, load ratios during fire and fire curves. It was shown that the slabs heated using the natural fire curves did not fail and survived the whole duration of fire exposure. The fire resistances of the prestressed hollow core concrete slabs predicted from the finite element analysis were compared with design resistances calculated using current codes of practice. The comparison has shown that the British Standards conservatively estimated the fire resistances of the prestressed hollow core concrete slabs investigated, except for the slabs heated using the standard fire curve under a higher load ratio of 0.7. On the other hand, the European code conservatively estimated the fire resistances for all the prestressed hollow core concrete slabs.

## References

- [1] J.C. Walraven and P. Mercx. The bearing capacity of prestressed hollow core slabs. *Heron*, 28 (3), 1983.
- [2] N. E. Andersen and D. H. Lauridsen. *Hollow Core Concrete Slabs*. Danish Institute of Fire Technology, Technical Report X52650, Part 2, Basismiddel project X52650, April 1999.
- [3] A. V. Acker. Shear resistance of prestressed hollow core floors exposed to fire. *Structural Concrete*, 4(2), 65-74, 2003.
- [4] A. L. Materazzi and M. Breccolotti. Fire behaviour of HPLWC hollow core slabs: full scale furnace tests and numerical modelling. *Proceedings of the workshop Held at Milan University of Technology*, Milan, Italy, 289-294, December 2-3, 2004.
- [5] N. Torić, V. Divić, and I. Boko. Behaviour of prestressed hollow-core concrete slab under fire – Experimental study. *Tehnički vjesnik*, 19 (4), 847-856, 2012.
- [6] J.H.H. Fellinger, J. Stark and J. Walraven. Shear and anchorage behaviour of fire exposed hollow core slabs. *Heron*, 50(4), 2005.
- [7] J.H.H. Fellinger. *Shear and anchorage behaviour of fire exposed hollow core slabs*. Dissertation TU Delft, Delft: Delft University Press, 2004.
- [8] DIANA. *DIANA Finite element analysis, user's manual, release 8.1*. Delft: TNO, 2003.
- [9] J. Chang, A. H. Buchanan, R. P. Dhakal and P. J. Moss. Hollow-core concrete slabs exposed to fire. *Fire and Materials* 2008, 32, 321-331, 2008.
- [10] E. Ellobody. Nonlinear behaviour of unprotected composite slim floor steel beams exposed to different fire conditions. *Thin-Walled Structures*, 49(6), 762-771, 2011.
- [11] E. Ellobody. Composite slim floor stainless steel beam construction exposed to different fires. *Engineering Structures*, 36(3), 1-13, 2012.
- [12] E., Ellobody and B. Young. Investigation of concrete encased steel composite columns at elevated temperatures. *Thin-Walled Structures*, 48(8), 597-608, 2010.
- [13] E. Ellobody and C.G. Bailey. Modelling of unbonded post-tensioned concrete slabs under fire conditions. *Fire Safety Journal*, 44(2), 159-167, 2009.
- [14] E. Ellobody and C.G. Bailey. Modelling of bonded post-tensioned concrete slabs in fire. *Structures and Buildings*, ICE proceedings, Thomas Telford Journals, 161(6), 311-323, 2008.

- [15] ABAQUS. *ABAQUS Standard/Explicit User's Manual*. Hibbit, Karlsson and Sorensen, Inc. Vol. 1, 2 and 3, Version 6.11-1, USA, 2011.
- [16] BS 8110-2. *Structural use of concrete. Code of Practice for Special Circumstances*. British Standards Institution, London, 1985.
- [17] Eurocode 2. *Design of concrete structures. General rules*. Structural fire design (together with United Kingdom National Application Document). British Standards Institution, BSEN 1992-1-2, London, 1992.
- [18] BS8110-1. *Structural use of concrete. Code of Practice for Design and Construction*. British Standards Institution, London, 1997.
- [19] Eurocode 1. *Actions on structures. General actions. Actions on structures exposed to fire*. British Standards Institution, BSEN 1991-1-2, London, 2002.
- [20] E. Ellobody and C.G. Bailey. Behaviour of unbonded post-tensioned concrete slabs. *Advances in Structural Engineering*, Vol. 11, No. 1, 107-120, 2008.
- [21] CEB. *RC Elements under cyclic loading*. Comite Euro-International Du Beton (CEB), Thomas Telford, 1996.
- [22] P. Klieger and J.F. Lamond. Significance of tests and properties of concrete and concrete making materials. *ASTM publication*, 1994.

# Behaviour of reinforced concrete slabs strengthened by concrete overlays

Wael IBRAHIM<sup>a,1</sup>, Mohamed El-adawy<sup>b</sup> and Gouda GHANEM<sup>b</sup>  
<sup>a</sup>*RWTH-Aachen University*  
<sup>b</sup>*Helwan University*

**Abstract.** This paper discusses the influence of three factors, the distribution of shear connectors, the concrete compressive strength, addition of new concrete thickness on the behavior of one-way composite pre-slabs. The experimental program involved nine tests to study flexure and cracking behaviour of reinforced concrete slabs strengthened with cast in- place new concrete layer. Three of them were reference monolithic slabs and the remaining six slabs were composite pre-slabs composed of two layers with different distributions of shear connectors according to shear force distribution. All slabs were tested under two line loads. The strengthening with cast in-place new concrete layer significantly increases the strength capacity of reinforced concrete (RC) slabs.

**Keywords.** Shear connectors, slabs, compressive strength, strengthening

## Introduction

RC structures are designed and built to perform adequately with respect to strength, serviceability and durability. During their service life however, they might (due to several reasons) behave unsatisfactorily with respect to these criteria. Rehabilitation and strengthening interventions are then necessary [1-3].

The objective of this paper is to present the results of an experimental investigation on the behaviour of one-way reinforced concrete slabs strengthened in flexure with a 4.0 cm concrete overlay. Shear transfer at the concrete interface was provided in one way to provide bonding between the overlay and concrete substrate by dowel action only acting as shear connectors [4-6]. Nine slabs were tested. All slabs were loaded up to failure except slabs S no. (2) and S no. (3). For slabs S no. (2) and S no. (3), a two-stage loading procedure was employed. Initially, these slabs were subjected to loads 25% and 75% of their service load level, respectively. This load was then removed and the slabs were strengthened. The rehabilitated slabs were tested twenty-eight days after casting the concrete overlays. During the experiments, displacements, interlayer slips and strains were measured. A design procedure for evaluating the behaviour of the slabs after the different interventions, both in service and at failure, is also presented.

---

<sup>1</sup>Corresponding author: RWTH – Aachen University, Aachen, Germany;  
Email: [Wael.ibrahim@rwth-aachen.de](mailto:Wael.ibrahim@rwth-aachen.de)

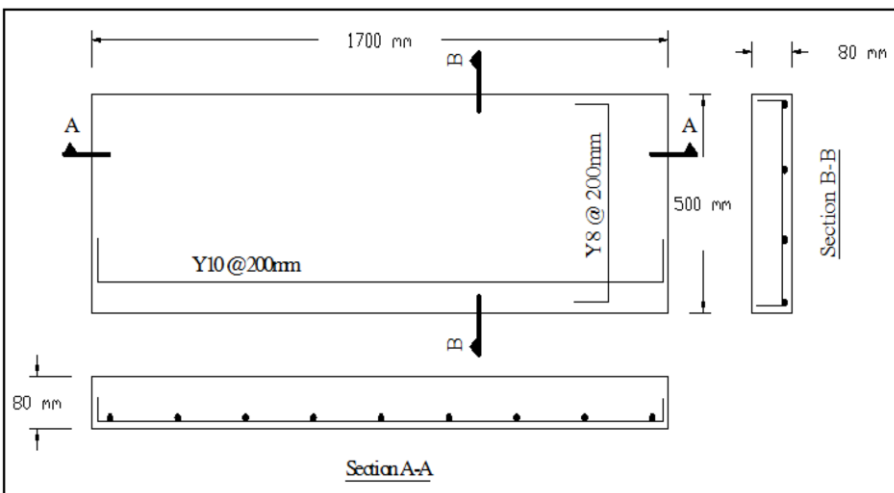
### 1. Experimental program

#### 1.1. Test Specimens

The experimental program consisted of nine one-way slabs. All slabs had the same flexural reinforcement. The details of the one-way slabs tested in the laboratory are shown in (Table 1 and Figure 1). The major variables of the specimen were shear connectors spacing, concrete overlay and compressive strength of concrete. Each specimen had the same concrete strength but different shear connectors spacing. Specimen no. 1 was the original slab without strengthening. Slab no. (2) and slab no. (3) Were first loaded to 25% and 75% of their service load level respectively, and then strengthened with a 40 mm concrete overlay. One repair method was used i.e. the concrete overlay was bonded to the original slab where the shear transfer at the concrete interface was provided by shear connectors with a bond breaker between the two concrete layers. The shear connectors were positioned as shown in Figure 2.

**Table 1.** Test matrix of the experimental program

Specimen ID	Concrete overlay [mm]	Shear connectors Spacing [mm]			Concrete compressive strength of overlay? [MPa]	
		L/3	L/3	L/3	First Layer	Second Layer
S1	-	-	-	-	-	-
S2	40	250	250	250	33	34
S3	40	250	250	250	33	34
S4	40	150	150	150	33	34
S5	40	250	250	250	33	34
S6	40	200	-	200	33	34
S7	40	200	250	200	33	34
S8	80	250	250	250	33	34
S9	40	250	250	250	33	38



**Figure 1.** Control slab S1

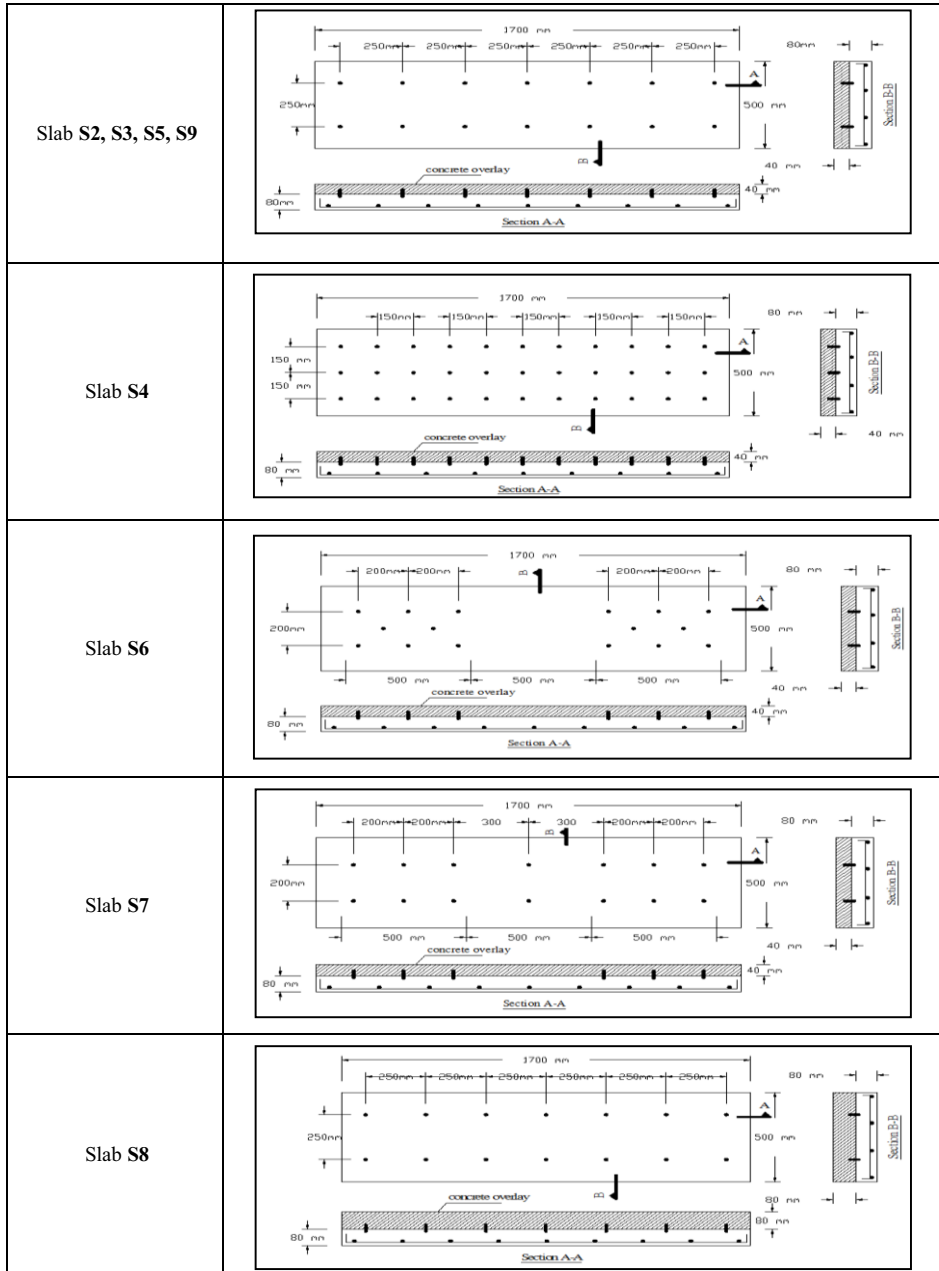


Figure 2. Test specimen details

### 1.2. Materials

Concretes of compressive strengths of  $f_c = 30$  MPa were used. Steel reinforcing bars of 400 MPa yield strength, 600 MPa ultimate strength, and a 200 GPa elasticity modulus were used. Steel reinforcing bars a nominal diameter of 12 mm and a length of 80 mm were used as shear connectors. A total of 14 to 33 connectors/specimen would be necessary in each shear span for the composite slab to reach its ultimate bending capacity. This number of connectors is considered reasonable when compared to the maximum values of 25 to 30 connectors/m<sup>2</sup> commonly used in practice [2] ). With this number of connectors, partial composite action should be expected at service load levels during the tests.

### 1.3. Strengthening procedures

The strengthening procedure consisted of initially machine grinding the top surface of the slab. Holes are then drilled for the shear connectors, which penetrated 6.0 cm into the original slab. The slab details i before casting the concrete overlay are shown in Figure. 2. The concrete overlay was cast manually and an internal vibrator was used for consolidation. The concrete slump averaged about 180 mm. The overlays were covered with wet burlap for 7 days.

### 1.4. Testing set-up

The slabs were tested in a simply supported condition with a two-point load equidistant from the two supports, as shown in Figure. 3. As a result, each slab had a region of constant bending moment (between the applied loads) and a region of constant shear force along the shear span. Throughout the loading tests, mid-span deflections and strains in the concrete as well as in the longitudinal reinforcement were measured. In the repaired slabs, the interlayer slip at the supports was also evaluated.



Figure 3. Test set-up



## 2. Test results and analysis

### 2.1. Effect of strengthening by concrete overlays

Generally, the overall behaviour of the strengthened slabs S no. (2) to S no. (9) with respect to the original slab S no. (1), compared through the load versus mid-span deflection relationship is shown in Figure 4. The repaired slabs exhibited a much larger stiffness and strength, which in turn led to the increases of load carrying capacity both in service and at failure. The new service load was around 66 % to 260 % higher than the original one. Thus, this rehabilitation procedure produced significant improvements in the performance of the slabs. This result emphasizes that the number of connectors at the interface between the overlay and substrate is enough to transfer the shear stresses.

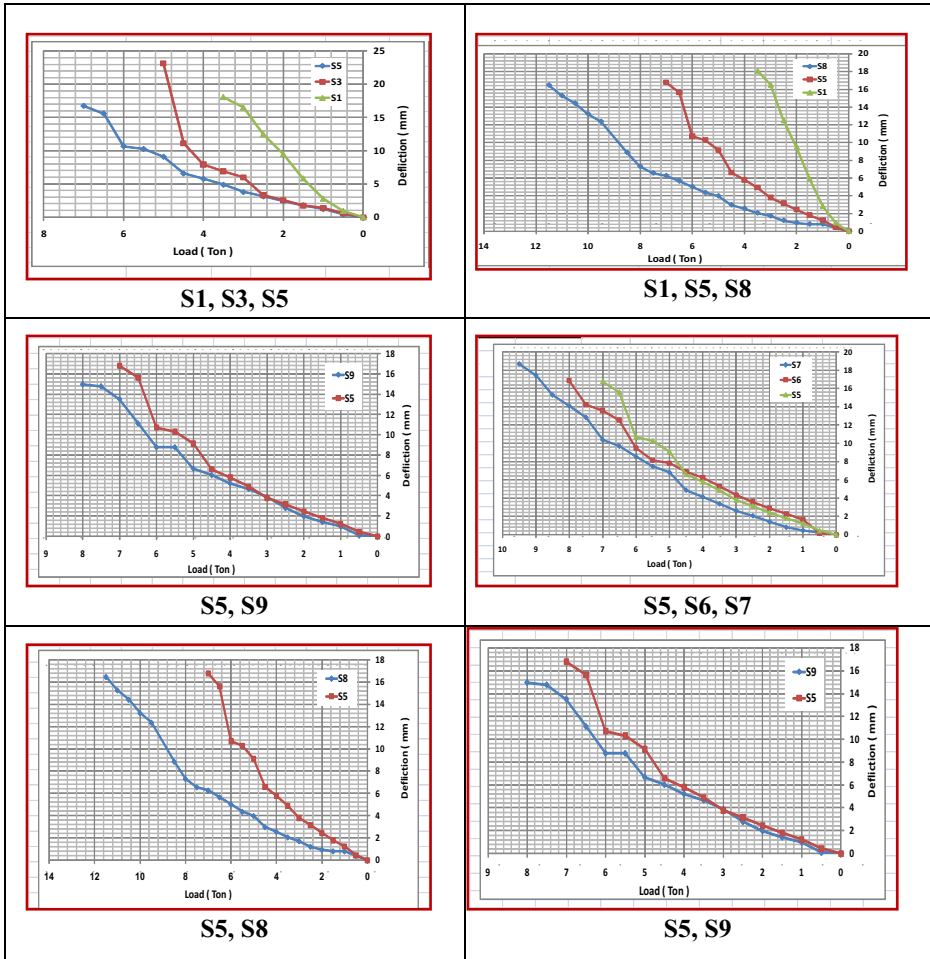


Figure 4. Load-deflection curves

## 2.2. Effect of number of shear connectors

As expected, strengthened slabs S no. (4), S no. (6) and S no. (7) with respect to the strengthened slab S no. (5) exhibited a much larger stiffness and strength, which in turn led to increases in load carrying capacity both in service and at failure. This result emphasizes that the number of connectors at the interface between the overlay and substrate is important to transfer the shear stresses. During these tests, no slip was observed over the supports of the slabs. This indicates that the bond strength at the interface between the different concretes was sufficient to withstand the shear stresses being transferred. Consequently, full composite action occurred up to failure. These strain measurements indicated yielding of the tensile reinforcement. Both slabs failed due to bending with crushing of the concrete in the overlay directly below the loading pads. The behaviour of the strengthened slab S no. (8) with respect to strengthened slab of the same number of connectors S no. (5) was also compared in Figure. 4. The load versus mid-span deflection relationship for the original slab S no. (1) is also presented in the plot. These results show that the slab S no. (8) was stiffer with respect to the original slab S no. (1) and strengthened slab S no. (5) for all loads. This larger stiffness resulted in smaller mid-span deflections up to failure. The partial composite action behaviour associated with the existence of the initial mid-span deflection and the fact that this strengthened slab S no. (8) was already cracked are the reasons for the differences in the load mid-span versus deflection relationship.

## 2.3. Effect of concrete overlay compressive strength

The test results indicate expressively the overall better performance, for both service and failure load, when the slabs are repaired with concrete overlay. Figure 4.3 presents the load versus mid-span deflection relationship for the slabs S no. (9) and S no. (5). Thus the values of the deflections and the cracking stage of the slab at the time of the repair are very important aspects to consider when assessing the behaviour of repaired slabs under service loads. More research is necessary to optimize the concrete overlay compressive strength.

## 3. Conclusion

The major conclusions deduced from this research are given below as follows:

1. Experimental study, as presented in this paper, emphasizes the influence of shear connectors on the structural behavior of strengthened slabs and on the debonding mechanism.
2. The overall analysis of the test results indicates expressively the better performance of slabs that are repaired with a larger number of shear connectors. These slabs exhibited increased stiffness and similar load carrying capacity compared to slabs containing a lower number of shear connectors of the same geometry.
3. Strengthening slabs by adding a concrete overlay of intermediate compressive strength indicates expressively the overall better performance, for both service and failure load.

4. The design procedures for evaluating the behavior of the strengthened slabs, at service and failure loads is still needed especially when shear connectors are used.
5. Deflection is significantly reduced in the strengthened slabs.
6. Finally, strengthening slabs by adding concrete overlays will only enhance their load carrying capacity as long as the existing tensile reinforcement is sufficient to accommodate the increased load.

## References

- [1] Bijen, J., Salet, T. Adherence of young concrete to old concrete development of tools for engineering, Wittman FW (ed) *Proceeding of 2nd Bolomey workshop on adherence of young on old concrete*, 1994.
- [2] Calixto, J. M., Pires, E. F., Lima, S. A., Piancastelli, E. M., Behavior of reinforced concrete slabs strengthened in flexure by concrete overlays, *ACI Structural Journal*, Vol. 229, 2003, p. 389-406
- [3] Mellinger, F. M. Structural design of concrete overlays, *ACI Journal* 60(2), 1963, p. 225-237
- [4] Perez, F., Bissonnette, B., Gagné, R. Parameters affecting the debonding risk of bonded overlays used on reinforced concrete slab subjected to flexural loading, *Materials and Structures Journal*, Vol. 42, 2009.
- [5] Saiidi, M., Vrontinos, S., Douglas, B. Model for the response of reinforced concrete beams strengthened by concrete overlay, *ACI Structural Journal* 87(6), 1990, p. 687-695
- [6] Silfwerbrand, J. Improving concrete bond in repaired bridge decks, *Concrete International Journal*, Vol. 12, Issue 6, 1990, p. 61-66

# Study on the mechanical property recovery of concrete subjected to elevated temperatures

Qingtao LI<sup>a,1</sup>, Guanglin YUAN<sup>b</sup> and Qianjin SHU<sup>b</sup>

<sup>a</sup>*Jiangsu Key Laboratory of Environmental Impact and Structural Safety in Engineering, China University of Mining and Technology, Jiangsu 221008, China*

<sup>b</sup>*China University of Mining and Technology, Xuzhou, Jiangsu 221008, China*

**Abstract.** This investigation was aimed at improving the recovery of the compressive strength, the splitting tensile strength and the static modulus of elasticity of concrete subjected to elevated temperature. Normal-strength concrete with water-cement ratio of 0.50 was prepared and exposed to 200 °C and 600 °C. Two cooling regimens were used including natural cooling and spraying water for 30 min. After cooling, the specimens were subjected to two post-fire-curing methods with and without performance-modifying agent (PMA) for a total duration of 180 days. The compressive strength, the splitting tensile strength and the static modulus of elasticity of concrete were measured to examine the changes in the mechanical properties of concrete. The test results indicated that the PMA could improve the recovery of the compressive strength, the splitting tensile strength and the static modulus of elasticity of concrete subjected to 200 °C and 600 °C.

**Keywords.** Concrete, recovery, mechanical property, elevated temperature

## Introduction

The mechanical properties of concrete deteriorate when it is subjected to high temperature such as in a fire because of the changes in the chemical composition of cement paste and the physical properties of aggregates. Experimental results showed that considerable loss in compressive strength occurred after exposure to 600 °C [1-3]. The decrease in compressive strength was greater when the concrete was cooled in water than when cooled in the air [1, 4, 5]. Concrete experienced a rapid loss of stiffness at elevated temperatures. When exposed to temperatures in the order of 200°C, the modulus of elasticity reduced to 70-80% of that measured at ambient temperatures and when exposed to temperatures in the order of 400°C, it reduced to 40-50% of its original value [6, 7]. Original strength of concrete and water cement ratio seems to have little influence on the elasticity-temperature relationship.

Experimental studies have been performed to investigate the strength recovery of concrete exposed to high temperatures [8, 9]. The compressive strength recovery, which depends on the type of concrete, method of re-curing and exposure temperature,

---

<sup>1</sup>Corresponding author: Email. lqt2003317@126.com, Tel. 0086-838995252

is faster and enhanced more after water re-curing, as compared to the air re-curing. Ichise et al. [10] observed that the compressive strength of high-strength concrete subjected to temperatures of up to 500 °C recovered up to 80% when subjected to underwater curing after this exposure. Matsudo [11] studied the recovery of the ultra-high strength concrete of which the compressive strength was above 100 N/mm<sup>2</sup>. After being exposed to 600 °C, it can be found that the recovery of compressive strength after two years was negligible, compared to concrete with high water-binder ratio.

Yiching Lin et al [8] reported that water curing of concrete specimens after exposure to high temperatures has a significantly positive influence on the residual strength recovery. For concrete with water-cement ratio of 0.58 subjected to 600 °C, the residual strength ratio of water-cured specimens at 180 days reaches 0.6 of the original strength. The compressive strength of concrete exposed to 600 °C almost can not recover along with the water curing period. Poon et al.[9] studied the effect of post-fire-curing on the strength, impermeability and porosity of concrete exposed to 600 °C. For concrete with water-cement ratio of 0.50 exposed to 600 °C, the test results indicated that the maximum residual strength ratio of was 0.66 after 56 days of water re-curing.

For concrete at ambient temperature, protection has been provided in aggressive environments. Surface coating is used to protect concrete [12, 13]. Results show that the durability of concrete was improved with calcium-silicate compound. The lack of enhancing properties of fire-damaged concrete related to inorganic coating leads to the necessity to investigate the performance recovery of concrete exposed to elevated temperature.

In this investigation, the recovery extents and influencing factors of the mechanical properties of concrete exposed to 200 °C and 600 °C were investigated. The compressive strength and modulus of elasticity of concrete were measured at different post-fire-curing periods.

## 1. Experimental details

### 1.1. Materials and mixture proportions

The cement used in this study was ordinary Portland cement CEM II, of which the specific gravity is 3.16. Coarse aggregate was crushed stone with a maximum size of 25 mm. Sea sand was used as fine aggregate in the study. The water used in this investigation was potable water which is free from injurious amount of deleterious materials. The polycarboxylate based superplasticizer was used to obtain workable concrete mixtures. Polypropylene fiber with an average length of 12 mm was used at an addition level of 0.1% per cubic meter to improve the spalling resistance of concrete during heating.

Details of the mixture proportions of concrete are given in Table 1. Cylindrical specimens with diameter of 100 mm and length of 200 mm were cast for mechanical properties testing. After a period of 28 days of curing in water at a temperature of 20 ± 2 °C, the specimens were placed in a curing room maintained at a temperature of 20 ± 2 °C and relative humidity (RH) 60 ± 5% for 90 days prior to being heated.

**Table 1.** Mix proportions of concrete

w/c ratio	Mixture proportion (kg/m <sup>3</sup> )				
	Water	Cement	Sea sand	Coarse aggregate	Superplasticizer
0.50	175	350	812	982	1.24

### 1.2. Heating and cooling regimes

On the 90<sup>th</sup> day, the concrete specimens were heated up to 200 °C and 600 °C by an electric furnace at an incremental rate of 5°C/min. The center temperature of the concrete specimen was measured by an embedded thermal couple. In order to make sure that the temperature in the center of the concrete specimens also reached the target temperature, the concrete specimens were maintained at the peak temperature of 200 °C and 600 °C for 360 min and 150 min, respectively. Then the concrete specimens were taken out from the electric furnace and cooled down to room temperature with two cooling regimens including cooling in the air and spraying water (at room temperature) for 30 min.

### 1.3. Post-fire-curing method

Afterward, all of the fire-damaged concrete specimens were stored in air ( at  $20 \pm 2$  °C and RH of  $60 \pm 5\%$  ) in the laboratory for 180 days. The heated concrete specimens were divided into two groups, one coated with PMA and another without the PMA coating. PMA is a product with a silicate-material system, and it is usually used on the surface of concrete to strengthen it or to repair cracks to lower the water ingress potential. The PMA reacts with cement hydrates such as  $\text{Ca}(\text{OH})_2$  and others in concrete to form C-S-H in the presence of water. The usage of PMA was about 0.3 kg/m<sup>2</sup>. The specimens coated with PMA were cured by sprinkling with water at a rate of about 1 lit/m<sup>2</sup> twice per day for 7 days.

## 2. Results and discussion

### 2.1. Recovery of compressive strength

The variation of the compressive strength of the concrete is shown in Figure 1. It is shown that the compressive strength of concrete exposed to 200 °C reduced slightly and recovered after re-curing for 180 days. However, at a higher temperature of 600 °C there was a great decrease in the compressive strength. It is possible that the recovery of the compressive strength was affected by the cooling method and application of PMA.

The recovery of compressive strength of concrete exposed to 200 °C is shown in Figure 1(a) and (b). After being exposed to 200 °C, the compressive strength of air-cooled and water-cooled concrete reduced to 94% and 92.6% of the initial compressive strength, respectively. Then the compressive strength of the air-cooled concrete exposed to 200 °C recovered to 96.0%, 98.4%, and 101.7% after re-curing for 30, 60

and 180 days, respectively. The compressive strength of the water-cooled concrete exposed to 200 °C recovered to 93.6%, 96.8%, and 103.8% after re-curing for 30, 60, and 180 days, respectively. The compressive strength of the PMA-coated concrete, after air-cooling, was 97.7%, 101.7% and 104.1% of the initial value after re-curing for 30, 60 and 180 days, respectively. The compressive strength of the PMA-cooled concrete, after water-cooling was 96.6%, 103.2% and 106.8% of the initial value after re-curing for 30, 60 and 180 days, respectively.

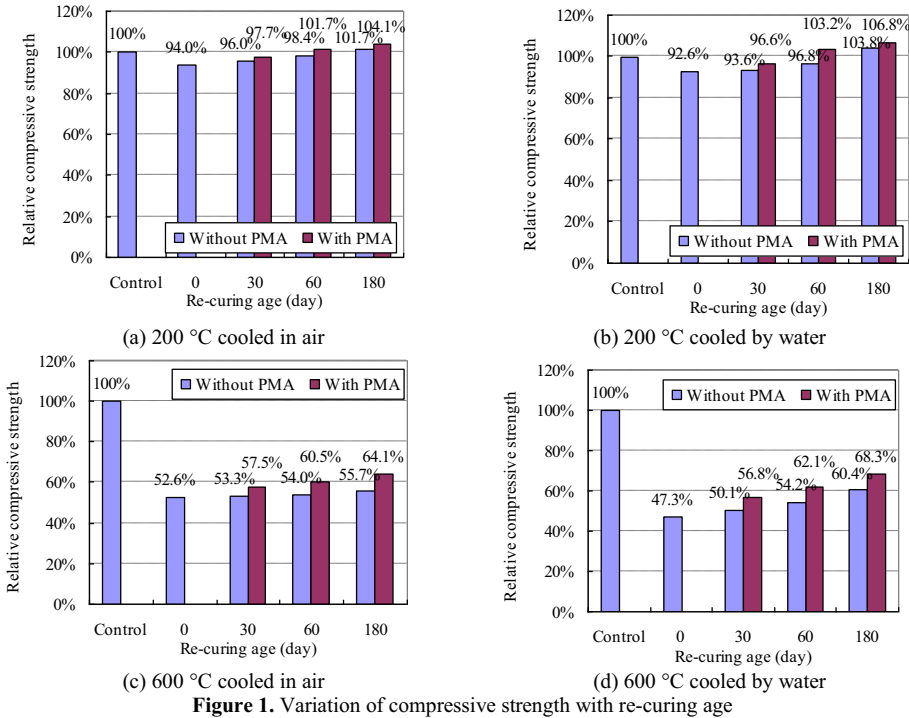


Figure 1. Variation of compressive strength with re-curing age

After exposure to 600 °C, the compressive strength of the concrete cooled in air and by water were 52.6% and 47.3% of the initial strength respectively. The reduction in the compressive strength immediately after the concrete was cooled down to room temperature by water was greater than that of concrete cooled in air. After re-curing for 30, 60 and 180 days, the relative compressive strength of the concrete cooled in air was 53.3%, 54% and 55.7%. The relative compressive strength of the concrete cooled by water was 50.1%, 54.2% and 60.4%. The compressive strength of the PMA-coated concrete cooled in air recovered to 64.1% of the original strength after re-curing for 180 days, while the relative compressive strength of the PMA-coated concrete cooled by water recovered to 68.3% of the initial strength.

Figure 1 demonstrates that the compressive strength of concrete coated with PMA, recovers more rapidly than that of the concrete without PMA coating. The recovery of the compressive strength of concrete coated with PMA, whether it was cooled in air or by water, was higher than that of the concrete without PMA coating. For concrete exposed to 200 °C, that without PMA coating recovered to about 101.7% to 103.8% of their original strength after re-curing for 180 days, while the concrete coated with PMA

recovered to about 104.1% to 106.8% of their initial strength. For the concrete exposed to 600 °C, that without PMA coating recovered to about 55.7% to 60.4% of their original strength after re-curing for 180 days, while that with PMA coating recovered to about 64.1% to 68.3% of their initial strength. The recovery of the concrete was due to the re-hydration reaction which can be improved by PMA. This result may be attributed to the cracks and pore structure of fire-damaged concrete cooled by water. The PMA permeated into the damaged concrete fissures thus greatly improved the compressive strength.

## 2.2. Recovery of splitting tensile strength

The recovery of the splitting tensile strength of the concrete is shown in Fig. 2. It can be seen that the splitting tensile strength of concrete exposed to 200 °C reduced but recovered slightly after re-curing for 180 days. However, the splitting tensile strength of concrete exposed to 600 °C decreased drastically. It is evident that the recovery of the splitting tensile strength was also affected significantly by the cooling method and application of PMA.

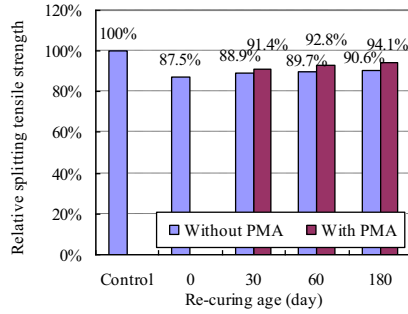
Figure 2 (a) and (b) shows the recovery of splitting tensile strength of concrete exposed to 200 °C. After being exposed to 200 °C, the splitting tensile strength of air-cooled and water-cooled concrete reduced to 87.5% and 82.5% of the initial splitting tensile strength, respectively. The splitting tensile strength of air-cooled concrete recovered to be 88.9%, 89.7%, and 90.6% after re-curing for 30, 60 and 180 days, respectively. While that of water-cooled concrete recovered to 84.4%, 86.6%, and 89.9% after re-curing for 30, 60, and 180 days, respectively. The splitting tensile strength of the concrete exposed to 200 °C, which was coated with PMA after air-cooling, was 91.4%, 92.8% and 94.1% of the initial value after re-curing for 30, 60 and 180 days, respectively. The splitting tensile strength of the water-cooled concrete coated with PMA was 89.8%, 92.0% and 95.5% of the initial value after re-curing for 30, 60 and 180 days, respectively.

From Figure 2 (c) and (d), it can be seen that the splitting tensile strength of concrete exposed to 600 °C cooled in air and by water was only 14.5% and 12.5% of the initial strength, respectively. The splitting tensile strength of water-cooled and air-cooled concrete was lower than 20% of the original strength. After re-curing for 30, 60 and 180 days, the relative splitting tensile strength of the air-cooled concrete was only 15.9%, 17.7% and 19.6% respectively. The relative splitting tensile strength of the water-cooled concrete was 14.4%, 16.6% and 19.9% respectively. With application of the PMA coating, the splitting tensile strength of the air-cooled concrete recovered to 37.1% of the original strength after re-curing for 180 days, while the relative splitting tensile strength of the water-cooled concrete recovered to 38.5% of the initial strength.

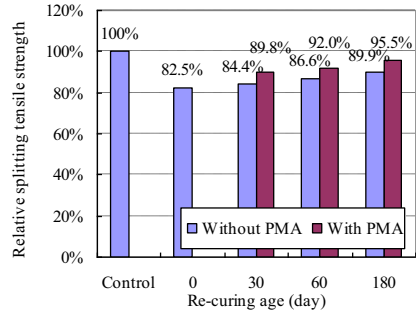
In Figure 2, it is demonstrated that the splitting tensile strength of the concrete coated with PMA, recovered more rapidly than that of the concrete without PMA coating. Considering the two cooling methods, the recovery of the splitting tensile strength of the concrete coated with PMA was higher than that of the concrete without PMA coating. For concrete exposed to 200 °C, that without the PMA coating recovered to about 89.9% to 90.6% of their original strength after re-curing for 180 days, while that coated with PMA recovered to about 94.1% to 95.5% of their initial strength. For the concrete exposed to 600 °C, that without PMA coating recovered to about 19.6% to 19.9% of their original strength, while that coated with PMA recovered to about 37.1% to 38.5% of their initial strength. The recovery of the concrete was due to the re-



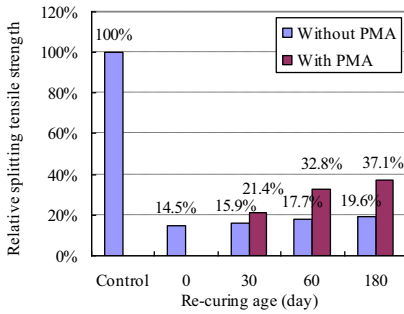
hydration reaction which can be improved by PMA. This can be attributed to the cracks and pore structure being filled by the PMA, thus the splitting tensile strength was improved.



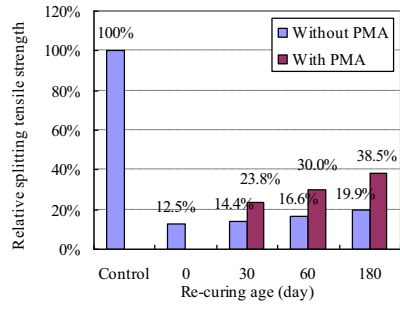
(a) 200 °C cooled in air



(b) 200 °C cooled by water



(c) 600 °C cooled in air



(d) 600 °C cooled by water

**Figure 2.** Variation of splitting tensile strength with re-curing age

### 2.3. Recovery of modulus of elasticity

Figure 3 shows the recovery of modulus of elasticity of concrete exposed to temperatures of 200 °C and 600 °C. It is shown that the modulus of elasticity of concrete decreased significantly due to these elevated temperatures. The recovery of modulus of elasticity of concrete is influenced significantly by the temperature and PMA.

After being exposed to 200 °C, the relative modulus of elasticity of air-cooled and water-cooled concrete was 54.0% and 51.5%, respectively. The residual modulus of elasticity of concrete after being heated at 600 °C was less than 15% of initial value. The modulus of elasticity of air-cooled and water-cooled concrete was 14.0% and 11.5% of the original modulus of elasticity, respectively. The reason for such drastic decrease in modulus of elasticity was because of gradual deterioration of concrete matrix due to high temperature.

As shown in Figure 3 (a) and (b), the modulus of elasticity of all concrete exposed to 200 °C increased slightly with the re-curing age. After re-curing for 30, 60 and 180 days, the modulus of elasticity of air-cooled concrete exposed to 200 °C was 54.8%, 56.9% and 58.4% of the initial value, respectively. The modulus of elasticity of water-cooled concrete exposed to 200 °C was 53.5%, 57.8% and 60.4% of the initial value, respectively. The modulus of elasticity for air-cooled concrete coated with PMA was

59.0%, 62.8% and 65.6% after re-curing for 30, 60 and 180 days, respectively. The modulus of elasticity for water-cooled concrete with PMA was 60.8%, 62.4% and 68.7% after re-curing for 30, 60 and 180 days, respectively.

From Figure 3 (c) and (d), it can be seen that the recovery of the modulus of elasticity of concrete with the PMA coating was more than that of the concrete without PMA coating. For concrete exposed to 600 °C, the relative modulus of elasticity of air-cooled concrete without PMA coating was 14.4%, 14.9%, 15.4%, after re-curing for 30, 60 and 180 days, respectively. The relative modulus of elasticity of water-cooled concrete without the PMA coating was 12.5%, 13.8%, 14.4%, after re-curing for 30, 60 and 180 days, respectively. The recovery in the modulus of elasticity of the concrete with PMA coating was higher than that of the concrete without the PMA coating. For the air-cooled concrete, that without PMA coating recovered to 15.4% of the original modulus of elasticity after 180 days, while the concrete coated with PMA recovered to 21.6% of the initial modulus of elasticity. For the water-cooled concrete, that without PMA coating recovered to 14.4% of their original modulus of elasticity after re-curing for 180 days, while that coated with PMA recovered to 25.7% of their initial modulus of elasticity.

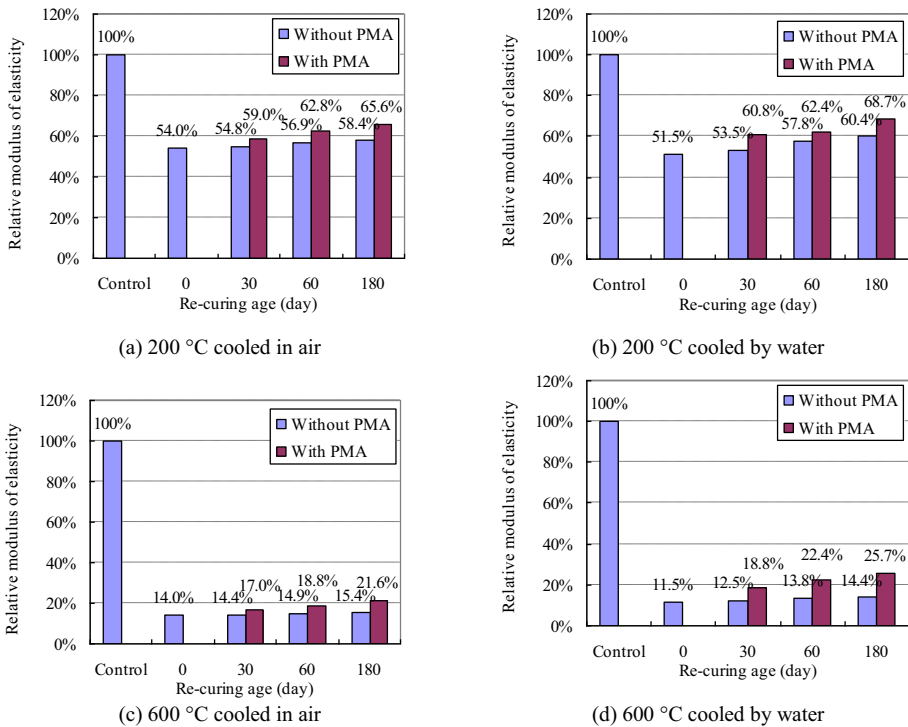


Figure 3. Variation of modulus of elasticity with re-curing age

### 3. Conclusions

The effects of cooling methods, re-curing age and the performance-modifying agent on the mechanical property recovery of concrete was examined. The following conclusions are made:

- (1) The mechanical properties of concrete exposed to 200 °C and 600 °C could recover to some extent after re-curing for 180 days, but the recovery extent was influenced by the cooling method.
- (2) The PMA could be used to improve the recovery extent and speed of the compressive strength of fire-damaged concrete exposed to temperatures of 200 °C and 600 °C.
- (3) The splitting tensile strength of water-cooled concrete decreased significantly after exposed temperatures above 200 °C and 600 °C. The splitting tensile strength of concrete exhibited a much larger loss than the compressive strength with the increase in heat temperature. The PMA can improve the recovery of splitting tensile strength of concrete exposed to elevated temperatures.
- (4) The modulus of elasticity reduced more significantly than the compressive of the concrete exposed to high temperatures. The recovery of the modulus of elasticity was proportional to the re-curing time, the use of PMA can improve the speed and the extent of the recovery.

### Acknowledgements

The authors wish to thank the financial support by the National Natural Science Foundation of China (Grant No. 51208504), and the Fundamental Research Funds for the Central Universities (Grant No. 2013QNB20).

### References

- [1] M. Husem, *The effects of high temperature on compressive and flexural strengths of ordinary and high-performance concrete*, *Fire Safety Journal* **41** (2006), 155-163.
- [2] Y.N. Chan, G.F. Peng and M. Anson, Residual strength and pore structure of high-strength concrete and normal strength concrete after exposure to high temperatures, *Cement and Concrete Composites* **21** (1999), 23-27.
- [3] H. Yang, Y. Lin, C. Hsiao and J.Y. Liu, Evaluating residual compressive strength of concrete at elevated temperatures using ultrasonic pulse velocity, *Fire Safety Journal* **44** (2009), 121-130.
- [4] S. Y. N. Chan, X. Luo and W. Sun, Effect of high temperature and cooling regimes on the compressive strength and pore properties of high performance concrete, *Construction and Building Materials* **14** (2000), 261-266.
- [5] L. Tanaçan, H. Y. Ersoy and Ü. Arpacioğlu, Effect of high temperature and cooling conditions on aerated concrete properties, *Construction and Building Materials* **23** (2009), 1240-1248.
- [6] F.P. Cheng, V.K.R. Kodur, and T.C. Wang: Stress-strain curves for high strength concrete at elevated temperatures, *Journal of Materials in Civil Engineering, ASCE* **1**(2004), 84-90.
- [7] M. Matsudo, H. Nishida, and T. Katayose: Mechanical properties of ultra-high strength materials after high temperature heating, *Fujita Technical Research Report* **40**(2004), 33-38(in Japanese).
- [8] Y. Lin, C. Hsiao, H. Yang and Y.F. Lin, The effect of post-fire-curing on strength-velocity relationship for nondestructive assessment of fire-damaged concrete strength, *Fire Safety Journal* **46** (2011), 178-185.
- [9] C.S. Poon, S. Azhar, M. Anson and Y.L. Wong, Strength and durability recovery of fire-damaged concrete after post-fire-curing, *Cement and Concrete Research* **31**(2001), 1307-1318.
- [10] K. Ichise et al: Strength Recovery of High Strength Concrete Subjected to High Temperature Heating,

*Proceedings of Japan Concrete Institute* **25**(2003), 353-358 (in Japanese).

- [11] M. Matsudo et al.: Mechanical properties of ultra-high strength concrete after heating, *Proceedings of Japan Architectural Institute*, **603** (2006), 171-177 (in Japanese).
- [12] H. Y. Moon, D. G. Shin and D. S. Choi, Evaluation of the durability of mortar and concrete applied with inorganic coating material and surface treatment system, *Construction and Building Materials* **21** (2007), 362-369.
- [13] A.A. Almusallam, F.M. Khan, S.U. Dulaijan and O.S.B. Al-Amoudi, Effectiveness of surface coatings in improving concrete durability, *Cement and Concrete Composites* **25** (2003), 473-481.

# Shear behavior of ultra-high-strength steel fiber-reinforced self-compacting concrete beams

Amr S. EL-DIEB<sup>1</sup>, Tamer A. EL-MAADDAWY and Omar AL-RAWASHDAH  
*Civil and Environmental Engineering Department, College of Engineering, United Arab Emirates University, UAE*

**Abstract.** Ultra-high-strength concrete (UHSC) is characterized with its high compressive strength, yet it shows very brittle failure compared to normal-strength concrete due to a limited post-crack behavior. The inclusion of steel fibers would enhance the post-crack response of this high class of concrete. Since UHSC is produced with very low water to cementitious materials ratio, the inclusion of steel fibers would reduce the concrete workability. The development of self-compacting concrete (SCC) opened the avenue for resolving the workability issue. In this study, the shear response of ultra-high-strength fiber-reinforced self-compacting concrete beams (UHS-FR-SCC) has been investigated. The impact of varying the steel fiber volume;  $V_f = 0.4\%$ ,  $0.8\%$  and  $1.2\%$ , on the shear response has been investigated. The shear response of the UHS-FR-SCC beams has been compared with that of similar beams made of normal strength concrete (NSC). The addition of steel fibers significantly increased the shear capacity of the concrete beams. The shear strength gain increased with an increase in the amount of steel fibers. The use of steel fibers had a more pronounced effect on the incremental shear strength gain of the NSC beams than the UHSC beams. Test results indicated that the inclusion of steel fibers with proper volume fraction can be used as a substitution of the internal steel stirrups. The obtained results could be used as input data to examine the validity of current models for shear strength prediction of UHS-FR-SCC beams.

**Keywords.** Ultra-high-strength fiber-reinforced self-compacting concrete (UHS-FR-SCC), steel fibers, shear, shear capacity, transverse reinforcement, ductility

## Introduction

Progress in concrete materials science and technology during the last 30 years has far exceeded that made during the previous 150 years [1]. The ultra-high-strength concrete (UHSC) is a new class of concrete that has been the result of such development. This new type of concrete is characterized with very high compressive strength; higher than 100 MPa. The UHSC shows very brittle failure behavior compared to normal-strength concrete (NSC) and therefore a limited post-crack behavior. UHSC fails explosively without any omen [2]. The addition of steel fibers to NSC can enhance the deformation capacity (i.e. axial strain or deflection) and consequently the ductility and fracture toughness can be improved [3-12]. The increase in fiber content improves the post-

---

<sup>1</sup>Corresponding author: Civil and Environmental Engineering Department, College of Engineering, United Arab Emirates University, P.O. Box 15551, Al Ain, UAE; E-mail: [amr.eldieb@uaeu.ac.ae](mailto:amr.eldieb@uaeu.ac.ae)

peak behavior and a more extended softening branch is observed [2]. The use of fibers to produce ultra-high-strength fiber-reinforced concrete (UHS-FRC) would provide the structures with innovative features and open new areas for the application of the UHSC.

Steel fibers would significantly reduce the workability of the UHSC. Any increase in the water-to-binder (w/b) ratio to maintain the workability would reduce the concrete strength. The development and use of self-compacting concrete (SCC) has opened the avenue for resolving the workability issue. The combination of technology and knowledge to produce UHS-FR-SCC was proved to be feasible [6].

The shear behavior and strength of reinforced concrete (RC) beams was found to be affected by the inclusion of steel fibers [7, 9-21]. These investigations concluded that the main parameters influencing the shear behavior and strength of RC beams made with steel fiber-reinforced concrete are:

- Shear span-to-depth ratio ( $a/d$ )
- Concrete compressive strength ( $f_c'$ )
- Steel fiber volume fraction ( $V_f$ )
- Main reinforcement ratio ( $\rho_s$ )

Most studies concluded that using steel fibers with volume fraction less than 0.75% will not contribute significantly to the shear behavior of beams [7, 9, 10, 12, 14, and 16]. Also, the minimum main reinforcement ratio should be higher than conventionally reinforced members in order to achieve sufficient ductility [11]. It was found that it is feasible to combine steel fibers and minimum shear reinforcement to achieve the shear strength of RC beams and improve its ductility [17, 18, and 20].

Few studies investigated the effect of incorporating steel fibers on the shear behavior of ultra-high-strength concrete RC beams [11, 18, 21], and self-compacting concrete (SCC) [16]. The interaction between the shear capacity, steel fiber content, shear span to depth ratio ( $a/d$ ), and the transverse shear reinforcement ratio ( $\rho_{st}$ ) needs more investigation in order to establish comprehensive understanding, and to be able to design RC beams with UHS-FR-SCC.

## 1. Study objectives

The aim of this study was to investigate the shear response of ultra-high-strength fiber-reinforced self-compacting concrete (UHS-FR-SCC) beams with different shear span to depth ratios ( $a/d$ ). The impact of varying the steel fiber volume on the shear response is investigated. The behavior of the UHS-FR-SCC beams was compared with that of similar beams made with normal strength concrete (NSC). The beam size, fiber type and longitudinal reinforcement ratio were kept unchanged.

## 2. Used materials

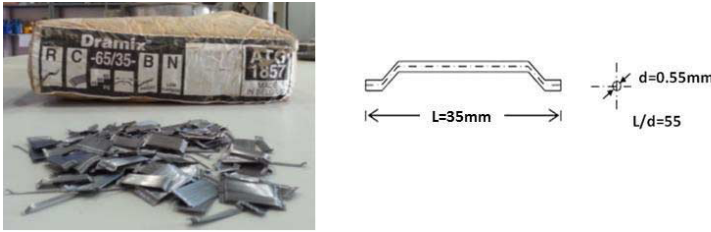
In this study, two mixtures were used to produce NSC and UHSC. The materials used in the mixtures included ordinary Portland cement (OPC, Type 1), local coarse crushed stone sand, dune sand, crushed stone aggregate (10 mm) and polycarboxylic based super-plasticizers. The concrete mixture proportions by weight are given in Table 1. The average cylinder compressive strengths of the concrete mixtures without the steel fibers were 28 MPa and 100 MPa for the NSC and UHSC mixtures, respectively.

The longitudinal steel reinforcement was No. 20 deformed bars with nominal yield strength of 520 MPa. The shear reinforcement outside the test region was No. 8 with nominal yield strength of 520 MPa. The shear reinforcement used in the test region was bars with measured yield strength of 344 MPa and a diameter of 5.5 mm.

**Table 1.** Concrete mixtures proportions for 1 m<sup>3</sup>

Constituent	NSC Mixture	UHSC Mixture
Cement (kg)	387.6	561.0
Silica Fume (kg)	12.4	99.0
Coarse Sand (kg)	472.2	470.3
Dune Sand (kg)	472.2	253.2
Coarse Agg. (kg)	757.2	927.5
Water (lit)	209.2	151.8
Superplasticizer (kg)	2.0	16.5

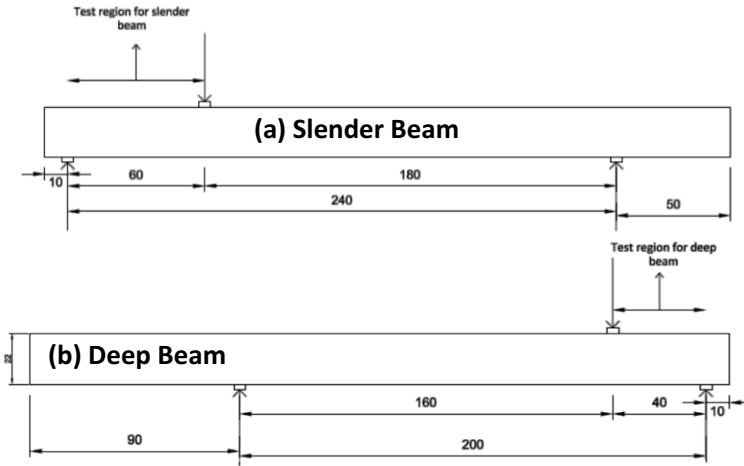
Dramix RC-65/35-BN were used as steel fiber which are manufactured by Bekaert cooperation. Steel fiber is hooked at its end as shown in Figure 1 and has a nominal tensile strength of 1100 MPa. The steel fiber has a length of 35 mm and a diameter of 0.55 mm which makes the aspect ratio ( $L/d$ ) equals 64. The fibers are not coated. Four different percentages of steel fiber were used (0 %, 0.4 %, 0.8%, and 1.2 %) of the concrete volume.



**Figure 1.** Dramix RC-65/35-BN fibers used in the study

### 3. Specimens configuration and testing

The loading regime adopted in this study allowed two tests to be performed on each beam as shown in Figure 2. The left shear span (slender beam specimen with  $a/d = 3.3$ ;  $a$ =shear span of 60 cm and  $d$ =effective beam depth of 18.2 cm) was first tested keeping the right end zone overhung and unstressed as shown in Figure 2-a. The right shear span (deep beam specimen with  $a/d = 2.2$ ;  $a$ =shear span of 40 cm and  $d$ =effective beam depth of 18.2 cm) was then tested keeping the left end zone, already tested previously, overhung and unstressed as shown in Figure 2-b. Each beam was three meter long ( $L = 300$  cm), the total height ( $h$ ) was 22 cm, effective depth ( $d$ ) was 18.2 cm and the width ( $b$ ) was 12 cm. The beams were designed to fail in shear. Four bars No. 20 were used as tensile steel and 2 bars No. 20 were used as compressive steel. The shear reinforcement outside the test regions was No. 8 with at spacing  $s = 10$  cm to assure that the shear failure will not occur outside the test region. For the beams with stirrups in the test region, the stirrups were plain double-legged with a nominal diameter of 6 mm spaced at a distance of  $s = 10$  cm.



**Figure 2.** Testing configuration and dimensions of beams; (a) slender beam and (b) deep beam (dimensions are in cm)

#### 4. Test matrix

Table 2 shows the test matrix of the study. The specimens were divided into two groups; Group (A) for the NSC specimens with 28MPa and Group (B) for the UHSC specimens with 100MPa. Group (A) consists of 10 tests; five tests for slender beams ( $a/d = 3.3$ ) and five tests for deep beams ( $a/d = 2.2$ ). Group (B) consists of five tests for slender beams ( $a/d = 3.3$ ). The main parameter changed in the five tests was the steel volume fraction ( $V_f$  %). Three volume fractions of steel fibers were investigated in this study (0.4%, 0.8% and 1.2%). Also, in each subgroup two tests were conducted on two control specimens without steel fibers; one specimen with internal stirrups and one specimen without internal stirrups.

### 5. Results and discussions

#### 5.1. Failure mode

Failure modes of the slender and deep specimens of group (A) are shown in Figures 3 and 4, respectively. All slender specimens of group (A) with the NSC, except S28-VF3, failed in a classical diagonal-tension shear mode of failure. Specimen S28-VF3 with the higher amount of steel fiber volume fraction of  $V_f = 1.2\%$  failed in a web-crushing shear mode of failure. The addition of the steel fibers in this specimen restricted growth and widening of the shear cracks developed in the shear span, and hence allowed the specimen to develop its full shear capacity. The deep specimen D28-VF0, D28-VF0-St, and D28-VF1 failed in a shear-compression mode of failure due to crushing of concrete at the head of the inclined shear cracks under the load point. Deep specimens D28-VF2 and D28-VF3 failed by crushing of the diagonal concrete struts. This was more evident in specimen D28-VF3 with higher steel fiber volume fraction of  $V_f = 1.2\%$ . All specimens of group (B), except S100-VF0, exhibited one major diagonal shear crack in the shear span. These specimens failed eventually in a diagonal-tension shear mode of



failure. Specimen S100-VF0 failed in a diagonal-splitting shear mode of failure. Failure modes of specimens of group (B) are shown in Figure 5.

**Table 2.** Test Matrix

Group	Shear Span to Depth Ratio	$V_f$ %	Beam I.D.
<b>A</b> $(f'_c = 28 \text{ MPa})$ (NSC)	Slender ( $a/d = 3.3$ )	0.0%	S28-VF0-St
		0.0%	S28-VF0
		0.4%	S28-VF1
		0.8%	S28-VF2
		1.2%	S28-VF3
	Deep ( $a/d = 2.2$ )	0.0%	D28-VF0-St
		0.0%	D28-VF0
		0.4%	D28-VF1
		0.8%	D28-VF2
		1.2%	D28-VF3
<b>B</b> $(f'_c = 100 \text{ MPa})$ (UHSC)	Slender ( $a/d = 3.3$ )	0.0%	S100-VF0-St
		0.0%	S100-VF0
		0.4%	S100-VF1
		0.8%	S100-VF2
		1.2%	S100-VF3



**Figure 3.** Failure modes of the slender specimens of group (A)



**Figure 4.** Failure modes of the deep specimens of group (A)

## 5.2. Deflection response

### 5.2.1. Group A (NSC)

The shear force versus deflection relationships of the slender and deep beam specimens of group (A) are depicted in Figures 6 and 7, respectively. It is evident that the addition

of steel fibers increased the shear resistance and energy absorption of the specimens. The shear resistances of the slender specimens with the steel fiber volumes of 0.4%, 0.8% and 1.2% were 20%, 48%, and 130% higher than the control specimen S28-VF0 that had neither steel fibers nor internal stirrups, respectively. For the deep specimens of this group, the addition of steel fibers with volume fractions of 0.4%, 0.8% and 1.2% resulted in increasing the shear resistance by 23%, 128%, and 110%, respectively relative to that of the control specimen S28-VF0. It is important to highlight that the shear resistances of specimens S28-VF2 and D28-VF2 with  $V_f = 0.8\%$  were higher than those of their counterpart specimens S28-VF0-St and D28-VF0-St with internal steel stirrups and no steel fibers. This indicates that the incorporation of steel fibers in the concrete mixture of NSC slender and deep beams can be used as a substitution for the internal steel stirrups.



Figure 5. Failure modes of slender specimens of group (B)

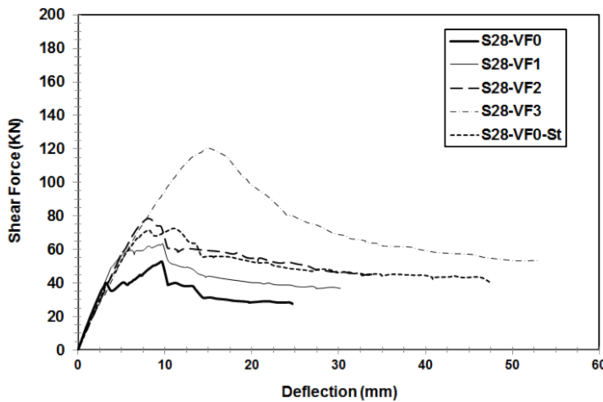


Figure 6. Shear force-deflection response of the slender specimens of group (A)

### 5.2.2. Group B (UHSC)

The shear force versus deflection relationships of the specimens of group (B) are depicted in Figure 8. The addition of steel fibers increased the shear resistance and energy absorption of the specimens. The shear resistances of the specimens of this group with the steel fiber volumes of 0.4%, 0.8% and 1.2% were 29%, 57%, and 94% higher than the control specimen S100-VF0 that had neither steel fibers nor internal stirrups, respectively. The addition of steel fibers with  $V_f = 0.8\%$  was not sufficient to increase the shear resistance to a level higher than that of specimen S100-VF0-St with internal steel stirrups and no steel fibers. This indicates that a minimum steel fiber volume fraction of  $V_f = 1.2\%$  shall be used to replace the internal steel stirrups for the UHSC beams.

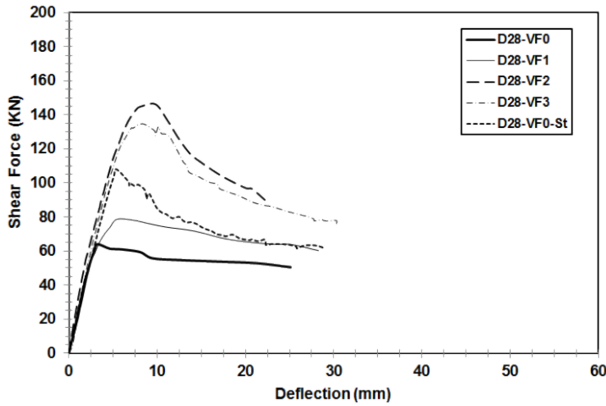


Figure 7. Shear force-deflection response of the deep specimens of group (A)

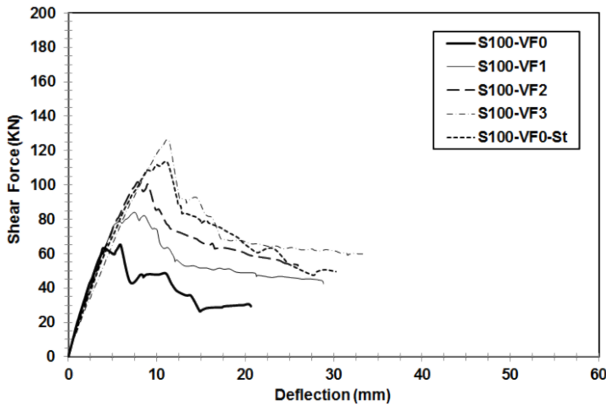


Figure 8. Shear force-deflection response of the slender specimens of group (B)

## 6. Conclusions

The inclusion of steel fibers in the concrete mixture significantly improved the shear resistance and energy absorption of both slender and deep beam specimens. Increasing the amount of the steel fibers increased the shear resistance of both NSC and UHSC beam specimens. The inclusion of steel fibers with  $V_f = 0.8\%$  in the mixture of the NSC beam specimens increased the shear strength to a level higher than that of a similar specimen with internal steel stirrups and no steel fibers. For the UHSC beam specimens, a minimum steel fiber volume fraction of  $V_f = 1.2\%$  was necessary to upgrade the shear resistance to a level higher than that of a corresponding specimen with internal steel stirrups and no steel fibers. The addition of the steel fibers in the concrete mixture restricted growth and widening of the shear cracks developed in the shear span, and hence allowed the specimens to develop a higher shear capacity.

## Acknowledgment

This work was financially supported by the UAEU Research Grant # 06-34-07-11/10. Also, the manufacturing and testing was conducted in the concrete and structural laboratories at the Civil and Environmental Engineering Department, UAEU, the help and effort of the laboratory specialists is very much appreciated.

## References

- [1] B.A. Graybeal, Material Property Characterization of Ultra-High-Performance Concrete, *Federal Highway Association, Report No. FHWA-HRT-06-103* (2006).
- [2] F. Bencardino, L. Rizzuti, G. Spadea and R.N. Swamy, Stress-Strain Behavior of Steel Fiber-reinforced Concrete in Compression, *ASCE Jour. of Materials in Civil Engineering* 20 (2008), 255-263
- [3] B.A. Graybeal, Compressive Behavior of Ultra-High Performance Fiber Reinforced Concrete, *ACI Materials Journal*, 104 (2007), 146-152.
- [4] F. Köksal, F. Altun, I. Yiğit and Y. Şahin, Combined Effect of Silica Fume and Steel Fiber on the Mechanical Properties of High-Strength Concretes, *Cons. and Build. Mat.*, 22 (2008), 1874-1880.
- [5] A. Sivakumar and M. Santhanam, Mechanical Properties of High-Strength Concrete Reinforced with Metallic and Non-Metallic Fibers, *Cement and Concrete Composites*, 29 (2007), 603-608.
- [6] A.S. El-Dieb, Mechanical, Durability and Microstructural Characteristics of Ultra-High-Strength Self Compacting Concrete Incorporating Steel Fibers, *Materials and Design* 30 (2009), 4286-4292.
- [7] C. Juárez, P. Valdez, A. Durán and K. Sobolev, The Diagonal Tension behavior of Fiber Reinforced Concrete Beams, *Cement and Concrete Composites* 29 (2007), pp.402-408.
- [8] Q. Chunxiang and I. Patnaikuni, Properties of High-Strength Steel-Fiber-Reinforced Concrete Beams in Bending, *Cement and Concrete Composites* 21 (1999) 73-81.
- [9] S. Furlanjr and J. Bento de Hanai, Shear behavior of Fiber Reinforced Concrete Beams, *Cement and Concrete Composites* 19 (1997), 359-366.
- [10] G. Campione and M.L. Mangiavillano, Fibrous Reinforced Concrete beams in Flexure: Experimental Investigation, Analytical Modelling and Design Consideration, *Eng. Structures* 30 (2008), 2970-2980.
- [11] Z. Savir and A.N. Dancygier, Flexural behavior of HSFRC with Low Reinforcement Ratios, *Eng. Structures* 28 (2006), 1503-1512.
- [12] F. Altun, T. Haktanir and K. Ari, Effects of Steel Fiber Addition on Mechanical Properties of Concrete and Rc Beams, *Cons. and Build. Mat.* 21 (2007), 654-661.
- [13] A.A.A. Hassan, K.M.A. Hossain and M. Lachemi, Behavior of Full-Scale Self-Consolidating Concrete in Beams, *Cement and Concrete Composites* 30 (2008), 588-596.
- [14] H.H. Dinh, G.J. Parra-Montensinos and J.K. Wight, Shear behavior of Steel Fiber-Reinforced Concrete beams without Stirrup reinforcement, *ACI Structural Journal* 107 (2010), 597-606.
- [15] D.M. Özcan, A. Bayraktar, A. Şahin, T. Haktanir and T. Türjer, Experimental and Finite Element Analysis on Steel Fiber-Reinforced Concrete (SFRC) Beams Ultimate Behavior, *Cons. and Build. Mat.* 23 (2009) 1064-1077.
- [16] T.H.-K. Kang, W. Kim, Y.-K. Kwak and S.-G. Hong, Shear Testing of Steel Fiber-Reinforced Lightweight Concrete Beams without Web Reinforcement, *ACI Structural Journal* 108 (2011), 553-561.
- [17] D.H. Lim and B.H. Oh, Experimental and Theoretical Investigation on Shear of Steel Fiber Reinforced Concrete Beams, *Eng. Structures* 21 (1999), 937-944.
- [18] H. Aoude, M. Belghiti, W.D. Cook and D. Mitchell, Response of Steel Fiber-Reinforced Concrete Beams with and without Stirrups, *ACI Structural Journal* 109 (2012), 359-367.
- [19] K. Choi, A.G. Sherif, M.M. Reda Taha and L. Chung, Shear Strength of Slender Reinforced Concrete Beams without Web Reinforcement, A Model using Fuzzy Set Theory, *Eng. Structures* 31 (2009) 768-777.
- [20] C. Cucchiara, L. La Mendola and M. Papia, Effectiveness of Stirrups and Steel Fibers as Shear Reinforcement, *Cement and Concrete Composites* 26 (2004), 777-786.
- [21] T.H.-K. Kang, W. Kim, L.M. Massone and T.A. Galleguillos, Shear-Flexural Coupling behavior of Steel Fiber-Reinforced Concrete Beams, *ACI Structural Journal* 109 (2012), 435-444.

# Static and dynamic testing of RC-slabs with high strength concrete overlay

Norbert RANDL<sup>a</sup> and Csaba SIMON<sup>b</sup>

<sup>a</sup>Carinthia University of Applied Sciences, Austria

<sup>b</sup>A-Hid Building Co., Hungary

**Abstract.** In the frame of a research project funded by the Austrian Research Foundation (FFG) the load bearing behavior of RC members upgraded with high strength concrete (HSC) overlays was investigated. HSC overlays provide – due to its decreased capillary porosity – a more durable and compact top layer and a higher resistance against mechanical abrasion. First, slant shear specimens were tested in order to determine the bond properties between normal concrete and the HSC overlay. Structural bending tests with reinforced concrete slabs with various overlay types and surface roughness categories were subsequently carried out. Because of the strong adhesive bond between HSC overlay and substrate, failure of the interface was not observed while some single delamination occurred with the normal strength concrete (NSC) overlay. With respect to retrofitting of bridges, a series of 4 slabs has been tested under fatigue loading as well, the HSC overlay applied on a high pressure water jetted surface.

**Keywords.** Concrete overlay, high strength concrete, high pressure water jetting, sand blasting, shear friction, slant shear test

## Introduction and research significance

As a part of the maintenance or due to the increased requirements of the new European Standards, the necessity of increasing loadbearing capacity of existing structures and/or the resistance against environmental actions may raise. In the field of reinforced concrete, a common and effective way to increase the performance of a structure is to apply a new concrete overlay. In this case the bond behavior between the old and new concrete is one of the key features. High strength concrete overlays provide a durable and compact top layer with increased resistance. Experimental studies performed at the Technical University of Munich [1, 2] indicate that the bond between a HSC overlay and an existing NSC-deck is much stronger than between two NSC-layers. A similar observation concerning bond strength is also made in on-going research on the application of overlays made of UHPC [3].

## 1. Overview of the testing program and test setup

The testing program contained different consecutive phases. After performing small scale tests with slant shear specimens, a number of large scale slab specimens were subject to static loading and, finally, several fatigue tests were conducted with another series of large scale slabs.

<sup>1</sup>Corresponding author: [n.randl@fh-kaernten.at](mailto:n.randl@fh-kaernten.at)

The surfaces of the substrates were treated with two different methods. A low to moderate roughness with a mean roughness depth  $R_t$  of about 0,8 - 1,1 mm was reached by sandblasting (SB), a stronger roughened surface with  $R_t \approx 2.4 - 3.6$  mm was produced by high pressure water jetting (HPW). The roughness was measured with the sand patch method. In case of two slant shear specimens and two slabs as well, short powder-actuated steel pins were applied in addition.

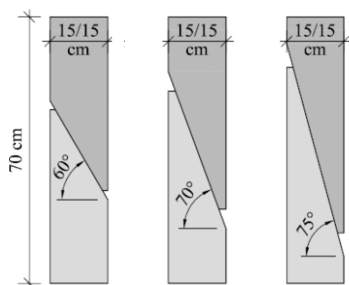
### 1.1. Material properties

All substrate structures were made of normal strength concrete (NSC) with a strength class in the upper range. The new concrete parts (overlays) were produced from a specially developed self-compacting high strength concrete (HSC) with a mean 28 days compressive cube strength of 124 MPa. For reference two slant shear specimens and two slabs were prepared with NSC overlays. As reinforcement for the slabs B 550 steel with a characteristic yield strength of 550 MPa and a minimum tensile strength of 620 MPa was applied.

### 1.2. Test set up

#### 1.2.1. Slant shear tests

In order to determine the interface bond strength between the new and old concrete parts, nine slant shear tests were carried out. To determine the relations between the normal and shear stresses along the interface, the inclination of the joint had to be varied with respect to the interaction of friction and adhesive bond. The dimensions of these specimens were 15 x 15 x 70 cm and the varied parameters were the angles of the interfaces, the surface treatment and the concrete qualities. The schematic and real illustrations of the specimens are shown in Fig. 1 and 2. The detailed properties of the slant shear specimens are given in Table 1.



**Figure 1.** Schematic illustration of the slant shear specimens



**Figure 2.** Real illustration of the slant shear specimens

The tests were carried out in a testing frame, the specimens were loaded by a hydraulic cylinder. The support on the bottom side contained a steel plate with a pin and the load introduction on the top side contained two sliding plates which provided a controlled pressure on the upper part of the specimen even when the joint started to shear off. The tests were displacement-controlled with a speed of 0,5 mm/min. To

measure the crack opening and the parallel displacements of the interface a set of four inductive displacement transducers (LVDT) were installed on the sides of the specimens in the middle of the joints.

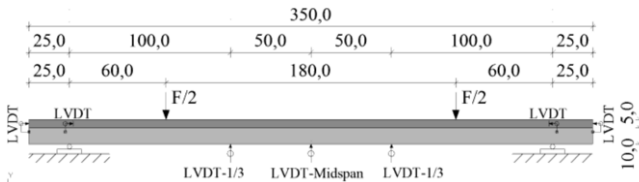
**Table 1.** Configurations of the slant shear specimens

No.	Joint angle [°]	Surface treatment	Mean roughness [mm]	$f_{cm,cube} \{1\}$ [MPa]	
				Substr.	Overlay
1	60	SB	0,934	50	126
2	60	SB	0,889	50	126
3	60	SB	0,980	50	52
4	70	SB + 1 stud	0,916	50	126
5	70	SB + 2 studs	0,899	50	126
6	70	HPW	3,299	50	126
7	75	HPW	3,643	50	126
8	75	HPW	2,669	50	126
9	75	HPW	3,240	50	52

{1} compressive strength  $f_{cm,cube}$  on testing day (150 mm cube)

*1.2.2. Slab bending tests*

For simulating old reinforced concrete slabs which are upgraded and strengthened with a concrete overlay, seven slab tests have been performed. The thickness and the reinforcement amount of the “old” precast concrete slabs were calculated based on Eurocode 2 principles [4], taking into account the standard load scenarios for buildings according to the code. The detailing of the one-way slabs was designed in a way, that the substrate slabs without the overlay were provided with a standard reinforcement amount (so that first the reinforcement would yield and afterwards the crushing of the concrete at the compression zone would follow). The reason was to simulate such a situation that the substrate slabs are existing old structures which need to be reinforced by a new overlay. For the longitudinal reinforcement  $\varnothing 10/15$  and for the transversal reinforcement  $\varnothing 8/25$  were applied with a concrete cover of 15 mm. Each slab test specimen had a dimension of 3,5 x 1,5 x 0,15 m, in which the overlay is included with a height of 5 cm of the total thickness h. The static system corresponds to a statically determined single-span beam with a span of 3,0 m (see Fig. 3). The different variations of the slab test specimens are given in Table 2.



**Figure 3.** Slab bending test setup

The tests were carried out as 4-point bending tests with the load introductions situated rather close to the supports in order to maximize the shear stress along the interface. A minimum distance to the supports ( $\geq 4h$ ) was kept in order to prevent direct load transfer and favorable effects from transverse pressure in the decisive

interface region. To measure possible lateral displacements in the interface, a set of six LVDTs were installed along the side faces of the slabs parallel to the interface. Three LVDTs at each longitudinal side were applied vertically to measure the deflections (Fig. 3).

**Table 2.** Configurations of the slab specimens

No.	Dimensions	Surface treatment	Mean roughness	$f_{cm,cube} \{1\}$ [MPa]	
			[mm]	Substr.	Overlay
1	Length 350 cm width 150 cm height 15 cm	SB + 144 studs	1,057	71	126
2		SB + 72 studs	0,838	71	126
3		SB	1,094	71	126
4		SB	1,105	71	52
5		HPW	3,24	71	126
6		HPW	2,376	71	126
7		HPW	3,099	71	52

{1} compressive strength  $f_{cm,cube}$  on testing day (150 mm cube)

### 1.2.3. Dynamic slab bending tests

Four HPW jetted slabs were subjected to high cycle fatigue testing in order to investigate the fatigue resistance of the bond between the two concrete layers. The test setup was the same four-point bending setup which was applied for the static tests. The load amplitudes have been chosen in relation to the mean ultimate load  $F_{m,u}$  of the slabs determined by the static bending tests (see applied load amplitudes in Table 3).

**Table 3.** Applied loads during the high cycle fatigue tests

Designation	Lower limit of the load amplitude	Upper limit of the load amplitude
Slab1	26,17 kN (0,1 $F_{m,u}$ )	196,24 kN (0,75 $F_{m,u}$ )
Slab2	26,17 kN (0,1 $F_{m,u}$ )	175,31 kN (0,67 $F_{m,u}$ )
Slab3	26,17 kN (0,1 $F_{m,u}$ )	154,37 kN (0,59 $F_{m,u}$ )
Slab4	26,17 kN (0,1 $F_{m,u}$ )	133,44 kN (0,51 $F_{m,u}$ )

The steering of the load was in that case load-controlled, with a frequency of 2,5 - 3 Hz depending on the magnitude of the deflection. When doing fatigue tests with RC members, high strain rates may have a favourable effect on the number of achieved load cycles. In the present tests the chosen frequency range is clearly below recommended frequency limits regarding this effect.



## 2. Test results and evaluation

### 2.1. Slant shear tests

In case of the slant shear tests the failure occurred in three different modes. The first mode was a distinct shear failure of the interface (see Fig. 4/a), the second one was a mixed interface / compression failure of the NSC part (see Fig. 4/b) and the third one was a mixed interface / shear failure of the NSC parallel to the inclined joint (see Fig. 4/c). However, an overall evaluation of all tests together was justified as also in the case of the mixed failure modes still a part of the failure surface propagated through the interface, with the maximum loads in the range of the measured interface shear resistance (first mode).

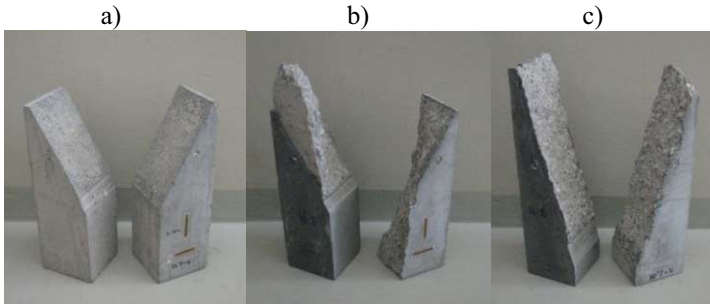


Figure 4. Slant shear tests: failure modes

Based on former investigations [5] and subsequently performed friction tests in undamaged zones of the already sheared off specimens a mean friction coefficient  $\mu$  of 1,1 for sandblasted and 1,5 for water jetted surfaces was determined. Applying these mean friction coefficients, based on the failure loads and the dimensions of the specimens, using formula (1) the adhesive bond-strength values of the joints  $\tau_{j,ad}$  were calculated.

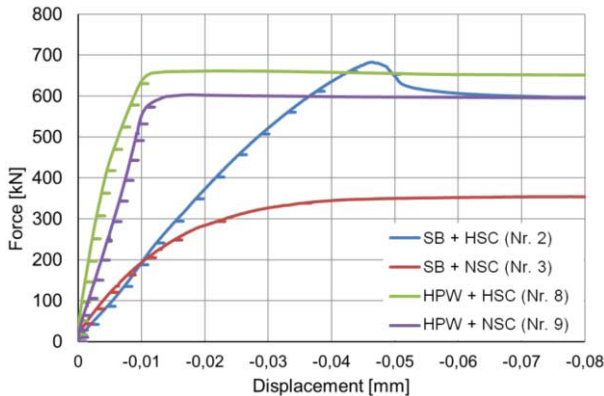


Figure 5. Force vs. parallel displacement

$$\tau_{j,ad} = \frac{F_{max} \cdot (\sin \beta - \mu \cdot \cos \beta)}{A_{interface}} \tag{1}$$

The specimens No. 4 and 5 had an additional shear resistance due to the installed studs. Based on test results provided by the manufacturer of the studs, the contribution of them (which was rather small due to the substantial and dominant adhesive bond) could be subtracted and the adhesive bond shear strength values of the slant shear specimens No. 4 and 5 were determined. Tab. 4 presents the determined mean adhesive bond strength  $\tau_{j,ad}$  and the appropriate friction coefficient which is also visible in the shear stress vs. normal stress diagram (see Fig. 6).

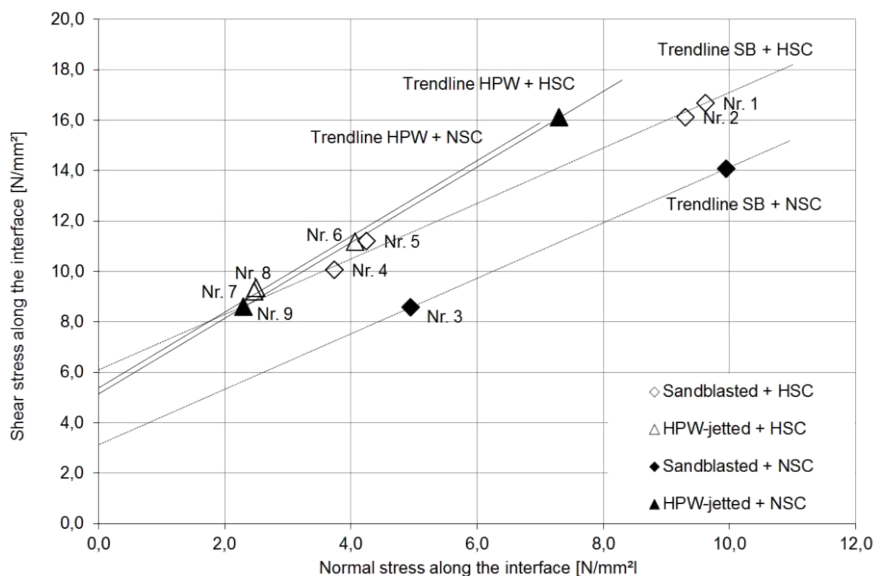


Figure 6. Shear stress vs. normal stress

Table 4. Friction coefficients and mean adhesive bond strengths

	SB + NSC	SB + HSC	HPW + NSC	HPW + HSC
$\mu$ [-]	1,1	1,1	1,5	1,5
$\tau_{j,ad}$ [MPa]	3,13	6,1	5,14	5,38

### 2.2. Static slab tests

In case of the slab tests all specimens failed finally due to bending. The failure always occurred between the load introduction points and was announced by the changing force-deflection characteristics as well. The load bearing capacities ranged from 246 to 310 kN. The first cracks appeared approximately at a load level of 50 kN on the bottom side of the slabs. At a load of about 150 kN shear cracks appeared between the supports and the load introductions. At the longitudinal faces sometimes crack offsets were observed when cracks crossed the interface (Fig. 7). Such crack offsets were observed in both cases with the HSC and the NSC overlays, however they were more pronounced in case of the NSC overlay and the same with the crack widths and deflections.

At one end face of the sandblasted slab with the NSC overlay some small lateral displacements at the joint were detected. They corresponded with a 0,73 m long crack along the interface, which indicated that some delamination process had started in these edge zones (Fig. 8).



Figure 7. Crack offset



Figure 8. Crack along the interface (SB slab with NSC overlay)

Table 5. Ultimate and service loads and the related deflections

No.	Surface treatment	$f_{cm,cube} \{1\}$ [MPa]		$F_{max}$ [kN]	$W_{F,max}$ [mm]	$F_{SLS}$ [mm]	$W_{F,SLS}$ [mm]
		Substr.	Overlay				
1	SB + 144 studs	71	126	259,6	52,92	123,6	12,71
2	SB + 72 studs	71	126	246,6	63,97	117,4	12,80
3	SB	71	126	279,5	59,96	133,1	12,92
4	SB	71	52	257,9	74,35	122,8	15,27
5	HPW	71	126	255,8	57,59	121,8	11,04
6	HPW	71	126	267,5	56,9	127,4	11,90
7	HPW	71	52	310,3	87,19	147,8	21,91

{1} compressive strength  $f_{cm,cube}$  on testing day (150 mm cube)

### 2.3. Dynamic slab tests

The main target of the test series was to investigate generally the behaviour of the interface under fatigue actions and to determine whether its resistance is lower compared to the fatigue behaviour of monolithic RC-structures. However, since the reinforcement ratio due to the reasons described in section 1.2 was relatively low, it was not surprising that in all the cases the final failure occurred due to the fatigue rupture of the longitudinal reinforcement. Nevertheless concerning the interface zone some important observations were made during the tests: in several cases after a significant number of cycles thin horizontal hairline cracks were detected along the interface between the supports and the load introductions, where the shear stresses in the interface are the maximum. A slight propagation of these cracks was observed in line with the increase of the number of load cycles.

After the stable main phase of the cycling, in all four tests just about 10.000-20.000 cycles before the actual failure a stepwise increase of the deflections was observed, reflecting pronounced damage propagation. Finally one of the bending cracks in the mid zone of the slabs between the load introduction points increased rapidly and the rupture of the longitudinal steel reinforcement took place in consequence. In Fig. 9 the test results are presented in relation to the steel stress amplitudes and the characteristic S-N curve of the applied Austrian reinforcing steel B 550 according to Eurocode. The number of cycles until failure for each test is displayed in Fig. 9 together with the applied cyclic stress range  $\Delta\sigma$  in the longitudinal reinforcing bars.

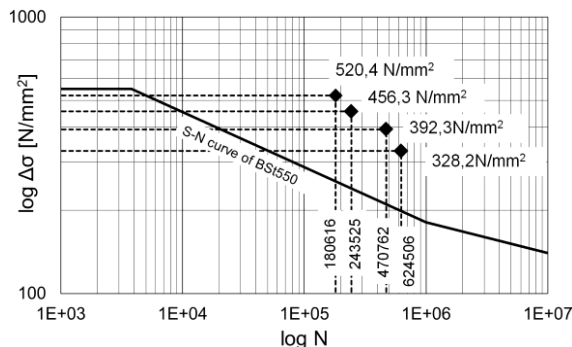


Figure 9. Fatigue resistance of the reinforcement

As mentioned above, during the fatigue tests horizontal cracks along the interface appeared more often compared to the slabs subjected to monotonic loading. As these cracks can be the sign of delamination processes between the two concrete layers, it can be concluded that, depending on the level and amplitude of cyclic loading, the shear resistance of the interface is expected to be more sensitive to cyclic actions than to static loading. A simplified design approach for interface shear design under fatigue loading is presented in Model Code 2010 [6, 7], differing between rigid bond-slip behaviour and non-rigid cracked interfaces.

### 3. Summary and conclusions

Slant shear tests and large scale structural tests with different interface roughness were performed to investigate the behaviour of high strength concrete overlays. In the slant shear tests it turned out that the bond strength in case of a low to moderate roughened (sandblasted) surface can be nearly doubled with the application of a HSC overlay instead of an NSC one. In case of a strongly roughened surface (high pressure water jetted) such an increase of the interface resistance was not observed (which can be traced back to the interfering effect of aggregate interlocking), but in general a high bond shear resistance was reached.

In the monotonic slab tests it was observed, that with the application of a HSC overlay the stiffness of a member subjected to bending increases somewhat compared to a member strengthened by a NSC overlay. In case of static bending actions, delamination of the HSC overlay can be nearly excluded due to the high bond strength.

High cycle fatigue tests with 4 slabs showed on the other hand that, even though delamination of the overlay is not likely to appear, the interface was more sensitive to fatigue actions than to static loading. Therefore such applications where fatigue loading occurs require an appropriate reinforcement along the edges even with HSC overlays.

### 4. Acknowledgement

This research was supported by the Austrian Research Foundation (FFG). The authors would like to thank the team in the laboratory, especially Michael Wirnsberger, Peter Druml, Thomas Steiner and Markus Graber for their contributions.

## References

- [1] R. Reinecke, *Haftverbund und Rissverzahnung in unbewehrten Betonschubfugen*, Doctoral Thesis, Technische Universität München, 2004.
- [2] A. Müller, *Zum Zug- und Schubtragverhalten von Betonfugen*, Doctoral Thesis, Technische Universität München, 2009
- [3] E. Brühwiler, E. Denarié, K. Habel, Bauteile aus ultrahochleistungsfähigem Faserbeton (UHPFRC) und traditionellem Stahlbeton, *Beton- und Stahlbetonbau*, Vol. 100, No. 2, pp. 124-131, 2005.
- [4] Austrian Standards Institute (ASI), ÖNORM EN 1992-1-1: *Eurocode 2: Design of concrete structures - Part 1-1: General rules and rules for buildings*, 2011.
- [5] N. Randl, *Untersuchung zur Kraftübertragung zwischen Alt- und Neubeton bei unterschiedlichen Fugenrauigkeiten*, Doctoral Thesis, Leopold-Franzens-Universität Innsbruck, Austria, 1997.
- [6] Fédération internationale du béton (fib), *Model Code 2010*, Lausanne, 2013.
- [7] N. Randl, Design recommendations for interface shear transfer in MC 2010, *Structural Concrete*, Vol. 14, No. 3, doi: 10.1002/suco.201300003, 2013.

# Effect of the loading condition on the restoring force characteristics of the rigid frame RC pier with the shear wall

Wenjun GAO<sup>a,1</sup>, Hisanori OTSUKA<sup>b</sup> and Yukihide KAJITA<sup>a</sup>

<sup>a</sup>*Department of Civil and Structural Engineering, Kyushu University, Japan*

<sup>b</sup>*Otsuka Research Institute for Infrastructure Co., Ltd, Japan*

**Abstract.** The rigid frame RC (reinforced concrete) pier with the shear wall is used as high piers of the expressway in mountainous area in Japan. The damage process and restoring force characteristics of this RC pier have not been sufficiently understood yet. In this study, the experiment work that the monotonic and cyclic loading on the RC specimens were carried out. Based on the test result, it is found that: axial compression force has influence on load carrying capacity of restoring force characteristic, and the load carrying capacity with axial compression force is greater than that without axial compression force; monotonic and cyclic loads show influence on deformation capacity of restoring force characteristic, and the deformation capacity of monotonic horizontal loading specimen is 2 times greater than that of cyclic horizontal loading specimen.

**Keywords.** Reinforced concrete pier, shear wall, restoring force characteristics, hysteresis properties

## Introduction

The rigid frame RC (reinforced concrete) pier with the shear wall is used as the high piers of expressway in mountainous area in Japan. This pier is flexible in the bridge axis direction and rigid in the perpendicular direction, and is expected to absorb earthquake energy in the perpendicular direction of bridge axis. The name of “Flexible Reinforced Concrete Pier (Flexible RC pier)” comes from the slenderness in the bridge axis direction, because the bearing support on the top of the pier is free in this direction.

Its large deformability in the perpendicular direction is not considered sufficiently in the seismic design, because the damage process and restoring force characteristics of this RC pier in the direction have not been sufficiently understood yet.

OTSUKA et al. [1] and GAO et al. [2] carried out laboratory tests and analysis to evaluate the performance of the flexible RC pier specimen under monotonic horizontal loading without axial compression force. In this study, further experimental work was conducted to indicate restoring force characteristics of the flexible RC pier specimen

---

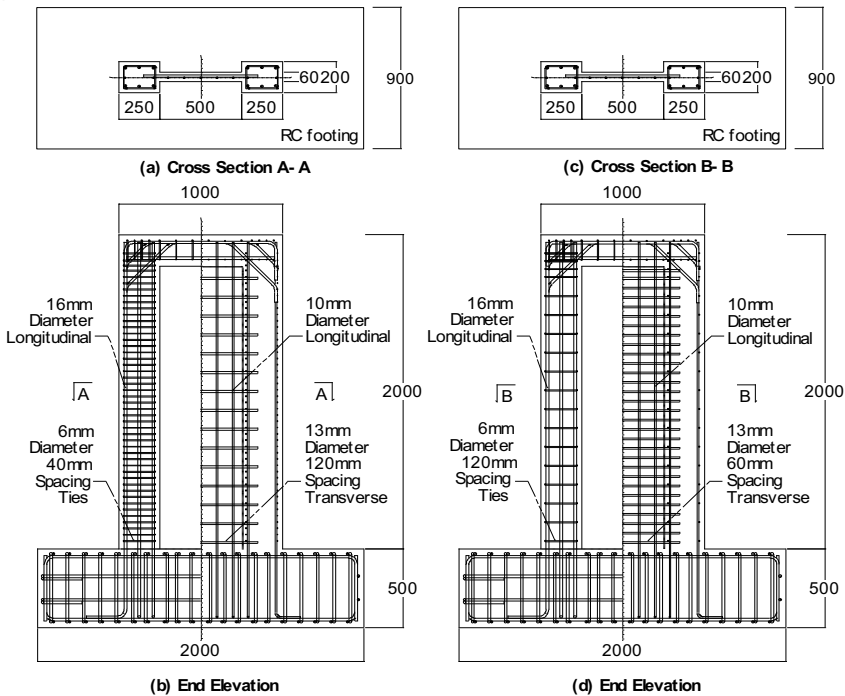
<sup>1</sup>Corresponding author: Kyushu University, W2-1101, 744, Motoooka, Nishi-ku, Fukuoka, Japan; Email: [gao@doc.kyushu-u.ac.jp](mailto:gao@doc.kyushu-u.ac.jp)

under the monotonic and cyclic loading with or without axial compression force. The result was analyzed from the aspects of damage process, hysteresis loops, and the yield and buckling of the steel bars on different loading condition. Finally, restoring force characteristic model is established based on experimental results.

### 1. Experimental procedures

#### 1.1 Test specimens

In this experimental study, the 1/10-scale Flexible RC pier test specimens were designed to represent a typical existing bridge pier. Five specimens were prepared. The specimen No. 1, 3, 4 had an increased volume of tie hoop of the side columns. The specimen No. 2, 5 had an increased volume of transverse reinforcement of the shear wall. **Figure 1**(a) and (b) show cross section and dimensions details of specimen No. 1, 3, and 4 respectively. Similarly, that of specimen No. 2 and 5 are shown in **Figure 1**(c) and (d) respectively. The total height of the specimen is 2,500 mm while its effective height is 1,900 mm, which is measured from the top of the footing to centerline of the applied horizontal force. The free height of the solid pier part of specimen is 2,000 mm; the width is 1,000 mm. The interior height of the shear wall is 1,800 mm, the interior width of the shear wall is 500 mm, and the thickness of the shear wall is 60 mm. The sectional size of the side columns is 250 mm × 200 mm. The height of the reinforced concrete footing is 500 mm, the width is 2,000 mm, and the thickness is 900 mm in all of the flexible RC pier specimens.



**Figure 1.** Sectional details of flexible RC pier specimen (Left: No. 1, 3 and 4; Right: No. 2 and 5; Dimensions in mm)

### 1.2 Test cases

The test cases are summarized in Table 1. The specimen No. 1, 3, 4 were assembled in similar longitudinal and transverse reinforcement, while specimen No. 2, 5 were in same reinforcement condition. Moreover, different loading conditions were applied to specimen No. 1, 3, 4 and specimen No. 2, 5 respectively. The specimen No. 1 and 2 were tested under monotonic horizontal loading without axial compression force. The specimen No. 3 was tested under monotonic horizontal loading with axial compression force. The specimen No. 4 and 5 were tested under cyclic horizontal loading with axial compression force.

**Table 1.** Test cases

Specimen No.	Side columns				Shear wall					
	Longitudinal reinforcement				Tie hoop		Longitudinal reinforcement		Transverse reinforcement	
	D* (mm)	N**	D (mm)	N	D (mm)	S*** (mm)	D (mm)	N	D (mm)	S*** (mm)
1, 3, 4	16	6	10	2	6	40	10	5	13	120
2, 5	16	6	10	2	6	120	10	5	13	60

\*D: Diameter; \*\*N: Number; \*\*\*S: Spacing.

Specimen No.	Axial compression force (kN)	Horizontal loading types
1, 2	0	Monotonic horizontal loading
3	156	Monotonic horizontal loading
4, 5	156	Cyclic horizontal loading

### 1.3 Material properties

According to specifications in the Japanese design code of concrete structures [3], a 28-day design cylinder compressive strength of 24 MPa was required. **Table 2** provides the actual material properties of the flexible RC pier specimens on the day of the testing. In addition, deformed bars were used in all specimens. The design yield strengths of reinforcement bars were expected to be 345 MPa [4]. The mechanical properties of deformed bars were tested before the quasi-static test. All the steel reinforcements used in this study are given in **Table 3**.

**Table 2.** Material properties of concrete used in specimens

Specimen No.	Compressive strength (MPa)	Tensile strength (MPa)	Elastic modulus (MPa)
1	31.5	3.0	$2.32 \times 10^4$
2	35.7	3.1	$2.35 \times 10^4$
3	30.1	2.9	$2.11 \times 10^4$
4	35.3	3.3	$2.44 \times 10^4$
5	38.2	3.3	$2.48 \times 10^4$

**Table 3.** Material properties of deformed bars used in specimens

Diameter (mm)	Yield stress (MPa)	Yield strain ( $\mu$ )	Elastic modulus (MPa)
6	409	2045	$2.00 \times 10^5$
10	363	1994	$1.82 \times 10^5$
13	345	2193	$1.79 \times 10^5$
16	385	2152	$1.84 \times 10^5$



### 1.4 Test setup

The test setup is shown in Figure 2. The flexible RC pier specimens were fixed to the strong test floor. The loading system of the vertical load assembly consisted of the hydraulic jack, roller shaft, and load spreader (H-shaped steel beam). A constant axial load was applied to specimens by means of an inversion 500 kN hydraulic jack that hanged from the reaction girder. The action point of axial compression force were designed to represent typical existing bearing support number of bridge pier, by four point loading at the top of specimens. To keep the vertical load throughout the test, the roller shaft was fixed on the reaction girder. The load spreader, namely H-shaped steel beam between the vertical jack and the specimen, was used to produce uniform compressive force on the specimen by the universal joint of the head of the vertical hydraulic jack. The loading system of the horizontal load assembly contained the horizontal hydraulic jack and the fixture assembly (prestressing bars and steel splint). The horizontal load was applied at the center of the top beam of the specimen. The horizontal hydraulic jack were fixed by post-tensioning its footing to the test specimen, and fixture assembly was used to set its fixation point, namely prestressing bars and steel splint on the top beam of the specimen. This was the condition of cyclic horizontal loading method. In contrast, monotonic horizontal loading method was relatively simpler. The fixture assembly of horizontal load was not necessary. The conditions without axial compression force did not need the vertical load assembly.

Before conducting cyclic horizontal loading test in existence of axial compression force, the predetermined vertical load was applied to the specimen and kept constant throughout testing. The cyclic horizontal excursions were applied in a displacement-control mode according to the specified horizontal deflection history shown in **Figure 3**. The displacement control was used in increments  $\Delta$  (one cycle to a peak deflection) of 2 mm, 4 mm, and 6 mm. Before performing a yield deflection of longitudinal reinforcement of side column, displacement control was used in increment of 2 mm; beyond the yield deflection, displacement control was used in increment of 4 mm, up to an approximately value 40 mm, it was followed by an increment of 6 mm, and so on until the specimen was unable to sustain the maximum load.

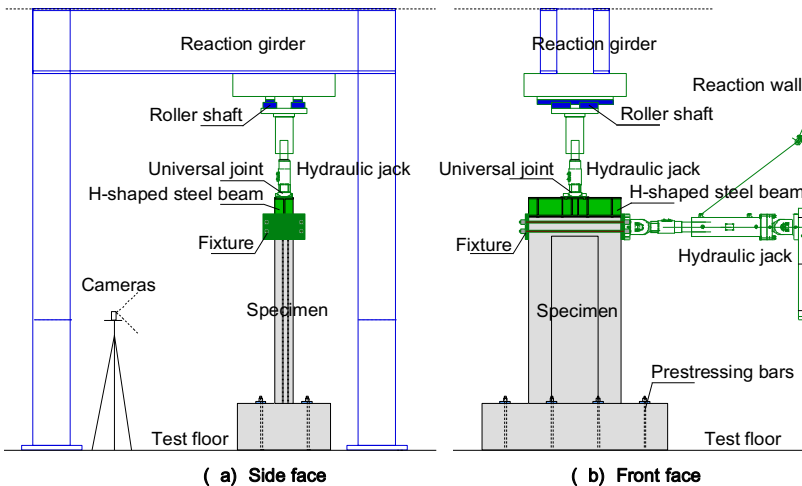


Figure 2. Test setup

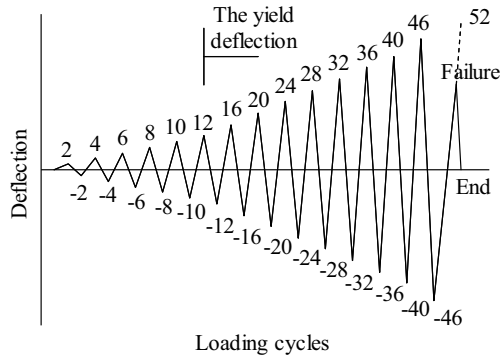


Figure 3. Specified deflection history (Specimen No. 4, dimensions in mm)

## 2. Experimental results and discussion

### 2.1 Failure pattern

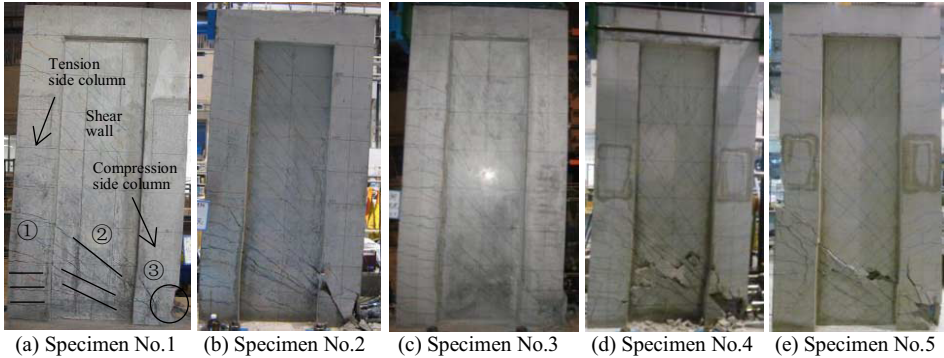
The final failure mode and crack pattern of these specimens are shown in **Photo 1**. Based on the result of the horizontal loading test, the damage process of the RC pier specimens is described in common as follows: the horizontal flexural crack, the diagonal shear crack, the yielding of the longitudinal reinforcement of side column and shear wall, the deterioration of the concrete cover, the failure of concrete on compression side column, the buckling of the longitudinal reinforcement and the bulging of the tie hoop in compressive column.

Under the monotonic horizontal loading (Specimen No. 1, 2), the first horizontal crack appeared at the bottom of the tension side column, namely the horizontal flexural crack. With increase of the monotonic horizontal load, the side column cracks extended to the shear wall, namely the diagonal shear crack. And then the cracks gradually developed toward to compression side column. Maximum value of the applied load was characterized by the yielding of the longitudinal reinforcement at the bottom of side column and shear wall, and the deterioration of the concrete cover. With the increase of the horizontal displacement, stiffness degradation of the specimens was relatively slower and the cracks developed fully, which showed that the RC pier specimens have good ductility. Finally, the failure of concrete on compression side column was observed in the specimen. Meanwhile, the compressive buckling of the longitudinal reinforcement and the bulging of the tie hoop in compression side column were observed in the specimens. Under the axial compression force and monotonic horizontal loading, the crack pattern and failure process of Specimen No. 3 was similar to that of Specimen No. 1. However, the maximum strength of Specimen No. 3 was relatively greater due to effect of the axial compression force.

Under the axial compression force and cyclic horizontal loading (Specimen No. 4, 5), a small amount of horizontal crack appeared at the bottom of the side columns and shear wall at the horizontal displacement  $\Delta = \pm 2$  mm. With the increase of the cyclic horizontal load, the longitudinal reinforcements yielded at  $\Delta = \pm 10$  mm. When load was close to the maximum value, the damage of the specimens mainly concentrated in the plastic hinge region, with the damage process similar to monotonic horizontal loading

tests. With the increase of the horizontal cyclic displacement, Specimen No. 4 and No. 5 lost the strength at  $\Delta=+52$  mm and  $\Delta=+46$  mm respectively.

Based on the experimental result, the failure pattern of the flexible RC pier member was shear failure after flexural yield with large toughness.



(a) Specimen No.1

(b) Specimen No.2

(c) Specimen No.3

(d) Specimen No.4

(e) Specimen No.5

**Photo 1.** Final failure mode and crack pattern

(In (a), ① is horizontal flexural crack; ② is diagonal shear crack; ③ is deterioration and failure of concrete)

## 2.2 Hysteresis properties

The hysteresis curves (load-displacement curves) of the RC pier specimens are shown in Figure 4. It can be seen that, (1) the horizontal load-displacement curves have four characteristic points, namely cracking point, yielding point, peak load point (the maximum load point), ultimate displacement point. (2) In each specimen, when the horizontal displacement is more than 7 mm, the reinforcement bars begin to yield. And the yielding sequence is the longitudinal reinforcement of the side column, the longitudinal reinforcement of the shear wall, the transverse reinforcement of the side column or shear wall. (3) Five specimens have sufficient hysteresis curve, indicating that these flexible RC pier specimens (side column and shear wall) have good energy absorption behavior. However, focusing on the ultimate displacement of these five specimens, the ultimate displacement in monotonic horizontal loading test was nearly a half comparing to that in the cyclic horizontal loading test. (4) The area of hysteresis curves of specimens No. 1 and 4 are greater than those of specimens No. 2 and 5, which shows that the deformation capacity and energy absorption behavior increased with the increase in volume of tie hoop of the side columns. (5) Peak load value of hysteresis curves of specimen No. 3 was greater than that of specimen No. 1, which shows that the yield strength and maximum strength force was increased by the existing of axial compression force.

## 3. Restoring force characteristics

Based on the result of **Figure 4**, the effects of different loading conditions on cracking point, yielding point and ultimate point are given in **Table 4** and **Table 5**, respectively. In Table 4, the values of the three points without axial force were treated as 1.0 comparing to the points with axial force, while in Table 5, the values of the three points towards monotonic loading were treated as 1.0. These three points were evaluated in

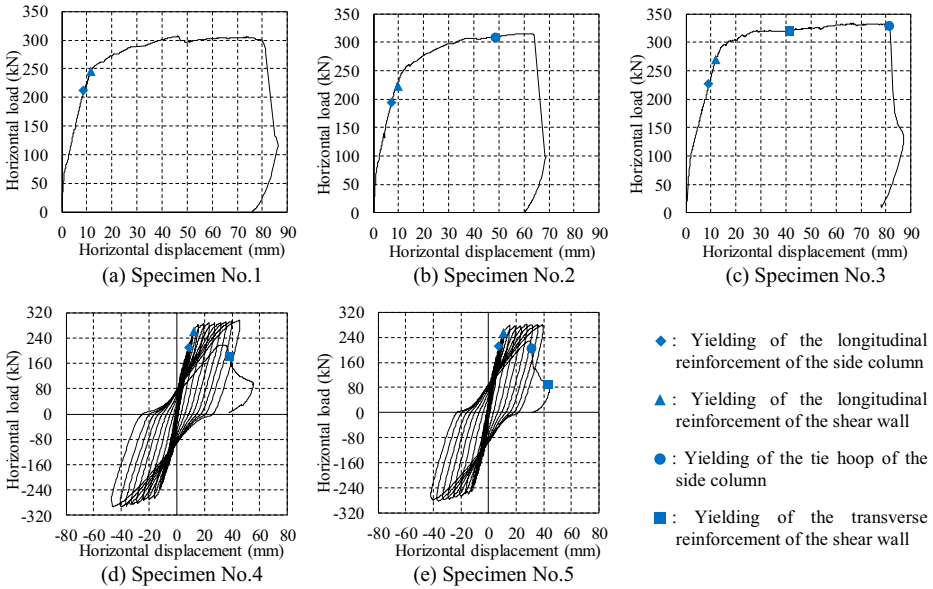


Figure 4. Hysteresis curves for the RC pier specimens

detail for this research.

The cracking point is defined as generation point of the horizontal flexural cracks. In monotonic horizontal loading specimens, the strength at the cracking point with axial compression force is 1.21 times greater than that of the cracking point without axial compression force. Moreover, the strength of cracking point of cyclic horizontal loading specimens is 1.34 times greater than that of monotonic horizontal loading specimens. In contrast, there is not much difference in the horizontal displacement value on different loading condition.

The yielding point is defined as the yielding of the longitudinal reinforcement of shear wall. In monotonic horizontal loading specimens, the yield load of the specimen with axial compression force is 1.14 times greater than that of the yielding load of the specimen without axial compression force. However, the yield load of cyclic horizontal loading specimens is 0.94 times lower than that of monotonic horizontal loading specimens. Moreover, the yield displacement with axial compression force is 1.12 times greater than that without axial compression force. The yield displacement of the cyclic horizontal loading specimens is 1.05 times greater than that of the monotonic horizontal loading specimens.

In monotonic horizontal loading specimens, the load value of the ultimate point is defined as the maximum load value, because the load value at the ultimate displacement point approximately equals to the load value at the maximum load point in test results. The load value of this point with axial compression force is 1.10 times greater than that of without axial compression force. In contrast, in cyclic horizontal loading specimens, the yielding load value is close to the maximum load value. The load value of this point of cyclic horizontal loading specimens is 0.83 times lower than that of monotonic horizontal loading specimens. From the aspect of ultimate displacement value, there is not much difference in the horizontal displacement value for the monotonic horizontal loading specimen. However, the ultimate displacement

(toughness) of this point of cyclic horizontal loading specimens is 0.50 times lower than that of monotonic horizontal loading specimens.

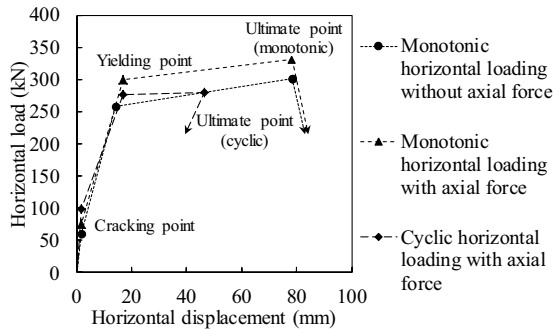
All these test result are summarized in **Figure 5**. In this figure, restoring force characteristic including the cracking point, the yielding point, and ultimate point are presented. As a result, the condition with or without axial compression force has an effect on load carrying capacity of restoring force characteristic, and the load carrying capacity of specimen with axial compression force is greater than that without axial compression force. Moreover, the difference of monotonic and cyclic load has an effect on deformation capacity of restoring force characteristic. The deformation capacity of monotonic horizontal loading specimen is 2 times greater than that of cyclic horizontal loading specimen.

**Table 4.** Comparison of the three points without or with axial force (the values in case of with axial force is the difference of No. 1 vs No. 3)

Loading condition	Cracking point		Yielding point		Ultimate point	
	Load	Displacement	Load	Displacement	Load	Displacement
Without axial force	1	1	1	1	1	1
With axial force	1.21	1	1.14	1.12	1.10	1

**Table 5.** Comparison of the three points towards monotonic loading or cyclic loading (the values in case of cyclic loading are the average between the difference of No. 1 vs No. 4 and that of No. 2 vs No. 5)

Loading condition	Cracking point		Yielding point		Ultimate point	
	Load	Displacement	Load	Displacement	Load	Displacement
Monotonic loading	1	1	1	1	1	1
Cyclic loading	1.34	1	0.94	1.05	0.83	0.50



**Figure 5.** Restoring force characteristic for RC pier specimens

### 4. Conclusions

In this study, the monotonic and cyclic loading on the RC specimens were carried out. The main findings can be summarized as follows:

- (1) The failure pattern of this type of RC pier member is shear failure after flexural yield with large toughness.
- (2) The RC specimens have sufficient hysteresis curve, indicating that these RC pier specimens (side column and shear wall) have good energy absorption behavior.

- (3) The restoring force characteristic behavior of the RC pier specimens includes the cracking point, the yielding point, ultimate point, which is established based on experimental results.
- (4) In this model, axial compression force has influence on load carrying capacity of restoring force characteristic, and the load carrying capacity with axial compression force is greater than that without axial compression force.
- (5) Monotonic and cyclic loads show influence on deformation capacity of restoring force characteristic, and the deformation capacity of monotonic horizontal loading specimen is 2 times greater than that of cyclic horizontal loading specimen.

## Acknowledgments

The authors gratefully acknowledge the financial support provided for this study by the West Nippon Expressway Company Limited and the FUJI P.S Corporation. Furthermore, this study was supported by JSPS KAKENHI Grant Number 24360181 and Kyushu University KIKIN H25.

## References

- [1] H. OTSUKA, W.J. GAO, Y. FUKUNAKA, T. IMAMURA, Study on Restoring Force Characteristics and Energy Absorption Capability of Flexible RC Pier with I Shape Section on Horizontal Loading, *Journal of JSCE* 68 (4), 2012, I\_556-I\_564. (in Japanese)
- [2] W.J. GAO, H. OTSUKA, J.H. CHOI, Study on Restoring Force Characteristics and Deformation Capacities of the Flexible Reinforced Concrete Pier with I-Shape Cross Section under Horizontal Load, *Proceedings of the Thirteenth East Asia-Pacific Conference on Structural Engineering and Construction (EASEC-13)*, September 11-13, 2013, Sapporo, Japan, 1-3-1.
- [3] JSCE, *Standard Specifications for Concrete Structures-2007, Design*, Japan Society of Civil Engineers, 34-57. (in Japanese)
- [4] JIS, *Standard Specifications for Concrete Structures-2007, Test Methods and Specifications*, Edited by Japan Society of Civil Engineers, Published by Japanese Standards Association, 291-297. (in Japanese)

# A study on behavior of reinforced concrete columns subjected to axial compression

P.K GUPTA<sup>1</sup> and V.K VERMA

*Department of Civil Engineering, IIT Roorkee, Roorkee, India*

**Abstract.** In the present study, a total of nine specimens of different diameters of 146 mm to 208 mm dia., were cast. Length of specimens was kept 800 mm. Length to diameter ratio varies from 3.85 to 5.48. The concrete of grade M30 was designed as per IS: 10262-2009 for the casting of specimens. The main reinforcement was taken from 2.0 to 4.05% of gross cross-sectional area. Bars of 12 mm dia. were used for main reinforcement and 8 mm dia. bars were used for lateral ties.

A three dimensional Finite element model was developed using ANSYS software to simulate the reinforced concrete columns (R.C.C.) under axial compression. To model the concrete core, a three dimensional eight node solid element 'SOLID 65' was used. The main reinforcement and lateral ties were modeled using 'LINK 8' element. In the present study, the minimum value of the ratio of cross-sectional area of lateral tie to the spacing between lateral ties ( $A_{tie}/S^2$ ) was decided for the effective confinement of concrete core in R.C. column. Effect of length to diameter (L/D) ratio on strength and ductility was studied. The test results indicate that as L/D decreases, ductility increases. The strain at failure was found approximately 0.0075 to 0.009.

**Keywords.** Finite element analysis, confinement, R.C.C., ductility

## Introduction

The transverse reinforcement in the form of lateral ties provides the confining pressure to the concrete core in the form of arch action. This action becomes more effective when the spacing between the lateral ties is smaller. The main parameters involved in the confinement are the ratio of the volume of transverse reinforcement to the volume of confined core, spacing between lateral ties, yield strength and pattern of lateral ties.

Roy and Sozen [1] conducted tests on reinforced concrete columns with different spacing of lateral ties. They found that the ultimate load capacity of R.C. column was not enhanced by the use of lateral ties with more spacing, but there was an increase in the ductility. They provided a relationships between strain corresponding to the decay of concrete resistance of up to 50% of maximum value, cross-sectional area of ties ( $A_{tie}$ ) at given spacing between ties (S). Kent and Park [2] developed stress-strain model for concrete confined by rectangular or square transverse reinforcement by using the test results of Roy and sozen [1]. They considered the same maximum stress for both unconfined and confined concrete. Popovics [3] proposed a stress-strain relation for the unconfined concrete and Mander et al. [4] tested circular, rectangular and square

---

<sup>1</sup>Corresponding author: [spramod\\_3@yahoo.com](mailto:spramod_3@yahoo.com)

R.C. columns to investigate the influence of different transverse reinforcement (spiral or lateral ties ) on the effectiveness of confinement. They presented a stress-strain model for concrete confined by transverse reinforcement. Mostafaei et al. [5] presented an approach to calculate the ultimate deformation and load capacity of R.C. columns.

This approach was based on axial-shear-flexure interaction. Subramanian [6] proposed an equation for the design of transverse reinforcement by considering the parameters such as confining pressure, concrete cover, longitudinal reinforcement and spacing between transverse reinforcement. Gramblička et al. [7] studied the influence of transverse reinforcement on the resistance of reinforced concrete column and verified the design guidelines for the detailing of transverse reinforcement. Early researchers [1-7] concluded that the confinement can be improved with the closer spacing of lateral reinforcement, proper distribution of longitudinal bars along the perimeter and by increasing the ratio of the volume of transverse reinforcement to the volume of confined concrete core. But still there is a question of determining the correct spacing, for which lateral ties would provide the effective confinement. In this paper some experiments were conducted and a numerical model of R.C. column was developed to get generate better understanding of the effect of confinement by lateral ties. With the help of this study a minimum value of the ratio  $A_{tie}/S^2$  is proposed for effective confinement of lateral ties.

## 1. Experiment details

### 1.1. Material

Ordinary Portland Cement produced as per IS: 8112-1989 [8], was used to prepare the desired grade of concrete. Mix designs for the concrete of grade M30 was prepared as per IS: 10262-2009 [9]. The concrete mix proportions and compressive strength of concrete cylinder specimens (150 mm x 300 mm) at 28 days ( $f_{ck}$ ) are given in Table 1. High Yield Strength Deformed (HYSD) bars with yield strength ( $f_y$ ) of 500 MPa were used for main reinforcement and lateral ties. The 12 mm dia. and 8 mm dia. bars were used for main reinforcement and lateral ties respectively. The main reinforcement was taken to be 2.0 to 4.05% of gross cross-sectional area.

**Table 1.** Concrete mix proportion

Mix	w/c ratio	Water (kg/m <sup>3</sup> )	Cement (kg/m <sup>3</sup> )	Fine Aggregate (kg/m <sup>3</sup> )	Coarse Aggregate (kg/m <sup>3</sup> )	Admixture (%)	Cylinder strength (MPa)
M30	0.45	171	380	673	1089	0.25	35.08

### 1.2. Specimens

A total of nine specimens of different diameters of 146 mm to 208 mm dia. were cast. Length of specimens (L) was kept at 800 mm. Length to diameter ratio varied from 3.85 to 5.48. Freshly prepared concrete was placed in three layers. Proper vibration and compaction was done in each layer. Typical nomenclatures are used to designate the specimens. For example specimen C-146: 146- stands for the diameter of specimen, C stands for the reinforced concrete column. Therefore, C-208 indicates the reinforced



concrete column specimen of 208 mm diameter. All the specimens were tested for axial compression.

### 1.3. Test instruments

All the column specimens were tested using INSTRON Universal testing machine having a capacity of 250 tonnes. During the testing, specimens were placed on bottom plate of the machine. The gauge length of the specimen was the entire length of the specimen. The test was conducted with the strain control method at a ramp rate of 0.2 mm/minute. The load-displacement curves were recorded by the machine automatically. Repeatability of the testing was assured by testing three samples of each type. The typical arrangement of loading is depicted in Figure 1(a) and testing of specimen is shown in Figure 1 (b).

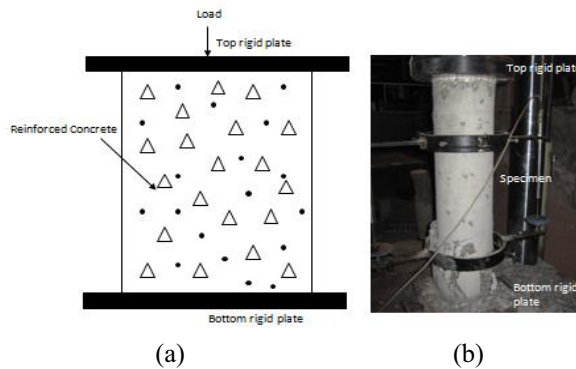


Figure 1. (a) Loading and (b) Testing arrangements

## 2. Computer modeling

### 2.1. Finite element model

A three dimensional Finite Element model was developed using ANSYS software to simulate the reinforced concrete column subjected to axial compression. Figure 2. shows a typical finite element model adopted for modeling of reinforced concrete columns. To model the concrete core, a three dimensional eight node solid element 'SOLID 65' was used. The main reinforcement and lateral ties were modeled by the link element 'LINK8'. Three techniques are available to model the steel reinforcement for reinforced concrete [10]: the discrete model, the embedded model, and smeared model (Figure 3). In the present case, the discrete model was used. The mesh size for the concrete core was chosen from 5 mm to 10 mm.

Load was applied as static uniform displacement through the top loading plate. The contact was defined as a surface to surface contact. Different friction factors (0.1 to 0.4) were taken for the contact surface and it was found that friction factor of 0.2 was suitable to achieve a quick convergence. In the finite element model, the lower rigid plate contacting the bottom of column was fixed in all six directions by a reference

node. The upper rigid plate at the top of the column was modeled fixed in five directions and only allowed movement in column axis at a reference node.

2.2. Material model of reinforcement

The Elastic perfectly plastic material behavior of the steel bars is adopted for modelling. Poisson’s ratio and elastic modulus of steel were taken as 0.3 and 200 GPa respectively. The yield stress ( $f_y$ ) was obtained from tensile test of material. Figure 4 shows the stress-strain variation used for steel bar.

2.3. Material model of concrete

In case of R.C. columns, the effectiveness of confining pressure depends upon the spiral or lateral ties used. The confining pressure will be less (or not effective) if the spacing of lateral ties is large. There may be a slight increase in concrete strength and ductility due to confinement with lateral ties [1]. In the present study, the spacing of 150 mm between the lateral ties considered to be large. Therefore an unconfined stress-strain model was used to model reinforced concrete. Figure 5 shows the uniaxial stress-strain curve for concrete proposed by [11].

The response of concrete was modeled by an elasto-plastic theory with associated flow and kinematic hardening rule. During plastic deformation, the expansion of the yielding surface can be guided by the uniaxial stress-strain curve. The stress-strain equation proposed by [11,12] is given as:

$$f = \frac{E_c \varepsilon}{1 + (R + R_E - 2) \left(\frac{\varepsilon}{\varepsilon_c}\right) - (2R - 1) \left(\frac{\varepsilon}{\varepsilon_c}\right)^2 + R \left(\frac{\varepsilon}{\varepsilon_c}\right)^3} \tag{1}$$

Where  $R = \frac{R_E(R_\sigma - 1)}{(R_E - 1)^2} - \frac{1}{R_E}$  ;  $R_E = \frac{E_c \varepsilon_c}{f_c}$  (2)

values of  $R_\sigma$  and  $R_\varepsilon = 4$

$$R_\sigma = \frac{f_c}{f_f} ; R_\varepsilon = \frac{\varepsilon_f}{\varepsilon_c} \tag{3}$$

Where  $f_c$  = Maximum stress ,  $\varepsilon_c$ = strain at maximum stress,  
 $f_f$ =stress at failure,  $\varepsilon_f$ =strain at failure

The value of  $\varepsilon_c$  may be taken as 0.003 and Young’s Modulus,  $E_c = 4700\sqrt{f_{cc}}$  MPa as per ACI-318, 1999 [13].

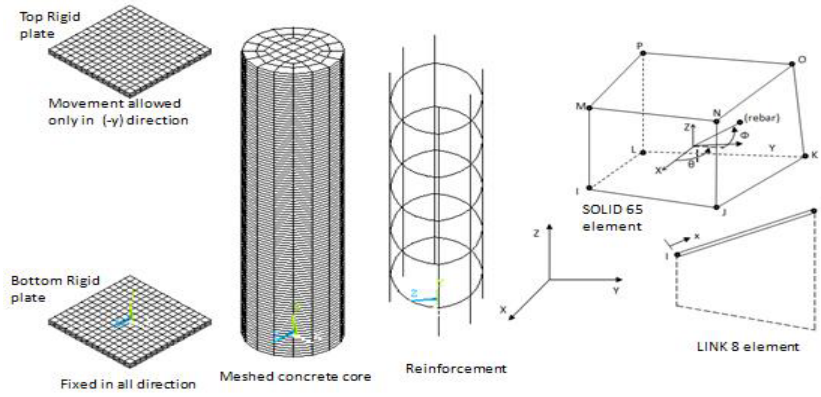


Figure 2. Typical details of Finite Element model for reinforced concrete column

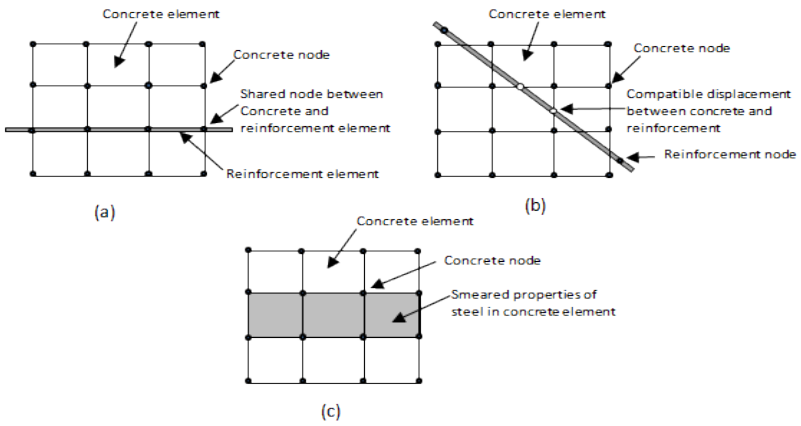


Figure 3. Models for steel reinforcement in reinforced concrete: (a) discrete (b) embedded and (c) smeared

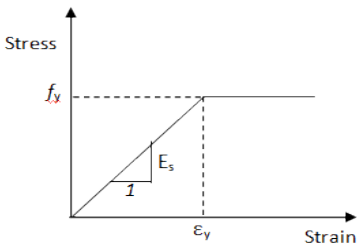


Figure 4. Stress-strain relationship for steel bar

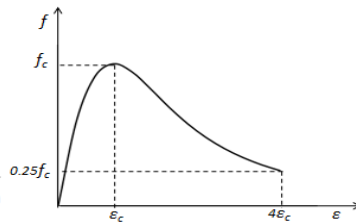


Figure 5. Stress-strain curve for concrete

### 3. Results and discussions

A total of nine specimens were cast and tested for axial compression. The 3D finite element modeling was carried out using ANSYS software. In the case of reinforced concrete column that contains the transverse reinforcement in the form of either spiral or lateral ties, confinement mainly depends upon the vertical spacing between spiral or lateral ties ( $S$ ) and on the ratio of the volume of transverse steel to the volume of confined concrete core ( $\rho_s$ ).

For the present study, the confining pressure ( $f_l$ ) was computed ( $f_l = 0.5k_e \rho_s f_y$ ) as given by Mander et al. [4] and it was found to be between 0.446 MPa to 0.996 MPa. Initially stress-strain model for reinforced concrete given by Mander et al. [4] was tried for the modeling of columns specimens. It was found that load-displacement curve obtained from the simulation did not show the strain softening behavior till 1% strain. It may be understood that since spacing of 150 mm between lateral ties is large and a less amount of confining pressure exists, so it would not provide effective confinement to the concrete core. Roy and Sozen [1] found that the confining pressure will be less (or not effective) if the spacing of lateral ties is large but there may be a slight increase in concrete strength and ductility. They provided a relationships between strain ( $\epsilon_{50}$ ) corresponding to the decay of concrete resistance of 50% of maximum value and cross-sectional area of ties ( $A_{tie}$ ) and spacing between ties ( $S$ ). The relation was given as  $\epsilon_{50} = 3 \frac{A_{tie}}{S^2}$ . This relation shows that the strain in the post peak region is governed

by the ratio  $A_{tie}/S^2$ . To determine the value of  $A_{tie}/S^2$  for which the specimen will be acted upon by the effective confining pressure, minimum value of  $\epsilon_{50}$  must be decided. For this purpose, a specimen (Column-4) was taken from the experimental data of Mander et al. [14]. This specimen was having the minimum value of confining pressure (0.85 MPa) among all the specimens. The diameter of lateral ties of this specimen was 10 mm and spacing between the ties was 119 mm. The value of  $\epsilon_{50}$  was calculated from the above equation  $\epsilon_{50} = 3 \frac{A_{tie}}{S^2}$  and found to be approximately equals to 0.017.

Therefore, it was concluded that, to get the effective confinement in R.C. column, the ratio  $A_{tie}/S^2$  should be more than  $0.017/3 \approx 0.006$ . In the present study, since the ratio  $A_{tie}/S^2$  was 0.0022 which is less than 0.006, the stress-strain model of unconfined concrete given by Saenz [11] was tried for the modeling of concrete in R.C. column specimens. It was found that the results obtained from the simulation were compatible with the experimental results. Table 2 shows the geometrical and material properties of reinforced concrete column specimens. The results of experiments and numerical simulations of R.C. Columns are given in Table 3. It can be seen that error in the results obtained from simulation is within 4%.

Load-displacement curves of few specimens and a typical deformed shape is plotted in Figure 6. The strain at failure was observed to be between 0.0075 to 0.009. Strain at maximum load  $\epsilon_{cc}$  was found to be 0.00285 to 0.003. The post peak part of the load-displacement curve shows the ductile behavior of composite material. From the load-displacement curve, it was found that about 0.6% strain develop in the post peak region. From the experiments, it was also observed that higher load capacity can be achieved with lower value of  $L/D$  and with lower percentage of longitudinal reinforcement.

**Table 2.** Geometrical and material properties of R.C. column specimens

Specimen	Geometrical properties			Properties of Reinforcement		
	(D) mm	L/D	$f_y$	Longitudinal (%)	steel	Ratio of area of longitudinal steel to area of confined concrete core ( $\rho_{cc}$ )
C146	146	5.48	500	4.05		0.0660
C149	149	5.37	500	3.89		0.0630
C152	152	5.26	500	3.74		0.0600
C182	182	4.4	500	2.61		0.0384
C184	184	4.35	500	2.55		0.0373
C188	188	4.25	500	2.44		0.0355
C204	204	3.92	500	2.08		0.0292
C206	206	3.88	500	2.04		0.0285
C208	208	3.85	500	2.00		0.0279

**Table 3.** Results of experiments and simulations

Specimen	Ultimate Load (kN)			Strain at failure	Confining pressure computed from Mander's model (Mander et al., 1988)		
	Experiment (kN)	Analysis (kN)	% Error		$\rho_s$	( $k_e$ )*	$f_c=0.5k_e \rho_s f_y$
C146	941	964	2.44	0.0075	0.0117	0.1524	0.446
C149	970	990	2.06	0.0081	0.0114	0.1650	0.470
C152	992	1014	2.22	0.0084	0.0111	0.1774	0.492
C182	1262	1306	3.49	0.0085	0.0089	0.2885	0.642
C184	1284	1326	3.27	0.0086	0.0088	0.2950	0.649
C188	1331	1376	3.38	0.0088	0.0086	0.3078	0.662
C204	1516	1576	3.96	0.0088	0.0078	0.3551	0.692
C206	1526	1585	3.87	0.0089	0.0077	0.3607	0.694
C208	1549	1610	3.94	0.0090	0.0076	0.3661	0.696

\* confinement coefficient 
$$k_e = \frac{\left(1 - \frac{s'}{2d_s}\right)^2}{1 - \rho_{cc}}$$

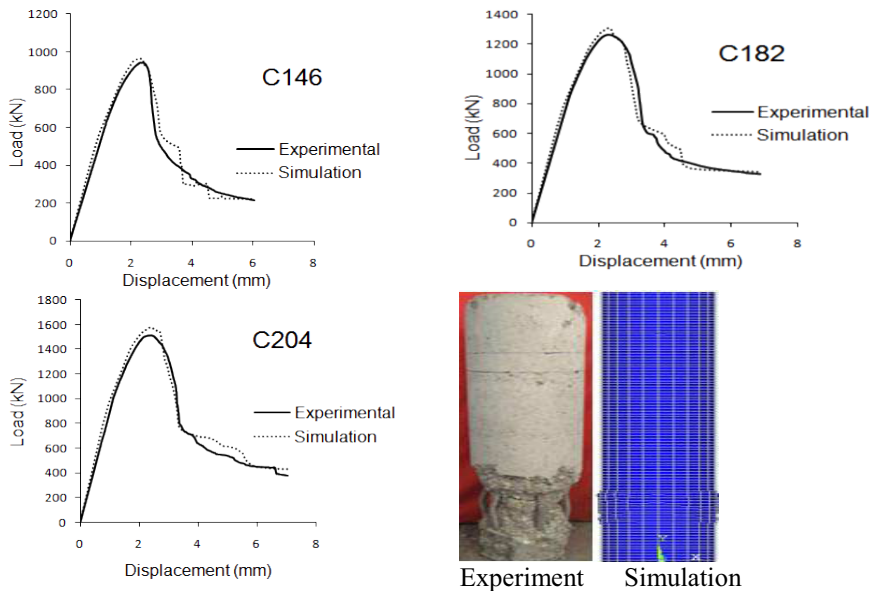


Figure 6. Load-displacement curves and deformed shape

#### 4. Conclusions

An effort was made to get an understanding of the effect of spacing of lateral ties in R.C. column for the effective confinement. On the basis of results obtained, following points can be concluded.

1. The value of  $A_{tie}/S^2$  greater than 0.006 may give the effective confinement.
2. There is no strength gain observed due to confinement though there is an enhancement in the column ductility. The strain at failure was obtained between 0.0075 and 0.009
3. The confining pressure, calculated based on equation given by Mander et al. [4] was found to be between 0.446 and 0.696.

#### References

- [1] H.E.H. Roy and M.A. Sozen, Ductility of concrete, *Proc., Int. Symp. on Flexural Mechanics of Reinforced Concrete*, ASCE-ACI, Maimi, (1964), 213-224.
- [2] D.C. Kent and R. Park, Flexural members with confined concrete, *J. Str. Engg.*, 97(1971), 1969-1990.
- [3] S. Popovics, A numerical approach to the complete stress-strain curves of concrete, *Cement and Concrete Research*, 35(1973), 583-599.
- [4] J. B. Mander, M. J. N. Priestley and R. Park, Theoretical stress-strain model for confined concrete, *J. Str. Engg.*, 114 (1988), 1804-1826.
- [5] H. Mostafaei, F. J. Vecchio and T. Kabeyasawa, Deformation capacity of reinforced concrete columns, *ACI Journal.*, 106 (2009), 187-195.
- [6] N. Subramanian, Design of confinement reinforcement for RC columns, *The Indian Concrete journal*, Point of View (2011), 1-8.

- [7] S. Gramblička and P. Veróný, Transverse reinforcement in reinforced concrete columns, *Journal of Civil Engg.* 8 (2013), 41-50.
- [8] IS: 8112-1989 (Reaffirmed 2005), 43 grade ordinary Portland cement-specification, Bureau of Indian Standard, New Delhi, India.
- [9] IS: 10262-2009, Concrete mix proportioning-guidelines, Bureau of Indian Standard, New Delhi, India.
- [10] Anthony J. Wolanski B.S., Flexural behavior of reinforced and prestressed concrete beam using finite element analysis, *Master's thesis, Marquette university, Milwaukee, Wisconsin* (2004).
- [11] L.P. Saenz, Discussion of 'Equation for the stress-strain curve of concrete', *ACI Journal.*, 61 (3) (1964), 1229-1235
- [12] A.A. Elwi and, D.W. Murray, A 3D hypoelastic concrete constitutive relationship, *Journal of Engg. Mech.*, 105 (1979), 623-641.
- [13] ACI-318, Building code requirements for structural concrete and commentary, Detroit (USA). American Concrete Institute (1999).
- [14] J. B. Mander, M. J. N. Priestley and R. Park, Observed stress-strain behavior of confined concrete, *J. Str. Engg.*, 114 (1988), 1827-1849.

# Parametric study of non-uniform thickness rectangular concrete filled steel tube in pure bending

P. K. GUPTA<sup>1</sup> and S. K. KATARIYA

*Department of Civil Engineering, Indian Institute of Technology Roorkee, India*

**Abstract.** This paper presents a parametric study using fiber element analysis method to investigate the effect of increasing steel area in tension side of concrete filled steel tube (CFST) beams. A computer code for fiber element analysis method has been written using Oracle-10g form-6i database. The developed code was validated by comparing its results with the experimental results from available literature for CFST beams having uniform thick steel tubes [1] and non-uniform thick steel tubes. After validation, the code is employed to perform a parametric study. The study will be helpful to decide the dimensions of steel tube thickness to obtain the balanced section. To obtain a balanced section in CFST flexural members having depth ranging from 150 to 230 mm, the area of steel in tension side should be approximately 3 to 7 times the steel area in compression side. Moreover, steel percentage area was found to be 9% to 15% of the composite sectional area to obtain balanced section.

**Keywords.** Fiber element analysis, non-uniform thickness, CFST, flexural capacity, ductility

## Introduction

Composite steel-concrete construction is widely used in the construction of buildings and bridges, even in earthquake prone area. The composite construction ideally combines the advantages of both steel and concrete to achieve high capacity, high stiffness, speed of construction, and economy [2-10]. Tomii and Sakino [3] performed tests on eight CFT-beam-column specimens with width to thickness ratio range from 23.5 to 45 for a strength study. Lu et al. [4] conducted an experimental study on the mechanical behavior of non-uni-thickness walled rectangular CFST beams subjected to

---

<sup>1</sup>Corresponding author: [pkgupfce@iitr.ernet.in](mailto:pkgupfce@iitr.ernet.in), [spramod\\_3@yahoo.com](mailto:spramod_3@yahoo.com), phone. 01332-285425, mobile 0919411500841, Fax. +91-1332-275568, 273560



pure bending. All specimens have width 140 mm and depth 160 mm. The thickness of steel tube on bottom side was 7.56 mm while rests three sides thickness were uniform as 4.72 mm. The span of each beam was 1800 mm. They concluded that a non-uni-thickness walled rectangular CFST beam exhibits adequate ductility, and the flexural strength of a non-uni-thickness walled CFST beam is superior to that of a uni-thickness walled CFST beam.

Experimental methods have been basic means of researching the behaviour of CFST, while numerical modelling methods become increasingly important because they can simulate cases that are difficult to be completed by experiments [5]. Calculation methods for flexural capacity of CFST beam have been proposed by a few researchers [3], [6] and [7]. Liang presented theory and algorithms of a performance-based analysis technique for the nonlinear analysis of thin-walled concrete-filled steel tubular beam-columns with local buckling effects [8]. In the present study, a parametric study has been conducted using fiber element analysis code developed in Oracle database to investigate the effects of balanced section on the flexural capacity of CFST beams.

## 1. Parametric study

It is not convenient to conduct the experiments for every case. Experiments consume time as well as materials costs. In such type of problems, to find the effect of change or variation in any parameter of the specimen it is better to use computer code after its validation. Computer code is best suitable tool for the parametric study. The main parameters of the study were area of steel, non-uniform thickness of steel tube and compressive strength of concrete. The main focus was to find the steel area and steel tube thickness to get the balanced section.

### 1.1 Computer code and its verification

The computer code based on fiber analysis method was written in Oracle-10g form 6i. The efficiency and accuracy of the developed computer code are demonstrated through comparisons between computer code results and experimental results have been validated in this paper. The details of the Specimens used for validation are given in Table1. The span of each validated CFST beam specimens was 1800 mm.

### 1.2 Stress-strain behaviour of steel and concrete

Stress-strain relationships for steel and concrete were used in computer code. The stress-strain relationship of structural steel is shown in Fig.1. The values of strain in steel at strain hardening ( $\epsilon_{st}$ ) and at ultimate point ( $\epsilon_{su}$ ) were taken as 0.005 and 0.2 respectively for mild steel (curve OABC).

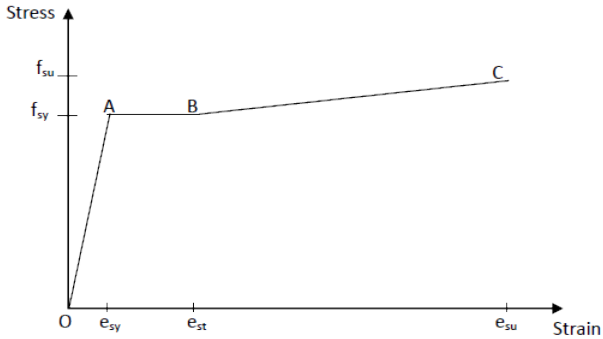


Figure 1. Stress-strain relationships for steel

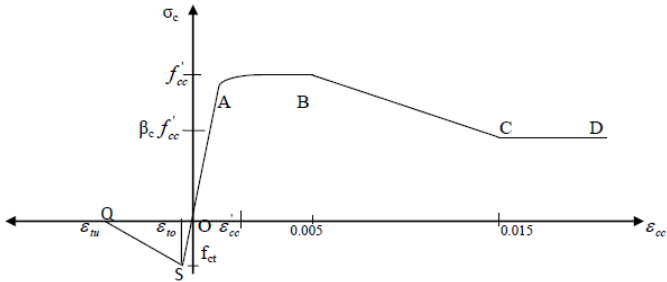


Figure 2. Stress-strain curve for concrete in concrete filled steel tube

The stress-strain relationship for confined concrete in both tension and compression is shown in Figure 2. The part QSO of the curve is in tension while part OABCD is in compression. The concrete stress from O to A can be calculated from the equation suggested by Mander et al. [9]

$$\sigma_c = \frac{f'_{cc} (\epsilon_{cc}/\epsilon'_{cc})}{\lambda - 1 + (\epsilon_{cc}/\epsilon'_{cc})^\lambda} \tag{1}$$

Where

$\sigma_c$  =longitudinal compressive stress in concrete at any part of compression

$\epsilon_{cc}$ =longitudinal compressive strain in concrete at any part of compression

$f'_{cc}$ =compressive cylinder strength of concrete in MPa

$\epsilon'_{cc}$ =strain in concrete corresponding to stress  $f'_{cc}$

$\epsilon_{to}$ =tensile strain in concrete at cracking

$\epsilon_{tu}$ = ultimate tensile strain in concrete

$\lambda$  is a parameter =  $E_c/(E_c - (f'_{cc}/\epsilon'_{cc}))$

The stress in the confined concrete stress-strain curve part AB, BC and CD is calculated as below:

$$\begin{aligned}
 \sigma_c &= f'_{cc} && \text{for } \epsilon'_{cc} < \epsilon_{cc} \leq 0.005 \\
 \sigma_c &= \beta_c f'_{cc} + 100 (0.015 - \epsilon_{cc}) (f'_{cc} - \beta_c f'_{cc}) && \text{for } 0.005 < \epsilon_{cc} \leq 0.015 \\
 \sigma_c &= \beta_c f'_{cc} && \text{for } \epsilon_{cc} > 0.015
 \end{aligned}
 \tag{2}$$

Parameter  $\beta_c$  depends upon ratio of larger lateral dimension to steel tube thickness. The above model has been explained in detail [1].

## 2. Beam specimens for parametric study

The span of each beam specimen was taken as 1000 mm. Width of beam specimen was kept fixed as 120 mm while depth is varied and taken as 150, 180, 200 and 230 mm. In this way four types of beam sections 120x150, 120x180, 120x200 and 120x230 mm are developed. In each beam section by keeping width and depth constant, steel tube thickness on tension side of the section was increased. To study the effect of strength of concrete, CFST beams were filled with concrete having cylinder strength 30 MPa, 50 MPa and 70 MPa.

Typical sectional view of beam is given in Figure 3. The steel tube thickness at bottom side was taken to get the balanced section while for rest of the three sides, the thickness was uniform as 1.5 mm. The yield strength ( $f_{sy}$ ) and ultimate tensile strength ( $f_{su}$ ) of the steel tubes were 260 MPa and 320 MPa respectively while the modulus of elasticity ( $E_s$ ) was 205 GPa. The concrete cylinder strengths ( $f'_{cc}$ ) were taken as 30 MPa, 50 MPa and 70 MPa to fill the tubes. The sectional dimensions of all CFST beam sections are given in Table 2.

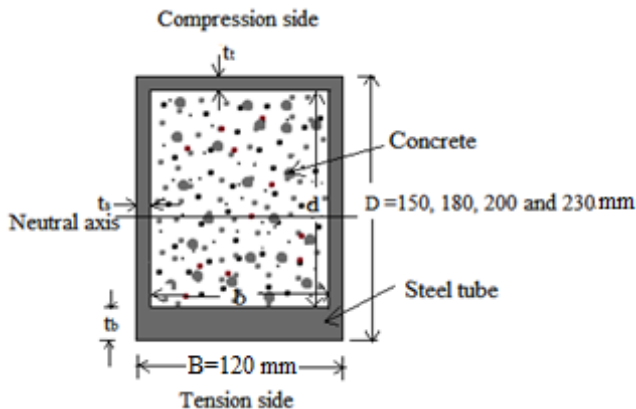


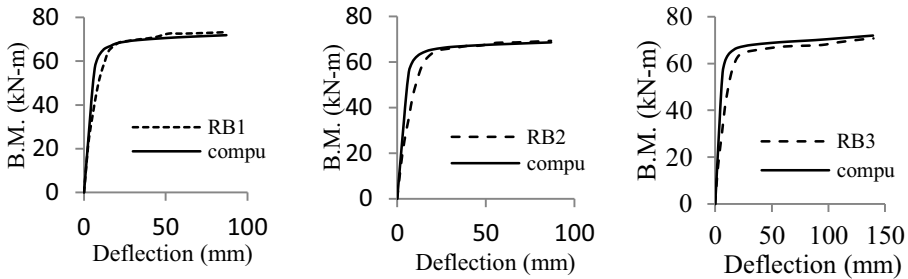
Figure 3. Typical view of non-uniformly walled CFST beam section

### 3. Results

#### 3.1. Validation of Computer Code for non-uniform thick CFST beams

**Table 1.** Details of the specimens used for validation [4]

Specimen	D (mm)	B (mm)	$t_t$ and $t_s$ (mm)	$t_b$ (mm)	$f_{sy1}$ (MPa)	$f_{sy2}$ (MPa)	$f_{su1}$ (MPa)	$f_{su2}$ (MPa)	$f'_{cc}$ (MPa)
RB1	140	120	4.72	7.56	316	395	418	525	38.70
RB2	140	120	4.72	7.56	316	395	418	525	25.10
RB3	140	120	4.72	7.56	316	395	418	525	30.40



**Figure 4.** Comparison of computational and experimental moment–deflection curve for specimens RB1, RB2 and RB3

Figure 4 shows good agreement between the experimental results and computational results.

#### 3.2. Results of simulated CFST beams

The following paragraphs summarises the salient findings of the parametric study. The results are covered in different structural aspects of the beam section.

##### 3.2.1. Flexural capacity

Since steel tube thickness is increased in tension side to obtain the balanced section of the CFST beam. Only steel tube sectional area increases. Hence the flexural capacity of CFST beams increases with the thickness increment of steel tube in tension side.

##### 3.2.2. Compressive strength of concrete

As the relatively high strength concrete is used in same section of CFST beam, the neutral axis shifts slightly towards compression side. To obtain the balanced section, the steel tube thickness is to be increased in tension side. Hence compressive strength also plays a role to decide the thickness the steel tube in tension side to obtain the balanced section.

**Table 2.** Details of non-uniform thick CFST beams

D (mm)	B (mm)	$t_t$ and $t_s$ (mm)	$t_b$ (mm)	$f_{sy}$ (MPa)	$f_{su}$ (MPa)	$f_{cc}$ (MPa)	$t_b/t_t$ ratio	$A_{st}/A_{sc}$ ratio	$A_s/A_g$ (%)	$A_{cc}/A_c$ (%)	Curvature	B.M. (kN-m)	B.M. ratio
150	120	1.5	9.75	260	320	30	6.50	3.41	9.81	52.97	0.00266	45.66	1
150	120	1.5	13.15	260	320	50	8.77	4.40	12.02	54.30	0.00266	57.87	1.27
150	120	1.5	17.91	260	320	70	11.94	5.79	15.12	56.28	0.00266	74.63	1.63
180	120	1.5	11.37	260	320	30	7.58	3.59	9.47	52.95	0.00222	63.74	1
180	120	1.5	15.80	260	320	50	10.53	4.76	11.87	54.39	0.00222	82.65	1.30
180	120	1.5	21.14	260	320	70	14.09	6.16	14.76	56.24	0.00222	106.87	1.68
200	120	1.5	12.20	260	320	30	8.13	3.63	9.18	52.87	0.00200	76.67	1
200	120	1.5	17.00	260	320	50	11.33	4.81	11.52	54.27	0.00200	100.20	1.31
200	120	1.5	23.51	260	320	70	15.67	6.42	14.69	56.29	0.00222	130.41	1.70
230	120	1.5	14.00	260	320	30	9.33	3.81	9.07	52.91	0.00172	100.10	1
230	120	1.5	19.54	260	320	50	13.03	5.06	11.42	54.32	0.00172	131.20	1.31
230	120	1.5	27.16	260	320	70	18.11	6.77	14.65	56.37	0.00172	171.62	1.71

Where  $A_g$ ,  $A_s$ ,  $A_c$ ,  $A_{cc}$ ,  $A_{st}$ , and  $A_{sc}$ , and are the area of composite section, steel tube area in composite section, sectional concrete area, concrete area in compression, area of steel tube in tension side and area of steel tube in compression side respectively.

### 3.2.3. Concrete utilization

Table 2 clearly indicates that using higher strength concrete, more concrete area may be utilised to increase the flexural capacity of CFST beams.

### 3.2.4. Steel area

It is clear that the area of steel in the tension side is 3.41 to 6.77 times the steel area in compression side and, steel percentage area required is 9.81% to 15.12% of the composite sectional area to obtain the balanced section. Table 2 shows the moment ratio range varies from 1.27 to 1.71, 1.30 to 1.68, 1.31 to 1.70 and 1.31 to 1.71 for 150 mm, 180 mm, 200 mm and 230 mm depth section respectively.

### 3.2.5. Curvature

CFST beams having same sectional dimensions filled with different strength of concrete, fail at same value of curvature.

## 4. Conclusions

A total of twelve CFST beams have been simulated to obtain the balanced section using different types of section filled with three concrete mixes having different compressive strength. A fiber element analysis computer code was prepared in Oracle database for this parametric study. It can be concluded that the bending capacity of a section increases with increase in steel tube sectional area. In a balanced section more than 50% area of concrete may be utilized by using high strength concrete. It can be concluded that extra steel should be provided on the tension side to obtain the balanced section to enhance the moment capacity of the CFST beams.

## References

- [1] P. K. Gupta and S. K. Katariya, "A study on concrete filled rectangular steel tubes subjected to bending," in *The 5th Asia and Pacific Young Researchers and Graduates Symposium on Current Challenges in Structural Engineering*, pp.309-319, Jaipur (India), 2013.
- [2] A. H. Verma, J. M. Ricles, R. Sause and L. W. Lu, "Seismic behaviour and modeling of high-strength composite concrete-filled steel tube (CFT) beam-columns," *Journal of Constructional Steel research*, vol. 58, pp. 725-758, 2001.
- [3] M. Tomii and K. Sakino, "Elasto-plastic behaviour of concrete filled square steel tubular beam-columns," *Architectural Institute of Japan*, p. 280, 1979.
- [4] F. W. Lu, S. P. Li, D. W. Li and G. Sun, "Flexural behavior of concrete filled non-uni-thickness walled rectangular steel tube," *Journal of Constructional Steel Research*, vol. 63, pp. 1051-1057, 2007.
- [5] H. Lu, L. H. Han and X. L. Zhao, "Analytical behaviour of circular concrete-filled thin-walled steel tubes subjected to bending," *Thin-Walled Structures*, vol. 47, pp. 346-358, 2009.
- [6] L. H. Han, "Flexural behaviour of concrete-filled steel tubes," *Journal of Constructional Steel Research*, vol. 60, pp. 313-337, 2004.

- [7] Q. Q. Laing, "Nonlinear analysis of short concrete-filled steel tubular beam-columns under axial load and biaxial bending," *Journal of Constructional Steel Research*, pp. 64,295-304, 2008.
- [8] Q. Q. Liang, "Performance-based analysis of concrete-filled steel tubular beam-columns, Part-II: Verification and applications," *Journal of Constructional Steel Research* 65, pp. 351-362, 2009.
- [9] J. B. Mander, M. Priestly and R. Park, "Theoretical stress-strain model for confined concrete," *Journal of Structural Engineering, ASCE*, pp. 117(3):657-66, 1991.
- [10] P. Gupta, S. Sarda and M. Kumar, "Experimental and computational study of concrete filled steel tubular columns under axial loads," *J. Constructional Steel Research*, pp. Vol. 63,182-193, 2007.

# Load-deflection curve prediction of RC beams strengthened by externally bonded CFRP wraps and strips

Asad-ur-Rehman KHAN<sup>1</sup> and Fawwad MASOOD

<sup>a</sup>*NED University of Engineering and Technology, Karachi-75270, Pakistan*

**Abstract.** Increasing emphasis on serviceability and limit design has created a need for better understanding of the moment-curvature relationship of Reinforced Concrete (RC) beams cross-section. Non-linear characteristics of stress-strain curve of steel and concrete has been the major concern for many researchers, and accurate load versus deflection response can only be predicted by incorporating the same. In addition, Fibre Reinforced Polymers (FRP) has emerged as a viable solution to enhance the performance of RC beams both in terms of loads and deflection. An analytical tool has been developed in the present study to predict load-deflection and moment-curvature characteristics of RC beams (normal and strengthened by externally bonded FRP). The developed tool predicts complete load-deflection response of RC beams, with and without externally bonded CFRP system, using strain compatibility and force equilibrium technique with emphasis on cracked, yield and ultimate behaviour of such beams with shear span to depth (a/d) ratios varying from 2 to 6. Range of a/d ratios is selected to cover flexure and shear dominant loading regimes. Good agreement is found between predicted load-deflection curves with experimental data available in literature.

**Keywords.** Externally bonded FRP, load deflection, shear strengthening, flexural strengthening

## Introduction

Strengthening of Reinforced Concrete (RC) structures has been of significant importance. Use of structural steel and cementitious materials in repairs has not always proved to be effective, durable and economical. At the same time they add to the self-weight of structure and often require longer periods of time as compared to Fibre Reinforced Polymers (FRP). FRP offers high elastic modulus, low density and excellent resistance against thermal, electromagnetic, chemical and environmental effects. They are easy to apply and are available in variety of forms which make them flexible and versatile to use. These attributes have made its use widespread. The growing use of FRP in construction industry has invited researchers to test new combinations of FRP laminates and wraps, which could suggest more efficient use of the material. Main objective of this study is to develop an analytical tool that can predict load-deflection curves for RC beams strengthened with externally bonded

---

<sup>1</sup>Corresponding author: [asadkhan@neduet.edu.pk](mailto:asadkhan@neduet.edu.pk)



Carbon Fibre Reinforced Polymer (CFRP) wraps and laminates in flexure and shear dominant regions using strain compatibility technique, before and after strengthening.

## **1. Methodology**

The tool for calculating load versus deformation is developed in MS-Excel through strain compatibility approach. The shear capacity of the flexure member is evaluated by a component within the tool developed according to guidelines of ISIS Educational Module 4 [1] and ACI 440.2R-02 [2], and is validated against published data. For concrete that is not cracked, a linear curve is assumed for the calculation of strains. For post cracking strains, Hognested's Curve [3] is used. Strength of concrete in tension is neglected, and its failure strain is taken as 0.0032. For steel, a linearly elastic and perfectly plastic stress-strain model is assumed, as suggested in ISIS Educational Module 2, 2003[4]. The FRP is taken as linear elastic until rupture. It is assumed that there is no relative slip between external FRP reinforcement and the concrete. The shear deformation within the adhesive layer is neglected since the layer is very thin [2].

Moment and Load carrying capacity of simply supported, singly reinforced concrete beam loaded in four point bending is calculated using strain compatibility technique as per ACI 318-05 [5] and Commentary ACI 318R-05 [6]. The deflections are calculated through moment area method to establish moment-curvature and load-deflection relationships. It is assumed that plane sections remain plane after bending, and that, there is a perfect bond between steel and adjoining concrete, thus having identical strains. The strain at initial cracking is obtained using the rupture stress, whereas yield strength is used while at yield, to obtain a tri-linear moment curvature, which is later utilized to calculate deflections. For the sake of verification, the nominal moment capacity using Whitney's stress block is also calculated as discussed in ACI 318-05 [5] and ISIS Module 4[1]. The shear resistance of the RC member is calculated as per guidelines of the ISIS Module 4[1]. The effective strain in CFRP is limited to  $\leq 0.004$  to ensure aggregate interlock in the concrete by preventing shear cracks from widening beyond acceptable limits. Due to long-term environmental exposure which eventually reduces tensile strength, creep-rupture and fatigue endurance of FRP laminates, the material properties in this study were reduced based upon the environmental exposure condition as suggested in ISIS Module 4[1].

The developed tool comprises of worksheets calculating strains starting from 0.0001 to 0.0032, with increments of 0.0002 for points beyond cracking, along with the initial cracking and yielding strains. The tool also computes the shear capacity under the guidelines of ISIS Educational Module 4 and ACI 440.2 [1, 2] for both strengthened and unstrengthened beams. Section and material properties, reinforcement details and shear-span to depth ratio ( $a/d$ ) are taken as input, and the result includes the load versus deflection, and moment versus deflection curves. The flowchart of the whole process is mentioned in Figure 1.

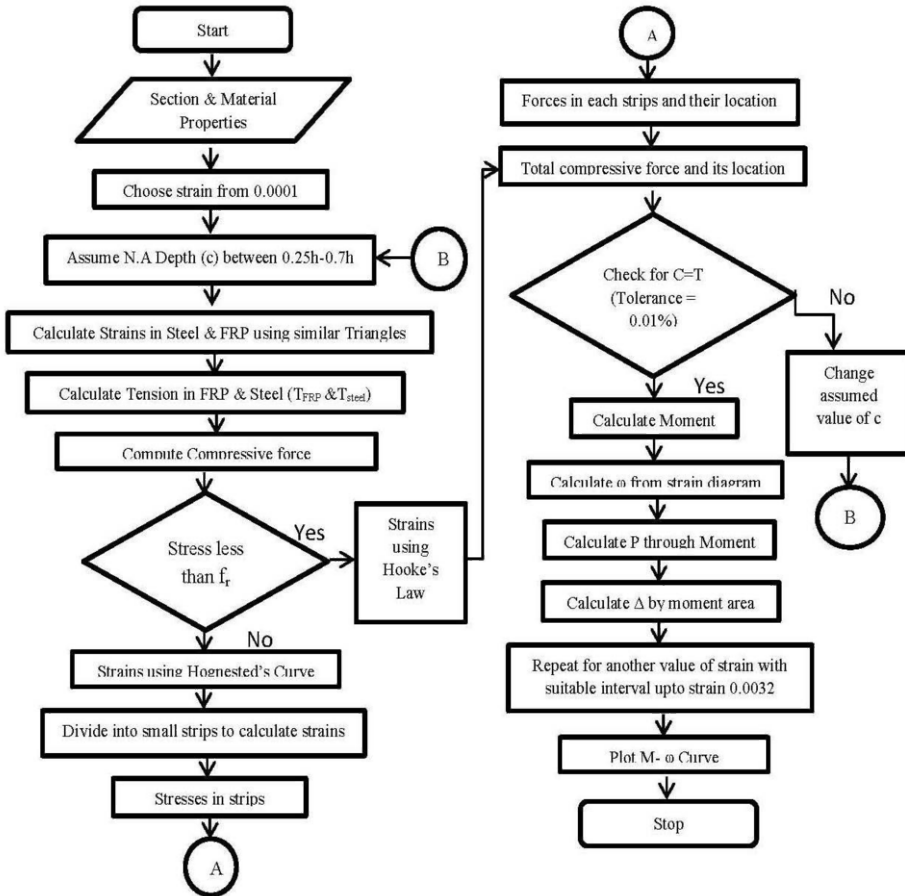


Figure 1. Flow chart for development of M-φ and P-Δ curves for the tool developed

## 2. Results and discussion

For the sake of verification, data from research papers [6-11] were utilized for validation of effectiveness of developed tool. Results of both experimental and predicted data were analysed and are discussed in the following sections. Verification is done for RC beams, normal and strengthened in flexure and shear.

### 2.1. Verification for flexure

A research paper entitled “Flexure Behaviour of RC Beams strengthened with CFRP sheets or fabric”, by P. Alagusundaramoorthy, I. E. Harik, and C. C. Choo [6] was used for verification of the predicted results in flexure. Appreciable agreement was found between the results predicted by the tool and the one published in the research paper. Data of the Beam CB7-1S was selected for the comparison. Beam profile and section are shown in Figure 2.

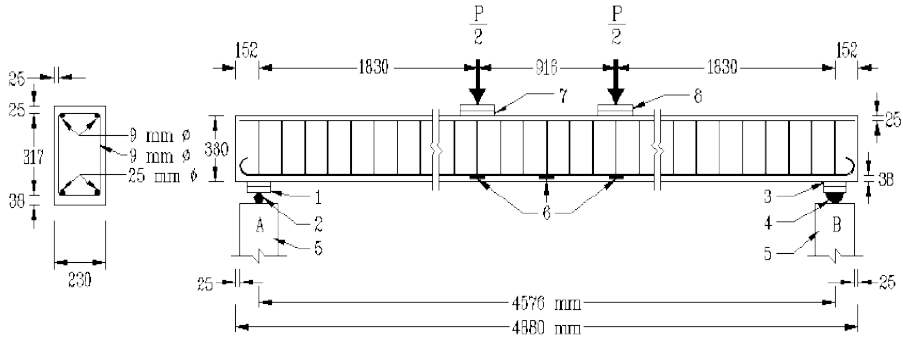


Figure 2. Section and profile of the beam [6]

Comparison of load-deflection curves for both normal and strengthened beams is shown in Figure 3. Experimental results are marginally deviating from what is predicted, due to the assumptions and limitations taken into account during the development of the tool. Up to 134 kN loads, all three load-deflection curves are overlapping till the yielding point. Beyond the yielding point there is a variation of 27.1% in the experimental and computational tool results. However, there is no significant difference in deflection in all three curves against the corresponding loads.

The post strengthening behaviour of the same beam is also in close agreement with the results reported in the paper. It can be seen that the computations and the results gathered from the study are close. Up to the load of 160 kN, all three curves shows almost same behaviour, while beyond this load, experimental result had 18.93% more load than the predicted models. Further verification of the tool was done via comparing the results obtained from the computational tool and the published data from focused prior studies. The difference in the ultimate loads and deformation is shown in Table 1.

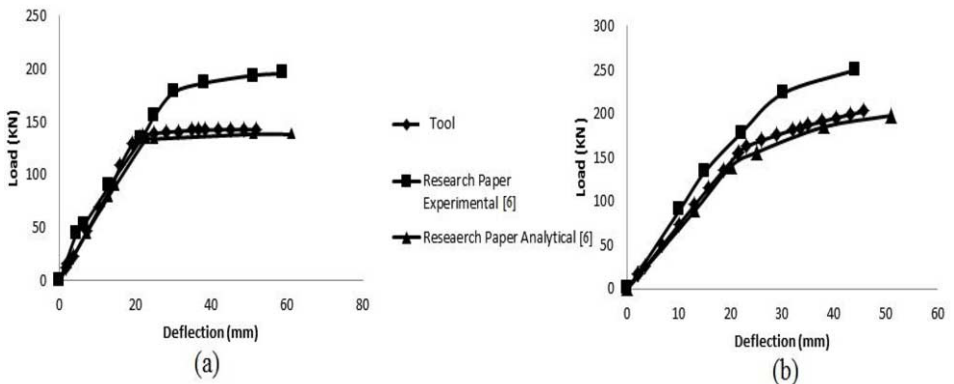


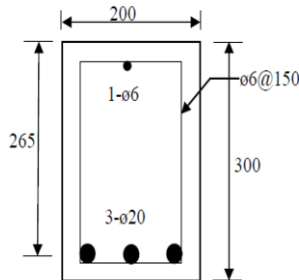
Figure 3. Load-deflection curve (a) unstrengthened (b) strengthened

**Table 1.** Comparison between published and predicted data: Flexural Dominant Region

Research Paper No.	Tool		Experimental		
	Ultimate Load (kN)	Ultimate Deflection (mm)	Ultimate Load (kN)	Ultimate Deflection (mm)	Difference in Load (%)
1 [6]	142.6	51.71	195.6	58.88	27.10
2 [6]	202.7	45.85	250	44	18.93
3 [7]	57.56	88.92	56	55	2.78
4 [8]	244.5	29.7	300	30.55	18.5
5 [9]	45.43	100.22	56.19	71.68	19.15

## 2.2 Verification for shear

A research paper entitled “Experimental investigation of RC beams strengthened with externally bonded FRP composites” by Nadeem A. Siddiqui [10] was used for verification of predicted results in shear. In this paper, two types of beams were tested; three beams were weak in flexure while the other three were deficient in shear. Out of these two groups of beams, one is control beam while the rest were strengthened with CFRP. Section properties are shown in Figure 4.

**Figure 4.** Section properties [10]

Shear capacity of the beams was calculated using procedures defined in ISIS module [4], which assisted in identifying the failure load. Experimental and predicted curves are shown in Figure 3. Predicted curve for unstrengthened beam shows a failure load of 154.6 kN with a corresponding deflection of 3.5 mm, which are close to the maximum experimental load and corresponding deflection. This, in fact, shows the limitation of the tool that it cannot accurately predict the load-deflection curve beyond the point where excessive shear cracking starts. Similar trend was observed in the comparison of load deflection curves for strengthened beam. Predicted curve shows a failure load of 187 kN with a corresponding deflection of 4.3 mm while the experimental failure is at the load of 189.6 kN and deflection at failure is 5.6 mm as shown in Figure 5. Comparison of predicted results with experimental values for other beams taken from the literature is shown in Table 2.

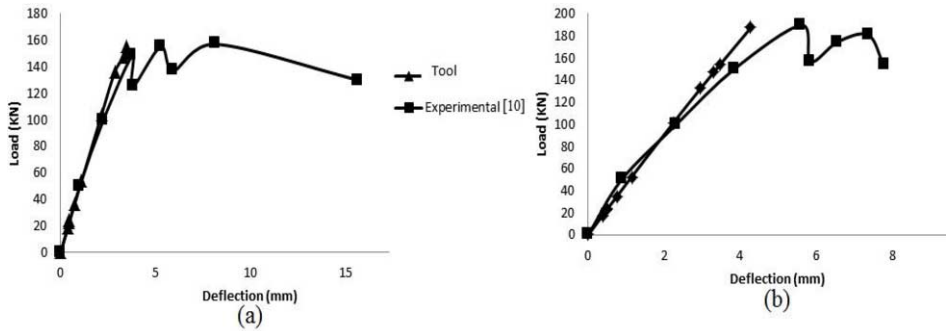


Figure 5. Load-deflection curve (a) unstrengthened (b) strengthened

Table 2. Comparison between published and predicted data for the shear dominant region

Research Paper No.	Tool		Experimental		
	Ultimate Load (kN)	Deflection at failure Load (mm)	Ultimate Load (kN)	Ultimate Deflection (mm)	Difference in Load (%)
6 [10]	154.6	3.5	148	3.75	4.46
7 [10]	187	4.3	189.6	5.6	1.37
8a [11]	132.7	1.78	110.5	2.93	20.1
8b [11]	193.4	4.31	224.9	10	14
8c [11]	219.8	2.44	182.8	4	20.2
8d [11]	219.8	2.44	190.7	6	15.25

### 3. Limitations of the tool

- Loads and deflections are calculated for simply supported beams with four points bending only.
- The tool is only applicable on the beams that have under-reinforced (tension controlled) section while for the over-reinforced section, the tool will not predict the yielding point.
- For percentages of steel up to 2%, the initial centroid value should be taken as 0.025h to 0.4h.
- For percentages of steel greater than 2%, the final centroid value should be changed by a value ranging from 0.4h to 0.9h.
- Effects of compression reinforcement have not been considered during the computation.
- Deflections are calculated at the centre of the beam considering the maximum deflection at that point.
- For shear deficient beams, the tool might not be able predict the true deflection at mid-span.

#### 4. Conclusions and recommendations

The tool is shown to be capable of predicting load-deflection curves of RC beams strengthened by externally bonded CFRP, which provides better insight of the post-strengthened behaviour of such beams.

On the basis of results, it can be inferred that prediction of load-deflection curves by the tool developed, shows appreciable agreement with the published data for beams deficient in flexural region, both for un-strengthened and strengthened beams. Predictions of flexure deficient beams include the post-yielding behaviour, which is found conservative in terms of load, due to the fact that the steel is considered to be elastic-perfectly plastic. The deviation percentage for failure loads in various beams in flexure critical beams was found to be ranging between 3 to 27%.

For load-deflection prediction for shear critical beams, a good agreement was found for a few beams, while there is a deviation in some of the beams. The post failure deflection was not obtained in the case of shear, due to sudden failure in case of shear critical beams. The deviation percentage for failure loads in various beams in shear critical beams was found to be ranging between 1.5 to 20%.

Further calibration of the tool by using additional experimental data is, therefore, recommended to improve load-deflection predictions especially for the case of shear deficient beams.

#### References

- [1] L.A. Bisby, *An Introduction to FRP Strengthening of Concrete Structures*, ISIS Educational Module 4, Canada, 2003
- [2] ACI Committee 440.2, *Guide for the Design and Construction of Externally Bonded FRP Systems for Strengthening Concrete Structures*, American Concrete Institute, Committee 440, 2002
- [3] E. Hognested, *Ultimate strength of Reinforced Concrete in American Design Practice, Symposium of the strength of concrete structures* (1956)
- [4] L.A. Bisby, *An Introduction to FRP Composites for Construction*, ISIS Educational Module 2, Canada, 2003.
- [5] ACI Committee 318, *Building Code Requirements for Structural Concrete*, American Concrete Institute, Committee (ACI 318-05), 2005
- [6] P. Alagusundaramoorthy, I.E Harik, C.C. Choo, Flexure Behaviour of RC Beams strengthened with CFRP sheets of Fabric, *J. Compos. Constr.* 7(4) (2003), 292-301
- [7] F. Bencardino, G. Spadea, R.N. Swamy, The problem of shear in RC beams strengthened with CFRP laminates, *Construction and Building Materials* (2006)
- [8] Hamid Saadatmanesh, RC Beams strengthened with GFRP Plates
- [9] W.-T. Jung, Y.-H. Park, J.-S. Park, J.-Y. Kang, Y.-J. You, Experimental investigation on flexural behaviour of RC Beams strengthened by NSM CFRP Reinforcement, *7th International Symposium on Fiber Reinforced Polymers for Reinforced Concrete Structures* (2005), 795-806
- [10] Nadeem A. Siddiqui, Experimental investigation of RC beams strengthened with externally bonded FRP composites, *Latin American Journal of Solids and Structures* (2009), 343-362
- [11] O. Chaalla, D. Perraton, Shear Strengthening of RC Beams by Externally Bonded Side CFRP Strips, *J. Compos. Constr.* 2(2) (1998), 111-113
- [12] G.N.J. Kani, *The Riddle of Shear Failure and its Solution*, 1964

# New investigations of butt-jointed precast and in-situ concrete columns

Daniel WOLFF<sup>1</sup>, Manuel KOOB, Markus BLATT and Jens MINNERT  
*Department of Civil Engineering, Technische Hochschule Mittelhessen, University of Applied Sciences, Giessen, Germany*

**Abstract:** The butt joint of the longitudinal reinforcement is the common way of joint for precast and in-situ concrete columns. The stresses, which occur in the joint area of butt-jointed columns out of normal strength up to high strength concrete and steel plate or end-face reinforcement, can be described very exactly nowadays. Design concepts as well as proposals for detailing are also available. However, still cases occur in practice for which the present design concept and engineering model is not applicable. At the *Technische Hochschule Mittelhessen* experimental investigations were carried out in order to determine the load-bearing capacity of butt-jointed columns with change of cross-section and misalignment of longitudinal reinforcement bars. The test specimens with change of cross-section reached at least 90 % of the load-bearing capacity of a column with continuous longitudinal reinforcement. Specimens with additional misalignment of the reinforcement bars reached clearly smaller failure loads. Further investigations are necessary to specify the stresses in the joint area of such columns.

**Keywords.** Butt joint, precast columns, in-situ columns, change of cross-section, misalignment of reinforcement bars

## Introduction

Butt-jointed columns are an extremely economical method for the joint of precast constructions as well as for in-situ constructions. The aim for more slender structural elements and greater field lengths results in higher loads of the columns. Columns out of ultra-high performance concrete (UHPC) are preferably produced as precast columns because of the controlled conditions of manufacturing in the precast factory. The butt joint is the simplest way for the construction of the joint in precast factories.

If normal strength concrete is used, however, high ratio of longitudinal reinforcement will be necessary for highly loaded columns. When the ratio of longitudinal reinforcement increases over 4.5 % no lapped joint of the longitudinal reinforcement is permissible according to Eurocode 2 ([1-2]), because the total cross-section of reinforcement must not be bigger than  $0.09 A_c$ . Because of this, the butt joint is also used for in-situ concrete columns.

In the following paper, the stresses that occur in the joint area of butt-jointed precast as well as in-situ concrete columns are explained and the available design concepts are presented initially.

---

<sup>1</sup>Corresponding author: [daniel.wolff@bau.thm.de](mailto:daniel.wolff@bau.thm.de)

Additionally results of a series of experiments are presented, which were carried out at the *Technische Hochschule Mittelhessen*. The aim of the investigations was to determine if the full load-bearing capacity of the butt-jointed columns can also be achieved when the longitudinal reinforcement bars of the upper column show a misalignment to the lower column (bars not in-line any more). Furthermore, the columns below the butt joint showed a different cross-section than above.

## 1. Stresses in the joint area of butt-jointed columns

### 1.1. Precast-concrete columns

For design and construction of butt-jointed precast columns with high strength concrete *Minnert* carried out extensive investigations in [4]. As a finding of the investigations, the stresses that occur in the joint area can be described with mechanical models. Besides a design concept and details of construction for the butt joint were developed. The investigations showed also validity for precast concrete columns out of normal strength concrete, as shown in [3].

For the description of the stresses in the joint area, two different kinds of butt joint must be distinguished. A less spread variant nowadays is the placing of reinforcement mats directly in the end face of the columns (end-face reinforcement). Mostly steel plates are placed in the end faces of the columns. In this case, the longitudinal reinforcement bars do not have to be connected directly to the steel plates; however, the distance should be as small as possible.

By placing end-face reinforcement only about 25 % of the load part of the longitudinal reinforcement is transferred directly by end bearing of the reinforcement bars across the mortar joint. The remaining load part (approx. 75 %) must be transferred into the core concrete by bond. For this purpose, a suitable transverse reinforcement for confinement and for increasing the load-bearing capacity of the core concrete is necessary. The end bearing of the reinforcement bars leads to transverse tensile stresses near the end of the bars, which has to be supported by the end-face reinforcement. Through the continuous further development of mortar, the today usual mortars show similar Young's modulus as concrete and that is why no stresses in the columns occur because of a weak behavior of the mortar joint. In figure 1, the stresses in the joint area are represented.

By using steel plates in the end-face of the columns, the stresses in the joint area differ. In this case the entire load part of the longitudinal reinforcement bars is transferred by end bearing across the mortar joint and no transverse tensile stresses arise in the field of the bar ends. Therefore, no increased transverse reinforcement is necessary to confine the core concrete.

A butt-jointed precast concrete column with steel plates in the end faces reaches the same full load as a continuous column in the normal area. The load-bearing capacity does not have to be decreased. A decrease of the load-bearing capacity of 10 % arises only with end-face reinforcement. The design value of load-bearing capacity of a butt-jointed precast concrete column according to Eurocode 2 ([1-2]) is given by:

$$N_{Rd} = \kappa \cdot (A_{c,netto} \cdot f_{cd} + A_{sl} \cdot f_{yd}) \quad (1)$$



with:

- $\kappa$  reduction factor for acceptable normal column force (1,0 steel plate; 0,9 for end-face reinf.)
- $A_{c,netto}$  cross-section of concrete
- $A_{sl}$  cross-section of longitudinal reinforcement
- $f_{cd}$  design value of concrete compressive strength
- $f_{yd}$  design value of yielding of reinforcement steel

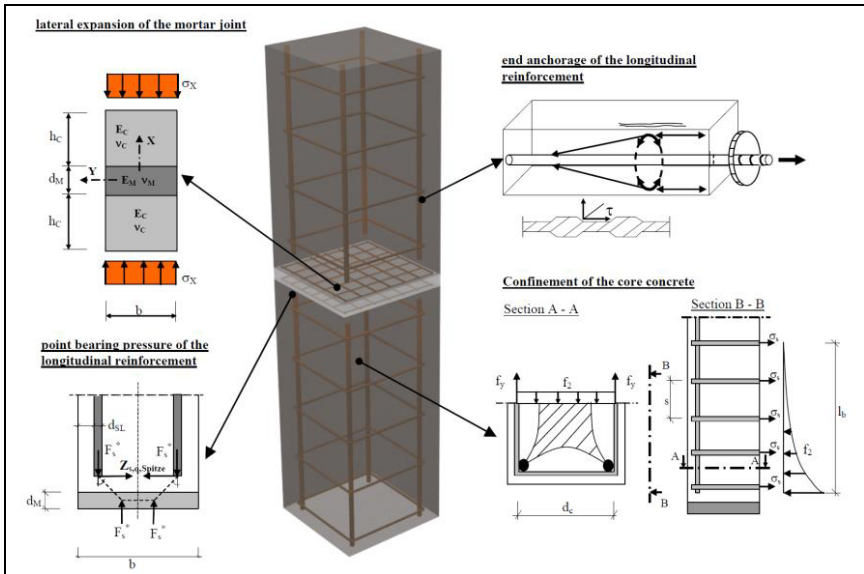


Figure 1. Mechanical models for the different stresses in the joint area of butt-jointed precast columns

### 1.2. In-situ concrete columns

For the application of the butt joint with in-situ concrete columns experimental and numerical investigations were carried out at the *Technische Hochschule Mittelhessen* ([5-6]). The investigations showed that butt-jointed in-situ concrete columns reached only about 90 % of the full load-bearing capacity of a comparable column with continuous longitudinal reinforcement in spite of an increased transverse reinforcement. The increased transverse reinforcement is necessary to support the stresses from end bearing of the longitudinal reinforcement bars and for confining the core concrete. For calculation of the design value of the load-bearing capacity of butt-jointed in-situ concrete columns the general factor  $\kappa=0,9$  for Eq. (1) is suggested. In this case an increased transverse reinforcement according to [4] must be arranged in the joint area.

## 2. Butt joint with change of cross-section and misalignment of the longitudinal reinforcement bars

The available engineering models and design concepts for butt-jointed precast and in-situ concrete columns cover the majority of occurring cases in practice. However, still cases occur, which are not covered by the available findings. Thus, it is not clear which stresses arise in the joint area if a change of cross-section occurs. This is possible, when

the column below has another cross-section than above the joint area. With increasing building height the load of a column decreases, for which smaller cross-sections can show a sufficient load-bearing capacity. In addition, creative wishes can require a change of the cross-section (for example a round column above the joint, a rectangular below). Which stresses arise through the change of cross-section and whether the so constructed columns show the full load-bearing capacity of a column with continuous longitudinal reinforcement is not known up to now.

The change of cross-section of the columns, usually results in a differing order of the longitudinal reinforcement bars above and below the joint. Thereby the longitudinal reinforcement bars show a longitudinal misalignment to each other. The bars are not in an axis with each other anymore. Because a great load part of the longitudinal reinforcement bars of the upper column must be transferred across the joint into the lower column, stresses in the joint area arise, which are not described in any design concept up to now. Moreover, it is not clear which influence the misalignment of the reinforcement bars has onto the load-bearing capacity of the joint area. The misalignment can also arise through inaccurate placing of the longitudinal reinforcement bars.

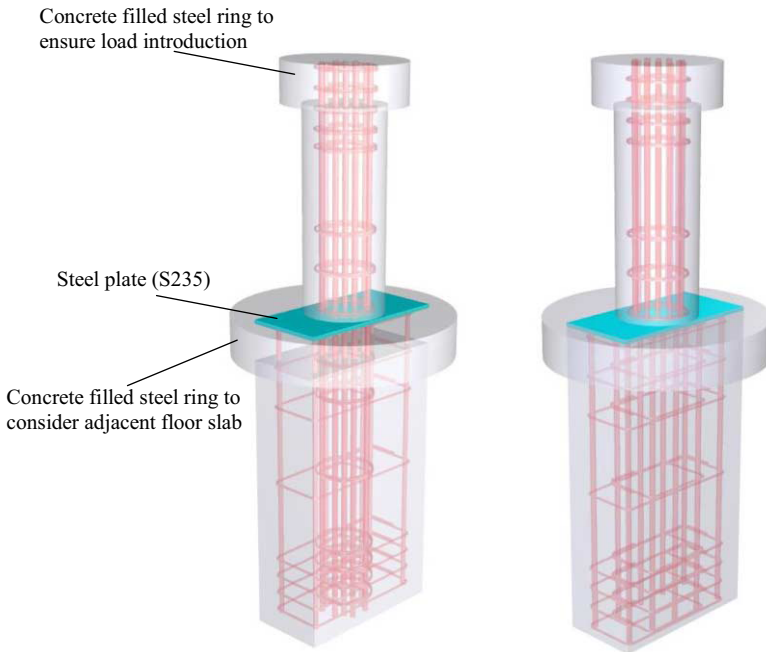
### **3. Experimental investigations of the butt joint with change of cross-section and misalignment of the reinforcement bars**

#### *3.1. Test description*

At the *Technische Hochschule Mittelhessen* experimental investigations were carried out to clarify the influence of a change of cross-section and the misalignment of the longitudinal reinforcement bars onto the load-bearing capacity of the joint area. In total six test specimens were manufactured. The two-part test specimens consist of a rectangular column with 40 x 20 cm edge length and a height of 80 cm in the lower part. In the upper part, a round column with a diameter of 20 cm and a height of 60 cm was arranged. Through the short length of the columns, the influences of the buckling effect are neglected in these investigations. The measurement of the deformations during the tests confirmed this. The columns consist of a concrete C25/30 with maximum aggregate size of 8 mm. A steel plate (steel grade S235) with the dimensions of the rectangular column with three different thicknesses was placed between the columns. The rectangular columns had a ratio of reinforcement of 2.3 %, the round columns of 5.9 %. The transverse reinforcement has been chosen according to Eurocode 2 ([1-2]). In the joint area, an additional steel ring filled with concrete C25/30 was placed to consider the influence of an adjacent floor slab. Near the upper press head, also such a steel ring was placed to ensure a secure load introduction. The material parameters of concrete and reinforcement were determined at additional concrete cubes and steel samples.

In order to be able to examine the influence of the change of cross-section separately from the misalignment of the longitudinal reinforcement bars, the test specimen V0 was produced, at which the reinforcement of the upper column was exactly continued in the lower column. The longitudinal reinforcement bars did not show any misalignment and stood (separated by the steel plate) directly onto each other. Furthermore, in the corners of the lower rectangular column additional reinforcement bars were placed.

The test specimens are represented in figure 2. An overview to the examined test specimens and the reached failure loads gives table 1 and table 2. Figure 3 shows two test specimens after failure.



**Figure 2.** Test specimens and reinforcement of the test series (left: specimen V0, right: specimen V1 – V3)

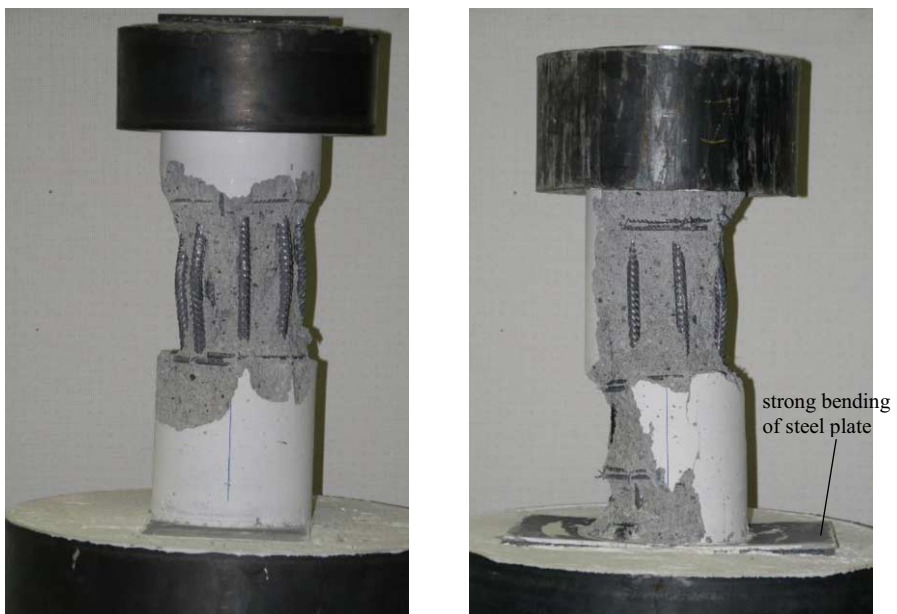
**Table 1.** Test program of the analyzed specimens

test type	rectangular column (bottom) h/b/t = 80/ 40/ 20 cm		round column (top) h/ Ø = 60/ 20 cm		f <sub>y</sub> [MPa]	thickness of steel plate [mm]	misalign-ment of reinforcement
	longitudinal reinforcement	f <sub>c,cube,bottom</sub> [MPa]	longitudinal reinforcement	f <sub>c,cube,top</sub> [MPa]			
	[mm]	[MPa]	[mm]	[MPa]			
V0.1	12 Ø 14 + 4 Ø 12	36.3	12 Ø 14	36.7	514	10	no
V0.2	12 Ø 14 + 4 Ø 12	33.0	12 Ø 14	32.1	489	10	no
V1	12 Ø 14	41.6	12 Ø 14	36.3	514	5	yes
V2.1	12 Ø 14	47.3	12 Ø 14	36.3	514	10	yes
V2.2	12 Ø 14	35.2	12 Ø 14	33.6	489	10	yes
V3	12 Ø 14	43.2	12 Ø 14	36.3	514	15	yes

**Table 2.** Failure loads of the analyzed specimens

test type	$F_{u,cont.}^{1)}$	failure load	$F_u / F_{u,cont.}$
	[kN]	$F_u$ [kN]	
V0.1	1,677	1,553	0.93
V0.2	1,539	1,395	0.91
V1	1,669	1,201	0.72
V2.1	1,669	1,402	0.84
V2.2	1,569	1,402	0.89
V3	1,669	1,405	0.84

- 1)  $F_{u,cont.}$  expected failure load of a column with continuous reinforcement [6]  
 $F_{u,cont.} = \alpha_1 \cdot \alpha_2 \cdot A_{c,netto} \cdot f_{c,cube,top} + A_{s,tot} \cdot f_y$   
 $\alpha_1 = 0.85$  conversion from laboratory strength to construction strength  
 $\alpha_2 = 0.80$  conversion from cube strength to prism strength in compression



**Figure 3.** Specimens after failure (left V0.2, right: V1)

### 3.2. Test results

The test specimens V0.1 and V0.2 with changes of cross-section but without misalignment of the reinforcement bars both failed in the normal column area outside the joint area (see figure 3, left). The remaining specimens failed originating from the joint area (see figure 3, right). Specimen V1 in addition showed strong bending of the steel plate with only 5 mm thickness.

The two test specimens V0.1 and V0.2 both reached at least 90 % of the load-bearing capacity of a column with continuous longitudinal reinforcement. By means of the investigations in [5] and [6] a general reduction factor of  $\kappa=0,9$  for butt-jointed in-situ concrete columns was suggested, cf. Eq. (1). Therefore, it can be considered that columns with changes of cross-section but without misalignment of longitudinal reinforcement bars can achieve the normal load-bearing capacity of butt-jointed in-situ

concrete columns and no significant stresses in the joint area occur that reduce the load-bearing capacity. The longitudinal reinforcement bars above and below the joint area of these specimens stand directly onto each other thus, the load part of the reinforcement bars can be transferred directly across the joint area. The concrete cross-section of the lower column has greater dimensions than the upper one. No overlap of the cross-section of the upper column across the edge of the cross-section of the lower column exists; hence, the load part of the concrete cross-section can also be transferred directly. The effect of overlapping of the upper column over the edge of the lower column must be the objective of further investigations.

The test specimens with change of cross-section and misalignment of the reinforcement bars (V1-V3) reached clearly smaller failure loads. With these specimens, the load part of the longitudinal reinforcement bars of the upper column cannot be transferred directly across the joint area and has to be introduced into the core concrete by bond. The here examined specimens had no increased transverse reinforcement as suggested in [5], because of this the core concrete cannot support the additional load from the introduction of the load part of the longitudinal reinforcement bars completely. Therefore, it can be stated that the full load-bearing capacity of a column with continuous reinforcement cannot be reached with butt-jointed columns with misalignment of the longitudinal reinforcement bars and normal transverse reinforcement according to Eurocode 2 ([1-2]) without special actions. In order to be able to describe the occurring stresses in the joint area more precisely and to develop proposals to increase the load-bearing capacity, further investigations are necessary.

#### **4. Conclusion**

At the *Technische Hochschule Mittelhessen* experimental investigations were carried out for the determination of the load-bearing capacity of butt-jointed columns with change of cross-section and misalignment of the longitudinal reinforcement bars. A change of cross-section can occur, because of smaller loads of the upper column or because of creative reasons. Both cases usually result in a misalignment of the longitudinal reinforcement bars above and below the joint. A misalignment can also occur through inaccurate placing of the reinforcement bars.

The test specimens with change of cross-section but without misalignment of the reinforcement bars reached at least 90 % of the load-bearing capacity of a column with continuous longitudinal reinforcement and failed in the normal column area.

The specimens with misalignment of the reinforcement bars showed clearly smaller failure loads. The failure of these specimens originated from the joint area of the upper round column. To develop proposals to increase the load-bearing capacity of these columns further investigations are necessary.

## References

- [1] Deutsches Institut für Normung: DIN 1992-1-1, Bemessung und Konstruktion von Stahlbeton- und Spannbetontragwerken, *Teil 1-1: Allgemeine Bemessungsregeln und Regeln für den Hochbau* (Jan 2011).
- [2] Deutsches Institut für Normung: DIN 1992-1-1/NA, Nationaler Anhang - Bemessung und Konstruktion von Stahlbeton- und Spannbetontragwerken, *Teil 1-1: Allgemeine Bemessungsregeln und Regeln für den Hochbau* (Apr 2013).
- [3] König, G., Minnert, J., Saleh, H.: Stumpf gestoßene Fertigteilstützen aus Normalbeton: *Beton- und Fertigteiljahrbuch 2001*. Wiesbaden & Berlin: Bauverlag.
- [4] Minnert, J.: Tragverhalten von stumpf gestoßenen Fertigteilstützen aus hochfestem Beton. *DAfStb Heft 499*. Berlin [u.a.]: Beuth 2000.
- [5] Minnert, J., Blatt, M.: Design Concept for Butt-Jointed In-Situ Concrete Columns in Imitation to Eurocode 2. In: ceb fib (Hg.): *The Third International fib Congress 2010*. PCI Annual Convention and Bridge Conference. Washington.
- [6] Minnert, J., Günther, G.: Bemessungsvorschlag für die verstärkte Querbewehrung bei mehrgeschossigen Ort betonstützen ohne Übergreifungsstoß der Längsbewehrung. "Stumpfstoß von Ort betonstützen". *Beton- und Stahlbetonbau 102* (2007), S. 88–97.

# Innovative structural frame using composite precast concrete components, the SMART frame

Won-Kee HONG<sup>a</sup>, Chaeyeon LIM<sup>a</sup>, Joongsoo PARK<sup>b</sup> and Sunkuk KIM<sup>a,1</sup>

<sup>a</sup>*Department of Architectural Engineering, Hyung Hee University, 1732 Deokyoungdaero, Giheung, Yongin 446-701, Republic of Korea*

<sup>b</sup>*Engineering and Construction Div., Samsung Everland, 67 Sejongdaero, Jung-gu, Seoul 100-742, Republic of Korea*

**Abstract.** Reinforced concrete (RC) structures have shown more economic efficiency and less constructability than steel structures even though construction technology of RC has evolved over the past 150 years. SMART frame is an innovative composite precast concrete (CPC) beam that has the merit of better constructability with respect to connections. SMART frame can be used for any building frames such as large size warehouses and pipe racks of industrial plants as well as residential, commercial buildings. It was found through numerous case studies that SMART frame reduces the embodied CO<sub>2</sub> by approximately 30%, the cost by 6% and the construction time when compared to existing structural systems.

**Keywords.** SMART frame, column-beam structure, composite precast concrete, economic efficiency, constructability

## Introduction

Reinforced concrete (RC) structures have shown more economic efficiency and less constructability than steel structures even though construction technology of RC and steel structures has been evolved over the past 150 years. SMART frame is an innovative structural frame that has the merit of the constructability of steel and the economy of RC. It is a column-beam structure formed by connecting a composite precast concrete (CPC) beam with a steel connection on the column side [1].

SMART Frame is a construction method that offers not only the advantages of precast concrete (PC) construction including shortening of construction time, maintaining quality and enhancing safety, but also additional economic and productive benefits by introducing the concept of in-situ production [2]. To improve these advantages of the SMART Frame, in-situ production, lifting, and installation of concrete members must be implemented based on precise and systematic plans. To erect SMART Frame in place requires implementation of constructability, economics,

---

<sup>1</sup>Corresponding author: [kimsuk@khu.ac.kr](mailto:kimsuk@khu.ac.kr)

and eco-friendliness as well as effectiveness of production and installation technologies of composite PC members.

Therefore this study aimed at evaluating the construction technology of SMART Frame and verifying its constructability, economy, and eco-friendliness through a case study project. To this end, a SMART Frame will be defined and technologies for the in-situ production and installation of SMART Frame will be described. Lastly, with the case study project reviewed to apply SMART Frame, its construction time, production costs, and CO<sub>2</sub> emissions will be examined by comparing them with those factors of existing methods. In the future, the research findings will be utilized as basic data for the analysis of constructability, economy, and eco-friendliness of new projects where SMART Frames may be applied.

### 1. Concept of SMART frame

SMART Frame is a column-beam frame system which consists of composite PC columns and beams. PC columns and PC beams retain the feature of post and lintel construction by steel connections, allowing fast and precise installation. Then structural integrity is secured by placing concrete columns along with slabs [3]. Therefore, SMART Frame is an innovative structural system that combines the benefits of concrete’s economics and steel-frame’s productivity. Existing cast-in-place RC structure has disadvantages in terms of construction time, safety, production costs, and quality while PC structure is costly. Moreover, a steel-frame structure is constructed fast, but costly and less resistant to fire. SMART Frame is designed to overcome such disadvantages to improve productivity and quality while reducing production costs, construction time, CO<sub>2</sub> emissions, and construction wastes.

SMART Frame has three hybrid functions as shown in Figure 1: structural hybrid, material hybrid, and construction hybrid. These three hybrid functions ensure the validity and economics of SMART Frame application.

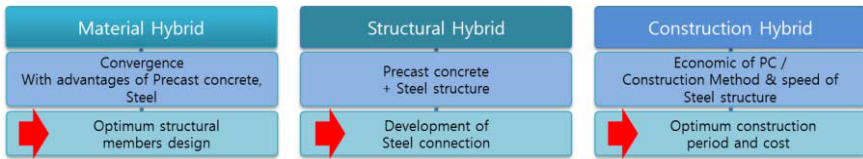


Figure 1. SMART engineering and management concept

The production and installation technologies were developed to satisfy the concept of SMART-SPACE. Here, SMART represents ‘Scientific, Measurable Attainable Reliable and ‘Timely’ technology, without relying on experience. SPACE represents S....., Productive Advanced Constructible and Economical technology, while meeting 3S (Safe, Simple, and Spotless) requirements.



## 2. Structural characteristics of SMART frame

### 2.1 SMART beam

A Smart Beam (Figure 2(a)) is a composite section consisting of a steel section, reinforcing steel, cast-in-place concrete and precast concrete members [4]. Precast concrete members minimize needs for formwork and scaffolding, thus improving constructability and scheduling in construction projects. In addition, as a slab is cast on the top of precast concrete members thereby encasing the beam steel sections. The hybrid composite beam structure can provide shallower section depths than steel beams. Relative to steel frame construction techniques, the Smart Beam significantly reduces the requisite quantity of steel sections, which come at a high unit price (Figure 3) [4]. Thus, the Smart Beam is a structural solution that offers advantages in structural stability, constructability and cost-effectiveness, relative to other types of structural members, by utilizing a convergence of structural engineering, materials, and construction engineering.

### 2.2 SMART columns

A Smart Column (Figure 2(b)) was developed to serve as an efficient connection between a column and a composite beam [4]. It is difficult to connect steel-framed reinforced concrete composite beams and RC columns. Such difficulties result in structural problems during construction. To resolve this issue, structural steel with a length equal to the depth of the beam is embedded in the column to serve as a point of connection with composite beams. That is, it is possible to connect the steel frame of the composite beam to the structural steel embedded in the column in the same manner as is used in a conventional steel frame connection. Since the upper reinforcing steel placed along the length of the beam is installed through the steel frame in the connection, constructability is improved and the structural safety of the connection is ensured. In addition, precast composite columns of up to three stories in height can be fabricated in a factory or onsite. Thus, the construction schedule can be shortened and the use of temporary construction materials such as formwork can be minimized.

A storied Smart Column is a combination of two precast (floor height) columns and a steel section that is inserted between columns in order to provide for connection to composite beams. The steel section is mechanically attached to precast columns by headed stud connectors. Smart Columns are manufactured offsite or onsite into 1, 2 or 3 story units and are assembled with Smart Beams at the construction site.

High strength bolts and welding are used for the connection of the steel beam flange to the steels inserted between columns, while reinforcing steels pass through the holes prepared in the steel web inserted between columns to resist moment at frame joint. Figure 4 describes Smart Frame beam and column joint.

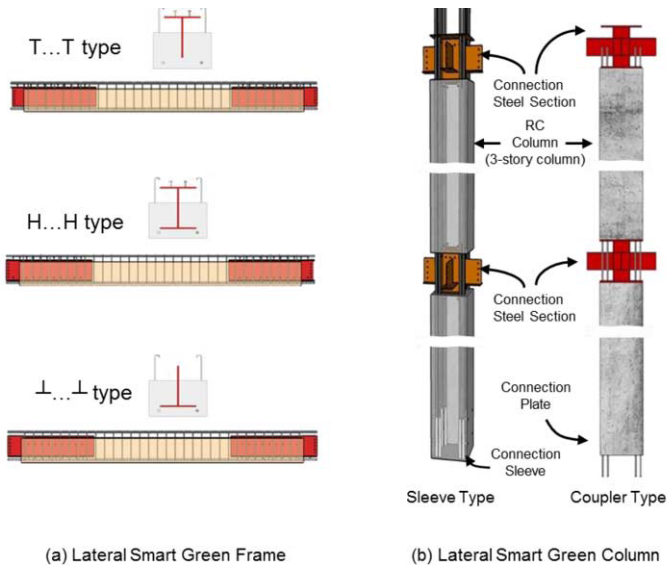


Figure 2. Smart beam and column

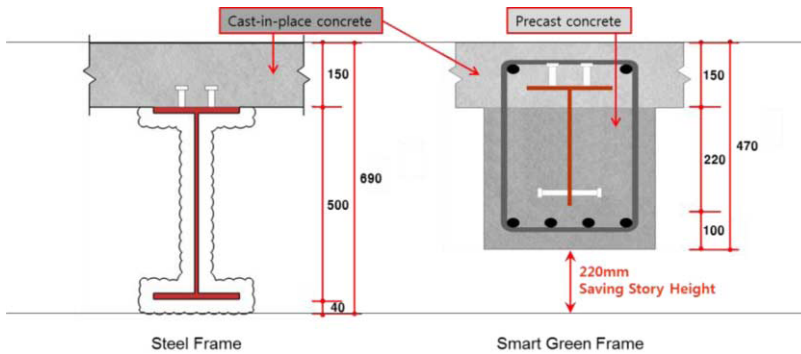
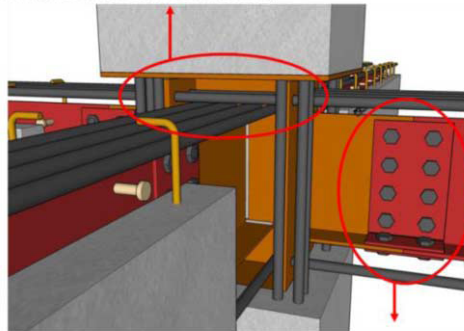


Figure 3. Reduction of effective floor height with Smart beam

-Passing top reinforcement through steel section  
(Identical with RC frame connection)



-Bolting or welding bottom flange  
(Identical with steel frame connection)

Figure 4. Smart frame beam-column connection

### 3. Construction technology of SMART Frame

#### 3.1 Relation between production and installation

To establish in-situ production and installation plans of composite PC members, various influential factors as shown in Figure 5 need to be considered. In case of a production plan, in-situ production and placement is the most influential factor and determining quantity of forms. In case of an installation plan, a lifting cycle is the most influential factor to determine production costs depending on the number of tower cranes required. Here, a lifting cycle refers to the time taken to lift one member. The in-situ production and placement plan is implemented through the algorithm suggested by Lee et al.[3?], and the installation plan using tower crane is developed according to variations of the production plan[5].

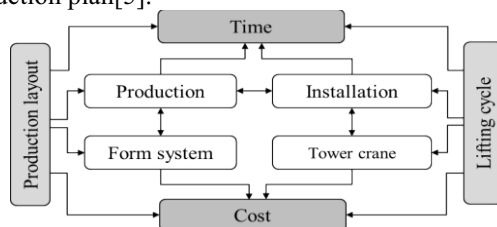


Figure 5. Production and installation simulation of SMART frame

#### 3.2 Production technology

##### 3.2.1 Form

A form is needed to produce composite PC members on the site. But if transferability is improved by modularizing the forms to make it applicable to PC members with diverse projects, the molds used in PC production factory, weight and volume will be increased, resulting in a decline in economics [6].

The form used for the in-situ production of composite PC members for SMART Frame is shown in Figure 6. The form consisted of sheathing board and frame. Steel sheathing board is reinforced by frames consisting of square pipes and angles.

##### 3.2.2 In-situ production layout

Unlike the plant production of PC members, for the in-situ production, the access road for workers, vehicles, the stockyard of materials and sufficient production area for safety need to be secured by considering the clearance area [1]; especially for the production in the limited site area. Furthermore, they should be placed within the working radius of tower cranes to transport and install the materials produced without horizontal mobility. To this end, this study used the in-situ production and placement algorithm of PC members which was developed in the preceding research [1].

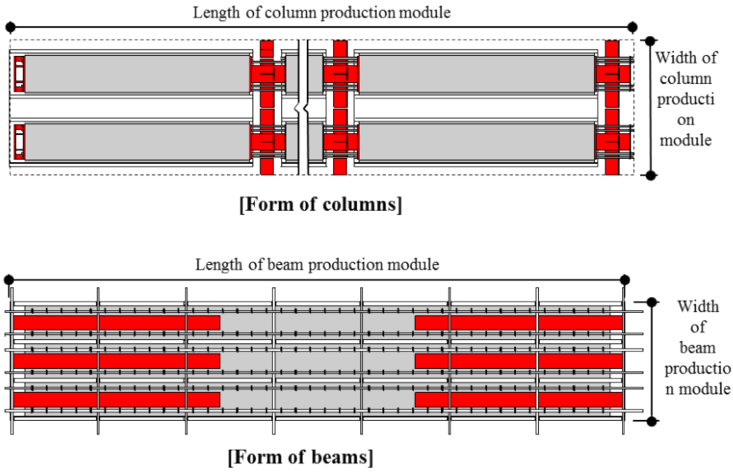


Figure 6. In-situ production form of SMART frame

### 3.2.3 Steam curing

For an efficient steam curing, it is necessary to optimize energy consumed for steam curing. To prevent strength degradation caused by moisture-freezing and quick cooling especially in winter, curing temperature needs to be maintained. An efficient way of controlling energy used for steam curing will reduce energy consumption. This study used the energy-efficient steam curing algorithm of composite PC members which was developed and presented in a preceding study [7].

## 3.3 Installation of SMART frame

### 3.3.1 Steel connection method

SMART Frame columns consisting of 3 story column unit can cause eccentricity due to construction error and beam weight. This eccentricity is insignificant from the standpoint of a single frame, yet may cause problems in installing additional beams or beams onto the upper floor with multiple frames of overall building [8].

To solve these problems, SMART Frame uses the steel connection method suggested by Lim [9] as shown in Figure 7. Beams positioned by lifting equipment pushes the column down by sliding along the inclined plane of steel frame. In other words, a quick and easy column-beam steel connection is possible through sliding when approaching the beam on the upper part of steel connection reinforced plate.

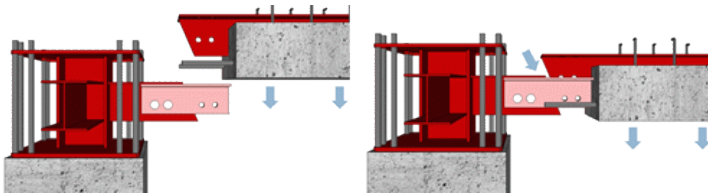


Figure 7. Steel connection method

### 3.3.2 Installation simulation

For the in-situ production and supply of a large quantity of PC members in the limited space, and for the efficient installation within a given time, a detailed construction plan needs to be developed. Especially it is required to develop a process control simulation model designed to maximize lifting tasks. For this reason, Lee et al.[5] developed a dynamic process control analysis model to optimize the productivity of SMART Frame. If the dynamic process control analysis model is used, it is possible to check an in-situ output and production cycle within a given construction time as well as the number of tower cranes within a planned budget [5].

## 4. Effects of SMART frame

In order to successfully apply a new type of structural system to apartment houses, there must be some improvement compared to existing construction methods, especially in terms of constructability and economy. SMART Frame introduced the concept of in-situ production and incorporated PC construction method's benefits such as shortening the construction time, maintaining quality, and enhancing safety. However, it is required to verify the effectiveness as well as constructability, economy, eco-friendliness of production and installation technologies of composite PC members which were developed to erect SMART Frame in place. This study selected the projects already completed, and conducted an analysis assuming that SMART Frame was used in the construction. Then construction time, production costs, and CO<sub>2</sub> emissions were estimated and compared with those of existing construction methods, presenting suggestions to be improved. The results are as shown in Table 1.

The existing methods applied to Case 1 to 3 took nine months on average to erect their frameworks. When SMART Frame was applied to case projects, construction time was shortened by about 55 days; production costs was reduced by about 6%; and CO<sub>2</sub> emissions were diminished by about 33%.

**Table 1.** Case projects and analysis of improvements

Project	Brief descriptions of project				Time saving (day)	Cost saving (%)	CO <sub>2</sub> reduction (%)
	Building Type	Location	No. of floors	Total floor area (m <sup>2</sup> )			
Case 1	Apartment Building	Suwon, Korea	B2, 26F	167,064	51	6.8	35
Case 2	Apartment Building	Suwon, Korea	B1, 15F	70,824	72	3.1	29
Case 3	Apartment Building	Incheon, Korea	B2, 37F	182,157	42	8.4	33

## 5. Conclusion

Interest in column-beam construction, which enables flexible architectural floor planning of apartment houses to maximize the efficiency of resources and energy, is growing [3]. SMART Frame was developed to reduce production costs, construction time, and skilled manpower while improving safety and constructability as well as eco-friendliness resulting from diminishing CO<sub>2</sub> emissions.

SMART frame can be used for any building frames including large size warehouses and pipe racks of industrial plants as well as residential, commercial buildings. It was confirmed through case studies that SMART frame reduces the embodied CO<sub>2</sub> by approximately 30%, reduces the cost by 6% and reduces construction time, when compared to existing structural systems.

This study was carried out centering on the super structure. If a SMART frame is applied to basement area, it is expected to make better use of space and save story height, greatly reducing construction costs and CO<sub>2</sub> emissions. In the future, the research findings will be utilized as basic data for the analysis of constructability, economics, and eco-friendliness of new projects where SMART Frame will be applied.

## Acknowledgment

This research was supported by the Ministry of Land, Infrastructure and Transport (MOLIT) of the Korea government and the Korea Agency for Infrastructure Technology Advancement (KAIA) (No. 13AUDP-B068892-01).

## References

- [1] W.K. Hong, G. Lee, S. Lee, S. Kim, Algorithms for in-situ production layout of composite precast concrete members, *Automation in construction* 41(2014), 50-59
- [2] C. Lim, S. Kim, An Analysis of Influence Factors on In-situ-production and Installation Schedule of Composite Precast Concrete Members, *The Korea Institute of Building Construction* (Academic Conference of spring) 13(1) (2013), 176-177
- [3] S. Lee, J. Joo, J.T. Kim, S. Kim, An analysis of the CO<sub>2</sub> reduction effect of a column-beam structure using composite precast concrete members, *Indoor Built Environ* 21(1) (2011), 150-162.
- [4] C.Y. Lim, S.H. Lee, D.H. Lee, S.K. Kim, Application study for the space efficiency improvement of the underground parking lots in the apartment building, *Academic Conference of the Korea Institute of Ecological Architecture and Environment* (2010), 63
- [5] S. Lee, Dynamic Scheduling Model for Column-Beam System Buildings by Composite Precast Concrete Members, doctorate thesis, Kyung Hee University (2013), 1~90
- [6] C.Y. Lim, J. Joo, G.J. Lee, S. Kim, Basic Analysis for Form System of In-situ Production of Precast Concrete Member, *Korea Institute of Construction Engineering and Management* (Academic Conference of fall) (2011), 137-138
- [7] I.W. Won, Y. Na, J.T. Kim, S.K. Kim, Energy-efficient algorithms of the steam curing for the in situ production, *Energy and Buildings*, 64(2013), 275-284
- [8] G.H. Kim, D.H. Lee, S.K. Kim, A basic study of steel-joint connection method of composite precast concrete members, *The Korea Institute of Building Construction* 13(1) (2013), 10-11
- [9] C.Y. Lim, K.H. Kim, Y.J. Na, S.K. Kim, Conceptual Study for Improvement of Connection Between Precast Concrete Members, *Journal of the Architectural Institute of Korea* (Academic Conference of spring) 32(1)(2012), 169-170

# Flexural behavior of RC Beams with local steel - experimental investigation

Shehab MOURAD<sup>1</sup>, Abdelhamid CHARIF and M. Iqbal KHAN

*Department of Civil Engineering, King Saud University, Kingdom of Saudi Arabia*

**Abstract.** Steel manufactures are always complying with the minimum code specifications. However in many countries the actual yield strength of the rebars can exceeds its nominal values by a significant factor, depending on the steel manufacturing processes. Such increase in yield strength can have negative effects on the flexural behavior of beams that are designed as tension controlled, and reduce its ductility, an essential property in seismic resisting structures. The present study experimentally investigated the effect of using rebars with yield strength exceeding its nominal values on the flexural behavior of beams. The study indicates that such increase in rebar yield strength needs to be considered in design in order to achieve the desired ductile failure mode of beams.

**Keywords.** Flexural behavior, reinforced concrete, yield strength, ductility

## Introduction

The quality and mechanical properties of steel are governed by the method of production, the chemical compositions, the mechanical working of rebars and the heat treatment [1]. Seismic standards have been developed in many countries following the design philosophy to allow the steel to deform but not fail during an earthquake. In this regard, most international specifications outline and control the mechanical property requirements for rebars to be used in seismic resistant systems [2]. This approach allows the structure to effectively absorb the energy of the earthquake without collapsing. In order to satisfy such behavior, rebars should possess high strength with sufficient ductility and low variation in yield strength to experience high number of inelastic cycles of deformation with high plastic strains. However, most rebars manufactured locally in the Gulf Area, as well as other areas, show high variability in steel yield strength that exceeds its nominal values. The increase in both yield and ultimate strength of rebars will certainly improve the member strength but it may also affect adversely the behavior and reduce its ductility. In most design codes, such as ACI-318R-08 [3], this is required to ensure a ductile flexural behavior, it is stated that steel should not only reach yielding stage but also needs to reach a minimum strain of 0.005. In addition, ACI-318R-08 states that the maximum allowed steel ratio in the beam should not exceed ( $\rho_{\max}$ ), given by;

---

<sup>1</sup>Corresponding author: [smourad@ksu.edu.sa](mailto:smourad@ksu.edu.sa)

$$\rho_{\max} = \frac{3}{8} \frac{0.85\beta_1 f'_c}{f_y} \quad (1)$$

Where,  $f'_c$  is the specified concrete compressive strength,  $f_y$  is the nominal steel yield strength and  $\beta_1$  is a factor relating depth of equivalent rectangular compressive stress block to neutral axis depth, and it equal to 0.85 for  $f'_c \leq 27.6$  MPa.

## 1. Experimental investigation

As part of the experimental investigation, random samples were taken from two different local steel producers. As the tensile strength of the rebars depends on the process of its manufacturing, an investigation was made to compare the tensile strength of rebars prepared by two different processes of tempering and quenching processes as obtained from two different producers. The grade of steel in both processes was Grade 60 with nominal yield stress of 420MPa and nominal ultimate strength of 620 MPa. Tensile tests were done on different rebar diameters for each type of steel. The ratios of the mean to nominal yield strength " $\gamma_y$ " and the ratio of mean to nominal ultimate strength " $\gamma_u$ " were computed as given in Table 1 for different rebars diameters. As can be noticed, the values of  $\gamma_y$  for rebars prepared by tempering process are almost approaching 1.00, while the values of  $\gamma_y$  for rebars prepared by quenching process are much higher and can reach up to 1.43. The values of  $\gamma_u$  for both types of steel rebars are within reasonable range of 1.00 to 1.15. The results indicate that rebars prepared by quenching process exhibit higher values of yield strength as compared to its nominal values. Typical stress-strain curves for 16mm and 20mm rebars manufactured by both tempering and quenching processes are shown in Figure 1. It was anticipated that such relatively high values of yield strength, will have a significant effect on the flexural behavior of beams.

**Table 1.** Comparison of mean-to-nominal strength values for tempered and quenched steel rebars

Bar Diameter (mm)	Tempered Steel rebars		Quenched Steel rebars	
	$\gamma_y$	$\gamma_u$	$\gamma_y$	$\gamma_u$
10	1.00	1.06	1.40	0.97
16	1.01	1.10	1.43	1.15
18	1.00	1.07	1.31	1.11
20	0.99	1.09	1.30	1.11



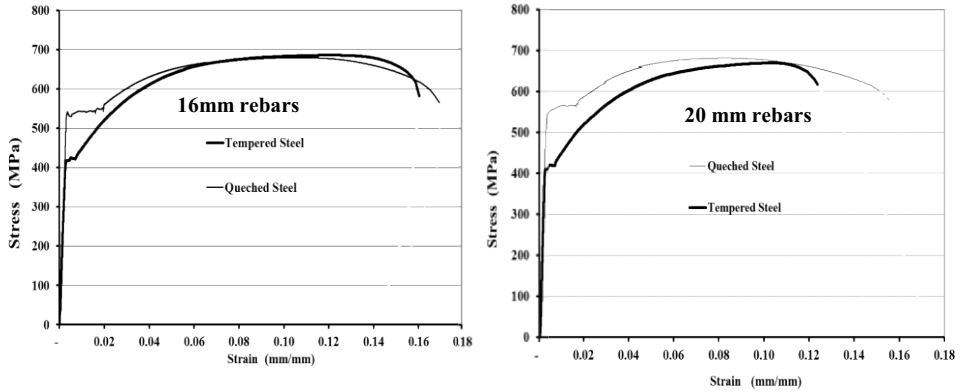


Figure 1 : Typical stress-strain curves for 16mm and 20 mm rebars

## 2. Flexural behavior of beam specimens

The experimental investigation on beam specimens was part of undergraduate-senior student project at King Saud University, [4]. A total of 4 specimens were divided in two groups (2 beams in each group). The first group of specimens was reinforced with Tempered steel rebars and designated at “T”, whereas the second group of specimens was prepared using Quenched steel rebars and designated as “Q”. The grade of steel in both groups was Grade 60 with nominal yield stress of 420MPa and nominal ultimate strength of 620 MPa. The beams were designed for a compressive strength of 25 MPa. Two specimens of each group were designed for two different failure strains (0.004 and 0.0065) in tension steel. The beam specimens of first group were designated as T-0.004 and T-0.0065, whereas specimens of second group were identified as, Q-0.004, and Q-0.0065 respectively. Details of beam specimens are shown in Figure 2. All beams were 3.1 m long with a width and depth of 200 mm and 500 mm respectively. The concrete cover at sides was 20 mm. Top and bottom covers were adjusted in order to achieve the desired effective depth that corresponds to the design failure strains in bottom steel. The flexural reinforcement was provided in two layers. One 8 mm bar was used in compression side to support the stirrups. Shear reinforcement of all the beams was designed according to ACI-318R-08. It was intended that flexural failure of beams will be prominent. The effective depth corresponding to each failure steel strain was computed based on the assumption that the ultimate compressive strain in concrete will reach 0.003, and the nominal yield stress of both groups was 420 MPa. The computed effective depths corresponding to groups “T” and “Q” were 425.9 mm and 444.0 mm respectively.

The specimens were instrumented to provide strain readings. Two strain gauges were installed on tension steel and compression steel of beam specimens at mid span. The strain gauges in the tension steel were placed in the bottom layer of the flexural reinforcement. One linear voltage differential transducer (LVDT) with 50 mm travel was used to measure mid span deflections. The load was monitored using load cells at third points. The beams were simply supported and two equal concentrated loads were

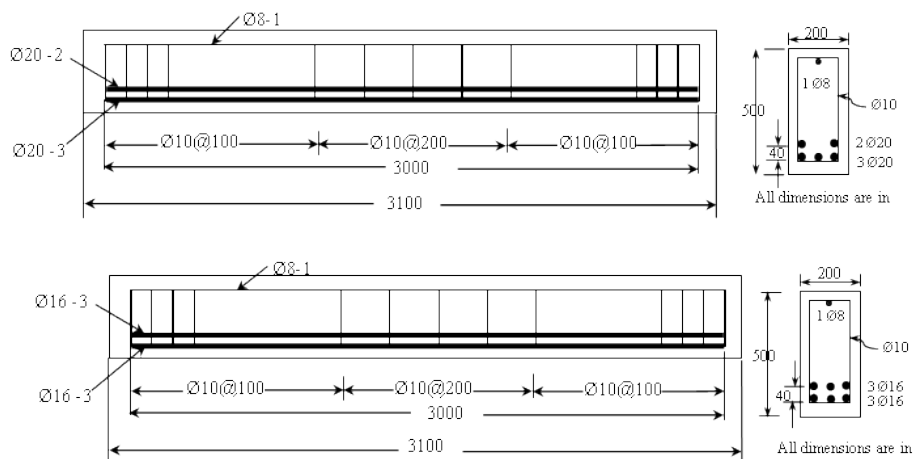


Figure 2. Details of beam specimens

applied at the third point of the span, as shown in Figure 3. The load was applied in a 10000 kN upgraded Amsler press with an electronic control using a 2000 kN measuring range option. Load was applied continuously at a displacement rate of 2 mm per minute up to failure. Load, deflections and strains were recorded using a data acquisition system.



Figure 3. Test setup

### 3. Test results

The resulted moment-curvature relationships of the four specimens are shown in Figure 4. The values of ultimate moments, curvatures and curvature ductility are given in Table 2. It is noticed that specimens T-0.0065 and Q-0.0065 exhibit higher curvature and ductility as compared to specimens T-0.004 and Q-0.004, due to the fact that its rebars have greater chance to yield before reaching the ultimate concrete strain. However, specimens made of quenched rebars; Q-0.004 and Q-0.0065, exhibit higher ultimate moments with less curvature and ductility as compared to those specimens made of tempered steel, T-0.004 and T-0.0065. Such behavior is attributed to the fact that the rebars manufactured by quenching process have higher yield strength and it will not be able to experience the whole yielding plateau before concrete failure.

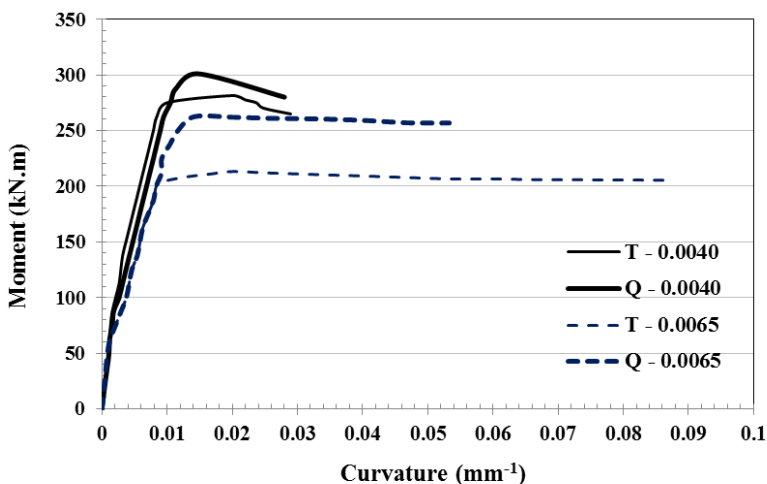


Figure 4. Moment-curvature relationship of the tested beam specimens

Table 2. Experimental results of beams reinforced with tempered and quenched steel

Specimen	Ultimate moment $M_u$ (kN.m)	Curvature at first yield of steel $\phi_y$ ( $\text{mm}^{-1}$ )	Ultimate curvature $\phi_u$ ( $\text{mm}^{-1}$ )	Curvature ductility $\mu_\phi = \phi_u / \phi_y$
T-0.040	281.4	0.009795	0.02895	2.96
T-0.065	213.15	0.009600	0.08670	9.03
Q-0.004	301.1	0.009979	0.02834	2.84
Q-0.065	262.5	0.008761	0.05330	6.08

The increase in steel yield strength has negative effect of reducing the beam's ductility capacity and positive effect of increasing the beam's moment capacity. However in seismic design, it is required to increase both the ductility and ultimate moment capacities. To achieve such goal with the increase in steel yield strength and utilizing the maximum steel ratio the following procedure is proposed.

The maximum steel ratio allowed in design " $\rho_{max}$ " as given by ACI-318R-08 [3], should account for the expected increase in the steel yield strength which can be indicated by the value of mean yield strength to nominal yield strength " $\gamma_y$ ". Therefore, the modified maximum steel ratio can be computed as  $(\rho_{max})_{modified}$  and given by;

$$(\rho_{max})_{modified} = \frac{\rho_{max}}{\gamma_y} \quad (2)$$

Equation (2) will reduce the  $\rho_{max}$  by the factor  $(1/\gamma_y)$ , and allows the beam to exhibit tension control failure and increase its ductility. However, it will reduce its moment capacity by the same factor. In order to increase the moment capacity in such case, additional compression steel can be utilized.

This work was extended to include an analytical investigation integrating stress resultants and predicting moment-curvature relationships, that is presented in an accompanying paper [5]

#### 4. Conclusions

Steel mechanical properties are usually exceeding the minimum nominal strength values for a specific grade of steel. The quality and mechanical properties of steel are governed by the method of production, chemical compositions, mechanical working of rebars and heat treatment. From the experimental tensile tests on rebars manufactured by both tempering and quenching processes, it was shown that mean to nominal value for yield strength “ $\gamma_y$ ” are higher for rebars manufactured by quenching process, and can reach values up to 1.40. The effect for such high yield strength was investigated experimentally on full-scale beams. Results showed its negative effect of reducing ductility especially when the beams were designed for high steel strain failure of 0.0065. Such negative effect on ductility can be resolved by reducing the maximum allowed steel ratio by a suggested factor “ $1/\gamma_y$ ”.

#### Acknowledgment

The authors gratefully acknowledge the support given by the structural laboratory technicians at the College of Engineering in King Saud University to complete all required tests in the present study.

#### References

- [1] Davis, H. E., et al., *The Testing of Engineering Materials*, McGraw-Hill, 4th ed., 1982.
- [2] Milbourn, D., Metallurgical Benefits of Vanadium Microalloying in Producing High Strength Seismic Grade Rebar, *Proceedings of International Seminar on Production and Application of High Strength Seismic Grade Rebar Containing Vanadium* Beijing China, (2010).
- [3] ACI Committee 318. *Building code requirements for structural concrete (ACI 318 2008)*, American Concrete Institute, Farmington Hill, Michigan, (2008)
- [4] Allorani, M., et al., Tensile Strain limits for ductile design of RC beams reinforced with Saudi rebars Senior Undergraduate Project No. CE 499-32/33-I-02/2, -Department of Civil Engineering- King Saud University, (2012).
- [5] A. Charif, S. Mourad, I. Khan: Flexural behavior of RC beams with local steel: Analytical investigation, *International Conference on Construction Materials and Structures*, ICCMATS, Johannesburg, November 24-26, 2014.

# Experimental study of time dependent bond transfer length under pure tension in slabs

Behnam VAKHSHOURI<sup>1</sup> and Felix Shami NEJADI

*Center for Built Infrastructures Research, University of Technology, Sydney, Australia*

**Abstract.** In a member subjected to pure tension, the stress in concrete is uniform over the whole concrete section. It is assumed that a local bond failure occurs at each crack and there are relative displacements or slip between the steel and the surrounding concrete. Compatibility of deformation between the two materials is thus not maintained. The bond transfer length is a length of reinforcement adjacent to a crack where the compatibility of deformation between the steel and concrete is not maintained because of partially bond breakdown and slip. It is an empirical measure of the bond characteristics of the reinforcement, incorporating bar diameter and surface characteristics such as texture-etc. Based on results from a series of long term tests on eight restrained reinforced concrete slab specimens and accurate measurements of material properties including the creep and shrinkage characteristics of two concrete batches, the ratio of final bond transfer length ( $d_0^f$ ) (after all shrinkage cracking) to  $d_0$  is presented. Experimental results show that shrinkage causes the bond to deteriorate with time.

**Keywords.** Bond transfer length, creep, shrinkage, pure tension, long-term

## Introduction

Due to the presence of steel in a reinforced concrete member, bar-concrete bond and interaction consideration is inevitable [1]. Concrete- reinforcement bond between one crack and another to carry a certain amount of the tensile force normal to the cracked plane is illustrated by tension stiffening that contributes to the overall stiffness of the member [2,3]. With perfect bond, no slip occurs between concrete and reinforcement, whereas with poor bond, relative displacement can occur. Good bond properties increase the stiffening effect [4].

Under sustained load,  $\sigma_c$  gradually reduces, due to cracking and bond breakdown caused by drying shrinkage and, to a lesser extent, due to tensile creep. Early shrinkage reduces the cracking load and, under sustained service loads, shrinkage makes additional primary cracks with time and causes a time-dependent decay of the steel-concrete bond. This decay is a short term effect which occurs particularly rapidly in large diameter specimens.

<sup>1</sup>Corresponding author: Behnam.Vakhshouri@student.uts.edu.au

## **1. Time dependent effects of creep and shrinkage on bond mechanism**

Creep and shrinkage over time affects the behavior of reinforced concrete members especially in cracked members. Similar results in cracked and uncracked sections are in experimental investigations emphasizing to account for shrinkage and creep effects in long term study of RC members [5].

Tension-stiffening relationships were coupled with shrinkage and accompanying creep effects and in most cases, tension stiffening relationships were derived from shrunk experimental RC members [2]. Concrete shrinkage strain, continues to increase with time at a decreasing rate [6]. Other internal events, such as bond slip or crack development around the bar, reduce the tension stiffening and there is no reason to suppose that this reduction will occur at the same rate as creep or shrinkage.

Among the different approaches used those which are more general and based on the bond stress–slip mechanism, are appropriate for studying the RC member under serviceability conditions. Several improvements in the analysis of concrete structures are reported in the literature [7]. The time-dependent effects of creep, shrinkage and temperature variation also exceeds the nonlinear behaviour of RC member due to bond-slip, aggregate interlock at a crack and dowel action of the reinforcing steel crossing a crack. A method of incorporating both cracking and time-dependent effects of creep and shrinkage in slab analysis, by assuming that cracks propagate only parallel to or perpendicular to orthogonal reinforcement, was reported [8].

## **2. Behavior after cracking and before yielding of steel**

First cracking occurs at the weakest part of the cross-section where the concrete tensile stress reaches the lower characteristic value of the direct tensile strength, so the stress in the concrete at the crack drops to zero. The bond characteristics of materials determine the position of subsequent cracks relative to the first. The zero tensile stress of concrete at each crack is rising with distance from the crack due to the steel-concrete bond, to a maximum value  $\sigma_c$  (less than the tensile strength of the concrete) mid-way between adjacent cracks. The next crack will then not form within  $S_0$  of the first crack as the stresses in the concrete are lower within this limit than outside. Slip at the concrete-steel interface in the region of significant bond stress ( $s_0$  on either side of the crack) causes the crack to open. When the bond from steel to concrete can no longer transfer sufficient tensile force to form an additional crack between two existing cracks, the final established cracking state is reached.

It was reported that a linear variation exists between steel strain (adjacent to a crack location) with load. As well there is a linear relation of bond stresses with load. This linear variation of stress implies a constant bond stress, which initially suggests some form of plastic behavior [9]

## **3. Bond transfer length**

When the tensile force carried by concrete is transferred to the steel bar, the steel stress at cracked section increase under restriction by bond forces developed along a certain length of steel bars called bond transfer length on either side of the crack. There are

just limited studies in the short-term definition of bond transfer length while long-term variation is almost unknown. Service loading, gradually moves the transfer region toward the unloaded end, and from the resulting strain curves, more or less bilinear decreasing trend are seen, with a transition point happening at the limit of the initial transfer region.

Among various formulae presented to estimate the bond strength of deformed steel reinforcement, the Orangun et al.'s equation [11] serves as the basis for the ACI 318-05 building code on the development length. Beeby and Scott (2004) [9] presented a method for calculating average strains in a tension member based on bond transfer length and crack spacing for short term loading as eq. 1.

$$w = S_0 \varepsilon_{s2} \quad (1)$$

Where;  $\varepsilon_{s2}$  is the strain in the reinforcement at a crack (concrete carries no tension) and  $S_0$  is bond transfer length.

Bizindavy et al (1999) [8] concluded that approximate bilinear relationship exists between the bond transfer length and the relative load level with a constant value in the range of service load levels (loads lower than the initial cracking load), followed by a linearly increasing function up to failure. In this regard, experimental study done at the University of Durham showed approximately constant bond stress over time under sustained loading.

#### 4. Experimental investigation on the ratio of long term bond transfer length to initial bond transfer length

A total eight of fully restrained slab specimens with four different reinforcement layouts were monitored for up to 150 days, to measure the effect of shrinkage on the development of time dependent direct tension cracking due to restrained deformation. Details of these specimens are shown in Table 1. According to Table 1, the slab specimens were effectively anchored at both ends to ensure the complete restraining of specimens. At the mid-span of each specimen, the section was locally reduced to ensure that first cracking always occurred at this location (Figure 1).

All tests of companion specimens were carried out in accordance with the relevant parts of the Australian standard AS1012. Two different batches of concrete were used for slabs through the test according to Table 2.

**Table 1.** Details of test specimens (reinforcement and dimensions)

Slabs	No. of Bars	Bar dia. (mm)	Ast (mm <sup>2</sup> )	Cs (mm)	S (mm)
RS1-a	3	12	339	109	185
RS1-b	3	12	339	109	185
RS2-a	3	10	236	110	185
RS2-b	3	10	236	110	185
RS3-a	2	10	157	145	300
RS3-b	2	10	157	145	300
RS4-a	4	10	314	115	120
RS4-a	4	10	314	115	120

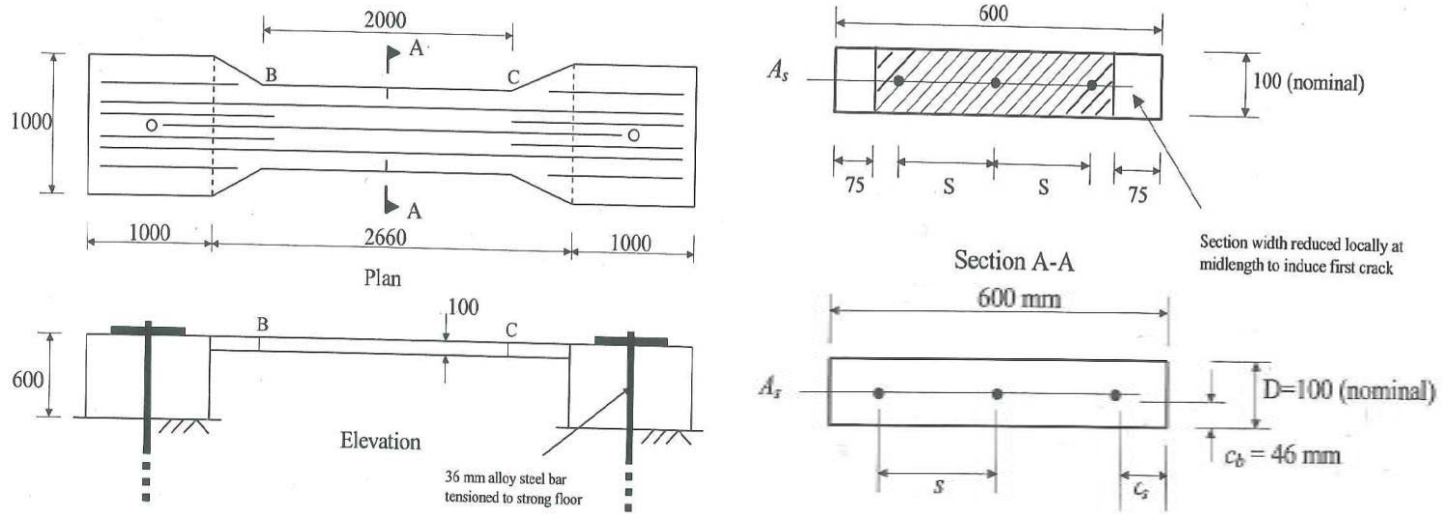


Figure 1. Restrained slab specimen details

Table 2. Material properties for concrete batch 1 (B.1) and batch 2 (B.2)

Material property	Age (days)									
	3		7		14		21		28	
	B.1	B.2	B.1	B.2	B.1	B.2	B.1	B.2	B.1	B.2
Compressive strength (MPa)	8.17	10.7	13.7	17.4	20.7	25	22.9	27.5	24.3	28.4
Flexural tensile strength (MPa)	1.91	2.47	3.15	3.1	3.43	3.77	3.77	3.97	3.98	4.04
Indirect tensile strength (Brazil test) (MPa)			1.55	1.6					1.97	2.1
Modulus of elasticity (MPa)	13240	16130	17130	18940	21080	21750	22150	22840	22810	23210



4.1 Analytical model

In a fully restrained RC member (Fig. 2), as concrete shrinks the restraining force  $N(t)$  gradually increases until the first crack appears. The resulting force reduces to  $N_{cr}$ , immediately after the first crack appears and the stress away from the crack is less than the tensile strength of concrete  $f_{ct}(t)$ . On either side of the crack the concrete shortens elastically, allowing the crack to open to a width  $w$ .

The slight increase in crack width with distance  $z$  from the steel bar can be obtained by integrating the reduction in elastic tensile strain in the concrete (from that at the level of the bar) over the half crack spacing on either side of the crack.

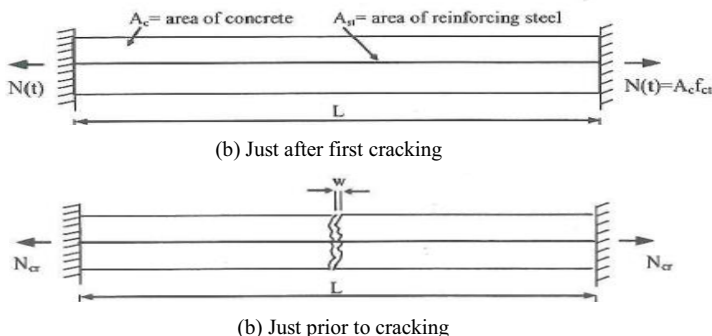


Figure 2. First cracking in a restrained direct tension member [10]

According to Fig. 3, Gilbert [10] derived the following expressions for the restraining force  $N_{cr}$ , the concrete and steel stresses away from the crack  $\sigma_{c1}$  and  $\sigma_{s1}$  respectively, and the steel stress at the crack  $\sigma_{s2}$ .

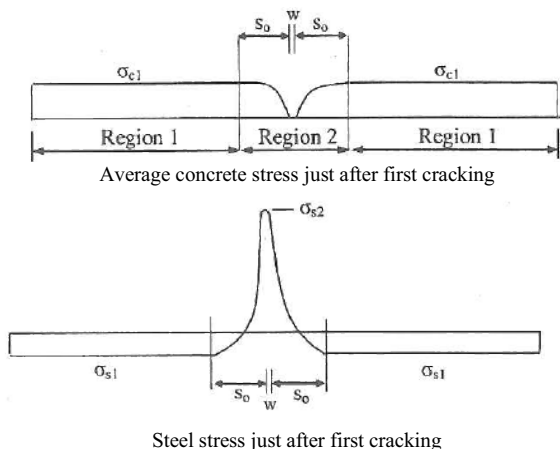


Figure 3. First cracking in a restrained direct tension member [10]

$$N_{cr} = \frac{npf_{ct}A_{ct}}{C_1 + n\rho(1+C_1)} \tag{2}$$

$$\sigma_{c1} = \frac{N_{cr} - \sigma_{s1}A_{st}}{A_c} = \frac{N_{cr}(1+C_1)}{A_c} \tag{3}$$

$$\sigma_{s1} = -\frac{2s_0}{3L-2s_0} \sigma_{s2} = -C_1 \sigma_{s2} \tag{4}$$

$$\sigma_{s2} = \frac{N_{cr}}{A_{st}} \tag{5}$$

$$C_1 = \frac{2s_0}{3L-2s_0} \tag{6}$$

$$\frac{\sigma_{s1}^*}{E_s} L + m \frac{\sigma_{s2}^* - \sigma_{s1}^*}{E_s} \left(\frac{2}{3}s_0 + w\right) = \Delta u \tag{7}$$

$$\sigma_{s1}^* = \frac{-2s_0 m}{3L-2s_0 m} \sigma_{s2}^* + \frac{3\Delta u E_s}{3L-2s_0 m} \tag{8}$$

$$\sigma_{s2}^* = \frac{N(\infty)}{A_{st}} \tag{9}$$

The bond transfer length  $s_0$  as eq. (10) in this study is related to bar diameter and ratio of reinforcement.

$$s_0 = \frac{d_b}{10\rho} \tag{10}$$

The code alterations regarding tension stiffening proposed by Beeby, Scott and Jones (2005) [9] are supporting the effect of bar diameter and reinforcement ratio on bond transfer length. Good bond increase the stiffening effect and is more significant for low reinforcement ratios than for higher ones, reported by Massicotte et al. (1990) [4]. Figure 4(a, b and c) respectively shows portion of a fully restrained member under direct tension when all the shrinkage has occurred and the final pattern of cracks has been established, it illustrates the average stresses in the concrete and steel caused by shrinkage. Gilbert [10] derived expressions for the final average spacing  $S_r$  and width in a fully restrained member, the final restraining force in a member, and the final concrete and steel stresses by enforcing the requirements for compatibility and equilibrium. With these derivations  $s_0$  was assumed to remain constant over time (eq. 2), and the supports of the member were presumed to be immovable. But these assumptions may introduce significant error because the results from this experimental program that indicated that shrinkage cause deterioration in the bond at the concrete steel interface and a gradual increase in  $s_0$  with time.

In the present study, the measured steel strains in region 1(measured by a demec gauge) and obtaining the average value for these regions along the steel bar, the steel stress remote from the cracks immediately after the first crack  $\sigma_{s1}$ , and after all shrinkage cracking  $\sigma_{s1}^*$ , was calculated. Similarly, from the measured steel strains in region 2 (measured by electric strain gauges) and obtaining the average value for these strain gauges between the reinforcement bars, the steel stress in the vicinity of the first crack immediately after the first cracking of  $\sigma_{s2}$ , and after all shrinkage cracking  $\sigma_{s2}^*$  was also calculated.

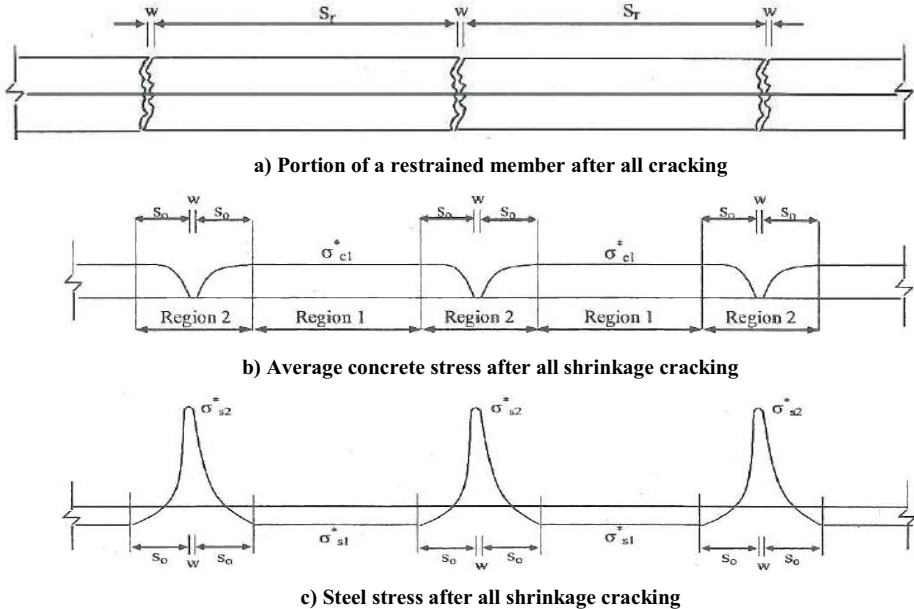


Figure 4. Final concrete and steel stresses after direct tension cracking [10]

Using eq. (5) and (9), the bond transfer length immediately after the first cracks  $s_0$ , and after all shrinkage cracking,  $s_0^*$ , was obtained. The results and ratio of  $s_0^*/s_0$  are presented in Table 3.

**Table 3.** Measured no-bond length after first and all shrinkage cracking

	Measured bond transfer length (mm)							
	RS1 (a)	RS1 (b)	RS2 (a)	RS2 (b)	RS3 (a)	RS3 (b)	RS4 (a)	RS4 (b)
After first cracking ( $s_0$ )	261	215	228	201	246	342	256	259
After 150days shrinkage ( $s_0^*$ )	366	290	290	292	323	454	332	319
$s_0^*/s_0$	1.4	1.35	1.27	1.45	1.31	1.33	1.29	1.23

From Table 3, the average ratio of the final bond transfer length  $s_0^*$  to the initial value after first cracking  $s_0$  is 1.33, so the final bond transfer length for long time calculations may be expressed as eq (11) :

$$s_0^* = 1.3 s_0 \quad (11)$$

From the test results, the extent to which shrinkage cracking can be controlled depends on limiting the desired crack width and the amount and distribution of bonded reinforcement across the crack.

The final crack width, crack spacing and steel stress at crack, are dependent on the steel area (or more precisely, the reinforcement ratio ( $\rho = A_{st}/A_c$ )). An increase in the steel area reduces the final crack width and with more cracks developing, reduces crack spacing. Details of crack width and spacing will be presented in another paper.

With an increase in the steel area, the loss of stiffness at first cracking reduces and, therefore the restraining force after cracking is greater, but stress in the steel decreases at each crack. With a larger restraining force, the stress in the concrete away from a crack tends to be higher and consequently further cracking is more likely

## 5. Conclusions

Despite world-wide research on cracking behavior of RC members, there are limited documents in bond transfer length study especially under sustained loading and long-term monitoring of tension stiffening under pure tension. Experimental study on fully restrained slabs presented in this paper, illustrate that due to the random nature of cracking, great accuracy in calculating the crack width and crack spacing is not achievable. Notwithstanding this, the measured widths of shrinkage cracks, and the steel and concrete stresses determined from the test data, agree well with the results from the analytical models in literature.

Experimental results also indicate that shrinkage causes deterioration in bond at the concrete steel interface. There is a gradual increase in the bond transfer length  $s_0$ , with time. The final value for  $s_0$  after all shrinkage has occurred is 1.33 times the initial value after first cracking.

## References

- [1] Wenkenbach I, Tension stiffening in reinforced concrete members with large diameter reinforcement, M.Sc. University of Durham (United Kingdom), 2011
- [2] Kaklauskas G., Gribniak V., Eliminating shrinkage effect from moment curvature and tension stiffening relationships of reinforced concrete members, *Structural engineering*, Vol. 137, No. 12, pp:1460–1469, 2011
- [3] Torres L., Almansa F.L., Bozzo L.M., Tension-Stiffening Model for Cracked Flexural Concrete Members, *Structural engineering*, Vol.130, No.8, pp:1242-1251, 2004
- [4] Massicotte B., Elwi A, McGregor J.G., Tension-Stiffening Model for Planar Reinforced Concrete Members, *Structural engineering*, Vol. 116, No. 11, pp:3039-3058, 1990
- [5] Behfarnia K, The effect of tension stiffening on the behaviour of RC beams, *Asian Journal of civil engineering* (Building and housing), Vol. 10, No. 3, pp:243-255, 2009
- [6] Wu H.Q., Gilbert R.I., Modelling short-term tension stiffening in reinforced concrete prisms using a continuum-based finite element model. *Engineering structures*, Vol. 31 No.10, pp:2380-239, 12009
- [7] Mihai P, H, Ioan, Rosca B., Numerical analysis of bonding between concrete and reinforcement using the finite element method, *Journal of applied sciences* (Faisalabad), Vol. 10, No. 9, pp:738-744, 2010
- [8] Bizindavyi L., Neale K. W., Transfer lengths and bond strengths for composites bonded to concrete. *Journal of composites for construction*, Vol. 3, No. 4, pp:153–160, 1999
- [9] Beeby A.W., Scott R.H., Cracking and deformation of axially reinforced members subjected to pure tension. In *Magazine of Concrete Research*, Vol. 57, pp:611-621, 2005
- [10] Gilbert R.I., Closure of "Tension Stiffening in Lightly Reinforced Concrete Slabs", *Structural Engineering*, Vol. 134, No. 7, pp:1264-1265, 2008
- [11] Wang H., An analytical study of bond strength associated with splitting of concrete cover, *Engineering structures*, Vol. 31, No. 4, pp:968-975,2009

# Condition assessment of a Johannesburg skyscraper

Willem F. van EDE<sup>a</sup> and Stephen EKOLU<sup>b</sup>

<sup>a</sup>*SMEC South Africa*

<sup>b</sup>*Department of Civil Engineering Science, University of Johannesburg, South Africa*

**Abstract.** This paper presents a condition assessment conducted on a Johannesburg skyscraper. It had become apparent that concrete spalling occurred in areas of the top 11m of the Southern and Western facades of the reinforced concrete skyscraper constructed in the 1970's. However, the extent of the problem was unknown. The only information available were two photographs showing spalled concrete and severely corroded reinforcement bars. Some literature search pertaining to the structure was conducted after which, visual inspection and mapping of spalled areas and cracks were conducted. This was followed by a cover meter survey, a half-cell potential survey, and the removal of 20 (twenty) cores for laboratory testing. It was found that the typical problems associated with carbonation and insufficient cover resulted in the corrosion of reinforcement which then led to the spalling observed.

**Keywords.** Reinforced concrete, spalling, carbonation, cover, site supervision

## Introduction

This paper illustrates the significance, methods and processes of conducting assessments in order to diagnose deterioration mechanisms in ageing infrastructure. Ageing of any structure leads to the need for repair and maintenance that has to be conducted with the intent to prolong the structure's lifetime. Concrete structures typically undergo numerous processes that lead to its deterioration, right from early age defaults to gradually developing physical or chemical attack processes. Corrosion of steel is the most widespread form of deterioration in reinforced concrete (RC) structures. Two attack processes, consisting of chloride attack and carbonation are responsible for steel corrosion in RC structures. The sources of chlorides may be external such as sea water, de-icer salts, salty groundwater and soils. Internal sources of chlorides may include chemical admixtures or construction materials, especially aggregates. Carbonation on the other hand arises from the ingress of atmospheric carbon dioxide into concrete. In both cases (of chloride attack and carbonation,) protection to steel reinforcement is provided by the concrete cover which normally has a high pH of about 12.5, as in the rest of the concrete material mass. At such a high pH, steel forms a protective passive film at its surface but once chlorides or carbon dioxide penetrates through the full cover depth to the level of steel, the alkalinity of concrete decreases, the protective passive film breaks down and steel corrosion ensues [1-2].

<sup>1</sup>Corresponding author: [Willem.vanEde@smec.com](mailto:Willem.vanEde@smec.com)

As the infrastructure which is essential for conduct of economic activities continues to be amassed worldwide, attention will in future shift more towards repair and maintenance of existing structures rather than new construction. However, prior to conduct of any meaningful repair actions, it is essential that the damage or active deterioration process(es) occurring in the structure is/are properly diagnosed through condition or structural assessment methods. The assessment usually involves insitu non-destructive testing (NDT) along with limited physical laboratory testing or analyses done on core or dust samples [1-3]. This paper is limited to a case study involving the use of various methods of condition assessment including visual inspection, insitu strength grade determination, ultrasonic pulse velocity (UPV), covermeter survey, half-cell potential, core testing and optical microscopy.

## 1. Background

The multi-storey reinforced concrete skyscraper in Johannesburg, estimated to have been constructed in the 1970's, is a multi-functional structure used for office and residential purposes, and a shopping precinct within the inner city. The owner was concerned of the severe concrete spalling that had occurred mainly at the south and west facades, causing speculation that chemical attack on concrete may have risen as a result of windblown dust from nearby mine dumps. Accordingly, engineering expertise was called upon to examine the condition of the structure and suggest the required repair and/or rehabilitation options. In the investigation, emphasis was placed on determining the structural integrity and material characteristics of the in-situ concrete. The engineering team then conducted the following assessments

- A condition survey entailing on-site inspection
- Laboratory testing and optical microscopy

Some past literature indicated that concrete mixes tested and used throughout the structure had compressive strengths of 40 MPa at 28 days, which at the time of construction, was considered to be high-strength concrete. The mixtures consisted of 37.5 mm Juskei granite stone and rod-milled reef quartzite sand of standard grading. However, no information was available regarding the cover to steel reinforcement, sizes of the structural members and steel reinforcement bars used in design or construction. The outer façade finishing consisted of sandblasted, exposed aggregate surface. The sandblasting operation was conducted in the early ages of insitu concrete placement. The main issues of concern that were identified for conduct of the investigation were:

- (a) Presence of severe cracking and exposed corroded steel bars on the outer surfaces of building walls
- (b) Uncertainty over the active deterioration processes, given the 40-year age of the structure
- (c) Potential environmental effects arising from extensive presence of previous and/or existing gold mining activities, to the South-West of the structure
- (d) Unknowns regarding the type of aggregates used. Some of the aggregates in Johannesburg are reactive and could cause alkali-silica reaction attack. This

phenomenon and its implications may not have been known during the time of construction of the structure.

The insitu investigation was therefore conducted to determine the cover to steel reinforcement, establish the condition and integrity of the existing structure. Considering the complexity of gaining access to conduct measurements, it was quite difficult to do several field measurements except those tests that were considered to be most essential, which included the cover to steel reinforcement and the half-cell potential measurements. Some rebound hammer measurements were also done.

In the laboratory investigation, different assessment methods were used to conduct the tests based on cores drilled from all four walls of the building. Firstly, the depth of carbonation that occurred over the past service life of the structure was measured along with compressive strengths, rebound hammer readings, and UPV. The UPV technique is a versatile method capable of establishing concrete characteristics to determine the soundness of concrete quality; it enables accurate estimation of elastic modulus, strength and crack depth. Excellent concrete quality typically gives a propagation speed of 4000 to 4800 m/s. A velocity of 3000 to 3500 m/s is satisfactory while < 3000 m/s indicates poor quality and lack of integrity.

## 2. Survey and field tests

### 2.1. Photographic survey and crack mapping

Photographic surveys, mapping of cracks wider than 0.3mm and mapping of areas of spalling were conducted. The surveys provided strong evidence that the problems were localized. **Photo 1** to **Photo 3** shows some of the problematic areas.



### 2.2. Extraction of cores

A total of 5 (five) cylindrical cores, from preselected locations, were extracted from each of the four facades. These 100mmdiameter cores of approximately 200mm length were sent for laboratory testing. **Photo 4** shows the coring process while **Photo 5** and **Photo 6** show some of the core samples.



2.3. Cover meter survey

The survey was conducted by scanning the facade with a cover meter instrument. A grid system was used to position the recordings and map the results. Vertical gridlines were spaced at 2m intervals and the horizontal construction joints were used as the horizontal gridlines. **Photo 7** shows a technician carrying out the cover meter survey.

The lowest cover reading for each block was recorded, thereby giving conservative measurements. The survey was able to identify areas that would require repair and maintenance in the short to medium term. The results of the South facade cover survey, which contained by far the most area of low cover, is shown in **Figure 1**.

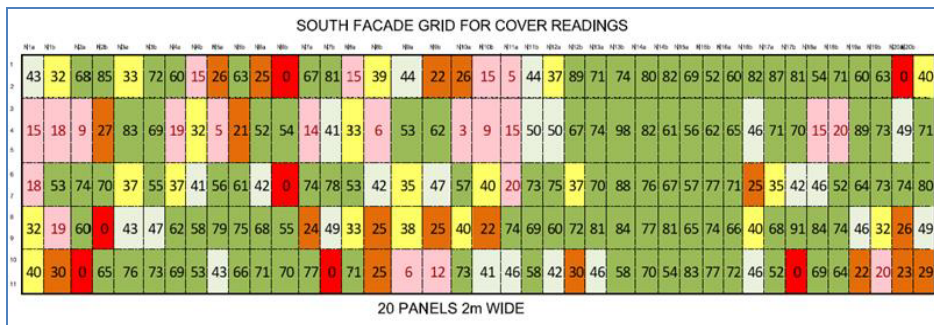
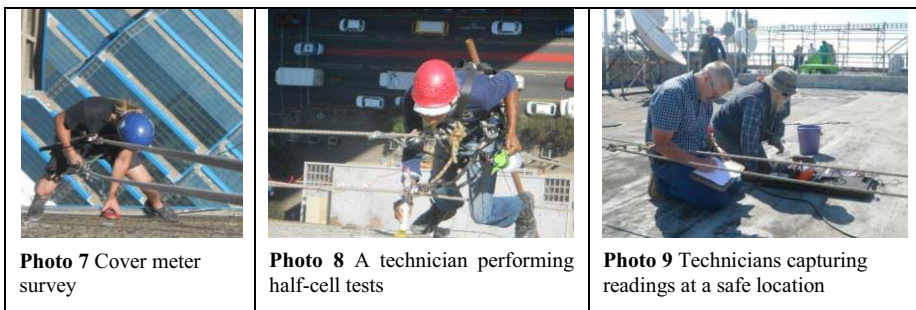


Figure 1. Minimum cover meter readings taken on the South Facade

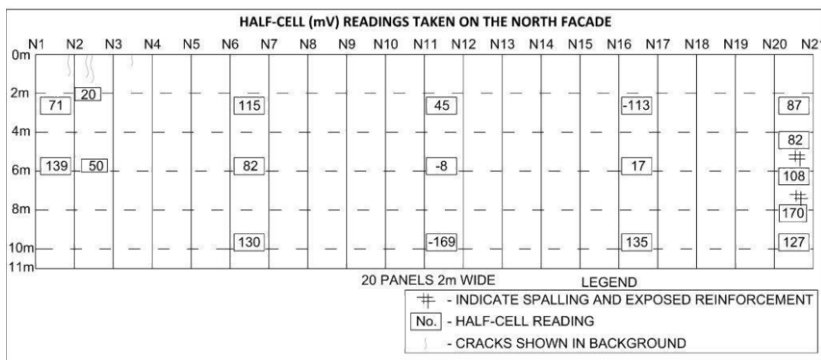
2.4. Half-cell potential tests

Half-cell potential measurements were conducted to assess the likely presence of corrosion activity, whether hidden or visible. Typically, readings of less than -350mV imply a 95% probability of corrosion occurring, whilst readings higher than -200 mV suggest less than 5% probability of any presence of corrosion[1-3]. Half-cell readings that were obtained, varied between -170mV to +180mV. The results indicated that no corrosion activity was occurring at the locations where measurements were taken[4]. **Photo 8** shows a technician performing the half-cell tests while the data was being captured at a safe location, as in **Photo 9**.





Half-cell readings were taken at random locations and also near cracks. **Figure 2** indicates the locations and readings of half-cell measurements taken on the South facade.



**Figure 2.** Half-cell potential measurements taken on the South facade

### 3. Laboratory tests

Several tests were conducted on the 20 core samples extracted from the building facades, as subsequently discussed.

#### 3.1. Core compressive strength and quality tests

A minimum of three cores per facade were used for concrete tests consisting of density, compressive strength, Ultrasonic Pulse Velocity, and rebound hammer. The tests were conducted in accordance with BS 1881:Part 203 and EN 13791[5-7].

The density of the concrete was determined to be 2384 kg/m<sup>3</sup>, which is typical of normal concretes. The insitu strength results were in the range of 35 to 44 MPa, averaging 38 MPa i.e approximately 40 MPa. The results obtained were in agreement with the literature information indicating that concrete mixtures of 40 MPa strength were used.

Ultrasonic Pulse Velocity measurements conducted on visually assessed defect-free cores gave velocity readings ranging from 4500 to 5000 m/s, which would indicate excellent quality characteristics[1].

### 3.2. Carbonation attack

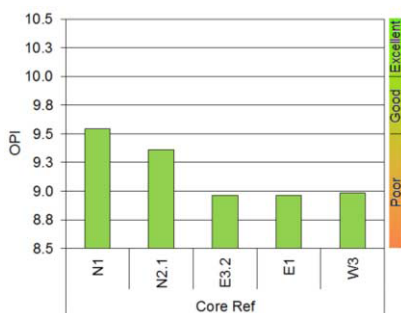
The depth of the carbonation front was determined on cores samples selected from each of the four façades. Carbonated concrete has a significantly lower pH than non-carbonated concrete. The samples were sprayed with phenolphthalein indicator solution. The carbonated concrete retained its natural colour while the non-carbonated concrete turned purple. The carbonation front was then measured and found to vary from 13mm to 24mm with an average of 19.3mm. Note that due to the rough exposed aggregate finish and the presence of stone aggregates inside the concrete, significant variability in the carbonation front measurements would be expected.

### 3.3. Concrete analysis for chlorides

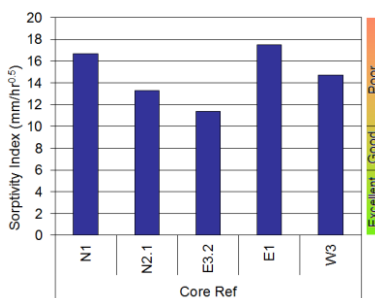
Dust samples, obtained from the core samples, were analysed for chloride concentrations. The total chloride contents were determined in accordance with the ASTM C1152 test method [8]. The chloride contents were found to be between 50 and 170 ppm, well below the 500ppm threshold beyond which chloride corrosion attack would normally occur [4].

### 3.4. Durability tests

Six core samples were selected for durability tests. Two durability index tests were conducted on the core samples namely, oxygen permeability and sorptivity tests [9]. The objective of conducting these tests was to obtain an indication of the potential performance of the concrete under mild exposure environment. The tests revealed generally poor durability performance, as shown in **Figures 3** and **4**. This was not surprising as the desk study revealed that no extenders were used in the concrete mix design[4]. However, the results should be examined in the context of the construction period of the 1970s when current understanding of the influence of extenders in concrete was not yet fully developed. Modern concrete technology usually requires the use of extenders in order to achieve good durability performance.



**Figure 3.** Oxygen permeability test results

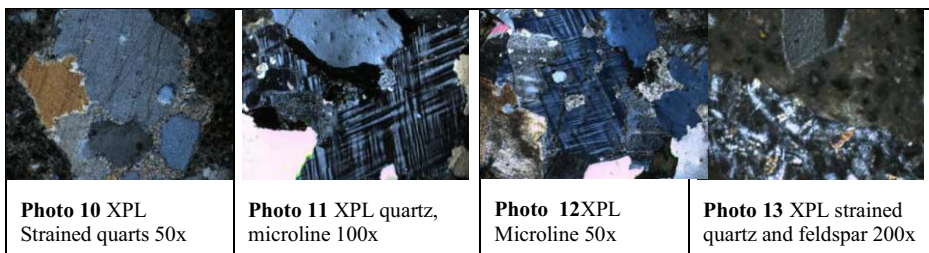


**Figure 4.** Sorptivity test results

### 3.5. Optical microscopy

The site photos gave no indication of possible alkali-aggregate reaction or sulphate attack. The desk study revealed that the stone aggregate were Jukskei granite from a quarry near Halfway House Midrand; Granite aggregate is typically non-reactive. The sand used was Rodmilled Reef Quartzite but no information could be found on the reactivity of the reef quartzite. The investigation team found no reason to suspect that the sand used could be reactive. Optical microscopy was however conducted to establish the potential for alkali-aggregate reaction. Any presence of sulphate attack would also be detected by microscopy [4].

Detailed examination of the concrete was done using thin section optical microscopy. Thin sections were prepared from different concrete cores and cut longitudinally in a direction parallel to core axis. Microscopic examination showed the aggregates to be predominantly quartz, microcline, feldspars and some opaque particles as shown in micrographs of **Photo 10** to **Photo 13**.



Strained particles such as seen in **Photo 10** and **Photo 13** may sometimes be associated with alkali aggregate reaction[4]. However, there was no evidence of any reactive phase(s) such as microcrystalline quartz commonly found in reactive aggregates in South Africa.

## 4. Conclusion

Site survey determined that the spalling was localized, in areas of very low cover. Carbonation attack was the mechanism identified to have caused corrosion of the reinforcement, which then resulted in spalling. In the 40 MPa concrete, carbonation had progressed to about 19.4 mm over the 40 years of the structure's lifetime. However, the cover in the façade varied significantly to the extent that the very low cover areas were severely affected by corrosion.

The concrete was intrinsically of excellent quality yet its durability characteristics were generally poor when evaluated based on durability indexes. This poor index performance is attributed to absence of extenders, whose use in concrete was not an established technology in the 1970's. No indication of chemical deterioration attack mechanism was found.

## References

- [1] J.H. Bungey and S.G. Millard, *Testing of concrete in structures*, Blackie Academic & Professional, Glasgow, 1996.
- [2] N. Delatte (Eds), *Failure, Distress and Repair of Concrete Structures*, CRC Press, 2009.
- [3] V.M. Malhotra and N.J. Carino, *Handbook on Nondestructive testing of concrete*, CRC Press, Boca Raton, London, New York, Washington, 2004.
- [4] S.O. Ekolu, Condition Assessment of Insitu Reinforced Concrete, A Technical Report submitted to SMEC Group, Johannesburg, 2012.
- [5] BSI, British Standards Institute, *Testing of Concrete Part 120: Method for determination of the compressive strength of concrete cores*, BS 1881:Part 120, 1983.
- [6] BSI, British Standards Institute, *Testing of Concrete Part 202: Method for determination of the compressive strength of concrete cores*, BS 1881:Part 202, 1986
- [7] BSI, British Standards Institute, *Assessment of in-situ compressive strength in structures and pre-cast concrete components*, BS EN 13791:2007
- [8] ASTM C1152, ASTM International, *Standard Test Method for Acid-Soluble Chloride in Mortar and Concrete*, 2006
- [9] M.G Alexander, Y. Ballim, and J.M. Mackechnie, Concrete durability index testing manual, Research Monograph No.4, Departments of Civil Engineering University of Cape Town and University of the Witwatersrand, March 1999.

# Understanding the influence of marine microclimates on the durability performance of RC structures

Olukayode O. ALAO<sup>1</sup>, Mark ALEXANDER and Hans BEUSHAUSEN  
*Department of Civil Engineering, University of Cape Town, South Africa*

**Abstract.** Innovative research in the use of concrete has made it one of the most commonly used materials in the construction industry globally, with about 25 billion tons consumed annually. The durability of concrete is strongly dependent on the interactions of its constituent materials with the environment, and determines its performance during the service life. Reinforced concrete (RC) structures in marine environments are subjected to chloride-laden exposure conditions which affect their durability. This paper reports on an investigative study that seeks to understand the influence of climatic conditions such as temperature, relative humidity, precipitation and wind speed etc. on the exposure of RC structures to airborne chloride deposition and ingress. The focus of the study is the marine environment of the Cape Peninsula in South Africa. The study showed that the durability of a RC structure is location-specific, and the microclimate of the location influences the severity of exposure.

**Keywords.** Durability performance, marine environment, reinforced concrete

## Introduction

Reinforced concrete (RC) structures are subjected to continuous ageing during their service life, and depending on the severity of environment or the deterioration mechanisms to which they are subjected, repair or rehabilitation of RC structures in many cases becomes necessary. Statistical data on the quantity of additional raw materials consumed during infrastructure repair is difficult to source; however, economically about R 11.8 billion is required annually in South Africa for the repair and maintenance of 8 246 bridges and culverts [1]. In 2013, this expenditure on repair and maintenance was about 3.8 % of the South African annual budget [2].

Most of the deterioration mechanisms from which RC structures suffer stem from their interaction with the service environment. For this reason, it is important to understand the influence of the environment (climate conditions) on catalysing and/or repressing the effects of the deterioration mechanism(s) on the RC structure.

## 1. Durability of Reinforced Concrete Structures

The durability of a RC structure is closely related to the structure's performance during its service life [3].

---

<sup>1</sup>Corresponding author: [alxolu001@myuct.ac.za](mailto:alxolu001@myuct.ac.za)

A simplistic definition of service life with the main focus on chloride-induced corrosion ‘...is the period of initiation or the time required for the chloride concentration at the reinforcement to reach the critical chloride level’ [4]. The durability of materials and structures is dependent mainly on the resistance of the material to the ingress of aggressive substances, and on the prevailing environmental conditions at the exposed surfaces of the [5]. This paper presents an investigative study on the influences of climatic elements such as wind, precipitation, temperature change and RH on the severity of exposure of RC structures to airborne chlorides in the marine environment and how these affect their durability performance.

## 2. Marine environmental characterization

### 2.1. Marine exposure zone classification

RC structures are subjected to a variety of exposure conditions in their service environments, which affects their durability. Examples of such service environments include marine, industrial and other severe environments. RC structures in the marine zone are categorised according to SANS as shown in Table 1.

**Table 1.** Classification of marine exposure categories for South Africa (SANS 10100-2, 2009) [6], compared with EN 206 categories

Marine exposure category	Description of exposure	Nearest matching exposure classes from EN 206-1
<i>Moderate</i>	<ul style="list-style-type: none"> <li>Surfaces protected by a waterproof cover or permanent formwork not likely to be subjected to weathering or corrosion</li> <li>Enclosed surfaces</li> <li>Structures or members permanently submerged</li> </ul>	XS 2: Permanently submerged Part of marine structure
<i>Severe</i>	<ul style="list-style-type: none"> <li>All exposed surfaces</li> <li>Surfaces on which condensation takes place</li> <li>Surfaces in contact with soil</li> <li>Surfaces permanently under running water</li> <li>Surfaces protected by permanent formwork not likely to be subjected to weathering or corrosion</li> </ul>	XS 1: Exposed to airborne salt but not in direct contact with sea water
<i>Very severe</i>	<ul style="list-style-type: none"> <li>All exposed surfaces of structures within 30 km from the sea</li> <li>Surfaces in rivers polluted by industries</li> <li>Cast in situ piles, wet-cast against casings</li> </ul>	XS 1: Exposed to airborne salt but not in direct contact with sea water XS 3: Tidal, splash and spray zones.
<i>Extreme</i>	<ul style="list-style-type: none"> <li>Surfaces in contact with sea water of industrially polluted water</li> <li>Surfaces in contact with marshy conditions</li> </ul>	XS 3: Tidal, splash and spray zones.

The service environment is a major factor to be considered when designing RC structures. It is important as the durability of a concrete structure is location-specific; in any particular location a structure can be durable, but in differing exposure conditions, the rate of deterioration for the same structure might vary. For this reason, it is essential

to assess the severity of exposure at each specific site, whether inland or in a coastal region, by determining the microclimatic conditions [7].

RC structures located along the coastline, which are exposed to airborne chlorides generated from the sea, are prone to a greater degree of corrosion than most inland structures [8–10]. This study focuses on a local marine environment: Cape Town (more generally the Cape Peninsula), located in the Western Cape Province of South Africa. The Cape Peninsula experiences a wet-cool winter and dry, summer, Mediterranean-type climate [11].

## *2.2. Airborne chloride transportation in marine environment*

Generally, the atmosphere in marine environments is salt-laden, generated from breaking wave action of seawater. The major source of atmospheric chlorides is marine aerosol, which is present in high proportions in coastal regions. The atmospheric chloride ions make up a significant part of the marine aerosol, and they are transported inland by the effects of environmental actions such as wind, precipitation, temperature and relative humidity [12–13]. The deposition of these chloride particles depends on their size and radius. Studies of the transport of aerosols inland have shown that the larger particles (which are  $>10\mu\text{m}$  in diameter) are typically deposited close to the shoreline (typically 400–600m), while finer particles travel further inland [14]. This implies that regions closer to the coast have a higher probability to be affected by corrosion inducing effects of chlorides.

### *2.2.1. Precipitation*

Precipitation may have a beneficial effect in washing away corrosive agents that have settled on exposed concrete surfaces, particularly in marine environments. However, if the rain collects in cracks or depressions on the surface of the concrete, it may accelerate corrosion by supplying continued wetness. Dew and condensation are undesirable from a corrosion viewpoint if not accompanied by frequent rain washing (wash effect) which dilutes or eliminates contamination [14]. A film of dew, saturated with sea salt or acid sulphates, and airborne chlorides provides an aggressive solution for the transportation of these species and the propagation of corrosion.

A broad view on the rainfall pattern for the Cape Peninsula indicates a moderately-high rainfall pattern during winter and a low rainfall in summer. It can be expected that concrete structures will remain wetted for a long period of time due to the high number of rain days during winter. During summer the number of rainy days is fewer and therefore the time that concrete structures are drier. Therefore it can be expected that during the cool wet months, chloride ingress will most likely be enhanced.

### *2.2.2. Wind*

Oceanic air is rich in marine aerosols resulting from the evaporation of drops of sea water, mechanically transported by the wind [15]. During winter, a north-westerly wind is experienced across the Cape Peninsula. The summer period on the other hand, experiences strong southerly and south-easterly winds over a longer period of time in comparison with winter winds [11]. Certain areas of the Cape, such as parts of the Southern Suburbs, are considered relatively windless [11]. The wind speed experienced around the Cape Peninsula is relatively high due to the exposure of the Peninsula to the

ocean winds, which transport sea spray on-shore and cause higher concentrations of chlorides in the atmospheres of the exposure zones that are bordered by the sea.

The seasonal differences in prevailing wind directions and speeds implies seasonal differences of RC exposure to airborne chloride deposition. During the high wind speed periods in summer, the generation of airborne chlorides will be expected to be high because larger waves develop on the sea. These larger waves break to form white foam which is rich in salt. But factors that could influence the distance which the airborne chloride travels include surface roughness such as the presence of vegetation and urban infrastructure.

### *2.2.3. Temperature*

Temperature also plays an important role in the corrosive severity of an environment [16]. There is an expected doubling in corrosion activity for every 10 °C rise in temperature [14], a phenomenon noted by [17-18]. Temperature also influences the relative humidity and affects the atmospheric residence time for airborne sea salts. The residence time of an airborne chloride particle in the atmosphere is the period of time between its generation from the breaking of an ocean wave to its deposition onto a surface.

The average annual temperature in the Cape Peninsula typically ranges from 20 – 30 °C, experiencing lower temperatures during the winter season and higher in summer [11]. The implication of lower temperatures in winter, is that it tends to be more corrosion prone for embedded reinforcement, as it provides enough moisture saturation duration for RC structures exposed to airborne chloride attack.

### *2.2.4. Relative humidity (RH)*

The RH of a location is dependent on the moisture content of the atmosphere and this is influenced by precipitation and temperature. At low environmental temperatures, the surrounding air is more saturated with moisture and hence a higher RH is measured. A study carried out in an environment with high RH indicated that higher airborne chloride concentrations were measured inland [9], as a result of the moisture present in the atmosphere giving the aerosol particles longer residence time. Marine environments typically have higher RH, as well as aerosols high in salt concentrations [14]. It was observed that at RH of 85-90 % corrosion activities in a concrete structure decreased and hence the rate of deterioration was slowed down [19]. This can be attributed to the blocking of pores at high RH [18]. RH is more important in the first stage of corrosion which is the diffusion of chloride ions through the concrete cover, while the temperature is influential in accelerating the rate of steel corrosion [19].

The average RH for the Cape Town area is 78% [20]. However, the RH for the Cape Peninsula is higher in winter than in summer. Hence, there is substantially more moisture in the atmosphere to improve the residence time of airborne chlorides in winter over the summer seasons.

## **3. A proposed marine environment characterization method for improved concrete durability performance**

The major shortcoming of the current marine exposure classifications in the SANS 10100-2 and EN 206-1:2013 is its generalist approach. As was previously shown in



Table 1, the standards do not give due consideration to the influence of climatic conditions on the severity of the deterioration mechanism(s). Therefore, there is a need to carry out location-specific studies to characterize the severity of the marine environment.

RC structures exposed to airborne chlorides are identified to be at a distance of 30 km from the coast in the current SANS RC design code [6]. This study analyzed the microclimate and estimated the concentration of airborne chlorides in select locations in the Cape Peninsula area, using two methods: the wet candle device, reviewed later, and analysis of data from previous chloride profiling investigations, which was collated for the purpose of categorizing the severity of exposure of RC structures to airborne chloride attack. In these studies, the local climate, with a focus on the dominating wind direction, was also reviewed.

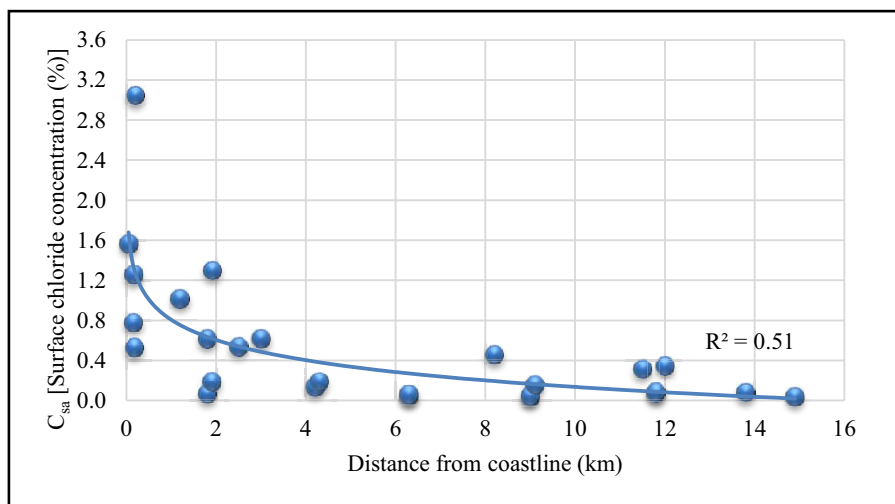
The wet candle device method which is a standardized ASTM method [21] of measurement is relatively simple. This technique uses a wet wick (bandage or gauze wrapped around test tube with loose ends) of a known diameter and surface area to measure aerosol deposition. The wick is maintained wet using a reservoir of water or 40% glycol or distilled (or deionized) water solution. Aerosol particles are trapped by the wet wick and retained. At intervals which need to be chosen carefully, quantitative determination of the chloride collected by the wick is made.

The study of previous forensic investigations on RC structures located in the Cape Peninsula involved a statistical analysis of chloride content datasets. The RC structures assessed included buildings and water reservoirs. These structures are all exposed to airborne chloride attack. A sample size of about 110 such datasets was retrieved for 38 RC structures examined. Representative data for each structure were deduced from either single observations or by accumulating results through averaging of 5 – 15 datasets.

In order to characterize the quality of concrete and the severity of the environment, an investigation of the interrelationship between the ages of structures, cement contents, compressive strengths, and surface chloride contents was carried out. The age of the RC structures examined ranged between 34 – 40 years, with only one structure estimated to be 70 years old. Also, their distances from the coast varied from 50 m to 15 km from the nearest coastline. The estimated cement content was between 280 – 420 kg/m<sup>3</sup> and because of the age of the structures, it was also assumed that pure Portland cement must have been the type of cement used.

Figure 1 illustrates a plot of distance of RC structure from coastline with respect to the measured average surface chloride concentration ( $C_{sa}$ ). From Figure 1, it can be observed that there is a significant reduction in the  $C_{sa}$  of the RC structures as distance increases from 2 – 14 km from the ocean. It must be noted that for the RC structures analysis, no information on exposure to prevailing wind direction and orientation could be retrieved. The  $C_{sa}$  in the RC structure at a distance of 16 km from the coast is almost zero. The logarithmic regression analysis also inferred a correlation of the data with regards to RC exposure severity to airborne chloride attack, where an  $R^2$  value of 0.51 was reported.

The second method involved setting up wet candle stations which were located at distances of 50 m, 150 m, 250 m, 2.7 km and 13.5 km from the nearest shore, in the Cape Town area with due consideration given to the NW or SE prevailing wind direction in the location selection.



**Figure 1.** Average surface chloride content vs distance of the RC structure from the coastline.

The period of exposure was 8 months from December 2013 – July 2014, which allowed for simulating the seasonal changes and their influence on deposition rate. The weather conditions during the period of monitoring were also retrieved from the South African Weather Service (SAWS). The average RH during winter and summer seasons were 75.7 % and 66.7 % respectively. Temperatures in winter averaged at 11 °C while it was much higher in summer at 28 °C. The average wind speed measured during both seasons was between 41.8-47.2 km/h and with a higher precipitation in winter of 107.9 mm with much lesser in summer at 10 mm. The aim of this experimental study was to correlate the generation of airborne chlorides from the sea, their transportation inland, and consequent deposition on RC structures.

Table 2 shows that at the station 2.7 km (2700 m) from the sea, the measured chloride deposited on the candle was only 9 % of the deposition rate of the station at 50 m. During the monitoring period, it was found that the location marked M, experienced a significant decrease in chloride deposition corresponding with the transition from summer to winter and the prevailing wind direction. However, locations labelled GB, PE, MG and B experienced an increased deposition in the winter period.

**Table 2.** Chloride deposition rate per monitored location

LOCATIONS	Granger Bay - GB	Muizenberg - M	Paarden Eiland - PE	Montague Gardens - MG	Bellville - B
Distance (m)	50	150	250	2700	13500
Total chloride deposition rate (mgCl/m <sup>2</sup> .day)	126.69	27.26	30.87	11.23	10.54

Based on site investigations and statistical analysis of previous forensic data for the Cape Peninsula location, Table 3 has been proposed. The severity of the exposure zones based on the measured airborne chloride deposition rates was adapted from the ISO 9223 [22].

**Table 3.** Classification for RC structures exposed to airborne chloride attack in the Cape Peninsula

Deposition rate of chlorides (mgCl/m <sup>2</sup> .day)	Category (ISO)	Airborne chloride exposure zones (ISO)	Distance of RC to nearest coastline (km)
$60 \leq S \leq 300$	S <sub>2</sub>	Severe	0 – 3
$3 \leq S \leq 60$	S <sub>1</sub>	Moderate	3 – 14
$S \leq 3$	S <sub>0</sub>	Insignificant	> 14

Chloride deposition rate in the S<sub>0</sub> category is usually regarded as being insignificant from the corrosion point of view for exposed metals. The airborne salinity in the monitored locations are within the S<sub>1</sub> and S<sub>2</sub> categories. This implies that the airborne chloride exposure severity in the Cape Peninsula ranged from ‘moderate’ to ‘severe’ from the distance of 0 – 13.5 km. In this proposed classification scheme, ‘very severe’ exposure has not been used in categorizing any exposure zone as it has been reserved to refer to RC structures which are in direct contact with seawater only.

#### 4. Conclusion

The Cape Peninsula marine environment is windy, relatively humid, cool and wet in winter, and dry and warm in summer. The main objective of this study was to assess the severity of RC exposure to airborne chloride attack in the Cape Peninsula marine environment. From the data analyzed and discussed in the preceding sections, the following conclusions can be inferred with specific reference to the Cape Peninsula location:

- RC structures more than 14 km distance from the coastline are exposed to minimal or insignificant airborne chloride attack
- The wet candle technique was effective in providing a basis for characterization for concrete structures exposure to deposition of atmospheric chlorides
- The winter season poses the most threat in terms of airborne chloride transportation from the sea as a result of high precipitation and RH and also accelerating the electrochemical process of reinforcement corrosion
- The changes in prevailing wind direction greatly influenced the distances travelled by airborne chlorides and either increased or decreased deposition rates.

Finally, the evaluation of the Cape Peninsula marine environment indicated that there is a limit to the extent of RC exposure to airborne chloride attack. Improper design of RC structures can decrease their service life but with proper evaluation of environmental loading the expected performance of the structure can be designed for.

#### References

- [1] SANRAL, 2013. The South African National Roads Agency SOC Limited - ANNUAL REPORT 2013, Pretoria. Available at: [http://sanral.ensight-cdn.com/content/Sanral\\_Annual\\_Report\\_13\\_LRES.pdf](http://sanral.ensight-cdn.com/content/Sanral_Annual_Report_13_LRES.pdf).
- [2] Statssa, 2014. Gross Domestic Product - Third quarter 2013. Statistical release P0441, 3(February),

- p.75.
- [3] Narasimhan, H. & Chew, M.Y.L., 2009. Integration of durability with structural design: An optimal life cycle cost based design procedure for reinforced concrete structures. *Construction and Building Materials*, 23(2), pp.918–929. Available at: <http://linkinghub.elsevier.com/retrieve/pii/S0950061808001177>
  - [4] Khatri, R. & Sirivivatnanon, V., 2004. Characteristic service life for concrete exposed to marine environments. *Cement and Concrete Research*, 34(5), pp.745–752. Available at: <http://linkinghub.elsevier.com/retrieve/pii/S0008884603000863>
  - [5] Alexander, M. & Mackechnie, J., 2003. Concrete Mixes for Durability in Marine Environment.pdf. *Journal of the South African Institution of Civil Engineering*, 45(2), pp.20–25.
  - [6] South African National Standards. SANS 10100-2: The structural use of concrete Part 2 : Materials and execution of work. Pretoria, South Africa: SANS; 2009.
  - [7] Wilmot, R., 2006. Corrosion protection of reinforcement for concrete structures. *The Journal of The Southern African Institute of Mining and Metallurgy*, 107(MARCH), pp.139–146.
  - [8] Anwar Hossain, K.M., Easa, S.M. & Lachemi, M., 2009. Evaluation of the effect of marine salts on urban built infrastructure. *Building and Environment*, 44(4), pp.713–722. Available at: <http://linkinghub.elsevier.com/retrieve/pii/S0360132308001303>
  - [9] Meira, G., Andrade, C., Alonso, C., Borba, J., Padilha, M., 2010. Durability of concrete structures in marine atmosphere zones – The use of chloride deposition rate on the wet candle as an environmental indicator. *Cement and Concrete Composites*, 32(6), pp.427–435. Available at: <http://linkinghub.elsevier.com/retrieve/pii/S0958946510000399>
  - [10] Hossain, K.M.A. & Easa, S.M., 2011. Spatial distribution of marine salts in coastal region. *International Journal of Research and Reviews in Applied Sciences*, 7(3), pp.228–235.
  - [11] Cowling, R., Macdonald, I. & Simmons, M., 1996. The Cape Peninsula, South Africa: physiographical, biological and historical background to an extraordinary hot-spot of biodiversity. *Biodiversity and Conservation*, Volume 5, pp. 527-550.
  - [12] Meira, G., Andrade, C., Alonso, C., Padaratz, I., Borba Jr, J., 2007. Salinity of marine aerosols in a Brazilian coastal area—Influence of wind regime. *Atmospheric Environment*, 41(38), pp.8431–8441. Available at: <http://linkinghub.elsevier.com/retrieve/pii/S1352231007006176>
  - [13] Gao, Y., Chen, S.B. & Yu, L.E., 2007. Efflorescence relative humidity of airborne sodium chloride particles: A theoretical investigation. *Atmospheric Environment*, 41(9), pp.2019–2023. Available at: <http://linkinghub.elsevier.com/retrieve/pii/S1352231006012714>
  - [14] Roberge, P.R., 2011. *Atmospheric corrosion*. In W. R. Revie, ed. Uhlig's Corrosion Handbook. John Wiley & Sons, Ltd, pp. 299 – 326. Available at: <http://onlinelibrary.wiley.com/doi/10.1002/9783527610426.bard040301/full>
  - [15] Blanchard, D.C. & Woodcock, A.H., 1980. *The production, concentration, and vertical distribution of the sea-salt aerosol\**. *Annals of the New York Academy of Sciences*, 338(1), pp.330–347. Available at: <http://dx.doi.org/10.1111/j.1749-6632.1980.tb17130.x>.
  - [16] Bertolini, L., Elsener, B. & Pedferri, P., 2013. *Corrosion of steel in concrete: prevention, diagnosis, repair*. 2nd ed., Weinheim, Germany: Wiley-VCH.
  - [17] Lindvall, A., 2007. Chloride ingress data from field and laboratory exposure – Influence of salinity and temperature. *Cement and Concrete Composites*, 29(2), pp.88–93. Available at: <http://linkinghub.elsevier.com/retrieve/pii/S0958946506001636>
  - [18] Alhozaimy, A., Hussain, R., Al-Zaid, R., Al-Negheimish, A., 2012. Coupled effect of ambient high relative humidity and varying temperature marine environment on corrosion of reinforced concrete. *Construction and Building Materials*, 28(1), pp.670–679. Available at: <http://linkinghub.elsevier.com/retrieve/pii/S0950061811005575>
  - [19] El Hassan, J., Bressolette, P., Chateau-neuf, A., El Tawil, K., 2010. Reliability-based assessment of the effect of climatic conditions on the corrosion of RC structures subject to chloride ingress. *Engineering Structures*, 32(10), pp.3279–3287. Available at: <http://linkinghub.elsevier.com/retrieve/pii/S0141029610002579>
  - [20] Alexander, M. & Beushausen, H., 2009. Deformation and volume change of hardened concrete. In G. Owens, ed. *Fulton's Concrete Technology*. Midrand, South Africa: *Cement and Concrete Institute*, pp. 111-154.
  - [21] American Society for Testing and Materials. ASTM G-140: Standard test method for determining atmospheric chloride deposition rate by wet candle method. Annual book of ASTM standards. Philadelphia (USA): ASTM; 2008
  - [22] International Organization for Standardization. 1992. Corrosion of metals and alloys - Corrosivity of atmospheres – Classification. (ISO 9223:1992). Geneva, Switzerland: International Organization for Standardization.

# Concrete filled double skin circular tubes: a review

Yoosuf ESSOPJEE and Morgan DUNDU<sup>1</sup>

*Department of Civil Engineering Science, University of Johannesburg, South Africa*

**Abstract.** A review of the research conducted on the compressive strength of concrete filled double skin circular tubes (CFDSCT) columns is conducted. Variables of the CFDSCT considered in this review include the concrete strength, steel strength, inner and outer tube diameter, steel thickness and length of the stub columns. Test results show that the composite columns had compressive strengths of up to 41% higher than the sum of the individual strengths of the section. All the outer tubes of these composite columns by failed local buckling. A review of the design equations proposed are presented and discussed. The paper also identifies gaps for further research for these types of columns.

**Keywords.** Concrete-filled tube, stub columns, local buckling, double skin, axial compression, CFDSCT, confinement effect.

## Introduction

In multi-storey buildings architects may detail downpipes or other services like electrical wiring in the centre of columns. This is done for aesthetic reasons. One way of achieving this is to use concrete filled double skin tubes (CFDSTs). Concrete filled double skin tubes (CFDSTs) are structural members that have a double steel skin with concrete sandwiched between the two steel tubes. These structural elements range from concrete filled double skin rectangular tubes (CFDSRTs), concrete filled double skin circular tubes (CFDSCTs) to concrete filled double skin square-circular tubes (CFDSSCTs), as shown in Figure 1.

These members are economical and quicker to construct when compared to conventional concrete reinforced columns because the steel tube serves as form-work. The concrete fill prevents the outer steel tube from buckling inwards whilst the steel prevents the concrete from deforming laterally, under compressive loads. CFDST columns have structural benefits similar to concrete filled tube (CFT) columns, however, CFDST are lighter, stronger and possesses better energy absorption when compared to CFT columns [1, 2].

Zhao and Han [2] have listed research work done in this field and Elchalakani et al. [1] have conducted research on stub CFSCT columns with a square hollow inner tubes and circular hollow outer tubes. The slenderness ratios of the stub columns tested by Elchalakani et al. [1] ranged from 35 to 90. It was found from this investigation that a simple arithmetic addition of the strengths of the steel tubes and concrete predicted the

---

<sup>1</sup>Corresponding author: University of Johannesburg, Department of Civil Engineering, P.O. Box 524, Auckland Park, 2006, South Africa; E-mail: [mdundu@uj.ac.za](mailto:mdundu@uj.ac.za)

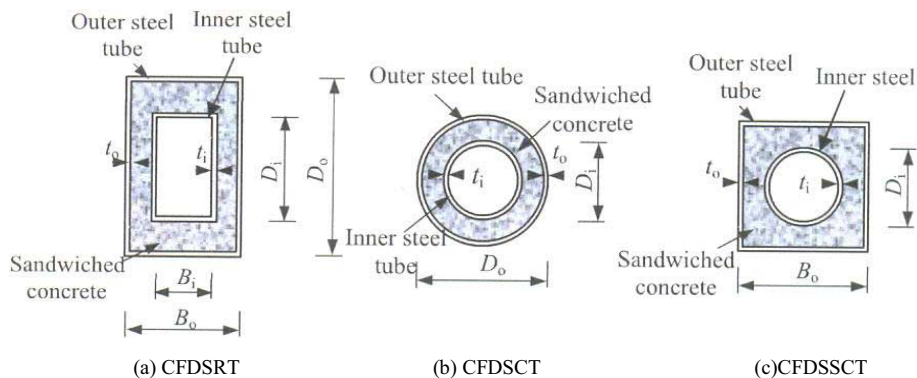


Figure 1. Cross section of CFDSTs

test results well. Yang et al. [4] conducted research on CFDST with an octagonal outer tube and a circular inner tube. From the results of this experiment, it was found that the axial capacity of the proposed CFDST columns was larger than CFDSTs with a square outer tube and a circular inner tube and smaller than CFDSTs with a circular outer tube and a circular inner tube. The CFDST's were modelled numerically and the results obtained agreed well with the proposed simple formula. This aim of this paper is to review CFDSCT only.

## 1. Literature review

### 1.1. Tested specimen

Tao et al. [4] conducted 12 tests on CFDSCT stub columns. The lengths of the stub columns varied from 342 and 900 mm. Two concrete filled circular tube (CFCT) columns were also tested in order to compare the results against the CFDST results. The concrete cube strength was 47 MPa at the time of the test and the yield strength of the steel inner tube ( $f_{yi}$ ) varied from 295 to 396 MPa, while that of the outer tube ( $f_{yo}$ ) was either 276 or 295 MPa. As given in Table 1 the outside tube diameters ( $D_o$ ) were 114, 180, 240 and 300 mm and the inside tube diameters ( $D_i$ ) were 48, 58, 88, 114, 140 and 165 mm.

Uenaka et al. [5] tested 12 stub columns in total. Nine out of the twelve samples were CFDSCT stub columns and the remainder were CFT columns. The concrete strength was 23 MPa. Outer tubes had an average dimension of 158 mm while the average dimensions of the inner tubes were 39, 77 and 114 mm. The inner and outer steel tubes' strengths ranged from 221 to 308 MPa and each stub column was 450 mm in length.

Wei et al. [6] conducted tests on CFDSCT with outer tube diameters ranging from 74.7 to 114.3 mm and inner tube diameters ranging from 61.2 to 88.9mm. The diameter-to-thickness ratio of the outer tubes varied from 43 to 169. Aggregates made up 86% of the polymer concrete in terms of its weight and the remaining 14% was polymer resin. The polymer concrete strength achieved was 75 MPa. As shown in Table 3, the yield strengths of the inner tubes and outer tubes ranged from 216 to 512 MPa and 255 to 524 MPa, respectively. All the stub columns were machined to have a length of 230 mm.

### 1.2. Failure modes

Uenaka et al. [5], Tao et al. [4] and Wei et al. [6], all found that the mode of failure of the outer tube was outward local buckling. The diameter-to-thickness ratios of these tubes ranged from 38 to 176. Uenaka et al. [5] and Wei et al. [6] also noted that the inner tubes failed by inward local buckling. After exposing the concrete infill, both authors found that the concrete infill had failed by shear. The diameter-to-thickness ratios for the inner tubes ranged from 19 to 146. Tao et al. [4], however, found that the inner tubes with larger diameter-to-thickness ratios failed by inward local buckling of the tube, whilst those with smaller diameter-to-thickness ratios showed no sign of local buckling.

### 1.3. Test strength results

The yield strengths of the steel used by all authors ranges from low to medium strength steel. Such steel is expected to achieve the required ductility. None of the researchers tested slender columns since the main aim of these testing programmes were to determine the behaviour and strength of stub columns. Simply supported end conditions were simulated in all the tests performed. The tests results for the stub columns conducted by Tao et al. [4], Uenaka et al. [5] and Wei et al. [6] are given in Tables 1, 2 and 3, respectively. In these tables  $N_T$  represent the test compressive strength and  $N_p$  represent the sum of the strengths of the individual components (two tubes plus the concrete infill).

Based on the test results in Table 1, Tao et al. [4] suggested that concrete confinement exist in CFDSCT, and proposed a basic formula, given in Equation 1, to define the strengths of these stub columns.

$$N_u = (C_1 \chi^2 f_{syo} + C_2 (1.14 + 1.02\xi) f_{ck}) A_{sco} + A_{si} f_{syi} \quad (1)$$

where  $\chi$  is the hollowness ratio of the inner tube over the outer tube,  $\xi$  is the confinement factor that is equal to the product of the area of steel and yield stress of steel divided by the product of the area of concrete and the yield stress of the concrete,  $f_{syo}$  is the yield strength for the outer tube,  $f_{ck}$  is the cylindrical strength for the concrete,  $A_{sco}$  is the area of the outer tube and sandwiched concrete,  $A_{si}$  is the area of the inner steel tube and  $f_{syi}$  is the yield strength of the inner tube,  $C_1 = \alpha / (1 + \alpha)$  and  $C_2 = (1 + \alpha) / (1 + \alpha_n)$ . In  $C_1$  and  $C_2$ ,  $\alpha$  is equal to the area of steel over the area of concrete and  $\alpha_n$  is the same with only the nominal area of concrete. Equation 1 is a modification of the sum of the individual strengths of the steel tubes and concrete and assumes that the inner steel tube only acts compositely when the hollowness ratio is less than 0.8. It is clear from the results in Table 1 that although Equation 1 suggests that the outer tube causes enhancement, there is little or no enhancement.

**Table 1.** Tao et al. test results

Test	D <sub>o</sub> (mm)	D <sub>i</sub> (mm)	D <sub>o</sub> /t <sub>o</sub>	D <sub>i</sub> /t <sub>i</sub>	f <sub>yi</sub> (MPa)	f <sub>vo</sub> (MPa)	N <sub>T</sub> (kN)	N <sub>P</sub> (kN)	N <sub>T</sub> /N <sub>P</sub>
1	180	-	60	-	-	276	1680	1547	1.09
2	180	-	60	-	-	276	1618	1547	1.05
3	180	48	60	16	396	276	1790	1633	1.10
4	180	48	60	16	396	276	1791	1633	1.10
5	180	88	60	29	370	276	1648	1566	1.05
6	180	88	60	29	370	276	1650	1566	1.05
7	180	140	60	47	342	276	1435	1285	1.12
8	180	140	60	47	342	276	1358	1285	1.06
9	114	58	38	19	375	295	904	830	1.09
10	114	58	38	19	375	295	898	830	1.08
11	240	114	80	38	295	276	2421	2376	1.02
12	240	114	80	38	295	276	2460	2376	1.04
13	300	165	100	55	321	276	3331	3283	1.01
14	300	165	100	55	321	276	3266	3283	0.99

Uenaka et al's [5] test-to-predicted strengths in Table 2, imply that there is significant concrete confinement in the CFDSCT and that the concrete confinement exists only because of the outer tube. According to Uenaka et al. [5] the effect of confinement became smaller as the internal diameter increased. In Uenaka et al. [5] results, strength enhancement ranges from almost 0 to 41%, and based on these experimental results, Equation 2 was developed.

$$N_u = [2.86 - 2.59(d_i/d_o)]A_{so}f_{yo} + A_{si}f_{yi} + A_c f'_c \quad 0.2 \leq d_i/d_o \leq 0.7 \quad (2)$$

where, N<sub>u</sub> is the axial capacity, D<sub>i</sub> is the inner tube diameter, D<sub>o</sub> is the outer tube diameter, A<sub>so</sub> is the area of the outer tube, f<sub>yo</sub> is the yield strength of the outer tube, A<sub>si</sub> is the area of the inner tubes, f<sub>yi</sub> is the yield strength of the inner tube, A<sub>c</sub> is the area of concrete and f'<sub>c</sub> is the cube strength of the concrete. Similarly to Equation 1, Equation 2 is a modification of the sum of the individual strengths of each material. As indicated above, the results obtained by Uenaka et al. [5] vary by a large margin. Such a large variation casts doubt on the accuracy of Equation 2.

**Table 2.** Uenaka et al. test results

Test	D <sub>o</sub> (mm)	D <sub>i</sub> (mm)	D <sub>o</sub> /t <sub>o</sub>	D <sub>i</sub> /t <sub>i</sub>	f <sub>yi</sub> (MPa)	f <sub>vo</sub> (MPa)	N <sub>T</sub> (kN)	N <sub>P</sub> (kN)	N <sub>T</sub> /N <sub>P</sub>
1	159	-	176	-	221	221	700	497	1.41
2	158	38	176	43	221	221	635	450	1.41
3	159	76	176	84	221	221	540	440	1.23
4	159	114	176	126	221	221	378	395	0.96
5	158	-	105	-	308	308	815	581	1.40
6	158	39	105	26	308	308	852	648	1.31
7	158	77	106	51	308	308	728	640	1.14
8	158	114	106	76	308	308	589	542	1.09
9	158	-	74	-	286	286	908	680	1.33
10	158	40	74	19	286	286	968	705	1.37
11	158	77	74	36	286	286	879	752	1.17
12	157	115	73	54	286	286	704	697	1.01

Wei et al. [6] found that the average test strength of the CFDSCT is 15% larger than the sum of the strengths of the individual components (Table 3). Most of the



results in this table are closer to Tao et al. [4] test results. Based on the variation of the strength results in Tables 1–3 and the discussion above, it inconclusive as to whether there is useful confinement in CFDSCT or not. The test-to-predicted strength in Tables 1 suggests that the test values can clearly be represented by the sum of the individual strengths of the materials.

**Table 3.** Wei et al. test results

Test	$D_o$ (mm)	$D_i$ (mm)	$D_o/t$	$D_i/t$	$f_{vi}$ (MPa)	$f_{vo}$ (MPa)	$N_T$ (kN)	$N_P$ (kN)	$N_T/N_P$
1	74.8	62.0	73	62	470	486	283	264	1.07
2	74.7	62.0	77	66	470	486	285	254	1.12
3	75.4	62.7	58	51	470	486	348	325	1.07
4	75.2	62.4	63	52	470	486	348	314	1.11
5	76.3	62.0	43	62	470	486	395	350	1.13
6	76.3	62.0	44	66	470	512	395	353	1.12
7	81.0	62.0	90	62	470	524	330	303	1.09
8	81.0	62.0	93	66	470	524	335	294	1.14
9	81.5	62.7	73	55	470	524	386	348	1.11
10	81.5	62.2	71	55	470	524	395	350	1.13
11	87.4	61.8	88	71	452	428	378	338	1.12
12	87.3	61.6	93	70	452	428	385	332	1.16
13	87.9	61.4	70	69	452	428	432	363	1.19
14	87.9	61.2	75	72	452	444	408	371	1.1
15	99.7	80.3	169	146	474	409	283	238	1.19
16	99.9	86.8	145	142	444	409	299	228	1.31
17	99.9	80.5	141	120	474	409	357	275	1.3
18	99.9	74.0	143	119	512	409	380	302	1.26
19	99.8	61.4	151	112	432	409	443	389	1.14
20	101.7	61.5	63	110	432	409	644	541	1.19
21	88.8	63.5	57	55	216	286	357	319	1.12
22	101.4	63.4	65	55	216	255	477	426	1.12
23	101.5	76.1	62	64	235	255	417	363	1.15
24	114.3	63.5	70	57	216	262	598	549	1.09
25	114.3	76.1	70	67	235	262	551	492	1.12
26	114.3	88.9	70	57	286	262	524	460	1.14

## 2. Conclusions

This paper provides a review of the literature available on CFDSCT short columns. The stub columns are intended to give guidance for the design of long columns. Important aspects of each paper are covered, which include the specimen dimensions and properties, failure modes, effects of confinement, test results and the proposed design formulations. As expected, the mode of failure of the outer tubes was outward local buckling. All authors reviewed also found that the inner tubes of some CSDSCT failed by inward local buckling and shear of the concrete infill. This was common in inner tubes with larger diameter-to-thickness ratio. The availability of concrete confinement varied from author to author. Tao et al. [4] results suggest that there is no enhancement; Uenaka et al. [5] results suggest that confinement ranges from 0 to 41%, and Wei et al. [6] results suggest that test specimen have an average of 15% confinement. Based on the discussions above it is inconclusive to judge whether there is useful confinement in CFDSCT or not.

## References

- [1] Elchalakani M, Zhao XL, Grzebieta R. Tests on concrete filled double-skin (CHS outer and SHS inner) composite short columns under axial compression. *J Thin-Wall Structures* 2002;40(5):415-41.
- [2] Zhao XL, Han LH. Double skin composite construction. *J Composite Construction* 2006;8:93-102.
- [3] Yang J, XU H, PENG G. Behaviour of concrete-filled double skin steel tubular columns with octagon section under axial compression. *J China Civil Engineering* 2007;40(2):33-38.
- [4] Tao Z, Han LH, Zhao XL. Behaviour of concrete-filled double skin (CHS inner and CHS outer) steel tubular stub columns and beam-columns. *J Constructional Steel Research* 2004;60(8):1129-58.
- [5] Uenaka K, Kitoh H, Sonoda K. Concrete filled double skin circular stub columns under compression. *J Thin-Walled Structures* 2010;48:19-24.
- [6] Wei S, Mau ST, Vipulanandan C, Mantrala SK. Performance of new sandwich tube under axial loading: experiment. *J Structural Engineering ASCE* 1995;121(12):1806-14.

# Flexural failure modes of steel plate-strengthened reinforced concrete elements

Akinropo Musiliu OLAJUMOKE and Morgan DUNDU<sup>1</sup>

*Department of Civil Engineering Science, University of Johannesburg, South Africa*

**Abstract.** Failure of plate strengthened flexural reinforced concrete (RC) member can be crushing of the concrete at the compression face or premature debonding of the plate from the concrete element at the tension face. Debonding can be classified into three groups; namely, intermediate crack debonding (ICD), delamination and plate-end debonding (PED). Intermediate crack debonding is caused by flexural or flexural-shear stress, and plate-end debonding and delamination are caused by interfacial stress. This paper reviews the failure modes of flexural strengthened RC elements in bending, using epoxy-bonded steel plates. It also attempts to establish the width-to-thickness ratios of plates that can achieve the full flexural strengths of the strengthened element and promote a ductile failure.

**Keywords.** Reinforced concrete, flexural strengthening, epoxy bonding, steel plates, premature failure, ductility and stiffness, width-thickness ratio.

## Introduction

The failure modes of normally reinforced concrete (RC) elements, in bending, are well established in literature and can be adequately taken care of in the design. Although the flexural failure modes of the steel plate-strengthened RC elements are identifiable, they are not yet adequately mitigated in design. Investigations have been ongoing for several decades to try and develop the design parameters for these elements. The structural behaviour of beams and slabs is similar in most respects, however, slabs have their own unique structural properties in that their thicknesses are considerably smaller than their other dimensions, shear reinforcement is not normally required due to higher shear span/depth ratio [1] and their flexural reinforcement spacing differs from that of beams. Due to these factors, the results of beams strengthening studies cannot be just extrapolated to slabs.

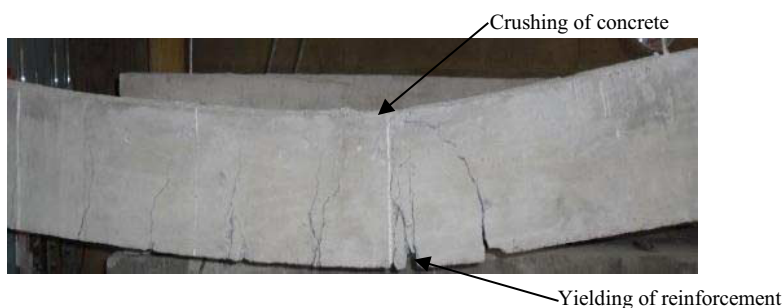
## 1. Failure modes

A structure is believed to have failed if it can no longer fulfil the purpose for which it was designed. For ordinary RC element in bending, failure is usually by flexure which occurs when the reinforcing bars at the tension face yield and the concrete at the compression face crushes as shown in Figure 1. However, in a plate strengthened

---

<sup>1</sup>Corresponding author: University of Johannesburg, Department of Civil Engineering Science, P.O. Box 524, Auckland Park, 2006, South Africa; E-mail. [mdundu@uj.ac.za](mailto:mdundu@uj.ac.za)

flexural RC member, failure can imply crushing of the concrete at the compression face or debonding of the plate from the concrete element at the tension face. The latter premature failure mode can be intermediate crack debonding (ICD), delamination or plate-end debonding (PED). According to Teng *et al* [2] this premature failure can be categorized into two main groups of (i) flexural or flexural-shear stress induced failure (intermediate crack debonding) and (ii) interfacial stress induced failure (plate-end debonding and delamination). It should be noted that cracking at the concrete-plate interface usually leads to slip (difference in strain between the plate and adjacent concrete), which is a partial interaction problem, and this precedes debonding [3].



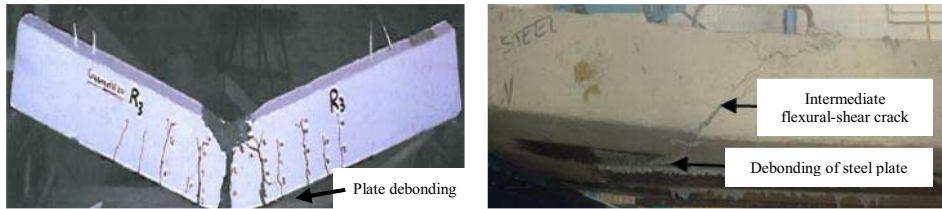
**Figure 1.** Yielding of reinforcement and crushing of concrete

### 1.1. Intermediate crack debonding

Intermediate crack debonding is the separation of a steel plate from the concrete surface in externally bonded (EB) elements. It occurs in zones of high bending moment or where both the bending moment and shear force are high, after the formation of flexural or flexural-shear cracks, and propagates towards the end of the strengthened RC element [4]. The strain in a bonded plate is high at the point of high moment of the element, and because the concrete has lower strength than the adhesive, this failure mode usually occurs in the concrete, at the adhesive-concrete interface [3]. As the crack forms and propagates, the tensile stress from the concrete is transferred to the externally bonded plate (EBP). This stress continues to increase as the loading increases until a critical level is reached at which debonding is initiated. Interfacial debonding commences from the high stress zone and propagates from the crack point towards the end of the plate [2, 4, 5]. If the failure is dominated by flexural crack as shown in Figure 2(a), then debonding will commence from the mid-span and propagation will be due to the widening of the flexural cracks [6]. This failure mechanism is often referred to as intermediate flexural crack (IFC) debonding, and is common in slender members [4].

When debonding is caused by flexural-shear cracks, as shown in Figure 2(b), it is called intermediate flexural-shear crack debonding. In this case, debonding propagation is due to the combination of widening of the crack and the induced stress caused by the relative vertical movement between the cracked faces of the beam before the formation of a diagonal shear crack [3]. It should be noted that intermediate crack debonding does not usually lead to complete peeling off of the steel plate from the entire beam length as the cracks never reaches the ends of the beam [5]. According to Liu *et al.* [3] intermediate crack debonding is difficult to prevent, but compared to plate-end and

critical diagonal crack debonding, it gives more ductile failure. The strain variation is not linear at the cracked section of a RC member, but linear at the uncracked section.



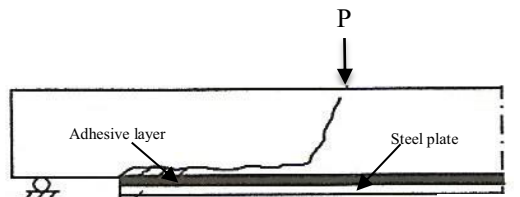
(a) Debonding caused by flexural cracks [6]

(b) Debonding caused by flexural-shear crack [7]

**Figure 2.** Intermediate crack debonding caused by flexural and flexural-shear failures

### 1.2. Delamination or rip-off failure

Delamination is partial separation of the steel plates from the concrete, together with a part of the concrete cover [8]. It is a common failure mode of externally bonded strengthened beams or slabs, and is usually initiated at the curtailment end of the strengthening plate if the epoxy glue is strong enough to prevent plate separation. This leads to a rip-off of the concrete cover [9], as shown in Figure 3. From Figure 3, it can be observed that the crack started as a small diagonal crack at the end of the plate, which then extended to the reinforcing bars. A possible cause of this crack is the abrupt change in stresses from the steel plate to the concrete. The presence of the reinforcing steel forced the crack to propagate along the bars, towards the mid-span. Due to the influence of the high shear and bending stresses (biaxial stress) at the loading point, the crack changed direction and propagated at about  $60^\circ$ , towards this point [9]. Since the crack is more than  $45^\circ$  (typical of unplated beams), this leads to reduced shear capacity. According to Jumaat et al. [4], the tearing of the concrete cover along the internal reinforcing bars in this failure mode is an indication of the existence of a strong bond between the concrete and the plate.



**Figure 3.** Delamination or rip-off failure [9]

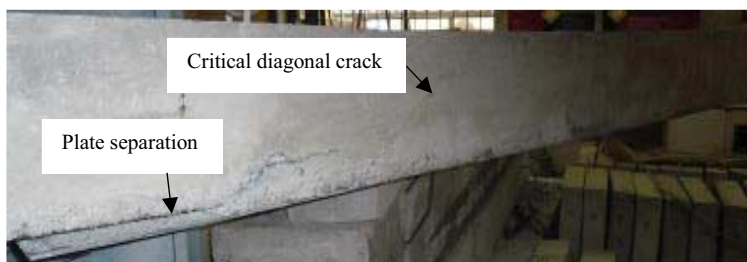
### 1.3. Plate-end debonding

Plate-end debonding or plate separation is caused by high interfacial normal and shear stresses at the end of the plate, and usually leads to the peeling off of the plate, with little or no concrete [8]. It usually occurs before yielding of the reinforcing steel bars and the steel plate at the tension face, and prior to crushing of the concrete at the compression face. This mode of failure can be initiated either by flexural or diagonal shear cracks, depending on the zone of plate end curtailment. If the plate-end curtailment is in the zone of maximum bending moment (center of the beam) the plate separation will be initiated by the formation flexural cracks [10]. Similarly, if the plate-

end curtailment is in the zone of high shear force, which is usually at the end of the beam, then plate separation will be initiated by the formation shear cracks [11]. The shear initiated plate separation is common for members of low overall span/depth ratio and with low plate width-to-thickness ratio.

Hollaway and Mays [12] showed that plate separation in steel plate strengthened beams is common if the shear span/depth ratio ( $a_v/h$ ) ranges from 2.22 and 5.00. For shear span/depth ratio greater than 3.5, flexural and shear cracks are narrower than that of unplated beam, and initiation of plate separation shifts from plate free end to any point of widest shear crack, within the shear span area. Shear plate-end debonding occurs within a short time, making it more problematic to handle than that of flexural crack [4, 10, 13]. The chances of occurrence of plate-end debonding failure increase with increase in the flexural strengthening steel plate thickness [5, 8].

Figure 4 shows an example of plate-end interfacial debonding due to shear cracks. It can be observed from the figure that as plate separation propagated towards the mid-span, it changed into a diagonal crack, which extended towards the loading point. The latter failure mechanism is called critical diagonal crack (CDC) debonding and usually occurs after the formation of large crack, which may be due to insufficient shear reinforcement [4].



**Figure 4.** Plate-end debonding failure

To mitigate these premature failures, bolts have been used as anchorages of plate strengthened RC elements [5, 14, 15]. Anchor bolts prevent separation of the plate from the concrete and improve the stiffness [5, 16], however, it has been concluded that anchor bolts do not prevent debonding or facilitate the achievement of full composite action [14]. According to Aykac et al. [5], the use of bolts to anchor thin plates actually had negative effects on the modulus of toughness (MOT) and ultimate load-carrying capacity of the beams. This was attributed to reduction in the cross-section of the thin plate as a result of the bolt-hole. Bolted plates may introduce localized stress concentration around the bolt-hole and may be obstructed by the internal reinforcing bars. This can be critical in situations where adequate cover was not provided at the initial construction phase and initial constructional detailed information is absent. In addition, bolting does not usually give good aesthetic finish, and additional work and cost of these complementary devices can make strengthening more expensive and discouraging.

Provision of other anchorage systems such as extended plates or sheets over the supports and bonded angle sections at the ends, to mitigate these failure modes has been reported from other investigations [10, 11, 12, 17]. According to Hollaway and Mays [12] strength improvement of anchored over unanchored plating is relevant only for  $a_v/h$  less than 4.0 and is of little benefit for higher ratios under serviceability loading.

It was also observed that cracks in the plated beams usually occur at the concrete-adhesive interface and are finer and more uniformly distributed within the constant moment zone than in the unplated beams [12]. Sena-Cruz et al. [17] reported on the use of mechanically fastened and externally bonded reinforcement (MF-EBR) technique with the aim of mitigating the premature failure in strengthened beams. It was shown that MF-EBR beams gave higher deflection (an indication of ductility) before failure, than those of EBR and NSM. Under monotonic loading, the load carrying capacities of MF-EBR beams over that of EBR beams were higher by about 37%, while NSM strengthened beam had the highest load carrying capacity under post-fatigue monotonic tests [17]. It should be noted that mitigation of these failure modes by extension of the plates or sheets over the supports can be difficult to achieve in an already built structure. In some cases this can actually damage the supports, which in most instances are RC supports.

## 2. Effects of plate dimensions on the failure modes

Aykac et al. [5] showed that there is inverse relationship between the strengthening steel plate thickness and the modulus of toughness (MOT) of strengthened beams, because the lower the plate thickness the higher was the beam's MOT. On the other hand, the rigidity of the strengthened beams was found to be directly proportional to the thickness of the plates. Strengthening with steel plates thicker than 5 mm increased the stiffness; however, the ductility was reduced, which usually led to premature failure [9]. In this work, flexural failure occurred in plate thickness up to 3 mm, at a curtailment distance not exceeding 500 mm from supports and with 5 mm thick plate, at a curtailment distance not exceeding 100 mm from supports. For higher plate thicknesses and curtailment distances, the failure was a combination of flexure and shear, and rip-off. This means that curtailment of the strengthening steel plates should be as close as possible to the supports. Bruwer and Dundu [7] achieved full composite action and yielding of the steel plates in RC slabs strengthened with 6 mm thick plates but had debonding and shearing failure in RC slabs strengthened with 8 mm thick plates. Hollaway and Mays [12] recommended the use of as wide as possible plates in beams of low ( $a_v/h$ ) for even distribution of flexural strain across the beam section. This emphasizes the need to establish some design parameters such as plate width/thickness ratio ( $b/t$ ) and safe ( $a_v/h$ ) for efficient use of steel plates in strengthening slabs, in particular.

Based on the above investigations, it can be concluded that for structural elements in which ductility requirements override that of stiffness, steel plates of thickness less or equal to 6 mm are considered better. On the other hand, where stiffness is of higher importance, thicker steel plates than 6 mm can be used. Whilst ductility is very important for general RC elements in bending, stiffness is also important in special structures like bridges which are constantly subjected to combination of static and dynamic loading. In addition, curtailment of the strengthening steel plates should be closer to the supports as much as practically possible.

### 3. Conclusions

This paper has highlighted premature failures [intermediate crack debonding (ICD), delamination and plate-end debonding (PED) associated with this technique and the need for further investigations. It is noted that most of the published investigations on the plate strengthening of RC elements are on beams of low shear span/beam depth ratios ( $a_v/h$ ), and very few studies have been carried out on slabs. In these investigations, the elements have been tested mainly under static loading while dynamic loading was rarely considered. As noted previously, slabs have unique structural properties that are different from the properties of beams. Slab thicknesses are considerably smaller than their other dimensions, shear reinforcement is not normally required due to higher shear span/depth ratio and their flexural reinforcement spacing differs from that of beams. Due to these factors, design parameters such as plate width/thickness ratio ( $b/t$ ) and plates spacing ( $s$ ) need to be developed for the slabs.

### References

- [1] F.K. Kong and R.H. Evans, *Reinforced and Prestressed Concrete*, ELBS, Third edition. Chapman and Hall, Hong Kong, 1990.
- [2] J.P. Teng, S.T. Smith, J. Yao and J.F. Chen, Intermediate crack-induced debonding in RC beams and slabs, *Construction and Building Materials* 17(6-7) (2003), 447 – 462.
- [3] I.S.T. Liu, D.J. Oehlers and R. Seracino, Study of intermediate cracking debonding in adhesively plated beams, *Journal of Composites for Construction*, ASCE 11 (2007), 175 – 183.
- [4] M.Z. Jumaat, M.A. Rahman M.A. Alam and M.M. Rahman, Premature failures in plate strengthened RC beams with emphasis on premature shear: A review, *International Journal of the Physical Sciences* 6(2) (2011), 156-168.
- [5] S. Aykac, I. Kalkan, B. Aykac, S. Karahan and S. Kayar, Strengthening and repair of reinforced concrete beams using external steel plates, *J. of Structural Engineering*, ASCE 139 (2013), 929 – 939.
- [6] A.E. Ajeel, R.H Ghedan and D.M. Hamza, Replacing of internal tension bars by external bonded plate, *Journal of Engineering and Development* 15(3) (2011), 90 – 103.
- [7] C.P.C. Bruwer and M. Dundu, Structural behavior of composite concrete-steel slabs, *4<sup>th</sup> International Conference on Steel & Composite Structures*, Sydney, Australia, 2010.
- [8] B.H. Oh, J.Y. Cho and D.G. Park, Failure behavior and separation criterion for strengthened concrete members with steel plates, *Journal of Structural Engineering*, ASCE 129 (2003), 1191 – 1198.
- [9] W. Lin, Shear capacity of plated beams by nonlinear finite element method, *IEEE* (2011), 1701 – 1704.
- [10] M.S.M. Ali, D.J. Oehlers and S-M. Park, Comparison between FRP and steel plating of reinforced concrete beams, *Composite: Part A: Applied science and manufacturing* 32 (2001), 1319 – 1328.
- [11] V. Narayanamurthy, J.F. Chen, J. Cairas and D.J. Oehlers, Plate end debonding in the constant bending moment zone of plated beams, *Composites: Part B* 43 (2012), 3361 – 3373.
- [12] L.C. Hollaway and G.C. Mays, Structural strengthening of concrete beams using unstressed composite plates, In: *Strengthening of reinforced concrete structures*, L.C. Hollaway and M.B. Leeming (editors), Boca Raton F.L.: CRC Press, (1999), 83 – 133.
- [13] H.N. Garden and L.C. Hollaway, An experimental study of the influence of plate end anchorage of carbon fibre composite plates used to strengthen reinforced concrete beams, *Composite Structures*, 42 (1998), 175 – 188.
- [14] T.M. Roberts and H. Haji-Kazemi, Strengthening of under-reinforced concrete beams with mechanically attached steel plates, *International Journal of Cement Composites and Lightweight Concrete* 11(1), (1989) 21.
- [15] R. Jones, R.N. Swamy and A. Charif, Plate separation and anchorage of reinforced concrete beams strengthened by epoxy bonded steel plates, *Structural Engineering*, 66(5), (1988), 85-94.
- [16] M. Hussain, A. Sharif, I.A. Basunbul, M.H. Baluch and G.J. Al-Sulaimani, Flexural behavior of precracked reinforced concrete beams strengthened externally by steel plates, *ACI Structural Journal* 92(1) (1995), 14 – 22.
- [17] J.M. Sena-Cruz, J.A.O. Barros, M.R.F. Coelho and F.F.T. Silva, Efficiency of different techniques in flexural strengthening of RC beams under monotonic and fatigue loading, *Construction and Building Materials* 29 (2012), 175 – 182.



# Methods for flexural strengthening of reinforced concrete elements using steel plates

Akinropo Musiliu OLAJUMOKE and Morgan DUNDU<sup>1</sup>

*Department of Civil Engineering Science, University of Johannesburg, South Africa*

**Abstract.** When reinforced concrete elements are incapable of safely sustaining the anticipated load, flexural strengthening may be necessary. Two major construction methods have been reported in literature for strengthening reinforced concrete (RC) elements in bending. These methods include Externally Bonded Reinforcement (EBR) and Near Surface Mounting (NSM). The aim of this paper is review these methods, including the extensive surface preparation that must be performed on bonded elements. Previous investigations have shown that these techniques are effective in salvaging old and distressed reinforced concrete structures. This paper identifies the problems associated with the utilisation of steel plates as strengthening material for RC elements in EBR and NSM techniques.

**Keywords.** Reinforced concrete, flexural strengthening, externally bonded reinforcement, near surface mounting, scabbling, epoxy bonding, steel plates

## Introduction

The most common structural elements that resist loads in bending only are beams and slabs. If these elements are not properly designed and constructed, some problems, such as excessive deflection, flexural and shear failure as well as materials degradation (for example, spalling of concrete and corrosion of steel) may occur. To prevent total collapse, the elements may require flexural strengthening. Flexural strengthening may also be required if there is a change in the use of a structure, and this change results in an increase in the applied loadings. Primarily, strengthening is a means of enhancing the structural performance of an existing structure beyond its current level. When the strength of a concrete structure is enhanced and its design life extended, several economic and environmental problems can be avoided since concrete is bulky and rarely recycled [1].

A steel plate is one of the materials used in the flexural strengthening of RC elements. This is usually carried out by gluing the plate to the concrete element's tension face, using epoxy glue. Essentially, two methods are available in which this task can be achieved, and these include Near Surface Mounting (NSM) and Externally Bonded Reinforcement (EBR) [2, 3]. A number of investigations on these methods have been reported in the literature, and these range from experimental, analytical to

---

<sup>1</sup>Corresponding author: University of Johannesburg, Department of Civil Engineering Science, P.O. Box 524, Auckland Park, 2006, South Africa; E-mail. [mdundu@uj.ac.za](mailto:mdundu@uj.ac.za)

field application of the technique [4-6]. From these studies it has been found that when adequate bond exist between the concrete elements and the epoxy-bonded steel plates, the ductility of the concrete element increases significantly [7]. Additional advantages of using steel plates for strengthening RC elements include enhanced ultimate strength capacity and flexural stiffness, tensile strain reduction resulting from composite action as well as improved serviceability performance through reduced deflection and crack control [8-9]. Strengthened RC beams with thin plates have been found to reach their full flexural capacity before failure and devoid of shear peeling [6-7]. Although some work on the influence of the plate parameters has been investigated this work is not comprehensive enough, and needs further investigations. This will assist to standardize the design and construction specifications.

Other strengthening materials include carbon fibre reinforced polymers (CFRP), glass fibre reinforced polymer (GFRP) and aramid fibre reinforced polymer (AFRP) [10, 11]. According to Jumaat *et al* [10], these advanced materials are used in special applications where other benefits of low maintenance, corrosion resistance, fire resistance, lightweight and long span, override any cost disadvantage. It should be noted that, fibre reinforced polymers (FRP) are very expensive and not readily available in Africa, as they have to be imported from advanced countries where they are being produced. The cost of FRP can be ten times as much as that of steel plates, and they are brittle at failure [6, 11]. Although the problem of corrosion of steel has been stated as one of the disadvantages of steel plating, grades of steel which are corrosion resistant are now available at much cheaper cost than FRP. Durability of steel can also be increased by using protective long-life coatings, such as hot-galvanizing or other coatings. The American Galvanizers Association [12] projected that hot-dipped galvanized (HDG) items will last 75 to 100 years in an aggressive marine environment. For steel plates that require painting it should be noted that today's paints are now expected to last for about 30 years before a major touch-up of a modern three coat paint system [13].

Strengthening with externally bonded (EB) plates has been practiced for more than 50 years, and today this method is still popular worldwide. The popularity of steel plates is due to the easiness of its application on site, little addition to the concrete element size and enhanced internal lever arm, which translates to increased moment capacity [11, 14]. It is observed that most of the investigations in this area have been carried out under static loading, but very few studies are available on investigations with dynamic loading. Analysis for dynamic loading is very important in the design and rehabilitation of bridge, stadium, dance hall and gallery structures. This paper reviews the various investigations on the use of externally bonded (EB) steel plates in strengthen RC elements in bending. This is done with a view to update information on the technique, identify some problems associated with the technique as well as identifying some missing gaps for further studies, in order to standardise this technique.

## **1. Overview of the flexural strengthening using plates**

The structural behaviour of beams and slabs is similar in most respects, however, slabs have their own unique structural properties in that their thicknesses are considerably smaller than their other dimensions, shear reinforcement is not normally required due to higher shear span/depth ratio [15] and their flexural reinforcement spacing differs from that of beams. Due to these factors, the results of beams strengthening studies

cannot be just extrapolated to slabs. Researchers [4, 10, 14] have credited the pioneering work in the post-construction strengthening of RC elements to L'Hermite and Bresson [16] who first reported on the use of epoxy to glue steel plates onto the concrete surface to improve its load carrying capacity. Research thereafter continued in this area until the 1990s, and during this period many RC structural members were successfully strengthened with steel plates in the Netherlands and United Kingdom [11, 14]. According to DOT BA 30/94 [17] the bridges that were successfully strengthened with steel plates in UK include (i) Quinton Bridge (M5) near Birmingham in 1975; (ii) Swanley Interchange (M25) in 1977; (iii) Brinsworth Road Bridge (M1) in 1982; (iv) Stainsby-Teversal Road bridge in 1986 and (v) Brandon Creek Bridge (A10) in 1985. Also, Fleming and King [18] used steel plates as externally bonded shear and flexural reinforcements in South African and reported an increase of both shear and bending strengths of the steel plated beams. Since then several buildings and bridges have been successfully strengthened in South Africa using steel plates. Two major construction methods have been reported in literature for strengthening reinforced concrete (RC) elements in bending. These methods include Externally Bonded Reinforcement (EBR) and Near Surface Mounting (NSM) [2, 19]. The use of either of these two methods does not have any adverse effect on the headroom.

### *1.1. Externally bonded (EB) steel plates*

This method involves mounting the strengthening steel plates at the tension surface of the concrete using adhesive of adequate properties. Most of the failure modes in plate strengthening are associated with the externally bonded (EB) or surface mounting technique. It is noted that most of the early investigations [4, 14, 20] have adopted EB technique for plate strengthening of RC elements due to the simplicity of its installation.

### *1.2. Near surface mounted (NSM) steel plates*

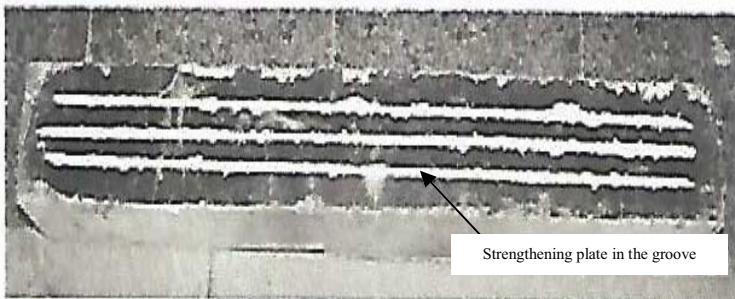
In this method, the strengthening steel plate is usually installed in pre-made groove on the tension face of RC element with the aid of an appropriate adhesive. This method has been adopted in recent studies to overcome some of the failure modes in the externally bonded (EB) reinforcement [20, 21]. The method gives a better aesthetic appearance to the structural element being strengthened as the steel plate could be fixed to completely level with the surface of the concrete. Another advantage is that the steel plate could be covered with thin layer of mortar to protect it from corrosion and/or fire effects. However, the effectiveness of this method depends on the provision of adequate cover to the original reinforcement bars; otherwise it would be difficult to develop a groove of adequate depth.

The NSM strengthening technique is an effective method, and epoxy grout or cement grout can be used for its surface finishing. It increases the stiffness and load carrying capacity of the strengthened beams as well as reduces debonding and other premature failures of the elements in bending [22].

## **2. Surface preparation (SP) of the materials**

The technique of bonding steel plates to concrete slabs surface requires high quality control and good workmanship. For composite action to exist between the concrete and

steel surfaces, both concrete and steel must be properly prepared. However, few authors [2, 6, 23] have given details in this regard. Chajes et al. [2] and Aykac et al. [6] used grinding wheel to prepare the concrete surface while Bruwer and Dundu [23] used scabbling machine for the same purpose. Zhang et al. [9] used chiseling method to roughen the concrete surface and electric grinder to roughen the steel plate surface. The use of scabbling machine for surface preparation of the concrete is considered better for effective exposure of the aggregates and for situation in which only certain portion is to be exposed, such as for slabs. Generally, the preparation of the bonded surfaces involves scabbling of the concrete and gritblasting of the steel plate surfaces, before gluing both materials together with an appropriate epoxy [14, 20, 22]. Wire-brushing and high pressure air must be applied to remove the dust and grid remnants from the concrete surface before the application of the primer and epoxy. Gritblasting of the steel plate surface to a white metal finish is done to remove any surface mill scales, grease or oil that may interfere with the gluing process. In the surface mounting (SM) or externally bonded (EB) reinforcement method, the scabbling of concrete surface is performed to remove the weak mortar laitance and expose the well bonded aggregates in order to increase the surface frictional grip between the RC element and epoxy laden plate [14, 23]. As for the near surface mounting (NSM) method, the groove is prepared to an appropriate depth within the concrete cover, to create space for the steel plates. Figure 1 shows the beams with the grooves and plates, installed into the grooves. It can be observed that the plates are levelled with the soffit of the beam and can be covered with a thin layer of adhesive or cement grout to achieve smoothness and better aesthetic finishing.



**Figure 1.** Near surface mounted strengthened reinforced concrete beams [22].

The epoxy consists of two coats; a primer adhesive and a two-part (resin and hardener) epoxy adhesive. The primer adhesive is mixed first and applied onto the prepared concrete surface. This gives it time to penetrate deep into the hairline cracks of the concrete and provide a surface ready for the application of the epoxy adhesive. The two-part epoxy adhesive is mixed thoroughly with low speed mechanical mixer to prevent entrained air that can adversely affect bonding and an appropriate thickness is applied on the grit-blasted steel plate. The resin and the hardener are usually of different colour, and the uniform colour of their mixture is an indication of adequate mixing [17]. Finally, the steel plate is pressed onto the soffit of the RC concrete slab and the two parts are allowed to bond for about 5 days. It should be noted that the thickness of the epoxy influences the composite action of the strengthened element. Thicker adhesive layer leads to stress lag [24, 25].

Figure 2 shows scabbled surfaces from the current investigation. The scabbled surfaces were achieved using the pneumatic machine. About 3 mm depth of scabbling was conveniently achieved, and it can be observed that this is adequate as the aggregates have been well exposed before the steel plate is bonded to the concrete surface. It should be noted that it may be necessary to putty fill any void or bug holes that might have been created by the removal of some loose aggregates during scabbling. This is done to prevent the formation of air bubbles at the concrete-epoxy interface that may adversely affect bonding between the steel plate and the concrete.



(a) Scabbling process



(b) Completed scabbled surface

**Figure 2.** Scabbled concrete slabs

### 3. Conclusions

This paper has shown that a lot of investigations have been carried out on the use of steel plates in strengthening and increasing the flexural strength of reinforced concrete elements, using Externally Bonded Reinforcement (EBR) and Near Surface Mounting (NSM) techniques. The techniques have been found to be very effective. The use of near surface mounting (NSM) of plates is a recent development but its effective usage may be jeopardized by inadequate concrete cover. Since the strengthening techniques are generally applied to old structures the information about the concrete cover and reinforcement arrangement may not be available. Even when the concrete cover is available it might not be adequate enough to accommodate the grooves required in near surface mounting method. NSM could also damage the reinforcing bars during the preparation of the grooves. Based on these shortcomings, the externally bonded (EB) strengthening technique has better practical application than the near surface mounting (NSM) technique.

### References

- [1] M. Dundu, Structural steel construction in South Africa, *Steel Construction Reports* 4(4) (2011), 259 – 268. DOI: 10.1002/stco.201110034.
- [2] M.J. Chajes, T.A. Thomson Jr, T.F. Januszka and W.W. Finch Jr, Flexural strengthening of concrete beams using externally bonded composite materials, *Construction and Building Materials* 8(3) (1994), 191 – 201.
- [3] I.S.T. Liu, D.J. Oehlers and R. Seracino, Tests on the ductility of reinforced concrete beams retrofitted with FRP and steel near-surface mount plates, *Journal of Composites for Construction, ASCE* 10 (2006), 106 – 114.
- [4] R. Jones, R.N. Swamy and T.H. Ang, Under- and over-reinforced concrete beams with glued steel plates, *The International Journal of Cement Composites and Lightweight Concrete* 4(1) (1982), 19 – 32.

- [5] J.P. Teng, S.T. Smith, J. Yao and J.F. Chen, Intermediate crack-induced debonding in RC beams and slabs, *Construction and Building Materials* 17(6-7) (2003), 447 – 462.
- [6] S. Aykac, I. Kalkan, B. Aykac, S. Karahan and S. Kayar, Strengthening and repair of reinforced concrete beams using external steel plates, *Journal of Structural Engineering, ASCE* 139 (2013), 929 – 939.
- [7] W. Lin, Shear capacity of plated beams by nonlinear finite element method, *IEEE* (2011), 1701 – 1704.
- [8] F. Sevuk and G. Arslam, Retrofit of Damaged Reinforced Concrete Beams by Using Steel Plate, *Structures Congress, ASCE* (2005), 1 – 8.
- [9] J.W. Zhang, J.G.Y. Teng, Y.L. Wong and Z.T. Lu, Behavior of two-way RC slabs externally bonded with steel plate, *Journal of Structural Engineering* 127 (2001), 390 – 397.
- [10] M.Z. Jumaat, M.A. Rahman, M.A. Alam and M.M. Rahman, Premature failures in plate strengthened RC beams with emphasis on premature shear: A review, *International Journal of the Physical Sciences* 6(2) (2011), 156-168.
- [11] H.N. Garden and L.C. Hollaway, An experimental study of the influence of plate end anchorage of carbon fibre composite plates used to strengthen reinforced concrete beams, *Composite Structures* 42 (1998), 175 – 188.
- [12] American Galvanizers Association, *Hot-dip Galvanizing for Corrosion Protection, A specifier's guide*, American Galvanizers Association, (2012).
- [13] FHWA-HRT-11-046, *Performance evaluation of one-coat, systems for new steel bridges*, Department of Transportation, USA, (2011)
- [14] W. Jansze, Strengthening of reinforced concrete members in bending by externally bonded steel plates: Design for shear and plate anchorage, PhD thesis submitted to Delft University of Technology, Delft University Press, 1997.
- [15] F.K. Kong and R.H. Evans, *Reinforced and Prestressed Concrete. ELBS*, Third edition, Chapman and Hall, Hong Kong, 1990.
- [16] R. L'Hermite J. Bresson, Concrete reinforced with glued plates, In: *RILEM International Symposium, Synthetic resins in building construction*, Paris, 1967, 175 – 203.
- [17] Department of Transport (DOT) BA 30/94, *Strengthening of concrete Highway structures using externally bonded plates*, UK Department of Transport Advice Note, 1994.
- [18] C.J. Fleming and G.E.M. King, The development of structural adhesives for three original uses in South Africa, *RILEM Bulletin* 37 (1967), 241 – 251.
- [19] J.M. Sena-Cruz, J.A.O. Barros, M.R.F. Coelho and F.F.T. Silva, Efficiency of different techniques in flexural strengthening of RC beams under monotonic and fatigue loading, *Construction and Building Materials* 29 (2012), 175 – 182.
- [20] L.C. Hollaway and G.C. Mays, Structural strengthening of concrete beams using unstressed composite plates, In: *Strengthening of reinforced concrete structures*, L.C. Hollaway and M.B. Leeming (editors). Boca Raton F.L.: CRC Press, (1999), 83 – 133.
- [21] H.M. Afefy and T.M. Fawzy, Strengthening of RC one-way slabs including cut-out using different techniques, *Engineering Structures* 57 (2013), 23 – 36.
- [22] D. Mostofinejad and S.M. Shamel, Externally bonded reinforcement in grooves (EBRIG) technique to postpone debonding of FRP sheets in strengthened concrete beams, *Construction and Building Materials* 38 (2013), 751 – 758.
- [23] C.P.C. Bruwer and M. Dundu, Structural behavior of composite concrete-steel slabs, 4<sup>th</sup> International Conference on Steel & Composite Structures, Sydney, Australia, 2010.
- [24] D. Lei, G.Y. Chen, Y.Q. Chen and Q.W. Ren, Experimental research and numerical simulation of RC beams strengthened with bonded steel plates, *SCIENCE CHINA Technological Science*, Science China Press and Springer-Verlag Berlin Heidelberg, (2012), 3271 – 3277.
- [25] R.N. Swamy, R. Jones and J.W. Bloxham, Structural behaviour of reinforced concrete beams strengthened by epoxy-bonded steel plates, *Structural Engineer* 65A(2) (1987), 59 – 68.

This page intentionally left blank

# Structural steel and other metals



This page intentionally left blank

# Behaviour and design of a double track open timber floor plate girder railway deck steel bridge

Ehab ELLOBODY<sup>1</sup>

*Department of Structural Engineering, Faculty of Engineering, Tanta University, Tanta, Egypt*

**Abstract.** This paper discusses the nonlinear behaviour and design of a double track open timber floor plate girder railway deck steel bridge. A 3-D finite element model has been developed for the bridge, which accounted for the bridge geometries, initial geometric imperfections, material nonlinearities of the bridge components, bridge boundary conditions, interactions between bridge components and bridge bracing systems. The simply supported double track railway steel bridge has a span of 30 m, a width of 7.2 m and a depth of 3.12 m. The bridge components comprising main plate girders, stringers, cross girders, connections, bracing members, stiffeners, bearings, and filed splices were designed following the design rules specified in the European Code for steel bridges. The live load acting on the bridge was Load Model 71, which represents the static effect of vertical loading due to normal rail traffic specified in the European Code. The finite element model of the double track bridge was developed depending on additional finite element models, developed by the author, for small and full-scale plate girder steel bridge tests previously reported in the literature. The small and full-scale tests had different geometries, different boundary conditions, different loading conditions and different failure modes. Failure loads, load-mid-span deflection relationships, failure modes, stress contours of the double track bridge as well as of the small and full-scale tests were predicted from the finite element analysis and compared well against test results. The comparison with test results has shown that the finite element models can be effectively used to provide more accurate analyses and better understanding for the behaviour and design of railway steel bridges. The paper presents a complete piece of work regarding the finite element analysis and design of railway steel bridges, which can be used for further parametric studies, finite element analyses and investigations of the bridges under different loading and boundary conditions. The study has shown that the design rules, loading and recommendations specified in the European Code provide accurate and conservative estimations for the design of railway steel bridges.

**Keywords.** Bridges, FE modelling, plate girders, railway, steel structures design

## Introduction

Finite element models were developed and reported in the literature highlighting the structural performance of different types of steel bridges subjected to different loadings and different boundary conditions. Earls and Shah [1] presented a combined experimental and numerical investigation on high performance steel I-shaped bridge girders. The investigations were assessed against the American bridge specification

---

<sup>1</sup>Corresponding author, [ehab.ellobody@f-eng.tanta.edu.eg](mailto:ehab.ellobody@f-eng.tanta.edu.eg)

(AASHTO) provisions for cross sectional compactness and adequate bracing. The study showed that the specifications may be inadequate owing to intense interactions between local and global buckling modes in the bridge girders. Shanmugam et al. [2] presented a combined experimental and numerical study on the ultimate load behaviour of plate girders curved in plan. The study indicated that the load-carrying capacity decreases with the increase in curvature. Floor beams of orthotropic plated bridge decks were investigated by Corte and Bogaert [3]. It was concluded that the shear deformations can be considerably large to be neglected. The behavior of bridge girders made of high performance steel (HPS 70W) was evaluated by Felkel et al. [4]. The findings of the study indicated that improved structural performance may be obtained when location of bracing was optimized and fabrication imperfection tolerances were minimized. Galvin and Dominguez [5] presented a theoretical and experimental research work on a cable-stayed bridge. Full-scale tests were carried out to measure the bridge dynamic response. Romeijn and Bouras [6] developed a finite element model of a tension-tie arch bridge to investigate the in-plane buckling length factor of the arches. Eldib [7] presented the shear buckling strength and design of curved corrugated steel webs for bridges considering material inelasticity. A finite element analysis was performed to study the geometric parameters affecting the shear buckling strength of curved corrugated steel webs for bridges. A new type of streamlined girder bridge with a thin-walled steel box girder was investigated by Zhang et al. [8]. The authors showed that the finite element analysis can be an effective method to predict properties of this class of bridges. Graciano et al. [9] studied the influence of initial geometric imperfections on the postbuckling behavior of longitudinally stiffened plate girder webs subjected to patch loading. Recently, Lin et al. [10] showed that the renovation of old railway bridges can greatly enhance the stiffness and reduce the stress levels of steel members, resulting in the extension of the service life of the railway bridge.

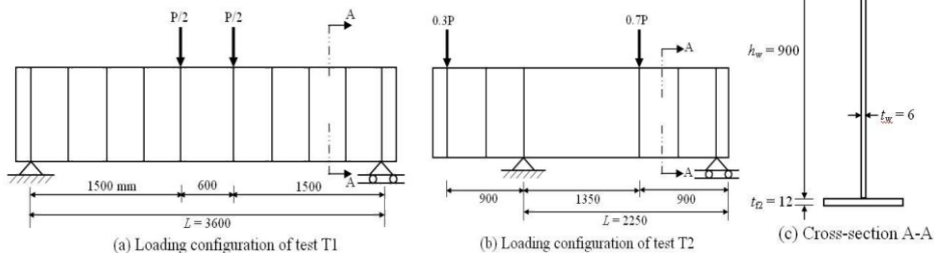
However, to date there is no detailed investigations on railway steel bridges combining the design and finite element modelling of the bridges, which is addressed in this study. The study will highlight for the first time that finite element modelling can complement design rules of railway steel bridges by incorporating initial geometric imperfections, actual geometries, loading and boundary conditions. This can reduce the time and effort used for the analysis of the bridges. The finite element models can be used to perform more detailed finite element analyses, which improve the safety and understanding of the behaviour of railway steel bridges. The main objective of this study is to highlight the finite element modelling and design of a double track open timber floor plate girder railway deck steel bridge. An efficient nonlinear 3-D finite element model was developed using the finite element program ABAQUS [11], which considered the inelastic material properties of bridge components, bridge geometries, bridge boundary conditions, actual bracing system, and initial geometric imperfections. In addition, finite element models of small and full scale plate girder steel bridge tests available in the literature were developed and acted as a basis for modelling the whole double track bridge. The bridge components were designed following the design rules specified in the European Code EC3-2 (BS EN 1993-2) [12] for steel bridges. The failure loads, failure modes and load-mid-span deflection relationships, stress contours were predicted using the finite element model and compared against published experimental results. The failure load of the bridge was compared with that predicted from EC3 [12], with detailed discussions and analyses presented.

### 1. Summary of experimental investigation

To verify the FE models developed, the small and full-scale plate girder bridge tests conducted by Nakamura and Narita [13] and Felkel et al. [4] were simulated. The test specimens were denoted T1-T5 as shown in Table 1. The tests carried out by Nakamura and Narita [13], T1 and T2, were small-scale built-up I-section plate girder steel bridges tested under bending and shear, respectively. The small-scale plate girder T1 was simply supported and had a length between supports of 3.6 m as shown in Fig. 1. The web of plate girder T1 was 900 mm high and 6 mm thick. While the flange of the plate girder was 200 mm wide and 12 mm thick. The web was stiffened by steel plates at the end supports and the loading positions, and also stiffened by intermediate stiffeners at intervals of 375 mm. The plate girder was restrained laterally at the end supports to resist lateral-torsional buckling. The yield and ultimate tensile strength of the steel used were 372.3 and 511.4 MPa, respectively. The plate girder T1 was loaded at two points as shown in Fig. 1. The deformed shape shows a typical lateral torsional buckling (LTB) shape of the plate girders. On the other hand, test T2 was a small-scale simply supported plate girder steel bridge with an overhanging cantilever from one end. The plate girder had a length between supports of 2.45 m and the overhanging length from the support to loading was 0.9 m as shown in Fig. 1. The plate girders were loaded at two points, as shown in Fig. 1, which subjected the plate girder to high shear forces. The main failure mode was buckling owing to shear stresses (SB).

**Table 1.** Dimensions and material properties of plate girder bridge test specimens.

Test	Dimensions (mm)					Material properties (MPa)			Reference
	$h_w$	$b_f$	$t_w$	$t_{f1}$	$t_{f2}$	$L$	$f_y$	$f_u$	
T1	900.0	200.0	6.0	12.0	12.0	3600	372.3	511.4	[13]
T2	900.0	200.0	6.0	12.0	12.0	2250	372.3	511.4	[13]
T3	914.4	228.6	7.9	20.6	25.4	12192	558.0	621.0	[4]
T4	914.4	228.6	7.9	20.6	25.4	12192	558.0	621.0	[4]
T5	914.4	228.6	7.9	20.6	25.4	12192	558.0	621.0	[4]



**Figure 1.** Layout of the small-scale plate girder bridge tests T1&T2 tested by Nakamura and Narita [13].

The tests carried out by Felkel et al. [4], T3-T5, were full-scale built-up I-section plate girder steel bridges tested under bending to study the effect of lateral bracing on the behaviour of the bridges. The full-scale plate girder steel bridge tests were simply supported and had an overall length of 12.192 m as shown in Fig. 2. The web of plate girder T3 was 914 mm high and 8 mm thick. While the flanges of the plate girder was 229 mm wide and thickness varying from 11-25mm, as shown in Fig. 2. The web was stiffened by steel plates at the end supports and the loading positions, and also stiffened by intermediate stiffeners. The plate girder T3 was restrained laterally at the end supports and loading position (three locations) to resist lateral-torsional buckling, while tests T4 and T5 were restrained at five locations as shown in Fig. 2. The yield and ultimate tensile strength of the steel used, which were 558 and 621 MPa,

respectively. The plate girders were loaded at mid-span. The failure mode of the specimen T3 was elastic lateral torsional buckling (LTB). The full-scale plate girder steel bridge specimen T4 failed due to lateral torsional buckling (LTB). This failure occurred suddenly in a bifurcation (snap through) fashion at the left flange transition zone. Finally, the failure mode of T5 was also owing to lateral torsional buckling (LTB) at one end of the specimen that initiated away from the flange transition zone.

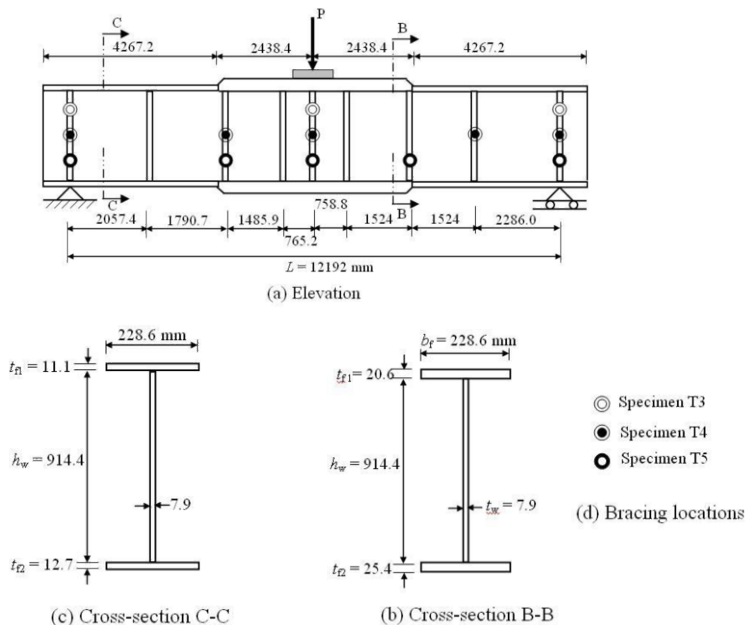


Figure 2. General layout of the full-scale plate girder bridge tests (T3-T5) tested by Felkel et al. [4].

## 2. Finite Element model

The finite element program ABAQUS [11] was used to develop finite element models for the small and full-scale plate girder steel bridge tests detailed in [13] and [4] as well as for the double track railway bridge investigated in this study. The models has accounted for the measured geometry, initial geometric imperfections and measured material properties of flange and web portions. Buckling investigation requires performing two types of analyses. The first is known as Eigenvalue analysis that estimates the buckling modes and loads. The second is called load-displacement nonlinear analysis and follows the Eigenvalue prediction. The 4-node doubly curved shell element with reduced integration (S4R) was used to model the plate girder steel bridges T1, T2 and T3-T5, as shown in Figs. 3, 4 and 5, respectively. The plate girder steel bridges investigated were modeled in full owing to unsymmetrical conditions. The top compression flange was prevented from lateral transitional displacement at the bracing positions. The load was applied in increments as static point load using the RIKS method available in the ABAQUS [11] library. The non-linear geometry was included to deal with the large displacement analysis.

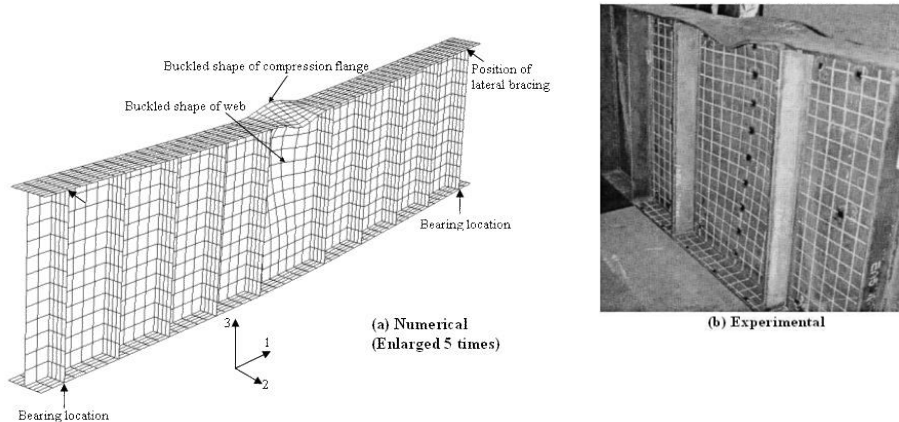


Figure 3. Comparison of failure modes of the plate girder bridge T1.

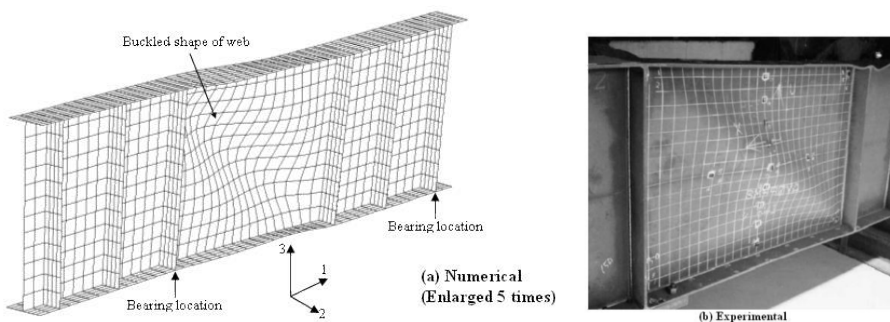


Figure 4. Comparison of failure modes of the plate girder bridge T2.

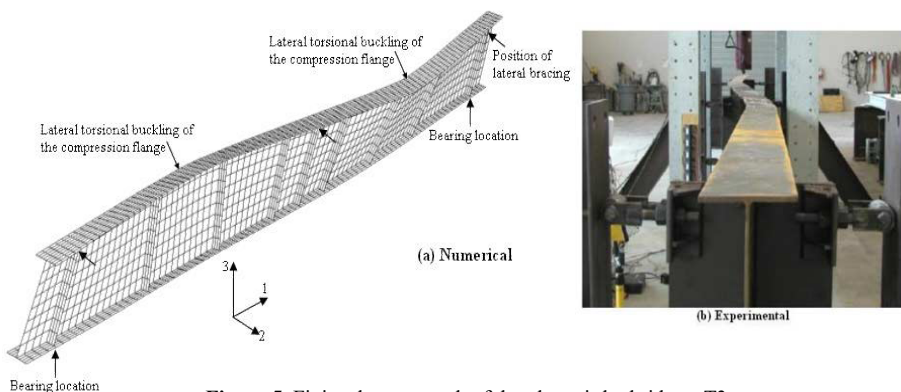


Figure 5. Finite element mesh of the plate girder bridges T3.

The stress-strain curves given in the EC3 [16] were used to model the steel used in the tests with measured values of the yield stress ( $f_y$ ) and ultimate stress ( $f_u$ ). Mainly two buckling modes for steel beams, detailed in [17, 18], could be identified as unrestrained and restrained lateral distortional buckling modes. Following the same approach, [14 and 15], the lateral distortional buckling modes could be obtained for the

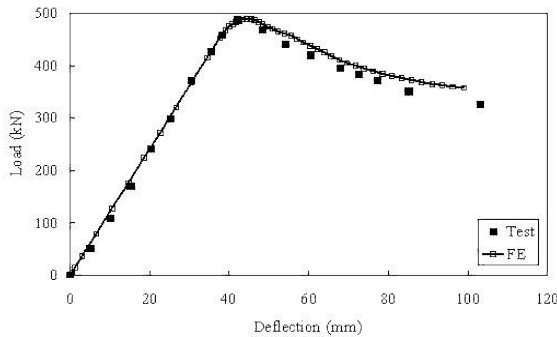
investigated plate girder steel bridges by performing Eigenvalue analysis. The buckling modes are factored by  $L_u/1000$ , where  $L_u$  is the length between points of bracing.

### 3. Verification of the FE model

In order to verify the developed models, the tests detailed in [13 and 4] were simulated. Table 2 shows a comparison between the failure loads ( $P_{Test}$ ) and mid-span deflections at failure ( $\delta_{Test}$ ) obtained from the tests and FE analyses ( $P_{FE}$ ) and ( $\delta_{FE}$ ), respectively. It can be seen that good agreement between the test and FE results. The load-mid-span deflection curves predicted experimentally and numerically were also compared in Fig. 6 for plate girder steel bridge test T3. It can be shown that generally good agreement was achieved between experimental and numerical curves. Furthermore, the deformed shapes at failure of the plate girder steel bridges observed experimentally and numerically were compared as shown in Figs. 3-5, as examples for T1-T3, respectively. It can be seen that there is good agreements between the deformed shapes.

**Table 2.** Comparison of test and finite element results.

Test [Ref.]	Test			Finite element analysis			$\frac{P_{Test}}{P_{FE}}$	$\frac{\delta_{Test}}{\delta_{FE}}$
	$P_{Test}$ (kN)	$\delta_{Test}$ (mm)	Failure mode	$P_{FE}$ (kN)	$\delta_{FE}$ (mm)	Failure mode		
T1 [13]	1474.0	15.0	LTB	1503.0	14.7	LTB	0.98	1.02
T2 [13]	1752.0	5.0	SB	1742.0	5.3	SB	1.01	0.94
T3 [4]	489.3	40.6	LTB	490.3	44.0	LTB	1.00	0.92
T4 [4]	1140.0	91.0	LTB	1144.7	97.4	LTB	1.00	0.93
T5 [4]	1157.0	93.0	LTB	1175.2	99.2	LTB	0.98	0.94
Mean	...	...	...	...	...	...	0.99	0.96
COV	...	...	...	...	...	...	0.013	0.042



**Figure 6.** Load-mid-span deflection curves for T3.

### 4. Layout and design of the double track railway steel bridge investigated

The general layout of the double track open timber floor plate girder railway deck steel bridge investigated is shown in Figs. 7 and 8. The bridge has simply supported ends, a length between supports of 30 m and an overall length of 31 m. The width of the bridge

(spacing between main plate girders) is 7.2 m as shown in Fig. 7. The railway steel bridge components were designed adopting the design rules specified in EC3 [12, 20]. The steel material of construction of the double track bridge had yield and ultimate stresses of 275 and 430 MPa, respectively. The bridge has upper and lower wind bracings of K-shaped truss as well as cross bracings of X-shaped truss as shown in Fig. 7. In addition, the bridge has lateral shock (nosing force) bracing for the stringers as well as braking force bracing at the level of upper wind bracing. The plate girder web is stiffened by vertical stiffeners, to safeguard against shear stresses and web buckling, spaced at a constant distance of 1.667 m. The expected live loads on the bridge conform to Load Model 71, which represents the static effect of vertical loading due to normal rail traffic as specified in EC1 [19]. The bolts used in connections and field splices are M27 high strength pretensioned bolts of Grade 8.8.

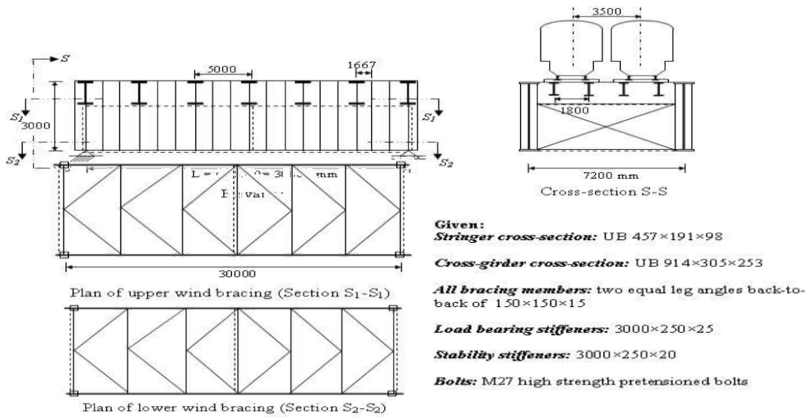


Figure 7. General layout of a double track open-timber floor plate girder railway deck steel bridge.

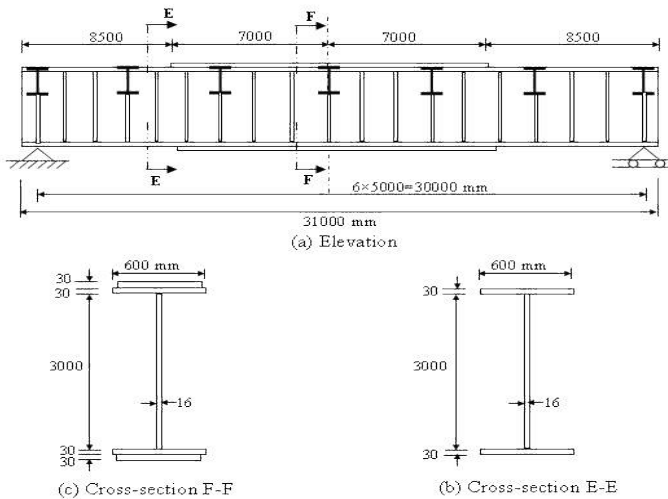
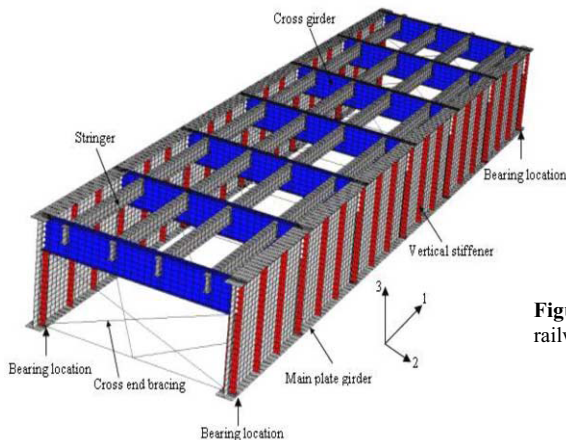


Figure 8. General layout of the full-scale plate girder of a double track open-timber railway steel bridge.

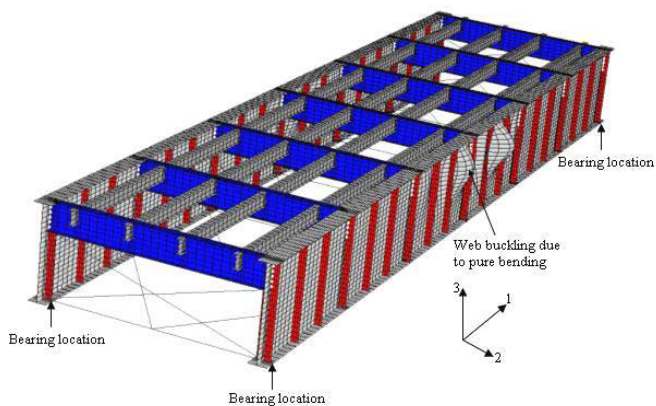


## 5. Finite element modelling of the railway bridge and discussions

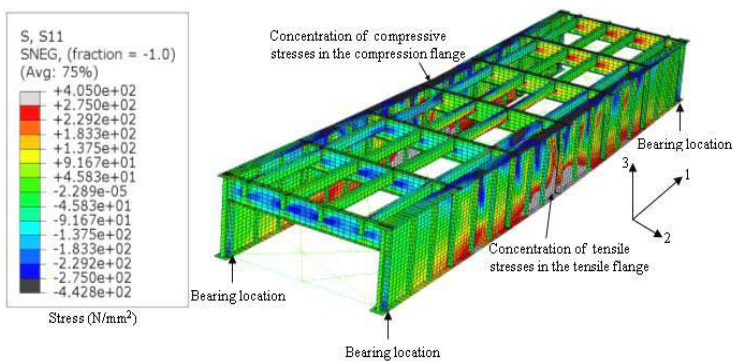
The double track railway bridge investigated can be modelled adopting the same approach detailed in Sections 2 and 3. The S4R shell element was used to model the flanges and webs of the stringers, cross-girders, stiffeners and main plate girders. The bracing members were modelled using structural 2-D truss elements (T2D2). The bolts were modelled using JOINTC joint elements having stiffnesses in two directions. The developed finite element model shown in Fig. 9 can be now used to study the bridge for any analysis, boundary conditions, geometries and loadings. As an example in this paper, the bridge was analysed to predict the ultimate load that can be carried by the bridge up to complete failure. The yield and tensile stresses of steel were 275 and 430 MPa, respectively. An Eigenvalue buckling analysis was performed for the whole bridge and the buckling mode predicted is shown in Fig. 10. It can be seen that a clear web buckling mode due to bending was predicted at mid span panel. The buckling modes are factored by a magnitude of  $L_u/1000$ , where  $L_u$  is the distance between web stiffeners. The deformed shape of the whole bridge analysed to failure is shown in Fig. 11. It can be seen that a clear combined lateral torsional buckling mode of the upper main plate girder flange and web buckling mode was predicted at mid-span owing to bending stresses. Fig. 11 also plotted the principal stresses in direction 1-1, contours at failure. It can be seen that the yield stresses were reached at mid-span in the upper and lower flanges of the main plate girder. The load-mid-span deflection curve predicted numerically was plotted in Fig. 12. The ultimate load that can be resisted by each main plate girder was 6683.7 kN at a deflection of 318.8 mm. The design load predicted using EC3 [12] for each main plate girder was also plotted in Fig. 12, which was 5763.3 kN. The finite element failure load was 16% higher than the design load, which shows that the design rules specified in the EC3 [12] are conservative and accurate.



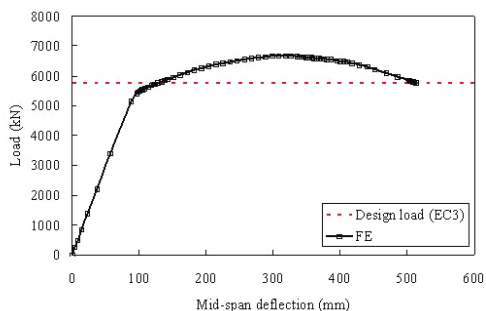
**Figure 9.** FE mesh of the double track railway steel bridge.



**Figure 10.** Elastic lateral buckling mode for the railway bridge.



**Figure 11.** Stress contours of the railway steel bridge at failure.



**Figure 12.** Load per one main girder-mid-span deflection curves for the railway steel bridge at ultimate limit state.

## 6. Conclusions

The nonlinear behaviour and design of a double track open timber floor plate girder railway deck steel bridge has been investigated and discussed in this paper. A 3-D finite element model has been developed for the bridge, which accounted for the bridge geometries, initial geometric imperfections, material nonlinearities of the bridge components, bridge boundary conditions, interactions between bridge components and bridge bracing systems. In addition, finite element models for small and full-scale plate girder steel bridge tests reported in the literature have been developed. The small and full-scale tests had different geometries, different boundary conditions, different loading conditions and different failure modes. Failure loads, load-mid-span deflection relationships, failure modes and stress contours of the bridge as well as of the tests have been predicted from and compared well against test results. The comparison with test results has shown that the finite element models can effectively provide more accurate analyses and better understanding for the behaviour and design of railway steel bridges. The finite element models can be used for further parametric studies, finite element analyses and investigations of the bridges under different loading and boundary conditions. The study has shown that the design rules specified in the European Code provide conservative predictions for railway steel bridges.

## References

- [1] C. J. Earls and B. J. Shah. High performance steel bridge girder compactness. *Journal of Constructional Steel Research*, 58, 859-880, 2002.
- [2] N. E. Shanmugam, M. Mahendrakumar and V. Thevendran. Ultimate load behaviour of horizontally curved plate girders. *Journal of Constructional Steel Research*, 59, 509-529, 2003.
- [3] W. D. Corte and P. V. Bogaert. The effect of shear deformations in floor beams on the moment distribution in orthotropic plated bridge decks. *Journal of Constructional Steel Research*, 62, 1007-1015, 2006.
- [4] J. P. Felkel, D. C. Rizos and P. H. Ziehl. Structural performance and design evaluation of HPS 70W bridge girders. *Journal of Constructional Steel Research*, 63, 909-921, 2007.
- [5] P. Galvin and J. Dominguez. Dynamic analysis of a cable-stayed deck steel arch bridge. *Journal of Constructional Steel Research*, 63, 1024-1035, 2007.
- [6] A. Romeijn and C. Bouras. Investigation of the arch in-plane buckling behaviour in arch bridges. *Journal of Constructional Steel Research*, 64, 1349-1356, 2008.
- [7] M. E. A. H. Eldib. Shear buckling strength and design of curved corrugated steel webs for bridges. *Journal of Constructional Steel Research*, 65, 2129-2139, 2009.
- [8] H. Zhang, R. DesRoches, Z. Yang and S. Liu. Experimental and analytical studies on a streamlined steel box girder. *Journal of Constructional Steel Research*, 66, 906-914, 2010.
- [9] C. Graciano, E. Casanova and J. Martínez. Imperfection sensitivity of plate girder webs subjected to patch loading. *Journal of Constructional Steel Research*, 67, 1128-1133, 2011.
- [10] W. Lin, T. Yoda, N. Taniguchi and M. Hansaka. Performance of strengthened hybrid structures renovated from old railway steel bridges. *Journal of Constructional Steel Research*, 85, 130-139, 2013.
- [11] ABAQUS. *ABAQUS Standard User's Manual*. Hibbit, Karlsson and Sorensen, Inc. Vol. 1, 2 and 3, Version 6.11-1, USA, 2011.
- [12] EC3. *Eurocode 3 – Design of steel structures – Part 2: Steel bridges*. Code of Practice for Design of Steel Bridges. BS EN 1993-2, British Standards Institution, 2006.
- [13] S. Nakamura and N. Narita. Bending and shear strengths of partially encased composite I-girders. *Journal of Constructional Steel Research*, 59, 1435-1453, 2003.
- [14] E. Ellobody. Interaction of buckling modes in castellated steel beams. *Journal of Constructional Steel Research*, 67(5), 814-825, 2011.
- [15] E. Ellobody. Nonlinear analysis of cellular steel beams under combined buckling modes. *Thin-Walled Structures*, 52(3), 66-79, 2012.

- [16] EC3. *Eurocode 3: Design of steel structures Part 1-1: General rules and rules for buildings*. British Standards Institution, BS EN 1993-1-1, London, UK, 2005.
- [17] M.A. Bradford. Lateral-distortional buckling of steel I-section members. *Journal of Constructional Steel Research*, 23, 97–116, 1992.
- [18] T. Zirakian and H. Showkati. Distortional buckling of castellated beams. *Journal of Constructional Steel Research*, 62, 863-871, 2006.
- [19] EC1. *Eurocode 1 – Actions on structures – Part 2: traffic loads on bridges*. BS EN 1991-2, British Standards Institution, 2003.
- [20] EC3. *Eurocode 3 – Design of steel structures – Part 1-5: Plated structural elements*. BS EN 1993-1-5, British Standards Institution, 2006.
- [21] EC1. *Eurocode 1: Actions on structures - General actions - Part 1-4: Wind actions*. BS EN 1991-4, British Standards Institution, 2004.

# Kinetic study of steel emissivity and its effect on steel behaviour under fire condition

Han FANG<sup>a,1</sup>, Man Biu WONG<sup>a</sup> and Yu BAI<sup>a</sup>

<sup>a</sup>*Department of Civil Engineering, Monash University, Australia*

**Abstract.** Steel emissivity is one of the key parameters for steel structure design for fire resistance since it affects the heat exchange between structural steel members and fire. Constant values of emissivity are usually given in design standards and used in computations for predicting steel structure temperatures under fire conditions. However, such steel temperature estimations would only be approximate due to the fact that variation of steel emissivity has been shown to be temperature dependent by previous research [7]. The temperature-dependent steel emissivity increases upon heating as a consequence of the occurrence of thermal oxidation on steel surface. In this study, the steel emissivity was measured experimentally. Besides, a model based on the kinetic theory for thermal oxidation was proposed for computing steel emissivity and used for kinetic study of steel emissivity variation. Both the experimental result and kinetic study show that steel emissivity is also dependent on the heating rate. Based on this new finding for computing steel emissivity, the kinetic model is recommended to be used for steel design at high temperature in order to obtain an accurate prediction of steel temperatures under fire condition.

**Keywords.** Steel emissivity, kinetic theory, thermal oxidation, fire, temperature

## Introduction

Steel is a most commonly used construction material especially for high-rise buildings because of its features of high strength, hardness, ease of fabrication and impact resistance. However, steel structure design against high temperature working conditions such as fire is essential for structural safety assessment due to its significant strength reduction at temperatures above 500°C [1]. In the design of steel structures at high temperatures, steel temperature prediction which is required for steel strength estimation is based on heat transfer between steel and fire due to convection and radiation [1-2]. In the heat transfer process, radiation that usually dominates is a function of emissivity, Stefan-Boltzmann constant, fire temperature and steel temperature. Among these parameters, emissivity is the most controversial one as its value varies in different design standards (e.g. 0.7 in Eurocode 3 [1] and 1.0 in [2]). Therefore, the variation of steel emissivity at high temperatures needs to be investigated for an accurate estimation of temperatures and strength of steel in fire.

---

<sup>1</sup>Corresponding author: [han.fang@monash.edu](mailto:han.fang@monash.edu)

In order to understand the variation of steel emissivity, a spectral method was adopted by many researchers to measure steel emissivity in an isothermal condition [3-5]. Unlike the steel emissivity measured isothermally, an indirect method based on the thermal energy equilibrium on a surface can be adopted to measure emissivity upon random heating in [6-7]. It was found that steel emissivity increases significantly from 0.2-0.3 to 0.7-0.8 from 400°C to about 550°C due to the occurrence of oxidation when steel is exposed to air. In the design of steel structures subject to fire, the temperature of steel increases and the rates of steel temperature development vary from time to time depending on the fire curve that is being used. The emissivity measured by using spectral method in an isothermal environment or under a random heating condition may cause inaccurate steel temperature estimation because of the uncertainty in steel temperature development. Therefore, it is essential to understand the emissivity variation due to oxidation upon heating at different rates.

## 1. Methodology

In this study, the indirect method used in [7] which includes direct steel temperature measurements and thermal analysis based on heat transfer theory was adopted to obtain steel emissivity. In the experiment conducted for this study, a carbon steel sample is heated at a specified rate and both the sample temperatures and furnace temperatures were recorded for further analysis. The analysis based on solving the energy equilibrium equation using finite difference method is applied to calculate steel emissivity. In the energy equilibrium equation, the net heat flux absorbed to increase steel temperature by  $\Delta T_s$  is described by

$$\dot{q}_{net} = C_p \rho \frac{V \Delta T_s}{A \Delta t} \quad (1)$$

where  $C_p$  = steel specific heat capacity;  $\rho$  = steel density;  $A$  = surface area of the member per unit length;  $V$  = volume of the member per unit length;  $\Delta T_s$  = steel temperature increment and  $\Delta t$  = time interval. The net heat flux stored in material is equal to the total energy flow due to convection and radiation. Thus:

$$\dot{q}_{net} = q_c + q_r \quad (2)$$

where  $q_c$  = convective heat flux and  $q_r$  = radiation heat flux. The expressions for the heat flux due to convection and radiation are given in equations (3) and (4) respectively.

$$q_c = h_c (T_f - T_s) \quad (3)$$

$$q_r = \varepsilon_s \sigma \left[ (T_f + 273)^4 - (T_s + 273)^4 \right] \quad (4)$$

where  $h_c$  = convective coefficient;  $\sigma$  = Stefan-Boltzmann constant;  $\varepsilon_s$  = steel emissivity;  $T_f$  = furnace temperature and  $T_s$  = sample temperature.

By substituting Eqs. (2), (3) and (4) into Eq. (1), the energy equilibrium equation, Eq. (1), can be rearranged into Eq. (5) which is used to obtain steel emissivity.

$$\varepsilon_s(T) = \frac{c_p \rho \frac{V}{A} - h_c (T_f - T_s)}{\sigma [(T_f + 273)^4 - (T_s + 273)^4]} \quad (5)$$

## 2. Experimental procedures

A high temperature test was carried out to obtain steel emissivity. The device used for the high temperature test was an electrical furnace with 800 mm × 350 mm × 350 mm internal dimensions shown in Fig.1. The specimens for high temperature tests were made up of 4130 steel with dimensions of 10 mm in diameter and 200 mm in length. The 4130 steel samples had the same specific heat capacity as the steel studied in [8].

Before starting the high temperature test, the sample surface was rinsed with acetone to get rid of the oils, grease, or dirt. A surface profilometer was used to measure the average surface roughness (Ra) since the surface roughness is one of the key factors that influence the steel emissivity [5, 9]. In order to measure the sample and furnace temperature, two thermocouples were used, one to measure the surface temperature of steel and the other one to monitor the temperature of the surrounding environment near the steel sample. Special care was taken to mount the thermocouple on the sample surface to avoid the effect of the heat flux intercepted directly by the thermocouple sensor. This was done by protecting the thermocouple with ceramic fiber tape as an insulation material.

During the high temperature test, the steel sample was heated up to 700°C which was chosen to achieve a complete thermal oxidation process for the steel samples. Two furnace heating rates of 35°C/min and 8°C/min respectively were used for the high temperature tests in order to investigate the heating rate effects on steel emissivity variation.

## 3. Results and discussions

With the measured furnace temperature ( $T_f$ ) and steel temperature ( $T_s$ ), the variation of steel emissivity with temperature can be obtained by using equation (5). Figure 2(a) and (b) depicts the temperatures of furnace and steel obtained from tests under two heating rates which were used to calculate steel emissivity in Eq. (5). Other heat transfer parameters such as  $\Delta t$ ,  $\sigma$  and  $A/V$  in Eq. (5) were based on Eurocode 3 [1] for unprotected steel members while the convective coefficient  $h_c$  was decided according to Eurocode 1 [10] for heating in an electric furnace. The density of 4130 steel is 7833.3 kg/m<sup>3</sup>. All these values are given in Table 1. The specific heat capacity of 4130 steel was studied in [8] and adopted in this study to estimate the steel emissivity.

**Table 1.** Heat transfer parameters used in Eq. (5)

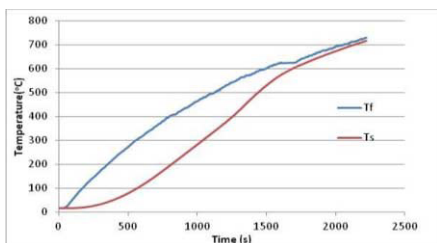
$\Delta t$ (s)	$\sigma$ (W/m <sup>2</sup> K)	$A/V$	$h_c$ (W/m <sup>2</sup> K)	$\rho$ (kg/m <sup>3</sup> )
5	5.67*10 <sup>-8</sup>	400	9	7833.3

The calculated steel emissivity from Eq. (5) is presented in Figure 3 based on the heating rates measured in the steel sample. The heating rates are 30.31°C/min and 6.14°C/min. The steel emissivity was obtained at temperatures from 50°C to 600°C. In Figure 3, it shows that the variation of steel emissivity is almost constant with a value of 0.29 at temperatures up to about 360°C. When the sample temperature is over 360°C,

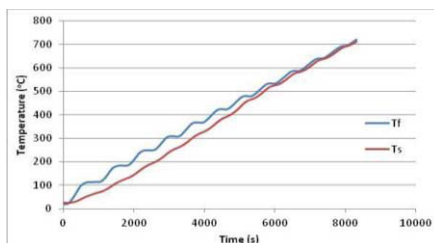
the emissivity of steel starts to increase dramatically from 0.29 up to 0.7 due to the increment of the surface roughness caused by the occurrence of thermal oxidation. This is confirmed by comparing the surface roughness measured before and after the test shown in Table 2. This agrees with the work done by others [4, 6, 7]. By comparing the steel emissivity measured under two heating rates, it is quite obvious that the developments of steel emissivity before the starting of thermal oxidation are almost the same for the two heating rates. However, the steel emissivity obtained at the rate of 6.14°C/min increases faster than that obtained at 30.31°C/min once the thermal oxidation starts.



Figure 1. Experimental setup



(a)



(b)

Figure 2.  $T_f$  and  $T_s$  from (a) 35°C/min test; (b) 8°C/min test

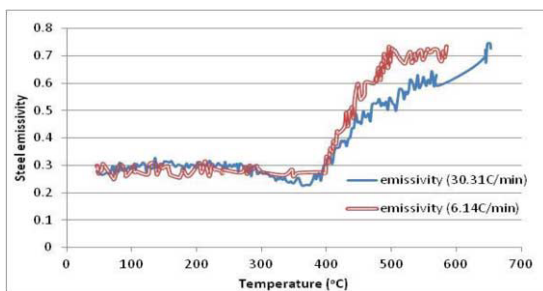


Figure 3. Steel (4130) emissivity

Table 2. Steel surface roughness (Ra) for test at 30.31°C/min

	Before test	After test
Ra (30.31°C/min)	0.525	6.72
Ra (6.14°C/min)	0.625	7.33



#### 4. Kinetic modelling of steel emissivity

In order to estimate the steel emissivity for fire design and investigate its dependency on heating rates, kinetic theory of thermal oxidation was used to analyze the variation of steel emissivity. The rate of the propagation of thermal oxidation can be modeled by the Arrhenius equation [4, 11] for non-isothermal heating:

$$\frac{d\alpha}{dT} = \frac{A}{\beta} * \exp\left(-\frac{E_A}{R*T}\right)(1 - \alpha)^n \quad (6)$$

where  $\alpha$  = conversion degree;  $A$  = pre-exponential factor;  $E_A$  = activation energy for thermal oxidation;  $\beta$  = heating rate;  $n$  = reaction order;  $T$  = steel temperature and  $R$  = gas constant. Knowing the degree of conversion, the temperature dependent steel emissivity can be calculated as:

$$\varepsilon_s = \begin{cases} \varepsilon_b, & \text{for } T < T_s \\ \varepsilon_b(1 - \alpha) + \varepsilon_f\alpha, & \text{for } T_s < T < T_f \\ \varepsilon_f, & \text{for } T > T_f \end{cases} \quad (7)$$

where  $\varepsilon_s$  = steel emissivity;  $T_s, T_f$  = starting and finishing temperature of oxidation;  $\varepsilon_b$  = steel emissivity without oxidation and  $\varepsilon_f$  = steel emissivity after the finishing of oxidation. In order to use this kinetic model to estimate steel emissivity, kinetic parameters ( $A, E_A$  and  $n$ ) in Eq. (6) need to be determined. The method proposed in [12] as a single curve method is adopted for the kinetic parameters calculation based on the steel emissivity obtained at a rate of 30.31°C/min and the results are summarized in Table 3. The computed kinetic parameters agree well with the values obtained in [4]. The  $T_s$  and  $T_f$  in Eq. (7) can be obtained by incremental calculation of Eq. (6) as the temperatures at which  $\alpha$  is zero and 1.0 respectively; the values are given in Table 4. By substituting the kinetic parameters into Eqs. (6) and (7), the steel emissivity at a rate of 6.14°C/min and 30.31°C/min can be calculated for the verification of the accuracy of this model. The steel emissivity calculated by using the kinetic model above is presented in Figure 4 for comparison with the test results. From Figure 4, it is shown that the modeled steel emissivity agrees with the test results reasonably well. Therefore, this model is recommended to be used for accurate steel emissivity estimation taking into account the effect of heating rate.

**Table 3.** Kinetic parameters for thermal oxidation

$E_A$ (KJ/mol)	$A$ ( $\text{min}^{-1}$ )	$n$
116.8117	$2.7*10^8$	1.36

**Table 4.** Calculated values for  $T_s$  and  $T_f$

Heating rates	$T_s$ (°C)	$T_f$ (°C)
6.14°C/min	349.4	514
30.31°C/min	369.7	570

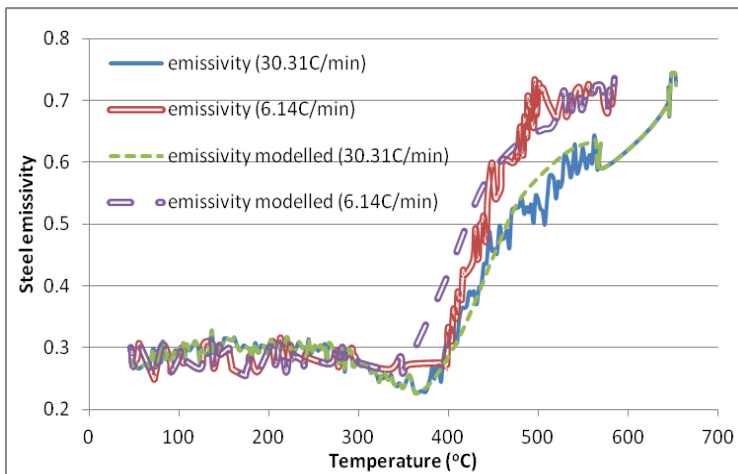


Figure 4. Steel (4130) emissivity model results

## 5. Conclusion

Steel emissivity is investigated in this study based on both experimental measurement and kinetic analysis. The steel emissivity was obtained indirectly from high temperatures tests conducted under continuous heating at different rates which is based on the practical working condition of steel structure subject to high temperature. From the results of steel emissivity estimation, it is shown that steel emissivity variation is not constant but temperature dependent. The steel emissivity is equal to 0.29 at temperatures approximately below 360°C and starts to increase from 0.29 to 0.7 at temperatures above 360°C. The build-up of steel emissivity is due to the occurrence of thermal oxidation at steel surface which causes the increment of surface roughness. Besides, it was also found that the steel emissivity heated at a lower rate starts to increase with a higher rate.

In addition to the determination of steel emissivity in experiment, a model based on kinetic theory of thermal oxidation was also proposed and used to analyze and estimate the steel emissivity for structural design. The rate of the increment of steel emissivity due to thermal oxidation is dependent on heating rates based on the kinetic theory. Compared with the test results, the modeled steel emissivity under different heating rates shows a reasonable agreement with steel emissivity obtained from high temperature tests. Therefore, this model is recommended to be used for an accurate estimation of steel emissivity in structural design for high temperatures.

## References

- [1] EN1993-1-2, *Eurocode 3: Design of Steel Structures-Part1-2: General rules-structural fire design*, 2005.
- [2] T.T. Lie, American Society of Civil Engineers and Committee on Fire Protection, *Structural fire protection, American Society of Civil Engineers*, New York, 1992.
- [3] L.D. Campo, R.B. Perez-Saez, X. Esquisabel, I. Fernandez and M.J. Tello, New experimental device for infrared spectral directional emissivity measurements in a controlled environment, *Review of Science Instruments* 77 (2006), 113111.

- [4] L.D. Campo, R.B. Perez-Saez and M.J. Tello, Iron oxidation kinetics study by using infrared spectral emissivity measurements below 570°C, *Corrosion Science* **50** (2008), 194-199.
- [5] C.D. Wen, Study of steel emissivity characteristics and application of multispectral radiation thermometry (MRT), *Journal of Materials Engineering and Performance* **20** (2011), 289-296.
- [6] T. Paloposki and L. Liedquist, Steel emissivity at high temperatures, *VTT Research Notes* 2299, 2006.
- [7] H. Sadiq, M.B. Wong, J. Tashan, R. Al-Mahaidi and X.L. Zhao, Determination of steel emissivity for the temperature prediction of structural steel members in fire, *Journal of Materials in Civil Engineering* **25** (2013), 167-173.
- [8] M. Li, J.A. Brooks, D.G. Atteridge and W.D. Porter, Thermophysical property measurements on low alloy high strength carbon steels, *Scripta Materialia* **36** (1997), 1353-1359.
- [9] F. Bierbrauer and J. Chen, A study on the surface emissivity of oxidized steel using a three layer model, *APMC* **2** (1993), 11-14.
- [10] EN1991-1-2, *Eurocode 1: Actions on structures-Part 1-2: General actions-actions on structures exposed to fire*, 2002.
- [11] Y. Bai, N.L. Post, J.J. Lesko and T. Keller, Experimental investigations on temperature-dependent thermo-physical and mechanical properties of pultruded GFRP composites, *Thermochimica Acta* **469** (2008), 28-35.
- [12] H. Fang, M.B. Wong and Y. Bai, A new kinetic model for steel specific heat during phase transformation, Chapter 129, *From Materials to Structures: Advancement through Innovation*, Proceedings of the 22<sup>nd</sup> Australian Conference on the Mechanics of Structures and Materials (ACMSM22), Sydney, Australia, 11-14 December 2012, *Taylor and Francis Group*, London, 2013.

# Low cycle fatigue performance of integral bridge steel H-piles subjected to earthquakes

Murat DICLELI<sup>a,1</sup> and Semih ERHAN<sup>b</sup>

<sup>a</sup>*Department of Engineering Sciences, METU, Ankara, Turkey*

<sup>b</sup>*Department of Civil Engineering and Arch., University of Bahrain*

**Abstract.** Under the effect of medium and large intensity ground motions, the seismically-induced lateral cyclic displacements in steel H-piles of integral bridges (IBs) could be considerable. As a result, the piles may experience cyclic plastic deformations following a major earthquake. This may result in the reduction of their service life due to low-cycle fatigue effects. Accordingly, low cycle fatigue in integral bridge piles is investigated under seismic effects in this study. For this purpose, an IB with two span is considered. Three dimensional nonlinear structural models of the IB including dynamic soil-bridge interaction effects are built. Then, time history analyses of the IB models are conducted using a set of ground motions with various intensities representing small, medium and large intensity earthquakes. In the analyses, the effect of various properties such as soil stiffness, pile size and orientation are considered. The magnitude of cyclic displacements of steel H-piles are then determined from the analyses results. In addition, using the existing data from experimental tests of steel H-piles, a fatigue damage model is formulated. This fatigue damage model is used together with the cyclic displacement obtained from seismic analyses to determine the remaining service life of IBs under cyclic displacement due to thermal effects. The fatigue analyses results reveals that earthquakes with large intensity may reduce the service life of the piles with non-compact sections.

**Keywords.** Low cycle fatigue, H-piles, earthquake, integral bridges, service life

## Introduction

An integral bridges is one in which the continuous superstructure, the abutments and the single row of flexible piles supporting the abutments are built monolithically to form a rigid frame structure. The most common types of piles used at the abutments are steel H-piles. Under the effect of medium and large intensity ground motions, the seismically-induced lateral cyclic displacements in steel H-piles of integral bridges (IBs) could be considerable. The piles may experience cyclic plastic deformations. This may result in the reduction of their service life due to low-cycle fatigue effects. Accordingly, low cycle fatigue in integral bridge piles is investigated under seismic effects in this study. For this purpose, IBs with two spans are considered. Three

---

<sup>1</sup>Corresponding author: Middle East Technical University, email. [mdicleli@metu.edu.tr](mailto:mdicleli@metu.edu.tr)

dimensional (3-D) nonlinear structural models of these IBs including dynamic soil-bridge interaction effects are built. Then, time history analyses of the IB models are conducted using a set of ground motions with various intensities representing small, medium and large intensity earthquakes. In the analyses, the effect of various properties such as soil stiffness and pile size are considered. The magnitude of cyclic displacements of steel H piles are then determined from the analyses results. Then, a fatigue damage model is used together with the cyclic displacement obtained from seismic analyses to determine the remaining service life of IB piles

### **1. Properties of integral bridge**

Two span IB was considered in the present work, for purposes of investigating the low cycle fatigue in integral bridge piles under seismic effects. The total length of the bridge is 82 m and the width is 16 m. The bridge has two spans with the lengths of 41 m each. The bridge has slab-on- prestressed concrete girder deck. There are seven AASHTO type VI girders [1] supporting a 225 mm thick reinforced concrete slab and are spaced at 2380 mm. A 75 mm thick asphalt pavement is provided on the deck surface. The bridge pier is composed of three reinforced concrete columns supporting a cap beam.

### **2. Parameters considered in this study**

A parametric study was conducted in this study to investigate the effects of the pile size and foundation soil properties on the low cycle fatigue of steel H-piles commonly used in the construction of IBs. Accordingly, two different pile sizes, HP 310 x 174 and HP 250 x 85 are assumed in the parametric study. Furthermore, the piles are assumed to be made of ASTM A36 steel [2], commonly use in steel H-piles. Orientation of the piles for bending about their strong axes is assumed. The foundation soil is assumed to be sand. Two different sand stiffness levels (medium and dense) were also included in the study.

### **3. Structural model of integral bridge**

The bridge superstructure was modelled using 3-D beam elements. The superstructure was divided into a number of segments and its mass (23.36 tons/m) was lumped at each nodal point connecting the segments. The in-plane translational stiffness of the deck is relatively much higher than that of the other members of the bridge. Accordingly, at the abutment and pier locations, the bridge deck was modelled as a transverse rigid bar of length equal to the center-to-center distance between the two exterior girders supporting the deck slab. The transverse rigid bar was used to simulate the interaction between the axial deformation of the columns and torsional rotation of the bridge deck as well as the interaction between the in-plane rotations of the deck and displacements of the bearings.

The cap beam and the columns are modelled as 3-D beam elements. The parts of the beam elements within the joint connecting the cap beam to the columns were

modelled as rigid elements. The tributary masses of the cap beam and the columns were lumped at the joints connecting them. The reinforced concrete piles underneath the pier column are modelled using 3-D beam elements as well. The nonlinear structural behaviour of the columns and piles is modelled using link elements with Takeda's hysteretic model.

The steel H-piles were modelled as 3-D beam elements and nonlinear link elements were used to represent interaction between the piles and the surrounding soil. The lateral soil resistance deflection (p-y) relationship for sand is defined at any specific depth H, by the following equation [3].

$$P = A.P_u \cdot \tanh \left[ \frac{k.H}{A.P_u} \cdot y \right] \tag{1}$$

where; A = a factor to account for cyclic or static loading condition and assumed as 0.9 for cyclic loading, P<sub>u</sub> = ultimate bearing capacity of foundation soil at the depth H, (kN/m) and k = initial subgrade reaction modulus (kN/m<sup>3</sup>) and may be obtained as a function of angle of inertial friction (φ) from a table given in API design code [1]. To simulate radiation damping, dashpots were placed at the nodal points along the pile. The radiation damping coefficient for these dashpots was obtained from the following equation [4].

$$c = A.\rho.V_s \tag{2}$$

where, A= the tributary area between the nodal points along the pile, ρ = mass density of the soil (1.85 ton/m<sup>3</sup> and V<sub>s</sub>= the shear wave velocity (250 m/s).

Nonlinear link elements are used to simulate abutment-backfill interaction in the structural model. The force deformation relationship of these link elements is obtained using hyperbolic p-y curves purposed by Duncan & Mokwa [5] for nonlinear abutment backfill modelling under seismic loadings as follows;

$$P = \frac{y}{\frac{1}{K_{max}} + R_f \frac{y}{P_{ult}}} \tag{3}$$

where, P = the passive resistance of backfill, P<sub>ult</sub> = the ultimate passive resistance, y = the backfill deformation, K<sub>max</sub> = the initial slope of the load-deformation curve and R<sub>f</sub> = defined as follows;

$$R_f = 1 - \frac{P_{ult}}{K_{max} \cdot y_{max}} \tag{4}$$

Duncan & Mokwa [5] have used a value of R<sub>f</sub> = 0.85 for hyperbolic load-deflection curves. Accordingly, in this study, a value of R<sub>f</sub> = 0.85 for hyperbolic load-deflection curves will be used. Hysteretic behaviour of the backfill soil is also considered and a similar approach proposed by Cole & Rollins [6] was used to simulate this hysteretic behaviour. The radiation damping effects for the abutment-backfill system are

simulated in the structural model using dashpots. The potential formation of a gap behind the abutment due to the inelastic cyclic movements is also considered in the analyses.

#### 4. Moment curvature relationships of H-piles

As the relative rotation or displacement capacity of a steel member is proportional to its curvature capacity, the moment curvature relationships of steel H-piles subjected to different levels of axial loads are obtained. The obtained moment-curvature relationships are then used as envelope curves to define the nonlinear hysteretic behaviour of steel H-piles under cyclic loading. The obtained moment-curvature relationships under zero axial load for HP sections considered in this study are illustrated in Fig.1.

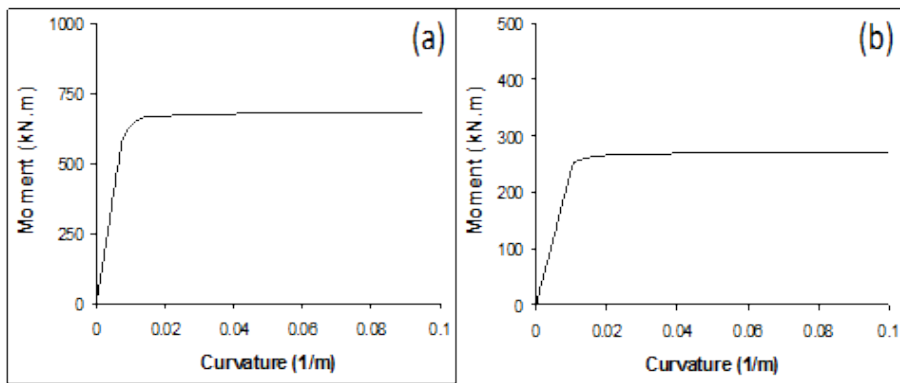


Figure 1. Moment curvature relationship for (a) HP310x174 (b) HP250x85 sections

#### 5. Strain-based low cycle fatigue

Low-cycle fatigue failure of structural components is caused by cyclic loads or displacements of relatively larger magnitude that may produce significant amounts of plastic strains in the structural component. Generally, the number of displacement cycles that leads to failure of a component is determined as a function of the plastic strains in the localized region of the component being analyzed. This is referred to as strain-based approach to fatigue life estimate of structural components. This approach is appropriate for determining the fatigue life of steel H-piles supporting the abutments as it considers the seismically-induced large plastic deformations that may occur in localized regions of the piles where fatigue cracks may begin. Koh & Stephens [7] proposed an equation to calculate the number of constant amplitude strain cycles to failure for steel sections under low cycle fatigue. This equation is based on the total strain amplitude,  $\varepsilon_a$ , and expressed as follows:

$$\varepsilon_a = M(2N_f)^m \quad (5)$$

where,  $M = 0.0795$ ,  $m = -0.448$  for steel H-pile sections and  $N_f$  is the number of cycles to failure. The above equation is used for the estimation of the maximum strain amplitude steel H-piles can sustain before their failure takes place due to low-cycle fatigue effects under seismically induced cyclic loadings. For a bridge to serve its intended purpose, it must sustain the effect of seismically-induced cyclic displacements during a seismic event. The seismically-induced strains in steel H-piles are assumed to have variable amplitudes. Therefore, Eq. (5), which is derived for constant amplitude cycles, cannot be used directly alone to obtain the number of cycles to failure to estimate the consumed life of the pile due to low cycle fatigue effects under seismic loading. Accordingly, Miner's rule [8] may be used in combination with Eq. (5) to obtain the consumed life of the pile due to low cycle fatigue. Miner [8] defined the cumulative fatigue damage induced in a structural member by load or displacement cycles of different amplitudes as:

$$\sum_i^n \frac{n_i}{N_i} \leq 1 \quad (6)$$

where,  $n_i$  is the cycles associated with the  $i^{\text{th}}$  loading (or displacement) case and  $N_i$  is the number of cycles to failure for the same case. The above equation states that if a load or displacement is applied  $n_i$  times (e.g. the number of strain cycles of a certain amplitude under seismic loading), only a fraction,  $n_i/N_i$  of the fatigue life has been consumed. The fatigue failure is then assumed to take place when  $n_i/N_i$  ratios of the cycles with different amplitudes add up to 1.

## 6. Analyses of the bridge models

A total of four IB models were built considering two different pile sizes and soil stiffness levels. Then, thermal analyses of these IBs were conducted. The analyses results revealed that the steel H-piles remain within the elastic limits under thermal induced displacements due to the small length of the IBs. Consequently, low cycle fatigue effects under thermal loading are not expected for this particular bridge. Hence, these effects are not considered together with seismic effects for low cycle fatigue life estimates of the IBs assessed in this study. Then, nonlinear time history analyses of the IB models are conducted using seven earthquake ground motions. The acceleration spectrums of selected earthquakes are represented in Fig. 2. The nonlinear time history analyses are repeated for peak ground accelerations of 0.2, 0.5, 0.8 and 1.0g for each selected earthquake. This led to a total of 32 different analyses cases. The analyses results are presented in the following sections.



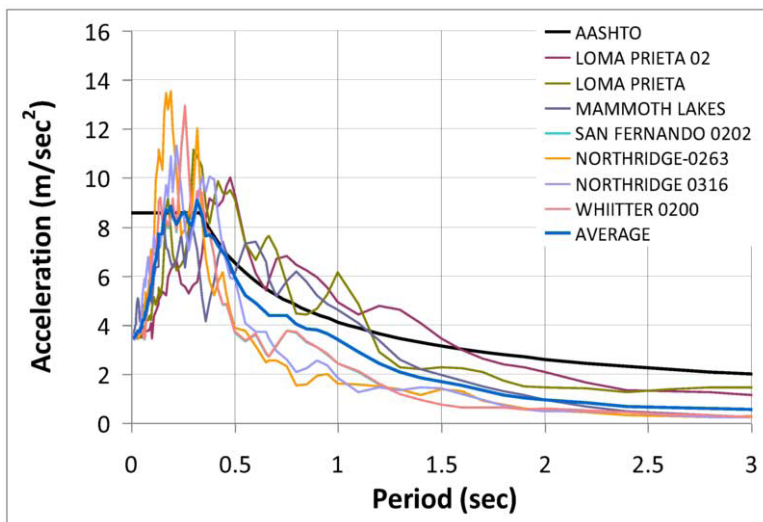


Figure 2. The comparison of the AASHTO design spectrum and acceleration spectra of selected earthquakes

### 7. Analyses results

The hysteric (cyclic) moment-rotation relationships of the steel H-piles are obtained from the nonlinear time history analyses results. Then, a Matlab algorithm was developed to calculate the amplitude of positive ( $\epsilon_{ap}$ ) and negative ( $\epsilon_{an}$ ) strain cycles using the moment rotation relationships obtained from nonlinear time history analyses. Then the strain amplitudes ( $\epsilon_a$ ) were calculated as follows;

$$\epsilon_a = \frac{|\epsilon_{pa}| + |\epsilon_{na}|}{2} \tag{7}$$

Next, the number of displacement cycles ( $N_f$ ) that leads to failure of a steel H-pile was determined using the method purposed by Koh and Stephens [5] as mentioned earlier. Furthermore, cumulative fatigue damage index for the H-piles are obtained using Miner’s rule [6]. The number of cycles and cumulative fatigue damage index for the H-piles of IBs are tabulated in Table 1 for different pile sizes and Table 2 for different soil stiffness values. The average values of cumulative fatigue damage indices obtained from seven ground motions are also illustrated in Figure 3. The analyses results are presented for peak ground accelerations of 0.5, 0.8 and 1g. In the case of peak ground acceleration of 0.2g, a hysteric (cyclic) behaviour is not observed due to the elastic behaviour of the H-piles under this small level of peak ground acceleration. In the following subsection, the effect of various pile sizes and soil stiffness on the low cycle fatigue damage of Steel H-piles of IBs is further studied.

#### 7.1. Effect of pile sizes and soil stiffness

In this section the effect of pile size on low cycle fatigue performance of steel H-piles is studied. The analyses results are tabulated in Table 1 in terms of cumulative fatigue damage index (ranging between 0 and 1.0 where 0 represents no damage, and 1 represents total failure) for various peak ground acceleration levels and earthquakes. The average fatigue damage indices obtained for different peak ground accelerations

are also compared in Fig. 3(a). The results presented in Table 1 clearly reveal that as the size of the pile increases, cumulative fatigue damage index decreases. For instance, in the case of the Northridge earthquake scaled to a peak ground acceleration of  $A_p=0.8g$ , cumulative fatigue damage index is calculated as 0.0013 for the larger pile. However, for the same bridge supported by smaller piles at the abutment and subjected to the same earthquake and peak ground acceleration level, the low cycle fatigue damage index is calculated as 0.0037. This obviously results from the greater bending capacity of larger piles that require larger displacements to reach their fatigue strain amplitude limit. However, in the case of the smaller piles, the piles may easily reach their fatigue strain amplitude limit at smaller displacements amplitudes. The effect of soil stiffness on low cycle fatigue performance of steel H-piles at the abutments is also studied in this section. The stiffness of the foundation soil is observed to have a remarkable effect on the cumulative fatigue damage index of steel H-piles under seismic loading (Fig. 3(b)). As the soil stiffness increases, cumulative fatigue damage index of steel H-piles also increases, as observed from Table 2. For example, in the case of the Northridge earthquake scaled to a peak ground acceleration of  $A_p=0.8g$ , the cumulative fatigue damage index is calculated as 0.0013 for medium sand. However, for the same earthquake and peak ground acceleration levels, the low cycle damage index is calculated as 0.0024 for dense sand.

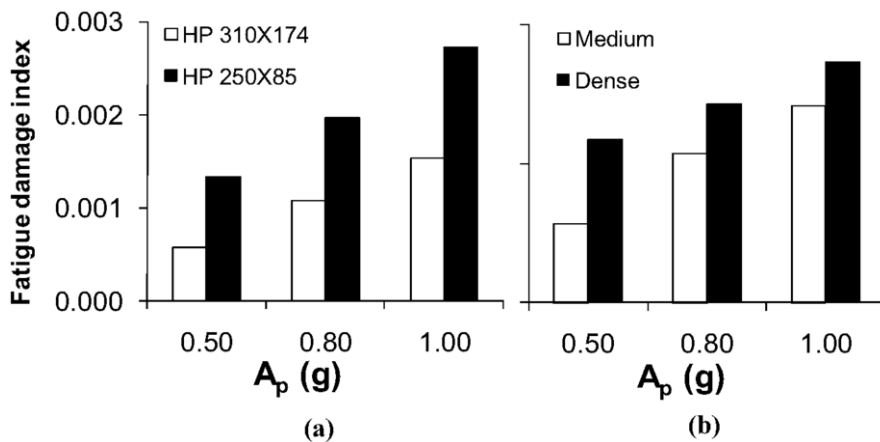


Figure 3. Average values of fatigue damage index vs.  $A_p$  for different (a) pile sizes (b) soil stiffness

**Table 1.** Number of cycles and fatigue damage index for different pile sizes.

Earthquake	Pile Size	Scaled $A_p=0.5g$		Scaled $A_p=0.8g$		Scaled $A_p=1.0 g$	
		Number of cycles	$\sum_i \frac{n_i}{N_i}$	Number of cycles	$\sum_i \frac{n_i}{N_i}$	Number of cycles	$\sum_i \frac{n_i}{N_i}$
		$n_i$		$n_i$		$n_i$	
<b>Loma Prieta</b>	HP 310x174	76	0.0003	59	0.0008	50	0.0013
<b>Actual</b>	HP 250x85	79	0.0005	62	0.0011	48	0.0017
<b>Ap=0.200 g</b>	HP 310x174	65	0.0007	62	0.0012	60	0.0018
<b>Loma Prieta</b>	HP 250x85	72	0.0011	86	0.0021	89	0.0026
<b>Actual</b>	HP 310x174	52	0.0005	42	0.0014	40	0.0020
<b>Ap=0.278 g</b>	HP 250x85	63	0.0012	45	0.0019	41	0.0027
<b>Mammoth Lake</b>	HP 310x174	52	0.0009	62	0.0013	66	0.0017
<b>Actual</b>	HP 250x85	58	0.0030	61	0.0037	65	0.0040
<b>Ap=0.263 g</b>	HP 310x174	88	0.0006	79	0.0012	72	0.0016
<b>Northridge</b>	HP 250x85	86	0.0021	84	0.0026	81	0.0031
<b>Actual</b>	HP 310x174	42	0.0008	46	0.0010	48	0.0014
<b>Ap=0.316 g</b>	HP 250x85	46	0.0018	49	0.0021	53	0.0035
<b>San Fernando</b>	HP 310x174	72	0.0002	67	0.0006	61	0.0009
<b>Actual</b>	HP 250x85	77	0.0005	81	0.0011	85	0.0015
<b>Whitter</b>	HP 310x174						
	HP 250x85						

**Table 2.** Number of cycles and fatigue damage index for different soil stiffness.

Earthquake	Soil stiffness	Scaled $A_p=0.5g$		Scaled $A_p=0.8g$		Scaled $A_p=1.0 g$	
		Number of cycles	$\sum_i \frac{n_i}{N_i}$	Number of cycles	$\sum_i \frac{n_i}{N_i}$	Number of cycles	$\sum_i \frac{n_i}{N_i}$
		$n_i$		$n_i$		$n_i$	
<b>Loma Prieta</b>	Dense	68	0.0008	83	0.0009	86	0.0012
<b>Actual</b>	Medium	76	0.0003	59	0.0008	55	0.0011
<b>Ap=0.200 g</b>	Dense	61	0.0013	63	0.0014	67	0.0016
<b>Loma Prieta</b>	Medium	65	0.0007	62	0.0012	60	0.0014
<b>Actual</b>	Dense	45	0.0014	45	0.0015	41	0.0019
<b>Ap=0.278 g</b>	Medium	52	0.0005	42	0.0014	40	0.0018
<b>Mammoth Lake</b>	Dense	79	0.0018	81	0.0024	86	0.0025
<b>Actual</b>	Medium	52	0.0009	62	0.0013	66	0.0017
<b>Ap=0.263 g</b>	Dense	80	0.0013	85	0.0021	86	0.0025
<b>Northridge</b>	Medium	88	0.0006	79	0.0012	74	0.0017
<b>Actual</b>	Dense	57	0.0009	61	0.0012	57	0.0015
<b>Ap=0.316 g</b>	Medium	42	0.0008	46	0.0010	48	0.0014
<b>San Fernando</b>	Dense	67	0.0007	73	0.0007	77	0.0009
<b>Actual</b>	Medium	72	0.0002	67	0.0006	64	0.0008
<b>Whitter</b>	Dense						
	Medium						

## 8. Conclusions

In this paper, a parametric study is conducted on the low cycle fatigue in IB piles under seismic effects. This parametric study reveals that soil stiffness and pile sizes have significant effects on the cumulative fatigue damage indices, typically used to assess fatigue failure and service life of structures. However, it is found that the cumulative fatigue damage indices calculated for steel H-piles of IBs due to seismic loading are negligible. In the design of small and medium span IBs, these low cycle fatigue effects do not need to be considered.

## References

- [1] AASHTO *Load and Resistance Factor Design (LRFD) Specifications*, Washington, D. C., USA, 2010
- [2] ASTM A36 Standard Specification for Carbon Structural Steel, 1999
- [3] A.Anandarajah, J.Zhang & C.Ealy Calibration of dynamic analysis methods from field test data, *Soil Dynamics and Earthquake Engineering* 25(7-10) 763-772, 2005.
- [4] API (American Petroleum Institute) Recommended Practice and Planning, Designing, and Constructing Fixed Offshore Platforms, Washington, D.C. USA, 2000.
- [5] M.J. Duncan, R.L. Mokwa Passive earth pressure: Theories and tests. *Journal of Geotechnical and Geoenvironmental Engineering* 127(3):248–257, 2001.
- [6] R.T. Cole, K.M. Rollins Passive earth pressure mobilization during cyclic loading *Journal of Geotechnical and Geoenvironmental Engineering* 132(9) 1154–1164, 2006.
- [7] S.K. Koh, R.I. Stephens Mean stress effects on low cycle fatigue for a high strength steel *Fatigue and Fracture of Engineering Materials and Structures* 14(4) 413–28, 1990.
- [8] M.A. Miner, Cumulative Damage in Fatigue, *ASME Journal of Applied Mechanics* 12: 159-164, 1945.

# Buckling behavior of 6082-T6 aluminum alloy columns with box-section and L-section under eccentric compression

Ximei ZHAI<sup>1</sup>, Lijuan SUN<sup>2</sup> and Yuanzheng ZHAO<sup>3</sup>

*School of Civil Engineering, Harbin Institute of Technology, China*

**Abstract.** Experimental studies of 29 pin-ended columns, including 13 box-type and 16 L-type, extruded from 6082-T6 aluminum alloy under eccentric compression, were performed in this paper. The buckling behavior, stability strength and deformation preformation of all the specimens were obtained. A numerical investigation of aluminum alloy columns under eccentric compression was conducted by using finite element analysis software ABAQUS, and the simulation results were verified with experimental results of 29 columns. The results showed that the FE model proposed by this paper can well predict the stability bearing capacity and the deformation characteristic for aluminum alloy columns under eccentric compression. Finally, based on the experimental data and a number of numerical calculation results, a revised interaction equation recommended by Chinese Code for Design of Aluminum Structures to predict the stability bearing capacity of 6082-T6 aluminum alloy specimens loaded by eccentric compression is proposed.

**Keywords.** Aluminum alloy, eccentric compression, finite element analysis, buckling behavior, stability bearing capacity

## Instruction

Aluminum alloy is widely used as a new structural material for its advantages such as the high strength-to-weight ratio, lightness, and corrosion-resistance. The stability strength of aluminum alloy structure components is predominant due to its low value of the elastic modulus. In China aluminum alloy has been applied as load-bearing structures in the past few years [1-3], later than America and Europe countries, due to the lack of experimental data and corresponding analysis, especially the study of the 6082-T6 high strength aluminum alloy. In consideration of practical use of 6082-T6 aluminum alloy in China, this paper reports experimental study of 13 box-type and 16 L-type 6082-T6 aluminum alloy specimens under eccentric expression with varying eccentricities in order to investigate the stability strength and deformation behavior of 6082-T6 aluminum alloy. This research developed a finite element (FE) model to study the buckling strength and stability behavior of aluminum alloy columns in eccentric compression by using FE analysis software ABAQUS and verified this FE analysis model with experimental results of 29 columns. A FE extensive parameter study by

---

<sup>1</sup> Corresponding author: ph. +86 451 86282081, fax. +86 451 86282704, E-mail. [xmzhai@hit.edu.cn](mailto:xmzhai@hit.edu.cn),

<sup>2</sup> [sunlijuan0304@163.com](mailto:sunlijuan0304@163.com)

<sup>3</sup> [804084297@qq.com](mailto:804084297@qq.com)

using this FE analysis model was performed to study the stability bearing capacity of eccentrically compressed B-type columns with different slenderness ratio and eccentricity ratio. The design formula of eccentrically compressed columns from the Chinese Code for Design of Aluminum Structures [4] had been modified based on the simulation results and experiments from this research.

### 1. Test summary

#### 1.1. Design of the specimens

Regularized slenderness ratio  $\bar{\lambda}$ , eccentricity  $e$  and eccentric direction were the main parameters to design the specimens. The details about all the specimens are shown in Table 1. and the sketches of the sections of specimens both B-type and L-type are shown in Figure 1., The regularized slenderness ratio  $\bar{\lambda}$  was then determined in the following expression:

$$\bar{\lambda} = \sqrt{\frac{P_{0.2}}{P_E}} \tag{1}$$

$$P_{0.2} = Af_{0.2} \tag{2}$$

$$P_E = \frac{\pi^2 E_0 I}{L_e^2} \tag{3}$$

Where  $A$  is the cross section area,  $f_{0.2}$  is the 0.2% proof stress,  $E_0$  is the initial Young’s modulus,  $I$  is the moment of inertia about the bending axis,  $L_e$  is the effective length of the specimen which means the distance between the top and the bottom hinges,  $P_{0.2}$  is yield load,  $P_E$  is the Euler load based on  $E_0$ , here  $E_0=68133.3\text{MPa}$ ,  $f_{0.2}=295.87\text{MP}$  according to material performance test [5].

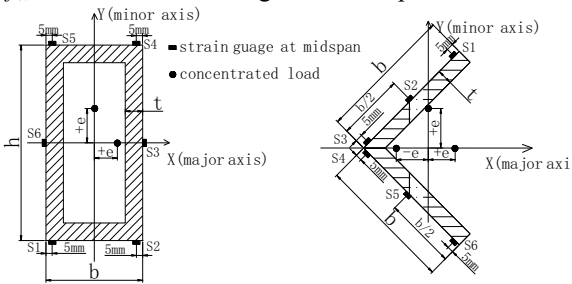


Figure 1. Details of sections

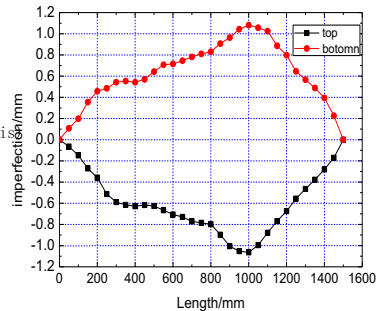


Figure 2. The imperfection of B2-2

#### 1.2. Testing set-up

An electric hydraulic servo control system of MTS Corporation with capacity of 2500kN was adopted for testing loading. The monotonic compressive load was applied to the specimens with loading velocity of 0.005 mm/s. All specimens were fixed to the

steel end plates using high-strength pattern stone with depth of approximate 10~20mm. Except the B-type columns around the minor axis of bending subjected to single-pole hinge, the other columns were subjected to double-pole hinge. Generally, a test was terminated when the compressive load decreased to 20% of the ultimate (maximum) load. Displacement transducers and strain gauges were installed on the mid-span of each specimen to monitor the strains and the deformation of the specimens.

**Table 1.** Details of specimens

Axis	NO.	e mm	b×h(b)×t mm	Le mm	$\bar{\lambda}$	imp mm	$\omega_d$	P <sub>u</sub> kN	P' <sub>u</sub> kN	P' <sub>u</sub> /P <sub>u</sub>	Fail mode
Minor axis	B1-2	10	49.86×99.84×3.94	840.0	0.86	0.38	0.92	169.8	160.2	0.94	F+L
	B3-1	15	49.80×99.80×3.91	1523.0	1.57	0.19	0.92	82.9	84.6	1.02	F+L
	B3-2	15	49.81×99.71×3.87	1520.8	1.56	0.34	0.92	78.3	83.0	1.06	F+L
	B4-1	15	39.72×79.53×3.83	680.0	0.89	0.27	0.72	92.0	94.2	1.02	F+L
	B4-2	15	39.75×79.71×3.88	680.1	0.89	0.05	0.72	96.5	96.1	1.00	F+L
	B5-1	10	39.89×79.83×5.95	424.1	0.58	0.06	0.73	212.8	200.1	0.94	F
	B5-2	10	39.84×79.82×5.92	424.3	0.58	0.08	0.73	181.4	199.3	1.10	F
	L1-1	-15	89.87×89.87×9.79	495.6	0.59	0.38	-	227.5	236.9	1.04	F
	L3-1	15	109.70×109.70×9.96	894.6	0.87	0.63	-	250.3	259.6	1.04	F+N
	L3-2	15	110.24×110.24×9.99	830.0	0.80	2.63	-	262.9	244.0	0.93	F+N
	L5-1	-10	109.64×109.64×9.89	1223.4	1.19	0.58	-	259.8	230.7	0.89	F
	L5-2	10	109.79×109.79×9.86	1294.7	1.25	1.28	-	227.8	221.8	0.97	F+N
	L7-1	-20	109.94×109.94×11.99	1736.3	1.69	1.29	-	157.6	155.0	0.98	F
	L7-2	20	109.94×109.94×11.90	1736.0	1.69	2.70	-	153.6	155.7	1.01	F
	L8-1	-15	69.88×69.88×7.90	1239.5	1.90	0.74	-	54.1	51.5	0.95	F
Major axis	B2-1	20	39.72×79.58×3.90	1595.8	2.10	0.32	0.72	56.6	56.6	1.00	F
	B2-2	20	39.86×79.87×3.91	1595.9	2.09	1.07	0.72	61.4	56.3	0.92	F
	B4-3	15	39.72×79.58×3.89	735.9	0.97	0.13	0.72	133.3	149.6	1.12	F+L
	B4-4	15	39.77×79.70×3.88	735.3	0.97	0.11	0.72	142.3	149.1	1.05	F+L
	B5-3	15	39.92×79.98×5.96	396.4	0.69	0.06	0.73	260.1	246.8	0.95	F
	B5-4	15	39.80×79.78×5.95	396.7	0.69	0.19	0.73	233.3	245.4	1.05	F
	L2-1	10	109.72×109.22×9.90	755.8	0.73	0.59	-	428.0	425.6	0.99	F+N
	L2-2	10	109.92×109.92×9.90	755.8	0.73	0.63	-	430.7	426.4	0.99	F+N
	L4-2	15	89.94×89.94×9.83	894.8	1.06	0.20	-	252.8	276.7	1.09	F
	L6-1	15	69.84×69.84×5.87	1016.3	1.55	0.20	-	89.8	83.2	0.93	F
	L6-2	15	69.86×69.86×5.88	1016.4	1.55	0.42	-	87.7	86.5	0.99	F
	L6-3	15	69.86×69.86×5.85	1015.6	1.55	0.18	-	97.5	85.0	0.87	F
	L8-2	20	69.92×69.92×7.97	1295.5	2.00	0.87	-	77.0	70.0	0.91	F
	L8-3	20	69.98×69.98×7.98	1296.6	1.99	1.41	-	73.0	68.9	0.94	F

Note: e=eccentricity, imp= amplitude of overall imperfection, F=flexural buckling, L=local buckling, N=torsional buckling, P<sub>u</sub>=ultimate load from tests, P'<sub>u</sub>=ultimate load from FEA.

### 1.3. Measurement of the initial imperfection

The residual stress of the specimens can be ignored because the 6082-T6 aluminum alloy were processed by extrusion forming [6], so only the initial geometric imperfection was measured in this research. The initial geometric imperfection was obtained every 5cm by the high-precision laser displacement along the longitudinal centerline of the webs of specimens. The imperfection curves of B2-2 were shown in Figure 2. and the amplitudes of the imperfection curves for all the specimens were shown in Table 1. As shown in Table 1, the initial imperfection of most specimens was less than 1/1000 of the effective length L<sub>e</sub>.

### 1.4. Results and analysis

All the box-type aluminum alloy specimens were observed to fail mainly by overall flexural buckling around the minor axis of bending no matter the eccentricity along minor axis or major axis, and several box-section columns with large width-thickness ratio or little slenderness ratio failed by the interaction of local and overall buckling.

All the local buckling appeared later than the overall buckling. The L-type specimens around minor axis of bending failed by overall flexural buckling around the minor axis, These L-type columns with little  $\bar{\lambda}$  and positive eccentricity failed by flexural buckling companied by torsional buckling later after ultimate load. As for L-type specimens around major axis of bending, the short specimens ( $\bar{\lambda} < 1.0$ ) failed by flexural-torsional buckling and the long specimens ( $\bar{\lambda} > 1.0$ ) failed by overall buckling around the minor axis shown in Table 1. The curves of load–displacement and strains of partial specimens are shown in Figure 3. and Figure 4.

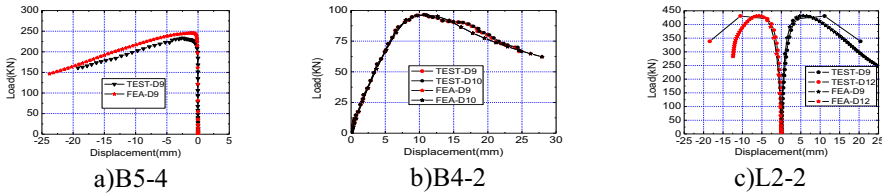


Figure 3. Load-mid span displacement

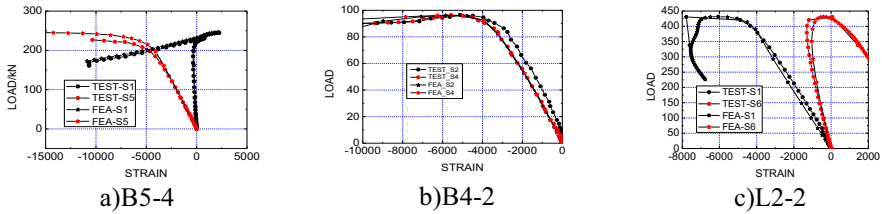


Figure 4. Load-mid span strain

## 2. Finite element analysis

### 2.1. Modeling

The Ramberg-Osgood expression [7], as shown in Eq. (4), was used to describe the stress-strain relationship. The parameters of the expression were based on the measured material properties of aluminum alloy 6082-T6 from tensile tests. Eq. (4) involves the initial Young’s modulus ( $E_0$ ), the 0.2% proof stress ( $f_{0.2}$ ) and a parameter  $n$  which can be determined using the 0.1% and 0.2% proof stress as shown in Eq. (5).

$$\varepsilon = \frac{\sigma}{E_0} + 0.002 \left( \frac{\sigma}{f_{0.2}} \right)^n \tag{4}$$

$$n = \frac{\ln(2)}{\ln(f_{0.2} / f_{0.1})} \tag{5}$$

In this research all specimens were fixed to the steel plates using pattern stone with depth of approximate 20mm. The pattern stone only contributed little to the equivalent end plate thickness and the pattern stone can be ignored as Young’s modulus of the pattern stone was only 1/40 of the steel. Thus only the thickness of the steel plate of 20mm, was considered as the equivalent thickness of the end plate. As shown in Figure 5. A 4-node shell element S4 with full integration was adopted for the modeling of



aluminum alloy specimens with the mesh size of 5mm×5mm, and the steel end plates were simulated using C3D8R, an 8-node linear brick element with reduced integration.

The measured amplitude of geometric imperfections and overall mode created by buckling analysis was adopted. Considering the local buckling which happened to the box-type specimens, the superposition of local and overall modes was introduced for the box-type specimens. The Walker expression<sup>[8]</sup> was used to determine the amplitude of the local imperfection  $\omega_d$  in the following form.

$$\omega_d = 0.3t\sqrt{f_{0.2}/\sigma_{cr}} \quad (6)$$

Where  $t$ , is the thickness of specimens section, and  $\sigma_{cr}$  is the elastic local buckling stress obtained from the built-in eigenvalue buckling analysis.

## 2.2. Comparison of test and numerical results

To demonstrate the feasibility and accuracy of the FE analysis method in this paper, the simulation results of all specimens are presented and compared with test results in Table 1. As shown in Table 1, the ratios of buckling load from test and simulation results, respectively for all specimens vary from 1% to 13%, and the FEA model proved by this paper can be capable of producing accurate buckling strength. The buckling failure modes of specimen B4-4 and L2-2 in test and in simulation are shown in Figure 5, respectively. In addition, Figure 5 and Figure 6 showed that the FE model can well predict the stability bearing capacity, the deformation characteristic and strain of aluminum alloy columns under eccentric compression. The failure modes from simulation about buckling of specimens are coincident with the observed phenomenon from test as shown in Figure 5.

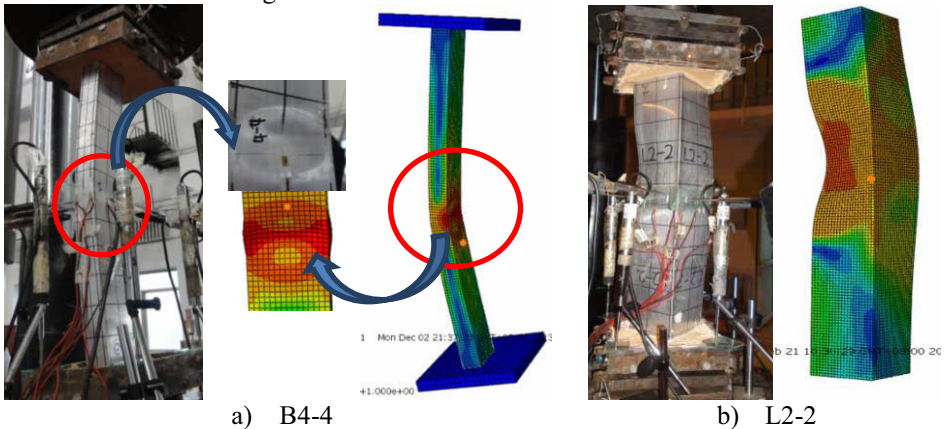


Figure 5. Failure mode comparison between test and FEA

## 3. FE extensive parameter study

Some factors including section dimension, slenderness ratio and eccentricity, influenced the buckling bearing capacity for the aluminum alloy columns. Three kinds of B-type columns with the dimension of 40×80×4 mm, 40×80×6 mm, 50×100×4 mm, were considered in the extensive parameter analysis. The regularized

slenderness ratio  $\bar{\lambda}$  ranged from 0.5 to 3.0. The eccentricity ratio (e/b) of the specimens around major axis of bending ranged from 0.1 to 10, and that of the specimens bending around the minor axis ranged from 0.1 to 6. The overall geometric imperfection of these specimens was Le/1000. The results were shown at Figure 6, and Figure 7. In the following figures,  $N_y = f_{0.2}A$ ,  $M_y = f_{0.2}W_{1x}$  (A : the area of the section;  $W_{1x}$  : the section modulus of in-plane).

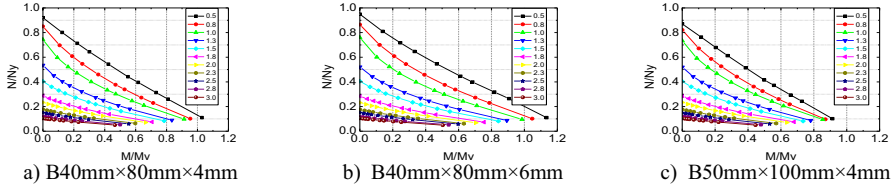


Figure 6.  $M/M_y-N/N_y$  interaction curve around the minor axis of bending

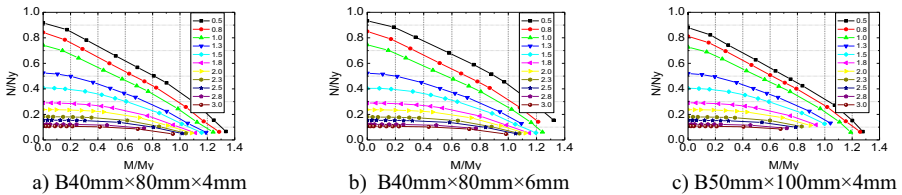


Figure 7.  $M/M_y-N/N_y$  interaction curve around the major axis of bending

As the results showed, the ultimate stability loads of the short specimen ( $0.5 < \bar{\lambda} \leq 1.8$ ) were insignificantly affected by the slenderness ratio, whereas, the ultimate loads of the long columns ( $\bar{\lambda} > 1.8$ ) were not sensitive to the increasing of slenderness ratio. It can be concluded from Figure 8, that the stability bearing capacity of B-type columns descends with the increasing of width-thickness ratio b/t.

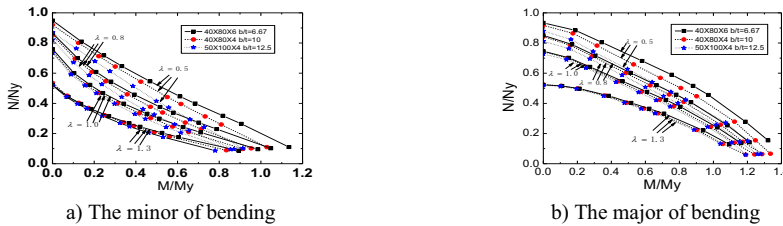


Figure 8.  $M/M_y-N/N_y$  interaction curve comparison of three sections

#### 4. Proposed design approach for stability bearing capacity

The interaction equation was recommended by Chinese Code for Design of Aluminum Structures [4] for eccentrically compressed columns, as shown in Eq. (7) and Eq. (8). The stability bearing capacity for columns around the minor axis of bending was calculated by Eq. (7). As for columns around the major axis of bending, Eqs.(7) and (8) should be checked. In this paper the parameters of the Eq. (7) and Eq. (8) were revised by FE extensive parameter study. The  $\eta_1$  in Eq. (7) was replaced by 0.45 from

0.75, while  $\eta$  in Eq. (8) was replaced by 0.5 from 0.7. As shown in Figure 9, the revised interaction curve was closer to the simulation results than the curve from Chinese codes, and for the short columns ( $\bar{\lambda} < 1.0$ ) around the minor axis of bending, the accuracy of the two approaches was neither high. It can be concluded from the Figure 10 and Figure 11, that the interaction equation of the Chinese codes was conservative compared with the test results and the simulation results, no matter for columns around the minor axis of bending or around the major axis of bending.

In-plane: 
$$\frac{N}{\varphi_x A} + \frac{\beta_{mx} M_x}{\gamma_x W_{1x} (1 - \eta_1 N / N'_{Ex})} \leq f_{0.2} \tag{7}$$

Out-plane: 
$$\frac{N}{\varphi_y A} + \eta \frac{M_x}{\varphi_b W_{1x}} \leq f_{0.2} \tag{8}$$

Where  $\beta_{mx}$  is the coefficient of bending moment ( $\beta_{mx} = 1$  for columns with the equal moments at the two sides);  $M_x$  is the maximum moment of the columns;  $\varphi_x$  and  $\varphi_y$  are the stability coefficients of columns under concentric compression both calculated by Eq. (9) ( $\varphi_x$  : in-plane;  $\varphi_y$  : out-plane);  $\gamma_x$  is the plastic adaption coefficient of cross section;  $\varphi_b$  is the stability coefficient of the flexural component ( $\varphi_b = 1.0$  for B-type section);  $N'_{Ex}$  is calculated by Eq.(10).

$$\varphi = \left( \frac{1}{2\bar{\lambda}^2} \right) \left\{ \left( 1 + 0.2(\bar{\lambda} - 0.15) + \bar{\lambda}^2 \right) - \left[ \left( 1 + 0.2(\bar{\lambda} - 0.15) + \bar{\lambda}^2 \right)^2 - 4\bar{\lambda}^2 \right]^{1/2} \right\} \tag{9}$$

$$N'_{Ex} = N_y / (1.2 \times \bar{\lambda}^2) \tag{10}$$

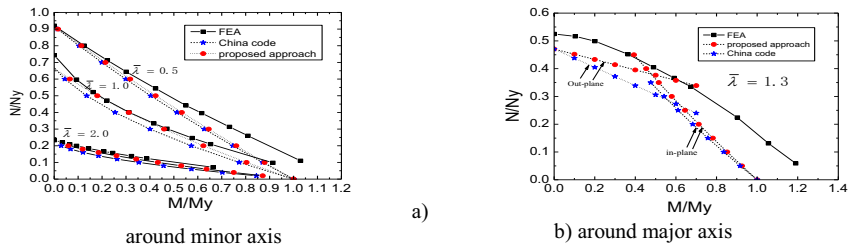


Figure 9. Comparison of FEA, Chinese codes and proposed approach

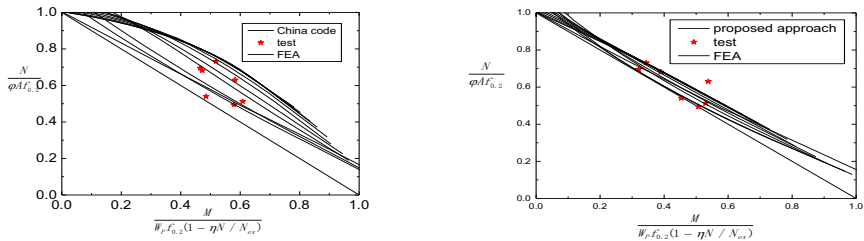
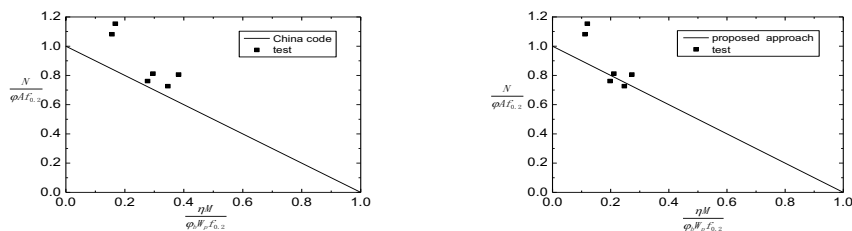


Figure 10. Comparison of in-plane stability bearing capacity



a) Chinese codes and test results

b) proposed approach and test results

**Figure 11.** Comparison of out-plane stability bearing capacity

## 5. Conclusions

- 1) All the box-type aluminum alloy specimens were observed to fail mainly by overall buckling around the minor axis, and several box-section columns with large width-thickness ratio or little slenderness ratio failed by the interaction of local and overall buckling. The L-type specimens around minor axis of bending failed by overall flexural buckling around the minor axis, and these L-type columns with little  $\bar{\lambda}$  and positive eccentricity failed by flexural buckling accompanied by torsional buckling later after ultimate load. As for L-type specimens around major axis of bending, the short specimens ( $\bar{\lambda} < 1.0$ ) failed by flexural-torsional buckling and the long specimens ( $\bar{\lambda} > 1.0$ ) failed by overall buckling around the minor axis.
- 2) The FE model proposed by this paper based on the ABAQUS can well predict the stability bearing capacity, the failure mode and the deformation characteristic of 6082-T6 aluminum alloy columns under eccentric compression.
- 3) The stability strength of the box-type columns decreased as the regularized slenderness ratio  $\bar{\lambda}$  and width-thickness ratio increased. Especially, the less the regularized slenderness ratio is, the greater the effect on stability bearing capacity.
- 4) The interaction equation of the stability strength for the 6082-T6 aluminum alloy columns with symmetrically bidirectional section in eccentric compression from the Chinese Code for Design of Aluminum Structures was conservative.

## Acknowledgments

The authors wish to acknowledge the support from National Nature Science Foundation of China under the Grant No. 51108126.

## Reference

- [1] Yujin Wang, Feng Fan, Hongliang Qian and Ximei Zhai. Experimental study on constitutive model of high-strength aluminum alloy 6082-T6, *Journal of Building Structures*, 2013, 34(6):113-120. (in Chinese)
- [2] Ximei Zhai, Yujin Wang, Hai Wu and Feng Fan. Research on stability of high strength aluminum alloy columns loaded by axial compressive load. *Advanced Materials Research*. 2010, Vols. 168-170: 1915-1920.

- [3] Ximei Zhai, Hai Wu and Lijuan Sun. Stability Strength of Aluminum Alloy Columns under Concentric Compression, *10th International Conference on Advances in Steel Concrete Composite and Hybrid structures*, 2012.6, 60-67, Singapore.
- [4] GB50429. Chinese Code for Design of Aluminum Structures. Beijing: *MOHURD, PRC* 2007. (in Chinese)
- [5] Yujin Wang, Hongliang Qian and Feng Fan. Experimental study on stress-strain relationship and mechanical properties of aluminum alloy 6082-T6, *Engineering Mechanics*, 2013, 30(6):309-313. (in Chinese)
- [6] Mazzolani F. M. Structures of aluminum alloy. Translated by Zhumei Tan. Beijing: *Metallurgical Industry Press*, 1992.
- [7] Ramberg W and Osgood W R. Description of stress-strain curves by three parameters. Washington, D.C.: National Advisory Committee for Aeronautics, TN-902, 1943.
- [8] ZHAI Ximei, WU Hai, FAN Fen. Numerical investigation of aluminum alloy column in concentric compression, *6th International Symposium on Steel Structures*, 2011.11, 738-745, Seoul, Korea.

# A different approach to the design of steel columns

Anthony F. GEE<sup>a</sup> and Primus V. MTENGA<sup>b,1</sup>

<sup>a</sup>Tony Gee International, FAMU/FSU College of Engineering

<sup>b</sup>FAMU/FSU College of Engineering

**Abstract:** The Paper describes a method of obtaining the entire non-linear elastic behavior of prismatic columns having an initial out-of-straightness and a variety of end restraints and loading conditions. It is shown that columns do not in fact ‘buckle’ due to instability but rather fail under the combined effects of axial load and bending. For over 250 years eminent researchers have attempted to reconcile empirical data with the Euler critical axial stress. Failure loads were consistent with this stress, although at a slightly lower level attributable to initial imperfections, up to a certain value, known as the ‘elastic limit’ and usually assumed to be slightly less than half the yield stress of the material. Clearly the strength of the material sets an upper limit to the capacity of a column but researchers have never produced a satisfactory theory to explain why failure loads deviate from the Euler critical stress above this ‘elastic limit’. Consequently most current specifications for the design of steel columns are based on ‘column curves’ relating the critical axial stress to the slenderness ratio and consisting of two distinct parts: below the ‘elastic limit’, the equation to the curve is related directly to the Euler equation and is therefore independent of the strength of the material, above this it is simply a mathematically derived curve joining this point to the yield strength of the material. The subject method is continuously applicable over the whole range of slenderness ratios. It also allows a range of end restraint and loading conditions to be analyzed. Although researchers have recognized the potential benefits of obtaining the non-linear behavior of a column, it has always been considered too time-consuming to be used in everyday engineering design. However, the method is codified and tabulated in terms of non-dimensional parameters to provide a practical design office tool.

**Keywords.** Buckling, column, slenderness ratio, steel

## Current methods

Current methods for calculating the strength of steel compression members, as exemplified by the *AISC Specification* [1], are based on the use of the ‘Column Curve’ developed by the Structural Stability Research Council, formerly the Column Research Council. The curve is empirically derived: the mathematical expression of the curve is given by Equations E3-2 and E3-3 of the *AISC Specification* and in the Commentary it is said that “the equations are based on a reasonable conversion of research data into strength equations”. Equation E3-3 simply states that, for values of  $F_e/F_y < 0.44$ ,  $F_{cr} = 0.877 F_e$ , where  $F_e$  is the Euler buckling stress for an idealized perfect strut and  $F_{cr}$  is the critical or ultimate design stress for a pin-ended column.

<sup>1</sup>Corresponding author: [mtenga@eng.fsu.edu](mailto:mtenga@eng.fsu.edu)

The factor 0.877 is intended, therefore, to account for initial imperfections in the member. In the Commentary to previous versions of the Specification, it was stated that it is based on an initial ‘out-of-straightness’ of  $L/1,500$ . Equation E3-2 is nothing more than the mathematical expression of a curve for  $F_e/F_y > 0.44$  providing a fit between Equation 3-3 at  $F_e/F_y = 0.44$  and the upper limit represented by the ‘squash load’,  $F_{cr} = F_y$  at  $L = 0$ .

The physical parameter forming the basis for the application of these equations is the ‘slenderness ratio’,  $L/r$  or, more properly, the ‘effective slenderness ratio’,  $KL/r$ , where  $K$  is a factor to account for end conditions. Values for  $K$  for various combinations of free-, pin- and fixed-ended conditions are given in Table C-C2.2 in the Specification but they are only recommended for use “when ideal end conditions are approximated” and because true fixity cannot be relied upon, they are necessarily conservative. The method is, therefore, at best arbitrary and empirical. It is also inflexible in that it does not allow the designer to select values for initial imperfections or end restraint and, for this reason, is probably overly conservative in application: the vast majority of steel compression members are, in practice, designed as pin-ended. It has, however, stood the test of time and because they are familiar with it, most practicing engineers may prefer to continue to use it for those cases where it is appropriate to treat the member as pin-ended.

Furthermore, it is essential that any proposed new method of design shall produce substantially similar results – for those cases in which direct comparison is possible – if it is to achieve universal acceptance within the industry.

## 1. Philosophical basis

The proposed method is based on the concept that real compression members, as opposed to idealized perfect pin-ended struts, do not ‘buckle’ when the axial stress reaches a critical value but fail under the combined effects of axial load and bending when the maximum combined stress reaches yield. In other words, whereas the acceptance criteria for a column under the AISC Specifications are:

$$\phi_c P_n \geq P_u \quad (\text{Load and Resistance Factor Design})$$

or:

$$\frac{P_n}{\Omega} \geq P \quad (\text{Allowable Stress Design})$$

where, in both cases:

$$P_n = A_g \cdot F_{cr}$$

the acceptance criteria under the proposed method are exactly the same except that, in

$$\text{both cases, } P_n \text{ is such that: } \frac{P_n}{A_g} + \frac{M_n}{S} \leq F_y$$

where  $M_n$  is the maximum bending moment in the member under an axial load  $P_n$ . It is only necessary, therefore, to find the relationship between the moment  $M_n$  and the load  $P_n$ .

In the *Guide to Stability Design Criteria for Metal Structures* [2] which summarizes the work of the SSRC, it is stated that: “To determine the failure load of an actual

(compression) member it is necessary to take the initial imperfections into account and to consider the entire nonlinear load-deflection curve of the member. Unfortunately, the process of obtaining such a curve is often too difficult and time consuming to be used in routine engineering design”.

This Paper describes how equations to these non-linear load-deflection curves up to the point of first yield have been obtained for a wide range of end conditions and the resulting load/maximum moment relationships tabulated in a general dimensionless way such that they can readily be used for routine engineering design [3].

## 2. Pin-ended column

To see how this works, consider the simple case of a pin-ended column, having an initial out-of-straightness  $e$ , subject to an axial compressive force  $P$ .

The equation of flexure is:

$$M = -EI \frac{d^2 y}{dx^2} = P(y + y_0)$$

or:

$$\frac{d^2 y}{dx^2} = -a^2 \left[ y + e \cdot \sin\left(\frac{\pi x}{L}\right) \right]$$

$$\text{where: } a = \sqrt{\frac{P}{EI}}$$

and the initial shape of the strut is assumed to be approximately:

$$y_0 = e \cdot \sin\left(\frac{\pi x}{L}\right)$$

The solution to this differential equation is:

$$y = \left[ \frac{(aL)^2}{\pi^2 - (aL)^2} \right] e \cdot \sin\left(\frac{\pi x}{L}\right)$$

so that:

$$M = P \cdot e \left[ \frac{\pi^2}{\pi^2 - (aL)^2} \right] \sin\left(\frac{\pi x}{L}\right)$$

$M$  is a maximum when:  $\sin\left(\frac{\pi x}{L}\right) = 1$  or:  $\left(\frac{\pi x}{L}\right) = \frac{\pi}{2}$  so that:

$$M_{\max} = P \cdot e \left[ \frac{\pi^2}{\pi^2 - (aL)^2} \right]$$

Note that:  $(aL^2) = \left(\frac{PL^2}{EI}\right)$  so that:  $M_{\max} \rightarrow \infty$  as:  $P \rightarrow \frac{\pi^2 EI}{L^2}$



i.e. the maximum moment tends to infinity as the load approaches the Euler critical load.

$\frac{M_{\max}}{P.e}$  can now be plotted against  $\frac{PL^2}{EI}$  so that the maximum moment in any given column having properties  $L, E, I$  and  $e$  can be obtained for any value of the load  $P$ , since both  $\frac{M}{P.e}$  and  $\frac{PL^2}{EI}$  are dimensionless functions. This becomes the new 'Column Curve'.

It can be seen that  $\frac{PL^2}{EI}$  replaces  $KL/r$  as the defining parameter in the design process.

### 3. General solution

In order to expand this principle to columns having a variety of end conditions and loadings, a solution was obtained for the general case of a column, having an initial out-of-straightness  $e$ , subject to an axial compressive force  $P$ , end moments  $M_1$  and  $M_2$  and end reactions  $R_1$  and  $R_2$ .

The equation of flexure is:

$$M = -EI \frac{d^2 y}{dx^2} = P(y + y_0) + R_1 x - M_1 \quad \text{or:}$$

$$\frac{d^2 y}{dx^2} = -a^2 \left[ y + e \cdot \sin\left(\frac{\pi x}{L}\right) + \frac{R_1}{P} x - \frac{M_1}{P} \right] \text{ where, as before: } a = \sqrt{\frac{P}{EI}}$$

and the initial shape of the strut is assumed to be approximately:

$$y_0 = e \cdot \sin\left(\frac{\pi x}{L}\right)$$

The solution to this differential equation is:

$$y = \frac{R_1}{P} \left[ \left( \frac{L}{\sin(aL)} \right) \sin(ax) - x \right] + \frac{M_1}{P} \left[ 1 - \left( \frac{1 - \cos(aL)}{\sin(aL)} \right) \sin(ax) - \cos(ax) \right] + \left[ \frac{(aL)^2}{\pi^2 - (aL)^2} \right] e \cdot \sin\left(\frac{\pi x}{L}\right)$$

There are two unknowns,  $R_1$  and  $M_1$ , in this equation so that, with the use of two appropriate boundary conditions, particular solutions can be derived for columns having a variety of end restraints and loadings. For example:

for a fixed ended column,  $\frac{dy}{dx} = 0$  when:  $x = 0$  and:  $x = L$  so that:

$$y = \left[ \frac{\pi a L}{\pi^2 - (aL)^2} \right] \left\{ \left[ \frac{\sin(aL)}{1 - \cos(aL)} \right] \cdot [1 - \cos(ax)] - \sin(ax) + \left( \frac{aL}{\pi} \right) \sin\left(\frac{\pi x}{L}\right) \right\}$$

and:

$$M = P.e \left[ \frac{\pi a L}{\pi^2 - (aL)^2} \right] \left\{ \left( \frac{\pi}{aL} \right) \sin\left(\frac{\pi x}{L}\right) - \left[ \frac{\sin(aL)}{1 - \cos(aL)} \right] \cos(ax) - \sin(ax) \right\}$$

$M$  is a maximum when:  $\frac{dM}{dx} = 0$ , i.e. when:  $x = 0$  or:  $x = L$  so that:

$$M_{\max} = P.e \left[ \frac{\pi aL}{\pi^2 - (aL)^2} \right] \left[ \frac{\sin(aL)}{1 - \cos(aL)} \right]$$

while for a column fixed at one end and pinned at the other,

$M_1 = 0$  when:  $x = 0$  and:  $\frac{dy}{dx} = 0$  when:  $x = L$  so that:

$$M = P.e \left\{ \left[ \frac{\pi^2}{\pi^2 - (aL)^2} \right] \sin\left(\frac{\pi x}{L}\right) - \left[ \frac{\pi \sin(ax)}{\sin(aL)} \right] \left[ \frac{(aL)^2}{\pi^2 - (aL)^2} \right] \left[ \frac{1}{aL \cdot \sin(aL) - \cos(aL)} \right] \right\} \quad M \text{ is a}$$

maximum when:  $\frac{dM}{dx} = 0$ , i.e. when:  $x = L$  so that:

$$M_{\max} = P.e \left[ \frac{\pi (aL)^2}{\pi^2 - (aL)^2} \right] \left[ \frac{\sin(aL)}{aL \cdot \cos(aL) - \sin(aL)} \right]$$

#### 4. Elastic (passive) end restraint

Two other cases are particularly useful for design purposes. The first is that of a column having an initial out-of-straightness  $e$ , subject to an axial compressive force  $P$  and to restraining moments  $\bar{M}$  at the ends which are proportional to the rotation. The moment/rotation characteristic is represented by a ‘stiffness’ parameter  $Q$  where:

$$Q = \frac{\bar{M}L}{EI} \left( \frac{1}{\theta} \right) \text{ so that: } \bar{M} = Q \cdot \left( \frac{EI}{L} \right) \cdot \theta \text{ and: } \theta = \left( \frac{dy}{dx} \right)$$

The two required boundary conditions are then:

$$M_1 = Q \cdot \left( \frac{EI}{L} \right) \cdot \left( \frac{dy}{dx} \right) \quad \text{when: } x = 0 \quad \text{and:}$$

$$M_2 = Q \cdot \left( \frac{EI}{L} \right) \cdot \left( \frac{dy}{dx} \right) \quad \text{when: } x = L$$

The solution is complex and the resulting equations very long but expressions have been obtained for the relationship between the non-dimensional parameters  $\frac{M_{\max}}{P.e}$  and

$$\frac{PL^2}{EI} \text{ for a range of values of } Q \text{ from } 0 \text{ (pinned) to } \infty \text{ (fixed) [Figure 1]}$$

The limitations of the mathematics restrict the solution to the case where both ends have the same ‘stiffness’  $Q$ . However, where the values of  $Q$  at the two ends are reasonably similar, use of an average value produces sufficiently accurate results. To cater for extreme cases, solutions were also obtained for struts elastically restrained at

one end and pinned at the other and elastically restrained at one end and fixed at the other. Armed with curves or tables corresponding to the three cases, judicious interpolation allows the strength of a prismatic compression member having a defined initial out-of-straightness and almost any combination of end restraint conditions to be obtained.

Where the member frames into other members at an end, the appropriate value of Q is obtained from:

$$Q = \frac{k_1 + k_2 + k_3, etc}{k} \text{ where: } k = \frac{EI}{L}$$

for the compression member and  $k_1, k_2, k_3, etc.$  are the corresponding values for the other members into which it frames.

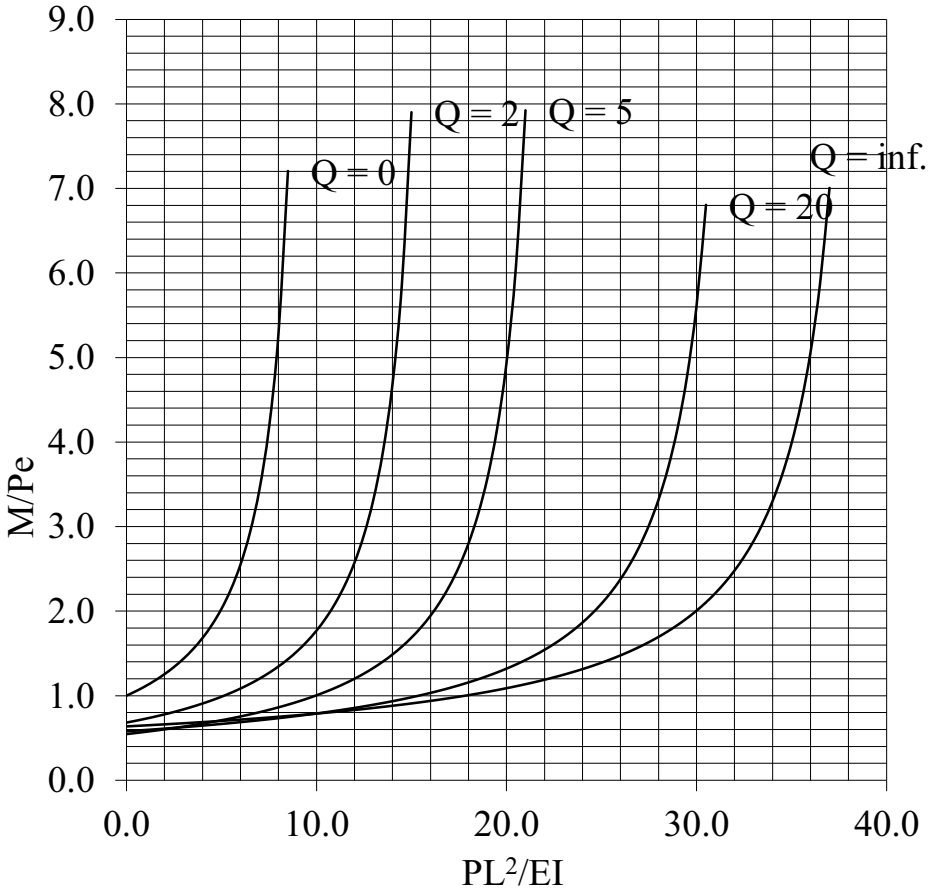


Figure 1. Column elastically restrained at both ends

### 5. Applied (active) end moments

The second case is that of a column subject to an axial compressive force  $P$  and applied moments  $M_1$  and  $M_2$  at the ends, the usual output from computerized analysis of structural frames.  $M_2$  is the larger of the two applied end moments  $M_1$  and  $M_2$ .

The maximum bending moment in the column is defined in terms of the non-dimensional parameters  $m$  and  $k$ :

$$m = \frac{M_{\max}}{M_2} \quad \text{and:} \quad k = \frac{M_1}{M_2} \quad \text{so that:} \quad -1 \leq k \leq 1$$

$k$  being positive if the member is in single bending, negative if it is in double bending.

Again, the solution is complex and the resulting equations very long but as before expressions have been obtained for the relationship between the non-dimensional

parameters  $m$  and  $\frac{PL^2}{EI}$  for a range of values of  $k$  [Figure 2]

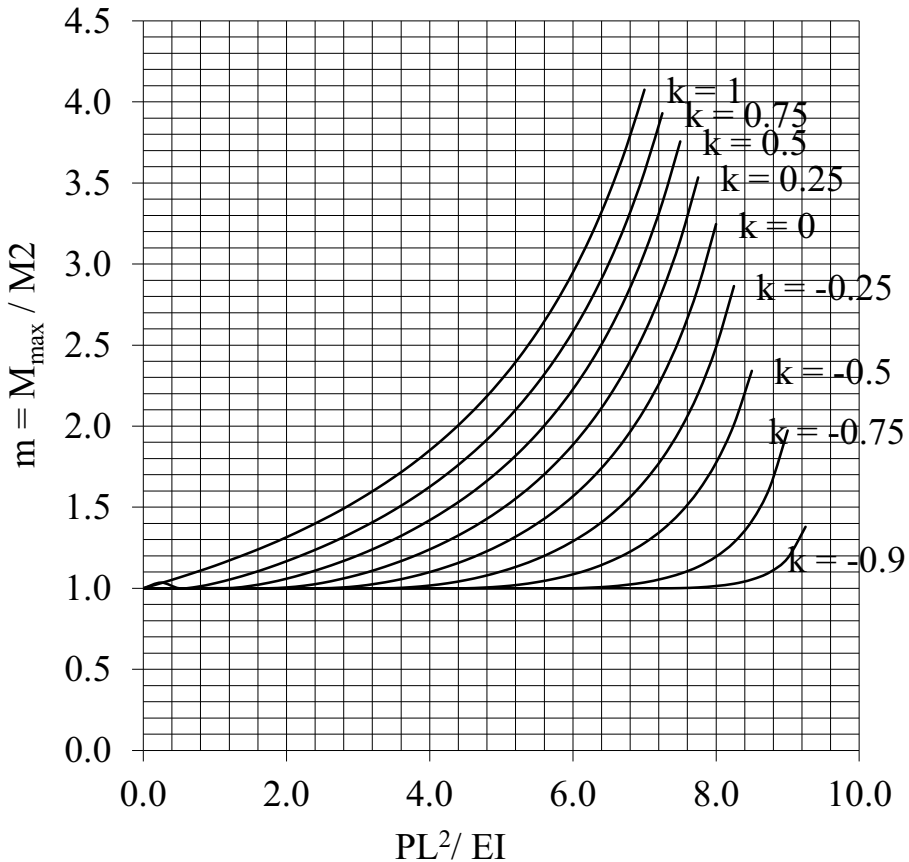


Figure 2. Column with applied end moments

## 6. Parametric studies

A large number of parametric studies have been carried out to confirm that for members having typical proportions, the proposed method gives very similar results to those obtained using current methods: in no case was there ever a difference of more than two section weights between the two methods. Moreover, since the proposed method is based on mathematical principles rather than empirical data, there might be some justification for concluding that any differences are due to shortcomings in the current system. In the case of long slender sections, the steep rise in maximum combined stress between the 'good' and 'no good' sections revealed by the proposed method shows clearly how close the sections are to a 'buckling' type failure, that is to say the deflection and hence the maximum bending moment are increasing rapidly.

## 7. Conclusions

The proposed method has considerable advantages over current methods. It enables the actual out-of-straightness of the member to be taken into account, it allows for variable degrees of elastic restraint between pinned and fully fixed to be assumed for the ends of the member and it enables designs to be obtained for columns subjected to lateral loading. In the case of compression members with applied end moments, it is significantly faster to use. Solutions have been obtained and design tables compiled for a large number of cases including:

- Both ends elastically restrained with initial out-of-straightness
- One end elastically restrained, one end pinned, with initial out-of-straightness
- One end elastically restrained, one end fixed, with initial out-of-straightness
- One end fixed, one end free, with initial out-of-straightness
- Both ends elastically restrained with uniformly distributed lateral loading
- One end elastically restrained, one end pinned, with uniform loading
- One end elastically restrained, one end fixed, with uniform loading
- One end fixed, one end free, with uniform loading
- Both ends elastically restrained with a single, central concentrated lateral load
- One end elastically restrained, one end pinned, with a concentrated load
- One end elastically restrained, one end fixed, with a concentrated load
- One end fixed, one end free, with a concentrated load
- Both ends fixed with applied relative lateral displacement
- One end fixed, one end pinned, with applied displacement
- One end fixed, one end free, with applied displacement
- Applied moments at both ends
- Applied moment at one end, pinned at the other
- Applied moment at one end, fixed at the other

Collected together, these tables would provide a very useful design office aid.

## **Acknowledgement**

The work described in this Paper formed the basis of a doctoral study by Anthony F. Gee in the Florida A&M University/Florida State University College of Engineering. Dr. Primus V. Mtenga is his supervising professor.

## **References**

- [1] American Institute of Steel Construction (2010), Specification for Structural Steel Buildings, *ANSI/AISC 360-10*,
- [2] Galambos, T.V. (1988), Guide to Stability Design Criteria for Metal Structures, 4<sup>th</sup> Edition, *John Wiley & Sons*, New York, NY. 15
- [3] Gee, Anthony F. (2013), Versatile Method for the Design of Steel Compression Members, *ASCE Practice Periodical on Structural Design and Construction*, May 2013

# A critical review on current and proposed structural fire engineering codes for steelwork in South Africa

Richard WALLS<sup>1</sup>, Celeste VILJOEN, Hennie DE CLERCQ and Johan RETIEF  
*University of Stellenbosch, South Africa*

**Abstract.** This paper presents a review on the code requirements in South Africa for steelwork exposed to fire conditions, both currently and the proposed changes to the codes. The SA hot-rolled steel design code, SANS 10162-1 [1], is based upon the Canadian steel code, CSA S16 [2], and contains negligible guidance in relation to fire design. It is currently being proposed that the updated Canadian code be adopted for the next revision of SANS 10162, along with its new fire engineering guidelines (Annex K). In this paper the proposed new guidelines are presented and investigated relative to local building code requirements as outlined in the National Building Regulations (described in SANS 10400: Part T [3]). They are also compared to the Eurocode suite of design guides [4,5], which are considered to be technically advanced codes. It can be seen that the Canadian guidelines can be effectively adopted in the next iteration of SANS 10162, and provide results consistent with the Eurocode design equations. However, in the long term it may be necessary to move towards or consult the Eurocodes because of the much broader scope they encompass.

**Keywords.** Fire engineering, structural steelwork, SANS 10400

## Introduction

In South Africa, fire engineering is rapidly moving from a topic addressed after designs are complete, to a core theme that has to be considered during the design phase of any structure. Internationally, great advances have been made in this field, but little has been transferred into South African design codes, especially in terms of structural steelwork. Options for transferring such advances to South Africa range from extending the adoption of the Canadian standard for structural steel to considering the comprehensive Eurocode provisions for structural fire design.

## 1. Code requirements

It is a fact that codes play an important part in fire design. However, designers should not be limited to blindly following codes as they cannot necessarily be applied in the same way in every situation. There needs to be sound engineering principles based on research and experience when going outside of standard code requirements.

---

<sup>1</sup>Corresponding author: richardwalls28@gmail.com. +27 (0)72-372-4096

South Africa's current design codes should not be used in isolation to go beyond basic prescriptive fire code requirements to produce true rational designs, because of their limited scope. Thus, as with most design codes in a relatively smaller economy like South Africa international codes may be adapted, adopted or consulted. The discussions below are centred around this situation.

The most recent version of the Canadian S16 code for hot rolled steel structures contains guidance for fire design. A minimal and effective way to provide for fire design is obviously to include these provisions when adopting CSA S16 as the future SANS 10162-1. At the other end of the scale, an equivalent transfer of the comprehensive Eurocodes on fire design would be a major undertaking.

### *1.1. South African building code - SANS 10400*

The primary source of information for any building requirement issue in South Africa is the National Building Regulations (NBRs), from which we get SANS 10400-T [3] "The application of the National Building Regulations. Part T: Fire Protection". SANS 10400-T covers a wide range of topics including requirements for buildings, fire escapes, sprinkler protection, occupancy and other information.

Steelwork within SANS 10400 is addressed very superficially. The primary guidelines relate directly to the fire resistance of steel columns and lists the minimum thickness of protection material that must be applied to give columns certain fire resistance ratings. However, this does not account for the thermal properties of the protective coating, the load on the member, the shape of the steel section and numerous other factors which influence the resistance of a steel section at elevated temperatures.

Other clauses in SANS 10400 relating to steelwork specifically include:

- "No unprotected steel shall be permitted in the structure of any basement". This recommendation could be ignored for secondary floor beams using various design methods developed internationally (e.g. the SPM by Clifton [6] or Bailey's [7] method), which permit the development of tensile membrane behavior in unprotected composite floor slabs.
- "Unprotected steel may be used in the structural system of all single-storey and certain double-storey buildings in spite of the fact that in many cases such structural members would not comply with the requirements of (the structural stability requirements presented in the code)". When true rational design is employed it might be shown that certain structures do or don't satisfy fire resistance requirements so this statement is not necessarily true.
- It is specifically noted that premature distortion or collapse should be guarded against. However, no information is provided regarding how this should be ensured.

Rational structural design is not specifically addressed within SANS 10400-T. However, Annex B allows for rational fire design to be undertaken by a competent person according to BS 7974 [7] in such a way that an equivalent fire resistance is achieved as the prescribed resistance, and that "Any relevant standards or technical documents can be used during the process" of designing to BS 7974. This opens the door for the use of any international standard, meaning that the new Eurocode or the Canadian code could be applied. Ultimately structural fire designs may be subject to review by a fire chief who could request proof that SANS codes are satisfied.



### 1.2. South African steel codes – SANS 10162

In South Africa hot-rolled structural steelwork is designed according to SANS 10162-1 [8] whilst cold-formed sections are designed to SANS 10162-2 [9]. Negligible information is provided in either document in terms of design for fire.

SANS 10162-1 is based upon the Canadian hot-rolled steel design code, CSA S16 [2]. Thus, it is currently proposed that for the next revision of SANS 10162-1 the provisions for fire design given in the Canadian code be adopted, as presented in Annex K [10]. Although these provisions are not as advanced as the Eurocode suite of documents they do provide a significant improvement and can be easily introduced as the calculations are consistent with the current design methodologies employed. Also, the South African loading code for buildings, SANS 10160, is aligned with the European basis of design, thus allowing designers to consult the Eurocodes for cases beyond the scope of the local standards (including future adoptions of the Canadian code).

From the above discussion on SANS 10400 it can be seen that even though the building regulations themselves do not provide information about rational design the concession that international codes of practice can be utilized means that CSA S16 could be used to satisfy equivalent fire resistance requirements.

### 1.3. Canadian steel design code for fire - CSA S16 Annex K

Topics such as principles for fire design, the consideration of localized and post-flashover fires, advanced analysis methods and active protection systems (such as sprinklers) are briefly addressed in Annex K of CSA S16. However, additional literature would be required by designers on most of these topics. Specific details relating to fire design in this code will now be discussed.

The change in the mechanical properties of steelwork at elevated temperatures is referenced by CSA S-16 directly to Eurocode 3 [5]. The change in the yield strength ( $f_y$ ) and Young's modulus ( $E$ ) of S355JR steelwork with increasing temperature is shown in Figure 1. These values are used to produce the graphs presented below.

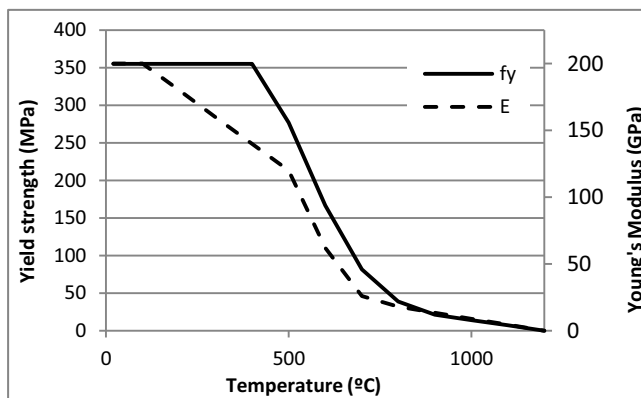


Figure 1. Change in yield strength and Young's modulus of S355JR steelwork with temperature [5]

The factored resistance of a member in compression,  $C_r$ , as a function of temperature  $T$ , is given by S16 as:

$$C_r(T) = (1 + \lambda(T)^{2dn})^{-1/dn} A f_y(T) \tag{1}$$

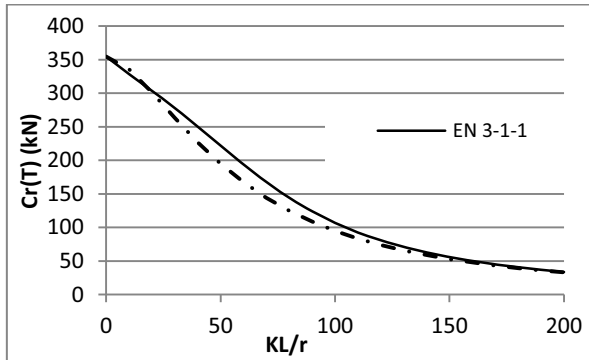
with:

$$d = 0.6$$

$$n = 1.34 \text{ for general steelwork}$$

The non-dimensional slenderness of a member is given by:

$$\lambda(T) = \frac{KL}{r} \sqrt{\frac{f_y(T)}{\pi^2 E(T)}} = \sqrt{\frac{f_y(T)}{F_e(T)}} \tag{2}$$



**Figure 2.** Comparison of compressive failure loads for a UC203x203x71 at  $T = 800^\circ\text{C}$  when the Eurocode [5] and the Canadian [2] codes are used

The resistance of a UC 203x203x71 column at  $800^\circ\text{C}$  is calculated using the CSA S16 equations and the equivalent expressions provided in EN 3-1-2 to produce Figure 2. It can be seen that the resistances are quite comparable, with the Canadian code being slightly more conservative in the slenderness range of around 20-130. The maximum difference is 16% at a slenderness of around 70.

According to S16 the resistance of a member in bending under lateral-torsional buckling is given as:

$$M_r(T) = C_K M_p(T) + (1 - C_k) M_p(T) \left( 1 - \left( \frac{C_k M_p(T)}{M_u(T)} \right)^{0.5} \right)^{C_z(T)} \tag{3}$$

where:

$$C_k = 0.12$$

$M_p(T)$  = Plastic moment at elevated temperature,  $T$

$M_u(T)$  = Elastic critical load at elevated temperature  $T$ , given by:

$$M_u(T) = \frac{\omega_2 \pi}{L} \sqrt{E(T) I_y G(T) J + I_y C_w \left( \frac{\pi E(T)}{L} \right)^2} \tag{4}$$

where:

$\omega_2$  = Factor to account for the bending moment shape, as defined in Clause 13.6 of CSA S-16.

$$C_z(T) = \frac{T+800}{500} \leq 2.4 \tag{5}$$

The bending resistance calculated for a UB 406 x 178 x 54 is shown in Figure 3 when the member is at  $20^\circ\text{C}$ ,  $400^\circ\text{C}$  and  $800^\circ\text{C}$ . It can be seen that the strength of the steel rapidly decreases with increasing temperature.

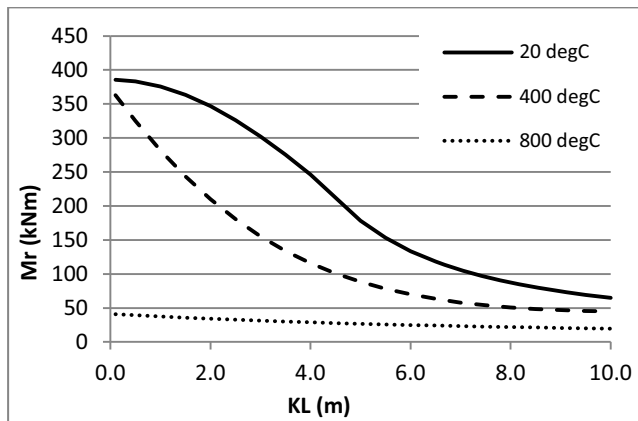


Figure 3. Bending resistance of a UB 406x178x54 member at different temperatures according to [2]

#### 1.4. Fire curves and heat transfer equations

Along with the main code annexure the Canadian Institute of Steel Construction has also published a commentary on Annex K [10], which could be utilized in the updated South Africa code. This provides useful information such as the reliability values used for design, heat transfer equations, details regarding testing and discussions regarding the level of structural analysis and design employed.

Heat transfer equations are important for determining the design temperature of a steel member exposed to a specific fire. However, to do this a time-temperature fire curve must be generated first. Historically the most well-known fire curve is the standard fire, otherwise known as the ISO 834 [11] curve. In Eurocode 1-1-2 [4] guidance and equations are now provided for parametric fire curves which consider the amount of fuel available, ventilation conditions, the cooling phase of a fire and other such important topics. To be able to effectively move in the direction of rational fire design South Africa would need to refer to these parametric curves, otherwise would remain using the standard fire. Since guidance is provided for converting parametric fires to equivalent standard fire ratings using equations from the CIB or Eurocode documents, the parametric curves can be used in conjunction with existing standard fire rating requirements.

Using the lumped heat mass transfer equations from the CSA S16 commentary and the fire curves from EN 1-1-2 [4] Figure 4 has been produced. This figure depicts a comparison between the gas temperature of a fire and the temperature of a UC 254 x 254 x 73 member in the fire. The temperature was calculated using CSA S16 and EN 3-1-2 for the member with no passive protection. It can be seen that the EN equations predict a temperature about 1.6% higher at the maximum point. The curve for the protected member had 13 mm of vermiculite applied to it, causing a 24% reduction in maximum temperature and more than doubling the time to reach the maximum.

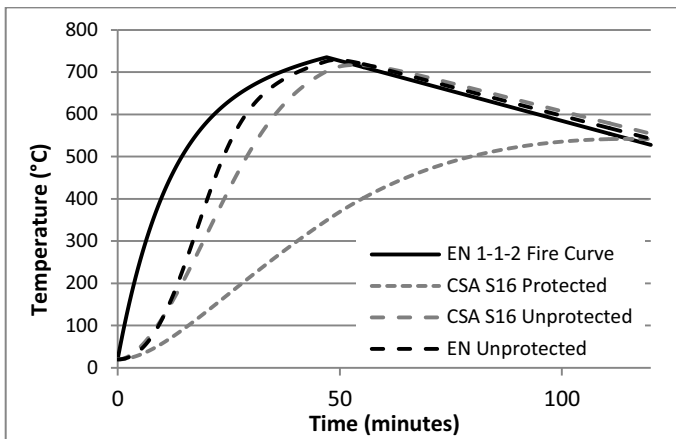


Figure 4. Comparison of fire and steel temperatures for an unprotected and protected UC 254x254x73

## 2. General comparison of CSA S16 and the Eurocodes

Overall, differences and similarities between the Canadian and European code requirements for steelwork include, but are not limited to, the following:

- An extremely important aspect to consider is that the Eurocodes provide a much more extensive set of guidelines for steelwork and other construction materials. The various documents have been harmonized to provide a consistent approach to structural fire engineering. However, the extensive nature of the Eurocodes can also make them complicated to apply and implement, especially for South Africa.
- Similar fire resistance values for members are calculated, with S16 being slightly more conservative than EN 3-1-2 (see Fig. 2). Also, Very similar maximum temperatures are calculated using the heat transfer equations (see Fig. 4). This highlights what appears to be a consistent design philosophy.
- The Canadian steel code obtains the mechanical properties of steelwork at elevated temperatures directly from the Eurocode (see Fig. 1).
- The partial load factor for live loads at the fire limit state is 0.5 for general buildings and 1.0 for storage structures in the Canadian code. In the Eurocodes the values are more specific to usage such as 0.5 for domestic buildings, 0.7 for shopping areas and 0.9 for storage areas. Hence, values are quite similar.

## 3. Conclusion and discussion regarding the direction for steel fire design in South Africa

From this paper it can be seen that South Africa is currently lagging far behind the rest of the world in terms of structural fire design. The Canadian hot-rolled steelwork design code could be easily adopted to provide the basics in terms of fire design, and methodologies would be consistent with existing design codes and building regulations. The Eurocodes are an extremely advanced set of fire design documents and could be consulted for structures outside the scope of the Canadian code. Results from CSA S16

are similar to those calculated in the Eurocodes, indicating that Eurocode based extensions need not be inconsistent with CSA S16 procedures. Also, Eurocode based extensions for composite construction may particularly be of interest.

#### 4. Acknowledgements

The financial assistance of the National Research Foundation (DAAD-NRF) towards this research is hereby acknowledged. Opinions expressed and conclusions arrived at, are those of the author(s) and are not necessarily to be attributed to the DAAD-NRF.

#### References

- [1] SABS, *SANS 10162-1:2005. The structural use of steel. Part 1: Limit-state design of hot-rolled steelwork*, Pretoria: South African Bureau of Standards, 2005.
- [2] CSA, *CSA S16-09 Design of steel structures*, Toronto: Canadian Standards Association, 2009.
- [3] SABS, *SANS 10400: The application of the National Building Regulations. Part T: Fire protection.*, Pretoria: South African Bureau of Standards, 2010.
- [4] BSI, *BS EN 1991-1-2:2002: Eurocode 1: Actions on structures - Part 1-2: General Actions - actions on structures exposed to fire*, London: British Standards Institute (BSI), 2002.
- [5] BSI, *BS EN 1993-1-2:2005: Eurocode 3: Design of steel structures – Part 1-2: General – Structural fire design*, London: British Standards Institute (BSI), 2005.
- [6] Clifton, G., *Design of Composite Steel Floor Systems for Severe Fires*, Manukau City : New Zealand Heavy Engineering Research Association, 2006.
- [7] BSI, *BS 7974: Application of fire safety engineering principles to the design of buildings - Code of practice*, London: British Standards Institute (BSI), 2001.
- [8] SABS, *SANS 10162-1:2005. The structural use of steel. Part 1: Limit-state design of hot-rolled steelwork*, Pretoria: South African Bureau of Standards, 2005.
- [9] SABS, *SANS 10162-2:2011 The structural use of steel. Part 2: Cold-formed steel structures*, Pretoria: SABS, 2011.
- [10] CISC, *CISC Commentary on CSA S16-09 Annex K Structural Design for Fire Conditions*, Ontario: Canadian Institute of Steel Construction, 2010.
- [11] ISO, *ISO 834 Fire-resistance tests -- Elements of building construction. Parts 1-12*, Geneva: International Organization for Standardization, 1999.

# Factors that influence friction in tendons of unbonded post-tensioning systems

Morgan DUNDU<sup>1</sup> and Michelle WARD

*Department of Civil Engineering Science, University of Johannesburg, South Africa*

**Abstract.** The coefficient of friction in an unbonded post tensioning system is influenced by many factors, and these factors include the thickness of lubricant or grease present in the system, clearance between the strand and the plastic sheath, surface characteristics of the strand and plastic sheath. In order to determine the effect of these factors, a series of friction tests were performed on two different diameters of strand, namely; 12.7 mm and 15.24 mm diameters. Through a regression analysis, it was found that the frictional force decreases with increase in the thickness of the grease and that friction increases with increase in the mass of the strand. The amount of friction was found to be dependent on the surface characteristics of the strand and plastic sheath, clearance between the plastic sheath and the strand and the extrusion process of the plastic sheath.

**Keywords.** Post-tensioning, 7-wire strand, grease, mass, plastic sheath, unbonded, coefficient of friction.

## Introduction

Post-tensioning consists of two systems, namely; bonded and unbonded tendon systems. The bonded multistrand system has been the method of choice in post-tensioning, however, in recent years the unbonded system has become more popular. This is because the unbonded system is versatile and is more economic than the bonded multistrand systems [1]. In an unbonded post-tensioning system, the tendon consists of a 7-wire mono-strand that is coated with a specified thickness of grease (Figure 1). Once coated with grease, the plastic sheath is extruded over the strand in order to protect the strand against chemical and mechanical damage. The grease allows the strand to move inside the plastic sheath, provides corrosion protection to the strand and reduces the amount of friction between the strand and the plastic sheath during post-tensioning. Although the friction in an unbonded tendon is greatly reduced, it is still necessary to estimate the friction loss.

Under-estimating the friction loss can lead to inadequate prestress and improper camber whilst over-estimation can lead to excessive shortening of the concrete member, excessive camber and horizontal movements [2].

---

<sup>1</sup>Corresponding author: University of Johannesburg, Department of Civil Engineering Science, P.O. Box 524, Auckland Park, 2006, South Africa; E-mail. [mdundu@uj.ac.za](mailto:mdundu@uj.ac.za)

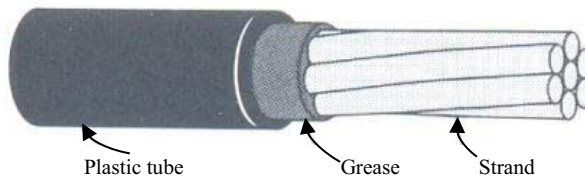


Figure 1. Unbonded tendon

The coefficient of friction, in an unbonded post-tensioning system, is influenced by many factors, and these include the thickness of lubricant or grease present in the system, clearance between the strand and the plastic sheath, surface characteristics of the strand and plastic sheath, and the size of the wires making up the 7 wire strand. Lack of consensus on the treatment of friction is shown by the large variation of the coefficient friction, which ranges from 0.05 to 0.15 (see Table 1). For an unbonded system SANS10100-1 [3] and EN 1992-1-1 [4] specifies one value for the coefficients of friction. Note that the value specified by EN 1992-1-1 [4] is twice the value specified by SANS10100-1 [3]. PTI [5] specifies a range of coefficients of friction and AASHTO [2] do not include a coefficient of friction for an unbonded system. The upper bound of the PTI [5] range is three times higher than the coefficient specified in SANS10100-1 [3], however, PTI [5] recommends a coefficient for an unbonded system of 0.07. The large variation in the coefficient of friction shows that there is no real consensus on its exact value that must be used, and the values given in Table 1 should only be considered as guidelines. According to AASHTO [2], the friction coefficient varies from project to project and is dependent on the quality of workmanship

Table 1. Coefficient of friction ( $\mu$ )

SANS10100-1	EN 1992-1-1	PTI	AASHTO
0.05	0.10	0.05-0.15 (0.07)	-

This investigation was performed in order to understand the factors that influence the coefficient of friction and establish why the variation of the coefficient of friction is large. Experiments were conducted on 5 different coils, and 3 strands were tested per coil. Of the coils provided, two different diameters of strand (12.7 mm and 15.24 mm) were tested with different thickness of grease. The aim of the experiment was to determine the amount of force required to pull the plastic sheath off the strand and relate this force to the amount of grease used in the system. Other factors that influence the coefficient of friction, such as the surface characteristics of the strand and plastic sheath, mass of the wires making up the 7 wire strand and the contact pressure between the strand and the plastic sheath, were also investigated.

## 1. Friction test

The friction test was conducted according to the test procedure outlined in EOTA ETAG 013 [6], Annex C. A total of 5 different coils were supplied and 3 specimens per coil were tested. All specimens were 1.2 meters long. For each specimen, the weight of

the strand, wires, grease and plastic sheath (including its thickness) had to be measured. The weight of the grease was established by weighing the lubricated strand. After that the grease was washed off the strand and the strand elements re-weighed. The apparatus required to perform this test are shown in Figure 2. Of the 1.2 m length of the strand, 0.2 m length was exposed to facilitate the clamping process. Once the strand was clamped the spring balance was then hooked to the plastic sheath. The spring balance was then pulled up by hand until the sheath started to move and the force on the spring balance was constant. The force required to move the sheath was recorded and the procedure repeated for other specimens [6].



**Figure 2.** Friction test apparatus

## 2. Results

The force required to pull the plastic sheath off the strand was related to the amount of grease used in the system and the mass of the wires as described below.

### 2.1 Relationship between friction and the amount of grease

Figure 3 shows the relationship between the mass of grease and the frictional force for the 12.7 mm and 15.24 mm strands. Each value on the graph is an average of 3 values from each coil. It can be seen from the figure that the thickness of grease varies from 32.4 g/m to 36.5 g/m for the 12.7mm diameter strand and 43 g/m and 48 g/m for the 15.24 mm diameter strand. The corresponding frictional force for the 12.7 mm diameter ranges from 30 N and 35 N and from 55 N to 76 N for the 15.24 mm diameter. It is clear from these results that the frictional force decreases with increase in the thickness of the grease.



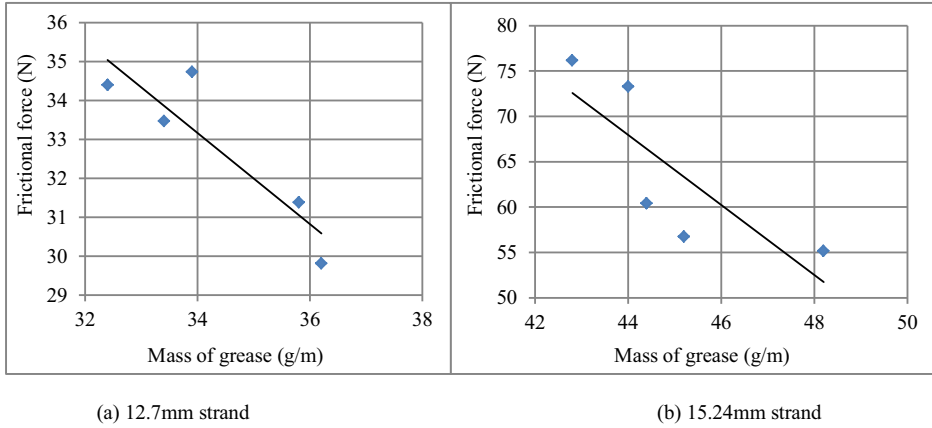


Figure 3. Relationship between friction and grease

2.2 Relationship between friction and the mass of the wires

The mass of the strands vary from coil to coil. This can be explained by the fact that when the strand is produced, there is a tolerance of  $\pm 0.03\text{mm}$  in the diameter of the wires of the strand. As shown in Figure 4, the friction increases with increase in the mass of the strand. This means that a strand of larger mass would yield a higher friction force than a lighter strand. The higher friction is caused by larger sag, resulting from the larger mass. In the extreme case of the strand reaching the plastic sheath, the contact pressure exerted by the strand on the plastic sheath is larger, resulting in higher friction generated.

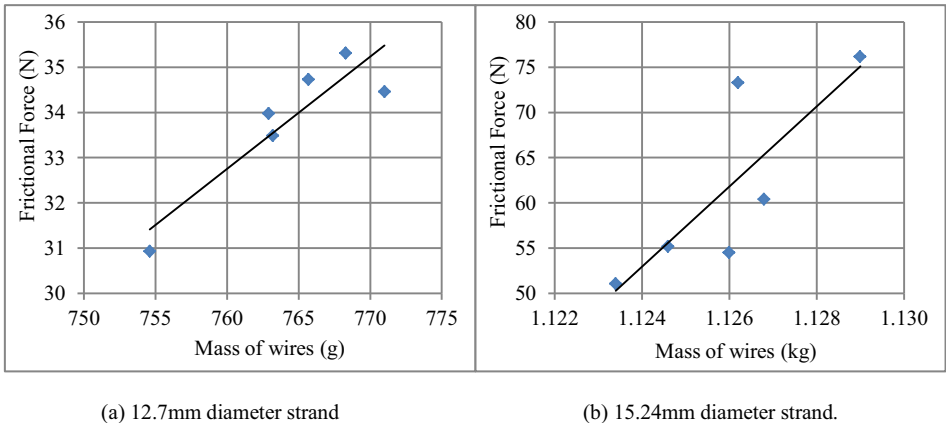


Figure 4. Relationship between friction and the mass of wires of a strand

### 2.3 Manufacturing process

The extrusion of the plastic sheath over the greased strand affects the clearance between the strand and the plastic sheath, and subsequently the free movement of the strand. In addition, when the clearance is not uniform, the amount of grease in the various strands varies. It was observed during the experiments that strands that had a smaller clearance required more force to pull the plastic sheath from the strand.

The internal surfaces of the plastic sheath of a few specimens were twisted or rifled during the extrusion process, in conformity with the spiral shape of the strand. Evidence of this behaviour is shown in Figure 5, and happens when the extrusion process is not precisely timed. The plastic sheath takes the profile of the strand if the strand is pushed through the production line faster than the extruded plastic sheath. This pulls or stretches the plastic sheath over the strand, making the plastic sheath tighter than is required. The plastic sheath takes the profile of the strand when it has hardened. Specimens that exhibited this behaviour had a higher pull-out force than those with smooth profiles. The ridges or rifled profile increased the friction.



Figure 5. Plastic sheath with a spiral profile

### 3. Coefficient of friction

A simple test was also performed to determine the coefficient of friction. In this test, a sheet of polyvinyl acetate (PVA), with properties that are similar to high density polyethylene or plastic sheath, was placed on a flat surface. The top surface of the polyvinyl acetate sheet represented the inside part of the plastic sheath. A steel plate, with grease applied to its bottom side, was placed on the Polyvinyl Acetate sheet. Several weights were then applied on the steel plate in order to induce a vertical or normal load. A spring balance was hooked to the steel plate, and to generate the friction force, the spring balance was pulled as shown in Figure 6. As soon as the plate started moving, the friction force was recorded. The process was repeated several times with different weights in order to obtain consistent coefficients of friction. An initial weight of 28.28N was applied on the steel plate. This weight was increased to 36.89kN the second series of tests. The results from this exercise are given in Table 2.



**Figure 6.** Test set-up to establish the coefficient of friction.

**Table 2.** Results from the coefficient of friction test

Weight (N)	Without Grease		With Grease	
	Pulling Force (N)	Coefficient of friction	Pulling Force (N)	Coefficient of friction
28.25	5.68	0.201	1.177	0.042
	6.08	0.215	1.373	0.048
	5.68	0.201	1.177	0.042
	5.68	0.201	1.177	0.042
36.89	7.358	0.200	1.569	0.042
	7.358	0.200	1.765	0.047
	6.671	0.180	1.472	0.040
	7.358	0.200	1.765	0.047

The results in Table 2 shows that the presence of the grease greatly reduces the amount of friction present in a system. The average coefficient of friction is 0.2 for the system without grease and varies from 0.040 to 0.048 (recommend a value of 0.042) for the system with grease. The recommended value is close to the lower bound coefficient of friction, provided by PTI [5] and SANS10100-1 [3]. The small difference between this experiment and the coefficient specified in the standards could be because the steel plate does not represent the shape of the strand. In addition, the coefficient of friction established from these tests did account for other friction factors, such as friction due to the curvature of the strand.

#### 4. Conclusion

From the tests carried out, the following conclusions can be made:

- 1) The frictional force between the strand and the plastic sheath is reduced by increasing the amount of grease. Slightly less grease yielded higher frictional forces.
- 2) Friction increases with increase in the mass of the strand. The higher friction is caused by larger sag and contact pressure, resulting from the larger mass.
- 3) Friction was found to be dependent on the surface characteristics of the strand and plastic sheath. Specimens with rifled profiles had much higher frictional forces than smooth profiles. The coefficient of friction is optimum if the profile of the plastic is smooth and the optimum amount of grease is present.

- 4) It was observed during the experiments that strands that had a smaller clearance required more force to pull the plastic sheath from the strand.
- 5) The recommended coefficient of friction of 0.042 is close to the lower bound coefficient of friction, provided by PTI [5] and SANS10100-1 [3]. The small difference between this experiment and the coefficient specified in the standards is because the steel plate does not represent the shape of the strand and that the coefficient of friction established from these tests did account for other friction factors, such as friction due to the curvature of the strand.

## References

- [1] N.H. Burns, J. Moon, Flexural Behaviour of member with unbonded tendons, *Journal of Structural Engineering*, ASCE 123(1997), 1087–1094.
- [2] AASHTO, *Bridge design specifications*, 6<sup>th</sup> edition, American Association of State Highway and Transportation Officials, Washington DC, 2012.
- [3] SANS 10100-1, Standardised specification for the structural use of concrete, South African Bureau of Standards, Pretoria, South Africa, 2000.
- [4] EN 1992-1-1, Design of concrete structures Part 1-1: General rules and rules for buildings, European Committee for Standardization, Brussels, 2004.
- [5] PTI, *Post Tensioning Manual*, Post Tensioning Institute, 6th Edition, 2006.
- [6] EOTA, Guideline for technical approval of post tensioning kits for pre stressing of structures, European Organization for Technical Approvals, Brussels, No. ETA-06/0226, 2007.

# Cold-formed circular hollow sections under axial compression

Morgan DUNDU<sup>1</sup> and Vongani CHABALALA

*Department of Civil Engineering Science, University of Johannesburg, South Africa*

**Abstract.** Two series of experiments were carried out to investigate the behaviour of pinned-ended circular hollow section (CHS) columns, subjected to axial compressive load. A total of 30 columns were tested in this investigation; 20 columns in Series 1 and 10 columns in Series 2. The outside diameter-to-thickness ratio ( $d/t$ ) and the slenderness ratio ( $KL/r$ ) ranged from 29.7 to 46.4 and 20.8 to 82.2 for Series 1, respectively, and from 55.0 to 62.9 and 10.7 to 34.9 for Series 2, respectively. In general, Series 1 columns failed by overall flexural buckling and, whilst Series 2 columns failed by local ring-type buckling. The test strengths of the columns were compared with the strengths predicted by the South African design standard (SANS10162-1) and the European design standard (EN 1993-1-1).

**Keywords.** Circular hollow sections, columns, diameter-to-thickness ratio, slenderness ratio, overall flexural buckling, local buckling.

## Introduction

The behavior of axially loaded circular hollow steel sections (CHSs) has been an area of extensive research over a long period of time. However, not much study has been performed on thinner cold-rolled carbon sections which are in use today. To fill this gap hot-rolled column curves and design formulae have been used to define the behavior of thin cold-rolled sections. Although both materials are made out of carbon steel and possess a bilinear stress-strain relationship, thin cold-rolled sections do not have a well-defined yield plateau and are affected by local buckling far much more than hot-rolled sections. In addition, the amount and distribution of residual stresses, exhibited by the thin cold-rolled sections, are completely different from hot-rolled sections. The aim of this paper is to study the behaviour of these sections and compare the experimental strengths of the columns with the design strengths predicted by the South African standard, SANS 10162-1 [1], and the European standard, EN 1993-1-1 [2]. SANS10162-1 [1] is based on the Canadian code, CAN/CSA-S16-09 [3], and any reference to SANS10162-1 [1] also refers to CAN/CSA-S16-09 [3].

## 1. Material properties

In order to determine the material properties of the CHSs, tensile tests were conducted on the coupons. A total of 45 coupons were machined from the lengths supplied (3

---

<sup>1</sup>Corresponding author: University of Johannesburg, Department of Civil Engineering Science, P.O. Box 524, Auckland Park, 2006, South Africa; E-mail. mdundu@uj.ac.za

coupons from each length) and tested according to the guidelines provided by European Standard, EN ISO 6892-1 [4]. The coupons were tested using the 100kN capacity Instron 1195 tensile testing machine, at a rate of 3mm/min. A calibrated extensometer was attached to each coupon during testing to measure the longitudinal strain of the coupons. The average values of the yield stress ( $f_y$ ), tensile strength ( $f_u$ ) and Young's modulus of elasticity (E) for the tested coupons are presented in Table 1. Since the tested carbon steel did not have a defined yield point, the yield stress ( $f_y$ ) of each coupon was determined from a 0.2% off-set line, parallel to the initial stress-strain curve. The average values of the yield stress ( $f_y$ ) and Young's modulus of elasticity (E) were used to predict the strengths of the columns using SANS 10162-1 [1] and EN 1993-1-1 [2].

**Table 1.** Average material properties

Series	Section	Length (m)	$f_y$ (MPa)	$f_u$ (MPa)	E (MPa)
Series 1	89.0×3.0mm	1.0-2.0	376.0	430.9	207018.2
	102.0×3.0mm	1.0-2.0	399.7	462.3	202602.1
	114.9×3.0mm	1.0-2.0	425.7	468.5	204245.4
	127.3×3.0mm	1.0-2.0	398.3	469.8	201876.0
	139.2×3.0mm	1.0-2.0	362.0	464.3	202667.8
Series 2	165.1×3.0mm	1.0-2.0	477.3	545.2	205079.0
	220.0×5.0mm	1.0-2.0	494.3	557.4	204803.8
		2.5	503.7	569.4	205695.6
	270.0×4.8mm	1.0-2.0	358.7	447.8	205542.6
		2.5	355.7	460.5	205844.3

## 2. Specimen preparation, test set-up and procedure

All columns were supplied in 6m lengths, except for the 165.1×3 mm section, where only one 5 m length was supplied. In order to provide a range of columns from short to slender columns the supplied lengths were cut into 1 m, 1.5 m, 2.0 m and 2.5 m columns. After cutting the columns to the required lengths, the ends were milled flat, so that the load could be applied uniformly over the cross-sectional area.

The column strength is reduced by imperfections such as initial out of straightness and residual stresses. SANS 10162-1 [1] and EN 1993-1-1 [2] limits the initial out of straightness for most general shapes to  $L/1000$ . In this investigation the initial out of straightness was measured at mid-height of the column, using a thin metal wire and a pair of vernier calipers. In all the columns measured there was no visible initial out-of-straightness between the metal wire and the columns. It was concluded that the columns were straight and that initial out-of-straightness should not be considered. Residual stresses were also not considered since the manufacturing process of CHSs tends to distribute residual stresses uniformly, which results in greater compressive resistance [5].

The smaller sections (Series 1 specimens) were tested at the University of Johannesburg's Civil Engineering Science laboratory using a 500kN capacity Instron and the larger sections (Series 2 specimens) were tested at the University of the Witwatersrand using a 1500 kN Schenck Trebel compression machine. The (CHS) columns were compressed under concentric axial loads, between pin-ended conditions, at a loading rate of 5 mm/min. The slow loading rate allowed good observation of the

failure modes during testing. In order to create pin-ended conditions, 2, 20 mm thick plates with spherical grooves and a steel ball were used at each end. Figure 5 shows typical experimental set ups for the two series of experiments.



**Figure 1.** Typical experimental set-up

### 3. Failure modes

All columns in Series 1, except 1 m and 1.5 m length columns, failed by overall flexural buckling (FB) followed by minor local buckling (LB) that occurred at mid-length of the columns (Figure 2(a)). Columns of larger outside diameter-to-thickness ratio (1 m and 1.5 m lengths) failed by interaction of local buckling and overall flexural buckling (L-FB) as shown in (Figure 2(b)).

Two sizes of columns (165.1x3.0 mm and 220.0x3.5 mm), tested with the Schenck Trebel machine, are classified as Class 4 or slender sections by both SANS 10162-1 [1] and EN 1993-1-1 [2]. As expected, these columns failed by local buckling (LB). Local buckling was manifested in these columns as an outward ring-type local buckle. Local ring-type buckling occurred at the bottom end of the 1 m length column of the 165.1x3 mm section (Figure 2(e)). For the 1.5 m and 2 m length columns, the local ring-type buckling occurred at a third of the column height, from the top, and mid-height, respectively (Figure 2(c)). All the 220.0x3.5 mm columns failed by local ring-type buckling, at the mid-height of the 1 m, 2 m, and 2.5 m column lengths (Figure 2(c)). Although the 270.0x4.8 mm section was not expected to fail by buckling, all the 1.0 – 2.0 m columns failed by local ring-type buckling at the top end of the columns (Figure 2(d)), whilst the 2.5 m length column failed by flexural buckling (Figure 2(a)).

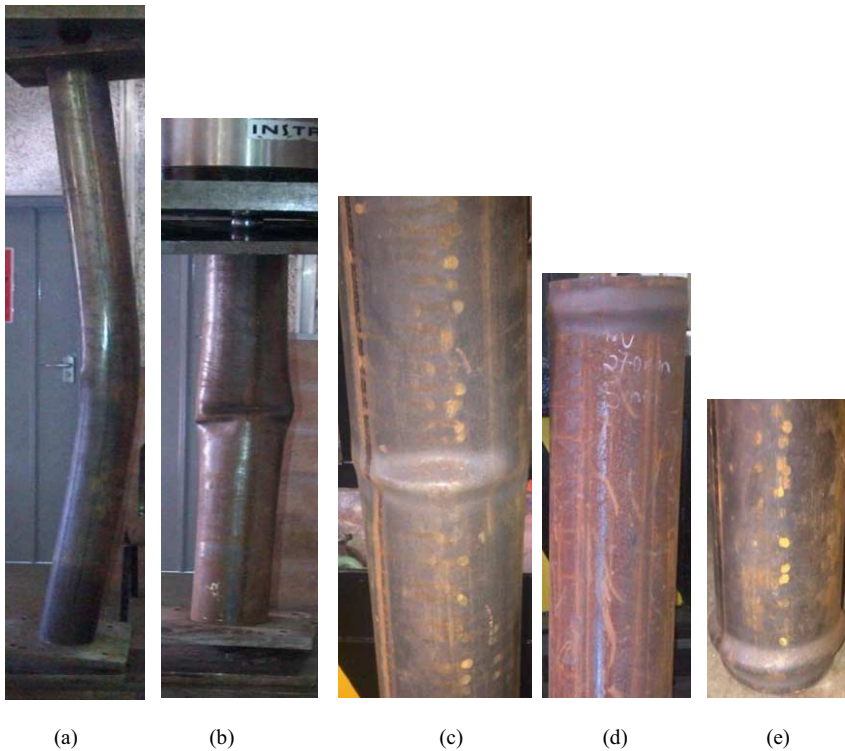


Figure 2. Typical failure modes

#### 4. Local buckling

CHSs, subject to increasing compression load may experience local failure. This mode of failure is called local buckling. Local buckling is influenced by the outside diameter-to-thickness ratio ( $d/t$ ) and the yield stress ( $f_y$ ) of the sections, whilst overall flexural buckling or instability is influenced by the length of the column. To prevent local buckling from occurring, the diameter-to-thickness ratios of the elements must be limited. The maximum diameter-to-thickness ratios depend on the classification of the cross-section. Column cross-sections are classified into Class 1 (plastic), 2 (compact), 3 (semi-compact) and 4 (slender) in accordance with their behaviour in compression. In SANS 10162-1 [1], Classes 1, 2 and 3 have the same limits. The approach adopted in this standard is to separate sections that are stocky enough to be able to resist an axial stress equal to the yield stress without local buckling and those that buckle before the yield stress is reached. For easier of reference the three classes will be referred as Class 3. It should be noted that the steel sections cannot be designed on the basis of overall failure if the limiting values of a Class 3 section are exceeded. Sections with width-to-thickness ratios exceeding these values are referred to as Class 4 sections.



**Table 2.** Slenderness and diameter-to-thickness ratios

Series	CHS (dxt)	L (mm)	r (mm)	KL/r	d/t	$f_y$ (MPa)	Limit (d/t)		Classification	
							SANS	EC3	SANS	EC3
Series 1	89.0x3.0	1000	30.4	32.9	29.7	375.2	61.3	31.3	Class 3	Class 1
		1500	30.4	49.3	29.7	375.2	61.3	31.3	Class 3	Class 1
		2000	30.4	65.7	29.7	375.2	61.3	31.3	Class 3	Class 1
	102.0x3.0	1000	35.0	28.6	34.0	392.5	58.6	41.9	Class 3	Class 2
		1500	35.0	42.8	34.0	392.5	58.6	41.9	Class 3	Class 2
		2000	35.0	57.1	34.0	392.5	58.6	41.9	Class 3	Class 2
	114.9x3.0	1000	39.6	25.3	38.3	416.2	55.3	39.5	Class 3	Class 2
		1500	39.6	37.9	38.3	416.2	55.3	39.5	Class 3	Class 2
		2000	39.6	50.5	38.3	416.2	55.3	39.5	Class 3	Class 2
	127.3x3.0	1000	44.0	22.7	42.4	395.9	58.1	53.4	Class 3	Class 3
		1500	44.0	34.1	42.4	395.9	58.1	53.4	Class 3	Class 3
		2000	44.0	45.5	42.4	395.9	58.1	53.4	Class 3	Class 3
	139.2x3.0	1000	48.2	20.8	46.4	362.1	63.5	58.4	Class 3	Class 3
		1500	48.2	31.1	46.4	362.1	63.5	58.4	Class 3	Class 3
		2000	48.2	41.5	46.4	362.1	63.5	58.4	Class 3	Class 3
Series 2	165.1x3.0	1000	57.3	17.4	55.0	484.7	47.5	43.6	Class 4	Class 4
		1500	57.3	26.2	55.0	484.7	47.5	43.6	Class 4	Class 4
		2000	57.3	34.9	55.0	484.7	47.5	43.6	Class 4	Class 4
	220.0x3.5	1000	76.6	13.1	62.9	494.3	46.5	42.8	Class 4	Class 4
		1500	76.6	19.6	62.9	494.3	46.5	42.8	Class 4	Class 4
		2000	76.6	26.1	62.9	494.3	46.5	42.8	Class 4	Class 4
	270.0x4.8	2500	76.6	32.7	62.9	503.7	45.7	41.0	Class 4	Class 4
		1000	93.8	10.7	56.3	354.4	64.9	59.7	Class 3	Class 3
		1500	93.8	16.0	56.3	354.4	64.9	59.7	Class 3	Class 3
		2500	93.8	26.7	56.3	348.6	66.0	60.7	Class 3	Class 3

For all the columns investigated (see Table 2), the outside diameter-to-thickness ratio ( $d/t$ ) and the slenderness ratio ( $L/r$ ) ranged from 29.7 to 46.4 and 20.8 to 82.2 for Series 1, respectively, and from 55.0 to 62.9 and 10.7 to 34.9 for Series 2, respectively. Parameters  $d$ ,  $L$  and  $t$ , in Table 2, represent the outside diameter, clear length (which ranges from 1000 mm-2500 mm) and thickness of the CHSs. The slenderness range is significantly smaller than the compression slenderness limit of 200, as prescribed by SANS10162-1 [1].

For yielding to take place before local buckling, SANS10162-1 (SANS) requires that the maximum diameter-to-thickness ratio for CHSs be  $d/t \leq 23000/f_y$ . The maximum width-to-thickness ratios, prescribed by EN 1993-1-1, for Class 1, 2 and 3 are  $d/t \leq 11750/f_y$ ,  $d/t \leq 16450/f_y$  and  $d/t \leq 21150/f_y$ , respectively. A comparison of the diameter-to-thickness ratios of the sections tested and the code-predicted limits in Table 2 suggest that all columns, except the 165.1x3.0 and 220.0x3.5 CHSs, will yield before local buckling failure takes place.

## 5. Test results

A comparison of the test strength of the CHSs with the code-predicted strength, calculated using SANS 10162-1 (SANS) [1] and EN 1993-1-1 (EC3) [2] is shown in Table 3. In Table 3,  $N_{TEST}$  represent the experimental strength,  $N_{SANS}$  represent the

strength predicted by SANS 10162-1 [1] and  $N_{EC3}$  represent the strength predicted by EN 1993-1-1 [2].

**Table 3.** Test and code-predicted strength of CHSs

Series	Size	d/t	KL/r	$f_y$ (MPa)	$N_{TEST}$ (kN)	$N_{SANS}$ (kN)	$N_{EC3}$ (kN)	$\frac{N_{TEST}}{N_{SANS}}$	$\frac{N_{TEST}}{N_{EC3}}$	Failure mode	
Series 1	89.0x3.0	29.7	32.9	375.2	268.43	281.02	265.98	0.96	1.01	L-FB	
		29.7	49.3	375.2	243.73	244.93	226.71	1.00	1.08	L-FB	
		29.7	65.7	375.2	198.48	201.95	184.35	0.98	1.08	FB	
	102.0x3.0	34.0	28.6	392.5	333.10	350.20	333.91	0.97	1.01	L-FB	
		34.0	42.8	392.5	328.60	313.71	291.66	1.06	1.14	L-FB	
		34.0	57.1	392.5	247.11	267.13	245.19	0.94	1.02	FB	
	114.9x3.0	38.3	25.3	416.2	398.71	427.30	410.50	0.95	0.99	L-FB	
		38.3	37.9	416.2	364.65	391.21	365.43	0.95	1.02	L-FB	
		38.3	50.5	416.2	336.81	342.40	315.66	1.00	1.08	FB	
	127.3x3.0	42.4	22.7	395.9	431.97	450.62	437.72	0.96	0.99	L-FB	
		42.4	34.1	395.9	376.40	422.65	397.90	0.90	0.95	L-FB	
		42.4	45.5	395.9	340.71	382.20	354.37	0.90	0.97	FB	
	139.2x3.0	46.4	20.8	362.1	453.14	453.63	445.95	1.00	1.02	L-FB	
		46.4	31.1	362.1	401.55	433.62	412.29	0.93	0.97	L-FB	
		46.4	41.5	362.1	354.28	403.06	376.23	0.88	0.94	FB	
Series 2	165.10x3.0	55.0	17.4	484.7	769.00	627.05	636.43	1.23	1.20	LB	
		55.0	26.2	484.7	733.00	605.91	593.80	1.21	1.23	LB	
		55.0	34.9	484.7	661.00	572.58	548.82	1.15	1.20	LB	
	220.0x3.5	62.9	13.1	494.3	1061.00	864.96	978.02	1.23	1.10	LB	
		62.9	19.6	494.3	1073.00	853.25	932.20	1.26	1.15	LB	
		62.9	26.1	494.3	1040.00	833.59	885.90	1.25	1.17	LB	
	270.0x4.8	62.9	32.7	503.7	997.00	805.95	845.12	1.24	1.18	LB	
		56.3	10.7	354.4	1349.00	1428.81	1477.51	0.97	0.95	LB	
		56.3	16.0	354.4	1362.00	1417.81	1425.20	0.99	0.98	LB	
			56.3	26.7	348.6	1296.00	1360.75	1311.60	0.97	1.01	FB

To show the accuracy of SANS10162-1 [1] and EN 1993-1-1 [2], the experimental results of CHSs are compared with the code-predicted compressive resistance (Table 3). Generally EN 1993-1-1 [2] tends to model the tests results of all non-slender columns better than SANS10162-1 [1]. Evidence of this is provided by the test-to-predicted ratios of Class 1-3 sections, which are close 1 (Tables 2 and 3). In this group of sections, SANS10162-1 [1] models stockier sections or sections that experienced interaction of local and overall flexural buckling better than moderate slender sections or sections that experienced overall flexural buckling. Generally in non-slender sections (89.0x3.0 mm, 102.0x3.0 mm, 114.9x3.0 mm, 127.3x3.0 mm and 139.2x3.0 mm CHSs), SANS10162-1 [1] tends to overestimate the strength of the CHSs. The level of overestimation increases with increase in the slenderness ratio and diameter-to-thickness ratio. The most overestimated compressive resistance obtained is for the 139.2x3.0 mm columns, with a length of 2.0 m.

As shown in Table 3 and Figure 3, both standards do not model the strengths of slender sections well. SANS10162-1 [1] and EN 1993-1-1 [2] underestimate the strengths of the columns by an average of 22% and 18%, respectively. As expected all slender sections (165.10x3.0 mm and 220.0x3.5 mm) failed by local buckling. Local buckling was manifested as an outward ring-type local buckle. In general, EN 1993-1-1 [2] is more conservative than SANS10162-1 [1].

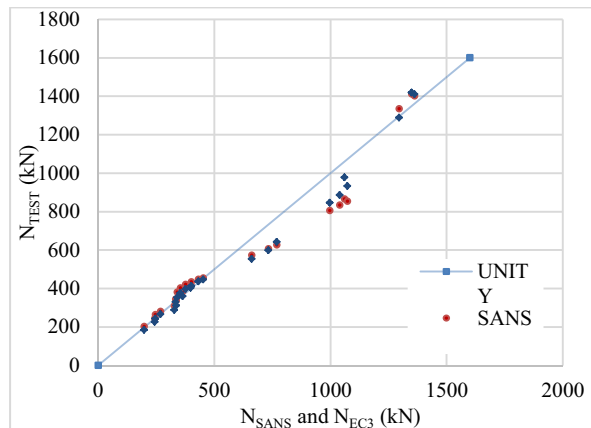


Figure 3. Comparison of experimental strength with the specified design strengths

## 6. Conclusions

All the Series 1 experiments specimens failed by flexural buckling accompanied by minor inward local buckling that occurred at the mid-length of the columns. Most Series 2 experiments specimens failed by local ring-type buckling and this was attributed to the large outside diameter-to-thickness ratio ( $d/t$ ) of the specimens. Columns with large diameter-to-thickness ratio failed in a ductile manner (Figure 6-7) while those with small diameter-to-thickness ratio experienced a sudden decrease in capacity after reaching the maximum load. All slender sections (165.10x3.0 mm and 220.0x3.5 mm) failed by local buckling. Local buckling was revealed as an outward ring-type local buckle.

The test-to-predicted ratios of Class 1-3 sections of almost 1 show that EN 1993-1-1 [2] tends to model the tests results of all non-slender columns better than SANS10162-1 [1]. For the same group of sections, SANS10162-1 [1] models stockier sections or sections that experienced interaction of local and overall flexural buckling better than moderate slender sections or sections that experienced overall flexural buckling. Both standards do not model the strengths of slender sections well. As shown in Table 3, SANS10162-1 [1] and EN 1993-1-1 [2] underestimate the strengths of the columns by an average of 22% and 18%, respectively.

## References

- [1] SANS 10162-1, The structural use of steel - Part 1: Limit-state design of hot-rolled steelwork, South Africa National Standards, Pretoria, South Africa, 2011.
- [2] EN 1993-1-1, Design of steel structures - Part 1.1: General rules and rules for buildings, British Standard Institution, 2005.
- [3] CAN/CSA-S16-09, Limit states design of steel structures, Canadian Standards Association, Rexdale, Ontario, Canada, 2009.
- [4] BS EN ISO 6892-1. Tensile testing of metallic materials: Part 1 - Method of test at room temperature. British Standard Institution; 2009.
- [5] Kurobane Y, Packer JA, Wardenier J, Yeomans N. *Design guide for structural hollow section column connections*. CIDECT series no. 9. Cologne, Germany; 200

# Structural masonry and timber

This page intentionally left blank

# Assessment of the unreinforced masonry shear wall stiffness

Nebojša MOJSILOVIĆ<sup>1</sup>

*Institute of Structural Engineering, ETH Zurich, Switzerland*

**Abstract.** One of the most challenging and still not satisfactorily solved issues in the design of structural masonry is the determination of the stiffness of shear walls. Determining the correct stiffness is of the utmost importance, for example for the deformation-based design of masonry structures. An assessment of the shear wall stiffness has been made, based on the results obtained from the full-scale testing of medium-size and large unreinforced masonry walls subjected to in-plane static-cyclic loading. This paper discusses the experimental results obtained and addresses the question of the influence of different parameters on the shear stiffness of unreinforced masonry walls. The selected parameters are mechanical (boundary conditions, vertical pre-compression, stiffness degradation), geometrical (aspect ratio, size effect) and constructional (presence of different layers in bed joints). A set of conclusions and recommendations for practical application and future research is also given.

**Keywords.** Deformation capacity, load test, masonry, shear wall, static-cyclic loading, stiffness.

## Introduction

One of the most challenging and still not satisfactorily solved issues in the (seismic) design of structural masonry is the assessment of the stiffness of shear walls. Determining, or rather estimating the correct stiffness is of utmost importance, for example for the deformation-based design of masonry structures [1]. In general, the response of masonry walls subjected to cyclic shear is nonlinear and dependent upon several parameters, e.g. the level of the pre-compression applied to the shear wall, boundary conditions etc. Moreover, the reduction in both strength and stiffness of masonry can be observed during cycling. Usually, the hysteresis curve such as those shown in Figure 1 are chosen as representative load-deformation characteristic for the evaluation of the deformation capacity of masonry. This relationship can be modelled by a simple (bilinear) linear-elastic ideal-plastic curve, see Figure 2. In order to determine the curve parameters, the ultimate value of the shear force  $H_u$  and two characteristic horizontal displacements, namely the value  $v_y$  at transition from elastic to plastic range and the ultimate plastic deformation  $v_u$  are needed. After setting the value of the ultimate shear force and estimating the effective stiffness  $K_{eff}$ , the displacement

---

<sup>1</sup> Corresponding author: [mojsilovic@ibk.baug.ethz.ch](mailto:mojsilovic@ibk.baug.ethz.ch)

$v_y$  can be readily calculated. The ultimate displacement corresponds to the strength degradation of 20% and the ultimate shear force,  $H_u$ , is obtained by equating the areas under the experimental and bilinear envelopes.

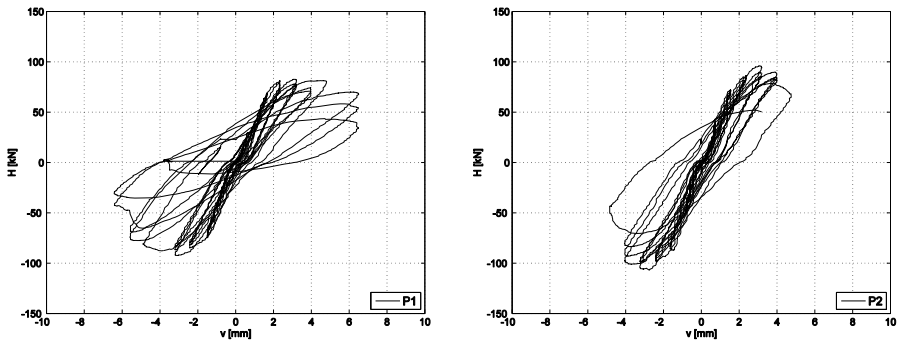


Figure 1. Typical hysteresis (shear force-horizontal displacement) of masonry shear wall [2].

In general, masonry wall stiffness is difficult to determine and for practical applications it is usually calculated based on the elastic beam theory incorporating also shear deformation; see e.g. [3]. The masonry material mechanical characteristics involved in this calculation are rarely determined through material tests, but are rather chosen based on experience or adopted from Structural Code provisions and recommendations. In the latter case, those characteristics, i.e. moduli of elasticity and shear are determined indirectly through their relation to the masonry compressive strength, see e.g. Swiss [4] or European Masonry Structural Code [5]. However, the compressive masonry strength is determined from pure compression tests and does not represent the actual stress state in the masonry wall subjected to (cyclic) shear loading.

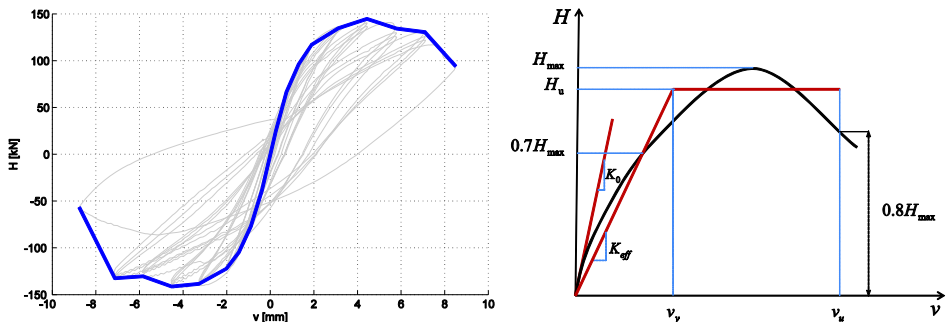


Figure 2. Hysteresis envelope and bi-linear idealization.

This paper presents and discusses the values of the shear stiffness obtained from several test series on clay block masonry walls subjected to static-cyclic shear loading [6-10]; cf. also Table 1. All tests except for the specimens of the Series C were performed in the structural laboratory of the Institute of Structural Engineering of ETH Zurich. The walls of Series C were tested in the structural laboratory of the Civil Engineering Department of the University of Newcastle, Australia within the joint research project with ETH Zurich.

### 1. Experimental data

Test Series P and T were performed within the framework of the research project on the deformation capacity of structural masonry [1, 2, 6]. Figures 1 and 3 show the (measured) hysteretic loops obtained from these tests. All wall specimens except for T7 were fixed at both upper and lower ends. Test T7 was tested as a cantilever beam (upper end was free to rotate).

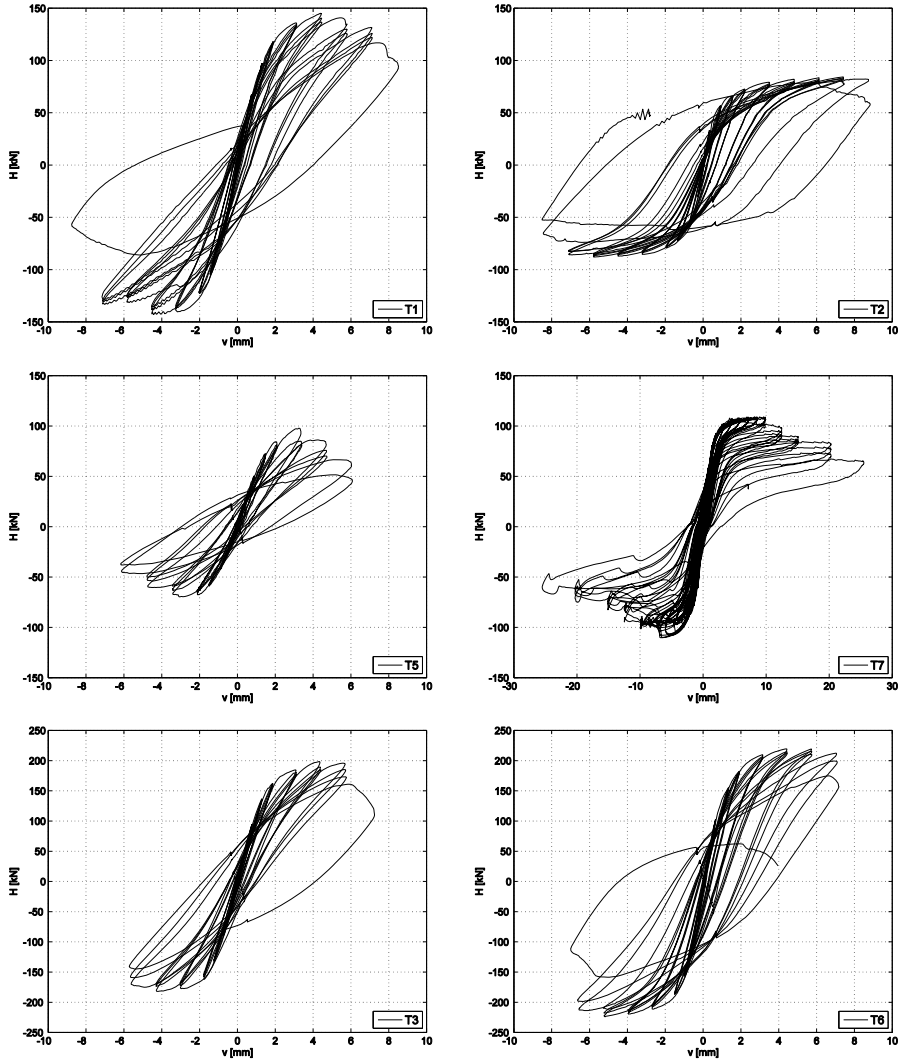


Figure 3. Shear force-deformation characteristics obtained from tests [6].

The latter boundary condition (cantilever), was implemented for all specimens of the Series W [7-9] and C [10]. These specimens were tested within the framework of the research projects on the behavior of the masonry walls with incorporated soft layers in one of the bed joints. Note that the walls W0.R and W0.10 were without soft layer



(control specimens). Their hysteretic behavior is shown in Figure 4. Other walls of the Series W had a soft layer incorporated in the bed joint made of extruded elastomer (E) or rubber granulate (G). In order to reveal the influence of the soft layer on the wall stiffness, the results of four of those tests are given in Table 1. Finally, walls of the Series C [10] shown in Table 1 were also control specimens and had no soft layer incorporated in the bed joints.

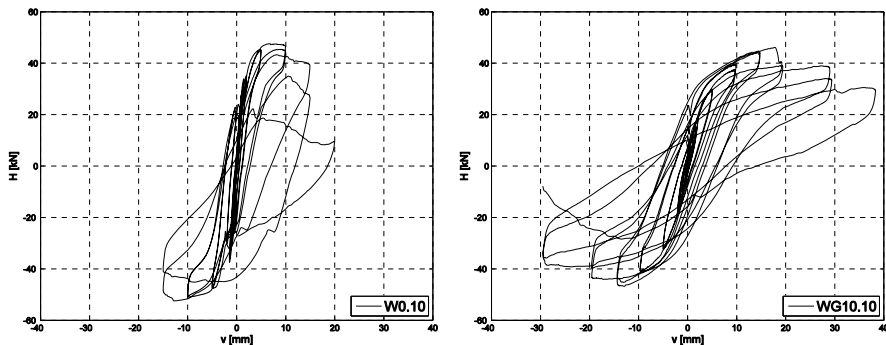


Figure 4. Shear force-deformation characteristics obtained from tests [8, 9].

From the analysis of the hysteretic behavior of the specimens obtained from experimental investigations [6-10] the shear wall stiffness has been assessed and is presented in Table 1. Note that all walls, except walls T5 and T6, had an aspect ratio (height over length) equal to one. Walls T5 and T6 had an aspect ratio of 2/3 and 4/3, respectively. In the Table 1  $\sigma_0$  is the pre-compression stress level,  $f_x$  is the mean compressive strength of the masonry (perpendicular to the bed joints),  $H_{max}$  is the maximal lateral load obtained from the test and  $H_u$  the ultimate shear strength obtained by equating the areas under the experimental and bilinear envelopes as previously described.

Table 1. Shear strength, ultimate story drift and stiffness (elastic, tangent and effective) of test specimens

Test	$\sigma_0/f_x$	$H_{max}$ [kN]	$H_u$ [kN]	$\delta_u$ [%]	$K_{el}$ [kN/mm]	$K_0$ [kN/mm]	$K_{eff}$ [kN/mm]
P1	0.10	92.00	81.38	0.38	230.30	76.64	64.89
P2	0.15	107.00	94.32	0.25	230.30	94.17	73.81
T1	0.10	145.15	135.0	0.27	230.30	98.94	70.48
T2	0.05	88.21	80.60	0.30	230.30	91.48	52.54
T3	0.20	198.40	185.13	0.22	230.30	131.48	103.83
T5	0.20	97.87	86.58	0.20	118.60	59.38	49.14
T6	0.10	224.00	211.47	0.26	342.30	158.06	121.95
T7	0.10	110.20	100.55	0.54	134.70	79.46	64.49
C1	0.10	93.28	93.28	1.66	107.10	15.10	14.04
C2	0.20	145.89	145.89	1.25	107.10	21.20	17.17
C3	0.05	53.37	53.37	2.50	107.10	8.20	7.42
W0.R	0.10	49.9	45.6	2.20	94.24	15.50	10.29
WG10	0.10	43.1	38.5	2.36	25.27	6.50	4.60
WE10	0.10	46.4	39.4	1.22	47.97	8.30	6.74
W0.10	0.10	47.6	42.1	1.01	91.74	28.60	24.62
WG10.10	0.10	46.8	41.5	2.20	25.16	11.00	5.12
WE10.10	0.10	43.1	37.9	1.20	46.89	19.20	16.08

In addition, the ultimate drift capacity, i.e. the ultimate displacement capacity divided by the height of the specimen,  $\delta_{us}$ , is also given and corresponds to the strength degradation of 20%, see Figure 2. For each test specimen three different values for stiffness are given: the elastic stiffness,  $K_{el}$ , which is calculated based on the elastic beam theory incorporating shear deformation; the tangent stiffness,  $K_0$ , which is calculated as the slope of the initial branch (first cycle) of the hysteresis; and the effective stiffness,  $K_{eff}$ , which is obtained as a slope of the secant of the cyclic envelope at  $0.7 H_{max}$ . Note that for the calculation of  $K_{el}$  the mechanical characteristics needed were determined according to [4]. Furthermore, values given for the specimens with soft layer (WEs and WGs) include also the deformation caused by a soft layer.

## 2. Discussion

The effective stiffness,  $K_{eff}$ , is the parameter of utmost importance for seismic design of masonry shear walls. In general, the effective stiffness is a complex parameter and difficult to determine. For practical applications, it is usually adopted as a certain percentage (usually 50%) of the elastic stiffness,  $K_{el}$ . However, as seen from Table 1 and as shown in Figure 5, the ratio between the tangent and the effective stiffness as well as between the elastic stiffness and the effective stiffness for clay block masonry walls, is scattered and the latter ratio is, in most cases, much smaller than 0.5. Furthermore, as can be clearly seen from the hysteretic behavior of the masonry walls (Figures 1, 3 and 4) a significant degradation of stiffness  $K_0$  during cyclic loading can be observed. Figure 5 shows exemplarily the (tangent) stiffness degradation for three tests of the Series T.

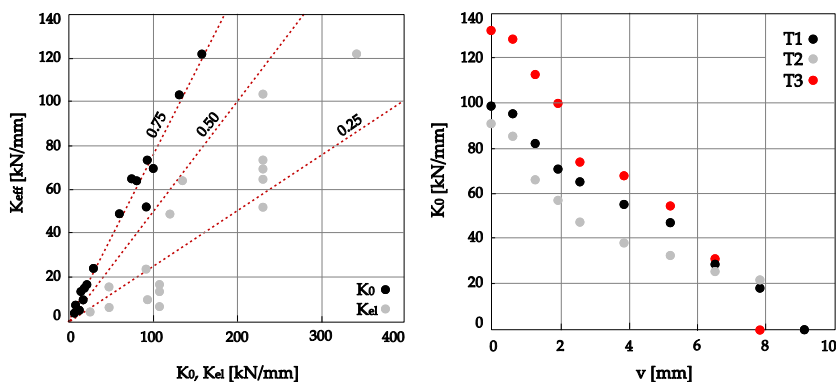


Figure 5. Stiffness comparisons and degradation.

It can also be seen from Table 1 (specimens P1 and P2, T1 to T3, and C1 to C3) that, as the vertical pre-compression level increases, the assessed stiffnesses (tangent and effective) increase, but the ultimate deformation capacity decreases. This is because increasing the pre-compression level postpones the formation of the tensile cracks, which reduce the effective area of the wall, but on the other hand, it accelerates the formation of the mechanisms that correspond to the collapse of the specimens, i.e. shear-compression failure at the toes and center of the specimens. The former

phenomenon causes the effective stiffness to increase and the later one causes the ultimate deformation capacity to decrease.

Walls with lower aspect ratio (height over length) exhibited lower shear stiffness, cf. tests T1, T6 and T7. Further, comparing the values of the stiffnesses of walls P1 and T1 (same pre-compression level and aspect ratio) it can be seen, that there is some size effect affecting the assessed wall stiffness: both tangent and effective stiffnesses are higher for a larger wall. Finally, changing the boundary conditions from fixed ends to cantilever (tests T1 and T7) significantly decreased the specimen's stiffness.

Considering the results of the wallets of the Series W it can be seen from Table 1 that, the presence of a soft layer in the bed joint (W0.R, WG10 and WE10) or between the wallette and underlying concrete element (W0.10, WG10.10 and WE10.10) reduces the stiffness considerably, compared to the conventional masonry. Moreover, the wall stiffness decreases with decreasing shear modulus of the soft layer.

### 3. Conclusions

The presented analysis and discussion of the results of static-cyclic tests on the several series of masonry walls allow the following conclusions to be drawn:

Based on the values obtained from tests, it seems that the effective shear stiffness of clay-block masonry walls can be estimated at 75% of the tangent stiffness. The correlation between effective and elastic stiffness, which is calculated based on the elastic beam theory incorporating shear deformation, exhibit a rather large scatter.

Shear stiffness of the specimens was highly influenced by pre-compression level, namely: the specimens with higher pre-compression were stiffer. Further, the shear stiffness decreases with decreasing aspect ratio of the wall and with placing the soft layers in one of the lower bed joints of the wall.

Shear stiffness undergoes considerable degradation during the static-cyclic loading. This fact should be taken into consideration when designing masonry walls subjected to seismic actions.

### References

- [1] A.H. Salmanpour, N. Mojsilović and J. Schwartz, Deformation capacity of unreinforced masonry walls subjected to in plane loading: a state-of-the-art review, *Journal of Advanced Structural Engineering* **5:22** (2013), SpringerOpen.
- [2] A.H. Salmanpour, N. Mojsilović and J. Schwartz, Experimental study of the deformation capacity of structural masonry. *Proceedings of the 12th Canadian Masonry Symposium (2013)*, Vancouver, British Columbia, June 2-5, Paper No. 161.
- [3] M. Tomažević, *Earthquake-resistant design of masonry buildings*, Imperial College Press, London; 1999.
- [4] SIA 266:2003, Swiss Structural masonry Code, *Swiss Society of Engineers and Architects*, Zurich, 2003.
- [5] CEN-EN 1052-1:1998, Methods of test for masonry, Part 1: Determination of compressive strength, 1998.
- [6] N. Mojsilović, Experimental study of the deformation capacity of structural masonry, *50<sup>th</sup> CIB W023 - Wall Structures Commission Meeting*, Eindhoven, Netherlands, 2013.
- [7] N. Mojsilović, B. Stojadinovic, A. Barandun and C. Vögeli, Seismic behavior of masonry walls with soft-layer wall bearings, *Proceedings of the 5th International Conference on Structural Engineering, Mechanics and Computation*, Cape Town, South Africa, September 2-4, 2013, pp. 1865-1870.

- [8] A. Barandun, Seismic Behavior of Unreinforced Masonry Walls with Soft Layer Strip Bearings, MSc Thesis, Institute of Structural Engineering, ETH Zurich, 2013.
- [9] C. Vögeli, Seismic Behavior of Unreinforced Masonry Walls with Soft Layer Strip Bearings, MSc Thesis, Institute of Structural Engineering, ETH Zurich, 2014.
- [10] N. Mojsilović, G. Simundic and A.W. Page, Masonry wallettes with damp-proof course membrane subjected to cyclic shear: An experimental study, *Construction and Building Materials* **24(11)** (2010), 2135–2144.

# A complete timber building system for multi-storey buildings

Per-Anders DAERGA<sup>a</sup>, Ulf Arne GIRHAMMAR<sup>b,1</sup> and Bo KÄLLSNER<sup>c</sup>

<sup>a</sup>*Building Engineering, Faculty of Science and Technology, Umeå University, Sweden*

<sup>b</sup>*Division of Structural and Construction Engineering-Timber Structures, Luleå University of Technology, Sweden*

<sup>c</sup>*Faculty of Technology, Linnæus University, Växjö, Sweden*

**Abstract.** The Masonite Flexible Building (MFB) system is a complete timber building system for commercial and residential multi-storey houses. The system is for tall and large buildings with long floor spans. The MFB system uses prefabricated wall, floor and roof elements which are delivered in flat packages and erected on the construction site. The MFB system might be classified as a panel construction, where the load-carrying structure consists of composite light-weight timber I-beams mechanically integrated with a composite laminated wood panel called PlyBoard™. The I-beams and the panel form a strong and rigid carcass for wall and floor elements, making the system well suited for high rise construction. A key feature of the MFB system is the connection technique which enables swift erection of the system units on site. The PlyBoard™ panels are provided with a continuous slot along the periphery. The slot is used as a general connection interface for the joining of the wall elements. The floor elements are suspended and hooked onto the bearing walls using sheet steel hangers, allowing swift assembling of the floor deck and enabling direct vertical wall-to-wall load transfer parallel to grain. The paper presents the construction principles, system components and units, erection technique, functional and architectural aspects of the Masonite Building System.

**Keywords.** Masonite flexible building system, multi-storey timber buildings, slotted-in connections, suspended connections, functionality requirements

## Introduction

Building systems and construction methods for multi-storey timber buildings have developed rapidly. Currently, timber construction technology uses prefabricated units, which are highly competitive with regard to cost efficiency, environmental impact and erection. The Masonite Flexible Building (MFB) system is one of several systems based on prefabricated units.

The MFB system is an open building system in the sense that the technical solutions and the building method are free to be employed by architects, designers, manufacturers and construction companies. The system meets current requirements

---

<sup>1</sup>Corresponding author: [ulf.arne.girhammar@ltu.se](mailto:ulf.arne.girhammar@ltu.se)

regarding fire safety, moisture conditions, strength and stabilization, thermal and acoustic insulation. This paper is an extended version of the one presented earlier [1].

## 1. Masonite flexible building system

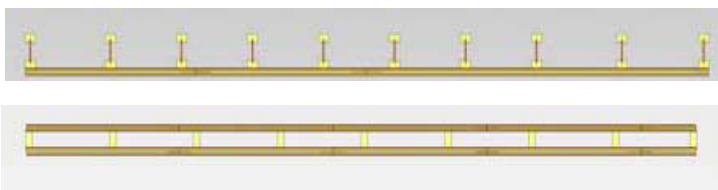
The MFB system consists of prefabricated wall, floor and roof elements which are delivered in flat packages and assembled storey by storey. The system is intended for multi-storey buildings up to eight storeys and floor spans of up to 8 m [2]. The system meets fire requirements of REI 60 minutes [3] and noise requirement class A [4].

Structurally, MFB is a combined panel and frame construction using a special PlyBoard™ panel together with I-shaped framing members. The prominent features of the system are the unified connection interface incorporated in the PlyBoard™ panel, the elimination of horizontal timber members in the walls to reduce settlement to a minimum and the suspended floor-to-wall connection. The carcass structure and the high quality of system components offer architectural freedoms and simple assembling.

### 1.1. Load-bearing structure

External wall and floor elements use a ribbed PlyBoard™ panel construction with ribs of composite I-studs and I-beams, respectively. Internal wall elements have boxed PlyBoard™ panel structure with ribs of timber studs. The different load-bearing structures are depicted in Figure 1. The PlyBoard™ panel is attached to the I-beams/I-studs mechanically by nails. The combination of PlyBoard™ and I-studs/I-beams forms a strong and rigid load-bearing structure well suited for high rise construction, see sections below for description of each of the structural members.

Usually in wall panel constructions, the individual studs carry the vertical loads from roof and suspended floors, whereas the sheathing resists the horizontal forces due to wind and accounts for the bracing. In this case, the PlyBoard™ panel is employed for carrying both vertical and horizontal loads, thus significantly increasing the load-bearing efficiency of the wall. The use of high quality engineered wood products offers new design options which improves many of earlier disadvantages for multi-storey timber buildings, such as vertical settlement due to loading perpendicular to grain of horizontal members, thermal bridges at wall-to-floor junction etcetera.



**Figure 1.** Examples of structural wall and floor carcasses: Ribbed PlyBoard™ panel with I-members used in external walls and floor, and boxed PlyBoard™ panel for load-bearing internal walls, respectively.

### 1.2. Material and system components

The structural components of the MFB system are a composite lightweight I-beam and PlyBoard™ panel. Together they constitute the structural skeleton of the building elements.

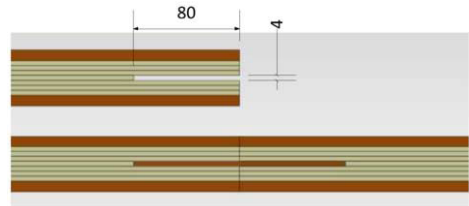
**Composite I-beams:** The composite I-beams and I-studs are used as structural members in wall, floor and roof elements. The flanges are made of machine graded structural timber, and the web is made of hard fibreboard or oriented strand board (OSB). The I-beams and I-studs are manufactured by Masonite Beams AB, Sweden.

**PlyBoard™ panel** is a three-layered wood composite panel with a core of laminated veneer lumber (LVL) and surface layers of hard fibreboard as shown in Figure 2. The veneer plies have a thickness of 3-4 mm and the grain orientation is parallel for all plies. The material composition gives the panel its high strength and stiffness, good form and dimensional stability and high moisture diffusion resistance. The panel is available with fibreboard thicknesses of 4 or 8 mm and number of LVL plies between 3 and 7. The nominal dimensions are 1200 × 2400 mm and are manufactured by IBC Group, Sweden.

The PlyBoard™ panels are spliced using a loose tongue joint which is glued to attain a strong joint. When used for external walls, the joint also ensures airtightness and serves as vapour barrier (see Figure 3).



**Figure 2.** The PlyBoard™ panel.



**Figure 3.** Peripheral slot and spliced panels using a glued board tongue joint (in mm).

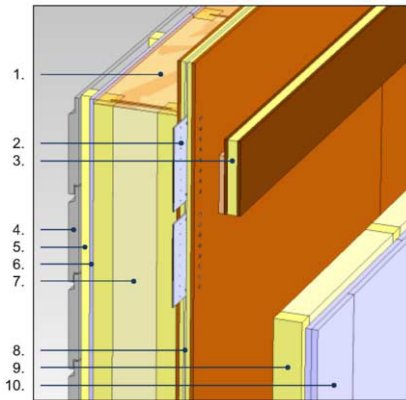
### 1.3. Wall and Floor Elements

The wall elements are delivered with preinstalled tubes for electric cables and power sockets and a support beam for the suspended floor. In addition, the external wall elements come with cladding, doors and windows. The maximum lengths of the wall elements are limited to 9 m, being the maximum length that can be transported by road.

**External wall elements:** The carcass is a ribbed panel structure according to Figure 1 with I-studs and a PlyBoard™ panel. Figure 4 shows a representative external wall construction with a description of each of the various layers and parts. The depth of the load-bearing layer normally depends on the demand of thermal insulation. The PlyBoard™ panel is attached to the inner side of the I-studs. This enables the vertical loads to be transferred directly to the foundation. The PlyBoard™ performs the triple functions of vertical load transfer, horizontal bracing and airtightness/vapour barrier respectively; the last function is achieved provided that the panel splices are sealed. Due to the continuous panel layer and the fact that the floor is suspended, the building envelope remains intact and unbroken, and thermal bridges are reduced to a minimum.

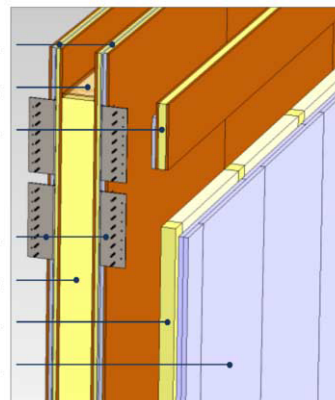
An issue of great importance for medium and high rise timber construction is the design of the wall-floor junction with respect to vertical load transfer capacity and settling. In contrast to typical designs of contemporary multi-storey timber buildings where the floor is fully or partly supported by the wall, see for example [2], and horizontal timber plates are used for load transfer (i.e. stresses perpendicular to grain direction), it can be argued that medium and high rise buildings require a design where the vertical load transfer is parallel to grain in order to maintain a high load transfer capacity and keep the amount of settling as small as possible.

Consequently, to achieve an optimal vertical load transfer capacity with minimum settling, the MFB system uses a design approach where the floor elements are structurally detached from the wall by means of a separate support beam on the wall and special floor hanger devices attached to the floor elements. This design allows for a clean and simple wall-floor interface without any horizontally installed timber members except for the top and bottom plates of thin hard fibre board, as shown in Figures 4 and 7.



1. Fibre board strip; 2. Slotted-in connection plate; 3. Support beam for suspended floor; 4/5/6. Cladding layers; 7. I-studs; 8. PlyBoard™ panel with perimeter slot; 9/10. Lining layers.

**Figure 4.** The MFB external wall element with carcass of PlyBoard™ panel and I-studs.



1. PlyBoard™ panels with perimeter slot; 2. Fibre board strip; 3. Support beam for suspended floor; 4. Slotted-in connection plate for transverse wall; 5. Timber studs; 6/7. Lining layers.

**Figure 5.** MFB internal load-carrying wall element with a boxed panel and works as a shear wall.

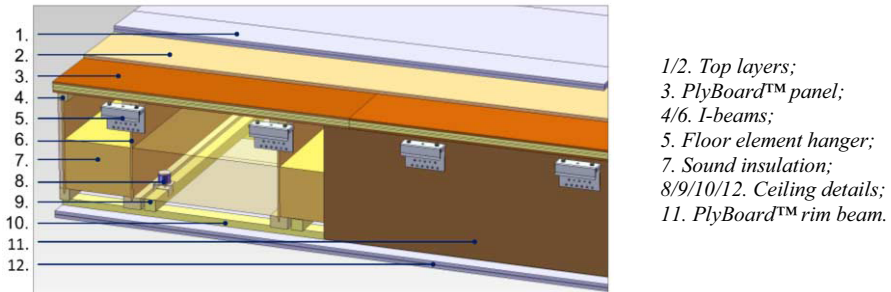
*Internal wall elements:* The carcass is a boxed panel structure according to Figure 1, with squared timber studs. Like the external walls, internal walls carry the loads from the roof, suspended floors and the dead load of the wall itself. Furthermore, they are used for bracing the building implying that they transfer the horizontal wind force and the wind induced uplift force. Figure 5 shows the internal wall including descriptions of each of the layers and parts.

*Floor element:* Floor structures have to offer adequate load-carrying capacity, minimal deflection and vibration, effective sound insulation and sufficient fire resistance. To satisfy these demands, the MFB suspended floor elements are designed as a multi-layered structure with an embedded load-bearing structure, a floor finish and a ceiling as illustrated in Figure 6. The structural floor layer is a composite ribbed PlyBoard™ panel according to Figure 1.

The MFB system uses sheet metal hangers that are pre-mounted on the ends of the floor element with mechanical fasteners and hooked on to a separate support beam on



the wall when the floor element is lifted in place. The design of the floor hanger is described more in a section 1.4 (Figure 10). The floor-to-wall connection is structurally disconnected from the external wall to avoid horizontal timber members loaded perpendicular to grain direction and to obtain an unbroken climate shield.

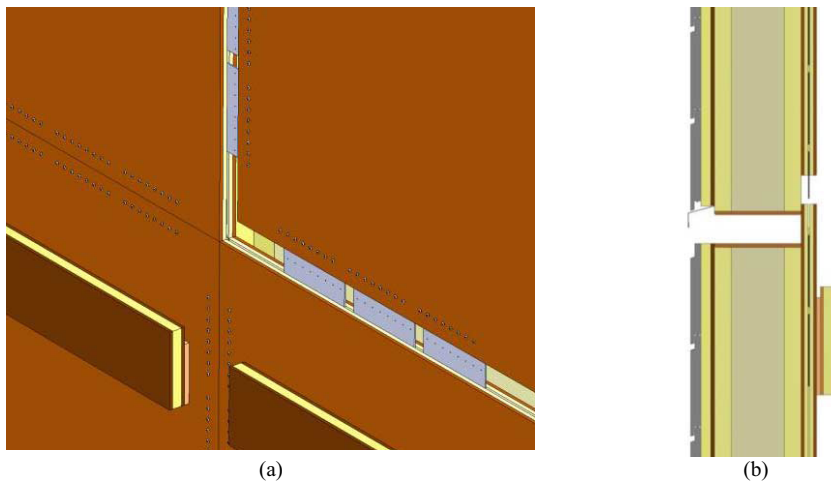


**Figure 6.** The MFB floor element with PlyBoard™ panel and I-beams.

#### 1.4. Structural connections

The MFB system has a unified interface for the inter-connection of wall elements and a hanger attachment from the suspended floor to the load-bearing walls. Depending on the type of wall intersection, different types of slotted-in steel plates are used

*The slotted-in wall connection:* The external and internal wall elements are spliced by slotted-in steel plates and screws. The connection interface is shown in Figure 7 for an external wall and in Figure 8 for a wall junction. The slotted-in plate connection resists both horizontal wind force (shear joint) and wind induced uplift forces (hold-down device). The structural features of the slotted-in connection are described in [5].

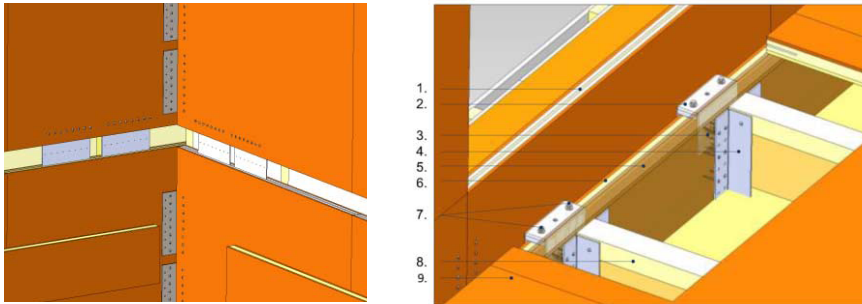


**Figure 7.** External wall-to-wall connection interface with slotted-in steel plates and screw connectors: (a) Steel plates used for horizontal and vertical connections between wall elements and (b) Detail of connecting elements vertically and use of hard fibreboard strips instead of timber rails.

*Wall junction and corner connections:* The slotted-in plates are also applied for wall junction and wall corner connections. In addition, the internal wall elements use slotted-in angle brackets on the gable sides; see Figure 5 and Figure 8. These brackets

enable an efficient stabilization of the building by transferring the wind induced up-lift forces from shear walls to transverse walls over the height of the wall.

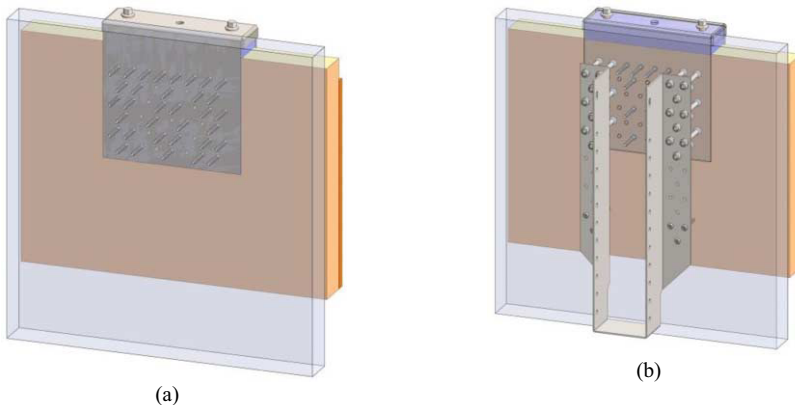
*The floor hanger connection:* The floor-to-wall connection is critical and needs special design attention as conflicting structural and functional demands coincide e.g. securing load transfer, avoiding acoustic flank transmission and fulfilling the fire safety regulations. The hangers are preinstalled on the ends of the floor elements and are fastened by screws to the rim beam as shown in Figure 6 and Figure 9. The internal spacing of the hangers corresponds to the spacing of the I-beams of the floor element, normally 600 mm. At erection, the hook of the hanger grabs around the support beam on the bearing walls (cf. Figure 7), enabling direct vertical wall-to-wall load transfer parallel to grain.



**Figure 8.** Wall junction – steel angle brackets connect shear walls to transverse walls (left). **Figure 9.** The floor hanger connection for the suspended floor to external wall.

1. External wall PlyBoard™ panel; 2. Floor hanger; 3. Hanger fasteners in rim beam; 4. Joist hanger; 5. Rim beam; 6. Support beam; 7. Screws fixed to support beam; 8. I-beam; 9. Floor PlyBoard™ panel.

It is noticed that the design of the hanger connection can be critical since there is no redundancy and the safety of the structure depends solely on the mechanical hanger connection in case of failure. The present design is examined and evaluated in [6] together with suggestions for improvements and a proposal for an alternative design.



**Figure 10.** An extract of the floor-to-wall connection showing the rim beam of the floor element (transparent in light blue), the support beam (light brown), the distance plate (dark brown) between the support beam and the wall element and the floor element hanger: (a) Original design of the floor element hanger screwed to the rim beam; and (b) Modified design where the floor element hanger is connected with the beam hanger in front of the rim beam through bolts and nuts to improve the load-bearing capacity and the ductility of the floor element hanger.

Normally, the floor hanger and the joist hanger are connected mechanically and independently of each other to the rim beam of the floor element as illustrated in Figure 10a, where only the floor hanger is shown. This imposes high stresses on the PlyBoard™ rim beam and especially on the outer board layers at the fasteners. In order to alleviate the stresses on the rim beam and obtain a safer connection, it is suggested that the two hangers are tied together by screws through the rim beam and secured with nuts on the other side as shown in Figure 10b. Experimental investigations (not yet reported) confirmed that both the ultimate load and ductility are improved.

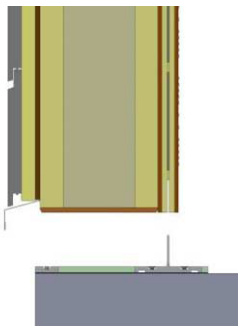
*The support beam connection:* The support beam for the floor elements transfers the floor load to the load-carrying walls. The support beam is mechanically attached to the wall panel at manufacturing by a set including both inclined and horizontal fasteners. The sets are intermittently distributed along the support beam with spacing equal to that of the vertical studs such that each set will be anchored to a stud.

The fasteners are the double-threaded and self-tapping screw types. The inclined fasteners are carrying the vertical load of the floor, and have a length that allows it to be anchored in the flange of the I-stud behind the wall panel.

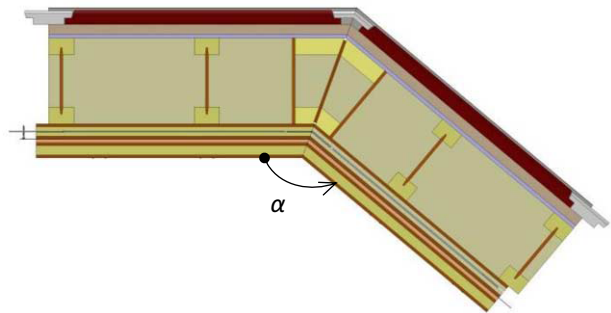
The horizontal fasteners prevent separation of the support beam from the wall panel due to induced moment from the load eccentricity introduced by the floor load.

*Anchorage to foundation:* A new concept of tying shear walls to the foundation using a metal T-profile inserted in the slot of the wall panel is developed, see Figure 11. The T-profile is mechanically fastened to both the bottom slab and the wall element and is used for both external and internal walls.

*Connecting wall corners with arbitrary angles:* The method used to join interconnecting external wall elements at corners with arbitrary angles is shown in Figure 12. The angle  $\alpha$  can vary between 90 to 270 degrees. The element uses the same docking interface as ordinary wall elements.



**Figure 11.** Holding down device for tying the shear wall to the foundation.



**Figure 12.** External wall corner element for arbitrary corner angles  $\alpha$  between 90 to 270 degrees.

## 2. Miscellaneous

The philosophy of the building system is to carry out all the erection procedures from the inside of the building while standing on the floor deck. The concept of suspended floor implies that the floor load is the same for all storeys, and that the same type of

acoustic damper can be used for all the hanger connections, which simplifies the design significantly.

The PlyBoard™ panel and the I-beams/I-studs constitute a strong and tight structure and building envelope characterized by efficient use of raw material, good thermal and building physical features, making the MFB system suitable for buildings with very high energy demands as those introduced by the EU Directive on energy performance of buildings (nearly zero-energy buildings) [7].

The prefabricated wall units have a modularized design and can be customized with respect to size and configuration of openings (number, size and location) providing flexibility in organizing the rooms' shape in plan, section and size. The wall elements allow the building envelope to be optimized regarding structural and physical performance, and both the wall and floor elements can be adjusted to meet specific safety and functional requirements (e.g. thermal, acoustic and fire performance) by modifying or changing the components and internal layer composition.

### 3. Conclusions

The Masonite Flexible Building System combines the slenderness of a timber light-frame system with the strength and robustness of a cross laminated timber system. The erection of the system elements is simple and done swiftly by using efficient slotted-in steel-plate connections for the walls and steel hangers for the floors. The system is well adapted for multi-storey buildings.

### Acknowledgement

The authors greatly acknowledge the financial support from the County Administrative Board of Norrbotten, the Regional Council of Västerbotten and The European Union's Structural Funds – The Regional Fund.

### References

- [1] Daerga P. A., Girhammar U. A., Källsner B., Masonite flexible building system for multi-storey timber buildings, *12th World Conference on Timber Engineering, 2012*.
- [2] Masonite Beams AB, *MFB Handbook*. Draft version 2010:1, 40 p. (in Swedish).
- [3] The Swedish National Board of Housing, Building and Planning: *Building regulations (BFS 2013:14), Building rules (BBR 5:221)*, Sweden 2013.
- [4] Swedish Standards Institute: *Acoustics - Measurement of Sound Insulation in Buildings*, Swedish Standard (SS 02 52 67), Sweden 2001.
- [5] Daerga P. A., Girhammar U. A., Källsner B., Slotted-In Steel-Plate Connections for Panel Wall Elements – Experimental and Analytical Study, *12th World Conference on Timber Engineering, 2012*.
- [6] Daerga P. A., Girhammar U. A., Källsner B., Suspended Floor Element Connections for the Masonite Flexible Building System, *12th World Conference on Timber Engineering, 2012*.
- [7] The European Parliament and the Council of 19 May 2010 on the energy performance of buildings, Directive 2010/31/EU, *Official Journal of the European Union*, 18.6.2010, L 153/13-35.

# Sheathing-to-framing fasteners in light wood-framed buildings as finite beam element

Michał BASZEN<sup>1</sup> and Czesław MIEDZIAŁOWSKI

*Department of Structural Mechanics, Białystok University of Technology, Poland*

**Abstract.** A proposition of 3D numerical model of light wood-framed structures is presented in the paper. To describe the behavior of fasteners, 6 degrees of freedom beam element was used. The model took into account the non-linear characteristics of the whole structure resulting from the non-linear behavior of individual connectors. There was made an assumption that only non-linear elements of the structure had sheathing-to-framing connectors. Sheathing and framing were described by shell elements and its stiffness matrixes had included orthotropic material characteristics of timber and chipboard. The function describing the P- $\Delta$  characteristics of fasteners was obtained on the basis of joint experimental researches. Verification of the proposed model was provided by comparative analyses of results obtained from the proposed model and full-scale experimental tests. The proposed model results have shown good agreement with the results of experimental studies, particularly in the range of destructive burden.

**Keywords.** Light wood-framed buildings, 3D FEM model, non-linear analysis, dowel type fastener, finite beam element, experimental tests

## Introduction

Although currently used timber framed construction has more than 60 years, still the issue is accurate analysis of its behavior. Using numerical models implementing FE and verifying them through the experimental studies allows the behavior of construction work to be specified. But still, a wide range of timber structure characteristics remain unexplored.

A very important issue is the need to define the work of joints, as well as its stiffness, which determines the stiffness of overall structure. The rigidity of joints determines the distribution of internal forces between the individual elements, affecting on the structures behavior and its capacity.

Nonlinear behavior of timber structures results from fasteners nonlinearity. A light wood-framed wall is able to carry external loads on the level dependent on the sheathing-to-framing connection type. The most common fasteners as nails, screws, dowels; despite their high strength, have a small cross-sectional area. That makes the connection be the most vulnerable component of the structure. The experimental

---

<sup>1</sup>Corresponding author: Department of Structural Mechanics, Faculty of Civil and Environmental Engineering, Białystok University of Technology, Wiejska 45E street, 15-351 Białystok, Poland; e-mail: [m.baszen@kmb.pb.edu.pl](mailto:m.baszen@kmb.pb.edu.pl)

studies highlighted that the  $P-\Delta$  (load-deflection) function of fasteners is decisive for resistance to destruction [1]. Destruction of joints could take different forms. It may involve the bending of the fastener and pulling it out of framing, or sheathing cut by nails as well as panel damage at the corners [2,3]. The way the structure is loaded also affect on the joints destruction. Static loads cause damage by peeling out the sheathing of the wood frame and pulling out nails while dynamic load causes the joint damage by breaking the nails [4].

Most models describing wall and floor elements of light wood-framed buildings used Finite Element Method to analyze the above problems discussed. Connection between sheathing and framing was usually presented as single spring or system of oriented springs [5-7].

Behavior of fasteners, its rigidity, deformability as well as its failure modes affect material characteristics used to simulate the fasteners as spring elements. However, using spring systems bring in some simplicities in presentation of fastener behavior.

## 1. Proposition of numerical model

In the present paper, a proposed 3D numerical model using finite elements was used to describe the behavior of light wood-framed structures as walls [8] or floor elements [8,9] (Figure 1).

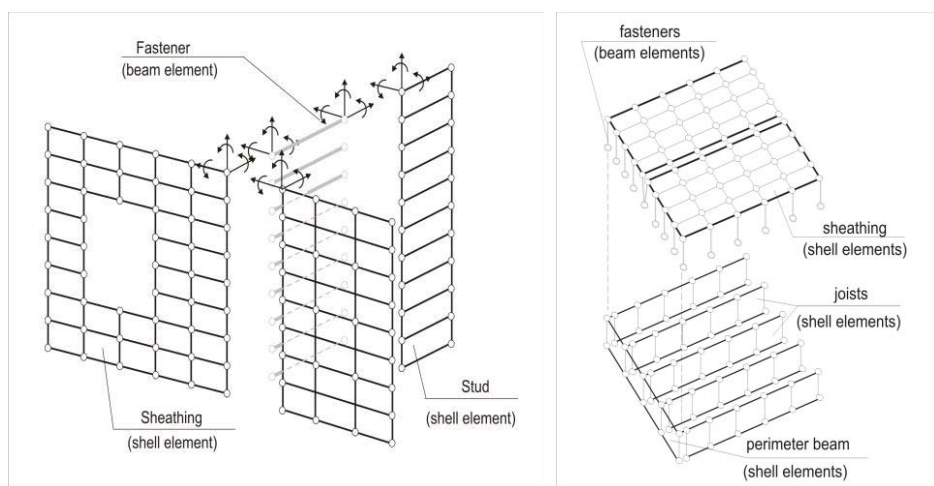


Figure 1. Proposed numerical model

The assumed timber frame and sheathing were described by 4-node shell elements. Timber and chipboard sheathing panels had been materials with different mechanical parameters in each direction. Due to these orthotropic properties, different values of elasticity moduli as well Poisson's ratios were used in the model. These mechanical parameters were taken from experimental study of material properties.

Eventually, the existing bearing between panels of sheathing as well as cooperation of double studs along the opening in walls, were described by simple one-dimensional bar elements with zero tension stiffness.

In opposition to previously realized models [5-7], where the fasteners were described by single spring or system of the springs simulating stiffness under bending, shear and compression-tension state, the proposed model used beam elements. The six degree of freedom beam element was incorporated. It was assumed that the connectors will be treated as miniature beams attached in the surrounding frame and sheathing.

Stress tensor for beam element is described by the formula:

$$\boldsymbol{\sigma} = \mathbf{E} \cdot \boldsymbol{\varepsilon} \quad (1)$$

where stiffness tensor  $\mathbf{E}$  is diagonal, so can be expressed as:

$$\mathbf{E} = \text{diag} \left[ EA, GA/k_y, GA/k_z, EJ_y, EJ_z, EJ_s \right] \quad (2)$$

The values of the EA, GA, EJ are the substitute stiffness of fastener calculated on the basis of the experimentally obtained curve [8] describing the fasteners slip (Figure 2b). The cross-section  $A$  is constant and independent of the connector deformation.

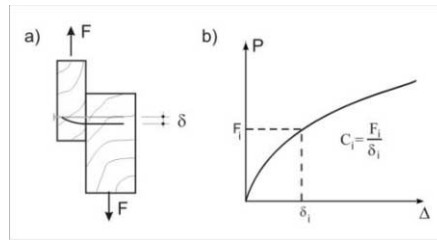


Figure 2. Load-slip experimental curve

Stiffness of the connection is calculated as:

$$C_i = \frac{F_i}{\delta_i} \quad (3)$$

The substitute stiffness of the fastener  $E$  is determined at the assumption that the beam element is attached on both sides.

Displacement  $\delta$  (Figure 2a) is obtained from the formula [8]:

$$\delta = \frac{Fl^3}{12EI} \left( 1 + \frac{12EI}{GA} \frac{\alpha}{l^2} \right) \quad (4)$$

where:  $l$  - length of fastener,  $I$  - moment of inertia,  $E, G$  - respectively the elasticity modulus and modulus of distortion,  $\alpha$  - aspect ratio.

By comparing Eqs. (3) and (4) the substitute elasticity modulus is calculated as:

$$E = \frac{l^3}{12I} \left[ 1 + \frac{3}{4}(1+\nu)\alpha \left( \frac{d}{l} \right)^2 \right] \cdot C \quad (5)$$

The behavior of fasteners in floor elements and in walls varies. The live load perpendicular to floor panel surface results in the bearing between sheathing and framing. The friction in the contact area also changes stiffness of connection.

Finally, the stiffness is described by:

$$C' = \alpha_1 \cdot \alpha_2 \cdot C \quad (6)$$

where:  $\alpha_1$  - coefficient related to the bearing of sheathing to joists,  $\alpha_2$  - coefficient related to friction in contact area.

The behavior of light wood-framed structure is nonlinear. The greater impact on this nonlinearity results from the fastener behavior. The proposed model assumed therefore that the only nonlinear component will be the beam describes sheathing-to-framing fasteners, while the other elements will operate in the linear range.

The nonlinearity is described by the function [10]:

$$N = (A + B \cdot \delta) \left[ 1 - e^{\left( \frac{-C}{A} \delta \right)} \right] \quad (7)$$

where: A, B, C are determined on the basis of experimental studies.

Elasticity modulus  $E$  for a particular nail in "i"-step of loading was determined from the relationship:

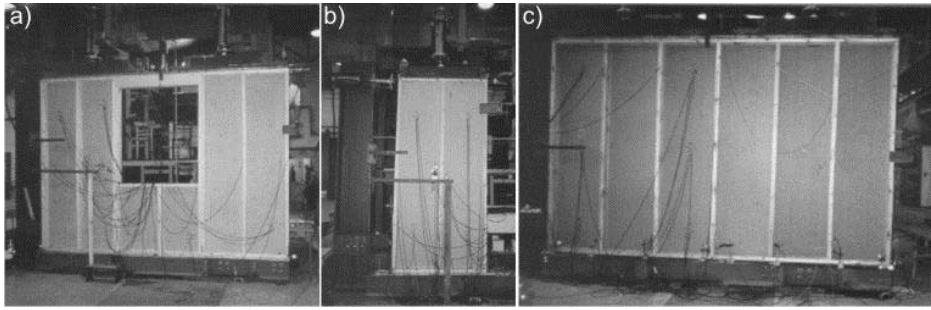
$$E_i = E_0 \cdot \frac{C_i}{C_0} \quad (8)$$

where:  $E_0$  - elasticity modulus calculated from Eq. (6),  $C_0$ ,  $C_i$  - respectively initial and "i"-step of loading stiffness.

## 2. Experimental verification

To verify the proposed numerical model, there were carried out comparison of the internal forces and displacements obtained from the model and experimental studies conducted at the Białystok University of Technology [9].





**Figure 3.** Wall and floor specimen

There were conducted full-scale experimental test of wall and floor elements. Four wall specimen with one sheathing panel 1,25 m long by 2,75 m high (Figure 3b) and three specimen 3,75 m long by 2,75 m high (Figure 3a) with three separate panels of sheathing and window opening were tested.

The floor element researches were also conducted. There were tested four specimen (Figure 3c) in two series by two elements. The dimensions of specimen was 2,75 x 3,75 m for first series and 2,75 x 3,6m for the second.

The wall elements have been loaded by system of vertical burden and horizontal force. Floor elements have been loaded in the plane parallel to the joists.

During the test were recorded the displacements in the plane of the elements as well the elements deformation in the timber frame and sheathing. Additionally in the external element of framing, there were recorded relative displacement between sheathing and framing to determine the sheathing-to-framing fastener effort. The external load, displacement and strain values were recorded using VISHEY 4000 and DAQ (data logger) system in 6 second intervals. The deformation of framing was recorded using single strain gauges while strain of sheathing panels were recorded using strain gauge rosette.

The external loads in wall elements were applied in three load phases. In the first phase, the specimen were loaded only vertically to the level of 40% of the expected ultimate load. The second phase was similar to first but horizontal load was applied. In the third phase, the vertical and horizontal load were applied simultaneous. This phase was divided into two stages. In first stage, the specimen was loaded to the level of 40% expected ultimate load while in second the specimen was loaded until it was damaged.

The floor elements were loaded in two phases according to one type of external load. The first phase was the structure loading to the level of 40% of the expected ultimate load. The second phase was similar to third phase of wall loading. The difference was that the specimen were not loaded to destruction but only to expected ultimate load.

### 3. Comparative analysis

#### 3.1. Deformability of the wall and floor elements

In view of static scheme and the way the external loads had been applied, the displacement in wall were recorded in horizontal direction at top corner of specimen opposite to lateral force. The measurements were carried out in *Phase-3* under mutual

horizontal and vertical loading until the specimen was destroyed. The load-slip characteristics for perforated wall elements are presented at Figure 4a.

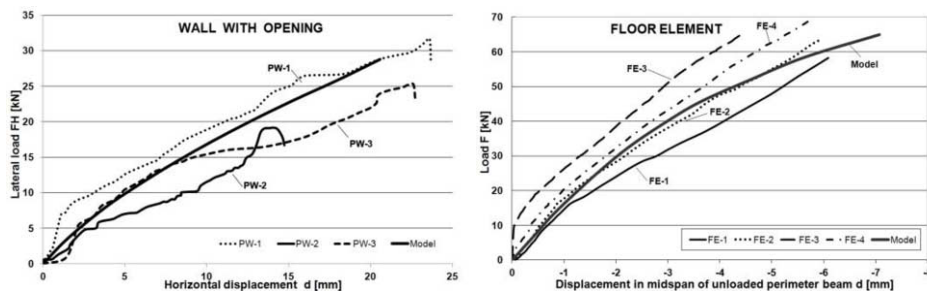


Figure 4. Experimental and numerical load-slip curves

The same testing stand was used to provide experimental researches on walls and floor elements. The floor elements were tested in vertical position and only in the plane direction external loads were applied. The loads perpendicular to floor surface were omitted. Due to different behavior of walls and floor, other boundary conditions were applied to floor specimen. The floor elements were supported in two external nodes of unloaded perimeter beam. That unloaded edge had freedom to deformation. The displacements of mid-span node of that beam were recorded to obtain load-slip curve of floor element (Figure 4b).

### 3.2. Stress in elements of framing

In stress calculation, the elastic behavior of wood was assumed. Using Hooke's law stress values were computed from experimentally obtained values of strain. The strain values in studs of single walls were recorded at 1/4 and 1/2 of wall height. In the case of perforated walls, the strain values were recorded at measurement points placed at half-height of the specimen studs. During the experimental test, single wall specimen SW-1 was damaged in Phase-2. In comparative analyses, only three single wall specimen were compiled. The selected results of stress in single walls are presented in Table 1.

Table 1. Stress in studs of single walls at 1/4 of height

Specimen	Stress [MPa]			Vertical load [kN]	Horizontal load [kN]
	Stud 1	Stud 2	Stud 3		
SW-2	1,338	3,363	1,850	55,99	4,12
SW-3	2,430	2,638	2,075	56,48	4,20
SW-4	1,438	4,063	2,163	56,80	2,68
Model	1,496	3,930	3,087	56,00	4,15

In floor elements, the measuring points were arranged near to the loaded and unloaded perimeter beams. In the last two specimen, additional measurement points were located at three middle joists at an equal distance from both edges. The values of strain in joists were recorded at a direction parallel to direction of external forces. The selected results of stress in floor elements are presented in Table 2.

**Table 2.** Stress in joists of floor elements near to unloaded beam perimeter

Specimen	Stress [MPa]							External load [kN]
	Joist 1	Joist 2	Joist 3	Joist 4	Joist 5	Joist 6	Joist 7	
FE-1	1,007	0,046	0,060	0,060	0,069	0,069	0,890	16,82
FE-2	1,156	0,085	0,083	0,080	0,086	0,086	1,031	16,70
FE-3	0,834	-	0,038	0,076	0,049	-	0,792	17,09
FE-4	0,868	-	0,011	0,071	0,019	-	0,602	16,29
Model	0,977	0,061	0,052	0,086	0,052	0,061	0,977	16,80

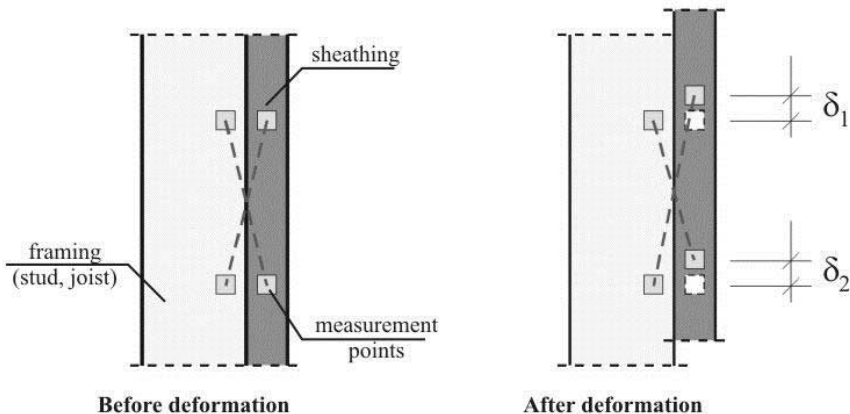
Differences in stress values in studs and joists of the analyzed elements show large heterogeneity of the wood and chipboard materials. However, the values are at the same range and show good agreement between model and tested specimen.

### 3.3. Shear in sheathing-to-framing fasteners

The deformability of the structure as well as the values of stress in framing and sheathing allow the overall proposed numerical model to be verified. The next step was to verify the assumption that the beam element correctly describes the behavior of dowel type fastener. Therefore the comparative analyses of shear in fasteners were conducted. The value of shear in nails was calculated using formula (7). The experimental data [10] allows to be adopted, values of necessary coefficient respectively as  $A = 599.75$ ,  $B = 100.91$ ,  $C = 2498.93$ , which results in the formula:

$$N = (599.75 + 100.91 \cdot \delta) \left[ 1 - e^{(-4.167\delta)} \right] \quad (9)$$

There were recorded values of displacements at measurement points (Fig. 5). To obtain the force in the fastener, the average displacement value were inserted to formula (9). The strain measurements were made using DEMEC Mechanical Strain Gauge.

**Figure 5.** Measuring system for determining the slip of sheathing-to-framing fastener

The measurement systems were placed at external stud or joist. The measurement points were applied at positions near 60cm to each end of framing elements.

**Table 3.** Shear in fasteners in external studs of single walls

Specimen	Shear [kN]		Vertical load [kN]	Horizontal load [kN]
	Fastener 1	Fastener 2		
SW-2	0,265	0,194	55,99	4,12
SW-3	0,141	0,186	56,48	4,20
SW-4	0,250	0,230	56,80	2,68
Model	0,219	0,251	56,00	4,15

**Table 4.** Shear in fasteners in external studs of walls with opening

Specimen	Shear [kN]		Vertical load [kN]	Horizontal load [kN]
	Fastener 1	Fastener 2		
PW-1	0,250	0,300	159,86	8,01
PW-2	0,158	0,170	167,90	8,50
PW-3	0,310	0,253	158,99	7,11
Model	0,189	0,261	160,00	7,90

**Table 5.** Shear in fasteners in external joist of floor element

Specimen	Shear [kN]		External load [kN]
	Fastener 1	Fastener 2	
FE-1	0,056	0,136	16,82
FE-2	0,083	0,104	16,70
FE-3	0,077	0,148	17,09
FE-4	0,118	0,096	16,29
Model	0,108	0,102	16,80

#### 4. Summary

The comparative analyses shows that the proposed numerical model exhibits high compliance in reproducing the deformation behavior of light wood-framed structures, and took into a count the redistribution of internal forces at a similar level to those obtained from experimental research.

The stress in the framing elements of the experimentally tested specimen was at the same level as obtained from the numerical analyses. This similarity leads to the conclusion that the model is in good agreement, representing the distribution of internal forces between elements of light wood-framed structures. The differences of stress and displacement between results taken from numerical and experimental data follow from heterogeneous material properties as well from the deviation of burden and measurement systems.

More sheathing-to-framing fasteners in floor elements than in walls, caused higher participation of sheathing in carrying the external loads.

During analyses, it was observed that shear in fasteners in numerical model as well as from experimental tests, were at similar level.

The slip-load curve taken from computational analyses had got a similar shape to  $P-\Delta$  characteristic obtained from full-scale experimental tests. The displacements of light wood-framed wall and floor elements taken from experimental and numerical analyses were most consistent in the range of destructive burden.

## References

- [1] W.J. McCutcheon, Racking Deformation in Wood Shear Walls, *Journal of the Structural Engineering*, 111(2) (1985), 257 – 269
- [2] J.D. Dolan, A.C. Johnson, *Monotonic Tests of Long Shear Walls with Openings*, Report No TE-1996-001, The American Forest & Paper Association, 1996.
- [3] C.P. Heine, *Effect of Overturning Restraint on the Performance of Fully Sheathed and Perforated Timber Framed Shear Walls*, MSc thesis, Virginia Polytechnic Institute and State University, Blacksburg, 1997.
- [4] D.W. Dinehart, H.W. Shenton III, Comparison of Static and Dynamic Response of Timber Shear Walls, *Journal of the Structural Engineering* 124(6) (1998), 686 – 695.
- [5] M. Li, R. Foschi, F. Lam, Modeling Hysteretic Behavior of Wood Shear Walls with a Protocol-Independent Nail Connection Algorithm, *Journal of Structural Engineering*, 138(1) (2012) , 99–108.
- [6] A.M. Tarabia, R.Y. Itani, Static and Dynamic Modeling of Light-Frame Wood Buildings, *Computers & Structures*, 63(2) (1997), 319 – 344.
- [7] M.W. White, J.D. Dolan, Non-linear shear-wall analysis, *Journal of the Structural Engineering*, 121(11) (1995), 1629 – 1635.
- [8] M. Malesza, *Redistribution of internal forces and deformability of shear wall with wooden frame and cooperating sheathing (only in Polish)*, PhD thesis, Bialystok University of Technology, Bialystok, 1997.
- [9] M. Baszeń, C. Miedziałowski, Experimental tests of light wood-framed constructions, in: *Lightweight structures in civil engineering*, ed. J.B. Obrębski, IASS Polish Chapter, Częstochowa 2004.
- [10] R.D. Hunt, A.H. Bryant A.H, Laterally Loaded Nail Joints in Wood, *Journal of Structural Engineering*, 116(1) (1990), 111 – 124

# Repair of masonry arch bridges with respect to longitudinal cracking and load assessment

Triona BYRNE<sup>1</sup> and Dermot O'DWYER

*Department of Civil, Structural and Environmental Engineering,  
Trinity College Dublin 2, Ireland*

**Abstract.** This paper outlines a case study on the rehabilitation of a masonry arch bridge on Woodhouse Estate, Co. Waterford, Ireland. The main structural defect with this bridge is longitudinal cracking, which has led to lateral spread of the spandrel walls. Different repair techniques are discussed and the most suitable repair technique for longitudinal cracking is identified. The resulting information is used to define a set of guidelines for repair of masonry arch bridges with respect to longitudinal cracking. A procedure is also developed for load assessment of a masonry arch bridge, based on Heyman's classic line of thrust assessment. Microsoft Excel's 'Solver' is used as an optimisation tool, to determine the maximum allowable imposed load on a masonry arch. These values can then be used in conjunction with Coulomb's analysis to identify the limits on the horizontal thrust under varying axle loads and under pre-repair and post-repair bridge conditions.

**Keywords.** Masonry arch, repair, longitudinal cracking, load assessment

## Introduction

Masonry arch bridges are ubiquitous in Ireland and all over the world, representing a large part of the global transport infrastructure. In Ireland and the UK, the MEXE method is primarily used to assess masonry bridge structures. MEXE (Military Engineering Experimental Establishment) is a conservative, semi-empirical method that proves so popular because of its extraordinary simplicity but there is a need for more robust methods [1]. Archie-M is another computer based model that is used but it is a somewhat expensive and complex software tool. One simple method of arch assessment is the traditional approach of superimposing a feasible line of thrust over the arch and verifying the arch's stability by demonstrating that the line of thrust is contained within the arch, based on Heyman's safe theorem [2].

In the present work, Microsoft Excel was used as an optimisation tool for a masonry arch bridge load assessment. The 'Solver' tool in Excel can be used to determine the maximum allowable axle load for a particular arch.

---

<sup>1</sup>Corresponding author: [byrnet2@tcd.ie](mailto:byrnet2@tcd.ie)

The use of Solver's suitability as an appropriate tool for determining the optimum horizontal forces on a masonry arch is assessed in this paper. The proposed analysis procedure also identifies the magnitude of the horizontal thrust developed in the arch under load. The magnitude of the horizontal thrust that is developed when an arch is loaded is required when assessing whether the arch's abutments are adequate.

The classic problem when studying the arch i.e finding the line of thrust that maximises the allowable load factor for the imposed load on the arch, is a non-linear optimisation problem.

Unfortunately, in contrast to systems of linear equations, there is no simple method for finding the solutions to systems of simultaneous non-linear equations. If the horizontal thrust is assumed and fixed in this problem, then the optimum line of thrust for that horizontal reaction can be deduced, because the problem in this case is linear and the Simplex algorithm will find an optimum feasible solution, if one exists. Coulomb's analysis of masonry arches can then be used to establish upper and lower limits on the magnitude of the horizontal reaction [3]. Thus a hybrid algorithm involving a gradient search combined with the Simplex algorithm should be able to provide good, if not optimal, solutions to this load assessment problem. However, Microsoft Excel, which is a tool that is readily available to all engineers, can solve well-conditioned optimisation problems with a fair degree of success. Hence its use has been investigated in this paper.

This paper also investigates the optimum repair procedure for the rehabilitation of masonry arch bridges where the spandrel walls have separated from the arch barrel, resulting in classic longitudinal cracks in the arch barrel. This defect is explored with respect to Woodhouse Bridge in County Waterford, Ireland. The repair procedure suggested in the paper was based on a study of the literature in the field and similar case studies [4-6]

## **1. The masonry arch and its assessment**

The masonry arch bridge is one of the most sustainable structures in existence, with many masonry arches in service for hundreds of years up to now without any need for significant repair. Documents have been prepared by government institutions and similar organisations, which outline technical methods for repair of masonry arch bridges, in order to increase the service life of such bridges. The earliest arch forms originated in Roman times and since then masonry arch bridges have become an important aspect of culture heritage worthy of rehabilitation and preservation [5].

Masonry arch bridges are such impressive structures because of their capacity to adjust to movement or deformation in their supporting structures and to adapt to greater loads than they were initially designed for. A masonry arch bridge has the ability to open and close cracks that form along the intrados or extrados, which are not harmful until they become substantial enough to form a hinge thus converting the arch into a mechanism. Therefore cracking is very common in masonry structures and does not necessarily affect the structural integrity of the arch [7].

Longitudinal cracks are a common structural defect in masonry arch bridges. They can occur anywhere within the arch barrel [8]. Diagonal cracking in a bridge structure is usually caused by spread of the abutments or non-uniform settlement, which induces torsion in the arch barrel. Masonry arches in historic bridges are susceptible to damage from several different physical factors. This compromises the structural integrity of the

bridge and could be a serious problem, leading to failure or collapse. Bridges that were in visibly poor condition were demonstrated to show greater deflections than bridges in good condition, almost regardless of the span length, as shown through tests done by Boothby et al. [9]. These tests showed that in particular, bridges in poor condition usually had appreciable horizontal movements of the abutments.

### *1.1 Masonry arch bridge assessment*

There are British Standards relating to conservation, which are defined in the British Standard 7913 "Guide to the Conservation of Historic Buildings". This document outlines the best practice for the management and treatment of historic buildings and structures. The Design Manual for Roads and Bridges (DMRB) is a document published by the UK Department of Transport, which outlines the current standards for Design and Construction of Roads and Bridges [10]. In 2003, it acknowledged for the first time the importance of old road structures by publishing a document titled "The conservation of highway structures". This document covers the listing of bridge structures in the UK, strategies for conservation, guidelines for application of principles and several other matters. This document suggests the use of modified MEXE method for assessment of short/medium, single span bridges primarily. The modified MEXE method is an empirical assessment based on the work of Pippard and is found in BA 16/97, "The Assessment of Highway Bridges and Structures" [10]. However, there are a number of limitations to this method stated in BA 16/97 in relation to the span length, span-to-rise ratios, multiple spans and the depth of fill [11]. For this particular project, the CIRIA (Construction Industry Research and Information Association) C656 manual [5] on appraisal and remedial treatment of masonry arch bridges is used to form a set of guidelines for the repair of masonry arch bridges with respect to longitudinal cracking. The C656 manual also outlines methods for structural assessment of masonry bridges, and it re-iterates the identification of the MEXE method as a simple and quick method of assessing the load carrying capacity of a bridge, in relation to the strength of the arch barrel only.

### *1.2 Heyman's Line of Thrust theory*

The theory of the 'line of thrust' of an arch was developed long before Heyman [2]. However, Heyman related the traditional 'line of thrust' approach to the plastic analysis of frames, which had been developed in the 1950s. In an un-cracked voussoir arch, if it is possible to draw a line of thrust that is in equilibrium with the applied loads and within the arch perimeter, then the arch is stable. The arch becomes unstable and fails when the line of thrust is no longer contained within the stonework and a mechanism occurs. Heyman states that this is the "basic stability statement for the stone skeleton".

In a cracked voussoir arch, loaded under its own weight, there are two limit situations that provide the minimum and maximum abutment thrust lines. Heyman assumed that the worst loading position was located approximately at the quarter-point of an arch, with hinges forming at the point of loading, the springings and the extrados of the arch between the loaded point and the most distant abutment. In his findings, Heyman also outlines the "safe" theorem of masonry arches, which is as follows: "*If a line of thrust can be found which is in equilibrium with the external loads and which lies wholly within the masonry, then the structure is safe*".



### *1.3 Microsoft Excel for non-linear problems*

Microsoft Excel's Solver tool was introduced in 1991 and combines the functions of a user-friendly interface, an algebraic modelling language and optimisers for linear (subject to linear constraints), non-linear (at least one of the constraints is non-linear) and integer problems [12]. These functions are integrated into the normal Microsoft Excel spreadsheet program. The Solver dialogue box requires the user to specify a target cell, changing variable cells and a set of constraints from within the spreadsheet.

As an algebraic modelling system, the optimisation function is defined by algebraic formulae, which are linked to cells in the spreadsheet. Excel can express a wide range of mathematical relationships but it cannot distinguish decision variables from other variables, or objectives or constraints from other formulae. Therefore, the Solver tool provides an interactive and user-friendly way to specify which spreadsheet cells are to be used for each of these roles (See Figure 1).

When solving linear problems, Solver uses a straightforward implementation of the Simplex method with bounded variables to find the optimal solution. For non-linear problems, Solver uses a Generalised Reduced Gradient (GRG) method. GRG guarantees a local optimum solution on problems with continuously differentiable functions, and it is considered to be a very robust method. Upon finding an optimum solution, the message "Solver found a solution" is displayed, or otherwise, "Solver could not find a feasible solution" is displayed.

## **2. Load assessment of the masonry arch**

### *2.1 Load assessment and repair of the masonry arch*

To produce an appropriate list of potential repair techniques for the Woodhouse Bridge, the CIRIA C656 manual on appraisal and remedial treatment of masonry arch bridges was consulted, along with a number of case studies from literature on the topic. For example, one case study considered Donim Bridge which is a masonry arch bridge with longitudinal cracking located in Guimarães, Portugal. The case study outlines the remedial work carried out [4].

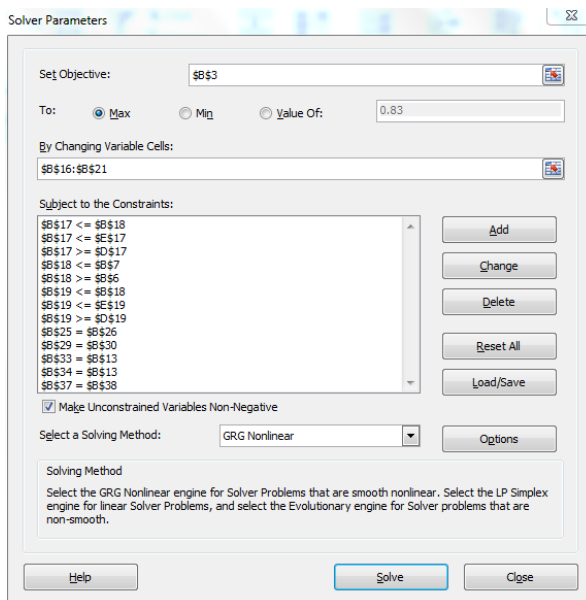


Figure 1. Microsoft Excel’s Solver interface

Guides such as “A Guide to the repair and strengthening of masonry arch highway bridges” by Page [13], which was produced by the Transport Research Laboratory, were also consulted, along with papers from the ‘Sustainable Bridges’ project carried out under the Sixth Framework programme [6-14].

### 2.2 Calculation of optimum load factor

The procedure outlined in the paper is based on the often used simplifying assumptions that: the voussoirs in the arch are incompressible, failure does not occur due to slipping of the voussoirs and the voussoirs have no tensile strength. The arch is modeled as two dimensional so that the imposed load is assumed to act as a line load across the arch thickness. These are the traditional assumptions and the limitations of analyses based on these assumptions are well known. There are a number of possible analyses that can be performed on such models. The first problem considered was to identify the maximum allowable load factor for an imposed load applied to a masonry arch. The variables in this case are the magnitude of the horizontal thrust,  $H$ , the line of thrust heights at the positions of the applied loads,  $y_2 \dots y_{n-1}$  the height of the line of thrust at the springing points,  $y_1$  and  $y_n$ , plus  $\lambda$ , the allowable load factor, which is the objective of the analysis. If the horizontal reaction is assumed then the problem is a linear one and is set up with the following constraints;

- The line of thrust must lie within the intrados and extrados heights,  $I_i$  and  $E_i$ .
- The line of thrust must be in equilibrium with the vertical applied loads at each load point.

$$E_i \geq y_i \geq I_i$$

$$L_{Self_i} + \lambda L_{Imposed_i} = H \left( \frac{-y_{i+1} + 2y_i - y_{i-1}}{\Delta x} \right)$$

Where  $\Delta x$  is the horizontal distance between the points of application of the applied load,  $L_{imposed}$ , and  $L_{Self_i}$  denotes self-weight of the arch structure.

Taking Woodhouse Bridge as a sample arch, and modeling the arch in the simplest manner with only three load application positions at the quarter points and the arch centre, the dimensions of the arch boundary were plotted on a graph on the Excel spreadsheet and upper and lower bounds for the horizontal thrust were calculated approximately by hand, giving 1425 kN and 950 kN respectively. An intermediate value of 1000 kN was then chosen and manually input into the Excel spreadsheet. As the problem is linear, Solver uses the Simplex method to find the optimum value for the load factor, the values for the line of thrust and the values of the vertical forces. The resulting arch with line of thrust is presented in Figure 2.

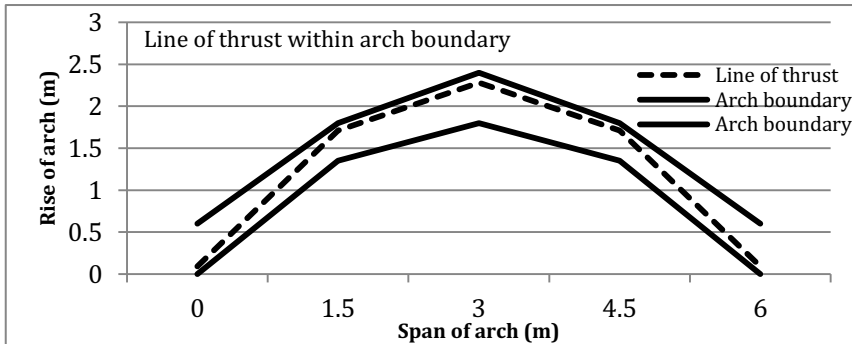


Figure 2. Line of thrust within arch boundary with optimum load factor

### 2.3 Calculation of optimum horizontal thrust on arch

The problem above was then re-formulated as a non-linear problem by unfixing the horizontal force and setting it as a variable. The GRG non-linear solving method was selected and Solver found values for the optimum horizontal thrust, the optimum load factor, the vertical support reactions and the line of thrust. The line of thrust is plotted on a graph along with the arch boundaries, to demonstrate where a hinge forms, at the point of contact of the line of thrust with the arch boundary, shown in Figure 3.

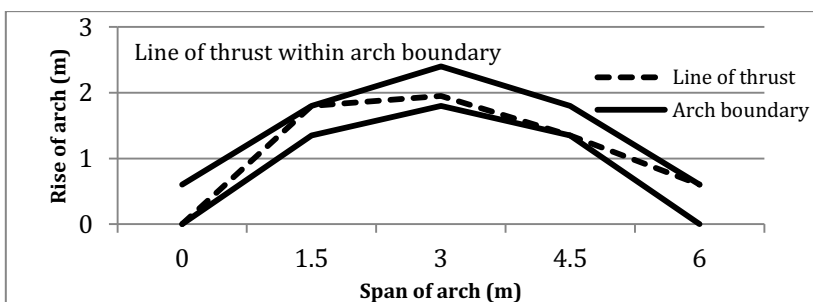


Figure 3. Line of thrust within arch boundary with optimum horizontal thrust

The hinging points in this case are evident in the diagram and the arch is clearly on the point of being transformed into a four-hinge mechanism thus proving that the arch is at the point of failure.

### 3. Analysis of results

#### 3.1 Guidelines for repair of longitudinal cracks in masonry arch bridge

For a bridge like Woodhouse Bridge, which suffers from a series of defects, there are several remedial works that should be carried out to prolong the service life of the bridge. Important general aspects to consider are management and removal of vegetation, repointing and patch repairs of deteriorating masonry. In the case of Woodhouse Bridge, there are visible longitudinal cracks that could be problematic for the bridge, as well as some scour around the piers, mortar washout and severe vegetation invasion.



**Figure 4.** Longitudinal cracking in Woodhouse Bridge

Although scour is extensive around the bridge abutments and piers, longitudinal cracking is the most critical defect. It should be addressed by means of transverse tie-bars connecting pattress plates on opposite spandrel walls. The disadvantages of tie-bars are the labour intensity and traffic disruption during construction, but as Woodhouse Bridge is on a private estate, it should not be an issue. Pattress plates can be disruptive to the bridge appearance so they should be avoided where possible, as preserving the bridge aesthetic is an important part of preserving the bridge heritage. Carrying out thorough research and a carefully designed site investigation should minimize risks associated with these remedial works, but the full extent of repairs necessary for a masonry arch bridge can never be determined in advance.

#### 3.2 Use of Solver for arch assessment

For the numerical example outlined above, the Solver tool was successful in finding an optimum load factor and associated optimum horizontal thrust for the arch structure. There are a variety of situations where this type of analysis could be useful. The analysis of masonry arch bridges is often described as a “black art” and one simple method of analysis is not sufficient to be able to make safe assumptions about the stability of the structure. Therefore this tool could be added to an engineer’s “toolbox” to help understand the load on a masonry arch.

One application of this tool could be in the analysis of multi-span masonry arch bridges. If the difference in horizontal thrust from either side of a pier is greater than the force the pier is capable of withstanding, toppling of the pier could ensue. The problem could also be modified to solve for different criteria by creating different constraints, e.g. if a geotechnical engineer stipulated certain limitations of horizontal thrust. Another use could be to test for different axle loads. The problem could also be

re-formulated to solve for the geometric factor of safety, by modifying the constraints to find the smallest factor that the ring thickness could be scaled by.

There are a number of limitations to the program in its current, basic state. The program currently requires the user to initially input good estimates of the values for vertical force and horizontal force, which requires a good understanding of the basic static equations of an arch and arch geometry. The program also needs to be manipulated manually to find the upper and lower limits for the load factor initially, although this problem is eliminated when the problem was tested as a non-linear one.

#### 4. Conclusions

The successful use of Excel's Solver tool for load assessment of the masonry arch is good news for engineers looking for a simple, readily available and inexpensive load assessment tool. Some simple examples of where this tool could be useful in a practical application include determination of the horizontal thrust being transmitted to the piers of a masonry arch bridge structure. If the Solver tool returns an unusually high value for the load factor, it could be appropriate to examine the bridge and check the fill for stability and loading conditions. This technique could also be used for other forms of plastic design.

This method ignores stresses in the structure completely but from the line of thrust analysis, it is possible to calculate stresses using equations of statics. There may also be many more applications for this program in relation to load assessment and optimisation of masonry arch bridges and it is an area worthy of further consideration for structural engineers.

#### References

- [1] Fanning, P. J., & Boothby, T. E. (2001). Three-dimensional modelling and full-scale testing of stone arch bridges. *Computers & Structures*, 79(29–30), 2645-2662.
- [2] Heyman, J. (1982). *The masonry arch*. Chichester: Ellis Horwood
- [3] Heyman, J. (1966). The stone skeleton. *International Journal of solids and structures*, 2(2), 249-279.
- [4] Oliveira, D. V., & Lourenço, P. B. (2004). *Repair of stone masonry arch bridges*. International conference on arch bridges, 4, Barcelona, 2004 - "arch'04 - 4th International Conference on Arch Bridges". Barcelona : CIMNE, 2004.
- [5] Melbourne, C., McKibbins, L.D., Sawar, N., Gaillard, C.S., *Masonry arch bridges: condition appraisal and remedial treatment*, CIRIA, London, 2006
- [6] Melbourne, C., Wang, J., Tomor, A., Holm, G., Smith, M., Bengtsson, P. E., . . . Molins, C. (2007). *Sustainable Bridges—Assessment for Future Traffic Demands and Longer Lives*. Integrated Project in the Sixth Framework Programme on Research, Technological Development and Demonstration of the European Union, FP6-PLT-001653,
- [7] L. Garmendia, San-José, J. T., García, D., & Larrinaga, P. (2011) *Rehabilitation of masonry arches with compatible advanced composite material*. *Construction and Building Materials*, 25(12), 4374-4385.
- [8] Fanning, P. J., Boothby, T. E., & Roberts, B. J. (2001) *Longitudinal and transverse effects in masonry arch assessment*. *Construction and Building Materials*, 15(1), 51-60.
- [9] Boothby, T. E., Domalik, D. E., & Dalal, V. A. (1998). *Service load response of masonry arch bridges*. *Journal of structural engineering*, 124(1), 17-23.
- [10] Design Manual for Roads and Bridges, vol. 3. Section 4, Part 4. *The Assessment of Highway Bridges and Structures*. London: 1997.

- [11] Gibbons, N., & Fanning, P. J. (2010). *Ten stone masonry arch bridges and five different assessment approaches*. Paper presented at the Proceedings of the 6th International Conference on Arch Bridges (ARCH'10), B. Chen and J. Wei, eds., Fuzhou, China.
- [12] Fylstra, D., Lasdon, L., Watson, J., & Waren, A. (1998). *Design and use of the Microsoft Excel Solver. Interfaces*, 28(5), 29-55.
- [13] Page, J. (1996). *A guide to repair and strengthening of masonry arch highway bridges*. Transport Research Laboratory, England.
- [14] Bién, J., Rawa, P., Jakubowski, K., & Kaminski, T. (2007). Sustainable Bridges—Assessment for Future Traffic Demands and Longer Lives. *Integrated Project in the Sixth Framework Programme on Research, Technological Development and Demonstration of the European Union, FP6-PLT-001653*,

# The conservation state of the wooden roof of the National Museum in Phnom Penh

Bartolomeo MEGNA<sup>1</sup> and Giovanni LIOTTA

*Laboratory of Materials for Restoration and Conservation, Dipartimento di Ingegneria Civile, Ambientale, Aerospaziale, dei Materiali, Università di Palermo*

**Abstract.** During a visit to the national Museum in Phnom Penh, the most important one in the Kingdom of Cambodia, the authors noted the presence of some signs of a termites attack in the secondary elements of the roof. According to this observation, a further investigation was performed in order to evaluate the phytosanitary condition of the wooden bearing element of the roof. According to these observations, an intervention of restoration, conservation and safeguard has to be considered as necessary and urgent. In this paper, the results of the investigation of the conservation state of the bearing wooden structures of the of the National Museum in Phnom Penh, Kingdom of Cambodia, are presented; moreover a proposal of an intervention properly designed for a long time safeguard against the termites is reported. Particularly, the presence and extension of a severe, in progress, termites' attack was documented, the termites' species involved was identified, finally a proposal for a long time conservation plan of the roof is presented.

**Keywords.** Termites, wooden structures, Cambodia

## Introduction

In February 2012, the authors got involved in the visit of the National Museum in Phnom Penh and noted signs of termite attack on the external wooden beams of the roof (figure 2a).

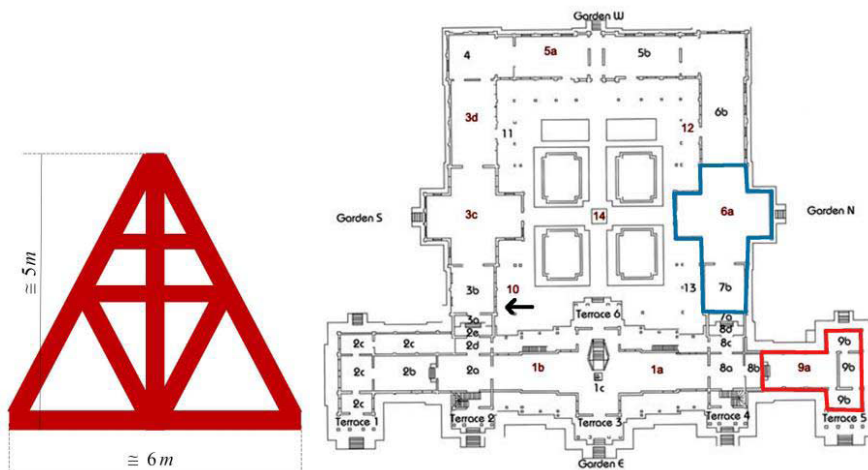
Considering the risk connected to the presence of such insects in a wooden structure, a preliminary investigation of the roof was performed in order to verify the presence of the termites in other parts of the roof. As in an anthropic environment, termites represent a high danger for wooden elements of structures and identify the termite species [1-10]. The drywood termites (e.g. Kalotermitidae) have their nest inside the wooden element they feed on, within a relatively limited space. Their colonies consist of few thousands of individuals of the various castes [11, 12]. The subterranean termites (e.g. Rhinotermitidae) have their nest in the soil and move back and forward to the wooden elements they feed on, by passing through light safe galleries that they build using excrements and soil grains glued together with saliva. Their colonies consist of several hundreds of thousands of individuals (up to more than one million). The latter are definitely the most destructive ones [11-15].

---

<sup>1</sup> Corresponding author: [bartolomeo.megna@unipa.it](mailto:bartolomeo.megna@unipa.it), mobile. 00393336243062

The National Museum in Phnom Penh is the largest Cambodian museum of cultural history and is the country's leading historical and archaeological museum. The museum roof bearing structure consists of wooden A-frame elements, a drawing of which is shown in figure 1. The Museum buildings, inspired by Khmer temple architecture to George Groslier, were constructed between 1917 and 1924. The wood used in the structure has not been identified as the available samples were too rotten to be observed under the microscope.

In the floor plan of figure 1b, all the inspected area are highlighted: the arrow indicates the colonnade, the red area is the north wing affected by termites infestation, the blu area is the west wing affected by fungi infestation.



**Figure 1.** a) schematic drawing of A frames of the roof; b) floor plan of the museum

## 1. Materials and methods

The main goal of this investigation was to verify the phytosanitary condition of the wooden roof of the National Museum in order to prepare, whereas needed, suggestions for its safeguard and the proper precautionary steps for its conservation. The investigation concerns the main and secondary wooden structures of the north wing of the roof of the Museum. The study consists of two parts. The first was an on situ visual examination, particularly focused on the heads of primary and secondary beams, as they usually suffer biologically induced decay due to water condensation on wood, caused by its contact with walls. The second part was a microscopic investigation of samples collected during the inspection, consisting of powdered material coming from every meaningful part of the structure.

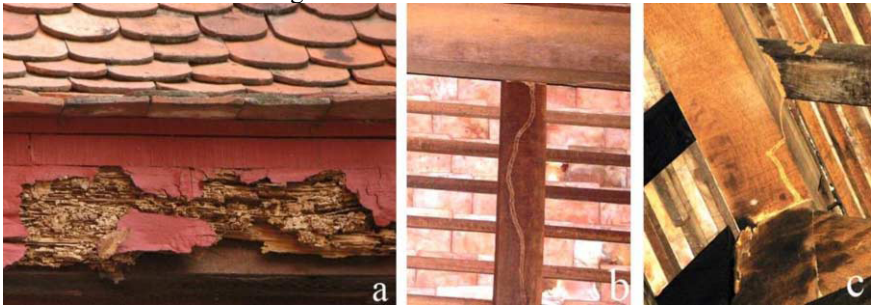
It has to be highlighted that a recent restoration intervention was performed in the north wing of the building due to the presence of a severe termites' infestation. The decayed wooden beams considered unfit to bear the required loading were substituted with brand new ones. The new beams underwent an insecticide treatment performed by brush application of a liquid insecticide, mostly in the end grain or in the joint of the beams. Signs of this treatment could be easily noted for the brown stain of the product used. Most of the original wooden elements weren't substituted even in presence of



termites' walkways on the surfaces, probably assuming that massive use of insecticide could stop the ongoing infestation. Unfortunately, it has not been considered that the pathways are used only to move from one feeding place to another one, while the main part of the termite population live safely within the nest, where it cannot be reached by a treatment performed from the surface.

## 2. Results of investigation

During the investigation, signs of termites' walkways were found both on the original wooden beams and on the new bearing elements (figure 2b-c). This finding highlights that termite infestation was currently active and were now spreading to the recently introduced wooden beams. The bearing structures of the roofs are installed over large beams going from one wall to the opposite wall, forming the base of the triangular structural truss element bearing the whole roof.



**Figure 2.** a) Roof tile decayed by termites; b, c) Termite walkways on old and new beams of the roof.

Some of the large beams rested over the brick walls showed a severe deterioration of end grain, induced by termites, while the remaining part of the beams appeared in good phytosanitary condition. Unfortunately, if the external wooden surface is hammered, the sound produced clearly indicates the presence of large voids in the wood: widespread termites' galleries could be observed by removing the thin wooden film on the surface in the whole beam. The galleries pass over the support area indicating a clear and present risk of failure (fig. 3a).

As previously described, in the interspace between ceiling and roof new wooden elements introduced during the recent restoration intervention stay side by side with the old wooden beams, even if the old ones are clearly deteriorated by termites. In addition to this, the presence of deteriorated wood, even if the infestation is not currently active on it, is an important risk factor old wood act as an attraction for further upcoming infestation.

The termites' galleries hollowed out the wood, reducing severely its section and consequently mechanical properties. The galleries were filled of termite cells, recently made; their presence suggested an active infestation. Going deeper in the wood beam, a large number of workers and soldiers of the species *Coptotermes gestroi* (figure 3c-d) were found. Going deeper in the removal of the termites' nest, it was possible to observe that there was no more wood in the beam's head (figure 3b). According to such observation, the whole roof was in a clear and present danger of collapse.



**Figure 3.** a) head of a beam decayed by termites; b) head of a beam completely destroyed by termites, c),d) *Coptotermes Gestroi* individuals.

Signs of termites walkways and tunnels were found also on the bearing beams of the roof, lying on the severely decayed horizontal beams and indicating a possible active infestation (figure 4a). A large number of termites galleries were identified by removing the surface wooden layer (figure 4b). Moreover even in this case, several workers and soldiers of the same species, i.e. *Coptotermes gestroi*, were found.

Moreover some of the roof prop beams showed clear signs of termites attack. Particularly one of the prop beams was found to be broken in the middle by the weight of the vertical poles connected on it, with no residual mechanical function which indicated that there was a presence of a large number of termites' galleries within (figure 4c).



**Figure 4.** a) termites pathways on a roof bearing beam; b) the same beam after the removal of wood surface; c), horizontal prop beam collapsed due to termites infestation.

Finally the pitches of the lateral colonnade of the inner garden was slightly sloped; according to this geometrical consideration, rain can reach the wooden structures under the roof in presence of heavy rain and strong wind. Actually these wooden beams showed clear signs of fungii infestation, due to a high water content, even if transient, figure 5a.

It's well known that a high water content of wood, particularly in the presence of fungi, attracts insects and particularly termites. According to this observation the presence of termites in the tie beams of the trusses of the colonnade roof was investigated. It was possible to note that all the shrinkage cracks were filled with a granular material, figure 5b. Sampling and direct observation of such material were performed and was identified as termite faeces, commonly used by termites to build their tunnels or walkways. Usually these walkaways or tunnels have to be perfectly sealed as termites are scared by light. The termite population was large and active, figure 5c, as clearly identified by breaking of the walkways along the whole beam, finding in every investigated point, a large number of living insects spreading out from wood. This observation confirmed that termite presence was widespread and abundant.



**Figure 5.** Colonnade beam: a) fungi signs; b) termites pathways; c) living termites.

The termites responsible for the attacks of the wooden structures of the roof of the National Museum in Phnom Penh belong to the family of Rhinotermitidae and to the species of *Coptotermes gestroi*. This species is native to South East Asia but nowadays is widespread in other continents. It's one of the most dangerous species for wood. The *Coptotermes gestroi*, as all the other species belonging to the family Rhinotermitidae, are subterranean termites, i.e. they build the nest in the soil and the workers spread all around to find wet wood to eat, reaching places quite far from the nest (dozens of meters). *Coptotermes gestroi* species can attack only wooden structure with a high moisture content. Once they start the infestation, they can spread to nearby dry wooden elements because these termites are able to create by themselves a proper environment for their activity, leading to a very severe potential damage. In the roof environment, the main cause of high humidity is probably the occurrence of condensation phenomena. The way to prevent humidity from condensation is to ensure good air circulation.

Moreover the investigation has been extended to the west wing of the roof. In this part of the structure no sign of termites were identified but a large fungi infestation was clearly present and active, figure 6. The visual investigation and knocking on the wood beams indicate that the decay is affecting only the surface of all the wooden elements. Nevertheless the restoration intervention on the roof has to be designed in order to reduce the relative humidity of the garret ensuring a good air circulation in all the parts of the roof. Particularly the tape sealing the open spaces between the two folds of the roof has to be removed urgently.



**Figure 6.** Detail of the fungi infestation found in the west wing of the museum roof.

### 3. Proposal of intervention

It has to be put into act, the measures suitable to maintain good air circulation in the garret of the museum, in order to reduce or avoid the settling of new termites infestation. The first step of the recovery will be the disinfection of all the termite infested beams in the roof and in the colomnade, by means of Cypermethrin (Cyano-(3-phenoxyphenyl)methyl]3-(2,2-dichloroethenyl)-2,2-dimethylcyclopropane-1-carboxylate) base product. The second step will be the removal of all elements showing signs of termites' attack. All the woods removed has to be set on fire. The insecticide has to be applied by pressure injection, an awkward operation that has to be performed by specialized operators. The beams severely attacked by fungi have to be removed too and all the surrounding wooden elements have to be treated with a 10% solution of Benzalkonium chloride, also known as alkyldimethylbenzylammonium chloride (ADBAC), applied by brushing.

The last step of the recovery intervention will be the sanitization of the soil all around the museum against the species *Coptotermes gestroi*. The way to reach this result is the use of a product like hexaflumuron, able to affect the growing process of termites leading to the destruction of the entire nest.

#### 3.1 Measures for long term safeguard and conservation

All the new beams need to be treated with the same products described for old members. The heads of the new beams should not be put in direct contact with the walls, in order to facilitate moisture exchange with air and avoid the settling and development of new termites' infestation or fungi infection. It's mandatory to create in all the garrets, a good air circulation system in order to avoid condensation phenomena and prevent new settling of biodeterioration agents. It looks to be enough, ensuring the presence of open gaps between the beams as shown in figures 7a, in all the parts of the roof. It also looks to be needed to avoid the mistakes highlighted in figures 7b and 7c, where the gaps are sealed with tape or mortar respectively. In order to increase the air circulation and to prevent a high humidity level in the garret, a 50 x 50 cm window has to be created at the top of every gable of the roof. These windows will be designed properly to prevent rain water from getting in.



**Figure 7.** Roof structure: a) open gap between the folds of the roof; b) open gap between the folds sealed with tape; c) open gap between the folds sealed with mortar.

#### 4. Conclusive remarks

In this paper the preliminary study for the conservation of the wooden roof of the National Museum in Phnom Penh is presented. The study started from visual inspection of external elements of the roof and goes to the identification of termites' species responsible for the decay. Moreover some proposal have been done to improve the environmental condition of the roof and to ensure a long term safeguard of the structure.

The observation reported in this case study offer the opportunity to develop some interesting advice on termites decayed wooden structures.

As a first point it's quite clear that the old restoration intervention wasn't effective, as the termites' infestation come back after one year and nowadays is more widespread than before. This fact appears to be related to some controversial decision in the previous intervention such as: old and new timbers were mixed in the structure, regardless the presence of termites walkways on some old elements; no modification occurs in the garret environment, no new opening were created to increase air circulation; old timber attacked by termites were stored closed to the building and the termites nest wasn't identified and eradicated. It's very important note that the use of an effective insecticide is not enough in treating subterranean termites infestation because the insecticide can kill only the termites present in the timber elements while the main part of the nest population is safe in ground.

As a second point the wood severely attacked by termites shows a clean apparently healthy surface even if the infestation is ongoing: it's very important to look at the small signs of termites presence, such as walkways in the wooden elements or in the walls, filling of shrinkage cracks. As shown in this paper the infestation could have totally decayed a wooden elements without affecting its surface.

As subterranean termites are quite widespread in Cambodia, the only effective long time safeguard consists in the environmental control of relative humidity in order to lowering wood moisture content in the wooden elements.

#### References

- [1] Harris. *Termites: Their Recognition and Control*. Longman Group Ltd., London, 1971.
- [2] Hichin. *Termites-a world problem*. Hutchinson, UK, 1971.
- [3] Edwards; Mill. *Termites in buildings. Their biology and control*. Rentokil Ltd, UK, 1986
- [4] Lee. Subterranean termite pests and their control in the urban environment in Malaysia. *Sociobiology* 2002
- [5] Pearce. *Termites: biology and pest management*. CAB International, UK, 1997.
- [6] Lee, Chung.. Termites,. In *Urban Pest Control - A Malaysian Perspective* University Sains Malaysia, 2003. pp. 99-111
- [7] Clement, Bagneres, Uva, Wilfert, Quintana, Reinhard and Dronnet, Biosystematics of Reticulitermes termites in Europe: Morphological, chemical and molecular data. *Insectes Sociaux* (2001) 202-215.
- [8] Constantino. The pest termites of South America: taxonomy, distribution and status. *Journal of Applied Entomology* (2002) 355-365.
- [9] Su, Scheffrahn. Termites as pests of buildings, *Termites: evolution, sociality, symbioses, ecology*. Kluwer Academic Publishers. 2000, pp. 437-453
- [10] Kambhampati, Eggleton - *Taxonomy and phylogeny of termites. Termites: evolution, sociality, symbioses, ecology*. Kluwer Academic, 2000
- [11] Roonwal. Termites of the Oriental Region., *Biology of Termites, vol. II*. Academic Press, New York and London, 1970, pp. 315-391.
- [12] Tho, Kirton. The economic significance of Coptotermes termites in Malaysian forestry. In, *Proceedings of the 3rd International Conference on Plant Protection in the Tropics*, Genting Highlands, Malaysia. Volume IV. 1992

- [13] Sornnuwat, Tsunoda, Yoshimura, Takashi, Vongkaluang. Foraging populations of *Coptotermes gestroi* (Isoptera: Rhinotermitidae) in an urban area. *J. Econ. Entomol.* 1996, 1485-1490
- [14] Ahmad Said, S. and Yaacob, A.W. Termites from selected building premises in Selangor, Peninsular Malaysia. *Malaysian Forester* (1997) 203-215.
- [15] Kirton, Wong. The economic importance and control of termite infestations in relation to plantation forestry and wood preservation in Peninsular Malaysia - an overview. *Sociobiology* 2001.
- [16] Chiappini, Liotta, Reguzzi, Battisti, *Insetti e Restauro*. Calderini Edagricole, Italy, 2001.
- [17] Liotta Le infestazioni termitiche nei monumenti di Palermo. *Atti XVIII Congr. naz. ital. Entomologia*, 281, 1998.
- [18] Liotta. Le termiti e i manufatti lignei. *I Congr. Naz. "Legno nel restauro e restauro del legno"* Palutan ed. Milano, 1987, 83-86.
- [19] Liotta, *Gli insetti e i danni del legno - Problemi di restauro*. Nardini Editore, Firenze, 1991.
- [20] Liotta, Le termiti agenti di degrado delle strutture lignee dei beni culturali *Proceedings of the International Conference "Conservation of Historic Wooden Structures"*. 2005. Vol 1, 3-10.
- [21] Liotta, - *Agli insetti piacciono le opere d'arte*. EDIMED, Palermo, 2007
- [22] Liotta, Agrò, Le Infestazioni termitiche nelle Biblioteche e negli Archivi di Palermo. *International Journal of the History and Conservation of the Book*. 1999. 73-81.
- [23] Miller. Caste differentiation in the lower termites. *Biology of Termites. Volume 1*. Academic Press, New York and London, 1969.
- [24] Sajap, Amit, and Welker. Evaluation of hexaflumuron for controlling the subterranean termite *Coptotermes curvignathus* (Isoptera: Rhinotermitidae) in Malaysia. *J. Econ. Entomol.* 2000, 429-433.
- [25] Su, Hillis-Starr, Ban, Scheffrahn. Protecting historic properties from subterranean termites: a case study with Fort Christiansvaern, Christiansted National Historic Site, United States Virgin Islands. *American Entomologist* 2003, 20-32

This page intentionally left blank

# Modelling, simulation and computation



This page intentionally left blank

# Macro vs mesoscale modelling of fracture in concrete beams: size effect and crack openings

N. AISSAOUI<sup>1</sup>, S. GHEZALI and M. MATALLAH  
*RisAM, Université de Tlemcen, BP 230 Algeria*

**Abstract.** The size effect in concrete structures is a well-known phenomenon. In the present paper both macro and meso scale approaches were used to numerically investigate the size effect on notched beams under three point bending. The scale effect is investigated on the nominal strength and on the crack openings. For the macroscopic approach, concrete is considered as a monophasic material described by a softening damage law whereas for the mesoscopic approach, concrete is considered as a biphasic material made of two components (the aggregates and the matrix phase). A damage based model is used to describe the behavior of both the aggregates particles and the matrix phase.

The main objective of this work is to investigate the size effect on crack openings. A numerical post processing method developed by Matallah et al [2] is used in order to study the crack openings process. The numerical results of the simulations of the both approaches are compared to those obtained experimentally by Y. Alam [3].

**Keywords.** Macro, meso, size effect, crack openings

## Introduction

Concrete has traditionally been known as the most commonly used material of construction throughout the world. As the need for structures made of concrete such as buildings and structures of civil engineering is rapidly growing, a thorough understanding of its mechanical behavior from the properties of its components, particularly the cracking and fracture behavior [1,4] is crucial to ensure safe and economic designs.

The scale effects in the mechanical behavior of concrete are important phenomena that have been the subject of numerous studies. One of the major objectives of size effect studies was reliable extrapolation from normal scale specimens to the very large structure. Cracking appears to be inevitable in structures made of concrete. For a more reliable design of structures made of concrete, it is important to understand the fracture properties of the material and take into account the phenomenon of scaling in the design to avoid damage and cracking. The design which is done on a global scale must evolve to reflect what is happening across the material.

<sup>1</sup>Corresponding author: [nassima2307@hotmail.fr](mailto:nassima2307@hotmail.fr)

The process of degradation in concrete structure is governed by several mechanisms which can occur in a scale lower than that of a Representative Volume Element (RVE). Hence, knowledge of concrete behavior over a wide range of scale is desired. In this sense and according to the level of observation, several scales of modeling could be envisaged.

In this paper, two types of approaches have been used to numerically study the size effect on crack openings. The first approach is based on a macroscopic model; the second modeling strategy is carried out at the mesoscopic scale. For the macroscopic approach, concrete is considered as a monophasic material described by a softening damage law whereas for the mesoscopic approach, concrete is considered as a biphasic material made of two components, where the cement paste and the aggregates are described with their own mechanical characteristics. The contribution of the present study is to compare two approaches of modeling, the mesoscopic modelling to the macroscopic one in order to show the capabilities of each model to predict the size effect in concrete structures. A set of experimental tests carried out by Alam [3] is considered. A practical method proposed by Matallah et al [2] is used to extract crack openings from a continuum-damage-finite element computation. Hence, the size effect on crack openings is also investigated on the crack opening process.

## 1. Numerical simulation

### 1.1. Description of the experimental tests

In [3], an experimental program has been achieved in order to study the size effect in concrete structures. Two types of concrete mixes were used : M1 with a maximum aggregate size of 20mm, and M2 with a maximum aggregate size of 12mm. Three notched beams which are geometrically similar in two dimensions were studied. The cross section of the specimens is rectangular, and the span to depth ratio is  $l/d = 3:1$  for all the specimens. The cross sectional height  $d$  is 100, 200 and 400mm respectively for the three specimens. The thickness  $b$  is kept constant at 100mm for all sizes. In the present study, only the beams of concrete mix M1 are investigated. As shown in Figure1, the beams dimensions are given in table 1.



Figure 1. Three beams with geometrically similar sizes.

Table 1. Beams dimensions

Size (mm)	Span S	Beam height D	Notch length a
D1	300	100	20
D2	600	200	40
D3	1200	400	80

In the present section two types of approaches were used to numerically study the size effect. The numerical results of the two simulations are compared with the results resulting from the experimentation. Simulations are carried out in plane stress by using the finite elements code Cast3M.

### 1.2. Macroscopic approach

In macroscopic approach the mesh is constructed with elements of different sizes. The elements are kept small in the area close the notch where damage is expected to occur. A gradual mesh is considered to have a smooth transition between the different macro zones. The parameters of the model are given in table 2.

**Table 2.** The model parameters of macroscopic approach

$f_t$ (MPa)	$G_f$ (N/m)	$E$ (GPa)
3	100	30

### 1.3. Mesoscopic approach

Since the pioneering work of Roelfstra et al. [9], meso-scale modelling using numerical concrete has been emerging as the most useful approach for studying the influence of the interactions between the concrete constituents on the macroscopic behavior. However, the main drawback of this approach remains the high computational cost. Mesoscopic modelling of concrete requires the generation of a numerical concrete with an aggregate structure which consists in randomly distributed aggregates and cement matrix. Concrete is considered as a bi-phasic material where the cement paste and the aggregates are described with their own mechanical characteristics. The aggregates are idealized with circular shapes. The aggregates are randomly placed into the concrete specimen, conforming to the aggregates size distribution curve and the aggregate/paste area ratio. Each phase has its own mechanical behavior. The parameters used in mesoscopic modeling are indicated in Table 3.

**Table 3.** The model parameters of mesoscopic approach

	$f_t$ (MPa)	$G_f$ (N/m)	$E$ (GPa)
Mortar	3	50	20
Aggregates	6	80	60

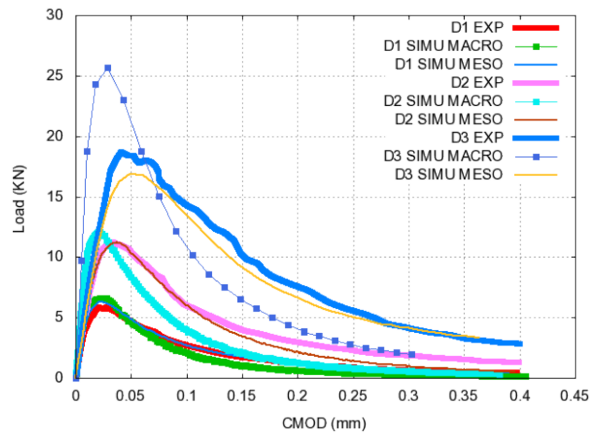
## 2. Discussion

### 2.1. Size Effect on Load-Cmod curve

The load-CMOD curves of the two approaches obtained in the analyses of the notched beams for the three sizes are compared with the experimental results in Figure 2. We note that modeling at the macroscopic scale does not perfectly reproduce the scale effect. Nevertheless, the results of beams D1 and D2 are globally well reproduced. For the largest beam D3, by using the same material parameters, the model overestimates

the scale effect. It is therefore clear that the macroscopic approach does not provide an accurate description of the scale effect for the larger beam.

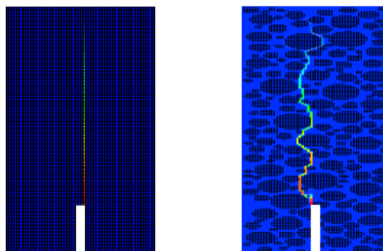
On the other hand, the size effect is well reproduced by using a mesoscopic modelling. The peak-Load values obtained numerically are similar to those obtained experimentally. Moreover, mesoscopic approaches have the advantage to facilitate the study of progressive cracking by taking into account the random distribution of aggregates. Using the mesoscopic model, we found that the inclusion of two specific laws of behavior for each component of concrete (mortar and aggregates) allows a realistic description of all stages of degradation. In contrast to the macroscopic model, mesoscopic model used is able to predict the full experimental curves (see Figure 2).



**Figure 2.** Comparison of the Numerical - Experimental results

## 2.2. Crack openings

In addition to the global results in the form of load-CMOD curves, local results like damage and cracks patterns are investigated. The procedure OUVFISS developed in [2] is used for the prediction of crack openings. In Figure 3 and 4, the crack opening and damage fields of the central parts of the beam D2 are illustrated (Macro left and Meso right). The mesoscopic approach reproduces very well the tortuosity of the crack path which depends on the aggregates random distribution.



**Figure 3.** Crack opening fields D2 Macro-Meso

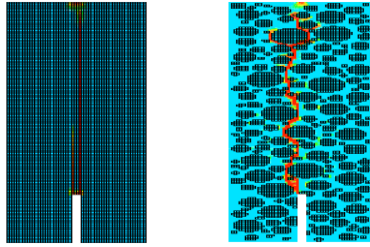


Figure 4. Damage at the central part of the beam D2 Macro-Meso

The experimental and numerical crack opening profile of the beam D2 at the end of loading stage is presented in Figure 5. The numerical crack opening profile obtained by the mesoscopic approach from the notch tip has the same slope that the experimental profile calculated from the digital images correlation [3]. The numerical result of crack openings approximates that obtained by the experiment.

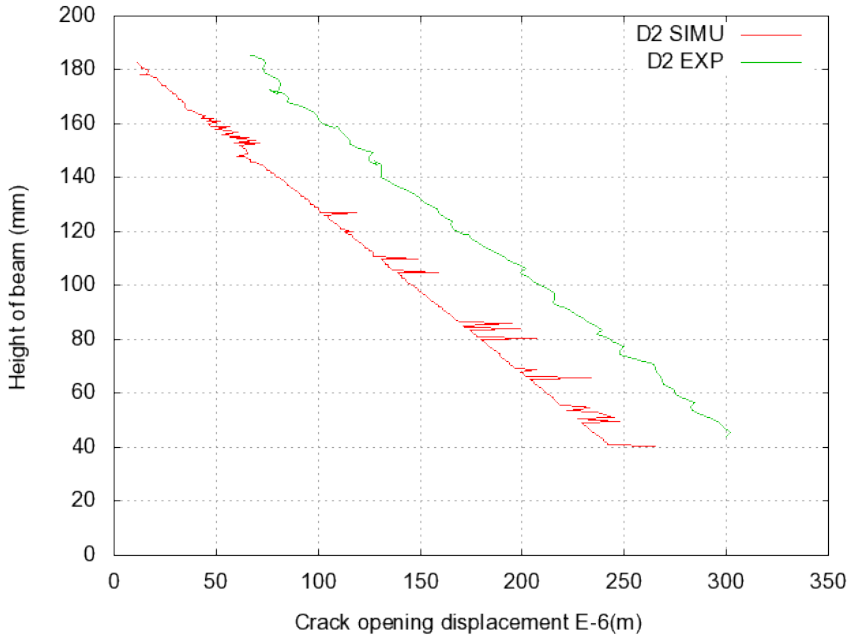


Figure 5. Crack opening profile of beam D2 at the end of loading

### 3. Conclusions

In this study, a comparison of two modeling approaches for predicting the fracture of concrete structures is presented. An isotropic damage model [10] is adopted to model the non-linear behavior of concrete. The fundamental bases of this model are given in [10]. The size effect has been studied to show the ability of each approach to reproduce this phenomenon. A post processing method in [2] has been used in order to study the cracking process in beams under three point bending test. At macroscopic scale, the size effect is partially reproduced. The macro-scale is still far from reproducing the scale effect if large size specimens are considered. At the mesoscopic scale, the size effect and the crack openings process are well reproduced.

### References

- [1] Z. P. Bazant and J. Planas, *Fracture and Size Effect in Concrete and Other Quasibrittle Materials*, CRC Press, Boca Raton and London, 1998.
- [2] M. Matallah, C. La Borderie, and O. Maurel. A practical method to estimate crack openings in concrete structures, *Int. J. Nume. Analy. Meth. Geomechanics.*, **43** (2010), 1615-33.
- [3] S. Y. Alam, *Experimental study and numerical analysis of crack opening in concrete*, PhD Thesis, Ecole Centrale de Nantes., France, 2011.
- [4] J.G.M. van Mier, *Fracture Processes of Concrete*, CRC Press, USA, 1997.
- [5] J. Oliver, A. Huespe, M.D.G. Pulido, and E. Blanco, Computational modeling of cracking of concrete in strong discontinuity settings, *Computers and Concrete*, 1(1) (2004), 61-67.
- [6] Sukumar, N., Moes, N., Moran, B., and Belytschko, T, Extended finite element method for three-dimensional crack modelling, (2000) *Int. J. Numer. Meth. Engng* 48(11), 1459-1570.
- [7] Dufour, F., Pijaudier-Cabot, G., Choinska, M., and Huerta, A, Extraction of a crack opening from a continuous approach using regularized damage models, (2008) *Computers & Concrete* 5(4), 375-388.
- [8] Bazant, Z.P., and Oh, B, Crack band theory for fracture of concrete, (1985) *Materials and Structures* 16(3), 155-177.
- [9] Roelfstra, P.E., Sadouki, H., Wittmann, F.H., Le béton numérique, *Materials and Structures* 18(107) (1985), 327-335.
- [10] Fichant, S., Laborderie, C., and Pijaudier Cabot, G., Isotropic and anisotropic description of damage in concrete structures, *Mech. Cohes.-Fric Mater* **4** (1999), 339-359.
- [11] Z.M. Wang, A.K.H. Kwan and H.C. Chan. Mesoscopic study of concrete I: generation of random aggregate structure and finite element mesh. *Computers and Structures*, **70** (1999), 533-544.

# Review of the strength theories

Ilmir VALIAKHMETOV

*Polytechnic Institute, Yugra State University, Khanty-Mansiysk, Russia*

**Abstract.** The paper deals with the classic and modern strength theories. Due to the fact that different materials under certain operating conditions have different ways of responding to the deformation (tension, compression, shear, torsion, bending), there are many theories of strength establishing a measure of the stress state, above which there is a transition from elastic state to the yield or failure.

The classical theories of strength are easy to use and were very popular at one time. They include the maximum principal stress theory, the maximum principal strain theory, the maximum shear stress theory, the maximum distortion energy theory, and the Mohr-Coulomb strength theory.

Research towards new theories should be attributed to the strength theories applicable to anisotropic materials, and theories of outgoing the basis of phenomenological prerequisites that are usually based on one of the classical theories with the added conditions. There are important criteria such as Hoek-Brown, Murell, Drucker-Prager, Hill, and other theories used by European, American, Chinese and Russian scientists.

**Keywords.** Strength theories, classical theories, anisotropic, materials

## Introduction

Strength theory is designed to determine the maximum stress state of a brittle or ductile solid material, at which a change in the mechanical properties of the material occurs, under various external loading conditions. Strength theory includes failure criteria, yield criteria, material models in computational mechanics and computer codes. It has been widely used in mechanics, engineering, materials engineering (also commonly known as materials science), and earth science. To obtain information on the strength properties of the material under complex stress states experienced, requires large amount of expensive experiments and will spend a lot of time. Strength theory has been the object of study by physicists, mechanical engineers, civil engineers, material scientist and earth scientist.

Some of history's greatest scientists have participated in the search for the strength theory. They were Leonardo da Vinci (1452-1519), Galileo Galilei (1564-1642), Charles-Augustin de Coulomb (1736-1806), Henri Edouard Tresca (1814-1885), Christian Otto Mohr (1835-1918), and Richard Edler von Mises (1883-1953). It has been studied for over a few hundred years, and hundreds of criteria and models have been proposed, ranging from the one-parameter criterion (model) to the multi-parameter criterion. Nonetheless, it is still an open subject of research.

Although there are some review books and articles about the strength theories, they are heavy and difficult to survey.

<sup>1</sup>Corresponding author: [mirvaliak@gmail.com](mailto:mirvaliak@gmail.com)



In the first half of the 20<sup>th</sup> century, some of the surveys were reviewed by Westergaard [1], Mohr [2], Nadai [3], Prager [4], Schleicher [5], Marin [6], Dorn [7], Gensamer [8], and Meldahl [9]. In the 1960s, this subject was also contributed by Filonenko-Boroditch [10], Freudental and Geiringer [11], Naghdi [12], Paul [13], Marin [14], Goldenblat and Kopnov [15]. It was further reviewed in the 1970s by Tsai and Wu [16], Michino and Findley [17], Krempl [18], Salencon [19], Bell [20], Geniev et al. [21]. Strength theories were subsequently contributed upon by Zyczkowski [22], Chen and Baladi [23], Hosford [24], Shaw [25], Rowlands [26], Ikegami [27], Desai [28], Hamza [29] and by Du [30], Klausner [31], Andreev [32], Brown [33], Munx and Fett [34], in the 1980s - 90s.

In this century the strength theory was surveyed by Hoek et al [35], Yu [36], Christensen [37], and others.

## 1. History of development of the strength theories and classical strength theories

Two of the world famous and talented Italian scientists such as Leonardo da Vinci (1452-1519) and Galileo Galilei (1564-1642) may have been among the first researchers of the strength of materials and structures. Da Vinci and Galilei did tensile tests of iron wire and stone, and also bending tests of beams. Galilei believed that the fracture of materials often happens at the condition when local normal stress equals to a critical value. He wrote his famous book "Two New Sciences", a portion of which is devoted to the mechanical properties of building materials and research strength of beams. This book represents the first printed work in the field of strength of materials [38].

Charles-Augustin de Coulomb (1736-1806) was a French physicist and engineer. He may be the first researcher in the maximum shear stress strength theory. Of all the scientists of the 18th century, Coulomb made the largest contribution to the science of mechanics of elastic bodies [38]. Coulomb gave the first description of the famous Mohr-Coulomb strength theory. Coulomb's Memoir Essay [39] describes conducted experiments for establishing the strength of some kind of sandstone and he gave a theoretical discussion of the compression of a prism, the bending of beams, and the stability of arches and walls. The Memoir Essay was published in Paris in 1776 [39].

### 1.1. Classical strength theories in the 19<sup>th</sup> century and early the 20<sup>th</sup> century.

In the 19<sup>th</sup> century, there were three strength theories such as the maximum principal stress theory, the maximum principal strain theory and the maximum shear stress theory.

The maximum principal stress theory was assumed by such scientists as Rankine (1820-1872) and Lamé (1795-1870). It was the first theory relating to the strength of materials under complex stress. It assumes that if maximum principal stress is the design criteria, then the maximum principal stress must not exceed the working stress for the material and only one principal stress,  $\sigma_1$  of the stresses  $\sigma_1$ ,  $\sigma_2$ , and  $\sigma_3$  was taken into account. This criterion was extended with the well-known textbook of Rankine's, "Manual of Applied Mechanics" [40].

The maximum principal strain theory was the second strength theory. Edme Mariotte (1620-1684) was a French physicist and he made the first statement on the maximum strain criterion or maximum elongation criterion [41]. Maximum strain theory was generally accepted, principally under the influence of such researches as the two French academicians Saint-Venant (1797-1886) and Poncelet (1788-1867) [42]. This theory says that a material begins to fail when maximum principal strain equals the yield point strain in simple compression. This theory was very famous at one point, but it does not agree well with most experiments, therefore no one uses it today.

The maximum shear stress theory also known as the Tresca yield criterion was the third strength theory. Henri Tresca French scientist presented two notes dealing with the flow of metals under great pressure to the French Academy [43], in 1864. He assumed that yield occurs when the shear stress exceeds the shear yield strength. This theory is simple to apply and suits well for the prediction of yield for some ductile materials.

The criterion of failure based on the assumption that anyone definite volume of material has only a limited capacity for absorbing and storing energy in the form of elastic strain was suggested by Beltrami in 1885 [44]. This theory has not been used in engineering because it does not agree with experiments. At the end of the 19th century, strength theory was also investigated by Guest [45], Foppl [46], and others.

The maximum distortion energy theory was the fourth strength theory. This theory was formulated by Maxwell in 1865 [38]. However, it is generally attributed to von Mises [47] and Huber [48]. This theory postulates that failure occurs when the distortion energy reaches the same energy for yield (or failure) in uniaxial testing.

Christian Otto Mohr (1835-1918) was very good German engineer and scientist. He conducted a more complete research of the strength of materials. He used the stress circle method [49] in perfecting his strength theory in 1900 [50]. Mohr's criterion was based on the assumption that the maximum shear stress is the only decisive indicator of impending failure. This criterion takes into account the principal stresses  $\sigma_1$ ,  $\sigma_3$  and considers that the average principal stress  $\sigma_2$  slightly affects on onset of limit state and therefore it can be ignored. Now this criterion is called the Mohr-Coulomb strength theory, because the idea of Mohr's criterion is similar to the idea Coulomb's (1773) [39].

## 2. Strength theories in the 20th century and early the 21th century

A basic postulate concerning the yield surfaces for the classification of a large number of failure criteria, yield criteria and material models was developed by Drucker [51, 52]; Hill and Bishop [53] with the convexity of yield surface determined in the 20<sup>th</sup> century. Later, Ilyushin generalized the convexity of yield surface to the strain space [54].

The convex domain and its two bounds are much interesting. One method used in the present paper for representing these theories is to use the normal stress  $\sigma_{13}$ ,  $\sigma_{12}$ ,  $\sigma_{23}$  and the principal shear stresses  $\tau_{13}$ ,  $\tau_{12}$ ,  $\tau_{23}$  acting on the same planes, such that:

$$\sigma_{ij} = \frac{1}{2}(\sigma_i + \sigma_j); \tau_{ij} = \frac{1}{2}(\sigma_i - \sigma_j); i, j = 1, 2, 3$$

### 2.1. First series of strength theory

First series of strength theory are simplest and the earliest series of strength theory. This series considers the influence of the normal stress,  $\sigma_{13}$  and the maximum shear stress,  $\tau_{13}$ , and it can be written mathematically as

$$F(\sigma_{13}, \tau_{13}) = C \quad (1)$$

#### 2.1.1. Maximum shear stress criterion

This is a one-parameter criterion of the maximum shear stress criterion (Tresca yield criterion). It is also referred to as the third strength theory in Chinese and in Russian. This criterion is applicable to materials subject to equal yield stress in compression and in tension  $\sigma_c = \sigma_t = \sigma_s$ , therefore Tresca criterion has been widely used in mechanical engineering and for metallic materials. This criterion is written mathematically as

$$F = \sigma_1 - \sigma_3 = \sigma_S, \text{ or } F = \tau_{13} = C \quad (2)$$

Davidenkov [55], Drucker [56] and others gave the generalization of the Tresca criterion [43] by adding a hydrostatic stress term,  $\sigma_m$ . The extended Tresca criterion is written mathematically as

$$F = \tau_{13} + \beta\sigma_m = C \quad (3)$$

#### 2.1.2. Mohr-Coulomb strength theory

The renowned Mohr-Coulomb strength theory is a two-parameter criterion written mathematically as

$$F = \tau_{13} + \beta\sigma_{13} = C, \text{ or } F = \sigma_1 - \alpha\sigma_3 = \sigma_t, \quad \alpha = \frac{\sigma_t}{\sigma_c} \quad (4)$$

This theory does not take into account the intermediate principal stress  $\sigma_2$  that is a disadvantage. Mohr-Coulomb strength theory is most widely used in soil mechanics.

#### 2.1.3. Nonlinear Mohr-Coulomb criteria

Nonlinear Mohr-Coulomb criteria is multi-parameter criteria used in rock mechanics. Some of the expressions are quation (5) given in Hoek-Brown [57], equation (6) in Murell [58], etc.

$$F = (\sigma_1 - \sigma_3) + \sqrt{m\sigma_1 - c} = 0 \quad (5)$$

$$F = \tau_{13} + \lambda\sigma_{13}^n = 0 \quad (6)$$

## 2.2. Second series of strength theory

The second series of strength theory take into consideration the influence of the octahedral normal stress  $\sigma_8$  and the octahedral shear stress  $\tau_8$ , and it can be written mathematically as

$$\tau_8 = f(\sigma_8), \text{ or } F(\sigma_8, \tau_8) = C \quad (7)$$

### 2.2.1. The von Mises Yield criterion

The expression is

$$F = \tau_8 = C, \text{ or } J_2 = C, \text{ or } \tau_m = C \quad (8)$$

It is a one-parameter criterion, also referred to as the von Mises criterion [47], or octahedral shear stress  $\tau_8$  yield criterion by Nadai [3]. It was also referred to as shear strain energy theory (energy of distortion) by Maxwell [38], Huber [48], Hencky [59]), or  $J_2$  theory, or mean square of principal stress deviations by Paul [13], or the fourth strength theory in Chinese, Russian, etc. All these expressions are the same, since

$$\begin{aligned} \tau_8 &= \frac{\sqrt{15}}{3} \tau_m = \frac{\sqrt{2}}{3} \sigma_e = \sqrt{\frac{2}{3} J_2} = \frac{2}{3} \sqrt{\tau_{12}^2 + \tau_{23}^2 + \tau_{13}^2} \\ &= \frac{1}{3} \sqrt{(\sigma_1 - \sigma_2)^2 + (\sigma_2 - \sigma_3)^2 + (\sigma_3 - \sigma_1)^2} \end{aligned} \quad (9)$$

### 2.2.2. Drucker-Prager criterion etc.

The expression is

$$F = \tau_8 + \beta \sigma_8 = C \quad (10)$$

It is a two-parameter criterion and it is an extension of the von Mises criterion. This criterion was expressed by Drucker-Prager [60] as a correction of the von Mises yield criterion by adding a hydrostatic stress term  $\sigma_8$  (or  $\sigma_m$ ). This criterion was used widely in soil mechanics and its many variants have been applied to concrete, rock, and other pressure-dependent materials.

### 2.2.3. Hill Yield criterion

The expression generalizing the yield criterion by Hill [61] is

$$\begin{aligned} f |\sigma_2 - \sigma_3|^m + g |\sigma_3 - \sigma_1|^m + h |\sigma_1 - \sigma_2|^m + a |2\sigma_1 - \sigma_2 - \sigma_3|^m \\ + b |2\sigma_2 - \sigma_1 - \sigma_3|^m + c |2\sigma_3 - \sigma_1 - \sigma_2|^m = \sigma_s^m \end{aligned} \quad (11)$$

Where  $m \geq 1$ , the six parameters  $f, g, h, a, b, c$  are constants characterizing the anisotropy. It is a three-parameter criterion,  $f=g=h, a=b=c$ , for the isotropic case. Its many variations of this criterion are in wide use for polymers, metals, and certain composites.

### 2.3. The other criteria and computational implementation

A large number of failure criteria and yield criteria was presented in the 20th century. The yield criteria are for metallic materials. The failure criteria are for anisotropic and composite materials, and for specific materials such as rock, concrete, soils, iron, high steel, alloy, ice, polymers, energetic materials (solid rocket propellant, TNT, etc.), ceramic, glass, biomaterials, powder, photoplastic materials, brick masonry and other materials.

Strength theory, being one of the most significant constitutive relations, has been implemented into various computational codes, mainly the non-linear computer codes based on the Finite Element Method (FEM).

The yield criteria have been implemented into the commercial FEM systems, such as Abaqus FEA (formerly ABAQUS), ADINA, ALGOR, ANSYS, COMSOL Multiphysics, LUSAS, LS-DYNA, RFEM, etc. The functions and the applied field of many powerful commercial FEM codes were limited to the choosing of failure criteria. More effective and systematic models of materials under complex stress are needed.

The results of research and designs depend strongly on the choice of strength theory in most cases. The selection of the correct strength theory becomes even more important than the calculations, as indicated by Sturmer, Schulz, and Wittig [62]. Therefore, it is very important to choose a reasonable strength theory in design and research.

## References

- [1] H.M. Westergaard, On the resistance of ductile materials to combined stresses, *J. Franklin of the Institute* 189 (1920), 627–640.
- [2] C.O. Mohr, *Abhandlungen aus den Gebiete der Technischen Mechanik*, Third Ed, Verlag von Wilhelm Ernst & Sohn, 1928.
- [3] A.L. Nadai, *Theory of Flow and Fracture of Solids*, Vol. 1, McGraw-Hill, New York, 1950.
- [4] W. Prager, Recent developments in the mathematical theory of plasticity, *J. Appl. Phys.* 20 (1949), 235–241.
- [5] F. Schleicher, *Z. Angew. Math. Mech.*, 5 (1925), 199.
- [6] J. Marin, Failure theories of materials subjected to combined stresses, *Proc. Am. Soc. Civ. Eng.* 61 (1935), 851–867.
- [7] J.E. Dorn, Effect of stress state on the fracture strength of metals, In: *Fracturing of metals ASM*, (1948), 32–50.
- [8] M. Gensamer, Strength of metals under combined stresses, *ASM* (1940), 38–60.
- [9] A. Meldahl, *Brown Boveri Rev. Zurich*, (1944), p. 260.
- [10] M.M. Filonenko-Boroditch, *Mechanical Theories of Strength*, Moscow Univ Press, Moscow, 1961.
- [11] A.M. Freudental and H. Geiringer, In: *Encyclopedia of Physics*, S. Flugge (ed), Vol 6, The mathematical theories of the inelastic continuum, *Elastizitat und Plastizitat*, Springer, Berlin, (1958), 229–433.
- [12] P.M. Naghdi, Stress-strain relations in plasticity and thermoplasticity, In: *Plasticity*, E.H. Lee and P.S. Symonds (eds), Pergamon Press, (1960), 121–169.
- [13] B. Paul, Macroscopic criteria for plastic flow and brittle fracture, In: *Fracture, An Advanced Treatise*, Vol 2, H. Liebowitz (ed) Academic Press, New York (1968), 313–496.
- [14] J. Marin, *Mechanical Behavior of Engineering Materials*, Printice-Hill, Englewood Cliffs, 1962.

- [15] I.I. Goldenblat and V.A. Kopnov, *Yield and Strength Criteria for Structural Materials*, Machine Manufacturing, Moscow, 1968.
- [16] S.W. Tsai and E.M. Wu, A general theory of strength for anisotropic materials, *J. Compos. Mater.*, 5(1), (1971), 58–80.
- [17] M.J. Michino and W.N. Findley, A historical perspective of yield surface investigation for metals, *Int. J. Non-Linear Mech.*, 11(1) (1976), 59–82.
- [18] E. Krempl, *The Influence of State of Stress on Low-cycle Fatigue of Structural Materials: A literature survey and interpretive report*, ASTM STP 649, ASTM, (1974).
- [19] J. Salencon, *Applications of the Theory of Plasticity in Soil Mechanics*, J. Wiley & Sons (1977), 158 pp.
- [20] J.F. Bell, *Mechanics of solids, Vol 1: The experimental foundations of solid mechanics*, In: *Encyclopedia of Physics*, Vol 6a/1, Springer, Berlin (1973), 483–512, and 666–690.
- [21] G.A. Geniev et al, *Strength of Lightweight Concrete and Porous Concrete under Complex Stress State*, Moscow Building Press, Moscow, 1978.
- [22] M. Zyczkowski, *Combined Loadings in the Theory of Plasticity*, Polish Scientific Publ, PWN, and Nijhoff, 1981.
- [23] W.F. Chen and G.Y. Baladi, *Soil Plasticity: Theory and Implementation*, Elsevier, Amsterdam, 1985.
- [24] W.F. Hosford, Comments on anisotropic yield criterion, *Int. J. Mech. Sci.* 27, (1985), 423.
- [25] M.C. Shaw, A critical review of mechanical failure criteria, *ASME J. Eng. Mater. Technol.*, 106 (1984), 219–226.
- [26] R.E. Rowlands, Strength (failure) theories and their experimental correlation, In: *Failure Mechanics of Composites*, G.C. Si and A.M. Skudra (eds), Elsevier Science Pub. (1985), 71–125.
- [27] K. Ikegami and Y. Niitsu, Fundamental experiments on plastic deformation of stainless steel at high temperature, In: *Advance in Constitutive Laws for Eng. Material*, Int. Acad. Publ. (1989), 920–933.
- [28] C.S. Desai, Single surface yield and potential function plasticity models: A review, *Computers and Geotechnics*, 7 (1989), 319–335.
- [29] H. Hamza, Critical strain energy as a failure and crack propagation criterion for ice, *Proc IAHR Int Symp on Ice Prob.* (1984).
- [30] Q.H. Du, *An Encyclopedia of Engineering Mechanics*, Higher Education Press, Beijing, 1994.
- [31] Y. Klauser, *Fundamentals of Continuum Mechanics of Soils*, Springer-Verlag (1991), 437–485.
- [32] G.E. Andreev, Brittle Failure of Rock Materials: Test results and Constitutive Models, AA Balkema (1995).
- [33] M.W. Brown and H. Gao, Multiaxial fatigue (in Chinese), *J. Mechanical Strength*, 18(1) (1996), 9–13.
- [34] D. Munz and T. Fett, *Ceramics: Mechanical Properties, Failure Behaviour, Materials Selection*, Springer Verlag, Berlin, 1999.
- [35] E. Hoek, C. Carranza-Torres, B. Corkum, Hoek-Brown criterion – 2002 edition, In: *Proceeding of the NARMS-TAC Conference, vol 1*, Toronto, (2002), 267–273.
- [36] M.H. Yu, *Unified Strength Theory and its Applications*, Springer, Berlin, 2004.
- [37] R.M. Christensen, *The Theory of Materials Failure*, Oxford University Press, United Kingdom, 2013.
- [38] S.P. Timoshenko, *History of Strength of Materials*, McGraw-Hill, New York, 1953.
- [39] C.A. Coulomb, Essai sur une application des regles de maximis et minimis a quelques problems de statique, relatifs a l'architecture, *Memoires de Mathematique et de Physique, presentes a l'Academie, Royale des Sciences par divers Savans, et lus dans ses Assemblees*, 7 (1773, 1776), 343–382, Paris.
- [40] W.J.M. Rankine, *Manual of Applied Mechanics* (1 edition, Ref. from Timoshenko, 1953, p. 198; 21st edition, 1921), 1861.
- [41] E. Mariotto, *Traite du mouvement des eaux, (posthumously)*, de la M. Hire ed; English transl by J.T. Desvaguliers, London, 1686.
- [42] de Saint-Venant, Memoire sur l'establissement des equations differentielles des mouvements interieurs operes dans les corps solides ductiles au dela des limites ou l'elasticite pourrait les ramener a leur premier etat., *Comptes Rendus hebdomadaires des Seances de l'Academie des Sciences* 70, (1870), 473–480.
- [43] H. Tresca, Sur l'ecoulement des corps solides soumis a de fortes pression, *Comptes Rendus hebdomadaires des Seances de l'Academie des Sciences, Rend* 59 (1864), 754–758.
- [44] E. Beltrami, *Rend Ist Lombardo Sci. Lettere* B18 (1885), 704–714.
- [45] J.J. Guest, On the strength of ductile materials under combined stress, *Philos. Mag.*, 50 (1900), 69–133.
- [46] A. Foppl, *Mitt Mech-tech Lab*, Munch, T Ackermann, vol 7 1900.
- [47] R.E. von Mises, Mechanik der festen Korper im plastisch deformablen Zustand, *Nachrichten von der Koniglichen Gesellschaft der wissenshaften zu Goettinger, Mathematisch-physikalische Klasse* (1913), 582–592.
- [48] M.T. Huber, Przyczynek do podstaw wytorymalosci, *Czasop Techn.*, 22, 81 (Lwow, 1904); Pisma, 2, PWN, Warsaw (1956).

- [49] O. Mohr, Über die Darstellung des Spannungszustandes und des Deformationszustandes eines Körperelementes und über die Anwendung derselben in der Festigkeitslehre, *Der Civilingenieur*, 28 (1882), 113–156.
- [50] O. Mohr, Welche Umstände bedingen die Elastizitätsgrenze und den Bruch eines Materials? *Zeitschrift des Vereins Deutscher Ingenieure* Band, 44 (1900), 1524–1530.
- [51] D.C. Drucker, A more foundational approach to stress-strain relations, *Proc. Of 1st OS-Natl Congress Appl. Mech.*, ASME (1951), 487–491.
- [52] D.C. Drucker and F. Edelman, Some extension of elementary plasticity theory, *J. Franklin Inst.*, 251(6), (1951), 581–605.
- [53] J.F.W. Bishop and R. Hill, A theory of the plastic distortion of a polycrystalline aggregate under combined stresses, *Philos. Mag.*, 42 (1951), 414–427.
- [54] A.A. Ilyushin, On the postulate of plasticity, *PMM* 25(3) (1961), 503–507.
- [55] N.N. Davidenkov, In favour and against a uniform theory of strength, *Bulletin Engineering and Technology*, 4 (1947), 121–129
- [56] D.C. Drucker, Limit analysis of two and three-dimensional soil mechanics problems, *J. Mech. Phys. Solids*, 1, (1953), 217–226.
- [57] E. Hoek and E.T. Brown, Empirical strength criterion for rock masses, *J. Geotech. Eng.*, 106(9) (1980), 1013–1035.
- [58] S.A.F. Murrell, The effect of triaxial stress system on the strength of rocks at atmospheric temperatures, *Geophys. J.*, 10 (1965), 231–282.
- [59] H. Hencky, Zur Theorie plastischer Deformationen und der Hierdurch im Material hervorgerufenen Nebenspannungen, *Proc. 1st Int. Congr. On Appl. Mechanics*, J. Waltman, (ed) Delft, Technische Boekhandel en Druckerij, (1925).
- [60] D.C. Drucker and W. Prager, Soil mechanics and plastic analysis for limit design, *Q. Appl. Math.*, 10(2) (1952), 157–165.
- [61] R. Hill, A user-friendly theory of orthotropic plasticity in sheet metals, *Int. J. Mech. Sci.*, 35 (1993), 19.
- [62] G.S. Sturmer, A. Schulz and S. Wittig, Life time prediction for ceramic gas turbine components ASME-Paper No 91-GT-96, 1991.

# Analysis of hopper eccentricity effect on granular flow in three-dimensional silos using discrete element method

M. BENYAMINE<sup>a,1</sup>, N. FEZZIOUTI<sup>b</sup>, O. HAMI<sup>a</sup>, M. DJERMANE<sup>a</sup> and A. SLIMANI<sup>b</sup>

<sup>a</sup>Laboratoire FIMAS, Université de Béchar, B.P 417 Béchar 08000, Algérie

<sup>b</sup>Laboratoire ENERGARID, Université de Béchar, B.P 417 Béchar 08000, Algérie

**Abstract.** Silos are widely used in industry and agriculture for the storage of different granular products. The discharge of granular matter from these containers is one of the most common phenomena of everyday life, but it has not yet been completely understood. Early studies of the discharge process were mainly concerned with the concentric silos. However, eccentric hoppers are frequently encountered in chemical and pharmaceutical industries. Then, it is of paramount importance to understand the physical phenomena that control the flow of grains in these silos to guarantee optimal discharge process. In this study, numerical simulation was performed using Discrete Element Method DEM in order to analyze the discharge process in three dimensional eccentric silos. The flow performance in centric and eccentric silos are also analyzed and compared and a clear effect of hopper eccentricities is shown. The results obtained for different hopper eccentricities reveal that flow of particle is slightly dependant on the position of exit aperture.

**Keywords.** Granular flow, eccentric discharge, silos and hoppers, discrete element method, flow rate

## Introduction

Granular materials present one of the most challenging areas of research in mechanics. The flow of coal down an inclined chute, the discharge of grain from hopper or motion of debris in a landslide are all examples of granular material flow. Granular materials are unlike solids, in that they conform to the shape of the vessel containing them, thereby exhibiting fluid like characteristic. It is well accepted that granular materials can sustain shear stresses in the absence of any deformation. The characteristics of individual particles that constitute the bulk solids are probably of major importance in influencing the characteristics of the bulk solids both at the rest and during flow [1].

Early research has mainly been focused on experimental investigations [2,3] and deriving approximate analytical methods for engineering design [4,5]. Due to their

---

<sup>1</sup>Corresponding author: [benyamine\\_mbk@yahoo.fr](mailto:benyamine_mbk@yahoo.fr); fax. +21349815244



difficult behaviour, modelling of granular materials is still a challenge. Accordingly, the discrete element method (DEM) offers a more natural way to simulate granular media and describes particle flow behaviours at individual particle level. This method was pioneered by Cundall and Strack [6] and since then, it has been widely employed in the simulation of discharge hopper/silo [7-8]. An understanding of granular flow behaviour is crucial to recognize the flow patterns developed in the material during eccentric discharge because it is an important cause of silo failure. Although, most of these studies [9-11] were devoted to the pressure measurements, also, the effect of the eccentricities on the flow pattern and velocity profiles have been analyzed by [12-14]. Seeing the industrial frequency of eccentric silos and the relatively limited existing researches of how this eccentricity affect discharge process, this work focused on using DEM model to simulate the granular flow in three dimensional centric and eccentric silos.

The aim of this work was to study the silo phenomena, especially how eccentricities affect the flow pattern developed in the granular material during the silo outflow process. In order to get more information about the eccentric discharge, the discharge rate was analyzed for various friction coefficients. Additionally, a comparison between the predicted results in the case of centric and eccentric silos was carried out.

**1. Discrete element method**

Discrete element method simulation is one of the emerging tools to investigate the behaviour of granular materials. The key aim of DEM is to explicitly model the particle-scale processes in a system. The basic assumption in DEM is that during a small time step, the disturbances cannot propagate from any particle to the others except its immediate neighbours [6]. The force and momentum equation balances, and material constitutive laws are evaluated for each particle at contacts.

$$m_i a_i = F_i + m_i g \text{-----(1)}$$

$$I_i \omega_i = M_i \text{-----(2)}$$

where  $m_i$  and  $a_i$  are the mass and the acceleration of the particle  $i$ ,  $F_i$  is the resultant forces acting on particle  $i$ ,  $g$  is the gravitational acceleration vector,  $I_i$  and  $\omega_i$  are the moment of inertia and angular velocity for particle  $i$ , respectively.  $M_i$  is the moment acting on particle  $i$ . These calculations are adopted for each particle in every time step [12,14]. The resultant forces acting on particle  $i$ ,  $F_i$  can be resolved into normal and shear components:

$$F_i = F_i^n + F_i^s \text{-----(3)}$$

The contact force in the normal direction is based on the total overlap  $\delta_n$  in the normal contact direction and the normal relative velocity  $u_n$ , and is given by:

$$F_i^n = -k_n \delta_n + c_n u_n \text{-----(4)}$$

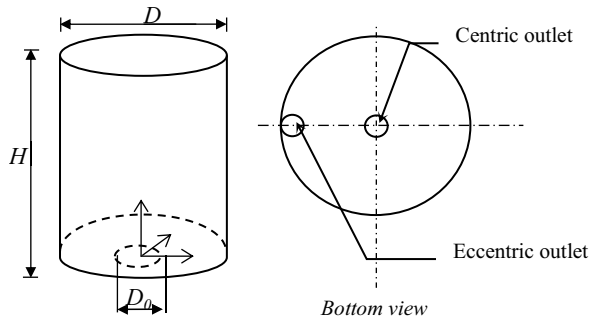
The contact shear force is based on the relative displacement increment  $\Delta x_s$  in the tangential contact direction and frictional slip. It is given by:

$$F_i^s = \min\{\mu F_i^n; k_s \Delta x_s + c_s u_s\} \text{-----(5)}$$

Where  $k_n$  and  $k_s$  are the normal and shear stiffnesses respectively,  $\mu$  is the friction coefficient,  $u_s$  is the tangential relative velocity,  $c_n$  and  $c_s$  are the normal and shear damping coefficient respectively. The shear component of the contact displacement increment, occurring over a time step  $\Delta t$  is given by  $\Delta x_s = u_s \Delta t$ .

## 2. Description of the problem

The discharge process of a silo filled with glass spheres beads was modeled. The principal data for particles and simulation parameters are shown in Table 1. These parameters were chosen mainly to be the same as those considered in [14] and they can be obtained generally by direct measurement using methods described in the literature [15,16]. At the beginning of the simulations, the non-overlapping particles were randomly generated. Then, these particles were allowed to settle under gravity onto the bottom of the silo. After a stable bed had been formed, the orifice at the bottom was opened and the particles began to flow out. The cylindrical hopper used for the analysis of flow patterns in silos with eccentricity, is defined by the hopper diameter  $D=0,3\text{ m}$ , hopper outlet diameter  $D_o=0,03\text{ m}$  and the height  $H=0,37\text{ m}$  as reported in Figure 1.



**Figure 1.** Geometry of studied silo showing a flat bottom hopper with schematic drawing of the eccentricity

**Table 1.** Material properties and simulation data

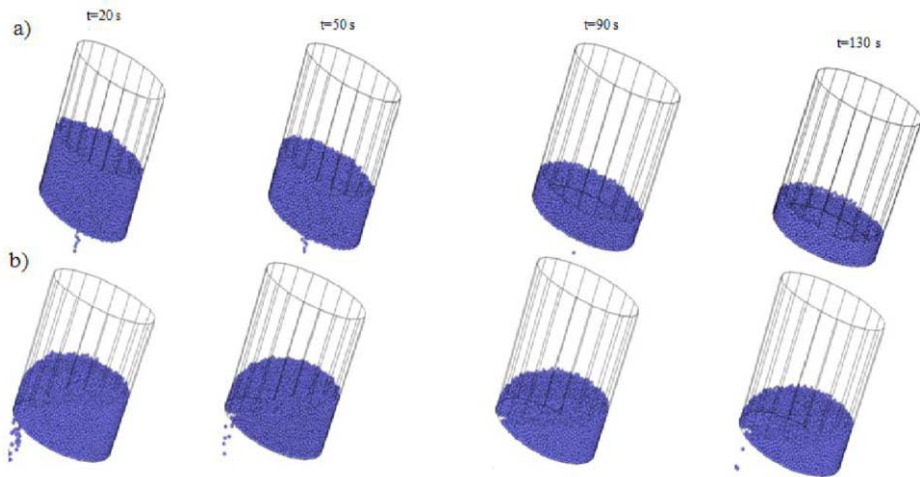
Particle diameter, $d$ (m)	0.003
Particle density, $\rho_p$ ( $\text{Kg/m}^3$ )	2500
Friction coefficient: particle/particle $\mu_p$	0., 0.5, 0.6
Friction coefficient: particle/wall $\mu_w$	0.05, 0.6
Spring coefficient: particle/particle $k_p$ ( $\text{Nm}^{-1}$ )	250000
Spring coefficient: particle/wall $k_w$ ( $\text{Nm}^{-1}$ )	250000
Number of particles, $N$	50000
Time step, $\Delta t$ (s)	$10^{-5}$

## 3. Results and discussions

In this investigation, the discrete element method is used to highlight the effect of the eccentricities on the emptying process.

Figure 2, shows a snapshot of out flowing particles in concentric and eccentric silos at different time steps. In this view, a rotation of the silo has been taken to show details of particles distribution within the centre of the silo. Figure 2a represents the discharge process for concentric silo. At the beginning, the top surface remains flat. The particles flowed as mass flow in the upper part of the silo. As the time elapses, almost a symmetric flow is observed and the upper surface changes its shape during the material flow. The region of flow broadens and reaches the upper surface. It can be said that the flow occurs in a cone shaped central region of the silo whereas the particles located in the regions near the side walls are stationary. The shape of this channel

indicates that the flow is radial in the upper part of silo confirming the Jenike's assumption of the radial flow [8]. From these figures, the flow of the particles can be characterized by the funnel flow. In the final phase, the flow of material channel vanished when the top surface reaches the bottom and stagnant zones were developed along the lateral and bottom walls. By examination of flow patterns in the fully eccentric silo (Figure 2b), the flowing zone above the orifice occurs near the left wall at the initiation of the emptying process. Afterwards, this zone deepens with progressing of the discharge. As it can be seen, the channel flow formed a semi-cone along the outlet. Its sides become more and more steeper and when the slope of these sides reaches the angle of repose some of the particles flow down to the left part of the material. In the later phase, the stagnant zone is localized only in the right and the bottom silo walls.



**Figure 2.** State of the particles during discharge at different simulation times:  
a) centric silo, b) eccentric silo

The flow rate in silo is an important topic of early research. The prediction of discharge rate is necessary for the operation effectiveness, control of granular material and for reliable design of silos. Numerous experiments have been made over the years to examine granular flow out of an orifice in the base of cylindrical silo. From these studies, there are many factors that affect the flow rate of grain through an orifice. Taking into account that the discharge rate ( $q$ ) is independent of the material height and the cylinder diameter, a dimensional analysis envisage that  $q$  is proportional to  $\rho g^{1/2} D^{5/2}$ . A very good review on the theoretical analysis that has been advanced to describe the discharge rate through orifices was written by Neddermann et al. [31]. The most widely used correlations that predict the flow rate of granular material through orifice is that of Beverloo et al. [4]. This correlation predicts the flow rate from flat bottom cylindrical silo as:

$$\dot{q} = C \rho g^{1/2} (D_0 - kd)^{5/2} \quad \text{-----}(6)$$

where  $(D_0 - kd)$  is the effective orifice diameter,  $k$  is an empirical constant depending on the size and shape of the particle typically equal to 1.5 for spherical particles,  $d$  is

the particle diameter,  $D_0$  is the orifice diameter,  $C$  is a constant that depends on the material type and commonly has a value close to 0.58,  $\rho$  is particle density and  $g$  is the acceleration gravity. The evolution of flow rate, in the analyzed cases, can be depicted as shown in Figure 3. In all cases, the flow rate exhibits some fluctuations. These fluctuations are possibly due to the formation and collapse of arches in the vicinity of the silo outlet. Moreover one can see from this figure, that the particles started with an accelerating flow, then the highest but fairly constant flow is carried out. Then the particles eventually fall as the silo is being emptied. By comparing the two profiles, the change in trends for different cases are almost similar. However, for all the cases studied, the flow rate increases with time at beginning of the discharge. This is due to dilation wave which is created at the opening of the orifice and spread rapidly over the entire ensiled material.

For fully eccentric silo, a higher flow rate is generated at the early stage of the discharge which indicates that this type of silo initiate flow more quickly. Therefore, it is believed that the augmentation of the flow rate is caused largely by the fact that rigid wall boundary facilitates the passage of particles when they approach beyond lower part of the silo. Hence in the cases of centric and half-eccentric silos, the effect of vertical wall improving the bridging action near the outlet is greater than the presence of the ensiled material in the proximity of the outlet. But when the height of material diminishes, the fully eccentric silo is characterized by lower flow rate in comparison to the half and centric ones.

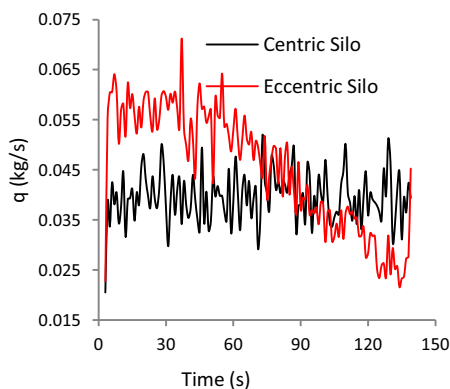


Figure 3. Discharging flow rate

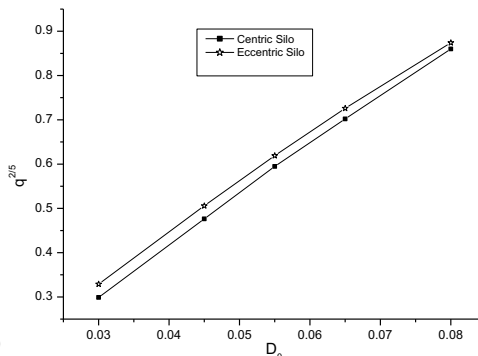


Figure 4. Discharging flow rate as function of outlet

Thus, at this time, the material does not move along the silo walls and most of the particles are located in the left part of the silo and under these circumstances, they are subject to elevated contact forces and, in turn, the flow is slowdown.

### 3.1 Effect of outlet diameter

The discharge rate for centric silo is measured from the DEM simulation for a range of silo diameter. Figure 4 display the flow rate obtained from the DEM simulation by

plotting  $\dot{q}^{5/2}$  against the orifice width  $D_0$ . As illustrated in this figure, the model gives a good prediction for the discharge rates by comparison with the Beverloo correlation, in which the flow rate merely increased with orifice diameter.

### 3.2 Effect of particle-wall friction

Figure 5 shows the results of a comparison between simulated flow rate with different coefficients of particle-wall friction during discharge process. As it can be seen, the flow rate is reduced with increasing particle-wall friction coefficient. Also these figures indicates that flow rate in the case of  $\mu_w = 0.6$  is approximately the same as the case of  $\mu_w = 0.32$  (Fig 3). These results suggest that particle- wall friction coefficient have a little effect on the flow rate as reported in many previous researches ([18]). The independence of the flow rate on the particle- wall friction coefficient can be interpreted by the permanent existence of the stagnant zones between the wall and the flowing region in the case of flat bottom silos.

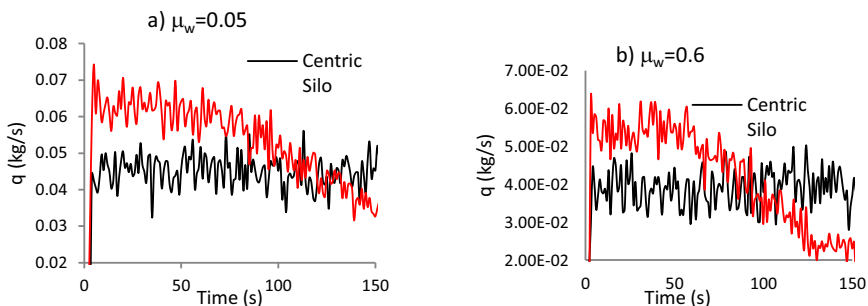


Figure 5. Discharging flow rate for various particle–wall friction coefficient: a)  $\mu_w=0.05$  and b)  $\mu_w=0.6$

### 3.3 Effect of particle-particle friction

The sensitivity of the flow parameters to ensiled material properties is examined for various particle-particle friction coefficients. From the simulation results depicted in figure 6 ( $\mu_p=0$ ,  $\mu_p=0.6$ ) (Figure 3  $\mu_p=0.5$ ), the decreasing of the particle friction exhibits diminishing of accelerating phase. On the other hand, comparison between centric and eccentric silos, reveals that the discharge rate is seen to be strongly affected by the value of particle friction coefficient. For smooth material ( $\mu_p = 0$ ), the flow of particles in fully eccentric silo is slightly faster at all time than the flow from the concentric one, the reason may be that the small friction coefficient results in good fluidity in the vicinity of vertical wall. When the coefficient of particle friction increases, the flow rate decreases and the fully eccentric silo produces a higher discharge rate only at the beginning of discharge process.

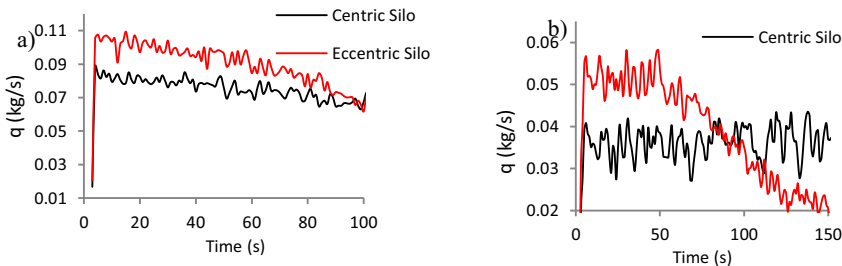


Figure 6. Discharging flow rate for various particle–particle friction coefficient: a)  $\mu_p=0$ . and b)  $\mu_p=0.6$

## 4. Conclusions

In the present study, three dimensional discrete element simulations have been carried out to investigate the behaviour of granular material in silos with central and eccentric exit. DEM simulations were used to investigate the effects of eccentricities on the granular flow in order to establish the distributions of diverse variables and to understand the dependency of these variables on the geometry of silos. The examination of the evolution of the flow rate indicates two flow stages: the acceleration phase and decelerating phase which takes the maximum of the discharge time. Moreover from these analyses, it was confirmed that the eccentricity has a great effect on granular flow. Also, the predicted results illustrate that the particles flow was faster in the case of fully eccentric silo than the centric one at the early stage of discharge process which indicates that this type of silo initiate flow more quickly. This augmentation of the discharge rate is due to the presence of rigid wall boundary which gives a reduced resistance to the passage of particles when they approach beyond lower part of the silo.

The flow rate was assessed for discharge particles from each silo for a variety of particle and wall friction coefficients. A comparison of simulation results show that for all friction coefficients, the discharge rate from fully eccentric silo is always greater than that from centric and half-eccentric ones at the beginning of the emptying process. Additionally, these results do not show great differences for large friction coefficient, while there are significant differences for lesser ones. As it has been reported by previous researches, this work proved that the DEM technique appears to be a sufficient diagnostic tool to investigate the granular flow in 3D silo to large extent.

## References

- [1] Jaeger, H.M., Nagel, S.R., Behringer, R.P.: Granular solids, liquids and gases, *Reviews of Modern Physics* 68, 1259–1273 (1996).
- [2] Lueptov, R.M., Akonur, A., Shinbrot, T.: PIV for granular flows, *Experiments in Fluids* 28, 183–186 (2000).
- [3] Bohrsen, J.U., Antes, H., Ostendorf, M., Schwedes, J.: Silo discharge: measurement and simulation of dynamic behavior in bulk solids, *Chemical Engineering Technology* 27, 71–76 (2004).
- [4] Beverloo, W.A., Leniger, H.A., Van de Velde, J.: The flow of granular solids through orifices *Chemical Engineering Science* 15, 260–269 (1961).
- [5] Drescher, A., Analytical Methods in Bin-Load Analysis, *Elsevier Amsterdam-Oxford-New York-Tokyo* (1991).
- [6] Cundall P.A. and Strack, O.D.L, A discrete numerical method for granular assemblies, *Geotechnique* 29, 47–65(1979).
- [7] Langston, P.A., Tüzün, U., Heyes, D.M, Continuous potential discrete particle simulations of stress and velocity-fields in hoppers—transition from fluid to granular flow, *Chemical Engineering Science* 49, 1259–1275 (1994).
- [8] Wu J., Binbo J, Chen, J. Yang, Y., Multi-scale study of particle flow in silos, *Advanced Powder Technology* 20, 62–73 (2009).
- [9] Jofriet, J.C., Negi, S.C., Lu, Z. A numerical model for flow of granular materials in silos—part 3: parametric study. *Journal of Agricultural Engineering Research* 68(3), 237–246 (1997).
- [10] Sadowski, A.J., Rotter, J.M., Steel silos with different aspect ratios: II — behaviour under eccentric discharge. *Journal of Constructional Steel Research* 67, 1545–1553 (2011).

- [12] Chou, C.S., Hsu, J.Y., Lau, Y.D., The granular flow in a two-dimensional flat-bottomed hopper with eccentric discharge, *Physica A* 308, 46–58 (2002).
- [13] Chou, C.S., Hsu, J.Y.: Kinematic model for granular flow in a two-dimensional fat-bottomed hopper, *Advanced Powder Technology* 14(3), 313–331 (2003).
- [14] Sielamowicz, I., Czech, M., Kowalewski, T., Empirical description of flow parameters in eccentric flow inside a silo model, *Powder Technology* 198, 381–394 (2010).
- [15] Hoomans B.P.B.: Granular dynamics of gas-solid two-phase flows, Twente University, *Enschede* (2000).
- [16] Balevičius, R., Sielamowicz, I., Mróz, Z., Kačianauskas, R.: Investigation of wall stress and outflow rate in a flat-bottomed bin: A comparison of the DEM model results with the experimental measurements, *Powder Technology* 214, 322–336 (2011).

# A constitutive model for shape memory alloys, visualizing internal deformability mechanism

Seyed Amirodin SADRNEJAD<sup>1</sup>

*Department of Civil Engineering, K.N. Toosi University of Technology, Tehran, Iran*

**Abstract.** The issue of intelligent structures and intelligent control systems has engaged researchers worldwide. So, analysis of these materials is of high importance in designing and for analysis of the structures in which these alloys have been utilized, a suitable behavioral constitutive law is required. The shape of crystal structure in shape memory alloys is dependent on the temperature and external tension imposed on them.

To assess the thermo-mechanical behavior of shape memory alloys and analyzing these special materials, a simple constitutive integrated model, named multi-plane, is proposed. The multi-plane framework is to asset the model assessment between macroscopic and macroscopic scale due to the possibility of choosing little and a high number in the main numerical integrand as sampling planes. The martensitic strain tensor in macro-scale are due to summation of shear displacement in multi-scale between crystals, therefore, a constitutive law for each multi-plane has been considered which its transformation surfaces are dependent on the shear direction and the vertical component in the multi-planes. Mechanical behavior of these materials is of high importance in designing and for analysis of the structures in which these alloys have been utilized; a suitable behavioral constitutive law is required.

To represent the capability of this model, the predicted different test data upon time rate and temperature domains are compared with the experimental results. The interesting well accuracy of results proves the strength and capability of the proposed model.

**Keywords.** Shape memory alloys, model, shape memory effect, super elasticity, micro-plane

## Introduction

Shape memory alloys are widely used for many variety applications such as medical devices and energy absorption and aerospace industries and even recently structural engineering. These materials exhibit a strongly nonlinear thermo-mechanic behavior due to abrupt changes in their lattice structure called martensite phase transformation. The lattice structural phases in high and low temperatures in these materials are respectively called austenite and martensite. The ability to transform into each other in different stresses and temperatures and consequently change of mechanical and electrical properties of these materials has encouraged researchers to use these alloys in smart structures.

<sup>1</sup>Corresponding author: [sadrnejad@kntu.ac.ir](mailto:sadrnejad@kntu.ac.ir)



The ability of returning into the initial shape through increasing the temperature after pseudo plasticity deformations in some temperatures below critical temperature, called *shape memory effect*, is one of the most distinctive features of these alloys. To this reason, these alloys are called shape memory alloys.

Another notable phenomenon is super elasticity in which Increase of the stress imposed on material in high temperature will turn the austenite phase into martensite phase and causes pseudo plasticity deformations. In this case after unloading, the martensite phase will be returned into austenite phase. For analyzing the structures made by these materials, a simple suitable 3D model is required so that it should be able to predict complicated behavior of one point of these materials under multi axial loading conditions.

In this paper, a three-dimensional model based on the multi-plane integrated method has been proposed as a more capable model predicting the special behavioral aspects of shape memory alloys. In continuation, first, the multi-plane method has been described, then the on plane constitutive law used in multi-plane framework has been introduced and in the next section simulation results have been presented and compared with experiments data qualitatively.

## 1. Multi-plane model

This multi-plane model has been used for development of the non-linear hardening properties of other complex behavior materials such as geomaterials, soils and stones [2-6]. Induced anisotropy as the history effects is generally, initiated and constructed during plastic shear deformation in materials and plays a key role in understanding the plastic behaviour of material in a general stress state, including the rotation of principal stress axes (e.g. Sadrnejad, 1990) [11-15].

In shape memory alloys , overall martensite strain of one polycrystalline point of materials is the sum of martensite shear deformation in the planes with different orientation related to the each single crystal in that point.

Below considerations have been assumed for facilitating the development of the model:

- Negligibility of thermal expansion
- Elasticity of volumetric strain

In multi-plane frame-work the stress components in the  $k_{th}$  multi-plane are obtained by transforming of the macro-scale stress tensor of  $\sigma_{ij}$  in the  $k_{th}$  multi-plane (Fig. 1). So, first the strain components of each plane are obtained using the constitutive law of that multi-plane and then the macro-scale strain tensor is obtained using the virtual work principle [7-10]. Stress components could be obtained as below (Figure 1):

$$T_i^k = \sigma_{ij} n_j^k \quad i, j = 1, 2, 3 \quad (1)$$

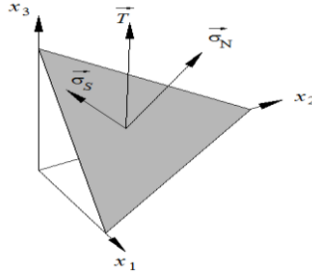


Figure 1. Components of stress tensor on multi-plane

$$\sigma_N^k = \sigma_{ij} n_i^k n_j^k \quad (2)$$

$$\sigma_s^k = \sigma_{ij} (s_i^k n_j^k + n_i^k s_j^k) / 2 \quad (3)$$

$$s_i^k = (T_i^k - \sigma_N^k n_i^k) / \sigma_s^k \quad (4)$$

$T_i^k$  is the  $i_{th}$  component of stress tensor and  $n_i^k$  is the  $i_{th}$  component of unit normal vector and  $\sigma_N^k$  is the vertical component of stress tensor and  $\sigma_s^k$  is shear component of stress tensor, all in the  $k_{th}$  multi-plane.

The vertical component  $\sigma_N^k$  could be divided in deviatoric term  $\sigma_D^k$  and volumetric term  $\sigma_V^k$  in the  $k_{th}$  multi-plane as below:

$$\sigma_V^k = \frac{\sigma_{ii}}{3} = \sigma_{ij} \times \delta_{ij} / 3 \quad (5)$$

$$\sigma_D^k = \sigma_N^k - \sigma_{ii} / 3 \quad (6)$$

Based on the virtual work principle:

$$\varepsilon_{ij} = \frac{3}{4\pi} \int_{\Gamma} \left[ \varepsilon_v^k \left( \frac{1}{3} \delta_{ij} \right) + \varepsilon_D^k \left( n_i^k n_j^k - \frac{1}{3} \delta_{ij} \right) + \frac{\varepsilon_s^k}{2} (s_i^k n_j^k + n_i^k s_j^k) \right] d\Gamma \quad (7)$$

$\Gamma$  is the surface of the unit hemisphere.

## 2. Constitutive law on multi-plane

Each substructure in material crystals includes several austenite and martensite multi-structures and each martensite multi-structure consists of variants of martensite with different orientations. The kinematic of multi-structure are represented by two parameters  $\lambda(x, t)$  named *volume fracture factor* and  $\varepsilon_m(x, t)$  named *the martensite strain tensor* for point  $x$  in time  $t$ . The *volume fracture factor* is equal to the volume of martensite multi-structure divided by total volume of that point of material which lie between two scalar values 0 and 1. The value of 0 is related to the full austenite and the value of 1 represents the full martensite multi-structure of one point of material.

The *martensite strain tensor*  $\varepsilon_m(x, t)$  could be obtained by multi-plane method in equation (8) and (9). This tensor include of two important distinctions: the direction of the unit martensite strain tensor  $E_{m_{ij}}$  and the scalar magnitude of the martensite strain tensor  $\bar{\varepsilon}_m$ . The unit martensite strain tensor  $E_{m_{ij}}$  obtains by normalizing the martensite strain tensor  $\dot{E}_{m_{ij}}$  from (10) and the martensite strain tensor  $\dot{E}_{m_{ij}}$  derives by superposing the on plane shear strains from (11) with considering only the shear component of planar strains in virtual work equation (7).

$$\dot{E}_{m_{ij}} = \dot{\lambda} \bar{\varepsilon}_m E_{m_{ij}} \quad (8)$$

$$\varepsilon_{m_{ij}} = \lambda \bar{\varepsilon}_m E_{m_{ij}} \quad (9)$$

$$E_{mij} = \dot{E}_{mij} / \sqrt{\dot{E}_{mij} : \dot{E}_{mij}} \quad (10)$$

$$\dot{E}_{mij} = \sum_{k=1}^{13} W_k \lambda_p^k F(k)_p \times \frac{1}{2} (s_i^k n_j^k + n_i^k s_j^k) \quad (11)$$

$F(k)_p$  in eq. (11) is the planar proportion factor which could be obtained by eq. (12).

$$F(k)_p = \Sigma_{ij} s_i^k n_j^k \quad (12)$$

$\Sigma_{ij}$  in eq. (12) is the unit stress tensor:

$$\Sigma_{ij} = \frac{1}{s} \sigma_{ij} \quad , \quad s = \sqrt{\sigma_{ij} : \sigma_{ij}} \quad (13)$$

It is obvious that the martensite strain tensor under every stress path, reaches to maximum value when the volumetric fracture factor  $\lambda$  reaches to 1 when the multistructure of the point become martensite completely.

$$\varepsilon_{mij(\max)} = \bar{\varepsilon}_m E_{mij} \quad (14)$$

The martensite strain tensors is a symmetric and trace free tensor so it has five independent components that lives in a five dimensional symmetry- trace free sub-space. Suppose the set  $P$  is a five dimensional sub-space that the martensite strain tensor growth interior it with deformation rapidly until reaches on boundary  $\partial P$ .

We define the set  $P$  as below:

$$\varepsilon_{mij} \in P \quad , \quad P = \{ \varepsilon_m | tr(\varepsilon_m) = 0, g(\varepsilon_m) \leq 0 \} \quad (15)$$

$g$  is a function as below:

$$g: R_{dev}^{3 \times 3} \rightarrow R \quad (16)$$

In an isotropic phase transformation for every rotational vector  $R$ , we can say:

$$g(\varepsilon_m) = (R^T \varepsilon_m R) \quad (17)$$

It implies that we can define the martensite strain function  $g(\varepsilon_m)$  by three invariant of the martensite strain tensor as below:

$$\begin{aligned} I_1(\varepsilon_m) &= tr(\varepsilon_m) = 0 \\ I_2(\varepsilon_m) &= \frac{1}{2} [tr(\varepsilon_m^2) - tr(\varepsilon_m^2)] = -\frac{1}{2} \times tr(\varepsilon_m^2) \\ I_3(\varepsilon_m) &= det(\varepsilon_m) \end{aligned} \quad (18)$$

For an alloy with asymmetry response in tension and compression, we can define the set  $P$  as below:

$$g(\varepsilon_m) = g(I_2(\varepsilon_m), I_3(\varepsilon_m)) \quad (19)$$

$$P = \{ \varepsilon_m | tr(\varepsilon_m) = 0, g(\varepsilon_m) = (-I_2(\varepsilon_m))^{\frac{3}{2}} - a I_3(\varepsilon_m) - b \leq 0 \} \quad (20)$$

$a, b$  could be obtained if we have the maximum values of martensite strain tensor  $\varepsilon_m$  on the boundary of  $\partial P$  for two different stress path. If we have two parameter  $a$  and  $b$ , then we can determine the total set of  $P$  and it's boundary  $\partial P$ . The boundary of function  $g$  for various value of  $a$  and  $b$  are presented in principle strain coordinate system in figure 2. As it could be seen, parameter  $a$  determines the intensity of asymmetry response in tension and compression and parameter  $b$  determines the magnitude of boundary surface of function  $g$ .

Having the increment of volume fracture factor  $\lambda$  for every increment of stress and the value of maximum magnitude of martensite strain  $\bar{\varepsilon}_m$  for stress path, the increment of strain tensor could be obtained for placement  $x$  at time  $t_i$ :

$$\dot{\varepsilon}(x, t_i) = \dot{\varepsilon}_e(x, t_i) + \dot{\varepsilon}_m(x, t_i) \quad (21)$$

$$\varepsilon_m(x, t_i) = \lambda(x, t_i) \bar{\varepsilon}_m(x, t_i) E_m(x, t_i) \quad (22)$$

$$\dot{\varepsilon}_m(x, t_i) = \varepsilon_m(x, t_i) - \varepsilon_m(x, t_{i-1}) \quad (23)$$

### 3. Constitutive law

The mentioned constitutive law relations in macro scale are as following:

$$\sigma = D(\varepsilon - \lambda \bar{\varepsilon}_m E_m) \tag{24}$$

$$\eta = \lambda \frac{\mathcal{L}}{\theta_{cr}} - c_p(1 + \ln\left(\frac{\theta}{\theta_0}\right)) \tag{25}$$

$$\omega(\theta) = \frac{\mathcal{L}}{\theta_{cr}}(\theta - \theta_{cr}) \tag{26}$$

$$d_\lambda = \sigma: \varepsilon_m - \omega(\theta) \tag{27}$$

$$d_{\varepsilon_m} = \lambda \sigma \tag{28}$$

$D$  is elastic modulus matrix,  $\varepsilon$  is the total strain tensor,  $\eta$  is the entropy density,  $\mathcal{L}$  is the latent heat of transformation,  $\theta_{cr}$  is the thermodynamic transformation temperature,  $c_p$  is the heat capacity (assumed to be equal in both the austenite and martensite),  $\theta_0$  is the initial temperature,  $\theta$  is the current temperature,  $\omega(\theta)$  is the difference of chemical energy between austenite and martensite phases,  $d_\lambda$  is the driving force associated with the volumetric fraction,  $d_{\varepsilon_m}$  is the driving force associated with the martensite strain. Equation (27) implies that the phase transformation from austenite to martensite in free stress state starts when:

$$d_\lambda^+ = -\omega(M_s) \tag{29}$$

Also, reverse phase transformation in free stress state happens when:

$$d_\lambda^- = -\omega(A_s) \tag{30}$$

In the above equations,  $A_s$  and  $M_s$  are the temperatures in which the transformation to austenite and martensite phase are started when the external tension is zero.

Hence, in macro scale, the stress induced phase transformation and reverse phase transformation occur when we reach the conditions as:

$$d_\lambda = \sigma: \varepsilon_m - \omega(\theta) \geq d_\lambda^+ \tag{31}$$

$$d_\lambda = \sigma: \varepsilon_m - \omega(\theta) \leq d_\lambda^- \tag{32}$$

In multi-plane scale, although, the conditions above are revolved to the following equations:

$$\sigma_s^k \cdot \bar{\varepsilon}_m^K \geq (d_\lambda^+ + \omega(\theta)) \times \frac{(\Sigma_{ij} s_i^k n_j^k)^2}{\Sigma_{ij}:E_{ij}} \tag{33}$$

$$\sigma_s^k \cdot \bar{\varepsilon}_m^K \geq (d_\lambda^- + \omega(\theta)) \times \frac{(\Sigma_{ij} s_i^k n_j^k)^2}{\Sigma_{ij}:E_{ij}} \tag{34}$$

The energy balance law in thermodynamic, results the relation of temperature evolution for adiabatic condition:

$$\theta(t) = \theta_0 \exp\left(\frac{(\lambda(t) - \lambda_0)\mathcal{L}}{c_p \theta_{cr}}\right) \tag{35}$$

The kinetic relation describes the evolution of martensite volume fraction in each multi-plane. We define it for time step  $i$ , by modifying the mathematical function used by sadjadpour [16] as following:

$$\dot{\lambda} = \begin{cases} \dot{\lambda}^+ \left(\frac{\Delta d_{\lambda i}}{\Delta d_{\lambda i-1}}\right) (1 + (d_\lambda - d_\lambda^+)^{-1})^{\frac{-1}{p}} & d_\lambda > d_\lambda^+ \\ \dot{\lambda}^- \left(\frac{\Delta d_{\lambda i}}{\Delta d_{\lambda i-1}}\right) (1 + (d_\lambda^- - d_\lambda)^{-1})^{\frac{-1}{p}} & d_\lambda < d_\lambda^- \\ 0 & \text{Other wise} \end{cases} \tag{36}$$

$\dot{\lambda}^+$  and  $\dot{\lambda}^-$  and  $p$  are the kinetic parameters that obtain by calibrating with experimental data. This kinetic law can represent the inherent loading rate effect behavior of these materials [6]. Another phenomenon that can affect the loading rate effect behavior in these materials is the evolution of temperature in adiabatic condition during phase

transformation. The developed model can represent it with considering the effect of increasing of temperature during phase transformation from equations (26) and (27).

#### 4. Modulus matrix, $C_{6 \times 6}$

In each multi-plane the relations are as follows:

$$\tilde{\sigma}_{3 \times 1}^k = \begin{pmatrix} \sigma_V^k \\ \sigma_D^k \\ \sigma_S^k \end{pmatrix} = T_{6 \times 3}^k T^T \times \tilde{\sigma}_{6 \times 1} \quad T_{6 \times 3}^k = \begin{bmatrix} \frac{1}{3} & (n_1^k)^2 - \frac{1}{3} & s_1^k n_1^k \\ \frac{1}{3} & (n_2^k)^2 - \frac{1}{3} & s_2^k n_2^k \\ \frac{1}{3} & (n_3^k)^2 - \frac{1}{3} & s_3^k n_3^k \\ 0 & 2n_1^k n_2^k & s_1^k n_2^k + n_1^k s_2^k \\ 0 & 2n_2^k n_3^k & s_2^k n_3^k + n_2^k s_3^k \\ 0 & 2n_1^k n_3^k & s_1^k n_3^k + n_1^k s_3^k \end{bmatrix}_{6 \times 3} \quad (37)$$

$$\varepsilon_{3 \times 1}^k = C_{3 \times 3}^k \sigma_{3 \times 1}^k \quad (38)$$

$$C_{3 \times 3}^k = C_{e_{3 \times 3}}^k + C_{m_{3 \times 3}}^k \quad (39)$$

$$C_{e_{3 \times 3}}^k = \frac{1}{E} \begin{bmatrix} 1 - 2\nu & 0 & 0 \\ 0 & 1 + \nu & 0 \\ 0 & 0 & 1 + \nu \end{bmatrix}, \quad C_{m_{3 \times 3}}^k = \begin{bmatrix} 0 & 0 & 0 \\ 0 & 0 & 0 \\ 0 & 0 & \frac{\varepsilon_m^k}{\sigma_s^k} \end{bmatrix} \quad (40)$$

$$\varepsilon_{3 \times 1}^k = C_{3 \times 3}^k \sigma_{3 \times 1}^k \quad (41)$$

Substituting the above equations to equation (7):

$$\tilde{\varepsilon}_{6 \times 1} = (6 \times \sum_{k=1}^{13} W_k T_{6 \times 3}^k C_{3 \times 3}^k T_{6 \times 3}^{k T}) \tilde{\sigma}_{6 \times 1} \quad (42)$$

$$C_{6 \times 6} = 6 \times \sum_{k=1}^{13} W_k T_{6 \times 3}^k C_{3 \times 3}^k T_{6 \times 3}^{k T} \quad (43)$$

$W_k$  is the weighted coefficient related to  $k^{th}$  multi-plane which are proportion with the area of each multi-plane. For this, we select *NiTi* alloy which studied by Mc Naney et al. [17]. The parameters of this alloy are as follows:

$$E = 35000 \text{ (MPa)}, \sigma_y = 1500 \text{ (MPa)}, M_s = -51.55^\circ\text{C}, A_s = -6.36^\circ\text{C}, \mathcal{L} = 63 \left(\frac{MJ}{m^3}\right) \quad c_p = 5.4 \left(\frac{MJ}{m^3 \cdot ^\circ\text{C}}\right), \nu = 0.2, \theta = 22^\circ\text{C} \quad (44)$$

The maximum of martensite strain tensor obtained by experimental results for tension and shear deformations are:

$$\varepsilon_{m_{max}}^t = \begin{bmatrix} 0.05 & 0 & 0 \\ 0 & -0.025 & 0 \\ 0 & 0 & -0.025 \end{bmatrix}, \quad \varepsilon_{m_{max}}^s = \begin{bmatrix} 0 & 0.04 & 0 \\ 0.04 & 0 & 0 \\ 0 & 0 & 0 \end{bmatrix} \quad (45)$$

Then by equations (18) and (19) and (20), then  $a$  and  $b$ :  $a=0.55$   $b=6.4 \times 10^{-5}$

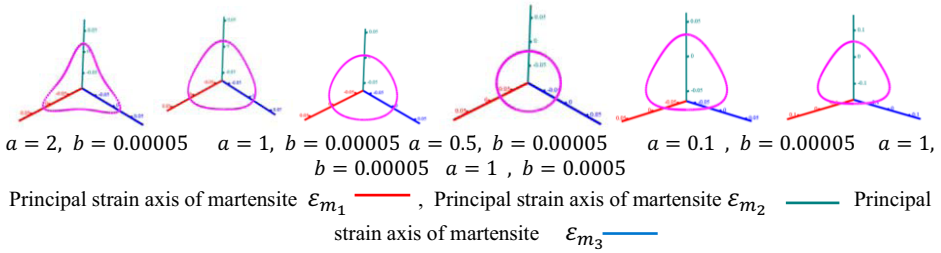
Now, we have the total boundary of set  $P$ , we say  $\partial P$ , that belongs to the set of maximum martensite strain tensors for every loading path.

The kinetic parameters have been obtained after calibrating with experimental data.

$$P = 2, \lambda^+ = -\lambda^- = 0.1, d_\lambda^+ = -\omega(M_s) = 5.836 \left(\frac{MJ}{m^3}\right), d_\lambda^- = -\omega(A_s) = -5.836 \left(\frac{MJ}{m^3}\right)$$

$$\text{And also, we consider: } \theta_{cr} = \frac{A_s + M_s}{2} = -28.955^\circ\text{C}$$

And finally we suppose that the system is in isothermal condition due to very small loading rate and the initial temperature  $\theta_0$  is equal to  $22^\circ\text{C}$ . It is obvious that since the ambient temperature is greater than austenite start temperature  $A_s$ , we are in austenite phase initially and under mechanical loading and unloading, we have super elasticity behavior.



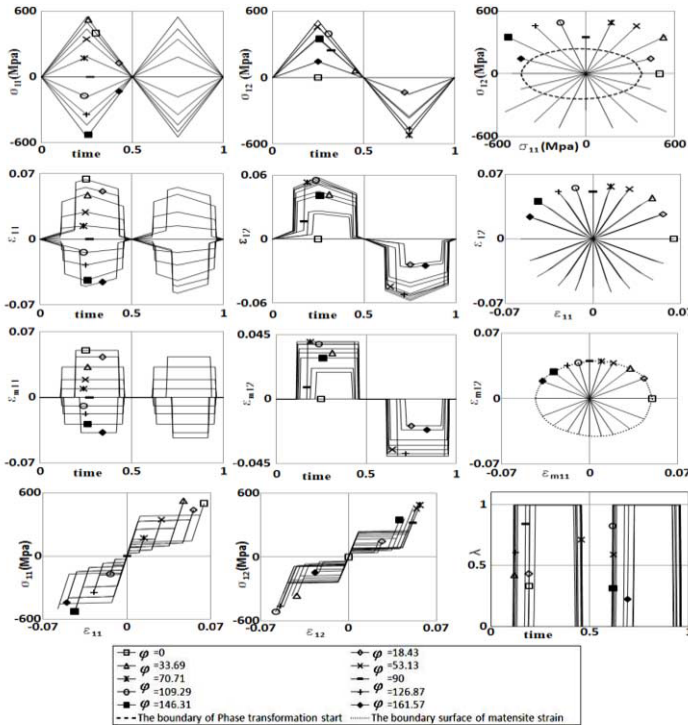
**Figure 2.** The effects of parameters  $a$  and  $b$  on the shape and size of the set of martensite strain in principal strain space

### 5. Proportional biaxial tension-torsion loading

The applied biaxial stress tensor has been assumed as tensor (53). We have considered ten different values of  $\varphi$  for ten different loading paths.

$$\sigma = \sigma_{max}(t) \begin{bmatrix} \cos \varphi & \sin \varphi & 0 \\ \sin \varphi & 0 & 0 \\ 0 & 0 & 0 \end{bmatrix} \tag{46}$$

The first simulation results have been presented in figure 3. The martensite strain path and the martensite volume fracture  $\lambda$  versus the time for each loading path have been tracked.



**Figure 3.** Stress controlled simulations of biaxial tension-torsion proportional for ten loading and unloading paths

More ever the boundary of phase transformation start and reverse phase transformation start which obtained from multi-plane model and also the boundary of martensite strain in the plane  $\varepsilon_{m11} - \varepsilon_{m12}$  have been shown. The first diagram at the top row in left of Figure 5 shows variation of the normal component of deviatoric stress increment to corresponding plane versus time. The slope if these stress histories are somethings for plane no. 1 and 4, while this slope is something different for plane 2 and 3. However, for the load case  $\varphi=0$  on plane no. 1, 2, 3 and 4, the normal component of both deviatoric stress and martensite strain are zero, while, for the load case  $\varphi=70.71$  on plane no. 1, 2, 3 and 4, the normal component rate of both deviatoric stress and martensite strain are maximum.

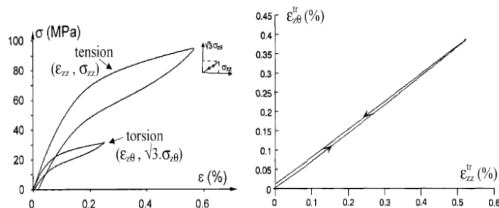


Figure 4. The measured results of tensile-shear proportional loading on Cu-Zn-Al alloy by LExcellent, C. et.al [18].

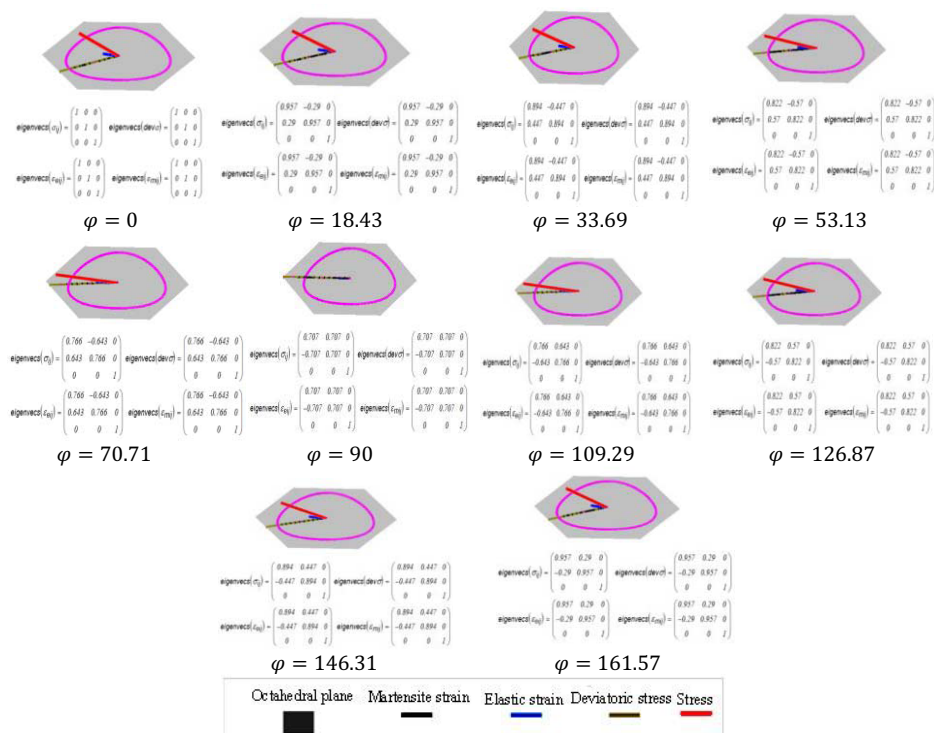


Figure 5. Diagrams showing stress, deviatoric stress, elastic strain, martensite strain and martensite strain boundary surface in principal stress/strain axes coordinate for 10 proportional loading paths upon  $\varphi$

The next at the same row shows the normal component of martensite strain increment on corresponding plane versus time. The last diagram in the same row shows

the normal component of deviatoric stress increment versus the normal component of martensite strain increment on corresponding plane. Martensite strain on plane no. 12 increases by time due to increase of axial tensile stress, however, upon the change of tensile to shear stress, this strain remains constant. The loading and opposite loading effect cycles are not symmetry for plane no. 11.

The second rows of Figures 5 shows variation of the shear component of deviatoric stress and martensite strain increments on corresponding plane versus time and the last diagram shows the variation of shear component of deviatoric stress increment versus the shear component of martensite strain increment on corresponding plane. The third rows of Figures 5 shows three view of the components of stress path increment of each plane upon different values of  $\varphi$ .

The fourth row shows three view of the components of martensite strain path increment of each plane upon different values of  $\varphi$ . Upon the third and fourth row diagram of 13 planes, it is concluded that the components of stress paths and martensite strain paths and also elastic strains, in proportional loadings are the same.

These model results are quite well comparable with the experiments measured on Cu-Zn-Al alloy and presented by LExcellent, C. et.al (2001-2002)[18] as shown in Figure 4. Figure 5 shows the orientation of stress, deviatoric stress, elastic strain, martensite strain and also martensite strain boundary surface in principal stress/strain axes coordinate for 10 proportional loading paths which have been obtained upon different values of  $\varphi$ .

## 6. Conclusion

A semi- micro-mechanical model based on thermo dynamic relations and multi-plane framework was proposed for predicting mechanical behavior of shape memory alloys. This model is able to visualize the internal mechanism, localized activities in different orientations, prefailure and failure mechanism and induced internal anisotropy and deformation histories distributions through the material. Also, the developed model can predict 3D response of one specimen of SMA under every complicated multi-axial loading. Further significant phenomenon of these capabilities provided due to partitioning any aspect into the aspects predicted of multi-planes and then summing the micro effects numerically and presenting the overall results at any single point. The obtained results from proposed model are in good agreement with the available experimental results qualitatively.

## References

- [1] O.C. Zienkiewicz, and G.N. Pande, Time dependent Multi-laminate Model of Rocks, *International Journal of Numerical and Analytical Methods In Geo-mechanics*, 1 (1977), 219-247.
- [2] S.A. SADRNEZHAD & G.N. PANDE, A Multilaminate Model For Sand, *Proceeding of 3rd International symposium on Numerical Models in Geomechanics*, NUMOG-III, 8-11 May 1989, Niagara Falls, CANADA.
- [3] S.A. Sadrnezhad, Multilaminate elastoplastic model for granular media, *Journal of Engineering*, Islamic Republic of Iran, vol.5, (1992), Nos.1&2, May, -11.



- [4] S.A. Sadrnezhad, A Multilaminate Elastic-plastic Model For Liquefaction Of Saturated Sand, *Proceeding of the Third International Conference on Seismology and Earthquake Engineering*, May 17-19, 1999, I.R.IRAN., p.561-568.
- [5] S.A. Sadrnejad, Induced Anisotropy Prediction Through Plasticity, *Proceeding of International Conference on Engineering Applications of Mechanics*, June 9-12, 1992, Teheran-Iran, p.598-605.
- [6] S.A. Sadrnezhad, A semi-micro-mechanical model for anisotropy of sand, *First conference on optimum use of land*, Tehran, Iran, March 2001, P. 437
- [7] P. C. Prat, and Z. P., Bazant, Microplane model for triaxial deformation of soils, *Journal of Engineering Mechanics-Asce*, Vol. 1989, (1989), 139-146.
- [8] Z. P. Bazant, F. C. Caner, F. C., Carol, M. D. Adley, and S. A., Akers, "Microplane model M4 for concrete. I: Formulation with work- conjugate deviatoric stress", *Journal of Engineering Mechanics-Asce*, Vol. 126, (2000), 944-953.
- [9] Z. P. Bazant & B.H. Oh, Crack band theory for fracture of concrete, *Mater. Struct.*, (1983) 16, 155-177.
- [10] I. Carol, and Z. P., Bazant, Damage and plasticity in microplane theory, *International Journal of Solids and Structures*, Vol. 34, (1997), 3807-3835.
- [11] S.A. Sadrnezhad, Numerical Identification of Failure Specifications of Soil", *4<sup>th</sup> International Conference on Civil Engineering*, 4-6 May 1997, Teheran, Iran, p. 100-111.
- [12] S.A. Sadrnezhad, Prediction of The Rotation of Principal Stress Axes in Porous Media by Multi-laminate Based Model, *Int. Journal of Univ. of Science & Tech. of IRAN*, (1998), VOL 9, No.1, pp. 15-33.
- [13] A. Roohbakhsh Davaran and S. A. Sadrnejad, A 3D multi-plane model for shape memory alloys, *IJE Transactions A: Basics Vol.21, No. 1, February 2008*.
- [14] S. A. Sadrnejad, Principles of soil plasticity, (1999), *K. N. T. University*, Tehran, Iran.
- [15] S.A. Sadrnejad, Mathematical approach to Non-associated Plasticity Compliance Matrix for Granular Medium As Continuum, *Proceeding of International Conference on Engineering Applications of Mechanics*, June 9-12, 1992, TEHERAN-IRAN, p.343-349.
- [16] Amir Sadjadpour and Kaushik Bhattacharya, A multimechanics inspired constitutive model for shape-memory alloys: The one-dimensional case, *Smart. Mat. Struct. accepted for publication*, (2006).
- [17] J. M. McNaney, V. Imbeni, Y. Jung, P. Papadopoulos and R.O. Ritchie, An experimental study of the superelastic  $\epsilon_{\text{ect}}$  in a shape-memory Nitinol alloy under biaxial loading, *IMEch. Mater.* (2003), 35 969-986.
- [18] C. A. LExcellent, C. Vivet, Bouvet, S. Calloch, P. Blanca, Experimental and numerical determinations of the initial surface of phase transformation under biaxial loading in some polycrystalline shape-memory alloys, *Journal of the Mechanics and Physics of Solids* (2002), 50 2717-2735.

# Brittle material damage pro-elasticity model for rock made structures

Seyed Amirodin SADRNEJAD<sup>1</sup>

*Department of Civil Engineering, K.N. Toosi University of Technology, Tehran, Iran*

**Abstract.** An important concern in brittle material engineering and in particular rock made structure mechanics is non-homogeneity as micro/macro cracks or joints. This noticeable feature of failures in rock is appearance of slip surfaces or shear bands, the characteristics of that are associated with deformation being concentrated in a narrow zones and the surrounding material remaining intact. Adopting the joints as fractures, fractures are well known for their effects on the mechanical and transport properties of rock in such structural material.

A damaged pro-elasticity multi-plane based model has been developed and presented to predict intact and damaged rock behavior. In this multi-plane model, the stress-strain behavior of a material is obtained by integrating the mechanical response of an infinite number of predefined oriented planes passing through a material point. Essential features such as the pro-elasticity hypothesis and multi-plane model are discussed.

The methodology to be discussed here is modeling of slip on the local and global levels due to the deformation procedure of the existing/probable micro/macro cracks or joints of rock and this method has a potential of using different parameters on different sampling planes to predict inherent anisotropy of rocks. Upon the presented methodology, more attention has been given to slip initiation and propagation through these joints. In particular, softening in non-linear behaviour of joints in going from the peak to residual strengths imparts a behaviour often associated with progressive failure. The predictions of the derived stress-strain model are compared to experimental results for marble, sandstone, Quartz mica schist and anisotropic schist. The comparisons demonstrate the capability of this model to reproduce accurately the mechanical behavior of rocks.

**Keywords.** Multi-plane model, pro-elasticity, damage, pre-failure mechanism, pre-failure mechanism

## Introduction

The identification of the post-peak behavior of rocks, in which the strain-softening or strain hardening occurs, under various confinement pressure is time-consuming and need to utilizing a special set up. Hence, the various elasto-plastic constitutive models based on the associated or non-associated flow rules developed for this purpose [1-6].

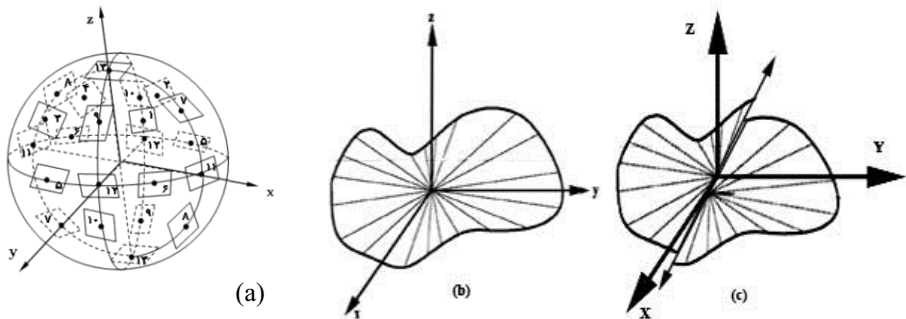
The multi-plane developed by Sadrnejad [7,8], is capable of predicting the behaviour of geo-materials such as rock on the basis of sliding mechanisms, elastic behaviour of intact parts and possibilities to see different plasticity models for the most possible sliding orientations.

<sup>1</sup>Corresponding author: [sadrnejad@kntu.ac.ir](mailto:sadrnejad@kntu.ac.ir)

The spatial strength distribution at a location as an approximation of probable mobilized sliding mechanism is proposed as an ellipsoid function built up on bedding plane. According to the proposed model, the interface asperity shapes that is identical to model based on the minimum energy level, identify the active sliding orientations, cracks, and joints. Furthermore, the sliding behavior of any predefined existing joints through the rock mass is introduced to the matrix of global mechanical behavior based on a realistic and logical way.

### 1. Strain distribution around a point

There is a further consideration in addition to the requirement that the displacements of a cemented or granular medium provide due to slippage/widening/closing between particles that make a contribution to the strain in addition to that from the compression of particles. Consider two neighboring points on either side of the point of contact of two particles. These two points do not in usual remain close to each other but describe complex trajectories. Fictitious average points belonging to the fictitious continuous medium can be defined which remain adjacent so as to define a strain tensor. In the most extreme case, the definition of a sphere shape element  $dr$  (instead of  $dx$ ,  $dy$ ,  $dz$  cube) carrying distributed strain similarly on its surface can reflect strain components on infinite orientation at a point when  $dr$  tends to zero.



**Figure 1.** a- isotropic sphere elements, b- deformed element, c- deformed jointed element

Figure 1 shows sphere elements and typical deformed shapes for joint less and jointed elements. Obviously there is a certain history of displacement on any random orientation through the elements. These are abbreviated in only three  $x$ ,  $y$  and  $z$  planes, when a box - shape  $dx dy dz$  element is employed. However, a predefined numerical integration may be employed to ease the solution.

Numerical integration generally simulates the smooth curved sphere surface to a composition of flat tangential planes, making an approximated polygon to sphere surface. The higher the number of sampling planes, the closer is the approximated surface to the sphere. Clearly, if the number of sampling planes is taken as six, the approximated surface is the same as the normal  $dx dy dz$  box element [20, 21, 22, and 23].

## 2. Damage multi-plane model for rock

Upon yield criterion in plasticity, the stress condition exceeds the yield limits, plastic sliding or widening/closing take place as an active plane. Therefore, one of the most important features of a multi-plane framework is that it enables the identification of the active planes as a matter of routine. The orientation of a sampling plane or micro-plane is characterized by the unit normal  $n$  of components  $n_i$  (indices  $i$  and  $j$  refer to the components in Cartesian coordinates  $x_i$ ). In the formulation with a kinematic constraint, which makes it possible to describe softening behavior of plane concrete in a stable manner, the strain vector  $\varepsilon_N$  on the micro-plane (Figure 2) is the projection of the macroscopic strain tensor  $\varepsilon_{ij}$ . So the components of this vector are  $\varepsilon_{Ni} = \varepsilon_{ij} n_j$ . The normal strain on the micro-plane is  $\varepsilon_N = n_i \varepsilon_{Ni}$ , that is

$$\varepsilon_N = N_{ij} \varepsilon_{ij} ; \quad N_{ij} = n_i n_j \tag{1}$$

Where repeated indices imply summation over  $i=1, 2, 3$ . The mean normal strain, called the volumetric strain  $\varepsilon_V$ , and the deviatoric strain  $\varepsilon_D$  on the micro-plane can also be introduced, defined as follows:

$$\varepsilon_V = \varepsilon_{KK} / 3 ; \quad \varepsilon_D = \varepsilon_N - \varepsilon_V \tag{2}$$

This separation of  $\varepsilon_V$  and  $\varepsilon_D$  is useful when the effect of the hydrostatic pressure for a number of cohesive frictional materials, such as concrete, needs to be captured. To characterize the shear strains on the micro-plane (Figure 2), we need to define two coordinate directions M and L, given by two orthogonal unit coordinate vectors  $m$  and  $l$  of components  $m_i$  and  $l_i$  lying on the micro-plane.

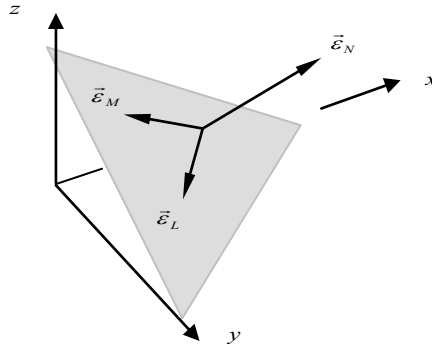


Figure 2. Strain components on a micro-plane

To minimize directional bias of  $m$  and  $l$  among micro-planes, one of the unit vectors  $m$  and  $l$  tangential to the plane is considered to be horizontal (parallel to  $x$ - $y$  plane).

The value of the shear strain components on the micro-plane in the direction of  $m$  and  $l$  are  $\varepsilon_M = m_i (\varepsilon_{ij} n_j)$  and  $\varepsilon_L = l_i (\varepsilon_{ij} n_j)$ . Because of the symmetry of tensor  $\varepsilon_{ij}$ , the shear strain components may be written as follows (e.g. Bažant et al., 1985, 1988) [10, 11]:

$$\varepsilon_M = M_{ij} \varepsilon_{ij} ; \quad \varepsilon_L = L_{ij} \varepsilon_{ij} \tag{3}$$

In which the following symmetry tensors were introduced:

$$M_{ij} = (m_i n_j + m_j n_i) / 2 ; \quad L_{ij} = (l_i n_j + l_j n_i) / 2 \tag{4}$$

Once the strain components on each micro-plane are obtained, the stress components are updated through micro-plane constitutive laws, which can be expressed in algebraic or differential forms. In the kinematic constraint micro-plane models, the stress

components on the micro-planes are equal to the projections of the macroscopic stress tensor  $\sigma_{ij}$  only in some particular cases, when the micro-plane constitutive laws are specifically prescribed in a manner such that this condition can be satisfied.

This happens for example in the case of elastic laws at the micro-plane level, defined with elastic constants chosen so that the overall macroscopic behavior is the usual elastic behavior [12]. In general, the stress components determined independently on the various micro-planes will not be related to one another in such a manner that they can be considered as projections of a macroscopic stress tensor. Thus the static equivalence or equilibrium between the micro level stress components and macro level stress tensor must be enforced by other means. This can be accomplished (as proposed in Bažant, 2004) [13] by application of the principle of virtual work, yielding :

$$\sigma_{ij} = \sigma_V \delta_{ij} + \frac{3}{2\pi} \int_{\Omega} \left[ \sigma_D \left( N_{ij} - \frac{\delta_{ij}}{3} \right) + \sigma_L L_{ij} + \sigma_M M_{ij} \right] d\Omega \quad (5)$$

Where  $\Omega$  is the surface of a unit hemisphere,  $\sigma_V$  and  $\sigma_D$  are the volumetric and deviatoric part of normal stress component and  $\sigma_L$  and  $\sigma_M$  are as shear stress components on the micro-planes respectively. Equation (5) is based on the equality of the virtual work inside a unit sphere and on its surface, rigorously justified by Bažant et al. 2004[13].

The integration in equation (5) is performed numerically by Gaussian integration using a finite number of integration points on the surface of the hemisphere. Such an integration technique corresponds to considering a finite number of micro-planes, one for each integration point. The use of this numerical integration technique for evaluation of integral statement in equation (5) yields:

$$\sigma_{ij} = \sigma_V \delta_{ij} + \frac{3}{2\pi} \int_{\Omega} s_{ij} d\Omega \approx \sigma_V \delta_{ij} + 6 \sum_{\mu=1}^{N_m} w_{\mu} s_{ij}^{(\mu)}, s_{ij} = \sigma_D \left( N_{ij} - \frac{\delta_{ij}}{3} \right) + \sigma_L L_{ij} + \sigma_M M_{ij} \quad (6)$$

$N_m$  is the number of integration points on hemisphere. Based on The formulation, macroscopic constitutive matrix in the proposed model is obtained as follows:

$$D_{ijkl} = \frac{3}{4\pi} \int_{\Omega} \left( \frac{E}{1+\nu} \right) \left[ \left( N_{ij} - \frac{\delta_{ij}}{3} \right) \left( N_{kl} - \frac{\delta_{kl}}{3} \right) + M_{ij} M_{kl} + L_{ij} L_{kl} \right] d\Omega + \frac{E}{1-2\nu} \frac{\delta_{kl}}{3} \delta_{ij} \quad (7)$$

$E$  and  $\nu$  are as elastic modulus and Poisson’s coefficient.

### 3. Proposed damage function formulation

Total deviatoric part of constitutive matrices is computed from superposition of its counterparts on the micro-planes that such counterparts in turn, are calculated based on the damages occurred on each plane depending on its specific loading conditions [8,9]. This damage is evaluated according to the five separate damage functions; each of them belongs to the particular loading states. This five loading conditions are as follows: 1. *hydrostatic compression* 2. *hydrostatic extension* 3. *pure shear* 4. *shear + compression* 5. *shear + extension*.

On each micro-plane at each time of loading history, there exists one specific loading situation that it may be in one of the five mentioned basic loading conditions. For every five mood, a specific damage function according to the authoritative laboratory test results available in the literature is assigned. Then, for each state of on plane loading,

one of the five introduced damage functions will be computed with respect to the history of micro-stress and strain components. These five damage functions are as below:

$$\omega_{HC} = 0.0 \tag{8}$$

$$\begin{cases} \omega_{HT} = 0.0 & \text{if } \varepsilon_{eq} \leq \sqrt{3}a \\ \omega_{HT} = 1.0 - \left(\frac{\sqrt{3}a}{\varepsilon_{eq}}\right) \times \exp\left[-\left(\frac{\varepsilon_{eq} - \sqrt{3}a}{b - \sqrt{3}a}\right)\right] & \text{if } \varepsilon_{eq} > \sqrt{3}a \end{cases} \tag{9}$$

$$\omega_{SH} = 0.5 \times (\omega_C + \omega_T) \tag{10}$$

$$\begin{cases} \omega_C = d \times \varepsilon_{eq} & \text{if } \varepsilon_{eq} \leq e \\ \omega_C = f(\varepsilon_{eq} - e)^2 + g(\varepsilon_{eq} - e) + h & \text{if } e < \varepsilon_{eq} \leq i \\ \omega_C = 1.0 - \left(\frac{j}{\varepsilon_{eq}}\right) \times \exp\left[-\left(\frac{\varepsilon_{eq} - i}{k - i}\right)\right] & \text{if } \varepsilon_{eq} > i \end{cases} \tag{11}$$

$$\begin{cases} \omega_T = 0.0 & \text{if } \varepsilon_{eq} \leq a \\ \omega_T = 1.0 - \left(\frac{a}{\varepsilon_{eq}}\right) \times \exp\left[-\left(\frac{\varepsilon_{eq} - a}{c - a}\right)\right] & \text{if } \varepsilon_{eq} > a \end{cases} \tag{12}$$

Parameters  $a$  to  $k$  in the above relations are computed according to laboratory results obtained for each specific rock. In equation (9),  $\varepsilon_{eq}$  is as average strain and in the other relations is as the magnitude of projected deviatoric strain vector on each micro-plane.

#### 4. Elasto-plastic behavior of Quartz mica schist

To show the capability of the proposed model in predicting the softening behavior, the tri-axial test results presented by Varadarajan, et al. [12,19] were produced and compared with the test results. Figure 3-a, b shows the comparison of the model result with tri-axial tests for Quartz mica schist as stress deviator versus axial strain.

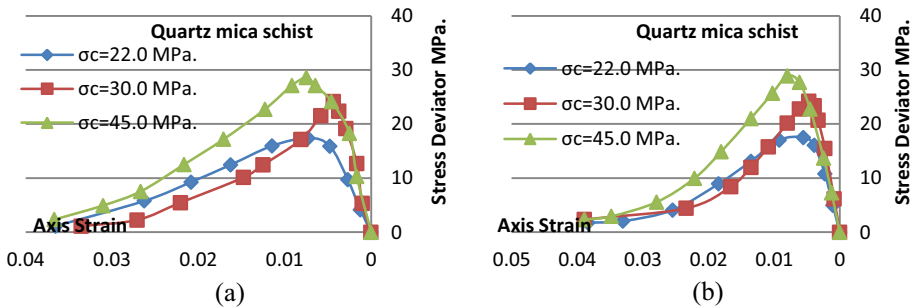


Figure 3. Comparison of experimental with model results for Quartz mica schist (different confining stress): (a) test results; and (b) model results

Also, the comparison of stress deviator versus lateral strain are shown in Figure 4-a, b. The model predicts a strain-softening phenomenon as it assumed, also a good accuracy was obtained between numerical simulations and experimental results. The presented comparisons show that the model has predicted comparable results as the effects of on plane shear stress axes orientation on the mechanical behavior of schistose structured rock. Whereas the model has predicted tally results for determination of the Elasto-Plastic behavior of marble, sandstone, Quartz mica and the behavior of orientation changes in anisotropic structured schist rock samples. Some prediction of model have been presented in Figures 5, 6 and 7. Therefore, it can be used to predict the Elasto-Plastic behavior of any rock with different potential of cracking.

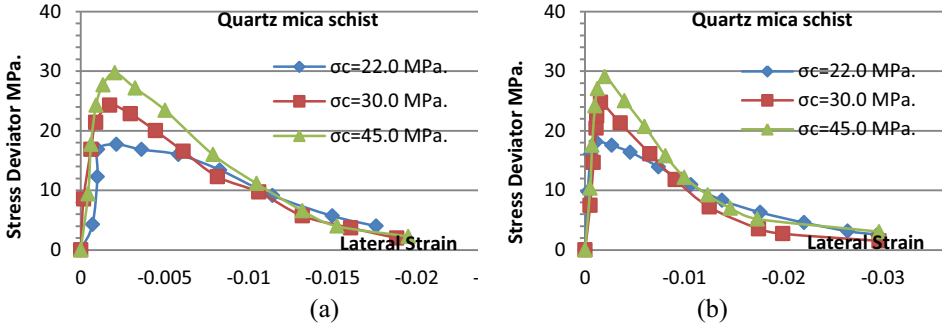


Figure 4. Comparison of experimental with model results for Quartz mica schist (different confining stress): (a) test results; and (b) model result

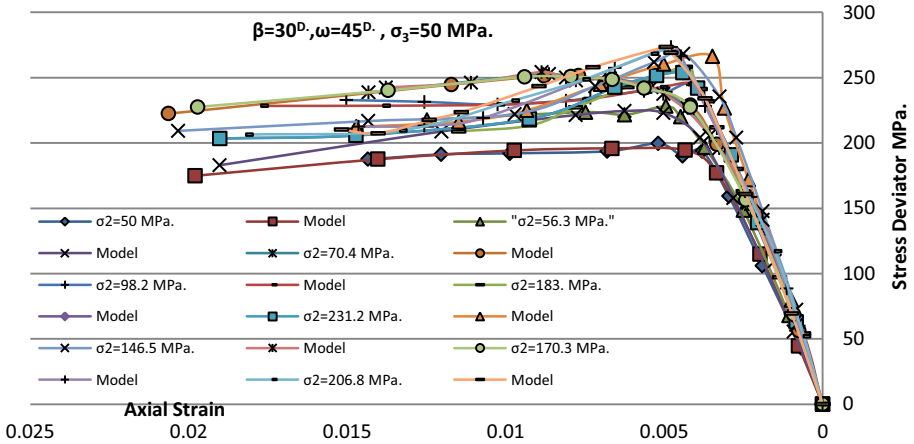


Figure 5. Stress deviator versus axial strain at different ( $\sigma_2$ )

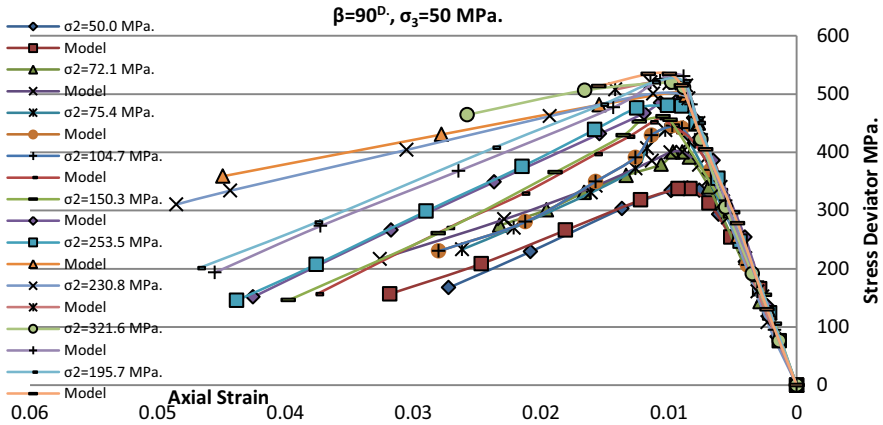


Figure 6. Stress deviator versus axial strain at different ( $\sigma_2$ )

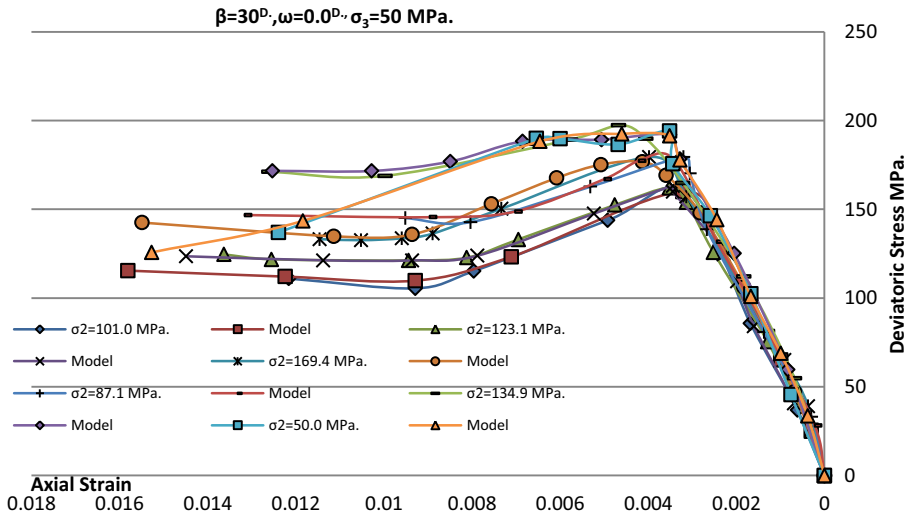


Figure 7. Stress deviator versus axial strain at different ( $\sigma_2$ )

### 5. Conclusion

A multi-plane based model incorporating the pro-elasticity hypothesis and five typical damaged planes was developed for the elasto-plastic with different potential of cracking behavior of rocks. Aside from modeling simplicity, the pro-elasticity and damage functions approach is more realistic and any aspect such as softening, hardening, effects of bedding plane and changes in the loading orientation and on plane shear stress direction can be predicted through the change of planar parameters.



There is also a possibility the whenever, the on plane loading conditions changes in such a way that existing crack starts to be closed, while the crack opening reaches to values smaller than critical crack opening, those mentioned stiffness components increase again and go back to its initial intact values.

A semi-micro-plane numerical algorithm is developed and presented for a better anticipation of load path effects through material. In this way, the directional information and effects of applied load orientation on mechanical behavior of material are addresses and considered. Further than possibility of predicting inherent anisotropy, this rational way facilitates to the model to predict induced anisotropy and a potential to solve anisotropy of material through considering of different mechanical behavior on different orientation. The sampling plane constitutive formulations provide convenient means to classify loading events generate history rules and formulate independent evolution rules for local variables.

To clarify the capability of the proposed model, the test results conducted on marble, sandstone, Quartz mica schist and anisotropic schist are produced by the model. A good accuracy was obtained between numerical simulations and experimental results.

Although the proposed model has excellent features such as pre-failure configuration of inside material, final failure mechanism, capability of seeing induced/inherent anisotropy and also any fabric effects on material behavior, in such a case that the basis of its formulation is simple, logical and has some physical insights that make it convenient to perceive.

## References

- [1] Chang C.S, Hicher P.Y., An elasto-plastic model for granular materials with microstructural consideration, *International Journal of Solids and Structures*, 2005, Vol. 42, pp. 4258–4277.
- [2] Drucker D.C., A definition of a stable inelastic material, *Journal of Applied Mechanics*, 1959, Vol. 26, pp. 101–106.
- [3] Mroz Z., Non-associated flow laws in plasticity, *Journal de Mechanique* 1963; Vol. 2, pp. 21–42.
- [4] Mroz Z., On forms of constitutive laws for elastic–plastic solids, *Archiwum Mechaniki Stosowanej* 1966; Vol. 18, 1–34.
- [5] Mandel J.: Conditions de Stabilite et Postulat de Drucker. In: Kravichenko, J., Sirieys, P.M. (Eds.), *Proceeding of the IUTAM Symposium on Rheology and Soil Mechanics* Springer-Verlag, Berlin, 1964, pp. 58–68.
- [6] Maier G, Hueckel T., Nonassociated and coupled flow rules of elastoplasticity for rock-like materials. *International Journal of Rock Mechanics*, Mineral Science & Geomechanics Abstract 1979, Vol. 16, pp. 77–92.
- [7] Lorig, L. J, Cundall, P. A. and Hart., R. D. (1984), Analysis of Block Test No. 1 — Inelastic Rock Mass Behavior — Phase 3 — Hexagonal, [www.winternet.com/~icg/net/rep/Cundall-rep.doc](http://www.winternet.com/~icg/net/rep/Cundall-rep.doc)
- [8] Sadrnejad, S. A. and Labibzadeh, M., (2005), A Continuum/discontinuum Micro Plane Damage Model for Concrete, *International Journal of Civil Engineering*, Oct. 2005, vol.5, No.3, paper138.
- [9] Sadrnejad, S. A., (2006), Numerical Evaluation of Non-homogeneity and Anisotropy due to Joints in Rock Media, *International Journal of Civil Engineering*. Vol.4 , No. 2, June 2006
- [10] Bazant, Z., B.Oh. Micro plane model for progressive fracture of concrete and rock, *J. E. Mech.*, 111, pp.559-582, 1985.
- [11] Bazant, Z., P. Prat. "Micro plane model for brittle plastic material: Part I & II." *J. E. Mech.*, 114, pp.1672-1702, 1988.
- [12] Carol, I., M. Jirasek and Z. P. Bazant, A thermodynamically consistent approach to micro plane theory. Part I: Free energy and consistent micro plane stresses, *Int. J. Solids & Structures*, 38, 2921-2931, 2001.

- [13] Bažant, Z. P., Giovanni, D. L., 2004. Nonlocal Micro-planes Model With Strain-Softening Yield Limits, *International Journal of Solids and Structures*, 41, pp. 7209-7240.
- [14] Varadarajan A, Sharma K.G, Hashemi M., Strain – softening behavior of a schistose rock mass under triaxial loading, *ISRM 2003-Technology roadmap for rock mechanics*, South Africa Institute of Mining and Metallurgy.
- [15] Kwasniewski, M. & K- Mogi 1990. Effect of the intermediate principal stress on the failure of a foliated anisotropic rock. *In H.P. Rossignol* (ed.) Mechanics of Jointed and Faulted Rock- 407-416, Rotterdam: Balkema.
- [16] Kwasniewski, M- & K. Mogi 1996. Finding of a foliated rock in a general triaxial field of compressive stresses, *Prace Naukowe UniwersyteHU głydes0 1602:209-232*.
- [17] Nakata Y, Hyodo M, Murata H, Yasufuku N., Flow deformation of sands subjected to principal stress rotation, *Soils and Foundations* 1998, Vol. 38, No. 2, pp. 115-128.
- [18] Nayeri, A., Fakharian, K., 2009. Study on Pullout Behavior of Uniaxial HDPE geogrids Under Monotonic and Cyclic Loads. *International Journal of Civil Engineering*, Vol. 7, No. 4, pp. 211-223.
- [19] Sadrnejad S.A. and Labibzadeh, M., (2005), A Continuum/discontinuum Micro Plane Damage Model for Concrete, *International Journal of Civil Engineering*, vol.5, No.3, paper138.
- [20] Sadrnejad S.A., (2006), Numerical Evaluation of Non-homogeneity and Anisotropy due to Joints in Rock Media, *International Journal of Civil Engineering*. Vol.4, No. 2.
- [21] Sadrnejad S.A. and Karimpour H., (2011), Drained and Undrained Sand Behaviour by Multilaminar Bounding Surface Model, *International Journal of Civil Engineering*, vol.9, No.2

# Target column overdesign factor of steel frames considering system reliability

Yan-Gang ZHAO<sup>1</sup>, Zhao-Hui LU and Mohammad SHARFUDDIN  
*Department of Architecture, Kanagawa University, Japan*

**Abstract.** Steel frames are usually designed with a column over design factor (COF) to ensure the yielding of all beams in flexure prior to possible yielding of columns, which is generally considered to be the preferable failure mode. In the present study, considering the uncertainties of earthquake load and strengths of structural members, the failure modes of multistory ductile frame structures are investigated probabilistically. First order reliability method (FORM) and Dimension Reduction Integration (DRI) with fourth moment standardization are mainly applied in the investigation. The  $A_i$  distribution of load along the height of the frame is taken into account. Comparing with the result of triangular distribution it is observed that target COF requirement is affected by the load considered in the evaluation. To evaluate the target COF requirement that probabilistically avoids the undesirable story collapse modes the consideration of system reliability is very essential. In the present paper, the concept of system reliability is introduced in determining the target COF. It is observed that target values of COF considering system reliability is different from than that of most likely failure modes. This study has been conducted for different reliability levels and the corresponding COF values have been presented in this paper.

**Keywords.** Frame structure, story mechanism, failure probability, column overdesign factor, system reliability

## Introduction

The design philosophy of “weak beam strong column” has been widely accepted in the seismic design of steel frame structures. In this concept, it is assumed that yielding of all beams in flexure will occur prior to possible yielding of columns which is considered to be the preferable failure mode, because of its large capacity to absorb earthquake energy before the structure actually collapses [1].

To ensure that a frame structure collapses according to the preferable beam-hinging failure mode, as shown in Fig. 1, the columns of the structure that receives forces from the beams are generally designed with a column overdesign factor (COF) greater than one to make the columns relatively stronger than the beams. However, it is difficult to specify the exact value of COF for a structure due to large uncertainty of the member strength and the earthquake loads.

Target values of COF that ensure probabilistically the preferable entire beam hinging failure mode of frames have been evaluated [2,3]. However, in previous studies, the target COF was evaluated considering only the most likely failure modes.

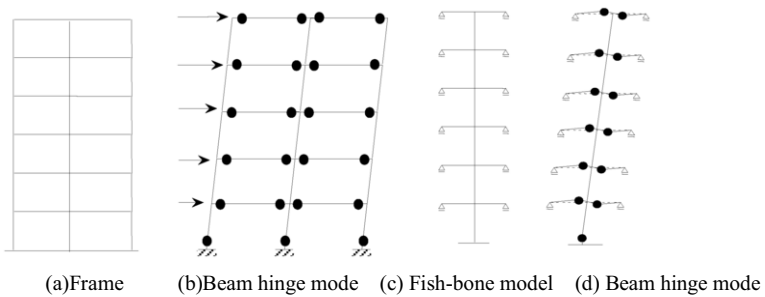
<sup>1</sup>Corresponding author: Dept. of Architecture, Kanagawa University, [zhao@kanagawa-u.ac.jp](mailto:zhao@kanagawa-u.ac.jp)

Since most like story mode is only one element of the system consists of many story failure modes, avoiding the most likely mode does not mean that all other story failure modes are avoided. Therefore the consideration of system reliability is very important.

The object of the present paper is to investigate the target COF requirement based on  $A_i$  distribution of load and also to implement the system reliability in the evaluation of target COF.

**1. Computational assumptions**

The fish-bone model [4], that condenses the columns and beams of each story into one column and one beam, respectively, employed in this study to simplify the computation. It has been shown that the second moment reliability index of the failure modes are not affected by the mean value of member strength or the number of bays; the high-order moment of the performance function is also independent of number of bays and mean value of member strength, thus, the reliability indices of story failure patterns do not vary with the change of number of bays and mean value of member strength [7]. Therefore, COF is not affected by the number of bays and COF based on fish-bone model and real frame should be same.



**Figure 1.** Entire beam hinging failure mode

In the fish-bone model, the COF is generally expressed by the floor COF, which is defined for each floor level as the ratio of the sum of mean strengths of columns to the sum of mean strengths of beams, as follows: :

$$COF = \frac{\sum_i \mu_{Mc_i}}{\sum_i \mu_{Mb_i}} = \mu_{Mc} / \mu_{Mb} \tag{1}$$

Where  $\mu_{Mc_i}$  and  $\mu_{Mb_i}$  are the mean plastic moment strength of the column and beam, respectively, connected to a specific floor of the original frame, and  $\mu_{Mc}$  and  $\mu_{Mb}$  are the mean plastic moment strength of the column and beam, respectively, of the fish-bone model.

For convenience of the investigation, the following basic assumptions are applied in this study.

- Elastic-plastic frame structures are considered. The failure of a section means the imposition of a hinge and an artificial moment at that section.
- The structural uncertainties are represented by considering only the moment capacities as random variables. The coefficient of variation of material strength is considered to be 0.1.
- Plastic moment capacities are statistically independent to one another and independent of the applied loads. All the random variables are assumed to follow the lognormal distribution.
- The geometrical second-order and shear effects are neglected. The effect of axial forces on the reduction of moment capacities is also neglected.
- The external load is considered to consist of only the static lateral earthquake loads. Ai distribution of loads along the height of the structure is taken into account. Some results of triangular distribution are also presented here.

## 2. Evaluation method

### 2.1 Evaluation index

To avoid probabilistically the story mechanisms, the probabilities of the story mechanisms should be controlled at least lower than that of the entire beam hinging failure mode. In the target COF evaluation, following evaluation index is used:

$$\gamma = P_{f2} / P_{f1} \quad (2)$$

where  $P_{f1}$  = the occurrence probability of the beam hinging failure mode and  $P_{f2}$  = the occurrence probability of the story collapse. If the above evaluation index is determined based on only likely failure mode and system reliability is not considered, in that case the  $P_{f2}$  corresponds to one failure mode with one performance function, which is not realistic and it does not necessarily mean that all other story failure modes are avoided. Therefore, the computation of  $P_{f2}$  considering system reliability is essential.

In the target COF evaluation, the reliability index of the entire beam hinging mode  $\beta_T$  should be given first to indicate the safety requirement of the structure.  $P_{f1}$  is the probability corresponding to the reliability index, namely

$$P_{f1} = \Phi(-\beta) \quad (3)$$

The method used in this paper is to assume a reliability index such as  $\beta_T=2$  or  $\beta_T=3$  for the entire beam hinging failure mode first to specify the safety level of the structure and then to compute the mean value of the earthquake load using reliability analysis method such as first order reliability method (FORM) or method of moments [6] to ensure that the first order reliability index becomes equal to the target reliability index  $\beta_T$  for frame structures designed with various COFs.

After obtaining the aforementioned evaluation index, to ensure probabilistically that the designed structure collapses according to the designed preferable failure mode, the relative occurrence rate of the most likely story mechanism  $\gamma$  should be controlled lower than a specific allowable level  $\gamma_0$  as follows:

$$\gamma = P_{f2} / P_{f1} \leq \gamma_0 \leq 1 \tag{4}$$

By conducting the failure mode analysis and the reliability analysis using a different COF for a frame structure, a  $\gamma$ -COF curve can be obtained and the target value of the COF for which Eq. 16 is satisfied can be determined. The larger the value of COF, the smaller the value of the relative occurrence rate of the undesirable failure modes.

When  $\gamma_0 = 1$ , the undesirable failure mode and the preferable entire beam-hinging mode have the same likelihood of occurrence, i.e., both probabilities are equal. A COF value lower than the value corresponding to  $\gamma_0 = 1$  enhances the story collapse, i.e., the probability of the story collapse is higher than that of the entire beam-hinging mode, therefore this value is not allowed.

2.2 Dimension reduction integration for system reliability

Considering likely failure modes the performance of the system is as follows:

$$G = \min\{G_{L1}, G_{L2}, G_{L3}, \dots, G_{LK}, G_{UK}\} \tag{5}$$

where  $K=n-1$  and  $n$  is the number of story.

Because of the difficulty in obtaining the sensitivity of the performance function and the mutual correlations among the failure modes, the derivative- based FORM is not applicable. In the present study, The Dimension Reduction Integration (DRI) based moment method is applied. The method does not require the computation of derivatives, nor the determination of the design point and nor computation of the mutual correlations among the failure modes; and thus computationally very effective for reliability assessment.

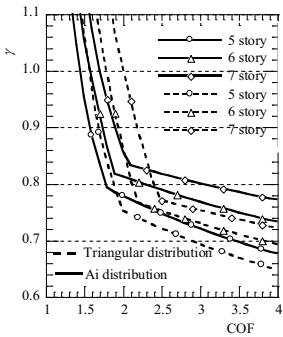


Figure 2.  $\gamma$ -COF Curve

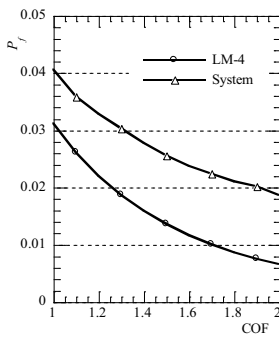


Figure 3.  $P_f$  of system and LM-4

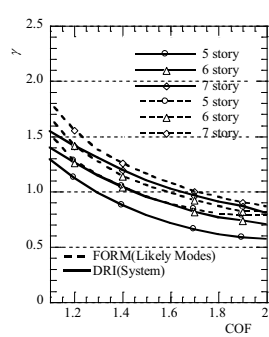


Figure 4.  $\gamma$ -COF Curve

**Table 1.** Target COF requirement for multi-story frames applying FORM

		Five story	Six story	Seven story
$\beta_T=2$	Ai	1.45	1.58	1.70
	Triangular	1.57	1.79	2.01
$\beta_T=3$	Ai	1.23	1.31	1.38
	Triangular	1.28	1.40	1.52

### 3. Target COF evaluation for multi-story frames

#### 3.1 Target COF using Ai distribution

Three basic frames are utilized in this analytical investigation: five story, six story and seven story frames. In this section, target values of COF for five to seven story frames are evaluated considering only the most likely failure modes applying FORM.

Fig. 2 shows the  $\gamma$ -COF curve for five to seven story frames based on Ai distribution of load under reliability level 2 ( $\beta_T=2$ ) applying FORM. COF based on triangular load also shown in this Fig. for comparison. From this Fig. it is observed that target COF requirement increases with the increase of the number of story.

The target COF values for five to seven story building frames under reliability level 2, and 3 ( $\beta_T=2$ , and  $\beta_T=3$ ) are presented in Table 1. Target COF based on triangular load previously published by Pu and Zhao [5] also shown in this Table for comparison. Target COF based on triangular distribution is higher than that of Ai distribution of load. From this table it is observed that target COF requirement is affected by the load distribution considered in the evaluation.

#### 3.2 Target COF considering system reliability

In this section, target values of COF for five to seven story frames are evaluated considering system reliability applying DRI. Initially the failure probability of the system and that of the failure modes are investigated. It is observed that failure probability of the system is always higher than that of any single mode.

Fig. 3 shows a comparison of failure probability of the system and that of a lower failure mode, LM-4 of a seven story frame under reliability level 2 ( $\beta_T=2$ ). After evaluation of the failure probability, the target values of COF are determined based on the evaluation index mentioned earlier. Fig. 4 shows the  $\gamma$ -COF curve for five story to seven story frames under reliability levels 2 ( $\beta_T=2$ ) considering system reliability applying DRI.

The target COF values considering system reliability for five to seven story building frames based on Ai distribution of load under reliability level 2, and 3 ( $\beta_T=2$ , and  $\beta_T=3$ ) are presented in Table 2.

**Table 2.** Target COF for multi-story frames considering system reliability

	Five story	Six story	Seven story
$\beta_T=2$	1.29	1.45	1.64
$\beta_T=3$	1.03	1.35	1.51

It is observed that under the same reliability level, the target COF requirement increases with the increase of the number of stories and decreases with the increase of the reliability level. A similar observation is found for all cases considered in this study.

The COF plays an important role in determining the building response during an earthquake. If the appropriate COF is not provided, then this can become a major reason for building damage during strong earthquakes. Therefore one should select carefully the target COF value for a specific frame.

From this study, the minimum values of the COF to probabilistically avoid the undesirable story collapse modes during an earthquake are obtained considering both likely failure modes and system reliability. It should be noted here that the restrictive assumptions considered in this study may affect the results to some extent.

#### 4. Conclusion

The COF requirement that probabilistically ensures the preferable entire beam hinging failure mode during earthquake and probabilistically avoids the undesirable story collapse modes of the frame structure has been evaluated in this paper considering both likely failure modes and system reliability. From the investigation it is observed that:

- (1) Target COF requirement is affected by the load distribution considered in the evaluation. Target COF based on triangular distribution is higher than that of Ai distribution of load.
- (2) Under the same reliability level the target COF requirement increases with the increase of the number of stories and decreases with the increase of the reliability level. A similar observation is found for all cases considered in this study.
- (3) Target COF requirement is also affected by the evaluation methods. Target COF based on likely modes and that of system reliability is different.

#### Acknowledgments

This study is partially supported by the National Natural Science Foundation of China (Grant No. U1134209, 51008313), and the Program of PCSIRT (grant no. IRT1296), for which we are grateful for the support.



## References

- 1) Anderson J.C. and Gupta R.P.: Earthquake resistant design of unbraced frames. *Journal of Structural Engineering*, ASCE 98(11), pp. 2523-2539, 1972.11
- 2) Ono T., Zhao Y. G. and Ito T.: Probabilistic evaluation of column overdesign factor for frames. *Journal of Structural Engineering*, ASCE 126(5), pp. 605-611, 2000.5
- 3) Zhao Y. G., Ono T., Ishii K. and Yoshihara K.: An investigation of column overdesign factors for steel framed structure. *Journal of Structural and Construction Engineering* 558, pp. 61-67, 2002.8
- 4) Ogawa K., Kamura H. and Inoue K.: Modeling of the moment resistant frame to fishbone- shaped frame for the response analysis. *Journal of Structural and Construction Engineering* 521, pp. 119-126, 1999.7
- 5) Zhao Y. G., Pu W.C. and Ono T.: Likely story mechanisms of steel frame structures. *Journal of Structural and Construction Engineering* 613, pp. 35-42, 2007.3
- 6) Zhao Y.G. and Ono T.: Moment methods for structural reliability. *Structural Safety*, 23(1), pp. 47-75, 2001

# Effect of shear wall in improving the reliability of RC frame buildings subjected to seismic loading

Mohamed A. DAHESH, Ahmet TUKEN and Nadeem A. SIDDIQUI<sup>1</sup>  
*Department of Civil Engineering, King Saud University, Riyadh, Saudi Arabia*

**Abstract.** In the past, several researches have been carried out to study the influence of shear walls on controlling the lateral stiffness/story drift of the RC buildings under seismic forces. But the level of increase in the reliability due to the implementation of shear walls was not studied much. In the present study, a simple Monte Carlo Simulation-based methodology has been presented by which increase in the reliability level due to the addition of shear walls in RC building frame was quantitatively assessed. In order to demonstrate the methodology, first a 10-story seismically deficient (in terms of lateral stiffness) rectangular RC frame building having no shear walls was subjected to an earthquake of known magnitude and its reliability against lateral drift was estimated. The building was then laterally stiffened by shear walls in the two orthogonal directions and reliability indices were estimated again in each direction. It was demonstrated that the shear walls improve the reliability against serviceability limit state of lateral drift dramatically. A parametric study was also carried out to obtain that value of story weight below which the building is as reliable as desired (i.e. reliability index  $\geq 3.0$ ).

**Keywords.** RC shear wall-frame building, seismic loading, serviceability limit state, Monte Carlo simulation

## Introduction

A reinforced concrete (RC) multistory frame building must possess adequate strength, lateral stiffness and ductility if it is likely to be subjected to moderate to severe earthquakes. The requirements of strength and ductility can easily be satisfied by selecting the adequate section sizes of the frame-members and required detailing of their reinforcements. However, in order to satisfy the requirements of lateral stiffness, a sufficient amount of shear walls should be provided in the building. In the past, several researches have been carried out to study the influence of shear walls on controlling the lateral stiffness/story drift of the RC buildings under seismic forces. Balasubramanian et al. [1] presented an improved method for estimation of stiffness of brick masonry shear walls with opening. Their proposed method was applicable to both strong spandrel-weak pier and weak spandrel-strong pier conditions. The results of the proposed method were in good agreement with the results of finite element analysis and experimental test results. Burak and Comlekoglu [2] performed an analytical study to evaluate the effect of shear wall area to floor area ratio on the seismic behavior of

---

<sup>1</sup> Corresponding author: [nadeem@ksu.edu.sa](mailto:nadeem@ksu.edu.sa)

mid-rise reinforced concrete structures. The analytical results indicated that, in order to control the drift, at least 1.0% shear wall ratio should be provided in the design of mid-rise buildings. They also found that when the shear wall ratio increases beyond 1.5%, the improvement of the seismic performance was not so significant. Tuken and Siddiqui [3, 4] proposed an easy to apply analytical method to determine the amount of shear walls necessary to make reinforced concrete buildings seismic-resistant against moderate to severe earthquakes. The analytical procedure was demonstrated by implementing it on a 10 story 3-D reinforced concrete (RC) building. Lee and Haldar[5] developed an efficient algorithm to evaluate the reliability of a steel frame and reinforced concrete shear wall structural system subjected to static loading. In a companion paper [6], the algorithm was extended to consider dynamic loading, including seismic loading.

The above review shows that a very limited research was conducted on reliability assessment of RC frame buildings containing shear walls. Also the level of increase in the reliability due to the implementation of shear walls was not studied much. In the present study, a simple Monte Carlo Simulation-based methodology has been presented by which increase in the reliability level due to the addition of shear walls was quantitatively assessed.

## 1. Reliability analysis

In order to carry out the reliability analysis of RC frame building, with and without shear walls, a limit state function describing the failure criterion is required. This function assumes a negative or zero value at the failure and a positive value when the structural system or member is safe. Thus we can define the probability of limit state violation (i.e. probability of failure) as

$$P_f = P[g(\underline{x}) \leq 0] \quad (1)$$

where,  $g(\underline{x})$  is the limit state function and  $\underline{x}$  is the vector of basic random variables. In the present study, the story drift of the structure is considered to be the serviceability limit state. For the serviceability criterion, the limit state function can be expressed as

$$g(\underline{x}) = \delta_{lim} - \delta_{cal} \quad (2)$$

Where  $\delta_{lim}$  = allowable story drift prescribed in the code. In the present study this value was taken as 0.02 times story height as described in SBC 301 [7]. The story drift ( $\delta_{cal}$ ) was computed as the difference of the lateral deflections at the top and bottom of the story under consideration (i.e.  $\delta_i = y_T - y_{i-1}$ ). This value was multiplied by a deflection amplification factor  $C_d$  (as per SBC 301,  $C_d = 6.5$  for special RC moment frames) and divided by the importance factor  $I$  (=1 for the present study) as per section 10.9.7.1 of SBC 301 [7].

After providing the shear walls, the lateral deflections at each story level was obtained by solving the following governing differential equation, derived considering the shear wall-frame interaction [4].

$$s^2 \frac{d^4 w}{dx^4} - \frac{d^2 w}{dx^2} + \frac{v^2 - 1}{v^2} M_0(x) - s^2 f(x) = 0 \tag{3}$$

Where,  $s^2 = K / (v^2 GA)$ ;  $GA$ = the shear rigidity of the frame per unit height (i.e. equivalent shear stiffness of the building);  $K = \Sigma K(\text{shear walls}) + \Sigma K(\text{columns})$ ;  $K = \Sigma EI$  = total stiffness of all shear walls within the story (since stiffness of the columns are very small compared to total stiffness of all the shear walls within that story,  $\Sigma K(\text{columns})$  term can be neglected);  $f(x)$  = distributed lateral force;  $M_0(x)$  = moment caused by the external loads at height  $x$ ;  $v^2 = 1 + \frac{K}{K_0}$ ;  $K_0$ = flexural rigidity

of the structure in the horizontal plane. The lateral deflections at each story level for the pure frame building (without shear walls) was obtained by solving the governing differential equation given by Baikov [8]. Having derived the limit state function the next step is the assessment of probability of failure and reliability (measured in terms of reliability index  $\beta$ ) of the frame structure. For this purpose, Monte Carlo Simulation technique [9] was employed.

## 2. Numerical study and discussion of results

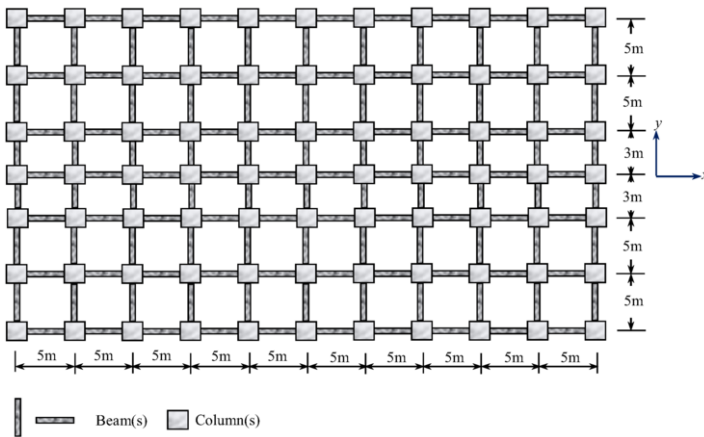
To study the effect of shear walls on the overall reliability of the building a typical 3-D regular frame building containing no shear walls was studied first (Fig. 1). The statistical characteristics of the selected random parameters, required for the reliability analysis are given in Table 1. In this study only these four parameters were considered random as they have considerable uncertainty in their values as given in Table 1; other values were assumed to be deterministic as shown in Table 2. The frame is subjected to dead, live, and horizontal seismic loads. To evaluate the reliability of the building against the serviceability limit state, the horizontal drift of the top floor was considered not to exceed 0.02 times  $h_s$ , where  $h_s$  is the story height (= 3m). Thus the limiting drift is equal to 60 mm in the present numerical study. The frame was then stiffened with shear walls in  $x$ - and  $y$ -directions as shown in Fig. 2. The thickness of all the shear walls were taken as 250 mm. Due to the presence of these shear walls, the lateral stiffness of the building increased substantially and thus the lateral drift reduced considerably.

**Table 1.** Basic random variables and their statistical values

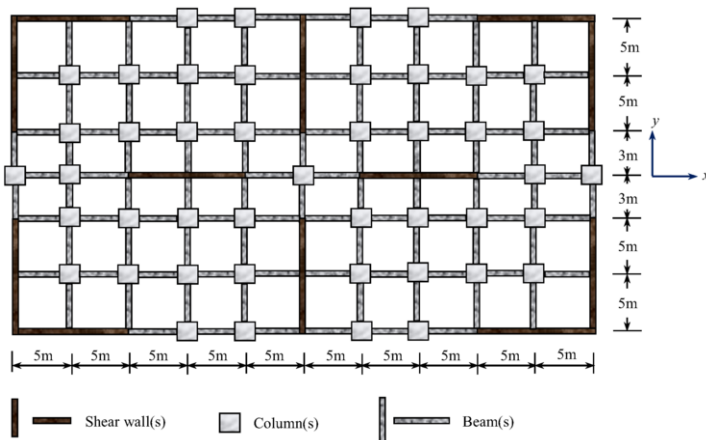
Random Variable	Nominal value	Bias factor	COV	Distribution
Story weights, $w_i$	7.0 kN/m <sup>2</sup>	1.05	0.125	Lognormal
Design spectral response acceleration, $S_{DS}$	2.2 m/s <sup>2</sup>	0.78	0.15	Normal
Modulus of elasticity of concrete, $E$	23500 MPa	1.0	0.18	Lognormal
Building height, $H$	30 m	1.05	0.05	Normal

**Table 2.** Deterministic values

Random Variable	Value
Column size	600×600 mm
Beam size, $b_w \times D$	250×450 mm
Slab thickness, $t$	120 mm
Compressive strength of concrete, $f_c'$	20 MPa
Yield strength of steel, $f_y$	420 MPa
Response modification factor, $R$	6.5
Occupancy importance factor, $I$	1.0



**Figure 1.** Typical floor plan of the 3-D building studied (without shear wall)



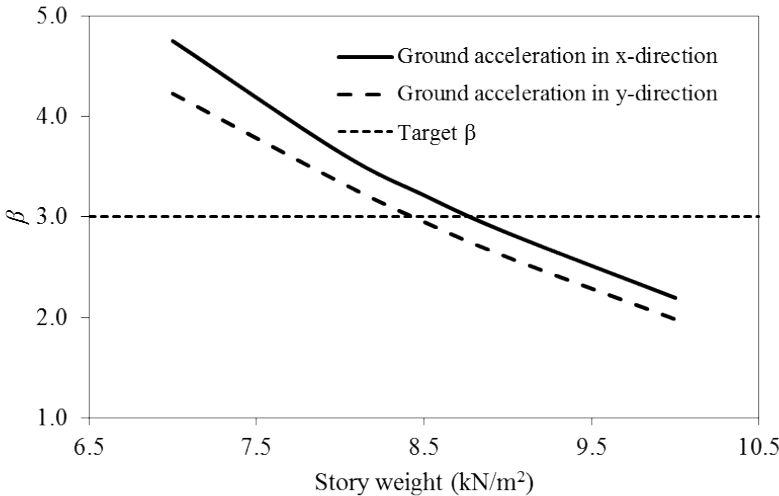
**Figure 2.** Typical floor plan of the 3-D building studied (with shear wall)

The Monte Carlo simulation results presented in Table 3 shows that, for the frame without shear walls, the probability of failure of the building frame when earthquake is considered from *x*-and *y*-directions are 0.99961 and 0.99980 respectively. These values show that it is almost certain that building drift will exceed the limiting value of the drift under present seismic loads. 100,000 simulation were used for carrying out the reliability analysis of building frame containing no shear walls and at least 1 million simulations were employed for carrying out the reliability analysis of building frames with shear walls. A substantially higher number of simulations were used for reliability analysis of shear wall-frame building, because the expected probability of failure of the shear wall-frame building was of the order of  $10^{-6}$ . Table 3 also shows that the probability of failure of the building in *x*-direction is lesser than the probability of failure in *y*-direction. This can be attributed to the higher stiffness of the building in *x*-direction compared to *y*-direction. This study thus clearly illustrates the beneficial effects of shear walls in carrying the seismic loads and controlling the lateral drift at the top of the building frame.

**Table 3.** Results of the reliability analysis of building frame without and with shear walls

Seismic ground acceleration in	Frame without shear wall		Frame with shear wall	
	$P_f$	$\beta$	$P_f$	$\beta$
<i>x</i> -direction	$9.9961 \times 10^{-1}$	-3.36	$1.00 \times 10^{-6}$	4.75
<i>y</i> -direction	$9.9980 \times 10^{-1}$	-3.54	$12.00 \times 10^{-6}$	4.22

It is also obvious from the table that when shear wall of almost equal quantity was provided in the two directions, the probability of failure reduced dramatically and reliability improved to an extent that it reached to the target value (generally 3.0, [9]).



**Figure 3.** Variation of reliability index  $\beta$  with story weight

The effect of story weight on reliability index of Shear-wall frame building was carried out to arrive at the results of design interest. For the design purposes, the parameters should be selected in such a manner so that  $(\beta - \beta_T)^2 \approx 0$ . Here  $\beta$  and  $\beta_T$  are the actual and target reliability index values.  $(\beta - \beta_T)^2 \approx 0$  is an indication that the reliability of the shear-wall frame building is equal to the target reliability value. Figure 3 shows that as the story weight is increasing reliability is continuously decreasing. This is due to the fact that with the increase of story weight base shear increases which in turn increases the story drift. Consequently probability of reaching to the limiting drift value increases; thus reliability decreases or probability of serviceability failure increases. This graph illustrates that reliability of shear-wall frame building is lesser when it is subjected to the earthquake from  $y$ -direction. This is so because building is less stiff in  $y$ -direction compared to  $x$ -direction. Figure 3 shows that the present building is reliable (against the seismic ground acceleration acting either in  $x$ - or in  $y$ -directions) to the desired extent provided the story weight is approximately less than or equal to  $8.5 \text{ kN/m}^2$ . Beyond this story weight, reliability will sharply decrease to a value less than 3.0.

### 3. Conclusions

In the present study, a simple Monte Carlo Simulation-based methodology was presented by which increase in the reliability level due to the addition of shear walls in RC building frame was quantitatively assessed. It was demonstrated that the shear walls improve the reliability against serviceability limit state of drift dramatically. Providing shear walls of even small magnitude (about 1% or less of shear wall to floor area ratio) can make a highly deficient RC frame building (against lateral drift) a safe and reliable RC frame building. The effect of story weight on reliability of RC shear-wall frame building was also studied to obtain that maximum story weight below which the building is as reliable as desired (i.e. reliability index  $\geq 3.0$ ).

### Acknowledgement

The work presented in this paper was funded by the Deanship of Scientific Research, Research Centre, College of Engineering, King Saud University, Riyadh, Saudi Arabia through Research Grant No. 19/434.

### References

- [1] S.R. Balasubramanian, K.B. Rao, D. Basu, M.B. Anoop, and C.V. Vaidyanathan, An improved method for estimation of elastic lateral stiffness of brick masonry shear walls with openings, *KSCE Journal of Civil Engineering*, 15(2011), 281-293.
- [2] B. Burak, and H.G. Comlekoglu, Effect of shear wall area to floor area ratio on the seismic behavior of reinforced concrete buildings, *Journal of Structural Engineering*, ASCE, 139(2013), 1928-1937.
- [3] A. Tuken and N.A. Siddiqui, A simplified analytical procedure to determine the amount of shear walls in reinforced concrete buildings, *7th International Conference on Analytical Models and New Concepts in Concrete and Masonry Structures*, AMCM 2011, Ktakow, Poland, June 13-15, 2011.

- [4] A. Tuken and N.A. Siddiqui, Assessment of shear wall quantity in seismic-resistant design of reinforced concrete buildings, *Arabian Journal for Science and Engineering, AJSE B-Engineering*, 38(2013), 2639-2648.
- [5] S.Y. Lee and A. Haldar, Reliability of frame and shear wall structural systems. I: Static Loading, *Journal of Structural Engineering*, ASCE, 129(2003), 224-232.
- [6] S.Y. Lee and A. Haldar, Reliability of frame and shear wall structural systems. II: Dynamic Loading, *Journal of Structural Engineering*, ASCE, 129(2003), 233-240.
- [7] SBC 301, *Loading and Forces Requirements*, Saudi Building Code, Riyadh, Saudi Arabia, 2007.
- [8] V.N. Baikov, *Reinforced Concrete Structures*, Mir Publishers, Moscow, 1974.
- [9] A.S. Nowak and K.R. Collins, *Reliability of Structures*, first edition, McGraw Hill, Singapore, 2000.
- [10] A. Tuken and N.A. Siddiqui, SBC-based assessment of shear wall quantity in moment resisting frame buildings. *KSCE Journal of Civil Engineering*, DOI 10.1007/s12205-014-0143-9 (In Press).



# Prediction on short-term burst pressure of plastic pipe reinforced by cross-winding steel wires

Xiangpeng LUO<sup>a</sup>, Jinyang ZHENG<sup>a</sup>, Ping XU<sup>b</sup>, Weican GUO<sup>a,c</sup> and Jianfeng SHI<sup>a,1</sup>

<sup>a</sup>*Institute of Process Equipment, Zhejiang University, Hangzhou 310027, P.R. China*

<sup>b</sup>*Institute of Applied Mechanics, Hangzhou 310027, P.R. China*

<sup>c</sup>*Zhejiang Special Equipment Insp & Research Institute, Hangzhou 310020, P.R. China*

**Abstract.** A plastic pipe reinforced by cross-winding steel wires (PSP) is composed of two layers of thermoplastic high density polyethylene (HDPE) matrix and a high strength cross-winding steel wire mesh skeleton. PSP has been widely used in construction materials and structures. Based on mechanical properties analysis of PSP and the fracture of steel wires as the failure criterion, the prediction model of short-term burst pressure at room temperature was established. It was revealed that the main factors influencing stress of steel wires were modulus of HDPE and elastic constants of composite layer. Burst experiments were conducted for PSP, and the results agree well with the theoretical results, which show that our proposed model can be employed to predict the burst pressure of PSP. Finally, the effects of the steel wire number and the winding angle on the burst pressure were analyzed.

**Keywords.** Plastic pipe, cross-winding steel wires, burst pressure, theoretical analysis

## Introduction

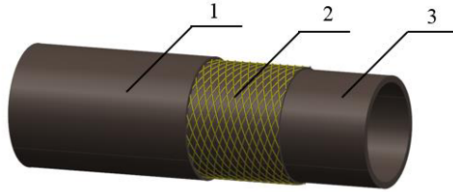
Polyethylene pipe reinforced by cross helically wound steel wires (PSP) is composed of two layers of thermoplastic high-density polyethylene (HDPE) and a composite layer, as shown in Figure 1. The composite layer contains steel wires tightly integrated with HDPE matrix by high performance cohesive resin. Combining the advantages of both plastic and metal, PSP has excellent mechanical performance, such as high strength and good corrosion resistance.

There exist several literatures on the investigation of mechanical properties of composite pipes subjected to inner pressure. Rosenow [1] employed the classical laminated-plate theory to predict the stresses and strains in the response of thin-wall filament-wound pipes. Wen et al. [2] used the elastic theory to calculate the intensity of a wire-netted colloidal pipe under inner pressure and he also studied the effect of the volume fraction and strength of steel wires on the loading-bearing ability of the pipe. On the base of the plane strain characterization, Kruijer et al. [3] proposed a new model on a nonimpregnated aramid fiber reinforced thermoplastic pipe. And according to the

---

<sup>1</sup>Corresponding author: [shijianfeng@zju.edu.cn](mailto:shijianfeng@zju.edu.cn)

netting analysis method, elastic constants in the fiber direction were obtained, as well as the mechanical properties. Zheng et al. [4] studied mechanical properties of PSP through experimental investigations, including burst test, flattening test and buckling test, but no systematic theoretical investigation was conducted in this work. For short-term properties of PSP, Zheng et al. [5] developed an analytical procedure to predict the short-term burst pressure. Li et al. [6] concentrated on the long-term mechanical properties of PSP, and proposed a viscoelastic mechanical model to describe the time-dependent mechanical response of PSP, and the proposed model was verified by long-term hydrostatic tests.



1. Outer HDPE layer, 2. Composite layer, 3. Inner HDPE layer

**Figure 1.** Structure of PSP

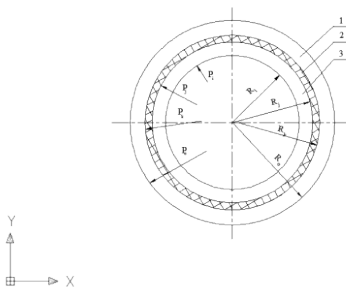
Since the short-term burst pressure is one of the important parameters for PSP loading-bearing capability, the mechanical calculation on the prediction of short-term burst pressure of PSP have some engineering significance. In this paper, two theoretical methods, force equilibrium method and strength analysis method, were introduced. Meanwhile, experimental investigations on the short-term burst pressure of PSP at room temperature were carried out to verify the proposed methods. Furthermore, based on the proposed theoretical method, the effect of steel wire number and winding angles on the short-term burst pressure were discussed.

## 1. Prediction method of burst pressure

In view of engineer utility, simplified model (Representative Volume Element) and approximate derivation of the real physical property are employed to obtain the equations of elastic constants of PSP. Several assumptions are made for the PSP structure and material properties.

- The PSP is considered to be a thick cylinder, with inner HDPE layer, composite layer and outer HDPE layer, and their interface is perfectly combined. The schematic diagram of the cross-section of PSP is shown in Figure 2.
- The cross-section of the PSP always stays perpendicular to its axis line.
- The steel wires and HDPE are homogeneous, continuous and isotropic, without flaws, and their properties do not vary throughout the composition process.
- The strains of steel wires and HDPE are continuous at the interface, which remains in good condition all the time. Also they are in small deformation and linear elastic state, with no initial stress. The time-dependent properties are not taken into account.

For the PSP produce, according to the current standards, its failure is mostly caused by the failure of steel wire. Hence, the maximum stress criterion is adopted to determine the failure of steel wire, and then the state of PSP.



1 Outer layer, 2 Composite layer, 3 Inner layer.

**Figure 2.** Schematic diagram of the cross section of PSP

1.1. Force equilibrium method

According to the axial loading equilibrium condition [7]:

$$\frac{\pi Nd^2}{4 \cos \alpha} \sigma_g \cos^2 \alpha + \sigma_p \left[ \pi (r_o^2 - r_i^2) - \frac{\pi Nd^2}{4 \cos \alpha} \right] = \pi r_i^2 P \tag{1}$$

Where,  $d$  is the diameter of the steel wire, mm;

$K$  is the coefficient,  $K = \frac{r_o}{r_i}$ ;

$N$  is the steel wire numbers;

$r_i$  is the inner radius of PSP, mm;

$r_o$  is the outer radius of PSP, mm;

$\alpha$  is the winding angle, degrees;

$\sigma_g$  is the aring stress of steel wire, MPa;

$\sigma_p$  is the bearing stress of HDPE, MPa.

Substituting the calculated strength of steel wire and HDPE into Eq.(1), the axial burst pressure of PSP is obtained:

$$P_B^x = \frac{Nd^2 (\sigma_{bg} \cos^2 \alpha - \sigma_{bp})}{4r_i^2 \cos \alpha} + \sigma_{bp} (K^2 - 1) \tag{2}$$

Where,  $\sigma_{bg}$  is the limit strength of steel wire, MPa;

$\sigma_{bp}$  is the calculated stress of HDPE, MPa.

According to the hoop loading equilibrium condition [7]:

$$\frac{\pi Nd^2}{2 \sin \alpha} \sigma_g \sin^2 \alpha + \sigma_p \left[ 2(r_o - r_i)L - \frac{\pi Nd^2}{2 \sin \alpha} \right] = 2r_i LP \tag{3}$$

Where,  $L = \frac{\pi(r_i + r_o)}{\tan \alpha}$ .

Substituting the calculated strength of steel wire and HDPE into Eq.(3), the hoop burst pressure of PSP is obtained:

$$P_B^\theta = \frac{Nd^2(\sigma_{bg} \sin^2 \alpha - \sigma_{bp})}{4r_i(r_i + r_o) \cos \alpha} + \sigma_{bp}(K - 1) \tag{4}$$

The short-term burst pressure of PSP is the minimum value of axial burst pressure and hoop burst pressure, namely

$$P_{B1} = \min(P_B^z, P_B^\theta) \tag{5}$$

1.2. Strength analysis method

The strength analysis method is based on the stress analysis of the PSP, and the predicted burst pressure is related to the loading condition. When the zero axial strain (plane strain) loading condition is considered, the corresponding burst pressure is  $P_{B2}$ .

The composite layer consists of two composite monolayers, which is presented in Figure 3. Since the layers of steel wires are in contact with each other, the thickness of a single monolayer is regarded as the steel wire diameter  $d_{st}$ , and the thickness of the whole composite layer is doubled. Firstly, single composite monolayer is analyzed, for it is the basic unit of the composite layer. There are three mutually perpendicular symmetry planes, so it is anisotropic. The lower monolayer is analyzed. The local coordinate system of the composite monolayer is designed as (T, L, r), where T is the winding direction of steel wire, L is the direction perpendicular to the steel wire in plane, and r is the normal direction of the composite monolayer plate. For the sake of simplified analysis process, the series-parallel model method is adopted. A rectangle outside and rectangle inside model is employed in this study, shown in Figure 4. Inside shaded rectangles represent the steel wires in Figure 3, and the volume fraction of each component remains unchanged.

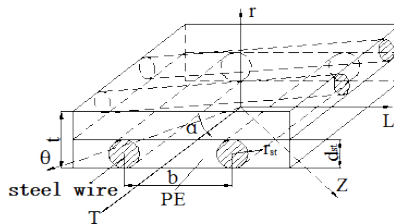


Figure 3. Schematic diagram of composite layer [8]

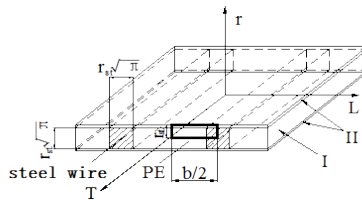


Figure 4. Simplified model of the single monolayer [8]

A representative volume element (RVE) is got from the simplified single monolayer model shown in Figure 5, which will be used in the mechanical analysis. Figure 5 shows the RVE model, its length is half of the distance between steel wire centers, and its width is the thickness of the composite monolayer plate, namely the radius of the steel wire  $r_{st}$ ; 1 represents the steel wire, and its area is 1/4 of the cross section of steel wire; 2, 3 and 4 represent PE. Labels 1 and 2 constitute the region I, and labels 3 and 4 constitute the region II.

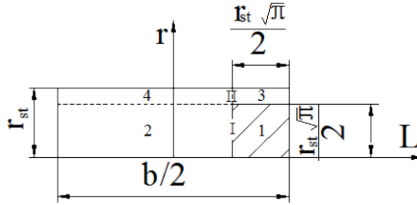


Figure 5. Representative volume element of the single monolayer [8]

The key of this method is the conforming of RVE model. Based on the determined RVE model, combining the mechanical properties of steel wire and HDPE, the elastic modulus, poisson's ratio and shear modulus of the single composite monolayer will be obtained. In the light of analysis method proposed by P. C. Chou, elastic properties of the composite layer can be obtained, the details can be found in reference [9].

Knowing the elastic properties of the composite layer, then combining the geometric equation and physical equation under the action of inner pressure, the radial stress is expressed as:

$$\begin{aligned} & \left( \frac{\mu_{\theta z c} \mu_{z \theta c} - 1}{E_{\theta c}} \right) r^2 \frac{d^2 \sigma_{rc}}{d^2 r} + \left( \frac{3\mu_{\theta z c} \mu_{z \theta c} - \mu_{r z c} \mu_{z \theta c} - \mu_{r \theta c} + \mu_{\theta r c} + \mu_{\theta z c} \mu_{z r c}}{E_{\theta c}} + \frac{\mu_{\theta r c} + \mu_{\theta z c} \mu_{z r c}}{E_{rc}} \right) r \frac{d \sigma_{rc}}{dr} \\ & + \left( \frac{\mu_{\theta z c} \mu_{z \theta c} - \mu_{r z c} \mu_{z \theta c} - \mu_{r \theta c} - 1}{E_{\theta c}} + \frac{\mu_{\theta r c} + \mu_{\theta z c} \mu_{z r c} - \mu_{z r c} \mu_{r z c} + 1}{E_{rc}} \right) \sigma_{rc} = (\mu_{r z c} - \mu_{\theta z c}) C_p \end{aligned} \quad (6)$$

Where,  $\mu_{zrc}$ ,  $\mu_{\theta rc}$  and  $\mu_{z\theta c}$  are the Poisson's ratios of composite layer in  $z-r$ ,  $\theta-r$ ,  $z-\theta$  plane, respectively;

$E_{\theta c}$ ,  $E_{z c}$  and  $E_{rc}$  are the elastic modulus of composite in  $\theta$ ,  $z$ ,  $r$  direction, MPa.

According to stress boundary condition,  $\sigma_c(r = R_j) = P_j$ ,  $\sigma_c(r = R_k) = P_k$ , and the equivalent axial strain  $C_p$  of each layer,  $P_j$ ,  $P_k$  and  $C_p$  will be obtained. Then, the hoop stress of composite layer  $\sigma_{\theta c}$  is also available.

On the other hand, according to Lamé's equation [10], stresses of inner and outer HDPE layer are expressed. Afterwards, through generalized Hooke's law, expressions of strains of each layer can be gained as functions of the inner and outer pressure of the corresponding layer [11].

Stress and strain of the composite layer obtained under the cylindrical coordinate system can be transformed into material coordinate system, and the strain in steel wire direction will be obtained, see Ep.(7). Because the thickness of the composite layer is small, the strain in steel wire direction is regarded as the steel wire strain, thereby one can obtain tensile stress of the steel wire, expressed as Ep.(8), detailed expression for each nomenclature is available in reference [11].

$$\begin{pmatrix} \varepsilon_{T_i} \\ \varepsilon_{L_i} \\ \gamma_{TL_i} \end{pmatrix} = [T]^{-T} \begin{pmatrix} \varepsilon_{\theta_i} \\ \varepsilon_{z_i} \\ \gamma_{z\theta_i} \end{pmatrix} \tag{7}$$

$$\sigma_{st_i} = E_{st} \times \varepsilon_{T_i} \tag{8}$$

When the tensile stress of the steel wire reaches its strength limit, the PSP is expected to be failure. Then the inner pressure at this moment is regarded as the burst pressure, which is expressed as follows.

$$P_{B2} = \frac{\frac{\sigma_{stb}}{E_{st}} - (S_1 - \pi R_i^2 P_i) \cdot AA_2 - AA_3}{\pi R_i^2 \cdot AA_2 - \frac{(2 - 2u^2 R_o^2)}{E_m (R_o^2 - R_k^2)} \cdot AA_1} \tag{9}$$

The specific expression of the above parameters can be found in reference [12].

## 2. Experiment and results

### 2.1. Material properties of PSP

The parameters of the matrix HDPE and the reinforced steel wire of a PSP used in this study are listed in Table 1 and Table 2.

**Table 1.** Physical and mechanical properties of PE100

Property	Value
Density / g/cm <sup>3</sup>	0.9600-0.9609
Yield stress $\sigma_{pe}$ /MPa (100mm/min)	>25
Young's modulus $E_{pe}$ /MPa	1002
Poisson's ratio $\mu_{pe}$	0.45
Elongation at break $\varepsilon_{max}$ /%	>600

**Table 2.** Physical and mechanical properties of steel wire

Property	Value
Young's modulus $E_{st}$ /MPa	210000
Density $\rho_{st}$ / g/cm <sup>3</sup>	7.8
Tensile breaking force $F_{st}$ /N	1491
Tensile strength $\sigma_{stb}$ /MPa	1900
Poisson's ratio $\mu_{st}$	0.26
Linear expansion factor $\alpha$ / m/(m.°C)	$1.14 \times 10^{-5}$

### 2.2. Burst experiment

To verify the theoretical method, burst experiments were carried out for 10 types (each type with 4 samples) of PSP at room temperature ( $23 \pm 2^\circ\text{C}$ ), using the reciprocating electric pressure pump. The seal of experimental equipment was done according to the standard GB6111-2003 [13]. The morphology of the crack and the value of the pressure when PSP burst were recorded.

With the properties of steel wire and HDPE, burst pressures of the PSP were calculated by the two methods mentioned above along with the experimental results, as listed in Table 3.

It can be seen from Table 3, the range of error percentage for the force equilibrium and strength analysis methods are -11.9 % to 2.3% and -4.8% to 4.5%, respectively, which is acceptable in engineering practice, and can be used as a referential parameter when short-term burst pressure is considered.

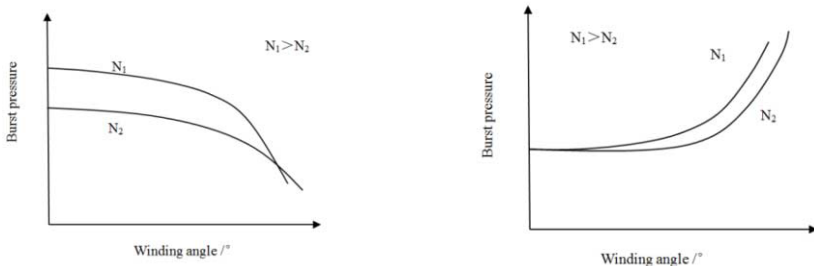
**Table 3.** Dimensions of PSP and their experimental and theoretical burst pressure [14]

Sample number	D <sub>o</sub> /mm	r <sub>st</sub> /mm	N	t <sub>tot</sub> /mm	P <sub>B0</sub> /MPa	Force equilibrium method		Strength analysis method	
						P <sub>B1</sub> /MPa	error /%	P <sub>B2</sub> /MPa	error /%
1	110	0.8	36	8.5	6.3	5.8	-7.9	6.3	0
2	110	0.8	56	10.0	8.0	8.1	1.3	8.2	2.5
3	160	0.8	60	9.5	4.4	4.2	-4.5	4.6	4.5
4	160	0.8	90	10.0	5.7	5.4	-5.3	5.6	-1.8
5	200	0.8	80	11.0	4.2	3.7	-11.9	4.0	-4.8
6	200	0.8	120	10.5	4.4	4.5	2.3	4.6	4.5
7	250	0.8	100	12.0	3.4	3.1	-8.8	3.4	0
8	250	0.8	200	12.5	4.6	4.5	-2.2	4.6	0
9	315	0.8	210	12.5	3.2	3.1	-3.1	3.2	0
10	315	0.8	280	12.5	3.8	3.7	-2.6	3.8	0

2.3. Steel wire number and winding angel

It is known that steel wires are the reinforced part of PSP, and its increment in number will increase the burst pressure, both in axial burst pressure and hoop burst pressure, which is verified in Figure 6, where N<sub>1</sub> > N<sub>2</sub>.

From the theoretical analysis, it is concluded that the two modes of the burst crack, axial and hoop crack, are related to the winding angle. With fixed steel wire number, axial burst pressure decreases and hoop burst pressure increases with the increment of steel wire winding angle, and there is an angle, at which the two burst pressure equals to each other, and then we call the angel an optical one. At this moment, the strength state of PSP is in good status.



(a) Axial burst pressure of PSP vs winding angle

(b) Hoop burst pressure of PSP vs winding angle

**Figure 6.** Axial and hoop burst pressure of PSP vs winding angle with differert steel wire numbers

### 3. Conclusions

Two theoretical methods, force equilibrium method and strength analysis method, were introduced to predict short-term burst pressure of PSP at room temperature. Good agreement between theoretical results and experimental results shows that both methods can be employed to predict burst pressure of PSP. According to the theoretical analysis, the effect of steel wire number and winding angle on burst pressure were analyzed; it was found that burst pressure increases with the increment of steel wire number, and there exists an optimal winding angle at which the strength of PSP is in a good state.

### References

- [1] Rosenow, M.W.K., Wind Angle Effects in Glass Fiber-Reinforced Polyester Filament Wound Pipe, *Composites*, 15 (1984), 144-152.
- [2] Wen, J.M., He, P.F., Feng, Q., Strength Analysis of Wire Braided Hose under Internal Pressure, *Fiber Reinforced Plastics/Composites*, 78(4) (2002), 11-12, and 21.
- [3] Kruijer, M.P., Warnet, L.L., Akkerman, R., Analysis of the Mechanical Properties of a Reinforced Thermoplastic Pipe (PTP), *Composites, Part A*, 36(2006), 291-300.
- [4] Zheng, J.Y., Lu, Y.B., Li, X., et al, Experimental Investigation on Mechanical Properties of Plastic Pipes Reinforced by Cross Helically Steel Wires, *Journal of Pressure Vessel Technology*, 130(2) (2008), 021401.
- [5] Zheng, J.Y., Gao, Y.J., Li, X., et al, Investigation on Short-Term Burst Pressure of Plastic Pipes Reinforced by Cross Helically Wound Steel Wires, *Journal of Zhejiang University SCIENCE A*, 9(5) (2008), 640-647.
- [6] Li, X., Zheng J.Y., Li, Y., et al. Long-Term Stress Analysis of Plastic Pipe Reinforced by Cross-Winding Steel Wire, ASME 2008 Pressure Vessels and Piping Conference. *American Society of Mechanical Engineers* (2008), 477-491.
- [7] Liu, H.W. Mechanics of Materials (I) [M], *Higher Education Press*, Beijing, 2004.
- [8] Lin, X.F., Strength Analysis and Optimal Design of Plastic Pipe Reinforced by Cross-Winding Steel Wires [D], *Zhejiang University*, Hangzhou, 2006.
- [9] Chou, P.C., Carleone, J., Hsu, C.M., Elastic constants of layered media, *Journal of Composite Materials*, 6(1972), 80-93.
- [10] Zheng, J.Y., Process Equipment Design [M], *Chemical Industry Press*, Beijing, 2010.
- [11] Zheng, J.Y., Li, X., Xu, P., Lin, X.F., Li, Y.X, Analyses on the short-term mechanical properties of plastic pipe reinforced by cross helically wound steel wires, *Journal of Pressure Vessel Technology-Transactions of The ASME*, 131(3) (2009), 031401.
- [12] Rao J, Study on Burst Pressure of Plastic Pipe Reinforced by Cross-Winding Steel Wires [D], Zhejiang University, Hangzhou, 2012.
- [13] GB/T6111, Thermoplastics Pipes for the Conveyance of Fluids-Resistance to Internal Pressure-Test Method, 2003.
- [14] Zhu, Y.C., Zheng, J.Y., Lu, Y.B., Lin, X.F., Li, X., Dong, H.Z., Chen, D.F., Experimental Investigation on Short-Term Burst Pressure of Plastic Pipes Reinforced by Cross Helically Wound Steel Wires, *China Plastics*, 05(2006), 49-52.



# Neural network model for predicting deterioration of bridge components using visual inspection data

Md Saeed HASAN<sup>1</sup>, Sujeeva SETUNGE and David W. LAW

*School of Civil, Envir and Chemical Engineering, RMIT University, Australia*

**Abstract.** As a primary component of a Bridge Management System (BMS), prediction models are crucial for planning the maintenance work, making budgetary decisions, life-cycle analysis and optimization of future maintenance works programs. In a BMS, planned decisions for conducting repairs and rehabilitation are based on inspection data collected for the bridges by trained inspectors following a condition rating method developed by the authority. There is a significant need to produce a practical system where these visual inspection data can be converted into a decision tool. To address this need, a study has been conducted to forecast deterioration of reinforced concrete bridge components using an Artificial Neural Network (ANN). Visual inspection data was sourced from Victoria, Australia and utilized to develop an ANN model using Levenberg-Marquardt optimization with the help of Bayesian regularization process. A neural network based model for prediction of bridge condition rating is proposed. The back-propagation algorithm was used to train the network to recognize the pattern of deterioration of bridges. The various factors which influence the deterioration rate are considered as input to the system. Deterioration of three major structural components was modeled and presented in this paper.

**Keywords.** Condition monitoring, bridge deterioration, Markov Chain, Neural Network

## Introduction

Whole life care of a bridge network requires an understanding of deterioration. Bridges are the key structural elements in the transportation system. They are considered to be vital links in any roadway network. Complete or partial failure to maintain these links paralyses the overall performance of the roadway network and causes excessive public and private losses. The structural condition of bridges continues to deteriorate due to aging, limited maintenance budgets, increased traffic loads and environmental exposure and corrosion. Maintaining their performance at an acceptable level and within safety ranges is a high priority for most of the road transport authorities around the world. Therefore, bridge networks need to be managed in a way that ensures their uninterrupted performance throughout their design life. Effective maintenance of road structures can be greatly improved by introducing automated asset management

---

<sup>1</sup>Corresponding author. [m.hasan@student.rmit.edu.au](mailto:m.hasan@student.rmit.edu.au), [sujeeva.setunge@rmit.edu.au](mailto:sujeeva.setunge@rmit.edu.au)

practices. Thus determining a reliable bridge maintenance and rehabilitation strategy is of great importance.

Visual inspection carried out by trained inspectors to establish the structural integrity of road structures is a common practice by many transportation agencies as part of their asset management and capital planning programs. In Victoria, Australia, the road transport authority Vicroads has a scheme of four state condition monitoring system carried out by expert inspectors. With time there has been a significant amount of data accumulated in the system which can now be used for proactive decision making as opposed to reactive current practice.

Previously the BMS in most cases used to be based on a deterministic approach and the assessment of reliability or safety in general was based on subjective statements [1]. There has been continuous effort coming from different researchers who have tried to implement different techniques into BMS [2, 3]. The most popular BMS introduced and widely applied in the USA are PONTIS and BRIDGIT, which are stochastically based systems with rational assessment procedures [1]. These procedures set guidelines for data collection and reduce the subjective nature of data.

Artificial intelligence (AI) is a relatively new technique introduced to model the deterioration of facility structures where computer techniques have been utilized to automate BMS from the condition monitoring data. Some researchers have tried to fit regression prediction models based on Artificial Neural Network (ANN) techniques and found that the average prediction errors are quite high [4, 5]. Other authors [6-8] have used Markov Chain techniques to model bridge deterioration. The Markov chain model is used for modeling the bridge deterioration in the analysis routines in the popular BMS PONTIS [9].

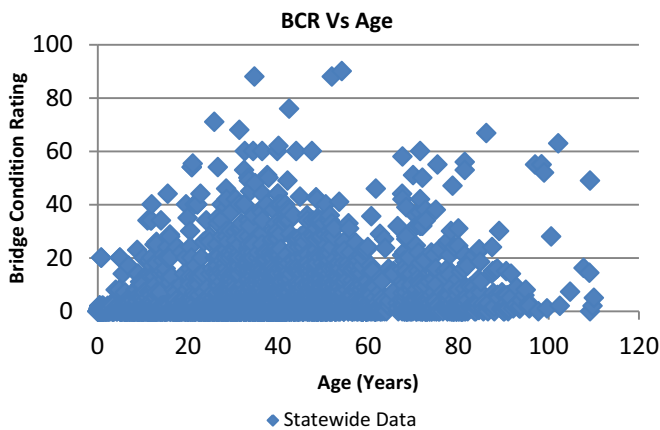
AI techniques encompass expert systems, artificial neural networks (ANN), genetic algorithm (GA), and case-based reasoning (CBR) to optimise the prediction of future conditions obtained through a set of observations. Researchers are using ANN to determine the expected deterioration of bridge structures from existing condition data and other input parameters with respect to age [2, 10]. In general, developing a model for a bridge structure is a complex task; one reason being that the causes and properties of deterioration are not well understood. At present, large visual inspection on concrete bridge structures and the performance databases have become available to the most authorities. However, such databases contain observed data but no accompanying theory and knowledge of rules of the observed behavior. Hence, the requirements of a technique adaptable to solve the functional relationships, which often feature non-linearities, become necessary. Many of the deterministic and stochastic models are not very well suited for this purpose. Neural Networks are suitable in such circumstances to predict the behavior of bridges where cause-effect relationships are little known.

## **1. Significance of research**

This research project aimed to use artificial neural network to model the deterioration of different components of concrete bridges in Victoria, Australia. The specific objective of the research is to develop a model to predict the future condition of concrete bridge structures from the available condition monitoring data. Effort has been made to utilize the most suitable algorithm to perform the calculation by the neural network. A supervised back-propagation learning algorithm has been deployed in this research work. This methodology has been used for deriving an ANN model for three

different components of concrete bridges namely precast deck, cast-in-situ abutment and precast girder.

The scope of the research was to identify the optimized algorithm, training and transfer function for the use of road authorities in order to develop a model from the available condition monitoring data which will significantly improve the reliability of the budgetary decisions. At present, drawing conclusions from the existing routine inspection data collected over a decade is very difficult, as a significant amount of data is staying in unchanged condition most of the time. In Figure 1, Bridge Condition Rating (BCR) is plotted against the age of the bridges. It was found that producing accurate forecasting models are not possible using a deterministic method as there is no pattern within the data. For this kind of approach, the coefficient of correlation is very poor for prediction purposes. Enhanced effort is required to understand and utilize this data.



**Figure 1.** Discrete relationship between age of the bridges and BCR when all records are considered

## 2. Methods of prediction

A Neural network has been applied in this research to model concrete bridge component deterioration. The mechanism of the deterioration process of concrete is complicated. A Neural Network model has the ability to learn the linear or non-linear relationship between inputs and outputs. An artificial neural network (ANN) also referred to as parallel distributed processing is an information-processing paradigm inspired by the parallel structure of the human brain processing information system. ANNs are biologically inspired computer programs designed to simulate the way in which the human brain processes information. ANNs gather their knowledge by detecting the patterns and relationships in data and learn (or are trained) through experience, not from programming. Natural neurons of the brain receive signals through synapses located on the dendrites or membrane of the neuron. If the neuron receives a strong signal which surpasses a certain threshold value, it will be activated and will emit a signal through the axon. This signal might be sent to another synapse,

and might activate other neurons. This way the information is processed and transferred. This process is schematically shown in Figure 2.

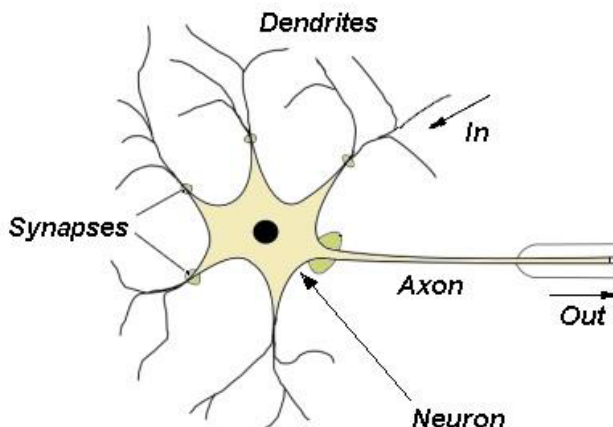


Figure 2. Schematic diagram of a biological neuron

The complexity of real neurons is highly abstracted when modeling artificial neurons. These basically consist of inputs (like synapses), which are multiplied by weights (strength of the respective signals), and then computed by a mathematical function which determines the activation of the neuron. Another function (which may be the identity) computes the output of the artificial neuron (sometimes in dependence of a certain threshold). ANNs combine artificial neurons in order to process information.

Recently, the neural network approach to data analysis and modeling has received much attention from researchers and practitioners. Over the past decade, there have been significant activities and important breakthroughs in the development of various theoretical and computational models for connectionist computing [11-13]. Neural networks were originally developed as tools for the exploration and reproduction of human information processing tasks such as speech, vision, olfaction, touch, knowledge processing and motor control. The feed-forward network, dynamic reconfigurable network [14] and counter propagation network [15] are some of the topologies of neural networks which are currently in use. Among them, multilayer feed-forward networks are most commonly used in engineering field. Here the flow of information is unidirectional, moving from input to the output layer. The network accepts continuous valued inputs and is used in a supervised learning environment [12].

ANN methods are being used to compute and solve different problems in civil engineering fields such as structural design, structural assessment, structural control, traffic engineering, and highway engineering [16-18]. While trying to model the deterioration of concrete bridges, several researchers have used ANN. For instance, Sobanjo [2] has endeavoured to model bridge deterioration from fifty concrete bridge superstructure inspection records where he considered the age of bridge as the only input. Similar work has been carried out by Cattani et al. [19] using neural network approach to predict the condition rating of railway bridges in the Chicago metropolitan area. In their work, several physical characteristics of the bridges were considered as the input vector while the overall condition of the bridge, which was on a rating scale of 1 to 5, was considered as the output of the ANN model. While modeling the bridge

abutment condition ratings in the state of Michigan, Li and Burgueno [20] compared several ANN methods to come up with a best model. The ANN model was able to predict the discrete condition rating of bridge abutments based on physical and operational bridge parameters.

Neural networks architecture has been classified into various types based on their learning mechanisms and other features. Multi-Layer Perceptron (MLP) architecture has been used in this research work to model the deterioration of bridge component. MLP architecture is widely used in prediction and classification tasks in engineering practice [21, 22]. MLP architecture is part of a back propagation method (BPM) which can handle stochastic behavior of data and can predict or classify them accordingly [22].

There are several layers in a MLP architecture, namely an input and an output layer accompanied by one or more hidden layers which are transitional layers. The hidden layer consists of the computational units called hidden neurons. The transitional computations are carried out by hidden layers before sending the input to the output layer. The input-hidden layer weights connect input layer neurons to the hidden layer neurons. Similarly, the hidden layer neurons are linked to the output layer neurons through the corresponding hidden-output layer weights. Figure 3 shows graphically the connectivity structure of a multilayer neural network with a single hidden layer. The input-output mapping of a multilayer perceptron can be formulated by the Eq. (1),

$$O = N_3[N_2[N_1[I]]] \quad (1)$$

Here  $N_1$ ,  $N_2$  and  $N_3$  represent nonlinear mapping provided by input, hidden and output layer respectively. The activity of neurons in the hidden layer is determined by the activities of the neurons in the input layer and the connecting weight between input and hidden units. Similarly, the activity of the output units depends on the activities of the neurons in the hidden layer and the connecting weight between hidden and output layers.

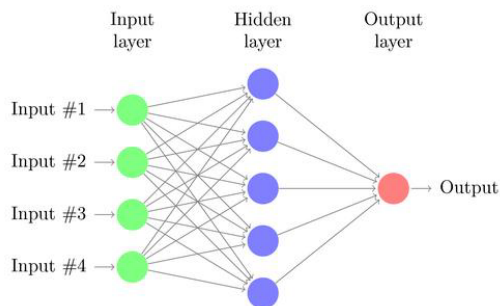


Figure 3. Neural Network connectivity between different layers.

### 3. ANN model

In this research paper, condition monitoring data of precast deck/slab (8P), precast girder (2P) and cast-in-situ abutment (24C) were analyzed. This study develops a

framework using feed forward neural networks to fit an input-output relationship and is designed to predict the state of deterioration or condition of bridge components. The neural network toolbox of MATLAB programs were used to develop the model.

### 3.1 Preprocessing of the data and selection of Input variables

The data has been sourced from the road authority of Victoria, Australia. The condition monitoring database has data which were collected over the period of 1995 to 2012. The database contains condition monitoring as well as other physical parameter data such as length, width, span, environmental exposure category, location, construction date and date of inspection. From the database, the average annual daily traffic (AADT) volume and the percentage of commercial vehicle were also collected. In this research paper an attempt has been made to use the database information to model the deterioration of three major components of concrete bridge structures. The three major structural components are precast deck, cast-in-situ abutment and precast girder which are denoted as 8P, 24C and 2P successively in the database system.

While developing ANN model it is very important to choose the input variables wisely. The input parameter should have significant influence on the output and thus able to predict the output. While choosing the input variables, the engineering judgment and experience has been applied. A similar study conducted by Huang [23], to identify the deterioration of concrete decks in Wisconsin considered 11 significant parameter as ANN input after ANOVA analysis. The parameters were maintenance history, age, previous condition, district, design load, length, deck area, AADT, environment, number of spans and degree of skew. Among this parameters, in this research work, five (5) parameters have been selected which are age, length, AADT, environmental exposure, and number of spans. In addition to this, two other parameters, percentage of commercial vehicle and width of the bridge were also considered using engineering judgment.

The maintenance history was not available (for this data set) although most of the bridges were experiencing regular routine maintenance. To overcome this problem in this analysis, the overall condition rating (OCR) of components were calculated and compared with the successive inspection record. The components which showed an improvement in the OCR were removed from the calculation. This was done to remove the unrecorded maintenance and repair work impact on the model. Hence only the bridges that indicated a deterioration trend in their condition data were considered. The OCR value 1.0 indicates that the bridge is in perfect condition which is also another indication of maintenance impact. To ensure the bridge is experiencing deterioration an attempt has been made to ignore the perfect condition bridges. Hence the data was filtered above a threshold value of OCR. Again, removing the perfect condition bridge data increases the likelihood of correctly predicting failures as the only true failures in the model, so all the bridges/components that are not deteriorating are ignored. Table 1 shows a typical sample raw data set.

After removing the probable maintenance impact using OCR, the size of the input matrix for the deck/slab was  $7 \times 92$ , for the abutment it was  $7 \times 132$  and for the girder it was  $7 \times 32$ . The output matrix size was  $4 \times 92$ ,  $4 \times 132$ ,  $4 \times 32$  respectively for deck, abutment and girder.

**Table 1.** Sample data for precast deck/slab component

ID	Year Built	Inspection Date	Condition				OCR	AA DT	CV %	L*	W*	*S
			1	2	3	4						
SN7521	30/06/1980	16/06/1997	0	85	15	0	2.15	101	0.26	7.6	12.1	1
SN7521	30/06/1980	1/08/2005	0	20	80	0	2.8	101	0.26	7.6	12.1	1
SN0174	2/04/1970	14/05/1997	45	55	0	0	1.55	412	0.13	7.5	19.9	1
SN0254	1/01/1970	15/08/2005	0	100	0	0	2	161	0.22	3.6	8.8	1
SN0254	1/01/1970	9/06/2012	0	0	100	0	3	161	0.22	3.6	8.8	1

\*L = length, W = width, S = span

### 3.2 Selection of Neural Network model properties

A Feedforward BP-MLP neural network was developed to predict the condition of the bridge components. To train the network with the training data a Bayesian Regularization function [24] has been used which is suitable for noisy widespread type of data. This function updates the weight and bias values according to Levenberg-Marquardt optimization [25]. The Bayesian regularization process minimizes a combination of squared errors and weights, and then determines the correct combination so as to produce a network that generalizes well for the optimized prediction. The hyperbolic tangent sigmoid function, specified as 'tansig' was selected as the transfer function for the networks both from input to hidden and hidden to output layers. The hyperbolic tangent sigmoid function is commonly used for continuous activation functions [11]. The range of output values of this 'tansig' function varies between -1 and 1. Seventy percent data has been allocated for the training the network using the random function available in Matlab and the rest of the input data were allocated for the testing of the network. The number of neurons in the hidden layer was selected to be eight after trial and error testing with the best training performance. Since the data corresponds to a time series, it is better to set sampling as a random process. Other methods will only use specific part of the time series for training which may result in lost information about the long-term exposure.

## 4. Results and discussions

Figure 4 – 6 represents the regression plot of all three models developed using ANN for three different bridge components, deck/slab, abutment and girder respectively. For the deck/slab component, the coefficient of determination (R-squared) value is 0.92 for training, 0.61 for testing and overall is 0.88. The R-square value is an indication of accuracy of prediction where close to 1 value indicates the higher accuracy and 1 as perfect prediction.

The R-squared value of the abutment model is 0.96 for training, 0.86 for testing and 0.94 for overall prediction. In the case of the girder, this values are 0.96, 0.80 and 0.92 respectively. The R-squared value indicates that the derived model had high accuracy during the training phase compared to testing. This is expected as it was not possible to ensure that the maintenance data was removed fully from the system. Hence, some inputs still remain as biased by the maintenance action. Although for a small sample size, splitting data randomly is better than dividing manually in terms of biasing the data, there might be a high probability that all the outlier data are parsed into the testing phase.

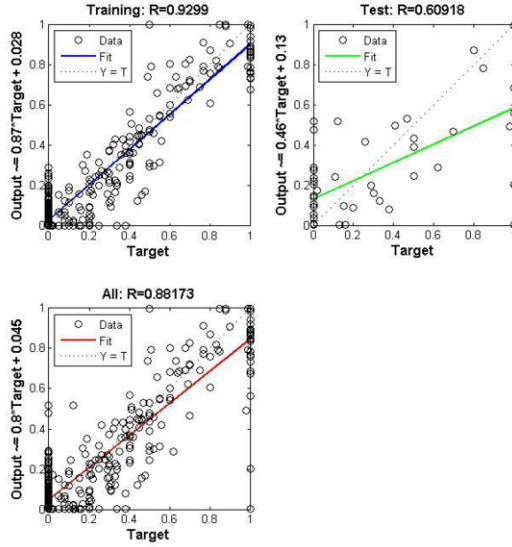


Figure 4. Regression plot of deck/slab (8P) predictive model during the training, testing stage and overall situation

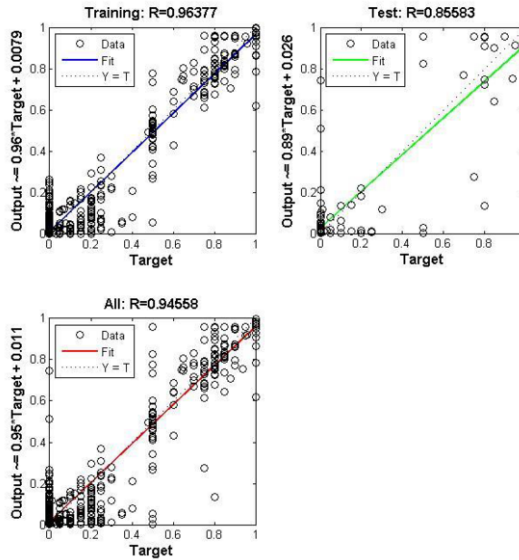
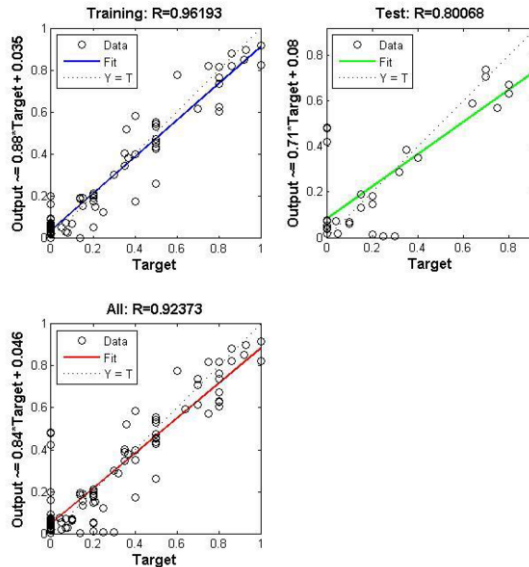


Figure 5. Regression plot of abutment (24C) predictive model during the training, testing stage and overall situation





**Figure 6.** Regression plot of girder (2P) predictive model during the training, testing stage and overall situation

## 5. Conclusion

This study developed an ANN prediction model for deck deterioration by adopting BP-MLP fitting utilities. Using historical data of bridges in Victoria, it developed an ANN model of 7 inputs in the input layer, one hidden layer with eight hidden neurons in hidden layer, and four output labels in the output layer. In the validation, the ANN model was able to predict the output with a reasonably good accuracy. These results indicate the potential of the ANN model with BP-MLP fitting tool as a prediction method for the deterioration of concrete bridge components.

The recording of maintenance work carried out on bridge components is a vitally important requirement for effective BMS. By considering maintenance impact, the quality of the prediction using ANN model can be further improved.

## References

- [1] P. Thoft-Christensen, Bridge Management Systems: present and future, *Recent Advances in Bridge Engineering* (1996), 13-37.
- [2] J.O. Sobanjo, A Neural Network Approach to Modeling Bridge Deterioration, *Proceeding 4th Congress on Computing in Civil Engineering*, ASCE (1997), 623–626.
- [3] O.B. Tokdemir, C. Ayvalik, J. Mohammadi, Prediction Of Highway Bridge Performance By Artificial Neural Networks And Genetic Algorithms, *Proceeding of the 17th International Symposium on Automation and Robotics in Construction ISARC* (2000).
- [4] M. Liu, D.M. Frangopol, Optimal bridge maintenance planning based on probabilistic performance prediction, *Engineering Structures* 26 (2004), 991-1002.

- [5] J.B. Son, J. Lee, M. Blumenstein, Y.-C. Loo, H. Guan, K. Panuwatwanich, Generating Historical Condition Ratings for the Reliable Prediction of Bridge Deteriorations, *IABSE Symposium Report*, International Association for Bridge and Structural Engineering (2009), 44-53.
- [6] G. Morcoux, Performance prediction of bridge deck systems using Markov chains, *Journal of Performance of Constructed Facilities* 20 (2006), 146-155.
- [7] P. Basheer, S. Chidiact, A. Long, Predictive models for deterioration of concrete structures, *Construction and Building Materials* 10 (1996), 27-37.
- [8] V. Patidar, S. Labi, K. Sinha, P. Thompson, NCHRP report 590: multiple-objective optimization for bridge management systems, *Transportation Research Board of the National Academies* (2007).
- [9] P.D. Thompson, E.P. Small, M. Johnson, A.R. Marshall, The Pontis bridge management system, *Structural Engineering International* 8 (1998), 303-308.
- [10] J. Cattan, J. Mohammadi, Analysis of bridge condition rating using neural networks, *Computer-Aided Civil and Infrastructure Engineering* 12 (1997), 419-429.
- [11] D.E. Rumelhart, G.E. Hinton, J.L. McClelland, A general framework for parallel distributed processing, *Parallel distributed processing* 1 (1986).
- [12] R.P. Lippmann, An introduction to computing with neural nets, *ASSP Magazine, IEEE* 4 (1987), 4-22.
- [13] K. Knight, Connectionist ideas and algorithms, *Communications of the ACM* 33 (1990), 58-74.
- [14] H.H. Szu, A Dynamic Reconfigurable Neural Network: Learning Principles, Paradigms, Rules and Morphology, *Auerbach publishers*, 1991.
- [15] D. Skapura, J.A. Freeman, Neural Networks Algorithms, Applications, and Programming Techniques, Addison-Wesley Publishing Company, 1991.
- [16] A. Mukherjee, J. Deshpande, J. Anmala, Prediction of buckling load of columns using artificial neural networks, *Journal of Structural Engineering* 122 (1996), 1385-1387.
- [17] S.H. Kim, C. Yoon, B.J. Kim, Structural monitoring system based on sensitivity analysis and a neural network, *Computer Aided Civil and Infrastructure Engineering* 15 (2000), 189-195.
- [18] M. Saito, J. Fan, Artificial Neural Network-Based Heuristic Optimal Traffic Signal Timing, *Computer-Aided Civil and Infrastructure Engineering* 15 (2000), 293-307.
- [19] J. Cattan, J. Mohammadi, Analysis of bridge condition rating using neural networks, *Computer Aided Civil and Infrastructure Engineering* 12 (1997), 419-429.
- [20] Z. Li, R. Burgueño, Using soft computing to analyze inspection results for bridge evaluation and management, *Journal of Bridge Engineering* 15 (2010), 430-438.
- [21] H. Adeli, Neural networks in civil engineering: 1989–2000, *Computer-Aided Civil and Infrastructure Engineering* 16 (2001), 126-142.
- [22] J. Bieñ, Neural Networks in Bridge Management Systems, *Advanced Technology in Structural Engineering*, ASCE (2004), 1-8.
- [23] Y.-H. Huang, Artificial Neural Network Model of Bridge Deterioration, *Journal of Performance of Constructed Facilities* 24 (2010), 597-602.
- [24] F. Dan Foresee, M.T. Hagan, Gauss-Newton approximation to Bayesian learning, *Proceedings of the 1997 international joint conference on neural networks, IEEE* 3 (1997), 1930-1935.
- [25] S. Roweis, Levenberg-marquardt optimization, Notes, University Of Toronto (1996).

# Information-based formulation of a creep model using a new experimental database

Wassim RAPHAEL<sup>a,1</sup>, Laurent TOUMA<sup>a</sup> and Alaa CHATEAUNEUF<sup>b</sup>

<sup>a</sup>*Ecole Supérieure d'Ingénieurs de Beyrouth (ESIB), Saint-Joseph University, Lebanon*

<sup>b</sup>*Clermont Université, Univ Blaise Pascal, Institut Pascal, BP 10448, F-63000, France*

**Abstract.** Creep and shrinkage strain of concrete can have prejudicial consequences in prestressed structures built by phases. But these uncontrolled strains appear, with values often clearly more important than the expected ones. In fact, there is not yet a physical explanation perfectly satisfactory of creep and the codified descriptions of this phenomenon are always unreliable. In the context of this study, and starting from an important experimental database from large centers of research in Europe, a new model of creep calculation was developed and allows to obtain results more satisfactory than those of BPEL, EC2 and CEB 78

**Keywords.** Creep, strains, concrete, experimental database, model

## Introduction

When tackling the issue of concrete performance, the emphasis is usually put on a single parameter, namely the strength. However, in some situations, some other parameters have an equal importance if not a greater one, such as time-variant deformations. The prediction of the behavior of concrete structures with time is an extremely complex task, as chemical, physical and mechanical properties of concrete are substantially altered. In particular, the rheological behavior of concrete is itself time dependent. More generally, the strains undergone by concrete can be classified into three categories: shrinkage strain, instantaneous strain and creep strain. Shrinkage strain appears immediately after the concrete has been cast, and it will continue, with monotonically decreasing rate, over the whole lifetime of concrete member. Instantaneous strain is defined as the strain that appears immediately when the load is applied, whether they belong to the elastic or inelastic domains. Creep is defined as the increase of strain with time, for concrete under sustained load [1-2]. The distinction between instantaneous strain and creep strain is not straightforward as it may seem, because the recorded instantaneous strain depends on the rate of application of the load and thus, inevitably, a portion of that strain is due to creep. However, such distinction will not be crucial in practical cases because what matters is the total strain incurred by the concrete member under study.

<sup>1</sup>Corresponding author: [wassim.raphael@usj.edu.lb](mailto:wassim.raphael@usj.edu.lb), CST Mkalles Mar Roukos, Po Box 11-514 Riad El Solh Beirut, 1107 2050, Lebanon, [Tel: 961 1 421354](tel:9611421354), Fax. 961 4 532645

The physical nature of creep is not yet well understood. Recent researches are focused on visco-elastic behavior of materials, but no major recent results of practical value have come out yet for concrete structures. Consequently, almost all creep code models are mainly of empirical nature, whose parameters are determined by experience. In 1978, Bazant and Panula started collecting, at the Northwestern University, shrinkage and creep data from all over the world [3]. Their database contained approximately 400 creep tests and 300 shrinkage tests, mostly from North America and Europe. After the ACI-CEB Hubert Rush workshop on concrete creep, Muller and Panula extended this database as part of the collaboration established between the ACI and the CEB [2]. A further expansion undertaken by the RILEM TC 107-CSP subcommittee 5 led to what is known as the RILEM database.

As one might have expected, several problems and shortcomings affected the use of this or that database to compare or to calibrate creep models. Bazant, Guang-Hua Li and Baweja pointed out several issues introducing biases in the results, namely: (i) highly non-uniform data distributions, the statistics were dominated by data with short load duration, low age at loading, and small specimen size; (ii) the statistics were also dominated by data for old types of concrete having low strength, which are seldom used anymore; (iii) the variability of concrete composition and other parameters in the database causes enormous scatter, masking the much lower scatter in the time evolution of creep and shrinkage. Moreover, since creep depends on the type of cement and since cement descriptions differ from country to country, the data obtained from European cement concretes may not be directly compared with that of United States cement concrete and so on [4]. Another problem is related to which data sets to include regarding the composition of the concrete. The problem of evaluating existing models and code procedures received extensive attention in the literature. Numerous papers proposed various statistical methods to evaluate and compare the predictive capability of these procedures.

In the present work, a large database has been constituted for creep testing carried out by many research institutes in Europe. The experimental results in this database are compared with three European design codes of practice: BPEL, CEB 78 and EUROCODE 2. As the comparison shows that these codes underestimate the long-term creep strain with errors of up to 300%, a new creep model is proposed in this work on the basis of the experimental database. The proposed model is then compared and validated with a practical case study.

## **1. Inaccuracy of creep codes**

### *1.1. Experimental database*

In Europe, the creep of concrete structures can generally be evaluated by one of the following design codes: the Eurocode 2 (EN 1992-1-1 or EC2) (Eurocode2 – EN 2004) [7], the Model-Code CEB 78 (Code-Modèle CEB – FIP 1978) [8], or the French code BPEL. Starting from a large experimental database that we have constituted during the last five years by collecting data from several research institutions in Europe (RILEM<sup>1</sup>,

---

LCPC<sup>2</sup>, CEBTP<sup>3</sup>), a comparison is performed between the results obtained by laboratory tests and those given by the models indicated in the design codes. The database includes 432 creep tests on samples of various shapes and dimensions, under different environmental conditions. It is to be mentioned that intensive negotiations were necessary to convince some institutions to allow for the access to their testing data. In order to allow for useful exploration, large effort has been spent in the uniformization and the classification of the laboratory test data. This database allows us to validate each creep model by quantified statistical analysis.

The parameters considered for the creep tests are [9-18-19-20] :

- the temperature,  $T$  (°C);
- the loading date,  $t_0$  (days);
- the compressive concrete strength at 28 days,  $f_{c28}$  (MPa);
- the relative ambient humidity,  $\rho_h$  (%);
- the mean radius,  $r_m$  (cm);
- the type of cement,  $\alpha$ ;
- the compressive strength of concrete at the loading date,  $f_{cm}(t_0)$  (MPa);
- the applied stress,  $\sigma$  (MPa).

The compressive strength of concrete at 28 days  $f_{c28}$  (MPa) varies between 11 MPa and 118 MPa while the mean radius  $r_m$  of the specimen varies between 1.75cm to 15.25 cm. Regarding the loading date  $t_0$ , it varies between 0.5 day and 3300 days. The relative ambient humidity  $\rho_h$  varies between 1% and 100%. The applied stress  $\sigma$  varies between 0.69 and 52.7 MPa. The duration of the test after the loading date ( $t-t_0$ ) exceeds for some experiments 3000 days.

It is to note that the tests in the database were performed for different types of cement (class *S*, *N* and *R*), which are equally distributed; i.e. practically one third of tests belongs to each type. Therefore, there is no bias in the consideration of the database regarding the cement type. For each test in the data, the cement class is identified according to ASTM and EC2 classifications (i.e. Types I, II and III for ASTM, and classes R, N and S for EC2); the equivalence is considered from two points of view: the type of use regarding hardening and the chemical requirements. Although classes *N* and *R* can be well identified (as they correspond to ASTM types I and III respectively), confusion may appear for specific cases in class *S* (i.e. slow hardening). Even when subjective classification may occur in some cases, the large size of the database makes the model assessment insensitive to particular cases. In the creep database, three categories of compliances  $J^4$  are identified:

- 126 tests corresponding to small creep values with  $J$  between 0 and  $60 \times 10^{-6} \text{ MPa}^{-1}$
  - 187 tests corresponding to moderate creep values with  $J$  between  $60 \times 10^{-6}$  and  $120 \times 10^{-6} \text{ MPa}^{-1}$
  - 119 tests corresponding to large values of creep with  $J > 120 \times 10^{-6} \text{ MPa}^{-1}$
-

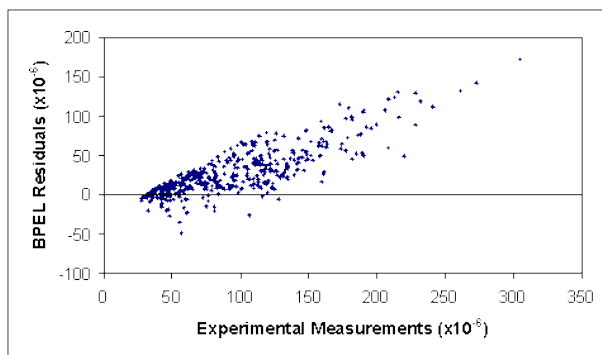
## 1.2. Residual method

In order to evaluate the accuracy of predictive methods on the basis of  $n$  experimental tests, the *Residual Method* has been applied on the creep compliance [10]. The residuals are calculated by the difference between the experimental and predicted compliances, as given in the following equation [15] :

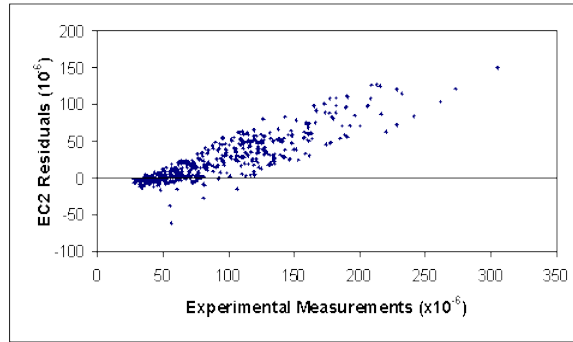
$$R_{ij} = (ObsX_{ij} - CalX_{ij}) \quad (1)$$

Where  $CalX_{ij}$  and  $ObsX_{ij}$  are respectively the predicted and the experimental creep compliance at time  $j$  of experiment  $i$ . In this study, as we are interested only in long-term creep, time-dependent variation is not involved in the code validation [3-11-12]. Therefore, only time at 3000 days after loading (i.e.  $j=3000$ ) has been considered. The graphical representation is given by plotting the residuals versus creep strains [13]. Figures 1 to 3 show the residuals obtained for the three creep models. Positive residuals indicate that the model underestimates the creep compliance whereas a negative residual means that the model overestimates the creep compliance. These figures have several common characteristics:

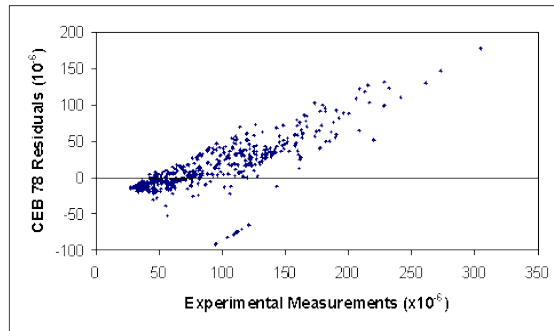
- they show clearly that creep models often underestimate the long-term strain.
- the residual magnitudes are very high for many creep tests, underlining the code inadequacy in creep prediction.
- the amplitude of residuals is smaller for the small values of creep compliance “J” than for large ones. It seems that the models are fitted for small creep strains.



**Figure 1.** Creep compliance residuals for model BPEL (J in MPa<sup>-1</sup>)



**Figure 2.** Creep compliance residuals for model EC2 (J in MPa<sup>-1</sup>)



**Figure 3.** Creep compliance residuals for model CEB 78 (J in MPa<sup>-1</sup>)

Table 1 summarizes the distribution of data points for various categories of long-term creep. The positive and negative signs indicate the residual type: underestimation or overestimation respectively. For a particular category, the values between brackets indicate the percentage of residuals in each category.

**Table 1.** Distribution of number and percentage of residual points for creep models

<i>Residual Range</i>	<b>Small Creep</b>		<b>Moderate Creep</b>		<b>Large Creep</b>	
	+	-	+	-	+	-
	95	31	177	10	118	1
BPEL	75%	25%	95%	5%	99%	1%
	60	66	168	19	119	0
EC2	48%	52%	90%	10%	100%	0%
	13	113	136	51	117	2
CEB 78	10%	90%	73%	27%	98%	2%

By analyzing the above results, we can state the following conclusions:

- The creep predicted by the design codes is not satisfactory for long-term creep predictions. For almost all the cases, the codes underestimate the creep and in some cases, the error can be very large.
- The residuals show a large dispersion, even when the mean value is adequately predicted, the wide confidence interval makes the prediction unreliable for practical use.
- There is a need for a predictive model with better performance, where most of the residuals are located in a narrow band equally distributed on positive and negative sides.

## 2. Phenomenological Creep Model PCM 2014

### 2.1. Proposed model

The proposed model is based on the observation of physical behavior of creep phenomenon. It aims at describing the creep compliance in terms of the structural and environmental parameters. The experimental observations show clearly two kinetic regimes in logarithmic time scale (Figure 4): a kinetic for short term (few days after loading) where the creep increases quickly and a kinetic for long-term where the creep increases with a lower rate which is almost constant, leading to large increase over structural lifetime. These two regimes suggest an additive form of the corresponding creep strains. That's why the proposed model is called **Phenomenological Creep Model (PCM 2014)**.

In order to determine the best fitting of creep evolution, we have considered the database specimens. The database will serve for both calibration and validation of the proposed model. For this reason, 50% of the creep tests have been randomly selected from the database in order to calibrate the proposed model, i.e. the PCM 2014, while the remaining 50% are used for the validation of the quality of the obtained predictions.

To consider the two creep kinetics within an additive expression, we have analyzed the experimental results in the database to develop the best nonlinear mathematical model for predicting the long-term creep. In a semi-logarithmic scale, our analyses have converged at the following expression for the compliance  $J$  [16-17] :

$$J - J_{init} = \mathbf{A} \cdot (1 - e^{-(t-t_0)/30}) + \mathbf{B} \cdot \log_{10}(t/t_0) \quad (2)$$

where  $t$  is the time in days,  $t_0$  is the loading time in days,  $J$  is the compliance which characterizes the creep strain per unit stress, and  $J_{init}$  is the compliance value at  $t = t_0$  ( $J_{init}$  is the instantaneous creep strain per unit stress); the units of  $J$  and  $J_{init}$  are  $\text{MPa}^{-1}$ . The parameters  $A$  and  $B$  have to be calibrated on the basis of experimental data. As shown in Figure 5, the parameter  $A$  represents the amplitude at short-term creep and the parameter  $B$  represents the long-term creep rate. Equation (2) is the sum of three terms (as it can be seen in figure 5):

- the first term is constant  $J_{init}$  allowing to take account for instantaneous creep strain at loading;
- the second term is exponential in elapsed time after loading, characterizing the evolution of short term creep;



- the third term is logarithmic in time, characterizing the evolution of long-term creep.

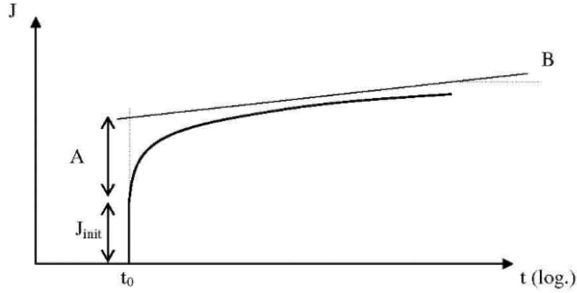


Figure 4. Shape of the curve of the total creep

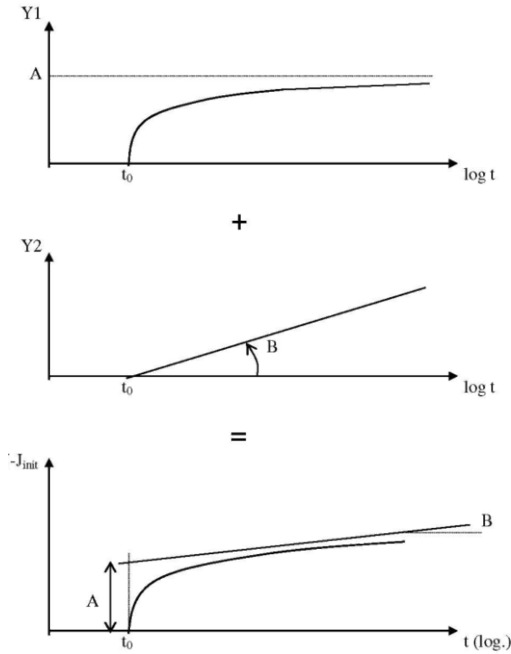


Figure 5. Shape of the creep curve, graphic sum of two terms (EXP + LOG)

In order to show the prediction capacity of the PCM 2014 in fitting the experimental data, Figure 6 compares the experimental results of creep testing with the curve given by equation 2, using the software Curve Expert. This same analysis was performed for a selected experimental set corresponding to 50% of the creep tests performed in the laboratories as mentioned previously. In all cases, the PCM 2014 gave

a very high fitting correlation, as in figure 6. It has been noticed that the correlation coefficients of the regression vary between 0.92 and 0.99 with a mean value of 0.98, which is very good for confidence in results.

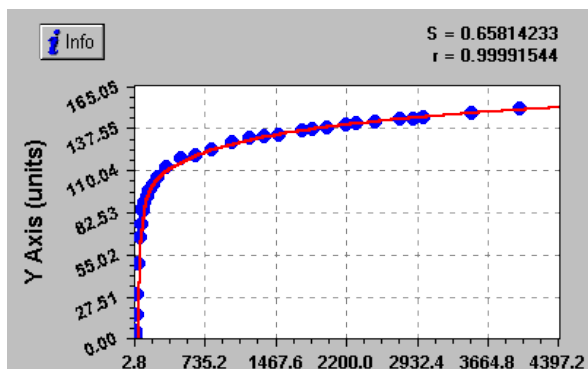


Figure 6. Example of PCM 2014 experimental fitting using the software Curve Expert.

## 2.2. Calibration of PCM 2014 parameters

The proposed creep model PCM 2014 (equation 2) depends on two parameters:  $A$  and  $B$  which should be calibrated using the experimental results. As mentioned previously, and using the software Curve expert, the values of the three parameters  $A$  and  $B$  are obtained by the minimization of the mean square error between predictive and experimental points, in addition to the determination of the optimal value of the initial compliance  $J_{init}$  at  $t = t_0$ . Therefore, we have a set of parameters ( $A, B, J_{init}$ ) for each experiment in the selected database tests. Each set ( $A, B, J_{init}$ ) depends on the corresponding test configuration, and instead of considering average values for all experiments, we have chosen to express these parameters in terms of testing conditions, which are identified as:

- the temperature,  $T$  ( $^{\circ}\text{C}$ )
- the loading date,  $t_0$  (days)
- the compressive concrete strength at 28 days,  $f_{c28}$  (MPa)
- the relative ambient humidity,  $\rho_h$  (%)
- the mean radius,  $r_m$  (cm)
- the type of cement,  $\alpha$
- The compressive strength of concrete at the loading date,  $f_{cm}(t_0)$  (MPa)
- The applied stress,  $\sigma$  (MPa)

For all the sets of parameters ( $A, B, J_{init}$ ), the regression procedure is applied to define the relationships between these parameters and the testing conditions influencing creep behavior. With a correlation coefficient of 0.95, the following coupled relationships have been obtained by Curve expert:

$$J_{init} = 32.963 - (0.0625 \times f_{c28}) + (0.542 \times r_m) - (0.0083 \times t_0) + (1.74 \times \alpha) - (0.12 \times f_{cm}(t_0)) + (0.225 \times A) \quad (3)$$

$$\mathbf{A} = -11.799 + (0.363 \times \mathbf{J}_{\text{init}}) + (0.25 \times \boldsymbol{\sigma}) - (0.144 \times \mathbf{f}_{\text{c28}}) + (0.122 \times \boldsymbol{\rho}_h) - (2.310 \times \mathbf{r}_m) - (0.0096 \times \mathbf{t}_0) + (0.233 \times \mathbf{T}) + (1.5 \times \mathbf{B}) \quad (4)$$

$$\mathbf{B} = 19.795 - (0.0910 \times \boldsymbol{\sigma}) - (0.168 \times \boldsymbol{\rho}_h) + (0.778 \times \mathbf{r}_m) + (0.006955 \times \mathbf{t}_0) - (0.0525 \times \mathbf{T}) + (0.356 \times \mathbf{A}) \quad (5)$$

The solution of the above coupled system of equations allows us to express the parameters A, B and  $\mathbf{J}_{\text{init}}$  as functions of the structural configuration:

$$\mathbf{J}_{\text{init}} = 9.0306 \times 10^{-2} \mathbf{T} + 2.1098 \boldsymbol{\alpha} + 6.6449 \times 10^{-2} \boldsymbol{\sigma} - 9.5765 \times 10^{-3} \mathbf{t}_0 - 7.6109 \times 10^{-2} \boldsymbol{\rho}_h - 1.1973 \times 10^{-2} \mathbf{r}_m - 0.1455 \mathbf{f}_{\text{cm}}(\mathbf{t}_0) - 0.16009 \mathbf{f}_{\text{c28}} + 50.444 \quad (6)$$

$$\mathbf{A} = 0.40136 \mathbf{T} + 1.6435 \boldsymbol{\alpha} + 0.29533 \boldsymbol{\sigma} - 5.6734 \times 10^{-3} \mathbf{t}_0 - 0.33826 \boldsymbol{\rho}_h - 2.4621 \mathbf{r}_m - 0.11334 \mathbf{f}_{\text{cm}}(\mathbf{t}_0) - 0.43373 \mathbf{f}_{\text{c28}} + 77.693 \quad (7)$$

$$\mathbf{B} = 9.0384 \times 10^{-2} \mathbf{T} + 0.58509 \boldsymbol{\alpha} + 1.4137 \times 10^{-2} \boldsymbol{\sigma} + 4.9353 \times 10^{-3} \mathbf{t}_0 - 0.28842 \boldsymbol{\rho}_h - 9.8508 \times 10^{-2} \mathbf{r}_m - 4.0349 \times 10^{-2} \mathbf{f}_{\text{cm}}(\mathbf{t}_0) - 0.15441 \mathbf{f}_{\text{c28}} + 47.454 \quad (8)$$

### 2.3. Validation of PCM 2014 creep model

As mentioned previously, the validation set is composed of 50% of database experiments which have not been selected for calibration. For this validation set, the 3000-days creep compliances for the proposed PCM 2014 are compared with the predictions obtained by the BPEL, the CEB 78 and the Eurocode 2, assuming that the creep strain is completed at this age. In order to evaluate the PCM 2014 accuracy, the  $M_{CEB}$  statistical method, suggested by Muller and Hilsdorf was applied [9-10-17]. The  $M_{CEB}$  method aims at calculating the mean deviation to indicate whether the model overestimates or underestimates the experimental values. The  $M_{CEB}$  is calculated as following:

$$M_i = \frac{1}{n} \sum_{j=1}^n \frac{CalX_{ij}}{ObsX_{ij}} \quad (9)$$

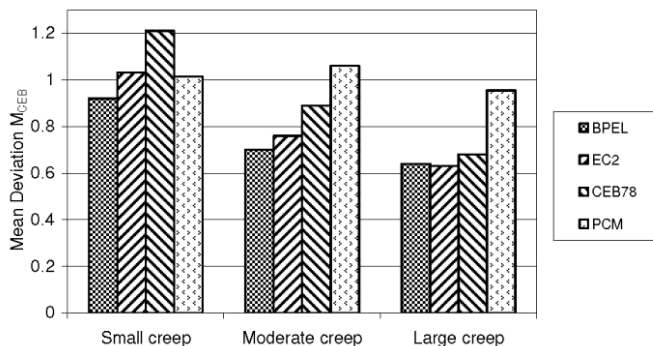
$$M_{CEB} = \frac{\sum_{i=1}^N M_i}{N} \quad (10)$$

where  $CalX_{ij}$  and  $ObsX_{ij}$  are respectively the predicted and the experimental creep compliance at time  $j$  of experiment  $i$ ,  $M_{CEB}$  is the mean deviation,  $n$  is the total number of values  $j$  of experiment  $i$  and  $N$  is the total number of data sets. The predicted creep results are better when this coefficient converges to 1, and close to the observed results; so the expected value for  $M_{CEB}$  is 1. If the coefficient is bigger than 1, this means that the theoretical predicted creep strain is greater than the experimental one.

In Table 2, the mean deviation  $M_{CEB}$  is calculated for the three categories of creep in the collected database: small, moderate and large, as defined in Section 2. The graphical illustration of  $M_{CEB}$  results is also presented in figure 7. It can be clearly observed that the PCM 2014 predictions are quite accurate as the mean deviations  $M_{CEB}$  for the three categories of creep are close to 1.

**Table 2.** Results of  $M_{CEB}$  for different design codes for the three categories of creep

$M_{CEB}$	<b>Proposed model PCM 2014</b>	BPEL	Eurocode	CEB 78
Small creep	<b>1.013</b>	0.922	1.029	1.213
Moderate creep	<b>1.059</b>	0.701	0.755	0.893
Large creep	<b>0.954</b>	0.641	0.631	0.678



**Figure 7.** Results of  $M_{CEB}$  for different design codes for the three categories of creep

For the validation set of the database, Figure 8 depicts the residuals obtained for the proposed model PCM 2014. It can be clearly observed that the PCM 2014 predictions are quite accurate as the residuals are close to zero. The analysis for the distribution of the residuals for various categories of long-term creep for the MPF is given in Table 3, where the values in brackets indicate the percentage of residuals among the points for each category. The comparison of these results with those given by the three design codes (Section 2 – Table 1) shows the large improvement in creep predictions.

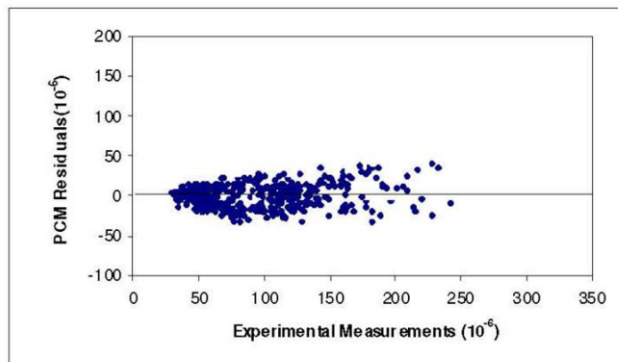


Figure 8. Creep compliance residuals for model MPF (J in MPa<sup>-1</sup>)

Table 3. Distribution of number and percentage of residual points for the new model MPF

	Small Creep		Moderate Creep		Large Creep	
<i>Residual Range</i>	+	-	+	-	+	-
	58	68	72	115	63	56
<b>PCM 2014</b>	46%	54%	39%	61%	53%	47%

The above results lead to the following conclusions:

- The proposed Phenomenological Creep Model PCM 2014 provides better results than other codes, in small, moderate and large creep strains. The advantage of PCM is mainly observed for large creep values.
- The PCM 2014 predictions are unbiased with respect to creep predictions. The remaining prediction scatter is explained by random testing conditions, such as measurement errors and information. The residual random error can be considered by Gaussian variable with mean equal to zero.
- The comparison with European codes of practice shows large improvements for moderate and large creeps.
- In addition to the above observations, the PCM 2014 allows us to evaluate accurately the initial creep compliance  $J_{init}$  by taking into account a number of structural parameters, not only the concrete strength as given in most of design codes, especially EC2, CEB78 and BPEL. Moreover, PCM 2014 considers the interdependence between compliance J and applied stress  $\sigma$ , which is not the case in the mentioned codes of practice.

### 3. Conclusion

In this work, a large creep database has been collected in order to develop and to validate a new model for long-term creep predictions. The comparison between the experimental results and three European codes of practice has shown that long-term creep strains are largely underestimated in these codes, which may lead to serious defects in infrastructure performance, especially when prestressing is considered.

The proposed model, called the Phenomenological Creep Model PCM 2014, is based on the analysis of creep tests in the database and on the physics of the creep behavior, which is divided into exponential time function for short-term creep evolution and logarithmic time function for long-term creep evolution. The proposed formulation is given as a function of the material, loading and environmental parameters. The PCM 2104 has been validated by experimental results, different from those used for model calibration. The comparison with experimental data shows the high accuracy of the proposed model, for various creep kinetics: small, moderate and large. The PCM 2014 improves largely the calculation of creep strains, compared to the existing codes of practice.

In the future, it would be also interesting to extend the comparison of the proposed model with other models that are not in the European codes, such as ACI and Canadian creep models. It would also be interesting to analyze the effect of prediction accuracy on the reliability assessment of existing infrastructures.

### 4. Acknowledgement

The authors gratefully acknowledge Professor Z.P. Bazant and all persons from RILEM, LCPC and CEBTP for their kind support for providing experimental and field measurement data.

### References

- [1] H.K. Hillsdorf, and D.J. Carreira, ACI-CEB conclusions of the Hubert Rüschi Workshop on Creep of Concrete, *Concrete international*, 2, 1980.
- [2] H.S. Muller, Z.P. Bazant, and C.H. Kuttner. Database on creep and shrinkage tests, *Rilem subcommittee 5 Report Rilem TC107-CSP, RILEM*, Paris, 81, 1999.
- [3] Z.P. Bazant and L. Guang-Hua. Unbiased Statistical Comparison of Creep and Shrinkage Prediction Models, *ACI Materials Journal*, 105, 2008.
- [4] D.B. McDonald, and Roper, H.,. Accuracy of prediction models for shrinkage of concrete, *ACI materials journal*, 3 (1993), 265-271.
- [5] Règles techniques de conception et de calcul des ouvrages et constructions en béton précontraint suivant la méthode des états limites, Règles BPEL 91, *Cahiers techniques du CSTB*
- [6] Modifsactions des règles de calcul du Béton Précontraint, 1999. *Fascicule 62, Titre II du CCTG - TRAVAUX* (Section 2).
- [7] Eurocode 2 – EN 2004. General rules and rules for building, *Design of concrete structures, Part 1*.
- [8] Code-Modèle CEB - FIP 78. Retrait et Fluage, *Bulletin d'information No 124/125*, Lausanne, 1980.
- [9] F.J. Ulm, M. Prat, JA Calgaro and I. Carol, Creep and shrinkage of concrete - *Editors : Special issue of Revue française de génie civil – Hermès Science Editions – France*, 1999.
- [10] W. Raphael, A. Chateaneuf, M. Lemaire, J.L. Favre and JA. Calgaro, Reliability based assessment of prestressed concrete structures subject to Creep – Application to a bridge, *Proceedings of the 9th International Conference on Applications of Statistics and Probability to Civil Engineering (ICASP 9)*, San Francisco, 2003.

- [11] W. Raphael, R. Faddoul, and A. Chateaneuf, Information-based formulation for Bayesian updating of the Eurocode 2 Creep Model, *Structural Concrete Journal – FIB - Thomas Telford Edition*, 10, 2009.
- [12] L. Vandewalle, Concrete creep and shrinkage at cyclic ambient conditions, *Cement & Concrete Composites* 22, ELSEVIER, Paris, France, (2000), 201-208.
- [13] W. Raphael & A. Chateaneuf, Etude des structures en béton armé et précontraint, Nouveau Modèle et Calculs fiabilistes. *Éditions Universitaires Européennes EUE.*, 2011.
- [14] ZP. Bažant and S. Baweja, Creep and Shrinkage Prediction Model for Analysis and Design of Concrete Structures: Model B3, *Materials and Structures*, 28 (1995), 357-367.
- [15] W. Raphael, R. Faddoul, F. Geara, and A. Chateaneuf, Improvement of the Eurocode 2 Shrinkage Model for Concrete Using a Large Experimental Database, *Journal of Structural Concrete – FIB*, 13, (2012), 174-181,
- [16] W. Raphael, B. Seif-El-Dine and A. Chateaneuf, Information based formulation for Bayesian concrete creep models updating, *Proceedings of the Icosar 9th International Conference on Structural Safety and Reliability*, 2005.
- [17] W. Raphael, Etude du fluage des structures en béton armé et précontraint – *PhD thesis – Ecole Centrale Paris – France*, 2002.
- [18] NJ. Gardner, Comparison of Prediction Provisions for Drying Shrinkage and Creep of Normal Strength Concretes, *Canadian Journal of Civil Engineering*, 31, (2004), 767-775.
- [19] A. Al-Manaseer and S. Lakshmikantan, Comparison between Current and Future Design Code Models for Creep and shrinkage of concrete, *Revue Française de génie civil*, 3, (1999), 39-59.
- [20] L. Jianyong and Y. Yan, A study on creep and drying shrinkage of high performance concrete - *Cement and Concrete Research*, Pergamon. 31, (2001), 1203-1206.

# Testing and nonlinear numerical modelling of fibre pull-out mechanism from cementitious materials

Faisal ABDULLE<sup>1</sup> and Robert XIAO

*Department of Urban Engineering, London South Bank University, 103 Borough Road, London, SE1 0AA, United Kingdom*

**Abstract.** The benefits of using micro-fibres as a crack controlling measure for concrete have encouraged their widespread use in the construction industry in recent years. However, there are currently no design standards that cover the specification of micro-fibres due to difficulties in quantifying their performance, owing to the random distribution and orientation characteristics of these fibres when added to the concrete mix. Therefore, the main focus of this research has been to carry out experimental testing and numerical simulation of single fibres, with different geometrical and mechanical properties, embedded in cementitious matrix and subjected to pull-out loading. A series of pull-out tests were carried out to study the main factors that affect the performance of fibres and to compare those with results from numerical analysis. Three-dimensional (3D) solid finite elements have been used to numerically model the matrix and fibres. Contact and target elements were used to create a bonded contact between the fibre and matrix models, and Cohesive Zone Material (CZM) model has been employed to simulate the failure mechanisms of the pull-out tests. Comparison of results revealed close agreements between the experimental tests and numerical simulations, and recommendations are made where significant differences between the results were identified.

**Keywords.** Fibre pull-out testing, numerical modelling, simulation

## Introduction

Concrete is a widely used structural material in the construction industry, due to its durability and ability to be mixed and moulded into any shape on site while its strength can be designed against compressive forces. However, concrete is weak in tension and shear and requires steel reinforcing bars to take these forces [1, 2]. As well as the reinforcing bars, steel mesh or micro-fibres may be incorporated into the concrete to inhibit crack propagation due to serviceability conditions [1- 4].

The use of micro fibres is preferred over other options as they are less hazardous and cost much less to include in concrete compared to their counterparts [5, 6]. However, their performance is not yet fully understood, despite being the subject of

---

<sup>1</sup>Corresponding authors: [abdullf8@lsbu.ac.uk](mailto:abdullf8@lsbu.ac.uk), [xiaor2@lsbu.ac.uk](mailto:xiaor2@lsbu.ac.uk)



extensive research over a long period. This is due to their random distribution and orientation characteristics when added to the concrete mix [2]. It is generally accepted, however, that single fibre pull-out testing is the most effective way of investigating fibre-matrix interface bond behaviour. It allows the adhesion quality of fibrous concrete to be investigated and characterised, enabling the effectiveness of fibres to be determined [7, 8].

Therefore, the aim of this research was to carry out experimental testing and numerical modelling and simulation of single fibres, with different shapes, dimensions and mechanical properties, embedded in cementitious matrix and subjected to pull-out loading. The objective was to develop a finite element (FE) model that is capable of predicting the pull-out strength and failure mechanisms of such fibres, so that their performance is better understood and the need to carry out laboratory testing for this purpose is largely reduced. ANSYS, finite element analysis (FEA) software suite, has been used for the numerical modelling study.

## 1. Design and testing of experimental specimens

Three different grades of mortar matrix were designed from Ordinary Portland Cement (OPC, grade 52.5N), beach sand and water [9]. Six (100x100x100 mm) cubes, three (150x300 mm) cylinders and nine (65x65x200 mm) pull-out test specimens (3 for each type of fibre) were cast from each mortar mix according to specifications [10]. The cubes and cylinders were tested to determine the compressive and tensile strengths of the specimens [11, 12]. These were needed as inputs in the numerical modelling of the fibre reinforced matrix. The pull-out tests were carried out in order to validate the results from the numerical simulation.

Three different types of fibres were used in the research (see Figure 1). Two of the fibres were steel, but had different shapes (hooked end - HE and undulated - UD) and dimensions. The third fibre was micro-synthetic polymer fibre (polypropylene - PP), which also had different shape (fibrillated) and dimension as well as mechanical properties different from those of steel fibres.

The fibres were added into the pull-out test specimens by being clamped to the centre of the moulds before casting the specimens. An artificial crack was deliberately formed across the middle of the specimens by a thin plastic membrane placed in the moulds. This was to ensure that the only connection between the two halves of the matrix (being pulled apart) was via the single fibres, see Figure 2.

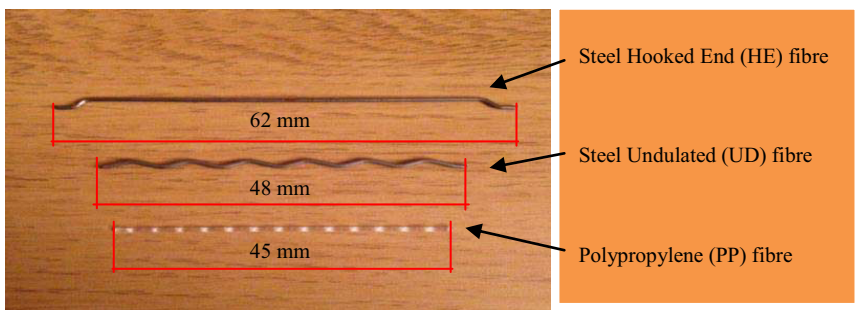


Figure 1. Fibres used in the research

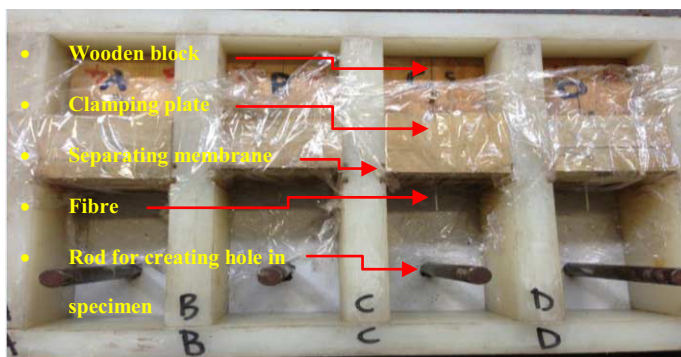


Figure 2. Fibre pull-out test specimen moulds ready for casting the first half

## 2. Nonlinear numerical modelling of fibre pull-out mechanism from matrix

### 2.1. Element types

Solid65 and Solid185 have been used to model the matrix and fibres respectively, and the interfacial bond between them has been created using Contact174 and the associated Target170 elements [13]. Cohesive Zone Material (CZM) model has been introduced to the contact element to activate debonding of fibres from the matrix using Mode II dominated Bilinear CZM Law, since the separation of the material interfaces is tangent to the interface [14, 15].

### 2.2. Material properties

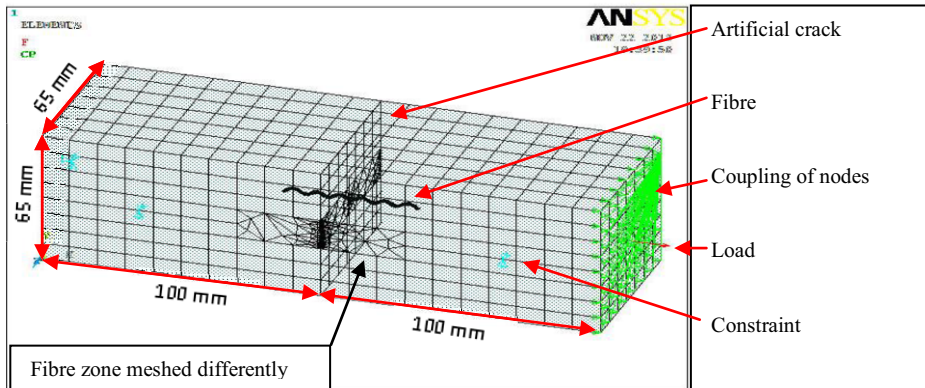
The properties shown in Table 1 and 2 have been used for the modelling of the specimens. The compressive and tensile strength values of the matrix were obtained from the experimental testing of the mortar cubes and cylinders, while the elastic modulus values for the different strengths of matrix were derived according to Table 3.1 of Eurocode 2 [1]. The material properties of the fibres were obtained from their manufacturers [3, 4]. Multilinear Isotropic (MISO) Hardening material model found in ANSYS has been used to model numerically the nonlinear behaviour of the matrix, and for the fibres Bilinear Isotropic (BISO) Hardening material model has been used [16]. Figure 3 shows the completed FE model.

Table 1. Material properties of matrix

Design Mix No.	Compressive strength (MPa)	Tensile strength (MPa)	Elastic Modulus (MPa)	Poisson's ratio
1	26.41	2.03	26561	0.2
2	41.23	2.72	29574	0.2
3	64.12	4.03	33163	0.2

**Table 2.** Material and geometrical properties of fibres

Properties	UD steel fibre	HE steel fibre	PP polypropylene
Elastic modulus (MPa)	210000	210000	10000
Tensile strength (MPa)	1050	1050	600
Poisson's ratio	0.3	0.3	0.3
Length (mm)	48	62	45
Diameter (mm)	1.04	0.98	Equiv. 1.08

**Figure 3.** Completed FE model

### 3. Comparison of FEA and experimental test results

#### 3.1. Fibre pull-out strength

Twenty seven pull-out specimens, having three different design strengths; 30 MPa (0.54 w/c), 40 MPa (0.42 w/c) and 60 MPa (0.30 w/c), and incorporating three different types of fibres, have been tested in total. There were generally two failure modes observed from the testing, pull-out failure and failure by rupture. The pull-out failure mode is associated with loss of bond between the fibre and matrix at the fibre-matrix interface. This type of failure occurred when test specimens with lower strengths were tested. The mechanically deformed fibres pulled out before reaching their ultimate strengths, but got straightened in the process (see Figure 4). This failure was classified as matrix failure.

However, rupture failure occurred when the tensile strength of fibres were exceeded. The failures were sudden and occurred just after peak loads. This type of failure was observed when mortar specimens with higher strengths were subjected to pull-out loading, which indicates that the bond strength of the matrix was greater than the strength of the failed fibres (see Figure 5). This is classified as fibre failure.

The load-displacement data from the FEA are superimposed on the experimental (EXP) test results in Figures 6 to 8. As can be seen in Figure 6, there is a very good agreement between the EXP and FEA results of the UD and PP fibres, with the ascending and descending slopes of the curves almost following the same path. In fact



Figure 4. Pull-out failure of fibres

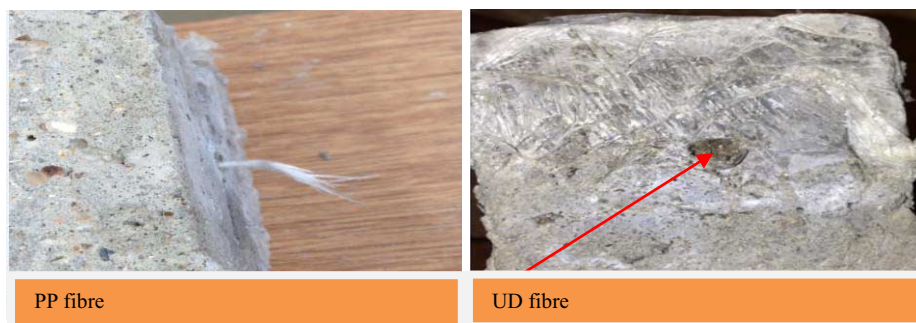


Figure 5. Rupture failure of fibres

the only difference in these curves is where there is a sudden increase in load in the descending region of the curves, due to bending/unbending of the fibres. However, the curves relating to the HE fibre are somewhat different with the biggest difference occurring during the pull-out process, where the resistance of the fibre is largely due to the mechanical anchorage of the hooks. The experimental results show considerable fluctuation of pull-out force beyond peak load, accounting for the fibre being pulled through hardened curved ducts. In comparison, the FEA results show a smooth curve, almost implying the only resistance of the HE fibre at this stage is frictional resistance, and do not capture well the additional energy required to bend/straighten the fibre hooks.

Figure 7 shows a similar trend with the FEA curves relating to the UD and PP fibres closely matching the EXP curves. The FEA curve for the PP fibre, however, shows more displacement at the beginning of loading than the EXP curve, with maximum difference of approx. 37% at 133 N pull-out load. This means that there is a 37% more elastic strain in the FE model of the PP fibre than there is in the actual fibre. As the load increases the FEA displacement decreases relative to the EXP displacement which increases, until they line up at peak load. It seems that minor difference in material properties is responsible for the slight deviation of the FEA results, as far as the displacement is concerned. In the case of the HE fibre, there is approx. 20% difference in peak load between the EXP and FEA results. Further improvements to the FEA data relating to the HE fibre can be seen in Figure 8.

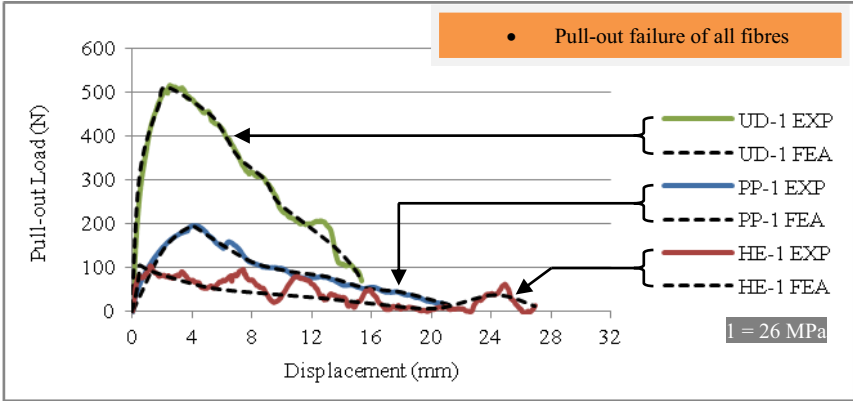


Figure 6. Load-displacement curves of different fibres: Test 1 (EXP vs. FEA)

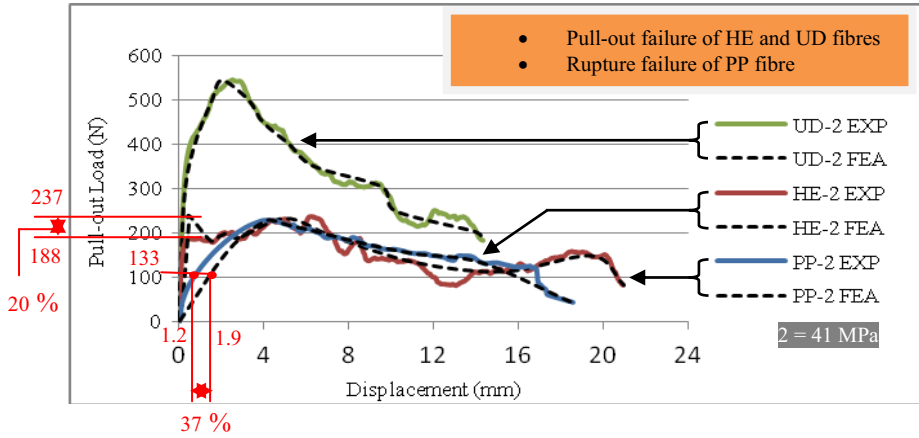


Figure 7. Load-displacement curves of different fibres: Test 2 (EXP vs. FEA)

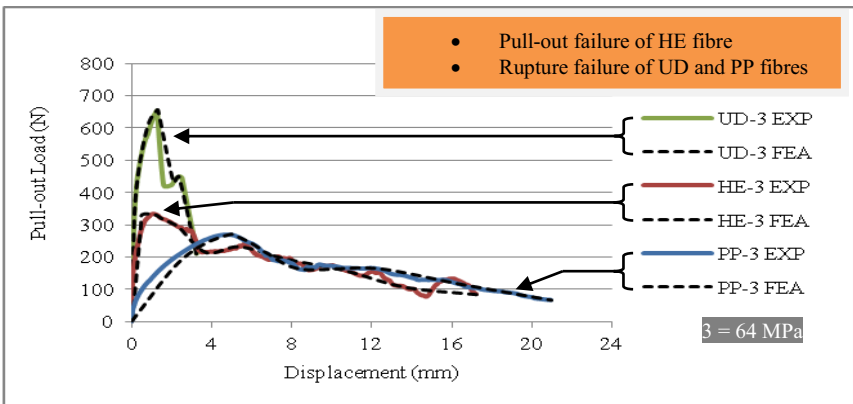


Figure 8. Load-displacement curves of different fibres: Test 3 (EXP vs. FEA)

3.2. Graphical simulation of interfacial fracture and fibre deformation

Figure 9a and 9b illustrate the damage sustained by the UD fibre when it failed. For comparison purposes, the state of the fibre is shown before and after the loading. It is clear from Figure 9b that the UD fibre had experienced the necking phenomenon (i.e. the cross-sectional area of the fibre decreased considerably due to plastic strains disproportionately localising in a relatively small area) as well as frictional sliding before the sudden failure (seen in Figure 8) occurred. As the cross-sectional area decreased considerably, the increased pull-out load due to bending or straightening of the fibre was enough to cause the failure of the fibre.

In an attempt to show the plastic deformation that the UD fibre had undergone as well as the fracture to the matrix along the interface, the FE model that consisted of this fibre type has been sliced through the middle and the fibre (still attached to one half of the matrix) is exposed as seen in Figure 10. Since the fibre is very small relative to the size of the matrix, the pull-out load did not affect much of the matrix. Only the region immediately adjacent to the fibre was affected.

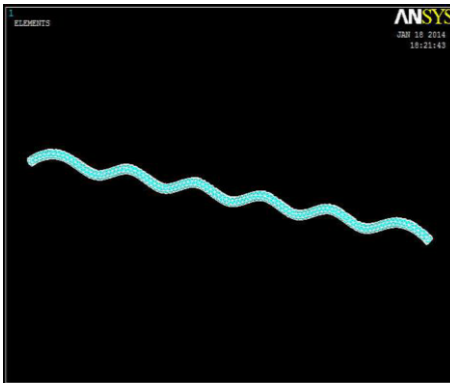


Figure 9a. UD fibre before loading

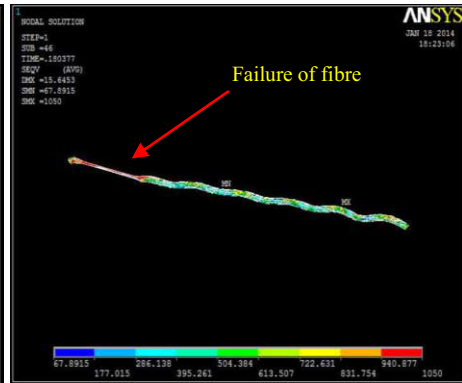


Figure 9b. UD fibre after loading

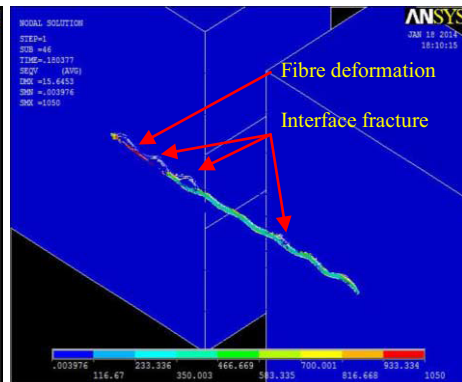
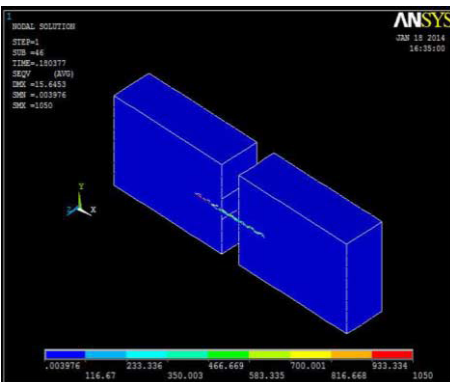


Figure 10. UD fibre-matrix model sliced through the middle

#### 4. Conclusions

The following conclusions can be drawn from the experimental and numerical investigations conducted:

- Pull-out load increases with increase in matrix strength due to improved interfacial bond between the fibre and matrix.
- Increase in length and diameter of fibre also increases the load required to cause debonding of fibres. However, it is more effective to increase the fibre diameter than length, as this increases the annular contact of the fibre with the matrix which in turn increases the pull-out load significantly.
- The HE fibre was found to be poorly proportioned and an increase in diameter is recommended.
- The Arc-Length nonlinear method used in the FEA allowed the full behaviour of the test specimens to be simulated and overcame the convergence difficulties encountered when materials reach their limit.
- It was concluded that the FE model is capable of predicting the load capacities and behaviour of the subject fibres, with the exception of the HE fibre whose resistance (after debonding) fluctuated considerably due to its deeper anchorage which the FEA did not capture well.

#### References

- [1] BS EN 1992-1-1 (Eurocode 2), *Design of concrete structures - Part 1-1: General rules and rules for buildings*, BSI Standard Publications, London, 2004.
- [2] The Concrete Society, *TR63 Guidance for the Design of Steel-fibre-reinforced Concrete*, The Concrete Society, Surrey, 2007.
- [3] Propex Concrete Systems, *Enduro 600 Product Data Sheet*. Retrieved 15 January 2014 from <http://www.fibermesh.com/downloads/Enduro%20600.pdf>
- [4] Dramix, 2010, *Data Sheet*. Retrieved 15 January 2014 from <http://www.bekaert.com/~media/Files/Download%20Files/Construction/Concrete%20reinforcement/Dramix%20General/Datasheet%20Dramix%20RC-6535-BN.ashx>
- [5] Elasto Plastic Concrete, *The History of Fibre Reinforcement*. Retrieved 25 October 2013 from <http://www.elastoplastic.com/index.php/the-history-of-fibre-reinforcement>.
- [6] G. Centonze, Steel Fibres from Waste Tyres as Reinforcement in Concrete: A Mechanical Characterization, *Construction & Building Materials* **36** (2012), 46 - 57.
- [7] R. Y. Xiao, and C. S. Chin, Finite Element Modelling of Fibrous Concrete Structures, *Trends in Civil and Structural Engineering Computing* **6** (2009) 131 - 148.
- [8] E. Zile, and O. Zile, Effect of the Fibre Geometry on the Pullout Response of Mechanically Deformed Steel Fibres, *Cement and Concrete Research* **44** (2012) 18 - 24.
- [9] Building Research Establishment (BRE), *Design of Normal Concrete Mixes*. Second ed. Construction Research Communications Ltd, Watford, 1997.
- [10] BS EN 12390-2, *Testing Hardened Concrete - Part 2: Marking and Curing Specimens for Strength Tests*, BSI Standard Publications, London, 2009.
- [11] BS EN 12390-3, *Testing Hardened Concrete - Part 3: Compressive Strength of Test Specimens*, BSI Standard Publications, London, 2009.
- [12] BS EN 12390-6, *Testing Hardened Concrete - Part 3: Tensile Splitting Strength of Test Specimens*, BSI Standard Publications, London, 2009.
- [13] ANSYS, Inc., *Modelling Composites*, ANSYS Release 14.0, USA, 2011.
- [14] ANSYS, Inc., *Modelling Interface Delamination with Contact Elements*, ANSYS Release 14.0, USA, 2011.
- [15] ANSYS, Inc., *Cohesive Zone Material Model*, ANSYS Release 14.0, USA, 2011.
- [16] ANSYS, Inc., *Modelling Material Nonlinearities*, ANSYS Release 14.0, USA, 2011.

# Parameter identification for supports and cracks in beams with non-classical boundary conditions

Ljubov FEKLISTOVA<sup>1</sup> and Helle HEIN  
*University of Tartu, J. Liivi 2, 50409, Tartu, Estonia*

**Abstract.** This article addresses parameter identification problem in vibrating Euler-Bernoulli beams with an open crack or elastic intermediate supports. The crack is simulated by a line spring model. The boundary value problem is solved by the aid of Haar wavelets. The characteristic parameters are predicted using the artificial neural networks. Two different approaches based on natural frequencies and Haar wavelets are compared. The significance of the second approach lies in its ability to make fast and trustworthy predictions on the selected parameters.

**Keywords.** Haar wavelet, neural networks, crack, elastic boundary conditions

## Introduction

A large number of studies has been conducted in the recent decades devoted to the health monitoring of the supports and cracks localization in vibrating beam-like structures [1-6]. Lau expanded Rutenberg's research on the free vibration of uniform beams with rotational constraint and presented a closed-form solution to the beam with rotational and translational supports at some point of the beam [7]. The exact closed-form solution of multi-cracked Euler-Bernoulli beam-like structures by means of Dirac's delta was proposed by Caddemi and Calio in 2008 [8] and further developed by Caddemi and Morassi in 2013 [9]. Alternatively, an analytical approach using a transfer matrix method was described by Attar [10].

The calculation of the stiffness parameters of the supports or characteristic parameters of the crack from the governing equation of the vibrating beams is an inverse problem and cannot be done analytically. Therefore, alternative methods have to be developed. A large number of numerical solutions are based on mesh methods, such as finite element method [13], finite difference method [12], spectral finite element method [11], etc [14]. Such methods have some deficiencies related to the mesh definition, calculation and computer storage.

The aim of this paper is to describe a mesh-free time-efficient method for parameter predictions of the supports and cracks in isotropic beams with arbitrary boundary conditions. Since the application of the interest falls into the low frequency region and a long slender beam, the Euler-Bernoulli beam theory is chosen. The

---

<sup>1</sup>Corresponding author. ljubov.feklistova@ut.ee, helle.hein@ut.ee



solution is based on the Haar wavelets and artificial neural networks (ANN). The integrity and computational efficiency of the method is demonstrated through a series of case studies.

### 1. Free vibration of beams with elastic constraints

A uniform Euler-Bernoulli beam of length  $L$  with elastic boundaries and an arbitrary number of intermediate elastic supports is shown in Figure 1. The restraints are provided by either a translational or rotational spring, or both, which are characterized by the spring constants  $K_t$  or  $K_r$ , respectively.

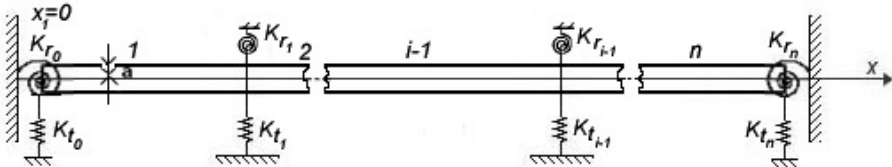


Figure 1. The beam with a crack and translational and rotational spring supports.

The governing differential equation of the  $i$ -th beam element of length  $l_i$  ( $i = 1, \dots, n$ ) is as follows [15]:

$$EI \frac{\partial^4 w_i(x_i, t)}{\partial x_i^4} + \rho A \frac{\partial^2 w_i(x_i, t)}{\partial t^2} = 0, \tag{1}$$

where  $w_i(x_i, t)$  is the transverse displacement of the  $i$ -th beam element,  $E$  is the Young's modulus,  $I$  is the moment of inertia,  $\rho$  is the mass per unit volume,  $A$  is the cross-sectional area and  $t$  is the time. By separating the variables, the solution of  $w_i(x_i, t)$  can be expressed as  $w_i(x_i, t) = W_i(x_i)T(t)$ , and the equation with regard to  $W_i(x_i)$  takes the following form:

$$\frac{d^4 W_i(x_i)}{dx_i^4} - k^4 W_i(x_i) = 0, \tag{2}$$

where  $\omega$  is the natural frequency and

$$k^4 = \frac{\omega^2 m}{EI}. \tag{3}$$

The boundary conditions of the beam at the left and right ends are as following:

$$\begin{aligned}
 K_{r_0} \frac{\partial w_1(0,t)}{\partial \alpha_1} &= EI \frac{\partial w_1^2(0,t)}{\partial \alpha_1^2}, & K_{t_0} w_1(0,t) &= -EI \frac{\partial w_1^3(0,t)}{\partial \alpha_1^3}, \\
 K_{r_n} \frac{\partial w_n(l_n,t)}{\partial \alpha_n} &= -EI \frac{\partial w_n^2(l_n,t)}{\partial \alpha_n^2}, & K_{t_n} w_n(l_n,t) &= EI \frac{\partial w_n^3(l_n,t)}{\partial \alpha_n^3},
 \end{aligned}
 \tag{4}$$

where  $K_{r_0}, K_{t_0}$  and  $K_{r_n}, K_{t_n}$  stand for the rotational and translational spring constants at the left and right ends, respectively.

The equations for the intermediate supports can be written as:

$$\begin{aligned}
 w_i(l_i,t) &= w_{i+1}(0,t), & K_{r_i} \frac{\partial w_i(l_i,t)}{\partial \alpha_i} &= -EI \left( \frac{\partial w_i^2(l_i,t)}{\partial \alpha_i^2} - \frac{\partial w_{i+1}^2(0,t)}{\partial \alpha_{i+1}^2} \right), \\
 \frac{\partial w_i(l_i,t)}{\partial \alpha_i} &= \frac{\partial w_{i+1}(0,t)}{\partial \alpha_{i+1}}, & K_{t_i} w_i(l_i,t) &= EI \left( \frac{\partial w_i^3(l_i,t)}{\partial \alpha_i^3} - \frac{\partial w_{i+1}^3(0,t)}{\partial \alpha_{i+1}^3} \right).
 \end{aligned}
 \tag{5}$$

In Eq. (5), the intermediate rotational restraints are characterized by the spring constants  $K_{r_i}, i = 1, \dots, n-1$  and the translational restraints by the spring constants  $K_{t_i}, i = 1, \dots, n-1$ .

### 2. Free vibration of beams with a crack

In the present research, it is assumed that an open crack with depth  $a$  is located at distance  $x_c$  from the left end of the Euler-Bernoulli beam. The crack is simulated by a massless spring with the bending constant  $c$  [16]:

$$c = 5.346 \frac{h}{EI} J\left(\frac{a}{h}\right),
 \tag{6}$$

where  $h$  is the height of the beam,  $a$  is the depth of the crack and  $J(a/h)$  is the dimensionless local compliance function proposed by Paipetis and Dimarogonas [16]:

$$\begin{aligned}
 J\left(\frac{a}{h}\right) &= 1.8624 \left(\frac{a}{h}\right)^2 - 3.95 \left(\frac{a}{h}\right)^3 + 16.375 \left(\frac{a}{h}\right)^4 - 37.226 \left(\frac{a}{h}\right)^5 + \\
 &+ 76.81 \left(\frac{a}{h}\right)^6 - 126.9 \left(\frac{a}{h}\right)^7 + 172 \left(\frac{a}{h}\right)^8 - 143.97 \left(\frac{a}{h}\right)^9 + 66.56 \left(\frac{a}{h}\right)^{10}.
 \end{aligned}
 \tag{7}$$

Due to localized crack effect, the cracked beam can be simulated as two uniform beams joined together by a spring at the crack. The continuity conditions have the form:

$$\begin{aligned}
 W_1(x_1) &= W_2(x_2) \\
 \frac{d^2W_1(x_1)}{d(x_1)^2} &= \frac{d^2W_2(x_2)}{d(x_2)^2} \\
 \frac{d^3W_1(x_1)}{d(x_1)^3} &= \frac{d^3W_2(x_2)}{d(x_2)^3} \\
 \frac{dW_1(x_1)}{d(x_1)^2} + c \frac{d^2W_1(x_1)}{d(x_1)^2} &= \frac{dW_2(x_2)}{d(x_2)^2},
 \end{aligned}
 \tag{8}$$

where  $W_1$  and  $W_2$  are the mode shapes of the left and right beam sections, respectively.

### 3. Haar wavelets

In the recent years, the wavelet transform has occasionally been implemented in structural health monitoring due to the fact that the wavelet transform does not require the analysis of the complete structure and has the ability to reveal some hidden parts of data that other signal analysis techniques fail to detect [17]. Lepik demonstrated that the Haar wavelets can be applied for numerical solving of differential equations [18].

The Haar wavelet family is a group of square waves [18]:

$$h_i(x) = \begin{cases} 1 & \text{for } x \in \left[ \frac{k}{m}, \frac{2k+1}{2m} \right), \\ -1 & \text{for } x \in \left[ \frac{2k+1}{2m}, \frac{k+1}{m} \right), \\ 0 & \text{elsewhere,} \end{cases}
 \tag{9}$$

where  $m$  is the index of delay and it is equal to  $2^j$ ;  $j=0,1,\dots,J$  indicates the level of the wavelet;  $k=0,1,\dots,m-1$  is the translation parameter. Integer  $J$  determines the maximal level of resolution. Index  $i$  is calculated according to the formula  $i = m + k + 1$ .

Proceeding from the definition above (9), any function  $y(x)$ , which is square integrable in the interval  $[0,1]$ , can be expanded into a Haar series with an infinite number of terms:

$$y(x) = \sum_{i=0}^{\infty} c_i h_i(x),
 \tag{10}$$

where the Haar coefficients are determined such that the integral square error  $\varepsilon$  is minimized

$$\mathcal{E} = \int_0^l \left[ y(x) - \sum_{i=1}^m c_i h_i(x) \right]^2 dx. \tag{11}$$

Any Haar function  $h_i(x)$  can be calculated in the collocation points:  $x_l = (l-0.5)/2M$ , where  $l = 1, 2, \dots, 2M$ . The matrix  $H(i, l) = h_l(x_i)$ , which is associated with the Haar wavelets, is obtained as following:

$$H(i, l) = \begin{vmatrix} h_1(x_1) & \dots & h_1(x_{2M}) \\ \dots & \dots & \dots \\ h_{2M}(x_1) & \dots & h_{2M}(x_{2M}) \end{vmatrix} = H. \tag{12}$$

If function  $y(x)$  is a piece-wise constant or it can be approximated as a piece-wise constant, the sum is terminated as:

$$y(x_l) = \sum_{i=1}^{2M} c_i h_i(x) = c'_{2M} h_{2M}, \tag{13}$$

where the coefficient vector is

$$c'_{2M} = y_{2M}^* H_{2M \times 2M}^{-1} \tag{14}$$

and

$$y_{2M}^* = [y(1/4M) y(3/4M) \dots y((4M-1)/4M)]. \tag{15}$$

Both matrices  $H$  and  $H^{-1}$  are calculated once and contain zeros; therefore, the Haar transform works faster than the Fourier transform.

#### 4. Numerical results

In this paper, several characteristic parameters of cracks and supports were predicted by ANNs for two unrelated dimensionless vibrating beams. Both case studies were investigated twice: for each example, the ANN was trained two times using two different data sets. The results of each approach were compared to each other.

In the first approach, six natural frequencies were fed into the inputs of the feedforward backpropagation ANN. In the second approach, at first, the mode shape amplitude comparison [19]

$$MSAC_q = \sum_{i=1}^k |W_{q,i}^u - W_{q,i}^d| \tag{16}$$

was obtained, where  $W_{q,i}$  define the modal displacement for the  $i$ -th mode shape at the coordinate  $q$ ; the upper index  $u$  denotes the structure without any intermediate support or crack; the upper index  $d$  indicates the structure with an intermediate support or crack. In the present paper,  $MSAC$  was transformed into 16 Haar coefficients and fed into the inputs of the ANN. In [15], only the first mode shape was used for delamination detection in composite structures.

In both approaches, 117 training patterns and ten test patterns were calculated numerically. Importantly, the test patterns were not shown to the ANNs in advance. The average results of ten trainings of the ANN by Levenberg-Marquardt method are explained below and shown in the tables.

Example 1. A vibrating beam with clamped end on the left side and free end with translational and rotational springs on the right side was considered. For the spring constraints, the following non-dimensional quantities were introduced

$$k_t = \frac{K_t L^3}{EI}, \quad k_r = \frac{K_r L}{EI} \tag{17}$$

The stiffness coefficients of the right end springs were fixed to 10.

Additional rotational and translational spring supports were placed at the distance of 0.4 units from the left end of the beam. The translational spring coefficient was fixed to 15. The ANN with one output and one hidden layer with 20 neurons on it (Figure 2a) predicted the stiffness coefficients of the rotational spring. In the case of frequencies, the number of inputs was 6; whereas in the case of Haar, there were 16 inputs. For  $MSAC$  in Eq. (17),  $k = 2$ . The results are shown in Table 1.

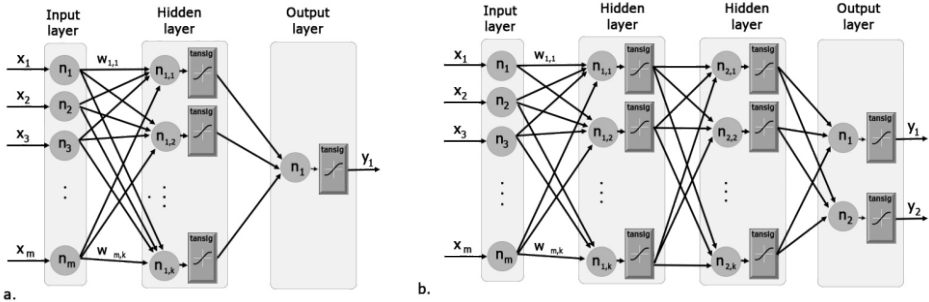


Figure 2. ANN training models: a. with one hidden layer; b. with two hidden layers.

Example 2. A homogeneous Euler-Bernoulli cantilever beam with one open crack was considered. The ANN with six or sixteen inputs, two outputs and two hidden layers with 15 neurons on each (Figure 2b) predicted the location and the depth of the crack. For  $MSAC$  in Eq. (17), it was taken  $k = 2$ . The results of two approaches are presented in Table 2. As it can be seen in Table 2, the advanced method with the use of Haar wavelets significantly improves the accuracy of the dynamic parameter predictions, and these results have a good agreement with the exact solutions.

**Table 1.** Prediction of the stiffness coefficient of the rotational spring placed in the intermediate of the beam with clamped right end and free left end with rotational and translational springs.

Rotational spring	Predictions based on six frequencies		Predictions based on Haar transform	
	Stiffness	Relative error	Stiffness	Relative error
97	97.2262	0.0023	96.9043	0.0010
209	209.3510	0.0017	209.6205	0.0030
305	304.9512	0.0002	306.7216	0.0056
385	385.1049	0.0003	385.2316	0.0006
449	449.2519	0.0006	445.8565	0.0070
585	585.1103	0.0002	585.2786	0.0005
729	728.2702	0.0010	726.4219	0.0035
873	872.6585	0.0004	873.6592	0.0008

**Table 2.** Prediction of the location and size of the crack in the cantilever.

Exact		Predictions based on six frequencies			Predictions based on Haar transform		
Location	Depth	Location	Depth	Relative error	Location	Depth	Relative error
0.18	0.21	0.1881	0.1932	0.0673	0.1806	0.2099	0.0021
0.26	0.37	0.2440	0.3677	0.0358	0.2611	0.3776	0.0169
0.34	0.37	0.3352	0.3647	0.0142	0.3426	0.3620	0.0167
0.52	0.13	0.4434	0.1368	0.0554	0.4232	0.1523	0.0512
0.50	0.49	0.5391	0.5001	0.0577	0.4835	0.4486	0.0636
0.58	0.25	0.5672	0.2565	0.0228	0.5796	0.2466	0.0054
0.66	0.25	0.6446	0.2418	0.0247	0.6594	0.2458	0.0060
0.74	0.17	0.7529	0.1689	0.0171	0.7384	0.1739	0.0056
0.82	0.33	0.8185	0.3383	0.0095	0.8164	0.3398	0.0118
0.90	0.25	0.8803	0.2475	0.0213	0.9007	0.2441	0.0064

## 5. Conclusions

A complex approach of ANNs trained by a set of natural frequencies or Haar coefficients is introduced in this paper for free vibration analysis of beams with various boundary conditions, intermediate elastic supports or a crack. The latter approach can analyze and precisely predict the characteristics of the beams with non-classical elastic boundary conditions or a crack with arbitrary depth-to-length ratio.

The case studies indicated that the results predicted by the ANNs and Haar wavelets method have a good agreement with the results obtained beforehand. Hence, the present approach can serve as a reference for future numerical research. Also the described approach has advantages over other numerical methods in time and calculation efficiency: once the system is created and trained, it can be used in practice without being reprogrammed.

## Acknowledgement

The work was supported by Tiigri Ülikool and the Estonian Science Foundation under Grant ETF 8830.

## References

- [1] H. Saito, K. Mori, Vibrations of a beam with non-linear elastic constraints, *Journal of Sound and Vibration*, 66-1 (1979), 1–8.
- [2] J.R. Banerjee, H. Su, Development of a dynamic stiffness matrix for free vibration analysis of spinning beams, *Computers & Structures*, 82-23:26 (2004), 891–2197.
- [3] L. Wang, J. Ma, J. Peng, L. Li, Large amplitude vibration and parametric instability of inextensional beams on the elastic foundation, *International Journal of Mechanical Sciences*, 67 (2013), 1–9.
- [4] M.-H.H. Shen, C. Pierre, Natural modes of Bernoulli-Euler beams with symmetric cracks, *Journal of Sound and Vibration* 138-1 (1990), 115–134.
- [5] [5] M.-H.H. Shen, Y.C. Chu, Vibrations of beams with a fatigue crack, *Computers & Structures* 45-1 (1992), 79–93.
- [6] C.A. Papadopoulos, The strain energy release approach for modeling cracks in rotors: A state of the art review, *Mechanical Systems and Signal Processing* 22-4 (2008), 763–789.
- [7] J. H. Lau, Vibration Frequencies and Mode Shapes for a Constrained Cantilever, *Journal of Applied Mechanics* 51 (1984), 182–187.
- [8] S. Caddemi, I. Calio, Exact solution of the multi-cracked Euler-Bernoulli column, *International Journal of Solids and Structures* 45-5 (2008), 1332–1351.
- [9] S. Caddemi, A. Morassi, Multi-cracked Euler-Bernoulli beams: Mathematical modeling and exact solutions, *International Journal of Solids and Structures* 50-6 (2012), 944–956.
- [10] M. Attar, A transfer matrix method for free vibration analysis and crack identification of stepped beams with multiple edge cracks and different boundary conditions, *International Journal of Mechanical Sciences* 57-1 (2012), 19–33.
- [11] J. Li, H. Hua, Spectral finite element analysis of elastically connected double-beam systems, *Finite Elements in Analysis and Design* 43-15 (2007), 1155–1168.
- [12] R. Ansari, R. Gholami, K. Hosseini, S. Sahmani, A sixth-order compact finite difference method for vibrational analysis of nanobeams embedded in an elastic medium based on nonlocal beam theory, *Mathematical and Computer Modelling* 54-11, 12 (2011), 2577–2586.
- [13] M. Skrinar, B. Lutar, A three-node beam finite element for transversely cracked slender beams on Winkler's foundation, *Computational Materials Science* 64 (2012), 260–264.
- [14] Y.I.Özdemir, Development of a higher order finite element on a Winkler foundation, *Finite Elements in Analysis and Design* 48-1 (2012), 1400–1408.
- [15] H. Hein, L. Feklistova, Computationally efficient delamination detection in composite beams using Haar wavelets, *Mechanical Systems and Signal Processing* 25-6 (2011), 2257–2270.
- [16] S.A. Paipetis, A.D. Dimarogonas, Analytical Methods in Rotor Dynamics, *Elsevier Applied Science* 48-1 (1986).
- [17] S.T. Quek, Q. Wang, L. Zhang, K.K. Ang, Sensitivity analysis of crack detection in beams by wavelet technique, *International Journal of Mechanical Sciences*, 43 (2001) 2899–2910.
- [18] Ü.Lepik, Numerical solution of differential equations using Haar wavelets, *Mathematics and Computers in Simulation*, (68) (2005) 127–143.
- [19] J.J. Sinou, A review of damage detection and health monitoring of mechanical systems from changes in the measurement of linear and non-linear vibrations, *Mechanical Vibrations: Measurement, Effects and Control*, R.C. Capri (Ed) (2009) 643–702.

# Effect of proximity on wind loads on tall buildings

Ashok Kumar AHUJA<sup>1</sup> and Ritu RAJ

*Deptt. of Civil Engg., Indian Institute of Technology Roorkee, Roorkee, India*

**Abstract.** An attempt has been made in the present study to find the effect of proximity between tall buildings on wind loads. Interference effect between two building blocks having different cross-sectional shapes is studied. Rigid models of tall buildings are made of timber and tested in an open circuit boundary layer wind tunnel. Models of the object buildings are placed on load cell one by one first under isolated condition and later under interference condition. Twisting moment developed due to wind is also measured in addition to base shear and base moment in along wind as well as across wind directions. Effects of percentage obstruction by the interfering buildings on wind loads on object buildings are studied. Results presented in the paper are of great use for the structural designers while designing closely spaced tall buildings.

**Keywords.** Tall buildings, wind loads, interference effect, base shear, base moment, twisting moment

## Introduction

While designing tall buildings for wind loads, it is necessary to consider the presence of neighboring buildings and their effects as wind force depend on the shape of the building as well as its exposure. The structural designers refer to relevant code of practices dealing with wind loads while designing tall buildings against wind. However, available information in code of practices regarding wind pressure coefficients and wind force coefficients is limited to isolated condition only. Information regarding variation in pressure and force coefficients values due to the presence of nearby building blocks is not available. Indian Standard for wind loads [IS – 875 (Part-3)-1987] has information about force coefficients for various cross-sectional shapes but for wind incidence angle perpendicular to one surface only.

Similarly limited information is available in standards of other countries also [2, 3 ...] Review of literature indicates that little work has been done in the field of effects of percentage obstruction by the interfering buildings on wind loads. The first study of interference effect of neighboring structures in relation to tall building was carried out by Harris [?]. Sykes [11] carried out an experiment to investigate the interference effects on the response of a tall building model. Blessmann (1985) studied the buffeting effects on neighboring tall buildings.

---

<sup>1</sup> Corresponding author: [ahujashok@gmail.com](mailto:ahujashok@gmail.com)

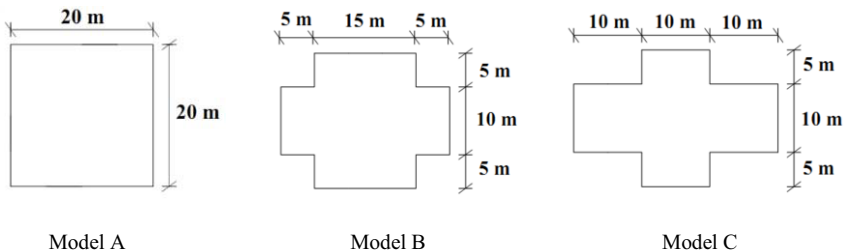


Blessmann and Riera (1985) carried out wind tunnel study of the interaction between two square prisms having equal aspect ratio. The interference effect of wind on the response of tall buildings was investigated by Zhang (1992). Zhang et. al (1995) reported the interference effects on torsional response of structurally asymmetric tall buildings. Interference effects from neighboring buildings on wind induced coupled translational-torsional motion of tall buildings was investigated by Thepmongkorn et. al (2002). Lam et. al (2008) studied the interference effects on wind loading of a row of closely spaced tall buildings. Amin and Ahuja [1] presented mean interference effects between two buildings. However most of the above studies focus on the interference effect on neighboring building with square or rectangular shapes only. Very few studies have been carried out in the area of interference effects on the closely spaced buildings with peculiar cross-sections.

## 1. Experimental programme

### 1.1. Details of models

Models used for the experimental study are made of plywood at a geometric scale of 1:100. One model has square shape and other two models are like plus shape. While making the models it was ensured that height and floor area of the models remains the same. Height of the models is kept as 600 mm with floor area of  $40,000 \text{ mm}^2$ . Cross-sectional dimensions of all models are shown in Fig. 1.



**Figure 1.** Cross-sections of building models

### 1.2. Characteristics of wind flow

Experiments are conducted in boundary layer wind tunnel (open circuit type) at the Department of Civil Engineering, Indian Institute of Technology Roorkee, India. The wind tunnel has a cross section of 2m (height) and 2m (width). Vortex generator, barrier wall and small cubical blocks are used to obtain wind velocity profile corresponding to terrain category-2. The wind velocity inside the tunnel during the tests was maintained as 9.78 m/s at the top level of the models.

1.3. Measurement technique

All plywood made rigid models (Photo. 1) are placed on load cell one by one first under isolated condition and later under interference condition. The arrangement of interfering building models are shown in Table 1.



Photo. 1. Wooden models of Tall buildings.

Table 1. Arrangement of interfering building models

Model No.	Full Blockage	Half Blockage	No Blockage
Model A			
Model B			
Model C			

Three cases of interference are considered, namely full blockage, half blockage and no blockage. The distance between the interfering model and instrumented model is kept as 1/10 of the height of models, i.e. 60 mm in each case. Base shear, base moment and twisting moment are measured at 0° wind incidence angle for isolated condition as well as for each interference condition. Observations are recorded for 60 sec at an interval of 1 sec and later the average values are calculated. In Table 1, the model sketch with hatch is instrumented model which is placed above the load cell one by one, and the plain sketch shows the position of interfering building model.

**2. Results and discussion**

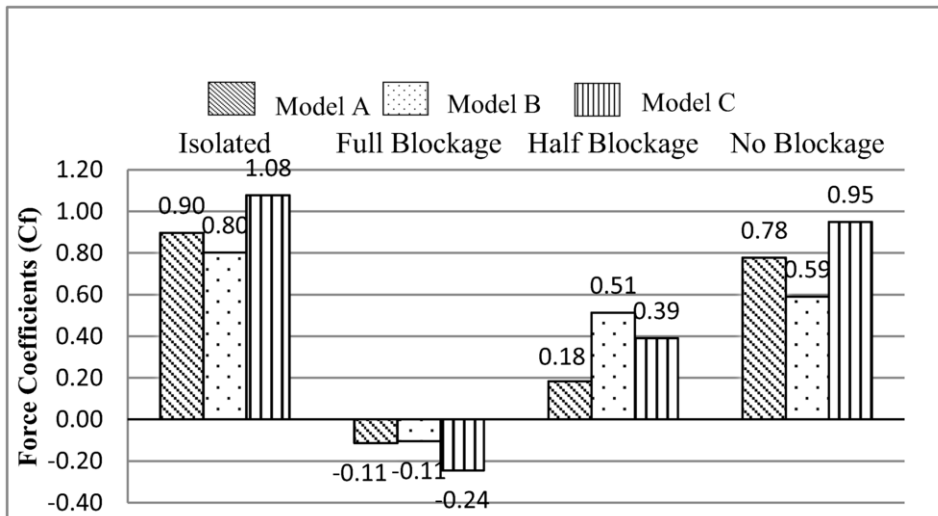
*2.1. Force coefficients*

Values of force coefficients ( $C_f$ ) are calculated from the measured values of along wind loads  $F_x$  at 0° wind incidence angle using Eq.(1), and are compared for all three models in Fig. 2.

$$C_f = \frac{F_x}{A \times P_{ref}} \tag{1}$$

Where  $P_{ref}$  is reference wind pressure which is calculated as:

$$P_{ref} = 0.6V_{ref}^2 = 0.6 \times (9.78^2) = 57.38 N/m^2$$



**Figure 2.** Comparison of force coefficient on all models at 0° wind incidence angle

Maximum value of force coefficient ( $C_f$ ) is obtained as 1.08 in case of model C under isolated condition because of its large exposed area. In case of model B, force coefficient is less than that for model A due to having cut corners although it has larger exposed area. Force Coefficient  $C_f$  is 0.9 for model A and 0.8 for model B.

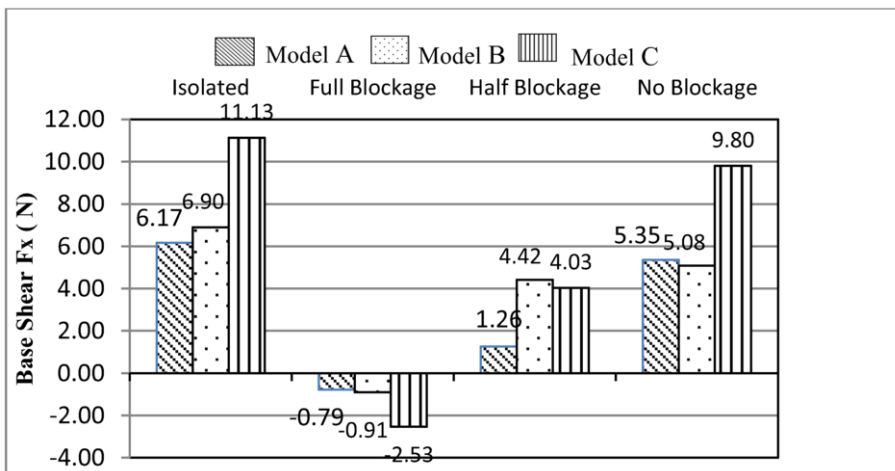
In case of full blockage interference condition, force coefficients for all models are negative. Values of  $C_f$  increase with decrease in blockage. These values are listed in Table 2.

**Table 2.** Force coefficients ( $C_f$ )

Model No.	Isolated	Full Blockage	Half Blockage	No Blockage
Model A	0.90	-0.11	0.18	0.78
Model B	0.80	-0.11	0.51	0.59
Model C	1.08	-0.24	0.39	0.95

2.2. Base shear and base moment

Figures 3 and 4 show the graph of base shear ( $F_x$ ) and base moment ( $M_y$ ) for all interfering conditions respectively. It is seen from the figures that values of base shear and base moment at  $0^\circ$  wind incidence angle are maximum for model C due to its large exposed area, and these are less in case of model A because the wind exposed area of model A is less as compared to models B and C. Similarly when interference cases of all models are considered, in full blockage condition wind acts on the interfering building model only and it passes through its sides. Thus wind creates negative pressure zone between the instrumented model and interfering building model which are very close to one another. The values of base shear and base moment are maximum in case of model C and its almost equal for model A and B.



**Figure 3.** Comparison of base shear on all models at  $0^\circ$  wind incidence angle

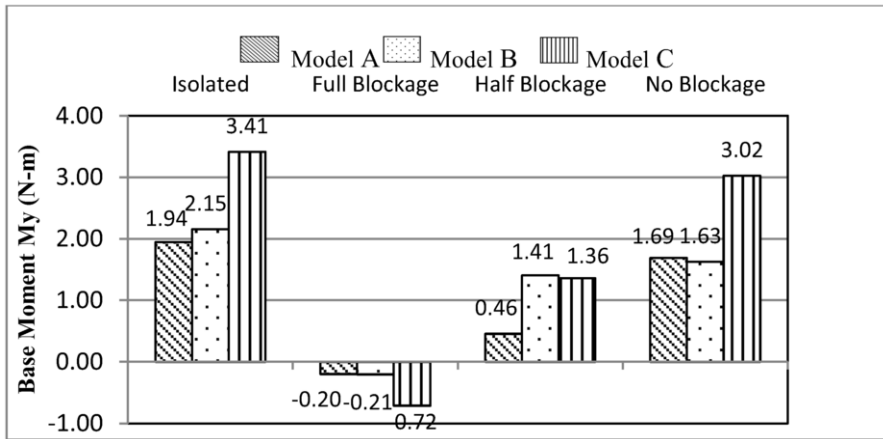


Figure 4. Comparison of base moment on all models at 0° wind incidence angle

In case of half blockage condition, half of the windward face of the instrumented building model is subjected to wind force such that the values of the base shear and base moment are positive but lesser than those in isolated cases for all models. In no blockage condition, the wind ward face is fully subjected to wind load, due to the presence of interfering building model on side of the instrumented building model. However, wind flow pattern in this case is slightly different from that of isolated case and hence the values of base shear and base moment are a bit smaller than those in isolated case.

2.3. Twisting moment

Figure 5 shows the Comparison of twisting moment ( $M_z$ ) in all four cases. It is noticed that twisting moment is maximum in case of half blockage condition for all models. The presence of the building on upstream side is affecting the wind flow.

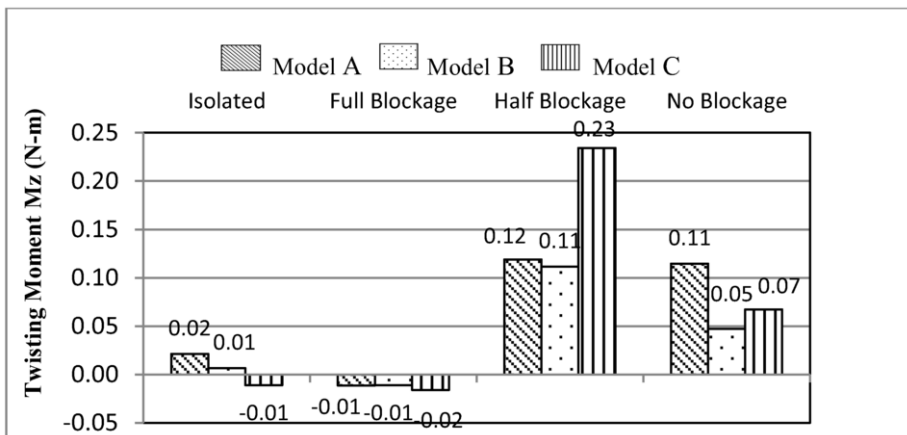


Figure 5. Comparison of twisting moment on all models at 0° wind incidence angle

In case of the half blockage case the wind is coming from upstream side and acting on 50% of the windward face of instrumented building model. Other 50% face of the model is covered by interfering model. This force creates the torsion in clockwise direction. In case of no blockage condition, the value of the twisting moment is maximum for model A and minimum for model B. In case of full blockage condition, whole of the instrumented building model is covered by the interfering model and hence the value of twisting moment is almost zero as in the case of isolated models.

### 3. Conclusions

- The force coefficient is maximum for model C in isolated cases.
- In interference cases, the force coefficient is maximum in no blockage condition and it becomes negative in case of full blockage condition.
- Effect of interference on base moment is similar to that of its effect on base shear.
- The presence of interfering building on upstream side change the flow pattern of wind and thus position of interfering building affect the twisting moment also. Further, its effect is maximum in half blockage condition.

### References

- [1] J.A. Amin and A.K. Ahuja, Mean interference effects between two buildings: effects of close proximity, *Structural Design of Tall and Special Buildings*, published online in Wiley Interscience, 2009.
- [2] AS/NZS: 1170.2 (2002), "Structural Design Actions, Part-2 : Wind Action"
- [3] ASCE: 7-02 (2002), "Minimum Design Loads for Buildings and Other Structures"
- [4] J. Blessmann, Buffeting effects on neighboring tall buildings, *Journal of Wind Engineering and Industrial Aerodynamics*, 18 (1985), 105-110.
- [5] J. Blessmann, and J.D. Riera, Wind excitation of neighboring tall buildings, *Journal of Wind Engineering and Industrial Aerodynamics*, 18 (1985), 91-103.
- [6] BS: 63699 (1995), "Loading for Buildings: Part 2 – Code of Practice for Wind Loads"
- [7] EN 1991-1-4 (2005), "Euro code 1: Actions on Structures - Wind Actions"
- [8] C.L. Harris, Influence of neighboring structures on the wind pressure on tall buildings, *Bureau of Standards, Journal of Research*, Vol. 12, (Research paper RP637), 1934.
- [9] IS:875-Part-3 (1987), "Code of Practice for Design Loads (other than Earthquake Loads) for Buildings and Structures- Wind Loads"
- [10] K.M. Lam, M.Y.H. Leung, and J.G. Zhao, Interference effects on wind loading of a row of closely spaced tall buildings, *Journal of Wind Engineering and Industrial Research*, 96 (2008), 562-583.
- [11] D.M. Sykes, Interference effects on the response of a tall building model, *Journal of Wind Engineering and Industrial Aerodynamics*, 11 (1983), 365-380.
- [12] S. Thepmongkorn, G.S. Wood, and K.C.S. Kwok, Interference effects on wind induced coupled motion of a tall building, *Journal of Wind Engineering and Industrial Aerodynamics*, 90 (2002), 1807-1815.
- [13] W.J. Zhang, Y.L. Xu, and K.C.S. Kwok, "Interference effects on aeroelastic torsional response of structurally asymmetric tall buildings", *Journal of Wind Engineering and Industrial Aerodynamics*, 57 (1995), 41-61.
- [14] X. Zhang, Interference effects of wind on the responses of tall buildings, *Journal of Wind Engineering and Industrial Aerodynamics*, 41 (1992), 867-879.

# Evaluation of the scale effect for the tensile strength of aligned flax fiber-reinforced composites

Jānis ANDERSONS<sup>1</sup>

*Institute of Polymer Mechanics, University of Latvia, Riga, Latvia*

**Abstract.** Confinement of concrete structural elements by fiber-reinforced polymer-matrix composite sheets is increasingly being used to strengthen or retrofit a structure. Along with carbon, glass, and basalt fiber reinforcement, natural fibers are being considered for such applications. Utilization of plant-derived natural fibers as the reinforcement of polymer-matrix composites is driven by economic and environmental reasons. When using composites in load-bearing applications, the dependence of strength on the material volume subjected to loading, i.e. the scale effect of strength, should be taken into account in design. Composite specimens of different sizes, produced from flax fiber/epoxy matrix prepregs, were tested in tension in fiber direction in order to elucidate the scale effect of the tensile strength. The strength distribution at a fixed specimen size was shown to deviate slightly from that of the Weibull strength statistics. A probabilistic weakest-link model of the strength in tension along the reinforcement direction was applied to theoretically evaluate the magnitude of scale effect.

**Keywords.** Flax fiber, polymer matrix composite, tensile strength, scale effect

## Introduction

Natural fiber-reinforced composites are increasingly being used in infrastructure applications [1, 2]. Such developments are driven by lower cost and production energy expenditure, as well as easier handling of natural fibers compared to the majority of synthetic fibers and their reasonable specific mechanical properties [3]. Notably, flax-fabric reinforced epoxy has been considered for confining concrete columns, demonstrating enhancement in column limit load, strain, and damping characteristics [4-6]. Alignment of the reinforcement along the hoop direction produces even more pronounced strengthening effect, as demonstrated experimentally in, e.g., [7], so application of unidirectionally reinforced (UD) natural-fiber composites should be preferable.

The efficiency of a UD composite confinement is determined primarily by its thickness, stiffness, and tensile strength in the hoop, i.e. reinforcing fiber direction. The latter is known to depend on specimen size exhibiting the so-called scale effect of

---

<sup>1</sup>Corresponding author: Institute of Polymer Mechanics, 23 Aizkraukles iela, Riga LV-1006, Latvia; E-mail: [janis.andersons@pmi.lv](mailto:janis.andersons@pmi.lv)

strength, i.e. reduction of failure stress with increasing specimen size. Since laboratory test specimens normally are much smaller than the size of the composite structure, an appropriate scaling method should be applied to estimate the strength of the latter using specimen strength test results.

Strength scaling based on the Weibull strength distribution can be applied for brittle materials, the fracture of which is initiation-controlled. Fiber-reinforced composites typically exhibit quasi-brittle fracture characterized by gradual development of a fracture process zone preceding the ultimate failure. Introducing a representative volume element (RVE) as a smallest material element the failure of which leads to ultimate fracture, the strength scatter of such materials can be described by a weakest-link strength distribution of a chain of RVEs [8]. It has been proposed in [8, 9] that the distribution of strength of the RVE of quasi-brittle materials should have a Weibull left tail grafted onto a normal distribution. Such a probabilistic model has been successfully applied to fiber-reinforced composite materials, e.g., for strength distribution of UD Thornel 300/5208 carbon/epoxy and life distribution of Kevlar/epoxy [9]. An indication of a grafting point has been observed also in quasi-UD flax/epoxy tensile strength distribution reported in [10]. In the current study, the applicability of the RVE-based scale effect model developed in [8, 9] to the tensile strength of an aligned flax fiber reinforced composite is considered.

## 1. Experimental

Materials, manufacturing procedure, and testing of flax/epoxy composites have been described in [10]. Below the essential data are briefly recapitulated for completeness and ease of reference. A composite plate was produced from LINEO flax/epoxy prepreg FLAXPLY<sup>®</sup>. The quasi-UD prepreg contained bonding weft yarns constituting a few percent of the total flax weight. Six UD prepreg plies of the areal density of 150 g/m<sup>2</sup> were aligned, stacked and cured in a thermopress for one hour at ~1 atm pressure and 130 °C temperature. Four groups of specimens, with widths  $w$  equal to 10, 20, 40, and 70 mm, were cut out of the plate along the fiber direction so that the gauge length to width ratio for all specimens amounted to 5. For 10-mm width, 26 specimens were produced, whereas for the other widths considered, the number of specimens varied from three to six. Fiberglass tabs were glued onto the specimen ends. The specimens were tested for strength by applying a stroke-controlled tensile loading in the fiber direction. The loading rate was varied according to specimen gauge length so that the nominal strain rate for all the specimens tested amounted to 0.75 %/min. The strength was evaluated from the failure load employing the average width of a specimen and the average plate thickness of the respective specimen group. The empirical strength distribution of the composite specimens with width  $w = 10$  mm is presented in Figure 1.

## 2. Model

It follows from the definition of the RVE that the probability of failure,  $P_N(\sigma)$ , of a composite specimen which contains  $N$  RVEs and is subjected to uniform tensile stress  $\sigma$  is given by the weakest-link relation Eq. (1)



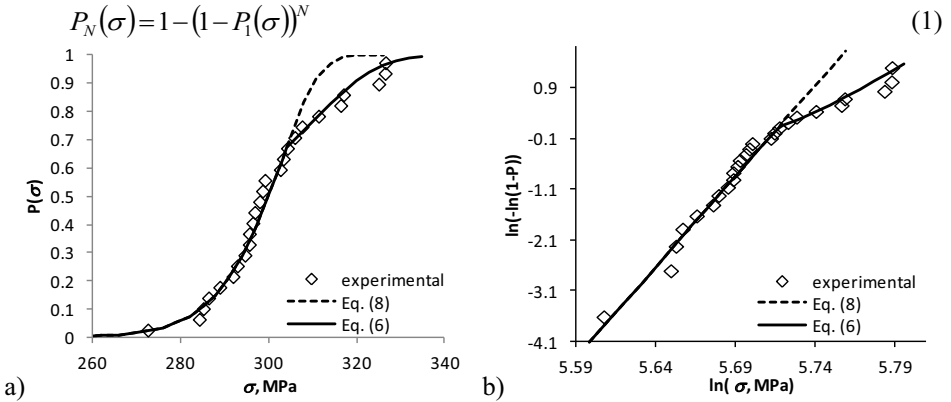


Figure 1. Strength distribution of specimens with  $w = 10$  mm in normal (a) and Weibull (b) co-ordinates.

where  $P_1(\sigma)$  designates strength distribution of the RVE. The latter is expressed as follows [9]

$$P_1(\sigma) = \begin{cases} 1 - \exp\left[-(\sigma/\beta)^\alpha\right] & \sigma < \sigma_{gr} \\ P_w(\sigma_{gr}) + \frac{r_f}{\delta\sqrt{2\pi}} \int_{\sigma_{gr}}^{\sigma} \frac{\exp\left[-(\sigma - \mu)^2\right]}{2\delta^2} d\sigma & \sigma \geq \sigma_{gr} \end{cases} \tag{2}$$

as consisting of a Weibull-distribution left tail grafted at a strength value designated as  $\sigma_{gr}$  onto a Gaussian distribution core. In Eq. (2) and below, the two-parameter Weibull distribution with the scale parameter  $\beta$  and shape parameter  $\alpha$  is designated as

$$P_w(\sigma) = 1 - \exp\left[-(\sigma/\beta)^\alpha\right] \tag{3}$$

and the normal distribution with mean  $\mu$  and standard deviation  $\delta$  as

$$P_G(\sigma) = \frac{1}{\delta\sqrt{2\pi}} \int_{-\infty}^{\sigma} \frac{\exp\left[-(\sigma - \mu)^2\right]}{2\delta^2} d\sigma \tag{4}$$

The value of the scaling parameter  $r_f$  in Eq. (2) is obtained by normalization of the grafted distribution, resulting in

$$r_f = [1 - P_w(\sigma_{gr})] / [1 - P_G(\sigma_{gr})] \tag{5}$$

Finally, taking into account Eqs. (2)-(5), strength distribution of a composite specimen Eq. (1) takes the form

$$P_N(\sigma) = \begin{cases} 1 - (1 - P_w(\sigma))^N & \sigma < \sigma_{gr} \\ 1 - (r_f [1 - P_G(\sigma)])^N & \sigma \geq \sigma_{gr} \end{cases} \quad (6)$$

For large-size specimens with dimensions exceeding considerably those of the RVE, the Weibull tail of the distribution Eq. (6) prevails [9], hence the average strength  $\langle \sigma \rangle$  depends on specimen size, expressed as the number  $N$  of RVEs it contains, as

$$\langle \sigma \rangle = \beta N^{-1/\alpha} \Gamma(1 + 1/\alpha) \quad (7)$$

### 3. Results and discussion

#### 3.1. Grafted Weibull distribution

It is seen in Figure 1b that the low-strength tail of the empirical strength distribution of the composite specimens with width  $w = 10$  mm is linear in Weibull co-ordinates whereas at higher stresses the distribution deviates from linearity in a manner similar to that expected for the grafted distribution Eq. (6) (and presented in [8, 9]), with the grafting point located at  $\sigma_{gr} = 304$  MPa. It follows from Eq. (6) that, for  $\sigma < \sigma_{gr}$ , strength distribution

$$P_N(\sigma) = 1 - \exp\left[-\left(\sigma/\beta^*\right)^\alpha\right] \quad (8)$$

holds, where  $\beta^* = N^{-1/\alpha} \beta$ . The parameters of the Weibull distribution Eq. (8) were determined by the maximum likelihood method (MLM) using the experimental strength values below  $\sigma_{gr}$  (i.e. treating them as right-censored observations), leading to  $\alpha = 35.7$  and  $\beta^* = 303$  MPa. The distribution Eq. (8) with these parameter values is plotted in Figure 1 by a dashed line. Good agreement with the empirical distribution up to the grafting point  $\sigma_{gr}$  and deviation for higher strength is seen, as expected.

If the scale effect of strength for large-size specimens is of primary interest, the obtained data are sufficient for its prediction according to Eq. (7) without specifying the number of RVEs,  $N$ , in each specimen. Indeed,  $N$  is proportional to the volume of a specimen. In the case considered, specimen thickness was kept constant and length varied proportionally to width, therefore  $N \sim w^2$ . Designating the 10-mm width as  $w_{10}$  and the number of RVEs such a specimen contains by  $N_{10}$ , for arbitrary specimen width  $N = N_{10} (w/w_{10})^2$ . Substituting this expression for  $N$  into Eq. (7), we arrive at

$$\langle \sigma \rangle = \beta^* (w/w_{10})^{-2/\alpha} \Gamma(1 + 1/\alpha) \quad (9)$$

The predicted variation of mean strength with specimen width according to Eq. (9) is compared with test results in Figure 2. It is seen that Eq. (9) agrees well with 10-mm width specimen strength, thus corroborating the dominance of the Weibull tail of

strength distribution seen in Figure 1. The agreement is also good for 20 and 40-mm width specimens, while being somewhat inferior for the largest, 80-mm ones. Such a discrepancy is likely to stem from the limited amount of strength data of 10-mm width specimens at  $\sigma < \sigma_{gr}$  available for the Weibull parameter estimation of Eq. (8).

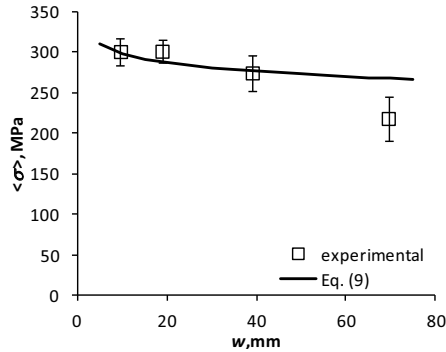


Figure 2. Average strength as a function of specimen width.

### 3.2. Gaussian core distribution

In order to evaluate the distribution parameters of the Gaussian core of Eq. (6), the number  $N$  of RVE's in a specimen, equal to the ratio of specimen and RVE volumes  $N = V/V_{RVE}$ , has to be known.  $V_{RVE}$  can be evaluated exactly if empirical strength distributions for specimens of two substantially different sizes are available. Alternatively, based on previous experience with microstructural simulation and testing, RVE volume can be roughly estimated using typical fracture process zone (FPZ) dimensions [8]. Since in the case considered, fracture develops in the plane of isotropy of the transversely isotropic UD composite, the FPZ length estimate obtained for isotropic materials as triple the maximum inhomogeneity size [8] should apply, the inhomogeneities being the reinforcing flax-fiber yarns. The width of the FPZ (i.e. its extent along the reinforcement direction) for UD composites is related to ineffective length of a yarn, typically 10 times the yarn diameter, leading to an estimate of RVE volume at  $V_{RVE} = 1.4 \text{ mm}^3$ . Using the average dimensions of 10-mm width specimens, the number of RVEs such a specimen contains is  $N_{10} = 505$ .

Having evaluated  $N$  for the specimens used to determine the parameters of the Weibull distribution Eq. (8), the scale parameter of the Weibull tail of the RVE strength distribution is obtained as  $\beta = N_{10}^{1/\alpha} \beta^* = 361 \text{ MPa}$ . The grafting probability for RVE according to Eq. (3) amounts to  $P_w(\sigma_{gr}) = 0.0022$ , which is within the expected grafting probability range [8]. Thus, the strength distribution of a single RVE, Eq. (2), of the flax/epoxy composite is heavily dominated by the Gaussian core with the grafted Weibull left tail applying only for very low fracture probability. Due to the weakest-link scaling, Eq. (1), with the increase of specimen size (i.e. the increase of the number  $N$  of the RVEs it contains) the extent of Weibull tail of the strength distribution Eq. (6) becomes more prominent as exemplified by Figure 1, until for  $N \gg 1$  Weibull distribution dominates reflecting a change from quasi-brittle to brittle fracture of the composite.

The distribution parameters of the Gaussian core of Eq. (6) were evaluated by the MLM, using the experimental strength data of the composite specimens with width  $w = 10$  mm. The assumption of continuity of the probability density function at the grafting point [8] was relaxed (i.e.  $dP_w(\sigma_{gr})/d\sigma \neq dP_G(\sigma_{gr})/d\sigma$  was allowed), and estimates of the mean and standard deviation obtained as  $\mu = 440$  MPa and  $\delta = 45$  MPa. A good fit of the empirical strength distribution by Eq. (6) was achieved at the parameter  $\alpha, \beta, \mu, \delta, \sigma_{gr}, V_{RVE}$  values given above, as seen in Figure 1. Although the distribution function employed contains a relatively large number of empirical parameters, it allows accurate description of strength variability for materials exhibiting quasi-brittle fracture.

#### 4. Conclusions

A probabilistic model of a finite chain of representative volume elements, proposed by Bažant et al. [8, 9] for materials exhibiting quasi-brittle fracture, has been applied to elucidate the scale effect of tensile strength of a quasi-unidirectionally reinforced flax/epoxy composite. The theoretical distribution was shown to closely approximate the empirical strength distribution of relatively small-size composite specimens used to evaluate model parameters. The predicted scale effect was in reasonable agreement with the experimentally evaluated dependence of mean strength on specimen size.

#### Acknowledgement

This work has been funded by ESF via project 2013/0025/1DP/1.1.1.2.0/13/APIA/VIAA/019.

#### References

- [1] D.B. Dittenber, H.V.S. GangaRao, Critical review of recent publications on use of natural composites in infrastructure, *Composites: Part A* **43** (2012), 1419–1429.
- [2] B. Singh, M. Gupta, H. Tarannum, A. Randhawa, Natural fiber-based composite building materials, In: *Cellulose Fibers: Bio- and Nano-Polymer Composites*, Springer-Verlag, Berlin, Heidelberg, 2011, pp. 701- 720.
- [3] D.U. Shah, Developing plant fibre composites for structural applications by optimising composite parameters: a critical review, *Journal of Materials Science* **48** (2013) 6083–6107.
- [4] L. Yan, N. Chouw, Behavior and analytical modeling of natural flax fibre-reinforced polymer tube confined plain concrete and coir fibre-reinforced concrete, *Journal of Composite Materials* **47** (2013), 2133-2148.
- [5] L. Yan, A. Duchez, N. Chouw, Effect of bond on compressive behaviour of flax fibre reinforced polymer tube-confined coir fibre reinforced concrete, *Journal of Reinforced Plastics and Composites* **32** (2013), 273-285.
- [6] L. Yan, N. Chouw, Dynamic and static properties of flax fibre reinforced polymer tube confined coir fibre reinforced concrete, *Journal of Composite Materials* (2013), DOI: 10.1177/0021998313488154.
- [7] T. Vincent, T. Ozbakkaloglu, Influence of fiber orientation and specimen end condition on axial compressive behavior of FRP-confined concrete, *Construction and Building Materials* **47** (2013), 814-826.
- [8] Z.P. Bažant, S.-D. Pang. Activation energy based extreme value statistics and size effect in brittle and quasibrittle fracture, *Journal of the Mechanics and Physics of Solids* **55** (2007), 91–131.

- [9] J.-L. Le, Z.P. Bažant, M.Z. Bazant, Unified nano-mechanics based probabilistic theory of quasibrittle and brittle structures: I. Strength, static crack growth, lifetime and scaling, *Journal of the Mechanics and Physics of Solids* **59** (2011), 1291–1321.
- [10] J. Andersons, E. Spāriņš, J. Modniks, Scale effect of the tensile strength of aligned-flax-fiber reinforced composite, In: *Proc. of 13th International Conference on Fracture*, Beijing, 2013, 7 p.

# Flexural behavior of RC beams with local steel: analytical investigation

Abdelhamid CHARIF<sup>1</sup>, Shehab MOURAD and M. Iqbal KHAN  
*Department of Civil Engineering, College of Engineering  
 King Saud University, Saudi Arabia*

**Abstract.** The paper presents the analytical part of a work also including an experimental part presented in a separate paper. An analytical integration method for stress resultants across any shaped section is presented. The area integrals are first transformed to boundary line integrals using Green's theorem and then analytical integration is performed. The method is then used to predict moment-curvature relationships and compare with experimental results.

**Keywords.** Reinforced concrete, bending, curvature, analytical integration

## Introduction

The experimental part of this work is presented in an accompanying paper [1]. An analytical integration method of stress resultants over an arbitrary shaped section was formulated and used to compute the axial force and moment. This method, dealing with biaxial bending combined with an axial force, described in detail in reference [2] and performs better than the various numerical integration techniques [3-10]. The main steps are summarized here. Using the direct sign convention shown in Figure 1, the normal stress resultants for a beam-column member, subjected to an axial force and biaxial bending, are given by:

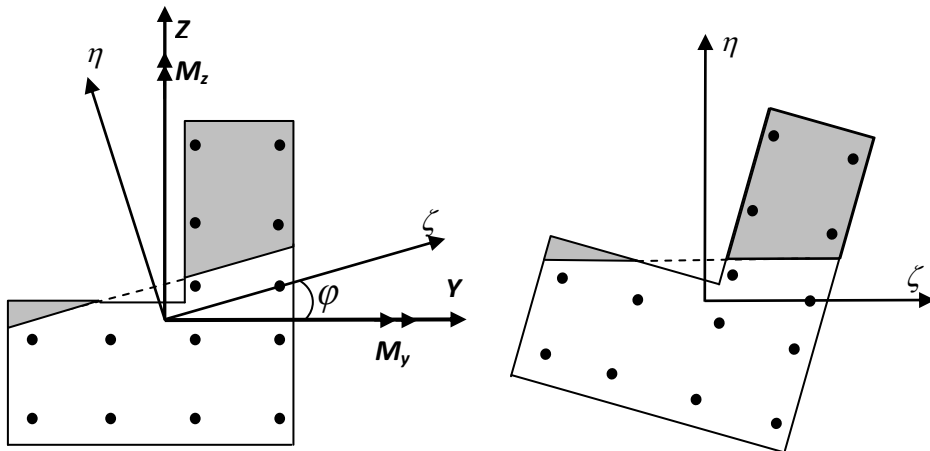
$$\begin{aligned}
 N &= \int \sigma dA = \iint \sigma dy dz \\
 M_y &= \int \sigma z dA = \iint \sigma z dy dz \\
 M_z &= -\int \sigma y dA = -\iint \sigma y dy dz
 \end{aligned}
 \tag{1}$$

## 1. Stress resultants for discrete bar reinforcement

Reinforcing bars are lumped at their centroid points with coordinates  $y_{bi}$  and  $z_{bi}$ . Their contribution is easily determined from the corresponding area and stress. To account for the displaced embedding concrete, an equivalent stress is subtracted.

---

<sup>1</sup>Corresponding author: [acharif@ksu.edu.sa](mailto:acharif@ksu.edu.sa)



**Figure 1.** General section under axial force and biaxial bending  
 (a): Inclined neutral axis in global axes  
 (b): Rotated section and use of local axes.

$$\begin{aligned}
 N_B &= \sum_i F_{bi} = \sum_i A_{bi}(\sigma_{bi} - \sigma_{ci}) \\
 M_{By} &= \sum_i F_{bi}z_{bi} = \sum_i A_{bi}(\sigma_{bi} - \sigma_{ci})z_{bi} \\
 M_{Bz} &= -\sum_i F_{bi}y_{bi} = -\sum_i A_{bi}(\sigma_{bi} - \sigma_{ci})y_{bi}
 \end{aligned}
 \tag{2}$$

Bar stress ( $\sigma_{bi}$ ) and concrete stress ( $\sigma_{ci}$ ) at the same point  $i$  are easily computed using corresponding stress-strain models. The capacity of a section with discrete reinforcement is obtained by combining equations (1) and (2). All other forms of non-discrete reinforcement use equations (1) by summing integrations over all the components of the section.

The axial force in (1) and (2) is independent of  $y$ - $z$  axis system whereas bending moments depend on the origin and orientations of these axes. It is common to express moments about the gross section centroid. This point is thus considered as the origin. With the assumption of plane sections and strain compatibility (perfect bond between various components), the total normal strain is a combination of axial force and bending moment effects:

$$\mathcal{E} = \mathcal{E}_0 + \mathcal{K}_y z - \mathcal{K}_z y
 \tag{3}$$

$\mathcal{E}_0$  is the centroidal normal strain, whereas  $\mathcal{K}_y$  and  $\mathcal{K}_z$  are curvatures about respective axes.

For dissymmetric sections, bending about one axis causes curvatures about both axes and bending angle  $\left(\frac{M_z}{M_y}\right)$  is in general different from neutral axis angle  $\left(\frac{\kappa_z}{\kappa_y}\right)$ .

**2. Expressions of integrals in local neutral coordinates**

Normal strain given by equation (3) and the resulting normal stress are functions of both  $y$  and  $z$  coordinates. There exists a system of axes  $(\zeta, \eta)$  as shown in Figure 1 where normal strain and stress depend on coordinate  $\eta$  only ( $\zeta$ -axis parallel to the neutral axis).

$$\varepsilon = \varepsilon_0 + \kappa\eta \tag{4}$$

Where  $\kappa = \kappa_y \cos \varphi + \kappa_z \sin \varphi$  and  $\varphi = \arctan\left(\frac{\kappa_z}{\kappa_y}\right)$  (5)

Integral relations (1) can be equally expressed with respect to coordinates  $(\zeta, \eta)$ , and then by virtue of relation (4) with respect to coordinates  $(\zeta, \varepsilon)$ . We obtain:

$$N = \frac{1}{\kappa} \iint \sigma(\varepsilon) d\zeta d\varepsilon$$

$$M_y = \frac{1}{\kappa} \iint \left( \zeta \sin \varphi + \frac{\varepsilon - \varepsilon_0}{\kappa} \cos \varphi \right) \sigma(\varepsilon) d\zeta d\varepsilon \tag{6}$$

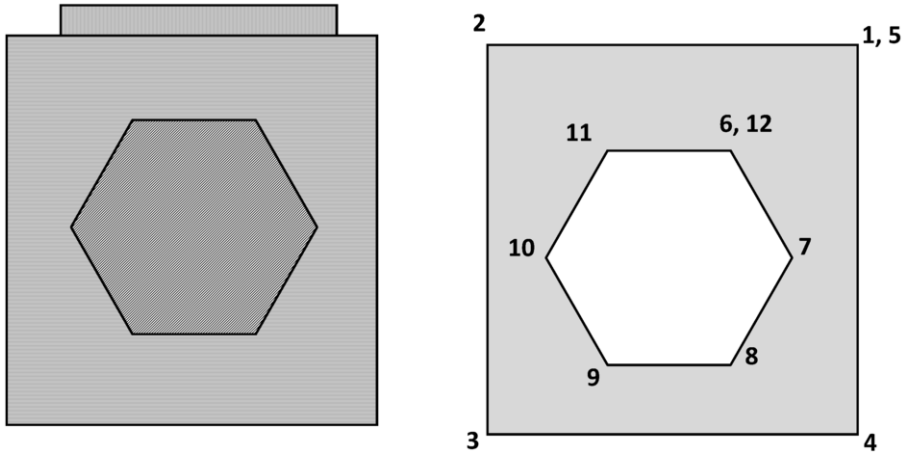
$$M_z = -\frac{1}{\kappa} \iint \left( \zeta \cos \varphi - \frac{\varepsilon - \varepsilon_0}{\kappa} \sin \varphi \right) \sigma(\varepsilon) d\zeta d\varepsilon$$

**3. Boundary integration of stress resultants**

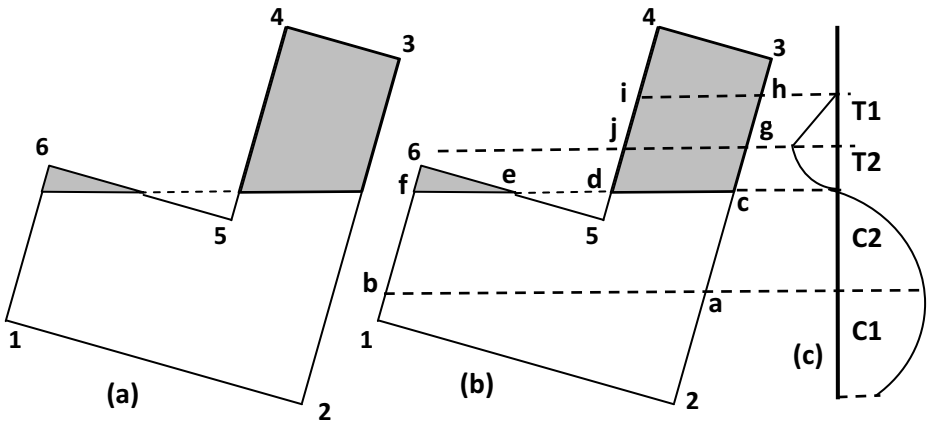
Green's theorem is a very useful tool as it reduces the problem dimension by replacing area integrals with path integrals along the border. The resulting boundary integration method offers many advantages and is very convenient for complex sections as it can elegantly handle various parts including voids. Figure 2 shows a composite section with three parts. The inner zone is either a void or a different material part. Figure 2b shows the appropriate vertex numbering (12 points) for the main part which eliminates the inner one, thanks to direction sign dependence of line integrals. If the inner part is not a void, it is dealt with similarly by a vertex numbering in the counterclockwise direction. The external skin reinforcement is also treated separately in the same way.



Figure 3 shows vertex numbering for the original section as well as identification of vertices for various parts. It is supposed in this case that both compression and tension models have two equations each as shown. The various parts are defined by lines parallel to the neutral axis, resulting in sub-polygons. The vertices for each part are shown in Table 1.



**Figure 2.** Border integration of a composite multi-polygon section  
 (a): Composite section (b): Vertex numbering for main part.



**Figure 3.** Identification of vertices for various parts of the section  
 (a) Full-Section vertices (b) Vertices of various parts  
 (c) Stress distribution across the section.

**Table 1.** Vertices for various polygons in Figure 3.

Polygon	Full section	Compr. Zone	Tension zone	Compr. Part C1	Compr. Part C2	Tension Part T1	Tension Part T2
Points	1-2-3-4-5-6	1-2-c-d-5-e-f	c-3-4-d-e-6-f	1-2-a-b	a-c-d-5-e-f-b	g-h-i-j	c-g-j-d-e-6-f

Applying Green transformations to equations (6) leads to:

$$\begin{aligned}
 N &= \frac{1}{\kappa} \oint_{\partial A} \zeta \sigma(\varepsilon) d\varepsilon \\
 M_y &= \frac{1}{\kappa} \oint_{\partial A} \left( \frac{\zeta^2}{2} \sin \varphi + \zeta \frac{\varepsilon - \varepsilon_0}{\kappa} \cos \varphi \right) \sigma(\varepsilon) d\varepsilon \\
 M_z &= -\frac{1}{\kappa} \oint_{\partial A} \left( \frac{\zeta^2}{2} \cos \varphi - \zeta \frac{\varepsilon - \varepsilon_0}{\kappa} \sin \varphi \right) \sigma(\varepsilon) d\varepsilon
 \end{aligned} \tag{7}$$

These integrations (7) are performed along the border lines of the section.

Assume a polygonal section with vertex coordinates expressed in  $(y, z)$  coordinates and then transformed to  $(\zeta, \eta)$  coordinates. Each polygon side is identified by two successive vertices  $(v)$  and  $(v+1)$  with a linear relation between their coordinates:

$$\zeta(\varepsilon) = s_v \varepsilon + t_v \quad \text{with} \quad s_v = \frac{\zeta_{v+1} - \zeta_v}{\varepsilon_{v+1} - \varepsilon_v} \quad \text{and} \quad t_v = \zeta_v - s_v \varepsilon_v \tag{8}$$

$N_v$  is the total number of vertices and point  $(N_v+1)$  refers to the first vertex in order to complete the closed boundary integral. Substitution and arrangement lead to:

$$\begin{aligned}
 N &= \frac{1}{\kappa} \sum_{v=1}^{N_v} (s_v I_{2v} + t_v I_{1v}) \\
 M_j &= \frac{1}{\kappa} \sum_{v=1}^{N_v} (c_{v1j} I_{3v} + c_{v2j} I_{2v} + c_{v3j} I_{1v}) \quad j = 2, 3
 \end{aligned} \tag{9}$$

With:

$$\begin{bmatrix} c_{v12} & c_{v22} & c_{v32} \\ c_{v13} & c_{v23} & c_{v33} \end{bmatrix} = \begin{bmatrix} \cos \varphi & \sin \varphi \\ \sin \varphi & -\cos \varphi \end{bmatrix} \begin{bmatrix} \frac{s_v}{\kappa} & \frac{t_v - s_v \varepsilon_0}{\kappa} & -\frac{t_v \varepsilon_0}{\kappa} \\ \frac{s_v^2}{2} & s_v t_v & \frac{t_v^2}{2} \end{bmatrix} \tag{10}$$

The three different integrals in the previous relations are:

$$I_{1v} = \int_{\epsilon_v}^{\epsilon_{v+1}} \sigma(\epsilon) d\epsilon \quad I_{2v} = \int_{\epsilon_v}^{\epsilon_{v+1}} \epsilon \sigma(\epsilon) d\epsilon \quad I_{3v} = \int_{\epsilon_v}^{\epsilon_{v+1}} \epsilon^2 \sigma(\epsilon) d\epsilon \quad (11)$$

#### 4. Analytical border integration of polynomial models

Nonlinear stress-strain models are usually expressed by one or two equations and the integrals (11) cannot be derived analytically in all cases. They are straightforward for polynomial models. For a polynomial stress-strain model of order  $k$ :

$$\sigma(\epsilon) = c_0 + c_1 \epsilon + c_2 \epsilon^2 + \dots + c_k \epsilon^k = \sum_{j=0}^k c_j \epsilon^j \quad (12)$$

The three integrals (11) become:

$$\begin{aligned} I_{1v} &= \int_{\epsilon_v}^{\epsilon_{v+1}} \sigma(\epsilon) d\epsilon = \sum_{j=0}^k \frac{c_j}{j+1} (\epsilon_{v+1}^{j+1} - \epsilon_v^{j+1}) \\ I_{2v} &= \int_{\epsilon_v}^{\epsilon_{v+1}} \epsilon \sigma(\epsilon) d\epsilon = \sum_{j=0}^k \frac{c_j}{j+2} (\epsilon_{v+1}^{j+2} - \epsilon_v^{j+2}) \\ I_{3v} &= \int_{\epsilon_v}^{\epsilon_{v+1}} \epsilon^2 \sigma(\epsilon) d\epsilon = \sum_{j=0}^k \frac{c_j}{j+3} (\epsilon_{v+1}^{j+3} - \epsilon_v^{j+3}) \end{aligned} \quad (13)$$

Relations (9) and (13) deliver closed-form solutions of normal stress resultants. It can be seen from (13) that all boundary lines parallel to the neutral axis ( $\epsilon_{v+1} = \epsilon_v$ ) have no contributions to force and moment resultants. This in fact is true by virtue of (11) and (9) whether the model is polynomial or not.

This formulation cannot however be used for non-integrable material models. An alternative to using numerical integration, is replacing the original model by an appropriate polynomial fit and then use the present method. This proved more efficient than performing numerical integration on original models [2].

Apart from the moment-curvature relationship for a given constant axial force, the preceding formulation can also be used to determine  $N$ - $M_y$ - $M_z$  interaction curves and surfaces, and the stress state for a given loading.

#### 5. Validation with experimental

The experimental part of this work is described in reference [1]. The present analytical formulation was used to predict moment-curvature relationships for four beams using

different steel ratio and different levels of yield stress. Figures 4 and 5 show the predicted and measured curves and the comparison is very good. The beam details and material data are described in reference [1].

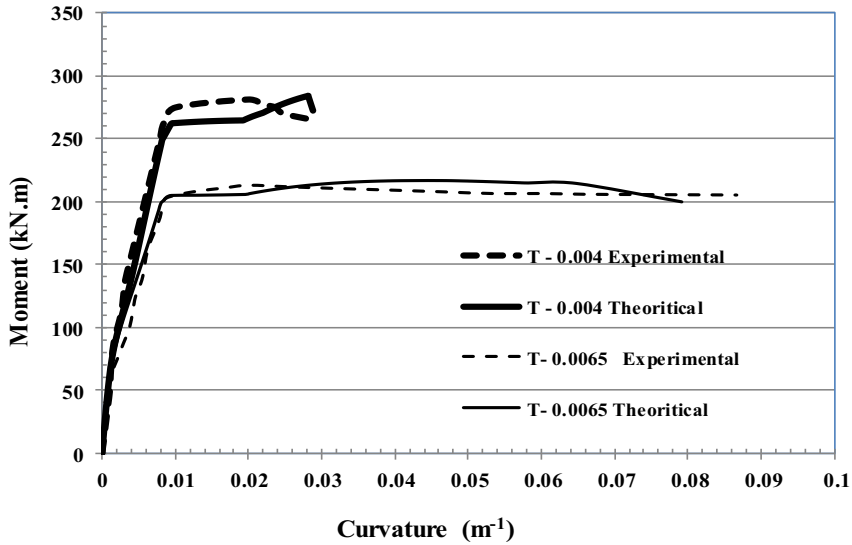


Figure 4. Predicted and measured moment-curvature for beams T (see reference [1]).

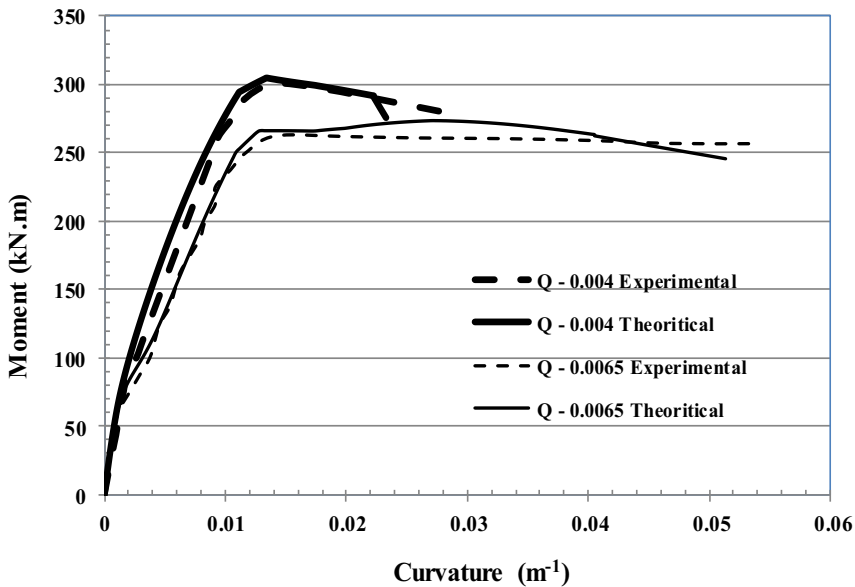


Figure 5. Predicted and measured moment-curvature for beams Q (see reference [1]).

## 6. Conclusions

The analytical integration method of stress resultants described in this work is very efficient. It deals with any complex shaped section. Analytical integration can be performed on any polynomial model and other specific models. Non-integrable models can also be approached by suitable polynomial fit and then integrated. The method was used to compare moment-curvature with experimental results and the comparison was very good. The effects of both yield value and reinforcement ratio observed in the experimental part are confirmed.

## Acknowledgment

The authors gratefully acknowledge the support given by the structural laboratory technicians at the College of Engineering in King Saud University to complete all required tests in the present study.

## References

- [1] S. Mourad, A. Charif, M.I. Khan, Flexural behavior of RC beams with local steel: Experimental investigation, *International Conference on Construction Materials and Structures*, ICCMS, Johannesburg, November 24-26, 2014.
- [2] A. Charif, M.J. Shannag, S. Dghaither, Ductility of lightweight concrete beams and columns, *Latin American Journal of Solids and Structures*, Vol.11, No 7, 2014, pp.1251-1274
- [3] D. Zupan, M. Saje, Analytical integration of stress field and tangent material moduli over concrete cross-sections, *Computers and Structures*, 2005 (85), pp.2368-80
- [4] J.M. Rotter, Rapid exact inelastic biaxial bending analysis, *Journal of the Structural Division – ASCE* 1985, 111, 2659-74
- [5] M.G. Sfakianakis, Biaxial bending with axial force of reinforced, composite and repaired concrete sections of arbitrary shape by fiber model and computer graphics, *Journal of Structural Engineering*, 1999;125(6):672–83.
- [6] A. Fafitis, Interaction surfaces of reinforced-concrete sections in biaxial bending, *Jnl Struct Eng, ASCE* 2001;127(7):840–6.
- [7] J.L. Bonet, M.L. Romero, P.F. Miguel, M.A. Fernandez, Analytical approach to failure surfaces in reinforced concrete sections subjected to axial load and biaxial bending, *Computers and Structures* 2004;82(2-3):213–25.
- [8] J.L. Bonet, M.H.F.M. Barros, M.L. Romero, Comparative study of analytical and numerical algorithms for designing reinforced concrete sections under biaxial bending, *Computers and Structures*, Vol.84, 2006, pp.2184-2193
- [9] J. Batista, M. Sousa Jr., C. Muniz, Analytical integration of cross-section properties for numerical analysis of reinforced concrete, steel and composite frames”, *Engineering Struct.*, 2007 (29),618-625.
- [10] A.E. Charalampakis, V.K. Koumousis, Ultimate strength analysis of composite sections under biaxial bending and axial load, *Advances in Engineering Software* 39 (2008) 923-936

# Simplified torsional strength of reinforced and prestressed concrete beams

Khaldoun N. RAHAL<sup>1</sup>

*Department of Civil Engineering, Kuwait University, Kuwait*

**Abstract.** A simple non-iterative model for the calculation of the torsional strength of reinforced and concentrically prestressed concrete beams is presented. The proposed model is based on a modification of a recently developed semi-empirical model suitable for non-prestressed members. The main equation relates the ultimate torsional moment to the amount and strength of the longitudinal and transverse reinforcement, the concrete compressive strength, and the geometrical properties of the cross section. The calculated strength is limited by an upper value calculated based on crushing of the concrete before the yielding of the reinforcement. The calculations of the model are compared to experimental data and good correlation is obtained.

**Keywords.** Beams, strength, torsion, reinforcement, prestressing

## Introduction

Structural members such as spandrel beams, beams curved in plan and bridge girder subjected to eccentric loading are subjected to a combination of stress resultants, including torsional moments.

There are numerous analytical models which study the torsional behavior. Some advanced models are capable of calculating the full response of reinforced concrete (RC) sections subjected to pure torsion [1] or torsion combined with other stress resultants [2–4]. Other simpler models concentrate on calculating the ultimate torsional capacity [5] or the ultimate torsional capacity and the mode of failure [6].

A significant number of the models for the torsional behavior are based on the hollow-tube analogy [7]. Figure 1 shows a hollow-tube model of a rectangular cross section reinforced using longitudinal and transverse hoop reinforcement. At ultimate, only the outer periphery is engaged in the resistance of the applied torque. This fact was supported by experimental results [5]. The shear flow (and shearing stresses) circulates around the periphery along an effective thickness  $a_0$ . The walls of the hollow tube are subjected to in-plane shearing stresses. In under-reinforced sections, one or both of the reinforcement (transverse and longitudinal) yield before crushing of the concrete. In over-reinforced sections, the concrete crushes before yielding in the reinforcement.

---

<sup>1</sup>Corresponding author: [Khaldoun.rahal@ku.edu.kw](mailto:Khaldoun.rahal@ku.edu.kw)

The basic equation for the torsional capacity of a reinforced concrete cross section is obtained using the following equation:

$$T_{ht} = 2A_o \sqrt{\frac{A_L f_{yL}}{p_h} \frac{A_t f_{yt}}{s}} \tag{1}$$

Where:

- $A_o$  = area enclosed by the shear flow
- $A_L$  = total area of longitudinal reinforcement
- $A_t$  = area of one leg of hoop reinforcement within spacing  $s$
- $f_{yL}$  = yield strength of longitudinal reinforcement
- $f_{yt}$  = yield strength of hoop reinforcement
- $p_h$  = perimeter of centerline of hoop
- $s$  = spacing of hoops reinforcement, parallel to axis of specimen

Building codes such as the ACI Code [8] and the Canadian CSA code [9] are based on the hollow-tube analogy. They relate the torsional capacity of under-reinforced sections to the transverse hoop reinforcement, inclination of diagonal stresses ( $\theta$ ) and the geometric properties of the cross section using the following equation:

$$T_{n-code} = 2A_o \frac{A_t f_{yt}}{s} \cot \theta \tag{2}$$

The amount of longitudinal reinforcement required for the torsional resistance is given by:

$$A_L = \frac{A_t}{s} p_h \left( \frac{f_{yt}}{f_{yL}} \right) \cot^2 \theta \tag{3}$$

A simple manipulation of Eqs. (2) and (3) leads to Eq. (1).

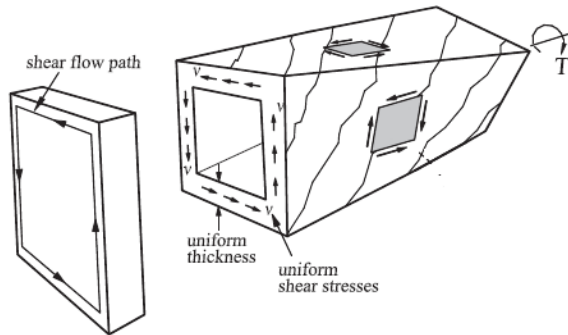


Figure 1. Hollow-tube model for torsion

A recent investigation [10] challenged two of the assumptions of the hollow-tube analogy. The first is a main assumption, stating that the shear flow is constant around the perimeter of the cross section. The second is that the torsional capacity is independent on the compressive strength of the concrete. Experimental evidence showed that strains in the concrete and steel on the longer sides of the cross sections are consistently larger than those in the short sides. In addition, beams with stronger concrete strength resisted relatively larger torsional moments. Based on experimental results, it was proposed [10] that the torsional strength can be calculated using the following equations:

$$T_n = 0.36(f'_c)^{0.16} A_c \left( A_L f_{yL} \frac{A_t f_{yt}}{s} \right)^{0.35} \tag{4-a}$$

$$\leq 2.5(f'_c)^{0.3} \frac{A_c^2}{p_c} \tag{4-b}$$

The first equation is suitable for under-reinforced sections. The second equation sets an upper limit that becomes critical when the amount of reinforcement exceeds the balanced reinforcement level.

The objective of this paper is to check the applicability of Eq. (4) to concentrically prestressed and partially prestressed beams. Adequate modifications to suit these types of members will be implemented.

### 1. Application to prestressed beams

Mitchell and Collins [1] have experimentally shown that the prestressing has a limited effect on the ultimate torsional capacity if the longitudinal prestressing steel yields at ultimate conditions. Based on that, it seems possible to apply Eq. (4-a) to prestressed and partially prestressed sections by a simple replacement of the term  $(A_L f_{yL})$  with  $(A_L f_{yL} + A_p f_{yp})$  where the terms  $A_p$  and  $f_{yp}$  are the area and yield strength of the prestressing steel. A similar approach has been successfully used by Mitchell and Collins [1] and Rahal [6].

A modification to Eq. (4-b) to make it more suitable to prestressed and partially prestressed beams is not feasible due to the limited experimental data on prestressed concrete beams which failed in an over-reinforced mode of failure. Hence, Eq. (4-b) remains unchanged in the proposed model.

In the original work [10], the development and evaluation of the model were based on concrete rectangular members adequately reinforced in the longitudinal and transverse directions. For the model proposed here, this will be ensured by calculating the cracking torque and setting it as a minimum value of the torsional capacity. The cracking torsional moment is based on a cracking stress equal to  $(0.4\sqrt{f'_c})$ . Hence, it is proposed that the torsional strength is calculated using:



$$T_n = 0.36(f'_c)^{0.16} A_c (A_L f_{yL} + A_p f_{yp})^{0.35} \left( \frac{A_t f_{yt}}{s} \right)^{0.35} \tag{5-a}$$

$$\leq 2.5(f'_c)^{0.3} \frac{A_c^2}{P_c} \tag{5-b}$$

$$\geq 0.4 \sqrt{f'_c} \frac{A_c^2}{P_c} \sqrt{1 + \frac{f_{pc}}{0.4 \sqrt{f'_c}}} \tag{5-c}$$

Where the term  $f_{pc}$  is the compressive stress in the concrete cross section due to prestressing.

### 2. Evaluation of the model

The test results from sixteen specimens [1,11] are used to evaluate the performance of the model as presented in Eqs. (5).

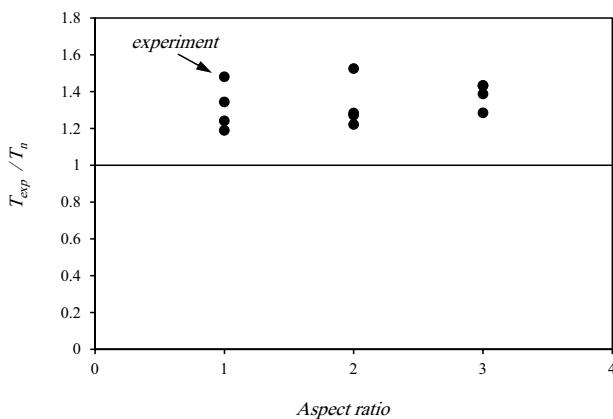


Figure 2. Correlation ratio of 12 specimens [11] versus aspect ratio

El-Degwy and McMullen [11] tested 12 partially prestressed beams to evaluate the effects of the aspect ratio and the amount of reinforcement on the torsional strength. The aspect ratio ranged from 1 to 3 in the three series. Figure 2 shows a plot of the ratio of experimental to calculated torsional strength (correlation ratio) versus the aspect ratio in the twelve specimens. In spite of the semi-empirical nature of the equations of the model, the results show that it captures the effect of the aspect ratio accurately.

Figure 3 shows a plot of the correlation factor versus the combined amount of reinforcement, as it appears in Eq. (5-a). Again, the comparison shows that the model accurately captured the effect of increasing amount of reinforcement on the torsional strength.

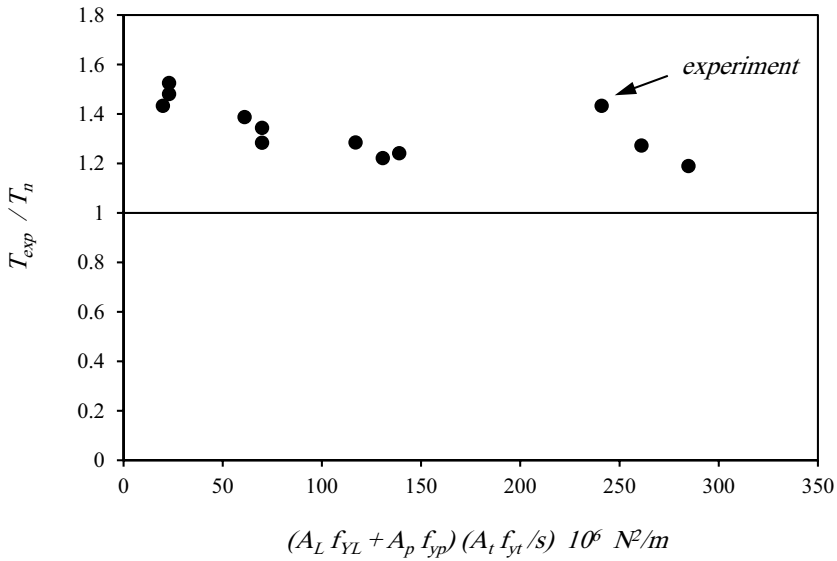


Figure 3. Correlation ratio of 12 specimens [11] versus amount of reinforcement

For the sixteen beams, the average of the correlation ratios was 1.29 and the coefficient of variation was 9.67%. For the 152 specimens used for the development of the original model, the average of the ratios was 1.07 and the coefficient of variation was 10.4%. The method seems to be more conservative for prestressed and partially prestressed concrete.

### 3. Conclusions

A recently developed semi-empirical model to calculate the torsional strength of reinforced concrete beams has been extended to cover the cases of concentrically prestressed beams. The equations were modified based on the assumption that the effect of prestressing is minimal if the prestressing steel yields at ultimate conditions.

The results of the proposed method were compared to the experimental results from sixteen specimens available in the literature. A good agreement was found. The average of the correlation ratios was 1.29 and the coefficient of variation was 9.67%.

### Acknowledgement

The research reported in this paper was supported by Research Sector, Kuwait University, Research Grant EV02/11. This support is gratefully acknowledged.

## References

- [1] D. Mitchell and M.P. Collins, *Behavior of structural concrete beams in pure torsion*, Publication No. 74-06, Department of Civil Engineering, University of Toronto, Toronto, 1974.
- [2] K.N. Rahal and M.P. Collins, *Effect of Cover Thickness on Shear and Torsion Interaction—An Experimental Investigation*, ACI Structural Journal, **92-3** (1995), 334-342.
- [3] K.N. Rahal and M.P. Collins, *Compatibility torsion in spandrel beams using Modified Compression Field Theory*, ACI Structural Journal, **103-3**, (2006), 328–338
- [4] J. Navarro-Gregori, P.M. Sosa, M.A.F. Prada and F.C. Filippou, *A 3D numerical model for reinforced and prestressed concrete elements subjected to combined axial, bending, shear and torsion loading*, Engineering Structures **29-12** ( 2007) , 3404–3419.
- [5] T.T.C. Hsu, *Torsion of structural concrete-behavior of reinforced concrete rectangular members*, Torsion of structural concrete, SP-18, American Concrete Institute, Detroit, Michigan, (1968), 261–306.
- [6] K.N. Rahal, *Analysis and design for torsion in reinforced and prestressed concrete beams*, Structural Engineering and Mechanics An International Journal, **11-6** (2001), 575–590.
- [7] J.G. MacGregor and M.G. Ghoneim, *Design for Torsion*, ACI Structural Journal **92-2** (1995), 211-218.
- [8] ACI Committee 318-11, *Building code requirements for structural concrete (ACI 318\_11) and commentary (318R-11)*, American Concrete Institute (2011).
- [9] CSA-A23.3, *Design of concrete structures (A23.3-04)*, Canadian Standards Association, Canada, ( 2004), 214 p.
- [10] K.N. Rahal, *Torsional strength of Normal and High-Strength Reinforced Concrete Beams*, Engineering Structures, **56** (2013), 2206–2216.
- [11] W.M. El-Degwy and A.E. McMullen, *Prestressed concrete tests compared with test theories*, PCI Journal, **30-5** (1985), 96-127.

# Effect of clay-concrete lining on canal seepage towards the drainage region - an analysis using Finite-Element method

Fitsum SOLOMON<sup>1</sup> and Stephen EKOLU

*Department of Civil Engineering Science, University of Johannesburg, South Africa*

**Abstract.** For proper design of a drainage system that utilizes lined canals, knowledge of the seepage into a soil substrate/drainage region is necessary so that the drainage blanket and /or filter type and thickness, and the size of collector pipes can all be designed. The work presented in this paper is based on the problem of steady-state seepage from a hypothetical irrigation canal into the substrate/drainage region towards asymmetrical trapezoidal concrete-lined canal. The problem is solved using a finite element based software program to determine the flow volume into the drainage region.

Typical values of soil permeability coefficients of single and two-layer subsoil from literature are used along with experimental results of a laboratory study done for the design seepage coefficient of clay-cement concrete as lining material. The water flow effect of canal seepage discharge analyzed shows that the effectiveness of canal lining in reducing seepage is less when drainage distance is large. This study may contribute towards a better understanding on design of hydraulic conductivity under hydraulic structures. It will systematically enumerate the many, often straightforward factors that determine coefficient of permeability for compliance purposes. This could also involve a re-estimation of the values of the permeability coefficient and the factors on which the coefficient depends.

**Keywords.** Drainage system, canals, seepage, water table, Finite Element method, canal linings

## Introduction

In most irrigation projects, it is critical to maintain not only a constant flow of water, but also a constant velocity. The design of a canal or ditch is a combination of its bed width and depth, together with the resulting mean velocity. Water is conveyed to the land to be irrigated by canals, with the attendant problem of water loss through seepage. Canal concrete liners normally decrease the conveyance losses or seepage through the bottoms and sides; prevent weed growth and retard moss accumulation. They also decrease erosion from high velocities; reduce maintenance costs; and increase the capacity of the canal to convey water. However, they do not eliminate seepage losses [1]. For the correct exploitation and management of groundwater, surface reservoirs and canals, it is necessary to estimate the seepage losses from canals.

---

<sup>1</sup>Corresponding author: [Fitsummoa@gmail.com](mailto:Fitsummoa@gmail.com)

A number of studies have assessed canal seepage losses using flow nets [2], analytical solutions [3-5] and numerical methods using the finite-element method, finite-difference method, and boundary-element method [6-8]. The problems considered mainly involved idealized conditions and only one or two layers of a largely homogeneous and isotropic medium as substrate/drainage region.

As mentioned previously, the concrete lining of a canal does not reduce seepage loss to zero, because of the development of fractures in the lining, and the lining material used is not completely impervious [1]. Among the aforementioned investigators, only [9] considered the problem of seepage from a lined canal founded on a stratified medium, toward fully penetrating drainages (case study).

## 1. Problem statement

Generally, fluid flow is investigated within the limits of Darcy's law, and capillary forces and surface tension are omitted for simplicity. In addition, the fluid is assumed to be incompressible and of constant density and viscosity. The problem of seepage from a lined canal toward asymmetrically placed drainages has been considered for solution. In this problem, the effect of canal lining on the canal seepage discharge has been investigated. The finite-element method (FEM) has been chosen to solve the governing partial differential equation on the steady-state seepage flow under lined canals, written as equation (1) for the saturated unconfined steady-state flow seepage in anisotropic medium.

$$K_x \delta^2 h / \delta x^2 + K_y \delta^2 h / \delta y^2 = 0 \quad (1)$$

Where,  $x$  and  $y$  = horizontal and vertical coordinates respectively,  $K_x$  and  $K_y$  = hydraulic conductivities in the  $x$  and  $y$  directions; and  $h = h(x,y)$  is the piezometric head above the datum. Because along the groundwater free surface, the atmospheric pressure is considered to be zero, the head of the points laid on this boundary is equal to their coordinate.

### 1.1. Finite Element Method

To solve the partial differential equation governing the seepage problem using FEM, first the domain is discretized to elements and nodes and then the approximation function is systematically derived over the given domain. Then, the Gaussian elimination solver type which approximates the governing equation, is derived over each element. Finally, the equations over all elements of the collection are converted by the continuity of primary variables. The boundary conditions of the problem are imposed and the connection set of equations is solved. The connection set of equations are of the general form as follows:

$$[A][H] = [Q] \quad (2)$$

Where  $[A] = [n \times n]$  elemental property matrix (generally referred to as the stiffness matrix in structural problems) and the permeability matrix in seepage problems ( $n$  is the number of nodes);  $[Q]$  = load vector in structural problems and is composed of known boundaries, source, and sink terms in seepage problems; and  $[H]$  = vector of known and unknown heads.

### 1.1.1. Computation of canal seepage discharge

Canal seepage discharge is the normal flux passing through the canal bed and canal sides. The normal flux across a node and the hydraulic heads at the nodes directly connecting to the node under consideration are interrelated by Eq. (3). The equation for a specified node (say, node  $i$ ) can be written as:

$$A_{ij}h = q_i \quad (3)$$

Where  $j$  = nodes directly connecting to node  $i$ , including node  $i$  itself [10].

In this paper, five common field cases for fluid flow characteristics of anti-seepage materials are analyzed based on design permeability coefficient obtained from the literature. In all cases, the seepage analysis was done using the finite element seepage module of the computer program Phase2 version 7.0 of Rocscience [11]. The analysis only considered the fluid flow behavior of anti-seepage materials, i.e. deformation of the canal is ignored and all displacement degrees of freedom are prescribed to zero. The roughly trapezoidal shaped canal was taken from literature [12]; it consists of a channel 154 km long built in 1908 using horses and mules. For this analysis, the channel shape was modified to be representative of a typical hypothetical trapezoidal canal of dimensions: top width ( $B$ ) of 17.8 m, and water depth ( $H_w$ ) (i.e the trapezoidal height of the canal) of 2.5 m, having a side slope angle,  $\alpha$  of  $45^\circ$ , and bottom width ( $W_b$ ) of 13.3 m. The total head in the canal was taken to be 52.5 m in order to simulate full ponding at steady state seepage, as shown in Figure 1.

## 2. Case studies of hypothetical irrigation canals

### 2.1. Unlined canal

**Case 1. Single-Layer Subsoil Unlined Irrigation canal:** The model condition beneath the unlined canal is a permeable layer. The hydraulic conductivity of the underlying single-layer subsoil silty sand was taken to be  $1.0 \times 10^{-5}$  m/s. The critical water head,  $h_1$  and differential heads of 10.75 m, 19.65 m and 28.55 m were used in the analysis. It was assumed that all the materials are isotropic.

### 2.2. Concrete irrigation canals

**Case 2. Hypothetical canal:** 50 mm thick clay-cement concrete founded on single-layer silty sand subsoil.

**Case 3. Hypothetical canal:** 75 mm thick clay-cement concrete founded on single-layer silty sand subsoil and two-layer subsoil fine sand underlying silty sand.

**Case 4. Hypothetical canal:** 100 mm thick clay-cement concrete founded on single-layer silty sand Subsoil and two-layer subsoil fine sand underlying silty sand.

For the concrete canals, the mix of clay, cement and aggregates used, was designed to correspond to the requirement of anti-seepage material. The mix should be workable and typically of composition: water/ (cement + clay) = 0.85 and clay/cement = 2/3 or 40% clay content. Its compressive strength is usually greater than 6 MPa while its water permeability ranges from  $5 \times 10^{-10}$  to  $1 \times 10^{-10}$  m/s [13]. Figure 1 indicates how the canal is installed in the canal for the control of seepage. In literature, large dams with slightly seeping core, were also built in Macedonia, Turiya dam [14].

In this paper, Case 1 represents unlined canals while the others, Case 2 to 4 are concrete lined canals. Table 1 gives the permeability coefficients applied in analysis of the cases.

### 3. Seepage analysis by Finite Element method

In the FEM of analysis, the foundation and different lining thicknesses of hypothetical irrigation canals are modeled using the computer software [11]. Typical values of soil permeability coefficients of single-layer subsoil from literature were used along with the experimental results from a laboratory study done for clay-cement concrete use as a lining material. The model set up extends below the thickness of lined canal and is fixed into an impervious layer. Material permeability is required in the finite element analysis in order to solve the seepage problem. Permeability,  $K_2/K_1$  is a factor which specifies the relative permeability in the direction orthogonal to the  $K_1$  direction. Note that the  $K_1$  permeability is the “primary” permeability defined by the saturated permeability  $K_s$ ; while  $K_1$  is the angle which specifies the direction of the  $K_1$  permeability and is given relative to the positive x (horizontal) direction. In the analysis, it is considered that,  $K_2/K_1 = 1$  (unity) and  $K_1$  angle = 0, i.e. the permeability in the horizontal direction =  $K_s$  (in saturated zone), and the permeability in the vertical direction =  $1 \times K_s$  (in saturated zone). The set boundary conditions are the total head (H), and zero pressure ( $p=0$ ) and hydraulic parameters are also given in the Table 1. An example of details of the Finite Element analysis set up is shown in the Figure 1.

#### 3.1. Presentation of results

The canal seepage was computed for different values of physical and hydraulic parameters. Canal seepage discharge was converted to dimensionless form by dividing,  $h_1$  and the hydraulic conductivity of the medium. All the physical parameters have been converted to dimensionless form by dividing by  $h_1$ . A summary of the results is presented along with Figures 1 to 3 giving the output results for each of the case studies. All cases can be further sub-categorized into two conditions (of lined and unlined canal) depending on the physical and hydraulic parameters employed.

**Table 1.** Hydraulic permeability properties of Case 1 to 4

Materials	Case 1		Case 2, 3, 4 Permeability(m/s)		
	Silty sand [15].	Silty Sand [15].	50 mm thick clay-cement concrete [13].	75 mm thick clay-cement concrete [13].	100 mm thick clay-cement concrete [13].
Coefficient of permeability (m/s)	$1 \times 10^{-5}$	$1 \times 10^{-5}$	$6.90 \times 10^{-10}$ (50 mm thick)	$5.00 \times 10^{-10}$ (75 mm thick)	$3.47 \times 10^{-10}$ (100 mm thick)

Drainage distances  $L/h_1$  are taken from top of trapezoidal height water head,  $H_w = 2.5$  m (i.e. the total head in the canal is 52.5 m) towards horizontal direction as shown Figure 1;  $k_L/k$  for non-lined canal (being earth liner) is such that  $k_L = k$ . The analysis is done for varied thicknesses of lining i.e 50 mm ( $k_L/k = 0.000069$ ), 75 mm ( $k_L/k = 0.00005$ ) and 100 mm ( $k_L/k = 0.0000347$ ). In order to examine the effect of the canal lining (with a thickness of  $d_L$  and a permeability of  $k_L$ ) on canal seepage discharge, the values of  $q/kh_1$  have been plotted (as shown in Fig.2) against the values of  $k_L/k$  for different drainage distances as shown in Figure 1.

The values of  $q_L/q_U$  have been plotted against the values of  $d_L/h_1$  for 50 mm lining ( $d_L/h_1 = 0.0047$ ), 75 mm lining ( $d_L/h_1 = 0.00698$ ) and for 100 mm lining ( $d_L/h_1 = 0.0093$ ) for different drainage distances shown in Figure 1, where  $q_L$  = value of canal discharge for lined canal, while  $q_U$  = canal discharge when everything is the same but there is no lining (NL) the result shown in Figure 3. The other two conditions follow the same procedure as condition 1 but  $h_1$  changes to 19.65 m and 28.55 m.

In the case of single layer subsoil condition, the total discharge velocity (m/s) is in the range of  $5.55 \times 10^{-07}$  to  $1.11 \times 10^{-05}$  m/s (see Fig.1a). Furthermore the discharge section can be selected for the different drainage distances to display the steady-state, volumetric flow rate of water, normal to the plane of the discharge section. At  $h_1 = 10.75$  m and drainage distances shown in Figure 1  $L_0 = 0$  m,  $L_1 = 7.1$  m,  $L_2 = 29.1$  m,  $L_3 = 51.1$  m and  $L_4 = 88.6$  m from the top of the water, the flow rates were calculated as  $1.38 \times 10^{-05}$ ,  $5.9661 \times 10^{-06}$ ,  $3.7228 \times 10^{-06}$  and  $6.9429 \times 10^{-06}$  m<sup>3</sup>/s respectively as shown in the Figure 1b.

Similar calculations were done for case studies at  $h_1 = 10.75$ , 19.65 m and  $h_1 = 28.55$  m, with and without a lining of 50 mm, 75 mm and 100 mm thick concrete. For instance, the 100 mm thick concrete lining at 10.75 m differential head elevation gave values of discharge flow rates of  $1.3991 \times 10^{-05}$ ,  $6.0695 \times 10^{-06}$ ,  $3.4714 \times 10^{-06}$ ,  $1.1307 \times 10^{-05}$  m<sup>3</sup>/s at distances  $L_1 = 7.1$  m,  $L_2 = 29.1$  m,  $L_3 = 51.1$  m and  $L_4 = 88.6$  m respectively. The water flow effect of canal seepage discharge analyzed shows that the effectiveness of canal lining in reducing seepage is less when drainage distance is large.

### 3.1.1. Effect of lining permeability on canal seepage

The effect of lining permeability on canal seepage (see Table 2) and effect of lining thickness (see Table 3) on canal seepage were analyzed and compared against the unlined canal. In order to examine the effect of the canal lining on canal seepage discharge, the values of  $q/kh_1$  have been plotted against the values of  $k_L/k$  for different drainage distances as shown on Figure 2.

### 3.1.2. Effect of lining thickness on canal seepage

Table 2 and corresponding Figure 2 indicate that when the thickness of lining is increased, the ratio of  $k_L/k$  decreases due to the nature of the anti-seepage barrier so that the greater the length, the longer the water paths, as follows: at drainage distance  $L_1 = 7.1$  m (Fig. 1) 75 mm thick concrete lining produces the lowest ratio of  $q/kh_1$  which is 0.1169, followed by the use of 50 mm lining ( $q/kh_1 = 0.1263$ ), NL ( $q/kh_1 = 0.1288$ ), and lastly 100 mm lining ( $q/kh_1 = 0.1301$ ). At  $L_2$  i.e. 29.1 m (Fig.1), the same trend was experienced that 75 mm gave lowest value ( $q/kh_1 = 0.0474$ ), followed by NL ( $q/kh_1 = 0.0555$ ), 100 mm ( $q/kh_1 = 0.0565$ ), and 50 mm lining ( $q/kh_1 = 0.0569$ ). For the further drainage distance  $L_3$  i.e. 51.1 m (Fig.1) the trend continues in favour of 75 mm ( $q/kh_1 = 0.0282$ ), followed by 100 mm ( $q/kh_1 = 0.0323$ ), 50 mm lining ( $q/kh_1 = 0.0334$ ), with the highest value being given NL ( $q/kh_1 = 0.0346$ ). Down further to the tail head water  $L_4$  i.e. at 88.6 m, the water flow effect changed. At  $L_4$  the lowest value of the dimensionless ratio, i.e  $q/kh_1$  was 0.0646 for NL, followed by 75 mm lining (0.0949), 100 mm (0.1052) and finally 50 mm lining (0.1504). In general, the 75 mm thick concrete was effective in reducing seepage up to drainage distance of approximately 50 m, but beyond this distance, it was not as effective as the NL. This is because as more water was discharged along the drainage distances, the water flow effect diminished.



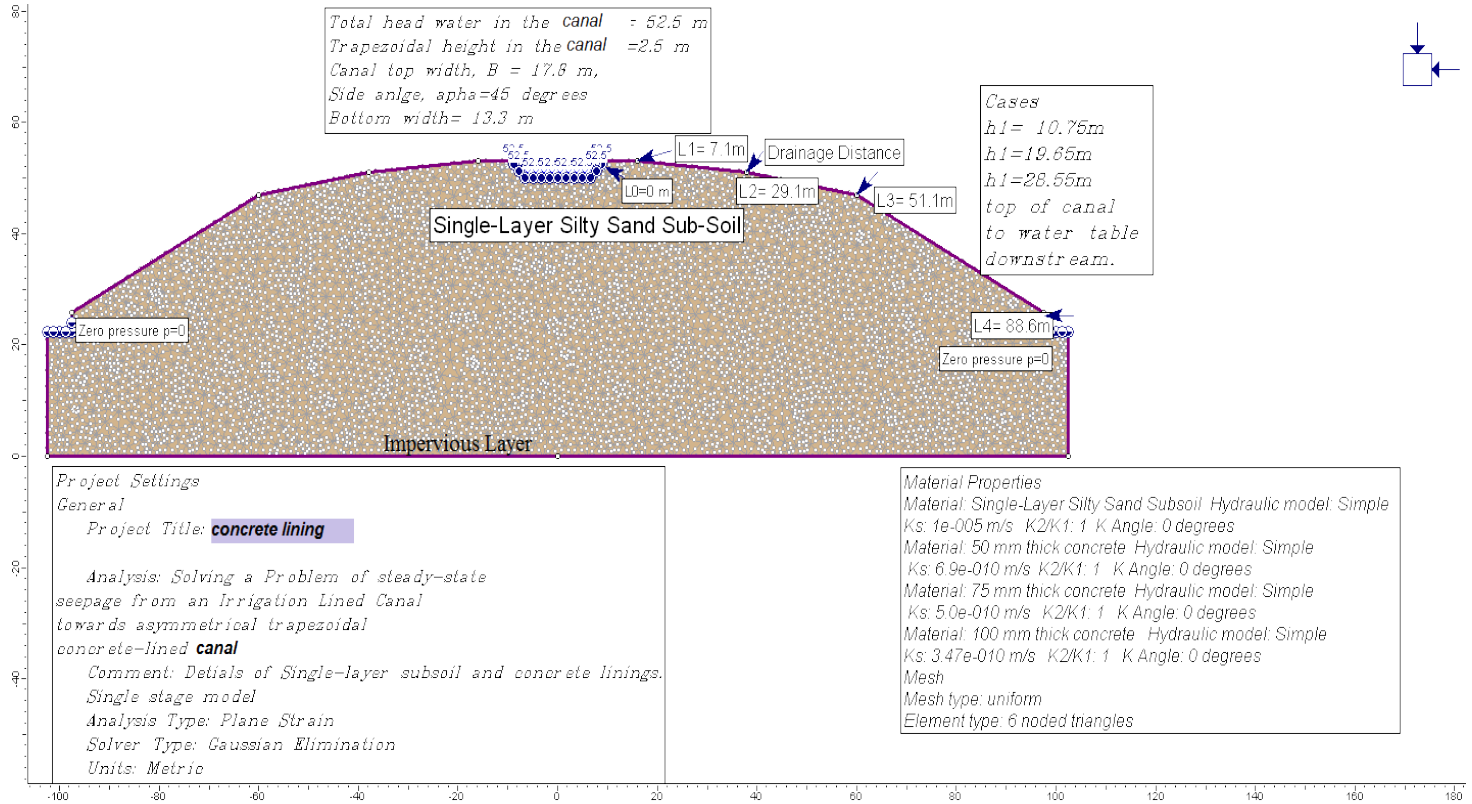


Figure 1. Details of case single-layer silty sand subsoil (case 1)

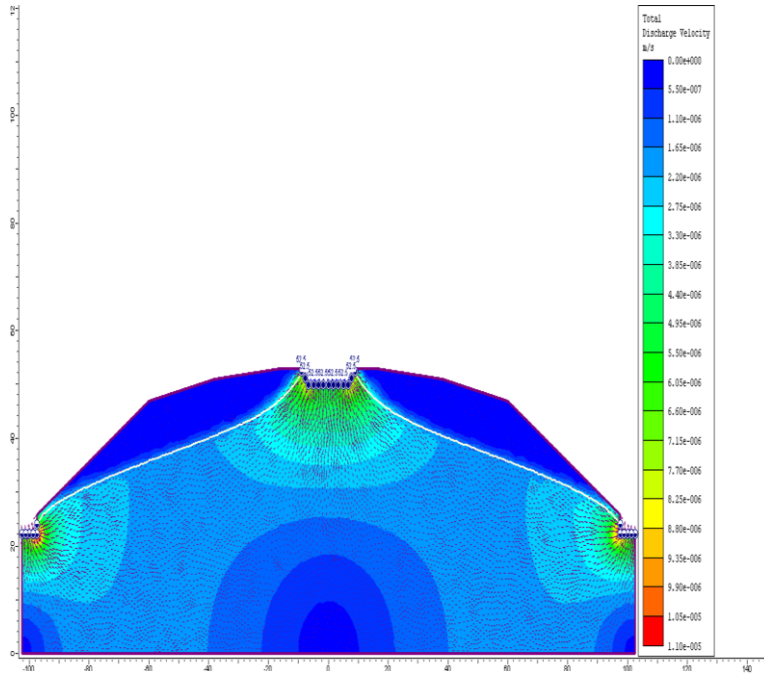


Figure 1a. Display of total discharge velocity ( $v_t$ ) and flow lines (case 1)

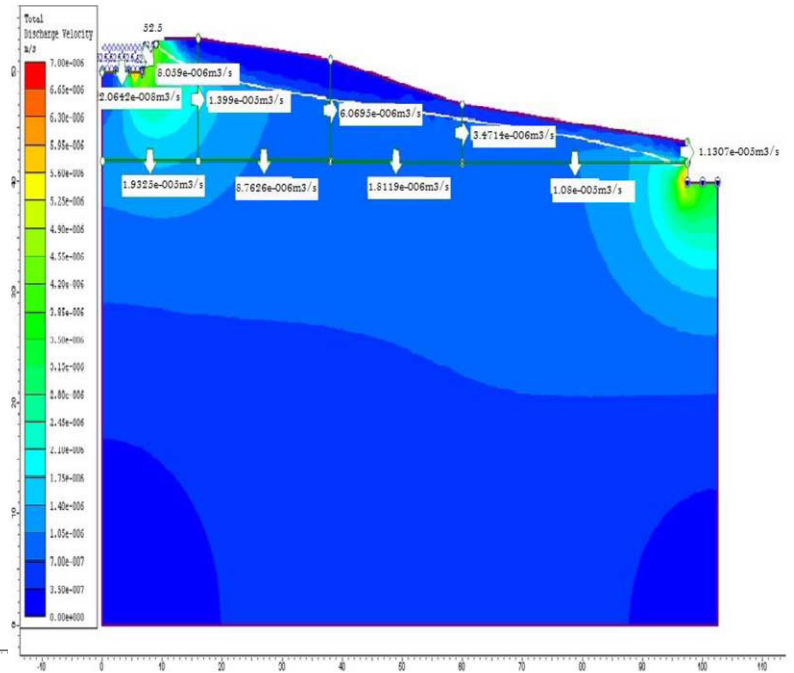


Figure 1b. Display of discharge section drainage distances across for case no lining and at  $h_1=10.75$  m

**Table 2.** Effect of lining permeability on canal seepage

Head to tail water table= $h_1$	On water table	Discharge section taken to simulate steady-state, volumetric flow of water, normal to drainage distances.				
		Non-lined (NL)	50 mm	75 mm	100 mm	
	Ratio	$K_L/k$	1	0.000069	0.00005	0.0000347
$h_1=10.75$ m	$L_1/h_1=142/215$	$q/kh_1$	0.1288	0.1263	0.1169	0.1301
	$L_2/h_1=582/215$	$q/kh_1$	0.0555	0.0569	0.0474	0.0565
	$L_3/h_1=1022/215$	$q/kh_1$	0.0346	0.0334	0.0282	0.0323
	$L_4/h_1=1772/215$	$q/kh_1$	0.0646	0.1504	0.0949	0.1052
$h_1=19.65$ m	$L_1/h_1=142/215$	$q/kh_1$	0.1776	0.1672	0.1719	0.1717
	$L_2/h_1=582/215$	$q/kh_1$	0.0983	0.0883	0.0912	0.0966
	$L_3/h_1=1022/215$	$q/kh_1$	0.0708	0.0658	0.0679	0.0694
	$L_4/h_1=1772/215$	$q/kh_1$	0.0708	0.0289	0.0311	0.0592
$h_1=28.55$ m	$L_1/h_1=142/215$	$q/kh_1$	0.1907	0.1885	0.1855	0.1821
	$L_2/h_1=582/215$	$q/kh_1$	0.1276	0.1331	0.1232	0.1196
	$L_3/h_1=1022/215$	$q/kh_1$	0.105	0.1016	0.0963	0.0907
	$L_4/h_1=1772/215$	$q/kh_1$	0.0947	0.0754	0.0187	0.0638

**Table 3.** Effect of lining thickness on canal seepage

Head to tail water table= $h_1$	On water table	Discharge section taken to simulate steady-state, volumetric flow of water, normal to drainage distances			
		Thickness(mm)	50 mm	75 mm	100 mm
	Ratio	$d_L$	0.0047	0.00698	0.0093
$h_1=10.75$ m	$L_1/h_1=142/215$	$d_L/h_1$	0.9799	0.907	1.01
	$L_2/h_1=582/215$	$q_L/q_U$	1.0241	0.8548	1.0173
	$L_3/h_1=1022/215$	$q_L/q_U$	0.9633	0.8134	0.9325
	$L_4/h_1=1772/215$	$q_L/q_U$	2.3284	1.4687	1.6286
$h_1=19.65$ m	<b>Ratio</b>	<b><math>d_L/h_1</math></b>	<b>0.0025</b>	<b>0.0038</b>	<b>0.0051</b>
	$L_1/h_1=142/215$	$q_L/q_U$	1.9913	1.9592	1.9233
	$L_2/h_1=582/215$	$q_L/q_U$	1.043	0.9654	0.9374
	$L_3/h_1=1022/215$	$q_L/q_U$	0.9676	0.9169	0.8652
$h_1=28.55$ m	$L_4/h_1=1772/215$	$q_L/q_U$	0.7969	0.1978	0.6747
	<b>Ratio</b>	<b><math>d_L/h_1</math></b>	<b>0.0018</b>	<b>0.0026</b>	<b>0.0035</b>
	$L_1/h_1=142/215$	$q_L/q_U$	1.9913	1.9592	1.9233
	$L_2/h_1=582/215$	$q_L/q_U$	1.043	0.9654	0.9374
$h_1=28.55$ m	$L_3/h_1=1022/215$	$q_L/q_U$	0.9676	0.9169	0.8652
	$L_4/h_1=1772/215$	$q_L/q_U$	0.7969	0.1978	0.6747

The effect of lining thickness on canal seepage can be determined by plotting the value of  $q_L/q_U$  against the values of  $d_L/h_1$  for different drainage as in Table 3 and Figure 3 where  $q_L$ = value of canal discharge for lined canal,  $q_U$ =canal discharge when all factors are the same but with no lining.

For  $h_1=19.65$  m (see Table 2). The lowest discharge ratio was experienced at the drainage distance  $L_1$  by a 50 mm lining giving ( $q/kh_1= 0.1672$ ), followed by 100 mm lining ( $q/kh_1= 0.1717$ ), 75 mm ( $q/kh_1= 0.1719$ ), while the highest value was given by NL ( $q/kh_1= 0.1776$ ).

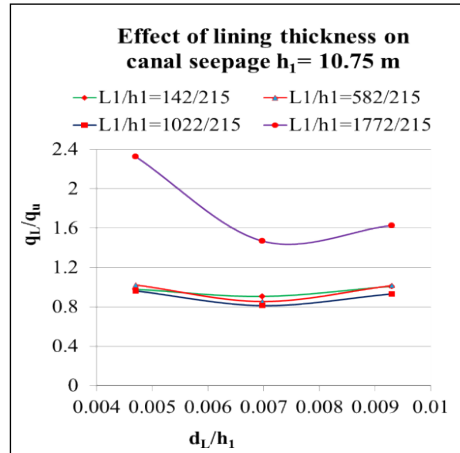
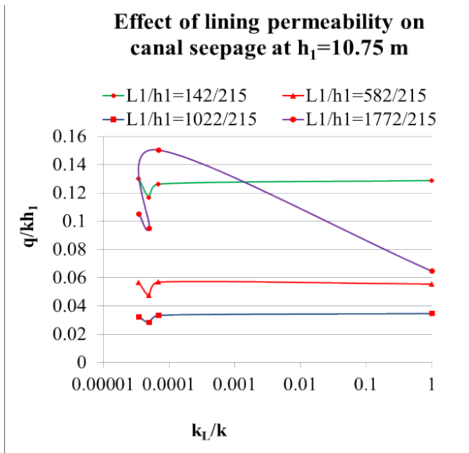
From the results, it was found that the lowest value of seepage was given by the 100 mm thick concrete lining applied all the way into the drainage region, except for the tail at the end, where 75 mm thick lining gave the lowest seepage. In the whole analysis, it is noticed that the values of the ratio  $q/kh_1$  did not vary by a large margin for  $h_1=28.55$  m, i.e 100 mm lining gave  $q/kh_1=0.1821$  compared to 75 mm lining which gave  $q/kh_1=0.1855$  at  $L_1$ . But a big margin except at the end i.e.  $L_4$  with 75 mm lining giving  $q/kh_1=0.0187$  and 100 mm giving  $q/kh_1=0.0638$ . This indicates that there is no significant difference in performance between 100 and 75 mm lining, of course the lower thickness has an effect on the economy especially when providing several kilometers of concrete canal lining constructed to upgrade the earlier earth canal.

The results also indicate that with a decrease in the permeability of the canal lining, the canal seepage decreases. However, the decrease in canal seepage is relatively more when the ratio of  $k_L/k$  is in the region of between 50 mm and 75 mm for  $h_1=10.75$  m and  $h_1=28.55$  m, the reductions being 36.9% and 75.2% respectively (see Table 2).

### 3.2. Discussion of results

The foregone analysis done, indicates that, with a decrease in the permeability of the canal lining, the canal seepage decreases as shown in Figure 2 for drainage distance  $L_4$  i.e. at 88.6 m. However, the decrease in canal seepage is relatively more when ratio of  $k_L/k$  lies in the range of  $6.9 \times 10^{-5}$  to  $5.0 \times 10^{-5}$ .

The effect of lining thickness on canal seepage has been assessed for different values of drainage distances at  $h_1=10.75$  m, 19.65 m and 28.55 m. Figure 3 shows that the initial decrease in canal seepage is very as the lining thickness increase up to 75 mm for a given drainage distance. However, with a further increase in lining thickness (beyond  $d_L/h_1 > 0.00698$  value for 75 mm lining, as shown Table 3), the decrease in canal seepage is less significant. After wards, the seepage gently increases with increase in thickness of canal. Therefore, the ratio of lining permeability to soil permeability should range between  $6.9 \times 10^{-5}$  to  $5.0 \times 10^{-5}$  and the lining thickness should be kept less than  $0.00698h_1$ , which is equivalent to 10.75 times 0.00698 i.e. 75 mm thick concrete. It is possible to conclude from Table 3 and Figures 3, that there is no significant difference in results regardless of whether the canal is lined or not. It is clear from Figure 3 that at, drainage distance  $L_4$  region the canal lining is not effective at all in reducing seepage, even with increase in thickness of the lining. A direct comparison is not of much value since the choice of canal type (concrete or earth canal) in the particular irrigation site is dependent on the subsoil type, particularly the quantity and type of clay present in the soil.



**Figure 2.** Effect of lining permeability on canal seepage **Figure 3.** Effect of lining thickness on canal seepage

#### 4. Conclusions

The foregone analysis illustrates the extent of the influence of lined canal seepage on the land drainage problem, which can be difficult to determine in most cases. Also, the effects of seepage are not always readily evident on site. The seepage water from canals that are on higher ground often disappears into pervious underground stratum and re-appears in a low-lying area at some distance from the canal. Thus, the land drainage problem exerts a marked influence on the justification for installation of canal lining to prevent seepage.

In the fluid flow problem from lined canal analysis, case studies of the effects of lining permeability and lining thickness on canal seepage were compared. With a decrease in permeability of the canal lining, the canal seepage also decreased. However, the decrease in canal seepage is more significant when the ratio of concrete lining permeability to subsoil permeability lies between  $6.9 \times 10^{-5}$  to  $5.0 \times 10^{-5}$ . The decrease in canal seepage is not very significant with initial increase in the lining thickness. However, further increase in the lining thickness must be kept to less than  $0.00698h_1$ , which in this case was less than 75 mm thickness. In general, water flow effect of canal seepage discharge is less when drainage distance is large.

#### References

- [1] Up Irrigation Research Institute, Report on estimation of seepage losses from canals by radio isotops, UPIRI, Reo. TM 54, RR (G15), Roorkee, India, 1984.
- [2] Harr, M.E., *Groundwater and seepage*, McGraw-Hill, New York, 1962.
- [3] Cedergren, H.R., *Seepage, drainage, and flow nets*, 2<sup>nd</sup> edition, Wiley, New York, 1977.
- [4] Goyale, R., and Chawla, A.S., Seepage from canals with infiltration from free surface zone, *Journal of Irrigation and Drainage Engineering*, Vol. 123, Issue 4, July 1997, pp.257-263.

- [5] Sharma, H.C., Kapoor, P.N., Chauhan, H.S., Transient ditch drainage of two-layered soil, *Journal of Irrigation and Drainage Engineering*, Vol.126, Issue 1, January 2000, pp.14-20.
- [6] Neuman, S.P., and Witherspoon, P.A., Finite element method for analyzing steady seepage with a free surface, *Water Resource Research*, Vol.6, Issue 3, June 1970, pp.889-897.
- [7] Desai, C.S., Approximate solutions for unconfined seepage, *Journal of Irrigation and Drainage Engineering*, Vol. 99, Issue 1, 1973, pp. 71-87.
- [8] Swamee, P.K., and Kashap, D., Design of minimum seepage loss nonpolygonal canal sections, *Journal of Irrigation and Drainage Engineering*, Vol. 127, Issue 2, 2001, pp.113-117.
- [9] Rastogi, A.K., and Joshi, S.C., Digital modeling to investigate the canal seepage losses, Indian Institute of Technology, Bombay, India, 1991.
- [10] Rastogi, A.K. and Joshi, S.C., Digital modeling to investigate the canal seepage losses, Indian Institute of Technology, Bombay, India, 1991.
- [11] Verification Manuel, *Two-Dimensional Finite Element Seepage from Trapezoidal Ditch*, Phase2 V 7.005, Rocscience Inc., Toronto, Ontario, Canada, 2008.
- [12] Harvey, E.F. and Steve, S.S., Delineating Ground Water Recharge from Leaking Irrigation canals using water chemistry and Isotops, *Ground water*, Vol..39, No.3, May-June 2001, pp. 408-421.
- [13] Solomon, F. H. and Ekolu, SO., Effect of fluid flow characteristics of anti-seepage materials in dam structures, Proceedings of the concrete society conference, Emperors Palace, Johannesburg, Republic of South Africa, 3<sup>rd</sup> – 4<sup>th</sup> August 2009, pp. 73-82.
- [14] Ljubomir, T., Dams and Appurtenant hydraulic structures, A.A.Balkema publishers, London, 2005.
- [15] Sherard, J.L., Woodward, R.J., Gizienski, S.F. and Cleverger, W.A., *Earth and Earth Rock Dams*, John Wiley and Sons, Inc. New York, 1963.

This page intentionally left blank

## 4. Sustainability, waste utilization and the environment



This page intentionally left blank

# Achieving building sustainability using sustainable building envelope

Joseph IWARO<sup>1</sup> and Abrahams MWASHA

*Department of Civil and Environmental Engineering, St. Augustine Campus  
University of West Indies, Trinidad and Tobago*

**Abstract.** In light of incorporating sustainability into building, the focus of many researchers has been on using existing assessment methods such as Leadership in Energy and Environment Design (LEED), Building Research Establishment Assessment Method (BREEAM), and Green Star to assess building sustainability. These tools focus on the building design with little focus on sustainable building envelope potentials to building sustainability. This shortcoming on the part of these tools has resulted into lack of consideration for durability, life cycle cost, life cycle energy performance, pre-mature failure of buildings and inability to assess the sustainable performance of building envelope. Besides, the possibility of achieving building sustainability through sustainable building envelope has been largely ignored due to lack of a comprehensive assessment method developed specifically for the building envelope. Therefore, this paper examines the potential of using sustainable building envelope as an effective alternative approach of achieving building sustainability based on life cycle analysis and sustainable performance assessment. This study was conducted using selected building envelope design case studies through a comprehensive assessment method known as Integrated Performance Model (IPM) developed for building envelope sustainable assessment and design. The findings indicated that the energy efficiency performance of a building envelope design is a major determinant of the building sustainability.

**Keywords.** Building, envelope, sustainable, performance, design

## Introduction

Building sustainability has been a major issue for building professionals just as the demand for sustainable building continues to increase [1]. The assessment of building sustainability using existing building performance assessment methods continues to be a challenge and is yet to be fully addressed. This is due to their single dimensional nature and the need to integrate important sustainable development values. Sustainable development values are the important performance indicators needed for sustainable performance assessment of building envelope. Such indicators include energy efficiency, material efficiency, environmental impact, external benefit, regulation efficiency, and economic efficiency. To date, there has been little research which

---

<sup>1</sup>Corresponding author: [iwaroayoola@yahoo.com](mailto:iwaroayoola@yahoo.com)

integrates energy analyses with the inclusion of energy efficiency measures, thermal modelling analysis, embodied energy analysis, environmental impact analysis, material efficiency analysis, life cycle energy analysis, and data on the life-cycle costs in residential building performance assessment [2]. As such, using a one dimensional approach to assess building sustainability may not be sufficiently effective and therefore may not satisfy all interests involved in sustainability assessment [3]. Therefore, there is need for an integrated approach that combines sustainable development values in a single performance framework to be developed. The purpose of this integrated approach is to assess the sustainable performance of building envelope in order to design a sustainable envelope that can help in achieving building sustainability.

### **1. The importance of the sustainable building envelope to building sustainability**

Achieving building sustainability is a major challenge for the construction industry in view of the many factors influencing the sustainable performance of the building as shown in Figure 1. Apart from external and internal factors which have significant impact on building sustainable performance, other factors influencing building sustainability include building envelope, thermal processes, building elements, and material properties. In all, the building envelope plays a major role in building sustainability since it serves as a regulator to other factors. Building envelope is the interface between the internal environment and external environment of building. Building envelope regulates the interactions between the building and the environment. In Figure 1, building envelope is shown to regulate building elements' impact, thermal processes, and material performance and it is centred to building design. This therefore provides indoor comfort conditions suitable for human activities [4]. According to the Lee and Tiong [5] building envelope is described as the first line of defence against the undesirable external impacts on the building. Also, it has been argued that building envelope, being the first line of defence is an important passive strategy of achieving building sustainability[6]. The building envelope protects buildings against undesirable environmental impacts such as pollution, climate change temperature, humidity, HVAC load, and lighting load etc. as illustrated in Figure 1. Therefore, the impact of the environment on building and the impact of building on the environment have necessitated the need for building envelopes to be made sustainable.

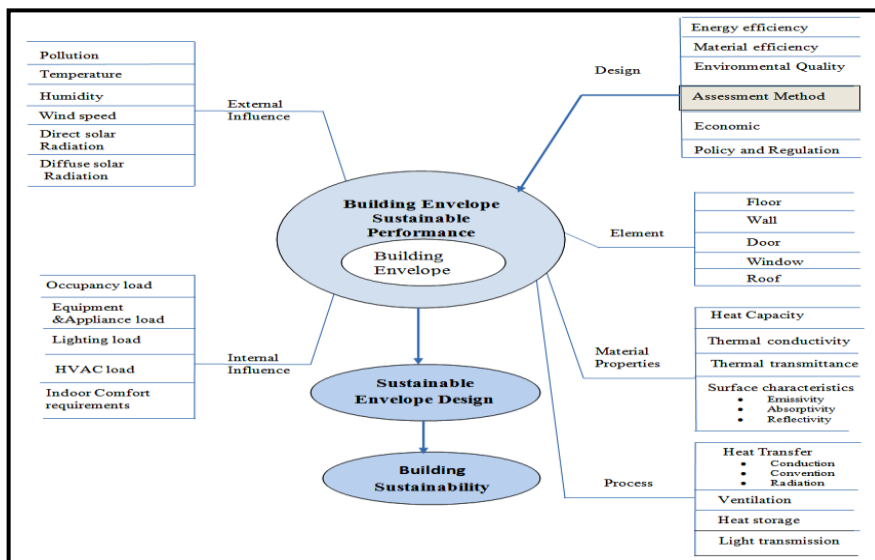


Figure 1. Factors influencing building sustainability

However, making the building envelope to be sustainable requires using an appropriate assessment method. The Assessment method, as illustrated in Figure 1, is central to sustainable performance assessment, sustainable envelope design and building sustainability. Assessment method regulates other factors listed in Figure 1 to achieve sustainable design. Sustainable design involves considering sustainability parameters such as energy efficiency, material efficiency, environmental quality, economic, policy and regulation factors during the designing process. In order to undertake sustainable design of building envelopes to achieve building sustainability, much effort must be placed on developing an integrated method such as Integrated Performance Model (IPM). IPM was developed for sustainable performance assessment and design of the building envelope [7].

## 2. Brief description of the Integrated Performance Model

The Integrated Performance Model is a sustainable performance assessment method and sustainable design rating system for residential building envelope. The IPM was developed by Iwaro and Mwashu [7] for the residential building envelope to fill the gap between existing building performance assessment methods and the current demand for building sustainability in Trinidad and Tobago and developing countries. The Model was developed to integrate sustainable performance values into a single framework. The IPM’s framework combines four conventional major evaluation frameworks such as Life Cycle Cost (LCC), Life Cycle Assessment (LCA), Life Cycle Energy Analysis (LCEA) and Multi Criteria Analysis (MCA) to derived six (6) sub-frameworks for the sustainable performance assessment and design of the building envelope. The IPM framework is developed based on six (6) major sustainable performance criteria: economic efficiency, material efficiency, external benefit, regulation efficiency, energy efficiency, and environmental impact; and sixty four (64) sub-criteria identified for this study. The process of selecting sustainable envelope design alternatives starts with the definition of envelope design requirements based on the input from policy makers and

building stakeholders such as clients, builders, engineers and architects etc. This input is used to define the criteria to be evaluated and identified design alternatives. Also, an integrated framework was developed for the sustainable envelope design problem since the sustainable performance assessment of building envelopes involves considering many sustainability factors. As such, the framework quantifies life cycle performance data for energy efficiency through Life Cycle Building Envelope Energy Analysis (LCBeEA) sub-index, economic efficiency performance data through Life Cycle Building Envelope Cost Analysis (LCBeCA) sub-index, environmental impact, material efficiency, regulation efficiency, and social impact data through Life Cycle Building Envelope Environmental Impact Analysis (LCBeEIA), Life Cycle Building Envelope Material Impact Analysis (LCBeMIA), Life Cycle Building Envelope Regulation Impact Analysis (LCBeRIA) and Life Cycle Building Envelope External Benefit Analysis (LCBeEBA) sub-indexes in IPM. These modelling processes as described above are illustrated in the model flow chart shown in Figure 2.

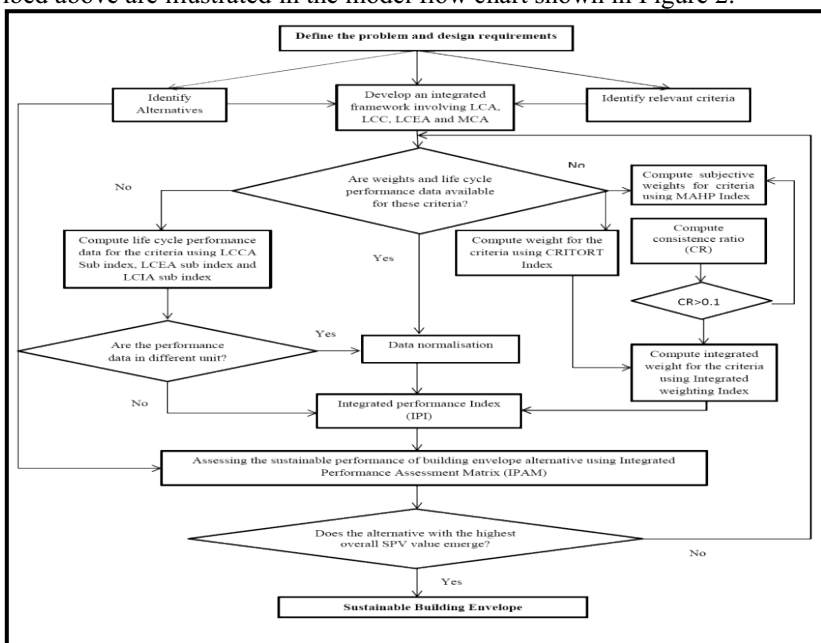


Figure 2. Model flow chart

The alternatives are to be assessed based on the overall sustainable performance values. However, the above process requires computing an integrated weight for each criterion to be used for the sustainable performance assessment. The integrated weight is computed through Modified Analytical Hierarchy Process (MAHP) method and Criteria Relative Important Through Objective Rating Technique (CRITORT) [7]. MAHP is used to derive the subjective weights while CRITORT is used to generate the objective weights for the decision making criteria based on the life cycle performance information. Also, the sustainable performance values generated through Integrated Performance Index for the criteria were used to compute the overall sustainable performance value for each alternative. The performance values derived from these sub-indexes are transferred to Integrated Performance Index (IPI) in equation (1) to generate sustainable performance values for the envelope alternatives.

$$IPI_i = \sum_{j=1}^n P_{ji} W_{Tj} \tag{1}$$

Where  $P_{ji} = f \{LCBeCA, LCBeEA, LCBeEIA, LCBeMIA, LCBeEBA, LCBeRIA\}$  ( $j = 1,2,3 \dots\dots\dots n$ )( $i = 1,2,3,\dots\dots,m$ ). Also,  $IPI_i$  denotes the Integrated Performance Index for envelope design alternatives as denoted by  $i$ . Also,  $W_{Tj}$  stands for the integrated weight for each criterion  $j$ , while  $P_{ij}$  represents the Life cycle performance values computed for envelope design alternatives,  $i$  based on the criteria performance values  $j$ . This means that the higher the values of  $P_{ji}$  and  $W_{Tj}$ , the better are the sustainable performance of the alternatives. Also, the higher the overall sustainable performance value from the IPI index, the more sustainable is the alternative. The Table 1 below present the overview of the envelope design alternative case studies used for practical demonstration of IPM.

**Table 1.** Overview of the proposed single family unit building envelopes

ENVELOPE ELEMENTS	MATERIAL USED		
	Alternative A	Alternative B	Alternative C
Roof Structure	50 X 150mm Timber frame	50 X 150mm Timber frame	50 X 150mm Timber frame
Roof Finishes	Red Clay tiles	Corrugated Aluminium roofing sheet	26 gauge AluZinc roofing sheet
External Wall	4”(inches) thick hollow vertical core concrete block	4” thick hollow core vertical clay block	6” thick hollow core vertical concrete block
External wall finishes (Wall insulation)	12mm plastered (both sides) with ceramic wall tiles for bathrooms	12mm plastered and painted both sides with ceramic wall tiles for bathrooms	12mm plastered and painted both sides with ceramic wall tiles for bathrooms
Windows	Sliding Aluminium glazed window(4”x4”) and 4” Louvre windows with solar shading and side fins	4” Louvre windows with glazing and Aluminium casement glass window with solar shading and side fins	Steel casement French type glazed windows(4”x4”), steel casement type glazed window (2”x4”) with solar shading and side fins
External Doors	Aluminium panel filled with Styrofoam; Hardwood patterned door	Hardwood framed and glazed panelled doors; Panel wooden door	Steel panel door with steel framework
Floor	3000psi concrete structure- 65BRC. 100mm thick reinforced concrete slab overlay	3000psi concrete structure- 65BRC. 100mm thick reinforced concrete slab overlay	3000psi concrete structure- 65BRC. 100mm thick reinforced concrete slab overlay
Floor finishes	1” thick ceramic tiles (12”x12”)	Terrazzo tiles (12”x12”) 1” thick ceramic tiles (12”x12”)	12mm thick Screed
Ceiling	Suspended Acoustic ceiling boards; Low sheen emulsion paint to ceiling	Suspended wood tile ceiling	Suspended gypsum ceiling boards

In Table 1, case studies of building envelope designs developed for a residential building project were used to demonstrate the practical application of IPM in selecting sustainable envelope design that can achieve building sustainability. As such, three (3) different building envelope design alternatives were proposed from which the best sustainable envelope design alternative was selected to satisfy the clients' needs using IPM index in equation (1) and methodologies described in Figure 2. Based on the modelling outcomes depicted in Table 2, alternative "A" recorded overall sustainable performance value of 25127, alternative "B" had a 18183 overall sustainable performance value while alternative "C" recorded a 22588 overall sustainable performance value. This means that alternative "A" is the most preferred sustainable option since it has the highest overall sustainable performance score. Also, in consideration of criteria performance and contribution to sustainable performance, energy efficiency criteria under alternative "A" emerged to be the most sustainable with the highest sustainable performance value of 3582 when compared with the other two alternatives. It means that alternative "A" has the lowest energy consumption, lowest embodied energy and possess better energy conservation strategies.

**Table 2.** Integrated performance assessment matrix

Criteria	Alternative A		Alternative B		Alternative C		Weight
	LPV	SPV	LPV	SPV	LPV	SPV	
External Benefit	15609	2602	15871	2645	15438	2573	0.166671
Energy Efficiency	21496	3582	20903	3483	20344	3390	0.166644
Environmental Impact	73892	12316	35430	5905	65479	10914	0.166673
Material Efficiency	19269	3212	18821	3137	17827	2971	0.166671
Regulation Efficiency	17994	2999	16571	2762	15938	2656	0.166669
Economic Efficiency	2500	417	1500	250	500	83	0.166673
<b>Overall sustainable performance value</b>		25127		18183		22588	$\Sigma = 1.000$

LPV= Life Cycle Performance Value, SPV= Sustainable Performance Value

### 3. Conclusion

The model's assessment in Table 2 revealed that the higher the energy efficiency performance of a building envelope design, the higher is the sustainable performance of that envelope design and the higher is the building sustainability. Also, the criteria performance tradeoff in Table 2 can be used to design a sustainable envelope that can achieve building sustainability by considering higher sustainable performance for design decision making. The application of IPM in this study has demonstrated the capability of IPM to assess, design, rank and selects the best sustainable building envelope design alternative taking into consideration the life cycle performance of envelope design alternative. This methodology can be used to predict the overall sustainable performance and sustainability of the whole residential building, using the building envelope data. It is therefore recommended that for any building envelope

design to be made sustainable, all the sustainable performance criteria also known as sustainable development values such as energy efficiency, economic efficiency, environmental impact, regulation efficiency, material efficiency, and external benefit must be assessed.

## References

- [1] K.C. Ding, Sustainable construction: The role of environmental tools', *Journal of Environment Management* 86(3)(2008), 451–464
- [2] J. Iwaro, A. Mwasha, R.G. Williams, Modelling the performance of residential building envelope: The role of sustainable energy performance indicators, *Energy and Buildings* 43(9)(2011), 2108 – 2117
- [3] D. Crookes, M. De Wit, Environmental economic valuation and its application in environmental: an evaluation of the status quo with reference to South Africa, *Impact and Project Appraisal* 20 (2) (2002), 127–134
- [4] K. Yeang, *Green Design in the hot humid tropical zone*, In J.-H. Bay & B. L. Ong (Eds. Tropical sustainable architecture: social and environmental dimensions (pp. xviii, 292). Oxford: Architectural/Elsevier, 2006
- [5] L. Irene, T. Robert, Examining the role of building envelopes towards achieving sustainable buildings, In: *International Conference on Whole Life Urban Sustainability And its assessment*, M. Horner, C. Hardcastle, A. Price, J. Bebbington (Eds) Glasgow 2007. <http://download.sue-mot.org/Conference-2007/Papers/Xing.pdf>
- [6] N. Kishnani, Climate, Buildings and Occupant Expectations: A comfort-based model for the design and operation of office buildings in hot humid conditions, *Unpublished PhD Thesis, Curtin University of Technology*, 2002
- [7] J. Iwaro, A. Mwasha, R.G. Williams, Development of an integrated approach for the assessment and sustainable design of residential building envelope, in *proceedings of 7th International Structural Engineering and Construction Conference*, Honolulu, USA. New Development in Structural Engineering and Construction, 2013 ([www.rpsonline.com.sg](http://www.rpsonline.com.sg)), Volume II



# On-site concrete waste minimization in the UK

Amir B. MEIBODI<sup>1</sup> and H. KEW

*School of Civil Engineering and Construction, Kingston University London*

**Abstract.** Over 1 billion tonnes of construction and demolition waste (C&DW) is generated every year worldwide. According to the Government's Waste Strategy for England, Construction industry is one of the biggest sources of waste in England. The construction, demolition and excavation (CD&E) sector generates more waste than any other sector in England, and it is the largest generator of hazardous waste, approximately 1.7 million tonnes, considering, the sector accounts for 9 to 10% of GDP (Gross Domestic Product). Concrete has been verified to be a leading construction material for more than a century. The production of concrete in the world has been estimated at an annual rate of 1 m<sup>3</sup> (approximately 2.5 tones) per capita. The Focus of this paper is in the particular area of concrete, to identify and illustrate the current methods and practices of onsite concrete waste minimizing in construction industry in the UK (United Kingdom). After literature reviews and researches in current and previous studies in waste minimization, a list of possible methods have been prepared. In addition, semi-structured face-to-face interviews were conducted in the study. The results illustrate "use of pre-fabricated building components", "Education and training", and "Purchase Management" as the most recommended methods (among the current practices) that promote waste minimization in the UK.

**Keywords.** On-site, concrete waste minimization, construction industry

## Introduction

According to the Government's Waste Strategy for England, construction industry is one of the biggest sources of waste in England. The construction, demolition & excavation (CD&E) sector generates more waste than any other sector in England, and it is the largest generator of hazardous waste, approximately 1.7 million tonnes, considering that the sector accounts for 9 to 10% of GDP (Gross Domestic Product) [1]. Over 1 billion tonnes of construction and demolition waste (C&DW) is generated every year worldwide [2]. Concrete has been proved to be a leading construction material for more than a century. It is estimated that the global production of concrete is at an annual rate of 1 m<sup>3</sup> (approximately 2.5 tonnes) per capita [3]. "A clear waste management policy, which includes effective recovery and recycling of resources, could enhance your reputation and give you the edge when tendering for new projects" [4]. Although great number of waste management and recycling programmes have been implemented in Europe between 1995 and 1998, the amount of waste generation

---

<sup>1</sup> Corresponding author. Tel: +44 7832003234,  
Email address: [amir.meibodi@yahoo.co.uk](mailto:amir.meibodi@yahoo.co.uk)

increased by approximately 15% while the gross domestic product grew by 10% in the same period. The situation particularly for construction waste management is also alarming. In many countries, the construction waste has already started to get out of control [5]. Construction and Demolition waste is considered as one of the major producers of the total waste stream due to its massive amount. Somehow, it is revealed that the material waste in the great number of construction sites is over the acceptable limits [6]. Most construction waste goes into landfills, increasing the burden on landfill loading and operation. Waste from sources such as solvents or chemically treated wood can result in soil and water pollution. Some materials can be recycled directly into the same product for re-use. Others can be reconstituted into other usable products. Also, Waste Minimisation (WM) is regularly identified as a key performance indicator of sustainable performance in construction [7-9]. Advocacy of waste management for construction activities, environmental protection, and recognition of waste generated from construction and demolition work have been promoted around the world [10]. More than 50% of waste deposited in a typical landfill in the United Kingdom came from construction waste [11]. Similarly, 29% of solid-waste in the United States is construction waste [12]. In recent years, the growing awareness of waste management concerns from construction and demolition waste has been directed to the expansion of waste management as an important role player of construction project management [13].

## 1. Aim and objective

The aim and objective of this paper was to determine the existing methods for onsite concrete waste minimization in the UK, in order to have updated information about current methods, which are being used by construction companies.

## 2. Methodology

Qualitative approach was used to collect the information about existing On-Site Concrete Waste Minimization methods. According to Saunders et al (2009), such research methodology including face-to-face, semi-structured interviews were conducted. Although most of onsite concrete waste minimization methods have been identified in literature reviews and recent studies, to be confident about most recent and updated data, face-to-face interviews were implemented. Further information about interviews has been explained below.

For doing in-depth study, interviews with experts in a relevant field are vital [14].

The collected data was analyzed using the following steps [14]:

- Comprehending the mining of data.
- Discovering regularities among data.
- Reflection.

The above three steps were employed for data unitizing, developing categories, and verifying the conclusion.

### 3. Recent studies

Recent studies illustrate different methods for minimizing the concrete waste in construction sites such as “Reuse and recycling operation”, “Improvements of on-site waste management practices” [15], “Environmental management system”, “On-site C&D waste sorting” [16], “Use of prefabricated building components”, “on-site reuse of materials”, “On-site waste conservation”, “Use of information technology on-site” [13]. Moreover, education and training, green building and design, green procurement, green roof technologies, lean construction, prefabrication and waste management are also considered as major methods for the promotion of sustainable construction [17].

### 4. Semi-structure interviews

Interviews are appropriate when quantitative study has been carried out, and qualitative information is required to clarify and complete the achievements [18-19]. The adopted method for data collection in this phase of the research was face-to-face semi-structured interview [14]. Interviewees were selected from identified 15 experts in the construction industry. Candidates from senior managers or executives were nominated for being interviewed. For having in-depth study and collecting feasible and useable data for this stage of research, between 5 and 25 interviews were considered suitable [20-21]. After corresponding with candidates, finally 5 interviews were fixed. Interviewees were chosen from candidates who have the enough reliable knowledge, experience, and success in construction industry.

#### 4.1. Interview's aim

In order to be confident about most accomplished and updated information face-to-face interviews were conducted. As mention previously, face-to-face interviews were conducted to obtained up to date data and add depth to study [14] using reliable, viable, and doable current methods. Moreover the results of this stage of study were allocated in the questionnaire for the next stage of the research.

#### 4.2. Interview template

The interview template contained 3 sections:

- Section 1: Interviewees background information (5 questions);
- Section 2: Existing policies and legislations of onsite concrete waste minimization (2 questions);
- Section 3: Existing methods of onsite concrete waste minimization, and any recommendations for them (2 questions).

Questions contained in section three were of an open-ended type. Questions in section two, and three were directly related to the findings of the literature reviews. The final version of the two-pages interview template has been finalized with a pilot study and a revision.

### *4.3. Interview sampling method*

For the interviews "purposive non-random sampling" [22] was adopted. This method is preferred as it selects the sample, which can deliver the best information without statistical analysis [22]. According to Kvale, 1996, 2009 in order to collect feasible and useable data for this stage of research, between 5 and 25 interviews are suitable. In order to have at least 5 interviews, contact with 15 experts in the construction industry had to be made. They included senior managers or executives of companies who have enough or reliable knowledge, experience, and success in construction industry. The companies were chosen from the list of 100 leading construction companies, 100 leading homebuilders, and 100 leading consulting firms in the UK. Top companies were nominated in order to reach the most reliable answers.

After corresponding with the 15 candidates, finally 5 individuals agreed to participate in interviews.

### *4.4. Interview process*

In order to enhance the clarity of questions, check the time required for answering the questions, and have a practice session prior to actual interviews, two pilot interviews were conducted with construction managers who are graduate from the Department of Civil and Building Engineering at Bolton University.

In order to allow the interviewees to be prepared for the interview, and to collect as much proper data (during the interview) relevant to the questions as possible, the interview schedule, participant information sheet and consent form were sent to the interviewees [23].

## **5. Validity and reliability**

In this research, validity was satisfied by using proper data collecting methods, and by ensuring the quality of data sources [14].

Reliability was achieved by clarifying general rules and adopting detailed procedures [24].

## **6. Ethical consideration**

This research complied with ethics regarding "participants right" and "Using works of other persons" [14].

## **7. Results**

During the interviews, the participants were asked to express their understanding and experiences about the approaches to minimizing the concrete waste on-site (In-Situ). The responses provided in-depth understanding about the possible and existing methods. Through clarifying and coding the responses, different methods were recognized. While most of the mentioned methods were already extracted through the

literature reviews some other methods such as "proper placing", and "Proper concrete formula" were introduced.

Result is shown in table 1. While the participants mentioned different possible and common approaches, most of them referred to "use of pre-fabricated components" and use of out of ready-mixed concrete" as the effective waste reducing methods.

**Table 1.** Current On-Site (In-Situ) concrete waste minimization methods in the UK

Methods	Number of positive responses
Use of pre-fabricated building components	5
Education and training	5
Purchase management (e.g. Better estimating of total concrete requirements, on-time ordering, etc.)	5
Onsite inventory management (include Onsite sorting of construction and demolition materials)	4
Waste prevention in onsite transport (Include use of volumetric trucks to handle the exact needs of the quantities)	4
Identification of available recycling facilities	4
Use of Information Technology onsite (e.g. BIM in order to avoid mistakes & misfit designs)	4
Implementation of environmental management systems	4
Onsite waste conservation	3
On site reuse	3
Governmental incentives for practices in reducing wastes	3
Quality Management (e.g. Use of concrete with proper characteristics such as slump, etc.)	3
Central area for cutting and storage	2
Onsite waste recycling operation	2
Proper site layout planning	2
Use of Ready mixed concrete (reducing direct production of concrete on construction sites)	1

## 8. Conclusion

Nowadays, Legislations and Regulations in the UK are the main drivers for construction waste reduction, for instance rising Landfill Tax, increasing cost for waste disposal, and compliance requirements with Site Waste Management Regulations 2008.

In this paper, possible initiatives for minimizing concrete wastes in construction sites (In-Situ) in the UK were introduced. The results were determined through semi-structured face-to-face interviews by applying qualitative data analyzing methods.

The result from the study found that "use of pre-fabricated building components" and "Education and training" and "Purchase Management" are the most recommended methods in the UK, based on current practices.

## References

- [1] Defra, 2012. Available at: <http://www.defra.gov.uk/environment/waste/topics/construction/index.htm>.
- [2] K. Amnon, Treatments for the improvement of recycled aggregate. Proc. Am. Soc. Civ. Engns, *Journal of Materials in Civil Engineering*, 16(6) (2004), 597-603.
- [3] A.M. Neville, Neville on concrete, Farmington Hills, Michigan, ACI International, 2003.
- [4] Reduce, Reuse, Recycle Managing your waste, by NSCC (National Specialist Contractors Council) Ltd 2007. <http://www.nsc.org.uk/docs/general/002fGuidanceonwaste.pdf>
- [5] J. Stenis, 2004, Construction Waste Management Based on Industrial Management Models: A Swedish Case Study, *Waste Management and Research*. 2005;23(1). In press. © 2004 ISWA
- [6] U. Kulathunga, D. Amaratunga, R. Haigh, and R. Rameezdeen, (2006), "Attitudes and perceptions of construction workforce on construction waste in Sri Lanka", *Management of Environmental Quality*, Vol. 17 No. 1, pp. 57-72.
- [7] R. Spence, and H. Mulligan, Sustainable development and the construction industry. *Habitat International* 19(3)(1995), 279-292.
- [8] BERR - Department for Business Enterprise and Regulatory Reform, *The strategy for sustainable construction*, 2008. [online]. [viewed 15/05/2011]. Available at: <http://www.berr.gov.uk/files/file46535>
- [9] C.J. Kibert, *Sustainable Construction: Green Building Design and Delivery*. 2nd ed. Hoboken, New Jersey: John Wiley & Sons, 2008.
- [10] L.Y. Shen, W.Y.V. Tam, Implementing of environmental management in the Hong Kong construction industry. *International Journal of Project Management* 20 (7)(2002), 535-543.
- [11] J. Ferguson, N. Kermode, C.L. Nash, W.A.J. Sketch, R.P. Huxford, *Managing and Minimizing Construction Waste: A Practical Guide*. Institution of Civil Engineers, London, 1995.
- [12] M.J. Rogoff, J.F. Williams, *Approaches to Implementing Solid Waste Recycling Facilities*. Noyes, Park Ridge, NJ, 1994.
- [13] W.Y.V. Tam, On the effectiveness in implementing a waste-management-plan method in construction, *Waste Management* 28 (2008) 1072-1080.
- [14] M. Saunders, P. Lewis, and A. Thornhill, *Research methods for business students*. Fifth edition. London : Prentice Hall, 2009.
- [15] M. Osmani, Construction Waste Minimization in the UK, International Conference on Asia Pacific Business Innovation and Technology Management, 2012
- [16] L. Weisheng, and Y. Hongping, Exploring critical success factors for waste management in construction projects of China. *Resources, Conservation and Recycling* 55 (2010) 201-208.
- [17] K.A. Bakhtiar, Y.S. LI, and S.H. Misnan, A framework for comparison study on the major methods in promoting sustainable construction practice, *Journal Alam Bina* 12(3)(2008), 55-69.
- [18] N. King, The Qualitative Research Interviews. In: CASSELL, C., and SYMON, G., *Qualitative Methods in Organisational Research: A Practical Guide*. London: Sage Publications, 1994.
- [19] S. Hannabuss, *Research Interviews*. New Library World 97 (1129)(1996), 22-30.
- [20] S. Kvale, *Interviews: An Introduction to Qualitative Research Interviewing*. Thousand Oaks, CA, USA: Sage Publications, 1996.
- [21] S. Kvale, S. Brinkmann, *InterViews Learning the Craft of Qualitative Research Interviewing, Second Edition*, 2009.
- [22] B. White, *Dissertation Skills For Business and Management Students*, South-Western Cengage Learning, 2000.
- [23] F.J. Fowler, *Survey Research Methods*. 3rd ed. Thousand Oaks, California, London: Sage Publications, 2002.
- [24] C. Voss, N. Tsiriktsis, and M. Frohlich, Case research in operations management, *International Journal of Operations & Production Management*, 22(2)(2002), p 205.

# Moisture transfer in three hemp concretes

Ines OTHMEN<sup>a,b,1</sup>, Philippe POUILLAIN<sup>b</sup> and Nordine LEKLOU<sup>b</sup>

<sup>a</sup>*French Environment and Energy Management Agency, France*

<sup>b</sup>*Institute of Research in Civil Engineering and Mechanics, UMR CNRS 6183, France*

**Abstract.** The immense stress on the world's environment means that measures must be taken today to safeguard natural resources for tomorrow. This is the challenge the construction industry faces. For that, recent research has found a solution in the use of bio-based materials. Hemp has renewed popularity due to its potential as a sustainable, eco-friendly resource. It's fast-growing, renewable, biodegradable and recyclable. The study investigates the measurement of the capillary absorption coefficient for three different hemp concretes. This coefficient will focus on the hydrophilic nature of these plant-derived particles and consequently the risk of mould growth.

**Keywords.** Lime hemp concrete, microstructure capillary action, moisture, mould growth

## Introduction

The shortage of natural resources and the impact of various human activities on the environment have led to a reflection on sustainable development. It is then important to develop new building materials with low environmental impact to replace conventional products. In this context, hemp-lime concrete (HC) constitutes a promising green building material. HC is made by mixing hemp shiv, a lime-based binder and water. Several studies investigated its properties [1–6]. Actually, it is a light material which provides good thermal insulation and hygric regulation. Those properties are attributed to its specific multi-scale porous structure [1].

Therefore, the aim of the current study is to compare the hygroscopic behavior of three hemp concretes used for building walls. These materials differ by the nature of the lime and the manufacturing method. Two HC were molded using two different limes: the first is a hydraulic lime, whereas the second contains pozzollans. Then, they are compared to a commercial HC. The investigations are based on the measurement of the capillary adsorption. This parameter can have significant effects on the heat loss and that the current standards lack the consideration of an important parameter [7].

---

<sup>1</sup>Corresponding author: [ines.othmen@univ-nantes.fr](mailto:ines.othmen@univ-nantes.fr)

Mailing: IUT de Saint Nazaire IEG-GeM, 58 rue Michel Ange BP 420 44606 Saint Nazaire- France

## 1. Materials and methods

Hemp–lime concrete is a carbon-negative building material. It was developed in France in the early 1990s and has been used in thermal upgrading of hundreds of buildings in Europe.

### 1.1. Materials

The current study deals with 3 different hemp concretes: two molded hemp concretes and a precast hemp concrete. Table 1 gives the mix proportions and the manufacturing method. Besides, the molded hemp concrete designated MHC–NHL and MHC–PF are obtained by mixing commercial non fibred shiv (Chanvribat) with St Astier NHL 3.5 and Tradical PF 70 respectively. The shivs are between 0.5 mm and 20 mm long and have a density of 100 kg.m<sup>-3</sup>. The properties of both lime used are given in Table 2.

**Table 1.** Mixes proportioning and manufacturing method for the studied hemp concretes

	MHC - NHL	MHC – PF	PHC
Hemp/binder mass ratio	0.45	0.45	0.65
Water/binder mass ratio	1.59	1.59	1.2
Manufacturing binder	Molding	Molding	Precasting

**Table 2.** Properties of the lime used

	CaO (%)	Hydraulic lime (%)	Pouzollans (%)
Tradical PF 70	75	15	10
Saint Astier NHL 3.5	25	75	-

The precast hemp concrete designated PHC is a commercial hempcrete whose binder exact composition is unknown but it is a certified material for insulation works. It is used as a reference to evaluate the performance of the molded mixes. The different concretes are stored in a curing room at 20°C±3°C and 50±10% relative humidity. Those conditions are considered as optimum conditions according to the studies [1,4].

### 1.2. Specimens

The representative elementary volume relative to hemp concrete was studied from the variation of the apparent density against volume [8] and from visual analysis [2]. Both studies showed that specimens of 100 cm<sup>3</sup> (cube with a side > 4.7 cm) take into account the specific pore and particle distribution of the material [1].

The specimens of the MHC are cylinders with a diameter of 11 cm and 22 cm high. For PHC, 7x7 cm<sup>2</sup> square-based and 18 cm high prismatic samples were cut from the blocks of PHC. We used them for the measurement of the apparent density and for capillary action. Cubes with an edge of 7 cm were used for porosity tests for the different studied hemp concretes.

### 1.3. Density and porosity

The density was closely controlled due to its significant effect on concrete properties especially for MHC. So it was necessary to make a gravimetric monitoring to ensure

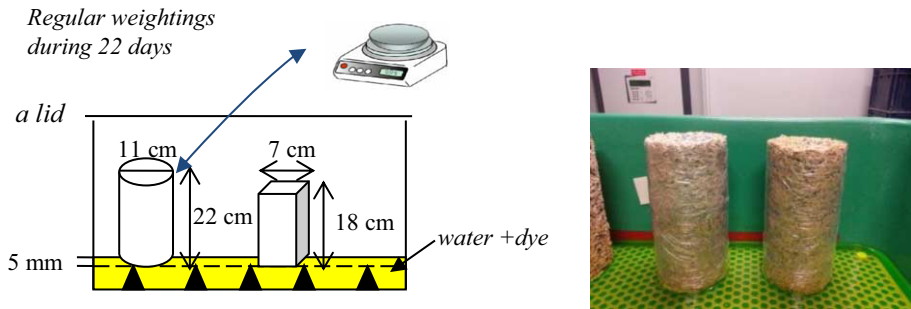


that the samples are of similar density. So, we checked the apparent density and standard deviation for the molded studied concretes during the 60 first days.

Due to the slow setting time of lime, the apparent density was measured during one year. The final values range between 442 and 455  $\text{kg}\cdot\text{m}^{-3}$ , as commonly used for building walls in France [9]. The porosity of the different materials was also measured on cubic samples with a volume of 343  $\text{cm}^3$  after a 400 days curing. The different samples have an average porosity of 65 %.

#### 1.4. Capillary action

The water absorption coefficient by capillarity was measured according to NF B 10-502 (Figure 1)



**Figure 1.** Description of the capillary action test, schematic diagram (left) and photo of the device(right)

The samples were placed on a perforated stainless steel sheet, in a container of colored water so that the water covered the lower 5 mm. The tray remains covered during the test period to maintain a relative humidity close to 100% around samples. The samples are weighed at regular intervals over time. The water absorption coefficient can be obtained from the measurement of the absorbed mass of water per unit area (specimen base surface area) during time.

## 2. Results and discussion

### 2.1. Microstructure

Whatever the lime used, HC are very light concretes. This is due to the low density and very high porosity, mainly accessible porosity. In addition, several studies [2,6,10] have shown that HC exhibits a multi-scale porous structure. Therefore, we investigated the different studied HC by means of Scanning Electron Microscope (SEM) analysis. The SEM views show that:

- At a macro scale, the porosity is due to the arrangement between the hemp shiv and the binder matrix (Figure 2)
- In the binder matrix, the porosity is due to hydrate arrangement during the setting process (Figure 3)
- Other porosity is intra particle, and it is in hemp shiv (Figure 4).

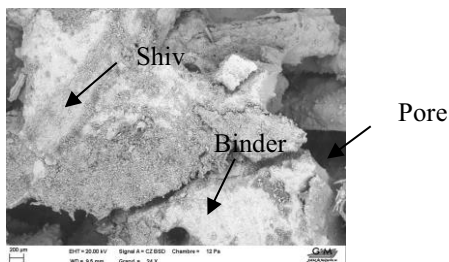


Figure 2. SEM view of PHC

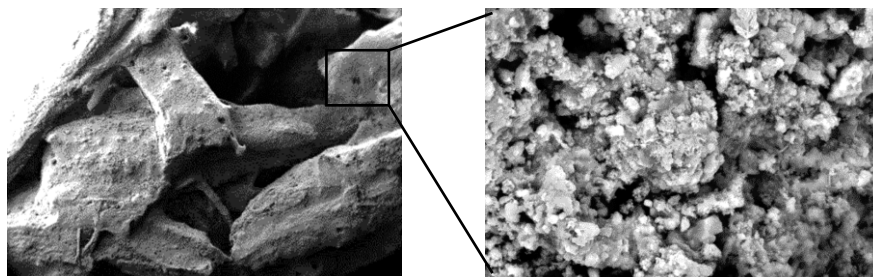


Figure 3. SEM view of MHC-NHL

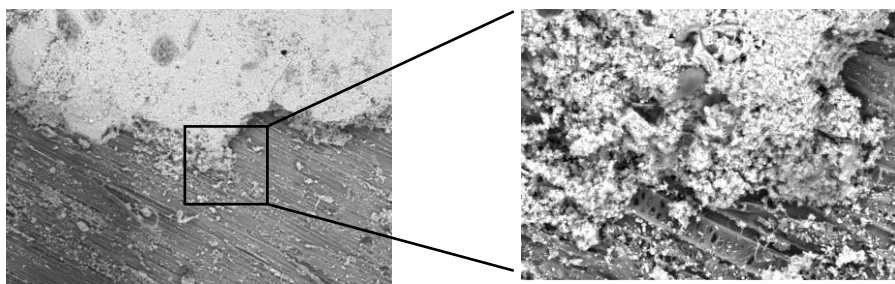


Figure 4. SEM view of MHC-PF

In fact, capillary absorption drops with increasing hydrates [3]. Therefore, it is important to analyze the microstructure of the binder in the hemp concretes.

## 2.2. Capillary action

Because of the highly porous nature of the concrete, the measurement was carried out during 22 days. The time evolution of the capillary water absorption is presented in Figure 5. As we can see from the results, the capillary behavior of all the concretes is similar. The mass increase due to water absorption is initially high and decreases with time, as can usually be observed. We can also deduce from monitoring of weight gain over time, the water absorption coefficient  $A$ . It is calculated using equation 1:

$$A = \frac{\Delta m}{S\sqrt{t}}$$

Where  $m$  is the mass in kg,  $S$  is the specimen surface area in  $m^2$  and  $t$  is the sorption time. It is consequently the slope of the first part of the curve ( $\Delta m/S=f(Vt)$ ). This coefficient is presented in table 3.

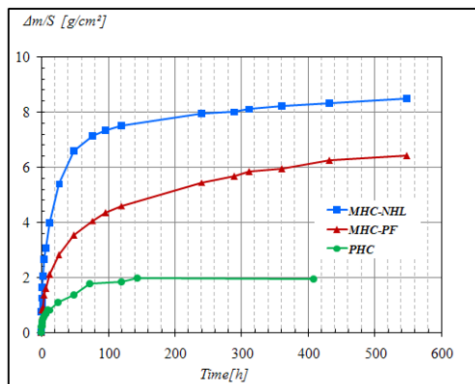


Figure 5. Water absorption by capillary suction over time

The water sorption coefficient obtained varies between 0.03 and 0.16  $kg.m^{-2}.s^{0.5}$  (1.8 and 9.6  $kg.m^{-2}.h^{-0.5}$ ). These values are of the same order of magnitude than those observed by Evrard [2], de Bruijn et al [5] and Walker et al [3]. They found 4.42  $kg.m^{-2}.h^{-0.5}$ , 9  $kg.m^{-2}.h^{-0.5}$  and 2.65 respectively. It is not possible to suggest a trend based on the results of former authors due to varying densities and composition (binder type and content)

Table 3. Water absorption coefficient in the first 24 h

	MHC-NHL	MHC-PF	PHC
$A [kg.m^{-2}.s^{0.5}]$	0.16	0.09	0.03

The very low value obtained for PHC was quite surprising. So we cut the specimens tested to observe the migration of water. We found that the industrial compaction of hempcrete has created a very dense zone in depth. We are then talking about a cut of the capillarity caused by excessive compaction.

### 3. Conclusion

The paper showed the influence of the binder nature on the capillary absorption coefficient. In fact, for three hemp concretes with almost the same apparent density and porosity, their water absorption coefficient ( $A$ ) is not the same which confirms the results found in other studies. Moreover, due to the high relative humidity, we observed mould growth from as early as 24h which continuously developed during the test (Figure 6). The mould type should be further investigated to determine favorable growing conditions and avoid them. In fact condensation or high relative humidity can cause mould growth and then a deterioration of the wall or insulating material.



**Figure 6.** Photos of developed microorganisms on test samples

## References

- [1] Collet F, Chamoin J, Pretot S, Lanos C. Comparison of the hygric behaviour of three hemp concretes. *Energy Build* 2013 (62)294–303.
- [2] Evrard A. Transient hygrothermal behaviour of Lime-Hemp Materials, Text *UCL*, 2008.
- [3] Walker R, Pavia S. Moisture transfer and thermal properties of hemp–lime concretes, *Constr Build Mater* 2014 (64)270–6.
- [4] Arnaud L, Gourlay E. Experimental study of parameters influencing mechanical properties of hemp concretes, *Constr Build Mater* 2012(28) 50–6.
- [5] De Bruijn PB, Jeppsson K-H, Sandin K, Nilsson C. Mechanical properties of lime–hemp concrete containing shives and fibres *Biosyst Eng* 2009 (103) 474–9.
- [6] Tran Le Anh. Etude des transferts hygrothermique dans le beton de chanvre et leur application au batiments, *Université de Reims Champagne Ardenne*, 2010.
- [7] Evrard A, Flory-Celini C, Claeys-Bruno M, De Herde A. Influence of liquid absorption coefficient on hygrothermal behaviour of an existing brick wall with Lime–Hemp plaster, *Build Environ* 2014 (79) 90–100.
- [8] Collet Florence. Caractérisations hydrique et thermique de matériaux de génie civil à faibles impacts environnementaux, *Université de Rennes*, 2005.
- [9] Béton de chanvre : des règles professionnelles validées par l’AQC - Règles techniques n.d.
- [10] Collet F, Pretot S. Thermal conductivity of hemp concretes: Variation with formulation, density and water content, *Constr Build Mater* 2014 (65) 612–9.

# Foam concrete production with şırnak mine waste claystone and fly ash

Yıldırım İ. TOSUN<sup>1</sup>

*Faculty of Engineering, Şırnak University, Şırnak, Turkey*

**Abstract.** Fly ash and Mine Waste clay stone thrown as waste in Şırnak City of Turkey were used in foam concrete production. Waste mixture at certain proportions decreasing instead of cement used, fine aggregate in specific proportions decreasing instead of fly ash used improved mechanical strength and porosity. Even fine clay stone aggregate minus 3 mm reducing porosity rather than fly ash, such as using three different size fractions are evaluated in foam concrete production. Effects of mechanical properties of waste clay stone and fly ash on foam concrete production were studied intensively. The main purpose of this study is to develop the ready-mixed foam mortar and concrete industry using local waste, Şırnak Coal Mine Waste clay stone and fly ash.

**Keywords.** Foam concrete, lightweight concrete, foam mortar, fly ash, claystone

## Introduction

Foam concrete is produced by aerated foaming slurry which containing cement sand and water mixtures. Low density concrete product may be so advantageous in construction works. Particularly, fly ash addition to foam shotcrete and mortar applications may provide very low density protective layer and aerating and even insulation layer concerns [1-5]. The beneficial properties of fly ash and use of foam concrete were defined in detail [6-8]. Pozzolans alone cannot bind pulverized calcium hydroxide at ordinary temperature and humid environments characterized by reacting chemically bonding materials such as fly ash and clay stone [9,10]. Pozzolans in foam concrete are used as mineral admixture. Mineral additives increasing the durability of foam concrete strength [11-14]. Concrete or cement added into the pozzolanic material may lead the heat of hydration to reduce the high target strength and low permeability ensures alkali silica reaction and sulfate attack [15-17]. Pozzolanic materials in foam concrete are commonly fly ash, silica fume and slag furnace [17,18].

Various researches [18-20] were evaluated sand, clay and fly ash cement mixtures. However, industrial wastes containing ash and sand were used as pozzolanic material or filler in foam concrete [21-22]. Influence of filler type on the properties of foam concrete fly ash instead of sand .economic and friendly ecological disposal of fly ash as waste. Comparison with air cured foam concrete made with cement-sand cement and fly ash showed higher strength. In the world today, 600 million tons of fly ash, but it is estimated that only 10% are evaluated in concrete technology [18].

<sup>1</sup>Corresponding author: [yildirimismailtosun@gmail.com](mailto:yildirimismailtosun@gmail.com)

Fly ash concrete to reduce the cost of providing energy conservation and environmental problems due to the reduction area has a wide use in concrete [23-25]. Fly ash concrete mixture for use in cement certain proportions decreasing instead of fly ash used , fine aggregate in specific proportions decreasing instead of fly ash used in or as fine aggregate and the cement in proportions to reducing rather than fly ash , such as using three different methods are performed [26-29]. Effects on mechanical properties of fly ash in concrete have been studied intensively over. In this study, the amount of fly ash on properties of fresh and hardened concrete to study briefly mentioned, but basically changes the amount of substitution of fly ash concrete workability and setting time was to determine the effect.

In this study, the amount of fly ash on properties of fresh and hardened foam concrete to study briefly mentioned, but basically changes the amount of substitution of fly ash concrete workability and setting time was to determine the effect.

### 1. Method

In this study, Cizre sand obtained from Dicle Stream and waste clay stone of Şırnak Coal Mine were used as fine aggregate, which was broken minus 3mm. Aggregate mixture ratios were set in four different size fractions and as given the limit values in the standards[29-32] between the 20% natural sand, 30% 0-5 mm crushed clay stone , 25% of 5-8 mm crushed clay stone and 25% of 8-12 mm were set in clay stone. The results of sieve analysis of aggregates used in the experiments are given in Figure 1, respectively.

CEM I 32,5 type cement as a binder was used. Silopi fly ash used in the experiments was supplied from power plant chemical composition of and the standard fly ash is given in Table 1, respectively.

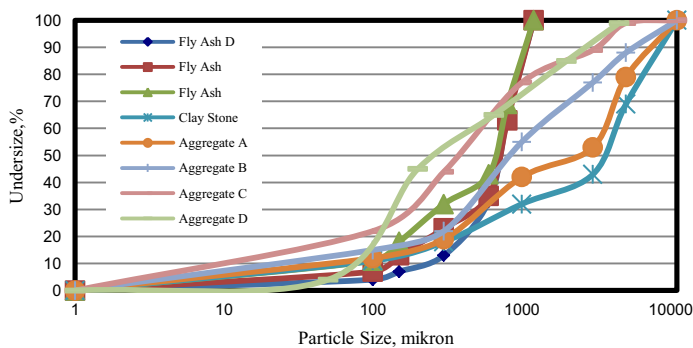


Figure 1. Sieve analysis of fly ash and fine aggregate used in tests

### 2. Results and Discussions

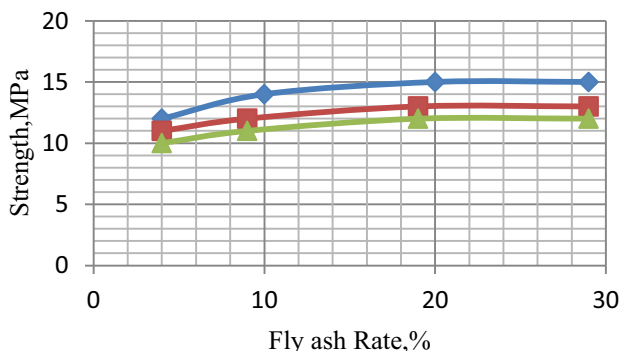
In order to determine the effect of amount of fine clay stone aggregate and Silopi fly ash on workability of the foam concrete, firstly 5 %, 10% , 20%, 30%, 40% clay stone added in to the foam concrete and secondly only 5 % , 10% , 20% and 30% of fly ash added in to the foam concrete. The curing time, strengths, densities and water

absorption amounts were determined as given in the standards. For each mixture, prepared by the method of penetration resistance of concrete and concrete stiffening time test 0.5 MPa till 3 MPa resisting the durations were observed. The concrete 10x10x10 cm blocks were prepared from every mixture and the 28-day compressive strength was determined. In the production of best foam concrete, concrete component quantities, dosage and suitable density value were selected [33-37].

This study was aimed to the production of low density 1200-1400 kg/m<sup>3</sup> grade foam concrete. The optimum water/cement (w/c) ratio in consideration was determined after 28 days regarding compressive strengths of concrete foam blocks to be produced have been selected as high water/cement ratio. Due to the high water absorption results of prior experiments on the w/c ratio, it was decided to be 3/1. TS 802 de [38] mentioned mixture of water and air flow by taking the amount of concrete components in the foam concrete. The results of fly ash addition on strength of foam concrete blocks are illustrated in Figure 2. 10% fly ash addition was sufficient in strength increase reaching 13-15 MPa replaced to cement. The fresh foam concrete for measuring the 1MPa resistance to penetration as given in ASTM C 403 standard, the determined comprising setting times were increased from 220 h to 317 h. That has showed that fly ash addition may improve workability time of foam concrete.

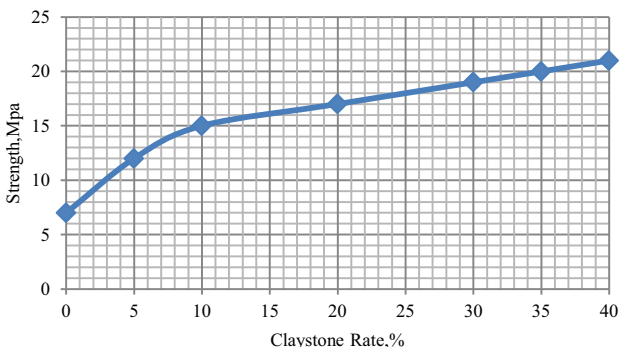
**Table 1.** Chemical composition of Silopi Fly Ash and standards

Oxide(%)	Fly Ash	TS EN 450 F	TS EN 197-1 F	TS 639 C	ASTM C 618
SiO <sub>2</sub>	48,53				
Al <sub>2</sub> O <sub>3</sub>	9,61				
Fe <sub>2</sub> O <sub>3</sub>	7,9				
S+A+F	67,04	> 70,00	> 70,00		> 50,00
CaO	23,8			< 5,00	
MgO	2,28			< 5,00	< 5,00
SO <sub>3</sub>	2,48	< 3,00	< 5,00		
K <sub>2</sub> O	2,51				
Na <sub>2</sub> O	0,35	<5,00	< 5,00	< 5,00	< 10,00
Ignition lost	1,79			< 6,00	< 6,00
Cl <sup>-</sup>	0,05			< 0,10	
Free CaO	2,1			< 1,00	
Reac. SiO <sub>2</sub>	35,2	> 25,00	> 25,00		> 25,00
Reac. CaO	21,7	7,5	< 10,00	> 10,00	



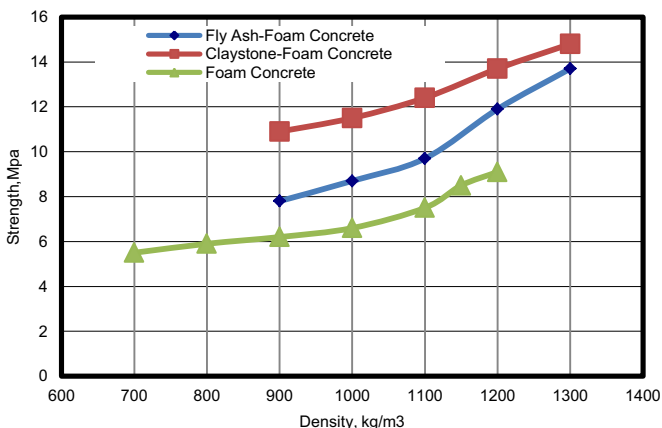
**Figure 2.** Uniaxial compressive strength results of Fly Ash addition on foam concrete at 28 day

After the determination 3/1of water/cement rate and effective amount of fly ash addition the foam concrete blocks, fine clay stone aggregate mixtures were prepared with the mixture of fine clay stone minus 3mm at weight rates of of 5%, 10%, 20% and 30% 40% with 10% fly ash replacing cement. For each foam concrete block, the compressive strength and water absorption rate were studied. The results are shown in Figure 3. At the end of the 28 days the compressive strength of foam concrete blocks with 20-30% fine clay stone aggregate raised to 17-19MPa. Water absorption rate decreased at 35 and 40 % fine aggregate addition to 23-33%.



**Figure 3.** Uniaxial compressive strength results Fine Clay Stone Addition on foam concrete at 28 day.

In order to determine the effect of apparent low density of foam concrete on strength, the produced foam concrete blocks without fly ash and fine clay stone aggregate were tested. As seen from Figure 4 only foam concrete densities ranged between 700 kg/m<sup>3</sup> and 1200 kg/m<sup>3</sup> and the strengths were changed between 7 MPa and 9 MPa. With fine clay stone aggregate addition that strength raised to 15 MPa.



**Figure 4.** The Effect of density on uniaxial compressive strength results of foam concrete at 28 day.



### 3. Conclusions

A 3/1 of water/cement rate and 10% Silopi fly ash addition in to the foam concrete was effective and water absorption rate of foam concrete was sufficient for thermal isolation. The high porosity and the lower densities of 900-1100 kg/m<sup>3</sup> values were provided in foam concrete production. The high amount of fly ash addition workability of the foam concrete blocks improved.

Fine aggregate clay stone mixtures provided much resistive compressive strength with the mixture of fine clay stone minus 3mm at weight rates of 30% 40% with 10% fly ash replacing cement.

At the end of the 28 days the compressive strength of foam concrete blocks with 20-30% fine clay stone aggregate raised to 17-19MPa. Water absorption rate decreased at 35 and 40 % fine aggregate addition to 23-33%.

In conclusion, depending on the amount used the fly ash in foam concrete, workability significantly changed and even significant the pressure increase in resistance values depending on the amount of fly ash and foam substituent were reduced. Also in the mixture of fly ash used concrete curing time depending on the amount of substitution was found to reduce the porosity.

### References

- [1] Hussin, M.W., Awal, A.S.M.A., 1996. Palm oil fuel ash-a potential pozzolanic material in concrete construction. In: *Proceedings of the International Conference on Urban Engineering in Asian Cities in the 21st Century*, Bangkok, Thailand, pp. D361-D366.
- [2] Isaia, G.C., Gastaldini, A.L.G., Moraes, R., 2003. Physical and pozzolanic action of mineral additions on the mechanical strength of high-performance concrete. *Cement and Concrete Composites* 25, 69-76.
- [3] Kiatikomol, K., Jaturapitakkul, C., Songpiriyakij, S., Chutubtim, S., 2001. Study of ground coarse fly ashes with different finenesses from various sources as pozzolanic materials. *Cement and Concrete Composites* 23, 335-343.
- [4] Mehta, P.K., 1977. Properties of blended cements made from rice-husk ash. *ACI Journal* 74, 440-442.
- [5] Paya, J., Monzo, J., Borrachero, M.V., Mora, E.P., 1996. Comparisons among magnetic and non-magnetic fly ash fractions: Strength development of cement-fly ash mortars. *Waste Management* 16, 119-124.
- [6] Bouzoubaa, N., Bilodeau, A., Sivasundaram, V., Fournier, B., Golden, D.M., 2004. Development of ternary blends of high-performance concrete. *ACI Materials Journal* 101, 19-29.
- [7] Cheerarot, R., Jaturapitakkul, C., 2004. A study of disposed fly ash from landfill to replace Portland cement. *Waste Management* 24, 701-709.
- [8] Chindaprasirt, P., Homwuttiwong, S., Sirivivatnanon, V., 2004. Influence of fly ash fineness on strength, drying shrinkage and sulfate resistance of blended cement mortar. *Cement and Concrete Research* 34, 1087-1092.
- [9] Gonzalez, M.A., Irassar, E.F., 1997. Ettringite formation in low C3A Portland cement exposed to sodium sulfate solution. *Cement and Concrete Research* 27, 1061-1072.
- [10] Singh, N.B., Singh, V.D., Rai, S., 2000. Hydration of baggase ashblended Portland cement. *Cement and Concrete Research* 30, 1485-1488.
- [11] Tay, J.H., 1990. Ash from oil-palm waste as concrete material. *Journal of Materials in Civil Engineering* 2, 94-105.
- [12] Udoeyo, F.F., Dashibil, P.U., 2002. Sawdust ash as concrete material. *Journal of Materials in Civil Engineering*, 173-176.
- [13] Tangchirapat W Saeting T Jaturapitakkul C Kiattikomol K Siripaniehgom A, 2007, Use of waste ash from palm oil industry in concrete, *Waste Management* 27 p81-88
- [14] Jumaat MZ, Alengaram U.J., Mahmud H., 2009, Shear strength of oil palm shell foamed concrete beams, *Materials and Design*, 30, p.2227-2238
- [15] Kim HK, Jeon JH, Lee HK, 2012, Workability, and mechanical, acoustic and thermal properties of lightweight aggregate concrete with a high volume of entrained air, *Construction and Building Materials*, 29, 193-200

- [16] Chen X, Yan Y, Liu Y, Hu Z, 2014, Utilization of circulating fluidized bed fly ash for preparation of foam concrete, *Construction and Building materials*, 54, p137-146
- [17] Ranjani GIS Ramamuthy K, 2012, Behaviour of foam concrete under sulphate environments, *Cement&Concrete Composites*,34, p825-834
- [18] Erdogan, T.Y.,2003, Concrete . METU Development Foundation Publishing and Communications, Inc. Ankara.
- [19] Simsek , O. , 2004. *Concrete and Concrete Technology* . Distinguished Publishing, Ankara,
- [20] Liu MYJ,Alengram UJ, Jumaat MZ, Mo KH, 2014, Evaluation of Thermal Conductivity mechanical and transport properties of leightweight aggregate foamed geopolymer concrete, *Energy and Buildings*,72, p238-245
- [21] Xia Y. Yan Y,Hu Z, 2013, Utilization of circulating fluidized bed fly ash in preparing non-autoclaved aerated concrete production, *Construction and Building Materials*, 47, p1461-1467
- [22] Sata , V., Jaturapitakkul ,C., Kiattikomol ,K., 2007, From Pozzolan of Influence on Mechanical Properties Of Various By- Product Materials High -Strength Concrete, *Construction and Building Materials*, p1589-1598 .
- [23] C. K. Park, M. H. Noh , T. H. Park, rheological Properties Of Materials Containing Mineral Admixtures cementitious , *Cement and Concrete Research* . In 2005. 842-849
- [24] Moulieu , M. , Khelafib H., 2008, Performance Characteristics of The Lightweight Aggregate Concrete Containing Natural Pozzolan Building and Environment, 43, p 31-36
- [25] Demirbog , R., Orung , I., Rose, R., 2001, Effects of expanded perlite aggregate and Mineral Admixtures on the compressive strength of low-density concretes. *Cement Concrete Research*, 31, 1627-32
- [26] Chen , B., Liu, J. , 2008 Application Of Experimental in Lightweight Concrete Admixtures With Mineral High Strength and Workability , *Construction and Building Materials*, 22,p 655-659
- [27] Hoek, E., 2013. Practical Rock Engineering, notes by Evert Hoek Hoek. My <http://www.rocsience.co>
- [28] B. W. Lang , K. Wenger , M. A. Ward, 2002, Effect Of Fly Ash Silica Fume And Heat Of Ten Of Portland Cement Hydration . *Cement and Concrete Research* . In 2002. From 1045 to 1051 .
- [29] ASTM C 403, 2001. Standard test method for time of setting of concrete mixtures by penetration resistance. *Annual Book of ASTM Standards*, 04.02, pp. 222–227.
- [30] ASTM C 618, 2001. Standard specification for coal fly ash and raw or calcined natural pozzolan for use as a mineral admixture in concrete. *Annual Book of ASTM Standards* 04.02, pp. 310–313.
- [31] ASTM, 1985, ASTM C 618-85 "Standard Specifications for Fly Ash and Raw Calcined Natural Pozzolan For Use As Our mineral admixture in Portland Cement Concrete ", *ASTM Philadelphia*.
- [32] TS 2987, 1978, Determination of Setting Time of Concrete , *The Turkish Standards Institute* , Ankara.
- [33] ASTM C 150, 2001, Standard specification for Portland cement. *Annual Book of ASTM Standards* 04.01, pp. 149–155.
- [34] ASTM C 403 , 1999, Standard test method for time of setting of concrete by penetration resistance Mixtures ', *American Society for Testing and Materials*, Pennsylvania.
- [35] TS EN 12350-3, 2002, Concrete - Fresh Concrete Testing-Part 3:V-B Experiment, TSE, Ankara.
- [36] TS EN 12350-2, 2002, Concrete - Fresh Concrete Testing-Part 2: Slump Experiment, TSE, Ankara.
- [37] TS EN 12390-3 , 2003. Concrete - Testing hardened concrete - Part 3: Determination of Compressive Strength of Test Specimens, *Turkish Standards Institute*, Ankara, 12p .
- [38] TS 802, 1985. Concrete Mixture Principles of Accounts . *Turkish Standards Institute*, Ankara

# Reducing CO<sub>2</sub> in concrete by half

Michiel HAAS<sup>1</sup>

*Faculty of Civil Engineering, TU Delft Netherlands*

**Abstract.** Concrete is the main construction material in the world with over 9 billion m<sup>3</sup>/year being produced. That leads to a CO<sub>2</sub> emission of over 5 billion tons of CO<sub>2</sub>/year, whereby more than half is caused by the OPC (Ordinary Portland Cement). It is expected that the concrete use will rise until 2050, an increase of 260%, that means the CO<sub>2</sub> emission will increase with the same percentage to 13 billion tons CO<sub>2</sub>. To reduce the immense CO<sub>2</sub> emission, it is necessary to use other binders than only OPC, for instance Supplementary Cementing Materials (SCM) and Non-Portland Cement (NPC). But it is also possible to make real bio-cement out of biomass, so bio-cement can be grown.

The authors did some pilot projects, of using only 85 kg cement/m<sup>3</sup> concrete, instead of the normal used 330-260 kg cement/m<sup>3</sup> concrete. That means the CO<sub>2</sub> emissions can be reduced by half already, in the present time. In the future, it will be possible to reduce it still more and that will be necessary for our world.

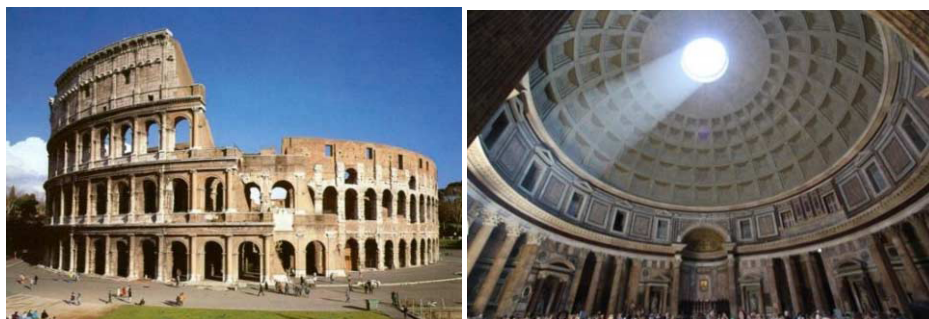
**Keywords.** Cement, OPC, reducing CO<sub>2</sub>, concrete

## Introduction

Concrete is widely used for making architectural structures, bridges/overpasses, highways, runways, parking structures, dams, foundations, brick/block walls, pavements, pools/reservoirs, pipes, footings for gates, fences and poles and even boats. Concrete technology was already known by the Ancient Romans and was widely used within the Roman Empire; the Colosseum is largely built of ancient concrete and the concrete dome of the Pantheon is the world's largest, shown in Figure 1. The concrete technology was of a sophisticated level which even with the current building regulations, it would not be possible to build the Pantheon nowadays. After the end of the Roman Empire, the technic of making concrete got lost, until the technology re-pioneered in the mid-18th century.

The usage of concrete worldwide is twice as much as steel, wood, plastics and aluminum combined. Concrete's use in the modern world is only exceeded by the usage of naturally occurring water [1]. Given the size of the concrete industry, and the fundamental way concrete is used to shape the buildings and infrastructure of the modern world, it is difficult to overstate the role this material plays today.

<sup>1</sup>Corresponding author: [m.haas@nibe.org](mailto:m.haas@nibe.org)



**Figure 1.** The Colosseum (left, source: [bezienswaardigheden.net](http://bezienswaardigheden.net)) and Pantheon (right, source: [commons.wikimedia.org](http://commons.wikimedia.org)) were already built in concrete during the Roman Empire

## 1. Composition of concrete

There are many types of concretes available, created by varying the proportions of the main ingredients as cement, aggregates, water, chemical admixtures, reinforcements and mineral admixtures. In this way or by substitution for the cementitious and aggregate phases, the finished product can be tailored to its application with varying strength, density, or chemical and thermal resistance properties.

**Cement:** commonly Portland cement, and other cementitious materials such as fly ash and slag cement, serve as a binder for the aggregate.

**Aggregate:** consists of large chunks of material in a concrete mix, generally a coarse gravel or crushed rocks such as limestone, or granite or recycled and crushed concrete, along with finer materials such as sand or recycled sand.

**Water:** is mixed with this dry composite (cement + aggregates), which produces a semi-liquid that workers can shape into a form. The concrete solidifies and hardens to rock-hard strength through hydration, a chemical process. The water reacts with the cement, which bonds the other components together, creating a robust stone-like material.

**Chemical admixtures:** are added to achieve varied properties. These ingredients may speed or slow down the rate at which the concrete hardens, and impart many other useful properties.

**Reinforcements:** are often embedded to concrete. Concrete can be formulated with high compressive strength, but always has lower tensile strength. For this reason it is usually reinforced with materials that are strong in tension (often steel). Concrete can be damaged by many processes, such as the freezing of trapped water.

**Mineral admixtures:** have become more popular in recent decades. The use of recycled materials as concrete ingredients has been gaining popularity because of increasingly stringent environmental legislation, and the discovery that such materials often have complimentary and valuable properties. The most conspicuous of these are fly ash, a by-product of coal-fired power plants, and slag, a by-product of industrial electric arc furnaces. The use of these materials in concrete reduces the amount of resources required as the ash and slag acts as a cement replacement. This displaces some cement production, an energetically expensive and environmentally problematic process, while reducing the amount of industrial waste that must be disposed of.

The mix design depends on the type of structure being built, how the concrete is mixed and delivered, and how it is placed to form the structure.

## 2. The environmental impact of concrete

The manufacture and use of concrete produces a wide range of environmental and social consequences. Some are harmful, some welcome, and some both, depending on circumstances. A major component of concrete is cement, which similarly exerts environmental and social effects.

The cement industry is one of the three primary producers of carbon dioxide, a major greenhouse gas. The other two are the energy production and transportation industries. Concrete is used to create hard surfaces that contribute to surface runoff, which can cause heavy soil erosion, water pollution, and flooding, but conversely can be used to divert, dam, and control flooding. Concrete is a primary contributor to the urban heat island effect, though less so than asphalt. Workers who cut, grind or polish concrete are at risk of inhaling airborne silica, which can lead to silicosis [2]. Concrete dust released by building demolition and natural disasters can be a major source of dangerous air pollution. The presence of some substances in concrete, including useful and unwanted additives, can cause health concerns due to toxicity and radioactivity. Wet concrete is highly alkaline and must be handled with proper protective equipment.

The cement industry is one of two primary industrial producers of carbon dioxide (CO<sub>2</sub>), creating at least 5% of worldwide man-made emissions of this gas, of which 50% is from the chemical process and 40% from burning fuel [3]. The carbon dioxide CO<sub>2</sub> produced for the manufacture of one ton of structural concrete (using ~14% cement) is estimated at 410 kg/m<sup>3</sup> (which is ~180 kg/ton CO<sub>2</sub> at density of 2.3 g/cm<sup>3</sup>). This CO<sub>2</sub> is reduced to 290 kg/m<sup>3</sup> with 30% fly ash replacement of cement [4]. The CO<sub>2</sub> emission from the concrete production is directly proportional to the cement content used in the concrete mix; 900 kg of CO<sub>2</sub> are emitted for the fabrication of every ton of cement [5]. Cement manufacture contributes greenhouse gases both directly through the production of carbon dioxide when calcium carbonate is thermally decomposed, producing lime and carbon dioxide [6], and also through the use of energy, particularly from the combustion of fossil fuels.

## 3. Design improvements

There is a growing interest in reducing carbon emissions related to concrete from both the academic and industrial sectors, especially with the possibility of future carbon tax implementation. Several approaches to reducing emissions have been suggested. One reason why the carbon emissions are so high is because cement has to be heated to very high temperatures in order to form the clinker. A major culprit of this is alite (Ca<sub>3</sub>SiO<sub>5</sub>), a mineral in concrete that cures within hours of pouring and is therefore responsible for much of its initial strength. However, alite also has to be heated to 1,500°C in the clinker-forming process. Some research suggests that alite can be replaced by a different mineral, such as belite (Ca<sub>2</sub>SiO<sub>4</sub>). Belite is also a mineral already used in concrete. It has a roasting temperature of 1,200°C, which is significantly lower than that of alite. Furthermore, belite is actually stronger once concrete cures. However, belite takes on the order of days or months to set completely, which leaves concrete

weak for an unacceptably long period of time. Current research is focusing on finding possible impurity additives, like magnesium, that might speed up the curing process. It is also worthwhile to consider that belite takes more energy to grind, which may make its full life impact similar to or even higher than alite [7].

Portland cement clinker contains four main minerals:

Alite: approximately tricalcium silicate (typically about 65% of the total)

Belite: approximately dicalcium silicate (typically about 15% of the total)

Aluminate: very approximately tricalcium aluminate (typically about 7% of the total)

Ferrite: very approximately tetracalcium aluminoferrite (typically about 8% of the total)

Another approach has been the partial replacement of conventional clinker with such alternatives as fly ash, bottom ash, and slag, all of which are by-products of other industries that would otherwise end up in landfills. Fly ash and bottom ash come from thermoelectric power plants, while slag is a waste from blast furnaces in the ironworks industry. These materials are slowly gaining popularity as additives, especially since they can potentially increase strength, decrease density, and prolong durability of concrete [8].

#### **4. EU SustCon project**

The SustCon EPV project [9] is an action co-funded by the European Community's Competitiveness and Innovation Framework Program (CIP) - Pilot and Market Replication Projects, under the Entrepreneurship and Innovation Program (EIP) - Eco-innovation.

Many national standards impose minimum ingredient components that are supplier oriented. This discourages the concrete producer from using other environmentally friendly materials. Durability aspects are often related to these prescriptive regulations. SustCon wants to assist the market in evolving from volume to quality, doing more with less. This is to the benefit of all stake-holders who gain from a value added innovation approach.

SustCon EPV facilitates the use of environmental friendly ingredients. Its environmental performance is quantified by the sustainability-index concrete (SI-C) and a related quality brand label.

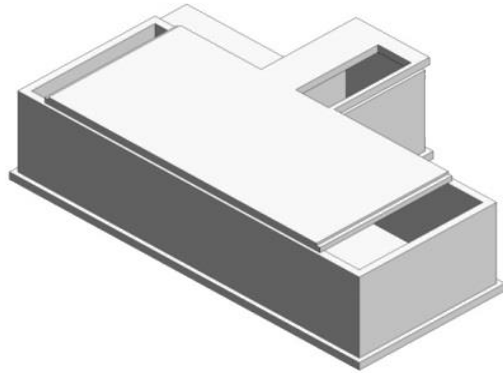
##### *4.1 Pilot 1: NL Watertight basement in Naarden*

The submerged basement is part of an extension of an existing house (a monument of cultural heritage, built by the famous architects Brinkman & Van der Vlugt, who built also Van Nelle factory Rotterdam), and, besides a living space, it serves as a foundation for a wooden and glass frame superstructure.

##### *4.1.1 Objective*

To build a watertight basement (figure 2) with alternative binders and low OPC cement content that fulfils the construction requirements and is significantly more sustainable than commonly used concrete mix designs in the Netherlands.

- I Prove technical performance of sustainable concrete mixes outside the standardized /regular Dutch concrete regulations.
- II Investigate the economic interest in the special concrete mixes and obtain information that will assist the business plan development
- III Utilize the case for developing a Sustainability Index Concrete.



**Figure 2.** The watertight basement (source: Michiel Haas)

#### 4.1.2 Technical demands

1. Foremost, the mix had to be water tight and be C20/25 strength.
2. Less than 100 kg cement per m<sup>3</sup> with low carbon footprint mix.
3. Workability F6, workability of the concrete mix, F6 = highly liquid
4. Low or no radon
5. Sidewall possibly of visual concrete.
6. Durable.

All the above elements are interwoven in the following description:

Since the mix was not according to the Dutch regulation NEN-EN 206-1 KOMO, the contractor retreated his guarantee immediately, but the concrete supplier assured the owner that this was not a problem. The guarantee was limited to the interface floor and sidewall joint. It was the intention to have a visual concrete sidewall, a smooth self-compacting ground calcium carbonate (GCC) light colored mix was the wish of the customer. For this reason, a different RMC plant and different mix was selected for the floors (Utrecht that did not have GCC) and the sidewalls (Gouda). The binder of the floor mixes (bottom and on top of pre-floor elements) were composed of 20% CEM I 52.5R (68 kg) and 80% (272 kg) GGBS, so total fines 340 kg. Strength results after 28 days gave C 38! This mix has a water/binder ratio of 0.49 since in the Netherlands GGBS of a certain supplier plus the CEM I of another supplier result in a so-called attest mix combination. As aggregate recycled washed railroad ballast was used.

The binder of the sidewall was 25% CEM I 52.5R, (85 kg), 135 kg GGBS and 120 kg GCC. Again “surprisingly” high 28 day strength of C/39 was obtained. With 165 kg water added, this mix had a water/binder ratio of 0.75 in the Netherlands and in Spain that would be 1.9! This provides yet another proof that the Water “cement” or “binder” ratio is a reasonable regulation but the Water Powder Ratio is a mix design guideline.

This would be 0.48, thus in relation with the obtained strength. With the obtained final strength, the consulting engineer could probably re-design the structure that could maybe result in either less cross-section (of the wall), less reinforcement or less required strength. Disappointing was that the RMC did not want to supply a Self Compacting Concrete as desired by the customer and that the GCC had changed to a grey type so that the visual aspects were less favorable. Later the customer invested in an adobe type stucco.

Workability of the mix revealed problems communicated between subcontractor and the producer. The first batch for the basement floor was considered too fluid (F 6-7), so the requested second batch for the sidewalls, originally requested as SCC, was ordered less fluid though it came from another plant! They obtained an F 4 (probably). The mix for the basement roof was a good F 6.

**Conclusion:** Three technical demands were obtained, the workability and aesthetical one were not achieved. More professional pilot project management should be effected.

#### 4.1.3 Economical interest

The jobsite was not in the regular economical range of the RMC. Yet, compared with a typical Dutch basement mix of 1/3 Cem I, 1/3 Cem III B and 1/3 fly-ash, (considered 100% cementitious content), both new mixes could be considered  $\pm 90$  mins? from departure plant. In other countries other criteria would govern. In Germany and Spain the difference would be greater. For the record, the owner had to pay € 800 more!

**Conclusion:** the initial buyer of the concrete, producer and/or contractor, may profit from the SustCon EPV initiative.

#### 4.1.4 Sustainability Index Concrete (SI-C)

LCA (Life Cycle Assessment) considerations: The precise carbon footprint of the binder ingredients have to be obtained from the concrete producer, but provisional figures are around 1000 kg CO<sub>2</sub>/T Cem I 52.5 (though the process is not yet known), 60 kg CO<sub>2</sub>/T GGBS and 40 kg CO<sub>2</sub>/GCC. The impact of the use of recycled aggregates is under discussion. Transportation impact is included in the index calculation.

**Conclusion:** at all times an index, when it is ready, can be attached to both type of concrete when all data is obtained. See Figure 3



**Figure 3.** The SI-C and other information from the tool of the concrete mix of the floor with 68 kg cement (source: Michiel Haas)



#### 4.1.5 Project conclusions

The following conclusions can be made:

- The sustainable concrete mix design outperformed the set objectives of early and 28 days compressive strength delivering.
- The mix design achieved good workability.
- Exposure and consistency classes requirement were met.
- For the most common concrete used (70 to 80 % of the Dutch market), the Naarden pilot has demonstrated that, instead of a global typical concrete using > 250 kg/m<sup>3</sup> Ordinary Portland Cement, less than 35 % OPC is needed (85kg/m<sup>3</sup>).

**This provides a base that ‘Reducing CO<sub>2</sub> in concrete by Half’ is possible.**



**Figure 4.** The result of NL/pilot1 inside the cellar with daylight on both sides. (source: Michiel Haas)

## References

- [1] What is the development impact of concrete? Cement Trust. Retrieved 10 January 2013.
- [2] Shepherd and Woskie - Controlling Dust from Concrete Saw Cutting. *Journal of Occupational and Environmental Hygiene*. Retrieved 14 June 2013.
- [3] The Cement Sustainability Initiative: Progress report, *World Business Council for Sustainable Development*, published 1 June 2002
- [4] A. Samarin (7 September 1999), Wastes in Concrete :Converting Liabilities into Assests, in Ravindra K. Dhir, Trevor G. Jappy, Exploiting wastes in concrete: *proceedings of the international seminar held at the University of Dundee*, Scotland, UK, Thomas Telford, p. 8
- [5] Mahasanan, Natesan; Steve Smith, Kenneth Humphreys, Y. Kaya (2003). The Cement Industry and Global Climate Change: Current and Potential Future Cement Industry CO2 Emissions. *Greenhouse Gas Control Technologies – 6th International Conference*. Oxford: Pergamon. pp. 995–1000. ISBN 978-0-08-044276-1. Retrieved 9 April 2008.
- [6] EIA – Emissions of Greenhouse Gases in the U.S. 2006-Carbon Dioxide Emissions
- [7] Amato, Ivan (2013). Green cement: Concrete solutions. *Nature* 494: 300–301. doi:10.1038/494300a. Retrieved 26 May 2013.
- [8] Kim, H.; Lee, H. (2013). Effects of High Volumes of Fly Ash, Blast Furnace Slag, and Bottom Ash on Flow Characteristics, Density, and Compressive Strength of High-Strength Mortar. *J. Mater. Civ. Eng.* 25 (5): 662–665.
- [9] M. Haas (2012). SustCon EPV Deliverable D2.0-D2.3, Sustainable Index Concrete and Pilots

# Embedded LCA information in BIM models

Joaquín DÍAZ, Laura ÁLVAREZ ANTÓN<sup>1</sup> and Kareem Tarek ANIS  
*Department of Architecture and Civil Engineering. Technische Hochschule  
Mittelhessen. Wiesenstrasse 14, 35390 Giessen, Germany*

**Abstract.** Construction industry, as it is well known, is one of the industries with the highest negative impacts on the environment concerning the amount of emissions generation and resources consumption. A major percentage of these generated emissions are a result of the massive amounts of different materials utilized and consumed during the different phases of construction processes. Targeting sustainable performance achievement, construction industry has to improve its behavior towards the environment, following the footsteps of other industries. Advanced technological solutions such as BIM and LCA can drive the construction industry towards achieving sustainability. These tools can improve the process of materials selection, alternatives comparison, etc, in order to follow sustainability principles. The creation of a link between LCA and BIM, as it is going to be explained, provides an easy and direct access to the information regarding environmental impacts of the different elements included in the proposed design. Therefore, this information can be considered during decision-making in the early project phases.

**Keywords.** Building Information Modeling (BIM), construction building materials, Construction Industry (CI), Life Cycle Assessment (LCA), smart-objects, sustainability

## Introduction

Nowadays issues regarding our environment and health have a vital concern all over the world. Realizing the impact of different human activities, its consequences on the surrounding nature and its relevance for our present and future well being, people became more conscious about the rationalization of their consumptions patterns and the need of measuring the environmental impacts of their activities [1].

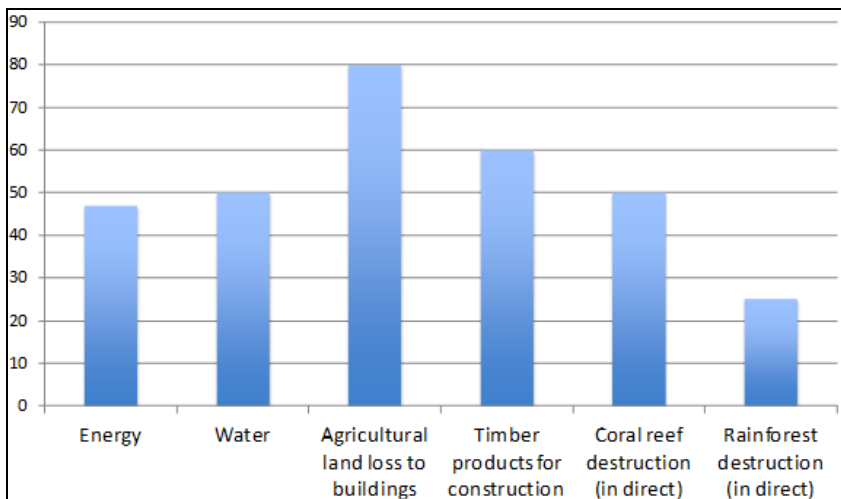
The awareness about the importance of developing sustainable thinking, and fulfilling its three main pillars, which are environmental, social and economic aspects, has been growing up worldwide, with a special attention on improving the performance of the different industries and their final products [2]. Many researches and statistics highlight that the current growing rate of the modern society is unsustainable, and if we keep on growing with this unconscious rate of resources consumption, therefore an equivalent of two planets will be needed by 2050. For example, it has been currently estimated that in the European Union almost 16 tones of materials resources are being consumed per person per year, taking into account that 6 tones of these consumed resources are wastes. Therefore it is clear that a change is needed [3].

<sup>1</sup>Corresponding author: [laura.alvarez.anton@bau.thm.de](mailto:laura.alvarez.anton@bau.thm.de)

Resources efficiency can be highlighted as one of the biggest challenges that the society is facing in the present. Different initiatives are being launched all over the world to address the current situation and how to reach sustainability; in Europe, the 2020 “a resource efficient Europe” initiative and the “Roadmap” can be mentioned as an example. These initiatives are trying to guide the development of a sustainable growth, with especial attention on resource-efficiency and low-carbon economy [4].

The construction industry (CI) is well known all over the world by its robust and fast growing, but on the other hand the environmental burdens are also increasing in a frightening way. As CI’s growth is based on consuming a massive amount of natural resources such as energy, land, raw materials, water, etc., which have negative influences and impacts on the environment [5]. It has been estimated that half of non renewable resources are consumed by mankind to be devoted for the sake of the construction industry.

Humanity spent the last decades trying to adapt the surrounding environment in order to fulfill its needs and requirements to have a better life quality. Therefore, today our daily life is carried on construction manufacture products such as houses to life in, roads to travel on, office buildings to work in, etc [6]. This makes the CI one of the most demanding industries for natural resources. The graph below shows the percentage of natural resources consumed by the construction sector.



**Figure 1.** Estimated percentage of global resources consumed by the construction industry [5].

It has been estimated that an improvement in construction industry could achieve in the European Union a 50% reduction of material consumption, and a 35% reduction of greenhouse gases emissions, among other environmental impacts. Therefore, it is one of the key sectors for improving environmental performance [3].

Therefore there is a need of reducing constructions environmental impacts, using a lifecycle approach. By selecting sustainable materials, increasing the rate of waste recycling and including environmental criteria during the design phase, the construction industry could become one of the engines for a sustainable development [3].

The weak performance of the construction sector towards achieving sustainability has been realized by several countries and organizations. Therefore many national and international initiatives and protocols were published to show the increasing concern about how to implement sustainability principles in the construction sector, in order to protect the surrounding environment and its resources for the next generations.

The construction industry is well known among all the other industries as the industry with the most complicated and unorganized nature, which influences its performance and it is the cause of many of its problems. The growth of these problems requires immediate solutions in order to integrate them into its current procedures and processes. These solutions have to address and take profit of the available opportunities and methods for achieving sustainability in the construction industry [7].

The construction sector remains as one of the sectors with the lowest adoption and implementation of sustainable principles and techniques compared to other industries such as automotive, pharmaceutical, etc. This is mainly related to some particular features of the industry such as the huge number of activities, processes, different stakeholders involved with different interests, projects' size, projects' long duration, costs, the lack of technological application and solutions, wastes produced, etc.[2]. In order to overcome all these issues the CI needs to reorganize all its processes in order to overcome them from a sustainable perspective.

The performance of the construction sector could be enhanced by different existing tools such as BIM and LCA, and profit from their implementation during the early project phases can be taken. For achieving sustainability and in particular improving the environmental performance of constructions, it is important to include environmental criteria since the early design phases.

The early design phases have the highest potential for influencing the project, because as the project evolves the chances of performing changes decreases. It is in the early design phases when different alternatives have to be analyzed in order to select the most suitable one [8]. Therefore it is important to have an effective decision-making tool in order to use it especially during the early project phases.

Moreover, as construction industry has a high rate of materials consumptions, special care should be taken when selecting them. Their environmental behavior should be checked while selecting the different materials and elements that are going to be included in the design in order to improve the overall environmental performance.

Therefore, it could be concluded that an effective decision-making tool that includes environmental criteria is required. Currently, already exist different methodologies that can contribute to this aim. BIM can improve information management and collaboration between the different stakeholders while LCA enables the environmental assessment of the construction during its whole life cycle.

In this paper special attention is going to be paid to LCA as an environmental assessment methodology and to BIM as an information management tool. Therefore there is a need to find a link between both of them in order to obtain an effective decision-making tool.

## **1. Life cycle assessment**

In order to achieve a wider approach of sustainability, environmental criteria have to be included during the design phases. Life Cycle Assessment could be highlighted as one of the most suitable methodologies for assessing environmental impacts. It is based on an

evaluation of the inputs and outputs during the whole life cycle of a product, highlighting its potential environmental impacts [9].

LCA methodology has an outstanding capacity for assessing decision making during the design phase of a sustainable construction, while it provides scientific bases for designer and engineers decisions [10]. It can also guide materials selection and highlight the main opportunities for improving the environmental performance of the construction. Including environmental criteria since the early design phases can also contribute to costs reduction due the avoidances of future changes caused by the poor environmental performance [11].

Despite of the fact that LCA has noticeable advantages, it is also a complex process with some drawbacks such as lack of data, time consumption, and lack of standardization. Moreover, due to these mentioned drawbacks, it is frequent to perform the LCA of constructions such as buildings in the late project phases when the building is being constructed or after its construction. For taking profit of the environmental assessment results they have to be used in the early design phases [12].

A question can come up related to the integration of environmental criteria in the early design phases: How can the environmental information be included in the decision-making process? A suitable approach to the answer of this question can be to search for a link between BIM models and LCA databases.

First of all taking into account the different existing LCA databases, it has to be mentioned that one of the main difficulties of LCA development is the lack of data. Moreover, the quality of the assessment results depends on the quality of these data [10]. The existing databases include a wide variety of fields, therefore, it is advisable in this case to use databases focused on the construction industry, such as the German database Ökobau.dat.

The complexity of the database and the different functional units used in the databases makes it complicated to directly link this information with the BIM model.

Therefore, if for every element that it is going to be included in the building model an LCA evaluation is performed and the results are presented using the same environmental indicators, this information could be included in the BIM libraries for every single element.

Currently, Environmental Product Declaration (EPD) is becoming also more frequent. EPD are developed following the international standard ISO 14025, which sets the need of following the ISO 14040 standards for the LCA performance [13]. The EPD includes a compilation of different environmental data calculated using the LCA methodology. The LCA results are presented using different types of environmental indicators such as global warming, acidification, eutrophication, renewable and non-renewable energy consumption etc. [14].

## **2. Building information modeling**

The Construction sector spent a long time trying to adopt new tools and processes based on the new technological solutions, and adapting them to the complicated and unorganized nature of the industry. These tools are implemented with the purpose of increasing communication between the different stakeholders involved in the project, decrease the total project cost, reduce project delivery time, enhance the impact of the final product/project on the surrounding environment, etc. [15].

Building information modeling appeared the last decade as one of the most compatible solutions that could lead these aims achievement. BIM is a digital representation based on the use and development of computer generated n-dimensional models, simulating the different phases and processes of the construction project (planning, designing, execution and operating). It helps the different key-players involved in the project (such as owner, architects, engineers, contractors, etc.) to imagine what is going to be built and how this building is going to behave in a simulated environment. Moreover, significant design, construction and operation issues can be identified since the early project phases and also the impacts of the proposed design can be simulated [15].

BIM can be defined according to the Construction Project Information Committee (CPIC) as “A digital representation of physical and functional characteristics of a facility creating a shared knowledge resource for information about it forming a reliable basis for decisions during its life cycle, from earliest conception to demolition” [16].

BIM allows the management of the whole life cycle of the constructed project supported by new digital technologies [17]. The capacity of BIM for supporting integrated design has to be highlighted. Through generating a digital model as a simulation of the real project, which will include relevant information and geometries needed to support the development of the project in the different stages and decision-making since the early phases.

Building information modeling is based on intelligent, rich data, object-oriented and digital parametric simulation of the project. This data can be analyzed and organized to provide information, which can help in making decisions, improving the quality of the final project, reducing the negative impact of the proposed design and achieving sustainable principles in the CI [15].

### *2.1. Smart-objects*

BIM model, consist of smart-objects which are defined as building elements and systems (such as walls, slabs, beams, columns, objects, etc.). Smart-objects can be considered as a digital representation or simulation of real existing items and manufactured products. Smart-objects are a representation of the physical characteristics of real items that can be seen or touched.

A Smart-Object is a composition of two main parts, first the 3D geometric definition, which describes the item or manufactured products shape and form. Secondly, a database definition based on alphanumeric information transfer for describing the objects properties. The object properties include: name, dimensions, etc. [18].

Nowadays there is a wide range of suppliers that provide readymade Smart-Objects libraries, which are based on real manufactured items. Some examples of these libraries are NBS National BIM Library, bimobject, etc.; these libraries contain Smart-Objects, which are a simulation of real existing products and also containing information about them (such as dimensions, materials, manufacturer, cost, etc).

### *2.2. Embedded information*

Smart-objects are not only about digital representation or simulation of real existing items and manufactured products, but also about the embedded information linked to

the different objects. The more information connected and added to the objects, the richer they become as a source of information for decision-making.

The embedded information in the BIM tools, allows the different users to compare and assess different design proposals and different materials selection, since the very early phases of the project, with respect to their cost, availability, quality, efficiency, time consuming, impact on the environment, etc. Using BIM starts to increase the contribution of the construction industry in implementing sustainable principles.

“BIM objects are much more than just graphical representations. Using them as medium to connect to a wider source of information provides for a powerful and rich source of information”[17].

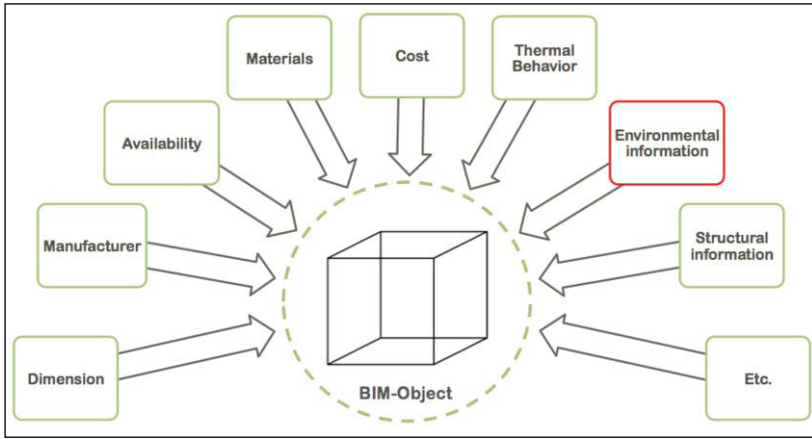


Figure 2. Information that could be included in the BIM object.

### 3. Suggested integration

The advantages of considering environmental information since the early design phases with the purpose of achieving a wider approach to sustainability are clear. Therefore, there is a need of finding an efficient link between the environmental information included in LCA databases and BIM models.

A new approach for linking LCA with BIM is going to be presented. This can provide a pre-design tool for materials and elements selection, in order to help in the decision-making process by enabling the comparison of different alternatives.

There is a need of finding an answer to the following question: How environmental information can be included in BIM models?

In order to find an answer to this question it is important to highlight on the one hand, that BIM models are composed of different smart objects. These objects, as it has already been explained, include information about the different features and properties of real elements represented in the form of smart objects. On the other hand, the environmental performance of an element can be calculated by using LCA methodology and the impacts can be represented by different environmental indicators.

By including the environmental information of the objects among their feature's information, the designer or engineer can check this information while selecting them. Therefore, the environmental criteria could be considered as the same level as any other decision-making criteria since the early design phases.

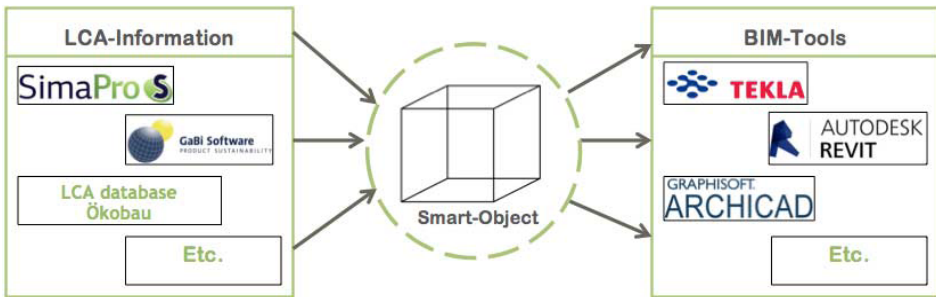


Figure 3. Proposing a link between LCA data and BIM tools.

The pictures below shows a trial that has been developed using Archicad software and a smart-object from one of the existing libraries that simulates a real manufactured chair.

Object Inventory List	
Object Name	Kinnarps_Task_Chair_5222
Quantity	3
2D Symbol	
3D Front Axonometry	
Length (A)	0,430
Width (B)	0,430
Total Height (Z Size)	1,040
Depth:	0,38
Height from ground (mm):	0,42
Object Weight Unit	kg
Backrest Material	Surf-Fabric Striped
Frame Material 2	Surf-Plastic Laminate
Frame	Paint-05
Material main:	Fabric
Seat Material	Surf-Fabric Striped
Material secondary:	Plastic
Production Year	
Date of publishing:	2013-05-07
BIMObject Category:	Office Furniture
BIMObject QR code url:	http://kinnarps.bimobject.com/...
Manufacturer:	Kinnarps
Manufacturer country:	Sweden
Design country:	Sweden
Installation instructions:	http://www11.kinnarps.com/Do...
Name of the object	Task chair 5000 5222
Product data url:	kinnarps.bimobject.com/5222
Product family:	Task chairs
Product group:	5000
Cost	0.00
Environmental information (LCA)	
Product certification:	
IFC Classification:	Furniture

Figure 4. BIM object used as a medium to include LCA information and transfer it to BIM tools.

An automatic object's List was compiled in the BIM software as shown in the figure above. This list included all the required information related to the object such as



dimensions, manufacturer, materials, etc., but it did not include any information related to environmental criteria.

As it is highlighted in the red box (environmental information LCA) in the figure above, we were able to adjust the object's information table manually to include in the table a new row where we can add LCA information.

Adding LCA information to the object's automatic list that could be compiled in the BIM software, will provided the users with early decision making information to assess and compare the different products and materials they selected.

#### 4. Conclusions

The pressure on the construction industry is increasing day by day, demanding an improvement of the quality of its final products by means of a sustainable approach and the implementation of new technological solutions. Building information modeling and life cycle assessment can be suggested as suitable methodologies for achieving a sustainable construction.

The efficient link between LCA and BIM is still under development. Nevertheless, the use of BIM-Objects as a medium to include LCA information in BIM tools could be considered as a step towards finding a way to link LCA databases with different BIM tools.

For the success of this idea several developments have to be done, first organize and simplify the LCA information, in order to overcome the issue of the complicity of the generated information. Secondly standardizing the process of creating smart-objects with the aim of including LCA information in its structure.

By achieving this linkage the awareness about environmental issues among the different stakeholders involved in the project will increase, and sustainable principles could be widely implemented in the construction industry. Moreover, the most important benefit is that it will provide the designers and engineers with a pre-decision making tool that allow them to consider environmental criteria while selecting different materials and products.

#### References

- [1] A.C. Tudora, Assessments criteria of building materials from ecological point of view, Universitatea Tehnică „Gheorghe Asachi”, Iași, 2011.
- [2] S. Asad & M.M.A. Khalfan, Integration of sustainability issues within construction processes, *Emirates Journal for Engineering Research* **12** (2007), 11-21.
- [3] European Commission, Roadmap to a Resource Efficient Europe, Communication from the commission to the European parliament, the council, the European economic and social committee and the committee of the regions (2011).
- [4] European Commission, Resource Efficiency Indicators, Science for Environmental Policy in-depth report, Issue 4 (2013).
- [5] G. Ofori, *Challenges of Construction Industry in Developing Countries: Lessons from Various Countries*, Department of Building, National University of Singapore, n.d.
- [6] Willmott Dixon, The impacts of construction and the built environment, WD Re-Thinking Ltd (2010).
- [7] D. Nirmal, *Environmental and Cost impact Analysis of Materials and Assemblies in Building Construction*, Master thesis, Florida International University, 2012.
- [8] R. Burke, *Project Management. Planning and Control Techniques*, John Wiley & Sons LTD, Third ed. Chichester, 2001.

- [9] ISO 14040:2006, Environmental management – Life cycle assessment- Principles and framework, [Online] Available at: [http://www.iso.org/iso/catalogue\\_detail.htm?csnumber=37456](http://www.iso.org/iso/catalogue_detail.htm?csnumber=37456) [Accessed 24<sup>th</sup> June, 2013].
- [10] C. Bayer & R. Gentry, A Guide to Life Cycle Assessment of Buildings, The American Institute of Architects, Washington, 2010.
- [11] M. Buyle, J. Braet & A. Audenaert, LCA in the construction industry: a review, *International Journal of Energy and Environment*6 (2012), 397-405.
- [12] W. Tritthart, et al., LoRe-LCA State of the art report – Use of Life Cycle assessment Methods and tools. LoRE-LCA-WP2-D2-IFZ report.doc, 2010.
- [13] ISO 14025:2006, Environmental label and declarations – Type III environmental declarations- Principle and procedures, [Online] Available at: [http://www.iso.org/iso/catalogue\\_detail?csnumber=38131](http://www.iso.org/iso/catalogue_detail?csnumber=38131) [Accessed 19<sup>th</sup> February, 2014].
- [14] The International EPD, What is an EPD? [Online] Available at: <http://www.environdec.com/es/What-is-an-EPD/> [Accessed 3<sup>rd</sup> March, 2014].
- [15] S. Ahar, A. Nadeem, J. Y.N. Mok & B. H. Y. Leung, *Building Information Modeling (BIM): A New Paradigm for Visual Interactive Modeling and Simulation for Construction Projects*, First International Conference on Construction in Developing Countries (ICCIDC-I), Karachi, Pakistan, 2008.
- [16] Royal Institute of British Architects, *BIM Overlay to the RIBA Outline Plan of Work*, RIBA Publishing, London, 2012.
- [17] Life-Cycle management of the built environment, BIM and Change Management- Sustainability and Life-cycle Management of the Built Environment, [Online] Available at: <http://buildinginformationmanagement.wordpress.com/2012/10/01/bim-in-chains-sustainability-and-life-cycle-management-of-the-built-environment-stalled/> [Accessed 25<sup>th</sup> February, 2013].
- [18] T. MacKnight, *Custom BIM Object Creation and the Bentley DataSet Files*, Bentley Architecture, s.d.

# Compressive strength and durability of fly ash stabilized dolomitic waste as a lightweight construction material

Ikechukwu F. ANEKE<sup>1</sup> and Felix N. OKONTA

*Department of Civil Engineering science, University of Johannesburg, P.O Box 524, Auckland Park 2006, South Africa*

**Abstract.** Due to the seriousness of environmental pollution and the production of huge energy consuming building and construction materials, the development of new eco-friendly and energy saving building materials to overcome these issues has been gaining increasing attention. South Africa has largest number of dolomite deposits in southern Africa, if not in the entire Africa. Nonetheless most of the dolomite in South Africa has some impurities of which they are neglected in dumping site (millions of tons). This paper looked at finding alternative use for this dolomitic waste (DW) by stabilizing this waste with another waste called fly ash (FA), introduction of gypsum as an activator will trigger a pozzolanic reaction in presences of water. As a result of this, the product of this reaction will be a useful material in construction and as well solve the difficulties i.e. environmental, social and cost often associated with storing and handling of this waste. This work went as far as providing an alternative for low-cost construction materials that can help deal with South African housing problems.

The waste material was analyzed from geomaterial and geochemistry view point, the chemical reaction between these materials: dolomitic waste and fly ash were illustrated. The XRF, SEM and EDS of the reacted product were looked at, the strength gained by the reaction after sample preparation for 28 days were also shown. However various geotechnical laboratory experiments were conducted ranging from proctor compaction test, compressive strength test and a mathematical model was generated to predict the compressive strength and these results were compared to compressive strength values obtained from the laboratory.

**Keywords.** Dolomitic waste, fly ash, geochemistry, SEM and compressive strength

## Introduction

Generally when a carbonate rock is composed of more than 95% of calcite, it is known as limestone, but otherwise it is called sedimentary rocks [1]. They originate from different natural sources such as dolomitic rocks dust, volcanic rock ([2] and [3]). The mineral dolomite derives its name from Deodat Dolomieu (1750-1801) named after a French engineer and mineralogist.

This dolomitic waste constitute mainly, of a chemical nomenclature (CaMg (CO<sub>3</sub>)<sub>2</sub>), which is an indication that it contains limestone that can be used as a source of calcium oxide (CaO). This calcium oxide is one of the major elements that contribute to pozzolanic reaction between dolomite and fly ash [4]. Although pozzolanic reaction is slow, but can be activated to be more reactive. The large volume of this waste after processing dolomite rock, forms lot of unwanted aggregates which are developed with many features depending on the primary rock properties, this can be used as a

---

<sup>1</sup>Corresponding author: [Frankaneke4@gmail.com](mailto:Frankaneke4@gmail.com)

lightweight material [5]. Lots of researchers have looked at the use of dolomite for lightweight construction material, but lightweight materials such as dolomitic waste-stabilized fly ash are gaining increasing interest over past years. Hence these wastes are natural materials and are granular with less bulk density [6]. Furthermore, there are growing interest in the development and utilization of both waste (dolomitic waste and fly ash). The example of this utilization is preparation of a ternary mix known as Dolomite-Fly ash- Gypsum (DO-FA-G) binder, a new cementitious binder based on dolomite, fly ash and gypsum. The hardening of this binder is developed by the means of chemical reactions between the dolomite, silica from the ash (fly ash) and water. The resultant reacted product, produces hydrated calcium silicates (C-S-H), as well as by means of reaction between the calcium sulphates from gypsum, CaO from dolomite and alumina from fly ash also reacts in presences of water to forms ettringite ( $3\text{CaO}\cdot\text{Al}_2\text{O}_3\cdot 3\text{CaSO}_4\cdot 32\text{H}_2\text{O}$ ). These hydration reactions in dolomite-fly ash-gypsum-water paste are very complex and are dependent on the fly ash mineralogical composition. The solubility of both the crystalline and non-crystalline fractions of the ash depends on the conditions in which the hydration reaction took place.

## 1. Experimental procedures

The dolomitic waste used in this paper, were collected from lyttelton mine in centurion South Africa and fly ash used for this work, was purchased from ULULA ash South Africa and it is a commercial available class 'F' fly ash that has a specific gravity of 2.0. Figure.1 shows the mine where the waste was collected.



**Figure 1.** Lyttelton dolomite mine

Gypsum was also used for this work and it was purchased from GypsealRhino borad sealant by BPB GypsumRhino board Division. The chemical compositions of these materials were determined by the use of XRF equipment. In certain cases, additional tests may be required such as XRD test which have been found to be important in the classification of specific material types. Standard procedures exist in most countries (ASTM or SABS) although slight variations might occur.

### 1.1 Chemical Composition of the materials

Chemical composition of a material is one of the most important indications that a material has a good or bad quality chemical composition for various applications. The detailed chemical compositions of materials used in this research paper are summarized in Table 1 below:

**Table 1.** Chemical composition of material

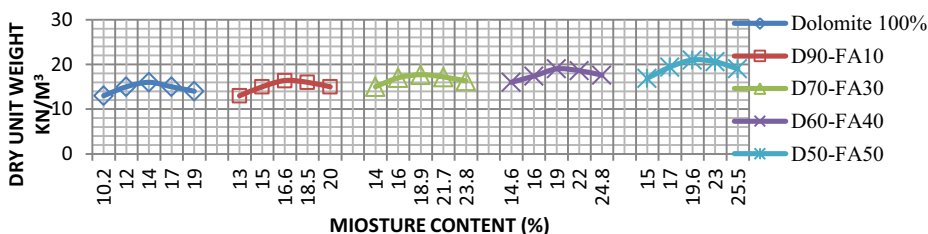
Oxide	Gypsum %	Fly ash %	Dolomitic waste %
SiO <sub>2</sub>	24	56	2.47
Al <sub>2</sub> O <sub>3</sub>	0.71	22.5	0.84
Fe <sub>2</sub> O <sub>3</sub>	0.35	6.8	0.34
CaO	32.3	3.8	31.5
MgO	0.38	2.3	19.12
SO <sub>3</sub>	42.8	0.25	<<<<
K <sub>2</sub> O	0.1	1.9	0.09
Na <sub>2</sub> O	<<<<	0.85	0.11
L.O.I	0.08	0.05	0.45

*1.2 Compaction*

Standard compaction test was performed in according with ASTM D698 to establish the relationship between the moisture content and dry density of the material. As a result of this, dolomitic waste and fly ash was chosen for some trial mixes and it was mixed with water thoroughly and stored in polythene bag for moisture equilibrium and remixed in accordance with ASTM D 698-91. The fly ash and dolomitic waste are compacted in the mould in three layers, giving an equal taps of 25 blows to each layer. Each trails using standard proctor apparatus, the values of the dry materials and corresponding trials mixes are inferred in Table 2 below. The results of the compaction with their corresponding dry densities and optimum moisture content are shown also in Figure 2. Nonetheless 6% gypsum was only added during sample preparation for casting.

**Table 2.** First mix of materials for compaction test

Material	Dolomitic waste mass (%)	Fly ash mass (%)	Gypsum (%)
1 <sup>st</sup> Trial	100	0	6
2 <sup>nd</sup> Trial	90	10	6
3 <sup>rd</sup> Trial	70	30	6
4 <sup>th</sup> Trial	60	40	6
5 <sup>th</sup> Trial	50	50	6



**Figure 2.** Compaction curves for different varying mixes of dolomitic waste and fly ash samples

The samples were prepared for their maximum densities at optimum water content based on compaction curves obtained as was calculated in Figure 2. 50x50x50 mm cube molds were used. These samples have various curing period for testing i.e. 7, 14 and 28 days. The samples prepared were labeled according to the trial combination chosen. Steam curing method was adopted for this research work. The samples were demolded and covered with plastic bags after 24hours of preparation and was carefully

positioned in hydro-autoclave with a constant temperature of 80°C for the curing period of 7, 14, and 28 days.

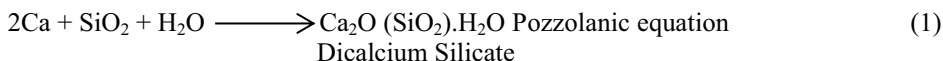
### 1.3 Compressive strength test

The compressive strength test were performed on the prepared samples according to ASTM D 695, by using mechanical testing machine, with automated fixtures in order to obtain the ultimate strength of the tested sample with respect to their stress-strain behaviors. The samples were loaded with 50 KN and utilized the speed rate of 5 mm/min. The compressive strength values are determined by the average of three samples tested for each different type of trial mixes. Scanning electron microscopy (SEM) was performed by using SEM Rigaku Ultimate, to study the microstructure of the base material (dolomitic waste) and the resulting samples. The test was carried out using secondary and backscattered electron detectors and a SEM sample was pulverized.

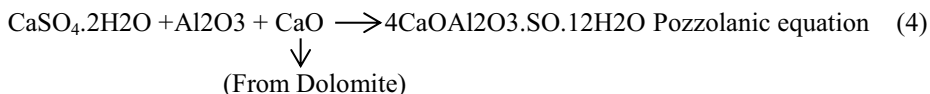
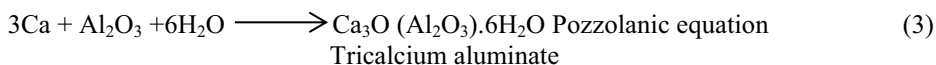
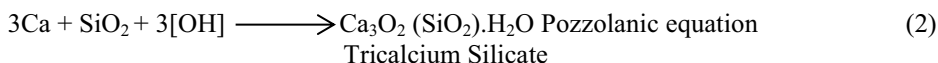
## 2. Results and discussion

### 2.1 Chemistry and mechanism of reactions

Fly ash has a reactive silica and aluminum of 22.5% and 56% respectively as presented in Table 1, while the dolomitic waste has 31.5% of free calcium {  $(CaMg(CO_3)_2)$  } and the samples for the first set was prepared using 6% gypsum. This sample reacts in the presence of water and temperature condition of 80°C as illustrated in the chemical equations below:



This reaction occurs during the first few days (3days) leading to a very significant strength gain; however the hydration reaction is the same to that of tricalcium silicate. But dicalcium silicate contributes little to the early strength of pozzolans; hence it makes substantial contributions to strength gain in later age.



The pozzolanic reaction of aluminate minerals is somewhat more complex than that of the calcium silicates minerals, and it takes place depending on sulfate ions that are present in the pore solution. Tricalcium is soluble, even more so than dicalcium silicate. In reaction that involves gypsum, this actually occurs with unduly reacted ettringite  $(Ca_6Al_2(SO_4)_3(OH)_{12}.26(H_2O))$  from  $C_3A$  and  $C_4AF$  when the gypsum is

consumed, the ettringite reacts with the remaining  $C_3A$  and  $C_4AF$  to form a new lower-sulfate phase known as Monosulphate with little or no ettringite.

## 2.2 Compaction results

The compaction results of the materials for the trial mixes of the compaction set as reported in Figure 2, when dolomitic waste was compacted the average results obtained shows that dolomitic waste recorded a maximum dry density (MDD) of  $16.0 \text{ KN/m}^3$  and corresponding optimum moisture content (OMC) of 14%.for the second trials in Table.2 (D90-FA10), this was done by replacing 10% of dolomitic waste with 10% of fly ash, after 10% of dolomitic waste was subtracted. This resulted in increased (MDD) and (OMC) giving the second trial a value of  $16.4 \text{ KN/m}^3$  and 16% respectively which was a clear evidence that fly ash is more denser than dolomite. In the 3<sup>rd</sup>, 4<sup>th</sup> and 5<sup>th</sup> trials when 30, 40 and 50% dolomitic waste was replaced with equal amount of fly ash the results subsequently lead to an increase in MDD and OMC giving value of  $17.7 \text{ KN/m}^3$  and 18.9%,  $20.5 \text{ KN/m}^3$  and 19%,  $22.0 \text{ KN/m}^3$  and 19.6% respectively. This simply shows that both the MDD and OMC are increasing as the mass% of the fly ash is increasing.

## 2.3 Compressive strength

The results for compressive strength test shows that the first set of mixtures (Table 2) without 6% gypsum have a strength gain in overall, But not as compare to those with 6% gypsum, which demonstrate a very good strength. However fly ash reactions with dolomitic waste enhanced strength development even after 7 days of curing, and the effect of 6%gypsum to compressive strength of the mixture of dolomitic waste and fly ash samples compacted to their respective maximum dry density at corresponding moisture content has been illustrated in (Figure 3 through 5) which shows that the compressive strength of dolomitic waste and fly ash mixtures for all the combination cured for 28 days. The combination of D50%+FA50%+G6% mix recorded strength of 2280 Kpa for 28days curing period from as low as 600Kpa of only dolomitic waste. The effect of pozzolanic reactions dominates strength gain at higher curing periods whereas the effect of density dominates strength gain at lower curing periods.

The dolomitic waste stabilized fly ash mixtures without gypsum have recorded strength up to 2080 Kpa after 28 days curing. The strength of the materials is very much dependent upon the pozzolanic reaction just as stated in equation (1) through equation (4). The addition of water and the method of curing play a critical role, particularly the amount used to prepare the sample. The strength of the materials increases when less water content was used. The pozzolanic reaction itself consumes a specific amount of water, but the water not consumed in the pozzolanic reaction will remain in the microstructure pore space and these pores usually make the end product weaker due to lack of strength-forming calcium silicate pozzolanic bonds. Although the samples were prepared at its OMC, which leads to high strength but low in workability. The perfect graphs of strength were shown for different curing ages, the compressive strength increases with an increase in age but the highest compressive strength were observed at 28 days age for all the different mixes, hence D<sub>50</sub>%+FA50%+G6% recorded a strength up to 2280 Kpa .

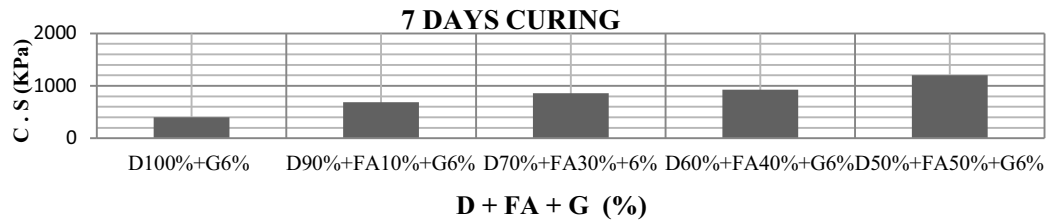


Figure 3. Compressive strength curve versus D<sub>0</sub> + Fa + G

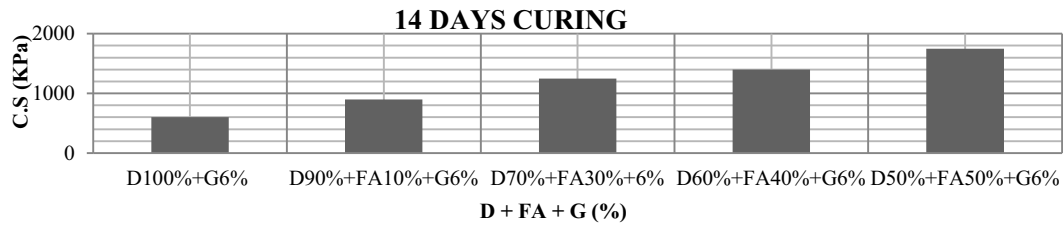


Figure 4. Compressive strength curve versus D + Fa + G

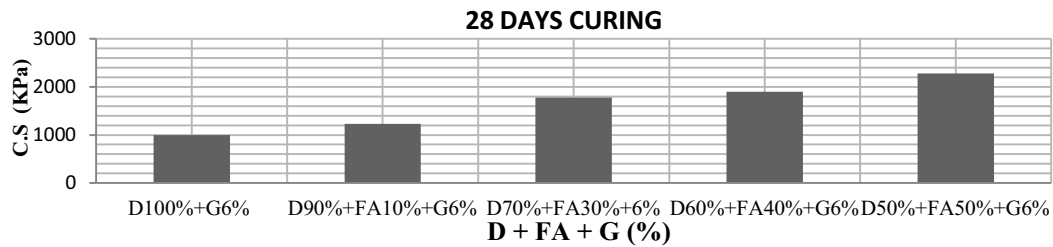


Figure 5. Compressive strength curve versus D + Fa + G



2.4 Stress-strain behavior

Compressive strength test were used to evaluate the stress-strain behavior properties of dolomitic waste, fly ash and gypsum mix propotion.it was seen that the density D, fly ash (FA), OMC, gypsum (G) affects not only the compressive strength, but also affects the stress-strain behavior. With increasing OMC in Figure 2; the specimen becomes stiffer and the stress-strain curves changes from ductile to brittle behavior. Figures 6 and 7 below shows that the mixture of (100% dolomitic D<sub>o</sub> waste) + (6% gypsum G) the compressive strength is low and the stress-strain curve is ductile to an extent. The behavior of the specimen at load failure is also shown in Figures 6 and 7 However when mix ratio of D<sub>o</sub>50% + FA50% + G6% was tested the compressive strength and stiffness is relatively high.

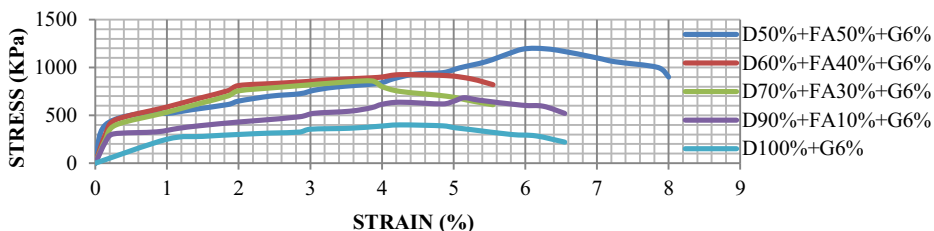


Figure 6. Stress-strain curve for 7 days test

The stress-strain curves become brittle in Figures 6 and 7 suggest that there is a difference between strength and ductility when the compressive strength is high. Its stress-strain behavior is less ductile and starts to be brittle as the level of stress begin to drop. Among mixed components affecting the stress-strain characteristic of dolomitic waste, fly ash, and gypsum of D50% + FA50% + G6% proportion have the most effect.

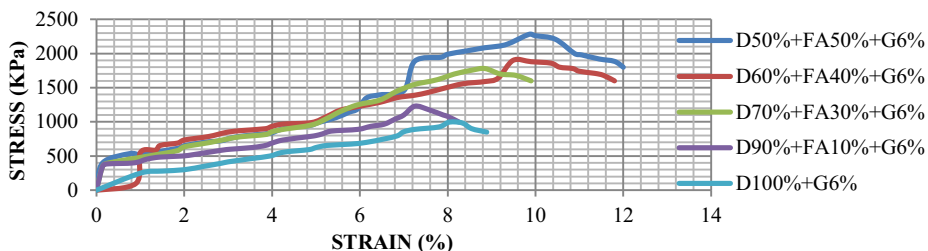


Figure 7. Stress-strain curve for 28 days test

2.5 Microstructure

The microstructure of dolomitic waste stabilized fly ash was analyzed using scanning electron microscope (SEM). In Figure 8, the microstructure of the stabilized material shows the formation of pore heterogenous matrix which does not exist in the original dolomitic waste. The formation of the matrix was due to the pozzolanic reaction occurred after mixing the original dolomitic waste with fly ash and gypsum as an activator.

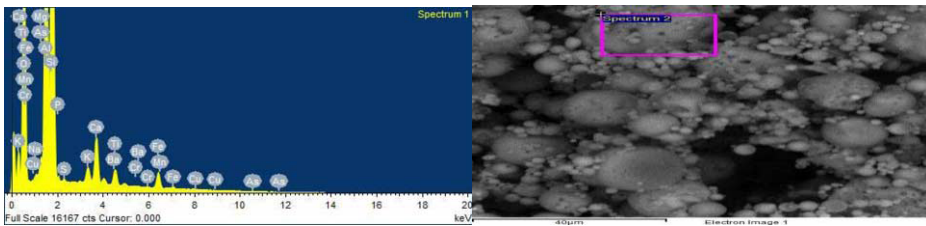


Figure 8. SEM of Do-Fa-G before and after 28 days curing

### 3. Regression analysis

Statistical model were generated and tested to show the relationship between variables for 6% gypsum only with respect to the compressive strength. Input parameters used in this study are based on the experimental result conducted in the laboratory. This includes the values of compressive strength, density, percentages of dolomitic waste, fly ash and finally the weight of water used to the ratio of prepared samples. Equation (5) below shows the regression analysis equation.

$$F = B_0 + B_1 \times \frac{b}{w} \tag{5}$$

Where F = compressive strength, B<sub>0</sub> and B<sub>1</sub> are the coefficients (Abram’s Law). The equation (6) below was used for this study:

$$Y = A_0 + B_{x1} + C_{x2} + D_{x3} \times \alpha \tag{6}$$

Where Y = Compressive strength, A<sub>0</sub>=1, B=Dolomitic waste, C= Fly ash, D = Density of the prepared specimen and α = Mass of H<sub>2</sub>O in the specimen (grams). However dolomitic waste, fly ash, density and mass of H<sub>2</sub>O are taken as independent variables, where compressive strength is taken as the dependent variables.

Table 3. Variables for 6% gypsum 7 days testing

Dolomite (%) X <sub>1</sub>	Fly ash (%) X <sub>2</sub>	Density (kN/m <sup>3</sup> ) X <sub>3</sub>	Mass of H <sub>2</sub> O (ml) α	C.S Lab values (Kpa) Y	C.S predicted values (kPa) Y
50	50	21.00	760	1200	1203.90
60	40	19.00	745	925	927.59
70	30	17.7	785	860	866.72
90	10	16.40	725	684	696.16
100	<<<	16.00	700	400	397.54

$$C.S (kPa) = 0.0208_{x1} + 0.01612_{x2} + 0.0751_{x3} \times 760 = 1203.9 \text{ kPa}$$

$$C.S (kPa) = 0.001248_{x1} + 0.0065_{x2} + 0.065_{x3} \times 745 = 927.59 \text{ kPa}$$

$$C.S (kPa) = 0.00874_{x1} + 0.001944_{x2} + 0.062_{x3} \times 785 = 866.72 \text{ kPa}$$

$$C.S (kPa) = 0.007866_{x1} + 0.0194_{x2} + 0.058_{x3} \times 725 = 696.16 \text{ kPa}$$

$$C.S (kPa) = 0.00791_{x1} + 0.035_{x3} \times 700 = 397.54 \text{ kPa}$$

Table 4. Variables for 6% gypsum 28 days testing

Dolomite (%) X <sub>1</sub>	Fly ash (%) X <sub>2</sub>	Density (kN/m <sup>3</sup> ) X <sub>3</sub>	Mass of H <sub>2</sub> O (ml) α	C.S Lab values (kPa) Y	C.S predicted values (kPa) Y
50	50	21.00	776	2280	2291.14
60	40	19.00	736.5	1900	1910.04
70	30	17.7	793	1780	1788.85
90	10	16.40	720	1230	1240.64
100	<<<	16.00	700	1000	1067.50

$$\text{C.S (kPa)} = 0.105_{x_1} + 0.275_{x_2} + 0.125_{x_3} \times 776 = 2291.14 \text{ kPa}$$

$$\text{C.S (kPa)} = 0.107_{x_1} + 0.623_{x_2} + 0.120_{x_3} \times 736.5 = 1910.04 \text{ kPa}$$

$$\text{C.S (kPa)} = 0.100_{x_1} + 0.324_{x_2} + 0.118_{x_3} \times 793 = 1788.85 \text{ kPa}$$

$$\text{C.S (kPa)} = 0.09_{x_1} + 0.0211_{x_2} + 0.10_{x_3} \times 720 = 1240.64 \text{ kPa}$$

$$\text{C.S (kPa)} = 0.085_{x_1} + 0.090_{x_3} \times 700 = 1067.5 \text{ kPa}$$

#### 4. Conclusions

- Dolomitic waste from lyttelton dolomite mine stabilized with fly ash can enhance the mechanical properties of lightweight construction materials. The mixture of D50%+FA50%+6% shows excellent result with highest compressive strength of 2280 Kpa in 28 days testing.
- The microstructure of the optimum strength pozzolanic material appears to be homogeneous and still have some minimum proportion of unreacted fly ash microspheres, with continuous matrices of aluminosilicate.
- The reaction between dolomitic waste and fly ash produces calcium silicate hydrates (C-S-H) which is responsible for strength gain, but the addition of 6% gypsum contributes to development for later age strength again. However the continuous addition of fly ash will be beneficial as the strength continues to increase.
- Some of the predicted values are slightly higher than the laboratory values, Thereby indicating the importance of the influence of mix constituents on the compressive strength of the specimens can be approved.

#### References

- [1] Fragoulis, D., Stamatakis, G., Chaniotakis, E., Columbus, G., 2004. Characterization of lightweight aggregates produced with clayey diatomite rocks originated from Greece. *Materials Characterization* 53, 307–316.
- [2] Riley, C.M., 1951. Relation of chemical properties to the bloating of clays. *Journal of the American Ceramic Society* 34, 121–128.
- [3] González-López., M Torres-Ruiz, J., López-Galindo, A., Delgado, A., 1994. Geochemistry of Spanish sepiolite– palygorskite deposits: genetic considerations based on trace elements and isotopes. *Chemical Geology* 112, 221–245
- [4] Davraz M, Gunduz L (2005).Engineering properties of amorphous silica as a new natural pozzolan for use in concrete.*Cem. Concr. Res*, 35:1251-1261.
- [5] A. Korjamins, G. Shakhmenko, Girts Bumanis, 2010. Utilization of bore-silicate glass waste as a micro-filler for concrete.
- [6] Cougny, G., 1990.specification on the clay raw materials for the manufacture of lightweight aggregate. *Bulletin of the International Association of Engineering Geology* 41, 47–55.

# Preliminary study of strength of coal composites

Lerato J. MOATLHODI<sup>1</sup> and Felix N. OKONTA

*Department of Civil Engineering Science, University of Johannesburg, South Africa*

**Abstract.** Large scale floor convergence and sudden failure of pillars in room-and-pillar underground mining have been reported in various countries over many years. Failure of these mines has been attributed, amongst other causes, to the stiffness criterion used by the mining operators and most importantly mine design practices, that tend to reduce the width-to-height ratio i.e. slender pillars in pursuit of greater coal recovery yields, in order to maximize coal recovery in the seam. It is recorded that the room-and-pillar method can leave behind about 40% of the total coal available for mining. The current study seeks to determine the appropriate width-height ratio for coal composite and stabilized coal pillars. Pure coal was mixed with granular soil and stabilized with cement to form cylindrical composite columns which were crushed to determine their unconfined compressive strength at different width-to-height ratios. The strength increased with the increase in W/H of the columns. Increase in coal percentage in a composite reduces the strength. The stabilized coal pillars mobilized less strength than the composite pillars. Based on limited data, relationships amongst column strength W/H and mix ratios were formulated and are proposed for the estimation of strength of mine support structures. More data is however required to formulate a general regression equation.

**Keywords.** Pillar failure, cement, unconfined compressive strength, stiffness

## Introduction

Coal has been the primary source of energy for many years and continues to be among the dominant sources of energy to date. It provides around 29.9% of global primary energy needs and generates around 41% of the world's electricity. Furthermore, it is used in the production of 70% of the world's steel according to the World Coal Association publication in 2013 [5]. This fossil fuel is formed through plant matter that accumulated over millions of years in swamps and peat bogs over the course of the Phanerozoic time period that was buried, compacted and lithified into coal seams. When coal seams are near the surface it is economical to use the open pit method to retrieve the coal, and this method affords the miner the benefit of recovery as much as up to 90% of the coal discovered. However when the seams are formed deep into the ground usually around 100m, depending also on density of the overburden and thickness of the seam, underground mining techniques are used as the method of coal extraction. Among the various methods employed in underground mining to extract coal, the room and pillar mining method is of interest in this study.

<sup>1</sup>Corresponding author: [ljmoatlhodi@uj.ac.za](mailto:ljmoatlhodi@uj.ac.za)

Coal seams are recovered in alternating sections leaving behind rectangular or square portions of in-situ coal as supports to the overburden. This method is normally done in seams that are relatively flat. It is important that the seams as well as the rooms are large enough to allow heavy machinery such as shuttle cars and tractors to pass through with ease [4]. The setback of this method is the valuable material that has to be left behind as supports, this can be up to 40% of the coal seam [5], however depending on the set production targets of the mining operations, the pillars can either be left in place or removed at the later stage of mining [4]. Mining of coal by this method has been dangerous throughout the years due to structural failures of the pillars that tend to occur, one such incident occurred on January 21 1960 at the Coalbrooke colliery in South Africa where 437 miners died from a collapsed mine [3]. The mine collapse was due to cascading pillar failure (CPF). Such tragedies accentuate the importance of understanding the structural and strength properties of coal, and the pillar failure mechanisms, in order to put a stop to the on-going disasters happening in mines [3]. This paper is subdivided into five parts, namely: introduction; materials and methods; results and discussions; and conclusion.

## **1. Materials and methods**

The pure coal (PC) used was sourced from one of the collieries at eMalahleni around Witbank in South Africa and the residually derived granular material (GM) was sourced from Johannesburg. The two materials were mixed and stabilized with Portland cement from Lafarge (Cem) to form the composite column samples. The composite material was split into 2 categories, the 46% PC, 46% GM and 8% Cem mix proportion, and the second consisted of 66% PC, 26% GM and 8% Cem by mass. Category 1 composite mix is referred to as 50/50 composite and the second 75/25 composite. PC was also stabilized with 8% cement and that formed the category 3 of test column samples referred to as stabilized coal (SC). Table 1 shows the different stabilized sample columns prepared for this study. A set of laboratory tests were conducted on the various categories of samples for classification purposes. These categories of soil materials were mixed separately at 30% moisture content and compacted in 150mm diameter moulds to produce several column samples with different heights to generate width/height (W/H) ratio groups of 0.25, 0.5, 1 and 2. The columns were cured in a humidity chamber for 7 days, and then crushed uniaxially under the Instron 5500R compression machine to determine their uniaxial compressive strength, and enabled the estimation of the columns' modulus of elasticity. Representative samples from the crushed material were reserved for moisture content determination at the time of crushing, there were a total of 16 sample columns tested.

Table 1. Sample preparation

Column Height (mm)	Column Diameter (mm)	Stabilized Material Composition	Material Composition ratio	No. of Columns
600	150	PC/GM	50/50	2
300	150	PC/GM	50/50	2
300	150	PC/GM	75/25	2
300	150	PC	100	2
150	150	PC/GM	50/50	2
150	150	PC/GM	75/25	2
150	150	PC	100	2
75	150	PC/GM	50/50	2
75	150	PC/GM	50/50	2
75	150	PC	100	2

Note: PC-pure coal, GM-granular material

## 2. Results and discussions

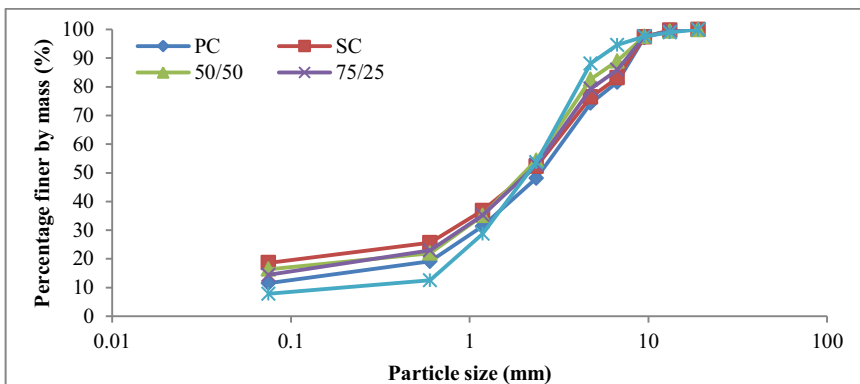


Figure 1. Particle size distribution

The PC and GM’s particle size distribution exhibited a narrow envelope, classified by Unified Soil Classification System (USCS) as poorly graded Sand with silt and gravel, which are non-plastic [1]. The Instron compression machine produced the stress – strain relationship shown in Figure 2 for all columns cast. The 75mm high columns showed a greater peak stress for a composite sample of 50/50 material. As the width of the columns was kept constant, an increase in height of column reduced the strength, ie the as the W/H ratio increases so does the compressive strength and this behavior was also observed by [2] in his study. [3] states that the shorter columns would retain most of their load even after failure, and also states that designing pillars with an adequate stability factor (greater than 2) minimizes risk of failure and that W/H ratios should be high enough to satisfy local mine stiffness criterion. Modulus of elasticity (E) being a measure of stiffness of the stabilized column and obtained as the ratio of uniaxial stress over the uniaxial strain from the unconfined compressive strength tests, as can be seen in Table 3 that increasing W/H ratio reduces the E.

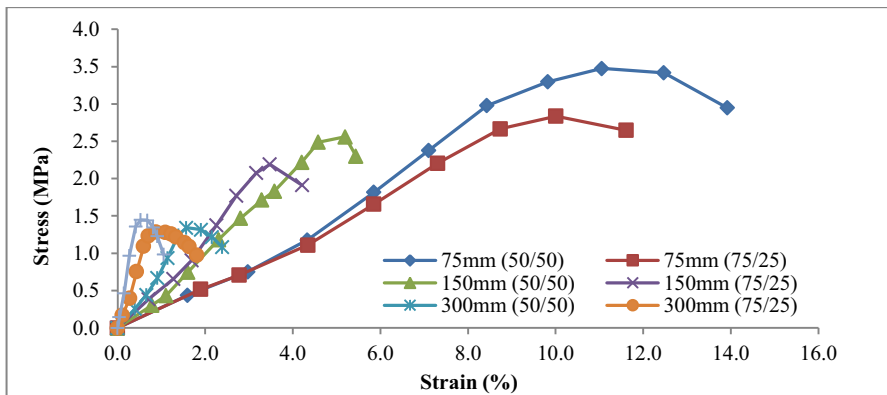


Figure 2. Stress-Strain relationship of columns with different heights

Table 2. Peak stress and estimated Modulus of Elasticity

Sample height (mm)	W/H	Peak Stress (MPa)			Modulus of Elasticity (MPa)	
		50/50	75/25	SC	50/50	75/25
600	0.25	1.45	1.21	0.88	319.12	37.23
300	0.5	1.34	1.28	0.86	119.47	21.94
150	1	2.56	2.20	1.44	58.56	65.30
75	2	3.48	2.84	1.64	43.89	37.01

Note: SC – stabilized coal

$$Sp = 1.123 W/H - 0.1625 CR + 1.316 \quad (R^2 = 0.928) \quad (1)$$

The pure coal stabilized with 8% cement achieved less compressive strength when compared to the stabilized composite as shown in Table 3; the cementation was more effective in holding together the composite particles than in the pure coal. A model with a coefficient of determination of 0.928 is proposed to predict the compressive strength (Sp) of pillars of varying W/H and composite ratio (CR). This indicates that though the strength of the pillar is dependent on the W/H ratio the composite variable contributes to the strength, with a negative slope coefficient where CR is defined as the ratio PC/PM. Figure 5 shows the quality of the fit between predicted values for Sp and the actual values from the laboratory. Figure 3 and 4 show the comparison of the actual results of this study to those from the empirical formulae from literature. The stabilized composite column strength is defined amongst the rest of the columns with same size specimen for the investigated W/H. However the witnessed lower strengths for 75/25 composite are attributed to higher content of PC in the composite.

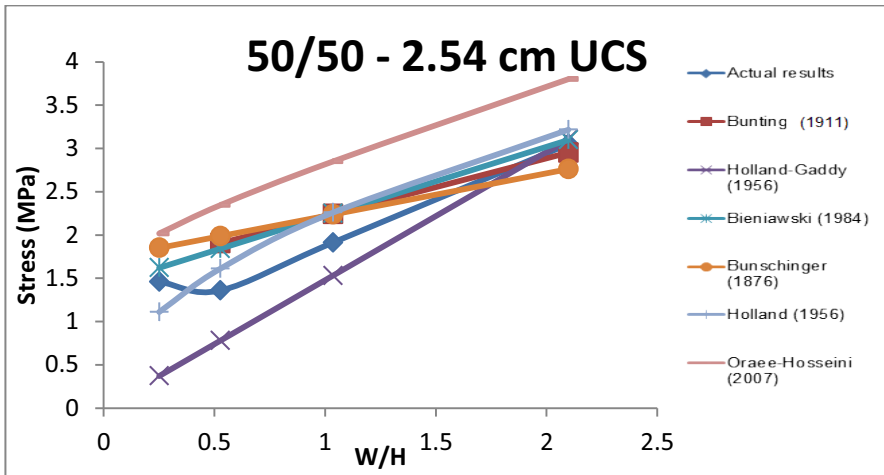


Figure 3. Comparison between actual results to empirical formulae for 50/50 – 15cm UCS specimen

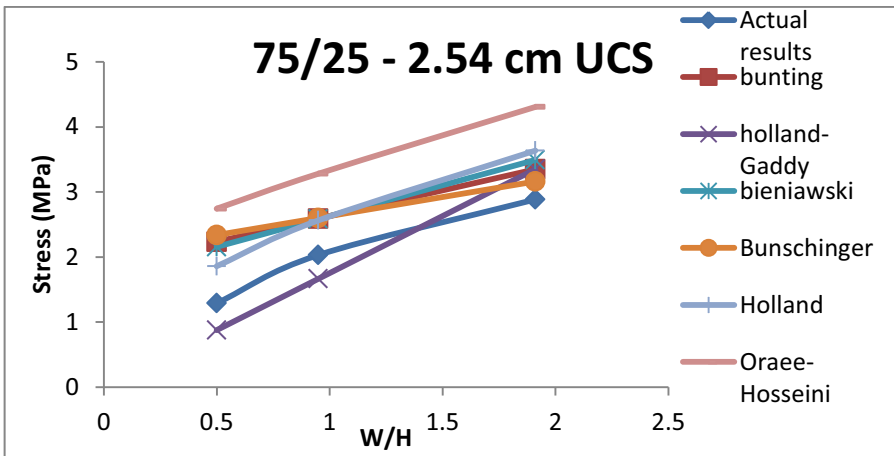


Figure 4. Comparison between actual results to empirical formulae for 75/25 – 15cm specimen



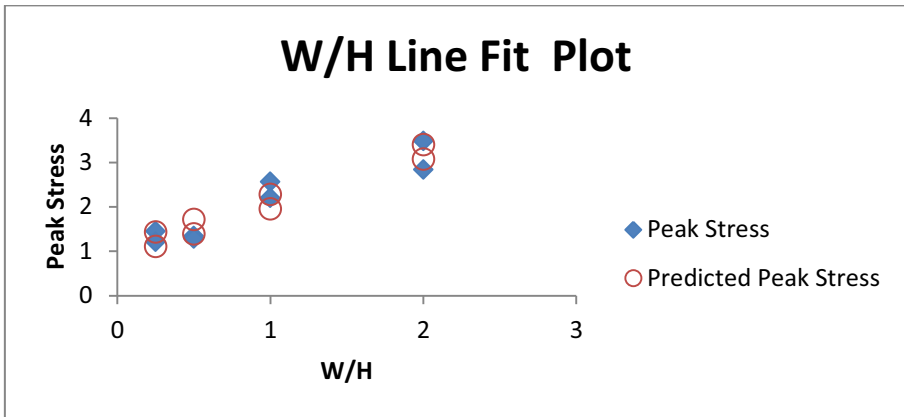


Figure 5. W/H best fit plot

### 3. Conclusions

Failure of pillars in the mining activity can be catastrophic. It occurs as a sudden collapse of supporting pillars leading to a transfer of load to the following pillars and thus a consecutive failure of remaining pillars. The strength of the pillars can be improved by as shown in literature as well as the current study increasing the W/H ratio and creating a composite of PC and GM and stabilizing it with cement. Shorter pillars have higher strength however lower E. Equation (1) with a coefficient of determination of 0.928 is proposed as an approximate expression to predict the compressive strength by W/H and CR.

### References

- [1] B.M. Das, *Principles of Geotechnical Engineering 7th Edition*, Cengage Learning, Stanford USA, 2009.
- [2] J.N. van der Merwe, A laboratory investigation into the effect of specimen size on the strength of coal samples from different areas, *The Journal of South African Institute of Mining and Metallurgy* **9** (2003), 273-280.
- [3] R.K Zipf Jr, C. Mark, Design Methods to Control Violent Pillar Failures in Room-and-Pillar Mines, *National Institute for Occupational Safety and Health*, (1997)
- [4] I.A. Given, W. Laird, J.W. Clark, S.F. Boshkov, F.D. Wright, R. L. Hafner, H. J.R., L. W.Casteel, A. Hoover, and C. Haycocks, *Underground Mining Systems and Equipment, SME Mining Engineering Handbook 3rd ed.* Port City Press, Baltimore, (1973), 12-95
- [5] World Coal Association. [Web:] [www.worldcoal.org](http://www.worldcoal.org) . [Date of access:] 01 July, 2013

# Use of ground waste glass in concrete production

Salim BARBHUIYA<sup>a,1</sup>, Aminul LASKAR<sup>b</sup> and Arnesh DAS<sup>c</sup>

<sup>a</sup>*Curtin University, Australia*

<sup>b</sup>*National Institute of Technology, Silchar India*

<sup>c</sup>*Delhi Technological University, India*

**Abstract.** Use of recycled waste glass in Portland cement and concrete has attracted a lot of interest worldwide due to the increased disposal cost and environmental concern. Being amorphous and containing relatively large quantities of reactive silica, glass is pozzolanic in nature when it is finely ground. Thus, it can be used as cement replacement as well as aggregate in cement and concrete. Attempt has therefore been made in the present work to investigate experimentally the effects of white ground glass on hardened properties of concrete. Experiments were conducted to study the feasibility of using glass sand and glass powder to substitute natural sand. It was observed that the mechanical properties such as compressive strength, splitting tensile strength decrease as the replacement level increases. However, the long-term trend is that the values of these properties tend to increase. Thus, it may be concluded that ground glass can be used in concrete to replace some part of and fine aggregate.

**Keywords.** Waste glass, compressive strength, splitting tensile strength, alkali-silica reaction, durability

## Introduction

The use of waste recycled glass in concrete is relatively a new concept that requires further study and investigation. This is needed in order to promote its application and introduce this to the construction market as an alternative to the primary materials used in concrete production. Over the years, substantial amount of research works have been carried out to exploit the potential use of waste or recyclable materials in concrete as a solution for waste materials problem, or to improve the properties of concrete. However, utilisation of these materials in concrete is not at a desired level. This is due to the lack of information and outcomes for these applications, in particular, the long-term observation. Therefore, this subject requires intensive research work to establish and define the accurate characteristics for recycled glass as sand/cement replacement in the concrete mix [1, 2].

Research on the use of crushed glass as a partial replacement for aggregate dates back to many decades [3, 4]. Although work on the use of finely ground glass as a pozzolanic material also started as early as 1970s [5], most of the works in this area are

---

<sup>1</sup>Corresponding author: Department of Civil Engineering, Curtin University, GPO Box U1987, Perth, WA 6845, Australia. Email. [Salim.Barbhuiya@curtin.edu.au](mailto:Salim.Barbhuiya@curtin.edu.au)

relatively recent [6-8], and has been encouraged as a result of continual accumulation of waste glass and its consequent environmental issues. Moreover, waste glass is potentially a very useful material and appropriate economical applications need to be found for it. Concerns about the use of glass aggregate in concrete relates to its susceptibility to alkali-aggregate-reaction (AAR) in concrete, and this aspect was also recognized and studied several decades ago, as indicated by the literature cited above or even earlier. Particle size of glass and alkali content of the mortar or cement are important factors influencing the reactivity of glass as aggregate. Attempt has therefore been made in the present work to investigate experimentally the effects of white ground glass on hardened properties of concrete

## 1. Experimental programme

### 1.1. Materials

Cement used throughout the experiment was Ordinary Portland cement (OPC). The physical properties of cement determined as per Indian Standard Code Practice IS: 12269-1987 are: specific gravity= 3.10, standard consistency= 29%, initial setting time= 55 minutes, 28 day compressive strength= 50.2 MPa. Locally available alluvial sand (specific gravity= 2.6) was used. The particle size distribution is summarised in Table 1. Sand was stored inside the laboratory throughout the experimental investigation. Graded crushed stone aggregate passing 20 mm sieve was stored in the laboratory. The physical properties as determined in the laboratory are: specific gravity= 2.6, Fineness modulus= 2.3, Aggregate crushing value= 20%. The particle size distribution of coarse aggregate is presented in Table 2. The superplasticiser used was a high range water-reducing admixture (HRWRA), which was Glenium 53. Ordinary tap water was used in all the mixes, to prepare the fresh concrete.

**Table 1.** Sieve analysis of sand

Sieve size, mm	4.75	2.36	1.70	1.18	0.60	0.30	0.15
% Passing	98.2	96.5	94.6	91.2	66.3	20.3	1.6

**Table 2.** Sieve analysis of coarse aggregate

Sieve size, mm	20	12.5	10	4.75
% Passing	83.2	16.7	1.0	0

Waste Glass (WG) used in the experiment was broken pieces of clear window panes, which is a type of soda glass. The specific gravity of the material is 2.5, fineness modulus is 3.2 and water absorption is 0.2%. Following the collection process, these pieces were kept in water for 5 minutes so as to remove any dirt on them. The glass pieces were finally washed in running water and dried completely in air and were then reduced to smaller size by crusher. These fragments were then put into a small crusher to prepare waste glass aggregates of less than 4.75 mm in size. The particle size distribution of glass sand is shown in Table 3. The chemical composition of glass determined by XRF is summarised in Table 4. The following three types of WG particles were used in the present study:

- Coarse ground glass sand (GS): particles in the range 4.75 mm- 150 micron
- Glass powder passing 150  $\mu$ m and retained 75  $\mu$ m (GP 150)
- Glass powder passing 75  $\mu$ m (GP 75)

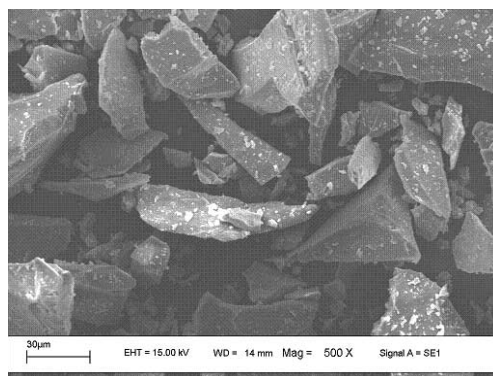
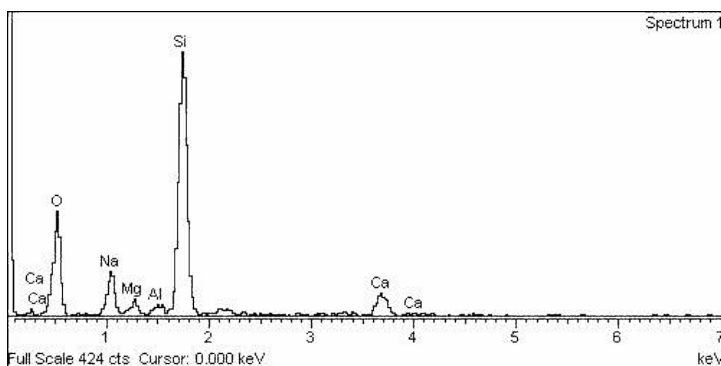
**Table 3.** Sieve analysis of glass sand

Sieve size, mm	4.75	2.36	1.18	0.60	0.30	0.15
% Passing	100	97.0	50.6	23.1	5.7	2.5

**Table 4.** Chemical composition of glass

Oxides	SiO <sub>2</sub>	Al <sub>2</sub> O <sub>3</sub>	Fe <sub>2</sub> O <sub>3</sub>	CaO	MgO	Na <sub>2</sub> O	K <sub>2</sub> O	SO <sub>3</sub>
%	72.4	1.45	0.48	11.5	0.65	13.0	0.43	0.09

Images of GP150 obtained from scanning electron microscope (SEM) at magnification 500 X and 1000 X is presented in Figure 1. It may be observed that they appear as elongated and angular particles of varying sizes. The EDXA pattern of GP is presented in Figure 2. It may be observed that GP mainly consist of silica as shown by peaks in EDXA patterns.

**Figure 1.** SEM image of ground glass at 500X**Figure 2.** EDXA pattern of glass powder

### 1.2. Mix proportions

The control mix was prepared without glass. The mix proportions of control concrete ( $\text{kg/m}^3$ ) were as follows: Cement = 450 Sand = 525 Coarse aggregate = 1125 Water including HRWRA = 202.7, HRWRA = 7.7; Water binder ratio= 0.40 and slump= 225 mm. Glass was used in the mixes in two different ways: part replacement of sand at 10%, 20%, 40%, 60% glass and part replacement of cement at 15%, 30%, and 45% glass. Cement was replaced by GS 150 and GS 75.

### 1.3. Test methods

Compressive strength of concrete was determined by crushing three 150mm cubes after 28 days of curing under water. Splitting tensile test was performed on cylinders as per IS 5816-1999 after 28 days of curing. Alkali silica reaction (ASR) test was carried out as per ASTM C1260 specification.

## 2. Results and discussion

### 2.1. Compressive and splitting tensile strength

The effects of ground glass on 28-day compressive strength and splitting tensile strength are shown in Figures 3 and 4. There is a continuous decrease in both the compressive and tensile strength of concrete up to 20% replacement level when natural sand was replaced by GS. This decrease may be due to the fact that GS has a poor shape and smooth surface compared to natural sand, and hence, there is a weak matrix-aggregate interfacial bond. GS is also more brittle compared to natural sand, which leads to cracking in concrete. The decrease in strength may also be related to possible inherent cracks in glass particles. However, beyond 20% replacement level, there is an increasing trend of compressive and tensile strength for concrete with GS. The GS used in the present study contains fines in the range 150 and 75 microns, which have pozzolanic property. The additional pozzolanic reaction compensates the otherwise reduction in compressive and tensile strength of concrete. Similar trends have also been observed by other researchers [1, 9].

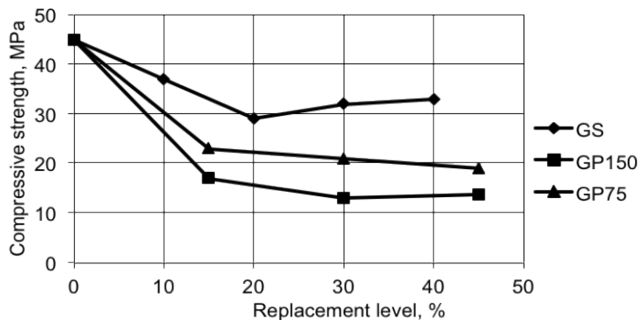
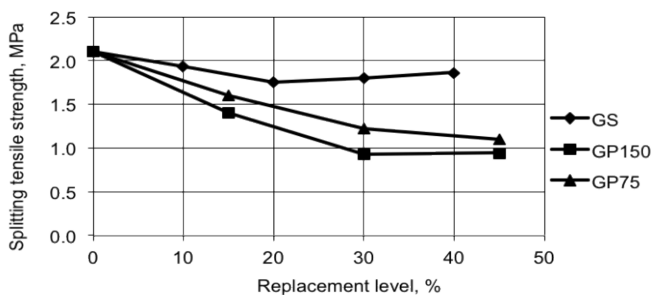
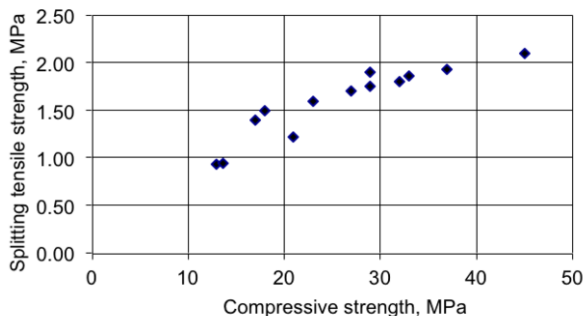


Figure 3. Variation in compressive strength with replacement level of ground glass



**Figure 4.** Variation in splitting tensile strength with replacement level of ground glass

The reduction in compressive and splitting tensile strength continues with the increase in cement replacement level up to 30%, beyond which there is a clear indication of increase in strength. Up to 30% replacement level, the decrease may be a short-term effect because in 28 days the pozzolanic effect is not evident. Beyond 30% level, further decrease might have been compensated by the pozzolanic reaction of large quantities of GP. When cement is replaced by GP75, there is also a reduction of both 28 days compressive strength and splitting tensile strength due to same reasons. However, strength at a particular replacement level is always more than the corresponding strength when cement is replaced by GP150. This implies that fineness plays an important role in pozzolanic activity of glass powder. It is known that pozzolanic reaction is slow at room temperature and a long curing period is needed to have positive benefits. Similar results have been reported by others [1, 10]. The relation between splitting tensile strength and 28 days compressive strength is shown in Figure 5. It may be observed that there is a good correlation between the two for concrete containing ground glass.



**Figure 5.** Variation of compressive strength with splitting tensile strength

## 2.2. ASR expansions

The percent expansion of mortar bars after 16 days immersion in NaOH at 80°C is presented in Figure 6. Each measure of a particular additive is an average of three samples. It may be observed that as the replacement level increases, the percent

expansion also increases in each case. Concrete mix containing GS has the highest expansion, while mix with GP75 has the least. However, there is no significant difference between the expansion of mix with GP150 and mix with GP75. Thus, the size effect of ground glass is also evident in alkali-silica reaction. This is because in case of finer glass particles, more pozzolanic reaction takes place thereby consuming the amount of alkali in the mix. Moreover, the greater the surface area of the glass particles the lower the quantity of alkali available per unit of this area, and the less alkali-silica gel can be formed [11]. Similar phenomenon was observed by others [1, 10, 12]. It may be observed from Figure 6 that the batches with GP150 and GP75 have 16 days expansion below 0.10% approximately up to 35% replacement level and therefore, the expansion was within acceptable limit according to ASTM C1260 specification.

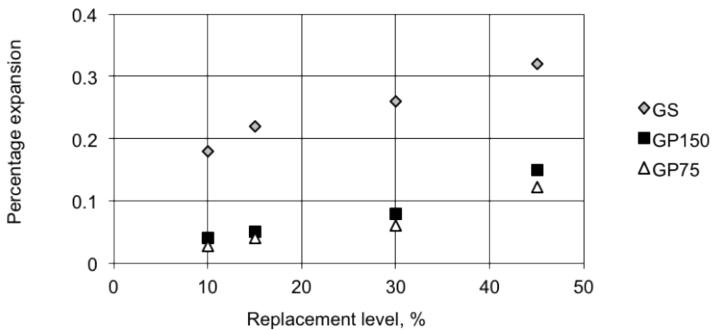


Figure 6. ASR with various replacement level of ground glass

### 2.3. Resistance to sulphate and chloride attack

Results of sulphate immersion test and chloride immersion test for concrete containing waste glass at 30% replacement level are shown in Figure 7. It may be observed that there is a gain in weight of concrete in both of the immersion cases. The magnitude of gain is higher in case of chloride immersion compared to sulphate immersion. The surfaces of the cylindrical specimens were also observed visually after five cycles (Figure 8) and it was found that the specimens had smooth surfaces without any defect. It may therefore be concluded that sulphate and chloride had no effect on concrete under investigation. Similar trend of gain in compressive strength after five cycles was also observed (Figure 9). The increase in weight and compressive strength for all the specimens was most likely due to additional curing during the test period. Similar results were obtained by Chen et al. [13] where E-glass was incorporated in concrete. However, Ozkan and Yuksel [14] observed loss in weight and compressive strength of concrete containing waste bottle glass.

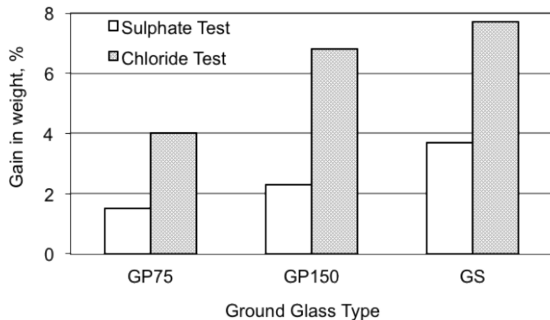


Figure 7. Effects of sulphate and chloride immersion test on weight gain after 24 hrs



Figure 8. Concrete surface after five cycle immersion in sulphate solution

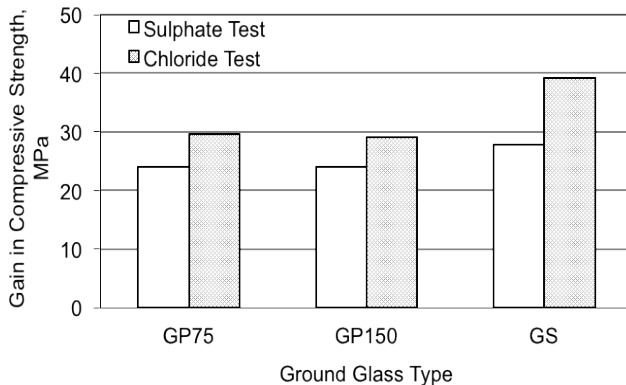


Figure 9. Effects of sulphate and chloride immersion test on compressive strength



### 3. Conclusions

The following conclusions can be drawn from the present study:

- There is a continuous decrease in both the compressive and tensile strength of concrete up to 20% replacement level when natural sand was replaced by glass sand. However, there is an increase beyond 20% replacement level.
- When cement is replaced by GP 75, and GP150 there is also a reduction of 28 days compressive strength and splitting tensile strength up to 30%.
- As the replacement level increases, the percent expansion increases in ASR. Concrete mix containing GS had the highest expansion while mix with GP75 has the least. Mix containing GS had expansion more than the specified limit in ASTM.
- There is a gain in weight and compressive strength of concrete in both sulphate and chloride emersion test.

### References

- [1] Shayan, A. and Xu, A. (2004) Value-added utilisation of waste glass in concrete. *Cem Con Res*, 34(1), pp 81–89.
- [2] Dhir, R.K., Dyer, T.D., Tang, A. and Cui, Y. (2004) Towards maximising the value and sustainable use of glass. *Conc Constr Ind*, 38(1), pp. 38–40.
- [3] Phillips, J.C., Cahn, D.S. and Keller, G.W. (1972) Refuse glass aggregate in Portland cement concrete. In *Proceedings of 3rd Mineral Waste Utilisation Symposium*, US Bureau of Mines, Chicago, IL. pp.386–390.
- [4] Johnston, C.D. (1974) Waste glass as coarse aggregate for concrete, *J of Test and Eval*, 2(5), pp 344–350.
- [5] Pattengil, M. and Shutt, T.C. (1973). Use of ground glass as a pozzolan. *Albuquerque Symp. On Utilisation of Waste Glass in Secondary Products*. Albuquerque, New Mexico, USA, pp. 137–153
- [6] Shayan, A. and Xu, A. (1999) Utilisation of glass as a pozzolanic material in concrete. *ARRB-TR Internal Report RC91132*, 11 pp.
- [7] Jin, W., Meyer, C. and Baxter, S. (2000) Glasscrete — concrete with glass aggregate, *ACI Mat Journal*, pp 208–213
- [8] Shi, C., Wu, Y., Shao, Y. and Riefler, C. (2004) Alkali-aggregate reaction of concrete containing ground glass powder. In *Proceedings of the 12th International Conference on AAR in Concrete* Beijing, pp. 789–795.
- [9] Topcu, I.B. and Canbaz, M. (2004) Properties of concrete containing waste glass. *Cem Con Res*, 34, pp. 267–274.
- [10] Shao, Y. Lefort, T., Moras, S. and Rodriguez, D. (2000) Studies on concrete containing ground waste glass. *Cem Con Res*, 30, pp 91-100.
- [11] Neville, A.M. *Properties of Concrete*, ELBS, Singapore Edition 2003, 653pp.
- [12] Topcu, I.B., Raif, A. and Bili, T. (2008) Alkali–silica reactions of mortars produced by using waste glass as fine aggregate and admixtures such as fly ash and  $\text{Li}_2\text{CO}_3$ . *Waste Management*, 28, pp 878–884.
- [13] Chen, C.H., Huang, R., Wu, J.K. and Yang, C.C. (2006) Waste E-glass Particles used in cementitious mixtures. *Cem Conc Res*, 36, pp. 449–456.
- [14] Ozkan, O. and Yuksel, I. (2008). Studies on mortar containing waste bottle glass and industrial by-products. *Const Build Mat*, 22(6), pp. 1288-1298.

# Radiological assessment of high density shielding concrete for neutron radiography

Stephen EKOLU<sup>a</sup> and Mokgobi A. RAMUSHU<sup>b,1</sup>

<sup>a</sup> Department of Civil Engineering Science, University of Johannesburg, South Africa

<sup>b</sup> Sasol Synfuels, Private Bag X1000, Secunda 2302, South Africa

**Abstract.** A radiation shield is a physical barrier placed between a source of ionizing radiation and the object to be protected from the radiation. In this research, concrete was selected as the best shielding material. An investigation was carried out to evaluate a specific concrete mixture developed in [1] for shielding of radiation energies. The high density shielding concrete (HDSC) concrete had 28-day compressive cube strength of 30 MPa, w/c (water/cementitious ratio) of 0.51 and density of 4231 kg/m<sup>3</sup>. It composed of CEM 52.5 N, silica fume, hematite aggregates, steel shots, colemanite and chemical admixtures.

This paper presents an evaluation of the shielding properties of the HDSC using foil activation method. It is shown that the HDSC mixture achieved the desired shielding capabilities within the first 250 mm thickness of the concrete block.

**Keywords.** Radiation shielding, curing, retardation, workability

## Introduction

Concrete possesses good compromise thickness requirements for neutron and photon and can be cast into almost any complex shape [1]. It was chosen as a shielding material based on existing knowledge and literature. The objective of this research was to develop and evaluate a special concrete shield that would be used to contain radiations emerging from the core of a nuclear reactor and being transported by a beam port into the neutron radiography experimental chamber. In order to achieve this objective, the program was divided into two phases.

- Phase 1: This phase consisted of identifying raw materials, mix design and its optimization, testing of mechanical properties.
- Phase 2: Involved Monte Carlo Neutron Particle (MCNP) simulations using the identified aggregates and radiological assessment of the mixture developed in phase 1, to validate radiation shielding capability of the HDSC mix.

The results of Phase 1 of this work are presented in another paper [1] while this paper presents the findings of Phase 2 of this research.

<sup>1</sup>Corresponding author: Sasol Synfuels, Private Bag X1000, Secunda 2302, South Africa, [ramushuma@gmail.com](mailto:ramushuma@gmail.com)

## 1. Background

A common industrial application of nuclear energy and related nuclear radiation issue is (but not exclusively) in power stations. Here, a radioactive material i.e uranium is used to produce electricity. However, in the process of their energy dissipation, radioactive materials are given out in form of energy referred to as radiation. It is a very powerful form of energy that is absorbed by all matter that it comes in contact with. Plants, animals, humans etc. are all affected by radiation. It attacks the cells which make up the body. Radiation energy remains active for a long time, as experienced in the nuclear explosion accident of 1986 at Chernobyl in the Soviet Union; Japan earthquake and Tsunami of March 2011. A report by the United Nations indicates that the natural exposure of a person to radioisotopes averages 2.0 millisievert (mSv) per year [4-5].

This study was geared towards shielding of radiations from nuclear reactors. In a nuclear reaction, the nucleus of heavy uranium-235 atoms absorbs a thermal neutron to initiate the fission process which splits into two nuclei called fission products. For each fission that occurs, between two or three neutrons are also emitted. These neutrons cause further fission of the enriched nuclei of uranium atom and hence release more energy, form more fission products and emit more neutrons, resulting in a chain reaction [3].

The HDSC concrete designed in this investigation was aimed at providing shielding against both, neutrons and photons emanating from a nuclear reactor. A literature survey on use of concrete for radiation shielding is given in another publication by the authors [1].

## 2. Materials and methods

Two techniques were used in the radiation shielding assessment namely, (1) the Monte Carlo Neutron Particle (MCNP-X) Simulation technique and (2) experimental radiological assessment of the designed HDSC.

### *2.1 Monte Carlo Neutron Particle simulations*

The purpose of this radiological safety assessment was to model the source of radiation and determine the efficiency of the shielding material in attenuating radiation as the radioactive particles travels through the shield. A target of 1  $\mu\text{Sv/h}$  instead of 10  $\mu\text{Sv/h}$  (regulatory requirement) was to be achieved at the other side of the shielding material.

#### *2.1.1. Inputs to the simulation model*

To perform the simulations, a mix design with defined proportions was required. In this case, a preliminary mix design needed to be produced. From the chemical analysis of concrete ingredients used, economic considerations, and availability of aggregates, it was decided that hematite, colemanite and steel shots would be the main aggregates to

be used in developing the HDSC. A mix design of 0.42 w/c (water/cementitious ratio) was used as an input into the MCNP simulation as shown in Table 1. The total (neutron and gamma) dose rate used was determined based on a model which included an equilibrium Low Enriched Uranium (LEU) core, internal geometry of the beam, layout and material composition of the experimental chamber.

**Table 1.** Mix input of the 0.42 w/c HDSC to MCNP simulations

Ingredients	OPC CEM 52.5 N	Water	Coarse hematite aggregates	Fine hematite aggregates	Fine Colemanite	Steel shots
Mass %	10.13	4.26	40.31	15.34	2.3	27.64

HDSC was modelled as per the mix composition given in Table 1, which gave the elemental composition summarized in Table 2. Although the density of about 4341 kg/m<sup>3</sup> was expected for this composition, the heavy weight concrete was modeled conservatively as 4000 kg/m<sup>3</sup>.

**Table 2.** Elemental composition of the high density concrete used in the MCNP calculations

Element	w%
Al	0.4292
Ca	5.0126
Fe	66.8533
H	0.5296
Mg	0.1222
B-10	0.0673
B-11	0.2960
O	25.6002

### 2.1.2. Outcomes of the MCNP-X simulations

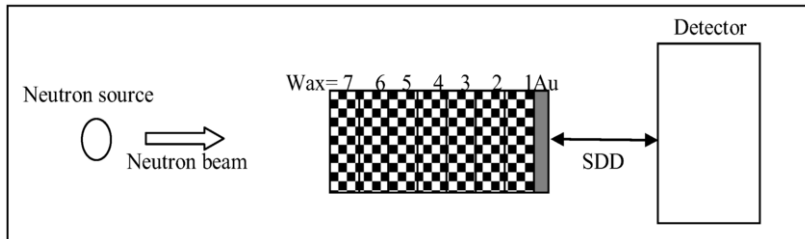
Calculations showed that the contact dose rates that were achieved, did meet the requirement of 1  $\mu$ Sv/h, with the only exception being the back wall (directly exposed to the open beam) where the contact dose rate at the hottest spot was more than 1  $\mu$ Sv/h but lower than 10  $\mu$ Sv/h. A thicker wall as well as a radiation beam stopper was included in the model in order to achieve the required dose rates.

### 2.2 Shielding experiment

The foil activation method was adopted for evaluating the attenuation properties of the shielding concrete, against radiations from the white spectrum neutron beam. Foils used in this experiment were made of gold. When a gold foil is activated by neutron beam, it emits characteristic gamma rays which can be counted and related to the neutron flux incident on the foil. By placing foils in front and between the shielding layers, the incident and transmitted neutron fluxes are obtained at each position of shielding thickness.

The simplified set-up of the experiment is given in Figure 1. The shielding material for evaluation consisted of 4230 kg/m<sup>3</sup> dense concrete blocks with surface area

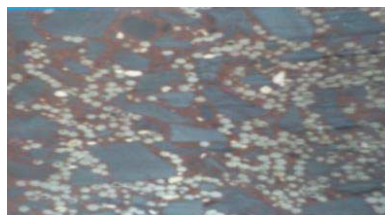
dimensions of 100 x100 mm. The thicknesses of the blocks used in the experiment are given in Table 3. The 20 mm thick slices were obtained by cutting the 100 x 100 x100 mm cubes using water jet cutting technology. This method was the only technique available that could cut through the hard (iron) aggregates of the concrete into slices, as shown in Figure 2.



**Figure 1.** Top view of the experimental setup (SDD - silicon drift detectors)

**Table 3.** Thickness of shielding material blocks used for measurements of transmitted neutron beam

Thickness (mm)	Quantity
20	5
100	7



**Figure 2.** 20 mm thick concrete slice showing steel shot aggregates

The beam size was limited from 300 mm to 50 mm diameter circular area using wax and cadmium. The wax cylinder was prepared carefully to fit into the protrusion of the external shutter. This way the biological shield would protect the scattered neutrons from the wax. The sequence of beam limiting material consisted of 200 mm thick wax and a cadmium sheet of 1 mm thickness. The beam limiter ensured that there was negligible neutron background, arising from the scattering neutron beam multiples.

Foils were cut into 0.5 cm radius discs of  $50 \times 10^{-4}$  cm thickness. After all layers of the shielding material were placed in the beam axis, ensuring that they are aligned to each other, foils were then placed between the shielding material as shown in Figures 3 and 4, positions F to B6. The 20 mm thick slices were employed in the set up except for the last position B6 where a 600 mm thick shielding concrete was used. Each foil was assigned a unique number and two foils were placed at each position on the left (L) and right (R) side. A thin foam was used to hold the foils in position and in line with

the beam axis. Figure 4 is a photograph of the actual shielding experiment that was conducted.

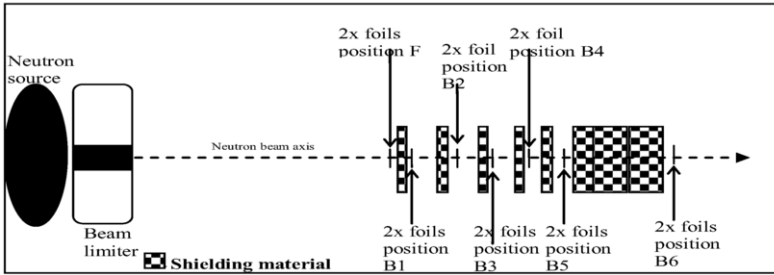


Figure 3. Side view of experimental set up



Figure 4. Experimental set up with foil

### 3. Experimental results

Measurements for flux calculation were conducted at thicknesses 0, 20, 40, 60, 80, 100 and 800 mm of the shielding material. The results for flux and dose rates are shown in Table 4. The linear attenuation coefficient was calculated to be  $0.62 \text{ cm}^{-1}$ , based on which the transmitted intensities after 200, 300, 400, 600 and 700 mm were calculated. The results in Figure 5 present a threshold line which is the dose rate threshold below which there is adequate estimated shielding for personnel safety from neutrons, as the dose rate is less than  $10 \text{ } \mu\text{Sv/h}$  ( $20 \text{ mSv/y}$ ).

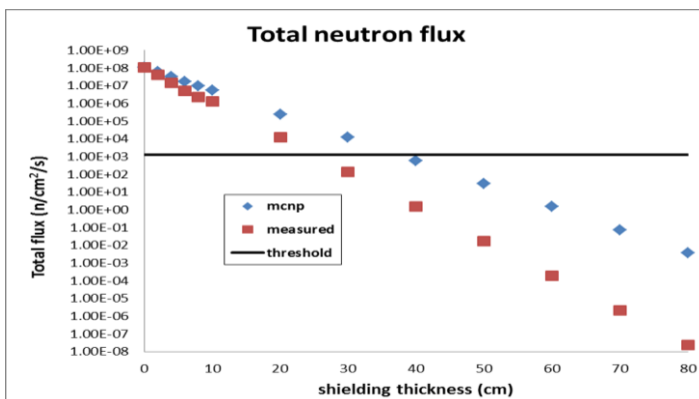


Figure 5. An extrapolated data of MCNP simulation and measured total flux at different thicknesses

**Table 4.** Experimental results showing dose rate attenuation

Foil position		Flux (n/cm <sup>2</sup> /s)			Dose rate (mSv/hr)	
Face	Shielding thickness (mm)	Value	% difference	Average	Value	Average
F-L	0	1.10E+08	2.2	1.11E+08	4.02E+03	4.07E+03
F-R	0	1.12E+08			4.11E+03	
B1-L	20	3.98E+07	11.6	4.22E+07	1.77E+03	1.88E+03
B1-R	20	4.47E+07			1.99E+03	
B2-L	40	1.34E+07	12.5	1.43E+07	5.97E+02	6.37E+02
B2-R	40	1.52E+07			6.77E+02	
B3-L	60	4.72E+06	14.2	5.09E+06	2.10E+02	2.26E+02
B3-R	60	5.45E+06			2.42E+02	
B4-L	80	2.11E+06	19.6	2.34E+06	9.39E+01	1.04E+02
B4-R	80	2.57E+06			1.14E+02	
B5-L	100	1.22E+06	7.5	1.27E+06	5.23E+01	5.43E+01
B5-R	100	1.31E+06			5.63E+01	
Calculated <sup>2</sup>	200	8.64E+03	-	8.64E+03	3.70E-01	3.70E-01
Calculated <sup>2</sup>	300	9.60E+01	-	9.60E+01	4.11E-03	4.11E-03
Calculated <sup>2</sup>	350	1.01E+01	-	1.01E+01	4.33E-04	4.33E-04
Calculated <sup>2</sup>	400	1.07E+00	-	1.07E+00	4.57E-05	4.57E-05
Calculated <sup>2</sup>	500	1.18E-02	-	1.18E-02	5.08E-07	5.08E-07
Calculated <sup>2</sup>	600	1.32E-04	-	1.32E-04	5.64E-09	5.64E-09
Calculated <sup>2</sup>	700	1.46E-06	-	1.46E-06	6.26E-11	6.26E-11
L	800	2.32E-08	No signal	2.32E-08	8.52E-13	0.00E+00

#### 4. Conclusions

The high density concrete mix that was developed [1] met all the requirements specified for shielding purposes. The aggregates used in the mix contained no long half-life decaying elements. The required minimum density of 4000 kg/m<sup>3</sup> as simulated in the MCNP was maintained

The performance of the concrete in shielding was more efficient than expected as the target levels of 1 µSv/h, which were more stringent than the regulatory limits of 10 µSv/h, were achieved at about 250 mm of the 600 mm thick wall of concrete.

## Acknowledgements

The authors acknowledge the National Research Foundation of South Africa for funding of the project, and are also grateful to NECSA (Nuclear Energy Corporation of South Africa) for supporting of the MSc study program of the second author.

## References

- [1] Ekolu S.O and Ramushu M.A, Material selection and mix design of radiation shielding concrete, *Proc. Intl Conf. on Construction Materials and Structures (ICCMATS)*, 24-26 November 2014, Johannesburg, South Africa.
- [2] Callan E.J., *Concrete radiation shielding*, Second edition. United States of America: American concrete Institute, 1962.
- [3] Kaplan M.F., *Concrete radiation shielding: nuclear physics, concrete properties, design and construction*, Longman group, United Kingdom, 1989.
- [4] United Nations Scientific Committee on the Effects of Atomic Radiation. Sources and Effects of Ionizing Radiation. UNSCEAR 2008. 219p, [http://www.unscear.org/docs/reports/2008/11-80076\\_Report\\_2008\\_Annex\\_D.pdf](http://www.unscear.org/docs/reports/2008/11-80076_Report_2008_Annex_D.pdf)
- [5] Sources and Effects of Ionizing Radiation. Volume I: Sources; volume II: Effects. United Nation Scientific committee on the Effects of Atomic Radiation. 2000 Report to the General Assembly, with scientific annexes. United Nations sales publication E.00.7X.3 and E.00.IX. United Nations, New York, 2000, 19p. [http://www.unscear.org/docs/GAreports/A-68-46\\_e\\_V1385727.pdf](http://www.unscear.org/docs/GAreports/A-68-46_e_V1385727.pdf)



# Permeable reactive barriers for acid mine drainage treatment: a review

Ayanda N. SHABALALA<sup>a,1</sup>, Stephen O. EKOLU<sup>b</sup> and Souleymane DIOP<sup>a</sup>

<sup>a</sup>*Council for Geoscience, Head Office, Engineering Geoscience Unit*

<sup>b</sup>*Department of Civil Engineering Science, University of Johannesburg, South Africa*

**Abstract.** Contaminated water flowing from abandoned mines is one of the most significant contributors to water pollution. Acid mine drainage (AMD) can have severe impacts on aquatic resources, can stunt terrestrial plant growth and harm wetlands, contaminate groundwater, raise water treatment costs, and damage concrete and metal structures. Permeable reactive barriers (PRBs) are one of the passive treatment technologies widely accepted for sustainable in situ remediation of contaminated groundwater and may be used in the management of localised seepage plumes from mine residues that contaminate shallow groundwater. These barriers provide chemical interactions with AMD as the polluted water flows through it. The ability of PRBs to remediate contaminants is dependent on the type of reactive material used. Some of the reactive media remove contaminants through physical contact while others work by altering the biogeochemical processes in the treatment zone, thus providing conditions conducive for contaminant immobilization or (bio) degradation. A variety of materials has been employed to remove contaminants including heavy metals, chlorinated solvents, aromatic hydrocarbons, and pesticides. This paper gives an overview of the PRB technology, which includes the advantages and limitations of the PRB, the types of reactive materials used, laboratory treatability tests used to evaluate suitable reactive materials and to aid in the designing and the implementation of the PRB and the installations schemes used in PRB field application.

**Keywords.** Passive treatment, acid mine drainage, permeable reactive barrier

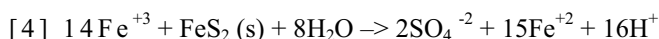
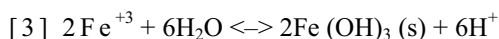
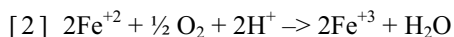
## Introduction

The formation of acid mine drainage (AMD) and the contaminants associated with it have been described as the largest environmental problem facing the mining industry. Commonly referred to as acid rock drainage (ARD) or AMD, acid drainage from mine waste rock, tailings, and mine structures such as pits and underground workings is primarily a function of the mineralogy of the rock material and the availability of water and oxygen [29]. It is a naturally occurring process of weathering and erosion of sulphur and iron (Fe) bearing material, as well as other metallic sulphidic materials. It occurs when groundwater comes into contact with remnant coal and rock that is rich in sulphide. These sulphide minerals oxidise in the presence of water and oxygen, the by-product being a usually but always acidic, typically sulphate ( $\text{SO}_4^{2-}$ ) rich drainage [8]. The resulting drainage usually has a low pH and high metal concentration.

---

<sup>1</sup>Corresponding author: Council of Geosciences, Water Geoscience Business Unit, 280 Pretoria Street, Silverton, Pretoria; Email: [ashabalala@geoscience.org.za](mailto:ashabalala@geoscience.org.za)

Contaminated water flowing from abandoned mines is one of the most significant contributors to water pollution. Acid mine drainage (AMD) can have severe impacts on aquatic resources, can stunt terrestrial plant growth and harm wetlands, contaminate groundwater, raise water treatment costs, and damage concrete and metal structures [8]. There are 4 commonly-accepted chemical reactions that represent the chemistry of pyrite weathering to form AMD [9]:



## 1. Brief review of related studies

### 1.1 Treatments technologies

Remediation of acid drainage is difficult and expensive. Treatment falls under two broad categories: active and passive. Active treatment involves physically adding a neutralising agent to the source of the AMD, or directly to the stream that has been impacted. Active treatment can be very successful; however, it necessitates a long-term and continuous commitment to treatment. Weather, equipment failure, and budget reductions can result in lapses in treatment [8].

Passive treatment encompasses a variety of techniques that are employed to raise the pH of AMD and consequently reduce metal loadings through a constructed treatment or containment project. While initial costs for passive treatment techniques can be higher than the costs of setting up active treatment, the former do not require continuous chemical inputs and they provide a controlled environment in which naturally occurring chemical and biological processes play a major role in the treatment of AMD [21, 27]. A widely accepted definition of Passive treatment is that it is a deliberate improvement of water quality using only naturally available energy sources (e.g., gravity, microbial metabolic energy, photosynthesis), in systems which require only infrequent maintenance in order to operate effectively over the entire system design life [34]. There are several types of passive treatment systems; they may be used on their own or in combinations, in order to treat difficult effluents. Generally, the selection of an appropriate passive system is based on water chemistry, flow rate, local topography and site characteristics. The primary passive technologies include constructed wetlands, anoxic limestone drains (ALD), successive alkalinity producing systems (SAPS), Limestone ponds and open limestone channels (OLC) [27].

### 1.2 Permeable reactive barriers

Permeable reactive barriers (PRB) usually consist of physical porous media that interact with specific chemicals of concern in the AMD. The PRB is placed in the path of polluted water flow, allowing the water to flow through it easily while the treatment process takes place through chemical or biochemical processes. These methods may

well be used in the management of localised seepage plumes from mine residues that contaminate shallow groundwater.

For PRBs designed to treat acid mine drainage (AMD) with sulphate contamination, the barrier is generally composed of solid organic matter, like municipal compost, leaf compost, and wood chips/sawdust [2]. Construction of PRBs involves the digging of a trench or pit in the flow path of contaminated groundwater, filling the void with reactive materials (a mixture of organic solids and possibly limestone gravel) that are sufficiently permeable to allow unhindered flow of the groundwater [19], as illustrated in Figure 1.

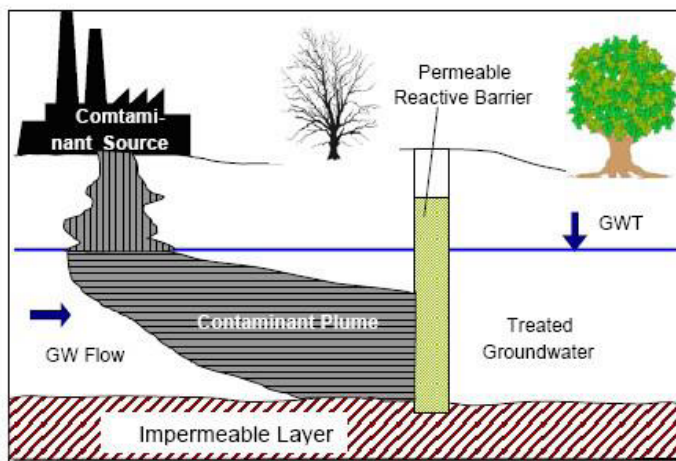
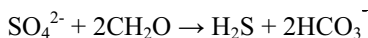
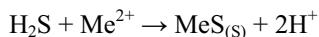


Figure 1. Diagrammatic representation of a PRB [11]

Iron, limestone, and carbon are common types of reactive materials that can be used. The reactive materials promote microbially mediated sulphate reduction, the generation of hydrogen sulphide, and the subsequent precipitation of sparingly soluble iron and other metals, such as Cd, Ni, Co, Cu, Zn, As sulphide minerals [31]. Sulphate-reducing bacteria (SRB) convert  $\text{SO}_4^{2-}$  to sulphide by catalysing the oxidation of organic carbon with the reduction of  $\text{SO}_4^{2-}$ :



The reaction between the  $\text{SO}_4^{2-}$  and the organic substrate consumes  $\text{SO}_4^{2-}$ , results in the production of  $\text{H}_2\text{S}$  and increases bicarbonate alkalinity and the pH. The sulphide produced reacts with dissolved metals ( $\text{Me}^{2+}$ ) and enhances the precipitation of metals as metal sulphides [20]:



The oldest full scale PRB technology was first used to remediate groundwater contaminated with chlorinated solvents. More recent work began in the 1970s and continued through the 1980s, culminating in a pilot-scale PRB installed in 1991 at Borden, Ontario site and a full-scale PRB installed in 1995 at the Intersil Site in Sunnyvale, CA. To date, PRBs have been used to treat a range of contaminants in

groundwater such as organohalogen compounds (e.g. tetrachloroethane (PCE), trichloroethene (TCE), dichloroethene (DCE), metals (e.g. chromium and arsenic), nitrate, and radionuclides such as uranium [4, 16]. The advantages and limitations of the PRB technology are summarized in Table 1 [4, 6, 13, 22, 23, 29, 32].

**Table 1.** The advantages and limitations of the PRB technology [4, 6, 13, 22, 23, 29, 32]

Advantages	Limitations
(a) Results in reduced costs due to the semi-permanent installation, low energy input, focused cleanup on only the area of contamination, conservation of clean water, and continued productive use of the site almost immediately after installation	(a) It can be expected that the long-term performance would be inhibited by clogging and armouring by aluminium and manganese precipitates. Armouring with aluminium hydroxide or manganese oxides would decrease the reactive surface area and may cause clogging of the pore spaces, restricting the flow of groundwater through the PRB
(b) They have the potential to mitigate the spread of contaminants that have proven difficult and expensive to manage with other cleanup methods	(b) Design flaws such as improper hydraulic and/or geological characterization of a site prior to PRB installation can result in limited capture of the plume, diversion and partial or total by-pass of the groundwater around the PRB and, overall, loss of hydraulic control
(c) Allows for treatment of multiple contamination plumes since more than one barrier can be used	(c) Limited field data concerning longevity of barriers
(d) Requires occasional monitoring to ensure that barriers are functioning properly	(d) Reactive media may have to be removed or be replaced during operation
(e) They typically rely on passive processes, and are considered an environmentally sustainable treatment technique	(e) Long time-frames (decades) may be required to manage risks associated with a long-lived or persistent contaminant source
(f) Minimise volume of soils and groundwater that need to be physically handled	(f) Deeper plumes can present problems for construction and monitoring
(g) They have potential operational lives of decades	

## 2. Materials and methods

### 2.1 Reactive media for heavy metal removal

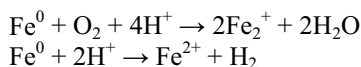
The ability of PRBs to remediate contaminants is dependent on the type of reactive material used. Some of the reactive media remove contaminants through physical contact while others work by altering the biogeochemical processes in the treatment zone, thus providing conditions conducive for contaminant immobilization or (bio) degradation. The choice of the reactive material is generally influenced by: (i) the type of contaminants to be treated (i.e., organic and/or inorganic), their concentrations, and the mechanisms needed for their removal (e.g. biodegradation, sorption or precipitation); (ii) the Hydrogeological and biogeochemical conditions of the aquifer; (iii) the environmental/ health impacts; (iv) mechanical stability (capacity of the material to preserve its hydraulic conductivity and reactivity over time), and (v) the availability

and cost of the material [22]. A suitable material must have the following characteristics [5, 12, 14, 24, 31]:

- Increase the pH of the groundwater to a level that causes metals such as Fe and Al to precipitate out of solution
- Provide reactive sites for the precipitation to take place
- Have a permeability and effective porosity that allows groundwater to pass freely through the barrier
- Longevity: with time, reactive materials may be consumed by reactions taking place and the reactive sites may become armoured by the precipitates that form
- Environmental compatibility: must not release toxins into the environment
- Must be abundant and low cost

### 2.1.1 Zero-valent iron

Zero-valent iron is currently the most common reactive material used in a PRB. It has been broadly used as a reactive material in PRBs for groundwater remediation and demonstrates very good removal efficiency for several inorganic (e.g. Cr, Cu, Ni, As, Zn) and organic contaminants. It consumes oxygen, establishing thus anaerobic conditions which favour growth of sulphate reducing bacteria. [3, 10, 33].



The first granular iron-filled wall was constructed inside a sheeted excavation by the University of Waterloo in 1991. This installation was monitored for a period of 5 years, and performed successfully and consistently. Granular iron has been effective in degrading a wide range of halogenated organic contaminants, such as trichloroethene, in groundwater and has now been implemented at over 20 sites [6].

Other types of media have been implemented in PRB. However, studies [16] have shown that particular media are more effective in removal of certain contaminants and not effective in others. For example, it has been shown that the effective media for removal of heavy metals are ZVI, apatite, bioreactors, and slag whereas only bioreactors are known to be capable of sulphate removal.

### 2.1.2 Pervious concrete

Pervious concretes are commonly used in parking lots, sidewalks and pathways, low traffic areas to reduce the peak flows along stream and drainage channels and reduces the risk of floods. They minimize stormwater-related flooding by allowing the infiltration of surface runoff through the pavement. Furthermore, these pavements are effective in reducing the pollutant loads in stormwater runoff. Runoff waters that pass through porous pavements contain lower pollutant loads than those from a reference catchment. This is said to be due to the accumulation of metallic micro-pollutants from runoff waters on the surface of the pervious pavement [28].

Absorption, straining and decomposition of microbiological organisms in soils have been suggested as the main removal mechanisms by pervious concrete pavements. Properly designed pervious concrete can be effective in treating polluted or acidic water, not only by raising its pH value but also by efficiently removing most of the

undesirable contaminants including sulfate, iron, zinc, sodium, magnesium, manganese and most other metals. Furthermore, the use of pervious concretes in pavements can lead to a reduction in oil and grease, and petroleum products (polycyclic aromatic hydrocarbons (PAHs)) from the water effluent drained through pervious concrete. For these reasons, pervious or permeable concrete is becoming more extensively promoted in light of its environmental sustainability impacts [7].

## *2.2 Batch and column tests*

In order to evaluate the suitability of the reactive materials, laboratory tests concerning the rate and mechanism (including the formation of by-products) of pollutant removal are performed. These laboratory treatability tests coupled with site characterization information are the basis for the design and the implementation of the PRB. These tests assess the effectiveness and rate of pollutants removal of potential barrier materials, evaluate the reaction products that are formed in the remediation process and their eventually toxicity and estimate the working life time of the reactor. The treatability tests can be performed under no flow conditions (batch tests) or under gravitational or imposed flow conditions (column tests). Batch studies evaluate the rate in the remediation of pollutants and the longevity of different materials under controlled conditions. It is the test more appropriated for the selection of the reactive materials for the barrier. Different samples consisting of a mixture of the reactive material to test and an aqueous solution containing dissolved contaminants are prepared. The mixtures react for a given period of time and the concentrations of the contaminants at the beginning and at the end of the contact time are measured [1].

In Column studies: the conditions of this test, like flow velocity, should be similar to those in the field site. Based on these studies, one can obtain the residence time of the contaminant in the reactive zone that can be used, with the flow rate, to determine the thickness of the media [26]. The test consists of the percolation of the solution of the contaminant through a cylindrical column filled with the reagent material. Concentration variation and physical–chemical parameters are typically monitored in the effluent and in different points along the height of the column. Hence, the profile of concentration of the contaminant and of its by-products along the column is obtained. Furthermore, distinct degradation rates can be determined for every value of flow rate. Samples of solutions from all recipients are collected and submitted to chemical analyses to determine concentration changes and to obtain physico–chemical parameters such as the pH, redox potential and electric conductivity [15]. A schematic diagram of a fixed-wall column is shown in Figure 2. Although batch tests are quick to perform, column experiments provide dynamic flow conditions which closely approximate those expected in a PRB system in field deployments and can be useful for the estimation of long term performance [1, 22].

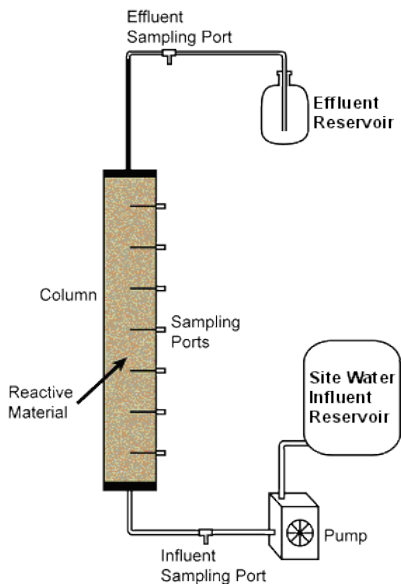


Figure 2. Schematic diagram of fixed-wall column [16]

Using results from the column tests, the residence time required to attain prescribed treatment follows a first-order decay equation [16, 21]

$$C_t = C_o e^{-kt}$$

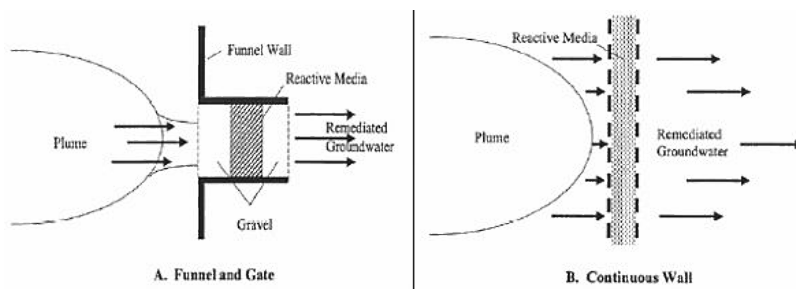
Where,  $C_o$  =the concentration of the contaminant entering the PRB,  $C_t$  = target concentration down-gradient of the PRB and  $k$  is the rate of reaction. If the decay rate (which depends on chemistry of the polluted water and media type), is known, only two sets of data are needed to estimate the residence time by re-arranging the decay equation into:

$$t = - \ln (C_t/C_o)/k$$

### 2.3 Installations schemes used in PRB field application

Two installation schemes are more frequently used in field applications of a PRB; Continuous and Funnel-and-Gate systems. The continuous PRB configuration consists of a single reactive zone installed across the contaminant plume, while the funnel-and-gate system consist of a permeable gate (reactive zone) placed between two impermeable walls that direct the contaminated plume towards the reactive zone. The choice between the two configurations is influenced by both the hydrogeological characteristics of the site and the reactive material cost. When a high cost reactive material is used, funnel-and gate configuration is preferred since the reactive zone requires less material. However, construction cost of continuous type barrier is much cheaper than funneland- gate system. Multi-sequenced reactive barriers are also being installed, especially on sites with multiple groundwater contaminants such as gas works sites. Multi-sequenced PRBs use multiple reactive materials in more than one reactive

zone to treat the contaminated groundwater [25, 30]. Diagrams of PRBs are shown in Figure 3.



**Figure 3.** Typical configurations of a permeable reactive barrier [18]

#### 2.4 Barrier design

Steps in the design of a permeable reactive barrier are shown in Figure 4. The main issues that need to be considered in the design of a permeable reactive barrier will be [4, 10, 17]:

- The selection of the treatment process and specification of reactive material including chemical composition, surface area, grain size, and density of placement
- The influence of the PRB on the groundwater flow and geochemical regime;
- The PRB's ability to retain its hydraulic properties (i.e. permeability) and treatment capacity in the long-term
- The location of the PRB in relation to contaminated groundwater and site constraints;
- The type and configuration of barrier
- The residence time to ensure that the contaminants of concern are treated to a level that protects identified receptors
- The treatment process does not result in any detrimental impacts to the environment, and in particular to groundwater quality or flow
- The seasonal and long-term variation in groundwater flow and contaminant flux can be accommodated by the PRB design;
- The treatment process can be monitored;
- The possible requirement to replace or rehabilitate the reactive media, as well as to decommission the PRB
- Whether a combination of remedial options may be required to meet the remedial objectives, i.e. the PRB forms part of an integrated treatment approach;
- Potential environmental impacts associated with implementing a PRB.



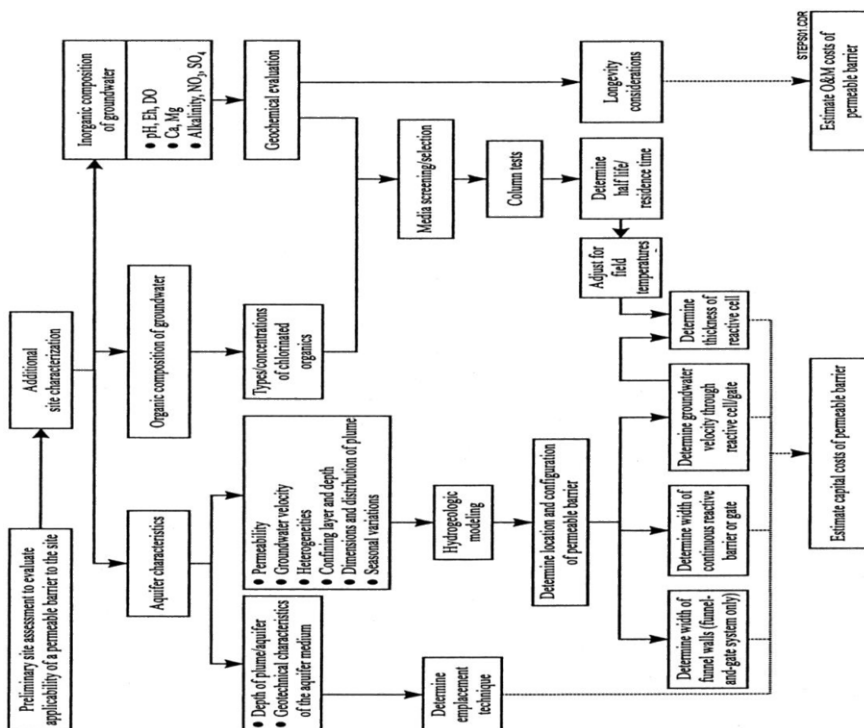


Figure 4. Steps in the design of a permeable reactive barrier [10]

### 3. Case studies

The PRB technology was first used to remediate groundwater contaminated with chlorinated solvents such as trichloroethylene (TCE), the three isomers of DCE (1,2-cis-, 1,2-trans- and 1,1-DCE) and vinyl chloride (VC) in the early stages. After proving to be effective in the treatment of these contaminants, its application was extended to include other contaminants such as halogenated aliphatic hydrocarbons, metals, metalloids, radionuclides, pesticides, petroleum hydrocarbons, and nutrients emanating from agricultural systems [22]. There are currently over 200 PRBs installed worldwide for different scenarios of contamination, but most of them rely on zero-valent iron (ZVI) and only a few on other materials such as modified zeolites, limestone, organic substrates and activated carbon [13]. Examples are pilot-scale PRBs used to treat contaminated groundwater and leachate from uranium mines in Hungary and Bulgaria, respectively. The PRB in Hungary which was installed 2002, is a continuous trench containing shredded  $\text{Fe}^0$  which removes uranium from the groundwater. The PRB in Western Bulgaria which was installed in 2004 is a ditch/continuous trench which treats acid drainage (pH 2.5–3.7) runoff from a uranium mine contaminated with radionuclides (mainly uranium and radium), heavy metals, arsenic and sulphates. Another example of a PRB is a funnel-and-gate PRB in Monkstown Northern Ireland, United Kingdom. This field-scale PRB, established in 1995, was developed to remediate a small but highly concentrated accumulation of a degreaser pollutant, trichloroethene (TCE), in glacial till on an industrial site [25].

#### 4. Conclusions

PRBs have been successfully used for the treatment of a variety of contaminants, including the treatment of AMD and the remediation of streams polluted by heavy metals. PRBs are practical, have low maintenance costs, require low energy input and are a more sustainable alternative to traditional pump and treat methods. Although Zero-valent iron is currently the most common reactive material used in a PRB, the spectrum of contaminants that can be treated has been broadened, owing to other types of media that have been implemented in PRB such as zeolites, limestone, organic substrates and activated carbon.

The selection of the reactive material is crucial; it must be chemically effective to eliminate the target contaminant(s) and must maintain an adequate permeability to ensure flow through the PRB. In order to evaluate the suitability of the reactive materials, treatability laboratory tests (batch and column) should be performed. These tests assess the effectiveness and rate of pollutants removal of potential barrier materials, evaluate the reaction products that are formed in the remediation process and their eventually toxicity and estimate the working life time of the reactor. Continuous and Funnel-and-Gate systems are two installation schemes frequently used in field applications of a PRB. Even though considerable laboratory-based research has been done on PRB technology, more research is still required to determine the long term-performance of PRBs, which have somewhat affected their acceptability and full-scale implementation.

#### References

- [1] Ambrosini, G. 2004. Reactive Materials for Subsurface Remediation through Permeable Reactive Barriers. Diss. ETHNo.15784 (2004).
- [2] Blowes, D. W., Ptacek, C. J., Benner, S. G., McRae, C.W.T., Bennett, T. A. and Puls, R. W. 2000. Treatment of inorganic contaminants using permeable reactive barriers. *Journal of Contaminant Hydrology*, 45, 123-137.
- [3] Bazdanis, G., Komnitsas, K., Sahinkaya, E. and Zaharaki, D. 2011. Removal of heavy metals from leachates using permeable reactive barriers filled with reactive organic/inorganic mixtures. Third International Conference on Environmental Management, Engineering, Planning and Economics, Skiathos island, Greece (June 19-24, 2011).
- [4] Carey, M.A., Fretwell, B.A., Mosley, N.G. and Smith, J.W.N. 2002. Guidance on the use of permeable reactive barriers for remediating contaminated groundwater. *National Groundwater & Contaminated Land Centre report NC/01/51*.
- [5] Cocos, L.A., Zagury, G.J., Clément, B., Samson, R. 2002. Multiple factor design for reactive mixture selection for use in reactive walls in mine drainage treatment. *Water Research* 32, 167-177.
- [6] Day, S.R., O'Hannesin, S.F. and Marsden, L.1999. Geotechnical techniques for the construction of reactive barriers. *Journal of Hazardous Materials* B67, 285-297.
- [7] Ekolu, S.O., Azene, F.Z. and Diop, S. 2013. A concrete reactive barrier for acid mine drainage treatment. *Institution of Civil Engineers publishing*. Paper 1300035.
- [8] Fripp, J., Sienkiewicz, P.F., Charkavorki, H. 2000. Acid mine drainage treatment. EMRRP Technical Notes Collection (ERDC TN-EMRRPSR-14), U.S. Army Engineer Research and Development Center, Vicksburg, MS.
- [9] Ford, K.L. (2003). Passive treatment systems for acid mine drainage. Technical Note 409. BLM/ST/ST 02/001+3596. Bureau of Land Management Web based report available online at <http://www.blm.gov/nstc/library/techno2.htm>
- [10] Gavaskar, A.R. 1999. Design and construction techniques for permeable reactive barriers. *Journal of Hazardous Materials* 68, 41-71.
- [11] Geranio, L. 2007. Review of Zero Valent Iron and Apatite as reactive materials for Permeable Reactive Barrier. Term Paper SS 07/08, major in Biogeochemistry and Pollutant Dynamics Department of Environmental Sciences, ETH Zurich.

- [12] Gibert, O., de Pablo, J., Cortina, J.L., Ayora, C. 2004. Chemical characteristics of natural organic substrates for biological mitigation of acid mine drainage. *Water Research* 38 (2004) 4186–4196.
- [13] Gibert, O., Rötting, T., Cortina, J.L., de Pablo, J., Ayora, C. and Carrera, J. 2011. In-situ remediation of acid mine drainage using a permeable reactive barrier in Aznalcóllar (Sw Spain). *Journal of Hazardous Materials* 191, 287–295.
- [14] Golab, A.N., Peterson, M.A. 2006. Selection of potential reactive materials for a permeable reactive barrier for remediating acidic groundwater in acid sulphate soil terrains. *Journal of Engineering geology and hydrogeology*, 39, 2006, 209–223.
- [15] Gusmão, A.D., Tácio Mauro Pereira de Campos, Manoel de Melo Maia Nobre and Eurípedes do Amaral Vargas Jr. 2004. Laboratory tests for reactive barrier design. *Journal of Hazardous Materials* 110, 105–112.
- [16] Henderson, A.D. and Demond, A.H. 2007. Long-Term Performance of Zero-Valent Iron Permeable Reactive Barriers: A Critical Review. *Environmental Engineering Science*, 24, 401–423.
- [17] ITRC Technology update team. 2011. Permeable Reactive Barrier: Technology Update. Technical/Regulatory Guidance. Retrieved from <http://www.itrcweb.org/GuidanceDocuments/PRB-51.pdf>
- [18] ITRC Mining Waste Team. (2005). Permeable Reactive Barrier Systems. ITRC. Retrieved from [http://www.itrcweb.org/miningwaste-guidance/to\\_permeable.htm](http://www.itrcweb.org/miningwaste-guidance/to_permeable.htm)
- [19] Johnson, D.B. and Hallberg, K.B. 2005. Acid mine drainage remediation options: a review. *Science of the Total Environment* 338, 3 – 14.
- [20] Ludwig, R.D., McGregor, R.G., Blowes, D.W., Benner, S.G., Mountjoy, K. 2002. A permeable reactive barrier for treatment of heavy metals. *Ground water*, vol. 40, No.1:59–66.
- [21] MEND. 1996. Review of passive systems for treatment of acid mine drainage Phase II. Prepared by Kilborn Inc. for Mine Environmental Neutral Drainage (MEND) programme.
- [22] Obiri-Nyarko, F., Grajales-Mesa, S.J. and Malina, G. 2014. An overview of permeable reactive barriers for in situ sustainable groundwater remediation. *Chemosphere* 111, 243–259.
- [23] Park, J., Lee, S., Lee, J. and Lee, C. 2002. Lab scale experiments for permeable reactive barriers against contaminated groundwater with ammonium and heavy metals using clinoptilolite (01-29B). *Journal of Hazardous Materials* B95, 65–79.
- [24] Pagnanelli, F., Viggi, C.C., Mainelli, S., Toro, L. 2009. Assessment of solid reactive mixtures for the development of biological permeable reactive barriers. *Journal of hazardous materials* 170, 998–1005.
- [25] Phillips, D.H. 2009. Permeable reactive barriers: A sustainable technology for cleaning contaminated groundwater in developing countries. *Desalination* 248, 352–359.
- [26] Powell, R.M., Puls, R.W., Blowes, D.W., Vogan, J.L., Gillham, R.W., Powell, P.D., Schultz, D., Sivavec, T. and Landis, R. 1998. Permeable reactive barrier technologies for contaminant remediation- *Environmental Protection Agency*, Office of research and development, Washington DC 20460, Office of Solid Waste and Emergency Response, Washington DC 20460, EPA/600/R-98/125.
- [27] Skousen, J. 1990. Overview of passive systems for treating acid mine drainage. West Virginia University. Retrieved 10/08/2010 from <http://www.wvu.edu/~agexten/landrec/passtr/passtr.htm>
- [28] Solpuker, U., Sheets, J., Kim, Y. and Schwartz, F.W. 2014. Leaching potential of pervious concrete and immobilization of Cu, Pb and Zn using pervious concrete. *Journal of Contaminant Hydrology* 161, 35–48.
- [29] USEPA (United States Environmental Protection Agency). 1998. Permeable reactive barrier technologies for contaminant remediation. USEPA, Washington, DC. 1 pp.
- [30] Thiruvenkatachari, R., Vigneswaran, S. and Naidu, R. 2008. Permeable reactive barrier for groundwater remediation. *Journal of Industrial and Engineering Chemistry* 14, 145–156.
- [31] Waybrant, K.R., Blowes, D.W., Ptacek, C.J. 1998. Selection of reactive mixtures for use in permeable reactive walls for treatment of mine drainage. *Environmental science and technology* 32, 1972–1979.
- [32] Wanner, C., Zink, S., Eggenberger, U. and Mäder, U. 2013. Unraveling the partial failure of a permeable reactive barrier using a multi-tracer experiment and Cr isotope measurements. *Applied Geochemistry* 37, 125–133.
- [33] Wilkin, R.T. and McNeil, M.S. 2003. Laboratory evaluation of zero-valent iron to treat water impacted by acid mine drainage. *Chemosphere* 53, 715–725.
- [34] Younger, P.L., Banwart, S.A. and Hedin, R.S. 2002. *Mine water*. Kluwer Academic Publishers London, 442 pp

# Bottom ash and fly ash wastes as alkalinising reagents for neutralising acid mine drainage

Stephen O. EKOLU<sup>a,1</sup>, Souleymane DIOP<sup>b</sup> and Firehiwot AZENE<sup>b</sup>

<sup>a</sup>*Department of Civil Engineering Science, University of Johannesburg, South Africa*

<sup>b</sup>*Council for Geoscience, Head Office, Engineering Geoscience Unit*

**Abstract.** Preliminary investigation was conducted to evaluate the utilization of bottom ash and fly ash by-products on a study limited to their role as alkalinising reagents, with the ultimate objective of examining their potential use for insitu treatment of acid mine drainage (AMD) in South African mines. Bottom ash (BA) and fly ash (FA) obtained from a coal-powered electricity generation station were used in varied combined proportions of 100/0, 90/10, 70/30 BA:FA reagent mixtures and used to conduct neutralization tests done at mix proportions varied from 20:1 to 1:1 AMD to reagent mixtures. Three types of acid mine drainage water from an underground gold mine (AMD-Wz), gold tailings dam (AMD-Lc) and a coal mine (AMD-MpK) were used in the investigation. Water quality tests were carried out before and after the neutralisation treatment.

It was found that both bottom ash and fly ash are effective alkalinising reagents for neutralising AMD. The materials were found to be most effective when mixed at a ratio no greater than 5:1 of mine water to reagent. Use of the coal ash wastes effectively removed up to 99% of iron from the AMD. The sulphate concentration was also reduced by the treatment but it remained fairly elevated. Manganese concentration reduced as the pH of the treated water increased, reaching a negligible concentration of < 1.0 mg/l at pH  $\geq$  11. Further investigations are underway to examine leaching and weathering characteristics of the reagents.

**Keywords.** Acid mine drainage, neutralization, bottom ash, fly ash, coal ash

## Introduction

Neutralization is one of the conventional methods of mitigating the impacts of acid mine drainage. However, the conventional method normally involves dosing the AMD water with chemicals, which is not only costly but also leaves inadequacies in water quality. For example, the AMD that is treated with lime typically does not result in efficient removal of sulphates although the pH may increase to desirable levels. These treatment options are not ideal techniques and alternative systems are continuously being sought that could provide more effective, sustainable solutions.

<sup>1</sup>Corresponding author: University of Johannesburg, Department of Civil Engineering, P.O. Box 524, Auckland Park, 2006, South Africa; E-mail. [sekolu@uj.ac.za](mailto:sekolu@uj.ac.za), [sekolu@gmail.com](mailto:sekolu@gmail.com)

Also, no single treatment system is universally applicable to all scenarios of acid mine water discharge. Lime dosing treatment is often used for active treatment of AMD that is discharging at the surface level, where water can then be pumped to the treatment plant. Over the past, alternative treatment systems have been sought whereby mine water could be neutralized or its acidity ameliorated at its source, such as underground locations of the abandoned mining activity. Moreover, acid mine discharge from abandoned mines normally have no foreseeable end, thereby implying that remedial measures of treatment have to be maintained indefinitely. It would be attractive and appealing if a permanent or semi-permanent treatment could be carried out at the source of acid mine discharge. This was the motivation behind the experimentation conducted in this investigation i.e to evaluate the material system for potential application as insitu AMD neutralizing treatment.

The environmental benefits along with potential efficiency of coal ash by-products in mine water neutralization has attracted some interest for insitu treatment of AMD. Coal-fired power stations generate enormous amounts of by-products consisting of bottom ash, fly ash, flue gas de-sulphurisation sludge and boiler slag. Fly ash and bottom ash have traditionally been used in a wide range of applications including structural fills in mines, road base or sub-base fills, waste stabilization. Fly ash is widely known for its use as a cement extender or pozzolan. But these products are always either underutilized or simply not employed to their full potential, leaving abundant quantities for disposal (which in South Africa have resulted in the infamous 'ash mountains'). Field experimentation on the use of coal ash combustion products (CCPs) for filling abandoned mines mostly started from the mid-1990s [1,2]. About 13 case studies of field experimentation have been reported in the US [2] where the CCPs have been applied either as: (1) a dry-fill (which may or may not intermix intimately with acid mine water) such as the treatment carried out at Wyodal mine (WY), Keenesburg mine (CO), Savage mine (MT), Storm strip mine (WV), Midwestern abandoned mine (IN); or (2) grouts or cementitious pastes such as the treatment that was applied at Big Gorilla Pit (PA), Clinton County (PA), Winding Ridge /Frazee Mine (MD) and Red Oak mine (OK). In almost all these cases, CCPs were applied. Field reports from monitoring of water quality have shown generally beneficial effects of using the by-products but there are indications of susceptibility to leaching of metal elements from the ash products. There are conflicting reports with some results showing no concerns of leaching while others give significant levels of metal leaching in metals and trace elements.

In almost all cases, there is pH increase which is attributable to the alkalinity derived from calcium and magnesium in the ash. The leaching of metals from CCPs has been attributed to the low pH of AMD which releases some metals from the ash, while the water acquires neutralization through the alkalis in the ash. If this explanation is correct, then leaching should cease or at least reduce after the AMD water has been neutralized [2]. However, leaching has also been reported in structural fills used for road bases and building foundations, both cases having shown increased levels of sulphates, iron, and manganese in the non-acidic ground water. It is evident therefore that leaching of chemical elements appears to be inherent in some or all ash products but may vary with the conditions of exposure i.e acidity of AMD, the mineralogy of ash, mixture formulation and method used in mine filling application. Monitoring of post-injection of CCPs shows that the immediate observations are quite different from

the long-term results. Immediately upon application of CCPs, the pH rises rapidly to levels as high as 12 in less than 24 hours, the alkalinity as  $\text{CaCO}_3$  also increases from 0 to a higher concentration. At this early stage, metal precipitation takes place. Thereafter, alkalinity decreases and pH drops and stabilizes in the long-term, while the concentration of metals in AMD remains steady. It can be speculated that the continuous supply of AMD will deplete the neutralizing capacity of the grouts, causing the water quality to degrade with time and eventually return to initial poor quality, perhaps over several years. No current studies have provided answers to this question and extensive research is needed to deal with durability and life of the insitu treatment [2].

## 1. Experimental

### 1.1 Materials and mix designs

The concept involves design of cementitious waste pastes (CWPs) capable of neutralising AMD during or after its formation. Since most heavy metals are leached out from the parent rocks during seepage of AMD, it is emphasized that this material system would be most effective when applied in-situ at the reaction sites of AMD. The cementitious pastes used in the experiments were the coal combustion products abundantly available from coal-power generating plants of ESKOM. The main CCP products used primarily consisted of fly ash and bottom ash. ESKOM alone produces 30 million tons of ash annually much of which is not beneficially used and has to be disposed off. In this laboratory investigation, different mixture combinations were prepared to study possible material systems that could be AMD ameliorants in form of cementitious filler paste. The neutralising coal ash material system was formulated through combinations of bottom ash and fly ash.

There were some specific considerations to the neutralisation investigation. Firstly, it was considered essential to establish the existence of inherent neutralising quality and capacity by the CWPs. This was investigated using a series of slurry mixtures that were constituted at different AMD to ash mix proportions varied from 20:1 to 1:1. The various mixtures used in preparation of the slurries are given in Table 1. Tests were done using the media solutions consisting of AMD from the gold mines and coal mines of South Africa. The results from the slurry study would be key to identifying those mixtures which have the potential and quality required to remediate AMD. The results are also useful in determining the short falls of the system and could be used to improve the formulations.

**Table 1.** Slurry mixtures of AMD-neutralising coal ash waste by-products

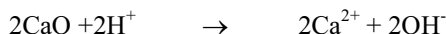
AMD-neutralising coal ash by-products (%)		AMD : BA/FA reagents ratio					
Bottom ash (BA)	Fly ash (FA)	20:1	10: 1	5:1	4:1	3:1	1:1
100	0	√	√	√	√	√	√
0	100	√	√	√	√	√	√
90	10	√	√	√	√	√	√
70	30	√	√	√	√	√	√

### 1.2 Neutralization tests

Slurry mixtures were prepared in AMD to CWP proportions of 20:1, 10:1, 5:1, 3:1, 1:1. The AMD solution was weighed into an open 2 litre beaker into which the CWP product was then added. The slurry mixture was stirred at regular intervals for a period of at least 30 minutes. Measurements of pH/EC were taken at different time intervals 5, 15, 30, 60 mins, 3, 6, 24 hrs or until steady readings were obtained. The mixtures were left to settle until the solid /liquid phases had separated and then stored away in sample bottles. The slurries were filtered using a 0.45  $\mu\text{m}$  pore membrane and the filtrate analysed for pH, EC, TDS,  $\text{SO}_4^{2-}$ , Fe, Ca, Na, Mn, Mg, Zn.

## 2. Results and discussions

As already discussed in the foregone, the neutralisation tests consisted of slurry mixtures prepared through proportional combination of alkalinising waste materials and the acidic mine water. The coal ash by-products of bottom ash and fly ash were used in different combinations to neutralise the AMD. Neutralisation of acidity occurs when the free lime (CaO) in bottom ash or fly ash dissolves in the water to form hydroxyl ions ( $\text{OH}^-$ ), directly increasing the pH.

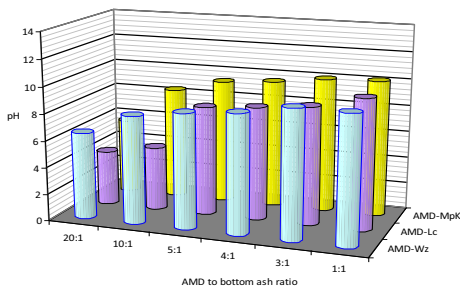


The contaminant elements (Fe, Al, Mg, Mn etc.) are insoluble at high pH and will therefore precipitate out of solution [3]. Immediate changes in pH and electrical conductivity were monitored prior to filtering of the treated water samples for chemical analysis.

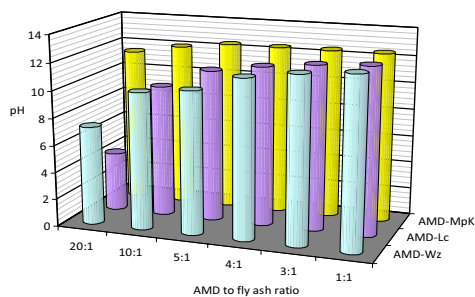
The bench scale neutralisation tests were done in two-litre beakers at normal temperatures. Bottom ash (BA) ground to pass 600  $\mu\text{m}$  was combined with fly ash (FA) or cement kiln dust, as described in the previous sections. The effects of bottom ash and fly ash on pH of the AMD were investigated using slurries that were prepared at varied AMD to ash ratios of 20:1 to 1:1. The results obtained are shown in Figures 1 and 2 for the bottom ash and fly ash respectively. Clearly, the AMD to ash ratio controls the maximum attainable pH, with high ratios of 20:1 and 10:1 giving lower neutralising capacity. It can be seen that neutralisation is most effective in achieving pH increase at a ratio of 5:1 or lower. It should however be noted that at the lower ratios, mixtures become less workable. From the results, the optimum mixture ratios would be 5:1 to 3:1. Overall, the fly ash was found to be more efficient in raising of the pH of AMD relative to its bottom ash counterpart. The ultimate pH values for bottom ash ranged from 8.6 to 9.6, 8.2 to 9.8, 9.3 to 10.2 for AMD-Wz, AMD-Lc, AMD-MpK respectively. The corresponding pH values for fly ash neutralisation were 10.5 to 12.4, 11.2 to 12.3, 12.4 to 12.5. It can be seen that the attainable pH through use of fly ash is 2 to 3 units higher than the corresponding pH achieved by use of bottom ash. There is also a significant difference in the response of the various AMD's drawn from different sources. Neutralisation of AMD-MpK from the coalfield occurred more rapidly and

achieved higher pH compared to AMD-Wz and AMD-Lc from the goldfields. It is evident in Figures 1 and 2 that AMD from the goldfields gave a gradual pH increase, attaining a relatively lower maximum pH level than the AMD from the coalfields.

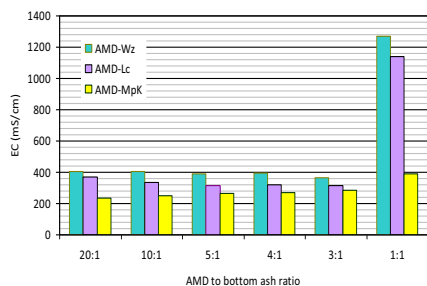
The electrical conductivity (EC) values of the neutralised solutions were also measured, as shown in Figures 3 and 4. These readings were taken after the solution had been allowed to settle for at least 30 mins. It can be seen that the EC generally increases as the AMD-ash ratio decreases from 20:1 to 1:1. The change in EC is strongly related to change in pH. Since pH increase results in precipitation of contaminant elements from solution, the EC of the treated solution should decrease. In this experiment, however, the precipitates were not filtered out of solution and so their presence may have influenced the EC readings in the reverse direction, increasing the measurements. As more of the elements precipitated from AMD into the slurry, there was increase in the EC values. Again, significant effects are observed for AMD to ash ratios of 5:1 or lower, with the effect on EC increasing as the ratios decreased. The AMD-MpK from the coalfields showed the lowest EC readings while the two AMD types from the goldfields showed higher EC measurements. AMD-MpK also gives the least change in EC, showing that the concentration of pollutant elements is much lower in the AMD-MpK compared to pollutants in AMD-Wz and AMD-Lc from the goldfields. The AMD-Wz had higher metal concentrations of Fe (281 mg/l), Mg (211 mg/l), and Mn (90 mg/l) compared to AMD-Lc which had Fe (124 mg/l), Mg (67 mg/l), Mn (17mg/l). The precipitation of these metals should be responsible for the higher EC measurements in AMD-Wz over those given by AMD-Lc.



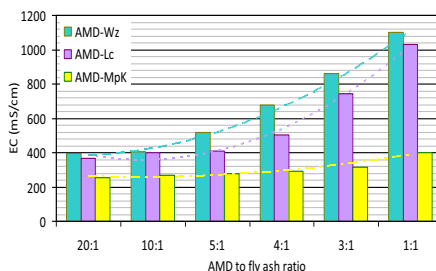
**Figure 1.** Effect of bottom ash on the pH of acid mine drainage from various sources



**Figure 2.** Effect of fly ash on the pH of acid mine drainage from various sources



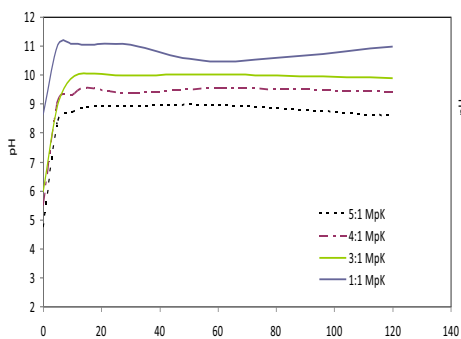
**Figure 3.** Effect of bottom ash on the pH of acid mine drainage from various sources



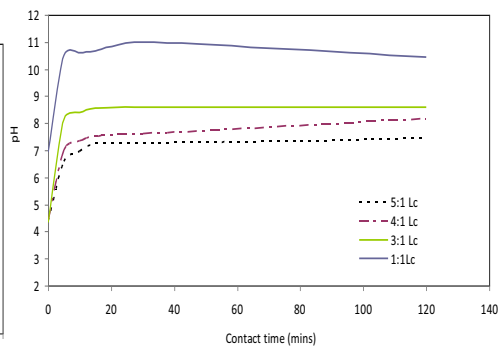
**Figure 4.** Effect of fly ash on the pH of acid mine drainage from various sources



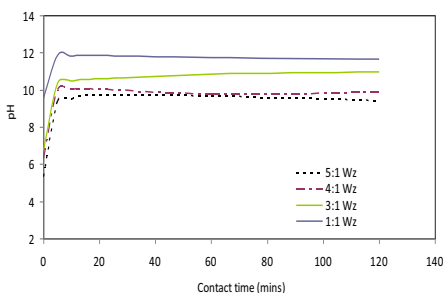
Figures 5 to 9 show the time-based change in pH of the AMD upon mixture with the ash powders. The figures give results for varied slurry proportions from 5:1 to 1:1 AMD to ash. In these results, bottom ash and fly ash were combined in proportions of 90:10 or 70:30 BA/FA for use in the beaker tests. The mixtures containing higher bottom ash proportions i.e. 90:10 BA/FA (Figures 5 and 6) attained a lower pH compared to that of 70:30 BA/FA (Figures 7 and 8), while the pH levels increased as the AMD: ash ratio reduced. In all cases (Figures 5 to 9) of the neutralisation tests, there is an immediate rapid increase in pH of the AMD, which comes to completion within 10 to 15 mins. At this point, however, the pH value reaches its peak forming a ‘kink’ and immediately decreases slightly before stabilising for the rest of the test period which was continued for up to 5 days. It is known that the particles of the neutralising ash can become coated with precipitates upon rise in pH [4]. As already mentioned, the pH increase results from neutralisation of the acidity of AMD. In this investigation, the mixtures were stirred at regular intervals, therefore limiting the possibility of armouring of the reacting particles by precipitates.



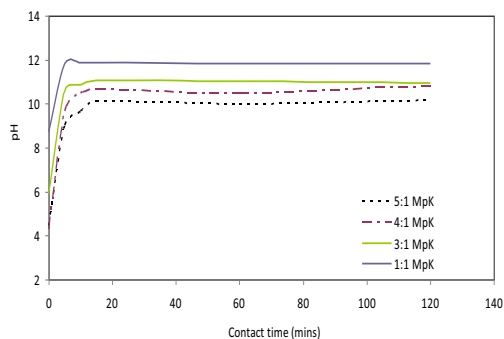
**Figure 5.** Effect of 90/10 BA-FA mixtures on pH change of AMD-MpK



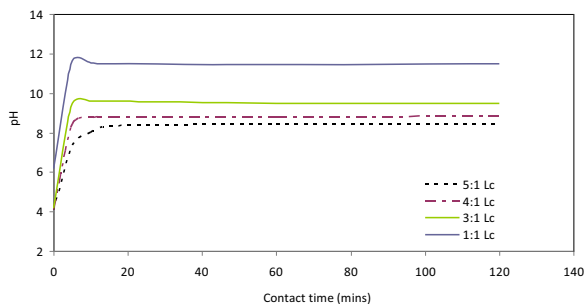
**Figure 6.** Effect of 90/10 BA-FA mixtures on pH change of AMD-Lc



**Figure 7.** Effect of 70/30 BA-FA mixtures on pH change of AMD-Wz



**Figure 8.** Effect of 70/30 BA-FA mixtures on pH change of AMD-MpK



**Figure 9.** Effect of 70/30 BA-FA mixtures on pH change of AMD-Lc

The slurries formed were left to settle, decanted and the solution filtered through a 0.45  $\mu\text{m}$  pore membrane then chemically analysed for changes in water chemistry. Table 2 gives results of chemical analyses done on selected mixtures of AMD: ash ratios. Nearly all iron was removed from the treated AMD to a concentration  $<1.0$  mg/l, decreasing as the pH increased. The concentration of manganese decreased significantly with reduction in the AMD: ash ratios, and with corresponding increase in pH especially to a level above 10.

In the slurry mixtures, Ca generally increased with rise in pH, that is, as the AMD:ash ratios decreased. Alkalis are highly soluble and may easily leach out from ash particles, causing rise of their chemical concentrations in the slurry mix. Changes in the Mg concentration did not appear to show a specific trend. But in the literature, reduction in Mg concentrations have been reported with suggestions of pH 10.5 to 11 as being ideal for Mg removal [4]. The concentration of sulphate ions generally decreased with increase in pH, but it remained significantly high.

### 3. Conclusions

A preliminary investigation was conducted in contribution to the potential utilization of the abundantly available bottom ash and fly ash waste by-products for insitu treatment of acid mine drainage in South African coal mines. In the foregone investigation:

1. It was found that both the bottom ash and fly ash were effective alkalinising reagents for neutralising acid mine drainage. The materials were more effective when mixed at a ratio no greater than 5:1 of mine water to reagent. The finely ground fly ash was found to be more effective, attaining a pH level 2 to 3 units higher than that of the relatively coarse bottom ash, being of fineness passing 600  $\mu\text{m}$ . Accordingly, fly ash is expected to possess greater alkaline potency than bottom ash.

**Table 2.** Composition of AMD water after treatment with cementitious wastes

Parameter	AMD-Lc	AMD-Wz	AMD-Mpk	AMD-Lc			AMD-Wz			AMD-MpK	
				100 BA	100 BA	100 BA	70 /30 BA-FA	70/30 BA-FA	70 /30 BA-FA	100 BA	100 BA
AMD: ash ratio				10:1	5:1	3:1	5:1	5:1	1:1	5:1	1:1
pH	2.6	3.0	2.8	6.9	8.7	8.9	10.9	11	11.4	9.8	10.8
Conductivity (mS/m)	230	240	254	322	327	310	294	351	305	264	386
Sulphate as SO <sub>4</sub> (mg/l)	3160	3100	1100	2390	2350	2290	2240	2610	2000	1450	2280
Calcium as Ca (mg/l)	840	1630	64	1640	1715	1740	1960	2200	1695	940	1360
Iron as Fe (mg/l)	124	218	33	0.36	0.08	0.15	0.2	0.19	0.39	0.34	0.38
Magnesium as Mg (mg/l)	211	67	54	130	130	130	57	89	0.37	77	120
Manganese as Mn (mg/l)	90	17	8.2	13	9.1	3.9	1.5	1	0.34	1.8	0.45

2. More rapid neutralisation treatment was exhibited in the acid mine drainage from the coalfields which attained higher final pH than its counterparts from the goldfields. The latter not only achieved lower final pH value but also did so more gradually than the former. Of the three types of acid mine drainage sources evaluated, the AMD from tailings dams was least responsive to neutralisation treatment.
3. The electrical conductivity increased with improved neutralisation efficiency as indicated by pH of the treated water. The rise in conductivity can be attributed to precipitation of the elements present in the acidic mine water into the slurry, as the pH level increased.
4. The neutralisation reaction is quite fast, increasing the pH rapidly and reaching completion within 10 to 15 minutes of mixing the alkaline reagents (cementitious wastes) and the acidic mine water. After this initial reaction period, the pH of the treated water remains practically constant.
5. Use of the cementitious coal ash wastes as alkalinizing reagents effectively removed up to 99% of iron from the acid mine water. The sulphate concentration was also reduced by the treatment but it remained fairly elevated. Manganese concentration reduced as the pH of the treated water increased, reaching a negligible concentration of < 1.0 mg/l at pH  $\geq$  11.
6. The change in concentration of magnesium varied with the pH. The calcium (and presumably other alkalis) concentration steadily increased with rise in pH of the treated water.

## References

- [1] Hogdes William K. and Keating Robert W. (1999), Maryland power plant research program promotes the beneficial use of CCPs as a means to protect Marylands natural resources, *International Ash Utilization Symposium, Center for Applied Energy Research, University of Kentucky*, paper #87, 5p
- [2] Murarka Ishwar P. (2006), Use of coal combustion products in mine-filling applications: a review of available literature and case studies, Final report, DOE Award No. 99-CBRC, 44p
- [3] Aube B., *The science of treating acid mine drainage and smelter effluents*, 361 Aumais, Ste-Anne-de-Bellevue, Quebec, Canada, 23p, [www.enviraube.com](http://www.enviraube.com)
- [4] Vadapalli V.R.K., Klink M.J., Etchebers O., Petrick L.F., Gitari W., White R.A., Key D., Iwuoha E. (2008), Neutralization of acid mine drainage using fly ash, and strength development of the resulting residues, Research Letters, *South African Journal of Science*, 104, July/August 2008, 317-322

# Potentiodynamic polarization study of the corrosion characteristics of acid mine drainage

Stephen O. EKOLU<sup>a,1</sup>, Souleymane DIOP<sup>b</sup> and Firehiwot AZENE<sup>b</sup>

<sup>a</sup>Department of Civil Engineering Science, University of Johannesburg, South Africa

<sup>b</sup>Council for Geoscience, Head Office, Engineering Geoscience Unit

**Abstract:** Potentiodynamic tests were carried out to evaluate the attacking characteristics of acid mine drainage (AMD) from South African mines. Tests were done using seven solutions of:- AMD water taken from the field and consisting of two AMD sources from the gold mines and two sources from the coal mines; sulphuric acid, distilled water, synthetic AMD prepared in the laboratory. Tests were done at normal room temperature of 23°C using mild steel and stainless steel samples.

Tafel plots were generated and corrosion current ( $I_{corr}$ ), corrosion potential ( $E_{corr}$ ), corrosion rates determined in each case. The corrosion rate of AMD from the coal mines was found to be similar to the corrosion of AMD from the gold tailings dam mine, both of which were significantly higher than the corrosion of AMD from the underground gold mine. It is, however, anticipated that the corrosion behaviour could be different under static conditions and further investigations in this regard are being conducted.

**Keywords.** Corrosion current, potential, acid mine drainage, potentiodynamic, polarization

## Introduction

With or without the presence of acid mine drainage, the mining environment is typically toxic and give rise to severe corrosion problems. But corrosion from mine-related activities becomes a much more enormous problem when acid mine drainage occurs, causing adverse effects to the environment, ecology and structural materials of engineering construction. It is well established that the pyritic ores exposed during mining, will over the years oxidise upon exposure to atmospheric conditions of oxygen and moisture. This normally happens several years after abandonment of mining activity. It is therefore usual that most problems of acid mine drainage are reported in abandoned mines.

In addition to the chemical process of AMD formation, iron and sulphide oxidizing bacteria are known to play a significant role in advancing AMD [1]. The Thiobacillus Ferro-oxidans and Thiobacillus Thiooxidans feed on the iron and sulphate found in the pyrites respectively, consequently accelerating the oxidation of these salts.

<sup>1</sup>Corresponding author: University of Johannesburg, Department of Civil Engineering, P.O. Box 524, Auckland Park, 2006, South Africa; E-mail. [sekolu@uj.ac.za](mailto:sekolu@uj.ac.za), [sekolu@gmail.com](mailto:sekolu@gmail.com)

Thiobacillus Thioxidans do not cause major influence but iron-feeding bacteria, typically crenothrix, gallionella, and others that use iron as an energy source that is fed upon and stored in their microbial protoplasm, tends to accelerate the oxidation of iron into ferric ion or rust.

The acidic and humid conditions in mines can be highly aggressive and may cause severe levels of corrosion in mining equipment infrastructure elements. Some of the common equipment that could experience corrosion problems are [2,3] piping systems and pumps which are widely used in underground mining operations, tunnel roof bolts, wire ropes for equipment, machinery and materials transportation assemblages, ore processing plants and structures. Other forms of infrastructure that could be affected include water handling equipment, pipes and dams [4]; highway structures

This paper presents an experimental study that was conducted using electrochemical polarization tests to assess the attacking nature of the AMD from coal mines and gold mines. The information generated through the study would provide understanding of the aggressiveness of the acid mine drainage attack on metals.

## 1. Experimental

The corrosion experiments were conducted by means of electrochemical polarization tests done with seven types of AMD solutions, and two types of steel consisting of mild steel and stainless steel. The experiment serves to provide rapid evaluation of the characteristics of corrosion behaviour of metals under the influence of AMD. Mild steel is a widely used structural material in civil engineering applications while stainless steel commands interest with respect to corrosion resistance. The chemical compositions of steel samples that were used in the corrosion study are given in Table 1.

**Table 1.** Chemical composition of mild steel and stainless steel samples

	Fe	C	Si	P	Mn	Cu	Al	Ni	Cr	Va
Mild steel	99.52	0.047	0.013	<0.005	0.24	0.013	0.044	0.008	0.026	<0.005
Stainless steel	70.84	0.049	0.49	0.027	1.20	0.39	<0.005	8.48	18.3	0.068

The six different media solutions that were used in the potentiodynamic tests, consisted of two AMD sources AMD-Wz, AMD-Lc from the gold mines; two AMD water sources AMD-MpK, AMD-MpT from the coal mines; synthetic AMD 3000/2.5 and sulphuric acid H<sub>2</sub>SO<sub>4</sub>/1.

Corrosion is an electrochemical process. Accordingly, rapid electrochemical techniques are typically applied to examine the process kinetics and the influence of environmental conditions. The test method allows measurement of instantaneous corrosion rates for metals under study which can be used to assess the corrosion resistance of the material. Such tests are also done in reinforced concrete structures subject to carbonation and/or chloride-induced corrosion attack. The instrument used in this investigation was an AUTOLAB PGSTAT 10 Electrical potentiostat with a glass corrosion cell, Ag/AgCl type reference electrode filled with 3M KCl solution. Installed in the instrument was the NOVA version 1.7 software that was used to perform data

capture and analyses throughout the tests. The working electrode consisted of specimens of 10 x 10 x 3 mm thick coupons. The specimens were mounted in epoxy resin moulds and the exposed surface area of the mounted coupon was measured. The working electrodes were then exposed to the test solution media and tests runs were then conducted at a scan rate of 0.1 mV/s, in order to obtain potentiodynamic anodic and cathodic polarization curves. The values of corrosion current ( $I_{\text{corr}}$ ) and corrosion potential ( $E_{\text{corr}}$ ) were determined from the Tafel plots of polarization curves. The  $I_{\text{corr}}$  is determined by extrapolating the linear portions of the anodic and cathodic curves of the Tafel plot. The  $I_{\text{corr}}$  values may also be used to calculate the corrosion rates. The polarisation resistance is related to the  $I_{\text{corr}}$  according to the Stern-Geary expression:

$$I_{\text{corr}} = \frac{\beta_a \times \beta_c}{2.3(\beta_a + \beta_c) R_p} = \frac{B}{R_p}$$

Where  $\beta_a$ ,  $\beta_c$  are anodic and cathodic Tafel constants. The corrosion rate (in  $\mu\text{m}/\text{yr}$ ) for mild steel can be calculated from [5]

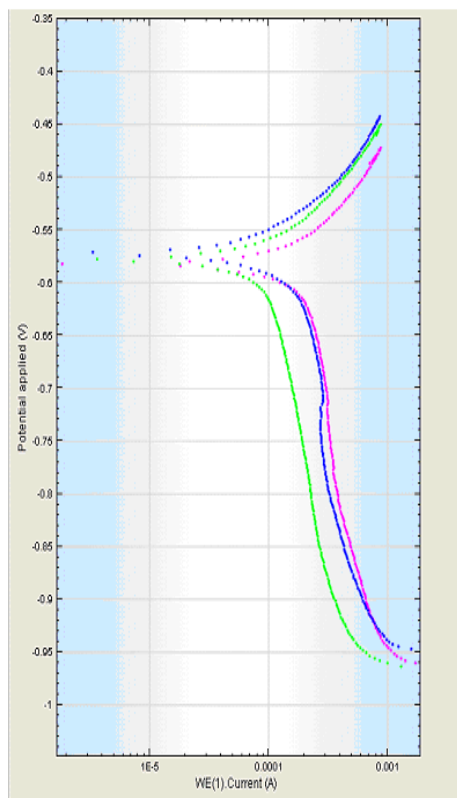
$$CR = 11 \times 10^6 \cdot \frac{B}{R_p} \cdot A$$

Knowing that 1 amp-hr consumes 1.04g Fe, the mass loss of steel can also be estimated from  $I_{\text{corr}}$ .

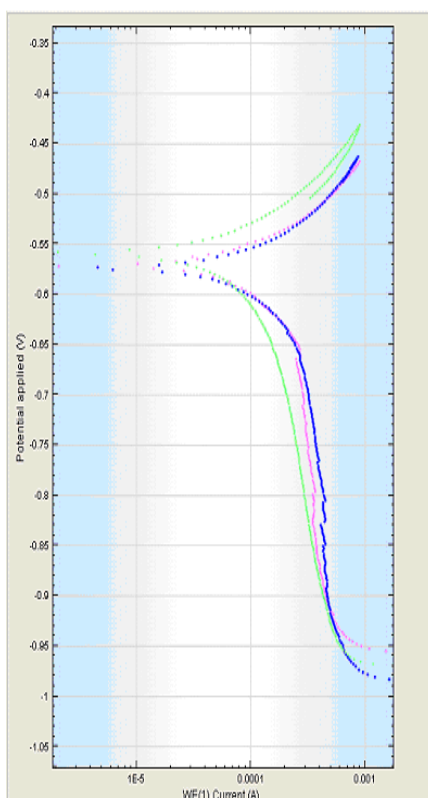
## 2. Results and discussion

The Tafel plots (potentiodynamic polarisation curves) were determined for mild steel and for stainless steel corrosion in the various AMD aqueous test solutions. Figures 1 and 2 show the polarization curves for mild steel in AMD-Lc and AMD-Wz respectively. From the Tafel plots, the values of parameters  $E_{\text{corr}}$ ,  $I_{\text{corr}}$ , Tafel constants  $\beta_a$  (anode slope) and  $\beta_c$  (cathode slope),  $R_p$ , and corrosion rate were determined as given in Table 2.

The potentiodynamic polarization measurements provide an assessment of corrosion behaviour under dynamic conditions. The measurements are instantaneous and provide rapid measurement of reactions involving rapid electron transfer. The pH range of the various AMD water is fairly close (2.6 to 3.1pH) and may not dominate corrosion influence. The relative corrosion behaviour between the AMD water types is likely to be largely determined by the differences in types and concentrations of elements or ions present in the AMD. As expected from classic corrosion theory, the lower pH of the aqueous solutions caused a right shift in the Tafel plots, directly increasing  $I_{\text{corr}}$  with increase in the acidity. This strong trend can be seen in Figure 3. The highly negative  $E_{\text{corr}}$  potentials of mild steel place the electrochemical reactions in the active regions. Some interesting observations can be seen with AMD-Wz. While its  $E_{\text{corr}}$  value is within the same range as the other AMD solutions, the sharply low current density led to relatively very low corrosion rate of 1.75 mm/yr, compared to 6.26 and 9.86 mm/yr for AMD-Lc and AMD -MpK.



**Figure 1.** Potentiodynamic polarization curves for mild steel in AMD-Lc



**Figure 2.** Potentiodynamic polarization curves for mild steel in AMD-Wz

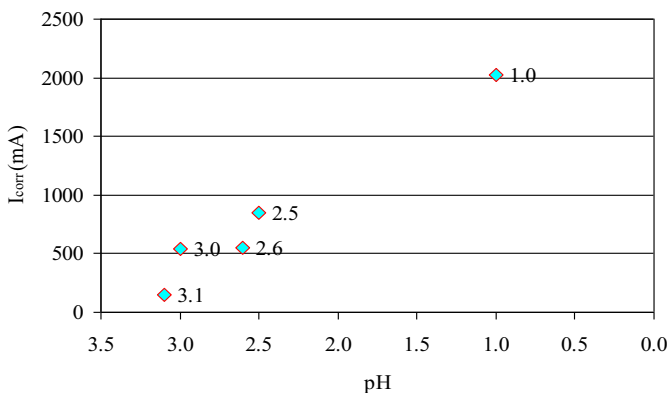
Unlike for static immersion tests, the dynamic conditions (solution agitation) of the potentiodynamic polarization measurements can be expected to increase corrosion rate. As such, the measured potentiodynamic rates of corrosion of 2 to 24 mm/yr, observed in the aqueous test solutions, are likely to be significantly higher than the rates for the static immersion tests determined at normal temperatures. From the potentiodynamic measurements, the ranking of corrosion in decreasing order is  $\text{H}_2\text{SO}_4 > \text{AMD-MpK} > \text{AMD-Lc} > \text{AMD-Wz}$ . The observed trends underscore the complexity of corrosion behaviour of metals under the influence of the metal characteristics, environmental conditions, and the aqueous solutions or the element concentrations in the solutions, for that matter.

The stainless steel showed positive (nobler) corrosion potentials and small current density, implying passivity as indicated by the generally negligible corrosion rates. Again the AMD-Wz, showed greater corrosive activity on stainless steel than the counterpart solutions of AMD-Lc and AMD-MpK. Clearly, the corrosive actions of AMD on metals are quite complex, being influenced by the metal characteristics in conjunction with exposure conditions.



**Table 2.** Potentiodynamic corrosion parameters for mild steel and stainless steel in acid mine drainage water

Sample	Aqueous solution	pH	$\beta_a$ (mV)	$\beta_c$ (mV)	$E_{corr}$ (mV)	$I_{corr}$ (mA)	Corrosion rate (mm/year)
Mild steel	AMD-Lc	2.6	69.1	248.0	-577.6	547.7	6.26
	AMD-Wz	3.1	508.2	135.7	-568.0	150.7	1.75
	AMD-MpK	3.0	-454.1	186.6	-586.7	545.2	6.39
	3000/2.5	2.5	246.6	110.2	-505.1	848.2	9.86
	H <sub>2</sub> SO <sub>4</sub>	1.0	-879.9	426.6	-604.2	2024.7	23.53
Stainless steel	AMD-Lc	2.6	278.6	787.0	179.5	2.8	0.03
	AMD-Wz	3.1	582.6	-1074.4	163.3	25.2	0.29
	AMD-MpK	3.0	274.4	578.4	118.6	1.3	0.02

**Figure 3.** Right shift of Tafel plots showing a direct increase in the  $I_{corr}$  with decrease in pH of the aqueous solutions

### 3. Conclusions

The corrosion of metals by acidic mine water from various sources was evaluated in the foregone investigation using electrochemical polarisation tests. Mild steel and stainless steel coupons were used in the investigation with a view of assessing the corrosivity of AMD from the coal mines and gold mines of South Africa. These AMD water sources consisted of underground gold mines, gold tailings, open pit coal mines.

From the potentiodynamic measurements, the ranking of corrosion attack by AMD, in decreasing order is AMD-MpK > AMD-Lc > AMD-Wz, with corrosion rates of 6.39, 6.26, 1.75 mm/yr respectively. As expected, sulphuric acid gave the highest corrosion rate while stainless steel showed negligible corrosion rates. However, it may be recalled that under dynamic conditions of the polarization tests, corrosion behaviour may be different than tests conducted under static conditions.

## References

- [1] Earlie J., Callaghan T. (1998), *Impacts of mine drainage on aquatic life, water uses, and man-made structures*, Chapter 4 of the book Coal Mine Drainage Prediction and Pollution Prevention in Pennsylvania, Department of Environmental Protection, Harrisburg, PA 17105, 12p, <http://www.dep.state.pa.us/dep/deputate/minres/districts/cmdp/main.htm>
- [2] DERM (2011), *Potential Impacts of acid sulphate Soils*, Department of Environment and Resource Management, Queensland Government, Australia. <http://www.derm.qld.gov.au/land/ass/impacts.html>, Accessed 28 Oct 2011
- [3] Mierzwa Aaron J., Appendix T-Mining, CC Technologies Laboratories Inc., Dublin Ohio, 12p.
- [4] Pankaj S., Sameer V., Sharma S.N, Mahure, N.V, Anil R., Sivakumar N., Murari R. (2011), Acid mine discharge – challenges met in hydro power project, *International Journal of Environmental Sciences*, Vol. 1, No. 6, 2011, ISBN 0976-4402, 9p
- [5] Broomfield John P., *Corrosion of steel in concrete: understanding, investigation and repair*, E & FN Spon, Chap 4, 29-84

This page intentionally left blank

## 5. Building science and construction

This page intentionally left blank

# Comparison of simple linear regression and multiple linear regression for estimating fuel use and emission rates for excavators

Heni FITRIANI<sup>a,1</sup> and Phil LEWIS<sup>b</sup>

<sup>a</sup>*Civil Engineering Department, University of Sriwijaya, Indonesia*

<sup>b</sup>*School of Civil and Environmental Engineering, Stillwater, Oklahoma, USA*

**Abstract.** Heavy-duty diesel (HDD) construction equipment consumes a significant amount of fuel and subsequently emits a substantial amount of pollutants into the environment. In most construction activities, HDD construction equipment is the primary source of emissions. The purpose of this paper is to demonstrate the comparative models for estimating fuel use and emission rates for HDD construction equipment specifically excavators. Second by second data were collected from portable emission measurement system (PEMS), containing fuel use and emission rates datasets along with engine performance data from three excavators. Emission pollutants include nitrogen oxides (NO<sub>x</sub>), hydrocarbons (HC), carbon monoxide (CO), carbon dioxide (CO<sub>2</sub>), and particulate matter (PM). For each excavator, predictive models were developed using simple linear regression (SLR) and multiple linear regression (MLR). Results yielded that the MLR accounted for the highest percentage of variability in the data compared to SLR based on the values of coefficient of determination (R<sup>2</sup>) for each model. In order to exhibit the significant impact of which engine data that may affect the emission rates, the variable impact analysis was also conducted.

**Keywords.** Heavy-duty diesel (HDD) construction equipment, fuel use, emission, portable emission measurement system (PEMS)

## Introduction

The construction sector plays an essential role in improving climate change due to the impact of greenhouse gas (GHG) emissions primarily caused by its major activities. Construction activities consume a significant amount of fuel and consequently emit a substantial amount of pollutants into the environment. According to the United States Environmental Protection Agency [2], there are approximately two million items of construction and mining equipment in the United States that spend about six billion gallons of diesel fuel annually. Furthermore, in most construction activities, heavy-duty diesel (HDD) construction equipment is the primary source of emissions. The EPA also estimates that in 2005, HDD construction vehicles produced U.S. national annual totals of 657,000 tons of NO<sub>x</sub>, 1,100,000 tons of CO, 63,000 tons of PM<sub>10</sub> and 94,000 tons of SO<sub>2</sub> [2].

<sup>1</sup>Corresponding author: [henifitriani79@yahoo.com](mailto:henifitriani79@yahoo.com)

Of these pollutants,  $\text{NO}_x$  and PM are the most prominent among HDD equipment [3]. Other pollutants found in diesel exhaust (DE) include hydrocarbons (HC) and carbon dioxide ( $\text{CO}_2$ ). In order to quantify and characterize the HDD emissions problem, reliable prediction models are needed; however, most emission prediction tools are based on engine dynamometer data and not real-world data [1]. The objective of this paper is to demonstrate two different predictive modeling methodologies for estimating fuel use and emission rates for HDD construction equipment, specifically excavators, based on real-world data.

## **1. Previous work**

As the need of conforming to emission standards has been largely increasing, numerous studies have been extensively piloted to quantify and characterize emissions and energy consumption of HDD construction equipment. Many studies have been completed using experimental designs such as dynamometer tests and real-world in-use measurements. Dynamometer tests are commonly used in quantifying emissions at steady-state conditions in the laboratory. Other studies conducted emission quantification by engaging Portable Emission Measurement Systems (PEMS), models, and simulations. The Environmental Protection Agency (EPA) and other government agency also develop other models such as the Nonroad model, the Offroad model, and the Urbemis model.

PEMS is generally used to gather fuel use and emissions field data of vehicles based upon real-world measurement. In-use emissions quantification enables data collection by capturing the actual duty cycle on second by second basis measurement. Commercial PEMS are obtainable for any kinds of applications as well as for different types of fuel use. Some of the most prominent real-world emissions measurements from HDD construction equipment were completed by the researchers at North Carolina State University [1, 5, 6, 7, 8]. Other researchers from West Virginia University and the University of California – Riverside also directed their studies on the use of on-board emission measurement for particular construction equipment.

## **2. Methodology**

This paper presents two different predictive modeling methodologies for estimating fuel use and emissions rates based on the real-world dataset from the research team at North Carolina State University. Simple linear regression (SLR) and multiple linear regression (MLR) models were developed and compared for three excavators. Engine performance data from the excavators, including manifold absolute pressure (MAP), revolutions per minute (RPM), and intake air temperature (IAT), were used to develop prediction models for fuel use and emission rates of  $\text{NO}_x$ , HC, CO,  $\text{CO}_2$ , and PM.

Table 1 displays the summary of engine attribute data for each excavator, including engine size (HP), displacement, model year, and EPA engine tier. The rated engine horsepower (HP) ranged from 93 HP to 254 HP and the model year ranged from 1998 to 2003; thus, all three of the excavators were either EPA engine tier 1 or 2.

**Table 1.** Summary of engine attribute data

Equipment	Horsepower	Displacement	Model	Engine
	(HP)	(Liters)	Year	Tier
Excavator 1	254	8.3	2001	1
Excavator 2	138	6.4	2003	2
Excavator 3	93	3.9	1998	1

### 3. Simple linear regression

Simple linear regression models were developed to determine the relationship between a single response variable and a single predictor variable. Since it has been shown by others that MAP is highly correlated to fuel use and emission rates [4, 5, 7], simple linear regression models were formulated based on the relationship between MAP as a predictor variable and fuel use as a response variable, as well as MAP and mass per time (grams per second) emission rates of NO<sub>x</sub>, HC, CO, CO<sub>2</sub>, and PM. These SLR models take the form of:

$$Y_{1-6} = ax + c \quad (1)$$

where:

- $Y_{1-6}$  = Fuel use or emission rate of NO<sub>x</sub>, HC, CO, CO<sub>2</sub>, or PM (g/s)
- $a$  = slope of the regression line
- $x$  = MAP (kilopascal)
- $c$  = y-intercept of regression line

### 4. Multiple linear regression

Multiple linear regression was used to model the relationship between three predictor variables based on engine performance data (MAP, RPM, IAT) and one response variable (either fuel use or emission rate of NO<sub>x</sub>, HC, CO, CO<sub>2</sub>, and PM).

The MLR equations for fuel use and emission rates for each pollutant take the form of:

$$Y_{1-6} = \beta_0 + \beta_1 X_1 + \beta_2 X_2 + \beta_3 X_3 \quad (2)$$

where:

- $Y_{1-6}$  = Fuel use or emission rate of NO<sub>x</sub>, HC, CO, CO<sub>2</sub>, or PM (g/s)
- $X_1$  = MAP (kilopascal)
- $X_2$  = Revolutions Per Minute (RPM)
- $X_3$  = Intake Air Temperature (Celsius degrees)
- $\beta_0, \beta_1, \beta_2, \beta_3$  = Coefficients of linear relationship



## 5. Results

This section presents the results for two predictive modeling methodologies – SLR and MLR- for excavators, as well as variable correlations and model comparisons for those models. The validation results for the models for all three excavators are presented in Table 5.

Table 2 shows the summary of the Pearson correlation coefficients for all three excavators, indicating the relationship between engine data, fuel use, and emission rates. MAP has a strong positive relationship with fuel use and emission rates of NO<sub>x</sub>, CO<sub>2</sub>, and PM, but a moderate positive relationship with HC and CO. RPM has the second strongest relationship with fuel use and emission rates. Meanwhile, IAT has the weakest relationship with fuel use and emission rates as indicated by the lower (and sometimes negative) values of correlation to the specified response variables.

**Table 2.** Summary of Pearson correlations coefficients

Equipment	Engine Data	Fuel Use	NO <sub>x</sub>	HC	CO	CO <sub>2</sub>	PM
EX 1	MAP	0.99	0.97	0.59	0.74	0.99	0.94
	RPM	0.80	0.74	0.63	0.85	0.79	0.74
	IAT	0.56	0.59	0.07	0.37	0.57	0.51
EX 2	MAP	0.98	0.92	0.62	0.47	0.98	0.94
	RPM	0.85	0.85	0.62	0.57	0.85	0.69
	IAT	0.55	0.56	0.33	0.30	0.55	0.44
EX 3	MAP	0.96	0.94	0.44	0.14	0.96	0.57
	RPM	0.84	0.79	0.42	0.23	0.84	0.47
	IAT	0.32	0.40	0.36	-0.12	0.32	0.44

### 5.1 Simple linear regression models

Based on their high correlation values, SLR models were developed using MAP as a predictor variable to predict fuel use and emission rates of each pollutant. Table 3 presents the results of the SLR models for all three excavators. These models are based on more than 19,000 observations of second-by-second, real-world fuel use and emissions data for excavator 2 and 3, and around 7,000 observations for excavator 1. Based on the coefficient of determination ( $R^2$ ), these models accounted for a high percentage of the variability in the data for fuel use, NO<sub>x</sub>, CO<sub>2</sub> and PM. HC and CO had the lowest  $R^2$  value, indicating much variability in the data, and therefore were more difficult to predict.

**Table 3.** Summary of SLR models for all excavators

Equipment	Response	Equations	R <sup>2</sup>
Excavator 1	Fuel Use	$Y_1 = 9.9429 X_1 + 0.4704$	0.982
	NO <sub>x</sub>	$Y_2 = 0.3545 X_1 + 0.0242$	0.948
	HC	$Y_3 = 0.0054 X_1 + 0.0024$	0.351
	CO	$Y_4 = 0.0175 X_1 + 0.0066$	0.543
	CO <sub>2</sub>	$Y_5 = 31.431 X_1 + 1.4720$	0.982
	PM	$Y_6 = 3.8619 X_1 + 0.1076$	0.881
Excavator 2	Fuel Use	$Y_1 = 6.4485X_1 + 0.5302$	0.963
	NO <sub>x</sub>	$Y_2 = 0.1202 X_1 + 0.0209$	0.850
	HC	$Y_3 = 0.0083 X_1 + 0.0031$	0.390
	CO	$Y_4 = 0.0239X_1 + 0.0142$	0.219
	CO <sub>2</sub>	$Y_5 = 20.358X_1 + 1.6475$	0.963
	PM	$Y_6 = 1.8463X_1 + 0.0354$	0.888
Excavator 3	Fuel Use	$Y_1 = 3.9492 X_1 + 0.1231$	0.930
	NO <sub>x</sub>	$Y_2 = 0.1231 X_1 + 0.0098$	0.876
	HC	$Y_3 = 0.0084X_1 + 0.0021$	0.194
	CO	$Y_4 = 0.0051X_1 + 0.0055$	0.018
	CO <sub>2</sub>	$Y_5 = 12.468 X_1 + 0.3748$	0.929
	PM	$Y_6 = 1.0842 X_1 - 0.0099$	0.333

$X_1 = \text{MAP}$

### 5.2 Multiple linear regression models

Based on the correlation matrix in Table 2, MAP and RPM are highly correlated to fuel use and emissions rate for most of pollutants. Even though IAT has a lower correlation to fuel use and emissions rate, IAT was still used as an input variable for the MLR models because it may still have some predictive power.

Table 4 summarizes the models for fuel use and emissions rates for all three excavators. Overall, the MLR models yielded higher R<sup>2</sup> values than the SLR models for their respective response variables. The MLR R<sup>2</sup> values for fuel use and emission rates for NO<sub>x</sub>, HC, CO<sub>2</sub> and PM indicate that the models perform well. The model for CO, however, accounted for less than 50% of the variability in the data; thus, the MLR models also indicate that emission rates of CO are more difficult to predict compared to fuel use and the other pollutants.

**Table 4.** Summary of MLR models for all excavators

Equipment	Response	Equations	R <sup>2</sup>
Excavator 1	Fuel Use	$Y_1 = -5.748 + 0.0728 X_1 + 0.000301X_2 - 0.0296X_3$	0.985
	NO <sub>x</sub>	$Y_2 = -0.2093 + 0.00247X_1 - 0.00002 X_2 + 0.000176X_3$	0.954
	HC	$Y_3 = 0.0056 + 0.000034 X_1 + 2.64E-6 X_2 - 0.00021X_3$	0.582
	CO	$Y_4 = -0.00003 + 0.000041 X_1 + 0.000011X_2 - 0.00018X_3$	0.801
	CO <sub>2</sub>	$Y_5 = -18.21 + 0.230X_1 + 0.00093 X_2 - 0.093X_3$	0.985
	PM	$Y_6 = -2.21 + 0.0293X_1 - 0.0136X_3$	0.880
Excavator 2	Fuel Use	$Y_1 = -5.07 + 0.0524 X_1 + 0.00069 X_2 - 0.0085 X_3$	0.972
	NO <sub>x</sub>	$Y_2 = -0.089 + 0.00082 X_1 + 0.000024 X_2 + 0.000134X_3$	0.884
	HC	$Y_3 = -0.0024 + 0.000048X_1 + 3.14E-6X_2 - 0.00008X_3$	0.402
	CO	$Y_4 = -0.0004 + 0.000013 X_1 + 0.000019 X_2 - 0.00024 X_3$	0.340
	CO <sub>2</sub>	$Y_5 = -16.05 + 0.166X_1 + 0.00213 X_2 - 0.0262 X_3$	0.972
	PM	$Y_6 = -1.53 + 0.021X_1 - 0.00026X_2 - 0.0064X_3$	0.913
Excavator 3	Fuel Use	$Y_1 = -2.343 + 0.0295X_1 + 0.00006X_2 - 0.007X_3$	0.935
	NO <sub>x</sub>	$Y_2 = -0.079 + 0.00096X_1 - 5.33E-6X_2 + 0.000096X_3$	0.880
	HC	$Y_3 = -0.0071 + 0.000034X_1 + 1.57E-6X_2 + 0.000094X_3$	0.250
	CO	$Y_4 = 0.0094 - 0.00005X_1 + 9.92E-6X_2 - 0.00018X_3$	0.096
	CO <sub>2</sub>	$Y_5 = -7.409 + 0.0932X_1 + 0.00017X_2 - 0.022X_3$	0.934
	PM	$Y_6 = -1.142 + 0.0081X_1 - 0.00013X_2 + 0.0104X_3$	0.390

**Table 5.** Comparison of validation results for SLR and MLR

Equipment	Pollutants	SLR			MLR		
		m	b	R <sup>2</sup>	m	b	R <sup>2</sup>
Excavator 1	Fuel Use	0.982	0.045	0.982	0.983	0.044	0.985
	NO <sub>x</sub>	0.948	0.005	0.948	0.944	0.004	0.951
	HC	0.352	0.002	0.351	0.573	0.002	0.575
	CO	0.542	0.005	0.543	0.773	0.003	0.759
	CO <sub>2</sub>	0.982	0.143	0.982	0.981	0.107	0.985
	PM	0.881	0.107	0.881	0.873	0.099	0.886
Excavator 2	Fuel Use	0.963	0.074	0.963	0.974	0.063	0.971
	NO <sub>x</sub>	0.850	0.007	0.850	0.887	0.006	0.879
	HC	0.392	0.003	0.390	0.441	0.003	0.434
	CO	0.220	0.015	0.219	0.322	0.013	0.327
	CO <sub>2</sub>	0.963	0.234	0.963	0.974	0.206	0.971
	PM	0.889	0.052	0.888	0.917	0.053	0.909
Excavator 3	Fuel Use	0.930	0.120	0.930	0.936	0.113	0.935
	NO <sub>x</sub>	0.875	0.007	0.876	0.878	0.007	0.878
	HC	0.193	0.004	0.194	0.243	0.004	0.239
	CO	0.018	0.008	0.018	0.105	0.007	0.100
	CO <sub>2</sub>	0.930	0.381	0.929	0.933	0.354	0.934
	PM	0.333	0.284	0.333	0.384	0.252	0.387

### 5.3 Model comparison

Model validations for the three excavators were developed in order to compare and evaluate the performance of SLR and MLR methodologies. The models were validated by plotting the predicted versus actual results for each model and fitting a trend line to

the data. For each trend line, the values of accuracy ( $m$ ), bias ( $b$ ), and precision ( $R^2$ ) were determined. As shown in Table 5, MLR produces higher  $R^2$  values compared to SLR for fuel use and all emissions rates. SLR has the lowest  $R^2$  value for fuel use and emissions rates. Overall, MLR outperformed SLR with respect to precision, accuracy, and bias. In most cases, the MLR approach produced highly precise models for  $\text{NO}_x$ ,  $\text{CO}_2$ , and PM; while the models for HC and CO were likely to be moderately precise with  $R^2$  values ranging from 0.50 – 0.87.

#### 5.4 Variable impact analysis

Using the MLR models, a variable impact analysis was conducted to determine the percentage of contribution of the input variables (MAP, RPM, and IAT) to the prediction of fuel use and emission rates of each pollutant. Table 6 presents the summary of the variable impact analysis for all three excavators. MAP is the most significant variable for fuel use, CO,  $\text{CO}_2$ , and PM which are 63.96%, 53.71%, 70.48% and 59.50%, respectively. RPM, however, has the most contribution for  $\text{NO}_x$ . IAT had the highest impact for HC.

**Table 6.** Variable impact analysis for average excavators

Engine Data	Fuel Use	$\text{NO}_x$	HC	CO	$\text{CO}_2$	PM
MAP	63.96%	40.13%	24.39%	53.72%	70.48%	59.50%
RPM	27.21%	43.20%	25.91%	35.02%	23.56%	19.67%
IAT	8.83%	16.57%	49.70%	11.26%	5.96%	20.83%

## 6. Conclusions and recommendations

The purpose of this paper was to demonstrate two different predictive modeling methodologies for estimating fuel use and emission rates of pollutants using real-world data. Based on the summary of Pearson correlation coefficients, MAP had a high positive correlation to fuel use and emission rates of  $\text{NO}_x$ ,  $\text{CO}_2$ , and PM, but had a moderate positive relationship with HC and CO. Although not as highly correlated, RPM had a strong positive relationship with fuel use and emissions. IAT was shown to have the least impact of the three engine performance variables on predicting fuel use and emission rates. It is recommended that other engine performance data, such as engine load or throttle position, be considered for future studies. For two modeling approaches, CO proved to be the most difficult pollutant emission rate to predict, as evidenced by its low  $R^2$  values. Typically, there is high variability in CO data which confounds the prediction effort, as well as the fact that CO did not have a strong correlation with any of the engine data predictor variables. It is recommended that strong relationships between CO and other variables be considered. For example, if there exists a strong relationship between CO and fuel use (which is accurately and precisely predicted by each of the three modeling approaches), then fuel use may be used as a predictor variable for CO.

With regard to variable impact analysis, it can be concluded that MAP has the highest percentage of contribution in the prediction of fuel use and emission rates, accounting for approximately 60% of total impact, although for HC and CO it had the second highest impact. For these two pollutants, RPM had the highest impact but it was second for fuel use, CO,  $\text{CO}_2$ , and PM. Although IAT had the lowest ranking impact among the three engine performance variables, it still may have some predictive power,

especially for CO. For strictly prediction purposes, it is recommended that all three engine performance variables be used to estimate fuel use and emission rates. Based on the model comparisons, MLR models generally performed better with respect to precision, accuracy, and bias. In most cases, the MLR approach produced highly precise models for NO<sub>x</sub>, CO<sub>2</sub>, and PM; while the models for HC and CO were moderately precise. These models are still useful. The simplicity of the one variable SLR models may be appealing to some users, such as fleet managers, that want to estimate the fuel use and emissions footprints of their equipment. Other users, such as engine manufacturers, may like the MLR approach because they would be able to reasonably estimate each of the engine performance variables.

Overall, the results of this study help to quantify and characterize the air pollution problem from HDD equipment used in construction. Although only excavators were addressed in this paper, the methodologies presented may certainly be used to develop fuel use and emissions models for other types of equipment. In order to further characterize this emissions problem, it is recommended that other types of equipment, such as backhoes, bulldozers, motor graders, track loaders, wheel loaders, and off road trucks, be targeted for future modeling efforts.

### Acknowledgement

The authors acknowledge the use of the real-world non-road equipment and emission database that was developed at North Carolina State University by Dr. H. Christopher Frey and Dr. William Rasdorf.

### References

- [1] Abolhasani, S., Frey, H. C., Kim, K., Rasdorf, W., Lewis, P., & Pang, S.-H, Real-World In-Use Activity, Fuel Use, and Emissions for Nonroad Construction Vehicles: A Case Study for Excavators. *Journal of the Air & Waste Management Association*, Vol 58(8), pp. 1033-1046, 2008.
- [2] EPA, *Users guide for the final NONROAD2005 model*, EPA-420-R-05-013, Ann Arbor, MI, 2005.
- [3] *Environmental Protection Agency Clean Air Act Advisory Committee (EPA CAAAC)*, Recommendations for reducing emissions from the Legacy Diesel Fleet. U.S. Environmental Protection Agency, Washington D.C, 2006.
- [4] Fitriani, H, Development of Predictive Modeling Tools for Estimating Fuel Use and Emissions Rates for Heavy-Duty Diesel Construction Equipment, *Doctor of Philosophy, Oklahoma State University*, Stillwater, OK, 2014.
- [5] Frey, H. C., Rasdorf, W., Kim, K., Pang, S.-H., Lewis, P., & Abolhassani, S, Real-World Duty Cycles and Utilization for Construction Equipment in North Carolina, Dept. of Civil, Construction, and Environmental Engineering, North Carolina State University, Raleigh, NC, 2008.
- [6] Kim, K., Operational Evaluation of In-Use Emissions and Fuel Consumption of B20 Biodiesel versus Petroleum Diesel-Fueled Onroad Heavy-Duty Diesel Dump Trucks and Nonroad Construction Vehicles. *Doctor of Philosophy, North Carolina State University*, Raleigh, NC, 2007.
- [7] Lewis, P. Estimating Fuel Use and Emission Rates of Nonroad Diesel Construction Equipment Performing Representative Duty Cycles. *Doctor of Philosophy, North Carolina State University*, Raleigh, NC, 2009.
- [8] Rasdorf, W., Frey, C., Lewis, P., Kim, K., Pang, S.-H., & Abolhassani, Field Procedures for Real-World Measurements of Emissions from Diesel Construction Vehicles, *Journal of Infrastructure Systems*, Vol 16(3), pp. 216-225, 2010.

# The effects of natural and artificial UV exposure on the physical properties of synthetic turf used for various sports fields

Adriano Coutinho ZUZARTE<sup>1</sup> and Deon KRUGER

*Department of Civil Engineering Science, University of Johannesburg, South Africa*

**Abstract.** Since its induction at the Astrodome, in 1965 synthetic turf has been improved and adapted to now be accepted as a playing surface for a variety of sports. These sports include Rugby, Soccer and Field hockey. As synthetic turf is most likely destined for outdoor use it will be subject to Ultra Violet (UV) degradation in the form of Ultra Violet light band A (UVA), Ultra Violet light band B (UVB) or a combination of both. Synthetic turf is a polymer based material, specifically polyethylene for this study. For this reason it is useful to investigate how polyethylene degrades due to UV. Absorbed UV causes a break in the intermolecular bonds of the polyethylene, which leads to cracking, inhibiting the material to perform as initially intended. Colour change is also a consequence of extended exposure to UV. Various UV stabilizers are used, by manufacturers, in order to slow this process down. These however are largely dependent on the type of UV being exposed.

Natural UV testing of new materials is time consuming, thus accelerated weathering testers such as the QUV/spray machines are used to simulate artificial UV and accelerate this process. A correlation between natural and artificial UV is sometimes difficult to achieve. For this reason both natural and artificial UV exposures were performed in this study. Through these various exposures to the samples, it was possible to indeed confirm that UV degrades synthetic turf as well as the processes leading to it. It was also confirmed that the samples would meet the sporting standards set out by the International Rugby Board (IRB), Fédération Internationale de Football Association (FIFA) and International Hockey Federation (FIH), for use as a playing surface. A correlation between natural and artificial UV in terms of colour change was achieved with UVA being found as the predominant type of natural UV exposure in Johannesburg, during the winter months. Solutions were also provided to mitigate the degrading effects of UV on synthetic turf, these solutions would however need further investigation

**Keywords.** UV, UV degradation, UV exposure, synthetic turf, synthetic yarn

## Introduction

What is natural UV? Natural UV, for the purposes of this study will be defined as UV that is emitted by the sun. Of the four types of UV emitted by the sun, only two eventually make it to the earth's surface, these being UVA and UVB. UVA makes up 95% of the UV that reaches the earth's surface and is characterized as the UV that allows your skin to tan. UVB on the other hand is characterized as the UV that causes human skin to burn causing skin cancer, due to its shorter wavelengths.

<sup>1</sup>Corresponding author: [adrianozuzarte@gmail.com](mailto:adrianozuzarte@gmail.com)

The intensity of UV exposure is affected by a variety of factors such as latitude, time of year, time of day, altitude, ozone levels and cloud cover [2]. What is artificial UV? Artificial UV, for the purposes of this study will be defined as UV that is emitted by the fluorescent bulbs used in the QUV/spray accelerated weathering tester. This piece of equipment does not try to replicate the entire spectrum of sunlight but rather the damaging effects of sunlight [3]. Through this piece of equipment it is possible to simulate months or years of outdoor exposure within weeks or months in the lab.

Two different types of lamps were used, UVA-340 and UVB 313. UVA-340 lamps emit a spectrum much the same as natural sunlight, with UVB-313 emitting a harsher spectrum [4]. What is synthetic turf? Synthetic turf is a polymer based material made using either polyethylene or polypropylene. Synthetic turf is formed through an extrusion process. The polymer is mixed together with a host of chemical additives such as colour dyes and UV stabilizers to form either a monofilament yarn or fibrillated yarn [5]. Many types of UV stabilizers can be used such as: UV reflectors, UV absorbers, Quenchers as well as HALS [6].

How does UV degrade synthetic turf? Synthetic turf degrades due to UV through a process known as photochemical degradation [7]. To understand how photochemical degradation occurs one needs to understand the three principles which govern this degradation. They are the Grotthus-Draper law, Stark-Einstein law and the bond dissociation energy [7]. Through these principles UV has the greatest potential to break the intermolecular bonds, due to its higher energy. Heat, oxygen and moisture then cause degradation through secondary reactions [8]. UVB with its shorter wavelengths and higher energy will have the greatest potential of breaking bonds when compared with UVA. Free radicals which exist in the synthetic turf due to impurities introduced during the manufacturing process attract and absorb the UV. The energy then excites and promotes the electrons from the highest occupied molecular orbital to the lowest unoccupied molecular orbital. This jump of electrons causes a rearrangement of atoms at this point with subsequent scission or crosslinking leading to degradation [9].

Through the degradation process the synthetic turf experiences the following effects to its physical properties. Cracks and crazing throughout the sample surface causing the material to become brittle. Gloss loss and chalking which through chemical reactions causes the material to lose its original colour [10]

## **1. Research methodology**

The research was broken down into three different types of UV exposure. Each type of exposure then had three tests performed both pre and post UV exposure for comparison. The three tests performed were a tensile strength test (BS EN 13864:2004), a colour change test (BS EN 20105-A02:1995) as well as micrographs taken using a scanning electron microscope (SEM). Through the various tests the following properties were compared: breaking force, percentage elongation, linear density and colour change. The samples used for the exposures are listed in Table 1 and supplied by Sportslabs Ltd.

**Table 1.** Synthetic yarn samples supplied by Sportslabs Ltd

Yarn SL Reference	Name	Yarn type
5644	MN Slide - Diamond Bright Green	Monofilament
5646	MN Ultra - White	Monofilament
5655	FB Ultra - Black	Fibrillated
5656	FB Ultra – Cardinal Red	Fibrillated

### 1.1. Exposure type 1 – Sportslabs Ltd.

The first type of exposure was performed by Sportslabs Ltd. The samples were exposed to artificial UV according to the BS EN 14836:2005. These results were compared against the standards set out by the IRB, FIFA and FIH for UV degradation of synthetic turf. It should be noted that the sporting bodies require samples to be exposed to the full period of artificial UVA in order to be compared to their standards.

### 1.2. Exposure type 2 – 80 days of natural UV exposure

The second type of exposure consisted of exposing the samples to 80 days of natural UV in Johannesburg, South Africa from the end of June till the beginning of September. The following climatic conditions were recorded for the exposure period: moderate to high levels of UV, clear skies, low rainfall, relatively dry conditions and mild to low temperatures.

### 1.3. Exposure type 3 – Equivalent 80 days artificial UVA and UVB exposure

The third type of exposure consisted of exposing the samples to an equivalent 80 days of artificial UVA and UVB. The equivalent times were calculated using the radiation rates for the two types of lamps used in the QUV machine as well as the kLangley rating for Johannesburg (170 kLangley/year)[11]. This gave the following equivalent exposure times:

- UVA @ 0.89 W/m<sup>2</sup> for 732 hours
- UVB @ 0.62 W/m<sup>2</sup> for 840 hours

## 2. Results

The results are presented in table format using percentages for each property investigated, for the various exposures. What should be noted is that a positive percentage indicates a gain in that particular property from pre to post UV exposure, with a negative percentage indicating a loss.

### 2.1. Exposure type 1 – Sportslabs Ltd.

**Table 2.** Percentage change in sample characteristics for artificial UVA, Sportslabs Ltd.

Sample	Tensile strength	Percentage elongation	Linear density	Colour change
5644	-17.36%	-17.41%	2.35%	Lighter
5646	-4.38%	6.49%	4.17%	Lighter
5655	-5.91%	6.42%	2.50%	Lighter
5656	-1.96%	6.53%	2.11%	Lighter



**Table 3.** Percentage change in sample characteristics for artificial UVB, Sportslabs Ltd.

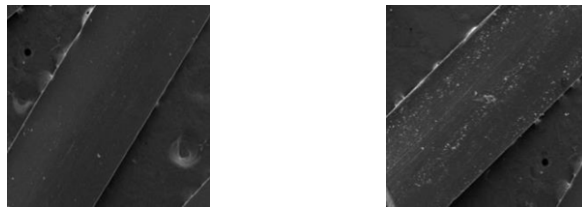
Sample	Tensile strength	Percentage elongation	Linear density	Colour change
5646	-4.38%	6.49%	4.17%	Lighter

**Figure 1.** SEM micrograph of sample 5644 both pre and post artificial UVA exposure

### 2.2. Exposure type 2 – 80 days of natural UV exposure

**Table 4.** Percentage change in sample characteristics for 80 days of natural UV exposure

Sample	Tensile strength	Percentage elongation	Linear density	Colour change
5644	-1.83%	-11.56%	6.85%	No change
5646	4.73%	2.91%	-2.86%	No change
5655	2.27%	-8.61%	0.90%	No change
5656	-2.62%	-12.68%	3.87%	Lighter

**Figure 2.** SEM micrograph of sample 5644 both pre and post 80 days natural UV exposure

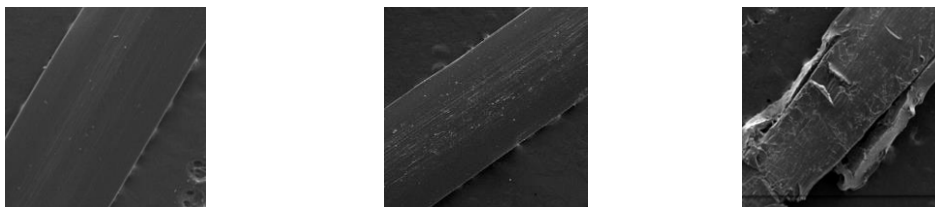
### 2.3. Exposure type 3 - Equivalent 80 days artificial UVA and UVB exposure

**Table 5.** Percentage change in sample characteristics for equivalent 80 days artificial UVA exposure

Sample	Tensile strength	Percentage elongation	Linear density	Colour change
5644	-2.34%	14.97%	2.74%	No change
5646	1.07%	11.61%	-6.67%	No change
5655	-4.52%	8.79%	0.54%	No change
5656	-10.70%	1.12%	3.49%	Lighter

**Table 6.** Percentage change in sample characteristics for equivalent 80 days artificial UVB exposure

Sample	Tensile strength	Percentage elongation	Linear density	Colour change
5644	-88.13%	-97.49%	16.44%	Lighter
5646	-33.31%	14.36%	29.52%	Lighter
5655	-27.06%	-18.37%	1.26%	Lighter
5656	-25.38%	3.16%	0.47%	Lighter



**Figure 3.** SEM micrograph of sample 5644 both pre and post equivalent 80 day artificial UVA and UVB exposure

### 3. Data analysis

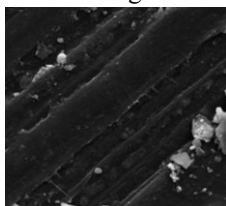
#### 3.1. Exposure type 1 – Sportslabs Ltd.

Through the various types of exposures investigated, there have been some noteworthy results. Firstly looking at Table 2 it can be seen that all the yarn samples are able to resist significant amounts of sustained UVA exposure, with minimal degradation. Figure 1 shows a SEM image taken both pre and post exposure with little changes seen. Since artificial UVA is more akin to natural UV exposure, it is used by the three sporting bodies to test the suitability of samples for use. Table 7 shows that all the samples would be fit for use as an artificial playing surface for Rugby, Soccer and Field Hockey. The standards (BS EN 14836:2005) require a change in tensile strength of no more than 50% and a grey scale rating of no less than 3 when exposed to UVA.

**Table 7.** Percentage change in sample characteristics for equivalent 80 days artificial UVA exposure

Sample	Sporting governing bodies					
	IRB		FIFA		FIH	
	Tensile strength	Colour change	Tensile strength	Colour change	Tensile strength	Colour change
5644	Yes	Yes	Yes	Yes	Yes	Yes
5646	Yes	Yes	Yes	Yes	Yes	Yes
5655	Yes	Yes	Yes	Yes	Yes	Yes
5656	Yes	Yes	Yes	Yes	Yes	Yes

Certain results recorded seem irrational. Certain samples increased their percentage elongation and linear density from pre to post UV exposure. Firstly the increase in percentage elongation can be explained through the initial crosslinking experienced during the degradation process actually increasing the elasticity of the material [9] with prolonged crosslinking eventually leading to a loss. The increases in linear density could be caused due to impurities left on the sample surface such as residue of evaporated water etc. as seen in Figure 4.



**Figure 4.** SEM micrograph depicting impurities left on the sample surface

All four samples experienced a loss in colour this would suggest that the colour pigments used in the samples are quite susceptible to erosion. When the samples were handled post UV exposure a sticky residue could be felt which would suggest Gloss loss occurred through the weeping process where the pigment is removed through a chemical reaction leaving a sticky residue.

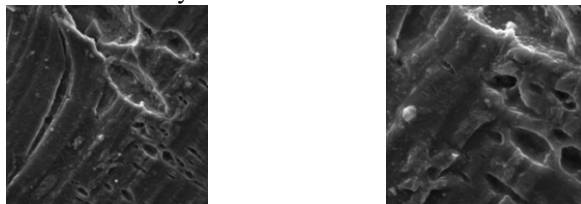
### 3.2. *Exposure type 2 – 80 days of natural UV exposure*

The results recorded in Table 4 show no consistency between all the samples. When one looks at the minimal losses experienced by the samples being exposed to artificial UVA for a substantial amount of time (Table 2) and compares this to the samples being exposed to natural UV, during winter months for substantially less amount of time (Table 4), it allows for the conclusion that no degradation has in fact occurred. This is confirmed by the SEM images in Figure 2 where no change can be seen from pre to post exposure. The increases and losses recorded can be explained by the fact that no one piece of sample is the same. No matter how small the difference it will be detected when measuring such a sensitive material.

### 3.3. *Exposure type 3 - Equivalent 80 days artificial UVA and UVB exposure*

The equivalent 80 day artificial UVA once again offered little in terms of degradation which for reasons explained above, is expected. One interesting comparison occurred with the colour change, where both the 80 day natural UV (Table 4) and equivalent 80 day artificial UVA exposures (Table 5) had the same results. The colour change measurement used was however qualitative and therefore subjective, a more quantitative measurement should be used in future for greater accuracy. The similar rates of degradation between the 80 day natural and equivalent 80 day artificial UVA suggest that UVA is the predominant type of UV exposure in Johannesburg in winter.

The equivalent 80 day artificial UVB exposure, offered some fascinating results and showed exactly how artificial turf degrades as well as the process leading to it. Figure 3 shows how severe the degradation is compared to UVA (post UVA is the center image and post UVB is the image on the right). Through the micrographs it was possible to see the crazing and cracking that occurs. The fibrillated samples actually melted and fused together with the monofilament samples snapping and warping due to the intensity of the UVB. Figure 5 shows a magnified image of sample 5644's surface illustrating how voids form and propagate into a crack. These cracks reduce the materials ability to perform as initially intended as seen in the results of Table 6.



**Figure 5.** Magnified SEM micrographs depicting cracking on sample 5644's surface

One interesting thing to note is how susceptible the samples were to degradation when exposed to artificial UVB as compared to UVA. Given that their energy and wavelengths are completely different with UVB being the harsher of the two but this

would suggest that the UV stabilizers are very much dependent on the type of UV being exposed.

UV stabilizers work much the same as sunscreens applied by humans. Sunscreens either offer UVB (SPF rating) protection or a broad spectrum protection. Broad spectrum protection means the sunscreen protects against both the shorter wavelengths of UVA as well as UVB [2, 12]. This phenomenon is illustrated with the monofilament samples. Sample 5644 suffered degradation with UVA and severe degradation with UVB suggesting a UVA stabilizer was used (Tables 5 and 6). Sample 5646 performed reasonably well against both UVA and UVB (Tables 5 and 6) suggesting a broad spectrum UV stabilizer was used. Sample 5646 was also the only sample to be exposed to artificial UVB for the required time stipulated by the sporting bodies (Table 3) where it performed reasonably well.

#### 4. Conclusions and recommendations

Through this study, it was possible to confirm the degrading effects that UV has on synthetic turf in terms of cracking, crazing and colour change. It was also possible to rate each sample against the standards set out by the sporting governing bodies (IRB, FIFA and FIH). These standards need to be revised, as they only cover UVA exposure, which is sufficient for low UV intensive areas. However synthetic turfs are being installed in UV intensive areas where UVB degradation becomes an issue.

The 80 days of natural UV exposure along with the equivalent 80 days of artificial UVA offered insight into a possible correlation between artificial and natural UV. These exposures confirm work done by Fredor and Brennan where an acceleration factor is highly dependent on location [13]. It is believed that should a full year of natural UV exposure be performed a correlation across all tests may be achieved.

These exposures revealed that the UV stabilizers effectiveness are largely dependent on the type of UV they are designed to resist. Consideration should be taken in terms of which type of UV stabilizer is suitable for the location where the turf will be used. Broad spectrum stabilizers should be used in UV intensive areas with UVA stabilizers in less intensive areas.

UV stabilizers, like sun screen, do not offer a permanent solution to UV degradation as over time they lose their effectiveness. The building of fully enclosed and semi enclosed sporting stadiums in conjunction with the use of UV stabilizers could offer a more permanent solution.

#### References

- [1] Target Technologies International, *Artificial / Synthetic Turf Infill & Materials: A Brief History of Artificial Turf*, Available from: [http://www.ttiionline.com/turf\\_industry\\_history.htm](http://www.ttiionline.com/turf_industry_history.htm) 7 October 2013
- [2] UV Awareness, *What is UV*, Available from: <http://www.uvawareness.com/uv-info/uv-information.php>, 5 July 2013.
- [3] Q-Lab, *Sunlight, Weathering & Light Stability Testing*. Q-Lab, Westlake, Ohio, USA, 2007.
- [4] Q-Lab, *Controlled Irradiance in Laboratory Weathering: Limitation in the State of the Art*. Q-Lab, Westlake, Ohio, USA, 1994.
- [5] swicoFil, *Vitagrass monofilament yarns*, Available from: <http://www.swicofil.com>, 5 July, 2013.
- [6] Harper, C, *Handbook of Plastics Technologies: The Complete Guide to Properties and Performance: Chapter 5 Plastic Additives*, McGraw-Hill Professional, Access Engineering, 2006.

- [7] Kitsinelis, S, *Light Sources Technologies and Applications*. Taylor & Francis. 12 materials and technology, 2010.
- [8] Vasile, P and Cornelia, M, *Practical guide to polyethylene*. Rapa technology limited. Shawbury, U.K, 2005.
- [9] Callister, W, *Materials science and engineering an introduction 7th ed*, United States of America: John Wiley & Sons, Inc. 9 swicofil, 2007.
- [10] Materials Technology, *UV Degradation Mechanisms*. Available from: <http://www.drb.mattech.co.uk/uv%20degradation.html>, 16 March 2013.
- [11] Heuvel - Folies bvba, *Levensduur (uv-starling)*. Available from: <http://heuvelfolies.be/CMS/Producten/Tunnel-%20en%20serrefolie/Folie-eigenschappen>, 13 July 2013.
- [12] American Cancer Society, *Skin cancer prevention and early detection – UV protection*. Available from: <http://www.cancer.org/cancer/skincancermelanoma/moreinformation/skin-cancer-prevention-and-early-detection-u-v-protection>, 5 July 2013.
- [13] Fedor, G and Brennan, P, *Comparison between Natural Weathering and Fluorescent UV Exposures: UVA-340 Lamp Test Results, Durability Testing of Non-Metallic Materials*, ASTM STP 1294, Robert J. Herling, Ed., American Society for Testing and Material, Philadelphia, 1996.

# Thermal characterization of heat reflective coating for building application

Bal Mukund SUMAN<sup>1</sup>

*CSIR, Central Building Research Institute Roorkee, Uttarakhand, India*

**Abstract.** The paper describes the measurement of thermal conductance and resistance of a reflective coating in the laboratory by guarded hot plate apparatus. Thermal resistance (R) of the coating and white wash was found 0.0012 m<sup>2</sup>K/W and zero respectively and reflectivity of heat reflective coating and white washing is 0.85 and 0.70. The maximum temperature difference of ceiling and the west wall surface between heat reflective coated room and the room treated with white wash were recorded as 6.0° C and 3.8° C respectively. The cooling load was reduced by 5.75% and 12.7% for heat reflective coated room on wall and for both the roof and walls respectively when compared to white wash application on wall and on roof and wall both when air-conditioner of 18000 Btu/hr capacity was used in each of the identical rooms maintaining indoor temperature at 23°C.

**Keywords:** Heat reflective coating, thermal conductance, cooling load, energy saving, set temperature

## Introduction

Energy conservation in the building sector is prominent in the era of energy shortage and escalations in energy cost as most of the energy is consumed in air conditioning of commercial building, office building, and cold storages particularly in summer season. Since most of the energy source of conventional form is depleting day by day, the application of heat reflective coating on building is important for saving in energy consumption. Energy saving in air conditioning may be achieved by reducing cooling load using quality heat reflective coatings or thermal insulation at roof and exposed surfaces of building or combination of both.

From olden days people use to get benefited of heat reflectivity by applying white wash on exposed surfaces of the building. Due to some drawback, such as non-durability, lower reflectivity and negligible thermal resistance, white wash application is discouraged. But due to low cost, white wash is still popular in rural areas to minimize effect of solar radiation on building. Reflective thermal coating is characterized for building application to drop indoor temperature improving inside thermal comfort condition during summer. Some of the important studies [1-3] made in which a reduced heat flux was noticed in the building with reflective coated roof. The heat gain into the building is required to minimize for improvement of indoor thermal condition. The application of white wash on external surfaces of the building can reduce heat gain up to some extent.

<sup>1</sup>Corresponding author: [bs\\_ashishh@rediffmail.com](mailto:bs_ashishh@rediffmail.com)

The heat reflective coating with high reflectivity (0.85 – 0.90) with its thermal resistance will be effective in reducing, power consumption in AC building and indoor temperature in non AC building. It was found from an experimental study conducted at Delhi that measured air temperatures within the white coated building were cooler than the dark building by more than 6°C on an average during summer. A comprehensive experimental study has been carried out to find actual influence of a typical heat reflective coating on thermal behavior of building. Two identical side by side rooms were monitored in which one had its wall and roof painted with a heat reflective coating. Other room was treated with simple white wash which is taken as reference room. The wall and roof of both the identical rooms have thermal transmittance of 2.3W/m<sup>2</sup>K and 3.66W/m<sup>2</sup>k respectively. Thermal transmittance (U) was determined by measuring K- value (Guarded hot plate method) of the materials used in different layers of wall and roof and using the equation,

$$U = \left( \frac{1}{h_i} + \sum_{j=1}^n \left( \frac{L_j}{K_j} \right) + \frac{1}{h_o} \right)^{-1} \quad \text{---} \quad \text{---} \quad (1)$$

Where  $h_i$  &  $h_o$  are inside and outside convective heat transfer coefficients respectively and L & K are thickness and thermal conductivity of the material layers.

### 1. Characterization of heat reflective coating (laboratory study)

Thermal conductance and thermal resistance of heat reflective coating are measured in the laboratory by Guarded hot plate apparatus [4] at heat transfer laboratory of Central Building Research Institute Roorkee. The required sample size for this equipment is 300 mmX300mmX50mm. Thermal conductance was measured of the substrate coated with and without heat reflective paints (HRP). The double coat of HRP was made on the substrate to measure thermal conductance. Roofing and walling materials are taken as substrate and thermal resistance of these substrates with and without HRP was also determined and given in Table 1.

**Table 1.** Thermal Resistance of the substrate, determined by Guarded hot plate apparatus

S. No	Name of the material	Thermal Resistance (m <sup>2</sup> K/W)
1.	Heat Reflective Paint (HRP)	0.0012
2.	23 cm Brick with 1.5 cm C.Pl each side	0.2836
3.	23 cm Brick with 1.5 cm C.Pl each side with HRP	0.2848
4.	10 cm RCC with 1.5 cm C.Pl at ceiling	0.0450
5.	10 cm RCC with 1.5 cm C.Pl at ceiling with HRP	0.0462

The application of heat reflective paint enhances thermal resistance of roof from 0.0450 m<sup>2</sup>K/W to 0.0462m<sup>2</sup>K/W and wall section from 0.2836 m<sup>2</sup>K/W to 0.2848 m<sup>2</sup>K/W, because thermal resistance of the heat reflective paint is measured as 0.0012 m<sup>2</sup>K/W. Thermal resistance was determined by the equation:

$$K_1 = \frac{V_1 \cdot I_1 \cdot L_1}{A (\Delta T)}, \text{ Or, } \frac{L_1}{K_1} = \frac{A (\Delta T)}{V_1 \cdot I_1} = R_1 \quad \text{---} \quad \text{---} \quad (2)$$

Where, V and I represents voltage and current and  $L_1$  and  $K_1$  denotes thickness and thermal conductivity respectively of the substrate material only. Similarly  $L_2$  and  $K_2$  of the substrate coated with Paint was taken to determine thermal resistance.

$$K_2 = V_2 \cdot I_2 \cdot L_2 / A (\Delta T), \text{ Or, } L_2 / K_2 = A (\Delta T) / V_2 \cdot I_2 = R_2 \quad \text{---} \quad \text{---} \quad (3)$$

Therefore, thermal resistance (R) of the coating will be,  $R = R_2 - R_1$

## 2. Characterization of heat reflective coating (field study)

### 2.1 Measurement of indoor and outdoor temperatures

Heat reflective coating has been made characterized by conducting experiments in the field. Two experimental rooms, identical in all respect i.e. orientation, dimension, specification etc. located in the campus of Central Building Research Institute; Roorkee was chosen for conducting experiments. The construction of walls is 23cm brick plastered both side and roof is 10cm RCC with plastered ceiling and the floor is normal cemented. The dimension of the identical rooms is 3.45m x 3.20m x 3.14m. The upper surface of roof and all the four walls of one of the room were treated with heat reflective coating. The outer surfaces of roof and wall were coated with ordinary white wash. This untreated room acts as a reference room for comparison purposes. The application of heat reflective coating enhances thermal resistance of roof and wall of the building by 0.012 m<sup>2</sup>K/W. Apart from thermal resistance; reflectivity is the important property which helps to bring down the cooling load of a building.

The indoor and outdoor surface temperatures of wall and roof were recorded in both the reference room and the treated room simultaneously along with the outdoor air temperatures during peak summer at an interval of half an hour throughout day and night. The observations were recorded with thermocouple fixed at various surfaces of roof and walls at both the external and internal points. Thermocouples were connected with 48 Channel Data logger. Roof temperature is an important parameter, which essentially determines the solar induced heat leakage through the roof into the building. As the upper surface temperature of roof decreases, heat flow into the building simultaneously reduces. As a result, lower peak temperature exists in the building with the application of heat reflective paint on roof. The inside surface temperature of roof and walls and outdoor air temperature profiles are given in graphical form depicted in Fig. 1 to Fig. 4 on a typical clear sunny day when ambient temperature varied between 38 to 42 degree Celsius and Relative humidity was 60 % approximately. The temperature profiles clearly indicate the effect of heat reflective paint application on wall and roof on indoor thermal environment. The difference of inside surface temperatures of wall and roof of both the treated and reference rooms are mainly due to higher reflectivity and thermal resistance of heat reflective paint than the conventional white wash. Temperature difference between ceilings of HRP coated roof of treated room and roof of reference room was 6°C. Similarly maximum temperature difference of inside surface of South, East, North and West wall between treated room and reference room were observed as 2 °C, 2.4 °C, 2.2 °C and 3.8 °C respectively.



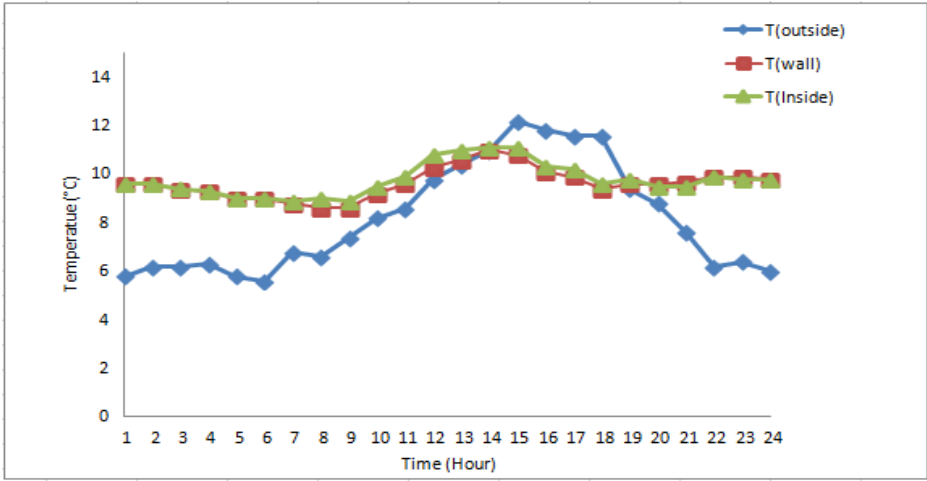


Figure 1. Thermal performance of heat reflective coating in winter months

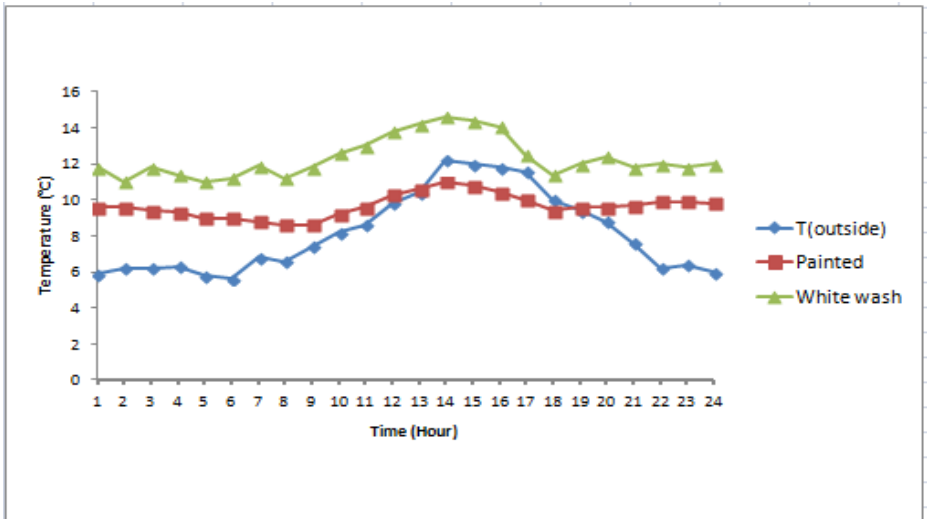


Figure 2. Comparison between thermal performance of heat reflective coating and white wash in winter

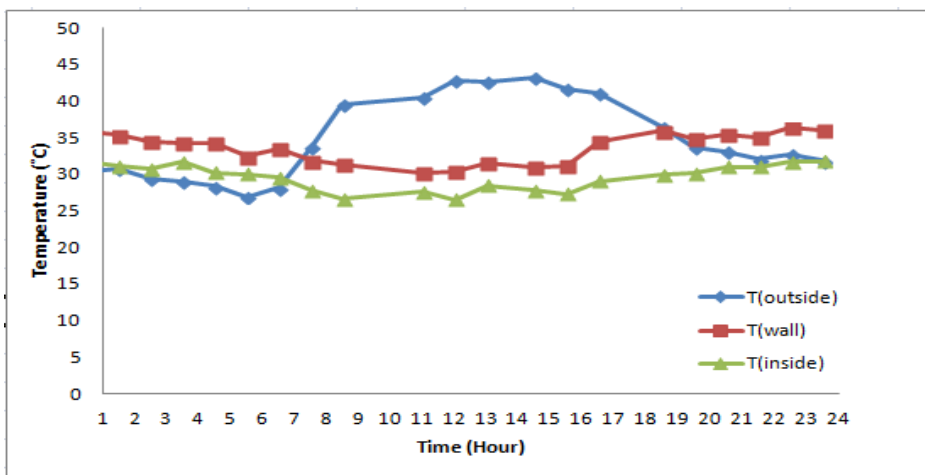


Figure 3. Thermal performance of heat reflective coating during summer

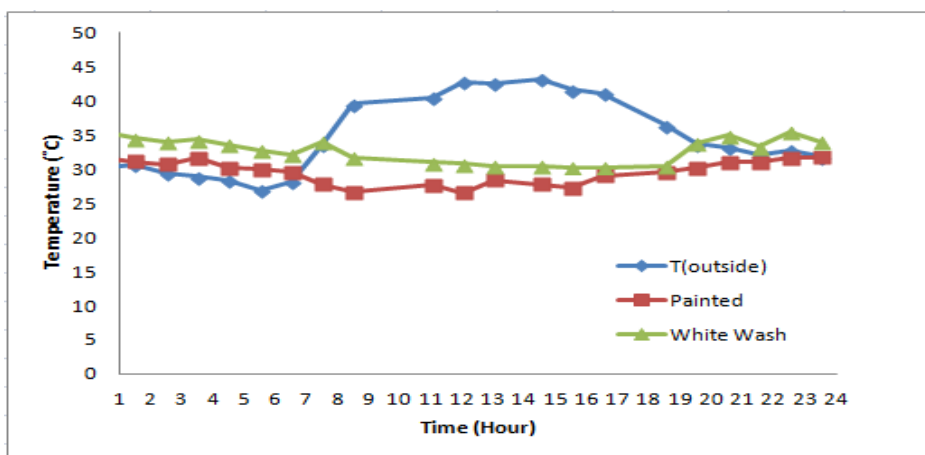


Figure 4. Comparison between thermal performance of heat reflective coating and whitewash in summer

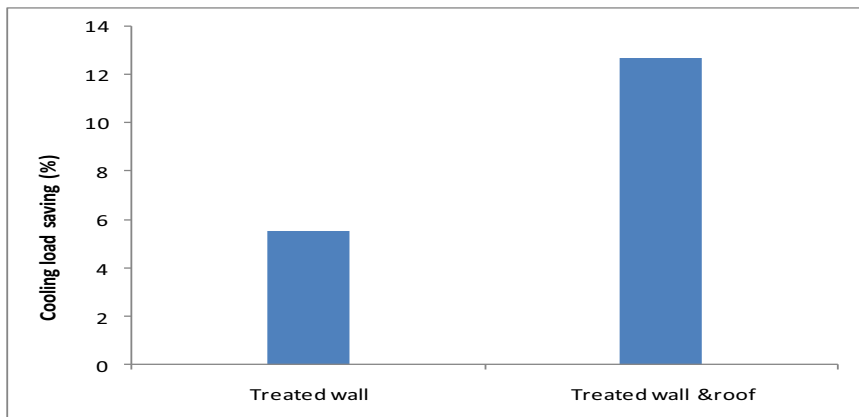
### 2.2 Cooling load observation

Two window type air conditioners of cooling capacity of 18000 Btu/hr each have been installed on the longer wall of both the treated room and reference room to assess the energy implications of HRP application. The base temperature of room has been set at 23°C which may be understood as the temperature of the thermostat setting below/above, which the air-conditioning unit will be switched off/on automatically. Electrical energy meters have been installed to measure the total electrical energy consumption in air conditioning system of each of the rooms separately. The difference in the consumption of electrical energy in treated and untreated reference room over the same period was measured for actual energy saving due to application of heat reflective paint in the treated room. In the first step, only

walls of treated room were treated by heat reflective paint and white washing was applied on walls of the reference room. In this case saving in electrical energy was recorded of the order of 5.56% in treated room over reference room. Similarly energy saving in electrical energy was recorded of the order of 12.73% when heat reflective paint was applied on both roof and walls of treated room and white washing was applied on walls and roof of the reference room. These results are shown in Table 2 and the percentage savings in energy consumption by application of HRP on roof and walls has been shown in fig. 5.

**Table 2.** Energy saving and temperature drop by paint coated on buildings

Application on Wall of treated room	Application on Roof of treated room	Energy Saving (%)	Maximum Indoor air temperature difference between treated room and reference room	Max. temperature difference between exterior and interior surface of the treated room
HRP	---	5.56	2.8	4.9
HRP	HRP	12.73	3.1	7.5



**Figure 5.** Saving in energy consumption (%) by application of heat reflective coating on roof and wall

### 3. Discussion

Experimental work was carried out in two phases as discussed in the previous section for evaluating the performance of heat reflective paint. The roof and walls of treated room was coated with heat reflective paint (HRP) and application of white wash was made on roof and walls of reference room. Indoor and outdoor temperatures of both the treated room and reference room have been recorded by using thermocouples and data logger device. Thermal conductance and thermal resistance of HRP has been determined in the laboratory. The thermal resistance of double coated HRP was  $0.0012\text{m}^2\text{K/W}$  where as white wash does not change any thermal resistance of the building section.

Temperature recorded for both the phases of experiments are given in fig 1 to fig 5. It is observed from these figures that there was low temperature difference between the north wall (2°C) and south wall (2.2°C) surfaces of treated room and reference room, because in summer, these walls receive lesser exposure of sun. The temperature differences are quite high for west (3.8°C) and east walls (2.4°C) between treated room and reference room. Sun travels through above middle path in the sky and hence roof gets maximum exposure. The temperature difference of ceilings between treated and reference room is found of the order of 6°C. One air-conditioner in each room (treated room and reference room) of 18000 Btu/hr capacities each was installed to record electrical energy consumption. In the first step only walls of treated room were treated by heat reflective paint and white washing was applied on walls of the reference room. In this case saving in electrical energy was recorded of the order of 5.56% in treated room over reference room. Similarly energy saving in electrical energy was recorded of the order of 12.73% when heat reflective paint was applied on both roof and walls of treated room and white washing was applied on walls and roof of the reference room.

#### 4. Conclusion

Thermal resistance of heat reflective coating is found 0.0012m<sup>2</sup>K/W. This gives an additional advantage to the reflectivity of HRP in lowering down the effect of solar radiation. The provision of HRP treatment on roof and wall brings down the indoor surface temperature of wall and roof by 2.2 to 6°C in comparison to the room with white wash application. The findings of the experiments are summarized as follow. It is observed that for AC buildings energy consumption in electrical energy was 5.56% lower in treated room than reference room when only wall was treated and the energy consumption was further reduced by 12.73% in treated room when compare to reference room when both roof and wall was treated. The application of HRP on roof and wall of the room improves the thermal environment conditions during summer in unconditioned building.

#### Acknowledgement

The study forms part of the regular R&D work done at CBRI Roorkee. The paper is sent for publication with permission of Director, CBRI.

#### Reference

- [1] Sharma M. R. and Sharafat Ali, "Assessment of Solar radiation on buildings" *Building Digest No. 108*, (1981), A CBRI Roorkee publication.
- [2] Anderson R W, Yarbrough D W, Graves R S & Wendit R L, Preliminary assessment of radiation control coatings for building: Testing and application *ASTM-STP*, Vol.2 (ASTM, Philadelphia, PA) 1991, pp.1116.
- [3] Bansal N K, Garg S N & Kothari S, Effect of exterior surface colour on thermal performance of buildings, *Build Environ*, 27 (1991), pp.31-36, Elsevier Ltd..
- [4] IS:3346, Method for the determination of thermal conductivity of thermal insulation materials.(Two-slab, guarded hot plat method) (1980), *Indian Standards Institution*, Manak Bhavan, New Delhi.

# Impact of traditional and modern building materials on the thermal behavior and energy consumption of a courtyard house in the hot and dry climate

Naïma FEZZIOUI<sup>a,1</sup>, Mébirika BENYAMINE<sup>b</sup>, Saleh LARBI<sup>c</sup>, Belkacem DRAOUI<sup>a</sup>,  
and Claude-Alain ROULET<sup>d</sup>

<sup>a</sup>*Energy Laboratory in Arid Zones ENERGARID, University of Bechar, Algeria,*

<sup>b</sup>*FIMAS Laboratory University of Bechar Algeria*

<sup>c</sup>*Mechanical Engineering and Development Laboratory, National Polytechnic School*

<sup>d</sup>*École Polytechnique Fédérale de Lausanne, EPFL*

**Abstract.** In this work, we studied the thermal behavior of mono or multilayer walls of various compositions consisting of traditional and modern building materials, in order to identify those that provide good comfort and better energy conservation in conditioning case in the context of a hot and dry climate for a courtyard house. The study is conducted with the TRNSYS-COMIS software. The thermo physical properties of modern building materials are those adopted by the Algerian regulations and those of adobe were determined in the laboratory LASIE at the University of La Rochelle. The results of this study show the impact of inertia on winter consumption, as well as the effectiveness of roof insulation in reducing cooling requirements. The adobe has good properties to improve comfort and energy savings but its stabilization with cement, to improve its mechanical properties decreases its thermal qualities.

**Keywords.** Adobe, roof insulation, multilayer walls, modern building materials, cooling requirements, TRNSYS-COMIS

## Introduction

The comfort of the buildings depends largely on the materials that constitute them and on the way they are used. Despite the important progress experienced by the construction industry, there is no clear methodology to implement a suitable selection of these materials [1]. The courtyard house "WAST Eddar" is the dominant model of space organization of Ksar Kenadsa (southwest of Algeria). This type of house, well suited to provide natural summer comfort is much less comfortable in winter [2], [3]. Several studies focused on wall insulation, some by calculating the improvement of the time constant in the wall [4]. Sambou [5] and Asan [6] look for an optimization by

---

<sup>1</sup>Corresponding author: [naifez@yahoo.fr](mailto:naifez@yahoo.fr), Fax. +213.49.81.52.44

genetic algorithm in hollow blocks walls offering the best combination insulation/inertia. Gossard [7] studied the equivalent thermophysical properties of the outer wall that maximize energy performance. Tsilingiris [8] optimizes the position of the two insulating wall inside a high inertia. In this work, we studied the thermal behavior of mono or multilayer walls of various compositions to identify those that provide a better natural comfort without conditioning [9], and greater energy savings in conditioning conditioned house in the city of Kenadsa. To ensure their general applicability, these expected solutions should be simple and easy to implement.

## 1. Simulation

The studied house is shown schematically in Figure 1. Table 1 describes the compositions of the walls chosen for this work, together with the thermal characteristics of materials (thermal conductivity  $\lambda$ ,  $\rho$  density and specific heat  $c$ ) and those of complete walls (heat transfer coefficient  $U$  according to EN 6984 and surface heat capacity  $\chi$  according to EN 13786 [10], this in accordance with the DTR C3-2 [11]. The simulations are performed for twenty types of walls (K1 to K20) and two types of roofings (L1 and L2).

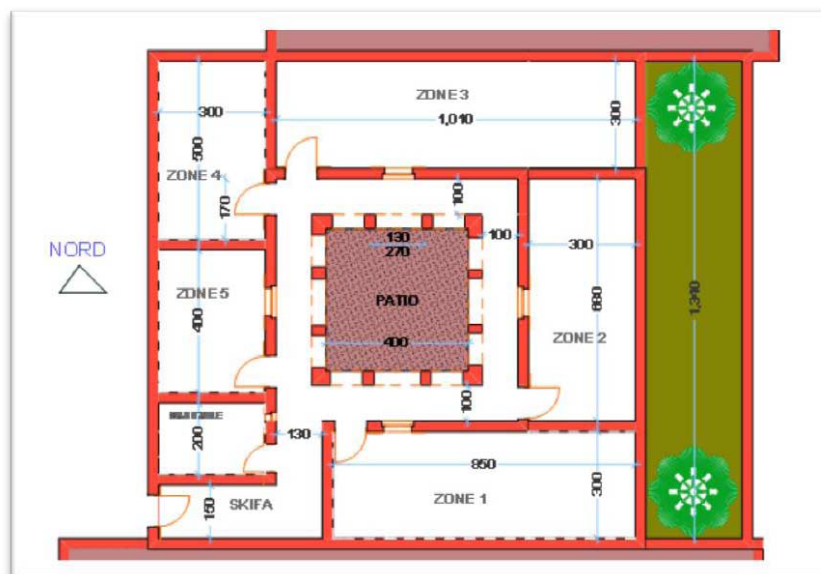


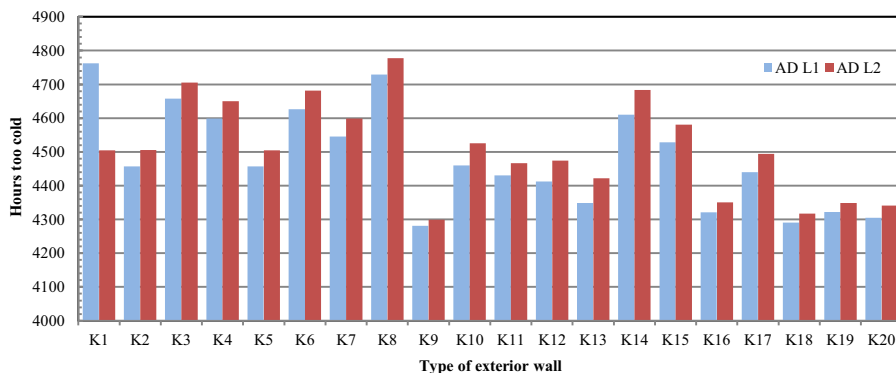
Figure 1. Plan of traditional "WAST Eddar "courtyard house studied

Table 1. Wall and roofs materials examined and their thermal characteristics [3]

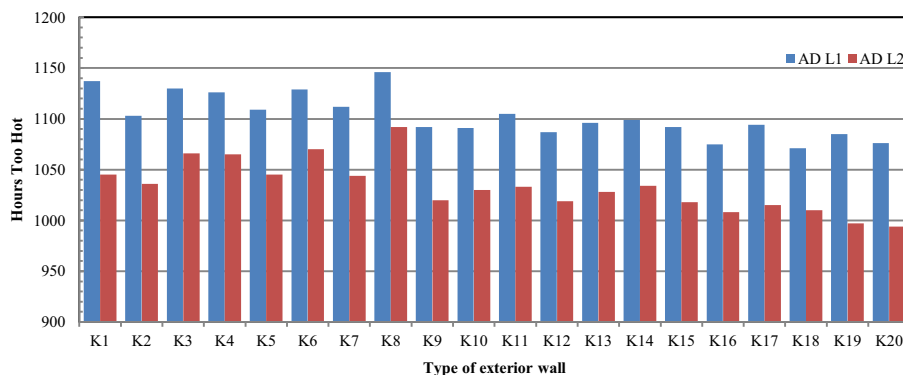
N°	Material and thicknesses	$\lambda$ W/m·K	$\rho$ kg/m <sup>3</sup>	c J/kg·K	U W/m <sup>2</sup> K	$\chi$ int kJ/m <sup>2</sup> K	$\chi$ ext kJ/m <sup>2</sup> K
K01	Stone: 40 cm	2.4	2350	936	2.97	89.8	173
K02	Brick : 40 cm	0.49	936	1692	0.979	56.8	83.9
K03	stabilized earth block: 40 cm	1.15	1700	900	1.953	74.2	120.7
K04	Sand-lime bric : 40 cm	0.8	1600	700	1.493	64.1	94.2
K05	Adobe : 40 cm	0.427	1594.2	687	0.903	50.5	69.0
K06	Full Concrete blocks: 40 cm	1.1	1700	999	1.666	73.8	121.7
K07	Hollow Concrete blocks: 40 cm	0.67	1200	888	1.349	59.8	85.3
K08	Concrete : 40 cm	1.8	2150	888	2.55	84.3	152
K09	SIPOREX : 40 cm	0.1805	600	1000	0.419	31.1	37.1
K10	inner coating: 2 cm	0.49	1450	888	0.798	70.2	95.4
	Stone	2.4	2350	936			
	Air space : 3 cm	0.3	1	1227			
	Brick : 20 cm	0.49	936	1692			
	Exterior coating: 2 cm	1.153	1700	1000			
K11	inner coating: 2 cm	0.49	1450	888	0.798	55.7	156.4
	Brick : 20 cm	0.49	936	1692			
	Air space : 3 cm	0.06	1	1227			
	Stone : 20 cm	2.4	2350	936			
	exterior coating: 2 cm	1.153	1700	1000			
K12	inner coating: 2 cm	0.49	1450	888	0.658	55.1	156.9
	Stone : 20 cm	2.4	2350	936			
	Polystyrene : 3 cm	0.0391	25	1380			
	Brick : 20 cm	0.49	936	1692			
	Exterior coating: 2 cm	1.153	1700	1000			
K13	inner coating: 2 cm	0.49	1450	888	0.658	70.4	94.9
	Brick : 20 cm	0.49	936	1692			
	Polystyrene : 3 cm	0.0391	25	1380			
	Pierre : 20 cm	2.4	2350	936			
	Exterior coating: 2 cm	1.153	1700	1000			
K14	Exterior coating: 2 cm	1.153	1700	1000	1.78	69.8	103.2
	Hollow Concrete blocks: 25cm	0.67	1200	888			
	Exterior coating: 2 cm	1.153	1700	1000			
K15	Exterior coating: 2 cm	1.153	1700	1000	1.358	66.7	99.5
	Brick : 25cm	0.49	936	1692			
	Exterior coating: 2 cm	1.153	1700	1000			
K16	inner coating: 2 cm	0.49	1450	888	0.559	44.0	103.6
	Siporex : 15 cm	0.1805	600	1000			
	Lame d'air : 3 cm	0.06	1	1227			
	Brique : 10 cm	0.49	936	1692			
	Exterior coating: 2 cm	1.153	1700	1000			
K17	inner coating: 2 cm	0.49	1450	888	0.924	64.2	105.8
	BSC: 10 cm	0.8	1600	700			
	Lame d'air : 3 cm	0.06	1	1227			
	Brick : 10 cm	0.49	936	1692			
	Exterior coating: 2 cm	1.153	1700	1000			
K18	inner coating: 2 cm	0.49	1450	888	0.511	25.2	95.2
	Glass wool :5cm	0.041	12	840			
	Brick : 25cm	0.49	936	1692			
	Exterior coating: 2 cm	1.153	1700	1000			
K19	inner coating: 2 cm	0.49	1450	888	0.511	55.5	35.0
	Brick : 25cm	0.49	936	1692			
	Glass wool: 5cm	0.041	12	840			
	Exterior coating: 2 cm	1.153	1700	1000			
K20	inner coating: 2 cm	0.49	1450	888	0.511	60.3	106.7
	Brick : 10cm	0.49	936	1692			
	Glass wool: 5cm	0.041	12	840			
	Brick : 15cm	0.49	936	1692			
	Exterior coating: 2 cm	1.153	1700	1000			
L1	inner coating: 2 cm	0.49	1450	888	2.19	67.88	122.15
	Hollow-core slab : 16 cm	1.23	1300	650			
	Reinforced concrete: 4 cm	1.8	2150	888			
	Sealing : 1 cm (sieved tuff)	0.2	1200	2100			
	Sable : 2 cm	0.625	1900	990			
	Portland cement mortar: 2 cm	1.4	2200	1080			
L2	dropped ceiling with tiles plaster: 3 cm	0.35	900	936	1.53	44.67	119.53
	Air space : 3 cm	1.11	1	1230			
	Hollow-core slab : 16 cm	1.23	1300	650			
	Reinforced concrete: 4 cm	1.8	2150	888			
	Sealing : 1 cm (sieved tuff)	0.2	1200	2100			
	Sand : 2 cm	0.625	1900	990			
	Portland cement mortar: 2 cm	1.4	2200	1080			

## 2. Simulation results and discussion

Simulations of the aero-thermal behavior of the house were carried out with TRNSYS [12] coupled with COMIS [13] using weather data of Bechar (southwest Algerian a hot and dry climate) obtained with Meteonorm. The dwelling is occupied by 7 persons and a likely occupation scenario has been assumed for the summer and winter. In the case of no-conditioning, we have assumed that the occupant closes the windows from 11h to 18h in summer and opens them for 15 minutes in winter mornings at 10am. To assess the heating and cooling needs in the conditioning case, we adopted the following set temperatures: 18 °C in winter and 28 °C in summer. As you can see, we did not want to impose conditions of comfort as high as in industrialized countries. We use the number of too cold hours (Figure 2) and hot hours (Figure 3) as indicators of thermal comfort. The energy needs for heating (Figure 3) and cooling (Figure 4) are used as energy performance indicators. The hot and cold hours adopted in this study correspond to the numbers of hours during which the temperature is outside the comfort category III, Which corresponds to 85% of occupants satisfied according to EN 15251 Annex A2.



**Figure 2.** Too cold hours according to EN 15251 in Zone 1 of the house for various exterior walls and for both roofs (AD L1 and L2)



**Figure 3.** Too hot hours according to EN 15251 in Zone 1 of the house for various exterior walls and for both roofs (AD L1 and L2)

As mentioned in the introduction for a courtyard house, Figures 2 and 3 show that the number of cold hours is much larger than the hot hours for the different studied



types of walls. This shows that this traditional type of construction is better adapted to summer than to winter comfort and this can be explained mainly by the lack of solar gains. Concrete wall K8 gives the worse results, followed by massive stone K1, both associated with an uninsulated roof. However this latter wall is greatly influenced by the insulation of the roof, which reduces the number of hot hours. Follow the brick K2 and aerated concrete K9 walls among the single layer but multilayer walls with an air gap or an insulation layer are better. Figure 1 shows that a dropped ceiling with an air layer under the roof deck increases the discomfort winter hours, except in the case K1 wherein a net decrease of approximately 36% is recorded, which can be explained by the contribution of the insulation in the increase of the use of internal heat gain. At the contrary, the dropped ceiling strongly improves the summer comfort in all cases. Thermal insulation in the stone wall K10 to get the double walls K11, K12 and K13 results in a smaller improvement than insulating the lightest walls: e.g the plastered brick wall K15 modified to K18 (interior insulation), K19 (external insulation) and K20 (double wall with insulation). This is not surprising because the reduction of the heat transfer coefficient is relatively low between K10 and K11, K12 or K13, while it is very important from K15 to K18, 19 or 20. The simulation results show that the monolayer walls (K1-K9) produce on average more discomfort hours than the multilayer family. The adobe K5 wall gave a number of hot hours rather close to that of K7, a monolayer hollow concrete blocks wall, and less cold hours. The Siporex K9 offers the best winter comfort, but its impact on summer comfort is similar to other layered case. His association with red brick and an air gap (K16) does not provide any improvement. The stabilization of adobe brick with cement (K3) increases its strength but decreases its thermal and energy performance especially in the cold season compared with the case K5. The sand-lime brick (K4) gives an lower comfort than adobe (K5).

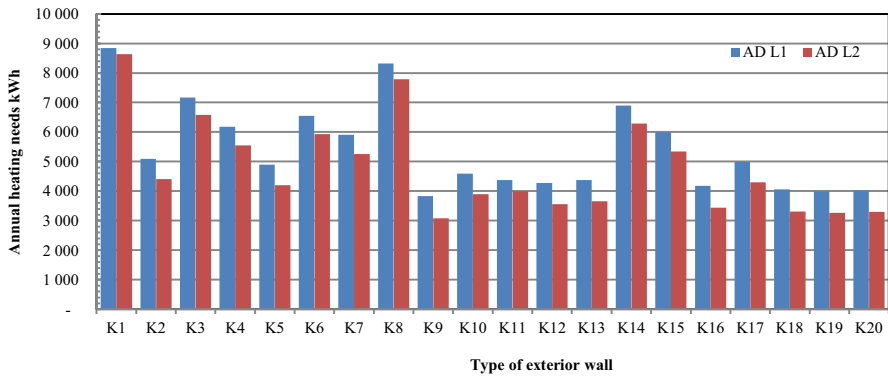


Figure 4. Annual heating needs of the house to various external walls and two cases of roofs

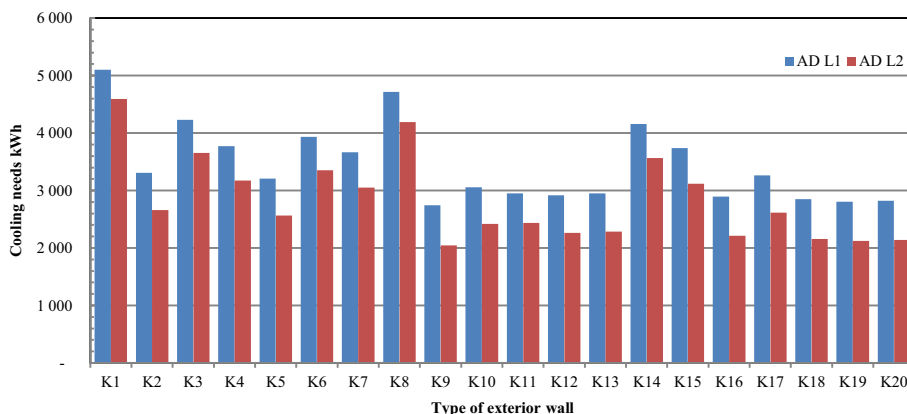


Figure 5. Annual cooling needs of the house to various external walls and two cases of roofs

On the other hand, simulations of such houses underscore the need for cooling in summer and probably also heating in the winter. Indeed, despite the fact that cold hours calculated in this type of construction are more likely than hot, their minimum average value does not exceed 2 ° C below the comfort limit. These hours are situated during nights when comfort can be achieved by the use of blankets or quilts. Furthermore, the parameters that affect the behavior of the conditioned building do not always act in the same way when not conditioned. Therefore, we did simulations to calculate the energy needs for cooling and heating different type of walls. Figures 4 and 5 show the annual heating and cooling needs for each variant and two kinds of roof insulation. The simulation results clearly show clearly that the insulation of the roof substantially reduces the energy requirements and that the insulation, regardless of its position in the vertical walls, reduces the heating needs by more than 30%. The position of the insulation does not substantially affect the energy required, as shown by the results of K18 (internal insulation), K19 (external insulation) and K20 (insulation between two walls) that give almost identical values. The use of stone wall K1 only in monolayer remains the largest energy consumer among the cases examined, followed by K8. Also replacing the air layer in the K10 and K11 by insulating material gave less desirable results for cooling requirements. The aerated concrete (K9) presents better results than in the case without conditioning, it is the component that has the lowest energy requirements. The adobe (K5) contributes to reducing energy needs, in particular when combined with an insulated. It is the second best among the r monolayer walls.

### 3. Conclusion

This work aimed to find solutions for improving the energy efficiency of a traditional courtyard house in a warm and dry climate in southern Algeria, testing various building envelope components. From this, we can draw the following conclusions:

- The most popular ways of constructing new buildings in South Algeria, i.e hollow concrete blocks for the walls and uninsulated hollow-core slab for the roof, does not provide the best natural comfort and needs much energy when cooling or heating.
- Adobe, a traditional local material, gives good results, but it remains to stabilize it without degrading its thermal properties.

- The roof insulation is necessary for reducing the need for cooling and heating, and greatly improves the summer comfort. However, it does not prove very effective in winter without heating.
- The position of the insulation in the wall does not impact substantially the energy needs, but influences the thermal comfort the external and distributed insulation giving the best results.
- Of course (but this is not new) the wall insulation improves the energy efficiency of the house.

## References

- [1] Chahwane L. ; Valorisation de l'inertie thermique pour la performance énergétique des bâtiments. *Thèse de doctorat, Université de Grenoble*, 2011
- [2] Bagneid A. The creation of a courtyard microclimate thermal model for the analysis of courtyard houses. *Thèse de doctorat, Office of Graduate Studies of Texas A&M University*, 2006
- [3] Fezzioui N. and al; Bioclimatic Architectural Design of Ksar de Kenadza: South-west Area of Algeria Hot and Dry Climate, *Architectural Science Review*, Volume 52.3, pp 183-190, 2009
- [4] Tittlein P. Environnements de simulation adaptés à l'étude du comportement énergétique de bâtiments à basse consommation. *PhD thesis, Université de Savoie*, 2008.
- [5] Sambou V. Transferts thermiques instationnaires : vers une optimisation de parois de bâtiments, *PhD thesis, Université Paul Sabatier, France*, 2008.
- [6] Asan H. Investigation of wall's optimum insulation position from maximum time lag and minimum decrement factor point of view, *Energy and Buildings*, 32(2) ,197 – 203, 2000.
- [7] GOSSARD D. and al ; Optimisation thermique de l'enveloppe de bâtiment en vue de maximiser sa performance énergétique, *Congrès français de thermique, SFT2012*, Talence, 29 mai - 1er juin 2012
- [8] Tsilingiris P. T. On the thermal time constant of structural walls, *Applied Thermal Engineering*, 24(5-6), 743 – 757, 2004.
- [9] Roulet C-A. Santé et qualité de l'environnement intérieur dans les bâtiments, *Presses polytechniques et universitaires romandes*, Lausanne, 2010
- [10] Thermal performance of building components - Dynamic thermal characteristics - Calculation methods. (*ISO/DIS 13786:1997*)
- [11] Rapport Technique, Document Technique Règlementaire, Règlement Thermique des Bâtiments d'Habitation - Règles de Calcul des Déperditions Calorifiques, *DTR C3-2*, Fascicule 1, CNERIB, Alger, 1998.
- [12] *TRNSYS version 16*, User Manual, Solar Energy Laboratory, University of Wisconsin- Madison. 2005
- [13] Feustel HE., COMIS-an international multizone air flow and contaminant transport model, *Energy and buildings*, 1999, 30 (1) , 3-18
- [14] Ben Habib R, A. Aït-Mokhtar and F. Allard ; Analyse Bioclimatique de l'Habitat Traditionnel des Régions Désertiques Nord Sahariennes, Conférence Européenne, *Performance Énergétique et Qualité des Ambiances dans le Bâtiment*, Lyon, Novembre 1994.

# Assessment of the involvement of qualified professionals in building supervision in Nigeria: Lagos and Ondo states as case studies

Catherine Mayowa IKUMAPAYI<sup>a,1</sup>, Chinwuba ARUM<sup>a</sup> and Reuben P. OMALE<sup>b</sup>

<sup>a</sup>*Civil Engineering Department, Federal University of Technology, Akure, Nigeria*

<sup>b</sup>*Architectural Department, Federal University of Technology, Akure, Nigeria*

**Abstract.** This research evaluates the involvement of qualified building professionals in building construction in Nigeria. Two methods were used in collecting the data used for the analysis. The data were collected by direct visitation to ongoing building sites and obtaining information through direct interaction with them. Secondly, questionnaires were administered to the contractors on different building sites to ascertain their view on the subject. The study revealed that less than 20% of building sites investigated involved qualified professionals (Architects, Engineers, Quantity Surveyors and Town Planners) in the supervision. Therefore it is recommended that there should be public awareness that qualified professionals on building construction sites are as important as the acquisition of the land for the building. These professionals should also be involved from onset of the construction. Furthermore, strict adherence to best practices in the production of Architectural and Structural drawings as well as Bill of Quantities should be ensured before the approval of building plans in the various relevant ministries.

**Keywords.** Professionals, building sites, supervision

## Introduction

The building and construction industries continual experience of increase rates of building collapse recently has called for thorough investigation of the causes behind the failure. Structural collapse occurs all over the world but that of Nigeria is on the high side [1]. Among the suggested reasons behind the failure are inadequate involvement of the professionals, inadequate supervision and professional incompetence [2,3]. A structure if properly handled by a professional is safely design to satisfy the owner's need and no failure will be experienced within the lifespan of the project. Hall (1984) identified the cause of building collapse to be faulty design, faulty execution of works and use of faulty materials as the major causes of building failure [4]. In Nigeria Building failure has also been attributed to be 50% of design fault, 40% of construction fault and 10% of product failure [5].

<sup>1</sup>Corresponding author: [mayowaik@yahoo.com](mailto:mayowaik@yahoo.com)

High rate of failure was verified for high rising buildings in Nigeria and directly related to the difficulties involved in realizing that such structures could only be adequately handled by highly skilled professionals [1]. Design fault and construction fault both involve lack of effective contribution of different professionals or lack of engagement of these professionals at one or both design and construction stages. For a successful building project realization, a professional project team is needed which should consist of Architect, surveyors, civil engineers, quantity surveyors, electrical engineers, mechanical engineers and structural engineers to deal with the time, money, equipment, technology, people and materials [7]. Thus this paper presents the result of professionals available on building constructions sites in Ondo state and Lagos state of Nigeria with their qualification and experience inclusive.

## **1. Stages of building process and the roles of the professionals**

Ayininuola and Olalusi [2] identify three stages of building process to be: conception-design stage, construction- supervision stage and post construction service stage and that for the realization of quality job in any of these stages of the building process, a high level of skill and professionalism is needed.

The conception—design stage is the planning and feasibility study stage where the owner's idea is translated into physical drawings called design having considered the technical and economical options available. The design consists of architectural drawings, structural drawings, mechanical and electrical drawings and the bill of quantity (BOQ). The architectural drawings are produced by the architect whose job at this stage is mainly to conceive the owner's idea and translate it to feasible drawings. The structural drawings are produced by structural engineers who will identify the expected load on the structure using the architectural drawings, select materials and proportion all the structural sections bearing in mind basic requirement like safety, aesthetic, economy and constructability using the appropriate code. The mechanical and electrical drawings are being handled by mechanical and electrical engineers who will study the architectural drawings and come up with a suitable design showing locations of all electrical appliances as well as plumbing works. The quantity surveyor prepares the BOQ using all the other drawings. The construction-supervision stage is the implementation where every effort is made to ensure compliance with the design and specification in the previous stage. It involves management of scheduling materials, human and technical resources. Certified engineers, architects, builders and skilled artisans all have their respective roles to play in this stage so as to enforce the quality assurance specifications. Service stage is the phase where the built structure is expected to serve the purpose in which it was built without any form of discomfort to the users. A management and monitoring team will continuously assess the true state of the structure and make recommendation for maintenance. Visual inspection and Non-Destructive testing could be used to assess the true state of the structure [6].

## **2. Methodology**

Two methods were used in collecting the data used for the analysis. The data were collected by direct visitation to ongoing building sites and obtaining information through direct interaction with them. Secondly, questionnaires were administered to the

contractors on different building sites to ascertain their view on the subject. The questionnaires include among other; site location, sex of the responder, discipline, qualification, site experience (years), time of involvement in supervision, type of building project ( one storey, two storeys etc),quality of the construction work, type of ownership (public or private), purpose of building (residential, school offices , hostel, others), building drawing available for construction ( Architectural drawing, structural drawing, Bill of quantity and others), availability of site office and problem encountered on site. Simple linear regression analysis was used for the analysis of the data so as to hypothesize a probabilistic relationship between quality of the construction work and year of experience of the professionals present on site.

### 3. Results and discussion

A total of 60 building sites were visited in both Ondo and Lagos states of Nigeria and their results are shown and discussed.

In all of the 60 sites visited the numbers of professionals involved were: 36 civil engineers, 4 builders, 3 architects, 3 electrical engineers, 3 mechanical engineers and 1 quantity surveyor. This is also graphically shown in Figure 1 as the percentage of professionals and their discipline. Figure 2 also shows that out of the 36 civil engineers employed on site only 8 (22%) of them were registered with COREN ( Council for the Regulation of Engineering in Nigeria), none of the architects nor quantity surveyors were registered with ARCON (Architects Registration Council of Nigeria) or QSRBN (Quantity Surveyors Registration Board of Nigeria) while one builder was registered with CORBON (Council of Registered Builders of Nigeria). The overall view shows that 18% of the professionals were actually registered and qualified for the supervision of the buildings in which they were involved.

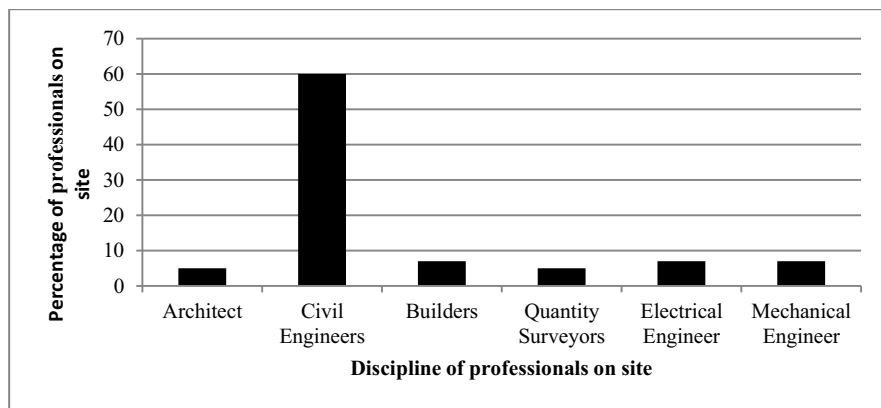


Figure 1. Percentage of professionals and their discipline as obtained from sites visited

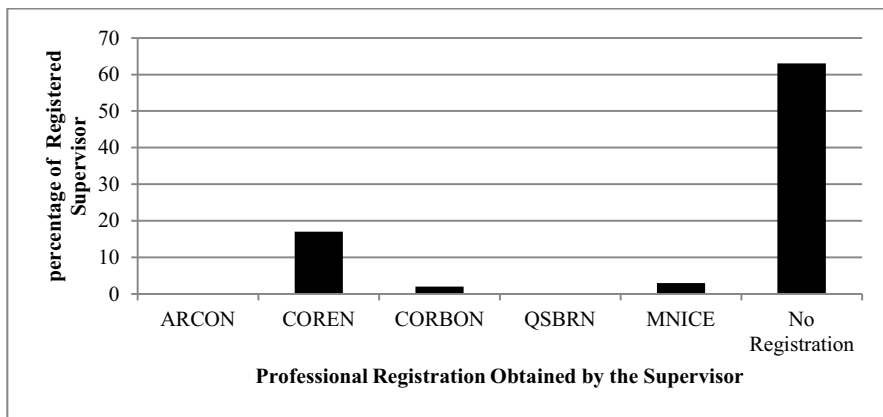


Figure 2. Percentage of the professionals registered with professionals bodies

Figure 3 shows that 48% of the professionals possess Higher National Diploma (HND) while 28% have bachelor’s degree, 7% have master’s degree and 8.33% have Ordinary National diploma (OND) while 8.33% have no qualification.

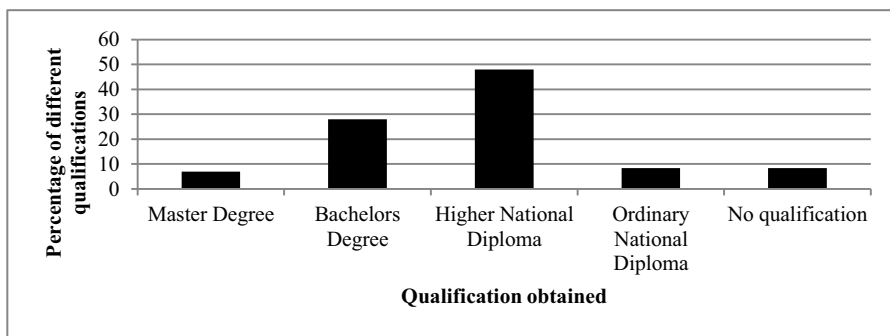


Figure 3. Percentage of various qualifications obtained

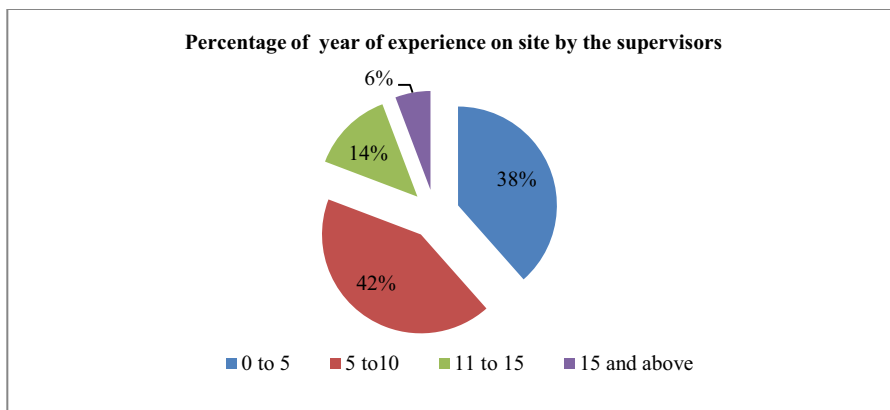


Figure 4. Percentage of year of experience on site by the supervisors

Most professionals site experience were below 10 years with 38% having 0-5 years experience, 42% have 6-10 years' experience, 14% have 11-15years experience and 6% have 16 and above years' experience as shown in Figure 4.

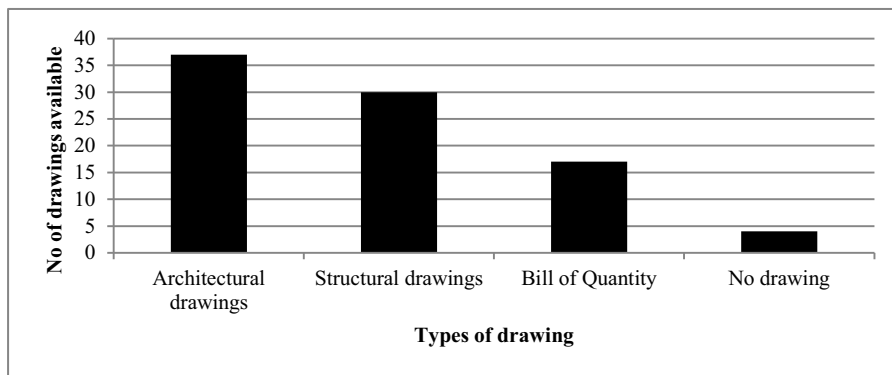


Figure 5. No and types of available drawings on site visited

It was also discovered that 37% of these professionals were involved from onset, 11% of half-way while 4% at finishing stage . Thirty seven sites have architectural drawings, thirty have structural drawings, and seventeen have Bill of quantity while four sites have no building drawing as shown in Figure 5. Two of the sites without drawing were one storey building type while the remaining two were bungalow.

Quality of work on site as well as the year of experienced of the professionals present was modeled using simple linear regression. The dependent variable was the quality of work (QOW) while the independent variable was year of experienced (YOE) of the professionals. The model obtained using Statistical Package for social sciences (SPSS) is shown in Eq. (1)

$$QOW = 1.255 + 0.224YOE \tag{1}$$

The model summary and the model coefficient are shown in Table 1 and Table 2. The coefficient of correlation (R) = 0.994 which shows that there is 99.4 % linear relationship between the dependent and independent variable. Also coefficient of determination (R<sup>2</sup>) = 0.988 which means that 98.8% of the dependent variable is explained by the independent variables .

Table 1. Model summary

Model	R	R Square	Adjusted R Square	Std. Error of the Estimate	Change Statistics				
					R Square Change	F Change	df1	df2	Sig. F Change
1	.994 <sup>a</sup>	.988	.982	.17496	.988	161.333	1	2	.006

a. Predictors: (Constant), YOE



Table 2. Model coefficients<sup>a</sup>

Model	Unstandardized Coefficients		Standardized Coefficients	t	Sig.	95% Confidence Interval for B	
	B	Std. Error	Beta			Lower Bound	Upper Bound
1 (Constant)	1.255	.197		6.364	.024	.407	2.104
YOE	.224	.018	.994	12.702	.006	.148	.301

a. Dependent Variable: QOW

#### 4. Conclusion and recommendations

Only 18% of the sites visited involved qualified professionals in their supervision. The reasons for this poor incidence of involvement of qualified professionals include developers' desire to save cost and their ignorance of the benefits associated with involvement of professionals as discovered on site. Therefore it is recommended that there should be public awareness of who a qualified professionals is and that qualified professionals on building construction sites are as important as the acquisition of the land for the building. These professionals should also be involved from onset of the construction. Furthermore, strict adherence to best practices in the production of Architectural and Structural drawings as well as Bill of Quantities should be ensured before the approval of building plans in the various relevant ministries.

Experienced professionals should be employed on any structural building who will in turn invite two or more young professionals to learn along with him/her. All building drawings should be made available at the commencement of the construction to enable the qualified professionals make use of them. Qualification, professional registration and year of experience should be used as criteria in selecting site supervisor as the quality of construction works on site depends on them.

#### References

- [1] A.N. Ede, Building Collapse in Nigeria: the Trends of Casualties in the Last Decade (2000-2010), *International Journal of Civil and Environmental Engineering IJCEE-IJENS*, **10**(6) (2010), 32-36.
- [2] G.M. Ayininuola and O.O Olalusi, Assessment of Building Failures in Nigeria: Lagos and Ibadan Case Studies, *African Journal of Science and Technology AJST: Science and Engineering Series* **5**(1) (2004), 73-78.
- [3] P.N. Opara, Building Failures and Collapses:A Case Study of Portharcourt, Nigeria, *Journal of Engineering and Technology in Nigeria*, **12**(1) 2007, 35-39.
- [4] G.T., Hall, Revision notes on Building and Adaptation, Butterwrths and Co., England, (1984) as cited by R.E Olagunju, S.C. Aremu and J. Ogundele, Incessant Collapse of Building in Nigeria: An Architect View, *Civil and Environmental Research*, **3**(4) 2013,
- [5] P. Ayuba, R.E Olagunju and O.K. Akande, Failure and Collapse of building in Nigeria: The role of Professionals and other Participants in Building Industry, *Interdisciplinary Journal of Contemporary Research Business IJCRB*, **4**(6), (2012), 1267-1272
- [6] A.N. Ede, Method to Reduce the High incidence of Structural Failure in Nigeria, *Journal of Sustainable Development in African*, **13**(1) (2011), 153-161.
- [7] A.A. Hussin and A. Omran, *Roles of Professionals in Construction Industry*, The International Conference on Economics and Administration, Faculty of Administration and Business, University of Bucharest, Romania, ICEA-FAA Bucharest, 14<sup>th</sup>-15<sup>th</sup> November, 2009, 248-256

# Thermal insulation of crumb-rubber mortar for building walls application

Mukaila Yinka SANNI<sup>1</sup>, Ocholi AMANA and PinderEjeh STEPHEN  
*Department of Civil Engineering Ahmadu Bello University, Zaria Nigeria*

**Abstract.** This research work reveals that the thermal properties of cement mortar are significantly affected with increase in crumb-rubber content, when used to partially replace sand in cement mortar mixes. The work is based on experimental study with replacement made at 5%, 10%, 15%, 20% and 25% crumb rubber by volume. Thermal properties were measured base on the transient line heat source (TLS) method using a KD 2 Pro-thermal analyzer. Thermal properties most especially the thermal conductivity of cement mortar (1.286W/mk) was greatly reduced to 0.351W/mk indicating 72.7% reduction with 25% crumb-rubber particles content, which makes it a better insulator. The specific heat capacity of cement mortar (2.791 MJ/m<sup>3</sup>.k) was reduced to 1.424MJ/m<sup>3</sup>k indicating 49% reduction with 25% rubber content, which may adversely reduce thermal mass effect. Other thermal properties such as thermal resistivity increased by 72.7%, thermal diffusivity decreased by 46.4% while thermal effusivity decreases by 66.4%. These results indicates that the potential use of such a composite material as an insulating mortar for building applications is viable.

**Keywords.** Crumb-rubber, mortar, density, strength, thermal properties

## Introduction

In order to reduce the problem of solid waste materials dumping in Nigeria and countries all over the world, it is imperative that solid waste materials should be utilized in an environmentally safe manner either as raw materials for other product or for some other beneficial purposes [1].

One of such material is automobile waste tyres which are non-biodegradable and can exist for a long time without any degradation.

According to [14], each year about 9 million tones of waste rubber-tyres are disposed of all over the world, which was also estimated to be around 1 billion tyres withdrawn from use in the world annually [9]. [8] Reported that an estimated 5 million scrap tyres from trucks, cars and motorcycles existed in Nigeria in 1983 with an annual generation rate of 15% each year. About 21million scrap tyres were estimated to exist in Nigeria by 2011.

Scientists, engineers and technologists look out for ways of using different types of solid waste as alternatives for some ingredients of civil engineering materials such as asphalt and concrete [10]. Many researchers have studied and developed various recycling methods for re-use of waste rubber-tyres in construction materials. Some of

---

<sup>1</sup>Corresponding author: [sannimukaila@yahoo.com](mailto:sannimukaila@yahoo.com)

these methods are: use of waste rubber-tyres in asphalt concrete mixture; use of waste rubber-tyres in some plastic and rubber products; utilizing waste rubber-tyres in Portland cement concrete; use of waste rubber-tyres as a visco-elastic material for vibration dampers and utilizing waste rubber-tyres in ordinary cement mortar [15].

Thermal properties of most cementitious materials are found to change with the presence of admixtures ([7]; [12]). The inclusion of processed waste rubber-tyre in mortar could also make the material a better thermal insulator, due to better thermal insulating properties of rubber-tyre which could be very useful especially in the wake of energy conservation requirements. This research further extends to look into thermal capabilities of rubber-mortar to efficiently exploit thermal performance in relation to conductivity, resistivity, diffusivity, heat capacity and effusivity. The study also aimed at developing some understanding of these and their potential application across building spectrum.

## **1. Materials and methods**

### *1.1 Materials*

Rubber-Mortar (RM) consists of Portland cement, fine aggregate (sand) and crumb-rubber particles with a good percentage of water. Mortar in general is different from concrete in that coarse aggregate are used in concrete while only fine aggregate (sands) are used in mortar.

Ordinary Portland Cement (OPC) with specific gravity of 3.15 was used throughout the investigation which was sourced from a retail outlet and tested to ensure that it conforms to [2]. Ordinary tap water (potable drinking water) which is fresh, colourless, odourless, tasteless and free from organic matter of any kind, sourced from Civil Engineering Laboratory Ahmadu Bello University at Zaria, Nigeria was used for all concrete mixes and curing. The water was therefore fit for concrete work [4]. Natural sharp river quartzite sand smaller than 4.76mm but larger than 75  $\mu\text{m}$ , that is, free of clay, loam, dirt and any organic or chemical matter was used. The sand with average specific gravity (SSD) of 2.65 and bulk density of 1,454  $\text{Kg/m}^3$  was used as fine aggregate. The fine aggregate (sand) falls in zone two (medium sand) according to [6] specification. Coarse rubber aggregate (ground rubber) from scrap tyres were further processed (with the aid of an electric grinding machine) into crumb-rubber of size 2.00 to 0.15mm with specific gravity of 1.12 and bulk density of 940 $\text{Kg/m}^3$ , which was then used for this research.



**Figure 1.** Materials for rubber-mortar mix

### 1.2 Mix proportions

A mix of water/cement ratio of 0.4 and sand/cement ratio of 3.0 was used to prepare mortar cubes by replacing mineral fine aggregate with crumb rubber of up to 25%. A total number of six (6) mixes were prepared: One control mortar mixes with no crumb-rubber aggregate and five mortar mixes in which fine aggregate (sand) was replaced by 2.00 - 0.15mm crumb rubber at 5%, 10%, 15%, 20% and 25% by volume. No mineral or chemical admixture was added.

The mix proportions was constant in terms of mix design ratio, water/cement ratio, sizes, type of natural and rubber-tyre aggregate used for the study as shown in Table 1. A total number of 72 mortar cubes were cast of which 54 mortar cubes samples 70.7x70.7x70.7mm were used for compressive strength test after 7, 14 and 28 days of standard curing in water. Also, 18 mortar cubes were used for conducting a thermal test after 28 days of curing in water.

**Table 1.** Quantities of materials for 12 mortar cubes mortars including 10% waste

Mix No	Mix Ratio	W/C Ratio	Rubber Aggregate		Cement (g)	Fine Aggregate (g)	Water (g)
			(%)	(g)			
A	1:3	0.4	0	0	2,240	6,720	896
B	1:3	0.4	5	217	2,240	6,384	896
C	1:3	0.4	10	434	2,240	6,048	896
D	1:3	0.4	15	652	2,240	5,712	896
E	1:3	0.4	20	869	2,240	5,376	896
F	1:3	0.4	25	1,086	2,240	5,040	896

### 1.3 Testing of mortar cubes samples

Tests were conducted to assess the density and compressive strength properties of rubber-mortar samples at the Department of Civil Engineering Concrete laboratory Ahmadu Bello University (A.B.U) Zaria. The test conducted includes: Determination of density of the hardened mortar which was established from the mortar cube samples after 7, 14 and 28 days of standard curing. The compressive strength tests of mortar cubes samples were determined after 7, 14 and 28 days of standard curing in water. KD 2 Pro-Thermal properties analyzer from the Department of Geology, University of Ibadan (U.I) was used to measure the thermal conductivity ( $k$ ), thermal resistivity ( $\rho$ ),

thermal diffusivity ( $\alpha$ ) and volumetric heat capacity ( $c$ ) of the mortar cubes sample after 28 days of standard curing in water while the thermal effusivity ( $\beta$ ) were computed from the relationship between thermal conductivity, density and specific heat capacity ( $\beta = \sqrt{k\rho c}$ ).



Figure 2. KD 2 Pro-Thermal properties analyzer



Figure 3. KD 2 Pro-Thermal analyzer during measuring of mortar properties



Figure 4. Mortar cubes

## 2. Results and discussion

### 2.1 Density

The density of the hardened mortar samples reduces with increase in percentage of crumb-rubber particles as shown in Table 2. Reduction in density can be linked to the low specific gravity of the rubber aggregate (1.12) compared to that of fine aggregate (2.65).

**Table 2.** Density of hardened mortar cubes

Samples	%Rubber Content	Mortars		
		Density(Kg/m3)		
		7 Days	14 Days	28 Days
A	0%	2,111	2,131	2,140
B	5%	2,086	2,093	2,094
C	10%	2,029	2,032	2,047
D	15%	1,881	1,887	1,874
E	20%	1,802	1,794	1,800
F	25%	1,755	1,729	1,741

### 2.2 Compressive strength

The compressive strength of mortar cubes samples were determined by a standard uniaxial compression test done on 70.7x70.7x70.7mm mortar specimens. The strength of mortar cubes, as shown in Table 3, reduces significantly with increase in the percentage crumb-rubber particles. Compressive strength of 38.1N/mm<sup>2</sup> was obtained for control mix after 28 days of standard curing, while a 25% rubber mix had strength of 5.35N/mm<sup>2</sup> indicating a percentage loss in strength of 86%.

**Table 3.** Compressive strength of control and rubber-mortar cubes

Specimen	Mix Ratio:1:3, Water-Cement Ratio (W/C): 0.4											
	Compressive Strength (N/mm <sup>2</sup> )			% Loss of Strength			Standard Deviation			Relative Strength Sr		
	7 Days	14 Days	28 Days	7 Days	14 Days	28 Days	7 Days	14 Days	28 Days	7 Days	14 Days	28 Days
A 0%	20.93	36.11	38.12	-	-	-	1.11	1.01	1.00	-	-	-
B 5%	15.25	20.53	22.27	27	43	42	0.72	1.03	0.92	0.73	0.57	0.58
C 10%	12.04	15.72	16.72	43	57	56	0.40	1.50	0.81	0.58	0.44	0.44
D 15%	7.76	8.16	8.96	63	77	77	0.51	0.62	0.50	0.37	0.23	0.24
E 20%	4.95	6.49	7.42	76	82	81	0.31	0.70	0.53	0.24	0.18	0.20
F 25%	3.41	4.89	5.35	84	87	86	0.20	0.31	0.31	0.16	0.14	0.14

### 2.3 Thermal properties

Thermal properties such as conductivity, heat capacity, diffusivity, resistivity and effusivity are critical in assessing the potential energy efficiency of rubber-mortar. The 70.7x70.7x70.7mm mortar cube specimens were tested for the thermal properties using KD2 Pro-Thermal properties. Average results obtained from the experimental measurements are presented in Table 4.

**Table 4.** Thermal properties of rubber-mortar cubes as a function of temperature (°C)

Sample	Density (Kg/m <sup>3</sup> )	Temp °C	Mix Ratio (1:3) Water-Cement Ratio ( W/C): 0.4				
			Thermal Properties @ 28 Days				
			Thermal Conductivity (W/mk)	Thermal Resistivity (Cm°c/W)	Thermal Diffusivity (mm <sup>2</sup> /S)	Heat Capacity (MJ/m <sup>3</sup> .K)	Thermal Effusivity (W/m <sup>2</sup> ks1/2)
A 0%	2,140	30.59	1.286	77.76	0.461	2.791	2.772
B 5%	2,094	29.79	1.094	91.41	0.384	2.847	2.554
C 10%	2,047	27.74	0.583	171.53	0.366	1.592	1.378
D 15%	1,874	27.09	0.507	197.23	0.306	1.658	1.255
E 20%	1,800	26.67	0.309	256.41	0.263	1.482	1.019
F 25%	1,741	27.32	0.351	284.90	0.247	1.424	0.933

### 2.3.1 Effect of crumb rubber on thermal conductivity

The results in Table 4 indicate that the value of mortar thermal conductivity decreases with an increase in the percentage of crumb-rubber, thereby improving their insulating value (R-value) which is attractive and indicates high potential for development most especially for a tropical, temperate and cold climate where low thermal conductivity construction materials are desirable in optimizing the heating/cooling load within the building space, and hence affecting the capacity of the mechanical equipment required in handling the load there in by enhancing thermal comfort. Thermal conductivity was also observed to increase with increase in density and temperature from the thermal analyzer (Conversely, thermal conductivity decreases with decrease in density and temperature). This indicates that density, temperature and aggregate type can influence thermal conductivity.

### 2.3.2 Effect of crumb rubber on thermal resistivity

The inverse of thermal conductivity value (1/conductivity) provided the thermal resistivity which indicates the resistance to heat flow through unit thickness of the mortar cube samples. The results, as shown in Table 4, reveal that thermal resistivity increases with increase in rubber content in the mortar.

### 2.3.3 Effect of crumb rubber on volumetric heat capacity

The heat capacity of the mortar reduces with increase in percentage replacement of crumb-rubber by volume of fine aggregate (sand). The heat capacity of control mixes (0% rubber mix) measured was 2.791MJ/m<sup>3</sup>k whereas 5%, 10%, 15%, 20% and 25% rubber-mortar had specific heat capacities of 2.847, 1.592, 1.658, 1.482 and 1.424 MJ/m<sup>3</sup>k respectively. This indicates that the volumetric heat capacity of mortar reduces significantly. Lower specific heat capacity (heat energy storing capacity) signifies lower thermal mass. In practical terms, it implies that in tropical and temperate climate this modified mortar will lose heat gained during the day faster, thereby enhancing thermal comfort within the confinement of a building space. But for cold climates this

thermal behavior will have an adverse effect because high heat storing capacity is always required in construction materials in order to store more heat which will aid in thermal cycle balance between the building and its environment there by keeping the residential and commercial buildings warm and in turn reducing the cost of heating and CO<sub>2</sub> emission.

#### *2.3.4 Effect of crumb rubber on thermal diffusivity*

In a manner slightly similar with the thermal conductivity variation, results in Table 4 indicate that the values of the thermal diffusivity of rubber mortar are lower than those of the control mixes (0% rubber mix). The decreasing values of both density and the specific heat capacity with addition of crumb-rubber content contributed to the decrease in the thermal diffusivity of the mortar. This effect implies that rubber-mortar will not undergo a faster temperature change i.e will or allow less rapid heat flow through the material when compared to the control mixes. Low thermal diffusivity also means a slower rate of heat transfer. Material with low thermal diffusivity like the rubber-mortar will respond slowly to an imposed temperature difference and can be used as effective thermal mass elements in a building [16].

#### *2.3.5 Effect of crumb rubber on thermal effusivity*

The thermal effusivity values measured are presented Table 4. The control mixes (0% rubber content) measured 2.772 W/m<sup>2</sup>Ks<sup>1/2</sup> whereas 5%, 10%, 15%, 20% and 25% rubber-mortar, had thermal effusivity of 2.554, 1.378, 1.255, 1.019 and 0.933 W/m<sup>2</sup>Ks<sup>1/2</sup> respectively. The result indicates that thermal effusivity of mortar decreases with the partial replacement of crumb-rubber by volume of fine aggregate (sand) in mortar. In practical terms, higher thermal effusivity of building materials increases its ability to conduct heat away from the building space faster thereby reducing the cooling load, and consequently increasing the period of thermal comfort. Low thermal effusivity such as the one obtained for rubber-mortar will reduce its ability to conduct heat away from the building faster, thereby reducing heating load most especially in cold climates. But maybe a disadvantage for tropical climates such as Nigeria due to increase in cooling load which has cost implications.

## **4. Conclusions**

The results of this investigation have evaluated the effect of crumb-rubber on the thermal insulation properties of mortar, with the following conclusions drawn:

- Density of hardened mortar cube was observed to reduce with increase in crumb-rubber content.
- Compressive strength of mortar cubes reduces with percentage increase in crumb-rubber content, when compared to the control mix.



- Thermal conductivity of mortar reduces significantly with the partial replacement of crumb-rubber by volume of fine aggregate (sand), thereby improving their insulating value (R-value).
- Thermal resistivity (inverse of thermal conductivity  $1/k$ ) increases as expected which indicate high resistance to heat transfer or flow.
- Thermal diffusivity reduces with percentage increase in crumb-rubber content.
- Volumetric heat capacity of mortar also reduces, which is likely to have an adverse effect on heat storing capability.
- Thermal effusivity of mortar reduces with percentage increase in crumb-rubber fines.

## References

- [1] F.A. Aisien, F.K. Hymore and , R.O. Ebewele *Application of Ground Scraps Tyre Rubbers in Asphalt Concrete Pavements*, Dept of Chemical Engineering University of Benin, Benin City Nigeria, 2006.
- [2] BS 12. *Portland cement*, British Standard Institution (BSI) London, 1991.
- [3] BS 1881: *Part 111: Method of Normal Curing of tests Specimens 20oC Method*, British Standard Institution (BSI) London, 1983.
- [4] BS 3148. *Methods of test for water for making concrete*, British Standard Institution (BSI) London, 1980
- [5] BS 4550: *Part 6: Method of Testing Cement (Standard Sand for Mortar Cubes)*, British Standard Institution (BSI) London, 1978
- [6] BS 882: *Aggregate from Natural Sources for Concrete (Specification)*, British Standard Institution (BSI) London, 1992.
- [7] I.K. Cisse, and M.Laguerbe *Mechanical characterization of filler sandcretes with rice husk ash additions*, Study applied to Senegal. Cem. Concr. Res. 2000, 30(1):13–18.
- [8] R.O. Ebewele, and L.H. Dzung, *Potential Application of Recycled Rubber*. Nigeria Journal of Engineering, 1990, 6(1) 1–3.
- [9] S.O. Erdogan, L. Mohammed, and K.S. K.S. Umur. *Compressive Strength Abrasion Resistance and Energy Absorption Capacity of Rubberized Concrete with and without slag*. 2010
- [10] B.N. Khalid, *Mechanical Properties of Fibre Waste Tyre Concrete*. International Journal of Civil Engineering IJCE-12th Issue 2008, pp. 97-110.
- [11] N.P. Khosla, and J.T. Trogdon, 1990, *Use of Ground Rubber in Asphalt paving mixtures*, Technical Report Department of Civil Engineering. North Carolina State University Raleigh, 1990.
- [12] D.C. Okpala, *Some engineering properties of sandcrete blocks containing rice husk ash*, Build. Environ. 1993. 28(3): 235-241.
- [13] M.Y. Sanni, *Characterisation of Rubber-Concrete and Mortar*, MSc Thesis in Civil Engineering, Ahmadu Bello University, Zaria – Nigeria. 2012. PP. 1 – 114.
- [14] Y. Yang, J. Chen, and G. Zhao, *Technical Advance on the Pyrolysis of Used Tires in China*, Dept. of Chem. Eng., Zhejiang University YuQuan Campus, Hangzhou, 310027, P.R.CHINA. 2000
- [15] X. Yunping, P. Meshin, N. Okpin, and L. Yue. *Premixed Rubberized Insulation Mortar (PRIM)*, University of Colorado at Boulder. 2010.
- [16] ACI Committee 122 *Guide to Thermal Properties of Concrete and Masonry Systems* ACI 122R-02.

# Precast concrete fencing units in low cost domestic housing in South Africa – a case study

Stella M. MLASI<sup>1</sup>

*Department of Civil and Chemical Engineering, University of South Africa*

**Abstract.** The rectangular flat concrete precast panels which are widely used as building blocks in fencing construction, have been introduced in the design and construction of low cost domestic housing. The use of masonry units has been the main option in the design and construction of domestic houses in South Africa. However, the use of precast concrete fencing panels, as an alternative, in domestic housing construction is spreading and undergoing improvement.

The objective of this paper was to investigate and analyse the extent of the use of precast concrete fencing panels in the construction of domestic housing. It has been found that this construction method is practiced mainly in remote and rural areas, and is based on the skill and intuition rather than formal design steps and agreed specifications. However, the product houses are usually appealing and the majority of users find them reliable. When compared to a masonry unit wall, the plastered precast concrete wall has several advantages, including a rapid construction process, material availability, durability, quality control, low cost construction, low maintenance and inspection, reduced impact on the environment and lower water demand during construction.

**Keywords.** Precast concrete panels, domestic housing, fencing, low cost maintenance

## Introduction

South Africa is one of the many developing countries facing huge challenges in housing. The population keeps growing, and the demand for dwelling units increases daily. The biggest challenge is from the economic standpoint, especially in remote or rural areas where communities need money for survival rather than for housing investments. In such areas, the common domestic dwelling units are usually constructed from handmade adobe bricks, which are formed using cement, sand and water. Their strength is usually lower than that of the widely used baked or burnt masonry units. However, of great interest is the emerging use of precast concrete fencing panels in domestic housing construction. This paper outlines some of the reasons why precast concrete fencing panels are chosen for house walls. It highlights the structural design integrity of such housing and also addresses future possibilities in long term and sustainable housing solutions. Special emphasis is placed on areas where such a construction concept has already been accepted and practiced. The data and

---

<sup>1</sup>Corresponding author: University of South Africa, Private Bag X6, Florida 1710, South Africa; E-mail: [mlasims@unisa.ac.za](mailto:mlasims@unisa.ac.za)

housing information used in this study was collected from the villages and rural townships around Brits and Rustenburg in the North West Province, though this type of construction is also practiced in other parts of the country. It was observed that in at least two out of five stands, there is a property constructed using precast concrete fencing panels.

## 1. Design and construction background

### 1.1. Construction processes and material availability

The construction of a common brick domestic house usually starts with some earth works and strip foundations, followed by the erection of walls. The plaster, in some cases, is applied to the walls for protection against moisture and for improving the strength, durability and aesthetics of the building. The precast concrete interlocking panels are staggered one on top of another using the interlocks provided and placed between two posts which form the walls as shown in Figure 1. There is no foundation for such a wall; instead the wall is built with approximately two of the panels below the natural ground level and a mass concrete around the bottom tip of each post so that it can hold the moments produced by the roof loading. The concrete slab is then cast to form the floor, which will prevent moisture from seeping under the wall.



**Figure 1.** (a) Precast concrete fence wall and (b) Complete precast concrete fence walled house

The usual wall, made of reinforced concrete, brick or masonry has the load bearing capacity to support both vertical and horizontal loads. The precast concrete fencing wall is capable of resisting horizontal wind load. The interlocks between the slabs and the posts act as hinged joints which transfer the load to the soil below. The roof is supported by the posts. To construct a brick wall, skilled personnel are always needed, in order to produce a straight and stable wall of the required joint strength. It could take up to 32 hours or more to lay the foundation, build a 3 m x 3m brick wall and coat it with plaster. However, to construct the precast concrete fencing panel wall, the person merely needs to follow the prescribed steps provided by the manufacturer. The interlocking nature of the precast concrete fence slabs and posts provides stability for the wall and for the whole house. One can believe that a complete system of concrete precast panels can be integrated to form a building frame that behaves monolithically

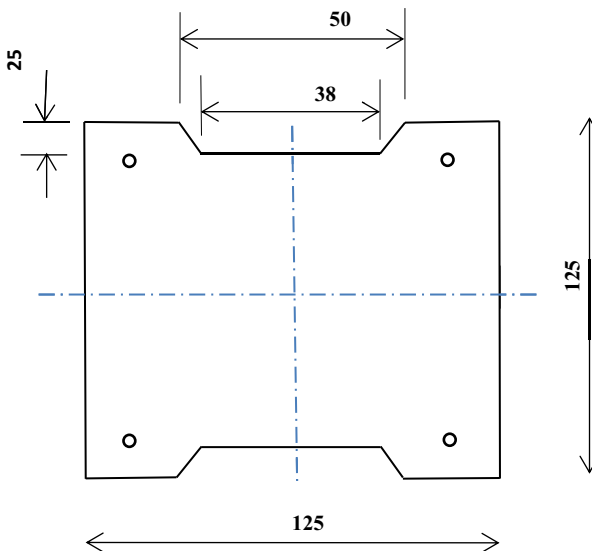
with sufficient strength, stiffness and durability [1]. Plastering of the precast concrete fence wall is necessary to prevent water from seeping in between the adjacent slabs, and to provide a straight and smooth finish on the inside and outside of the wall. The precast concrete units are cast and cured under controlled laboratory conditions. Where there is no requirement for rapid strength gain of the precast structural elements, the choice of cement and aggregates should be based on the economy [2].

## 1.2. A brief review of the housing regulations in South Africa

### 1.2.1. Basic design

The loading must be computed, designed for and checked for the precast concrete fence wall with reference to SANS 10160-3 Clause 5.5 [3]. In a precast concrete fencing panel, each precast post is designed to support the slabs through the interlocks, but when it is used in a building as a column, it should support the roof. Hence the designer should ensure that precast posts have sufficient compression and flexural capacity, and that slenderness limits are not exceeded.

Figure 2 shows a cross section of the outer-middle post or column of a house wall. The column is braced in the direction of the major x-axis by the wall. Outlined in the Appendix are the design calculations for the analysed column. All dimensions and cover to the 6 mm diameter reinforcing bars in the post or column were estimated on site and can change per manufacturer.



**Figure 2.** Cross section of a column

The column was found to be slender in both axis, and the moment produced at the base of the column is due to the dead weight of the steel sheeting, wooden rafter and purlins. The maximum design moment about the major and minor axis were 0.322 kNm and 0.379 kNm, respectively (refer to the Appendix). The calculations also show

that the area of steel in the column on site is more than 40% of the required area based on the design moments.

### *1.2.2 Connections and joints*

The connections and joints between the slabs and posts govern the thermal effects and differential settlement of post foundations. It is imperative for the designer to check the amount of settlement and the bending of the columns supporting the roof, especially because the posts are thin and can easily penetrate soft soils. The movement due to shrinkage is of no concern, since all the components used in the precast concrete wall are already dry during their application. When applying the plaster to the precast concrete fence wall, the builder should be careful not to put the paste into the joints which would prevent necessary movement. Damage can occur during transportation, handling, storage and erection, and reference on the guidelines and standards should be made to SABS 0100-1 Clauses 5.3.1.2 and 6.1.2.2 and SABS 0100-2 [4].

## **2. Discussion**

### *2.1 Quality control and durability*

The precast concrete units are cast and cured under controlled conditions, and samples are tested for strength and durability. The usual concerns arising during construction such as levelling and stability have been significantly reduced by the use of interlocks.

### *2.2 Maintenance and inspection*

It is convenient to use precast concrete, since it already has a smooth surface finish. In some cases, the precast concrete fence wall is left as it is; in some cases builders plaster the wall and even paint it. This increases the life span of the structure and reduces maintenance. The joints between the slab units and the post should be sealed with an elastic waterproof sealant to prevent moisture from entering, especially in areas of the wall closer to the roof, where plaster cannot be applied properly.

### *2.3 Economic considerations*

The use of precast concrete accelerates the construction process, since the number of components to be assembled is minimized and the process is pre-specified by the manufacturer. In a simple domestic housing construction, materials and labour are usually the main cost factors, though there are often other cost related factors such as transportation and consultation which may add to the total building costs. The construction of a precast concrete building in general requires fewer labourers compared to an in situ construction, a disadvantage in terms of employment creation.

Table 1 shows a cost breakdown comparison between brick and precast concrete room walls. The size of each wall is approximately 3 x 3 m<sup>2</sup> maximum. It should be noted that the cost of the precast concrete units are not readily available from published sources; the prices stated in Table 1 are the estimates from the contractors and are subject to change.

With the labour cost included, the total initial cost for building a single room with precast concrete slabs would total approximately R19 000, considering the fact that it is less time consuming to complete but it is still the uneconomical option. The brick walled room would take a few more days to complete, with less cost, but with a more negative environmental impact. The type of brick used in the calculations in Table 1, is a 210 x110 x 60 mm, handmade from cement, sand and water, and then burned in the sun after being daily cured by water. Other types of common bricks of good quality were available in the nearest towns, but this case study is based on the two most common types of building units in the chosen area.

**Table 1.** Initial cost of a standard room size 3 x 3 x 3 m height with one door and one window

Brick walled room		Precast concrete fence wall room	
1000 x bricks @ R5.50 each	R 5 500.00	60 x precast units @ R178.00 each + 10 posts @ R375.00	R 14 430.00
10 m <sup>3</sup> of soil @ R40/m <sup>3</sup>	R 400.00	6 m <sup>3</sup> of soil @ R40/m <sup>3</sup>	R 240.00
12 x cement bags @ R90.00 each	R 1 080.00	6 x cement bags @ R90.00 each	R 540.00
water	R 20.00	water	R 10.00
Total	<u>R 7 000.00</u>		<u>R 15 220.00</u>

It is not easy to disassemble the brick wall with the intention of reusing the material somewhere, because often the bricks break or suffer damage on the edges. However, the precast concrete slabs and posts can be easily disassembled and reused without being damaged. In other words, the low cost bricks could be used just once whilst the precast concrete units are reusable and have lower maintenance costs. During production, admixtures and other cementitious materials could be used to reduce cement quantities used in precast concrete units. This usually leads to more durable and economic products. In contrast, during the production of bricks, it is difficult to control waste and the quality of the products.

### 3. Conclusion and recommendation

In the construct of housing using precast concrete fence panels, savings come from reduced labour cost, less water usage, short construction time, flexibility and simplicity in the construction processes. The design steps and a code of practice need to be developed for such dwelling units, because small construction companies and individuals are practicing the construction of precast concrete fence panels housing.

### Acknowledgements

The author greatly appreciates the specific residents of the villages and townships in Brits and in Rustenburg for their generous and thoughtful participation in this study and for every question they answered. I am also thankful for the financial assistance of the University of South Africa.

## References

- [1] A. A. Yee, Structural and economic benefits of precast/pre-stressed concrete construction, *PCI Journal* 46 (2001), 34–42.
- [2] Brian Addis, Cementitious materials, Fulton's concrete technology, Eighth edition, Cement & concrete institute (2001), 5
- [3] South African National Standard SANS 10160-3, *Basis for structural design and actions for building and industrial structures*, The South African Bureau of Standard, Republic of South Africa, Pretoria, 2010.
- [4] South African Standard SABS 0100-1, *The structural use of concrete*, The South African Bureau of Standard, Republic of South Africa, Pretoria, 2000.

# The environmental performance of a reinforced precast concrete slab with void forming system

Magdalena HAJDUKIEWICZ<sup>a,b,c,1</sup>, Jérémy LEBRÊNE<sup>d</sup> and Jamie GOGGINS<sup>a,b</sup>

<sup>a</sup>Department of Civil Engineering, National University of Ireland Galway, Ireland

<sup>b</sup>Ryan Institute, National University of Ireland Galway, Ireland

<sup>c</sup>IRUSE, National University of Ireland Galway, Ireland

<sup>d</sup>Département Thermique & Énergétique, Polytech Nantes, France

**Abstract.** In some climates people spend approximately 90% of their lives indoors. Thus, it is very important to maintain healthy and comfortable conditions in buildings. The building sector is responsible for about 40% of the energy consumption and contributes related CO<sub>2</sub> emissions worldwide. Knowledge about the heat transfer and storage in concrete components of the building envelope and materials that comprise the envelope is vital in evaluating the environmental and energy performance of buildings. Providing sufficient thermal properties of the building envelope is crucial in delivering optimal indoor conditions while reducing the energy consumption in buildings.

This paper presents a case study that focuses on evaluating the environmental performance of a reinforced precast concrete slab that incorporates the void forming system. Numerical analysis and field measurements were performed to investigate thermal properties of the floor slab in the operating demonstration Engineering Building at the National University of Ireland Galway in Ireland. Firstly, the numerical finite volume models of the slab in the demonstration building were developed and validated with the 'real-time' physical measurements. Those measurements were obtained from the demonstration building, including temperature sensors embedded in the slab, outdoor air temperatures, thermal imaging, etc. Those validated models allowed investigation of the phenomena of heat transfer and storage in the slab and their influence on indoor environmental conditions, including occupants' health and comfort. The numerical models and 'real-time' field measurements were also supported by detailed laboratory experiments regarding the material properties of concrete. The proposed analysis will (i) identify possible design/operation drawbacks; (ii) suggest optimised, cost-effective and sustainable designs; and (iii) allow for the development of new environmentally friendly and energy efficient structural building components.

**Keywords.** Precast slab, void forming system, numerical model, environmental performance

## Introduction

The building sector is responsible for about 40% of the total European energy consumption and related CO<sub>2</sub> emissions in the European Union (EU) [1]. In 2009, EU leaders and the G8 specified a reduction in greenhouse emissions by at least 80% below 1990 levels by 2050 [2].

<sup>1</sup>Corresponding author: [magdalena.hajdukiewicz@nuigalway.ie](mailto:magdalena.hajdukiewicz@nuigalway.ie)



In addition, the EU adopted the Directive on Energy Performance of Buildings [3], which requires a 'nearly-zero energy building' target for new public buildings from 2018 and from 2020 for all new buildings. This puts pressure on the building sector to consider aggressive energy efficiency measures.

In some climate regions people spend approximately 90% of their lives indoors [4]. While reducing the energy consumed by buildings, consideration must also be given to providing healthy and comfortable indoor conditions for the occupants. Knowledge about the transport of various phenomena through multi-layered building components is vital in evaluating the components' structural and environmental performance. Providing sufficient thermal mass of the building envelope is crucial in delivering satisfactory indoor conditions while reducing the energy consumption in buildings.

In summary, it is vital to give consideration to both the environmental and energy aspects in buildings. This should be done in order to maintain safe, healthy and comfortable environments for the occupants of energy efficient and sustainable buildings.

Numerical methods have been previously used to investigate the thermal performance of building structural components (e.g. [5-7]). The most common methods include finite difference, finite element and finite volume numerical analyses. Those methods can help understand and predict phenomena that are often difficult to test experimentally, resulting in cleaner, healthier, better controlled and sustainable internal environments. It is important that numerical simulation tools are validated with physical measurements. However, there is a dearth of measured data for buildings. Experimental investigations in isolation do not provide a comprehensive picture of buildings performance. Furthermore, such investigations may be time consuming and expensive. On the other hand, numerical models can quickly offer rich information about the influence of the building structural elements on indoor environmental conditions. Validated with physical measurements, numerical models allow for many opportunities to test and optimise designs. This is done in order to ensure building owners and occupants enjoy high air quality, thermal comfort, minimal noise levels and energy efficiency.

The European Standards and building regulations for precast building products specify in detail the design and construction of precast elements in terms of their structural and environmental performance. However, there can be a gap between the intended design and the final product. This gap can be bridged by validated numerical models to predict if the designed product may perform as intended.

## **1. Demonstration building**

### *1.1. A living laboratory*

The Engineering Building (EB) at the National University of Ireland (NUI) Galway (Figure 1) is a state of the art academic facility that integrates all engineering activities on campus. The 14 250 m<sup>2</sup> building has been opened to public in July 2011 and accommodates over 1100 students and 110 staff. The building provides a learning environment and also acts as a teaching/learning tool. The EB is a 'living laboratory' for engineering, where live data sets from numerous types of sensors are provided to illustrate structural and environmental building performance concepts in undergraduate

teaching and in the development of full-scale research. Structural and environmental characteristics of the building are systematically captured, transformed and monitored throughout the building's entire life cycle. Those characteristics include the measurement of building's (i) structural behaviour (strains, temperatures and movements in the building structure); (ii) energy demands (electrical loads such as lighting, computing and HVAC equipment); and (iii) environmental behaviour (thermal comfort, air quality and water consumption). The information gathered from the building is then used to create interactive tools for students, form the basis for ongoing/future research projects and facilitate the advancement of engineering teaching methods.



Figure 1. Engineering building (EB) at NUI Galway.

### 1.2. Void-form concrete slab system

The research presented here investigates the environmental performance, i.e. heat transfer through the void-form concrete slab built in the Cobiax system technology [8]. The Cobiax slabs are the reinforced concrete slabs with implemented high-density polyethylene hollow void formers (Figure 2). Those hollow void formers not only reduce the structural dead load of the slab (resulting in saving on the material cost and allowing larger slab spans), but also increase the thermal resistance of the slab.

The investigated void-form concrete slab was a floor slab located on the third floor in the west wing of the EB. This novel form of flat slab system was implemented for the first time in Ireland in the EB. The slab (12.65 m x 7.50 m) consisted of the precast lattice girder element manufactured off site and the in-situ element (Figure 3). The bottom surface of the slab was exposed (with no finish applied to it), while the top surface of the slab was hidden under the suspended panel floor.

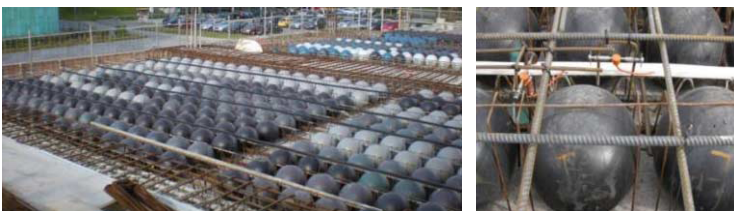


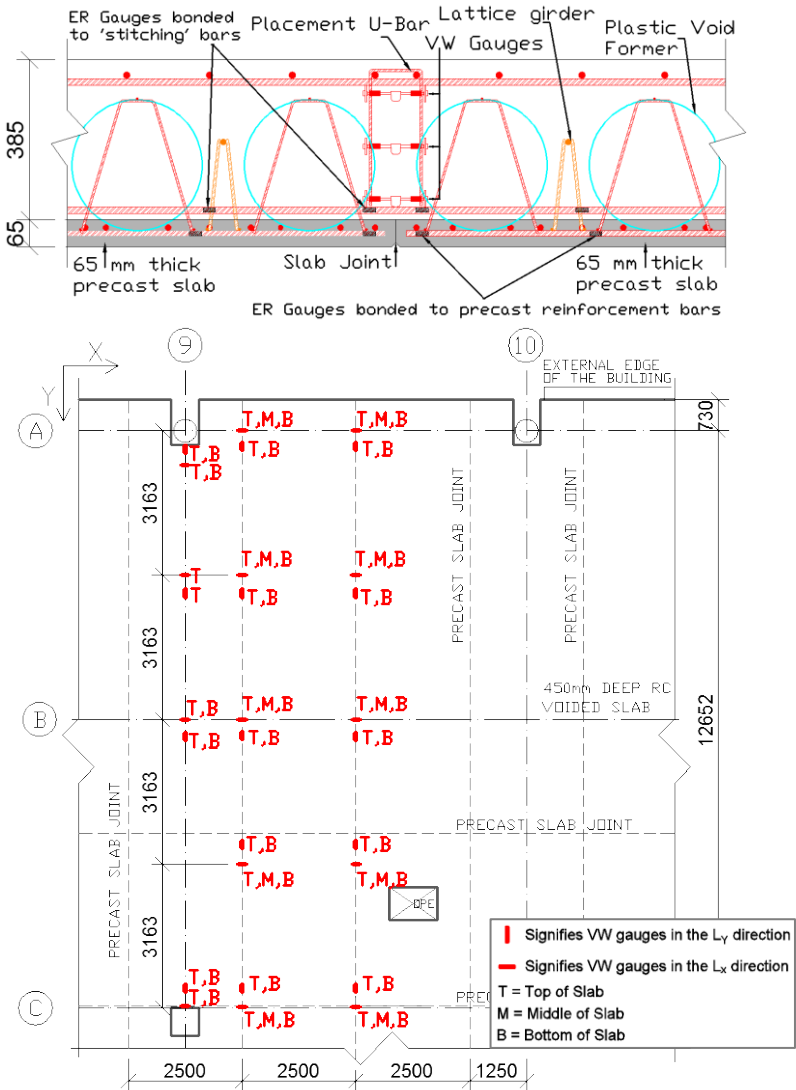
Figure 2. Cobiax voided concrete slab system being installed in the EB (left) and with gauges installed (right) [9].

## 2. 'Real-time' measurements

There were 164 sensors embedded in the slab, i.e. 64 vibrating wire (VW) gauges (Gage Technique model TES/5.5/T [10] measuring strain and temperature of concrete) and 100 electrical resistance gauges (Tokyo Sokki Kenkyujo model FLA-6-120-11-

3LT [11] measuring strain of reinforcement). The aim of embedding sensors in this novel form of slab was to investigate its structural (two-way spanning action) and environmental (heat transfer) performance.

This paper focuses on the experimental and numerical investigation of the heat transfer through the void-form slab in the EB. The experimental measured data were used to validate the numerical model of the heat transfer in the Cobiax slab. The slab temperature has been constantly monitored by the VW gauges located between grid locations 9A and 9.5C (Figure 3). In order to observe the slab temperature profile across its thickness, the gauges were attached to the reinforcement bars in the top, middle and bottom in-situ part of the slab as shown in Figure 3. The operating temperature of the VW gauges ranged from  $-20\text{ }^{\circ}\text{C}$  to  $80\text{ }^{\circ}\text{C}$ .



**Figure 3.** Section (top) and plan (bottom) of the Cobiax slab showing the location of VW gauges [9].

This paper focuses on the measurements taken by the gauges located in the middle of the slab/room (intersection of grid lines 9.5/B) and thus the most representative for the whole slab. At this location there were two gauges (TempX,Y\_B) located at the bottom of the slab (100 mm from the bottom surface of the slab), one gauge (TempX\_M) in the middle of the slab (227 mm from the bottom surface of the slab), and two gauges (TempX,Y\_T) at the top of the slab (354 mm from the bottom surface of the slab).

Data measured by the VW gauges have been collected and stored on a data acquisition system consisting of CR1000 data loggers, AVW200 vibrating wire interface and AM16/32B multiplexers [12]. This system has been automatically logging data from the sensors embedded in the void-form concrete slab since their initial installation. During the construction phase, data were stored on a flash memory card and manually downloaded onto a laptop weekly and backed-up on a server. Since the commissioning of the EB, data communication has been relayed through the use of the NL115 Ethernet and Compact Flash Module [12] and allowed for data collection over a local network. Additionally to the building structure performance measurement, outdoor air temperatures were monitored by the automatic weather station located at the NUI Galway campus [13]. Since, the rooms below and above the slab were both naturally ventilated, it was expected that the outdoor air temperature would influence the temperature distribution in the slab.

This paper presents the measurements taken throughout the full day of July 3<sup>rd</sup>, 2013. The measurements between 10 am and 4 pm were used to develop the numerical model of the slab (Section 3). Figure 4 compares the profiles of the outdoor air temperature and the slab temperatures. It is evident that with the increase in the outdoor air temperature, the temperature of the slab increased as well, particularly in the lower part of the slab (TempX,Y\_B). In the middle (TempX\_M) and upper (TempX,Y\_T) parts of the slab, the temperature increased with a visible thermal lag. This might have been due to the fact that the room above the slab had the suspended panel floor installed, which provided additional insulation from the influence of the outdoor air.

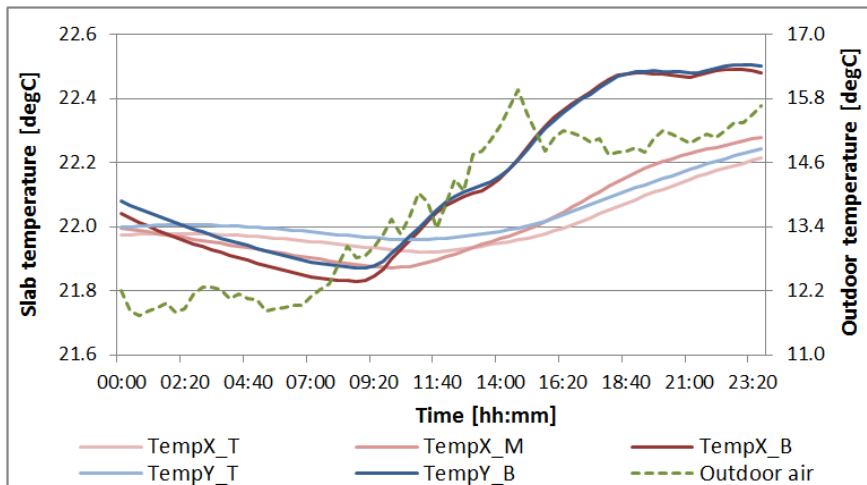


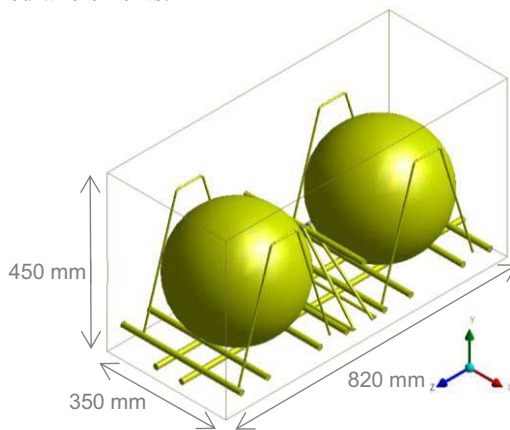
Figure 4. Outdoor air and slab temperature measurements recorded on July 3<sup>rd</sup>, 2013.

### 3. Numerical analysis

In this paper, a 3D finite volume model was developed in order to investigate the heat transfer through the Cobiax void-form slab. The commercial finite volume analysis software ANSYS CFX [14] was utilised. The numerical model was then validated with the ‘real-time’ measurements from the demonstration EB at NUI Galway (Section 2).

#### 3.1. Geometry and mesh

The 3D geometry of the slab was reduced in order to decrease the number of mesh elements to be solved and, thus, minimise the computational time. The geometry consisted of the 450 mm thick reinforced concrete slab with two void formers secured by the light metal mesh (Figure 5). The unstructured mesh of the model contained 2 337 162 tetrahedral elements.



**Figure 5.** Geometry of the modelled Cobiax slab.

#### 3.2. Material properties and boundary conditions

The steady state conditions were used in the analysis. The mass, momentum and energy governing equations were solved for all mesh elements in the model. The high resolution advection scheme (that denotes a class of numerical discretisation for solving partial differential equations) was applied. The high resolution scheme is essentially a second order accurate scheme, for which values of blend factor vary throughout the domain based on the local solution field. Satisfactory convergence was achieved using the criteria of 0.01% of root mean square residuals for mass, momentum and energy equations, 1% of the energy conservation target and the numerical results at points of interest no longer changing with additional iterations.

The air in the void formers was modelled as an ideal gas with the reference buoyancy density of  $1.185 \text{ kg/m}^3$  and the reference pressure of 1 atm. The full buoyancy model was applied (where the fluid density was a function of temperature or pressure) and the Reynolds averaged Navier-Stokes (RANS) eddy-viscosity two-equation standard  $k-\varepsilon$  turbulence model [15] was chosen. The other materials described in the model included (i) high-density polyethylene void formers ( $\rho = 950 \text{ kg/m}^3$ ), (ii) steel reinforcement bars (density,  $\rho = 7\,854 \text{ kg/m}^3$ ), and (iii) concrete ( $\rho = 2\,406 \text{ kg/m}^3$ ). The densities of the precast and in-situ concrete were experimentally

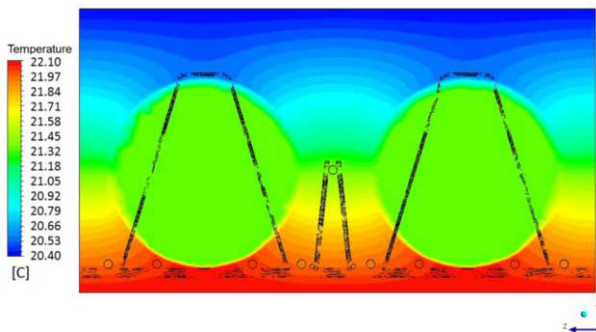
investigated in the laboratory environment based on the samples taken from the precast manufacturing plant and the building site [9].

The surface temperature boundary condition was set on the top and bottom horizontal surfaces of the model ( $t_{top} = 20.40\text{ }^{\circ}\text{C}$ ,  $t_{bottom} = 22.10\text{ }^{\circ}\text{C}$ ). Those temperatures were the average slab surface temperatures, measured with the thermal camera FLIR T335 [16] during the experiment on 3<sup>rd</sup> July 2013 between 10 am and 4 pm. Since there was no access available to the slab from the room above it, the top surface temperature of the slab was assumed the same as the temperature of the suspended panel floor. The measurement accuracy of the camera was  $\pm 2\text{ }^{\circ}\text{C}$  or 2% of the reading. Despite the fact that the room below the slab and the room above it were both naturally ventilated and operated in the same manner, the temperature of the bottom surface of the slab was higher than the temperature of the top surface. This was due to the temperature stratification inside those rooms and resulted in higher temperature at the ceiling level (in the room below the slab) than the temperature at the floor level (the room above the slab).

The symmetry boundary condition was set at the four vertical surfaces of the model in order to simulate the conditions in the middle of the slab (at the intersection of grid lines 9.5/B). The interface fluxes were set in order to model the heat transfer between the different materials in the model.

### 3.3. Validated results

Figure 6 shows the temperature distribution in the modelled Cobiax slab. Temperatures in the slab decreased evenly from the  $22.10\text{ }^{\circ}\text{C}$  at the bottom surface of the slab to  $20.40\text{ }^{\circ}\text{C}$  at its top surface. The average temperature of: (i) the air in the void formers was  $21.33\text{ }^{\circ}\text{C}$ , (ii) the polyethylene of the void formers was  $21.57\text{ }^{\circ}\text{C}$ , (iii) the reinforcement was  $21.59\text{ }^{\circ}\text{C}$ , and (iv) the concrete was  $21.53\text{ }^{\circ}\text{C}$ .



**Figure 6.** Temperature distribution in the void-form slab.

In order to validate the numerical model, the measurements on 3<sup>rd</sup> July 2013, taken every 20 min between 10 am and 4 pm were considered. The measurements over this 6-hours period were relatively steady (standard deviation not exceeding  $0.13\text{ }^{\circ}\text{C}$ ) and, thus, suitable for use in the validation of the steady state numerical simulation. Table 1 compares measured and simulated temperatures in the slab. The numerical results showed a very good agreement with the measurements in the lower parts of the slab (TempX,Y\_B) with an error of less than 2%. In the upper part of the slab (TempX,Y\_T) the error between measured and simulated temperatures increased up to 6%. This might have been due to the fact that the boundary condition at the top surface

of the slab was not specified accurately (it was assumed as the measured surface temperature of the suspended panel floor) and, thus, influenced the modelled temperatures in the upper part of the slab the most.

**Table 1.** Measured and simulated temperatures in the Cobiax slab at 9.5/B grid lines.

Location	Measured temp. [°C]	Simulated temp. [°C]	Error [%]
TempX_B	22.11	21.77	1.5
TempY_B	22.12	21.75	1.7
TempX_M	21.94	21.19	3.4
TempX_T	21.94	20.68	5.7
TempY_T	21.98	20.69	5.9

#### 4. Conclusions and future work

This paper presents a case study that focused on evaluating the environmental performance of a reinforced precast concrete slab that incorporated the void forming system. The initial field measurements and numerical models were performed to investigate thermal properties of the floor slab in the operating demonstration building.

The proposed analysis, such as presented in this paper, may be utilised to (i) identify possible design/operation drawbacks; (ii) suggest optimised, cost-effective and sustainable designs; and (iii) allow for the development of new environmentally friendly and energy efficient structural building components. Furthermore, validated numerical models can also be used to investigate the thermal behaviour of the void-form concrete slab, including fire resistance and cooling time after extinguishing the fire.

#### References

- [1] European Union. Official website of the European Union. 2014. Available: <http://www.europa.eu>.
- [2] European Climate Foundation. Roadmap 2050: a practical guide to prosperous, low carbon Europe. Brussels, Belgium, 2010.
- [3] European Union. The Directive 2010/31/EU of the European Parliament and of the Council of May 2010 on the energy performance of buildings. *Official Journal of the European Union*, Brussels, 2010.
- [4] US EPA. United States Environmental Protection Agency. 2012. Available: <http://www.epa.gov/>.
- [5] J. Sun and L. Fang. Numerical simulation of concrete hollow bricks by the finite volume method. *Int. J. Heat Mass Transf.*, 52(23–24):5598–5607, 2009.
- [6] A. Zaidi, R. Masmoudi, and M. Bouhicha. Numerical analysis of thermal stress-deformation in concrete surrounding FRP bars in hot region. *Constr. Build. Mater.*, 38: 204–213, 2013.
- [7] J. Ožbolt, J. Bošnjak, G. Periškić, and A. Sharma. 3D numerical analysis of reinforced concrete beams exposed to elevated temperature. *Eng. Struct.*, 58: 166–174, 2014.
- [8] Cobiax. 2014. Available: <http://www.cobiax.ch/>.
- [9] D. Byrne. The analysis of shear and load transfer in void form flat slab systems, through in-situ measurements from buildings and numerical modelling. PhD Thesis, College of Engineering and Informatics, National University of Ireland Galway, 2014.
- [10] Gage Technique. 2014. Available: <http://www.gage-technique.com/>.
- [11] TML. Tokyo Sokki Kenkyujo Co. Ltd. 2014. Available: <http://www.tml.jp/>.
- [12] Campbell Scientific Inc. 2014. Available: <http://www.campbellsci.co.uk/>.
- [13] IRUSE weather website. 2014. Available: <http://weather.nuigalway.ie/>.
- [14] Ansys, Inc. 2013. Available: <http://www.ansys.com/>.
- [15] B. E. Launder and D. B. Spalding. The numerical computation of turbulent flows. *Comput. Methods Appl. Mech. Eng.*, 3(2): 269–289, 1974.
- [16] FLIR. Thermal imaging. 2014. Available: <http://www.flir.com/IE/>.

# Foam geopolymers: state of the art and preliminary experimental results

Zahra ABDOLLAHNEJAD<sup>1</sup>, F. Pacheco TORGAL and J.L. Barroso DE AGUIAR  
*Department of Civil Engineering, University of Minho, Guimarães, Portugal*

**Abstract.** Buildings are responsible for more than 40% of the energy consumption and greenhouse gas emissions. Thus increasing building energy efficiency is the most cost effective way to reduce emissions. The use of thermal insulation materials constitutes the most effective way of reducing heat losses in buildings thus reducing heat energy needs. These materials have a thermal conductivity factor,  $k$  (W/m.K) lower than 0.065 while other insulation materials like for instance aerated concrete can go up to 0.11. Current insulation materials are associated with negative impacts in terms of toxicity. Polystyrene, for example contains anti-oxidant additives and ignition retardants, additionally, its production involves the generation of benzene and chlorofluorocarbons. Polyurethane is obtained from isocyanates, which are widely known for their tragic association with the Bhopal disaster. Besides current insulation materials releases toxic fumes when subjected to fire. This paper reviews literature on foam geopolymers that could constitute a lower toxicity alternative to current commercial insulator. Current methods use foaming agents (blowing agents) such as hydrogen peroxide ( $H_2O_2$ ), sodium perborate ( $NaBO_3$ ), silica fume, powder alumina. Results of an experimental research on foam hybrid alkaline cements are reported.

**Keywords.** Foam agents, hybrid alkaline cements, compressive strength, thermal conductivity, density

## Introduction

Energy consumption is one of the greatest problems of the human civilization being responsible for high greenhouse gas emissions. Energy efficiency is the most cost effective way to reduce emissions. Since buildings are responsible for more than 40% of the energy consumption it's reduction is of paramount importance not only environmental speaking as well as to reduce electric bills [1]. In this context the development of innovative thermal insulators constitutes a research priority [2].

Current insulation materials are associated with negative impacts in terms of toxicity. Polystyrene, for example contains anti-oxidant additives and ignition retardants, additionally, its production involves the generation of benzene and chlorofluorocarbons. Polyurethane is obtained from isocyanates, which are widely known for their tragic association with the Bhopal disaster [3].

---

<sup>1</sup>Corresponding author. [tolumahvash@gmail.com](mailto:tolumahvash@gmail.com)



Foamed materials are produced by using either cement paste or mortar in which large volumes of air are entrapped by using foam agents. Giannakau and Jones explored the potential of foam concrete to enhance the thermal performance of low rise building has shown that the foam concrete ground supported slab foundation possess better thermal insulation and lower sorptivity properties while producing satisfactory strength [4].

Using foam concrete instead of inner leaf leads to increase thermal insulation of brick wall by 23%. Furthermore, insulation is more or less inversely proportional to density of foam concrete [5]. The heat transfer at high temperature is done through porous materials which are affected by radiation. Heat transfer is an inverse function of the number of air–solid interfaces traversed [6].

In this context the first part of this paper reviews the state of the art of these materials followed by the disclosure of some preliminary experimental results on the influence of several foam agents on the properties of hybrid alkaline cements.

## 1. State-of-the-art

Proportioning and the preparation process of foam concrete are usually achieved by a trial and error process to obtain the desired mechanical properties of foam concrete [7]. Most proposed methods result in calculation of batch quantities. In this direction, McCormick based on solid volume calculations proposed a rational proportioning method [8]. Kearsley and Mostert have proposed a set of equations for calculating the foam volume and cement content [9].

Porosity network, permeability and pore size distribution affect compressive strength and durability properties of foam concrete [10]. The porosity of foam concrete consists of gel pores and capillary pores which is affected by volume, size, size distribution, shape and spacing between air-voids. Narrower air-void distribution leads more compact foam concrete which subsequently higher compressive strength is achieved. Using finer filler materials such as fly ash results in more uniformity of air void distributions. The compressive strength of foam concrete is significantly functioned to the density [10].

Therefore, the density of composition for foam concrete is adjusted by compressive strength. The type of mixer and batching and mixing sequences of foam concrete depends upon pre-formed foam method or mix-foaming method [11].

Pre-formed foaming is preferred to mix-forming technique due to the lower foaming agent requirement and a close relationship between amount of foaming agent used and air content of mix [12]. Foam concrete with density  $1000 \text{ kg/m}^3$  has one-sixth thermal conductivity of typical cement-sand mortar [13].

The name 'geopolymer' was introduced by Davidovits in the 1970s, however the technology of alkali-activation predates this terminology by more than 60 years [14]. According to the rigorous definition of Provis [14] these materials "*are produced through the reaction of an aluminosilicate—normally supplied in powder form as an industrial by-product or other inexpensive material—with an alkaline activator, which is usually a concentrated aqueous solution of alkali hydroxide, silicate, carbonate or sulphate*".

Despite all the investigations published on these materials in the last decades some aspects still needed to be further investigated especially concerning durability performance [15]. Foam geopolymer constitutes a recent research field with high

potential in the development of low toxicity thermal insulators with thermal conductivity value around 0.22 W/mK [16].

The discovery of one-part geopolymers (also known as hybrid alkaline cements) is considered a key event on the evolution of low carbon geopolymer technology, however they were associated with very low compressive strength [17, 18]. Some authors recently investigated these materials having reported a 28 days curing compressive strength of 27 MPa by using fly ash and 30% OPC [19]. These mixtures are used in this paper to produce foam materials. The influence of the foam agent is highlighted.

## 2. Experimental

Hybrid alkaline cements are based on kaolin, fly ash, ordinary Portland cement (OPC), sodium hydroxide, calcium hydroxide ( $\text{Ca}(\text{OH})_2$ ), water and superplasticizer (Table 1). As previously reported [18] the kaolin and sodium hydroxide were calcined in a furnace at 650 °C during 140 minutes being termed as calcined stuff.

**Table 1.** Mixture proportions (%)

Cement	Fly ash	$\text{Ca}(\text{OH})_2$	Calcined stuff	Water/Powder	SP/Powder	Sand
30	58.3	7.7	4	35	0.8	80

Two foam agents in three percentages (1%, 2% and 3%) were used, namely hydrogen peroxide ( $\text{H}_2\text{O}_2$ ) and sodium perborate ( $\text{NaBO}_3$ ). Figure 1 shows how foaming agents induce the increase in open porosity.

### 2.1 Testing description

To study foamed hybrid alkaline cement four parameters were considered bulk density; open porosity (water absorption); thermal conductivity and compressive strength. Bulk density was assessed according to the ASTM C 373-78. Thermal conductivity was assessed using an Alambeta instrument developed at the Technical University of Liberec, Czech Republic. During the measurements, the initial temperature of the samples and the base of the Alambeta were kept at 22-24 °C, and the relative humidity was in the range of 55-65%. To investigate the effect of the temperature drop on the thermal properties of the samples, the temperature of the measuring head at first was 10 °C higher than the environmental temperature. During the second set of measurements, the measuring head was 40 °C higher than the base plate.

For water absorption the specimens were immersed in water until their weights become stable. After they were then rolled lightly on a wet cotton cloth to remove all excess water from their surfaces to reach the status of saturated-surface-dry (SSD), and were weighed and denoted by  $W_{\text{SSD}}$ . Furthermore, the saturated IPF specimens were dried to constant weight by heating in an oven at 150 °C, and the resulting oven-dry (OD) specimens were then weighed and recorded as  $W_{\text{OD}}$ . The water absorption of each specimen can be calculated from the relation of  $W^* = (W_{\text{SSD}} - W_{\text{OD}})/W_{\text{OD}}$ .

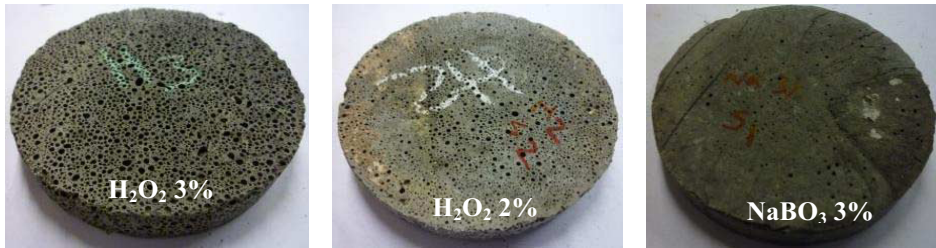


Figure 1. Porosity aspect in hybrid alkaline cement with different foam agents

Compressive strength tests were performed on  $50 \times 50 \times 50 \text{ mm}^3$  concrete specimens according to NP EN 195-1. The specimens were located in the chamber room at  $23 \text{ }^\circ\text{C}$  for 28 days. Compressive strength for each mixture was obtained from an average of 3 cubic specimens. The compressive strength after exposure to high temperatures was also assessed. The specimens were exposed during two hours at  $600 \text{ }^\circ\text{C}$  and  $800 \text{ }^\circ\text{C}$ . After two hours the specimens were removed from the furnace and tested after 4 hours at the laboratory controlled temperature.

### 3. Results and discussion

Figure 2-4 shows the open porosity (water absorption), bulk density and thermal conductivity results of mixtures with hydrogen peroxide ( $\text{H}_2\text{O}_2$ ) and sodium perborate ( $\text{NaBO}_3$ ).

Sodium perborate addition shows a higher influence on the increase of open porosity than hydrogen peroxide. The increase of sodium perborate content from 1% to 2% leads to just a minor increase in the open porosity while the increase to 3% even reduced it. A higher reduction in open porosity is noticed when hydrogen peroxide content increases from 2% to 3%.

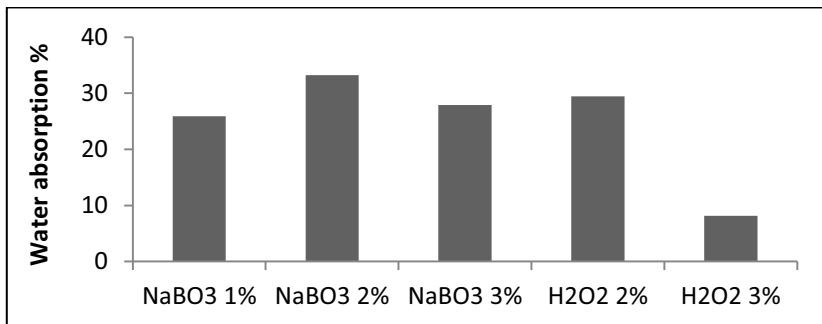


Figure 2. Water absorption (open porosity)

Concerning bulk density the increase in the sodium perborate from 1% to 3% content seems to have had little influence on the bulk performance. A not very different behaviour takes place when hydrogen peroxide content increases from 2% to 3%.

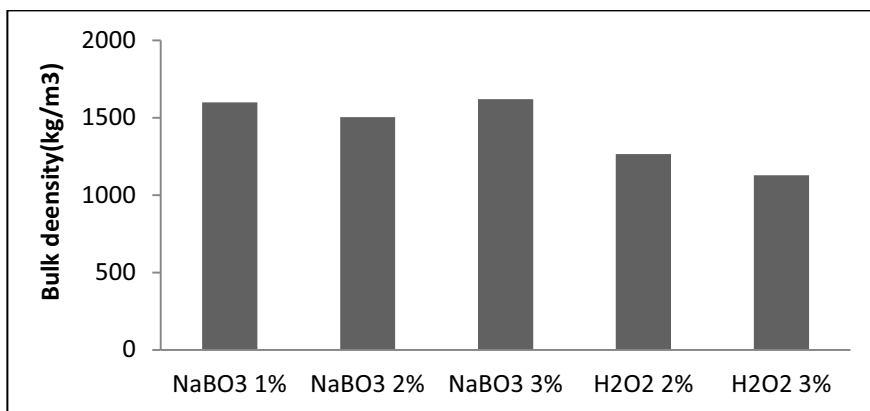


Figure 3. Bulk density

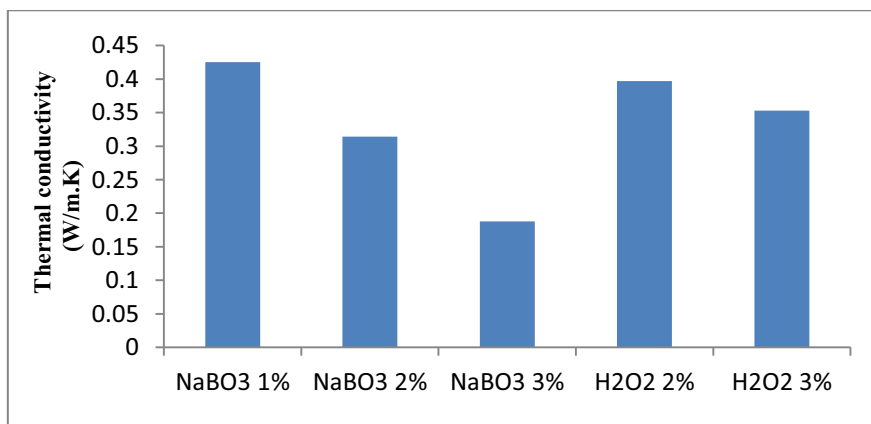


Figure 4. Thermal conductivity

The best thermal conductivity performance was obtained in the mixture with 3% sodium perborate. Still this performance is unsatisfactory because the thermal conductivity of commercial foamed masonry blocks (Ytong) are below 0.2 W/m.K and some aerated concrete mixtures have a thermal conductivity around 0.11 W/m.K. Further investigations concerning the use of higher contents of sodium perborate are therefore needed. Figure 5 shows the 28 days compressive strength at ambient temperature and after the specimens were submitted to a high temperature (600 °C and 800 °C).

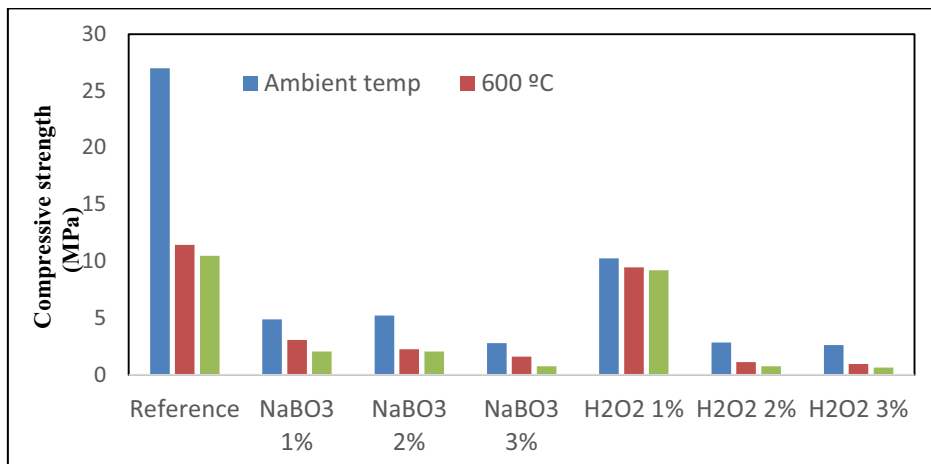


Figure 5. Compressive strength of specimens at 23 °C, 600 °C and 800 °C

Only the mixtures with 1% hydrogen peroxide and mixtures with 2% and 3% sodium perborate have a 28 days compressive strength above 6MPa. The exposure to high temperature leads to a severe compressive strength reduction for the reference mixture while the reduction is much less severe for foam mixtures. Further investigations concerning the use of higher contents of sodium perborate are therefore needed. The study of optimal foam agent percentage is currently ongoing.

#### 4. Conclusions

Foam materials can contribute to building thermal insulation being important materials in the context of building energy efficiency. This paper discloses preliminary results on the influence of several foam agents on the properties of hybrid alkaline cements.

Sodium perborate addition shows a higher influence on the increase of open porosity than hydrogen peroxide. The increase of sodium perborate content from 1% to 2% leads to just a minor increase in the open porosity while the increase to 3% even reduced it. Concerning bulk density the increase in the sodium perborate from 1% to 3% content seems to have little influence on the bulk performance.

The best thermal conductivity performance was obtained in the mixture with 3% sodium perborate (0.18 W/mK). Still this performance is unsatisfactory because the thermal conductivity of commercial foamed masonry blocks (Ytong) are below 0.2 W/m.K and some aerated concrete mixtures have a thermal conductivity around 0.11 W/m.K. The exposure to high temperature leads to a severe compressive strength reduction for the reference mixture while the reduction is much less severe for foam mixtures. Further investigations concerning the use of higher contents of sodium perborate are therefore needed. The study of optimal foam agent percentage is currently ongoing.

## References

- [1] F. Pacheco-Torgal, L. Cabeza, M. Mistretta, A. Kaklauskas, G. Granqvist, Nearly zero energy building refurbishment. A multidisciplinary aproch Springer Verlag, London, UK, 2013
- [2] F. Pacheco-Torgal, A. Fucic, S. Jalali, Toxicity of Building Materials. Woodhead Publishing Limited Abington Hall, Cambridge, UK, 2012
- [3] F. Pacheco-Torgal, Eco-efficient construction and building materials research under the EU Framework Programme Horizon 2020. *Construction and Building Materials* 51 (2014), 151-162.
- [4] A. Giannakou, M.R. Jones, Potentials of foamed concrete to enhance the thermal performance of low rise dwellings. In: Dhir RK, Hewelett PC, Csetenyi LJ, editors. Innovations and development in concrete materials and construction. UK: Thomas Telford; 533–44, 2002.
- [5] W. H. Taylor, Concrete technology and practice. London: Angus and Robertson; 1969.
- [6] R.C. Valore, Cellular concrete. Part I composition and methods of production. *ACI J* 50 (1954) 773–96.
- [7] M. Nehdi, Y. Djebbar, A. Khan, Neural network model for preformed foam cellular concrete. *ACI Mater J* 98 (2001) 402–409.
- [8] F.C. McCormick, Rational proportioning of preformed foam cellular concrete. *ACI Material Journal* 64 (1967) 104–109.
- [9] E.P. Kearsley, H.F. Mostert, Designing mix composition of foamed concrete with high fly ash contents. In: Dhir RK, Newlands MD, McCarthy A, editors. Use of foamed concrete in construction. London: Thomas Telford, 29–36, 2005.
- [10] K. Ramamurthy, E. Nambiar, G. Ranjani, A classification of studies on properties of foam concrete. *J Cement & Concrete Composites* 31 (2009) 388–396.
- [11] S. Karl, J.D. Worner, Foamed concrete-mixing and workability. In: Bartos PJM, editor. Special concrete-workability and mixing. London: E&FN Spon; 217–24, 1993.
- [12] K.J. Byun, H.W. Song, S.S. Park, Development of structural lightweight foamed concrete using polymer foam agent. ICPC-98; 1998.
- [13] Y.M. Hunaiti, Composite action of foamed and lightweight aggregate concrete. *J Mater Civ Eng* 8 (1996) 111–113.
- [14] J.L. Provis, Geopolymers and other alkali activated materials: why, how, and what? *Materials and Structures* 47 (2014) 11-25.
- [15] F. Pacheco-Torgal, Z. Abdollahnejad, A. Camões, M. Jamshidi, Y. Ding, Durability of alkali-activated binders. A clear advantage over Portland cement or an unproven issue ? *Construction and Building Materials* 30 (2012) 400-405
- [16] E. Prud'homme, P. Michaud , E. Joussein, C. Peyratout, A. Smith, S. Arrii-Clacens, J.M. Clacens, S. Rossignol, Silica fume as porogent agent in geo-materials at low temperature, *Journal of the European Ceramic Society* 30 (2010) 1641-1648.
- [17] D. Kolousek, J. Brus, M. Urbanova, J. Andertova, V. Hulinsky, J. Vorel, Preparation, structure and hydrothermal stability of alternative (sodium silicate-free) geopolymers. *Journal of Materials Science* 42 (2007) 9267-9275.
- [18] Peng, M.-X.; Wand, Z.-H.; Shen, S.-H.; Xiao, Q.-G., Synthesis, characterization and mechanisms of one-part geopolymeric cement by calcining low-quality kaolin with alkali. *Materials and Structures* (in press) 2014
- [19] Z. Abdollahnejad, P. Hlavacek, S. Miraldo, F. Pacheco-Torgal, A. Aguiar, Compressive strength, microstructure and hydration products of hybrid alkaline cements. *Materials Research* (in press) 2014

# Quality assurance in low-cost housing construction projects in the metropole

Manelisi RARANI<sup>1</sup> and Stanley FORE<sup>2</sup>

*Management and Project Management Department, Faculty of Business, Cape Peninsula, University of Technology, South Africa*

**Abstract.** In South Africa, to protect the beneficiaries of housing against the inferior workmanship, unsuitable material and inappropriate construction methods, building standards and regulations have been introduced. The housing inspectors have been given power to enforce and ensure that the building standards and regulations are followed and met by contractors. Regardless of the measures, low-cost houses built through government programmes are known to have many quality problems. Hence, this research assesses the effectiveness and adequacy that inspection process contributes to quality assurance in low-cost housing construction projects in the South African metropole. Data for the analysis were collected through questionnaires administered to low-cost housing inspectors in the South African metropolis. IBM Statistical Package for Social Sciences (SPSS) Statistics 21 version was used in analysing the data collected. This paper concludes that the low-cost housing inspectors lack training in housing inspection, and have limited knowledge in building standards and regulations. It is recommended that standard continuous training and education for low-cost housing inspectors be established. Such a program would provide courses and training of low-cost housing inspectors to improve their level of knowledge in building standards and regulations, review their roles and responsibilities, and establish awareness of their roles among the affected parties.

**Keywords.** Housing South Africa, quality, quality assurance, inspection, inspectors

## Introduction

In 1994, the South African government introduced low-cost housing projects through its Reconstruction and Development Programme (RDP), as an integral part of South African government's commitment to reduce poverty, improve the quality of people's lives, and address the inequalities arising from past injustices of apartheid era. Henceforth the houses built through this programme were commonly known as RDP houses [12]. Through the programme, many low-cost houses were built and delivered to beneficiaries. This was in line with what people expected after the first democratic elections [7]. The South African government has spent billions of Rand in low-cost housing since and the National Human Settlements Department (NHSD) spends millions of Rand on low-cost housing construction projects every financial year [13].

---

<sup>1,2</sup>Corresponding author: [manelisir@cput.ac.za](mailto:manelisir@cput.ac.za), [fores@cput.ac.za](mailto:fores@cput.ac.za)

However, concerns regarding the quality of low-cost houses built through government projects have been raised. Over the years, many communities have shown their growing disapproval about quality of low-cost houses delivered. This issue has become regular news items, as a number of articles have been sighted in the media [2] and also have been raised in numerous forums at both national and provincial levels [6] and [14]. South Africa's Public Protector reported that the low-cost housing problems that her office encountered included houses that lacked foundations and were built from weak materials which crumbled upon touching [1]. The Public Protector also reported that in two months in the year 2013, her office received over 5000 complaints with regard to poor quality of low-cost housing [1].

Given that the majority of South Africans are beneficiaries of low-cost housing, and also given the importance of housing construction sector to the South African economy, this issue seems to present an interesting area for investigation. The primary objective of this research was to investigate and determine the effectiveness of the current inspection process applied by low-cost housing inspectors, in assuring quality in low-cost housing construction projects in the metropole.

## **1. Literature review**

### *1.1. Housing and the housing role*

Housing is a broad concept; it does not only relate to the walls of the physical structure. There are other appropriate factors that make up a house. The Botshabelo Accord [16] stipulates that government must strive for the establishment of viable, socially and economically integrated communities which are situated in areas allowing convenient access to economic opportunities, health, educational and social amenities and within which South Africa's people will have access on a progressive basis to [7]:

- A permanent residential structure with secure tenure, ensuring privacy and providing adequate protection against the elements
- Portable water, adequate sanitary facilities, including waste disposal and domestic electricity supply.

In 1994, it was agreed that housing should play a pivotal role in economic growth and development. According to this view the delivery of housing does not just satisfied basic needs but also simultaneously stimulates the economy of the country [3]. It does so by the imperative role it plays in the economy, by generating income and employment. Secondly, housing construction creates demand with high levels of employment-intensity, across different sectors [3].

### *1.2. Housing quality*

ISO [15] define quality as a degree to which a set of inbuilt characteristics fulfil the initial requirements of the product or service. Mpambane [8] on his unpublished research integrates Lawrence and Morris measures of quality and identified three areas of housing quality:

- Structural quality, which refers primarily to durability of the house.
- Service quality, which is concerned with the kinds of equipment, facilities, and conveniences which the dwelling provides.



- The state of maintenance and caretaking.

### *1.3. Quality assurance in housing construction*

Quality assurance is the process of auditing or inspecting the quality requirements and the results from quality control measurements to ensure appropriate quality standards; operational definitions are used throughout the project [10]. Inspection process is the most vital process in assuring quality during housing construction. According to SABS [11], inspection is done (at such intervals as might be necessary and in accordance with accepted professional practice) for a system or measure or installation of a building, or part thereof; to validate whether they satisfy the design assumptions, and/or whether the design is being correctly interpreted and the work being executed generally in accordance with the designs, appropriate construction techniques and good practice.

In cases where the minimum requirements are not met, the inspection procedure offers an opportunity to begin the necessary action to bring the existing conditions up to a level that will be acceptable under provisions of the regulations [9]. The person who carries out inspection in housing construction is referred to as a housing inspector.

### *1.4. Housing inspectors*

The best legislation, designs and contracts will be of little use if those responsible for monitoring compliance during construction are unable to carry out their tasks. Therefore, Inspectors are in the front line of service delivery including housing. They are charged with the day to day interpretation of building regulations and enforcement of regulations. Inspectors decide, subject to the purpose of any given inspection, what to inspect, what changes to require, and whether or not to issue stop work orders or formal notification of violation [5].

Hence, a competent housing inspector is a person who is qualified by virtue of his or her education, training, experience and contextual knowledge to make a determination regarding the performance of a building or part thereof, in relation to a functional regulation or to undertake such duties as may be assigned to him or her in terms of these regulations [11].

### *1.5. Housing quality failure*

Achievement of acceptable levels of quality in the construction industry has long been a problem. The situation is even worse in the case of low-cost and mass housing projects in South Africa [7]. The National Department of Human Settlement spends over 10% of the housing budget every year, for tearing down and reconstructing badly built government houses. Hence, it is vital to highlight that the fundamental worth of housing programmes cannot only be measured in terms of the amount of units delivered, but the quality of the units being delivered [3].

## **2. Research methodology**

A plan on how the important factors such as information gathering, population sampling, data collection and analysis are to be carried out were devised. Quantitative

research method was used as it is good at providing information in breadth, from large number of units. The use of open-ended, closed-ended and scaled-response questions in a quantitative research method provided some advantages in this research, as the method is too shallow when the researcher wants to explore a problem or concept in depth. The focus of interest of the research was the low-cost housing inspectors in the South African Metropolis. The low-cost housing inspectors who participated in this research had an experience between 0 to 25 years in housing inspection and construction industry. The questionnaire was prepared in such a way that it covered the research questions and the specific objectives of the research. All respondents received the same set of questions in an attempt to maintain uniformity. The questionnaires were self-administered to the respondents. The completion and return timeline for the questionnaires was agreed upon between the researcher and the participants beforehand. There were 40 questionnaires that were distributed and 28 questionnaires were returned, giving a rate of response of 70%. It is unclear why only 28 questionnaires were returned. Once the researcher had completed the data collection, the data was captured in the IBM Statistical Package for Social Sciences (SPSS) Statistics 21 version. SPSS assisted with analysing the data collected. The results are presented in the form of tables and graphs.

### **3. Results and discussion**

In order to assess the competency of the respondents, the following data were collected: years of experience as an inspector and in construction industry, previous occupation, professional registration, highest qualifications, continued education and training.

The data in table 1 shows that all the respondents were appropriately experienced as housing inspectors in the construction industry. The majority of the respondents (72%) had between 1 to 5 years of experience as housing inspectors and 45% had between 6 to 10 years of experience in the construction industry. The majority of respondents had indicated to have National Trade Certificate (35%) as their highest qualification, followed by Bachelor's Degrees (30%), National Diploma (21%), Matriculation Certificate (8%), and Honours' Degrees (6%).

To establish whether housing inspectors participated in continuing education and training programmes (to ensure that their skills were continually improved), the respondents were asked whether they had undertaken any continuation education and training, of which the majority of respondents (68%) reported that they had indeed undertaken a continuation education and training. The results further revealed that even though some of the respondents had undertaken continuing education and training, none of them had undertaken continuing education and training in housing inspection.

To establish whether the housing inspectors were aware of their functions or not, the respondents were asked to state what they believed to be the functions of a housing inspector. The responses were combined and summarised to the following: site inspections, site meetings, quality assurance/acceptance or rejection of work, monitoring progress, writing technical reports, maintenance of stocks, and verifying claims. All respondents mentioned one to three of the functions. From this, it was evident that the respondents had an idea of what their functions are as housing inspectors, but they are not fully aware of them. To establish the respondents level of knowledge in building legislations, several statements were presented to which the respondents had to respond on a 5-point Likert scale of agreement, where 1 = None, 2

= Slightly Knowledgeable , 3 = Neutral, 4 = Knowledgeable, and 5 = Extremely Knowledgeable. Table 2 shows the details of response.

**Table 1.** Knowledge Building regulations

Characteristics	Percentage
<i>Years of Experience as an Inspector</i>	
0 to 5	72
6 to 10	25
21 to 25	3
<i>Years of Experience in Construction Industry</i>	
0 to 5	14
6 to 10	45
11 to 15	21
16 to 20	11
21 to 25	9
<i>Previous Occupation</i>	
Teacher	3
Building Consultant	5
Technician	9
Community Officer	9
Project Manager	10
Student	17
Architectural Technologist	20
Quantity Survey	27
<i>Professional Registration</i>	
Yes	4
No	96
<i>Highest Qualifications</i>	
Matriculation Certificate	8
Trade Certificate	35
National Diploma	21
Bachelor's Degrees	30
Honours' Degrees	6
<i>Continuation Education and Training</i>	
Yes	68
No	32

**Table 2.** Knowledge Building regulations

Statements	Percentage of Responses				
	1	2	3	4	5
Knowledge of the Housing Consumer Protection Measures Act		14	43	29	14
Knowledge of the National Building Regulation and Building Standards Act 103 of 1977 legislation			43	29	28
Knowledge of the National Building Regulation		14	29	29	28
Knowledge of the SABS 0400		14	43	14	29

Table 2 reveals that the +/- 50% of respondents have positively responded that they are knowledgeable on Consumer Protection Measures Act, National Building

Regulation and Building Standards Act 103 of 1977 legislation, National Building Regulation and SABS 0400. About +/-50% either indicated that they are not sure (neutral) and/or they are slightly knowledgeable. This is evidence that a certain percentage of the housing inspectors have weak knowledge of the building standards and regulations.

To establish whether during housing construction the foundation, insulation and drywall stage, the framing and walling, and paint, trim and finishing was inspected, the respondents were asked to indicate what they inspect during housing construction. 71% of respondents indicated that they did inspect the trenches, concrete, footings, foundation walls, backfilling and compaction. All respondents indicated that they inspected the foundation slab and walls. While 55% of the respondents indicated that they inspected the underground plumbing. The majority of the respondents (86%) indicated that they inspected framing, exterior walls, interior walls, roof sheathing, windows, interior and exterior doors. The respondents indicated that 57% of them inspected the exterior trim and finishes on their last inspection. Further shows that 71% of the respondents did not inspect insulation and drywall, only 29% did.

#### **4. Conclusion and recommendation**

The research established that the inspection objectives can only be achieved by competent housing inspectors. And it is evident that housing inspectors are adequately and appropriately qualified and possessed a level of experience in the construction industry that demonstrates their ability to apply the knowledge and skills gained and applied. However, it is evident that the housing inspectors have not received continuous education and training relating to housing inspection.

Evidence further shows that housing inspectors are not fully aware of their roles and responsibilities, meaning that they do not execute their roles and responsibilities effectively. This is supported by the fact that there is uncertainty among housing inspectors about what to inspect or not to inspect.

Although it is an accepted practice that housing inspectors must accustom themselves with building legislation and professional codes that govern the housing construction industry. The findings give evidence that almost half of the housing inspectors have insufficient knowledgeable of building standards and regulations that they are supposed to enforce for compliance.

From above, a conclusion can be drawn that the inspection process applied for low-cost housing inspectors in assuring quality in low-cost housing construction projects in the metropole ineffective.

#### **Acknowledgement**

I wish to thank the Management and Project Management Department in the Faculty of Business at the Cape Peninsula University of Technology as this article is written as a result of a dissertation submitted in fulfilment of the requirements for the degree in Master of Technology of Business Administration in Project Management.

## References

- [1] Fokazi, S. 2013. Madonsela exposes horrors of RDP homes. [www.iol.co.za/news/politics/](http://www.iol.co.za/news/politics/). Cape Town: iol news. 21 February 2013.
- [2] Govender, M. 2009. We'll fix rotten builders, vows Sexwale: *The Daily News*. 17 November 2013.
- [3] Hassen, E. K. 2003. When more means less: Low income Housing and Macroeconomic Policy in South Africa. Heinemann.
- [4] Kazaz, A. and Birgonul, M.T. 2005. The evidence of poor quality in high rise and medium rise housing units: a case study of mass housing projects in Turkey. *Building and Environment*, Vol. 40 No 11.
- [5] May, P. J. and Wood, R.S. 2003. At the Regulatory Frontlines: Inspectors' Enforcement Styles and Regulatory Compliance, *Public Administration Research and Theory*, Vol. 1.
- [6] Makhaye, D. 2000. Department of Housing: Department budget speech and policy statement of the Minister of Housing for the 2000/2001 financial year. KwaZulu-Natal.
- [7] Mkuzo, T. Z. 2011. An Assessment of the Quality of Housing Delivery in the Nelson Mandela Bay Municipality: The Beneficiaries' Perspective (2008 -2010). *Masters of Arts: Public Administration*. Nelson Mandela Metropolitan University. Nelson Mandela Metropolitan: Unpublished Dissertation.
- [8] Mpambane, S. 2008. An Investigation into the Effectiveness of the Inspectorate in the South African Home Building Industry. *Cape Peninsula University of Technology*. Cape Town: Unpublished Dissertation.
- [9] National Centre for Environmental Health. 2000. Standard Occupational Classification Manual. Springfield: VA.
- [10] Project Management Institution. 2008. *A guide to the Project Management Body of Knowledge*. Fourth Edition. United States of America: Newtown Square Inc.
- [11] SABS. 1990. 0400: *Code of Practice for the application of the National Building Regulations*. South African Bureau of Standards. Pretoria: Government Printers.
- [12] South Africa Year Book. 2003. *Government Communication and Information System*. Pretoria: Government Printers.
- [13] Product Development. 2010. *Research Report: Investigating Challenges in Adherence to Industry Norms and Standards*. Kwazulu Natal. Kwazulu Natal: Human Settlement.
- [14] Mabandla, B. 2003. Vote 29 Housing, National Assembly. Pretoria: Department of Housing.
- [15] ISO 9001. 2008. *Quality Management Systems*. United States of America.
- [16] David Kithakye. 2013. Housing the Nation: South Africa's National Housing Strategy. *Human Settlements*. South Africa.

# Performance measurement of quality of houses: development of a building quality index for houses

Jeffrey MAHACHI<sup>1</sup>

*Centre for Research and Housing Innovation, NHBRC  
Johannesburg, Republic of South Africa*

**Abstract.** The risk of structural failures of residential housing in South Africa is determined by the effectiveness of implementation of the relevant technical regulations. This risk has to be managed proactively in order to ensure consistent quality of the product. However, internationally, very little has been done to quantify the quality of a housing product. In this paper, a quality assessment system is presented, referred to as the Building Quality Index for Houses (BQIH). The quality assessment is carried out by measuring the constructed works against the workmanship standards and specifications. The measurements are comprehensive, straight-forward, consistent and effective. Furthermore, the assessments are carried out systematically and within reasonable cost and time. Of particular importance in the development of this system is the research and involvement in Conquas 21, the internationally acknowledged quality system for commercial buildings which was developed by CIDB in Singapore. A study into the applicability of Conquas 21 into the South African home construction market was carried out and the information which was obtained formed the basis for developing the BQIH.

**Keywords.** Building quality inspection index, Conquas, quality assessment

## Introduction

In South Africa a large pool of technical and legislative information on good house-construction practices is available. Nevertheless, inadequate quality is apparent throughout the entire spectrum of housing (i.e. low- to high-income dwellings). Over the years, there have been several cases of problems with, and failures of, South African house construction. These have typically been investigated by the National Home Builders Registration Council (NHBRC), a regulator and home warranty provider.

<sup>1</sup>Corresponding author: [tinash.mahachi@gmail.com](mailto:tinash.mahachi@gmail.com)

A multitude of other problems of less significance and consequence does not receive much attention and follow-up (e.g. water penetration, quality of cements, etc.). Despite the huge housing stock in South Africa (estimated at over 2.2 million housing units) there are no formal mechanisms, methodology or socially accepted platform either for proactive and consistent monitoring of its quality or the development of relevant performance statistics. A need was therefore identified for the development and implementation of a comprehensive and straightforward quality-appraisal system to measure housing quality standards.

Since 1994 the issues of the quality of house construction and risk management have been the concern of the NHBRC [refs 1 and 2]. In 2003, the NHBRC in liaison with the Research Council (CSIR) developed a system, referred to as the Building Quality Index for Houses (BQIH) for assessing the quality of houses.

The philosophy and principles of the BQIH were based on an internationally accepted quality control scheme, Conquas 21 [3], which was developed and implemented by the Construction Industry Development Board of Singapore. However, owing to the pronounced contextual and technological differences between the residential sectors of both countries, the two systems differ significantly.

## **1. Development process of the Building Quality Index for Houses (BQIH)**

The development process of the BQIH system is summarized below.

Initially, following several interactions with the Singapore Construction Industry Development Board (CIDB), Conquas 21 was analysed in the context of the South African situation. On the basis of that, the principles of the proposed system applicable to local conditions were identified. Based on the review of South African practice and standards the scoring system was developed. A series of initial appraisals were carried out, and their analysis served as the basis of an iterative process of calibrating and improving the scoring system and developing scoring sheets. The information obtained from the analysis also formed inputs to developing the user manual.

A Pocket Digital Assistant (PDA) for calculating the scores was developed. A pilot study was then undertaken in order to evaluate the applicability and relevance of the proposed system. The PDA was used to develop relevant performance statistics on the quality of houses.

### *1.1. Conquas 21*

Over the last 50 years or so, the focus and emphasis of the home-building industry worldwide has gradually shifted from quantity to quality in sustainable human shelter. Most countries have developed and introduced sets of policies, regulations and documentation relevant to their particular situation and aimed at safeguarding the interests of the consumer. Nevertheless, relatively few quality-assessment systems are in place to monitor and capture aspects of construction quality in a structured and consistent way.

Perhaps the most internationally accepted and established is the Construction Quality Assessment System (Conquas), which was launched in 1989 in Singapore where, until recently, nearly two thousand construction projects have been assessed. Within eight years of its implementation the average Conquas score improved steadily

from about 68% to 75%, which reflects a significant improvement in the quality of construction in Singapore [4].

The main objectives of the introduction of the system were:

- to introduce a standard quality-assessment system for construction projects,
- to render the quality assessment objective, by measuring against standards and specifications, using a sampling approach to suitably represent the entire project, and
- to enable the assessment to be carried out systematically, within reasonable cost and time.

The version of Conquas 21 [3] used had three main components, namely structural, architectural, and mechanical/electrical works. The system was aimed at all commercial type buildings and is based on selective sampling, as opposed to assessment of the entire project. The extent of sampling is proportional to the floor areas of buildings.

In view of its attractiveness, an analysis of the applicability of Conquas 21 to South African conditions, and in particular this country's house-construction industry, was carried out. Several contextual differences were identified, including: Geographical/climatic; Socio-economic; Spatial; Developmental and Technical.

### *1.2. Principles of BQIH*

Several aspects of the proposed system applicable to the South African situation and its needs were considered and investigated. These led us to the belief that:

- The system should follow the broad philosophy of Conquas in respect of its aims, the structure and the principle of relative weights.
- Both structural and architectural aspects of house construction should be considered. However, in line with the NHBRC mandate, the system should focus on assessing aspects of the quality of basic construction that affect the structural performance and safety of housing units.
- Important aims applicable to the South African situation were identified as:
  - ✓ the provision of an objective method for evaluating the performance of building contractors,
  - ✓ the identification of good and bad construction practices, and
  - ✓ identification of the training needs of contractors.
- The system should be inclusive of the entire spectrum of the housing industry – from the low- to the high-income sector.
- The system should be self-contained, straightforward, concise and practicable.
- Our research has shown that a large pool of information on required minimum construction standards is available in the relevant codes of practice, building regulations, construction guides and requirements of national/local authorities, in South Africa.
- The appraisal should be based on visual assessment of relevant items with no destructive testing being permitted.
- Following the initial research, one of the critical matters identified was the issue of subjectivity of assessment, with the obvious counter-measure being the appropriate training of the inspectors.



### 1.3. Benefits

There are several important benefits from implementing the proposed system. These benefits relate to various features of the society and the relevant role-players, as summarised below.

- The contractors will also benefit from the system, which will serve as a tool to identify the problem areas in their business.
- Perhaps the most obvious are the benefits to the consumer – i.e. the house owners.
- For local authorities the most important benefit is the ability to make an independent comparison of the relative performance of various contractors involved in the construction process.

## 2. Score sheets

The system includes score sheets, which include building components and items.

### 2.1. Building components

Five basic building components were adopted, as shown in Table 1.

**Table 1.** Building components

Reference	Description	Weighting (%)
1	Foundations	30
2	Floors & stairs	15
3	Walls	25
4	Roofs	20
5	Electrical & plumbing	10

The above division forms a substantial departure from Conquas 21, as regards the number of components, the inclusion of foundations, the exclusion of separate components related to architectural finishes, as well as the relative allocation of weighting percentages. In particular, the distribution of weightings shifts the emphasis of the assessment system away from architectural issues towards structural works. The performance of floors (15% weight), for example, is of less importance to the overall stability of a house than the performance of walls (25% weight).

### 2.2. Assessment

#### 2.2.1. Criteria

The investigation into a suitable and reasonable set of assessment criteria was preceded by a comprehensive review of South African sources of technical data regarding minimum quality requirements in construction. This involved a review of relevant codes of practice, technical guides, specifications and national regulations.

### 2.2.2. Appraisals

In Conquas 21 each of the components contains a detailed list questions regarding compliance with specific items, and facilitates only two options of scoring – namely, 0 for non-compliance and 1.0 for compliance.

It was felt that in the South African context the direct application of this approach would be too restrictive and, in fact, could disqualify large portions of housing units. Furthermore, our initial trial tests using Conquas 21 indicated that this type of philosophy is suited for the assessment of individual aspects of finishes, and tends to distort the appraisal of structural elements as well as items of a more generic nature.

It was therefore decided that, for certain building items (where possible and feasible), other than 0 and 1 ratings, to introduce an intermediate rating of 0.50, which enables a more graduated scoring of an item. This rating refers to the quality that is generally acceptable, with a few permissible non-compliances, which have been noted.

### 3. Pilot study

A pilot study was conducted to test the consistency and objectivity of the system. About 179 of the houses were ‘social houses with a footprint of 32m<sup>2</sup>’ built using concrete masonry blocks, and 19 were ‘middle to high income houses’ using clay masonry bricks. All housing developments were located in a provincial area of Gauteng.

The assessment project was carried out after the end of the rainy season. Nevertheless, an unexpected intense thunderstorm at the time of inspection process resulted in significant rainfall and enabled us to validate our concerns regarding the problem of water penetration through the roofs and walls of the houses.

An average index of 65% was obtained and Figure 1 presents the distribution of indices obtained from the survey.

An average index of 63,2% was obtained for the social houses and 82,4% for middle and high income houses. A difference of nearly 20 points clearly indicates the disparity in quality of product delivered to these two ends of the housing market.

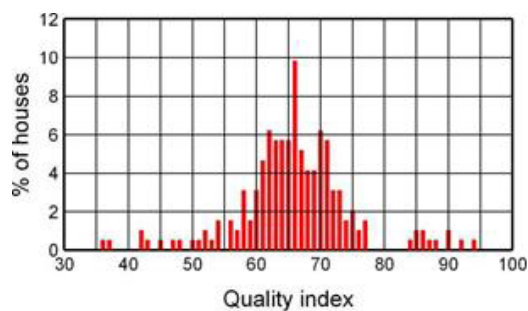


Figure 1. Distribution of quality indexes (all houses)

### 3.1. Evaluation of building components

In Table 2 a comparative analysis of average index values obtained for various building components defined in the system, is presented. It can be seen that, on average, the lowest index (60% of the maximum score) has been measured for roof structures, followed by walls (64% of the maximum score). Foundations and floors reflect overall results in the region of 70% of the maximum score and higher.

The results of electrical and plumbing works do not reflect the true situation, since for this summary only the middle and high income house were considered. This is due to the fact that electricity installation was not provided in all subsidy houses and in many cases the plumbing installation was incomplete.

**Table 2.** Summary of building components

Component Ref. Number	Description of Component	Average Index Obtained	Maximum Score	% Maximum Score Obtained
1	Foundations	20.6	30	69
2	Floors & stairs	11.3	15	75
3	Walls	16.1	25	64
4	Roofs	12.0	20	60
5*	Electrical & plumbing	9.0	10	90

\* For this comparison only the middle and high income houses are considered

The above trend offers an important insight into the current quality standards relevant to these building components, and also indicates the possible strategy for improvement. This is, in a sense, that any future efforts should be directed at improving the lower standards (i.e. shifting the tail of the distribution to the right). A similar shift in the peak of distribution towards the right will require much more input and effort (i.e. training, site controls, improvements in materials and design).

### 3.2. Correlation between building components

Figure 2 presents a comparison of all scores obtained for floors and walls. In order to enable a fair comparison, both sets of data were normalised by the respective maximum overall weights so the percentage values, which were obtained, represent the relative and comparable accomplishment of quality for both components.

The data is plotted in a way in which, for specific houses, the overall normalised score corresponding to floors is projected along the horizontal axis and the score for walls along the vertical axis. Each house is then represented by a single data point. The diagonal line at 45 degrees (referred to as the regression line of unity) represents the situation in which both relative quality scores are the same. A point below the unity-regression line denotes a house in which the quality of the floors is superior to the walls. The opposite situation is reflected by a point being above the diagonal line.

It can be seen in Figure 2 that most of the data points are scattered below the regression line, which indicates that for most of the houses more of the quality problems relate to walls. This finding suggests that more efforts (e.g. training) should be concentrated on the construction of walls, and not the floors. A similar comparison of walls and roofs suggests that the relative construction quality of both components is similar.

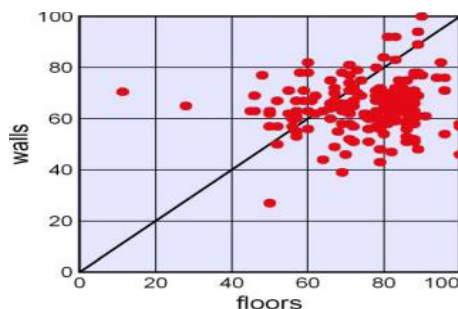


Figure 2. Comparison of scores obtained for floors and walls – *Correlation analysis*

#### 4. Conclusions

The paper has presented a summary of the principles and process of development of a post-construction appraisal system for houses in South Africa, referred to as the Building Quality Index for Houses.

The BQIH system offers a straightforward and concise assessment tool for the quality assessment of houses across the entire spectrum of the housing market in South Africa. Implementation of the system enables the comparison of quality outputs by various contractors and developers and, furthermore, produces a consistent and statistically based measure of quality performance by the entire industry.

#### References

- [1] Housing Consumer Protection Measure Act 1998. Act No. 95, 1998. *Government Gazette* No. 19418, Cape Town, RSA
- [2] Mahachi J, Goliger A M and Wagenaar F. Risk management of structural performance of housing in South Africa. Editor A. Zingoni. *Proceedings of 2<sup>nd</sup> International Conference on Structural Engineering, Mechanics and Computation*, July 2004, Cape Town.
- [3] CONQUAS 21. *The CIDB Construction Quality Assessment System*. Singapore, 5<sup>th</sup> Edition, 1998.
- [4] K Ho (2002). Presentation, Senior Development Officer, Quality Assessment Dept., Building and Construction Authority, Singapore.
- [5] NHBRC (1999). *Home Building Manual*. National Home Builders Registration Council, South Africa.

This page intentionally left blank

## Subject Index

3D FEM model	1172	blowing system	526
7-wire strand	1141	bond	347
abrasion resistance	848	bond test	932
accelerators admixtures	113	bond transfer length	1044
acid concentration	764	bond-slip diagram	932
acid mine drainage	1416, 1427, 1436	bottom ash	1427
acoustic emission	888	brick aggregate	378
additives	601	brick characterization	668
admixture(s)	398, 749	brickmaking	662
adobe	1468	bridge(s)	47, 544, 1089
aggregate packing	629	bridge deterioration	1264
air permeability	848	bucking behavior	1116
air voids	637	buckling	1125
aircrete	647	building	1345
alkali activation	136	Building Information Modeling	
alkali-silica reaction	1401	(BIM)	1377
alkaline activated binder	511	building quality inspection	
aluminium scrap recycling waste	136	index	1517
aluminum alloy	1116	building sites	1475
ambient	904	burst pressure	1256
analytical integration	1317	butt joint	1022
Andersen & Andreassen model	384	by-products	99
anisotropic	1207	C&DW	370
artificial aggregate	703	calcium sulfate	220
Artificial Neural Network	613	calorimetric techniques	220
asphalt concrete	601	calorimetry	268
asphalt pavements	620	Cambodia	1190
autoclaved aerated concrete	647	canal linings	1331
axial compression	1068	canals	1331
Bain distortion	691	carbon nanotubes	697
base moment	1303	carbonation	1052
base shear	1303	causes and sources	76
beams	871, 1325	cement	220, 676, 683, 1370, 1395
bending	1317	cement paste	339
bending test	888	ceramic	370
bentonite	662	ceramic powder	487
$\beta$ cyclodextrin	825	ceramic waste	208
binder	232, 518	CFDSCT	1068
black cotton oil	575	CFST	1007
blast furnace slag	475	change of cross-section	1022
blended cement(s)	152, 305, 370, 835	characterization	16, 608
blended cement-cassava peel ash	764	chemical attack	835

chloride ingress	3	coordination number	629
chloride penetration	819	core density	637
circular hollow sections	1148	corrosion	749, 788, 939
classical theories	1207	corrosion current	1436
clay stone	226, 1364	corrosion inhibitors	749
clinkering	703	corrosion rate	939
CO <sub>2</sub>	320	corrosion resistance	835
coal ash	1427	cover	1052
coarse aggregate	581	cover depth	354
coefficient of friction	1141	crack	1295
coefficient of thermal expansion	47	crack openings	1201
coir	544	crack pattern	871
collapse	881	crack width	939
column(s)	1125, 1148	cracking	354, 888
column overdesign factor	1242	cracks	3
column-beam structure	1030	creep	1044, 1274
combined load	819	cross-winding steel wires	1256
compaction	575	crumb rubber	601, 1481
composite precast concrete	1030	crushed bricks	320
compression	899	CTE optimization	47
compressive load	819	curing	404, 1409
compressive strength	121, 127, 253, 284, 311, 327, 378, 398, 420, 427, 436, 445, 475, 481, 487, 655, 709, 718, 764, 956, 1401, 1503	curing conditions	453
compressive strength prediction	293	curing time	575
concrete	47, 76, 121, 420, 718, 772, 780, 825, 861, 881, 888, 904, 917, 963, 1274, 1370	curvature	1317
concrete overlay	980	damage	1233
concrete property	162	damper	68
concrete waste minimization	1352	deformation capacity	1157
concrete-filled tube	1068	delamination	904
condition monitoring	1264	density	1481, 1503
confinement	998	design	946, 1345
confinement effect	1068	detwinning	691
Conquas	1517	diagnostic	904
constructability	1030	diameter-to-thickness ratio	1148
construction	99	dicalcium monoaluminate	113
construction building materials	1377	diffusion	3
construction defects	3	dimensional stability	86
construction demolition waste	587	direct tensile strength	436
construction failures	76	discrete element method	1215
construction industry	1352	Discrete Element Method (DEM)	629
Construction Industry (CI)	1377	dolomitic waste	1386
contrasts	904	domestic housing	1489
cooling load	1461	double skin	1068
cooling requirements	1468	Double-Punch Test	917
		dowel type fastener	1172
		drainage system	1331
		dry shake	848
		drying shrinkage	196, 848

ductility	145, 972, 998, 1007, 1038	fiber-reinforced concrete	917
ductility and stiffness	1074	fibre cement	893, 899
durability	16, 47, 86, 276, 347, 466, 835, 917, 1401	fibre pull-out testing	1287
durability performance	1060	fibre-reinforced cement composites	932
early age	162	fine aggregates	939
early age cracking	362	finite beam element	1172
earthquake	27, 1107	finite element analysis	998, 1116
East Africa	76	finite element method	1331
eccentric compression	1116	fire	946, 1100
eccentric discharge	1215	fire engineering	1134
economic efficiency	1030	fired ceramic tiles waste	152
EDX analysis	311	flame retardant	526
elastic boundary conditions	1295	flax fiber	544, 1310
elastic moduli	503	flexible pavement	560
elastic modulus	495, 734	flexural behavior	1038
electrical resistivity	487	flexural capacity	1007
elevated temperature	963	flexural strength	436, 647, 718
elongation	734	flexural strengthening	1015, 1074, 1080
elongation variation	740	flexure	871, 893
emission	1445	flow rate	1215
energy dissipation	910	flowability	145
energy saving	1461	fly ash	226, 445, 453, 481, 495, 503, 683, 703, 825, 1364, 1386, 1427
engineered cementitious composites	189	foam agents	1503
envelope	1345	foam concrete	226, 1364
environmental exposure	861	foam mortar	226, 1364
environmental performance	1495	fracture	888
epoxy bonding	1074, 1080	frame structure	1242
equal-channel angular pressing (ECAP)	35	fresh and hardened properties	168
European cement standards	391	fresh concrete	362
EVA (ethylene vinyl acetate)	526	friction	734, 740
expansion	806	FRP sheet	347
experimental database	1274	fuel use	1445
experimental tests	1172	functionality requirements	1164
externally bonded FRP	1015	furfuryl alcohol	461
externally bonded reinforcement	1080	general use cement	772
FA- $\beta$ -CD composite	825	geochemistry	1386
failed	553	geopolymer	466, 475, 487, 495, 503, 511
failure probability	1242	geopolymer mortar	481
fatigue behavior	601	gradients	904
fatigue test	613	grading	253
FE modelling	946, 1089	grain boundary	728
fencing	1489	grain boundary dislocation	728
fiber element analysis	1007	granular flow	1215
fiber reinforcement cementitious composite	196	gravel	608
		grease	1141



grinding	305	iteration	910
ground granulated blast furnace slag (GGBS)	518	Karacahisar castle	668
H-piles	1107	kinetic theory	1100
Haar wavelet	1295	laterite	608
hardening	532	layered structures	691
hardening mechanism	183	Life Cycle Assessment (LCA)	1377
headway	613	light wood-framed buildings	1172
heat of hydration	208	lightweight aggregate	411
heat reflective coating	1461	lightweight aggregate concrete	411
heavy-duty diesel (HDD) construction equipment	1445	lightweight concrete	202, 226, 1364
high alumina cement	113	lightweight green concrete	284, 427
high alumina slag	788	lime hemp concrete	1358
high early strength cement	772	limestone filler	772
high pressure water jetting	980	limit strength	411
high speed mill	305	load assessment	1181
high strength	145	load capacity	881
high strength cement	899	load deflection	1015
high strength concrete	980	load test	1157
high volume	780	loading frequency	613
high-performance steel fibers	917	local buckling	1068, 1148
highway bridges	861	long-term	1044
historic brick	668	long-term deformation	925
hollow core concrete slabs	946	longitudinal cracking	1181
housing South Africa	1510	Los Angeles abrasion test	568
hybrid alkaline cements	1503	low cost maintenance	1489
hybrid compo-site	526	low cycle fatigue	1107
hydration	16, 268, 532	low density blockwork	647
hydraulic mortars	320	low density polyethylene (LDPE)	560
hydroxide (OH)	518	low-strength application	175
hysteresis properties	989	macro	1201
ignition loss of bricks	668	magnesium sulphate attack	788
in-situ columns	1022	manufactured sand	475, 481
indirect tensile strength	595	marine environment	1060
industrial waste	575	marine exposure	749
infrared	904	Markov Chain	1264
inhomogeneous shear	691	Marsh cone test	333, 758
initial compressive strength	797	Marshall compaction	637
inspection	1510	Marshall stability	568
inspectors	1510	martensitic transition	691
insulation material	136	Masonite flexible building system	1164
integral bridges	1107	masonry	655, 1157
interfacial transition zone	718	masonry arch	1181
interference effect	1303	mass	1141
interlocking block	27	mass concrete	47
interlocking bricks	676	mass gain	806
internal curing	57, 453	mass loss	788
intumescent agent	526		

materials	99, 1207	natural pozzolan(s)	175, 835
mechanical property(ies)	86, 183, 189, 202, 378, 453, 963	near surface mounting	1080
meso	1201	neural network(s)	1264, 1295
Mi Panel	893, 899	neutralization	1427
micro fine	339	nickel	728
micro-plane	1223	non-destructive method	293
microscopic structure	183	non-linear analysis	1172
microstructure	189, 247, 276, 487, 532	non-uniform thickness	1007
microstructure and		numerical model	1495
super-plasticizer demand	697	numerical modelling	1287
microstructure capillary action	1358	Obimo sand	121
microtexture	581	on-site	1352
mineralogical composition	232	optimized grading curve	384
mini slump	339	ordinary Portland cement (OPC)	261, 1370
mining sand	481	overall flexural buckling	1148
misalignment of reinforcement bars	1022	packing density and self-consolidating mortars (SCM)	384
mix design	411	palm nut shell	284, 427
mixed-type boundary	728	palm oil fuel ash	475, 481, 511, 780
mixing proportion	240	particle size	247
mixture design	86	passive treatment	1416
model	1223, 1274	pavement	47, 608
modeling	532	pavement deterioration	620
modern building materials	1468	pavement materials	587
modified bituminous mix	568	PC	532
modulus of elasticity	127	PCC	532
moist-curing	276	penetration test	568
moisture	1358	performance	1345
moisture diffusion	925	performance specifications	3
molecular dynamics	728	periodic curing	276
monocalcium hexa aluminate	113	permeability	825
monocalcium monoaluminate	113	permeable reactive barrier	1416
monotonic tests	587	phosphonate superplasticizer	333
Monte Carlo simulation	1249	physical property(ies)	121, 668
mortar(s)	253, 261, 398, 655, 825, 1481	Piliostigma Thonningii (PTA)	398
mortar expansion	797	pillar failure	1395
mortar free	27	plastic pipe	1256
mortar/concrete prisms	806	plastic settlement	354
mould growth	1358	plastic sheath	1141
multi walled carbon nanaotubes	718	plate girders	1089
multi-plane model	1233	polarization	1436
multi-storey timber buildings	1164	polycarboxylate	327, 333
multilayer walls	1468	polymer	196, 568
nanoclays	709	polymer coated aggregates (PCA)	560
nanocrystalline structure	35	polymer matrix composite	1310
nanoparticles	16	polymer modified bitumen	620

polymer-concrete composite	544	recycled glass	305
polypropylene fibres	202	recycling	99, 370
polystyrene	893, 899	red clay	662
poorly dried aggregates	595	reducing CO <sub>2</sub>	1370
porosity and sorptivity	825	reinforced concrete	1038, 1052, 1060, 1074, 1080, 1317
porous asphalt mixture	629	reinforced concrete pier	989
porous building material	136	reinforced concrete structures	76
portable emission measurement system (PEMS)	1445	reinforcement	1325
portland cement	208	relative movement	27
portland cement pastes	214	repair	1181
post-tensioning	740, 1141	residual moisture	595
potential	1436	resilient modulus	595, 608
potential strength	411	resilient modulus tests	587
potentiodynamic	1436	restoration	320
power plant	703	restoring force characteristics	989
pozzolan	370	retardation	404, 1409
pozzolanic activity of bricks	668	reuse	196
pozzolanic non-pozzolanic additions	214	rheological performance	240
pozzolanicity	175	rheology	16, 214, 327, 339
pozzolanity	305	rigid frame bridge with corrugated steel webs	910
pozzolans	232	road	99
pre-failure mechanism	1233, 1233	road and drainage	553
precast columns	1022	roof insulation	1468
precast concrete panels	1489	SABS cement standards	391
precast slab	1495	sand	420
premature failure	1074	sand blasting	980
prestressed	946	sand lightweight concrete	293
prestressing	1325	sandcrete	683
pro-elasticity	1233	SANS 10400	1134
processing	16	saturation point	333, 758
professionals	1475	SBS	601
pulverized fuel ash (PFa)	518	scabbling	1080
pure tension	1044	scale effect	1310
quality	1510	scaling	461
quality assessment	1517	SCC (self-compacting concrete)	240, 445, 871
quality assurance	1510	scoria	835
quarry dust	481, 676	scoria rocks	247
R.C.C.	998	screed	848
radiation	904	seepage	1331
radiation shielding	404, 1409	segregation ratio	445
railway	1089	seismic	68
RC shear wall-frame building	1249	seismic intensity	910
RCPT	276	seismic loading	1249
rebound hammer	861	seismic response	544
reclaimed rubber	601	self-compacting geopolymer concrete (SCGC)	518
recovery	963		
recycled aggregate(s)	168, 453		

self-compacting paste systems	697	splitting tensile strength	1401
self-consolidating concrete	772	stability bearing capacity	1116
self-curing concrete	276	stabilization	575, 676
SEM	532	standard sand	253
SEM and compressive strength	1386	static-cyclic loading	1157
service life	1107	steam cured	772
service life of concrete	819	steel	76, 1125
serviceability limit state	1249	steel chip	196
set temperature	1461	steel emissivity	1100
setting	268	steel fibers (fibres)	145, 871, 972
severe plastic deformation (SPD)	35	steel filing particle	420
shape memory alloys	1223	steel plates	1074, 1080
shape memory effect	691, 1223	steel structures design	1089
shear	972	steel-reinforced concrete	925
shear bond strength	709	steel-slag	511
shear capacity	881, 972	stiffness	683, 1157, 1395
shear connectors	956	story mechanism	1242
shear friction	980	strains	1274
shear strength	709	strength	16, 268, 553, 595, 917, 1325, 1481
shear strengthening	1015	strength activity indices	247
shear wall	989, 1157	strength tests of aggregates	560
shredded rubber	871	strength theories	1207
shrinkage	466, 511, 1044	strengthening	956
silicate (Si)	518	stress-related material damping	910
silos and hoppers	1215	structural integrity	861
simulation	1287	structural steelwork	1134
site supervision	1052	structure	68, 881
size effect	1201	stub columns	1068
skid resistance	581	subbase	608
slabs	956	subgrade	553
slant shear test	980	sulphate attack	780, 806, 835
slenderness ratio	1125, 1148	sulphate concentration	797
slotted-in connections	1164	sulphate resistance	788, 797
slump	764	sulphuric acid solution	764
SMART frame	1030	super elasticity	1223
smart-objects	1377	superabsorbent polymers	57
sodium (Na)	518	superplasticizer	327, 445, 758
sodium hydroxide activator	487	supervision	1475
sodium sulphate	788	supplementary cementitious materials	57, 813
softening point test	568	suspended connections	1164
solar	904	sustainability	1377
solid waste	511	sustainable	1345
solid waste management (SWM)	560	synthetic turf	1453
sonication	718	synthetic yarn	1453
South African slag	797	system reliability	1242
spacing	354	tall buildings	1303
spalling	1052	temperature	240, 461, 904, 1100
specific surface area	305		
split-tensile strength	718		

temperature effect	220	uncertainty	3
tendon	734, 740	unconfined compressive strength	683, 1395
tensile material properties	362	uplift	27
tensile strain capacity	189	UV	1453
tensile strength	495, 503, 709, 1310	UV degradation	1453
tension	740	UV exposure	1453
termites	1190	variation	734
theoretical analysis	1256	very low water-cement ratio	183
thermal	904	viscosity	339
thermal conductance	1461	viscosity modifying agent	333, 758
thermal conductivity	261, 1503	void forming system	1495
thermal oxidation	1100	volcanic ash	232
thermal properties	1481	volcanic cones	247
thermal stress(es)	47, 162	waste	99
thermal stress device	162	waste ceramic aggregate	453
thermography	904	waste glass	1401
thickness	461	waste management	168
thin layer mortar	655	water absorption	378, 487
thin spray rock liner	709	water permeability	276
tilt boundary	728	water reducers	220
time	461	water table	1331
torsion	1325	water vapor sorption isotherms	813
traffic wander	613	water-binder ratio	764
transverse reinforcement	972	water-soluble polymers	276
triple junction	728	wearing course	581
TRNSYS-COMIS	1468	weight and strength loss	780
twinning	691	width-thickness ratio	1074
twisting moment	1303	wind loads	1303
two-stage concrete	127	wobble	734, 740
Uganda	76	wood ash	261
UHPC	86	wooden structures	1190
ultra high performance ductile concrete	145	workability	284, 404, 420, 427, 445, 495, 503, 1409
ultra-high-strength fiber-reinforced self-compacting concrete (UHS-FR-SCC)	972	X-ray powder diffraction (XRD) analysis	311
ultrafine grain structure	35	XRD-ray	208
ultrasonic pulse velocity	293	yield strength	1038
unbonded	1141		

## Author Index

Abdelgader, H.S.	127	Angelescu, N.	113, 127
Abdollahnejad, Z.	1503	Anis, K.T.	1377
Abdulle, F.	1287	Aqel, M.	772
Abiola, O.S.	575	Arum, C.	1475
Adamou, A.	121	Arunachalam, A.	311
Adebisi, N.O.	553	Asensio, E.	370
Adeniji, S.A.	553	Attwell, C.	466
Adiguzel, O.	691	Awal, A.S.M.A.	780
Afolayan, J.O.	881	Azene, F.	1427, 1436
Agbenyeku, E.-O.E.	284, 427	Bai, Y.	1100
Ahmad, Z.A.	511	Bajare, D.	136
Ahmed, A.	647, 655	Bakamwesiga, H.	861
Ahuja, A.K.	1303	Balqis, M.Y.	819
Aissaoui, N.	1201	Balu-Tabaaro, W.	232
Ajiboye, O.S.	420	Baodong, L.	910
Akintayo, F.O.	553	Barbhuiya, S.	1401
Akinteye, I.A.	261	Barisanga, F.	587
Al Hawat, W.	327	Bashar, I.I.	475, 481
Alao, O.O.	1060	Baszeń, M.	1172
Alawad, O.A.	247	Bayrak, O.	917
Albitar, M.	495, 503	Benmiloud, A.	888
Alengaram, U.J.	202, 475, 481	Benyamine, M.	1215, 1468
Alexander, M.	1060	Beushausen, H.	1060
Al-Ghazali, A.	620	Bier, T.A.	384, 697
Alhozaimy, A.	247	Biswal, D.R.	608
Ali, M.S.M.	495, 503	Blatt, M.	1022
Ali, N.Z.	697	Bogas, J.A.	293, 411
Alinaitwe, H.M.	76	Booyesen, C.J.	709
Aliyan, S.D.	835	Boshoff, W.P.	354, 362
Al-Martini, S.	327	Bratu, V.	113
Almuwbber, O.	445	Bukasa, G.M.	893, 899
Al-Negheimish, A.	247	Bumanis, G.	136
Al-Rawashdah, O.	972	Byrne, T.	1181
Al-Sallamin, A.	276	Cabrera, O.A.	939
Alswaidani, A.M.	835	Castellano, C.	208
Altinsapan, E.M.	668	Černý, R.	208
Álvarez Antón, L.	1377	Cerny, V.	703
Amana, O.	1481	Cha, S.L.	162
Amin, Sh.K.	152	Chabalala, V.	1148
Amtsbüchler, R.	391	Chao, S.-H.	917
An, G.-H.	925	Charif, A.	1038, 1317
Andersons, J.	1310	Chateaufneuf, A.	1274
Aneke, I.F.	1386	Chen, M.	629

Choi, H.-C.	526	Fowler, D.W.	47
Choi, J.-Y.	526	Frias, M.	370
Chouw, N.	27, 544	Fridrichová, M.	305
Combrinck, R.	354, 362	Fujiwara, H.	35
Daerga, P.-A.	1164	Ganesan, N.	871
Daghighi, A.	601	Gao, W.	989
Dahesh, M.A.	1249	Gao, X.	v, 240
Dahou, Z.	888	Gee, A.F.	1125
Das, A.	1401	Ghanem, G.	956
Dash, S.R.	608	Ghezali, S.	1201
Dave, U.V.	339	Girhammar, U.A.	1164
Dawneerangen, A.	168	Goggins, J.	1495
De Aguiar, J.L.B.	1503	Gomes, M.G.	293, 411
De Clercq, H.	1134	Güldoğan, İ.	668
De Sutter, S.	932	Gunesh, N.R.	568
Dey, G.	378	Güney, Y.	668
Diabdenkov, V.	728	Guo, W.	1256
Díaz, J.	1377	Gupta, P.K.	998, 1007
Dicleli, M.	68, 1107	Haas, M.	1370
Diop, S.	1416, 1427, 1436	Hajdukiewicz, M.	1495
Dippenaar, J.D.	362	Haldenwang, R.	445
Djermane, M.	1215	Hami, O.	1215
Dmitrienko, D.	728	Hasan, M.S.	1264
Dobrovolný, P.	305	Hein, H.	1295
Donza, H.	220, 939	Hlatshwayo, S.	391
Draoui, B.	1468	Hong, S.	196
Drochytka, R.	703	Hong, W.-K.	1030
Dundu, M.	v, 734, 740, 893, 899, 1068, 1074, 1080, 1141, 1148	Hooton, R.D.	3
Dvořák, K.	305	Huo, L.	183, 189
Ekolu, S.O.	v, 76, 253, 333, 404, 637, 758, 788, 797, 806, 848, 1052, 1331, 1409, 1416, 1427, 1436	Ibrahim, W.	956
El-adawy, M.	956	Ikotun, B.D.	825
El-Baden, A.S.	127	Ikumapayi, C.M.	1475
El-Dieb, A.S.	276, 487, 972	Irassar, E.	208, 214
Ellobody, E.	946, 1089	Islam, A.	475, 481
El-Maaddawy, T.A.	276, 972	Iwaro, J.	1345
Ercoli, L.	320	Jang, H.-M.	526
Erhan, S.	1107	Jayakumar, K.	311
Essopjee, Y.	1068	Jenkins, K.	587
Fang, H.	1100	Jirsa, J.	917
Fanourakis, G.C.	825	Joel, M.	676
Fares, G.	247	Johari, M.A.M.	511
Feklistova, L.	1295	Jonkers, H.M.	819
Fezzioui, N.	1215, 1468	Jumaat, M.Z.	202, 475, 481
Fitriani, H.	1445	Kajita, Y.	989
Fokeerbux, N.A.	560	Källsner, B.	1164
Fore, S.	1510	Kaneko, Y.	196
		Karki, N.	917
		Katariya, S.K.	1007
		Kazurikanyo, J.-B.	333

Keith, K.P.	268	Meddah, M.S.	453
Kerali, A.G.	175	Medina, C.	370
Kew, H.	1352	Megna, B.	320, 1190
Khan, A.-u.-R.	145, 1015	Meibodi, A.B.	1352
Khan, M.I.	436, 1038, 1317	Miedziałowski, C.	1172
Khodaii, A.	613	Mikrukov, V.	728
Kim, H.-J.	526	Milani, A.S.	68
Kim, J.K.	162	Minnert, J.	1022
Kim, J.-K.	925	Mishra, S.	825
Kim, S.	1030	Miyamoto, H.	35
Kimura, S.	196	Mlasi, S.M.	1489
Kizyalla, L.K.	637	Moatlhodi, L.J.	683, 1395
Klemm, A.J.	57	Mohammad, S.	780
Klingner, R.	917	Mojsilović, N.	1157
Koob, M.	1022	Mourad, S.	436, 1038, 1317
Korjakins, A.	136	Mtenga, P.V.	1125
Kruger, D.	904, 1453	Muhammad, R.	35
Kumar, R.	461	Mwakali, J.	861
Kupolati, W.K.	575	Mwasha, A.	1345
Larbi, S.	1468	Nahvi, A.	601
Lasisi, S.A.	261	Najim, O.F.	327
Laskar, A.	1401	Naturinda, D.N.	175
Law, D.W.	1264	Naz, A.	697
Lebrêne, J.	1495	Ndambuki, J.M.	575
Lee, J.-H.	526	Nejadi, F.S.	1044
Leklou, N.	1358	Ngwenya, A.	788, 797
Lewis, P.	1445	Nnebe, M.U.	121
Li, G.	189	Nukushina, T.	453
Li, M.	347	Ocholi, A.	676
Li, Q.	963	O'Dwyer, D.	1181
Lim, C.	1030	Okonta, F.N.	284, 427, 683, 1386, 1395
Lin, X.	183	Olajumoke, A.M.	764, 1074, 1080
Liotta, G.	1190	Olanitori, L.M.	881
Liu, M.	347	Olonade, K.A.	420, 764
Liu, Y.	347	Omale, R.P.	1475
Lomboy, G.R.	16	Omotosho, A.O.	764
Lu, Z.-H.	1242	Ortega, N.F.	939
Luo, X.	1256	Othman, A.M.	127
Mafokoane, T.T.	718	Othmen, I.	1358
Mahachi, J.	1517	Otsuka, H.	989
Mahumapelo, N.P.	662	Oyekunle, F.A.	764
Makhathini, B.N.	168	Panesar, D.	772
Maneli, A.	575	Panseriya, M.M.	339
Mannir, S.	398	Park, J.	1030
Masalova, I.	445	Park, J.-W.	526
Maslehuddin, M.	511	Paul, S.	378
Masood, F.	1015	Pavlík, Z.	208
Matallah, M.	1201	Pedrajas, C.	214
McKenzie, W.	518		



Pengfei, L.	910	Siddiqui, N.A.	1249
Poletaev, G.	728	Sikora, K.S.	57
Pontes, J.	293, 411	Simon, C.	980
Poullain, P.	1358	Slimani, A.	1215
Rahal, K.N.	1325	Solomon, F.	848, 1331
Raheem, A.A.	261	Song, Z.	183
Rahhal, V.	208, 214, 220	Stancu, C.	113
Raj, B.	871	Starostenkov, M.	728
Raj, R.	1303	Stephen, P.	1481
Ramushu, M.A.	404, 1409	Sulaiman, A.	780
Randl, N.	980	Suman, B.M.	1461
Raphael, W.	1274	Sun, L.	1116
Rarani, M.	1510	Taha, R.	99
Real, S.	293, 411	Talero, R.	214
Retief, J.	1134	Thelandersson, S.	861
Rizwan, S.A.	384, 697	Tiwari, A.K.	339
Rizzo, G.	320	Torgal, F.P.	1503
Robertson, I.N.	749	Tosun, Y.İ.	226, 1364
Roulet, C.-A.	1468	Touma, L.	1274
Rudman, C.	587	Traversa, L.P.	939
Rughooputh, R.	560, 568	Tuken, A.	1249
Rupieper, S.	734, 740	Tysmans, T.	932
Sabouni, R.	620	Ullah, H.	697
Sadek, D.M.	152	Usman, N.	595
Sadrnejad, S.A.	1223, 1233	uz Zaman, Q.	384
Sahoo, U.C.	608	Vakhshouri, B.	1044
Salau, M.A.	420	Valiakhmetov, I.	1207
Sánchez de Rojas, M.I.	370	van Ede, W.F.	1052
Sanni, M.Y.	1481	Van Gemert, D.	532
Sato, R.	453	van Tonder, P.	709, 718
Sato, Y.	196	Vantomme, J.	932
Schindler, A.K.	268	Verma, V.K.	998
Schlangen, E.	819	Viljoen, C.	1134
Scott, M.	904	Visintin, P.	495, 503
Seaidpour, M.	813	Wadsö, L.	813
Seiki, S.	453	Walls, R.	1134
Sele, L.	136	Wang, D.	86
Sengendo, S.	861	Wang, F.	347
Setunge, S.	1264	Wang, H.	240
Shabalala, A.N.	1416	Wang, K.	16
Sharfuddin, M.	1242	Ward, M.	1141
Shashikala, A.P.	871	Wasilewska, M.	581
Shehab, E.E.	487	Weilong, L.	910
Shehu, I.A.	780	Wenjuan, L.	910
Shi, C.	86	Wiggins, D.E.	57
Shi, J.	1256	Wolff, D.	1022
Shohniwa, A.T.	168	Wong, M.B.	1100
Shu, Q.	963	Wong, Y.D.	629
Siddiqui, M.S.	47	Woods, A.P.	917

Wozniak, M.	932	Yuan, G.	963
Wu, L.	86	Yusuf, M.O.	511
Wu, Z.	86	Zahra, T.	145
Xiao, R.	1287	Zhai, X.	1116
Xu, P.	1256	Zhang, T.	183, 189
Yan, L.	544	Zhao, Y.	1116
Yao, H.	189	Zhao, Y.-G.	1242
Yap, S.P.	202	Zheng, J.	1256
Ye, H.	240	Zonouzy, A.H.	613
Youssef, N.F.	152	Zuzarte, A.C.	1453

This page intentionally left blank